COMPUTATIONAL PLASTICITY XI

Fundamentals and Applications

E. Oñate, D.R.J. Owen, D. Peric and B. Suárez (Eds.)

COMPUTATIONAL PLASTICITY XI
Fundamentals and Applications

COMPLAS XI

COMPUTATIONAL PLASTICITY XI
Fundamentals and Applications

Volumen containing the full length papers accepted for presentation at the XI International Conference on Computational Plasticity. Fundamentals and Applications
Barcelona, Spain
07-09 September 2011

Edited by:

E. Oñate
Universitat Politècnica de Catalunya, Spain

D.R.J. Owen
Swansea University, United Kingdom

D. Peric
Swansea University, United Kingdom

B. Suárez
Universitat Politècnica de Catalunya, Spain

A publication of:

International Center for Numerical Methods in Engineering (CIMNE)
Barcelona, Spain

International Center for Numerical Methods in Engineering (CIMNE)
Gran Capitán s/n, 08034 Barcelona, Spain
www.cimne.com

Computational Plasticity XI – Fundamentals and Applications
E. Oñate, D.R.J. Owen, D. Peric and B. Suárez (Eds.)

First edition, December 2011

Printed by: Artes Gráficas Torres S.L., Huelva 9, 08940 Cornellà de Llobregat, Spain

Depósito legal: B-42317-2011
ISBN: 978-84-89925-73-1

SUMMARY

Preface 7
Acknowledgements 9
Contents 11

Plenary Lectures 23

INVITED SESSIONS 56

Advances in Damage Modelling at Large Inelastic Deformations: Theory and Computational Aspects 56
Organized by José César de Sá and Khemais Saanouni

Applications of Computational Methods to Product and Process Designs for Industry 80
Organized by Takashi Iizuka and Masayoshi Akiyama

Computational Algorithms for Contact and Interfaces 135
Organized by Tod Laursen

Computational Analysis of Masonry Structures 159
Organized by Pere Roca

Computational Challenges in Multiscale Inelasticity and Instability 189
Organized by Herbert Mang and Christian Hellmich

Computational Modeling of Forming Processes 221
Organized by Jean-Philippe Ponthot and Carlos Agelet de Saracibar

Computational Strategies for Metal Cutting & Forming Operations 275
Organized by Miguel Vaz

Continuous – Discontinuous Approaches to Failure of Quasi-brittle Materials 330
Organized by Gilles Pijaudier-Cabot and Frédéric Dufour

Energy-based Variational Principles and Applications in Constitutive Modeling 354
Organized by Jörn Mosler and Laurent Stainier

Inelastic Processes in Heterogeneous Materials 410
Organized by Hermann Matthies and Adnan Ibrahimbegovic

Modeling of Damage Evolution and Propagating Discontinuities at Failure 442
Organized by Ekkehard Ramm, Francisco Armero and Christian Linder

Multiresolution Science Based Mechanics of Complex Material 532
Organized by Wing-Kam Liu, Ji Hoon Kim and Lars-Erik Lindgren

Multiscale Modeling for Microstructure Design of Materials 587
Organized by Tomohiro Takaki and Kisaragi Yashiro

Non-conventional Modeling and Simulation of Materials and Processes 676
Organized by Francisco Chinesta and Elias Cueto

Novel Computational Approaches in Biomechanics at Different Length Scales 700
Organized by Gerhard A. Holzapfel

Numerical Modelling of Concrete Structures 788
Organized by Pavao Marovic and Nenad Bicanic

Shape Memory Materials: Theory and Computation 820
Organized by Edoardo Artioli and Robert Taylor

CONTRIBUTED SESSIONS 830

Advanced Material Models 830

Composites 944

Contact Problems 964

Damage, Fracture and Fatigue 1007

Forming Processes Simulations 1092

Geomechanics 1165

High Velocity Impact 1284

Innovative Computational Methods 1306

Multi-physics/Multiscale Material Problems 1502

Numerical Modelling of Concrete Structures 1595

Thermal-Mechanical Models and Applications 1637

AUTHORS INDEX 1661

PREFACE

This volume contains the full papers presented at the XI International Conference on Computational Plasticity (COMPLAS XI), held in Barcelona on 7-9 September, 2011. The first ten conferences in the series were also held in Barcelona; in April 1987, September 1989, April 1992, April 1995, March 1997, September 2000, April 2003, September 2005, September 2007 and September 2009. The continuing importance of this research topic is demonstrated by the fact that the number of papers presented has increased from just over 100 papers in the first conference to over 330 papers at this meeting.

The ever increasing rate of development of new engineering materials required to meet advanced technological needs poses fresh challenges in the field of constitutive modelling. The complex behaviour of such materials demands a closer interaction between numerical analysts and material scientists in order to produce thermodynamically consistent models which provide a response, while keeping with fundamental micromechanical principles and experimental observations. This necessity for collaboration is further highlighted by the continuing remarkable developments in computer hardware which makes the numerical simulation of complex deformation responses increasingly possible.

The developments that have taken place in these directions are illustrated by the contents of the papers included in these Proceedings. A stronger interaction between the phenomenological and micromechanical modelling of plasticity behaviour is apparent. The development of efficient and accurate computational methods for plasticity problems continues to be challenging goal, while it is interesting to note the permanence of element modelling as a research issue. The blending of classical FEM with new particle-based and discrete element methods appears as one of the more prominent areas of research. Industrial forming processes, geo-mechanics, bio-mechanics, steel, concrete and masonry structures form the core of the applications of the different numerical methods presented.

This volume includes contributions sent directly from the authors. The editors can not accept responsibility for any inaccuracies, comments and opinions contained in the papers.

The organizers would like to thank all authors for submitting their contributions, as well as the supporting organizations for their help in making COMPLAS XI possible.

Roger Owen
Djordje Peric
Swansea University
Swansea, Wales, United Kingdom

Eugenio Oñate
Benjamín Suárez
Universitat Politècnica de Catalunya
Barcelona, Spain

ACKNOWLEDGEMENTS

The editors and the congress organizers acknowledge the support towards the publication of the Proceedings and the organization of the COMPLAS XI Conference to the following organizations:

European Community on Computational Methods in Applied Sciences (ECCOMAS)

International Association for Computational Mechanics (IACM)

Swansea University

International Center for Numerical Methods in Engineering (CIMNE), Spain

Universitat Politécnica de Catalunya, Spain

Ajuntament de Barcelona

CONTENTS

Plenary Lectures

Development of Crystallographic Process Technology for Piezoelectric Actuator for Bio-MEMS Device 23
E. Nakamachi

Generalized Plasticity for Geomaterials with Double Structure 32
A. Gens*, M. Sánchez and B. Valleján*

Optimization of Metal Forming Processes for Improving Final Mechanical Strength 42
J-L. Chenot*, P-O. Bouchard, L. Fourment, P. Lasne and E. Roux*

Invited Sessions

Advances in Damage Modelling at Large Inelastic Deformations: Theory and Computational Aspects

Invited Session organized by José César de Sá and Khemais Saanouni

2D Adaptive Fem Simulation of Failures in High-speed Impacts.....56
M. Issa, K. Saanouni, C. Labergère and A. Rassineux

A Micromechanical Constitutive Model for Ductile Fracture: Numerical Treatment and Calibration Strategy 66
L. Malcher, F.M. Andrade Pires and J.M.A. César de Sá

Applications of Computational Methods to Product and Process Designs for Industry

Invited Session organized by Takashi Iizuka and Masayoshi Akiyama

Effect of Temperature in Formability of Composite Composed of Overlapped Fibre Bundle, Thermoplastic Resin and Metal.....80
T. Kuboki, S. Uematsu and M. Murata

Estimation of Response of Steel Sheet Plated with Thin Hard Layer.....91
T. Uchimura, T. Yamamoto and M. Akiyama

Estimation of Springback of Stainless Steel Sheet Part Taking Influence of Anisotropic Property of Plastic-Deformation-Dependent Young's Modulus into Account.....99
K. Hayakawa, K. Sawano, T. Nakamura, Y. Kubota, Y. Nanba and Y. Tabuchi

Experimental and Numerical Analyses on The Characteristics of Twin Skew Rolling 107
T. Uchimura, Y. Okuda and M. Akiyama

Influences of Finished Geometry of Specimen for Compression Test on the Stability of Testing and Precision of Measured Stress and Strain 117
J. Miyagawa, S. Ohba and M. Akiyama

Spring-back Prediction by Combination of the Finite Element Analysis and Bent Beam Theory Considering Bauschinger Effect 126
T. Matsumoto, S. Gotoh, T. Kuboki, M. Murata and Y. Jin

Computational Algorithms for Contact and Interfaces

Invited Session organized by Tod Laursen

Energy Frictional Dissipating Algorithm for Rigid and Ellastic Body's Contact Problems.....135
R. Bravo and J.L. Pérez-Aparicio

On a Contact between Curves and Rigid Surfaces – From Verification of the Euler-Eytelwein Problem to Knots 147
A. Konyukhov, K. Schweizerhof and A. Metzger

Computational Analysis of Masonry Structures

Invited Session organized by Pere Roca

A new Formulation to Assess the Seismic Demand of Masonry Structures by Means of Input Energy 159
M. Meza and F. Peña

Comparison between Minor Destructive Tests Results and Finite Element Models: The Case of a Sandstone Masonry Wall Tested in Laboratory 170
C. Liaño, I. Lombillo and L. Villegas

Computational Modeling of Hybrid Masonry Systems 181
I. Stanciulescu and Z. Gao

Computational Challenges in Multiscale Inelasticity and Instability

Invited Session organized by Herbert Mang and Christian Hellmich

Computational Modelling of Progressive Failure of Composite Materials and Structures Including Plasticity Effects 189
E.V. Morozov, J. Chen and K. Shankar

Multi-scale Analysis of Asphalt Mixture in Layered Road Structure 201
R. Valenta and M. Šejnoha

Multiscale Modelling of Masonry Structures under Extreme Loading 210
B.A. Izzuddin and L. Macorini

Computational Modeling of Forming Processes

Invited Session organized byJean-Philippe Ponthot and Carlos Agelet de Saracibar

Determination of the High Strain Rate Forming Properties of Steel Sheet 221
P. Verleysen, J. Peirs and L. Duchêne

Experimentally-based Identification of Sheet-metals Plastic Anisotropy, with a View to Obtaining Improved Predictions in Forming Simulations 229
G. Ferron, I. Charpentier, M. Martiny and M. Teaca

Identification of Orthotropic Plastic Material Parameters for Deep-Drawing Steel using DIC and FEMU 241
S. Schmaltz and K. Willner

Influence of the Material Hardening Model on the Simulation Results for the Equal Channel Angular Extrusion - ECAE - Process 251
R. Puff and M. Vaz Jr.

Johnson-Cook Parameter Identification for AISI 304 Machining through Nelder Mean Method 263
C.M. Giorgio Bort, P. Bosetti and S. Bruschi

Computational Strategies for Metal Cutting & Forming Operations

Invited Session organized by Miguel Vaz

Numerical Model of Warm Drawing of the Biocompatible Mg Alloys Accounting for Ductility of the Material 275
A. Milenin and P. Kustra

Numerical Simulation Study of the Knoop Indentation Test 287
M.I. Simões, A.X. Martins, J.M. Antunes, N.A. Sakharova, M.C. Oliveira and J.V. Fernandes

Parameter Identification and Elastic-plastic Problems: Optimization Strategies 295
J. Stahlschmidt, M. Vaz Jr., P.A. Muñoz-Rojas and E.L. Cardoso

Predictive Capability of Constitutive Model Outside the Range of Calibration 307
D. Wedberg and L-E. Lindgren

Process Analysis based on Experimental Tests and Numerical Modelling of Single Point Incremental Forming of Sheet Metal: Effect of the Principal Process Parameters....318
R. Bahloul, H. Arfa and H. BelHadj Salah

Continuous - Discontinuous Approaches to Failure of Quasi-brittle Materials

Invited Session organized by Gilles Pijaudier-Cabot and Frédéric Dufour

Stress Based Nonlocal Interactions....330
C. Giry, F. Dufour and J. Mazars

Thermodynamic Consistent Gradient-Poroplasticity Theory for Porous Media....342
G. Etse and J.L. Mroginski

Energy-based Variational Principles and Applications in Constitutive Modeling

Invited Session organized by Jörn Mosler and Laurent Stainier

A Variationally Consistent Approach for Non-associative Thermoplasticity at Finite Strain....354
M. Canadija and J. Mosler

Accelerated Energy-minimization in the Quasicontinuum Method with Application to Nanopillar Compression....360
B. Eidel, A. Stukowski and J. Schröder

Energy-based Variational Modeling of Adiabatic Shear Bands Structure....368
S. Su and L. Stainier

On the Thermodynamical and Variational Consistency of Cohesive Zone Models at Finite Strains....379
J. Mosler and I. Scheider

Plasticity Described by Uncertain Parameters - A Variational Inequality Approach....385
B. Rosic and H.G. Matthies

Simulation of the Dynamics of Bio-membranes in a Viscous Fluid with a Phasefield Variational Lagrangian Approach....397
C. Peco, A. Rosolen and M. Arroyo

Inelastic Processes in Heterogeneous Materials

Invited Session organized by Hermann Matthies and Adnan Ibrahimbegovic

A Deterministic Filter for Estimation of Parameters Describing Inelastic Heterogeneous Media....410
H.G. Matthies and B. Rosic

Multiscale Modelling of Masonry Structures using Domain Decomposition Techniques....422
K. Heyens, B. Vandoren and L. Schueremans

Two-scale Parameter Identification for Heterogeneous Elastoplastic Materials....432
U. Schmidt, J. Mergheim and P. Steinmann

Modeling of Damage Evolution andPropagating Discontinuities at Failure

Invited Session organized by Ekkehard Ramm, Francisco Armero and Christian Linder

Comparative Investigation and Application of 3D Constitutive Models for Concrete....442
B. Valentini and G. Hofstetter

Crack Propagation in Shells due to Impact Against Sharp Object....454
M. Pagani and U. Perego

Discontinuous Failure in a Gradient-enhanced Continuous Damage Model: a Regularised Displacement Framework....466
E. Tamayo-Mas and A. Rodríguez-Ferran

Exponential Finite Element Shape Functions for a Phase Field Model of Brittle Fracture....478
C. Kuhn and R. Müller

Finite Deformation Damage Modelling in Challenging Applications - Forming Limit Diagrams and Life Time Analysis for a Rocket Thrust Chamber 490
V. Tini, I.N. Vladimirov, Y. Kiliclar and S. Reese

Multiscale Strain Localization Modeling in the Gurson-Tvergaard-Needleman Plasticity Model....502
S. D'hers and E.N. Dvorkin

Numerical Simulations of Vickers Indentation Crack Growth in Ferroelectric Single Crystals: Effect of Microstructure on the Fracture Process 514
A. Abdollahi and I. Arias

On Micro-to-macro Connections in Strong Coupling Multiscale Modelling of Softening Materials....521
O. Lloberas-Valls, D.J. Rixen, A. Simone and L.J. Sluys

Multiresolution Science Based Mechanics of Complex Material

Invited Session organized by Wing-Kam Liu, Ji Hoon Kim and Lars-Erik Lindgren

A Comparative Study of Failure Criteria in Sheet Metal Forming Analysis....532
N-T. Nguyen, D-Y. Kim and H.Y. Kim

A Micromorphic Continuum Formulation for Finite Strain Inelasticity 540
S. Skatulla, C. Sansour and H. Zbib

Application of Finite Element Code to Characterize Mechanical Properties of Complex Microstructured Materials 552
N-T. Nguyen, S. Kang, D-Y. Kim and H.Y. Kim

Rapid Multiaxial High Cycle Fatigue Limit Predictions using Self-heating-based Probabilistic Multiscale Models 564
M. Poncelet, C. Doudard, S. Calloch, B. Weber and F. Hild

Simplified Multiscale Resolution Theory for Elastic Material with Damage 576
L-E. Lindgren, H. Qin, W.K. Liu and S. Tang

Multiscale Modeling for Microstructure Design of Materials

Invited Session organized by Tomohiro Takaki and Kisaragi Yashiro

A Dynamic Recrystallization Simulation Based on Phase-field and Dislocation-crystal Plasticity Models 587
M. Muramatsu, S. Sato, Y. Aoyagi and K. Shizawa

A New Crystal Plasticity Constitutive Equation Based on Crystallographic Misorientation Theory 594
H. Kuramae, Y. Nakamura, H. Sakamoto, H. Morimoto and E. Nakamachi

Application of Homogenization Method Considering Crystal Plasticity for Prediction of Mechanical Properties for Copper and Low Carbon Steel....603
T. Sueoka, T. Kuboki, M. Murata, K. Kuroda and K. Terada

Dynamic Recrystallization Model during Hot Working by Coupling Phase-Field Method and Finite Element Method.....610
T. Takaki

Molecular Dynamics Simulations on Interaction between Dislocation and Y2O3 Nanocluster in Fe 618
K. Yashiro, T. Mutsukado, M. Tanaka, A. Yamaguchi, K. Koga, T. Segi and T. Okuda

Multi-scale Modelling for Ferrite-Pearlite Composite Steel....630
I. Watanabe, D. Setoyama and N. Iwata

Numerical Investigations of Mechanical Stress Caused in Dendrite by Melt Convection and Gravity 642
H. Kashima, T. Takaki, T. Fukui and K. Morinishi

Numerical Prediction of Mechanical Properties of Dual-Phase Steel by using Multi-Phase-Field Method and Homogenization Method....652
A. Yamanaka and T. Takaki

Relationship between Deformation and Stability Switching in Amorphous Metal: Local Lattice Instability Analysis.....664
M. Nishimura, K. Yashiro and M. Arai

Non-conventional Modeling and Simulation of Materials and Processes

Invited Session organized by Francisco Chinesta and Elías Cueto

Neural Network Based Material Description of Uncured Rubber for use in Finite Element Simulations.....676
C. Zopf, S. Freitag and M. Kaliske

Towards a Numerical Simulation of Direct Manufacturing of Thermoplastic Parts by Powder Laser Sintering.....688
D. Defauchy, G. Regnier, I. Amran, P. Peyre, A. Ammar and F. Chinesta

Novel Computational Approaches in Biomechanics at Different Length Scales

Invited Session organized by Gerhard A. Holzapfel

A Microstructural Approach to Modelling Inelastic Effects in Fibred Biological Tissues 700
E. Peña, P. Sáez, M. Doblaré and M.A. Martínez

An Anisotropic Pseudo-elastic Model for the Mullins Effect in Arterial Tissue 713
E. Gultová, L. Horný, H. Chlup and R. Žitný

Collagen Orientation and Waviness Within the Vein Wall 720
J. Veselý, L. Horný, H. Chlup and R. Žitný

Computational Homogenization for Two-scale Modeling of Large Deforming Perfused Tissues 729
E. Rohan and V. Lukes

Determining the Constitutive Parameters of the Human Femoral Vein in Specific Patients 741
G. Fortuny, B. Herrera, F. Marimón and J. Marcé

nteractions Between Self Penetrating Neural Interfaces and Peripheral Nerves 748
P.N. Sergi and S. Micera

Longitudinal Prestrain in Male Abdominal Aorta from Pulse Wave Velocity Viewpoint.....757
L. Horný, T. Adámek, H. Chlup, R. Žitný, E. Gultová and J. Veselý

Modeling of Damage in Soft Biological Tissues and Application to Arterial Walls 764
D. Balzani, G.A. Holzapfel and S. Brinkhues

Numerical Analysis of Pulsatile Blood Flow in Realistic Coronary Bypass Models 776
J. Vimmr, A. Jonasova and O. Bublik

Numerical Modelling of Concrete Structures

Invited Session organized by Pavao Marovic and Nenad Bicanic

A Combined Finite-Discrete Element Model for Reinforced Concrete under Seismic Load.....788
N. Živaljić, Ž. Nikolić and A. Munjiza

Microplane Model M6f for Fiber-Reinforced Concrete.....796
F.C. Caner and Z.P. Bažant

Numerical Modelling of a RC Beam-column Connection Subjected to Ciclic Loading by Coupling 808
Different Non Linear Models
J. Pérez-Mota and N. Domínguez

Shape Memory Materials: Theory and Computation

Invited Session organized by Edoardo Artioli and Robert Taylor

Thermomechanical Simulation of Shape Memory Alloys Structures: Variational Methods and Associated Numerical Tools 820
M. Peigney

Contributed Sessions

Advanced Material Models

3D Modelling of the Elasto-plastic Behaviour of Adhesively Bonded Joints over a Wide Range of Tensile-shear Loads 830
J. Maurice, J-Y. Cognard, R. Créac'hcadec, L. Sohier, P. Davies, G. Meirinhos and S. Mahdi

An Efficient Numerical Integration Algorithm for the Single Mode Compressible Leonov Model 841
S.M. Mirkhalaf Valashani, F.M. Andrade Pires and R. Simões

Computational Modelling of a Multifield Single-Crystal Gradient Plasticity Formulation 852
C. B. Hirschberger and B. D. Reddy

Compression Behaviors of Low-Density Porous Materials under Multiaxial Stress Conditions 863
A. Sakuma and S. Nagaki

Implementation of a Material Model for a Cast TRIP-steel 869
S. Prüger, M. Kuna, K. Nagel and H. Biermann

Influence of the Plastic Potential on the Mechanical Response of Thermoplastic Components 881
M. Polanco-Loria and M. Hinrichsen

Johnson-Cook Parameter Identification from Machining Simulations using an Inverse Method 887
A. Shrot and M. Bäker

Plastic Torsional Analysis of Steel Members 899
Y.L. Pi and M.A. Bradford

Rheological Method for Constructing Constitutive Equations of One-phase Granular and Porous Materials 909
V. Sadovskiy

Smoothing of Yield Surfaces and a Reformulation of Multisurface Plasticity 921
J.M. Gesto, A. Gens and J. Vaunat

The Tikhonov Regularization Method in Elastoplasticity 932
H. Parente Azikri de Deus, C. Roberto Ávila da Silva Júnior, I. Moura Belo and J.C. Arantes da Costa Júnior

Composites

Discrete meso-modeling of Steel Fiber Reinforced Concrete: simulation of flexural behavior 944
A. Pros, P. Díez and C. Molins

Numerical Modelling of Behaviour of Carbon Nanotube-Reinforced Composites 952
F. Otero, S. Oller, X. Martínez and O. Salomon

Contact Problems

A Dual Mortar-based Contact Formulation Applied to Finite Plastic Strains 964
T. Doca, F.M. Andrade Pires and J.M.A. César de Sá

Halfspace Modeling of Elastic-plastic Contact of Rough Surfaces 976
F. Hauer and K. Willner

Numerical Analysis of Elastic-plastic Contact Problems 987
O. Sadovskaya

The Contact Temperature and Deformation Area of Asperities on Rough Surface for Three-Body Contact Situation 999
J. Horng, C. Wei, Y. Chen and S. Chern

Damage, Fracture and Fatigue

3D Modeling of Damage Growth and Ductile Crack Propagation using Adaptive Fem Technique 1007
H. Moslemi and A.R. Khoei

Cyclic Viscoelastoplasticity and Fatigue Fracture of Polymer Composites 1019
A.D. Drozdov

Non Intrusive Technique Based on a Discrete Element Approach to Extract Crack Opening from 3D Finite Element Computations 1031
B. Richard, C. Oliver, A. Delaplace and F. Ragueneau

Numerical Study on Interfacial Damage of Sprayed Coatings due to Thermo-Mechanical Fatigue..... 1043
S. Roth and M. Kuna

Plastic Deformation of Heterogeneous Materials: Numerical Simulation Study 1055
R.M. Branco, P.A. Prates, M.C. Oliveira, N.A. Sakharova and J.V. Fernandes

Prediction of Damage Intensity in Moment Frames by using Wavelet Analysis 1063
F. Raufi and O. Bahar

Prediction of Strain Localization during Sheet Metal Forming using Bifurcation Analysis and Gurson-type Damage 1072
L.Z. Mansouri, H. Chalal, F. Abed-Meraim and T. Balan

Stiffness and Strength of Hierarchical Polycrystalline Materials with Imperfect Interfaces 1082
M. Paggi and P. Wriggers

Forming Processes Simulations

An Arbitrary Lagrangian-Eulerian (ALE) Approach for the Modelling of Tension Levelling Processes 1091
L. Steinwender, A. Kainz, K. Krimpelstätter and K. Zeman

Analysis of Profile and Flatness in Flat Hot Rolling Based on Non-linearly Coupled Models for Elastic Roll Stack Deflection and Pseudo-steady-state Elasto-viscoplastic Strip..... 1104
A. Kainz, M. Widder, E. Parteder, G. Hein, K. Schörkhuber and K. Zeman

Numerical and Experimental Study of Sandwich Plates with Metallic Foam Cores 1116
H. Mata, M. Parente, A. Fernandes, R. Natal Jorge, R. Valente and A. Santos

On Standard Predictions of Reformability and Collapse Resistance for Expandable Tubulars based on Elasto-Plasticity Model 1124
T. Srisupattarawanit and G.P. Ostermeyer

On the Prediction of the Curvature of Cross Roll Straightened Bars..... 1136
A. Mutrux, B. Berisha and P. Hora

Reproduce Diameter Reduction Process of a Powder Filled Tube in Finite Element Analysis 1145
B. Böck, B. Buchmayr, S. Wallner and G. Posch

Validation of Thermal-Mechanical Modeling of Stainless Steel Forgings 1153
A.A. Brown, T.D. Kostka, B.R. Antoun, M.L. Chiesa, D.J. Bammann, S.A. Pitts, S.B. Margolis, D.T. O'Connor and N.Y.C. Yang

Geomechanics

3D Modelling of Geomaterials Accounting for an Unconventional Plasticity Approach 1165
V.A. Salomoni and R. Fincato

A Structured Constitutive Model for Simulating the Behaviour of an Overconsolidated Bonded Clay 1177
N.A. González, A. Gens, M. Arroyo and M. Rouainia

A Theoretical Approach to the Study of Compaction Bands in Porous Rocks..... 1189
A. Das, G.D. Nguyen and I. Einav

An Elastoplastic-Viscoplastic Soil Model for Cyclic Loading 1201
J.R. Maranha and A. Vieira

Effect of Large Displacements on the Numerical Analysis of an Embankment on Soft Soils..... 1212
P.J. Venda Oliveira and L.J.L. Lemos

Explicit Integration Scheme for Generalized Plasticity Constitutive Models with Automatic Error Control..... 1222
M.M. Stickle, P. De la Fuente and C. Oteo

Micromechanical Analysis of Damage and Fracture in Sandstone Rock Specimens, using Zero-thickness Interface Elements..... 1233
D. Garolera, I. Carol and C.M. López

Numerical Analysis and Safety Evaluation of a Large Arch Dam Founded on Fractured Rock, using Zero-thickness Interface Elements and a c-φ Reduction Method 1244
I. Aliguer, I. Carol and E. Alonso

Numerical Implementation of an Elastoplastic Model for Unsaturated Soils 1255
N.A. González and A. Gens

Numerical Simulation of Dynamic Pore Fluid-solid Interaction in Fully Saturated Non-linear Porous Media..... 1263
H. Sabetamal, M. Nazem, S.W. Sloan and J.P. Carter

Soldier Pile Walls – 3D Numerical Analysis of Soldier Pile Embedment..... 1274
J. Chalmovsky, R. Fiala and L. Mica

High Velocity Impact

A Computational Study on the Overload Characteristic Curves of Projectile Penetrating Metal Object 1284
D. Qiong, F. Long and Q. Wei

Dynamic Localizations in Structural Steel at High Strain Rates and Temperatures 1295
F.H. Abed and F.S. Makarem

Innovative Computational Methods

A Computational Procedure for the Cyclic Steady State Elastoplastic Analysis of Structures 1306
K.V. Spiliopoulos and K.D. Panagiotou

A Generalized Finite Element Method for Modelling Arbitrary Interfaces in Large Deformation Problems 1317
S.O.R. Biabanaki and A.R. Khoei

A Mixed Algorithm for Incremental Elastoplastic Analysis 1329
A. Bilotta, L. Leonetti and G. Garcea

An Efficient FETI Based Solver for Elasto-plastic Problems of Mechanics 1341
M. Cermak, T. Kozubek and A. Markopoulos

An Improved Accuracy Analysis of Elastoplastic Integration Algorithms 1353
F. Karaoulanis

Application of Sensitivity Analysis – Preliminary Step of the Process Parameters Estimation..... 1359
D. Szeliga

Assessment of the Enhanced Assumed Strain (EAS) and the Assumed Natural Strain (ANS) Techniques in the Mechanical Behavior of the SSH3D Solid-Shell Element 1368
L. Duchêne, A. Ben Bettaieb and A.M. Habraken

Elastic-plastic Analyses using the Solid-shell Finite Element SHB8PS and Evaluation on Sheet Forming Applications 1380
A. Salahouelhadj, H. Chalal, F. Abed-Meraim and T. Balan

Elastoplastic Analysis of Plane Steel Frames under Dynamic Loading 1391
A. Silva, W. Fernandes, R. Silveira and P. Gonçalves

Global Equilibrium Triangular Element for Lower Bound Limit Analysis 1403
D. Sodré and E. Lucena Neto

Interior-Point Algorithm for Shakedown Analysis Accounting for Limited Kinematical Hardening 1415
J.W. Simon and D. Weichert

Non-linear Analysis with the Boundary Element Method 1427
E. Pineda, I. Villaseñor and J. Zapata

Nonlinear Dynamic Model for Elastic Structures – A New Approach 1437
S.A. David and C. Oliveira

Non-linear Finite Element Assessment Analysis of a Modern Heritage Structure 1446
S. Sorace and G. Terenzi

Numerical Implementation of a Generalized Plasticity Model at Finite Strains 1458
F. De Angelis and R.L. Taylor

On the Performances of Different Nodal Integration Techniques and Their Stabilization 1466
F. Greco, L. Filice, I. Alfaro and E. Cueto

Predictive Models for Bolted T-stub Connections combining FEM with Intelligent Artificial Techniques 1478
J. Fernández-Ceniceros, R. Lostado-Lorza, R. Fernández-Martínez, A. Sanz-García and F.J. Martínez-de-Pisón

Shape Optimization for Anisotropic Elastoplasticity in Logarithmic Strain Space 1490
S. Germain and P. Steinmann

Multi-physics/Multiscale Material Problems

A Comparison between the Total Lagrangian Scheme (TLS) and the Predominat Twin Reorientation (PTR) Methods to Analyze the Twinning Deformations in a Rate Dependent Crystal Plasticity Model 1502
K. Kitayama, R. Cardoso, J. Yoon, T. Uemor and F. Yoshida

Discontinuity Layout Optimization in Upscaling of Effective Strength Properties in Matrix-inclusion Materials 1509
S. Bauer and R. Lackner

Finite-Temperature Nanovoid Deformation in Copper Under Tension 1517
M.P. Ariza, M. Ponga, I. Romero and M. Ortiz

Hydro-mechanical Modeling of Two-phase Fluid Flow in Deforming, Partially Saturated Porous Media With Propagating Cohesive Cracks using the Extended Finite Element Method 1527
T. Mohammadnejad and A.R. Khoei

Multi-scale Failure for Heterogeneous Materials: Link with Morphological Modeling 1539
E. Roubin, M. Bogdan and J.B. Colliat

Pore-space Controlled Hardening Model in Plasticity of Porous Materials: Application to The Analysis of Indentation Experiments 1551
R. Traxl and R. Lackner

Simulation of DP-Steels based on Statistically Similar Representative Volume Elements and 3D EBSD Data 1563
D. Brands, D. Balzani, J. Schröder and D. Raabe

Time-dependent Mesoscopic Modelling of Masonry using Embedded Weak Discontinuities 1575
B. Vandoren, K. Heyens and K. De Proft

Towards the Effective Behaviour of Polycrystalline Microstructures at Finite Strains.....1584
E. Lehmann, S. Loehnert and P. Wriggers

Numerical Modelling of Concrete Structures

An Elasto-plastic Damage Model for Concrete.....1595
E. Lale and M. Aydogan

High temperature effects in mortar and concrete specimens using a meso-mechanical model with fracture based zero-thickness interface elements 1607
M. Rodríguez, C.M. López, I. Carol and J. Murcia

Meso-macro Numerical Approach to Macroscopic Permeability of Fractured Concrete 1618
X. Jourdain, A. Vallade, J.B. Colliat, C. De Sa, F. Benboudjema and F. Gatuingt

The Influence of Load Misalignment on FRP-Concrete Bond Behaviour, a Numerical Study.....1625
P. Neto and J. Alfaiate

Thermal-Mechanical Models and Applications

A Method of Two-Scale Chemo-Thermal-Mechanical Coupling for Concrete 1637
T. Wu, I. Temizer and P. Wriggers

Multi-surface Description of Temperature and Strain Rate-dependent Damage Initiation and Growth in Ductile Viscoplastic Materials 1649
P. Longère, A-G. Geffroy, B. Leblé and A. Dragon

Authors Index.....1661

PLENARY LECTURES

XI International Conference on Computational Plasticity. Fundamentals and Applications
COMPLAS XI
E. Oñate, D.R.J. Owen, D. Peric and B. Suárez (Eds)

DEVELOPMENT OF CRYSTALLOGRAPHIC PROCESS TECHNOLOGY FOR PIEZOELECTRIC ACTUATOR FOR BIO-MEMS DEVICE

EIJI NAKAMACHI*

* Department of Biomedical Engineering
Doshisha University
Kyotanabe, Kyoto 610-0394, Japan
e-mail: enakamac@mail.doshisha.ac.jp, http//biomate.doshisha.ac.jp

Key words: Computational Plasticity, Forming Process, Composites, Nano-mechanics.

Abstract. Recently, the lead free piezoelectric material, which could be used for the actuator and the sensor of medical care devices, such as the health monitoring system (HMS) and the drug delivery system (DDS), is strongly required. In this study, we try to find a new biocompatible and lead-free piezoelectric material, by using the three-scale process-crystallographic analyses scheme, which consists of the first-principles calculations, the homogenization based finite element method, and the process optimization algorithm. After numerical calculations, we found an optimum biocompatible element combination and a tetragonal crystal structure of candidate material $MgSiO_3$. As a result of process crystallography simulation to adjust with the selected substrate Au(111), lattice parameters of $MgSiO_3$ with tetragonal structure were obtained as $a=b=0.3449$nm and $c=0.3538$nm, and its aspect ratio was 1.026. The piezoelectric stress constants of a non constraint $MgSiO_3$ crystal, $e_{33}=4.57\text{C/m}^2$, $e_{31}=-2.20\text{C/m}^2$ and $e_{15}=12.77\text{C/m}^2$, were obtained. Macro homogenized piezoelectric stress constants of $MgSiO_3$ thin film were obtained as $e_{33}=5.10\text{C/m}^2$, $e_{31}=-3.65\text{C/m}^2$ and $e_{15}=3.24\text{C/m}^2$. We confirmed the availability of our process crystallographic simulation scheme for a new biocompatible piezoelectric material design through the comparison with the experimental observation of a newly generated $MgSiO_3$ thin film material.

1 INTRODUCTION

Recently, the lead-based piezoelectric materials, such as $PbTiO_3$ and $Pb(Zr,Ti)O_3$, have been applied to various actuators [1] and sensors [2] in Micro Electro Mechanical System (MEMS) devices due to their high piezoelectric and dielectric properties. However, these materials contain the lead. Recently, lead and hazardous material are prohibited to use by Restriction of Hazardous Substances (RoHS) regulation [3]. Recently, the lead-free and biocompatible piezoelectric materials for Bio-MEMS devices have been developed by using the computational and the experimental approaches [4].

Zhang S. et al. [5] doped Ca and Zr in $BaTiO_3$ and succeeded in generating the piezoelectric material with high piezoelectric and dielectric constants. Fu P. et al. [6] doped La_2O_3 in Bi based $(Bi_{0.5}Na_{0.5})_{0.94}Ba_{0.06}TiO_3$ and succeeded in generating the piezoelectric

material with high piezoelectric constant and spontaneous polarization. However, these materials had problem of biocompatibility, and were not adequate for Bio-MEMS devices. Especially, ions of the composition element of a piezoelectric material invade the human body, when piezoelectric materials are applied to the implanted Bio-MEMS device. Therefore, piezoelectric materials should be constructed by biocompatible elements.

In previous study, we have developed a new three-scale analysis algorithm for a new piezoelectric material design, which consists of the first-principles calculation [7] and the process-crystallographic analyses scheme [8]. $MgSiO_3$, which was a candidate for a new biocompatible piezoelectric material and had the perovskite tetragonal structure, was found by using this numerical scheme, and it showed a high piezoelectric constant. Before a new material $MgSiO_3$ design and generation, we confirm the availability of our newly developed simulation scheme to analyze the epitaxial growth process of the perovskite tetragonal crystal structure and the piezoelectric properties of the existence piezoelectric material $BaTiO_3$. Numerical results showed a good agreement with the experimental ones.

In this study, we apply our three-scale process-crystallographic analyses scheme to design a new biocompatible $MgSiO_3$ piezoelectric thin film. Then, this thin film is generated by using the radio-frequency (RF) magnetron sputtering. Finally, the crystallographic orientation and the piezoelectric strain constant d_{33} are measured by using the X-ray diffracto-meter (XRD) and the ferroelectric measurement system to confirm the availability of our process-crystallographic design algorithm.

2 FIRST-PRINCIPLES AIDED THREE-SCALE ANALYSIS

2.1 Three-scale modeling of a piezoelectric thin film

Figure 1 shows the schematic description of the first-principles aided three-scale modeling of the piezoelectric thin film, which is grown on a substrate. It shows the three-scale structures, such as a “crystal structure”, a “micro structure” and a “macro structure.”

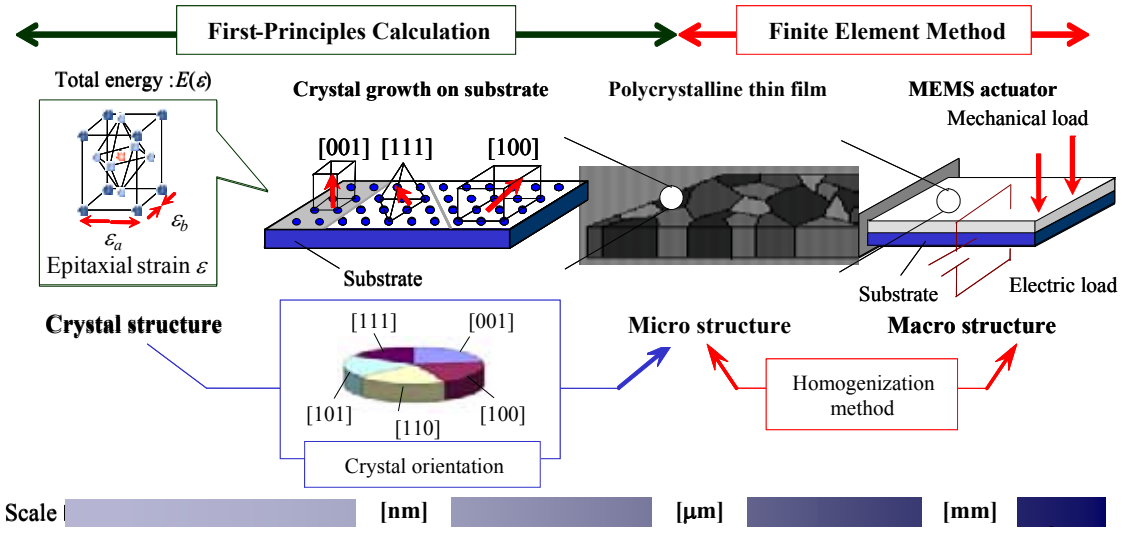

Figure 1: First-principles aided three-scale modeling of piezoelectric thin film on substrate

In the crystal structure scale, the stable structure and the crystal properties are evaluated by using the first-principles calculation. Next, the preferred orientations and their fractions are determined by considering the epitaxial strains, caused by the lattice mismatches between the thin film and the substrates. Additionally, the calculated crystal morphology is introduced into the micro structure and properties of the macro structure, which consist the thin film and the substrate, are calculated by the two-scale finite element analysis, which is derived based on the homogenization theory.

2.2 Process crystallography simulation algorithm

Thin film crystal is strained by mismatch between lattice constant of thin film and one of substrate, when thin film is grown epitaxially. Virtual crystal clusters with various orientations and conformations are generated by our process crystallography simulation, because thin film crystal has various conformations on a substrate as shown in Figure 2(a) and (b). Total energies of virtual clusters are varied by the crystal strain. Therefore, total energies of strained crystals are calculated by using the density functional theory (DFT), and total energies of virtual clusters are calculated. Total energies of virtual clusters are compared with one of stable state and total energy increments of virtual crystals are also calculated. In order to calculate the possibility of growth of the virtual cluster P_i, total energy increment ΔE is introduced into the canonical distribution as flows:

$$P_i = \frac{\exp[\Delta E_i / k_B T]}{\sum_n \exp[\Delta E_n / k_B T]} \tag{1}$$

where, k_B is the Boltzmann constant and T the absolute temperature.

The existing lead-free $BaTiO_3$ piezoelectric material with (111) orientation, which has perovskite type tetragonal structure as same as $MgSiO_3$, shows highest piezoelectric properties. In this study, we find the best substrate of $MgSiO_3$(111) with the minimum energy is found.

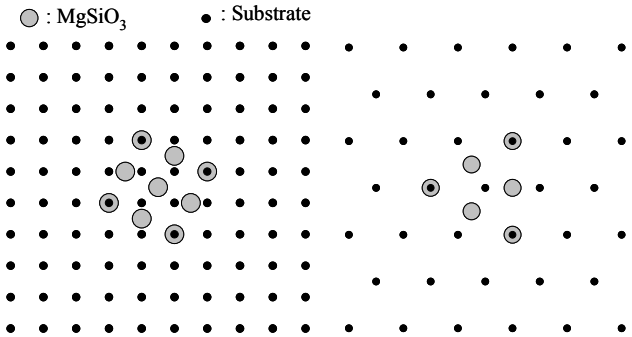

(a) $MgSiO_3$/Mo(100) (b) $MgSiO_3$/Au(111)

Figure 2: Schematic diagram for some conformations of $MgSiO_3$ crystal cluster on substrates

2.3 Numerical characterization process of the macro homogenized piezoelectric thin film

In order to evaluate the macro homogenized properties of the thin film, the micro structure of the thin film with a preferred orientation is applied to the two-scale finite element analysis on basis of crystallographic homogenization theory as shown in Fig.1. The crystal orientation fraction of the thin film is determined by frequency distribution of each grown cluster, which is calculated by the canonical distribution. The crystal orientation is introduced in the micro structure. For simplicity, the micro structure is divided evenly by eight-node rectangular solid elements and crystal orientations are assigned at the integration points of each element. For $BaTiO_3$, we employ experimentally obtained properties in the micro structure, and for $MgSiO_3$, computational properties obtained by the first-principles are employed for the micro structure.

3 DESIGN OF A NEW BIOCOMPATIBLE MATERIAL

3.1 The first-principles calculation

To calculate the crystal structure of perovskite $MgSiO_3$, energy cutoff was set as 500eV and k-point was generated by 8×8×8 Monkhurst-Pack mesh. We calculated the cubic structure as shown in Figure 3. Lattice constants a=b=c=0.3459nm were obtained.

The eigenfrequency of the cubic structure of $MgSiO_3$ was obtained as -112cm^{-1} by using phonon vibration analysis. This result indicated that $MgSiO_3$ crystal had possibility of phase transition to another phase, due to the eigenfrequency with negative value. Table I shows eigenvectors of each atom. It indicated that $MgSiO_3$ cubic crystal had possibility to change to the tetragonal structure, because all eigenvectors were existed along c axis only.

In order to calculate the stable tetragonal structure, initial structure was determined by employing eigenvectors. As a result, lattice parameters were obtained as a=b=0.3449nm and c=0.3538nm. The aspect ratio a/c=1.026 was obtained from 1.011 of $BaTiO_3$ thin film [9] to 1.049 of $PbTiO_3$ thin film [10]. Table 2 shows internal coordinates of the tetragonal $MgSiO_3$. We obtained reasonable result, because displacements of all internal atoms of the tetragonal structure had good agreement with direction of eigenvectors of the cubic structure as show in Table 1.

Furthermore, the variation of polarization and piezoelectricity of $MgSiO_3$ caused by the assigned small strain was calculated. The piezoelectric stress constants of $MgSiO_3$ crystal were determined as e_{33}=4.57C/m^2, e_{31}=-2.20C/m^2 and e_{15}=12.77C/m^2.

3.2 Determination of the best substrate

Biocompatible elements have bio-essential elements (Ca, Fe, Ge, Mg, Mn, Mo, Na, Ni, Sn and Zn) and elements (Si, Ta, Ti and Zr), which have been used in the human body. In previous study, we calculated reactivity with biological molecules and found new biocompatible elements (Li, Ba, K, Au, Rb, In) [11]. In these 20 biocompatible elements, we selected Au, Mo and Ta for candidates of the substrate, because these elements satisfied four terms, such as (1) the melting point is over sputtering temperature, (2) element dose not react to other elements under sputtering condition, (3) element is able to be use the under electrode and (4) element is cubic structure. Lattice parameters of Au with FCC cubic structure are

a=b=c=0.4080nm, ones of Mo with BCC cubic structure are a=b=c=0.3147nm and ones of Ta with BCC cubic structure are a=b=c=0.3289nm.

Table 3 shows result of crystallography simulation on (100), (110) and (111) oriented three substrate candidates. Total energies and orientation fractions of epitaxially grown $MgSiO_3$ thin films were different depend on conformations as shown in Figure 4. It shows an example of conformations of $MgSiO_3$(001)/Au(100).

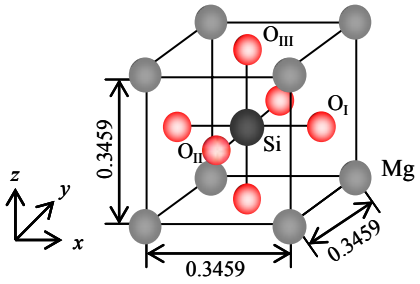

Figure 3: Schematic diagram for some conformations of $MgSiO_3$ crystal cluster on substrates

Table 1: Eigenvectors of interior atoms in $MgSiO_3$ Crystal

Atom	Eigenvector		
	ξ_x	ξ_y	ξ_z
Mg	0.00	0.00	0.88
Si	0.00	0.00	-0.13
O_I	0.00	0.00	-0.37
O_{II}	0.00	0.00	-0.37
O_{III}	0.00	0.00	-0.22

Table 2: Internal coordinates of $MgSiO_3$ crystal

Atom	x	y	z
Mg	0.00	0.00	0.00
Si	0.50	0.50	0.42
O_I	0.00	0.50	0.38
O_{II}	0.50	0.00	0.38
O_{III}	0.50	0.50	0.90

Table 3: Internal coordinates of $MgSiO_3$ crystal

Substrate		$MgSiO_3$		
Atom	Facet	Facet	Energy [eV]	Fraction [%]
Au	(100)	(001)	0.075	87.7
		(001)	0.126	12.3
	(110)	(101)	0.343	92.0
		(101)	0.406	8.0
	(111)	(111)	0.539	100.0
Mo	(100)	(100)	0.093	61.5
		(001)	0.105	38.5
	(110)	(001)	0.254	70.1
		(001)	0.287	20.2
		(101)	0.305	9.7
	(111)	(111)	0.774	100.0
Ta	(100)	(001)	0.001	90.8
		(001)	0.061	9.1
		(001)	0.172	0.1
	(110)	(101)	0.329	99.8
		(101)	0.488	0.2
	(111)	(101)	0.929	100.0

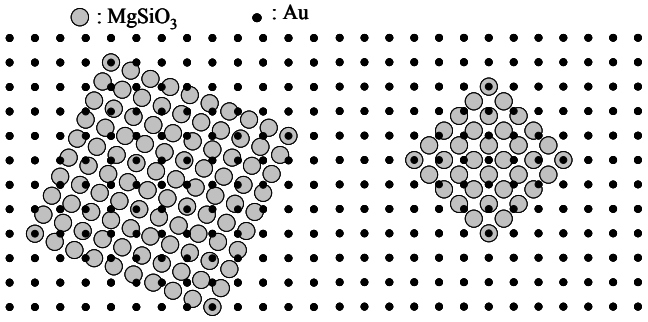

Figure 4: Conformations of $MgSiO_3$/Au(100) calculated by process crystallography simulation

Therefore, we summarized numerical results of independent orientations, total energies and fractions in Table 3. It shows that $MgSiO_3$(111) with highest piezoelectric property could be grown on Au(111) and Mo(111) substrates. Here, Au(111) was the best substrate of biocompatible $MgSiO_3$ thin film, because the total energy of $MgSiO_3$ on Au(111) was smaller than one on Mo(111) substrate.

Finally, the macro homogenized piezoelectric property of $MgSiO_3$ thin film on the best substrate, Au(111), was calculated by using the two-scale finite element analysis on basis of crystallographic homogenization theory. As a result, macro homogenized piezoelectric stress constants were calculated as e_{33}=5.10C/m^2, e_{31}=-3.65C/m^2 and e_{15}=3.24C/m^2.

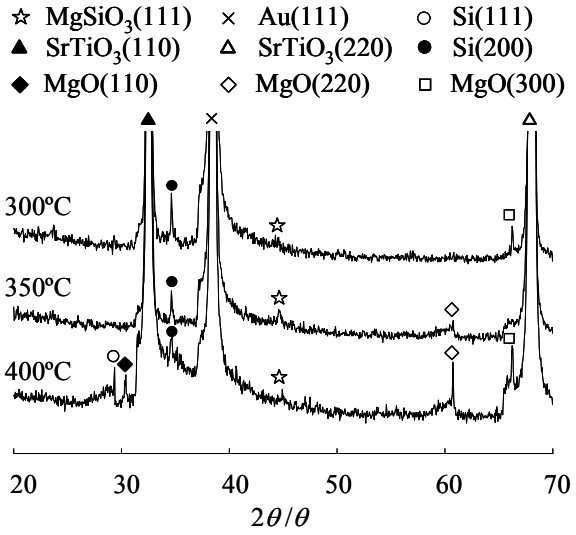

Figure 5: XRD $2\theta/\theta$ patterns for $MgSiO_3$ thin films generated at T_a=650ºC and T_s =300, 350 and 400 ºC

4 EXPERIMENTAL RESULTS OF THIN FILM GENERATION BY SPUTTERING

In order to confirm the availability of our process-crystallographic simulation scheme, $MgSiO_3$ thin film with the perovskite tetragonal crystal structure was generated by using RF

magnetron sputtering apparatus. We employed the simple search algorithm, such as the experimental design algorithm, by employing two design parameters, such as the substrate temperature T_s and post annealing temperature T_a.

Figure 5 shows $2\theta/\theta$ patterns for $MgSiO_3$ thin film generated at T_a=650ºC and T_s =300, 350 and 400 ºC. The peak of MgSiO (111) crystal was obtained.

The displacement-voltage curves were measured by using the ferroelectric measurement system in six cases of combinations with T_a=600, 650 and 700 ºC and T_s =300 and 350 ºC. Figure 6 shows displacement-voltage curves of generated piezoelectric $MgSiO_3$ thin films. It means that all films showed the piezoelectric property because of typical butterfly-type hysteresis curves. The piezoelectric strain constant d_{33} can be calculated by the gradient at cross point of the curve. Figure 7 shows measurement results of d_{33} under conditions of T_s =300, 350 and 400 ºC, and T_a=650 ºC.

Finally, the optimum condition, T_s=300ºC and T_a=650ºC, was found and the piezoelectric strain constant was d_{33}=346.7pm/V.

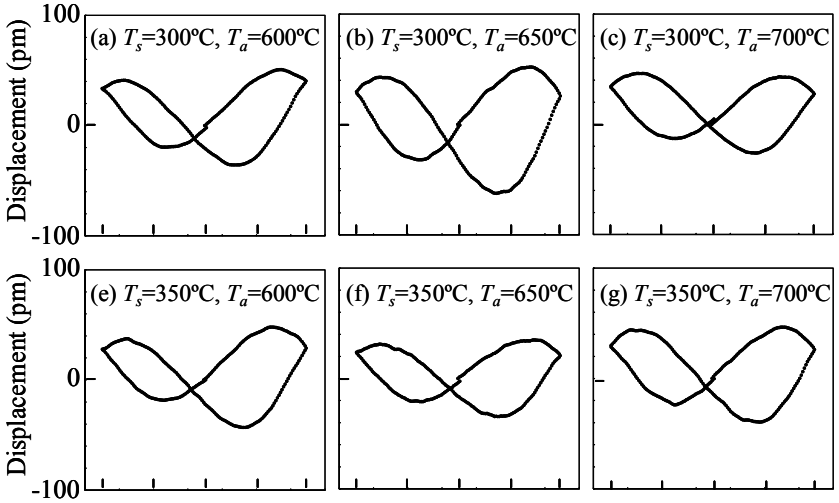

Figure 6: Displacement-voltage curves of $MgSiO_3$ thin film

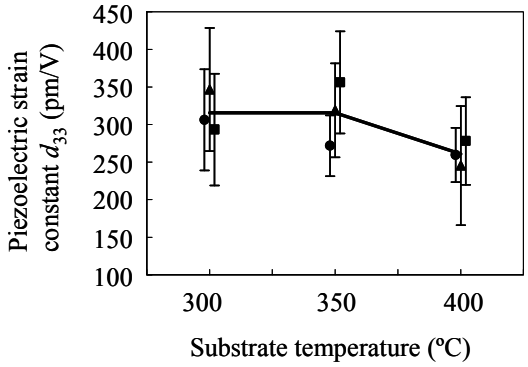

Figure 7: Relationship between piezoelectric strain constant d_{33} and substrate temperature under the condition of the post-anneal temperature 650ºC

5 CONCLUSION

In order to generate a new biocompatible $MgSiO_3$ piezoelectric thin film, which can apply to the Bio-MEMS device, our three-scale process-crystallographic simulation scheme for a new material generation was applied. Further, $MgSiO_3$ was generated by using RF magnetron sputtering apparatus and confirm the availability of our simulation scheme through the comparison with the experimental results. Finally, following results were obtained.

(1) Lattice constants of $MgSiO_3$ with tetragonal structure were obtained as $a=b=0.3449$nm and $c=0.3538$nm, and its aspect ratio is 1.026.
(2) The piezoelectric stress constants of $MgSiO_3$ crystal, $e_{33}=4.57C/m^2$, $e_{31}=-2.20C/m^2$ and $e_{15}=12.77C/m^2$, were obtained.
(3) Au(111) was the best biocompatible substrate, on which $MgSiO_3$(111) thin film with minimum total energy can be grown.
(4) Macro homogenized piezoelectric stress constants of $MgSiO_3$ thin film on Au(111) substrate were obtained as $e_{33}=5.10C/m^2$, $e_{31}=-3.65C/m^2$ and $e_{15}=3.24C/m^2$.
(5) An optimum condition was obtained as T_s=300ºC and T_a=650ºC, and its piezoelectric strain constant was $d_{33}=346.7$pm/V.

Consequently, we indicated that a new biocompatible $MgSiO_3$ thin film could be applied to actuators and sensors in Bio-MEMS.

ACKNOWLEDGEMENTS

I gratefully appreciate Ph. D. Hwisim Hwang for his analytical and experimental works on this subject. Further, I would like to acknowledge the financial support of the Grant-in-Aid for Scientific Research (B) (23360059) by the Ministry of Education, Culture, Sports, Science and Technology of Japan.

REFERENCES

[1] Tsai, J.Z., Chen, C.J. , Chen, W.Y., Liu, J.T., Liao, C.Y. and Hsin, Y.M. A new PZT piezoelectric sensor for gravimetric applications using the resonance-frequency detection. *Sens. Act. B.* (2009) **139**:259-264.
[2] Watson, B. , Friend, J. and Yeo, L. Piezoelectric ultrasonic micro/milli-scale actuators. *Sens. Act. A*. (2009) **152**:219-233.
[3] European Parliament, On the restriction of the use of certain hazardous substances in electrical and electric equipment. *Official J. Eur. Union.* (2003) **37**:19-23.
[4] Lin, D., Kwok, K.W. and Chan, H.L. Dielectric and piezoelectric properties of $K_{0.5}Na_{0.5}NbO_3$-$AgSbO_3$ lead-free ceramics. *J. Appl. Phys.* (2009) **106**:034102.1-034102.5.
[5] Zhang, S.W., Zhang, H., Zhang, B.P. and Zhao, G. Dielectric and piezoelectric properties of $(Ba_{0.95}Ca_{0.05})(Ti_{0.08}Zr_{0.12})O_3$ ceramics sintered in a protective atmosphere. *J. Eur. Ceram. Soc.* (2009) **29**:3235-3242.
[6] Fu, P., Xu, Z., Chu, R., Li, W., Zhang, G. and Hao, J. Piezoelectric, ferroelectric and dielectric properties of La_2O_3-doped $(Bi_{0.5}Na_{0.5})_{0.94}Ba_{0.06}TiO_3$ lead-free ceramics. *Mater. Des.* (2009) **31**:796-801.
[7] Uetsuji, Y., Hwang, H., Tsuchiya, K. and Nakamachi, E. First-principles study on crystal structure and piezoelectricity of perovskite-type silicon oxides. *J. Solid Mech. Mater. Eng.* (2008) **2**:1427-1435.

[8] Hwang, H., Uetsuji, Y., Sakata, S., Tsuchiya, K. and Nakamachi, E. Crystal growth prediction by first-principles calculations for epitaxial piezoelectric thin films. *J. Comput. Sci. Technol.* (2009) **3**:267-274.
[9] Schubert, J., Siegert, M., Faradmanesh, M., Zander, W., Prompers, M., Buchal, C., Lisoni, J. and Lei, C.H. Superconducting and electro-optical thin films prepared by pulsed laser deposition technique. *Appl. Surf. Sci.* (2000 **168**:208-214.
[10] Satoh, T., Wasa, K., Tabata, K., Adachi, H., Ichilawa, Y. and Setsune, K., Microstructures of sputtered $PbTiO_3$ thin films. *J. Vac. Sci. Technol. A*. (1995) **13**:1022-1026.
[11] Parr, R.G. and Pearson, G. Absolute hardness: companion parameter to absolute electronegativity. *J. Am. Chem. Soc.* (1983) **105**:7512-7516.

XI International Conference on Computational Plasticity. Fundamentals and Applications
COMPLAS XI
E. Oñate, D.R.J. Owen, D. Peric and B. Suárez (Eds)

GENERALIZED PLASTICITY FOR GEOMATERIALS WITH DOUBLE STRUCTURE

ANTONIO GENS*, MARCELO SÁNCHEZ† AND BEATRIZ VALLEJÁN*

* Department of Geotechnical Engineering and Geosciences
Universitat Politècnica de Catalunya
Jordi Girona 1-3, Edifici D-2, 08034 Barcelona, Spain
e-mail: antonio.gens@upc.edu, beatriz.vallejan@snclavalin.com web page: http://www.upc.edu

† Department of Civil Engineering
Texas A&M University
College Station, Texas, USA
e-mail: msanchez@civil.tamu.edu, web page: http://www.tamu.edu/

Key words: Generalized plasticity, double structure, swelling clays, sealing material

Abstract. The paper presents a double structure constitutive model based on a generalized plasticity formalism. The behaviour of macrostructure, microstructure and their interactions are described. A coupled hydromechanical formulation is then presented that assumes no hydraulic equilibrium between structural levels. Constitutive law and formulation are applied to the simulation of the behaviour during hydration of a heterogeneous mixture of bentonite powder and bentonite pellets. A satisfactory reproduction of observed behaviour is achieved.

1 INTRODUCTION

The behaviour of swelling clays is better understood if the effect of the pore size structure on their hydromechanical behaviour is taken into account. In compacted (and therefore unsaturated) swelling clays, the pore size structure is set up during compaction but it may change significantly in response to various actions such as loading and hydration. Although the distribution of pore sizes is of course continuous, useful insights can be obtained by considered only two structural levels: microstructural and macrostructural as well as their interactions. This dual material aspect is reinforced when the material is composed of a mixture of powder and highly compacted pellets. This mixture is an attractive sealing material in radioactive waste disposal schemes because, even when only modest compaction efforts are applied, a sufficiently high density value is achieved after hydration has taken place. However, the heterogeneity of the material gives rise to a complex hydromechanical behaviour that must be well understood if a sufficient degree of confidence in the performance of the seal is to be achieved.

The generalized plasticity model adopted for the description of the behaviour of the double structure material is presented first followed by the formulation of the hydromechanical problem. Constitutive law and formulation are then applied to description of a number of swelling pressure tests of a mixture of bentonite powder and highly compacted bentonite pellets being studies as a potential sealing material for a dep geological repository for high level nuclear waste.

2 GENERALIZED PLASTICITY CONSTITUTIVE MODEL

In strongly swelling clays, there are plastic mechanisms giving rise to irreversible behaviour in addition to those observed in non-swelling materials. Those additional mechanisms can often be attributed to the interaction between the macrostructure and the microstructure. This kind of irreversible behaviour generally appears at any value of applied suction and it is difficult to determine the initiation of the yielding. Those facts encourage the use of the generalized plasticity theory to describe these plastic mechanisms. In a generalized plasticity model the yield function is not defined or it is not defined in an explicit way [1]. The advantages in using the generalized plasticity theory to model the plastic mechanisms ascribed to the interaction between structures are presented in detail in [2].

The model is defined in terms of the three stress invariants (p, J, Θ) and suction (s). To formulate the double structure model is necessary to define laws for: i) the macrostructural level, ii) the microstructural level, and iii) the interaction between both structural levels.

2.1 Macrostructural level

The inclusion of this structural level in the analysis allows the consideration of phenomena that affect the skeleton of the material, for instance deformations due to loading and/or collapse of the macrostructure. The *BBM* (Barcelona Basic Model) has been adopted to describe the macrostructural behaviour [3]. The *BBM* considers two stress variables to model the unsaturated behaviour: the net stress ($\boldsymbol{\sigma}$) computed as the excess of the total stresses over the gas pressure, and the matric suction (s), computed as the difference between gas pressure and liquid pressure (p_g-p_l). The *BBM* yield surface (F_{LC}) is defined as follows:

$$F_{LC} = 3J^2 - \left[\frac{g(\theta)}{g(-30^o)}\right]^2 M^2 \left(p + p_s\right)\left(p_0 - p\right) = 0 \tag{1}$$

where M is the slope of the critical state, p_o is the apparent unsaturated isotropic pre-consolidation pressure at a specific value of suction, and p_s considers the dependence of shear strength on suction. To complete the definition of the yield surface as set out in (1), it is possible, in principle, to adopt any suitable Lode's angle function, g(θ).

The trace of the yield function on the isotropic p-s plane is called *LC* (Loading-Collapse) yield curve because it represents the locus of activation of irreversible deformations due to loading increments or to hydration collapse. The position of the *LC* curve is given by the pre-consolidation yield stress of the saturated state, p_o^* (hardening variable) that varies with plastic volumetric strain according to the following hardening law:

$$\dot{p}_0^* = p_0^* \frac{(1+e)}{(\lambda_{(0)} - \kappa)} \dot{\varepsilon}_v^p \tag{2}$$

where e is the void ratio, ε_v^p is the volumetric plastic strain, κ is the elastic compression index for changes in p and $\lambda_{(0)}$ is the stiffness parameter for changes in p for virgin states of the soil in saturated condition.

2.2 Microstructural level

The microstructure is the seat of the basic physico-chemical phenomena occurring at clay particle level. The strains arising from microstructural phenomena are considered nonlinear

elastic and volumetric. The microstructural strains are proportional to the microstructural effective stress ($\hat{p}$) through a microstructural bulk modulus according to:

$$\hat{p} = p + \chi s \tag{3}$$

$$\dot{\varepsilon}_{vm} = \frac{\dot{\hat{p}}}{K_m} = \frac{\dot{p}}{K_m} + \chi \frac{\dot{s}}{K_m} \tag{4}$$

where the subscript *m* refers to the microstructural level, the subscript *v* refers to the volumetric component of the strains, K_m is the microstructural bulk modulus and χ is a parameter dependent on the degree of saturation of the microstructure. The parameter χ is included only to account for the possibility that the microstructure may become unsaturated. However, generally a constant value of $\chi = 1$ is adopted since the micro-structural level, associated with the behaviour of expansive clay particles, is very likely to be saturated. In very active expansive clays this assumption can be supported by the high affinity of the active clay minerals by water, which maintain the interlayer space and micro-pores saturated even at relatively high suction. Under this condition mean effective stress controls the mechanical behaviour at microstructural level.

The concept of a Neutral Line (*NL*) is introduced corresponding to constant $\hat{p}$ and no microstructural deformation (Fig. 1). The *NL* divides the *p*-*s* plane into two parts, defining two main generalized stress paths, which are identified as: *MC* (microstructural contraction) when there is an increase in $\hat{p}$ and *MS* (microstructural swelling) in the opposite case.

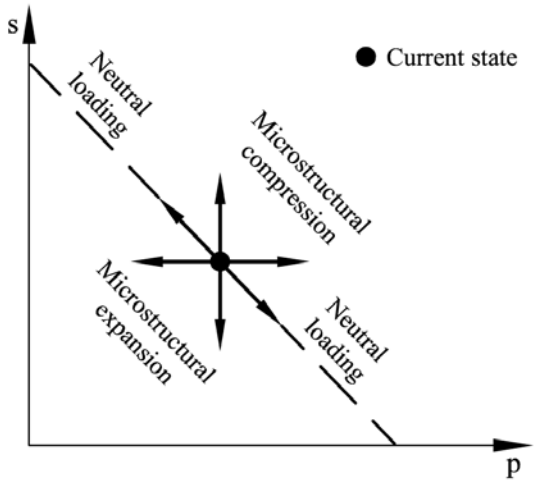

Figure 1: Neutral line and load directions in the microstructural model.

2.3 Interaction between microstructural and macrostructural levels

Based on experimental evidence, it is assumed that the macrostructure is affected by microstructural deformations generally in an irreversible way [4]. A hypothesis of the model is that the plastic deformations of the macrostructure (ε_{vM}^{p}) induced by microstructural effects are proportional to the microstructural strains (ε_{vm}) according to interaction functions *f* [2].

The total plastic macrostructural strains (i.e. the sum of the plastic strains induced by the yielding of the macrostructure, ε^{p}_{LC}, plus that induced by the microstructure, $\varepsilon^{p}_{vM\to m}$) are evaluated using:

$$\dot{\varepsilon}^{p}_{vM} = \dot{\varepsilon}^{p}_{vLC} + \dot{\varepsilon}^{p}_{vM\to m} = \dot{\varepsilon}^{p}_{vLC} + f\,\dot{\varepsilon}_{vm} \tag{5}$$

Two interaction functions f are defined: f_c for *MC* paths and f_S for *MS* paths. The interaction functions depend on the ratio p/p_o (Fig. 2). The ratio p/p_o is a measure of the degree of openness of the macrostructure relative to the applied stress state. When this ratio is low, it implies a dense packing of the material and it is expected that, under this condition (dense macrostructure), the microstructural swelling (*MS* path) affects strongly the global arrangements of clay aggregates, inducing large macrostructural plastic strains. In this case the microstructure effects induce a more open macrostructure, which implies a macrostructural softening. On the other hand, when the microstructure contracts (*MC* path) the induced macrostructural plastic strains are larger with open macrostructures, that is, for values of p/p_o close to 1. Under this path the clay tends towards a more dense state, which implies a hardening of the macrostructure. The result of the coupling between macro and micro levels is reflected in the value of p_o^*, the hardening variable of the macrostructure. In this way the effect of microstructural processes on the global arrangements of aggregates is taken into account.

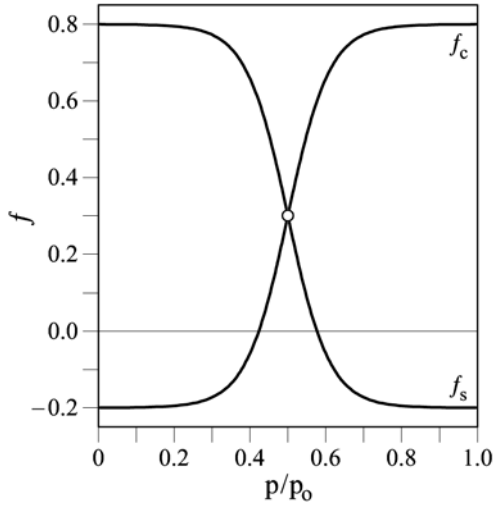

Figure 2: Interaction functions

To fully describe the soil behaviour, the definition of specific elasto-plastic laws for each domain is required according to the microstructural stress path followed (*MC* or *MS*). Generalized plasticity theory can deal with such conditions, allowing the consideration of two directions of different behaviour and the formulation of proper elasto-plastic laws for each region. Thus, a complete description of a generalized model includes the definition of the: i) loading and unloading direction, ii) plastic flow direction, and iii) a plastic modulus. Equivalent to loading/unloading directions in conventional stress/strain formulations, two

vectors may be defined at every point of the stress space. One vector indicates the *MC* direction and the other the *MS* direction. Given a generalized stress state and stress increment, the criterion to identify the microstructural stress path is illustrated in Figure 1.

2.4 Stress-strain relations

The constitutive model described contains two plastic mechanisms: i) a plastic mechanism associated with the yield of the macrostructure defined by a classical plasticity law, and ii) a plastic mechanism associated with the interaction between microstructure and macrostructure described by a generalized plasticity approach.

In classical plasticity theory, it is assumed that the material behaves either as an elastic or an elasto-plastic solid. The yield surface defines the transition from elasticity to plasticity, stress states inside the yield surface are considered as elastic ($F < 0$). In generalized plasticity theory, the state of the material is determined directly from the control variables: generalized stresses, strains and a finite number of internal variables. A process of loading is defined as elastic if the set of internal variables remains unchanged.

In the case of a purely (nonlinear) elastic loading, the stress increment is related to the increment of strains and suction by the following relationship:

$$\dot{\boldsymbol{\sigma}} = \mathbf{D}_e \cdot \dot{\boldsymbol{\varepsilon}}^e + \boldsymbol{\alpha}_s \dot{s} \tag{6}$$

where $\mathbf{D}_e$ is the global elastic matrix that considers the elastic component of both structural levels. $\boldsymbol{\alpha}_s$ is the elastic vector associated to suction.

When a loading process is inelastic, the material behaviour is described by the elasto-plastic mechanisms that are activated during the loading process. A multidissipative approach [5] has been adopted to derive the general elasto-plastic relations that can be expressed as follows:

$$\dot{\boldsymbol{\sigma}} = \mathbf{D}_{ep} \cdot \dot{\boldsymbol{\varepsilon}} + \boldsymbol{\gamma}_s \dot{s} \tag{7}$$

where D_{ep} is the global elasto-plastic matrix and γ_s is the elasto-plastic vector associated with suction. The expressions for the vectors and matrices in (6) and (7) together with the details of numerical implementation are presented in [6].

3 HYDROMECHANCIAL FORMULATION

The overall media is assumed to consist of two overlapping but distinct continua. In the following, subscript *M* will stand for the macrostructure and subscript *m* for the microstructure. Accordingly, macroporosity and microporosity are denoted as ϕ_M and ϕ_m respectively. Macroporosity and microporosity are defined as the volume of macropores and micropores, respectively, divided by the total volume of the soil. Thus, total porosity ϕ equals $\phi_M + \phi_m$. The degree of saturation of the macroporosity, $S_{wM,}$ is the volume of macropores occupied by water over the volume of the macropores; an equivalent definition holds for the microporosity degree of saturation, S_{wm}.

An important feature of the formulation is that hydraulic equilibrium between the two continua is not assumed, i.e. at each point of the domain the water potentials in the two continua may be different leading to an exchange of water between them. For simplicity, a linear relationship is assumed (e.g. [7]) where water exchange is described by:

$$\Gamma^w = \gamma(\psi_M - \psi_m) \tag{8}$$

where Γ^w is the water exchange term, γ is a parameter (often called the leakage parameter) and ψ is the total water potential. It is assumed that only matric and gravitational potential contribute to the total potential of the macrostructure but an additional osmotic component may also contribute to the microstructural potential [8]. Here, potential is defined in pressure units. As the water exchange is local in space, the gravitational potential will be the same for the two media. Water exchange will therefore be driven by suction differences alone.

Using the concept of material derivative, the balance equation for the solid phase can be written, for the case of a single porosity medium, as:

$$\frac{D\phi}{Dt} = \frac{(1-\phi)}{\rho_s}\frac{D\rho_s}{Dt} + (1-\phi)\dot{\varepsilon}_v \tag{9}$$

where *D(.)/Dt* denotes material derivative, ρ_s is the solid density, $\dot{\varepsilon}_v$ is the volumetric strain increment and *t* is time. For the case of double porosity equation (9) becomes:

$$\frac{D\phi}{Dt} = \frac{D\phi_M}{Dt} + \frac{D\phi_m}{Dt} = \frac{(1-\phi)}{\rho_s}\frac{D\rho_s}{Dt} + (1-\phi_M-\phi_m)(\dot{\varepsilon}_{vM} + \dot{\varepsilon}_{vm}) \tag{10}$$

where it has been assumed that the total volumetric deformation is the sum of the volumetric deformations of each medium.

3.1 Balance equations

The water mass balance equation for the case of two overlapping flow media is:

$$\frac{\partial}{\partial t}\left(\rho_w S_{wj}\phi_j\right) + \nabla\cdot\left(\mathbf{j}_{wj}\right) \pm \Gamma^w = f_j^w \;\; ; \; j = M, m \tag{11}$$

where S_{wj} is the liquid saturation of medium *j*, $\mathbf{j}_{wj}$ is the total mass fluxes of water in the liquid phase and f_j^w is the external mass supply of water per unit volume in medium *j*. The possible presence of dissolved air in the liquid phase is neglected for simplicity.

Finally, it is assumed that total stresses for the overall medium affect equally the macro and the microstructure. The equilibrium equation is:

$$\nabla\cdot\boldsymbol{\sigma} + \mathbf{b} = \mathbf{0} \tag{12}$$

where $\boldsymbol{\sigma}$ is the total stress tensor and $\mathbf{b}$ is the vector of body forces. In contrast, the total deformation of the medium is obtained from the sum of the deformations of each domain.

3.2 Hydraulic relationships

Liquid flow is governed by Darcy's law:

$$\mathbf{q}_{wj} = -\mathbf{K}_{wj}\left(\nabla\psi_j\right) = -\mathbf{K}_{wj}\left(\nabla p_{wj} - \nabla\rho_{wj}\mathbf{g}\right) \;\; ; \; j = M, m \tag{13}$$

where $\mathbf{q}$ is the mass liquid flow (with respect to the solid phase), $\mathbf{K}_l$ is the liquid permeability tensor, p_l is the liquid pressure, ρ_l is the liquid density and $\mathbf{g}$ is the gravity vector. The permeability tensor is expressed as

$$\mathbf{K}_{wj} = \mathbf{k}_j \frac{k_{rj}}{\mu_j} \;\; ; \; j = M, m \tag{14}$$

where $\mathbf{k}$ is the intrinsic permeability and k_r is the relative permeability that expresses the effect of degree of saturation (or suction) on global permeability. Intrinsic permeability

depends on many factors such as pore size distribution, pore shape, tortuosity and porosity. Here a dependence of intrinsic permeability on porosity is adopted:

$$\mathbf{k}_j = k_o \exp\left(b(\phi_j - \phi_o)\right) \; ; \; j = M, m \tag{15}$$

where ϕ_o is a reference permeability for which the intrinsic permeability is k_o. Relative permeability and retention curves are also defined for the two porosity levels using standard relationships. .

4 APPLICATION

The double-structure constitutive law and hydromechanical formulation is applied to the modelling of the behaviour of a mixture of 50% bentonite powder and 50% bentonite pellets, by dry weight, during hydration as observed in a number of laboratory swelling pressure tests [9]. FoCa clay, a calcium bentonite from the Paris Basin has been selected for the study. The major component of the clay fraction is an interstratified clay mineral of 50% calcium beidellite and 50% kaolinite. Pellets are manufactured by dynamic compaction of the powder between two rotating wheels. The dimensions of the pellets are 25 x 25 x 15 mm and their average dry density is 1.89g/cm^3. Compaction water content lies in the range of 4% to 5%.

In particular, three tests performed on samples with a dry density of 1.60 g/cm^3 (RS2B, RS2E and RS2F) are considered. Their lengths are 5, 10 and 12 cm respectively. Computed evolutions of swelling pressures compared with the measured values are shown in Figures 3a, 3b and 3c. Testing times ranged from 150 to 500 days depending on specimen length. The model reproduces very satisfactorily the observed behaviour. The evolution of water intake is also well matched (Figures 3d, 3e and 3f), some discrepancies at the end of the test have been attributed to small leakages in some of the very long term tests.

The evolutions of macrostructural and microstructural suctions at three different points (bottom, middle and top of the specimen) of test RS2E obtained in the analysis are plotted in Figure 4. It can be observed that, at the bottom boundary, the macrostructural and microstructural suctions reduce rapidly but they differ at the beginning of the test because of the delay in water transfer between the two porosities. Eventually, however, they come together and remain in equilibrium for the remainder of the test. Interestingly, at the other two points the two porosities come into equilibrium before they are reached by the hydration front, i.e. before they exhibit any suction reduction. They also maintain this equilibrium condition throughout the rest of the test. The analysis suggests, therefore, that non-equilibrium between the two porosity levels is only likely to affect the early stages of the test.

The cause underlying the characteristic temporary drop in swelling pressure is the collapse of the macrostructure that, in the constitutive model, corresponds to reaching the LC yield surface in the BBM. This is illustrated in Figure 5, where the stress paths (in macrostructural suction – vertical net stress space) followed by the same three points of test RS2E are plotted. The initial position of the LC yield surface is also shown. In the section of the stress path that moves towards the LC surface, stress increase appears to be more significant than suction reduction. Once the LC yield surface is reached, the vertical stress drops to compensate the tendency of the macrostructure to collapse so that the sample length is kept constant. It can also be noted that the point of start of the collapse does not coincide exactly with the plotted LC; this is because, by then, the yield surface has moved slightly due to the interaction with

the microstructural strains (MS, microstructure swelling) that develop from the very start of the test.

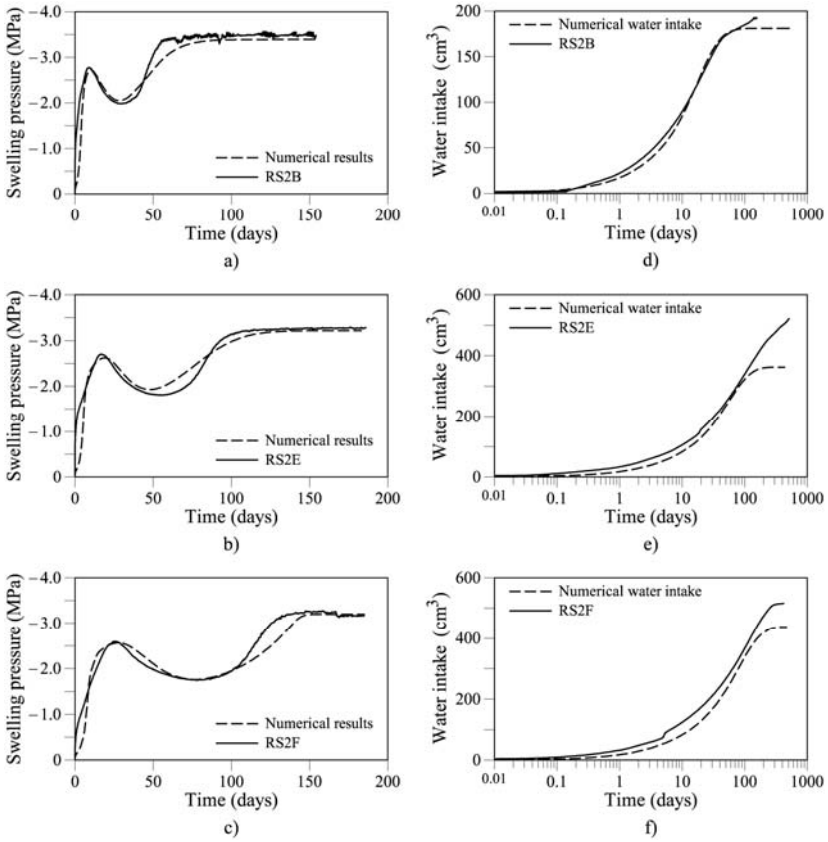

Figure 3: Observations vs. computed results for tests on samples of 1.60 g/cm^3 dry density. a), b) and c) Swelling pressure evolution for tests RS2B, RS2E and RS2F. d), e) and f) Evolution of accumulated water intake for tests RS2B, RS2E and RS2F.

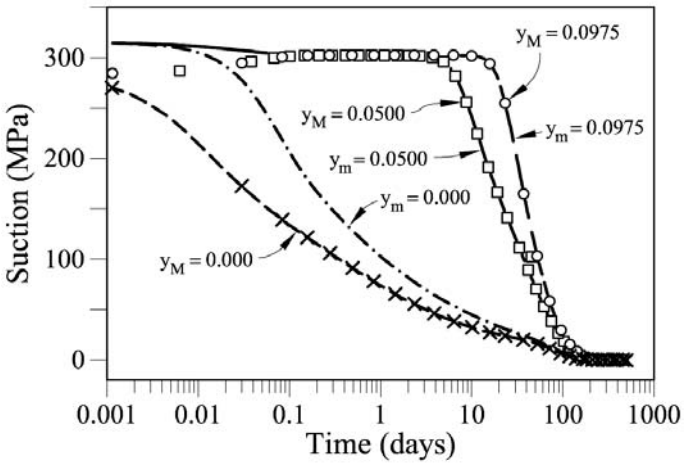

Figure 4: Computed evolution of macrostructural and microstructural suctions at three different points of test RS2E.

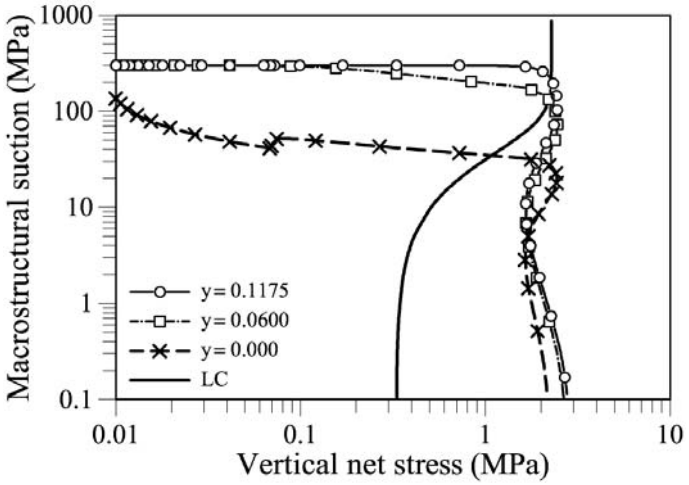

Figure 5: Computed stress path (macrostructural suction – vertical stress) for three different points of sample RS2E.

5 CONCLUSIONS

A double-porosity numerical formulation and a constitutive model have been developed to deal with the coupled hydromechanical behaviour of swelling clays exhibiting two levels of structure. The formulation is especially appropriate to reproduce the behaviour of mixtures of bentonite pellets and powder; a material that is receiving much attention as a potential component of sealing systems. It has been shown that the formulation results in a close quantitative reproduction of a number of swelling pressure tests performed on samples of different lengths. In addition, a detailed examination of the computational results provides valuable insights and understanding of the basic processes that underlie the observed macroscopic behaviour. The formulation is thus validated for use in analysis of field problems [10]

ACKNOWLEDGEMENTS

The work reported has been co-funded by ANDRA, CIEMAT, ONDRAF-NIRAS and the European Commission (EC contract FIKW-CT-2000-00010). The support of the Spanish Ministry of Science and Innovation trough grant BIA 2008-06537 is also gratefully acknowledged.

REFERENCES

[1] Pastor M, Zienkiewicz O. and Chan A. Generalized plasticity and the modelling of soil behaviour. *Int J Numer Anal Methods in Geomech* (1990) **14**:151-190.

[2] Sánchez M, Gens A, Guimarães L and Olivella S. A double structure generalized plasticity model for expansive materials. *Int J Numer Anal Methods in Geomech* (2005) **29**:751-787.

[3] Alonso E, Gens A. and Josa A. A constitutive model for partially saturated soils. *Géotechnique* (1990) **40**:405-430.

[4] Gens A. and Alonso, EE. A framework for the behaviour of unsaturated expansive clays. *Canadian Geotech* J (1992) **29**:1013–1032.
[5] Rizzi E, Giulio M and Willam K. On failure indicators in multi-dissipative materials. *Int J Sol Struct* (1990) **33**:3187-3124.
[6] Sánchez M, Gens A, Guimarães L. and Olivella S. Implementation algorithm of a generalised plasticity model for swelling clays. *Computers and Geotechnics* (2008) **35**:860-871.
[7] Wilson, R. and Aifantis, E. On the theory of consolidation with double porosity. *Int. J. Engng Sci*. (1982) **20**:1019-1035.
[8] Gens, A. Soil-environment interactions in geotechnical engineering. 47th Rankine Lecture, *Géotechnique* (2010) **60**:3-74
[9] Imbert, V. and Villar, M.V. Hydro-mechanical response of a bentonite pellets/powder mixture upon infiltration. *Applied Clay Science* (2006) **32**:197-209
[10] Gens, A., Valleján, B., Sánchez, M., Imbert, C., Villar, M.V. and Van Geet, M. Hydromechanical behaviour of a heterogeneous compacted soil: experimental observations and modelling. *Géotechnique* (2011) **61**: 367-386.

XI International Conference on Computational Plasticity. Fundamentals and Applications
COMPLAS XI
E. Oñate, D.R.J. Owen, D. Peric and B. Suárez (Eds)

OPTIMIZATION OF METAL FORMING PROCESSES FOR IMPROVING FINAL MECHANICAL STRENGTH

J.-L. CHENOT[*], P.-O. BOUCHARD[*], L. FOURMENT[*], P. LASNE[†] AND E. ROUX[*]

[*] CEMEF – Mines Paristech, UMR CNRS n° 7635
BP 207 – 06904 Sophia Antipolis Cedex, France
e-mail: Jean-loup.chenot@mines-paristech.fr, web page: http://www.cemef.mines-paristech.fr/

[†] Transvalor S.A., Parc de Haute Technologie, Sophia Antipolis , 694, av. du Dr. Maurice Donat
06255 Mougins Cedex, France
Email: patrice.lasne@transvalor.com - Web page: http://www.transvalor.com/index_gb.php

Key words: Metal forming, Finite element, Optimization, Identification, Mechanical properties.

Abstract.

The fundamental mechanical assumptions and the basic principles of 3-dimensional FE discretization are briefly summarized. Several important numerical developments for efficient and accurate computation of large plastic deformation are discussed. Material behavior must be known precisely: material parameters of the constitutive law, thermal law and friction law must be determined by experimental tests and identification procedures by inverse modeling. Is it also necessary to avoid the possible onset of defects, such as crack opening, by introducing damage modeling in the cost function. A parameter sensitivity analysis is utilized in order to select the most important factors: shape of the preform, tools geometry, etc. The practical optimization is carried out by a genetic algorithm technique or by a surface response method. Moreover, for assessing the fatigue behavior, a more local approach is necessary in order to take into account material evolution at the micro scale.

1 INTRODUCTION

Optimization of industrial forming processes has received a growing attention to increase competitiveness. Until recently this objective was the result of a long and expensive procedure, mostly achieved by trial and error, using industrial equipments and real materials. Finite element simulation of metal forming processes started in the 70's for 2D problems [1-4] and in the 80's for 3D configurations [5]. To-day commercial simulation codes facilitate trial and error optimization. However, in view of the continuous improvement of softwares and computing facilities, including parallel computing, it is now possible to consider *automatic optimization*, where the optimal solution is mostly found by computation.

A software, called MOOPI (MOdular software dedicated to Optimization and Parameters Identification) has been developed in CEMEF to address these issues. MOOPI, presented in Figure 1, is based on 4 different layers. The basic layer 0 represents the direct model, which is the finite element computation Forge in our case. Layer 1 deals with sensitivity analyses and enables us to check the influence of input parameters on output observables. Layer 2 is the optimization layer in order to find optimal parameters of any kind of numerical simulations. Finally layer 3 deals with inverse analysis for automatic materials parameters analysis by comparing experimental and numerical observables. Each layer can use the algorithms implemented in the other layers. For example, inverse analysis uses the optimization algorithms developed in the second layer in order to minimize the cost function, defined as the sum of the squared differences between experimental and numerical observables. If response surfaces are needed in the optimization algorithm, the sensitivity analysis layer can also be used to give the initial database using DoE (Design of Experiment) techniques.

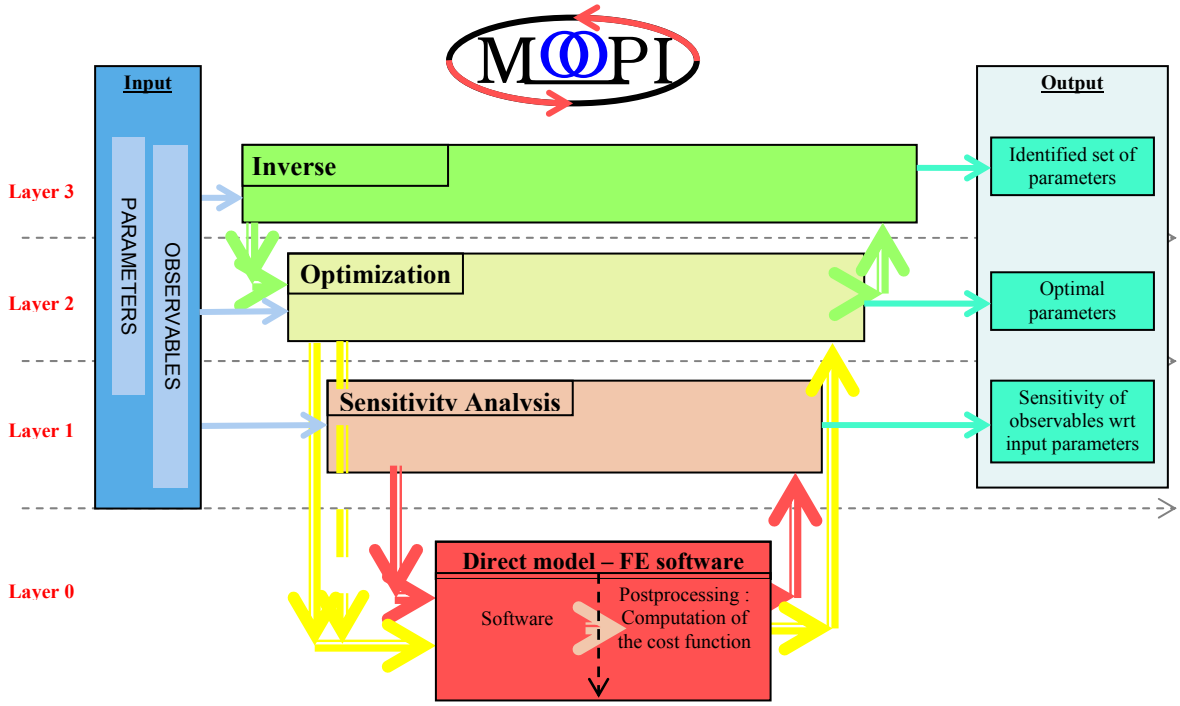

Figure 1 : Flowchart of the MOOPI software

2 MECHANICAL AND NUMERICAL APPROACH

The finite element approach of metal forming processes was described in [6], to which the interested reader is referred for more details.

2.1 – Mechanical and Thermal Description

Introducing an additive decomposition of the strain rate tensor $\dot{\varepsilon}$ into an elastic part $\dot{\varepsilon}^e$ and a plastic (or viscoplastic) one $\dot{\varepsilon}^p$:

$$\dot{\varepsilon} = \dot{\varepsilon}^{\mathrm{e}} + \dot{\varepsilon}^{\mathrm{p}} \tag{1}$$

Utilizing the Jauman objective derivative of the stress tensor , the hypo elastic law is written:

$$\frac{\mathrm{d}\sigma_{\mathrm{J}}}{\mathrm{dt}} = \lambda^{\mathrm{e}}\mathrm{trace}(\dot{\varepsilon}^{\mathrm{e}})\mathrm{I} + 2\mu^{\mathrm{e}}\dot{\varepsilon}^{\mathrm{e}} \tag{2}$$

where λ^e and μ^e are the Lamé coefficients. The plastic or viscoplastic component of the strain rate tensor obeys a general Perzyna rule of the form:

$$\dot{\varepsilon}^{p} = 3/2\sigma_{\mathrm{eq}}\left\langle(\sigma_{\mathrm{eq}} - \mathrm{R})/\mathrm{K}\right\rangle^{1/m}\ \boldsymbol{\sigma'} \tag{3}$$

where σ_{eq} is the equivalent strain, σ' is the deviatoric stress tensor, $\dot{\bar{\varepsilon}}$ is the equivalent strain rate and $\bar{\varepsilon}$ is the equivalent strain, K, R and m are material parameters.
At the interface between part and tool, the friction shear stress can be modeled by a "viscoplastic Coulomb" law, in term of the normal stress σ_n and the tangential velocity Δv :

$$\tau = -\alpha_{\mathrm{f}}\left|\sigma_{\mathrm{n}}\right|\Delta\mathrm{v}/\left|\Delta\mathrm{v}\right|^{1-\mathrm{p}} \tag{4}$$

Where α_f and p are friction coefficients.
For a quasi incompressible material flow, a mixed formulation in term of velocity v and pressure p is chosen in the domain Ω; for any virtual velocity and pressure fields $\boldsymbol{v}^*, p^*$:

$$\int_{\Omega}\sigma' : \dot{\varepsilon}^*\,\mathrm{dV} - \int_{\Omega}\mathrm{pdiv}(\mathrm{v}^*)\mathrm{dV} - \int_{\partial\Omega_{\mathrm{c}}}\tau\mathrm{v}^*\,\mathrm{dS} = 0 \tag{5}$$

Introducing the material compressibility κ; the mass conservation equation is written:

$$-\int_{\Omega}(\kappa\mathrm{div}(\mathrm{v}) + \dot{\mathrm{p}})\mathrm{p}^*\mathrm{dV} = 0 \tag{6}$$

The total time of the process is decomposed into small increments Δt, and the displacement field is assumed to be proportional to the velocity field at the beginning of the increment:

$$\Delta\mathrm{u} = \Delta\mathrm{t}\,\mathrm{v} \tag{7}$$

In the same way the stress increments are introduced, so that eqs. (5) and (6) are rewritten:

$$\int_{\Omega}(\sigma' + \Delta\sigma') : \dot{\varepsilon}^*\,\mathrm{dV} - \int_{\Omega}(\mathrm{p} + \Delta\mathrm{p})\mathrm{div}(\mathrm{v}^*)\mathrm{dV} - \int_{\partial\Omega_{\mathrm{c}}}\tau\mathrm{v}^*\,\mathrm{dS} = 0 \tag{8}$$

$$-\int_{\Omega}(\mathrm{p}\Delta\mathrm{t}/\kappa + \mathrm{div}(\Delta\mathrm{u})) : \mathrm{p}^*\,\mathrm{dV} = 0 \tag{9}$$

For hot forming process the heat equation is introduced:

$$\rho\mathrm{c}\,\mathrm{dT}/\mathrm{dt} - \mathrm{div}(\mathrm{k}\,\mathrm{grad}(\mathrm{T})) - \mathrm{r}\sigma : \dot{\varepsilon} = 0 \tag{10}$$

Where ρ is the material density, c the heat capacity, k the thermal conductivity and r the fraction of plastic work transformed into heat. The thermal and mechanical coupling originates from heat generation by plastic work, thermal dilatation which modifies eq. (9), and the dependency of the material parameters on temperature, e.g.:

$$K = K_0 \left(\varepsilon_0 + \bar{\varepsilon}\right)^n \exp(\beta / T), \;\; m = m_0 + m_1 T \tag{11}$$

2.2 – Finite Element Discretization

To achieve robustness and compatibility with other numerical requirements, a mixed displacement (or velocity) and pressure formulation with P1+P1 stabilized elements is chosen. The pressure field is discretized using tetrahedral elements with 4 linear shape functions M_n, while the velocity, or the displacement field, uses 5 shape functions N_n: the linear functions plus a bubble function. The discretized mixed integral formulation for the mechanical problem is:

$$R_n^U = \int_\Omega (\sigma' + \Delta\sigma') : \mathbf{B}_n dV - \int_\Omega (p + \Delta p)\, \mathrm{trace}(B_n)\, dV + \int_{\partial\Omega_c} \alpha_f |\sigma_n| \frac{\Delta v}{|\Delta v|} N_n dS = 0 \tag{12}$$

$$R_m^P = \int_\Omega \left(\frac{\kappa}{\Delta t} div(\Delta u) + p\right) M_m dV = 0 \tag{13}$$

To which the discretized heat equation is added:

$$\mathbf{C}.\Delta\mathbf{T} + \mathbf{H}'.\mathbf{T}\,\Delta t + \mathbf{F}\,\Delta t = 0 \tag{14}$$

Where **C** is the heat capacity matrix, **H'** is the conduction matrix and **F** is a vector gathering the boundary conditions and the heat source terms. Equations (12) and (13) on one hand and equation (14) on the other hand can be solved separately until convergence or using a global Newton Raphson algorithm.

2.3 - Numerical problems

2.2.1 Remeshing

Remeshing steps are compulsory when deformation of the work-piece results in too distorted elements and when contact occurs progressively between tools and the part. An iterative method is designed to remesh locally where it is necessary. Moreover, for a more reliable control of accuracy, an estimation of the discretization error is performed and the elements must be refined locally in the zones where the strain is higher. This is achieved by prescribing a local size of the elements and rebuilding the mesh accordingly [7]. But this approach may lead to generate a very large number of elements. This drawback can be partly overcome, by introducing anisotropic meshes having narrow elements in the direction of high strain gradient and elongated ones in the orthogonal direction [8].

2.2.2 Equations Solving

At each time increment several linear systems are generated by the Newton-Raphson procedure, their resolutions representing the more expensive contribution to the total CPU

time. Iterative methods are effective on the reasonably well conditioned systems we get due to the stabilization induced by the choice of $P1^{+}P1$ elements. These methods can be parallelized, provided a domain partitioning is defined, each sub domain being treated on a separate processor [8].

2.2.3 Multi Material Coupling

The problem of multi material coupling appears when the tools are considered as elastically deformable, or when a part is formed with several materials. At the interface between different materials, we must impose a unilateral contact condition with friction (and possibly with a force of cohesion). However challenging numerical problems appear to take into account this situation with non coincident meshes at the interface between materials. In the "master and slave approach", a Lagrange multiplier contribution of the non linear equations to solve is introduced to avoid penetration of the slave surface $\partial\Omega_{\mathrm{B}}^{\mathrm{contact}}$, into the master surface $\partial\Omega_{\mathrm{A}}^{\mathrm{contact}}$. But this approach is effective only when the surface mesh of the slave is more refined than the surface mesh of the master in contact. A quasi symmetric Lagrange multiplier formulation, was proposed by Fourment et al in [9] in which the additional term is written:

$$\Lambda^{QSYM} = \frac{1}{2}\left(\int_{\partial\Omega_B^{contact}} h_A(\Delta u_B)\lambda^B ds_B + \int_{\partial\Omega_A^{contact}} h_B(\Delta u_A)\overline{\lambda}^B ds_A \right) \tag{15}$$

Where λ^{A} is the Lagrange multiplier defined on $\partial\Omega_{\mathrm{A}}^{\mathrm{contact}}$ and $\overline{\lambda}^{\mathrm{B}}$ is the projection of λ^{B} on the surface $\partial\Omega_{\mathrm{A}}^{\mathrm{contact}}$. With a nodal formulation, the quasi symmetric approach imposes a number of constraints equal to the number of nodes of the slave mesh in contact. This method was applied successfully to forging with deformable tools.

2.2.4 Multi grid and multi mesh.

A major concern in numerical simulation is to reduce CPU time in order to be able to solve more complex problems, involving more refined meshes. However the CPU time is not a linear function of the number of unknowns, even for iterative solvers. The multi grid method is a way to achieve a quasi linear dependence of resolution time and consequently to reduce dramatically the computational cost. In ref. [10] a promising node-nested Galerkin multigrid method is described for solving very large linear systems originating from linearization of 3D metal forming problems. The smoothing and coarsening operators are built, using node-nested meshes made of unstructured tetrahedra. The coarse meshes are built by an automatic coarsening algorithm based on node removal and local topological remeshing techniques. A research version of the Forge finite element software was utilized to test the effectiveness of the multigrid solver, for several large scale industrial forging problems and it was shown that the decrease of CPU time can reach a factor higher than 7.

Another method for saving computational cost is to utilize different meshes as developed in ref. [11]. In hot incremental forming, such as cogging or ring rolling, a unique mesh for mechanical and thermal simulation is not the optimal choice. A Bimesh method will use different finite element meshes for the resolution of the different physical problems:

- a main fine mesh to store the results and to carry out the linear thermal computations with one unknown per node,
- a less refined mesh for the non-linear mechanical calculations with 4 unknowns per node.

The numerical development of the Bimesh method consists mainly in building the embedded meshes and managing the data transfer between the meshes. The Bimesh method leads to a CPU reduction of about 4 on industrial examples and is compatible with parallel calculations.

2.2.5 Finite Element modeling at the micro scale

It is well known that the micro (or nano) structure of metals is a key factor for determining the constitutive law during forming and for predicting the final properties of the work-piece. To treat in an average way, the evolution of the material micro structure during thermal and mechanical treatments, the classical method is based on a macro description, selecting representative material parameters (grain size, phase percentage, precipitates, etc.) and to identify physical laws which govern the evolution of these parameters, and their influence on the mechanical behavior [12]. The macro approach is quite convenient for coupling thermal, mechanical and physical computation, but it suffers severe limitations and needs a large amount of experiments to identify the physical laws describing micro structure evolution. On the other hand, computation at the micro scale is now possible and is developed for a more realistic description of materials. Micro modeling is potentially much more accurate but, due to heavier computer cost at the local micro level, direct coupling with macro thermal and mechanical simulations seems limited to 2D problems and simple parts, even with large clusters of computers. One way to view the middle term applications is to use micro modeling of material in post processing, to predict micro structure evolution for a limited number of locations in the work piece, neglecting coupling effects. Another method is to utilize the micro approach to help identification of macro laws. The basic ingredients of the general micro model developed at CEMEF are summarized in [13].

3 INVERSE METHOD FOR MATERIAL PARAMETERS IDENTIFICATION

For a given material law, inverse analysis is used to determine the best parameters that fit experimental data. Identification of the parameters is achieved by minimizing a least square cost function which evaluates the difference between computed and experimental values. In the past differentiation methods were mostly utilized [14], but for a more general approach it was realized that optimization methods using only the evaluation of the least square function must be preferred.

A parallel optimization algorithm based on EGO (Efficient Global Optimization Algorithm) suggested by Jones et al. [15], has been developed for identification and integrated in the MOOPI software. A flowchart of this algorithm is presented in Figure 2. The main idea of this extension is the following: instead of evaluating exactly the cost function of one new set of parameters at each iteration, the idea is to temporally set the cost function value to an approximate value regarding the kriging meta-model. This temporally approximation of the cost function value is not time consuming and enables to extract a new set of parameters from the meta-model without exact evaluation. N set of parameters can thus be extracted from the meta-model without any exact evaluation. The final step is to evaluate exactly the cost function value of these N new points, which can be done simultaneously using parallel computing.

The EGO algorithm implemented in MOOPI is well suited for parameters identification by inverse analysis. This software is able to work with multiple experimental observables and

multiple mechanical tests. The optimization procedure gives the set of identified parameters. Another useful information is a map of the objective function all over the parameters design space. This map is particularly interesting to understand the sensitivity of the observable regarding each parameter of the model.

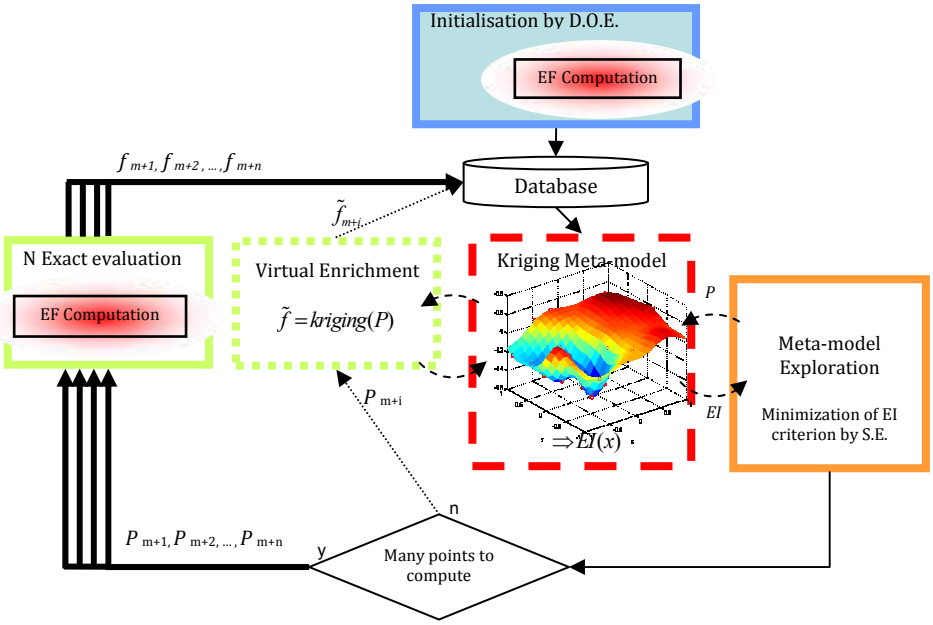

Figure 2: Flowchart of the parallel extension of the EGO algorithm implemented in the MOOPI software

As an example, we identified both elastic-plastic materials behavior law and Lemaître ductile damage parameters, in order to study the final mechanical strength of the clinched component. Figure 3 shows the identified and experimental load-displacement curves, and necking-displacement curves.

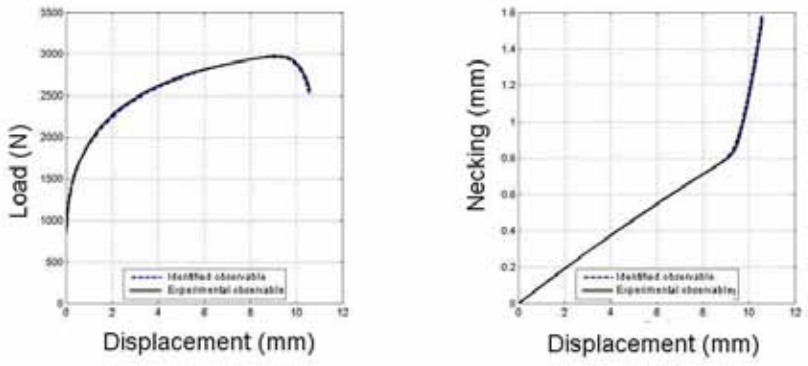

Figure 3: Identified and experimental load-displacement and necking-displacement curves

4 SENSITIVITY ANALYSIS

For any kind of manufacturing processes, input data are always subjected to variability or uncertainty. These variability issues can be experimental (prescribed load, temperature, lubrication, exact materials behaviour, friction, etc.) or numerical (mesh size, time step, etc.). Sensitivity analysis studies are essential to evaluate the impact of input data variability on output results and possibly to select the more important parameters for optimization. In our MOOPI software, finite element computations can be run iteratively with different input data. Observables are stored and compared to check the influence of input data on final results. The modification of input parameters can be done manually by the user, or can be obtained through a Design of Experiments (DoE). Sensitivity analysis is applied here to the study of the clinching process, where a sheet is deformed by the tools illustrated in Figure 4a. The idea is to find the clinching process parameters that have the highest influence on the final mechanical strength of the joined component. A sensitivity analysis has been done on the punch and lower die geometries, as shown in Figure 4a. A 5% modification has been applied to each parameter and the influence on the mechanical strength to pull-out has been measured. Figure 4b shows that two parameters have a major influence on the mechanical strength: the punch radius Rp and the lower die depth Pm.

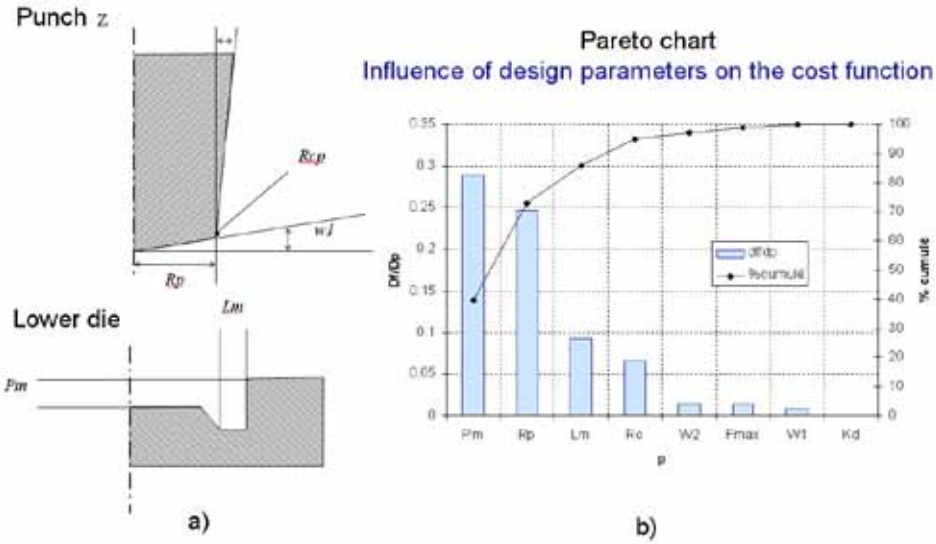

Figure 4: a) Clinching tools geometry and b) Influence of clinching process parameters on the final mechanical strength to pull-out.

5 PROCESS OPTIMIZATION

The numerical problem is to find the minimum of the cost function which represents the practical objective of the optimization. Several methods were attempted using complex derivatives of the cost function (see e. g. [16, 17]). However it is now preferred to use optimization algorithms that require only computation of the cost function. In the following, two examples are presented in order to illustrate the different approaches which are developed in the laboratory.

5.1 Optimization with a single objective

Here the objective is to find the clinching tools geometry that maximizes the final mechanical strength of the clinched component. The sensitivity analysis of section 4 allows us to select two parameters: the punch radius Rp and the lower die depth Pm. Using the MOOPI software, our methodology is summarized in Figure 5.

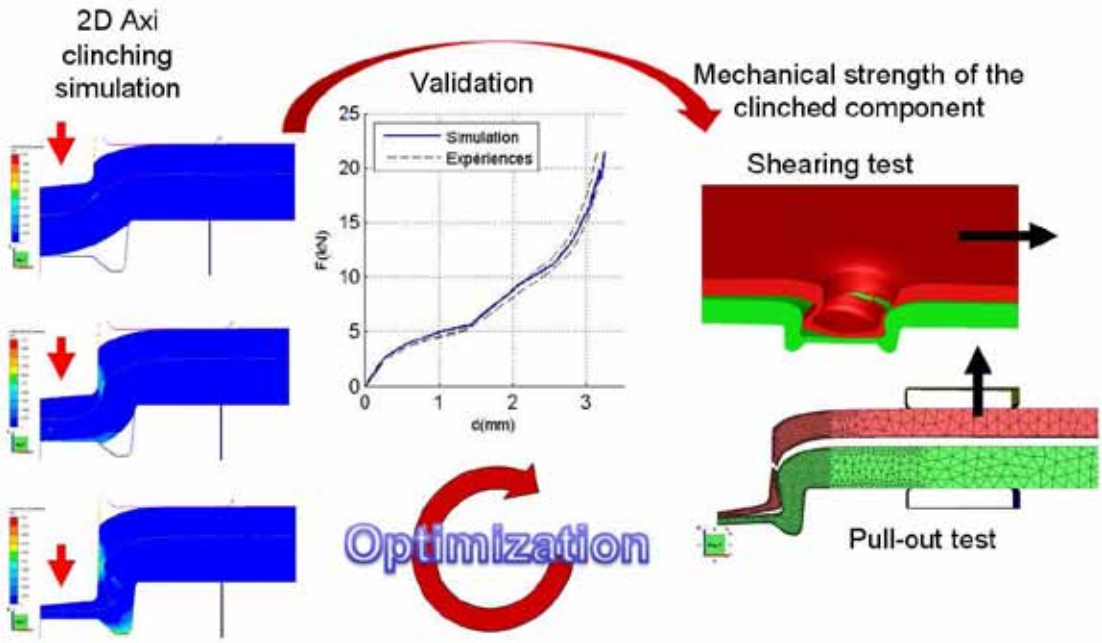

Figure 5 : Optimization of the whole chain of simulation, including the clinching process and the simulation of the shearing and pull-out test.

Table 1 shows the nominal values of the two parameters, the research space and the final optimal values identified by MOOPI.

	Nominal value	Research space	Optimal identified value
Rp (mm)	1.9	[1.6, 2.2]	1.96
Pm (mm)	0	[-0.3, 0.6]	0.16

Table 1 : Nominal values, research space and optimal values associated to the punch radius and the lower tool depth

In Figure 6a it can be seen that damage has been significantly decreased in the upper sheet thanks to the tools geometry modification. Figure 6b shows the response surface associated to the fracture strength to pull-out, that has been maximized. It is interesting to stress that in addition to a higher mechanical strength, the optimal solution is also surrounded by a smooth maximal area, so that a slight perturbation (or variability) of Rp and Pm will not have much

influence on the final mechanical strength.

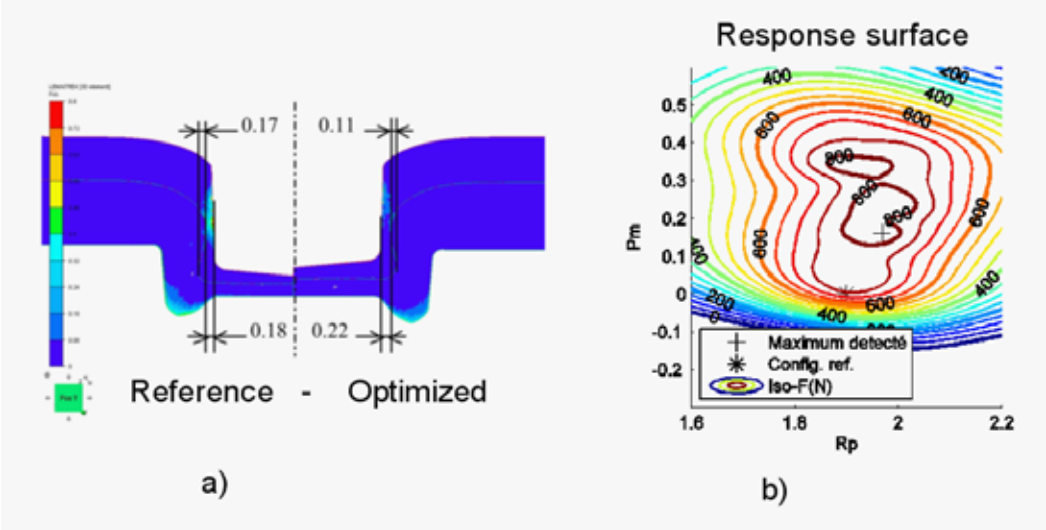

Figure 6 : a) Map of the final damage field, and b) Response surface associated of the final mechanical strength of the clinched component (* for reference, + for optimized configurations).

Table 2 shows the mechanical strength associated with the reference and optimal configurations. It can be seen that the optimized configuration induces an increase of 13.5% of the mechanical strength to pull-out, and of 42% of the mechanical strength to shearing.

	Mech Strength **Pull-out** (N)	Mech Strength **Shearing** (N)
Reference configuration	737	814
Optimized configuration	840	1193
Benefit (%)	**13.5%**	**42.1%**

Table 2 : Mechanical strengths for a pull-out and shearing test associated with the reference and optimal configurations

5.2 Multi objective optimization

Traditionally, in wire-drawing industry uses the optimization of the drawing force to design wire-drawing dies. The optimum die semi-angle is claimed to be 6°, or more generally is in a range between 4° and 8°. A second objective raises ambiguities, as the risk of ductile fracture should be estimated on a damage criterion. For instance, high-carbon drawn wire may show brittleness either during the drawing process, or at the cabling stage, or during wire service life. Then we have a multi-objective framework, the solution consists in a family of non-dominated solutions that constitute the Pareto optimal set, or the decision space *S*.
The industrial wire drawing process has been simulated following Bobadilla et al [18]. The mechanical analysis of the drawing process is performed by a 2D axi symmetric simulation. Dies are assumed non deformable and the drawing speed is constant. In Figure 7 the mesh

size is 0.5mm and the total nodes number is about 10,000. The wire is long enough to reach the mechanical steady state.

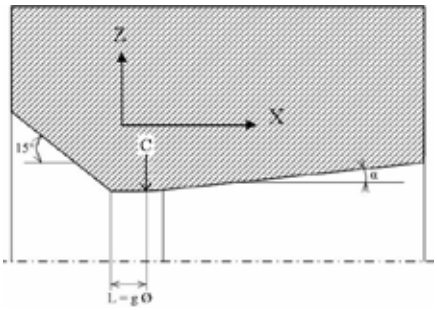

Figure 7 : Wire drawing mesh - Die geometry and corresponding design parameters

The Latham and Cockcroft (L&C) damage criterion is used as one of the objective function:

$$D_{max} = \underset{\Omega}{Max}\left(\int_0^{\varepsilon_f} \frac{max(\sigma_1, 0)}{\sigma_{eq}} d\varepsilon_p \right) \tag{16}$$

Alternatively, the wire drawing force F will be taken as an objective function. Bi-objective optimization (force and damage) will finally be addressed.

The shape parameters describe the geometry of the wire drawing die: reduction ratio R, die semi-angle α and the die length L as illustrated in Figure 7. The land length has no significant impact on the minimization of F or D_{max}. In single pass optimization, reduction ratio cannot be an optimization parameter, which leaves one optimization parameter: the die semi-angle α with values included in the range [1.2°; 22.5°]; this wide range has been selected not to exclude non-conventional solutions.

The selected multi-objective evolutionary algorithm (MOEA) is the Non Sorting Genetic Algorithm, NSGA-II, which is considered one of the most efficient MOEA to find Pareto optimal sets. In order to reduce computational costs, NSGA-II is coupled [19] to a metamodel based on the Meshless Finite Difference Method (MFDM). After initiating the metamodel with a reduced number of individuals, the metamodel is continuously updated during the algorithm iterations. This way, quite accurate Pareto fronts can be obtained by approximately the same number of function evaluations as in the single-objective case.

Optimization provides different optimal die semi-angle (α_{opt}) depending on the objective function. Indeed, an optimal die angle minimizing the non-dimensional drawing stress is found only when friction is non-zero (see Figure 8). On the other hand, no optimal die angle is observed in damage minimization, as the lowest damage is found on the lower bound ($\alpha = 1.2°$ here, see Figure 8). Finally, L&C damage criterion and the non-dimensional wire drawing force have been coupled into a bi-objective approach. The Pareto Optimal Front has been accurately constructed in a single optimization operation, showing these two objective functions to be in conflict. This curve in Figure 9 enables the user to set his priority either on damage or on drawing force. In this case, accepting a 2.1% increase of the drawing force

could save as much as 51% damage, at a die semi-angle $\alpha = 3.46°$. Therefore, damage can be strongly decreased with a slight increase of the reduced drawing force.

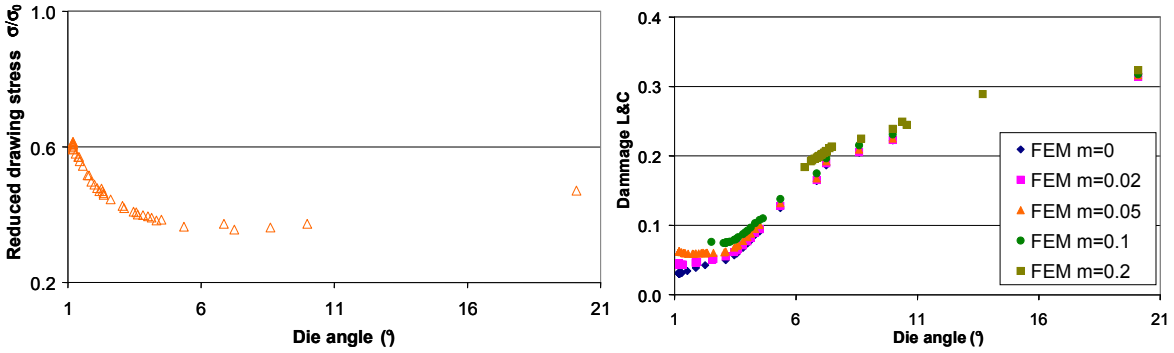

Figure 8 : Wire drawing force (left) and damage (right) versus die angle from a single objective optimization.

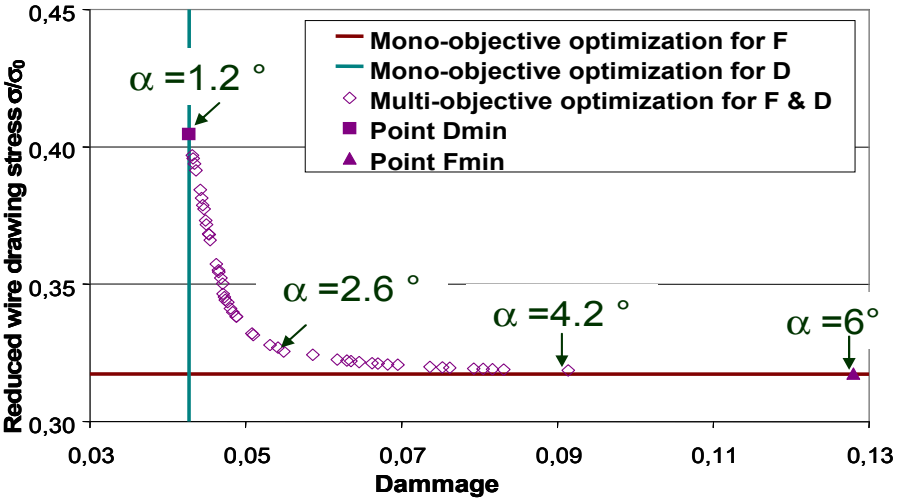

Figure 9 : Pareto front (wire drawing force versus damage) of the multi-objective optimization problem.

6 TOWARD PREDICTION AND OPTIMIZATION OF LOCAL MECHANICAL PROPERTIES

Forged components are recognized for their excellent mechanical strength and fatigue properties. The methodology presented here consists in improving fatigue analyses of forged components by accounting for the forging simulation stage. Kneading rate and grain flow orientation are two consequences of the forging process. Using the FORGE software, grain flow orientation is computed all along the forming process simulation. This grain flow orientation, as well as residual stresses, are input data for predicting fatigue, using an anisotropic extension of the Papadopoulos fatigue criterion. It is based on experimental fatigue results obtained on samples extracted at 0°, 45° and 90° with respect to the grain flow orientation. A numerical modelling is performed at the microscale using the DIGIMICRO

software. These simulations give a better understanding on the influence of elongated particles and cluster of particles on high cycle fatigue mechanisms. A virtual simulation chain is set-up to work on real industrial components. This simulation chain, together with microscale numerical modelling demonstrate the positive influence of the grain flow orientation of forged components on high cycle fatigue properties of industrial parts. The general methodology is schematically illustrated in Figure 10 and the complete description of the work is given in ref. [20].

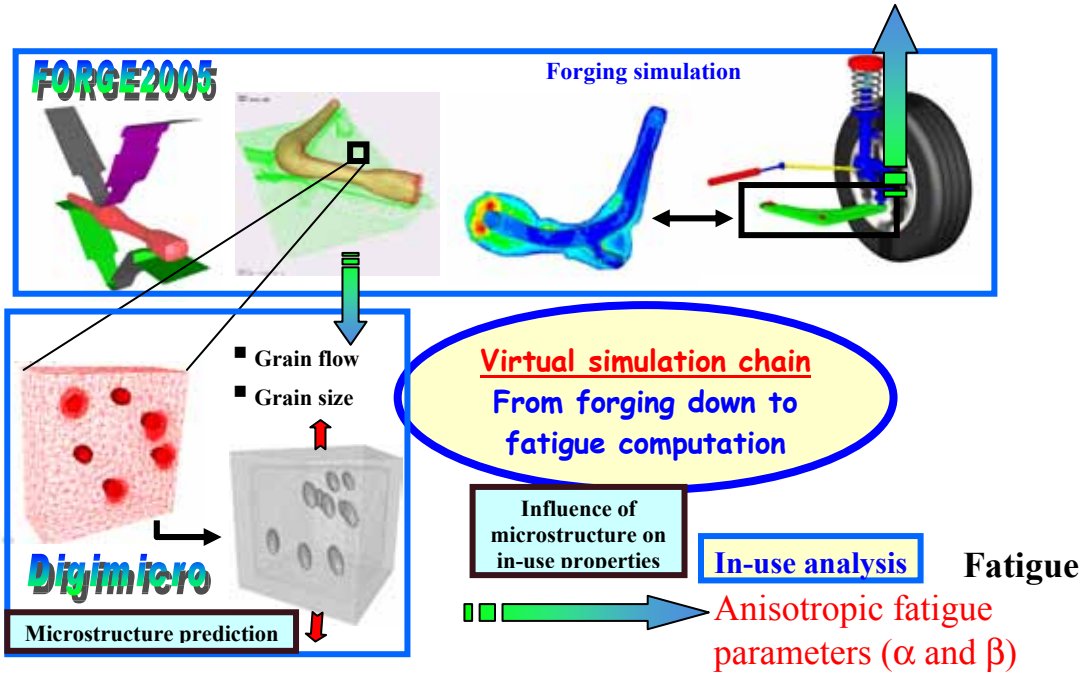

Figure 10 : Prediction and optimization of fatigue for forged components

7 CONCLUSIONS

The basic scientific ingredients were reviewed for accurate simulation of metal forming processes with a finite element computer code. A general software system was presented which will allow the user not only to simulate industrial processes but also to identify material parameters by inverse modeling, to assess the sensitivity of the results to process parameters and to optimize the whole forming sequence. An example of multi scale prediction of fatigue properties of a forged part was given as a first step toward optimization of the final properties of the work-pieces.

REFERENCES

[1] Iwata K., Osakada K. and Fujino S., *Transactions of the ASME*, Ser. B, 94-2, 1972, pp. 697-703.
[2] Cornfield G. C. and Johnson R. H., *J. Iron Steel Inst.*, 211, 1973, p. 567.
[3] Lee C. H. and Kobayashi S., *J. Eng. Ind.*, 95, 1973, p. 865.

[4] Zienkiewicz O. C., and Godbole K., *Int. J. Numer. Meth. Eng*., 8, 1974, p. 3.
[5] Surdon G. and Chenot J.-L., *Int. J. Numer. Meth. Eng*, 24, 1987, pp. 2107-2117.
[6] Wagoner R. H. and Chenot J.-L., *Metal Forming Analysis*, Cambridge University Press, Cambridge (2001).
[7] Fourment L. and Chenot J.-L., *Computational Plasticity. Fundamentals and Applications*, ed. by Owen D. R. J. et al., Pineridge Press, Swansea, U.K. (1992) 199-212.
[8] Coupez T., Digonnet H. and Ducloux R., *Appl. Math. Model* (2000) **25**:153-175.
[9] Fourment L., Popa S. and Barboza J., *8th Conference On Numerical Methods in Industrial Forming Processes*, Columbus, Ohio, USA, (2004) June
[10] Rey B., Mocellin K. and Fourment L., 8th *European Multigrid Conference EMG 2005*, Scheveningen The Hague, (2005) 27-30 September.
[11] Ramadan M., Fourment L. and Digonnet H., *The 13th International ESAFORM Conference on Material Forming - ESAFORM 2010*, Brescia Italy (2010) April 7-9
[12] Chenot J.- L. and Chastel Y., *J. Mat. proc. Tech.* (1996) **60**:11-18.
[13] Bernacki M., Chastel Y., Coupez T. and Logé R.E., *Scripta Mater.* (2008) **58**:1129-1132.
[14] Gavrus A., Massoni E. and Chenot J.-L., *J. Mat. proc. Tech*. (1996) **60**:447-454.
[15] Jones D. R., Schonlau M. and Welch W. J., *Journal of global optimization* (1998) **13**:455-492.
[16] Fourment L. and Chenot J.-L., *Int. J. Num. Meth. in Engng*. (1996) **39**, 1:33-50.
[17] Fourment L., Balan T. and Chenot J.-L., *Int. J. Num. Meth. in Engng*. (1996) **39**, 1:51-66.
[18] Bobadilla C., Persem N. and Foissey S., *Published by AIP Conf. Proc*., (2007) **907**:535-540.
[19] Ejday M. and Fourment L., *Int. J. Mater. Form*. (2010) **3**-1:5-8.
[20] Milesi M., Chastel Y., Hachem E., Bernacki M., Loge R.E., and Bouchard P.O., *Mater. Sci. Engng. A* (2010) **527**, 18-19:4654-4663.

XI International Conference on Computational Plasticity. Fundamentals and Applications
COMPLAS XI
E. Oñate, D.R.J. Owen, D. Peric and B. Suárez (Eds)

2D ADAPTIVE FEM SIMULATION OF FAILURES IN HIGH-SPEED IMPACTS

M.Issa[1], K.Saanouni[1], C.Labergère[1], A.Rassineux[2]

[1]ICD/LASMIS, UMR CNRS 6279, Université de Technologie de Troyes, BP 2060, 10010 Troyes Cedex, France
mazen.issa@utt.fr, saanouni@utt.fr, labergere@utt.fr
[2]Laboratoire Roberval de Mécanique, UMR CNRS 6259, Université de technologie de Compiègne, BP 20529, 60205 Compiègne Cedex, France.
alain.rassineux@utc.fr

Key words: thermo-elasto-visco-plasticity, finite strains, ductile damage, mixed hardening, full coupling, 2D adaptive mesh, error estimates, high velocity impact, FEM.

Abstract. The simulation of high-speed impacts needs the use of advanced constitutive equations required for the accurate prediction of the different thermomechanical fields and their mutual interactions (temperature, large strains, hardening, damage, friction …). Since these fields localize inside intense shear bands (ISB), ductile micro-cracks initiate inside these ISB leading to the initiation of macroscopic crack and its fast propagation until the final fracture occurs. Accordingly, these advanced constitutive equations should take into account not only the strong thermomechanical coupling but also the ductile damage and its strong effect (coupling) on the other thermomechanical fields. In this work a complete set of advanced and fully coupled thermo-elasto-viscoplastic-damage constitutive equations accounting for mixed nonlinear isotropic and kinematic hardening fully coupled with the ductile isotropic damage and the thermal softening for time dependent finite plasticity is presented. Related numerical aspects in the framework of a fully adaptive 2D finite element strategy are developed and briefly discussed. This adaptive procedure is applied to the simulation of simple high velocity impact of thick sheets with dynamic ductile fracture occurrence. Attention is paid to the localization of the main thermomechanical fields inside the ISB as well as to the macroscopic cracks initiation and growth under high velocity impact.

1 INTRODUCTION

High speed impact is mostly used to investigate the material behaviour under dynamic (high velocity) loading conditions where the strain rates can locally reach 10^8 s^{-1}. For strain rates in between 10 s^{-1} and 10^4 s^{-1} the impact tests can be investigated using the Hopkinson bar facilities, and between 10^4 s^{-1} and 10^8 s^{-1} the so called Taylor impact experimental

procedure should be used where the data analysis is more complex to investigate. Note that Taylor [1] was the first who developed analytical method to assess the dynamic yield stress at different strain rates for various materials. Other research works have investigated the high speed impacts on several metals like steel, aluminium and cooper [2-4]**.** More information about recent high speed experimental studies can be found in [5-8] where many of high speed impact works are reviewed.

The numerical simulations of high speed impact should take into account the highly severe thermomechanical conditions i.e.: high temperature which can exceeds the melting temperature, high strain rates reaching the 10^8 s^{-1}, large viscoplastic strains and complex contact and friction conditions. These fully coupled phenomena and their interactions should be accounted for in any constitutive equations used for their numerical simulation. Recently, different material behaviour models are used to simulate the high speed machining processes. These constitutive equations often propose a weak thermal coupling and isotropic viscoplastic flow with isotropic hardening of Norton-Hoff or Johnson-Cook types. In these models, many numerical formulations have been used like updated Lagrangian formulation ([10], [12-22], [25]), Eulerian formulation [9] or arbitrary Lagrangian Eulerian (ALE) formulations ([11-12]) have been used. Other works use specific meshless based numerical approaches to avoid the mesh adaptivity ([20]-[22]). In this work, an adaptive 2D FE-based numerical methodology using advanced constitutive equations which account for the ductile damage and its effect on the other thermomechanical fields at finite strain is presented. The coupling between thermal aspects, thermo-elasto-viscoplasticity and ductile damage including the mixed isotropic and kinematic non-linear hardening are included in this model previously developed by Saanouni et al. ([23]-[28]). Using the Vumat subroutine, the developed model is implemented into ABAQUS/EXPLICIT. Using this fully coupled methodology, the typical example of dynamic impact is investigated and attention is paid to the prediction of the thermomechanical fields' localization inside ISB where macroscopic cracks initiate and evolve with high velocity until the final fracture occurs.

2 THERMO-ELASTO-VISCOPLASTIC DAMAGE MODEL

In the framework of the thermodynamics of irreversible processes with state variables, and assuming small elastic and large viscoplastic strains, fully coupled thermo-elasto-visco-plastic-damage constitutive equations accounting for the micro-cracks closure are developed. Two external state variables are used: ($\underline{\varepsilon} = \int_t \underline{D} dt$, $\underline{\sigma}$) for mechanical aspects and (T, s) for thermal phenomena. For 'internal' state variables and their conjugate forces we have: ($\underline{\varepsilon}^e$, $\underline{\sigma}$) for small elastic strain tensor and the Cauchy stress tensor; ($\vec{q}, \vec{g} = \overrightarrow{grad(T)}$) for heat flux vector and its conjugate force; ($\underline{\alpha}$, $\underline{X}$) for the kinematic hardening (i.e. translation of the yield surface center); (r, R) for the isotropic hardening (i.e. variation of the yielding surface size) and (D,Y) for isotropic damage and its conjugate force.

Following this approach, a complete set of fully coupled constitutive equations is deduced in which the state relations (1) to (4) and the evolution equations (5) to (8) are summarized as following:

- **State relations:**

$$\underline{\sigma} = <\underline{\sigma}>_+ + <\underline{\sigma}>_- \text{ where } \begin{cases} <\underline{\sigma}>_+ = & \frac{\nu E(1-D)}{(1+\nu)(1-2\nu)} <\underline{\varepsilon}^e : \underline{1}>_+ <\underline{1}>_+ + \frac{E(1-D)}{(1+\nu)} <\underline{\varepsilon}^e>_+ \\ & -\frac{E}{(1-2\nu)} \xi\sqrt{1-D}(T-T_0) <\underline{1}>_+^{\varepsilon} \\ <\underline{\sigma}>_- = & \frac{\nu E(1-hD)}{(1+\nu)(1-2\nu)} <\underline{\varepsilon}^e : \underline{1}>_- <\underline{1}>_- + \frac{E(1-hD)}{(1+\nu)} <\underline{\varepsilon}^e>_- \\ & -\frac{E}{(1-2\nu)} \xi\sqrt{1-hD}(T-T_0) <\underline{1}>_-^{\varepsilon} \end{cases} \quad (1)$$

$$s = \frac{1}{\rho}\frac{E}{(1-2\nu)}\xi\sqrt{1-D} <\underline{\varepsilon}^e : \underline{1}>_+ + \frac{1}{\rho}\frac{E}{(1-2\nu)}\xi\sqrt{1-hD} <\underline{\varepsilon}^e : \underline{1}>_- + C_v\frac{(T-T_0)}{T_0} \quad (2)$$

$$\underline{X} = \frac{2C(1-D)}{3}\underline{\alpha} \quad \text{(a)} \qquad R = (1-D^m)Qr \quad \text{(b)} \quad (3)$$

$$\begin{cases} Y = <Y_{el}>_+ + <Y_{el}>_- + Y_{in} \\ <Y_{el}>_+ = \frac{\nu E}{2(1+\nu)(1-2\nu)} <\underline{\varepsilon}^e : \underline{1}>_+^2 + \frac{E}{2(1+\nu)} <\underline{\varepsilon}^e>_+ : <\underline{\varepsilon}^e>_+ - \frac{E}{2\sqrt{1-D}(1-2\nu)}\xi(T-T_0) <\underline{\varepsilon}^e : \underline{1}>_+ \\ <Y_{el}>_- = h\left[\frac{h\nu E}{2(1+\nu)(1-2\nu)} <\underline{\varepsilon}^e : \underline{1}>_-^2 + \frac{hE}{2(1+\nu)} <\underline{\varepsilon}^e>_- : <\underline{\varepsilon}^e>_- - \frac{hE}{2\sqrt{1-hD}(1-2\nu)}\xi(T-T_0) <\underline{\varepsilon}^e : \underline{1}>_-\right] \\ Y_{in} = \frac{1}{3}C\underline{\alpha} : \underline{\alpha} + mD^{(m-1)}\frac{1}{2}Qr^2 \end{cases} \quad (4)$$

where: (E, ν): Young modulus and Poisson coefficient, T: temperature, T_0: reference temperature, ξ: thermal expansion coefficient, C: kinematic hardening modulus, Q: isotropic hardening modulus, C_v: specific heat coefficient, ρ: material density, Y_{el}: the elastic part of the damage energy release rate and Y_{in}: its inelastic counter part, m a material parameter and $0 < h < 1$ is the micro-cracks closure parameter.

- **Evolution equations:**

$$\underline{D}^{vp} = \dot{\lambda}_{vp}\underline{n} \quad \text{(a)} \qquad \underline{n} = \frac{3}{2\sqrt{1-D}}\frac{\left(\underline{\sigma}^{dev} - \underline{X}\right)}{\left\|\underline{\sigma} - \underline{X}\right\|_M} \quad \text{(b)} \quad (5)$$

$$\dot{\underline{\alpha}}^{vp} = \dot{\lambda}_{vp}(\underline{n} - a\underline{\alpha}) \quad \text{(a)} \qquad \dot{r} = \dot{\lambda}_{vp}\left(\frac{1}{(1-D^m)} - br\right) \quad \text{(b)} \quad (6)$$

$$\dot{D} = \frac{\dot{\lambda}_{vp}}{(1-D)^{\beta}}\left[\frac{\langle Y - Y_0\rangle}{S}\right]^s \quad \text{(a)} \qquad \vec{q} = -k\overrightarrow{gradT} \quad \text{(b)} \quad (7)$$

$$f_{vp}(\underline{\sigma}, \underline{X}, R, \dot{p}; D) = f(\underline{\sigma}, \underline{X}, R; D) - K_2 Arc\sinh\left(\frac{\sqrt{1-D}\,\dot{p}}{K_1}\right) \le 0 \quad (8)$$

$$f(\underline{\sigma},\underline{X},R;D)=\frac{\left\|\underline{\sigma}-\underline{X}\right\|_M}{\sqrt{1-D}}-\frac{R}{\sqrt{1-D^m}}-\sigma_y \tag{9}$$

In these equations a and b are the material parameters governing the non-linearity of kinematic and isotropic hardening respectively. S, s, Y_0 and β are the ductile damage parameters.

$\dot{\lambda}_{vp}$ is the viscoplastic multiplier defined by $\dot{\lambda}_{vp}=K_1 Sinh\langle f/K_2\rangle$ which in fact is taken as the main unknown to be determined numerically at each integration point. K_1 and K_2 are the viscous parameters and f_{vp} is the viscoplastic yield function defined in Eq.8. The deviatoric tensor $\underline{n}$ in Eq.5b defines the outward normal to this yield function. The equivalent viscoplastic deformation rate is defined by $\dot{p}=\sqrt{(2/3)\underline{\dot{\varepsilon}}^{vp}:\underline{\dot{\varepsilon}}^{vp}}=\dot{\lambda}_{vp}/\sqrt{1-D}$ and the von Mises equivalent stress is given by: $\left\|\underline{\sigma}-\underline{X}\right\|_M=\sqrt{(3/2)(\underline{\sigma}-\underline{X})^{dev}:(\underline{\sigma}-\underline{X})^{dev}}$.

Combining Eq.7b (where k is the thermal conductivity) with the first law of thermodynamics leads to the generalized heat equation governing the temperature evolution under the form:

$$\rho C_v\dot{T}-k\Delta T=\underline{\sigma}:\underline{D}^{vp}-\underline{X}:\underline{\dot{\alpha}}-R\dot{r}+Y\dot{D}+\pi+T\left[\frac{\partial\underline{\sigma}}{\partial T}:\underline{\dot{\varepsilon}}^{e}-\frac{\partial Y}{\partial T}\dot{D}+\frac{\partial\underline{X}}{\partial T}:\underline{\dot{\alpha}}+\frac{\partial R}{\partial T}\dot{r}\right] \tag{10}$$

Note that, in this study, only the following material properties: E, C, Q, S, K_1 and σ_y, are taken as temperature dependent according to the simple relation of the form:

$$p=p_0\left[1-\left((T-T_0)/T_f-T_0\right)^{\chi}\right] \tag{11}$$

where $P\in\{E,C,Q,S,K_1,\sigma_y\}$ is the value of any of these parameters at the temperature T, P_0 its value at the reference temperature T_0, T_f is the melting temperature of the material and χ is a temperature independent material parameter.

The numerical aspects of the presented model and their implementation in ABAQUS/EXPLICIT is detailed in ([24-27]). A dynamic explicit scheme is used for the resolution of the global equilibrium and temperature equations, for the numerical integration of the fully coupled constitutive equations at each Gauss point of each element, the stress tensor as well as the overall state variables at each time increment, is calculated by iterative implicit algorithm using the elastic prediction and viscoplastic correction procedure with radial return mapping algorithm applied to a reduced number of differential equations.

A 2D mesh generator named DIAMESH2D is used for the 2D adaptive analysis following the procedure described in [26]. Based on appropriate error indicators with 2D linear and quadratic Quadrangular and Triangular elements, this procedure adapts the mesh size and the loading sequence with respect to the local curvature of the contact surfaces and to the distribution of the plastic and damage dissipations.

3 Application to high speed shear impact

This example concerns a typical dynamic (high speed) impact test performed using AISI4340 steel cylindrical sample composed from a hollow cylinder connected with a solid one, as schematically shown in Fig.1. Basing on the force displacement curves given in [28] for the AISI4340 stainless steel, the material parameters of the sample are determined using a classical inverse approach. The obtained values are: E=205000 MPa, ν=0.3, Cv=457 J/kg°C, ξ=1.37 10^{-5} °C^{-1} for the thermo elasticity. σ_y=792 MPa, Q=320 MPa, C= 5000 MPa, b=0.6, a=20, K_1=48.9, K_2=79.38 MPa for the viscoplastisity and S= 20, s=2, β=1, Y_0=7 for the damage evolution equations. All these parameters are identified at the reference temperature T_0= 20°C and their evolutions with respect to the temperature are governed by Eq. (11) in which the parameter χ=1.03 for all parameters except for the parameter S where χ=1.08 and the parameter E for which χ=4. The melting temperature for AISI4340 steel is taken equal to T_f=1520 °C and its conductivity k=5 W/m/°C in order to favour the adiabatic condition. The sample is impacted at a speed of 1600 mm/s, on its lower part (hollow cylinder) by a projectile made by fully thermoelastic material with the following parameters: $E = 450\ GPa$, $\nu = 0.22$, $C_v = 400\ J/Kg/°C$, $\xi = 1{,}37.10^{-5}\ °C^{-1}$ and k=50W/m/°C.

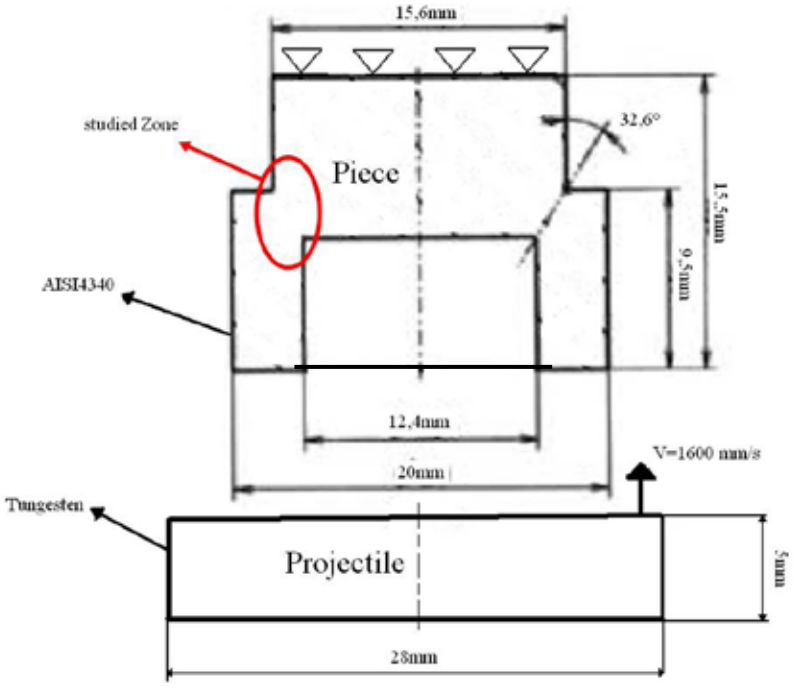

Figure 1. Schematization of the Impact test.

The geometric parameters required by the adaptive meshing procedure [26] are: $h^p_{\max}$=0.55 mm, $h^p_{\min}$=0.4 mm and $h^d_{\min}$=0.06 mm.

In this example we focus on the numerical prediction of the thermomechanical fields' localization as well as the initiation and propagation of macroscopic cracks under the impact

loading. The mesh adaptation and the distribution of the different thermomechanical fields will be investigated.

The Fig.2 shows the evolution of the mesh for different displacements of the projectile. The mesh is first refined inside the ISB where the temperature and the plastic strain are highly localized (as can bee seen in Fig 3 to 7) and mainly around the macroscopic crack where the damage has reached its maximum value. Clearly, the mesh refinement precedes the macroscopic crack path since its initiation for u = 1.95 mm (Fig. 3a) till the final fracture of the sample for u=3.26 mm (Fig. 2-c) and through the intermediate configuration as for u=2.75 mm (Fig. 2-b).

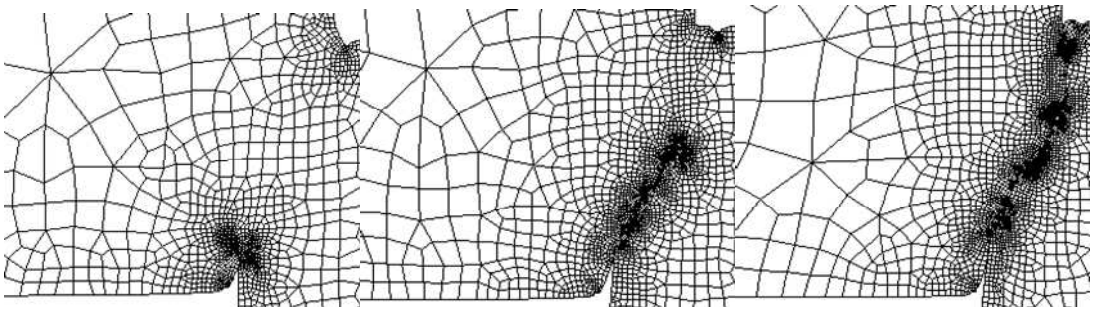

a) u=1.95 mm b) u=2.75 mm c) u=3.26 mm

Figure 2. Mesh adaptation during the macroscopic crack evolution for three different values of the projectile displacement

As shown in Fig. 3, the equivalent von Mises stress is, first, maximum with a value of 1220 MPa inside the ISB before the damage occurrence (Fig. 3a). It decreases and goes to zero as the damage increases and the macroscopic crack evolves as shown in Fig. 3a for u=1.95 mm and in Fig. 3b for u=2.75 mm. However, when the sample is completely fractured the von Mises stress is near zero every where around the crack except some zones where the contact between the crack lips generates normal stresses (Fig. 3.c). Note that this stress relaxation inside the ISB is not only due to the damage induced softening but also to the temperature increase from T_0=20 °C to T_{max}=924 °C (see Fig. 6) generated by the plastic work converted to heat.

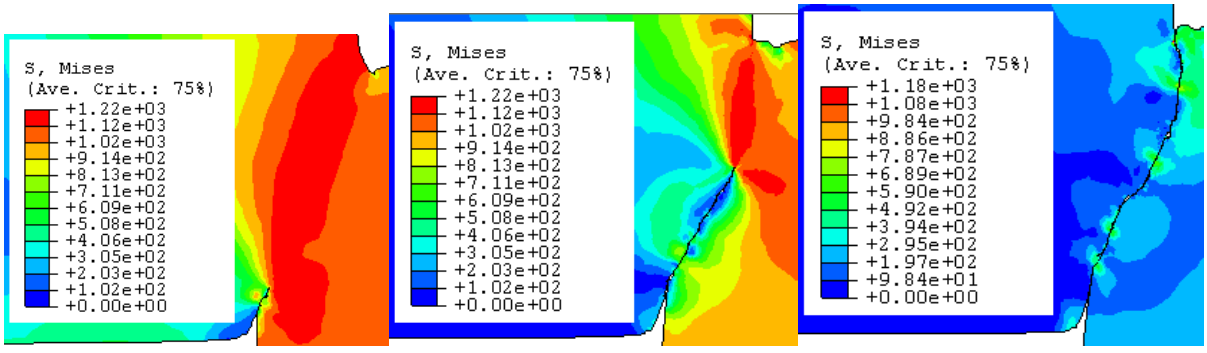

a) u=1.95 mm b) u=2.75 mm c) u=3.26 mm

Figure 3. Distribution of the von Mises equivalent stress for three different values of the projectile displacement

Similarly, the equivalent plastic strain distribution is shown in Fig.4. It is worth noting that the equivalent plastic strain localizes inside the ISB with a relatively homogeneous value around $p_{max} = 60\,\%$ every where before the macroscopic crack initiation as indicated in Fig. 4. However, once the macroscopic crack is initiated the equivalent plastic strain strongly localizes inside a very small zone located at the crack-tip where it reaches $p_{\max} = 206\,\%$ inside a small area of $p_{\max} = 155\,\%$ for u=1.95 mm as shown in Fig. 4.a. As the macroscopic crack evolves inside the ISB, the accumulated plastic strain diffuses around the crack tip and its maximum decreases to reach $p_{\max} = 137\,\%$ inside a relatively large area with $p_{\max} = 100\,\%$ for u=2.75 mm (Fig. 4b); and $p_{\max} = 132\,\%$ with a large area of $p_{\max} = 90\,\%$ for u=3.26 mm at the final fracture of the sample (Fig. 4c). This accumulated plastic strain distribution is confirmed by the equivalent plastic strain rate distribution shown in Fig. 5 where $\dot{p}_{\max} = 5.85\ 10^4\ s^{-1}$ for u=1.95 mm (Fig.5a), $\dot{p}_{\max} = 8.04\ 10^4\ s^{-1}$ for u=2.75 mm (Fig.5b) and $\dot{p}_{\max} = 3.00\ 10^5\ s^{-1}$ for u=3.26 mm (Fig.5c).

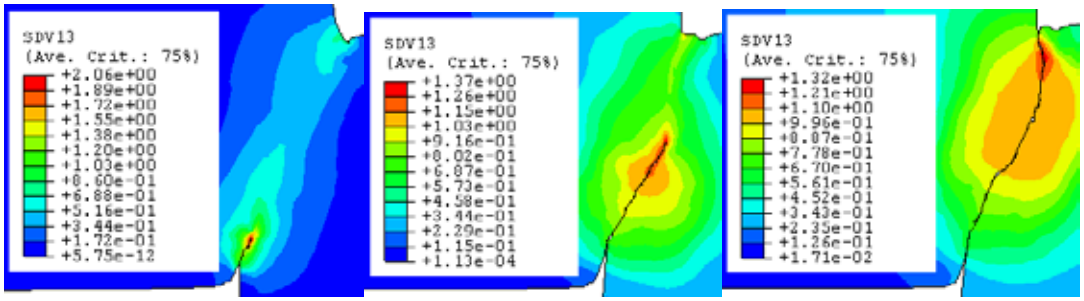

a) u=1.95 mm b) u=2.75 mm c) u=3.26 mm

Figure 4. Distribution of the equivalent plastic strain for three different values of the projectile displacement

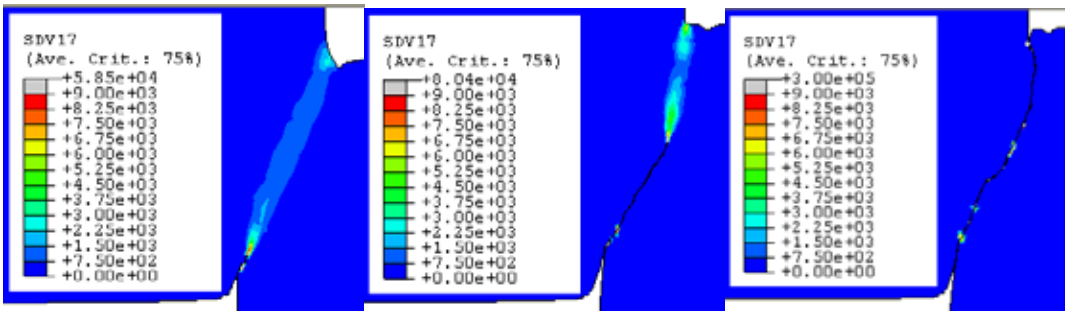

a) u=1.95 mm b) u=2.75 mm c) u=3.26 mm

Figure 5. Distribution of the equivalent plastic strain rate for three different values of the projectile displacement

The Fig.6 shows the evolution of temperature during the impact test. For the displacement u = 1.95 mm (Fig.6-a), the highest temperatures (500 ° C and 900 ° C) locate on both ends of the adiabatic shear band, for two reasons. The first is the concentration of high plastic strain rate on both ends of the band (between 3.10^3 and $9.10^3\ s^{-1}$) (Fig.6-a). The second reason is related to intense friction between the two sides of the crack which maintains high

temperatures on the edges of the crack even after the passage of the shear band (Fig.6-b) and Fig.6-c),.

The temperature localizes also inside the ISB as can be seen in Fig. 6. However, due to the friction between the crack lips, the maximum of the temperature is still located at the initial crack-initiation location with T_{max}=924 °C for u=1.95 mm (Fig. 6a), T_{max}=790 °C for u=2.75 mm (Fig. 6b) and T_{max}=817 °C for u=3.26 mm at the final fracture of the sample (Fig. 6c).

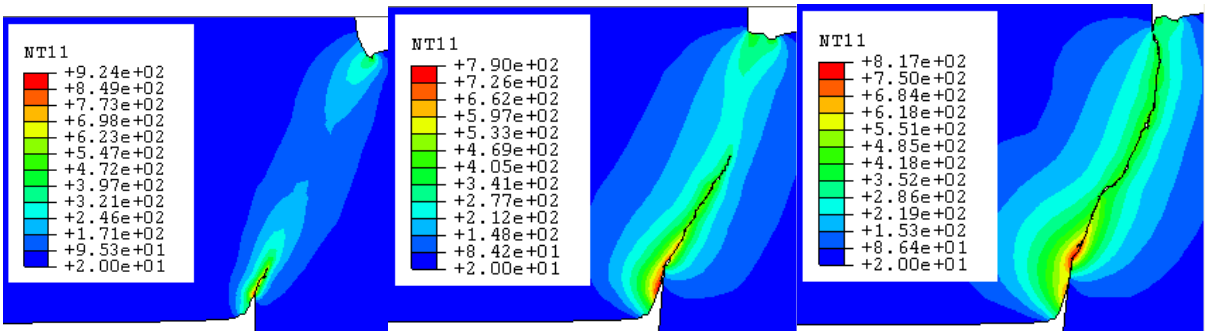

a) u=1.95 mm b) u=2.75 mm c) u=3.26 mm

Figure 6. Distribution of the temperature for three different values of the projectile displacement

Finally, the Fig.7 shows the distribution of the ductile damage including the macroscopic crack defined by killing the fully damaged elements having the smallest mesh size h_d=0.06 mm. The macroscopic crack length can be estimated to 0.5 mm for u = 1.95 mm (Fig. 7-a), 1.9 mm for u = 2.75 mm (Fig.7-b), and 3.31 mm for u = 3.26 mm (Fig. 7-c).

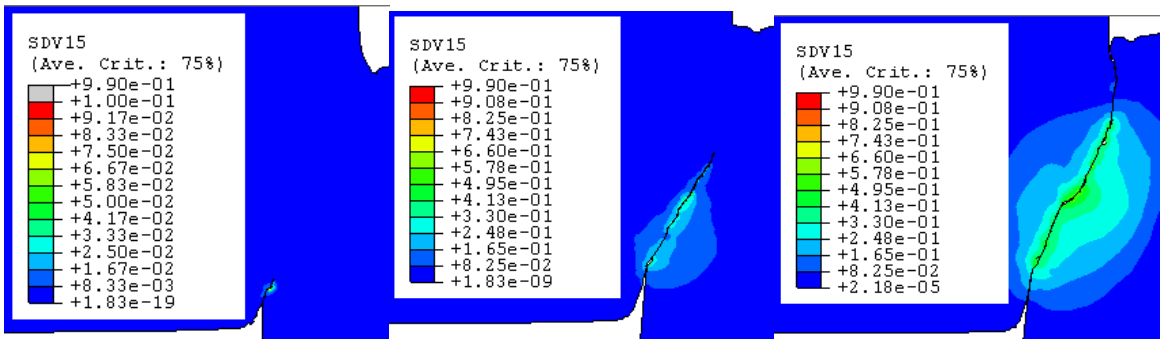

a) u=1.95 mm b) u=2.75 mm c) u=3.26 mm

Figure 7. Distribution of the ductile damage for three different values of the projectile displacement

4 CONCLUSION

An advanced thermo-elasto-viscoplastic-damage model accounting for non-linear isotropic and kinematic hardening, thermal and ductile damage effects including the micro-cracks closure under compressive phase of the loading has been briefly presented. Using the ABAQUS/EXPLICIT user's subroutine where this model has been implemented, the efficiency of this adaptive numerical methodology to simulate the dynamic fracture under high velocity impact has been shown. Particularly, this model is shown to be efficient to

capture the thermomechanical fields' localization inside an intensive shear band as well as the strong localization of the damage giving rise to the initiation and propagation of macroscopic cracks until the final fracture of the structure.

References:

[1] Taylor, G. I., " The use of flat ended projectile for determining dynamic yield stress." Par(I) Theoretical Considerations, Proc. Royal Sot Ser A194, London, 1948 pp 289-299.

[2] Lee, E. and Wolf, H., "Plastic wave propagation effects in high speed testing" J App Mech, Dec 1951 pp379-386.

[3] Ting, T. and Symonds, P, "Longitudinal Impact on Viscoplastic rods-Linear stress-strain rate law." J App Mech, June 1964 pp 199-207.

[4] Wiffens, A., "the use of flat ended projectile for determining dynamic yield stress." Par(II) Experimental Consideration, Proc. Royal Soc Ser A194, London, 1948 pp 300-322.

[5] Field JE, Walley SM, Bourne NK, Huntley JM. Experimental methods at high rates of strain. J Phys IV France 1994;4(C8):3–22.

[6] Field JE, Walley SM, Bourne NK, Huntley JM. Review of experimental techniques for high rate deformation studies. In: Proceedings of the Acoustics and Vibration Asia '98. Singapore: Acoustics and Vibration Asia 98 Conference; 1998. p. 9–38.

[7] Field JE, Proud WG, Walley SM, Goldrein HT. Review of experimental techniques for high rate deformation and shock studies. In: Nowacki WK, Klepaczko JR, editors. New experimental methods in material dynamics and impact. Warsaw, Poland: Institute of Fundamental Technological Research; 2001. p. 109–77.

[8] J.E.Field, S.M. Walley, W.G. Proud, H.T. Goldrein, C.R. Siviour, "Review of experimental techniques for high rate deformation and shock studies", International Journal of Impact Engineering 30 (2004), pp 725–775.

[9] Mackerle J., Finite-element analysis and simulation of machining: an addendum a bibliography (1996-2002), International Journal of Machine Tools and Manufacture, 2003, 43:103-114

[10] Kulak RF, Schwer LE, editors. Computational aspects of contact, impact and penetration. Lausanne: Elmepress Intl., 1991.

[11] Pantalé , O., Bacaria, J.L., Dalverny, O., Rakotomalala, R. and Caperaa, S. (2004). "2D and 3D Numerical Models of Metal Cutting with Damage Effects", Computer Methods in Applied Mechanics and Engineering, 193: 4383_4399.

[12] De Micheli, P., "Formulation explicite en tétraèdres linéaires pour la modélisation 2D et 3D de l'usinage à grande vitesse", Thèse Doctoral, Ecole nationale supérieurs des Mines de Paris. 2009.

[13] Maurel A., Fontaine M., Thibaud S., Michel G. et Gelin J.C., "Experiments and 3D FEM simulations of milling on a 304L Stainless steel, Metalforming 2008 ; Krakow.

[14] Ceretti E., Lazzaroni C., Menegardo L. et Altan T., Turning simulations using a three-dimensional FEM code, Journal of Materials Processing Technology, 2000, 98:99-103.

[15] Delalondre F., Guerdoux S., Fourment L., 3 D Simulation of Adiabatic Shear Bands in High Speed Machining, Proceeding of the 10th International Workshop on Modeling of

Machining Operations (CIRP), Reggio Calabria, 2007.
[16] Delalondre, F., "Modélisation et étude 3D des phénomènes de cisaillement adiabatiques dans les procédés de mise en forme à grande vitesse", thèse Doctorale, Ecole nationale supérieure des mines de Paris, 2008.
[17] Lin Z.C. et Yarng Y.D., A study of three-dimensional cutting model, International Journal of Computational Applications in Technology, 1996, 9(5/6):31-343.
[18] Maekawa K., Maeda M. et Tikagawa T., Simulation analysis of threedimensional continuous chip formation processes (Part1), International Japanese Society for Precision Engineering, 1997, 31(1):39-46.
[19] Molinari J.F., Three-dimensional finite-element analysis of high-speed machining, from Metal cutting and high speed machining, edited by D. Dudunski et al., Kluwer Academic/Plenum Publishers, 2002.
[20] Limido J., Espinosa C., Salaun M., Lacome J.L. "A new approach of high speed cutting modelling: SPH method", journal de physique IV, Vol. 134, 2006, pp. 1195-1200.
[21] Limido J., Espinosa C., Salaun M., Lacome J.L. "SPH method applied to high speed cutting modelling", international journal mechanical sciences, Vol. 49, 2007, pp. 898-908.
[22] Y. Chen, A. Eskandarian, M. Oskard and J.D. Lee, Meshless analysis of plasticity with application to crack growth problems, Theoretical and Applied Fracture Mechanics 41 (2004), pp. 83–94.
[23] Saanouni K., Chaboche J.L., "Computational Damage Mechanics. Application to Metal Forming", Chapter 7 of the Volume 3 : "Numerical and Computational methods" (Editors: R. de Borst, H. A. Mang), in "Comprehencive Structural Integrity", Edited by I. Milne, R.O. Ritchie and B. Karihaloo, ISBN: 0-08-043749-4, 2003.
[24] Issa M., K. Saanouni, C. Labergère, A. Rassineux, Prediction of serrated chip formation in orthogonal metal cutting by advanced adaptive 2D numerical methodology. To appear in IJMMM, 2010.
[25] Saanouni K., Lestriez P., Labergere C., « 2D adaptive FE simulations in finite thermo-elasto-viscoplasticity with ductile damage : Application to orthogonal metal cutting by chip formation and breaking »international Journal od damage Mechanics, vol 20, pp 23-61, 2011.
[26] Labergere C., Rassineux A., Saanouni K., 2D adaptive mesh methodology for the simulation of metal forming processes with damage, DOI 10.1007/s12289-010-1001-z, article in Press, 2011
[27] Rassineux A., "An automatic mesh generator for planar domains", StruCome 91, p. 519-531.
[28] Mabrouki T., Rigal J. F., "A contribution to a qualitative understanding of thermo-mechanical effects during chip formation in hard turning", J. Materials processing technology, Vol. 176, 2006.

XI International Conference on Computational Plasticity. Fundamentals and Applications
COMPLAS XI
E. Oñate, D.R.J. Owen, D. Peric and B. Suárez (Eds)

A MICROMECHANICAL CONSTITUTIVE MODEL FOR DUCTILE FRACTURE: NUMERICAL TREATMENT AND CALIBRATION STRATEGY

L. Malcher *, F.M. Andrade Pires†, J.M.A. César de Sá†

* Automotive Engineering Area, Faculty UnB Gama, University of Brasilia,
Distrito Federal, Brazil
e-mail: malcher@unb.br

† Department of Mechanical Engineering, Faculty of Engineering, University of Porto
Rua Dr. Roberto Frias, Porto 4200-465, Portugal

Key words: Micromechanical Model, Ductile Fracture, Two Damage Parameters.

Abstract. This contribution describes the numerical treatment and calibration strategy for a new micromechanical damage model, which employs two internal damage variables. The new micromechanical model is based on Gurson's theory incorporating the void volume fraction as one damage parameter and a shear mechanism, which was formulated considering geometrical and phenomenological aspects, as the second internal damage variable. The first and the second damage variables are coupled in the constitutive formulation in order to affect the hydrostatic stress and deviatoric stress contributions, respectively. Both internal damage variables are independent and, as a consequence, they also require independent nucleation mechanisms for each one in order to trigger the growth contribution. These mechanisms require the determination of material parameters that are obtained through two calibration points: one for high and the other for low stress triaxiality. This is in contrast to other damage models that typically require one calibration point. In the first part of this paper, theoretical aspects of the constitutive formulation are presented and discussed. Then, an implicit numerical integration algorithm is derived, based on the operator split methodology, together with a methodology to perform the calibration of all material parameters. In order to assess the performance of the new model, the "butterfly" specimen was used and the 1045 steel was employed under a wide range of stress triaxiality. The results obtained from the numerical simulations are presented such as: the evolution of both damage parameters, the evolution of the equivalent plastic strain, the reaction versus displacement curve and the contour of the effective damage parameter. From the comparison of the numerical results with experimental evidence, it will be highlighted that the present formulation is able to predict accurately the location of fracture onset and the level of the associated equivalent plastic strain at fracture.

1 INTRODUCTION

Ductile fracture in metals is an important subject to be improved in order to predict the correct location of crack initiation in machine components and rupture in general structures. The fracture phenomenon can be studied by its separated evolution contribution as the initiation and growth of general micro defects which is induced by large deformations. Some

researchers like McClintock [15] and Rice & Tracey [21] developed pioneering work undertaken on the subject, where the nature of defect was taken into account the study of ductile damage by analyzing its geometry in a continuous matrix.

The degradation of material properties is an irreversible process and starts from the formation of micro defects which can be voids, cracks and others, that already exist or that will be formed in the material matrix. However, the evolution of material degradation is dependent on macroscopic loading conditions which can cause a volumetric void growth such as in tensile loading condition or a preferential elongation of micro defects which can be observed in pure shear loading conditions. The ductile fracture phenomenon can be described, based on a micromechanical analysis of micro cavity growth, especially for the fracture computation within local approaches of fracture, (see Pineau [19]; Mudry [16]; Rousselier [23]; Besson [3]) or based on the Continuum Damage Mechanics theory and a thermodynamic framework, either phenomenological or micromechanically based, as Lemaitre [12].

The formulations proposed by Lemaitre and Gurson are the most important coupled damage ductile models to describe the above two methodologies, see Chaboche [7]. Since then, motivated by the limitations of these classical models, such as in prediction of the correct fracture location or in determination of the correct values of the internal variables at fracture, many researchers have proposed improvements in both methodologies, by introducing more effects in the constitutive formulation or in the damage evolution law like the pressure effect, temperature, Lode angle dependence, viscoplastic effects, crack closure effect, shear mechanisms, among others (Tvergaard & Needleman [27]; Rousselier [22;24]; Xue [28]; Nahshon & Hutchinson [17]; Lemaitre & Chaboche [13]; Chaboche [6]; Andrade Pires [1]; Chaboche et al. [7] ; Besson [4]).

These classical coupled damage models have the ability to predict the correct fracture location under a specific range of stress triaxialities (see Xue [28]; Nahshon [17]; Teng [26]) and are extremely accurate for loading conditions close to the calibration point, see Malcher [14]. For example, within range of high levels of stress triaxialities, where the spherical void growth is the predominant mechanism, the models based on Gurson theory, like the Gurson-Tvergaard-Needleman model, have good performance in prediction of fracture location and parameters in fracture as equivalent plastic strain and displacement. However, under shear dominated loads, where failure is mainly driven by the shear localization of plastic strain of the inter-voids ligaments due to void rotation and distortion, the model does not perform well, see Engelen [9] and Chaboche [7].

Due to these two types of ductile failure mechanisms, it is expected that the population of micro defects, that can be nucleated, would be higher in void sheeting than in internal necking. Motivated by these short comings, in this contribution, a new extension to the GTN model is proposed in order to improve the ability to predict the correct fracture location and determinate the internal parameters in the fracture. A new independent damage parameter is suggested to capture elongation of micro-defects and coupled to constitutive model to affect only the deviatoric stress part. A nucleation of general micro defects is introduced to trigger the shear mechanism and gives more accuracy to the model in prediction of ductile failure under mixed loading condition.

2 CONTITUTIVE FORMULATION

One of the most popular versions of Gurson's model is the Tvergaard–Needleman modification (Tvergaard and Needleman [27]). The model assumes isotropic hardening and isotropic damage, represented by the effective porosity f^*. The constitutive formulation for GTN's model can be better expressed as:

$$\Phi(\boldsymbol{\sigma}, k, f) = J_2(\boldsymbol{S}) - \frac{1}{3}\left\{1 + q_3.f^{*2} - 2.q_1.f^*.\cosh\left(\frac{q_2.3.p}{2.\sigma_y}\right)\right\}.\sigma_y{}^2 \tag{1}$$

where, the parameters q_1, q_2 and q_3 are introduced to bring the model predictions into closer agreement with full numerical analyses of a periodic array of voids.

The damage evolution, in this formulation, is reproduced by three simultaneous or successive mechanisms that can be described as the nucleation, growth and coalescence of voids as

$$f^* = \begin{cases} f, & f < f_c \\ f_c + \left(\frac{1}{q_1} - f_c\right)\frac{(f - f_c)}{(f_f - f_c)}, & f \geq f_c \end{cases} \tag{2}$$

where, f^* represents the effective damage, f_c denotes the critical volume void fraction and f_f is the volume void fraction at fracture. The effective damage is determined based on both nucleation and growth mechanisms if the volume void fraction is less than critical value. The coalescence is active only if the volume void fraction is higher than the critical value. The volume void fraction rate, $\dot{f}$, is a sum of the nucleation and growth mechanism as.

$$\dot{f} = \dot{f}^n + \dot{f}^g \tag{3}$$

The nucleation mechanism can be driven by either the plastic strain or the hydrostatic pressure. Equation 4 represents the nucleation mechanism based on the equivalent plastic strain:

$$\dot{f}^n = \frac{f_N}{s_N.\sqrt{2\pi}}.\exp\left[-\frac{1}{2}\left(\frac{\bar{\varepsilon}^p - \varepsilon_N}{s_N}\right)^2\right]\dot{\bar{\varepsilon}}^p \tag{4}$$

where, f_N represents the volume fraction of all second-phase particles with potential for microvoid nucleation, ε_N and s_N are the mean strain/pressure for void nucleation and its standard deviation. The variable $\bar{\varepsilon}^p$ represents the equivalent plastic strain and $\dot{\bar{\varepsilon}}^p$ is the rate of the accumulated plastic strain. The nucleation mechanism is valid only if the hydrostatic pressure is great to zero, $p > 0$. If $p \leq 0$, the nucleation mechanism rate is equal to zero. The evolution of growth mechanism in GTN's model is determined as:

$$\dot{f} = (1 - f).\dot{\varepsilon}_v^p \tag{5}$$

where, the elastic strain rate contributions is represented by $\dot{\varepsilon}_v^e$.

In order to improve the micromechanical models like Gurson and GTN to predict failure when void sheeting mechanism plays the main role, researchers as Xue [28], Nahshon & Hutchinson [17], Butcher et al. [5] have suggested the introduction of another mechanism as

shear, in the evolution law of the Gurson's damage parameter. Both researchers have initially formulated shear mechanisms based on phenomenological and geometrical aspects resulting in expression dependent on the equivalent plastic strain and its rate and a Lode angle function. Both formulations have shown a very nice performance in pure loading conditions, regarding the prediction of the crack initiation, but in combined load path, the models have failed either in prediction of the fracture location or in level of equivalent strain and displacement at fracture, see Malcher [14] and Reis & Malcher [20]). Xue [28], based on volume conservation of a representative square cell contains a cylindrical void at the center, has proposed a shear mechanism when this cell structure is subjected a pure shear loading condition. The evolution law for the shear mechanism proposed by Xue is represented by Equation 6

$$\dot{D}_{shear} = q_4 f^{q_5} \varepsilon_{eq} . \dot{\varepsilon}_{eq} \tag{6}$$

where, q_4 and q_5 are geometrical parameters and can be defined according to two or three dimensional problem. For two dimensional problem, $q_4 = \frac{3}{\sqrt{\pi}}$ and $q_5 = (1/2)$ and for three dimensional problem, $q_4 = \frac{3}{2}\left(\frac{6}{\pi}\right)^{(1/3)}$ and $q_5 = (1/3)$.

The shear mechanisms can be coupled in GTN's model and a so called Lode angle function is required to active the mechanism only when the shear strain is detected in a general loading condition. Xue [28] defines the Lode angle function as a linear expression of the normalized Lode angle, as:

$$g_0 = (1 - |\bar{\theta}|) \tag{7}$$

where, g_0 represents the so called Lode angle function and $\bar{\theta}$ is the normalized Lode angle. Thus, the damage internal variable rate (Equation 3) can be re-written according Equation 8.

$$\dot{f} = \dot{f}^n + \dot{f}^g + \dot{D}_{shear} \tag{8}$$

Authors as Reis & Malcher [20], Malcher [14], Xue [28] and Nahshon & Hutchinson [17] have shown that the original GTN's model has limitations, such as: no ability to predict failure in pure shear loading condition, due to the fact that the growth rate of the volume void fraction, which plays the damage parameter role, has no evolution; the coupled damage models have got good performance only for loading conditions close to calibration point; the nucleation of micro-voids mechanism does not have a physical meaning in low stress triaxiality, since the nucleation of micro-defects, in general, can be better appointed; and, in the plastic flow rule, the deviatoric stress tensor contribution is not affected by the damage parameter and the volume void fraction affects only the hydrostatic stress term. However, in order to try to solve the above problems, in this paper, a new formulation for GTN original model is suggested, giving ability to predict the correct location to crack initiation and the determination of the values of the internal variables at fracture.

The proposition starts from the way that the shear damage parameter is coupled in the GTN yield function. In the GTN original model (see Tvergaard and Needleman [27]) or in the GTN improved model (see Xue [28]; Nahshon & Hutchinson [17]), the damage parameters, such as only porosity or porosity and shear damage, affect mainly the hydrostatic pressure

contribution (see Equation 1). Hence, in this case, the plastic flow rule is expressed by an unbalanced equation, which the deviatoric contribution is free of the damage parameters. In this contribution, the volume void fraction and the shear damage will be coupled disconnectedly in the yield surface. The volume void fraction will affect exclusively the hydrostatic pressure and the shear damage will be coupled affecting the deviatoric stress contribution. Thus, Equation 1 can be re-written as follow:

$$\Phi(\boldsymbol{\sigma}, k, f) = \frac{J_2(\boldsymbol{S})}{(1 - D^{shear})} - \frac{1}{3}\left\{1 + q_3.f^2 - 2.q_1.f.\cosh\left(\frac{q_2.3.p}{2.\sigma_y}\right)\right\}.\sigma_y{}^2 \tag{9}$$

The new yield function would still be a function of the set of parameters $[\boldsymbol{\sigma}, k, f]$, since than the shear mechanism would still be a function of the volume void fraction.

In this paper, it is suggested an uncoupling between both shear damage and volume void fraction as well as the creation of a new nucleation of micro defects mechanism, responsible to trigger the shear damage parameter. Thus, the new constitutive formulation will get two independent damage parameters and the yield function established by Equation 9 would be a function of the set of parameters $[\boldsymbol{\sigma}, k, f, D]$. The volume void fraction, as defined by Tvergaard & Needleman [27] would be the first damage parameter and shear damage with a new nucleation of micro defect mechanism, the second one. Hence, the evolution of the new damage parameter can be expressed as:

$$\dot{D} = \dot{D}^n + q_6.\dot{D}^{shear} \tag{10}$$

where $\dot{D}$ represents the rate of the new damage parameter, $\dot{D}^n$ represents the rate of the nucleation of micro defects mechanism, $\dot{D}^{shear}$ denotes the rate of the shear contribution and the parameter q_6 can be introduced to calibrate the rate of the shear contribution, bringing more flexibility to suit the critical shear damage with the experimental critical displacement.

The nucleation of micro defects mechanisms, by the authors, will be considered a normal distribution of all second-phase particles with potential for micro defect nucleation and can be expressed as:

$$\dot{D}^n = \frac{D_N}{s'_N.\sqrt{2\pi}}.\exp\left[-\frac{1}{2}\left(\frac{\bar{\varepsilon}^p - \varepsilon'_N}{s'_N}\right)^2\right]\dot{\bar{\varepsilon}}^p \tag{11}$$

where, D_N represents the fraction of all second-phase particles with potential for micro defect nucleation, ε'_N and s'_N are the mean strain for defect nucleation and its standard deviation. The set of parameters $[D_N, \varepsilon'_N, s'_N]$, required to the nucleation of micro defect, need to be calibrated for a point in pure shear loading condition. This contribution added a new calibration point further the already required, which can come a very nice accuracy for the formulation within the all range of stress triaxiality.

Regarding the same simplification adopted by Gurson [11], in order to vanish the elastic contribution in the definition of the volume void fraction rate for a rigid plastic matrix (see Equation 5), the authors can suggest that in the rate of the shear mechanisms (Equation 6)

contribution, both equivalent strain and equivalent strain rate would be changed by the equivalent plastic strain and equivalent plastic strain rate. This simplification is reasonable in the majority of problems involving ductile damage since the elastic strains can be considered negligible. Thus, the expressions can be re-written, as:

$$\dot{D}^{shear} = q_4 D^{q_5} \bar{\varepsilon}^p . \dot{\bar{\varepsilon}}^p \tag{12}$$

By the authors and through the experimental evidence, the stress triaxiality effect can be introduced by an exponent in the previous Lode angle functions suggested by Xue.

$$g_0'(\xi,\eta) = [g_0(\xi)]^{1/\|\eta\|+k} \tag{13}$$

where, g_0' is the new function that now will be called by balance function, η represents the stress triaxiality and k is a constant that need to be calibrated. Figure 1 represents the behavior of the balance function on the space of the set of parameters $[g_0, \xi, \eta]$. The influence of the stress triaxiality can be observed manly in the range of stress triaxiality between $[-1/3 ; 1/3]$.

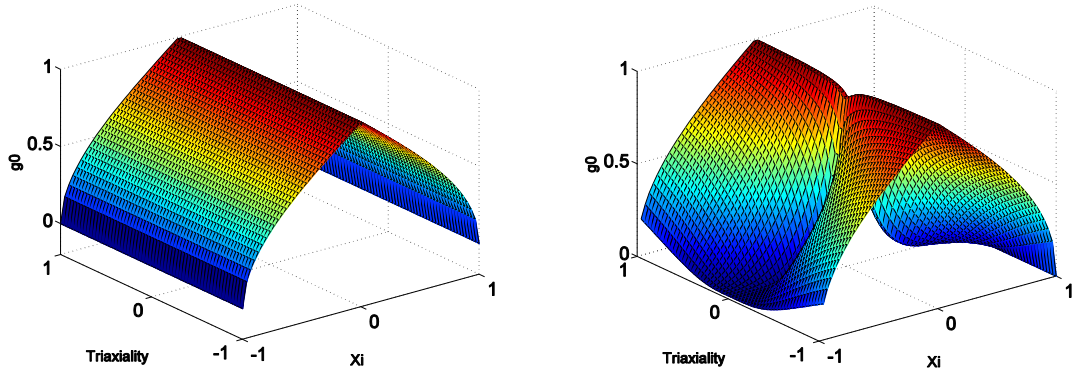

(a) (b)

Figure 1: Three dimensional representation of the balance function suggested by the authors.

Regarding this new model, two independents nucleation mechanisms are introduced, first one to trigger the growth rate of the volume void fraction and the second one to trigger the growth rate of the shear mechanism. In order to active or not each one contribution when pure shear or pure tensile loading condition is applied or to balance the value of it when both shear/tensile or shear/compression loading condition is present, the authors suggest the introduction of the Lode angle function, g_0, in the nucleation mechanisms

How was previously discussed, based on the modified formulation, two calibration points are required. First one for high stress triaxiality, which the smooth bar specimen can be used to determine the hardening law, σ_y, for undamaged model, the void nucleation parameters as f_N, ε_N and S_N and the critical volume void fraction f_c. A specimen in pure shear loading condition is also required to calibrate the general micro defects nucleation parameters as D_N, ε_N^s and s_N^s, the accelerator damage parameter, q_6, and the critical shear damage parameter, D_c. In Box 1, the basic constitutive equations and evolution law for internal variable and damage parameters are summarized:

Box 1. GTN's modified model including nucleation and elongation of micro shear defects.

(i) Elasto-plastic split of the strain tensor:

$$\boldsymbol{\varepsilon} = \boldsymbol{\varepsilon}^{e} + \boldsymbol{\varepsilon}^{p}$$

(ii) Elastic law

$$\boldsymbol{\sigma} = \mathbb{D}^{e} : \boldsymbol{\varepsilon}^{e}$$

(iii) Yield function

$$\Phi(\boldsymbol{\sigma}, r, f, D) = \frac{J_2}{1-D} - \frac{1}{3}.\left[1 + q_3.f^2 - 2.q_1.f.\cosh\left(\frac{3.q_2.p}{2.\sigma_y}\right)\right].\sigma_y^2$$

(iv) Plastic flow and evolution equations for R, f and D

$$\dot{\boldsymbol{\varepsilon}}^{p} = \dot{\gamma}.\boldsymbol{N}$$

$$\dot{R} = -\dot{\gamma}.\frac{\partial \Phi}{\partial k}$$

$$\dot{f} = (1-g_0).\frac{f_N}{S_N\sqrt{2.\pi}}.\exp\left[-\frac{1}{2}\left(\frac{\bar{\varepsilon}^{p} - \varepsilon_N}{S_N}\right)^2\right].\dot{\bar{\varepsilon}}^{p} + (1-f).\dot{\varepsilon}_v^{p}$$

$$\dot{D} = g_0.\frac{D_N}{s'_N.\sqrt{2\pi}}.\exp\left[-\frac{1}{2}\left(\frac{\bar{\varepsilon}^{p} - \varepsilon'_N}{s'_N}\right)^2\right].\dot{\bar{\varepsilon}}^{p} + q_6.\dot{D}^{shear}.[g_0(\xi)]^{1/\|\eta\|+k}$$

where,

$$\dot{D}^{shear} = q_3 D^{q_4}\bar{\varepsilon}^{p}.\dot{\bar{\varepsilon}}^{p}$$

$$g_0 = 1 - |\bar{\theta}|$$

and,

$$\dot{\bar{\varepsilon}}^{p} = \sqrt{\frac{2}{3}(\dot{\boldsymbol{\varepsilon}}^{p} : \dot{\boldsymbol{\varepsilon}}^{p})} \qquad \dot{\varepsilon}_v^{p} = \mathrm{tr}(\dot{\boldsymbol{\varepsilon}}^{p})$$

(v) Loading/unloading criterion

$$\dot{\gamma} \geq 0, \qquad \Phi \leq 0, \qquad \dot{\gamma}\Phi = 0$$

3 NUMERICAL INTEGRATION ALGORITHM

Algorithms based on operator split methodology are especially suitable for the numerical integration of the evolution problem and have been widely used in computational plasticity (see Simo & Hughes [25]; De Souza Neto et al. [8]). This method, which is used for our development, consists of splitting the problem in two parts: an elastic predictor, where the problem is assumed to be elastic and, a plastic corrector, in which the system of residual equations comprising the elasticity law, plastic consistency and the rate equations is solved, taking the results of the elastic predictor stage as initial conditions. In the case of the yield condition has been violated, the plastic corrector stage is initiated and the Newton- Raphson

procedure is used to solve the discretised equations. The Newton-Raphson procedure was chosen motivated by the quadratic rates of convergence achieved which results in return mapping procedures computationally efficient, see Simo & Hughes [25] and De Souza Neto et al. [8]. The implicit algorithms were proposed initially based on the infinitesimal strain theory and here, both numerical models are extended to the finite strain through the framework based on a logarithmic strain measure, rather than the elastic deformation gradient, see Peric´ et al. [18] and Eterovic et al. [10]). The overall algorithm for numerical integration is summarized in Box 2.

Box 2. Fully implicit Elastic predictor/Return mapping algorithm.

(i) Evaluate elastic trial state: Given the incremental strain $\Delta\boldsymbol{\varepsilon}$ and the state variables at t_n:

$$\begin{array}{lll} \boldsymbol{\varepsilon}^{e\,trial}_{n+1} = \boldsymbol{\varepsilon}^{e}_{n} + \Delta\boldsymbol{\varepsilon} & ; & \bar{\varepsilon}^{p\,trial}_{n+1} = \bar{\varepsilon}^{p}_{n} \quad ; \quad R^{trial}_{n+1} = R_n \\ f^{trial}_{n+1} = f_n & ; & D^{trial}_{n+1} = D_n \quad ; \quad \boldsymbol{S}^{trial}_{n+1} = 2G\,\boldsymbol{\varepsilon}^{e\,trial}_{n+1} \\ p^{trial}_{n+1} = K\varepsilon^{e\,trial}_{v\,n+1} & ; & \sigma^{trial}_{y} = \sigma_y\left(R^{trial}_{n+1}\right) \end{array}$$

(ii) Check plastic admissibility:

IF $\Phi^{trial} = \frac{J_2^{trial}}{1-D^{trial}_{n+1}} - \frac{1}{3}.\left[1 + q_3.f^{trial\,2}_{n+1} - 2.q_1.f^{trial}_{n+1}.\cosh\left(\frac{3.q_2.p^{trial}_{n+1}}{2.\sigma^{trial}_{y}}\right)\right].\left(\sigma^{trial}_{y}\right)^2 \leq 0$

THEN set $(\cdot)_{n+1} = (\cdot)^{trial}_{n+1}$ ***(elastic step)*** and go to *(v)*

ELSE go to (iii)

(iii) Return mapping ***(plastic step)***: *Solve the system of equations below for* $\Delta\gamma, p_{n+1}, f_{n+1}$, R_{n+1} and D_{n+1}, *using Newton-Raphson method:*

$$\left\{\begin{array}{c} \dfrac{J_{2\,n+1}^{trial}}{\left[1+\left(\frac{2G.\Delta\gamma}{1-D_{n+1}}\right)\right]^2.(1-D_{n+1})} - \dfrac{1}{3}.\left[1 + q_3.{f_{n+1}}^2 - 2.q_1.f_{n+1}.\cosh\left(\dfrac{3.q_2.p_{n+1}}{2.\sigma_y}\right)\right].\sigma_y^2 \\ p_{n+1} - p^{trial}_{n+1} + \Delta\gamma.K.\sigma_y.q_1.q_2.f_{n+1}.\sinh\left(\dfrac{3.q_2.p_{n+1}}{2.\sigma_y}\right) \\ f_{n+1} - f^{trial}_{n+1} - \Delta f^{n} - \Delta f^{g} \\ R_{n+1} - R^{trial}_{n+1} - \Delta R \\ D_{n+1} - D^{trial}_{n+1} - \Delta D^{n} - q_6.\Delta D^{shear} \end{array}\right\} = \left\{\begin{array}{c} 0 \\ 0 \\ 0 \\ 0 \\ 0 \end{array}\right\}$$

where,

$$\Delta f^{n} = (1 - g_{0\,n+1}).\frac{f_N}{S_N\sqrt{2.\pi}}.\exp\left[-\frac{1}{2}\left(\frac{\bar{\varepsilon}^{p}_{n+1} - \varepsilon_N}{S_N}\right)^2\right].\Delta\bar{\varepsilon}^{p}$$

$$\Delta f^{g} = (1 - f_{n+1}).\Delta\gamma.\sigma_y.q_1.q_2.f_{n+1}.\sinh\left(\frac{3.q_2.p_{n+1}}{2.\sigma_y}\right)$$

continue Box 2.

$$\Delta R = \frac{\Delta\gamma}{(1-f_{n+1}-D_{n+1})}.\left\{q_1.q_2.f_{n+1}.p_{n+1}.\sinh\left(\frac{3.q_2.p_{n+1}}{2.\sigma_y}\right) + \frac{2}{3}.\sigma_y.\left[1+q_3.{f_{n+1}}^2-2.q_1.f_{n+1}.\cosh\left(\frac{3.q_2.p_{n+1}}{2.\sigma_y}\right)\right]\right\}$$

$$\Delta D^n = g_{0\,n+1}.\frac{D_N}{S'_N\sqrt{2.\pi}}.\exp\left[-\frac{1}{2}\left(\frac{\bar{\varepsilon}^p_{n+1}-\varepsilon'_N}{S'_N}\right)^2\right].\Delta\bar{\varepsilon}^p$$

$$\Delta D^{shear} = [g_0]^{(1/\|\eta\|+k)}.q_4 D^{q_5}.\bar{\varepsilon}^p.\Delta\bar{\varepsilon}^p \qquad g_0 = (1-\xi^2_{n+1})$$

(iv) Update the others state variables:

$$\boldsymbol{\varepsilon}^e_{n+1} = \boldsymbol{\varepsilon}^{e\,trial}_{n+1} - \Delta\gamma.\left[\frac{\boldsymbol{S}^{trial}_{n+1}}{\left[1+\left(\frac{2G.\Delta\gamma}{1-D_{n+1}}\right)\right].(1-D_{n+1})} + \frac{1}{3}.\sigma_y.q_1.q_2.f_{n+1}.\sinh\left(\frac{3.q_2.p_{n+1}}{2.\sigma_y}\right).\boldsymbol{I}\right]$$

(v) Exit

4 CALIBRATION PROCEDURE

In order to determine the materials parameters for the proposed constitutive model, two calibration points are required. The first point is taken from a specimen at high level of stress triaxiality, where a smooth bar specimen can be used. In this step, the hardening law, $\sigma_y(R)$, for the undamaged model is determined as well as the set of parameters for nucleation of micro void mechanism $[f_N, S_N, \varepsilon_N]$. The second calibration point can be taken from a specimen in pure shear loading condition, where the accelerator parameter, q_6, is determined as well as the set of parameters for the nucleation of micro defects mechanism $[D_N, S'_N, \varepsilon'_N]$. Here, a butterfly specimen can be used under pure shear loading condition.

4.1 Geometry and mesh definition

Regarding the material properties for the first calibration point, a classical smooth bar specimen is used and the following dimensions were employed (see Figure 2a). In order to trigger necking, a dimensional reduction of 5% in the central diameter of the specimen is used. For a steel 1045, a gauge section 20.6 mm is used. The standard eight-nodded axsymmetric quadrilateral element, with four Gauss integration points, is adopted. The initial mesh discretisation is illustrated in Figure 2b, where only one symmetric quarter of the problem, with the appropriate symmetric boundary conditions imposed to the relevant edges, is modeled. A total number of 1800 elements have been used in the discretisation of both the smooth specimens, amounting to a total of 5581 nodes.

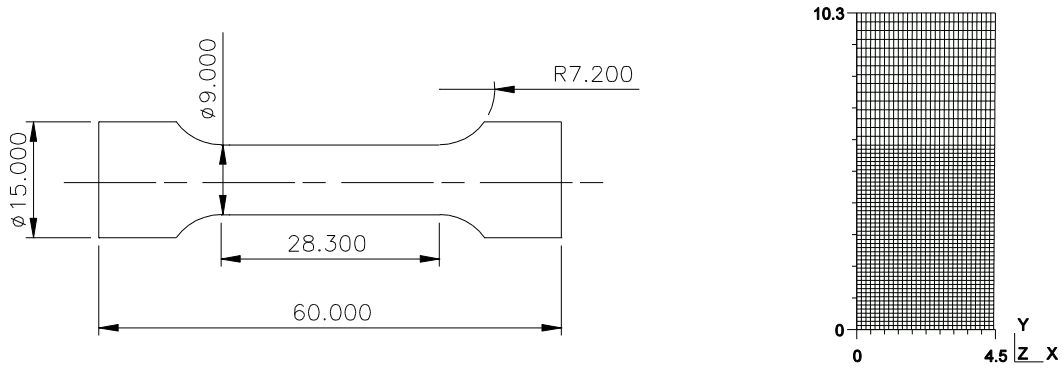

(a) (b)

Figure 2. Geometry for the smooth bar specimen. Dimension in (mm). Taken from Teng [26].

For the second calibration point and the numerical tests that will be presented, a butterfly specimen is used. The specimen was initially designed by Bai [2] and the geometry and general dimensions can be verified by Figure 3. In this case, a three dimensional finite element mesh of 3392 twenty nodded elements, with nine Gauss integration points, is used amounting to 17465 nodes.

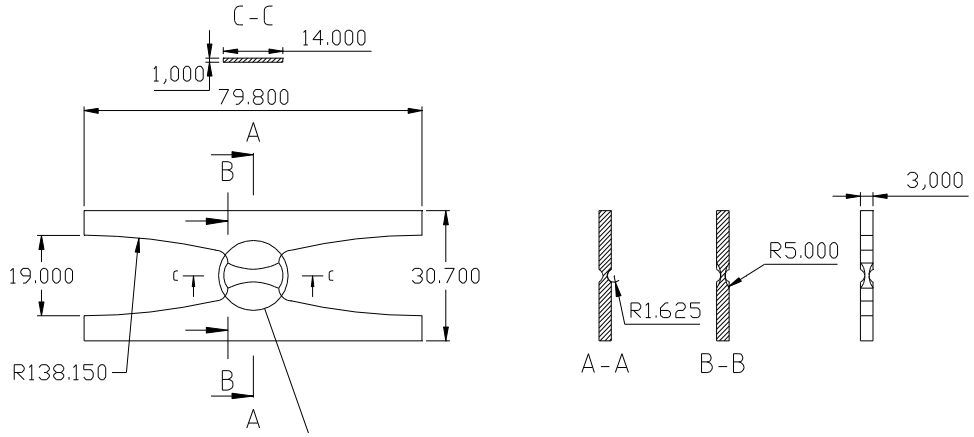

Figure 3. The geometry for butterfly specimen. Dimension in (mm). Taken from Bai [2].

4.2 Material parameters

In the present section, the stress-strain curve, the parameters required for modeling micro void nucleation mechanism from the GTN model are calibrated by tensile tests in cylindrical smooth bars. Through experimental data (see Bai [2]), the reaction versus displacement curve is determined as well as the stress-strain curve for an elasto-plastic model of von Mises type. The inverse method is adopted in order to calibrate the material parameters for coupled damage model by forcing the numerical solution to be, as close as possible to the experimental results. Figure 4a shows reaction curve for the model determined after the application of inverse method. A good agreement between the experimental and numerical results can be observed. Furthermore, the critical volume void fraction is also determined in the point where the model attains the displacement to fracture, experimentally observed (see Figure 4b). The critical values obtained is $f_c = 0.076$, for aluminum a steel 1045.

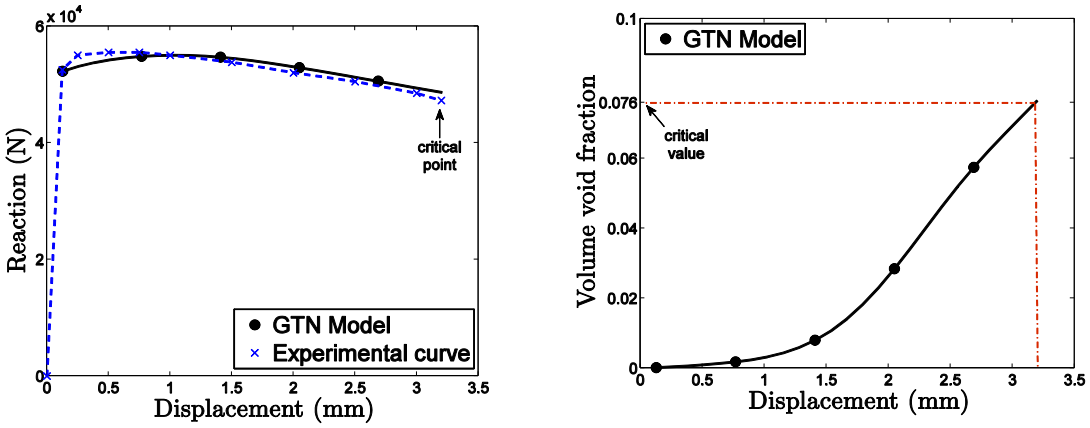

(a) (b)

Figure 4. (a) Reaction versus displacement curve for GTN model and experimental results for steel 1045. (b) Critical volume void fraction parameter calibrated for the material.

The results of the calibration procedure, in terms of stress-strain curve, can also be observed in Figure 5, where for uncoupled and coupled damage models, were determined.

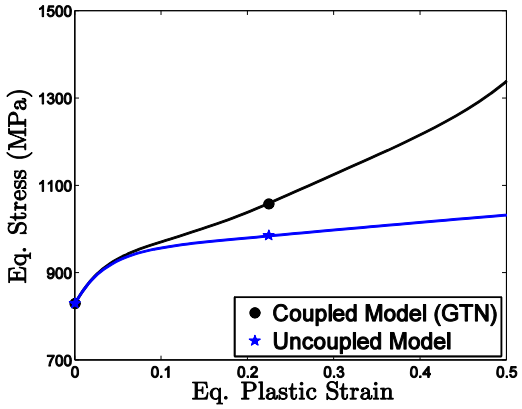

Figure 5. Stress-strain curve determined for an uncoupled and coupled models.

Regarding the second calibration point, the parameters related with the micro defects nucleation mechanism are determined as well as the critical value for the shear damage. The butterfly specimen is here used under pure shear loading condition and the displacement at fracture was suggested by Bai [2]. An inverse method is also adopted, regarding the calibration of the parameters by forcing the numerical results to be as close as possible to the experimental data. Table 2 contents the best materials parameters suggested after some inverse numerical tests. The parameters will be used during all numerical simulations.

Table 1: Materials parameters for steel 1045.

High stress triaxiality	f_N	S_N	ε_N	q_1	q_2	q_3	f_c	E (MPa)	υ
	0.05	0.2	0.1	1.5	1.0	2.25	0.076	220.000	0.33
Low stress triaxiality	d_N	S_N	ε_N	q_6		k	D_c		
	0.10	0.15	0.10	1.00		0.10	0.16		

5 NUMERICAL RESULTS

Regarding a consistent analysis for the new constitutive formulation at low level of stress triaxiality, some numerical tests are performed using the butterfly specimen and the implicit algorithm developed in above sections. Three different loading conditions are taken as: pure shear (0º), shear/tensile (10º) and shear/compression (-5º), taken hand the materials properties for a steel 1045. The performance of some internal variable and the ability to predict the correct fracture location are evaluated. At the end, the numerical results determined by the new formulation can be compared with the results obtained by other shear mechanisms as Xue [28] and Nahshon & Hutchinson [17].

Table 2: Numerical results for butterfly specimen, regarding different loading conditions.

Angle	Experimental data		Numerical results			
	u_f	$\bar{\varepsilon}^p$	u_f	$\bar{\varepsilon}^p$	f	d
0º	1.03	0.50	1.03	0.522	0.000	0.160
10º	0.42	0.36	0.44	0.353	0.026	0.053
-5º	1.71	0.60	1.71	0.612	0.000	0.126

Figure 6 represents a comparative illustration for the ability to predict the fracture location in combined shear/tensile (10º) loading condition using 1045 steel, regarding different shear mechanisms. Figure 6a illustrate the contour of damage parameter for Nahshon & Hutchinson shear mechanism, Figure 6b for Xue shear mechanism and Figure 6c for the new proposition. We can observer that only the new proposition predicts fracture onset in agreement with experimental evidence. The prediction by Xue is in complete disagreement with experimental evidence and by Nahshon & Hutchison, the contour is somewhat spread around the critical section, which may suggest a certain vagueness to the model.

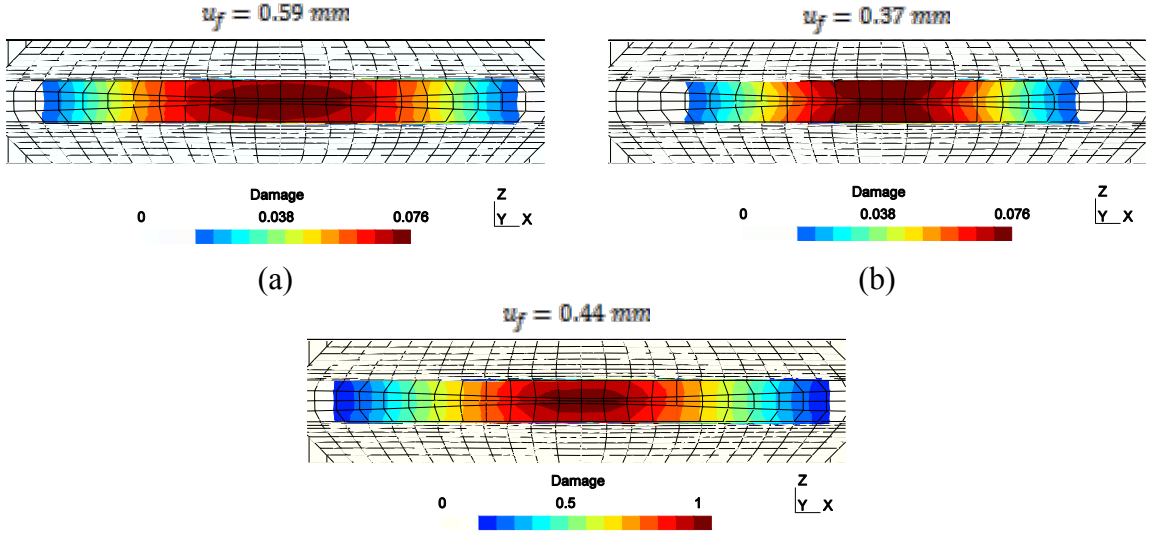

Figure 6. Damage parameter contour, (a) Nahshon & Hutchinson shear mechanism, (b) Xue shear mechanism and (c) new proposition. Section CC in the critical zone.

6 CONCLUSIONS

In this contribution, it was proposed a new formulation for improve the original GTN model, regarding the ability to predict ductile fracture in low level of stress triaxialities. The new formulation has two damage parameters, first one affecting only the hydrostatic stress part and another affecting the deviatoric part.

Numerical tests were provided, based on implicit integration algorithm, in order to evaluate the formulation in prediction the crack formation. A butterfly specimen was required, besides to a steel 1045. The model behaves well, whether in the determination of the correct level of equivalent plastic strain and displacement at fracture, or in prediction of the location to crack formation.

The proposition of create two damage parameters affecting separated stress contribution brings a balance in the evolution of internal variables so the more precise values at time of crack formation. Furthermore, the creation of a new micro-defects nucleation mechanism allowed a better calibration model and thus a good performance within wide range of stress triaxialities.

REFERENCES

[1] Andrade Pires, F.M., César de Sá, J.M.A., Costa Sousa, L., Natal Jorge, R.M. (2003). Numerical Modeling of ductile plastic damage in bulk metal forming, *International Journal of Mechanical Sciences*, 45:273–294.

[2] Bai, Y. (2008). Effect of Loading History on Necking and Fracture. Ph.D Thesis, *Massachusetts Institute of Technology*.

[3] Besson, J., Steglich, D. and Brocks, W. (2001). Modeling of crack growth in round bars and plane strain specimens. *International Journal of Solids and Structures*, 38(46–47):8259–8284.

[4] Besson, J., (2010). Continuum Models of Ductile Fracture: A Review. *International Journal of Damage Mechanics*, 19:3-52.

[5] Butcher, C., Chen, Z., Bardelcik, A., Worswick M. (2009). Damage-based finite-element modeling of tube hydroforming. *International Journal of Fracture*, 155:55–65.

[6] Chaboche, J.L. (2003). Damage mechanics. *In: Milne, I., Ritchie, R.O. and B. Karihaloo (eds.) Comprehensive Structural Integrity*, vol. 2. Elsevier-Pergamon, pp. 213–284.

[7] Chaboche, J.L., Boudifa, M., Saanouni, K., (2006). A CDM approach of ductile damage with plastic compressibility. *International Journal of Fracture*, 137:51–75.

[8] De Souza Neto, E.A., Peri´c, Owen, D.R.J. (2008). Computational methods for plasticity: theory and applications. *John Wiley & Sons Ltd*.

[9] Engelen, Roy A.B. (2005). Plasticity-induced Damage in Metals / nonlocal modelling at finite strains. PhD Thesis – Eindhoven : Technische Universiteit Eindhoven.

[10] Eterovic, A.L., & Bathe, K.-J. 1990. A Hyperelastic Based Large Strain Elasto-Plastic Constitutive Formulation with Combined Isotropic-Kinematic Hardening Using the Logarithmic Stress and Strain Measures. Int. *J. Num. Meth. Engng.*, 30, 1099–1114.

[11] Gurson, A.L. (1977). Continuum Theory of ductile rupture by void nucleation and growth - Part I. Yield criteria and flow rules for porous ductile media. *J. Engrg. Mat. Tech.,* 99:2-15.

[12] Lemaitre, J. (1985). A continuous damage mechanics model for ductile fracture. *Journal of Engineering Materials and Technology - Trans. of the ASME*, 107:83–89.
[13] Lemaitre, J., Chaboche, J.L. (1990). Mechanics of Solid Materials. Cambridge Univ. Press.
[14] Malcher, L.; Andrade Pires, F.M.; César de Sá, J.M.A. (2011). An Assessment of Isotropic Damage Constitutive Models under High and Low Stress Triaxialities. *International Journal of Plasticity*.
[15] McClintock, F. A. (1968). A Criterion for Ductile Fracture by the Growth of Holes. J. Appl. Mech., 35, 363–371.
[16] Mudry, F. (1985). Methodology and application of local criteria for prediction of ductile tearing. D.Reidel Publishing Co.
[17] Nahshon, K., Hutchinson, J. (2008). Modification of the Gurson model for shear failure. *European Journal of Mechanics A/Solids,* 27:1–17.
[18] Peric, D., Owen, D.R.J., & Honnor, M.E. (1992). A Model for Finite Strain Elasto-Plasticity Based on Logarithmic Strains: *Computational Issues. Comp. Meth. Appl. Mech Engng.*, 94:35–61.
[19] Pineau, A. (1981). Review of fracture mechanisms and local approaches to predicting crack resistance in low strength steels. In: Franc¸ois, D. et al. (ed.) Advances in Fracture Researches. New-York, Pergamon Press, ICF5. Cannes.
[20] Reis, F.J.P.; Malcher, L. ; Andrade Pires, F.M. ; César de Sá, J.M.A. (2010). A modified GTN model for the prediction of ductile fracture at low stress triaxialities. *International Journal of Structural Integrity*.
[21] Rice, J. R., Tracey, D., M. (1969). On the ductile enlargement of voids in triaxial stress fields. *Journal of the Mechanics and Physics of Solids*, 17:201–217.
[22] Rousselier's, G. (1980). Finite deformation constitutive relations including ductile fracture damage. In: Nemat-Nasser (ed.) Three-Dimensional Constitutive Relations and Ductile Fracture. North-Holland Publ. Comp., 1981 pp. 331–355.
[23] Rousselier's, G. (1987). Ductile fracture models and their potential in local approach of fracture. *Nuclear Engineering and Design* 105: 97–111.
[24] Rousselier's, G. (2001). The Rousselier model for porous metal plasticity and ductile fracture. In: Lemaitre, J. (ed.) Handbook of Materials Behavior Models, vol. 2. Academic Press, New York, chapter 6.6, pp. 436–445.
[25] Simo, J.C., & Hughes, T.J.R. (1998). Computational Inelasticity. NY: Springer-Verlag.
[26] Teng, X. (2008). Numerical prediction of slant fracture with continuum damage mechanics. *Engineering Fracture Mechanics*, 75:2020–2041.
[27] Tvergaard, V. and Needleman, A. (1984). Analysis of the cup-cone fracture in a round tensile bar. *Acta Met.* 32:157–169.
[28] Xue, L. (2007). Ductile Fracture Modeling – Theory, Experimental Investigation and Numerical Verification, Ph.D Thesis, *Massachusetts Inst. of Technology*. Ph.D Thesis, *Massachusetts Inst. of Technology*.

XI International Conference on Computational Plasticity. Fundamentals and Applications
COMPLAS XI
E. Oñate, D.R.J. Owen, D. Peric and B. Suárez (Eds)

EFFECT OF TEMPERATURE IN FORMABILITY OF COMPOSITE COMPOSED OF OVERLAPPED FIBRE BUNDLE, THERMOPLASTIC RESIN AND METAL

TAKASHI KUBOKI[*], SHUN-ICHI UEMATSU[†] AND MAKOTO MURATA[*]

[*] Dept. of Mechanical Engineering & Intelligent Systems
University of Electro-Communications
1-5-1 Chofu Gaoka, Chofu-shi, Tokyo, 182-8585, Japan
email: kuboki@mce.uec.ac.jp, www.uec.ac.jp

[†] Design Center, Heavy Duty Pump and Motor Business Unit
Caterpillar Japan, Ltd.
3700, Tana, Sagamihara-shi, Kanagawa, 229-1192, Japan

Key words: Fibre–Metal Laminate, Overlap, Thermoplastic Resin, Sandwich Structure.

Abstract. A structure for a composite of fibre-metal laminate (FML) has been proposed, which is composed of reinforcing fibre bundles, thermoplastic resin as the matrix and metal plates. The reinforcing fibre bundles are discontinuous, and are intentionally overlapped in the longitudinal direction. The resin including fibre bundles was sandwiched between the metal plates. The application concept for the industry is composed of three stages. At the 1st stage, FML is fabricated by lamination of reinforcing fibre bundles, thermoplastic resin and metal plates. At the 2nd stage, FML is formed into the final shape of the product by secondary forming processes, such as stretching or bending under a heated condition which melts the thermo resin. At the 3rd stage, the formed product is expected to have high strength. In the present paper, the effect of heating temperature on the deformation of FML at the 2nd stage was clarified. Firstly, the numerical examination was shown on the effect of overlap length on the fracture mode and the reinforcing mechanism in the proposed FML. Based on the result, the minimum bare length for the overlapped part for the discontinuous fibre bundles was determined so that the tensile strength might be as high as that with FMLs with continuous fibre bundles at the 3rd stage. Finally actual FML was experimentally fabricated, and subjected to all though the 1st to 3rd stages to verify the efficiency of the FML. In particular, the effect of heating temperature was focused upon to realize the forming process at the 2nd stage.

1 INTRODUCTION

It would be meaningful to develop materials, including composites, which have both high formability in plastic deformation and high strength after forming. It would be important particularly when the material is employed as structural components for vehicles or

architecture. The material should have higher formability and lower flow resistance during forming. On the other hand, the material should have high strength once it is formed into its final shape and used as structural components.

Many research trials have been conducted to develop such kinds of materials which have contradictory properties: high formability and high strength. Ultra-fine-grained metal is one of the most popular materials recently. Several new technologies have been proposed and have successfully formed ultra-fine-grained metals [1]. However, formability and tensile strength still have a contradictory tendency, and that is to say that fine-grained metals with higher strength tend to have lower elongation. Bake hardening is an effective method to satisfy the contradictory requirements [2]. Before bake hardening, the metal plate is relatively soft and easily deformed by cold working processes. After the metal plate is formed into its final shape, bake hardening is conducted to strengthen the metal.

Composites are very efficient materials which realise high strength while suppressing total weight [3]. The efficiency has been evaluated in terms of both mechanical properties and formability in the forming processes [4, 5]. However, it is generally difficult to subject the formed composite to secondary forming processes which require plastic deformation.

Discontinuous reinforcing fibres are inevitably used for composites to secure secondary deformation. Some composites with short fibres are proposed using an aluminium matrix, and their manufacturing methods are presented [6, 7]. However, short fibres would lead to lower strength than long fibres. "Stampable sheets" which are composed of a net of fibres and a thermoplastic matrix, have been proposed with emphasis on the formability at secondary deformation [8, 9]. "Stampable sheets" would enhance the flexibility in forming under the condition that the deformation is bending and the length is kept constant during the deformation. However, "stampable sheets" would not be applicable for forming processes where the composites are elongated because the fibres are woven into the shape of a net.

Fibre–metal laminates (FMLs) have been developed as hybrid structures, which have the durability of metals with the impressive fatigue and fracture properties of fibre-reinforced composite materials. The mechanical properties of FMLs have been investigated [10, 11]. There are also some research studies focusing upon the blast response of FMLs [12, 13]. Even though the fatigue and fracture properties of FMLs are excellent, the formability of FMLs is not secured.

In the present research, a structure of FML has been proposed for the purpose of maintaining substantial elongation at the secondary forming process as well as providing high strength [14]. The structure is composed of reinforcing fibre bundles, thermoplastic resin as the matrix and metal plates. The reinforcing fibre bundles are discontinuous, and are intentionally overlapped in the longitudinal direction. The resin including fibre bundles was sandwiched between the metal plates. Finite element analyses were carried out for the examination of the structure in terms of stress distribution and composite strength. Based on the analytical results, experiments were carried out to verify the formability in secondary forming under a heated condition as well as the strength after being cooled to room temperature. In particular, the effect of heating temperature was focused upon to realize the forming process at the 2nd stage.

2 INTRODUCTION OF A STRUCTURE FOR FIBRE–METAL LAMINATE (FML)

FML has been proposed by the authors, which is able to be greatly elongated at secondary forming and which provides a high level of strength in one direction after the secondary forming [14]. **Figure 1** shows the application image of the FML and the verification procedure by laboratory experiment. At the 1st stage of the application, FML is formed by lamination of reinforcing fibre bundles, thermoplastic resin and metal plates. At the 2nd stage, FML is formed into the final shape of the product by secondary forming processes, such as stretching or bending under a heated condition which melts the thermo resin. At the 3rd stage, the formed product is expected to have high strength. In the laboratory experiments for verification, FML is firstly formed by lamination into the shape for a tension test. The FML is elongated under a heated condition. After being cooled, the FML is subjected to a tension test for the measurement of mechanical properties.

In the proposed structure, the reinforcing fibre bundles are discontinuous, and are intentionally overlapped in the longitudinal direction. When the overlap length is satisfactorily long, the FML would have enough strength at the 1st stage. If the FML is heated at an appropriately warm temperature to melt the thermoplastic resin, the FML would be elongated with reduction of overlap length at the 2nd stage. If the overlap length is still long, the FML would maintain strength at the 3rd stage.

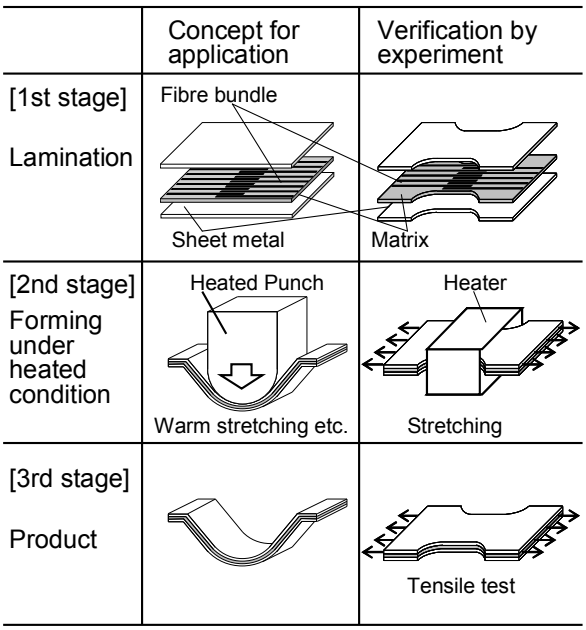

Figure 1: Concept and experimental procedure for FML

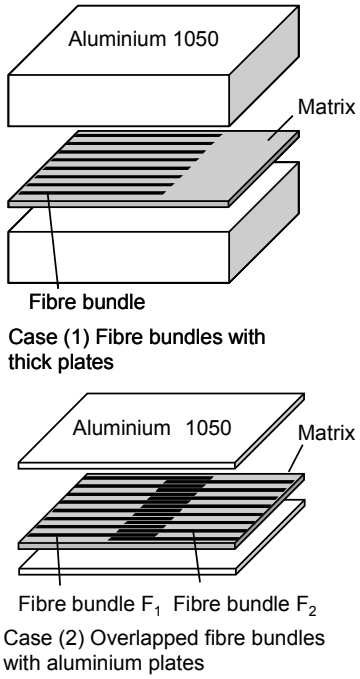

Figure 2: Schematic illustration of composites examined in FE analysis

3 FINITE ELEMENT ANALYSIS OF FML

3.1 FEA model for FML

The unique point of the proposed FML is the existence of overlapped fibre bundles.

Thermoplastic resin around the overlapped fibre bundles is required to withstand certain stress for maintaining the high strength of FML. In order to clarify the role of the overlapped part, a series of analyses was carried out.

Two types of models were adopted for the analyses as shown in **Fig. 2**. The fibre-bundle diameter was fixed at 0.43 mm, which was the same as the actual one used in the experiment. The thickness of the matrix of thermoplastic resin was 0.56 mm, which was determined from the measured value of tentatively formed FML. In the analyses, FMLs are elongated in the parallel direction to the fibre bundles by applying displacement at one of the FML ends.

Fibre bundles and thermoplastic resin are sandwiched by two metal plates of 5 mm thickness in Case (1). While one of the fibre-bundles ends is connected to one end of the FML, the other end is embedded into the resin. As the metal plates are much thicker than the fibre-bundle diameter, the FML is supposed to deform almost homogeneously without being affected by the existence of the fibre bundle. Therefore, Case (1) would simulate the behaviour of fibre bundles and resin in homogeneous deformation, i.e. in idealistic deformation of the composite. Fibre bundles, supplied from two directions, are sandwiched by two metal plates of 0.49 mm thickness in Case (2).

Numerical models in finite element analysis (FEA) are shown in **Fig. 3** taking Case (2) as an example. Elastic-plastic analysis was carried out using the commercial code ELFEN, which was developed by Rockfield Software Limited, Swansea. Implicit scheme was used. Metal plates and thermoplastic resin were treated as elasto-plastic material and fibre bundles were assumed to be elastic material. A von Mises' yield criterion was adopted for elasto-plastic materials, and the normality principle was applied to the flow rule. Constraints were dealt with by the penalty function method. The F-bar method was applied to the hexahedra element for overcoming volumetric locking with simple brick-type elements [15].

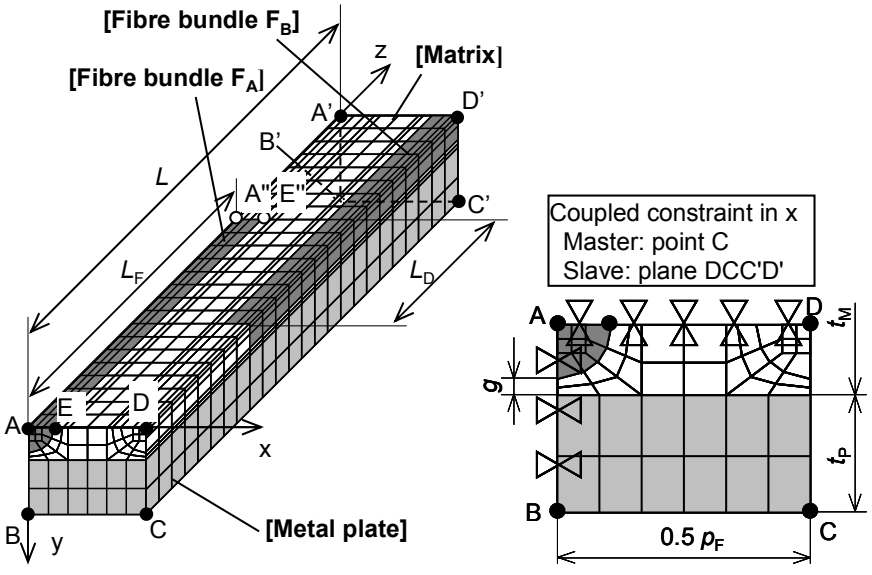

Figure 3: FEM model for composite

As the nodes between different materials belong to both materials, no slippage occurs, i.e. the materials are assumed to stick together completely. A half model was adopted in the thickness direction considering the symmetry. Only two fibres are modelled considering the periodicity in width direction. As the centre axis of fibre would be straight if a number of fibres exist periodically, surface ABB'A' is fixed in x direction as shown in Fig. 3. Although the other surface CDD'C' is not fixed in x direction, the movement of nodes on the surface are coupled so that the displacement of the surface CDD'C' should be the same. While surface A'B'C'D' is fixed in z direction, displacement is given to surface ABCD during tension test.

3.2 Stress distribution during numerical tensile test

A series of analyses was carried out for clarifying the reinforcing mechanism of the proposed FML by comparing stress distribution between different structures. The geometry of FML is shown in **Table 1**. If stress concentrates at some area, the tensile strength would decrease due to localized deformation. As stress concentration would occur at either the fibre bundle or boundaries between the fibre bundle and matrix, axial stress σ_F along the axis of the fibre bundle and shear stress τ_M on the boundary were evaluated. The evaluation lines for σ_F and τ_M are A-A" and E-E", respectively, in Fig. 3.

Table 1: geometry of FML

Total length (L), mm		60
Fibre bundle	Diameter (D_F), mm Length (L_F), mm Overlap length (L_D), mm Pitch (p_F), mm	0.43 28 - 40 (Case 1) 6, 20 (Case 1) 1.0 (Case 2) 1.0 at overlapped part
Matrix	Thickness (t_M), mm	0.56
Plate	(Case 1) Annealed aluminium 1050, thickness t_P=5.0 mm (Case 2) Annealed aluminium 1050, thickness t_P=0.49 mm	

Figure 4 shows the result for Case (1) which would simulate the behaviour of fibre bundles and matrix in homogeneous deformation. With increase of nominal strain ε of the laminate, axial stress σ_F of the fibre increases while the length L_S of the area, where shear stress τ_M is equal to yield shear stress of matrix τ_{My}, expands. At the same time, the length of part L_A, where axial stress σ_F changes at a constant rate at the end of the fibre bundle, also expands. Once nominal strain ε of FML reaches 0.0256, axial stress σ_F reaches rupture level. This phenomenon of stress slope would be explained by the following equation (1).

$$d\left(\frac{\pi}{4}D_F^2\sigma_F\right) = \pi D_F \tau_M dz \tag{1}$$

where, D_F = Diameter of fibre bundle [mm].

The left-hand side is increase of tension given by axial stress σ_F of the fibre bundle, while the right-hand side is the total force given by shear stress τ_M on the boundary. At the beginning of elongation of the laminate, shear stress τ_M reaches yield shear stress τ_{My} on the

boundary at the tip of the fibre bundle. With increase of elongation, the length L_S of τ_{My} expands, and axial stress σ_F has a slope following equation (1) at the end of the fibre bundle embedded in resin. Axial stress σ_F reaches σ_{FP} at the end of the slope and σ_F is constant at σ_{FP} at the plateau area, which is denoted by P_1 for ε=0.012 in Fig. 4. When nominal strain ε is larger than 0.0256, σ_{FP} reaches rupture level. When σ_{FP} reaches rupture level σ_{BF}, the length of axial-stress slope L_C is calculated following equation (2) derived from equation (1).

$$L_C = \frac{D_F \sigma_{BF}}{4\tau_{My}} \tag{2}$$

In the remaining section, let L_C be called critical length.

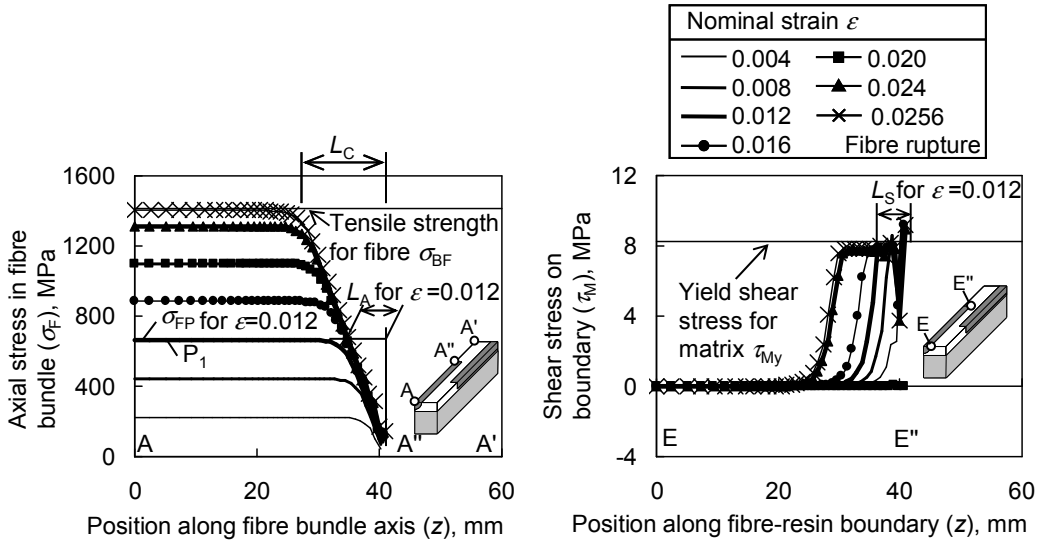

Figure 4: Stress distribution for Case (1)

Figure 5(a) shows the result for Case (2) where fibre bundles, supplied from two directions, are sandwiched by two metal plates, and the overlap length L_D is longer than critical length L_C. The shear-stress field is confined within the overlapped part L_D. Axial stress σ_F of the fibre bundle has two plateaus, P_1 and P_2, and two slopes following equation (1). As the plates also play a role of supporting tensile load, the stress proportion is not simple and the axial stress at the overlapped part P_2 is larger than half of the axial stress at P_1. As a result, shear stress τ_M is larger around z =40 mm than around z =20 mm.

Figure 5(b) shows the result for Case (2) when the overlap length L_D is shorter than critical length L_C. It is noteworthy that the shear-stress field expands beyond the overlapped part L_D. Even in the single-way-bundle part, axial stress continues to increase in the left-side direction in the area denoted by α. It is thought that the supporting plates have a role to convey stress to the single-way-bundle part. The existence of surplus length α is the reason why FML can reduce the minimum bare overlap length L_{DN} for maintaining tensile strength less than L_C calculated by equation (2).

Based on the numerical study above, the role of the overlap part was clarified. Shear stress τ_M on the boundary changes corresponding to axial stress σ_F of the fibre bundle which should

be 0 at the tip of the bundle and should be a certain constant value in single-way-bundle part P_1. Due to this stress distribution, the whole laminate can withstand the applied load, even if the fibre bundles are not continuous. The relationship between shear stress and axial stress should comply with equation (1). When the plate does not exist, the overlapped part L_D should be longer than critical length L_C, which is calculated by equation (2) in order to maintain strength of the laminate as high as the value predicted by the law of mixture [16]. However, the supporting plate would reduce the needed length for the maintenance of strength by surplus length α in Fig. 5(b). Surplus length α would change depending on the mechanical properties and thickness of the plates.

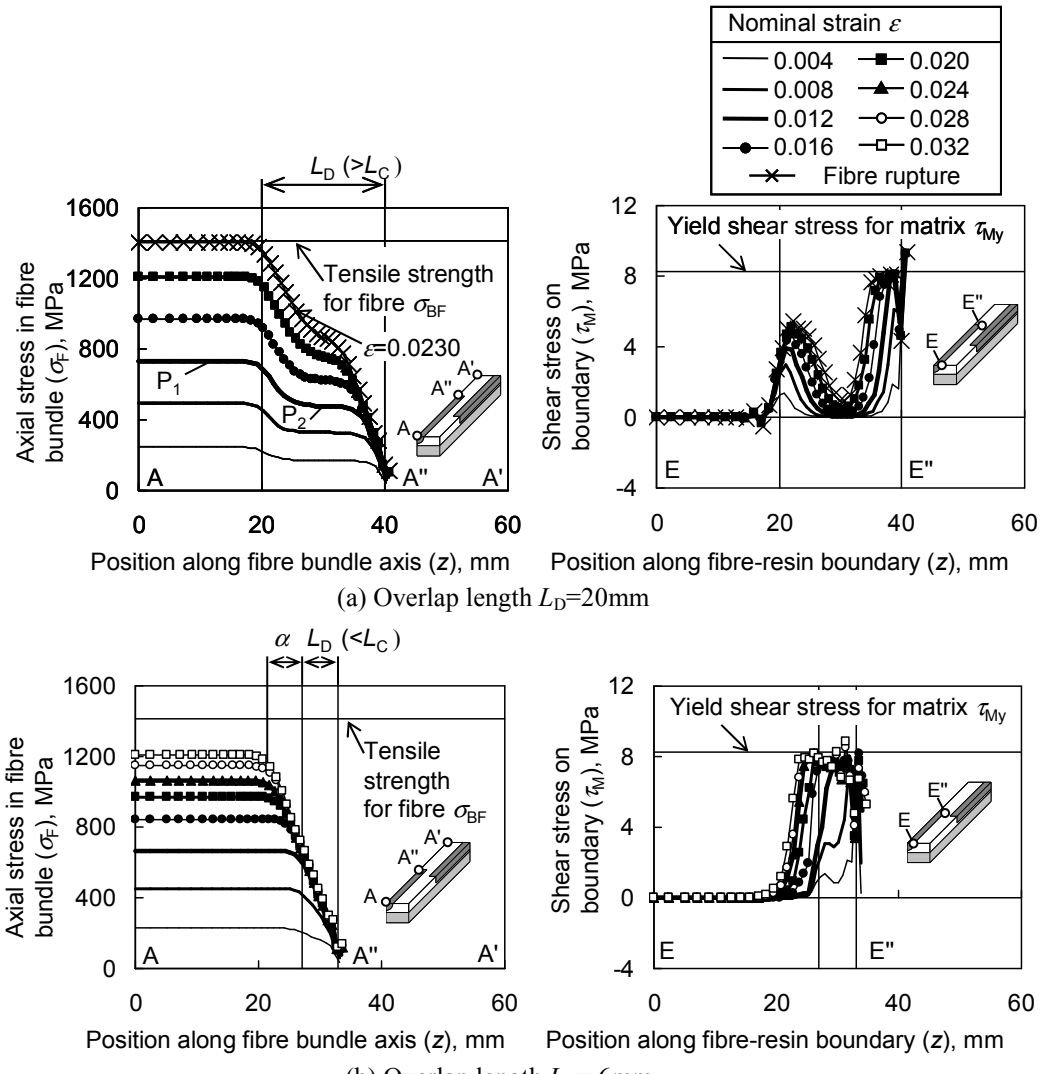

Figure 5: Stress distribution for Case (2)

4 EXPERIMENTAL RESULTS

4.1 Effect of temperature in 2nd stage of deformation

According to equation (1), when yield shear stress τ_{My}, which is the maximum value of τ_y, is enough low, axial stress σ_F would not be increased as the deformation will not conveyed between fibre bundles. This situation is easily realized by heating FML because the matrix is a thermoplastic resin, which melts completely over 100 degrees Celsius [17]. The effect of temperature on the formability of FML of case (2) is tested using device in **Fig. 6.** 4 rod heaters were used for heating FML. After the temperature at the surface of FML reached a saturated value, the temperature was recorded as heating temperature *T*. The experimental result is shown in **Fig. 7** in the form of stress-strain diagram with overlap length L_D of 30 mm. Overlap L_D of 30 mm is much longer than critical value L_C calculated equation (1) for room temperature.

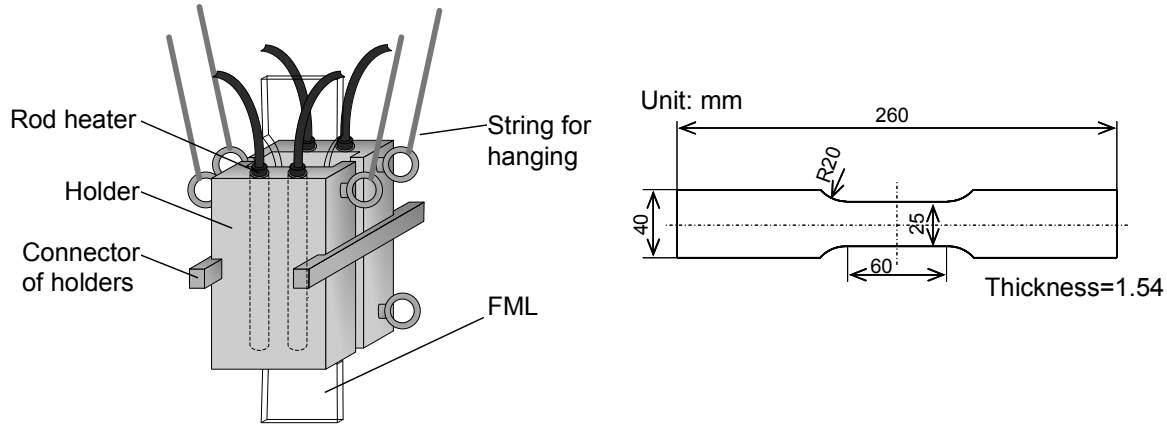

Figure 6: Schematic illustration of heating device and geometry of FML for tension test

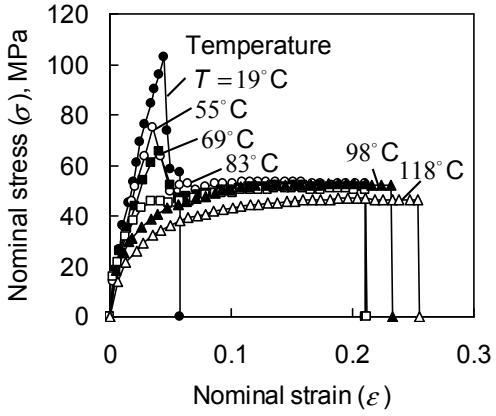

Figure 7: Effect of temperature on Stress-strain diagram for Case (2) with overlap length of 30 mm at 2nd stage of heating temperature

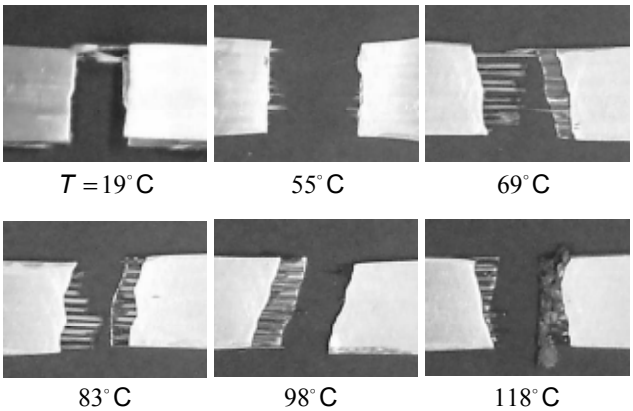

Figure 8: Effect of heating temperature on fracture mode of FML at 2nd stage

When the heating temperature T is at room temperature, the thermoplastic resin conveyed shear stress completely, the fibre bundles are tightly elongated so that tensile strength reached over 100 MPa and suddenly dropped due to rupture at the fibre bundles. With increase of heating temperature T, tensile strength decreased and total elongation increases. When the heating temperature is over 80 degrees, as the thermoplastic soften satisfactory, FML elongated more than 0.2 at nominal strain.

Figure 8 shows effect of heating temperature on fracture mode of FML at the 2nd stage of deformation. When the heating temperature T is lower than 60 degrees Celsius, the thermoplastic resin conveyed shear stress to fibre bundles, rupture occurred at the fibre bundles. On the other hand. The temperature T is over 60 degrees Celsius, the thermoplastic resin could not convey shear stress to the fibre bundles, and the bundles were pulled out from the resin.

4.2 Effect of overlap length on strength at 3rd stage

In order to verify the function of the proposed FML, Case (2), experiments were carried out by a strategy as explained in Fig. 1, which is composed of three stages, i.e. (1st stage) lamination, (2nd stage) forming under a heated condition and (3rd stage) tension test at room temperature. The geometry of test piece was the same as that shown in Fig. 6. Overlap length L_D was fixed at 20 mm.

At the 1st stage, FML was laminated at a temperature of 120℃, which melts the thermoplastic resin. At the 2nd stage, FML was elongated at a constant temperature of 120℃, after being re-heated by a heater which was mounted to the tension test machine as shown in Fig. 6. At the 3rd stage, FML was elongated again at room temperature and the stress-strain relationship was measured. Pre-elongation ΔL_p at the 2nd stage ranges from 0 to 18 mm against overlap length L_D of 20 mm.

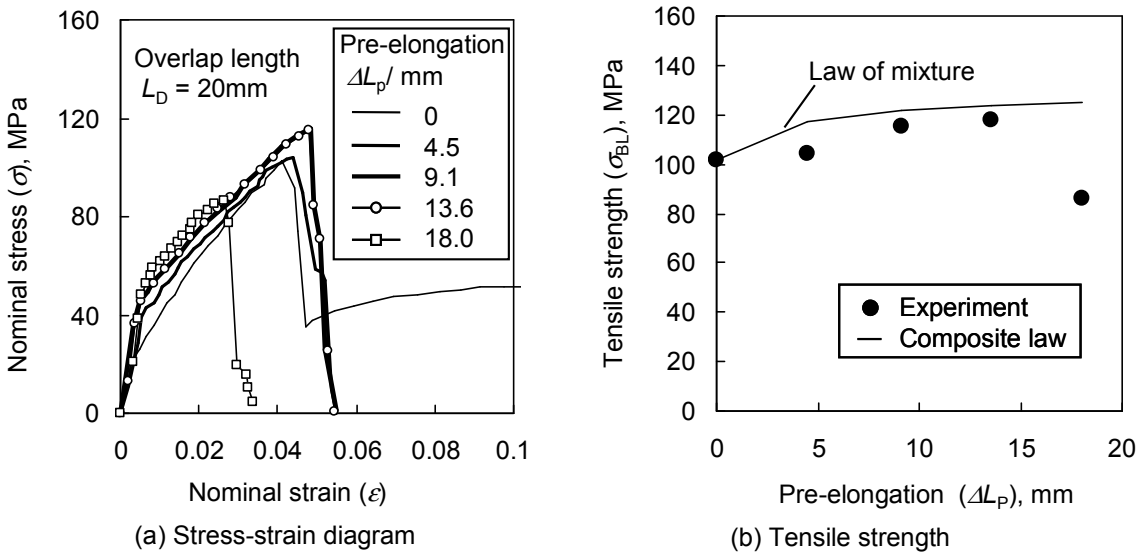

Figure 9: Effect of pre-elongation on mechanical properties of FML at 3rd stage of room temperature

According to the FEA result, which is not shown in the authors' previous paper [14], as the minimum bare length L_{DN} of the overlapped length should be around 8 mm, pre-elongation ΔL_p could be up to 12 mm (=20 - 8) while maintaining tensile strength. **Figure 9**(a) shows the effect of pre-elongation at the 2nd stage for a stress-strain diagram at the 3rd stage. Regardless of pre-elongation, stress increases with increase of strain and abruptly drops at some strain value. **Figure 9**(b) shows the effect of pre-elongation ΔL_p on tensile strength σ_{BL} of FML. With increase of pre-elongation ΔL_p, tensile strength σ_{BL} increases according to the law of mixture [16], up to ΔL_p =13.6 mm, which is almost equal to, but a little bit longer than predicted by FEA.

Judging from the result of the tension test and observation of rupture, the FML with proposed structure has a funct ion of being able to be elongated up to 9.1 mm at the 2nd stage while maintaining sound tensile strength and bonding condition at the 3rd stage. This ability of elongation and formability is much higher than other FML structures.

5 CONCLUSIONS

- A structure for FML was introduced, which is composed of reinforcing fibre bundles, thermoplastic resin as the matrix and metal plates.
- The reinforcing fibre bundles are discontinuous, and are intentionally overlapped in the longitudinal direction. The resin including fibre bundles was sandwiched between the metal plates.
- FEA results show that when overlap length is appropriately long, the axial stress of the fibre bundle has a distribution with two slopes. This would provide tensile strength of FML as high as a composite of continuous fibre bundles which comply with the law of mixture.
- The rupture would occur at the single-way-bundle part.
- On the other hand, when overlap length is short, the shear strength reaches the yield value on the boundary through the whole overlapping area. Rupture would occur on the boundary.
- Experimental results showed when FML is heated at appropriate temperatures at the second stage of deformation, it would be elongated much longer than conventional composites.
- Experimental results also showed FML has as high tensile strength with sound bonding condition as expected even after pre-elongation up to 9.1 mm against the parallel part of 60 mm, which is much longer than other structures of FML.

ACKNOWLEDGEMENT

The present paper benefited partially through association with Rockfield Software Limited, Wales, UK. The analysis part of this research work was expedited thanks to Drs Rance, Armstrong, Dutko and other members.

REFERENCES

[1] Kiuchi, M. Development of manufacturing technologies for ultra-fine grained steel sheets, Proc. of NAGOYA TUBE 2007, (2007) 9-23.

[2] Waterschoot, T., Verbeken, K., DE Cooman, B.C. Tempering kinetics of the martensitic

phase in DP steel, ISIJ Int, (2006) 46-1:138-146.
[3] Kaufmann, M., Zenkert, D., Mattei, C. Cost optimization of composite aircraft structures including variable laminate qualities, Compos Sci Technol, (2007) 67:357-366.
[4] O'higgins, R.M., Mccarthy, M.A., Mccarthy, C.T. Comparison of open hole tension characteristics of high strength glass and carbon fibre-reinforced composite materials, Compos Sci Technol, (2008) 68:2770-2778.
[5] Lee, J.S., Hong, S.J., Yu, WR., Kang, T.J. The effect of blank holder force on the stamp forming behavior of non-crimp fabric with a chain stitch, Compos Sci Technol, (2007) 67:357-366.
[6] Torralbaa, J.M., da Costab, C.E., Velasco, F. P/m aluminum matrix composites: an overview, J. Mater. Proc. Technol., (2003) 133:203-206.
[7] Mandal, D., Dutta, B.K., Panigrahi, S.C. Influence of mechanical working on properties of aluminium base short steel fiber reinforced composites, J. Mater. Sci., (2007) 42:8622-8628.
[8] Araki, Y., Suzuki, T., Hanatani, S. Composite material for automotive headliners - expandable stampable sheet with light weight and high stiffness-, JFE report, (2004) 4:77-82.
[9] Haque, E. Development of low density glass mat thermoplastic composites for headliner applications, SAE Technical Paper Series, SAE 2000 World Cong, (2006) 1:Detroit (USA), Paper no. 1129.
[10] Carrillo, J.G., Cantwell, W.J. Scaling effects in the tensile behavior of fiber-metal laminates, Compos Sci Technol, (2007) 67:1684-1693.
[11] Corte's, P., Cantwell, W.J. The prediction of tensile failure in titanium-based thermoplastic fibre-metal laminates, Compos Sci Technol, (2006) 66:2306-2316.
[12] Langdon, G.S., Cantwell, W.J., Nurick, G.N. The blast response of novel thermoplastic-based fibre-metal laminates - some preliminary results and observations, Compos Sci Technol, (2005) 65:861-872.
[13] Langdon, G.S., Nurick, G.N., Lemanski, S.L., Simmons, M.C., Cantwell, W.J., Schleyer, G.K. Failure characterisation of blast-loaded fibre-metal laminate panels based on aluminium and glass-fibre reinforced polypropylene, Compos Sci Technol, (2007) 67:1385-1405.
[14] Kuboki, T., Uematsu, S., Murata, M. Composite structure composed of overlapped fibre bundles, thermoplastic resin and metal plate for secondary forming process, Compos. Sci. and Technol., (2010) 70-9:1338-1345.
[15] de Souza Neto, E.A., Peric, D., Dutko, M., Owen, D.R.J. Design of simple low order finite elements for large strain analysis of nearly incompressible solids, Int. J. Solids Struct., (1996) 33-20-22:3277-3296.
[16] Kelly, A., Tyson, W.R. Tensile properties of fibre-reinforced metals: copper/tungsten and copper/molybdenum, J. Mech. Phys. Solids, (1965) 13:329-350.
[17] Kaneda, K., Watanabe, K. Japan Patent, (2007), P2007-30053A, in Japanese.

XI International Conference on Computational Plasticity. Fundamentals and Applications
COMPLAS XI
E. Oñate, D.R.J. Owen, D. Peric and B. Suárez (Eds)

ESTIMATION OF RESPONSE OF STEEL SHEET PLATED WITH THIN HARD LAYER

TAKASHI UCHIMURA*, TETSUYA YAMAMOTO†, MASAYOSHI AKIYAMA††

* Department of Mechanical and System Engineering
Kyoto Institute of Technology (KIT)
Goshokaido-cho, Matsugasaki, Sakyo-ku, Kyoto, 606-8585, Japan
email: m1623008@edu.kit.ac.jp, www.mesh.kit.ac.jp

† Product Engineering Group, Manufacturing Division, Semicon System Business Unit,
Canon Machinery Inc.,
85 Minami Yamada-cho, Kusatsu-shi, Shiga 525-8511, Japan
email: te-yamamoto@canon-machinery.co.jp

†† Department of Mechanical and System Engineering
Kyoto Institute of Technology (KIT)
Goshokaido-cho, Matsugasaki, Sakyo-ku, Kyoto, 606-8585, Japan
email: akiyama@mech.kit.ac.jp, www.mesh.kit.ac.jp

Key words: Elastic-Plastic Response, Steel Sheet, Thin Hard Layer, Plated Layer, Cantilever.

Abstract. Elastic and elastic-plastic responses were examined of cantilevers made from a cold rolled steel sheet and made from the same sheet plated with a thin hard layer. Tension test of these sheets showed a non-linear behaviour even in the area of small strain and conventional linear theory of cantilever had to be modified. By extending this theory to a sheet plated with a thin hard layer Young's modulus of plated layer was estimated. The range of estimated Young's modulus was similar to those in previous works but material non-linearity, especially on the compression side, must be measured more precisely.

1 INTRODUCTION

Metallic materials such as steels are deemed to be a linear elastic body at the beginning stage of its deformation and to deform plastically as soon as the stress reaches the intrinsic yield limit of the material [1]. However, precise observation showed that microscopic plastic deformation influences the macroscopic elastic response even after annealing and the elastic stress-strain curve becomes slightly non-linear [2]. Numerical investigation was carried out on this phenomenon by using homogenization method [3]. It is known for a metallic material that the Young's modulus decreases after plastic deformation [4] and for inverse loading this phenomenon is known as the Bauschinger's effect [5]. The response after plastic deformation is seemingly linear elastic but precise observation shows that the response is non-linear [6,7]. In the present work influence of this intrinsic non-linearity of material is evaluated on the response of bulk material with and without a thin hard coated layer taking an example on a bending experiment of a cantilever. Finally the Young's modulus of a thin hard coated layer is estimated on an assumption that the response of base material is non-linear.

2 BASIC EXPERIMENT

2.1 Theory

It is assumed in tension test that specimen of uniform cross sectional area in the axial direction elongates uniformly under the tensile force F. When the loading is on the linear elastic stage Young's modulus E is the coefficient that links stress σ, which is the force F divided by cross sectional area, and strain ε, which is the elongation per unit length in the axial direction. Schematic illustration is given in Figure 1. The stress-strain relationship is written by equation (1).

$$\sigma = E \cdot \varepsilon \tag{1}$$

If the specimen has a thin plated layer of a different material on the surface the force undertaken by two materials are F_b and F_p as it is illustrated in Figure 1. The distributions of stress for these two cases are illustrated in Figure2. If the materials of plated layer and the base are the same the distribution of stress is uniform in the cross section but if the Young's modulus of the hard layer is higher the stress is higher in the hard layer than in the base.

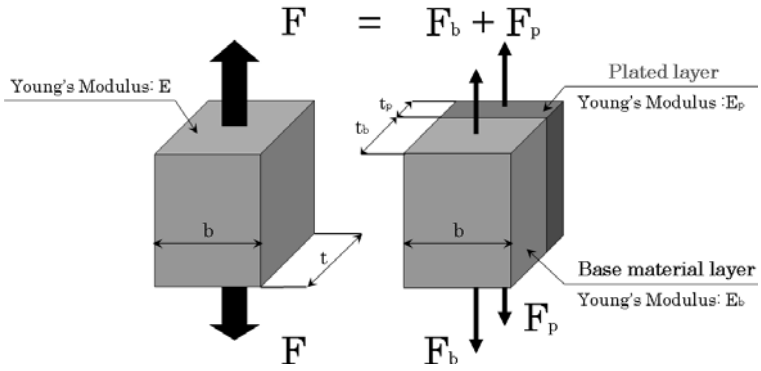

Figure 1: Schematic illustration of responses of specimens with and without thin hard plated layer

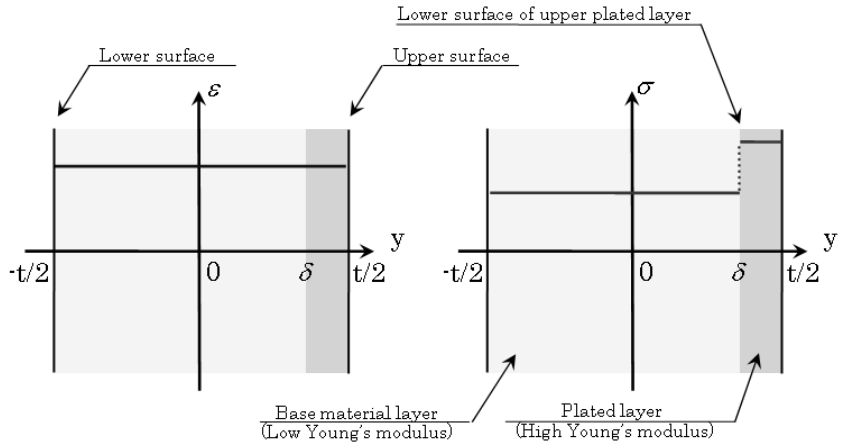

Figure 2: Schematic comparison of distribution of stress in specimens with and without thin plated layer

The average Young's modulus E_a of the whole material with a plated layer can be calculated by equation (2)

$$Ea = (Eb + Ep (tp / tb)) / (1 + (tp / tb)) \quad (2)$$

where E_b, E_p, t_b, t_p are the Young's module and the thicknesses of the base and the hard plated layer respectively. It is easy to understand that E_a is nearly equal to E_b if t_p is much smaller than t_b, and the value E_a obtained by tension test may give a considerably precise value of E_b regardless of the Young's modulus E_p of the hard plated layer.

2.2 Tension test

Tension tests were carried out on small specimens with and without a thin hard plated layer in a manner shown in Figure3. A couple of strain gauges of which gauge length was 0.3mm were placed at the centre of specimen. The major concern was the elastic response or a nearly elastic response and the tension test was stopped when the stress was estimated to reach the yield limit. The thickness of base sheet was a cold-rolled steel sheet with 0.8mm in thickness and the thickness of plated CrN layer was 2 μm, and the value of t_p / t_b is 0.0025, which is small enough to grant that E_a is nearly equal to E_b in equation (2). The results of base sheet and plated sheet are shown in Figure 4.

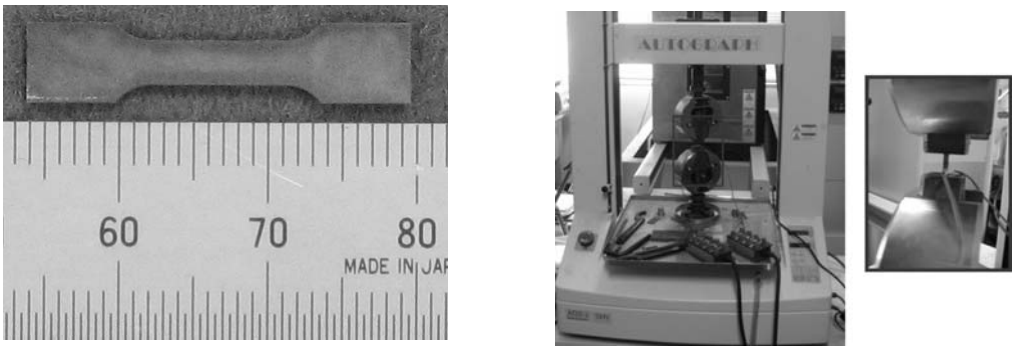

Figure 3: Specimen geometry and view of tension test

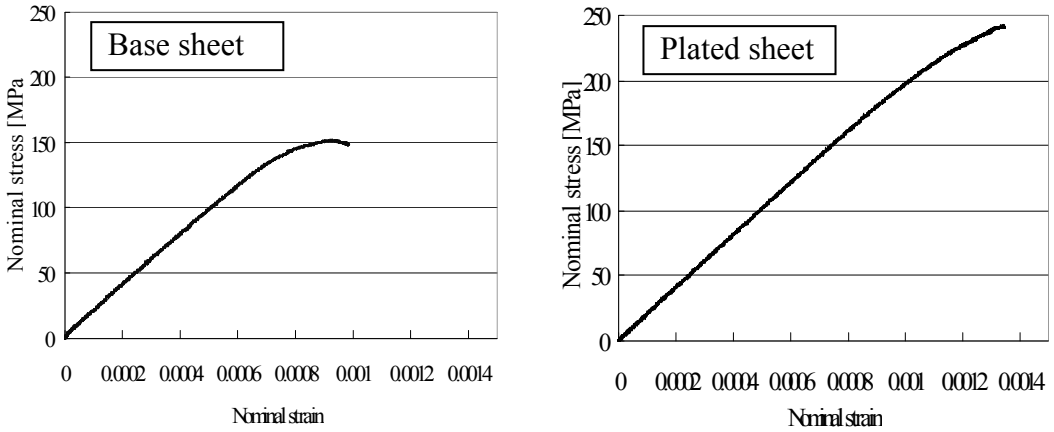

Figure 4: Stress-strain curves of specimens with and without thin hard plated layer

The stress-strain curve of the base sheet in Figure 4 can be deemed linear but detailed observation shows that it is non-linear. Piecewise measurement of the tangent of this curve showed that the tangent gradually decreases according to the increase in strain. The result is indicated in Table 1. After annealing treatment the Young's modulus of steel may lie usually between 200 and 210 MPa and the tangent for the lowest strain range in Table 1 may be an appropriate value. It is known that the Young's modulus decreases according to the increase in plastic strain [4,5] and the tendency of the change in the tangent value in Table 1 suggests that similar phenomenon can be observed depending upon the range of strain adopted for calculating the Young's modulus.

Table 1: Piecewise tangent values of stress-strain curve of base sheet

Range of strain	0.0000-0.0002	0.0002-0.0004	0.0004-0.0006	0.0006-0.0008
Tangent (MPa)	207	189	180	144

The response of the base sheet is not that of linear elastic material but it is non-linear when a wide range of strain is taken. It is only a phenomenological approach but it is curious to note that the stress-strain relationship is well expressed by equation (3)

$$\sigma = a\ (\varepsilon)^2 + b\ \varepsilon \tag{3}$$

where σ and ε are stress and strain, and a and b are coefficients [7]. Examples of the values of a and b are shown by equations (4) and (5) for a case such that the range of strain is 0.0 and 0.0008. The maximum difference between the measured stress and the calculated stress by equation (3) was 1 MPa and the approximation may be fairly good.

$$a = -4.48\times 10^{7} \tag{4}$$

$$b = 2.16\times 10^{5} \tag{5}$$

The base sheet can be granted a non-linear elastic material, but it can be granted an elastic-plastic material as it was suggested by using the homogenization method [8]. The base sheet can be granted this kind of material, i.e. linear elastic material under the strain of 0.0002 and plastically deforms after that with an extremely high work-hardening ratio until the value of strain reaches 0.0012. Linear elastic approach may be useful when one simulates the behaviour of base sheet under loading, but elastic-plastic approach may be useful depending upon the problem that one simulates.

Compared to the stress-strain curve for base sheet the curve for a plated sheet seems to be straight in Figure 4. The piecewise tangent values of this curve is indicated in Table 2. The plated sheet shows harder response than the base sheet. It is assumed that the plating operation might have given heat to the base sheet and the heat affected the recovery of Young's modulus [4]. It depends upon the accuracy required on the predicted result but it can be possible to grant the plated sheet a linear elastic body.

Table 2: Piecewise tangent values of stress-strain curve of plated sheet

Range of strain	0.0000-0.0002	0.0002-0.0004	0.0004-0.0006	0.0006-0.0008
Tangent (MPa)	209	199	199	196

3 THEORY OF BENDING

3.1 Linear elastic body

In the conventional theory of elastic bending of a cantilever strain is defined by equation (6) [9], where y, η and ρ are coordinate value in the thickness direction, the coordinate value of neutral plane and the radius of curvature of the neutral plane respectively. If the cantilever is a linear elastic body the axial stress σ is related to strain ε as given by equation (7) via the Young's modulus E.

$$\varepsilon = (y - \eta)/\rho \tag{6}$$

$$\sigma = E \cdot \varepsilon \tag{7}$$

By solving two equations (8) and (9) for the equilibriums of axial force and moment in a cross section the values of η and ρ are determined, where h, A and w are half thickness, cross sectional area and width of cantilever, and M is the moment by the external force exerting at the top of cantilever. The deflection of cantilever the can be calculated by using the values of E, η and ρ.

$$\int_{-h}^{h} \sigma \, dA = \int_{-h}^{h} (E \cdot (y - \eta)/\rho) \, w \, dy = 0 \tag{8}$$

$$\int_{-h}^{h} \sigma \cdot (y - \eta) \, dA = \int_{-h}^{h} (E \cdot (y - \eta)^2/\rho) \, w \, dy = M \tag{9}$$

The moment is calculated by equation (10) where F, L and x are the external force exerting on the free end of cantilever, the length of cantilever and the axial position of cross section after taking the origin at the fixed end of cantilever respectively.

$$M = F \cdot (L - x) \tag{10}$$

For a plated sheet equations (8) and (9) are modified as shown in (11) and (12), where k, Eb and Ep are the y-coordinate value of the boundary of the base and the plated layer and the elastic module of the base and the plated layer. In a manner similar to that for a linear elastic material the deflection is calculated.

$$\int_{-h}^{k} (E_b \cdot (y - \eta)/\rho) \cdot w \, dy + \int_{k}^{h} (E_p \cdot (y - \eta)/\rho) \cdot w \, dy = 0 \tag{11}$$

$$\int_{-h}^{k} (E_b \cdot (y - \eta)^2/\rho) \cdot w \, dy + \int_{k}^{h} (E_p \cdot (y - \eta)^2/\rho) \cdot w \, dy = M \tag{12}$$

When the Young's modulus E_p of the plated layer is unknown and that of the base sheet E_b is known, it is possible to determine the value by carrying out a bending experiment to measure the deflection of cantilever.

3.2 Non-linear body

If the base material reveals a non-linear behaviour described by equation (3), the equilibrium equations of axial force and moment corresponding to equations (8) and (9) are given by equations (13) and (14). What is important here is that it is not specified whether the material is an elastic body or not. Similarly to the elastic material η and ρ are determined by solving these two equations, and the deflection of cantilever is calculated.

$$\int_{-h}^{h} (a \cdot (y - \eta)^2/\rho^2 + b \cdot (y - \eta)/\rho) \, w \, dy = 0 \tag{13}$$

$$\int_{-h}^{h} (a \cdot (y - \eta)^3/\rho^2 + b \cdot (y - \eta)^2/\rho) \, w \, dy = M \tag{14}$$

4 BENDING TEST

Bending tests of a cantilever was carried out by using the base sheet of which thickness was 0.8mm and the sheet with a plated layer of CrN of which thickness was 2 μ m. The size of specimen was 5mm in width and 150mm in length. Two pieces of cantilever of the same dimensions were sectioned from the parent sheet to check the repeatability. End portion of 20mm in length was sandwiched in between heavy steel blocks and weight was loaded on the other end in an incremental manner. The view of experiment is shown in Figure 5.

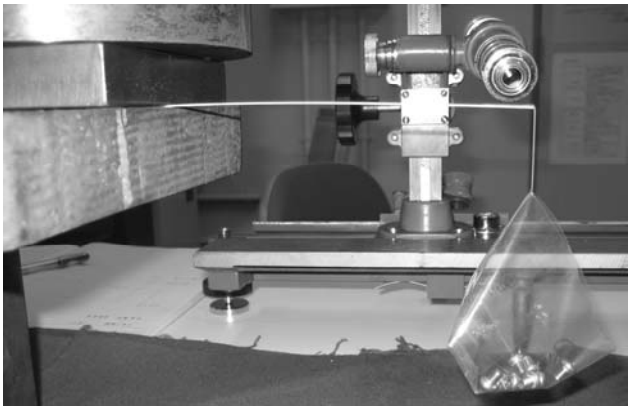

Figure 5: View of bending experiment of cantilever

5 RESULTS

The deflection of cantilever is plotted against the weight in Figure 6. Good repeatability is observed between the two cantilevers and between the cases when the front side of the sheet was used upward and when the back side was used upward. If the basic equations (12) and (13) of linear elasticity are used and the Young's modulus is 209 GPa in Table 2 the maximum deflection of the top end must be 6.2 mm which is much less than the measured value in Figure 6.

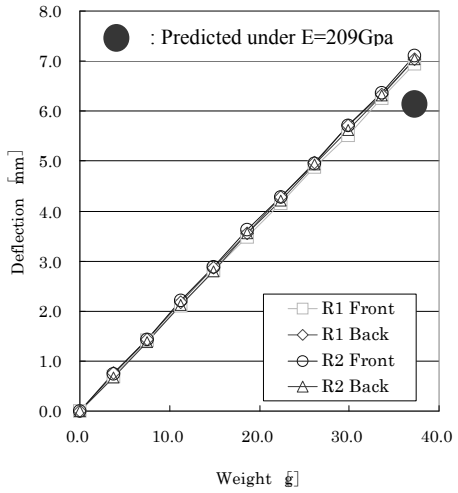

Figure 6: Responses of parent sheet

It is shown in the references [4, 5, 6] the Young's modulus of a plastically deformed material on the reverse loading side is smaller. If smaller value of Young's modulus is adopted on the compression side the discrepancy between the predicted and the measured deflections becomes smaller. The value of Young's modulus on the compression side may be slightly below 160GPa, but it is recommended to measure it by experiment.

For the sheet with a thin hard layer of CrN bending experiment was carried out in the same manner. The measured Young's modulus was 209 GPa as it was shown in Table 2 and the predicted deflection of the top end of cantilever never meets the measured deflection when the maximum weight of 37.3g was applied. If a value about 160 GPa is given to the Young's modulus on the compression side of the base steel of the plated sheet the estimated Young's modulus may lie within a range of 300 and 650 GPa. In order to determine the precise value of the Young's modulus of thin layer of CrN it is necessary to carry out a compression test of plated sheet to know the Young's modulus of the plated sheet.

6 DISCUSSIONS

If the material shows a non-linear behaviour use of equations (3), (4), (5), (13) and (14) may be recommended, but in the present work elastic-plastic FEA was carried out on the bending of a cantilever of base sheet assuming that the material behaves elastically when the strain is under 0.0002 and plastically deforms after that as it was indicated in Table 1. The results are shown in Figure 7. The software used for the analyses was ELFEN [10] developed at University of Wales. Basically the stress-strain curves on tension and compression sides are regarded as point symmetry and the Young's modulus has the same values both on the tension and compression sides. The difference in the deflection at the top was 14% smaller for linear elastic body than elastic-plastic body, but the difference was still large. Measurement of compressive S-S curve is necessary.

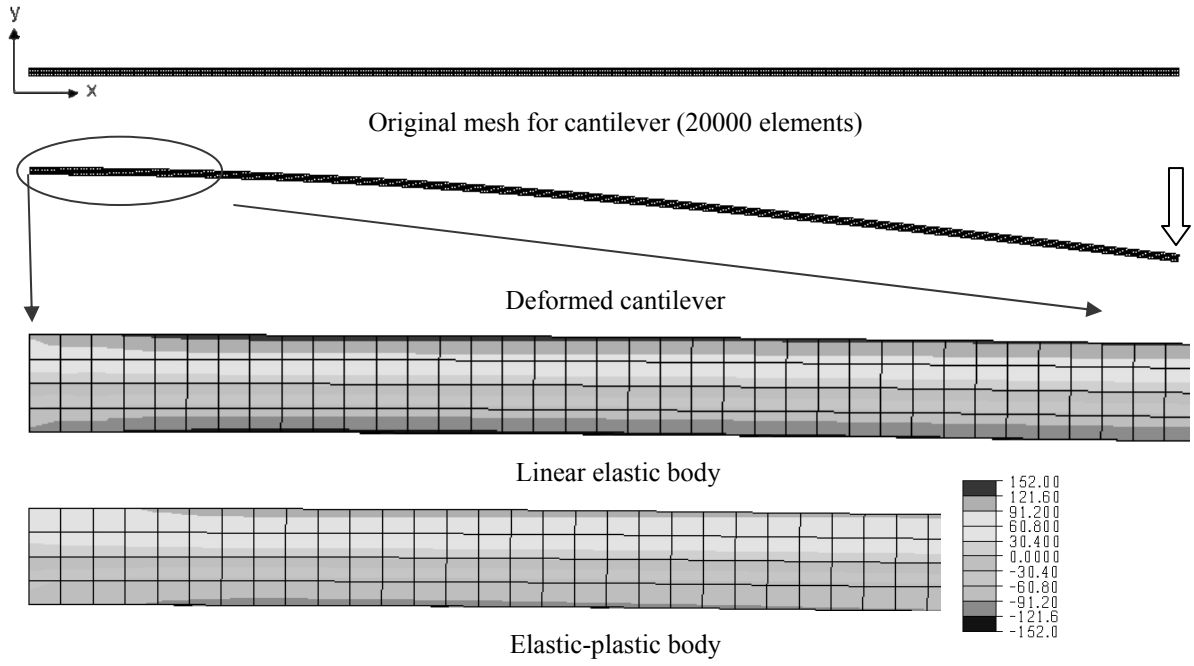

Figure 7: Comparison of axial stress levels in response of bending of base sheet

7 CONCLUSIONS

The stress-strain curve of a cold-rolled steel sheet was measured by a tension test and the response of cantilever made of the sheet was predicted assuming the sheet as linear elastic and elastic-plastic bodies. Assumption of linear elastic body gave smaller deflection at the top of the cantilever than that of the experimental result. Even when the deflection is predicted on the assumption such that the sheet is an elastic-plastic body with extremely high work-hardening ratio the difference was still large. It was assumed that the key to the precision of prediction was the measurement of the Young's modulus or the stress-strain curve on the compression side. When a smaller value of Young's modulus is given on the compression side than the tension side the predicted value came closer to the measured value. By using this technique for predicting the deflection the Young's modulus of a thin plated layer of CrN on the steel sheet was estimated to give a moderate value.

NOTE

Some part of this research work was carried out by Mr. Tetsuya Yamamoto, the second author when he was a student in Kyoto Institute of Technology and this paper has nothing to do with his present work at his present affiliation Canon Machinery Inc..

REFERENCES

[1] Hill, R. *The Mathematical Theory of Plasticity*, Clarendon Press, Oxford, (1950).
[2] Luong, M.P., Fatigue limit evaluation of metals using an infrared thermographic technique, *Mech. Mater.* (1988) **28**:155-163
[3] Akiyama, M., Matsui, K. and Terada, K. Analysis of Microscopic Yielding Behaviour of Carbon Steel under Macroscopic Loading, *Tetsu-to-Hagane*, (2005) **91**:803-808 (in Japanese)
[4] Yamaguchi, K., Adachi, H. and Takakura, N. Effects of Plastic Strain and Strain Path on Young's Modulus of Sheet Metals, *Met. Mater.* (1998) **4**:420-425
[5] Iida, K. and Akiyama, M. Influence of plastic strain history on Young's modulus, *COMPLAS-X* (2009), 449
[6] Bauschinger, J. Ueber die Veraenderung der Elasticitaetsgrenge und der Festigkeit des Eisens und Stahls durch Strechen und Quetschen, durch Erwaermen und Abkuehlen und durch oftmal wiederholte Beanspruchung., *Mitt. Mech.-Tech Lab., Muenchen* (1886) **XV**:1-116
[7] Akiyama, M., Kobayashi, K. and Nakai T. Optimum Design of Roll Radius for Tube Benging, *The Sumitomo Search* (1989) **40**:71-80
[8] Matsui, K., Terada, K., Akiyama, M., Kuboki, T. and Oikawa, K. Mechanism of the Bauschinger Effect by the Multi-Scale Modeling, *J. of JSME (A)*, (2002) **68**:1559-1566 (in Japanese)
[9] Timoshenko, S. and Goodier, J.N. *Theory of Elasticity*, McGraw Hill (1951)
[10] Rockfield Software Limited, *http://www.rockfield.co.uk/*

XI International Conference on Computational Plasticity. Fundamentals and Applications
COMPLAS XI
E. Oñate, D.R.J. Owen, D. Peric and B. Suárez (Eds)

ESTIMATION OF SPRINGBACK OF STAINLESS STEEL SHEET PART TAKING INFLUENCE OF ANISOTROPIC PROPERTY OF PLASTIC-DEFORMATION-DEPENDENT YOUNG'S MODULUS INTO ACCOUNT

KUNIO HAYAKAWA[*], KENTARO SAWANO[*], TAMOTSU NAKAMURA[*]
YOSHIHIRO KUBOTA[*], YASUO NANBA[†] AND YUSUKE TABUCHI[†]

[*] Department of Mechanical Engineering
Shizuoka University
3-5-1 Johoku, Naka-ku 432-8561, Hamamatsu, Japan
e-mail: tmkhaya@ipc.shizuoka.ac.jp

[†] Calsonic Kanse Co.Ltd.
2-1917 Nisshin-cho, Kita-ku, Saitama 331-0823, Japan

Key words: Sheet metal forming, Springback, Stainless steel sheet, Yoshida-Uemori model.

Abstract. A kinematic hardening model proposed by Yoshida and Uemori (Y-U model) was applied to the prediction of springback of stainless steel sheet part. From the experiments for the determination of the material constants, an anisotropic property of change in Young's modulus was observed; namely, the anisotropy was different at 0°, 45° and 90° from the rolling direction. The Y-U model for the stainless steel sheet was used to a calculation of a forming process of a part to examine the accuracy of the prediction of the springback by compar-ing the calculated result with the actual part formed. In order to consider the anisotropic property of change in Young's modulus, the calculated result to the actual part formed. In order to consider the anisotropic property of the change in Young's modulus, the calculations were performed using the different material constants at 0°, 45° and 90° from the rolling direction. With the material constants at 90° from the rolling direction, which was the direction of springback of the part, the prediction accuracy can be improved. Therefore, the consideration of the anisotropic property of the change in Young's modulus was found to be effective for more accurate prediction of the springback of the stainless steel part.

1 INTRODUCTION

Stainless steel sheets have been commonly used for automobile exhaust parts due to the excellent feature of corrosion resistance, heat resistance and design. The sheet metal part has become complicated in geometry and forming process due to the current demand of the strength and the lightness as an automobile part. Therefore, finite element analysis has widely used effectively nowadays for designing a sheet metal forming process. However, the precise prediction of springback has still been open problem. Many researches have been reported on the improvement of the accuracy. It is well known nowadays that the plastic constitutive

model developed by Yoshida and Uemori (Y-U model) can furnishes more accurate prediction of springback in the case of sheet metal forming of high-strength steel than conventional isotropic or kinematic hardening models in FE analysis [1-4].

In the present paper, the Y-U model was applied the part by stainless steel sheet for more presice prediction of the springback. First, the experiments of the materials were performed to determine the material constants used in the Y-U model. From the experiments, the anisotropic behavior of plastic-deformation-dependent Young's modulus in which the apparent Young's modulus decreases after preloading was confirmed in stainless steel sheet. Therefore, a method of calculation considering of the anisotropic property of the change in Young's modulus in Y-U model was examined by comparing the calculated results of springback with actual sheet metal part.

2 EXPERIMENTAL METHOD FOR TENSILE-COMPRESSIVE BEHAVIOR OF SHEET METAL

Several experiments have been reported for the tensile-compressive behavior of sheet metal without buckling under compressive loading [1, 5]. In the present paper, an electro-hydraulic controlled fatigue testing machine SHIMADZU Servopulser EHF-EV 100KN/TV 1KN/m-A20 was used for tensile-compressive tests of the materials. Figure 1 shows the geometry of specimen used for tensile-compressive tests. Figure 2 show Schematics of setup for tensile-compressive tests of stainless steel sheet. The specimen was clamped between clamp A, B and clamp C, D in order to prevent buckling. The extensometer SHI-MADZU SG10-100 was used with a jig shown in Figure 2 to measure the elongation of the specimen from the thickness direction without touching the clamps. The material used was SUS304 and SUS430. The angles of loading direction of the specimen were at 0°, 45° and 90°from the rolling direction (RD).

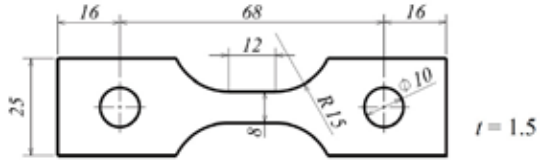

Figure 1: Geometry of specimen (unit: mm)

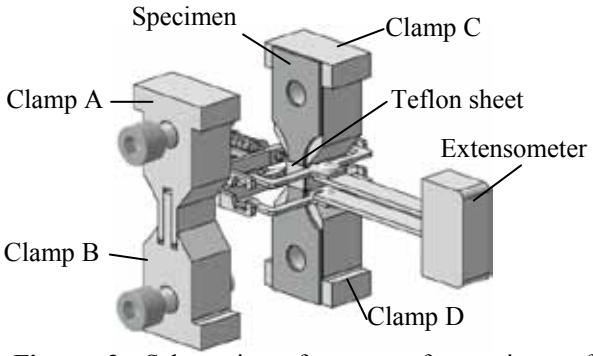

Figure 2: Schematics of setups of experiment for tensile-compressive tests of stainless steel sheet.

Figures 3 and 4 show experimental results of tensile tests of SUS304 and SUS430. Figure 5 shows a result of tensile-compressive loading test of SUS304, in which strain was subjected to 2.5%→-2.5%→5%→-5%. Figure 6 shows a result of loading-unloading tests of SUS304 for the evaluation of plastic-deformation-dependent Young's modulus.

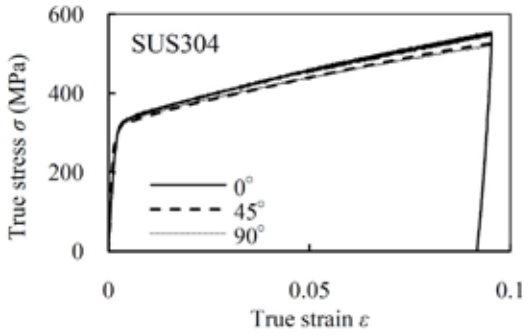

Figure 3: Stress- strain curves of SUS304 loading

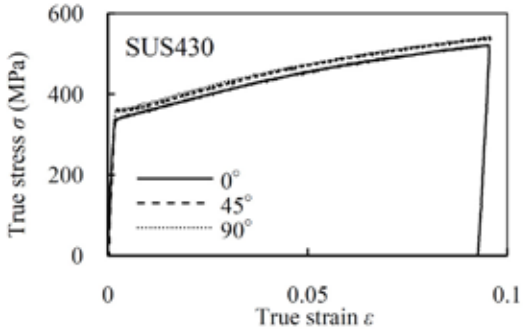

Figure 4. Stress-stain curves of SUS430 under tensile under tensile loading

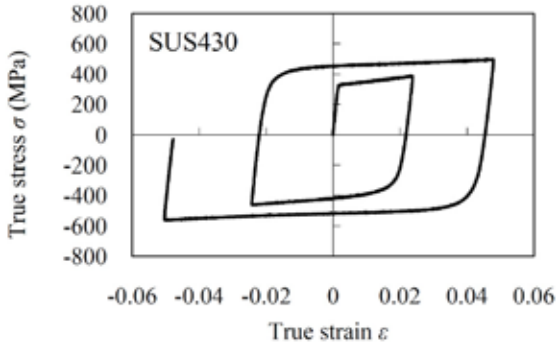

Figure 5. Stress-strain curve of SUS430 under tensile-compressive test

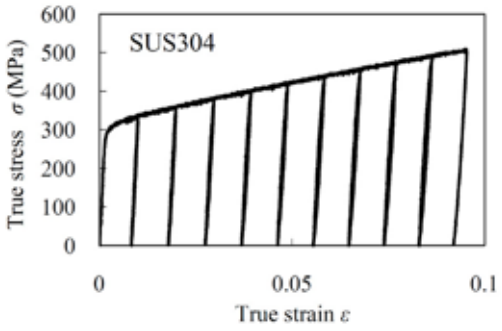

Figure 6. Result of loading-unloading tests of SUS304

3 ANISOTROPIC PROPERTY OF PLASTIC-DEFORMATION-DEPENDENT YOUNG'S MODULUS

Anisotropic property of plastic-deformation-dependent Young's modulus is a phenomenon in which apparent Young's modulus after plastic deformation decreases with the increase of equivalent plastic strain.

Figures 7 and 8 show the change in Young's modulus E_{av} as a function of equivalent plastic strain of SUS304 and SUS430. Moreover, for the sake of comparison, the change in Eav of high tensile strength steel sheet JSC980YN is shown in Figure 9. The stress range of stress used for the calculation of E_{av} was $0 \leq \sigma \leq 0.95\sigma_0$, where σ_0 is the stress from which the unloading began.

In case of JSC980YN, it seems that plastic-deformation-dependent Young's modulus is almost isotropic. In case of SUS304 and SUS430, however, the anisotropic behaviors in change in the E_{av} were observed obviously. For SUS430, the dependence tendency at 45° is the same as the tendency at 90°, only the tendency at 0° is different from the others. On the other hand, for SUS304, the different tendency was observed in the range of $0 \leq \overline{\varepsilon^p} \leq 0.04$ in each specimen. As the strain become larger, only the tendency of at 45° is different from at 0° and 90°.

In the Y-U model, the Eav can be given in the following expression using initial Young's

modulus E_0 and its asymptotic value E_a:

$$E_{av} = E_0 - \left(E_0 - E_a\right)\left\{1 - \exp\left(-\xi\overline{\varepsilon^p}\right)\right\} \tag{1}$$

where, ξ is a material constant. Material constants for equation (1) at 0°, 45° and 90° from the RD were obtained as shown in Table 1.

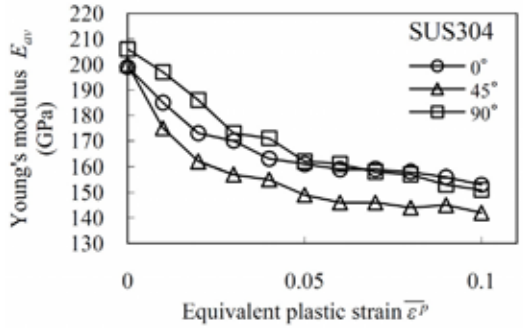

Figure 7: Change in plastic-deformation-dependent Young's modulus of SUS304

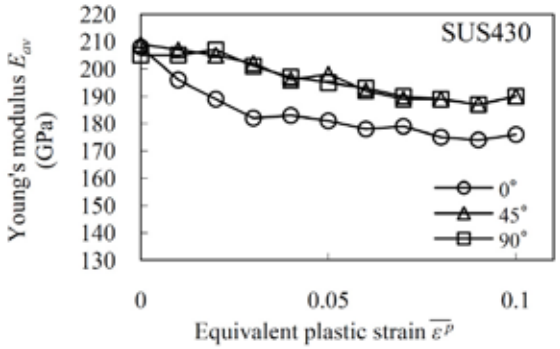

Figure 8: Change in plastic-deformation-dependent Young's modulus of SUS430.

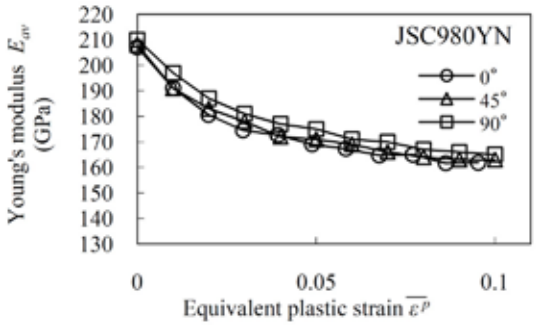

Figure 9. Change in plastic-deformation-dependent Young's modulus of JSC980YN.

Table 1: Material constants for change in Young's modulus

Material	Loading direction	E_0 (GPa)	E_a (GPa)	ξ
SUS304	0°	203	154	40
	45°	200	143	40
	90°	206	148	20
SUS430	0°	208	175	40
	45°	209	183	17
	90°	212	183	18

4 MATERIAL CONSTANTS OF HARDENING MODEL OF Y-U MODEL

In the present study, the calculation was performed using the Y-U model that can represent the work hardening stag-nation, plastic-deformation-dependent cyclic hardening and plastic-deformation-dependent Young's modulus. In Y-U model, the yield surface f and the bounding surface F are expressed by the following equation:

$$f = \phi\left(\boldsymbol{\sigma}, \boldsymbol{\alpha}\right) - Y = 0 \tag{2}$$

$$F = \phi\left(\boldsymbol{\alpha}, \boldsymbol{\beta}\right) - \left(B + R\right) = 0 \tag{3}$$

where ϕ is the function expressing equivalent stress, Y is the radius of f, $\boldsymbol{\alpha}$ is the center of f, $\boldsymbol{\beta}$ is the center of F, B is the initial radius of F, and R is the amount of isotropic hardening of F.

For the type of *f*, the anisotropic yield function by Hill in 1948 (Hill '48-type) was assumed.

The backstress $\boldsymbol{\alpha}^*$ expressing the relative kinematic motion of the center of *f* against the center of *F* is given by

$$\boldsymbol{\alpha}^* = \boldsymbol{\alpha} - \boldsymbol{\beta} \tag{4}$$

The evolution equation of $\boldsymbol{\alpha}^*$, $\boldsymbol{\beta}$ and *R* is given by

$$d\boldsymbol{\alpha}^* = C\left[\left(\frac{a}{Y}\right)(\boldsymbol{\sigma}-\boldsymbol{\alpha}) - \sqrt{\frac{a}{\overline{\alpha^*}}}\boldsymbol{\alpha}^*\right]\overline{d\varepsilon^p} \tag{5}$$

$$\overline{\alpha^*} = \sqrt{(3/2)\boldsymbol{\alpha}^* : \boldsymbol{\alpha}^*} \tag{6}$$

$$a = B + R - Y = (B - Y) + R = X_{sat} + R \tag{7}$$

$$d\boldsymbol{\beta} = m\left[\left(\frac{b}{Y}\right)(\boldsymbol{\sigma}-\boldsymbol{\alpha}) - \boldsymbol{\beta}\right]\overline{d\varepsilon^p} \tag{8}$$

$$dR = m(R_{sat} - R)\overline{d\varepsilon^p} \tag{9}$$

where $\overline{d\varepsilon^p}$ is the equivalent plastic strain increment, *C*, *b*, R_{sat} and *m* are material constants. *C* has two values C_1 and C_2. The C_1 is used only the visitnity of the initial yielding, then it switches to $C = C_2$ in the subsequent deformation [2]. The material constants are determined so that calculation can express the experimental results of tensile-compressive test as shown in Table 2.

The Lankford value for SUS304 and SUS430 was also obtained as shown in Table 3 in order to represent the anisotropic property of the materials.

Table 2: Material constants of hardening model of Y-U model

Material	*Y* (MPa)	X_{sat} (MPa)	C_1	C_2	*b* (MPa)	R_{sat} (MPa)	*m*
SUS304	284	26	260	135	150	540	4
SUS430	300	50	260	280	60	230	10

Table 3: Lankford values

Material	0°	45°	90°
SUS304	0.989	1.089	0.932
SUS430	1.202	0.951	1.632

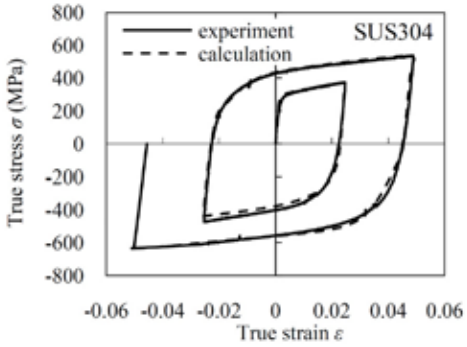

Figure 10. Comparison between experiment and analysis of SUS304 under tensile-compressive loading.

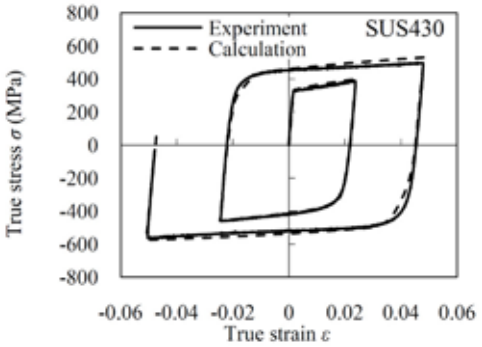

Figure 11. Comparison between experiment and analysis of SUS430 under tensile-compressive loading

Figures 10 and 11 show the comparison between experimental and calculated results of tensile-compressive loading using Y-U model with the material constants in Tables 2 and 3 of SUS304 and SUS430. The calculated results show good agreement with the experiments in both SUS304 and SUS430.

5 COMPARISON OF SPRINGBACK OF ACTUAL SHEET METAL PART WITH CALCULATION

Forming-springback analyses were performed by the part a using a finite element software ESI PAM-STAMP2G with the shell element. Forming process analysis was performed by stamping a blank sheet with a punch and a die by moving the die to the punch. The thickness of sheet metal is 1.5mm, Blank holder force (BHF) is 100kN, and Coulomb friction coefficient μ was set as 0.08.

Although the anisotropic characteristics on the change in Young's modulus was observed in stainless steel sheet from the experiments, equation (1) cannot express such anisotropy in single calculation. Therefore, in the present paper, three calculations were performed using material constants on the change in Young's modulus at 0°, 45° and 90°as shown in Table 1. The direction that springback of the part occur was at almost 90° from the RD, as the longitudinal direction of the part was along to RD. In the present case, therefore, the accuracy can be expected to be highest at the calculation by the material constants at 90°.

Prediction accuracy evaluation was performed by comparing the radius of curvature ρ_A and ρ_B of the calculated and the actual part formed at each section along the longitudinal direction in every 5 mm as shown in Figure 12. The 3-dimensional digital laser measurement system Konica-Minolta VIVID-9i was used for the measurement of the geometry of the actually formed part.

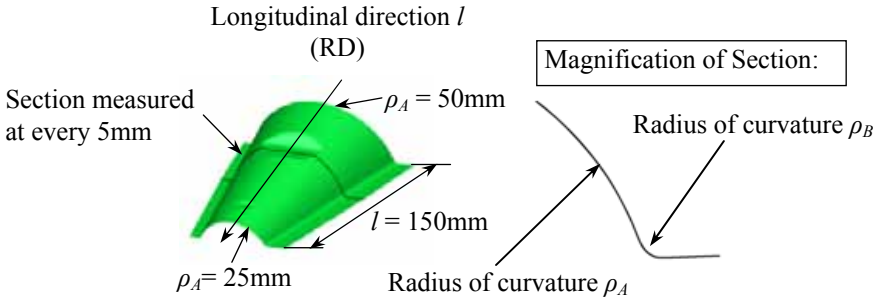

Figure 12. Shape of Part and Radius of curvature measured.

Figures 13 to 16 show the comparison of the values between calcualted and actual part in SUS304 and SUS430. The calculated result using the material constants of 90 from RD show the higher accuracy than the others. In the present case, the direction in which the springback occur is almost 90° from RD as expected. For SUS430 in Figures 15 and 16, the large difference can be observed. This is because the difference of the Young's modulus at 0 and 90 was significant as shown in Figure 8. From the results, the consideration of the anisotropic property of the change in Young's modulus was found out effective for more accu-rate prediction of the springback of the stainless steel sheet.

6 CONCLUSIONS

The normal text should be written single-spaced, justified, using 12pt (Times New) Roman in one column. The first line of each paragraph must be indented 0.5cm. There is not inter-paragraph spacing.

The Y-U model was applied to stainless steel sheet SUS304 and SUS430 for more precise prediction of springback. From the tensile-compressive loading test for determination of the material constants of the Y-U model, the anisotropic property of plastic-deformation-dependent Young's modulus and the tendency was shown. Moreover, influence of consideration of the anisotropic property of the change in Young's modulus was investigated by com-paring calculated result with the actual part formed. The following results were obtained:

1. The anisotropic characteristics on Plastic-deformation-dependent Young's modulus were shown in SUS304 and SUS430. In SUS430, the dependence tendency at 45° is the same as the tendency at 90°, only the tendency at 0° is different. In SUS304 each tendency shows different tendency.
2. The consideration of the anisotropic property of the change in Young's modulus in the Y-U model was found out to be effective for more accurate prediction of the springback of the stainless steel sheet.

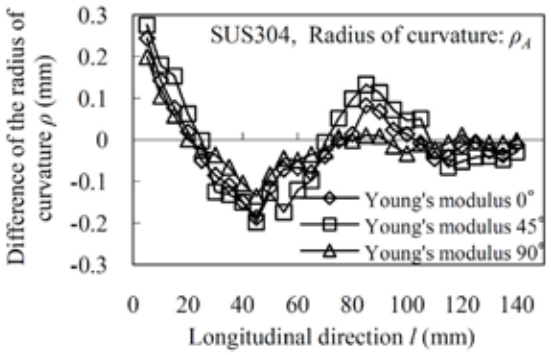

Figure 13: Difference of radius of curvature between experiment and analysis (SUS304, ρ_A)

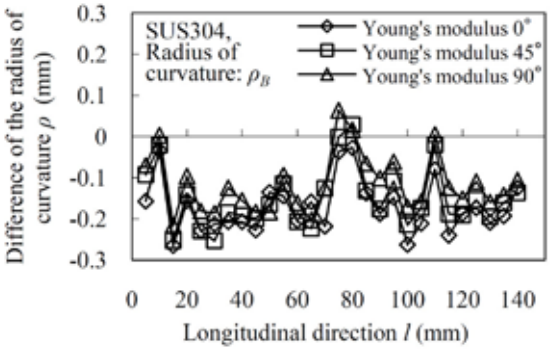

Figure 14: Difference of radius of curvature between experiment and analysis (SUS304, ρ_B)

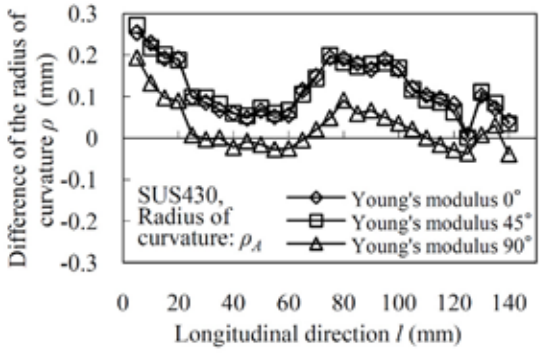

Figure 15: Difference of radius of curvature between experiment and analysis (SUS430, ρ_A)

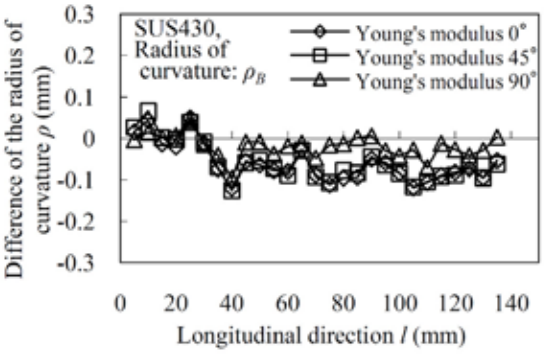

Figure 16: Difference of radius of curvature between experiment and analysis (SUS430, ρ_B)

REFERENCES

[1] F. Yoshida, T. Uemori, K. Fujiwara: Int. J. Plasticity, 18(2002), 633-659.
[2] F. Yoshida, T. Uemori: Int.J.Plasticity,18(2002),661-686.
[3] F. Yoshida, T. Uemori: Int. J. Mech. Sci., 45(2003), 1039-1043.
[4] F. Yoshida: Press Working, 48(2010), pp. 36-39 (in Japanese).
[5] T. Kuwabara, Y. Kumano, J. Ziegelheim, I. Kurosaki, Int. J. Plasticity, 25(2009), 1759-1776.

XI International Conference on Computational Plasticity. Fundamentals and Applications
COMPLAS XI
E. Oñate, D.R.J. Owen, D. Peric and B. Suárez (Eds)

EXPERIMENTAL AND NUMERICAL ANALYSES ON THE CHARACTERISTICS OF TWIN SKEW ROLLING

TAKASHI UCHIMURA*, YOKI OKUDA† , MASAYOSHI AKIYAMA‡

* MSc Course Student, Department of Mechanical and System Engineering
Kyoto Institute of Technology, Gosho-Kaido-cho, Matsugasaki, Sakyo-ku, Kyoto, 606-8585, Japan
e-mail: m1623008@edu.kit.ac.jp, http://www.mesh.kit.ac.jp

† Retinal Imaging Group, Retinal Instruments Department, Eye Care Business Unit,
TOPCON CORPORATION, 75-1, Hasunuma-cho, Itabashi-ku, Tokyo, 174-8580, Japan
email: y.okuda@topcon.co.jp

‡ Department of Mechanical and System Engineering, Kyoto Institute of Technology,
Gosho-Kaido-cho, Matsugasaki, Sakyo-ku, 606-8585, Kyoto, Japan
email: akiyama@mech.kit.ac.jp, http://www.mesh.kit.ac.jp

Key words: Twin Skew Rolling, Flat Rolls, Blooming Mill, Porosity, Infiltration of strain.

Abstract. Elastic-plastic FEA was carried out on the rolling process of twin skew rolling for a blooming mill to evaluate the influences of roll diameter, skew angle, and coefficient of friction on the suppression effect of porosities in the vicinity of centre axis of the material. Rolling by using a proto-type mill and modelling clay was then carried out to verify the validity of numerical analysis. Both results showed that the larger the roll diameter, and also the larger the coefficient of friction, the higher the suppression effect of porosities.

1 INTRODUCTION

Technology development for suppressing the porosities in blooming mill has a long history and many trials have been tried out mainly on the groove geometry of a pair of rolls [1], but there has been something more to do for the complete suppression. Recently a trial was proposed from a different point of view in which adoption of a pair of cone-type rolls showed a considerable effect in suppressing the porosities [2,3]. It is concluded in this proposal that use of a pair of cone rolls has a high advantage and the higher the skew angle the larger the effect. However, one important viewpoint has been missing from this result. According to the increase in the skew angle the working roll diameter increases and direct comparison of the results must be carefully done. In the present work rolling by a pair of simple cylindrical rolls was carried out both numerically and experimentally and influence of skew angle was evaluated on two sets of rolls; a pair of cylindrical rolls and a pair of skew rolls of which working diameter at the roll centre is the same as that of the cylindrical roll. In the experiment modelling clay was used for a parent billet and the parent billets were rolled through a proto-type rolling stand manufactured for this experiment.

2 MILL CONCEPT

The features of twin skew rolling method are illustrated in Figure 1. The major component of the mill is a pair of conical rolls of which half cone angle is θ and the difference in roll peripheral speed in the roll axis allows the three dimensional distribution of shearing force exerting on the billet surface and makes it possible to ease the generation of plastic deformation. This mechanism enhances the infiltration of compressive deformation to the billet centre that leads to the suppression of porosities [2,3]. Three features other than the roll geometry with half skew angle θ are that the roll axes are parallel each other, the angular velocities of two rolls are the same, and two rolls have the same geometry.

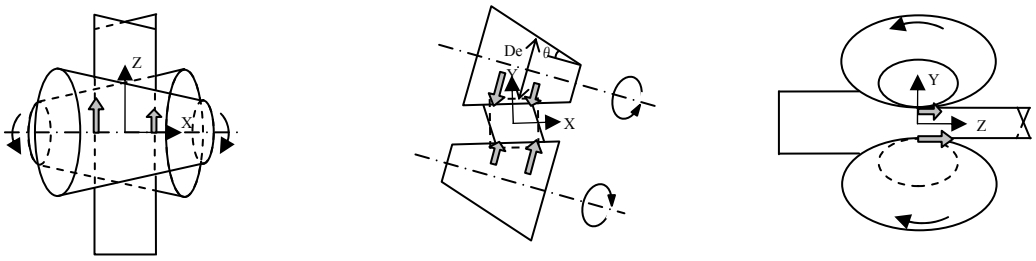

(a) Plane view (b) Elevation (c) Side view

Figure 1: Schematic illustrations of roll configuration for twin skew rolling method

In the previous work attention was focused on the effect of cone angle on the infiltration of deformation to the billet centre and a wide range of rolls with different cone angles were used to investigate the effect in the laboratory. However, roll diameter changes in the roll axis when cone angle is given and the lager the cone angle, the larger the working diameter of roll is. In a strict sense, therefore, influence of roll diameter and that of cone angle must be evaluated separately.

In the present work four pairs of rolls with a simple cylindrical geometry (flat roll) were manufactured corresponding to the skew rolls with different skew angles. The roll diameter of each cylindrical roll was the same as that of a skew roll measured at the centre in the axial direction.

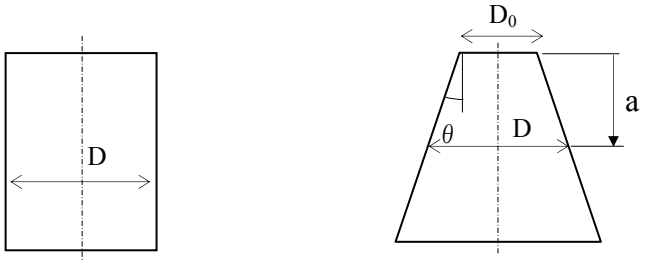

D=*Const.* $D=D_0+2a\tan\theta$

(a)Conventional roll (b)Skew roll

Figure. 2: Schematic illustration of flat roll and conical roll

3 NUMERICAL ANALYSES

Elastic-plastic FEA was carried out on the hot rolling by the twin skew rolling. The software used for the analyses was ELFEN [4] developed at University of Swansea, U.K.. A pair of rolls was assumed rigid and the parent billet was regarded an elastic-plastic material. Figure 3 shows a schematic illustration of rolling. The billet centre coincides with the roll centre in the axial direction. At the initial stage of analysis the tail end of billet was pushed by a rigid plane to urge the bite and as soon as the rolling starts the constraint by rigid plane was released. The material was hot medium carbon steel and the flow stress was calculated by the Misaka's equation [5] that is given by equation (1) that is often used in the analyses of hot steel rolling, where C, T, ε, $\dot{\varepsilon}$ are carbon content, temperature, strain and strain rate.

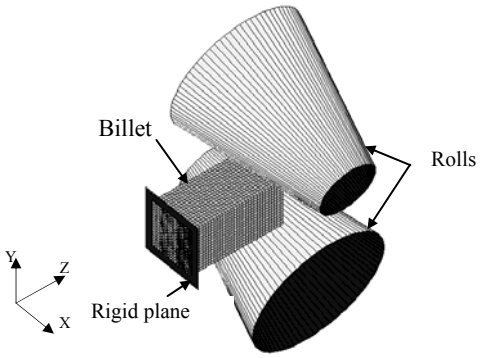

Figure 3: Configuration of rolls and billet.

$$\sigma = 9.8 \cdot \exp\left[0.126 - 1.75C + 0.594C^2 + \frac{2851 + 2968C - 1120C^2}{T}\right] \cdot \varepsilon^{0.21} \cdot \dot{\varepsilon}^{0.13} \qquad (1)$$

Coulomb friction rule was assumed on the contact surface and 0.3 and 0.4 were the values of the coefficient of friction. The skew angle was 15 degrees that was found optimum in the previous work [2,3]. The list of condition of numerical rolling is shown in Table 1.

Table 1: Conditions of numerical analyses

Material	S45C
Rolling temperature, T	1273K
Friction coefficient, μ	0.3, 0.4
Mesh division	16×16×64
Specimen size	35mm×35mm×70mm
Draft	10%
Skew angle, θ	0°, 15°
Centre diameter of roll	φ70mm, φ140mm
Strain late, $\dot{\varepsilon}$	$30s^{-1}$

4 RESULTS OF NUMERICAL ANALYSES

4.1 Influence of roll diameter

Distributions of equivalent plastic strain in a cross section where the state of rolling is steady are compared in Figure4. When a pair of skew roll is adopted clear shear deformation is observed but the intensity of equivalent plastic strain increases in the vicinity of centre axis. Axial distributions of equivalent plastic strain are compared in Figure5. It is clearly observed that infiltration of compressive deformation is higher for the rolling by twin skew rolling.

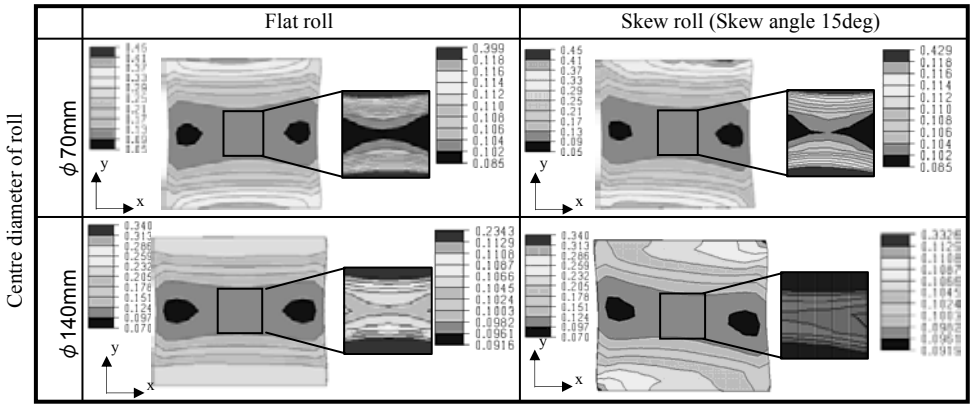

Figure 4: Distribution of equivalent plastic strain in cross-section after rolling

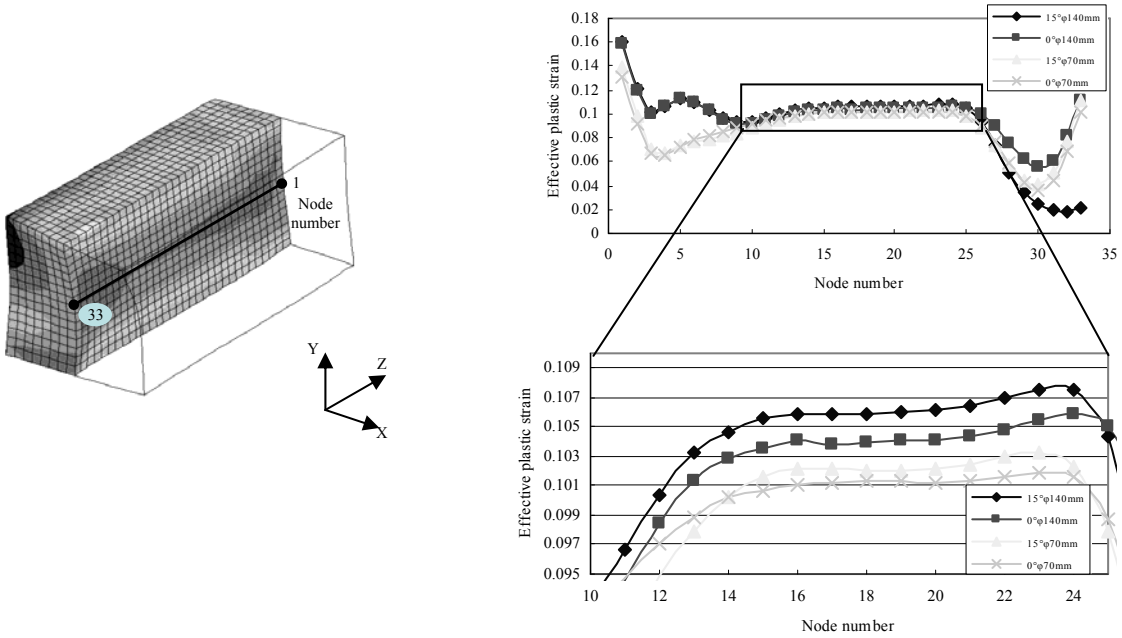

Figure 5: Distribution of effective plastic strain on centre axis of billet

4.2 Influence of friction

Influences of friction on deformation in a cross section and on the rolling axis are illustrated in Figure 6 and Figure 7 respectively. The tendencies of both rolling methods are very close and equivalent plastic strain increases according to the increase in friction, but the intensity of this tendency is higher for twin skew rolling. Distribution of roll peripheral speed due to the existence of skew angle realizes stronger three dimensional deformation that leads to higher infiltration of compressive deformation near to the billet axis.

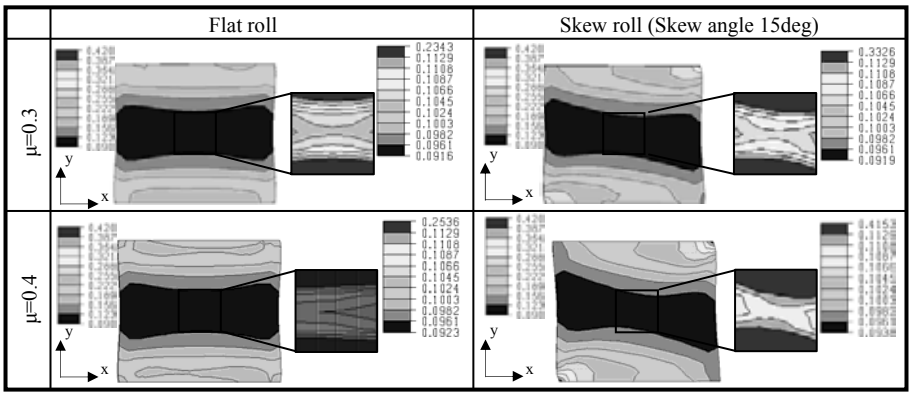

Figure 6: Comparison of influence of friction on distribution of equivalent plastic strain

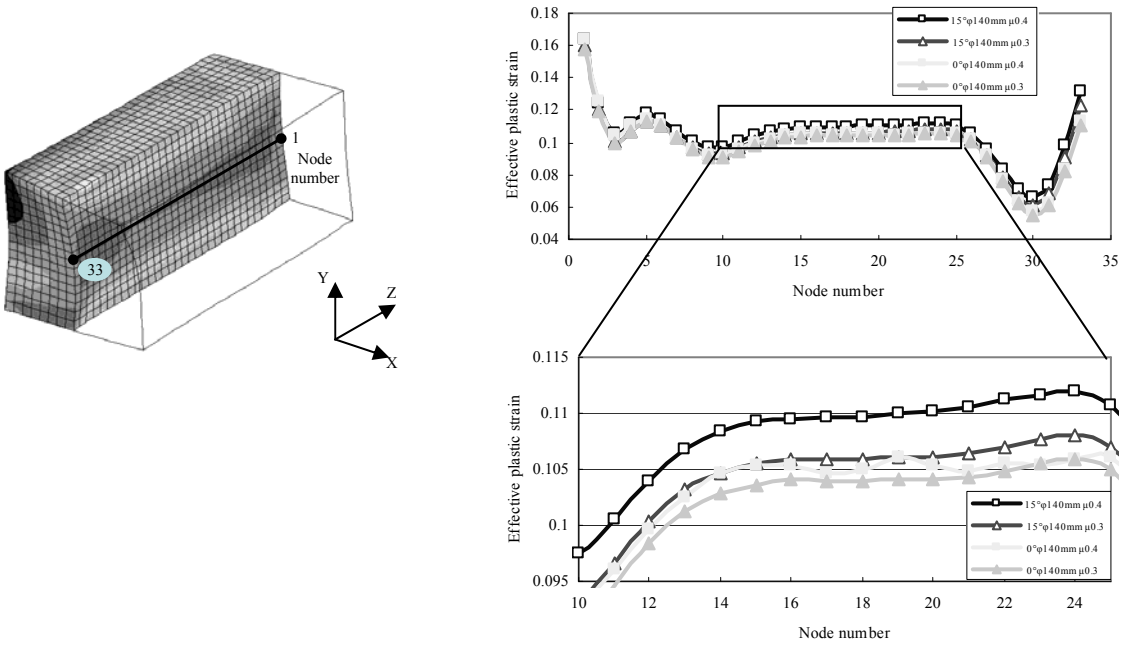

Figure 7: Distributions of equivalent plastic strain on rolling axis in steady state rolling

5 EXPERIMENT

5.1 Evaluating influence of roll diameter

A proto-type mill used for laboratory experiment is shown in Figure 8, and a set of four skew rolls and corresponding flat rolls are shown in Figure 9. The roll diameters of flat rolls were equal to the roll diameters of corresponding skew rolls at the centre in the axial direction. In Figure 10 an example of parent billet is shown that has a square cross section with a hole around the centre axis. The parent billet was made of a modelling clay, of which relationship between the flow stress and plastic strain resembles to that of hot steel, and the size of billet was 35mm×35mm×120mm and the diameter of centre hole was 5mm.

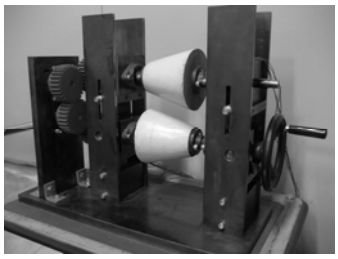

Figure 8: Twin skew rolling mill

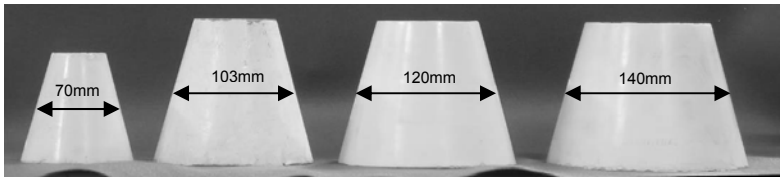

Skew rolls

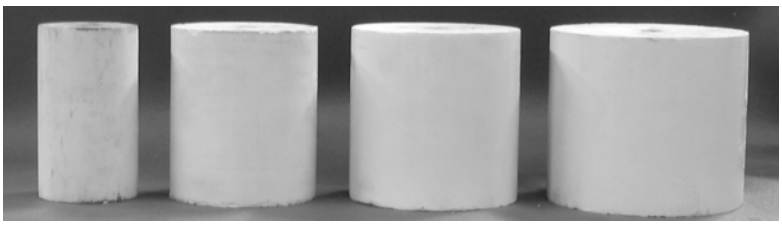

Flat rolls

Figure 9: Comparison of geometry of skew and flat rolls used for laboratory experiment

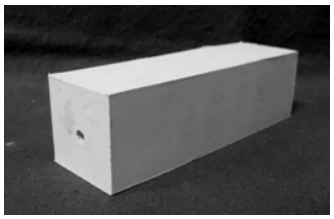

Figure 10: Modelling clay specimen

Similarly to the previous work [2,3] intensity of infiltration of compressive deformation was evaluated by measuring the ovality, i.e. aspect ratio, of the centre hole b/a as it is shown in Figure11. The smaller the ovality is, the higher the influence is.

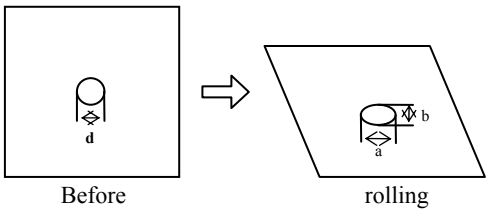

Figure 11: Schematic illustrations of initial round hole in cross-section and oval hole after rolling

The basic lubricant adopted was $CaCO_3$ that is often used for a laboratory experiment using modelling clay for simulating the rolling phenomenon of hot steel. Conditions of the rolling experiments are given in Table 2.

Table2: Conditions of rolling experiment in laboratory

Material	Modelling clay
Rolling temperature	293K
Specimen size	35mm×35mm×120mm
Round hole size	ϕ 5mm
Draft	10%, 20%
Skew angle	0°, 15°
Centre diameter of roll	ϕ 70mm, ϕ 103mm, ϕ 120mm, ϕ 140mm
Lubricant	$CaCO_3$

5.2 Evaluating influence of friction

Similarly to the previous work [2,3] influence of friction was evaluated by changing the lubrication condition. As it is shown in Table 3 three types of lubrication condition were adopted on the rolling using modelling clay billet; no lubricant, $CaCO_3$ and solution of soap.

Table 3: Condition of rolling experiment by changing friction

Material	Modelling clay
Rolling temperature	293K
Specimen size	35mm×35mm×120mm
Round hole size	ϕ 5mm
Draft	20%
Skew angle	0°, 15°
Centre diameter of roll	ϕ 103mm
Lubricant	No lubricant, $CaCO_3$, Solution of soap

6 RESULTS OF EXPERIMENT

6.1 Influence of roll diameter

Examples of cross section at the steady state rolling are compared in Figure 12. The ovality of centre hole by twin skew rolling is larger when the working diameter of roll is the same, and the ovality becomes larger according to the increase in roll diameter regardless of the type of rolling. These results are summarized and shown in Figure 13.

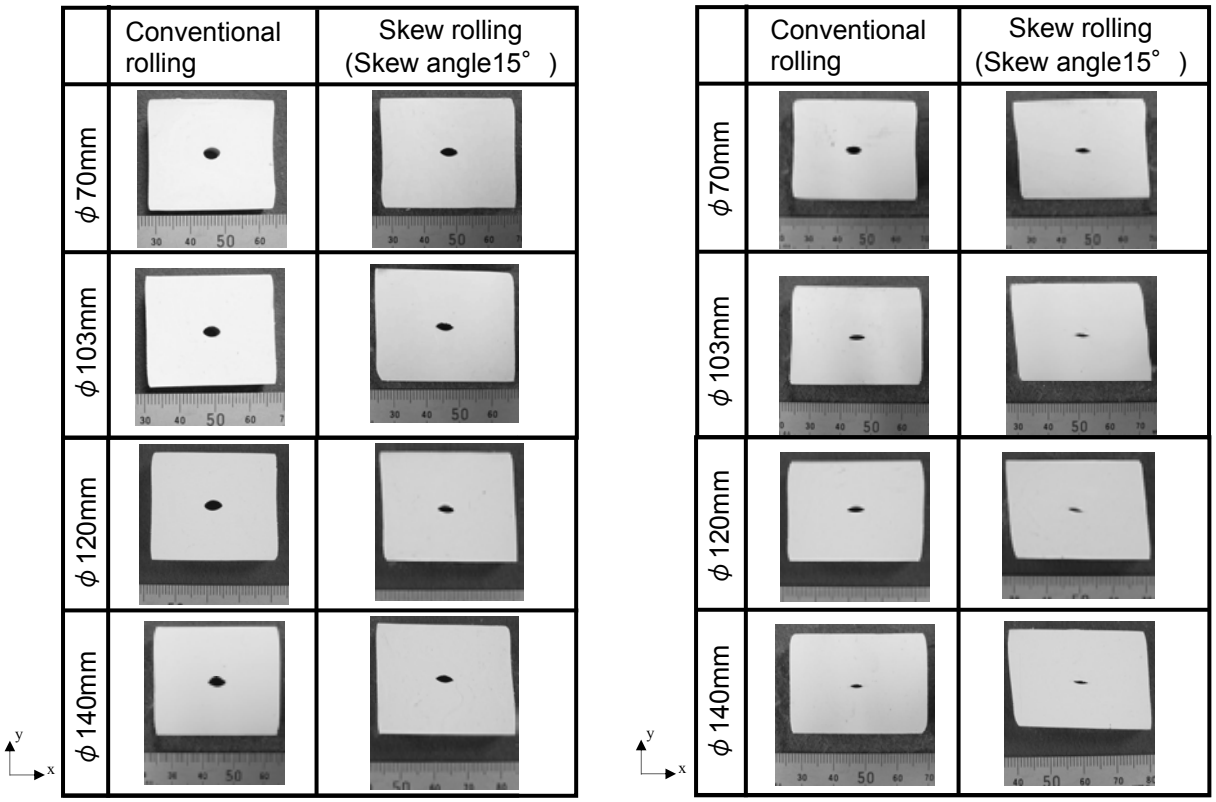

(a): Rolling reduction 10% **(b)**: Rolling reduction 20%

Figure 12: Deformation pattern of round hole in centre of specimen

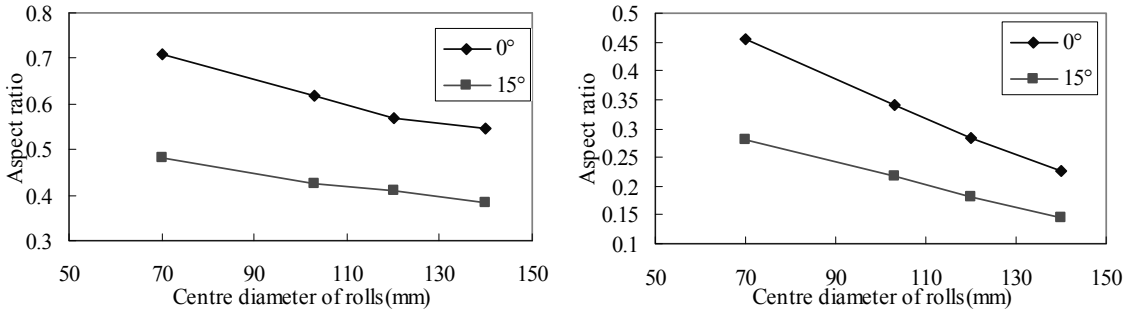

(a) Rolling reduction 10% **(b)** Rolling reduction 20%

Figure 13: Relationship between centre diameter and aspect ratio

6.2 Influence of friction condition

Influence of friction condition on infiltration of compressive deformation near to the centre axis is shown in Figure 14. As it was shown in Table 3 three conditions of lubrication were tried but lubrication by solution of soap failed only for twin skew rolling and only two other conditions by no lubricant and CaCO3 were successful. The reason of the failure was assumed as follows. Use of soap solution lead to too much decrease in friction coefficient on the contact surface and transmission of distributed shearing force on the roll surface was difficult, i.e. the distribution of shearing force was mainly used for the generation of lateral metal flow of billet surface ant the biting force in the rolling direction becomes poorer. This result suggests that slightly high coefficient of friction may be necessary for the twin skew rolling compared to the conventional rolling by a pair of flat rolls. Regarding the effect of high infiltration of compressive deformation near to the billet centre the results clearly shows the superiority of twin skew rolling similarly to the results by FEA.

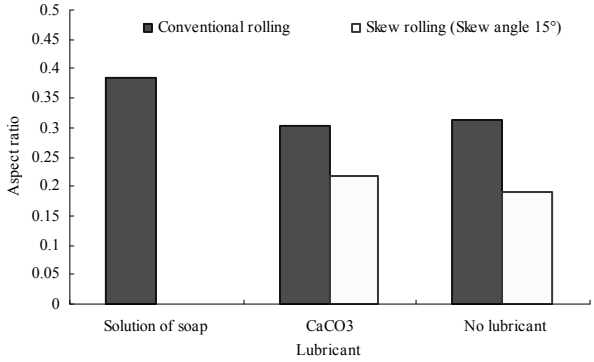

Figure 14: Influence of lubricity on infiltration of compressive deformation near to centre axis

7 CONCLUSIONS

In the present work influences of roll diameter of twin skew rolling and friction on the deformation near the centre axis of billet were evaluated numerically and experimentally. It was clarified that higher intensity of deformation is obtainable by the twin skew rolling method when the roll diameter of skew roll at the roll centre is the same as that of flat roll. Numerical results showed that concentration of strain in the vicinity of contact surface fades out according to the increase in roll diameter and the intensity of the concentration of equivalent plastic strain in the vicinity of billet centre increases. The results of experiment proved the validity of the numerical results. Friction on the contact surface is an important factor that generates the three dimensional shear deformation that is typical for the twin skew rolling method. Influence of friction on the infiltration of deformation to the billet centre was evaluated by changing the coefficient of friction in the numerical analysis and by changing the lubricant in the laboratory experiment. The results showed that the higher the friction is, the larger the infiltration of deformation to the centre is. Friction is more influential on the twin skew rolling than on the ordinary flat rolling. One important point to emphasize is that too low friction leads to failure in biting and rolling does not start in the twin skew rolling method.

NOTE

Some part of this work was carried out by the second author Mr. Yoki Okuda when he was a student at Kyoto Institute of Technology and this paper has nothing to do with his present work at his present affiliation Topcon Corporation.

ACKNOWLEDGEMENT

This research project was financially supported by The Amada Foundation, and the authors would like to express their deep gratitude for all the support.

REFERENCES

[1] R.E.Beynon, Roll Design and Mill Layout, AISE, (1956).
[2] Y. Okuda, M. Akiyama, Evaluation of new rolling method ensuring high reduction near billet centre, COMPLAS X, (2009), 448.
[3] Y. OKUDA, and M. AKIYAMA, Effect of variable roll peripheral speed to ensure high reduction in vicinity of billet centre (in Japanese), 2009, CAMP-ISIJ, 22, 434
[4] Rockfield Software Limited, Technium, Kings Road, Prince of Wales Dock, Swansea, SA1 8PH, West Glamorgan, U.K., http://rsazure.swan.ac.uk/profile.htm.
[5] Y. Misaka, T. Yoshimoto, Formularization of Mean Resistance to Deformation of Plain Carbon Steels at Elevated Temperature, J. of JSTP, 8-79 (1967), 414-422.

XI International Conference on Computational Plasticity. Fundamentals and Applications
COMPLAS XI
E. Oñate, D.R.J. Owen, D. Peric and B. Suárez (Eds)

INFLUENCES OF FINISHED GEOMETRY OF SPECIMEN FOR COMPRESSION TEST ON THE STABILITY OF TESTING AND PRECISION OF MEASURED STRESS AND STRAIN

JUNKI MIYAGAWA*, SHIGERU OHBA†, MASAYOSHI AKIYAMA††

* Taisei Kako Co., Ltd.
2-11-12, Fujinosato, Ibaraki city, Osaka 567-0054, Japan
e-mail: ewhfocenj@yahoo.co.jp, web page: www.taisei-g.co.jp

† Sumitomo Metals Technology Ltd. 1-8 Fuso-cho, Amagasaki, 660-0891, Japan
e-mail: ooba-sgr@smt-co.jp

†† Department of Mechanical and System Engineering, Kyoto Institute of Technology (KIT)
Goshokaido-cho, Matsugasaki, Sakyo-ku, Kyoto, 606-8585, Japan
email: akiyama@mech.kit.ac.jp, web page: www.mesh.kit.ac.jp

Key words: Compression Test, Cylinder, ASTM-E9 89a, Precision, Stress-Strain Curve.

Abstract. This paper deals with the influence of the specimen geometry on the precision of measured stress-strain curve on the compression side. Cylindrical specimen is adopted after ASTM-E9 89a and laboratory experiment and elastic-plastic FEA are carried out to evaluate the influence of the degree of parallelism of end surfaces. Present tolerance value of 0.5/1000 for the inclination of end surface can be relieved up to 6/1000.

1 INTRODUCTION

Stress-strain curve is an essential characteristic when one analyzes the plastic deformation of a material. Usually only a tension test is carried out to know the stress-strain curve on an assumption such that the stress-strain curve is point symmetric around the origin. This assumption is approximately correct, but in an exact sense two curves are slightly different [1]. If the difference is not negligibly small the assumption of point symmetry may lead to a discrepancy between the experimental and analytical results and prediction by the analysis of the forming process fails. For the prevention of this failure one ought to carry out a compression test as well as the tension test prior to the analysis [2]. Compression test specified by ASTM-E9 89a [3] is a commonly used compression test. For this test a cylindrical specimen is prepared in a manner such that the degree of parallelism of end surfaces must lie within the tolerance value of 0.5/1000, although the background of this tolerance value is not clear. If it is possible to loosen the tolerance value it will help specimen preparation. In the following part of this paper experiments and numerical analyses are carried out to evaluate the influence of specimen geometry on the precision of measured stress and strain and expansion of tolerance value is discussed. The code for numerical analysis is ELFEN [4] developed at University of Swansea, U.K.

2 PREPARATIONS

2.1 Specimen preparations

Figure 1 shows the manufacturing process for specimen. Parent bar was subjected to turning after thermal treatment at 680℃ and the end surface was finished by a sandpaper.

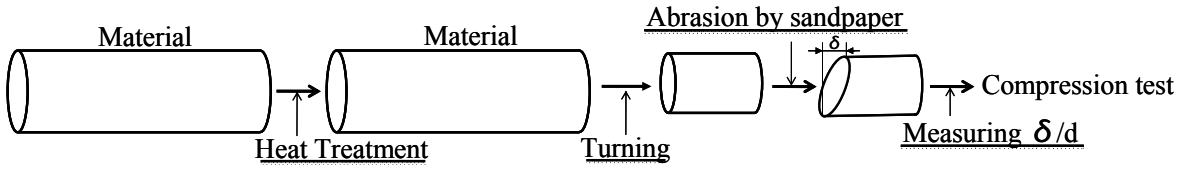

Figure 1: Flow of processing for preparing specimen for compression test

2.2 Theory

Inclination of end surface was measured by using the following theory. It was assumed that both end surfaces were flat planes and one end surface that was exactly perpendicular to the axis was placed on a flat table that was spanned by X and Y axes as is illustrated in Figure 2. The plane showing the top flat surface may cross the X-Y-plane, and the inclination angle α and parallelism (δ /*d*) of the top flat surface is calculated by determining the line AB.

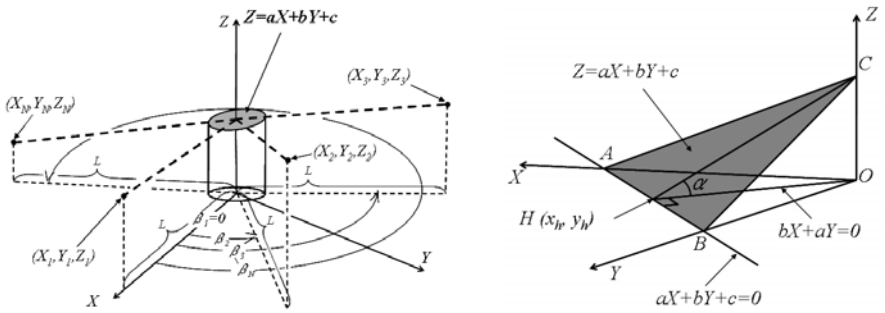

Figure 2: Illustrated image for measuring geometry of inclined upper surface

The equation of top flat surface is given by equation (1). Using the least square method the constants *a*, *b* and *c* are calculated, i.e. minimization process of the error S given by equation (2) leads to a set of equations (3), (4) and (5). Precise measurement of N sets of coordinate values (*Xi*, *Yi*, *Zi*) determines the plane ABC, where N must be larger than 2.

$$Z = aX + bY + c \tag{1}$$

$$S = \sum_{i=1}^{N} \left(Zi - aXi - bYi - c \right)^2 \tag{2}$$

$$\frac{\partial S}{\partial a} = 0 \tag{3}$$

$$\frac{\partial S}{\partial b} = 0 \tag{4}$$

$$\frac{\partial S}{\partial c} = 0 \tag{5}$$

Once a, b and c are determined the coordinate values of (*Xh, Yh*) of point H are calculated by solving a set of equations (6) and (7). The inclination angle α of the top flat surface is then calculated by using equation (8) and the parallelism (δ /d) is also calculated.

$$aX + bY + c = 0 \tag{6}$$

$$bX - aY = 0 \tag{7}$$

$$\alpha = \tan^{-1}\left(\frac{OC}{OH}\right) \tag{8}$$

2.3 Measurement

Figure 3 shows the outline of the measuring system. Coordinate values of (Xi, Yi) of each data points were calculated according to the angle β i and the fixed length L and the value Zi was the height of the spot of a laser pointer mounted on the top flat surface of the specimen.

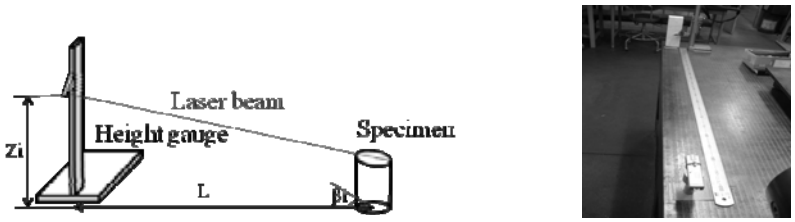

Figure 3: Illustration and view of measuring height of laser spot Zi

2.4 Result

Table 1 shows the measured values of parallelism of specimens. The range of parallelism lies between naught and 50/1000, and plural number of specimens were prepared for each geometrical conditions in Table 1.

Table 1: Calculated degree of inclination angle α of specimen

Specimen number	1	2	3	4	5	6	7	8
Parallelism of end surface (δ /*d*)	1 /1000	2 /1000	6 /1000	7 /1000	15 /1000	23 /1000	40 /1000	48 /1000

2.5 Tooling

A protector and a set of toolings for compression test were manufactured as shown in Figure 4. Compression test may endanger the operator because the specimen can suddenly become a bullet, and the protector prevents this danger from occurring. On the side of the protector there is a hole that is smaller than the specimen size and the cables from strain gauges placed on the specimen are drawn through this hole. The material of toolings was 0.45 mass % carbon steel and was prepared according to the thermal treatment illustrated in Figure 5 [5].

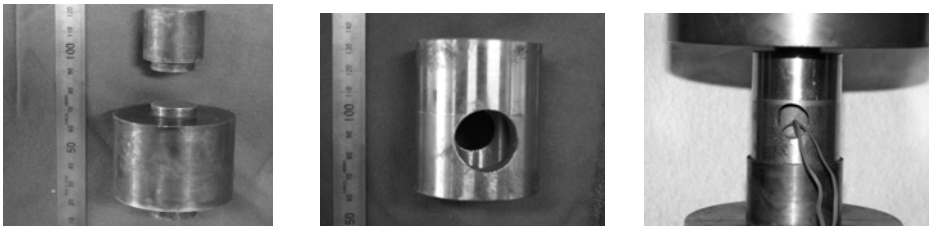

Figure 4: Tooling and protector for compression test

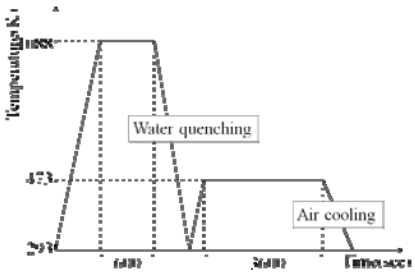

Figure 5: Diagram for quenching and tempering operations for toolings

3 EXPERIMENT

Compression test was carried out using a universal testing machine shown in Figure 6. The aspect ratio of specimens was 2.5 following the previous work on the uniformity of measured stress and strain in compression test [6,7]. Test was conducted until 5% strain was reached. Strain was measured by using four strain gauges placed at the specimen centre in a pitch of 90 degrees. Stress was a nominal stress. Cross head speed was 1mm/min.

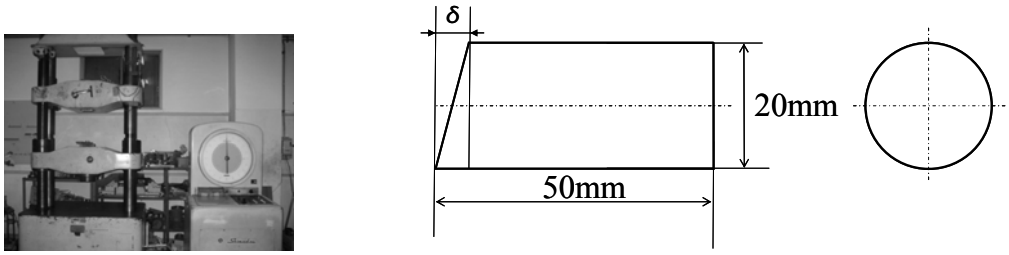

Figure 6: Machine and prepared specimen for compression test

Lubricant was prepared according to the previous work [8,9]. Soap mixed with powdered mild detergent for washing was placed on the specimen surface prior to the test.

Figure 7: View of lubricant

4 RESULT

4.1 Stability of experiment

No specimen flew as a bullet and the compression test was stable, but buckling occurred in accordance with the increase the index of parallelism (δ /d). Examples of normal and buckled specimens are shown in Fig. 8. All the specimens were observed under the back light after the test and the specimen was esteemed buckled when an opening was observed.

(a) Example of specimen with no buckling (b) Example of buckled specimen

Figure 8: Comparison of non-buckled and buckled specimens

Figure 9 shows the influence of the index of parallelism (δ /d) on buckling. Ordinate is the buckling index. The buckling index is 1 when buckling occurs on all the specimens and 0.5 when buckling occurs on 50% specimens and 0 when no buckling occurs. The critical value of the index of parallelism (δ /d) may be 7/1000 above which buckling occurs.

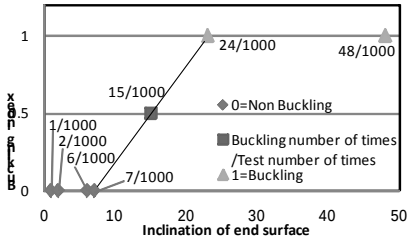

Figure 9: Influence of inclination of end surface upon on buckling

4.2 Stress-strain curves

Figure 10 shows the positions of four strain gauges placed in the circumferential direction at the specimen centre. No-1 gauge was placed on the longest portion of specimen and No-3 gauge on the shortest portion. Examples of four stress-strain curves are drawn in Figure 11. They were drawn by using the signals of four gauges, and three curves in Figure 11b are drawn by using the average strains. Three stress-strain curves in Figure 11b are almost the same and it can be recommended to take an average value of measured strains.

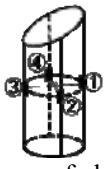

Figure 10: Illustrated image of placement of strain gauges

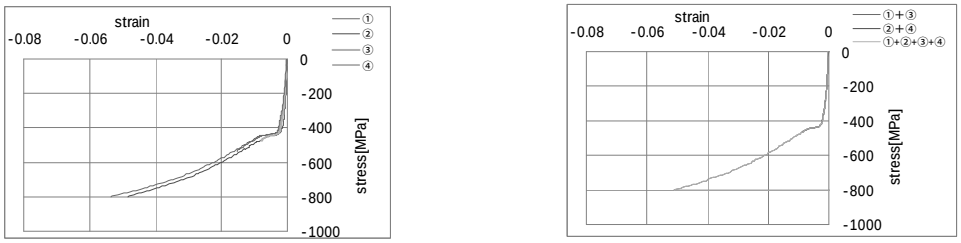

(a) Example of stress-strain curves for four strains (Inclination 6/1000)

(b) Comparison of average stress-strain curves on opposite angle (Inclination 6/1000)

Figure 11: Influence of inclination of end surface upon on stress-strain curves

The tangents of elastic region of stress-strain curves in Figure 11a lie in a wide range and it is unrealistic. However the tangents in Figure 11b measured within the stress range of -200 and -300MPa was a reasonable value of 206GPa.

Figure 12 is a comparison of stress-strain curves among specimens with different value of the index of parallelism (δ/d). It may be concluded that difference in the index of parallelism does not seriously influence the measured stress-strain curve as long as the value of index lies within the range of under (6/1000).

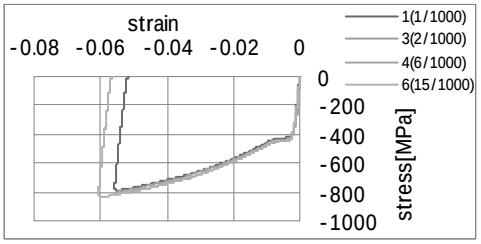

Figure 12: Comparison of raw stress-strain curves for all none buckling specimens

5 NUMERICAL ANALYSIS

5.1 Conditions for analysis

In order to examine the precision of measured stress and strains elastic-plastic FEA were carried out on the compression tests. The stress-strain curve was that given in Figure 11b. The stress-strain curve was assumed point-symmetric on the tension side. The parameter changed in the analyses was the inclination index δ of the end surface in Figure 6 and the response of specimen was examined.

Figure 13 shows an example of 3D initial mesh for the analysis. The centre portion was divided into 6 times 6 small squares. The outside layer was divided into 5 thin layers and the division in the circumferential direction was 24. The mesh division in a cross section was 156. The mesh division in the longitudinal direction was 24, and the total number of elements was 3744. Displacement constraint was given in the axial direction on all the nodes on the lower end surface and upper surface was compressed by a rigid ram as shown in Figure 14.

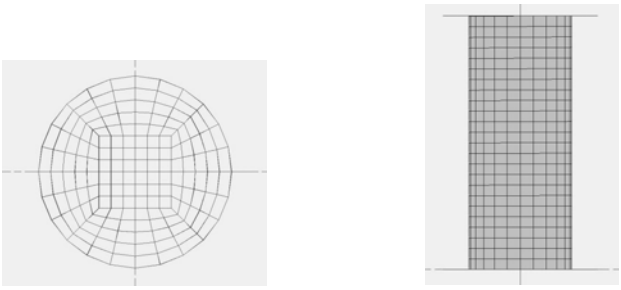

Figure 13: Illustrated image of dividing mesh

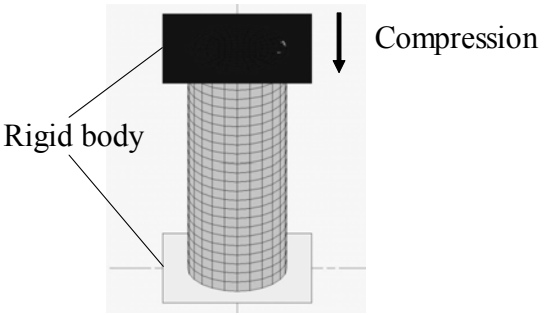

Figure 14: **L**oading procedure

5.2 Distribution of stress

Figure 15 shows examples of distribution of axial stress on the elastic and plastic stages for a specimen with the index (δ */d)* of 6/1000 on the centre plane of specimen. On the elastic stage, there is a clear distribution of stress according to the inclination of end surface, but it gradually fades out on the plastic stage. The average value of stress is equal to the compressive force divided by the cross sectional area of the centre plane.

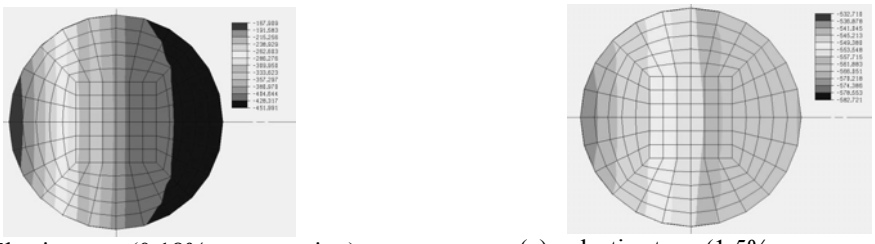

(a) Elastic stage (0.18% compression) (a) plastic stage (1.5% compression)

Figure 15: Examples of stress distributions on elastic and plastic stages

5.3 Distribution of strain

Figure 16 shows examples of distribution of axial strain on the centre plane of the specimen on the elastic and plastic stages. Figure 18-(a) and (b) show the distributions on the elastic and plastic stages respectively. Similarly to the distribution of axial stress distribution of axial strain on the elastic stage is slightly large but it gradually fades out on the plastic stage. There is also a distribution of other strain components but the intensity of those components is much smaller than that of the axial strain.

(a) Elastic stage (0.18% compression) (b) Elastic stage (1.5% compression)

Figure 16: Comparison of Distribution of strain in elastic stage and plastic stage

5.4 Stress-strain curve

Figure 17 shows four stress-strain curves drawn for each calculated stress and strain on the four points placed in the same pitch of 90 degrees around the specimen corresponding to the measuring points of strain in the compression test in a laboratory. As was expected four stress-strain curves on the elastic stage are totally different, but those are nearly the same on the plastic stage. Three average stress-strain curves drawn by using the average value of two strains all the four strains show an excellent matching one another. The Young's modulus of the average stress-strain curves sampled within the stress range of -200 and -300 GPa was 201GPa.

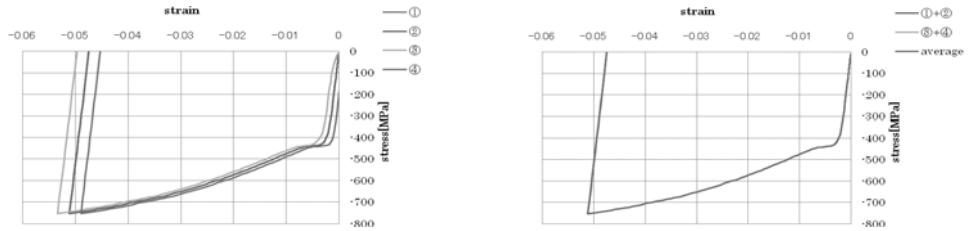

(a) Comparison of four stress-strain curves (b) Comparison of average stress-strain curves

Figure 17: Comparison of average stress-strain curves (Inclination 6/1000)

Figure 18 is a comparison between the analytical and measured stress-strain curves on the compression side. The material is a medium carbon steel with 0.45 mass % carbon content. Good agreement has been achieved and it may be concluded that by taking the average value of at least two strains around the circumferential direction of specimen. Especially excellent matching is obtainable when the stress state is plastic.

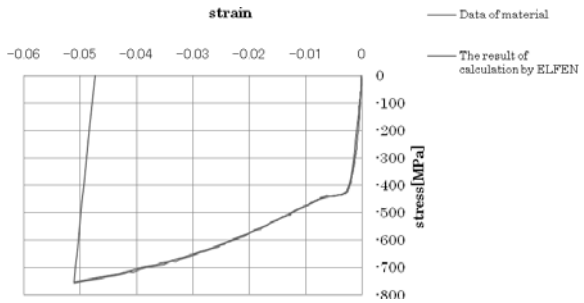

Figure 18: Comparison of result of experiment and numerical analysis

6 CONCLUSIONS

In the present work influence of parallelism of end surfaces on specimen for compression test on the precision of stress-strain curve on the compression side was evaluated numerically and experimentally. None of the specimens of which parallelism ranged from 1/1000 to 48/1000 suddenly flew as a bullet throughout the test, but buckling was observed when the parallelism exceeded 7/1000. If average strain is adopted on the centre plane of the cylindrical specimen the stress-strain curve obtained is almost the same as the true stress-strain curve of the material. The number of signals of strain should be at least two that face each other in the circumferential direction in a pitch of 180 degrees. If the number is four by placing the strain gauge in a pitch of 90 degrees, stress-strain curve drawn by using this average strain is exactly the same as the true stress-strain curve. It is specified in ASTM E9-89a that the parallelism of end surfaces must lie within a range of 0.5/1000, but this specified value can be until 6/1000 as long as the strain is measured in the circumferential direction on the centre plane in the same pitch of 90 or 180 degrees. In the present work influence of parallelism of end surfaces on specimen for compression test on the precision of stress-strain curve on the compression side was evaluated numerically.

ACKNOWLEGEMENT

This project was carried out with the financial assistance of The Amada Foundation, Japan, and the authors would like to express their deep gratitude for the support.

REFERENCES

[1] Shinji Fukui, Hideaki Kudo, Kiyota Yoshida, and Kunio Abe. Methods of Obtaining the Stress-Strain Curves of Ductile Metals for Large Strain Region, *The reports of the Institute of Science and Technology*, The University of Tokyo, No.8, Vol.3 (1954), pp.135-151.

[2] M. Akiyama, Proposal of a project for the prediction of anisotropy, *ISO TC67/SC5*, Washington, U.S.A., (2004).

[3] ASTM International, *Designation: E9-89a* (Reapproved 2000), pp.90-98.

[4] Rockfield Software Limited, URL: www.rockfield.co.uk

[5] Toru Araki, Heat-treatment Technology of Steel(in Japanese), *Vol. 8 of Lecture Series on Iron and Steel Engineering*, Asakura Publishing Co., Ltd, (1969), pp.1-20.

[6] Atsushi Ichijo, Masayoshi Akiyama, Numerical Re-examination of Simple Compression Test, *Proceedings of COMPLAS X*, (2009).

[7] Atsushi ICHIJO, Masayoshi AKIYAMA. Precision of Measured Stress and Strain in Compression Test for Cylindrical Specimen, *to be published in SOSEI-TO-KAKOU. J. of The Japan Society for Technology of Plasticity, Vol.52, no. 604*, (2011-5).

[8] Hiroshi Ohyama, Masayoshi Akiyama, Evaluation of Environment-Friendly Lubricant by Erichsen Test, *Proceedings of COMPLAS X*, (2009).

[9] Hiroshi OHYAMA, Masayoshi AKIYAMA. Development and Evaluation of Environmentally Friendly Lubricant for Cold metal Working, *SOSEI-TO-KAKOU. J. of The Japan Society for Technology of Plasticity, Vol.52, no.603,* (2011-4), pp.474-479.

XI International Conference on Computational Plasticity. Fundamentals and Applications
COMPLAS XI
E. Oñate, D.R.J. Owen, D. Peric and B. Suárez (Eds)

SPRING-BACK PREDICTION BY COMBINATION OF THE FINITE ELEMENT ANALYSIS AND BENT-BEAM THEORY CONSIDERING BAUSCHINGER EFFECT

TORU MATSUMOTO*, SHINNTAROU GOTOH*, TAKASHI KUBOKI*, MAKOTO MURATA* AND YINGJUN JIN†

*Dept. of Mechanical Engineering & Intelligent Systems
University of Electro-Communications
1-5-1 Chofu Gaoka, Chofu-shi, Tokyo, 182-8585, Japan
E-mail: matumoto@mt.mce.uec.ac.jp
gotoh@mt.mce.uec.ac.jp
kuboki@mt.mce.uec.ac.jp
murata@mt.mce.uec.ac.jp
Web page: http://www.mt.mce.uec.ac.jp/index.html

†Amada Co. Ltd
200, Ishida, Isehara-shi, Kanagawa 259-1196 Japan
Web page: http://www.amada.co.jp/index.html

Key words: Bauschinger Effect, Spring-back Prediction, V-bending, Finite Element Analysis.

Abstract. Plate bending is a common plastic working. High-precision bending would require the accurate prediction of spring-back, which is affected by Bauschinger effect. In the present study, an analysis of spring-back prediction was conducted by a combination of the finite element method (FEM) and bent-beam theory. The characteristic of this analysis is that the FEM is used to analyze bending behavior and the bent-beam theory is used to predict spring-back. This combination would reduce calculation time and skip the identification procedure of parameters which is needed in conventional phenomenological approach. The proposed method predicted spring-back more accurately than conventional analysis without kinematic hardening. Furthermore, the proposed numerical method was able to conduct analysis as accurate as that by the conventional FEM, which is implemented with numerical description of kinematic hardening, within much shorter calculation time.

1 INTRODUCTION

Plate bending is a concise, basic and common metal forming process used in industry. Plate bending is used to manufacture chassis and boxes for vehicles, electronic devices and so on. Recently, bent metals are often used for medical instruments, and they are required to be bent with severely high precision. When metal is formed by forging within many constraints in dies, it would be easy to deform metal precisely by considering volumetric constancy. However, as larger free surfaces exist in the case of plate bending, precise deformation would be very difficult due to spring-back caused by elastic recovery and the existence of tensile and compressive stresses on the two surfaces of the plate. Bauschinger effect complicates the

spring-back behaviour significantly.

In order to solve the problem, numerical models describing Bauschinger effect have been proposed by Armstrong and Frederic [1], Chaboche [2], and so on. These theories have been implemented into the finite element analysis and some improvement has been reported on the prediction of spring-back in plate bending. However, when the finite element method is applied for bending problems, it takes much time, in particular for the analysis of spring-back where the metal slides and rustles against tools. Imai et al. proposed a more practical method for the prediction of spring-back [3]. In the method, plate is pre-released just before the final release of the plate. During pre-release, spring-back behaviour is observed, and the final working conditions are determined based on the spring-back behaviour during the pre-release. However, this method is not general or versatile.

Therefore, the present study, a prediction method is proposed for the prediction of spring-back by a combination of the finite element analysis and bent-beam theory. The finite element method is used to calculate the bending shape and longitudinal stress distribution in the bent plate just before spring-back. The bent-beam theory is used to calculate spring-back based on the simulated results by the finite element method considering Bauschinger effect, which is described by a table of data. The table does not need the time-consuming identification trial of coefficients which are required for the ordinary numerical models of Bauschinger effect. This concise analysis method would be conducted for reduction of calculation time or operational convenience.

2 EXPERIMENTAL PROCEDURE

2.1 Plate bending

V-bending which is one of the most popular and common bending processes for plate is selected in this research. V-bending is classified into three methods, which includes air bending, bottoming, and coining. With increase of stroke of punch, contact area tends to increase, and bending state changes from air bending to bottoming and coining. In air bending as stoke is not so large, there are three line contacts. Bend angle and spring-back increase with increase of stroke. In bottoming, there are more than 5 line contacts, and area contact might start to appear depending conditions. As bending directions are opposite at different positions, spring-back becomes small. In coining, area contact governs the bending phenomena and the plate is high-pressured between die and punch at the end of bending leading to levelling of stress inside of the plate. This, air bending which is the most common and has high general versatility is used. Among the three methods, air bending is selected for investigation, as it is the most popular and concise method.

A common air bending is shown in Figure 1. Bending is conducted by pushing down a punch to the plate on a die. At this time, tensile stress appears on extrados of bending arc and compressive stress on intrados of bending arc. Plate is released after bent to a certain prescribed angle θe. After the release, the moment of external force is zero, and spring-back is occurred so that the moment of internal stress should be also zero. This spring-back is affected from Bauschinger effect because the strain of this spring-back is small. Experiment condition is shown in Table 1.

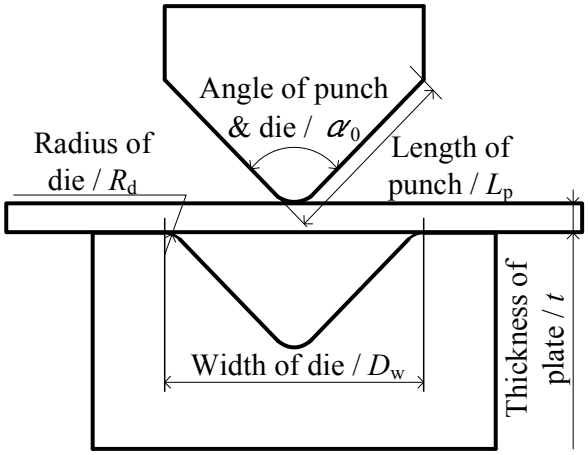

Figure 1: Schematic illustration of plate bending

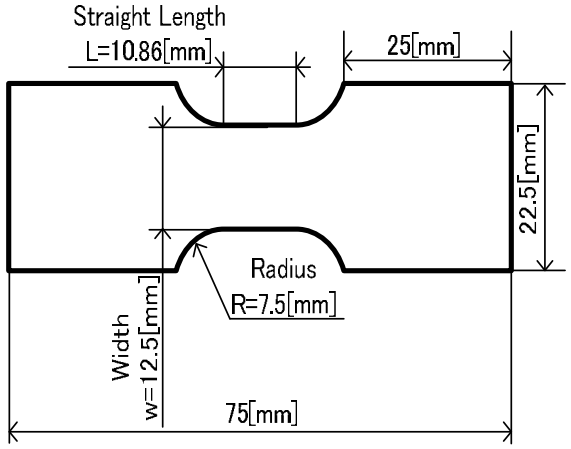

Figure 2: Test-piece for tensile-compressive test

Table 1: Parameter of bendind experiment

Parameter	Description
Material	SPCC
Angle of punch & die / α_p	88 [deg]
Length of punch / L_p	11.3 [mm]
Radius of die / R_d	1.5 [mm]
Width of die / D_w	18 [mm]
Thickness of sheet / t	1.17 [mm]

2.2 Measurement of stress-strain relationship

Tensile-compressive experiment was conducted to evaluate Bauschinger effect quantitatively. The shape of test piece which is used in tensile-compressive experiment is shown in Figure 2. The characteristic of this test piece is shorter parallel part than traditional test piece of industrial standard. However Stress-Strain diagram gained by using this test piece are similar to diagram gained by using traditional test piece.

3 ANALYSIS METHOD

A new numerical analysis was conducted by carrying out the finite element analysis followed by calculation based on bent-beam theory. The finite element method was applied for the first stage of bending, where the plate was pushed down by the punch up to a prescribed value. Based on stress distribution and the bent shape of the plate, analysis was conducted by bent-beam theory, whereby the curvature change is iteratively calculated so that the moment becomes zero through the whole plate in the longitudinal direction.

A flowchart of the analysis is shown in Figure 3, which would be explained as follows:

(1) Bending conditions are input, including characteristics of Bauschinger effect, which is given in the form of a table of data.

(2) The finite element analysis is carried out to calculate stress distribution and the shape of the plate.
(3) At the beginning of bent-beam analysis, the distribution of curvature change during spring-back is assumed.
(4) Based on the curvature change, the distribution of longitudinal strain change is calculated.
(5) Longitudinal stress is calculated from the strain change, using the table, which describes the relationship between strain and stress during unloading.
(6) By integrating the stress, moment distribution is estimated.
(7) If the moment is not zero through the plate, the assumed curvature distribution is modified. Steps from (4) - (7) are iterated until the moment is zero through the plate.

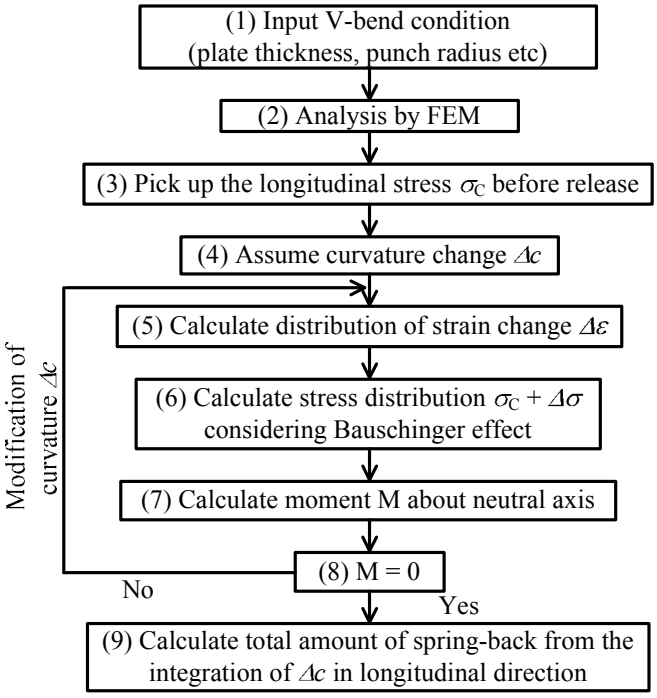

Figure 3: Method of building Bauschinger effect into analysis

3.1 FEM analysis

The commercial code ELFEN [5], which was developed by Rockfield Software Limited, Swansea, was used for the analysis of plate bending. Plane-strain elastic-plastic analysis was carried out using an implicit method. Von Mises yield criterion was adopted, and the normality principle was applied to the flow rule. Constraints were dealt with by the penalty function method. A quadrilateral element was used because of the simplicity of the material deformation. The F-bar method was applied to the element for overcoming volumetric locking with simple 4-node quadrilateral elements [6].

3.2 Bent-beam theory

Moment and spring-back were calculated by bent-beam theory. Firstly, curvature change Δc is assumed in the longitudinal position of the plate. Change of longitudinal strain $\Delta\varepsilon$ will be calculated from curvature change Δc as

$$\Delta\varepsilon = y\Delta c \ , \tag{1}$$

where, y = distance from neutral plane.
If the relationship between strain change $\Delta\varepsilon$ and stress change $\Delta\sigma$ as in Figure 4 during unloading is know as:

$$\Delta\sigma = f(\Delta c) \ , \tag{2}$$

the moment M will be calculated as

$$M = \int (\sigma_C - \Delta\sigma) y w dy \ , \tag{3}$$

where, σ_C = longitudinal stress at the end of bending and before spring-back, and w = plate width. Moment M should be zero after spring-back at any point in longitudinal position.

In bent-beam theory, spring-back angle $\Delta\theta$ is calculated from curvature change as shown in equation (4) [7]

$$\Delta\theta = \int_{S0}^{S1} \Delta c \, dS \ , \tag{4}$$

where, S = longitudinal position along the plate, S_0 = centre of the plate, S_1 = right end of the plate in FEM mesh in Figure 5.

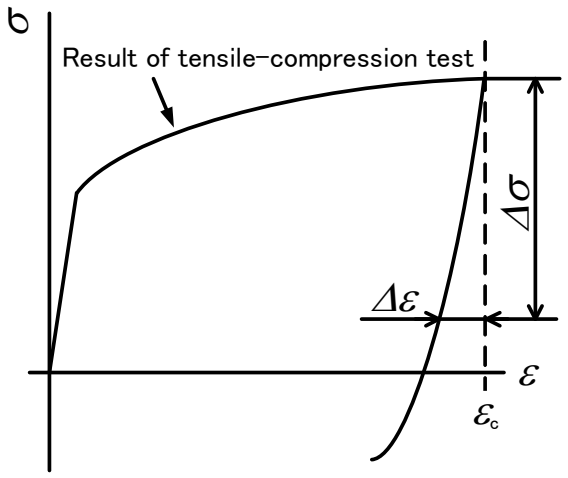

Figure 4: Definition of $\Delta\varepsilon$ and $\Delta\sigma$

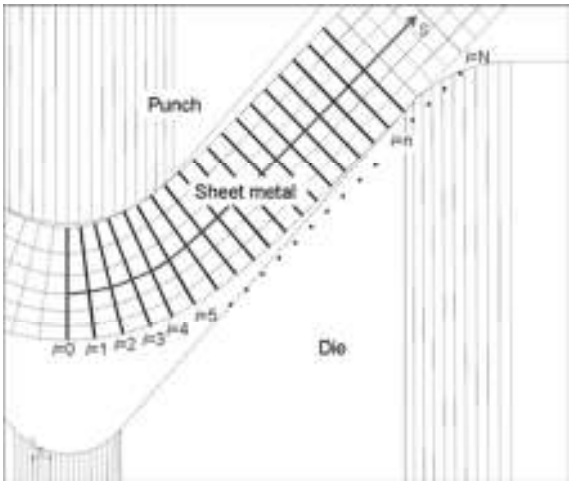

Figure 5: Calculation of curvature through plate

3.3 Experimental data on Bauschinger effect

The relationship between stress and strain during unloading, which is expressed by function $f(\varepsilon)$, was determined by tensile-compressive test. The results are shown in Figure 6. Conventional phenomenological description by Fredric and Armstrong is shown in Figure 7 for comparison with the proposed method. Armstrong and Frederic model is numerical expression being able to express Stress-Strain diagram including Bauschinger effect by combining nine parameters as shown in Table 2.

Bauschinger effect was certainly observed, i.e. absolute value of flow stress in compressive side is less than that in tensile side in experiment. Furthermore, Bauschinger effect increases with increase of deformation or strain ε, which cannot be expressed by the conventional phenomenological descriptions by Fredric and Armstrong.

As the experimentally obtained data was discrete as in Figure 8, $f(\varepsilon)$ should be determined. Approximation by some equation, such as quadratic curve, might be effective as in the literature [8]. Young's modulus E during unloading is equal to that during loading. Longitudinal plastic strain change $\Delta\varepsilon_p$ was calculated by subtracting elastic strain as

$$\Delta\varepsilon_p = \Delta\varepsilon - \frac{\Delta\sigma}{E} \tag{5}$$

$\Delta\sigma$ is non-dimensionalized by the maximum stress σ_{max}. The relationship between $\Delta\varepsilon_p$ and $\Delta\sigma / \sigma_{max}$ is shown in Figure 9. In the present research, $f(\varepsilon)$ was interpolated using experimental data as shown in Figure 10 in order to skip the identification procedure. Using data in the figure, intermediate data was interpolated in terms of pre-strain x, which is given during loading. Based on the interpolated data, $f(\varepsilon)$ was obtained by reconverting $\Delta\varepsilon_p$ and $\Delta\sigma / \sigma_{max}$ to $\Delta\varepsilon$ and $\Delta\sigma$.

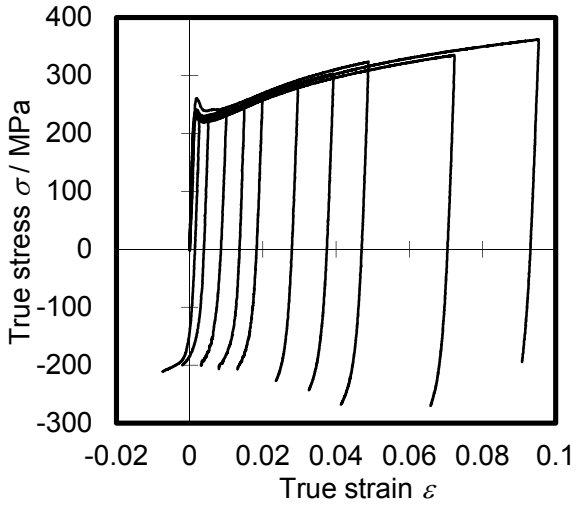

Figure 6: Experimental results of tensile-compressive test

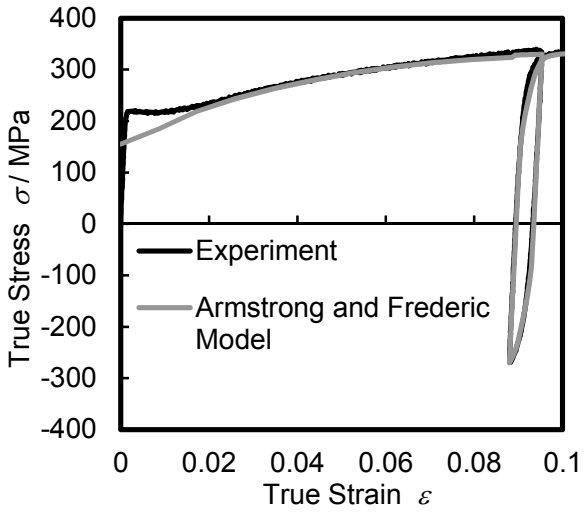

Figure 7: Discrete strain-stress diagram

Table 2: Function of each parameter

Description		Parameter
Young's modulus	E / MPa	210,000
Initial yield stress	σ_y / MPa	40
Limit of isotropic hardening	R_{inf} / MPa	275
Modulus commanding stress-strain curve of the part of compression	$\gamma_1, \gamma_2, \gamma_3$ / MPa	700, 100, 10
	χ_1, χ_2, χ_3	76, 30, 5

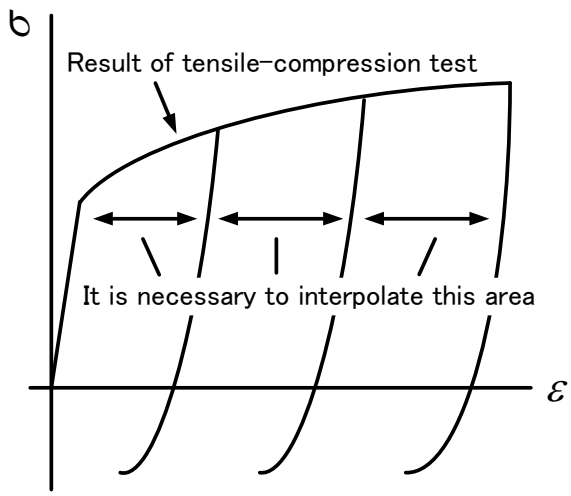

Figure 8: Discrete strain-stress diagram

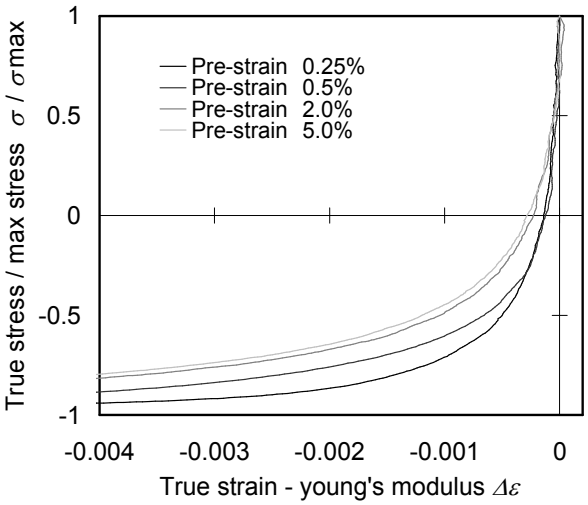

Figure 9: Stress and strain during unloading

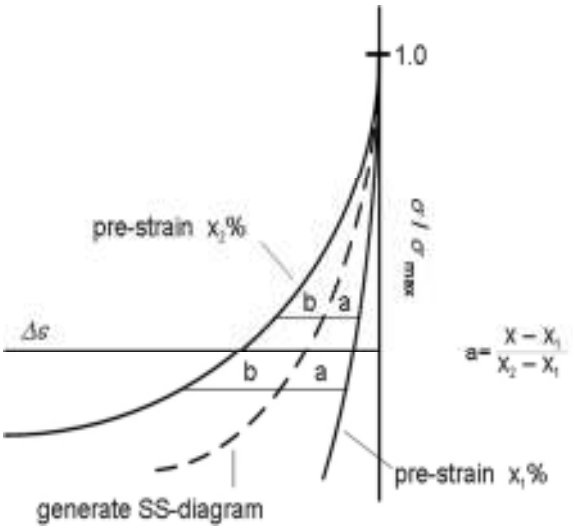

Figure 10: Interpolation of diagrams for intermediate pre-strain

4 COMPARISION BETWEEN ANALYTICAL AND EXPERIMENTAL RESULTS

Figure 11 shows the results on spring-back obtained by experiment, conventional FEM without kinematic hardening, FEM implemented with Fredric and Armstrong description of kinematic hardening, and proposed method whereby bent-beam theory was used for spring-back analysis following FEM of bending. The proposed method and FEM with kinematic hardening show a good agreement, and the calculation time for proposed method is about half of that for the latter method. There is still a discrepancy between analytical and experimental results. This might be attributed to dynamic effect, such as inertia and strain-rate dependency of material properties, because the bending speed is quite high in the experiment.

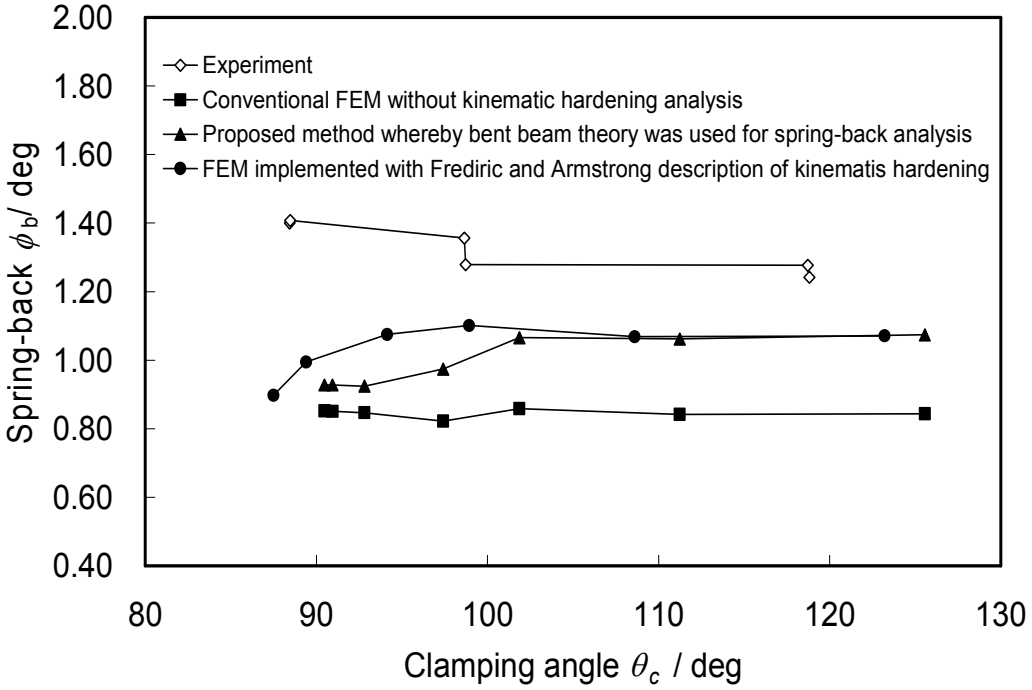

Figure 11: Comparison between experimental and analytical results (SPCC)

5 CONCLUSIONS

- A prediction method is proposed for the prediction of spring-back by a combination of the finite element analysis and bent-beam theory.
- The finite element method is used to calculate the bending shape and longitudinal stress distribution in the bent sheet metal just before spring-back.
- The bent-beam theory is used to calculate spring-back angle, which is described by a table of experimental data.
- The proposed method shows a good agreement with FEM result implemented with numerical description of kinematic hardening.
- The proposed method has an advantage on the calculation time against FEM.

ACKNOWLIDGEMENT

The present paper benefited partially through association with Rockfield Software Limited, Wales, UK. The analysis part of this research work was expedited thanks to Drs Rance, Armstrong, Dutko and other members.

REFERENCES

[1] Armstrong, P.J., Frederick, C.O. A mathematical representation of the multiaxial effect, CEGB Report RD/B/N731, (1966).
[2] Chaboche, J.L., Rousselier, G. On the plastic and viscoplastic constitutive equations, part i and II, J. Press. Vessel Technol.-Trans. ASME, (1983) 105-:153-164.
[3] Imai, K., Koyama, J., Jin, Y., Murata, M., Kuboki, T. Computational method for calculation of flange dimension in v-bending, Steel Res. Int., 2008, Vol. 79, pp. 209-216.

[4] Yskou, T. Iron and steel no.11, (1984), 1551-1558.
[5] Mullet, P., Rance, J. Applied discrete element technology, Bench Mark, 1996, 1, pp. 17-24.
[6] de Souza Neto, E.A., Peric, D., Dutko, M., Owen, D.R.J. Design of simple low order finite elements for large strain analysis of nearly incompressible solids, Int. J. Solids Struct., 1996, 33-20-22, pp. 3277-3296.
[7] Timoshenko, S. Strength of Materials, June 1940, D. Van Nostrand Company, Inc.
[8] Akiyama, M., Kobayashi, K., Nakai, T. Optimum Design of Roll Radius for Tube Bending, the Sumitomo Research, No. 40, 1989, pp.71-80.

XI International Conference on Computational Plasticity. Fundamentals and Applications
COMPLAS XI
E. Oñate, D.R.J. Owen, D. Peric and B. Suárez (Eds)

ENERGY FRICTIONAL DISSIPATING ALGORITHM FOR RIGID AND ELLASTIC BODY'S CONTACT PROBLEMS

R. Bravo* and J.L. Pérez–Aparicio†

* Department Structural Mechanics and Hydraulic Engineering
University of Granada Campues de Fuentenueva, 18071 Granada, Spain
e-mail: rbravo@ugr.es

† Department of Continuum Mechanics and Theory of Structures
Universidad Politécnica de Valencia
46022 Valencia, Spain
e-mail: jopeap@upvnet.upv.es

Key words: Contact, Time integration scheme, Consistent Dissipation, Friction

Abstract. An Energy Frictional Dissipating Algorithm (EFDA) for time integration of Coulomb frictional impact–contact problems is presented. Using the Penalty Method, and in the context of a conserving framework, linear and angular momenta are conserved and energy is consistently dissipated.

Published formulations were stable, forcing the energy dissipation to be monotonic in order to prevent unstable energy growth. The shortcoming of many was that they were not able to reproduce the real kinematics and dissipation of physical processes, provided by analytical formulations and experiments. EFDA formulates a conserving framework based on a physical energy dissipation estimator. This framework uses an enhanced Penalty contact model based on a spring and a dashpot, enforcing physical frictional energy dissipation, controlling gap vibrations and modifying the velocities and contact forces during each time step. The result is that the dissipated energy, kinematics and contact forces are consistent with the expected physical behavior.

1 INTRODUCTION

The numerically accurate analysis of frictional dynamic contact problems has been a challenge for the last 30 years. Complex problems do not have analytical solution and due to their high nonlinearity, non–smooth unilateral restriction and the presence friction, they are hard to model. Therefore, numerical time–stepping schemes are developed to emulate the conservative properties of the corresponding continuous problem.

Previous authors have addressed frictionless contact problems, for instance [7] focused on iterative but no time–stepping formulations, [1] and [3] for implicit. These authors

intended to create robust and stable algorithms for the enforcement of the contact constraints, while recent formulations have focused on frictional formulation and proposed unconditionally positive energy dissipation. Ref. [3] developed a positive energy dissipating algorithm, stable for friction with the Penalty Method and showed an artificial energy transfer between bodies–penalty springs in which the final energy was always lower than the initial for Stick and Slip cases. Therefore the behavior of the simulation was not consistent with the physical contact problem. Ref. [1] minimized that artificial energy transfer between body and penalty spring. For the non–sliding situation the energy after contact was equal to the initial and lower during contact while for the Slip case obtained a rigorous positive energy dissipation. The dissipation in both references was not based on a consistent conserving framework: the dissipation, although decreasing monotonically, was not in accordance to that of the continuous problem. Ref. [5] developed a conservative framework that enforced the impenetrability condition, eliminated the artificial energy transfer between body–penalty spring and took into account the frictional dissipation through an energy estimator. This formulation used a contact velocity that modified a predictor–corrector scheme, then the contact response agreed in velocities but not in forces and positions, not being accurate for persistent contact.

This article presents an Energy Frictional Dissipating Algorithm (EFDA) based on the frictionless algorithm of [2]. For Penalty contact problems, the new formulation conserves momenta, simulates the kinematics, contact forces and dissipates energy consistently, according to the physical problem in each time step. The algorithm key is a conservative framework based on updating contact forces and momenta for every contact. The framework takes into account dissipation by an energy estimator based on frictional Coulomb law, and is able to enforce energy conservation for the Stick contact and the right dissipation for the Slip contact.

2 DEFINITION OF THE PROBLEM AND GOVERNING EQUATIONS

2.1 Hamiltonian description of motion

The Hamiltonian Mechanics permit to obtain the equations of motion for multiple bodies that interact by contact. This subsection briefly describes the Hamiltonian equations for a continuous problem. Consider a manifold $\boldsymbol{Q}$ that describes the configuration of a mechanical system whose phase space is $\boldsymbol{P} = T^{\star}\boldsymbol{Q}$, the tangent space of $\boldsymbol{Q}$. This space is composed for each point of body i by positions $\boldsymbol{Q}^i(x, y, t)$ and linear momenta $\boldsymbol{P}^i(x, y, t)$ as function of time t. The Hamiltonian function $H\big[\boldsymbol{Q}^i(x, y, t), \boldsymbol{P}^i(x, y, t)\big]$ defines the total energy of the system and is assumed to be separable in kinetic $K(\boldsymbol{P}^i(x, y, t))$ and potential $V(\boldsymbol{Q}^i(x, y, t))$ energies, Eqs. 1.

$$H\big[\boldsymbol{Q}^i(x,y,t),\boldsymbol{P}^i(x,y,t)\big]=\sum_{i=1}^{n_{bd}}\big[K\big(\boldsymbol{P}^i(x,y,t)\big)+V\big(\boldsymbol{Q}^i(x,y,t)\big)\big]$$
$$K\big(\boldsymbol{P}^i(x,y,t)\big)=\frac{1}{2}\int_{\Omega^i}\frac{\boldsymbol{P}^i(x,y,t)^2}{\rho}\,\mathrm{d}\Omega \tag{1}$$

where n_{bd} is the total number of bodies, Ω^i the domain of body i and ρ the density. The kinetic energy is a real function $K:\boldsymbol{P}\rightarrow R$ and the potential $V:\boldsymbol{Q}\rightarrow R$ is an arbitrary function. The motion is governed by the Hamiltonian canonical equations, Eqs. 2.

$$\begin{aligned}\dot{\boldsymbol{Q}}^i(x,y,t) &= \frac{\partial H(x,y,t)}{\partial \boldsymbol{P}^i} &&= \int_{\Omega^i}\frac{\boldsymbol{P}^i(x,y,t)}{\rho}\,\mathrm{d}\Omega\\ \dot{\boldsymbol{P}}^i(x,y,t) &= -\frac{\partial H(x,y,t)}{\partial \boldsymbol{Q}^i} &&= -\nabla V\big(\boldsymbol{Q}^i(x,y,t)\big)\end{aligned} \tag{2}$$

The continuum variables from Eqs. 2 may be discretized, giving Eqs. 3.

$$\boldsymbol{Q}^i(x,y,t)=\sum_{A=1}^{n_{nod}}\boldsymbol{N}^A(x,y)\;\boldsymbol{q}^A(t)\;;\qquad \boldsymbol{P}^i(x,y,t)=\sum_{A=1}^{n_{nod}}\boldsymbol{N}^A(x,y)\;\boldsymbol{p}^A(t) \tag{3}$$

For the rigid bodies used in the current paper, this discretization is based on first order shape functions $N^A(x,y)$; for the elastic case they may be extended to higher order. For these first order functions, the discretization is based on only one node, $n_{nod}=1$, usually defined at the center of gravity x^i, y^i of each particle. The nodal displacements and linear momenta of all bodies i to k are grouped in the vectors $\boldsymbol{q}(t)$, $\boldsymbol{p}(t)$. For each body i, the discretization Eqs. 3 applied to Eqs. 2 produce the system of equations:

$$\dot{\boldsymbol{q}}^i=\boldsymbol{M}_i^{-1}\;\boldsymbol{p}^i\;;\qquad \dot{\boldsymbol{p}}^i=\boldsymbol{f}_c^i+\boldsymbol{f}_{ext}^i \tag{4}$$

where $\boldsymbol{M}_i$ is a diagonal mass matrix, with entries: $\boldsymbol{M}_i=\int_{\Omega^i}\rho\;[N^A(x,y)]^t N^A(x,y)\;\mathrm{d}\Omega$. Although contact forces $\boldsymbol{f}_c^i$ are applied in the contact points, the discretization considers an equivalent force applied to the nodes. The same thing can be said for the external forces $\boldsymbol{f}_{ext}^i$.

3 NEW ALGORITHM FORMULATION AND ENERGY–MOMENTUM CONSERVATION

The aim of this section is the discretization in time of Eqs. 4. The new equations will enforce the impenetrability condition and discretely inherit the conservation properties

through the conserving framework of section 4. The main three characteristic of this algorithm are: i) energy conservation for normal contact, ii) consistent dissipation for tangential Slip and iii) conservation for tangential Stick.

3.1 Time–discrete formulation

The frictional development of EFDA is based on the Simo–Tarnow's algorithm from [6], an energy–momentum conserving time integration scheme. This scheme is a discrete approximation of a Hamiltonian system (Eqs. 5) in time configuration $n+1/2$. Considering the interval $[t_n, t_{n+1}]$, the first set of equations of this algorithm relates displacements $\boldsymbol{q}^i_n$, $\boldsymbol{q}^i_{n+1}$ and linear momenta $\boldsymbol{p}^i_n$, $\boldsymbol{p}^i_{n+1}$; the second, is the discrete approximation of second Newton's law at $n + 1/2$:

$$\begin{array}{rclcrcl} \dot{\boldsymbol{q}}^i & = & \boldsymbol{M}_i^{-1}\, \boldsymbol{p}^i & \rightarrow & \dfrac{\boldsymbol{q}^i_{n+1} - \boldsymbol{q}^i_n}{\Delta t} & = & \boldsymbol{M}_i^{-1} \boldsymbol{p}^i_{n+\frac{1}{2}} \\ \dot{\boldsymbol{p}}^i & = & \boldsymbol{f}^i_{cN} + \boldsymbol{f}^i_{cT} & \rightarrow & \dfrac{\boldsymbol{p}^i_{n+1} - \boldsymbol{p}^i_n}{\Delta t} & = & \boldsymbol{f}^i_{cN\, n+\frac{1}{2}} + \boldsymbol{f}^i_{cT\, n+\frac{1}{2}} \end{array} \tag{5}$$

where $\Delta t = t_{n+1} - t_n$, $\boldsymbol{q}^i_n \approx \boldsymbol{q}^i(t_n)$, $\boldsymbol{p}^i_n \approx \boldsymbol{p}^i(t_n)$, $\boldsymbol{q}^i_{n+1} \approx \boldsymbol{q}^i(t_{n+1})$, $\boldsymbol{p}^i_{n+1} \approx \boldsymbol{p}^i(t_{n+1})$ and $\boldsymbol{p}^i_{n+1/2} = (\boldsymbol{p}^i_{n+1} + \boldsymbol{p}^i_n)/2$. The terms $\boldsymbol{f}^i_{cN\, n+1/2}$ and $\boldsymbol{f}^i_{cT\, n+1/2}$ are the discrete approximations of the resulting normal and tangential contact force vectors.

In order to obtain a conserving and a right kinematic response for contact between two bodies i, k, in EFDA additional linear momenta $\boldsymbol{p}^{ik}_{cN\, n+1/2}$, $\boldsymbol{p}^{ik}_{cT\, n+1/2}$ and contact forces $\boldsymbol{f}'^{ik}_{cN\, n+1/2}$, $\boldsymbol{f}'^{ik}_{cT\, n+1/2}$ (updating variables) are added to Eqs. 5, giving Eqs. 6. For these four variables, in the following the subscript $n + 1/2$ will be omitted for simplicity. The role of these new variables is to enforce bodies' energy conservation for normal contact and conservation–consistent dissipation for tangential, respectively:

$$\begin{array}{rclcrcl} \dfrac{\boldsymbol{q}^i_{n+1} - \boldsymbol{q}^i_n}{\Delta t} & = & \boldsymbol{M}_i^{-1} \left[\boldsymbol{p}^i_{n+\frac{1}{2}} + \displaystyle\sum_{\substack{k=1 \\ k\neq i}}^{n_{bd}} \left(\boldsymbol{p}^{ik}_{cN} + \boldsymbol{p}^{ik}_{cT} \right) \right] & = & \boldsymbol{M}_i^{-1} & \left(\boldsymbol{p}^i_{n+\frac{1}{2}} + \boldsymbol{p}^i_{cN} + \boldsymbol{p}^i_{cT} \right) \\ \dfrac{\boldsymbol{p}^i_{n+1} - \boldsymbol{p}^i_n}{\Delta t} & = & \displaystyle\sum_{\substack{k=1 \\ k\neq i}}^{n_{bd}} \left(\boldsymbol{f}^{ik}_{cN} + \boldsymbol{f}'^{ik}_{cN} + \boldsymbol{f}^{ik}_{cT} + \boldsymbol{f}'^{ik}_{cT} \right) & = & \boldsymbol{f}^i_{cN} + \boldsymbol{f}'^i_{cN} + \boldsymbol{f}^i_{cT} + \boldsymbol{f}'^i_{cT} & \end{array} \tag{6}$$

The expressions for the updating variables are now formulated in local contact coordinates and transformed to global by the unit normal and tangential vectors $\boldsymbol{N}^{ik}_{n+1/2}$, $\boldsymbol{T}^{ik}_{n+1/2}$, both at the contact point. To obtain from Eqs. 6 a conservative solution for Stick and dissipative for Slip, the updating variables must fulfill the discrete conserving equations defined in section 4. These variables are defined for both contact directions as:

$$
\begin{array}{ll}
\text{NORMAL} & \\
\boldsymbol{p}^{ik}_{cN} = \dfrac{\psi^{ik}_{2N}}{2} \boldsymbol{N}^{ik}_{n+\frac{1}{2}} \boldsymbol{N}^{ik\,t}_{n+\frac{1}{2}} (\boldsymbol{p}^{i}_{n+1} - \boldsymbol{p}^{i}_{n}); & \boldsymbol{f}'^{ik}_{cN} = \dfrac{\psi^{ik}_{1N}}{2} \boldsymbol{N}^{ik}_{n+\frac{1}{2}} K_N \ (g^{ik}_{Nn+1} - g^{ik}_{Nn}) \\
\text{TANG. STICK} & \\
\boldsymbol{p}^{ik}_{cT} = \dfrac{\psi^{ik}_{2T}}{2} \boldsymbol{T}^{ik}_{n+\frac{1}{2}} \boldsymbol{T}^{ik\,t}_{n+\frac{1}{2}} (\boldsymbol{p}^{i}_{n+1} - \boldsymbol{p}^{i}_{n}); & \boldsymbol{f}'^{ik}_{cT} = \dfrac{\psi^{ik}_{1T}}{2} \ \boldsymbol{T}^{ik}_{n+\frac{1}{2}} \ K_T \ (g^{ik}_{Tn+1} - g^{ik}_{Tn}) \\
\text{TANG. SLIP} & \\
\boldsymbol{p}^{ik}_{cT} = 0 \ ; \qquad \boldsymbol{f}'^{ik}_{cT} = 0; & \boldsymbol{f}^{ik}_{cT} = -\mu \ \Psi \ \left| \boldsymbol{f}^{ik}_{cN} + \boldsymbol{f}'^{ik}_{cN} \right| \ \boldsymbol{T}^{ik}_{n+\frac{1}{2}}
\end{array}
\tag{7}
$$

where K_N, K_T are user–defined penalties for normal and tangential contact, g^{ik}_{Nn+1}, g^{ik}_{Nn}, g^{ik}_{Tn+1}, g^{ik}_{Tn} normal and tangential gaps at n and $n+1$, $\Psi = \pm 1$ the Slip direction, μ the friction coefficient and $\psi^{ik}_{1N}, \psi^{ik}_{1T}, \psi^{ik}_{2N}$ and ψ^{ik}_{2T} proportionality parameters of the updating variables. Notice that $\boldsymbol{p}^{ik}_{cN}$, $\boldsymbol{f}'^{ik}_{cN}$, $\boldsymbol{p}^{ik}_{cT}$, $\boldsymbol{f}'^{ik}_{cT}$ (at $n+1/2$) enforce the conservative response for normal and tangential Stick contacts. On the other hand, for Slip $\boldsymbol{p}^{ik}_{cT} = \boldsymbol{f}'^{ik}_{cT} = 0$ since no tangential penalty spring is present; the new Coulomb friction force $\boldsymbol{f}^{ik}_{cT}$ is computed with the absolute value of the total (contact plus updating) normal contact forces. The normal and tangential–Stick contact forces $\boldsymbol{f}^{ik}_{cN}$, $\boldsymbol{f}^{ik}_{cT}$ are defined in Eqs. 8 using the [4] derivative, providing a discrete expression that conserves the artificial penalty energy.

$$
\begin{aligned}
\boldsymbol{f}^{i}_{cN} = \sum_{\substack{k=1 \\ k\neq i}}^{n_{bd}} \boldsymbol{f}^{ik}_{cN} = \sum_{\substack{k=1 \\ k\neq i}}^{n_{bd}} \frac{V(g^{ik}_{Nn+1}) - V(g^{ik}_{Nn})}{g^{ik}_{Nn+1} - g^{ik}_{Nn}} \ \boldsymbol{N}^{ik}_{n+\frac{1}{2}} = \sum_{\substack{k=1 \\ k\neq i}}^{n_{bd}} K_N \ \boldsymbol{N}^{ik}_{n+\frac{1}{2}} \ (g^{ik}_{Nn+1} + g^{ik}_{Nn}) \\
\boldsymbol{f}^{i}_{cT} = \sum_{\substack{k=1 \\ k\neq i}}^{n_{bd}} \boldsymbol{f}^{ik}_{cT} = \sum_{\substack{k=1 \\ k\neq i}}^{n_{bd}} \frac{V(g^{ik}_{Tn+1}) - V(g^{ik}_{Tn})}{g^{ik}_{Tn+1} - g^{ik}_{Tn}} \ \boldsymbol{T}^{ik}_{n+\frac{1}{2}} = \sum_{\substack{k=1 \\ k\neq i}}^{n_{bd}} K_T \ \boldsymbol{T}^{ik}_{n+\frac{1}{2}} \ (g^{ik}_{Tn+1} + g^{ik}_{Tn})
\end{aligned}
$$

where $V(g^{ik}_{Nn+1}) = K_N (g^{ik}_{Nn+1})^2/2, V(g^{ik}_{Nn}) = K_N (g^{ik}_{Nn})^2/2$ are the normal and $V(g^{ik}_{Tn+1}) = K_T (g^{ik}_{Tn+1})^2/2$, $V(g^{ik}_{Tn}) = K_T (g^{ik}_{Tn})^2/2$, the tangential penalty potential contact energies.

4 DISCRETE LINEAR, ANGULAR MOMENTUM CONSERVATION AND CONSISTENT BODY ENERGY DISSIPATION

This section develops the discrete conserving framework of EFDA to obtain the body energy conservation for normal contact and conservation–dissipation for tangential.

4.1 Discrete linear momentum balance

The discrete variation of the linear momentum of EFDA is defined through the second of Eqs. 6, the discrete counterpart of second Newton's law. Therefore, for body i the resultant of the normal contact forces $\boldsymbol{f}^{i}_{cN}$, $\boldsymbol{f}'^{i}_{cN}$ plus the tangential $\boldsymbol{f}^{i}_{cT}, \boldsymbol{f}'^{i}_{cT}$ is equal to the discrete linear momentum balance between n and $n+1$. Also, the total linear momentum

balance (Eq. 8) is the summation over that of each body and equals the resultant of the contact forces on n_{bd}.

$$\frac{\boldsymbol{p}^{tot}_{n+1} - \boldsymbol{p}^{tot}_{n}}{\Delta t} = \sum_{i=1}^{n_{bd}} \left(\boldsymbol{f}^{i}_{cN} + \boldsymbol{f}'^{i}_{cN} + \boldsymbol{f}^{i}_{cT} + \boldsymbol{f}'^{i}_{cT} \right) = \sum_{i=1}^{n_{bd}} \sum_{\substack{k=1 \\ k \neq i}}^{n_{bd}} \left(\boldsymbol{f}^{ik}_{cN} + \boldsymbol{f}'^{ik}_{cN} + \boldsymbol{f}^{ik}_{cT} + \boldsymbol{f}'^{ik}_{cT} \right) \quad (8)$$

Given two bodies i, k in contact, due to the AR principle: $\boldsymbol{f}^{ik}_{cN} = -\boldsymbol{f}^{ki}_{cN}$, $\boldsymbol{f}'^{ik}_{cN} = -\boldsymbol{f}'^{ki}_{cN}$, $\boldsymbol{f}^{ik}_{cT} = -\boldsymbol{f}^{ki}_{cT}$, $\boldsymbol{f}'^{ik}_{cT} = -\boldsymbol{f}'^{ki}_{cT}$ for Stick and $\boldsymbol{f}^{ik}_{cT} = -\boldsymbol{f}^{ki}_{cT}$, $\boldsymbol{f}'^{ik}_{cT} = \boldsymbol{f}'^{ki}_{cT} = 0$ for Slip. Then, the right term of Eq. 8 is zero in all situations and $\boldsymbol{p}^{tot}_{n+1} = \boldsymbol{p}^{tot}_{n}$.

4.2 Discrete angular momentum balance

We again redefine the variables $\boldsymbol{q}^{i}_{n+1}$, $\boldsymbol{q}^{i}_{n}$ as the positions of the contact point. From the second of Eqs. 6 and multiplying by the cross product $\times(\boldsymbol{q}^{i}_{n+1} - \boldsymbol{q}^{i}_{n})$, the discrete angular momentum balance for a body i is:

$$\frac{\boldsymbol{p}^{i}_{n+1} - \boldsymbol{p}^{i}_{n}}{\Delta t} \times (\boldsymbol{q}^{i}_{n+1} - \boldsymbol{q}^{i}_{n}) = \frac{\boldsymbol{J}^{i}_{n+1} - \boldsymbol{J}^{i}_{n}}{\Delta t} = \sum_{\substack{k=1 \\ k \neq i}}^{n_{bd}} \left(\boldsymbol{f}^{ik}_{cN} + \boldsymbol{f}'^{ik}_{cN} + \boldsymbol{f}^{ik}_{cT} + \boldsymbol{f}'^{ik}_{cT} \right) \times (\boldsymbol{q}^{i}_{n+1} - \boldsymbol{q}^{i}_{n}) \quad (9)$$

Invoking the AR principle and expressing the position's increments as function of the normal gap $(\boldsymbol{q}^{i}_{n+1} - \boldsymbol{q}^{i}_{n}) - (\boldsymbol{q}^{k}_{n+1} - \boldsymbol{q}^{k}_{n}) = g^{ik}_{Nn+1/2}\ (\boldsymbol{N}^{ki})^{t}$, the total angular momentum balance for n_{bd} is:

$$\frac{\boldsymbol{J}^{tot}_{n+1} - \boldsymbol{J}^{tot}_{n}}{\Delta t} = \sum_{i=1}^{n_{bd}} \sum_{k=i+1}^{n_{bd}} \left(\boldsymbol{f}^{ik}_{cN} + \boldsymbol{f}'^{ik}_{cN} + \boldsymbol{f}^{ik}_{cT} + \boldsymbol{f}'^{ik}_{cT} \right) \times g^{ik}_{Nn+\frac{1}{2}} (\boldsymbol{N}^{ki})^{t} \quad (10)$$

Since vectors $\boldsymbol{f}^{ik}_{cN} + \boldsymbol{f}'^{ik}_{cN}$, and the normal gap are collinear, their cross product is zero. The product between $\boldsymbol{f}^{ik}_{cT} + \boldsymbol{f}'^{ik}_{cT}$ and this gap is also zero since the tangential contact forces depend on the tangential gap: after some algebra we arrive to the triple product $(\boldsymbol{T}^{ik}_{n+1/2})^{t}\ \boldsymbol{T}^{ik}_{n+1/2} \times g^{ik}_{Nn+1/2} (\boldsymbol{N}^{ki})^{t}$ that is zero since the first vector is orthogonal to the cross product.

4.3 Discrete total bodies' energy balance

This equation is obtained by premultiplying both Eqs. 6 by $(\boldsymbol{p}^{i}_{n+1} - \boldsymbol{p}^{i}_{n})^{t}$ and $-(\boldsymbol{q}^{i}_{n+1} - \boldsymbol{q}^{i}_{n})^{t}$ respectively, then added for all contacting bodies n_{bd}. After some algebra:

$$\begin{aligned}\Delta E_{kin} = & \sum_{i=1}^{n_{bd}} \underbrace{(\boldsymbol{p}_{n+1}^{i} - \boldsymbol{p}_{n}^{i})^{t}\ \boldsymbol{M}_{i}^{-1}\ \boldsymbol{p}_{n+\frac{1}{2}}^{i}}_{\Delta E_{kin}^{i}} = -\sum_{i=1}^{n_{bd}} \sum_{\substack{k=1 \\ k\neq i}}^{n_{bd}} \Big[- \underbrace{(\boldsymbol{q}_{n+1}^{i} - \boldsymbol{q}_{n}^{i})^{t}\ \boldsymbol{f}_{cT}^{ik}}_{\Delta E_{\boldsymbol{f}_{cT}^{ik}}} \Big] \\ & + \sum_{i=1}^{n_{bd}} \sum_{\substack{k=1 \\ k\neq i}}^{n_{bd}} \Big[\underbrace{(\boldsymbol{q}_{n+1}^{i} - \boldsymbol{q}_{n}^{i})^{t}\ \boldsymbol{f}_{cN}^{ik}}_{\Delta E_{\boldsymbol{f}_{cN}^{ik}}} - \underbrace{(\boldsymbol{p}_{n+1}^{i} - \boldsymbol{p}_{n}^{i})^{t}\ \boldsymbol{M}_{i}^{-1}\ \boldsymbol{p}_{cN}^{ik}}_{\Delta E_{\boldsymbol{p}_{cN}^{ik}}(\psi_{2N}^{ik})} \\ & - \underbrace{(\boldsymbol{p}_{n+1}^{i} - \boldsymbol{p}_{n}^{i})^{t}\ \boldsymbol{M}_{i}^{-1}\ \boldsymbol{p}_{cT}^{ik}}_{\Delta E_{\boldsymbol{p}_{cT}^{ik}}(\psi_{2T}^{ik})} - \underbrace{(\boldsymbol{q}_{n+1}^{i} - \boldsymbol{q}_{n}^{i})^{t}\ \boldsymbol{f}_{cN}^{\prime ik}}_{\Delta E_{\boldsymbol{f}_{cN}^{\prime ik}}(\psi_{1N}^{ik})} - \underbrace{(\boldsymbol{q}_{n+1}^{i} - \boldsymbol{q}_{n}^{i})^{t}\ \boldsymbol{f}_{cT}^{\prime ik}}_{\Delta E_{\boldsymbol{f}_{cT}^{\prime ik}}(\psi_{1T}^{ik})} \Big] \end{aligned} \tag{11}$$

where $\Delta E_{kin}^{i} = E_{n+1}^{i} - E_{n}^{i}$ is the kinetic body energy balance between n and $n+1$ when bodies are rigid and external forces are not applied. Then, $\Delta E_{\boldsymbol{f}_{cN}^{ik}}$, $\Delta E_{\boldsymbol{f}_{cT}^{ik}}$ are the contact forces energy balance and $\Delta E_{\boldsymbol{p}_{cN}^{ik}}(\psi_{2N}^{ik})$, $\Delta E_{\boldsymbol{p}_{cT}^{ik}}(\psi_{2T}^{ik})$, $\Delta E_{\boldsymbol{f}_{cN}^{\prime ik}}(\psi_{1N}^{ik})$, $\Delta E_{\boldsymbol{f}_{cT}^{\prime ik}}(\psi_{1T}^{ik})$, all functions of the proportionality parameters, are the updating variables energy balance.

This equation is the conserving framework that relates the total bodies' energy balance with that of the updating variables. The role of energy conservation for normal contact is included in the terms $\Delta E_{\boldsymbol{f}_{cN}^{ik}}$, $\Delta E_{\boldsymbol{f}_{cN}^{\prime ik}}(\psi_{1N}^{ik})$, $\Delta E_{\boldsymbol{p}_{cN}^{ik}}(\psi_{2N}^{ik})$, while dissipation–conservation for Slip and Stick is included in the terms $\Delta E_{\boldsymbol{f}_{cT}^{ik}}$, $\Delta E_{\boldsymbol{f}_{cT}^{\prime ik}}(\psi_{1T}^{ik})$, $\Delta E_{\boldsymbol{p}_{cT}^{ik}}(\psi_{2T}^{ik})$. Therefore, the energy loss is always consistent since the dissipation is included in the energy balance.

Notice that ΔE_{kin} is the total energy for all bodies. Since the energy related to normal contact is conserved, ψ_{1N}^{ik}, ψ_{2N}^{ik} may be positive or negative, and $\Delta E_{\boldsymbol{p}_{cN}^{ik}}$, $\Delta E_{\boldsymbol{f}_{cN}^{\prime ik}}$ add or subtract energy. The same can be said for ψ_{1T}^{ik}, ψ_{2T}^{ik} for the Stick and Slip cases:

STICK: the energy is conserved since the contact force does not create–dissipate tangential work. This condition is enforced by zeroing the right part of Eq. 11:

$$0 = \sum_{i=1}^{n_{bd}} \sum_{\substack{k=1 \\ k\neq i}}^{n_{bd}} \Big[\Delta E_{\boldsymbol{f}_{cT}^{ik}} + \Delta E_{\boldsymbol{f}_{cN}^{ik}} + \Delta E_{\boldsymbol{p}_{cN}^{ik}} + \Delta E_{\boldsymbol{p}_{cT}^{ik}} + \Delta E_{\boldsymbol{f}_{cN}^{\prime ik}} + \Delta E_{\boldsymbol{f}_{cT}^{\prime ik}} \Big] \tag{12}$$

This equation provides infinite relationships that satisfy the total bodies' energy conservation for ψ_{1N}^{ik}, ψ_{2N}^{ik}, ψ_{1T}^{ik}, ψ_{2T}^{ik}. Using the AR principle and the reciprocities $\psi_{1N}^{ik} = \psi_{1N}^{ki}$, $\psi_{2N}^{ik} = \psi_{2N}^{ki}$, $\psi_{1T}^{ik} = \psi_{1T}^{ki}$ and $\psi_{2T}^{ik} = \psi_{2T}^{ki}$, Eq. 12 may be decoupled for the normal (Eq. 13) and tangential (Eq. 14) contacts between bodies i, k as:

$$\begin{aligned} & \underbrace{(\boldsymbol{p}_{n+1}^{i} - \boldsymbol{p}_{n}^{i})^{t}\ \boldsymbol{M}_{i}^{-1}\ \boldsymbol{p}_{cN}^{ik}}_{\Delta E_{\boldsymbol{p}_{cN}^{ik}}(\psi_{2N}^{ik})} + \underbrace{(\boldsymbol{p}_{n+1}^{k} - \boldsymbol{p}_{n}^{k})^{t}\ \boldsymbol{M}_{k}^{-1}\ \boldsymbol{p}_{cN}^{ki}}_{\Delta E_{\boldsymbol{p}_{cN}^{ki}}(\psi_{2N}^{ik})} + \underbrace{\big[(\boldsymbol{q}_{n+1}^{i} - \boldsymbol{q}_{n}^{i})^{t} - (\boldsymbol{q}_{n+1}^{k} - \boldsymbol{q}_{n}^{k})^{t}\big]\ \boldsymbol{f}_{cN}^{ik}}_{\Delta E_{\boldsymbol{f}_{cN}^{ik}}} \\ & + \underbrace{\big[(\boldsymbol{q}_{n+1}^{i} - \boldsymbol{q}_{n}^{i})^{t} - (\boldsymbol{q}_{n+1}^{k} - \boldsymbol{q}_{n}^{k})^{t}\big]\ \boldsymbol{f}_{cN}^{\prime ik}}_{\Delta E_{\boldsymbol{f}_{cN}^{\prime ik}}(\psi_{1N}^{ik})} = 0 \end{aligned} \tag{13}$$

$$\underbrace{(\boldsymbol{p}^i_{n+1}-\boldsymbol{p}^i_n)^t\ \boldsymbol{M}_i^{-1}\ \boldsymbol{p}^{ik}_{cT}}_{\Delta E_{\boldsymbol{p}^{ik}_{cT}}(\psi^{ik}_{2T})}+\underbrace{(\boldsymbol{p}^k_{n+1}-\boldsymbol{p}^k_n)^t\ \boldsymbol{M}_k^{-1}\ \boldsymbol{p}^{ki}_{cT}}_{\Delta E_{\boldsymbol{p}^{ki}_{cT}}(\psi^{ik}_{2T})}+\underbrace{\left[(\boldsymbol{q}^i_{n+1}-\boldsymbol{q}^i_n)^t\ -(\boldsymbol{q}^k_{n+1}-\boldsymbol{q}^k_n)^t\ \right]\ \boldsymbol{f}^{ik}_{cT}}_{\Delta E_{\boldsymbol{f}^{ik}_{cT}}}$$
$$+\underbrace{\left[(\boldsymbol{q}^i_{n+1}-\boldsymbol{q}^i_n)^t-(\boldsymbol{q}^k_{n+1}-\boldsymbol{q}^k_n)^t\right]\ \boldsymbol{f}'^{ik}_{cT}}_{\Delta E_{\boldsymbol{f}'^{ik}_{cT}}(\psi^{ik}_{1T})}=0 \tag{14}$$

Both imply that the energy transferred to the normal and tangential penalty springs is recovered by the updating variables. The energies $\Delta E_{\boldsymbol{p}^{ik}_{cN}}$, $\Delta E_{\boldsymbol{p}^{ik}_{cT}}$ enforce the total bodies' energy conservation, while $\Delta E_{\boldsymbol{f}'^{ik}_{cN}}$, $\Delta E_{\boldsymbol{f}'^{ik}_{cT}}$ adjust the contact forces to the conservative solution.

SLIP: from physical considerations, the total energy dissipated by friction must be equal to the increment of total energy, $E_{n+1}-E_n=-\sum_{i=1}^{n_{bd}}\ \sum_{\substack{k=1\\k\neq i}}^{n_{bd}}\Delta E_{\boldsymbol{f}^{ik}_{cT}}$. This equality is enforced by EFDA zeroing the last summation of Eq. 11. Also, $\Delta E_{\boldsymbol{p}^{ik}_{cT}}(\psi^{ik}_{2T})=\Delta E_{\boldsymbol{f}'^{ik}_{cT}}(\psi^{ik}_{1T})=0$ and $\psi^{ik}_{1T}=\psi^{ik}_{2T}=0$ since there is no penalty spring in the tangential direction, see the Slip condition in Eq. 7. Therefore, the equation that provides the infinite (therefore undetermined) relations between ψ^{ik}_{1N}, ψ^{ik}_{2N} is:

$$\sum_{i=1}^{n_{bd}}\ \sum_{\substack{k=1\\k\neq i}}^{n_{bd}}\left[\underbrace{(\boldsymbol{p}^i_{n+1}-\boldsymbol{p}^i_n)^t\ \boldsymbol{M}_i^{-1}\ \boldsymbol{p}^{ik}_{cN}}_{\Delta E_{\boldsymbol{p}^{ik}_{cN}}(\psi^{ik}_{2N})}+\underbrace{(\boldsymbol{q}^i_{n+1}-\boldsymbol{q}^i_n)^t\ \boldsymbol{f}^{ik}_{cN}}_{\Delta E_{\boldsymbol{f}^{ik}_{cN}}}+\underbrace{(\boldsymbol{q}^i_{n+1}-\boldsymbol{q}^i_n)^t\ \boldsymbol{f}'^{ik}_{cN}}_{\Delta E_{\boldsymbol{f}'^{ik}_{cN}}(\psi^{ik}_{1N})}\right]=0 \tag{15}$$

that represents a normal contact energy balance for all bodies. As in the previous case, this balance is enforced for every contact; using again AR, reciprocities $\psi^{ik}_{1N}=\psi^{ki}_{1N}$, $\psi^{ik}_{2N}=\psi^{ki}_{2N}$ and decoupling Eq. 15 for every contact, one arrives to relationships between ψ^{ik}_{1N}, ψ^{ik}_{2N}:

$$\underbrace{(\boldsymbol{p}^i_{n+1}-\boldsymbol{p}^i_n)^t\ \boldsymbol{M}_i^{-1}\ \boldsymbol{p}^{ik}_{cN}}_{\Delta E_{\boldsymbol{p}^{ik}_{cN}}(\psi^{ik}_{2N})}+\underbrace{(\boldsymbol{p}^k_{n+1}-\boldsymbol{p}^k_n)^t\ \boldsymbol{M}_k^{-1}\ \boldsymbol{p}^{ki}_{cN}}_{\Delta E_{\boldsymbol{p}^{ki}_{cN}}(\psi^{ik}_{2N})}+$$
$$\underbrace{\left[(\boldsymbol{q}^i_{n+1}-\boldsymbol{q}^i_n)^t-(\boldsymbol{q}^k_{n+1}-\boldsymbol{q}^k_n)^t\right]\ \boldsymbol{f}^{ik}_{cN}}_{\Delta E_{\boldsymbol{f}^{ik}_{cN}}}+\underbrace{\left[(\boldsymbol{q}^i_{n+1}-\boldsymbol{q}^i_n)^t-(\boldsymbol{q}^k_{n+1}-\boldsymbol{q}^k_n)^t\right]\ \boldsymbol{f}'^{ik}_{cN}}_{\Delta E_{\boldsymbol{f}'^{ik}_{cN}}(\psi^{ik}_{1N})}=0 \tag{16}$$

The condition at the beginning of the SLIP item and the last equation, enforce both the energy conservation of the normal contact and the dissipation for tangential contact.

5 DYNAMIC CONTACT, ENHANCED PENALTY METHOD

For every contact, Eqs. 13, 14, 16 provide a non–unique relation between $\psi^{ik}_{1N},\psi^{ik}_{2N}$ and $\psi^{ik}_{1T},\psi^{ik}_{2T}$ respectively that automaticaly conserve or dissipate consistently the total

energy for the tangential Stick and Slip cases. Using modal analysis decomposition, [2], it is possible to obtain the second order dynamic equation associated with the descriptive algorithm of Eqs. 6, defining an enhanced penalty contact model. The model described by Eqs. 17 consists of a spring and dashpot that control the gap and the penetration velocity, respectively.

$$\begin{aligned} 0 &= \ddot{q}_{Nn+1/2} + \overbrace{\omega_N^2\ \Delta t\ \frac{\psi_{1N}+\psi_{2N}}{2}}^{2\xi_N\omega_N}\dot{q}_{Nn+1/2} + \omega_N^2\ q_{Nn+1/2} \\ 0 &= \underbrace{\ddot{q}_{Tn+1/2}}_{\text{Inertia}} + \underbrace{\overbrace{\omega_T^2\ \Delta t\ \frac{\psi_{1T}+\psi_{2T}}{2}}^{2\xi_T\omega_T}\dot{q}_{Tn+1/2}}_{\text{Dashpot}} + \underbrace{\omega_T^2\ q_{Tn+1/2}}_{\text{Spring}} \end{aligned} \tag{17}$$

The variables $q_{Nn+1/2}$, $q_{Tn+1/2}$ represent the particle motion in normal and tangential direction. The dashpots are controlled by the user–defined parameters ξ_N, ξ_T, a penalization for penetration velocities that approximately enforce the consistency Kuhn–Tucker condition. Eqs. 17 provide the relations that can be easily generalized for any contact between rigid bodies i, k:

$$\psi_{1N}^{ik} + \psi_{2N}^{ik} = \frac{4\xi_N}{\Omega_N^{ik}}\ ; \qquad \psi_{1T}^{ik} + \psi_{2T}^{ik} = \frac{4\xi_T}{\Omega_T^{ik}} \tag{18}$$

where $\Omega_N^{ik} = \omega_N^{ik}\ \Delta t$, $\Omega_T^{ik} = \omega_T^{ik}\ \Delta t$, $\omega_N^{ik} = \sqrt{K_N/m}$, $\omega_T^{ik} = \sqrt{K_T/m}$, and m is the largest of the two contacting masses. The combination of Eqs. 13, 14, 16 with Eq. 18 provide the unique explicit expressions for $\psi_{1N}^{ik}, \psi_{2N}^{ik}$ and $\psi_{1T}^{ik}, \psi_{2T}^{ik}$. The insertion of these expressions in Eqs. 6 enforces a conservative response for Stick and consistent dissipative for Slip.

6 NUMERICAL SIMULATIONS

6.1 Elliptical particle Carom problem

In this subsection, the trajectory of the successive impacts of a rigid ellipse inside a one–meter square is simulated. The ellipse, of axes 15/6 cm is initially positioned at $(0.45, 0.1)$ m, inclination $\alpha = 50°$ as seen in Fig. 1 top, and it is subjected to initial velocity $V_x = 1, V_y = -0.4$ m/s in direction $\theta = -22°$, without spin. The friction angle is $\phi = 15°$ and the rest of the numerical parameters are the same as those in the previous simulation. To visualize the rotation of the ellipse, the orientation is defined by the largest semiaxis.

Figs. 1 depict the evolution of trajectory (top), linear velocities (left), rotational velocity and energy (right) from EFDA and from the analytical solution reproduced in the

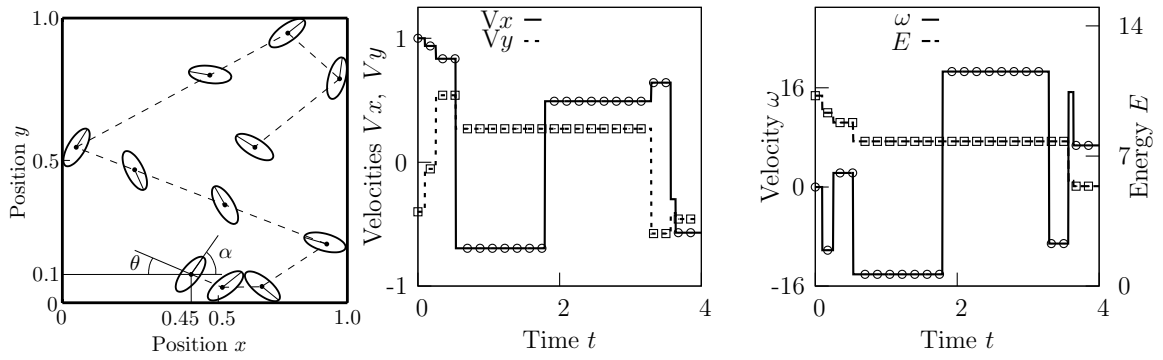

Figure 1: Carom problem with an elliptical particle: trajectory (top), linear velocities (bottom left), rotational velocity and total energy (bottom right). In the three, analytical (symbols) and numerical (lines) distributions coincide.

Appendix. First, the ellipse impacts against the bottom side of the box and consequently rotates since the line of action of the resultant contact force does not intersect the center of gravity, Figs. 1 top and bottom right. The initial V_x is larger than V_y, therefore, the contact point Slips along the horizontal side dissipating energy. Successive impacts decrease the tangential (with respect to any side) velocity, Fig. 1 bottom left. It is important to note that impacts may be conservative for one contact and dissipative for others: the velocity relation changes in every impact. This can be appreciated in Fig. 1 bottom right, where for impacts at $t \approx 1.8$, $t \approx 3.2$ s the energy is conserved, and at others dissipated, such as those before $t \approx 0.4$ and at $t \approx 3.5$, $t \approx 3.7$ s. Numerical and analytical results coincide perfectly since both EFDA and the analytical formulation are developed enforcing the energy conservation for normal contact and conservation–consistent dissipation for tangential.

6.2 The concave pendulum problem

The motion decay of two symmetrical positioned rigid disks resting on a semicircular rough surface under the action of gravity is analyzed, Fig. 2. In this problem, there are two sources of energy dissipation: friction between disk and surface, and frictional impact between disks. After every impact both disks periodically return to a lower height, until the motion stops. The disk and surface radii are 0.1, 0.5 m respectively, the friction angle is $\phi = 15°$, the initial position is defined by the angle $\gamma_{t0} = 45°$ and the initial velocity is zero.

In Figs. 3 left and right, results at the center of gravity are shown for only one of the disks, since the problem is symmetric. The left graphic depicts the polar position γ and velocity $\dot{\gamma}$, while the right one, the total energy E and the rotational velocity ω.

With the prescribed initial conditions, both disks slide from the beginning (dissipating energy) and eventually impact right at the bottom at $t \approx 0.3$ s. Before this first impact,

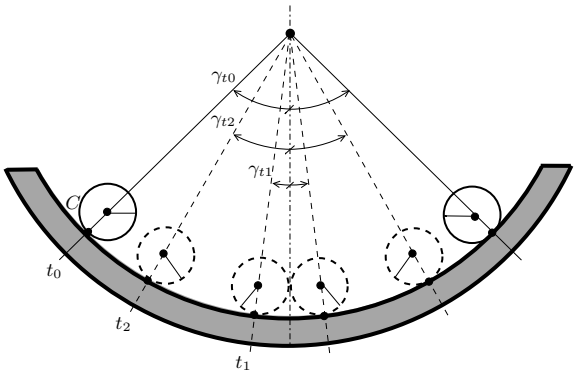

Figure 2: Pendulum problem. Initial, impact and maximum height after first impact defined by γ_{t_0}, γ_{t_1} and γ_{t_2}.

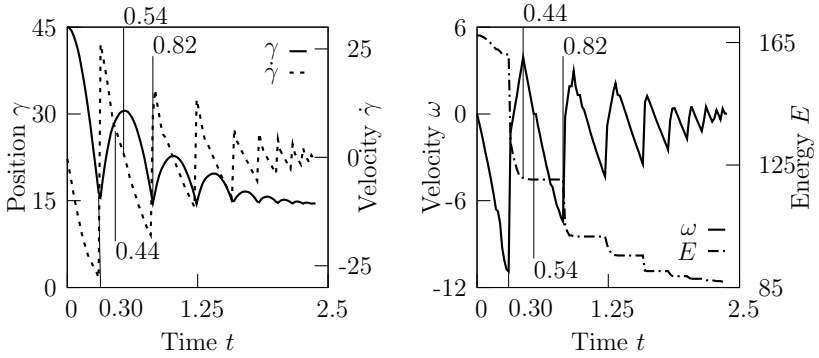

Figure 3: Pendulum problem. Evolution of center of gravity position γ, velocity $\dot{\gamma}$, rotational velocity ω and energy E with time t.

ω and $\dot{\gamma}$ increase (in modulus), while E decreases. At the moment of the first impact, $\dot{\gamma}$ and ω suddenly increase and reverse their values (abrupt change in the distributions) and the total energy E decreases also suddenly. As expected, the angular velocity ω reaches a maximum when the velocity of the contact point is zero $V_C = 0$ at $t_{roll} \approx 0.44$ s, then the disks start rolling and stop dissipating energy by friction. During rolling $\omega, \dot{\gamma}$ decrease to zero at $t \approx 0.54$ s the disks achieves its maximum height for the oscillation and therefore γ is maximum. Immediately, the disks continue rolling although downwards, increasing $\dot{\gamma}$ and ω until $t \approx 0.82$ s, when a new impact occurs. This sequence repeats continuously with a motion decay after every impact; the simulation stops when the energy loss is smaller than a fixed tolerance.

7 CONCLUSIONS

- The development of an energy frictional dissipating algorithm for contact problems (EFDA), that conserves momenta and dissipates energy according to the frictional Coulomb law, is presented. The key of EFDA is that conservation–dissipation is consistently enforced in a conserving framework through the modification of the contact kinematics with an additional linear momentum and a contact force.

- The energy of the normal contact is also conserved, therefore EFDA accurately obtains the real normal contact force and therefore, the real tangential contact force for the Slip case. This consistent energy conservation–dissipation ensure stability of the algorithm.

- For the more complex situation of the pendulum problem (two disks on a curved rough surface), EFDA also shows good stability simulating the impacts, transitions from sliding to rolling and motion decay until rest.

REFERENCES

[1] F. Armero and E. Petocz. A new dissipative time-stepping algorithm for frictional contact problems: Formulation and analysis. *Computer Methods in Applied Mechanics and Engineering*, 179(1-2):151–178, 1999.

[2] R. Bravo, J. L. Pérez-Aparicio, and T. A. Laursen. An enhanced energy conserving time stepping algorithm for frictionless particle contacts. *International Journal for Numerical Methods in Engineering*, 2010.

[3] V Chawla and T.A Laursen. Energy consistent algorithms for frictional contact problems. *International Journal for Numerical Methods in Engineering*, 42(5):799–827, 1998.

[4] O. Gonzalez. Exact energy and momentum conserving algorithms for general models in nonlinear elasticity. *Computer Methods in Applied Mechanics and Engineering*, 190(13-14):1763–1783, 2000.

[5] G.R. Love and T.A. Laursen. Improved implicit integrators for transient impact problems - dynamic frictional dissipation within an admissible conserving framework. *Computer Methods in Applied Mechanics and Engineering*, 192(19):2223–2248, 2003.

[6] J.C. Simo, N. Tarnow, and K.K. Wong. Exact energy-momentum conserving algorithms and symplectic schemes for nonlinear dynamics. *Computer Methods in Applied Mechanics and Engineering*, 100(1):63–116, 1992.

[7] R. L. Taylor and P. Papadopoulos. On a finite element method for dynamic contact/impact problems. *International Journal for Numerical Methods in Engineering*, 36(12):2123–2140, 1993.

XI International Conference on Computational Plasticity. Fundamentals and Applications
COMPLAS XI
E. Oñate, D.R.J. Owen, D. Peric and B. Suárez (Eds)

ON CONTACT BETWEEN CURVES AND RIGID SURFACES – FROM VERIFICATION OF THE EULER-EYTELWEIN PROBLEM TO KNOTS

ALEXANDER KONYUKHOV*, KARL SCHWEIZERHOF† AND ANDREAS METZGER†

*Institute of Mechanics
Karlsruhe Institute of Technology
Kaiserstrasse 12, 76131 Karlsruhe, Germany
e-mail: Alexander.Konyukhov@kit.edu, http://www.ifm.kit.edu/14_203.php/

†Institute of Mechanics
Karlsruhe Institute of Technology
Kaiserstrasse 12, 76131 Karlsruhe, Germany
http://www.ifm.kit.edu/

Key words: Curve-To-Curve Contact, Curve-To-Surface contact, Euler-Eytelwein Problem, Belt Friction Problem, Knots

Abstract. A general theory for the Curve-To-Curve contact is applied to develop a special contact algorithm between curves and rigid surfaces. In this case contact kinematics are formulated in the local coordinate system attached to the curve, however, contact is defined at integration points of the curve line (Mortar type contact). The corresponding Closest Point Projection (CPP) procedure is used to define then a shortest distance between the integration point on a curve and the rigid surface. For some simple approximations of the rigid surface closed form solutions are possible. Within the finite element implementation the isogeometric approach is used to model curvilinear cables and the rigid surfaces can be defined in general via NURB surface splines. Verification of the finite element algorithm is given using the well-known analytical solution of the Euler-Eytelwein problem – a rope on a cylindrical surface. The original 2D formula is generalized into the 3D case considering an additional parameter H-pitch for the helix. Finally, applications to knot mechanics are shown.

1 INTRODUCTION

In many engineering devices such capstan and belt drives frictional interaction between structure and ropes, cables or belts can be modeled as the interaction between rigid surfaces and deformable curvilinear beams or ropes without loss of tolerance. Several

developments are required for this problem: a robust cable finite element and a contact algorithm for the Curve-To-Rigid Surface contact interaction. The isogeometric approach, see [1], is employed together with a special finite beam element formulation allowing both finite rotations, see in [2] in order to obtain cable finite elements. The theory for Curve-To-Curve contact interaction developed in [3] is applied to obtain a contact algorithm describing the contact between a deformable curve (representing either the center-line of the beam or an edge of a solid body) and a rigid surface.

The classical Euler-Eytelwein solution of the belt friction problem, see e.g. in [4], is first employed to verify the developed algorithm. The solution of this problem was reported by Euler in his *Remarks on the effect of friction on equilibrium* and has been first published by the Berlin Academy of science [5] in 1769. Since the first time publishing the Euler solution by Eytelwein [6] in his *Handbuch der Statik fester Körper* in 1808 the problem is spread through the practical applications and became known as Euler-Eytelwein problem in many books of technical mechanics. Here we are proposing a generalization of the classical 2D solution into the 3D case under the assumption that the rope is forming a spiral line on a rigid cylinder. This solution in due course is used for verification.

Finally, combination of both Curve-To-Curve and Curve-To-Rigid Surface contact algorithms allows to step into modeling of more complex see-man knots (beginning of study see in [7]) such as the clove-hitch knot. Numerical examples are illustrating the tying-up-processes.

2 CURVE-TO-RIGID ANALYTICAL SURFACE CONTACT ALGORITHM

The theory for Curve-To-Curve contact developed in [3] is employed to obtain a contact algorithm between a deformable curve and a rigid surface as follows. A rigid surface is assumed to have arbitrary analytical description, e.g. via NURBS surfaces. All contact parameters for the Curve-To-Rigid Suface algorithm are defined similar to the Curve-To-Curve contact algorithm in the Serret-Frenet frame, see [3], obtained by the tangent vector $\boldsymbol{\tau}$, the normal vector $\boldsymbol{\nu}$ and the bi-normal $\boldsymbol{\beta}$ of the curve line, see Fig. 1. A vector $\mathbf{e}$ is defining the shortest distance.

In order to describe contact between deformable curves and rigid surfaces a Segment-To-Analytical-Surface (STAS) algorithm, discussed in [9], is modified using the projection of the integration points which is set up on the "slave" curve onto the rigid "master" surface. The combination of this strategy with the Curve-To-Rigid (analytical) Surface contact algorithm leads to the following definition of the coordinate system on the master surface:

$$\boldsymbol{\rho}_s(\xi) = \mathbf{r}(\alpha_1, \alpha_2) + p\mathbf{n}(\alpha_1, \alpha_2), \tag{1}$$

where $\boldsymbol{\rho}_s(\xi)$ is defining an integration point positioned on the mid-line of the curvilinear beam element, $\mathbf{r}(\alpha_1, \alpha_2)$ is parameterization of the rigid "master" surface. The integration point $\boldsymbol{\rho}_s(\xi)$ is found in the direction of the normal $\mathbf{n}(\alpha_1, \alpha_2)$ to the rigid "master" surface. The shortest distance between integration points and the surface denoted as p plays

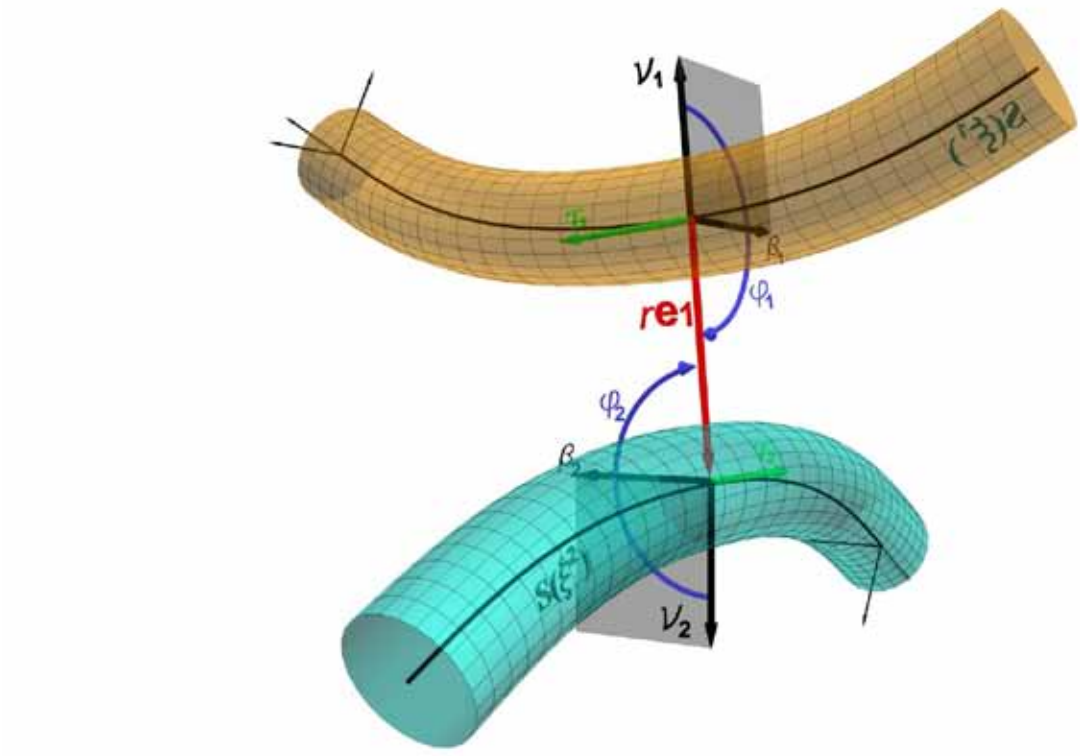

Figure 1: Curve-To-Curve contact algorithm is defined in the Serret-Frenet frame for both curves.

the role of a penetration. The Closest Point Projection (CPP) procedure, which is the standard contact local searching algorithm now turns into the determination of the surface convective coordinates α_1, α_2 defined by equation (1). In general, Newtons method is exploited to solve eqn. (1) defining then a point on the rigid surface and the penetration p between this surface and the selected integration point S. An analytical solution is possible for some surfaces – one of the important examples for further verification is the contact of a curve with a rigid cylindrical surface. Here, the rigid cylindrical surface with the radius R is given as $\mathbf{r} = \mathbf{R}_C + z\mathbf{e}_z + R\mathbf{e}_\varphi(\varphi)$ with the normal vector $\mathbf{n} = \mathbf{e}_\varphi(\varphi)$, see Fig. 2.

The distance p and thereby penetration into the cylinder is defined as

$$p = \begin{cases} \|\mathbf{R}_C - \boldsymbol{\rho}_s - \left((\mathbf{R}_C - \boldsymbol{\rho}_s)\cdot \mathbf{e}_z\right)\mathbf{e}_z\| - R & \text{– for an outward normal} \\ R - \|\mathbf{R}_C - \boldsymbol{\rho}_s - \left((\mathbf{R}_C - \boldsymbol{\rho}_s)\cdot \mathbf{e}_z\right)\mathbf{e}_z\| & \text{– for an inward normal} \end{cases} \tag{2}$$

It should be noticed that for the contact between the cylinder and a cable with a circular cross-section with radius R_{cable}, the penetration is, of course, computed as $penetration = p - R_{cable}$.

A coordinate z is used as a measure of tangential interactions for the definition of frictional interaction.

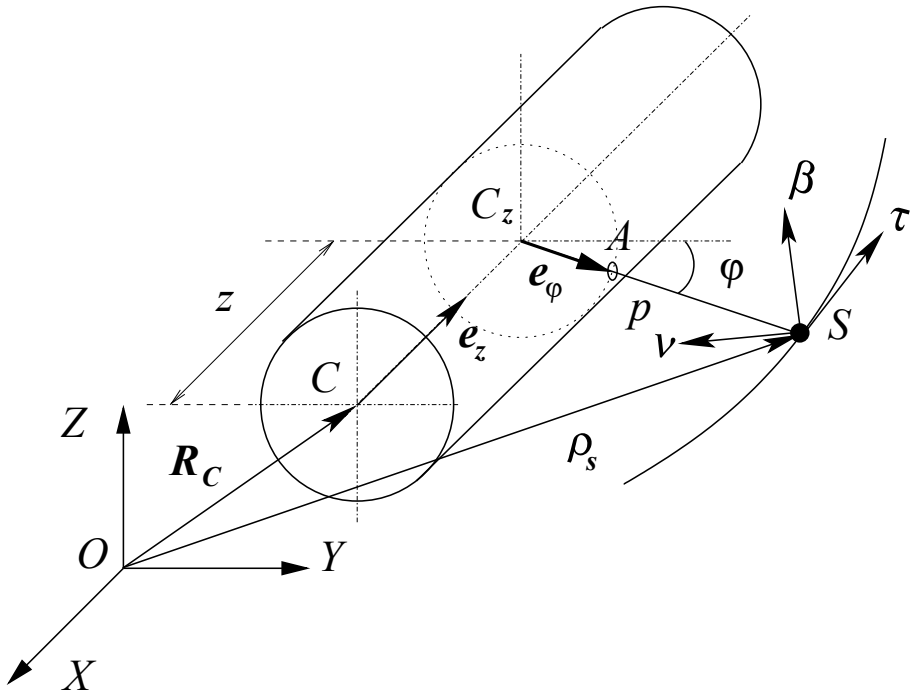

Figure 2: Contact with a rigid cylinder given by an analytical equation.

The contact integral is representing then the virtual work of contact traction along the curve L and is computed numerically using the integration formula of Lobatto or Gauss type depending on modeling purposes. Thus, e.g. the part responsible only for the normal contact is represented by

$$\delta W = \int_L N \delta p ds. \tag{3}$$

For the derivation of tangent matrices results from the Curve-To-Curve contact approach, see in [3], are employed directly. Thus, the tangent matrix derived from the linearized part of eqn. (3) is given as

$$\mathbf{K}^N = \int_L \varepsilon_r \, \mathbf{A}^T \left[\mathbf{e} \otimes \mathbf{e} \right] \mathbf{A} ds \tag{4a}$$

$$+ \int_L N \, \mathbf{A}^T \left\{ \frac{k \cos \varphi_1}{(1 - rk \cos \varphi)} \boldsymbol{\tau} \otimes \boldsymbol{\tau} - \frac{1}{r} \mathbf{g} \otimes \mathbf{g} \right\} \mathbf{A} ds. \tag{4b}$$

Here, N is a normal contact force, ε_r is a normal penalty parameter, $\mathbf{e}$ is a vector defining the shortest distance, $\mathbf{g} = \boldsymbol{\tau} \times \mathbf{e}$ is an orthogonal vector, r is the shortest distance between the integration point and the rigid surface, k is the curvature of the curve, φ is the angle between the normal curve vector $\boldsymbol{\nu}$ and the unit vector of the shortest distance $\mathbf{e}$ ($\mathbf{e} = \mathbf{e}_1$ in Fig. 1 and $\mathbf{e} = -\mathbf{e}_\varphi$ in Fig. 2). For all geometrical parameters see Fig. 1. $\mathbf{A}$ is an approximation operator for the curve line. The frictional tangential force T is computed

via the return-mapping algorithm. For the derivation of the tangential force T and other parameters including the tangent matrices and more details see [3].

3 GENERALIZATION OF THE EULER-EYTELWEIN FORMULA INTO THE 3D CASE CONSIDERING PITCH H

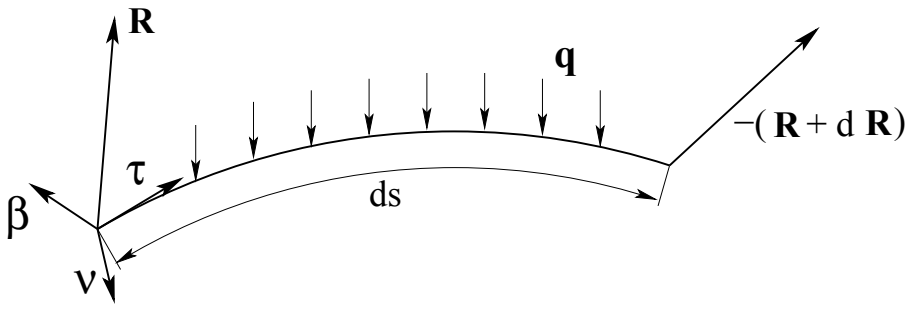

The equilibrium equation of the elementary part of the rope with length ds, see Fig. 3, is given in the following vector form

$$\frac{d\mathbf{R}}{ds} = \mathbf{q} \tag{5}$$

The force vector $\mathbf{R}$ can be expanded in the natural Serret-Frenet coordinate system used in the differential geometry of curves, see e.g. in [8], built by the unit tangent $\boldsymbol{\tau}$, the unit normal $\boldsymbol{\nu}$ and the unit bi-normal $\boldsymbol{\beta}$ vectors

$$\mathbf{R} = T\boldsymbol{\tau} + N\boldsymbol{\nu} + B\boldsymbol{\beta}, \tag{6}$$

with T – a tangential force, N – a normal force, and B – a bi-normal force. The full derivative of the force vector includes also a part due to changing the basis vectors $\boldsymbol{\tau}$, $\boldsymbol{\nu}$, $\boldsymbol{\beta}$ and is obtained via the Serret-Frenet formula, see e.g. in [8] and the application for this problem in [11]. Taking this formula into account, the projection of eqn. (5) onto the axes $\boldsymbol{\tau}$, $\boldsymbol{\nu}$, $\boldsymbol{\beta}$ results then in the system of ordinary differential equations:

$$\begin{cases} \dfrac{dT}{ds} + kN = q_\tau & \text{– equilibrium in } \boldsymbol{\tau} \text{ direction} \\ \dfrac{dN}{ds} - kT + \varkappa B = q_\nu & \text{– equilibrium in } \boldsymbol{\nu} \text{ direction} \\ \dfrac{dB}{ds} - \varkappa N = q_\beta & \text{– equilibrium in } \boldsymbol{\beta} \text{ direction} \end{cases} \tag{7}$$

where k is the curvature and $\varkappa$ is the torsion of the curve, which are in general functions of the arc-length parameter s.

3.1 Solution of the equilibrium equation for a spiral line (helix)

Now we consider a special case with the following conditions:

(i) the rope is positioned on the rigid surface.

(ii) the rope is loaded only by tangential forces $T_0\boldsymbol{\tau}_0$ and $T_1\boldsymbol{\tau}_1$ at both ends.

(iii) the rope is beginning to slide preserving its geometrical shape, i.e. only a motion along $\boldsymbol{\tau}$ is possible. Thus the form of the helix is conserved.

(iv) sliding is subjected to the Coulomb friction law such that $T(s) = \mu N(s)$, where μ is a coefficient of friction.

Thus, due to condition (iii), the first equilibrium equation in (7) is transferred into the equation of motion according to D'Alemberts principle with

$$q_\tau = -\rho \frac{\partial^2 u}{\partial t^2}, \tag{8}$$

where u is a tangential component of the displacement and ρ is the linear mass density. However, equilibrium along $\boldsymbol{\nu}$ and $\boldsymbol{\beta}$ axis is fulfilled and we consider the absence of the distributed forces $q_\nu = 0$, $q_\beta = 0$. The problem is then described by the system of ordinary differential equations:

$$\left\{ \begin{array}{lcl} \dfrac{dN}{ds} - kT + \varkappa B & = & 0 \\ \dfrac{dB}{ds} - \varkappa N & = & 0 \end{array} \right. \tag{9}$$

with the following initial conditions at $s = 0$ resulting from condition (ii):

$$T(0) = T_0, \quad N(0) = N_0, \quad B(0) = 0. \tag{10}$$

Now, we consider a case with a constant curvature k and a constant torsion $\varkappa$ of the curve. This is a case of the spiral line – a helix – on the cylinder. The system of equations (9) is transformed into a single differential equation of second order by taking the derivative of the first equation in (9):

$$\frac{d^2N}{ds^2} - k\frac{dT}{ds} + \varkappa \frac{dB}{ds} = 0 \tag{11}$$

and then using the second equation in (9) we obtain

$$\frac{d^2N}{ds^2} - k\frac{dT}{ds} + \varkappa^2 N = 0. \tag{12}$$

Now taking into account the sliding condition (iv) we obtain a second order differential equation :

$$\frac{d^2N}{ds^2} - \mu k \frac{dN}{ds} + \varkappa^2 N = 0 \tag{13}$$

with the initial conditions:

$$N(0) = N_0, \quad \frac{dN(0)}{ds} = kT_0. \tag{14}$$

The solution of the ordinary differential equation (13) is obtained by using the characteristic equation

$$\lambda^2 - \mu k \lambda + \varkappa^2 = 0 \tag{15}$$

$$\lambda_{1,2} = \frac{\mu k \pm \sqrt{\mu^2 k^2 - 4\varkappa^2}}{2} \tag{16}$$

Depending on the determinant $D = \mu^2 k^2 - 4\varkappa^2$ three solutions are possible. We consider these values for the spiral line (helix). The geometrical characteristics for this line are defined as follows, see Fig. 3

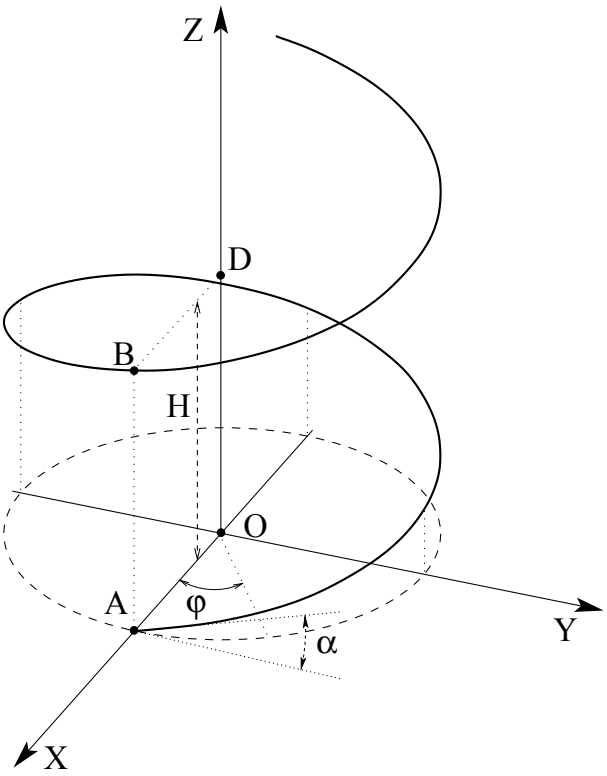

Figure 3: Spiral line (helix) with a pitch H.

Parametrization of the spiral line (helix):

$$\mathbf{r} = \left\{ \begin{array}{c} R\cos\varphi \\ R\sin\varphi \\ \dfrac{H}{2\pi}\varphi + const \end{array} \right\}. \tag{17}$$

Within $0 \leq \varphi \leq 2\pi$ the line is making a full turn around the OZ-axis raising by the pitch $z = H$ with the following geometrical items: arc-length of the spiral line (helix) $s = \sqrt{R^2 + \left(\frac{H}{2\pi}\right)^2}\varphi, \quad \varphi \in [0, ...)$; curvature of the helix $k = \dfrac{R}{R^2 + \left(\dfrac{H}{2\pi}\right)^2}$; torsion of the spiral line (helix) $\varkappa = \dfrac{H/2\pi}{R^2 + \left(\dfrac{H}{2\pi}\right)^2}$. Then positivity of the determinant can be expressed via the geometrical parameters of the helix as

$$D \geq 0 \implies = \mu k \geq 2\varkappa \implies \mu \geq \frac{H}{\pi R}. \tag{18}$$

Omitting details of transformations we discuss the expressions for the force ratio $\dfrac{T}{T_0}$ for all three possible cases.

3.1.1 Case 1. Positive determinant $D > 0$, $\mu > \dfrac{H}{\pi R}$

Since with $H = 0$ the determinant is positive $D > 0$, then this case is representing a spiral line with a very small pitch H in comparison with the radius R. The solution is given by the exponential functions as:

$$\frac{T}{T_0} = \left(\frac{\mu k}{2\omega} \sinh \omega s + \cosh \omega s \right) e^{\dfrac{\mu k}{2} s}, \tag{19}$$

with ω

$$\omega = \frac{\sqrt{\mu^2 k^2 - 4\varkappa^2}}{2}. \tag{20}$$

If we consider the 2D case with $H = 0$ in eqn. (19) **the classical Euler-Eytelwein for the rope on the cylinder is recovered**

$$\frac{T}{T_0} = \left[\sinh\left(\frac{\mu\varphi}{2}\right) + \cosh\left(\frac{\mu\varphi}{2}\right) \right] e^{\dfrac{\mu\varphi}{2}} = e^{\mu\varphi}. \tag{21}$$

3.1.2 Case 2. Negative determinant $D < 0$, $\mu < \dfrac{H}{\pi R}$

The case is representing either a case with a spiral line with large pitch H, or with a small coefficient of friction. The solution is given by the trigonometrical and exponential functions:

$$\frac{T}{T_0} = \left[\frac{k\mu}{2\tilde{\omega}}\sin\tilde{\omega}s + \cos\tilde{\omega}s\right] e^{\dfrac{\mu k}{2}s}, \tag{22}$$

with $\tilde{\omega}$

$$\tilde{\omega} = \frac{\sqrt{4\varkappa^2 - \mu^2 k^2}}{2}. \tag{23}$$

3.1.3 Limit case 3. Determinant is zero $D = 0$, $\mu = \dfrac{H}{\pi R}$

This case can be obtained just by the limit process with $\omega \to 0$ with the solution in eqn. (19) or in eqn. (22) as

$$\lim_{\omega\to 0}\frac{T}{T_0} = \left[\frac{k\mu}{2}s + 1\right] e^{\dfrac{\mu k}{2}s}. \tag{24}$$

A numerical computation for the cases with $D > 0$, $D = 0$, $D < 0$ and the classical Euler formula with $H = 0$ is presented in Fig. 4 for the angle $\varphi \in [0, 2\pi]$. The computation is given with a coefficient of friction $\mu = 0.3$ and radius $R = 1.0$ for the following cases:

- Classical Euler case $H = 0$;
- Positive determinant $D < 0$ with $H = 0.75$
- Zero determinant $D = 0$ with $H = \mu\pi R = 0.9424$
- Negative determinant $D < 0$ with $H = 1.2$

One can see, that if the pitch H is increasing then the ratio of forces T/T_0 is decreasing, thus, the standard 2D Euler case is representing the upper limit of the forces ratio T/T_0 with regard to the pitch H.

The derived formula is used further for the verification of the Curve-To-Rigid Suface contact algorithm.

4 APPLICATION TO KNOTS

Both the Curve-To-Curve (CTC) contact algorithm, see in [3], [7], and the developed Curve-To-Rigid-Surface (CTRS) contact algorithm are used to model the Clove-Hitch knot, see Fig. 5, presented also in [10].

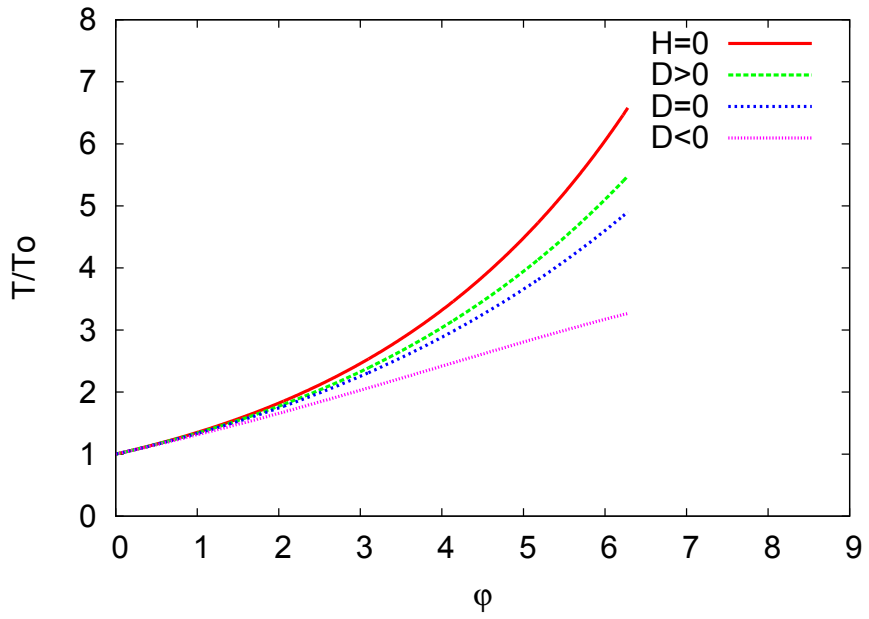

Figure 4: Comparison of all cases with determinant $D > 0$, $D = 0$, $D < 0$ and the classical Euler formula with $H = 0$.

The developed model allows to describe the tying-up mechanics of the Clove Hitch knot: during the tying up both loops of the knot are approaching each other. The upper loop of the knot is enforcing this motion. The knot is tying up and is not sliping because of the large frictional forces appearing between the two approaching loops.

5 CONCLUSIONS

- A special Curve-To-Rigid-Surface (CTRS) contact algorithm is developed in the current contribution based on the application of the Curve-To-Curve contact theory and Segment-To-Analytical Surface (STAS) contact algorithm.

- Rigid surfaces can be approximated with arbitrary NURBS surfaces – in this case an iterative solution of the corresponding Closest Point Projection (CPP) procedure is necessary to define the contact point as well as the penetration.

- An analytical closed form solution for the CPP procedure is possible for some simple cases e.g. for a cylinder.

- The Euler-Eytelwein problem is generalized into the 3D problem as a frictional sliding of a spiral line (helix) on a cylinder. It is shown that consideration of the pitch H leads to the reduction of the force ratio T/T_0. The formula is used as a basis for the verification of the Curve-To-Rigid-Surface (CTRS) contact algorithm.

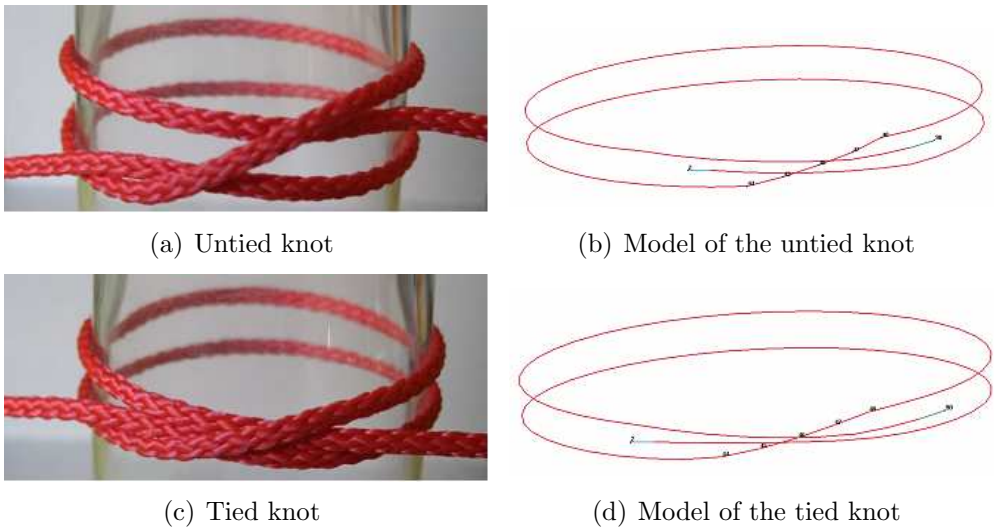

(a) Untied knot (b) Model of the untied knot

(c) Tied knot (d) Model of the tied knot

Figure 5: Illustration and finite element model of an untied and tied Clove-Hitch knot

- The developed Curve-To-Rigid (analytical) Surface (CTRS) contact algorithm together with the Curve-To-Curve (CTC) contact algorithm is applied to study the kinematics of the tying up of the Clove Hitch knot.

REFERENCES

[1] J.A. Cottrell, T.J.R. Hughes and Y. Bazilevs, *Isogeometric Analysis: Toward Integration of CAD and FEA*, John Wiley & Sons, 2009.

[2] A. Ibrahimbegovic, On finite element implementation of geometrically nonlinear Reissner's beam theory: three-dimensional curved beam elements. *Computer Methods in Applied Mechanics and Engineering* (1995) **122**:11–26.

[3] Konyukhov A., Schweizerhof K. Geometrically exact covariant approach for contact between curves, *Computer Methods in Applied Mechanics and Engineering* (2010) **199**:2510–2531.

[4] *E. R. Maurer, R. J. Roark, Technical mechanics: statics, kinematics, kinetics.* -5. ed. New York: Wiley, 1944.

[5] L. Euler, *Remarques sur l'effet du frottement dans l'equilibre*, Memoires de l'academie des sciences de Berlin, 18 (1769), pp. 265–278.

[6] J. A. Eytelwein, *Handbuch der Statik fester Körper. Mit vorzüglicher Rücksicht auf ihre Anwendung in der Architektur.* Vol. 2, Berlin, 1808, pp. 21–23.

[7] Konyukhov A., Schweizerhof K. Geometrically exact theory for contact interactions of 1D manifolds. Algorithmic implementation with various finite element models.

Computer Methods in Applied Mechanics and Engineering available online 2 April 2011, doi:10.1016/j.cma.2011.03.013

[8] Kreyszig E. *Differential geometry*. New York: Dover Publications, 1991.

[9] Konyukhov A. Geometrically Exact Theory for Contact Interactions, *Habilitationsschrift*, Karlsruhe, KIT, 2010.

[10] Metzger A., Konyukhov A., Schweizerhof K. Finite element implementation for Euler-Eytelwein-problem and further use in FEM-simulation of common nautical knots. *GAMM, 82nd Annual meeting* 18-21 April 2011, Graz, Austria.

[11] Konyukhov A., Schweizerhof K. Frictional interaction of a spiral rope and a cylinder – 3D-generalization of the Euler-Eytelwein formula considering pitch. *submitted*.

XI International Conference on Computational Plasticity. Fundamentals and Applications
COMPLAS XI
E. Oñate, D.R.J. Owen, D. Peric and B. Suárez (Eds)

A NEW FORMULATION TO ASSESS THE SEISMIC DEMAND OF MASONRY STRUCTURES BY MEANS OF INPUT ENERGY

MEZA J. MIGUEL[*], PEÑA FERNANDO[†]

[*] Instituto de Ingeniería (IdeI)
Universidad Nacional Autónoma de México
Circuito Escolar, s/n, Ciudad Universitaria, 04510 México D.F., México
Email: jmeza.mendez@gmail.com, www.iingen.unam.mx

[†] Instituto de Ingeniería (IdeI)
Universidad Nacional Autónoma de México
Circuito Escolar, s/n, Ciudad Universitaria, 04510 México D.F., México
Email: fpenam@iingen.unam.mx, www.iingen.unam.mx

Key words: Input Energy, Spectrum, Seismic demand, Unreinforced masonry.

Abstract. The main objective of this paper is to evaluate the elastic input energy of unreinforced masonry structures by means of the input energy spectrum. The energy is a novel approach which allows evaluating in a global and easily way the performance of the masonry structures. Structures modeled with non frame elements require of a great number of 2D or 3D elements, thereby making the calculation of the input energy a complicated issue. In this context, a new formulation that calculates the input energy using an input energy spectrum and the balance of energy is proposed. Two examples of application of unreinforced masonry structures were considered to evaluate the input energy and compare it with the proposed formula. The formula proposed shows interesting results that allowed identify the key features of the accelerograms that influence the input energy into structures.

1 INTRODUCTION

There are several methods proposed in the literature to quantify the severity, intensity or earthquake damage potential. Currently, all terms are intended to measure the same property of the ground motion: its effect on the structure. The only observed effect of ground motion on the structure is the permanent damage, so this measure is usually assessed by the degree of correlation with the observed damage. This can lead to a mistake, because the amount of damage depends on the qualities in building on the site. For this reason, macro-seismic scale of Modified Mercalli Intensity is not a reliable measurement of destructiveness potential (Orosco and Alfaro, 2008), though it is very used to describe the distribution of damage to the affected area. A rational correlation between a measure of intensity and observed structural damage could be established only if in the affected site buildings were uniformly designed in accordance with standard building code.

Unreinforced masonry buildings are structures with a particularly complex structural behavior. This complexity is given by the mechanical properties of the masonry, specially, by

the low tensile strength of the material. Taking into account the uncertainties in the masonry, it is not easy to deal with a dynamic analysis by finite element programs, even with the current structural analysis programs. The masonry is one of the most complex materials to be represented numerically on an analytical model, due to the variability of behavior, type of material and workmanship. This characteristic of material, together with the unreinforced masonry structures are usually represented by a large number of elements, causes that a dynamic analysis utilizes high computing resources, taking several days, even weeks to be achieved (Lourenço, 2002).

Generally, most of the simplified analyses establish that the response of the structure can be calculated by considering the fundamental mode. The unreinforced masonry structures do not meet this requirement, because a single mode is not sufficient to determine an approximate response. To interpret the structure's response, two parameters are reviewed: displacement and base shear. However, the unreinforced masonry structures exhibit the phenomenon of softening, which excludes the base shear as a reliable indicator of the structural response. In the same way, the displacement has the problem that does not reflect the overall behavior of the structure, because every part of the structure may have different values. So, it is necessary to use other parameters. In this paper, the use of the energy as the main parameter to assess the potential damage of an earthquake is proposed.

Energy is a physical quantity that can be represented by a scalar, an appropriate quantity to synthesize the behavior of the structure. The main problem lies in figuring out how the input energy is distributed into the structure. At the end of an earthquake, all the input energy must have been dissipated by the structure through some dissipation mechanism. Some energy is absorbed by the structure through elastic dissipation mechanisms, such as viscous damping, and another part is absorbed by the mechanisms of inelastic energy dissipation, which is responsible of the structural damage. Therefore, the energy of a structure will be dissipated at the end of an earthquake in some kind of energy.

This paper addresses analysis of historic structures by using the concept of energy. Both, input energy and robust models (macroelements) for masonry structures, that are currently available, can be successfully used for the analysis of historic structures. For evaluating churches, it will be necessary evaluate each macroelement that it is composed of. In this paper just macroelement façades is analyzed. Façades of two typical churches from Mexico were selected. Input energy for different earthquakes will be shown and studied.

2 DESTRUCTIVINESS POTENTIAL OF EARTHQUAKES

This section is a review of proposed parameters for evaluating the potential damage of the earthquakes. Structural seismic analysis requires that the seismic action is properly defined for the purposes of obtaining reliable results. It is common to specify such a dynamic load using response spectra or acceleration histories, according to the selected method of analysis. Idealization of the action must reflect the characteristics of motions at the site of construction. Intensity measures discussed here are evaluated considering the peak acceleration, duration of strong motion and frequency content of earthquake ground motion.

2.1 Housner intensity

Housner (1952) proposed as a measure of the intensity the area under the pseudo-velocity spectrum in the range of 0.1 to 2.5s periods, for 5% damping ratio (Eq. 1).

$$I_H = \int_{0.1}^{2.5} S_v dT \tag{1}$$

Its biggest shortcoming is the inability to consider the effect of duration of strong motion. Spectral velocity is insensitive to the duration, while the energy entered to the structure increases monotonically with duration. On the other hand, the influence of the ratio v/a, or the duration of the pulse in case of impulsive excitation, is well represented by the velocity spectrum. The frequency content of the earthquake is implicitly represented by the spectral distribution of the pseudovelocity.

2.2 Arias intensity

Arias (1970) introduced the measure of the intensity of ground motion (Eq. 2) as:

$$I_A = \frac{\pi}{2g}\int_0^t a^2(t)dt \tag{2}$$

Where t is the duration of the registration of ground acceleration $a(t)$. Arias intensity (I_A) is closely connected with the root mean square acceleration and corresponds to the area below the total energy spectrum absorbed by the system of a single degree of freedom (SDF) at the end of the earthquake excitation. The I_A is not sensitive to frequency content and long acceleration pulses of the excitation. However, the accumulated energy of I_A brings out the impulsive character of the earthquake.

2.3 Araya destructive potential

Araya and Saragoni (1985) modified the Arias intensity to take into account the frequency content (Eq. 3). Defined the destructiveness potential (P_D) as:

$$P_D = \frac{I_A}{v_0^2} \tag{3}$$

In this expression, v_0 is the number of crossings per unit of time.

2.4 Energy dissipation Index

The parameters explained above depend only of earthquake characteristics and have implicit in the definition considerations of energy since they are directly related to the mean square acceleration. However, the structural response depends of the structural characteristics and the site where the structure is based. Therefore, damage potential indexes must considering explicitly the structural response. In view of this, Sucuoglu and Nurtug (1995) proposed an index of the destructiveness of an earthquake based on the energy dissipated by a system of one degree of freedom (Eq. 4), which is expressed as,

$$E_I = \frac{1}{T_{max}}\int_0^{Tmax} V_e dT \tag{4}$$

$$V_e = \sqrt{\frac{2E_d}{m}}\ ; \quad E_d = 2\xi m\omega_n \int_0^{y(t)} \dot{y}dy$$

Where E_I can be interpreted as the average energy dissipated by the spectral velocity of the system equivalent to SDF subject to earthquake motions. The energy dissipated by a simple oscillator during the seismic action is sensitive to the parameters that describe dynamic characteristics of the earthquake: effective duration, peak values and frequency content. However, damage potential index is sensitive to the v/a, to peak values, spectral content, but does not show a direct relationship to the duration of the earthquake.

2.5 Some remarks of these formulae

The input energy of family of linear SDF systems can be taken as a measure of potential earthquake damage. An attempt was make to consider the hysteretic energy dissipation to measure the intensity of the earthquake, but that is only true to quantify structural damage but not the damage potential of earthquake. The damage potential is the ability of the seismic excitation to cause damage, while the damage does depend heavily on structural characteristics. Seismic excitation with a given damage potential may cause different levels of damage on different systems, depending on the structural characteristics of the system. When using the input energy all the energies are included into, so that is the reason for proposes a formula to evaluate input energy. Additionally, the input energy combines the structural and earthquake characteristics.

3 NEW FORMULATION TO ASSESS THE EARTHQUAKE DEMAND

A new formulation is proposed to assess the damage seismic potential and to know the demand imposed on the structure. This equation expresses the balance of energy of the structure and allows us to interpret their earthquake demand from the concept of energy. The equation governing a SDF system subject to a horizontal seismic ground motion comes from the dynamic equilibrium equation, as shown in Equation 5.

$$mx(t) + cx(t) + kx(t) = -ma_g(t) \tag{5}$$

Where m is the mass; c the damping; k the stiffness of the system; $\ddot{x}(t)$, $\dot{x}(t)$, $x(t)$ are the acceleration, velocity and relative displacement, respectively; $a_g(t)$ is the ground acceleration. If equation 5 is multiplied by the differential increment of relative displacement dx (or $\dot{x}dt$) and integrating it throughout the duration of earthquake $(0, t)$, it is obtained a equation, which contains the integrated or cumulative vibration and represents the energy balance (Akiyama, 2003). The energy balance of SDF system for a given time t is,

$$\int_0^t m\ddot{x}\dot{x}dt + \int_0^t c\dot{x}^2 dt + \int_0^t kx\dot{x}dt = \int_0^t -ma_g\dot{x}dt \tag{6}$$

$$W_k(t) + W_d(t) + W_s(t) = E(t)$$

Where E (input energy) is the work imposed by the dynamic forces at time t, W_{ek} the kinetic energy, W_{dd} the energy of dissipation by damping and, W_{es} the elastic strain energy. On the range of periods ranging from 0.2 to 5.0s, the relative input energy values are quite similar to the values of absolute input energy (Uang and Bertero, 1990). Therefore, it is no necessary for any differentiation between both energies. The input energy in the elastic range for a SDF can be calculated by adding the input energy contribution of each mode of vibration, for example for the mode 1, then,

$$\sum_{j=1}^{M}\{\int_0^t m_{1j}\ddot{x}_{1j}\dot{x}_{1j}dt+\int_0^t 2m_{1j}\xi_j\omega_j\dot{x}_{1j}^2dt+\int_0^t m_{1j}\omega_j^2x_{1j}\dot{x}_{1j}dt\}=\sum_{j=1}^{M}\int_0^t m_{1j}a_g\dot{x}_{1j}dt \quad (7)$$

When the structure is composed of several degrees of freedom, by adding the energy of each node, the total energy of the system is obtained (Eq. 8).

$$\sum_{j=1}^{M}\{\int_0^t m_{1j}\ddot{x}_{1j}\dot{x}_{1j}dt+\int_0^t 2m_{1j}\xi_j\omega_j\dot{x}_{1j}^2dt+\int_0^t m_{1j}\omega_j^2x_{1j}\dot{x}_{1j}dt\}=\sum_{j=1}^{M}\int_0^t m_{1j}a_g\dot{x}_{1j}dt$$

$$\sum_{j=1}^{M}\{\int_0^t m_{2j}\ddot{x}_{2j}\dot{x}_{2j}dt+\int_0^t 2m_{2j}\xi_j\omega_j\dot{x}_{2j}^2dt+\int_0^t m_{2j}\omega_j^2x_{2j}\dot{x}_{2j}dt\}=\sum_{j=1}^{M}\int_0^t m_{2j}a_g\dot{x}_{1j}dt$$

$$\vdots$$

$$\sum_{j=1}^{M}\{\int_0^t m_{Nj}\ddot{x}_{Nj}\dot{x}_{Nj}dt+\int_0^t 2m_{Nj}\xi_j\omega_j\dot{x}_{Nj}^2dt+\int_0^t m_{Nj}\omega_j^2x_{Nj}\dot{x}_{Nj}dt\}=\sum_{j=1}^{M}\int_0^t m_{Nj}a_g\dot{x}_{Nj}dt$$

$$E_{ti}=\sum_{j=1}^{M}\sum_{i=1}^{N}\left\{\int_0^t m_{ij}\ddot{x}_{ij}\dot{x}_{ij}dt+\int_0^t 2m_{ij}\xi_j\omega_j\,\dot{x}_{ij}^2dt+\int_0^t m_{ij}\omega_j^2x_{ij}\dot{x}_{ij}dt\right\}$$

$$=\sum_{j=1}^{M}\sum_{i=1}^{N}\int_0^t m_{ij}a_g\dot{x}_{ij}dt \quad (8)$$

Where E_{ti} is the total input of energy multi-degree of freedom (MDF) system, ξ is the damping ratio or fraction of critical damping, and ω is the natural circular frequency of vibration. Substituting the modal expansion of the displacement ($\Gamma\phi q$), the velocity ($\Gamma\phi\dot{q}$) and the acceleration ($\Gamma\phi\ddot{q}$) of each mode, we have the following general equation to determine the input energy for a structure that behaves in the elastic range:

$$E_{ti}=\sum_{j=1}^{M}\sum_{i=1}^{N}\left\{\int_0^t m_{ii}\Gamma_j^2\ddot{q}_j\dot{q}_j\phi_{ij}^2dt+\int_0^t 2m_{ii}\xi_j\omega_j\Gamma_j^2\dot{q}_j^2\phi_{ij}^2dt+\int_0^t m_{ii}\omega_j^2\Gamma_j^2q_j\dot{q}_j\phi_{ij}^2dt\right\}=$$
$$\sum_{j=1}^{M}\sum_{i=1}^{N}\int_0^t m_{ii}a_g\Gamma_j^2\dot{q}_j\phi_{ij}^2dt \quad (9)$$

Grouping common terms and using the orthogonality properties of natural modes,

$$E_{ti}=\sum_{j=1}^{M}\sum_{i=1}^{N}m_{ii}\phi_{ij}^2\Gamma_j^2\{\int_0^t\ddot{q}_j\dot{q}_jdt+\int_0^t 2\xi_j\omega_j\dot{q}_j^2dt+\int_0^t\omega_j^2q_j\dot{q}_jdt\}=$$

$$=\sum_{j=1}^{M}\sum_{i=1}^{N}m_{ii}\phi_{ij}^2\Gamma_j^2\int_0^t a_g\dot{q}_jdt$$

$$\sum_{i=1}^{M}\sum_{i=1}^{N}m_{ii}\phi_{ij}^2=1$$

$$E_{ti}=\sum_{j=1}^{M}\Gamma_j^2\int_0^t a_g\dot{q}_jdt=\sum_{j=1}^{M}\Gamma_j^2E(T_j) \quad (10)$$

$$E_{ti}/M=\sum_{j=1}^{M}(\sum_{i=1}^{N}\phi_{ij})\Gamma_j\int_0^t a_g\dot{q}_jdt=\sum_{j=1}^{M}(\sum_{i=1}^{N}\phi_{ij})\Gamma_jE(T_j) \quad (11)$$

Where E_{ti}/M is the total input energy normalized respect to the mass of (MDF) system. ϕ_{ij} are the generalized modal coordinates of each node, Γ is the participation factor, and $E(T_j)$ is the spectral input energy of a SDF system for each period T_j. Equation 10 and 11 determine the elastic energy input from modal dynamic characteristics of the structure.

Should be noted that the equations 10 and 11 are applied along the earthquake acts, this means that, if it is necessary to calculate the input energy to an earthquake applied in the direction "x", modal coordinates and participation factors are used of the direction "X". Likewise, along the direction "Y" and "Z". When apply two accelerograms simultaneously in different directions, it is necessary calculates the input energy for each direction and sum both to obtain the total input energy.

4 NUMERICAL EXAMPLES

The churches built in Mexico during the Colonial Era, between the 16th and 18th centuries, are typical structures of unreinforced masonry. These buildings vary in size and in architectural style; however, it is possible to find a general basic typologies. An important factor which influenced the architectural style was the experience of the ancient builders due to the seismic activity of the country. Generally, in the Pacific's coast and more specifically in the State of Oaxaca, the recurrent destruction of the first constructions caused an evolution of the churches towards edifications of not much height, with big buttresses and little outer ornamentation. By this reason, the churches of Oaxaca are rectangular, with one nave. On the other hand, regions where the seismic activity is smaller, the churches remained higher and slender. It is the reason the churches of the State of Puebla are bigger, with a plant of Latin cross. Both churches have a simple façade that has attached one or two small towers

The façades are one of the most vulnerable parts of the churches due to the bell towers and their belfries. Hence, this section presents the analysis of two façades. These models do not belong to any particular church but are representative of the global features of churches in both states. Both façades were analyzed applying different earthquakes of significant magnitude that occurred worldwide in different dates. The structural analysis program SAP2000 was used to obtain the input energy of models and compare them with the proposed formula.

4.1 Models for analysis

Two finite element models were performed; which correspond to the typical churches of the states of Oaxaca and Puebla (Fig. 1). Geometrically, the façade of Oaxaca's church has a lower height than Puebla's. Other important difference that stands out is the height of the towers of the façade of Puebla. The towers are relatively higher compared to the central part of the façade. The finite element model of Oaxaca's façade has 1002 elements and 2204 degrees of freedom, whereas the Puebla's façade has 1578 elements and 3482 degrees of freedom. The mechanical characteristics of the masonry material are: Elascity´s modulus = 1962 MPa; mass density = 1600 kg/m3; Poisson´s ratio = 0.20.

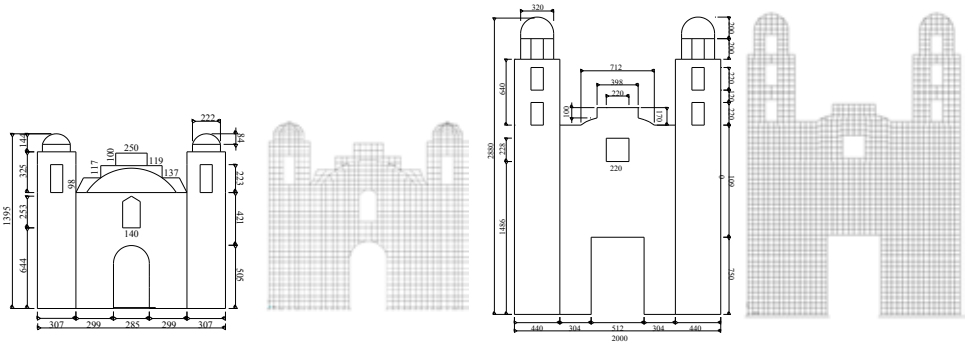

Figure 1: Dimension and finite element models of façades; State of Oaxaca (left), and Puebla (right).

Table 1 shows the modal characteristics of both façades. The Oaxaca's façade have a

fundamental period lesser than Puebla's façade, but both have approximately equal participating mass ratios (Mass %). Considering only ten modes, mass percent is 90.73 to Oaxaca and 91.34 to Puebla. It is necessary to indicate that considering only the first mode, the response of facades will be not approximated. This shows that both facades are different in modal characteristics. Analyses of both façades showed the influence of the modal characteristics in the input energy.

Table 1: Modal characteristics of façades

	Oaxaca			*Puebla*		
Mode	*Period*	*MPF*	*Mass(%)*	*Period*	*MPF*	*Mass (%)*
1	0.12016	16.2058	61.43	0.26563	26.1514	61.95
2	0.08352	0.0002	0.00	0.17979	0.0001	0.00
3	0.05939	8.8028	18.13	0.13182	15.1881	20.90
4	0.04417	0.0036	0.00	0.08989	0.00012	0.00
5	0.04145	3.9645	3.68	0.08149	7.1166	4.59
6	0.03480	0.0068	0.00	0.05256	0.0001	0.00
7	0.02823	0.0045	0.00	0.04719	4.2646	1.65
8	0.02462	5.6116	7.37	0.04637	0.0010	0.00
9	0.02131	0.7029	0.12	0.03953	4.9854	2.25
10	0.02029	0.0005	0.00	0.03894	0.0003	0.00

4.2 Earthquakes

The façades were analyzed by applying the earthquakes of different sites of the world. Table 2 summarized the earthquake characteristics. These earthquakes differ in terms of location, magnitude, duration and peak ground acceleration.

Table 2: Earthquake Characteristics

Earthquake	*Site registration*	*Duration (s)*	*PGA (m/s2)*	*Magnitude*	*Event*	*Date*
Oax990615	Oaxaca	70.00	1.07	6.5	Puebla	15-VI-1999
Oax990930	Oaxaca	50.00	1.86	7.5	Oaxaca	30-IX-1999
Pue990615	Puebla	47.50	1.95	6.5	Puebla	15-VI-1999
Pue990930	Puebla	100.00	0.42	7.5	Oaxaca	30-IX-1999
Gem760915	Gemona	9.50	6.23	6.5	Friuli	15-IX-1976
Kob950116	Kobe	20.00	5.87	6.9	Kobe	16-I-1995
Sct850918	SCT. D.F.	90.00	1.75	8.1	Michoacan	18-IX-1985
Stu760506	Sturno	45.00	3.22	6.5	Friuli	6-V-1976
Tol760506	Tolmezzo	12.00	2.89	6.5	Friuli	6-V-1976
Bol991211	Bolu	16.00	8.07	7.3	Turkey	11-XII-1999

These accelerograms have different features that allow reviewing their influence on the structures. Some are very similar in time and other in acceleration. The largest peak ground acceleration is from Turkey, but it has shortest duration, compared to the rest of the earthquakes, that mean it is an impulsive earthquake motion. On the other hand, the

Pue990930 earthquake has longest duration, but the peak ground acceleration is lower.

4.3 Analysis and earthquake evaluation

Figure 2 shows the energy spectra for different earthquakes used. It can be seen for long-period structures, the SCT850918 earthquake demand much more energy than other earthquakes. This is consistent with the damage observed in 1985 in Mexico City, where the period of the structures was amplified by the soil type where they are built. Gem760915, Kob950116 and Bol991211 earthquakes are demanding greater energy for low-periods buildings (0.6-1.0s). Coincidentally these earthquakes also have the largest ground acceleration. Bol991211 earthquake motion has a longer duration and higher acceleration than the Gem760915 and Kob950116 earthquakes, but as it can see in Figure 2, it demanded less energy. This indicates that the duration and maximum ground acceleration are not parameters that dominated at all the energy input of structures. Fundamental periods is plotted to locate the energy demand on the façades, according the figure 2 (left) this would not have a high energy demand for any earthquake. The figure 2 (right) display a close up of the spectra that shows the location of both fundamental periods.

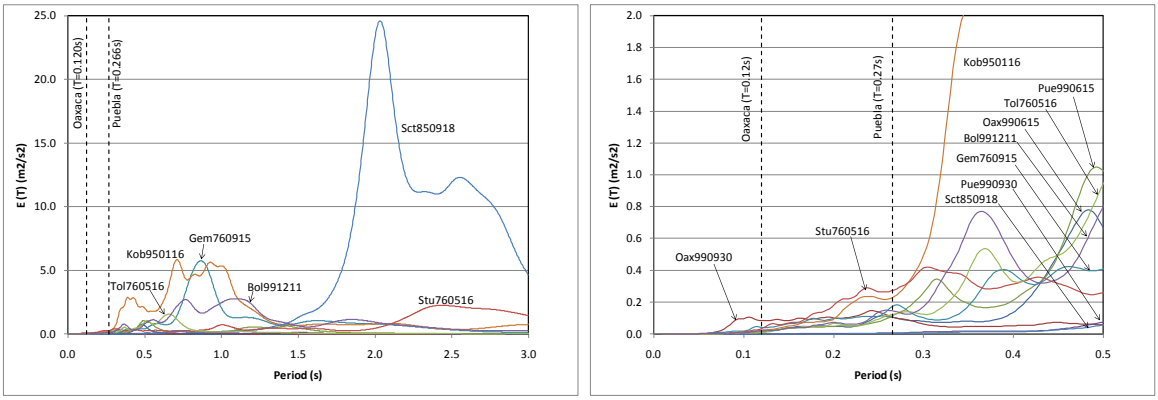

Figure 2: Spectra´s input energy of earthquakes (left), figure amplification (right).

Figure 3 shows, as an example, the energy of the earthquake in Bol991211 obtained with SAP2000 analysis program and the energy obtained with the proposed formula. The energy is not normalized, because the SAP2000 analysis program gave no normalized energies. As can be seen in the figure 3 the energy calculated with the formula 10 is near to the energy obtained with the SAP2000. It should be appreciated that the formula gives the energy at the end of the earthquake. The history of earthquake input energy shows a peak value around the 6s, which is slightly larger than the final input energy, the formula do not reflect those peaks. However, this increase is produced by the strain energy which is recoverable when elastic, but when the behavior is inelastic, peak strain energy is converted into hysteretic energy and reflected at the end of the duration of earthquake. The advantage of the formula is that it is possible to know the input energy at the end of earthquake duration, including all type of energies. Moreover, the formula can exclude the influence of mass; the normalized energy can be converted into equivalent velocity (Sucuoglu and Nurtug, 1995).

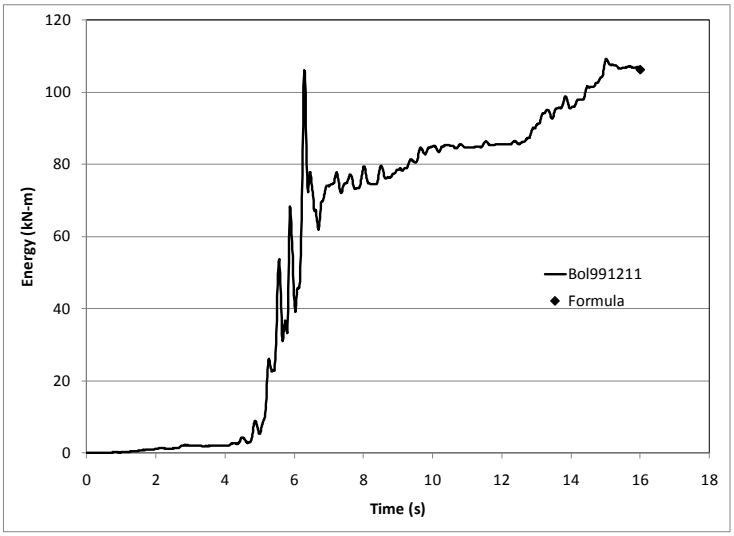

Figure 3: Comparison between energy obtained with the proposed formula and the SAP2000 software

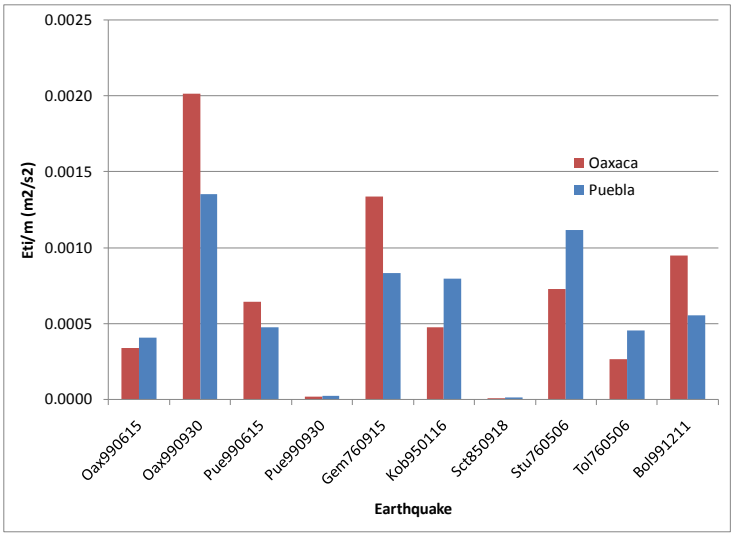

Figure 4: Demand of energy for the façades from Oaxaca and Puebla

Figure 4 shows the energy demand for both façades, obtained with the proposed formula. The highest energy demand was caused by the Oax990930 earthquake. On the other hand, the Sct850918 earthquake demands lowest energy. The Oax990930, Pue990615, Gem760915 and Bol991211 earthquakes had higher destructiveness potential on the Oaxaca´s façade. The Oax990615, Pue990930, Kob950116, Sct850918, Stu760506 and Tol760506 earthquakes demand high energy to Puebla's façade. According to results and the earthquake magnitude (Table 2), there are no relation between input energy and earthquake magnitude. All of them have an approximated magnitude of 7.5, but the input energies are not approximated. Table 3 shows the comparison between both input energies. The error between the SAP2000 program and the formula is in the range 0 to 10%. Energies obtained with the code SAP2000 were always bigger than the formula. Because the formula considers only the 90% of the mass of

the structure at take into account only ten modes. However, the results between both were very approximate and can be considered equal. It is clear that taking more modes in the calculations, the error will tend to zero.

Table 3: Comparison of input energy

	Oaxaca			*Puebla*		
Case	*Formula*	*Sap2000*	*Error (%)*	*Formula*	*Sap2000*	*Error (%)*
Oax990615	4.01	4.10	2.20	76.17	76.61	0.57
Oax990930	21.96	22.87	3.98	94.70	96.20	1.56
Pue990615	3.69	3.78	2.38	84.60	85.04	0.52
Pue990930	0.14	0.14	0.00	4.90	4.93	0.61
Gem760915	11.16	11.43	2.36	130.81	131.57	0.58
Kob950116	5.55	5.99	7.34	163.63	166.48	1.71
Sct850918	0.07	0.07	0.00	3.25	3.29	1.22
Stu760506	9.32	9.51	2.00	202.86	204.00	0.56
Tol760506	2.72	2.77	1.81	89.94	90.40	0.51
Bol991211	6.67	6.84	2.49	106.27	106.86	0.55

5 CONCLUSIONS

A novel formula to assess the destructiveness potential of earthquakes by using the input energy was proposed. It is very easy to calculate the maximum energy input with the proposed formula, because only needed the modes of vibrating of the structure and the energy spectrum.

The results showed that an earthquake not have the same destructiveness potential for two different structures. The duration and maximum acceleration of an earthquake are not parameters that dominate at all the energy input of structures. In general, the proposed formula to calculate the input energy gave a much better approximation than the modal time-history analysis. The proposed formula to calculate the input energy is only valid for the linear elastic range, since the formula does not include damage and elastic energy spectrum is used.

ACKNOWLEDGEMENT

The first author acknowledges the Ph.D. grant of Consejo Nacional de Ciencia y Tecnología – CONACyT of Mexico.

REFERENCES

[1] Akiyama, H., Earthquake-resistant Design Method for Buildings Based on Energy Balance, Gihoudou, Syuppan Press. (1999).

[2] Arias, A. A measure of earthquake intensity. *Seismic Design for Nuclear Plants*. R.J. Hansen ed., MIT Press, Cambridge, MA. (1970) 438–469.

[3] Housner, G.W. Spectrum intensities of strong motion earthquakes, *Proc. Symp. of earthquake and blast effect on structures*, EERI, Los Angeles, CA. (1952) 835–842.

[4] Lourenço, P. Computations on historic masonry structures, *Prog. Struct. Engng Mater.* (2002) **4:**301–319.
[5] Sucuoglu H. and Nurtug A. Earthquake ground motion characteristics and seismic energy dissipation, *Earthq. Eng. Struc. Dyn* (1995) **24**:1195–1213.
[6] Uang, C. and Bertero, V. Evaluation of seismic energy in structures. *Earthquake Engineering and Structural Dynamic* (1990) **19**:77-90.
[7] Orosco, L. and Alfaro, I. Potencial destructivo de sismos (segunda parte). Notebook of Engineering faculty, Universidad Nacional de Salta, Salta, Argentina, (2008) 34–45.

XI International Conference on Computational Plasticity. Fundamentals and Applications
COMPLAS XI
E. Oñate, D.R.J. Owen, D. Peric and B. Suárez (Eds)

COMPARISON BETWEEN MINOR DESTRUCTIVE TESTS RESULTS AND FINITE ELEMENT MODELS: THE CASE OF A SANDSTONE MASONRY WALL TESTED IN LABORATORY.

CLARA LIAÑO*, IGNACIO LOMBILLO, LUIS VILLEGAS

* Grupo de Tecnología de la Edificación (GTED)
Universidad de Cantabria
Avda. Castros s/n. 39005 Santander, Spain
e-mail: clara.liano@unican.es, web page: http://www.gted.unican.es

Key words: masonry, numerical modeling, flat jack.

Abstract. *This work is a comparative between stress and strain results obtained from Minor Destructive Tests (MDT) for several load tests on a sandstone masonry wall performed in laboratory, and the numerical results obtained from finite element models, in order to draw conclusions about the challenges and kindness of the experimental technique employed.*
Laboratory tests correspond to simple flat jack tests performed on a masonry wall.
In regard to the model, a macromodel has been used, assuming it consists of a single isotropic material with elastic behavior, pretending to be a first approximation from which the results can be refined. The parameters characterizing the material have been taken from laboratory results obtained from double flat jack tests. It is therefore a two-way analysis, where laboratory results are compared with those obtained from numerical calculation, and these, in turn, are fed with previous results.
By numerical modeling we obtain the stress distribution on the wall, resulting, first, from the load application, and after, induced by the pressure on the flat jack. Thus, we can compare the stress distribution resulting from the application of the load with the values obtained from the simple flat jack tests to validate them, and then study the evolution of stress and strain the wall during the test in order to achieve a better understanding of the process.

1 INTRODUCTION

The purpose of this work is to do a comparison between the experimental results obtained in the laboratory, concerning the state of stress and deformations of a masonry wall, and the theoretical ones, obtained from numerical modeling. The laboratory tests carried out were part of the Doctoral Thesis "Theoretical - Experimental Research about Minor Destructive Tests (MDT) applied to the Mechanical on-site Characterization of Historical Masonry Structures" [1].

For this, the study is focused on a masonry wall modeling the simple flat jack tests [2], [3], [4], [5], [6], [7].

With this aim, a macromodel of the wall has been used, assuming it consists of a single homogeneous material [9], [10], [11]. The parameters characterizing the material have been obtained, in turn, from the laboratory results from the double flat jack test. It is therefore an

analysis, bidirectional, in which laboratory records are compared with those obtained from numerical calculation, and these, in turn, fed with previous results.

2 TEST DESCRIPTION

The simple flat jack test, whose results are intended to be validated in this study, consists of a minor destructive test to obtain an approximate stress distribution in a structural element. To do this, the steps are:

- Mark on the wall two rows of control points. Measure the distance between them.
- Make a groove on the wall in the middle plane between the two rows of the control points.
- Measure the new distance between points (which will be closer after the groove's execution).
- Introduction of the flat jack in the groove and pressure's applying.
- Measure the distance between the points of control until it recovers the initial.

According to the test's methodology, the pressure applied on the flat jack at the moment in which the distance between the control points is recovered can be related with the existing stress on the wall before the test.

For this study, this test has been reproduced in the laboratory by applying a vertical load on a masonry wall. In Figure 1 some photographs of the test developed are shown.

General view of the masonry wall.

Measure of the initial distance between the control points.

Implementation of the groove.

Pressure's application on the flat jack.

Measure of the distance's evolution between the control points.

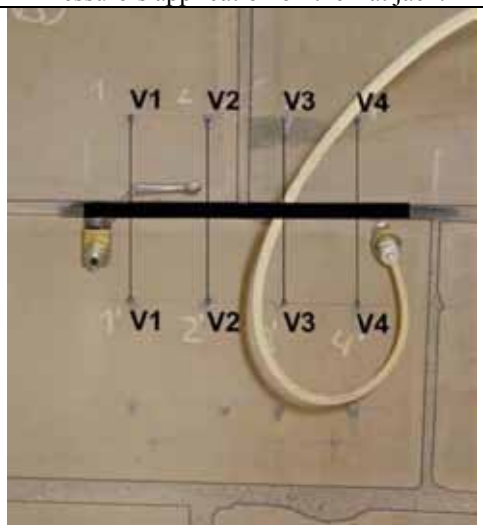

View of the groove, the flat jack and the control points considered.

Figure 1. Photographs of the laboratory tests carried out.

3 INITIAL DATA

To model the behavior of the wall it has been considered that it consists of a single linear material behavior, elastic and isotropic. This has been defined by the values of the Modulus of Elasticity (E) and Poisson's ratio (ν) obtained in the laboratory from double flat jack tests performed in the sandstone masonry. The values used in the calculation are:

$E=3{,}11.10^9$ N/m^2

$\nu=0{,}19$

The density (ρ) was estimated from a specimen of sandstone, which dominates the wall material under study. The value obtained was:

$\rho=2227$ kg/m^3

The loads considered have been the weight of the wall and the load applied on the upper side of the wall. To determine the weight, the value of the density referenced was taken, and to determine the vertical load it was taken into account the load supplied by the hydraulic jacks and the beam's weight that is used for a better distribution of loads. With the addition of these values the load applied is:

P=90.430,4 kp=904.304 N

With this load it results the following pressure applied on the upper side of the wall:

p=2.917.109,68 N/m^2

4 CALCULATION METHODOLOGY

For the numerical modeling of the experiments conducted in the laboratory, the program used has been ANSYS v11 [8].

The first step given was to define a model with the geometry of the masonry wall tested in laboratory whose main dimensions are shown in Figure 2.

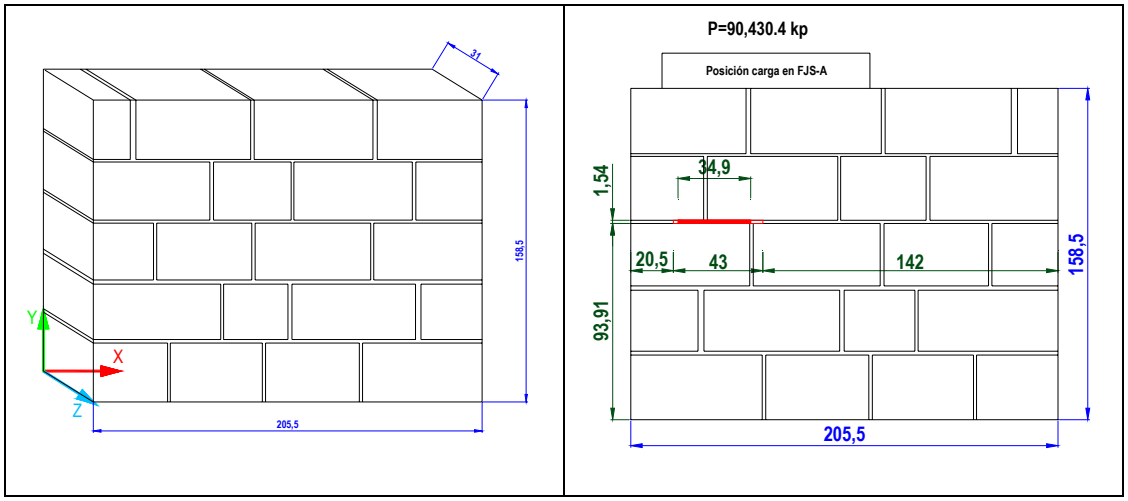

Figure 2. Wall's geometry (cm).

The next step was to define a space discretization which consists on dividing the solid wall in elements within the different parameters are evaluated (stresses, displacements, etc). The element's types used were SOLID45, when the discretization is performed with hexahedral elements, and type SOLID92 for tetrahedral elements. In both cases these elements are three dimensional, whose degrees of freedom correspond to the movements in three directions at each of its nodes (UX, UY, UZ).

As boundary conditions, it is considered coerced the displacement in the three directions on the base of the wall.

With these considerations three different approximations have been developed. A first one considering a hexahedral groove covering the entire wall's wide, a second one considering the real groove and jack's shape with the jack's pressure applied on all its surface and a third one considering the jack's pressure applied only on a fraction of its surface.

In Figure 3 images of the models used are shown. The first model was used in the first calculation (considering a hexahedral groove) and the second one for the other two

(considering the real shape of the groove). The real shape for the groove and for the flat jack was obtained after the laboratory test, removing the upper part of the wall marking the outline of both the groove and the flat jack. In Figure 4 these outlines are represented.

In the three cases the steps given have been the followings:

- Obtaining the stress distribution after the application of the load on the upper face of the wall.
- Implementation of the groove (by removing the corresponding elements).
- Flat jack's pressure application by steps.
- Stress and strains' distribution for each pressure step.
- Comparison between the results obtained from the numerical calculations and the ones obtained in laboratory.

Each of these steps will be described in detail in the next sections.

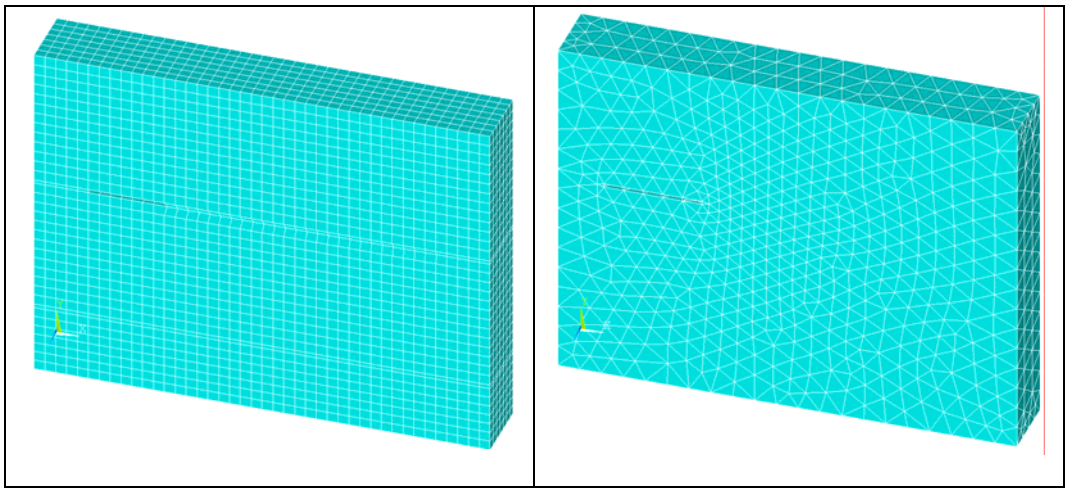

Figure 3. Models used for the calculations.

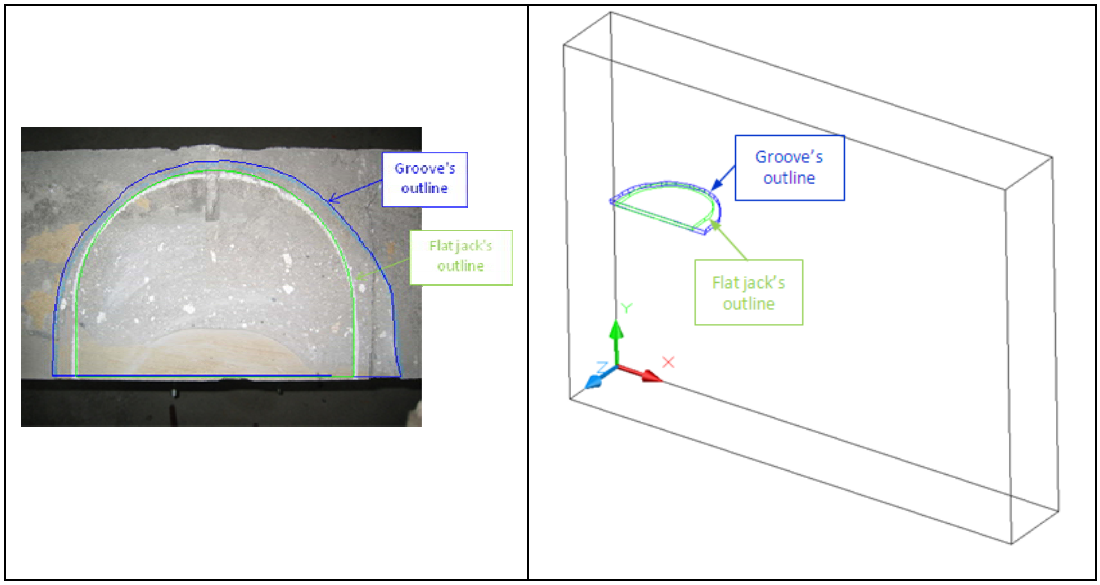

Figure 4. Groove and flat jack's outlines.

5 INITIAL STRESS DISTRIBUTION

As explained above, the first step given was to obtain the stress distribution after the load's application in order to know, before the calculation, the approximate result we should arrive to. The results obtained are shown graphically in Figure 5.

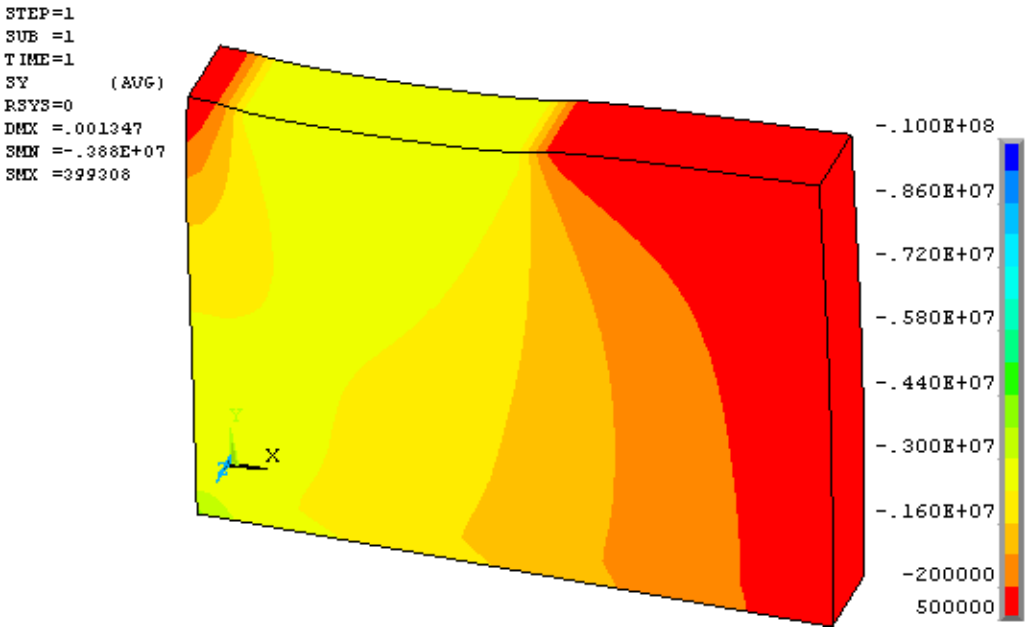

Figure 5. Stress distribution after the load's application.

From the calculations done we obtain that the approximate stress at the groove's height is $24{,}0.10^5$ N/m^2. According to the test methodology, this value should be similar to the pressure applied to the flat jack for which the distance between the control points is recovered.

6 IMPLEMENTATION OF THE GROOVE

In the calculations the implementation of the groove consists on the elimination of the elements corresponding to its volume. With this, we obtain a new stress distribution and a vertical displacements distribution in which we can appreciate the decrease in the distance between the control points.

In Figure 6 we represent the stress distributions for the two models used, once the elements of the groove have beene removed, and in Figure 7 the distributions for the vertical displacements.

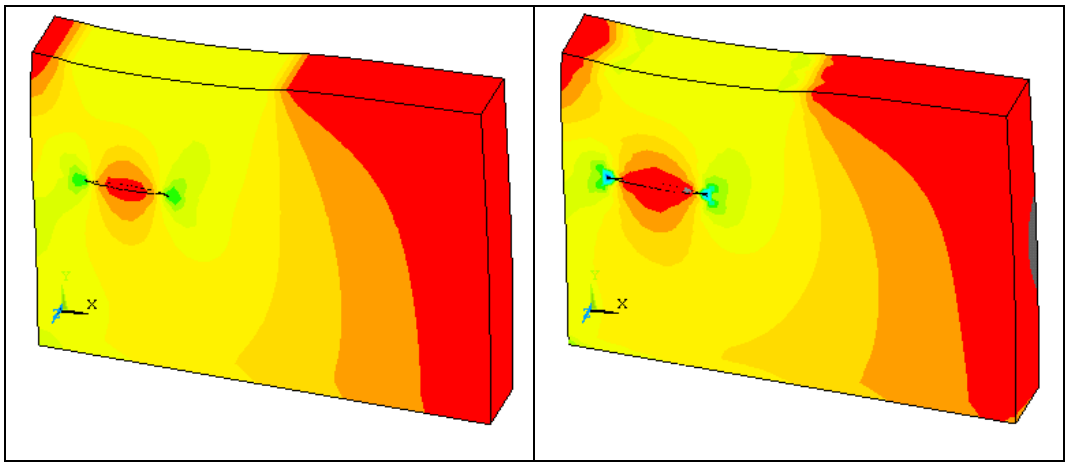

Figure 6. Stress distributions after the implementation of the groove for the two models: hexahedral groove and real shape of the groove.

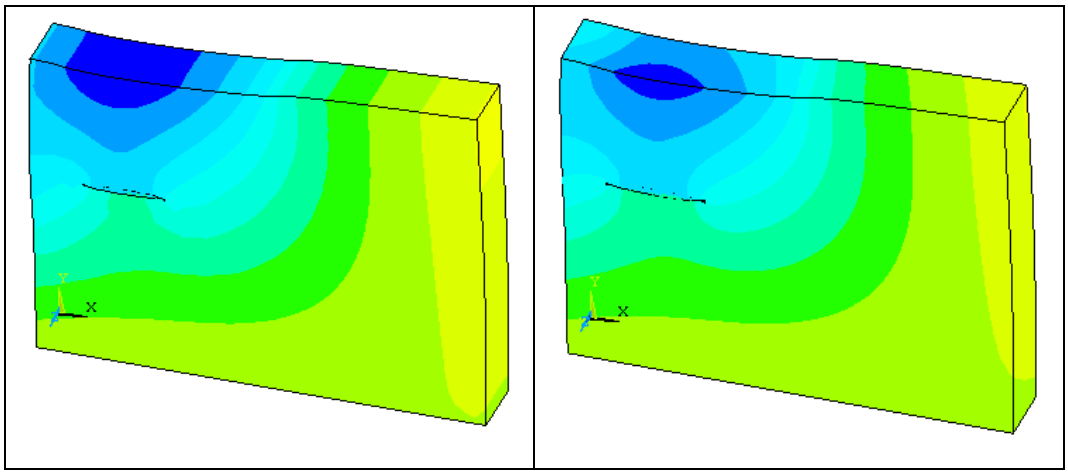

Figure 7. Vertical displacements distributions after the implementation of the groove for the two models: hexahedral groove and real shape of the groove.

7 PRESSURE'S APPLICATION AND STRESS DISTRIBUTIONS OBTAINED

In the next calculation's steps given, a pressure is applied on the flat jack's surfaces. In these steps is when the differences between the three calculations done are more obvious. In the first one the pressure is applied in a hexahedral surface which covers all the wall's wide, in the second one the pressure is applied only in the surface that corresponds to the real shape of the flat jack, and at last, in the third calculation, the pressure is applied in a portion of this surface which corresponds to an approximation of the contact surface obtained in the laboratory tests. In Figure 8 the area of the pressure's application is represented for each case.

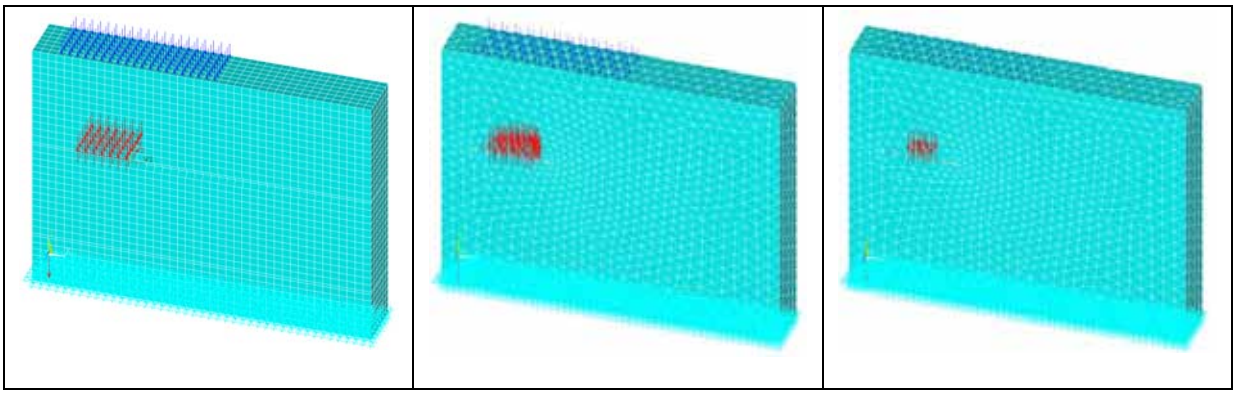

Figure 8. Different areas considered for the pressupre's application

For the third case, the surface in which the pressure is applied was obtained from the laboratory test, placing a tracing sheet on the flat jack so that the pressure's surface would be represented on it. In Figure 9 we can see the area used for this calculation.

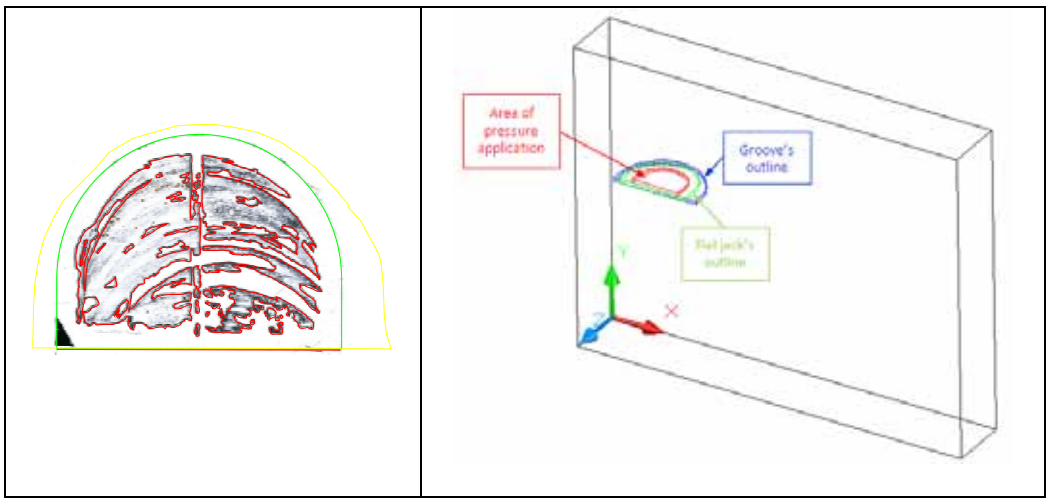

Figure 9. Area of pressure application

For these three different hypotheses we have obtained the stress distributions for two flat jack's pressures: one corresponding to the initial stress obtained at the groove's height ($24,0.10^5$ N/m^2), which should be the value for which the distance between the control points should be restored (Step 9); and other corresponding to the real pressure for which this distance coincides with the initial one measured (Step 10).

In Figure 10 the results for the stress distributions in each case are shown.

	STEP 9 $p=24.10^5$ N/m^2	STEP 10
First calculation	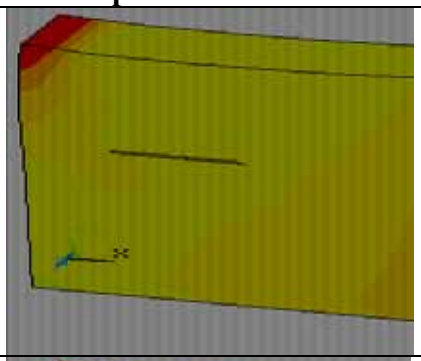	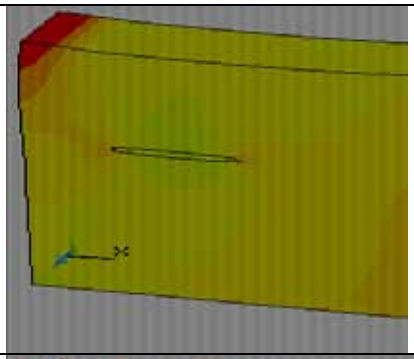
Second calculation	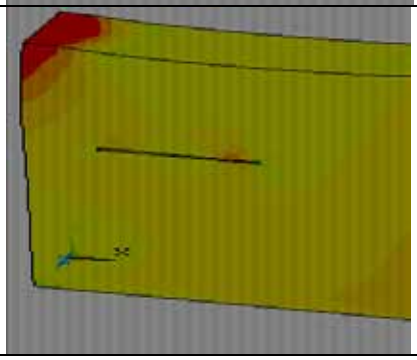	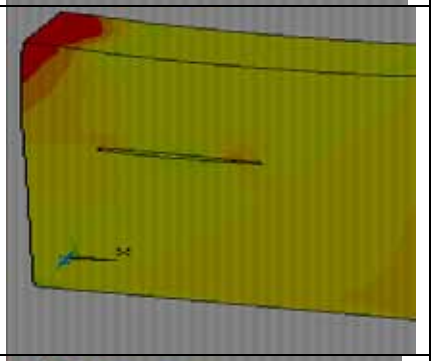
Third calculation	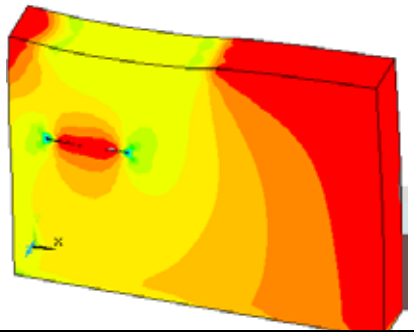	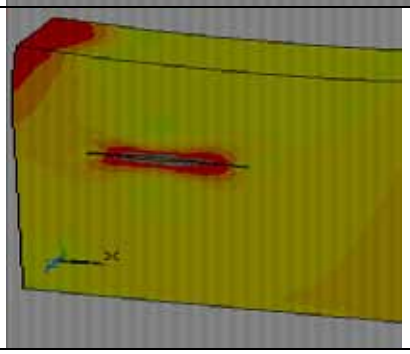

Figure 10. Stress distributions for the three calculations done for two flat jack's pressures.

Analyzing the different figures, we can notice that for Step 9, the stress distribution in the first and second calculations is similar to the initial one, even if the distance between the control points is not completely recovered. It doesn't occur the same in the third case, in which an area with tensile stresses appear around the groove.

In what concerns to Step 10, results for the first and second calculations are closer although it should be noticed a compression area around the groove, due to the pressure applied with the flat jack, bigger, and therefore less realistic, in first calculation. Again the stress distribution obtained with the third calculation doesn't reproduce the expected behavior of the wall during the test.

8 COMPARISON BETWEEN EXPERIMETAL AND NUMERICAL RESULTS

In the test carried out in laboratory, the resulting stress was $34{,}9.10^5$ N/m^2, value higher than the theoretical one expected ($24.\ 10^5$ N/m^2). Comparing it with the results obtained from the numerical simulation, we can conclude that the first approximation gives us a very similar value ($35.\ 10^5$ N/m^2) so it could be used to get a sufficiently accurate result.

However, the second calculation carried out gives us a nearest result to the theoretical one ($30.\ 10^5$ N/m^2).

The third calculation is not useful to simulate the test as it considers an area in which the pressure is applied too small to reproduce the real behavior of the wall during the test.

9 CONCLUSIONS

After all the calculations done, we can conclude that the simple flat jack test gives a reasonable result for the stress level in a masonry wall.

In what concerns to the numerical simulation, the results are also sufficiently. Anyway, it is important to emphasize that the calculation carried out is a first approach, having used a macromodel and considering an isotropic material with linear elastic behavior. It is expected that considering plastic behavior, nonlinearity and anisotropy, would improve the accuracy of the results achieved.

Even if the results obtained are not exactly the existing ones, we should not forget that the objective of this type of test is to obtain an order of magnitude of the stress situation of the wall with the least destructive testing possible, without considering it necessary, in general, to get the exact value of the stress at one point.

It is remarkable that in onsite tests the results would be even more accurate, taking into account that effects due to boundary conditions, as the size of the wall, disappear in a real wall.

10 REFERENCES

[1] Ignacio Lombillo. Doctoral Thesis "*Theoretical - Experimental Research about Minor Destructive Tests (MDT) applied to the Mechanical on-site Characterization of Historical Masonry Structures*". Universidad de Cantabria, (2010).

[2] Binda, L., Saisi, A. y Zanzi, L. (2003a). "Sonic tomography and flat jack tests as complementary investigation procedures for the stone pillars of the temple of S. Nicolo` l'Arena (Italy)". NDT & E International, 36(4): 215–227.

[3] Binda L. y Tiraboschi C. (1999a). "Flat-Jack Test as a Slightly Destructive Technique for the Diagnosis of Brick and Stone Masonry Structures". Int. Journal for Restoration of Buildings and Monuments, Int. Zeitschrift fur Bauinstandsetzen und Baudenkmalpflege, Zurich, pp. 449-472.

[4] de Veckey R.C. y Skandamoorthy J.S. (1997). "Measurement of stress in Sandstone blockwork using flat jacks". Journal of Brittish Masonry Society 11 (2), pp. 56-59. Presented al BMS meeting, Stoke on Trent, UK, 11/1996, BRE PD 248/96.

[5] Ronca P., Tiraboschi C. y Binda L. (1997). "In-situ flatjack tests matching new mechanical interpretations". 11th International Brick/Block Masonry Conference. Tongji University, Shanghai, China 14-16 October 1997, pp. 357 – 366.

[6] Rossi P. P. (1987). "Recent developments of the flatjacks test on masonry structures". Proceedings of the Second joint USA-Italy Workshop on Evaluation and Retrofit of Masonry Structures.
[7] Rossi P. P. (1982). "Analysis of mechanical characteristics of brick masonry tested by means of nondestructive in-situ tests". Proceedings of the 6th International Brick Masonry Conference (IBMaC). Rome, Italy.
[8] *"ANSYS User's Manual"*. Version 13.0 (2010).
[9] R. Martinez Barea, J. Yuste. *"Validación teórica mediante macro y micromodelos estructurales a escala de muros históricos"*. Jornadas Técnicas REHABEND (2009).
[10] M. Acito, L. Binda et al. *"Experimental and numerical study on the application of the flat-jack tests to masonry walls"*. Structural Analysis of Historic Construction-D'Ayala&Fodde (eds) (2008).
[11] P. Roca. *"Aplicación de técnicas experimentales y numéricas al estudio del patrimonio arquitectónico"*. Jornadas Técnicas REHABEND (2006).

XI International Conference on Computational Plasticity. Fundamentals and Applications
COMPLAS XI
E. Oñate, D.R.J. Owen, D. Peric and B. Suárez (Eds)

COMPUTATIONAL MODELLING OF HYBRID MASONRY SYSTEMS

Ilinca Stanciulescu* **and Zhenjia Gao†**

* Assistant Professor of Civil Engineering, Rice University, 208 Ryon Laboratory, MS 318
6100 Main Street, Houston, Texas 77005, USA
e-mail: ilinca.s@rice.edu/

† Ph.D. Student Civil Engineering, Rice University, 207 Ryon Laboratory, MS 318
6100 Main Street, Houston, Texas 77005, USA

Key words: Hybrid masonry, computational modelling, inelastic behaviour, damage

Abstract. In this work we investigate the seismic strength, behavior, and performance of the hybrid masonry structural system. The computational modeling efforts aim to characterize the inelastic behavior of hybrid masonry panels. In particular, we study the influence of the boundary conditions (gap or no gap, reinforced or bearing contact zone), the story shear, overturning moment, and the influence of the panel aspect ratio.

Several computational models with various levels of complexity are used in our study in an effort to identify the simplest model capable of capturing the salient features of these structural systems. A non-linear (plastic) constitutive model for the simulation of masonry is considered; this constitutive model is coupled with a damage mechanics model to simulate both the inelastic deformation of masonry in normal compression and tension and the damage due to cracking and micro-cracking.

In what we call type I hybrid masonry, the masonry does not make direct contact with the beams or columns of the steel frame. The frame and the masonry are connected only through connector plates. The hybrid masonry provides many advantages, such as improving the resistance to seismic loads, impeding the extent of the damage in the masonry and so on. There is no gap between beam and masonry for Type II, so the masonry shares the gravity load with the steel frame and benefits from the vertical compression. Type III is an extension of Type II systems with the addition of connectors along the sides of the panel, which resist vertical shear forces. For Type II and Type III hybrid masonry, because the beam is in contact with the masonry, another very important aspect needs to be considered for the numerical simulation: we require a contact formulation capable of modelling the transfer of normal and tangential forces between steel and masonry.

Preliminary computational results are presented in this paper that will be in the future correlated with laboratory test results from the large-scale tests done at the University of Illinois at Urbana Champaign.

1 INTRODUCTION

Reinforced masonry panels can be designed as stiff, strong and ductile panels, interacting with the surrounding steel frame to resist lateral seismic forces. In the hybrid masonry structural system, the panels are not only used to provide spatial functionality in a building, but they also be enhance the seismic performance. This structural system is designed in such a manner that steel frames are attached to masonry panels and will transfer part of the loading (e.g., gravity forces, story shears and overturning moments) to the masonry. The panel itself can be reinforced with horizontal and vertical bars. In what we call type I hybrid masonry, the masonry does not make direct contact with the beams or columns of the steel frame. The frame and the masonry are connected only through connector plates.

The hybrid masonry system improves the resistance to seismic loads and limits the extent of the damage. Because of the panel reinforcement, the deformation in the masonry is small. Two other systems, designated as Type II and Type III may be considered. There is no gap between beam and masonry for Type II, so the masonry share the gravity load with the steel frame and benefits from the vertical compression. Type III is an extension of Type II systems with the addition of connectors along the sides of the panel, which resist vertical shear forces. For the simulation of Type II and Type III hybrid masonry, due to the transmission of forces between the steel frame (beams) and the masonry panels through direct contact, a formulation capable of modelling the transfer of normal and tangential forces between steel and masonry needs to be considered for the numerical simulation.

For the numerical simulation we use FEAP [1], an open source finite element code, which provides a framework for finite element simulations; specific constitutive models and solution schemes are included via user functions. The formulations used in this study are a mix of FEAP original elements and user routines.

The rest of this paper is organized as follows: In the next section we briefly introduce various computational models that will be utilized in our study. The following section then introduces some preliminary numerical simulations. Through several parametric studies we investigate the influence of nonlinearity, of damage and of panel aspect ratio on the transfer of loads between the frame and the panel. The paper concludes with a summary of the important features of computational models for hybrid masonry, a discussion of the influence of nonlinearities and damage on the distribution of loads between the frame and the panels and a discussion of future work.

2 COMPUTATIONAL FRAMEWORK

An isotropic model is used to describe the linear elastic constitutive behavior of the steel frame. The formulation can account for shear deformation. Extensions to large deformations are also available (with or without shear effects). Through the built-in FEAP elements, we also have access to a more complex model for the frame that includes

plasticity and also accounts for geometric nonlinearities. For this option the inelastic behaviour is accounted for in the bending and axial effects but the element retains elastic response in the transverse shear terms.

The masonry panels are modeled with 2D plane strain or plane stress continuum elements. Constitutive models ranging from linear elasticity to large deformation plasticity are considered. The damage and the plastic deformation effects are included in a homogenized framework. From a numerical implementation point of view, the standard predictor corrector approach is used. In a first step, an elastic predictor is calculated. Then a plastic corrector is used to obtain the stress by an implicit Euler backward integration scheme. The stress can be expressed [2] as

$$\sigma_{n+1} = \sigma_n + D(\Delta\epsilon_{n+1} - \Delta\epsilon^p_{n+1}) = \sigma^{trial}_{n+1} - \Delta\lambda_{n+1} D \frac{\partial g}{\partial \sigma}|_{n+1}, \tag{1}$$

where subscripts indicate the step number, σ and ϵ are the stress and strain tensors, $\Delta\lambda$ is the increment of the plastic multiplier rate, and g is the plastic potential. Considering the additional equation enforcing the yield condition, we have a system of nonlinear equations having as unknowns the stress and the plastic multiplier rate that can be solved at every integration point using a local Newton-Raphson iteration. Different plastic potentials can be used to model masonry, such as the J2 or Mohr-Coulomb flow rule [2, 3].

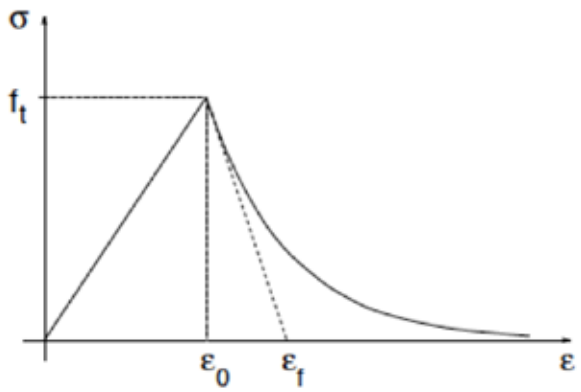

Figure 1: Uniaxial stress-strain curve based on an exponential softening model

Due to the brittle behavior of masonry, the computational framework should also include a damage mechanics model to simulate both the inelastic deformation of masonry in normal compression and tension and the damage due to cracking and micro-cracking. An effective simulation of the progressive deterioration of the mechanics properties of masonry panels under increasing loading can be obtained in the conventional framework of continuum damage mechanics. For this study, a scalar damage model is adopted with a single parameter, the damage coefficient d used to evaluate the effective stress $\sigma_d = (1 - d)\sigma$ (where σ_d is the stress in the damaged configuration, and σ is the stress corresponding to

an undamaged state). A possible expression for d [4] that models the case of exponential softening is given below and requires the definition of two parameters, ϵ_0, the strain at the peak stress and ϵ_f a strain parameter controlling the initial slope of the softening branch (Figure 1).

$$d(\epsilon) = \quad 0 \quad if \quad \epsilon < \epsilon_0 \tag{2}$$

$$d(\epsilon) = \quad 1 - \frac{\epsilon_0}{\epsilon} exp(-\frac{\epsilon - \epsilon_0}{\epsilon_f - \epsilon_0}) \quad if \quad \epsilon_0 < \epsilon \tag{3}$$

In this context, d has the role of a reduction factor that accounts for the effect of damage in the material: $d = 0$, corresponds to a state where no damage is present in the material, while $d = 1$ represents a completely damaged state. In other words, d can be seen as the ratio of damaged area to the total cross sectional area [5].

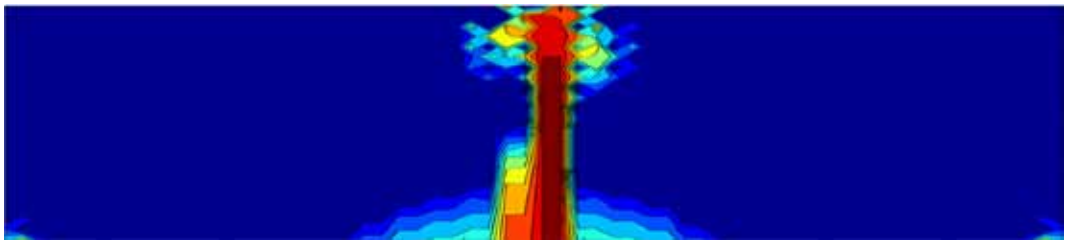

Figure 2: Distribution of damage in a simply supported unnotched beam subject to a concentrated load at mid span (blue: no damage to dark red: complete damage/ crack)

Figure 2 shows the distribution of damage in a simply supported beam under a concentrated load captured with our current implementation of such formulation (using a local damage model). This implementation is used for all numerical results that include damage presented in the next section. Work is currently underway to extend this model to a nonlocal model in order to avoid the mesh size effects that are characteristic for local formulations.

In the case of the type I hybrid masonry, there is no direct contact between the masonry and the steel frame. The transmission of loads can only occur through the masonry-frame (beam) connectors in this case. Type II and III hybrid systems however, reduce or even eliminate the gaps and direct contact becomes possible. Two fundamentally different approaches can be used to model contact in the finite element framework. The traditional formulation uses the so-called node-to-surface approach where the contact constraints are enforced strongly at every node in contact. This approach is computationally efficient but numerically not very robust, in particular, in the presence of large sliding or of significant difference in the stiffness properties of the bodies in contact. An alternate approach relies on the use of a mortar formulation [6, 7]. Both formulations are available as user subroutines in our code.

3 NUMERICAL RESULTS

We present in this section some preliminary numerical results obtained for a reduced scale (1:5) model that will be used by our collaborators at the University of Illinois, Urbana-Champaign to calibrate the experimental setup for the full-scale systems testing planed for the near future. The first study that we performed investigated the effect

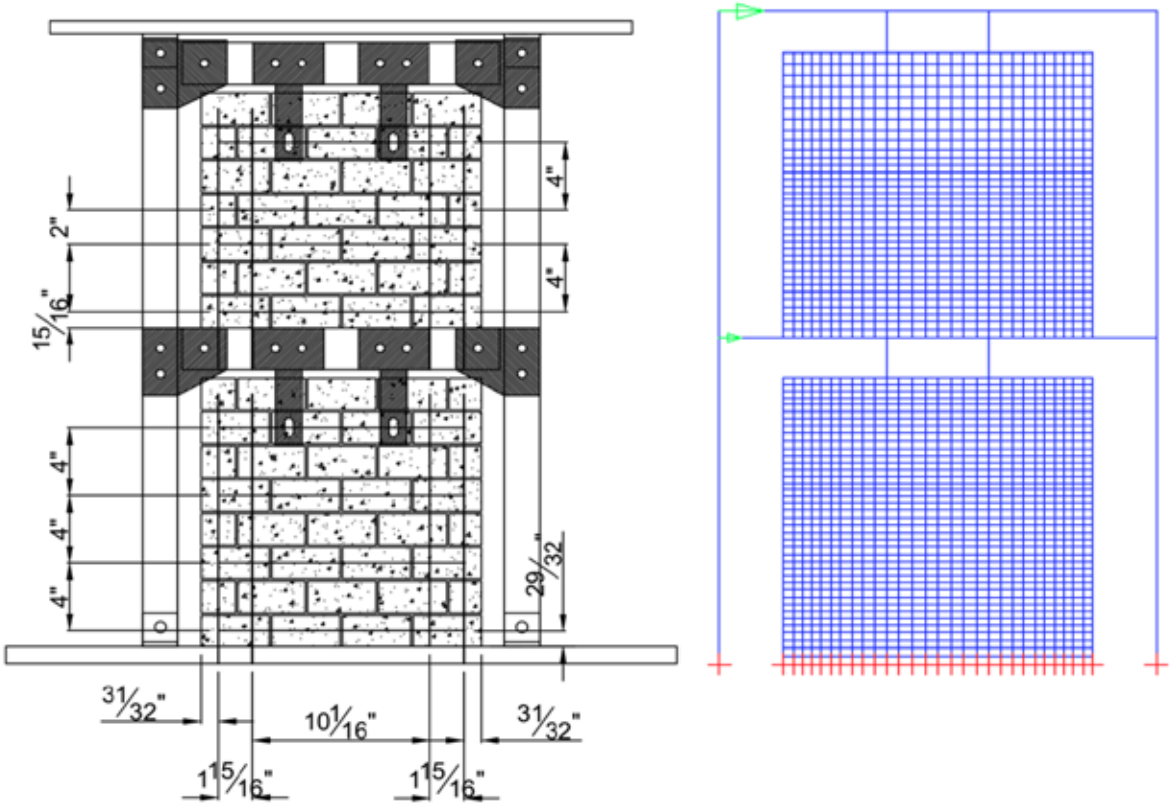

Figure 3: Reduced scale model of a type I hybrid masonry wall: Geometry (left) and finite element discretization (right)

of material and geometrical nonlinearities on the distribution of loads between the steel frame and the masonry panel. The structure presented in Figure 3 is of type I (no loads are transferred through direct contact). The connectors are in this example considered to transfer loads both vertically and horizontally. A controlled displacement loading sequence is considered. Three cases were simulated that consider different material behavior for steel and masonry: (1) linear elastic, (2) small deformation plasticity, and (3) large deformation plasticity.

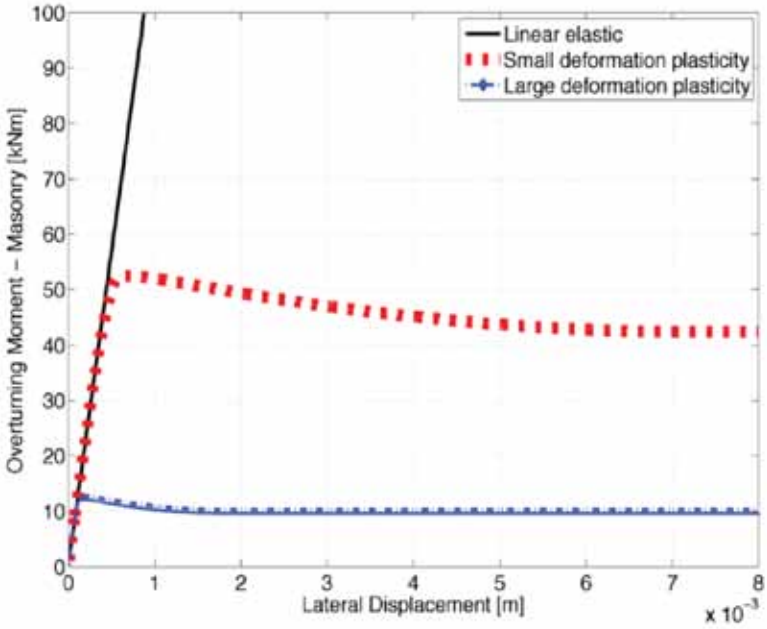

Figure 4: Overturning moment for the masonry panel

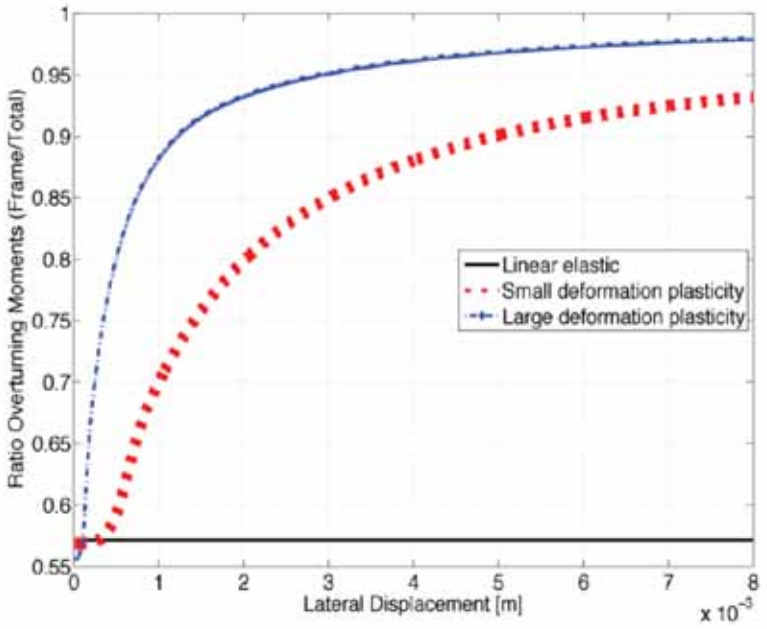

Figure 5: Ratio of overturning moment frame/masonry

Figures 5 and 4 show the total overturning moment of the masonry panel and the ratio of moments as functions of the lateral displacement at the second story beam. It is clearly seen that, while some loads are transmitted to the masonry panel in this system, there is a limited range of displacements for which the contribution of masonry in the overall behavior is significant. In the large deformation range, a significant percentage of the overturning moment has to be resisted by the steel frame. A more realistic assumption was used next, where it is assumed that the connectors transfer only horizontal loads to the masonry and that the masonry can undergo damage.

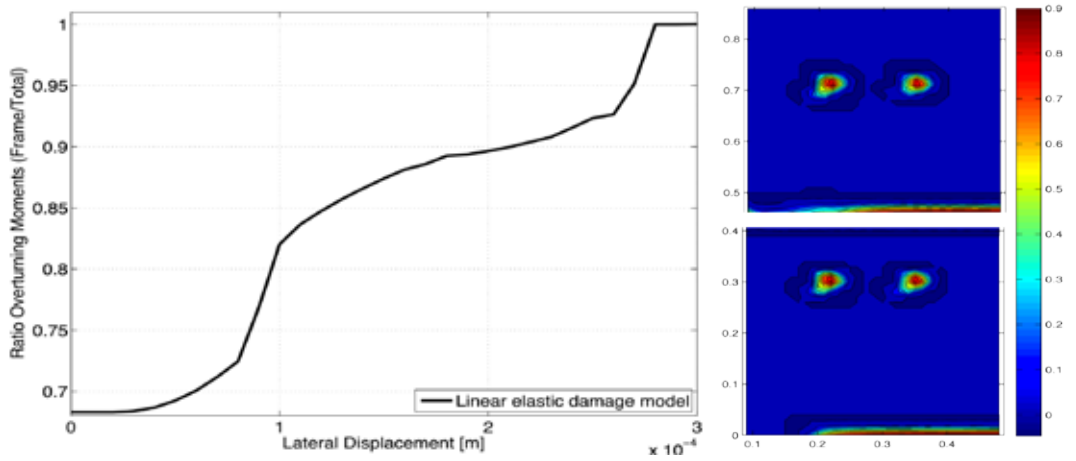

Figure 6: Ratio of overturning moment frame/masonry (left) and distribution of damage (right)

Figure 6 indicates that at relatively small lateral displacements, the ability of the masonry panel to provide resistance to the overturning moment is lost and quite rapidly the whole load needs to be supported by the frame. At this stage, we can only use such simulations for qualitative analyses since most material parameters that we used as input are approximate values for simple masonry. When experimental data will become available from the hybrid systems testing, the material parameters will be calibrated and quantitative conclusions will be drawn.

4 CONCLUSIONS

A computational framework for the analysis of hybrid masonry systems was established. The effect of nonlinearity on the structural response of a small scale hybrid masonry wall was investigated in this preliminary study. We studied both material nonlinearities (by using elasticity and plasticity models) and geometrical nonlinearities by also incorporating the effect of large deformations. The influence of damage in the masonry panel on the overall distribution of the overturning moment was investigated. The crack pattern is significantly influenced by the refinement of the mesh. Such mesh size effects associated with the use of local damage formulations require the investigation/ implementation of a

nonlocal damage algorithm to alleviate the stress softening problem. Future simulations of type II and type III systems will also require use of contact formulations.

REFERENCES

[1] Taylor, R. L., *FEAP A Finite Element Analysis Program* (2006).

[2] Lourenco, P.B., *Analysis of Masonry Structures with Interface Elements* (1994).

[3] Zucchini, A., Lourenco, P.B., A micro-mechanical homogenization model for masonry: Application to shear walls, *International Journal of Solids and Structure* (2009), 871–886.

[4] Jirasek, M. , Non-local damage mechanics with application to concrete, *Failure, degradation and instabilities* (2004), pp 683–707

[5] Faleiro, J., Oller, S., Barbat, A.H., Plastic-damage analysis of reinforced concrete frames, *International Journal for Computer-Aided Engineering and Software* (2010), Vol. 27, No. 1, 57-83.

[6] Wriggers, P., *Computational Contact Mechanics*, Springer, 2006.

[7] Yang, B., Laursen, T. A., Meng, X, Two Dimensional Mortar Contact Methods for Large Deformation Frictional Sliding, *International Journal of Numerical Methods in Engineering* (2005), Vol 62, 1183–1225

XI International Conference on Computational Plasticity. Fundamentals and Applications
COMPLAS XI
E. Oñate, D.R.J. Owen, D. Peric and B. Suárez (Eds)

COMPUTATIONAL MODELLING OF PROGRESSIVE FAILURE OF COMPOSITE MATERIALS AND STRUCTURES INCLUDING PLASTICITY EFFECTS

EVGENY V. MOROZOV*, JINGFEN CHEN, KRISHNAKUMAR SHANKAR

*School of Engineering and Information Technology
University of News South Wales at the Australian Defence Force Academy
Northcott Drive, 2600 Canberra ACT, Australia
e-mail: e.morozov@adfa.edu.au, web page: http://www.unsw.adfa.edu.au

Key words: Progressive Failure Analysis, Plasticity Effects, Composite Materials, Return Mapping Algorithm

Abstract. The paper is concerned with the development and verification of the computational algorithm enabling the progressive failure simulation that takes into account plasticity effects in addition to the damage progression to be performed for composite materials and structures.

The numerical approach is based on the combined elastoplastic damage model that accounts for the irreversible strains caused by plasticity effects and material properties degradation due to the damage initiation and development. The strain-driven implicit integration procedure is developed using equations of continuum damage mechanics, plasticity theory and includes the return mapping algorithm. A tangent operator that is consistent with the integration procedure is derived to ensure a computational efficiency of the Newton-Raphson method in the finite element analysis. The algorithm is implemented in ABAQUS as a user-defined subroutine. Prediction of the damage initiation in the laminated composite takes into account various failure mechanisms making use of Hashin's failure criterion. The plasticity effects in composite material are modelled using the approach developed by C. T. Sun and J. L. Chen.

The efficiency of the modelling approach and computational procedure is verified using the analysis of the progressive failure of composite laminates made of carbon fibre reinforced plastic and subjected to in-plane uniaxial tensile loading. It has been shown that the predicted results agree well with the experimental data.

1 INTRODUCTION

Laminated composite materials are widely used in aerospace, civil engineering, military vehicles, marine and many other industries due to their high strength and stiffness to weight ratios, good fatigue resistance and high energy absorption capacity. In many

applications, the progressive failure analysis of composite laminates is required to predict their mechanical behaviour under various loadings.

The development of an appropriate constitutive model for fibre reinforced composite materials normally involves the consideration of their mechanical response prior to the initiation of damage, the prediction of damage initiation and the modelling of postfailure behaviour. Continuum damage mechanics (CDM) provides a tractable framework for modelling damage initiation and development, as well as stiffness degradation. It is based on mesoscale, where a laminate is regarded as consisting of orthotropic plies. Several material models using continuum damage mechanics have been reported in literature [1–6]. Most of the CDM-based material approaches are based on elastic-damage models which are suitable for modelling the mechanical behaviour of elastic-brittle composites that do not exhibit noticeable nonlinearity or irreversible strains prior to the initiation of damage development. However, they may be insufficient in describing the nonlinear or plastic behaviour that some thermoset or thermoplastic composites might exhibit under transverse and/or shear loading. For example, research undertaken by Xiao [7] shows that material models that do not take into account the plastic features of composites failures might underestimate the energy absorbtion capacity of composite structures.

In addition to plasticity effects, material properties deterioration under loading is another significant feature of composite laminates. Defects such as fibre rupture, matrix cracks, fibre/matrix debonding developing in a ply do not lead to the collapse of a laminate immediately as they come up. These defects can accumulate gradually within the laminates. As a consequence, the material properties degrade progressively. Thus, the consideration of postfailure behaviour is important for an accurate prediction of failure loads.

Physically, the nonlinearity and/or irreversible deformations of fibre reinforced composites stem from the various mechanisms, such as the nonlinearity of each individual constituents, damage accumulation resulting from fibre or matrix cracking, and fibre/matrix interface debonding. Drucker [8] has proposed that such micromechanical phenomena can be described macroscopically within the framework of the plasticity theory. In combined plasticity and damage theories, the plastic strain represents all the irreversible deformations including those caused by microcracks. This approach is adopted in this study using an equivalent form of Sun and Chen plastic model [9]. The Hashin's failure criterion [10] is adopted to characterize the damage initiation and development.

Once damage initiates in the material, local stresses are redistributed in the undamaged area. As a result, the effective stresses in the undamaged area are higher than the nominal stresses in the damaged material. Plasticity is assumed to be developed in the undamaged area of the damaged material. So the effective stresses are used in the plastic model. Since the nominal stresses in the postfailure branch of the stress-strain curves decrease with the increase in strain, the use of these stresses in the failure criteria does not provide the prediction for further damage growth. Thus, the effective stresses are also applied in the Hashin's failure criteria.

2 ELASTOPLASTIC DAMAGE CONSTITUTIVE MODEL

The constitutive model is presented for an elementary orthotropic ply and consists of a plastic part which describes the plastic behaviour of composites under transverse and/or shear loading, failure criteria that are used to predict the thresholds for damage initiation and growth, and damage evolution laws that account for the development of damage.

2.1 Stress-strain relationship

Damage affects the behaviour of fibre-reinforced composite materials considerably. Material properties, such as elastic moduli and Poisson's ratio, degrade due to damage accumulation and growth. These effects are taken into account by introducing damage variables in the stiffness matrix using the CDM-based approaches. For example, the relation between the nominal stress and effective stress under uniaxial loading is given as

$$\sigma = (1-d)\bar{\sigma} \tag{1}$$

where $\sigma = P/A_0$ is the Cauchy nominal stress (P is the normal internal force applied to the resisting surface, A_0 is the original area), $\sigma = P/A_{\text{eff}}$ is the effective stress (A_{eff} is the effective resisting area of the damaged surface).

For composite materials exhibiting plasticity response, the total strain tensor $\boldsymbol{\varepsilon}$ is decomposed into the elastic and plastic strain parts $\boldsymbol{\varepsilon}^e$ and $\boldsymbol{\varepsilon}^p$ as

$$\boldsymbol{\varepsilon} = \boldsymbol{\varepsilon}^e + \boldsymbol{\varepsilon}^p \tag{2}$$

where the plastic strain $\boldsymbol{\varepsilon}^p$ represents all the irreversible deformations including those caused by microcracks.

According to the continuum damage mechanics theory, the stress-strain relationships for the damaged and undamaged composite materials are written in the following forms:

$$\boldsymbol{\sigma} = \mathrm{S}(d) : \boldsymbol{\varepsilon}^e; \quad \bar{\boldsymbol{\sigma}} = \mathrm{S}_{\mathbf{0}} : \boldsymbol{\varepsilon}^e \tag{3}$$

where bold-face symbols are used for variables of tensorial character and symbol (:) denotes inner product of two tensors with double contraction, e.g. $(\mathrm{S}(d) : \boldsymbol{\varepsilon}^e)_{ij} = \mathrm{S}(d)_{ijkl}\boldsymbol{\varepsilon}^e_{kl}$, where the summation convention is applied to the subscripts; $\boldsymbol{\sigma}$, $\bar{\boldsymbol{\sigma}}$ are the Cauchy nominal stress tensor and effective stress tensor (both are the second order tensors); $\mathrm{S}_{\mathbf{0}}$ is the fourth-order constitutive tensor for linear-elastic undamaged unidirectional laminated composite; $\mathrm{S}(d)$ is the one for the associated damaged material. The explicit form of $\mathrm{S}_{\mathbf{0}}$ is determined by elasticity theory for orthotropic materials. The form of the $\mathrm{S}(d)$ adopted in this model is similar to that presented by Matzenmiller et al. [2]

$$\mathrm{S}(d) = \frac{1}{D}\begin{bmatrix} (1-d_1)E_1^0 & (1-d_1)(1-d_2)\nu_{21}^0 E_1^0 & 0 \\ (1-d_1)(1-d_2)\nu_{12}^0 E_2^0 & (1-d_2)E_2^0 & 0 \\ 0 & 0 & D(1-d_3)G_{12}^0 \end{bmatrix} \tag{4}$$

where $D = 1 - (1 - d_1)(1 - d_2)\nu_{12}^0\nu_{21}^0$, d_1, d_2, d_3 denote damage developed in the fibre and transverse directions, and under shear (they are scalar damage variables that remain constant throughout the ply thickness); E_1^0, E_2^0, G_{12}^0 and ν_{12}^0, ν_{21}^0 are the elastic moduli and Poisson's ratios of undamaged unidirectional composite laminae.

In order to track the different failure mechanisms, namely, matrix microcraking and fibre rupture developed in the composite ply under tensile and compressive stresses, the damage variables are given as follows:

$$d_1 = \begin{cases} d_{1t} & \text{if } \sigma_1 \geq 0 \\ d_{1c} & \text{if } \sigma_1 < 0 \end{cases} \qquad d_2 = \begin{cases} d_{2t} & \text{if } \sigma_2 \geq 0 \\ d_{2c} & \text{if } \sigma_2 < 0 \end{cases} \tag{5}$$

where d_{1t}, d_{1c} denote damage developments caused by tension/compression in the fibre direction, and, d_{2t}, d_{2c} denote damage developments caused by tension/compression in the transverse direction.

It is assumed that the shear stiffness reduction results from the fibre and matrix cracking. To take this into account, the corresponding damage variable d_3 is expressed as:

$$d_3 = 1 - (1 - d_6)(1 - d_{1t}) \tag{6}$$

where d_6 represents the damage effects on shear stiffness caused by matrix cracking.

As mentioned before, all the irreversible deformations are represented by the plastic strain $\boldsymbol{\varepsilon}^p$. These effects are allowed for by the plastic model which includes the yield criterion, plastic flow rule, hardening variable flow rule, and the hardening law.

2.2 Plastic model

In the damaged materials, internal forces are resisted by the effective area. Thus, it is reasonable to assume that plastic deformation occurs in the undamaged area of the damaged composites. According to this, the plastic flow rule and hardening law are expressed in terms of effective stresses $\bar{\boldsymbol{\sigma}}$, equivalent plastic strain $\tilde{\varepsilon}^p$, and equivalent stress $\tilde{\sigma}$, which are based on the effective stress space concept.

The plastic yield function is given by:

$$F(\bar{\sigma}, \tilde{\varepsilon}^p) = F^p(\bar{\sigma}) - \kappa(\tilde{\varepsilon}^p) = 0 \tag{7}$$

where F^p is the plastic potential; κ is the hardening parameter which depends on the plastic deformations and is expressed in terms of equivalent plastic strain $\tilde{\varepsilon}^p$.

Due to its simplicity and accuracy, an equivalent form of the one-parameter plastic potential for plane stress condition proposed in [9] is adopted in this study to describe the irreversible strains exhibited by composites under transverse and/or shear loading:

$$F(\bar{\boldsymbol{\sigma}}, \tilde{\varepsilon}^p) = \sqrt{\frac{3}{2}(\bar{\sigma}_2^2 + 2a\bar{\sigma}_3^2)} - \tilde{\sigma}(\tilde{\varepsilon}^p) = 0 \tag{8}$$

where a is a material parameter which describes the level of plastic deformation developed under shear loading compared to the transverse loading, $\bar{\sigma}_2$ is the effective stress in the

transverse direction, $\bar{\sigma}_3$ is the effective in-plane shear stress, and $\tilde{\sigma}(\tilde{\varepsilon}^p)$ is the isotropic hardening law for composites materials. Selecting the plastic criterion in the form of Eq.(8) improves efficiency and accuracy of the computational algorithm.

The equivalent stress is expressed in terms of $\bar{\sigma}_2$ and $\bar{\sigma}_3$ as follows [9]:

$$\tilde{\sigma} = \left[\frac{3}{2}(\bar{\sigma}_2^2 + 2a\bar{\sigma}_3^2)\right]^{\frac{1}{2}} \tag{9}$$

Assuming the associated plastic flow rule for composite materials, the plastic strain rate $\dot{\boldsymbol{\varepsilon}}^p$ is expressed as:

$$\dot{\boldsymbol{\varepsilon}}^p = \dot{\lambda}^p \partial_{\bar{\boldsymbol{\sigma}}} F \tag{10}$$

where $\dot{\lambda}^p \geq 0$ is a nonnegative plastic consistency parameter; hereafter $\partial_x y = \partial y / \partial x$.

Substituting Eq.(8) into Eq.(10), the following explicit form of plastic strain rate is derived:

$$\begin{bmatrix} \dot{\varepsilon}_1^p \\ \dot{\varepsilon}_2^p \\ \dot{\varepsilon}_3^p \end{bmatrix} = \dot{\lambda}^p \partial_{\bar{\boldsymbol{\sigma}}} F = \dot{\lambda}^p \begin{bmatrix} 0 \\ \dfrac{\bar{\sigma}_2}{\sqrt{\frac{3}{2}(\bar{\sigma}_2^2 + 2a\bar{\sigma}_3^2)}} \\ \dfrac{3a\bar{\sigma}_3}{\sqrt{\frac{3}{2}(\bar{\sigma}_2^2 + 2a\sigma_3^2)}} \end{bmatrix} \tag{11}$$

In a similar fashion, the associated hardening rule is also assumed for the equivalent plastic strain rate and is presented as follows:

$$\dot{\tilde{\varepsilon}}^p = \dot{\lambda}^p h^p = \dot{\lambda}^p \partial_{\tilde{\varepsilon}^p} F \tag{12}$$

where h^p defines the evolution direction of the equivalent plastic strain.

The equivalent plastic strain rate can be obtained from the equivalence of the rates of the plastic work per unit volume W^p

$$\dot{W}^p = \bar{\boldsymbol{\sigma}} : \dot{\varepsilon}^p = \tilde{\sigma}\dot{\tilde{\varepsilon}}^p \tag{13}$$

Substituting Eq.(11) and Eq.(9) into Eq.(13), the following relation is derived

$$\dot{\tilde{\varepsilon}}^p = \dot{\lambda}^p \tag{14}$$

It follows from the comparison of Eq.(12) and Eq.(14) that the value of h^p is unity. Note that this result does not hold if the original quadratic form of the Sun and Chen yield criterion is adopted [9]. As a result, the application of the original yield criterion involves more computational efforts in the integration procedure. The current approach based on the use of Eq.(8) is free from this deficiency.

For the sake of simplicity, an isotropic hardening law expressed in terms of effective plastic strain $\tilde{\varepsilon}^p$ is adopted in this study. The following formulation of the isotropic hardening law proposed by Sun and Chen [9] is used to represent the equivalent stress versus equivalent strain hardening curve:

$$\kappa(\tilde{\varepsilon}^p) = \tilde{\sigma}(\tilde{\varepsilon}^p) = \beta(\tilde{\varepsilon}^p)^n \tag{15}$$

where β and n are coefficients that fit the experimental hardening curve. These parameters together with the material parameter a are determined using an approach based on the linear regression analyses of the off-axis tensile tests performed on the unidirectional composite specimens [9, 11].

2.3 Damage model

2.3.1 Damage initiation and propagation criteria

In order to predict the initiation and propagation of each intralaminar failure of the material and evaluate the effective stress state, the loading functions are adopted in the form of Hashin's failure criteria [10]. The damage initiation and propagation criteria f_I are presented in the following form:

$$f_I(\phi_I, r_I) = \phi_I - r_I \leq 0 \quad I = \{1t, 1c, 2t, 2c, 6\} \tag{16}$$

where ϕ_I is the loading function and r_I is the damage threshold corresponding to each failure mechanism. The damage threshold r_I controls the size of the expanding damage surface and depends on the loading history. The damage development in the material initiates when ϕ_I exceeds the initial damage threshold $r_{I,0}$. Further damage growth occurs when the value of ϕ_I in the current stress state exceeds r_I in the previous loading history. The damage variable d_6 represents the damage effect on shear stiffness due to matrix fracture caused by a combined action of transverse and shear stresses. However, the compressive transverse stress has beneficial effects on the matrix cracking. Thus, it is reasonable to assume that the damage effects are governed by the tensile matrix cracking only, i.e. f_6=f_{2t}.

According to Hashin's failure criteria, the loading functions for different failure mechanisms are given as:

$$\begin{aligned}
\phi_{1t} &= \left(\frac{\bar{\sigma}_1}{X_t}\right)^2 && (\bar{\sigma}_1 \geq 0) \quad \text{(tensile fibre damage mode)} \\
\phi_{1c} &= \left(\frac{\bar{\sigma}_1}{X_c}\right)^2 && (\bar{\sigma}_1 < 0) \quad \text{(compressive fibre damage mode)} \\
\phi_{2t} &= \left(\frac{\bar{\sigma}_2}{Y_t}\right)^2 + \left(\frac{\bar{\sigma}_3}{S_c}\right)^2 && (\bar{\sigma}_2 \geq 0) \quad \text{(tensile matrix damage mode)} \\
\phi_{2c} &= \left(\frac{\bar{\sigma}_2}{Y_c}\right)^2 + \left(\frac{\bar{\sigma}_3}{S_c}\right)^2 && (\bar{\sigma}_2 < 0) \quad \text{(compressive matrix damage mode)}
\end{aligned} \tag{17}$$

where X_t and X_c are the tensile and compressive strengths in fibre direction; Y_t and Y_c are the transverse tensile and compressive strengths; S_c is the shear strength.

Once the damage initiation is predicted, the evolution of damage variable d_I is determined by the damage flow rule and the damage evolution law.

2.3.2 Damage evolution

Under damage loading (i.e. when Eq.(16) is converted to equality) the damage consistency condition $\dot{f}(\phi_I, r_I) = 0$ is satisfied. Then the following expressions for damage thresholds r_I can be derived:

$$r_I = \max\{1, \max\{\phi_I^\tau\}\} \quad I = \{1t, 1c, 2t, 2c, 6\} \quad \tau \in [0, t] \tag{18}$$

Since damage is irreversible, the damage evolution rate should satisfy the following condition: $\dot{d}_I \geq 0$. The exponential damage evolution law is adopted for each damage variable and expressed in the following form [12]

$$d_I \quad = 1 - \frac{1}{r_I}\exp(A_I(1 - r_I)) \quad I = \{1t, 1c, 2t, 2c, 6\} \tag{19}$$

where A_I is parameter that defines the exponential softening law. This parameter is determined by regularizing the softening branch of the stress-strain curve to ensure the computed damage energy within an element is constant and thus avoid mesh dependency. The regularization is based on the Bazant's crack band theory [13]. According to this, the damage energy dissipated per unit volume g_I for uniaxial loading or shear is related to the critical strain energy release rate $G_{I,c}$ along with the characteristic length of the finite element l^* as follows

$$g_I = \frac{G_{I,c}}{l^*} \quad I = \{1t, 1c, 2t, 2c, 6\} \tag{20}$$

The critical strain energy release rates $G_{2t,c}$ and $G_{6,c}$ in this work are referred to as the intralaminar mode I and mode II fracture toughness parameters. The parameter $G_{2c,c}$ is the intralaminar model I fracture toughness under compression. The parameters $G_{1t,c}$ and $G_{1c,c}$ correspond to the mode I fracture energies of fibre breakage under tension and compression, respectively. The ways of identification of these parameters including the characteristic length l^* are described in [4, 14].

The damage energy dissipated per unit volume for uniaxial stress conditions is obtained from the integration of the damage energy dissipation during the damage process:

$$g_I = \int_0^\infty Y_I \dot{d}_I \mathrm{d}t; \quad Y_I = -\frac{\partial \psi}{\partial d_I}; \quad \psi = \frac{1}{2}\boldsymbol{\sigma} : \boldsymbol{\varepsilon} \quad I = \{1t, 1c, 2t, 2c, 6\} \tag{21}$$

where Y_I is the damage energy release rate, $\dot{d}_I$ is the rate of damage development defined as $\dot{d}_I = \mathrm{d}d_I/\mathrm{d}t$, and ψ is the Helmhotlz free energy. Equating Eq.(20) and Eq.(21), the parameter A_I is calculated numerically.

The loading/unloading stress strain curves of the present elastoplastic damage model are shown in Figure 1. Under longitudinal loading, the material is assumed to exhibit linear elastic brittle behaviour and the irreversible strain is not developed. Beyond the damage initiation, the elastic modulus E_1 is assumed to degrade gradually. It is assumed, that under transverse and shear loading, the irreversible deformations are exhibited prior to the damage initiations, however, there is no stiffness degradation. Beyond the damage initiation points, both irreversible deformations and stiffness degradations are taken into account.

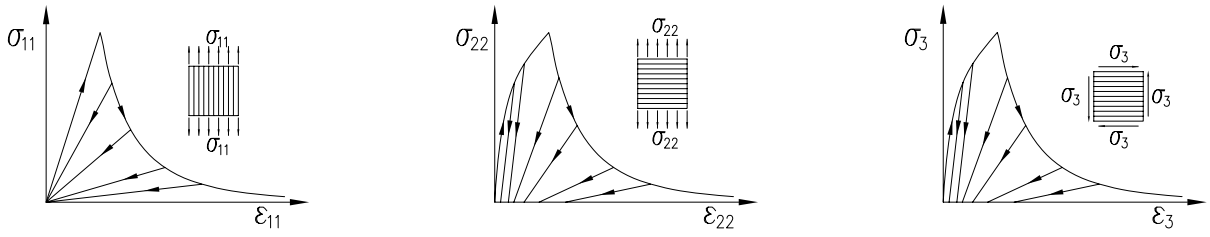

(a) longitudinal (b) transverse (c) in-plane shear

Figure 1: Loading/unloading stress-strain curves.

3 NUMERICAL IMPLEMENTATION

The proposed elastoplastic damage material model is embedded in Abaqus/Standard finite element software package using the user-defined subroutine UMAT. The numerical integration algorithms updating the Cauchy nominal stresses and solution-dependent state variables are derived as well as the tangent matrix that is consistent with the numerical integration algorithm ensuring the quadratic convergence rate of the Newton-Raphson method in the finite element procedures.

3.1 Integration algorithm

The solution of the nonlinear inelastic problem under consideration is based on the incremental approach and is regarded as strain driven. The loading history is discretized into a sequence of time steps $[t_n, t_{n+1}], n \in \{0, 1, 2, 3...\}$ where each step is referred to as the $(n+1)$th increment. Driven by the strain increment $\triangle\varepsilon$, the discrete problem in the context of backward Euler scheme for the elastoplastic damage model can be stated as: for a given variable set $\{\boldsymbol{\varepsilon}_n, \boldsymbol{\varepsilon}^p_n, \tilde{\varepsilon}^p_n, \bar{\boldsymbol{\sigma}}_n, \boldsymbol{\sigma}_n, r_{I,n}, d_{I,n}\}$ at the beginning of the $(n+1)$th increment, find the updated variable set $\{\varepsilon^p_{n+1}, \tilde{\varepsilon}^p_{n+1}, \bar{\boldsymbol{\sigma}}_{n+1}, \boldsymbol{\sigma}_{n+1}, r_{I,n+1}, d_{I,n+1}\}$ at the end of the $(n+1)$th increment. The updated stresses and solution-dependent state variables are stored at the end of the $(n+1)$th increment and are passed on to the user subroutine UMAT at the beginning of the next increment.

The effective stress strain relationship Eq.(3), the yield criterion Eq.(8), the associated plastic flow rule Eq.(10), and the hardening power law Eq.(15) constitute the nonlinear plastic constitutive material model. Using the backward Euler implicit integration procedure, the corresponding integration algorithm is formulated as follows:

$$\begin{aligned}
\boldsymbol{\varepsilon}_{n+1} &= \boldsymbol{\varepsilon}_n + \triangle\boldsymbol{\varepsilon} \\
\boldsymbol{\varepsilon}^p_{n+1} &= \boldsymbol{\varepsilon}^p_n + \triangle\lambda^p_{n+1}\partial_{\bar{\boldsymbol{\sigma}}_{n+1}} F^p_{n+1} \\
\tilde{\varepsilon}^p_{n+1} &= \tilde{\varepsilon}^p_n + \triangle\lambda^p_{n+1} \\
\bar{\boldsymbol{\sigma}}_{n+1} &= \mathrm{S}_0 : (\boldsymbol{\varepsilon}_{n+1} - \boldsymbol{\varepsilon}^p_{n+1}) \\
F_{n+1} &= F(\bar{\boldsymbol{\sigma}}_{n+1}, \tilde{\varepsilon}^p_{n+1}) \leq 0
\end{aligned} \tag{22}$$

where $\triangle\lambda^p_{n+1} = \dot{\lambda}^p_{n+1}\triangle t$ is the increment of the plastic consistency parameter.

The closest point return mapping algorithm is employed to solve this nonlinear coupled system. The solutions $\{\varepsilon^p_{n+1},\ \tilde{\varepsilon}^p_{n+1},\ \bar{\boldsymbol{\sigma}}_{n+1}\}$ are the converged values at the end of the $(n+1)$th increment. They ensure that upon yielding, the determined stress state lies on the yield surface and prevent the drift from the yield surface due to the unconverged solutions obtained from the forward Euler integration scheme.

The nonlinear system Eq.(22) is linearized and solved iteratively using the Newton-Raphson scheme. The iterations are performed until the final set of state variables $\{\bar{\boldsymbol{\sigma}}^{(k+1)}_{n+1}, \varepsilon^{p,(k+1)}_{n+1}, \tilde{\varepsilon}^{p,(k+1)}_{n+1}\}$ in the $(k+1)$th iteration fulfil the yield criterion $F(\bar{\boldsymbol{\sigma}}^{(k+1)}_{n+1}, \tilde{\varepsilon}^{p,(k+1)}_{n+1}) \leq$ TOL, where TOL is the error tolerance which is set to 1×10^{-6}.

Substituting the effective stresses $\bar{\boldsymbol{\sigma}}_{n+1}$ into the damage model, the damage variables are updated. According to Eq.(3), the Cauchy stresses are calculated as $\boldsymbol{\sigma}_{n+1} = \mathrm{S}(d_{n+1}) : \boldsymbol{\varepsilon}^e_{n+1}$.

3.2 Consistent tangent stiffness matrix

The consistent tangent matrix for the proposed constitutive model is derived in the following form:

$$\frac{\mathrm{d}\boldsymbol{\sigma}_{n+1}}{\mathrm{d}\varepsilon_{n+1}} = [M_{n+1} + \mathrm{S}(d_{n+1})] : C_0 : \mathrm{S}^{\mathrm{alg}}_{n+1} \tag{23}$$

in which M_{n+1} can be presented in the indicial form as follows:

$$M_{ik}|_{n+1} = \left.\frac{\partial \mathrm{S}(d)_{ij}\varepsilon^e_j}{\partial \varepsilon^e_k}\right|_{n+1} = \varepsilon^e_j \frac{\partial \mathrm{S}(d)_{ij}}{\partial d_p}\frac{\partial d_p}{\partial r_t}\frac{\partial r_t}{\partial \phi_t}\frac{\partial \phi_t}{\partial \bar{\boldsymbol{\sigma}}_q}\left.\frac{\partial \bar{\boldsymbol{\sigma}}_q}{\partial \varepsilon^e_k}\right|_{n+1} \quad p,q,k = \{1,2,3\};\ t = \{1,2\} \tag{24}$$

where matrix M_{ik} of is asymmetric. This results in the asymmetry of the consistent tangent matrix of the elastoplastic damage model. In Eq.(23), C_0 is the compliance matrix of the undamaged composite materials and $\mathrm{S}^{\mathrm{alg}}_{n+1}$ is the consistent tangent matrix for the discrete plastic problem Eq.(22). The latter is expressed as:

$$\mathrm{S}^{\mathrm{alg}}_{n+1} = \frac{\mathrm{d}\bar{\boldsymbol{\sigma}}_{n+1}}{\mathrm{d}\boldsymbol{\varepsilon}_{n+1}} = \tilde{\mathrm{S}}_{n+1} - \frac{(\tilde{\mathrm{S}}_{n+1} : \partial_{\bar{\boldsymbol{\sigma}}} F^p_{n+1}) \otimes \{\tilde{\mathrm{S}}_{n+1} : \partial_{\bar{\boldsymbol{\sigma}}} F_{n+1}\}}{\partial_{\bar{\boldsymbol{\sigma}}} F_{n+1} : \tilde{\mathrm{S}}_{n+1} : \partial_{\bar{\boldsymbol{\sigma}}} F^p_{n+1} - \partial_{\tilde{\varepsilon}^p} F_{n+1}} \tag{25}$$

where $\tilde{\mathrm{S}}_{n+1} = (C_0 + \triangle\lambda^p_{n+1}\partial^2_{\bar{\boldsymbol{\sigma}}\bar{\boldsymbol{\sigma}}} F^p_{n+1})^{-1}$, $\triangle\lambda^p_{n+1}$ is the increment of plastic consistent parameter in the $(n+1)$th increment, $(\otimes)$ denotes a tensor product.

3.3 Viscous regularization

Numerical simulations based on the implicit procedures, such as Abaqus/Standard, and the use of material constitutive models that are considering strain softening and material stiffness degradation often abort prematurely due to convergence problems. In order to alleviate these computational difficulties and improve convergence, a viscous regularization scheme has been implemented in the following form [5]:

$$\dot{d}^v_m = \frac{1}{\eta}(d_m - d^v_m), \quad m = \{1,2,3\} \tag{26}$$

where d_m is the damage variable obtained as described previously, d_m^v is the regularized viscous damage variable, and η is the viscosity coefficient.

The corresponding regularized consistent tangent matrix is derived as:

$$\left.\frac{\mathrm{d}\boldsymbol{\sigma}_{n+1}}{\mathrm{d}\boldsymbol{\varepsilon}_{n+1}}\right|_v = [M_{n+1}^v + \mathrm{S}(d_{n+1}^v)] : \mathrm{C}_0 : \mathrm{S}_{n+1}^{\mathrm{alg}}; \quad M_{n+1}^v = M(d_{n+1}^v) \cdot \frac{\triangle t}{\eta + \triangle t} \tag{27}$$

4 NUMERICAL RESULTS AND VERIFICATIONS

Numerical simulations of the progressive failure of 12 sets of T300/1034-C carbon/epoxy composite laminates with different geometries and different layups, containing a central circular hole and subjected to uniform in-plane tensile loading, were performed using the numerical procedure presented in previous sections. Three material layups were considered, namely, $[0/(\pm 45)_3/90_3]_s$, $[0/(\pm 45)_2/90_5]_s$, $[0/(\pm 45)_1/90_7]_s$ with the material properties listed in Table 1 along with other model parameters used in the finite element simulations. The geometry of the laminates is illustrated in Figure 2(a). The hole diameters D and widths of the laminates W are listed in Table 2. The predicted failure stresses σ_u ($\sigma_u = P_u/(WH)$, P_u is the failure load) were compared with the experimental results reported by Chang et al. [15] along with the numerical results obtained by Chang and Chang [16], Tan [17], and Maimí [4]. As shown in Table 2, the results demonstrates that the predicted failure stresses correlate well with the test data and generally more accurate in comparison with predictions made by Chang [16], and Tan [17]. Figure 2(b) illustrates the comparison of the load versus displacement curves corresponding to the cases labeled ✠ in Table 2.

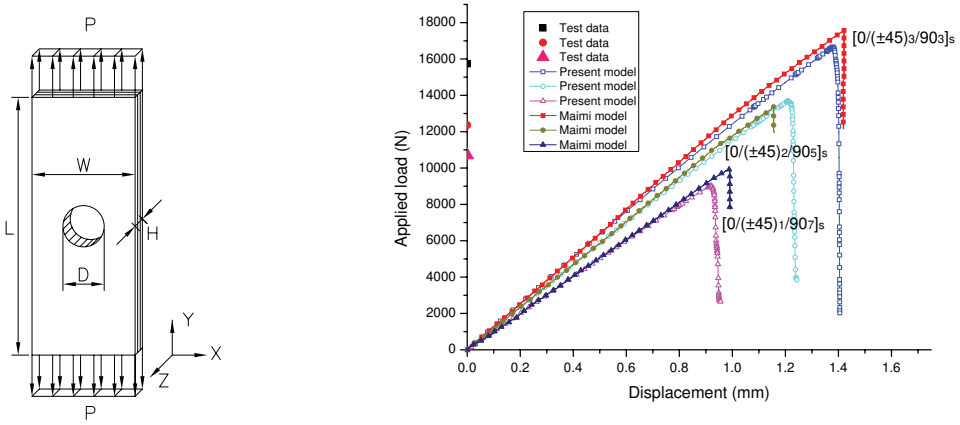

(a) (b)

Figure 2: (a) Geometry of the laminate ($L = 203.2\ mm$, $H = 2.616\ mm$); (b) load vs. displacement curves.

Table 1: Material properties of T300/1034-C and plastic model parameters

E_1^0	E_2^0	G_{12}^0	ν_{12}^0	X_t	X_c	Y_t	Y_c	S_c
146.8 GPa	11.4 GPa	6.1 GPa	0.3	1730.0 MPa	1379.0 MPa	66.5 MPa	268.2 MPa	58.7 MPa
$G_{1t,c}$	$G_{1c,c}$	$G_{2t,c}$	$G_{2c,c}$	$G_{6,c}$	a	β	n	η
89.83 N/mm	78.27 N/mm	0.23 N/mm	0.76 N/mm	0.46 N/mm	1.25	567.9092	0.272405	0.0002

Table 2: Comparison of the tensile failure stresses of T300/1034-C carbon/epoxy laminates

				Failure stress σ_u MPa					Error %			
Lay-up	Label	D (mm)	W (mm)	Present	Chang †	Tan †	Maimí	Test data	Present	Chang	Tan	Maimí
$[0/(\pm45)_3/90_3]_s$	a	3.175	19.05	293.07	227.53	275.75	—	277.17	5.74	-17.91	-0.5	—
$[0/(\pm45)_3/90_3]_s$	b	6.35	38.1	252.22	206.84	275.79	—	256.48	-1.66	-19.35	7.53	—
$[0/(\pm45)_3/90_3]_s$	c	3.175	12.7	269.05	206.84	262.00	—	226.15	18.97	-8.54	15.85	—
$[0/(\pm45)_3/90_3]_s$	d	6.35	25.4	238.30 ✱	179.26	248.21	263.1✱	235.80 ✱	1.06	-23.98	5.26	11.6
$[0/(\pm45)_2/90_5]_s$	a	3.175	19.05	239.13	193.05	186.16	—	236.49	1.12	-18.37	-21.28	—
$[0/(\pm45)_2/90_5]_s$	b	6.35	38.1	214.30	172.37	186.16	—	204.08	5.00	-15.54	-8.78	—
$[0/(\pm45)_2/90_5]_s$	c	3.175	12.7	216.28	165.47	172.37	—	177.88	21.58	-6.98	-3.10	—
$[0/(\pm45)_2/90_5]_s$	d	6.35	25.4	205.83 ✱	151.68	158.58	200.1✱	185.47 ✱	10.98	-18.22	-14.50	7.7
$[0/(\pm45)_1/90_7]_s$	a	3.175	19.05	171.03	144.79	227.53	—	190.98	-10.45	-24.19	19.13	—
$[0/(\pm45)_1/90_7]_s$	b	6.35	38.1	150.36	124.11	227.53	—	158.58	-5.18	-21.74	43.48	—
$[0/(\pm45)_1/90_7]_s$	c	3.175	12.7	154.96	124.11	213.74	—	134.45	15.25	-7.69	58.97	—
$[0/(\pm45)_1/90_7]_s$	d	6.35	25.4	135.67 ✱	103.42	199.95	148.2✱	159.96 ✱	-15.19	-35.34	25.00	-7.4

† Chang and Chang [16] and Tan [17].
✱ The load vs. displacement curves of these two sets of simulations are shown in Figure 2(b)

5 CONCLUSIONS

An elastoplastic damage constitutive model capable of simulating progressive failure of composite laminates has been developed. The model takes into account various failure mechanisms and plasticity effects. The corresponding numerical method based on the finite element formulation was developed and applied to the solution of the related nonlinear problems. The approach has been verified using numerical simulations of the progressive failure of the various laminates containing the central through hole. It has been shown that the proposed solution procedure provides sufficiently accurate predictions of the failure loads for the composite laminates made from the carbon fibre reinforced plastic.

REFERENCES

[1] Ladeveze, P. and Le Dantec, E. Damage modelling of the elementary ply for laminated composites. *Compos. Sci. Technol.* (1992) **43**(3) : 257–267.

[2] Matzenmiller, A., Lubliner, J. and Taylor, R. L. A constitutive model for anisotropic damage in fiber-composites. *Mech. Mater.* (1995) **20**(2):125–152.

[3] Maimí, P., Camanho, P. P., Mayugo, J. A. and Dávila, C. G. A continuum damage model for composite laminates: Part I - Constitutive model. *Mech. Mater.* (2007) **39**(10):897–908.

[4] Maimí, P., Camanho, P. P., Mayugo, J. A. and Dávila, C. G. A continuum damage model for composite laminates: Part II - Computational implementation and validation. *Mech. Mater.* (2007) **39**(10):909–919.

[5] Lapczyk, I. and Hurtado, J. A. Progressive damage modeling in fiber-reinforced materials. *Composites Part A* (2007) **38**(11):2333–2341.

[6] Van Der Meer, F. P. and Sluys, L. J. Continuum models for the analysis of progressive failure in composite laminates. *J. Compos. Mater.* (2009) **43**(20):2131–2156.

[7] Xiao,X. Modeling energy absorption with a damage mechanics based composite material model. *J. Compos. Mater.* (2009) **43**(5):427–444.

[8] Drucker, D. C. Yielding, flow and failure. In C. T. Herakovich, editor, *Inelastic behaviour of composite materials* (1975) volume 13 of *AMD*, 1–15. Houston, Texas.

[9] Sun, C. T. and Chen, J. L. A simple flow rule for characterizing nonlinear behavior of fiber composites. *J. Compos. Mater.* (1989) **23**(10):1009–1020.

[10] Hashin, Z. Failure criteria for unidirectional fiber composites. *J Appl. Mech-T ASME*(1980) **47**(2):329–334.

[11] Winn, V. M. and Sridharan, S. An investigation into the accuracy of a one-parameter nonlinear model for unidirectional composites. *J. Compos. Mater.* (2001) **35**(16):1491–1507.

[12] Faria, R., Oliver, J. and Cervera, M. A strain-based plastic viscous-damage model for massive concrete structures. *Int. J. Solids Struct.*(1998) **35**(14):1533–1588.

[13] Bazant, Z. and Oh, B. Crack band theory for fracture of concrete. *Mater. Struct.* (1983) **16**:155–177.

[14] Pinho, S. T. *Modelling failure of laminated composites using physically-based failure models.* PhD thesis. Department of Aeronautics, Imperial College, London, UK. (2005).

[15] Chang, F. K., Scott, R. A. and Springer, G. S. Strength of bolted joints in laminated composites. Technical Report AFWAL-TR-84-4029, Air Force Wright Aeronautical Laboratories, (1984).

[16] Chang, F. K. and Chang, K. Y. A progressive damage model for laminated composites containing stress concentrations. *J. Compos. Mater.* (1987) **21**:834–55

[17] Tan, S. C. A progressive failure model for composite laminates containing openings. *J. Compos. Mater.* (1991) **25**(5):556–577

XI International Conference on Computational Plasticity. Fundamentals and Applications
COMPLAS XI
E. Oñate, D.R.J. Owen, D. Peric and B. Suárez (Eds)

MULTI-SCALE ANALYSIS OF ASPHALT MIXTURE IN LAYERED ROAD STRUCTURE

RICHARD VALENTA* AND MICHAL ŠEJNOHA†

*Centre for Integrated Design of Advances Structures (CIDEAS)
Czech Technical University in Prague
Thákurova 7, 166 29 Praha 6, Czech Republic
e-mail: richard.valenta@hitest.cz, www.cideas.cz/

†Department of Mechanics, Faculty of Civil Engineering
Czech Technical University in Prague
Thákurova 7, 166 29 Praha 6, Czech Republic
e-mail: sejnom@fsv.cvut.cz, www.fsv.cvut.cz

Key words: Mastic asphalt mixture, Multiscale analysis, First order homogenization, Mori-Tanaka method

Abstract. The Mori-Tanaka averaging scheme is introduced in the place of demanding finite element analysis to assess the time-dependent macroscopic response of asphalt mixture as a part of the multi-layered road construction. In this computational framework the Mori-Tanaka method [1] is chosen to substitute the macroscopic constitutive model, which is not available in general. Instead we expect that the local constitutive laws of individual phases are known which allows for the derivation of macroscopic stresses and an instantaneous homogenized stiffness matrix of an asphalt layer through homogenization. The choice of the Mori-Tanaka method is supported by micromechanical analysis of a real microstructure of Mastic Asphalt mixture showing reasonable agreement with finite element simulations employing certain statistically equivalent periodic unit cell. This makes the application of the Mori-Tanaka method particularly attractive owing to computationally demanding nonlinear analysis of the layered system with subsoil deformation being governed by one of the available constitutive models for soils. Comparison with application of the macroscopic constitutive model for asphalt mixture, provided by detailed multi-scale homogenization, is also presented.

1 INTRODUCTION

As seen in Fig. 1(a), asphalt mixtures represent in general highly heterogeneous material with complex microstructure consisting at minimum of mastic binder, aggregates and voids. When limiting our attention to Mastic Asphalt mixtures, used typically in traffic

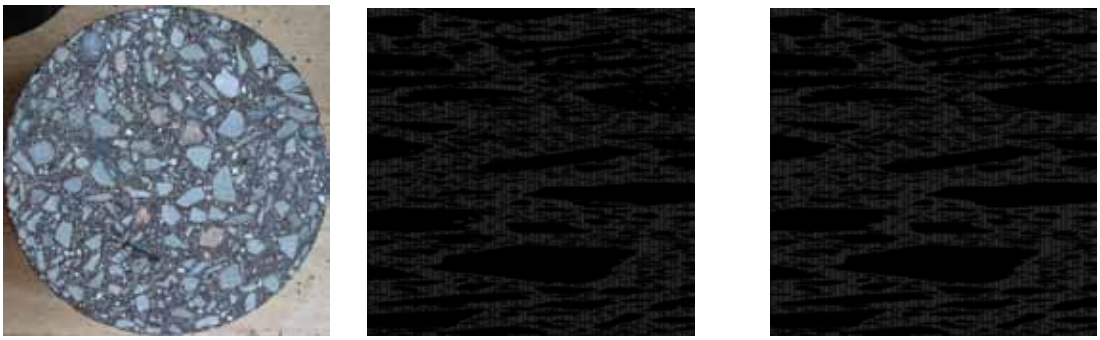

(a) (b) (c)

Figure 1: (a) A real microstructure of an asphalt mixture, (b) Original binary image, (c) Improved binary image

arteries of substantial importance, the fraction of voids becomes negligible. A binary image of such a two-phase material system plotted in Fig. 1(b) is then readily available.

Our contribution integrates various aspects of micromechanical modeling into a relatively simple, yet reliable and efficient computational scheme. The solution strategy relies on uncoupled multiscale homogenization approach and combines advanced simulation based homogenization techniques enabling detailed analysis of a certain representative volume element (RVE), here presented in the form of so called statistically equivalent periodic unit cell (SEPUC), and classical micromechanics based averaging techniques such as the Mori-Tanaka (MT) method in search for a reliable macroscopic constitutive law enabling a computationally efficient analysis of full scale structures.

Rendering the desired macroscopic constitutive model that describes the homogenized response of Mastic Asphalt mixture (MAm) to general loading actions thus endeavors to the formulation of a suitable micromechanical model on individual scales and to associated experimental work being jointly the building blocks of the upscaling procedure. Three particular scales shown in Fig. 2 are considered in the present study. It will be assumed that at each computational level the homogenized response can be described by the nonlinear viscoelastic generalized Leonov (GL) model, see [5, 6] for details . While mastic properties are derived from an extensive experimental program [7], the macroscopic properties of MAm are fitted to virtual numerical experiments performed on the basis of first order homogenization scheme. To enhance feasibility of the solution of the underlying nonlinear problem a two-step homogenization procedure is proposed. The introduced concept of *Virtual Testing Tool* (VTT) make possible to avoid expensive and often intricate large scale laboratory measurements and takes into account details of the microstructure of the analyzed heterogeneous material. The VTT is currently in the forefront of engineering interest [6].

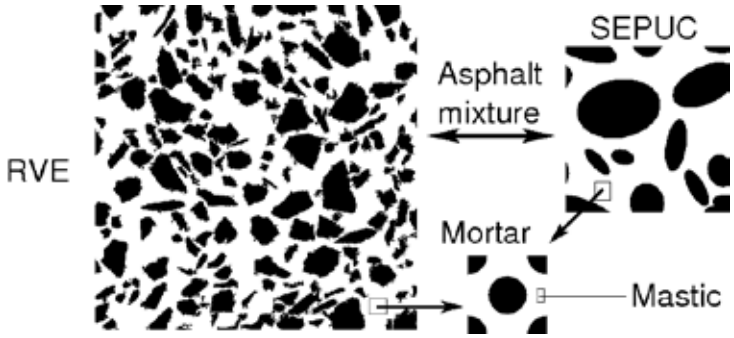

Figure 2: Three distinct scales of Mastic Asphalt mixture

2 VIRTUAL TESTING TOOL

The concept of VTT introduced in [6] assumes the experimental program to be carried out only on the level of the individual constituents - stones and mastic. Although the mastic-phase itself is a composite consisting of a filler and a bituminous binder, it is assumed in the present study to be well represented by a temperature and rate dependent homogeneous isotropic material. Since limiting our attention to moderate and elevated temperatures exceeding 0°C the GL model is exploited to provide for experimentally observed nonlinear viscoelastic behavior of bituminous matrices. The required experimental program to calibrate the model parameters on the one hand and on the other hand to address the homogenized macroscopic response is outlined in [7, 6].

2.1 Response of mortar from virtual experiments

In the framework of VTT approach we introduce a virtual set of experiments to arrive at a homogenized master curve and associated temperature and stress dependent shift factors on the scale of mortar. The concept of first order homogenization of periodic fields outlined in [7] is given the preference to deliver the homogenized creep response of the mortar phase at different temperature and stress levels. The mortar-phase naturally arises through the process of removing aggregates from original microstructure, Fig. 1(b), passing 2.26 mm sieve. Simplified periodic hexagonal array model plotted in Fig. 2 allows us to derive the model parameters on the mortar-scale by running a set of virtual numerical experiments. The selection of this geometrical representation of the mortar composite is purely an assumption building upon the conclusion that at least for the mastic-phase and low-temperature creep the response is independent of the filler shape and mineralogy [4].

First, a uniformly distributed range of temperatures from 0°C to 100°C was considered to provide for a temperature dependent viscoelastic behavior of mortar loaded in shear by the remote stress $\Sigma_{yx} = 1$kPa. Individual curves plotted in Fig. 3(a) were then horizontally shifted to give the homogenized creep compliance master curve seen in Fig. 3(b).

The stiffening, observed for high temperatures, is attributed to a volumetric locking

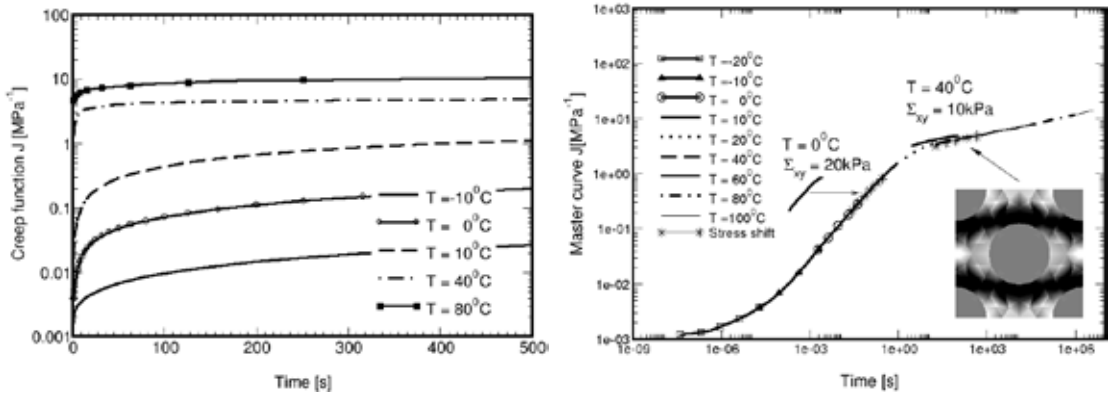

(a) (b)

Figure 3: (a) Creep data at different temperatures for reference stress $\Sigma_{xy} = 1$kPa, (b) Master curve for reference temperature $T = 40°$C

owing to a very low shear modulus approaching to zero. This in turn yields the Poisson ratio close to 0.5 in a finite zone of the binder phase that is progressed over the entire unit cell as seen in Fig. 3(b).

The second set of creep experiments was conducted at two different temperatures and two different levels of the remote stress Σ_{xy}. The two representative results, [40°C, 10kPa] and [0°C, 20kPa], are plotted as solid lines in Fig. 3(b). The indicated horizontal shifts identified with the corresponding star-lines then supplement the necessary data for the derivation of stress dependent shift factor a_σ. Note that prior to shifting the curves the result derived for 0°C was thermally adjusted to be consistent with the 40°C master curve.

2.2 Response of MAm from virtual experiments

Derivation of the macroscopic creep compliance master curve for a Mastic Asphalt mixture follows the general scheme sketched in the previous section. A SEPUC also seen in Fig. 2, is selected to predict the macroscopic response of MAm, where large aggregates are bonded to a mortar-phase being homogeneous and isotropic. The elliptical shape of aggregates has already been successfully used in detailed micromechanical simulations presented in [2]. The issue of constructing SEPUC by comparing the material statistics, e.g. the two point probability function, of the most appropriate representative of the real microstructure and the periodic unit cell is suggested in [9, 7, 6]. The underlying optimization problem was solved with the help of the evolutionary algorithm GRADE [3].

To address this issue, four SEPUCs all having the same statistics but different geometrical details, were subjected to a remote shear strain rate $\dot{E}_{xy} = 10^{-4}$. The resulting homogenized stress-strain curves for temperature $T = 20°$C are shown in Fig. 4(a). Although no "perfect match" is observed, the difference in estimated load bearing capacities is not exceeding 10%. On the contrary, the distribution of local fields varies considerably

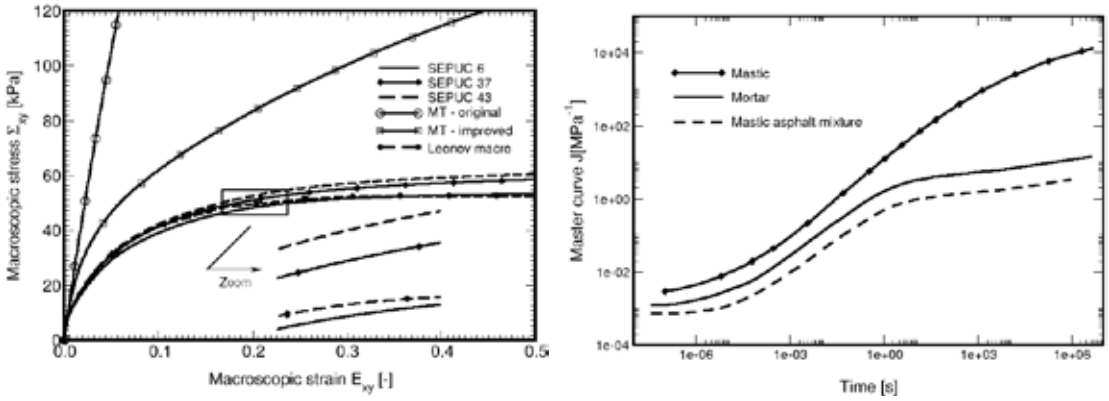

(a) (b)

Figure 4: (a) Macroscopic response for various SEPUCs $T = 20°\text{C}$, $\dot{E}_{xy} = 10^{-4}$, (b) Master curves on individual scales for reference temperature $T = 40°\text{C}$

as seen in Fig. 5. While a highly localized distribution of shear strain γ_{xy}^m in the mortar phase, identified with the lowest bearing capacity in Fig. 4(a), is evident in Fig. 5(a), the variation of this quantity in Fig. 5(c) shows a rather distributed character consequently resulting in a slightly stiffer response on the macroscale.

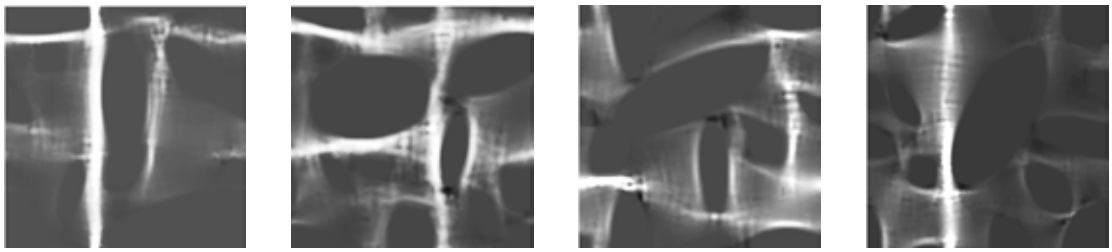

(a) (b) (c) (d)

Figure 5: Distribution of local shear strain: (a) SEPUC 6, (b) SEPUC 37, (c) SEPUC 43, (d) SEPUC 48

Although certainly more accurate, the detailed finite element simulations are in general computationally very expensive and often call for less demanding alternatives such as the Mori-Tanaka method outlined in [7]. Unfortunately, the corresponding results also plotted in Fig. 4(a) clearly expose essential limitations of the two-point averaging schemes, unable to capture localization phenomena observed in composites with a highly nonlinear response of the binder phase [8]. The presented results in Fig. 4(a) correspond to a classical formulation with the localization and transformation tensors calculated only once being functions of elastic properties of individual constituents (MT-original), and to the formulation where these tensors are updated after each time step taking into account increasing compliance of the mortar phase with time (MT-improved). Note that even the

latter case produces much stiffer response, although at a fraction of time, when compared to the FE results. A certain improvement has been achieved when putting on the same footing the localized character of matrix deformation, recall Fig. 5, and debonding of stone aggregates, both reducing the stress transfer from the matrix phase into the stones. This issue is addressed in Section 2.3.

Regarding the "similarity" of macroscopic response from various SEPUCs, the SEPUC No. 43 was selected to provide data needed in the calibration of the macroscopic GL model. Virtual numerical tests identical to those in the previous section were again performed to give first the homogenized master curve displayed in Fig. 4(b). The response of the homogenized asphalt mixture to the applied remote shear strain labeled as "Leonov macro" appears in Fig. 4(a) suggesting a reasonable agreement at least for this type of loading. Further applications are available in [6].

2.3 Augmented Mori-Tanaka method

Fig. 4(a) revealed essential limitations of the two-point averaging schemes hidden in their inability to properly capture the correct stress transfer between phases when highly localized deformation in the matrix is encountered. Here, we attempt to minimize this impact of the MT method on macroscopic predictions by introducing a damage like parameter ω into the local constitutive equation of stones thus controlling the amount of stress taken by stones. The stress increment in the stone phase is calculated as

$$\Delta\boldsymbol{\sigma}_s = \omega \mathbf{L}_s : \Delta\boldsymbol{\varepsilon}_s, \tag{1}$$

where the damage parameter ω being equal to one for intact material and zero for fully damaged material assumes the form

$$\omega = \left[\frac{\tau_{eq}^t}{N\tau_0} \Big/ \sinh\left(\frac{\tau_{eq}^t}{N\tau_0} \right) \right]^M, \tag{2}$$

where τ_{eq} is the current equivalent deviatoric stress and M, N are model parameters. In the present study, these were found by comparing the MT predictions with the results provided by the homogenized macroscopic Leonov (MGL) model under strain control condition for the prescribed macroscopic shear strain rate $\dot{E}_{xy}$.

Comparison of the resulting macroscopic predictions including the results from various SEPUCs are available in Fig. 6(a) whereas evolution of damage parameter ω is plotted for illustration in Fig. 6(b). Considerable improvement of the behavior of MT method is evident particularly when compared to the original predictions presented in Fig. 4(a).

Another strong motivation for mastering the MT method, apart from avoiding the mesoscopic virtual tests, is the possibility to estimate at least the local phase averages. These estimates are compared separately with predictions from individual SEPUCs in Fig. 7. Realizing that parameters of the damage model were fitted against the homogenized response the agreement of local fields is quite satisfactory. A closer match might be

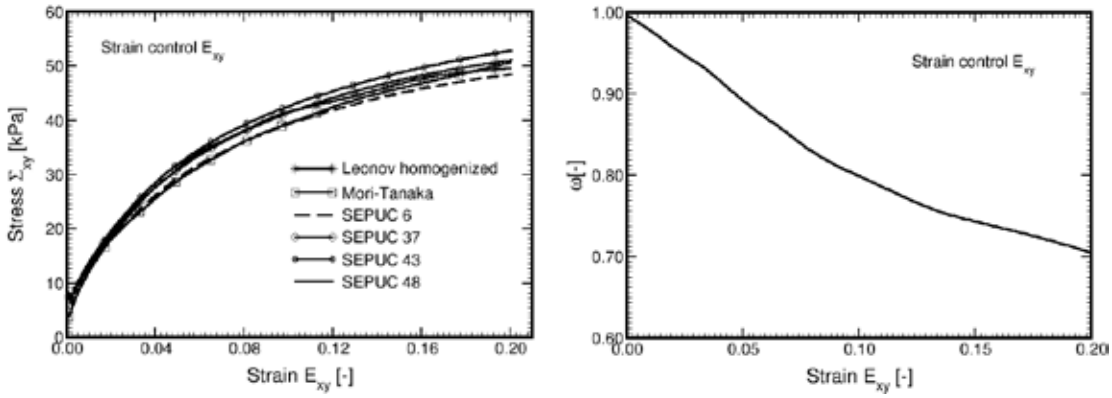

Figure 6: (a) Macroscopic response for various SEPUCs, MGL model and MT method, (b) variation of damage parameter ω: $T = 20\text{C}$, $\dot{E}_{xy} = 10^{-4}$ s^{-1}

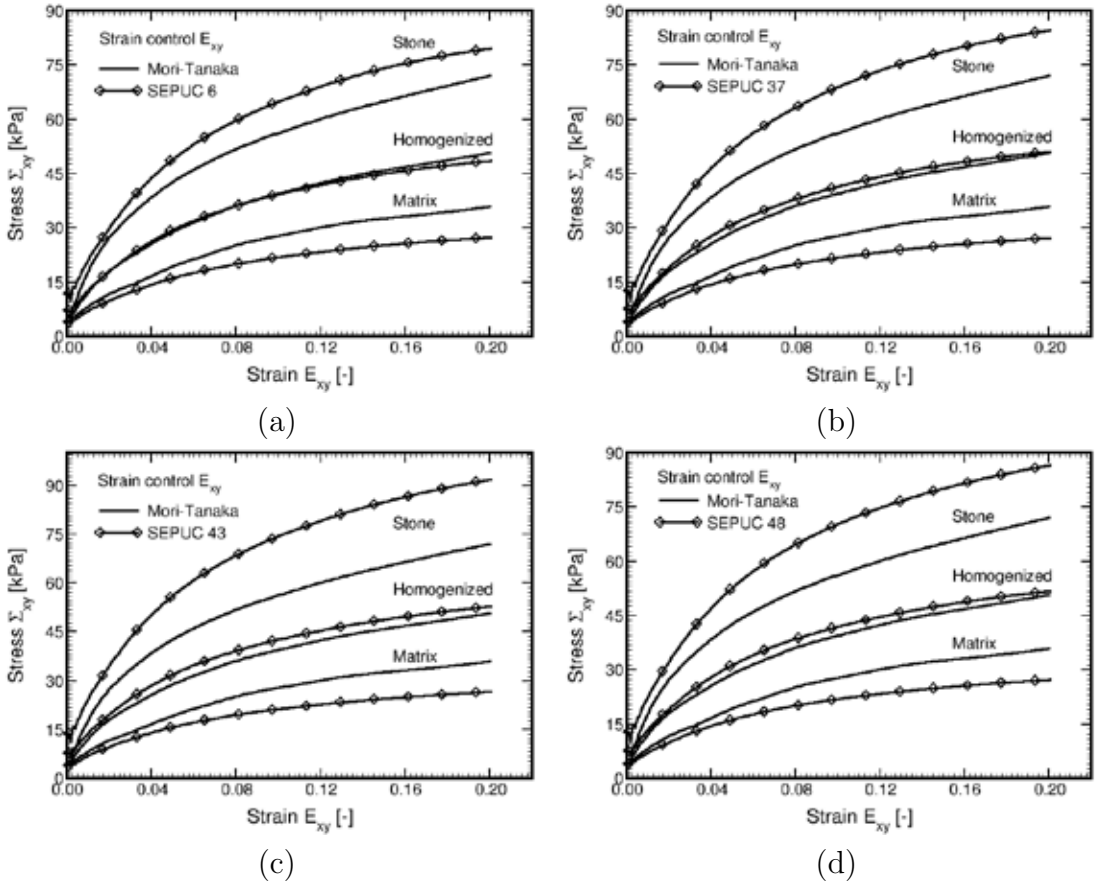

Figure 7: Phase averages of local fields from various SEPUCs and MT method, $T = 20\text{C}$, $\dot{E}_{xy} = 10^{-4}$ s^{-1}: (a) SEPUC 6, (b) SEPUC 37, (c) SEPUC 43, (d) SEPUC 48

expected if deriving the damage model parameters directly from the local matrix stress averages provided one of the periodic unit cell.

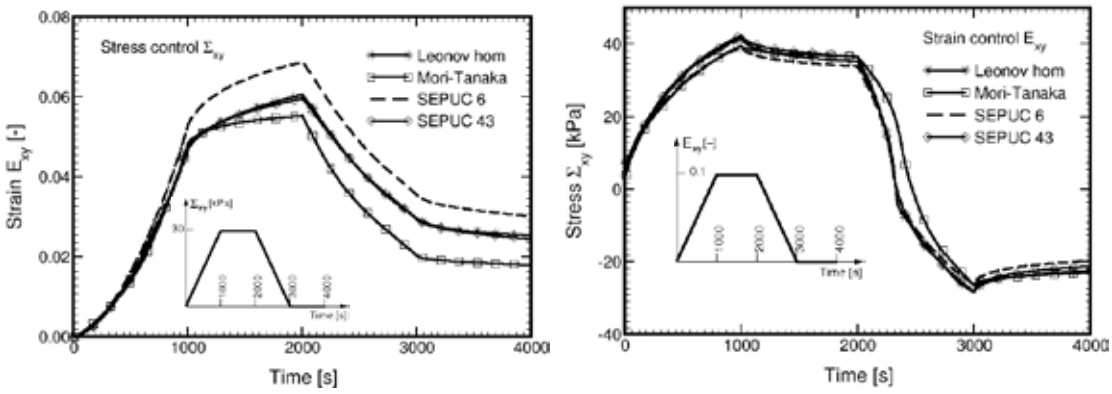

(a) (b)

Figure 8: Macroscopic response for reference temperature $T = 40$C (a) Stress control: loading–creep–unloading–recovery, (b) Strain control: loading–relaxation–unloading–recovery

At last we inspected the predictive capability of the MT method for loading conditions dominating the creep or relaxation response. The creep response is examined in Fig. 8(a). As expected, there is almost a perfect match between the results found from the MGL model and the finite element analysis of SEPUC No. 43. Considerable deviation of the results provided by SEPUC No. 6 agrees well with already observed deviations evident in stress control conditions. What is, however, more disturbing are the predictions pertinent to the Mori-Tanaka method associated especially with the interval of constant load (creep response). Its inability to predict a correct creep behavior is quite pronounced. The loading, as well as, unloading branches controlled by the damage parameter ω are on the other hand captured relatively well. Somewhat better agreement is provided by strain control loading visible in Fig. 8(b).

3 SUMMARY

Although research interests on flexible pavements have been quite intense in the past two decades, the field is still very much in development and will certainly witness considerable activity in the coming decade particularly in connection to hierarchical modeling and micromechanics. Within this framework, the present work provides theoretical tools for the formulation of macroscopic constitutive law reflecting the confluence of threads coming from experimental work, image analysis, statistical mechanics and traditional disciplines of micromechanics and the first order computational homogenization. Here, the totally uncoupled multiscale modeling approach is favored to enable an inexpensive analysis of real world large scale structures, which is the principle objective of our work.

The results from the proposed two-step homogenization scheme, promoted the SEPUC as a suitable computational model and in combination with the finite element formulation of the first order homogenization method to set a plausible route for the nonlinear viscoelastic homogenization. It is often desirable to identify local stress and strain fields in individual phases of the composite developed for various macroscopic loading conditions. However, fully coupled analysis employing detailed microsctructures, e.g SEPUC, is still often computationally prohibitive. Therefore, a simple Mori-Tanaka averaging scheme was examined to either support or decline its use in the framework of efficient coupled multiscale analysis. The presented results are in favor of this approach but at the same time suggest caution in applications where strong creep behavior is expected.

REFERENCES

[1] Y. Benveniste. A new approach to the application of Mori-Tanaka theory in composite materials. *Mechanics of Materials*, 6:147–157, 1987.

[2] Q. Dai, M.H. Saad, and Z. You. A micromechanical finite element model for linear and damage-coupled viscoelastic behaviour of asphalt mixture. *International Journal for Numerical and Analytical Methods in Geomechanics*, 30:1135–1158, 2006.

[3] A. Kučerová. *Identification of nonlinear mechanical model parameters based on soft-computing methods*. PhD thesis, Ecole Normale Supérieure de Cachan, Laboratoire de Mécanique et Technologie, 2007.

[4] R. Lackner, M. Spiegl, R. Blab, and J. Eberhardsteiner. Is low-temperature creep of asphalt mastic independent of filler shape and mineralogy? - arguments from multi-scale analysis. *Journal of Materials in Civil Engineering, ASCE*, 15:485–491, 2005.

[5] A. I. Leonov. Non-equilibrium thermodynamics and rheology of viscoelastic polymer media. *Rheol. Acta*, 15:85–98, 1976.

[6] R. Valenta. *Modeling of asphalt mixtures*. PhD thesis, Czech Technical University in Prague, Faculty of Civil Engineering, 2011.

[7] R. Valenta, M. Šejnoha, and J. Zeman. Macroscopic constitutive law for mastic asphalt mixtures from multiscale modeling. *International Journal for Multiscale Computational Engineering*, 8(1):131–149, 2010.

[8] M. Šejnoha, R. Valenta, and J. Zeman. Nonlinear viscoelastic analysis of statistically homogeneous random composites. *International Journal for Multiscale Computational Engineering*, 2(4):645–673, 2004.

[9] J. Zeman and M. Šejnoha. From random microstructures to representative volume elements. *Modelling and Simulation in Materials Science and Engineering*, 15(4):S325–S335, 2007.

XI International Conference on Computational Plasticity. Fundamentals and Applications
COMPLAS XI
E. Oñate, D.R.J. Owen, D. Peric and B. Suárez (Eds)

MULTISCALE MODELLING OF MASONRY STRUCTURES UNDER EXTREME LOADING

B.A. IZZUDDIN*, L. MACORINI†

Department of Civil and Environmental Engineering
Imperial College London, South Kensington Campus, London, UK
*e-mail: b.izzuddin@imperial.ac.uk
†e-mail: l.macorini@imperial.ac.uk

Key words: Multiscale modelling, partitioning approach, 3D mesoscale model, unreinforced masonry, geometric and material nonlinearity.

Summary. This paper presents an effective multiscale modelling approach for unreinforced masonry (URM). To date, only few attempts have been made to use multiscale strategies for investigating the nonlinear response of URM structures. The formulations developed so far are mainly based on computational homogenisation and on the definition of a representative volume element (RVE) at the mesoscale, which is often linked to the integration points for continuous elements at the structural scale. Such an approach has successfully been employed only for investigating running bond masonry, where a simple definition for the RVE can be employed. However, its use for the analysis of masonry structures characterized by a more complex texture, as in the case of multi-leaf masonry, could prove to be impractical. The proposed multiscale approach for URM is substantially different from previous multiscale models, as it does not rely on the definition of a RVE and considers strong coupling between the two scales. According to this formulation, an URM structure is represented by a parent structure which consists of super-elements representing the partitioned subdomains. Each partition is modelled by a detailed 3D mesoscale model, which accounts for material and geometric nonlinearity. Dual super-elements are used for modelling the partitions as separate processes, where two-way communication between each pair of dual parent/child super-elements allows effective parallelisation of the nonlinear structural analysis simulation.

1 INTRODUCTION

Masonry is a heterogeneous composite material made of blocks and mortar. Under extreme loading conditions, its response is strongly nonlinear, depending not only on the mechanical properties of the component materials, but also on the specific arrangement used to connect different blocks through mortar joints to form structural elements. The macroscopic nonlinear response, associated with the structural scale, is governed by the development of cracks and damage, which take place at the scale of the component material, hereinafter referred to as mesoscale. Cracks usually follow continuous paths along mortar joints, and in some cases spread through blocks. The development of cracks gives rise to damage induced anisotropy, which is an important characteristic of the macroscopic nonlinear response, as it determines the stress redistribution in damaged masonry elements [1].

In recent years, a significant research effort has been devoted to developing accurate and effective numerical models for unreinforced masonry (URM) structures. Two alternative strategies, based on either macroscale or mesoscale formulations, have been mainly employed so far [2]. Macroscale models, which consider masonry as a homogeneous material, assume complete separation between meso- and structural scales and employ close-form laws for describing material nonlinearity. Sophisticated macroscopic constitutive relationships can be formulated either considering the outcomes of experimental tests on masonry panels, or using the homogenisation approach to derive material properties for macroscale models directly from the mechanical and geometrical characteristics of blocks and mortar joints. However, even though macroscopic models are computationally efficient and can be used for the analysis of large structures, they do not provide an accurate representation of the structural response under extreme loading, because they do not account for damage induced anisotropy. Conversely, mesoscale models, which are based on an accurate description of masonry texture, can represent most of the failure modes for URM with high accuracy, but they are computationally demanding. Thus their use is prohibitively demanding for nonlinear analyses of real URM structures. Recently, a few attempts [3,4,5] have been made to bridge the two scales of representation through a multiscale strategy, so as to guarantee high accuracy and computational efficiency.
In the following, the proposed multiscale modelling strategy for URM is described, pointing out the main differences from other multiscale formulations. The proposed approach is based on the domain partitioning method [6] and on the use of a detailed 3D mesoscale model. Advanced 2D nonlinear interface elements [7] are employed at the mesoscale, which allow an accurate representation of crack development and collapse of URM elements under extreme loading condition. The potential and effectiveness of the proposed computational strategy is demonstrated through numerical examples.

2 MULTISCALE STRATEGY FOR URM

Multiscale modelling is an effective numerical strategy for investigating the nonlinear response of structures made of heterogeneous materials. According to this formulation, the macroscopic or structural scale is linked to the mesoscale during the entire numerical simulation. Depending on the degree of coupling between the scales, different approaches can be used [8]. When the two scales are only weakly coupled and their characteristic lengths are very different, a two-level finite element (FE) procedure, often called FE^2 method [9], can be effectively used. In this approach, a first FE continuous model is used at structural scale, while a second FE mesoscale description, which is associated with a representative volume element (RVE) for the analysed heterogeneous material, is linked to each integration point for continuous elements at the structural scale (Fig. 1). Key aspects in this approach are the definition of a suitable RVE and the choice of the operator for the two-way transformation of local mesoscale quantities (strain, stress, stiffness) into global macroscale variables. This approach have been recently successfully used to analysed the in-plane [4,5] and out-of-plane response [10] of running bound masonry structures. For this common typology of URM, a realistic and simple RVE can be defined. Periodicity properties of the characteristic mesoscale texture are used to define boundary conditions to the mesoscale model for the RVE, while average field homogenisation principles are employed to transform local stress and stiffness

values into macroscale quantities. In previous mesoscale formulations for URM, continuous elements are employed at both scales. The material nonlinearity associated with the quasi-brittle nature of the masonry component behaviour is considered at both scales employing suitable plasticity/damage models.

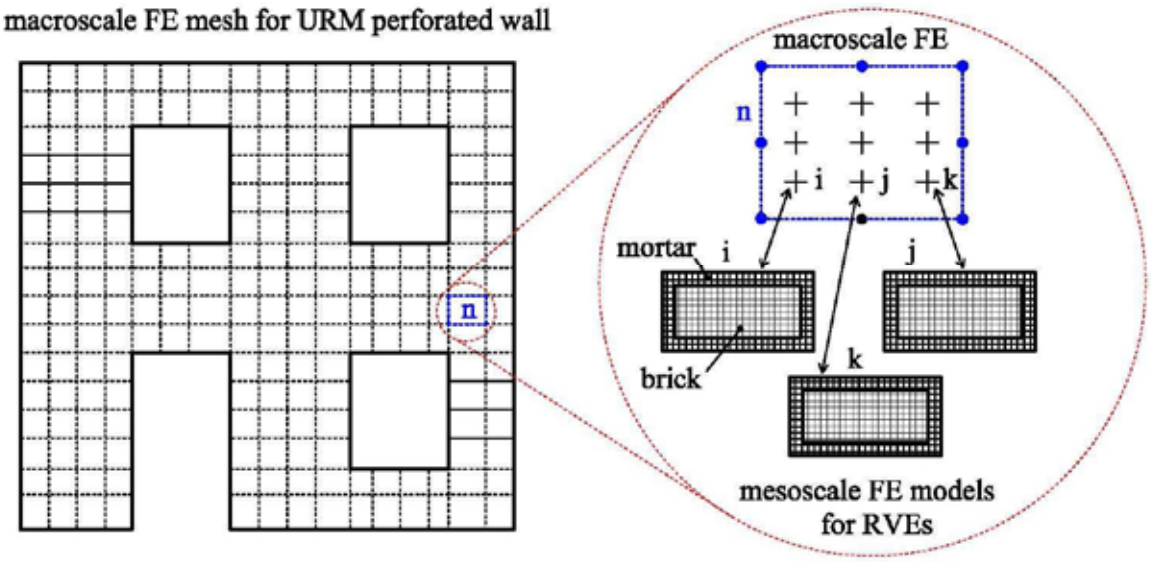

Figure 1: FE^2 strategy for modelling a running bond masonry perforated wall

Even though such an approach is accurate and suitable for the analysis of running bond masonry, its effectiveness has yet to be demonstrated under general conditions, when URM structures with more complex textures are analysed under extreme loading. In such cases, the dimensions of the RVEs could become significantly bigger, thus the use of continuous elements for mortar and blocks could be prohibitive, even when using parallel computing resources in the structural analysis. Moreover, in general, when the size of the RVE for URM is comparable with the characteristic length of the finite elements used at the structural scale, the use of the FE^2 strategy is questionable. In this situation, the spacing of integration points at the structural scale could be significantly smaller than the RVE size, leading to an overlapping of different RVEs and thus to an unrealistic modelling of the actual URM structure. This can happen in many real situations: i) in the case of historical structures made of relatively large stone blocks, ii) when modelling narrow piers in perforated walls, or iii) when using a fine mesh at structural scale to capture stress concentrations, e.g. close to openings, where the propagation of cracks and damage usually initiate.
Finally, the use of standard continuous elements is effective for representing crack development and collapse of URM elements when accounting for material nonlinearity only. Conversely, the consideration of geometric nonlinearity requires the introduction of significant enhancements to the continuous formulation, so as to guarantee a realistic representation of large deformations at fracture zones. This is an important modelling consideration, which can be crucial when investigating the response of URM under extreme loading. In fact, in some practical situations, geometric nonlinearity determines the response at collapse of masonry walls, e.g. when masonry panels are loaded out-of-plane by dynamic

forces under earthquakes and collapse due to geometric instabilities.
The proposed mutiscale numerical approach allows the analysis of URM in the most general conditions, as it is based on a strong coupling between the two scales and accounts for both material and geometric nonlinearity. Moreover, it is not founded on the definition of a RVE communicating with a macroscale model, but on the use of a domain partitioning approach, thus avoiding some intrinsic shortcomings of more standard multiscale formulations.

2.1 Proposed multiscale modelling for URM

When the characteristic lengths of macroscale and mesoscale are very close, as in the case of URM with large RVEs, the FE^2 strategy is not effective. Alternative approaches should be used to account for the strong coupling between the two scales [8]
The proposed multiscale modelling for URM employs domain partitioning techniques to connect the structural and mesoscale, where a detailed 3D model, based on the discrete approach, is used for representing cracks and accounting for geometric nonlinearity.

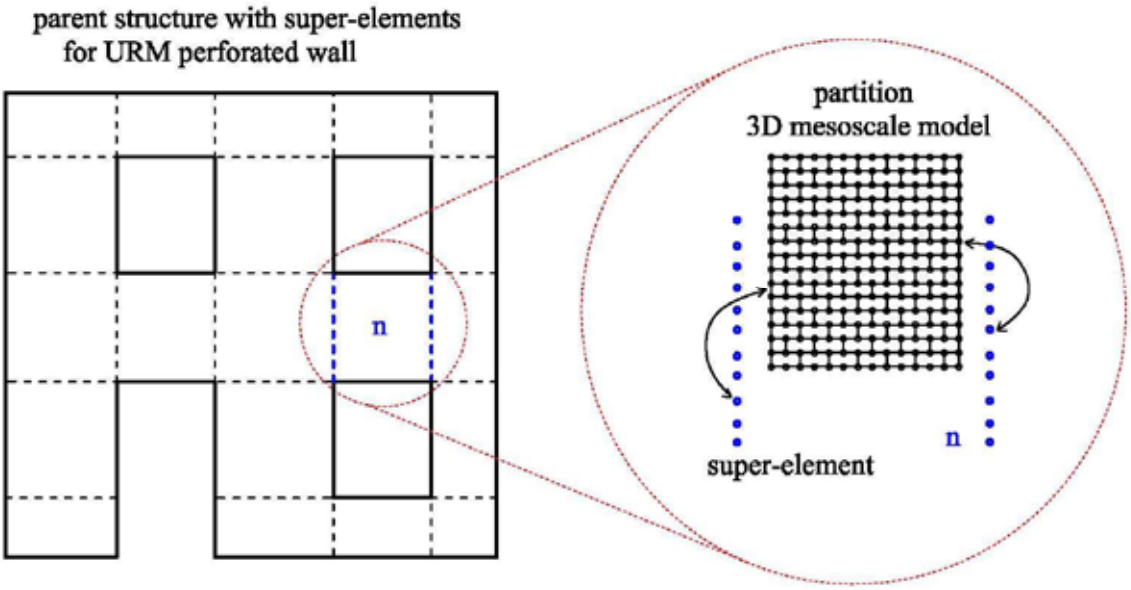

Figure 2: Multiscale modelling with domain partitioning approach for a perforated URM wall

According to the proposed formulation [6], an URM structure is represented by a parent structure which consists of super-elements representing the partitioned subdomains. Dual super-elements are used for modelling the partitions as separate processes, where two-way communication between each pair of dual parent/child super-elements allows effective parallelisation of the nonlinear structural analysis simulation [11]. Each partition is represented by a detailed 3D mesoscale model, which uses an advanced 2D nonlinear interface element [7] recently developed for representing crack development in URM elements. In the proposed approach, the definition of damage at the structural scale benefits directly from the accuracy guaranteed by the mesoscale model. Furthermore, the macroscale model considers only the partition boundaries, where a specific macro-element is introduced to reduce the number of freedoms leading to further computational savings. In defining the

macro-element, particular attention should be paid to allowing discontinuities at the partition boundary so as to maintain a similar level of accuracy in the prediction of crack propagation as in a monolithic model.
The employed macroelement does not correspond to a standard finite element but is a simple collection of single nodes, which are connected to the joints at the partition boundaries of each subdomain. When analysing the nonlinear response of URM structures using the proposed approach, a standard incremental/iterative strategy is used to solve the nonlinear equilibrium equations for the unknown displacement parameters. The process associated with the parent structure transfers the global displacements at the partitioned boundary nodes to all the partitions (Fig. 2). Then the boundary value problem associated with the mesoscale representation for each partition is solved though different processes in parallel. Finally, each partition transfers its boundary forces and the associated global consistent stiffness matrix to the parent structure where the global equilibrium is checked at each iteration.

2.2 Constraints at partition boundaries for improved efficiency

When analyzing real URM structures using the proposed multiscale strategy with a large number of CPUs for parallel computation, the most critical process becomes that of the parent structure. Therefore a significant improvement in the numerical performance and thus a considerable saving in wall-time can be achieved by reducing the freedoms at the boundary for each partition, so as to limit the communication overhead and size of the parent structure.

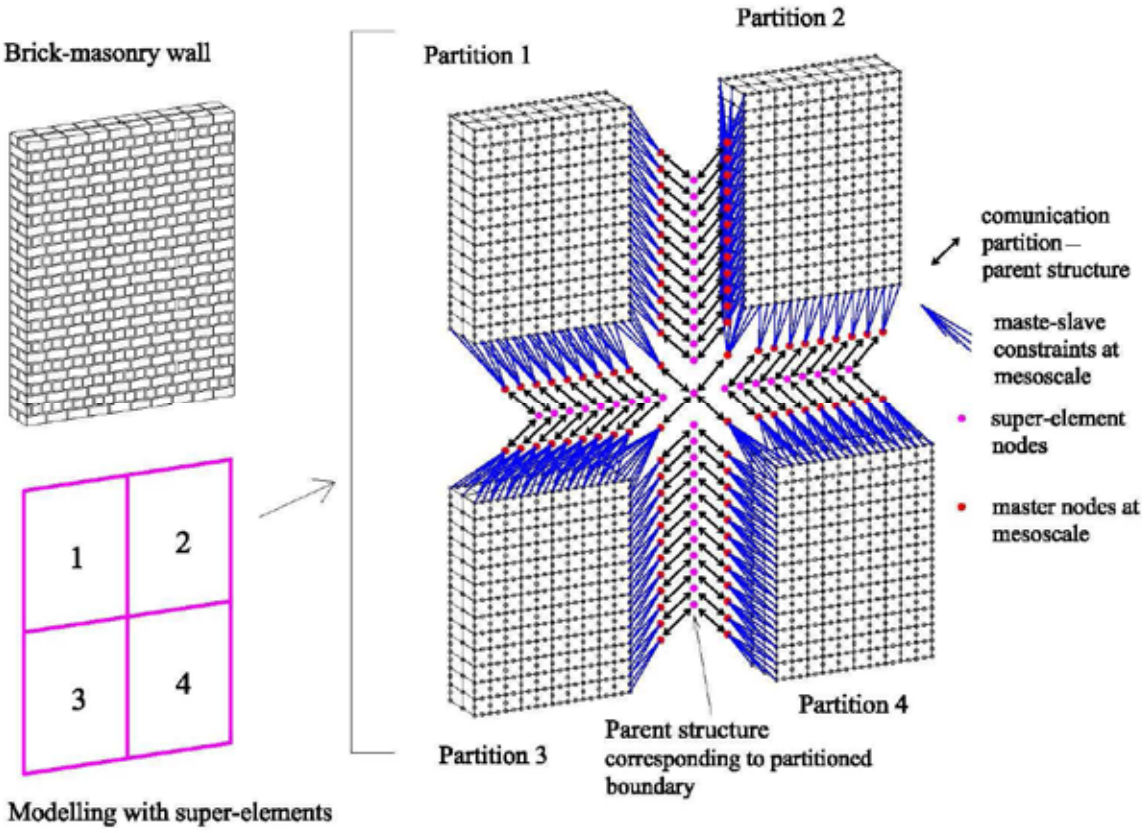

Figure 3: The enhanced multiscale modelling with 3D mesoscale description for URM structures

Thus a significant improvement for the proposed numerical strategy, which is currently under development, is based on the introduction of specific constraints in the mesoscale description for each partition, where several nodes of one or more faces of a solid or a 2D interface element at the partition boundary are connected to a single node. In this respect, two limiting cases are considered. The first case consists of hard coupling using a master-slave approach, where the three freedoms for each node on the slave surface/s are fully determined by the six freedoms of the master node. The second case is based on soft coupling using a Lagrangian multiplier approach, where the displacements of the 'master' node are associated with the average of the nodal displacements of the considered 'slave' surface. Using such coupling, the number of freedoms at the partition boundary of each partition and therefore the total freedoms of the parent structure can be significantly reduced (Fig.3).

3 MESOSCALE DESCRIPTION

A detailed 3D mesoscale model is used for representing URM nonlinear behaviour. Such a mesoscale approach enables the representation of any 3D arrangement for brick-masonry, accounting for the in-plane stacking mode and the through-thickness geometry, and importantly it allows the investigation of both the in-plane and the out-of-plane response of unreinforced masonry panels.

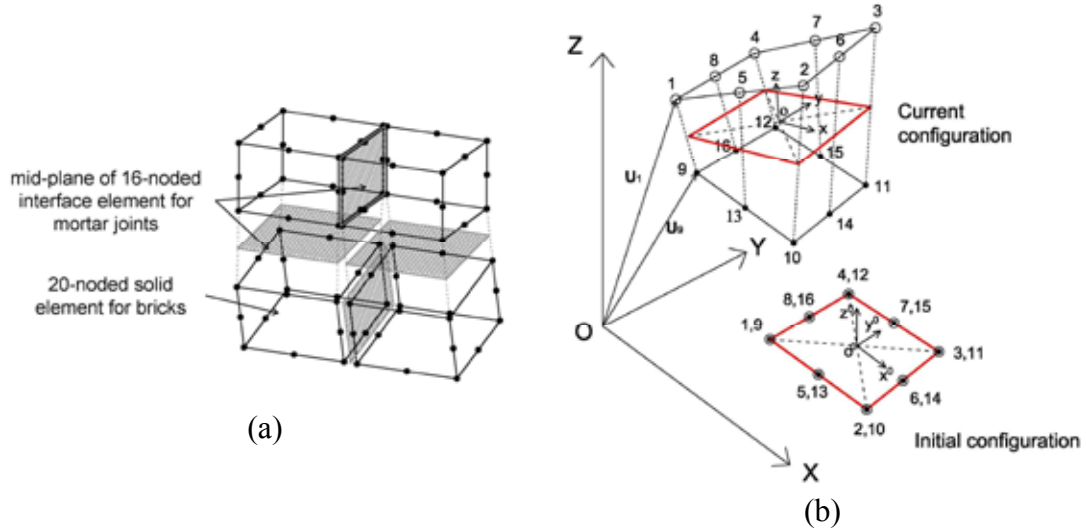

Figure 4: (a) 3D mesoscale modelling, (b) interface element kinematics

In the mesoscale model (Fig.4 a), blocks are modelled using 3D elastic continuum solid elements, while mortar and brick-mortar interfaces are modelled by means of 2D nonlinear interface elements. Furthermore, zero-thickness interface elements are also arranged in the vertical mid-plane of all blocks along the direction of the shorter horizontal dimension so as to account for possible unit failure in tension and shear.

The employed 20-noded 3D solid element is based on standard finite element techniques, considering linear elastic material behaviour based on Green's strain, which allows a simple treatment of large-displacement small-strain 3D continuum problems. The interface element, which accounts for both geometric and material nonlinearity, employs 16-nodes with 3

translational freedoms for each node. In order to account for large displacements that could characterise the response of interfaces at failure in actual URM panels, a co-rotational approach is employed.

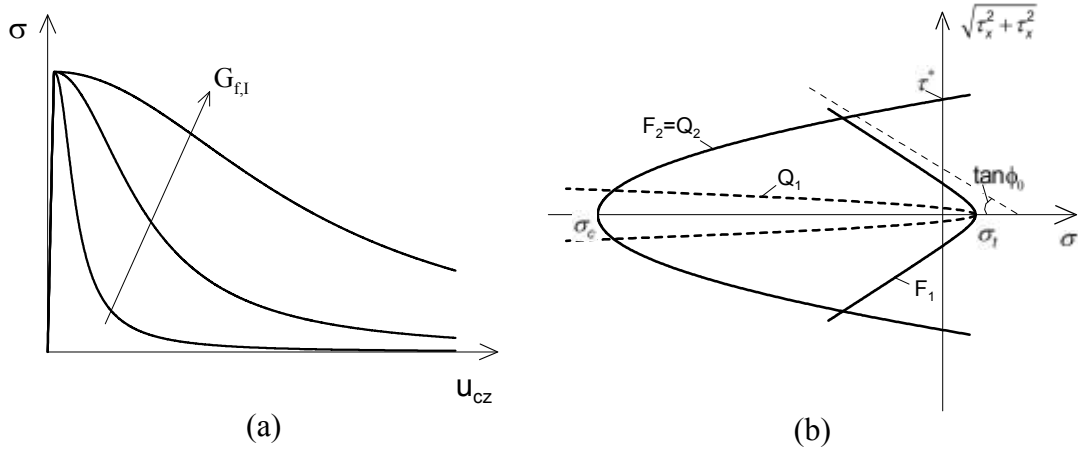

Figure 5: (a) Initial plastic surfaces and potentials, (b) traction-separation curve in tension.

With regard to the constitutive model for the interface element, this enables not only separations and damage to be evaluated, but it also accounts for the actual elastic deformations of mortar and brick-mortar interfaces. The inelastic response at the interfaces is simulated by means of a cohesive fracture model based on a multi-surface plasticity criterion. An elasto-plastic contact law which follows a Coulomb slip criterion is used to model the response in tension and shear, while a cap model is employed to account for crushing in compression (Fig. 4b). A formulation that considers energy dissipation, de-cohesion and residual frictional behaviour has been employed [7]. Moreover, a non-associated plastic flow with a plastic potential different from the yield function has been introduced for modelling inelastic deformation due to shear. This enables the direction of plastic deformations to be independent from the yield function. A specific plastic potential can be defined to account for the actual dilatancy which is due to the roughness of the fractured shear surface and can be measured in tests on interfaces. Figure 5a shows traction-separation curves in tension, which depend of tensile strength and mode-I fracture energy $G_{f,I}$, while Figure 5b depicts the hyperbolic plastic surfaces $F_{1(2)}$ and potentials $Q_{1(2)}$, which are employed for representing the material nonlinearity at interfaces.

4 NUMERICAL EXAMPLES

The performance of the developed numerical strategy, based on the use of domain partitioning approach, which is associated with the detailed 3D mesoscale model for URM, has been investigated considering the wall-clock time required by different models for determining the elastic response of a large URM solid wall. A monolithic model (m), where the FE problem is solved using a serial code, and models with an increased number of partitions (Pi, i=1,2,4,8,16,32,64) have been considered in the numerical simulations (Fig. 6b). Figure 6a shows the mesh employed for the whole wall together with the super-elements (partitions) used in the different models. When using the proposed numerical

strategy, the parent structure is represented only by the nodes at the partitions boundaries (Fig. 2), while each partition includes the detailed mesoscale model with solid and interface elements for a portion of the analysed structure, which is indentified by a super-element. Conversely, in the monolithic simulation, the parent structure corresponds to the complete FE model for the whole wall. In all the simulations, a vertical displacement is applied at the top of wall in one step first, and then a horizontal displacement is applied in five steps.

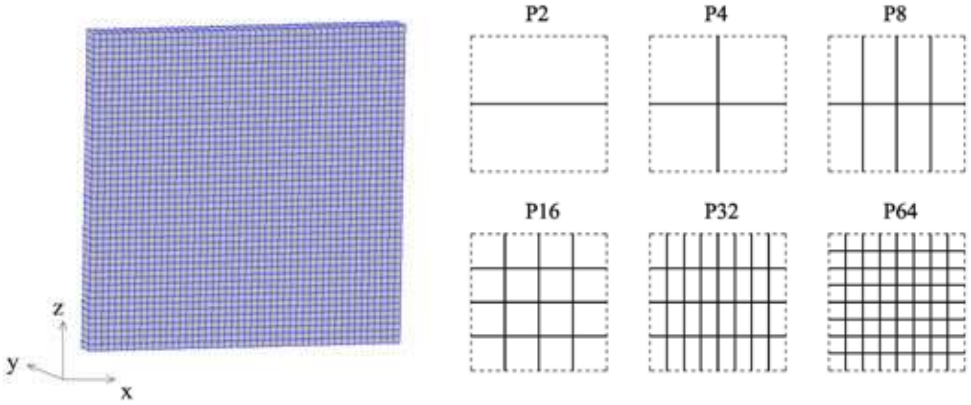

Figure 6: (a) Mesh with solid elements and 2D interfaces for the whole structure, (b) Super-elements schemes used for the different models

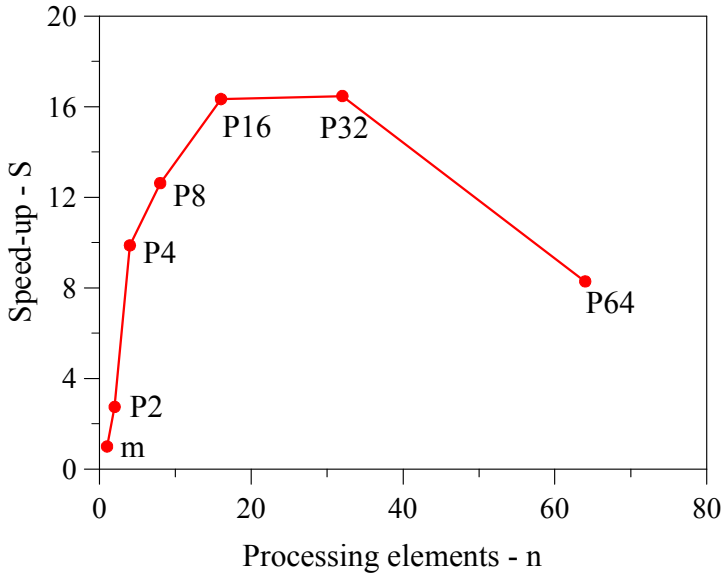

T_m = 20220 s

	n	S_i
P2	3	2.75
P4	5	9.88
P8	9	12.62
P16	17	16.33
P32	33	16.46
P64	65	8.28

Figure 7: Speed-up achieved using an increased number of partitions

The numerical results achieved in the different analyses are exactly the same. This confirms that when using the proposed partitioning approach, the accuracy guaranteed by the detailed 3D mesoscale model can be maintained also at structural scale, where the analysed structural system is represented by a parent structure with a reduced number of freedoms.

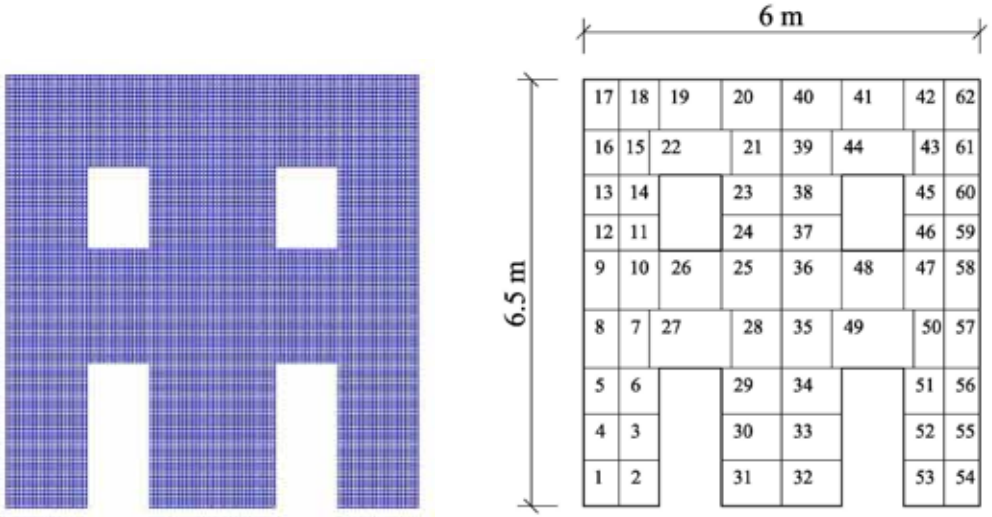

Figure 8: Mesh and partitions scheme used for representing a full-scale URM perforated wall

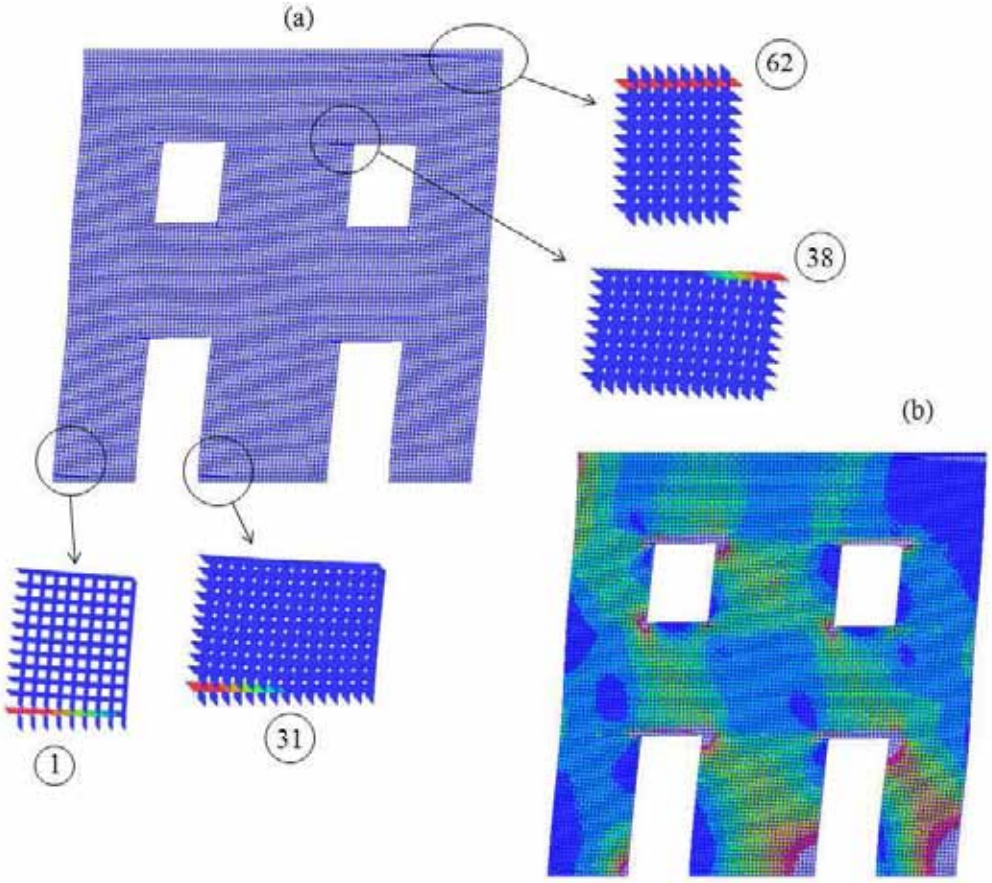

Figure 9: (a) Representation of cracks in the full-scale URM perforated, (b) maximum principal stresses in solid elements at the end of the numerical analysis

The effectiveness of a specific subdivision is related to the number of operations required to solve the linear system for each partitions and parent structures. It does not depend only on their dimension, but also on the specific strategy used to divide the original structure with super-elements. This is illustrated in Figure 7, where the speed-up achieved using models with a different number of partitions is s. It can be observed that when dividing the structure in two partitions, the total wall-clock time is more than halved (S2=2.75>2), thanks to a more efficient use of the frontal algorithm used to calculate the solution of the equation linear system of equations. Further benefit is achieved when using four partitions (S4/S2=3.59>2) and the gain in speed is maintained up to 16 partitions. Then increasing the number of partitions from 16 up to 32 guarantees only a limited improvement in the overall computing time, while the use of 64 sub-divisions leads even to a reduction in speed-up. This is caused by a relevant increase in the dimension of the parent structure which implies high overheads because of data communication. This confirms the potential of the proposed reduction of partition boundary freedoms through coupling elements, which is currently under development and will be reported in future work.
In a second numerical simulation, the proposed numerical strategy for URM structures has been used to investigate the nonlinear response of a full-scale perforated URM wall under in-plane loading. Considering the large dimension of the structure (Fig. 8), the detailed 3D mesoscale strategy, which requires 162840 nodes to represent the whole URM perforated wall, cannot be employed in a monolithic model using ordinary memory and CPU resources, thus requiring the use of the developed multiscale strategy with partitions and different processors. Figure 8 shows the mesh with solid and interface elements for the whole structure and the arrangement for the 62 super-elements employed for representing the structural system. The deformed shape including the cracks in the wall with details of damage at interface elements is displayed in Figure 9a, while the contours of maximum principal stresses in solid elements are shown in Figure 9b. The results achieved confirm the potential of the proposed numerical strategy, which allows the investigation of full-scale URM structures, ensuring the accuracy characteristics of mesoscale models for a realistic representation of cracks and damage.

5 CONCLUSIONS

An effective multiscale modelling strategy for URM structures has been presented in this paper. The domain partitioning approach is coupled with an accurate 3D mesoscale model for representing the nonlinear behaviour of URM structure under general loading conditions. The potential benefits of including specific coupling constrains in the mesoscale description to reduce the size of the parent structure have been discussed. The effectiveness of the proposed method is demonstrated through a significant speed-up that can be achieved by analysing a large URM wall considering a sufficient number of partitions. It is shown that significant computational benefits can be derived from using a small number of partitions, mostly because of the significant reduction in computation required by the frontal method at the parent structure level combined with a moderate communication overhead with the partitions. The computational benefits of the method are demonstrated by obtaining the nonlinear response of an URM solid wall and through a nonlinear simulation for a full-scale URM façade. The various studies show clearly that the proposed method can be used for the

realistic and efficient nonlinear analysis of large URM structures, importantly with a high simulation accuracy as provided by a detailed mesoscale description. Current research is focussing on the development of the proposed coupling elements for reducing the number of partition freedoms at the mesoscale boundary, and this will be reported in future work.

Acknowledgements

The authors gratefully acknowledge the support provided for this research by the 7th European Community Framework Programme through a Marie Curie Intra-European Fellowship (Grant Agreement Number: PIEF-GA-2008-220336) and the High Performance Computing (HPC) Services at Imperial College London for providing and supporting the required computing facilities.

REFERENCES

[1] Massart, T.J., Peerlings, R.H.J and Geers, M.G.D. Mesoscopic modeling of failure and damage-induced anisotropy in brick masonry, *European Journal of Mechanics A/Solids* (2004) **23**:719-735.

[2] Lourenço, P.B. *Computational strategy for masonry structures*, PhD Thesis Delft University of Technology, Delft, the Netherlands, (1996).

[3] Uva, G. and Salerno, G. Towards a multiscale analysis of periodic masonry brickwork: a FEM algorithm with damage and friction, *Int J Solids Struct* (2006) **43**: 3739-3769.

[4] Massart, T.J., Peerlings, R.H.J. and Geers, M.G.D. An enhanced multi-scale approach for masonry wall computations with localizations of damage, *Int. J. Numer. Meth. Engng*. (2007) **69**:1022-1059.

[5] Taylor, R. L. And De Bellis, M. L. Multi-scale analysis of masonry structures, CMM 2011 – Computer Methods in Mechanics, , Poland, (2011).

[6] Macorini, L. and Izzuddin, B.A. Nonlinear analysis of masonry structures using mesoscale partitioned modelling, PARENG2011, Ajaccio, France, (2011).

[7] Macorini, L. and Izzuddin, B.A. A non-linear interface element for 3D mesoscale analysis of brick-masonry structures, *Int. J. Numer. Meth. Engng*. (2011) **85**:1584:1608.

[8] Markovic, D. and Ibrahimbegovic, A. On micro-macro interface conditions for micro scale based FEM for inelastic behavior of heterogeneous materials, *Comput Method Appl M* (2003) **193**:5503-5523.

[9] Feyel, F. A multilevel finite element method (FE2) to describe the response of highly non-linear structures using generalized continua, *Comput. Methods Appl. Mech. Engrg*. (2003) **192**: 3233-3244.

[10] Mercatoris B.C.N. and Massart, T.J. A coupled two-scale computation scheme for the failure of periodic quasi-brittle thin planar shells and its application to masonry, *Int. J. Numer. Meth. Engng*. (2011) **85**:1177-1206.

[11] Jokhio, G. and Izzuddin, B.A. Parallelisation of nonlinear structural analysis using dual partition super-elements, PARENG2011, Ajaccio, France, (2011).

XI International Conference on Computational Plasticity. Fundamentals and Applications
COMPLAS XI
E. Oñate, D.R.J. Owen, D. Peric and B. Suárez (Eds)

DETERMINATION OF THE HIGH STRAIN RATE FORMING PROPERTIES OF STEEL SHEET

P. VERLEYSEN[*], J. PEIRS[*] AND L. DUCHENE [†]

[*] Department of Materials Science and Engineering
Faculty of Engineering
Ghent University
Technologiepark 903, 9052 Zwijnaarde (Ghent), Belgium
e-mail: Patricia.Verleysen@UGent.be, www.ugent.be/ir/dmse/en

[†] Mécanique des Solides, des Fluides et des Structures
Department ArGEnCO
University of Liege
Sart Tilman B52, 4000 Liège 1, Belgium
e-mail: L.Duchene@ulg.ac.be

Key words: Forming Process, Steel Sheets, Forming Limit Diagram.

Abstract. The strain rate dependence of the plastic yield and failure properties displayed by most metals affects energies, forces and forming limits involved in high speed forming processes. In this contribution a technique is presented to assess the influence of the strain rate on the forming properties of steel sheets. In a first step, static and high strain rate tensile experiments are carried out in order to characterize the materials strain rate dependent behaviour. In a second step, the phenomenological Johnson-Cook model and physically-based Voce model are used to describe the constitutive material behaviour. The test results are subsequently used to calculate the forming limit diagrams by a technique based on the Marciniak-Kuczynski model. With the developed technique, static and dynamic forming limit diagrams are obtained for a commercial DC04 steel and a laboratory made CMnAl TRIP steel. The results clearly indicate that increasing the strain rate during a forming process can have a positive or negative effect.

1 INTRODUCTION

In forming processes such as magnetic pulseforming, hydroforming and explosive forming, high rates of deformation are obviously obtained. However, also in more conventional sheet forming techniques, such as deep drawing, roll forming and bending, locally strain rates are occurring deviating from the ones occurring in static material tests. As the strain rate increases most materials present significantly higher plastic flow stresses, however much lower deformation levels. Other materials combine an increase in flow stresses with an increase in elongation values (Van Slycken et al., 2006). Materials which experience no strain rate sensitivity at all are exceptional. In the study here a commercial and laboratory made steel are considered. The commercial DC04 (EN 10027-1) is an unalloyed deep-drawing steel. This steel grade is frequently used in the production of body components in the automotive

industry. The laboratory made CMnAl-TRIP steel is a multiphase steel in which, under certain conditions, the austenite phase transforms to martensite during plastic straining [1].

In a first step, static and dynamic tensile experiments are carried out using a classical tensile test device and a split Hopkinson tensile bar facility respectively. The stress-strain curves obtained for the two steels clearly show that their mechanical behaviour is strain rate dependent. With increasing strain rate, plastic stress levels increase, however, as opposed to the TRIP-steel, for the DC04 steel the deformation capacity decreases. Subsequently, to allow simulation of forming processes, Johnson-Cook and Voce material model parameters are determined [2]. Finally, the influence of the strain rate on the forming limits is assessed using the uni-axial tensile test results. Indeed, performing multi-axial experiments at high strain rates is not obvious. Prediction of the initiation of necking in the steel sheets subjected to multi-axial strain states is based on the Marciniak-Kuczynski model. The thus obtained forming limit diagrams show a non-negligible effect of the strain rate. For the DC04 material, the reduced ductility at higher strain rates is reflected into an unfavourable downward shift of the forming limit diagram. Certainly, the left-hand side is adversely affected. The behaviour of the TRIP steel is as opposed to that of DC04: the dynamic FLD is higher than the static one.

2 EXPERIMENTAL PROGRAM

2.1 EXPERIMENTAL SETUPS

Static and dynamic tensile experiments are carried out at room temperature (around 22˚C). test bench. The *static experiments* are carried out on a classical screw driven electromechanical Instron tensile machine according to the European standard specifications EN 10002-1:2001. A tensile specimen, with a gage length of 120mm, is used in the tests. The tensile tests are carried out with an initial strain rate of 5.6 $10^{-4}s^{-1}$, in the gage section of the specimen, which is increased to 5.6 $10^{-3}s^{-1}$ at 3.4% of deformation until rupture.
For the *dynamic experiments* the split Hopkinson tensile bar (SHTB) setup of the department of Materials Science and Engineering at the Ghent University in Belgium is used. A schematic representation of the setup is given in the Figure 1, a photograph in the Figure 2.

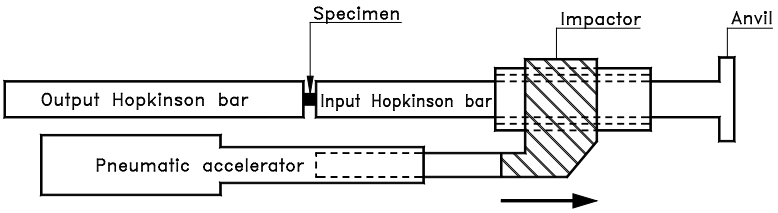

Figure 1: Schematic representation of split Hopkinson tensile bar device at Ghent University

The setup consists of two long bars, an input bar and an output bar, between which a specimen is sandwiched. For tensile tests a tube-like impactor is put around the input bar and is accelerated towards an anvil at the outer end of the input bar. Thus a tensile wave, the so-

called incident wave, is generated and propagates along the input bar towards the specimen. The incident wave interacts with the specimen, generating a reflected wave and a transmitted wave. The strain histories $\varepsilon_i(t)$, $\varepsilon_r(t)$ and $\varepsilon_t(t)$ corresponding to respectively the incident, reflected and transmitted wave are usually measured by means of strain gages at well chosen points on the Hopkinson bars. The history of the stress, the strain and the strain rate in the specimen are derived from the measured waves, using the following expressions [3]:

$$\sigma(t) = \frac{A_b E_b}{A_s} \varepsilon_t(t) \tag{1}$$

$$\varepsilon(t) = \frac{U_{ob} - U_{ib}}{L_s} = -\frac{2C_b}{L_s} \int_0^t \varepsilon_r(\tau) d\tau \tag{2}$$

$$\dot{\varepsilon}(t) = \frac{V_{ob} - V_{ib}}{L_s} = -\frac{2C_b}{L_s} \varepsilon_r(t) \tag{3}$$

with E_b the modulus of elasticity of the Hopkinson bars, A_s and A_b the cross section area of the specimen and of the Hopkinson bars respectively, C_b the velocity of propagation of longitudinal waves in the Hopkinson bars and L_s the gage length of the specimen. U_{ib} and U_{ob} are the displacements of the interface between the specimen and, respectively, the input bar and the output bar; V_{ib} and V_{ob} are the corresponding velocities.

Figure 2: SHTB setup at Ghent University. Its total length is 11m.

The DC04 sheet steel has a thickness of 1.5mm, the TRIP-steel 1.2mm. Specimens are cut by spark erosion along the rolling direction. Geometry and dimensions used for the split

Hopkinson tensile bar experiments can be found in Figure 3.

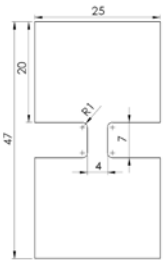

Figure 3: Geometry of test specimen used for the SHTB experiments. The 4mm wide section, with a gage length of 5mm, is actually submitted to the high strain rate load.

3.2 Results

Several static and dynamic tests have been carried out. In Figure 4 representative engineering stress-strain curves can be found. For the DC04 steel the static and dynamic curves have a different overall shape. For the static curve a clear strain hardening is observed during the first stages of plastic deformation and uniform elongation is achieved after 24% of deformation. The dynamic curves on the other hand, show a very high yield stress, again followed by few strain hardening. Between the dynamic curves differences are less pronounced.
The static and dynamic engineering stress-strain curves for the CMnAl TRIP steel are very similar. The stress increases, however not as much as for the DC04 steel. The main effect of the strain rate is seen in the higher uniform elongation during dynamic loading: ±30% vs ±22%.

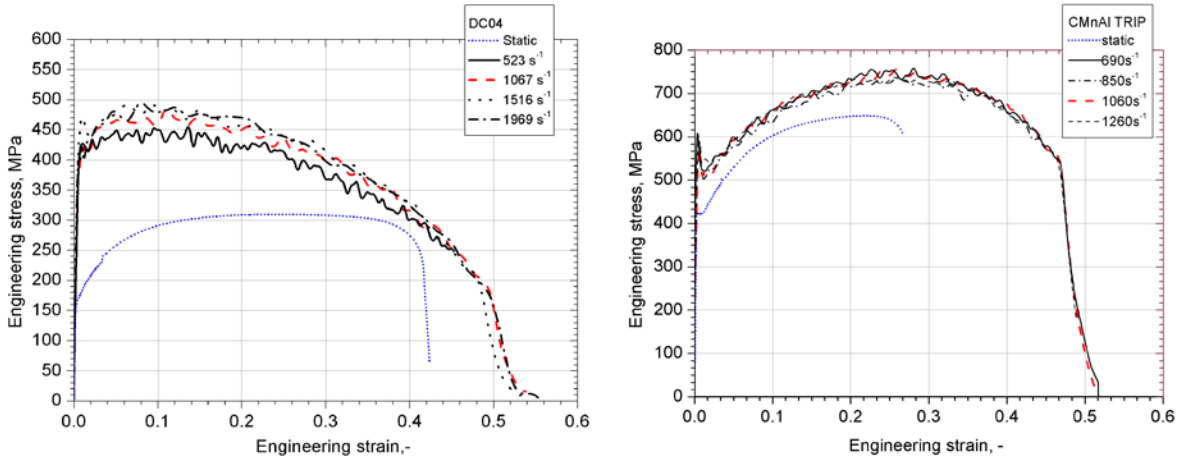

Figure 4: Representative static stress-strain curve and dynamic curves obtained for the investigated steels

3 MODELLING OF THE HIGH STRAIN RATE BEHAVIOUR

The experimental results are used to model the constitutive material behaviour. Two different frequently used models are used: Voce law and the Johnson-Cook model [2]. Voce law describes the relation between the stress σ and plastic strain ε_p. The model contains only three parameters σ_0, K and n which can easily be determined from only one experiment.

$$\sigma = \sigma_0 + K(1 - e^{-n\varepsilon_p}) \tag{4}$$

The Voce flow rule does not explicitly describe the material's strain rate and temperature dependence. Both can be taken into account by making the model parameters strain rate and/or temperature dependent.

The Johnson-Cook phenomenological model does take into account strain rate and temperature dependent material behaviour:

$$\sigma = \left(\mathrm{A} + \mathrm{B}\varepsilon_p{}^{\mathrm{n}} \right) \left(1 + C \ln \frac{\dot{\varepsilon}}{\dot{\varepsilon}_0} \right) \left(1 - \left[\frac{T - T_{room}}{T_{melt} - T_{room}} \right]^m \right) \tag{5}$$

The first term of the right hand side describes the isothermal static material behaviour. Consequently, the parameters A, B and n are determined using the static tensile tests. The initial (for ε<3.4%) strain rate during the static tensile test is the reference strain rate $\dot{\varepsilon}_0$ used in the second term, expressing the strain rate hardening with parameter C. The last factor, including m, represents thermal softening. C and m are calculated using the high strain rate tensile tests.

The quasi-adiabatic temperature increase in the specimen during high strain rate plastic deformation is calculated using the following formula:

$$\Delta T = \frac{\beta}{\rho c} \int \sigma d\, \varepsilon_p \tag{6}$$

In this equation ρ is the mass density, c the specific heat and β the Taylor-Quinney coefficient indicating the fraction of plastic work converted into heat. This β-value is usually assumed to have a value between 0.9 and 1. Constant values for c and β can be used regarding the modest temperature range acquired during these tests. During the high strain rate tests the temperature will gradually change from room temperature to approximately 100°C depending on the material.

In table 2 values for the parameters of Voce model σ_0, K and n and Johnson-Cook model A, B, n, C and m can be found. The parameters are calculated by a least square method. For the Voce law two sets of parameters are given: one for the static behaviour at room temperature and one for a dynamic, adiabatic experiment at $1000s^{-1}$.

In Figure 5 a comparison is made between experimental and modelled stress-strain curves. Both models succeed in describing the experimental behaviour. The Voce model appears to perform better than the Johnson-Cook model which is not surprising regarding the use of two Voce law parameter sets for the static and dynamic loading compared with one parameter set for the JC model. Indeed, the large differences between the overall shape of the static and dynamic stress strain curves complicates modelling of the material behaviour with one parameter set. Nevertheless, the agreement between the experiments and models is very good. Because the Voce model performs better at higher strains, it will be used for calculation of the FLDs in the next section.

Table 2: Values for the Voce and Johnson-Cook material model parameters

Model	Parameter	DC04	CMnAl TRIP
Voce (static/dynamic)	σ_0 (MPa)	163.5/383.1	394/501
	K	226.2/137.5	468/574
	n	13.2/31.7	9.2/5.4
Johnson-Cook	A (MPa)	162	394
	B (MPa)	598	1395
	n	0.6	0.72
	C	2.623	0.013
	m	0.009	0.62

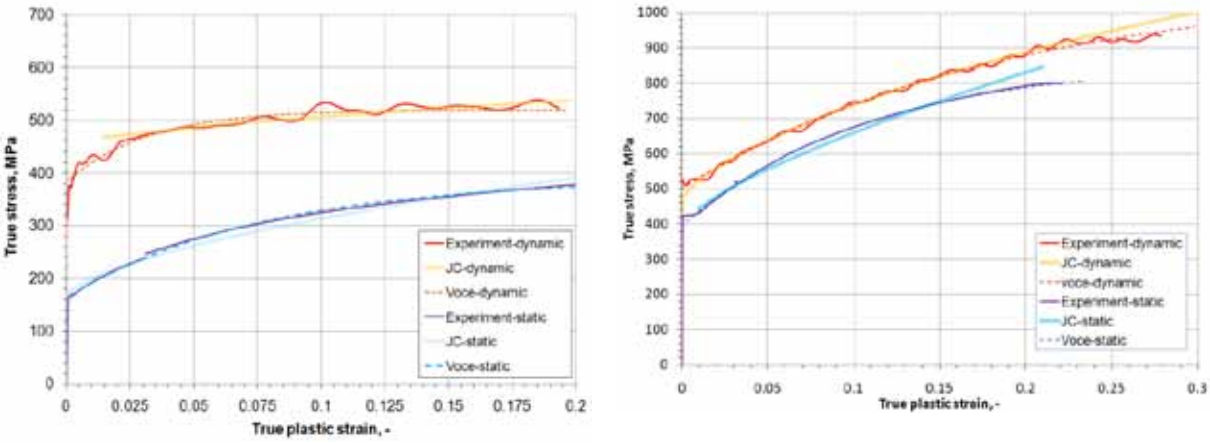

Figure 5: Experimental static and dynamic tensile curves and curves simulated with the Johnson-Cook model for the DC04 (left) and the TRIP (right) steel

4 CALCULATION OF STRAIN RATE DEPENDENT FLD

4.1 Marciniak-Kuczynski method

The uniaxial tensile test results at different strain rates are used to predict the forming limits of the studied steel grades. Onset of necking under the multi-axial strain conditions occurring in forming processes is predicted using the well-known Marciniak–Kuczinski model [5].

In the Marciniak-Kuczynski (MK) method, it is assumed that an initial imperfection is present in the sheet metal. The imperfection is modelled by a band b of smaller thickness than the surrounding zone a, as schematically represented in Figure 6. The orientation of the band is characterized by the angle ψ. The initial imperfection can originate from a real thickness variation, surface roughness, a local variation of the strength or a combination. Physical meaning of this assumption is given in [6]. The imperfection parameter, f_0, is defined as the ratio of the reduced thickness t_{b0} to the initial thickness of the sheet t_{a0} ($f_0=t_{b0}/t_{a0}$). During a biaxial straining process, the imperfection zone deforms more than the uniform zone. Therefore, the strain path of the imperfection zone is continuously ahead of the strain path of

the uniform zone. At a certain point, when the strain localization takes place, the difference between the strain path of the imperfection and the uniform zone begins to increase drastically. If the ratio of strain in the zone b to that of the perfect sheet reaches a presumed critical value, the sheet is considered to have failed. This critical value has low impact on the calculated forming limit because the strain in zone a does not change much once there is strain localization in b. The failure strain is calculated for different orientations of b. The lowest failure strain from these calculations is the forming limit. Once the strain localization is detected, the sheet metal is assumed to have failed.

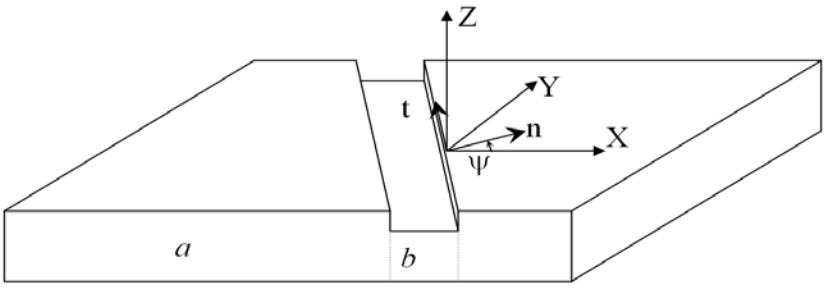

Figure 6: Schematic representation of the Marciniak-Kunczynski sheet with imperfection

In this study, the critical ratio of the strain increment in the region b to that of the region a is 4. The Voce hardening law fitted to the experimental stress-strain curves (see previous section) and von Mises yield criterion are adopted. Instead of optimizing the the imperfection parameter f_0, itis set on 0.99 for both materials for reasons of comparability.

4.2 Static and dynamic FLDs

The results of the FLD calculations are shown in Figure 7. Each chart presents a graph for static and a graph for dynamic ($1000s^{-1}$) deformation of the sheet.

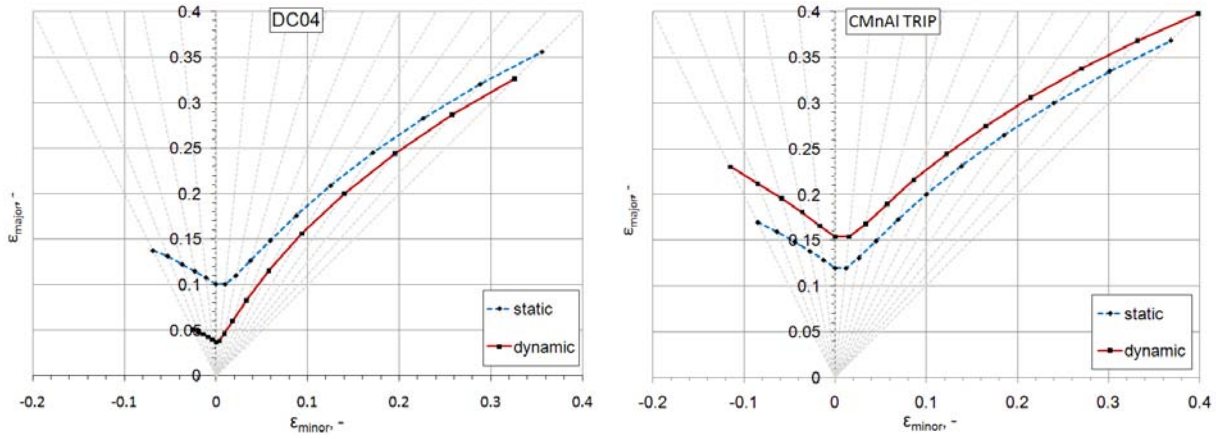

Figure 7: Comparison of static and dynamic FLD's for the considered steels

5 CONCLUSIONS

The influence of the strain rate on the forming properties of the commercial steels DC04 and a laboratory made CMnAl TRIP steel is studied. Static and high strain rate tensile experiments are performed to assess the influence of the strain rate on the mechanical behaviour. Going from static to dynamic loading rates, the plastic stresses increase. Concerning deformation before necking values are roughly halved for the DC04 steel. In contrast, the TRIP steel shows an increase of uniform strain when dynamically loaded. Subsequently, the Johnson-Cook and Voce models are used to describe the strain rate and temperature dependent constitutive behaviour of the studied steels. These constitutive models combined with the corresponding material parameters can be used to calculate the energies and forces occurring in a high speed forming process.

Finally, the influence of the strain rate on the forming limits is assessed using the uni-axial tensile test results. Prediction of the initiation of necking in the steel sheets subjected to multi-axial strain states is based on the Marciniak-Kuczynski model. The resulting forming limit diagrams show a non-negligible effect of the strain rate. The reduced ductility at higher strain rates is reflected into an unfavourable downward shift of the forming limit diagrams for the DC04 steel grade. For the TRIP steel, an important upward trend in the forming limits can be observed if the strain rate is increased.

REFERENCES

[1] Van Slycken, J., Verleysen, P., Degrieck, J., et al. High-strain-rate behavior of low-alloy multiphase aluminum- and silicon-based transformation-induced plasticity steels. *Met. Mat. Trans. A-Phys. Met. Mat. Sc.* (2006) **37A**:1527-1539.

[2] Liang, R.Q. and Khan, A.S. A critical review of experimental results and constitutive models for BCC and FCC metals over a wide range of strain rates and temperatures. *Int. J. Plast.* (1999) **15**:963-980.

[3] Kolsky, H. An investigation of the mechanical properties of materials at very high rates of loading Proc Phys Soc Lond Sec B (1949) **62**:676-700.

[4] Marciniak, Z. and Kuczynski, K. Limit strains in the processes of stretch-forming sheet metal, *Int. J. Mech.* (1967) **9**:609-620.

[5] Marciniak, Z., Kuczynski, K., and Pokora, T. Influence of plastic properties of a material on forming limit diagram for sheet-metal in tension. *Int. J. Mech. Sci.* (1973) **15**:789-800.

XI International Conference on Computational Plasticity. Fundamentals and Applications
COMPLAS XI
E. Oñate, D.R.J. Owen, D. Peric and B. Suárez (Eds)

EXPERIMENTALLY-BASED IDENTIFICATION OF SHEET METALS PLASTIC ANISOTROPY, WITH A VIEW TO OBTAINING IMPROVED PREDICTIONS IN FORMING SIMULATIONS

G. FERRON, I. CHARPENTIER, M. MARTINY, M. TEACA

Laboratoire d'Étude des Microstructures et de Mécanique des Matériaux, LEM3, UMR CNRS 7239,
Université Paul Verlaine - Metz, Ile du Saulcy, 57045 Metz, France

E-mail: gerard.ferron@univ-metz.fr

Key words: Sheet Metals, Plastic Anisotropy, Experimental Characterization.

Summary. Experimental tests developed to characterize sheet metals plastic anisotropy are reviewed in this paper, with particular emphasis on those dedicated to the identification of advanced yield surfaces capable of improving the predictions in forming simulations. The direct identification methods using a variety of tests that cover a wide range of proportional stress states are first discussed. Inverse methods based on experiments on complex-shaped specimens are next presented. With these methods, the parameters of a selected material model are determined by minimizing the discrepancies between numerically-predicted results and experimental ones.

1 INTRODUCTION

Sheet metal forming processes are widely used in automotive and domestic appliance industries to manufacture complex-shaped structural components. In view of the complexity of textural and micro-structural evolutions associated with plastic yielding, the optimization of these processes should be performed by means of finite element (FE) simulations in which only the most important aspects of anisotropic plasticity are selected in relation with the expected predictions.

In addition to the initial yield surface, two main kinds of surfaces can be defined in stress space, depending on the experimental procedure applied for their determination.

The subsequent yield surfaces (SYSs) are obtained by exploring the whole stress space after a given pre-strain has been applied to the material. The determination of SYSs reveals the anisotropic character of strain-hardening. The Bauschinger effect is one of the manifestations of anisotropic hardening, which is expected to play an appreciable role on the springback of the piece when the stamping tools are removed [1].

The constant work contours (CWCs) are defined in stress space by joining the points obtained under different quasi-linear strain-paths or stress states at a given value of expended plastic work. With the CWCs, emphasis is given to initial anisotropy and to possible differential hardening effects that manifest by differences in strain-hardening along different strain-paths, leading to an evolution of the shape of the CWCs with the level of plastic work. Experimental evidence [2] tends to indicate that the directions of plastic strain increments are

normal to the CWCs, which explains that they are commonly modeled by a yield function and its associated flow rule. Among many anisotropic yield functions proposed during the last decades, Hill's quadratic function [3] is the best known and remains the most widely used in industrial context.

The present paper focuses on the experimental methods that can be used to identify anisotropic yield surfaces and/or CWCs, which play a prominent role in the predictions of strain distributions and defects in the formed part. Two main methods are examined : first, direct methods for identifying the CWCs, in which a variety of tests are performed to cover a wide range of linear or quasi-linear strain-paths (see also the excellent review on sheet metals experimental characterization by Kuwabara [4]) ; second, inverse methods using experiments on complex-shaped specimens, where the parameters of a material model are determined by minimizing the discrepancies between numerically-predicted results and experimental ones.

2 DIRECT IDENTIFICATION METHODS

Direct identification methods of the three-dimensional plastic behavior of metals were developed concurrently with modern plasticity theories. A pioneering example is given by the work of Lode [5], who tested thin tubes under combined axial tension and internal pressure in order to examine the influence of the intermediate principal stress on yielding. A number of tests covering a wide range of biaxial stress states have also been proposed for a long time for sheets in order to define an appropriate anisotropic yield function fitting experimental data. These classical tests are critically reviewed in this section, together with more recent experiments conducted on biaxially stretched specimens.

2.1 Uniaxial tension tests

The uniaxial tension test is accepted as an unquestionable experiment for characterizing strain-hardening and plastic anisotropy. Its main limitation comes from the occurrence of necking, which restricts its straightforward analysis to strain levels corresponding to the point of maximum load. An example of uniaxial stress-strain curves taken from [6] is given on Fig. 1a for annealed 1050A aluminum specimens cut along the rolling direction (RD), the diagonal direction (DD) and the transverse direction (TD). The total logarithmic surface strains ε_1 and ε_2 along the tensile and the width directions, respectively, were determined during the tests as the average values obtained over a central zone of the specimens by using an image correlation method. The Lankford coefficient R measuring the ratio between plastic strains in the width direction (ε_2^p) and in the thickness direction (ε_3^p) was then calculated by taking into account the contribution of elastic strains and the assumption of plastic incompressibility. The evolutions of R as a function of plastic strain ε_1^p along the tensile direction are shown on Fig. 1b. It can be observed that the stress-strain curve along TD exhibits a slightly lower hardening rate, as compared to RD and DD, Fig. 1a. Besides, the Lankford coefficient slightly evolves during the tests, Fig. 1b. These observations indicate that the assumption of isotropic hardening is not rigorously satisfied.

The angular variations of the Lankford coefficient (measured at $\varepsilon_1^p = 0.1$) and of the flow stress at different values of plastic work are shown on Figs 1c and 1d, respectively. The

relation between strain anisotropy, Fig. 1c, and stress anisotropy, Fig. 1d, cannot be accounted for with Hill's quadratic criterion [3], which only involves 3 parameters for describing the adimensional plane-stress yield surface. The FMM model proposed by Ferron et al. [7] is used in Fig. 1d to fit the variations of both $R(\alpha)$ and $\sigma(\alpha)$.

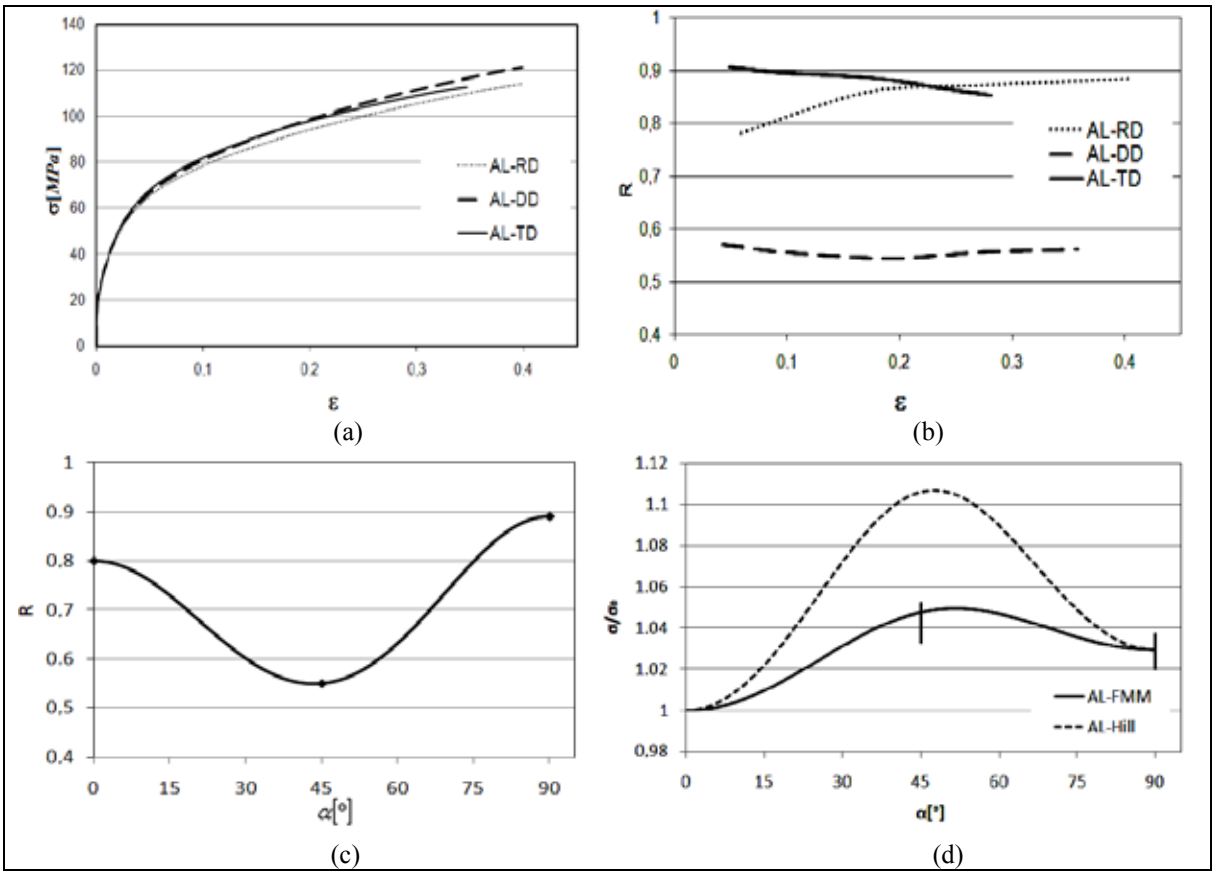

Figure 1: Uniaxial stress-strain curves (a), evolution of the Lankford coefficient (b), and angular variations of the Lankford coefficient (c) and of normalized flow stress (d) for annealed 1050A aluminum (after [6]).

More complex angular evolutions of the Lankford coefficient and of the flow stress can be obtained in dual phase steels [8] or in aluminum alloys [9]. An asymmetric yield behavior in tension and compression can also be observed in some advanced materials [9].

2.2 Shear tests

The simple shear test can be performed on a conventional testing machine by means of a device imposing a parallel displacement of two lateral grips, which leads to a shear strain γ as shown on Fig. 2a (from [10]). Compared with the uniaxial tension test, much larger homogeneous strains can be obtained with this test. Also, the stress can easily be reversed by inverting the relative displacement of the grips. Further flexibility for analyzing strain-induced anisotropy is obtained by cutting samples in prestrained sheets [10]. Simple shear results are illustrated on Fig. 2b for a low-carbon steel with 20% tension prestrain along RD.

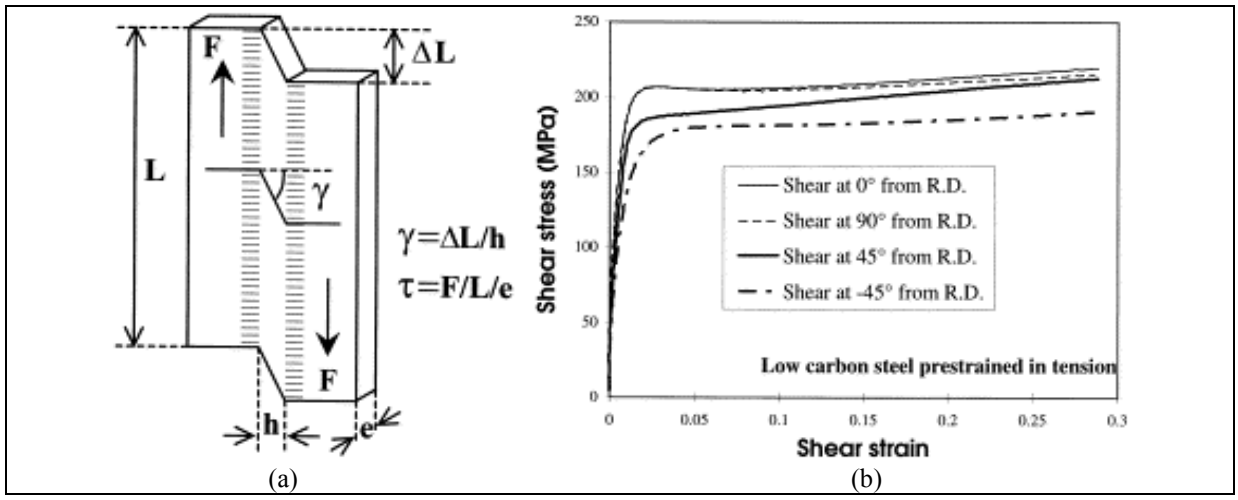

Figure 2: Geometry of a simple shear sample (a) and experimental shear stress–shear strain curves for a low-carbon steel after 20% prestrain in tension along RD (b) (from [10]).

2.3 Plane-strain tension tests

The tension test on wide specimens (Fig. 3a) can be used to obtain strain states close to plane-strain tension in the middle section of minimal cross-sectional area [11]. With the assumption of plane-strain tension, the plane-strain stress-strain curve can be directly estimated by recording the load and the (average) axial strain in the middle section. However, an extensive study by Dournaux et al. [12] clearly shows that uniform stress- and strain-states are not obtained in the middle section. Strain field analysis by means of optical full-field measurement techniques further shows that the degree of strain field homogeneity is strongly sensitive to specimen geometry. An optimized geometry can be searched by FE analysis, but the results depend on the yield function [12]. Finally, this test could alternatively be used to analyze the ability of selected constitutive models to reproduce the inhomogeneous strain fields.

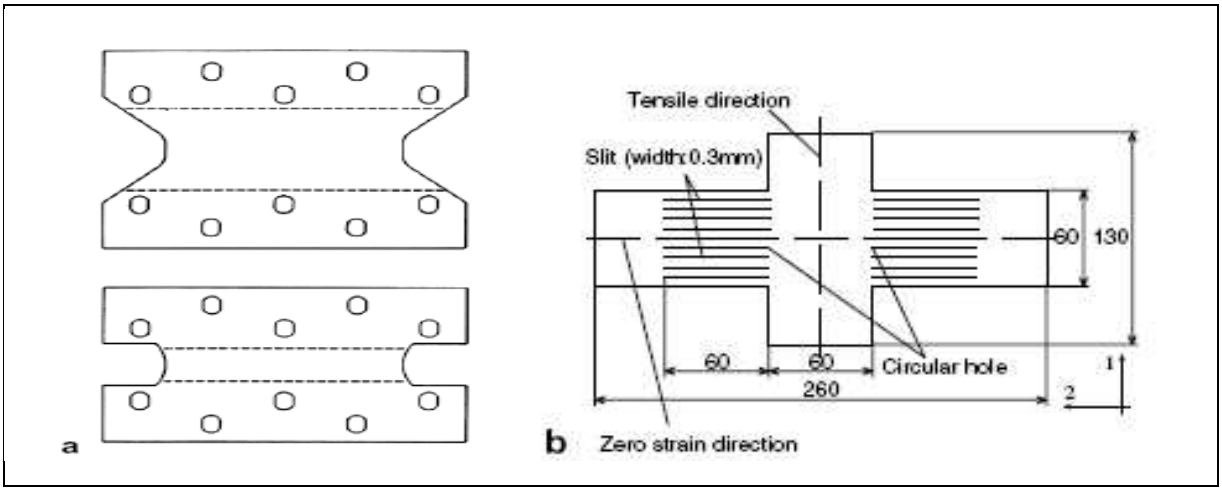

Figure 3: Plane-strain tension wide specimens proposed by Wagoner [11] (a);
plane-strain tension cruciform specimen proposed by Kuwabara and Ikeda [13] (b).

Cruciform specimens (Fig. 3b) also have been designed for plane-strain stretching, with slits machined along the direction normal to the loading direction, while the elongation along this normal direction is maintained equal to zero during the test [13].

2.4 Bulge test

Following the earlier work of Mellor [14], the plastic bulging of a blank clamped along a circular contour and submitted to the action of a lateral fluid pressure is widely used in industrial and academic laboratories. Large plastic strains are obtained with this test at the apex of the dome. The biaxial flow stress σ_b at the apex is estimated by measuring fluid pressure p and calculating the thickness and curvatures at the pole, via appropriate measurements and assumptions. The surface strains ε_1 and ε_2 and curvatures $(1/R_1)$ and $(1/R_2)$ along RD and TD, respectively, are determined as average values measured over a certain area around the pole by means of either extensometers and spherometers, or optical systems allowing a continuous recording of the coordinates of a grid applied on the sheet. The through-thickness strain ε_3 is estimated with the assumption of incompressibility :

$$\varepsilon_3 = -(\varepsilon_1 + \varepsilon_2) \tag{1}$$

and the thickness t is determined as :

$$t = t_0 \exp(\varepsilon_3) \tag{2}$$

where t_0 is the initial thickness.

The biaxial stress at the pole is determined using the membrane equilibrium equation :

$$\frac{\sigma_1}{R_1} + \frac{\sigma_2}{R_2} = \frac{p}{t} \tag{3}$$

where σ_1 and σ_2 are the membrane stresses.

The local shape of the deformed sheet around the pole is often approximated by a sphere. Then, under the assumptions $R_1 \approx R_2 \equiv R$ and $\sigma_1 \approx \sigma_2 \equiv \sigma_b$, equation (3) reduces to :

$$\sigma_b = \frac{pR}{2t} \tag{4}$$

Apart from experimental accuracy, several elements can affect the determination of the biaxial stress-strain law. First, the strain and the curvature depend on the position along the profile. Thus, the determination of surface strains and curvatures at the pole may depend on the size of the zone used for their determination. Second, the determination of the thickness using the strains measured on the upper face of the sheet ignores the strain gradients through the thickness, which arise from the combination of stretching and bending for thick sheets. Third, the membrane equilibrium equations (3) and (4) represent an approximation for thick sheets.

In order to evaluate the accuracy of the bulge test analysis, Lemoine et al. [15] performed virtual experiments in which the results obtained by FE calculations are used as input data for determining the biaxial stress-strain law in agreement with the experimental procedure. In this way, the experimental procedure can be evaluated by comparing the "experimental" stress-strain curve with the "reference" one introduced in the simulations. The $\sigma_1(|\varepsilon_3|)$ curves predicted for an isotropic (von Mises) material with a die diameter of 108 mm and for different sheet thicknesses are shown on Fig. 4a. A progressive overestimate of the stress-strain curve is observed with the experimental determination. This effect is more significant for materials with a lower hardening rate, and it is clearly much more important for thick sheets. The strain gradients through the thickness partly explain this effect, as a result of a progressive underestimate of the thickness when it is computed with the value of the upper surface strain ε_1 [15]. For thick sheets, it is also observed that the calculated stress is far too low in the early stages of bulging (Fig. 4a). This effect can be explained by the initial predominance of bending. This may be observed on Fig. 4b where the evolution of stress σ_1 at the apex is plotted as a function of dome height *H* for different nodes through the thickness of the sheet.

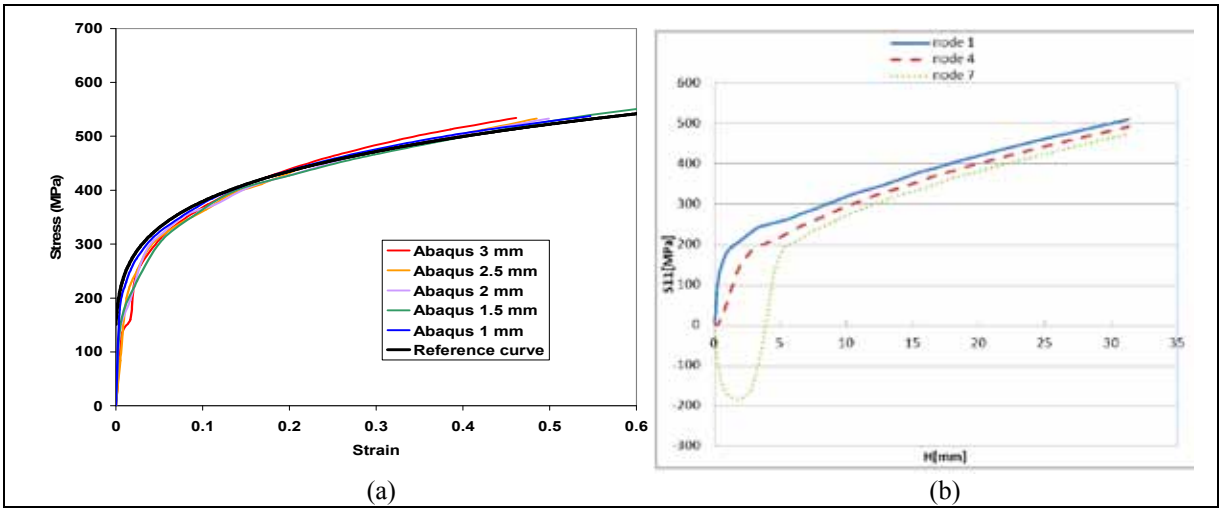

(a) (b)

Figure 4: Comparison between the "reference" curve and "experimental" curves (Abaqus) for different thicknesses (a); evolution of apex stress σ_1 as a function of dome height *H* for the upper node 1, mid node 4 and lower node 7 through the thickness (b) (from [15]).

For in-plane anisotropic materials, the approximation $\sigma_1 = \sigma_2$ in the equilibrium equation (4) is an additional source of error, because the strain and stress states at the apex neither exactly correspond to equibiaxial states [15].

2.5 Compression tests

Biaxial compression tests can be performed on adhesively bonded blocks of sheet specimens [16]. Generally, these tests are analyzed by assuming pressure-insensitive plastic yielding, which allows the direct prediction of in-plane loading behavior. Some difficulties

possibly arise from friction, from lack of parallelism between the specimen and the tools and from elasticity effects [17].

2.6 Biaxial tension tests

Reviews of cruciform specimens designed for determining yield stress or stress-strain curves in biaxial tension can be found in [4,18]. Some examples of cruciform specimens are shown on Fig. 5. With these specimens, a direct identification of the stress-strain law in biaxial tension is performed by measuring the deformation in the central gauge part and by determining the stress from equilibrium considerations. The main difficulty with this kind of specimens consists of obtaining significant levels of biaxial stretching in the central part. This difficulty can be overcome by machining slits in the specimen arms and creating a thinner central part [20,21]. Kuwabara et al. [2] avoided this thinning by machining very narrow slits in the arms, so that the cross-sectional area of arms is almost the same as that of the central gauge part. However, the amount of stretching in the central part is limited in this case to a few percents of elongation.

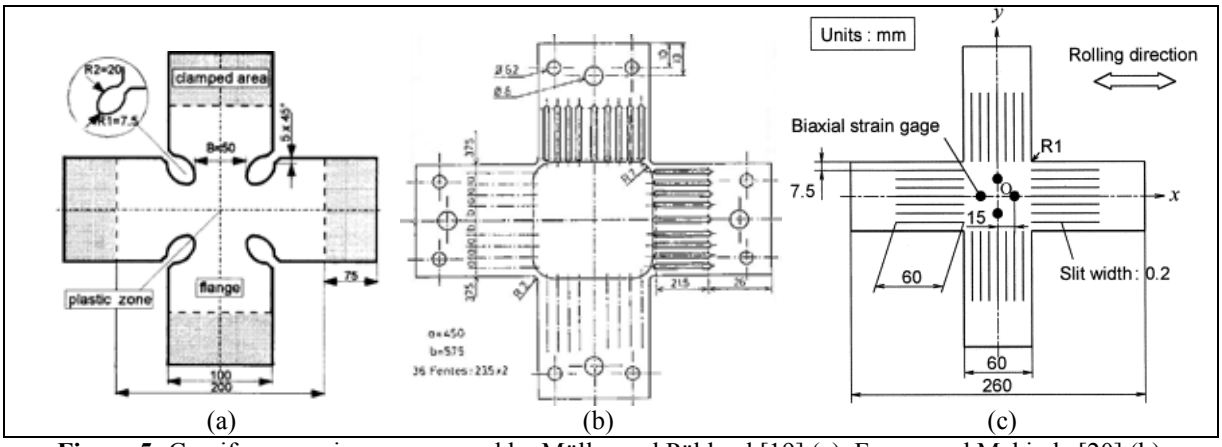

(a) (b) (c)

Figure 5: Cruciform specimens proposed by Müller and Pöhland [19] (a), Ferron and Makinde [20] (b) and Kuwabara et al. [2] (c).

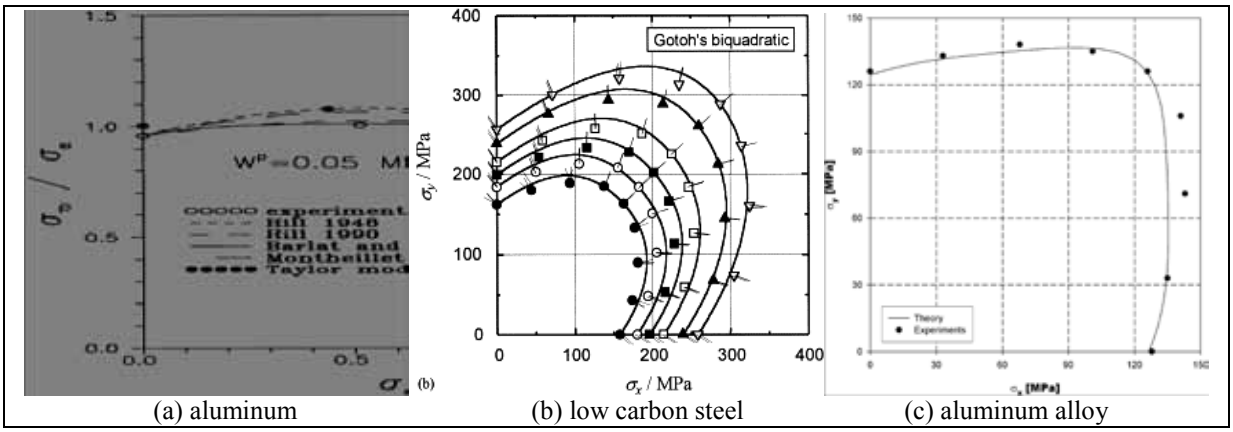

(a) aluminum (b) low carbon steel (c) aluminum alloy

Figure 6: Constant works contours determined with cruciform specimens by Green et al. [22] (a), Kuwabara et al. [2] (b) and Banabic et al. [23] (c).

Examples of CWCs determined in the biaxial stretching range are shown on Fig. 6. The biaxial devices used for these experiments consist of two sets of opposite actuators, which are servo-controlled at either a given strain ratio [22] or a given load ratio [2,23] to obtain one point of the CWC. Referring to the denominations used in Fig. 5, specimens are of either type (b) [22] or type (c) [2,23].

3 INVERSE IDENTIFICATION METHODS

Inverse identification methods are carried out by using an optimization procedure in which the parameters of the constitutive law introduced in FE simulations are adjusted in order to minimize the discrepancies between numerically predicted results and experimental ones. Theoretical formulations of the identification problem can be found in [24,25]. For plastically deformed anisotropic sheet metals, the global results related to the load-displacement response were first analyzed. Owing to the advances in optical full-field measurement techniques, the analysis of heterogeneous strain fields obtained on specifically-designed specimens is now increasingly used for the identification of material parameters.

3.1 Global results analysis

Load-displacement results have been analyzed in a variety of situations by Ghouati and Gelin [25] to identify strain-hardening parameters and Hill's quadratic yield function parameters. Experiments used for identification include uniaxial tension tests, bulge tests and deep-drawing tests. Another example of global results analysis is given in [26], where plane-strain tension tests are analyzed by recording the load as a function of the thickness in the centre of the specimen. Plastic yielding is modeled using Hill's quadratic model with the assumptions of either associated or non-associated flow rule, and Barlat's yield function (Yld91) [27]. Improved results could be obtained with this latter yield function.

3.2 Strain fields analysis

More informative and discriminant results are expected from full-field displacement and strain measurements. One of the first studies using full-field displacement measurements on plastically-stretched sheet metals was performed by Meuwissen et al. [28]. These authors designed non-standard tensile specimens with dissymmetric notches (Fig. 7a). The displacement fields were measured optically with retro-reflective markers on the specimen surface. Belhabib et al. [29] also used notched specimens (Fig. 7b). These authors performed full-field optical strain measurements and FE analysis to determine the strain-hardening parameters and Hill's quadratic yield function parameters. Kajberg and Lindkvist [30] performed a numerical optimization of strain measurements on notched specimens with the aim of determining the stress-strain law at large strains.

A much wider range of stress states can be covered using biaxially-stretched cruciform specimens. For a pertinent identification based on strain fields analysis, the design of cruciform specimens should be guided by the following prescriptions [31]:

- obtain a wide range of stress-states over the surface of the specimen,
- obtain a satisfactory compromise between a significant strain level in all the regions of the specimen and a high sensitivity of strain fields to plastic anisotropy.

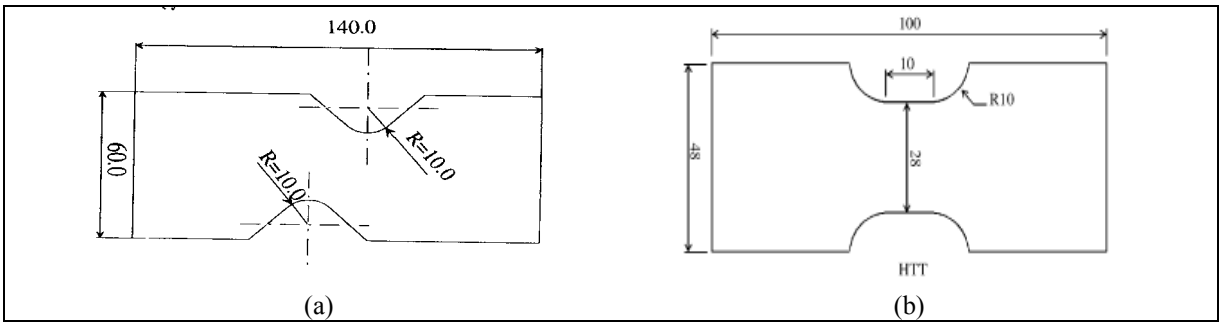

(a) (b)

Figure 7: Non-standard tensile specimens designed by Meuwissen et al. [28] (a) and Belhabib et al. [29] (b).

Two types of cruciform specimens designed according to the above objectives [31,32] are presented on Fig. 8. Both types exhibit the same external shape. The geometry of the first type is simply defined by a hole machined in its centre (Fig. 8a). The stress-state is close to uniaxial tension in the major part of specimen arms (UT region), and close to plane-strain tension along the lines oriented at 45° from the specimen axes (PST region). The second type of specimens (Fig. 8b) is designed to enforce different stress states along the symmetry axes:

- equibiaxial tension (EBT) in the centre of the specimen, defined by the Lagrangian coordinate $X = 0$,
- plane-strain tension (PST) at the points at $X \approx \pm 10\,\text{mm}$, where a strain peak is observed between the ends of the slots oriented at 45° from the symmetry axes,
- uniaxial tension (UT) in the regions defined by $25\ \text{mm} < |X| < 40\ \text{mm}$, where a strain plateau is observed along the central ligaments of the arms.

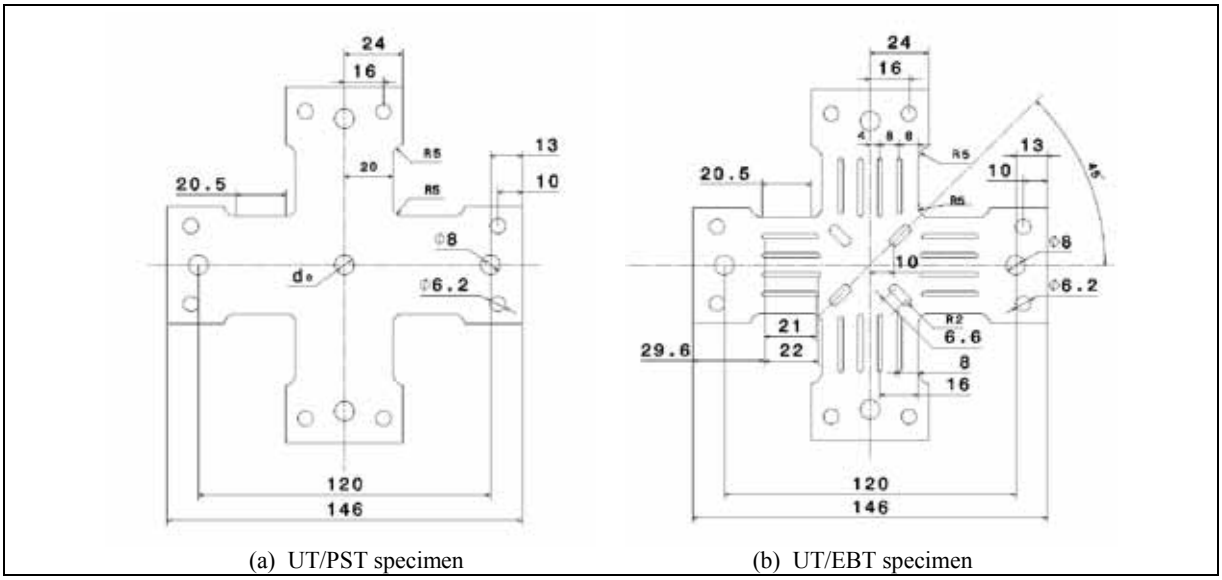

(a) UT/PST specimen (b) UT/EBT specimen

Figure 8: Cruciform specimens with stress states ranging from uniaxial tension to plane-strain tension (a) and from uniaxial tension to equibiaxial tension (b) [31,32].

The identification procedure [31,32] is performed with a 8-parameter yield function [7] by combining the results of uniaxial tension tests and biaxial tension tests on cruciform

specimens. Uniaxial tension tests along the directions at 0°, 45° and 90° from the rolling direction are carried out to determine the strain-hardening parameters and yield function parameters related to transverse strain- and stress-anisotropy. Strain distributions measured in biaxial tension tests by an image correlation method are used as input data in an optimization procedure allowing the determination of yield function parameters related the shape of the yield surface in biaxial tension. As an illustration, the plot of major principal strains measured for various materials along the symmetry axis corresponding to the rolling direction of UT/EBT specimens (Fig. 9a) displays the high sensitivity of strain fields to material anisotropy. The yield surfaces obtained by the identification procedure are shown on Fig. 9b.

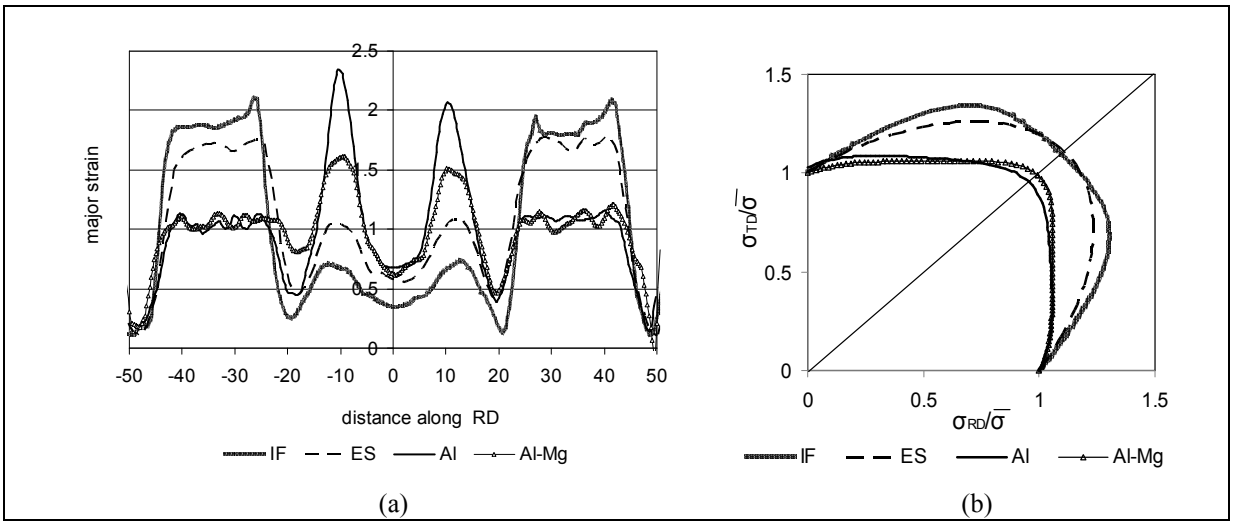

Figure 9: Normalized distributions of major principal strain measured along the rolling direction of UT/EBT specimens (a) and identified yield surfaces in the biaxial stretching range (b) (from [31]).

4 CONCLUSIONS

The aspects of sheet metals plastic anisotropy reviewed in this paper mainly deal with the experimental identification of yield surfaces, and more specifically of constant work contours. To improve numerical predictions of strain distributions and to assess the feasibility of a forming process, these experiments should bring accurate information about:

- the *orientation* dependence of yielding, both concerning transverse *strain*- and *stress*-anisotropy, which plays a prominent role in processes with draw-in, as is the case for the formation of ears in the cup drawing test,
- the *stress-ratio* dependence of yielding, particularly the shape of the yield surface in the biaxial stretching range, which controls the strain distributions obtained in stampings that present a wide range of stress states. The use of biaxially stretched specimens, designed either for a direct or an inverse identification, represents an efficient mean for this characterization.

The yield surfaces can be modeled by choosing one of the anisotropic yield functions developed during the last 30 years concurrently with ever more accurate characterizations of sheet yielding, see, e.g., the reviews of Banabic [33] and Barlat et al. [34].

REFERENCES

[1] B. Tang, X. Lu, Z. Wanga and Z. Zhao, "Springback investigation of anisotropic aluminum alloy sheet with a mixed hardening rule and Barlat yield criteria in sheet metal forming", *Materials and Design*, **31**: 2043-2050 (2010).

[2] T. Kuwabara, S. Ikeda and K. Kuroda, "Measurement and analysis of differential work hardening in cold-rolled steel sheet under biaxial tension", *J. Mater. Proc. Technol.*, **80-81**: 517-523 (1998).

[3] R. Hill, "A theory of the yielding and plastic flow of anisotropic metals", *Proc. Royal Soc. London*, **A193**: 281-297 (1948).

[4] T. Kuwabara, "Advances in experiments on metal sheets and tubes in support of constitutive modeling and forming simulations", *Int. J. Plast.*, **23**: 385-419, (2007).

[5] W. Lode, "Versuche über den Einfluss der mittleren Hauptspannung auf das Fliessen der Metalle Eisen, Kupfer und Nickel", *Z. Physik*: **36**, 913 (1926).

[6] M. Teaca, "Caractérisation expérimentale et modélisation de la déformation plastique des tôles métalliques", *PhD thesis*, Metz (2009).

[7] G. Ferron, R. Makkouk and J. Morreale, "A parametric description of orthotropic plasticity in metal sheets", *Int. J. Plast.*, **10**: 431-449 (1994).

[8] M. Rabahallah, T. Balan, S. Bouvier, B. Bacroix, F. Barlat, K. Chun and C. Teodosiu, "Parameter identification of advanced plastic strain rate potentials and impact on plastic anisotropy prediction", *Int. J. Plast.*, **25**: 491-512, (2009).

[9] B. Plunkett, O. Cazacu and F. Barlat, "Orthotropic yield criteria for description of the anisotropy in tension and compression of sheet metals", *Int. J. Plast.*, **24**: 847-866 (2008).

[10] E.F. Rauch, "Plastic anisotropy of sheet metals determined by simple shear tests", *Mat. Sci. Engng*, **A241**: 179-183 (1998).

[11] R.H. Wagoner, "Measurement and analysis of plane-strain work hardening", *Met. Trans.*, **11A**: 165-175 (1980).

[12] J.L. Dournaux, S. Bouvier, A. Aouafi and P. Vacher, "Full-field measurement technique and its application to the analysis of materials behavior under plane-strain mode", *Mat. Sci. Engng*, **A500**: 47-62 (2009).

[13] T. Kuwabara and S. Ikeda, "Measurement and analysis of work hardening of sheet steels subjected to plane strain tension", *Tetsu-to-Hagane*, **88 (6)**: 334-339 (2002).

[14] P.B. Mellor, "Stretch forming under fluid pressure", *J. Mech. Phys. Solids*, **5:** 41-56 (1956).

[15] X. Lemoine, A. Iancu and G. Ferron, "Flow curve determination at large plastic strain levels: limitations of the membrane theory in the analysis of the hydraulic bulge test", *Esaform 2011*, Belfast, 27-29 april 2011.

[16] Y. Tozawa, "Plastic deformation behavior under the compression of combined stress", in *Mechanics of Sheet Metal Forming*, eds D.P. Koistinen and N.M. Wang, pp. 81-110, Plenum Press, New York (1978).

[17] Y. Maeda, M. Yanagawa, F. Barlat, K. Chung, Y. Hayashida, S. Hattori, K. Matsui, J.C. Brem, D.J. Lege, S.J. Murtha and T. Ishikawa, "Experimental analysis of aluminum yield surface for binary Al-Mg alloy sheet samples", *Int. J. Plast.*: **14**, 301-318 (1998).

[18] A. Hannon and P. Tiernan, "A review of planar biaxial tensile test systems for sheet metal", *J. Mater. Proc. Technol.*, **198**: 1-13 (2008).
[19] W. Müller and K. J. Pöhlandt, "New experiments for determining yield loci of sheet metal", *J. Mater. Process. Technol.*, **60**: 643-648 (1996).
[20] G. Ferron and A. Makinde, "Design and development of a biaxial strength testing device", *J. Test. Evaluat.*, **16**: 253-256 (1988).
[21] J.P. Boehler, S. Demmerle and S. Koss, "A new direct biaxial testing machine for anisotropic materials", *Exp. Mech.*, **34**: 1-9 (1994).
[22] D.E. Green, K.W. Neale, S.R. MacEwen, A. Makinde and R. Perrin, "Experimental investigation of the biaxial behaviour of an aluminum sheet", *Int. J. Plast.*, **20**: 1677-1706 (2004).
[23] D. Banabic, T. Kuwabara, T. Balan, D.S. Comsa and D. Julean, "Non-quadratic yield criterion for orthotropic sheet metals under plane-stress conditions", *Int. J. Mech. Sci.*, **45**: 797-811 (2003).
[24] R. Mahnken and E. Stein, "A unified approach for parameter identification of inelastic material models in the frame of the finite element method", *Computer Methods Appl. Mech. and Engng*, **136**: 225-258 (1996).
[25] O. Ghouati and J.C. Gelin, "A finite element-based identification method for complex metallic material behaviour", *Comput. Mater. Sci.*, **21**: 57-68 (2001).
[26] A. Khalfallah, H. Bel Hadj Salah and A. Dogui, "Anisotropic parameter identification using inhomogeneous tensile test", *Eur. J. Mech. A/Solids*, **21**: 927-942 (2002).
[27] F. Barlat, D.J. Lege and J.C. Brem, "A six-component yield function for anisotropic materials", *Int. J. Plast.*, **7**: 693-712 (1991).
[28] M.H.H. Meuwissen, C.W.J. Oomens, F.P.T. Baaijens, R. Petterson and J.D. Janssen, "Determination of the elasto-plastic properties of aluminium using a mixed numerical-experimental method", *J. Mater. Process. Technol.*, **75**: 204-211 (1998).
[29] S. Belhabib, H. Haddadi, M. Gaspérini and P. Vacher, "Heterogeneous tensile test on elastoplastic metallic sheets: Comparison between FEM simulations and full-field strain measurements", *Int. J. Mech. Sci*., **50**: 14-21 (2008).
[30] J. Kajberg and G. Lindkvist, "Characterisation of materials subjected to large strains by inverse modeling based on in-plane displacement fields", *Int. J. Solids Struct.*, **41**: 3439-3459 (2004).
[31] M. Teaca, M. Martiny, I. Charpentier and G. Ferron, "Heterogeneous biaxial tensile tests for the characterization of sheet metals plastic anisotropy", *AIP Conference Proceedings* **1315:** 57-62 (2011).
[32] M. Teaca, I. Charpentier, M. Martiny and G. Ferron, "Identification of sheet metal plastic anisotropy using heterogeneous biaxial tensile tests", *Int. J. Mech. Sci*., **52**: 572-580 (2010).
[33] D. Banabic, "Formability of metallic materials", Springer, Heidelberg (2000).
[34] F. Barlat, J.W. Yoon and O. Cazacu, "On linear transformations of stress tensors for the description of plastic anisotropy", *Int. J. Plast.*, **23**: 876-896 (2007).

XI International Conference on Computational Plasticity. Fundamentals and Applications
COMPLAS XI
E. Oñate, D.R.J. Owen, D. Peric and B. Suárez (Eds)

IDENTIFICATION OF ORTHOTROPIC PLASTIC MATERIAL PARAMETERS FOR DEEP-DRAWING STEEL USING DIC AND FEMU

Stefan Schmaltz*, Kai Willner*

*Chair of Applied Mechanics, Department of Mechanical Engineering
Friedrich-Alexander University Erlangen-Nuremberg
Egerlandstr. 5, 91058 Erlangen, Germany
e-mail: stefan.schmaltz@ltm.uni-erlangen.de, willner@ltm.uni-erlangen.de
Web page: http://www.ltm.uni-erlangen.de

Key words: Computational Plasticity, Parameter Identification, Sheet steel, FEMU

Abstract. In this paper the deep-drawing sheet steel DC04, representative for sheet-bulk metal forming processes, is characterized through uni- and biaxial tensile and compression tests. The orthotropic plastic material parameters for the Hill 1948 yield surface are identified in two different ways. The first one utilizes uniaxial tensile experiments with specimen in three angles to the rolling direction of the sheet (0, 45 and 90 degree) and the plastic material parameters are calculated through the Lankford coefficients. Second a Finite Element Model Updating (FEMU) procedure is introduced. By taking the measured full-field displacement data and the forces of the biaxial tensile experiments better fitting parameters are identified at reasonable experimental costs.

1 INTRODUCTION

In engineering disciplines the complexity of produced parts and therewith of manufacturing processes increases steadily. In addition the product life cycle of many products gets shorter, which results in a need of reliable and fast numerical simulations. This coincides with the need of material parameters being optimized for the utilized material, load type and constitutive law.
The goal of our research is to present a procedure to get optimal material parameters at modest experimental costs. The chosen material, a deep-drawing sheet steel (DC04), which is representative for sheet-bulk metal forming processes, is characterized through uni- and biaxial tensile and compression tests. The plastic material parameters are identified in two different ways. At first the direct approach is taken, which uses the experimentally measured values of the different tests for the calculation of the yield surface. Then our Finite Element Model Updating (FEMU) procedure is introduced, applied and the results are discussed.

2 EXPERIMENTAL SET-UP AND DATA ACQUISITION

The used sheet metal is fabricated in a cold-rolling process and therefore shows orthotropic elastic and plastic material characteristics. To capture and verify this behavior, experiments based on different load types were performed, see fig. 1. For the uniaxial tensile test standardized specimen[1] were utilized. To prevent buckling the uniaxial compression test is performed on micro-specimen using hydraulic clamping with bearing extensions. In the biaxial tension and compression experiments a self-designed specimen is employed. Utilizing bearing plates, with friction reduction plates made out of Teflon®, in the biaxial compression tests, the initial compression yield point can be determined without buckling of the structure. The machines for the uniaxial testing are based on an

Figure 1: Specimen for the experimental testing

electro-mechanical principle. For the biaxial loading type a hydraulic machine is utilized where the cylinders of the vertical and horizontal axis can be controlled separately.

For the identification of the plastic material parameters with our FEMU procedure full-field displacement data and the experimentally determined forces of the experiments are essential. Therefore the deformation of the specimen during the experiments is captured with an optical full-field measurement system. On each specimen a stochastic spray pattern is applied which deforms with the specimen. In the course of the experiment a certain amount of pictures of the deforming specimen is taken and the full-field displacement data can be calculated through Digital Image Correlation (DIC).
There, a homogeneous mesh is layed onto the stochastic spray pattern in the initial state of the analysis. The elements are fitted to the deformed state by minimizing the deviation of the brightness distribution from previous to actual state. Having the elements in each state, the displacement field is identified.
Combined with each picture taken through the full-field measurement system the present force level is captured.

[1]Tensile Specimen DIN 50125 – H 12.5×50 of 2.0 mm sheet steel DC04

3 MATERIAL CHARACTERIZATION

The analyzed material shows orthotropic elastic and plastic characteristics without rate dependency. As sheet steel with a width of 2.0 mm is used, the plane stress element formulation is assumed to be valid. Having large deformation at small strains, the total strain $\boldsymbol{\epsilon}$ can be decomposed additively out of the elastic $\boldsymbol{\epsilon}^{\mathrm{el}}$ and the plastic part $\boldsymbol{\epsilon}^{\mathrm{pl}}$. In rate form this equation reads as

$$\dot{\boldsymbol{\epsilon}} = \dot{\boldsymbol{\epsilon}}^{\mathrm{el}} + \dot{\boldsymbol{\epsilon}}^{\mathrm{pl}}. \tag{1}$$

The elastic behavior is linear, utilizing Hooke's Law $\dot{\boldsymbol{\sigma}} = \boldsymbol{C}\dot{\boldsymbol{\epsilon}}^{\mathrm{el}} = \boldsymbol{C}(\dot{\boldsymbol{\epsilon}} - \dot{\boldsymbol{\epsilon}}^{\mathrm{pl}})$, with the stress tensor $\dot{\boldsymbol{\sigma}}$ in rate form and the compliance tensor $\boldsymbol{C}^{-1}$. The linearly independent, orthotropic elastic material parameters are identified by an iterative FEMU procedure to be $E_1 = 199,290\,\mathrm{MPa}$, $E_2 = 212,996\,\mathrm{MPa}$ and $\nu_{12} = 0.3356$. More detailed information can be found in [5]. The shear modulus G_{12} is defined as mean value.

$$\boldsymbol{C}^{-1} = \begin{bmatrix} \frac{1}{E_1} & -\frac{\nu_{12}}{E_1} & 0 \\ -\frac{\nu_{21}}{E_2} & \frac{1}{E_2} & 0 \\ 0 & 0 & \frac{1}{G_{12}} \end{bmatrix}, \quad \frac{\nu_{12}}{E_1} = \frac{\nu_{21}}{E_2}, \quad G_{12} = \frac{E_1 E_2}{E_1 + E_2 + 2\nu_{12}E_2} \tag{2}$$

For the solution of the inelastic part of the problem further equations have to be defined. To be able to describe the actual state internal variables Φ_i are applied. With their evolution equations

$$\dot{\Phi}_i = \dot{h}_i(\boldsymbol{\sigma}, \theta, \boldsymbol{\Phi}), \tag{3}$$

the yield function $F(\boldsymbol{\sigma}, \theta, \boldsymbol{\Phi}) = 0$ and the associative flow rule

$$\dot{\boldsymbol{\epsilon}}^{\mathrm{pl}} = \dot{\mu}\frac{\partial F}{\partial \boldsymbol{\sigma}}, \tag{4}$$

with the plastic multiplier $\dot{\mu}$, is defined. The plastic multiplier has to meet the following conditions

$$\dot{\mu}F = 0, \quad \dot{\mu} \geq 0, \quad F \leq 0. \tag{5}$$

As common practice for deep-drawing sheet steel, the orthotropic yield surface is modeled with the Hill 1948 ansatz [1]. It reads as:

$$F = a_1(\sigma_2 - \sigma_3)^2 + a_2(\sigma_3 - \sigma_1)^2 + a_3(\sigma_1 - \sigma_2)^2 + 3a_4\sigma_{31}^2 + 3a_5\sigma_{23}^2 + 3a_6\sigma_{12}^2 - 2\bar{\sigma}_{\mathrm{F}}^2. \tag{6}$$

The variables a_1 to a_6 describe the shape of the yield surface and $\bar{\sigma}_{\mathrm{F}}$ represents the current equivalent flow stress. For the plane stress configuration the Hill 1948 yield surface in the principal axes σ_1, σ_2 is described through an ellipse symmetric to the coordinate origin. The yield function reduces to

$$F = a_1\sigma_2^2 + a_2\sigma_1^2 + a_3(\sigma_1 - \sigma_2)^2 + 3a_6\sigma_{12}^2 - 2\bar{\sigma}_{\mathrm{F}}^2. \tag{7}$$

The remaining parameters a_1, a_2, a_3 and a_6 can be determined directly through evaluation of the Lankford coefficients $r^{(0°)}$, $r^{(45°)}$ and $r^{(90°)}$ from uniaxial tensile tests [1]. The Lankford coefficients, also called anisotropy parameters, are obtained by

$$r^{(d)} = \frac{\epsilon^{(d)}_{\text{width}}}{\epsilon^{(d)}_{\text{thickness}}}, \quad d = 0°, 45°, 90°. \tag{8}$$

The index d stands for the values of tensile tests with specimen from angles of 0, 45 and 90 degree to the rolling direction of the sheet metal.

The evolution of the yield surface, the hardening of the material, is modeled through a Hockett-Sherby law

$$\bar{\sigma}_{\text{F}}(\bar{\epsilon}_{\text{pl}}) = \bar{\sigma}_{\infty} - [\bar{\sigma}_{\infty} - \bar{\sigma}_0] \exp\left(A \cdot \bar{\epsilon}^{B}_{\text{pl}}\right). \tag{9}$$

In this equation $\bar{\sigma}_{\text{F}}$ represents the current equivalent flow stress, $\bar{\epsilon}_{\text{pl}}$ the current equivalent plastic strain, $\bar{\sigma}_{\infty}$ the equivalent stress to which the yield curve converges, $\bar{\sigma}_0$ the equivalent initial yield stress and A and B are further material parameters. The parameters vary for the different load types and are fitted individually with a curve fitting algorithm.

Utilizing the performed uniaxial tensile experiments the Hill 1948 initial yield surface for our sheet steel can be identified. It is plotted in fig. 2 and labeled as *Lankford*. In this

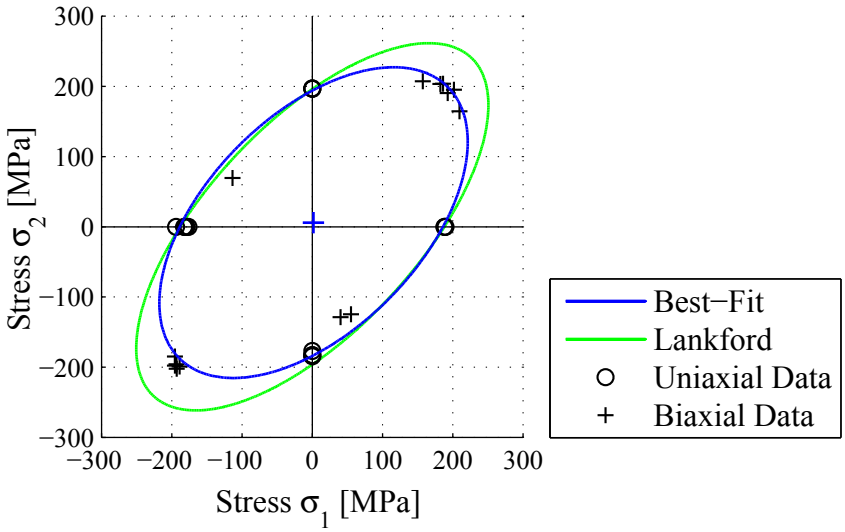

Figure 2: Experimentally determined Hill 1948 and *Best-Fit* yield surfaces

stress-stress diagram (fig. 2) also the initial yield stresses for the different experiments are plotted. To verify that the Hill 1948 yield surface is a sufficiently good model for our material a general ellipse equation is fitted to the experimental yield values. The

Best-Fit ellipse is obtained by a Least-Squares Fit using the Galerkin-Method to solve the overdetermined system of equations. The mid-point of the fitted ellipse lays almost in the coordinate origin as in the Hill 1948 model and the ellipse fits the data points very well.
Comparing the *Lankford* to the *Best-Fit* yield surface, a discrepancy for the biaxial yield stress can be found. To get a better fitting yield surface, without performing a large amount of experiments, our iterative FEMU procedure is utilized.

4 IDENTIFICATION PROCEDURE

For the identification procedure simulations of the performed experiments are set up. Here the biaxial tension test is chosen and modeled in the commercial Finite Element Method (FEM) software tool MSC.Marc. As having sheet metal, four-node, isoparametric, bilinear, plane-stress quadrilateral elements are utilized. The total amount of degrees of freedom is reduced by employing symmetric boundary conditions. The rolling direction is modeled through a rotation of the element coordinate system and the experimentally measured forces are applied as boundary condition, see fig. 3.

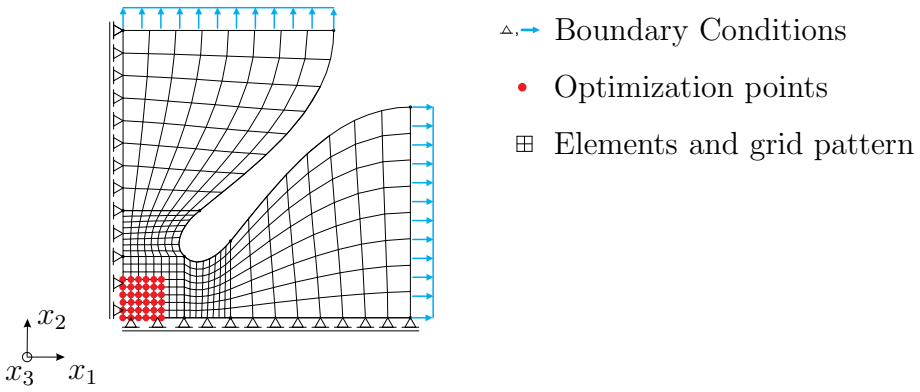

Figure 3: Modeled region of the biaxial tensile specimen

As we do have the measured full-field data sets and the simulations, the FEMU procedure for the parameter identification can be set up. Basic principles of the FEMU method and an overview over existing identification methods can be found in [2].
For our procedure the experimentally measured displacements u_1 and u_2 are required at a certain subset of nodes of the FE mesh. These optimization points are indicated in red in fig. 3. The values are calculated through a coordinate transformation and a data interpolation of the experimentally determined displacements.

The schedule of the FEMU procedure is depicted in fig. 4. It is controlled by an optimization routine which starts the FEMU procedure with a pre-defined set of initial material parameters. In our case the variational parameters are a_1, a_2, a_3 and a_6 of the plane stress Hill 1948 yield surface, see equation (7). With these parameters a FEM simu-

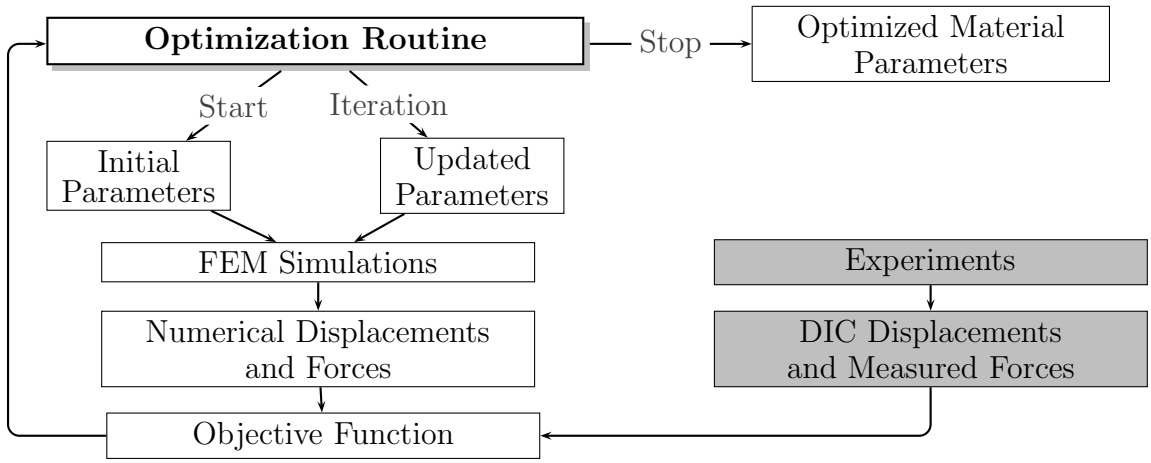

Figure 4: Schedule of the iterative FEMU procedure using experimental data

lation is run and the numerically and experimentally determined displacements and forces are processed by the objective function. Depending on the used optimization algorithm, a resulting vector or a scalar value is passed back to the optimization routine. If a certain stopping criterion is missed, the material parameters are updated and another iteration is initiated. Otherwise the optimized material parameters are identified which define the Hill 1948 yield surface.

The FEMU procedure is performed utilizing the biaxial tensile tests and their simulation.

5 PROCEDURE VERIFICATION

To verify the convergence of our identification procedure two optimization algorithms with different initial starting points are utilized [3]. The first algorithm is a gradient-free Nelder-Mead Simplex Method [4]. The utilized objective function $f(\boldsymbol{x}) = \Phi_{\mathrm{U}}(\boldsymbol{x}) + \Phi_{\mathrm{K}}(\boldsymbol{x})$ is a sum of the weighted least-squares sums of the experimentally and numerically determined displacements (10) and the forces (11).

$$\Phi_{\mathrm{U}}(\boldsymbol{x}) = \frac{1}{2NM} \sum_{i=1}^{M} \sum_{j=1}^{N} \sum_{k=1}^{2} w_{\mathrm{U},k} \left[(u_k^{(\mathrm{exp})})_{ij} - (u_k^{(\mathrm{num})}(\boldsymbol{x}))_{ij} \right]^2 \tag{10}$$

$$\Phi_{\mathrm{K}}(\boldsymbol{x}) = w_{\mathrm{K}} \frac{1}{M} \sum_{i=1}^{M} \left[(K^{(\mathrm{exp})})_i - (K^{(\mathrm{num})}(\boldsymbol{x}))_i \right]^2 \tag{11}$$

In the equations (10) and (11) $u_k^{(\ldots)}$ are the displacements, K are the forces and $w_{\mathrm{U},1}$, $w_{\mathrm{U},2}$ and w_{K} are the weighing factors. The indices stand for the steps in the numerical simulation (i), the number of optimization points (j) and the space directions (k).
The second optimization algorithm is the gradient-based Levenberg-Marquardt Trust Region Method [4]. An approximation of the objective function is minimized in a certain

Trust Region r, see equation (12).

$$\min_{\boldsymbol{s}} \frac{1}{2}\|\boldsymbol{J}(\boldsymbol{x})\boldsymbol{s} + \boldsymbol{v}(\boldsymbol{x})\|_2^2, \text{ subject to } \|\boldsymbol{s}\| \leq r \tag{12}$$

$$v_i(\boldsymbol{x}) = \begin{cases} w_{\mathrm{U},k}\left[(u_k^{(\mathrm{exp})})_i - (u_k^{(\mathrm{num})}(\boldsymbol{x}))_i\right], & \text{for } 1 \leq i < l. \\ w_{\mathrm{K}}\left[(K^{(\mathrm{exp})})_i - (K^{(\mathrm{num})}(\boldsymbol{x}))_i\right], & \text{for } l \leq i < m. \end{cases} \tag{13}$$

The parameter $v_i(\boldsymbol{x})$ is a column vector of the weighted least-squares sums of the forces and the displacements and $\boldsymbol{J}(\boldsymbol{x}) = \left[\frac{\partial v_j}{\partial x_i}\right]$ is its Jacobian. The value l is the number of steps times the number of optimization points and $(m-l)$ represents the number of steps. As no gradient is accessible in the used commercial FE code it is calculated through an evaluation of Finite Differences.

In order to show that the above described identification setup is reasonable and to test the FEMU procedure a numerical experiment is performed. An orthotropic Hill 1948 yield surface which is conform to the *Best-Fit* ellipse is defined. Boundary conditions equal to the measured ones of the biaxial tensile tests are applied and the resulting displacements and forces are recorded. Then a FEMU procedure is initiated. The numerically determined forces and displacements are taken as input-data and the parameters a_1, a_2, a_3 and a_6 are re-identified. Table 1 shows the pre-defined material parameters and the identified ones with the FEMU procedures with their standard deviations. Two runs were performed. In the first FEMU procedure the gradient-based Levenberg-Marquardt optimization algorithm is utilized. In order to verify the convergence of our procedure, three different initial starting parameter sets are employed, see fig. 5. The three runs converge to the same results with a small standard deviation (table 1). In the second FEMU cycle

Table 1: Identified material parameters of the numerical example from gradient-free and gradient-based methods with standard deviation

	a_1	a_2	a_3	a_6
Pre-defined Parameters	9.38e-01	9.49e-01	1.02e+00	1.10e+00
Ident. Param. gradient-based	9.40e-01	9.51e-01	1.02e+00	1.09e+00
Standard Deviation	1.82e-03	2.12e-03	2.77e-03	2.05e-02
Ident. Param. gradient-free	9.32e-01	9.43e-01	1.02e+00	1.09e+00
Standard Deviation	5.07e-03	5.42e-03	4.22e-03	3.29e-02

the gradient-free Nelder-Mead Simplex optimization algorithm is employed. This algorithm is started with three different initial material parameter sets. It converges to the values shown in table 1. However, the number of function evaluations needed to converge is higher than the one of the gradient-based algorithm and convergence is reached only if the initial parameters are within a small region around the optimal values.

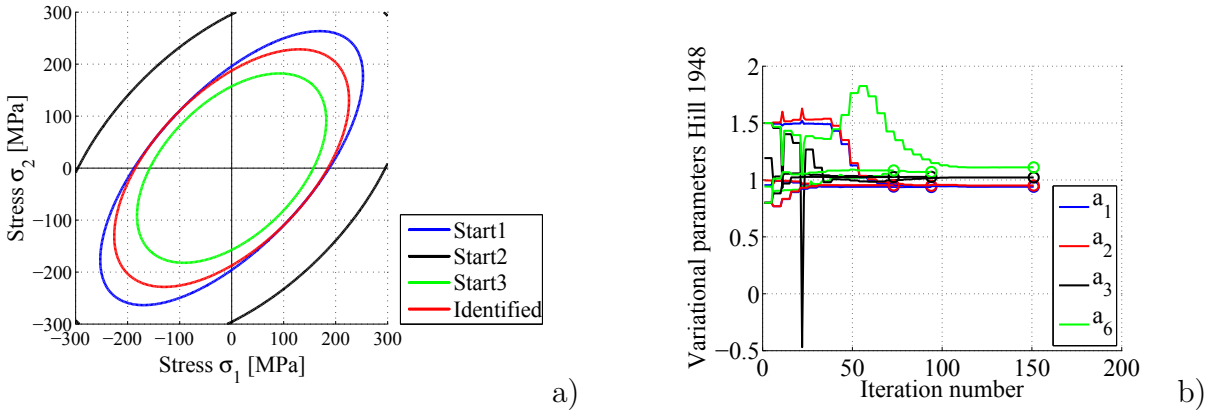

Figure 5: Numerical biaxial tension experiment, gradient-based method: **a)** Initial and identified yield surfaces. **b)** Variational parameters over iteration number.

6 IDENTIFIED PARAMETERS

Having verified that our FEMU procedure is capable of identifying the proper orthotropic plastic material parameters the experimentally determined displacements and forces of three biaxial tension tests are employed as input data. As in the numerical example the FEMU procedure is run with the two optimization algorithms starting from different initial material parameter sets. Fig. 6a) depicts that four different starting sets are utilized. Comparing fig. 6b) to fig. 5b) it is obvious that the convergence with the experimental data set is faster. This effect is caused by the inhomogeneities in the measured

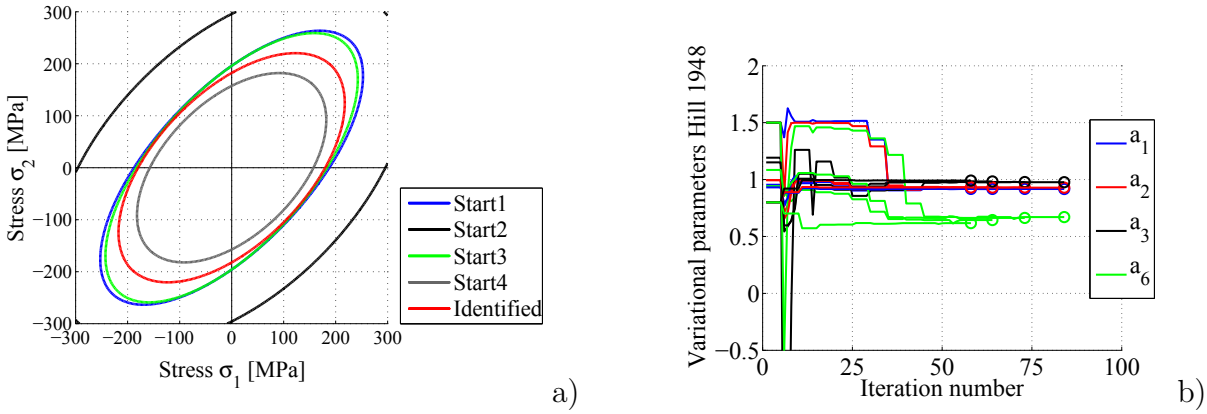

Figure 6: Biaxial tension experiment, gradient-based method: **a)** Initial and identified yield surfaces. **b)** Variational parameters over iteration number.

data. As being not perfectly biaxially loaded over all time steps, like in the numerical

example, and using three different experimental data sets in one FEMU procedure the iteration number decreases.
The identified material parameters for the Hill 1948 yield surface are written down in table 2. The standard deviations of the gradient-free optimization cycles are smaller than the gradient-based ones. However, convergence with the gradient-free method is reached only if good starting parameter sets are chosen.

Table 2: Identified material parameters of the experimental data sets from gradient-free and gradient-based methods with standard deviation

	a_1	a_2	a_3	a_6
Ident. Param. gradient-based	9.18E-01	9.30E-01	9.82E-01	6.49E-01
Standard Deviation	4.82E-04	6.28E-04	6.36E-03	2.37E-02
Ident. Param. gradient-free	9.18e-01	9.30e-01	9.78e-01	6.64e-01
Standard Deviation	1.61e-03	6.82e-04	1.57e-03	6.11e-03

Fig. 7 depicts the via FEMU identified Hill 1948 yield surface together with the *Lankford* and *Best-Fit* surfaces. Especially the biaxial yield stress is represented more accurately as through the *Lankford* yield surface. Therewith only biaxial tensile tests are

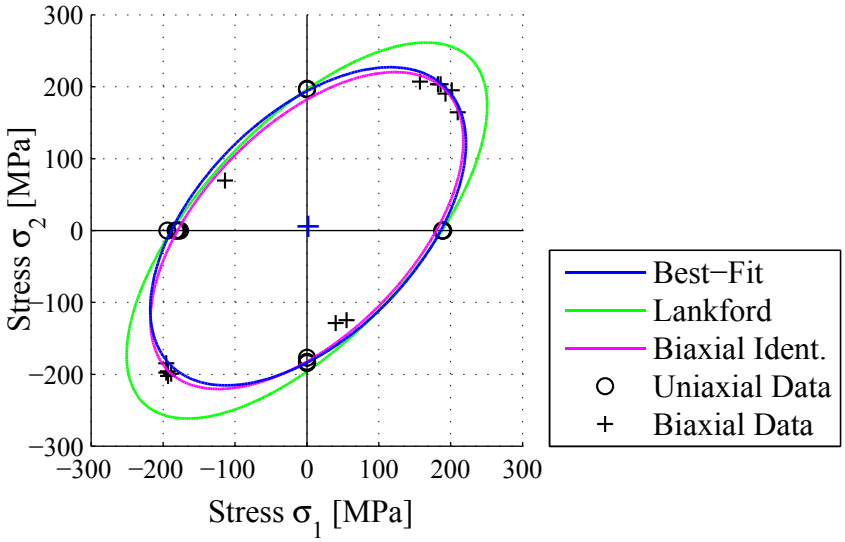

Figure 7: Identified Hill 1948 yield surface

needed to be able to identify the initial yield surface almost as precisely as performing various different tensile and compression experiments and fitting a general ellipse to this data set.

7 CONCLUSION AND OUTLOOK

The paper characterizes the orthotropic plastic behavior of the sheet steel DC04 through uni- and biaxial tension and compression tests. The plastic material parameters for the Hill 1948 yield criterion are identified directly and by an iterative FEMU procedure employing full-field displacement data and forces from experiments. Utilizing this FEMU procedure the amount of experiments needed for the material characterization is minimized, while the accurateness of the identified material parameters is maximized.
In order to accelerate the convergence and to increase the precision more complex specimen resulting in inhomogeneous loading are to be generated. Furthermore a combined anisotropic and kinematic hardening function has to be implemented to be able to represent the hardening behavior of the sheet metal more accurately.

Acknowledgements. This work is supported by the German Research Foundation (DFG) under the Transregional Collaborative Research Centre SFB/TR73.

REFERENCES

[1] Lecompte, D. et al., Identification of yield locus parameters of metals using inverse modeling and full field information, *Proc. of the 7th USNCTAM*, (2006).

[2] Avril, S. et al., Overview of Identification Methods of Mechanical Parameters Based on Full-field Measurements, *Exp. Mech.*, (2008) **48**: 381–402

[3] Chaparro, B.M. et al., Material parameters identification: Gradient-based, genetic and hybrid optimization algorithms, *Comp. Mater. Sci.*, (2008) **44**: 339–346.

[4] Nocedal, J., Wright, S. J., Numerical Optimization (Second Edition), *Springer Science+Business Media, New York*, (2006).

[5] Schmaltz, S., Willner, K., Optimization of elastic material parameters of sheet metal with FEMU and DIC, Submitted to: *PAMM*, (2011)

XI International Conference on Computational Plasticity. Fundamentals and Applications
COMPLAS XI
E. Oñate, D.R.J. Owen, D. Peric and B. Suárez (Eds)

INFLUENCE OF THE MATERIAL HARDENING MODEL ON THE SIMULATION RESULTS FOR THE EQUAL CHANNEL ANGULAR EXTRUSION – ECAE – PROCESS

R. PUFF[*] AND M. VAZ JR.[†]

[*] Whirlpool S.A.
Hermetic Compressor Unit – Embraco
e-mail: Rinaldo_Puff@embraco.com.br

[†] State University of Santa Catarina
Campus Universitário, 89223-100 Joinville, Brazil
e-mail: M.Vaz@joinville.udesc.br

Key words: Computational Plasticity, Forming Process, Equal Channel Angular Extrusion, Hardening Rules.

Abstract: The objective of this article is to present a comparison of the results achieved for the Equal Channel Angular Extrusion – ECAE – process, using a so called *"quick start"* approach, followed by simulation using material parameters defined by Swift´s [1] and Voce´s [2] relations. The comparison was made considering extrusion force, equivalent stresses and equivalent plastic strain quantities. Two angles (90 and 120^{o}), two channel concordance radii relations (0.2, 2 and 2, 5mm) and two friction coefficients (0.05 and 0.15) were used. ANSYS 12.1 commercial package was applied for this work.

1 INTRODUCTION

Equal Channel Angular Extrusion – ECAE – is a powerful deformation technique that was first studied and developed by Segal in 1981 [3]. It is an innovative process that allows engineers and researchers to obtain improved mechanical properties for some materials, by forcing its passage through an angular channel with constant cross section. The improvement of the mechanical properties is a result of severe plastic deformation with consequent grain refinement. The advantage of this process is that the cross section of the material remains constant, and reduced forming forces are required when comparing to other cold working processes.

In recent years many researchers have investigated angular extrusion processes under experimental and numerical perspectives. Some works are focused on experimental techniques aiming to optimize die and process conditions and evaluate different materials. Numerical techniques and commercial FEM – Finite Element Method – packages have also been used to study specific details of the process in order to obtain better processing conditions and improved material characteristics.

Krishnmaiah *et al.* [4] applied the ABACUS commercial FEM package to study the process for 99.8% pure normalized cooper, in order to evaluate the influence of the friction coefficient on the die filling and in other mechanical properties. In their analysis, four-node elements in plane strain mode, with reduced integration were applied.

Aour *et al.* [5] numerically investigated polymer extrusion applying MARC FEM software, using also four-node elements and reduced integration. The work aimed at evaluating the results of the process in the form of equivalent plastic strain and process characteristics, such as channel angle, internal and external radii, friction coefficient and number of passages through the die.

Son, Jin and Im [6] applied FEM to investigate the influence of friction on the load required to perform the extrusion through an angular channel, and also on the strain distribution in the workpiece. In this case a mixed formulation was used, with linear tetrahedral elements, and constant shear friction. In this work, a remeshing process based on an effective strain measure was also applied.

Lee *et al*. [7] performed a non-isothermal 3D simulation of a titanium workpiece to evaluate the effect of process parameters on the strain distribution. Rotation of the workpiece in 90 and 180º between passages through the die was considered. In the 3D formulation of the problem, hexahedral and tetrahedral elements were used to model the workpiece and channel, respectively. A constant friction model was used combined to a rigid-thermo-visco plastic constitutive relation for the material.

Hu, Zhang and Pan [8] used FEM to optimize the die structure for the ECAE process for a magnesium alloy (AZ31). In their work, a rigid die was considered, and the workpiece was described by an elastic-perfectly plastic material. As process parameters, the friction coefficient, angle between channels and internal and external radii were accounted for.

Nagasekhar *et al.* [9] performed a comparative analysis between FEM simulation and experimental approach in order to verify the effectiveness of the computational model. The authors used pure cooper, which mechanical properties were evaluated using a standard stress-strain test. The result of the work is focused on the load required to perform the process. The simulation was performed using explicit 3D ABACUS software. Some process parameters, like the Coulomb friction coefficient, were also varied through the analysis. The authors also applied tetrahedral elements with reduced integration and adaptive meshing.

Kaushik, Karaman and Srinivasa [10] used FEM simulation to study the Cooper powder pressing with the ECAE process. In their work, the explicit ABACUS software was used. The material porosity was modeled using the Gurson [11] and Duva & Crow [12] models. The authors used the friction coefficient and interaction conditions as process parameters. They applied 2D and 3D formulations to evaluate specific process details.

Semiatin and Delo [13], studied the deformation and failure of several difficult-to-work alloys, like commercial-purity titanium and AISI 4340 steel during ECAE process. Their work was mostly experimental, but FEM was applied in order to study specific failure modes and the effects of chilling on non-uniform flow during non-isothermal ECAE.

Yang and Lee [14], used the commercial package MARC to analyze strain conditions after ECAE. They varied the channel angle and the extrusion direction during consecutive passages through the process. The effect of friction was also evaluated.

As it can be noticed, numerous works and analysis have been performed in recent years using FEM simulation as the main analysis tool. Different classes of materials were evaluated,

and, in certain cases, experimental material evaluation was performed in advance to verify their mechanical properties. In most cases, the analysis aims to assess process characteristics for the different materials using numerical approach. In addition, the brief survey showed that, in simulations using a single passage, the main parameters that affect the workability of the materials in general, are the angle between the channels, the friction coefficient and the internal and external concordance radii.

In the industry perspective, in the search for new materials, optimized components and new strategies to design metal forming operations, oftentimes research engineers are confronted with no detailed material data to start the tooling development. In such conditions, it is not uncommon to use material properties, such as Young's modulus, Poisson's ratio, yield and ultimate stresses and elongation at rupture, obtained from general material libraries, tables, standards and even internet sources. This strategy is sometimes referred as "*quick start*" and has been used when no stress-strain curve for the material is available. For sure, there are some errors to be considered when taking this approach, instead of devising experiments to evaluate mechanical parameters of the material, and yield stress curves, such as Swift´s [1] and Voce´s [2] relations. This activity takes time and consumes laboratory resources.

The objective of this article is to present and discuss a comparison of numerical experiments performed for a given carbon steel, using constitutive parameters determined via classical approaches and parameter identification techniques. The Swift´s [1] parameters were determined using tensile tests by assuming uniform stress-strain distribution within the specimen, whereas a parameter identification technique [15] was used in conjunction with a modified Voce´s [2] equation.

2 HARDENING MODELS

The *"quick start"* using FEM usually considers two hardening models: elastic-perfectly plastic and bilinear hardening [16]. The former requires only three properties, which can be easily found for general materials in many references (books and internet sites): the Young's modulus, Poisson's ratio and Yield Strength. The model considers that, once the equivalent stress in the simulation reaches the material yield stress, the material presents perfect plasticity. The latter requires two additional properties: Ultimate Stress and Elongation at breakage. This makes it possible to establish the bilinear hardening model for the material, computing the Tangent Hardening Modulus and approximating the real material hardening behaviour by two linear curves, as shown in Figure 1.

The material chosen for this analysis is the same used in Stahlschmidt *et al*. [17], which is a cold rolled carbon steel without further heat treatment. In the work, the authors used a parameter identification methodology based on optimization, to determine hardening parameters of a modified Voce [2] yield stress curve. The basic properties considered for the *"quick start"* hardening models were obtained from MatWeb website [18] and are presented in the Table 1.

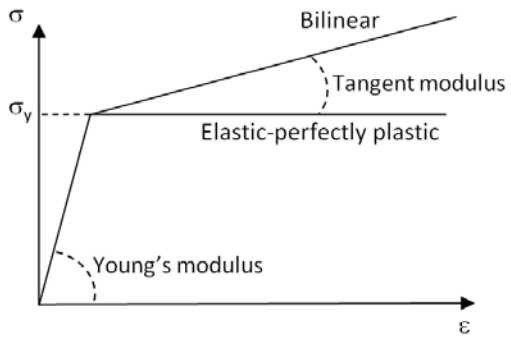

Figure 1: Two "*quick start*" approaches considered in the analysis.

Table 1: Mechanical properties for the "*quick start*" approach.

Material	Symbol	Value
Young Modulus	E	200GPa
Poisson Ratio	ν	0.3
Yield Stress	σ_Y	530MPa
Ultimate Stress	U	625MPa
Elongation	e	12%

According to [17], the Swift's [1] hardening model is defined as:

$$\sigma_y = \sigma_i \left(\varepsilon_0 + \varepsilon_p\right)^n , \tag{1}$$

where σ_i, ε_0 and n are the material parameters. Also from the same reference [17], Voce's modified hardening model is defined as:

$$\sigma_y = \sigma_0 + \zeta\varepsilon_p + \left(\sigma_\infty - \sigma_0\right)\left[1 - \exp\left(-\delta\varepsilon_p\right)\right] , \tag{2}$$

in which σ_0, σ_∞, δ and ζ are the hardening parameters obtained by an identification technique based on an Hybrid Genetic–BFGS optimization method [17]. Table 2 shows the hardening parameters for both equations, determined by using tensile tests with specimens prepared according to the Brazilian NBR-ISO 6892 standard.

Table 2: Material parameters identified by Stahlschmidt *et al*. [17], for the cold rolled steel used in this analysis.

Swift's yield curve		Voce's yield curve	
σ_i	1175.7 MPa	σ_0	425.9 MPa
ε_0	0.0018733*	σ_∞	720.66 MPa
n	0.1821	δ	34.9928
		ζ	552.25 MPa

*value corrected to accomplish for the elastic curve

3 SIMULATION DETAILS

All the simulations were performed with the use of the commercial FEM software ANSYS, version 12.1. A 2D approach using axis-symmetric formulation was used to model the NBR-ISO specimen, and plane strain for the ECAE process. The geometry selected for the ECAE workpiece was a square section with 10mm edge, and length of 40mm. The extrusion distance inside the die was 35mm in order to achieve a significant portion of the workpiece extruded. The element used in the simulations was an eight-node, non-linear quadratic element, referenced in ANSYS [16] as PLANE183. The die was modeled as rigid walls without heat transfer. Thermal effects were also not considered in the workpiece. The contact between the workpiece and die walls was modeled using Augmented Lagrangean´s Method [16], which is a combination of the pure penalty method in the tangential direction and pure Lagrange's Method in the normal direction [16]. Initially, it uses the contact stiffness state in the equilibrium. Afterwards, the resulting penetration is minimized by using the Lagrangean part of the algorithm. Coulomb friction was used to model the friction between the workpiece and die, which allows shear stresses on both contact surfaces.

4 RESULTS AND DISCUSSION

4.1 Results for the NBR-ISO workpiece

As a first analysis, in order to evaluate comparatively the different hardening rules, a simulation was performed for one of the geometries evaluated by Stahlschmidt *et al*. [17]. Figure 2 shows results for the equivalent plastic strain, plotted in the final stage of deformation. It is possible to observe that Voce´s model was the only one that could truly predict the actual deformation process of the workpiece. This is mainly because it is able to predict the final deformation region of the stress/strain curve, in which there is the neck formation and consequently the stress reduction. Nevertheless, it is also important to evaluate the loading force, once it is a major feature in stress analysis carried out by engineers in industry. Therefore, Figure 3 presents the comparison among the four models in terms of Force x Elongation. In this case, one first observation is that the elastic-perfectly plastic and bilinear models predict loading forces unrealistically smaller than the forces measured in the tensile tests [17]. As already observed by Stahlschmidt *et al*. [17], use of Swift´s model brings a better correlation, and Voce's model provides the best numerical results. Due to the best agreement with the experiments, when addressing the ECAE process, the latter should be considered as the reference when comparing the results obtained by using the other yield curves.

4.2 Simulation of the ECAE process

Most references describe the main influencing variables on the ECAE process as the angle between the channels, the inner and outer radii and the friction coefficient between the workpiece and the channel walls. According to the analysis performed by Krishnmaiah *et al.* [4]; Son, Jin and Im [6] and Hu, Zhang and Pan [8], a *"soft"* process would be performed using an angle of 120^{o} together with larger inner and outer radii and low friction coefficient. Considering the aforementioned conditions, two cases were evaluated, as indicated in Table 3.

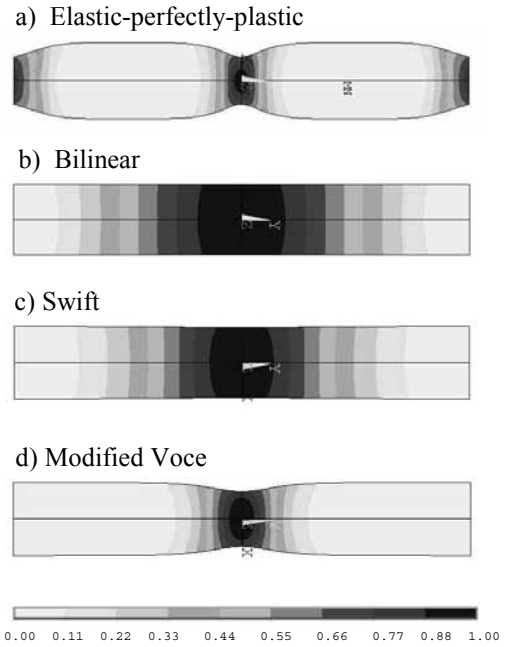

Figure 2: Normalized equivalent strain, $(\varepsilon - \varepsilon_{min}) / (\varepsilon_{max} - \varepsilon_{min})$, plotted on the deformed configuration.

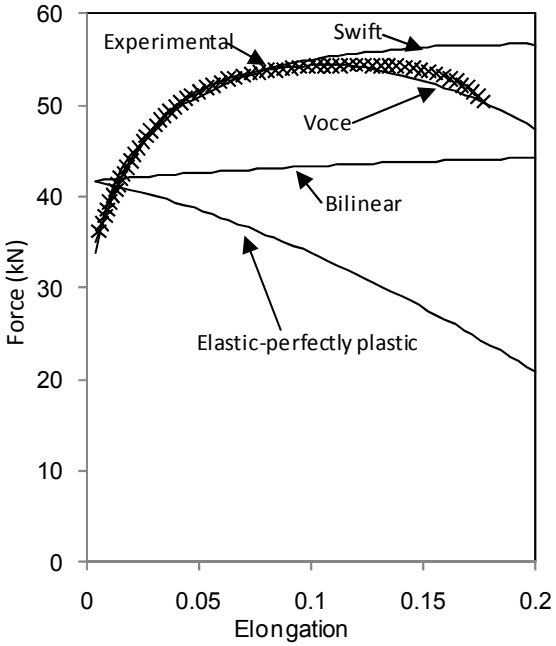

Figure 3: Force x Elongation curves for the hardening models compared to the experimental results [17].

Table 3: The *"soft"* and *"hard"* simulation parameters chosen for the comparison.

Parameter	*"soft"* process	*"hard"* process
Angle	120^o	90^o
Radii	2 and 5	0.2 and 2
Friction coefficient	0.05	0.15

The evaluated results were:

- Equivalent plastic strain and von Mises stress plotted on the deformed configuration.
- The extruding force and integrated work.
- The equivalent strain at the middle of the workpiece in the short and the long direction.
- The equivalent von Mises stress in the same directions.

Figure 4 presents the equivalent plastic strain and von Mises stress plotted on the deformed configuration for the *"soft"* process simulation. It can be clearly observed the region where the shear of the workpiece is taking place. Also, there is some major strain concentration at the upper side of it. One can also notice high von Mises stress concentration at the shear region and at the upper side.

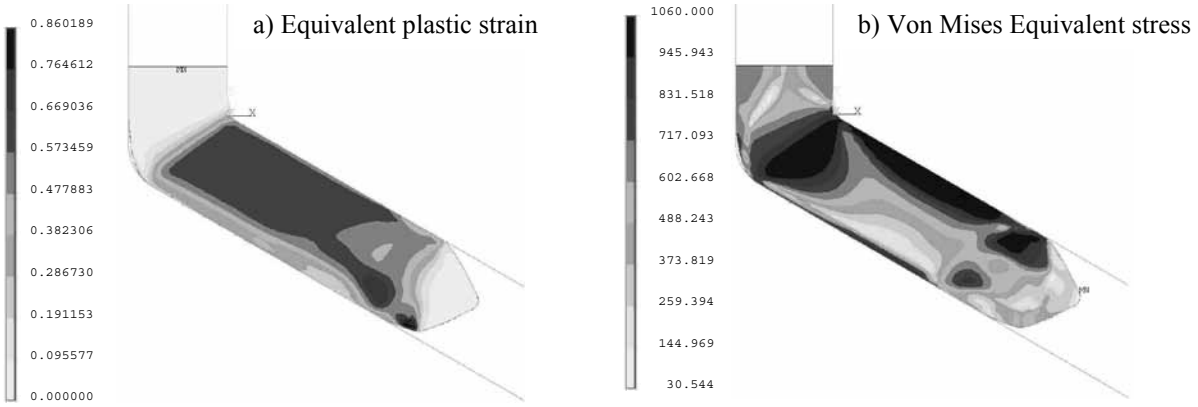

Figure 4: Results for the *"soft"* condition plotted on the deformed configuration for the modified Voce's model.

Figure 5 presents the equivalent plastic strain and equivalent von Mises stress plotted on the deformed configuration for the *"hard"* process simulation. In this case, the 45^{o} shear of the workpiece can be clearly observed, as well as the much higher strains and stresses compared to the *"soft"* condition. The maximum plastic strain achieved in this case is around 1.6, against 0.86 for the *"soft"* condition. The maximum von Mises stress is 1468 MPa, against 1060 MPa for the *"soft"* condition. It shows that the chosen *"soft"* and *"hard"* conditions are representative for the purpose of this analysis.

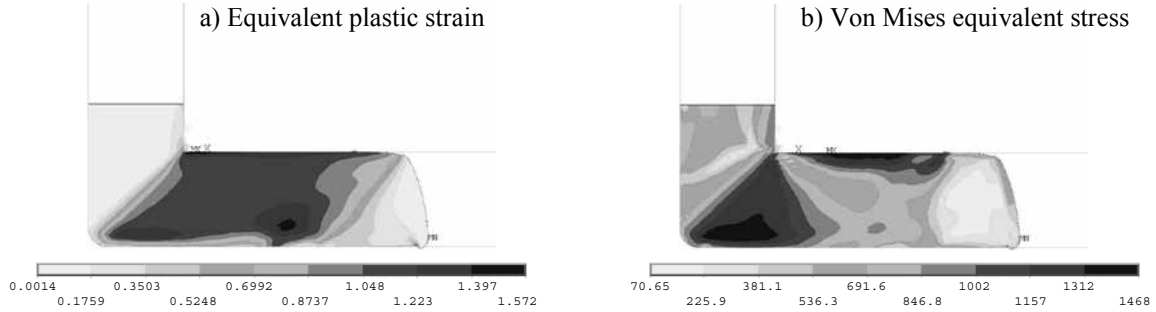

Figure 5: Results for the *"hard"* condition plotted on the deformed configuration for the modified Voce's model.

When comparing the results of the extrusion force for the two conditions and four hardening models considered, it can be observed in the figure 6 that, as expected, there is a huge difference between the *"soft"* and *"hard"* maximum forces necessary for performing the extrusion. For the *"soft"* condition, Figure 6a, Swift's model presents a fairly good agreement with modified Voce's equation, considering the latter as reference. Nevertheless, the bilinear model presented some qualitative similarity, but a lower force level. In the same case, elastic-perfectly plastic's model presented much lower results. The force results for the *"hard"* condition are presented in Figure 6b. It can be observed that Swift´s and Bilinear models present good correlation with Voce's equation, however, the results for the elastic-

perfectly plastic's model were markedly unrealistic.

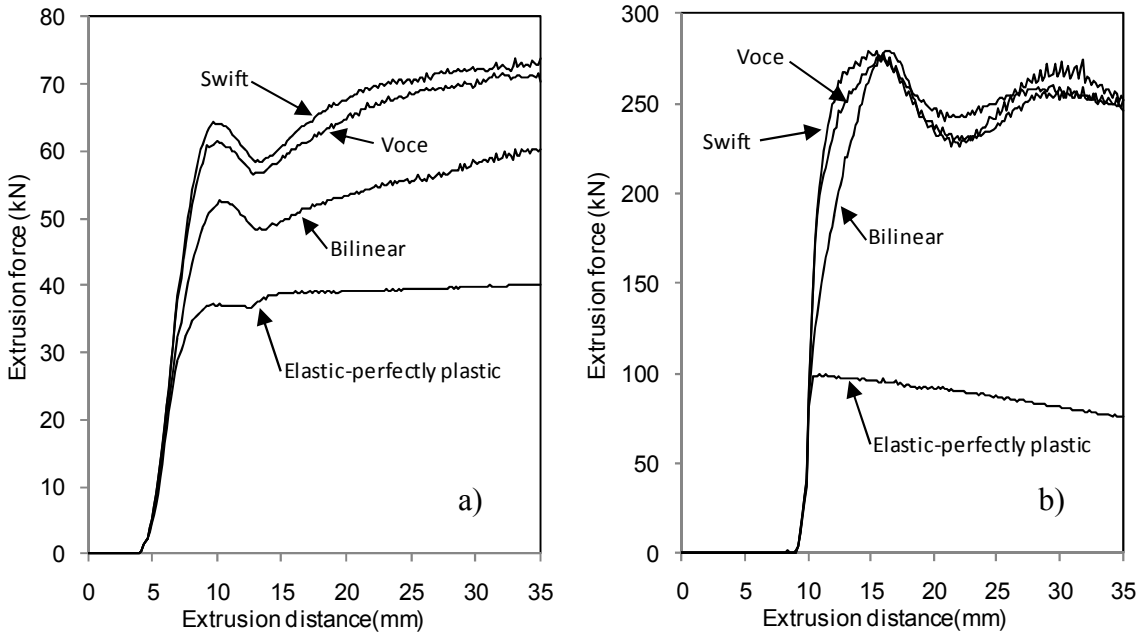

Figure 6: Comparison of the simulated extruding force using the four hardening models. a) *"soft"* condition. b) *"hard"* condition.

Table 4: Simulated extrusion work for the two conditions and four hardening models.

	Extrusion work [J]						
Condition	**Voce**	**Swift**	**Difference [%]**	**Bilinear**	**Difference [%]**	**Elastic-perfectly plastic**	**Difference [%]**
"soft"	12.3	12.9	4.9	10.6	-13.8	7.0	-43.1
"hard"	44.1	43.1	-2.3	44.0	-0.2	13.3	-69.8

As a resume of the observations, it is better to represent the total extrusion work, shown comparatively in Table 4. It can be observed that Swift´s and Bilinear models presented acceptable differences lower than 5% in the most cases. For the *"soft"* condition, Bilinear model presented a higher discrepancy of 13.8%, but still acceptable for a *"quick start"* approach. In the other hand, Elastic-perfectly plastic model presented discrepancies higher than 40%, which are completely unacceptable.

Figure 7a and b, show the equivalent plastic strain distribution along the centerlines of the workpiece for the *"soft"* condition. It can be observed that, for both horizontal and vertical directions, there is a good agreement of Voce's, Swift's and Bilinear models. Elastic-perfectly plastic model predicts higer plastic strain levels, and a more uniform distribution. The reason lies on the fact that once the yield stress is reached during the simulation process, a further increase on the load would cause continuous plastic deformation without any hardening. For the *"hard"* condition, Figure 7c and d, one may notice that in the horizontal direction, the plastic strain at the lower and upper regions of the workpiece was more affected by the

models, whereas a smaller effect was observed inside the workpiece. In the vertical direction, major differences were found at the lower part, which is the region directly affected by the initial deformation experienced by the workpiece when introduced in the angular channel. It is reasonable to expect that the hardening rule is more influent in this region.

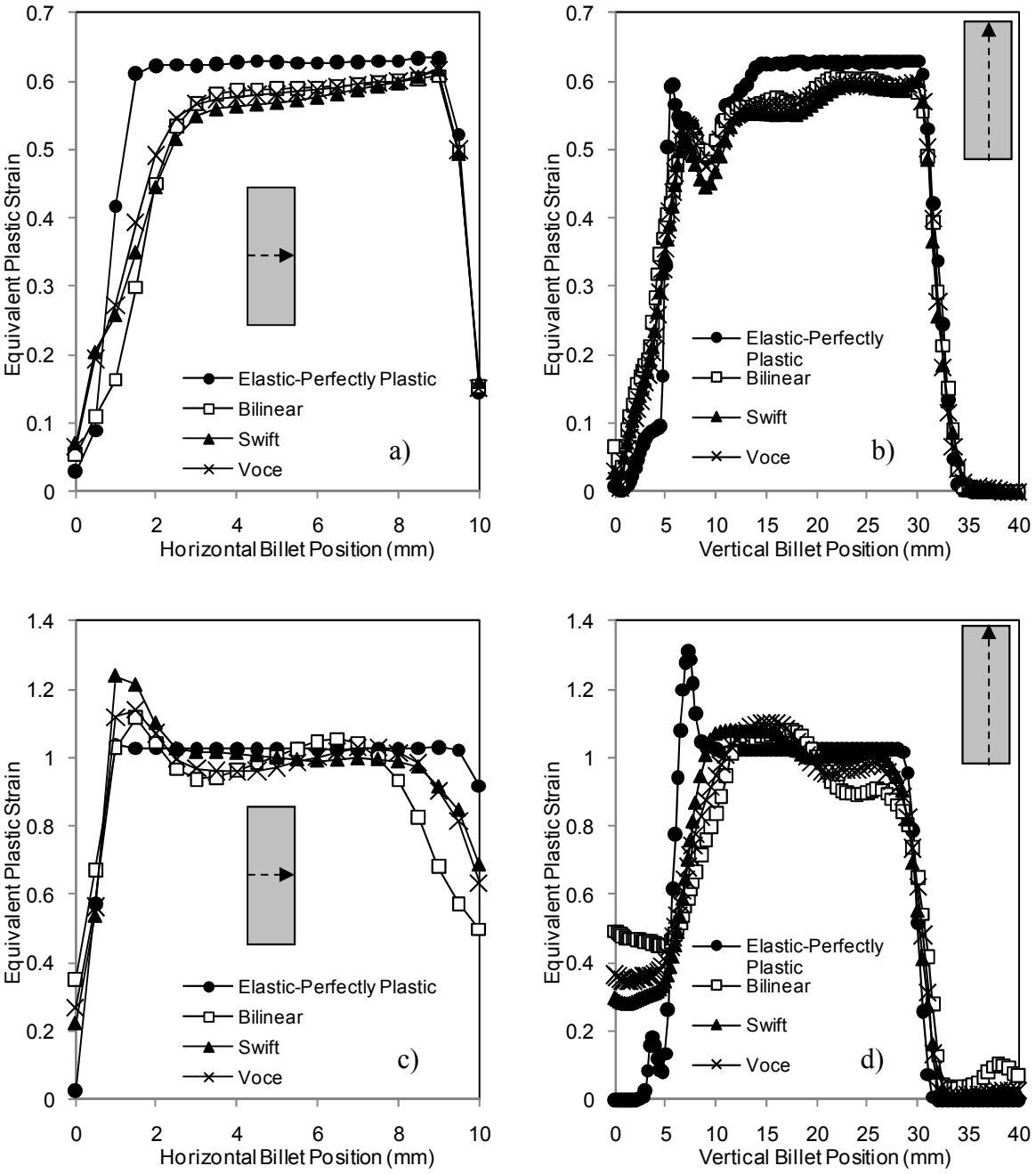

Figure 7: Equivalent plastic strain for the two conditions along the horizontal and vertical centerlines. a) *"Soft"* condition – horizontal. b) *"Soft"* condition – vertical. c) *"Hard"* condition – horizontal. d) *"Hard"* condition – vertical.

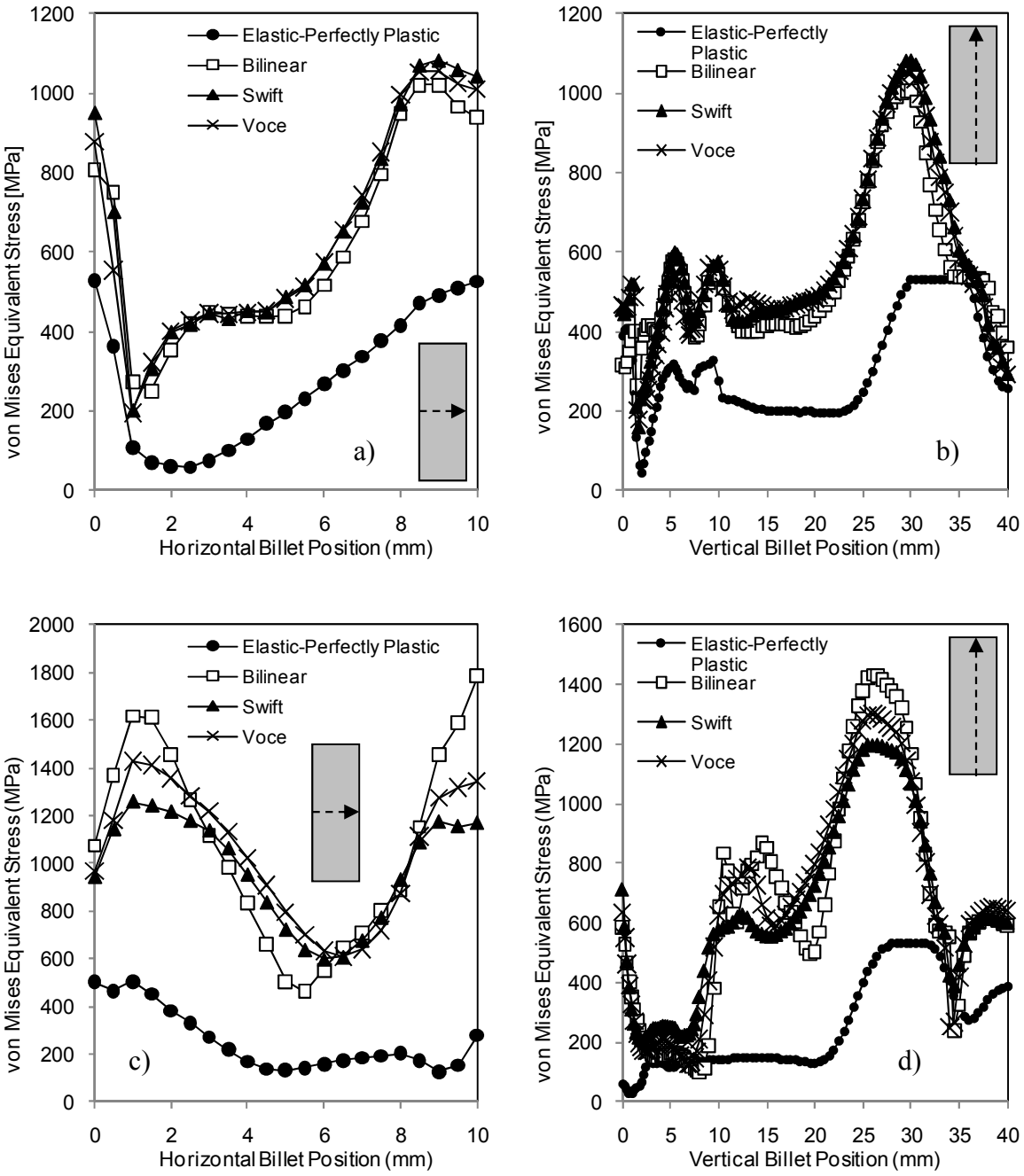

Figure 8: von Mises equivalent stress for the two conditions along the horizontal and vertical centerlines. a) *"Soft"* condition – horizontal. b) *"Soft"* condition – vertical. c) *"Hard"* condition – horizontal. d) *"Hard"* condition – vertical.

The comparison has also been performed for the stress results, once, in many cases, it is important to evaluate the residual stresses present in the workpiece after each passage through the angular channel. It can be observed in Figure 8a and b that, for the *"soft"* condition, Swift's and Bilinear models yield good agreement with the reference along horizontal and

vertical directions; however the Elastic-perfectly plastic model presented a huge difference. The same behaviour can be observed in Figure 8c and d for the *"hard"* condition. Although presenting much higher stress levels, there is also for this condition a good agreement with the reference for Swift's and Bilinear models, whilst the Elastic-perfectly plastic material presented larger differences.

12 CONCLUSIONS

Within the industrial perspective, when conceiving new forming operations, designing new mechanical components or using new materials, research engineers generally use a modeling strategy known as "*quick start*". In such cases, in a first stage, material is described in a simplified manner in order to obtain preliminary results used to validate or not the design concept. In a second stage, experiments aiming at determining material parameters are designed and new round of simulations are performed aiming at achieving the primary design objectives. This work is inserted within this framework, which aims to assess simplified material models against a more complex constitutive relation and determine how accurate are the results obtained using such models.

- The ECAE process was used in this article to compare four different yield curves: modified Voce, Swift, Bilinear and Elastic-perfectly plastic. The main objective was to determine whether a simpler yield curve could be used in conjunction with the ECAE process, which in turn, is recommended to achieving better mechanical properties for materials.

- Voce's and Swift's parameters were taken from Stahlschmidt *et al*. [17], which were determined by applying optimization methods. In the reference, Voce's hardening model presented the best agreement with the experimental results and was used in the present work as a reference for comparison.

- The results were compared based on three information normally required during the planning phase of the ECAE process: the required extrusion force and work, plastic strains and residual stresses present in the workpiece.

- Swift's equation presented good correlation with the reference (modified Voce) in most cases, but as well as the latter, requires initial experimental testing for determining parameters for the simulation.

- The Bilinear model requires only the knowledge of five properties: Young Modulus; Poisson's ratio; Yield and Ultimate stresses and elongation, which, in most cases, can easily be found in the literature or web sites. This approximation presented a fairly good correlation with Voce's model. Therefore, it is a good choice for this initial evaluation of the ECAE process and its desired results.

- The elastic-perfectly plastic´s model presented a very poor agreement with Voce's results, thereby indicating that it is a bad choice, mainly for the type of material considered in the analysis. Some hardening needs to be considered with the risk of making poor predictions for the process planning.

REFERENCES

[1] Swift, H.W. Plastic instability under plane stress. *J Mech. Physics Solids* (1952) **1**:1-18.

[2] Voce, E. The relationship between stress and strain for homogeneous deformation, *J. Inst.*

Metals (1948), **74**:537-562.
[3] Segal, V.M. Materials processing by simple shear, *Mat. Sci. Eng*. (1995) **A197**:157-164.
[4] Krishnaiah, A.; Kumaran, K.; Chakkingal, U. and Venugopal, P., Finite element analysis of equal channel angular extrusion (ECAE) process, *Metallurgical and Materials Engineering* (2004) **1**:1-8.
[5] Aour, B.; Zairi, F.; Gloaguen, J.; Naitabdelaziz, M. and Lefebvre, J. Numerical investigation on equal channel angular extrusion process of polymers, *Computational Materials Science* (2006) **37(4)**:491-506.
[6] Son, I.H.; Jin, Y.G. and Im, Y.T. Finite element investigations of friction condition in equal channel angular extrusion, *Journal of Achievements in Materials and Manufacturing Engineering* (2006) **17(1-2) Jul-Aug**:285-288.
[7] Lee, J.; Son, I.; Im, Y.; Chon, S. and Park, J. Design guideline of multi-pass equal channel angular extrusion for uniform strain distribution, *Journal of Materials Processing Technology* (2007) **191(1-3)**:39-43.
[8] Hu, H.-jun; Zhang, D.-fei and Pan, F.-sheng. Die structure optimization of equal channel angular extrusion for AZ31 magnesium alloy based on finite element method, *Transactions of Nonferrous Metals Society of China* (2010) **20(2)**:259-266.
[9] Nagasekhar, A.V.; Yoon, S.C.; Tick-Hon, Y. and Kim, H.S. An experimental verification of the finite element modeling of equal channel angular pressing, *Computational Materials Science* (2009) **46(2)**:347-351.
[10] Kaushik, A.; Karaman, I. and Srinivasa, A.R. Simulation of powder compaction using equal channel angular extrusion at room temperature: Comparison of two constitutive theories, *International Journal* (2009) **1(1)**:211-226.
[11] Gurson, A.L. Continuum theory of ductile rupture by void nucleation and growth: Part I – Yeld criteria and flow rules for porous ductile materials, *Journal of Engineering Materials and Technology* (1977) **99**:2-15.
[12] Duva, J.M. and Crow, P.D. The densification of powders by power-law creep during hot isostatic pressing, *Acta Metallurgica Et Materialia* (1992) **40(1)**:31-35.
[13] Semiatin, S. and Delo, D., Equal channel angular extrusion of difficult-to-work alloys, *Materials & Design* (2000) **21(4)**:311-322.
[14] Yang, Y. and Lee, S. Finite element analysis of strain conditions after equal channel angular extrusion, *Journal of Materials Processing Technology* (2003) **140(1-3)**:583-587.
[15] Stahlschmidt, J. *Parameter Identification of Elastic-Plastic Parameters*, M.Eng. Dissertation, UDESC, Joinville, (2010).
[16] ANSYS Manual, Release 12.0 - © (2009).
[17] Stahlschmidt, J.; Vaz Jr., M.; Muñoz-Rojas, P.A. and Cardoso, E.L. Uma estratégia numérico-experimental para a determinação de parâmatros materiais, *6th Brazilian Conference on Manufacturing Engineering* (2011).
[18] AISI 1045 Steel, cold drawn, 19-32 mm (0.75-1.25 in) round, <http://www.matweb.com/search/DataSheet.aspx?MatGUID=cbe4fd0a73cf4690853935f52d910784&ckck=1>, visited on Apr/30th/2011.

XI International Conference on Computational Plasticity. Fundamentals and Applications
COMPLAS XI
E. Oñate, D.R.J. Owen, D. Peric and B. Suárez (Eds)

JOHNSON-COOK PARAMETER IDENTIFICATION FOR AISI-304 MACHINING THROUGH NELDER MEAD METHOD

C. M. GIORGIO BORT*, P. BOSETTI* AND S. BRUSCHI*

*Department of Mechanical and Structural Engineering (DIMS)
University of Trento
Via Mesiano 77, 38123 Trento, Italy
e-mail: dims@ing.unitn.it, www.unitn.it/en/dims

Key words: Orthogonal Cutting, Parameter identification, Johnson Cook, Nelder Mead Method

Abstract. The finite elements method (FEM) represents a useful tool for simulating machining processes, nevertheless numerical models are very sensible to the adopted material model and related constants. The paper reports a novel approach for the identification of the material parameters of the Johnson-Cook (JC) plasticity model, which is currently utilized in modeling material behavior during machining operations thanks to its capability to account for the material sensitivity to strain, strain rate, and temperature. The presented approach is based on the use of the Nelder Mead Method (NMM) to identify both the parameters of the simplified JC model and the friction factor of the Tresca law. NMM is a non-linear heuristic technique that affords to find local minima. Compared to the evolutionary approach typically used in parameter identification, the main benefit of this method consists in the low number of iterations necessary to achieve a good match between the experimental and numerical process outputs.
The reference process is the Orthogonal Tube Cutting (OTC) test of AISI 304 thin tubes. Although the AISI 304 is a well-known material and many data are available in literature, its reported JC parameters are characterized by a large dispersion, making necessary to develop a robust parameter identification procedure to have reliable material data to calibrate the numerical model.
OTC tests were carried out on an instrumented lathe and their numerical model developed through the commercial FEM software Deform^{TM} 2D v.10.1. The optimization problem was implemented in the language programming Ruby. The comparison between experiments and numerical results was made with regard to the cutting force, the tool-chip contact length, and the chip morphology.

1 INTRODUCTION

In the last decades, many efforts have been made in modeling machining processes, and different approaches have been used implying the development of statistical processes, theoretical and numerical models. Among the latter, the finite elements method (FEM) is the more utilized, since it is capable to handle a large number of process inputs and to represent as well several outputs, such as the temperature distribution in the workpiece, chip and tool, forces, chip morphology, residual stresses [1], and tool wear [2]. On the contrary, numerical models of machining operations can be computationally expensive and are highly sensible to the model parameters, especially as regards the rheological and tribological data. In machining operations the workpiece is in fact highly stressed in the primary and secondary shear zones, and it undergoes strains higher than 200 % at strain rates of more than 10^6 $1/s$. However rheological and tribological data are generally unknown at high strains and strain rates, therefore it is necessary to develop a robust strategy to identify these model unknowns.
The workpiece flow stress model commonly used for machining simulations is the Johnson-Cook constitutive equation [3]. It correlates the flow stress to the workpiece temperature, strain, strain rate, and is represented by the following equation:

$$\sigma(T, \epsilon, \dot{\epsilon}) = (A + B\,\epsilon^n)\left[1 + C\,ln\left(\frac{\dot{\epsilon}}{\dot{\epsilon}_0}\right)\right]\left[1 - \left(\frac{T - T_r}{T_m - T_r}\right)^m\right] \tag{1}$$

where T (^oC) is the workpiece temperature, T_m (^oC) the melting temperature, T_r (^oC) the room temperature, ϵ the plastic strain, $\dot{\epsilon}$ ($1/s$) the strain rate, A (MPa) the yield strength, B (MPa) and n the hardening modulus and the hardening coefficient respectively, C the strain rate sensitivity, and m the thermal softening coefficient. The friction model commonly used for machining simulations is the Tresca law due to high local pressure involved at the tool-workpiece contact. The Tresca law is represented by:

$$\tau = t\,\tau_{max} \tag{2}$$

where τ (MPa) is the tangential friction stress, τ_{max} (MPa) the maximum admissible tangential stress, and t the friction factor.

The reference process utilized in this paper for the identification of the Johnson Cook parameters is the Orthogonal Tube Cutting (OTC) test carried out on $AISI\,304$ thin tubes. The scientific literature reports different approaches for the identification of the Johnson Cook parameters of the stainless steel $AISI\,304$. Chandraserkaran *et al.* [4] demonstrated that the Split-Hopkinson pressure bar test can achieve a limited range of strains and, for this reason, this kind of test cannot be used in the parameter identification of the material model for machining processes. They stated that to identify the correct flow stress law at high strains and strain rates a combination between numerical simulations and experimental tests must be used. Lee *et al.* [5] combined quasi static and dynamic compressive tests with FEM simulations to fit the measured flow stress with the

Johnson Cook law, at three different strain rates, up to 10^3 $1/s$. Higher strain rates, up to 5×10^4 $1/s$, where achieved by Vural *et al.* [6] developing a new shear compression specimen. Nevertheless, even when modeling the same material, it is possible to find in literature that different sets of material parameters have been used in process simulations [7]-[9].
The sets of the JC parameters found in literature for the stainless steel AISI 304 were used in the FEM simulations of the OTC test, and a comparison between their outputs and the OTC results is presented in this study. The observable parameters are the cutting force, the chip thickness and curvature, and the tool-chip contact length. Very different results were obtained, proving that it is necessary to identify the material model parameters and the tribological factor through a more robust method. Shrot [11] utilized FEM machining simulations and the Levenberg-Marquardt optimization algorithm to identify the coefficients A, B and n of the equation 1. The hypotheses assumed in the Shrot's study deal with the process considered adiabatic and the neglection of the friction phenomena, which, however, can hardly describe the mechanical phenomena characterizing the real cutting processes.
The purpose of this work is to develop an approach dedicated to the simultaneous identification of the rheological and tribological parameters to be implemented in the numerical model of a machining operation. This is achieved by minimizing, through a customized Nelder Mead Method (NMM) [12], the sum square error between the calculated cutting force and chip morphology through FEM simulations, and those measured in an experimental OTC test. NMM is a simplex-based technique that can require a low number of iterations to converge to local minima, compared to the derivatives and evolutionary approaches typically used in parameter identification. On the contrary, NMM is highly sensible to the initial simplex, thus some considerations were made in choosing the starting simplex.

2 EXPERIMENTAL SET-UP

The OTC test consists on a rotating tube and a translating tool with a feed rate orthogonal to the cutting speed. The test was carried out on an industrial lathe (figure 1). The tube was made of $AISI\,304$, its external diameter was 50 mm and its wall 1 mm thick. The tool was made of high speed steel (HSS) with a TiN coating, its rake angle was $18° \pm 2°$ and its inclination angle zero. The process parameters were chosen accordingly to the data sheet given by the tool manufacturer, setting the cutting speed to 26,77 m/min, and feed rate to 0.09 mm/rev.
The chosen observables parameters were the cutting force, the chip thickness and curvature, and the tool-chip contact length. The force was measured by means of a Kistler™ multicomponent dynamometer $9257B$ placed below the toolholder (figure 1). The acquired average value of the cutting force was 182 N, identified at the attainment of the test steady state condition. The chip thickness and curvature were evaluated at the

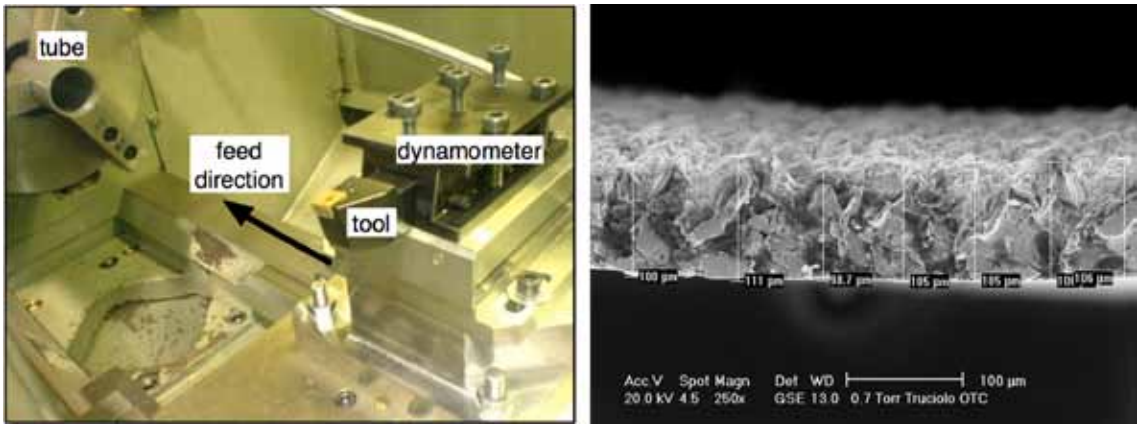

Figure 1: The experimental set-up used in the OTC test (left) and the measured chip (right).

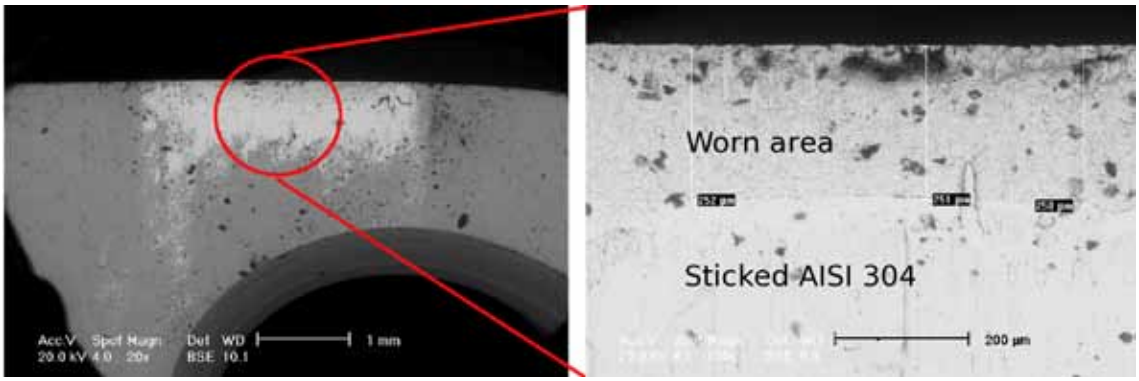

Figure 2: The tool flank at ESEM microscope (left) with a particular of the tool wear with the worn area and the $AISI\,304$ sticking zone (right).

ESEM microscope: seven different sections of the chip were considered measuring an average thickness of 105 μm, while the curvature radius was 1.51 mm^{-1}. Also the tool-chip contact length was measured at the ESEM microscope, by considering the tool wear after several cuts. In figure 2 it is possible to associate the clearest zone on the insert flank to the worn area. Focussing the attention to the wear zone, two different regions can be distinguished: the one nearest to the cutting edge is the real worn area in which the TiN coating has been removed, while the second one is evident due to the sticked $AISI\,304$ deposited during the cut. The latter is not a worn zone and for this reason is not considered in the measurements. The average chip contact length was 250 μm.

3 NUMERICAL MODEL

Due to the reduced feed rate compared to the thickness of the tube, it was possible to assume a plane strain condition for the above described machining process. A bi-dimensional

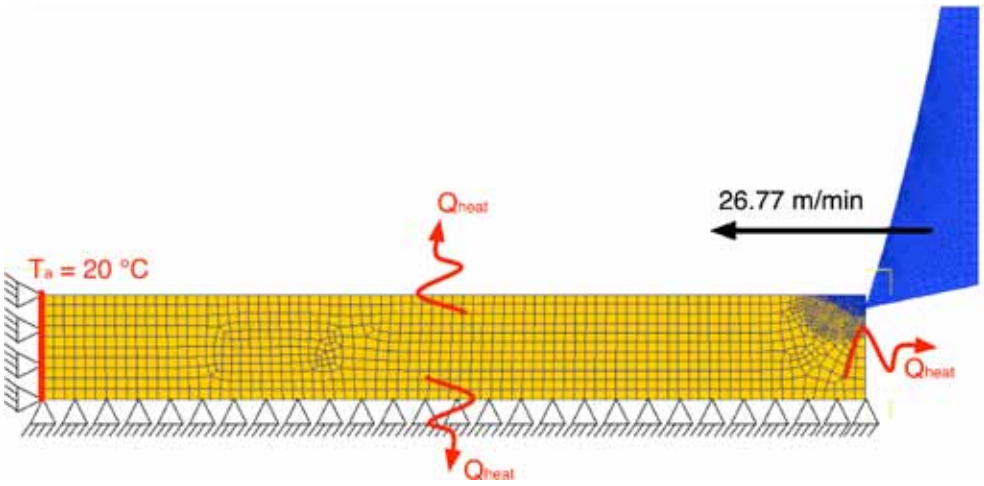

Figure 3: The OTC test model implemented in Deform^{TM} 2D.

numerical model was implemented in the commercial FEM software Deform^{TM} 2D (figure 3), which solves the thermo-mechanical problem using a Lagrange implicit method. The time step was set to 5 μs and the cutting length was 5 mm to ensure the achievement of the steady state condition. The process parameters were chosen accordingly to those used in the experimental test: depth of cut of 0.09 mm, cutting speed of 26,77 m/min, tool rake angle of 18°. The tool was considered as a rigid material and the workpiece as a plastic one since the residual stresses were not chosen as observables parameters.
An adaptive mesh was used, with tetrahedral quadratic elements. At the beginning of the simulation the workpiece was discretized with 1700 elements and the tool with 1600 elements, but due to the adaptive re-meshing, the number of the workpiece elements at the end of the simulation was approximately 3500. One finer mesh window was set on the workpiece moving together with the tool to have always an higher number elements in the workpiece zone nearest to the cutting edge: in this zone the length of the element edge was set to 6 μm. Null horizontal and vertical speeds were imposed at the workpiece's bottom and left edges. Moreover, the workpiece edge at left was considered at room temperature (i.e. 20°C) and the others exchanged heat with the environment or the tool. The convection coefficient was set equal to 10 $W/m^2\,K$. Accordingly to the literature review, the heat transfer coefficient between the workpiece and the tool was set equal to 3000 $W/m^2\,K$. The used friction model was the Tresca law by considering that in OTC, as it is for the machining processes, the real and the apparent contact areas between the chip and the tool are almost equal.
Two model features remain unknown and must be determined: the friction factor of the Tresca law, and the workpiece material parameters of flow stress law (i.e. the five material parameters of the JC model). The identification of these parameters was performed by using the optimization algorithm proposed in the next section.

3.1 Model sensitivity to JC parameters from literature

In order to analyze the model sensitivity to the rheological parameters, numerical simulations of the OTC test with the above described model were carried out by using the JC parameters found in literature for $AISI\,304$ and the experimental flow stress law implemented in the Deform^{TM}'s material library. The further parameters were used in modeling different processes with different strain rates. As it can be seen in table 1, the J-C parameters differ significantly from each other. For all the simulations, the friction factor was set equal to 0.9, representative of dry conditions [13].
The table 2 summarizes the results obtained with the simulations carried out. Due to the high percentage error associated to all the calculated observables, neither the set of parameters available in literature nor the data of the Deform^{TM}'s material library could be considered valid for developing a reliable numerical model.

Table 1: JC parameters for $AISI\,304$ from literature.

	Processes	Strain rates	A	B	C	n	m
Ocana	Pulse laser microforming	10^3	350	275	0.022	0.36	1.0
Aquaro [8]	Peen forming	$> 10^6$	239	522	0.1	0.65	0.63
Mori [9]	Impulsive loads	10^3	310	1000	0.07	0.65	1

Table 2: Results from the simulations carried out with the JC parameters from literature.

Output	Measurements	Ocana [7]	Aquaro [8]	Mori [9]	Deform
Cutting force $[N]$	182	118	394	425	238
Error %	-	35	116	133	31
Chip thickness $[mm]$	0.105	0.241	0.369	0.460	0.3348
Error %	-	129	251	338	219
Chip contact length $[mm]$	0.250	0.173	0.501	0.617	0.3259
Error %	-	308	100	147	219
Chip curvature $[1/mm]$	1.510	0.524	0.0	0.0	0.01
Error %	-	65	100	100	99

4 OPTIMISATION ALGORITHM

The block diagram 4 schematizes the optimization software architecture, which utilizes two programming environments: Ruby [14] and Deform^{TM} 2D. The further has been chosen in this study since it is an object-oriented programming language, it is freeware, and thanks to its capabilities in handling regular expressions and blocks it is possible to develop a compact-high efficient code. In the following section a brief introduction to the modified Nelder Mead Method (NMM) and to the processing procedure developed in Ruby is presented.

4.1 The modified Nelder Mead Method

The optimization is carried out through the Nelder Mead Method. This is a simplex method useful for local minimization and it was implemented in a simplified version. Typically, NMM starts from an initial simplex and moves the vertices, accordingly to its image value, in the direction of the minimum. Four different operations can be performed to change the vertices: reflection, expansion, contraction and shrink. At each minimization step, the centroid M of hyper-face opposed to the worst point and the reflected point R are computed through the equations 3 and 4 respectively:

$$M = \frac{\sum_{i=1}^{N} V_i}{N-1} \tag{3}$$

$$R = 2\,M - W \tag{4}$$

where V_k is the k-th vertex of the simplex with N vertices and W is the vertex with the highest image. The reflection consists in moving the worst vertex on the opposite side of the line between the two best vertices. The expansion acts as the reflection, but the new vertex is moved farther, and it is performed when the new reflected vertex is lower than the lowest point in the simplex. The expanded point E can be evaluated by:

$$E = 2\,R - M \tag{5}$$

If the reflected vertex is higher or equal than the worst point in the simplex, then a contraction is executed. The contracted point C_1 is equal to:

$$C_1 = \frac{W+M}{2} \tag{6}$$

The last possible condition is that the reflected point is higher than the second best vertex and lower than the worst vertex. If these conditions are satisfied, a different contraction is performed:

$$C_2 = \frac{W+R}{2} \tag{7}$$

In the presented algorithm the shrink was not implemented because this operation requires two evaluations of the target function at each optimization step. As a consequence, the convergence would become slower than for the standard method, even if the algorithm would require a lower number of simulations to achieve a satisfactory solution. The convergence criteria is based on the simplex norm, i.e. the sum of the differences of all possible combinations of vertices values.
In the developed numerical model, six unknowns have to be determined, meaning that the dimension of the simplex is seven. Since the solution found by NMM is strongly dependent from the first simplex choice, the first set of vertices was composed by the JC parameters found in literature [8]-[9] (with a friction factor t of 0.9) and others five points randomly chosen. The starting simplex is reported in table 3.

Table 3: The starting simplex used for the optimization.

Vertex No.	A	B	C	n	m	t
1	350	275	0.022	0.36	1.000	0.60
2	310	1000	0.070	0.65	1.000	0.50
3	1000	1500	0.014	0.36	1.000	0.90
4	239	522	0.100	0.65	1.000	0.70
5	129	85	0.023	0.97	0.458	0.40
6	784	812	0.459	0.51	0.196	0.69
7	649	1136	0.372	0.73	0.207	0.80

4.2 The optimization procedure

The main tasks performed by the Ruby Optimization Procedure (ROP) are to run the optimization and to interact with Deform^{TM} in batch mode, giving the chance to automate the pre-processing phase, simulation execution and post-processing analysis.
The output of the optimization step is a configuration file used as input for the numerical model. The ROP runs the pre-processor to generate the model database file, representing the numerical model. Then the ROP executes Deform^{TM} 2D and waits until the simulation comes to an end.
If no errors occur at the end of the simulation, the procedure extracts the nodal coordinates of the final geometry of the chip. Then the nodes on the external and internal chip edges are identified (figure 4). The chip thickness is estimated as the difference between the radius of the circumferences interpolating the points on external and internal chip edges. The mean radius between these two circumferences gives the chip curvature. The chip contact nodes are identified by the contact boundary condition applied on them, and they are used to calculate the tool-chip contact length. Finally, the cutting force

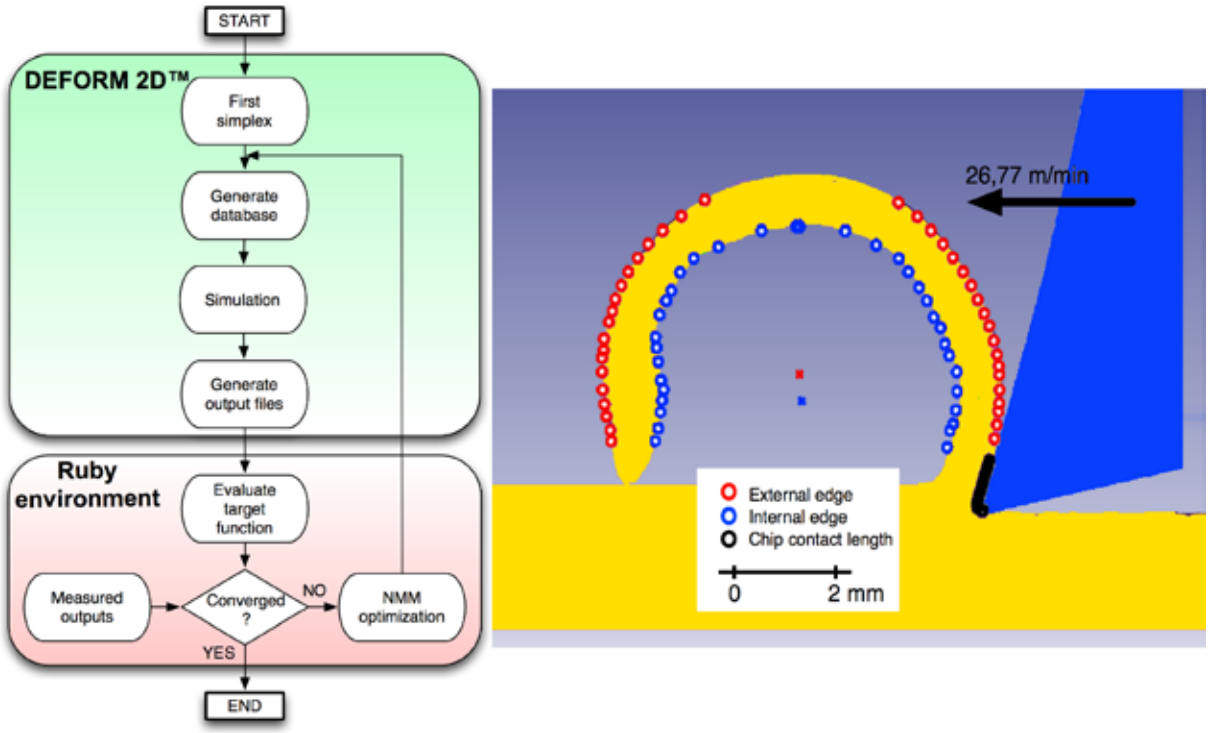

Figure 4: The scheme of the optimization software developed under Deform^{TM} 2D and Ruby environments (left). The identified chip contact nodes, external and internal edges (right).

is obtained by calculating the average of the cutting force values when the steady state conditions are reached. The target function is defined as the sum of the percentage error between the measured outputs and the calculated ones. Penalty functions are used to avoid negatives rheological and tribological parameters. Let Y_m and Y_c be the vectors of four elements containing respectively the measured outputs and the calculated ones, and let X be the vector of six elements with the optimized parameters, the target function can be evaluated as:

$$f(X) = \sum_{i=1}^{4} \frac{|Y_{mi} - Y_{ci}|}{Y_{ci}} + \sum_{j=1}^{6} min(0, X_i)^2 \tag{8}$$

The first term in the equation represents the percentage error, and the second one the penalty function applied to all the rheological and tribological parameters. The algorithm ends when the simplex norm is less than 10.

5 RESULTS

After 20 iterations the optimization algorithm converged to the solution, being the last norm of the simplex 1.18. The convergence plot is reported in figure 5, where it can be seen that the simplex norm tends to zero. In the same figure the comparison between

the measured cutting force and the calculated one is shown: the fitting is satisfactory expecially if it is compared with the results obtained with the sets of Johnson-Cook parameters reported in literature and with flow stress data of the Deform^{TM}'s material library (see table 1). Figure 6 shows a qualitative comparison between the experimental chip morphology and the numerically calculated one: the results are acceptable. The set of Johnson-Cook parameters of the best vertex is reported in table 4, while the outputs calculated with these parameters are in table 5.

Table 4: The optimized set of parameters.

A	B	C	n	m	t
740	630	0.28	0.53	0.26	0.61

Table 5: The outputs obtained with the optimized set of parameters.

	Cutting force $[N]$	Chip thickness $[mm]$	Chip contact length $[mm]$	Chip curvature $[1/mm]$
Measured	182	0.11	0.25	1.51
Calculated	197	0.13	0.12	2.01
Error %	8	20	51	33

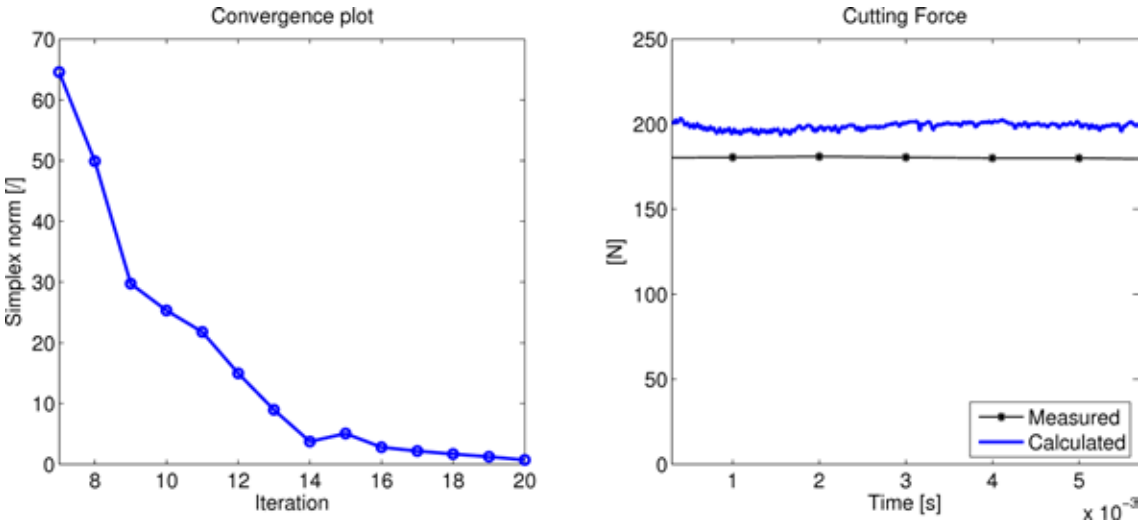

Figure 5: The convergence plot (left), the comparison between the measured cutting force and the calculated one (right).

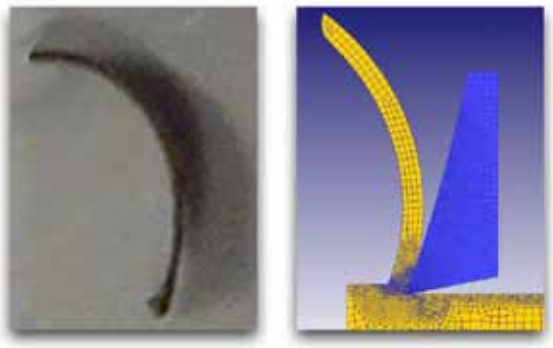

Figure 6: The measured chip (left) and the calculated one (right).

6 CONCLUSIONS

In this paper a numerical model of the orthogonal tube cutting test and a procedure for the material rheological parameters identification have been presented. The numerical model was developed in Deform^{TM} 2D and the optimization procedure was implemented in the programming language Ruby. The analyzed outputs were: the cutting force, the chip thickness and curvature, and the contact length between the tool and the chip. The coefficients of the Johnson Cook constitutive model and the friction factor of Tresca law were identified at the same time by minimizing the percentage error between the measured outputs and the calculated ones. Through the Nelder Mead Method, after 20 iterations, an optimal set of rheological and tribological parameters was found, and the calculated outputs were compared with experimental ones. The results can be considered acceptable compared to the ones obtained with sets of Johnson-Cook parameters available in literature. However, the evaluation of chip morphology is still not satisfactory: more analyses are going on to decrease the errors. Nevertheless, the developed approach can represent a useful tool in identifying the rheological behaviour of materials processed at high strain rates.

REFERENCES

[1] D. Umbrello, R. M'Saoubi and J.C. Outeiro, The influence of Johnson-Cook material constants on finite element simulation of machining of AISI 316L steel. *International Journal of Machine Tool & Manufacture* (2001) **47**:461–470.

[2] A. Attanasio, E. Ceretti and C. Giardini, 3D FEM simulation fo flank wear in turning. *Esaform proceedings* (2011), 561–566.

[3] G.R. Johnson and W.H. Cook, A constitutive model and data for metals subjected to large strains, high strain rate, and temperatures. **International Symposium on Ballistics** (1983), 1-7

[4] H. Chandrasekaran, R. MSaoubi and H. Chazal, Modelling of material flow stress in chip formation process from orthogonal milling and split Hopkinson bar tests. **Machining Science and Technology** (2005), **9**:131-145.

[5] S.Lee, F. Barthelat, J. W. Hutchinson and H.D. Espinosa, Dynamic failure of metallic pyramidal truss core materials Experiments and modeling. *International Journal of Plasticity* (2001), **22**:2118–2145.

[6] M. Vural, D. Rittel and G. Ravichandran, Large Strain Mechanical Behavior of 1018 Cold-Rolled Steel over a Wide Range of Strain Rates. **Metallurgical and materials transactions** (2003), **34A**:2873–2885.

[7] J.L. Ocaña, M. Morales, C. Molpeceres, O. Garca and J.A. Porro, J.J. Garca-Ballesteros, Numerical modelling and experimental characterization of short pulse laser microforming of thin metal sheets. **Multi-Material Micro Manufacture** (2008).

[8] D. Aquaro, Erosion rate of stainless steel due to the impact of solid particles. *AITC-AIT 2006 International Conference on Tribology* (2006).

[9] L. F. Mori, S. Lee, Z. Y. Xue, A. Vaziri, D. T. Queheillalt, K. P. Dharmasena, H. N. G. Wadley, J. W. Hutchinson and H. D. Espinosa, Deformation and fracture model os sandwich structures subjected to underwater impulsive loads. **Journal of mechanics of materuals and structures** (2007), textbf10:1981–2006.

[10] S. Y. Ahmadi-Brooghani, H. Hassanzadeh and P. Kahhal, Modeling of single-particle impact in abrasive water jet machinning. **World Academy of Science, Engineering and Technology** (2007), **36**:243–248.

[11] , A. Shrot and M. Bärker, How to identify Johnson-Cook parameters from machinning simulations. *Esaform proceedings* (2011), 29–34.

[12] J. H. Mathews and K. D. Fink, *Numerical methods using Matlab, 4^{th} Edition.* Prentice-Hall Inc., (2004), 430–436.

[13] C. M. Giorgio Bort, S. Bruschi and P. Bosetti, Modelling sawing of metal tubes through FEM simulation. *Esaform proceedings* (2011), 651–655.

[14] D. Thomas, *Programming Ruby, the pragmatic programmers' guide.* The Pragmatic Programmers, 2*nd* edition (2004).

XI International Conference on Computational Plasticity. Fundamentals and Applications
COMPLAS XI
E. Oñate, D.R.J. Owen, D. Peric and B. Suárez (Eds)

NUMERICAL MODEL OF WARM DRAWING OF THE BIOCOMPATIBLE MG ALLOYS ACCOUNTING FOR DUCTILITY OF THE MATERIAL

ANDRZEJ MILENIN*, PIOTR KUSTRA*

* AGH University of Science and Technology
Department of Applied Computer Science and Modelling
Al. Mickiewicza 30, 30059 Krakow, Poland
e-mail: milenin@agh.edu.pl, www.isim.agh.edu.pl

Key words: Magnesium alloys, Drawing Process, Fracture, Workability, Finite Element Simulation.

Abstract. Due to high compatibility and solubility in human organism, special magnesium alloys are applied in bioengineering. Production of surgical threads to integration of tissue can be application of these types of alloys. This sort of application calls for fine wires with diameters from 0.1 to 0.9 mm. The warm drawing process in heated dies was proposed to increase the workability of the Mg alloys. The purpose of this paper is development and experimental validation of a mathematical model of a warm drawing process of wires made of MgCa0.8, Ax30 and ZEK100 alloys and determination of optimal parameters with the objective function defined as maximum of workability. The first part of investigation is focused on development of a numerical model, which is based on FE solution. The second part of paper is focused on experimental upsetting and tensile tests. Basing on these tests the flow stress and fracture models were obtained. The materials models are implemented into the Authors' FE code, which is dedicated to modelling of drawing processes. For experimental verification of model the thermo visual analysis of wire drawing and tests of mechanical properties of wire were performed. With help of model the dependence between technological parameters of drawing and ductility function was obtained. The technical problem defined as determination of optimal drawing velocity, which is helpful to obtain the temperature in deformation zone taking into account fracture criterion, was solved. The optimum drawing schedule for Mg alloys was proposed.

1 INTRODUCTION

Magnesium alloys with high bio-compatibility are applied in medicine because of their high compatibility and solubility in the human body [1-3]. The production of surgical threads by wire drawing is an example of an application of these types of materials (for example, MgCa08, Ax30 and ZEK100 alloys), which act as alternatives to bio-inert materials such as titanium, tantalum or 316L steel. Corrosion research performed on Mg alloys *in vivo* showed the possibility for implant solubility, which could eliminate implant extraction [3]. Some promising properties of the special Mg alloys with respect to these applications include its

strength and biological stability, which make it suitable for a long-term implantation and are the focus of interest in [4]. However, the magnesium alloys have low technological plasticity during cold deformation; therefore, the drawing of thin wires is difficult [5]. In work [6] a new manufacture technology of wire made of Mg alloys is proposed. In this technology the metal is heated by a hot die and the process of warm deformation is performed. The description of this process is represented in the papers [6-8].

The model of ductility is very important element of FE program for simulation of Mg alloys wire drawing. It enables the optimization of the process of wire drawing on the basis of simulations. The problem of prediction of fracture for the magnesium alloys is described in the literature [9-11]. However, these works account only for few parameters of drawing, such as the die angle and the reduction ratio. Aluminium and zinc containing magnesium alloys (eg. AZ31, AZ80) are the well-investigated materials, which have a bigger technological plasticity than MgCa0.8 and Ax30 alloys [11]. The yield stress and fracture models of the latter alloys for warm deformation are not available in the literature.

The purpose of this paper is the development of mathematical models of yield stress and ductility for MgCa0.8, Ax30 and ZEK100 alloys, implementation these models into FE code [12] and simulations of wire drawing processes in heated die. Experimental validation of model is based on thermo visual measurement of wire temperature during drawing. The practical conditions of drawing processes for thin wire made of Mg alloys are proposed in the paper.

2 COUPLED FEM MODEL OF WIRE DRAWING

The FE code Drawing2d developed by A. Milenin [12-14] is used. The FE model solves a boundary problem considering such phenomena as metal deformation, heat transfer in die and wire, metal heating due to deformation and friction.

2.1 Model of plastic deformation

Solution of boundary problem is obtained using variation principle of rigid-plastic theory:

$$J = \int_V \int_0^{\xi_i} \sigma_s(\varepsilon_i, \xi_i, t) d\xi_i dV + \int_V \sigma_0 \xi_0 dV - \int_S \sigma_\tau v_\tau dS \tag{1}$$

where: ξ_i – effective strain rate, σ_s – yield stress, ε_i – effective strain, t – temperature, V – volume, σ_0 – mean stress, ξ_0 – volumetric strain rate; S – contact area between the alloy and the die, σ_τ – friction stress, v_τ – alloy slip velocity along area of die.

The friction stress is determined according to law:

$$\sigma_\tau = f_{tr} \frac{\sigma_s}{\sqrt{3}} \left[1 - \exp\left(-\frac{1.25\sigma_n}{\sigma_s} \right) \right] \tag{2}$$

where: f_{tr} – friction coefficient, σ_n – normal stress on contact between the alloy and the die.

The stress tensor σ_{ij} is calculated on the basis of strain rate tensor ξ_{ij} according to following equation:

$$\sigma_{ij} = \delta_{ij}\sigma_0 + \frac{2\sigma_s}{3\xi_i}\xi_{ij} \tag{3}$$

The stationary formulation of the boundary problem is used. The strain tensor ε_{ij} is calculated by integration of strain rate tensor along the flow lines:

$$\varepsilon_{ij} = \int_0^{\tau} \xi_{ij}(\tau)d\tau = \sum_{p=1}^{p=p_\tau} \xi_{ij}^{(p)} \Delta\tau^{(p)} \tag{4}$$

where: $\Delta\tau^{(p)}$ – time increment, $\xi_{ij}^{(p)}$ – strain rate tensor determined according to equation:

$$\xi_{ij}^{(p)} = \sum_{n=1}^{n_{nd}} N_n \xi_{ijn} \tag{5}$$

where: N – finite element shape functions, ξ_{ijn} – nodal strain rate tensor for current finite element, n_{nd} – number of nodes in element.

The points of flow lines are determined on the basis of the values of the velocity at point p, which are calculated according to the formula:

$$v_i^{(p)} = \sum_{n=1}^{n_{nd}} N_n v_{in} \tag{6}$$

The calculation of the position of the next point (p+1) of flow line is carried out according to the equation:

$$x_i^{(p+1)} = x_i^{(p)} + v_i^{(p)}\Delta\tau \tag{7}$$

2.2 FEM solution of thermal problem in metal

This problem was solved by applying the following method. The passage of the section through the zone of deformation was simulated. For this section at each time step the non-stationary temperature problem was examined:

$$\lambda\left(\frac{\partial^2 t}{\partial r^2} + \frac{1}{r}\frac{\partial t}{\partial r}\right) + Q_d = c\rho\frac{dt}{d\tau} \tag{8}$$

where: $Q_d = 0.9\sigma_s\xi_i$ – deformation power, c – specific heat; ρ – alloy density, τ – time, λ – thermal conductivity coefficient (the following values are used for MgCa0.8, Ax30 and ZEK100 alloys: c = 624 J /kgK, ρ = 1738 kg /m^3, λ = 126 J /mK). Heat exchange between the alloy and the die is defined as:

$$q_{conv} = \alpha\left(t - t_{die}\right) \tag{9}$$

where: t_{die} – die temperature, α – heat exchange coefficient.

The generation of heat from the friction is calculated according to the formula:

$$q_{fr} = 0.9\sigma_\tau v_\tau \tag{10}$$

2.3 FEM solution of thermal problem in die

The model of temperature distribution in the die is based on the solution of Fourier

equation in the cylindrical coordinate system:

$$\lambda\left(\frac{\partial^2 t}{\partial r^2}+\frac{1}{r}\frac{\partial t}{\partial r}+\frac{\partial^2 t}{\partial y^2}\right)+Q_h=0 \tag{11}$$

where: Q_h – power of the heating element.

The heat Q_h is generated in the finite elements, which correspond to the position of heating device. The boundary problem is solved on the basis of the variation formulation of equation (11). For the areas, which are in contact with the metal, the temperature of the alloy is obtained from the solution of the thermal problem for the metal.

3 MATERIALS MODELS

3.1 Yield stress model

For obtaining the model of flow stress the load-displacement curves from upsetting tests were used. Model of yield stress σ_s was proposed as a modified Henzel-Spittel equation:

$$\sigma_s = Ae^{-m_1 t}\varepsilon_i^{m_2}\xi_i^{m_3\left(\frac{t-20}{280}\right)^{m_6}}e^{\frac{m_4}{\varepsilon_i}}\left(1+\varepsilon_i\right)^{m_5 t}e^{m_7\varepsilon_i}\xi_i^{m_8 t}t^{m_9} \tag{12}$$

where: A, m_1 - m_9 – empirical coefficients.

3.2 Fracture model

The key parameter, which presents fracture, is called ductility function [8]. This parameter is defined by the following formula:

$$\psi=\frac{\varepsilon_i}{\varepsilon_p\left(k,t,\xi_i\right)}<1 \tag{13}$$

where: k – triaxility factor, $k=\sigma_0/\sigma_s$.

Critical deformation function $\varepsilon_p(k,t,\xi_i)$ is obtained on the basis of experimental results for the upsetting and the tension tests. In the Drawing2d FEM code [10] equation (13) is implemented as an integral:

$$\psi=\int_0^{\tau}\frac{\xi_i}{\varepsilon_p\left(k,t,\xi_i\right)}d\tau\approx\sum_{m=1}^{m=m_\tau}\frac{\xi_i^{(m)}}{\varepsilon_p\left(k,t,\xi_i\right)}\Delta\tau^{(m)} \tag{14}$$

where: τ – time of deformation, $\Delta\tau^{(m)}$ – time increment, $\xi_i^{(m)}$ – the values of the strain rate in the current time, m – a index number of time step during numerical integration along the flow line.

The numerical integration of function (14) along the flow lines is carried out according to formulas (4)-(7). The following function of critical deformation is proposed:

$$\varepsilon_p=d_1\exp\left(-d_2k\right)\exp\left(d_3t\right)\xi_i^{d_4} \tag{15}$$

The wire breaking outside the deformation zone was modeled by follow criteria (for drawing with out braking):

$$\frac{\sigma_y}{\sigma_s} \leq 1 \tag{16}$$

where: σ_y – drawing stress.

4 MATERIALS TESTS

In the present paper, the flow stress and fracture models for MgCa0.8 (Mg 99.2 %, Ca 0.8 %), Ax30 (Mg 96.2%, Al 3.0%, Ca 0.8%) and ZEK100 (Mg 98%, Zn 1 %, rare earths 0.5 %, Zr 0.5 %) alloys were obtain. Upsetting and tensile tests were performed on the Zwick Z250 machine at the AGH University of Science and Technology. Results of the upsetting tests were used to determine the flow stress model and results of both tests were used for identification of fracture (workability) model.

4.1 Conditions and results of experiment

Cylindrical samples ø8 mm, h = 10 mm were used for upsetting tests. The sample for the tensile tests is presented in the figure 1. Conditions and selected results of experiment are presented in table 1 (upsetting tests) and table 2 (tensile tests). For the upsetting samples 1u and 2u (table 1) the destruction of the sample wasn't occurred.

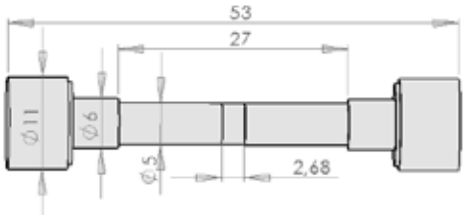

Figure 1: Shape of sample for tensile tests

The coefficients in equation (12) were determined using the inverse approach [15-16] with the least squares method. The objective function was formulated as the root-mean-square difference between experimental and predicted loads. The following values of coefficients were obtained:

MgCa0.8: A=447.4; m_1=0.0007542; m_2=0.4485; m_3=0.2867; m_4=-0.0001899; m_5=-0.009392; m_6=2; m_7=0.8318; m_8=-0.0004359; m_9=0.007962.

Ax30: A=656.5; m_1=0.001210; m_2=0.4445; m_3=0.05207; m_4=-0.0006153; m_5=-0.009350; m_6=2; m_7=0.5107; m_8=0.0002455; m_9=0.01805.

ZEK100: A=656.5; m_1=0.001210; m_2=0.4445; m_3=0.05207; m_4=-0.0006153; m_5=-0.009350; m_6=2; m_7=0.5107; m_8=0.0002455; m_9=0.01805.

Parameters d_1-d_4 of equation (15) were obtained using fracture test for different values of k,t,ξ_i, which are described above. Interpretation of results of tensile and upsetting tests was done using the inverse algorithm [16]. The FEM models of all tests were made for determining conditions of fracture initiation (k,t,ξ_i). Change of values k,t,ξ_i during deformation was calculated in that part of the sample, where initiation of fracture occurred in test. Ductility function for each test was calculated on the basis of formulas (14) and (15). The

difference between experimental and calculated value of ductility function at the moment of the fracture is used as the objective function. The minimum of the objective function is reached by a variation of the coefficients. The following values of coefficients were obtained:

MgCa0.8: $d_1 = 0{,}03313$; $d_2 = 2{,}130$; $d_3 = 0{,}01167$; $d_4 = -0{,}3130$.
Ax30: $d_1 = 0{,}04517$; $d_2 = 1{,}172$; $d_3 = 0{,}01109$; $d_4 = -0{,}1725$.
ZEK100: $d_1 = 0.05503$; $d_2 = 0.1388$; $d_3 = 0.01036$; $d_4 = -0.1216$.

Table 1: Conditions and results of upsetting tests for MgCa08, Ax30 and ZEK100

Sample	Initial temperature, ^{0}C	Tool velocity, mm/min	The deformation, which corresponds to destruction of sample, mm (MgCa0.8 /Ax 30/ ZEK100)	Samples (MgCa0.8 /Ax 30 / ZEK100)		
1u	300	60	6.08* / 6.8* / 5.13*			
2u	300	600	5.79* / 6.5* / 5.77*			
3u	250	60	6.70 / 6.9 / 4.33			
4u	250	600	5.0 / 6.7 /4.33			
5u	200	60	3.40 / 3.8 / 3.01		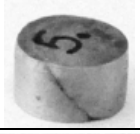	
6u	200	600	2.80 / 2.85 / 2.27			
7u	100	60	2.2 / 1.8 / 1.61			
8u	20	10	1.9 / 1.5 / 1.63			

*The destruction of the sample did not occur

Table 2: Conditions and results of upsetting tests for MgCa08, Ax30 and ZEK100

Sample	Initial temperature, ^{0}C	Tool velocity, mm/min	The elongation, which corresponds to destruction of sample, mm (MgCa0.8 / Ax30 / ZEK100)
1t	300	60	22.5 / 12.8 / 16.9
2t	300	600	16.0 / 12.8 / 13.37
3t	250	60	14.0 / 10.5 / 14.15
4t	250	600	8.50 / 9.4 / 10.68
5t	200	60	6.4 / 7.2 / 11.35
6t	200	600	- / 6.15 / 9.42
8t	20	10	2.66 / 4.15 / 3.78

Ductility functions for MgCa08 alloy is presented on figure 2. The obtained models of materials were implemented in the FEM model of the wire drawing.

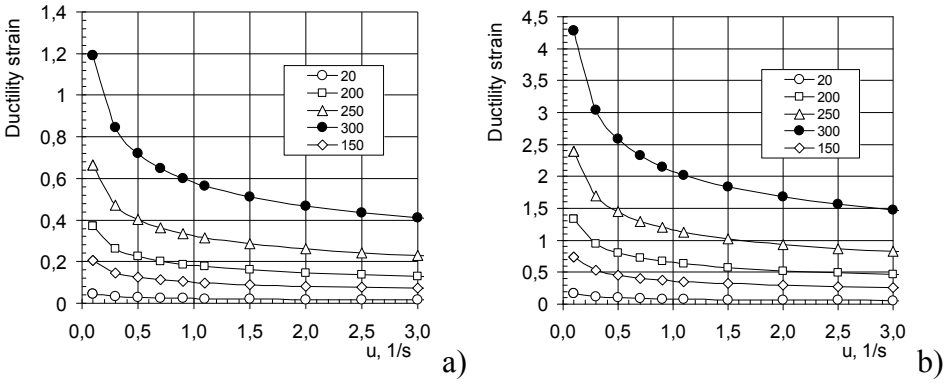

Figure 2: Ductility function for MgCa08: a) k=0.3; b) k=-0.3

5 VERIFICATION OF NUMERICAL MODELS

An experimental study of the process of wire drawing was performed for the purpose of the verification of mathematical model. The following data were used in experiment:
- Initial diameter of wire $d_0 = 1$ mm; final diameter of wire $d_1 = 0.92$ mm;
- Length of calibration part of tool $0.3d_1$; die semi-angle 5°;
- Drawing velocity in range 10 ÷ 500 mm /min; tool temperature in range 250 ÷ 410 °C;

Variants of tests for MgCa0.8 magnesium alloy are shown in table 3. For the verification of the wire temperature at the output from the zone of deformation the data of infrared camera were used. The measurement results for the alloy are shown in table 3 for MgCa0.8.

Table 3: Variants of drawing parameters and measurement results of temperature wire and tool with the infrared cameras for MgCa0.8

Variant	1	2	3	4	5	6
V, mm/s	10	10	100	200	200	500
t_{die}, C	410	350	350	340	260	250
Comment	wire breaking	passed	passed	passed	passed	passed
Tool temperature (thermocouple) [C]	410	350	350	340	260	250
Temperature of tool (infrared camera) [°C]	440	365	360	340	260	225 (oscillation)
Temperature of wire (infrared camera) [°C]	-	320	310	290	210	190

The selected results of the numerical simulation of variants 1 and 2 from the table 3 are shown on figure 3. The calculated temperature of metal for variant 2 was 311 ^{0}C. The temperature, obtained in the experiment was 320 ^{0}C. The break of wire was observed for variant 1 in the experiment. The results of calculation for this variant show an increase in the deformation at the end of the wire (figure 3, d), which corresponds to the break of wire.

Experiment show that numerical model is working correctly that why can be used to design drawing schedule.

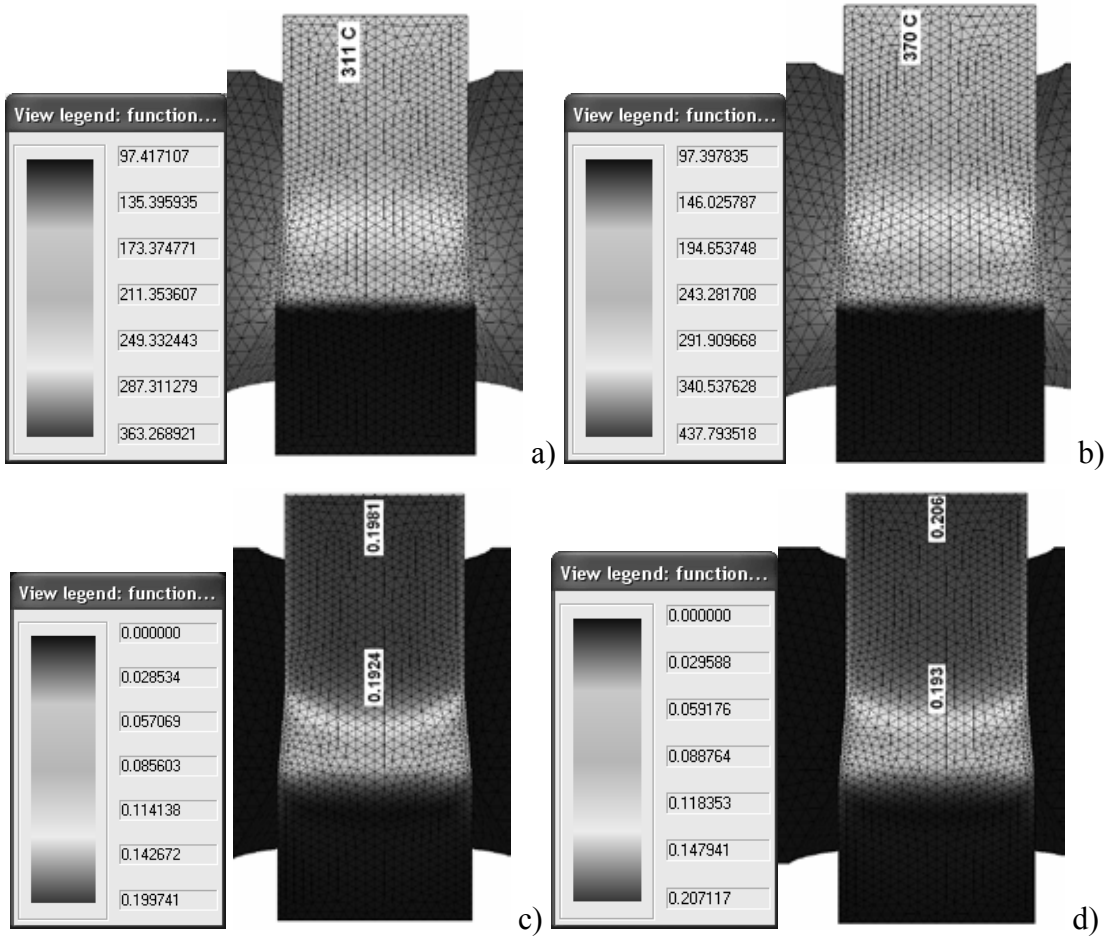

Figure 3: Results of numerical analysis of drawing process of MgCa0.8 magnesium alloys: a,b – distribution of temperature, c,d – distribution of strain intensity for drawing process a,c variant 2 of table 3 and b,d variant 1 of table 3

6 DETERMINATION OF OPTIMAL DRAWING PARAMETERS

After implementation of the models (12)-(15) into the FEM code Drawing2d, the simulation of the wire drawing was performed. Example of results is shown above. The initial wire diameter was 0.5 mm. The following parameters of the process were changed: velocity (0.01 - 2.0 m/s), die semi-angle (4^0, 5^0 and 6^0). Final diameter of wire was 0.44 mm (elongation 1.29). Temperature of die was 400 ^{0}C. On figure 4 dependence between ductility function, temperature of wire in exit cross-section, drawing force, relative drawing stress and die semi-

angle, drawing velocity was shown. Smaller values of ductility function in this case related to die semi-angle 4^0. The critical technological parameter was a drawing velocity. If drawing velocity is small (not more 0.01-0.05 mm/s), the drawing process is possible, because time of contact between metal and hot die is relatively long and temperature of metal is above 250 ^{0}C. From other side, for velocities 0.01-0.05 mm/s gives minimums of drawing load and relative drawing stress was observed (figure 4,c and figure 4,d). Conclusion of those simulations is existence of optimum drawing parameters from point of view of fracture, wire braking and wire temperature.

The next step of research was related to determinate of drawing maps for Mg alloys by numerical simulations. The value of ductility function (13), value of wire braking criteria (16) and temperature conditions were accepted as the objective functions. On figure 5 developed drawing maps for MgCa08 was shown. Figure 5,a is related to possible variants of drawing from point of view satisfaction of criteria (13). According this relationship, if drawing velocity increase, the possible elongation must be smaller (decreased). The breaking prognoses is shown on diagram in figure 5,b. In this case, if velocity increases, temperature of wire decreases and wire in exit of die is stronger in compare with metal in deformation zone. That's way possibility of braking decrease for biggest values of drawing velocity. The mechanism of influence temperature on wire breaking is complicit. From one side, increasing of temperature is related to increase of plasticity. This phenomena is take into account in diagrams on figure 5,a. From another side, high temperature of metal is related to high temperature of metal after deformation zone and special case of wire braking. This braking was observed in experiment for variant 1 in table 3. The summary map was shown on figure 5, d.

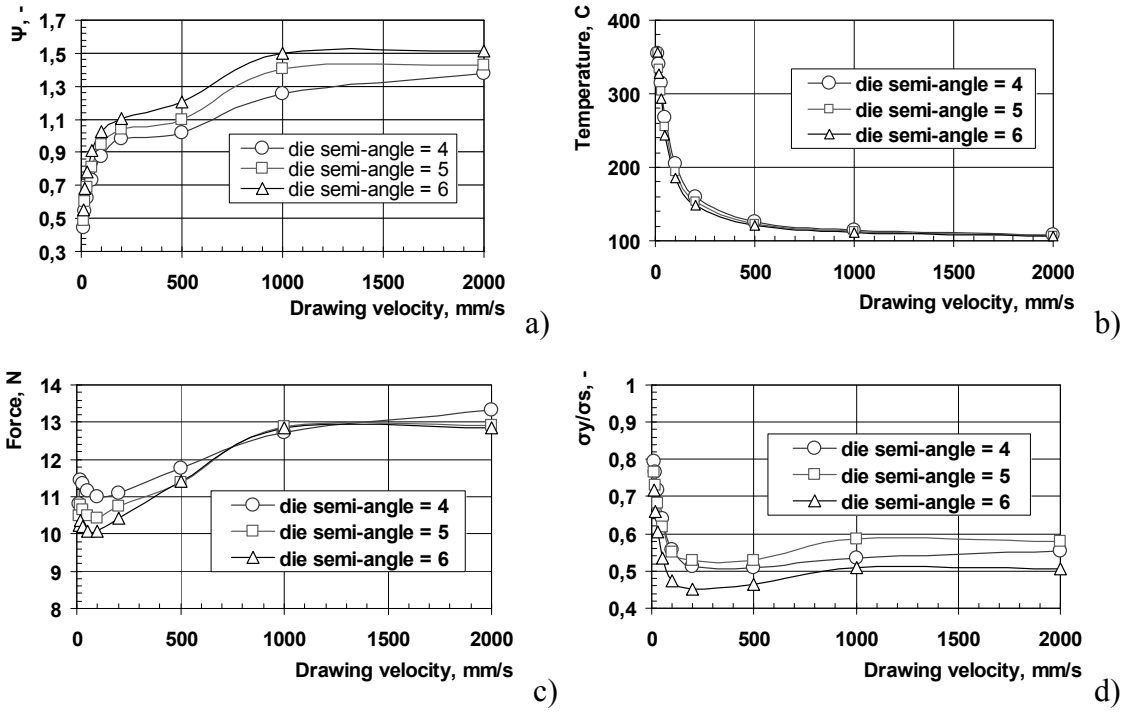

Figure 4: Dependence between ductility function (a), temperature of wire in exit cross-section (b), drawing force (c), relative drawing stress (d) and die semi-angle, drawing velocity

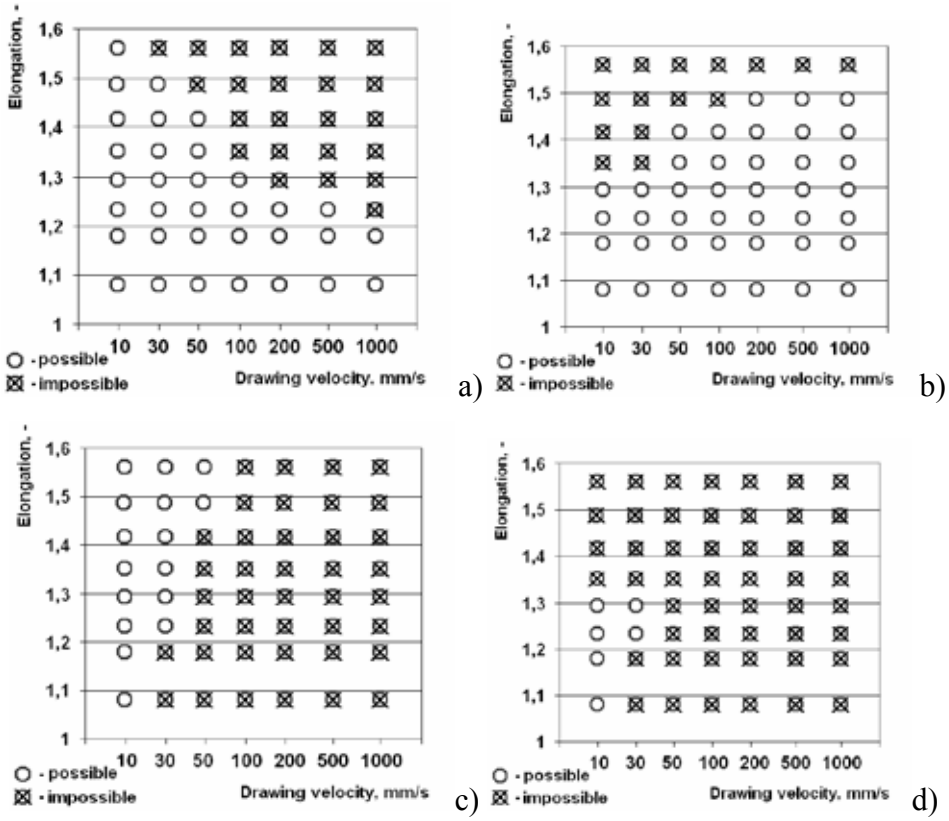

Figure 5: Maps of possible elongations per pass: (a) – because the fracture criteria (13); (b) – because the relationship σ_y/σ_s criteria (wire breaking); (c) – because temperature conditions; (d) – summary map

With help of these maps, the follow drawing schedule was proposed: 1.000→0,921→0,849→0,782→0,720→0,663→0,611→0,563→0,518→0,478→0,440→0,405→0,373→0,344→0,317→0,292→0,269→0,248→0,228→0,210→0,193→0,178→0,164→0,151→0,139→0,128→0,118→0,109→0,100 with drawing velocity 0.01 m/s. The angle of die was 4^o and friction coefficient 0.03. According this schedule wire from MgCa08 (figure 6) and Ax30 were produced in laboratory of AGH University of Science and Technology.

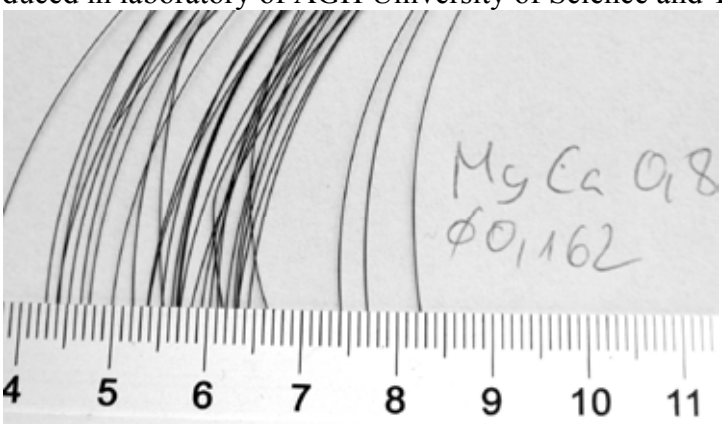

Figure 6: Wires from MgCa08 after drawing, d=0.16 mm

7 CONCLUSIONS

- Experimental - theoretical methodology to determinate parameters of empirical yield stress and ductility models of MgCa0.8, Ax30 and ZEK100 alloys were developed.
- Ductility of MgCa0.8, Ax30 and ZEK100 alloys is strongly dependent on temperature and strain rate.
- Experiment show that numerical model is working correctly that why can be used to design draft schedule. Verification shows that parameters of yield stress function and ductility model were correctly calculated.

ACKNOWLEDGMENTS

The authors would like to thank the Ministry of Science and High Education of Poland, project no. 416/N-DFG-SFB/2009/0.

REFERENCES

[1] Bach F.-W., Kucharski R., Bormann D., Magnesium compound structures for the treatment of bone defects, *Engineering of Biomaterials*, (2006), 56-57, 58-61.

[2] Heublein, B., Rohde, R., Niemeyer, M., Kaese, V., Hartung, W., Röcken, C., Hausdorf, G., Haverich A., Degradation of magnesium alloys: A new principle in cardiovascular implant technology, Paper TCT-69, 11 Annual Symposium Transcatheter Cardiovascular Therapeutics, *The American Journal of Cardiology*, (1999), Expcerpta Media Inc., New York.

[3] Haferkamp, H., Kaese, V., Niemeyer, M., Phillip, K., Phan-Tan, T., Heublein, B., Rohde, R,. *Exploration of Magnesium Alloys as New Material for Implantation*; (2001), Mat.-wiss. u. Werkstofftech, 32: Wiley-VCH Verlag GmbH, Weinheim, 116-120.

[4] Wan, Y., Xiong, G., Luo, H., He, F., Huang, Y., Zhou, X. Preparation and characterization of a new biomedical magnesium-calcium alloy, *Materials and Design*, (2008), 29, 2034-2037.

[5] Eickemeyer J., Guth A., Falter M., Opitz R., Drawing of magnesium wires at Ambient temperature, Proc. *6th Int. Conf., Magnesium alloys and their Applications,* (2004), WILEY-VCH, 318 – 323.

[6] Milenin A. Seitz J.-M, Bach Fr.-W., Bormann D., Kustra P.: Production of thin wires of magnesium alloys for surgical applications// *Proc. Conf. Wire Expo 2010*, (2010), Milwaukee, Wisconsin, USA, May 2010, Wire Ass. Int. Inc. P. 61-70.

[7] Bach Fr.-W., Milenin A., Kucharski R., Bormann D., Kustra P., Modelowanie za pomocą MES procesu ciągnienia drutów ze stopu magnezu wykorzystywanych w chirurgii, *Hutnik-Wiadomości Hutnicze*, (2007), 74, 8-11 (in Polish).

[8] Milenin A., Kustra P. The multiscale FEM simulation of wire fracture phenomena during drawing of Mg alloy, *Steel Research International,* (2008), vol. 79, spec. issue Conf. Metal Forming 2008, 1, 717-722.

[9] Yoshida K.: Cold drawing of magnesium alloy wire and fabrication of microscrews. *Steel Grips*, 2 (2004), 199-202.

[10] Grosman F., Tkocz M.: Zastosowanie funkcji odkształcalności granicznej do prognozowania utraty spójności materiału. *Mat. 11 Konf. Informatyka w Technologii Metali*, Zakopane (2004), 339-346 (in Polish).

[11] A. Milenin, D. Byrska, O. Gridin The multi-scale physical and numerical modeling of fracture phenomena in the MgCa0.8 alloy // *Computers and Structures*, (2011), vol. 89 iss. 11–12, 1038–1049, DOI 10.1016/j.compstruc.2011.01.003.
[12] Milenin A. Program komputerowy Drawing2d – narzędzie do analizy procesów technologicznych ciągnienia wielostopniowego. *Hutnik*, (2005), nr 2, vol. 72, 100-104, (in Polish).
[13] Mroz S. Milenin A. Numerical modelling of the metal flow and stock bending during the rolling of unequal angle bar // *Journal of Materials Processing Technology*, (2006), Vol: 177 Iss. 1-3, 561-565, DOI: 10.1016/j.jmatprotec.2006.04.027.
[14] Milenin A., Muskalski Z., Kustra P. The multi-scale FEM simulation of wire fracture during drawing of perlitic steel //*Materials Science Forum*, (2008), Vol.: 575-578, 1433-1438.
[15] Milenin A., Kustra P. Mathematical model of warm drawing process of magnesium alloys in heated dies// *Steel Research International*, (2010), vol. 81, no. 9, spec. ed. 1251-1254.
[16] A. Milenin, P. Kustra, M. Paćko Mathematical model of warm drawing of MgCa0.8 alloy accounting for ductility of the material// *Computer Methods in Materials Science*: quarterly, (2010), vol. 10, no. 2: 69-79.

XI International Conference on Computational Plasticity. Fundamentals and Applications
COMPLAS XI
E. Oñate, D.R.J. Owen, D. Peric and B. Suárez (Eds)

NUMERICAL SIMULATION STUDY OF THE KNOOP INDENTATION TEST

M.I. SIMÕES[*], A.X. MARTINS[†], J.M. ANTUNES[*†], N.A. SAKHAROVA[†], M.C. OLIVEIRA[†] AND J.V. FERNANDES[†]

[*]Escola Superior de Tecnologia de Abrantes, Instituto Politécnico de Tomar
Rua 17 de Agosto de 1808, 2200 Abrantes, Portugal
e-mail: {isabel.simoes, jorge.antunes}@ipt.pt, web page: http://www.esta.ipt.pt

[†] CEMUC – Department of Mechanical Engineering, University of Coimbra,
Rua Luís Reis Santos, Pinhal de Marrocos, 3030-788 Coimbra, Portugal
e-mail: {marta.oliveira, nataliya.sakharova, valdemar.fernandes}@dem.uc.pt,
web page: http://www2.dem.uc.pt/cemuc/

Key words: Knoop Indentation, Ultramicrohardness, Numerical simulation.

Abstract. This paper presents a study of the influence of the mechanical properties of materials on the surface indentation geometry and on the depth-sensing indentation results with a Knoop indenter. Three-dimensional numerical simulations of this indention test were performed for several materials, with different mechanical properties, using the in-house finite element simulation code, DD3IMP. In order to obtain accurate results, the numerical model of the Knoop indenter was prepared, taking into account the optimization of the finite element mesh.

1 INTRODUCTION

Depth-sensing indentation tests have been employed like a standard technique for the mechanical characterization of bulk and composite materials. Experimental hardness tests are mainly performed using pyramidal Vickers and Berkovich indenters. The Knoop indenter differs from Vickers indenter merely in the indenter pyramid shape. The Knoop indenter geometry, with lozenge-based pyramid, leads to a more extended and shallower indentation impression than the Vickers indenter with square-based pyramid geometry. This makes the Knoop indentation attractive for determining the intrinsic thin film hardness [1] and for material anisotropy determination.

At our knowledge, studies of depth-sensing indentation using the Knoop indenter are unusual and further investigation is needed. Few examples are the experimental work conducted by Riester et al. [2, 3] and the numerical studies performed by Li Min *et al*. [4] and Giannakopoulos *et al*. [5].

Due to the scarce number of experimental and numerical studies, concerning the Knoop indenter, their enlargement could become very valuable in the characterization of some type of materials, such as thin films and anisotropic materials. In this context, the goal of the present study is to contribute for an improved understanding of the influence of the materials

mechanical properties on the indentation geometry and, consequently, on the mechanical properties evaluation by the Knoop hardness test.

2 THEORETICAL ASPECTS

The Knoop indenter has a pyramid-shaped geometry with apical angles of 130° and 172.5°, and a base with one diagonal, L, 7.11 times longer than the other, m, [6]. The Knoop indenter geometry is shown in Figure 1.

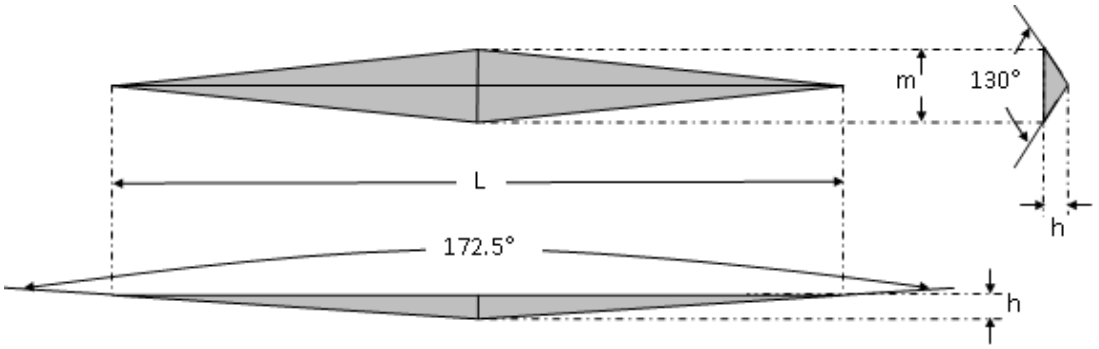

Figure 1: Geometry of the Knoop Indentation

The Knoop indenter contact area, A, as a function of the indentation depth, is given by:

$$A = 2h_c^2 \tan\theta_1 \tan\theta_2 = 65.4h_c^2, \quad (1)$$

where h_c is the indentation contact depth and θ_1=65°, θ_2=86.25° are the semi-apical angles of the indenter.

Marshall *et al.* [7] investigated the Knoop indentations and observed that, during the unloading period, the short diagonal of indentation (m) contracts, due to the elastic recovery, while the long diagonal (L) remains unchanged (see Figure 2).

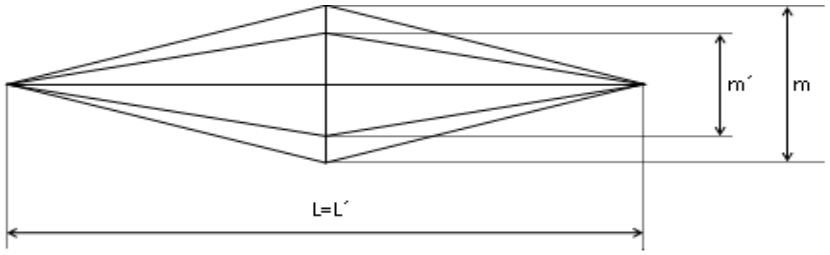

Figure 2: The short diagonal m reduces to m´, the long diagonal remains unchanged L=L´ after unloading

In the study of Marshall *et al.* [7], an equation for the recovered indentation size, which takes into account the indenter's geometry and the material mechanical properties, was proposed:

$$\frac{m'}{L'} = \frac{1}{7.11} - 0.45\frac{H}{E}, \quad (2)$$

where H is the hardness and E is the Young's modulus. Based on Marshall *et al.* [7] work, the

H and E values obtained by traditional methods are overestimated due to the substantial elastic recovery of the short diagonal compared with negligible elastic recovery of the long axis direction. In order to improve the mechanical properties results, an iterative procedure based in Equation (2) was proposed [7]: the initial values of H and E are calculated by the traditional methods and the ratio H/E is adjusted until convergence.

In this context, the aim of the current study is to investigate the Knoop indentation test. A detailed study concerning to the Knoop indentation surface geometry, at maximum load and after unloading, is performed. To attain this objective, three-dimensional numerical simulation of several fictitious materials was performed.

3 NUMERICAL SIMULATION AND MATERIALS

In order to perform the numerical simulations of the Knoop hardness test, the finite element DD3IMP in-house code was used. This code was developed to simulate processes involving large plastic deformations and rotations, considers the hardness tests a quasi-statistic process and makes use of a fully implicit algorithm of Newton-Rapson type [8,9]. The code allows the three-dimensional numerical simulations of the hardness test using any type of indenter geometry and takes into account the friction between the indenter and the deformable body. A detailed description of the DD3IMP simulation code has previously been given [10].

The test sample used in the numerical simulations of the indentation test has both radius and thickness of 40 μm. Figure 3 shows a global view and a detail of the indentation region of the finite element mesh. The discretization was performed using three-linear eight-node isoparametric hexahedrons. Due to geometrical and material symmetries in the X=0 and Z=0 planes, only a quarter of the sample was used in the numerical simulation of the Knoop hardness test. The finite element mesh was composed by 17850 elements. The mesh refinement was chosen in order to provide accurate values of the indentation contact area, and consequently of the mechanical properties.

In all the numerical simulations, the contact with friction between the indenter and the deformable body was considered, with a Coulomb's coefficient equal to 0.16 [10].

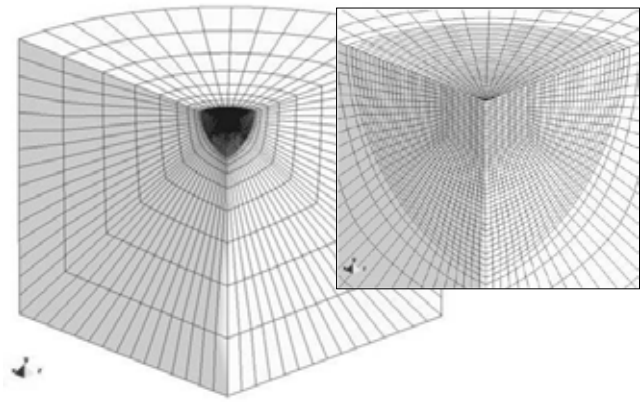

Figure 3: Finite element mesh for the test sample used in the numerical simulations.

The Knoop indenter geometry was modelled using parametric Bezier surfaces, which allow a fine description of the indenter tip, namely an imperfection such as the one that occurs in the real geometry, similar to the case of the Vickers indenter [11]. The model of the indenter has a tip imperfection, which consists in a plane normal to the indenters' axis with an area equal to 0.0032 μm^2. Figure 4 shows a global view of the Knoop geometry and a detail of the indenter tip.

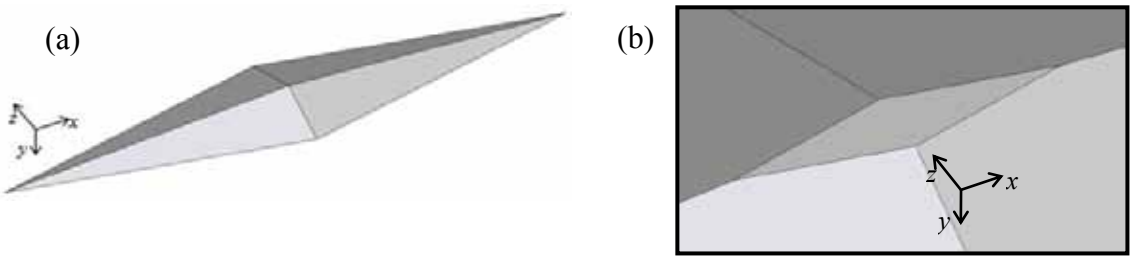

Figure 4: Knoop indenter modelled with Bezier surfaces. (a) general view; (b) detail of the indenter tip

Due to the tip imperfection, the indenter area function disagrees from the ideal. The following equation provides the Knoop indenter area function used in the analysis of the numerical results:

$$A = 65.4377h_c^2 + 0.9152h_c + 0.0032 \tag{3}$$

The numerical simulations of the Knoop hardness test were carried out on 10 fictitious materials, up to the same maximum indentation depth, $h_{max} = 0.2\,\mu m$. Table 1 resumes the mechanical properties of the materials considered. The plastic behaviour of the materials was modelled considering that the true-stress, σ, and the logarithmic plastic strain, ε, relationship was described by the Swift law: $\sigma = k(\varepsilon + \varepsilon_0)^n$, where k, ε_0 and n (strain hardening parameter) are material constants (the material yield stress is given by: $\sigma_y = k\varepsilon_0^n$). The constant ε_0 was considered to be 0.005 for all materials.

Table 1: Mechanical properties of the fictitious materials used in the numerical simulations

Material	σ_y (GPa)	n	E (GPa)	ν	h_f / h_{max}
M1	2	0.01	200	0.3	0.83
M2	10				0.49
M3	20				0.28
M4	2	0.3			0.70
M5	6				0.41
M6	20				0.15
M7	10	0.01	400		0.66
M8	20				0.49
M9	2	0.3			0.82
M10	20				0.24

3 RESULTS AND DISCUSSION

The fictitious materials considered (see Table 1) had two different Young' modulus (200 GPa and 400 GPa). Two different cases of work-hardening coefficient, n (on one side, the materials were assumed elastic-perfectly plastic (n ≈ 0) and by the other side, the materials had high work-hardening coefficient (n=0.3)), and different yield stress values σ_y were studied. In order to study the mechanical properties influence on the results of the Knoop indentation, the surface indentation profiles were analysed along both diagonals, the long diagonal, L, and the short one, m, as shown in Figures 5 and 6, respectively. Moreover, these figures show the indentation profiles at the maximum load (open symbols) and after unloading (solid symbols).

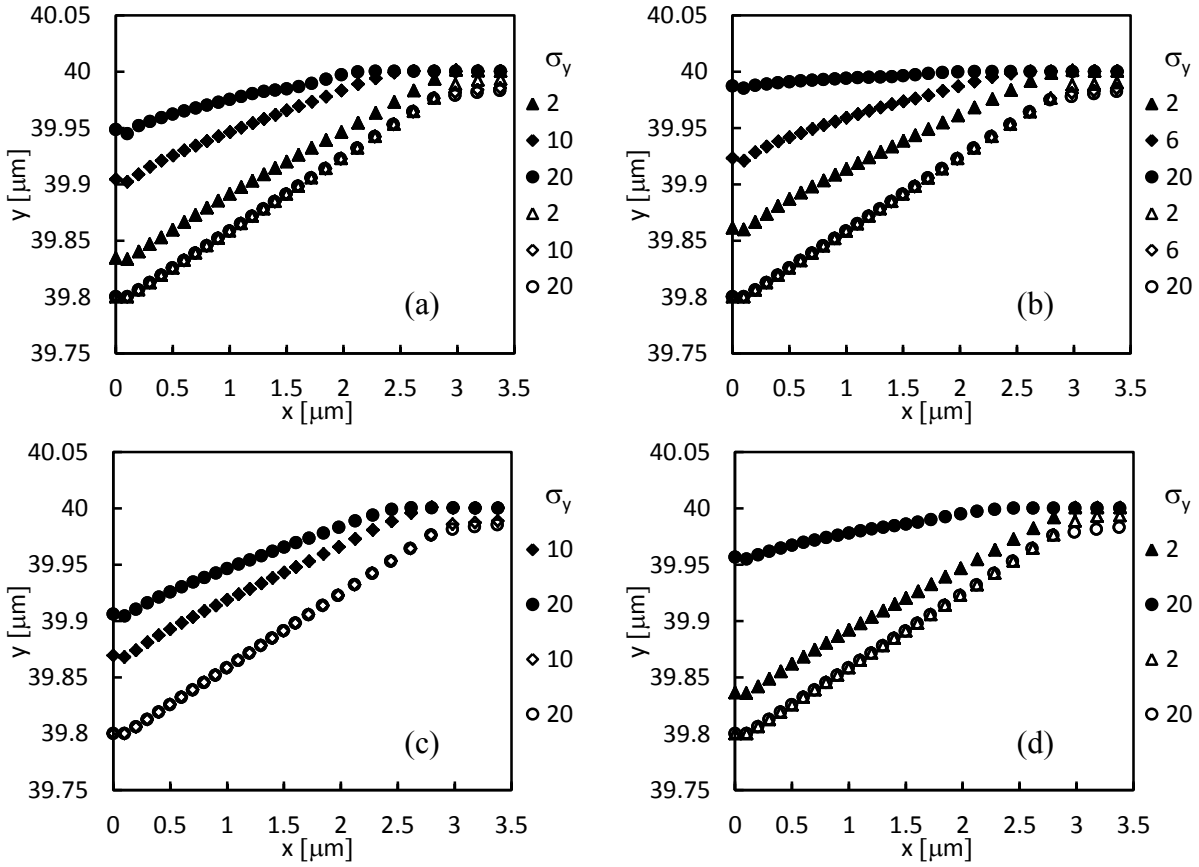

Figure 5: Surface indentation profiles at the maximum load along the longer diagonal, L, for the following materials: (a) M1, M2 and M3; (b) M4, M5, M6; (c) M7 and M8; (d) M9 and M10

Figures 5 and 6 show that the "sink-in" appears on the indentation surface at the maximum load, except in case of the M1 material, where the surface tends to form "pile-up". This fact certainly is related with a ratio h_f/h_{max} equal 0.83 (where h_f is the indentation depth after unload and, h_{max} the indentation depth at the maximum load) and the low value of the work-hardening coefficient. In fact, in case of Vickers indentation, the indentation profiles are related to the h_f/h_{max} ratio and the "pile-up" formation appears when this ratio is higher than

0.8, for low values of the work-hardening coefficient (n ≈ 0). So, the current results for the Knoop indentation are in agreement with previous studies for Vickers indenter [10]. It should be noted that, for a given material, the h_f/h_{max} ratio does not depends on the indentation depth and has a correlation with the value of the H/E ratio, between the hardness and the Young's modulus, which slightly depends on the work-hardening coefficient (the h_f/h_{max} ratio decreases when the H/E ratio increases).

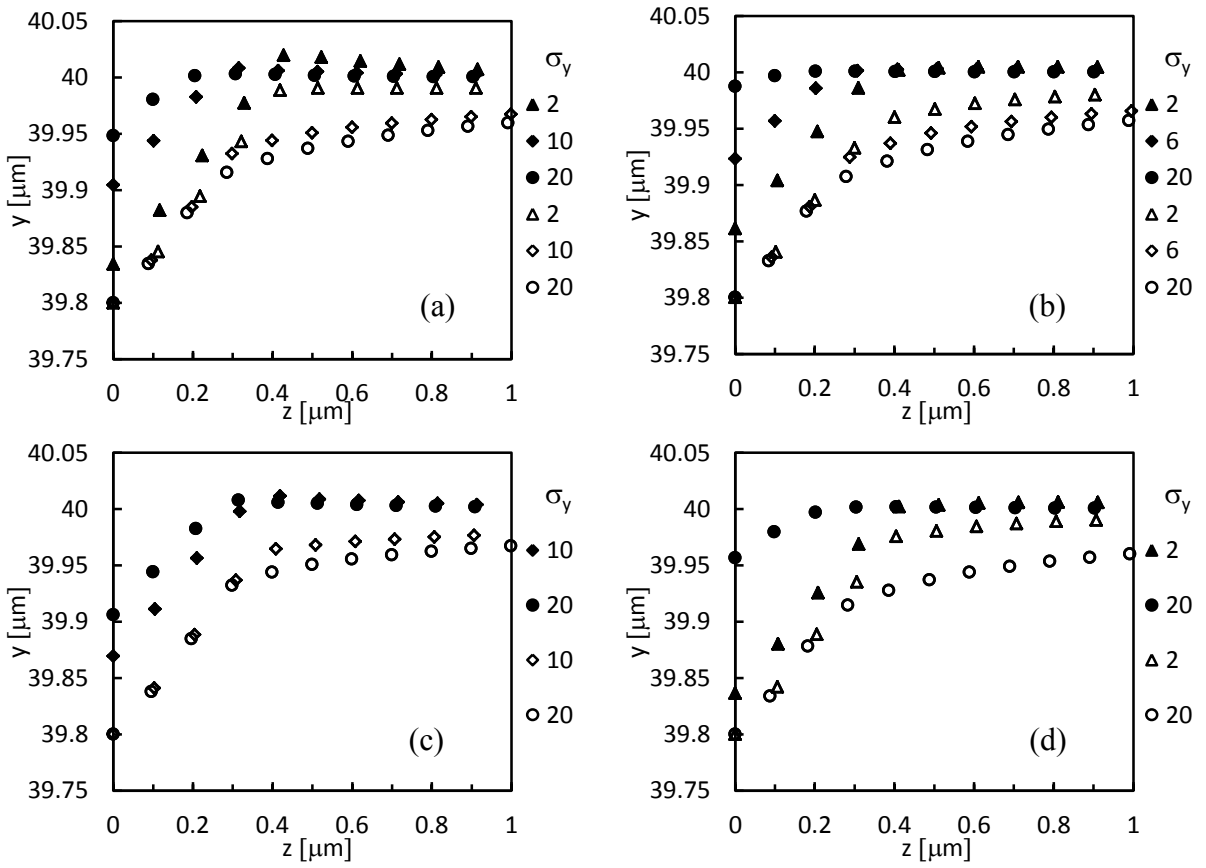

Figure 6: Surface indentation profiles at the maximum load along the short diagonal, m, for following materials: (a) M1, M2 and M3; (b) M4, M5, M6; (c) M7 and M8; (d) M9 and M10

After unloading, for materials with the same value of Young's modulus (E=200 GPa, Figures 5, 6 (a, b); E=400 GPa, Figures 5, 6 (c, d)), the surface indentation profiles show an elastic recovery along both diagonals that increases with the increase of the material yield stress, σ_y, and the work-hardening coefficient, n. Figures 5 and 6 also show that the increasing of the Young's modulus value leads to a decrease of the elastic recovery. Moreover, in the case of the short diagonal, for the materials M1 and M7, the indentation surface tends to form "pile-up". This is probably connected with the small elastic recovery.

As a general conclusion, the results presented in Figures 5 and 6 show that both indentation diagonals have elastic recover after unloading, as opposed to the conclusion by Marshall *et al*. [7]. In this context, the application of Equation (2) for the determination of the mechanical properties, namely the hardness and the Young's modulus, cannot be quite appropriate. This

becomes critical for materials with high work-hardening coefficient and higher values of the H/E ratio, between the hardness and the Young's modulus.

4 CONCLUSIONS

- This is an exploratory study concerning the numerical simulation of the Knoop indentation tests, in order to understand how to obtain accurate results concerning the mechanical properties of materials, namely the hardness and the Young's modulus;
- The surface indentation profiles shows "sink-in" formation for all materials except of ones with the h_f/h_{max} ratio slightly higher than 0.8;
- Elastic recovery for both diagonals of Knoop indentation is observed, although the elastic recovery along the short diagonal is inferior than the one along the long diagonal;
- The recovery along the indentation diagonals should be considered for determination of the mechanical properties by Knoop indentation test, especially for materials with high work-hardening coefficient and high ratio between the yield stress and Young's modulus; that is, it may be worth reexamining the use of the traditional equations for hardness and Young's modulus evaluation, providing that an adequate value of correction factor of indenter geometry is considered.

REFERENCES

[1] Chicot, D., Bemporad, E., Galtieri, Roudet, G. F., Alvisi, M. and Lesage, J. Analysis of data from various indentation techniques for thin films intrinsic hardness modelling. *Thin Solid Films* (2008) **516**:1964–1971.

[2] Riester, L., Blau, P. J., Lara-Curzio, E. and Breder, K. Nanoindentation with a Knoop indenter. *Thin Solid Films* (2000) **377-378**: 635-639.

[3] Riester, L., Bell, T.J. and Fischer-Cripps, A.C. Analysis of depth-sensing indentation tests with a Knoop indenter. *J. Mater. Res*. (2001) **16**:1660-1667.

[4] Li, M, Chen, W.M., Liang, N.G. and Wang, L.D. A numerical study of indentation using indenters of different geometry. *J. Mater. Res*. (2004) **19**: 73-78.

[5] Giannakopoulos, A.E. and Zisis, Th. Analysis of Knoop indentation. *Int. J. Solids Struct*. (2011) **48**:175-190.

[6] Knoop, F., Peters, C.G. and Emerson, W.B. A sensitive pyramidal-diamond toll for indentation measurements. J. *Res. Nat. Bur. Stand*. (1939) **23**:39–61.

[7] Marshall, D.B., Noma, T. and Evans, A.G. A simple method for determining elastic modulus to hardness ratios using Knoop indentation. *Int. J. Am. Ceram. Soc. A* (1982) **65**: C175–C176.

[8] Menezes, L.F. and Teodosiu, C. Three-dimensional numerical simulation of the deep-drawing process using solid finite elements. *J. Mater. Processing Technol.* (2000) **97**:100–106.

[9] M.C. Oliveira, J.L. Alves and L.F. Menezes, Algorithms and strategies for treatment of large deformation frictional contact in the numerical simulation of deep drawing process. *Arch. Comput Method* (2008) **E15**:113-162.

[10] Antunes, J.M., Menezes, L.F. and Fernandes, J.V. Three-dimensional numerical

simulation of Vickers indentation tests. *Int. J. Solids Struct.* (2006) **43**: 784–806.
[11] Sakharova, N.A., Fernandes, J.V., Antunes, J.M. and Oliveira, M.C. Comparison between Berkovich, Vickers and conical indentation tests: A three-dimensional numerical simulation study, *Int. J. Solids. Struct.* (2009) **46**:1095-1104.

XI International Conference on Computational Plasticity. Fundamentals and Applications
COMPLAS XI
E. Oñate, D.R.J. Owen, D. Peric and B. Suárez (Eds)

PARAMETER IDENTIFICATION AND ELASTIC-PLASTIC PROBLEMS: OPTIMIZATION STRATEGIES

J. STAHLSCHMIDT[*], M. VAZ JR.[*], P.A. MUÑOZ-ROJAS[*], E.L. CARDOSO[*]

[*] Department of Mechanical Engineering
Centre for Technological Sciences, State University of Santa Catarina
Campus Universitário Prof. Avelino Marcante
89223-100, Joinville, Brazil

Key words: Parameter Identification, Optimization, Genetic Algorithm.

Abstract. Parameter identification is a technique which aims at determining model parameters based on a combination of experimental and numerical procedures. This work addresses identification of material parameters for elastic-plastic problems using optimization methods. Firstly, a comparative study is presented in which optimization techniques based on Genetic Algorithms, Univariate, Steepest Descent and BFGS methods are discussed. Identification of Carbon steel parameters based on tensile tests illustrates application of the BFGS, GA and GA-BFGS hybrid methods.

1 INTRODUCTION

In recent years, the development of robust computational models has made possible to efficiently simulate a wide range of metal forming processes. Such progress has been translated into the release of commercial packages able to simulate forming processes such as forging, rolling, deep drawing and extrusion amongst many others. However, the success of the simulations is directly linked to the capacity of constitutive models and respective parameters to accurately represent the experimental behaviour of the material. In general, industries have determined such parameters by means of mechanical tests described in technical standards using the assumption of homogeneous deformation. For instance, the material parameters obtained using tensile tests are determined for strains up to the necking onset, thereby severely limiting the level of plastic strain above which the results are no longer valid. Therefore, use of such material parameters in the simulation of metal forming operations involving large plastic strains would compromise the results.

The numerical-experimental technique known as parameter identification has emerged as the best approach to determine material parameters at large strains. The recent literature shows many works on the determination of constitutive parameters of elastic-plastic problems[1]. The investigation presents further studies on the application of optimization strategies to this class of problems. In a first part, a comparative study of the *Univariate* technique, *gradient-based* methods and *Genetic Algorithms* (GA) is discussed based on experimental data available in the literature. In a second part, a *hybrid strategy* combining *GA* with a *gradient-based* optimization method is assessed. The technique is illustrated for tensile tests of cylindrical specimens prepared according to the ASTM and NBR technical standards.

2 PARAMETER IDENTIFICATION AND THE OPTIMIZATION PROBLEM

Conceptually, parameter identification consists of finding a set of parameters, defined in this work as $\boldsymbol{p}$, which minimizes the difference between an experimental measure and a corresponding computed response with respect to a given norm. In this work, the computed response is obtained by solving the direct problem using a non-linear finite element approximation whereas the experimental response corresponds to measurement of selected variables of the experiment.

Parameter identification, therefore, can be formulated using optimization techniques, which consists of finding a minimum of the general problem

$$\begin{array}{lll} \text{Minimize} & g_0(\boldsymbol{p}) & \boldsymbol{p} \in R^n \\ \text{Subject to} & h_l(\boldsymbol{p}) = 0 & l = 1 \ldots m_h \\ & g_j(\boldsymbol{p}) \le 0 & j = 1 \ldots m_g \\ & p_i^{\inf} \le p_i \le p_i^{\sup} & i = 1 \ldots n \end{array} , \tag{1}$$

in which $\boldsymbol{p} \in R^n$ is the *design vector* (a vector containing *n design variables*), $p_i^{\inf}$, and, $p_i^{\sup}$, are upper and lower bounds of the design variables, respectively, $g_o(\boldsymbol{p})$ is the *objective function* to be minimized, subjected to *equality*, $h_l(\boldsymbol{p})$, and *inequality* $g_j(\boldsymbol{p})$ constraints.

The initial problem is complemented by the definition of the *objective function*, which in this work is based on the relative quadratic difference between experimental and computed response evaluated over the deformation process, so that

$$g_0(\boldsymbol{p}) = \sqrt{1/N \sum_{k=1}^{N} \left[\left(R_k^{MEF}(\boldsymbol{p}) - R_k^{Exp} \right) / R_k^{Exp} \right]}, \tag{2}$$

where R^{Exp} is the experimental response, $R^{MEF}(\boldsymbol{p})$ is the corresponding numerical response computed using a set of *design variables* $\boldsymbol{p}$, and N is the number of experimental points. In the present case, the measured and computed tensile loading are used to evaluate $g_o(\boldsymbol{p})$, and the hardening parameters correspond to $\boldsymbol{p}$. Therefore, in the identification process, the loading curve is computed using Finite Elements based on a given set of hardening parameters. The optimization process subsequently changes $\boldsymbol{p}$, so that, at the end of the identification procedure, g_o is minimum.

The literature shows several principles upon which optimization methods are based for multidimensional problems[2,3,4]. The most common approaches are *mathematical programming techniques, evolutionary methods* and, to a lesser extent, the *univariate approaches*. The *gradient-based algorithms* fall within the former, in which the gradient of $g_o(\boldsymbol{p})$ with respect to $\boldsymbol{p}$ is computed at each iterative step. *Gradient-based algorithms*, therefore, requires a continuous and twice differentiable objective function and constraints (the Hessian must be continuous). A disadvantage of such methods is the influence of the initial parameters on the process when the problem is noncovex. Moreover, the nonconvexity of parameter identification problems favours existence of multiple local minima.

Evolutionary methods consist of optimization algorithms based upon a generic *population* and use concepts inspired in biological mechanisms. The idea behind all variants of evolutionary algorithms is that each candidate plays the role of an *individual*, part of a *population*, and that some individuals are selected to generate the next *generations*. Selection and evolution of the population takes place by a recursive application of operators mimicking

biological evolution, such as *mutation* and *combination*. Besides no requirement of differentiability of the objective function and restrictions, the advantage of evolutionary algorithms is their theoretical capacity to determine the global minimum despite the existence of multiple local minima and plane regions (very small gradients). However, their obvious disadvantage lies on the high computational cost due to the large number operations required.

In addition to the *gradient-based* algorithms and *evolutionary* methods, the *univariate strategy* can also be used to multidimensional problems. In this case, a one-dimensional optimization technique is used to minimize one design variable at a time, seeking to produce a sequence of improved approximations to the minimum point.

2.1 Univariate methods

The concept of the method is described in Rao[3] for general optimization problems. In this method, one seeks to produce improved approximations to the minimum point by changing only one design variable at time and assuming that the remaining variables are constant during the process. The procedure is repeated successively for each design variable until a global convergence criterion is reached. This strategy requires application of a *one-dimensional* optimization method, giving rise to several possible combinations. In this work, this strategy is used is conjunction with the *Golden Section* one-dimensional strategy[2]. It is worthy to mention that the *Golden Section* method does not require computation of the gradient of the objective function. Convergence for the present implementation of the *Univariate* method is established by the mean quadratic relative difference of the current and previous set of material parameters, $\phi(\boldsymbol{p})$ (please, see Eq. (6)).

2.2 Gradient-based methods

Gradient-based methods are iterative in their essence, so that, at each iteration a new set of design variables are determined leading to minimization of the objective function. The iterative procedure is repeated until convergence is reached. The optimization literature indicates many mathematical strategies to account for the gradient in the iterative process. This work addresses the *Steepest Descent* and *modified Newton* with Hessian matrix computed using the *BFGS* equations.

For the sake of objectivity, this section presents a summary of the methods and the reader is referred to Arora[2] and Rao[3] for further insights on general purpose optimization methods. In this class of problems, the necessary conditions for a design vector $\boldsymbol{p}$ be a local minimum are established by the *Karush–Kuhn–Tucker* conditions (or *KKT* conditions). Most parameter identification techniques constitute unconstrained problems and the KKT conditions require only a null gradient of the objective function at the optimum point. Therefore, in order to ensure that $\boldsymbol{p}^*$ is a local minimum, $g_0(\boldsymbol{p})$ is expanded in a Taylor series in the neighbourhood of $\boldsymbol{p}^*$ so that

$$g_0(\boldsymbol{p}) - g_0(\boldsymbol{p}^*) = \frac{1}{2}\boldsymbol{d}^T\boldsymbol{Q}(\boldsymbol{p}^*)\boldsymbol{d}\,, \quad \text{where} \quad \nabla g_0(\boldsymbol{p}^*) = \boldsymbol{0} \quad \text{and} \quad \boldsymbol{d} = \boldsymbol{p} - \boldsymbol{p}^*\,, \tag{3}$$

in which $\boldsymbol{p}$ is sufficiently close to $\boldsymbol{p}^*$, $\boldsymbol{Q}$ is known as *Hessian* matrix and corresponds to the second derivative of the objective function with respect to the design variables, and $\boldsymbol{d}$ is the

search direction in the design space. Noticeably, since $g_0(\boldsymbol{p}) - g_0(\boldsymbol{p}^*) \geq 0$, the procedure leads to a minimum $\boldsymbol{p}^*$ only if the *Hessian* is positive definite. Therefore, Equation (3) suffices to ensure that $\boldsymbol{p}^*$ is a local minimum. Convergence for gradient-based optimization techniques are usually defined by the norm of the gradient of the objective function, $\phi(\boldsymbol{p}) = \| \nabla g_0(\boldsymbol{p}) \|$, however, in this work, some comparative examples adopt the same criterion established for the *Univariate* method (please, see section 3.1).

Steepest Descent method: The *Steepest Descent* method uses the negative of the gradient of the objective function as a search direction based on the fact that, in a given point $\boldsymbol{p}$, the direction opposite to $\nabla g_0(\boldsymbol{p})$ is the direction of fastest decrease of the objective function[2]. The optimization process is iterative so that the design variables at iteration k+1 are computed using the gradient of the objective function and the optimum step length, α. In the present case, a normalized search direction, $\boldsymbol{d}$, is used, so that

$$\boldsymbol{p}^{(k+1)} = \boldsymbol{p}^{(k)} + \alpha^{(k)} \boldsymbol{d}^{(k)} \qquad \text{and} \qquad \boldsymbol{d}^{(k)} = -\nabla g_0(\boldsymbol{p}^{(k)}) / \| \nabla g_0(\boldsymbol{p}^{(k)}) \| . \tag{4}$$

Computation of the gradient of the objective function, $\nabla g_o(\boldsymbol{p})$, known as sensitivity analysis, can be accomplished by using analytical, semi-analytical or numerical strategies. In this work $\nabla g_o(\boldsymbol{p})$ is computed using central finite differences. The optimal step size, α, represents the scaling along the search direction, being computed by solving a one-dimensional minimization problem and assuming that $\nabla g_o(\boldsymbol{p})$ is orthogonal to the search direction. In the present implementation, the *Golden Section* method is utilised to calculate α along the search direction.

Newton's method: The classical Newton's method is derived from the second-order expansion of the objective function in a Taylor series by assuming that the gradient of the objective function is null for iteration k+1. Contrasting to the *Steepest Descent* algorithm, Newton's method presents a quadratic rate of convergence in the vicinity of the optimal point. However, to ensure convergence under such condition, the Hessian must remain positive definite and computation of the optimum step size must be included. Therefore, the *modified Newton's method* using a normalized search direction can be represented as

$$\boldsymbol{p}^{(k+1)} = \boldsymbol{p}^{(k)} - \alpha^{(k)} \boldsymbol{Q}^{(k)^{-1}} \nabla g_0(\boldsymbol{p}^{(k)}) / \| \nabla g_0(\boldsymbol{p}^{(k)}) \| = \boldsymbol{p}^{(k)} + \alpha^{(k)} \boldsymbol{d}^{(k)} . \tag{5}$$

An evident drawback of the *modified Newton's method* is the requirement to calculate the Hessian matrix at each iteration. The search for alternative approaches to evaluate the Hessian gave rise to the so-called *Quasi-Newton* methods, which use approximations of $\boldsymbol{Q}^{-1}$ computed from the gradient of the objective function. In this work, the strategy proposed by *Broyden, Fletcher, Goldfarb and Shanno*[2] (*BFGS*) was used to calculate the inverse of the Hessian.

2.3 Evolutionary methods

Evolutionary methods are heuristic search strategies inspired in natural phenomena and biological mechanisms. One of the most widely used methods is the *Genetic Algorithm* (*GA*), which attempts to mimic natural evolution of a generic population[4]. In such techniques, the optimization process evaluates only $g_o(\boldsymbol{p})$ and does not require a continuous and differentiable

objective function. When convexity can not be ensured in advance, as most parameter identification problems, *GA* methods yield good approximation to obtaining the global minimum within the design space. In addition, the algorithm can be easily parallelized, making possible to use multiprocessor and distributed computing. It is relevant to mention that *GA*s have been used in areas as widely different as economics, task scheduling, Computer Aided Design (CAD), state assign problems, robot trajectory generation, routing in telecommunications network and many others. Application of *GA* to parameter identification is a relatively new endeavour, especially when addressing finite strain elastic-plastic problems. The recent works of Chaparro et al.[5], Munõz-Rojas et al.[1,6] and Aguir et al.[7] illustrate application of *GA* to this class of problems.

Genetic Algorithms account for two fundamental steps: *selection* and *reproduction*. The former is the process of choosing parents for reproduction, whereas the latter creates offspring from one or two parents. Initially, the *initial population*, *i.e.* a set of design vectors containing the material parameters $\{\boldsymbol{p}_1 , \boldsymbol{p}_2 , \ldots , \boldsymbol{p}_{ni}\}$, is randomly generated within the design space. In general, the literature designates each design vector, $\boldsymbol{p}_i$, as an *individual* (or *phenotype*). The number of individuals of a population, *ni*, is a variable of the method defined *a priori*. The most usual structure of *GA* encodes the design vector (or an *individual*) in a binary string upon which the genetic operations can be easily applied. The *gene* of an *individual* corresponds to a single material parameter, and is represented by a number of binary units (1 or 0) – *number of bits*. The accuracy of the search is determined by the number of bits used to encode a *gene* (or a single material parameter).

Generation of the initial *population* is followed by computation of the objective function for every *individual* and application of the *selection*. The *fitness proportionate selection*, also known as *roulette-wheel* selection, was used in this work to select parents. This method assigns a proportion of the roulette wheel according to the value of the objective function, *i.e.* smaller objective functions yield larger proportions, thereby increasing the probability of selection after a random rotation of the roulette wheel.

The formation of a new *generation* is completed by application of the genetic operators of *combination* and *mutation* to the selected individuals. In the process of *combination,* two new *individuals* (referred as *offspring*) are generated from a random combination of genes of pre-selected parents. The *mutation* operation randomly alters the values of genes of the individual according to a given rate. *Mutation* prevents the *GA* to reach an early convergence to a local minimum. The processes of selection and reproduction are subsequently applied to form new generations until a convergence or stopping criterion is reached.

2.4 GA-BFGS hybrid method

Hybrid methods can be generally defined as a combination of two or more optimization methods. This strategy is mainly used to improve the accuracy of results and convergence of the optimization process. The literature shows just a few works devoted to application of hybrid approaches to parameter identification of elastic-plastic problems. Ponthot and Kleinermann[8] investigated application of the *conjugate gradient*, *BFGS*, a modified *Globally Convergent Method of Moving Asymptotes*, *Levenberg-Marquardt* and *Gauss-Newton* optimization methods to identification of hardening parameters of a von Mises material. The

authors discussed also several possible combinations of the aforementioned methods aiming at avoiding local minima.

Hybrid approaches combining *Genetic Algorithms* and *gradient-based* optimization procedures were proposed by Chaparro *et al.*[5] and Muñoz-Rojas *et al.*[1,6]. Chaparro *et al.*[5] combine a *Genetic Algorithm* and the *Levenberg-Marquardt* method to determine hardening parameters of anisotropic materials. Muñoz-Rojas *et al.*[1,6], aiming at the GTN damage model, proposed a combination of *GA* with either *Sequential Linear Programming* or *Globally Convergent Method of Moving Asymptotes* methods. In both works the *Genetic Algorithm* is used with the objective of reducing the design space of the gradient based method by providing initial parameters closer to the global minimum. A hybrid identification procedure using *artificial neural networks* was developed by Aguir *et al.*[7] as an alternative to the finite element calculations to evaluate the objective functions within the *Genetic Algorithm*. The authors used also a multi-objective strategy to account for experimental results for uniaxial and biaxial tensile tests.

In addition to the positive characteristics highlighted is section 2.3, *GA* can be used to assess the design space, making possible to define new lateral restrictions of the search region. On the other hand, stringent convergence requirements, large initial population, generations and number of bits demand higher computing resources and processing time. Therefore, aiming at improving the efficiency of the optimization process, a hybrid strategy combining *GA* and the *modified Newton – BFGS* gradient-based method is proposed. The procedure can be described as follows: (*i*) Initially, the *Genetic Algorithm* is applied seeking to reduce the search region of the gradient-based method (*i.e.* improve estimation of the initial parameters). This strategy intends to circumvent the well-known convergence problems and convergence to local minima associated with defining initial parameters in gradient-based methods. There are no established rules on defining the best initial population size or other *GA*-related parameters. (*ii*) The second step consists of using the *modified Newton – BFGS* method with initial parameters, $\boldsymbol{p}^{(0)}$, given by the best individual (*i.e.* smallest value of the objective junction) provided by the last generation of the GA. This strategy has proven to be robust and accurate since the *modified Newton – BFGS* method presents high convergence rate in the neighbourhood of the optimal point.

3 NUMERICAL EXAMPLES AND DISCUSSIONS

The parameter identification techniques, including the convergence process, depend upon (*i*) the finite element approximation, (*ii*) the optimization method, (*iii*) the finite element mesh (*iv*) the number of increments of the non-liner mechanical solution, (*v*) the initial parameters, and (*vi*) the convergence or stopping criteria. The following sections address some of the aforementioned aspects for the identification techniques summarized in section 2. The first example presents an assessment of the identification strategies (*i*) *Univariate – Golden section*, (*ii*) *Gradient-based – Steepest Descent*, (*iii*) *Gradient-based – modified Newton-BFGS* and (*iv*) *Genetic Algorithm,* using experimental data available in the literature. Emphasis is placed on the *BFGS* method, for which effects of the number of mechanical increments and mesh size is discussed. The second example shows application of the *modified Newton – BFGS* method and *hybrid GA-BFGS* strategy to determining constitutive parameters

based on uniaxial tensile tests. The effects of the specimen geometry and initial parameters are also investigated.

3.1 Assessment of individual techniques

The experimental load *vs.* displacement curve presented by Ponthot and Kleinermann[5], corresponding to a special steel used in piping manufacture for the nuclear industry (Steel A-533, Grade B, Class 1), is adopted as reference in this example. The initial radius and reference length of the specimen are $r = 6.413$ *mm* and $\ell_0 = 26.67$ *mm* ($2\,\ell_0 = 53.34$ *mm* is the gauge length), respectively. The problem is assumed isothermal and axisymetrical. The finite element mesh used in the simulations attempts to reproduce reference [8] and contains 400 elements and 451 nodes with refinement at the necking region. The same yield stress curve was utilised in this example,

$$\sigma_Y = \sigma_0 + \zeta\varepsilon_p + (\sigma_\infty - \sigma_0)\left[1 - \exp\left(-\delta\varepsilon_p\right)\right] , \tag{6}$$

in which σ_∞, σ_0, ζ and δ are the parameters to be determined. The Young modulus and Poisson's ratio are assumed $E = 206.9$ *GPa* and $\nu = 0.29$, respectively. The initial set of material parameters for each method is presented in Table 1. Noticeably, the *Steepest Descent* and *BFGS* methods require only initial values, whereas the *Univariate* and *GA* techniques demand a search interval delimited by maximum and minimum values. The *GA* parameters used in this example are the following: population of 80 individuals, parameters encoded with 20 bits, 85 % of combination probability and 5 % of mutation.

Table 1. Initial and maximum/minimum values.

Method		σ_∞ [*MPa*]	σ_0 [*MPa*]	ζ [*MPa*]	δ [*m/m*]	Step size
BFGS Steepest Descent	Initial	650	500	325	20	0.5
Univariate – Golden Section	Maximum	800	600	400	30	-
Genetic Algorithm	Minimum	500	400	250	10	-

The perturbation adopted by the *Steepest Descent* and *BFGS* methods is defined by multiplying the initial parameters by a constant factor $f = 2\times10^{-6}$. The different nature of the optimization strategies used in this work recommends specific convergence or stopping criteria. However, in an attempt to harmonize the convergence assessment, a global quadratic measure of the relative uncertainty interval was used for the *Univariate*, *Steepest Descent* and *BFGS* methods. Notwithstanding, the characteristics of the *GA* prevent definition of similar stopping criterion. Therefore, in the present simulations, the stopping criterion for the *GA* is the difference of $g_o(\boldsymbol{p})$ computed for the worst and best individual. Thus

$$\textit{Univariate, Steepest Descent, BFGS}: \quad \phi(\boldsymbol{p}) = \sqrt{\frac{1}{n}\sum_{i=1}^{n}\left(\frac{p_i^{(k+1)} - p_i^{(k)}}{p_i^{(k+1)}}\right)^2} \le 10^{-3} , \tag{6}$$

$$\textit{Genetic Algorithm}: \quad \varepsilon_{GA} = \left| g_0^{(l)}(\boldsymbol{p}^{\text{worst}}) - g_0^{(l)}(\boldsymbol{p}^{\text{best}}) \right| \le 10^{-5} , \tag{7}$$

in which p_i is an individual parameter, n is the number of constitutive parameters and superscripts k and l indicate the iteration step and generation number, respectively. It is relevant to mention that assessment of the convergence for gradient-based methods can also be defined by using the norm of the gradient of the objective function.

Table 2. Final parameters and process convergence data.

Method	σ_∞ [MPa]	σ_0 [MPa]	ζ [MPa]	δ [m/m]	$g(p)$	CPU / CPU_{BFGS}
Genetic Algorithm	667.63	434.77	254.75	20.002	0.00956408498	21.52
Univariate – Golden Section	669.23	479.91	250.00	16.314	0.00986779019	17.39
Steepest Descent	668.02	450.60	252.53	18.764	0.00938025222	9.67
BFGS	678.19	471.25	218.13	15.524	0.00881813074	1
Ponthot and Kleinermann[8]	657.7	458.5	311.4	18.868	-	-

Table 2 presents the final parameter set, objective function and relative CPU time (with respect to the *BFGS* method) for each identification technique, whereas Figure 1 shows the corresponding loading curves. Ponthot and Kleinerman's[8] parameters are also indicated in Table 2. For the initial parameter set given in Table 1, the *BFGS* presented the best results owing to the smaller objective function (*i.e.* smaller relative errors between the experimental and numerical loading curves) and smaller processing time (*i.e.* higher convergence rate). It is relevant to mention that, despite its best performance, the *BFGS* method is highly sensitive to the initial parameters, as discussed in section 3.2. The initial *GA* internal parameters (*number of bits* and *population size*) lead to a relatively smaller objective function. However, the large number of evaluation of the objective function imposes a prohibitively high CPU time when using single-processor computing. In this example, the *Univariate* method required also high processing time without any significant gain in the objective function. The advantage of such method is its dependence on the maximum/minimum initial interval instead of a parameter set.

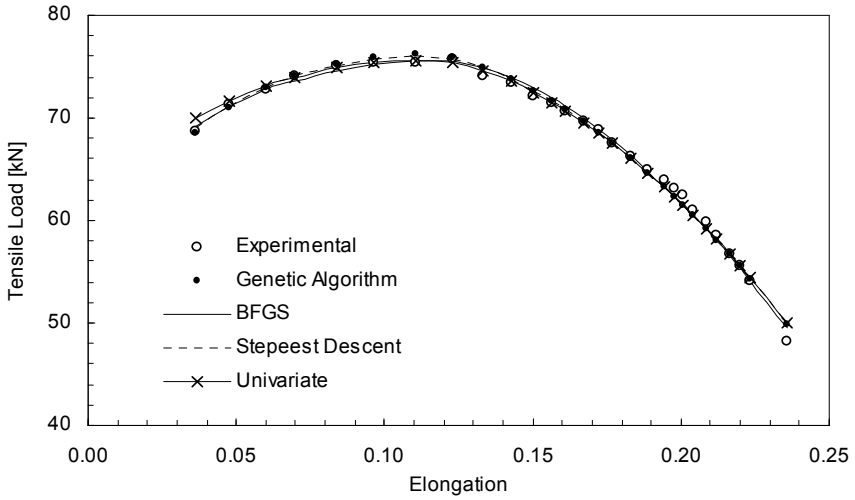

Figure 1: Loading curve.

3.2 Hybrid methods: Genetic Algorithm and BFGS technique

The best results provided by the *BFGS* optimization technique recommends further investigation on its application to parameter identification. However, the well-known dependence of gradient-based optimization methods on initial parameters and possibility of many local minima suggest use of alternative optimization techniques to estimate improved initial parameters for the *BFGS* method. This work uses a *Genetic Algorithm* in an attempt to determine initial parameters for the *BFGS* method closer to the global minimum. In this section, a brief assessment of the influence of the initial parameters in the identification process is presented, followed by the application of the *GA-BFGS* hybrid approach. Furthermore, the effects of the specimen geometry are also discussed.

Aiming at evaluating the effects of variations of geometry in the parameters, tensile tests were performed using specimens prepared according to the American ASTM E 8M-01 and Brazilian NBR ISO 6892 standards (referred in this work as ASTM and NBR, respectively). Figure 2(a) shows the ASTM and NBR specimens. The Brazilian NBR defines specimens with diameter and gauge length $d = 10 \pm 0.1\ mm$ and $\ell_0 = 70 \pm 0.15\ mm$, respectively, whereas the ASTM establishes $d = 12.5 \pm 0.2\ mm$ and $\ell_0 = 62.5 \pm 0.2\ mm$. Six NBR and ASTM specimens were prepared and tested, so that the corresponding median *tensile load x elongation* curves, shown in Figure 2(b), were used in the identification process.

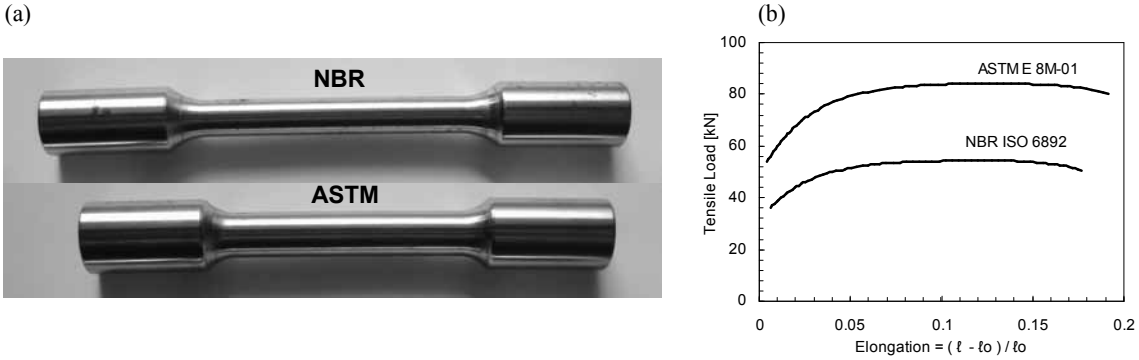

Figure 2: (a) Specimens prepared according to NBR and ASTM standards; (b) Tensile loading.

Table 3. Initial and maximum/minimum values.

Method		σ_∞ [*MPa*]	σ_0 [*MPa*]	ζ [*MPa*]	δ [m/m]	Step size
BFGS	Case (1)	1050	900	750	50	0.5
	Case (2)	700	600	500	30	
	Case (3)	250	210	180	10	
GA – BFGS Hybrid method	Maximum	1050	900	750	50	-
	Minimum	250	210	180	10	-

The geometrical models used in the simulations were defined according to actual measurements of the specimens. In this example radial symmetry and axisymetry were also assumed. A finite element mesh of 200 elements and 231 nodes, with progressive refinement at the centre region, was used for both NBR and ASTM specimens. The Young modulus and Poisson's ratio were $E = 200\ GPa$ and $\nu = 0.3$, respectively.

Table 3 shows the initial parameters used for the *BFGS* optimization strategy and the search region defined for the *GA-BFGS hybrid method*. The same set of initial parameters was used for identification based on NBR and ASTM specimens. The perturbation in this example was defined as in section 3.1. On the other hand, in this case, convergence for the *BFGS* was assessed by the norm of the gradient of the objective function, i.e. $\phi(\boldsymbol{p}) = \| \nabla g_0(\boldsymbol{p}) \| = 2 \times 10^{-6}$.

Results obtained by sole application of the *BFGS* method are presented in Table 4 for *Cases (1)* to *(3)*. One can observe that parameters obtained for *Case (2)* are close for both ASTM and NBR specimens. As well remarked in the literature, convergence for the *BFGS* optimization strategy is strongly dependent upon the initial parameters. No convergence was achieved in *Cases (1)* and *(3)* for the NBR and ASTM specimens within 50 iteration steps. Evolution of $\| \nabla g_0 \|$, shown in Figure 3, illustrates the convergence process for all cases.

Table 4. Parameters determined for ASTM and NBR specimens using the *BFGS* optimization method.

Method	Case	σ_∞ [*MPa*]	σ_0 [*MPa*]	ζ [*MPa*]	δ [*m/m*]	$g_0(p)$	CPU
ASTM	Case (1)	–	–	–	–	*No convergence*	2 h 11 m
	Case (2)	708.40	421.98	592.60	35.424	0.00266693349	38 m
	Case (3)	–	–	–	–	*No convergence*	1 h 52 m
NBR	Case (1)	–	–	–	–	*No convergence*	2 h 26 m
	Case (2)	720.65	426.61	552.82	35.042	0.00480087739	37 min
	Case (3)	–	–	–	–	*No convergence*	2 h 14 m

The *GA – BFGS* hybrid method is introduced as a possible solution for the convergence problem (owing to initial parameters) of gradient-based optimization strategies. Initially, in a first stage (A), the *Genetic Algorithm* is applied aiming at obtaining a point close to the global minimum (thereby avoiding local minima). The second stage (B) consists of application of the *BFGS* method to search for a minimum even closer to the global minimum.

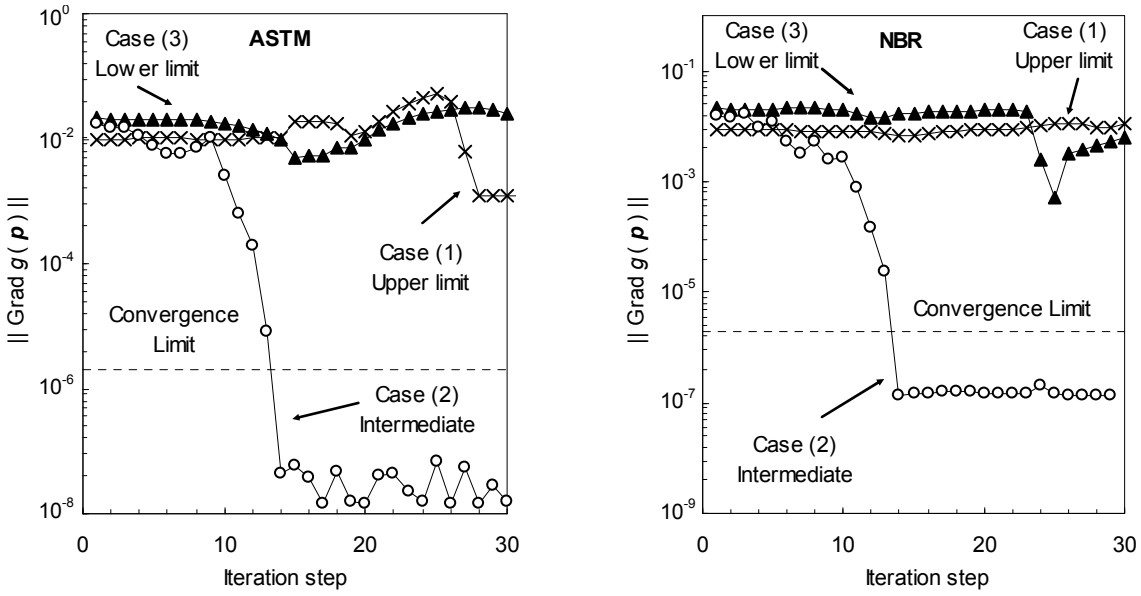

Figure 3: Evolution of $\|\nabla g_0\|$ for the initial set of parameters given in Table 3 for the BFGS method.

Table 5. Final parameters determined for ASTM and NBR specimens using the *GA – BFGS* hybrid approach.

Method	Stage	σ_∞ [*MPa*]	σ_0 [*MPa*]	ζ [*MPa*]	δ [m/m]	*g*(*p*)	CPU
ASTM	(A) *GA*	731.72	440.00	505.95	26.540	0.01200340080	1 h 26 m
	(B) *BFGS*	708.40	421.98	592.60	35.429	0.00266693349	32 m (*)
NBR	(A) *GA*	737.98	437.30	469.74	31.075	0.00802597455	1 h 57 m
	(B) *BFGS*	720.65	426.61	552.82	35.042	0.00480087739	30 (*)

(*) The total CPU time are: ASTM = 1 h 58 m and NBR = 2 h 27 m.

In this example, the parameters used for the *GA* are as follows: population of 60 individuals, parameters encoded with 10 bits, 85 % of combination probability and 5 % of mutation. It is interesting to note that smaller number of bits leads to "convergence" (difference between $g_0(\boldsymbol{p})$ of the worst and best individuals, ε_{GA}) at smaller number of generations, but with larger errors. In this case, larger errors are not relevant since the parameters obtained by applying the *GA* are used only as an initial approximation for the *BFGS* method. The stopping criterion used in this example is $\varepsilon_{GA} = 10^{-2}$.

Table 5 presents the parameter set obtained after stages (A) and (B) for ASTM and NBR specimens. The initial parameter set for the *BFGS* method, stage (B) of Table 5, were obtained after the *GA* reaches the stopping criterion. It is worthy to note that stricter stopping criteria would require larger number of generations, as indicated in Figure 4, without any improvement of the overall performance of the identification process.

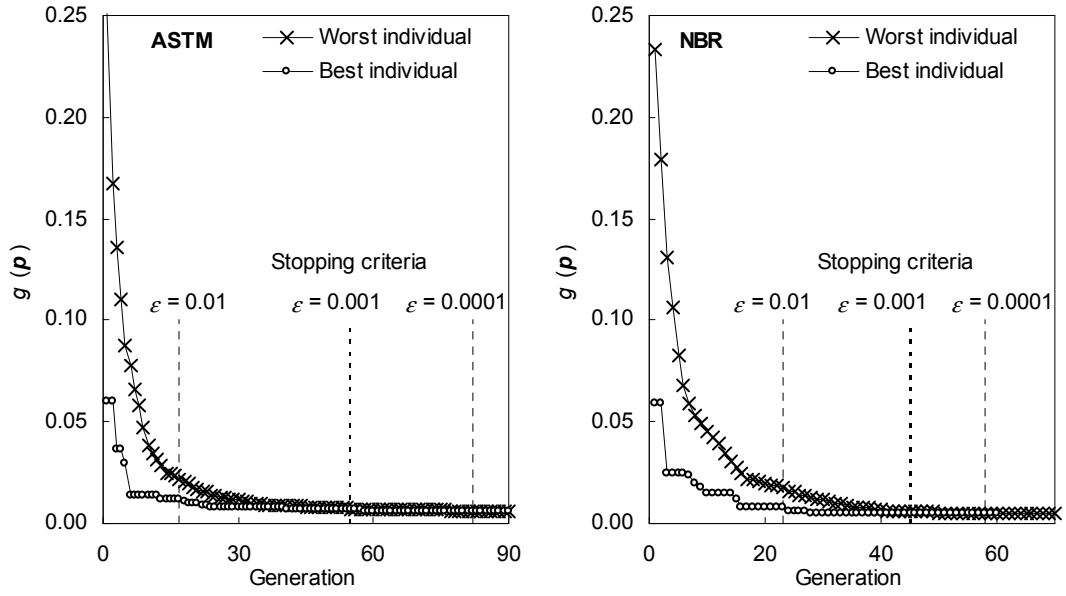

Figure 4: Evolution of the GA during Stage (A) and indication of the stopping creteria.

Case (2) of Table 4 (both ASTM and NBR) and Table 5 show that the *GA – BFGS hybrid method* yields the same parameters as the direct application of the *BFGS* technique. Therefore, it is possible to infer that such set of parameters indeed represent the global

minimum of the problem. Although the direct application of the *BFGS* method required less CPU time, its success is strongly dependent upon the initial parameters. On the other hand, in spite of requiring additional processing time, no convergence problems were observed when using the *GA – BFGS hybrid method*.

3 FINAL REMARKS

Parameter identification has become an essential task when developing new constitutive models. Direct measurement of constitutive parameters is not always possible thereby recommending use of inverse problem strategies, which in turn, are based upon optimization methods. In a first part, this work addressed identification procedures based on the *Univariate* approach, *Steepest Descent* and *BFGS* gradient-based methods and a *Genetic Algorithm*. A comparison of the aforementioned identification strategies shows that the *BFGS* method provided the best results (lower CPU time and objective function). However, this technique, as all gradient-based optimization methods, are strongly dependent upon the initial parameters and, therefore, liable to convergence problems, as discussed in a second example. Therefore, a *GA-BFGS* hybrid approach is proposed, i.e., the *GA* is applied first in order to estimate initial parameters for the *BFGS* method closer to the global minimum. The strategy was able to circumvent the convergence problems when attempting to determine material parameters of Carbon steel.

ACKNOWLEDGEMENTS

M. Vaz Jr. gratefully acknowledges the support provided by CNPq (National Council for Scientific and Technological Development – Project 301991/2009-0).

REFERENCES

[1] Muñoz-Rojas, P.A., da Cunda, L.A.B., Cardoso, E.L. , Vaz Jr., M, Creus, G.J. A mixed optimization approach for parameter identification applied to the Gurson damage model, in: Vaz Jr., M, de Souza Neto, E.A., Muñoz-Rojas, P.A., (Eds.), *Advanced Computational Materials Modeling: from Classical to Multi-scale Techniques*, Wiley-VCH, (2011) 165-204.

[2] Arora, J.S. *Introduction to Optimum Design*. McGraw-Hill (2001).

[3] Rao, S.S. *Engineering Optimization*. John Wiley & Sons (2009).

[4] Holland, J.H. *Adaptation in Natural and Artificial Systems*. MIT Press (2004).

[5] Chaparro, B.M., Thuillier, S., Menezes, L.F., Manach, P.Y. and Fernandes, J.V. Material parameters identification: Gradient-based, genetic and hybrid optimization algorithms. *Comput. Mater. Science* (2008) **44**: 339-346.

[6] Muñoz-Rojas, P.A., Cardoso, E.L. and Vaz Jr., M., Parameter identification of damage models using genetic algorithms. *Exp. Mech.* (2010) **50**: 627-634.

[7] Aguir, H., Belhadjsalah, H. and Hambli, R. Parameter identification of an elasto-plastic behaviour using artificial neural networks–genetic algorithm method. *Mat. Design* (2011) **32**:48-53.

[8] Ponthot, J.-P. and Kleinermann, J.-P., A cascade optimization methodology for automatic parameter identification and shape/process optimization in metal forming simulation. *Comput. Meth. Appl. Mech. Eng.* (2006) **195**: 5472-5508.

XI International Conference on Computational Plasticity. Fundamentals and Applications
COMPLAS XI
E. Oñate, D.R.J. Owen, D. Peric and B. Suárez (Eds)

PREDICTIVE CAPABILITY OF CONSTITUTIVE MODEL OUTSIDE THE RANGE OF CALIBRATION - COMPLAS XI

DAN WEDBERG*, LARS-ERIK LINDGREN†

* AB Sandvik Coromant, Metal Cutting Research, 811 81 Sandviken, Sweden
e-mail: dan.wedberg@sandvik.com, www.sandvik.com

† Division of Material Mechanics
Luleå University of Technology, SE-971 87 Luleå, Sweden
email: lars-erik-lindgren@ltu.se, www.ltu.se

Key words: Machining, Material model, Dislocation density, Extrapolation, High strain rates.

Abstract. Machining one of the most common manufacturing processes within the industry but it is also a process with extreme conditions in the vicinity of the cutting insert. Due to diversity of physical phenomena involved machining has proven to be complex and difficult to simulate. The chip formation process is in the vicinity of the cutting insert associated with highly localized severe deformations accompanied by high local temperatures rise. Furthermore, the strain rate can in the primary zone be very high (>50000 s^{-1}), far beyond what can be reached with conventional mechanical material tests. Therefore, the possibility to extrapolate the material model outside the calibration range with respect to strain rate is a wanted feature. It is recognized that the mechanical behavior at high strain rate differs considerably from that observed at low strain rates and that the flow stress increase rapidly with the strain rates above ~1000 s^{-1}. The predictive abilities outside as well as inside the calibration range of the empirical Johnson-Cook plasticity model and a dislocation density based model are compared and discussed with reference to AISI 316L stainless steel. The results clearly show the difficulty of obtaining a comprehensive material model that predicts the material behavior across the loading conditions that can occur in machining with good accuracy and that the accuracy of extrapolation is uncertain.

1 INTRODUCTION

Machining is a well recognized manufacturing process and one of the most common within the industry. Understanding of the material removal process is highly important and the ability to simulate machining are several, including determination and optimization of cutting tools design, cutting parameters, residual stresses and cutting process robustness to name a few. Machining has however proven to be particularly complex to simulate due to several numerical as well as modelling complications [1]. The work piece material during machining is forced to quickly change flow direction at the cutting edge vicinity to subsequently form a chip. These prerequisite give mainly rise to two main deformation zones, which are usually called the primary and the secondary deformation zone [1]. A third deformation zone can also be identified opposite the flank of the insert [2]. The major shearing of the work piece material takes place in the primary deformation zone and in addition to severe plastic

deformation and dissipated heat generations the strain rate can reach > 50000 s^{-1} within this zone [3]. The secondary deformation zone occurs in the contact between the chip and the insert after the material has gone through the first deformation zone. Due to the severe contact conditions with sticking and sliding at high pressure the local temperature is high within this zone. Heat is generated due to plastic generation and friction. Hence during machining the workpiece material locally experience severe strains, high strain rates and high temperatures causing hardening and softening. A material model must handle the involved complex interactions phenomena as plasticity, friction, heat generation, heat flow, material damage and microstructural changes of the workpiece material in order to be able to handle a wide range of strains, strain rates and temperatures.

The calibration of any material model is usually done based on data from material testing covering the relevant range of loading conditions of the intended application. The magnitude of strains, strain rate and temperatures involved in machining are however several orders higher than can be generated from conventional material tension and compression testing. Despite the fact that Split-Hopkinson is a technology that is becoming more common and that a strain rate of 10000 s^{-1} with large plastic strains [4] can be reached it is not sufficient to reach the extreme conditions that arise in the area around the cutting insert. Therefore the possibility to extrapolate the material model outside the calibration range without loss of accuracy is a highly wanted feature. This is not entirely trivial since materials exhibit different strain hardening and softening characteristic at different strain, strain rate and temperatures and that a marked increase in the strain rate sensitivity has been noticed for strain rates higher than approximately 1000 s^{-1} [5,6]. This significant increased strain rate sensitivity has been interpreted to different mechanisms for example increased dominance of dislocation drag [5], enhanced rate of dislocation and twin generation [6].

Considerable amount of work has been devoted to develop material models. The models can be divided into two major categories, empirical material models and physically based material models. The empirical models are solely based on curve fitting without any interpretation of the underlying physics and the deformation mechanisms. Hence the need for material data is relatively small which together with few parameters making them easy to use. The Johnson-Cook, J-C, plasticity model is an empirical material model that has been widely used to characterize the material response and is commonly used in FE-simulation of metal cutting. The physical based material models are on the other hand related to the underlying physics of deformation and the evolution of the microstructure. The predictive capabilities beyond the calibration range are therefore expected to be larger and more suitable for simulation of manufacturing processes involving large range and severe conditions of deformation, deformation rate and temperature. The predictive abilities outside as well as inside the calibration range of the empirical J-C plasticity model and a dislocation density based model, physical based, are in this study compared and discussed with reference to 316L stainless steel.

2 MATERIAL MODELS

2.1 Johnson-Cook plasticity model

The flow stress response of the J-C plasticity model is a multiplication of the individual strain, strain rate and temperature effects and is written

$$\sigma_y = \left(A + B\bar{\varepsilon}^{p^n} \right) \left[1 + C \ln\left(\frac{\dot{\bar{\varepsilon}}^p}{\dot{\bar{\varepsilon}}_{ref}} \right) \right] \left[1 - \left(\frac{T - T_{room}}{T_{melt} - T_{room}} \right)^m \right] \tag{1}$$

where $\bar{\varepsilon}^p$ is the effective plastic strain, $\dot{\bar{\varepsilon}}^p$ is the effective plastic strain rate, $\dot{\bar{\varepsilon}}_{ref}$ represents a reference strain rate, T_{melt} is the melting temperatures, T_{room} is the room temperature. Parameters A, B, C, n and m are fitted user defined material parameters.

2.2 Dislocation density model

Dislocations and their motions have a decisive role in inelastic deformation of metals and alloys, especially at room temperatures. Their motion through the crystals of a polycrystalline material and their interaction is however a complex phenomenon. The model presented here assumes that dislocation glide is the dominant contribution to plastic straining. Climb is also included. The dislocation density model includes a coupled set of evolution equation for the state variables, dislocation density and vacancy concentration, in order to keep track of the hardening/softening behavior of the material [7,8,9].

The macroscopic flow stress is assumed to consists of additive components as in this case consists of three components according to

$$\sigma_y = \sigma_G + \sigma^* + \sigma_{drag} \tag{2}$$

where σ_G and σ^* are the long-range athermal component respectively the short-range contributions to the flow stress. The last component, σ_{drag}, accounts for phonon and electron drag. The first component, σ_G, is the stress needed to overcome the long-range interactions lattice distortions due to the dislocation substructure and grain boundaries. The second component, σ^*, is the stress needed for the dislocation to pass through the lattice and to pass short-range obstacles. Thermal vibrations will then also assist the dislocation when passing these obstacles. The long-range stress component is commonly written as

$$\sigma_G = m\alpha G b \sqrt{\rho_i} \tag{3}$$

where m is the Taylor orientation factor, α is a proportionality factor, G is the temperature dependent shear modulus, b is the magnitude of Burgers vector and ρ_i is the immobile dislocation density.

The short-range stress components may be written as,

$$\sigma^* = \tau_0 G \left(1 - \left(\frac{kT}{\Delta f_0 G b^3} \ln\left(\frac{\dot{\bar{\varepsilon}}_{ref}}{\dot{\bar{\varepsilon}}^p} \right) \right)^{1/q} \right)^{1/p} \tag{4}$$

where Δf_0 denote the required free energy needed to overcome the lattice resistance or obstacles without assistance from external stress, τ_0 denote the athermal flow strength required to move the dislocation past barriers without assistance of thermal energy,

$\dot{\bar{\varepsilon}}_{ref}$ denote the reference strain rate. The exponent p and q characterize the barrier profiles and usually have values between $0 \le p \le 1$ respectively $1 \le q \le 2$.

The component that accounts for phonon and electron drag is written as [8]

$$\sigma_{drag} = G\left(C_e + C_p \frac{T}{300}\right)\dot{\bar{\varepsilon}}^p \tag{5}$$

where T denotes the temperature, G the shear modulus, C_e and C_p is the electron drag respectively the phonon drag coefficient.

The evolution of the structure is considered to consist of a hardening and a recovery process. The total dislocation density may be characterized by the creation process, the immobilization process where dislocation get stucked, the re-mobilization process where the opposite occur and the annihilation process [7]. The total dislocation density in this model is considered to consist of both immobile dislocation density and mobile dislocation density. The used model assumes that the mobile dislocation density is stress and strain independent and much smaller than the immobile ones. Hence the evolution equation is written

$$\dot{\rho}_i = \dot{\rho}_i^{(+)} - \dot{\rho}_i^{(-)} \tag{6}$$

where index i denotes the immobile dislocations. It has been observed that dislocation tends to cluster into cells and subgrains during plastic deformation [10] and forming LEDS (Low-Energy Dislocation Structures) [11]. This structure evolution influences both the hardening and the recovery. The increase in immobile dislocation density is assumed to be related to the plastic strain rate and may therefore be written according to

$$\dot{\rho}_i^{(+)} = \frac{m}{b}\frac{1}{\Lambda}\dot{\bar{\varepsilon}}^p \tag{7}$$

where Λ denote the mean free path which is a function of the size of the grains and the dislocation subcell diameter. The mean free path is assumed to be a combination of the distance between the grain boundaries, g, and the dislocation subcell diameter, s, as

$$\frac{1}{\Lambda} = \left(\frac{1}{g} + \frac{1}{s}\right) \tag{8}$$

where s is defined as

$$s = K_c \frac{1}{\sqrt{\rho_i}} + s_\infty \tag{9}$$

Reduction in dislocation densities may occur by different processes eg by dislocation glide and/or climb. This model takes into account the recovery by dislocation glide and climb. The former is described by

$$\dot{\rho}_i^{(-)} = \Omega \rho_i \dot{\bar{\varepsilon}}^p \tag{10}$$

where Ω is a recovery function which may depends on the temperature and strain rate. Altough in this model only of the temperatur. Recovery by climb is describe by

$$\dot{\rho}_i^{(-)} = 2c_\gamma D_v \frac{c_v}{c_v^{eq}} \frac{Gb^3}{kT} \left(\rho_i^2 - \rho_{eq}^2 \right) \tag{11}$$

where c_v is the vacancy fraction, c_v^{eq} is the thermal equilibrium vacancy concentration, D_v is the diffusivity and c_γ is a calibration parameter. More details are found in [9].

2.3 Calibration procedure

The calibration of the presented dislocation density model and the J-C model was based upon uniaxial compression tests of SANMAC 316L at low strain rates, with a maximum strain rate and elevated temperature of 10 s^{-1} respectively 1300 °C, and at high strain rates, with a maximum strain rate and elevated temperature of 9000 s^{-1} respectively 950 °C. The temperatures were measured during the test at the low strain rates while computed assuming adiabatic heating for the tests at higher strain rates. The tests at the higher strain rates were performed via a Split-Hopkinson pressure bar (SHPB). The actual parameter determinations were done by an error minimization method via a developed toolbox in Matlab in combination with a subset of test data.

The parameters that need to be determined in the dislocation density model are shown in Table 1. Of these are the parameters K_c and Ω temperature dependent. A linear interpolation has been used between each test temperature and therefore each one of them has 9 values to be calibrated. Thermal expansion, Young's modulus, Poisson's ratio and shear modulus are also needed along with other physical constants. More details are given in [9]. The five parameters to be determined for the J-C model are given in section 2.1.

Table 1: Parameters to be determined in the dislocation density model

α	K_c	s_∞	ρ_{i0}	Ω	c_γ	τ_0	Δf_0	p	q	c_s^{Cr}	h^{Cr}	c_s^{Ni}	h^{Ni}	C_p	B_e/B_p

3 RESULTS AND DISCUSSIONS

The dislocation density model has shown to give an overall good agreement with measured stress-strain curves in the strain rate range from 0.01 to 10 s^{-1} and from room temperature up to 1300 °C [9]. But if this material model with the optimized parameters at low strain rates are extrapolated and compared with measured stress-strain curves at high strain rates the same good agreement are not obtained. This was shown in [12]. Hence this discrepancy indicates that new physics are entering during deformation at these high strain rates and extrapolation from these conditions did not work. The observed increased strain rate sensitivity has been interpreted to different mechanisms for example increased dominance of dislocation drag [5], enhanced rate of dislocation and twin generation [6]. In an attempt to improve the predictability of the model throughout the strain rate range from low to high the physical phenomena dislocation drag has been implemented followed by a re-calibration of the model with given conditions. Some examples of measured stress-strain curves compared with predicted response of the dislocation density model at low strain rates and high strain rates are shown in Figure 1 at some different temperatures. The presented strain rate is the average strain rate.

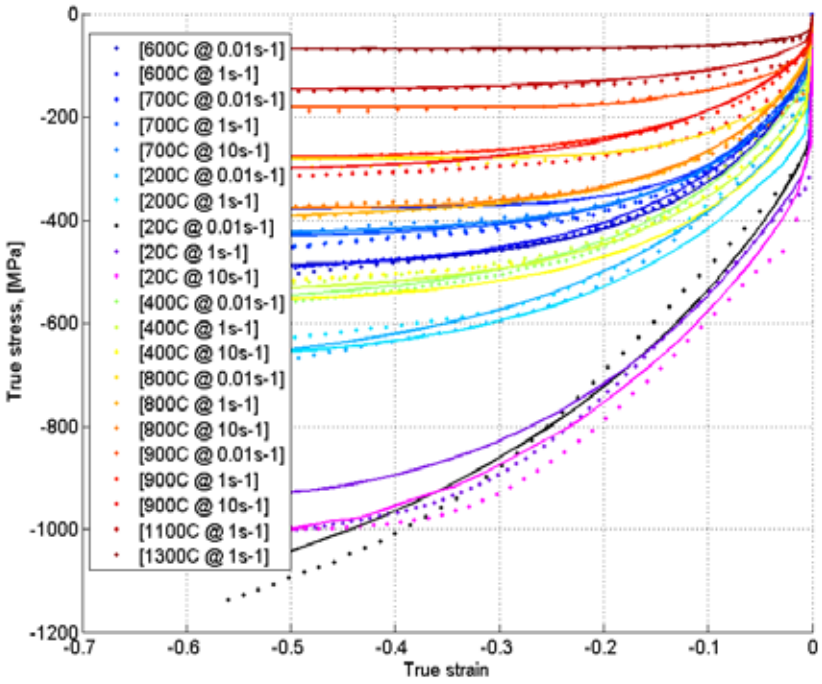

a)

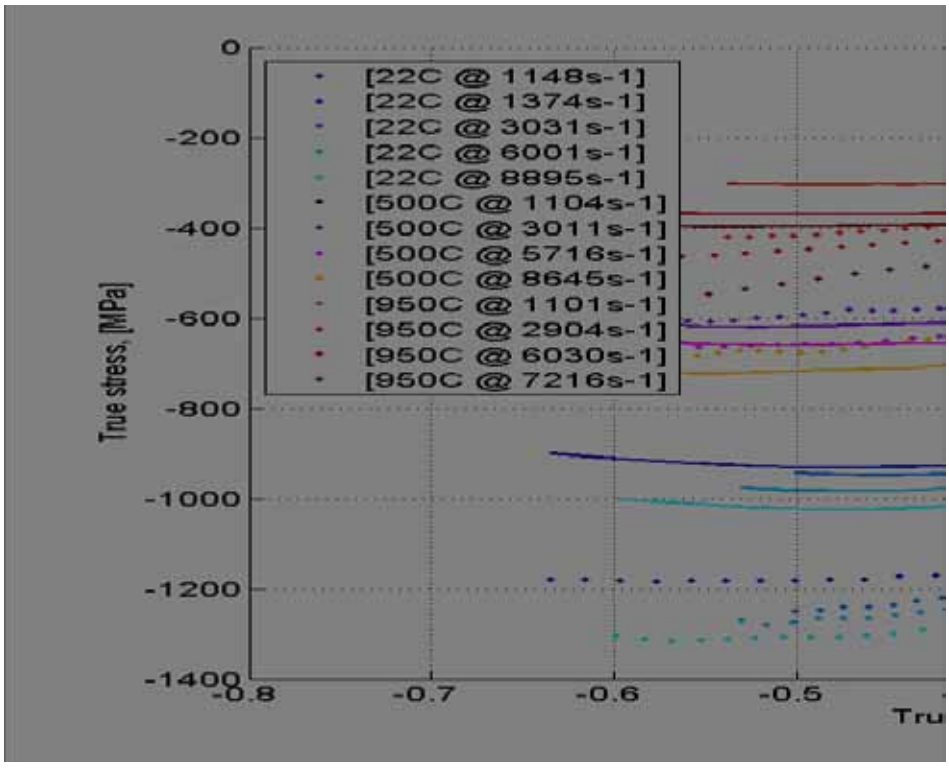

b)

Figure 1: Measured stress-strain curves and predicted response of the dislocation density model, lines, a) at low strain rates and b) high strain rates. Note: the vertical sequence of the curves fall with increased strain rate and reduced temperature.

The consistency at low strain rates is still good but the same consistency is not obtained at high strain rates. The predicted responses at 500 °C are little to high while little too low at room temperatures within the high strain rate range. Hence, dislocation drag followed by the re-calibration is not sufficient in order to cover the whole strain rate range from low to high. This indicates that additional and/or other deformation mechanisms are active and that the underlying dominated deformation mechanism changes. This will not be discussed further here. However, it is possible to get a relatively good consistency within the high strain rates range. Figure 2 shows the results from a re-calibration of K_c and Δf_0 based on data at high strain rates.

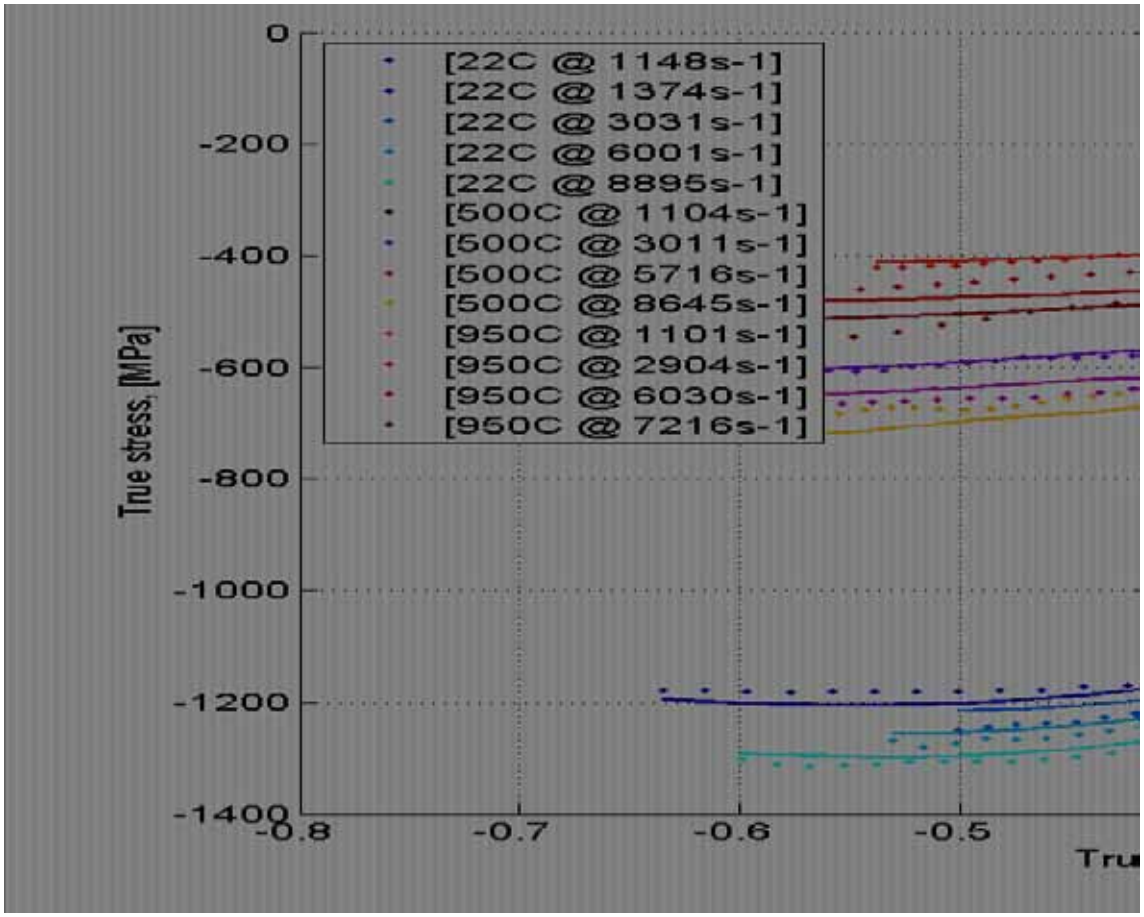

Figure 2: Measured stress-strain curves and predicted response of the dislocation density model, lines, where the latter is re-calibrated based on high strain rate data. Note: the vertical sequence of the curves fall with increased strain rate and reduced temperature.

The J-C plasticity model did not show the same consistency as the dislocation density model when subjected to the entire test data at low strain rate in [9] and it also failed to predict the material response at high strain rates with good agreements [12]. Better agreement, but far from satisfactory, was obtained if the parameters where re-calibrated based on only high strain data. The parameter and the predicted response are shown in Table 2 and Figure 3. The predicted responses at 950 °C and at room temperature are too low together with

significant differences in the work hardening rate at the latter temperature.

Table 2: Parameters for J-C plasticity model within the high strain rate range

Case	A	B	n	C	$\dot{\varepsilon}_{ref}$	m
High	245 MPa	580 MPa	0.587	0.117	1 s^{-1}	0.733

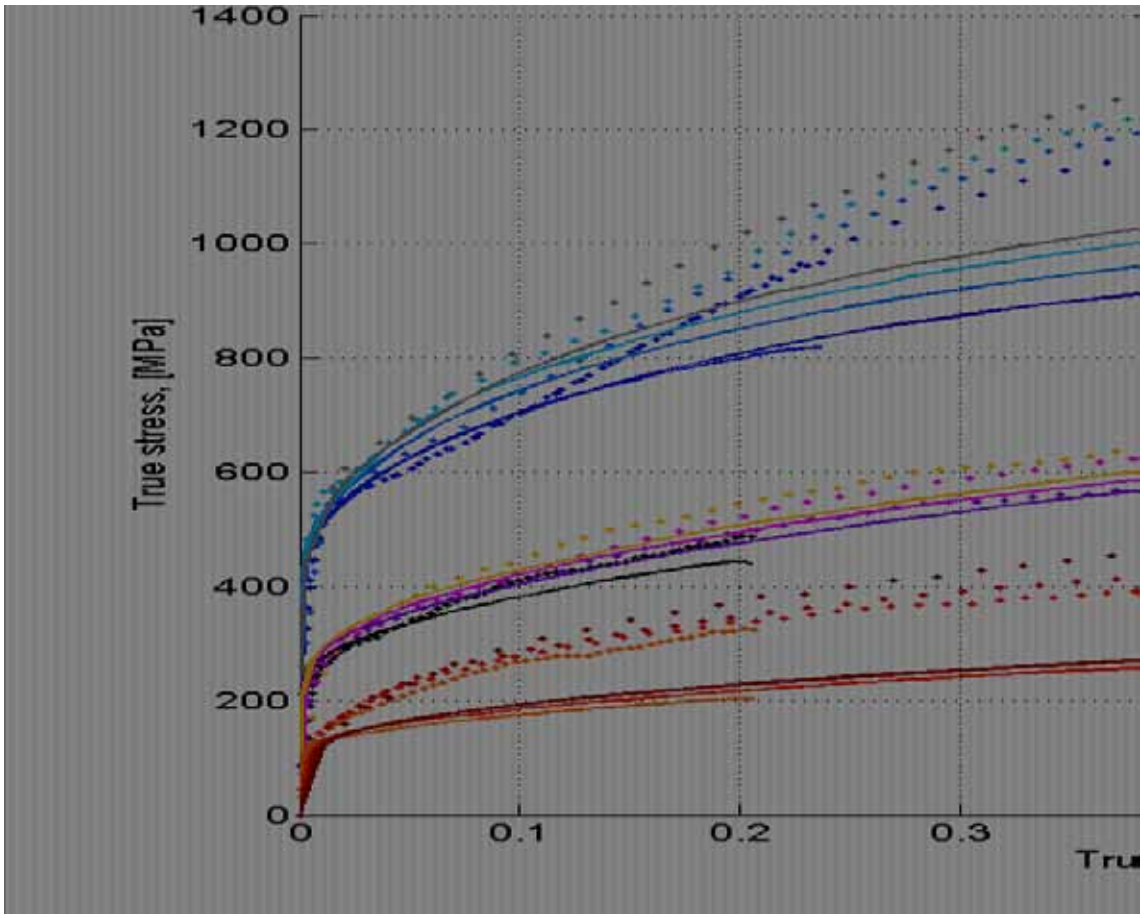

Figure 3: Measured stress-strain curves and predicted response of the J-C plasticity model, lines, where the latter has been re-calibrated based on high strain rate data. Note: the vertical sequence of the curves fall with reduced strain rate and increased temperature.

The reliability of extrapolation has so far proven to be uncertain. Although a wide available strain rate data range with a maximum strain rate of about 10000 s^{-1} extrapolation to even higher strain rates is needed to cover the loading conditions that may appear in machining simulations. Lack of material data at these extreme strain rates means that it is neither possible to calibrate or check the predictability range of the material model and it makes it even more uncertain. Despite this an extrapolation to strain rates up towards 50000s^{-1} were performed based on the calibrated dislocation density model and the J-C plasticity model at high strain rates shown in Figure 2 and 3. The results are shown in Figure 4 together with presented results from SHPB-testing of 316L at a plastic strain of 0.1 and room temperature in

[12]. The difference in the predicted results between the dislocation density model and the J-C model, when extrapolated to these extreme strain rates, is noticeable. The predicted strain rate sensitivity is higher in the latter and has an appearance that complies with the current perception of increased strain rate sensitivity > 1000 s^{-1} but how precisely the extrapolation corresponds with the behavior of the material is difficult to say. More research is still needed.

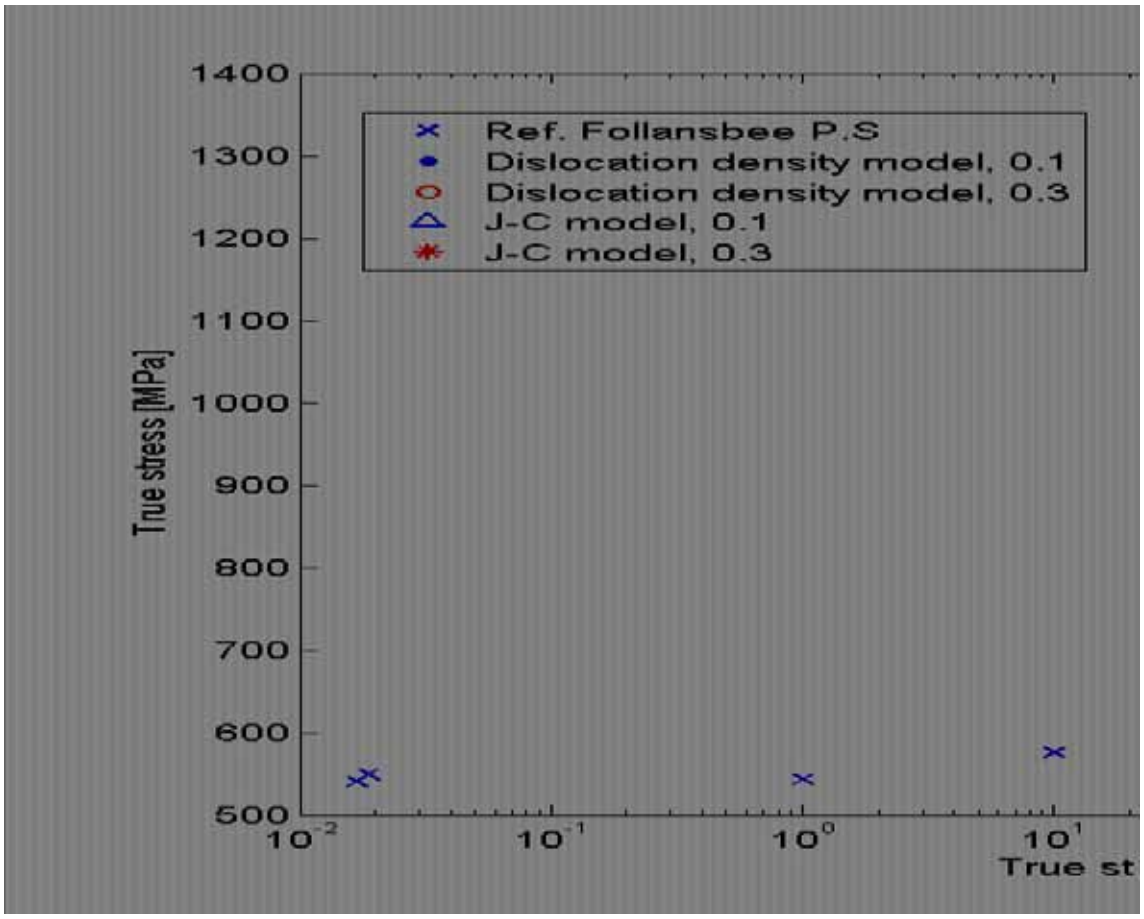

Figure 4: Measured flow stress, presented in [12], and predicted flow stress of the dislocation density model and the J-C plasticity model as function of strain rate at true strain of 0.10, 0.30 and room temperature. The dislocation density model and the J-C model are based on calibration at high strain rate data.

4 CONCLUSION

- The J-C plasticity model did not show the same good ability as the dislocation density model to reproduce the material behavior in the strain rate range and temperature range from 0.01 to 10 s^{-1} respectively from room temperature to 1300 °C. Neither the dislocation density model without phonon drag nor the J-C model predicted the material behavior at high strain rates particularly well when extrapolated.
- Inclusion of phonon and electron drags within the dislocation density model improved the accuracy in the high strain rate range without any major changes in its prediction capability at low strain rates as the effects of phonon and electron drags

are small at these strain rates. The predictability is much better than the J-C plasticity model. However, we still consider the agreement with measurements to be somewhat unsatisfactorily. The discrepancy may be due to other deformation mechanisms or can be due to uncertainties and assumptions in the SHPB-testing.

- Extrapolated dislocation density model, calibrated with stress-strain data at high strain rates, shows higher strain rate sensitivity within the strain rate range of 10000-50000 s^{-1} than the extrapolated J-C plasticity model calibrated within the same data range. This is due to the linear dependency on strain rate for the phonon-term whereas the J-C model has a logarithmic dependency. However, we have not data available to validate the predictable ability.
- The work clearly shows the difficulty of obtaining a comprehensive material model that predicts the material behavior across the loading conditions that can occur in machining with good accuracy.

ACKNOWLEDGEMENT

Swedish Research Council, grant no 1397-2005.

REFERENCES

[1] Vaz, Jr., Owen, D., Kalhori, V., Lundblad, M., Lindgren, L-E. Modelling and simulation of machining processes. *Arch Comput Methods Eng* (2007) **14**:173-204.

[2] Altintas, Y. *Manufacturing automation.* Cambridge University Press, (2000).

[3] Poulachon, G., Moisan, A., Jawahir, I.S. On modelling the influence of thermo-mechanical behavior in chip formation during hard turning of 100Cr6 bearing steel. *Annals of CIRP* (2001) **50/1**:31-36.

[4] ASM Handbook. *Mechanical testing and evaluation.* Vol. 8., (2000).

[5] Regazzoni, G., Kocks, U.F., Follansbee, P.S. Dislocation kinetics at high strain rates. *Acta Metall* (1987) **35**:2865-2875.

[6] Lee, W.S., Lin, C.F., Liu, T.J. Strain rate dependence of impact properties of sintered 316L stainless steel. *Journal of Nuclear Materials* (2006) **359**:247-257.

[7] Bergström, Y. A dislocation model for the stress-strain behavior of polycrystalline α-Fe with special emphasis on the variation of the densities of mobile and immobile dislocations. *Materials Science & Engineering* (1969/70) **5**:193-200.

[8] Frost, H.J., Ashby, M.F. *Deformation-Mechanism Maps – The Plasticity and Creep of Metals and Ceramics*. Pergamon Press.

[9] Lindgren, L.-E., Domkin, K., Hansson, S. Dislocation, vacancies and solute diffusion in physical based plasticity model for AISI 316L. *Mech. of Materials* (2008) **40**:907-919.

[10] Holt, D. Dislocation cell formation in metals. *Journal of Applied Physics* (1970) **41**(8):3197-3201.

[11] Kuhlman-Wilsdorf, D. Q:Dislocation structure – how far from equilibrium? A: Very close indeed. *Materials Science & Engineering* (2001) **A315**:211-216.

[12] Lindgren, L.-E., Wedberg, D. Material modelling and physical based models with particular emphasis on high strain rates, in: A, K. (Ed), *International Symposium on Plasticity* (2009). NEAT, Inc, St Thomas, USA.

[13] Follansbee, P.S. High-strain-rate deformation of FCC metals and alloys, in

Metallurgical applications of shock-wave and high-strain-rate phenomena, Murr, L.E., Staudhammer K.P., Meyers, M.A. (Ed) (1986).

XI International Conference on Computational Plasticity. Fundamentals and Applications
COMPLAS XI
E. Oñate, D.R.J. Owen, D. Peric and B. Suárez (Eds)

PROCESS ANALYSIS BASED ON EXPERIMENTAL TESTS AND NUMERICAL MODELLING OF SINGLE POINT INCREMENTAL FORMING OF SHEET METAL: EFFECT OF THE PRINCIPAL PROCESS PARAMETERS

R. BAHLOUL*, H. ARFA* AND H. BELHADJ SALAH*

* Laboratoire de Génie Mécanique (LGM)
Ecole Nationale d'Ingénieurs de Monastir (ENIM)
Université de Monastir
Avenue Ibn Eljazzar, 5019 Monastir, Tunisia
E-mail: bahloul_riadh@yahoo.fr, Web page: http://www.lgm.rnu.tn

Key words: Single Point Incremental Forming (SPIF), CNC Programming, Experimental Investigation, Finite Element Modelling, Punch Force Evolutions.

Abstract. Incremental sheet forming (ISF) is a very promising technology to manufacture sheet metal products by the CNC controlled movement of a simple forming tool. It is considered as an innovative and flexible sheet metal forming technology for small batch production and prototyping, which does not require any dedicated die or punch to form a complex shape. Although incremental sheet forming is a slow process, the cost reduction linked to the fact that punches or dies are avoided, makes it a very suitable process for low series production, in comparison with the traditional stamping or drawing processes. This paper investigates the process of single point incremental forming of aluminum truncated cones and square pyramids geometries both experimentally and numerically. Concerning the numerical simulation, the finite element models are established to simulate the process by using a static implicit finite element code ABAQUS/Standard. In this article, the reported approaches were mainly focused on the influence of some crucial computational parameters. The influence of several parameters will be discussed: the initial sheet thickness and the workpiece geometry. The output of the simulation is given in terms of the punch forces evolution generated in this forming process and the final geometry. A comparison between the simulation results and the experimental data is made to assess the suitability of the numerical models. Experimental and numerical results obtained allow having a better knowledge of mechanical responses from different parts manufactured by SPIF with the aim to improve their accuracy. Predicted results show good agreement with experimental data for these geometries of the cones and pyramids. It is also concluded that the numerical simulation might be exploited for optimization of the incremental forming process of sheet metal.

1 INTRODUCTION

Single point incremental forming (SPIF) is an innovative process which allows to produce complex sheet components by CNC movement of a simple tool, with or without the combined use of simple dies [1]. Blank material is completely clamped by a simple frame and an

hemispherical punch is used as deforming tool (Figure 1). In this context, Single Point Incremental Forming may constitute a suitable industrial alternative, especially if one or few parts have to be produced, since no expensive dies are required. In the mean time, process mechanics is mainly characterised by stretching condition [2]: therefore a relevant sheet thinning occurs, which penalizes process suitability. More in detail, sheet thinning in the deformed zone may be approximated through the well known sine law, which relates the final thickness to the slope of the formed surface [3]. Actually some relevant deviations from this simple model are highlighted carrying out simple SPIF experiments.

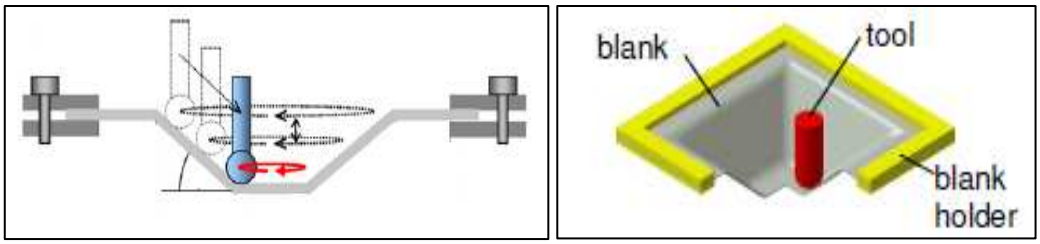

Figure 1: Single point incremental forming SPIF

Many papers have been published on the incremental forming process of sheet metal, most of which are concerned with the experimental work [4-6]. In this context and since the 2005 review article, Ham and Jeswiet [7,8] performed an experimental investigation on the effects of process variables on formability of various aluminum alloys in a systematic way using two factorial designs of experiments. They used the maximum formable angle as the measure of formability. Process variables studied included feed rate, spindle rotation speed, step size and forming angle. It was reported that faster spindle rotation speed improves formability and step size has little effect on the maximum forming angle, whereas the material thickness, tool size and the interaction between material thickness and tool size have a considerable influence on maximum forming angle. Kopac and Kampus [9] presented in their work the process controlled by CNC milling machine-tool together with CAD/CAM Master Cam system and a smooth forming tool. With experimental testing and measurements the limits of forming without a full-size model were defined. By using a simple full-size model and the concept where the sheet metal can move vertically in the clamping device, better results and products were obtained. An evaluation of the maximum slope angle of simple geometries was carried out by Capece Minutolo et al. [10] by means of an incremental forming process of aluminum alloy sheets. In their applications, maximum slope angle of frustums of pyramid and cone has been evaluated. This evaluation has been performed by an experimental tests program, that has foreseen the carrying out of geometries for different slope angles, up to the observation of fractures. In the specific case, afterwards the mechanical characterization and the evaluation of the sheets formability, frustums of pyramid and cone, with different slope angles, have been carried out, up to the appearance of fractures in the sheet. Numerical simulation of incremental forming of sheet metal has been also carried out in some papers [11,12], in which however the tool path is relatively simple. Effect of tool path on the deformation behavior has not been discussed. Since there is no article to which can be referred for the practical use of the numerical simulation for this process, the authors think that it is of great worth to check its applicability from the view point of making the production process more efficient. Very recently some researchers have focused their attention on modelling and numerical simulation

in incremental forming. Hirt et al. [13] presented in their work two major process limits, namely the limitation on the maximum achievable wall angle, and the occurrence of geometric deviations. They proposed some forming strategies and process modelling for CNC incremental sheet forming to overcome these process limits, including the processing of tailor rolled blanks. Additionally, finite element modelling of the process is presented and discussed with respect to the prediction of the forming limits of ISF. In 2004, Bambach et al. [14] developed a finite element modelling of the ISF process. In particular, the outcome of different multistage strategies is modelled and compared to collated experimental results regarding aspects such as sheet thickness and the onset of wrinkling. Moreover, the feasibility of modelling the geometry of a part is investigated as this is of major importance with respect to optimizing the geometric accuracy. Experimental validation is achieved by optical deformation measurement that gives the local displacements and strains of the sheet during forming as benchmark quantities for the simulation. The numerical simulation may provide technical support to the designers only if the simulation time is comparable with the trial and error tests. With this aim, both experimental tests and three-dimensional FE model of single point incremental forming (SPIF), derived by the application of an explicit approach, have been developed by Ambrogio et al. [15] and a suitable application for the process design has been defined in their applications. Single point incremental forming (SPIF) suffers from process window limitations which are strongly determined by the maximum achievable forming angle [16]. In this subject, an experimentally explored multi-step tool paths strategy is reported and the resulting part geometries compared to simulation output. Sheet thicknesses and strains achieved with these multi-step tool paths were verified and contributed to better understanding of the material relocation mechanism underlying the enlarged process window. In the present research, deformation behaviour of sheet metal in single point incremental forming process (SPIF) is numerically simulated using a static implicit finite element code ABAQUS/Standard. Furthermore, several incremental forming tests were carried out on Al 3003-O Aluminum Alloy blanks utilizing a properly designed fixture mounted on a 3-axis controlled CNC milling machine equipped with a special tool. The objective of this study is to investigate the effects of two commonly varied forming process parameters on the force required to form the sheet metal. These are the initial sheet thickness and the workpiece geometry. A useful control of the process by determining and monitoring the forces between the punch and the sheet is aimed. The effect of the initial thickness variation on the evolution of the efforts provided by tool is studied in addition to the influence of the final workpiece geometry on the thickness distribution of final product is also considered.

2 EXPERIMENTAL PLATFORM

The research activity was carried out through the two following phases: first of all a set of experiments [17], characterized by different geometrical conditions, were carried out using a 3-axis CNC vertical milling machine (Figure 2) as a platform to develop the ISF process. The forming tool consists in a cylindrical rotating punch with 10 mm diameter and hemispherical end shape which it was used simply as a tool (one-point incremental forming). The tool path was specified on the CNC milling machine through a part program: for each test a subroutine has been developed to describe the tool trajectory from CAM procedure depending on the testing conditions. Such trajectory includes both the movement in the horizontal plane (i.e. the x-y table of the milling machine) and the tool depth at each loop along the Z-axis. The blank,

which had square shape and dimensions equal to 200 mm×200 mm, was clamped using a properly designed framework; in this way the punch determines the extension of the blank which undergoes plastic deformation due to the punch movement.

Figure 2: The experimental equipment for SPIF experiments (three-axis milling machine tool - SPIF tooling system) [17]

To analyse the punch load, the force measuring set-up is shown in figure 2. It consists of a table type force sensor which was mounted between a steel fixture and the milling machine work-surface. This was a Kistler 9265B six-component force dynamometer and connected to it was a complementary Kistler 5017A 8-channel charge amplifier. The measuring system also includes charge amplifiers, data acquisition cards and a PC. The sampling rate in force measurement was 50 Hz.

3 NUMERICAL MODELLING OF SINGLE POINT INCREMENTAL FORMING

In this study we consider the single point incremental forming operations (SPIF). It is a progressive sheet metal forming operation characterised by large displacements and strains, and located deformations. The punch is a simple smooth ended tool with a diameter far smaller than the dimension of the part being made. Proceeding in an incremental way, the tool is moved along contours which follow the shape of the final geometry as described by CAD and CAM of CATIA software. It is very difficult in general to predict the forming loads applied by the tools and the thickness strain distribution of the final state of a deformation after the accumulation of numerous incremental deformation passes. Recently, finite element method (FEM) has facilitated the calculation of the punch forces during the whole deformation process and the thickness strain. In this investigation, elasto-plastic analysis of SPIF process by finite element method (FEM) was performed using a finite element code ABAQUS© software capable of handling large deformation. Finite element models are established to simulate aluminum truncated cones and pyramids.

3.1 The parts geometry of the applications

Reported simulations are mainly based on the production of simple workpiece geometry, a right truncated cone at 40 mm depth with circular base having the initial diameter of D = 180 mm. The second model shape to undertake the numerical study represents a truncated pyramid at 40 mm depth starting from the square base side length of l = 180 mm. These geometries for both the frustums of cone and pyramid are carried out with different

thicknesses and slope angles beginning from a square sheet with a side of 200 mm. The tool paths, whose examples are reported in figure 3, are characterized, for the frustums of cone, by a sequence of circular coils, the first of which presents D = 180 mm, while the feed along an edge has a step size p = 0.5 mm; for the frustums of pyramid, a sequence of square coils generates the tool path, the first of which presents l = 180 mm, and the feed along a Z direction has a step size p = 0.5 mm. For both of them, the maximum drawing depth is z = 40 mm.

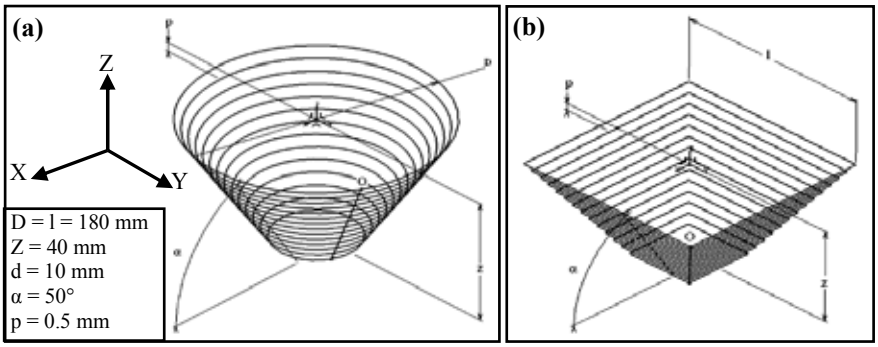

Figure 3: Geometries and dimensions carried out for some parts formed (a) Representative conical frustums with tool path and (b) Representative frustums square pyramid with tool path

The standard process parameters applied are 0.5 mm vertical step size, 10 mm tool diameter, 50° wall angle and the standard material used is 1.2 mm thick Al 3003-O [17]. Unless the parameter is being varied, these will be the constant values used.

3.2 Contour tool path generation using CATIA software

The determination of the trajectory defining the tool path becomes increasingly difficult depending strongly on the complexity of the final geometry of parts and the minimization of the incremental step size. In fact, the implementation of the trajectory in numerical model remains very difficult if a traditional methods based on manual calculation will be considered. Within the framework, we have to generate the trajectory describing the desired geometries characterizing the truncated cones and pyramids. Therefore in the present study, the parts were modelled in a commercial 3D CAD-CAM software CATIA V5R17, and the trajectories to control the tool motion in order to form the desired shapes were automatically generated with the CAM module. This software generates the tool path after defining all the parameters that characterize the working operation such as the tool dimensions, the step depth, etc... The path generation is automatic: the software evaluates and identifies the best tool path for the operation we want to do. Finally the 3D CAD/CAM uses a specific postprocessor to convert the trajectory of the tool so obtained into a numerical file. Figure $4a_1$ shows the trajectory, described by the tool during the forming of frustum of cone. In the analysis, the tool path is of type discontinuous represented by a series of contours generated along the Z-axis of the cone. A detailed view on the discontinuity zone is displayed in figure $4b_1$. The geometrical shape of a pyramidal model and the corresponding discontinuous tool path are reported in figure $4a_2$. In the same manner as the first geometry of the conical model, a zooming view on the discontinuity zone of the trajectory is presented by figure $4b_2$. It is characterized by square tool paths with constant step depth forming a pocket. In the case, the forming tool moves from the top to the bottom of the pocket, in which it follows a series of consecutive Z constant

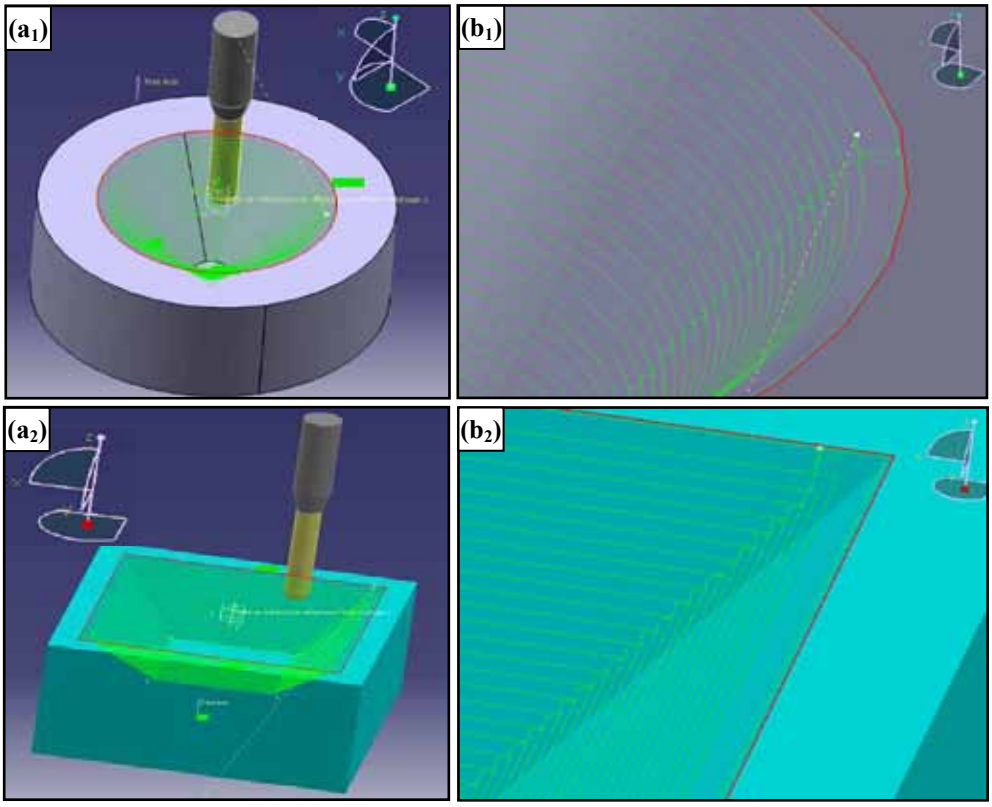

Figure 4: (a_1) Discontinuous trajectory for conical model; (b_1) A detailed view on the discontinuity zone; (a_2) A tool path for pyramidal geometry: discontinuous trajectory and (b_2) A detailed view on the discontinuity zone

contours with fixed step depth Δz constant during all the tool path. The steps shown are in sequential order and they are for incremental, unidirectional steps.

3.3 Description of the numerical model

As sheet metal forming involves large material rotation as well as strain, suitable algorithm should be employed in the FEA. In this investigation, a three-dimensional, elasto-plastic FE model is set up for the simulation of the SPIF process. Therefore, static simulations were conducted in this work by using the implicit FE package Abaqus/Standard like calculation algorithm capable of handling large deformation. Figure 5a reports the developed numerical model for the process in the initial position of tools. It shows the undeformed sheet modelled in this context. Modelling the interaction between the tool and the sheet is one of the most important considerations necessary to simulate the incremental forming process correctly. The punch, the blank-holder and the backing plate are modelled by adopting the assumption of an analytical rigid body hypothesis, while the sheet material is considered as elastic-plastic object. Since in the experiments the sheet was flooded with lubricant, the contact at the interface between sheet and tools follows Coulomb's friction law:

$$\tau_f = \mu\sigma_n \tag{1}$$

where τ_f is friction shear stress, σ_n is normal stress at interface and μ is the friction coefficient. Friction conditions between the forming tool and the sheet metal part have been accounted by considering sliding friction with a small relatively friction coefficient equal to $\mu_p = 0.09$. On the other hand, the value of the friction coefficient at the contact interfaces of blank-holder, sheet and designed backing plate is chosen to be equal to $\mu_b = 0.15$. Concerning the processing conditions including a punch displacement, the tool is considered as a rigid body and the corresponding boundary conditions are related to the defined path.

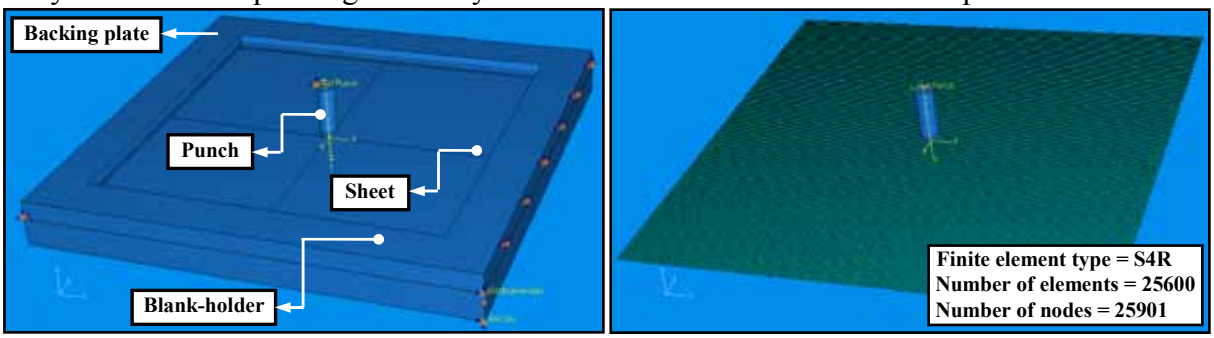

Figure 5: (a) Three-dimensional numerical simulation of single point incremental forming of sheet metal and (b) The finite element meshing configuration of the initial blank

Due to the 3D tool path movement, a fully three-dimensional spatial analysis has been realized. The finite element meshing configuration of the initial blank is shown in figure 5b. As a consequence, quadrilateral shell elements with 4 nodes and 6 degrees of freedom per node (S4R) and five Gaussian reduced integration points through the thickness direction were used. This is suitable for nonlinear material models and widely used in the forming problems of large deformation and large rotation. Al 3003-O sheets with a size of 200 mm×200 mm have been considered for different thicknesses. In the FE model, the global size of elements is 1.25 mm×1.25 mm and the blank was initially meshed with 25600 finite shell elements and 25901 nodes. In this way, for each node, both displacements and rotations (i.e. 6 degrees of freedom for each node) are taken into account. Furthermore, the element is subjected to both tractions and moments at each step of the deformation path. All simulations were performed on Windows XP PC Core 2 Quad with 2.5GHz processor and a read/write memory performance of 2096 Megabytes. The CPU time required to simulate the single point incremental forming process of truncated cone or square pyramid mentioned previously takes on average 5 days.

4 RESULTS AND DISCUSSION

This section provides information about the results obtained in the frame of the present work, with regards to the influence of different process parameters on the characteristics of the parts produced by incremental sheet forming and the comparison between the results predicted by the numerical model and the ones obtained experimentally. The objectives of these studies are to identify and analyze the effects of the principal geometrical parameters related to the initial sheet thickness, the wall angle and the part shape on the characterization of the process.

4.1 Force components acting on traveling punch during the incremental forming process

The graphs of figure 6 summarize the time plot of punch forces attained during the single point incremental forming process of the Al 3003-O Aluminum Alloy blanks. The evaluations of the magnitude of the loads provided by the punch in incremental CNC sheet metal forming process were investigated by applying two approaches: experimental analysis and numerical modelling on forces determination for improving knowledge of single point incremental forming. Both figures $6a_1$ and $6a_2$ represent the evolution of the three force components measured and predicted by experimental and numerical approaches respectively throughout the incremental forming process by producing a cone with standard process parameters by using a 10 mm diameter tool. The tool path used in this part of analysis follows a discontinuous trajectory. The initial thickness of the sheet metal before its working is fixed at a value equal to 1.2 mm. As it can be concluded from these graphs, a typical force curves start at zero once forming is initiated. As the tool pushes deeper into the metal, the force quickly increases until a depth is reached where the forces tend to remain approximately constant.

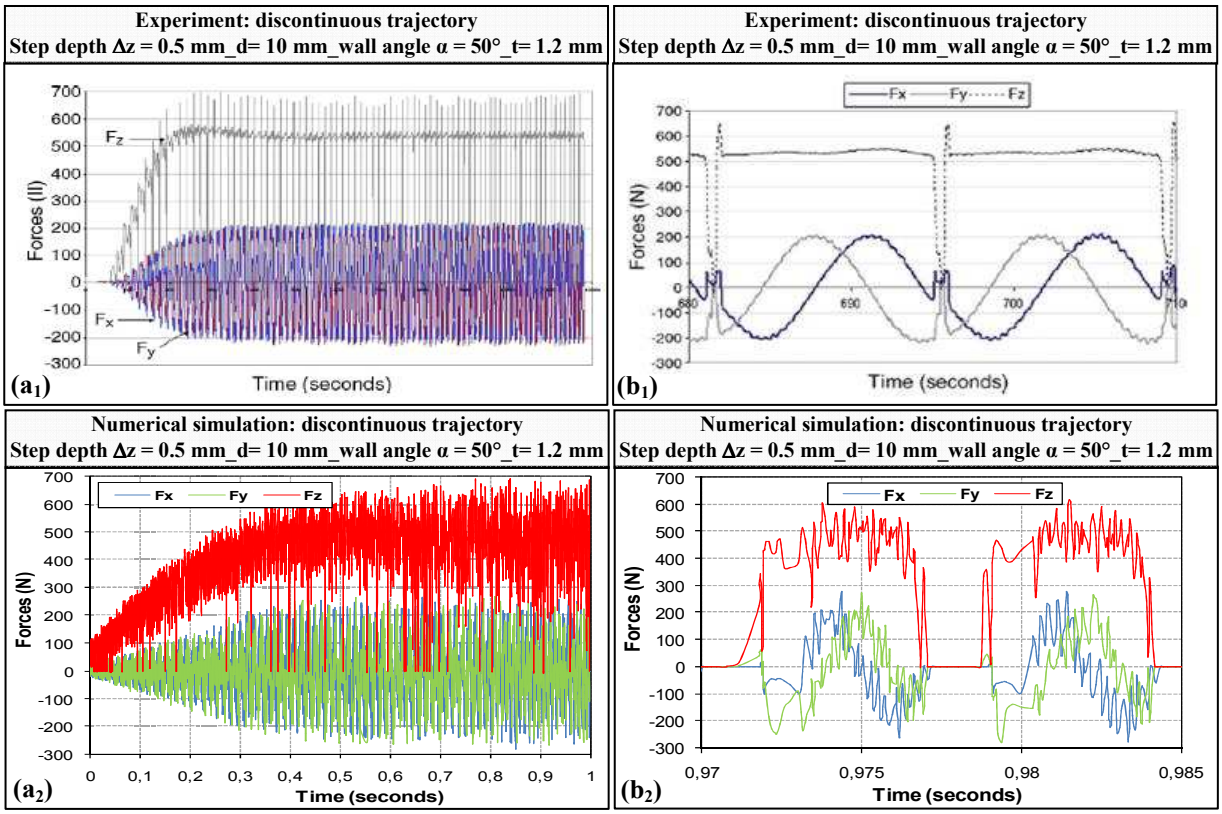

Figure 6: Experimental and numerical results for punch forces during the SPIF process by producing a cone with standard process parameters (a_i) Evolution of three forces components (F_x, F_y and F_z) exerted on the sheet metal (b_i) A detailed views of the forces measured experimentally and predicted by numerical simulation

This occurs for a number of reasons. Firstly, the tool does not have a contact area that is fully evolved until a number of contours have been made, and secondly, any effect induced by starting near the edge of the backing plate must be overcome. Comparing the force components measured in the experiment shown by figure $6a_1$ and the force diagram calculated

by using FEA described in figure $6a_2$, it can be said that the force patterns in the X and Y directions are not equal. This is due to sheet anisotropy and non-symmetric deformation mode. With an aim of validating the developed numerical model, we chose to make a localized enlargement of the preceding figures (Figures $6a_1$ and $6a_2$). This was meant to establish a more detailed comparison of the results determined by means of the two experimental and numerical approaches. Detailed views of the measured and simulated force components for two contours are demonstrated by figures $6b_1$ and $6b_2$. It can be observed from these two results that after completion of one contour, the F_z component first drops to zero when the tool finishes a contour radius and it moves to the next one, before reaching its peak value at the step down. It finally stabilizes when the tool moves along the contour. F_x and F_y forces change between their minimum and maximum values in a sinusoidal way according to the tool position relative to the dynamometer axis within one contour. A comparison of the numerical efforts of various components illustrated in figure $6b_2$ shows a fairly good agreement with collated experimental data (Figure $6b_1$). In fact, it can be noted a resemblance on the shape levels of curves into various representations. Except that we expect a minimal error of approximately 8% between the experimental amplitudes and those which are obtained from numerical calculations.

The square pyramid shaped box was formed on CNC milling machine, and it has been modelled by means of FEA. The force components were measured in X, Y and Z directions. Figures 7a and 7b show a detailed view of the experimental measures and the numerical prediction of three forces components (F_x, F_y and F_z) for two contours of the pyramid tool path. Unlike the forces in figure 6, F_x and F_y forces are approximately constant with changing sign depending on the tool position relative to the dynamometer. When the tool travels along the x-axis of the dynamometer, the F_x force reaches its maximum value, while the F_y force is at its maximum when the feed direction corresponds to the y-axis of the dynamometer. When the F_x/F_y force is at the maximum value, which corresponds to friction as well as to the limited forming action in the feed direction, the corresponding F_y/F_x force maintains an intermediate level. As it can be seen from the comparison of figures 7a and 7b, the force values are generally in agreement, except for high peak values in numerical study.

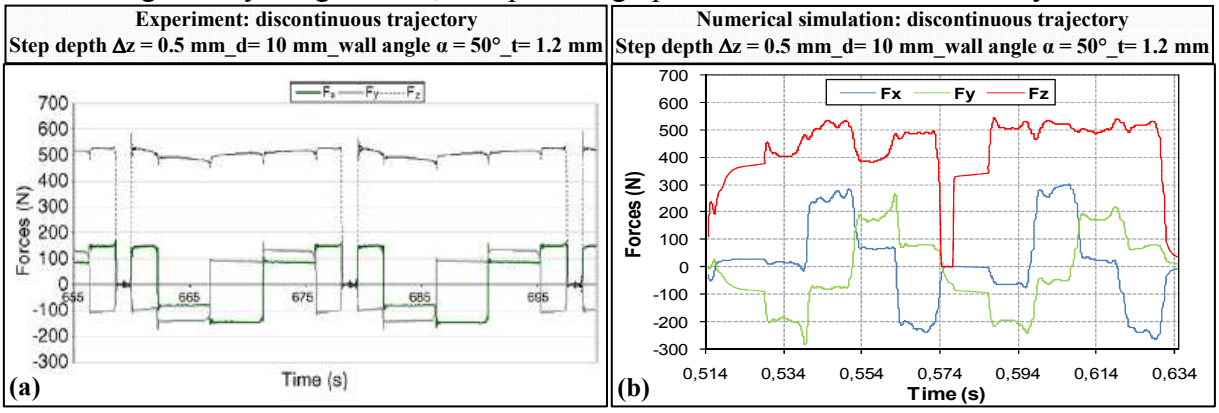

Figure 7: A detailed views of the forces F_x, F_y and F_z for two contours of the pyramid tool path (a) Experimental investigation (b) Numerical prediction

Note that the time in figures 7a and 7b is not in scale, i.e. the comparison can be made considering the patterns of load curves. Generally these peaks occur in the corners of the

pyramid when the tool is making the vertical step downwards, as the tools' moving direction changes rapidly. Moreover, we find the points of discontinuity of the trajectory. The latter correspond to the zero values of the efforts and the resumption of a new cycle when a new incrementing is controlled by the tool.

4.2 Influence of sheet thickness: force trend at the variation of initial sheet thickness

In order to make a comparison between the results obtained for conical and pyramidal geometry, we chose to represent all force vector sum curves in the same figure. Examples of the Abaqus predicted total forces acting on the traveling tool during forming operation are presented in figure 8 for cones and pyramids parts formed by using 1.2, 1.5 and 2 mm thick. From figure 8, it can be seen that the resultant forces for cones and pyramids evolve according to identical trends. The force vector sums for pyramids are of the same order of magnitudes as for cones for identical process parameters, although the individual F_x, F_y and F_z force components show different patterns. First of all, the instantaneous simulated force value depends on the sheet thickness as shown in figure 8. Besides, a strong correlation exists between the forming load and the thickness: to put it in a more detailed way, the increase in the above-mentioned geometrical parameter leads to the increase of the numerically predicted load as well.

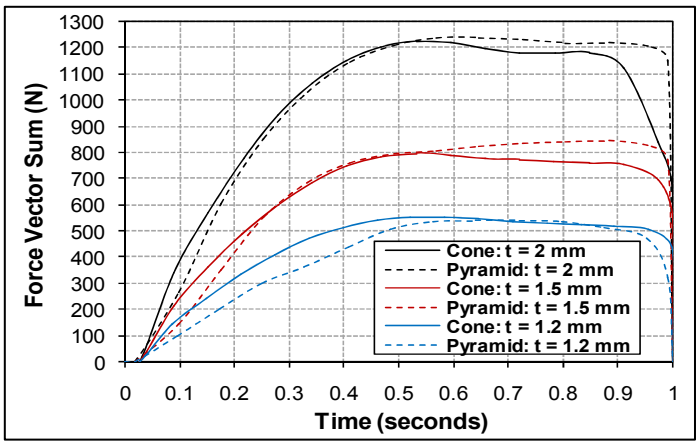

Figure 8: Simulated force curves for cones and pyramids parts formed using 1.2, 1.5 and 2 mm thick Al 3103-O: a comparison between the two parts geometry for discontinuous tool path

Figure 9 shows the results obtained in the force measurements performed in the way described previously, in comparison with the values of the magnitude of force required to form a given part predicted by the FEM process model. As the sheet thickness increases, it is apparent that this magnitude also rises. That is, the magnitude of force is directly proportional to the initial sheet thickness and fits well with the linear trends shown in the figure. As it can be noticed, experimental values are slightly lower than predictions, but results are very good, showing a discrepancy between the experimental results and the predictions of the model. The results obtained by two approaches make it possible to give the relative variation of the force amplitude compared to the experiment and expressed by: $\Delta F(\%) = \left[(F_{\text{Exp}} - F_{\text{Num}}) / F_{\text{Exp}} \right] \times 100$. They are 2% and 3%, respectively for the smallest and greatest values of sheet thickness (1.2 mm and 2 mm). Consequently, the peak load evolution curve determined by the numerical

approach is thus in good agreement with the experimental one.

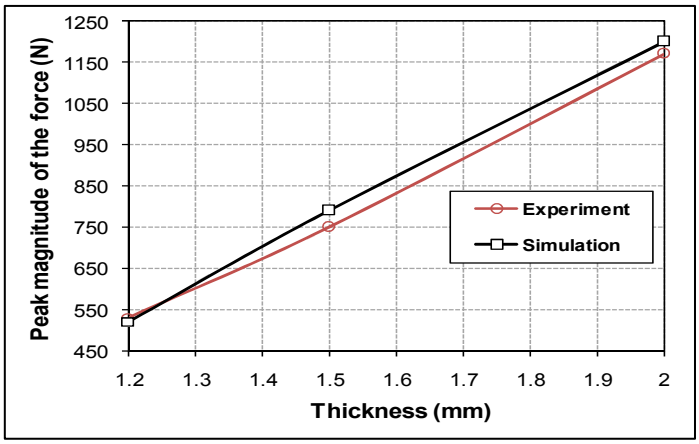

Figure 9: Influence of initial sheet thickness on the peak magnitude of the forming loads acting on the punch

5 CONCLUSIONS

This paper investigates the process of single point incremental forming of truncated cones and pyramids formed of an aluminum alloy sheet Al 3003-O both experimentally and numerically. In the first part of this paper, a deeper assessment of the process was developed following a set of numerical simulations and experimental tests in order to find the influence of some relevant process parameters, on the estimation and the repartition of the forming force components and to make a comparison between them. The obtained experimental and numerical results are found to be in agreement for the two models: conical and pyramidal geometries. In the second part of the work, a campaign of numerical tests has been carried out in a parametric form by varying systematically at each test the initial value of the sheet thickness during forming process. In this investigation, three FE simulations of the considered process were performed for the conical and pyramidal models, each having varied the material thickness. In particular, this study examines the effect of the considered geometrical parameter on the evolution of the resultant forming forces acting on the traveling tool. The results of the tests were analyzed quantitatively, and some observations were made as follows below:

- The forming force tends to increase with the sheet thickness, and this cannot be a negligible aspect.
- For a better comparison between the two conical and pyramidal shapes we chose to represent in the same figure the evolution of the corresponding resultant force curves parameterized in sheet thickness. According to the obtained results, it could be noted that the different efforts evolve in the same way. In fact, when the sheet thickness is increased, the forces will increase accordingly.

REFERENCES

[1] Bambach, M., Hirt, G. and Junk, S. Modelling and experimental evaluation of the incremental CNC sheet metal forming process. *In Proceedings of the seventh International Conference on Computational Plasticity ITCP* (2003).

[2] Ambrogio, G., Filice, L., Fratini, L. and Micari, F. Some relevant correlations between

process parameters and process performance in incremental forming of metal sheets. *In Proceedings of the sixth International Conference on Material Forming ESAFORM* (2003) 175-178.

[3] Kitazawa, K., and Nakajima, A. Cylindrical incremental drawing of sheet metals by CNC incremental forming process. *In Proceedings of the sixth International Conference on Computational Plasticity ICTP* (1999) 1495-1500.

[4] Mori, K., Yamamoto, M. and Osakada, K. Determination of hammering sequence in incremental sheet metal forming using a genetic algorithm. *J. Mater. Process. Technol* (1996) **60**:463-468.

[5] Dai, K., Wang, Z.R. and Fang, Y. CNC incremental sheet forming of an axially symmetric specimen and the locus of optimization. *J. Mater. Process. Technol* (2000) **102**:164-167.

[6] Kim, Y.H. and Park, J.J. Effect of process parameters on formability in incremental forming of sheet metal. *J. Mater. Process. Technol* (2002) **130/131**:42-46.

[7] Ham, M. and Jeswiet, J. Single point incremental forming and the forming criteria for AA3003. *Annals of the CIRP - Manufacturing Technology* (2006) **55(1)**:241-244.

[8] Ham, M. and Jeswiet, J. Single point incremental forming limits using a box-behnken design of experiment. *Key. Eng. Mater* (2007) **344**:629-636.

[9] Kopac, J. and Kampus, Z. Incremental sheet metal forming on CNC milling machine-tool. *J. Mater. Process. Technol* (2005) **162-163**:622-628.

[10] Capece Minutolo, F., Durante, M., Formisano, A. and Langella, A. Evaluation of the maximum slope angle of simple geometries carried out by incremental forming process. *J. Mater. Process. Technol* (2007) **194**:145-150.

[11] Iseki, H. An approximate deformation analysis and FEM analysis for the incremental bulging of sheet metal using a spherical roller. *J. Mater. Process. Technol* (2001) **111**:150-154.

[12] Shim, M.S. and Park, J.J. The formability of aluminum sheet in incremental forming. *J. Mater. Process. Technol* (2001) **113**:654-658.

[13] Hirt, G., Ames, J., Bambach, M. and Kopp, R. Forming strategies and process modeling for CNC incremental sheet forming. *Annals of the CIRP - Manufacturing Technology* (2004) **53(1)**:203-206.

[14] Bambach, M., Hirt, G. and Ames, J. Modeling of optimization strategies in the incremental CNC sheet metal forming process. *In Proceedings of the eighth International Conference on Numerical Methods in Industrial Forming Processes NUMIFORM* (2004) **712**:1969-1974.

[15] Ambrogio, G., Filice, L., Gagliardi, F. and Micari, F. Three-dimensional FE simulation of single point incremental forming: experimental evidences and process design improving. *In Proceedings of the eighth International Conference on Computational Plasticity COMPLAS* (2005) Barcelona, Spain.

[16] Duflou, J.R., Verbert, J., Belkassem, B., Gu, J., Sol, H., Henrard, C. and Habraken, A.M. Process window enhancement for single point incremental forming through multi-step toolpaths. *Annals of the CIRP - Manufacturing Technology* (2008) **57(1)**:253-256.

[17] Duflou, J.R., Tunçkol, Y., Szekeres, A. and Vanherck, P. Experimental study on force measurements for single point incremental forming. *J. Mater. Process. Technol* (2007) **189**:65-72.

XI International Conference on Computational Plasticity. Fundamentals and Applications
COMPLAS XI
E. Oñate, D.R.J. Owen, D. Peric and B. Suárez (Eds)

STRESS BASED NONLOCAL INTERACTIONS

C. GIRY*, F. DUFOUR AND J. MAZARS

*3SR, Grenoble-INP/UJF/CNRS
Domaine universitaire, BP 53, 38041 Grenoble cedex 9, France
Email: cedric.giry@hmg.inpg.fr

Key words: Damage, nonlocality, interactions, stress state

Abstract. The progressive degradation of quasi-brittle materials can be reproduced efficiently by means of damage models. The presence of microcracks in the media gives a nonlocal aspect to the evolution of damage. By interacting with each other under loading, it leads to stress amplification (singularity) or decrease (shield effect) at a given location. In the framework of damage models, the nonlocal integral method [1] or the gradient enhanced media [2] introduce this notion of interactions between points by means of an internal length.

However, they are still some pending issues regarding these methods [3] (e.g., treatment of free boundaries, description of the damage state close to complete failure). In this paper, a modification of the nonlocal integral regularization method is proposed. The influence of a point on its neighbourhood is evolving during the loading and its intensity and direction depend on the stress state it encounters.

Through several numerical simulations, we show that our proposition improves the treatment of free boundaries and gives physically sound damage and strain field in the fracture process zone up to complete failure. The latter being a key parameter of durability analysis.

1 INTRODUCTION

Quasi-brittle materials show the presence of microcracks in their media. Under loading, these microcracks interact with each other, leading to nonlocal interactions. During the cracking, strain localization appears with a size and an orientation of the localized band as well as its evolution that can be directly linked to the nonlocal interactions due to microcracks.

In continuous media, the microcracks are not explicitly represented. As a consequence, additional generalized constitutive equations need to be introduced in the models to take into account the nonlocal character of the propagation and coalescence of microdefects. These models replace the local internal variable by its nonlocal counterpart. For the

nonlocal gradient model [2], the nonlocal internal variable fulfills a differential equation whereas for the nonlocal integral model [1], the nonlocal internal variable is a weighted spatial average.
In addition to restoring the objectivity of the numerical modeling for strain softening behavior, these models aim at describing the behavior of quasi-brittle materials for microcracked area which do not degenerate into a widely opened crack and size effect through the introduction of an internal length.
However, several drawbacks arise from the original models (e.g., description of the kinematic fields in the FPZ, damage initiation in crack tip-problem, description of the interactions in the vicinity of boundaries). To overcome these problems, we propose a new nonlocal integral method in which the weighting is enhanced by introducing the influence of the stress state on the interactions.
First, the original model associated to a damage model is recall. Then, the stress based nonlocal model is presented. Finally, several tests are performed addressing the different drawbacks quoted previsouly.

2 NONLOCAL DAMAGE MODEL

2.1 Continuum damage theory

A scalar isotropic damage model for describing the non linear behavior of concrete under monotonic loading is used. The general stress-strain relationship is:

$$\sigma_{ij} = (1 - D)C_{ijkl} : \varepsilon_{kl} \tag{1}$$

where σ_{ij} and ε_{kl} are the components of the Cauchy stress tensor and the strain tensor, respectively (i, j, k, l $\in [1, 3]$) and C_{ijkl} are the components of the fourth-order elastic stiffness tensor.
The evolution of D is driven by an equivalent strain ε_{eq} that quantifies the local deformation state in the material. Among several definitions, we consider here the equivalent strain defined by Mazars with its corresponding evolution law [6].
The damage scalar variable D is a function of the internal variable Y. This parameter equals the damage threshold ε_{D_0} initially. Its evolution is governed by the Kuhn-Tucker condition:

$$\varepsilon_{eq} - Y \leq 0 \ , \ \dot{Y} \geq 0 \ , \ \dot{Y}(\varepsilon_{eq} - Y) = 0 \tag{2}$$

Mazars has introduced a local measure ε_{eq} of the strain tensor defined by:

$$\varepsilon_{eq} = \sqrt{\sum_{i=1}^{3} \langle \varepsilon_i \rangle_+^2} \tag{3}$$

$\langle \varepsilon_i \rangle_+$ denotes the positive principal strains. This model considers that damage is driven by positive strains, i.e. extension. It allows to accurately reproduce the behavior of

quasi-brittle materials such as concrete. In this model, damage is determined as a linear combination of two damage variables (Eq. 4): D_t and D_c which are damage due to tension and compression respectively [6]:

$$D = \alpha_t D_t + \alpha_c D_c \tag{4}$$

The parameters α_t and α_c depend on the stress state (e.g. $\alpha_t = 1$ in pure traction). The damage evolution is characterized by the following exponential law:

$$D_{c,t} = 1 - \frac{\varepsilon_{D_0}(1 - A_{c,t})}{Y} - \frac{A_{c,t}}{\exp^{\left(B_{c,t}(Y - \varepsilon_{D_0})\right)}} \tag{5}$$

A_t, B_t, A_c and B_c are the parameters governing the shape of the evolution law. The constitutive relation exhibits strain softening and as a consequence, needs a regularization technique.

2.2 Original integral nonlocal approach

In the nonlocal damage model, the equivalent strain given in Eq. 3 is replaced by an average equivalent strain $\overline{\varepsilon}_{eq}$ over a volume Ω in the equation governing the growth of damage as defined by Pijaudier-Cabot and Bažant [1].

$$\overline{\varepsilon}_{eq}(\boldsymbol{x}) = \frac{\int_\Omega \phi(\boldsymbol{x} - \boldsymbol{s})\varepsilon_{eq}(\boldsymbol{s})d\boldsymbol{s}}{\int_\Omega \phi(\boldsymbol{x} - \boldsymbol{s})d\boldsymbol{s}} \tag{6}$$

$\phi(\boldsymbol{x} - \boldsymbol{s})$ is the weight function defining the interaction between the considered point located at $\boldsymbol{x}$ and the neighboring points located at $\boldsymbol{s}$. The most used nonlocal weight function is taken as the Gauss distribution function:

$$\phi(\boldsymbol{x} - \boldsymbol{s}) = \exp\left(-\left(\frac{2\left\|\boldsymbol{x} - \boldsymbol{s}\right\|}{l_c}\right)^2\right) \tag{7}$$

where l_c is the internal length of the model.

2.3 Stress based nonlocal integral approach

In the proposed approach, the point of view of the calculation of nonlocal quantities is slightly different. *We no longer consider what a point located at $\boldsymbol{x}$ can receive but what a point located at $\boldsymbol{s}$ can distribute*. The nonlocality is defined as a quantity given by each point located at $\boldsymbol{s}$ along its principal stress direction with an intensity depending on the level of the principal stress. We introduce in the nonlocal regularization both the notion of directionality as shown by Pijaudier and Dufour [7] in the limited case of the vicinity of boundaries and the variation of the intensity depending on the state of loading in the structure. The stress field allows the direct description of the presence of free boundary and the development of fracture process zone that are at the origins of

the modification of the nonlocal interactions. During the calculation, the evolution of the interactions between points is considered through a single scalar ρ that, multiplied by the characteristic length l_c, defines the internal length of the model. This internal length evolves from zero for stress-free material up to l_c when maximum principal stress is reached. It is important to notice that this coefficient depending on the stress state of the distributed points does not introduce any parameter in the model.
Let us denote $\boldsymbol{\sigma}_{prin}(\boldsymbol{s})$, the stress state of the point located at $\boldsymbol{s}$, expressed in its principal frame. The vectors forming this frame are $\boldsymbol{u}_1(\boldsymbol{s})$, $\boldsymbol{u}_2(\boldsymbol{s})$, and $\boldsymbol{u}_3(\boldsymbol{s})$ with the associated principal stresses $\sigma_1(\boldsymbol{s})$, $\sigma_2(\boldsymbol{s})$ and $\sigma_3(\boldsymbol{s})$.

$$\boldsymbol{\sigma}_{prin}(\boldsymbol{s}) = \sum_{i=1}^{3} \sigma_i(\boldsymbol{s})(\boldsymbol{u}_i(\boldsymbol{s}) \otimes \boldsymbol{u}_i(\boldsymbol{s})) \tag{8}$$

where $\otimes$ is the tensor product. We define an ellipsoid centered at point $\boldsymbol{s}$, corresponding to a homothety of the original interaction domain with a ratio $|\frac{\sigma_i(\boldsymbol{s})}{f_t}|$ along principal stress direction $\boldsymbol{u}_i(\boldsymbol{s})$. f_t denotes the tensile strength of the material.
The choice of f_t leads to no modification of the interactions at the tensile stress peak, in the direction associated to the maximum tensile stress. The characteristic length l_c associated to the material defines the maximum size of the domain of interactions and so the internal length ρl_c of the stress based nonlocal model can not exceed this value. As a consequence, we need to limit in compression the value of ρ to one under loading directions for which $|\sigma_i(\boldsymbol{s})|$ is higher than f_t.
By using the spherical coordinates (ρ, θ and ϕ), the following equation describes the ellipsoid associated to the stress state of the point located at $\boldsymbol{s}$ (Fig. 1).

$$\rho(\boldsymbol{x}, \boldsymbol{\sigma}_{prin}(\boldsymbol{s}))^2 = \frac{1}{f_t^2 \left(\frac{\sin^2\varphi\cos^2\theta}{\sigma_1^2(\boldsymbol{s})} + \frac{\sin^2\varphi\sin^2\theta}{\sigma_2^2(\boldsymbol{s})} + \frac{\cos^2\varphi}{\sigma_3^2(\boldsymbol{s})} \right)} \tag{9}$$

where θ is the angle between $\boldsymbol{u_1}$ and the projection of $(\boldsymbol{x}-\boldsymbol{s})$ onto the plane defined by $\boldsymbol{u_1}$ and $\boldsymbol{u_2}$ and φ is the angle between $\boldsymbol{u_3}$ and $(\boldsymbol{x}-\boldsymbol{s})$. Considering, these angles, we obtain:

$$\cos\theta = \frac{\boldsymbol{u}_1.(\boldsymbol{u}_3 \wedge ((\boldsymbol{x}-\boldsymbol{s}) \wedge \boldsymbol{u}_3))}{\|\boldsymbol{u}_3 \wedge ((\boldsymbol{x}-\boldsymbol{s}) \wedge \boldsymbol{u}_3)\|} \qquad \sin\theta = \frac{\boldsymbol{u}_2.(\boldsymbol{u}_3 \wedge ((\boldsymbol{x}-\boldsymbol{s}) \wedge \boldsymbol{u}_3))}{\|\boldsymbol{u}_3 \wedge ((\boldsymbol{x}-\boldsymbol{s}) \wedge \boldsymbol{u}_3)\|} \tag{10}$$

$$\cos\varphi = \frac{\boldsymbol{u}_3.(\boldsymbol{x}-\boldsymbol{s})}{\|\boldsymbol{x}-\boldsymbol{s}\|} \qquad \sin\varphi = \frac{(\boldsymbol{x}-\boldsymbol{s}).(\boldsymbol{u}_3 \wedge ((\boldsymbol{x}-\boldsymbol{s}) \wedge \boldsymbol{u}_3))}{\|(\boldsymbol{x}-\boldsymbol{s})\| \, . \, \|\boldsymbol{u}_3 \wedge ((\boldsymbol{x}-\boldsymbol{s}) \wedge \boldsymbol{u}_3)\|}$$

where $\wedge$ is the vector product and "." is the scalar product. The weight function now reads:

$$\phi(\boldsymbol{x}-\boldsymbol{s}) = \exp\left(-\left(\frac{2\,\|\boldsymbol{x}-\boldsymbol{s}\|}{l_c\ \rho(\boldsymbol{x}, \boldsymbol{\sigma}_{prin}(\boldsymbol{s}))} \right)^2 \right) \tag{11}$$

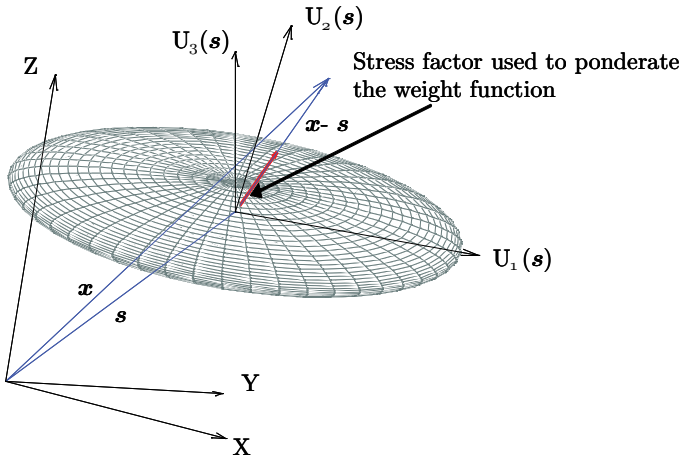

Figure 1: Definition of the ρ coefficient giving the influence of $\boldsymbol{s}$ on $\boldsymbol{x}$

with $\rho(\boldsymbol{x}, \boldsymbol{\sigma}_{prin}(\boldsymbol{s}))$ equal to the radial coordinate of the ellipsoid defined previously in the direction $(\boldsymbol{x} - \boldsymbol{s})$.
The intensity of the influence of a point at $\boldsymbol{s}$ on its neighborhood depends on the magnitude and direction of the principal stresses at $\boldsymbol{s}$.

3 INITIATION OF FAILURE

In the framework of nonlocal elasticity, Eringen and coworkers [4] have pointed out that the point encountering the maximum stress is not located at the crack tip. Simone and coworkers [3] have extended this study to nonlocal damage models, showing that the bad description of the nonlocal field leads to a wrong initiation of damage. To illustrate this problem and to compare the numerical solution of the original and the stress based nonlocal method, a notched plate under tension is studied (Fig. 2) with a pre-existing crack of length $h = 0.0005$ m. Due to symmetry, only half of the specimen is described.

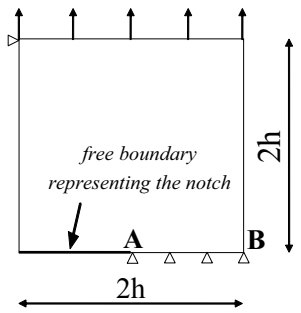

Figure 2: Compact Tension Specimen (CTS)

The notch is described geometrically by letting free the boundary. The influence of the

internal length of the model on the location of the maximum nonlocal equivalent strain is studied. The following parameters are used for the material: E = 1000 MPa; $\nu = 0.2$; $l_c = 0.0001$, 0.0002 or 0.0005 m.
The equivalent strain defined by Mazars is calculated from the strain field obtained under an imposed displacement. The nonlocal equivalent strain is then computed according to Eq. 3. The evolution along the line AB in front of the crack is given on Fig 3 for both nonlocal methods. These results, obtained by Simone et al., show a shift of the

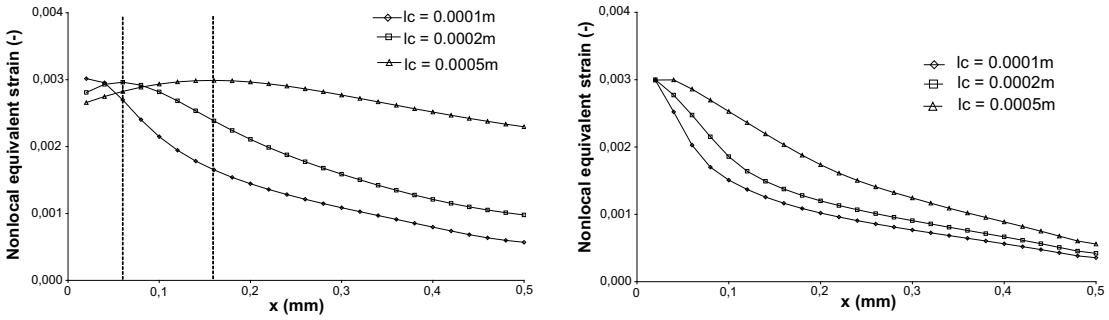

(a) (b)

Figure 3: CTS: Evolution of the nonlocal equivalent strain along AB. (a) Original nonlocal method; (b) Stress based nonlocal method.

maximum nonlocal equivalent strain with the original nonlocal method leading thus to a wrong location of damage initiation. Furthermore, this shift is proportional to the internal length.
In the original nonlocal method, the domain of interactions depends only on the distance between points. So, a point at the crack tip will be influenced in the same way by points in the shadow zone of the notch than by points in front of the notch. Since the strain gradient is smaller in front of the notch than at the back, the maximum nonlocal equivalent strain is shifted to the notch front.
For the same test, with the stress based nonlocal method, the shift is null whatever the characteristical length l_c chosen. Indeed, the points in the shadow zone of the notch no more influence the point at the crack tip since they encounter a low stress state.
This study shows the capability of the stress based nonlocal method to correctly locate the inception of material nonlinearities in mode I problem with a pre-existing crack. This result is a key issue for size effect analysis.

4 SIZE EFFECT ANALYSIS: 3 POINT BENDING TEST

Size effects have been widely studied in the past regarding concrete structure and it is a key issue when one wants to transcript the material behavior identified at the scale of a laboratory specimen to a real structure.
The use of nonlocal models allows to reproduce this size effect by introducing an internal

length. However, we can observe that the parameters obtained depend a lot on the geometry and the stress state. Indeed, it has been shown the original nonlocal model show discrepancies when we compare results from one type of test to another (e.g. notched and unnotched beam) [5]. A first attempt to improve the results regarding size effect has been made by Krayani and coworkers [5]. By modifying the area of regularization close to free boundaries, a better redistribution of the state parameter was obtained leading to an improvement of the results.
We compare the original and the stress based nonlocal damage formulation through 3 point bending test on unnotched and notched beams with three geometrically similar sizes. The specimens with constant depth (b = 1 m), various heights (D = 80, 160, 320 mm) and corresponding lengths (L = 3D) are referred to as small, medium and large beam, respectively. Simulations are performed in 2D plane stress conditions. The model parameters used for these simulations are the same as the one in [5] : $E = 3.85 \times 10^4 MPa,\ \nu = 0.24,\ A_t = 0.95,\ A_c = 1.25,\ B_t = 9200,\ B_c = 1000,\ \varepsilon_{D_0} = 3.0 \times 10^{-5}$ and $l_c = 10$ mm.

4.1 Size effect on unnotched specimens

From the peak load P_u, we estimate the nominal strength σ_N, according to the elastic beam theory (Tab. 1):

$$\sigma_N = \frac{9}{2}\frac{P_u}{bD} \tag{12}$$

We notice that the results are quite close to each other, since the main difference is

Table 1: Unnotched beam: Peak load and nominal strength for the two nonlocal methods

	Original nonlocal		Stress based nonlocal	
D(mm)	P_u(kN)	σ_N(MPa)	P_u(kN)	σ_N(MPa)
80	65.732	3.70	64.380	3.62
160	123.792	3.48	122.240	3.43
320	240.440	3.38	218.360	3.07

only for the interactions perpendicular to the lower free boundary. With the stress based nonlocal model, the interactions are along lines parallel to the bottom side of the beam thus to a smaller domain of interactions and a lower peak load.
We use now the Bazant's size effect law for the case of unnotched beams [8]:

$$\sigma_N = f_{r\infty}\left(1 + \frac{D_b}{D}\right) \tag{13}$$

where D_b and $f_{r\infty}$ are constants. These two constants are obtained from a linear regression.

Table 2: Unnotched beam: Identification of D_b and $f_{r\infty}$ for the two nonlocal methods

	Original nonlocal	Stress based nonlocal
$D_b(mm)$	10.34	18.31
$f_{r\infty}(MPa)$	3.30	2.98

4.2 Size effect on notched specimens

The size effect analysis is now performed on notched specimen with a $0.2D$ high notch located at mid-span. From the peak load P_u, we estimate the nominal strength σ_N, according to the elastic beam theory (Tab. 3):

$$\sigma_N = \frac{9}{2}\frac{P_u}{bD(0.8^2)} \tag{14}$$

Again using the Bazant's size effect law for notched beams [8]:

Table 3: Notched beam: Peak load and nominal strength for the two nonlocal methods

	Original nonlocal		Stress based nonlocal	
D (mm)	P_u (kN)	σ_N (MPa)	P_u (kN)	σ_N (MPa)
80	42.316	3.72	35.630	3.13
160	64.426	2.83	59.130	2.60
320	97.454	2.14	94.440	2.07

$$\sigma_N = \frac{Bf_{r\infty}}{\sqrt{\left(1+\frac{D}{D_0}\right)}} \tag{15}$$

where B is a dimensionless geometry-dependent parameter and D_0 is a characteristic size. For each formulation, D_0 and $Bf_{r\infty}$ are obtained from a linear regression. B can

Table 4: Notched beam: Identification of D_0 and $Bf_{r\infty}$ for the two nonlocal methods

	Original nonlocal	Stress based nonlocal
$D_0(mm)$	42.42	110.87
$Bf_{r\infty}(MPa)$	6.25	4.08

be calculated according to Rilem recommendations ($B = 1.08$) [9]. One can compare the values of $Bf_{r\infty}$ obtained with unnotched and notched specimen and give an error committed by the model regarding the description of size effect. Indeed, $f_{r\infty}$ is a parameter

Table 5: Comparison of the values $Bf_{r\infty}$ obtained from unnotched and notched specimens for the two nonlocal method

$Bf_{r\infty}$(MPa)	Original nonlocal	Stress based nonlocal
Computed from unnotched	3.56	3.21
Fit from notched	6.25	4.08
Relative error	76%	27%

relative to the material and should not be affected by size effect. Another mean to observe the consistency of the formulations regarding size effect is to use the Bazant's universal size effect law [8]:

$$\sigma_N = \frac{Bf_{r\infty}}{\sqrt{\left(1+\frac{D}{D_0}\right)}}.\left(1+\left(\left(\eta+\frac{D}{D_b}\right).\left(1+\frac{D}{D_0}\right)\right)^{-1}\right) \tag{16}$$

We consider in this formula the parameters linked to the unnotched specimen as known with the first analysis and we fit the value of D_0 in order to retrieve the values of the nominal strength of the notched specimens. The best fits are obtained for $D_0 = 300$ mm

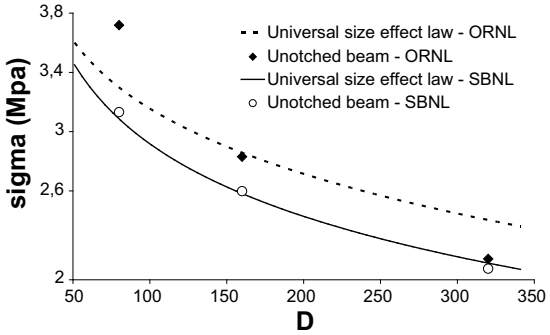

Figure 4: Fits of the universal size effect law on notched specimens for the original nonlocal method (ORNL) and the stress based nonlocal method(SBNL)

with the original nonlocal formulation and $D_0 = 255$ mm with the stress based nonlocal formulation. A better fit of the universel size effect law on the notched beam results is obtained with the stress based nonlocal model. It confirms the results obtained with the first method of error estimator in the description of size effect.
This analysis shows the internal length, that is linked to the size of the FPZ and allows to describe size effect, depends on the material through a characteristical length l_c as it is defined in the original version but also on the stress state as it is introduced in the stress based nonlocal model.

5 CRACKING EVOLUTION IN A 3 POINT BENDING TEST OF A NOTCHED BEAM

The efficiency of the stress based nonlocal method to describe the failure process of quasi-brittle material is explored through the comparison with experimental results on the evolution of crack opening along the height of a notched beam under three point bending test (3PBT). This beam tested at the GEM laboratory in Nantes by the second author is depicted in Fig. 5(a) with the associated mesh used for the numerical investigation. This beam has been modeled in 2D under plane stress conditions. The loading has been

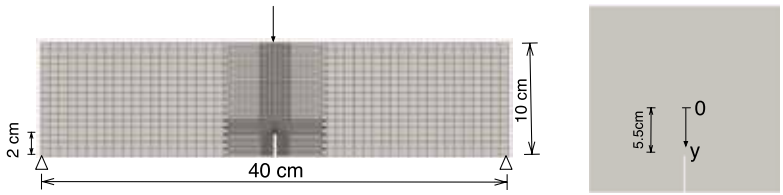

(a) (b)

Figure 5: Three point bending test: (a) Mesh of the specimen. (b) Axis of the crack opening.

applied via displacement control. Both nonlocal methods have been successively used with the same set of parameters for the damage model describing concrete (see Eq. 5): E = 30,000 MPa; $\nu = 0.24$; $\varepsilon_{D_0} = 0.00004$; $\beta = 1.06$; $A_t = 0.9$; $B_t = 4000$; $A_c = 1.25$; $B_c = 1000$ and $l_c = 0.008$ m.

The beam is composed of isoparametric elements with linear interpolation. A peculiar attention was taken to describe finely the notch tip where stress concentration occurs.

Image correlation technique was used during the experiment to follow the strain localisation process. Fig. 5(b) gives the orientation and the origin along the height of the beam of the measured cracking. We compare hereafter these experimental results with the one obtained from numerical calculations using the post treatment method proposed by Dufour and coworkers [10]. Fig. 6b, c and d show the crack opening along the height at different CMOD levels. One can observe that for the lowest CMOD considered, we have a cracking prediction close between the original and stress based nonlocal method. We are still in a diffused microcracking far from the crack tip that leads to a strain field similar between both methods. During the localisation process, the stress level and the internal length of the stress based nonlocal decreases, as a consequence we obtained a sharper strain profile that is closer to the one of a macrocrack for higher CMOD [11]. It leads so to a better estimation of the crack opening. A reason for the constant shift (error around 10%) between the experimental and the numerical results regarding the crack opening can be due to the 2D approximation used for the calculation. Indeed, experimentally, the crack opening was measured on surface and we can expect to have different values in the depth.

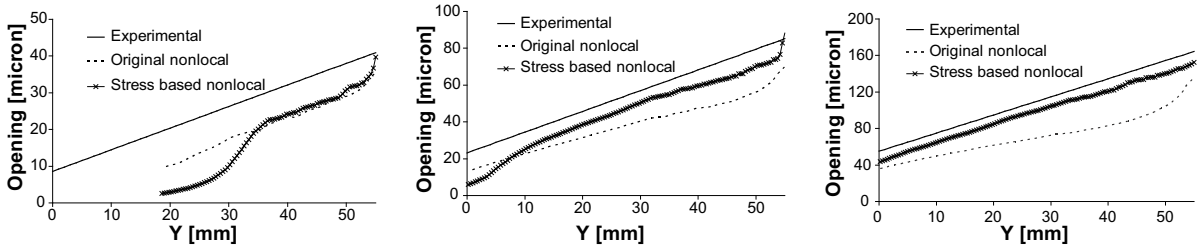

Figure 6: 3PBT: Crack opening along the height of the beam at different loading level. (a) 50 µm; (b) 100 µm and (c) 200 µm

6 CONCLUSIONS

We have proposed in this paper a modification of the integral nonlocal model in order to adapt the regularisation close to free boundary and during the cracking process. The stress state of each point is used during the calculation in order to create an evolution of the interaction between points. Each point interacts with its neighborhood in function of the intensity and direction of its principal stress values. All these improvments are made with no additional parameter that would be difficult to calibrate and the computational cost is similar to the original nonlocal method since the connectivity maxtric is identical. This can be easily implemented in any FE code that already includes nonlocal approach. The modification has been illustrated through several examples. The stress based nonlocal approach provides a better solution to model damage initiation. The proposed approach is capable to perfectly locate the damage initiation which is badly estimated with any other regularisation techniques. This result is a key issue when considering size effect analysis. The proposed approach gives a better description of size effect compared to the original one.

Furthermore, damage and strain profiles across a fracture process zone are more physically sounded. The result objectivity is conserved and our proposal allows to obtain a weak discontinuity that gets close to strong discontinuity upon mesh refinement. As a result the estimate of crack opening is much improved. This is a key issue as information on crack opening is a hot topic in structural engineering for durability analysis or the leakage rate estimation for confining vessels. It has been shown that continuous modelling can provide this kind of information. By improving the FE calculation and more particularly by taking into account the effect of a damaged zone on its vicinity, crack opening estimation are greatly improved.

In future works, loaded interface between two materials and loaded boundaries will be investigated. This will be of great interest for structural analysis with interaction between a crack in concrete and rebars.

REFERENCES

[1] Pijaudier-Cabot, G. and Bažant, Z. Nonlocal damage theory, *J. of Eng. Mech.* (1987) **113**:1512-1533.

[2] Peerlings, R. H. J., de Borst, R., Brekelmans, W. A. M. and de Vree, J. H. P. Gradient enhanced damage for quasi-brittle materials. *Int. J. for Num. Meth. in Eng.* (1996) **39**:937–953

[3] Simone, A., Askes, H. and Sluys, L. J. Incorrect initiation and propagation of failure in nonlocal and gradient enhanced media. *Int. J. Solid. Struc.* (2004) **41**:351-363.

[4] Eringen, A. C., Speziale, C. G. and Kim, B. S. Crack-tip problem in non-local elasticity. *J. Mech. Phys. Sol.* (1977) **25**:255–339

[5] Krayani, A., Pijaudier-Cabot, G. and Dufour, F. Boundary effect on weight function in non-local damage model. *Eng. Frac. Mech.* (2009) **76**:2217-2231.

[6] Mazars, J. A description of micro- and macroscale damage of concrete structures. *Eng. Fract. Mech.* (1986) **25**:729–737

[7] Pijaudier-Cabot, G. and Dufour, F. Nonlocal damage model: boundary and evolving boundary effects. *Eur. J. of Env. and Civ. Eng.* (2010) **14**.6-7:729–749

[8] Bažant, Z.P. *Scaling of Structural Strength.* Hermes Penton Science (Kogan Page Science), London,(2002).2nd updated ed., Elsevier, London 2005

[9] Shah, S. Size-effect method for determining fracture energy and process zone size of concrete. *Materials and Structures* (1990) **23**:461–465

[10] Dufour, F., Pijaudier-Cabot, G., Choinska, M. and Huerta, A. Extraction of a crack opening from a continuous approach using regularized damage models. *Computers and Concrete* (2008) **5(4)**:375–388.

[11] Giry, C., Dufour, F. and Mazars J. Stress based nonlocal damage model. *Int. J. Solid. Struc.* (under review).

XI International Conference on Computational Plasticity. Fundamentals and Applications
COMPLAS XI
E. Oñate, D.R.J. Owen, D. Peric and B. Suárez (Eds)

THERMODYNAMIC CONSISTENT GRADIENT-POROPLASTICITY THEORY FOR POROUS MEDIA

GUILLERMO ETSE* AND JAVIER L. MROGINSKI†

*CONICET and Center for Numerical and Computational Methods in Engineering (CEMNCI)
Faculty for Exact Sciences and Technology, Tucuman National University
Av. Roca 1800, (4000) Tucumán, Argentina
e-mail: getse@herrera.unt.edu.ar

†CONICET and Applied Mechanics Department
Faculty of Engineering, Northeaster National University
Av. Las Heras 727, Resistencia, Chaco, Argentina
e-mail: javierm@ing.unne.edu.ar

Key words: localizad failure, gradient theory, wave propagation, porous media, MEF

Abstract. Complex degradation processes of partial saturated media like soils during post-peak regime are strongly dependent on humidity, stress state, boundary conditions and material parameters, particularly porosity. To realistically and objectively describe the dramatic change from diffuse to localized failure mode or from ductile to brittle ones, accurate constitutive theories and numerical approaches are required. In this paper, a non-local gradient poroplastic model is proposed for partial saturated media based on thermodynamic concepts. A restricted non-local gradient theory is considered, following (Mroginski, et al. Int. J. Plasticity, 27:620-634) whereby the state variables are the only ones of non-local character. The non-local softening formulation of the proposed constitutive theory incorporates the dependence of the gradient characteristic length on both the governing stress and hydraulic conditions to realistically predict the size of the maximum energy dissipation zone. The material model employed in this work to describe the plastic evolution of porous media is the Modified Cam Clay, which is widely used in saturated and partially saturated soil mechanics. To evaluate the dependence of the transition point between ductile and brittle failure regime in terms of the hydraulic and stress conditions, the localization indicator for discontinuous bifurcation is formulated for both drained and undrained conditions, based on wave propagation criterion.

1 INTRODUCTION

The mechanic of porous media constitutes a discipline of great relevance in several knowledge areas like the Geophysics, the Civil Engineering, the Biomechanics and the Materials Science. The main purpose of the mechanic of porous media is the deformation modelling and pore pressure prediction, when the body is been subjected to several external actions and physical phenomena. By the way, the complexity of the real engineering materials implies that for its appropriate modelling they should be included in the concept or theory of partially saturated porous media with cohesive-frictional properties diverse. Besides, the failure behaviour of engineering materials during monotonic loading processes demonstrate a strong dependence on both the stress state and the hydraulic conditions governed during the process. In spite of this fact most of the proposals for continuous formulations of engineering materials like concrete and soils are based on non-porous continua theory [9, 12]. In fact, the traditional formulations commonly accepted by the scientific community for the study of this kind of materials are experimental evidences founded, and a consistent elastoplastic thermodynamic framework is not fully considered [8, 14, 18]. Although it provides a general useful approach for a lot of engineering problems.

Even though noteworthy theoretical developments based on the theory of porous media were recently presented [4, 5, 10]. Nevertheless, it can be observed a necessity of new non-local formulations based on the theory of porous media in order to solve the critical problem of uniqueness loss of the numerical solution in post-peak regime or in pre-peak regime when the volumetric elastoplastic behavior is non-associate.

In this work the thermodynamically consistent formulation for gradient-based elastoplasticity by [22] that follows general thermodynamic approach by [19] for non-local damage formulation is extended for porous media. Main feature of present proposal is the definition of a gradient-based characteristic length in terms of both the governing stress and hydraulic conditions to capture the variation of the transition from brittle to ductile failure mode of cohesive-frictional porous materials with the level of confinement pressure and saturation. Relevant items in this work are, on the one hand, the particularization of the proposed thermodynamically consistent theory for non-local elastoplastic porous media to partially saturated soils. On the other hand, the formulation of the discontinuous bifurcations condition and related failure indicator as well as their evaluations for different hydraulic conditions.

2 POROUS MEDIA DESCRIPTION

Porous media are multiphase systems with interstitial voids in the grain matrix filled with water (liquid phase), water vapor and dry air (gas phase) at microscopic level [6, 9] (see Fig. 1a).

Key argument to reconcile continuum mechanics with the intrinsic microscopic discontinuities of porous like materials composed by several interacting phases, is to consider

them as thermodynamically open continuum systems (see Fig. 1b). Thus, their kinematics and deformations are referred to those of the skeleton. Contrarily to mixture theories based upon an averaging process [13, 14], the representation of porous media is made by a superposition, in time and space, of two or more continuum phases. In case of non-saturated porous continua we recognize three phases, the skeleton, the liquid and the gaseous phases.

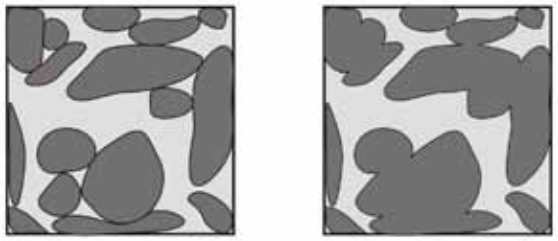

Figure 1: Porous media description. a) Microscopic level ; b) Macroscopic level

2.1 Stress tensors

The mechanical behavior of partially saturated porous media is usually described by the effective stress tensor $\boldsymbol{\sigma}'$, as follows

$$\boldsymbol{\sigma}' = \boldsymbol{\sigma} - \boldsymbol{\delta} p^w = \boldsymbol{\sigma}^n + \boldsymbol{s} \tag{1}$$

being $\boldsymbol{\sigma}$, $\boldsymbol{s} = \boldsymbol{\delta}\,(p^a - p^w)$ and $\boldsymbol{\sigma}^n = \boldsymbol{\sigma} - \boldsymbol{\delta} p^a$ the total, net, and suction stress tensors, respectively, while $\boldsymbol{\delta}$ is the Kronecker delta. Moreover, p^a and p^w are the gas and water pore pressures, respectively. In several geotechnical problems the gas pore pressure can be considered as a constant term that equals the atmospheric pressure [18]. In these cases the suction tensor is counterpart to the water pore pressure, p.

2.2 Flow theory of poroplasticity

Plasticity is a property exhibited by various materials to undergo permanent strains after a complete process of loading and unloading. Hence, poroplasticity is that property of porous media which defines their ability to undergo not only permanent skeleton strains, but also permanent variations in fluid mass content due to related porosity variations. To characterize current stages of thermodynamically consistent poroelastoplastic media and to describe their irreversible evolutions, internal variables such as the plastic porosity ϕ^p or the plastic fluid mass content m^p must be considered in addition to the plastic strain $\boldsymbol{\varepsilon}^p$, and the irreversible entropy density s^p.

Assuming the additive decomposition of Prandtl-Reuss type to the thermodynamic variables into elastic and plastic parts

$$\begin{aligned}\dot{\boldsymbol{\varepsilon}} &= \dot{\boldsymbol{\varepsilon}}^e + \dot{\boldsymbol{\varepsilon}}^p \\ \dot{m} &= \dot{m}^e + \dot{m}^p \\ \dot{s} &= \dot{s}^e + \dot{s}^p\end{aligned} \tag{2}$$

Both, the rate of skeleton plastic strains $\dot{\boldsymbol{\varepsilon}}^p$ and the rate of plastic fluid mass content $\dot{m}^p$ are related to the irreversible evolution of the skeleton. Indeed, let $\dot{\phi}^p$ be the rate of plastic porosity

$$\dot{\phi}^p = \frac{\dot{m}^p}{\rho_0^{fl}} \tag{3}$$

with ρ_0^{fl} the initial fluid mass density.

3 GRADIENT-POROPLASTICITY

In this section the fundamentals of the thermodynamically consistent gradient plasticity theory for porous media by Mrognski, Etse and Vrech (2011) [15] are shortly described.

3.1 Dissipative stress in non-local porous media

Based on previous studies developed by [6, 19], we assume that arbitrary thermodynamic states of the dissipative material during isothermal processes are completely determined by the elastic strain tensor $\boldsymbol{\varepsilon}^e = \boldsymbol{\varepsilon} - \boldsymbol{\varepsilon}^p$, and the internal variables q_α with $\alpha = s, p$ for solid or porous phase, respectively, which are considered here as scalar variables. When considering poroplastic materials the elastic variation of fluid mass content $m^e = m - m^p$ needs also to be included as a thermodynamic argument of the free energy, see [6]. Also, in order to capture non-local effects produced by monotonic external actions on each phase of the porous media we further assume that the gradient of the internal variables ∇q_α, are the only ones of non-local character [15, 19, 22]. The extension to more than two scalar internal variables is straightforward. Hence, both q_α and ∇q_α will appear as arguments in the Helmholtzs free energy

$$\Psi = \Psi\left(\boldsymbol{\varepsilon}^e, m^e, q_\alpha, \nabla q_\alpha\right) \tag{4}$$

While the Clausius-Duhem inequality (CDI),

$$\int_\Omega \frac{1}{\theta}\left[\left(\boldsymbol{\sigma} - \rho\partial_{\boldsymbol{\varepsilon}^e}\Psi\right) : \dot{\boldsymbol{\varepsilon}} + \left(p - \rho\partial_{m^e}\Psi\right)\dot{m} + \rho\partial_{\boldsymbol{\varepsilon}^e}\Psi : \dot{\boldsymbol{\varepsilon}}^p + \rho\partial_{m^e}\Psi\dot{m}^p + \right.$$
$$\left. - \sum_\alpha \rho\partial_{q_\alpha}\Psi\dot{q}_\alpha - \sum_\alpha \rho\partial_{\nabla q_\alpha}\Psi\nabla\dot{q}_\alpha\right] \mathrm{d}\Omega \geq 0 \tag{5}$$

where $\boldsymbol{\sigma}$ is the stress tensor, p is the pore pressure and ρ the mass density. Also, a following compact notation for partial derivative was adopted, $\partial_x(\bullet) = \frac{\partial(\bullet)}{\partial x}$. By, integrating the gradient term by parts and using de Divergence Theorem results

$$\int_\Omega \frac{1}{\theta}\left[(\boldsymbol{\sigma} - \rho\partial_{\boldsymbol{\varepsilon}^e}\Psi) : \dot{\boldsymbol{\varepsilon}} + (p - \rho\partial_{m^e}\Psi)\,\dot{m} + \rho\partial_{\boldsymbol{\varepsilon}^e}\Psi : \dot{\boldsymbol{\varepsilon}}^p + \rho\partial_{m^e}\Psi\dot{m}^p + \right.$$
$$\left. + \sum_\alpha Q_\alpha \dot{q}_\alpha\right] \mathrm{d}\Omega + \int_{\partial\Omega}\sum_\alpha Q_\alpha^{(b)}\dot{q}_\alpha \,\mathrm{d}\partial\Omega \geq 0 \quad (6)$$

Where the dissipative stresses Q_α and $Q_\alpha^{(b)}$ defined in the domain Ω and on the boundary $\partial\Omega$, respectively, as

$$Q_\alpha = -\rho\partial_{q_\alpha}\Psi - \nabla\cdot(\rho\partial_{\nabla q_\alpha}\Psi) \qquad \text{in } \Omega \quad (7)$$
$$Q_\alpha^{(b)} = -\rho\partial_{\nabla q_\alpha}\Psi\mathbf{n} \qquad \text{on } \partial\Omega \quad (8)$$

where introduced.

In the standard local theory it is postulated that the last inequality of Eq. (6) must hold for any choice of domain and for any independent thermodynamic process. As a result, Colemans equation are formally obtained like in local plasticity.

$$\boldsymbol{\sigma} = \rho\partial_{\boldsymbol{\varepsilon}^e}\Psi \quad (9)$$
$$p = \rho\partial_{m^e}\Psi \quad (10)$$
$$\mathfrak{D} = \boldsymbol{\sigma} : \boldsymbol{\varepsilon}^e + p\dot{m}^p + \sum_\alpha Q_\alpha\dot{q}_\alpha \geq 0 \qquad \text{in } \Omega \quad (11)$$
$$\mathfrak{D}^{(b)} = \sum_\alpha Q_\alpha^{(b)}\dot{q}_\alpha \geq 0 \qquad \text{on } \partial\Omega \quad (12)$$

In case of $p = 0$ above equations takes similar form to those obteined by [19, 22] for non-porous media. Also, from Eqs. (11) and (12) it can be concluded that the dissipative stress Q_α can be decomposed into the local and non-local components

$$Q_\alpha = Q_\alpha^{loc} + Q_\alpha^{nloc} = -\rho\partial_{q_\alpha}\Psi - \rho\nabla\cdot(\partial_{\nabla q_\alpha}\Psi) \quad (13)$$

3.2 Thermodynamically consistent gradient-based constitutive relationship

Based on previous works [19, 22], the following additive expression is adopted for the free energy density of non-local gradient poroplastic materials

$$\Psi(\boldsymbol{\varepsilon}^e, m^e, q_\alpha, \nabla q_\alpha) = \Psi^e(\boldsymbol{\varepsilon}^e, m^e) + \Psi^{p,loc}(q_\alpha) + \Psi^{p,nloc}(\nabla q_\alpha) \quad (14)$$

with the elastic energy density,

$$\rho\Psi^e = \boldsymbol{\sigma}^0 : \boldsymbol{\varepsilon}^e + p^0 m^e + \frac{1}{2}\boldsymbol{\varepsilon}^e : \mathbf{C}^0 : \boldsymbol{\varepsilon}^e + \frac{1}{2}M\left(\mathbf{B} : \boldsymbol{\varepsilon}^e - m^e\right)^2 \tag{15}$$

$\Psi^{p,loc}$ and $\Psi^{p,nloc}$ are the local and non-local gradient contributions due to dissipative hardening/softening behaviors, which are expressed in terms of both the internal variables and their gradient, q_α and ∇q_α, respectively.

3.3 Non-local plastic flow rule

For general non-associative flow and hardening rule, we introduce the dissipative potential Φ^* such that non-associative flow and hardening rules are defined

$$\dot{\boldsymbol{\varepsilon}}^p = \dot{\lambda}\partial_{\boldsymbol{\sigma}}\Phi^* = \dot{\lambda}\mathbf{m}_\sigma \quad ; \quad \dot{m}^p = \dot{\lambda}\partial_p\Phi^* = \dot{\lambda}\mathrm{m}_p \quad ; \quad \dot{q_\alpha} = \dot{\lambda}\partial_{Q_\alpha}\Phi^* = \dot{\lambda}\mathrm{m}_{Q_\alpha} \tag{16}$$

where $\mathbf{m}_\sigma = \partial_{\boldsymbol{\sigma}}\Phi^*$, $\mathrm{m}_p = \partial_p\Phi^*$ and $\mathrm{m}_{Q_\alpha} = \partial_{Q_\alpha}\Phi^*$, being Φ^* the plastic dissipative potential. To complete problem formulation in Ω, the Kuhn-Tucker complementary conditions are introduced as follow

$$\dot{\lambda} \geq 0 \qquad ; \qquad \Phi\left(\boldsymbol{\sigma}, p, Q_\alpha\right) \leq 0 \qquad ; \qquad \dot{\lambda}\Phi\left(\boldsymbol{\sigma}, p, Q_\alpha\right) = 0 \tag{17}$$

3.4 Rate constitutive equations

In the undrained condition and considering the additive decomposition of the free energy potential in Eq. (14) and the flow rule of Eq. (16), the following rate expressions of the stress tensor $\dot{\boldsymbol{\sigma}}$ and pore pressure $\dot{p}$ are obtained

$$\dot{\boldsymbol{\sigma}} = \mathbf{C} : \dot{\boldsymbol{\varepsilon}} - \dot{\lambda}\mathbf{C} : \mathbf{m}_\sigma - M\mathbf{B}\dot{m} + \dot{\lambda}M\mathbf{B}\mathrm{m}_p \tag{18}$$

$$\dot{p} = -M\mathbf{B} : \dot{\boldsymbol{\varepsilon}} + \dot{\lambda}M\mathbf{B} : \mathbf{m}_\sigma + M\dot{m} - \dot{\lambda}M\mathrm{m}_p \tag{19}$$

being M the Biot's module, $\mathbf{B} = b\mathbf{I}$ with b the Biot coefficient and $\mathbf{I}$ the second-order unit tensor, and $\mathbf{C} = \mathbf{C}^0 + M\mathbf{B} \otimes \mathbf{B}$, whereby $\mathbf{C}^0$ is the fourth-order elastic tensor which linearly relates stress and strain.

After multiplying Eq. (19) by $\mathbf{B}$ and combining with Eq. (18), a more suitable expression of the rate of the stress tensor for drained condition is achieved

$$\dot{\boldsymbol{\sigma}} = \mathbf{C}^0 : \dot{\boldsymbol{\varepsilon}} - \mathbf{B}\dot{p} - \dot{\lambda}\mathbf{C}^0 : \mathbf{m}_\sigma \tag{20}$$

while the evolution laws of the local and non-local dissipative stress in Eq. (13) results

$$\dot{Q}_\alpha^{loc} = -\dot{\lambda}H_\alpha^{loc}\mathbf{m}_Q \tag{21}$$

$$\dot{Q}_\alpha^{nloc} = l_\alpha^2\nabla\cdot\left(\mathbf{H}_\alpha^{nloc}\nabla\dot{\lambda}\mathrm{m}_{Q_\alpha} + \dot{\lambda}\mathbf{H}_\alpha^{nloc}\cdot\nabla Q_\alpha\mathbf{m}_Q^2\right) \tag{22}$$

where $\mathbf{m}_Q^2 = \partial^2\Phi^*/\partial Q^2$. Thereby, local hardening/softening module H_α^{loc} have been introduced as well as the new non-local hardening/softening tensor $\mathbf{H}_\alpha^{nloc}$ as defined in [19]

$$H_\alpha^{loc} = \rho\frac{\partial^2\Psi^{p,loc}}{\partial q_\alpha^2} \quad , \quad \mathbf{H}_\alpha^{nloc} = \rho\frac{1}{l_\alpha^2}\frac{\partial^2\Psi^{p,nloc}}{\partial\nabla q_\alpha\partial\nabla q_\alpha} \tag{23}$$

with $\mathbf{H}_\alpha^{nloc}$ a second-order positive defined tensor. For the characteristic length l_α three alternative definitions can be given, see [16, 19, 20]. On the one hand, it can be defined as a convenient dimensional parameter so as H_α^{loc} and $\mathbf{H}_\alpha^{nloc}$ will get the same dimension. On the other hand, l_α can be interpreted as an artificial numerical stabilization mechanism for the non-local theory. Alternatively, as a physical entity that characterizes the material microstructure. In this last case, and for calibration porpuse, specific numerical analysis on the representative volume element (RVE) need to be performed at micro scale level.

4 MODIFIED CAM CLAY CONSTITUTIVE MODEL FOR GRADIENT PLASTICITY

The modified Cam Clay plasticity model was originally proposed by [17] for normally consolidated clays. However, due to accurate predictions of consolidated clay mechanical behavior obtained with this model and the reduced number of involved parameters it has been extended to a wide range of soils including unsaturated soils [1, 3].

The main characteristics of the modified Cam Clay plasticity model are:

a- The yield function is an ellipse on the (σ', τ) plane

b- The volumetric component of the plastic strain on the Critical State Line (CSL) is null while the plastic flow develops under constant volume

c- Associated plasticity is assumed

The yield function is defined by

$$\Phi\left(\sigma', \tau, Q_\alpha\right) = \left(\sigma' + \frac{\tau^2}{m^2\sigma'}\right) - Q_\alpha \tag{24}$$

where $\sigma' = I_1/3 - \beta p$ is the effective hydrostatic stress, $\tau = \sqrt{3J_2}$ the shear stress, m the CSL slope and Q_α thermodynamically consistent dissipative stress equivalent to the preconsolidation pressure p_{co}. Also I_1 and J_2 are the first and second invariants of the stress tensor and the deviator tensor, respectively.

To avoid overestimation of the volumetric compressibility coefficient K_0 by the conventional critical state model a non-associated flow rule was introduced by [11, 2]. Thereby, the following plastic potential function is proposed

$$\Phi^{*}\left(\sigma',\tau,Q_{\alpha}\right)=\eta\left(\sigma'^{2}-\sigma'Q_{\alpha}\right)+\left(\frac{\tau}{m}\right)^{2} \tag{25}$$

The η coefficient is a restriction function limiting the influence of the volumetric pressure on the softening regime,

$$\eta=\eta_{0}+\frac{a\left(1+m\,\exp\left(\frac{-(\sigma+\beta p)}{\upsilon}\right)\right)}{1+n\,\exp\left(\frac{-(\sigma+\beta p)}{\upsilon}\right)} \tag{26}$$

being a, n and m internal parameters of the exponential function, $\eta_0 = 1$ and $\upsilon = \mathrm{abs}\left(p_{co}/2\right)$.

The thermodynamic consistency is achieved by assuming the following expression for the dissipative part of the free energy in Eq. (14)

$$\rho\Psi^{p}\left(\varepsilon^{p},\nabla\varepsilon^{p}\right)=\rho\Psi^{p,loc}\left(\varepsilon^{p}\right)+\rho\Psi^{p,nloc}\left(\nabla\varepsilon^{p}\right)=-\frac{1}{\chi}p_{co}^{0}\exp\left(\chi\varepsilon^{p}\right)-\frac{1}{2}l_{\alpha}^{2}\mathbf{H}^{nloc}\nabla^{2}\varepsilon^{p} \tag{27}$$

where ε^p is the volumetric plastic strain of the continuous solid skeleton expressed as a function of the internal variables which describe the plastic evolution of the porous and solid phases, in terms of the plastic porosity ϕ^p and the plastic volumetric strain of soil grain ε_s^p, respectively

$$\varepsilon^{p}=\phi^{p}+\left(1-\phi_{0}\right)\varepsilon_{s}^{p} \tag{28}$$

From Eq. (13) the following expressions for local and non-local dissipative stresses are obtained

$$Q_{\alpha}^{loc}\left(\varepsilon^{p}\right)=-\rho\partial_{\varepsilon^{p}}\Psi=p_{co}^{0}\exp\left(\chi\left(\phi^{p}+\left(1-\phi_{0}\right)\varepsilon_{s}^{p}\right)\right) \tag{29}$$

$$Q_{\alpha}^{nloc}\left(\nabla\varepsilon^{p}\right)=-\rho\nabla\cdot\left(\partial_{\nabla\varepsilon^{p}}\Psi\right)=l_{s}^{2}\mathbf{H}_{s}^{nloc}\nabla^{2}\varepsilon_{s}^{p}+l_{p}^{2}\mathbf{H}_{p}^{nloc}\nabla^{2}\phi^{p} \tag{30}$$

where l_s and l_p are the characteristic length for solid and porous phase, respectively.

5 INSTABILITY ANALYSIS OF POROUS MEDIA

The global failure in a continuous media is generally preceded by local discontinuities taking place in areas or regions where the constituent material is subjected to a post-pick stress state. A large number of materials failure studies have been developed in the framework of continuous mechanics. Thereby, a succession of events that begins at microscopic scale and cause the progressive deterioration of the medium, which is initially treated as a continuous one, until transforming it in a discontinuous medium. Therefore, the following failure shapes are defined:

1. *Discrete failure*: this type of analysis lies beyond to the continuum mechanics and belongs the fracture mechanics. The discontinuity is presented in the displacement velocity field, i.e. $[[\dot{\boldsymbol{u}}]] \neq 0$ [1]

2. *Localized failure*: this analysis is characterized by the continuity in the displacement velocity field, while its gradient exhibits the discontinuity, i.e. $[[\dot{\boldsymbol{u}}]] = 0$ and $[[\dot{\boldsymbol{\varepsilon}}]] \neq 0$

3. *Diffuse failure*: this behaviour is generally presented in ductile materials. In this case the both velocity and deformation rate remains continuous, i.e. $[[\dot{\boldsymbol{u}}]] = 0$ and $[[\dot{\boldsymbol{\varepsilon}}]] = 0$.

These concepts of the solids mechanics can be appropriately extrapolated to the mechanics of porous media considering that the medium is composed by a solid skeleton surrounded, in the general case, by several fluids phases. The influence of these fluids phases is taken into account by its corresponding pore pressure.

Considering the Kuhn-Tucker complementary condition, the incremental constitutive equations Eq. (18) and Eq. (19), and the decomposition of the dissipative stress rate Eq. (21) and Eq. (22), the following expression for the plastic multiplier can be obtained

$$\dot{\lambda} = \left(\dot{\Phi}^{e} + \dot{\Phi}^{nloc}\right)/h \tag{31}$$

with

$$\dot{\Phi}^{nloc} = l_{\alpha}^{2}\partial_{Q_\alpha}\Phi\left\{\partial_{Q_\alpha}\Phi^{*}\left[\mathbf{H}_{\alpha}^{nloc}\nabla^{2}\dot{\lambda} + \nabla\mathbf{H}_{\alpha}^{nloc}\nabla\dot{\lambda}\right] + 2\partial_{Q_\alpha}^{2}\Phi^{*}\nabla Q_{\alpha}\mathbf{H}_{\alpha}^{nloc}\nabla\dot{\lambda}\right\} \tag{32}$$

$$\dot{\Phi}^{e} = \dot{\Phi}_{s}^{e} + \dot{\Phi}_{p}^{e} = (\partial_{\boldsymbol{\sigma}}\Phi\mathbf{C}\dot{\boldsymbol{\varepsilon}} - \mathrm{M}\partial_{p}\Phi\mathbf{B}\dot{\boldsymbol{\varepsilon}}) + \dot{m}/\rho_{0}^{fl}\left(\mathrm{M}\partial_{p}\Phi - \partial_{\boldsymbol{\sigma}}\Phi\mathbf{B}\right) \tag{33}$$

$$h = h_{s} + h_{p} + \bar{H} = \partial_{\boldsymbol{\sigma}}\Phi\mathbf{C}\partial_{\boldsymbol{\sigma}}\Phi^{*} + \mathrm{M}\left(-\partial_{\boldsymbol{\sigma}}\Phi\mathbf{B}\partial_{p}\Phi^{*} - \partial_{p}\Phi\mathbf{B}\partial_{\boldsymbol{\sigma}}^{*} + \partial_{p}\Phi\partial_{p}\Phi^{*}\right) + \bar{H}_{\alpha}^{loc} \tag{34}$$

with $\bar{H}_{\alpha}^{loc} = H_{\alpha}^{loc}\partial_{Q_\alpha}\Phi\partial_{Q_\alpha}\Phi^{*}$.

Since we shall only concerned with the possibility of bifurcations in the incremental solution, the difference between two possible solutions of $\dot{\boldsymbol{\sigma}}$ must satisfy the homogeneous equilibrium equations, i.e. $\nabla\dot{\boldsymbol{\sigma}} = 0$.

An infinitive domain is considered and the solutions for the displacement rate $\dot{\boldsymbol{u}}$, the plastic multiplier $\dot{\gamma}$ and the mass content $\dot{\gamma}$ are expressed in terms of plane waves, as follows [19]

[1] $[[\bullet]]$ is the jump operator, defined by $[[\bullet]] = \bullet^{+} - \bullet^{-}$

$$\dot{u}\left(\boldsymbol{x},t\right)=\dot{\mathcal{U}}\left(t\right)\exp\left(\frac{i2\pi}{\delta}\boldsymbol{n}\cdot\boldsymbol{x}\right) \tag{35}$$

$$\dot{\gamma}\left(\boldsymbol{x},t\right)=\dot{\mathcal{M}}\left(t\right)\exp\left(\frac{i2\pi}{\delta}\boldsymbol{n}\cdot\boldsymbol{x}\right) \tag{36}$$

$$\dot{\lambda}\left(\boldsymbol{x},t\right)=\dot{\mathcal{L}}\left(t\right)\exp\left(\frac{i2\pi}{\delta}\boldsymbol{n}\cdot\boldsymbol{x}\right) \tag{37}$$

being $\boldsymbol{x}$ the position vector, $\boldsymbol{n}$ is the normal direction of the wave and δ is the wave length. Also, $\dot{\mathcal{U}}$, $\dot{\mathcal{M}}$ and $\dot{\mathcal{L}}$ are spatially homogeneous amplitudes of the wave saolutions.

Upon introducing the Eq. (31) into the incremental constitutive equations, Eq. (18), satisfying the equilibrium equation on the discontinuity surface, and considering the assumed solutions given in Eqs. (35)-(37), it is concluded that this equation is satisfied for each $\boldsymbol{x}$ if

$$\left(\frac{2\pi}{\delta}\right)^{2}\mathbf{n}\cdot\left\{\mathbf{C}^{0}-\frac{\mathbf{C}^{0}\partial_{\boldsymbol{\sigma}}\Phi^{*}\otimes\partial_{\boldsymbol{\sigma}}\Phi\mathbf{C}^{0}}{h+\bar{h}^{nloc}}\right\}\cdot\mathbf{n}\,\dot{\mathcal{U}}=0 \tag{38}$$

for drained conditions ($\dot{p}=0$), and

$$\left(\frac{2\pi}{\delta}\right)^{2}\mathbf{n}\cdot\left\{\mathbf{C}-\frac{\mathbf{C}\partial_{\boldsymbol{\sigma}}\Phi^{*}\otimes\partial_{\boldsymbol{\sigma}}\mathbf{C}}{h+\bar{h}^{nloc}}-\mathrm{M}^{2}\frac{\partial_{p}\Phi^{*}\mathbf{B}\otimes\mathbf{B}\partial_{p}\Phi}{h+\bar{h}^{nloc}}+\mathrm{M}\left(\frac{\mathbf{C}\partial_{\boldsymbol{\sigma}}\Phi^{*}\otimes\mathbf{B}\partial_{p}\Phi}{h+\bar{h}^{nloc}}+\frac{\partial_{p}\Phi^{*}\mathbf{B}\otimes\mathbf{C}\partial_{\boldsymbol{\sigma}}\Phi}{h+\bar{h}^{nloc}}\right)\right\}\mathbf{n}\,\dot{\mathcal{U}}=0 \tag{39}$$

for undrained conditions ($\dot{m}=0$), where $\bar{h}^{nloc}$ is the generalized gradient module.

$$\bar{h}^{nloc}=\bar{h}_{s}^{nloc}+\bar{h}_{p}^{nloc}=\mathbf{n}\cdot\left[l_{s}^{2}\left(\partial_{Q_{s}}\Phi\partial_{Q_{s}}\Phi^{*}\mathbf{H}_{s}^{nloc}\right)+l_{p}^{2}\left(\partial_{Q_{p}}\Phi\partial_{Q_{p}}\Phi^{*}\mathbf{H}_{p}^{nloc}\right)\right]\cdot\mathbf{n}\left(\frac{2\pi}{\delta}\right)^{2} \tag{40}$$

By calling $\mathbf{A}^{d,nloc}$ and $\mathbf{A}^{u,nloc}$ to the expressions into the bracket of Eq. (38) and Eq. (39), respectively, the acoustic tensor for gradient-regularized plasticity under drained and undrained conditions are deduced. It is clear that these expressions differs from the local counterpart only by the additional term $\bar{h}^{nloc}$. Thereby, when $l_{\alpha}=0$ the acoustic tensor for local plasticity is recovered, $\mathbf{A}^{d,loc}=\mathbf{A}^{d,nloc}$ and $\mathbf{A}^{u,loc}=\mathbf{A}^{u,nloc}$.

6 CONCLUSIONS

In this work a general thermodynamically consistent gradient constitutive formulation to describe non-local behaviour of porous media is proposed. The proposal is an extension

of the gradient-based thermodynamically consistent theories by [19] and [22] for non-porous continua particularized to the Modified Cam Clay constitutive model. Porous materials in this work are modelled from the macroscopic level of observation. They are considered to defined open thermodynamic systems characterized by the presence of occluded sub regions.

Discontinuous bifurcation theory to predict localized failure modes is consistently extended to porous media. As a result, the analytical expression of the localization tensor for gradient regularized plasticity in porous media is obtained. This failure indicator is particularized for both drained and undrained hydraulic conditions.

REFERENCES

[1] Alonso, E. E., Gens, A. and Josa, A. A constitutive model for partially saturated soils. *Geotechnique* (1990) **40**(3):405–430.

[2] Balmaceda, A. R. *Compacted soils, a theoretical and experimental study (in spanish).* Pdh Thesis. Universidad Politecnica de Catalunya (1991)

[3] Bolzon, G, Schrefler, B. A. and Zienkiewicz, O. C. Elastoplastic soil constitutive laws generalized to partially saturated states. *Geotechnique* (1996) **46**(2):279–289.

[4] Borja, R. I. and Koliji, A. On the effective stress in unsaturated porous continua with double porosity. *J. Mech. Phys. Solids.* (2009) **57**:1182–1193.

[5] Coussy, O. and Monteiro, P.J.M. Poroelastic model for concrete exposed to freezing temperatures. *Cement Concrete Res.* (2008) **35**:40–48.

[6] Coussy, O. *Mechanics of Porous Continua*. John Wiley & Sons. (1995).

[7] de Borst, R. and Muhlhaus, H. B Gradient-dependent plasticity: Formulation and algorithmic aspects. *Int. J. Numer. Meth. Eng.* (1992) **35**:521–539.

[8] Di Giuseppe, E.,Moroni, M. and Caputo, M. Flux in Porous Media with Memory: Models and Experiments. *Transport Porous Med.* (2009) **83**:479–500.

[9] Di Rado, H. A., Beneyto, P. A., Mroginski, J. L. and Awruch, A. M. Influence of the saturation-suction relationship in the formulation of non-saturated soils consolidation models. *Math. Comput. Model.* (2009) **49**:1058–1070.

[10] Ehlers, W. and Blome, P. A Triphasic Model for Unsaturated Soil Based on the Theory of Porous Media. *Math. Comput. Model.* (2003) **37**:507–513.

[11] Gens, A. and Potts, D.M. A theoretical model for describing the behaviour of soils not obeying Rendulic's principle. *Int. Sym. on Numerical Models in Geomechanics, Zurich* (1992)

[12] Gawin, D., Baggio, P. and Schrefler, B.A. Coupled heat, water and gas flow in deformable porous media. *Int. J. Numer. Meth. Fl.* (1995) **20**:969–987.

[13] Lewis, R. W., Schrefler, B. A. *The Finite Element Method in the Static and Dynamic Deformation and Consolidation of Porous Media*. John Wiley & Sons. (1998).

[14] Mroginski, J. L., Di Rado, H. A., Beneyto, P. A. and Awruch, A. M. A finite element approach for multiphase fluid flow in porous media. *Math. Comput. Simul.* (2010) **81**:76–91.

[15] Mroginski, J. L., Etse, G. and Vrech, S. M. A thermodynamical gradient theory for deformation and strain localization of porous media. *Int. J. Plasticity* (2011) **27**:620–634.

[16] Pamin, J. *Gradient-dependent plasticity in numerical simulation of localization phenomena*. PhD. Thesis., TU-Delft, The Netherlands. (1994).

[17] Roscoe, K.H. and Burland, J.B. *On the generalized stress-strain behaviour of wet clay*. In Engineering Plasticity, eds. J. Heyman and F.A. Leckie. Cambridge University Press. (1968)

[18] Schiava, R. and G. Etse, G. Constitutive modelling and discontinuous bifurcation assessment in unsaturated soils. *J. Appl. Mech.* (2006) **73**:1039–1044.

[19] Svedberg, T. and Runesson, K. A thermodynamically consistent theory of gradient-regularized plasticity coupled to damage. *Int. J. Plasticity* (1997) **13**:669–696.

[20] Vrech, S. and Etse, G. Geometrical localization analysis of gradient-dependent parabolic Drucker-Prager elatoplasticity. *Int. J. Plasticity* (2005) **22**:943–964.

[21] Vrech, S. and Etse, G. FE approach for thermodynamically consistent gradient-dependent plasticity. *Latin Am. Appl. Res.* (2007) **37**:127–132.

[22] Vrech, S. and Etse, G. Gradient and fracture energy-based plasticity theory for quasi-brittle materials like concrete. *Comput. Meth. Appl. Mech.* (2009) **199**:136–147.

XI International Conference on Computational Plasticity. Fundamentals and Applications
COMPLAS XI
E. Oñate, D.R.J. Owen, D. Peric and B. Suárez (Eds)

A VARIATIONALLY CONSISTENT APPROACH FOR NON-ASSOCIATIVE THERMOPLASTICITY AT FINITE STRAIN

MARKO CANADIJA* AND JÖRN MOSLER†

* Faculty of Engineering
University of Rijeka
Vukovarska 58, HR-51000 Rijeka, Croatia
e-mail: markoc@riteh.hr, http://www.riteh.hr

† Helmholtz-Zentrum Geesthacht
Zentrum für Material- und Küstenförschung
Institut für Werkstoffforschung
D-21502 Geesthacht, Germany
e-mail: joern.mosler@hzg.de, http://www.hzg.de

Key words: Thermoelastoplasticity, variational consistent updates, cyclic plasticity

Abstract. The present paper deals with nonisothermal plasticity at finite strain. Both isotropic and kinematic hardening are included through a non-associative model of Armstrong-Frederick-type. The model proposed in the present contribution is based on the recent works [1, 2]. Within the papers [1, 2], a variationally consistent update was proposed. This update allows computing the state of a thermomechanical solid by minimizing a certain energy potential. The non-trivial extension of [1, 2] to non-associative evolution equations was realized through the introduction of an extended principle of maximum dissipation augmented by a suitable parameterization of evolution equations. The latter formulation was recently presented in [3] within the context of isothermal plasticity. Recently, these authors have extended this approach to non-isothermal plasticity [4]. The predictive capabilities of this model are critically analyzed and demonstrated in the present contribution.

1 INTRODUCTION

Thermomechanically coupled problems were traditionally solved by decoupling the total problem into two sequential steps – the mechanical step in which the temperature is held fixed and the thermal step in which the configuration is fixed. The cornerstone of the aforementioned isothermal step was the radial return method. For capturing the heat dissipation due to plastic deformation, the most common model is the empirical rule of Taylor and Quinney. Unfortunately, this approach can violate the second law of thermodynamics, particularly if cyclic plasticity is considered. A further shortcoming of this approach is that the resulting thermomechanically coupled problem does not show a variational structure, cf. [1]. A variationally consistent reformulation of the thermomechanically coupled problem was recently given in [1]. In the present paper, the formulation presented in [1] is extended to non-associative evolution equations. This extension is based on a modified principle of maximum

dissipation. Concerning isothermal plasticity, such a principle was advocated in [3].

2 A NOVEL VARIATIONALLY CONSISTENT FORMULATION FOR THERMOMECHANICALLY COUPLED PROBLEMS

Without going too much into detail, the variational principle governing the thermomechanically coupled problem as originally proposed in [1] and further elaborated in [4] is defined by the incremental potential

$$I_{inc} = \int_{B_0} \left[E_{n+1} - E_n - \Theta_{n+1}\left(N_{n+1} - N_n\right) + \left[\int_{t_n}^{t_{n+1}} D dt \right] \right] dV \tag{1}$$

$$- \int_{B_0} \Delta t \chi_{n+1} dV - \Delta t P_{\mathbf{F},n+1} + \Delta t P_{\Theta,n+1} \,.$$

Here, E is the internal energy, D is the dissipation, N is the entropy, Θ is the so-called external temperature, χ is a Fourier-type dissipation potential, $P_{\mathbf{F}}$ is a potential defining the mechanical power associated with external forces, P_{Θ} is the counterpart potential for temperature effects, t denotes the time and B_0 is the domain of the considered body. As shown in [1], the state of a deforming body can be described by the stationary conditions of functional (1) for standard dissipative solids (solids fulfilling the normality rule).

For a family of constitutive models showing non-associative evolution equations, the framework proposed in [1] was extended in [4]. This extension is also the focus of the present paper. Conceptually and in line with [3], the idea is an extended principle of maximum dissipation. More precisely, the dissipation functional D, the flow rule and the evolution equations are chosen independently. For enforcing evolution equations different than those implied by the unconstrained principle of maximum dissipation, the concept of pseudo stresses is employed here. Such stresses are denoted as $\tilde{\boldsymbol{\Sigma}}$ in what follows. These stresses are inserted into the desired flow rule. By doing so, all constraints such as plastic incompressibility are automatically fulfilled, cf. [3].

Using the aforementioned parameterization, the unknown deformation φ and the unknown temperature Θ at time t_{n+1} can be computed from the saddle point problem

$$\left(\varphi_{n+1}, \Theta_{n+1}\right) = \arg \inf_{\varphi_{n+1}} \sup_{\Theta_{n+1}} \left\{ \inf_{\Delta\lambda, \tilde{\boldsymbol{\Sigma}}_{n+1}, N_{n+1}} I_{inc} \right\}. \tag{2}$$

Here, $\Delta\lambda$ is the integrated plastic multiplier. Problem (2) can be conveniently solved in a staggered fashion. For that purpose, a minimization with respect to the fully locally defined variables is performed first. This gives rise to the local constitutive update

$$\left(\Delta\lambda, \tilde{\boldsymbol{\Sigma}}_{n+1}, N_{n+1}\right) = \arg \inf_{\Delta\lambda, \tilde{\boldsymbol{\Sigma}}_{n+1}, N_{n+1}} I_{inc}\big|_{\varphi_{n+1}=const.,\Theta_{n+1}=const.} \,. \tag{3}$$

It can be conveniently solved by applying Newton-type procedures. Subsequently, the stresses follow from the relaxed energy as partial derivatives with respect to the conjugate strain variable.

3 EVOLUTION LAWS AND YIELD FUNCTION

When minimization problem (3) is to be solved, the evolution equations and the stresses have to be specified.

For defining the stresses, the Helmholtz energy is introduced via the classical Legrende-Fenchel transformation

$$\Psi\left(\mathbf{F},\Theta,\boldsymbol{\alpha}\right)=\inf_{N}\left[E\left(\mathbf{F},N,\boldsymbol{\alpha}\right)-N\Theta\right], \tag{4}$$

where $\boldsymbol{\alpha}$ is a set of strain-like internal variables describing plastic deformation. If the set of internal variables is specified as $\boldsymbol{\alpha}=\left\{\mathbf{F}^{p},\boldsymbol{\alpha}_{k},\alpha_{i}\right\}$, the Helmholtz energy reads $\Psi=\left\{\mathbf{F}^{e},\Theta,\boldsymbol{\alpha}_{k},\alpha_{i}\right\}$, where $\mathbf{F}^{e},\mathbf{F}^{p}$ are the elastic and the plastic part of the deformation gradient. Based on Ψ, the stresses are introduced in standard manner, i.e., as derivatives of Ψ with respect to the deformation gradient.

Having defined the stresses, the internal dissipation inequality can be written as (see [4])

$$D_{\text{int}}=\boldsymbol{\Sigma}:\mathbf{L}^{p}+\mathbf{Q}_{k}:\dot{\boldsymbol{\alpha}}_{k}+Q_{i}\dot{\alpha}_{i}\geq 0, \tag{5}$$

where $\mathbf{L}^{p}$ is plastic velocity gradient, $\boldsymbol{\Sigma}$ is the Mandel stress tensor and $\mathbf{Q}_{k},Q_{i}$ are stress-like internal variables conjugate to the strain-like kinematic hardening variable $\boldsymbol{\alpha}_{k}$ and the strain-like isotropic hardening variable α_{i}, respectively.

With (5) the temperature evolution can be defined from the balance of energy. After a straightforward computation it is given by

$$c\dot{\Theta}=\rho_{0}Q_{\Theta}-\text{DIV}\mathbf{H}+D_{\text{int}}+\Theta\partial^{2}_{\Theta\mathbf{F}^{e}}\Psi:\dot{\mathbf{F}}^{e}, \tag{6}$$

where c is the heat capacity at constant strain, $\mathbf{H}$ is the outward heat flux vector and Q_{Θ} is heat source per unit mass. The last term governs thermoelastic heating and it is frequently neglected.

According to (5), the internal dissipation depends crucially on the considered state. For distinguishing between plastic and elastic deformation, the by now classical a yield function is considered. In the present paper, this yield function is assumed to be of the type

$$\phi\left(\boldsymbol{\Sigma},\mathbf{Q}_{k},Q_{i},\Theta\right)=\boldsymbol{\Sigma}^{eq}\left(\boldsymbol{\Sigma}-\mathbf{Q}_{k}\left(\boldsymbol{\alpha}_{k}\right)\right)-Q_{i}\left(\alpha_{i}\right)-Q_{0}^{eq}\left(\Theta\right)\leq 0. \tag{7}$$

Here, the initial yield stress $Q_{0}^{eq}\left(\Theta\right)$ is chosen as temperature dependent. The function $\boldsymbol{\Sigma}^{eq}$ defining the shape of the yield function is assumed to be convex and positively homogenous function of degree one, i.e.,

$$\boldsymbol{\Sigma}^{eq}\left(c\left(\boldsymbol{\Sigma}-\mathbf{Q}_{k}\right)\right)=c\boldsymbol{\Sigma}^{eq}\left(\boldsymbol{\Sigma}-\mathbf{Q}_{k}\right). \tag{8}$$

Finally, the evolution equations are defined. For that purpose and in line with the framework of generalized standard solids, a plastic potential is introduced. In the present paper, this potential is of the type

$$g\left(\boldsymbol{\Sigma},\mathbf{Q}_{k},Q_{i},\Theta\right)=\phi\left(\boldsymbol{\Sigma},\mathbf{Q}_{k},Q_{i},\Theta\right)+\overline{\phi}\left(\mathbf{Q}_{k}\right). \tag{9}$$

The evolution equations are gradients of g. More precisely,

$$\mathbf{L}_{\boldsymbol{\alpha}}^{p} = \lambda \partial_{\boldsymbol{\Sigma}} \bar{\phi}, \quad \dot{\mathbf{Q}}_k = -\dot{\boldsymbol{\alpha}}^{p} + \lambda \partial_{\mathbf{Q}_k} \bar{\phi}, \quad \dot{\alpha}_i = -\lambda \,. \tag{10}$$

(10) is supplemented by the standard Karush-Kuhn-Tucker conditions.

In the case of a von Mises yield function and applying the concept of pseudo stresses $\tilde{\boldsymbol{\Sigma}}$, (10) can be re-written as

$$\mathbf{L}_{\boldsymbol{\alpha}}^{p} = \lambda \frac{\mathrm{Dev}\tilde{\boldsymbol{\Sigma}}}{\left\| \mathrm{Dev}\tilde{\boldsymbol{\Sigma}} \right\|}, \quad \dot{\mathbf{Q}}_k = -\lambda \frac{\mathrm{Dev}\tilde{\boldsymbol{\Sigma}}}{\left\| \mathrm{Dev}\tilde{\boldsymbol{\Sigma}} \right\|} + \lambda \partial_{\mathbf{Q}_k} \bar{\phi}, \quad \dot{\alpha}_i = -\lambda \,. \tag{11}$$

If the yield function is now combined with the dissipation inequality (5), the internal dissipation takes the form

$$D_{\mathrm{int}} \overset{\phi=0}{=} \lambda Q_0^{eq} + \lambda \mathbf{Q}_k : \frac{\partial \bar{\phi}}{\partial \mathbf{Q}_k} \geq 0 \,. \tag{15}$$

Accordingly, the second law of thermodynamics is automatically fulfilled, if the plastic potential (9) is convex. That can be guaranteed by using a convex yield function (which is the case for the von Mises model) and a convex function $\bar{\phi}$.

4 EXAMPLE AND CONCLUSIONS

For demonstrating the efficiency of the discussed framework, the cyclic tension test is numerically analyzed, cf. [3, 5]. In line with [1, 2] adiabatic conditions are considered. The material response is defined by a Helmholtz energy of the type

$$\Psi = W\left(\bar{\mathbf{C}}^{e}\right) + U(J) + T(\Theta) + M(J,\Theta) + \Psi^{p}\left(\boldsymbol{\alpha}_k\right), \tag{16}$$

where the potential $W\left(\bar{\mathbf{C}}^{e}\right)$ defining the elastic deviatoric response as a function of the deviatoric elastic right Cauchy-Green tensor $\bar{\mathbf{C}}^{e}$, the potential $U(J)$ depending on the Jacobian determinant of the deformation gradient characterizing the elastic volumetric response, the part $T(\Theta)$ associated with thermal effects, the part $M(J,\Theta)$ related to thermoelastic effects and the potential $\Psi^{p}\left(\boldsymbol{\alpha}_k\right)$ corresponding to kinematic hardening are chosen as

$$W\left(\bar{\mathbf{C}}^{e}\right) = \frac{1}{2}\mu\left[\mathrm{tr}\left(\bar{\mathbf{C}}^{e}\right) - 3\right], \; U(J) = \frac{1}{2}\kappa\left[\frac{1}{2}\left(J^2 - 1\right) - \ln J\right], \tag{17}$$

$$T(\theta) = c_0\left[\left(\Theta - \Theta_0\right) - \Theta \ln\frac{\Theta}{\Theta_0}\right], \; M(J,\Theta) = \left(\Theta - \Theta_0\right)\left[-3\alpha U'(J)\right], \; \Psi^{p} = \frac{1}{2}c\boldsymbol{\alpha}_k : \boldsymbol{\alpha}_k \,.$$

Thermal softening is accounted for by a temperature-dependent initial yield stress of type

$$Q_0^{eq}(\theta) = y_0(\theta_0)\left[1 - \omega_0\left(\theta - \theta_0\right)\right]. \tag{18}$$

The plastic response is completed by a von Mises yield function

$$\phi\left(\boldsymbol{\Sigma},\mathbf{Q}_k,\Theta\right)=\left\|\mathrm{Dev}\boldsymbol{\Sigma}-\mathbf{Q}_k\right\|-Q_0^{eq} \tag{19}$$

including kinematic hardening and the evolution equations and the flow rules are defined by the gradients of the convex plastic potential

$$g\left(\boldsymbol{\Sigma},\mathbf{Q}_k,\Theta\right)=\phi\left(\boldsymbol{\Sigma},\mathbf{Q}_k,\Theta\right)+\bar{\phi}\left(\mathbf{Q}_k\right);\quad \bar{\phi}\left(\mathbf{Q}_k\right)=\frac{1}{2}\frac{b}{c}\left\|\mathbf{Q}_k\right\|^2 \tag{20}$$

with respect to their dual variables. Finally, the thermal problem is governed by the Fourier dissipation potential

$$\chi=\frac{1}{2}k\mathrm{GRAD}\,\Theta\cdot\mathrm{GRAD}\,\Theta\,. \tag{21}$$

The material parameters used in the numerical simulations are summarized in Tab. 1.

Table 1: Material parameters

μ, GPa	κ, GPa	α, GPa	b
80	173.333	$1.15\cdot10^{-5}$	8.5
c, GPa	y_0, MPa	c_0, N/mm^{2}K	ω_0, K^{-1}
1.9	244.95	3.7518	0.002

Within the variational framework, the part of the mechanical dissipation which is transferred to heat is consistently governed by the first law of thermodynamics. However, by assuming the classical Taylor-Quinney coupling, a Taylor-Quinney factor can be computed as a post-processing step, cf. [1]. The respective results for the first loading stage are shown in Fig. 1. Accordingly and as already mentioned in [1], the assumption of a constant factor is not in line with the first law of thermodynamics. More precisely, the evolution of this factor is highly non-linear. That confirms that the classical Taylor-Quinney assumption is not valid in general and can usually only be justified by a mean value of the more complex and physically more sound evolution shown in Fig. 1. Such problems can be conveniently and naturally solved by using the advocated variationally consistent thermomechanically coupled model.

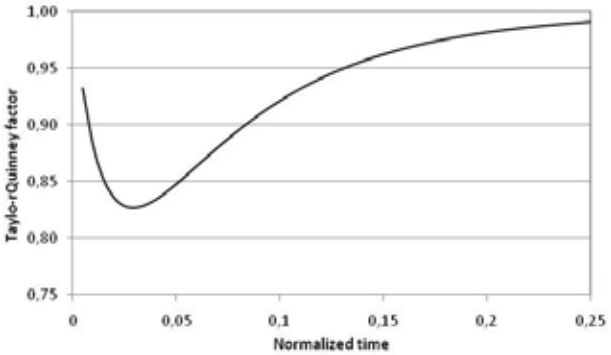

Figure 1: Evolution of the Taylor-Quinney factor as predicted by the variationally consistent model

REFERENCES

[1] Q. Yang, L. Stainier and M. Ortiz, "A variational formulation of the coupled thermo-mechanical boundary-value problem for general dissipative solids", *J. Mech. Phy. Solids,* **54**, 401-424, (2006).

[2] L. Stainier and M. Ortiz, "Study and validation of thermomechanical coupling in finite strain visco-plasticity*", Int. J. Solids Struct*., **47**, 705-715, (2010).

[3] J. Mosler, "Variationally consistent modeling of finite strain plasticity theory with non-linear kinematic hardening", *Comput. Meth. Appl. Mech. Eng.*, **199**, 2753–2764, (2010).

[4] M. Canadija and J. Mosler, "On the thermomechanical coupling in finite strain plasticity theory with non-linear kinematic hardening by means of incremental energy minimization", *Int. J. Solids Struct.*, **48**, 1120-1129, (2011).

[5] J.C. Simo and C. Miehe, "Associative coupled thermoplasticity at finite strains: formulation, numerical analysis and implementation", *Comput. Meth. Appl. Mech. Eng.*, **98**, 41–104, (1992).

XI International Conference on Computational Plasticity. Fundamentals and Applications
COMPLAS XI
E. Oñate, D.R.J. Owen, D. Peric and B. Suárez (Eds)

ACCELERATED ENERGY-MINIMIZATION IN THE QUASICONTINUUM METHOD WITH APPLICATION TO NANOPILLAR COMPRESSION

B. EIDEL*, A. STUKOWSKI† AND J. SCHRÖDER*

*Institute for Mechanics, Faculty of Engineering Sciences
University of Duisburg-Essen
Universitätsstr. 15, 45141 Essen, Germany
e-mail: bernhard.eidel@uni-due.de, www.uni-due.de/mechanika/

†Lawrence Livermore National Laboratory (LLNL)
7000 East Avenue, Livermore, CA 94550, USA
e-mail: stukowski1@llnl.gov, https://www.llnl.gov/

Key words: Multiscale Materials Modeling, Atomic-to-Continuum Coupling, Energy-Minimization, Finite Element Method, Quasicontinuum

Abstract. The focus of this contribution is on a novel, improved technique for energy minimization in atomic simulations and its adaption to a variationally consistent formulation of the quasicontinuum (QC) method. The optimization algorithm called FIRE for Fast Inertial Relaxation Engine can be understood as a modification of the Steepest Descent (SD) method, which improves SD by accelerating the system in the direction of the force, making the minimization more aggressive. The performance of FIRE is assessed in the example of nanopillar compression with respect to efficiency and stability against competitive optimization methods.

1 MODELING

1.1 Fully nonlocal QC method based on energy calculation in clusters.

The main conceptual ingredients of the fully nonlocal QC-method which drastically reduce the computational burden of fully atomistic models are visualized in Fig. 1. Firstly, it is a finite element discretization ('coarse-graining') reducing the number of degrees of freedom in the crystal. Secondly, and even more important for reducing the computational costs, it is the calculation of atomic energies $E_{\boldsymbol{k}}$ at lattice sites $\boldsymbol{k}$ in spherical sampling clusters $\mathscr{C}_{\boldsymbol{i}}$ of radius R_c defined as $\mathscr{C}_{\boldsymbol{i}} = \{\boldsymbol{k} : |\boldsymbol{X}_{\boldsymbol{k}} - \boldsymbol{X}_{\boldsymbol{i}}| \leq R_c(\boldsymbol{i})\}$ instead of in the entire crystal. The energy of each cluster is multiplied with a weighting factor $n_{\boldsymbol{i}}$ accounting for the energy contributions of atoms outside the cluster. The summation over all mesh

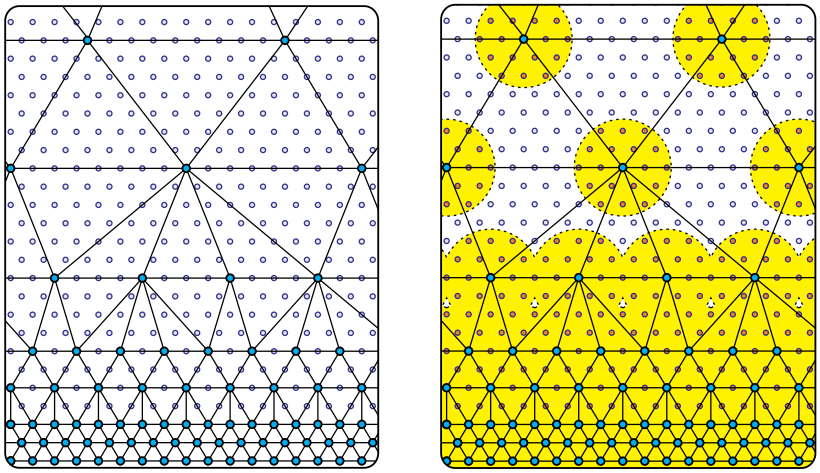

Figure 1: Approximations in the cluster-based QC method: (Left) Finite element discretization of the crystal where atoms in the interior of elements smoothly follow the deformation of the representative atoms (mesh nodes) by linear interpolation. (Right) Energy sampling in spherical clusters.

nodes $\boldsymbol{i} \in \mathscr{L}_h$ and therefore over all clusters yields the QC-approximation of the total energy

$$E^{\mathrm{QC}} = \sum_{\boldsymbol{i}\in\mathscr{L}_h} n_{\boldsymbol{i}} \sum_{\boldsymbol{k}\in\mathscr{C}_{\boldsymbol{i}}} E_{\boldsymbol{k}}\,. \tag{1}$$

The atomic energies $E_{\boldsymbol{k}}$ are calculated using pair functionals of the Embedded Atom Method (EAM). Note, that the cluster radius R_c is a purely numerical parameter controlling the accuracy of the cluster summation rule, whereas the cut-off radius is a physical parameter and cannot be arbitrarily chosen. The weighting factors $n_{\boldsymbol{i}}$ are calculated such that the sum of the shape function values in the clusters multiplied with the weighting factors equals the sum of the shape function values at all lattice sites in the crystal, it reads

$$\sum_{\boldsymbol{i}\in\mathscr{L}_h} n_{\boldsymbol{i}} \sum_{\boldsymbol{k}\in\mathscr{C}_{\boldsymbol{i}}} \varphi_{\boldsymbol{j}}(\boldsymbol{X}_{\boldsymbol{k}}) = \sum_{\boldsymbol{k}\in\mathscr{L}} \varphi_{\boldsymbol{j}}(\boldsymbol{X}_{\boldsymbol{k}}) \qquad \forall \quad \boldsymbol{j} \in \mathscr{L}_h\,. \tag{2}$$

Stable equilibrium configurations of the crystal are minimizers of the total energy and correspond to configurations for which the resultant force at every finite element node $\boldsymbol{a}$ is zero, hence

$$\min_{\{\boldsymbol{x}_{\boldsymbol{a}}\}} E^{\mathrm{QC}} \quad \Longrightarrow \quad \boldsymbol{f}_{\boldsymbol{a}}^{\mathrm{QC}} = -\frac{\partial E^{\mathrm{QC}}}{\partial \boldsymbol{x}_{\boldsymbol{a}}} = \boldsymbol{0} \qquad \forall \quad \boldsymbol{a} \in \mathscr{L}_h\,. \tag{3}$$

For more details about the cluster-based QC method, we refer to [7] and [4], a comparison with the QC method based on Cauchy-Born elasticity can be found e.g. in [5] and [6].

1.2 Energy minimization based on acceleration and inertia

Energy minimization in atomic simulations at zero temperature is used to find the (inherent) equilibrium structure of a solid without the "noise" of thermal vibrations. When the equilibrium structure is searched at finite temperature, an established technique is to carry out molecular dynamics (MD) calculations, but then, to remove continuously kinetic energy from the system, a process called numerical "quenching". In [1] a simple MD scheme for structural relaxation was proposed which belongs to this class of minimizers. The algorithm dubbed FIRE for *Fast Inertial Relaxation Engine* (FIRE) crucially relies on inertia as its precursor Quick-Min (QM) does, see [2], but makes effective improvements. The strategy to descent to a minimum of the total energy is to follow an equation of motion given by

$$\dot{\boldsymbol{v}}(t) = 1/m\, \boldsymbol{F}(t) - \gamma(t)|\boldsymbol{v}(t)| \left[\hat{\boldsymbol{v}}(t) - \hat{\boldsymbol{F}}(t)\right], \tag{4}$$

with mass m, velocity $\boldsymbol{v} = \dot{\boldsymbol{x}}$, force $\boldsymbol{F} = -\nabla E^{\mathrm{QC}}(\boldsymbol{x})$, and where the hat denotes a unit vector. Hence, the strategy is to accelerate in a direction that is "steeper" than the current direction of motion via the function $\gamma(t)$, if the power $P(t) = \boldsymbol{F}(t) \cdot \boldsymbol{v}(t)$ is positive. To avoid uphill motion the algorithm stops as soon as the power becomes negative. The parameter $\gamma(t)$ must be chosen appropriately but should not be too large, because the current velocities carry information about the reasonable 'average' descent direction and energy scale, see [1]. The numerical treatment of the algorithm is based on an MD integrator like the Velocity Verlet algorithm providing the propagation of the trajectories due to conservative forces. The MD trajectories are continuously readjusted by a mixing rule of the velocities according to

$$\boldsymbol{v} \to (1-\alpha)\boldsymbol{v} + \alpha \hat{\boldsymbol{F}}|\boldsymbol{v}| \tag{5}$$

which follows from an Euler-step of the second term on the right in eq. (4) with time step size Δt and $\alpha = \gamma \Delta t$. The propagation rules for the FIRE algorithm can be summarized as follows (initialization: set values for Δt, $\alpha = \alpha_{\mathrm{start}}$, the global vectors $\boldsymbol{x}$ and set $\boldsymbol{v} = \boldsymbol{0}$):

1. MD integrator: calculate $\boldsymbol{x}$, $\boldsymbol{F} = -\nabla E^{\mathrm{QC}}(\boldsymbol{x})$ and $\boldsymbol{v}$ using any common MD integrator (here: Velocity Verlet); check for convergence.
2. calculate force power $P = \boldsymbol{F} \cdot \boldsymbol{v}$.
3. set $\boldsymbol{v} \to (1-\alpha)\boldsymbol{v} + \alpha|\boldsymbol{v}|\hat{\boldsymbol{F}}$.
4. if $P > 0$ and the number of steps since P was negative is larger than N_{min}, increase the time step $\Delta t \to \min(\Delta t f_{\mathrm{inc}}, \Delta t_{\mathrm{max}})$ and decrease $\alpha \to \alpha f_{\alpha}$.
5. if $P \leq 0$, decrease time step $\Delta t \to \Delta t f_{\mathrm{dec}}$, freeze the system $\boldsymbol{v} \to \boldsymbol{0}$, and set α back to α_{start}.
6. Return to MD integrator.

The FIRE-parameters used in the present work are set to $N_{\min} = 5$, $\alpha_{\text{start}} = 0.1$, $f_{\text{inc}} = 1.1$, $f_{\text{dec}} = 0.5$ and $f_\alpha = 0.99$.

Remark.
The differences of FIRE compared with its precursor QM are twofold. Both algorithms take dynamical steps starting in the direction of the steepest descent. Furthermore they both reset the velocity if the force and velocity are in opposite directions. The first difference is, however, that FIRE employs variable time step sizes. The second difference is that QM projects the velocity onto the force vector according to

$$\boldsymbol{v} \rightarrow (\boldsymbol{v} \cdot \hat{\boldsymbol{F}})\hat{\boldsymbol{F}} \tag{6}$$

whereas FIRE only projects a component of the velocity in the force direction, while maintaining momentum in other directions, see eq.(5), which avoids to adjust the direction of descent too hastily.

2 EXAMPLE: COMPRESSION OF A NANOPILLAR

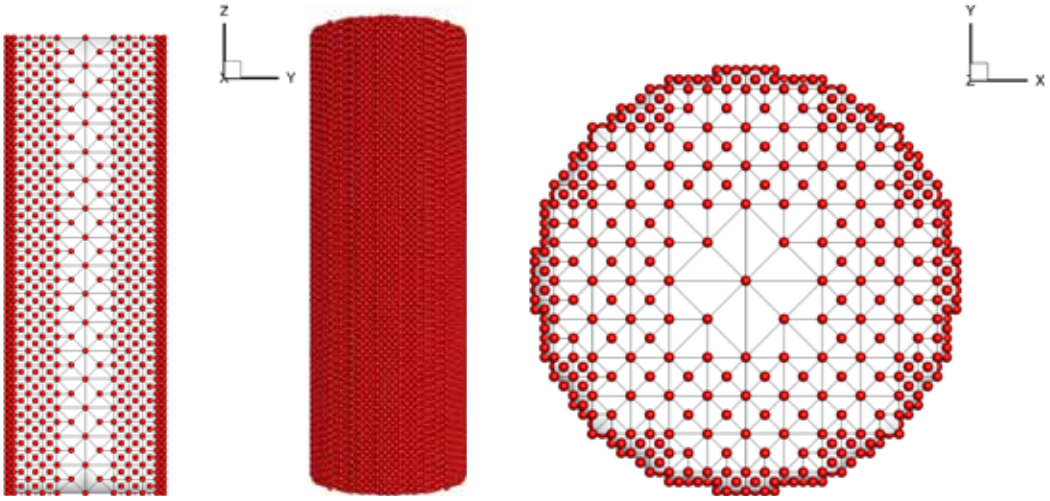

Figure 2: Nanopillar compression, (left) lateral cross sectional view of the discretization, (center) outer face, (right) cross sectional view of discretization reveals the approximation of the circle by a polygon due to the small size of the fcc pillar.

The single-crystalline, fcc nanopillar made of aluminum is of cylindrical shape and exhibits height $H = 64\,a_0$, diameter $D = 16\,a_0$ with lattice constant $a_0 = 4.032$ Å. Crystallographic $< 001 >$-axes align with cartesian X-, Y- and Z-axes. The pillar is supported at the bottom in z-direction and all faces are free surfaces. After initial relaxation of the crystal without the presence of external forces, the top surface is loaded by a compressive force, which is mediated by displacement control in z-direction. For a proper geometry description the curved surface is in full atomic resolution, whereas the interior of the pillar

is initially coarse-grained by finite elements. The cluster radius in the simulations is set to $R_c = a_0/\sqrt{2}$, for the energy calculation an EAM-potential for aluminum is used.

The novel FIRE minimizer is tested against the performance of the Steepest Descent (SD) method, a nonlinear version of the Conjugate Gradient (CG) method and the Limited-memory Broyden-Fletcher-Goldfarb-Shanno (L-BFGS) algorithm. The total deformation range can be decomposed into three distinct ranges.

(I) For *surface relaxations* the energy landscape is typically rather flat, the process of energy-minimization using conventional optimization algorithms tends to get trapped in shallow holes representing local energy minimizers as indicated by residuals toggling up and down but cannot go below an accuracy threshold. FIRE in contrast, by virtue of its inertia can pass these local minima and can achieve virtually arbitrary accuracy. For the surface relaxation in the present example the performance of FIRE is in between L-BFGS and the CG method, the convergence of SD is very slow, see the top diagram in Fig. 3.

(II) The range of *elastic compression* is very ample and extends to a maximum compressive strain of 7.7%. The reason is that the pillar exhibits no initial dislocations which can serve as carriers of plastic deformation. Therefore, the present compression simulation probes the strength of the material rather than giving an example of classical, dislocation-mediated plasticity on the nanoscale. The diagram in the center of Fig. 3 belongs to a single loading step which is representative for the performance of the minimization algorithms in the entire elastic deformation range. FIRE performs better than the other optimizers and is even considerably faster than L-BFGS.

(III) At the point of *material instability*, where strain localizes in a crystallographic slip band coinciding with a {111} plane, CG and SD diverge, whereas L-BFGS and FIRE can pass the point of bifurcation. Here, FIRE is faster than L-BFGS, see the bottom in Fig. 3.

2.1 A note on the mechanics of nano-/micropillars

The mechanics of small-sized (diameter D in the range of approximately 100 nm – 2 μm), single-crystalline pillars has attracted considerable interest in recent years. The reason is that for these pillars subject to compression a size-dependence of the flow stress in the sense of "smaller is stronger" has been measured, which was first reported in [3]. This behavior seems to be at odds with an earlier understanding, according to which size-dependence requires structural obstacles to dislocation motion like grain-boundaries or other interfaces (cf. Hall-Petch relationship). A single-crystalline specimen with a deformation state assumed to be quasi-homogeneous in contrast, was not expected to exhibit that size-dependence.

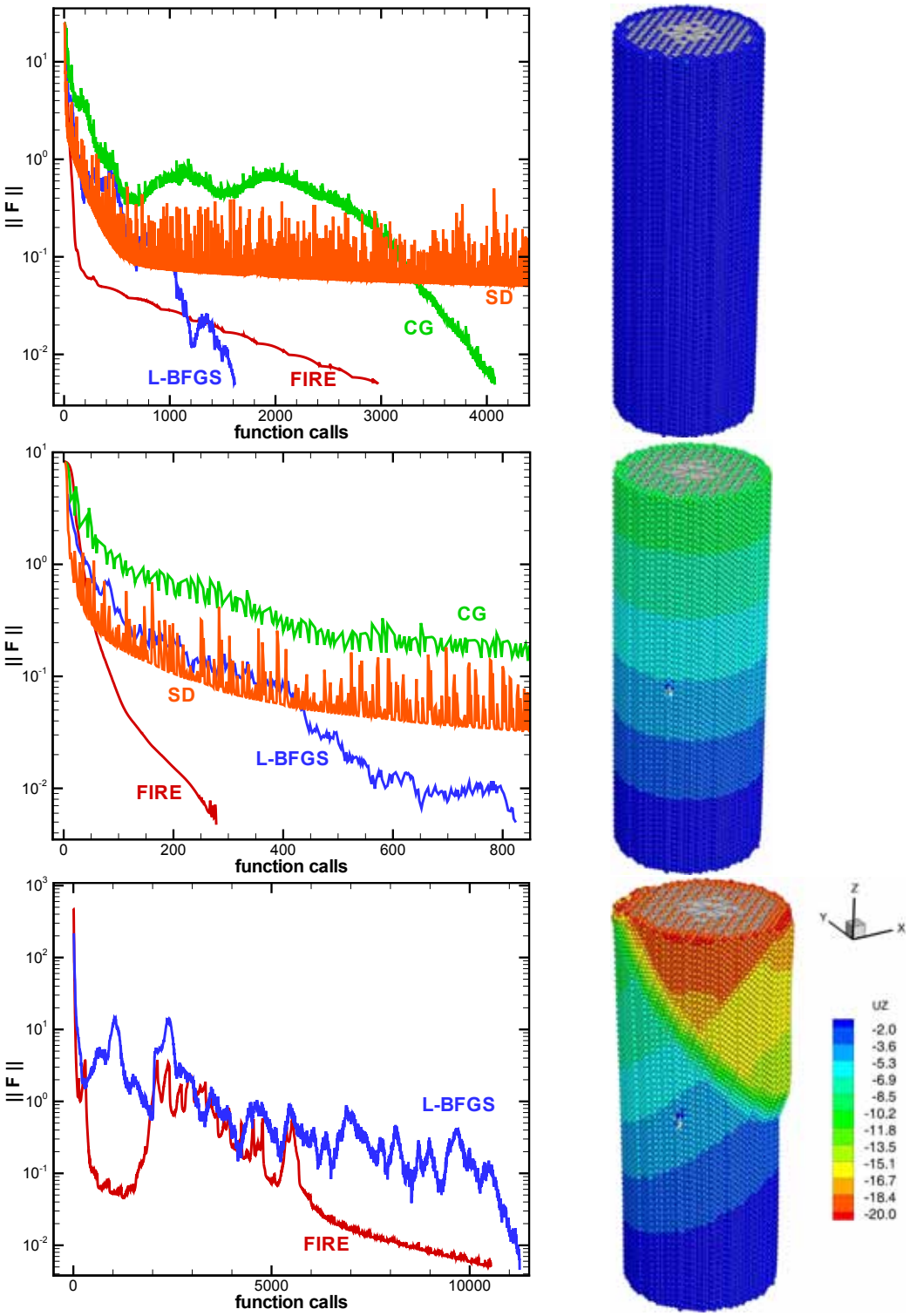

Figure 3: Convergence diagrams for different optimizers at characteristic deformation stages of the compressed nanopillar (left), contour plots for displacement component u_z [Å] (right).

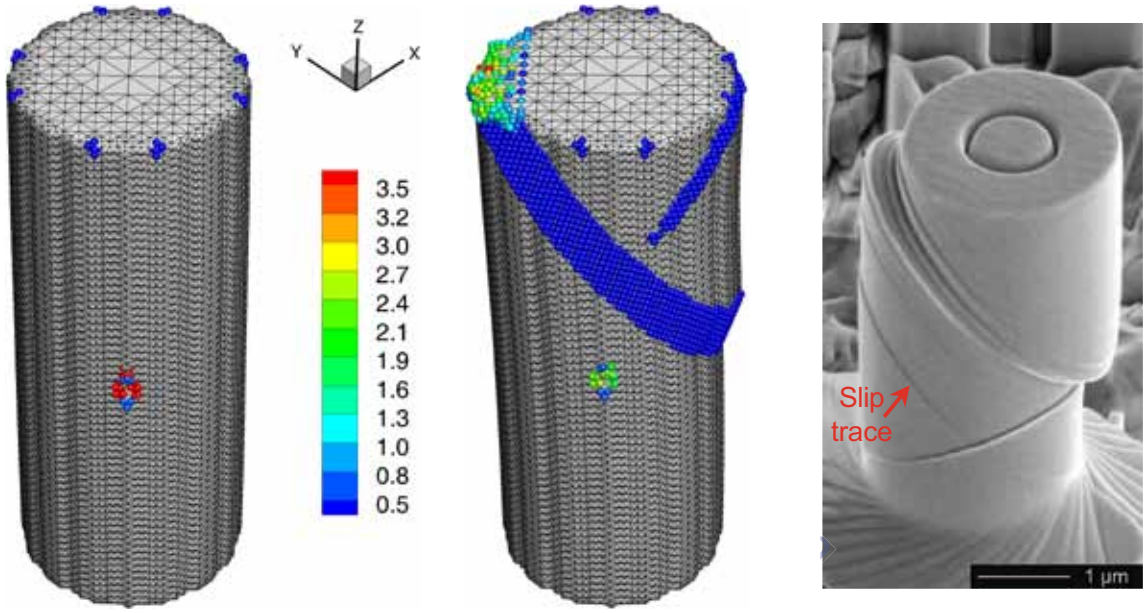

Figure 4: Compression of single-crystalline fcc nano-/micropillar. Deformed pillar right before (Left) and right after bifurcation (centre) with contour plots for $II(\mathrm{dev}\boldsymbol{E}) > 0.3$ in QC-simulation for Al and (right) in the experiment of a Ni-micropillar, picture from [3].

Note, that for the present simulations one atom has been removed from the middle of the pillar's surface in order to attract stress at that local defect and thereby to trigger localization. This can be best seen in the left of Fig. 4, where atoms are displayed that exhibit a value for the second invariant of the Green-Lagrangian strain tensor $II(\mathrm{dev}\boldsymbol{E}) > 0.3$. Note that right before localization the largest deviatoric strain is observed at the site where the atom is removed. Nevertheless, localization starts from the intersecting surfaces at the loaded top, Fig. 4 (center), which indicates that this geometrical defect is stronger than the artificially introduced surface defect. Furthermore the contour plot of $II(\mathrm{dev}\boldsymbol{E})$ in Fig. 4 reveals that right after the first microband has formed, a second slip system is activated.

3 CONCLUSION

Summarizing, in its modified formulation within the quasicontinuum method, FIRE is competitive with, in some cases superior to well-established efficient minimization algorithms like L-BFGS. Beyond its superior behavior with respect to *efficiency* and *stability* FIRE is easy to implement and can be operated intuitively. These benefits and promising results suggest to use FIRE in various other models, especially when stability issues are a major concern.

REFERENCES

[1] Bitzek, E., Koskinen, P., Gähler, F., Moseler, M., and Gumbsch, P. Structural relaxation made simple. *Phys. Rev. Lett.* (2006) **97**:170201(4).

[2] Della Valle, R.G. and Jonsson, H.C. Molecular dynamics simulation of silica liquid and glass. *J. Chem. Phys.* (1992) **97(4)**:2682–2689.

[3] Dimiduk, D.M., Uchic, M.D., and Parthasarathy, T.A. Size-affected single-slip behavior of pure nickel microcrystals. *Acta Mater.* (2005) **53**:4065–4077.

[4] Eidel, B. and Stukowski, A. A variational formulation of the quasicontinuum method based on energy sampling in clusters. *J. Mech. Phys. Solids* (2009) **57**:87–108.

[5] Eidel, B. Coupling atomistic accuracy with continuum effectivity for predictive simulations in materials research - the Quasicontinuum Method. *Int. J. Mat. Res.* (2009) **100**:1503–1512.

[6] Eidel, B., Hartmaier, A., and Gumbsch, P. Atomistic Simulation Methods and their Application on Fracture, In: *Multiscale Modelling of Plasticity and Fracture by Means of Dislocation Mechanics*. CISM International Centre for Mechanical Sciences, Courses and Lectures, Vol. 522, 1–58, Springer, (2010).

[7] Knap, J. and Ortiz, M. An analysis of the quasicontinuum method. *J. Mech. Phys. Solids* (2001) **49**:1899–1923.

XI International Conference on Computational Plasticity. Fundamentals and Applications
COMPLAS XI
E. Oñate, D.R.J. Owen, D. Peric and B. Suárez (Eds)

ENERGY-BASED VARIATIONAL MODELING OF ADIABATIC SHEAR BANDS STRUCTURE

Shaopu SU, Laurent STAINIER

Institut de recherche en Génie Civil et Mécanique (GeM - UMR 6183 CNRS)
Ecole Centrale de Nantes
1 rue de la Noë, BP 92101, 44321 Nantes cedex 3
e-mail: Shaopu.Su@ec-nantes.fr, Laurent.Stainier@ec-nantes.fr

Key words: adiabatic shear band, variational approach, thermo-viscoplasticity

Abstract. A modeling approach of the shear localization in thermoviscoplastic materials is developed in the framework of an energy-based variational formulation. The shear band structure in the layer (1D) sustaining a simple shearing deformation has been analysed in stationary and transient regimes. Starting from the optimization problem characterizing our variational formulation, we seek an approximate solution by way of a semi-analytical approach to predict the profiles of velocity and temperature in the band and obtain the evolution of some characteristic parameters, such as shear band width and maximum temperature, showing a good consistency with the solution obtained by the finite element method. Indeed, the results converge to the steady solution, in agreement with the canonical analytical solution [1].

1 INTRODUCTION

We have recently proposed a variational formulation of coupled thermo-mechanical boundary-value problems [2], allowing to write mechanical and thermal balance equations under the form of an optimization problem of a scalar function. This formulation applies to a wide range of material behaviors, possibly irreversible and dissipative, as long as they fit in the framework of Generalized Standard Materials [3]. The proposed variational structure brings several advantages. Beyond unifying a wide range of constitutive models in a common framework, the variational formulation also presents interesting mathematical properties. Among these, an important property is that of symmetry, inherent to all variational formulations, but which lacked to alternative coupled thermo-mechanical formulations previously proposed in the literature.

An adiabatic shear band is an intense shearing zone appearing in large plastic deformation with thermal instability at high strain rates. It's encountered in many engineering problems: forming processes and impact loading of metallic materials, but also in thermoplastic polymers. Understanding and predicting their onset and evolution is critical since

they usually are a precursor to macroscopic ductile fracture. Much work has thus been published on the topic. Molinari ([1], [4]), Wright ([5]) have derived the analytical expressions for velocity and temperature profiles (1D) in the steady state, but the results are based on specific constitutive relations. In general, the small width of the shear band and the material softening effect associated with the local heating bring a lot of difficulties to numerical simulations, such as mesh dependence, model quality and interactions between multiple bands. Many methods (XFEM [6], meshless method [7], interface element [8], $\cdots$) have been used for bypassing these problems. However, it is necessary to know the approximate domain of the shear band width in most of these approches. Here, we aim at constructing a semi-analytical model able to predict the internal structure of an adiabatic shear band and its evolution with time (and loading), starting from the variational formulation described in [2]. Indeed, thermo-mechanical coupling effects and conduction play a fundamental role in determining the velocity and temperature profiles within an adiabatic shear band.

2 Variational model in the steady state

We simplify the shear band model as its 1D problem illustrated in Fig.1: a layer of thickness $2H$ subjected to a simple shearing force. The velocity imposed on the boundary is V_0, and isothermal conditions ($T = T_0$) at $y = \pm H$ are considered. The material is chosen as a steel having thermoviscoplastic properties with parameters of the material described in [1]. Here, the elastic and the hardening effects are neglected to simplify the model. First, we consider the problem in case of the steady state, when the stress and the entropy in the layer are stationary.

2.1 Variational formulation

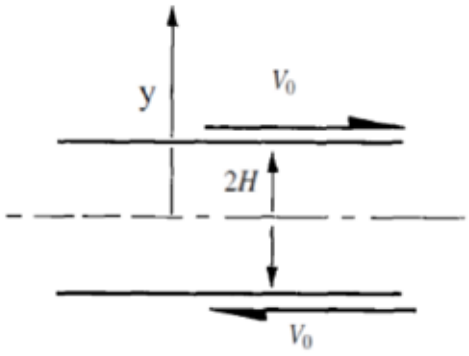

Figure 1: 1D shear band problem [1]

Using the total pseudo-potential function proposed by Yang et al.[2], and combined

with the stationary conditions, the power density function is reduced to :

$$\Phi(V,T) = \int_{-H}^{H} \Psi^*(\frac{T}{\Theta}V_{,y};\Theta) - \chi(-\frac{T_{,y}}{T};\Theta)dy$$

where Ψ^* is a dissipation pseudo-potential describing the viscoplasticity with thermal softening:

$$\Psi^*(\frac{T}{\Theta}V_{,y};\Theta) = \frac{1}{m+1}\frac{\tau_0}{(\dot{\gamma}_0)^m} exp\left[-\beta\left(\left(\frac{\Theta}{T_0}\right)-1\right)\right]\left(V_{,y}\frac{T}{\Theta}\right)^{m+1} \qquad m \in [0,1] \tag{1}$$

Parameters m and β are the strain rate sensitivity exponent and the thermal softening coefficient, and τ_0 and $\dot{\gamma}_0$ are the reference stress and strain rate. $\Theta(y)$ is the equilibrum temperature introduced to satisfy the symmetry property of the power density function. χ is a thermal conduction pseudo-potential obeying the Fourier law:

$$\chi(-\frac{T_{,y}}{T};\Theta) = \frac{1}{2}\lambda\Theta\left(\frac{T_{,y}}{T}\right)^2 \tag{2}$$

where the parametrer λ is the thermal conductivity. Thus the problem of the shear band (Fig. 1) can be described as an optimization problem of the power density function:

$$\inf_V \max_T \{\Phi(V,T)\} \tag{3}$$

Taking variation with respect to the velocity, we can obtain the mechanical equilibrium equation, while the heat equation is obtained from stationarity condition on T. In addition, thermal equilibrium requires that $\Theta = T$.

2.2 Semi-analytical method

Considering boundary conditions in the 1D problem:

$$V|_{\pm H} = V_0; \quad T|_{\pm H} = T_0;$$

and taking advantage of the solutions obtained by Leroy and Molinari [1], the profiles of velocity and temperature can be written as follows with parameters h and T_{max}:

$$V(y) = V_0\frac{\tanh(y/h)}{\tanh(H/h)}, \quad T(y) = T_{max} - (T_{max}-T_0)\frac{\ln(\cosh(y/h))}{\ln(\cosh(H/h))} \tag{4}$$

where h is the shear band width, and T_{max} is the central temperature. We introduce a new parameter T_{max} to replace the material parameters used in [1], since this change avoids the limitation to specific constitutive relations and gives us a more general description of velocity and temperature in the layer.

Finally, the variational model of the shear band in the steady state is restated as follows:

$$\inf_h \max_{T_{max}} \{\Phi(h,T_{max})\} \tag{5}$$

2.3 Results

In our calculations, a trust region method is used in view of the strong non-linearity of the Euler-Lagrange equations of (5). Table (1) shows the shear band widths and the central temperatures for different material parameters, in good agreement with the analytical solutions.

Table 1: Shear band width and central temperature (dimensionless) ($\beta = 0.38; V_0 = 0.1108$ m/s)

	variational model $[h\ T_{max}]$		analytical $[h\ T_{max}]$	
$m = 0.12; \kappa = 1/0.242373$	0.312643	775.026	0.312643	775.020
$m = 0.012; \kappa = 1/0.403788$	0.031073	896.626	0.031072	896.656
$m = 0.06; \kappa = 1/0.3218$	0.153552	851.299	0.153552	851.303

Fig. 2 illustrates the influence of the imposed velocity V_0 on h and T_{max}. With the velocity increased, the shear band width h decreases and the central temperature in the band increases. Obviously in a thermal softening material, a higher strain rate causes a smaller band width, and also brings more dissipation and heat generation in the band. In addition, the time of the formation of the shear band is so short that the heat cannot go out of the layer by conduction, leading to a higher central temperature.

3 Variational model in transient regime

For thermoviscoplastic materials under high strain rates, the rapid evolution of the shear band and its small width complicate numerical simulations. In this section, we will extend the stationary variational modeling to transient regime, establishing a variational update form of the 1D shear band problem.

3.1 Incremental variational formulation

The variational framework proposed in Yang et al.[2] also includes a time-discretized incremental variational problem, and it can be applied to the 1D shear band problem, yielding an incremental optimization problem. In particular, considering a time increment $[t_n, t_{n+1}]$, and assuming that $[\mathbf{F}_n, T_n, \mathbf{F}^p_n]$ is known, we proceed to obtain the variational update at time t_{n+1}. $\mathbf{F}$ is the gradient of deformation, and we consider the conventional multiplicative decomposition:

$$\mathbf{F} = \mathbf{F}^e\mathbf{F}^p$$

If the material satisfy the Von Mises law, the gradient of plastic deformation $\mathbf{F}^p_{n+1}$ verifies the following equalities:

$$\mathbf{F}^p_{n+1} = \exp[(\bar{\varepsilon}^p_{n+1} - \bar{\varepsilon}^p_n)\mathbf{M}]\mathbf{F}^p_n$$

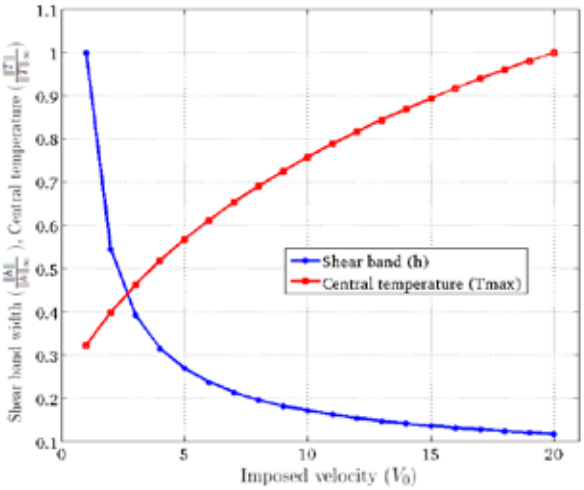

Figure 2: Influence of the imposed velocity V_0 about the shear band width and the central temperature

$$tr(\mathbf{M}) = 0, \quad \mathbf{M} \cdot \mathbf{M} = \frac{3}{2}$$

where $\overline{\varepsilon}^p$ is the cumulated plastic deformation. In general, $\mathbf{F}$ is written:

$$\mathbf{F}_{n+1} = \mathbf{I} + \frac{\partial \overrightarrow{u_{n+1}}}{\partial \overrightarrow{x}}$$

Considering the 1D shear band problem, it reduces to:

$$\mathbf{F}_{n+1} = \begin{bmatrix} 1 & \frac{\partial u_{n+1}}{\partial y} & 0 \\ 0 & 1 & 0 \\ 0 & 0 & 1 \end{bmatrix}$$

Following [2], the total pseudo-potential for the thermo-mechanical coupled problem is then:

$$\Phi_n = \int_{-H}^{H} \left[\mathcal{W}_n - \Delta t \chi \left(\frac{1}{T_{n+1}} \frac{\partial T_{n+1}}{\partial y} \right) \right] dy$$

where $\mathcal{W}_n$ is the optimized potential about $\overline{\varepsilon}^p_{n+1}$ and $\mathbf{M}$:

$$\begin{aligned} \mathcal{W}_n \left(\mathbf{F}_{n+1}, T_{n+1}; \mathbf{F}_n, T_n, \mathbf{F}^p_n, \overline{\epsilon}^p_n \right) \quad = \quad & \inf_{\overline{\epsilon}^p_{n+1}, \mathbf{M}} [W \left(\mathbf{F}_{n+1}, T_{n+1}, \mathbf{F}^p_{n+1}, \overline{\epsilon}^p_{n+1} \right) \\ & - W \left(\mathbf{F}_n, T_n, \mathbf{F}^p_n, \overline{\epsilon}^p_n \right) + \eta_n \left(T_{n+1} - T_n \right) \\ & + \int_{t_n}^{t_{n+1}} \Psi^* \left(\frac{T_{n+1}}{T_n} \frac{\Delta \overline{\epsilon}^p}{\Delta t}; T(t) \right) dt] \end{aligned} \tag{6}$$

where $W \left(\mathbf{F}_{n+1}, T_{n+1}, \mathbf{F}^p_{n+1}, \overline{\epsilon}^p_{n+1} \right)$ is the free energy, which includes the elastic energy, stored plastic energy and the heat storage capacity of the material [9]. In addition, the

notations Ψ^* and χ are the same as previously: the dissipation pseudo-potential and the Fourier pseudo-potential. The entropy η_n is defined by :

$$\eta_n = -W_{,T_n}\left(\mathbf{F}_n, T_n, \mathbf{F}_n^p, \overline{\epsilon}_n^p\right)$$

and $\Delta\overline{\epsilon}^p = \overline{\epsilon}_{n+1}^p - \overline{\epsilon}_n^p$. Note that $\mathcal{W}$ appears as a thermo-elastic pseudo-potential. Indeed Piola-Kirchhoff stress can be written as:

$$\frac{\partial \mathcal{W}_n}{\partial \mathbf{F}_{n+1}} = \mathbf{p}_{n+1}$$

and the heat equation in the adiabatic form is given by taking variation about T:

$$\frac{\partial \mathcal{W}_n}{\partial T_{n+1}} = -\Delta\eta + \frac{\Delta t}{T_{n+1}} D_{int}$$

where D_{int} is the internal dissipation.

In view of the above variational framework, the incremental 1D problem of the shear band described in Fig.1 is written as:

$$\inf_{u_{n+1}} \max_{T_{n+1}} \Phi_n\left(u_{n+1}, T_{n+1}; u_n, T_n, \mathbf{F}_n^p, \overline{\epsilon}_n^p\right) \tag{7}$$

When the time step tends towards 0, Euler-Lagrange equations of (7) are consistent with continuous mechanical and thermal equilibrum equations.

3.2 Numerical validation

In this section, we will use the finite element method (FEM) and a semi-analytical method to simulate the evolution of velocity and temperature in the layer. On the one hand, FEM gives us a more precise simulation of the formation of the shear band. However, it cannot avoid the difficulty of mesh dependence, the domain where the shear band occurs requiring a very fine mesh; on the other hand, the semi-analytical method, although less precise in early stages of shear band formation, shows a good convergence of the shear band width and is consistent with the results obtained by FEM. In addition, it has a better efficiency compared with FEM.

3.2.1 Finite element method

Thanks to the symmetry of the total pseudo-potential, the tangent matrix of the FEM is also symmetrical, which is different from the traditional thermal-mechanical problem, and this character brings some algorithmic advantages. In the FEM model, elasticity and thermal capacity are considered [9]. But hardening effect is neglected for comparing with analytical results. Because of the thermal softening in the dissipation pseudo-potential, we choose the following form for its time-discretization [10]:

$$\frac{1}{\triangle t}\int_{t_n}^{t_{n+1}} \Psi^*\left(\frac{T_{n+1}}{T_n}\frac{\Delta\overline{\epsilon}^P}{\Delta t}; T(t)\right) dt \approx \frac{T_n}{T_{n+1}}\Psi^*\left(\frac{T_{n+1}}{T_n}\frac{\Delta\overline{\epsilon}^P}{\Delta t}; T_n\right) + \frac{\Delta T}{T_{n+1}}\Psi^*\left(\frac{T_{n+1}}{T_n}\frac{\Delta\overline{\epsilon}^P}{\Delta t}; T_{n+\alpha}\right)$$

The parameter α is choosen equal to 0.5. In the latter simulation by the semi-analytical method, we also use this form to approximate the dissipation, but α is choosen equal to 0.

Fig.3 gives us the results for profiles of velocity and temperature in the layer ($H = 1.25mm, V_0 = 0.01108m/s, T_0 = 300K$). As time increases, profiles of velocity change from a linear form to a nonlinear form, and step by step concentrate in the central zone, arriving at a steaty state when time reaches 0.1 s. The stationary shear band width is 0.247 mm, and $T_{max} = 395K$.

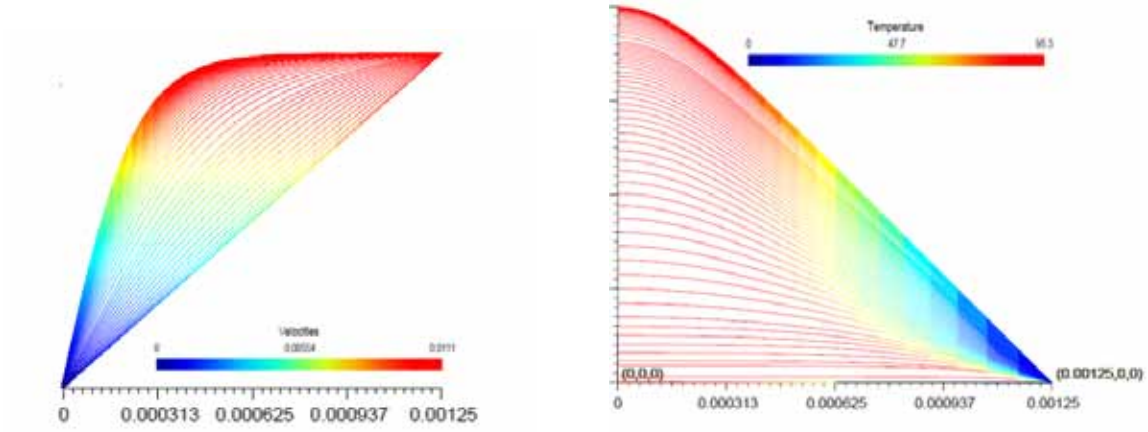

Figure 3: Evolution of the profiles of velocity and temperature($V_0 = 0.01108m/s$)

We also analyse the evolution of the shear band when the imposed velocity is $1m/s$ (Fig.4). Compared with $V_0 = 0.01108m/s$, the time when the material reaches a steady state is shorter, the shear band width is smaller ($h = 0.014583mm$), and the central temperature is higher ($T_{max} = 2047K$), which is in agreement with the analytical solution. In addition, we can observe a heat affected zone in the process of the formation of the shear band because of the locally lower strain and the local annealing due to the temperature increase [4]. This transient effect is less obvious in the case of $V_0 = 0.01108m/s$.

For illustrating the evolution of shear band width and comparing it with the semi-analytical method, we choose two parameters to measure the shear localization: the kinematic width h_v from the velocity distribution and the thermal width h_T from the temperature distribution. Refering to the analytical formulation, they are calculated by:

$$\begin{aligned} h_{V_{n+1}} \quad & \text{such that} \quad V_{n+1}(h_{V_{n+1}}) \simeq V_0 \tanh(1) \\ h_{T_{n+1}} \quad & \text{such that} \quad \frac{2m}{\beta} \log(\cosh(\frac{H}{h_{T_{n+1}}})) = \frac{T_{max}}{T0} - 1 \end{aligned}$$

Fig.5 presents the convergence of the kinematic width and the thermal width when $H = 1.25mm, V_0 = 0.01108m/s, T_0 = 300K$. With the time increased, the two widths decrease

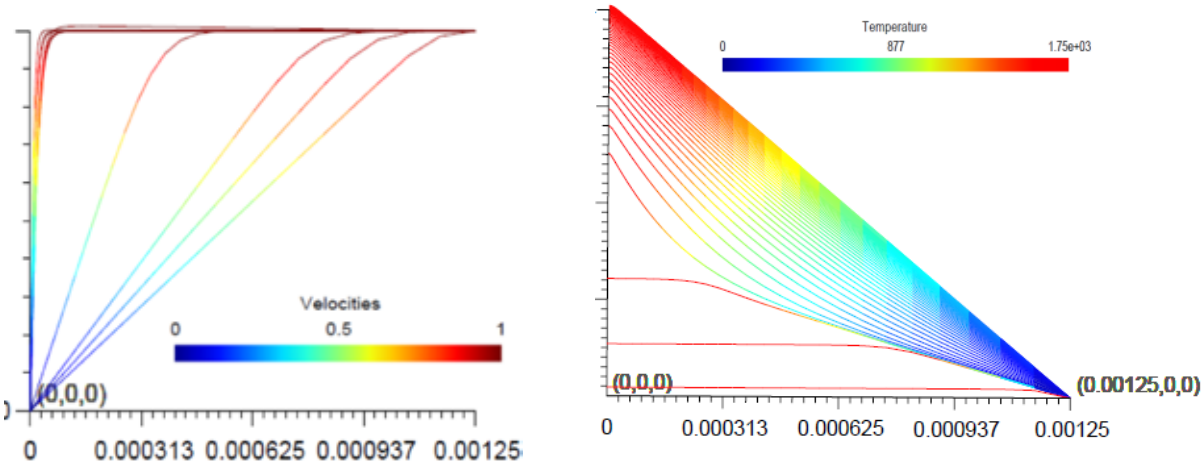

Figure 4: Evolution of the profiles of velocity and temperature ($V_0 = 1m/s$)

gradually and tends towards the same stationary value, which is consistent with the analytical solution.

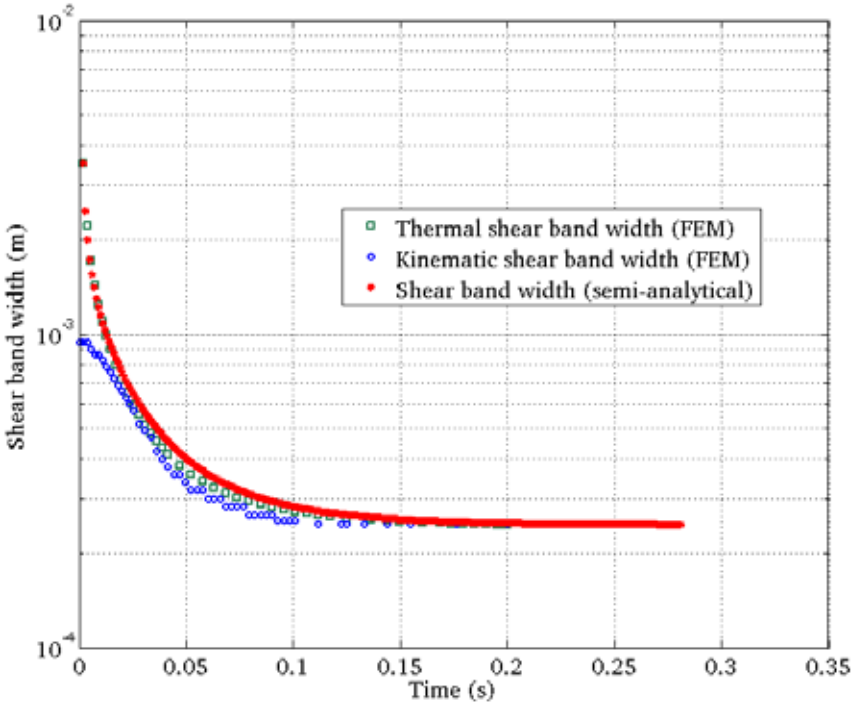

Figure 5: Convergence of the shear band width ($V_0 = 0.01108m/s$)

3.2.2 Semi-analytical method

The strong shear localization causes difficulties in the simulation of the shear band by FEM. Indeed, it is necessary to have an approximation of the width before constructing the mesh. Therefore, we follow an idea initially proposed by Yang et al.[8], who derived a simple model of shear bands based on a linear velocity and a Gaussian temperature profiles. Neglecting the heat affected zone, and supposing that at each time step the distributions of velocity and temperature satisfy the canonical solutions, we write at $t = t_{n+1}$:

$$V(y) = V_0 \frac{\tanh(y/h_{n+1})}{\tanh(H/h_{n+1})}, \quad T(y) = T_0 - \frac{2m}{\beta} T_0 \ln \frac{\cosh(y/h_{n+1})}{\cosh(H/h_{n+1})} \tag{8}$$

where m, β are the material parameters, the same as the analysis in the steady state. We then obtain the incremental optimization problem for the 1D shear band (Fig.1) as:

$$\operatorname*{stat}_{h_{n+1}} \Phi_n(h_{n+1}) \tag{9}$$

It is important to note that, in contrast to previous approaches, the shear band width figures among the unknowns, and will be determined by computation. It is an important feature, since this width is controlled by the combined effect of internal dissipation and conduction, and we will use an example to illustrate that it can evolve as the shear band evolves towards its stationary structure.

In general, there is no shear band in the plane at the initial time, so we choose:

$$h_0 = H$$

Fig.6 shows us the evolution of velocity profiles and temperature profiles compared with the analytical stationary solutions when $H = 1.25mm, V_0 = 0.01108m/s, T_0 = 300K$. Here the time step is chosen as $\triangle t = 1e-3s$. Results obtained by the semi-analytical approach are consistent with those obtained by FEM. In addition, returning to Fig.5, we can get the comparison about the convergence of shear band width. The widths evolutions are in agreement with the results by FEM. Furthermore, computation time is reduced compared to that of FEM. Therefore the semi-analytical method presents a higher efficency besides not requiring a mesh.

4 CONCLUSIONS

Considering a simplified 1D model of shear band in thermoviscoplastic materials, we have developped an energy-based variational semi-analytical approach to predict shear band internal structure. In stationary or transient regimes, the shear band width and the central temperature are determined and in good agreement with the work of Leroy et al.[1]. Compared with the finite element method, we not only got the validation of the variational modeling in the analysis of the formation of the shear band, but have also shown the efficiency and feasibility of the proposed semi-analytical method.

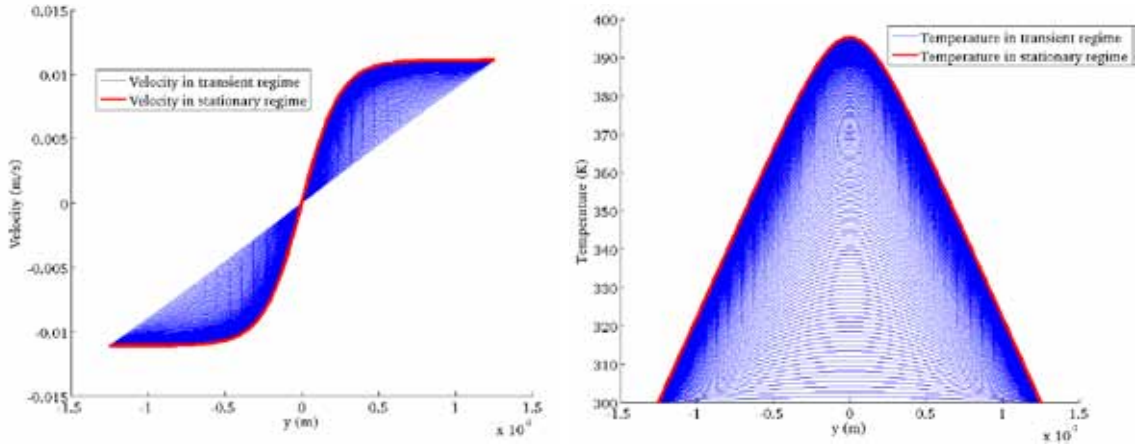

Figure 6: Evolution of the profiles of velocity and temperature by semi-analytical method ($V_0 = 0.01108m/s$)

REFERENCES

[1] Y.M. Leroy and A. Molinari, Stability of steady states in shear zones. *J. Mech. Phys. Solids*(1992). **40**:181-212.

[2] Yang, Q., Stainier, L., Ortiz, M., A variational formulation of the coupled thermo-mechanical boundary-value problem for general dissipative solids. *J. Mech. Phys. Solids*(2006). **54**:401-424.

[3] Halphen, B., Nguyen, Q.S., Sur les matériaux standard généralisés. *Journal de Mcanique*(1975). **14**:39-63.

[4] F. Dinzart, A. Molinari, Structure of adiabatic shear bands in thermo-viscoplastic materials. *Eur. J. Mech. A/Solids*(1998), **17**:923-938.

[5] T.W. Wright, G. Ravichandran, Canonical aspects of adiabatic shear bands. *International Journal of Plasticity*(1997). **13**:309-325.

[6] P. M. A. Areias, T. Belytschko. Two-scale method for shear bands : Thermal effects and variable bandwidth. *Int. J. Numer. Meth. Engng*(2007). **72**:658-696.

[7] S. Li, W. K. Liu, A. J. Rosakis, T. Belytschko, W. Hao. Mesh-free Galerkin simulations of dynamic shear band propagation and failure mode transition. *International Journal of Solids and Structures*. **39**:1213-1240.

[8] Q. Yang, A. Mota, M. Ortiz. A class of variational strain-localization finite elements, *J. Int. J. Numer. Meth Engng* (2005). **62**:1013-1037.

[9] L. Stainier, M. Ortiz. Study and validation of a variational theory of thermo-mechanical coupling in finite visco-plasticity, *Int. J. Solids Struct*(2010). **47**:705-715.

[10] L. Stainier. Consistent incremental approximation of dissipation pseudo-potentials in the variational formulation of thermo-mechanical constitutive updates, *Mechanics Research Communications*(2011). In press(doi: 10:1016/j.mechrescom.2011.03.011).

XI International Conference on Computational Plasticity. Fundamentals and Applications
COMPLAS XI
E. Oñate, D.R.J. Owen, D. Peric and B. Suárez (Eds)

ON THE THERMODYNAMICAL AND VARIATIONAL CONSISTENCY OF COHESIZE ZONE MODELS AT FINITE STRAINS

J. MOSLER AND I. SCHEIDER

Helmholtz-Zentrum Geesthacht
Centre for Materials and Coastal Research
Institute for Materials Research, Materials Mechanics,
D-21502 Geesthacht, Germany
e-mail: joern.mosler@hzg.de

Key words: Cohesive zone model, finite strains, damage mechanics, thermodynamical consistency, variational constitutive updates

Abstract. In the present contribution, the thermodynamical and variational consistency of cohesive zone models is critically analyzed. Starting from cohesive zone models suitable for fully reversible deformation, the restrictions imposed by the second law of thermodynamics are investigated. It will be shown that a naive modeling approach leads to a contradiction of the dissipation inequality, even if a purely elastic response is desired. Based on such findings, a thermomechanically consistent model including dissipative effects is proposed. This model is finally recast into a variationally consistent form. Within the resulting model, all state variables are naturally and jointly computed by minimizing an incrementally defined potential. The predictive capabilities of this model are demonstrated by means of selected examples.

1 INTRODUCTION

Cohesive interface models dating back to the pioneering works [1, 2, 3] represent one of the most powerful and versatile tools available for the analysis of material failure. Within such models, the stress vector acting at a crack, usually given in terms of the crack width, resist the separation of the bulk material across the crack.

While the number of different cohesive interface models in the literature is tremendous (for an overview, see [4, 5] and references cited therein), interface laws specifically designed for material failure at finite strains are still relatively rare – particularly for anisotropic solids. However, geometrically nonlinear effects and anisotropic mechanical responses do play an important role in many applications, e.g., in delamination processes, cf. [6].

Clearly, considering a geometrically exact description, the constraints imposed by the fundamental principles of constitutive modeling such as those related to the principle

of objectivity are not automatically fulfilled and thus, they require special attention. However and as shown in [7], such principles are often not carefully considered. More precisely, except for the framework presented in [7], the existing cohesive zone models described with respect to the current, i.e., deformed, configuration which account for an anisotropic mechanical response, do not fulfill all of the aforementioned physical principles. Particularly, the second law of thermodynamics is not fulfilled. In the present paper, a physically sound framework complying with these fundamentals of physics is discussed.

2 KINEMATICS

In what follows, a body Ω is considered to be separated during deformation into the two parts Ω^- and Ω^+ by means of a crack or a shear band denoted as $\partial_{\mathrm{s}}\Omega$, i.e., $\Omega = \Omega^- \cup \Omega^+ \cup \partial_{\mathrm{s}}\Omega$. The orientation of $\partial_{\mathrm{s}}\Omega$ with respect to the undeformed configuration is locally defined by its normal vector $\boldsymbol{N}$. In line with standard notation, the normal vectors are postulated as $\boldsymbol{N}^- = -\boldsymbol{N}^+ = \boldsymbol{N}$.

The motion of the sub-bodies Ω^- and Ω^+ is described by the deformation mapping $\boldsymbol{\varphi}$ which can be written as $\boldsymbol{\varphi} = \mathrm{id} + \boldsymbol{u}$ with id being the identity mapping and $\boldsymbol{u}$ being the displacement field. Denoting $\boldsymbol{u}^{\pm}$ as the displacement field in Ω^+ and Ω^- and H_{s} as the Heaviside function of $\partial_{\mathrm{s}}\Omega$, a displacement field $\boldsymbol{u}$ characterizing a crack or a shear band is discontinuous and thus, it is of the type

$$\boldsymbol{u} = \boldsymbol{u}^- + H_{\mathrm{s}} \left(\boldsymbol{u}^+ - \boldsymbol{u}^- \right). \tag{1}$$

With Eq. (1), the displacement discontinuity $[\![\boldsymbol{u}]\!]$ at $\partial_{\mathrm{s}}\Omega$ can be defined as

$$[\![\boldsymbol{u}]\!] = \boldsymbol{u}^+ - \boldsymbol{u}^- \quad \forall \boldsymbol{X} \in \partial_{\mathrm{s}}\Omega. \tag{2}$$

Since the deformation in Ω^- and that in Ω^+ are in general uncoupled, the normal vectors $\boldsymbol{n}^-$ and $\boldsymbol{n}^+$ on both sides of a crack are usually not parallel. For this reason, a fictitious intermediate configuration $\bar{\boldsymbol{x}}$ between $\boldsymbol{x}^-$ and $\boldsymbol{x}^+$ is frequently introduced as

$$\bar{\boldsymbol{x}} = (1-\alpha)\, \boldsymbol{x}^- + \alpha\, \boldsymbol{x}^+, \quad \alpha \in [0;1]. \tag{3}$$

In most cases, α is set to $\alpha = 1/2$.

3 CONSTITUTIVE MODELING

3.1 Elastic interfaces

In the most general case, the mechanical response of an elastic interface can be defined by means of a Helmholtz energy of the type

$$\Psi = \Psi([\![\boldsymbol{u}]\!], \boldsymbol{a}_1, \ldots \boldsymbol{a}_n). \tag{4}$$

Here, $\boldsymbol{a}_i$ are structural vectors describing the material's symmetry. By introducing the surface deformation gradient associated with the fictitious intermediate configuration of

a deformed crack as

$$\bar{\boldsymbol{F}} = (1-\alpha)\ \boldsymbol{F}^- + \alpha\ \boldsymbol{F}^+, \qquad \alpha \in [0;1], \tag{5}$$

Eq. (4) can be re-written as

$$\Psi = \Psi(\llbracket \boldsymbol{u} \rrbracket, \boldsymbol{F}^-, \boldsymbol{F}^+, \boldsymbol{A}_1, \dots \boldsymbol{A}_n), \quad \text{with} \quad \dot{\boldsymbol{A}}_i = \boldsymbol{0}. \tag{6}$$

Here, $\boldsymbol{A}_i$ are the vectors obtained by applying a pull-back to the spatial vectors $\boldsymbol{a}_i$. With Eq. (6), the rate of the Helmholtz energy is computed as

$$\dot{\Psi} = \frac{\partial \Psi}{\partial \llbracket \boldsymbol{u} \rrbracket} \cdot \dot{\llbracket \boldsymbol{u} \rrbracket} + \frac{\partial \Psi}{\partial \bar{\boldsymbol{F}}} : \left[(1-\alpha)\ \dot{\boldsymbol{F}}^- + \alpha\ \dot{\boldsymbol{F}}^+ \right]. \tag{7}$$

It bears emphasis that the deformation gradients $\boldsymbol{F}^{\pm}$ and the displacement discontinuity $\llbracket \boldsymbol{u} \rrbracket$ are only weakly coupled ($\boldsymbol{F}^+ = \boldsymbol{F}^- + \mathrm{GRAD}\, \llbracket \boldsymbol{u} \rrbracket$)). Hence, the stress power consists of three terms in general. By introducing two stress tensors $\boldsymbol{P}^{\pm}$ of first Piola-Kirchhoff type being conjugate to the deformation gradients $\boldsymbol{F}^{\pm}$, the stress power can thus be written as

$$\overset{o}{w} = \boldsymbol{T} \cdot \dot{\llbracket \boldsymbol{u} \rrbracket} + \boldsymbol{P}^- : \dot{\boldsymbol{F}}^- + \boldsymbol{P}^+ : \dot{\boldsymbol{F}}^+. \tag{8}$$

Consequently, by applying the standard Coleman & Noll procedure, cf. [8], the constitutive equations

$$\boldsymbol{T} = \frac{\partial \Psi}{\partial \llbracket \boldsymbol{u} \rrbracket}, \quad \boldsymbol{P}^- = \frac{\partial \Psi}{\partial \boldsymbol{F}^-} = (1-\alpha)\ \frac{\partial \Psi}{\partial \bar{\boldsymbol{F}}}, \quad \boldsymbol{P}^+ = \frac{\partial \Psi}{\partial \boldsymbol{F}^+} = \alpha\ \frac{\partial \Psi}{\partial \bar{\boldsymbol{F}}} \tag{9}$$

are derived. As a result, two boundary-like laws are also implicitly defined by the Helmholtz energy (6) in addition to the classical constitutive model $(9)_1$, see also [9]. These additional tensors are required for thermomechanical consistency. This can be seen more explicitly by ignoring them. In this case, the dissipation reads

$$\mathcal{D} = \boldsymbol{T} \cdot \dot{\llbracket \boldsymbol{u} \rrbracket} - \dot{\Psi} = -\frac{\partial \Psi}{\partial \bar{\boldsymbol{F}}} : \left[(1-\alpha)\ \dot{\boldsymbol{F}}^- + \alpha\ \dot{\boldsymbol{F}}^+ \right] \neq 0. \tag{10}$$

Consequently, the dissipation would be non-vanishing, even in case of a hyperelastic-type model. It bears emphasis that these additional stress tensors have not been considered in any of the existing cohesive zone models.

3.2 Dissipative effects

In this section, the hyperelastic model described before is combined with damage mechanics. For that purpose, a Helmholtz energy of the type

$$\Psi = \sum_{i=1}^{n} \prod_{j=1}^{n} (1 - d_i^{(j)})\ \Psi_i(\llbracket \boldsymbol{u} \rrbracket, \boldsymbol{F}^+, \boldsymbol{F}^-) \tag{11}$$

is adopted. Here, $d_i^{(j)} \in [0;1]$ are damage variables. The underlying idea corresponding to Eq. (11) is that the energy is decomposed into that related to the different relevant failure modes. One typical example is given by the decomposition of the energy into mode-I and mode-II/III failure energies. Application of the Coleman & Noll procedure to Eq. (11) yields the stress response

$$\begin{aligned} \boldsymbol{T} = \sum_{i=1}^{n} \prod_{j=1}^{n} (1 - d_i^{(j)}) \, \frac{\partial \Psi_i}{\partial \left[\!\left[\boldsymbol{u} \right]\!\right]} \qquad & \begin{aligned} \boldsymbol{P}^{-} &= (1-\alpha) \sum_{i=1}^{n} \prod_{j=1}^{n} (1 - d_i^{(j)}) \, \frac{\partial \Psi_i}{\partial \bar{\boldsymbol{F}}} \\ \boldsymbol{P}^{+} &= \quad \alpha \sum_{i=1}^{n} \prod_{j=1}^{n} (1 - d_i^{(j)}) \, \frac{\partial \Psi_i}{\partial \bar{\boldsymbol{F}}}, \end{aligned} \end{aligned} \tag{12}$$

together with the reduced dissipation inequality

$$\mathcal{D} = \mathring{w} - \dot{\Psi} = \sum_{i=1}^{n} \sum_{j=1}^{n} \prod_{k=1, k\neq j}^{n} (1 - d_i^{(k)}) \, \Psi_i(\left[\!\left[\boldsymbol{u} \right]\!\right], \boldsymbol{F}^{+}, \boldsymbol{F}^{-}) \, \dot{d}_i^{(j)} \geq 0. \tag{13}$$

Since the elastic energies Ψ_i are assumed to be non-negative and $d_i^{(j)} \in [0;1]$, the second law of thermodynamics is automatically fulfilled, if $d_i^{(j)}$ is monotonically increasing, i.e.,

$$\dot{d}_i^{(j)} \geq 0. \tag{14}$$

For fulfilling Ineq. (14) and also for accounting for cross-softening, the damage evolution is defined as

$$d_i^{(j)} = d_i^{(j)}(\kappa_j). \tag{15}$$

with

$$\kappa_i(t_{n+1}) = \max\{\kappa_i(t_n); \Psi_i(t_{n+1})\}, \qquad \kappa_i(t=0) = \kappa_{i(0)}. \tag{16}$$

Accordingly, κ_i is the history of the maximum stored elastic energy related to failure mode i and thus, it is monotonically increasing. Hence, if $d_i^{(j)}(\kappa_j)$ is also chosen as a monotonically increasing function, the second law of thermodynamics is automatically fulfilled. The term cross-softening results from Eq. (15) and means that mode-I crack opening leads to a reduction in the shear stiffness as well.

4 VARIATIONAL CONSTITUTIVE UPDATES

Following [7], the variational principle

$$\inf I_{\text{inc}}^{\partial_{\text{s}}\Omega}, \quad I_{\text{inc}}^{\partial_{\text{s}}\Omega} := \int_{t_n}^{t_{n+1}} \mathcal{E} \, \mathrm{d}t = \Psi(t_{n+1}) - \Psi(t_n) + \int_{t_n}^{t_{n+1}} \mathcal{D} \, \mathrm{d}t. \tag{17}$$

is equivalent to the proposed constitutive modeling framework. Thus, all state variables follow naturally from energy minimization. More explicitly,

$$(\kappa_1(t_{n+1}),\dots,\kappa_n(t_{n+1})) = \arg\inf I_{\text{inc}}^{\partial_{\text{s}}\Omega}(\llbracket \boldsymbol{u} \rrbracket_{n+1}, \bar{\boldsymbol{F}}_{n+1}, \kappa_1(t_{n+1}),\dots,\kappa_n(t_{n+1}))\big|_{\boldsymbol{u}=\text{const}}. \tag{18}$$

Finally, the reduced potential as implicitly introduced by Eq. (18) defines the stress response in the hyperelastic-like manner

$$\boldsymbol{T} = \frac{\partial \tilde{I}_{\text{inc}}^{\partial_{\text{s}}\Omega}}{\partial \llbracket \boldsymbol{u} \rrbracket}, \quad \boldsymbol{P}^{\pm} = \frac{\partial \tilde{I}_{\text{inc}}^{\partial_{\text{s}}\Omega}}{\partial \boldsymbol{F}^{\pm}}, \quad \text{with} \quad \tilde{I}_{\text{inc}}^{\partial_{\text{s}}\Omega} = \inf_{\{\kappa_i\}} I_{\text{inc}}^{\partial_{\text{s}}\Omega}. \tag{19}$$

With these notations, the total energy (work) of the considered structure is given by

$$I_{\text{total}} = I_{\text{total}}(\boldsymbol{\varphi}) = \int_{\Omega} \tilde{I}_{\text{inc}}^{\Omega}\, \mathrm{d}V - I_{\text{ext}} + \int_{\partial_{\text{s}}\Omega} \tilde{I}_{\text{inc}}^{\partial_{\text{s}}\Omega}\, \mathrm{d}A \tag{20}$$

where the potential I_{ext} is associated with external forces, while the potential $\tilde{I}_{\text{inc}}^{\Omega}$ is the bulk's counterpart of the interface-related potential $\tilde{I}_{\text{inc}}^{\partial_{\text{s}}\Omega}$. As straightforward computations shows that a minimization of potential (20) results in the classical equilibrium conditions in weak form, i.e.,

$$\delta I_{\text{total}} = 0 = \int_{\Omega} \boldsymbol{P} : \delta \boldsymbol{F}\, \mathrm{d}V - \frac{\partial I_{\text{ext}}}{\partial \boldsymbol{\varphi}} \cdot \delta \boldsymbol{u} + \int_{\partial_{\text{s}}\Omega} \left[\boldsymbol{T} \cdot \delta \llbracket \boldsymbol{u} \rrbracket + \boldsymbol{P}^{\pm} : \delta \boldsymbol{F}^{\pm} \right] \mathrm{d}A, \ \forall \delta \boldsymbol{u} \tag{21}$$

Here, Eqs. (12), together with $\boldsymbol{P} := \partial_{\boldsymbol{F}} \tilde{I}_{\text{inc}}^{\Omega}$, has been inserted. The term $\partial I_{\text{ext}}/\partial \boldsymbol{\varphi}$ is a generalized force. Eq. (21) can be conveniently discretrized by finite elements. Further details are omitted here. They can be found in [7] and will be discussed in the respective presentation.

REFERENCES

[1] G.I. Barenblatt. The mathematical theory of equilibrium cracks in brittle fracture. *Adv. Appl. Mech.*, 7:55–129, 1962.

[2] A. Hillerborg, M. Modeer, and P.E. Petersson. Analysis of crack formation and crack growth in concrete by means of fracture mechanics and finite elements. *Cement and Concrete Research*, 6:773–782, 1976.

[3] D.S. Dugdale. Yielding of steel sheets containing slits. *Journal of the Mechanics and Physics of Solids*, 8:100–108, 1960.

[4] W. Brocks, A. Cornec, and I. Scheider. *Comprehensive Structural Integrity. Fracture of Materials from Nano to Macro, volume 3*, chapter 03, pages 127–209. Elsevier, Oxford, 2003.

[5] J. Mosler. On the modeling of highly localized deformations induced by material failure: The strong discontinuity approach. *Archives of Computational Methods in Engineering*, 11(4):389–446, 2004.

[6] M.J. van den Bosch, Schreurs P.J.G., and M.G.D. Geers. Identification and characterization of delamination in polymer coated metal sheet. *Journal of the Mechanics and Physics of Solids*, 56:3259–3276, 2008.

[7] J. Mosler and I. Scheider. A thermodynamically and variationally consistent class of damage-type cohesive models. *Journal of the Mechanics and Physics of Solids*, 2011. in press.

[8] B.D. Coleman and M.E. Gurtin. Thermodynamics with internal state variables. *J. Chem. Phys*, 47:597–613, 1967.

[9] P. Steinmann. On boundary potential energies in deformational and configurational mechanics. *Journal of the Mechanics and Physics of Solids*, 56(3):772–800, 2008.

XI International Conference on Computational Plasticity. Fundamentals and Applications
COMPLAS XI
E. Oñate, D.R.J. Owen, D. Peric and B. Suárez (Eds)

PLASTICITY DESCRIBED BY UNCERTAIN PARAMETERS - A VARIATIONAL INEQUALITY APPROACH -

BOJANA V. ROSIĆ and HERMANN G. MATTHIES

Institute of Scientific Computing
Technische Universität Braunschweig
38106 Braunschweig
e-mail: wire@tu-bs.de

Key words: stochastic plasticity, polynomial chaos expansion, stochastic variational inequality, Karhunen-Loève expansion

Abstract. In this paper we consider the mixed variational formulation of the quasi-static stochastic plasticity with combined isotropic and kinematic hardening. By applying standard results in convex analysis we show that criteria for the existence, uniqueness, and convergence can be easily derived. In addition, we demonstrate the mathematical similarity with the corresponding deterministic formulation which further may be extended to a stochastic variational inequality of the first kind. The aim of this work is to consider the numerical approximation of variational inequalities by a "white noise analysis". By introducing the random fields/processes used to model the displacements, stress and plastic strain and by approximating them by a combination of Karhunen-Loève and polynomial chaos expansion, we are able to establish stochastic Galerkin and collocation methods. In the first approach, this is followed by a stochastic closest point projection algorithm in order to numerically solve the problem, giving an intrusive method relying on the introduction of the polynomial chaos algebra. As it does not rely on sampling, the method is shown to be very robust and accurate. However, the same procedure may be applied in another way, i.e. by calculating the residuum via high-dimensional integration methods (the second approach) giving a non-intrusive Galerkin techniques based on random sampling—Monte Carlo and related techniques—or deterministic sampling such as collocation methods. The third approach we present is in pure stochastic collocation manner. By highlighting the dependence of the random solution on the uncertain parameters, we try to investigate the influence of individual uncertain characteristics on the structure response by testing several numerical problems in plain strain or plane stress conditions.

1 Introduction

The deterministic description of the inelastic behaviour [4, 10] is not applicable to heterogeneous materials due to the uncertainty of corresponding characteristics at the

micro-structural level. Namely, the deterministic approach has one disadvantage: the description of the material parameters is given by the first order statistical moment called a mean value or mathematical expectation. However, such representation neglects the most important property of material characteristics — their random nature. Due to this reason, we consider a mathematical model which approximates material parameters as random fields and processes in order to closely capture the real nature of the random phenomena.

The history of the stochastic elastoplasticity begins with the work of Anders and Hori [1]. They declared elastic modulus as the source of the uncertainty and treated all following subsequent uncertainties with the help of a perturbation technique. Thereafter, Jeremić [6] introduced the Fokker-Plank equation approach based on the work of Kavvas [85], who obtained a generic Eulerian-Lagrangian form of the Fokker-Plank equation, exact to second-order, corresponding to any nonlinear ordinary differential equation with random forcing and random coefficient. In other words, Jeremic and his co-workers have obtained the deterministic substitute of the original stochastic partial differential equation. However, these methods are or mathematically very complicated to deal with or not enough accurate to be used for. Namely, the perturbation technique is limited only on the problems described by small variation of input properties. Its another disadvantage is known as a "closure-problem " or dependence of the lower-order moments on the higher-order moments. Similarly, the Fokker-Planck method predicates the mean behaviour exactly but it slightly over-predicates the standard deviation of the solution. The main reason for this are the Dirac delta initial conditions. The error may be minimised only by a better approximation of the Dirac initial condition on the expense of the computational cost.

In this paper we introduce the spectral stochastic finite element methods into the uncertainty quantification of stochastic elastoplastic material. The difficulty arising in this case comparing to other problems considered until now is the tensorial representation of some material characteristics such as constitutive tensor. Thus, we introduce the new method which is able to overcome this difficulty.

2 STRONG FORMULATION OF EQUILIBRIUM EQUATIONS

Consider a material body occupying a bounded domain $\mathcal{G} \in \mathbb{R}^d$ with a piecewise smooth Lipschitz continuous boundary $\partial\mathcal{G}$ on which are imposed boundary conditions in Dirichlet and Neumann form on $\Gamma_D \subseteq \partial\mathcal{G}$ and $\Gamma_N \subset \partial\mathcal{G}$ respectively, such that $\Gamma_D \cap \Gamma_N = \varnothing$ and $\partial\mathcal{G} = \bar{\Gamma}_N \cup \bar{\Gamma}_D$. The probability space is defined as a triplet $(\Omega, \mathcal{B}, \mathbb{P})$, with $\mathcal{B}$ being a σ-algebra of subsets of Ω and $\mathbb{P}$ a probability measure. The balance of momentum localized about any point x in domain $\mathcal{G}$ in time $t \in \mathcal{T} := [0, T]$ leads to an equilibrium equation

and boundary conditions required to hold almost surely in ω, i.e. $\mathbb{P}$-almost everywhere:

$$\begin{aligned} \operatorname{div} \boldsymbol{\sigma} + \boldsymbol{f} &= \mathbf{0} \quad \text{on } \mathcal{G}, \\ \boldsymbol{\sigma} \cdot \boldsymbol{n} &= \boldsymbol{g}, \quad \text{on } \Gamma_N, \\ \boldsymbol{u} &= \mathbf{0}, \quad \text{on } \Gamma_D \end{aligned} \tag{1}$$

where $\boldsymbol{u}$ and $\boldsymbol{v}$ denote the displacement and velocity fields over $\mathcal{G}$, $\boldsymbol{f}$ the body force, $\boldsymbol{\sigma}$ stress tensor, $\boldsymbol{n}$ the exterior unit normal at $x \in \mathit{\Gamma}_N$, and $\boldsymbol{g}$ a prescribed surface tension. For the sake of simplicity we use homogeneous Dirichlet boundary conditions and under the assumptions of small deformation theory we introduce the strain $\boldsymbol{\varepsilon}(\boldsymbol{u}) = D\boldsymbol{u}$, with the linear bounded operator defined as a mapping $D : \boldsymbol{u}_1(x)\boldsymbol{u}_2(\omega) \to (\nabla_S \boldsymbol{u}_1(x))\boldsymbol{u}_2(\omega)$ [10, 5, 4].

3 VARIATIONAL FORMULATION

The strong formulation is not suitable for solving and thus one introduces the mixed formulation of elastoplastic problem, given by next theorem:

Theorem 3.1 *There are unique functions, $w \in H^1(\mathcal{T}, \mathcal{Z}^*)$ and $w^* \in H^1(\mathcal{T}, \mathcal{Z}^*)$ with $w(0) = 0$ and $w^*(0) = 0$, which solve the following problem a.e. $t \in \mathcal{T}$:*

$$\forall z \in \mathcal{Z} : \; a(w(t), z) + \langle\!\langle w^*(t), z \rangle\!\rangle = \langle\!\langle f(t), z \rangle\!\rangle \tag{2}$$

and

$$\forall z^* \in \mathcal{K} : \; \langle\!\langle \dot{w}(t), z^* - w^*(t) \rangle\!\rangle \leq 0. \tag{3}$$

Here $a(w(t), z)$ represents the bilinear form, $\boldsymbol{w}$ is the primal variable, $\boldsymbol{z}$ is the test function, $\boldsymbol{f}(t)$ the loading, $\boldsymbol{w}^*$ the dual variable and the duaility operator $\langle\!\langle \cdot, \cdot \rangle\!\rangle$ is defined as:

$$\langle\!\langle \boldsymbol{y}_1, \boldsymbol{y}_2 \rangle\!\rangle = \mathbb{E}\left(\int_{\mathcal{G}} \boldsymbol{y}_1 \cdot \boldsymbol{y}_2 \, \mathrm{d}y \right). \tag{4}$$

The first equation represents the equilibrium equation, while the second is the flow rule describing the rate of change of the plastic deformation. If the stress stays inside the domain $\mathcal{K}$ one has elastic response, otherwise the response is plastic.

4 STOCHASTIC CLOSEST POINT PROJECTION

Computationally the solution of the elastoplastic problem collapses to the (iterative) solution of a convex mathematical programming problem, which has goal to find the closest distance in the energy norm of a trial state to a convex set $\mathcal{K}$ of elastic domain, known as a closest point projection. In other words, one search for:

$$\boldsymbol{\Sigma}_n(\omega) = \underset{\boldsymbol{\Sigma}(\omega) \in \mathcal{K}}{\arg\min} \, \mathcal{I}(\omega), \tag{5}$$

where $\mathcal{I}$ is given as:

$$\mathcal{I} := \arg\min_{\boldsymbol{\Sigma}\in\mathcal{K}} \frac{1}{2}\langle\langle \boldsymbol{\Sigma}^{trial} - \boldsymbol{\Sigma}_n, \boldsymbol{A}^{-1} : (\boldsymbol{\Sigma}^{trial} - \boldsymbol{\Sigma}_n)\rangle\rangle \tag{6}$$

in the time step n described by an implicit Euler difference scheme. Here, $\boldsymbol{\Sigma}^{trial}$ describes the trial stress leading to the typical operator split of the closest point projection algorithm into two steps: elastic predictor and plastic corrector.

Predictor step The predictor step calculates the polynomial chaos expansion of displacement u_n^k (in iteration k) by solving the equilibrium equation Eq. (1) [9, 8]. The displacement is then used for the calculation of the strain increment $\triangle E_n^k$ and the trial stress $\Sigma_n^{k,tr}$ assuming step to be purely elastic. If the stress $\Sigma_n^{k,tr}$ lies outside of the admissible region $\mathcal{K}$ we proceed with the corrector step. Otherwise, $\Sigma_n^k = \Sigma_n^{k,tr}$ represents the solution and we may move to the next step.

Corrector step The purpose of the corrector step is to project the stress outside of admissible region back onto a point in $\mathcal{K}$. To do this, we define the corresponding Lagrangian to a minimisation problem Eq. (5):

$$\mathcal{L}(\omega) = \mathcal{I}(\omega) + \lambda(\omega)\varphi(\boldsymbol{\Sigma})(\omega), \tag{7}$$

where the function $\varphi(\boldsymbol{\Sigma})(\omega)$ represents the yield function describing the convex set $\mathcal{K} := \{\boldsymbol{\Sigma}(\omega) \in \mathcal{S} \mid \varphi(\boldsymbol{\Sigma}) \leq 0 \text{ a.s. in } \Omega\}$. Hence, the standard optimality conditions [7] become:

$$\mathbf{0} \in \partial_{\boldsymbol{\Sigma}}\mathcal{L} = \partial_{\boldsymbol{\Sigma}}\mathcal{I}(\omega) + \lambda\partial_{\boldsymbol{\Sigma}}\varphi(\omega) \quad \text{a.s..} \tag{8}$$

The problem of closest point projection becomes complicated since we deal with uncertain parameters, i.e. polynomial chaos variables (PCV), which require the introduction of the polynomial chaos algebra called PC algebra.

5 NUMERICAL RESULTS

Two test problems in plane strain conditions are considered: rectangular strip with hole Fig. (1) under extension and Cooke's membrane Fig. (2) excited by a shear force on the right edge. The finite element discretisation is done using eight-nodded quadrilateral elements. For random parameters are declared the shear and bulk modulus, yield stress and the isotropic hardening. Due to the positive definiteness of these properties, we model them as lognormal random fields, i.e. the piecewise exponential transformation of a Gaussian random field with prescribed covariance function and correlation lengths.

5.1 Plate with Hole

The geometry and the boundary conditions for this particular problem are given in Fig. (1). The extension force is of deterministic nature, and in the initial state doesn't depend on the parameter ω. However, in each iteration it gets mixed with the uncertainty

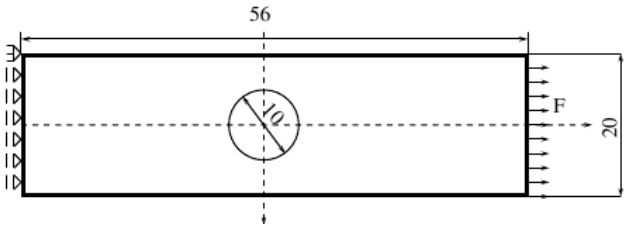

Figure 1: Geometry of the problem: plate with hole

of input parameters and hence becomes random. The randomness in input parameters depend on the choice of the values of the standard deviations as well as correlation lengths. The more large correlation length is, the less random field oscillates. Two representative examples of input random fields are given in Fig. (2), where the values of correlation lengths are chosen as moderate, 3 times less then the dimension of a plate.

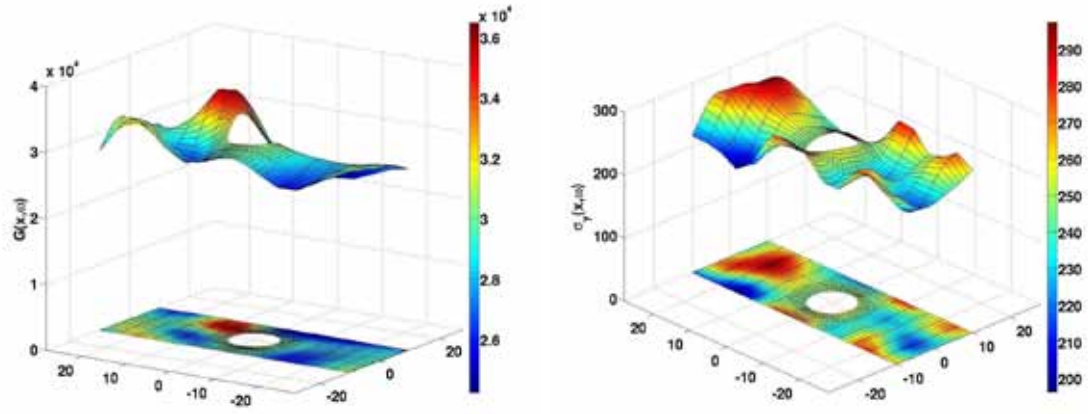

Figure 2: Two realisations of input random fields: shear modulus and yield stress

Solving the equilibrium equation, one obtains the displacement as a solution. In Fig. (3) we compared it with the initial configuration as well as with the deterministic value. Further more, we have calculated the shear stress, whose first two statistical moments are given in Fig. (4). Similarly, the Von Mises stress gives the statistical moments in Fig. (5).

The problem is solved in few different ways: by a pure sampling technique such as Monte Carlo or Latin Hypercube sampling [3], then by intrusive stochastic Galerkin method relying on white noise analysis and corresponding algebra [9] and non-intrusive variant of this method which uses the sparse grid collocation points [2]. The accuracy of these methods in the mean sense is almost the same, and hence we give the comparison of the variance convergence in Fig. (6). As one may notice, the normalised residual error is the smallest in a case of latin hypercube technique, while the intrusive method has the same convergence rate until certain error. In that point the method converges satisfying

less strict criteria. The reason is the numerical error introduced by a polynomial algebra, as well as in the span space of the basis functions needed for the local Galerkin projections.

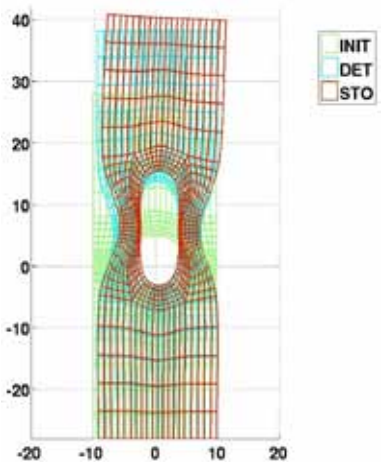

Figure 3: Comparison of the mean value of the total displacement in stochastic configuration with the deterministic and initial value

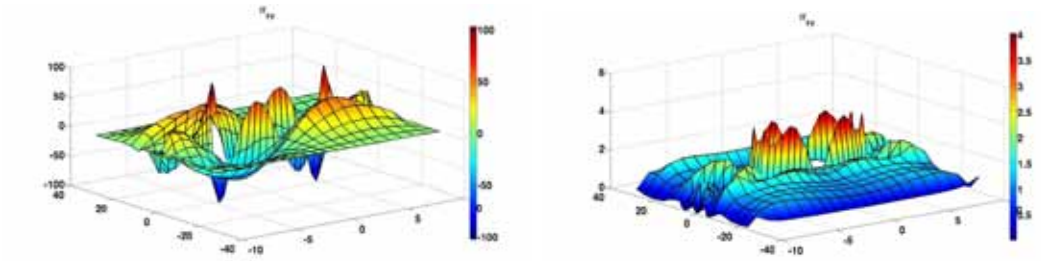

Figure 4: The shear stress σ_{xy}: mean vaalue and standard deviation

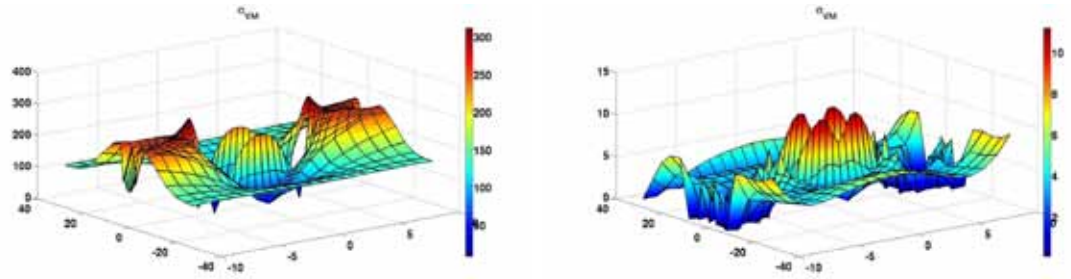

Figure 5: Von Mises stress: the mean value and standard deviation

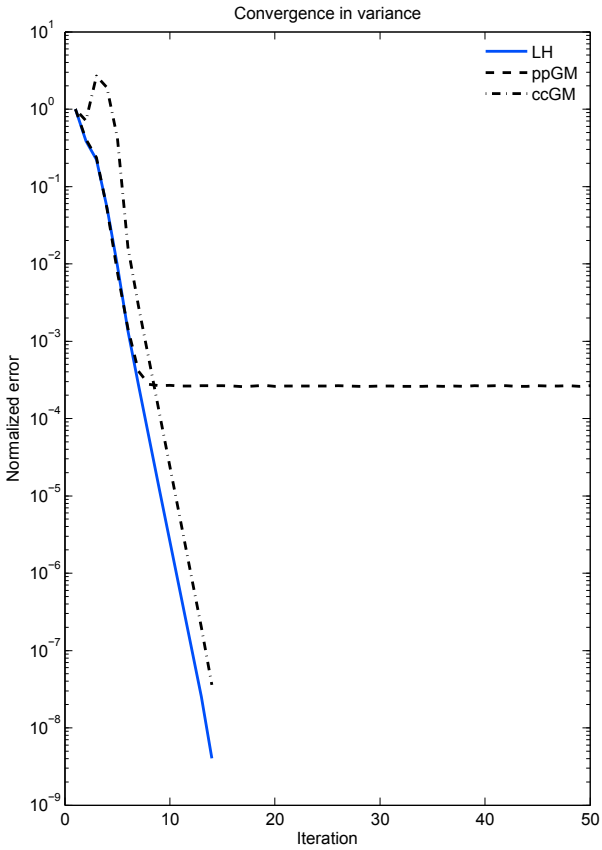

Figure 6: Comparison of the converegence of variance between latin hypercube sampling (LH), intrusive stochastic Galerkin method (ppGM) and non-intrusive stochastic Galerkin method (ccGM)

In practice very often one has to calculate the probability of stress taking the value less than some critical point. In Fig. (7) we show three probabilities schemes with respect to three different yield stress values. If the value is bigger, one has smaller probability to exceed the limit, which is expected.

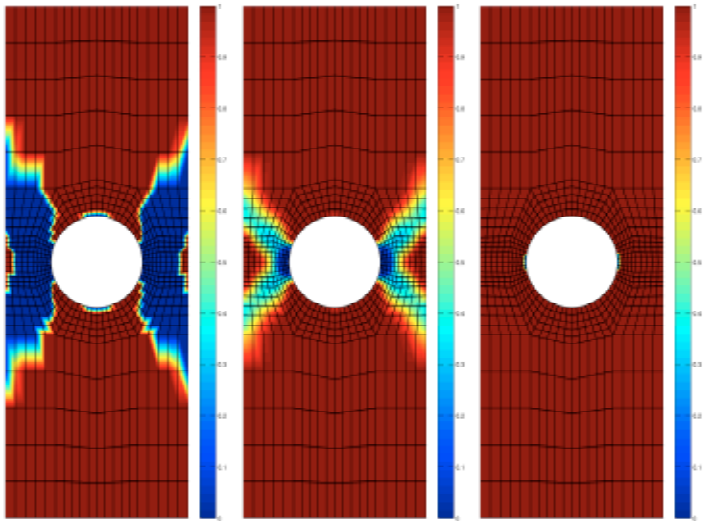

Figure 7: The probability excideence for different values of yield stress: $\sigma_y = 200$,$\sigma_y = 250$ and $\sigma_y = 300$

5.2 Cooke's membrane

The Cooke's membrane is subjected to load in y direction on the right boundary and constrained on the left as it is shown in Fig. (8). As in previous case, the random parameters are chosen in the same way, just with different mean values, and hence standard deviations.

The comparison of the mean displacements is given in Fig. (9), and as one may notice the difference is large enough not to be neglected.

The influence of the correlation lengths on the structure response is given in Fig. (10) and Fig. (11) for the xx component of deformation. In the case of large covariance lengths the random field fluctuates less and the response is more similar to deterministic one. However, in a case of small correlation lengths the field of compression grows into the larger area.

Besides the mean stastistics of the response structure, one may show the variance of the deformation ε_{xx} in Fig. (12).

6 CONCLUSION

The idea of random variables as functions in an infinite dimensional space approximated by elements of finite dimensional spaces has brought a new view to the field of stochastic

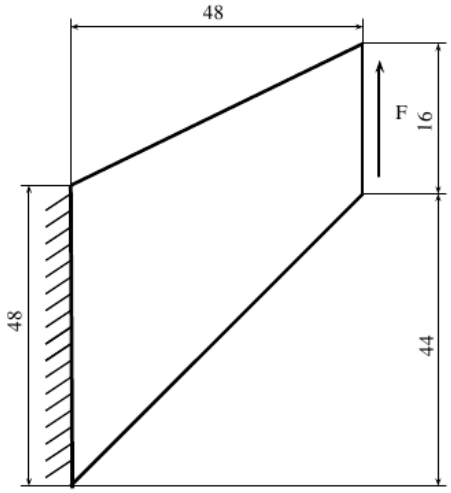

Figure 8: Geometry of the problem: Cooke's membrane

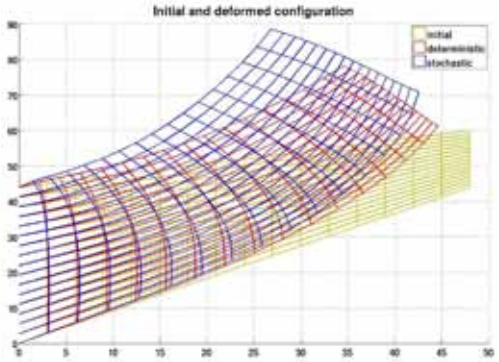

Figure 9: Comparison of the mean values of the displacement for initial, deterministic and stochastic configuration

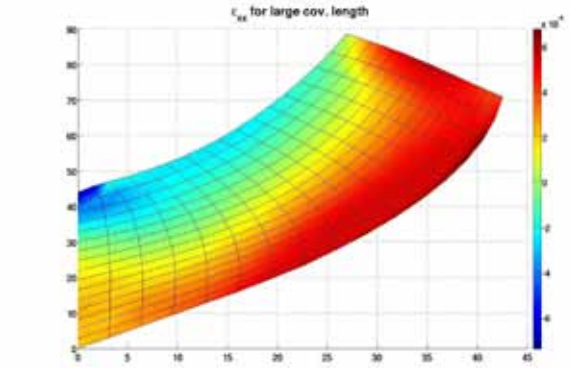

Figure 10: The mean value of deformation ε_{xx} for the large covariance length $l_c = 20$

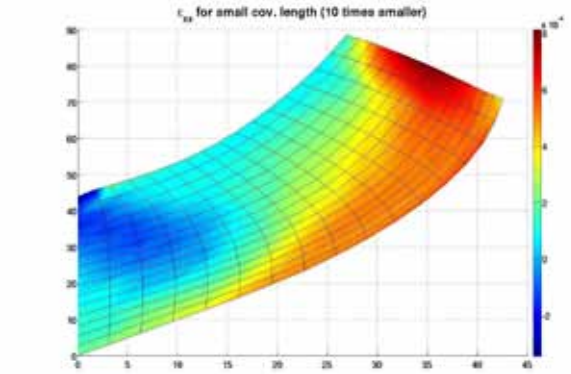

Figure 11: The mean value of deformation ε_{xx} for the small covariance length $l_c = 2$

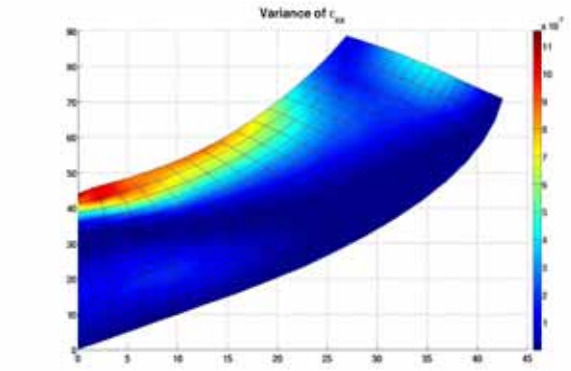

Figure 12:

elastoplasticity. In this paper, we have proposed an extension of stochastic finite element method and related numerical procedures to the resolution of inelastic stochastic problems in the context of Galerkin methods. In some way this strategy may be understood in a sense of model reduction technique due to the applied Karhunen Loève and polynomial chaos expansion. A Galerkin projection minimises the error of the truncated expansion such that the resulting set of coupled equations gives the expansion coefficients. If the smoothness conditions are met, the polynomial chaos expansion converges exponentially with the order of polynomials. In contrast to the Monte Carlo the Galerkin approach, when properly implemented, can achieve fast convergence and high accuracy and can be highly efficient in particular practical computations.

REFERENCES

[1] M. Anders and M. Hori. Stochastic finite element methods for elasto-plastic body. *International Journal for Numerical Methods in Engineering*, 46:1897–1916, 1999.

[2] I. Babuska, F. Nobile, and R. Tempone. A s stochastic collocation method for elliptic partial differential equations with random input data. *SIAM J. Numer. Anal.*, 45:1005–1034, 2007.

[3] R. E. Caflisch. Monte Carlo and Quasi-Monte-Carlo methods. *Acta Numerica*, 7:1–49, 1998.

[4] W. Han and B. Daya Reddy. *Plasticity: Mathematical Theory and Numerical Analysis*. Springer, New York, 1999.

[5] A. Ibrahimbegović. *Nonlinear Solid Mechanics*. Springer, Berlin, 2009.

[6] B. Jeremic, K. Sett, and M. Levent Kavvas. Probabilistic elasto-plasticity: Formulation of evolution equation of probability density function. 2005.

[7] D. G. Luenberger. *Optimization by Vector Space Methods*. John Wiley and Sons, New York, 1969.

[8] H. G. Matthies and B. Rosić. Inelastic Media under Uncertainty: Stochastic Models and Computational Approaches. In *Daya Reddy, IUTAM Bookseries*, volume 11, pages 185–194, 2008.

[9] B. Rosić and H. G. Matthies. Computational approaches to inelastic media with uncertain parameters. *Journal of Serbian Society for Computational Mechanics*, 2:28–43, 2008.

[10] J. C. Simo and T. J. R. Hughes. *Computational Inelasticity*. Springer Verlag, New York, 1998.

XI International Conference on Computational Plasticity. Fundamentals and Applications
COMPLAS XI
E. Oñate, D.R.J. Owen, D. Peric and B. Suárez (Eds)

SIMULATION OF THE DYNAMICS OF BIO-MEMBRANES IN A VISCOUS FLUID WITH A PHASEFIELD VARIATIONAL LAGRANGIAN APPROACH

C. Peco[1*], A. Rosolen[1] and M.Arroyo [1]

1: Laboratory of Computational Methods and Numerical Analysis. (LaCàN)
Universitat Politècnica de Catalunya
Campus Nord UPC, 08034 Barcelona, Spain
e-mail: christian.peco@upc.edu, web page: www-lacan.upc.edu

Key words: Bio-membranes, maximum-entropy, meshfree, Stokes, coupling, lagrangian, phase-field

Abstract. Bio-membranes are the basic separation structure in animal cells. Their complex behaviour, rich physical properties, formation and dynamics have been the object of experimental and theoretical investigation for biologists, chemists and physicists for many years. Bio-membranes are made out of several kinds of lipids self-assembled in a fuid bilayer, which presents a fluid behaviour in-plane and solid out-of-plane (curvature elasticity). Vesicles are closed fluid membranes, which play an important role in biophysical processes such as transfer of proteins, antibodies or drug delivery into the cells. Vesicles serve as simplified models of more complex cell membranes, as well as the basis for bio-mimetic engineered systems. Bio-membranes only exist in solution and intimately interact with the surrounding fluid, which owing to the characteristic sizes and velocities, can be modeled with the incompressible Stokes equations. The aim of our work is to simulate the dynamics of the interaction between a bio-membrane and the fluid media surrounding. We take as basis our previous work on bio-membrane simulations [1], in which the solution of the fourth order PDE governing the bending elasticity of a vesicle is tackled with a phase-field or diffuse interface approach. The nonlinear, fourth-order PDE governing the phase field are conveniently solved using the local maximum-entropy (LME) approximants, a type of meshfree shape functions [2]. We merge the phase field model with the Stokes fluid media to treat naturally the coupling between the viscous forces in the fluid, the elastic forces due to the membrane, and the various constraints in the problem. The dynamics arise from a variational principle, and dictate the Lagrangian motion of the particles, convecting the phase field.

1 INTRODUCTION

Biomembranes or biological membranes have been object of experimental and theoretical investigation for biologists, chemists and physicists during many years. Biomembranes are composed by several kinds of lipids self-assembled in a fluid bilayer , which presents a liquid behaviour in-plane and solid out-of-plane. Vesicles are closed biomembranes which play an important role in biophysical processes and serve as simplified models of cell membranes to study aspects of the interaction between the lipid bilayer structure and the surrounding fluid. To simulate the dynamic behaviour of a vesicle both biomembrane solid structure and surrounding fluid have to be properly modelled. The Canham-Helfrich bending energy model is normally used to describe the solid behaviour, while the fluid is modelled as a Stokes flow. Two different approaches can be used to describe the equations for equilibrium shapes of vesicles in the continuum media approach, sharp-interface and phase-field or diffuse-interface models. In this work a phase-field model proposed by Du et al. [4] is used. This kind of models represent the interface between the inner and outer fluid as a diffuse-interface whose thickness is controlled by a transition parameter e. The derived equations are highly non-linear and involve fourth-order spatial partial differential operators. The weak form of the equations necessitates piecewise smooth and globally C^1 continuous basis functions because products of second derivatives are involved in the integration of the variational formulation. The equations are discretized with LME [1] approximation schemes because they present interesting features such as positivity, monotonicity, variation diminishing property (the interpolation is not more wiggly than the data) and smoothness (C^∞). Adaptivity strategies are also required to make computationally affordable the phase-field approach. The fluid is commonly modelled as a Stokes flow because the Reynolds number is low. The idea is to apply the same numerical scheme to compute both the phase-field bending energy and the bulk effect of the fluid field surrounding the membrane. It is well-known that the Stokes problem lacks pressure stability if velocity and pressure are described with the same interpolation space, which demands a stabilization method to handle the problem. We borrowed finite element method (FEM) stabilization strategies to develop a LME stabilizing method. The structure of this paper is as follows. Section 2 introduces the formulation of the phase-field model and its numerical treatment. The capability of the adaptive strategy is also illustrated. In Section 3, we describe the Stokes flow problem and the stabilizing LME method, whose performance is tested through numerical benchmarks. Some concluding remarks are collected in Section 4.

2 MODEL OF THE BIOMEMBRANE: A PHASE-FIELD APPROACH

The phase-field model of a biomembrane is presented in this section. The numerical treatment, which includes discretization, nonlinear solver and adaptivity strategy, is also introduced. A numerical example of a dumbbell shape is set to evaluate the performance of the proposed scheme.

2.1 Problem formulation and numerical treatment

The phase-field model describing the equilibrium shapes for vesicles can be possed as an energy constrained-minimization problem:

Minimize

$$E(\phi) = f_E \frac{k}{2\epsilon} \int_\Omega \left[\epsilon \Delta\phi + \left(\frac{1}{\epsilon}\phi + C_0\sqrt{2} \right) \left(1 - \phi^2 \right) \right]^2 \, d\Omega \tag{1}$$

subject to

$$V(\phi) = \frac{1}{2} \left(Vol(\Omega) + \int_\Omega \phi \, d\Omega \right) = V_0 \tag{2}$$

$$A(\phi) = f_A \int_\Omega \left[\frac{\epsilon}{2} |\nabla\phi|^2 + \frac{1}{4\epsilon}(\phi^2 - 1)^2 \right] \, d\Omega = A_0 \tag{3}$$

where ϕ is the phase-field, ϵ the transition parameter, C_0 the spontaneous curvature, $f_E = \frac{3}{8\sqrt{2}}$, $f_A = \frac{3}{2\sqrt{2}}$, k the bending rigidity, V_0 and S_0 the volume and area constraints, respectively.

These equations are discretized with LME approximation schemes, augmented Lagrangian methods are used to impose the linear and nonlinear constraints, while L-BFGS and Newton-Rahpson techniques are applied to solve the nonlinear problem. An adaptive algorithm based on Centroidal Voronoi Tesselations [5] is proposed to reduce the computational cost. A detailed explanation about the approximants, the discretization procedure, the numerical strategy to solve the problem and the adaptive algorithm is given in [6].

2.2 Numerical example

The energies computed for the dumbbell equilibrium shape considering different values of ϵ and several levels of refinement for uniform grid of points can be seen in Table 1. The number of nodes for each grid and the values of the average nodal spacing $\bar{h}$ (average element size in FEM terminology) are denoted in the first and second column, respectively. The remaining columns correspond to the values of energies for different values of transition parameter ϵ.

It is remarkable that the accuracy of phase-field results is intrinsically associated to the value of the transition parameter ϵ, which is in turn directly related with the size of the discretization: we consider that the relation $\epsilon \geq 2h$ is quite reasonable. In Table 1 it is shown that values of energy converge for each fixed ϵ (columns) and the error becomes gradually less as the grid of points is refined. The largest errors are presented by the values of the upper supra-diagonal, and it happens because they do not fulfill the mentioned relation between the transition paremeter and the discretization size.

The effect of the adaptive strategy applied to a grid of 6124 points is shown in Figures 1 and 2, respectively. Former illustrates the grid of points, while latter the phase-field

# nodes	$\bar{h}$	$\epsilon = 0.05$	$\epsilon = 0.04$	$\epsilon = 0.03$	$\epsilon = 0.02$	$\epsilon = 0.01$
6124	0.024	9.29504	9.15560	–	–	–
12271	0.017	9.30167	9.15918	9.00361	–	–
24597	0.012	9.30627	9.16106	9.00310	8.87045	–
49145	0.0084	9.31053	9.16315	9.00362	8.86669	–
98388	0.0059	9.31307	9.16407	9.00331	8.86445	8.81432
146545	0.0048	9.31439	9.16421	9.00217	8.86005	8.77677
296344	0.0034	9.31650	9.16512	9.00251	8.86033	8.77359

Table 1: Energies of the dumbbell equilibrium shape for different uniform grids of points and several values of ϵ.

solutions. The value of the transition parameter ϵ, and thus the value of the average nodal spacing $\bar{h}$, is decreased in each step. The accuracy obtained at the end of the process reaches that obtained with a uniform grid of 296344 points.

The effect of the adaptive strategy applied to a grid of 6124 points is shown in Figures 1 and 2, respectively. Former illustrates the grid of points, while latter the phase-field solutions. The value of the transition parameter ϵ, and thus the value of the average nodal spacing $\bar{h}$, is decreased in each step. The accuracy obtained at the end of the process reaches that obtained with a uniform grid of 296344 points.

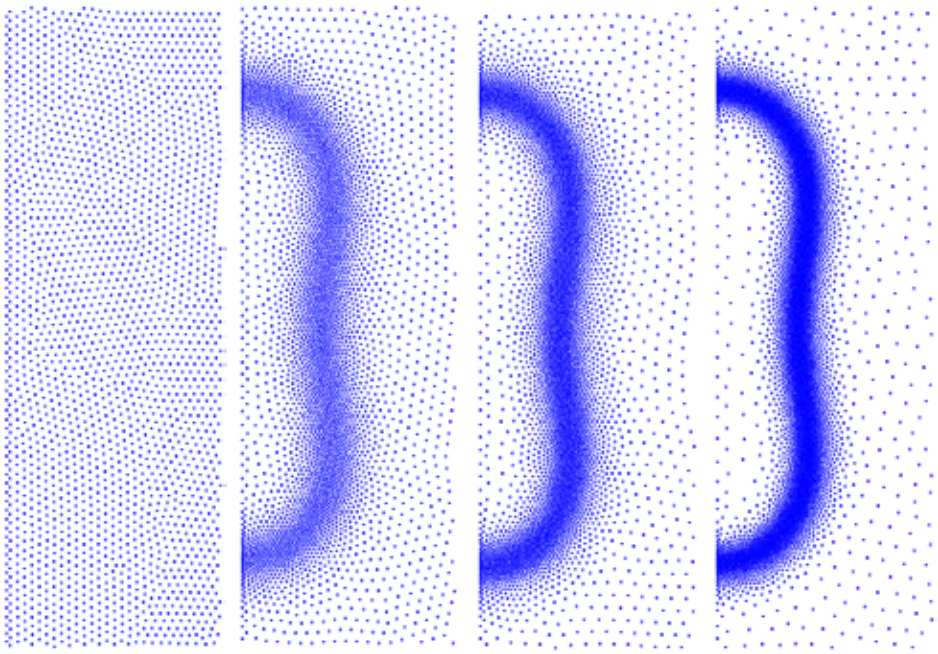

Figure 1: Adapted grid of 6124 points corresponding to the dumbbell equilibrium shape. The average nodal spacing $\bar{h}$ decreases from left to right.

Three-dimensional views of the dumbbell equilibrium shape are illustrated in Figure 3.

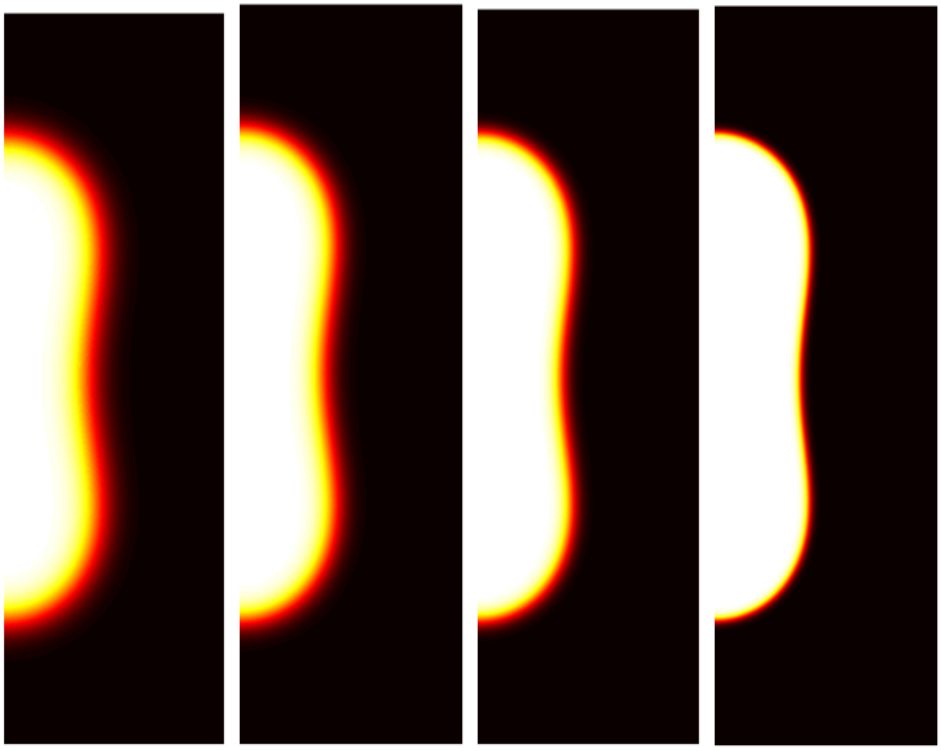

Figure 2: Phase-field density for different grids of 6124 points corresponding to the dumbbell equilibrium shape.

3 MODEL OF THE FLUID: STOKES FLOW

The Stokes flow problem and the stabilization with LME approximation schemes are explained in this section. The performance of the method is illustrated with classical benchmark tests.

3.1 Introduction

The Stokes problem can be formulated in general form as:

$$-\nu\triangle u + \nabla p = f \quad \text{in } \Omega \quad \nabla \cdot u = 0 \quad \text{in } \Omega \quad u = u_d \quad \text{on } \Gamma_d \tag{4}$$

where v is the velocity, p the pressure, f the vector of body forces, ν the kinematic viscosity, and $\Omega \subset R^d$.

Let be $V = H_0^1(\Omega)^d$ and $Q = L_2(\Omega)/R$ the velocity and pressure spaces, respectively. Then, the weak form is set to find $u \in V$ and $p \in Q$ such that:

$$a(u,v) - b(p,v) = l(v) \quad v \in V \quad b(q,u) = 0 \quad q \in Q \tag{5}$$

This weak form is widely studied in literature, and it is well-known that the existence and uniqueness of the solution require equations to satisfy the Ladyzhenskaya-Babuška-

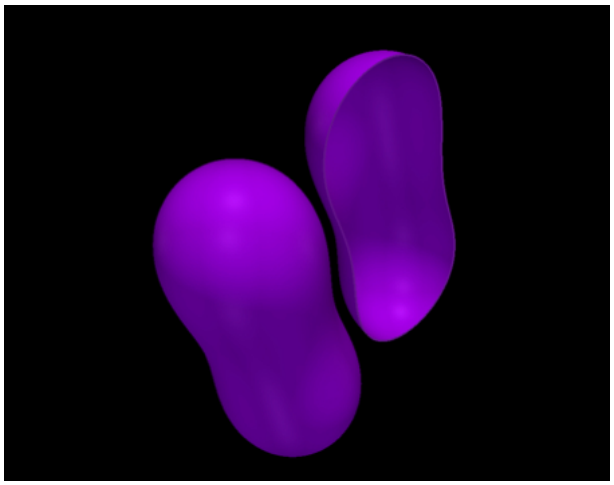

Figure 3: 3D view of the dumbbell equilibrium shape.

Brezzi (LBB) condition. This rule states that the following inf-sub condition has to be fulfilled to guarantee the stability of the system (matrix of the system derived non singular):

$$\inf_{q\in Q}\sup_{v\in V}\frac{b(q,v)}{\|q\|_Q\|v\|_V}\geq K_b>0 \tag{6}$$

This condition holds true if $b(q,v)=(q,\nabla\cdot v)$, $q\in Q=L_2(\Omega)/\ R$ and $v\in V=H_0^1(\Omega)^d$, properties which are always kept by the Stokes problem at a continuous level. Unfortunately, when the equations are discretized with restrictive spaces, that is, $Q_h\subset Q$ and $V_h\subset V$, the LBB condition can fail and the pressure become unbounded. In particular, it is proven that using the same discretization space for both pressure and velocity results in a loss of stability, which is the cardinal issue of numerical methods for solving the Stokes problem.

3.2 Stabilization of Stokes equations

Main strategies to deal with this obstacle are mixed formulations and stabilization of Stokes equations. The mixed formulations tackle the problem by seeking admissible pairs of spaces that fulfill the inf-sup condition. Stabilization techniques use a discretization based on a single space for both pressure and velocity, and add terms to the original weak form to give coercivity to the resulting matrix.

We are interested in the coupled problem posed by the bending model of biomembranes and the Stokes flow in which they are immersed. LME approximants present nice characteristics to solve the phase-field governing the structure behaviour and, to earn simplicity in the numerical scheme and reduce the computational cost, we find convenient to use the same discretization space for the fluid problem.

Stabilization techniques have undergone a large and satisfactory development in the FEM context [3]. We develop a LME stabilization method inspired in FEM stabilization ideas. Because of the noticeable differences between FEM and LME, the application of the FEM based methods is not direct and redefinition of parameters is needed. The discretization of the Stokes problem leads to the following system:

$$\begin{bmatrix} K & -D^T \\ D & 0 \end{bmatrix} \begin{bmatrix} U \\ P \end{bmatrix} = \begin{bmatrix} F \\ 0 \end{bmatrix} \tag{7}$$

where K comes from the Laplacian velocity and it is definite positive, while D corresponds to the pressure terms and introduces the inestability to the total matrix. To stabilize the system we need to add an extra term to the weak form [3]:

$$\int_\Omega \tau \ \mathcal{P}(w,q) \ \mathcal{R}(u,p) \ d\Omega \tag{8}$$

where $\mathcal{R}(u,p)$ is the residual or strong form of the problem (which ensures the consistency of the new weak form), τ is a parameter which controls the measure of the stabilization to be applied and $\mathcal{P}$ is a partition of the differential operator. Different choices of this partition lead to different stabilization methods.

To summarize the effect of the stabilization methods and to provide an integrated way of implementation in the code, the following general term becomes adequate from now on [2]:

$$\int_\Omega \tau_1 \ (-\alpha\nu\Delta w + \beta_1 \nabla q) \ (-\nu\Delta u + \nabla p - f) \ d\Omega \tag{9}$$

where α and β_1 are parameters that take values $1, 0, -1$ the former, and $1, -1$ the latter. The different combinations of the values enable the user to jump from one stabilization method to another while mantaining the same term structure.

This last expression can be developed in a larger group of terms to add their discretized matrices to the original matrix form of the Stokes problem, resulting:

$$\begin{bmatrix} K + \alpha K_{st} & -D^T - \alpha D_{st}^T \\ \beta_2 D - \beta_1 D_{st} & \beta_1 L_{st} \end{bmatrix} \begin{bmatrix} U \\ P \end{bmatrix} = \begin{bmatrix} F - \alpha F'_{st} \\ \beta_1 F''_{st} \end{bmatrix} \tag{10}$$

where $\beta_2 = -\beta_1$ and L_{st} is a positive definite matrix since comes from a pressure Laplacian. This matrix gives to the global matrix the stabilization needed to be non singular and subsequently provide a solution for the system.

The parameter τ is a stabilization parameter that have to be defined by the the method, an which usually involves a constant to be calibrated by the user. In FEM, some expressions that work element wise have been developed, performing very well. Since in LME we work with a set of points instead of a mesh, some redefinition of the parameter has to be worked out. In FEM, the normal parameter to use is the nodal spacing. In meshless methods, this nodal spacing is usually interpreted as a the range of the shape functions,

creating functions-wise parameters. Here we propose an expression based on this concept but defining a pointwise parameter, which show a fairly direct way for implementation and excellent results in simulations.

$$\tau_1 = \frac{C}{\nu}\bar{\rho}^2; \tag{11}$$

where $\bar{\rho}$ is the mean over the neighbors, $N\bar{\rho} = \sum_{i=1}^{N} \rho_i$ with $1, 2, .., N$ the list of neighbors of gauss point.

3.3 Numerical examples

We select and apply the GLS-LME stabilization technique ($\alpha = 1$ and $\beta_1 = 1$) to the classical Poiseouille and Colliding flows benchmark tests for the Stokes problem. Here we only illustrate the performance of the method for the Colliding flow, but similar results were obtained for the Poiseouille problem. Since these tests have analytical solution we can accurately compare the results of the simulations.

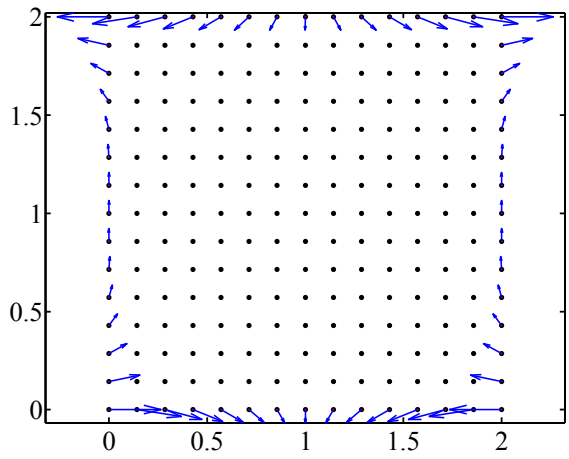

Figure 4: Definition of the Colliding flow problem.

The essential boundary conditions of the problem are plotted in Figure 4. The velocity field is illustrated in the Figure 5 without the application of stabilizing method (left) and after stabilization (right). Although we have illustrated the solutions corresponding to a coarse grid of points for clearness purposes, the observed patterns are maintained in refined grids. The velocity stabilized solutions do no present a strange physical behaviour when compared with the analytical one. The same behaviour can be seen in the Figure 6 where we plot the pressure for the solution without stabilization. Disproportionate values of pressure and oscillations are observed. This anomalous behaviour dissapears after the

stabilization and the obtained solution recovers the smoothness, matching the analytical field.

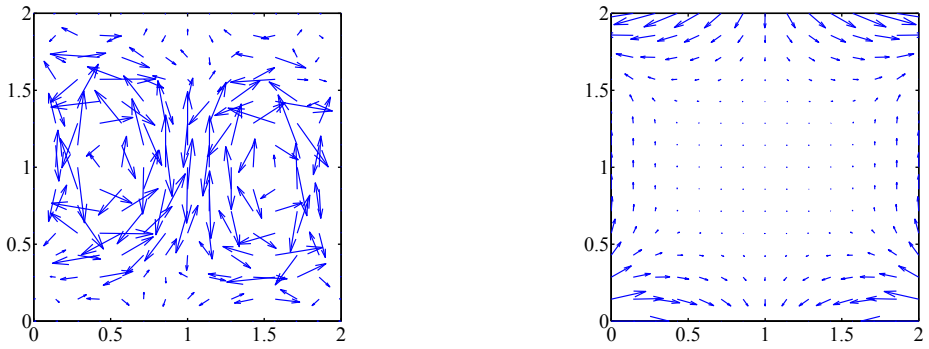

Figure 5: Colliding flow velocity stabilization: (left) Velocity field with no stabilization computed with 225 nodes, and (right) Velocity field stabilized computed with GLS-LME, 225 nodes and $\gamma = 1.0$.

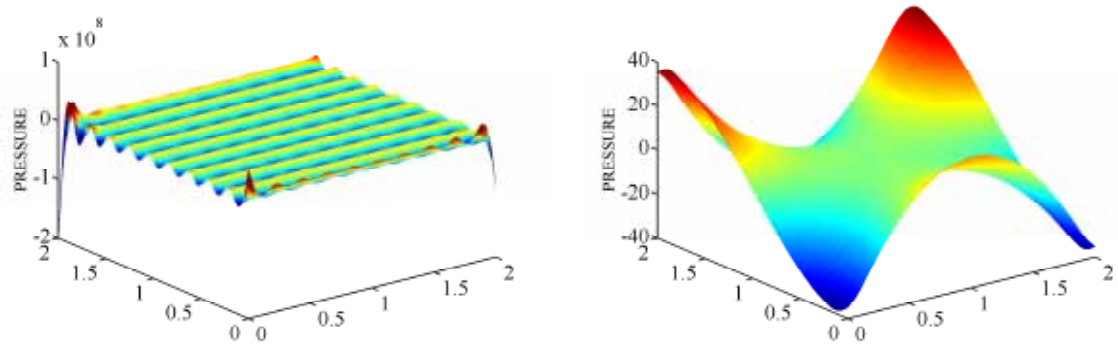

Figure 6: Colliding flow pressure stabilization: (left) Pressure field with no stabilization computed with 625 nodes, and (right) Pressure field stabilized computed with GLS-LME, 625 nodes and $\gamma = 1.0$.

This fact is reflected in detail with the recovery of the optimal rate after the stabilization in the convergence charts for L_2 norm, as it is illustrated in the Figure 7.

Another set of simulations have been run over an unstructured grid in order to test the capability of the point-wise τ_C parameter introduced before. As can be observed in 7, both for pressure and velocity the optimal slopes are recovered. This important result enables the use of this fairly direct implementation parameter to manage adaptive processes which are needed in high accurate or tridimensional computations.

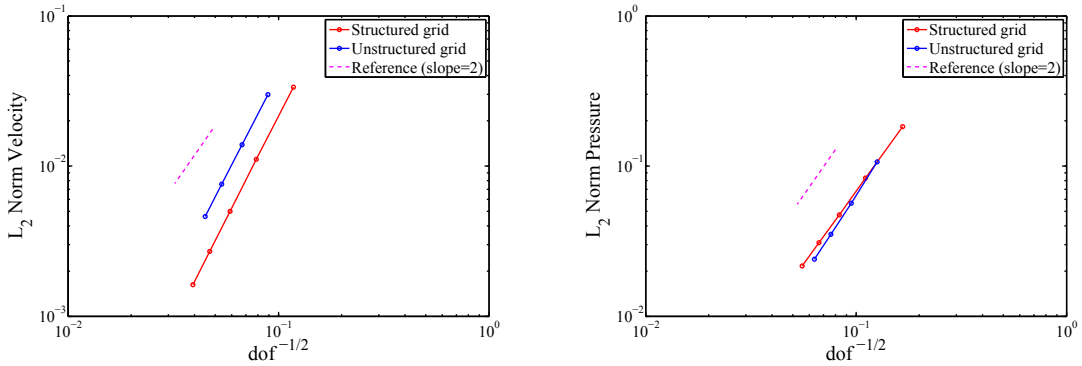

Figure 7: Colliding flow velocity stabilization: (left) Velocity field with no stabilization computed with 225 nodes, and (right) Velocity field stabilized computed with GLS-LME, 225 nodes and $\gamma = 1.0$.

4 COUPLING STRATEGY AND NUMERICAL EXAMPLES

Once the main two ingredients of the numerical simulation have been tested and performed separately, a coupling strategy have to be set in order to generate and efficient algorithm which can represent the evolution of a biological process. The idea we present here is a change of scope from a phase-field eulerian approach to a fully lagrangian one where the phase-field no longer will be solved over a stacionary set of points, but will be considered as a material property which is transported within the fluid and therefore solved in terms of its final position. This inmediately generates a coupled monolithic algorithm where the Stokes equations are solved considering the potential forces coming from the phase-field bio-membrane.

We state the dynamic problem form a variational standpoint (stokes) by setting an optimization over the total system incremental energy $\dot{W}$ (biomembrane bending energy change and Stokes bulk fluid dissipation)

$$\dot{W} = \dot{E} + D \tag{12}$$

Being E the bending elastic energy of the biomembrane in terms of a phase-field ϕ, and D the dissipation, which become described as:

$$E = \frac{k}{2\epsilon} \int_{\Omega_t} (\epsilon \, \triangle_t \, \phi_t + (\frac{1}{\epsilon}\phi_t + c_0\sqrt{2})(1 - \phi_t^2))^2 d\Omega_t \tag{13}$$

$$\mathcal{D} = \int_{\Omega_t} 2\mu\Delta{:}\,\Delta + \kappa(\nabla \cdot v)^2 d\Omega_t \tag{14}$$

Where $\Delta = \frac{1}{2}(\nabla v + \nabla v^T) - \frac{1}{3} I(\nabla \cdot v)$ and Ω_t the space domain at time t.

This expression can be worked out taking into account the incompressibility of the media, leading to the following simplified expression

$$\mathcal{D} = \int_{\Omega_t} \mu |\nabla v|^2 d\Omega_t \tag{15}$$

Which will be used from now on as the dissipation expression for the bulk Stokes fluid.

We discretize the original time interval for a process in smaller time steps $[t_0..t_k, t_{k+1}..t_{end}]$, and calculate the evolution between two generic states t_k and t_{k+1}, by applying a minimization over the incremental energy,

$$\Delta\mathcal{E}_{k\to k+1} = \int_{t_k}^{t_{k+1}} W dt \approx W_{k\to k+1}\Delta t \tag{16}$$

We define,

$$W_{k\to k+1} = \dot{E}_{k\to k+1} + \mathcal{D}_{k\to k+1} \tag{17}$$

The differential equation is

$$\partial_\varphi \partial_t E(\varphi, \varphi_t) + \partial_\varphi \dot{D}(\varphi_t) = 0 \tag{18}$$

If we use a classic alpha-method to integrate through time, we have

$$\dot{W_{k\to k+1}} = \theta \dot{W_{k+1}} + (1-\theta)\dot{W}_k \tag{19}$$

The aim of the algorithm is to minimize the whole energy action at a given step, setting all the expressions in terms of an unknown deformation mapping. The calculations will be brought to the reference state, in which the spatial discretization will take place, by means of mesh-free shape functions. A numerical simulation over an axisymmetric cilinder with a bio-membrane embedded can be observed in figure 8, where the forces of the elastic potential coming fron the phase-field can be seen over the fluid domain, governing the evolution for the shape, which can be identified following the line where forces are stronger.

5 CONCLUSIONS

We explain how the biomembranes structural behaviour can be modeled through an energy constrained-minimization phase-field problem. We indicate algorithms to solve the problem and also propose an adaptive strategy based on LME approximants and Centroidal Voronoi Tessellations. We illustrate the performance of the proposed method with a representative example of a dumbbell equilibrium shape.

We propose a stabilization technique inspired in the well-known FEM stabilization methods to solve the Stokes problem with LME. We design a pointwise stabilization parameter suitable for the new environment and we illustrate the capability of the proposed scheme in the classical Colliding flow benchmark problem.

We present a coupling algorithm based on a lagrangian variational approach which enable us to represent the dynamics of an evolution by means of a monolithic scheme, using the deformation mapping to solve both the membrane and the fluid.

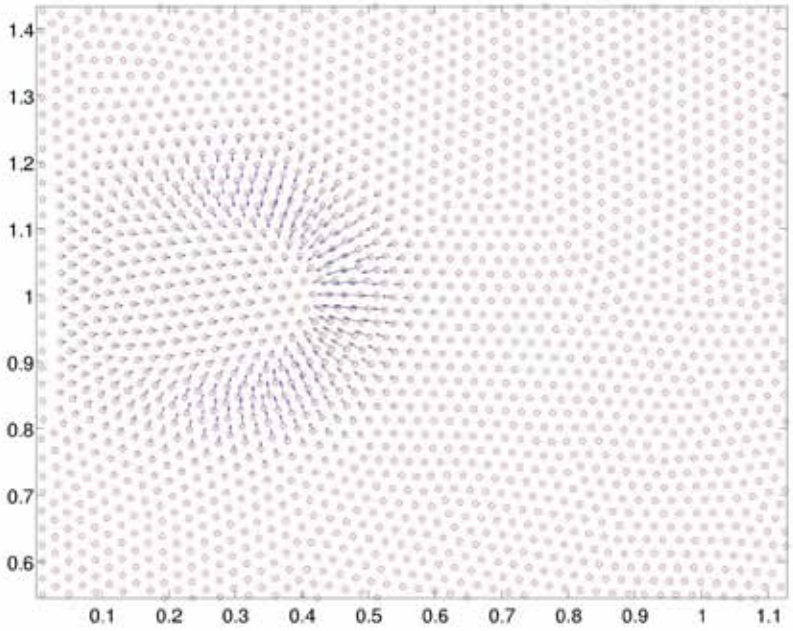

Figure 8: Elastic forces over fluid domain of 6124 nodes and $\gamma = 0.8$.

REFERENCES

[1] M. Arroyo and M. Ortiz, *Local maximum-entropy approximation schemes: a seamless bridge between finite elements and meshfree methods*, International Journal for Numerical Methods in Engineering **65** (2006), no. 13, 2167–2202.

[2] T. Barth, P. Bochev, M. Gunzburger, and J. Shadid, *A taxonomy of consistently stabilized finite element methods for stokes problem*, Siam Journal on Scientific Computing 25 (2004), 1585-1607.

[3] R. Codina, *Comparison of some finite element methods for solving the diffusion-convection-reaction equation*, Computer Methods in Applied Mechanics and Engineering 156 (1998), 185-210.

[4] Q. Du, C. Liu, and X. Wang, *A phase field approach in the numerical study of the elastic bending energy for vesicle membranes*, Journal of Computational Physics **198** (2004), 450–468.

[5] Q. Du, V. Faber, and M. Gunzburger, *Centroidal Voronoi Tessellations: Applications and Algorithms*, SIAM Review **41** (1999), no. 4, 637–676.

[6] A. Rosolen and C. Peco and M. Arroyo, *An adaptive maximum–entropy meshfree method for phase–field models of axisymmetric biomembranes*, To be submitted to Journal of Computational Physics (2011).

XI International Conference on Computational Plasticity. Fundamentals and Applications
COMPLAS XI
E. Oñate, D.R.J. Owen, D. Peric and B. Suárez (Eds)

A DETERMINISTIC FILTER FOR ESTIMATION OF PARAMETERS DESCRIBING INELASTIC HETEROGENEOUS MEDIA

HERMANN G. MATTHIES and BOJANA V. ROSIĆ

Institute of Scientific Computing
Technische Universität Braunschweig
38106 Braunschweig
e-mail: wire@tu-bs.de

Key words: Bayesian linear estimation, uncertainty updating, stochastic plasticity

Abstract. We present a new, fully deterministic method to compute the updates for parameter estimates of quasi-static plasticity with combined kinematic and isotropic hardening from noisy measurements. The materials describing the elastic (reversible) and/or inelastic (irreversible) behaviour have an uncertain structure which further influences the uncertainty in the parameters such as bulk and shear modulus, hardening characteristics, etc. Due to this we formulate the problem as one of stochastic plasticity and try to identify parameters with the help of measurement data. However, in this setup the inverse problem is regarded as ill-posed and one has to apply some of regularisation techniques in order to ensure the existence, uniqueness and stability of the solution. Providing the apriori information next to the measurement data, we regularize the problem in a Bayesian setting which further allow us to identify the unknown parameters in a pure deterministic, algebraic manner via minimum variance estimator. The new approach has shown to be effective and reliable in comparison to most methods which take the form of integrals over the posterior and compute them by sampling, e.g. Markov chain Monte Carlo (MCMC).

1 INTRODUCTION

The deterministic description of the properties of heterogeneous material and their parameter identification are not quite suitable having in mind the uncertainties arising at the micro-structural level. Thus, we may consider them as unknown and try to identify from the given experimental data in a Bayesian manner. By measuring some quantities of interest such as deformation, one cannot estimate the material characteristics (Young's modulus, shear and bulk modulus, etc) straightforwardly since the problem is ill-posed and suffers from the issues of the existence, uniqueness and stability of the solution. In order

to regularize the problem, we may give additional information next to the measurement data in a form of distribution function of unknown characteristics — so called a priori information. This kind of regularization technique is known as Bayesian.

In recent studies [2, 8, 9, 11, 13, 21], the Bayesian estimates of the posterior density are taking the forms of integrals, computed via asymptotic, deterministic or sampling methods. The most often used technique represents a Markov chain Monte Carlo (MCMC) method [5, 9, 13], which takes the posterior distribution for the asymptotic one. This method has been improved by introducing the stochastic spectral finite element method [14] into the approximation of the prior distribution and corresponding observations [11, 13]. This group of methods is based on Bayes formula itself. Another group belongs to so-called 'linear Bayesian' [6] methods, which update the functionals of the random variables. The simplest known version represents the Kalman-type method [4, 1, 3, 22].

In order to avoid the sampling procedure required by previous methods, we describe the minimum variance estimator based on 'white noise' analysis. Starting with a probabilistic model for the uncertain parameters (the maximum entropy principle) we cast the identification problem in a direct algebraic estimation framework, which has shown to be effective and reliable. In this way not only that the sampling at any stage of the identification procedure is avoided but also the assumption of gaussianity.

The paper is organized as follows: in first section we briefly describe the forward problem [1], then we introduce the update procedure concentrating on one parameter, i.e. shear modulus and give the numerical results for two test problems in plain strain conditions.

2 FORWARD PROBLEM

Consider a material body occupying a bounded domain $\mathcal{G} \in \mathbb{R}^d$ with a piecewise smooth Lipschitz continuous boundary $\partial\mathcal{G}$ on which are imposed boundary conditions in Dirichlet and Neumann form on $\Gamma_D \subseteq \partial\mathcal{G}$ and $\Gamma_N \subset \partial\mathcal{G}$ respectively, such that $\Gamma_D \cap \Gamma_N = \varnothing$ and $\partial\mathcal{G} = \bar{\Gamma}_N \cup \bar{\Gamma}_D$ [20, 7, 10]. The probability space is defined as a triplet $(\Omega, \mathcal{B}, \mathbb{P})$, with $\mathcal{B}$ being a σ-algebra of subsets of Ω and $\mathbb{P}$ a probability measure. The balance of momentum localized about any point x in domain $\mathcal{G}$ in time $t \in \mathcal{T} := [0, T]$ leads to an equilibrium equation and boundary conditions required to hold almost surely in ω, i.e. $\mathbb{P}$-almost everywhere:

$$\begin{aligned} \operatorname{div} \boldsymbol{\sigma} + \boldsymbol{f} &= \mathbf{0} \quad \text{on } \mathcal{G}, \\ \boldsymbol{\sigma} \cdot \boldsymbol{n} &= \boldsymbol{g}, \quad \text{on } \Gamma_N, \\ \boldsymbol{u} &= \mathbf{0}, \quad \text{on } \Gamma_D \end{aligned} \tag{1}$$

where $\boldsymbol{u}$ and $\boldsymbol{v}$ denote the displacement and velocity fields over $\mathcal{G}$, $\boldsymbol{f}$ the body force, $\boldsymbol{\sigma}$ stress tensor, $\boldsymbol{n}$ the exterior unit normal at $x \in \Gamma_N$, and $\boldsymbol{g}$ a prescribed surface tension. For the sake of simplicity we use homogeneous Dirichlet boundary conditions and under

[1] The paper with this subject is also part of the proceedings, search for authors

the assumptions of small deformation theory we introduce the strain $\boldsymbol{\varepsilon}(\boldsymbol{u}) = D\boldsymbol{u}$, with the linear bounded operator defined as a mapping $D : \boldsymbol{u}_1(x)\boldsymbol{u}_2(\omega) \to (\nabla_S \boldsymbol{u}_1(x))\boldsymbol{u}_2(\omega)$.

The strong form of equilibrium equation given by Eq. (1) may be reformulated in a variational setting, which includes the uncertain parameters such as the elastic and hardening properties, yield stress, loading etc. These quantities are modeled as random fields/processes approximated by polynomial chaos and Karhunen Loève expansions [14], which further allow the use of the stochastic Galerkin projection procedures in low-rank and sparse format [16]. In other words, the problem collapses to the constrained-stochastic optimization one, where the closest distance in the energy norm of a trial state to the convex set of the elastic domain is found by a stochastic closest point projection algorithm[15, 19].

3 ESTIMATION OF SHEAR MODULUS VIA DIRECT GENERAL BAYESIAN APPROACH

In the scope of this paper we show the procedure of identifying one representative property q of elastoplastic material called shear modulus, often denoted by G. As this property is regarded as positive definite, we take the lognormal distribution with appropriate covariance function as a corresponding a priori information and solve the forward problem in Eq. (1) in order to obtain the solution (stress, displacement, etc.). The functional of the solution represents the 'forecast' measurement y further used in the update procedure. Besides this, one employs the information gathered by experimental (here simulated) measurements which are disturbed by some additional independent noise ϵ.

Let us define the random variable q as a measurable mapping [18]:

$$q : \Omega \to \mathcal{Q}, \tag{2}$$

where $\mathcal{Q}$ is a deterministic Hilbert space. If we denote the space of random variables with finite variance as $S := L_2(\Omega)$, then $\mathcal{Q}$-valued random variables belong to a space $L_2(\Omega, \mathcal{Q}) := \mathcal{Q} \otimes S$, obtained as a tensor product of corresponding deterministic and stochastic spaces.

According to previous definitions, we may define the linear measurement as a random variable/field:

$$z = \hat{y} + \epsilon, \tag{3}$$

where

$$\hat{y} = Y(q, u), \quad \hat{y} \in \mathcal{Y} \tag{4}$$

represents some functional of the solution linear in parameter q. The measurement error is here assumed to be Gaussian with prescribed covariance C_ϵ. Thus, the measurement is random and belongs to a subspace $\mathscr{Y}_0 \subseteq \mathscr{Y} := \mathcal{Y} \otimes S$.

In the same manner, the a priori information q_f belongs to a closed subspace $\mathscr{Q}_f \subset \mathscr{Q}$, allowing the prediction of the observation y via linear mapping $H : \mathcal{Q} \to \mathcal{Y}$, i.e.

$$y = Hq_f, \quad y \in \mathscr{Q}_0 = H^*(\mathscr{Y}_0). \tag{5}$$

Collecting these two informations, we are able to estimate the posterior $q_a \in \mathscr{Q}$ as the orthogonal or minimum variance projection of q onto the subspace $\mathscr{Q}_f + \mathscr{Q}_0$ [18, 17, 12]:

$$q_a(\omega) = q_f(\omega) + K(z(\omega) - y(\omega)), \quad K := C_{qfy}\,(C_y + C_\epsilon)^{-1} \tag{6}$$

where q_f is the orthogonal projection onto $\mathcal{Q}_f$, K the "Kalman gain"operator and C appropriate covariances.

In order to numerically compute the previous estimate Eq. (6) one introduces a projection operator P, which projects the parameter set onto the subspace $\hat{\mathscr{Q}} := \mathcal{Q}_N \otimes S_J$. Here $\mathcal{Q}_N$ is a finite element discretization of a deterministic space $\mathcal{Q}$ and S_J the discretization of the stochastic space, obtained by taking the polynomial chaos expansion (PCE) of the solution space as the ansatz function. The projection of Eq. (6) then reads:

$$\hat{q}_a(\omega) = \hat{q}_f(\omega) + K(\hat{z}(\omega) - \hat{y}(\omega)), \tag{7}$$

giving the PCE of posterior $\hat{q}_a(\omega)$ as the final estimate, from which all other further properties, such as statistical moments, probability density functions, etc. are efficiently computed.

4 NUMERICAL RESULTS

Two test problems in plane strain conditions are considered: rectangular strip with hole Fig. (1) and Cooke's membrane Fig. (6). Due to lack of measurement data, we describe the virtual reality by constant value of shear modulus (deterministic truth), and simulate experiment by measuring the shear stress as the most suitable quantity (depends linearly on parameter). The measurements are preformed in all nodal points (including boundary conditions) obtained by finite element discretization of the domain of consideration with the help of eight-noded quadrilateral elements.

4.1 Plate with hole

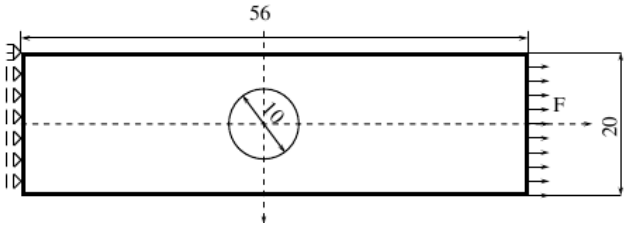

Figure 1: Geometry of the problem: plate with hole

The update procedure is performed as a sequential row of several measurements and updates. In each sequential step the loading is changed by its intensity and sign in prescribed manner. In this particular example the loading changes such that the force is

first of extension type, and then compression. The identification starts by measuring the shear stress Fig. (2) in the sensors positions, assuming the a priori distribution Fig. (3) as a lognormal random field and then updating the parameter to q_a which is in the next update taken as a priori distribution. This new update is characterized by a new loading and hence new measurement set of data. This cycle repeats until the convergence is achieved.

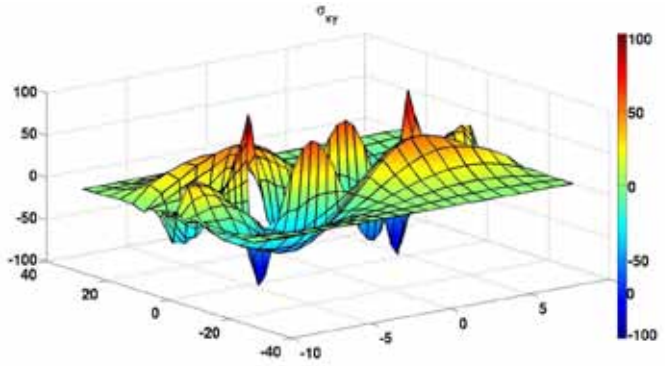

Figure 2: The shear stress as a measurement

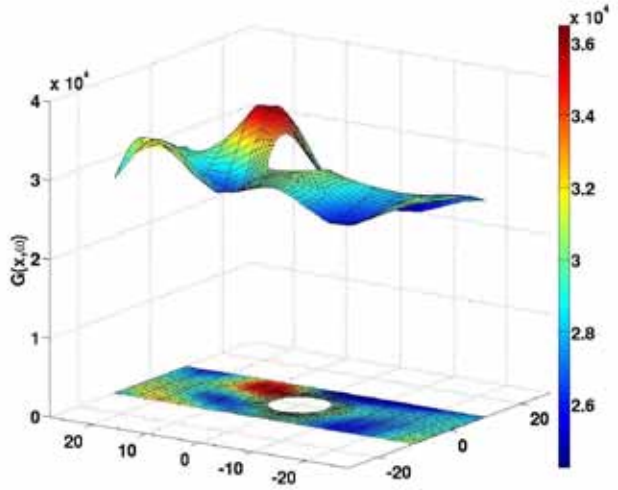

Figure 3: Apriori G - one realisation

The posterior distribution with each update changes in the direction of the truth, which is reflected in the convergence given by a RMSE (root mean squared error) between the

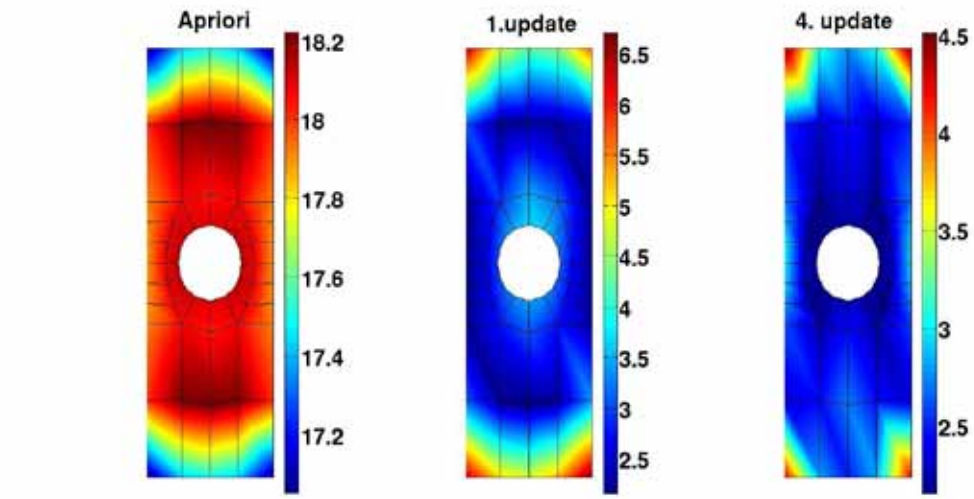

Figure 4: Relative RMSE of variance [%] after 4th update in 10% equally distributed measurement points

PCEs of the posterior $\hat{\boldsymbol{q}}_f^i$ and truth $\hat{\boldsymbol{q}}_t$ in each update i:

$$\varepsilon^i = \frac{\|\hat{\boldsymbol{q}}_f^i - \hat{\boldsymbol{q}}_t\|_{L_2(\Omega)}}{\|\hat{\boldsymbol{q}}_t\|_{L_2(\Omega)}}, \quad i = 1, .., I \tag{8}$$

As one may see in Fig. (4) the error decreases with each update, such that in 4th step one obtains the error circa 2% in almost all points besides the corners where it increases a bit. The possible explanation of such behavior is the existence of the boundary conditions imposed in these nodes.

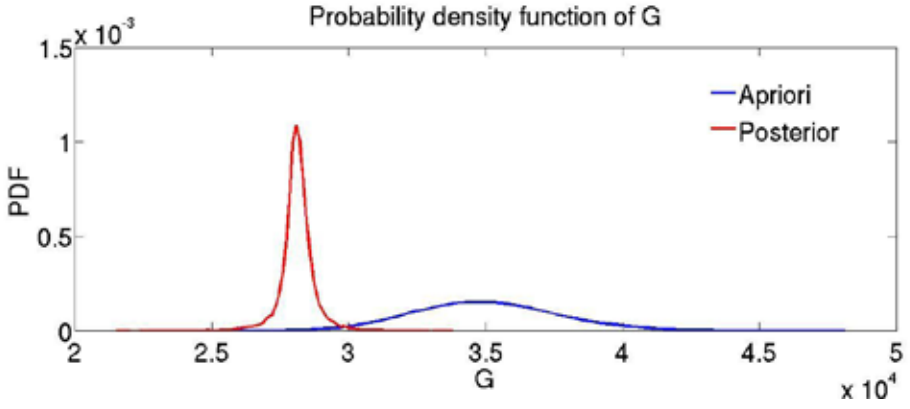

Figure 5: Comparison of apriori and posterior distribution

The comparison of probability density functions of prior and posterior after first update

lead us to the same conclusion, since the posterior is much more narrowed and goes in the direction of the truth which is deterministic.

4.2 Cooke's membrane

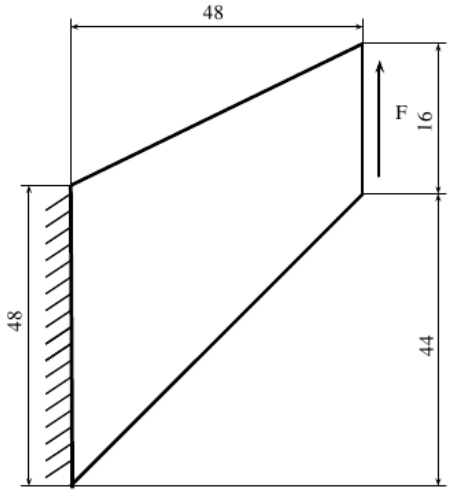

Figure 6: Geometry of the problem: Cooke's membrane

The Cooke's membrane is subjected to load in y direction on the right boundary and constrained on the left as it is shown in Fig. (6). The identification of shear modulus is done in the similar manner as in previous example, by sequential procedure. Thus, the measurement in each update changes since the loading alters according to some prescribed scheme. This change one may see in Fig. (7) from the first up to the third update.

After the third update in Fig. (8) one may notice that the initial lognormal field changes to a uniform value of shear modulus over spatial domain with the small variation on the boundary (see Fig. (9)). The same conclusion is made by calculating the root mean square error as before (see Fig. (10)), as well as comparison of probability density functions, see Fig. (11).

5 CONCLUSION

The mathematical formulation of the stochastic inverse elasto-plastic problem is recast via projection of the minimum variance linear Bayesian estimator onto the polynomial chaos basis. The update requires one solution of the stochastic forward problem via stochastic Galerkin method based on model reduction techniques together with the stochastic closest point projection method. The estimation is purely deterministic and doesn't require sampling at any stage, as well as assumption of linearity in the forward model and Gaussian statistics.

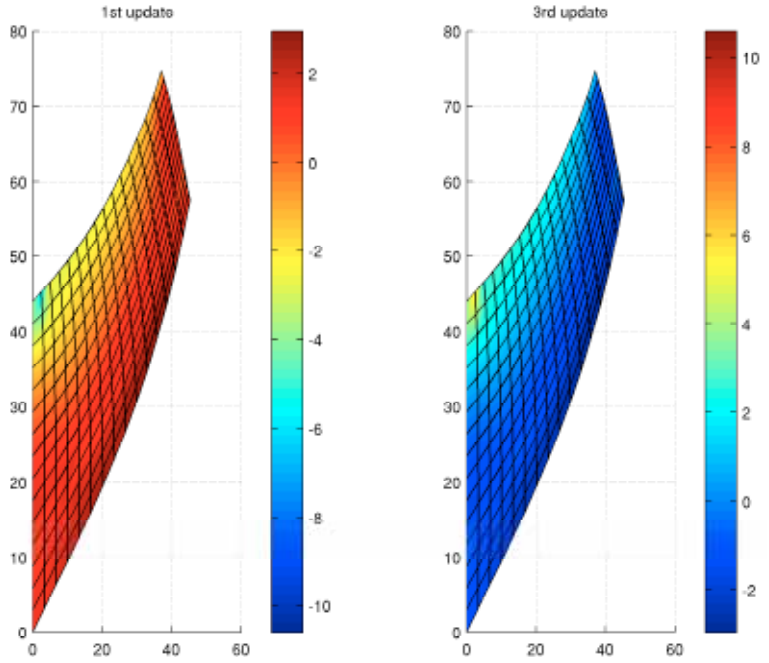

Figure 7: The measurment mean value in a case of plate with hole

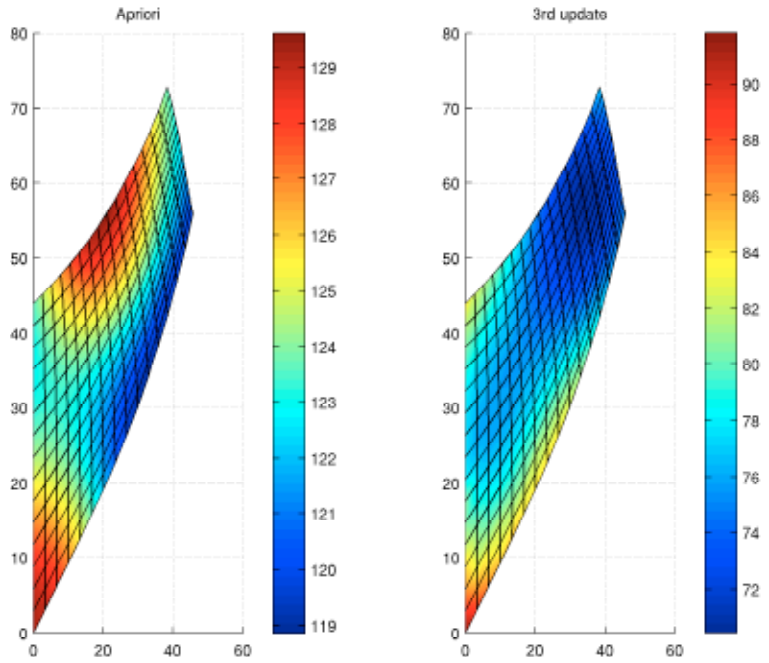

Figure 8: The realisations of apriori of shear modulus and its update

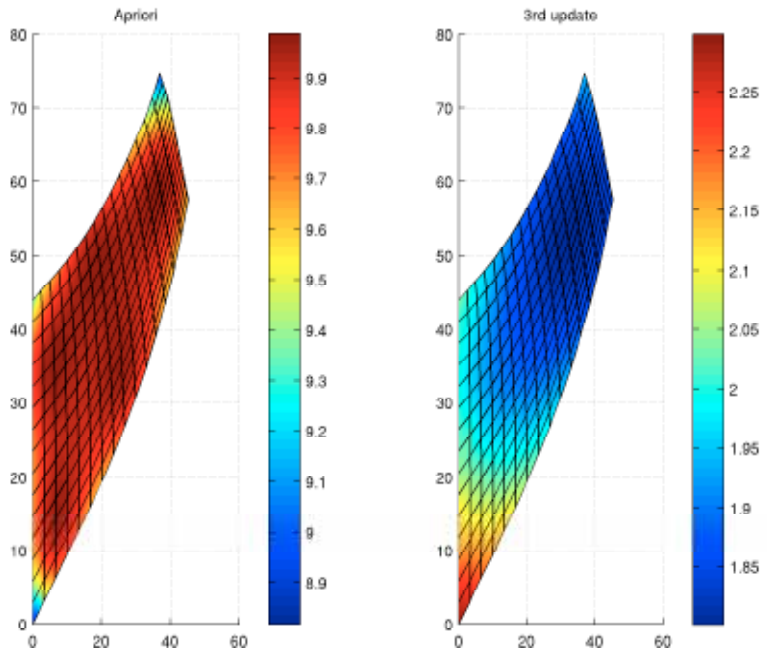

Figure 9: Change of variance of shear modulus from apriori to 3rd update

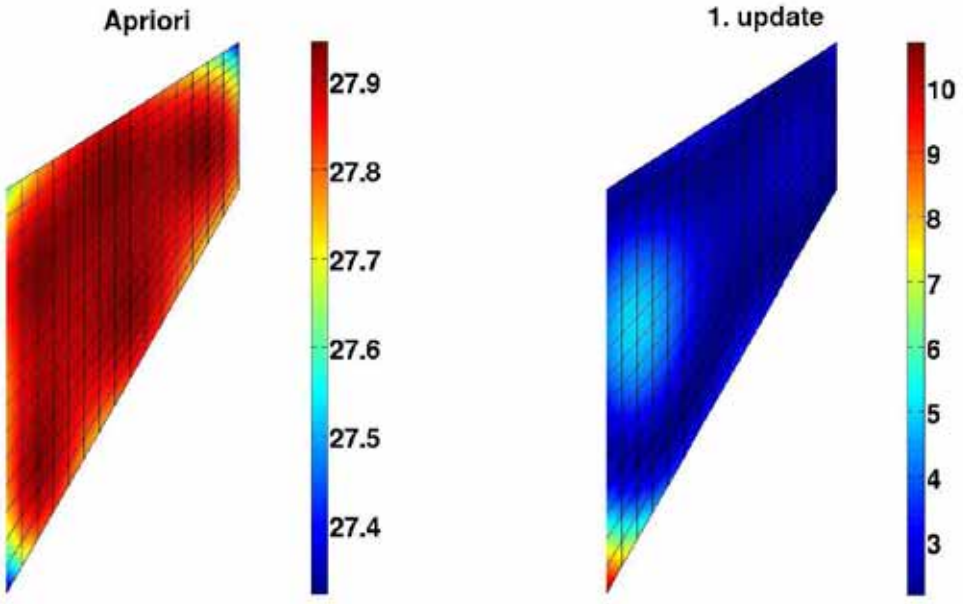

Figure 10: RMSE [%] of variance after first update for the case when mean is larger 30% than truth

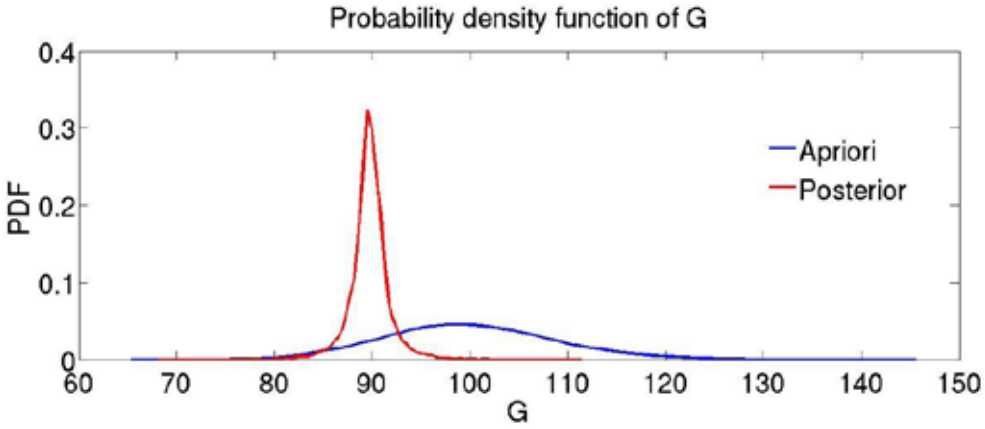

Figure 11: Comparison of apriori and posterior distribution

REFERENCES

[1] Jeffrey L. Anderson. An ensemble adjustment Kalman filter for data assimilation. *Monthly Weather Review*, 129:2884–2903, 2001.

[2] M. Arnst, R. Ghanem, and C. Soize. Identification of Bayesian posteriors for coefficients of chaos expansions. *Journal of Computational Physics*, 229(9):3134 – 3154, 2010.

[3] Craig H. Bishop, Brian J. Etherton, and Sharanya J. Majumdar. Adaptive sampling with the ensemble transform Kalman filter. Part I: Theoretical aspects. *Monthly Weather Review*, 129(3):420–436, March 2001.

[4] Geir Evensen. The ensemble Kalman filter for combined state and parameter estimation. *IEEE Control Systems Magazine*, 29:82–104, 2009.

[5] D. Gamerman and H. F. Lopes. *Markov Chain Monte Carlo: Stochastic Simulation for Bayesian Inference*. Chapman and Hall/CRC, 2006.

[6] Michael Goldstein and David Wooff. *Bayes Linear Statistics - Theory and Methods*. Wiley Series in Probability and Statistics. John Wiley & Sons, Chichester, 2007.

[7] W. Han and B. Daya Reddy. *Plasticity: Mathematical Theory and Numerical Analysis*. Springer, New York, 1999.

[8] S. B. Hazra, H. Class, R. Helmig, and V. Schulz. Forward and inverse problems in modeling of multiphase flow and transport through porous media. *Computational Geosciences*, 8(1):21–47, 2004.

[9] D. Higdon, H. Lee, and C. Holloman. Markov chain Monte Carlo-based approaches for inference in computationally intensive inverse problems. *Bayesian Statistics*, (7):181–197, 2003.

[10] A. Ibrahimbegović. *Nonlinear Solid Mechanics*. Springer, Berlin, 2009.

[11] A. Kučerová and H. G. Matthies. Uncertainty updating in the description of heterogeneous materials. *Technische Mechanik*, 30((1-3)):211–226, 2010.

[12] D. G. Luenberger. *Optimization by Vector Space Methods*. John Wiley and Sons, New York, 1969.

[13] Y. M. Marzouk and D. Xiu. A stochastic collocation approach to Bayesian inference in inverse problems. *Communications in Computational Physics*, 6(4):826–847, 2009.

[14] H. G. Matthies. Stochastic finite elements: Computational approaches to stochastic partial differential equations. *Zeitschrift für Angewandte Mathematik und Mechanik (ZAMM)*, 88(11):849–873, 2008.

[15] H. G. Matthies and B. Rosić. Inelastic Media under Uncertainty: Stochastic Models and Computational Approaches. In *Daya Reddy, IUTAM Bookseries*, volume 11, pages 185–194, 2008.

[16] H. G. Matthies and E. Zander. Solving stochastic systems with low-rank tensor compression. *Linear Algebra and Application, submitted*, 2010.

[17] O. Pajonk, B. Rosić, A. Litvinenko, and H. G. Matthies. A deterministic filter for non-gaussian bayesian estimation. *Physica D: Nonlinear Phenomena, submitted, http://www.digibib.tu-bs.de/?docid=00038994*, 2011.

[18] B. Rosić, A. Litvinenko, O. Pajonk, and H. G. Matthies. Direct bayesian update of polynomial chaos representations. *Journal of Computational Physics, submitted, http://www.digibib.tu-bs.de/?docid=00039000*, 2011.

[19] B. Rosić and H. G. Matthies. Computational approaches to inelastic media with uncertain parameters. *Journal of Serbian Society for Computational Mechanics*, 2:28–43, 2008.

[20] J. C. Simo and T. J. R. Hughes. *Computational Inelasticity*. Springer Verlag, New York, 1998.

[21] A. Tarantola. Popper, Bayes and the inverse problem. *Nature Physics*, 2(8):492–494, August 2006.

[22] Michael K. Tippett, Jeffrey L. Anderson, and Craig H. Bishop. Ensemble square root filters. *Monthly Weather Review*, 131:1485 – 1490, 2003.

XI International Conference on Computational Plasticity. Fundamentals and Applications
COMPLAS XI
E. Oñate, D.R.J. Owen, D. Peric and B. Suárez (Eds)

MULTISCALE MODELLING OF MASONRY STRUCTURES USING DOMAIN DECOMPOSITION TECHNIQUES

K. HEYENS*‡,B. VANDOREN‡ AND L. SCHUEREMANS†

*‡Departement IWT, vakgroep Bouwkunde
Xios Hogeschool Limburg
Universitaire campus gebouw H, B-3590 Diepenbeek, Belgium
e-mail: koen.heyens@xios.be

†Department of Civil Engineering,
KULeuven
Kasteelpark Arenberg 40-bus 2448, B-3001 Heverlee, Belgium
e-mail: luc.schueremans@bwk.kuleuven.be

Key words: computational plasticity, masonry, domain decomposition, FETI, GFEM, cohesive zone

Abstract. This paper describes the application of a domain decomposition technique for multiscale modelling of fracture behaviour in masonry. The use of multiple domains allows for a difference in employed mesh sizes for the macro- and mesoscale. For domains which play a crucial role in the failure process, we apply a mesoscale level meshing, while less critical components can be modelled by a less computationally expensive macroscale mesh. The crack behaviour is modelled by using the GFEM method, while the joint degradation is described using a plasticity based cohesive zone model, with a smooth yield surface. For the purpose of domain decomposition, we propose the use of a FETI method.

1 INTRODUCTION

The design of masonry structures, as it is done today, is still based on codebooks and rules of thumb, which often lead to a lack of control over safety factors and non-optimal structure dimensions. As such, it would be useful to develop reliable numerical tools that predict the behaviour of masonry structures.

The majority of numerical tools currently available for constitutive description of masonry structures are proven to be accurate on small scale structures, but when used on large scale structures, excessive computational effort is required and numerical instabilities occur [14, 7, 5]. Hence, in order to lower the computational cost it is more efficient to focus on regions of the masonry structure where cracks occur. It is also known that the mortar phase is relatively weak, which due to the periodic arrangement of the phases leads

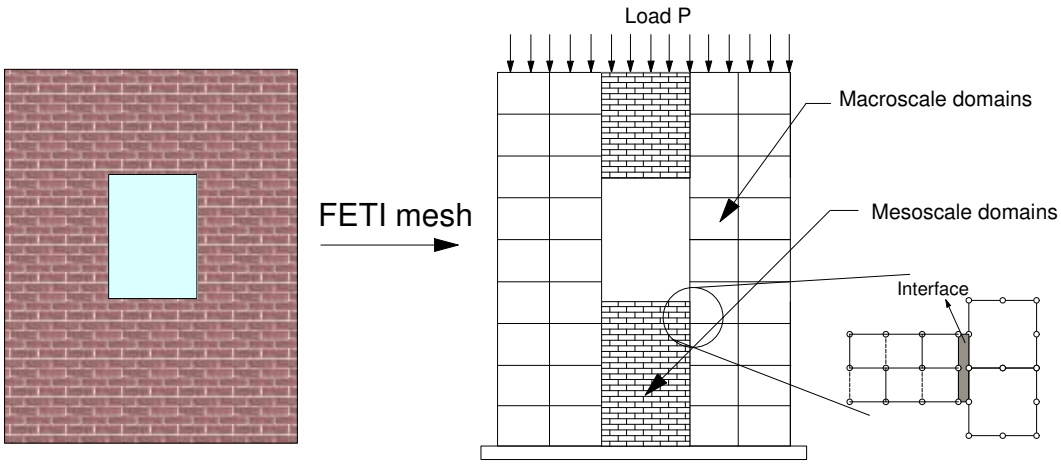

Figure 1: Multiscale approach masonry wall subjected to compression forces

to a stiffness degradation along preferential orientations, i.e. the crack path in masonry (often) follows the joints. A domain decomposition method can be employed to decompose the masonry structure into several domains, and concentrate our computational efforts on the domains which undergo inelastic behaviour.

It is possible to adopt such a technique in two different ways to describe a multiscale model for masonry structures. The first approach consists of initializing the discretized masonry structure as a coarse grid consisting of several domains. Once a domain meets a given criterion, indicating the occurrence of inelastic behaviour, it will be isolated and evaluated on a mesoscale using a finer background mesh. Afterwards, the results from the mesoscale computation will be integrated into the macroscale parent grid using a domain decomposition technique. An other way to use the domain decomposition technique is to define the regions in the discretized structure where possible inelastic behaviour could occur beforehand. These domains will be meshed at mesoscale, while the remainder of the structure will be meshed with a coarse grid on macroscale.

In this contribution the second approach will be presented, as illustrated in Figure 1. As shown in the figure, the mesoscale domains are concentrated under and above the window, since under uniform compression the inelastic behaviour most likely will occur in those regions. The evaluation at macroscale is done with an homogenized stiffness, as described in [14], and the mesoscale crack behaviour is modelled using a discontinuous model based on the Generalized Finite Element Method (GFEM) [18, 10, 5]. Crack growth is given by a plasticity based cohesive zone model, in terms of tractions and displacements. This approach does not constitute a completely new method, but rather an application of domain decomposition techniques on masonry structures, in order to reduce the computational effort and increase the numerical stability within the inelastic regions. The proposed method will serve as a good basis for the future development of

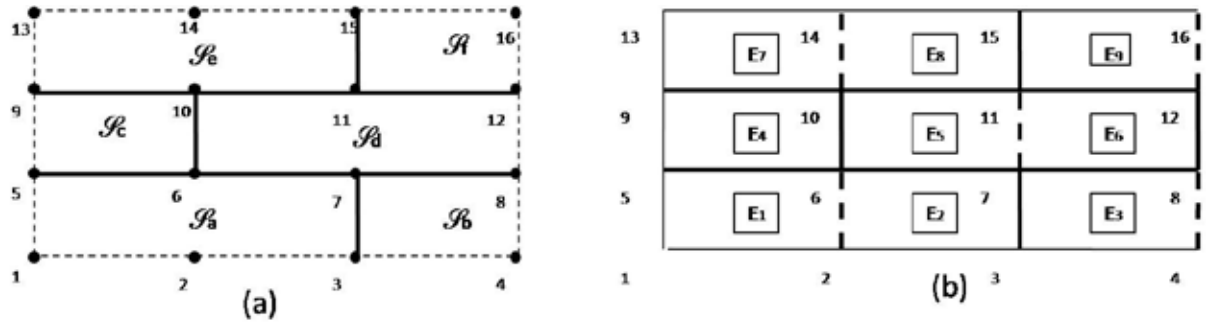

Figure 2: (a) GFEM cells in masonry; (b) background mesh

the automated 'detect-and-refine' approach we have mentioned earlier.

2 THE GENERALIZED FINITE ELEMENT METHOD

The generalized finite element method belongs to the numerical family of discontinuous models. These models are classified as discontinuous, because displacements are represented as discontinuities.
The basic idea of this approach is to enhance the displacement field by discontinuous functions that allow for jumps along the discontinuity surface. A key feature of this method is that the behavior of the crack can be completely captured within the discontinuity, while the surrounding continuum remains elastic. Such a discontinuous function can be added using the partition of unity property of finite element shape functions φ_i [1, 20].

$$\sum_{i=1}^{n} \varphi_i(\boldsymbol{x}) = 1 \qquad \forall \boldsymbol{x} \in \Omega \tag{1}$$

When using GFEM, it is necessary to know the possible locations of the crack path before computation. This results in a topology which consists of a number of cells $\mathscr{S}_i$, defined by possible cracks. Within the partition of unity method, the discontinuity information is processed on the level of a cell [18]. The displacement field for a cell reads

$$\boldsymbol{u}(\boldsymbol{x}) = \hat{\boldsymbol{u}}(\boldsymbol{x}) + \sum_{i=1}^{N_H} \mathscr{H}_i \tilde{\boldsymbol{u}}(\boldsymbol{x}) \tag{2}$$

where: $\hat{\boldsymbol{u}}(\boldsymbol{x})$ equals the regular set of displacements en $\tilde{\boldsymbol{u}}(\boldsymbol{x})$ equals the enhanced set of displacements.

$$\mathscr{H}_i = \begin{cases} 1 & \text{if} \quad \boldsymbol{x} \in \mathscr{S}_i \\ 0 & \text{otherwise} \end{cases} \tag{3}$$

It is logical to use the GFEM to describe crack behaviour in masonry walls, as the topology of a masonry wall is mostly known, and it is easy to fit a background mesh where the joints coincide with boundaries of an element boundary (see Figure 2).

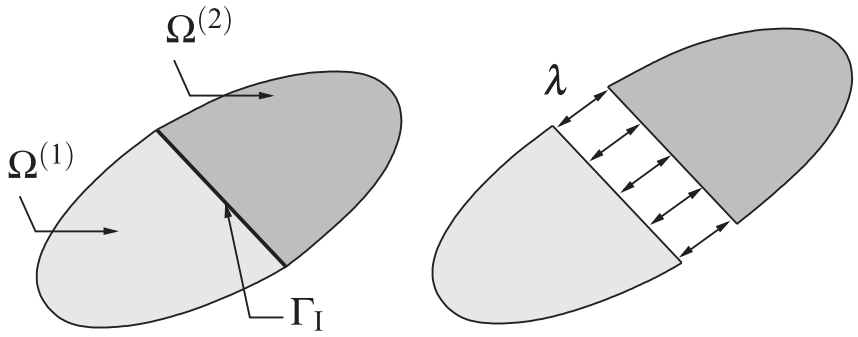

Figure 3: Decomposition in two domains with interface forces λ

3 THE DOMAIN DECOMPOSITION APPROACH

In this section a basic formulation of the Finite Element Tearing and Interconnecting (FETI) method is introduced, a method which belongs to the family of dual domain decomposition methods. Here the given formulation is adopted for a finite element analysis, further details on this method can be found in Farhat et al. [6].

Consider a body divided in two domains ($N_s = 2$) as shown in Figure 3, each domain $\Omega^{(s)}$ has a displacement field $\boldsymbol{u}^{(s)}$ and after discretization the local equilibrium reads,

$$\boldsymbol{K^{(s)}u(x)^{(s)}} = \boldsymbol{f^{(s)}} \tag{4}$$

where (s) is the number of the respective domain, $\boldsymbol{K^{(s)}}$ the stiffness matrix and $\boldsymbol{f^{(s)}}$ the external force vector. For the two domains given in Figure 3, the continuity of the solution field is given by:

$$\boldsymbol{u^{(1)}} = \boldsymbol{u^{(2)}} \qquad \text{at} \qquad \Gamma_I \tag{5}$$

When incorporating the continuity requirement of (5) with (4), the solution reads

$$\begin{bmatrix} \boldsymbol{K^{(1)}} & \boldsymbol{0} & \boldsymbol{B^{(1)^T}} \\ \boldsymbol{0} & \boldsymbol{K^{(2)}} & \boldsymbol{B^{(2)^T}} \\ \boldsymbol{B^{(1)}} & \boldsymbol{B^{(2)}} & \boldsymbol{0} \end{bmatrix} \begin{bmatrix} \boldsymbol{u^{(1)}} \\ \boldsymbol{u^{(2)}} \\ \boldsymbol{\lambda} \end{bmatrix} = \begin{bmatrix} \boldsymbol{f^{(1)}} \\ \boldsymbol{f^{(2)}} \\ \boldsymbol{0} \end{bmatrix} \tag{6}$$

where the matrices $\boldsymbol{B^{(s)}}$ contain the values +1 or -1 at those positions that correspond to the interface of the respective domain $\Omega^{(s)}$, and Lagrange multipliers λ are introduced to enforce the compatibility constraints. Since the domains can be part of the macroscale, where the displacement field is continuous or part of the mesoscale, where a discontinuity can be incorporated in the displacement field [1, 5]. This results in two expressions of the displacement vector,

$$\boldsymbol{u(x)^{(s)}} = \begin{cases} \boldsymbol{\hat{u}(x)^{(s)}} & \text{if x} \in \text{macroscale} \\ \boldsymbol{\hat{u}(x)^{(s)}} + \sum_{i=1}^{N_H} \mathscr{H}_i \boldsymbol{\tilde{u}(x)^{(s)}} & \text{if x} \in \text{mesoscale} \end{cases} \tag{7}$$

To solve the interface problem, we solve this for the local displacement field $\boldsymbol{u(x)^{(s)}}$

$$\boldsymbol{u(x)^{(s)}} = \boldsymbol{K^{(s)^+}} \left(\boldsymbol{f^{(s)}} - \boldsymbol{B^{(s)^T}} \boldsymbol{\lambda} \right) - \boldsymbol{R^{(s)}} \boldsymbol{\alpha^{(s)}} \tag{8}$$

where $\boldsymbol{K^{(s)^+}}$ is the inverse of the stiffness matrix for a domain $\Omega^{(s)}$ with no rigid modes or a generalized inverse if the domain s is floating, in which case $\boldsymbol{R^{(s)}}$ are the rigid body modes. $\boldsymbol{\alpha^{(s)}}$ are the amplitudes of the rigid body modes [13].

4 A PLASTICITY BASED COHESIVE ZONE MODEL

In a cohesive zone model, the fracture behaviour is regarded as a gradual phenomenon in which separation takes place across a cohesive zone. Such a cohesive zone does not represent any physical material, but rather the cohesive forces which occur when material elements are being pulled apart [2, 20].

The constitutive relationship for the cohesive zone is defined in terms of tractions and separations. First, the basic equations of the plasticity theory in the traction space are presented. Next, the proposed material model will be discussed, based on the plasticity yield surface which was proposed in earlier work [9].

4.1 The cohesive zone model

In this study, the plasticity theory is embedded in a finite element environment using a cohesive zone model. Hence, it is necessary to describe the mathematical relation between the tractions $\boldsymbol{T}$ and separations $\boldsymbol{\Delta}$, each with a normal and tangent component. Following classical elasto-plasticity, the total deformation rate vector of a discontinuity can be decomposed in two parts, an elastic and a plastic component:

$$\dot{\boldsymbol{\Delta}} = \dot{\boldsymbol{\Delta}}^{\boldsymbol{e}} + \dot{\boldsymbol{\Delta}}^{\boldsymbol{p}} \tag{9}$$

where the elastic deformation rate is related to the traction rate by the elastic stiffness matrix $\boldsymbol{D}$ as

$$\dot{\boldsymbol{T}} = \boldsymbol{D} \dot{\boldsymbol{\Delta}}^{\boldsymbol{e}} \tag{10}$$

A definition of a yield surface is used to bound the elastic region, and can be used as a fracture criterion. As the constitutive model is expressed in terms of tractions and separations, the yields surface needs to be defined in the traction space $\{T_n, T_t\}$, where T_n stands for the normal component of the traction vector, and T_t for the tangential component of the traction vector. A suitable mathematical description for a smooth yield surface F is given by a cubic Bézier function [9, 19], as illustrated in Figure 4.

4.2 Proposed material model

All simulations of plastic deformation are based on the notion of a yield function f, such that $f < 0$ in the elastic regime, $f = 0$ on the yield locus, and $f > 0$ when plastic

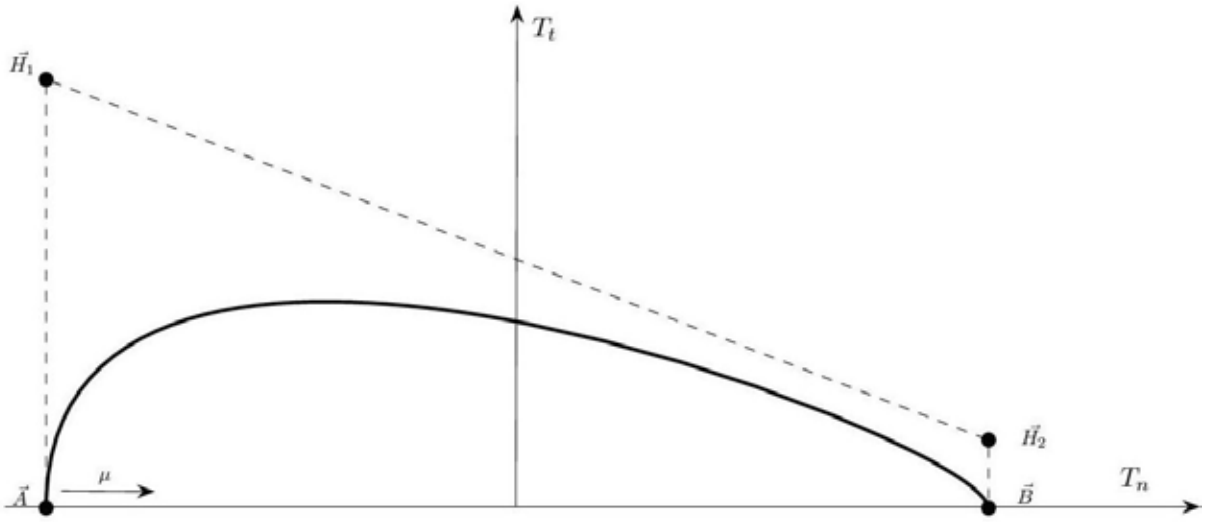

Figure 4: Cubic Bézier curve with two control points $\{\boldsymbol{A}, \boldsymbol{B}\}$ and two hinge points $\{\boldsymbol{H_1}, \boldsymbol{H_2}\}$

deformation occurs. Our employed yield function is described by

$$f(\boldsymbol{T}, \boldsymbol{T^{\mu}}) = \sqrt{T_n^2 + T_t^2} - \sqrt{\left(T_n^{\mu}\right)^2 + \left(T_t^{\mu}\right)^2} \tag{11}$$

In case $f > 0$, the computed traction vector $\boldsymbol{T}^{(t)}$ is located outside the yield surface, and plastic deformation occurs. For the adopted yield surface, its evolution throughout the computation is governed by the decrease of tensile strength, compression strength and cohesion. The decrease of compression strength is not implemented and remains constant in this work, since the influence of the decrease of tensile strength and cohesion in masonry cracking is substantial in comparison with the decrease of compression strength.

The decrease of tensile strength and cohesion are given by the following expressions:

$$f_t = f_t^p \cdot \exp\left[\frac{-\beta_n \cdot f_t^p}{G_f^I} \cdot \Delta_n^{pl}\right] \;;\; \Delta_n^{pl} = \int_0^t \dot{\Delta}_n^{pl} dt \tag{12}$$

$$c = c_r + \left(\frac{C}{c^p} - c_r\right) \cdot \exp\left[\frac{-\beta_t \cdot \frac{C}{c^p}}{G_f^{II}} \cdot (\Delta_t^{pl})\right] \;;\; \Delta_t^{pl} = \int_0^t \dot{\Delta}_t^{pl} dt \tag{13}$$

where f_t^p is the initial tensile strength, G_f^I the mode I fracture energy, G_f^{II} the mode II fracture energy, c^p is the value of the cohesion obtained before plastic deformation occurs, c_r is the residual cohesive strength and $\frac{C}{c^p}$ is the initial cohesive strength. The material parameters $\beta_n$and β_t control the rate of softening for each internal variable. Δ_t^{pl} and Δ_n^{pl} are respectively the tangent- and normal plastic deformations of the displacement vector $\boldsymbol{\Delta}$.

5 IMPLEMENTATION NON-LINEAR ANALYSIS

The algorithms described in the previous sections are implemented in a Matlab® environment. An algorithm outline of the implemented code considering the non-linear analysis with a domain decomposition technique is presented in Table 1.

6 CONCLUSIONS

In this paper, we have presented a multiscale approach to modelling masonry fractures using a domain decomposition technique. The fracture behaviour is based on a plasticity cohesive zone model with a smooth yield surface, and discontinuities are incorporated using the Generalized Finite Element Method. Implementation of the algorithms was done in a Matlab® environment and the domains are chosen in such way that there is a minimal computational effort.

ACKNOWLEDGMENTS

The authors would like to thank the Xios Hogeschool limburg, departement IWT for funding for this work and the KU Leuven, Department of Civil engineering for collaboration in this research.

Algorithm outline of the non-linear conversion analysis

For each loading step Δt do:

1. Initialize solution field $\boldsymbol{\Delta u_0^{(s)}}$ and interface connectivity $\boldsymbol{B^{(s)}}$
2. Compute strain $\Delta\boldsymbol{\epsilon_i^n} \longleftarrow \Delta\boldsymbol{u}_i^{(s)}$ and the displacement jumps $\boldsymbol{\Delta_i} \longleftarrow \Delta\boldsymbol{u}_i^{(s)}$ in the cohesive zones for each integration point n in $\Omega^{(s)}$.
3. Compute stress $\Delta\boldsymbol{\sigma_i^n} \longleftarrow \Delta\boldsymbol{\epsilon_i^n}$ and the tractions $\boldsymbol{T_i} \longleftarrow \boldsymbol{\Delta_i}$ in the cohesive zones for each integration point n in $\Omega^{(s)}$.
   - check if $f < 0$ else plastic deformation occurs
4. Compute internal force vector $\Delta\boldsymbol{f_{int,i}^{(s)}}$
5. Update internal force vector $\boldsymbol{f_{int,i+1}^{(s)}} = \boldsymbol{f_{int,i}^{(s)}} + \Delta\boldsymbol{f_{int,i}^{(s)}}$
6. Apply prescribed displacements or forces.
7. FETI solver
   - compute rigid body modes $\boldsymbol{R^{(s)}}$.
   - compute Lagrange multipliers $\boldsymbol{\lambda_i}$ and the amplitudes $\boldsymbol{\alpha_i^{(s)}}$.
   - update external force vector with interdomain forces $\boldsymbol{f_{ext,t+\Delta_t}^{(s)}} = \boldsymbol{f_{ext,t+\Delta_t}^{(s)}} - \boldsymbol{B^{(s)^T}\lambda_i}$
   - Compute displacements increment $\delta\boldsymbol{u_{i+1}^{(s)}} = \boldsymbol{K_i^{(s)^+}}\left(\boldsymbol{f_{ext,t+\Delta_t}^{(s)}} - \boldsymbol{f_{int,i+1}^{(s)}}\right) - \boldsymbol{R^{(s)}\alpha_i^{(s)}}$
8. Update displacement vector $\boldsymbol{u_{i+1}^{(s)}} = \boldsymbol{\Delta u_i^{(s)}} + \delta\boldsymbol{u_{i+1}^{(s)}}$
9. Assemble domain quantities $\boldsymbol{u_{i+1}^{(s)}}$ in global quantities $\boldsymbol{u_{i+1}}$
10. check for convergence $\parallel \delta\boldsymbol{u_{i+1}} \parallel \leq \epsilon \cdot \parallel \boldsymbol{\Delta u_1} \parallel$ Else go to 2 if criterion is met go to the next loading step

Table 1: Algorithm outline of the non-linear conversion analysis

References

[1] I. Babuška and J. M. Melenk. the Partition of Unity Method. *International Journal for Numerical Methods in Engineering*, 40(4):727–758, February 1997.

[2] R. Borst, M. Gutiérrez, Garth N. Wells, J. Remmers, and H. Askes. Cohesive-zone models, higher-order continuum theories and reliability methods for computational failure analysis. *International Journal for Numerical Methods in Engineering*, 60(1):289–315, May 2004.

[3] K. De Proft. *Combined experimental - computational study to discrete fracture of brittle materials*. PhD thesis, Vrije Universiteit Brussel, 2003.

[4] K. De Proft. Modelling masonry using the partition of unity method. In *VIII International Conference on Computational Plasticity*, 2005.

[5] K. De Proft, K. Heyens, and L.J. Sluys. Mesoscopic modelling of masonry failure. *Proceedings of the ICE - Engineering and Computational Mechanics*, 164(1):41–46, March 2011.

[6] C. Farhat and F. Roux. A method of finite element tearing and interconnecting and its parallel solution algorithm. *International Journal for Numerical Methods in Engineering*, 32(6):1205–1227, October 1991.

[7] G. Giambanco. Numerical analysis of masonry structures via interface models. *Computer Methods in Applied Mechanics and Engineering*, 190(49-50):6493–6511, October 2001.

[8] M. Hestenes and E. Stiefel. Methods of Conjugate Gradients for Solving Linear Systems 1. *Journal Of Research Of The National Bureau Of Standards*, 49(6), 1952.

[9] K. Heyens, K. De De Proft, and L. J. Sluys. A smooth yield surface based on interpolation of bezier curves for masonry modelling. In *X International Conference on Computational Plasticity*, pages 2–5, 2009.

[10] K. Heyens and L. Schueremans. A meso-scale model for masonry. Technical report, KULeuven, 2010.

[11] B. Kim, Y. Sakai, and A. Sakoda. Modeling Masonry Structures using the Applied Element Method. *Young*, pages 581–584, 2003.

[12] O. Lloberas-Valls, D. Rixen, A. Simone, and L. J. Sluys. Applications of domain decomposition techniques for the multiscale modeling of softening materials. *International Journal*, pages 1–4, 2009.

[13] O. Lloberas-Valls, D.J. Rixen, A. Simone, and L.J. Sluys. Domain decomposition techniques for the efficient modeling of brittle heterogeneous materials. *Computer Methods in Applied Mechanics and Engineering*, 200(13-16):1577–1590, March 2011.

[14] P. Lourenço. *Computational strategies for masonry structures*. PhD thesis, Delft University of Technology, 1996.

[15] J. Oliver. Strong discontinuities and continuum plasticity models: the strong discontinuity approach. *International Journal of Plasticity*, 15(3):319–351, March 1999.

[16] J. Oliver. From continuum mechanics to fracture mechanics: the strong discontinuity approach. *Engineering Fracture Mechanics*, 69(2):113–136, January 2002.

[17] D. Rixen. Extended preconditioners for the FETI method applied to constrained problems. *International Journal for Numerical Methods in Engineering*, 54(1):1–26, May 2002.

[18] A. Simone, C. a. Duarte, and E. Van der Giessen. A Generalized Finite Element Method for polycrystals with discontinuous grain boundaries. *International Journal for Numerical Methods in Engineering*, 67(8):1122–1145, August 2006.

[19] H. Vegter and A. Vandenboogaard. A plane stress yield function for anisotropic sheet material by interpolation of biaxial stress states. *International Journal of Plasticity*, 22(3):557–580, March 2006.

[20] G. N. Wells and L. J. Sluys. A new method for modelling cohesive cracks using finite elements. *International Journal for Numerical Methods in Engineering*, (June 2000):2667–2682, 2001.

XI International Conference on Computational Plasticity. Fundamentals and Applications
COMPLAS XI
E. Oñate, D.R.J. Owen, D. Peric and B. Suárez (Eds)

TWO-SCALE PARAMETER IDENTIFICATION FOR HETEROGENEOUS ELASTOPLASTIC MATERIALS

U. SCHMIDT*, J. MERGHEIM AND P. STEINMANN

*Chair for Applied Mechanics
University of Erlangen-Nuremberg
Egerlandstr. 5, 91058 Erlangen, Germany
e-mail: ulrike.schmidt@ltm.uni-erlangen.de
www.ltm.uni-erlangen.de

Key words: Homogenization, Parameter Identification, Inverse Problem, Multi-Scale, Computational Plasticity

Abstract. The aim of this paper is to describe a method for identifying micro material parameters using only macroscopic experimental data. The FE^2 method is used to model the behavior of the complex materials with heterogeneous micro-structure. The resulting least squares problem, with the difference of the simulated and the measured macroscopic data in the objective function, is minimized using gradient-based optimization algorithms with respect to the microscopic material parameters. The gradient information is derived analytically within the discretized scheme.

1 INTRODUCTION

Advanced materials are characterized by their heterogeneity and diverse functionality at multiple scales. In order to use and employ these new materials and exploit their whole potential a good understanding of the functioning and mechanism is necessary. Mechanical modeling of heterogeneous materials is an essential part of this, but still presents a challenge for computational mechanics. Computational homogenization is designed to handle heterogeneity at different scales.

The concept of (computational) homogenization requires separated scales, that means macro phenomena appear on a much larger length scale than the micro scale and its phenomena. Thus the material behavior of each macroscopic point is determined by an underlying microscopic domain. It is assumed that there exists a subdomain of finite volume on the micro scale, which is representative for the mechanical behavior of the entire microscopic domain, thus often called representative volume element (RVE). In contrast to the macro scale, the material behavior on the micro scale is determined directly by a constitutive law and the micro material parameters. The mechanical equilibrium equations at macro and micro scale are further complemented by a scale linking condition,

often called macro homogeneity condition. An appropriate choice of the boundary condition on the microscopic scale leads to the formulation for the macroscopic stresses and strains as the volumetric means (or more general, some adequate boundary integrals) of their microscopic counterparts.

Since the micro material parameters are an important ingredient for this two-scale simulation, knowledge of the parameters and its acquisition is quite an important topic. Classical parameter identification and its macroscopic experiments are well established and one might want to utilize this experience, when given the task to identify microscopic material parameters. Ultimately, the task at hand is to identify microscopic material parameters using only macroscopic experiments.

The identification of micro parameters in a two-scale homogenization problem is also investigated in [1, 2, 3], using numerical sensitivities or gradient-free optimization techniques together with miscellaneous homogenization techniques. This paper couples classical parameter identification [4] and computational homogenization, more precisely the FE^2 method [5]. Gradient-based optimization is used to solve the resulting two-scale parameter identification problem.

In a previous work [6] a two-scale parameter identification using analytical gradient-information was investigated for elasticity, which yields simplifications and less computational costs compared to the present extension to plasticity. The main focus of this work is on the derivation of the gradient information in a two-scale FE scheme.

The paper is structured as follows: In section 2 a short overview of the direct problem, the FE^2 method and a fix of notation is given. In section 3 the two-scale parameter identification problem is defined and the gradient information derived. An example in section 4 illustrates the functionality of the method. The paper is concluded in the last section with a discussion and an outlook on further investigation.

2 DIRECT PROBLEM

For the equilibrium at the macro domain $\bar{\Omega}$ we have a standard quasi-static problem (1) with body forces $\bar{\mathbf{b}}$ and stresses $\bar{\boldsymbol{\sigma}}$ and adequate boundary conditions. Herein macroscopic quantities are marked by an overbar. At the micro scale neglecting body forces leads to the equilibrium equation (2) in the micro domain $\Omega(\bar{\mathbf{X}})$ at the macroscopic point $\bar{\mathbf{X}}$. The continuous formulation is complemented by the macro homogeneity condition (4). The micro boundary condition on e.g. the displacements $\mathbf{u}$ (3) links the macro strain $\bar{\boldsymbol{\varepsilon}}$ to the microscopic scale. The up-scaling of the micro stresses leads to the definition of the macro stresses (5) as the boundary integral of the dyadic product of the reference point

and the tractions $\mathbf{t}$ at the micro scale. In summary:

$$\nabla \cdot \bar{\boldsymbol{\sigma}} = \bar{\mathbf{b}} \qquad \text{in } \bar{\Omega} \quad \text{with } \bar{\mathbf{u}}|_{\partial\bar{\Omega}_D} = \bar{\mathbf{u}}_p,\ (\bar{\boldsymbol{\sigma}} \cdot \bar{\mathbf{n}})|_{\partial\bar{\Omega}_N} = \bar{\mathbf{t}}_p \tag{1}$$

$$\nabla \cdot \boldsymbol{\sigma} = \mathbf{0} \qquad \text{in } \Omega(\bar{\mathbf{X}}) \quad \text{with appropriate b.c., e.g.} \tag{2}$$

$$\mathbf{u} = \mathbf{X} \cdot \bar{\boldsymbol{\varepsilon}} \qquad \text{on } \partial\Omega(\bar{\mathbf{X}}) \quad \text{(down-scaling)} \tag{3}$$

$$(\delta\bar{\boldsymbol{\varepsilon}} : \bar{\boldsymbol{\sigma}})(\bar{\mathbf{X}}) = \int_{\Omega(\bar{\mathbf{X}})} \delta\boldsymbol{\varepsilon} : \boldsymbol{\sigma}\, \mathrm{d}V \tag{4}$$

$$\bar{\boldsymbol{\sigma}}(\bar{\mathbf{X}}) = \int_{\partial\Omega(\bar{\mathbf{X}})} \mathbf{X} \otimes \mathbf{t}\, \mathrm{d}A \qquad \text{(up-scaling)} \tag{5}$$

The material behavior on the micro scale is modeled by the common von Mises plasticity for small strains with linear isotropic hardening, whereas the material behavior on the macro scale is solely determined by the micro scale and has no constitutive law of its own. The micro material parameters are compression modulus K and shear modulus μ for the elastic part and yield stress σ_Y and hardening modulus h for the plastic part. For the convenience in the subsequent analysis the parameters are summarized in vector $\boldsymbol{\alpha} = (K, \mu, \sigma_Y, h)$.

Application of the standard FE^2 method [5] results in the vectorial residuals $\bar{\mathbf{R}}(\bar{\mathbf{u}}(\boldsymbol{\alpha}), \boldsymbol{\alpha})$ and $\mathbf{R}(\mathbf{u}(\bar{\boldsymbol{\varepsilon}}(\boldsymbol{\alpha}), \boldsymbol{\alpha}), \boldsymbol{\alpha})$ on the macro and micro scale, respectively. The residuals vanish in equilibrium (6), (7). The discrete down-scaling (8) is now defined at each boundary node j of the RVE. The discrete macroscopic stresses can be computed as the sum over the boundary nodes of the discrete quantities (9).

After application of the FE^2 method, the following discrete equations for the direct problem are important for the parameter identification:

$$\bar{\mathbf{R}}(\bar{\mathbf{u}}(\boldsymbol{\alpha}), \boldsymbol{\alpha}) = \mathbf{0} \tag{6}$$

$$\mathbf{R}(\mathbf{u}(\bar{\boldsymbol{\varepsilon}}(\boldsymbol{\alpha}), \boldsymbol{\alpha}), \boldsymbol{\alpha}) = \mathbf{0} \tag{7}$$

$$\mathbf{u}_j = \mathbf{X}_j \cdot \bar{\boldsymbol{\varepsilon}}(\boldsymbol{\alpha}) \tag{8}$$

$$\bar{\boldsymbol{\sigma}} = \sum_j \mathbf{X}_j \otimes \mathbf{f}_j \tag{9}$$

A short remark on the microscopic boundary conditions: There are other appropriate choices besides the 'linear displacement' boundary condition given here. The 'periodic' (periodic fluctuations and anti-periodic tractions) boundary condition is often chosen. However, the resulting discretized problem can be transformed in such a way that the structure is the same as for the system resulting from the 'linear displacement' boundary condition. After the transformation of the system to contain only the independent nodes one has prescribed displacements $\mathbf{u}_J = \mathbf{X}_J \cdot \bar{\boldsymbol{\varepsilon}}$ at the nodes J spanning the RVE, while the forces on the remaining nodes vanish.

3 INVERSE PROBLEM

3.1 Problem formulation

The objective function measures the difference between simulated and measured displacements $\bar{\mathbf{u}}$ and forces $\bar{\mathbf{f}}$ of the macro scale. Both contributions have weighting factors, w_u and w_f, to compensate for dimension differences.

$$f = w_u \sum_i \|\bar{\mathbf{u}}_i(\boldsymbol{\alpha}) - \bar{\mathbf{u}}_i^{\text{measured}}\|^2 + w_f \sum_j \|\bar{\mathbf{f}}_j(\boldsymbol{\alpha}) - \bar{\mathbf{f}}_j^{\text{measured}}\|^2 \tag{10}$$

Displacements and forces can be measured at different points, which is indicated by the different indices i and j. The goal is to identify the microscopic material parameters, which minimize the difference for the given data. Then the task at hand can be described as a minimization problem under certain constraints, namely that the material parameters are feasible and the mechanical equilibria on micro and macro scale are satisfied.

$$\min f(\boldsymbol{\alpha}) \quad \text{s.t. } \boldsymbol{\alpha} \text{ is feasible and } \bar{\mathbf{u}}, \mathbf{u} \text{ in equilibrium} \tag{11}$$

The model with the identified parameters can be validated if the objective function is sufficiently small also for a separate data set of measured displacements and forces resulting from a different experiment.

3.2 Gradient information

In order to employ gradient-based optimization techniques to minimize the objective function, the gradient information is required. Due to better convergence behavior and lower computational costs the analytical derivation is preferred over a numerical calculation, e.g. using finite differences. The necessary gradient information is calculated as a total derivative of the objective function with respect to the parameter vector $\boldsymbol{\alpha}$, denoted by $\frac{\mathrm{d}}{\mathrm{d}\boldsymbol{\alpha}}$.

$$\frac{\mathrm{d}f}{\mathrm{d}\boldsymbol{\alpha}} = w_u \sum_i (\bar{\mathbf{u}}_i(\boldsymbol{\alpha}) - \bar{\mathbf{u}}_i^{\text{measured}}) \cdot \frac{\mathrm{d}\bar{\mathbf{u}}_i(\boldsymbol{\alpha})}{\mathrm{d}\boldsymbol{\alpha}} + w_f \sum_j (\bar{\mathbf{f}}_j(\boldsymbol{\alpha}) - \bar{\mathbf{f}}_j^{\text{measured}}) \cdot \frac{\mathrm{d}\bar{\mathbf{f}}_j(\boldsymbol{\alpha})}{\mathrm{d}\boldsymbol{\alpha}} \tag{12}$$

A look at the macroscopic residual $\bar{\mathbf{R}}(\bar{\mathbf{u}}(\boldsymbol{\alpha}), \boldsymbol{\alpha}) = \bar{\mathbf{R}}^{\text{int}}(\bar{\mathbf{u}}(\boldsymbol{\alpha}), \boldsymbol{\alpha}) - \bar{\mathbf{R}}^{\text{ext}}(\boldsymbol{\alpha}) = \mathbf{0}$, consisting of an internal part $\bar{\mathbf{R}}^{\text{int}}$ and an external part $\bar{\mathbf{R}}^{\text{ext}}$, is necessary in order to determine the derivatives of the simulated quantities. The force term $\mathbf{f}_j$ in the objective function incorporates the external forces contained in $\bar{\mathbf{R}}^{\text{ext}}$ in an way appropriate to the experiments and available measurements. The degrees of freedom (DOFs) of the macroscopic residual are partitioned into prescribed displacement DOFs (p) and remaining DOFs (r). Here the remaining DOFs contain DOFs at internal nodes, where the body forces are prescribed and DOFs at the boundary, where tractions are prescribed. The vectorial residual at the macro scale is differentiated w.r.t. the material parameters, the partial derivatives

are denoted as $\frac{\partial}{\partial \bar{\mathbf{u}}}$ and $\frac{\partial}{\partial \boldsymbol{\alpha}}$, respectively. The assumption, that the prescribed terms are independent of the material parameters, i.e. $\frac{\mathrm{d}\bar{\mathbf{u}}_p}{\mathrm{d}\boldsymbol{\alpha}} = \mathbf{0}$, $\frac{\mathrm{d}\bar{\mathbf{R}}_r^{\mathrm{ext}}}{\mathrm{d}\boldsymbol{\alpha}} = \mathbf{0}$, finally leads to

$$\mathbf{0} = \frac{\partial \bar{\mathbf{R}}_p^{\mathrm{int}}}{\partial \bar{\mathbf{u}}_r} \cdot \frac{\mathrm{d}\bar{\mathbf{u}}_r}{\mathrm{d}\boldsymbol{\alpha}} + \frac{\partial \bar{\mathbf{R}}_p^{\mathrm{int}}}{\partial \boldsymbol{\alpha}} - \frac{\mathrm{d}\bar{\mathbf{R}}_p^{\mathrm{ext}}}{\mathrm{d}\boldsymbol{\alpha}} \tag{13}$$

$$\mathbf{0} = \frac{\partial \bar{\mathbf{R}}_r^{\mathrm{int}}}{\partial \bar{\mathbf{u}}_r} \cdot \frac{\mathrm{d}\bar{\mathbf{u}}_r}{\mathrm{d}\boldsymbol{\alpha}} + \frac{\partial \bar{\mathbf{R}}_r^{\mathrm{int}}}{\partial \boldsymbol{\alpha}} \tag{14}$$

With the assumption that $\bar{\mathbf{K}}_{rr} := \frac{\partial \bar{\mathbf{R}}_r^{\mathrm{int}}}{\partial \bar{\mathbf{u}}_r}$, a part of the stiffness matrix of the direct problem, is regular, we can calculate the derivative of the displacements w.r.t. the material parameters:

$$\frac{\mathrm{d}\bar{\mathbf{u}}_p}{\mathrm{d}\boldsymbol{\alpha}} = \mathbf{0}, \quad \frac{\mathrm{d}\bar{\mathbf{u}}_r}{\mathrm{d}\boldsymbol{\alpha}} = -\bar{\mathbf{K}}_{rr}^{-1} \cdot \frac{\partial \bar{\mathbf{R}}_r^{\mathrm{int}}}{\partial \boldsymbol{\alpha}} \tag{15}$$

Furthermore, one can calculate the total derivative of the macroscopic external forces from (13) using $\bar{\mathbf{K}}_{pr} := \frac{\partial \bar{\mathbf{R}}_p^{\mathrm{int}}}{\partial \bar{\mathbf{u}}_r}$ and equation (15) as

$$\frac{\mathrm{d}\bar{\mathbf{R}}_r^{\mathrm{ext}}}{\mathrm{d}\boldsymbol{\alpha}} = \mathbf{0}, \quad \frac{\mathrm{d}\bar{\mathbf{R}}_p^{\mathrm{ext}}}{\mathrm{d}\boldsymbol{\alpha}} = \frac{\partial \bar{\mathbf{R}}_p^{\mathrm{int}}}{\partial \boldsymbol{\alpha}} - \bar{\mathbf{K}}_{pr} \cdot \bar{\mathbf{K}}_{rr}^{-1} \cdot \frac{\partial \bar{\mathbf{R}}_r^{\mathrm{int}}}{\partial \boldsymbol{\alpha}} \tag{16}$$

Now it can be seen, that the determination of the derivatives is similar to solving the linearized direct problem with an artificial load $\frac{\partial \bar{\mathbf{R}}^{\mathrm{int}}}{\partial \boldsymbol{\alpha}}$. In order to construct this artificial load vector, the partial derivative of the macroscopic stresses w.r.t. microscopic parameters will be determined in the following. The element-wise contributions to the internal residual consist of the derivatives of the macro shape functions, summarized in the B-matrix $\bar{\mathbf{B}}_e^T$ (independent of material parameters) and the macro stresses $\bar{\boldsymbol{\sigma}}(\bar{\boldsymbol{\varepsilon}}, \boldsymbol{\alpha})|_e$

$$\frac{\partial \bar{\mathbf{R}}^{\mathrm{int}}(\bar{\mathbf{u}}, \boldsymbol{\alpha})|_e}{\partial \boldsymbol{\alpha}} = \int_{\bar{\Omega}_e} \bar{\mathbf{B}}_e^T \cdot \frac{\partial \bar{\boldsymbol{\sigma}}(\bar{\boldsymbol{\varepsilon}}, \boldsymbol{\alpha})|_e}{\partial \boldsymbol{\alpha}} \mathrm{d}V \tag{17}$$

In the classical one scale parameter identification the derivative of the stresses can be obtained by differentiating the constitutive law. However, the use of a two-scale modeling scheme in the present work necessitates further calculations at this point. By definition (9) we calculate the macro stresses as the sum of dyadic products of the reference position and the reaction forces at boundary nodes and thus its derivative can be expressed as

$$\frac{\partial \bar{\boldsymbol{\sigma}}(\bar{\boldsymbol{\varepsilon}}, \boldsymbol{\alpha})}{\partial \boldsymbol{\alpha}} = \sum_j \mathbf{X}_j \otimes \frac{\partial \mathbf{f}_j(\bar{\boldsymbol{\varepsilon}}, \boldsymbol{\alpha})}{\partial \boldsymbol{\alpha}} \tag{18}$$

Clearly, it is necessary to calculate the derivatives at the micro scale. Starting once again with the vectorial residual, but now for the microscopic problem, and its total derivative w.r.t. the material parameters, we use the partitioning into prescribed displacement DOFs and prescribed force DOFs. An illustration is given in figure 1.

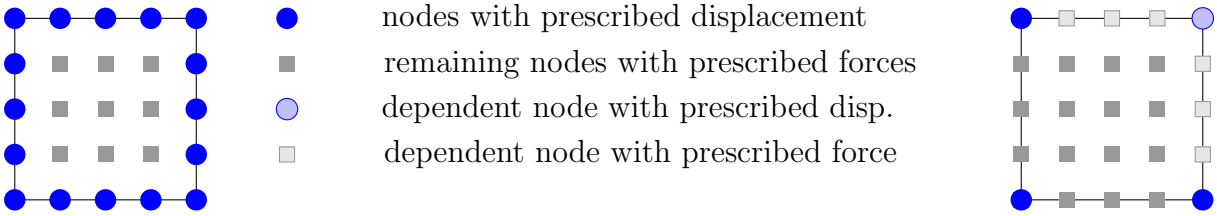

Figure 1: Schematic distribution of prescribed displacements/forces for 'linear displacement' (left) and 'periodic' (right) boundary conditions in 2D

On the micro scale the prescribed forces do not depend on the material parameters, but the prescribed displacements do. The prescribed displacements on the micro scale depend on the macro strain and therefore on the material parameters. Their derivative follows from equation (8) as

$$\frac{\mathrm{d}\mathbf{u}_p}{\mathrm{d}\boldsymbol{\alpha}} = \mathbf{X}_p \cdot \frac{\mathrm{d}\bar{\boldsymbol{\varepsilon}}}{\mathrm{d}\boldsymbol{\alpha}}. \tag{19}$$

Therefore, the total derivative of the micro residual can be expressed as

$$\mathbf{0} = \frac{\mathrm{d}\mathbf{R}}{\mathrm{d}\boldsymbol{\alpha}} = \frac{\partial \mathbf{R}^{\mathrm{int}}}{\partial \mathbf{u}} \cdot \frac{\mathrm{d}\mathbf{u}}{\mathrm{d}\boldsymbol{\alpha}} + \frac{\partial \mathbf{R}^{\mathrm{int}}}{\partial \boldsymbol{\alpha}} - \frac{\mathrm{d}\mathbf{R}^{\mathrm{ext}}}{\mathrm{d}\boldsymbol{\alpha}} \tag{20}$$

$$= \begin{pmatrix} \mathbf{K}_{pp} & \mathbf{K}_{pr} \\ \mathbf{K}_{rp} & \mathbf{K}_{rr} \end{pmatrix} \cdot \begin{pmatrix} \mathbf{X}_p \cdot \frac{\mathrm{d}\bar{\boldsymbol{\varepsilon}}}{\mathrm{d}\boldsymbol{\alpha}} \\ \frac{\mathrm{d}\mathbf{u}_r}{\mathrm{d}\boldsymbol{\alpha}} \end{pmatrix} + \begin{pmatrix} \frac{\partial}{\partial \boldsymbol{\alpha}} \mathbf{R}_p^{\mathrm{int}} \\ \frac{\partial}{\partial \boldsymbol{\alpha}} \mathbf{R}_r^{\mathrm{int}} \end{pmatrix} - \begin{pmatrix} \frac{\mathrm{d}}{\mathrm{d}\boldsymbol{\alpha}} \mathbf{R}_p^{\mathrm{ext}} \\ \mathbf{0} \end{pmatrix}. \tag{21}$$

The derivative of the internal residual w.r.t. the displacement $\frac{\partial \mathbf{R}^{\mathrm{int}}}{\partial \mathbf{u}}$ is the stiffness matrix $\mathbf{K}$ of the direct micro problem, containing the submatrices $\mathbf{K}_{pp}, \mathbf{K}_{pr}, \mathbf{K}_{rp}, \mathbf{K}_{rr}$ related to prescribed or remaining nodes, respectively. One can reformulate the second line associated with the prescribed force DOFs in (21) by using the assumption that $\mathbf{K}_{rr}$ is regular and arrive at an expression for the total derivative of the displacements.

$$\mathbf{0} = \mathbf{K}_{rp} \cdot \mathbf{X}_p \cdot \frac{\mathrm{d}\bar{\boldsymbol{\varepsilon}}}{\mathrm{d}\boldsymbol{\alpha}} + \mathbf{K}_{rr} \cdot \frac{\mathrm{d}\mathbf{u}_r}{\mathrm{d}\boldsymbol{\alpha}} + \frac{\partial \mathbf{R}_r^{\mathrm{int}}}{\partial \boldsymbol{\alpha}} \tag{22}$$

$$\Rightarrow \frac{\mathrm{d}\mathbf{u}_r}{\mathrm{d}\boldsymbol{\alpha}} = -\mathbf{K}_{rr}^{-1} \cdot \left(\mathbf{K}_{rp} \cdot \mathbf{X}_p \cdot \frac{\mathrm{d}\bar{\boldsymbol{\varepsilon}}}{\mathrm{d}\boldsymbol{\alpha}} + \frac{\partial \mathbf{R}_r^{\mathrm{int}}}{\partial \boldsymbol{\alpha}} \right) \tag{23}$$

Inserting this in the first line of (21) and reordering of the terms leads to

$$\frac{\mathrm{d}\mathbf{R}_p^{\mathrm{ext}}}{\mathrm{d}\boldsymbol{\alpha}} = \mathbf{K}_{pp} \cdot \mathbf{X}_p \cdot \frac{\mathrm{d}\bar{\boldsymbol{\varepsilon}}}{\mathrm{d}\boldsymbol{\alpha}} - \mathbf{K}_{pr} \cdot \mathbf{K}_{rr}^{-1} \cdot \left(\mathbf{K}_{rp} \cdot \mathbf{X}_p \cdot \frac{\mathrm{d}\bar{\boldsymbol{\varepsilon}}}{\mathrm{d}\boldsymbol{\alpha}} + \frac{\partial \mathbf{R}_r^{\mathrm{int}}}{\partial \boldsymbol{\alpha}} \right) + \frac{\partial \mathbf{R}_p^{\mathrm{int}}}{\partial \boldsymbol{\alpha}} \tag{24}$$

$$= \left(\mathbf{K}_{pp} - \mathbf{K}_{pr} \cdot \mathbf{K}_{rr}^{-1} \cdot \mathbf{K}_{rp} \right) \cdot \mathbf{X}_p \cdot \frac{\mathrm{d}\bar{\boldsymbol{\varepsilon}}}{\mathrm{d}\boldsymbol{\alpha}} - \mathbf{K}_{pr} \cdot \mathbf{K}_{rr}^{-1} \cdot \frac{\partial \mathbf{R}_r^{\mathrm{int}}}{\partial \boldsymbol{\alpha}} + \frac{\partial \mathbf{R}_p^{\mathrm{int}}}{\partial \boldsymbol{\alpha}} \tag{25}$$

When we express $\frac{\mathrm{d}\mathbf{R}_p^{\mathrm{ext}}}{\mathrm{d}\boldsymbol{\alpha}}$ by means of partial derivatives

$$\frac{\mathrm{d}\mathbf{R}_p^{\mathrm{ext}}}{\mathrm{d}\boldsymbol{\alpha}} = \frac{\partial \mathbf{R}_p^{\mathrm{ext}}}{\partial \bar{\boldsymbol{\varepsilon}}} \cdot \frac{\mathrm{d}\bar{\boldsymbol{\varepsilon}}}{\mathrm{d}\boldsymbol{\alpha}} + \frac{\partial \mathbf{R}_p^{\mathrm{ext}}}{\partial \boldsymbol{\alpha}} \tag{26}$$

we can identify by comparison of coefficients the following terms

$$\frac{\partial \mathbf{R}_p^{\text{ext}}}{\partial \bar{\boldsymbol{\varepsilon}}} = \left(\mathbf{K}_{pp} - \mathbf{K}_{pr} \cdot \mathbf{K}_{rr}^{-1} \cdot \mathbf{K}_{rp}\right) \cdot \mathbf{X}_p \tag{27}$$

$$\frac{\partial \mathbf{R}_p^{\text{ext}}}{\partial \boldsymbol{\alpha}} = \frac{\partial \mathbf{R}_p^{\text{int}}}{\partial \boldsymbol{\alpha}} - \mathbf{K}_{pr} \cdot \mathbf{K}_{rr}^{-1} \cdot \frac{\partial \mathbf{R}_r^{\text{int}}}{\partial \boldsymbol{\alpha}}. \tag{28}$$

The sum to calculate the macro stress is constructed over the boundary nodes, where displacements are prescribed, i.e. $\frac{\partial \mathbf{f}_j}{\partial \boldsymbol{\alpha}} = \left(\frac{\partial \mathbf{R}_p^{\text{ext}}}{\partial \boldsymbol{\alpha}}\right)_j$. Therefore we only need (28) to construct the partial derivative of the macro stresses. It remains to calculate the partial derivative of the internal residual w.r.t. the material parameters. For this the internal variables like plastic strain, back stress and hardening evolution are summarized in the vector $\boldsymbol{\beta}$. The inelastic material model is dealt with by using a recursive strategy to differentiate w.r.t. the material parameters, described in detail in [4]. The key point of this strategy is to view the stress and internal variables $\boldsymbol{\beta}$ as dependent on the current and last load steps as well as the material parameters, i.e. $\boldsymbol{\sigma}^k = \boldsymbol{\sigma}^k(\boldsymbol{\varepsilon}^k, \boldsymbol{\varepsilon}^{k-1}, \boldsymbol{\beta}^k, \boldsymbol{\beta}^{k-1}, \alpha)$, and $\boldsymbol{\beta}^k = \boldsymbol{\beta}^k(\boldsymbol{\varepsilon}^k, \boldsymbol{\varepsilon}^{k-1}, \boldsymbol{\beta}^{k-1}, \alpha)$, and differentiate accordingly. The partial derivatives needed for parameter identification consider all dependencies but the strain of the current step, i.e. $\frac{\partial \boldsymbol{\sigma}^k(\boldsymbol{\varepsilon}^k, \alpha)}{\partial \boldsymbol{\alpha}}$ and $\frac{\partial \boldsymbol{\beta}^k(\boldsymbol{\varepsilon}^k, \alpha)}{\partial \boldsymbol{\alpha}}$. The total derivatives from the last step are a vital ingredient for this calculation and are constructed at the beginning of the current step using the results from the last step. The total derivative of the microscopic displacements w.r.t. the material parameters (23) can be constructed by means of the partial derivatives

$$\frac{\partial \mathbf{u}_r(\bar{\boldsymbol{\varepsilon}}(\boldsymbol{\alpha}), \boldsymbol{\alpha})}{\partial \boldsymbol{\alpha}} = -\mathbf{K}_{rr}^{-1} \cdot \frac{\partial \mathbf{R}_r^{\text{int}}}{\partial \boldsymbol{\alpha}}, \quad \frac{\partial \mathbf{u}_r(\bar{\boldsymbol{\varepsilon}}(\boldsymbol{\alpha}), \boldsymbol{\alpha})}{\partial \bar{\boldsymbol{\varepsilon}}} = -\mathbf{K}_{rr}^{-1} \cdot \mathbf{K}_{rp} \cdot \mathbf{X}_p \tag{29}$$

as $\frac{\mathrm{d}\mathbf{u}_r}{\mathrm{d}\boldsymbol{\alpha}} = \frac{\partial \mathbf{u}_r}{\partial \bar{\boldsymbol{\varepsilon}}} \cdot \frac{\mathrm{d}\bar{\boldsymbol{\varepsilon}}}{\mathrm{d}\boldsymbol{\alpha}} + \frac{\partial \mathbf{u}_r}{\partial \boldsymbol{\varepsilon}}$, once $\frac{\mathrm{d}\bar{\boldsymbol{\varepsilon}}}{\mathrm{d}\boldsymbol{\alpha}}$ is known. Thus, we have a classical parameter identification step in the integration points. The special dependency of the prescribed micro displacements on the material parameters resulting from the two-scale homogenization scheme influences only the global microscopic equations (23) and (25).

3.3 Algorithm

The iteration procedure to calculate micro material parameter derivatives of displacements and forces at macroscopic scale and its steps are illustrated by the following scheme.

INIT ($k = 0$): Initialize the derivatives of the macro displacements $\frac{\mathrm{d}\bar{\mathbf{u}}^0}{\mathrm{d}\boldsymbol{\alpha}} = \mathbf{0}$. Furthermore, initialize the derivatives of the micro displacements $\frac{\partial \mathbf{u}^0}{\partial \boldsymbol{\alpha}} = \mathbf{0}$, $\frac{\partial \mathbf{u}^0}{\partial \bar{\boldsymbol{\varepsilon}}^0} = \mathbf{0}$, and of the micro internal variables $\frac{\partial \boldsymbol{\beta}^0}{\partial \boldsymbol{\alpha}} = \mathbf{0}$, $\frac{\partial \boldsymbol{\beta}^0}{\partial \boldsymbol{\varepsilon}^0} = \mathbf{0}$ on all micro domains.

ITERATION

I) set $k \to k+1$, known: $\frac{\mathrm{d}\bar{\mathbf{u}}^{k-1}}{\mathrm{d}\boldsymbol{\alpha}}$

II) after macro equilibrium calculations, on each macro element for each integration point:

A) construct $\frac{\mathrm{d}\bar{\boldsymbol{\varepsilon}}^{k-1}}{\mathrm{d}\boldsymbol{\alpha}}$ from $\frac{\mathrm{d}\bar{\mathbf{u}}^{k-1}}{\mathrm{d}\boldsymbol{\alpha}}$

B) invoke subproblem on micro scale for each integration point

i) known: $\frac{\mathrm{d}\bar{\boldsymbol{\varepsilon}}^{k-1}}{\mathrm{d}\boldsymbol{\alpha}}, \frac{\partial \mathbf{u}^{k-1}}{\partial \boldsymbol{\alpha}}, \frac{\partial \mathbf{u}^{k-1}}{\partial \bar{\boldsymbol{\varepsilon}}^{k-1}}, \frac{\partial \boldsymbol{\beta}^{k-1}}{\partial \boldsymbol{\alpha}}, \frac{\partial \boldsymbol{\beta}^{k-1}}{\partial \boldsymbol{\varepsilon}^{k-1}}$

ii) construct $\frac{\mathrm{d}\mathbf{u}^{k-1}}{\mathrm{d}\boldsymbol{\alpha}} = \frac{\partial \mathbf{u}^{k-1}}{\partial \bar{\boldsymbol{\varepsilon}}^{k-1}} \cdot \frac{\mathrm{d}\bar{\boldsymbol{\varepsilon}}^{k-1}}{\mathrm{d}\boldsymbol{\alpha}} + \frac{\partial \mathbf{u}^{k-1}}{\partial \boldsymbol{\alpha}}$

iii) after micro equilibrium calculations, on each micro element for each integration point:

a) construct $\frac{\mathrm{d}\boldsymbol{\varepsilon}^{k-1}}{\mathrm{d}\boldsymbol{\alpha}}$ from $\frac{\mathrm{d}\mathbf{u}^{k-1}}{\mathrm{d}\boldsymbol{\alpha}}$

b) construct $\frac{\mathrm{d}\boldsymbol{\beta}^{k-1}}{\mathrm{d}\boldsymbol{\alpha}} = \frac{\partial \boldsymbol{\beta}^{k-1}}{\partial \boldsymbol{\varepsilon}^{k-1}} \cdot \frac{\mathrm{d}\boldsymbol{\varepsilon}^{k-1}}{\mathrm{d}\boldsymbol{\alpha}} + \frac{\partial \boldsymbol{\beta}^{k-1}}{\partial \boldsymbol{\alpha}}$

c) calculate $\frac{\partial \boldsymbol{\sigma}^{k}}{\partial \boldsymbol{\alpha}}, \frac{\partial \boldsymbol{\beta}^{k}}{\partial \boldsymbol{\varepsilon}^{k}}, \frac{\partial \boldsymbol{\beta}^{k}}{\partial \boldsymbol{\alpha}}$ and save $\frac{\partial \boldsymbol{\beta}^{k}}{\partial \boldsymbol{\varepsilon}^{k}}, \frac{\partial \boldsymbol{\beta}^{k}}{\partial \boldsymbol{\alpha}}$ for next step

d) calculate $\frac{\partial \mathbf{R}^{\mathrm{int,k}|_e}}{\partial \boldsymbol{\alpha}}$

iv) assemble global artificial load vector $\frac{\partial \mathbf{R}^{\mathrm{int,k}}}{\partial \boldsymbol{\alpha}}$

v) determine $\frac{\partial \mathbf{u}^{k}}{\partial \boldsymbol{\alpha}}, \frac{\partial \mathbf{u}^{k}}{\partial \bar{\boldsymbol{\varepsilon}}^{k}}$ (29), $\frac{\partial \mathbf{f}^{k}}{\partial \boldsymbol{\alpha}}$ (28) and save $\frac{\partial \mathbf{u}^{k}}{\partial \boldsymbol{\alpha}}, \frac{\partial \mathbf{u}^{k}}{\partial \bar{\boldsymbol{\varepsilon}}^{k}}$ for next step

vi) calculate $\frac{\partial \bar{\boldsymbol{\sigma}}^{k}}{\partial \boldsymbol{\alpha}}$ (18) from $\frac{\partial \mathbf{f}^{k}}{\partial \boldsymbol{\alpha}}$ and give it back to macro scale

C) use $\frac{\partial \bar{\boldsymbol{\sigma}}^{k}}{\partial \boldsymbol{\alpha}}$ to calculate $\frac{\partial \bar{\mathbf{R}}^{\mathrm{int,k}|_e}}{\partial \boldsymbol{\alpha}}$ (17)

III) assemble global artificial load vector $\frac{\partial \bar{\mathbf{R}}^{\mathrm{int,k}}}{\partial \boldsymbol{\alpha}}$

IV) solve for $\frac{\mathrm{d}\bar{\mathbf{u}}^{k}}{\mathrm{d}\boldsymbol{\alpha}}$ (15), $\frac{\mathrm{d}\bar{\mathbf{f}}^{k}}{\mathrm{d}\boldsymbol{\alpha}}$ (16) and go to step I).

4 NUMERICAL EXAMPLE

In a first investigation on the functionality of the proposed multi-scale method for parameter identification, reidentification for numerical examples is considered. Therefore the numerical simulations are carried out for given material parameters on the micro scale. Then the optimization algorithm is employed to solve the problem for several starting points.

The example setting is illustrated in figure 2. The geometry at the macroscopic scale is a punched disk, which is elongated in five steps to a total of 1.5 % elongation. The hole has a radius of 1 mm and is centered at the quadratic disk with base length 4 mm and thickness 1 mm. The microscopic domain consists of a cube with an ellipsoidal void. The ellipsoid with radii $a = 4.8, b = 3.2, c = 4.0$ is placed at the center of a cube with base length 10. 'Linear displacement' boundary conditions were employed.

We assume a microscopic material law of von Mises plasticity with linear isotropic hardening. For the reference solution the material parameters at the micro scale are given as $K = 73.53, \mu = 28.20, \sigma_Y = 0.30, h = 15.00$ in GPa. The displacements at the

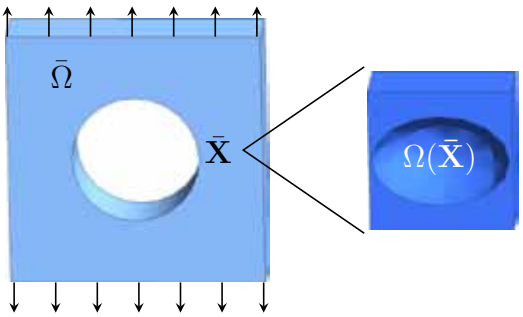

Figure 2: Example setting

front and back as well as the resultant force on top and bottom of the macro disk are the entries in the objective function. The optimization algorithm `lsqnonlin` from MATLAB's Optimization Toolbox is used to minimize the optimization problem. Four starting points are presented: 1 (80.47, 31.63, 0.27, 16.86), 2 (84.23, 34.07, 0.28, 18.50), 3 (69.26, 33.93, 0.23, 17.85), 4 (88.90, 30.61, 0.25, 15.94).

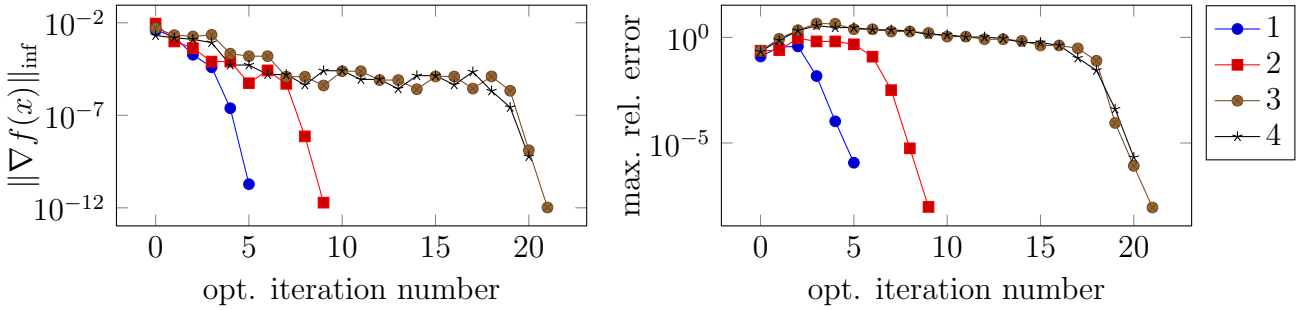

Figure 3: Optimization characteristics

Results for each stating point are shown in figure 3. The plot on the left depicts the infinity norm of the gradient of the objective function against the iterations of the optimization. The decrease indicates the convergence to a stationary point. The plot on the right depicts the maximal relative error of the identified material parameters with respect to the reference parameters, also against the iterations of the optimization. In both plots the y-axes use a logarithmic scale. As can be seen, the optimization convergences and the identified micro parameters indeed coincide with the reference parameters.

5 CONCLUSIONS

In this paper the coupling of classical parameter identification and the FE^2-method is described. The gradient information of the objective function is derived leading from macroscopic derivatives down to microscopic derivatives. A calculation scheme covering

the main steps within the recursive approach at the two scales is shown. The example illustrates that the correct material parameters of the micro scale, both elastic and plastic ones, can be identified using only the macroscopic data. The optimization converges successfully in a small to moderate number of steps. Thus we conclude that the two-scale parameter identification can be solved using the proposed scheme.

However, more research into the stability and robustness of the method is required. The method relies on observable nonlinear effects at the macro scale. If the plastic effects on the micro structure appear only very locally confined, the effects on the macro scale may become negligible small and therefore pose only insufficient data.

Furthermore, for improving the computational costs we will investigate the effects of separate identification of elastic and plastic materials as well as the effects of the coupling of 2-D macro to 3-D micro simulations.

Acknowledgments
The authors gratefully acknowledge the support of the Cluster of Excellence 'Engineering of Advanced Materials' at the University of Erlangen-Nuremberg, which is funded by the German Research Foundation (DFG) within the framework of its 'Excellence Initiative'.

REFERENCES

[1] Burczyński, T. and Kuś, W. Identification of material properties in multi-scale modeling. *J. Phys. Conf. Ser.* (2008) **135**:012025.

[2] Ilic, S. and Hackl, K. Inverse Problems in the Modelling of Composite Materials. *Proceedings of the 7th Int. Conference on Engineering Computational Technology.* (2010) Paper 122.

[3] Oskay, C. and Fish, J. On calibration and validation of eigendeformation-based multiscale models for failure analysis of heterogeneous systems. *Comput. Mech.* (2008) **42**:181–195.

[4] Mahnken, R. and Stein, E. A unified approach for parameter identification of inelastic material models in the frame of the finite element method. *Comput. Meth. Appl. Mech. Eng.* (1996) **136**:225–258.

[5] Feyel, F. and Chaboche, J.-L. FE2 multiscale approach for modelling the elastoviscoplastic behaviour of long fibre SiC/Ti composite materials. *Comput. Meth. Appl. Mech. Eng.* (2000) **183**:309–330.

[6] Schmidt, U. and Mergheim, J. and Steinmann, P. Multi-Scale Parameter Identification. *Int. J. Multiscale Comput. Eng.* accepted (2010).

XI International Conference on Computational Plasticity. Fundamentals and Applications
COMPLAS XI
E. Oñate, D.R.J. Owen, D. Peric and B. Suárez (Eds)

COMPARATIVE INVESTIGATION AND APPLICATION OF 3D CONSTITUTIVE MODELS FOR CONCRETE

Bernhard Valentini and Günter Hofstetter

Unit for Strength of Materials and Structural Analysis
Institute of Basic Sciences in Civil Engineering
University of Innsbruck
Technikerstraße 13, A-6020 Innsbruck, Austria
e-mail: Guenter.Hofstetter@uibk.ac.at, www.uibk.ac.at/bft/

Key words: concrete model, constitutive model, concrete structure, finite element method, numerical simulation

Abstract. This contribution deals with a comparative investigation of two 3D material models for concrete. The models under consideration are a modified version of the Extended Leon model and the damage-plasticity model proposed by Grassl and Jirásek. The results of extensive comparisons of the model response with test data motivated some modifications of both concrete models, in particular, regarding the evolution of damage.

1 INTRODUCTION

Several 3D constitutive models for concrete were proposed in the last decade. E.g., Pivonka [2] developed a modified version of the Extended Leon model [1], which is formulated within the framework of plasticity theory, and applied it to the numerical simulation of pull-out tests of anchor bolts. Schütt [3] proposed a non-smooth multi-surface damage-plasticity model and employed it for the analysis of composite structures. Huber [4] compared a 3D multi-surface plasticity model for concrete with a 3D gradient enhanced damage model. Recently, a 3D concrete model, based on a combination of plasticity theory and damage theory, was proposed by Grassl and Jirásek [5].

This contribution focuses on a comparative investigation of the modified Extended Leon model [2] and the damage-plasticity model [5]. To this end, the models are implemented into the commercial FE-analysis program system ABAQUS [6] by means of a return mapping algorithm, which is enhanced by substepping and error-control in order to improve robustness and accuracy of the stress update.

The results of extensive validation of the model response by material tests motivated some modifications of both concrete models, in particular, regarding the evolution of

damage. Furthermore, the numerical simulation of a well-known 3D benchmark test demonstrates the capabilities of an enhanced version of the damage-plasticity model for the analysis of concrete structures.

2 3D CONSTITUTIVE MODELS FOR CONCRETE

2.1 Modified Extended Leon Model

The Extended Leon model is a single-surface plasticity model with nonlinear hardening and softening. It was developed by Etse [1] and modified later by Pivonka [2]. The latter version is described and employed in this paper.

The yield function of the Extended Leon (EL) model

$$f_{EL}(\sigma^m, \rho, \theta; \alpha_h, \alpha_s) = \left[\frac{1 - q_h(\alpha_h)}{f_{cu}^2}\left(\sigma^m + \frac{\rho\, r(\theta)}{\sqrt{6}}\right)^2 + \sqrt{\frac{3}{2}}\frac{\rho\, r(\theta)}{f_{cu}}\right]^2 + \\ + \frac{q_h^2(\alpha_h)}{f_{cu}} m_s(\alpha_s)\left(\sigma^m + \frac{\rho\, r(\theta)}{\sqrt{6}}\right) - q_h^2(\alpha_h)\, q_s(\alpha_s) \tag{1}$$

is formulated in terms of the hydrostatic stress σ^m, the deviatoric radius ρ, the Lode angle θ, the strain-like internal hardening variable α_h and the strain-like internal softening variable α_s; f_{cu} denotes the uniaxial compressive strength of concrete and $r(\theta)$ a deviatoric shape function, with the limiting cases of a triangular and circular yield function in the deviatoric plane.

The plastic strain rate is described by a flow rule, which is associated in the deviatoric plane and non-associated in the meridional plane.

Hardening behavior of the Extended Leon model is described by the normalized strength parameter

$$q_h(\alpha_h) = \begin{cases} q_{h_0} + (1 - q_{h_0})\sqrt{\alpha_h\,(2 - \alpha_h)} & \text{if } \alpha_h < 1 \\ 1 & \text{if } \alpha_h \geq 1 \end{cases}, \tag{2}$$

where $q_{h_0} = f_{cy}/f_{cu}$ denotes the initial value of q_h, which represents the ratio of the elastic limit stress under compressive loading, f_{cy}, and the uniaxial compressive strength.

The evolution law of the strain-like internal hardening variable is given as

$$\dot{\alpha}_h(\sigma^m, \rho, \theta; \alpha_h, \alpha_s) = \frac{\|\dot{\boldsymbol{\varepsilon}}^p\|}{x_h(\sigma^m)} = \dot{\gamma}\, h_h(\sigma^m, \rho, \theta; \alpha_h, \alpha_s) \tag{3}$$

with $x_h(\sigma^m)$ denoting the hardening ductility parameter, which increases with increasing hydrostatic pressure. Hence, the rate of the internal hardening variable α_h is decreasing for increasing values of the confining pressure.

Softening behaviour is controlled by the decohesion parameter

$$q_s(\alpha_s) = \begin{cases} 1 & \text{if } \alpha_h < 1 \\ e^{-(\alpha_s/\alpha_u)} & \text{if } \alpha_h \geq 1 \end{cases} , \tag{4}$$

which is driven by the strain-like internal softening variable α_s; $\alpha_u = G_f^I/(l_{char}\, f_{tu})$ is employed for regularizing the softening behavior with G_f^I as the specific mode I fracture energy of concrete, l_{char} as the characteristic length of the finite element and f_{tu} as the uniaxial tensile strength.

The evolution law of the strain-like internal softening variable α_s is defined as

$$\dot{\alpha}_s(\sigma^m, \rho, \theta; \alpha_h, \alpha_s) = \frac{\| \langle \dot{\boldsymbol{\varepsilon}}^p \rangle \|}{x_s(\sigma^m)} = \dot{\gamma} h_s(\sigma^m, \rho, \theta; \alpha_h, \alpha_s) \ , \tag{5}$$

with $x_s(\sigma^m)$ denoting the softening ductility parameter depending on the maximum value of the mean stress.

The friction parameter m_s in (1) is defined as

$$m_s(\alpha_s) = \begin{cases} m_0 & \text{if } \alpha_h < 1 \ , \\ m_r - (m_r - m_0)\, q_s(\alpha_s) & \text{if } \alpha_h \geq 1 \end{cases} , \tag{6}$$

where m_0 and m_r are the initial and the residual friction parameter, respectively.

2.2 Damage-plasticity model by Grassl and Jirásek

The damage-plasticity model by Grassl and Jirásek [5] is a single-surface model with nonlinear isotropic hardening, formulated within the framework of plasticity theory, and nonlinear isotropic softening, described on the basis of damage theory. The yield function of the damage-plasticity (DP) model is given in terms of the effective mean stress $\bar{\sigma}^m$, the effective deviatoric radius $\bar{\rho}$ and the effective Lode angle $\bar{\theta}$ and the strain-like internal hardening variable α_p:

$$\begin{aligned} f_{p,DP}(\bar{\sigma}^m, \bar{\rho}, \bar{\theta}; \alpha_p) = \left[\frac{1 - q_h(\alpha_p)}{f_{cu}^2} \left(\bar{\sigma}^m + \frac{\bar{\rho}}{\sqrt{6}} \right)^2 + \sqrt{\frac{3}{2}} \frac{\bar{\rho}}{f_{cu}} \right]^2 + \\ + \frac{m_0\, q_h^2(\alpha_p)}{f_{cu}} \left(\bar{\sigma}^m + \frac{\bar{\rho}}{\sqrt{6}} r(\bar{\theta}) \right) - q_h^2(\alpha_p) \ . \end{aligned} \tag{7}$$

The shape of the yield function in the deviatoric plane is controlled by a deviatoric shape function $r(\bar{\theta})$; m_0 denotes a friction parameter. The plastic strain rate is described by a flow rule, which is non-associated in both the deviatoric and the meridional plane.

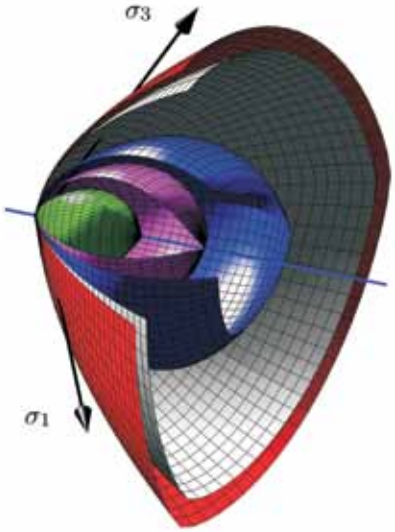

Figure 1: Yield surface of the damage-plasticity model by Grassl and Jirásek, plotted in the principal stress space for five different states during hardening

Hardening is described by the normalized strength parameter

$$q_h(\alpha_p) = \begin{cases} q_{h_0} + (1 - q_{h_0})\,\alpha_p \left(\alpha_p^2 - 3\alpha_p + 3\right) & \text{if } \alpha_p < 1 \\ 1 & \text{if } \alpha_p \geq 1 \end{cases} . \tag{8}$$

The evolution of the strain-like internal hardening variable is given as

$$\dot{\alpha}_p(\bar{\sigma}^m, \bar{\rho}, \bar{\theta}; \alpha_p) = \frac{\|\dot{\boldsymbol{\varepsilon}}^p\|}{x_h(\bar{\sigma}^m)} 4\cos^2(\bar{\theta}) = \dot{\gamma} h_p(\bar{\sigma}^m, \bar{\rho}, \bar{\theta}; \alpha_p) \tag{9}$$

with the hardening ductility parameter $x_h(\bar{\sigma}^m)$, defined in a different manner from the Extended Leon model (cf. [5]). The yield surface (7) in the principal stress space is shown for five different states during hardening in Fig. 1.

Softening material behavior of the damage-plasticity model is described by an isotropic damage law. The damage loading function is formulated in the strain-space as

$$f_{d,DP}(\boldsymbol{\varepsilon}, \boldsymbol{\varepsilon}^p; \alpha_d) = \tilde{\varepsilon}(\boldsymbol{\varepsilon}, \boldsymbol{\varepsilon}^p) - \alpha_d \ , \tag{10}$$

where $\tilde{\epsilon}$ represents the equivalent strain and α_d the strain-like internal softening variable.

Since the original version of the evolution law of the damage variable produces sharp bends of compressive stress-strain curves at the transition from hardening to softening, it is replaced in the present work by

$$\omega(\overline{\sigma}_d^m; \alpha_d) = 1 - X(\overline{\sigma}_d^m) \frac{1}{\left(1 + \dfrac{\alpha_d}{\varepsilon_{f,t}}\right)^2} - \left[1 - X(\overline{\sigma}_d^m)\right] e^{-\left(\alpha_d/\varepsilon_{f,c}\right)^2} \tag{11}$$

with $\varepsilon_{f,t}$ and $\varepsilon_{f,c}$ controlling the slope of the softening curve and

$$X(\overline{\sigma}_d^m) = \begin{cases} 0 & \text{if } \overline{\sigma}_d^m \leq -\frac{f_{cu}}{3} \\ \frac{3\overline{\sigma}_d^m}{f_{cu}} + 1 & \text{if } -\frac{f_{cu}}{3} < \overline{\sigma}_d^m < 0 \\ 1 & \text{if } \overline{\sigma}_d^m \geq 0 \end{cases} \tag{12}$$

determining the weight of the second and third term in (11) on the damage variable. Since $\overline{\sigma}_d^m$ is equal to the effective mean stress at the onset of softening, X is a constant parameter. For tensile loading with $\overline{\sigma}_d^m \geq 0$ the shape of the softening curve is controlled only by the hyperbolic function which results in a steeper initial descent of the softening envelope. In contrast, for compressive loading with $\overline{\sigma}_d^m \leq -\frac{f_{cu}}{3}$ the shape of the softening curve is controlled only by the quadratic exponential function. Thus, the sharp bend of stress-strain curves at the transition from hardening to softening, produced by the original damage law, is avoided. For $-\frac{f_{cu}}{3} < \overline{\sigma}_d^m < 0$ multi-axial combined tension-compression loading is controlled by a combination of both functions.

The rate of the strain-like internal softening variable is given as

$$\dot{\alpha}_d = \begin{cases} 0 & \text{if } \alpha_p < 1 \\ \dfrac{\dot{\varepsilon}^{p,vol}}{x_s(\dot{\varepsilon}^{p,vol})} & \text{if } \alpha_p \geq 1 \end{cases}, \tag{13}$$

where $\dot{\varepsilon}^{p,vol} = \dot{\varepsilon}_{ij}^p \, \delta_{ij}$ denotes the volumetric plastic strain rate and the softening ductility parameter $x_s(\dot{\varepsilon}^{p,vol})$ controls the evolution of the strain-like internal softening variable.

3 STRESS UPDATE ALGORITHM

For both concrete models the implicit backward Euler method is employed for integrating the constitutive rate equations. The resulting nonlinear system of equations is solved at each integration point for the stresses, the internal variables and the consistency parameters by means of Newton's method. The consistent (damage-)elasto-plastic tangent moduli are employed for achieving a quadratic rate of asymptotic convergence at the structural level.

In order to increase the robustness of the stress update for larger strain increments the return mapping algorithm is enhanced by a substepping method proposed by Pérez-Foguet et al. [7]. It is characterized by subdividing the total strain increment of the time step under consideration into m subincrements and performing the return mapping algorithm consecutively for all subincrements of the total strain increment by analogy to the well known single step method. Fig. 2 shows a comparison of the robustness of the single-step return mapping algorithm with the subincremented version of the return mapping algorithm for a set of trial stresses consisting of a grid of 51×51 equally spaced points. The grid is defined by $\sigma_m^{trial} = [-80, 20]$ N/mm^2, $\rho^{trial} = [0, 40]$ N/mm^2 and

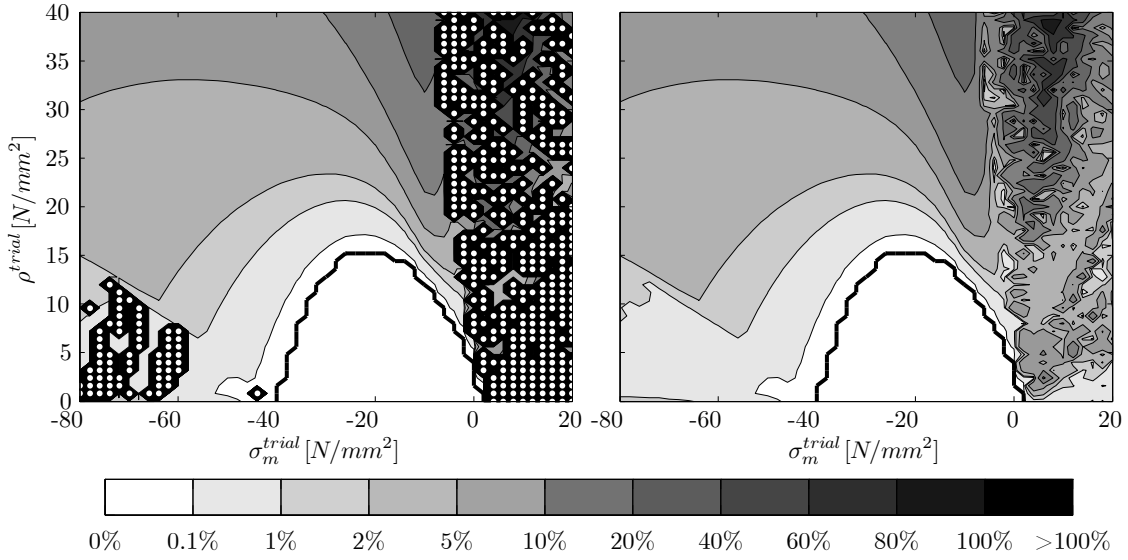

Figure 2: Iso-error maps for the stress update by the single-step Newton method (left) and the Newton method with subincrementation (right); white dots indicate points with failure of convergence

$\theta^{trial} = \pi/3$. For all stress points of this grid the initial values of the stresses, internal variables and damage variables are chosen as zero.

Fig. 2 clearly shows that in contrast to the single-step stress update, the stress update with subincrementation converges for all investigated trial stresses. In the hardening region the relative errors of the stresses are increasing with increasing distance from the boundary of the elastic domain, indicated in Fig. 2 by the black curve. In the softening domain the relative errors are larger than in the hardening domain because the nonlinearity of the underlying problem in tension is more pronounced than in compression.

In order to avoid larger integration errors as shown in Figure 2 (right), the size of the initial subincrement is determined according to a user-defined error threshold value for the stresses. To this end, for the time step under consideration two solutions for the stresses are computed based on different subincrement sizes. If the relative error of the stresses is smaller than the user-defined threshold value, then the solution is accepted, otherwise the number of subincrements is increased.

The single step integration and the subincrement integration mainly differ by the computation of the consistent tangent moduli, since the latter method requires additional terms resulting from the variation of the stresses and internal variables of the previous subincrement [7, 8] and, in addition, the consistent tangent moduli for the actual subincrement depend on those of the previous subincrement. Hence, computing the consistent elasto-plastic tangent moduli for the substepping method is more expensive than computing those for the single-step method.

4 VALIDATION AND APPLICATION

The modified Extended Leon model by Pivonka and the damage-plasticity model by Grassl and Jirásek were validated by experimental data of several test series on concrete specimens subjected to different stress paths, which are available in the literature. The investigation is documented in [8]. This validation confirmed the superiority of the damage-plasticity model. In the following, exemplarily, only a comparison of the results of triaxial compression tests with different levels of confinement, described in [9], with the respective model response is presented.

In a further validation step the modified damage-plasticity concrete model is applied to the numerical simulation of well-known 3D benchmark tests, including cylindrical concrete specimens subjected to torsional loading, cyclic loading tests of RC squat bridge columns and tests on beam-shaped concrete specimens, subjected to combined bending and torsional loading. In the following, only the latter benchmark test is addressed briefly. The analysis of all benchmark tests is documented in [8].

4.1 Validation by material tests

The material parameters of the concrete specimens, tested by Imran and Pantazopoulou [9], are given in Table 1. In this table G_f^I is estimated according to [10] from the maximum aggregate size of $d_{max} = 10$ mm.

Table 1: Material parameters for the triaxial compression tests according to [9]

parameter	(mean) value	
E_c	30000.00	N/mm^2
ν_c	0.15	
f_{cu}	47.40	N/mm^2
f_{tu}	4.74	N/mm^2
G_f^I	0.0780	Nmm/mm^2

Fig. 3 shows a comparison of experimental data and the computed response for triaxial compression tests with different levels of confinement. The peak stresses at different levels of confinement are predicted well by both models. However, the modified Extended Leon model (ELM) underestimates both, the axial and lateral strain, in particular, for higher levels of confinement.

In contrast to the modified Extended Leon model, the damage-plasticity model (DPM) by Grassl and Jirásek yields good agreement of measured and predicted axial and lateral strains for different levels of confinement. A further slight improvement is achieved by the enhanced softening law (11), as the artificial sharp bends are eliminated (DPM-enh.).

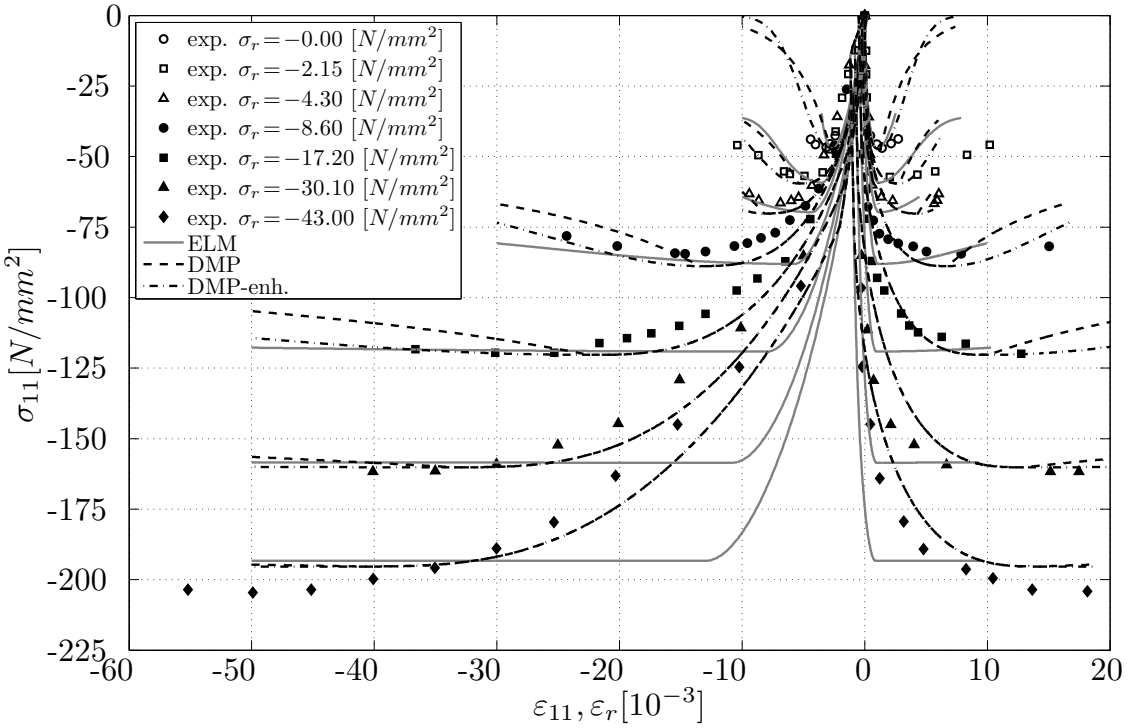

Figure 3: Experimental and numerical results of triaxial compression tests according to [9]

4.2 Benchmark test: the PCT-3D test

In the PCT-3D tests, conducted at the University of Innsbruck, prismatic concrete specimens with dimensions of $180 \times 180 \times 600$ mm were subjected to combined bending and torsional loading. The test layout is described in detail in [11]. Fig. 4 shows the FE-mesh of the concrete specimen, the support rollers and the load application roller. The concrete specimen and the steel components are discretized by altogether 69372 3D isoparametric 20-node elements with reduced numerical integration.

A notch of isosceles triangular shape of 60 mm length in both vertical and horizontal direction with a notch width of 5 mm was provided at midspan of the specimen at the tensile faces for triggering crack initiation. At an offset of 30 mm from the front face of the specimen a concentrated vertical load was applied to the load application roller, which resulted in combined bending and torsional loading. In the numerical simulation after application of the dead load the concentrated load is applied by prescribing a vertical displacement at a single node of the load application roller.

The material parameters are summarized in Table 2. The uniaxial tensile strength and the specific mode I fracture energy of concrete are estimated according to [10].

The scatter of the experimental results regarding the load-crack mouth opening curve and the respective mean value as well as the numerical results for the PCT-3D test are

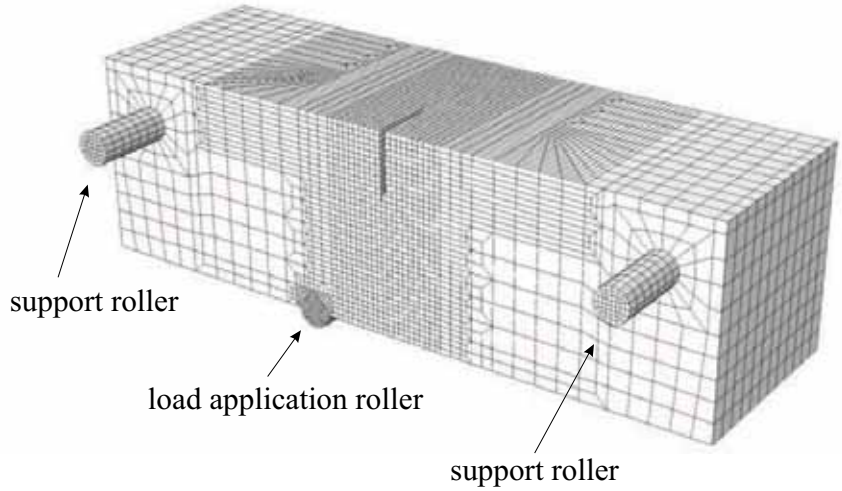

Figure 4: Finite element mesh of the PCT-3D test

Table 2: Material parameters for the numerical simulation of the PCT-3D test

concrete				steel		
param.	mean value		stand. dev.	param.	mean value	
ρ_c	2449	kg/m^3		ρ_s	7850	kg/m^3
E_c	37292	N/mm^2	$\pm$ 2055	E_s	210000	N/mm^2
ν_c	0.19		$\pm$ 0.014	ν_s	0.30	
f_{cu}	40.1	N/mm^2	$\pm$ 0.83			

shown in Fig. 5. In the numerical simulation the onset of cracking is predicted at the center of the base of the triangular notch. With increasing vertical displacement of the point of load application, the crack starts propagating along the base of the triangular notch and subsequently along the top face towards the rear face. At peak load the predicted crack extends from the notch to the rear side of the specimen. In contrast to the front face, at the top face the crack propagates in one row of elements (see Fig. 6). However, in the experiments a slightly curved crack was observed at the top face. Hence, the present model shows some mesh induced bias as a consequence of the employed smeared crack approach. Nevertheless, the overall structural behavior is predicted very well by the present model.

5 CONCLUSIONS

The comparison of the response of two constitutive models for concrete, consisting of a modified version of the Extended Leon model by Pivonka and the damage-plasticity model by Grassl and Jirásek, conducted for several sets of experimental material data, clearly revealed the superiority of the damage-plasticity model. Both models were implemented

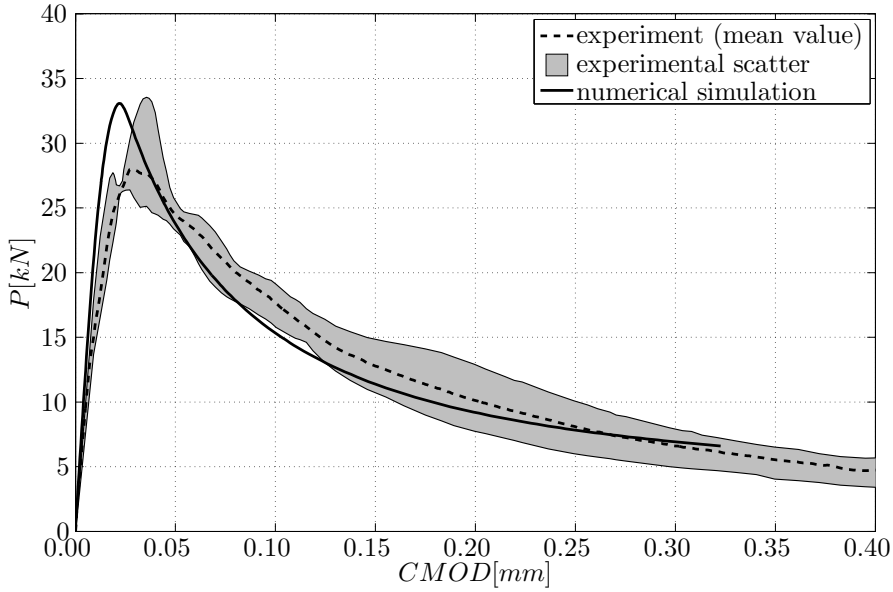

Figure 5: Measured and computed load-crack mouth opening displacement curves for the PCT-3D test

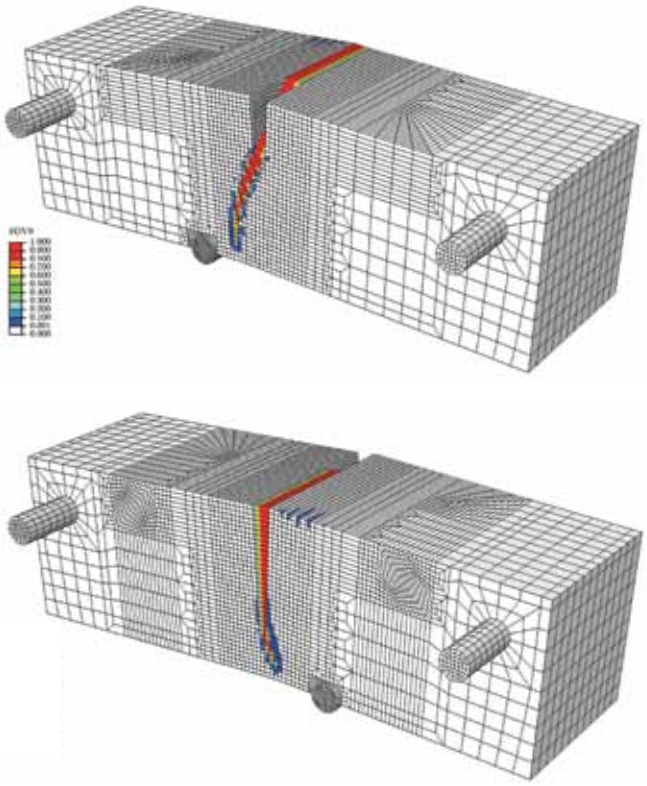

Figure 6: Predicted crack pattern at failure of the PCT-3D test ($SDV9 \equiv \omega$, deformations 50-fold magnified)

into the commercial finite element program ABAQUS, employing the return mapping algorithm, enhanced by substepping and error control, for the stress update. Several benchmark tests conducted on concrete specimens with loadings producing pronounced 3D stress states were analyzed to thoroughly check both the model response and the robustness of the stress update algorithm. The benchmark tests confirmed the capabilities of the enhanced version of the damage-plasticity model for solving large-scale problems in Civil Engineering. An example for the latter is the numerical simulation of an ultimate load test on a 3D model of a concrete arch dam on a scale of 1:200. It allowed a comparison of the predicted response with test data. The finite element mesh, shown in Fig. 7, comprises both the arch dam and the adjacent rock foundation. It consists of about 267 000 3D linear finite elements with altogether 914 000 degrees of freedom. The test setup, the numerical model and the comparison of the predicted response with the test data are described in detail in [8].

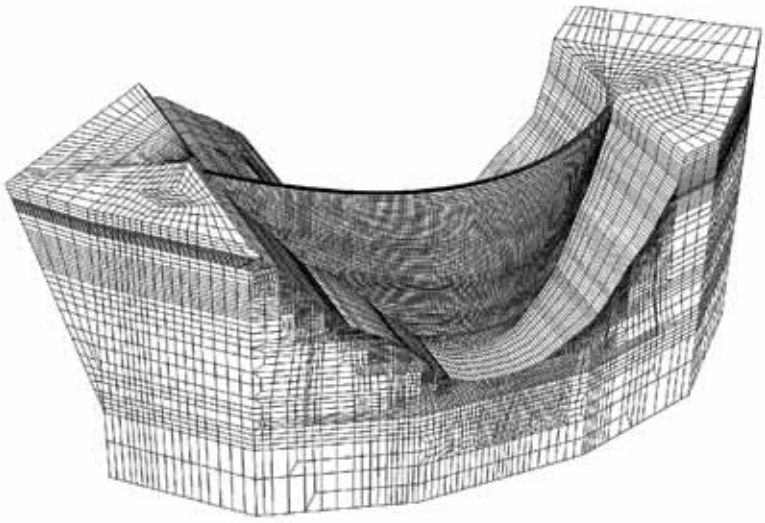

Figure 7: Finite element mesh of the arch dam model

REFERENCES

[1] Etse, G., and Willam, K., Fracture energy formulation for inelastic behavior of plain concrete, *J. Eng. Mech.* (1994) **120**: 1983-2011.

[2] Pivonka, P., Constitutive modelling of triaxially loaded concrete considering large compressive stresses: application to pull-out tests of anchor bolts, *Ph.D.-thesis*,

Vienna University of Technology, Austria, 2001.

[3] Schütt, J., Ein inelastisches 3D-Versagensmodell für Beton und seine Finite-Element-Implementierung, *Ph.D.-thesis*, University of Karlsruhe, Germany, 2005.

[4] Huber, F., Nichtlineare dreidimensionale Modellierung von Beton- und Stahlbetontragwerken, *Ph.D-thesis*, University of Stuttgart, Germany, 2006.

[5] Grassl, P., and Jirásek, M., Damage-plastic model for concrete failure, *Int. J. Solids & Struct.* (2006) **43**: 7166-7196.

[6] ABAQUS User's Manual. Dessault Systemes Simulia Corp., Providence, RI, USA, 2009.

[7] Pérez-Foguet, A., Rodriguez-Ferran, A., and Huerta, A., Consistent tangent matrices for substepping schemes, *Comp. Meth. Appl. Mech. Eng.* (2001) **190**: 4627-4647.

[8] Valentini, B., A three-dimensional constitutive model for concrete and its application to large scale finite element analyses, *Ph.D. thesis*, University of Innsbruck, Austria, 2011.

[9] Imran, I., and Pantazopoulou, S.J., Experimental Study of Plain Concrete under Triaxial Stress, *ACI Material Journal* (1996) **93**: 589-601.

[10] CEB-FIP model code 1990. Bulletin information 203 du Committee Euro-International du Beton, 1991.

[11] Feist, C., and Hofstetter, G., Validation of 3D crack propagation in plain concrete. Part I: Experimental investigation - the PCT3D test, *Computers & Concrete* (2007) **4**: 49-66.

XI International Conference on Computational Plasticity. Fundamentals and Applications
COMPLAS XI
E. Oñate, D.R.J. Owen, D. Peric and B. Suárez (Eds)

CRACK PROPAGATION IN SHELLS DUE TO IMPACT AGAINST SHARP OBJECTS

MARA PAGANI* **and UMBERTO PEREGO***

*Department of Structural Engineering
Politecnico di Milano
Piazza Leonardo da Vinci, 20133 Milan, Italy
e-mail: pagani@stru.polimi.it, umberto.perego@polimi.it

Key words: Cohesive Elements, Crack Propagation, Solid-Shell Elements

Abstract. The present paper is concerned with the development of an effective finite element tool for the simulation of crack propagation in thin structures, induced by contact or impact against sharp objects. In particular the purpose is the refinement and further development of a recently proposed finite element approach for the simulation of the blade cutting of thin membranes [1]. Standard cohesive interface elements are not suited for the simulation of this type of cutting, dominated by the blade sharpness and by large failure opening of the cohesive interface. The new concept of "directional" cohesive element, to be placed at the interface between adjacent shell elements, where the cohesive forces can have different directions on the two sides of the crack whenever the cohesive region is crossed by the cutting blade, was introduced in [1] for elastic 4-node full-integration shell elements with dissipation localized inside the interface elements, in the framework of an explicit dynamics formulation. In the present paper the computational efficiency of the proposed approach is investigated by considering applications to different test problems, modifying the shell element kinematics. Some considerations about a reduced integration solid-shell element are here reported; the interaction between this kind of element and directional cohesive elements is under study.

1 INTRODUCTION

Thin structures are typically modeled using shell finite elements. Since many years, most explicit commercial finite element codes (see e.g. Abaqus and LS-Dyna) offer the possibility to simulate crack propagation in shells by eliminating from the model those finite elements where developing damage has reached a critical threshold. While this approach provides good results for the simulation of diffused damage due to explosions or crashes against large obstacles, it is not convenient for the simulation of the propagation of isolated cracks in large structures or of localized damages produced by sharp obstacles

(see e.g. [2]). This type of problems appear to be better tackled by approaches based on the use of cohesive fracture models, capable to transmit cohesive forces across either an intra-element or inter-element displacement discontinuity [3],[4]. Among the different types of crack propagation problems in thin structures, the mechanics of cutting a shell with a sharp object or tool has attracted particular attention in view of its engineering interest [5]. Standard cohesive interface elements are not suited for the simulation of this type of cutting, dominated by the blade sharpness and by large failure opening of the cohesive interface. The new concept of "directional" cohesive element, to be placed at the interface between adjacent shell elements, where the cohesive forces can have different directions on the two sides of the crack whenever the cohesive region is crossed by the cutting blade, was introduced in [1] for elastic shells with dissipation localized inside the interface elements, in the framework of an explicit dynamics formulation. In the present paper the proposed approach is briefly summarized and used to simulate the cutting of a thin rubber sheet, on the basis of the experimental test discussed in [6]. In [1] the interface element was applied in conjunction with full integration 4-node shell elements (MITC4 elements [7]). For future application to elastoplastic laminated shells, the kinematics of a computationally effective reduced integration solid shell element is discussed and its possible use in the present explicit dynamics context is investigated.

2 COHESIVE ELEMENTS

2.1 Model description

In standard finite element approaches to fracture, based on the introduction of a cohesive interface between adjacent shell elements, due to the crack propagation opposite cohesive forces develop across the displacement discontinuity. The direction of the opposite forces depends only on the direction of the displacement jump and on the adopted cohesive law. When the material is quasi-brittle and/or the impacting object is blunt, there is no interference between the object and the cohesive region because the ultimate cohesive opening displacement is much smaller than the typical size of the cutter. On the contrary, when the material is very ductile or the cutting blade is sharp, it may well happen that the blade intersects the trajectory of the cohesive forces, giving rise to inaccurate predictions of the crack propagation. For these reasons, a new concept of "directional" cohesive interface element, where the cohesive forces acting on the crack opposite faces have different directions when the process zone is crossed by the cutting blade, has been proposed in [1] and is briefly recalled below.

The implementation of these "directional" cohesive elements follows the following steps. When the selected fracture criterion is met at a given node, the node is duplicated and it is assumed that cohesive forces $\mathbf{F}_i^{\pm}$ are transmitted between the newly created pair of nodes $i^{\pm}$ by a massless "cable", i.e. a truss element ad hoc introduced in the model in correspondence of each pair of separating nodes. In the current implementation, the cohesive cables are attached to nodes lying in the middle surface of the shell. Contact of

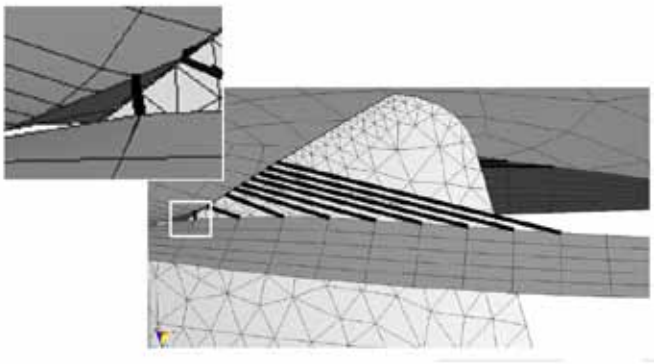

Figure 1: Cohesive forces between detaching elements.

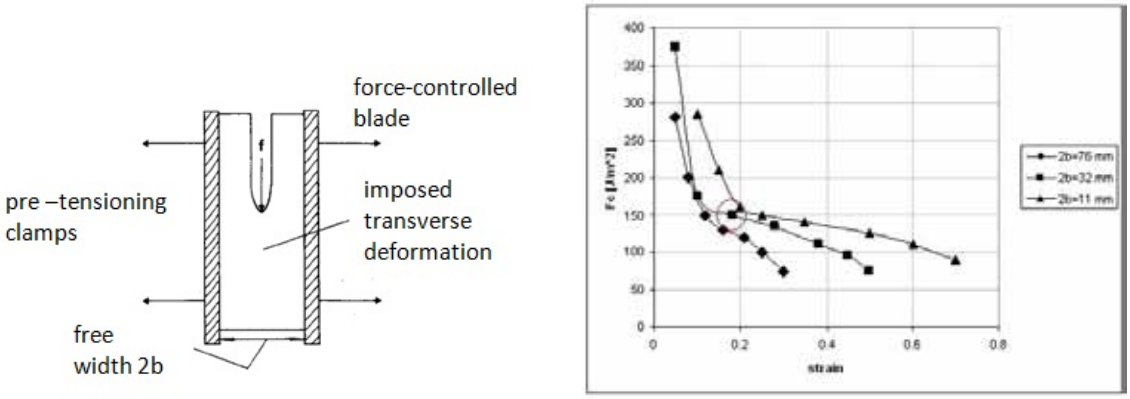

(a) (b)

Figure 2: Cutting of a rubber sheet: (a) test setup and (b) experimental results.

cable elements (which are geometric entities) against the cutting blade is checked. When a point of a cable element is detected to be in contact with the blade, the cable element is subdivided into two elements by introducing a joint in correspondence of the contact point (see Fig. 1). The force transmitted by the cables depends on their length (rather than on the distance between opposite crack nodes as in standard cohesive elements) according to the adopted cohesive law. When the current total cable length exceeds the limit value, the cable is removed and no forces are anymore transmitted between the opposite nodes.

2.2 Model validation

In order to validate this new approach, the force-controlled cutting of a pre-tensioned rubber sheet is simulated. The test setup and the recorded [6] cutting force at unstable propagation onset are shown in Fig. 2 for varying pre-tensioning and rubber sheet width. The test geometry and mesh shown in Fig. 3a have been considered, with length $L =$

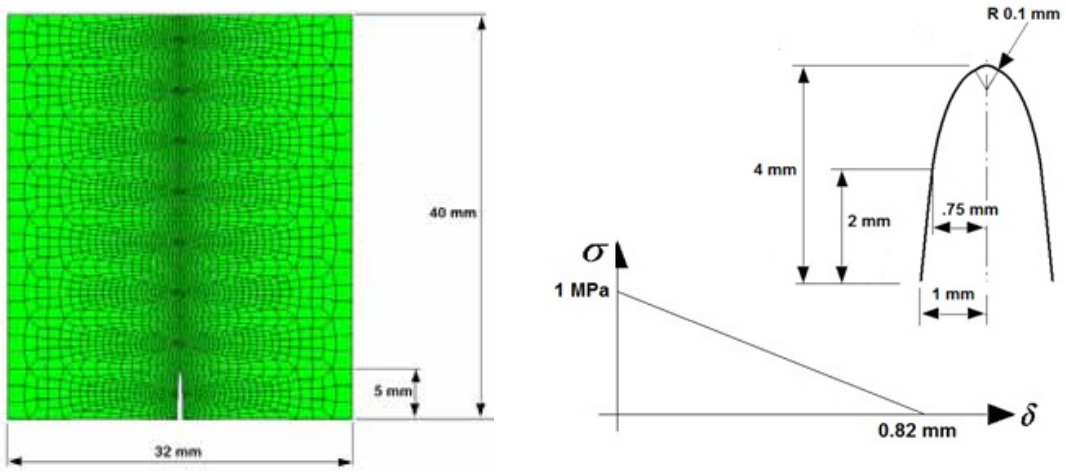

(a) (b)

Figure 3: Cutting of a rubber sheet: (a) dimensions and mesh of the rubber sheet and (b) cohesive law and blade shape.

40 mm, width $D = 32$ mm, thickness $t = 0.1$ mm, initial defect $a = 5$ mm, Young modulus $E = 1$ MPa, Poisson ratio $\nu = 0.45$ and the cohesive law shown in Fig. 3b. Imposing a transverse tensile strain of 18%, a cutting force at unstable crack propagation equal to about 150 N/m is expected to be obtained (see circled dot in Fig. 2b).

The numerical results of the explicit dynamics simulation are shown in Fig. 4. The first plot shows the evolution of the vertical reaction force at the lateral clamps. The first part of the plot concerns the initial pre-tensioning phase. The second part concerns the cutting phase. The second plot shows the time evolution of the contact force at the blade tip. As it can be observed, this oscillates about the experimentally measured value of 0.015 N, which confirms the good accuracy of the simulation.

3 SOLID-SHELL ELEMENTS

The MITC4 shell elements used in the previous example need four integration points in the shell plane and at least two integration points along the thickness for a total of eight integration points. The introduction of material non-linearities, requires a higher number of Gauss points, leading to increasing computational costs.

Several types of 8-node solid-shell elements have been recently proposed in the literature. Among these, the SHB8PS element proposed by Abed-Meraim and Combescure [9] has eight nodes, only one integration point in the plane and an arbitrary number of integration points, with a minimum of two, distributed along the thickness direction and it is based on the assumed strain stabilization proposed by Belytschko and Bindeman[8]. Combescure's element is here reconsidered with some modifications aimed at improving its computational effectiveness, especially in explicit dynamics analyses (see [9] for a detailed

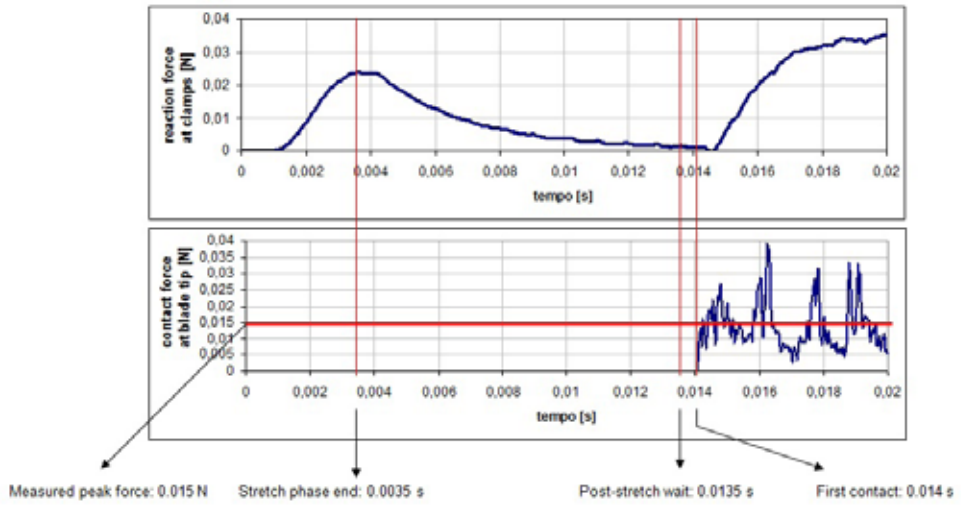

Figure 4: Cutting of a rubber sheet. Numerical results: vertical reaction force evolution at lateral clamps (upper plot); evolution of contact force at cutter tip (lower plot).

SHB8PS element presentation).

3.1 SHB8PS element

SHB8PS is a hexahedral, 8-node, isoparametric element with three-linear interpolation. It makes use of a set of n_{int} integration points distributed along the ζ direction in the local coordinate frame as shown in Fig. 5.

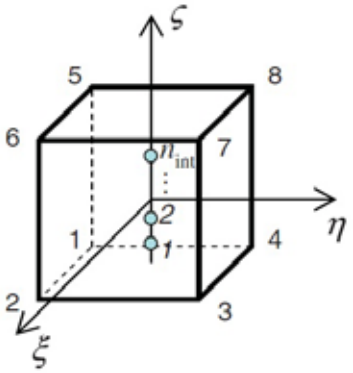

node	ξ	η	ζ
1	-1	-1	-1
2	1	-1	-1
3	1	1	-1
4	-1	1	-1
5	-1	-1	1
6	1	-1	1
7	1	1	1
8	-1	1	1

Figure 5: SHB8PS reference geometry, integration points location and nodal coordinates.

Indicating with $\mathbf{d}_i$ and $\mathbf{x}_i$ the vectors of nodal displacements and coordinates for each element, Belytschko and Bindeman have shown that the nodal displacements can be

expressed as :

$$\mathbf{d}_i = a_{01}\mathbf{s} + a_{1i}\mathbf{x}_1 + a_{2i}\mathbf{x}_2 + a_{3i}\mathbf{x}_3 + c_{1i}\mathbf{h}_1 + c_{2i}\mathbf{h}_2 + c_{3i}\mathbf{h}_3 + c_{4i}\mathbf{h}_4 \tag{1}$$

where

$$\begin{array}{l}
\mathbf{s}^T = (1,1,1,1,1,1,1,1) \\
\mathbf{h}_1^T = (1,1,-1,-1,-1,-1,1,1) \\
\mathbf{h}_2^T = (1,-1,-1,1,-1,1,1,-1) \\
\mathbf{h}_3^T = (1,-1,1,-1,1,-1,1,-1) \\
\mathbf{h}_4^T = (-1,1,-1,1,1,-1,1,-1) \\
a_{ji} = \mathbf{b}_j^T \cdot \mathbf{d}_i, \qquad c_{\alpha i} = \boldsymbol{\gamma}_\alpha^T \cdot \mathbf{d}_i, \qquad i,j = 1\ldots 3
\end{array}$$

and $\boldsymbol{\gamma}_\alpha$ and the mean form $\mathbf{b}_i$ of Flanagan and Belytschko [10] are defined as ($\mathbf{N}$ being the shape functions):

$$\begin{array}{l}
\boldsymbol{\gamma}_\alpha = \dfrac{1}{8}\left[\mathbf{h}_\alpha - \displaystyle\sum_{j=1}^{3}(\mathbf{h}_\alpha^T \cdot \mathbf{x}_j)\mathbf{b}_j\right], \qquad \alpha = 1,\ldots,4 \\
\mathbf{b}_i = \frac{1}{\Omega_e}\int_{\Omega_e} \mathbf{N}_{,i}(\xi,\eta,\zeta)\mathrm{d}\Omega, \qquad i = 1,2,3
\end{array} \tag{2}$$

Defining the four functions

$$h_1 = \eta\zeta, \quad h_2 = \zeta\xi, \quad h_3 = \xi\eta, \quad h_4 = \xi\eta\zeta \tag{3}$$

this allows to express the discrete gradient operator relating the strain field to the nodal displacements as

$$\begin{array}{rcl}
\nabla(\mathbf{u}) & = & \mathbf{B}\cdot\mathbf{d} \qquad \text{with} \\
\mathbf{B} & = & \left[\begin{array}{ccc}
\mathbf{b}_x^T + h_{\alpha,x}\boldsymbol{\gamma}_\alpha^T & \mathbf{0} & \mathbf{0} \\
\mathbf{0} & \mathbf{b}_y^T + h_{\alpha,y}\boldsymbol{\gamma}_\alpha^T & \mathbf{0} \\
\mathbf{0} & \mathbf{0} & \mathbf{b}_z^T + h_{\alpha,z}\boldsymbol{\gamma}_\alpha^T \\
\mathbf{b}_y^T + h_{\alpha,y}\boldsymbol{\gamma}_\alpha^T & \mathbf{b}_x^T + h_{\alpha,x}\boldsymbol{\gamma}_\alpha^T & \mathbf{0} \\
\mathbf{0} & \mathbf{b}_z^T + h_{\alpha,z}\boldsymbol{\gamma}_\alpha^T & \mathbf{b}_y^T + h_{\alpha,y}\boldsymbol{\gamma}_\alpha^T \\
\mathbf{b}_z^T + h_{\alpha,z}\boldsymbol{\gamma}_\alpha^T & \mathbf{0} & \mathbf{b}_x^T + h_{\alpha,x}\boldsymbol{\gamma}_\alpha^T
\end{array}\right]
\end{array} \tag{4}$$

For a set of n_{int} integration points ($I = 1,\ldots,n_{int}$), with coordinates $\xi_I = \eta_I = 0, \zeta \neq 0$, the derivatives $h_{\alpha,i}$ ($\alpha = 3,4; i = 1,2,3$) vanish, so that (4) reduces to a matrix $\mathbf{B}_{12}$ where the sum on the repeated index α only goes from 1 to 2, leading to six hourglass modes in the element stiffness matrix $\mathbf{K}_e$:

$$\mathbf{K}_e = \int_{\Omega_e} \mathbf{B}^T \cdot \mathbf{C} \cdot \mathbf{B}\mathrm{d}\Omega = \sum_{I=1}^{n_{int}} \omega(\zeta_I) J(\zeta_I) \mathbf{B}^T(\zeta_I) \cdot \mathbf{C} \cdot \mathbf{B}(\zeta_I) \tag{5}$$

where $\omega(\zeta_I)$ are Gauss' weights, $J(\zeta_I)$ is the geometry Jacobian, and $\mathbf{C}$ the matrix of elastic moduli.

The stabilization of the hourglass modes is obtained assuming a modified compatibility operator $\bar{\mathbf{B}}$:

$$\bar{\mathbf{B}} = \mathbf{B}_{12} + \mathbf{B}_{34} \tag{6}$$

where $\mathbf{B}_{34}$ is a stabilization term, computed in a co-rotational system, having the following expression [9]:

$$\mathbf{B}_{34} = \begin{bmatrix} \sum_{\alpha=3}^{4} h_{\alpha,x}\boldsymbol{\gamma}_\alpha^T & \mathbf{0} & \mathbf{0} \\ \mathbf{0} & \sum_{\alpha=3}^{4} h_{\alpha,y}\boldsymbol{\gamma}_\alpha^T & \mathbf{0} \\ \mathbf{0} & \mathbf{0} & h_{3,z}\boldsymbol{\gamma}_3^T \\ \mathbf{0} & \mathbf{0} & \mathbf{0} \\ \mathbf{0} & \mathbf{0} & \mathbf{0} \\ \mathbf{0} & \mathbf{0} & h_{4,x}\boldsymbol{\gamma}_4^T \end{bmatrix} \tag{7}$$

The elastic stiffness matrix is then given by the sum of the following contributions:

$$\mathbf{K}_{12} = \int_{\Omega_e} \mathbf{B}_{12}^T \cdot \mathbf{C} \cdot \mathbf{B}_{12} \mathrm{d}\Omega = \sum_{I=1}^{n_{int}} \omega(\zeta_I) J(\zeta_I) \mathbf{B}_{12}^T(\zeta_I) \cdot \mathbf{C} \cdot \mathbf{B}_{12}(\zeta_I) \tag{8}$$

$$\mathbf{K}_{STAB} = \int_{\Omega_e} \mathbf{B}_{12}^T \cdot \mathbf{C} \cdot \mathbf{B}_{34} \mathrm{d}\Omega + \int_{\Omega_e} \mathbf{B}_{34}^T \cdot \mathbf{C} \cdot \mathbf{B}_{12} \mathrm{d}\Omega + \int_{\Omega_e} \mathbf{B}_{34}^T \cdot \mathbf{C} \cdot \mathbf{B}_{34} \mathrm{d}\Omega \tag{9}$$

The stabilization terms are evaluated in a co-rotational system allowing to compute the integrals analytically, in this way improving accuracy and saving computing time.

3.2 Enhanced Assumed Strain EAS

Solid-shell elements are well known to be affected by volumetric locking and by the so-called Poisson thickness locking. Volumetric locking occurs when the material approaches incompressibility. Poisson thickness locking reveals itself in out-of-plane bending, e.g. about the η-axis (see Fig. 6). The analytical solution of the problem leads to a transverse normal strain $\varepsilon_{\zeta\zeta}$, which is constant within the shell plane but linear in the thickness direction ζ, while the assumed displacement model leads to $\varepsilon_{\zeta\zeta}$ constant through the thickness. To avoid Poisson thickness locking and volumetric locking, the strain terms $\varepsilon_{\xi\xi}$, $\varepsilon_{\eta\eta}$ and $\varepsilon_{\zeta\zeta}$ must be modeled through the thickness by polynomials of the same order. This can be achieved by enhancing the strain component $\varepsilon_{\zeta\zeta}$ in ζ direction by use of the EAS concept, as proposed e.g. in [11] and [12]. The covariant strain enhancement is expressed as

$$\boldsymbol{\varepsilon}_{enh} = \mathbf{B}_{enh} W_{enh} \tag{10}$$

where

$$\mathbf{B}_{enh} = [0, 0, \zeta, 0, 0, 0]^T \tag{11}$$

and W_{enh} is the enhancement degree-of-freedom of the considered element, which enriches $\varepsilon_{\zeta\zeta}$ linearly in ζ. The computationally inexpensive EAS approach avoids to make use of the modified plane-stress elastic tensor, used to this purpose in [9], which requires the definition of an additional material co-rotational reference frame.

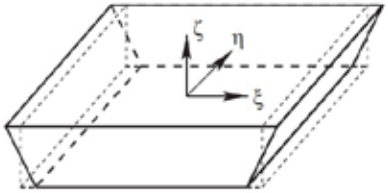

Figure 6: Bending about η-axis.

Application of the enhanced SHB8PS element to the cantilever plate strip under a tip load proposed in [13] (see Fig. 7) produces the results shown in Fig. 8.

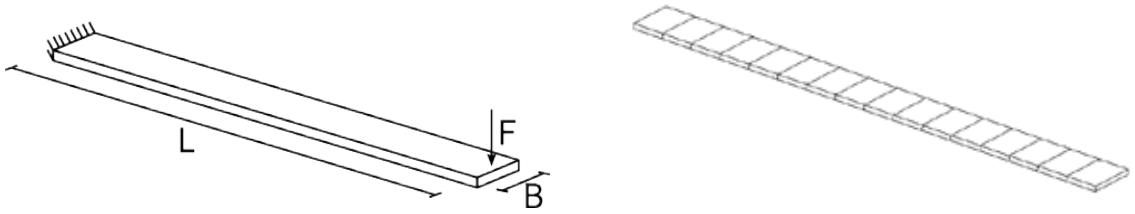

(a) (b)

Figure 7: Cantilever plate strip: (a) geometry and load; (b) mesh.

Table 1: Plate strip parameters

L	B	T	E
10 mm	1 mm	0.1 mm	10^7 N/mm^2

The plate strip is characterized by the geometric and material parameters reported in Table 1. The small-displacements out-of-plane bending behavior in the near incompressible limit is studied. The mesh consists of 16 regular elements while a total tip force of 40 N is applied in 10 time steps. Poisson's ratio is varied between $\nu = 0$ and $\nu = 0.499$, and load vs. displacement diagrams are shown in Figs. 8. It can be noted that while the SHB8PS element without any correction of the behavior in the thickness direction is

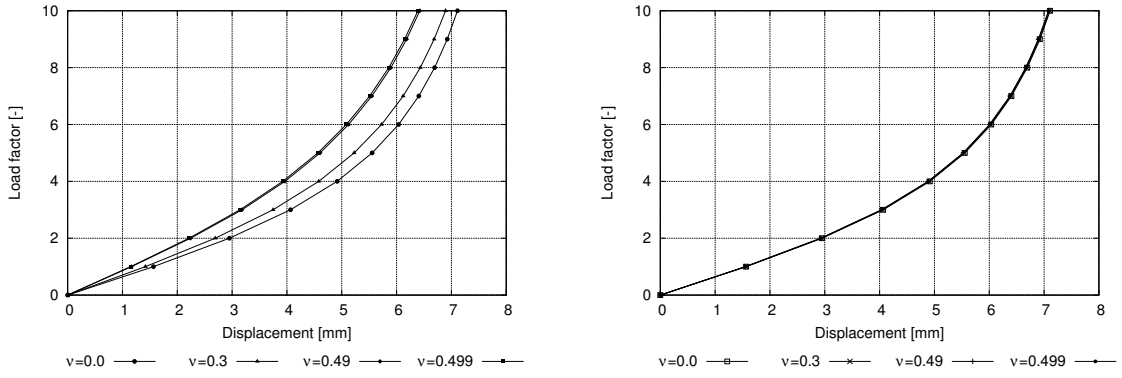

Figure 8: Cantilever plate strip under tip load: (a) SHB8PS element without EAS enhancement; (b) with EAS enhancement.

sensitive to Poisson's ratio variations (Fig. 8a), complete insensitivity of the response is shown by its enhanced version (Fig. 8b). A similar insensitivity is also obtained using the modified plane-stress elastic tensor as proposed in [9], though at the cost of computing a new co-rotational frame at each increment.

3.3 Element modification for explicit dynamics

For application to problems of the type considered in section 2, with contact and crack propagation, explicit dynamics approaches are usually preferred. However, the incorporation of solid-shell elements into an explicit code leads to very small time increments due to the element small thickness compared to the in-plane dimensions. Time-step sizes of the same order of magnitude of those required by normal shell elements, such as the MITC4 used in section 2, can be obtained by means of a variable transformation, where new translational and rotational degrees of freedom in the element middle plane are introduced according to the following definition:

$$\mathbf{u}_i = \frac{\mathbf{u}_a + \mathbf{u}_b}{2} \qquad i = 1,\dots,4 \qquad a = 1,2,3,4 \qquad b = 5,6,7,8 \tag{12}$$

$$\boldsymbol{\phi}_i = \frac{\mathbf{u}_b - \mathbf{u}_a}{2} \qquad i = 1,\dots,4 \qquad a = 1,2,3,4 \qquad b = 5,6,7,8 \tag{13}$$

$$\tag{14}$$

where $a = 1,2,3,4$ and $b = 5,6,7,8$ indicate nodes belonging to the lower and upper element faces, respectively, as depicted in Fig. 5. In this way it is possible to introduce a selective scaling of masses corresponding to the ϕ_i degrees of freedom, as is usually done in shell elements [14]. The effectiveness of this provision is studied by simulating the cantilever beam described in Fig. 9, impulsively loaded by a uniformly distributed transverse load. The beam has length $L = 10$ mm, a rectangular cross section of width

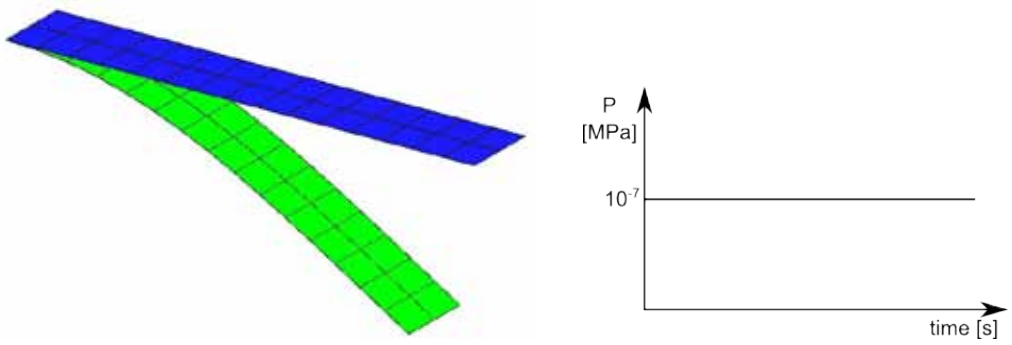

(a) (b)

Figure 9: Impulsively loaded cantilever beam: (a) Finite element undeformed/deformed mesh and (b) applied load.

$B = 2.5$ mm and thickness $T = 0.0074$ mm, Young modulus $E = 1768$ MPa, Poisson ratio $\nu = 0.3$, density $\rho = 3 \cdot 10^{-9}$ T/mm^3. The problem has been analyzed using three different types of elements: MITC4, SHB8PS and improved SHB8PS. The stable time increments obtained in the three cases according to Gerschgorin's theorem are reported in Table 2. It can be seen that the SHB8PS with transformed degrees of freedom leads to a stable time step of the same order of the MITC4, two orders of magnitude smaller than the standard SHB8PS. The displacement evolution of the beam tip, obtained by MITC4 and improved SHB8PS elements, is shown in Fig. 10. An almost complete agreement between the two analyses can be observed.

Table 2: Stable time increments

Element type	**Time increment**
MITC4	$5.17 \cdot 10^{-7}$ s
SHB8PS	$7.26 \cdot 10^{-9}$ s
Improved SHB8PS	$5.95 \cdot 10^{-7}$ s

4 CONCLUSIONS

The development of an effective numerical tool for the simulation of the cutting process of thin membranes has been discussed. It has been shown how the cutting of a rubber pre-tensioned membrane can be accurately simulated by using "directional" cohesive elements in conjunction with standard shell elements. In a more general case, inelastic dissipation due to plasticity and delamination takes place in the cutting region of thin laminates. The description of these nonlinear phenomena is more conveniently achieved by using solid-shell elements. Reference has been made to the SHB8PS element [9], recently proposed

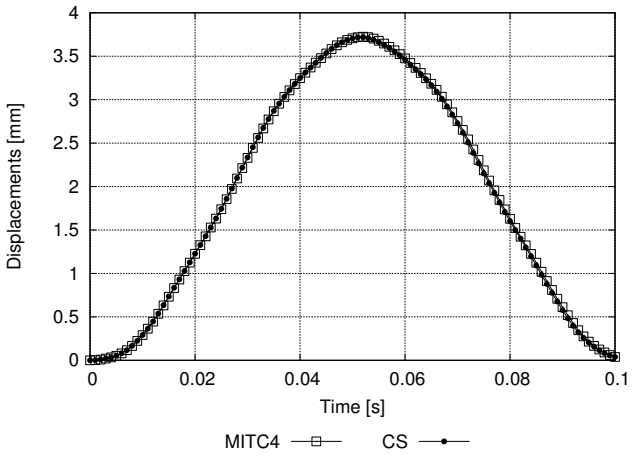

Figure 10: Impulsively loaded cantilever beam: tip displacements evolution obtained by MITC4 and SHB8PS elements.

in the literature. Two modifications of the element have been proposed to improve its performance: the adoption of an enhanced strain approach in the thickness direction, to avoid volume locking and Poisson's thickness locking, and a linear variable transformation, to allow for mass scaling and consequent increase of the time-step size in explicit dynamics. The application of this modified solid-shell element to cutting problems is currently in progress.

REFERENCES

[1] Frangi, T., Pagani, M., Perego, U. and Borsari, R. Directional Cohesive Elements for the Simulation of Blade Cutting of Thin Shells. *Computer Modeling in Engineering & Sciences*. (2010) **57:3**:205-224.

[2] Iqbal, M.A., Gupta, G. and Gupta, N.K. 3D numerical simulations of ductile targets subjected to oblique impact by sharp nosed projectiles. *International Journal of Solids and Structures*. (2010) **47(2)**:224-237.

[3] Song, J.H. and Belytschko, T. Dynamic fracture of shells subjected to impulsive loads. *Journal of Applied Mechanics*. (2009) **76**:051301_1 051301_9.

[4] Areias, P.M.A., Song, J.H. and Belytschko, T. Analysis of fracture in thin shells by overlapping paired elements. *Computer Methods in Applied Mechanics and Engineering*. (2006) **95(41-43)**:53435360.

[5] Atkins, T. *The science of engineering of cutting*. Buttenworth Heinemann, (2009).

[6] Lake, G. J. and Yeoh, O. H. Measurement of rubber cutting resistance in the absence of friction. *International Journal of Fracture* (1978) **14(5)**:509-526.

[7] Bathe, K. *Finite element procedures*. Prentice-Hall Int., Englewood Cliffs, NJ, USA, (2009).

[8] Belytschko, T. and Bindeman, L.P. Assumed strain stabilization of the eight node hexahedral element. *Computer Methods in Applied Mechanics and Engineering*. (1993) **105**:225-260

[9] Abed-Meraim, F. and Combescure, A. An improved assumed strain solid-shell element formulation with physical stabilization for geometric non-linear applications and elastic-plastic stability analysis. *International Journal for Numerical Methods in Engineering*. (2009) **80**:1640-1686.

[10] Flanagan, D. P. and Belytschko, T. A uniform strain hexahedron and quadrilateral with orthogonal hourglass control, *International Journal for Numerical Methods in Engineering*. (1981) **17(5)**:679-706.

[11] Schwarze, M. and Reese, S. A reduced integration solid-shell finite element based on the EAS and the ANS concept-Geometrically linear problems. *International Journal for Numerical Methods in Engineering*. (2009) **80**:1322-1355.

[12] Cardoso, R.P.R., Yoon, J.W., Mahardika, M., Choudhry, S., Alves de Sousa, R.J. and Fontes Valente, R.A. Enhanced assumed strain (EAS) and assumed natural strain (ANS) methods for one-point quadrature solid-shell elements. *International Journal for Numerical Methods in Engineering*. (2008) **75**:156-187.

[13] Schwarze, M. and Reese, S. A reduced integration solid-shell finite element based on the EAS and the ANS concept-Large deformation problems. *International Journal for Numerical Methods in Engineering*. (2010) **85**:289-329.

[14] Key, S.W. and Beisinger, Z.E. Transient Dynamic Analysis of Thin Shells by Finite Element Methods. *Proceedings of Third Conference Matrix Methods in Structural Analysis*, Wright-Patterson Air Force Base, Ohio (1971) .

XI International Conference on Computational Plasticity. Fundamentals and Applications
COMPLAS XI
E. Oñate, D.R.J. Owen, D. Peric and B. Suárez (Eds)

DISCONTINUOUS FAILURE IN A GRADIENT-ENHANCED CONTINUOUS DAMAGE MODEL: A REGULARISED DISPLACEMENT FRAMEWORK

ELENA TAMAYO-MAS, ANTONIO RODRÍGUEZ-FERRAN

Laboratori de Càlcul Numèric (LaCàN)
Departament de Matemàtica Aplicada III
Universitat Politècnica de Catalunya (UPC)
Campus Nord UPC, 08034, Barcelona, Spain
e-mail: {elena.tamayo, antonio.rodriguez-ferran}@upc.edu

Key words: Gradient damage model, Cohesive cracks, Smoothed displacements, Energy balance

Abstract. To simulate numerically a failure process, a new kind of model which combines the two traditional approaches (damage and fracture mechanics) has been proposed in the literature. The basic idea of these hybrid strategies is to employ regularised continuous models to describe the first stages of failure and discontinuous models to deal with the possible development of cracks.

Here, a new combined approach is presented. In order to describe damage inception and its diffuse propagation, an implicit gradient-enhanced continuum model based on smoothed displacements is used, where two different displacement fields coexist: (a) the standard displacements $\boldsymbol{u}$ and (b) the gradient-enriched displacement field $\widetilde{\boldsymbol{u}}$, which is the solution of a partial differential equation with $\boldsymbol{u}$ as the source term. Once the damage parameter exceeds a critical value, the continuous model is coupled to a discontinuous one. The eXtended Finite Element Method (X-FEM) is used to describe the growing cracks, whose direction of propagation is prescribed by the steepest descent direction of the damage profile and whose cohesive law is defined according to an energy balance. Therefore, the energy not yet dissipated by the continuous bulk is transmitted to the cohesive interface thus ensuring that the energy dissipated by the structure remains constant through the transition.

1 INTRODUCTION

To simulate numerically failure of quasi-brittle materials, two different kinds of approaches have usually been employed: (a) damage mechanics, which belongs to the family of continuous models and (b) fracture mechanics, which belongs to discontinuous models.

On the one hand, if damage mechanics analyses are carried out, the first stages of a failure process can be described. But these continuous models, which are characterised by a strain softening phenomenon, do not correctly reflect the energy dissipated in the fracture process zone [1]. Numerically, if stress-strain laws with softening are used, physically unrealistic results are obtained. To overcome this limitation, regularisation techniques may be employed to introduce non-locality into the model, either by integral-type [2, 3] or gradient-type [4, 5] approaches. However, if continuum models are used to describe the final stage of failure, numerical interaction between the physically separated parts of the body remains thus obtaining unrealistic results.

On the other hand, by means of fracture mechanics analyses, the last stages of failure may be described. These discontinuous models, which are based on the cohesive zone concept [6], can deal with evolving cracks and material separation but do not allow to describe neither damage inception nor its diffuse propagation [7].

In order to achieve a better description of the entire failure process, a new kind of model which combines these two traditional strategies has emerged [8–12]. The basic idea of these hybrid strategies is to use damage mechanics in order to characterise strain localisation and the accumulation of damage and fracture mechanics in order to deal with the possible formation of evolving macrocracks.

In this work, a new contribution in this direction is presented, see Figure 1. A gradient-enhanced damage model based on smoothed displacements [13] is used for the continuum. When the damage parameter exceeds a critical threshold D_{crit}, this regularised continuum model is coupled to a discontinuous one: a propagating crack, which is modelled by means of the X-FEM [14, 15], replaces the damaged zone and avoids formation of spurious damage growth. The discontinuity is completely characterised by the regularised continuum. On the one hand, the crack evolves according to the direction dictated by the steepest descent direction of the already formed damage profile. On the other hand, its cohesive law is defined by means of an energy balance in such a way that the energy which would be dissipated by the continuum is transferred to the crack.

An outline of this paper follows. The new continuous-discontinuous methodology is formulated in Section 2. In Section 3, the energy criterion used to define the cohesive crack is presented. To validate the proposed methodology, a three-point bending test is carried out in Section 4. In order to restrict attention to the proposed energy balance, a local continuum bulk is considered in Section 4.1. In Section 4.2, the same benchmark test is carried out with a non-local continuum bulk. The concluding remarks of Section 5 close this paper.

2 MODEL FORMULATION

2.1 Discontinuous displacements

Consider the domain Ω bounded by $\Gamma = \Gamma_u \cup \Gamma_t \cup \Gamma_d$, as shown in Figure 2. Prescribed displacements are imposed on Γ_u, prescribed tractions are imposed on Γ_t and the boundary

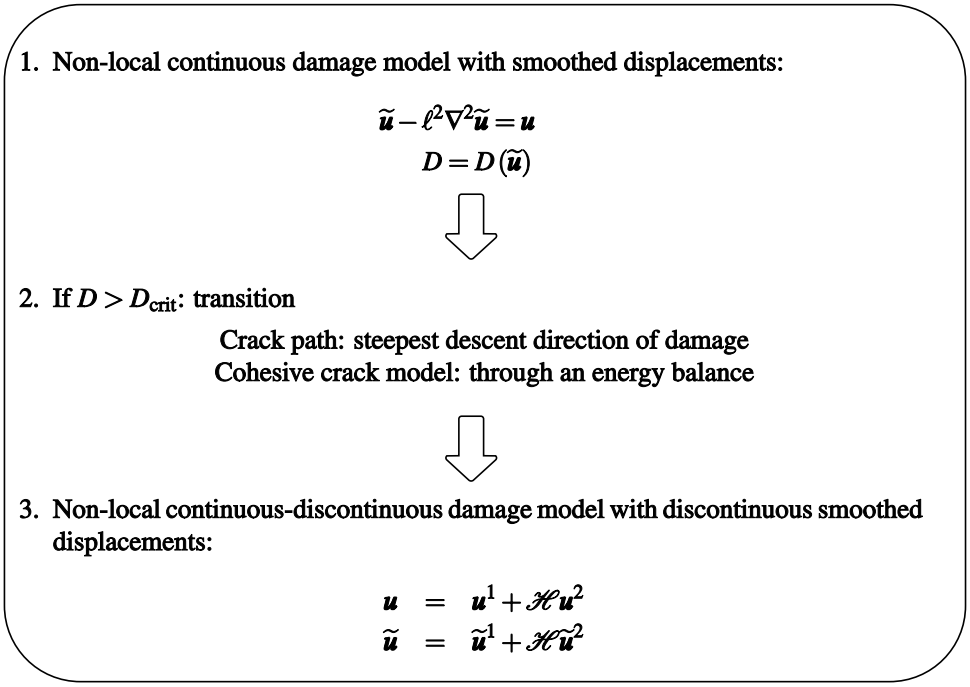

Figure 1: Proposed continuous-discontinuous strategy.

Γ_d consists of the boundary of the crack.

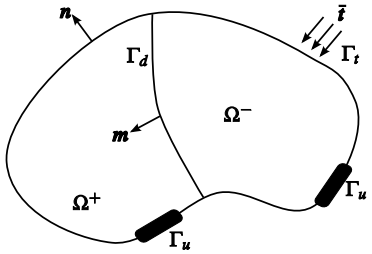

Figure 2: Notations for a body with a crack subjected to loads and imposed displacements.

By means of the X-FEM, the displacement field $\boldsymbol{u}$ can be decomposed as

$$\boldsymbol{u}(\boldsymbol{x}) = \boldsymbol{u}^1(\boldsymbol{x}) + \mathcal{H}(\boldsymbol{x})\,\boldsymbol{u}^2(\boldsymbol{x}) \qquad \text{in } \bar{\Omega} = \Omega \cup \Gamma \tag{1}$$

where $\boldsymbol{u}^i(\boldsymbol{x})$ $(i = 1, 2)$ are continuous fields and

$$\mathcal{H}(\boldsymbol{x}) = \begin{cases} 1 & \text{if} \quad \boldsymbol{x} \in \bar{\Omega}^+ \\ -1 & \text{if} \quad \boldsymbol{x} \in \bar{\Omega}^- \end{cases} \tag{2}$$

is the Heaviside function centred at Γ_d. The continuous part $\boldsymbol{u}^1(\boldsymbol{x})$ corresponds to the displacement field without any crack, while is the discontinuous displacement $\mathcal{H}(\boldsymbol{x})\,\boldsymbol{u}^2(\boldsymbol{x})$ the additional field that models the crack.

A similar decomposition holds for the smoothed displacements $\widetilde{\boldsymbol{u}}$

$$\widetilde{\boldsymbol{u}}\left(\boldsymbol{x}\right)=\widetilde{\boldsymbol{u}}^{1}\left(\boldsymbol{x}\right)+\mathcal{H}\left(\boldsymbol{x}\right)\widetilde{\boldsymbol{u}}^{2}\left(\boldsymbol{x}\right) \tag{3}$$

where $\widetilde{\boldsymbol{u}}^{i}\left(\boldsymbol{x}\right)$ $(i=1,2)$ are continuous fields.

2.2 Governing equations

The strong form of the equilibrium equation and boundary conditions for the body $\bar{\Omega}$ without body forces is given by

$$\begin{aligned}
\nabla\cdot\boldsymbol{\sigma} &= \mathbf{0} \quad \text{in } \Omega && \text{(4a)}\\
\boldsymbol{\sigma}\cdot\boldsymbol{n} &= \bar{\boldsymbol{t}} \quad \text{on } \Gamma_t && \text{(4b)}\\
\boldsymbol{\sigma}\cdot\boldsymbol{m} &= \bar{\boldsymbol{t}}_d \quad \text{on } \Gamma_d && \text{(4c)}\\
\boldsymbol{u} &= \boldsymbol{u}^{*} \quad \text{on } \Gamma_u && \text{(4d)}
\end{aligned}$$

where $\boldsymbol{\sigma}$ is the Cauchy stress tensor, $\boldsymbol{u}^{*}$ is a prescribed displacement, $\bar{\boldsymbol{t}}$ is the load on the boundary and $\bar{\boldsymbol{t}}_d$ is the load on the discontinuity surface. Note that $\boldsymbol{n}$ is the outward unit normal to the body and $\boldsymbol{m}$ is the inward unit normal to Ω^{+} on Γ_d, see Figure 2.

For convenience, and to complete the strong form of the mechanical problem, only an isotropic damage model

$$\boldsymbol{\sigma}\left(\boldsymbol{x}\right)=\left[1-D\left(\boldsymbol{x}\right)\right]\boldsymbol{C}:\boldsymbol{\varepsilon}\left(\boldsymbol{x}\right) \tag{5}$$

is considered, where $\boldsymbol{\varepsilon}\left(\boldsymbol{x}\right)=\nabla^{s}\boldsymbol{u}\left(\boldsymbol{x}\right)$ is the small strain tensor, $\boldsymbol{C}$ is the fourth-order tensor of elastic moduli and D is the isotropic damage parameter ($0\leq D\leq 1$ and $\dot{D}\geq 0$). Nevertheless, the gradient formulation based on smoothed displacements may be extended to other models such as plasticity [16].

In order to regularise the problem, the second-order diffusion partial differential equation

$$\widetilde{\boldsymbol{u}}-\ell^{2}\nabla^{2}\widetilde{\boldsymbol{u}}\left(\boldsymbol{x}\right)=\boldsymbol{u}\left(\boldsymbol{x}\right)\qquad \text{in}\,\Omega\setminus\Gamma_d \tag{6}$$

is coupled with the mechanical equations. Both for the standard and the enhanced displacement fields, combined boundary conditions

$$\left.\begin{aligned}
\widetilde{\boldsymbol{u}}^{i}\cdot\boldsymbol{n} &= \boldsymbol{u}^{i}\cdot\boldsymbol{n}\\
\nabla\left(\widetilde{\boldsymbol{u}}^{i}\cdot\boldsymbol{t}\right)\cdot\boldsymbol{n} &= \nabla\left(\boldsymbol{u}^{i}\cdot\boldsymbol{t}\right)\cdot\boldsymbol{n}
\end{aligned}\right\}\ \text{on }\Gamma
\qquad
\left.\begin{aligned}
\widetilde{\boldsymbol{u}}^{i}\cdot\boldsymbol{m} &= \boldsymbol{u}^{i}\cdot\boldsymbol{m}\\
\nabla\left(\widetilde{\boldsymbol{u}}^{i}\cdot\boldsymbol{t}\right)\cdot\boldsymbol{m} &= \nabla\left(\boldsymbol{u}^{i}\cdot\boldsymbol{t}\right)\cdot\boldsymbol{m}
\end{aligned}\right\}\ \text{on }\Gamma_d \tag{7}$$

where $i=1,2$, are proposed: Dirichlet boundary conditions are prescribed for the normal component of the displacement field whereas non-homogeneous Neumann boundary conditions are imposed for the tangential one. These combined conditions satisfy the necessary properties for regularisation: (a) reproducibility of order 1 ($\boldsymbol{u}=\widetilde{\boldsymbol{u}}$ if $\boldsymbol{u}$ is a linear field), (b) displacement smoothing along the boundary and (c) volume preservation [17].

2.3 Variational formulation

The space of trial standard displacements is characterised by the function defined in Eq. (1), where

$$\boldsymbol{u}^1, \boldsymbol{u}^2 \in \mathcal{U}_{\boldsymbol{u}} = \left\{ \boldsymbol{u} \mid \boldsymbol{u} \in H^1(\Omega) \text{ and } \boldsymbol{u}_{|\Gamma_u} = \boldsymbol{u}^* \right\} \tag{8}$$

with $H^1(\Omega)$ a Sobolev space. Analogously, the space of admissible displacement variations is defined by the weight function $\boldsymbol{\omega}(\boldsymbol{x}) = \boldsymbol{\omega}^1(\boldsymbol{x}) + \mathcal{H}(\boldsymbol{x})\boldsymbol{\omega}^2(\boldsymbol{x})$ with

$$\boldsymbol{\omega}^1, \boldsymbol{\omega}^2 \in \mathcal{W}_{\boldsymbol{u},\boldsymbol{0}} = \left\{ \boldsymbol{\omega} \mid \boldsymbol{\omega} \in H^1(\Omega) \text{ and } \boldsymbol{\omega}_{|\Gamma_u} = \boldsymbol{0} \right\} \tag{9}$$

Following standard procedures, the equilibrium equation (4a) can be cast in a variational form, thus leading to

$$\int_\Omega \nabla^s \boldsymbol{\omega}^1 : \boldsymbol{\sigma} \, \mathrm{d}\Omega = \int_{\Gamma_t} \boldsymbol{\omega}^1 \cdot \bar{\boldsymbol{t}} \, \mathrm{d}\Gamma \qquad \forall \boldsymbol{\omega}^1 \in H^1(\Omega) \tag{10a}$$

$$\int_\Omega \mathcal{H} \nabla^s \boldsymbol{\omega}^2 : \boldsymbol{\sigma} \, \mathrm{d}\Omega + 2 \int_{\Gamma_d} \boldsymbol{\omega}^2 \cdot \bar{\boldsymbol{t}}_d \, \mathrm{d}\Gamma = \int_{\Gamma_t} \mathcal{H} \boldsymbol{\omega}^2 \cdot \bar{\boldsymbol{t}} \, \mathrm{d}\Gamma \qquad \forall \boldsymbol{\omega}^2 \in H^1(\Omega) \tag{10b}$$

where at the discontinuity Γ_d,

$$\dot{\bar{\boldsymbol{t}}}_d = f\left([\![\dot{\boldsymbol{u}}]\!] \right) \tag{11}$$

with f relating traction rate $\dot{\bar{\boldsymbol{t}}}_d$ and displacement jump rate $[\![\dot{\boldsymbol{u}}]\!]$.

Similarly to the equilibrium equation, the regularisation PDE (6) is also cast in a weak form. Characterising the space of trial smoothed displacements $\widetilde{\boldsymbol{u}}$ by the function defined in Eq. (3), with $\boldsymbol{u}^1, \boldsymbol{u}^2 \in \mathcal{U}_{\boldsymbol{u}}$, one obtains

$$\begin{aligned}
\int_\Omega \boldsymbol{\omega}^1 \cdot (\widetilde{\boldsymbol{u}}^1 + \mathcal{H}\widetilde{\boldsymbol{u}}^2) \, \mathrm{d}\Omega \;+\; & \ell^2 \int_\Omega \nabla \boldsymbol{\omega}^1 : \left(\nabla \widetilde{\boldsymbol{u}}^1 + \mathcal{H} \nabla \widetilde{\boldsymbol{u}}^2 \right) \mathrm{d}\Omega + 2\ell^2 \int_{\Gamma_d} \omega_t^1 \left(\nabla \left(\boldsymbol{u}^2 \cdot \boldsymbol{t} \right) \cdot \boldsymbol{m} \right) \mathrm{d}\Gamma = \\
= \; & \int_\Omega \boldsymbol{\omega}^1 \cdot (\boldsymbol{u}^1 + \mathcal{H}\boldsymbol{u}^2) \, \mathrm{d}\Omega + \ell^2 \int_{\Gamma \setminus \Gamma_d} \omega_t^1 \left(\nabla \left(\boldsymbol{u}^1 \cdot \boldsymbol{t} \right) \cdot \boldsymbol{n} + \mathcal{H} \nabla \left(\boldsymbol{u}^2 \cdot \boldsymbol{t} \right) \cdot \boldsymbol{n} \right) \mathrm{d}\Gamma
\end{aligned} \tag{12a}$$

$$\begin{aligned}
\int_\Omega \boldsymbol{\omega}^2 \cdot (\mathcal{H}\widetilde{\boldsymbol{u}}^1 + \widetilde{\boldsymbol{u}}^2) \, \mathrm{d}\Omega \;+\; & \ell^2 \int_\Omega \nabla \boldsymbol{\omega}^2 : \left(\mathcal{H} \nabla \widetilde{\boldsymbol{u}}^1 + \nabla \widetilde{\boldsymbol{u}}^2 \right) \mathrm{d}\Omega + 2\ell^2 \int_{\Gamma_d} \omega_t^2 \left(\nabla \left(\boldsymbol{u}^1 \cdot \boldsymbol{t} \right) \cdot \boldsymbol{m} \right) \mathrm{d}\Gamma = \\
= \; & \int_\Omega \boldsymbol{\omega}^2 \cdot (\mathcal{H}\boldsymbol{u}^1 + \boldsymbol{u}^2) \, \mathrm{d}\Omega + \ell^2 \int_{\Gamma \setminus \Gamma_d} \omega_t^2 \left(\mathcal{H} \nabla \left(\boldsymbol{u}^1 \cdot \boldsymbol{t} \right) \cdot \boldsymbol{n} + \nabla \left(\boldsymbol{u}^2 \cdot \boldsymbol{t} \right) \cdot \boldsymbol{n} \right) \mathrm{d}\Gamma
\end{aligned} \tag{12b}$$

$\forall \boldsymbol{\omega}^1, \boldsymbol{\omega}^2 \in \mathcal{W}_{\boldsymbol{u},\boldsymbol{0}}$, where $\boldsymbol{t}$ is the unit tangent to the boundary.

2.4 Finite element discretisation

In combined strategies, the transition between the continuous and the discontinuous approach takes place when a critical situation is achieved. In a damaging continuum approach, for example, this critical situation occurs when the damage parameter at one integration point exceeds a critical damage value set *a priori*. Employing an extended

finite element strategy to prevent remeshing and other kinds of techniques, Eq. (1) and (3) read, in the domain of an element with enhanced nodes,

$$\mathbf{u}(\boldsymbol{x}) = \mathbf{N}(\boldsymbol{x})\mathbf{u}^1 + \mathcal{H}(\boldsymbol{x})\mathbf{N}(\boldsymbol{x})\mathbf{u}^2 \tag{13a}$$

$$\widetilde{\mathbf{u}}(\boldsymbol{x}) = \mathbf{N}(\boldsymbol{x})\widetilde{\mathbf{u}}^1 + \mathcal{H}(\boldsymbol{x})\mathbf{N}(\boldsymbol{x})\widetilde{\mathbf{u}}^2 \tag{13b}$$

where $\mathbf{N}$ is the matrix of standard finite element shape functions, $\mathbf{u}^1$, $\widetilde{\mathbf{u}}^1$ are the basic nodal degrees of freedom and $\mathbf{u}^2$, $\widetilde{\mathbf{u}}^2$ are the enhanced ones. The discrete format of the problem fields leads to the four discrete weak governing equations

$$\int_\Omega \mathbf{B}^T\boldsymbol{\sigma}\,\mathrm{d}\Omega = \int_{\Gamma_t} \mathbf{N}^T\bar{\boldsymbol{t}}\,\mathrm{d}\Gamma \tag{14a}$$

$$\int_\Omega \mathcal{H}\mathbf{B}^T\boldsymbol{\sigma}\,\mathrm{d}\Omega + 2\int_{\Gamma_d} \mathbf{N}^T\bar{\boldsymbol{t}}_d\,\mathrm{d}\Gamma = \int_{\Gamma_t} \mathcal{H}\mathbf{N}^T\bar{\boldsymbol{t}}\,\mathrm{d}\Gamma \tag{14b}$$

$$(\mathbf{M}+\ell^2\mathbf{D})\widetilde{\mathbf{u}}^1 + (\mathbf{M}_\mathcal{H}+\ell^2\mathbf{D}_\mathcal{H})\widetilde{\mathbf{u}}^2 = (\mathbf{M}+\ell^2\boldsymbol{C}^{\Gamma\setminus\Gamma_d,\boldsymbol{n}})\mathbf{u}^1 + (\mathbf{M}_\mathcal{H}+\ell^2(\boldsymbol{C}_\mathcal{H}^{\Gamma\setminus\Gamma_d,\boldsymbol{n}} - 2\boldsymbol{C}^{\Gamma_d,\boldsymbol{m}}))\mathbf{u}^2 \tag{14c}$$

$$(\mathbf{M}_\mathcal{H}+\ell^2\mathbf{D}_\mathcal{H})\widetilde{\mathbf{u}}^1 + (\mathbf{M}+\ell^2\mathbf{D})\widetilde{\mathbf{u}}^2 = (\mathbf{M}_\mathcal{H}+\ell^2(\boldsymbol{C}_\mathcal{H}^{\Gamma\setminus\Gamma_d,\boldsymbol{n}} - 2\boldsymbol{C}^{\Gamma_d,\boldsymbol{m}}))\mathbf{u}^1 + (\mathbf{M}+\ell^2\boldsymbol{C}^{\Gamma\setminus\Gamma_d,\boldsymbol{n}})\mathbf{u}^2 \tag{14d}$$

where $\mathbf{B}$ is the matrix of shape function derivatives and

$$\mathbf{M} = \int_\Omega \mathbf{N}^T\mathbf{N}\,\mathrm{d}\Omega \qquad \mathbf{D} = \int_\Omega \nabla\mathbf{N}^T\nabla\mathbf{N}\,\mathrm{d}\Omega \tag{15a}$$

$$\mathbf{M}_\mathcal{H} = \int_\Omega \mathcal{H}\mathbf{N}^T\mathbf{N}\,\mathrm{d}\Omega \qquad \mathbf{D}_\mathcal{H} = \int_\Omega \mathcal{H}\nabla\mathbf{N}^T\nabla\mathbf{N}\,\mathrm{d}\Omega \tag{15b}$$

$$\boldsymbol{C}^{\Gamma,\boldsymbol{n}} = \int_\Gamma \mathbf{N}^T\boldsymbol{t}\boldsymbol{t}^T\left[\frac{\partial\mathbf{N}}{\partial x}n_x + \frac{\partial\mathbf{N}}{\partial y}n_y\right]\mathrm{d}\Gamma \qquad \boldsymbol{C}_\mathcal{H}^{\Gamma,\boldsymbol{n}} = \int_\Gamma \mathcal{H}\mathbf{N}^T\boldsymbol{t}\boldsymbol{t}^T\left[\frac{\partial\mathbf{N}}{\partial x}n_x + \frac{\partial\mathbf{N}}{\partial y}n_y\right]\mathrm{d}\Gamma \tag{15c}$$

Some remarks about the discretisation:

- Eq. (14a) is the standard non-linear system of equilibrium equations, while Eq. (14b) deals with the contribution of the crack, which is multiplied by a factor of two due to the chosen definition of the Heaviside function, see Eq. (2).

- Matrices $\mathbf{M}$ and $\mathbf{D}$ are the constant mass and diffusivity matrices already obtained in [13]. The enriched matrices $\mathbf{M}_\mathcal{H}$ and $\mathbf{D}_\mathcal{H}$ are also constant, once the finite element is cracked.

- Matrices $\boldsymbol{C}^{\Gamma\setminus\Gamma_d,\boldsymbol{n}}$, $\boldsymbol{C}_\mathcal{H}^{\Gamma\setminus\Gamma_d,\boldsymbol{n}}$ and $\boldsymbol{C}^{\Gamma_d,\boldsymbol{m}}$ contain contributions from the combined boundary conditions (7). Since Dirichlet boundary conditions are prescribed for the normal component of the displacement field on Γ, the normal component of the weight function $\boldsymbol{\omega}$ vanishes on the boundary thus leading to

$$\int_\Gamma \boldsymbol{\omega}\nabla\widetilde{\boldsymbol{u}}\cdot\boldsymbol{n}\,\mathrm{d}\Gamma = \int_\Gamma \omega_t\nabla\left(\widetilde{\boldsymbol{u}}\cdot\boldsymbol{t}\right)\cdot\boldsymbol{n}\,\mathrm{d}\Gamma = \int_\Gamma \omega_t\nabla\left(\boldsymbol{u}\cdot\boldsymbol{t}\right)\cdot\boldsymbol{n}\,\mathrm{d}\Gamma \tag{16a}$$

  Again, $\boldsymbol{C}^{\Gamma_d,\boldsymbol{m}}$ is multiplied by a factor of two because of the Heaviside function.

- The symmetry of the resulting discretisation is due to the property $\mathcal{H}\mathcal{H} = +1$, which is derived from Eq. (2).

3 ENERGETICALLY EQUIVALENT CRACKS

In the proposed strategy, the transition between the continuous and the combined approach takes place when a critical situation is achieved, whose definition depends on the underlying continuous model. If a damage model is considered, the transition takes place when the damage value exceeds a critical threshold D_{crit}. Once this critical value is reached, a crack described by a cohesive law is initiated, damage value is fixed to D_{crit} and the bulk material unloads.

We propose to characterise the evolving crack by the regularised bulk. On the one hand, the direction of propagation must be determined. Although in a regularised continuous model, the crack growth cannot be analytically derived, the background can be used to deduce it. Here, the discontinuity is extended according to the steepest descent direction of the damage profile, thus avoiding the use of special tracking techniques. On the other hand, the cohesive law must be defined. The strategy here used is based on the idea that the energy which would be dissipated by a continuum approach is conserved if a combined strategy is used, see [8, 9].

Consider first the continuous approach and a damaged band λ_D. Then, in this zone of the structure, the dissipated energy can be expressed as

$$\Psi_C = \int_{\lambda_D} \psi_C \, \mathrm{d}\Omega = \int_{\lambda_D} \int_0^{t_f} \boldsymbol{\sigma}_C \cdot \dot{\boldsymbol{\varepsilon}}_C \, \mathrm{d}t \, \mathrm{d}\Omega \tag{17}$$

where the subscript C stands for *Continuous strategy* and $\dot{\boldsymbol{\varepsilon}}_C$ is the tensor of the strain rate.

Consider now the combined approach. In λ_D, the dissipated energy can be decomposed into two contributions

$$\Psi_{CD} = \Psi_{CD}^{\text{bulk}} + \Psi_{CD}^{\text{crack}} = \int_{\lambda_D} \int_0^{t_f} \boldsymbol{\sigma}_{CD} \cdot \dot{\boldsymbol{\varepsilon}}_{CD} \, \mathrm{d}t \, \mathrm{d}\Omega + \Psi_{CD}^{\text{crack}} \tag{18}$$

where the subscript CD stands for *Continuous-Discontinuous strategy*, Ψ_{CD}^{bulk} is the dissipated energy of the bulk and Ψ_{CD}^{crack} is the fracture energy.

Hence, imposing energy balance

$$\Psi_C = \Psi_{CD} \tag{19}$$

see Figure 3, the fracture energy

$$\Psi_{CD}^{\text{crack}} = \Psi_C - \Psi_{CD}^{\text{bulk}} \tag{20}$$

is computed and can be transferred to the crack at the moment of the transition.

In order to estimate the fracture energy, different techniques can be employed. In [9], an analytical estimation of Ψ_{CD}^{crack}, and thus, of the crack stiffness, is computed. Nevertheless, with this procedure, the fracture energy is overestimated. Indeed, by means of these

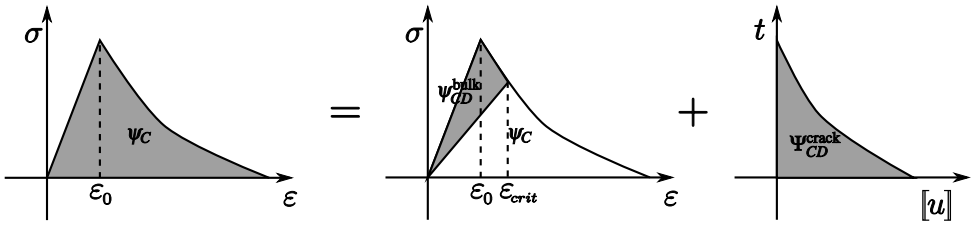

Figure 3: Energy balance.

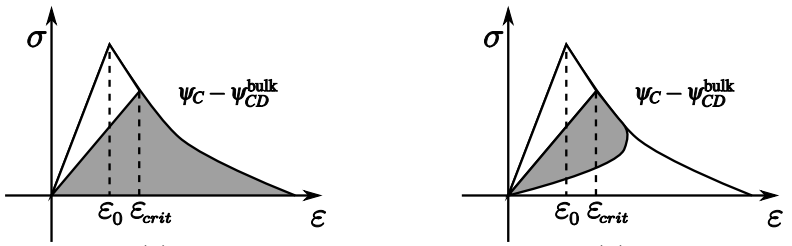

Figure 4: Energy not yet dissipated in the damage band which is transmitted to the cohesive crack and is dissipated by the continuous-discontinuous model, considering that by the continuous strategy, (a) all the points of λ_D download following the softening branch and (b) points of λ_D download following both softening and elastic branches.

assumptions, in all points across the damage band λ_D, the energy $\Psi_C - \Psi_{CD}^{\text{bulk}}$ depicted in Figure 4(a) is transferred to the crack. However, in some of these points, the continuous strategy would dissipate less energy, see Figure 4(b).

As suggested by this discussion, we propose to employ a new methodology which takes into account, for each point across the damage band λ_D, the unloading behaviour (both softening and secant) of the continuous bulk. Since the continuous unloading branch is only known up to the activation of the continuous-discontinuous strategy, we propose to approximate it by the tangent to the transition point. By means of this strategy, the dissipated energy Ψ_{CD}^{crack} is more accurately estimated, although it cannot be exactly computed. Again, as in [9], the accuracy of this strategy increases considerably if the crack is activated at a later stage of the failure process.

4 APPLICATION TO A THREE-POINT BENDING TEST

The new methodology is illustrated on a three-point bending test. In order to cause localisation, a weakened region is considered, see Figure 5. The test is carried out according to a simplified Mazars criterion and the trilinear softening law

$$D = \begin{cases} 0 & \text{if} \quad 0 \le Y \le Y_0 \\ \frac{Y_f}{Y_f - Y_0}\left(1 - \frac{Y_0}{Y}\right) & \text{if} \quad Y_0 \le Y \le Y_f \\ 1 & \text{if} \quad Y_f \le Y \end{cases} \tag{21}$$

Based on this damage evolution, the linear traction-separation law

$$\bar{\boldsymbol{t}}_d = \left\{ \begin{array}{c} \bar{t}_n \\ \bar{t}_s \end{array} \right\} = \mathbf{T} \left\{ \begin{array}{c} [\![\boldsymbol{u}]\!]_n \\ [\![\boldsymbol{u}]\!]_s \end{array} \right\} + \left\{ \begin{array}{c} t_{\text{crit}} \\ 0 \end{array} \right\} = \left(\begin{array}{cc} T_n & 0 \\ 0 & 0 \end{array} \right) \left\{ \begin{array}{c} [\![\boldsymbol{u}]\!]_n \\ [\![\boldsymbol{u}]\!]_s \end{array} \right\} + \left\{ \begin{array}{c} t_{\text{crit}} \\ 0 \end{array} \right\} \tag{22}$$

is prescribed, where imposing $\Psi_{CD}^{\text{crack}} = \int_0^\infty t_n \, \mathrm{d}[\![\boldsymbol{u}]\!]_n$, $T_n = -\frac{1}{2} \frac{t_{\text{crit}}^2}{\Psi_{CD}^{\text{crack}}}$.

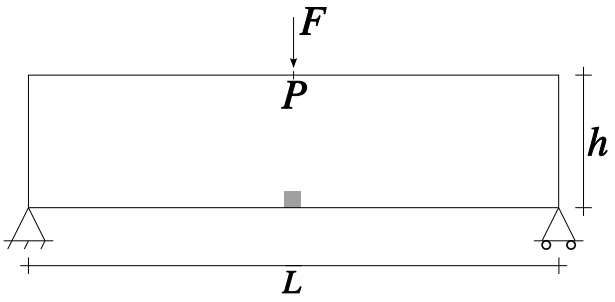

Figure 5: Three-point bending test: problem statement.

The geometric and material parameters for this test are summarised in Table 1.

Table 1: Three-point bending test: geometric and material parameters.

Meaning	Symbol	Value
Length of the specimen	L	3 mm
Width of the specimen	h	1 mm
Young's modulus	E	30 000 MPa
Idem of weaker part	E_W	27 000 MPa
Damage threshold	Y_0	10^{-4}
Final strain	Y_f	1.25×10^{-2}
Poisson's coefficient	ν	0.0
Critical damage	D_{crit}	0.995

4.1 Local bulk

First, and in order to focus on the proposed energy balance, a local continuum damage model is considered. The force-displacement curves and the damage profiles with the deformed meshes are shown in Figure 6. For comparison purposes, three kinds of results are shown. On the one hand, the continuous (C) results are plotted. On the other hand, two different continuous-discontinuous (CD) results are shown: the ones obtained with (a) the analytical estimation of the dissipated energy and (b) the proposed methodology, which does not overestimate the fracture energy. As seen, it increases the accuracy when estimating Ψ_{CD}^{crack}.

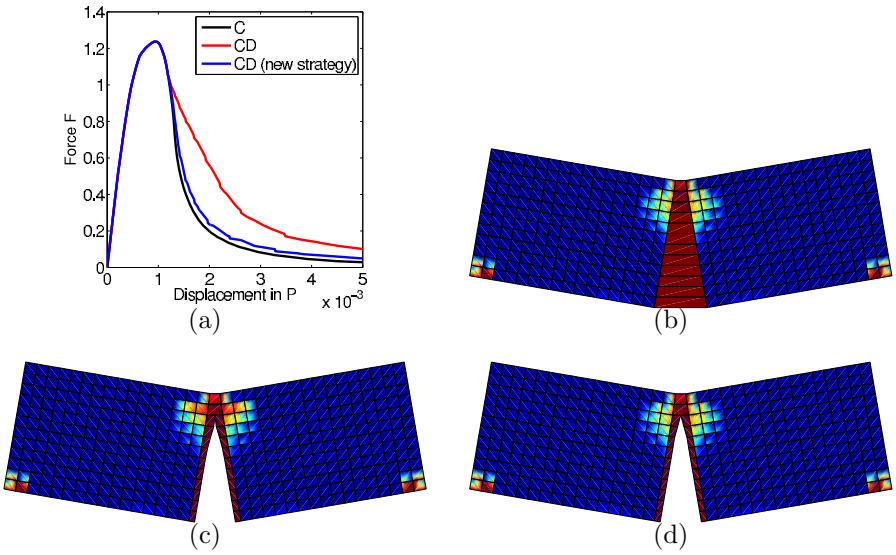

Figure 6: Three-point bending test with a local damage bulk: (a) force-displacement curves; final damage profiles with deformed meshes (×50) obtained with (b) the C strategy, (c) the CD strategy which overestimates the fracture energy and (d) the CD strategy based on the new proposed methodology.

4.2 Non-local bulk

As a second test, the same benchmark example is carried out with a non-local damage bulk. Results are shown in Figure 7. Again, three kinds of results are shown. As seen, the proposed methodology allows to estimate properly Ψ_{CD}^{crack} making the continuous and the continuous-discontinuous strategies energetically equivalent.

5 CONCLUSIONS

A new strategy to simulate an entire failure process is proposed: a gradient-enriched formulation based on smoothed displacements is enhanced with a discontinuous interpolation of the problem fields in order to describe its final stages, where macroscopic cracks can arise.
The main features of this new combined strategy are summarised here:

- The gradient-enhanced approach with smoothed displacements is able to obtain physically realistic results. Combined boundary conditions must be imposed on the boundary to solve the regularisation PDE.

- At the end of each time step, the strategy checks if the critical situation is achieved. If the transition criterion is satisfied, a discrete crack whose properties depend on the underlying continuous, is introduced.

  – This evolving crack propagates across the bulk according to the direction determined by the already damage profile.

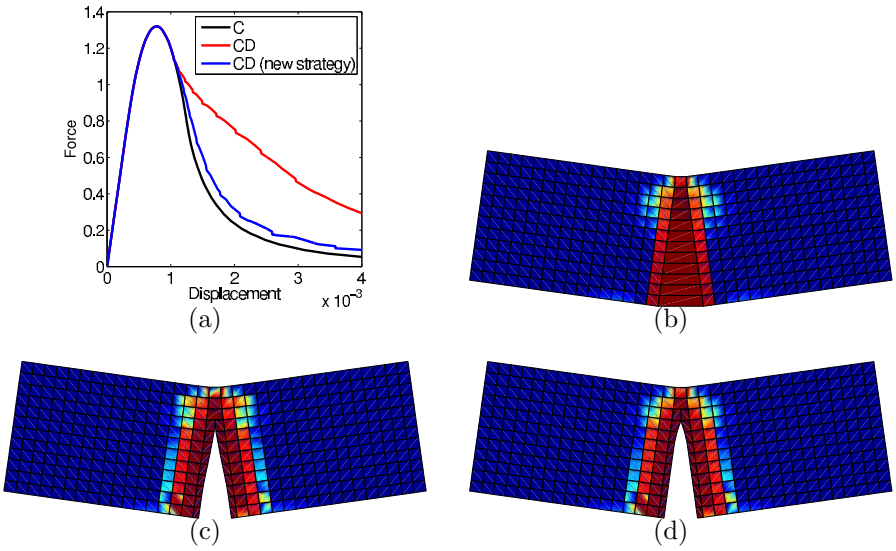

Figure 7: Three-point bending test with a non-local damage bulk: (a) force-displacement curves; final damage profiles with deformed meshes (×50) obtained with (b) the C strategy, (c) the CD strategy which overestimates the fracture energy and (d) the CD strategy based on the new proposed methodology.

  - The cohesive law is defined through an energy balance: the energy remaining to be dissipated by the continuum approach is transmitted to the cohesive zone.

- Once the crack is introduced, both standard displacements $\boldsymbol{u}$ and gradient-enhanced displacement field $\widetilde{\boldsymbol{u}}$ may admit discontinuities.

References

[1] M. Jirásek. Mathematical analysis of strain localization. *Revue Européenne de Génie Civil*, 11(7-8):977–991, 2007.

[2] Z. P. Bažant and M. Jirásek. Nonlocal integral formulations of plasticity and damage: survey of progress. *Journal of Engineering Mechanics*, 128(11):1119–1149, 2002.

[3] G. Pijaudier-Cabot and Z. P. Bažant. Nonlocal damage theory. *Journal of Engineering Mechanics - ASCE*, 118(10):1512–1533, 1987.

[4] R. de Borst, J. Pamin, R. H. J. Peerlings, and L. J. Sluys. On gradient-enhanced damage and plasticity models for failure in quasi-brittle and frictional materials. *Computational Mechanics*, 17(1-2):130–141, 1995.

[5] R. H. J. Peerlings, R. de Borst, W. A. M. Brekelmans, and M. G. D. Geers. Gradient-enhanced damage modelling of concrete fracture. *Mechanics of Cohesive-frictional Materials*, 3(4):323–342, 1998.

[6] A. Hillerborg, M. Modeer, and P. A. Petersson. Analysis of crack formation and crack growth in concrete by means of fracture mechanics and finite elements. *Cement and Concrete Research*, 6(6):773–782, 1976.

[7] J. Mazars and G. Pijaudier-Cabot. From damage to fracture mechanics and conversely: a combined approach. *International Journal of Solids and Structures*, 33(20-22):3327–3342, 1996.

[8] F. Cazes, M. Coret, A. Combescure, and A. Gravouil. A thermodynamic method for the construction of a cohesive law from a nonlocal damage model. *International Journal of Solids and Structures*, 46(6):1476–1490, 2009.

[9] C. Comi, S. Mariani, and U. Perego. An extended FE strategy for transition from continuum damage to mode I cohesive crack propagation. *International Journal for Numerical and Analytical Methods in Geomechanics*, 31(2):213–238, 2007.

[10] A. Simone, G. N. Wells, and L. J. Sluys. From continuous to discontinuous failure in a gradient-enhanced continuum damage model. *Computer Methods in Applied Mechanics and Engineering*, 192(41-42):4581–4607, 2003.

[11] M. Jirásek and T. Zimmermann. Embedded crack model: II. combination with smeared cracks. *International Journal for Numerical Methods in Engineering*, 50(6):1291–1305, 2001.

[12] G. N. Wells, L. J. Sluys, and R. De Borst. Simulating the propagation of displacement discontinuities in a regularized strain-softening medium. *International Journal for Numerical Methods in Engineering*, 53(5):1235–1256, 2002.

[13] A. Rodríguez-Ferran, I. Morata, and A. Huerta. A new damage model based on nonlocal displacements. *International Journal for Numerical and Analytical Methods in Geomechanics*, 29(5):473–493, 2005.

[14] N. Moës, J. Dolbow, and T. Belytschko. A finite element method for crack growth without remeshing. *International Journal for Numerical Methods in Engineering*, 46(1):131–150, 1999.

[15] T. Belytschko and T. Black. Elastic crack growth in finite elements with minimal remeshing. *International Journal for Numerical Methods in Engineering*, 45(5):601–620, 1999.

[16] A. Rodríguez-Ferran, T. Bennett, H. Askes, and E. Tamayo-Mas. A general framework for softening regularisation based on gradient elasticity. *International Journal of Solids and Structures*, 48(9):1382–1394, 2011.

[17] E. Tamayo-Mas and A. Rodríguez-Ferran. Condiciones de contorno en modelos de gradiente con desplazamientos suavizados. *Submitted*.

XI International Conference on Computational Plasticity. Fundamentals and Applications
COMPLAS XI
E. Oñate, D.R.J. Owen, D. Peric and B. Suárez (Eds)

EXPONENTIAL FINITE ELEMENT SHAPE FUNCTIONS FOR A PHASE FIELD MODEL OF BRITTLE FRACTURE

CHARLOTTE KUHN* AND RALF MÜLLER†

Institute of Applied Mechanics
Technische Universität Kaiserslautern
P.O.B. 3049, 67653 Kaiserslautern
http://mechanik.mv.uni-kl.de/
*e-mail: chakuhn@rhrk.uni-kl.de

†e-mail: ram@rhrk.uni-kl.de

Key words: Phase Field Model, Fracture, Finite Elements, Exponential Shape Functions

Abstract. In phase field models for fracture a continuous scalar field variable is used to indicate cracks, i.e. the value 1 of the phase field variable is assigned to sound material, while the value 0 indicates fully broken material. The width of the transition zone where the phase field parameter changes between 1 and 0 is controlled by a regularization parameter. As a finite element discretization of the model needs to be fine enough to resolve the crack field and its gradient, the numerical results are sensitive to the choice of the regularization parameter in conjunction with the mesh size. This is the main challenge and the computational limit of the finite element implementation of phase field fracture models. To overcome this limitation a finite element technique using special shape functions is introduced. These special shape functions take into account the exponential character of the crack field as well as its dependence on the regularization length. Numerical examples show that the exponential shape functions allow a coarser discretization than standard linear shape functions without compromise on the accuracy of the results. This is due to the fact, that using exponential shape functions, the approximation of the surface energy of the phase field cracks is impressively precise, even if the regularization length is rather small compared to the mesh size. Thus, these shape functions provide an alternative to a numerically expensive mesh refinement.

1 INTRODUCTION

Variational formulations of brittle fracture as suggested by Francfort and Marigo [1] overcome some of the limitations of classical Griffith theory. However, a direct discretization of such fracture models is faced with significant technical difficulties. A regularized approximation by means of Γ-convergence as presented by Bourdin [2] offers a new

perspective towards the computational implementation of the model. The core of the regularization is the approximation of the total energy functional, in which a continuous scalar field variable is introduced to indicate cracks, i.e. the value of 1 is assigned to sound material and a value of 0 indicates fracture. With this crack field the regularized model resembles a phase field model for fracture, where additionally a Ginzburg–Landau type equation is used to describe the evolution of the crack field and cracking is addressed as a phase transition problem. Similar phase field fracture models have been introduced e.g. in [3, 4, 5, 6, 7, 8]. Differing in technical details all of these models introduce a regularization length which controls the width of the transition zone where the crack field interpolates between broken and unbroken material; i.e. the smaller the regularization parameter, the smaller the transition zone and the higher the gradients of the crack field in the vicinity of the cracks.

Numerical implementations are faced with the difficulty that the spacial discretization has to be fine enough to resolve these high gradients of the crack field, which leads to high computational costs for small values of the regularization parameter. On the other hand the regularization length needs to be chosen sufficiently small in conjunction with the global geometric dimension of the sample in order to get reasonable results. The most common approach to meet the requirement for a sufficiently fine resolution on the one hand and to keep the computation time within bounds on the other hand are adaptive mesh refinement techniques as used e.g. in [9], where the mesh is only refined where it is necessary, i.e. in the vicinity of a crack. Another approach to increase the efficiency of the computations was introduced in [5], where Fourier transforms are used to solve the linear part of the problem. However, this technique restricts the simulations to problems with periodic boundary conditions.

In this work we follow a different approach which is inspired by [10], where exponential finite element (FE) shape functions are introduced as an alternative to an extensive mesh refinement in the simulation of extrusion processes. These special shape functions qualitatively capture the shape of the solution and thus allow a much coarser discretization than the standard discretization using linear shape functions. In contrast to the simulation of the extrusion process, where the exponential shape functions are used in one distinct direction only, the discretization of the crack field in a two dimensional setting requires an extension of the concept to the full 2d case.

2 A PHASE FIELD MODEL FOR FRACTURE

2.1 Governing Equations

The present phase field model of fracture is based on a regularized version of the variational formulation of brittle fracture by [1] which was introduced in [11]. The core of the regularization is the approximation of the total energy of a cracked linear elastic

body Ω, with the stiffness tensor $\mathbb{C}$ and the cracking resistance $\mathcal{G}_c$, by the functional

$$E(\boldsymbol{\varepsilon}, s) = \int_\Omega \psi(\boldsymbol{\varepsilon}, s)\, dV = \int_\Omega \underbrace{\frac{1}{2}(s^2+\eta)\boldsymbol{\varepsilon}\cdot(\mathbb{C}\boldsymbol{\varepsilon})}_{=\psi^{\mathrm{e}}(\boldsymbol{\varepsilon},s)} + \underbrace{\mathcal{G}_c\left(\frac{1}{4\epsilon}(1-s)^2 + \epsilon|\nabla s|^2\right)}_{=\psi^{\mathrm{s}}(s)}\, dV\,. \tag{1}$$

This energy as well as the energy density ψ are functions of the linearized strain tensor $\boldsymbol{\varepsilon} = \frac{1}{2}(\nabla\boldsymbol{u} + (\nabla\boldsymbol{u})^T)$, i.e. the symmetric part of the gradient of the displacements $\boldsymbol{u}$ and the continuous scalar crack field s, which takes the value 1, if the material is undamaged, and 0 if there is a crack. The degradation of the elastic energy in the bulk $E^{\mathrm{e}} = \int_\Omega \psi^{\mathrm{e}}\, dV$ upon cracking is modeled by the factor $(s^2+\eta)$, where the small positive parameter η is introduced to obtain an artificial rest stiffness $\eta\mathbb{C}$ at fully broken state ($s = 0$) in order to circumvent numerical difficulties. The parameter ϵ, appearing twice in the surface energy $E^{\mathrm{s}} = \int_\Omega \psi^{\mathrm{s}}\, dV$, has the dimension of length and controls the width of the transition zone between broken and unbroken material, where s interpolates between 0 and 1.

If body forces and inertia terms are neglected, the mechanical part of the problem is described by the local balance law for the Cauchy stress tensor $\boldsymbol{\sigma}$

$$\mathrm{div}\boldsymbol{\sigma} = \mathbf{0}\,, \tag{2}$$

plus the according boundary conditions $\boldsymbol{\sigma}\boldsymbol{n} = \boldsymbol{t}_n^*$ on $\partial\Omega_t$, where $\boldsymbol{n}$ is the outer normal vector, and the material law (3) derived from the energy density ψ

$$\boldsymbol{\sigma} = \frac{\partial\psi}{\partial\boldsymbol{\varepsilon}} = (s^2+\eta)\mathbb{C}\boldsymbol{\varepsilon}\,. \tag{3}$$

Interpreting s as order parameter of a phase field model, its evolution in time is assumed to follow a Ginzburg–Landau type evolution equation, where $\dot{s}$ is proportional to the variational derivative of the energy density ψ with respect to s.

$$\dot{s} = -M\cdot\frac{\delta\psi}{\delta s} = -M\left[s\boldsymbol{\varepsilon}\cdot(\mathbb{C}\boldsymbol{\varepsilon}) - \mathcal{G}_c\left(2\epsilon\Delta s + \frac{1-s}{2\epsilon}\right)\right] \tag{4}$$

The mobility factor M is a positive constant, which controls the dissipation in the process zone. For sufficiently large values of M the solution of the evolution equation can be considered as stationary. In order to take into consideration the irreversible character of cracking, $s(\boldsymbol{x}, t)$ is fixed to 0 for all future times $t > t^*$ if it becomes 0 at any time t^*.

2.2 Evolution Equation in 1d

In a 1d setting, the evolution equation for a stationary ($\dot{s} = 0$) crack field reduces to

$$s'' - \frac{s}{4\epsilon^2} = -\frac{1}{4\epsilon^2}\,, \tag{5}$$

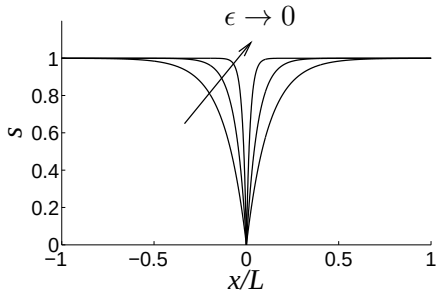

Figure 1: 1d stationary crack field

if elastic contributions are neglected. With boundary conditions $s(0) = 0$ and $s'(\pm\infty) = 0$ the analytic solution of Eq. (5) is given by

$$s(x) = 1 - \exp\left(-\frac{|x|}{2\epsilon}\right) \tag{6}$$

Figure 1 illustrates the impact of the regularization length ϵ on the crack field $s(x)$. The smaller ϵ gets, the higher gradients and curvatures of the solution $s(x)$ appear in the vicinity of the crack at $x = 0$. The limit $\epsilon \to 0$ yields a discontinuous function, which is 0 at $x = 0$ and 1 elsewhere.

3 NUMERICAL IMPLEMENTATION

3.1 Weak Forms

Starting point for the FE implementation of the coupled problem of mechanical balance equation (2) and evolution equation (4) are the weak forms of these field equations. With virtual displacements $\delta\boldsymbol{u}$ and δs, they read

$$\int_\Omega \nabla\delta\boldsymbol{u} \cdot \boldsymbol{\sigma}\, dV = \int_{\partial\Omega_t} \delta\boldsymbol{u} \cdot \boldsymbol{t}_n^*\, dA \tag{7}$$

with prescribed surface traction $\boldsymbol{t}_n^*$ on part $\partial\Omega_t$ of the boundary and

$$\int_\Omega \left[\delta s \frac{\dot{s}}{M} - \nabla\delta s \cdot \boldsymbol{q} + \delta s \left(s\boldsymbol{\varepsilon} : [\mathbb{C}\boldsymbol{\varepsilon}] + \frac{\mathcal{G}_c}{2\epsilon}(s-1)\right)\right] dV = 0 \tag{8}$$

with $\boldsymbol{q} = -2\mathcal{G}_c\,\epsilon\,\nabla s$. The normal flux $\boldsymbol{q} \cdot \boldsymbol{n}$ is assumed to vanish on the boundary $\partial\Omega$.

3.2 Finite Element Discretization

In a 2d setting the weak forms of the field equations (7) and (8) are discretized with 4 node quadrilateral elements with 3 degrees of freedom (u_x, u_y, s) per node. The displacements $\boldsymbol{u}$, the crack field s, as well as their virtual counterparts $\delta\boldsymbol{u}$ and δs are approximated

by shape functions $N_I^{\boldsymbol{u}}$, N_I^s, $N_I^{\delta\boldsymbol{u}}$, and $N_I^{\delta s}$, which interpolate the respective nodal values $\hat{\boldsymbol{u}}_I$, $\hat{s}_I$, $\delta\hat{\boldsymbol{u}}_I$, and $\delta\hat{s}_I$. Using Voigt–notation - denoted by an underline in the following - the approximations read

$$\underline{\boldsymbol{u}} = \sum_{I=1}^{N} N_I^{\boldsymbol{u}} \underline{\hat{\boldsymbol{u}}}_I \,, \quad s = \sum_{I=1}^{N} N_I^s \hat{s}_I \,, \quad \underline{\delta\boldsymbol{u}} = \sum_{I=1}^{N} N_I^{\delta\boldsymbol{u}} \underline{\delta\hat{\boldsymbol{u}}}_I \,, \quad \text{and} \quad \delta s = \sum_{I=1}^{N} N_I^{\delta s} \delta\hat{s}_I \,. \tag{9}$$

Accordingly the approximations of the gradient expressions yield

$$\underline{\boldsymbol{\varepsilon}} = \sum_{I=1}^{N} [\underline{B}_I^{\boldsymbol{u}}] \underline{\hat{\boldsymbol{u}}}_I, \quad \underline{\nabla s} = \sum_{I=1}^{N} [\underline{B}_I^s] \hat{s}_I, \quad \underline{\delta\boldsymbol{\varepsilon}} = \sum_{I=1}^{N} [\underline{B}_I^{\delta\boldsymbol{u}}] \underline{\delta\hat{\boldsymbol{u}}}_I, \quad \text{and } \underline{\nabla\delta s} = \sum_{I=1}^{N} [\underline{B}_I^{\delta s}] \delta\hat{s}_I \,, \tag{10}$$

where the derivative matrices

$$[\underline{B}_I^{\boldsymbol{u}}] = \begin{bmatrix} N_{I,x}^{\boldsymbol{u}} & 0 \\ 0 & N_{I,y}^{\boldsymbol{u}} \\ N_{I,y}^{\boldsymbol{u}} & N_{I,x}^{\boldsymbol{u}} \end{bmatrix}, \; [\underline{B}_I^s] = \begin{bmatrix} N_{I,x}^s \\ N_{I,y}^s \end{bmatrix}, \; [\underline{B}_I^{\delta\boldsymbol{u}}] = \begin{bmatrix} N_{I,x}^{\delta\boldsymbol{u}} & 0 \\ 0 & N_{I,y}^{\delta\boldsymbol{u}} \\ N_{I,y}^{\delta\boldsymbol{u}} & N_{I,x}^{\delta\boldsymbol{u}} \end{bmatrix}, \text{ and } [\underline{B}_I^{\delta s}] = \begin{bmatrix} N_{I,x}^{\delta s} \\ N_{I,y}^{\delta s} \end{bmatrix} \tag{11}$$

are obtained from the derivatives of the shape functions.

By a standard argument for finite element approximations the nodal values $\delta\hat{\boldsymbol{u}}_I$ and $\delta\hat{s}_I$ of the virtual quantities $\delta\boldsymbol{u}$ and δs drop out of the system of equations, leading to the nodal residuals

$$[\underline{R}_I] = \begin{bmatrix} \underline{R}_I^{\boldsymbol{u}} \\ R_I^s \end{bmatrix} = \int_\Omega \begin{bmatrix} [\underline{B}_I^{\delta\boldsymbol{u}}]^T \underline{\boldsymbol{\sigma}} \\ N_I^{\delta s} \dfrac{\dot{s}}{M} - [\underline{B}_I^{\delta s}]^T \underline{\boldsymbol{q}} + N_I^{\delta s} \left(s\, \underline{\boldsymbol{\varepsilon}}^{T\cdot} (\underline{\mathbb{C}}\, \underline{\boldsymbol{\varepsilon}}) + \dfrac{\mathcal{G}_c}{2\,\epsilon}(s-1) \right) \end{bmatrix} dV \,. \tag{12}$$

The time integration of the transient terms is performed with the implicit Euler method. Together with the nonlinear character of the phase field model this yields a nonlinear system of equations, which has to be solved in every time step Δt. This is done with a Newton–Raphson algorithm, which requires the derivation of the consistent tangent matrix $\left[\underline{S}_{IJ}\right]$ which has the following structure:

$$\left[\underline{S}_{IJ}\right] = \left[\underline{K}_{IJ}\right] + \frac{1}{\Delta t} \left[\underline{D}_{IJ}\right] \,. \tag{13}$$

The stiffness matrix $\left[\underline{K}_{IJ}\right]$ and the damping matrix $\left[\underline{D}_{IJ}\right]$ are obtained by derivation of the nodal residuals $\left[\underline{R}_I\right]$ with respect to the nodal values $(\underline{\hat{\boldsymbol{u}}}_J, \hat{s}_J)$ and $(\underline{\dot{\hat{\boldsymbol{u}}}}_J, \dot{\hat{s}}_J)$, respectively.

$$\left[\underline{K}_{IJ}\right] = \int_\Omega \begin{bmatrix} [\underline{B}_I^{\delta\boldsymbol{u}}]^T (s^2+\eta)\, \underline{\mathbb{C}}\, [\underline{B}_J^{\boldsymbol{u}}] & [\underline{B}_I^{\delta\boldsymbol{u}}]^T 2s\, \underline{\mathbb{C}}\, \underline{\boldsymbol{\varepsilon}} N_J^s \\ N_I^{\delta s} 2s (\underline{\mathbb{C}}\, \underline{\boldsymbol{\varepsilon}})^T [\underline{B}_J^{\boldsymbol{u}}] & 2\mathcal{G}_c\, \epsilon\, [\underline{B}_I^{\delta s}]^T [\underline{B}_J^s] + N_I^{\delta s} \left(\underline{\boldsymbol{\varepsilon}}^{T\cdot} \underline{\mathbb{C}}\, \underline{\boldsymbol{\varepsilon}} + \dfrac{\mathcal{G}_c}{2\,\epsilon} \right) N_J^s \end{bmatrix} dV \tag{14}$$

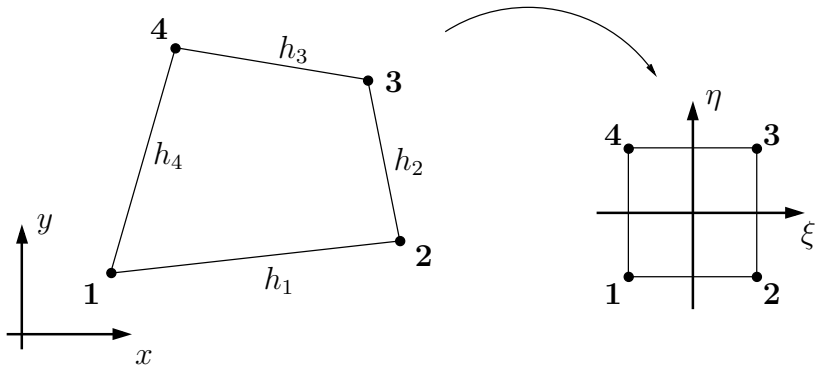

Figure 2: Node and edge numbering of the quadrilateral element in global (left) and natural coordinates (right)

and

$$\left[\underline{D}_{IJ}\right] = \int_\Omega \begin{bmatrix} 0 & 0 \\ 0 & \frac{1}{M} N_I^{\delta s} N_J^s \end{bmatrix} dV \,. \tag{15}$$

If the same shape functions are chosen for the approximation of actual values and the virtual quantities, i.e. $N_I^{\boldsymbol{u}} = N_I^{\delta \boldsymbol{u}}$ and $N_I^s = N_I^{\delta s}$, the system matrix $\left[\underline{S}_{IJ}\right]$ becomes symmetric. This is due to the fact, that the constitutive law (3) as well as the evolution equation (4) are derived from a potential. Different shape functions however, render a non-symmetric system matrix $\left[\underline{S}_{IJ}\right]$.

4 EXPONENTIAL SHAPE FUNCTIONS

The standard implementation with 4 node quadrilateral elements makes use of the linear Lagrangian shape functions

$$N_I^{\text{lin}}(\xi, \eta) = \frac{1}{4}(1 + \xi_I \xi)(1 + \eta_I \eta), \qquad I = 1, ..., 4 \tag{16}$$

with (ξ_I, η_I) according to Fig. 2 for all the shape functions $N_I^{\boldsymbol{u}}$, $N_I^{\delta \boldsymbol{u}}$, N_I^s, and $N_I^{\delta s}$ as well as for the approximation of the geometry in the isoparametric concept

$$\boldsymbol{x} = \sum_{I=1}^{N} N_I^{\text{lin}} \hat{\boldsymbol{x}}_I. \tag{17}$$

In [12] it is shown that triangular elements with linear shape functions overestimate the surface energy by a factor

$$f(h/\epsilon) = 1 + h/4\epsilon \,, \tag{18}$$

where h is the edge length of the elements. As a sufficiently good approximation of the surface energy is crucial in order to obtain reasonable results, this yields the necessity of a

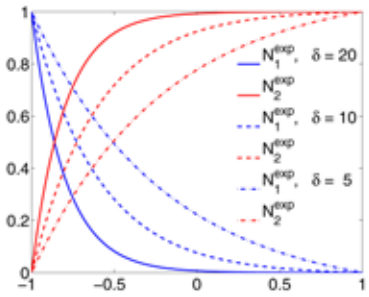

Figure 3: 1d exponential shape functions for different values of δ

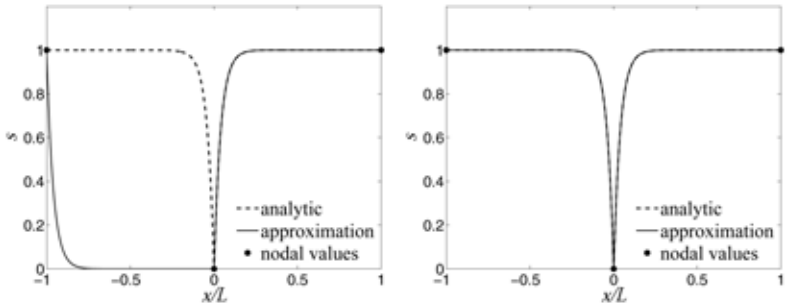

Figure 4: Approximation with unswitched shape functions (left), and switched shape functions (right)

very fine resolution of the transition zones. In different numerical simulations with linear shape functions in a 2d setting, $h \approx \epsilon$ was empirically found as an upper bound for the element size, [13, 8].

4.1 1d Exponential Shape Functions

The simulation of extrusion processes is faced with a similar problem, as shear boundary layers which exhibit an exponential velocity profile need to be resolved. In [10] exponential shape functions, that qualitatively capture the shape of the sharp velocity field, are proposed as an alternative to a fine spacial resolution. Adapted to the present phase field model these 1d shape functions read

$$\bar{N}_1^{\exp}(\xi,\delta) = 1 - \frac{\exp\left(-\frac{\delta(1+\xi)}{4}\right) - 1}{\exp\left(-\frac{\delta}{2}\right) - 1} \qquad \text{and} \tag{19}$$

$$\bar{N}_2^{\exp}(\xi,\delta) = \frac{\exp\left(-\frac{\delta(1+\xi)}{4}\right) - 1}{\exp\left(-\frac{\delta}{2}\right) - 1} \tag{20}$$

in natural coordinates on the interval $[-1, 1]$. Through their dependence on the ratio $\delta = h/\epsilon$ of the element size h and the regularization parameter ϵ, these shape functions are able to capture the analytic solution (6) for any values of h and $\boldsymbol{\varepsilon}$. In the limit case $\delta \to 0$ or equivalently $h \to 0$ these shape functions converge to the one dimensional linear shape functions, see also Fig. 3.

$$\lim_{\delta\to 0} \bar{N}_1^{\exp}(\xi,\delta) = \frac{1-\xi}{2} = N_1^{\text{lin}}(\xi) \qquad \lim_{\delta\to 0} \bar{N}_2^{\exp}(\xi,\delta) = \frac{1+\xi}{2} = N_2^{\text{lin}}(\xi) \tag{21}$$

The exponential shape functions (19) and (20) are unsymmetric with respect to ξ, i.e. $\bar{N}_1^{\exp}(-\xi) \neq \bar{N}_2^{\exp}(\xi)$, and are designed to match the analytical solution (6), if $\hat{s}_1 \leq \hat{s}_2$ (presuming node numbering from left to right) holds for the according nodal values, see Fig. 4. Due to their non-symmetry the shape functions need to be switched according to

the nodal values of s in order to obtain good approximations for arbitrary nodal values of s.

$$N_1^{\exp}(\xi) = \begin{cases} \bar{N}_1^{\exp}(\xi,\delta) & \text{if } \hat{s}_1 \leq \hat{s}_2 \\ \bar{N}_2^{\exp}(-\xi,\delta) & \text{if } \hat{s}_1 > \hat{s}_2 \end{cases} \quad \text{and} \quad N_2^{\exp}(\xi) = \begin{cases} \bar{N}_2^{\exp}(\xi,\delta) & \text{if } \hat{s}_1 \leq \hat{s}_2 \\ \bar{N}_1^{\exp}(-\xi,\delta) & \text{if } \hat{s}_1 > \hat{s}_2 \end{cases} \tag{22}$$

4.2 Extension to the 2d Setting

The 2d linear shape function (16) of each single element node can be obtained by multiplying the 1d linear shape functions belonging to the adjacent edges of the respective node. Replacing the 1d linear shape functions by the exponential shape functions (22) this strategy yields

$$\begin{aligned} N_1^{\exp}(\xi,\eta,\delta_i) &= N_1^{\exp}(\xi,\delta_1)\cdot N_1^{\exp}(\eta,\delta_4), \quad N_2^{\exp}(\xi,\eta,\delta_i) = N_2^{\exp}(\xi,\delta_1)\cdot N_1^{\exp}(\eta,\delta_2), \\ N_3^{\exp}(\xi,\eta,\delta_i) &= N_2^{\exp}(\xi,\delta_3)\cdot N_2^{\exp}(\eta,\delta_2), \quad N_4^{\exp}(\xi,\eta,\delta_i) = N_1^{\exp}(\xi,\delta_3)\cdot N_2^{\exp}(\eta,\delta_4), \end{aligned} \tag{23}$$

where the element nodes and the element edges are numbered according to Fig. 2. Each shape function depends on the ratio $\delta_i = \frac{h_i}{\epsilon}$ of both adjacent element edges. For an appropriate approximation behavior, it is postulated that the orientation of the 1d shape functions of opposite edges must be the same. The so constructed shape functions possess the Kronecker delta property, i.e. $N_I^{\exp}(\xi_J,\eta_J,\delta_i) = \delta_{IJ}$. Continuity across element borders holds, if the orientation of the shared edge of two neighbor elements is the same. However, the partition of unity property does not hold in general, i.e. it holds only if

$$\delta_1 = \delta_3 \qquad \text{or} \qquad \delta_2 = \delta_4\,. \tag{24}$$

For the sake of simplicity, we restrict the element shape at this point to square and rectangular elements for which condition (24) holds. For a more general framework allowing for arbitrarily shaped quadrilateral elements, as well as for some more technical details of the implementation, the reader is referred to [14].

5 NUMERICAL EXAMPLES

The performance of the exponential shape functions is tested in this section. In all simulations, linear shape functions (16) were used for the approximation of the geometry and the actual and virtual displacements, i.e. $N_I^{\boldsymbol{u}} = N_I^{\delta\boldsymbol{u}} = N_I^{\text{lin}}$. Three different versions of approximating the crack field s and its virtual counterpart δs are compared to each other: The standard approximation with linear shape functions $N_I^s = N_I^{\delta s} = N_I^{\text{lin}}$ (labeled lin/lin), the complete approximation with exponential shape functions $N_I^s = N_I^{\delta s} = N_I^{\exp}$ (labeled exp/exp), and a mixed formulation with $N_I^s = N_I^{\exp}$ but $N_I^{\delta s} = N_I^{\text{lin}}$ (labeled lin/exp).

5.1 Evolution Equation in 1d

As a first test, the 1d stationary evolution equation (5) is solved for a regularization parameter $\epsilon = 0.01L$. The superior performance of the exponential shape functions becomes apparent in the plots of the numerical solutions with different numbers of elements

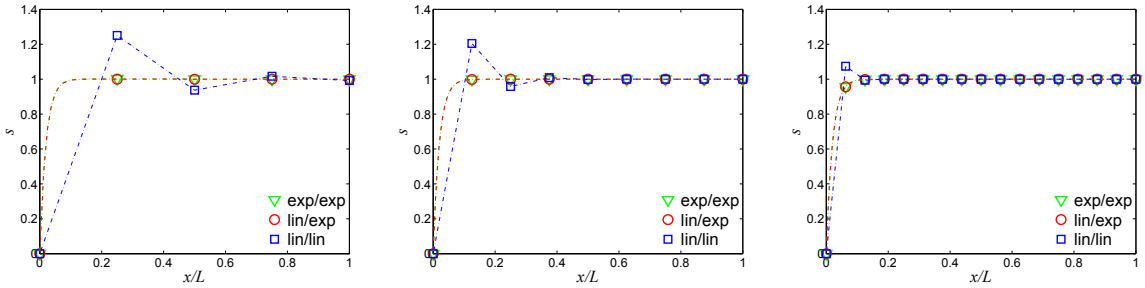

Figure 5: Solution of the 1d stationary evolution equation with $n = 4$ (left), $n = 8$ (middle) and $n = 16$ elements (right)

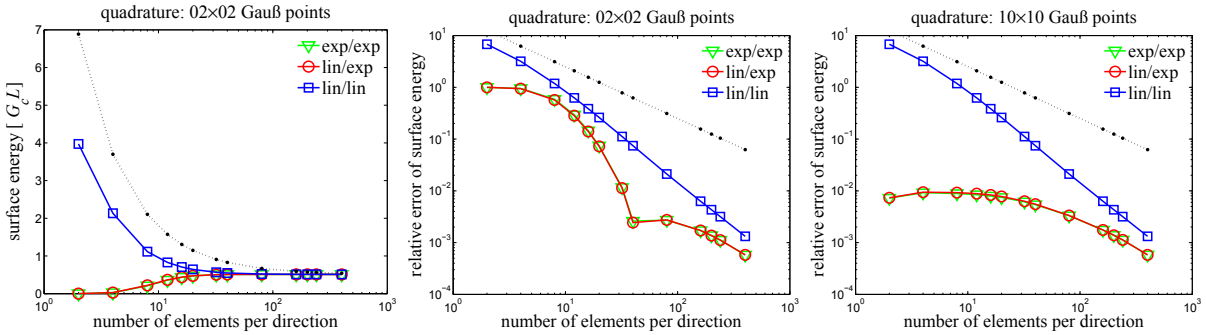

Figure 6: Evaluation of the surface energy

in Fig. 5. While there is almost no visible error in the solutions with exponential shape functions, the linear shape functions fail to adequately resolve the transition zone even for the smallest tested element size $h = L/16$.

5.2 Surface Energy of an Edge Notched Sample

For the first numerical assessment of the 2d exponential shape functions, the stationary evolution equation is solved on the domain $L \times L$ under the constraint $s(x, y) = 0$ if $(x, y) \in [0, L/2] \times \{0\}$. Again, the regularization length is set to $\epsilon = 0.01L$, and no mechanical loads are applied. A regular mesh with square elements is used for the discretization.

Figure 6 shows an evaluation of the surface energy E^{s} associated with the computed crack field. Regular meshes within the range of 2×2 to 400×400 elements were used for the discretization. The results are compared to the error estimate (18) for the triangular elements with linear shape functions (black dotted line). The reference solution $E^{\mathrm{s}} = 0.51017344300\, \mathcal{G}_c L$ was computed with standard linear shape functions and a non-uniform mesh with square elements of edge length $h = 7.1429 \cdot 10^{-4} L$ in the vicinity the crack. The performance of the tested linear shape functions is slightly better than it is to be expected from the error estimate. However, especially for discretizations with only few

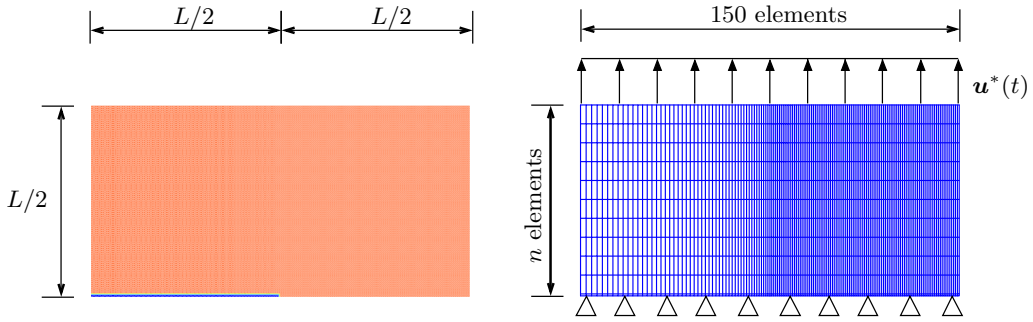

Figure 7: Simulation setup: contour plot of initial crack field (left) and finite element mesh (right)

elements both versions using the exponential shape functions perform significantly better. A crucial point for the performance of the exponential shape functions is a sufficiently precise computation of the integrals in the residuals (12), the stiffness matrix (14), and the damping matrix (15). For standard linear 4 node elements, usually the Gauß quadrature formula with 2 integration points per direction is used to compute the integrals. Yet, the performance of the exponential shape functions can easily be improved by employing a higher order quadrature method, e.g. a quadrature with 10×10 Gauß points as was used to obtain the results in the right plot of Fig. 6. Thus, a major part of the error in the surface energy computed with exponential shape functions and 2×2 Gauß points (Fig. 6, middle) is due to the quadrature error.

5.3 Peel Off Test

In this simulation the performance of the exponential shape functions is tested under mechanical loading, i.e. the whole set of coupled equations has to be solved..e. the whole set of coupled equations has to be solved. The mixed formulation (lin/exp) yields an unsymmetric system matrix, which is computationally more expensive. As the results obtained by the pure exponential formulation in sections 5.1 and 5.2 are very similar, the mixed formulation is dismissed in the following. The sample depicted in Fig. 7 is loaded by a linear increasing displacement load $\boldsymbol{u}^*(t) = \sqrt{\frac{\mathcal{G}_c L}{2\mu}} \cdot t$. A dimensional analysis shows that with this scaling of the displacements, the geometric length L and the cracking resistance $\mathcal{G}_c$ can be factored out of the equations. If additionally the mobility M is chosen large enough to assume quasi-static cracking, the solution of the coupled problem only depends on the ratio of the Lamé constants λ/μ (here: $\lambda = \mu$) and the regularization parameter ϵ in conjunction with L (here: $\epsilon = 0.0005L$). The discretization in x-direction is done with 150 elements. A varying number of n elements plus one row of elements of fixed height, to model the initial crack, discretize the structure in y-direction, see Fig. 7. Gauß quadrature with 5×5 integration points was used for the integration.

The two left plots in Fig. 8 show the evolution of the elastic energy with respect to the load factor t for different values of n. The elastic energy increases with the loading

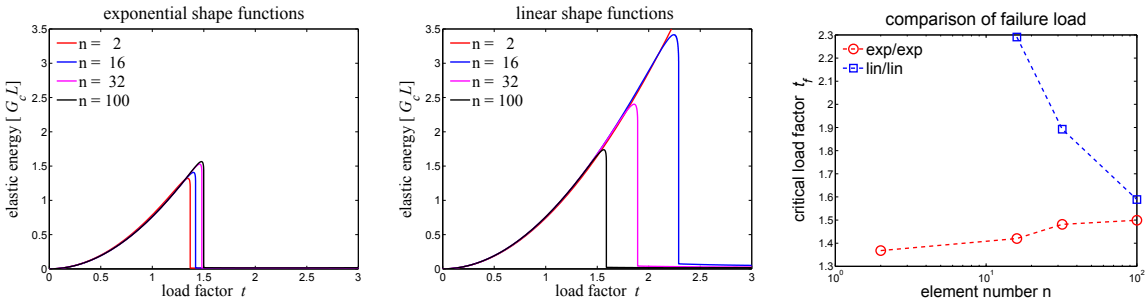

Figure 8: Elastic energy and failure load

until rupture occurs and it drops to zero. Impressively, the simulation with only $n = 2$ elements in y-direction already gives a qualitatively good result, when the exponential shape functions are employed. Using the standard linear shape functions, no rupture is observed in the simulation with $n = 2$ elements up to a load factor of $t = 3$, which is about twice the actual critical loading. Also the simulation with $n = 16$ elements still overestimates the critical loading by far. Only the simulations with more elements produce as accurate results as the simulations with the exponential shape functions. The right plot of Fig. 8 compares the computed failure loads. The overestimation of the critical load value of the linear shape functions stems from the overestimation of the surface energy associated with the initial crack.

6 SUMMARY

The aim of this work was to provide an alternative to expensive mesh refinement in finite element simulations of a phase field model for fracture in cases where the regularization parameter is very small. To this end special shape functions, which capture the analytical stationary solution of the 1d crack field, were derived and implemented into a 2d element of a finite element code. Through their dependence on the ratio of element size and regularization parameter, the exponential shape functions are able to adjust to the crack field for virtually arbitrarily small values of the regularization length. This allows for computations with very small values of the regularization parameter, which would require an extensive mesh refinement, when standard linear shape functions are used.
The effectiveness of the proposed technique has been demonstrated in numerical examples. In all simulations the usage of the exponential shape functions resulted in a considerable reduction of the level of refinement, yet their full potential only reveals itself if a sufficiently precise quadrature method is employed for the computation of the occurring integrals.

REFERENCES

[1] Francfort, G. A. and Marigo, J.-J. Revisiting brittle fracture as an energy minimization problem. *J. Mech. Phys. Solid.* (1998) **46**:1319–1342.

[2] Bourdin, B., Francfort, G. A. and Marigo, J.-J. Numerical experiments in revisited brittle fracture. *J. Mech. Phys. Solid.* (2000) **48**:797–826.

[3] Aranson, I. S., Kalatsky, V. A. and Vinokur, V. M. Continuum field description of crack propagation. *Phys. Rev. Let.* (2000) **85**:118–121.

[4] Karma A., Kessler, D. A. and Levine, H. Phase-field model of mode iii dynamic fracture. *Phys. Rev. Let.* (2001) **87**:45501.

[5] Eastgate, L. O., Sethna, J. P., Rauscher, M., Cretegny, T., Chen, C.-S. and Myers, C. R. Fracture in mode i using a conserved phase-field model. *Phys. Rev. E* (2002) **65**:036117.

[6] Brener, E. A. and Spatschek, R. Fast crack propagation by surface diffusion. *Phys. Rev. E* (2003) **67**:016112.

[7] Spatschek, R., Hartmann, M., Brener, E., Müller-Krumbhaar, H. and Kassner, K. Phase field modeling of fast crack propagation. *Phys. Rev. Let.* (2006) **96**:015502.

[8] Miehe, C., Welschinger, F. and Hofacker, M. Thermodynamically consistent phase-field models for fracture: Variational principles and multi-field fe implementations. *Int. J. Numer. Meth. Eng.* (2010) **83**:1273–1311.

[9] Welschinger, F., Hofacker, M. and Miehe, C. Configurational–force–based adaptive fe solver for a phase field model of fracture. In *PAMM* (2010) **10**:689–692.

[10] LaZghab, S., Aukrust, T. and Holthe, K. Adaptive exponential finite elements for the shear boundary layer in the bearing channel during extrusion. *Comput. Meth. Appl. Mech. Eng.* (2002) **191**:1113–1128.

[11] Bourdin, B. Numerical implementation of the variational formulation of quasi-static brittle fracture. *Interfaces Free Bound.* (2007) **9**.

[12] Bourdin, B., Francfort, G. and Marigo, J.-J. The variational approach to fracture. *J. Elasticity* (2008) **91**:5–148.

[13] Amor, H., Marigo, J.-J. and Maurini, C. Regularized formulation of the variational brittle fracture with unilateral contact: Numerical experiments. *J. Mech. Phys. Solid.* (2009) **57**:1209–1229.

[14] Kuhn, C. and Müller, R. A new finite element technique for a phase field model of brittle fracture. *J. Theor. Appl. Mech* (2011) in press.

XI International Conference on Computational Plasticity. Fundamentals and Applications
COMPLAS XI
E. Oñate, D.R.J. Owen, D. Peric and B. Suárez (Eds)

FINITE DEFORMATION DAMAGE MODELLING IN CHALLENGING APPLICATIONS - FORMING LIMIT DIAGRAMS AND LIFE TIME ANALYSIS FOR A ROCKET THRUST CHAMBER

VIVIAN TINI*, IVAYLO N. VLADIMIROV*, YALIN KILICLAR* AND STEFANIE REESE*

*RWTH Aachen University
Institute of Applied Mechanics
Mies-van-der-Rohe Str. 1, D-52074 Aachen, Germany
e-mail: stefanie.reese@rwth-aachen.de, www.ifam.rwth-aachen.de

Key words: Finite Deformation Damage, Forming Limit Diagram at Fracture, Lifetime Analysis, Rocket Thrust Chamber

Abstract. This paper presents the coupling of a recently developed finite anisotropic elastoplastic constitutive model with isotropic ductile damage. The feasibility of the model for failure prediction purposes is presented in two challenging applications. The first one concerns the prediction of forming limit diagrams at fracture (FLDF) by means of finite element simulations of the so-called Nakajima stretching test. In the second application, the model is utilized in a thermomechanical analysis of a rocket combustion chamber segment. In both applications, the potential of the model for failure prediction purposes is discussed.

1 INTRODUCTION

In some engineering applications, such as in forming processes of metal sheets, it is common to have more than ten percent of plastic strain at failure. On applications involving polymers, failure can occur at a very large value of strain, i.e. a few hundred percent. In these cases, small strain damage formulations are no longer sufficient to provide a reliable failure prediction. For this purpose, a continuum damage formulation in the framework of finite deformations is necessary.

In this paper, the coupling of an anisotropic finite elastoplastic constitutive model with isotropic damage will be introduced. The complete derivation of the anisotropic elastoplastic model has been published recently [1]. The triple multiplicative split of the deformation gradient is performed to incorporate nonlinear kinematic hardening according

to the Armstrong-Frederick concept [2]. The most important steps of the derivation and the extension of the model to include isotropic damage will be presented in Section 2.

The model is implemented as a user subroutine UMAT into the Abaqus finite element analysis software. Upon successful numerical validations by means of a number of uniaxial, multiaxial, monotonic and cyclic loadings, the model is applied to challenging finite element simulations which will be described in Section 3 and Section 4.

In Section 3 the application of the model to generate forming limit diagrams at fracture (FLDF) will be discussed. The prediction of FLDF is especially important when forming is limited by fracture rather than necking. In cases where the strain path approaches equibiaxial stretching, ductile fracture due to void formation might be induced before the onset of localized necking. In such situations it is essential to predict the occurence of fracture. For this purpose, the simulation of the so-called Nakajima stretching test are performed. The results are used to generate the forming limit diagrams at fracture.

The second application concerns failure which occurs at the cooling channel wall of a rocket thrust chamber. The extreme thermomechanical loadings during the operation of the rocket lead to the thinning and bulging of the cooling channel wall, which eventually causes the so-called "dog house" failure mode [3]. A transient heat transfer analysis is performed to obtain the temperature history of the modelled chamber segment. Afterwards a series of static analyses is performed to obtain the stress-strain field as well as the cyclic evolution of the damage. The computation results show the potential of the model to predict the end shape of the cooling channel wall.

2 FINITE STRAIN DAMAGE MODELLING

This part will summarize the most important steps of the derivation of the anisotropic elastoplastic model and its coupling with an isotropic damage variable following the principle of strain equivalence as elaborated by Lemaitre [4].

The constitutive model uses the triple multiplicative decomposition of the deformation gradient $\mathbf{F} = \mathbf{F}_e \, \mathbf{F}_{p_e} \, \mathbf{F}_{p_i}$ into elastic ($\mathbf{F}_e$), plastic-elastic ($\mathbf{F}_{p_e}$) and plastic-inelastic ($\mathbf{F}_{p_i}$) parts. The additional multiplicative split of the plastic part of the deformation gradient into elastic and inelastic parts is performed for the modelling of nonlinear kinematic hardening according to the Armstrong-Frederick concept [2]. This split can be physically motivated by taking into account the dislocation-induced lattice rotations and stretches and local plastic deformations on the microscale.

Based on the principle of material objectivity and the concept of material isomorphism the Helmholtz free energy per unit volume can be written in the form

$$\psi = \psi_e \left(\mathbf{C}_e, D \right) + \psi_{kin} \left(\mathbf{C}_{p_e}, D \right) + \psi_{iso} \left(\kappa, D \right) \tag{1}$$

where $\mathbf{C}_e = \mathbf{F}_e^T \, \mathbf{F}_e = \mathbf{F}_p^{-T} \, \mathbf{C} \, \mathbf{F}_p^{-1}$ represents the elastic right Cauchy-Green deformation tensor and $\mathbf{C}_{p_e} = \mathbf{F}_{p_e}^T \, \mathbf{F}_{p_e} = \mathbf{F}_{p_i}^{-T} \, \mathbf{C}_p \, \mathbf{F}_{p_i}^{-1}$ the elastic part of the plastic right Cauchy-Green tensor. The first part ψ_e describes the macroscopic elastic material properties. The terms ψ_{kin} and ψ_{iso} represent the amounts of stored energy due to kinematic and

isotropic hardening, respectively. The variable κ refers to the accumulated plastic strain. The scalar D represents the isotropic ductile damage variable, where $D = 0$ holds for a virgin (undamaged) material point and $D = 1$ for a completely damaged material point.

The constitutive equations of the model are obtained from the derivation based on the Clausius-Duhem form of the second law of thermodynamics $-\dot{\psi} + \mathbf{S} \cdot \frac{1}{2}\dot{\mathbf{C}} \geq 0$. Inserting the Helmholtz free energy and differentiating with respect to time yields

$$-\left(\frac{\partial \psi_e}{\partial \mathbf{C}_e} \cdot \dot{\mathbf{C}}_e + \frac{\partial \psi_{kin}}{\partial \mathbf{C}_{p_e}} \cdot \dot{\mathbf{C}}_{p_e} + \frac{\partial \psi_{iso}}{\partial \kappa}\,\dot{\kappa} + \frac{\partial \psi}{\partial D}\,\dot{D}\right) + \mathbf{S} \cdot \frac{1}{2}\,\dot{\mathbf{C}} \geq 0 \tag{2}$$

The specific forms of the energy contributions ψ_e, ψ_{kin} and ψ_{iso} are given as $\psi_e = (1-D)\,\bar{\psi}_e$, $\psi_{kin} = (1-D)\,\bar{\psi}_{kin}$ and $\psi_{iso} = (1-D)\,\bar{\psi}_{iso}$, where

$$\bar{\psi}_e = \frac{\mu}{2}\,(\operatorname{tr}\mathbf{C}_e - 3) - \mu\,\ln\left(\sqrt{\det \mathbf{C}_e}\right) + \frac{\Lambda}{4}\,(\det \mathbf{C}_e - 1 - 2\,\ln\left(\sqrt{\det \mathbf{C}_e}\right) \tag{3}$$

$$\bar{\psi}_{kin} = \frac{c}{2}\,(\operatorname{tr}\mathbf{C}_{p_e} - 3) - c\,\ln\left(\sqrt{\det \mathbf{C}_{p_e}}\right) \tag{4}$$

$$\bar{\psi}_{iso} = Q\,(\kappa + \frac{e^{\,-\beta\,\kappa}}{\beta}) \tag{5}$$

are the parts of the Helmholtz free energy corresponding to the undamaged state. Note that due to the Neo-Hookean form of $\bar{\psi}_e$ the material model is capable of describing finite elastic strains. Here μ and Λ refer to the Lamé constants and c is the stiffness-like kinematic hardening parameter. The expression for $\bar{\psi}_{iso}$ corresponds to the saturation-type isotropic hardening rule of Voce [5] where Q and β are the isotropic hardening parameters. The relation for the second Piola-Kirchhoff stress tensor $\mathbf{S} = 2\,\mathbf{F}_p^{-1}\,(\partial \psi_e / \partial \mathbf{C}_e)\,\mathbf{F}_p^{-T}$ is obtained by making use of standard arguments [6].

The numerical implementation of the model is carried out in the reference configuration. The constitutive equations obtained from the thermodynamically consistent derivation are summarized below:

- Stress tensors

$$\mathbf{S} = (1-D)\left(\mu\,(\mathbf{C}_p^{-1} - \mathbf{C}^{-1}) + \frac{\Lambda}{2}\,(\det \mathbf{C}\,(\det \mathbf{C}_p)^{-1} - 1)\,\mathbf{C}^{-1}\right) \tag{6}$$

$$\bar{\mathbf{S}} = \frac{1}{1-D}\,\mathbf{S} \tag{7}$$

$$\mathbf{X} = c\,(\mathbf{C}_{p_i}^{-1} - \mathbf{C}_p^{-1}) \tag{8}$$

$$\mathbf{Y} = \mathbf{C}\,\bar{\mathbf{S}} - \mathbf{C}_p\,\mathbf{X}, \quad \mathbf{Y}_{kin} = \mathbf{C}_p\,\mathbf{X} \tag{9}$$

- Evolution equations

$$\dot{\mathbf{C}}_p = \dot{\lambda}\,\frac{\mathrm{sym}\Big(\mathbf{C}_p\left(\mathcal{A}\left[(\mathbf{Y}^D)^T\right]+(\mathcal{A}^T\left[\mathbf{Y}^D\right])^T\right)^D\Big)}{\sqrt{\mathbf{Y}^D\cdot(\mathcal{A}\left[(\mathbf{Y}^D)^T\right])}} \tag{10}$$

$$\dot{\mathbf{C}}_{p_i} = 2\,\dot{\lambda}\,\frac{b}{c}\,\mathbf{Y}^D_{kin}\,\mathbf{C}_{p_i},\quad \dot{\kappa}=\sqrt{\frac{2}{3}}\,\dot{\lambda} \tag{11}$$

$$\dot{D} = \dot{\lambda}\sqrt{\frac{2}{3}}\,\frac{1}{1-D}\left(\frac{Y}{s}\right)^k H(\kappa-p_D) \tag{12}$$

- Yield function

$$\Phi=\sqrt{\mathbf{Y}^D\cdot(\mathcal{A}\left[(\mathbf{Y}^D)^T\right])}-\sqrt{\frac{2}{3}}\left(\sigma_{y0}+Q\left(1-e^{-\beta\,\kappa}\right)\right) \tag{13}$$

- Fourth-order anisotropy tensor

$$\begin{aligned}\mathcal{A} &= a_1\,\mathcal{I}+a_2\,\mathbf{M}_1\otimes\mathbf{M}_1+a_3\,\mathbf{M}_2\otimes\mathbf{M}_2+a_4\left(\mathbf{M}_1\otimes\mathbf{M}_2+\mathbf{M}_2\otimes\mathbf{M}_1\right) \quad (14)\\ &+ a_5\,\mathcal{D}_1+a_6\,\mathcal{D}_2\\ D^\alpha_{ijkl} &= \frac{1}{2}\left(M^\alpha_{ik}\delta_{jl}+M^\alpha_{jl}\delta_{ik}+M^\alpha_{il}\delta_{jk}+M^\alpha_{jk}\delta_{il}\right),\quad \alpha=1,2 \quad (15)\\ \mathbf{M}_i &= \mathbf{N}_i\otimes\mathbf{N}_i,\quad i=1,2 \quad (16)\end{aligned}$$

- Kuhn-Tucker conditions

$$\dot{\lambda}\geq 0,\quad \Phi\leq 0,\quad \dot{\lambda}\,\Phi=0 \tag{17}$$

Here, $\mathbf{C}_p=\mathbf{F}_p^T\,\mathbf{F}_p$ and $\mathbf{C}_{p_i}=\mathbf{F}_{p_i}^T\,\mathbf{F}_{p_i}$ are right Cauchy-Green deformation-like tensors, $\mathbf{X}$ is the back stress tensor in the reference configuration, $\mathbf{Y}$ (not to be confused with the scalar quantity Y thermodynamically conjugate to D) and $\mathbf{Y}_{kin}$ represent non-symmetric second-order stress tensors. $\mathcal{A}$ is the fourth-order orthotropy tensor in the reference configuration written in terms of the second-order structure tensors $\mathbf{M}_1$ and $\mathbf{M}_2$. $\mathbf{N}_1$ and $\mathbf{N}_2$ are the privileged directions of the material in the reference configuration. The pre-factors a_i $(i=1,...,6)$ can be determined based on the classical Hill coefficients as elaborated in [7].

The evolution of the isotropic damage variable in (12) is applied following the work of Lemaitre [4]. Here, s and k are two positive material parameters describing the rate at which damage evolves. The Heaviside step function $H(\kappa-p_D)$ with properties $H=0$ if $\kappa<p_D$ and $H=1$ if $\kappa\geq p_D$ is utilized here to describe the threshold p_D where damage begins to evolve. The scalar Y is defined in [8] as the energy density release rate and is given here as

$$Y = \frac{R_\nu}{2E}\,\mathbf{Y}^D \cdot (\mathcal{A}\,[(\mathbf{Y}^D)^T]) \tag{18}$$

where R_ν is the so-called triaxiality function:

$$R_\nu = \frac{2}{3}(1+\nu) + 3(1-2\nu)\left(\frac{1/3\,\mathrm{tr}\,\mathbf{Y}}{\sqrt{\mathbf{Y}^D \cdot (\mathcal{A}\,[(\mathbf{Y}^D)^T])}}\right)^2 \tag{19}$$

In (18), $E = \mu(3\Lambda + 2\mu)/(\Lambda + \mu)$ represents Young's modulus of elasticity and $\nu = \Lambda/2(\Lambda + \mu)$ the Poisson's ratio.

The coupling between the anisotropic elastoplastic model and the Lemaitre-type isotropic damage model is carried out according to the effective stress concept: $\bar{\mathbf{S}} = 1/(1 - D)\,\mathbf{S}$. $\bar{\mathbf{S}}$ is the local effective stress which increases as damage develops in the material. Further, the stress tensor $\mathbf{Y}$ that appears in the yield function (13) depends on the effective stress $\bar{\mathbf{S}}$. Through the yield function and the plastic flow rule the plastic deformation as well as the hardening internal variables are also affected by the damage development in the material. In this way, a coupled framework of finite strain anisotropic damage-elastoplasticity is obtained, where the damage behaviour strongly depends on the anisotropically evolving plasticity in the material. Thus, the damage evolution shows induced anisotropy although from the mathematical point of view the damage formulation is isotropic.

The internal variables of the coupled damage-plasticity model are $\mathbf{C}_p$, $\mathbf{C}_{p_i}$, κ and D which describe the evolution of plastic deformation, kinematic hardening, isotropic hardening and damage, respectively. The tensor-valued evolution equations are discretized by a type of the exponential map algorithm (see [9]) that satisfies plastic incompressibility and uses the spectral decomposition to evaluate the exponential tensor functions in closed form. The discretization of the scalar evolution equations for κ and D is performed by the classical implicit backward Euler scheme.

3 THE NAKAJIMA STRETCHING TEST

This section discusses the application of the coupled damage-elastoplasticity model to simulate the so-called Nakajima test where six specimens are used to obtain six distinct points of the FLDF. The test represents a stretching operation up to fracture used to experimentally determine forming limit diagrams. The tools used in the Nakajima test include a hemispherical punch, a blankholder (Fig. 1(a)) and a die (Fig. 1(b)). For the simulation, six different blank specimens with varying width of the middle section (15, 25, 35, 45, 55 and 100 mm) are created. The corresponding Nakajima tests are performed for each specimen. The major and minor strains recorded at the end of each of these simulations correspond to a point on the FLDF. The specimens with widths of 15, 45 and 100 mm correspond essentially to strain states of uniaxial, plane and biaxial tension,

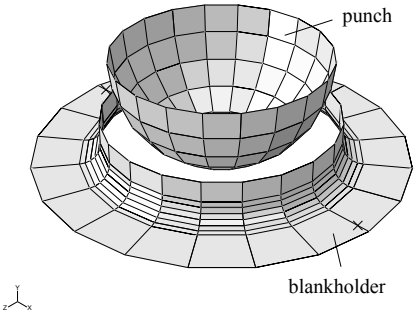

(a) Punch and blank holder.

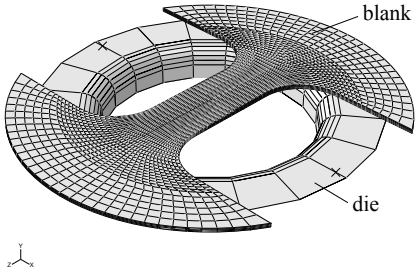

(b) Die and undeformed blank.

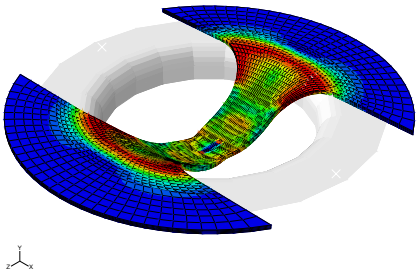

(c) Die and deformed blank.

Figure 1: Tools for the Nakajima test.

respectively. The specimen with a width of 15 mmm is depicted in Fig. 1(b) and in Fig. 1(c) in the undeformed and deformed configuration, respectively.

The material degradation in the element where failure occurs can be seen from the stress-strain curves up to fracture in Fig. 2. The corresponding evolution of the damage variable are shown in Fig. 3. Contour plots in Fig. 4(a) to Fig. 4(f) shows the bottom view distribution of damage for each specimen.

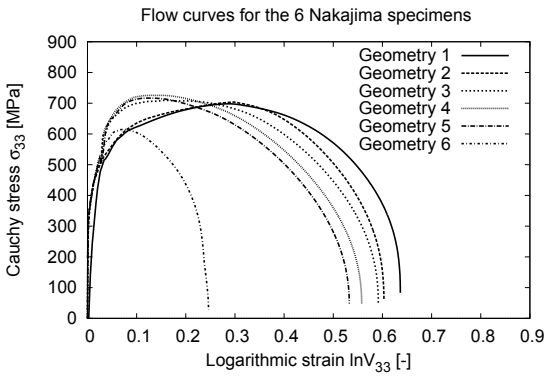

Figure 2: Flow curves - specimens 1 to 6.

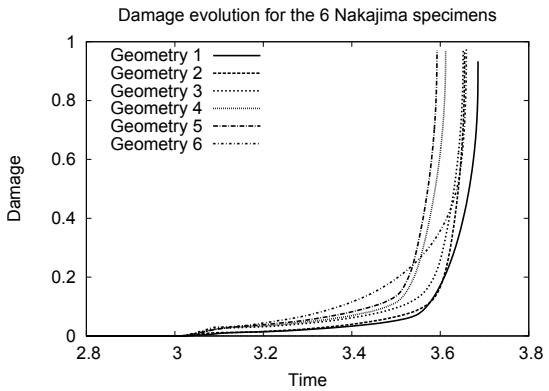

Figure 3: Damage evolution - specimens 1 to 6.

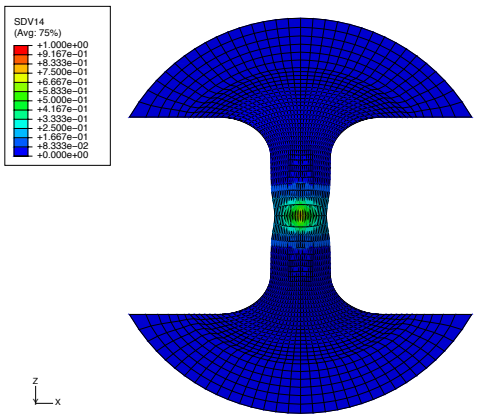

(a) Geometry 1, width 15 mm.

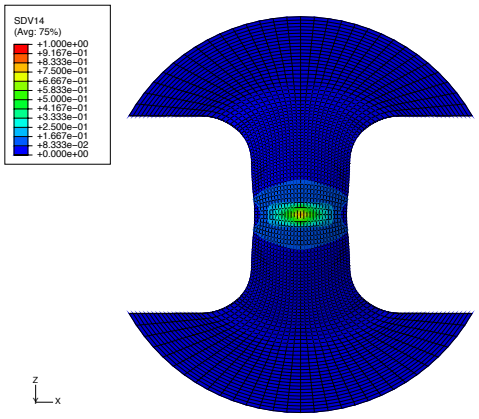

(b) Geometry 2, width 25 mm.

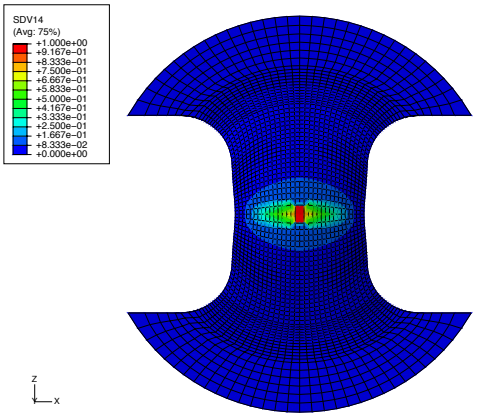

(c) Geometry 3, width 35 mm.

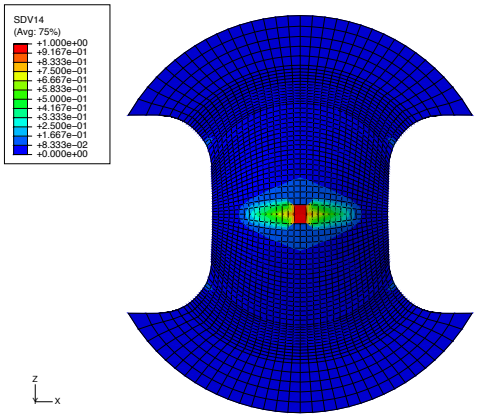

(d) Geometry 4, width 45 mm.

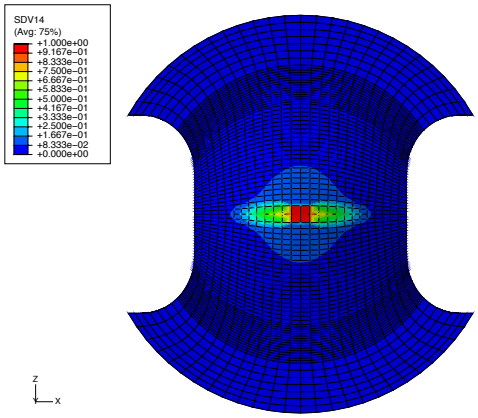

(e) Geometry 5, width 55 mm.

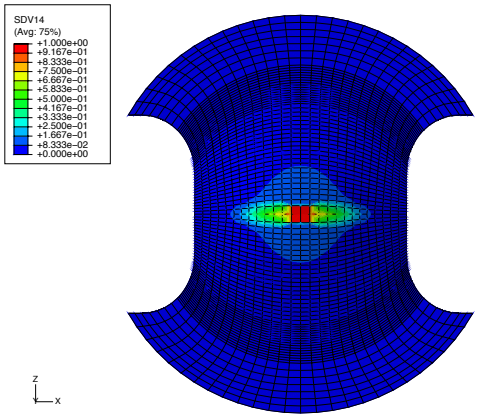

(f) Geometry 6, width 100 mm.

Figure 4: Damage distribution from the six Nakajima test specimens.

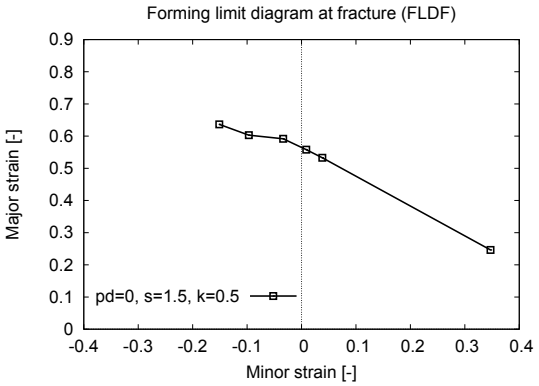

Figure 5: FLDF obtained by Nakajima tests.

Finally, the FLDF can be constructed by recording the major and minor strains for the ruptured element and by plotting them as points in the limit strain space. The six Nakajima test simulations give six combinations of major and minor strains ranging from uniaxial tension to biaxial tension. The FLDF is shown in Fig. 5. The major strain is 0.246 whereas the minor strain is 0.347. It is worth noting, that this difference occurs due to the considered plastic anisotropy in the FE computations.

4 THERMOMECHANICAL ANALYSES OF A ROCKET COMBUSTION CHAMBER SEGMENT

This section discusses the application of the presented model for the lifetime prediction of a rocket combustion chamber segment. Fig. 6(a) shows a typical rocket combustion chamber. The schematic cross section of the chamber is shown in Fig. 6(b). The outer wall is made out of nickel alloy. The cooling channel walls are made out of copper alloy. The hot gas resulting from the combustion of the propellants (liquid oxygen and liquid hyrogen) flows through the center of the chamber. The coolant (liquid hydrogen) flows through the small cooling channel passages. There can be up to 360 cooling channels in the circumference direction. The geometry of the modelled segment is the quasi Vulcain geometry following the work of Kuhl et al. [10]. First of all, a transient thermal analysis of the combustion chamber segment is performed to obtain the temperature field of the entire chamber segment. The obtained temperature history is then used as input for the user subroutine in the static analyses.

4.1 Transient heat transfer analysis

Convective thermal boundary conditions are employed at the inner and outer radii as well as in the cooling channel similar to the work of Riccius et al. [11]. The left and right sides have zero flux boundary conditions to ensure symmetry of the thermal field. The thermal cycle described in Table 1 is applied in the analysis. Fig. 7 shows some snapshots of the temperature field resulting from the transient thermal analysis.

4.2 Static analyses

The goal of the static analysis is to see the feasibility of the implemented damage model to describe the dog-house failure mode qualitatively. The pressure cycle in Table 2 is applied as load in the static analyses. For the static analyses 8-node brick elements

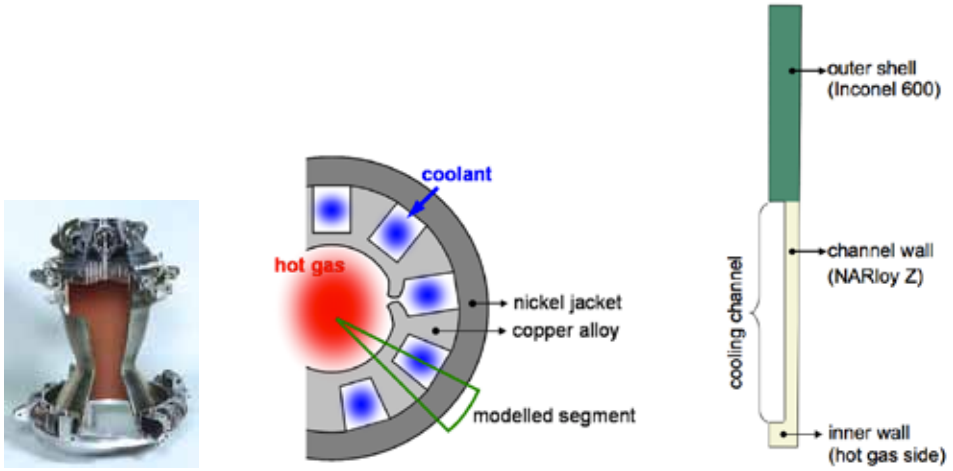

(a) A typical rocket combustion chamber.

(b) A schematic cross section of a typical rocket combustion chamber.

(c) Modelled segment of the quasi Vulcain thrust chamber at the throat.

Figure 6: Schematic cross section of a typical rocket combustion chamber and the modelled segment.

Phase	Time [s]	T_{hotgas} [K]	$T_{coolant}$ [K]
Pre-cooling	0 - 2	40	40
Hot run	3 - 603	950	40
Post-cooling	604 - 605	40	40
Relaxation	605 - 620	293.15	-

Table 1: Thermal cycle applied for the transient thermal analysis.

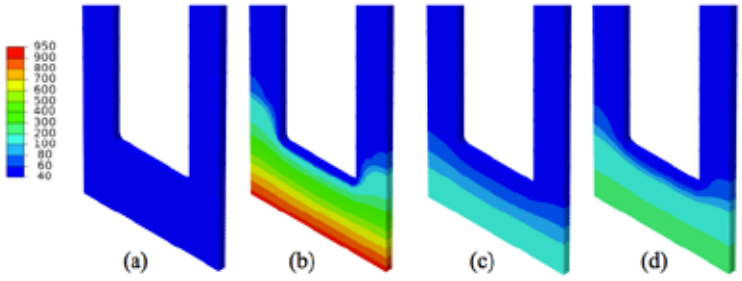

Figure 7: Temperature distribution at different phases of the assumed operational cycle: (a) pre cooling (b) hot run (c) post cooling (d) relaxation.

with reduced integration were applied. The critical area of interest is the cooling channel wall at the hot gas side. Two different meshes were used. The coarser and the finer mesh

Phase	Time [s]	P_{hotgas} [MPa]	$P_{coolant}$ [MPa]
Pre-cooling	0 - 2	0	2
Hot run	3 - 603	10	14.5
Post-cooling	604 - 605	0	2
Relaxation	605 - 620	0	0

Table 2: Pressure cycle applied for the static analyses.

have in total 1338 and 4014 elements respectively. Fig. 8 shows the discretization of the hot gas side wall using both meshes. The corner of the cooling channel passage is rounded with 0.1 mm fillet radius.

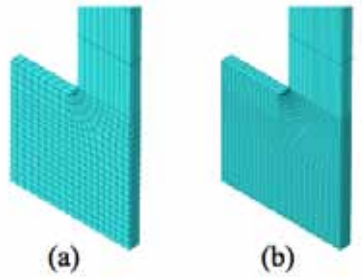

Figure 8: (a) Mesh 1 with 1338 elements. (b) Mesh 2 with 4014 elements.

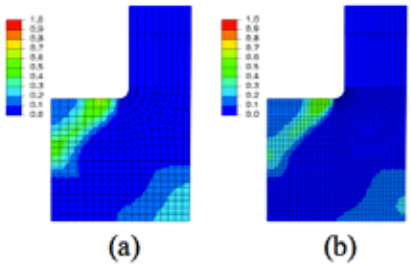

Figure 9: Damage distribution obtained from the static analyses: (a) Mesh 1 at the 16th cycle. (b) Mesh 2 at the 13th cycle.

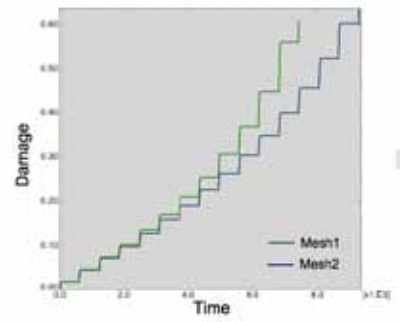

Figure 10: The cyclic evolution of the damage over time.

The damage distribution obtained from the analyses are shown in Fig. 9. The computation using Mesh 1 could be performed up to 16 cycles. Applying Mesh 2 the computation could be performed up to 13 cycles. As the damage increases, the local iteration within the user subroutine requires smaller and smaller time steps. The corresponding cyclic damage evolutions over time are shown in Fig. 10. Here it can be seen that with the coarser mesh, the damage evolves slightly faster, in comparison to the one obtained using the finer mesh.

This indicates a mesh dependency of the result. On the one hand this phenomenon could be attributed to the well-known localization effect in elastoplasticity coupled with damage. Another possible explanation is that simply the mesh is still too coarse to yield a converged result. An investigation which clarifies these issues is under way. In any case, improvement of the robustness of the computation shall enable the computation of more

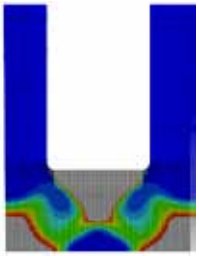

(a) Predicted end shape of the cooling channel segment.

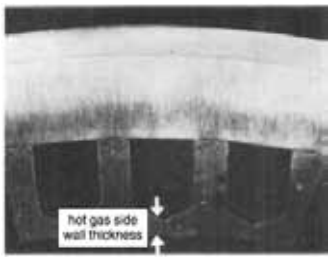

(b) The dog-house failure mode occured in a NARloy-Z thrust chamber [12].

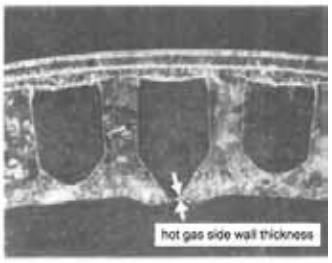

(c) The dog-house failure mode occured in an OFHC thrust chamber [12].

Figure 11: The predicted end shape of the channel segment from the simulation and the dog-house failure mode.

loading cycles. It is important to eliminate the convergence problem in the solution of the time discretized equation system to determine the internal variables. Fig. 11(a) shows the predicted end shape of the cooling channel segment. The grey area represents the area mostly affected by damage. Fig. 11(b) and Fig. 11(c) show cross sections of combustion chambers made out of NARloy-Z copper alloy and OFHC (oxygen free copper) alloy respectively. It is concluded by Hannum et al. [12] that depending on the liner material, the causes of the failure are different. In a NARloy-Z combustion chamber, the hot gas side wall does not bulge so much towards the chamber. Failure is then caused by low cycle fatigue. In an OFHC combustion chamber, the wall becomes significantly thinner. Cracking occurs after a necking phenomenon.

5 CONCLUSIONS

The coupling of a finite anisotropic elastoplastic model with isotropic ductile damage has been presented. The implementation of the model for finite element simulations in two challenging applications has shown the good potential of the model for failure prediction purposes.

6 ACKNOWLEDGEMENTS

The authors gratefully acknowledge the support provided by the German Science Foundation within the projects TP3 of the PAK343 "Methods for quasistatic-dynamic combined forming processes" and TP D3 of the CRC/Transregio 40 "Fundamental Technologies for the Development of Future Space-Transport-System Components under High Thermal and Mechanical Loads".

References

[1] I. N. Vladimirov, M. P. Pietryga, and S. Reese. Anisotropic finite elastoplasticity with nonlinear kinematic and isotropic hardening and application to sheet metal forming. *International Journal of Plasticity*, 26:659–687, 2010.

[2] C. O. Frederick and P. J. Armstrong. A mathematical representation of the multiaxial bauschinger effect. *Materials at High Temperatures*, 24:1–26, 2007.

[3] Jr. Daniel T. Butler and Marek-Jerzy Pindera. Analysis of factors affecting the performance of rlv thrust cell liners. Technical report, NASA Glenn Research Center, 2004.

[4] J. Lemaitre. *A Course on Damage Mechanics*. Springer, Berlin, 1992.

[5] E. Voce. The relationship between stress and strain for homogeneous deformation. *Journal of Institute of Metals*, 74:537–562, 1948.

[6] B. D. Colemann and M. Gurtin. Thermodynamics with internal variables. *Journal of Chemical Physics*, 47(597–613), 1967.

[7] I. N. Vladimirov, M. P. Pietryga, and S. Reese. On the influence of kinematic hardening on plastic anisotropy in the context of finite strain plasticity. *International Journal of Material Forming*, 2011.

[8] J. Lemaitre and J. L. Chaboche. *Mechanics of Solid Materials*. Cambridge University Press, Cambridge, 1995.

[9] I. N. Vladimirov, M. P. Pietryga, and S. Reese. On the modeling of nonlinear kinematic hardening at finite strains with application to springback - comparison of time integration algorithms. *International Journal of Numerical Methods in Engineering*, 75:1–28, 2008.

[10] D. Kuhl, Jörg Riccius, and O.J. Haidn. Thermomechanical analysis and optimization of cryogenic liquid rocket engines. *Journal of Propulsion and Power*, 18:835–846, 2002.

[11] Jörg R. Riccius and E. B. Zametaev. Stationary and dynamic thermal analyses of cryogenic liquid rocket combustion chamber walls. In *38th AIAA/ASME/SAE/ASEE Joint Propulsion Conference and Exhibit*, 2002.

[12] Ned P. Hannum and Jr. Harold G.P̃rice. Some effects of thermal-cycle-induced deformation in rocket thrust chambers. Technical report, NASA Langley Research Center, April 1981.

XI International Conference on Computational Plasticity. Fundamentals and Applications
COMPLAS XI
E. Oñate, D.R.J. Owen, D. Peric and B. Suárez (Eds)

MULTISCALE STRAIN LOCALIZATION MODELING IN THE GURSON-TVERGAARD-NEEDLEMAN PLASTICITY MODEL

SEBASTIÁN D'HERS* **AND EDUARDO DVORKIN†**

*Computational Mechanics Lab., Instituto Tecnológico de BuenosAires
Av. E. Madero 399, C1106ACD, Buenos Aires, Argentina
e-mail: sdhers@itba.edu.ar, web page: www.itba.edu.ar

† Facultad de Ingeniería , Universidad de Buenos Aires
Av. Las Heras 2214, C1127AAR Buenos Aires, Argentina web page: www.fi.uba.ar
SIM&TEC, Pueyrredón 2130, C1119ACR Buenos Aires, Argentina
e-mail: edvorkin@simytec.com, web page: www.simytec.com

Key words: Plasticity, Localization, Strong discontinuity, Multiple scales, Gurson-Tvergaard-Needleman

Abstract. The modeling of strain localization requires the use of different scales to describe the evolution of the material of the overall structure and the material inside the localized region. Focusing on the Gurson-Tvergaard-Needleman material we develop a multiscale formulation that uses strong discontinuity modes to model the development of a localization zone and the material degradation and void growth inside it. We present a strong discontinuity mode formulation able to capture the band kinematics that consists of a combination of sliding and opening modes. Then we derive an heuristic inter-scale factor to set a proper connection between the localized and the continuum scales.

This approach describes the evolution of the accumulated plastic strain and the void content inside and outside the localization band. The localization scale evolution is effectively controlled by the proposed heuristic rule. To illustrate on the formulation capabilities, a test case is presented and the behavior of the inter-scale connection factor is analyzed. The resulting formulation does not require a specific mesh refinement to model strain localization, provides mesh independent results and can be calibrated using experimental results.

1 INTRODUCTION

The Gurson-Tvergaard-Needleman plasticity model[1–5] incorporates to the standard J_2 plasticity model the material degradation that is due to the nucleation, growth and coalescence of voids. This material model is usually used for modeling ductile fracture phenomena, where the void content is used as an indicator of crack initiation.

Most ductile fracture processes are preceded by a strain localization, that takes place in a narrow band shaped region. In most cases the band width results much smaller than the problem domain, therefore forcing the two opposing sides of the region to open and/or slide relatively to each other (depending on the material considered). This inserts in the problem domain a kinematic mechanism that conditions its response.

Due to that, the modeling of strain localization phenomena via finite element formulations requires to use different scales for the description of the global deformation in the continuum and the localized deformation inside the localization bands and to use of physically meaningful laws to describe the evolution of the material inside the latter ones.

These issues have been addressed in the literature by many numerical techniques: the enhanced strain field method[6,7] the extended finite element method (X-FEM),[8,9] the strong discontinuity approach[10] and the embedded strong discontinuity modes.[11,12] The last two techniques were applied in the framework of G-T-N materials[13,14]

2 THE G-T-N MATERIAL MODEL

The Gurson plasticity model was first developed by Gurson.[1,2] It has been modified through time to adjust the model parameters[3,4] and received new inclusions like the addition of a void coalescence mechanism.[5] The complete set is known as the Gurson-Tvergaard-Needleman (G-T-N) material model. Herein we recall the equations required for the present development.[15]

The G-T-N yield surface, ${}^t\Phi$, depends on the hydrostatic stress, ${}^t\sigma_h$, the J_2 equivalent stress ${}^t\sigma_e$, the volume void fraction, ${}^t f$, and the actual yield stress,${}^t\sigma_y$, *

$$ {}^t\Phi\left({}^t\sigma_h, {}^t\sigma_e, {}^t f, {}^t\bar{\varepsilon}^P\right) = \left(\frac{{}^t\sigma_e}{{}^t\sigma_y}\right)^2 + 2\ {}^t f\ q_1\ \cosh\left(\frac{3}{2} q_2 \frac{{}^t\sigma_h}{{}^t\sigma_y}\right) - 1 - \ {}^t f\ {}^2\ q_1^2 = 0 \tag{1} $$

$$ {}^t\sigma_h = \frac{1}{3}\ {}^t\underline{\underline{\sigma}} :\ {}^t\underline{\underline{\mathbf{g}}}, \tag{2} $$

$$ {}^t\sigma_e = \sqrt{\frac{3}{2}\ {}^t\underline{\underline{\mathbf{s}}}\ :\ {}^t\underline{\underline{\mathbf{s}}}}, \tag{3} $$

being ${}^t\underline{\underline{\mathbf{s}}}$ the deviatoric stress tensor and ${}^t\underline{\underline{\mathbf{g}}}$ the metric tensor. The parameters q_1 and q_2 were set to fit the experimental results. We adopt $q_1 = 1.5$ and $q_2 = 1$ for the present study.

During yielding ${}^t\Phi = 0$; hence we can obtain an equivalent stress that takes into account the void effect,

$$ {}^t\bar{\sigma}^2 = \ {}^t\sigma_y{}^2 \left(1 + \ {}^t f\ {}^2\ q_1^2 - 2\ {}^t f\ q_1\ \cosh\left({}^t\alpha\right)\right) \tag{4} $$

*We indicate the tensorial product between two tensors as a b (in other references it is indicated as $a \bigotimes b$) and the number of underlines indicates the tensor order.

For the evolution of ${}^t\sigma_y$ we adopt an implicit hardening law from,[15]

$$\frac{{}^t\sigma_y}{{}^0\sigma_y} = \left(\frac{{}^t\sigma_y}{{}^0\sigma_y} + \frac{3\ G}{{}^0\sigma_y}\ {}^t\bar{\varepsilon}^P\right)^N \tag{5}$$

where ${}^0\sigma_y$ is the initial yield stress, ${}^t\bar{\varepsilon}^P$is the equivalent plastic strain (to be defined in Eqn. (11)), N is the hardening exponent and G is the elastic shear modulus.

The increment of void volume fraction is attributed to:

- Growth of existing voids driven by the bulk plastic deformation,

$$df_{growth} = \left(1 -\ {}^t f\right)\ d\underline{\underline{\varepsilon}}^P :\ {}^t\underline{\underline{\mathbf{g}}}. \tag{6}$$

- Nucleation of new voids driven by the accumulated plastic strain evolution,[16]

$$df_{nucleation} =\ {}^t A\ d\bar{\varepsilon}^P \tag{7}$$

with:

$${}^t A = \frac{f_N}{S_N\sqrt{2\pi}} exp\left[-\frac{1}{2}\left(\frac{{}^t\bar{\varepsilon}^P - \varepsilon_N}{s_N}\right)^2\right], \tag{8}$$

where, f_N is the void volume fraction of nucleation particles, S_N its standard deviation and ε_N the mean strain for void nucleation. We adopt $s_N = 0.1$, $f_N = 0.04$ and $\varepsilon_N = 0.3$.

- Coalescence of voids is modeled by modifying ${}^t f$ once a critical void fraction, $f_{Critical}$, is reached.[5]

The evolution of the internal variables, ${}^t f$ and ${}^t\bar{\varepsilon}^P$, of the G-T-N material depends on the volumetric $\left(\varepsilon_h^P\right)$ and distortive $\left(\varepsilon_e^P\right)$ equivalent plastic strains. Those equivalent strains are defined decomposing the plastic strain increment as follows,

$$\underline{\underline{\varepsilon}}^P =\ {}^{t+\Delta t}\underline{\underline{\varepsilon}}^P -\ {}^t\underline{\underline{\varepsilon}}^P = \frac{1}{3}\varepsilon_h^P\ {}^{t+\Delta t}\underline{\underline{\mathbf{g}}} + \varepsilon_e^P\ \frac{3}{2}\frac{{}^t\underline{\underline{\mathbf{s}}}}{{}^t\sigma_e}, \tag{9}$$

Hence the increment between t and $t+\Delta t$ of the void volume fraction and the equivalent plastic strain becomes,

$${}^{t+\Delta t}f -\ {}^t f = f = \left(1 -\ {}^{t+\Delta t}f\right)\ \underline{\underline{\varepsilon}}^P :\ {}^{t+\Delta t}\underline{\underline{\mathbf{g}}} +\ {}^{t+\Delta t}A\ \bar{\varepsilon}^P, \tag{10}$$

$$\bar{\varepsilon}^P\ =\ {}^{t+\Delta t}\bar{\varepsilon}^P -\ {}^t\bar{\varepsilon}^P = \frac{{}^{t+\Delta t}\sigma_h\ \varepsilon_h^P +\ {}^{t+\Delta t}\sigma_e\ \varepsilon_e^P}{\left(1 -\ {}^{t+\Delta t}f\right)\ {}^{t+\Delta t}\sigma_y}. \tag{11}$$

3 FINITE ELEMENT FORMULATION

3.1 Displacement and strain decomposition

We solve the nonlinear elastoplastic problem using an incremental procedure where we decompose the strain and displacement increments from time t to time $t + \Delta t$ as,

$$ {}^{t+\Delta t}\underline{\underline{\varepsilon}} = {}^{t}\underline{\underline{\varepsilon}} + \underline{\underline{\varepsilon}} \quad \wedge \quad {}^{t+\Delta t}\underline{u} = {}^{t}\underline{u} + \underline{u}, $$

and discretize the continuum using the standard element shape functions,[17] $\underline{\mathbf{H}}$, and the nodal displacements, $\underline{\mathbf{U}}$,

$$ \underline{u} = \underline{\mathbf{H}}\ {}^{t+\Delta t}\underline{\mathbf{U}} - \underline{\mathbf{H}}\ {}^{t}\underline{\mathbf{U}} = \underline{\mathbf{H}}\underline{\mathbf{U}}. $$

At the elements where the localization indicator triggers a discontinuity, we decompose the displacement field into continuous and localized contributions,[11,12]

$$ \underline{u} = \underline{u}_{continuum} + \underline{u}_{localized} = \underline{\mathbf{H}}\ \underline{\mathbf{U}}_{continuum} + \underline{\mathbf{H}}\ \underline{\mathbf{U}}_{localized} \tag{12} $$

Assuming infinitesimal strains analysis, we also decompose the deformation increment into elastic and plastic components. Since we assume the localization behaves as rigid-plastic, the elastic deformation only contributes to the continuum scale, and the plastic deformation contributes to the continuum and to the localized scales. Hence,

$$ \underline{\underline{\varepsilon}} = \underline{\underline{\varepsilon}}^{E} + \underline{\underline{\varepsilon}}^{P} = \underline{\underline{\varepsilon}}^{E}_{continuum} + \underline{\underline{\varepsilon}}^{P}_{continuum} + \underline{\underline{\varepsilon}}^{P}_{localized}. \tag{13} $$

The displacement $\underline{u}_{localized}$ has to be designed as to reproduce the localized deformation kinematics, thus we adopt,[11]

$$ \underline{u}_{localized} = \underline{\mathbf{H}}\ \underline{\mathbf{U}}_{localized} = \underline{\mathbf{H}}\ \gamma\ \underline{\mathbf{\Theta}} \tag{14} $$

where $\underline{\mathbf{\Theta}}$ are the nodal displacements corresponding to the strong discontinuity mode to be defined later in this work and γ is the increment of a scalar parameter which is part of the problem unknowns. The evolution of this parameter is written as,

$$ {}^{t+\Delta t}\gamma = {}^{t}\gamma + \gamma. \tag{15} $$

Replacing Eqn. (14) into Eqn. (12) results,

$$ \underline{u} = \underline{\mathbf{H}}\ \underline{\mathbf{U}} = \underline{\mathbf{H}}\,(\underline{\mathbf{U}} - \gamma\ \underline{\mathbf{\Theta}}) + \underline{\mathbf{H}}\gamma\ \underline{\mathbf{\Theta}}. \tag{16} $$

Thus the resulting strain fields, using Voight notation, are,

$$ \underline{\varepsilon}_{continuum} = \underline{\varepsilon}^{E}_{continuum} + \underline{\varepsilon}^{P}_{continuum} = \underline{\mathbf{B}}\,(\underline{\mathbf{U}} - \gamma\ \underline{\mathbf{\Theta}}) \tag{17} $$

$$ \underline{\varepsilon}_{localized} = \underline{\varepsilon}^{P}_{localized} = \underline{\mathbf{B}}\ \underline{\mathbf{U}}_{localized} = \underline{\mathbf{B}}\ \gamma\ \underline{\mathbf{\Theta}} \tag{18} $$

were $\underline{\mathbf{B}}$ is the adopted element strain-displacement matrix.

Summarizing this derivation, we now can build a strong discontinuity mode, $\underline{\mathbf{\Theta}}$, that can generate a localized displacement field $\underline{u}_{localized}$ with a related strain field strain $\underline{\underline{\varepsilon}}^{P}_{localized}$.

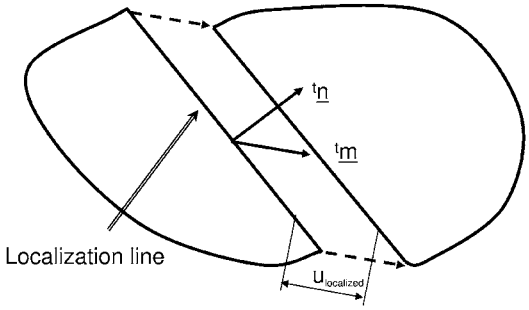

Figure 1: Continuous with an active localization.

3.2 Localization definition

A localization line in plane problems can be characterized by a line with normal ${}^t\underline{\mathbf{n}}$ and a propagation direction ${}^t\underline{\mathbf{m}}$ along which the displacement jump,[19] $\underline{u}_{localized}$, is found (i.e. if ${}^t\underline{\mathbf{n}} \parallel {}^t\underline{\mathbf{m}} \Longrightarrow$ the kinematics is Mode I and if ${}^t\underline{\mathbf{n}} \perp {}^t\underline{\mathbf{m}} \Longrightarrow$ the kinematics is Mode II). In Fig. 1 we draw a schematic representation of the above definitions, considering a general displacement jump; the band has no width.

To describe the induced localization strain we use the Maxwell conditions, so we necessitate that the discontinuity jump satisfies,[6]

$$\underline{\nabla}\, \underline{\mathbf{u}}_{localized} = \gamma\, {}^t\underline{\mathbf{n}}\, {}^t\underline{\mathbf{m}}$$

where γ is a scalar increment of the discontinuity jump. Hence the strain jump becomes,

$$\underline{\underline{\varepsilon}}^{P}_{localized} = \frac{1}{2}\,\gamma\left({}^t\underline{\mathbf{n}}\, {}^t\underline{\mathbf{m}} + {}^t\underline{\mathbf{m}}\, {}^t\underline{\mathbf{n}}\right) \tag{19}$$

3.3 Bifurcation analysis

It has been shown[18,19] that the triggering of bifurcation in the material behavior and the respective band orientation can be determined from the singularity of the acoustic tensor, which is defined as,

$${}^t\underline{\underline{\mathbf{Q}}} = {}^t\underline{\mathbf{n}} \cdot {}^{\mathbf{t}}\underline{\underline{\underline{\underline{\mathbf{C}}}}}^{\mathbf{EP}} \cdot {}^t\underline{\mathbf{n}} \tag{20}$$

where ${}^{\mathbf{t}}\underline{\underline{\underline{\underline{\mathbf{C}}}}}^{\mathbf{EP}}$ is the constitutive tensor.

The bifurcation condition requires that,[6,18]

$${}^t\underline{\underline{\mathbf{Q}}} \cdot {}^t\underline{\mathbf{m}} = \left({}^t\underline{\mathbf{n}} \cdot {}^{\mathbf{t}}\underline{\underline{\underline{\underline{\mathbf{C}}}}}^{\mathbf{EP}} \cdot {}^t\underline{\mathbf{n}}\right) \cdot {}^t\underline{\mathbf{m}} = 0 \tag{21}$$

what is satisfied when,

$$\det\left({}^t\underline{\underline{\mathbf{Q}}}\right) = \det\left({}^t\underline{\mathbf{n}} \cdot {}^{\mathbf{t}}\underline{\underline{\underline{\underline{\mathbf{C}}}}}^{\mathbf{EP}} \cdot {}^t\underline{\mathbf{n}}\right) = 0. \tag{22}$$

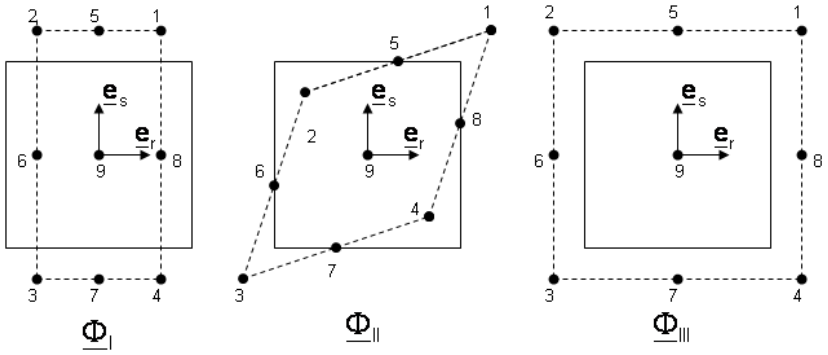

Figure 2: Base of modes for a 9-node element in the isoparametric element space.

Eqn.(22) implies that at least one of ${}^t\underline{\underline{\mathbf{Q}}}$ eigenvalues to be zero and the respective eigenvector ${}^t\underline{\mathbf{m}}$ to be the band growth direction according to Eqn.(21). Since it is difficult to precisely determine when Eqn.(22) is satisfied during an incremental procedure we use,[6]

$$\det\left({}^t\underline{\underline{\mathbf{Q}}}\right) = \det\left({}^t\underline{\mathbf{n}} \cdot {}^{\mathbf{t}}\underline{\underline{\underline{\underline{\mathbf{C}}}}}^{\mathbf{EP}} \cdot {}^t\underline{\mathbf{n}}\right) \leq 0 \tag{23}$$

and the growth direction can be obtained from the eigenvector ${}^t\underline{\mathbf{m}}$ belonging to the smallest eigenvalue of ${}^t\underline{\underline{\mathbf{Q}}}$.

3.4 Strong discontinuity modes definition

To build a strong discontinuity mode, ${}^t\underline{\mathbf{\Theta}}$, able to model the localization when scaled by γ, we use a base of displacement modes, ${}^t\underline{\mathbf{\Psi}}_A$, constituted by two shear modes and a volume change mode[11,12,14] . Subindex $A = I...III$ indicates the deformation mode.

To construct each of them, we use three different sets of nodal coordinates, ${}^t\underline{\mathbf{\Phi}}_A$, and the unstrained nodal coordinates $\left(r^k, s^k\right)$ and build them as,

$${}^t\underline{\mathbf{\Psi}}_A^k = \left[\left({}^t\Phi_A^k\right)_r - r^k\right]\ \underline{\mathbf{e}}_r\ +\ \left[\left({}^t\Phi_A^k\right)_s - s^k\right]\ \underline{\mathbf{e}}_s. \tag{24}$$

In the above equation $(\underline{\mathbf{e}}_r; \underline{\mathbf{e}}_s)$ are orthonormal base vectors shown in Fig.2 along the (r, s) natural directions and the upper index $k = 1...N$ indicates the node. As an illustrative example we plot the displacement modes in the element isoparametric space coordinates (r,s) for a 9-node element in Fig.2. To complete the definition we generalize Eqn.(24) in the (x_1, x_2) structural coordinate system using the element shape functions h_j,

$${}^t\underline{\mathbf{\Psi}}_A^k = \left[\ h_j\left(\left({}^t\Phi_A^k\right)_r, \left({}^t\Phi_A^k\right)_s\right)\ x_i^j - x_i^k\right]\underline{\mathbf{e}}_i\ . \tag{25}$$

With this displacement modes, ${}^t\underline{\mathbf{\Psi}}_A$, we compute their respective strains at the element center,

$$\underline{\varepsilon}_A = \underline{\mathbf{B}}_c\ \ {}^t\underline{\mathbf{\Psi}}_A \tag{26}$$

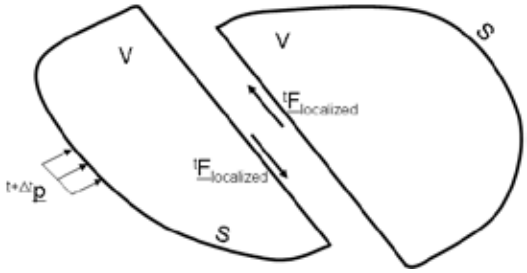

Figure 3: Continuous with an active localization band

where $\underline{\mathbf{B}}_c$ is the strain-displacements matrix calculated at the element center. By linearly combining the above defined strain fields we obtain the $\underline{\varepsilon}^P_{localized}$ defined in Eqn. (19),

$$\underline{\varepsilon}^P_{localized} = \beta_I \underline{\varepsilon}_I + \beta_{II} \underline{\varepsilon}_{II} + \beta_{III} \underline{\varepsilon}_{III} \cdot, \tag{27}$$

where β_A parameters have to be determined.

Therefore the modes ${}^t\underline{\mathbf{\Psi}}_A$ can also be linearly combined and normalized to get the localization strong discontinuity mode, ${}^t\underline{\mathbf{\Theta}}$,

$${}^t\underline{\mathbf{\Theta}} = \frac{\beta_I \ {}^t\underline{\mathbf{\Psi}}_I + \beta_{II} \ {}^t\underline{\mathbf{\Psi}}_{II} + \beta_{III} \ {}^t\underline{\mathbf{\Psi}}_{III}}{|\beta_I \ {}^t\underline{\mathbf{\Psi}}_I + \beta_{II} \ {}^t\underline{\mathbf{\Psi}}_{II} + \beta_{III} \ {}^t\underline{\mathbf{\Psi}}_{III}|} \tag{28}$$

3.5 Element equilibrium equations

We apply the virtual work principle in order to obtain the finite element equations. In Fig. 3 we show a scheme of a solid with a localization line and the localization line forces (band forces). For the equilibrium at time $t + \Delta t$ we get,

$$\int_V \delta \left[\underline{\varepsilon}_{continuum}\right]^T \ {}^{t+\Delta t}\underline{\sigma}_{continuum} \, dv \ + \ \delta \left[\underline{\mathbf{U}}_{localized}\right]^T \ {}^{t+\Delta t}\underline{\mathbf{F}}_{localized} = \int_S \delta \underline{\mathbf{u}}^T \ {}^{t+\Delta t}\underline{\mathbf{p}} \, ds. \tag{29}$$

Replacing Eqns. (12), (14) and (17) into Eqn. (29) and since $\delta\underline{\mathbf{U}}$ and $\delta\underline{\gamma}$ are arbitrary we obtain set of equations[12] that has to be solved iteratively; therefore, a Newton-Raphson scheme is implemented at the global level. The parameters γ are condensed at the element level.

The only undefined variable is ${}^{t+\Delta t}\underline{\mathbf{F}}_{localized}$ for which we propose[11] that,

$$\frac{{}^t\underline{\mathbf{\Theta}}^T \ {}^{t+\Delta t}\underline{\mathbf{F}}_{localized}}{{}^t\underline{\mathbf{\Theta}}^T \ {}^t\underline{\mathbf{F}}_{localized}} = \frac{{}^{t+\Delta t}\bar{\sigma}_{localized}}{{}^t\bar{\sigma}_{localized}}, \tag{30}$$

where the localization equivalent stress ${}^{t+\Delta t}\bar{\sigma}_{localized}$ is unknown. To calculate it, we relate the localization volumetric and distortive equivalent plastic strains to the band incremental parameter γ, through a set of positive factors ζ and φ. These factors relate the continuum and the localization scales. Hence,

$$\left(\varepsilon^P_{h \ loc}\right)^2 = \zeta^2 \gamma^2 \ , \tag{31}$$

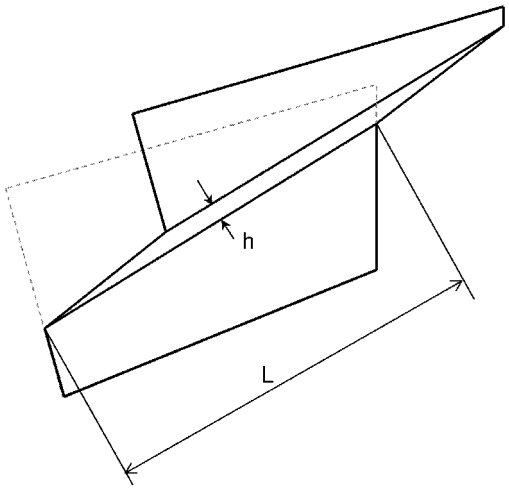

Figure 4: Scheme of a band in a localized element

$$\left(\varepsilon^P_{e\ loc}\right)^2 = \varphi^2\gamma^2. \tag{32}$$

To determine the inter-scales factors we request the distortive dissipated energy in the band to be equal to the energy dissipated by the distortive part of the localization mode. For this we calculate a purely distortive strong discontinuity mode, ${}^t\underline{\mathbf{\Theta}}_d$, as was done for the localization mode ${}^t\underline{\mathbf{\Theta}}$, hence,

$$\int_{t_\gamma}^{t+\Delta t_\gamma} \underline{\Theta}_e^T\ {}^\tau\underline{\mathbf{F}}\ d\gamma = \int_{V_{loc}} \int_{t_{\varepsilon^P_{e\ loc}}}^{t+\Delta t_{\varepsilon^P_{e\ loc}}} {}^\tau\bar{\sigma}_{loc}\ d\varepsilon^P_{e\ loc} dV_{loc}\ . \tag{33}$$

The same reasoning is applied to the hydrostatic contribution, but with the volumetric strong discontinuity mode, $\underline{\Theta}_h$.

To solve Eqn.(33) and the respective volumetric equations, we construct an heuristic rule for what we depict in Fig 4 an element shaped domain that has a localization line across it. The localization line splits the domain in two subdomains that slide along the localization line. Assuming unitary thickness, the volume of material comprised in the localization is,

$$V_{loc} = \ h\ L, \tag{34}$$

where h is a reference bandwidth and L is the band length across the element.

Using in Eqn.(33) an Euler backward time integration scheme together with Eqn. (34) and the corresponding volumetric equations leads to,

$$\gamma\ \ {}^t\underline{\Theta}_e^T\ \ {}^{t+\Delta t}\underline{\mathbf{F}}\ =\ {}^{t+\Delta t}\bar{\sigma}_{loc}\ \varepsilon^P_{e\ loc}\ h\ L\ , \tag{35}$$

and

$$\gamma\ \ {}^t\underline{\Theta}_h^T\ \ {}^{t+\Delta t}\underline{\mathbf{F}} = \ {}^{t+\Delta t}\bar{\sigma}_{loc}\ \varepsilon^P_{h\ loc}\ h\ L\ . \tag{36}$$

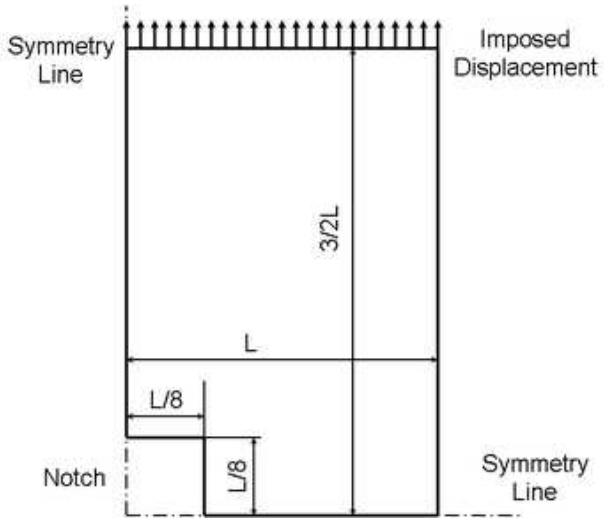

Figure 5: Test case notched sample

Replacing $\varepsilon^P_{e\ loc}$ and $\varepsilon^P_{h\ loc}$definitions into Eqns. (31) and (32) we get the inter-scales factors,

$$\varphi = \left| \frac{{}^t\underline{\boldsymbol{\Theta}}_e^T \ {}^{t+\Delta t}\underline{\mathbf{F}}_{loc}}{h\ L\ {}^{t+\Delta t}\bar{\sigma}_{loc}} \right| , \tag{37}$$

$$\zeta = \left| \frac{{}^t\underline{\boldsymbol{\Theta}}_h^T \ {}^{t+\Delta t}\underline{\mathbf{F}}}{h\ L\ {}^{t+\Delta t}\bar{\sigma}_{loc}} \right| . \tag{38}$$

Now that a proper scale is defined for the band strains, we determine $\varepsilon^P_{h_{loc}}$ and $\varepsilon^P_{e_{loc}}$ from Eqns. (31) and (32). Finally we determine the internal variables increments using Eqns. (5), (10) and (11), and replace them into Eqn. (4) to get ${}^{t+\Delta t}\bar{\sigma}_{localized}$.

The h parameter is added in Eqn. (34) to incorporate a regularization that takes into account the strain concentration inside the band. It is a bandwidth yet not a physical one. It can be interpreted as the width a band should have in order to have uniform strains inside the band with the same overall effect to the continua. This allows for parameter h to control the unloading path of the structure, as it is shown in the next section.

4 NUMERICAL EXAMPLE

To test our finite element formulation we use a plane strain pure traction test. A specimen with a central notch, used to fix the initiation of the localization, is considered as shown in Fig. 5. The element adopted for the analysis is a 4 node quadrilateral with mixed interpolated tensorial components (QMITC4)[20,21] and due to the specimen symmetry only one quarter is modeled. For time evolution we use imposed displacements with automatic time stepping up to a 4% of elongation. To focus on strain localization and not in material fracture or crack opening phenomenon, the analyzes are stopped when ${}^tf$ grows beyond 2/3. The material parameters are set to $E = 200GPa$, $\sigma_y = 600MPa$. Nor initial void volume fraction nor hardening are considered.

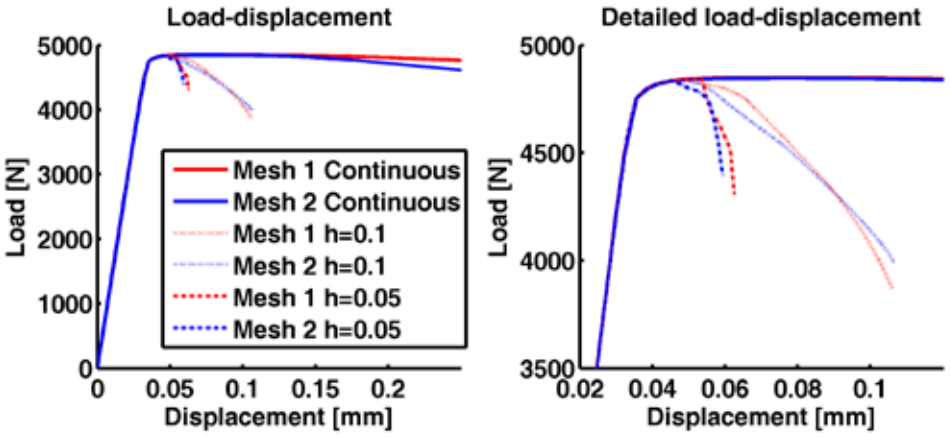

Figure 6: Load displacement results

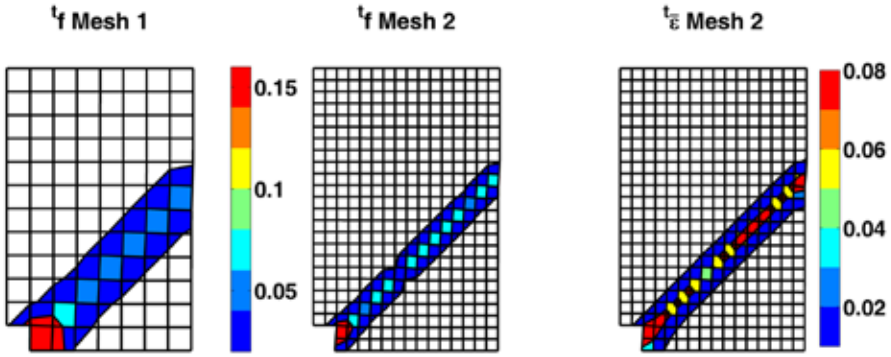

Figure 7: ${}^t f_{loc}$ and ${}^t \bar{\epsilon}^P_{loc}$ for some meshes

Two mesh densities are analyzed each for two h parameters (Eqn. 34) are used. In the load-displacement plot shown in Fig. 6 it can be seen that the use of a continuous formulation (standard finite elements) leads to mesh dependent results, while the use of the present formulation shows no mesh dependency. The parameter h has the role of scaling the material deterioration inside the band, thus controlling the load downslope. Sample band plots of the ${}^t f_{loc}$ and ${}^t \bar{\epsilon}^P_{loc}$ variables are shown in Fig. 7.

5 CONCLUSIONS

We have applied the strong discontinuity modes formulation[11,12,14] for modeling strain localization in G-T-N materials. The required inter-scales connection, between the continuum and the localization scales is achieved using an equivalent dissipated work criteria distinguishing between distortive and volumetric contributions. We introduced a length-scale (h) to heuristically model the material damage evolution inside the band. This h-parameter controls the damage-induced unloading behavior and therefore it can be determined from actual experimental data. The resulting formulation does not require a

specific mesh refinement to model a localization, provides mesh independent results and allows the control of the downslope part of the load-displacement path via the h-parameter. The actual implementation uses the same order of the Gauss integration required for calculating the element stiffness matrix and does not introduce extra d.o.f. in the assembled numerical model.

We gratefully acknowledge the support of TENARIS and ITBA for this research.

REFERENCES

[1] Gurson, A.L., *Plastic flow and fracture behavior of ductile materials incorporating void nucleation, growth and coalescence*. Ph.D. thesis, Brown University, (1975).

[2] Gurson, A.L., Continuum theory of ductile rupture by void nucleation and growth: Part 1 - yield criteria and flow rules for porous ductile materials, *J. Eng. Matl. Tech.* (1977) **99**:2-15.

[3] Tvergaard V., Influence of voids on shear band instabilities under plane strain conditions, *Int. J. Fract.* (1981) **17**:389-407.

[4] Tvergaard, V., On localization in ductile materials containing spherical voids, *Int. J. Fract.* (1982) **18**:237-252.

[5] Tvergaard, V. and Needleman, A., Analysis of the cup-cone fracture in a round tensile bar, *Acta Metallica* (1984) **32**:157-169.

[6] Ortiz, M., Leroy, Y. and Needleman, A., A Finite-Element Method for Localized Failure Analysis, *Comput. Meth. Appl. Mechs. Engng.*, (1987) **61**:189-214.

[7] Armero, F. and Garikipati K., Recent Advances in the Analysis and Numerical Simulation of Strain Localization in Inelastic Solids, *Proc. Computational Plasticity COMPLAS IV*, (Ed. by D.R.J Owen, E. Oñate and E. Hinton), Barcelona, (1995).

[8] Samaniego, E. and Belytschko, T., Continuum–discontinuum modelling of shear bands, *Int. J. Num. Methods in Engng.*, (2005), **62**:1857-1872.

[9] Areias, P.M.A. and Belytschko T., Two-scale shear band evolution by local partition of unity, *Int. J. Numerical Methods in Engng.*, (2006) **66**:878-910.

[10] Oliver, J., Modeling strong discontinuities in solid mechanics via strain softening constitutive equations. Part 1: Fundamentals, *Int. J. Numerical Methods in Engng.*, (1996) **39**:3575-3600.

[11] D'hers, S. and Dvorkin, E.N., Modeling shear bands in J2 plasticity using a two-scale formulation via embedded strong discontinuity modes, *Int. J. Numer. Meth. Engng*, (2009) **77**:1015-1043.

[12] D'hers, S. and Dvorkin, E.N.,On the modeling of shear bands formation in J2 materials with damage evolution, *Engineering Computations*, (2011) **28-2**:130-153.

[13] Sánchez, P.J. ,Huespe, A.E. and Oliver, J., On some topics for the numerical simulation of ductile fracture, *International Journal of Plasticity*, (2008), **24**:1008-1038.

[14] D'hers S., *On localization modeling for ductile materials*, Doctoral thesis, University of Buenos Aires, (2010).

[15] Aravas N., On the numerical integration of a class of pressure-dependent plasticity models, *International Journal for Numerical Methods in Engineering*, (1987) **24**:1395-1416.

[16] Chu, C.C. and Needleman, A., Void nucleation effects in bi-axially stretched sheets, *J. Eng. Mater. Technol.*, (1980) **102**:249-256.

[17] Bathe K. J., *Finite Element Procedures*, Prentice Hall, New Jersey, (1996).

[18] Rice, J.R., The Localization of Plastic Deformation, in Theoretical and Applied Mechanics, *Proceedings of the 14th International Congress on Theoretical and Applied Mechanics*, (ed. W.T. Koiter) (1976), Delft, North-Holland Publishing Co., Vol. 1, pp.207-220.

[19] Ottosen, N.S. and Runesson K., Properties of discontinuous bifurcation solutions in elasto-plasticity, *Int. J. Solids Structures*, (1991) **27**:401-421.

[20] Dvorkin, E.N. and Vassolo S.I., A quadrilateral 2D finite element based on mixed interpolation of tensorial components, *Engng. Computations*, (1989) **6**:217-224.

[21] Dvorkin, E.N., Assanelli, A.P. and Toscano R.G.,Performance of the QMITC element in 2D elasto-plastic analyzes, *Computers & Structures*, (1996) **58**:1099-1129.

XI International Conference on Computational Plasticity. Fundamentals and Applications
COMPLAS XI
E. Oñate, D.R.J. Owen, D. Peric and B. Suárez (Eds)

NUMERICAL SIMULATIONS OF VICKERS INDENTATION CRACK GROWTH IN FERROELECTRIC SINGLE CRYSTALS: EFFECT OF MICROSTRUCTURE ON THE FRACTURE PROCESS

AMIR ABDOLLAHI AND IRENE ARIAS

Laboratori de Càlcul Numèric (LaCàN)
Departament de Matemàtica Aplicada III
Universitat Politècnica de Catalunya (UPC)
Campus Nord UPC-C2, E-08034 Barcelona, Spain
e-mail: irene.arias@upc.edu, http://www-lacan.upc.edu

Key words: Ferroelectricity, Fracture, Phase-field models, Finite element analysis

Abstract. The Vickers indentation technique is commonly used to investigate the fracture toughness of ferroelectric single crystals. Experiments show that the radial cracks perpendicular to the poling direction of the material propagate faster than the parallel ones. Using a phase-field model, we perform numerical simulations to show this anisotropy attributed to interactions between material microstructure and radial cracks. This model is based on a modified regularized formulation of the variational brittle fracture and domain evolution in ferroelectric materials.

1 INTRODUCTION

Ferroelectric materials exhibit strong electro-mechanical coupling which make them ideal materials for use in electro-mechanical devices such as sensors, actuators and transducers. To assure optimum reliability of these devices, understanding of the fracture behavior in these materials is essential. The complex nonlinear interactions of the mechanical and electrical fields in the vicinity of the crack, with localized switching phenomena, govern the fracture behavior of ferroelectric materials. Experimental techniques have been used to study fracture in ferroelectrics, including Vickers indentation to investigate the fracture toughness anisotropy [1–5]. Experiments show that cracking along the poling direction of the material has a shorter length and consequently a higher effective fracture toughness than that normal to the poling direction.

In this paper we introduce a model able to capture the anisotropic crack growth under Vickers indentation loading. This anisotropy is obtained by linking the crack propagation with the microstructural phenomena. The model treats in a coupled phase-field energetic

fashion both the brittle crack propagation and the microstructure evolution. We have recently presented a model, showing that the interaction of the microstructure and the crack leads to a slow-fast crack propagation behavior observed in experiment [6]. In Ref. [7], we have introduced a modification in the formulation to endow the phase-field model with the ability to simulate the aforementioned anisotropic crack growth. We present here the highlights of that work.

The theory of the coupled phase-field model is summarized in Section 2. Simulation results are presented and discussed in Section 3. The last Section is the conclusion of this paper.

2 PHASE-FIELD MODEL

The proposed approach to brittle fracture in ferroelectrics relies on the coupling of two energetic phase-field models, namely a time-dependent Ginzburg-Landau model for ferroelectric domain formation and evolution [8], and a variational regularized model of Griffith's fracture [9]. The electro-mechanical enthalpy density h is written as [6]

$$\begin{aligned} h(\varepsilon, \mathbf{p}, \mathbf{E}, v) &= (v^2 + \eta_\kappa)\left[U(\nabla \mathbf{p}) + W(\mathbf{p}, \varepsilon)\right] + W_e(\varepsilon, v) + \chi(\mathbf{p}) - \frac{\varepsilon_0}{2}|\mathbf{E}|^2 - \mathbf{E}\cdot\mathbf{p} \\ &+ G_c\left[\frac{(1-v)^2}{4\kappa} + \kappa|\nabla v|^2\right], \end{aligned} \tag{1}$$

where $\mathbf{p}$ is the polarization, $\mathbf{E}$ is the electric field defined as $\mathbf{E} = -\nabla\phi$, ϕ is the electrical potential, G_c is the critical energy release rate or the surface energy density in Griffith's theory and κ is a positive regularization constant to regulate the size of the fracture zone. The scalar field v provides a diffuse representation of the fracture zone, $v = 1$ and $v = 0$ indicating unbroken and broken material, respectively. The parameter η_κ is a small residual stiffness to avoid the singularity of the elastic energy in fully fractured regions of the domain. The domain wall energy density U, the electroelastic energy density W and the phase-separation potential χ in Eq. (1) are given in Ref. [7]. Note that here the energy functional W does not include the elastic energy and it is only associated with coupling terms between the strain and the total polarization $\mathbf{p}$. The elastic energy density W_e is written in [9] as

$$W_e(\varepsilon, v) = \kappa_0 \frac{\mathrm{tr}^-(\varepsilon)^2}{2} + (v^2 + \eta_\kappa)\Big(\kappa_0 \frac{\mathrm{tr}^+(\varepsilon)^2}{2} + \mu\ \varepsilon_D \cdot \varepsilon_D\Big), \tag{2}$$

where κ_0 and μ are the bulk and shear modulus of the material, respectively. The decomposition of the trace of the strain tensor ε in positive and negative parts are $\mathrm{tr}^+ = \max(\mathrm{tr}(\varepsilon), 0)$ and $\mathrm{tr}^- = \max(-\mathrm{tr}(\varepsilon), 0)$ and ε_D are the deviatoric components of the strain tensor. This decomposition is introduced to prevent crack nucleation, propagation and interpenetration in compressed regions by accounting for asymmetric behavior

in traction and compression. Note that here only the expansion and shear terms are multiplied by the jump set function $(v^2 + \eta_\kappa)$.

The stresses and electric displacements are derived from the electrical enthalpy as $\sigma = \partial h/\partial \varepsilon$ and $\mathbf{D} = -\partial h/\partial \mathbf{E}$. This particular formulation of the phase-field model encodes the traction-free, electrically permeable and free-polarization boundary conditions of a sharp-crack model [6].

The time evolution of the system results from the gradient flows of the total electromechanical enthalpy with respect to the primary variables v and $\mathbf{p}$, assuming that the displacement and the electric field adjust immediately to mechanical and electrostatic equilibrium (with infinite mobility), i.e.

$$\alpha \int_\Omega \dot{p}_i \delta p_i \mathrm{d}\Omega = -\int_\Omega \frac{\partial h}{\partial p_i} \delta p_i \, \mathrm{d}\Omega, \tag{3}$$

$$\beta \int_\Omega \dot{v} \delta v \mathrm{d}\Omega = -\int_\Omega \frac{\partial h}{\partial v} \delta v \, \mathrm{d}\Omega, \tag{4}$$

$$0 = \int_\Omega \sigma_{ij} \delta \varepsilon_{ij} \, \mathrm{d}\Omega, \tag{5}$$

$$0 = \int_\Omega D_i \delta E_i \, \mathrm{d}\Omega, \tag{6}$$

where $1/\alpha > 0$ and $1/\beta > 0$ are the mobilities of the processes. The weak form of the evolution and equilibrium equations is discretized in space with standard finite elements. Equations (3) and (4) are discretized in time with a semi-implicit scheme. A simple algorithm to solve the coupled system in a straightforward staggered approach is presented in Ref. [6].

3 NUMERICAL SIMULATIONS

We consider a rectangular domain with boundary conditions as shown in Fig. 1. The indentation is included in the model by considering a square inner boundary. The indentation faces are pulled by a monotonically increasing mechanical load w and electrical potential $\phi = 0$ is considered for these faces. The outer four edges of the simulated region are assumed to satify the following conditions: (1) $\boldsymbol{\sigma} \cdot \mathbf{n} = \mathbf{0}$, (2) $\nabla\phi \cdot \mathbf{n} = 0$ and (3) $\nabla\mathbf{p} \cdot \mathbf{n} = \mathbf{0}$, where $\mathbf{n}$ is the unit normal to the outer edges. The vertical initial polarization $\mathbf{p}_0 = (0, 1)$ is assigned to the sample in Fig. 1. The normalized dimensions of the domain are 200×200 ($L = 40$). The constants are chosen to fit the behavior of single crystals of barium titanate ($BaTiO_3$). The normalized constants are presented in Ref. [6]. The nomalized critical surface energy density is chosen as $G_c' = 15.6$. Fifty load steps are computed with load increments of $\Delta w = 5 \times 10^{-2}$. The normalized time step $\Delta t' = 10^{-2}$ leads to convergent and accurate solutions for the time integration of gradient flow equations in Equations (3) and (4). The simulations are carried out using the finite element library of the Kratos multi-physics package [10].

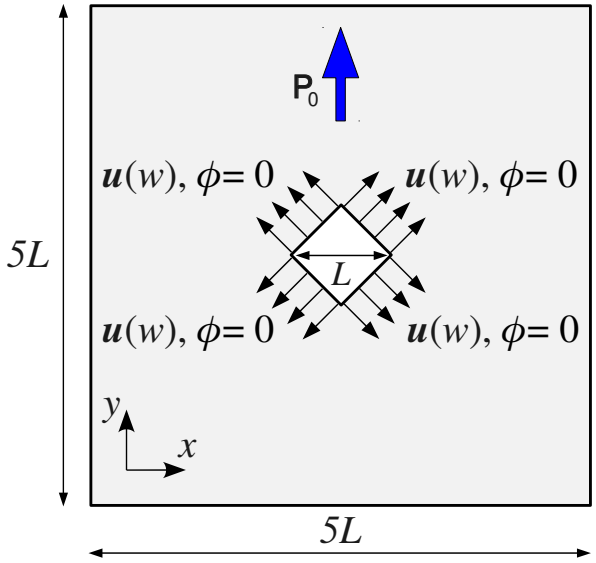

Figure 1: A schematic of the computational model.

Fig. 2 presents two snapshots of the crack propagation. The fracture zone grows along the four radial directions by increasing the load step as shown in two sample load steps $w = 1.5$ and $w = 2.5$.

The value of surface energy (integral over the domain of the last term in Eq. (1)) is obtained and presented in Fig. 3 for each of the four equal zones marked in Fig. 2(b). The surface energies of zones 1 and 3 follow nearly the same path. This also holds for zones 2 and 4. Interestingly, the surface energies of zones 2 and 4 are smaller than zones 1 and 3, i.e. the cracks propagating parallel to the polarization are shorter than those propagating perpendicularly. This is a clear evidence of the anisotropic crack propagation in agreement with experimental observations [1–5].

Fig. 4 presents the contours of polarization components in the load step $w = 1.8$. The x components of the polarization vectors indicate wing-shaped domains or twins around the tip of the parallel cracks in Fig. 4(a). This kind of ferroelastic domain switching is induced by the high tensile stresses near the crack tip which tend to elongate the material in the x direction in front of the parallel cracks. Since the polarization vectors are initialized in the direction of the tensile stresses near the perpendicular cracks, Fig. 4(b) does not show any twin formation around these cracks. Due to the absence of ferroelastic domain switching, the perpendicular cracks propagate longer than parallel ones and the fracture toughness is lower in the perpendicular direction to the initial polarization. The domain switching-induced toughening is also reported in other experiments of crack propagation in $BaTiO_3$ [11, 12].

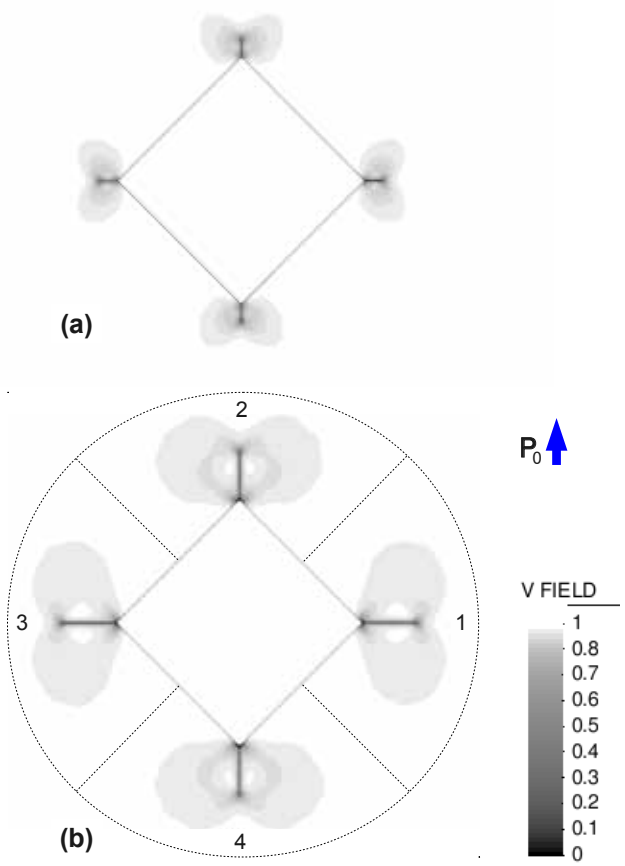

Figure 2: Contour plots of the field v for two snapshots of the fracture evolution at load steps (a) $w = 1.5$ (b) $w = 2.5$. Four equally large areas around the corners of the indentation are considered to obtain the surface energy evolution of the four radial cracks (zones $1 - 4$) shown in Fig. 3.

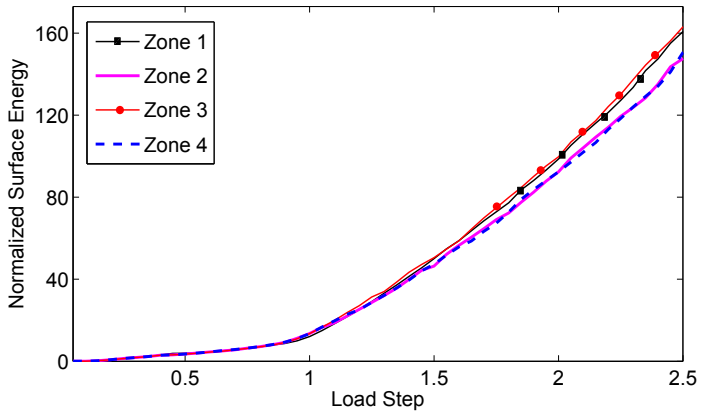

Figure 3: Evolution of the normalized surface energy of four zones as a function of the load step.

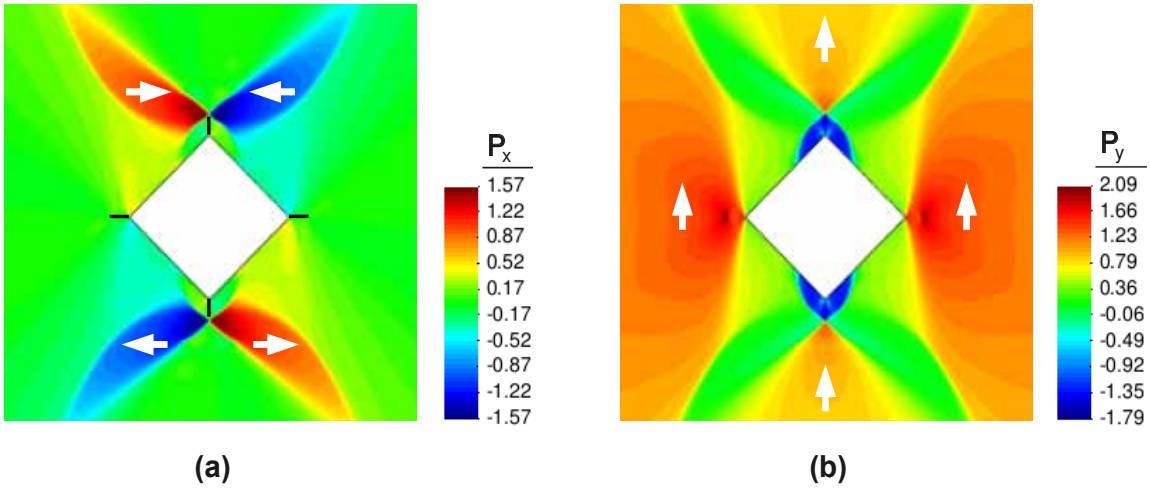

Figure 4: Distribution of polarization components in an area near the indentation in the load step $w = 1.8$ (a) x and (b) y components. Black lines in (a) indicate the position of the cracks ($v = 0$). Domain orientations are indicated with arrows.

4 CONCLUSIONS

We present a general formulation of coupled phase-field model based on variational formulations of brittle crack propagation and domain evolution in ferroelectric materials. Using this model, the simulation of Vickers indentation crack growth in ferroelectric single crystals is performed. The simulation results show that radial cracks parallel to the poling direction of the material propagate slower than perpendicular ones, which is in agreement with experimental observations. Ferroelastic switching induced by the intense crack-tip stress field is observed near the parallel cracks, which is believed as the main fracture toughening mechanism in ferroelectric materials.

References

[1] Pisarenko, G.G., Chushko, V.M. and Kovalev, S.P. Anisotropy of fracture toughness of piezoelectric ceramics. *J. Am. Ceram. Soc.* (1985) **68**:259–265.

[2] Tobin, A.G. and Pak, Y.E. Effect of electric fields on fracture behavior of PZT ceramics. *Proc. SPIE, Smart Struct. Mater* (1993) **1916**:78–86.

[3] Wang, H.Y. and Singh, R.N. Crack propagation in piezoelectric ceramics: Effects of applied electric fields. *J. Appl. Phys.* (1997) **81**:7471–7479.

[4] Lynch, C.S. Fracture of ferroelectric and relaxor electro-ceramics: Influence of electric field. *Acta Mater.* (1998) **46**:599–608.

[5] Schneider, G.A. and Heyer, V. Influence of the electric field on vickers indentation crack growth in BaTiO3. *J. Eur. Ceram. Soc.* (1999) **19**:1299–1306.

[6] Abdollahi, A. and Arias, I. Phase-field modeling of the coupled microstructure and fracture evolution in ferroelectric single crystals. *Acta Mater.* (2011) DOI: 10.1016/j.actamat.2011.03.030.

[7] Abdollahi, A. and Arias, I. Phase-field simulation of anisotropic crack propagation in ferroelectric single crystals: effect of microstructure on the fracture process. *Modelling Simul. Mater. Sci. Eng.* (2011), in press.

[8] Zhang, W. and Bhattacharya, K. A computational model of ferroelectric domains. Part I: model formulation and domain switching. *Acta Mater.* (2005) **53**:185–198.

[9] Amor, H., Marigo, J.J. and Maurini, C. Regularized formulation of the variational brittle fracture with unilateral contact: Numerical experiments. *J. Mech. Phys. Solids* (2009) **57**:1209–1229.

[10] Dadvand, P., Rossi, R. and Onate E. An object-oriented environment for developing finite element codes for multi-disciplinary applications. *Arch. Comput. Methods Eng.* (2010) **17**:253–297.

[11] Meschke, F., Raddatz, O., Kolleck, A. and Schneider G.A. R-curve behavior and crack-closure stresses in barium titanate and (Mg,Y)-PSZ ceramics. *J. Am. Ceram. Soc.* (2000) **83**:353–361.

[12] Fang, D.N., Jiang, Y.J., Li, S. and Sun, C.T. Interactions between domain switching and crack propagation in poled BaTiO3 single crystal under mechanical loading. *Acta Mater.* (2007) **55**:5758–5767.

XI International Conference on Computational Plasticity. Fundamentals and Applications
COMPLAS XI
E. Oñate, D.R.J. Owen, D. Peric and B. Suárez (Eds)

ON MICRO-TO-MACRO CONNECTIONS IN STRONG COUPLING MULTISCALE MODELING OF SOFTENING MATERIALS

O. LLOBERAS-VALLS*, D. J. RIXEN†, A. SIMONE* AND L. J. SLUYS*

*Faculty of Civil Engineering and Geosciences
Delft University of Technology
P.O. Box 5048, 2600 GA Delft, The Netherlands
e-mail: O.LloberasValls@tudelft.nl

†Faculty 3mE
Delft University of Technology
Mekelweg 2, 2628 CD Delft, The Netherlands

Key words: Concurrent multiscale analysis, micro-to-macro connection, FETI, strain localization and softening

Abstract. In this contribution we describe a methodology for the multiscale analysis of heterogeneous quasi-brittle materials. The algorithm is based on the finite element tearing and interconnecting FETI [1] method cast in a non-linear setting. Adaptive multiscale analysis is accounted for with the use of selective refinement at domains that undergo non-linear processes. We focus on the micro-to-macro connection method which constitutes the strategy to handle incompatible interfaces arising from the connection of non-matching meshes. The behaviour of standard collocation and average compatibility techniques is assessed for a multiscale analysis of damage propagation in a quasi- brittle material. The choice of the connection strategy has an influence on the overall response and the computational cost of the analysis.

1 INTRODUCTION

The adopted methodology to enforce interscale relations in multiscale analysis certainly influences the overall mechanical response. Early examples of interscale relations in multiscale approaches are found in classical homogenization theory [2]. In this context, closed-form expressions are derived in order to synthesize effective properties from a heterogeneous microstructure. Examples of such techniques constitute the constant strain and stress assumptions at the microscale. Such assumptions, in combination with Hill's energy condition [3], lead to the well known Voigt and Reuss bounds. The study of complex microstructures undergoing non-linear behaviour has resulted in more sophisticated

homogenization techniques. In many cases, a closed-form expression can not be explicitly derived, however, numerical and computational homogenization techniques [4, 5, 6] are used to synthesize "on the fly" the constitutive behaviour of a representative microstructural sample. Constant strain and stress assumptions together with periodic conditions are well established micro-to-macro transition strategies which evolve from the earlier classical homogenization theory.

Similar strategies concerning interscale relations can be employed in concurrent multiscale techniques [7, 8, 9]. In these methodologies, coarse and fine scale regions are processed simultaneously. Hence, interscale constraints are designed to connect two incompatible meshes. The simplest choice corresponds to the well established collocation technique. Several weak versions of the collocation approach are represented by the family of mortar methods [10, 11]. Their effect in the multiscale analysis of elastic large scale structural analysis has been investigated in [12]. However, the influence of such constraints on the adaptive multiscale analysis of damage growth is accounted for in the present study.

2 MULTISCALE APPROACH

The multiscale approach adopted in this manuscript is based on an extension of the FETI framework presented in [13]. Below, the basic formulation and the adaptive multiscale features are summarized for completeness.

2.1 Basic formulation

Consider a body Ω with heterogeneous underlying structure and boundary conditions depicted in Figure 1. The body Ω is divided into N_{s} non-overlapping domains $\Omega^{(s)}$ connected by the interface Γ_{I}.

In a general concurrent multiscale analysis, where coarse (c) and fine (f) material resolutions co-exist, the resulting interface satisfies $\Gamma_{\mathrm{I}} = \Gamma_{\mathrm{I}}^{\mathrm{cc}} \cup \Gamma_{\mathrm{I}}^{\mathrm{ff}} \cup \Gamma_{\mathrm{I}}^{\mathrm{cf}}$, where the superscripts denote coarse to coarse mesh connection (cc), fine to fine mesh connection (ff) and coarse to fine mesh connection (cf). Note that in the present approach $\Gamma_{\mathrm{I}}^{\mathrm{cc}}$ and $\Gamma_{\mathrm{I}}^{\mathrm{ff}}$ are conforming whereas $\Gamma_{\mathrm{I}}^{\mathrm{cf}}$ is non-conforming except for the common nodes. These nodes are referred to as independent since they all meet a corresponding pair at the adjacent mesh. Dependent nodes are found at the non-conforming interfaces $\Gamma_{\mathrm{I}}^{\mathrm{cf}}$ and their nodal solution can be expressed as a function of the solution field at independent nodal points.

Continuity of the incremental solution field $\delta\mathbf{u}$ at the interface Γ_{I} between two different adjacent domains s and p reads

$$\delta\mathbf{u}^{(s)} = \delta\mathbf{u}^{(p)} \quad \text{at } \Gamma_{\mathrm{I}}, \tag{1}$$

and is satisfied with the introduction of linear multipoint constraints (LMPC). The set of LMPC is cast in a matrix form using modified Boolean matrices $\bar{\mathbf{B}}^{(s)}$. These matrices are constructed by row-wise concatenation of the tying relations between independent and

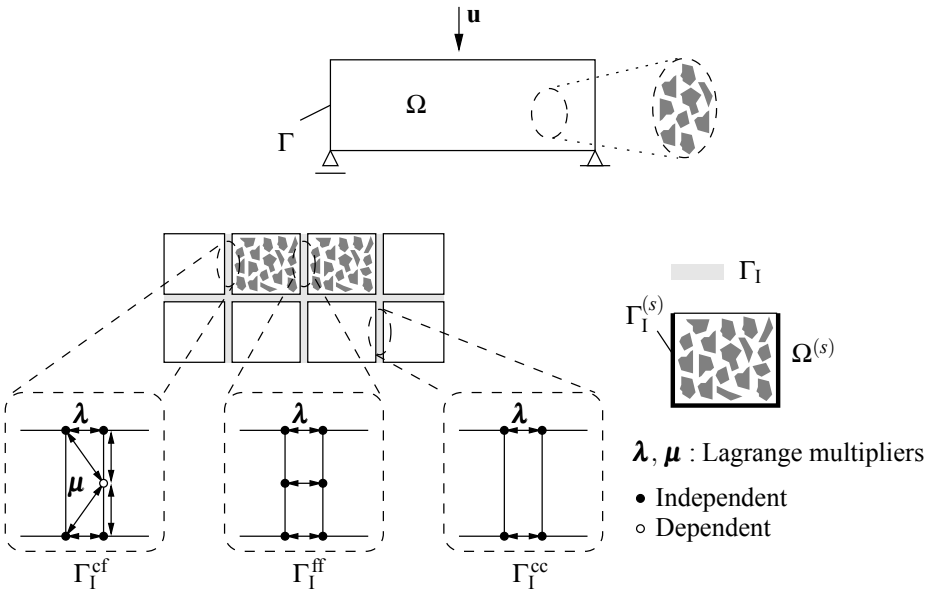

Figure 1: Beam with heterogeneous solid Ω (top). Decomposition in N_s domains (bottom).

dependent interface nodes as

$$\left[\begin{array}{ccc} \bar{\mathbf{B}}^{(1)} & \dots & \bar{\mathbf{B}}^{(N_s)} \end{array} \right] = \left[\begin{array}{ccc} \mathbf{B}^{(1)} & \dots & \mathbf{B}^{(N_s)} \\ \mathbf{C}^{(1)} & \dots & \mathbf{C}^{(N_s)} \end{array} \right]. \tag{2}$$

The matrices $\mathbf{B}^{(s)}$ correspond to the standard signed Boolean matrices of the FETI method while $\mathbf{C}^{(s)}$ contains the LMPC concerning dependent nodes.

Enforcement of the above mentioned continuity constraints is accomplished by the introduction of a heterogeneous Lagrange multiplier field

$$\delta\boldsymbol{\Lambda} = \left[\begin{array}{c} \delta\boldsymbol{\lambda} \\ \delta\boldsymbol{\mu} \end{array} \right] \tag{3}$$

in which $\delta\boldsymbol{\lambda}$ accounts for the independent nodes while $\delta\boldsymbol{\mu}$ represent the forces acting to constrain the dependent nodes.

The final linearized system of equilibrium equations for the decomposed solid with different resolutions can be written as

$$\left[\begin{array}{cccc} \mathbf{K}^{(1)} & \mathbf{0} & \mathbf{0} & \bar{\mathbf{B}}^{(1)^{\mathrm{T}}} \\ \mathbf{0} & \ddots & \mathbf{0} & \vdots \\ \mathbf{0} & \mathbf{0} & \mathbf{K}^{(N_s)} & \bar{\mathbf{B}}^{(N_s)^{\mathrm{T}}} \\ \bar{\mathbf{B}}^{(1)} & \dots & \bar{\mathbf{B}}^{(N_s)} & \mathbf{0} \end{array} \right] \left[\begin{array}{c} \delta\mathbf{u}^{(1)} \\ \vdots \\ \delta\mathbf{u}^{(N_s)} \\ \delta\boldsymbol{\Lambda} \end{array} \right] = \left[\begin{array}{c} \mathbf{f}_{\mathrm{ext}}^{(1)} - \bar{\mathbf{B}}^{(1)^{\mathrm{T}}}\boldsymbol{\Lambda} - \mathbf{f}_{\mathrm{int}}^{(1)} \\ \vdots \\ \mathbf{f}_{\mathrm{ext}}^{(N_s)} - \bar{\mathbf{B}}^{(s)^{\mathrm{T}}}\boldsymbol{\Lambda} - \mathbf{f}_{\mathrm{int}}^{(N_s)} \\ \mathbf{0} \end{array} \right], \tag{4}$$

where $\mathbf{K}^{(s)}$,$\mathbf{f}_{\mathrm{ext}}^{(s)}$ and $\mathbf{f}_{\mathrm{int}}^{(s)}$ refer to the tangent stiffness matrix, external and internal force vectors, respectively.

The augmented system in (4) is transformed into an interface flexibility problem following a standard FETI implementation [1].

2.2 Adaptive multiscale modeling

A multiscale analysis starts with a set of coarse scale domains with effective properties for the elastic bulk. Such effective properties can be computed with the use of classical homogenization theory [2] or numerical homogenization techniques [4, 14] on a Representative Volume Element (RVE) [3].

Adaptivity is accounted for by monitoring or anticipating the need for a highly detailed analysis at particular regions. Since our focus is directed to a study of crack growth and coalescence in brittle heterogeneous materials, a methodology is employed to anticipate the initiation of such phenomena and trigger a fine scale analysis in these particular regions. The resolution is upgraded domain-wise by mesh refinement when non-linearities are expected at domain $\Omega^{(s)}$. Consequently the interface tying relations need to be recomputed each time after a zoom-in. The reader is referred to the work in [13, 15] for a detailed formulation of strain/stress-based predictors for non-linear behaviour and zoom-in techniques for domain decomposition analysis.

3 STRONG AND WEAK MICRO-TO-MACRO CONNECTIONS

In the present approach, the interscale relations are defined employing a set of LMPC at non-conforming interfaces. These constraints enforce continuity of the incremental solution field $\delta\mathbf{u}(\mathbf{x})$ through the interface $\Gamma_{\mathrm{I}}^{\mathrm{cf}}$. A general weak form for such compatibility condition reads

$$\int_{\Gamma_{\mathrm{I}}^{\mathrm{cf}}} w(\mathbf{x})(\delta\mathbf{u}^{\mathrm{f}}(\mathbf{x}) - \delta\mathbf{u}^{\mathrm{c}}(\mathbf{x}))\, \mathrm{d}\Gamma_{\mathrm{I}}^{\mathrm{cf}} = \mathbf{0}, \quad \forall \mathbf{x} \in \Gamma_{\mathrm{I}}^{\mathrm{cf}}, \tag{5}$$

where $w(\mathbf{x})$ represents a weighting function. By setting $w(\mathbf{x})$ equal to the Dirac function $\delta(\mathbf{x})$ at all nodes, the standard collocation method is recovered. In this view the relations concerning independent (ind) and dependent (dep) nodes at the interface depicted in Figure 2 read

$$\mathbf{u}^{\mathrm{f}}_{\mathrm{ind},i} = \mathbf{u}^{\mathrm{c}}_{\mathrm{ind},i}, \quad i = 1, 2, \tag{6a}$$

$$\mathbf{u}^{\mathrm{f}}_{\mathrm{dep},i} = \mathbf{u}^{\mathrm{c}}(\mathbf{x}_i), \quad i = 1, nf. \tag{6b}$$

Note that the selection of linear or bilinear coarse scale elements leads to a linear distribution of the displacement field at the interface. Consequently, the resulting strains are constant at $\Gamma_{\mathrm{I}}^{\mathrm{cf}}$ between independent nodes. For this reason, such interscale relations present similarities with the constant strain approach typically adopted in classical homogenization theory.

Other choices of the weight function $w(\mathbf{x})$ lead to the so-called mortar methods [10]. In the present study, $w(\mathbf{x})$ is set to a constant which is an adequate choice for the case of

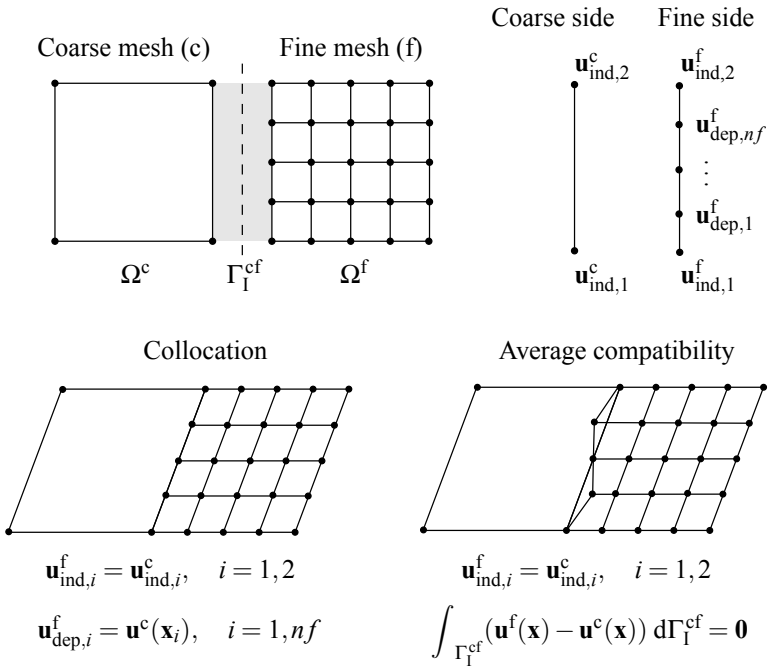

Figure 2: Strong and weak micro-macro connections.

linear shape functions as argued in [12]. The resulting relations are referred to as average compatibility in the remaining of the text and read

$$\mathbf{u}^{\mathrm{f}}_{\mathrm{ind},i} = \mathbf{u}^{\mathrm{c}}_{\mathrm{ind},i}, \quad i = 1,2, \tag{7a}$$

$$\int_{\Gamma_{\mathrm{I}}^{\mathrm{cf}}} (\mathbf{u}^{\mathrm{f}}(\mathbf{x}) - \mathbf{u}^{\mathrm{c}}(\mathbf{x}))\, \mathrm{d}\Gamma_{\mathrm{I}}^{\mathrm{cf}} = \mathbf{0}. \tag{7b}$$

The set of constraints in (7) enforce continuity of the solution field in a weak sense for the interface segment bounded by the independent nodes, the independent nodes satisfying the strong compatibility (7a). This can be adequate when the fine scale solution field at the interface cannot be properly captured with the coarse scale shape functions. For this reason there is a gain in flexibility at the non-conforming interface. Note that the weak constraint in (7b) is obtained by choosing a constant distribution of Lagrange multipliers $w(\mathbf{x})$ in the standard weak form of interface compatibility used in the FETI method. In this view, the interscale relation based on average compatibility preserves some similarities with the constant stress assumption in the classical homogenization theory.

Besides the nature of strong and weak compatibility constraints, the number of equations involved in (6) and (7) are significantly different. Enforcement of collocation constraints (6b) at the interface $\Gamma_{\mathrm{I}}^{\mathrm{cf}}$ requires a set of $nf \times N_{\mathrm{dof}}$ equations (refer to Figure 2), nf being the number of dependent nodes and N_{dof} the number of degrees of freedom per node. However, the number of equations concerned in (7b) is N_{dof}. Both collocation and

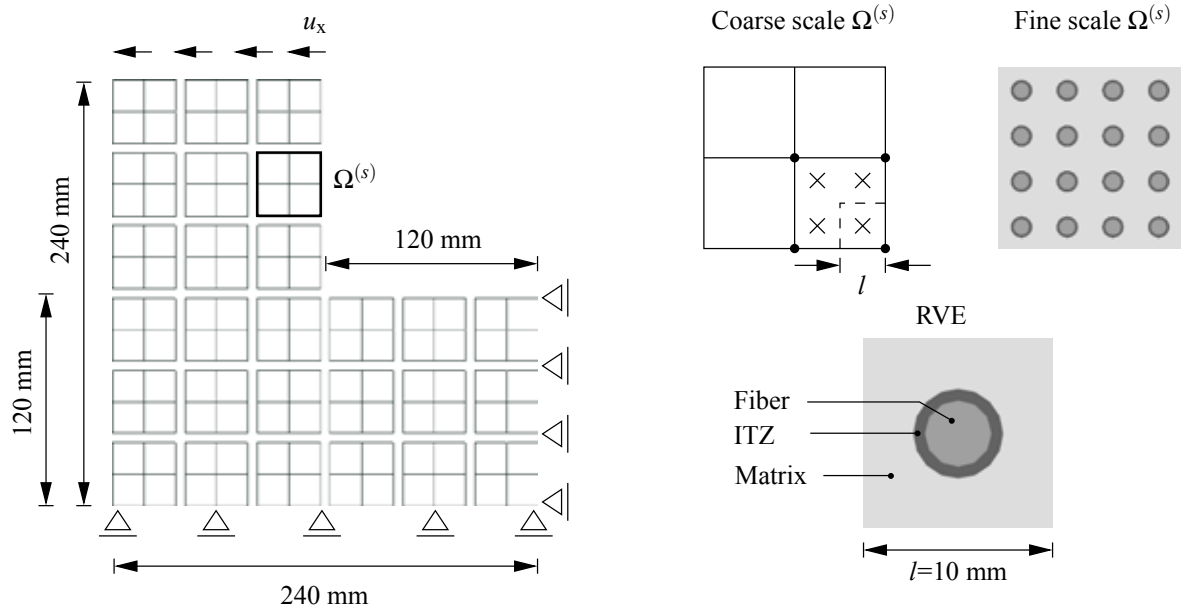

Figure 3: Set-up of the multiscale domain decomposition analysis.

average compatibility constraints can be cast in a matrix form for each domain $\Omega^{(s)}$ as

$$\mathbf{C}^{(s)}\mathbf{u}^{(s)} = \mathbf{0}. \tag{8}$$

The matrices $\mathbf{C}^{(s)}$ are used in the assembly of the modified Boolean matrices $\bar{\mathbf{B}}^{(s)}$ as shown in (2). Since the number of rows of $\mathbf{C}^{(s)}$ depends on the micro-to-macro connection method, the size of the resulting interface problem becomes lower for the choice of average compatibility constraints.

4 EXAMPLES

A multiscale analysis of an L-shape specimen with heterogeneous mesostructure is performed using the presented domain decomposition framework. The specimen is meshed using a coarse discretization and partitioned into 27 non-overlapping domains. The underlying heterogeneous structure consists of a number of regularly distributed steel fibers. Computations are performed considering a two-dimensional slice of the structure in which plane strain conditions are assumed. The regular distribution of fibers allows the retrieval of effective elastic properties from a simple unit cell which is treated as an RVE. The problem set-up is summarized in Figure 3. Non-linear behaviour is linked to crack nucleation and propagation in our study and is simulated by means of a gradient-enhanced damage model [16]. Tensile failure is modeled adopting a Mazars [17] definition for the equivalent strain $\tilde{\varepsilon}$. An exponential evolution of damage ω with the maximum strain κ is considered. A summary of the material parameters is given in Table 1. The non-local equivalent strain $\tilde{\varepsilon}_{\mathrm{nl}}$ is adopted as the internal variable invariant used to construct the

	Material parameters		Soft inclusion	Matrix	Coarse bulk
E	Young's modulus	[N/mm^2]	20.0×10^2	40.0×10^3	Effective
ν	Poisson's ratio	[−]	0.2	0.2	Effective
$\tilde{\epsilon}_{\text{nl}}$	Non-local equivalent strain	[−]	Mazars	Mazars	Mazars
κ_0	Damage initiation threshold	[−]	5.0×10^{-5}	8.5×10^{-5}	5.0×10^{-5}
c	Gradient parameter	[mm^2]	1.5	1.5	1.5
$\omega(\kappa)$	Damage evolution law	[−]	Exponential	Exponential	[−]
α	Residual stress parameter	[−]	0.999	0.999	[−]
β	Softening rate parameter	[−]	400	400	[−]

Table 1: Material parameters.

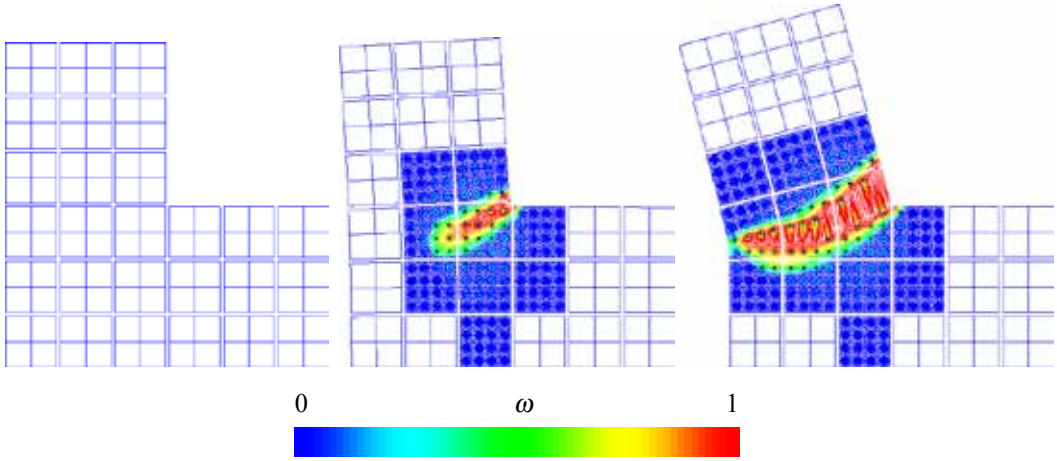

Figure 4: Evolution of damage growth during multiscale analysis.

non-linear domain predictor [13]. Upon increasing load, damage grows and propagates from the re-entrant corner of the L-shape specimen as shown in Figure 4. The interscale relations used in this analysis correspond to the collocation constraints (6). Due to the adaptive nature of the interface it is possible to capture the development of non-linearity satisfying continuity of the solution throughout the complete specimen.

The load-displacement curves depicted in Figure 5 show the sensitivity of the method to different elastic effective properties for the coarse bulk. In these tests, collocation is adopted at $\Gamma_{\text{I}}^{\text{cf}}$ and the effective elastic moduli are retrieved by classical homogenization, i.e. Voigt, Reuss and Mori-Tanaka averaging schemes, and computational homogenization, i.e. fully prescribed forces, displacements and periodic boundary conditions. All multiscale analyses (gray area) are plotted together with the direct numerical solution (DNS). The agreement between multiscale analyses and DNS depends on the choice of effective elastic properties for the coarse bulk. The differences between multiscale analysis and DNS are higher in the pre-peak region since the overall behaviour is dominated by the chosen effective elastic properties. However, in the post-peak region, these differences

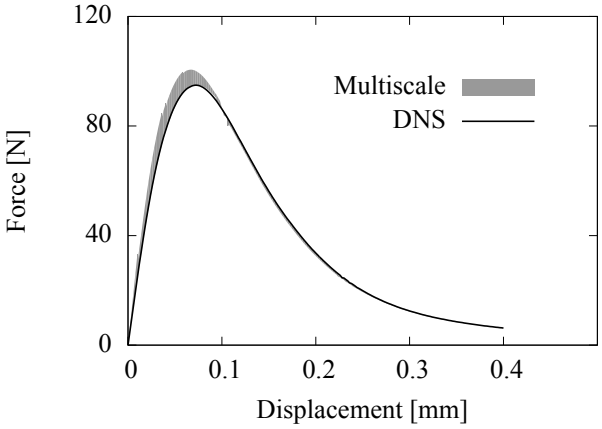

Figure 5: Load-displacement curves for the DNS and multiscale analysis.

become smaller due to the fact that non-linear areas are fully considered.

An assessment of collocation and average compatibility interscale relations is carried out by comparing the damage field between multiscale analysis and DNS at ultimate loading stage (Figure 9). The absolute error in ω is defined as

$$E_\omega = |\omega_{\text{DNS}}| - |\omega_{\text{Mult}}|\,, \quad 0 \leq E_\omega \leq 1. \tag{9}$$

A small increase of E_ω is observed for the average compatibility constraint although differences remain in an acceptable range. The error E_ω is higher around the domain interfaces where a steep damage gradient needs to be captured. The overall cost of the interscale relation in the multiscale analysis is found by computing the size of the interface problem (Figure 7). The active interface is defined as the ratio between the number of degrees of freedom involved in the interface Γ at load step t and the maximum number obtained by considering all fine scale domains. In both collocation and average compatibility the active interface grows with the activation of fine scale domains. However, the interscale relations based on average compatibility constraints lead to a lower active interface and this has a beneficial impact on the overall cost of the analysis.

5 CONCLUSIONS

A multiscale domain decomposition framework for the analysis of heterogeneous quasi-brittle materials is presented. The multiscale strategy provides results which are in agreement with a reference DNS and results in a much lower computational cost. The analyses are influenced by the choice of the effective elastic properties for the coarse bulk and the micro-to-macro connection strategy. The tests performed on a steel reinforced L-shape specimen reveal that both interscale relations give similar results although the accuracy is higher for the collocation constraint. However, average compatibility techniques provide a cheaper overall cost which might be preferred in large scale computations.

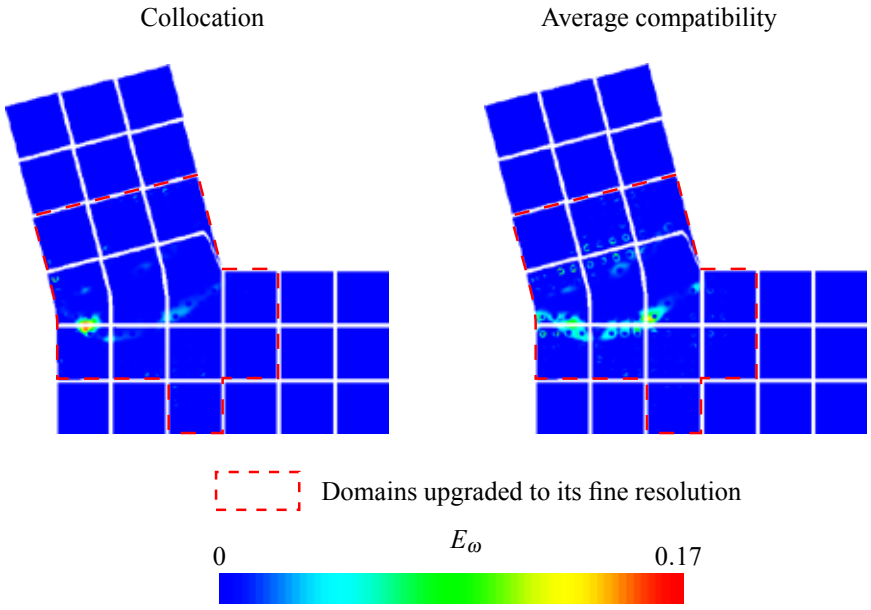

Figure 6: Damage field error E_ω between DNS and multiscale analyses.

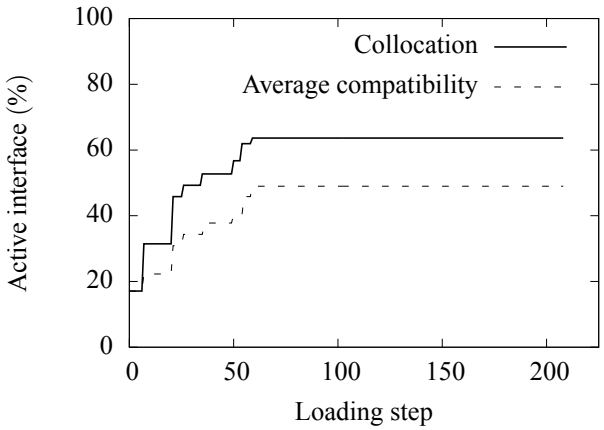

Figure 7: Evolution of the size of the interface problem.

REFERENCES

[1] C. Farhat and F. X. Roux. A method of finite element tearing and interconnecting and its parallel solution algorithm. *International Journal for Numerical Methods in Engineering*, 32(6):1205–1227, 1991.

[2] S. Nemat-Nasser and M. Hori. *Micromechanics: Overall properties of heterogeneous materials*. North-Holland, 1993.

[3] R. Hill. Elastic properties of reinforced solids: Some theoretical principles. *Journal of the Mechanics and Physics of Solids*, 11(5):357–372, 1963.

[4] H. Moulinec and P. Suquet. A numerical method for computing the overall response of nonlinear composites with complex microstructure. *Computer Methods in Applied Mechanics and Engineering*, 157(1-2):69–94, 1998.

[5] F. Feyel and J. L. Chaboche. FE^2 multiscale approach for modelling the elastoviscoplastic behaviour of long fibre SiC/Ti composite materials. *Computer Methods in Applied Mechanics and Engineering*, 183(3-4):309–330, 2000.

[6] V. Kouznetsova, W. A. M. Brekelmans, and F. P. T. Baaijens. An approach to micro-macro modeling of heterogeneous materials. *Computational Mechanics*, 27(1):37–48, 2001.

[7] T. J. R. Hughes, G. R. Feijóo, L. Mazzei, and J. B. Quincy. The variational multiscale method–a paradigm for computational mechanics. *Computer Methods in Applied Mechanics and Engineering*, 166(1-2):3–24, 1998.

[8] A. Hund and E. Ramm. Locality constraints within multiscale model for non-linear material behaviour. *International Journal for Numerical Methods in Engineering*, 70(13):1613–1632, 2007.

[9] P. Ladevèze, O. Loiseau, and D. Dureisseix. A micromacro and parallel computational strategy for highly heterogeneous structures. *International Journal for Numerical Methods in Engineering*, 52(12):121–138, 2001.

[10] C. Bernardi, Y. Maday, and A. Patera. A new nonconforming approach to domain decomposition: The mortar element method. In H. Brezis and J. L. Lions, editors, *Nonlinear Partial Differential Equations and Their Application*, Pitman, 1989.

[11] F. B. Belgacem. The mortar finite element method with lagrange multipliers. *Numerische Mathematik*, 84(2):173–197, 1999.

[12] A. Mobasher Amini, D. Dureisseix, and P. Cartraud. Multi-scale domain decomposition method for large-scale structural analysis with a zooming technique: Application to plate assembly. *International Journal for Numerical Methods in Engineering*, 79(4):417–443, 2009.

[13] O. Lloberas-Valls, D. J. Rixen, A. Simone, and L. J. Sluys. Domain decomposition techniques for the efficient modeling of brittle heterogeneous materials. *Computer Methods in Applied Mechanics and Engineering*, 200(13–16):1577–1590, 2011.

[14] C. Miehe and A. Koch. Computational micro-to-macro transitions of discretized microstructures undergoing small strains. *Archive of Applied Mechanics*, 72(4):300–317, 2002.

[15] O. Lloberas-Valls, D. J. Rixen, A. Simone, and L. J. Sluys. Multiscale domain decomposition analysis of quasi-brittle heterogeneous materials. *International Journal for Numerical Methods in Engineering*, 2010. (Submitted, October 19, 2010).

[16] R.H.J. Peerlings, R. de Borst, W. A. M. Brekelmans, and J.H.P. de Vree. Gradient enhanced damage for quasi-brittle materials. *International Journal for Numerical Methods in Engineering*, 39(19):3391–3403, 1996.

[17] J. Mazars and G. Pijaudier-Cabot. Continuum damage theory–application to concrete. *Journal of Engineering Mechanics*, 115(2):345–365, 1989.

XI International Conference on Computational Plasticity. Fundamentals and Applications
COMPLAS XI
E. Oñate, D.R.J. Owen, D. Peric and B. Suárez (Eds)

A COMPARATIVE STUDY OF FAILURE CRITERIA IN SHEET METAL FORMING ANALYSIS

NGOC-TRUNG NGUYEN, DAE-YOUNG KIM AND HEON YOUNG KIM

Department of Mechanical and Biomedical Engineering, Kangwon National University,
192-1, Hyoja2-dong, Chuncheon, Gangwon-do, 200-701, Korea
e-mail: ntnguyen@kangwon.ac.kr, dae-young@kangwon.ac.kr, khy@kangwon.ac.kr
Web page: cae.kangwon.ac.kr

Key words: Sheet Metal Forming, Formability, Failure Criteria, Necking, Ductile Fracture.

Abstract. Development of predictive capabilities of forming failure can help not only to reduce the experimental effort of formability characterization but also to accelerate the development of new or improved sheet metal alloys. This paper presents a comparative study on prediction of failures in sheet metals which leads to undesirable localized straining and/or fracture during the stamping process. The theoretical diffuse and localized necking models were applied. Several classical fracture criteria were also studied in the finite element analysis. All these models were used to predict the onset of failure and compare with the experimental cases. Comparison and validity of different failure criteria was discussed.

1 INTRODUCTION

In sheet metal forming analysis, the criterion using Forming Limit Diagram (FLD) is widely used for failure prediction since it was originally introduced by Keeler (1965) and Goodwin (1968) [1, 2]. FLD has been commonly applied to evaluate the formability of sheet metals for diagnosing the possible production problems in sheet metal stamping. It indicates the limit strains corresponding to the onset of localized necking over a range of major-to-minor strain ratios. Although the concept of FLD is simple, its experimental implementation is not trivial. Therefore, analytical and numerical predictions of FLD have been intensively studied as the alternative methods. Recently, ductile fracture criteria have been used to determine the limit forming states [3]. The limit states were calculated by plugging the values of stress and strain histories obtained from the simultaneous finite element simulations into the integral form of different ductile fracture criteria. Several successful predictions for the fracture process have been reported. Some fracture criteria can be used to determine the FLD successfully whereas some others fail with this effort.

This paper presents a comparative study on prediction of failures in sheet metals which leads to undesirable localized straining and/or fracture during the stamping process. More detailed discussion on each single topic can be found in [4, 5]. The theoretical diffuse and localized necking models according to Swift-Hill (1952) and Stören-Rice (1975) were applied. Several classical fracture criteria such as Rice-Tracey (1969), Cockcroft-Latham (1968), Brozzo et al. (1972), Oh *et al.* (1979), and Wilkins *et al.* (1980) were also studied in the finite element analysis. All these models were used to predict the onset of failure and

compare with the experimental cases. To determine the FLD experimentally, we conducted the Nakajima tests following the ISO 12004-2 standard [6].

2 EXPERIMENT SETUP

In order to determine the FLD of metal sheet, limiting dome height (LDH) tests were performed. The die set of the NUMISHEET '96 benchmark model was used. Experimental setup including the formability tester and the die set is depicted in Fig. 1. Four kinds of specimens were cut into so-called Nakajima specimens from the same material sheet, the narrowest widths of which were 25, 50, 75 and 175mm, with a length of 175mm in the rolling direction. Fig. 2 shows different blank shapes used in this study. The ASIAS scanning system was used to measure principal strains.

The formability tester Die set

Figure 1: The formability tester and die set

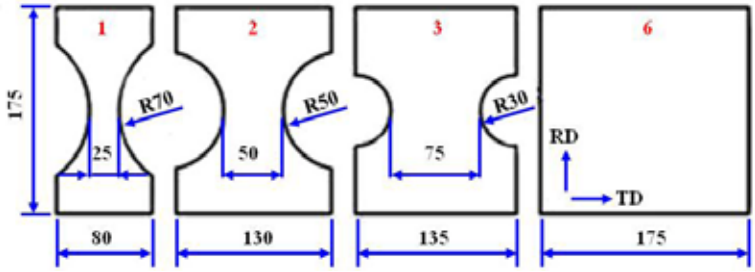

Figure 2: Blank shapes of the LDH test

3 FAILURE CRITERIA

3.1 Necking criteria

Under significant plastic deformation the onset of localization, which is often referred to as *diffuse necking*, occurs. Diffuse necking, which ends the initially uniform deformation in a wide thin sheet, involves contraction in both the lateral and width directions. The diffuse neck is accompanied by contraction strains in both the width and thickness direction and develops

gradually thus still allowing considerable extension [7]. Diffuse necking is usually predicted by, e.g. the Considère (1885) and Swift-Hill (1952) criteria [8]. Upon further deformation the necking region further localizes in an infinitesimal band which is related to the material instability or the *localized necking*. During localized necking the specimen thins without further width contraction [7]. Localized necking can be predicted by, e.g. the model of Hill (1952). Different approaches to predict necking have been introduced from different perspective views of the phenomenon, e.g. maximum load, zero extension line, bifurcation from point vertex on the yield surface or pre-existing imperfections.

Critical thinning or thickness reduction is commonly used in press shop to determine the necking and it is assumed that necking occurs when the thickness strain is around 18–20% [9]. Even though that critical thinning criterion is frequently used in industry, there is not much research has done into this area.

3.2 Fracture criteria

Based on general observations from ductile tests that the load carrying capacity is reduced during the process, the materials are considered to be damaged. Damage indicators and damage rules for the ductile materials have been defined in different ways. It is postulated that fracture occurs when the damage, D, exceed a critical value. In the normalized form, the condition of fracture is expressed as:

$$D = 1 \tag{1}$$

Cockcroft and Latham (1968) developed a ductile fracture criterion based on the concept of "true ductility" [10]. Cockcroft-Latham stated that fracture will not occur until the product of maximum principal stress and equivalent strain is accumulated to a critical value. The *reduced form* of the Cockcroft-Latham criterion is given by:

$$D = \frac{1}{D_{\text{crit.}}^{\text{C-L}}} \int_0^{\bar{\varepsilon}^f} \sigma_1 d\bar{\varepsilon}^p \tag{2}$$

where σ_1 is the highest tensile stress, $\bar{\varepsilon}^p$ is the equivalent plastic strain, $\bar{\varepsilon}^f$ is the equivalent fracture strain. The critical value, $D_{\text{crit.}}^{\text{C-L}}$, is determined experimentally. Brozzo *et al.* (1972) modified the Cockcroft-Latham criterion fracture condition to express the effect of principal stress and hydrostatic stress [11].

$$D = \frac{1}{D_{\text{crit.}}^{\text{B}}} \int_0^{\bar{\varepsilon}^f} \frac{2\sigma_1}{3(\sigma_1 - \sigma_m)} d\bar{\varepsilon}^p \tag{3}$$

where $\sigma_m = (\sigma_1 + \sigma_2 + \sigma_3)/3$ is the hydrostatic stress. The Cockcroft-Latham criterion was later modified by Oh *et al.* (1979) to have the so-called *normalized form* as given below [12]:

$$D = \frac{1}{D_{\text{crit.}}^{\text{Oh}}} \int_0^{\bar{\varepsilon}^f} \frac{\sigma_1}{\bar{\sigma}} d\bar{\varepsilon}^p \tag{4}$$

Wilkins *et al.* (1980) suggested a damage function that includes a hydrostatic pressure weighting term, w_1, and an asymmetric-strain weighting term, w_2. Fracture is postulated to occur when the damage function D exceeds a critical value D_C over a critical material volume R_C, leading to discontinuous macro crack creation and stepwise growth [13]. The criterion is rewritten in the normalized form as:

$$D = \frac{1}{D_{\text{crit.}}^{\text{W}}} \int_0^{\bar{\varepsilon}^f} w_1 w_2 d\bar{\varepsilon}^p \tag{5}$$

The hydrostatic pressure weighting term accounts for the growth of holes during loadings that consists of large stress triaxiality and small strain. The asymmetric-strain weighting term accounts for the observation that, after initiation, the holes can link up as a band if subsequent loading is shear. The two weighting terms are defined by:

$$w_1 = \left(\frac{1}{1 - a\sigma_m} \right)^{\alpha}; \qquad w_2 = \left(2 - A\right)^{\beta} \tag{6}$$

where a is a constant and relates to a so-called limit pressure, P_{lim}; A is the asymmetric-strain factor. These terms are calculated by:

$$a = \frac{1}{P_{\text{lim}}}; \qquad A = \max\left(\frac{s_2}{s_3}, \frac{s_2}{s_1} \right), \quad s_1 \geq s_2 \geq s_3 \text{ are deviatoric stresses} \tag{7}$$

4 RESULTS AND DISCUSSION

The aluminum alloy (AA6061-T6) sheet of 0.8mm thickness was used to prepare specimens for the experimental tests in this paper. The mechanical properties and material constants are obtained from the tensile test of flat type dog-bone and shear specimens as shown in Fig. 3. The inverse method was applied to determine the failure strains at fracture of the tensile specimen using finite element simulation. The analysis was conducted with the assumptions that the material is isotropic and follows the von Mises plasticity theory.

The fracture uniaxial tensile test of the dog-bone specimens could not only provide the information about stress-strain relation and the fracture strains of the material but also help to calculate the material parameters through the inverse method with stress and strain result outputs of a parallel finite element simulation. As an example, the thickness strain record of the loaded specimen was used to identify the critical thinning value which was later applied as a criterion to predict failure. Such process is illustrated in Fig. 4 which shows the bifurcation point as failure occurs.

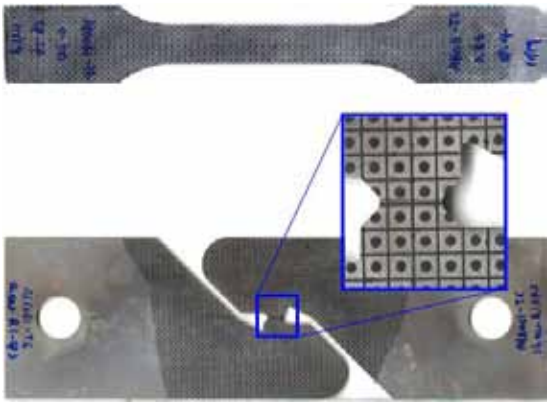

Figure 3: Dog-bone and shear specimens

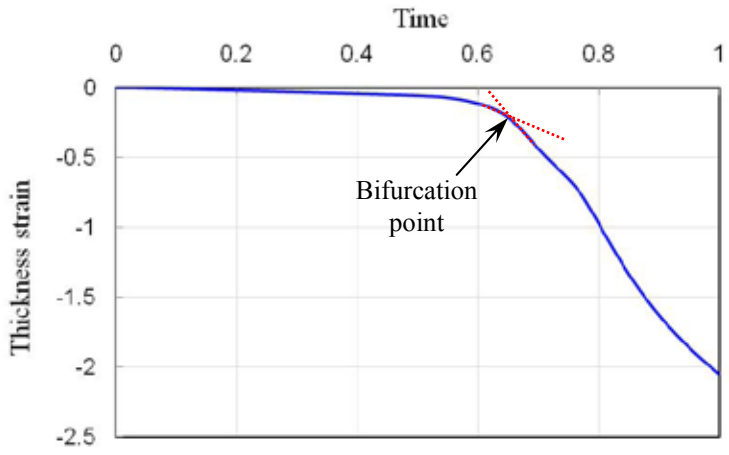

Figure 4: Determination of the failure point using the thickness strain record

The experiment data and the FLD of AA6061-T6 obtained from the reference paper [14] are given in Fig. 5. The experimental data and the reference FLD agree pretty well except for the proximity of biaxial stretch mode. The calculated limit strains using necking criteria together with the experimental FLD from reference [14] are shown in Fig. 6. The left-hand side of the experimental FLD is parallel to the calculated curve for localized necking by Hill's criterion. For positive values of ε_2, the calculated curve using Swift's criterion has similar shape and is in accord with the experimental one. In both sides, the experimental curve is higher than the analytical ones. The Stören-Rice curve approaches the experimental FLD in the modes of uniaxial tension and biaxial stretch. But for plane strain condition, it predicted the limit strain that is far below the true value. It reflects a fact that necking has developed much earlier than it can be detected as depicted in Fig. 6 (a). An identical observation was reported for the forming limit diagram of a low-carbon steel [7].

Applying the inverse method for the finite element simulation of the tensile test of this material, the flat type dog-bone specimen failed at about 21.5% thickness strain. Limit strains of the 17.5, 20, 22.5 and 25% thickness strains conditions were also obtained from the finite element simulation and shown in Fig. 6 (b). On the left side of FLD, necking occurs when the thickness strain is about 20%. It is reasonable to predict localized necking occurs before the

critical value of thickness strain at which the material was failed in the tensile test. However, the thinning criterion underestimated failures on the right hand side of FLD.

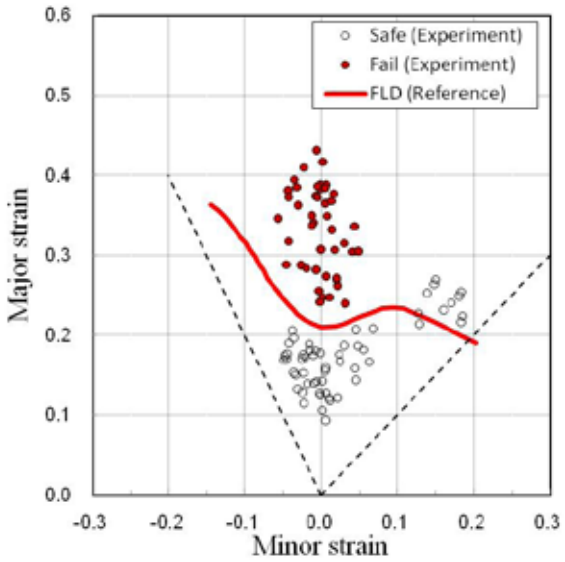

Figure 5: The forming limit diagram: experimental results and the reference FLD

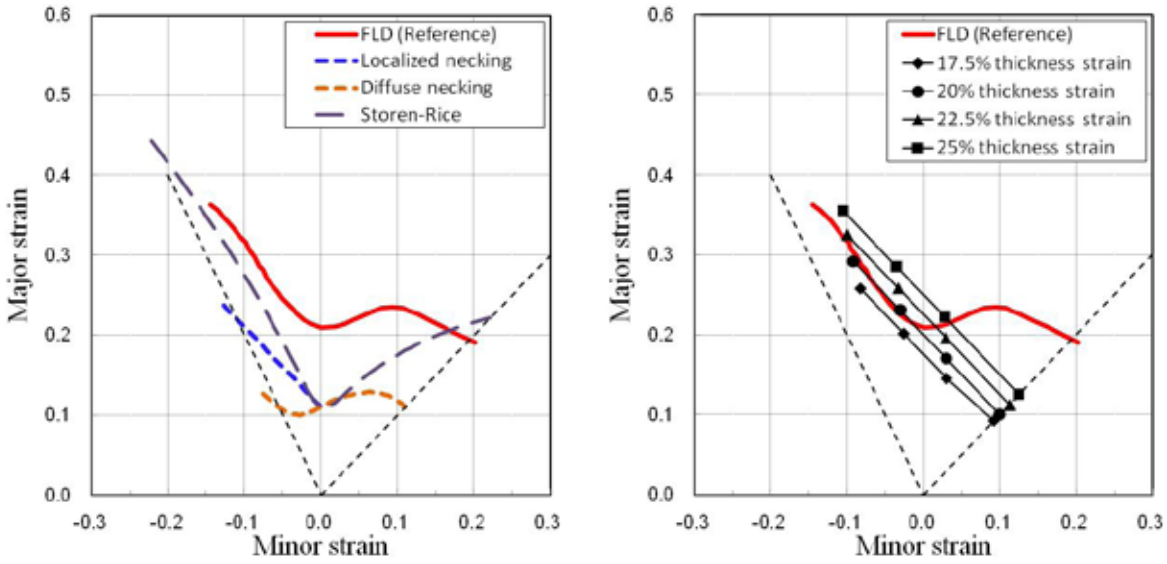

Figure 6: Predictions of the FLD: (a) with necking criteria, (b) with thinning criterion

Comparison between limit strain due to ductile fracture criteria and that of the experimental FLD is given in Fig. 7. Only predictions with the criteria proposed by Rice-Tracey, Brozzo *et al.*, Oh *et al.*, and Wilkins *et al.* are presented. More criteria including the proposed criterion by the present authors are discussed in [5]. The calculated strains of all models are located on or above the FLD. This makes sense as necking, which is followed by fracture, occurs earlier than the observed fracture. Among the four investigated fracture models in this study, the Wilkins *et al*. criterion is able to predict pretty well the forming

limit. Other models seem to overestimate the failure strains. Besides, as can be seen from Fig. 7, the distance from the fracture points to the FLD following Wilkins *et al.* is relative small reflecting the experimental observation that soon after necking fracture occurs. Especially, for uniaxial and biaxial stretch modes fracture follows almost right after necking.

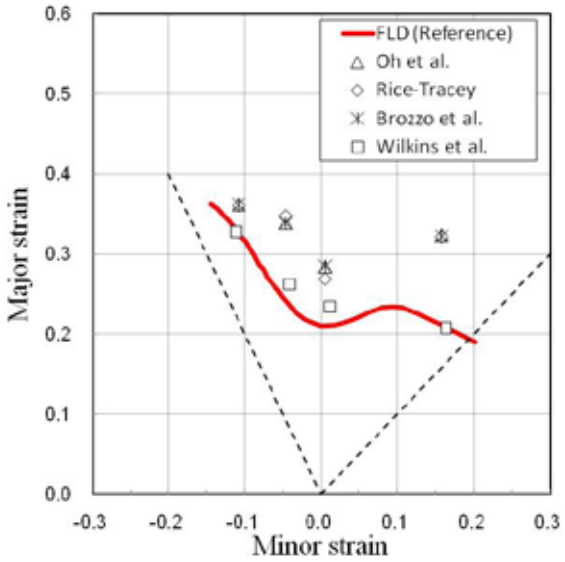

Figure 7: Predictions of the FLD using ductile fracture criteria

5 SUMMARY

Failures in the LDH tests were predicted by several necking and ductile fracture criteria in order to establish a calculated FLD and then compare that with the experimental curve. The following conclusions were made:

- Swift and Hill necking criteria underestimated the limit strains but these calculated curves have the similar shape with the FLD.
- The left side of the FLD was well predicted by thinning and the Wilkins *et al.* criterion.
- Whereas the neighbor of uniaxial and biaxial stretch modes can be calculated by Stören-Rice criterion, the prediction for plane strain condition is far to be satisfied.
- In all cases, the ductile fracture criteria tended to overestimate the failure which is initiated by necking in practice. Even though the calculated FLD is not well shaped, the prediction by the Wilkins *et al.* fracture criterion for the low ductility material in this study is acceptable.
- At the current time the work on sensitivity of the forming limit with different yield conditions is undertaken.

ACKNOWLEDGEMENTS

This work was supported by the Basic Science Research Program (2010-0017090) and the World Premiere Materials program (10037929) funded by the Korean government (Ministry of Education, Science and Technology, and Ministry of Knowledge Economy).

REFERENCES

[1] Keeler, S. P., and Backhofen, W. A., Plastic instability and fracture in sheet stretched over rigid punches. *ASM Transactions Quarterly* (1964) **56**: 25-48.

[2] Goodwin, G. M. Application of strain analysis to sheet metal forming in the press shop. *SAE technical paper 680093* (1968).

[3] Ozturk, F., and Lee, D. A New Methodology for Ductile Fracture Criteria to Predict the Forming Limits. *Journal of Materials Engineering and Performance* (2007) **16**(2): 224-228.

[4] Nguyen, N.-T., Kim, D.-Y., and Kim, H. Y. Numerical prediction of failure in sheet metal forming process: Part I. Necking (in preparation). (2011).

[5] Nguyen, N.-T., Kim, D.-Y., and Kim, H. Y. Numerical prediction of failure in sheet metal forming process: Part II. Ductile fracture (in preparation). (2011).

[6] International Standard, ISO 12004-2:2008 (E).

[7] Hosford, W. F., and Caddell, R. M. *Metal Forming: Mechanics and Metallurgy*. Cambridge University Press, New York, (2007).

[8] Considère, M. L'emploi du fer et de l'acier dans les constructions. *Ann. Ponts Chausseés* (1885) **9**: 574-775.

[9] Esche, S. K., Kinzel, G. L., and Altan, T. *Review of failure analysis in sheet metal forming simulation*. In: J. K. Lee, G. L. Kinzel, and R. H. Wagoner (Eds.), *Proceedings of the Numisheet '96.* Dearborn, Michigan, USA (1996): 270-279.

[10] Cockcroft, M. G., and Latham, D. J. Ductility and the workability of metals. *Journal of the Institute of Metals* (1968) **96**: 33-39.

[11] Brozzo, P., de Luca, B., and Rendina, R. *A new method for the prediction of formability in metal sheets*. In: (Eds.), *Proceedings of the Proceedings of the Seventh Biennial Conference of International Deep Drawing Research Group on Sheet Metal Forming and Formability.* (1972).

[12] Oh, S. I., Chen, C. C., and Kobayashi, S. Ductile Fracture in Axisymmetric Extrusion and Drawing. *J. Eng. Ind. Trans. ASME* (1979) **101**: 36-44.

[13] Wilkins, M. L., Streit, R. D., and Reaugh, J. E. Cumulative-strain-damage model of ductile fracture: simulation and prediction of engineering fracture tests. Lawrence Livermore National Laboratory, Report UCRL-53058, (1980).

[14] Djavanroodi, F., and Derogar, A. Experimental and numerical evaluation of forming limit diagram for Ti6Al4V titanium and Al6061-T6 aluminum alloys sheets. *Materials & Design* (2010) **31**(10): 4866-4875.

XI International Conference on Computational Plasticity. Fundamentals and Applications
COMPLAS XI
E. Oñate, D.R.J. Owen, D. Peric and B. Suárez (Eds)

A MICROMORPHIC CONTINUUM FORMULATION FOR FINITE STRAIN INELASTICITY

S. SKATULLA*, C. SANSOUR† AND H. Zbib‡

*CERECAM, Department of Civil Engineering, University of Cape Town
7701 Rondebosch, South Africa, e-mail: sebastian.skatulla@uct.ac.za

†Division of Materials, Mechanics, and Structures
The University of Nottingham, Nottingham NG7 2RD, UK, carlo.sansour@nottingham.ac.uk

‡School of Mechanical and Materials Engineering
Washington State University Pullman, WA 99164-2920, USA, zbib@wsu.edu

Key words: Generalized continua, Micromorphic continuum, Finite strain inelasticity, Scale effects

Abstract. This work proposes a generalized theory of deformation which can capture scale effects also in a homogenously deforming body. Scale effects are relevant for small structures but also when it comes to high strain concentrations as in the case of localised shear bands or at crack tips, etc. In this context, so-called generalized continuum formulations have been proven to provide remedy as they allow for the incorporation of internal length-scale parameters which reflect the micro-structural influence on the macroscopic material response. Here, we want to adopt a generalized continuum framework which is based on the mathematical description of a combined macro- and micro-space [8]. The approach introduces additional degrees of freedom which constitute a so-called micromorphic deformation. First the treatment presented is general in nature but will be specified for the sake of an example and the number of extra degrees of freedom will be reduced to four. Based on the generalized deformation description new strain and stress measures are defined which lead to the formulation of a corresponding generalized variational principle. Of great advantage is the fact that the constitutive law is defined in the generalized space but can be classical otherwise. This limits the number of the extra material parameters necessary to those needed for the specification of the micro-space, in the example presented to only one.

1 Introduction

Decades ago, it has been recognized that for some materials the kinematics on meso- and micro-structural scales needs to be considered, if the external loading corresponds

to material entities smaller than the *representative volume element* (RVE) and the statistical average of the macro-scopical material behaviour does not hold anymore. In this sense the fluctuation of deformation on micro-structural level as well as relative motion of micro-structural constituens, such as granule, crystalline or other heterogeneous aggregates, influence the material response on macro-structural level. Consequently, field equations based on the assumption of micro-scopically homogeneous material have to be supplemented and enriched to also include non-local and higher-order contributions.

In particular, generalized continua aim to describe material behaviour based on a deeper understanding of the kinematics at smaller scales rather than by pure phenomenological approximation of experimental data obtained at macro-scopical level. The meso- or micro-structural kinematics and its nonlocal nature is then treated either by incorporating higher-order gradients or by introducing extra degrees of freedom. For the latter, the small-scale kinematics at each material point can be thought to be equipped with a set of directors which specify the orientation and deformation of a surrounding a micro-space. This results in a *micromorphic continuum* theory [3], if the directors are allowed to experience rotation, stretch and change of angles to each other.

Geometrically nonlinear micromorphic formulations are sparsely found in literature, e.g. in [5] issues related to material forces of in the hyperelastic case were discussed, or in [7] micromorphic plasticity two-scale models have been proposed addressing micro-structural damage as well as granular material behaviour.

So far formulations of generalized continua are faced with two major problems. The first one relates to the fully non-linear and inelastic material behaviour. Classical inelastic formulations are based on decompositions of strain measures. Since generalized continua exhibit more than one strain or deformation measure the question arises as to how these can be decomposed into elastic and inelastic parts. Few suggestions were made in [11, 4, 2]. These formulations remained, however, less satisfactory since the decomposition of the two deformation measures were, strictly speaking, independent of each other, which raises many questions regarding the adequate formulation of evolution laws for the inelastic parts. The second problem relates to the observation of scale effects also in a homogenously deforming specimen. *Cosserat* and higher gradient theories cannot predict such scale effects, because the extra strain measures are identically zero for homogenous deformation. Furthermore, it is desirable to set out from a general and unified formulation of continua with meso- and micro-structure. We propose a framework based on the mathematical concept of fibre bundles embedded into a generalized continuum formulation. More specifically, we want to consider the Cartesian product of the macroscopic and further meso- or microscopic spaces and, accordingly, the generalized deformation is composed of a macro-, meso- and/or micro-components. In principle, every point of the macroscopic space would have an infinite number of degrees of freedom and dimensions. In practice, the number of degrees of freedom is finite corresponding to the chosen level of accuracy. In this sense the micromorphic continuum appears just as special approximation of the general case [8]. From the micromorphic deformation description nonlinear strain

measures are derived and corresponding stress measures are defined which allow for the formulation of generalized variational principles and corresponding Dirichlet boundary conditions.

The paper is organized as follows. In Sec. 2 the theory of the generalized continuum is outlined. Subsequently, in Sec. 3 a generalized micromorphic principle of virtual work is proposed. The approach allows for the incorporation of any conventional constitutive law, this fact is exemplified using an inelastic material law. Details of the inelastic formulation are elaborated in Sec. 4.1 and Sec. 4.2. Finally, the excellent performance is demonstrated by an example of scale effects in homogenously deforming body as well as by that of a shear band formation in Sec 5.

2 Generalized deformation and strain

The basic idea is that a generalized continuum $\mathcal{G}$ can be assumed to inherit the mathematical structure of a fibre bundle. In the simplest case, this is the Cartesian product of a macro space $\mathcal{B} \subset \mathbb{E}(3)$ and a micro space $\mathcal{S}$ which we write as $\mathcal{G} := \mathcal{B} \times \mathcal{S}$. This definition assumes an additive structure of $\mathcal{G}$ which implies that the integration over the macro- and the micro-continuum can be performed separately. The macro-space $\mathcal{B}$ is parameterized by the curvilinear coordinates ϑ^i, $i = 1, 2, 3$ and the micro-space or micro-continuum $\mathcal{S}$ by the curvilinear coordinates ζ^α. Here, and in what follows, Greek indices take the values 1, ... or n. The dimension of $\mathcal{S}$ denoted by n is arbitrary, but finite. Furthermore, we want to exclude that the dimension and topology of the micro-space is dependent on ϑ^i. Each material point $\tilde{\mathbf{X}} \in \mathcal{G}$ is related to its spatial placement $\tilde{\mathbf{x}} \in \mathcal{G}_t$ at time $t \in \mathbb{R}$ by the mapping $\tilde{\boldsymbol{\varphi}}(t) : \mathcal{G} \longrightarrow \mathcal{G}_t$. For convenience but without loss of generality we identify $\mathcal{G}$ with the un-deformed reference configuration at a fixed time t_0 in what follows. The generalized space can be projected to the macro-space in its reference and its current configuration by

$$\pi_0(\tilde{\mathbf{X}}) = \mathbf{X} \qquad \text{and} \qquad \pi_t(\tilde{\mathbf{x}}) = \mathbf{x} \tag{1}$$

respectively, where π_0 as well as π_t represent projection maps, and $\mathbf{X} \in \mathcal{B}$ and $\mathbf{x} \in \mathcal{B}_t$. The tangent space $\mathcal{TG}$ in the reference and current configuration, respectively, are defined by the pairs $(\tilde{\mathbf{G}}_i \times \mathbf{I}_\alpha)$ and $(\tilde{\mathbf{g}}_i \times \mathbf{i}_\alpha)$, respectively, given by

$$\tilde{\mathbf{G}}_i = \frac{\partial \tilde{\mathbf{X}}}{\partial \vartheta^i}\,, \quad \mathbf{I}_\alpha = \frac{\partial \tilde{\mathbf{X}}}{\partial \zeta^\alpha}\,, \quad \tilde{\mathbf{g}}_i = \frac{\partial \tilde{\mathbf{x}}}{\partial \vartheta^i} \quad \text{and} \quad \mathbf{i}_\alpha = \frac{\partial \tilde{\mathbf{x}}}{\partial \zeta^\alpha}\,, \tag{2}$$

where the corresponding dual contra-variant vectors are denoted by $\tilde{\mathbf{G}}^i$ and $\mathbf{I}^\alpha$, respectively. The generalized tangent space can also be projected to its corresponding macro-space by

$$\pi_0^*(\tilde{\mathbf{G}}_i) = \mathbf{G}_i \qquad \text{and} \qquad \pi_t^*(\tilde{\mathbf{g}}_i) = \mathbf{g}_i \tag{3}$$

respectively, where the tangent vectors $\mathbf{I}_\alpha$ are assumed to be constant throughout $\mathcal{S}$ for simplicity. Note that the definition of a projection map is not trivial. The tangent of the projection map defines the geometry of the extra space and so the metric which is to be used to evaluate the integral over the generalized space. The concept is rich in its structure.

Now, we assume that the placement vector $\tilde{\mathbf{x}}$ of a material point P ($\tilde{\mathbf{X}} \in \mathcal{G}$) is of an additive nature and is the sum of its position in the macro-continuum $\mathbf{x} \in \mathcal{B}_t$ and in the micro-continuum $\boldsymbol{\xi} \in \mathcal{S}_t$ as follows

$$\tilde{\mathbf{x}}\left(\vartheta^k, \zeta^\beta, t\right) = \mathbf{x}\left(\vartheta^k, t\right) + \boldsymbol{\xi}\left(\vartheta^k, \zeta^\beta, t\right) . \tag{4}$$

Thereby, the macro-placement vector $\mathbf{x}$ defines the origin of the micro co-ordinate system such that the micro-placement $\boldsymbol{\xi}$ is assumed to be relative to the macro-placement. The definition of the generalized continuum and so of the extra degrees of freedom depends directly on the choices to be made for the micro deformation $\boldsymbol{\xi}\left(\vartheta^k, \zeta^\beta, t\right)$. The theory is based on the fact that the dependency on the micro co-ordinates ζ^β must be determined apriori. Specific choices define specific continua. The following quadratic ansatz

$$\tilde{\mathbf{x}} = \mathbf{x}\left(\vartheta^k, t\right) + \zeta^\alpha \left(1 + \zeta^\beta \chi_\beta\left(\vartheta^k, t\right)\right) \mathbf{a}_\alpha\left(\vartheta^k, t\right) . \tag{5}$$

results adequate strain measures of full rank shown in [10]. The vector functions $\mathbf{a}_\alpha\left(\vartheta^k, t\right)$ and scalar functions χ_α, with their corresponding micro co-ordinates ζ^α, are independent degrees of freedom. The number α must be chosen according to the specific topology of the micro-space as well as depending on the physical properties of the material due to its intrinsic structure.

In computations we have to deal with four additional independent functions per micro co-ordinate. These are the three components of the vector $\mathbf{a}_\alpha$ as well as the independent displacement-like functions χ_α. Note, however, $\mathbf{a}_\alpha$ as well as χ_α are constant over $\mathcal{S}$. While the functions χ_α contribute to the definition of the strains, their special importance lies in the fact that they allow for the complete definition of linear distribution of strain in the extra dimensions. Also, it is important to realize that the dimension of the micro-space does not have to coincide with the dimension of the macro-space.

Now we proceed to define the strain measures. Taking the derivatives of $\tilde{\mathbf{x}}$ (Eq. 5) with respect to the macro-coordinates ϑ^i as well as with respect to the micro co-ordinates ζ^α, the generalized deformation gradient tensor can be expressed as follows

$$\begin{aligned}
\tilde{\mathbf{F}} \;=\; & \Big[\mathbf{x}_{,i}\left(\vartheta^k, t\right) + \zeta^\alpha \zeta^\beta \chi_{\beta,i}\left(\vartheta^k, t\right) \mathbf{a}_\alpha\left(\vartheta^k, t\right) \\
& \qquad + \zeta^\alpha \left(1 + \zeta^\beta \chi_\beta\left(\vartheta^k, t\right)\right) \mathbf{a}_{\alpha,i}\left(\vartheta^k, t\right)\Big] \otimes \tilde{\mathbf{G}}^i + \\
& \Big[\mathbf{a}_\alpha\left(\vartheta^k, t\right) + \zeta^\beta \left(\chi_\beta\left(\vartheta^k, t\right) \mathbf{a}_\alpha\left(\vartheta^k, t\right) + \chi_\alpha\left(\vartheta^k, t\right) \mathbf{a}_\beta\left(\vartheta^k, t\right)\right)\Big] \otimes \mathbf{I}^\alpha .
\end{aligned} \tag{6}$$

Similar to its classical definition, a generalized right *Cauchy-Green* deformation tensor based on Eq. (6) is formulated as $\tilde{\mathbf{C}} = \tilde{\mathbf{F}}^T \tilde{\mathbf{F}}$ and neglecting higher order terms in ζ^α and

extracting only the dominant parts of $\tilde{\mathbf{C}}$ (constant and linear in ζ^α) we arrive at

$$\begin{aligned}\tilde{\mathbf{C}} &= \Big(\mathbf{x}_{,k}\cdot\mathbf{x}_{,l}+\zeta^\alpha\,(\mathbf{a}_{\alpha,k}\cdot\mathbf{x}_{,l}+\mathbf{x}_{,k}\cdot\mathbf{a}_{\alpha,l})\Big)\;\tilde{\mathbf{G}}^k\otimes\tilde{\mathbf{G}}^l\\ &+\Big(\mathbf{x}_{,k}\cdot\mathbf{a}_\beta+\zeta^\alpha\,\mathbf{a}_{\alpha,k}\cdot\mathbf{a}_\beta+\zeta^\alpha\,\mathbf{x}_{,k}\cdot(\chi_\alpha\,\mathbf{a}_\beta+\chi_\beta\,\mathbf{a}_\alpha)\Big)\Big(\tilde{\mathbf{G}}^k\otimes\mathbf{I}^\beta+\mathbf{I}^\beta\otimes\tilde{\mathbf{G}}^k\Big)\\ &+\Big(\zeta^\alpha\,(\chi_\gamma\,\mathbf{a}_\alpha\cdot\mathbf{a}_\beta+\chi_\beta\,\mathbf{a}_\alpha\cdot\mathbf{a}_\gamma)+2\,\zeta^\alpha\,\chi_\alpha\,\mathbf{a}_\beta\cdot\mathbf{a}_\gamma+\mathbf{a}_\beta\cdot\mathbf{a}_\gamma\Big)\;\mathbf{I}^\beta\otimes\mathbf{I}^\gamma=\mathbf{C}+\zeta^\alpha\,\mathbf{K}_\alpha\,. \end{aligned}\tag{7}$$

Note in order to obtain Eq. (7) the geometry of the micro-space must be specified. Specifically, one has to decide about the projection map $\pi_0^*(\tilde{\mathbf{G}}_i)$ which defines the transition from the tangent vectors $\tilde{\mathbf{G}}^i$, defined in the generalized space, to the tangent vectors $\mathbf{G}^i$, defined in $\mathcal{TB}$.

3 Generalized principle of virtual work

A micromorphic variational principle is established based on the generalized strain tensor $\tilde{\mathbf{C}}$ (Eq. 7). From a non-linear boundary value problem in the domain $\mathcal{B}\times\mathcal{S}$ considering the static case and considering only mechanical processes, the *first law of thermodynamics* provides the following variational statement

$$\delta\Psi-\mathcal{W}_{ext}=0\,. \tag{8}$$

The external virtual work $\mathcal{W}_{ext}$ is defined in the Lagrangian form as follows

$$\mathcal{W}_{ext}\,(\mathbf{u})=\int_{\mathcal{B}}\mathbf{b}\cdot\delta\mathbf{u}\;dV+\int_{\mathcal{B}}\mathbf{l}^\alpha\cdot\delta\mathbf{a}_\alpha\;dV+\int_{\partial\mathcal{B}_N}\mathbf{t}^{(\mathbf{n})}\cdot\delta\mathbf{u}\;dA+\int_{\partial\mathcal{B}_N}\mathbf{q}^{(\mathbf{n})\,\alpha}\cdot\delta\mathbf{a}_\alpha\;dA \tag{9}$$

where the external body force and moment $\mathbf{b}$ and $\mathbf{l}$, respectively, acting in $\mathcal{B}$ and the external traction and surface moment $\mathbf{t}^{(\mathbf{n})}$ and $\mathbf{q}^{(\mathbf{n})}$, respectively, acting on the Neumann boundary $\partial\mathcal{B}_N$ are obtained by integrating corresponding quantities over the micro-space $\mathcal{S}$. For more details refer to [10].

With Eq. (7) the internal virtual power in the Lagrangian form is given by

$$\delta\Psi=\int_{\mathcal{B}}\int_{\mathcal{S}}\tilde{\rho}_0\,\frac{\partial\psi(\tilde{\mathbf{C}})}{\partial\tilde{\mathbf{C}}}\,dS\,dV=\int_{\mathcal{B}}\frac{1}{2}\Big\{\,\mathbf{S}:\delta\mathbf{C}+\mathbf{M}^\alpha:\delta\mathbf{K}_\alpha\,\Big\}\;dV\,, \tag{10}$$

with the force stress and the higher-order size-scale relevant stress

$$\mathbf{S}\left(\vartheta^k\right)=\frac{1}{V_{\mathcal{S}}}\int_{\mathcal{S}}2\,\tilde{\rho}_0\,\frac{\partial\psi(\tilde{\mathbf{C}})}{\partial\tilde{\mathbf{C}}}\;dS\,,\quad\mathbf{M}\left(\vartheta^k\right)=\frac{1}{V_{\mathcal{S}}}\int_{\mathcal{S}}2\,\zeta^\alpha\,\tilde{\rho}_0\,\frac{\partial\psi(\tilde{\mathbf{C}})}{\partial\tilde{\mathbf{C}}}\,dS\,. \tag{11}$$

Then, substituting Eqs. (10) and (9) into Eq. (8) we end up with a micromorphic variational principle:

$$\int_{\mathcal{B}}\Big\{\,\mathbf{S}:\delta\mathbf{C}+\mathbf{M}^\alpha:\delta\mathbf{K}_\alpha\,\Big\}\;dV-\mathcal{W}_{ext}=0\,. \tag{12}$$

The generalized principle of virtual work is supplemented by essential boundary conditions, the so-called Dirichlet boundary conditions

$$\mathbf{u} = \mathbf{h}_u \quad \text{on } \partial\mathcal{B}_D\,, \qquad \mathbf{a}_\alpha = \mathbf{h}_{\gamma,\alpha} \quad \text{on } \partial\mathcal{B}_D\,, \tag{13}$$

where $\mathbf{h}_u$ and $\mathbf{h}_{\gamma,\alpha}$ are prescribed values at the boundary $\partial\mathcal{B}_D$.

4 The inelastic formulation

As discussed in the introduction, the inelastic constitutive law can be any classical one which is now to be defined at the level of the micro-continuum. In what follows we adopt and tailor to our purposes the formulation of finite strain inelasticity based on unified constitutive models as developed in ([9]). While the choice is convenient we stress that any alternative inelastic law could serve the purpose as well.

4.1 Generalized kinematics of the elastic-inelastic body

A point of departure for an inelastic formulation constitutes the multiplicative decomposition of the generalized deformation gradient Eq. (6) into an elastic and an inelastic part

$$\tilde{\mathbf{F}} = \tilde{\mathbf{F}}_e \tilde{\mathbf{F}}_p. \tag{14}$$

For metals, the above decomposition is accompanied with the assumption $\tilde{\mathbf{F}}_p \in SL^+(3,\mathbb{R})$ which reflects the incompressibility of the inelastic deformations, where $SL^+(3,\mathbb{R})$ denotes the special linear group with determinant equal one.

The following generalized right *Cauchy-Green*-type deformation tensors are defined

$$\tilde{\mathbf{C}} := \tilde{\mathbf{F}}^T \tilde{\mathbf{F}}\,, \qquad \tilde{\mathbf{C}}_e := \tilde{\mathbf{F}}_e^T \tilde{\mathbf{F}}_e\,, \qquad \tilde{\mathbf{C}}_p := \tilde{\mathbf{F}}_p^T \tilde{\mathbf{F}}_p\,. \tag{15}$$

Since the deformation gradient $\tilde{\mathbf{F}}$ is also an element of $GL^+(3,\mathbb{R})$ with positive determinant, we can attribute to its time derivative a left and right rate

$$\dot{\tilde{\mathbf{F}}} = \tilde{\mathbf{l}}\tilde{\mathbf{F}}\,, \qquad \dot{\tilde{\mathbf{F}}} = \tilde{\mathbf{F}}\tilde{\mathbf{L}}\,. \tag{16}$$

Both rates are mixed tensors (contravariant-covariant). They are related by means of the equation

$$\tilde{\mathbf{L}} = \tilde{\mathbf{F}}^{-1}\tilde{\mathbf{l}}\tilde{\mathbf{F}}\,. \tag{17}$$

Since $\tilde{\mathbf{F}}_p \in SL^+(3,\mathbb{R})$ we can define a right rate according to

$$\dot{\tilde{\mathbf{F}}}_p = \tilde{\mathbf{F}}_p \tilde{\mathbf{L}}_p \tag{18}$$

which proves more appropriate for a numerical treatment in a purely material context.

4.2 The constitutive model

4.2.1 General considerations

Let $\tilde{\boldsymbol{\tau}}$ be the generalized *Kirchhoff* stress tensor. Consider the expression of the internal power in terms of spatial and material tensors, respectively

$$\mathcal{W} = \tilde{\boldsymbol{\tau}} : \tilde{\mathbf{l}}\,, \qquad \mathcal{W} = \tilde{\boldsymbol{\Gamma}} : \tilde{\mathbf{L}} \tag{19}$$

where $\tilde{\mathbf{l}}$ is defined in Eq. (16a). The comparison of Eq. (19a) with (19b) leads with the aid of Eq. (17) to the definition equation of the material stress tensor $\tilde{\boldsymbol{\Gamma}}$:

$$\tilde{\boldsymbol{\Gamma}} = \tilde{\mathbf{F}}^{\mathrm{T}} \tilde{\boldsymbol{\tau}} \tilde{\mathbf{F}}^{-T}\,. \tag{20}$$

The tensor $\tilde{\boldsymbol{\Gamma}}$ is, accordingly, the mixed variant pull-back of the generalized *Kirchhoff* tensor. It coincides with Noll's intrinsic stress tensor and determines up to a spherical part the Eshelby stress tensor.

A common feature of inelastic constitutive models is the introduction of phenomenological internal variables. We denote a typical internal variable as $\boldsymbol{Z}$. Assuming the existence of a free energy function according to $\psi = \psi(\tilde{\mathbf{C}}_e,\, \boldsymbol{Z})$, the localized form of the dissipation inequality for an isothermal process takes

$$\mathcal{D} \;=\; \tilde{\boldsymbol{\tau}} : \tilde{\mathbf{l}} - \tilde{\rho}_{\mathrm{ref}}\, \dot{\psi} = \tilde{\boldsymbol{\Gamma}} : \tilde{\mathbf{L}} - \tilde{\rho}_{\mathrm{ref}}\, \dot{\psi} \geq 0\,, \tag{21}$$

where ρ_{ref} is the density at the reference configuration. This inequality can be transferred to (see [10])

$$\begin{aligned} \mathcal{D} = &\left(\tilde{\boldsymbol{\Gamma}} - 2\tilde{\rho}_{\mathrm{ref}} \tilde{\mathbf{C}} \tilde{\mathbf{F}}_p^{-1} \frac{\partial \psi(\tilde{\mathbf{C}}_e,\, \boldsymbol{Z})}{\partial \tilde{\mathbf{C}}_e} \tilde{\mathbf{F}}_p^{-T} \right) : \tilde{\mathbf{L}} \\ &+ 2\tilde{\rho}_{\mathrm{ref}} \tilde{\mathbf{C}} \tilde{\mathbf{F}}_p^{-1} \frac{\partial \psi(\tilde{\mathbf{C}}_e,\, \boldsymbol{Z})}{\partial \tilde{\mathbf{C}}_e} \tilde{\mathbf{F}}_p^{-T} : \tilde{\mathbf{L}}_p - \tilde{\rho}_{\mathrm{ref}} \frac{\partial \psi(\tilde{\mathbf{C}}_e,\, \boldsymbol{Z})}{\partial \boldsymbol{Z}} \cdot \dot{\boldsymbol{Z}} \;\geq\; 0\,. \end{aligned}$$

By defining $\boldsymbol{Y}$ as the thermodynamical force conjugate to the internal variable $\boldsymbol{Z}$

$$\boldsymbol{Y} := -\tilde{\rho}_{\mathrm{ref}} \frac{\partial \psi(\tilde{\mathbf{C}}_e,\, \boldsymbol{Z})}{\partial \boldsymbol{Z}}, \tag{22}$$

and making use of standard thermodynamical arguments, from Eq. (22) follows the elastic constitutive equation

$$\tilde{\boldsymbol{\Gamma}} = 2\tilde{\rho}_{\mathrm{ref}} \tilde{\mathbf{C}} \tilde{\mathbf{F}}_p^{-1} \frac{\partial \psi(\tilde{\mathbf{C}}_e,\, \boldsymbol{Z})}{\partial \tilde{\mathbf{C}}_e} \tilde{\mathbf{F}}_p^{-T} = 2\tilde{\rho}_{\mathrm{ref}} \tilde{\mathbf{F}}_p^{T} \tilde{\mathbf{C}}_e \frac{\partial \psi(\tilde{\mathbf{C}}_e,\, \boldsymbol{Z})}{\partial \tilde{\mathbf{C}}_e} \tilde{\mathbf{F}}_p^{-T} \tag{23}$$

as well as the reduced local dissipation inequality

$$\mathcal{D}_p := \tilde{\boldsymbol{\Gamma}} : \tilde{\mathbf{L}}_p + \boldsymbol{Y} \cdot \dot{\boldsymbol{Z}} \geq 0\,, \tag{24}$$

where Eq. (22) has been considered. $\mathcal{D}_p$ is the plastic dissipation function. From Eq. (24) follows as an essential result that the stress tensor $\tilde{\boldsymbol{\Gamma}}$ and the plastic rate $\tilde{\mathbf{L}}_p$ are conjugate variables. Observe that the tensor $\tilde{\mathbf{L}}_p$ is defined in Eq. (18).

4.2.2 The elastic constitutive model

Further we assume that the elastic potential can be decomposed additively into one part depending only on the elastic generalized right *Cauchy-Green* deformation tensor $\tilde{\mathbf{C}}_e$ and the other one depending only on the internal variable $\boldsymbol{Z}$

$$\psi = \psi_{\mathrm{e}}(\tilde{\mathbf{C}}_e) + \psi_{\mathrm{Z}}(\boldsymbol{Z})\,. \tag{25}$$

Defining the logarithmic strain measure

$$\boldsymbol{\alpha} := \ln \tilde{\mathbf{C}}_{\mathrm{e}}\,, \qquad \tilde{\mathbf{C}}_e = \exp \boldsymbol{\alpha} \tag{26}$$

and assuming that the material is elastically isotropic, one can prove that the relation holds

$$\tilde{\mathbf{C}}_e \frac{\partial \psi_e(\tilde{\mathbf{C}}_e)}{\partial \tilde{\mathbf{C}}_e} = \frac{\partial \psi_{\mathrm{e}}(\boldsymbol{\alpha})}{\partial \boldsymbol{\alpha}}\,, \tag{27}$$

where $\psi_{\mathrm{e}}(\boldsymbol{\alpha})$ is the potential expressed in the logarithmic strain measure $\boldsymbol{\alpha}$. Eq. (23) results then in

$$\tilde{\boldsymbol{\Gamma}} = 2\rho_{ref}\, \tilde{\mathbf{F}}_p^T \frac{\partial \psi_{\mathrm{e}}(\boldsymbol{\alpha})}{\partial \boldsymbol{\alpha}} \tilde{\mathbf{F}}_p^{-T}\,. \tag{28}$$

Note that ψ_{e} is an isotropic function of $\boldsymbol{\alpha}$. The last equation motivates the introduction of a modified logarithmic strain measure

$$\bar{\boldsymbol{\alpha}} := \tilde{\mathbf{F}}_p^{-1} \boldsymbol{\alpha} \tilde{\mathbf{F}}_p\,. \tag{29}$$

Since the following relation for the exponential map holds

$$\tilde{\mathbf{F}}_p^{-1} (\exp \boldsymbol{\alpha}) \tilde{\mathbf{F}}_p = \exp \bar{\boldsymbol{\alpha}}, \tag{30}$$

Eq. (28) takes

$$\tilde{\boldsymbol{\Gamma}} = 2\rho_{ref}\, \frac{\partial \psi(\bar{\boldsymbol{\alpha}})}{\partial \bar{\boldsymbol{\alpha}}}\,. \tag{31}$$

It is interesting to note that Eq. (30) together with Eqs. (26), (15a), and (15c) lead to a direct definition of $\bar{\boldsymbol{\alpha}}$. The relation holds

$$\bar{\boldsymbol{\alpha}} = \ln(\tilde{\mathbf{C}}_p^{-1} \tilde{\mathbf{C}}). \tag{32}$$

For computational simplicity a linear relation is assumed and therefore the elastic constitutive model Eq. (31) takes its final form

$$\tilde{\boldsymbol{\Gamma}} = K \,\mathrm{tr}\, \bar{\boldsymbol{\alpha}}^T\, \mathbf{1} + \mu\, \mathrm{dev} \bar{\boldsymbol{\alpha}}^T \tag{33}$$

where

$$\bar{\boldsymbol{\alpha}}^T = \ln(\tilde{\mathbf{C}}\tilde{\mathbf{C}}_p^{-1})\,, \tag{34}$$

and K is the bulk modulus and μ the shear modulus.

It should be stressed that the reduction of the elastic constitutive law to that given by Eq. (31) results in a considerable simplification of the computations necessary for the formulation of the weak form of equilibrium and its corresponding linearisation. The only assumption we used was the very natural one of having an internal potential depending on $\tilde{\mathbf{C}}_e$. The following reduction is carried out systematically.

4.2.3 Inelastic constitutive model

The presented framework of generalized continua allows for the application of any set of classical constitutive laws. In what follows we confine ourselves to a unified constitutive law of the Bodner and Partom type as generalized in the first author's previous work (see e.g. [9]). We concluded from Eq. (24) that the tensors $\tilde{\mathbf{\Gamma}}$ and $\tilde{\mathbf{L}}_p$ are conjugate. Essentially we have to consider the stress tensor $\tilde{\mathbf{\Gamma}}$ as the driving stress quantity, while the plastic rate for which an evolution equation is to be formulated is taken to be $\tilde{\mathbf{L}}_p$. This leads to the following set of evolution equations

$$\begin{aligned}
\tilde{\mathbf{L}}_p &= \dot{\phi}\boldsymbol{\nu}^{\mathrm{T}}\,, \quad \dot{Z} = \frac{M}{Z_0}(Z_1 - Z)\dot{W}_p\,, \quad \dot{W}_p = \Pi_{\mathrm{dev}\tilde{\mathbf{\Gamma}}}\dot{\phi}(\Pi_{\mathrm{dev}\tilde{\mathbf{\Gamma}}},\, Z)\,, \quad \boldsymbol{\nu} = \frac{3}{2}\frac{\mathrm{dev}\tilde{\mathbf{\Gamma}}}{\Pi_{\mathrm{dev}\tilde{\mathbf{\Gamma}}}} \\
\Pi_{\mathrm{dev}\tilde{\mathbf{\Gamma}}} &= \sqrt{\frac{3}{2}\mathrm{dev}\tilde{\mathbf{\Gamma}} : \mathrm{dev}\tilde{\mathbf{\Gamma}}}\,, \quad \dot{\phi} = \frac{2}{\sqrt{3}}D_0 \exp\left[-\frac{1}{2}\frac{N+1}{N}\left(\frac{Z}{\Pi_{\mathrm{dev}\tilde{\mathbf{\Gamma}}}}\right)^{2N}\right]\,.
\end{aligned} \tag{35}$$

Here, Z_0, Z_1, D_0, N, M are material parameters. The choice of the transposed quantity in Eq. (35a) reflects the form given by associative viscoplasticity, when the classical flow functions are generalized and formulated in terms of nonsymmetric quantities.

5 Numerical examples

In this section two numerical examples are presented to demonstrate the applicability of the micromorphic theory. In this specific case the micro-deformation and so micro-continuum are assumed to be one-dimensional, i.e. we consider only $\alpha = 1$ in Eq. 5). There vector $\mathbf{a}$ in the generalized reference configuration is defined to be parallel to the $x-$axis. The material parameters, typical for metals, are chosen as follows: $K = 1.64206E02$ N/mm^2, $\mu = 1.6194E02$ N/mm^2, $D_0 = 10000$ 1/sec, $Z_0 = 1150$ N/mm^2, $Z_1 = 1400$ N/mm^2, $N = 1$ and $M = 100$. The inelastic parameters are reported in the literature for titanium; e.g. [1].

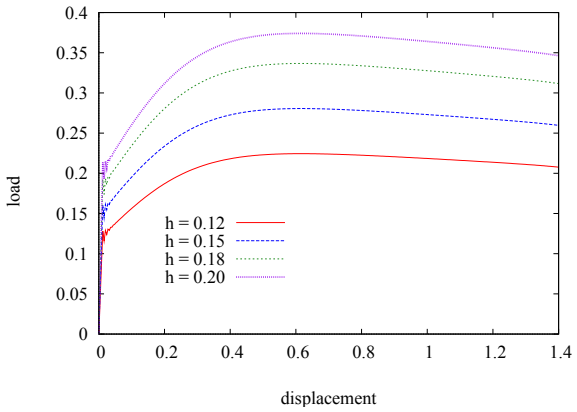

Figure 1: load displacement graph illustrating size-scale effects for different values of the internal length parameter h

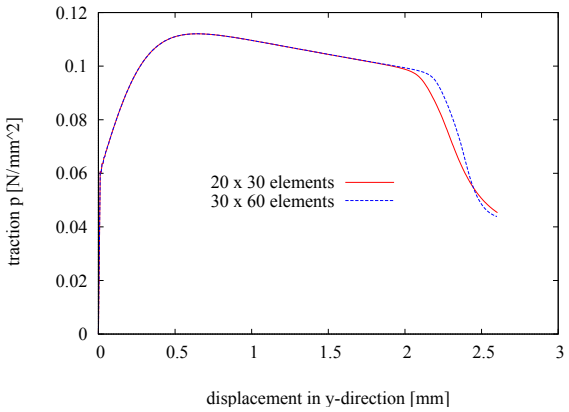

Figure 2: load displacement graph illustrating computations using 20×30 elements and 30×60 elements

5.1 Simple tension

The first example is a thin sheet of dimensions 26×10 subjected to simple tension. One quarter of the sheet is discretised using 5×5 enhanced 4-node finite elements of the type developed in [9], which, in this specific case, are equivalent to three-dimensional enhanced 8-node elements with thickness 1. The aim here is to illustrate size-scale effects in the viscoplastic regime at homogenous deformations. We consider four different internal length-scale parameters, denoted by h, which are nothing but the size/length of the microspace $\mathcal{S}$, and take them to be of the values 0.12, 0.15, 0.18 and $0.20\,mm$. The time step used is $0.1sec$ for the displacement at the top increasing by a velocity of $0.02N/sec$. While the specimen is under force loading with no prescribed displacements at the loading side, the computations are carried out displacement-controlled with the value of the external loading being scaled and determined to provide the prescribed displacement velocity.

The corresponding load-displacement graphs are depicted in Fig. 1. With increasing internal length-scale parameter it can be clearly seen that the onset of the plastic deformation takes place at larger loading values. During the plastic deformation the relative loading offset between the curves is maintained.

Now, this case of simple tension particularly illustrates the attractiveness of the proposed generalized theory as it predicts scale effects also in a homogenously deforming specimen. In fact alternative theories, such as micropolar (Cosserat) or strain gradient approaches, lack the means to predict this kind of scale effect. This is clear, because the former necessitates the rotation gradient and the latter the deformation gradient of higher order not to vanish. In this example, however, both of them do not arise and consequently, no scale effects would be observed.

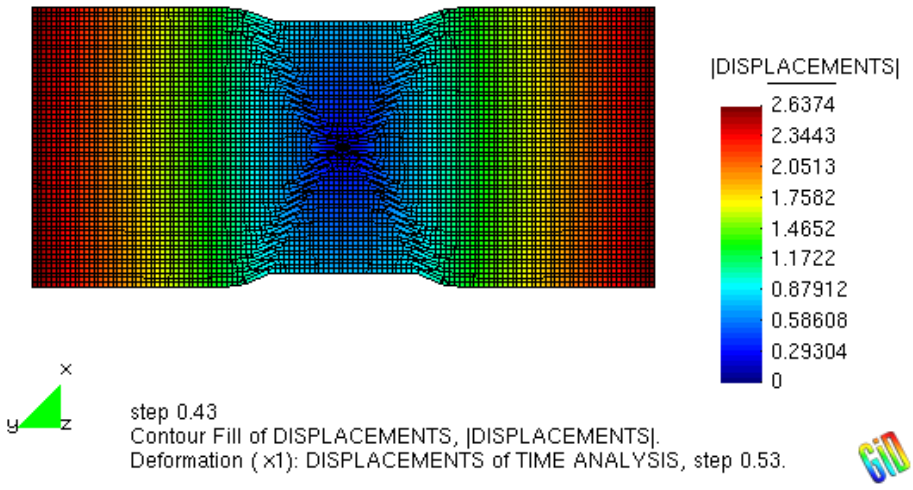

Figure 3: final deformed configuration displaying the shearband formation using 30×60 elements

5.2 Shearband formation

The second numerical example is the same as before in terms of geometry, loading, and time step - a thin sheet under tension. Shearbanding is initialized by decreasing the material parameter Z_0 by 10% within the first element (at the centre of the specimen). The internal length is considered to be $h = 0.1\,mm$. One quarter of the sheet is modeled using 20×30 and 30×60 4-node elements of the type described above. From the load-displacement curve in Fig. (2) it is clear that heavy softening related to the shearband formation takes place. This softening is independent of the mesh since both meshes give essentially the same results. The deformed configuration is pictured in Fig. (3).

Note that the constitutive law is of the viscoplastic type. However, the Bodner-Partom model covers in the limit the time-independent case as well. The present choice of material parameters together with the applied loading velocity renders the time-dependent effect rather very small. Also, from the previous example we can conclude that the scale effect due to the micromorphic formulation is dominant here.

6 Conclusion

A general framework for a micromorphic continuum has been developed which is especially attractive for non-linear material behaviour. This approach motivates research into experimental verification of the mentioned extra degrees of freedom which is still elusive at large. While it is clear that generalized degrees of freedom and the internal lengths as well as the scale effects associated with them are related to the internal structure of the material, the direct deformation mechanisms at the micro-scale giving rise to such degrees of freedom are widely subject to intensive research in many areas of mechanics

and physics with many open questions. It is very likely that more than one mechanism could lead to a certain type of degrees of freedom. While these questions are beyond the scope of the present work we do acknowledge their importance. Multi-scale modelling and experimentation will be at the heart of any answer.

REFERENCES

[1] Bodner, S., and Partom, Y., "Constitutive equations for elastic-viscoplastic strain-hardening materials", *ASME, J. Appl. Mech.* (1975) **42**:385–389.

[2] Chambon, R., Caillerieа, D., and Tamagnini, C., "A strain space gradient plasticity theory for finite strain", *Computer Methods in Applied Mechanics and Engineering* (2004) **193**:2797–2826

[3] Eringen, A.C., "Theory of micromorphic materials with memory", *International Journal of Engineering Science* (1972) **10**:623–641

[4] Forest, S., and Sievert, R., "Nonlinear microstrain theories", *International Journal of Solids and Structures* (2006) **43**:7224–7245

[5] Hirschberger, C.B., Kuhl, E., and Steinmann, P., "On deformational and configurational mechanics of micromorphic hyperelasticity - theory and computation", *Computer Methods in Applied Mechanics and Engineering* (2007) **196**:4027–4044

[6] Kröner, E., "Allgemeine kontinuumstheorie der versetzungen und eigenspannungen", *Archive for Rational Mechanics and Analysis* (1960) **4**:273–334.

[7] Regueiro, R.A., "Finite strain micromorphic pressure-sensitive plasticity", *Journal of Engineering Mechanics* (2009) **135**:178–191

[8] Sansour, C., "A unified concept of elastic-viscoplastic cosserat and micromorphic continua". *Journal de Physique IV Proceedings* (1998) **8**:341–348

[9] Sansour, C., and Kollmann F. G., "On theory and numerics of large viscoplastic deformation". *Comp. Meth. Appl. Mech. Engrg.* (1997) **146**:351–369.

[10] Sansour, C. and Skatulla, S., "A micromorphic continuum-based formulation for inelastic deformations at finite strains. application to shear band formation", *International Journal of Solids and Structures* (2010) **47**:1546–1554

[11] Steinmann, P., "A micropolar theory of finite deformation and finite rotation multiplicative elastoplasticity", *International Journal of Solids and Structures* (1994) **31**:1063–1084

XI International Conference on Computational Plasticity. Fundamentals and Applications
COMPLAS XI
E. Oñate, D.R.J. Owen, D. Peric and B. Suárez (Eds)

APPLICATION OF FINITE ELEMENT CODE TO CHARACTERIZE MECHANICAL PROPERTIES OF COMPLEX MICROSTRUCTURED MATERIALS

N.-T. NGUYEN[*], S. KANG[†], D.-Y. KIM[*] AND H. Y. KIM[*]

[*] Department of Mechanical and Biomedical Engineering, Kangwon National University,
192-1, Hyoja2-dong, Chuncheon, Gangwon-do, 200-701, Korea
e-mail: ntnguyen@kangwon.ac.kr, dae-young@kangwon.ac.kr, khy@kangwon.ac.kr
Web page: cae.kangwon.ac.kr

[†] Department of Mechanical Engineering, Yonsei University, Korea
134 Shinchon-dong, Seodaemoon-ku, Seoul, 120-749, Korea
E-mail: snlkang@yonsei.ac.kr

Key words: homogenization, complex microstructure, eigenstrain technique, periodicity.

Abstract. A technique to solve the periodic homogenization problem is described systematically in this work. The method is to solve the cell problems by imposing eigenstrains in terms of a thermal or a piezoelectric strain to the representative volume element (RVE). Homogenized coefficients are then calculated from stress solutions of those cell problems. As a dual approach, an imposed stress field can also be applied to solve the cell problems. Numerical examples of characterization mechanical properties of complicated microstructure materials are examined. The obtained results show good agreements with the published data. Comparisons show that the technique in this study can be effectively used to characterize the mechanical properties of complex microstructured materials.

1 INTRODUCTION

Mechanical properties of complex microstructured materials can be characterized with the homogenization method which is a process of finding a homogeneous 'effective' material that is energetically equivalent to a microstructured heterogeneous material [1]. That means an object of the equivalent homogenized material behaves in the same manner as the origin one when it is subjected to usual loadings. Specifically, homogenization method aims to calculate effective elastic properties of highly heterogeneous media by averaging over an assumed statistical homogeneous volume. The conditions for such a volume to be chosen as a Representative Volume Element (RVE) are sufficiently large at the microscale and sufficiently small at the macroscale and structurally typical of the entire composite material on average [2]. For different approach, the RVE size affects the obtained results [3, 4]. However, when the ratio of the RVE size to the body dimensions under consideration tends to zero the results converge to exact solution. Among various approaches to predict the effective properties of composites, the mathematical homogenization method with the periodicity assumption over a basic cell (or a representative volume element) is preferable due to its rigorous mathematical background and the ease to implement [5-7]. Based on this method,

different approaches can be used to obtain the equivalent properties of the highly heterogeneous periodic media. Researches on the homogenization problems are devoted to either making an in-house code [5, 6] or writing user-subroutines in commercial softwares [8] to study some particular cases. These approaches, on one hand, are flexible and facilitated to the researchers and skillful software users, but on the other hand, can be burdensome to engineers who have less skill.

In the present work we focus on a so-called eigenstrain technique to solve the homogenization problems using commercial FEM softwares. The eigenstrain technique solves the basic cell problems by applying a prescribed eigenstrain as a given local macroscopic scale strain at the material point associating with the basic cell. In co-operation with commercial FEM softwares, the eigenstrain technique can solve the homogenization problems regardless of using any user-subroutine. The method is then used to characterize the mechanical properties of some composite materials having complex microstructures.

2 THE HOMOGENIZATION PROBLEM

Generally, there are two different scales associated with microscopic and macroscopic behaviors to describe a microstructured heterogeneous composite material [9, 10]. The first one is a *macroscale*, denoted by the slowly varying *global variables* $\mathbf{x}$, at which the heterogeneities are invisible. The other is for the material micro-architecture of heterogeneities size and referred as the *microscale*, denoted by the rapidly oscillating *local variables* $\mathbf{y}$. To model a structure of such kind of material using the finite element method (FEM) one should utilize models with very fine mesh so that the details at the microscale size of heterogeneities can be captured. That leads to a very expensive computational cost and sometimes it is impossible to perform the analysis due to extremely high requirements of computer resources. Instead, a so-called homogenization process can be used to characterize the heterogeneous material as a homogenized one and then, the equivalent material properties are used in the simulation of the whole structure as in a normal FEM analysis [7].

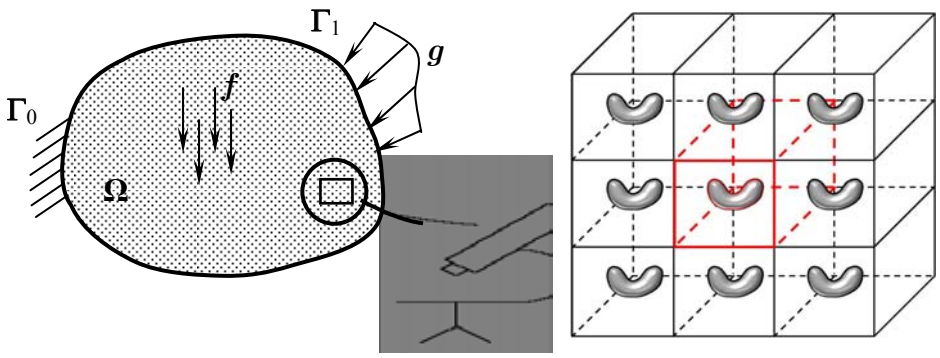

Figure 1: The macroscale and microscale of the homogenization problem

2.1 The problem formulation

From the asymptotic expansion [7, 11], the homogenized elasticity tensor can be determined explicitly by:

$$a_{ijkh}^{\hom} = \frac{1}{|Y|}\int_{Y}\left(a_{ijkh}(\boldsymbol{y}) + a_{ijrs}(\boldsymbol{y})e_{rs}(\boldsymbol{\chi}^{kh})\right)dy \tag{1}$$

where, $\mathbf{Y} = \left\{\mathbf{y} \in \mathbb{R}^n; 0 \le y_i \le Y_i, i = \overline{1,n}\right\}$, $|\mathbf{Y}|$ is the "volume" of the unit cell, $\langle \bullet \rangle = \frac{1}{|\mathbf{Y}|}\int_{\mathbf{Y}}(\bullet)d\mathbf{y}$ denotes the arithmetic mean over the unit cell $\mathbf{Y}$.

χ^{kh} in (1) is the solution of the *cell problem*:

$$\begin{cases} -\dfrac{\partial}{\partial y_j}a_{ijrs}(\mathbf{y})e_{rs}(\chi^{kh}) = \dfrac{\partial}{\partial y_j}a_{ijkh}(\mathbf{y}) \\ \chi^{kh} \text{ is } \mathbf{Y}\text{-periodic} \end{cases} \tag{2}$$

with the periodicity condition defined by: If $\mathbf{y} \in \mathbf{Y} \mapsto v_i(\mathbf{y}) : \mathbf{Y}\text{-periodic}$ or $v_i(\mathbf{y}) \in V_{\text{per}}(\mathbf{Y})$ then $v_i(\mathbf{y})$ takes equal values on the opposite faces of $\mathbf{Y}$.

Generally, we can obtain the solution $\mathbf{v}_E = \chi^{kh}$ by solving the six cell problems and then compute the homogenized elasticity coefficients according to (1). As an alternative, the homogenization problem (2) with periodicity conditions can be formulated in the following forms:

For a given macroscopic strain $\mathbf{E}$,

$$(P_{\mathbf{E}})\begin{cases} Find\ \mathbf{v}_{\mathbf{E}} \in V_{\text{per}}(\mathbf{Y})\ such\ that \\ J_{\mathbf{E}}(\mathbf{v}_{\mathbf{E}}) \le J_{\mathbf{E}}(\mathbf{v}),\ \forall \mathbf{v} \in \mathbf{V}_{\text{per}}(\mathbf{Y}) \end{cases} \tag{3}$$

where $J_{\mathbf{E}}(\mathbf{v}) = \frac{1}{2|\mathbf{Y}|}\int_{\mathbf{Y}}\mathbf{a}(\mathbf{E}+\mathbf{e}(\mathbf{v}))(\mathbf{E}+\mathbf{e}(\mathbf{v}))d\mathbf{y}$

Note that the problems (2) and (3) are equivalent. Moreover, the variational formulation (3) is equivalent to a problem of minimization with constraints:

$$\begin{cases} Find\ \mathbf{v} \in V_{\text{per}}(\mathbf{Y})\ such\ that\ J(\mathbf{v}) \to \min \\ J(\mathbf{v}) = \frac{1}{2}\mathbf{a}(\mathbf{v},\mathbf{v}) - \mathbf{l}(\mathbf{v}) \end{cases} \tag{4}$$

where $\mathbf{a}(\mathbf{v},\mathbf{v}) = \frac{1}{|\mathbf{Y}|}\int_{\mathbf{Y}}\mathbf{a}\mathbf{e}(\mathbf{v}_{\mathbf{E}})\mathbf{e}(\mathbf{v})d\mathbf{y}$; $\mathbf{l}(\mathbf{v}) = -\frac{1}{|\mathbf{Y}|}\int_{\mathbf{Y}}\mathbf{a}\mathbf{E}\mathbf{e}(\mathbf{v})d\mathbf{y}$

Again, by solving 6 problems of formulation (3) or (4) with the imposed macroscopic strains $E_{ij} = \left(T^{kh}\right)_{ij} = \frac{1}{2}\left(\delta_{ik}\delta_{jh} + \delta_{ih}\delta_{jk}\right)$, where δ_{ij} is the Kronecker delta symbol; the

homogenized coefficients are determined by:

$$a_{ijkh}^{\hom} = \left\langle \sigma_{ij}^{kh} \right\rangle = \frac{1}{\left|\mathbf{Y}\right|} \int_{\mathbf{Y}} \sigma_{ij}^{kh} d\mathbf{y} = \frac{1}{\left|\mathbf{Y}\right|} \int_{\mathbf{Y}} \mathbf{a}\left(\mathbf{T}^{kh} + \mathbf{e}\left(\mathbf{v}_{\mathbf{T}^{kh}}\right)\right) d\mathbf{y} \tag{5}$$

2.2 Periodicity conditions

Due to the periodicity of the composites, the microscopic displacement and stress fields are the $\mathbf{Y}$ periodic solution. In the homogenization, the periodic boundary conditions must be imposed on the RVE to reflect the repeatability of the microstructure. For the symmetric inclusion or RVE, the periodic boundary condition leads to the ordinary constraints on the boundary of the RVE [6, 12]. For the non-symmetric inclusion or RVE, appropriate multi-point constraints are imposed on the displacements of nodes on the boundary of RVE in order to produce the periodic boundary conditions [12, 13].

The internal constraints among nodal degrees of freedom can be expressed by a set of constraint equations that must be introduced into the finite element equations. That is, the periodic boundary conditions can be treated as a set of constraint equations. To specify identical displacement for corresponding nodes on opposite edges, the elimination method can be used [12, 14]. The pairs of nodes on the opposite edges of the RVE can be linked by a constraint equation so that the opposite edges have identical deformed shapes. The periodicity conditions can be described by two sets of indices:

$$I^1 = \left\{ i_1^1, i_2^1, ..., i_M^1 \right\}, \qquad I^2 = \left\{ i_1^2, i_2^2, ..., i_M^2 \right\} \tag{6}$$

and a set of M constraint equations:

$$u_{i_k^1} = u_{i_k^2} \qquad k = 1, 2, ..., M \tag{7}$$

The multi-point constrains for RVE can be equivalently expressed in the matrix form by [12]

$$\mathbf{Pu} = \mathbf{0} \tag{8}$$

where $\boldsymbol{P}$ is the transformation matrix whose entries are equal to zero except

$$\begin{aligned} P_{ij} &= 1 \quad \forall i \in I^1 \cup I^2 \\ P_{i_k^1 i_k^2} &= -1 \quad \forall k \in \left\{1, 2, ..., M\right\} \\ P_{i_k^2 i_k^1} &= -1 \quad \forall k \in \left\{1, 2, ..., M\right\} \end{aligned} \tag{9}$$

For the system of N degree of freedom (DOF) with M constraint equations, the resulting transformation matrix should be $N \times \left(N - M\right)$. Figure 2 illustrates the periodicity conditions with constraints on the boundary of the RVE in a 2D case with 2 DOFs at each node. The arrows represent the coupling degrees of freedom for identical nodes on opposite sides. The displacements at corner nodes are fixed.

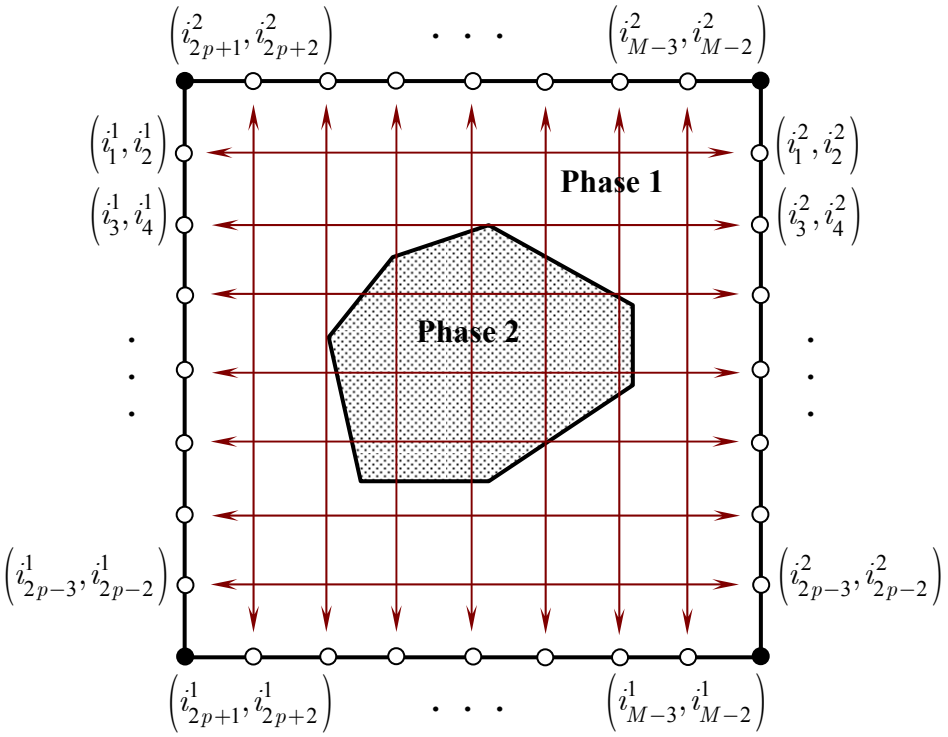

Figure 2: The periodicity constraints on boundary of a 2D RVE

Let u^1 be the free components of $\mathbf{u}$, and u^2, u^3 the components that are linked by the periodicity conditions. Then, we have the cell problem in discretized form:

$$\begin{cases} Find\, \mathbf{u} \in \mathbb{R}^N \, such\, that\, \mathbf{Pu} = \mathbf{0} \; and \\ \mathbf{v}^T\mathbf{Ku} = \mathbf{v}^T\mathbf{L} \quad \forall \mathbf{v} \in \mathbb{R}^N \, such\, that\, \mathbf{Pv} = \mathbf{0} \end{cases} \tag{10}$$

The elimination method to handle the periodicity conditions is easy to implement. However, the bandwidth of the stiffness matrix is seriously increased. It is recommended to use the skyline or sparse storage method for a better computing performance. Commercial FEM softwares supply utilities to handle with such constraint. The **`CP`** command in ANSYS® and **`MPC`** function in MSC. PATRAN® can be used to define the periodicity conditions. Moreover, for particular problems with symmetric microstructure, only a part of the unit cell is modeled and the periodicity conditions can be reduced to the conventional boundary conditions [6]. A study on alternative methods and comparison of computing time among them can be found in [15]. Method to ensure strain-periodicity for a hexagonal unit cell by imposing the kinematic boundary conditions is also introduced [16].

2.3 The eigenstrain technique

The eigenstrain terminology is first defined by Mura [17] to indicate non-elastic strains as thermal expansion, phase transformation, initial strains, plastic strains, etc. The eigenstrain method is named due to the fact that this technique solves the basic cell problems of homogenization by applying an eigenstrain as a given local macroscopic scale at the material point associating with the basic cell. The fact that the elementary macroscale strain state is achieved by applying an appropriate eigenstrain makes this method distinct to the isostrain method in which specific displacements are imposed on the boundary to obtain the macroscale strain states. The displacements imposed on the corresponding boundary in the cell problems to achieve the elementary macroscale strain states are

$$\phi_i^{kl} = \delta_{ik} y_l \tag{11}$$

The corresponding macroscale (average) strain components due to the imposed displacements are given by

$$\begin{aligned} T_{ij}^{kl} &= \left\langle e\left(\phi^{kl}\right)\right\rangle_{ij} = \frac{1}{|Y|}\int_Y e_{ij}\left(\phi^{kl}\right)dy \\ &= \frac{1}{|Y|}\int_Y \frac{1}{2}\left(\frac{\partial \phi_i^{kl}}{\partial y_j} + \frac{\partial \phi_j^{kl}}{\partial y_i}\right)dy = \frac{1}{|Y|}\int_{\partial Y}\frac{1}{2}\left(\phi_i^{kl} n_j + \phi_j^{kl} n_i\right)ds \end{aligned} \tag{12}$$

It is worth noting that, for the isostrain method, the periodicity condition of the fluctuating displacement in the cell problem doesn't hold strictly, i.e.

$$\left\langle \mathbf{e}\left(\mathbf{v}^{kl}\right)\right\rangle \neq 0 \tag{13}$$

This is because the imposed displacements constraint to obtain the elementary macroscale strain and the periodicity condition constraint cannot be applied simultaneously on the same boundary.

To achieve at the same time the macroscale elementary strain state and the periodicity condition, the eigenstrain method shows to be a most suitable way. An applied eigenstrain plays the role of the macroscale elementary strain and the periodicity condition discussed in Section 3 will be satisfied by constraining the displacements of nodes on the boundary.

The eigenstrain $\mathbf{T}^{kl}$ can be either a thermal strain as in [18] or a piezoelectric strain:

$$\mathbf{T}^{kl} = \mathbf{e}_{thermal}^{kl} = \boldsymbol{\alpha}^{kl}\Delta T \qquad \text{or} \qquad \mathbf{T}^{kl} = \mathbf{e}_{piezo}^{kl} = \mathbf{d}^{kl}\overline{\mathbf{E}} \tag{14}$$

where $\boldsymbol{\alpha}^{kl}$ is the thermal expansion coefficient vector, ΔT is the temperature difference, $\mathbf{d}^{kl}$ is the piezoelectric strain matrix and $\overline{\mathbf{E}}$ is the electric field vector. For example, to obtain the macroscale strain state $\mathbf{T}^{11}$ the corresponding thermal expansion coefficient is $\boldsymbol{\alpha}^{11} = \left\{1,0,0,0,0,0\right\}^{\mathrm{T}}$ and the temperature $\Delta T = 1$ if the eigenstrain is chosen as a thermal strain. If a piezoelectric strain is applied then the piezoelectric strain matrix is

$$\mathbf{d}^{11} = \begin{bmatrix} 1 & 0 & 0 & 0 & 0 & 0 \\ 0 & 0 & 0 & 0 & 0 & 0 \\ 0 & 0 & 0 & 0 & 0 & 0 \end{bmatrix}^T \tag{15}$$

and the electric field vector is $\bar{\mathbf{E}} = \{1,0,0\}^T$. Similarly, the other macroscale strain states can be achieved by applying an appropriate eigenstrain with the corresponding fictitious material properties $\boldsymbol{\alpha}^{kl}$ or $\mathbf{d}^{kl}$. In general, the steps to solve the cell problems with a commercial FE software using the eigenstrain technique can be summarized as follows

1. Build the model of the basic cell.
2. Define and assign the material properties for each constituent.
3. Control the meshing process so that nodes are identical located on opposite faces/sides of the cell model.
4. Apply the periodicity conditions.
5. Assign the fictitious material properties to the whole model to achieve a desired elementary macroscale strain state (the eigenstrain).
6. Solve the problem.
7. Calculate the homogenized elasticity coefficients using stresses at Gauss points of the elements according to:

$$\begin{aligned} a_{ijkl}^{\hom} &= \frac{1}{|\mathbf{Y}|}\int_{\mathbf{Y}} \sigma_{ij}^{kl} dy \\ &= \frac{1}{|\mathbf{Y}|}\sum_{GP=1}^{NGP} \sigma_{ij}^{kl}\left(y_{GP}\right) w\left(y_{GP}\right) J\left(y_{GP}\right) \end{aligned} \tag{16}$$

where $\sigma_{ij}^{kl}\left(y_{GP}\right)$ is the stress component, $w\left(y_{GP}\right)$ and $J\left(y_{GP}\right)$ are the weight and Jacobian at the sampling points y_{GP}, respectively.

3 NUMERICAL EXAMPLES

In this section, two numerical examples are investigated to validate the proposed technique. The demonstrations are done by using various commercial softwares.

3.1 Composite material with randomly distributed spherical particle

The unit cell model is first generated by GeoDict2009® (licensed by Dr. Andreas Wiegmann at ITWM, Germany, www.geodict.com) and then transferred into the FE environment, e.g. MSC. PATRAN® as shown in Figure 3. The particle volume fraction is 30%, the radius of particles to unit cell length size ratio is chosen as $L/D = 10/3$ [19]. The

material properties of constituents are given in Table 1.

Table 1. Material properties of constituents

	E (GPa)	ν
Particle	450	0.17
Matrix	70	0.3

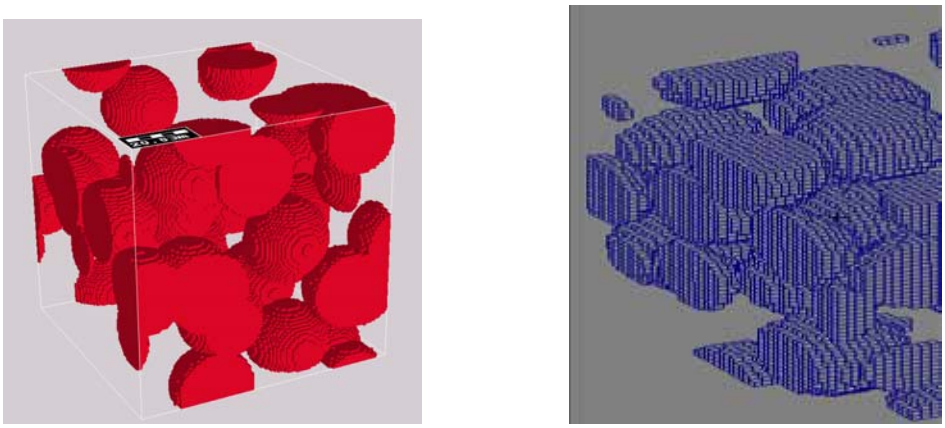

(a) The GeoDict2009® model (b) The FE model showing inclusions

Figure 3: The GeoDict2009® model and the FE model of the RVE

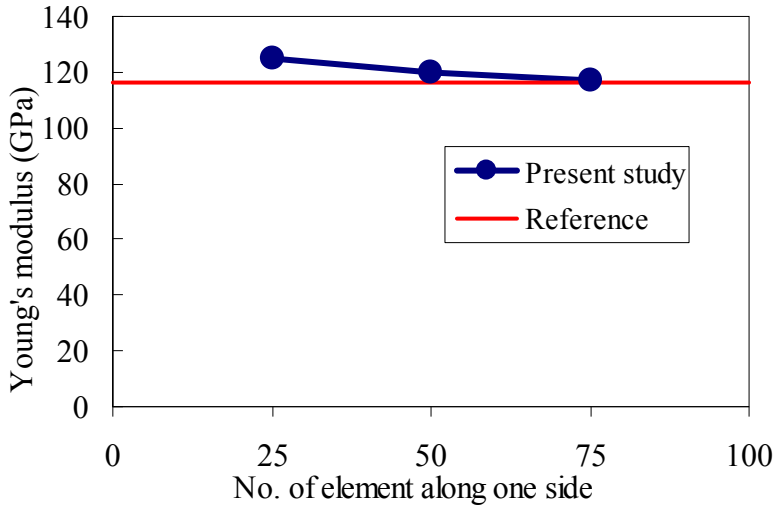

Figure 4: Converged results with respect to the mesh density

The GeoDict2009® program generates voxel (cubic) elements with the periodic option in x, y and z direction to guarantee the periodicity constraints of opposite faces. Calculation has been made with different mesh configurations and reported in Figure 4. Due to the random property of the distribution of particles in the model and the usage of voxels to approximate

the spherical geometry, the obtained results have a slight difference compared to the referred ones. However, the discrepancy is acceptable, about 7%, 3% and less than 1% for the 25x25x25, 50x50x50 and 75x75x75 mesh configurations, respectively.

Although the GeoDict2009® model approximates the geometry with certain errors by using voxel elements, we can have a benefit of using such cubic elements. The homogenized coefficients determined by equation (16) are now evaluated with less effort by using the constant value 1/8 of the element volume for the Jacobian.

3.2 Glass/alumina two phase material with imperfect bonding

In previous example, matrix and inclusion in the composite are assumed to be perfectly bonded and, therefore, there is no separation between them. However, consideration of the damage of the interface is necessary to accurately predict the behavior of multiple phase composites. One of the methods to consider the debonding at the interface is to use interface elements (or cohesive elements) which are currently provided in several commercial softwares to simulate the onset and propagation of delamination. These elements have zero thickness and are modeled at the interface of the constituents of a composite material. The constitutive behavior of these elements is usually expressed in terms of tractions versus relative displacements between the top and bottom edge/surface of the elements (traction-separation curves). Several constitutive laws have been proposed in the literature to express the behavior of these elements [20].

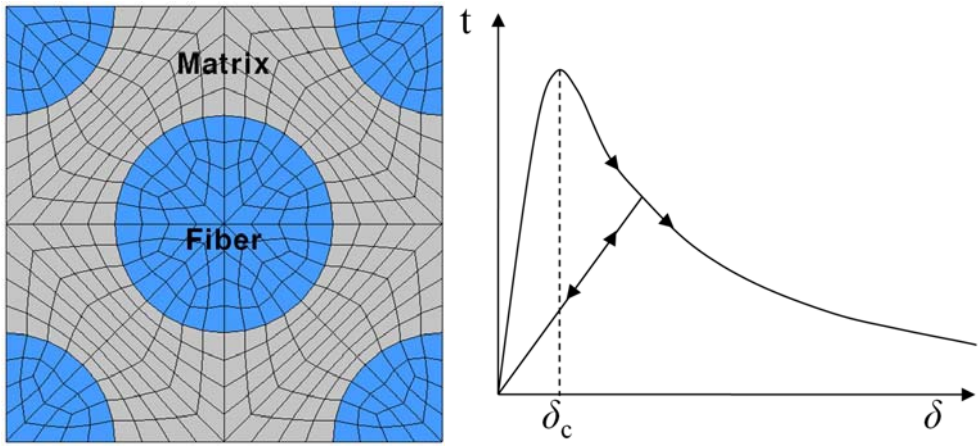

(a) (b)

Figure 5: (a) The RVE model; (b) A typical exponential traction-separation curve to model the decohesive phenomenon at the fiber/matrix interface

In this example we characterize the properties of the glass/alumina composite with consideration of the imperfect bonding of the constituents. The model in this example is based on the reference [21] where the isostrain method is used to obtain the homogenized properties. The cohesive elements are modeled along the interface of constituents. A typical FE model of the RVE with the fiber volume fraction of 45% is shown in Figure 5a. The matrix ($E_m = 68$ GPa, $\nu_m = 0.21$) and the fiber ($E_f = 340$ GPa, $\nu_f = 0.24$) are considered as isotropic materials. A typical exponential traction-separation curve, shown in Figure 5b, is applied for

the constitutive behavior of the cohesive elements. The maximum normal traction at the interface is $t_{\max} = 1000\text{MPa}$, the corresponding critical normal and shear opening displacement are $\delta_n = \delta_t = 1\ \mu\text{m}$. These two cohesive parameters are identified from the experiment work in [21].

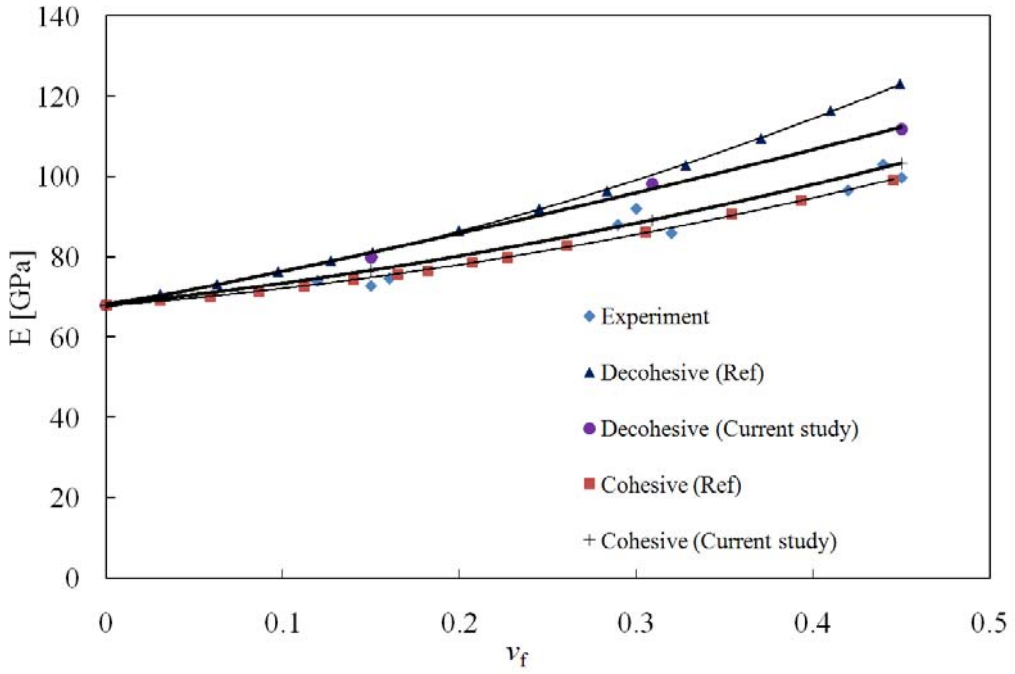

Figure 6: Elastic modulus of the composite with different fiber volume fractions

An increase of the fiber volume fraction, in a natural way, increases the elastic modulus of the material as shown in Figure 6. The imperfectly bonded interface made the structure softer and, therefore, the predicted modulus is smaller than that in the case of the perfectly bonded interface. When a perfect bonding is assumed, the prediction using the current method and the one in the reference are very close to each other up to a value of the fiber volume fraction about 20%. After that value, the results by the isostrain method in [21] are always higher than the predictions by the eigenstrain method in this study. The gaps keep increasing when the fiber volume fraction is larger. In the case of the imperfect bonding at the interface, results from the current method and the reference one are both well matched to the experimental data.

4 CONCLUSIONS

The eigenstrain technique to characterize mechanical properties of complex microstructured materials is presented in the current study. The method can be applied with conventional FE softwares. Numerical examples have been investigated to verify the method. The main advantage of this method is simplicity and applicability for engineers who have less programming skills to use any commercial software at hand to characterize the mechanical properties of multiphase composite materials with complex microstructure regardless of using any user-subroutine.

ACKNOWLEDGEMENTS

This work was supported by the BK21 program (핵C6B1110) funded by the Korean government (Ministry of Education, Science and Technology).

REFERENCES

[1] Tartar, L. (1978). Quelques remarques sur l'homogénéisation. *Functional analysis and numerical analysis*, Fujita, ed., Japan Society for the Promotion of Science, Tokyo.

[2] Hill, R. Elastic properties of reinforced solids: Some theoretical principles. *Journal of the Mechanics and Physics of Solids* (1963) **11**(5): 357-372.

[3] Böhm, H. J. A short introduction to basic aspects of continuum micromechanics. *ILSB Report/ILSB-Arbeitsbericht 206*, Institute of Lightweight Design and Structural Biomechanics (ILSB), Vienna University of Technology, (2007).

[4] Hollister, S. J., and Kikuchi, N. A comparison of homogenization and standard mechanics analyses for periodic porous composites. *Computational Mechanics* (1992) **10**: 73-95.

[5] Guedes, J. M., and Kikuchi, N. Preprocessing and postprocessing for materials based on the homogenization method with adaptive finite element methods. *Computer Methods in Applied Mechanics and Engineering* (1990) **83**(2): 143-198.

[6] Hassani, B. A direct method to derive the boundary conditions of the homogenization equation for symmetric cells. *Communications in Numerical Methods in Engineering* (1996) **12**(3): 185 - 196.

[7] Sanchez-Palencia, E., and Zaoui, A. Homogenization Techniques for Composite Media. Springer, (1987).

[8] Peng, X., and Cao, J. A dual homogenization and finite element approach for material characterization of textile composites. *Composites Part B: Engineering* (2002) **33**(1): 45-56.

[9] Kwon, Y. W., Allen, D. H., and Talreja, R. Multiscale Modeling and Simulation of Composite Materials and Structures. Springer (2007).

[10] Cioranescu, D., and Donato, P. *An Introduction to Homogenization*. Oxford, (1999).

[11] Bensoussan, A., Lions, J.-L., and Papanicolaou, G. *Asymptotic analysis for periodic structures*. North-Holland Publishing Company, (1978).

[12] Bornert, M., Bretheau, T., and Gilormini, P. Homogénéisation en mécanique des matériaux 1: Matériaux aléatoires élastiques et milieux périodiques. Hermes Science, Paris (2001).

[13] Yang, Q.-S., and Becker, W. Numerical investigation for stress, strain and energy homogenization of orthotropic composite with periodic microstructure and non-symmetric inclusions. *Computational Materials Science* (2004) **31**(1-2): 169-180

[14] Léné, F. Contribution à l'étude des matériaux composites et de leur endommagement. Ph.D., Université Paris 6, Paris (1984).

[15] Debordes, O., Licht, C., Marigo, J. J., Mialon, P., Michel, J. C., and Suquet, P. Charges limites de milieux fortement heterogenes. *Note Technique No. 85-3*, Laboratoire de Mechanique Generale des Milieux Continus, Universite des Sciences et Techniques du Languedoc, (1985).

[16] Taliercio, A., and Coruzzi, R. Mechanical behaviour of brittle matrix composites: a

homogenization approach *International Journal of Solids and Structures* (1999) **36**(24): 3591-3615.
[17] Mura, T. *Micromechanics of defects in solids*. Springer, (1987).
[18] Yuan, Z., and Fish, J. Toward realization of computational homogenization in practice. *International Journal for Numerical Methods in Engineering* (2008) **73**: 361-380.
[19] Kari, S., Berger, H., Rodriguez-Ramos, R., and Gabbert, U. Computational evaluation of effective material properties of composites reinforced by randomly distributed spherical particles. *Composite Structures* (2007) **77**(2): 223-231.
[20] Chandra, N., Li, H., Shet, C., and Ghonem, H. Some issues in the application of cohesive zone models for metal–ceramic interfaces. *International Journal of Solids and Structures* (2002) **39**(10): 2827-2855.
[21] Mathias, J. D., and Tessier-Doyen, N. Homogenization of glass/alumina two-phase materials using a cohesive zone model. *Computational Materials Science* (2008) **43**(4): 1081-1085.

XI International Conference on Computational Plasticity. Fundamentals and Applications
COMPLAS XI
E. Oñate, D.R.J. Owen, D. Peric and B. Suárez (Eds)

RAPID MULTIAXIAL HIGH CYCLE FATIGUE LIMIT PREDICTIONS USING SELF-HEATING-BASED PROBABILISTIC MULTISCALE MODELS

MARTIN PONCELET[*], CEDRIC DOUDARD[†], SYLVAIN CALLOCH[†], BASTIEN WEBER[††] AND FRANCOIS HILD[*]

[*] LMT-Cachan (ENS Cachan/CNRS/Université Paris 6/PRES UniverSud Paris)
61 avenue du Président Wilson, F-94235 Cachan Cedex, France
Email: poncelet@lmt.ens-cachan.fr, hild@lmt.ens-cachan.fr, www.lmt.ens-cachan.fr

[†] LBMS EA 4325 (E.N.S.I.E.T.A./Université de Brest/E.N.I.B.)
2 rue François Verny, F-29806 Brest Cedex, France
Email: cedric.doudard@ensieta.fr, sylvain.calloch@ensieta.fr, www.ensieta.fr/lbms/

[††] ArcelorMittal Maizières Research
Voie Romaine BP 30320, F-57283 Maizières-lès-Metz, France
Email: bastien.weber@arcelormittal.com, www.arcelormittal.com

Key words: Thermomechanical process, Probability, Metallic materials, Multiaxial Fatigue.

Summary Thermal measurements under multiaxial cyclic loadings are used herein to predict multiaxial fatigue properties. Two models describing random microplasticity activation via a Poisson Point Process. The thermal response is interpreted as the "mean" behaviour of the microplastic activity, whereas the fatigue limit relies on the weakest link assumption. The first model is based upon a yield surface approach to account for stress multiaxiality at a microscopic scale. The second one relies on a probabilistic modelling of microplasticity at the scale of slip-planes. Both models are identified on thermal results and a uniaxial mean fatigue limit, and then validated using fatigue limits as well as thermal responses in the case of tension-torsion loadings on tubular specimens made of medium carbon steel. They predict well hydrostatic stress, volume and proportional multiaxial effects. The model with microplasticity described at the scale of slip-planes also offers a good prediction of non-proportional mean fatigue limits (~ 5% error) whereas the other model is less predictive (~ 17% error).

1 INTRODUCTION

The thermal measurements under cyclic loadings, usually referred to as "self-heating tests," [1-10] offer a neat and pragmatic way to predict high cycle fatigue properties without the drawback of the long-lasting traditional fatigue tests. Several models, from early empirical to recent approaches [11] based on microplasticity activation have been proposed to better understand and consolidate this link.

This paper focuses on two of these two-scale models developed for multiaxial loadings.

The first model is based upon a yield surface approach [12,13] to account for stress multiaxiality at a microscopic scale. The second one relies on a probabilistic modelling of microplasticity at the scale of slip-planes [14-16].

Both probabilistic descriptions are based on a Poisson Point Process. With this type of approach, the thermal response is linked to the "mean" behaviour of the microplastic activity, whereas the fatigue limit relies on the weakest link assumption. For the presented models, this implies that the fatigue limit is eventually described by a well-known Weibull model, which directly explains the influence of the stress heterogeneity and the volume effect on the fatigue results. From a thermal point of view, the influence of the stress heterogeneity is also taken into account, but with different formulae. Last, the influence of the hydrostatic stress is also described, thanks to the chosen intensity of the Poisson Point Process. For the first model, this intensity depends on the mean hydrostatic stress, and the normal stress to the considered plane for the second model.

Both models are validated using fatigue limits as well as thermal responses in the case of tension-torsion loadings on tubular specimens made of medium carbon steel. Both thermal effects and mean fatigue limit predictions are in good agreement with experimental results for proportional and non-proportional tension-torsion loadings. The conceptual difference between the two models implies a major difference of prediction capacity when non-proportional loadings are concerned, the mean fatigue limit prediction error of the critical shear stress approach being three times less than that with the yield surface approach. A notable advantage of the proposed models is that their identifications do not require non-proportional fatigue results, though they can predict them.

2 PROBABILISTIC BASIS OF THE MODELS

In metallic polycrystalline alloys, the physical process of damage initiation is usually governed by intragranular microplasticity. At that scale, the microplastic activity is not homogeneous because of local stress fluctuations (grain orientation and surrounding influence) and local plastic threshold. To model the onset of microplasticity, a set of elastoplastic sites randomly distributed within an elastic matrix is considered. For the sake of simplicity, no spatial correlation is considered herein. HCF damage is assumed to be localized at the mesoscopic scale and is induced by microplastic activity (in the grains whose orientation is favourable). The distribution of active sites (*i.e.*, sites where microplasticity occurs) of volume V_s is modelled by a Poisson Point Process [17-21]. The probability of finding k active sites in a domain Ω of volume V reads

$$P_k^*(\Omega) = \frac{\left[-\lambda^* V\right]^k}{k!} exp\left[-\lambda^* V\right] \tag{1}$$

where λ^* is the intensity of the Poisson Point Process and $\lambda^* V$ is the mean number of active sites. The intensity of the process depends on the loading level, and its form is detailed later.
The relationship between the stress tensor in a site where microplasticity occurs, $\underline{\underline{\sigma}}$, and the macroscopic stress tensor $\underline{\underline{\Sigma}}$ is given by the localisation law [22,23]

$$\underline{\underline{\sigma}} = \underline{\underline{\Sigma}} - 2\mu(1-\beta)\underline{\underline{\varepsilon_p}} \tag{2}$$

where $\underline{\underline{\varepsilon}}^p$ is the corresponding plastic strain tensor (assumption of additive decomposition of strain with an elastic and a plastic part) and μ the shear modulus. β is given by Eshelby's analysis of a spherical inclusion in an elastic matrix [24].

3 ELASTOPLASTIC BEHAVIOUR

3.1 Yield surface approach

The assumptions of the first model are chosen so that it presents a reduced number of parameters and closed-form formulae as its uniaxial predecessor [4]. Microplasticity is modelled at a microscopic scale and is described by a yield surface, normality rule and linear kinematic hardening

$$\begin{aligned} &\mathrm{f} = \mathrm{J}_2\left(\underline{\underline{\mathrm{S}}} - \underline{\underline{\mathrm{X}}}\right) - \sigma_\mathrm{y} \le 0 \\ &\dot{\underline{\underline{\varepsilon}}}^{\mathrm{p}} = \dot{\chi}\,\frac{\partial \mathrm{f}}{\partial \underline{\underline{\mathrm{S}}}} \\ &\dot{\underline{\underline{\mathrm{X}}}} = \frac{2}{3}\,\mathrm{C}\,\dot{\underline{\underline{\varepsilon}}}^{\mathrm{p}} \quad \textit{and} \quad \underline{\underline{X}}\left(\underline{\underline{\varepsilon}}^p = \underline{\underline{0}}\right) = \underline{\underline{0}} \end{aligned} \tag{3}$$

where J_2 is the second stress invariant, $\underline{\underline{\mathrm{S}}}$ the deviatoric stress tensor, $\underline{\underline{\mathrm{X}}}$ the back stress, C the hardening parameter, σ_y the yield stress and $\dot{\chi}$ the plastic multiplier.

The magnitude of the intrinsic dissipated energy $\delta\left(\Sigma_0^{eq}, \sigma_y\right)$ in a site over a loading cycle is calculated for a given value of the yield stress, von Mises' equivalent stress amplitude $\Sigma_0^{eq} = \max_t J_2\left(\underline{\underline{\Sigma}}(t) - \underline{\underline{\Sigma}}_m\right)$, and a mean stress $\underline{\underline{\Sigma}}_m$ given by

$$\underline{\underline{\Sigma}}_m = \underline{\underline{S}}_m + I_{1,m}\underline{\underline{I}} = \underset{Y}{Min}\left[\underset{t}{Max}\, J_2\left(\underline{\underline{\Sigma}}(t) - \underline{\underline{Y}}\right)\right] + \frac{1}{3}\underset{z}{Min}\left[\underset{t}{Max}\left(trace\left(\underline{\underline{\Sigma}}(t)\right) - z\right)\right]\underline{\underline{I}} \tag{4}$$

As for previous models proposed by the authors, the intensity of the Poisson Point Process describing the activation of microplasticity follows a power law of the equivalent stress amplitude

$$\lambda = \frac{1}{\mathrm{V}_0}\left(\frac{\Sigma_0^{eq}}{S_0 + \alpha I_{1,m}}\right)^m, \tag{5}$$

where α, m and $V_0 S_0^m$ are three material parameters, and $I_{1,m}$ the mean hydrostatic stress over a given cycle. Von Mises' equivalent stress amplitude is chosen because of the isotropy of the material tested hereafter. The power-law dependence is chosen because the onset of microplasticity follows a power-law of the applied stress [25] and because this form leads to a Weibull model when combined with the weakest link assumption [4,11]. The hydrostatic stress dependence is introduced to account for the mean stress effect on self-heating measurements and on fatigue properties.

It is now possible to calculate the global (mean) dissipated energy Δ in a domain Ω of

volume V, *i.e.*, first calculate the intrinsic dissipated energy $\delta\left(\Sigma_0^{eq},\sigma_y\right)$ of one site, integrate it over the whole population of active sites [11] to obtain the total dissipated energy $D\left(\Sigma_0^{eq}\right)$, and then integrate it over the whole domain Ω. In the case of uniform proportional loading, this calculation is straightforward and a closed-form solution is found [26]

$$\Delta = \frac{4\mathrm{m}\,\mathrm{V_S}}{\mathrm{h}(\mathrm{m}+1)(\mathrm{m}+2)}\frac{\left(\Sigma_{effdiss}\right)^{m+2}}{V_0\,S_0^m} \text{ with } \Sigma_{effdiss} = \frac{G_{m+2}^{1/(m+2)}\Sigma_{0M}^{eq}}{\left(1+\frac{\alpha}{S_0}I_{1,mM}\right)^{m/(m+2)}}, \tag{6}$$

where h is a parameter gathering the different thermal-related parameters.

This expression is identical to uniaxial homogeneous situation, except that uniaxial stress amplitude is changed to $\Sigma_{effdiss}$, the effective dissipative stress amplitude, where G_{m+2} is a *dissipation* heterogeneity factor. The latter factor can be calculated in the case of proportional loading

$$G_{m+2} = \frac{1}{\mathrm{V}}\int_\Omega \left(\frac{S_0+\alpha I_{1,mM}}{S_0+\alpha I_{1,m}(M)}\right)^m \left(\frac{\Sigma_0^{eq}(M)}{\Sigma_{0M}^{eq}}\right)^{\mathrm{m}+2} \mathrm{dV}, \tag{7}$$

and requires a numerical integration for non-proportional loadings.

3.2 Critical shear stress approach

From now on and for the sake of clarity, every variable of the present model having an equivalent in the yield surface approach is denoted with $\tilde{\cdot}$, *e.g.* Σ_0^{eq} and $\tilde{\Sigma}_0^{eq}$. Microplasticity is here modelled at the scale of slip planes based on Schmid's criterion

$$\tau - \tau_y \le 0, \tag{8}$$

with τ_y the critical shear stress and $\tau = \underline{\underline{\sigma}} : \underline{\underline{a}}$ the (resolved) shear stress for the considered direction defined by

$$\underline{\underline{a}} = \frac{1}{2}\left(\underline{n}^t\,\underline{m} + \underline{m}^t\,\underline{n}\right), \tag{9}$$

where $\underline{n}$ is the direction normal to the considered plane, and $\underline{m}$ the in-plane slip direction. The shear stress τ for the considered direction is related to the macroscopic shear stress T by the same localization law as before [15]

$$\tau = T - \mu(1-\beta)\gamma^p, \tag{10}$$

where γ^p is the plastic slip ($\underline{\underline{\varepsilon}}^p = \gamma^p\,\underline{\underline{a}}$). One direction thus becomes active when the shear stress amplitude T_0 is greater than the critical shear stress τ_y, which is assumed to be a random variable.

The same sequence of calculation is needed to express the global dissipated energy $\tilde{\Delta}$,

except that now an angular integration over all directions in space is necessary. The intensity of the Poisson Point Process follows a power law of the macroscopic shear amplitude integrated over all angular directions in space (defined by the solid angle Θ) [15]

$$\widetilde{\lambda} = \frac{1}{\widetilde{V}_0\left(\widetilde{S}_0 + \widetilde{\alpha}\, I_{1,max}\right)^{\tilde{m}}} \int \left(2T_0(\Theta)\right)^{\tilde{m}} d\Theta \quad , \tag{11}$$

where $\tilde{m}$, $\tilde{\alpha}$ and $\tilde{V}_0\left(\tilde{S}_0\right)^m$ are three parameters depending on the considered material, and $I_{1,max}$ the maximum hydrostatic stress over a given cycle. The global dissipated energy $\tilde{\Delta}$ is expressed in a similar way as for the first model

$$\tilde{\Delta} = \frac{4\tilde{m}\,\tilde{V}_S}{\tilde{h}(\tilde{m}+1)(\tilde{m}+2)} \frac{\left(\tilde{\Sigma}_{effdiss}\right)^{\tilde{m}+2}}{\tilde{V}_0\,\tilde{S}_0^{\tilde{m}}} \text{ with } \tilde{\Sigma}_{effdiss} = \frac{\tilde{G}_{\tilde{m}+2}^{1/(\tilde{m}+2)}\tilde{\Sigma}_{0M}^{eq}}{\left(1+\frac{\tilde{\alpha}}{\tilde{S}_0} I_{1,\max M}\right)^{\tilde{m}/(\tilde{m}+2)}}, \tag{12}$$

where $\tilde{h}$ is a parameter gathering the different thermal-related parameters of the model. The dissipation heterogeneity factor is defined as

$$\tilde{G}_{\tilde{m}+2} = \frac{1}{V}\int_{\Omega}\left(\frac{\tilde{S}_0 + \tilde{\alpha} I_{1,\max M}}{\tilde{S}_0 + \tilde{\alpha} I_{1,\max}(M)}\right)^{m}\left(\frac{\tilde{\Sigma}_0^{eq}(M)}{\tilde{\Sigma}_{0M}^{eq}}\right)^{\tilde{m}+2}\Gamma(\tilde{m}+2)\,dV \text{ with } \kappa(\tilde{m}+2) = \int\left(\frac{2T_0(M,\Theta)}{\widetilde{\Sigma}_0^{eq}(M)}\right)^{\tilde{m}+2} \tag{13}$$

where $\kappa(\tilde{m}+2)$ represents the distribution of activated directions.

The definitions of equivalent stresses are not the same for the two models (Σ_0^{eq} is von Mises' equivalent stress, whereas $\widetilde{\Sigma}_0^{eq}$ is Tresca's equivalent stress). Moreover the expression of $\tilde{G}_{m+2}$ is different from G_{m+2} since it includes the integration of the distribution of activated directions. This implies a numerical calculation, and a complete closed-form solution is no longer available. Aside from this little drawback, the hypotheses of this model make it intrinsically more relevant from a non-proportional point of view as will be shown in the next sections.

4 SELF-HEATING RESPONSE

The thermal response of the model corresponds to the "mean" point of view of the previous described microplastic onset, *i.e.*, the temperature is linked to the global dissipated energy. The * notation is used in the following equations of the section to clarify that they may be used for any of the two models (heat conduction equation is the same in both cases). Since the uniformity of the temperature in the specimen is a relevant assumption in the present case [27], the mean dissipation Δ^* is introduced in the following simplified heat conduction equation

$$\dot{\theta} + \frac{\theta}{\tau_{eq}} = \frac{f_r\,\Delta^*}{\rho\, c}, \tag{14}$$

where $\theta = T_{specimen} - T_{ref}$ is the mean temperature variation with respect to the reference temperature T_{ref}, τ_{eq} a characteristic time depending on the heat transfer boundary conditions [28], ρ the mass density, c the specific heat and f_r the loading frequency. The thermoelastic term is not considered since it vanishes over one cycle and only mean steady-state temperatures are needed. For both models, the mean (uniform) steady-state temperature $\bar{\theta}$ reads

$$\bar{\theta} = \eta^* \frac{m^*}{(m^*+1)(m^*+2)} \frac{\left(\Sigma_{effdiss}{}^*\right)^{m^*+2}}{V_0^* \left(S_0^*\right)^{m^*}} \text{ with } \eta^* = \frac{4 f_r \tau_{eq}}{\rho c} \frac{V_S^*}{h^*}. \tag{15}$$

This expression is similar to that for uniform tensile loading except for $\Sigma_{effdiss}{}^*$ term, and only three parameters are needed to describe the thermal response.

5 HIGH CYCLE FATIGUE RESPONSE

The weakest link theory is considered to describe the fatigue limit. The failure probability is then given by the probability of finding at least one active site in domain Ω. From Equation (1), the failure probability is thus given for both models by

$$P_F^* = 1 - exp\left[\int_\Omega -\lambda^* V \, dV\right]. \tag{16}$$

5.1 Yield surface approach

By using Equation (5), the failure probability is related to the loading amplitude

$$P_F = 1 - \exp\left[\int_\Omega -\frac{V}{V_0}\left(\frac{\Sigma_0^{eq}(M)}{S_0 + \alpha I_{1,m}(M)}\right)^m dV\right]. \tag{17}$$

which corresponds to Weibull's model [29,30]. This expression is simplified using a *stress* heterogeneity factor H_m, defined by

$$H_m = \frac{1}{V}\int_\Omega \left(\frac{\left(S_0 + \alpha I_{1,mM}\right)}{\left(S_0 + \alpha I_{1,m}(M)\right)} \frac{\Sigma_0^{eq}(M)}{\Sigma_{0M}^{eq}}\right)^m dV. \tag{18}$$

Equation (16) becomes

$$P_F = 1 - \exp\left[-\frac{V_{eff}}{V_0}\left(\frac{\Sigma_{0M}^{eq}}{S_0 + \alpha I_{1,mM}}\right)^m\right]. \tag{19}$$

where $V_{eff} = V H_m$ denotes the effective volume. From this expression, and as for the previous self-heating models proposed by the authors [4], the fatigue limit features are derived

$$\overline{(\Sigma_0^{eq})_\infty} = \overline{\Sigma}_\infty = \left(S_0 + \alpha I_{1,mM}\right)\left(\frac{V_0}{V_{eff}}\right)^{(1/m)} \Gamma\left(1+\frac{1}{m}\right) \text{ and } CV = \frac{\overline{\overline{\Sigma}}_\infty}{\overline{\Sigma}_\infty} = \frac{\sqrt{\Gamma\left[1+\frac{2}{m}\right] - \Gamma^2\left[1+\frac{1}{m}\right]}}{\Gamma\left(1+\frac{1}{m}\right)} \tag{20}$$

where $\overline{\Sigma}_\infty$ is the mean fatigue limit, $\overline{\overline{\Sigma}}_\infty$ the standard deviation and CV the coefficient of variation.

The stress H_m and dissipation G_{m+2} heterogeneity factors have intrisincally different meanings. However their expressions are very similar in the case of proportional loadings [see equations (18) and (7)]. Moreover the high value of the exponent m (m = 12 for the present material) induces very close values of these factors, even more for loadings with uniform mean hydrostatic stresses. This means that the combined effects of direction and heterogeneity of loading are nearly the same for fatigue and self-heating results, which makes easier the interpretation of self-heating results.

On the contrary, H_m and G_{m+2} can be very different for non-proportional loadings. Considering two uniform loadings with the same equivalent stress amplitude and the same mean hydrostatic stress, the first one proportional and the second one non-proportional, H_m factors are identical but G_{m+2} factors can be very different.

5.2 Critical shear stress approach

With the second model the failure probability corresponds to the probability of finding at least one active *slip direction* in the given volume. The failure probability is thus related to the shear stress amplitude by

$$\tilde{P}_F = 1 - \exp\left[-\frac{1}{\tilde{V}_0}\int_\Omega\int\left(\frac{2T_a}{\tilde{S}_0 + \tilde{\alpha} I_{1,max}}\right)^{\tilde{m}} d\Theta\, dV\right] . \tag{21}$$

A stress heterogeneity factor $\widetilde{H}_{\tilde{m}}$ is again introduced,

$$\widetilde{H}_{\tilde{m}} = \frac{1}{V}\int_\Omega\left(\frac{\left(\widetilde{S}_0 + \tilde{\alpha} I_{1,max\,M}\right)}{\left(\widetilde{S}_0 + \tilde{\alpha} I_{1,max}(M)\right)}\frac{\widetilde{\Sigma}_0^{eq}(M)}{\widetilde{\Sigma}_{0M}^{eq}}\right)^{\tilde{m}} \kappa(\tilde{m})\, dV , \tag{22}$$

so that equation (20) becomes

$$\tilde{P}_F = 1 - \exp\left[-\frac{\tilde{V}_{eff}}{\tilde{V}_0}\left(\frac{\tilde{\Sigma}_{0M}^{eq}}{\tilde{S}_0 + \tilde{\alpha} I_{1,max}}\right)^{\tilde{m}}\right]. \tag{23}$$

Last the mean fatigue limit is expressed (CV is the same as for the previous model)

$$\overline{(\widetilde{\Sigma}_0^{eq})}_\infty = \widetilde{\overline{\Sigma}}_\infty = \left(\widetilde{S}_0 + \tilde{\alpha} I_{1,max\,M}\right)\left(\frac{\widetilde{V}_0}{\widetilde{V}_{eff}}\right)^{(1/\tilde{m})} \Gamma\left(1+\frac{1}{\tilde{m}}\right). \tag{24}$$

Note that $\widetilde{G}_{\tilde{m}+2}$ and $\widetilde{H}_{\tilde{m}}$ are *a priori* different because of the influence of the hydrostatic stress. The values of these factors are however again nearly identical because of the high value of $\tilde{m}$ for proportional and non-proportional loadings.

The identication of m^* is performed using equation (15), so that the values of m and $\tilde{m}$ are identical, and so the relative fatigue scatter is the same for both models (*i.e.*, same *CV* value). The mean fatigue limits are different because equations (20) and (24) account for the influence of several parameters on fatigue properties in different ways.

6 EXPERIEMENTAL APPLICATION

Both models depend on three parameters to predict the fatigue limits, and a last one to account for self-heating under cyclic loadings. They are applied to the case of AISI 1045 medium carbon steel tubes under tension-torsion loadings. In that case, the macroscopic stress tensor depends only on the radius r of the specimen and is defined by

$$\Sigma_{zz} = \Sigma_{11,0}\sin(2\pi f_r t) + \Sigma_m \qquad (25)$$

$$\Sigma_{\theta z} = \Sigma_{12,0}\frac{r}{R_e}\sin(2\pi f_r t + \varphi)$$

where $\Sigma_{11,0}$ and $\sqrt{3}\,\Sigma_{12,0} = \tan(\phi)\,\Sigma_{11,0}$ are the tensile and shear stress amplitudes, φ the phase lag between shear and normal stresses, Σ_m the mean tensile stress, and R_e the external radius of the specimen. The hydrostatic pressure is uniform over the volume of the specimen, so that the two heterogeneity factors of the both models have the same expression for proportional loadings, *i.e.* $G_m = H_m$ and $\widetilde{G}_{\tilde{m}} = \widetilde{H}_{\tilde{m}}$. In the next section, the identification procedure is presented, and a comparison of predictions with experimental fatigue results.

6.1 Identification

Identification is based on self-heating curves obtained with the same procedure as for previous self-heating tests [4,11,12,27]. During the test, the amplitude of loading is step-wise constant, and increases once the differential temperature is stabilised. One pure torsion loading and one pure tension with non-zero mean stress are applied. The steady-state temperature is plotted as a function of the loading amplitude in Figure 1. As for other steels [4,11,12,27], each curve has a first part that shows virtually no change in temperature, whereas in the second part the temperature increases significantly with the stress amplitude. This transition is reported to be a rather good estimation of the mean fatigue limit for steels in uniaxial homogeneous case [4,6,7,8]. Moreover it has been shown that the gradual increase of temperature is linked to the fatigue scatter [4]. The relatively short duration of self-heating tests (in comparison with traditional fatigue tests) makes them not only interesting for academic studies, but also very attractive for industrial purposes.

Both models depend exactly on the same parameters, namely, m^* describes the scatter of fatigue results and the slope (in a log-log plot) of the self-heating temperature response, η^* a scale parameter for the thermal response, α^* accounts for the effect of the mean hydrostatic stress on self-heating and fatigue properties, and $V_0^*\left(S_0^*\right)^{m^*}$ the scale parameters for the fatigue

response. All parameters are identified using the 2 self-heating tests and one fatigue limit that may concern any type of geometry or loading. Figure 1 shows the identification for both approaches.

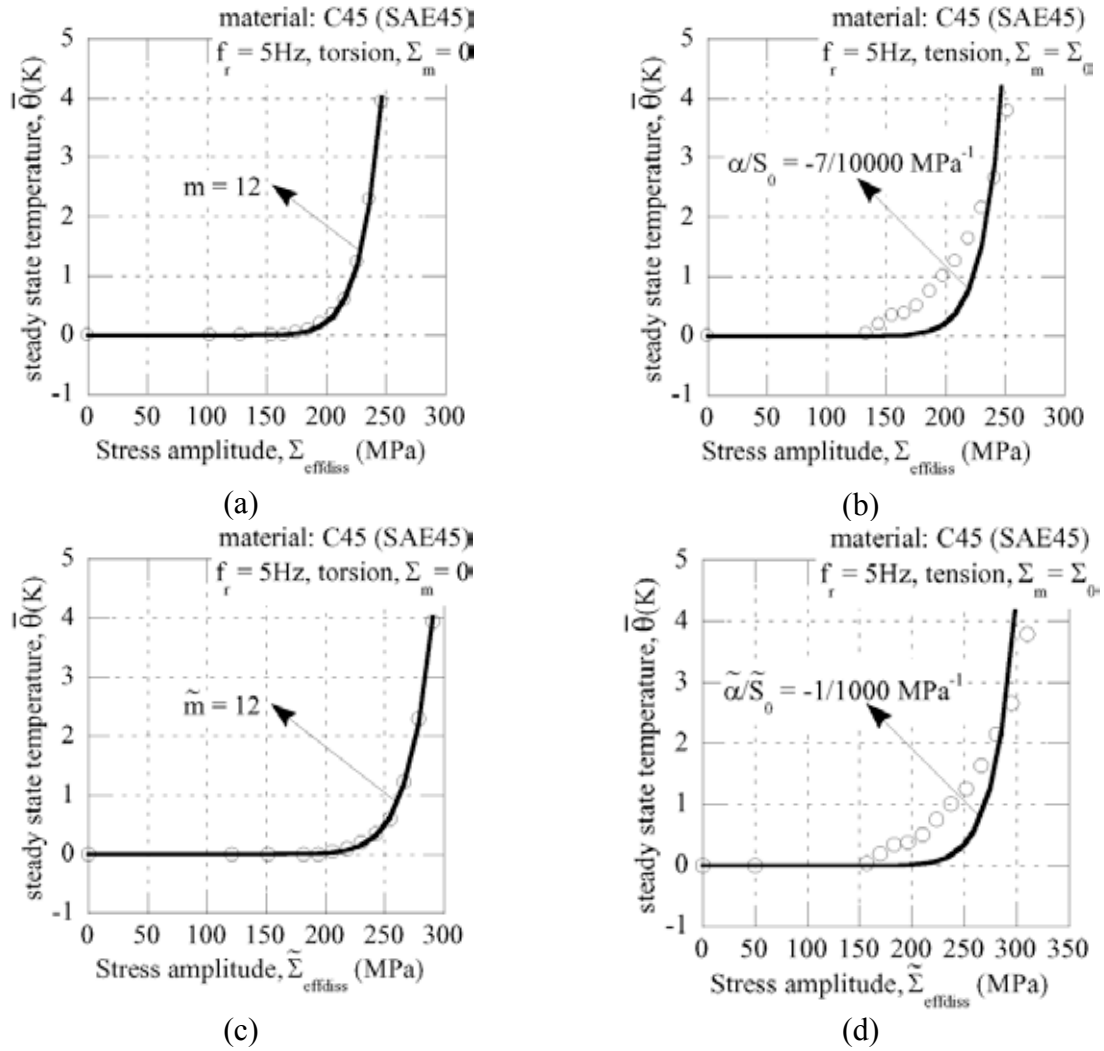

Figure 1: Identification of m and α using torsion (a) and tension with mean stress (b) self-heating curves. Identification of $\tilde{m}$ (c) and $\tilde{\alpha}$ (d) using the same curves.

No non-proportional loading results are needed for this identification. Any couple of loading paths may be used to identify parameters m^*, η^* and α^* as long as their mean (resp. maximum) hydrostatic stresses over a given cycle are different.

The last (scale) parameter of each model is obtained by using a mean fatigue limit and Equation (20) for the yield surface approach, or Equation (24) for the critical shear stress approach. This value is obtained for tensile loadings ($\phi = 0°$ and $\Sigma_m = 0$) when fatigue limits are evaluated for 5×10^6 cycles. Staircase tests are performed on 15 smooth and round

samples machined from the same steel bar as before. Stress steps are equal to 10 MPa. The measured mean fatigue limit is 262 MPa.

6.2 Validation

Models are first validated from a thermal point of view. A pure tension (zero mean stress) and a non-proportional (constant von Mises' equivalent stress at mean radius ($\phi = 48°$, $\varphi = 90°$)) self-heating tests are performed. Figure 2 shows self-heating curves as a function of von Mises (a), yield surface (b) and critical shear stress (c) equivalent stress amplitudes. For both models all curves collapse onto one another when the definition of the equivalent stress is used. This result means that both hydrostatic stress and non-proportional thermal effects are well predicted.

Mean fatigue limit prediction is then checked using three different series of staircase tests (target: 5 x 10^6 cycles). The first one is a pure torsion loading, the second one a proportional loading ($\phi = 48°$ and $\Sigma_m = 0$) and last one a non-proportional loading ($\phi = 48°$, $\varphi = 90°$). Comparison between experimentally obtained mean fatigue limits and predicted ones is shown in Table 1, using the relative prediction error defined as $\left(\overline{\Sigma}_\infty^{exp} - \overline{\Sigma}_\infty^{pre}\right)/\overline{\Sigma}_\infty^{exp}$. Predictions are in good agreement with experimental results, except for the yield surface model, which is non-conservative for non-proportional loading.

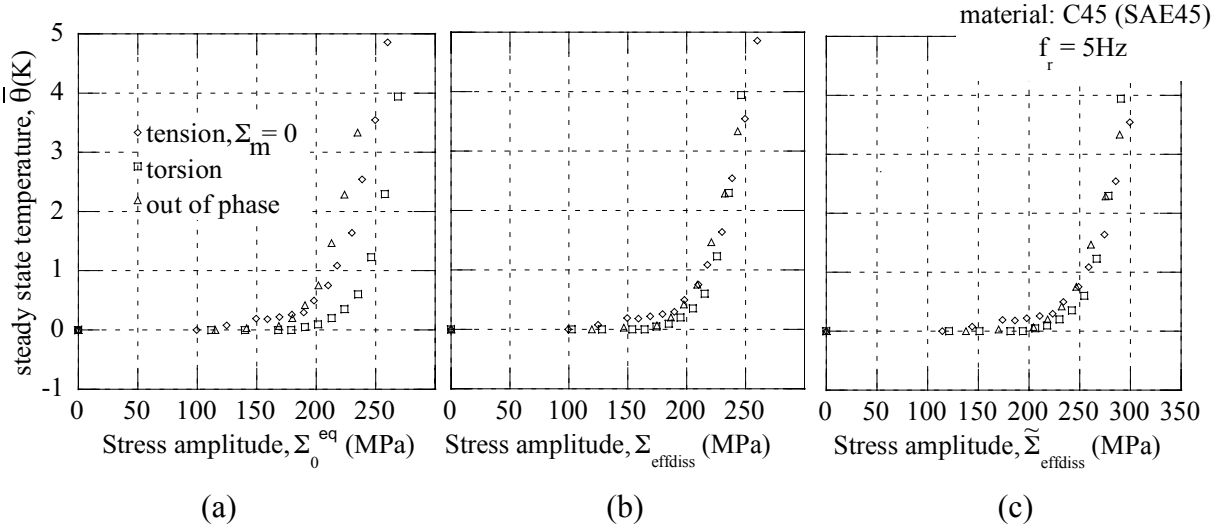

Figure 2: Thermal validation: self-heating curves for different equivalent stress amplitude.

Table 1: Fatigue validation. Relative prediction errors of both models.

Loadings ($\Sigma_m = 0$)	Prop. ($\phi = 90°$)	Prop. ($\phi = 48°$)	N-prop. ($\phi = 48°$, $\varphi = 90°$)
Σ_0^{eq} (MPa)	277	267	205
Critical shear stress model	6%	7%	-5%
Yield surface model	9%	6%	-17%

7 CONCLUSION

The present paper was focused on a comparison of two multiscale models whose parameters are tuned thanks to self-heating data, and subsequently used to predict multiaxial high cycle fatigue properties. The first model uses an equivalent stress to account for stress multiaxiality at the microscopic scale, whereas the second one relies on a description of microplasticity at the scale of slip-planes.

Both thermal and fatigue behaviours are well described by each model. They account for the influence of the stress heterogeneity, the volume effect and the hydrostatic stress. Relative errors are small for each experimental validation, even though the "identification cost" is low (and the same for each model), thanks to the information extracted from the self-heating tests.

The distinction between the yield surface and critical shear stress approaches is nearly impossible from a thermal point of view (see Figures 2 (b) and (c)), whereas an important difference appears as along as non-proportional fatigue limit is concerned. The interest of the critical shear stress approach is clearly shown, lowering (in absolute value) the prediction error from –17% to –5% without the addition of new parameters. This is due to its microplastic activation description, combining probabilistic onset and slip-planes approach, which leads to very close *dissipation* and *stress* heterogeneity factors.

A next step of this work will be the prediction of multiaxial fatigue life with the critical shear stress approach and the application to industrial cases.

REFERENCES

[1] Bérard, J.-Y., Rathery, S., and Béranger, A.-S., Détermination de la limite d'endurance des matériaux par thermographie infrarouge. *Mat. Techn*. (1998) **1-2**:55-57.

[2] Cura, F., Curti, G. and Sesana, R., A new iteration method for the thermographic determination of fatigue limit in steels. *Int. J. Fat.* (2005) **27[4]**:453-459.

[3] Dengel, D. and Harig, H., Estimation of the fatigue limit by progressively-increasing load tests. *Fat. Fract. Eng. Mat. Struct.* (1980) **3[1]:**113.

[4] Doudard, C., *Détermination rapide des propriétés en fatigue à grand nombre de cycles à partir d'essais d'échauffement*. PhD thesis, ENS Cachan, France, (2004).

[5] Galtier, A., Bouaziz, O. and Lambert, A., Influence de la microstructure des aciers sur leurs propriétés mécaniques. *Méc. Ind.* (2002) **3[5]**: 457-462.

[6] Krapez, J.-C., Pacou, D. and Bertin, C., Application of lock-in thermography to a rapid evaluation of the fatigue limit in metals. 5th AITA, Int. Workshop on Advanced Infrared Techn. and Appl., Venezia (Italy), ed. E. Grinzato et al. (1999), 379-385.

[7] La Rosa G. and Risitano, A., Thermographic methodology for rapid determination of the fatigue limit of materials and mechanical components. *Int. J. Fat.* (2000) **22[1]**: 65-73.

[8] Luong, M.P., Infrared thermographic scanning of fatigue in metals. *Nuclear Engineering and Design.* (1995) **158[2-3]**:363-376.

[9] Mabru, C. and Chrysochoos, A., Dissipation et couplages accompagnant la fatigue de matériaux métalliques. Photomécanique 2001, ed. Y. Berthaud, M. Cottron, J.-C. Dupré, F. Morestin, J.-J. Orteu and V. Valle, GAMAC, (2001) 375-382.

[10] Stromeyer, C.E., A machine for determining fatigue limits calorimetrically. *Rep. Brit. Ass.* (1915) 638.

[11] Doudard, C., Calloch, S., Cugy, P., Galtier, A. and Hild, F., A probabilistic two-scale model for high cycle fatigue life predictions. *Fat. Fract. Eng. Mat. Struct.* (2005) **28**:279-288.
[12] Doudard, C., Poncelet, M., Calloch, S., Boué, C., Hild, F. and Galtier, A., Determination of an HCF criterion by thermal measurements under biaxial cyclic loading, Int. J. Fatigue. (2007) **29[4]**:748-757.
[13] Lemaitre, J. and Doghri, I. Damage 90: a post processor for crack initiation. *Comput. Methods Appl. Mech. Engrg.* (1994) **115**: 197-232.
[14] Dang Van, K., *Sur la résistance à la fatigue des métaux. Sciences et techniques de l'armement*, Mémorial de l'artillerie française, 3ème fascicule (1973).
[15] Doudard, C., Hild, F., and Calloch, S., A probabilistic model for multiaxial high cycle fatigue. *Fat. Fract. Eng. Mat. Struct.* (2007) **30**:107-114.
[16] Morel, F., A fatigue life prediction method based on a mesoscopic approach in constant amplitude multiaxial loading. *Fat. Fract. Eng. Mat. Struct.* (1998) **21**:241-256.
[17] Curtin W.A., Exact Theory of Fiber Fragmentation in Single-Filament Composite, *J. Mater. Sci.* (1991), **26**:5239-5253.
[18] Gulino, R. and Phoenix, S.L., Weibull strength statistics for graphite fibres measured from the break progression in a model graphite/glass/epoxy microcomposite. *J. Mater. Sci.* (1991) **26**:3107-3118.
[19] Jeulin, D., *Modèles morphologiques de structures aléatoires et changement d'échelle*. thèse d'Etat, Université de Caen, France, (1991).
[20] Fedelich B., A stochastic theory for the problem of multiple surface crack coalescence, *Int. J. Fract.* (1998) **91**:23-45.
[21] Denoual, C. and Hild, F., Dynamic fragmentation of brittle solids: A multi-scale model. *Eur. J. Mech. A/Solids.* (2002) **21**:105-120
[22] Berveiller, M. and Zaoui, A., An extension of the self-consistent scheme to plastically flowing polycristals. *J. Mech. Phys. Solids.* (1979) **26**:325-344.
[23] Kröner, E., On the plastic deformation of polycristals. *Acta Met.* (1984) **9**:155-161.
[24] Eshelby, J.D., The Determination of the Elastic Field of an Ellipsoidal Inclusion and Related Problems. *Proc. Roy. Soc. London A.* (1957) **241**:376-396.
[25] Cugy, P. and Galtier, A., Microplasticity and temperature increase in low carbon steel, in: Proceedings of the 7th Int. Fat. Conf., Stockholm (Sweden), (2002).
[26] Poncelet, M., Doudard, C., Calloch, S., Weber, B. and Hild, F., Probabilistic multiscale models and measurements of self-heating under multiaxial high cycle fatigue, *Jal Mech. Phys. Sol.* (2010) **58**:578-593
[27] Poncelet, M., Doudard, C., Calloch, S., Hild, F., Weber, B. and Galtier, A., Prediction of self-heating measurements under proportional and non-proportional multiaxial cyclic loadings, *C. R. Mécanique.* (2007) **335**:81-86
[28] Chrysochoos, A. and Louche, H., An infrared image processing to analyse the calorific effects accompanying strain localisation, *Int. J. Engrg. Sci.* (2000) **38**:1759-1788,
[29] Weibull, W., A Statistical Theory of the Strength of Materials, *Roy. Swed. Inst. Eng. Res. (*1939) Report 151.
[30] Weibull, W., A statistical distribution function of wide applicability, *ASME J. Appl. Mech.* (1951) **18**:293-297.

XI International Conference on Computational Plasticity. Fundamentals and Applications
COMPLAS XI
E. Oñate, D.R.J. Owen, D. Peric and B. Suárez (Eds)

SIMPLIFIED MULTISCALE RESOLUTION THEORY FOR ELASTIC MATERIAL WITH DAMAGE

LARS-ERIK LINDGREN[*], HAO QIN[*], WING KAM LIU[†] AND SHAN TANG[†]

[*]Luleå University of Technology
Engineering Sciences and Mathematics
971 87 Luleå, Sweden
e-mail: lars-erik.lindgren@ltu.se, www.ltu.se

[†]Northwestern University
Mechanical Engineering
2145 Sheridan Rd, Evanston, IL 60208-3111, USA
email : w-liu@northwestern.edu , www.tam.northwestern.edu

Key words: Multiscale, Damage, Localisation.

Abstract. The multiscale resolution continuum theory (MRCT) is a higher order continuum mechanics. A particle is represented by a point that is deformable. This enables the possibility to include the effect of microstructure features in the continuum model on the deformation behavior through additional nodal variables for the higher order scale. This reduces the need for a very fine mesh in order to resolve microstructure details. It is possible to further reduce the computational effort by keeping the additional degree of freedoms to a minimum by tailoring the theory to specific phenomena. The latter is illustrated in a simplified context for an elastic material with damage.

1 INTRODUCTION

The multiscale resolution continuum theory (MRCT) is a higher order continuum mechanics theory. It is a generalization of the micromorphic theory [1-3]. MRCT introduces length scales useful for application to localization problems. It has additional nodal parameters for the information about the deformation on the microstructural scale. This relieves the problem of having an extremely fine mesh. However, still very small elements are required and this together with the additional nodal variables adds to the computational burden. This paper demonstrates the method for an elastic material with brittle damage.

2 BACKGROUND

The multiscale approach belongs to the field of generalized continuum theories. Cosserat already 1909 introduced a generalized continuum. The Cosserat continuum, also named micropolar, introduced higher order terms. There are several papers [4-7] that describe different variants of generalized continuum theories. Eringen is the originator of the micromorphic theory and summarized his work in [1]. The micromorphic continuum includes the relative deformation of a subdomain at a specific point. Thus the particle represented by a

point is deformable. This enables the possibility to include the effect of microstructure features in the continuum model on the deformation behavior. The size of the subdomain determines a length scale l^i that influences the behavior at a given point. This domain is called a microdomain. The right superscript, i, denotes the level or scale of the microdomain as explained in the next section.

Eringen [1] indicated the possibility of formulating a theory for higher grades of continua but limited his description to the first grade. Germain [8] used a more elegant approach by utilizing the principle of virtual power. He showed how to include higher order terms in the deformation of the RVE. Liu with co-workers [9, 10] have developed a multiscale resolution continuum theory based on nested scales. The starting point for their derivation is also the principle of virtual power. The use of embedded RVEs or length scales facilitate the formulation of scales of higher order in the Multiscale Continuum Resolution Theory (MCRT).

3 MULTISCALE CONTINUUM RESOLUTION THEORY

The starting point for deriving the MCR theory is the principle of virtual power [11, 3, 10]. The internal virtual power is decomposed into a homogeneous and inhomogeneous part. The latter is due to the local stress variation within N nested RVEs within a point.

$$\delta p_{\text{int}}^{\text{hom}} + \delta p_{\text{int}}^{inh} = \sigma^0 : \delta \mathbf{l}^0 + \sum_{i=1}^{N} \int_{\Omega^i} \left({}_m\sigma^i : \delta {}_m\mathbf{l}^i - \sigma^0 : \delta \mathbf{l}^0 \right) d\Omega \tag{1}$$

, where $\mathbf{l}^0$ is the spatial velocity gradient and σ^0 is the Cauchy stress tensor on the macroscopic scale. The corresponding quantities, ${}_m\mathbf{l}^i$ and ${}_m\sigma^i$, are set up for each microdomain i. The scales are assumed to be separable so that ${}_m\mathbf{l}^i$ and ${}_m\sigma^i$ are constant for all smaller scales Ω^j, $j > i$. Eq. (1) is approximated to

$$\delta p_{\text{int}}^{\text{hom}} + \delta p_{\text{int}}^{inh} = \sigma^0 : \delta \mathbf{l}^0 + \sum_{i=1}^{N} \frac{1}{\Omega^i} \int_{\Omega^i} \left({}_m\beta^i : \left(\delta {}_m\mathbf{l}^i - \delta \mathbf{l}^0 \right) \right) d\Omega \tag{2}$$

A linear varying spatial velocity gradient within each subscale is assumed.

$${}_m\mathbf{l}^i \left(\mathbf{x} + \mathbf{y} \right) = \mathbf{l}^i \left(\mathbf{x} \right) + \mathbf{g}^i \left(\mathbf{x} \right) \cdot \mathbf{y}^i \tag{3}$$

where $\mathbf{y}^i$ is a local coordinate system at $\mathbf{x}$ in the microdomain. The term $\mathbf{l}^i$ gives the microstrain and $\mathbf{g}^i$ is its gradient. This leads after some manipulations to

$$\delta p_{\text{int}}^{\text{hom}} + \delta p_{\text{int}}^{inh} = \sigma^0 : \delta \mathbf{l}^0 + \sum_{i=1}^{N} \beta^i : \left(\delta \mathbf{l}^i - \delta \mathbf{l}^0 \right) + \mathbf{m}^i : \delta \mathbf{g}^i \tag{4}$$

where average microstresses are

$$\beta^i = \frac{1}{\Omega^i} \int_{\Omega^i} \beta_m^i \, d\Omega \tag{5}$$

and microcouples are

$$\mathbf{m}^i = \frac{1}{\Omega^i} \int_{\Omega^i} \beta_m^i \otimes \mathbf{y} \, d\Omega \tag{6}$$

Thus it is assumed that the microstresses and their couples can be related to the symmetric

part of the relative velocity gradient, $\mathbf{d}^i - \mathbf{d}^0$, and second velocity gradient $\mathbf{g}^i$, respectively. We use a hypoelastic approach. Notice that we limit the description to elastic deformations. The macroscopic stress update is written as

$$\sigma^{0\nabla} = \mathbf{C}_\sigma \mathbf{d}^0 \tag{7}$$

where $[\ ]^\nabla$ denotes an objective rate. $\mathbf{C}_\sigma$ is the elasticity tensor. The microstresses are updated by

$$\left(\beta^i\right)^\nabla = \mathbf{C}^i_\beta \left(\mathbf{d}^i - \mathbf{d}\right) + \mathbf{C}^i_{\beta m}\mathbf{g}^i \tag{8}$$

and the couples are updated by

$$\left(\mathbf{m}^i\right)^\nabla = \mathbf{C}^i_{\beta m} \left(\mathbf{d}^i - \mathbf{d}\right) + \mathbf{C}^i_{m}\mathbf{g}^i \tag{9}$$

Including the external virtual power and setting the total virtual power to zero leads to the following coupled equations of motion [3]

$$\begin{aligned} &\nabla\cdot\left(\sigma^0 - \sum_{i=1}^{N}\beta^i\right) = \rho\dot{\mathbf{v}}^0 \\ &\nabla\cdot\mathbf{m}^i - \beta^i = \gamma^i I^i \qquad i = 1..N \end{aligned} \tag{10}$$

where $\mathbf{v}^0$ is the macroscopic velocity field, ρ is the macroscopic density, ρ^i is the density in microdomain i, and γ^i is the micro-acceleration defined as

$$\gamma^i = \dot{\mathbf{l}}^i + \mathbf{l}^i\cdot\mathbf{l}^i \tag{11}$$

and the inertia tensor is

$$I^i = \frac{1}{\Omega^i}\int_{\Omega^1}\rho^i\mathbf{y}^i\otimes\mathbf{y}^i d\Omega \tag{12}$$

4 SIMPLIFIED MCRT FOR ELASTIC-DAMAGE MODEL

It is possible to reduce the computational cost by adapting the theory to specific phenomena. Kadowaki and Liu [12] demonstrated this for the case of granular media. We are here considering an elastic material with local softening/fracture with one additional scale (N=1). Elastic behavior is assumed. The damaged regionin the microdomain, gray in Figure 1, is assumed to completely lose its strength. Then homogenized the constitutive equation is

$$\mathbf{C}^1_\beta = \frac{1}{\Omega^1}\int_{\Omega^1}\mathbf{C}_\sigma d\Omega = \mathbf{C}_\sigma\left(1-\omega\right) \tag{13}$$

where ω is the fraction of the damaged volume in the microdomain. The coupling matrix may be non-zero when the damage is unsymmetric in the microdomain. We assume it is symmetric and thus have

$$\mathbf{C}^1_{\beta m} = \frac{1}{\Omega^1}\int_{\Omega^1}\mathbf{C}_\sigma\otimes y^1 d\Omega = \mathbf{0} \tag{14}$$

The constitutive matrix for the couple terms becomes

$$\mathbf{C}^1_m = \mathbf{C}^e_\sigma \otimes \frac{\left(l^1\right)^2}{12}\mathbf{D} \tag{15}$$

where

$$\mathbf{D} = \begin{bmatrix} (Z_1)^3 Z_2 Z_3 & 0 & 0 \\ 0 & Z_1 (Z_2)^3 Z_3 & 0 \\ 0 & 0 & Z_1 Z_2 (Z_3)^3 \end{bmatrix} \tag{16}$$

with

$$\mathbf{Z}_i^1 = \frac{y_i^+ + y_i^-}{l^1} = \frac{2y_i}{l^1} \tag{17}$$

The parameters $y_i^{\pm}$ are the distances from origin to where damage has reached into the microdomain, see Figure 1. We have symmetric damage in the current one-dimensional implementation, ie. $y_i^+ = y_i^-$. The damage can be unsymmetric for when several stress or strain components are used. The subscript *i* denotes the coordinate direction of the normal to this surface.

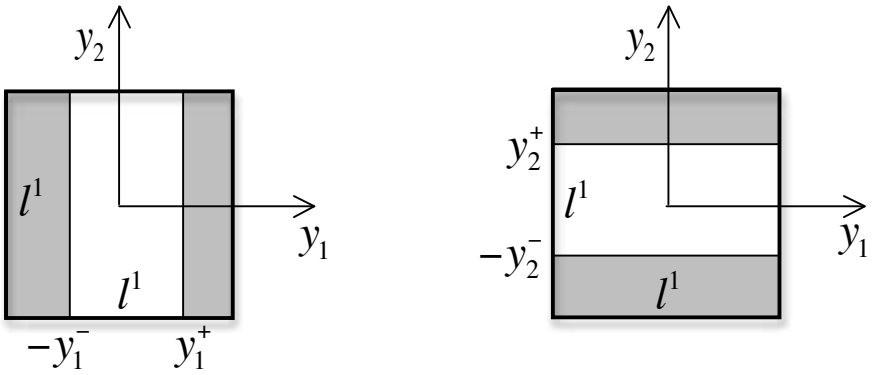

Figure 1: Two-dimensional view of damage volumes (gray) that are growing into the microdomain.

The fraction of damage volume is

$$\omega = \prod_{i=1}^{R} \left(1 - \frac{2y_i}{l^1}\right) \tag{18}$$

where *R* is the number of dimensions of the problem. We have R=1 in the case below. Damage is assumed to be due to the volumetric deformation in the microdomain. Therefore, all shear components of higher order degree of freedoms are excluded. The reduced microstress/deformation are

$$\begin{aligned} \beta^1 &= \begin{bmatrix} \beta_{11}^1 & \beta_{22}^1 & \beta_{33}^1 \end{bmatrix}^T \\ \mathbf{d}^1 &= \begin{bmatrix} d_{11}^1 & d_{22}^1 & d_{33}^1 \end{bmatrix}^T \end{aligned} \tag{19}$$

and the corresponding couples/gradients are reduced to

$$\begin{aligned} \mathbf{m}^1 &= \begin{bmatrix} m_{111}^1 & m_{112}^1 & m_{113}^1 & m_{221}^1 & m_{222}^1 & m_{223}^1 & m_{331}^1 & m_{332}^1 & m_{333}^1 \end{bmatrix}^T \\ \mathbf{g}^1 &= \begin{bmatrix} d_{11,1}^1 & d_{11,2}^1 & d_{11,3}^1 & d_{22,1}^1 & d_{22,2}^1 & d_{22,3}^1 & d_{33,1}^1 & d_{33,2}^1 & d_{33,3}^1 \end{bmatrix}^T \end{aligned} \tag{20}$$

Computing the gradients from the first derivatives of the microstrain over a finite element reduces the number of independent nodal degrees of freedom (dof) further. Thus the three

dimensional finite element will have six (three displacements and three normal microstrains) unknowns for each node. The one-dimensional example below has only two dofs per node.

Different damage criterion can be applied. A simple linear increase in damage when the macroscopic strain exceeds a given criterion and the damage becomes complete ($\omega = 1$) when a fracture strain is reached.

5 FINITE ELEMENT IMPLEMENTATION

The implementation of the above outlined theory is shown for a one-dimensional rod with two nodes.

5.1 Kinematics

The finite element interpolation of nodal velocities and rate of microstrains is written as

$$\mathbf{v}(\mathbf{x}) = \begin{bmatrix} N_1^0 & N_2^0 & 0 & 0 \\ 0 & 0 & N_1^1 & N_2^1 \end{bmatrix} \begin{bmatrix} v_{x1} \\ v_{x2} \\ d^1_{xx1} \\ d^1_{xx2} \end{bmatrix} = \begin{bmatrix} \mathbf{N}^0 & 0 \\ 0 & \mathbf{N}^1 \end{bmatrix} \begin{bmatrix} \mathbf{v}^0 \\ \mathbf{d}^1 \end{bmatrix} = \mathbf{N}\mathbf{v} \tag{21}$$

N_n^0 and N_n^1 indicates that we may use different functions to interpolate the microstrain than the nodal velocity, or use different number of integration points when evaluating them. This is not utilized in the following.

The gradient of microstrain is computed as

$$\mathbf{g}^1(\mathbf{x}) = g^1_{xxx} = d^1_{xx,x} = \begin{bmatrix} \dfrac{\partial N_1^1}{\partial x} & \dfrac{\partial N_2^1}{\partial x} \end{bmatrix} \begin{bmatrix} d^1_{xx1} \\ d^1_{xx2} \end{bmatrix} = \mathbf{B}^1\mathbf{d}^1 \tag{22}$$

The macroscopic spatial velocity gradient is obtained by

$$\mathbf{d}^0(\mathbf{x}) = d^0_{xx} = \begin{bmatrix} \dfrac{\partial N_1^0}{\partial x} & \dfrac{\partial N_2^0}{\partial x} \end{bmatrix} \begin{bmatrix} v_{x1} \\ v_{x2} \end{bmatrix} = \mathbf{B}^0\mathbf{v}^0 \tag{23}$$

The needed rates of the macroscopic strain, microstrain and its gradient can now be written as

$$\begin{aligned} \mathbf{d}^0(\mathbf{x}) &= \mathbf{B}^0\mathbf{v}^0 \\ \mathbf{d}^1(\mathbf{x}) &= \mathbf{N}^1\mathbf{d}^1 \\ \mathbf{g}^1(\mathbf{x}) &= \mathbf{B}^1\mathbf{d}^1 \end{aligned} \tag{24}$$

The generalized strain rate vector is introduced

$$\Delta(\mathbf{x}) = \begin{bmatrix} \mathbf{d}^0(\mathbf{x}) \\ \mathbf{d}^1(\mathbf{x}) - \mathbf{d}^0(\mathbf{x}) \\ \mathbf{g}^1(\mathbf{x}) \end{bmatrix} = \begin{bmatrix} \mathbf{B}^0 & 0 \\ -\mathbf{B}^0 & \mathbf{N}^1 \\ 0 & \mathbf{B}^1 \end{bmatrix} \begin{bmatrix} \mathbf{v}^0 \\ \mathbf{d}^1 \end{bmatrix} = \mathbf{Q}\mathbf{v} \tag{25}$$

5.2 Kinetics

Kinetic variables that are energy conjugate kinetic with those in Eq. (25) are

$$\Sigma = \begin{bmatrix} \sigma_x^0 \\ \beta_{xx}^1 \\ m_{xxx}^1 \end{bmatrix} \tag{26}$$

Their (objective) rates are obtained from the constitutive model as described below. We want to continuously update their values, as they are needed for the internal force calculations.

5.3 Constitutive equations

We specialize the matrices in section 4 for the uniaxial stress case. Then we have

$$\sigma_{xx}^{\nabla} = \mathbf{C}_{\sigma}\mathbf{d}^0 \Leftrightarrow \dot{\sigma}_{xx}^0 = Ed_{xx}^0 \tag{27}$$

The higher order constitutive relations are given by

$$\left(\beta^1\right)^{\nabla} = \mathbf{C}_{\beta}^1\left(\mathbf{d}^1 - \mathbf{d}\right) + \mathbf{C}_{\beta m}^1\mathbf{g}^1 \Leftrightarrow \dot{\beta}_{xx}^1 = C_{\beta}^1\left(d_{xx}^1 - d_{xx}^0\right) + C_{\beta m}^1 g_{xxx}^1 \tag{28}$$

and

$$\left(\mathbf{m}^1\right)^{\nabla} = \mathbf{C}_{\beta m}^1\left(\mathbf{d}^1 - \mathbf{d}\right) + \mathbf{C}_{m}^1\mathbf{g}^1 \Leftrightarrow \dot{m}_{xxx}^1 = C_{\beta m}^1\left(d_{xx}^1 - d_{xx}^0\right) + C_{m}^1 g_{xxx}^1 \tag{29}$$

The objective rates are equal to time rates in case of one-dimensional formulation, as we have no rotations. The microdomain properties are calculated based on assuming elastic behavior and a damaged zone without and stiffness. Symmetry of damaged region gives

$$C_{\beta m}^1 = \frac{1}{l^1}\int_{-y_1^-}^{y_1^+} E^1 y^1 dy^1 = \left[\text{as } y_1^+ = y_1^- = y_1\right] = 0 \tag{30}$$

The microstrain elasticity is

$$\mathbf{C}_{\beta}^1 = \frac{1}{l^1}\int_{-y_1^-}^{y_1^+} E^1 dy = E^1\frac{\left(y_1^+ + y_1^-\right)}{l^1} = E^1\frac{2y_1}{l^1} = E^1\left(1-\omega\right) \tag{31}$$

where it has been used that the fraction of damage material, ω ,is

$$\left(1-\omega\right) = \frac{2y_1}{l^1} \tag{32}$$

The microcouple constitutive relation is

$$C_m^1 = \frac{1}{l^1}\int_{-y_1^-}^{y_1^+} E^1\left(y^1\right)^2 dy^1 = \left[y_1^+ = y_1^- = y_1\right] = \frac{E^1\left(l^1\right)^2}{12}\left(2\frac{y_1}{l^1}\right)^3 = \frac{E^1\left(l^1\right)^2}{12}\left(1-\omega\right)^3 \tag{33}$$

The extended constitutive matrix becomes then

$$\Sigma^{\nabla} = \begin{bmatrix} E^0 & 0 & 0 \\ 0 & E^1\left(1-\omega\right) & 0 \\ 0 & 0 & \dfrac{E^1\left(l^1\right)^2}{12}\left(1-\omega\right)^3 \end{bmatrix}\Delta = \mathbf{C}\Delta \tag{34}$$

5.4 Element internal force vector

The internal forces are computed as

$$\mathbf{f}_{\text{int}} = \begin{bmatrix} f_1^0 \\ f_2^0 \\ f_1^1 \\ f_2^1 \end{bmatrix} = \int_{V^e} \mathbf{Q}^T \Sigma \, dV = \int_{x_1}^{x_2} \begin{bmatrix} \frac{\partial N_1^0}{\partial x} & -\frac{\partial N_1^0}{\partial x} & 0 \\ \frac{\partial N_2^0}{\partial x} & -\frac{\partial N_2^0}{\partial x} & 0 \\ 0 & N_1^1 & \frac{\partial N_1^1}{\partial x} \\ 0 & N_2^1 & \frac{\partial N_2^1}{\partial x} \end{bmatrix} \begin{bmatrix} \sigma^0 \\ \beta^1 \\ m^1 \end{bmatrix} a \, dx \tag{35}$$

Where a is the area of the cross-section of the rod. The internal forces can be split it up into macroscopic forces and microscopic forces

$$\mathbf{f}_{\text{int}}^0 = \begin{bmatrix} f_1^0 \\ f_2^0 \end{bmatrix} = \int_{x_1}^{x_2} \begin{bmatrix} \frac{\partial N_1^0}{\partial x}\left(\sigma^0 - \beta^1\right) \\ \frac{\partial N_2^0}{\partial x}\left(\sigma^0 - \beta^1\right) \end{bmatrix} a dx \tag{36}$$

respectively

$$\mathbf{f}_{\text{int}}^1 = \begin{bmatrix} f_1^1 \\ f_2^1 \end{bmatrix} = \int_{x_1}^{x_2} \begin{bmatrix} N_1^1 \beta^1 + \frac{\partial N_1^1}{\partial x} m^1 \\ N_2^1 \beta^1 + \frac{\partial N_2^1}{\partial x} m^1 \end{bmatrix} a dx \tag{37}$$

5.5 Element tangent stiffness matrix

The tangent stiffness matrix is

$$\mathbf{K} = \frac{d\left(\mathbf{F}_{\text{int}} - \mathbf{F}_{\text{ext}}\right)}{d\mathbf{V}} = \frac{d\mathbf{F}_{\text{int}}}{d\mathbf{V}} \tag{38}$$

where $\mathbf{F}_{\text{int}}$ is the global internal force vector and $\mathbf{F}_{\text{ext}}$ is the external forces. $\mathbf{V}$ is the global vector of nodal values corresponding $\mathbf{v}$ in Eq. (20). It is approximated by computing the element contribution as

$$\mathbf{k} = \frac{d\left(\mathbf{f}_{\text{int}}\right)}{d\mathbf{v}} = \frac{d\mathbf{f}_{\text{int}}}{d\mathbf{v}} \approx \int_{V^e} \mathbf{Q}^T \frac{d\Sigma}{d\Delta} \mathbf{Q} dV \tag{39}$$

where

$$\frac{d\Sigma}{d\Delta} = \begin{bmatrix} E^0 & 0 & 0 \\ 0 & E^1\left(1-\omega\right) & 0 \\ 0 & 0 & \frac{E^1\left(l^1\right)^2}{12}\left(1-\omega\right)^3 \end{bmatrix} \tag{40}$$

We use a fixed damage during an increment and update between the increments. This requires small time steps but removes this nonlinearity from the iterative process and simplifies the derivation of the consistent constitutive matrix in Eq. (39). The stiffness matrix can be split into three separate contributions. The macroscopic part is

$$\mathbf{k}^0 = \int_{x_1}^{x_2} E^0 \begin{bmatrix} \left(\frac{\partial N_1^0}{\partial x}\right)^2 & \frac{\partial N_1^0}{\partial x}\frac{\partial N_2^0}{\partial x} & 0 & 0 \\ \frac{\partial N_1^0}{\partial x}\frac{\partial N_2^0}{\partial x} & \left(\frac{\partial N_2^0}{\partial x}\right)^2 & 0 & 0 \\ 0 & 0 & 0 & 0 \\ 0 & 0 & 0 & 0 \end{bmatrix} a\,dx \tag{41}$$

The coupling matrix is

$$\mathbf{k}^{01} = \int_{x_1}^{x_2} E^1(1-\omega) \begin{bmatrix} \left(\frac{\partial N_1^0}{\partial x}\right)^2 & \frac{\partial N_1^0}{\partial x}\frac{\partial N_2^0}{\partial x} & -\frac{\partial N_1^0}{\partial x}N_1^1 & -\frac{\partial N_1^0}{\partial x}N_2^1 \\ \frac{\partial N_1^0}{\partial x}\frac{\partial N_2^0}{\partial x} & \left(\frac{\partial N_2^0}{\partial x}\right)^2 & -\frac{\partial N_2^0}{\partial x}N_1^1 & -\frac{\partial N_2^0}{\partial x}N_2^1 \\ -\frac{\partial N_1^0}{\partial x}N_1^1 & -\frac{\partial N_2^0}{\partial x}N_1^1 & \left(N_1^1\right)^2 & N_1^1 N_2^1 \\ -\frac{\partial N_1^0}{\partial x}N_2^1 & -\frac{\partial N_2^0}{\partial x}N_2^1 & N_1^1 N_2^1 & \left(N_2^1\right)^2 \end{bmatrix} a\,dx \tag{42}$$

The higher order contribution is

$$\mathbf{k}^1 = \int_{x_1}^{x_2} \frac{E^1\left(l^1\right)^2}{12}(1-\omega)^3 \begin{bmatrix} 0 & 0 & 0 & 0 \\ 0 & 0 & 0 & 0 \\ 0 & 0 & \left(\frac{\partial N_1^1}{\partial x}\right)^2 & \frac{\partial N_1^1}{\partial x}\frac{\partial N_2^1}{\partial x} \\ 0 & 0 & \frac{\partial N_1^1}{\partial x}\frac{\partial N_2^1}{\partial x} & \left(\frac{\partial N_2^1}{\partial x}\right)^2 \end{bmatrix} a\,dx \tag{43}$$

6 RESULTS

The formulation in the previous section has been implemented in Matlab™. A rod is subject to tension by prescribing opposite motions of each end. The microstress β_{xx}^1 is set to zero at the ends, ie microstrain is equal to the macroscopic strain there. The used properties are given in Table 1. A simple damage model is used. It is

$$\omega = \left\langle \frac{\varepsilon^0 - \varepsilon_{init}}{\varepsilon_{fracture} - \varepsilon_{init}} \right\rangle \tag{44}$$

The symbol $\langle\ \rangle$ denotes that the expression is zero for negative arguments. The damage is only applied in the center region of the rod, $x \in [-0.005L, 0.005L]$. x is the coordinate of the integration point at the center of the element. The model is set up so that there is always one element centered around x=0.

The macroscopic stress for the problem follows the analytic solution

$$\sigma^0 = E^0 \ln\left(1 + \frac{u}{L}\right) \tag{45}$$

where u is the total elongation of the rod and L=0.1 m is its initial length. The logarithmic strain definition has been used.

The results below are plotted at different instances in time. The strain computed according to Eq. (44) is 0.0, 0.26, 0.47, 0.64, 0.79, 0.91, 1.03, 1.13, 1.31 and 1.39 for each of the lines, respectively. The macroscopic strain and stress are shown in Figure 2. All plots are based on averaged nodal values when they show element data. The number of elements was 101 and the center element is subject to damage. The overall strain and stress follow the analytic solution. The localization in the center element is obvious. The micro-stress and damage can be seen in Figure 3. The damage weakens the microdomain and the micro-stress decreases.

Splitting the element in the centre of the rod into four elements gives

Table 1: Used material properties

E^0	2.10^{11} Pa
E^1	$= E^0$
l^1	$2.\ 10^{-6}$ m
ε_{init}	0.05
$\varepsilon_{fracture}$	0.30

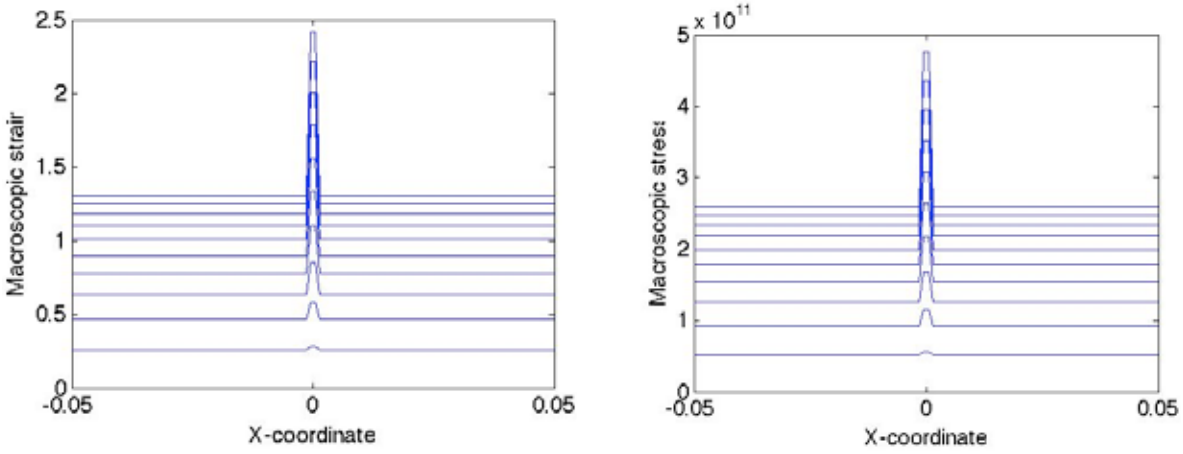

Figure 2: Macroscopic strain and stress during loading.

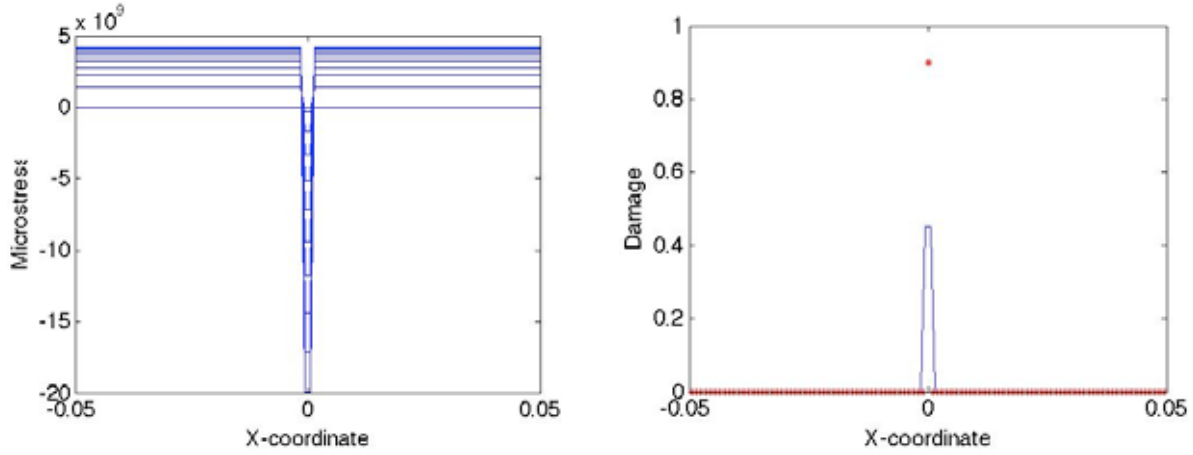

Figure 3: Micro-stress and damage during loading. The crosses in the damage plot denote values at element center. There it can be seen that the damage reaches 0.9.

7 DISCUSSIONS

Hardening and softening behavior of materials depends in a wide range of scales. Despite this, macroscopic models have been successfully used to describe the hardening behavior of materials. However, softening behavior that is determined by the weakest link in the material poses a challenge for these models. Model that brings in a length scale is one step forward in creating convergent finite element models. The MCRT is an approach that does this and also reduces the need for a very fine mesh in the localization zone. However, this is at the additional cost of additional nodal degree of freedoms. Therefore, it is of particular interest to develop constitutive models for the microdomain with a minimum of higher order degrees of freedoms for specific problems. The preliminary evaluated damage model is one example. The convergence behavior of the model need be evaluated as well as the effect on the condition number of the stiffness matrix for different combinations of element sizes and size of microdomain.

ACKNOWLEDGMENTS

The L-E Lindgren would like to acknowledge the financial support from the Steel Research Programme of the Swedish Steel Producers Association (Jernkontoret) financed by the Swedish Agency for Innovative Systems (VINNOVA) and Sandvik Materials Technology (SMT) together with Swedish Steel (SSAB). H Qin has been financially supported by the Centre of High-performance Steel (CHS). WK Liu and S Tang are supported by NSF CMMI Grant 0823327 and the ARO.

REFERENCES

[1] Eringen, A., *Microcontinuum field theories. I: Foundations and solids.*, Springer Verlag, (1997).
[2] Kadowaki, H. and Liu, W., A multiscale approach for the mircopolar continuum model, *Computer Methods in Engineering & Sciences* (2005) **7**:269-282.
[3] Vernerey, F., Liu, W. K. and Moran, B., Multi-scale micromorphic theory for hierarchical

materials, *Journal of the Mechanics and Physics of Solids* (2007) **55**:2603-2651.
[4] Skatulla, S., Arockiarajan, A. and Sansour, C., A nonlinear generalized continuum approach for electro-elasticity including scale effects, *Journal of the Mechanics and Physics of Solids* (2009) **57**:137-160.
[5] Lazar, M. and Maugin, G. A., On microcontinuum field theories: The eshelby stress tensor and incompatibility conditions, *Philosophical Magazine* (2007) **87**:3853 - 3870.
[6] Forest, S., Micromorphic approach for gradient elasticity, viscoplasticity, and damage, *Journal of Engineering Mechanics* (2009) **135**:117-131.
[7] Lakes, R., Experimental methods for study of cosserat solids and other generalized elastic continua, *Continuum models for materials with micro-structure*, H. Mulhaus (Editor), J. Wiley, (1995).
[8] Germain, P., The method of virtual power in continuum mechanics. Part 2: Microstructure, *SIAM Journal on Applied Mathematics* (1973) **25**:556-575.
[9] Liu, W. and McVeigh, C., Predictive multiscale theory for design of heteregeneous materials, *Computational Mechanics* (2008) **42**:147-170.
[10] Vernerey, F. J., Liu, W. K., Moran, B. and Olson, G., A micromorphic model for the multiple scale failure of heterogeneous materials, *Journal of the Mechanics and Physics of Solids* (2008) **56**:1320-1347.
[11] McVeigh, C. and Liu, W. K., Multiresolution modeling of ductile reinforced brittle composites, *Journal of the Mechanics and Physics of Solids* (2009) **57**:244-267.
[12] Kadowaki, H. and Liu, W., A multiscale approach for the micropolar continuum model, *Computer. Modeling in Engineering & Sciences* (2005) **7**:269-282.

XI International Conference on Computational Plasticity. Fundamentals and Applications
COMPLAS XI
E. Oñate, D.R.J. Owen, D. Peric and B. Suárez (Eds)

A DYNAMIC RECRYSTALLIZATION SIMULATION BASED ON PHASE-FIELD AND DISLOCATION-CRYSTAL PLASTICITY MODELS

MAYU MURAMATSU[*], SHINICHI SATO[**], YOSHITERU AOYAGI[***] AND KAZUYUKI SHIZAWA[****]

[*] Department of Mechanical Engineering
Keio University
3-14-1 Hiyoshi Kohoku-ku, Yokohama 223-8522, Japan
Email: muramatsu@mech.keio.ac.jp

[**] Graduate School of Science and Technology
Keio University
3-14-1 Hiyoshi Kohoku-ku, Yokohama 223-8522, Japan

[***] Nuclear Science and Engineering Directorate
Japan Atomic Energy Agency
2-4 Shirane Shirakata, Tokai-mura, Naka-gun 319-1195, Japan
Email: aoyagi.yoshiteru@jaea.go.jp

[****] Department of Mechanical Engineering
Keio University
3-14-1 Hiyoshi Kohoku-ku, Yokohama 223-8522, Japan
Email: shizawa@mech.keio.ac.jp

Key words: Dynamic Recrystallization, Phase-field Model, Dislocation-crystal Plasticity Model, Multiphysics Simulation.

Abstract. In this paper, so as to reproduce the dynamic recrystallization, the dislocation-crystal plasticity model devotes to a deformation analysis and multi-phase-field one to nucleus growth calculation. First, we place a few nuclei on the parent grain boundaries, i.e., high dislocation density site. Next, carrying out the simulation, dislocations start to accumulate in accordance with the deformation. Introducing the energy of dislocations stored locally in the matrix into the phase-field equation, the placed nuclei begin growing. In the region where the phase transitions from the matrix to the recrystallized phase, the values of dislocation density, crystal orientation and slip are reset. Moreover, applying the above information to the hardening modulus and crystal bases of the crystal plasticity model, the deformation is calculated again. With the progress of deformation, the dislocation density increases even inside the growing nuclei. Also, on the basis of the results obtained by the multiphysics simulation, we discuss the microstructure formations dependent on applied deformation.

1 INTRODUCTION

The mechanical properties of metals are significantly affected by microstructures formed during recrystallization in rolling processes. Especially, the nucleus growth that occurs during the warm- or hot-rolling is known as the dynamic recrystallization (See fig. 1). First, applying plastic deformation to materials, cell structure is formed and then, subgrains are formed by pair annihilation and rearrangement of dislocations in the dynamic recovery stage. Next, in the nucleation stage, subgrain groups on the boundaries between parent grains coalesce to nuclei due to grain boundary migration. This mechanism is called bulging. During this process, stress-strain curve describes the hardening because of dislocation accumulation due to plastic deformation shown in fig. 2. However, once nucleus growth starts and recrystallized phase expands, decrease of dislocation density causes softening of materials. If a further deformation is given to the materials, the stress-strain curve sifts to the rehardening due to dislocation accumulation in the recrystallized new phase. With this mechanism, stress-strain curve during dynamic recrystallization is known to have multi-peaks. For control of mechanical properties in materials design, it is industrially important to predict numerically the dynamic recrystallization.

In the previous work [1], the authors developed a simple multiphysics model of the dynamic recrystallization by coupling the KWC type phase-field model and dislocation-crystal plasticity one that can express the dislocation accumulation by calculating GN crystal defects (GN dislocation density and GN incompatibility). Also, we conducted a computation for a single nucleus on the basis of this model. However, it cannot predict the growth of a number of nuclei because the KWC type phase-field model hardly deals with different nuclei. In addition, there still exists a problem about how to update the crystal orientation of the region that change into recrystallized phase from matrix since the initial orientation was given to such area in the previous simulation.

So as to work out the above problems, in this study, we adopt a multi-phase-field model to extend the material model to an enhanced type suitable for a lot of nuclei. Therein, a modification is conducted for the free energy of bulk to be a double well type considering the stored dislocation energy as a driving force of recrystallization. Next, we develop a multiphysics model combining the multi-phase-field model and dislocation-crystal plasticity one through the crystal orientation and the dislocation density. Using the present model, a

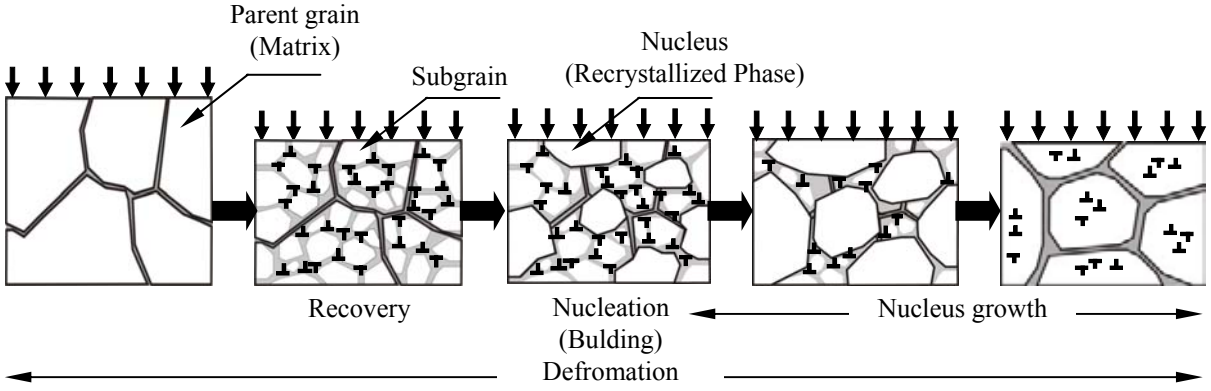

Figure 1 Illustration of dynamic recrystallization

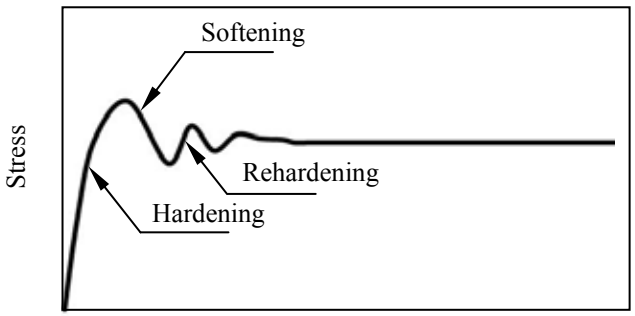

Figure 2 Illustration of stress-strain curve during dynamic recrystallization

numerical simulation is carried out assuming a FCC polycrystal with a few nuclei on the parent boundaries subject to a compressive load in hot-rolling. In this calculation, the current orientation considering deformation is given to the region where the phase changes into recrystallized phase from matrix.

2 MATERIAL MODELS

2.1 Phase-field model

In order to express the growth of a number of nuclei, the multi-phase-field model is adopted in this study. By use of the model, it is possible to calculate growth of a lot of grains simultaneously. Setting the order parameter for grain α as $\phi^\alpha (0 \le \phi^\alpha \le 1)$, and considering the interface field [2] defined as $\psi^{\alpha\beta} \equiv \phi^\alpha - \phi^\beta$ and sum of ϕ^α all over the phases, such as $\sum_\alpha \phi^\alpha = 1$, the evolution equation of ϕ^α is obtained as

$$\frac{\partial \phi^\alpha}{\partial t} = -\sum_{\beta=1}^{N} \frac{M_\phi^{\alpha\beta}}{N} \sum_{\gamma=1(\gamma\neq\alpha)}^{N} \{\frac{1}{2}(\alpha^{\alpha\gamma^2} - \alpha^{\beta\gamma^2})\nabla^2\phi^\gamma + \frac{\partial f(\phi^\alpha,\phi^\gamma)}{\partial \phi^\alpha} - \frac{\partial f(\phi^\beta,\phi^\gamma)}{\partial \phi^\beta}\} \tag{1}$$

where N is the total number of the grains, $M_\phi^{\alpha\beta}$ the mobility of the interface between grains α and β and $\alpha^{\alpha\beta}$ the diffusion constant of the interface between grains α and β. For the free energy of bulk $f(\phi^\alpha,\phi^\beta)$, the function is employed such that

$$f(\phi^\alpha,\phi^\beta) = p(\phi^\alpha,\phi^\beta) f_r(\rho) + \{1 - p(\phi^\alpha,\phi^\beta)\} f_m(\rho) + W^{\alpha\beta} q(\phi^\alpha,\phi^\beta) \tag{2}$$

where $W^{\alpha\beta}$ is the energy barrier between grains α and β. In addition, $f_r(\rho)$ and $f_m(\rho)$ are stored dislocation energies in recrystallized grain and matrix, respectively. Because of $f_r(\rho) \ll f_m(\rho)$, Eq. (2) can rewritten in the form

$$f(\phi^\alpha,\phi^\beta) = \{1 - p(\phi^\alpha,\phi^\beta)\} f(\rho) + W^{\alpha\beta} q(\phi^\alpha,\phi^\beta) \tag{3}$$

where $f(\rho)$ is the difference between stored dislocation energies in recrystallized phase and matrix defined as $f(\rho) \equiv f_m(\rho) - f_r(\rho)$. Using the local stored energy of dislocations $E_s^{\alpha\beta}$, $f(\rho)$ can be represented as $f(\rho) = E_s^{\alpha\beta} = E_s^\alpha - E_s^\beta$. For simplify, we set $E_s^{\alpha\beta} = E_s$ when the phase α is the recrystallized grain and β the matrix, and $E_s^{\alpha\beta} = -E_s$ when the phase α is the matrix and β the recrystallized phase, where E_s is the local energy of stored dislocation

calculated by

$$E_s = \sum_{\alpha} E_s^{\alpha} = \sum_{\alpha^*} \frac{1}{2} \mu \rho^{(\alpha^*)} \tilde{b}^2 \tag{4}$$

where $\rho^{(\alpha^*)}$ is the dislocation density for the slip system α^* (explained later.), μ the shear modulus and $\tilde{b}$ the magnitude of burgers vector. First, we consider a bi-phase problem to obtain $p(\phi)$ and $q(\phi)$. The conditions that $f(\phi)$ is the double well function with the driving force of $E_s^{\alpha\beta}$ are $f(0) = E_s^{\alpha\beta}$, $f(1) = 0$, $f'(0) = 0$ and $f'(1) = 0$. On the above conditions, $q(\phi)$ is determined as $q(\phi) = \phi^2 (1-\phi)^2$. While, we choose $p(\phi)$ as $p(\phi) = \{(2\phi e^{\phi} e^{1-\phi} / e) - (2e^{\phi} e^{1-\phi} / e) + 3\}(1-\phi)^2$. Moreover, replacing ϕ and $1-\phi$ with ϕ^{α} and ϕ^{β} respectively to extend these functions to suitable forms for a multi phases problem, $p(\phi^{\alpha}, \phi^{\beta})$ and $q(\phi^{\alpha}, \phi^{\beta})$ are obtained as follows.

$$\{1 - p(\phi^{\alpha}, \phi^{\beta})\} = (\frac{2}{e} \phi^{\alpha} e^{\phi^{\alpha}} e^{\phi^{\beta}} - \frac{2}{e} e^{\phi^{\alpha}} e^{\phi^{\beta}} + 3) \phi^{\beta 2} \tag{5}$$

$$q(\phi^{\alpha}, \phi^{\beta}) = \phi^{\alpha 2} \phi^{\beta 2} \tag{6}$$

2.2 Dislocation-crystal plasticity model

The elastic-viscoplastic constitutive equation of crystal plasticity model is given by

$$\overset{\nabla}{\boldsymbol{T}} = \boldsymbol{C}^e : (\boldsymbol{D} - \sum_{\alpha^*} \boldsymbol{P}_s^{(\alpha^*)} \dot{\gamma}^{(\alpha^*)}) \tag{7}$$

where $\overset{\nabla}{\boldsymbol{T}}$, $\boldsymbol{C}^e$, $\boldsymbol{D}$, $\boldsymbol{P}_s^{(\alpha^*)}$ and $\gamma^{(\alpha^*)}$ denotes the Mandel-Kratochvil rate of Cauchy stress, the anisotropic elastic modulus tensor, deformation rate tensor, Schmid tensor and the slip for slip system α^*, respectively. The evolution equation of flow stress $g^{(\alpha^*)}$ and the hardening modulus $h^{(\alpha^*\beta^*)}$ dependent on dislocation density are written in the forms

$$\dot{g}^{(\alpha^*)} = \sum_{\beta^*} h^{(\alpha^*\beta^*)} \| \dot{\gamma}^{(\beta^*)} \| \tag{8}$$

$$h^{(\alpha^*\beta^*)} = \frac{1}{2} \frac{ac\mu \Omega^{(\alpha^*\beta^*)}}{L^{(\beta^*)} \sqrt{\rho^{(\beta^*)}}} \dot{\gamma}^{(\beta^*)} \tag{9}$$

where $\Omega^{(\alpha^*\beta^*)}$ is the interaction matrix, $L^{(\beta^*)}$ the dislocation mean free path, and a and c the numerical parameters. A model depending on dislocation density is adopted for $L^{(\beta^*)}$. The dislocation density $\rho^{(\alpha^*)}$ is defined by $\rho^{(\alpha^*)} = \rho_0^{(\alpha^*)} + \rho_G^{(\alpha^*)} + \rho_{\eta}^{(\alpha^*)} + \rho_R^{(\alpha^*)}$, where $\rho_0^{(\alpha^*)}$ is the initial dislocation density, $\rho_G^{(\alpha^*)}$ and $\rho_{\eta}^{(\alpha^*)}$ the norms of GN dislocation density tensor and GN incompatibility tensor, respectively and $\rho_R^{(\alpha^*)}$ the density of annihilated dislocations [3].

3 SIMULATION METHOD

In the multiphysics simulation, crystal deformation and nucleus growth are taken into account simultaneously. First, the dislocation-crystal plasticity simulation is conducted for

prediction of formation of subdivisions and micro shear bands induced by plastic compression. On the basis of the information of nucleation obtained by the above calculation, it is reproduced that the nuclei generated at a nucleation site start to grow by the driving force, i.e., the stored dislocation energy, through the phase-field simulation. The evolution of order parameter due to nucleus growth can be obtained. During this process, in the area where the phase transition from matrix to new phase, the dislocation density should be initialized so as to be the value of sufficiently annealed metal. The information of nucleus growth such as the dislocation density is introduced into the dislocation-crystal plasticity simulation again. The dislocation density and the crystal orientation are changed by deformation. Giving the updated information back to Eq. (1), the nucleus growth simulation can be carried out. The information of dislocation density is introduced into Eq. (1) through the stored dislocation energy expressed by Eq. (4). Same operations are repeated, and dynamic recrystallization simulation is conducted.

4 SIMULATION RESULTS AND DISCUSSIONS

In this simulation, 10% compressive deformation is applied to 80μm×80μm polycrystal aluminum plate under plane strain condition. Considering hot worming process, 2 nuclei are placed on the parent grain boundaries in the initial condition (See figs. 3). The Asaro's 2-slip model is employed and the values of the initial dislocation densities in the matrix and the nuclei are $\rho_0 = 1\mu\,\mathrm{m}^{-2}$ and $\rho_0 = 0.001\mu\,\mathrm{m}^{-2}$, respectively (See fig. 4). In this study, the dislocation-crystal plasticity simulation is carried out by FEM and multi-phase-field model by FDM so that the developed dynamic recrystallization model is calculated by the FEM-FDM hybrid analysis. The number of the finite elements is 2682 and the number of the finite difference grid 40401. In this paper, following 2 cases of simulations are performed: (a) the case that the recrystallization area has the initial crystal orientation and (b) the case that the recrystallization area has the current crystal orientation, i.e., the crystal orientation averaged among the values of neighbor elements.

Figure 5 depicts stress-strain curve obtained by this simulation. In the both cases of simulations, stress-strain curves with oscillations are observed, in which the hardening and softening occur by deformation and by grain growth, respectively. In fig. 5, the arrow of (a) shows the result of the simulation in the case that the recrystallization area has the initial

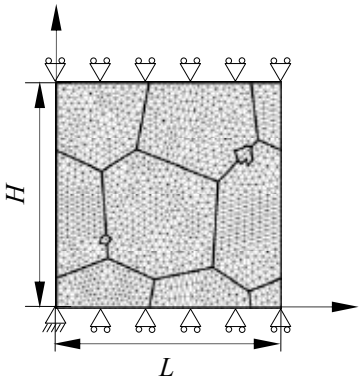

Figure 3 Analysis model

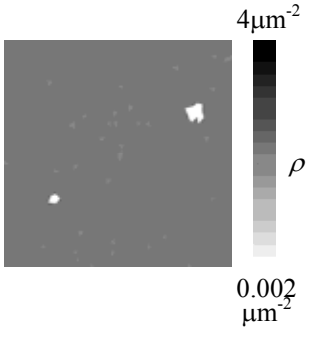

Figure 4 Initial distribution of dislocation density

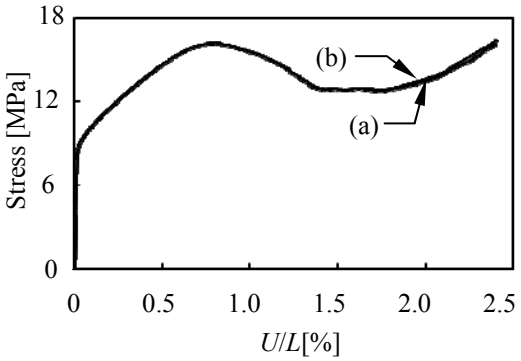

Figure 5 Nominal stress-strain curve

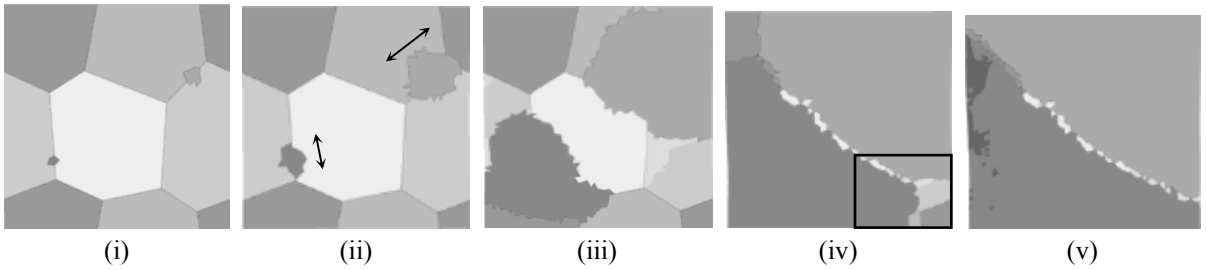

(a) Case that t the recrystallized area has initial crystal orientation

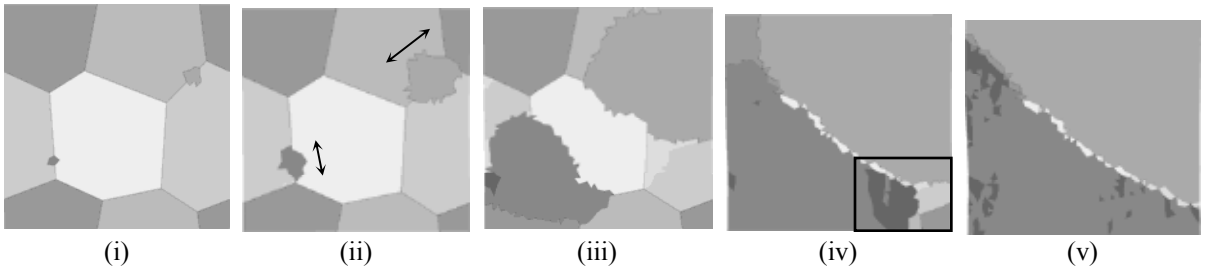

(b) Case that the recrystallized area has current crystal orientation

Figure 6 Distributions of crystal orientation
(U/L[%]: (i) 0.0, (ii) 0.6, (iii) 1.3, (iv) 2.1, (v) 4.2)

crystal orientation while (b) the result of the simulation in the case that the recrystallization area has the current crystal orientation. It can be seen that the case (b) describe slightly higher rate of hardening than the case (a). The above difference might be explained that the simulation (b) shows higher rehardening rate than (a) because the deformation is taken into account in the simulation (b) more than (a). Also, fig. 6 describes the temporal distributions of crystal orientation. In the both results from the simulations (a) and (b), the nuclei grow along the parent grain boundaries where the dislocations store significantly, shown as the arrows in figs. 6 (a) (ii) and (b) (ii). Furthermore, figs. 7 are the enlarged figures of the rectangulars in figs. 6 (a) (iv) and (b) (iv). Figures 7 (i) and (ii) denote the distributions of dislocation density and crystal orientation, respectively. From figs. 7 (a) (i) and (b) (i), it is noted that the distributions of dislocation density are similar to each other. On the other hand, from the

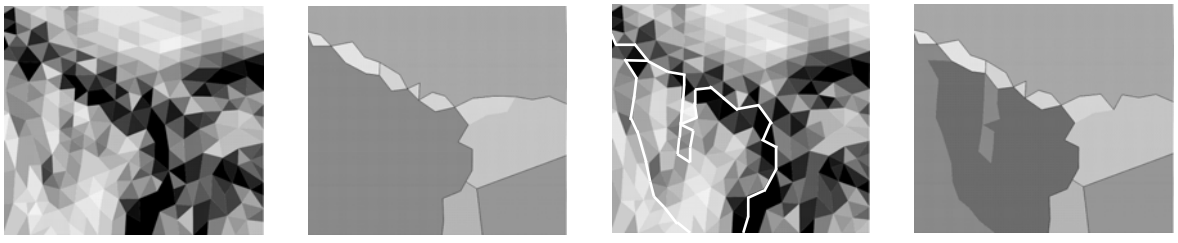

(a) Case that the recrystallized area has initial crystal orientation

(b) Case that the recrystallized area has current crystal orientation

Figure 7 Distributions of (i) dislocation density and (ii) crystal orientation at U/L=2.1%

distributions of crystal orientation in figs. 7 (a) (ii) and (b) (ii), the growing nucleus at the lower left is not affected by deformation while the one in fig. 7 (b) is affected by deformation. Here, the white lines in fig. 7 (b) (i) mean nucleus-matrix boundaries and the boundaries between the recrystallized area whose crystal orientation does not change from its initial crystal orientation and the one whose crystal orientation does change from its initial crystal orientation. The area surrounded by white lines would be a nucleation site if the grain boundary misorientation were higher than 15˚.

5 CONCLUSIONS

- Simulating dynamic recrystallization by coupling the multi-phase-field model and the dislocation-crystal plasticity model, it can be reproduced that a few nuclei grow responding to the distribution of dislocation density and crystal orientation.
- Givining the averaged value of neighbor elements to the region that transitions to recrystallized phase from matrix, it can be possible to calculate considering the change of crystal orientation due to deformation.

ACKNOWLEDGEMENTS

This study is supported in part by Grant-in-Aid for Scientific Research from Japan Society for the Promotion of Science.

REFERENCES

[1] Muramatsu, M., Aoyagi, Y. and Shizawa, K., “Multiscale Modeling and Simulation on Dynamic Recrystallization Based on Phase-Field Method and Dislocaiotn-Crystal Plasticity Theory”, *The 16th International Symposium on Plasticity and Its Current Applications*, (2010): 10-12.

[2] Steinbach, I. and Pezzolla, F., “A Generalized Field Method for Multiphase Transformations Using Interface Fields”, *Physica D*, (1999) **139**: 385-393.

[3] Aoyagi, Y. and Shizawa, K., “Multiscale Crystal Plasticity Modeling Based on Geometrically Necessary Crystal Defects and Simulation on Fine-Graining for Polycrystal”, *Int. J. Plasticity*, (2007) **23**: 1022-1040.

XI International Conference on Computational Plasticity. Fundamentals and Applications
COMPLAS XI
E. Oñate, D.R.J. Owen, D. Peric and B. Suárez (Eds)

A NEW CRYSTAL PLASTICITY CONSTITUTIVE EQUATION BASED ON CRYSTALLOGRAPHIC MISORIENTATION THEORY

HIROYUKI KURAMAE[*], YASUNORI NAKAMURA[†], HIDETOSHI SAKAMOTO[$]
HIDEO MORIMOTO[‡] AND EIJI NAKAMACHI[§]

[*] Department of Technology Management, Faculty of Engineering,
Osaka Institute of Technology,
5-16-1 Omiya, Asahi-ku, Osaka, 535-8585, Japan
e-mail: kuramae@dim.oit.ac.jp, www.oit.ac.jp

[†] Department of Mechanical Engineering, Faculty of Engineering,
Osaka Sangyo University,
3-1-1 Nakagaito, Daito, Osaka, 574-8530, Japan
Email: nkmr@mech.osaka-sandai.ac.jp, www.osaka-sandai.ac.jp

[$] Department of Mechanical System Engineering, Faculty of Engineering,
Kumamoto University,
2-39-1 Kurokami, Kumamoto, 860-8555, Japan
Email: sakamoto@mech.kumamoto-u.ac.jp, www.kumamoto-u.ac.jp

[‡] Yokohama R&D Laboratories,
Furukawa Electric Co. Ltd.,
2-4-3 Okano, Nishi-ku, Yokohama, 220-0073, Japan
Email: morimo@yokoken.furukawa.co.jp, www.furukawa.co.jp/

[§] Department of Biomedical Engineering, Faculty of Life and Medical Sciences,
Doshisha University,
1-3 Tatara-Miyakodani, Kyotanabe, Kyoto, 610-0394, Japan
Email: enakamac@mail.doshisha.ac.jp, www.doshisha.ac.jp

Key words: Constitutive Equation, Crystal Plasticity, Multi-scale Analysis, Misorientation Theory.

Abstract. Since plastic deformation of polycrystal sheet metal is greatly affected by its initial and plastic deformed textures, multi-scale finite element (FE) analysis based on homogenization with considering micro-polycrystal morphology is required [1]. We formulated a new crystal plasticity constitutive equation to introduce not only the effect of crystal orientation distribution, but also the size of crystal grain and/or the effect of crystal grain boundary for the micro-FE analysis. The hardening evolution equation based on strain gradient theory [2], [3] was modified to introduce curvature of crystal orientation based on crystallographic misorientation theory. We employed two-scale structure, such as a microscopic polycrystal structure and a macroscopic elastic/plastic continuum. Our analysis

code predicts the plastic deformation of polycrystal metal in the macro-scale, and simultaneously the crystal texture and misorientation evolutions in the micro-scale. In this study, we try to reveal the relationship between the plastic deformation and the microscopic crystal misorientation evolution by using the homogenized FE procedure with the proposed crystal plasticity constitutive equation. The crystallographic misorientation evolution, which affects on the plastic deformation of FCC polycrystal metal, was investigated by using the multi-scale FE analysis. We confirmed the availability of our analysis code employing the new constitutive equation through the comparison of a uniaxial tensile problem with the numerical result and the experimental one.

1 INTRODUCTION

Recently, multi-scale finite element (FE) analyses code are developed to evaluate macroscopic material properties such as the strength, the yield loci and the formability, by employing a realistic three-dimensional (3D) microscopic polycrystal structure obtained by using the scanning electron microscopy and the electron backscattering diffraction (SEM-EBSD) measurements [4]. The experimental determination, interpretation, and the numerical simulation for polycrystal texture analyses at the micro-scale have been attracting the attention of researchers in the field of sheet metal forming [5-6]. Further, the progress of computer technology, such as parallel computing [7], promises an unprecedented means for a large-scale numerical calculation in this multi-scale analysis for the industrial applications. For the crystal plasticity constitutive equation, the isotropic and kinematical hardening evolutions are introduced [8]. In our two-scale homogenization theory to assess the sheet material formability, a realistic 3D representative volume element (RVE) is employed, which is determined by SEM-EBSD measurement.

Until now, we have found many “virtual” RVE models, such as Voronoi polyhedron grain models, but they do not have the necessary crystal grain characteristic of location, size or orientation in 3D space. Since the deformation and hardening are very much affected by the neighboring crystal grains, orientation and the grain size themselves.

In this study, a new hardening evolution equation is proposed for assessment of crystal orientation rotation and misorientation evolution. Our model is considered misorientation between adjacent regions across a boundary. This involves a model, which assumes a simple geometrical relationship between crystal slip systems responsible for the rotation and misorientation.

2 ELAST/VISCO-CRYSTAL PLASTICITY CONSTITUTIVE EQUATION BASED ON MISORIENTATION THEORY

2.1 Definition of equivalent misorientation

We calculated curvature of crystallographic misorientation to express geometrically necessary (GN) dislocation storage [9]. When the GN dislocation is stored during plastic deformation, sheet metal shows work hardening. Thus, consideration of misorientation into hardening evolution equation is able to analyze sheet metal forming and to assess the deformation characterization accurately.

We defined the three normal orthogonal coordinate systems for calculation of

crystallographic misorientation as shown in Fig. 1. One is the sample coordinate system ($\boldsymbol{e}_i$ - x_i). The second is the crystalline coordinate system ($\boldsymbol{i}_i$ - y_i), and third is (111) plane coordinate system ($\boldsymbol{j}_i$ - θ_i). Relationship between the sample coordinate system and the crystalline coordinate system, the representative (111) plane coordinate system are expressed as $\boldsymbol{i}_i = \Theta_i^j \boldsymbol{e}_j$, $\boldsymbol{j}_i = \Omega_i^j \boldsymbol{e}_j$, where Θ_i^j, Ω_i^j are coordinate transformation matrices.

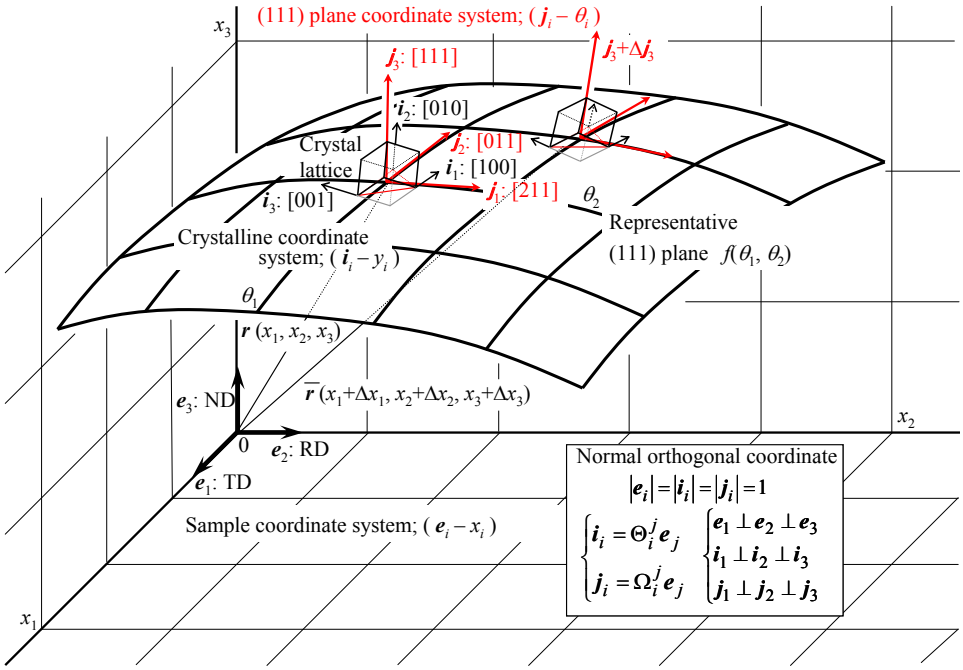

Figure 1: Definition of the three normal orthogonal coordinate systems

In the Fig. 2, $\boldsymbol{j}_1$, $\boldsymbol{j}_2$ and $\boldsymbol{j}_3$ express $[2\bar{1}\bar{1}]$, $[01\bar{1}]$ and $[111]$ vectors on the (111) plane coordinate system ($\boldsymbol{j}_i$ - θ_i), which belongs with the crystalline coordinate system ($\boldsymbol{i}_i$ - y_i). Rate of [111] direction $\Delta\boldsymbol{j}_3$ is defined by using $\boldsymbol{j}_i$ as follow:

$$\Delta\boldsymbol{j}_3 = -b_{\alpha\beta}\boldsymbol{j}_\alpha \Delta\theta_\beta \tag{1}$$

where $b_{\alpha\beta}$ (α, β = 1, 2) is the second fundamental metric tensor, which corresponds to a curvature tensor of crystal orientation, and is expressed as follows:

$$b_{\alpha\beta} = -\frac{\partial \boldsymbol{j}_3}{\partial \theta_\beta} \cdot \boldsymbol{j}_\alpha \tag{2}$$

$$\boldsymbol{b} = b_{\alpha\beta}\boldsymbol{j}_\alpha \otimes \boldsymbol{j}_\beta \tag{3}$$

The curvature tensor $b_{\alpha\beta}$ corresponds to rate of normal direction of tangential plane, and is transformed by the coordinate transformation matrices $\Omega_k^\alpha, \Omega_l^\beta$ to the sample coordinate system as follows:

$$\boldsymbol{b} = b_{\alpha\beta}\Omega_k^\alpha \Omega_l^\beta \boldsymbol{e}_k \otimes \boldsymbol{e}_l = \bar{b}_{kl}\boldsymbol{e}_k \otimes \boldsymbol{e}_l \tag{4}$$

$$\bar{b}_{kl} = -\boldsymbol{j}_{3,l} \cdot \boldsymbol{j}_k \tag{5}$$

where $\bar{b}_{kl}$ is misorientation tensor. Equivalent misorientation K is defined by the second invariant value of $b_{\alpha\beta}$ as follow:

$$K = \sqrt{\frac{1}{2}\bar{b}_{kl}\bar{b}_{kl}} \tag{6}$$

This scalar value K depends on crystal orientation distribution and grain size.

2.2 Introducing equivalent misorientation into crystal plasticity constitutive equation

In this study, the equivalent misorientation caused by crystal orientation distribution is introduced into the crystallographic homogenized multi-scale FE procedure, which is based on the dynamic explicit scheme [1]. The strain rate dependent crystal plasticity constitutive equation [2, 8] is employed to the micro-FE analysis. The crystalline viscoplastic shear strain rate $\dot{\gamma}^{(a)}$ of the power law form defined on the slip system (a) is expressed as follow:

$$\dot{\gamma}^{(a)} = \dot{\gamma}_0^{(a)} \left[\frac{\tau^{(a)}}{g^{(a)}} \right] \left[\left| \frac{\tau^{(a)}}{g^{(a)}} \right| \right]^{\frac{1-m}{m}} \tag{7}$$

where $\tau^{(a)}$ is the resolved shear stress, $g^{(a)}$ is the reference shear stress, $\dot{\gamma}_0^{(a)}$ is the reference shear strain rate, and m is the coefficient of strain rate sensitivity. In this study, $\dot{\gamma}_0^{(a)} = 0.033$ and $m = 0.01$ are employed for FCC metal, respectively.

The equivalent misorientation K is introduced into the hardening evolution equation as follow:

$$\dot{g}^{(a)} = \left\{ \frac{1}{\tanh C_2} \tanh\left(C_1 |K| + C_2\right) \right\} \sum_{b=1}^{N} h_{ab} \left| \dot{\gamma}^{(b)} \right| \tag{8}$$

where N is the total number of slip systems for the FCC crystal $N = 12$, C_1 and C_2 are constants of hardening parameters. The hardening coefficient h_{ab} for the nth power equation is expressed as follows:

$$h_{ab} = q_{ab} h(\gamma) + (1 - q_{ab}) h(\gamma) \delta_{ab} \tag{9}$$

$$h(\gamma) = h_0 n C \{ C(\gamma_0 + \gamma) \}^{n-1} \tag{10}$$

where the matrix q_{ab} is introduced to describe the self and latent hardenings. The γ is the accumulated shear strain over all the slip systems, h_0 is the initial hardening modulus, and n and C are the hardening exponent and the hardening coefficient, respectively. These values including C_1 and C_2 in Eq. (8) are determined by the parameter identification calculation through the comparison with the experimental results.

When $K = 0$, which is uniform crystal orientation distribution condition, the hardening evolution equation (8) becomes the conventional equation as follow:

$$\dot{g}^{(a)} = \sum_{b=1}^{N} h_{ab} \left| \dot{\gamma}^{(b)} \right| \tag{11}$$

3 NUMERICAL RESULTS

3.1 Material parameter identification by using 3D-EBSD measured polycrystal model

We obtained distribution of crystal orientation in a 3D parallelepiped box region of the aluminum alloy sheet metal A5182-O by SEM-EBSD measurement, which is a material of the NUMISHEET 2008 benchmark problem [10], and developed a RVE-FE model as shown in Fig. 2. The RVE-FE model is 5×5×5 voxel FEs by using 8-node solid element with 1000 Gaussian integration points. The crystal orientation distribution of the sheet metal measured by SEM-EBSD is assigned into the integration points on the RVE-FE model.

Figure 3 shows comparison of stress-strain curves obtained by the experiment of the rolling direction (RD) tensile test and its multi-scale FE analyses by using identified parameters as summarized in Table 1. In the multi-scale FE analyses, proportional loading is applied to macro-FE model, which consists of one 8-node solid element, combined with the micro RVE-FE model to obtain the homogenized stress. It is good agreement of stress-strain relationships between the experiment and FE analyses. In the multi-scale FE result by misorientation theory, the critical (initial) resolved shear stress (CRSS) τ_0 and the initial hardening modulus h_0 are smaller than conventional ones due to effect the misorientation hardening parameters C_1 and C_2.

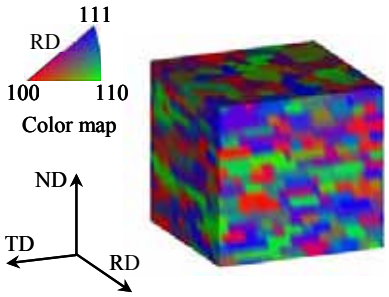

Figure 2: RVE-FE model of A5182-O (111×111×111μm^3)

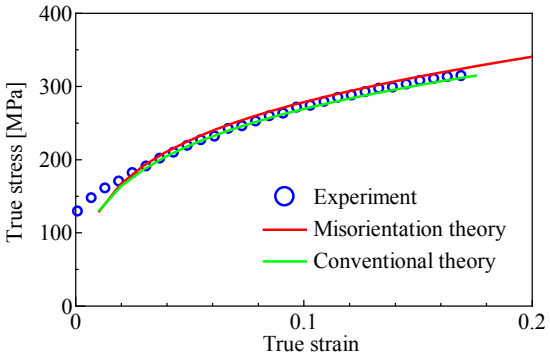

Figure 3: Relationships between true stress and true strain of experimental and identification results

Table 1: Material parameters obtained by multi-scale FE analysis

	n	τ_0 [MPa]	h_0 [MPa]	C	γ_0 [MPa]	C_1	C_2
Misorientation	0.19	13.0	49.0	17.0	0.10	5.0	0.8
Conventional	0.19	15.0	72.0	17.0	0.10	–	–

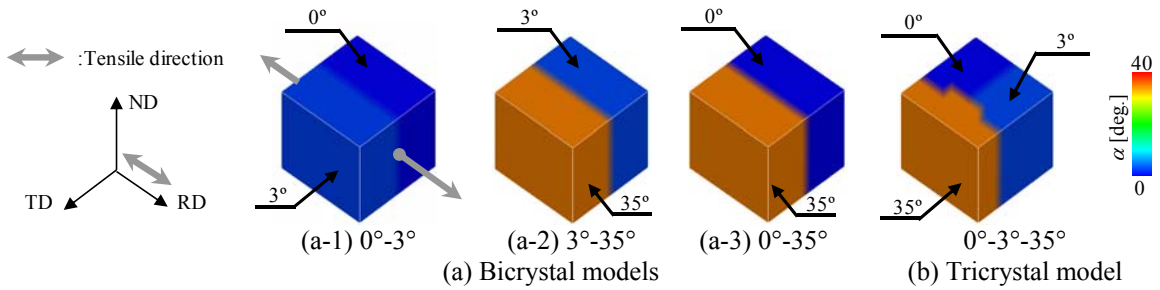

Figure 4: Initial crystal orientation angle α distributions of micro-models

Table 2: Euler angle (φ_1, Φ, φ_2) and crystal orientation angle α

	φ_1	Φ	φ_2	α
Grain 1	–12.3°	54.5°	44.7°	0.3°
Grain 2	12.5°	57.7°	43.3°	3.2°
Grain 3	89.6°	69.0°	8.84°	34.7°

3.2 Multi-scale analysis by using bicrystal and tricrystal micro-models

In order to consider the newly developed constitutive equation based on misorientation theory, simple initial crystal models, such as bicrystal and tricrystal models are employed to the micro-FE analysis, as shown in Fig. 4. Three crystal orientations are selected from the SEM-EBSD crystal orientation distribution of A5182-O sheet metal as summarized in Table 2. Micro-FE model is $111\times111\times111\mu m^3$ volume with $5\times5\times5$ FEs, which is same as the polycrystal A5182-O RVE-FE model. A crystal orientation angle α is defined as angle between crystal [111] direction and normal direction (ND) of sheet metal. Consequently, a low tilt angle boundary model as shown in Fig. 4 (a-1) and high tilt angle boundary models as shown in Fig. 4 (a-2) and (a-3) are constructed in the bicrystal models, respectively. In addition, tricrystal model as shown in Fig. 4 (b) is also constructed. It has mixed with low and high tilt angle boundaries. Figure 5 shows initial equivalent misorientation distribution on the center cross-section surface of the ND direction (ND = 55.5μm) of micro-models. The tilt angle is clearly described by the equivalent misorientation distribution.

Figure 6 shows comparison of stress-strain curves obtained by the multi-scale FE analyses of the RD tensile problem by using three types of bicrystal models and the tricrystal model. The material parameters of A5182-O polycrystal sheet metal are used for these models. In the tilt angle 0°-3° bicrystal model, the highest stress is achieved because the model has larger amount of active slip systems by smaller α value than the others, which means the crystal

(111) plane coincides with sheet plane. The 35° single crystal model is the lowest stress. The high tilt 0°-35° and 3°-35° bicrystal models, and the 0°-3°-35° tricrystal model are combination behavior between the low tilt model and the 35° single crystal model.

Figure 7 shows texture evolution on {111} pole figures compared with the initial texture and after 0.5 tensile deformation. The textures are evoluted to toward preferred orientation of tensile deformation such as the Copper orientation {112}<111>. The crystal angle α is also rotated by tensile deformation as shown in Fig. 8. According to crystal angle rotation, equivalent misorientation distribution is also changed as shown in Fig. 9. In the 0°-3° low tilt angle bicrystal model, grain boundary is disappearance and crystal binding each other. In the high title angle bicrystal models 0°-35° and 3°-35°, however, grain boundary has been remained during tensile deformation.

Since there is a triple point in the tricrystal model and interaction of each grain, the subgrain growth and localization of misorientation are occurred as shown in Fig. 9 (b). Figure 10 shows history of crystal angle α rotation of tricrystal model during tensile deformation. While the crystal $\alpha = 35°$ as red solid line did not almost rotate, crystals $\alpha = 0°$ and 3° as blue and purple solid lines rotated toward 15° and then low tilt angle boundary between 0° and 3° is disappeared. It could predict physical evidence that crystal rotations and misorientation effect on material hardening by using our multi-scale analyses with the new hardening evolution equation.

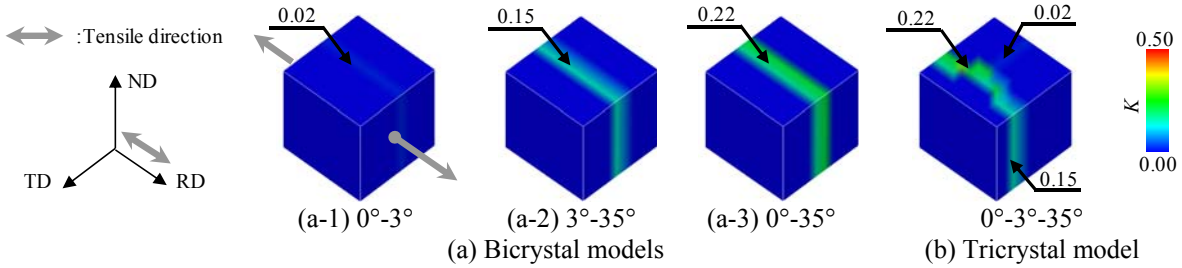

Figure 5: Initial equivalent misorientation distributions of micro models

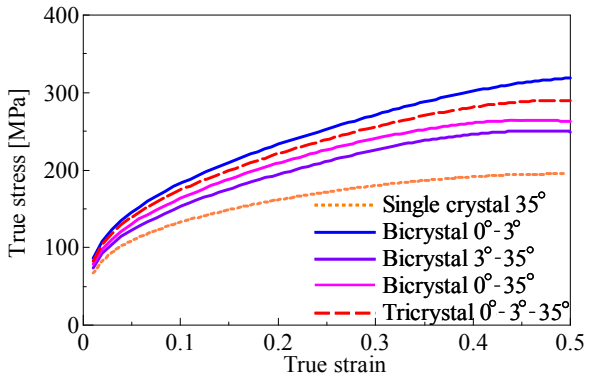

Figure 6: Relationships between true stress and true strain of multi-scale FE analyses

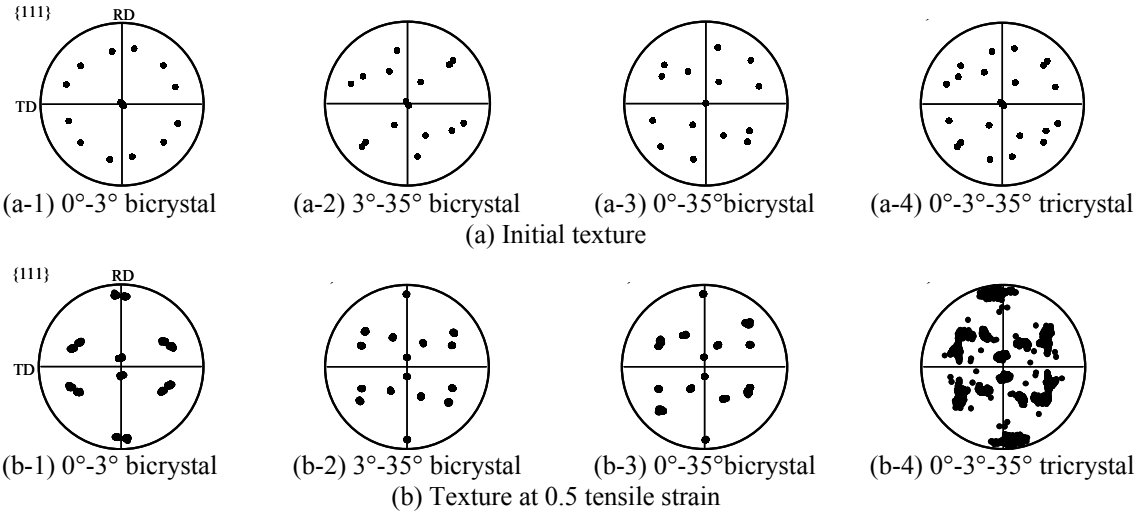

Figure 7: Texture evolution on {111} pole figures

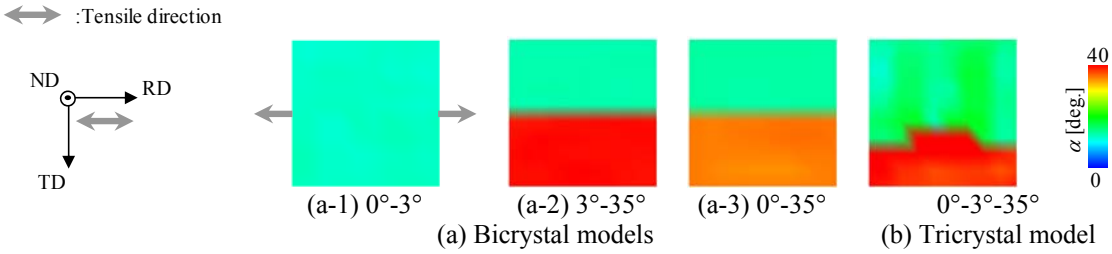

Figure 8: Distributions of Crystal orientation angle α evolutions at 0.5 tensile strain

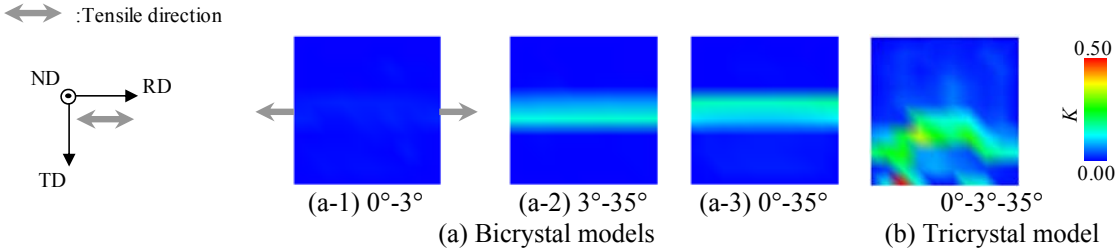

Figure 9: Distributions of equivalent misorientation evolutions at 0.5 tensile strain

4 CONCLUSIONS

We suggest the new hardening evolution equation based on crystallographic misorientation and carried out tensile analyses. Misorientation evolution and forming subgrain boundary were expressed. We conclude that consideration of misorientation is necessary for crystal plastic analysis.

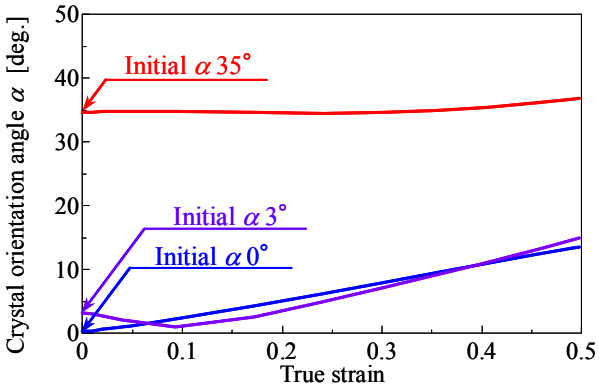

Figure 10: Crystal rotation histories of tricrystal model

ACKNOWLEDGEMENT

One of the authors (H. Kuramae) was financially supported by the Amada Foundation for Metal Work Technology and the Grant-in-Aid for Scientific Research (C) (23560106) by the Ministry of Education, Culture, Sports, Science and Technology, Japan.

REFERENCES

[1] Nakamachi, E., Tam, N.N. and Morimoto, H. Multi-scale finite element analyses of sheet materials by using SEM-EBSD measured crystallographic RVE models. *Int. J. Plasticity* (2007) **23**:450-489.

[2] Asaro, R.J. and Needleman, A. Texture development and strain hardening in rate dependent polycrystals. *Acta Metallurgica* (1985) **33**:923–953.

[3] Fleck, N.A., Muller, G.M. and Hutchinson, J.W., Strain gradient plasticity: theory and experiment. *Acta Mater.* (1994) **42**:475-487.

[4] Adam, J., Mukul, K. and Brent, L.A. (Eds.) *Electron Backscatter Diffraction in Materials Science*, Kluwer Academic Press, (2000).

[5] Maniatt, A.M., Dawson, P.R. and Lee, Y.S. A time integration algorithm for elasto-viscoplastic cubic crystals applied to modeling polycrystalline deformation. *Int. J. Num. Meth. Engng.* (1992) **35**:1565-1588.

[6] Nakamachi, E. and Dong, X. Study of texture effect on sheet failure in a limit dome height test by using elastic/crystalline viscoplastic finite element analysis. *J. of App. Mech.* (1997) **64**:519-524.

[7] Kuramae, H., Ikeya, Y., Sakamoto, H., Morimoto, H., and Nakamachi, E. Multi-scale parallel finite element analyses of LDH sheet formability tests based on crystallographic homogenization method. *Int. J. Mech. Sci.* (2010) **52**:183-197.

[8] Harder, J. A crystallographic model for the study of local deformation processes in polycrystals. *Int. J. Plasticity* (1999) **15**:624-625.

[9] Lange, F.F. Mathematical characterization of a general bicrystal. *Acta Metal.* (1996) 15:331-318.

[10] Hora, P., Volk, W., Roll, K., Griesbach, B., Kessler, L. and Hotz, W. (Eds.), *Proc. 7th International Conference and Workshop on Numerical Simulation of 3D Sheet Metal Forming Process*, Vol. B, (2008).

XI International Conference on Computational Plasticity. Fundamentals and Applications
COMPLAS XI
E. Oñate, D.R.J. Owen, D. Peric and B. Suárez (Eds)

APPLICATION OF HOMOGENIZATION METHOD CONSIDERING CRYSTAL PLASTICITY FOR PREDICTION OF MECHANICAL PROPERTIES FOR COPPER AND LOW CARBON STEEL

TAKUYA SUEOKA[*], TAKASHI KUBOKI[*], MAKOTO MURATA[*]

KOUICHI KURODA[†1], KENJIRO TERADA [†2]

[*] Dept. of Mechanical Engineering & Intelligent Systems
University of Electro-Communications
1-5-1 Chofu Gaoka, Chofu-shi, Tokyo, 182-8585, Japan
e-mail: sueoka@mce.uec.ac.jp
kuboki@mce.uec.ac.jp
murata@mce.uec.ac.jp

[†1] Corporate Research & Development Laboratories
Sumitomo Metal Industries, Ltd.
1 Fusho-cho, Amagasaki-shi, Hyogo, 660-0891, Japan
email: kuroda-kui@sumitomometals.co.jp

[†2] S Department of Civil Engineering
Tohoku University
6-6 Aza-Aoba, Aramaki, Sendai 980-8579, Japan
email: tei@civil.tohoku.ac.jp

Key words: Multi-Scale Analysis, Crystal Plasticity, Periodic Boundary Condition.

Abstract. The homogenization method considering crystal plasticity was taken as a prediction method of mechanical properties after metal forming. Copper and low carbon steel were taken as raw materials. It was experimentally clarified that low carbon steel showed stronger Bauschinger effect than copper. At the first trial of analysis, the homogenization method considering crystal plasticity showed a similar behavior to that of copper of single phase metal rather than low carbon steel. However, addition of small amount of carbide in low carbon steel inside the crystals, just as in the actual steel, significantly improved the prediction accuracy.

1 INTRODUCTION

Materials are subjected to various processes of plastic deformation before shaped into final products. The mechanical properties would be affected by the history of deformation in the previous processes. It would be important to predict the mechanical properties in advance in terms of safety and strength assessment for the final products. Even in the middle of

manufacturing, the prediction of mechanical properties would be helpful for the decision of appropriate working conditions in the following processes.

There are many numerically description methods proposed by many researchers for description of mechanical properties during deformation. For example, mixed hardening combines work hardening and kinematic hardening [1].Armstrong and Frederic [2], and Chaboche [3] proposed numerical models which can describe complex history of stress-strain. These phenomenological methods would supply only numerical description of kinematic hardening. On the other hand, multi-scale analysis considering crystal plasticity would be another trend for the explanation of appearance of kinematic hardening as well as quantitative prediction [4]. Although efficiency of these proposed description have been discussed in literature, it would still be meaningful to examine the applicability of the analyses in metal forming.

In the present research, the homogenization method considering crystal plasticity was taken as a prediction method of mechanical properties after metal forming. Copper and low carbon steel was taken as raw materials. Analyses were tried to predict local mechanical properties after metal forming, taking nosing as an example, after identifying material constantans. Firstly, material constants which were needed in the analysis, was identified by tension test. Macro scale analysis was conducted on tube nosing to pick up deformation history at local points of nosed tubes. Based on the calculated history in macro scale, multi-scale analysis was carried out for the prediction of local mechanical properties of nosed tubes.

2 ANALYSIS METHOD

2.1 Analysis model

Homogenization method was applied in a cube of representative volume element (RVE). Crystal plasticity was considered and a periodic boundary condition was applied. Figure 1 shows the analysis models. There are 54 crystals in the RVE. The orientation of crystals was given at random. The material properties of 54 crystals are all the same except the crystal orientation for Case1. While actual copper is a single phase metal, low carbon steel includes carbide, though it is small amount. Case2 in Figure 1 is the finite element model of dual phase metal. While Case 1 was applied for copper and the low carbon steel, Case 2 was for the low carbon steel. Case 2 recreated the low carbon steel, whereby the amount of carbide is equal to that of actual low carbon steel. The volumes which are surrounded by white lines denote carbide, while the remainder part denotes ferrite.

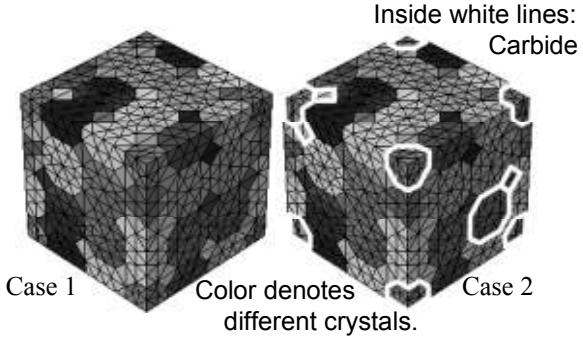

Figure 1: analysis model

2.2 Periodic boundary condition

In the analysis model, a periodic boundary condition is applied assuming each REV of crystal grains is dimensionless point and infinite number of grains exists at one point in macro scale. Figure 2 shows conceptual diagram of periodic boundary condition. Material constant for the grain should be determined in advance for the execution of analysis. In Case 1, the identification of coefficients was carried out by comparing the analytical and experimental results in uni-axial tension test. In Case 2, identification on carbide was firstly tried referring mechanical properties of carbide in the literature [5]. Identification on ferrite was continuously carried out by comparing stress-strain diagrams of the whole low carbon steel in the numerical and experimental uni-axial tests. n the analysis model, a periodic boundary condition is applied so that it might be assumed each representative volume of crystal grains is dimensionless point and infinite number of grains exists at one point in macro scale. Figure 2 shows conceptual diagram of periodic boundary condition. Material constant for the grain should be determined in advance for the execution of analysis.

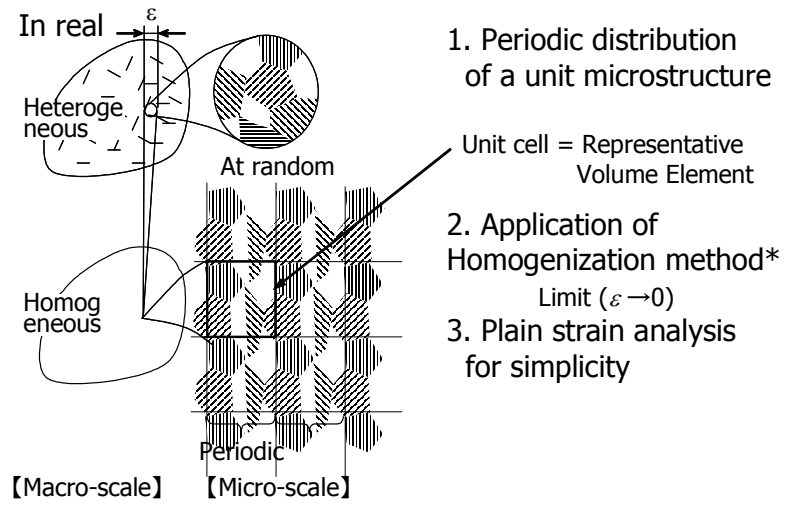

Figure 2: Conceptual diagram of periodic boundary condition

2.3 Crystal-plastic constitutive law

For the description of crystal plasticity, the following Peirce's equation [6] was employed.

$$\dot{\gamma}^{(\alpha)} = \dot{\gamma}_0 \frac{\tau^{(\alpha)}/g^{(\alpha)}}{\left|\tau^{(\alpha)}/g^{(\alpha)}\right|^{1-n}} \tag{1}$$

$$\dot{g}^{(\alpha)} = \sum_{\beta} h_{\alpha\beta}\dot{\gamma}^{(\alpha)} \tag{2}$$

$$h_{\alpha\alpha} = h(\gamma) = h_0 \sec h^2 \left|\frac{h_0\gamma}{\tau_s - \tau_0}\right| \tag{3}$$

$$h_{\alpha\beta} = qh(\gamma) \quad (\alpha \neq \beta) \tag{4}$$

2.4 Finite element method analysis

The commercial code ELFEN [7], which was developed by Rockfield Software Limited, Swansea, was used for the analysis of tube nosing. This analysis assumes that the macroscopic analysis. Microscopic analysis was carried out by the commercial code Abacus, which was developed by SIMULIA.

2.5 Determination procedure of material constants

Mechanical properties of low carbon steel were determined by uni-axial tensile test, which was sectioned out from the parent bar rod, which is annealed in advance. The specimen geometry is shown in Figure 3. After nosing, the same geometry of test piece was sectioned out along circumferential direction as show in Figure 4, for evaluation of mechanical properties after the metal forming. Stress-strain diagrams of raw materials were experimentally obtained.

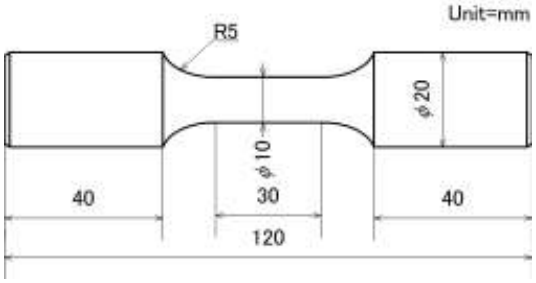

Figure 3: Specimen for tensile test

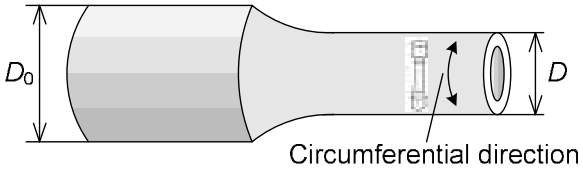

Figure 4: Positions of tension-test specimen

2.6 Determination results on the material constants for analysis

The stress-strain diagram was numerically obtained and compared with experimental result as shown in Figure 5.Identification was conducted on the following parameters; peed dependence parameter n, slip ratio[s^{-1}], initial hardening parameter h_0[MPa], saturation stress τ_s[MPa], yield stress τ_0[MPa], hardening parameter q, difference parameter θ. For the examination of the effect of material parameters in crystal, a series of numerical analyses was carried out by changing these parameters, based on the values determined in the previous section.

The combination of parameters for numerical examinations was given as Table 1. These analytical parameters were adjusted so that calculated stress-strain diagram might become the same value as experimental one in the uni-axial tensile test. Stress-strain diagrams were shown in Figure 5. Copper has a higher hardening ratio than low carbon steel. While low carbon steel reached uniform elongation at $\varepsilon = 0.07$, copper still harden with increase of ε when ε is over 0.1. Numerical identified and experimental diagrams are in good agreement when ε is less than 0.1.

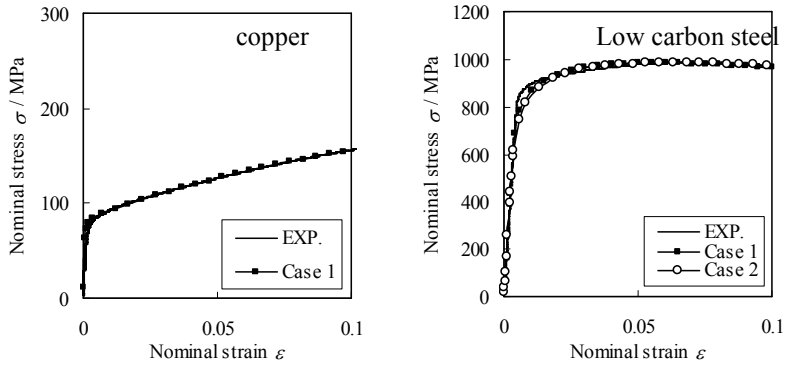

Figure 5: EXP. and FEM result of tensile test

Table 1: Calibrated parameters for analyses

Material	copper	Low carbon steel	
Analysis model	Case 1	Case 1	Case 2
Slipping velocity dependence parameter n	30.0	30.0	30.0
Average level of slipping velocity $\dot{\gamma}_0$ / s^{-1}	0.001	0.001	0.001
Hardening parameter in initial stage h_0 / MPa	100	380	380 (200)
Saturation stress t_s / MPa	72	315	265 (2400)
Yield stress t_0 / MPa	25.5	285	255 (1200)
Hardening parameter q	1.0	1.0	1.0

3 PREDICTION OF MECHANICAL PROPERTIES AFTER NOSING

Figure 6 and Figure 7 shows stress-strain diagrams obtained by experiment and analysis of the test pieces sectioned out of nosed tubes. Nosing ratio κ defined by

$$\kappa = \frac{D_0 - D_1}{D_0} \tag{5}$$

was changed form … to …., where D_0: initial diameter of tube, D_1: tip diameter after nosing.

Some differences were experimentally observed between copper and the low carbon material on the behaviour of stress-strain diagram attendant upon nosing ratio κ. Flow stress of copper increased with increase of nosing ratio κ, which would be attributed to strain hardening. On the other hand, it is noteworthy that with increase of nosing ratio κ, flow stress decreased in spite of accumulation of strain for the low carbon steel, which is dual phase metal.

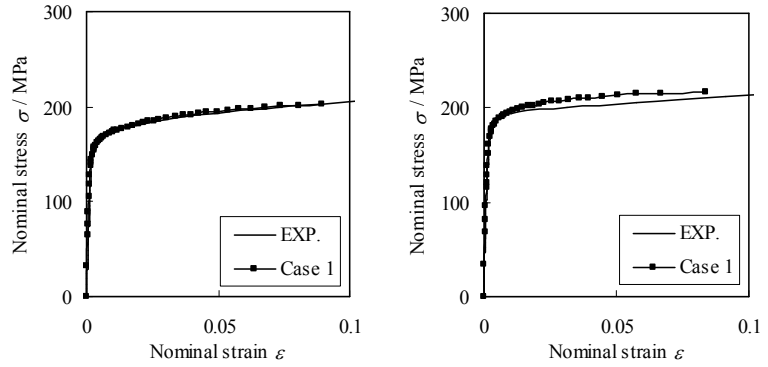

(a) Nosing ratio 4.8% (b) Nosing ratio 7.2%

Figure 6: EXP. and FEM stress-strain diagrams .of Copper after nosing

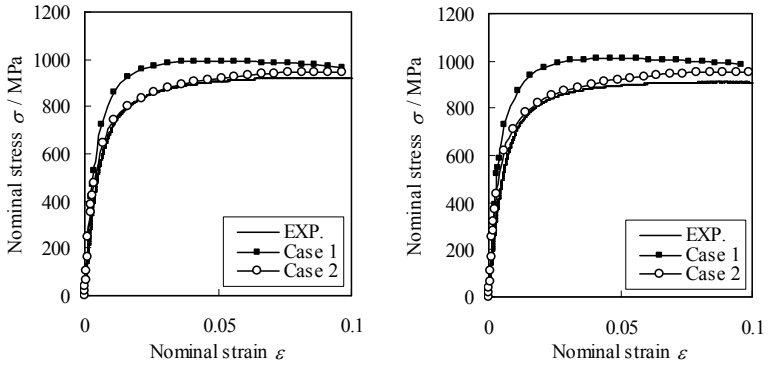

(a) Nosing ratio 4.9% (b) Nosing ratio 6.7%

Figure 7: EXP. and FEM stress-strain diagrams of Low carbon steel after nosing

Table 2: Proof stress after nosing [MPa]

Copper	EXP.	Case 1	Case 2
Nosing ratio κ=4.8%	157	161	
Nosing ratio κ=7.2%	175	176	
Low carbon steel	EXP.	Case 1	Case 2
Nosing ratio κ=4.9%	552	716	591
Nosing ratio κ=6.7%	585	733	592

The numerical method of Case 1 predicted well the behaviour of stress-strain diagram for copper. The flow stress increases with increase of nosing ratio. However, Case 1 could not predict the stress-strain behaviour for the low carbon steel. On the other hand, Case 2 predicted well the behaviour of stress-strain diagram of the low carbon steel. In other words, 2nd phase of material, which might be included in a small amount, would affect the mechanical properties after metal forming. It is needed to consider the existence of 2nd phase material, and that consideration considerably enhances the prediction accuracy in analysis.

Table 2 shows proof stress obtained by the experiment and the analysis. The value of

analysis is improved by considering the 2nd phase material of carbide. Case 1 predicted proof stress of copper within error of 3.8 %. Case 2 predicted that of the low carbon steel within error of 7.1 %.

4 CONCLUSIONS

- Prediction of mechanical properties of nosed metallic tube was attempted for copper and low carbon steel, which is widely employed in industry. The predicted value was compared to experimental results.
- It was noteworthy that flow stress decreased attendant upon intensity of deformation, in spite of accumulation of strain in the case of the low carbon steel, which is dual phase metal.
- The homogenization method with consideration of crystal plasticity was adopted for the prediction of mechanical properties.
- The numerical method predicted well the stress-strain behaviour of copper.
- It was needed to consider the existence of the 2nd phase material for accurate prediction for the low carbon steel. The consideration considerably improved accuracy of analysis.
- Homogenization method with crystal plasticity predicted proof stresses within error of 7.2 %.

5 ACKNOWLEDGEMENT

The present paper benefited partially through association with Rockfield Software Limited, Wales, UK. The analysis part of this research work was expedited thanks to Drs Rance, Armstrong, Dutko and other members. The present paper were also benefited partially through association with Dassault Systemes Simulia Corp.

REFERENCES

[1] de Souza Neto, E. A., Peric, D., Owen, D. R. J., Computational Methods for Plasticity: Theory and Applications, (2009).
[2] Armstrong, P.J., Frederick., C.O. A mathematical representation of the multiaxial Bauschinger effect, CEGB Report RD/B/N731, (1966).
[3] Chaboche, J.L., Rousselier, G. On the plastic and viscoplastic constitutive equations, part Ⅰ and II, J. Press. Vessel Technol.-Trans. ASME, (1983) 105-:153-164.
[4] Watanabe, I., Terada, K., Terada, K., Akiyama, M., Neishi, Y. Multi-scale analysis for polycrystalline metals, (2003), 6:239-246,in Japanese.
[5] Umemoto, M. Current Advances in Materials and Processes, (2001), 14-3:554, in Japanese.
[6] Peirce, D., Asaro, R.J., and Needleman, A., Material rate dependence and localized deformation in crystaline solids, *Acta metall*, Vol. 31, No. 12, pp. 1951-1976, (1983).
[7] Timoshenko, S. Strength of Materials, June 1940, D. Van Nostrand Company, Inc.

XI International Conference on Computational Plasticity. Fundamentals and Applications
COMPLAS XI
E. Oñate, D.R.J. Owen, D. Peric and B. Suárez (Eds)

DYNAMIC RECRYSTALLIZATION MODEL DURING HOT WORKING BY COUPLING PHASE-FIELD METHOD AND FINITE ELEMENT METHOD

TOMOHIRO TAKAKI*

*Mechanical and System Engineering, Graduate School of Science and Technology
Kyoto Institute of Technology
Matsugasaki, Sakyo, Kyoto 606-8585, Japan
e-mail: takaki@kit.ac.jp, http://www.cis.kit.ac.jp/˜takaki/

Key words: Dynamic Recrystallization, Hot Working, Microstructure, Multi-Phase-Field Method, Finite Element Method, Multiscale Modeling

Abstract. Multiscale model for hot–working, which can investigate the macroscopic mechanical behavior based on the microstructure evolution, has been developed by coupling the finite element (FE) method and phase–field (PF) method. Here, the microstructure evolutions in dynamic recrystallization are simulated by the multi–phase–field-dynamic recrystallization (MPF–DRX) model. The microscopic simulations are performed in every element used in the finite element simulations to calculate the macroscopic mechanical behaviors.

1 INTRODUCTION

During hot–working of low–to–medium stacking fault energy metal, the dynamic recrystallization (DRX) occurs, where the plastic deformation due to dislocation accumulation and the nucleation and growth of recrystallized grain occur simultaneously [1]. The macroscopic mechanical behavior during DRX shows a characteristic stress – strain curve, or single and/or multiple peak curves are generated depending on the initial grain size, the strain rate and the temperature [2]. Because these macroscopic stress – strain curves are largely affected by the microstructure evolution, it is key for the working process design to develop a multiscale numerical model for the hot–working. There are roughly two kinds of multiscale method: one is by finite element method [3, 4, 5, 6, 7], which mainly focuses on the macroscopic mechanical behavior, and the other is by grain growth model [9, 10, 11, 12, 13, 14, 15, 16, 17], which focuses on the microstructure evolution.

In finite element simulations considering the DRX microstructure evolution during hot–working [3, 4, 5, 6, 7], the information of microstructure, such as average grain size, recrystallization volume fraction, stored energy (or dislocation density) and so on, is incorporated into the model through the constitutive equation and the DRX microstructural

information is updated as a function of strain, strain rate and temperature. To increase the accuracy of these models in more practical hot–working, it is key to properly incorporate the information of DRX microstructure evolutions, which largely depends on the stress and thermal history, into the constitutive equation.

In DRX simulations using grain growth model [9, 10, 11, 12, 13, 14, 15, 16, 17], the nucleation and growth of DRX grains, or realistic DRX microstructure evolution, are simulated and the macroscopic stress–strain curve is calculated from the average dislocation density in the computational domain. As a grain growth model, Cellular Automata (CA) is widely employed [9, 10, 11, 12, 13, 14, 15]. We have developed the MPF–DRX model [16, 17] using multi–phase–field (MPF) method instead of CA and confirmed that the MPF-DRX model can be applied to the transient deformation where strain and temperature change rapidly during deformation [18].

In this study, we develop multiscale DRX model coupling above two types of DRX models, where the DRX microstructure evolution is simulated by MPF–DRX model and the macroscopic mechanical behavior is calculated by large deformation finite element analysis, where the conventional J_2–flow theory is used as the constitutive equation.

2 COUPLING OF MPF–DRX MODEL AND FE METHOD

Figure 1 shows an image of the multiscale simulation using MPF–DRX model and FE method.

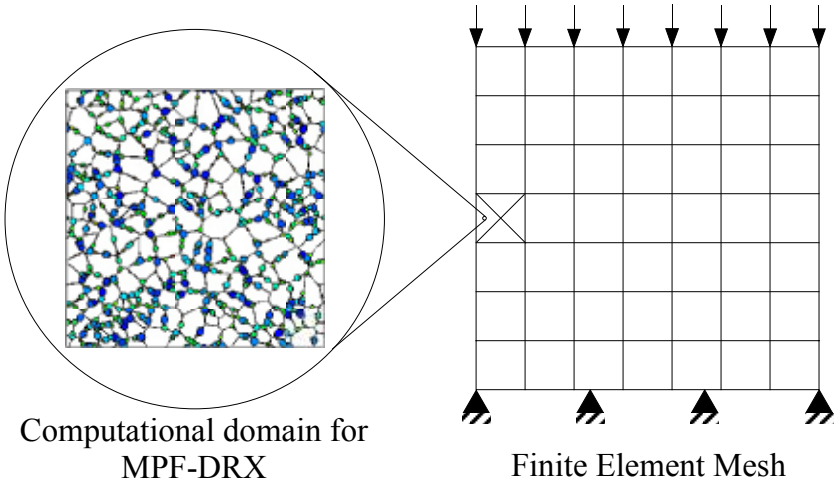

Figure 1: Image of multiscale simulation

The MPF–DRX simulations are performed in all finite elements used in FE simulation. Because the crossed-triangle element is employed in the present FE simulation, in the example of Fig.1, the computational domains with 196 numbers ($= 7 \times 7 \times 4$) are prepared and the MPF–DRX simulations are performed in all 196 domains. The equivalent strain rate $\dot{\bar{\varepsilon}}$ and temperature T, which are different in every element, are transferred from

FE simulation to MPF–DRX simulation and the tangent modulus $d\bar{\sigma}/d\bar{\varepsilon}$ which is the slope of the uniaxial stress–strain curve is transferred from MPF–DRX simulation to FE simulation.

3 MPF–DRX MODEL

In the MPF–DRX model [16], the grain growth driven by stored energy is simulated by the MPF method [21] and the local dislocation density evolution due to plastic deformation and dynamic recovery (DRV) is expressed by the Kocks–Mecking (KM) model [19]. A macroscopic stress-strain curve is obtained from the Bailey–Hirsch equation [20] using average dislocation density in all computational domain.

3.1 MPF model

A polycrystalline system including N grains is indicated by N phase–field variables. The ith grain is indicated by the phase field ϕ_i, where ϕ_i takes values of 1 inside the ith grain, 0 inside the other grains, and $0 < \phi_i < 1$ at the grain boundary. The evolution equation of ϕ_i is expressed by [21]

$$\dot{\phi}_i = -\sum_{j=1}^{n} \frac{2M_{ij}^{\phi}}{n} \left[\sum_{k=1}^{n} \left\{ \left(W_{ik} - W_{jk}\right) \phi_k + \frac{1}{2} \left(a_{ik}^2 - a_{jk}^2\right) \nabla^2 \phi_k \right\} - \frac{8}{\pi} \sqrt{\phi_i \phi_j} \Delta f_{ij} \right]. \quad (1)$$

where n is the number of phase–field variables larger than 0 at the lattice point, a_{ij}, W_{ij}, and M_{ij}^{ϕ} are the gradient coefficients, the height of double–well potentials and the phase–field mobilities related to the grain boundary thickness δ, grain boundary energy γ and grain boundary mobility M, respectively, by

$$a_{ij} = \frac{2}{\pi} \sqrt{2\delta\gamma}, \quad W_{ij} = \frac{4\gamma}{\delta}, \quad M_{ij}^{\phi} = \frac{\pi^2}{8\delta} M. \quad (2)$$

Here, δ, γ and M are assumed to be constant at all boundaries and Eq.(2) is true only for $i \neq j$ and the diagonal components are zero. The driving force Δf_{ij} can be obtained as $\Delta f_{ij} = 1/2\mu b^2(\rho_i - \rho_j)$, where μ is the shear modulus, b is the magnitude of the Burgers vector, and ρ_i and ρ_j are the dislocation densities in ith and jth adjacent grains, respectively.

3.2 Dislocation evolution and macroscopic stress

The accumulation of dislocations due to plastic deformation and DRV is expressed by the KM model [19] as the relationship between the local dislocation density ρ_i in the ith grain and the true strain ε;

$$\frac{d\rho_i}{d\varepsilon} = k_1 \sqrt{\rho_i} - k_2 \rho_i. \quad (3)$$

Here, the first term on the right–hand side expresses the work hardening, where k_1 is a constant that represents hardening. The second term is the DRV term, where k_2 is a

function of the temperature T and the strain rate $\dot{\varepsilon}$. [9] . Macroscopic stress is related to the average dislocation density $\bar{\rho}$ as

$$\sigma = \alpha\mu b\sqrt{\bar{\rho}}, \tag{4}$$

where α is the dislocation interaction coefficient of approximately 0.5. From eqs. (3) and (4), a macroscopic stress–strain curve can be determined.

3.3 Nucleation of DRX grains

It is assumed that the nucleation of recrystallized grains occurs only with the bulging of a grain boundary in the present model. Therefore, when the dislocation density at a grain boundary exceeds its critical value ρ_c, or

$$\rho_c = \left(\frac{20\gamma\dot{\varepsilon}}{3blM\tau^2}\right)^{1/3}, \tag{5}$$

nuclei are in placed at a grain boundary by following the nucleation rate per unit area of a grain boundary [9]

$$\dot{n} = c\dot{\varepsilon}^d \exp(-\frac{\omega}{T}), \tag{6}$$

where $\tau = 0.5\mu b^2$ is the line energy of a dislocation, l is the mean free path of mobile dislocation expressed by $l = 10/(0.5\sqrt{\rho_0})$, [9] and c, d and ω are constants.

4 FINITE ELEMENT METHOD

To evaluate the macroscopic mechanical behavior during hot–working process, the elasto–plastic large deformation simulation is performed by finite element method. Here, the conventional J_2–flow theory is employed as the constitutive equation, where the elastic strain rate $\dot{\varepsilon}^e_{ij}$ and plastic strain rate $\dot{\varepsilon}^p_{ij}$ are derived from the generalized Hook's low and the flow low and the Mises yield function, respectively. The relation between the Jaumann rate of Kirchoff stress S_{ij} and strain rate $\dot{\varepsilon}_{ij}$ is indicated as follow:

$$S_{ij} = \left(D^e_{ijkl} - \frac{2G}{g}\sigma'_{ij}\sigma'_{kl}\right)\dot{\varepsilon}_{kl}, \tag{7}$$

where D^e_{ijkl}, σ'_{ij} and G are the elastic coefficient tensor, the deviatoric Cauchy stress tensor and shear modulus expressed as $G = E/\{2(1+\nu)\}$, respectively. In addition, g is expressed by

$$g = \frac{2}{3}\bar{\sigma}^2\left(1 + \frac{h}{2G}\right), \quad \bar{\sigma}^2 = \frac{3}{2}\sigma'_{ij}\sigma'_{ij}, \tag{8}$$

where, taking into account the uniaxial test and non–compressibility,

$$\frac{1}{h} = \frac{3}{2}\left(\frac{1}{E_t} - \frac{1}{E}\right), \tag{9}$$

can be obtaind. Here, E_t is the tangential coefficient in the true stress and true strain curve, or $E_t = d\sigma/d\varepsilon$, and is calculated in the MPF–DRX simulation. Therefore, in the present FE simulation, we don't need the uniaxial constitutive equation obtained by uniaxial test, which is required in the normal FE simulation.

Because the strain rate dependency is contained in the MPF–DRX simulation, the strain rate independent constitutive equation is used in the FE simulation. In this study, furthermore, an isothermal condition is assumed and, therefore, the thermal conduction equation is not shown here.

5 NUMERICAL SIMULATIONS

To confirm the accuracy of the present model, the uniaxial compression simulations in a plane stress condition of copper [18] are performed for a single crossed–triangle element. The constant strain rates $\dot{\varepsilon}$ are set to be 0.001, 0.003, 0.01, 0.03 and 0.1/s in the isothermal condition $T = 800$ K. The time step is determined as $\Delta t = \Delta x^2/\left(4a^2M^{\phi}\right)$ from Eq.(1). Because the strain increment $\Delta\varepsilon$ is calculated as $\Delta\varepsilon = \dot{\varepsilon}\Delta t$, $\Delta\varepsilon$ changes depend on the $\dot{\varepsilon}$. Young's modulus E is derived as $E = 0.5\alpha\mu bk_1$ from Eqs.(3), which is a gradient of true stress and true strain curve at $\varepsilon = 0$, and (4) and Poisson's ration is set to be 0.3.

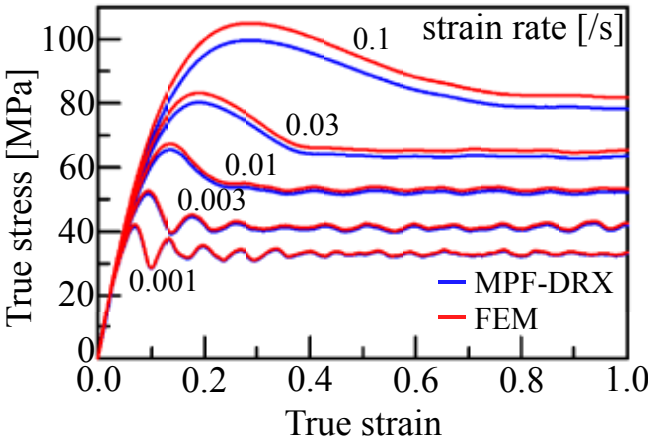

Figure 2: Stress–strain curves calculated by MPF–DRX model and FE method

Figure 2 shows the true stress and true strain relations for five different strain rates. Although the present simulation is compression, stress and strain are indicated as positive value. From Fig.2, the characteristic stress–strain curves in DRX, where the transition from the multiple peaks to the single peak occurs with increasing the strain rate, can be observed. Red lines are the results of MPF–DRX simulation and blue lines are the results of FE simulation used the results of MPF–DRX simulation. The good agreements between red and blue lines are confirmed especially in slow strain rate region.

Figure 3 shows the DRX microstructure evolution for $\dot{\varepsilon} = 0.01$/s. The color indicates the DRX cycle defined in Ref. [17].

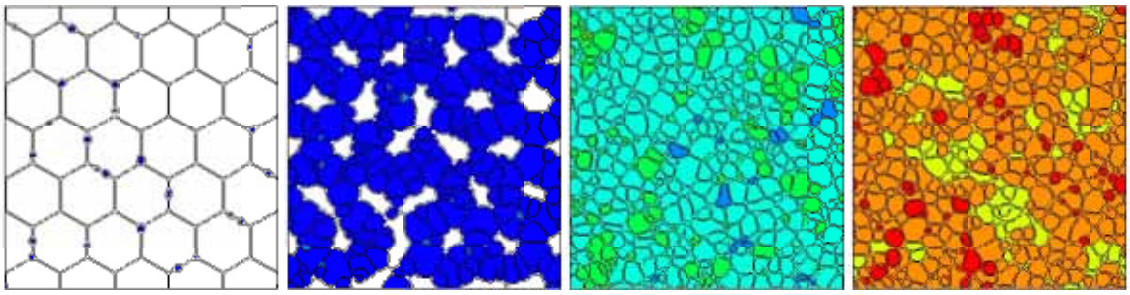

(a) ε = -0.1 (b) ε = -0.2 (c) ε = -0.5 (d) ε = -1.0

Figure 3: DRX microstructure evolutions ($\dot{\varepsilon} = 0.01$)

From Figs.2 and 3, it is confirmed that the present model can simulate the microstructure evolution and the macroscopic mechanical behavior simultaneously. However, the results shown in Figs.2 and 3 can be calculated only by the MPF–DRX model. The novel point of the present coupling model is that the model can simulate the different microstructure evolution for every finite element in the nonuniform deformation simulation.

6 CONCLUSIONS

The novel multiscale model, which can evaluate the macroscopic mechanical behavior based on the microstructure evolution considering the DRX in hot–working process, has been developed. Here, the MPF–DRX model has been incorporated into the large deformation FE method with the conventional J_2 flow theory as the constitutive equation. The uniaxial compression simulations using one crossed–triangle element were performed to confirm the accuracy of the developed model.

As future work, the model will be extended to the nonuniform and nonisothermal deformation condition.

REFERENCES

[1] F. J. Humphreys and M. Hatherly: Recrystallization and Related Annealing Phenomena, Elsevier, (2004), 415.

[2] T. Sakai and J. J. Jonas, Dynamic recrystallization: mechanical and microstructural considerations, *J. Mater. Process. Technol.*, (1984) **32**:189–209.

[3] K. Karhausen and R. Kopp, Model for integrated process and microstructure simulation in hot forming, *Steel Res.*, (1992) **63**:247–256.

[4] M. Glowacki, R. Kuziak, Z. Malinowski and M. Pietrzyk, Modelling of heat transfer, plastic flow and microstructural evolution during shape rolling, *Acta Metall.*, (1995) **53**:159–166.

[5] F. P. E. Dunne, M. M. Nanneh and M. Zhou, Anisothermal large deformation constitutive equations and their application to modelling titanium alloys in forging, *Philos. Mag. A*, (1997) **75**:587–610.

[6] E. P. Busso, A continuum theory for dynamic recrystallization with microstructure-related length scales, *Int. J. Plast.*, (1998) **14**:319–353.

[7] C. M. Sellars and Q. Zhu, Microstructural modelling of aluminium alloys during thermomechanical processing, *Mater. Sci. Eng., A*, (2000) **280**:1–7.

[8] J. R. Cho, H. S. Jeong, D. J. Cha, W. B. Bae and J. W. Lee, Prediction of microstructural evolution and recrystallization behaviors of a hot working die steel by FEM, *J. Mater. Process. Technol.*, (2005) **160**:1–8.

[9] R. Ding and Z. X. Guo, Coupled quantitative simulation of microstructural evolution and plastic flow during dynamic recrystallization, *Acta Mater.*, (2001) **49**:3163–3175.

[10] R. Ding and Z. X. Guo, Microstructural evolution of a Ti–6Al–4V alloy during thermomechanical processing, *Mater. Sci. Eng. A*, (2004) **365**:172–179.

[11] M. Qian and Z. X. Guo, Cellular automata simulation of microstructural evolution during dynamic recrystallization of an HY-100 steel, *Mater. Sci. Eng. A*, (2004) **365**:180–185.

[12] G. Kugler and R. Turk, Modeling the dynamic recrystallization under multi-stage hot deformation, *Acta Mater.*, (2004) **52**:4659–4668.

[13] R. L. Goetz, Particle stimulated nucleation during dynamic recrystallization using a cellular automata model, *Scr. Mater.*, (2005) **52**:851–856.

[14] N. Xiao, C. Zheng, D. Li and Y. Li, A simulation of dynamic recrystallization by coupling a cellular automaton method with a topology deformation technique, *Comp. Mater. Sci.*, (2008) **41**:366–374.

[15] C. Zheng, N. Xiao, D. Li and Y. Li, Microstructure prediction of the austenite recrystallization during multi-pass steel strip hot rolling: A cellular automaton modeling, *Comp. Mater. Sci.*, (2008) **44**:507–514.

[16] T. Takaki, T. Hirouchi, Y. Hisakuni, A. Yamanaka and Y. Tomita, Multi-Phase-Field Model to Simulate Microstructure Evolutions during Dynamic Recrystallization, *Mater. Trans.*, (2008) **49**:2559–2565.

[17] T. Takaki, T. Hirouchi, Y. Hisakuni, A. Yamanaka and Y. Tomita, Multi-phase–field simulations for dynamic recrystallization, *Comput. Mater. Sci.*, (2009) **45**:881–888.

[18] T. Takaki, A. Yamanaka and Y. Tomita, Multi-Phase-Field Simulations of Dynamic Recrystallization during Transient Deformation, *ISIJ Int.*, (2011), *submitted*.

[19] H. Mecking and U. F. Kocks, Kinetics of flow and strain-hardeningstar, *Acta Metall.*, (1981) **29**:1865–1875.

[20] J. E. Bailey and P. B. Hirsch, The dislocation distribution, flow stress, and stored energy in cold-worked polycrystalline silver, *Philos. Mag.*, (1960) **5**:485–497.

[21] I. Steinbach and F. Pezzolla, A generalized field method for multiphase transformations using interface fields, *Physica D*, (1999) **134**:385–393.

[22] Q. Yu and S. K. Esche, A multi-scale approach for microstructure prediction in thermo-mechanical processing of metals , *J. Mater. Process. Technol.*, (2005) **169**:493–502.

[23] H. W. Lee and Y.-T. Im, Numerical modeling of dynamic recrystallization during nonisothermal hot compression by cellular automata and finite element analysis, *Int. J. Mech. Sci.*, (2010) **52**:1277–1289.

XI International Conference on Computational Plasticity. Fundamentals and Applications
COMPLAS XI
E. Oñate, D.R.J. Owen, D. Peric and B. Suárez (Eds)

MOLECULAR DYNAMICS SIMULATIONS ON INTERACTION BETWEEN DISLOCATION AND Y_2O_3 NANOCLUSTER IN FE

KISARAGI YASHIRO*, TAKANORI MUTSUKADO†, MINORU TANAKA†, AKIHIRO YAMAGUCHI †, KENJI KOGA ‡, TAKASHI SEGI ‡ AND TAKANARI OKUDA ‡

*Graduate School of Engineering, Kobe University
1-1, Rokkodai, Nada, Kobe, 657-8501, Japan
e-mail: yashiro@mech.kobe-u.ac.jp, http://mm4.scitec.kobe-u.ac.jp/~yashiro/

†Student of Graduate School of Engineering, Kobe University

‡Kobelco Research Institute, Inc.
1-5-5, Takatsukadai, Nishi-ku, Kobe, Hyogo 651-2271, Japan

Key words: Yttria Oxide, ODS Steels, Dislocation, Nano Precipitates, Molecular Dynamics Simulation

Abstract. For a new insight on the mechanical properties of oxide dispersion strengthened (ODS) steels from atomistic viewpoints, we have implemented molecular dynamics simulations on the interaction between Y_2O_3 nanocluster and dislocation in bcc Fe. There is so far no all-round interatomic potential function that can represent all the bonding state, i.e. metal, ion and covalent systems, so that we have adopted rough approximation. That is, each atom in Y_2O_3 is not discriminated but treated as "monatomic" pseudo-atom; and its motion is represented with the simple pairwise potential function as same as Johnson potential for Fe. The potential parameters are fitted to the energy change in the hcp infinite crystal, by using the ab-initio density functional theory (DFT) calculation for explicitly discriminated Y and O. We have set edge/screw dislocation in the centre of periodic slab cell, and approached it to the "YO" monatomic nano-cluster coherently precipitated in bcc-Fe matrix. The dislocation behavior is discussed by changing the size and periodic distance of the nano-cluster. Among the many useful results, we have obtained a conclusion that the edge dislocation is strongly trapped by YO sphere larger than the diameter of $d = 0.9\,\mathrm{nm}$, while the screw dislocation shows various behavior, *e.g.* it cuts through the precipiate without remarkable resistance if the dislocation line tension is high, or it changes the slip plane leaving jogs at the position anterior to the precipiate with loose line tension.

1 INTRODUCTION

Oxide dispersion strengthened (ODS) steels are potential next-gen materials for fuel cladding tubes at nuclear power plants. For the engineering application and further developments of desired steels, it is urgent to understand the key mechaism of their superior properties against neutron irradiation and high temperature. Starting from the pioneering report for alloying elements and mechanical alloying process of ODS steels in 1989 [1], experimental studies have revealed the relationship between internal microstructure and mechanical properties [2], improvement of tensile and creep properties by extremely fine Y-Ti-O clusters with Ti addition [3], quantitative evaluation of nanosized oxides [4], and so on. So far the fine oxides, of a few nanometer size, are expected to prevent the free dislocation motion; however, due to the complexity of mechanical alloying and recrystalization process, it is still difficult to show the direct evidence even with the recent advancement of experimental technique such as TEM *in situ* test.

Computational approach would be one answer to tackle these difficulties. In the field of physics of crystal plasticity, various dislocation-obstacle problems have long been discussed using molecular dynamics (MD) and discrete dislocation dynamics (DDD) simulations; and we have also discussed the dislocation motion in γ/γ' microstructure in Ni-based superalloys [5, 6]. However, there is no suitable potential function which can represent all the bonding state, i.e. metal, ion and covalent systems with sufficient number of atoms needed for deformation simulation. Of course the ab-initio density functional theory (DFT) calculation can treat mixing of any atom species, however, the calculation is so far limited to very small system at most a few hundred atoms. Thus quite a few atomistic simulations can be found for ODS steels except for lattice Monte Carlo (LMC) simulation, in which atom position is restricted on regular lattice site, so that the limited combination of local bonding can be precisely determined by ab-initio DFT calculation. Alinger et al. [7] performed the LMC simulation of Fe-Y-Ti-O system and discussed the structure and morphology of precipitated nanocluster. Hin et al. [8] simulated more realistic precipitation by kinetic LMC, considering the different diffusion mechanism (O atoms by interstitial jumps and Fe and Y atoms by vacancy jumps). Both studies apply finer lattice mesh than the usual bcc lattices and their results should be appreciated as accurate prediction based on DFT data. However, we would confront to drastic increase in the combination of local bonding if we applied these DFT-LMC analysis to many alloy elements system for real ODS steel design. Moreover, we never apply these DFT-LMC scheme to disordered structure, such as dislocations and grain boundaries, since we should consider enormous mesh much more than the number of atoms involved. From an engineering point of view, we need an atomistic simulator in which the potential functions have differentiable form for dynamic simulation and they are also easy to fit for new elements interest. The 2-body potential form is the simplest way and there are many resources fitted for various elements; however, obviously we would fail to represent the bonding between oxygen and metallic atoms if we fitted them separately in the 2-body form. Thus, in the present study, we don't

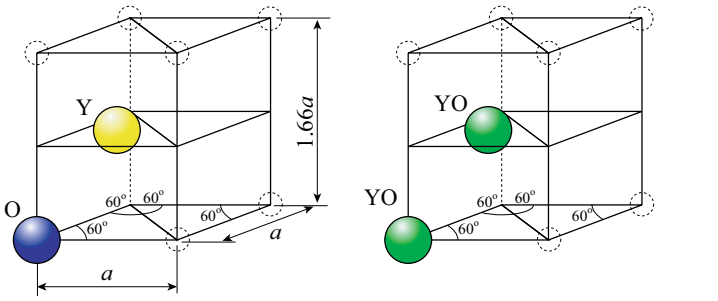

(a) hcp unit cell for DFT calculation (b) hcp unit cell for monatomic "YO"

Figure 1: Rhombohedral unit cells for hcp structure.

distinguish the Y and O atoms in Y_2O_3 but treat as "monatomic" pseudo-atom of YO, in the fitting of Johnson potential parameters against the DFT calculation for explicitly discriminated Y and O. By virtue of this rough approximation, we can easily implement atomistic simulation using conventional resources, *e.g.* Johnson potential parameters for Fe, keeping the rough characteristics of oxides such as lattice parameters and bulk modulus. Although we cannot validate the physical meaning of the isolated pseudo-atom nor discuss the formation and structure of new oxidation products, we can perform MD simulation on the interaction between edge/screw dislocation and oxide nano-cluster. In the present study, we show the brief fitting process and MD simulations of edge/screw dislocation approaching the nano-clusters coherently precipitated in bcc-Fe matrix, changing the size and distances of precipitates.

2 POTENTIAL FITTING PROCEDURE

DFT calculations for potential fitting are implemented using the Vienna Ab-initio Simulation Package (VASP) developed by Kresse and Hafner [9]. Although the Y_2O_3, M_2X_3 type metal oxide, is reported to form the C-rare earth oxide structure [10], it is very difficult to directly consider such a low-symmetric irregular structure by DFT calculation. Thus we have roughly approximated the structure of Y_2O_3 by simple hcp lattice, which is close to the corundum structure or the second candidate of M_2X_3 metal oxide. Figure 1 shows the rhombohedral unit cells for hcp lattice. The supercell for DFT calculation has one Y-atom and one O-atom at the lattice point as shown in Fig. 1(a). Keeping the atom position at the lattice point, or statically, we have changed the lattice parameter a and performed DFT calculation to obtain the energy–lattice parameter curve. The ultrasoft pseudopotential [11] is adopted and the exchange correlation term is treated in the formulation of GGA (generalized gradient approximation) [12]. The cutoff energy and number of **k** points are 296.9 eV and $15 \times 15 \times 15$, respectively.

Johnson potential expresses the system energy, E_{tot}, by the following form:

$$E_{\mathrm{tot}} = \sum_i \sum_{j>i} \left[-C_1 (r_{ij} - C_2)^3 + C_3 r_{ij} - C_4 \right] \tag{1}$$

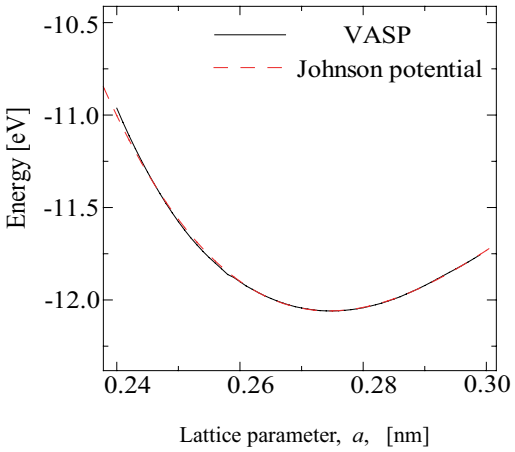

Figure 2: Free-energy curves against lattice expansion/compression by DFT calculation for discriminated Y and O in the hcp structure and by Johnson potential fitted as monatomic YO mean-atom.

Table 1: Potential parameters for Fe and YO pseudo-atom.

Element	Range [nm]	C_1	C_2	C_3	C_4
Fe	$0.19 < r_{ij} < 0.24$	2.1960	3.0979	2.7041	7.4365
	$0.24 < r_{ij} < 0.30$	0.6392	3.1158	0.4779	1.5816
	$0.30 < r_{ij} < 0.344$	1.1150	3.0664	0.4669	1.5480
YO	$0.19 < r_{ij} < 0.344$	0.523	3.090	0.194	1.560

here r_{ij} is the distance between atoms i and j, and the potential parameter $C_1 \sim C_4$ should be found for yttria oxide. We have expressed the infinite YO hcp crystal with monatomic YO pseudo-atoms in Fig. 1(b) under the periodic boundary, and fitted its energy change to the DFT result (Fig. 2). By this fitting process, the equilibrium lattice length and the bulk modulus, or energy change rate against lattice expansion/compression, are precisely represented for monatomic YO pseudo-atoms. On the Fe-YO interaction, simple arithmetic average rule is adopted, i.e., $(C_i^{\mathrm{Fe}}+C_i^{\mathrm{YO}})/2$. All the potential parameters are listed in Table 1.

3 SIMULATION ON EDGE DISLOCATION

3.1 Simulation procedure

Figure 3 shows the dimensions and introduction of edge dislocation. The x, y and z axes are orinented to the [111], [$\bar{1}$12] and [$\bar{1}$10] directions in the bcc structure. For the precipitate–edge dislocation problem, we have replaced Fe atoms with YO ones, in the sphere at the position shown in Fig. 3(a). That is, the precipitate has initially bcc structure or coherently precipitated in the bcc matrix. Different sphere diameter d is

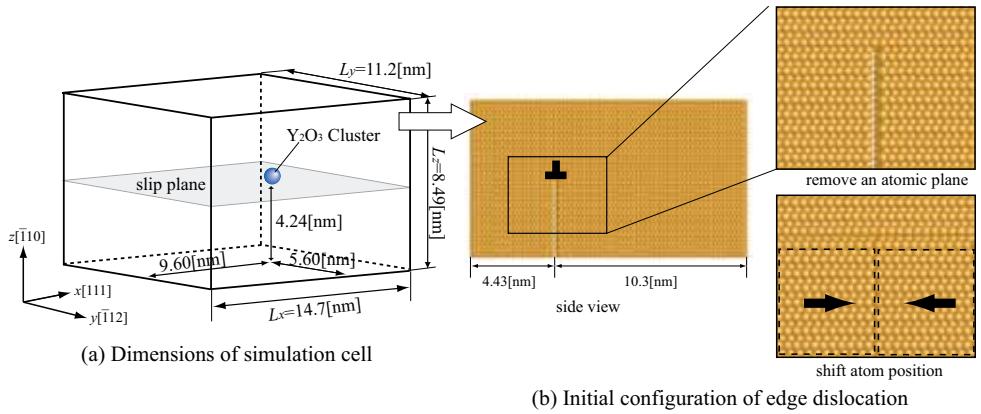

(a) Dimensions of simulation cell

(b) Initial configuration of edge dislocation

Figure 3: Simulation model for edge dislocation.

considered, i.e., 0.6, 0.9, 1.5, 3.0 and 5.0 nm. The edge dislocation is also introduced by eliminating one atomic plane as shown in Fig. 3(b). The periodic boundary condition is applied in the x and y axes, i.e. dislocation motion and line directions, while the z boundary is basically free surface but also has restriction for deformation control. The initial structure is relaxed by MD calculation of 100 000 fs under $T = 10$ K. Then, we apply the small displacement of 1.0×10^{-6} nm at every MD step in the [111] direction for upper z surface atoms and in the opposite for lower ones, in order to approach the edge dislocation to the precipitate. For comparison, we have also performed same shear simulation *without* precipitate. Furthermore, we have also implemented same simulation with different cell length L_y in the y direction to check the effect of the periodic distance between the precipitates. Note that the temperature is so far intentionally controlled to very-low value since we would include not only the mechanical effects but also thermal fluctuation under high temperature, and we couldn't seperate the both effects if we had started from high temperature.

3.2 Results and discussion

Figure 4 summarizes the result of simulations with the cell length of L_y=11.2 nm. Fig. 4(a) shows the position of dislocation core while Fig. 4(b) does the shear stress, τ_{zx}, on the simulation cell. The abscissa is time and the shear simulation starts from $t = 0$ fs. The position of dislocation core is evaluated from the atoms with high energy as marked in Fig. 5(a), one example of dislocation motion. In the figure, only the dislocation and precipitate are visualized with a certain threshold for potential energy. Back to Fig. 4(a), the dislocation begins to glide around $t = 20\,000$ fs and reaches to constant speed before $t = 50\,000$ fs, if there is no precipitate anterior to the dislocation (thick solid line). The shear stress also peaks out and shows constant flow stress at that point of steady motion (Fig. 4(b)). In the case of the YO diameter of $d = 0.6$ nm, the position–time and stress–time curves are very similar to those of without precipitate (dashed lines). That is, the

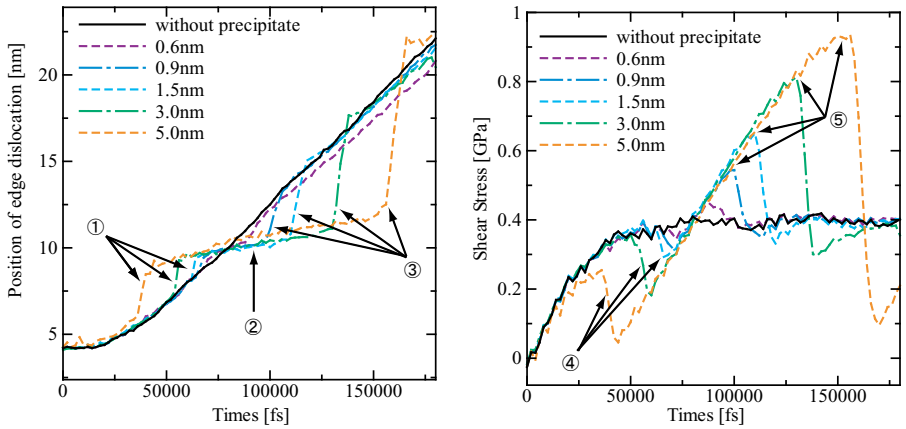

(a) Time–position curves (b) Time–shear stress curves

Figure 4: Change in the core position and shear stress (edge dislocation, $L_y = 11.2\,\mathrm{nm}$).

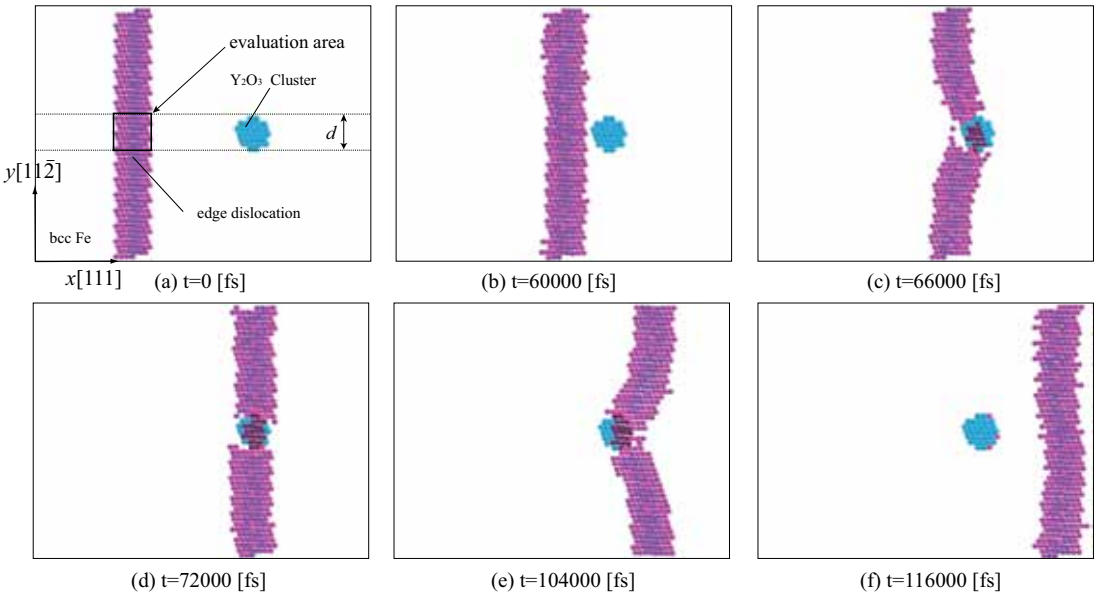

Figure 5: Motion of edge dislocation on the slip plane ($d = 1.5\,\mathrm{nm}$, L_y =11.2 nm).

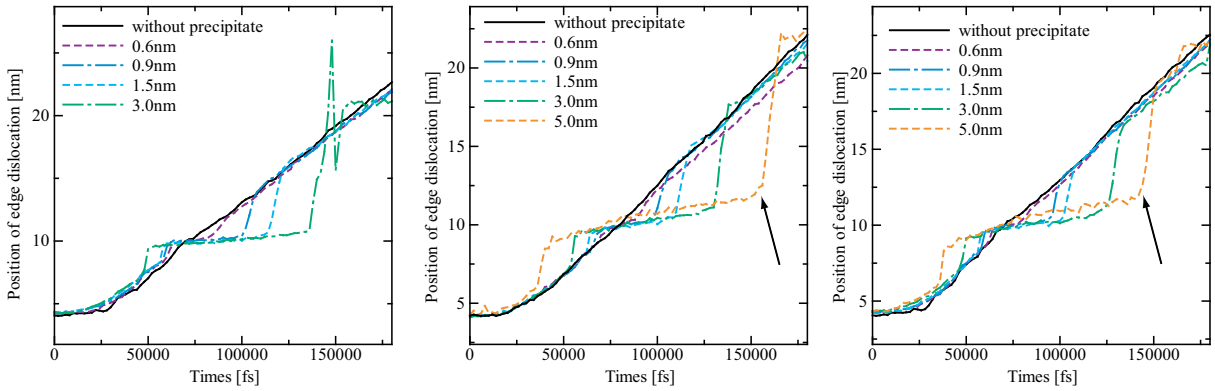

(a) 4.9[nm] (b) 11.2[nm] (c) 25.2[nm]

Figure 6: Position–time curves with different periodic length between precipitates (edge dislocation).

edge dislocation receives no resistance from such small precipitates of $d = 0.6\,\mathrm{nm}$. On the other hand, the dislocation motion is clearly affected by the YO precipitate larger than $d = 0.9\,\mathrm{nm}$, as previously shown in Fig. 5 for $d = 1.5\,\mathrm{nm}$. In the approaching process, the precipitate attracts the edge dislocation as shown in Fig. 5(c). On the other hand, the edge dislocation should largely bend to unlock the pinning (Fig. 5(e)). Both of them are the evidence that the YO precipitate has attractive effect on the edge dislocation. These tendency becomes more remarkable with the precipitate size, as indicated Arrows ① and ③ in Fig. 4(a). It is also noteworthy that the increased shear stress is first relaxed by the collision of dislocation and precipitate as indicated Arrows ④ in Fig. 4(b), while the unlock stress of Arrow ⑤ drastically increases with the precipitate size.

Figure 6 shows the position–time curves with different simulation cells of $L_y = 4.9, 11.2$ and $25.2\,\mathrm{nm}$. Fig. 6(b) is identical to Fig. 4(a). On Fig. 6(a), there is no space between YO precipitates of the diameter $d = 5\,\mathrm{nm}$ in the smallest cell length $L_y = 4.9\,\mathrm{nm}$, so that we omit the simulation. The diameter $d = 3\,\mathrm{nm}$ might be still large for the cell length $L_y = 4.9\,\mathrm{nm}$, since there is large oscillation around $t = 150\,000\,\mathrm{fs}$ where the trapped dislocation is unlocked and proceeds again. With the larger periodic distance or larger spacing between precipitates, the locked dislocation can largely bend. Thus the unlock time becomes shorter as shown with Arrow in Figs. 6(b) and 6(c) with the help of line tension of largely bent dislocation. On the other hand, the smallest precipitate $d = 0.6\,\mathrm{nm}$ is always similar to the case without precipitate, despite of the precipitate spacing.

4 SIMULATION ON SCREW DISLOCATION

4.1 Simulation procedure

Figure 7 shows the simulation model for screw dislocation. The slab cell looks like same as the previous simulation; however, the slip plane is set normal to the $[\bar{1}12]$ direction (y-axis) and periodicity is only set to the [111] direction (x-axis). As mentioned later, the

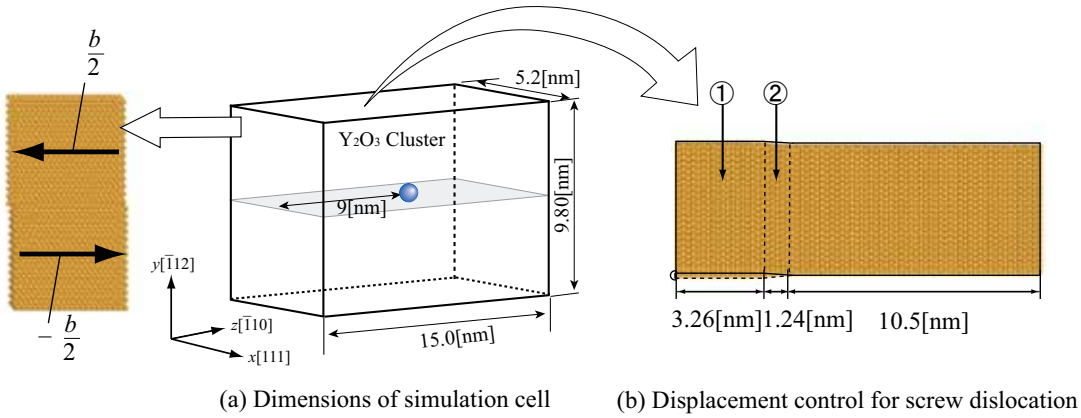

Figure 7: Simulation model for screw dislocation.

screw dislocation tends to change the slip plane so that we adopt narrow periodic length $L_x = 5.2\,\mathrm{nm}$ as the standard length. Atoms in the upper and lower half of $z < 3.26\,\mathrm{nm}$ from the front edge (Area ①) are alternately shifted in the x-axis, with the magnitude of $b/2$ (b; Burgers vector). Atoms in Area ② are also linearly shifted to connect the slipped and non-slipped area. As same as the previous simulations, the initial configuration is relaxed with 100 000 fs MD calculation under $T = 10\,\mathrm{K}$, for both cases with and without YO precipitate. The maximum diameter of the precipitate is $d = 3\,\mathrm{nm}$. Then, small displacement of $3.0 \times 10^{-6}\,\mathrm{nm}$ is applied in the [111] and $[\bar{1}\bar{1}\bar{1}]$ directions alternately on the upper and lower surfaces of the cell, to proceed the screw dislocation by the xy shear.

4.2 Results and discussion

Figure 8 shows the position–time and shear stress-time curves in the cell width of $L_x = 5.2\,\mathrm{nm}$. The horizontal dashed line in Fig. 8(a) indicates the center of YO precipitate. Also, the vertical broken lines in Figs. 8(a) and 8(b) mark the same time points. Contrary to the edge dislocation, there is no remarkable difference even with the large ($d \geq 0.9\,\mathrm{nm}$) precipitate. Figure 9 shows one example of dislocation motion in the simulation of $d = 1.5\,\mathrm{nm}$. Despite of the similar line tension as the previous Fig. 6(a), the screw dislocation feels no resistance to cut through the precipitate, leaving high energy atoms around the YO atoms. On the other hand, if we use the wider simulation cell of $L_x = 10.4\,\mathrm{nm}$, the dislocation shows various motion as indicated in the position of dislocation core in Fig. 10(b). Here Fig. 10(a) is identical to Fig. 8(a). The mechanism for the variation in Fig. 10(b) is different case by case; for example, the screw dislocation changes its slip plane and drags the jog-like high energy atoms at the point far away from the precipitate, and passes the precipitate–matrix interface as shown in Fig. 11 of $d = 0.9\,\mathrm{nm}$. In the case of $d = 3.0\,\mathrm{nm}$, the screw dislocation does change the slip plane too, but is attracted and trapped by the precipitate and leaves Orwan loop like defect around the precipitate

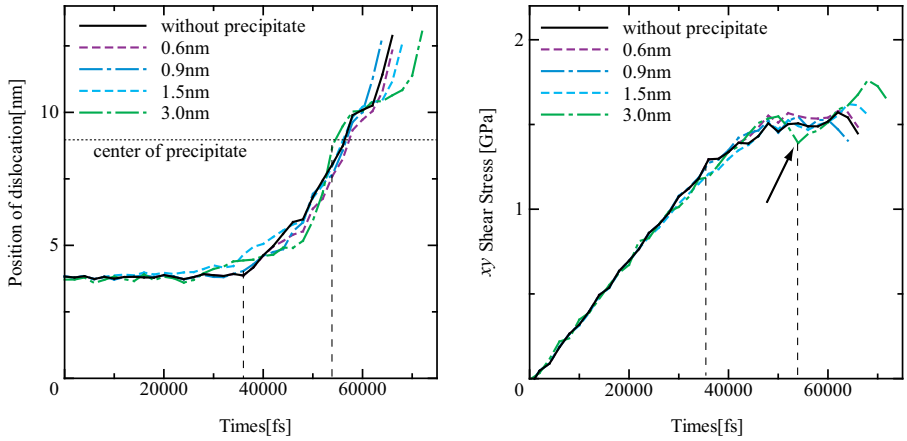

(a) Time–position curves (b) Time–shear stress curves

Figure 8: Change in the core position and shear stress (screw dislocation, $L_x = 5.2\,\mathrm{nm}$).

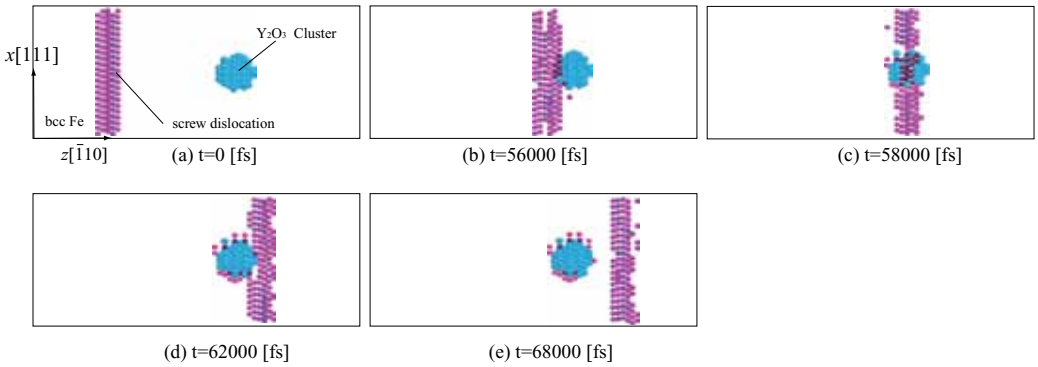

Figure 9: Motion of screw dislocation (L_x=5.2 nm, $d = 1.5\,\mathrm{nm}$).

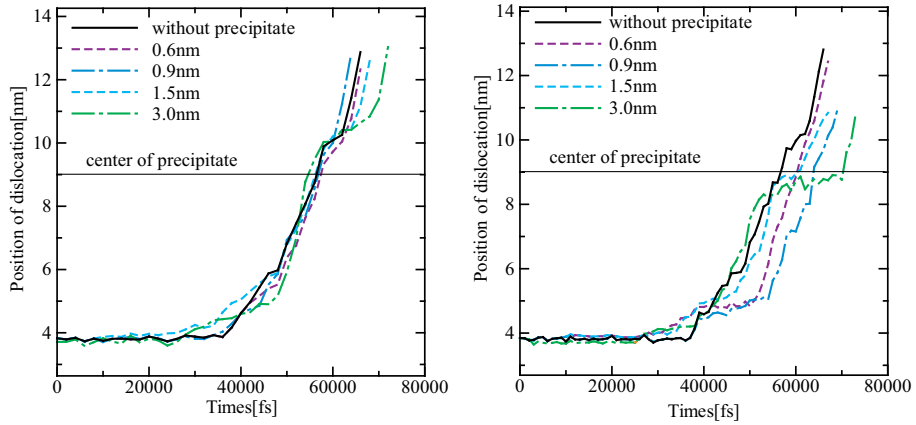

(a) 5.2[nm] (b) 10.4[nm]

Figure 10: Position–time curves with different periodic length between precipitates (screw dislocation).

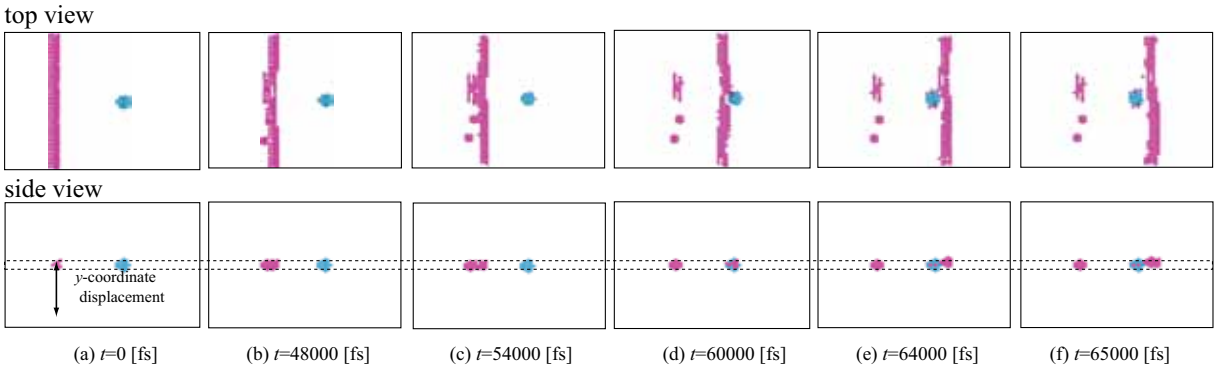

Figure 11: Motion of screw dislocation (L_x=10.4 nm, d = 0.9 nm).

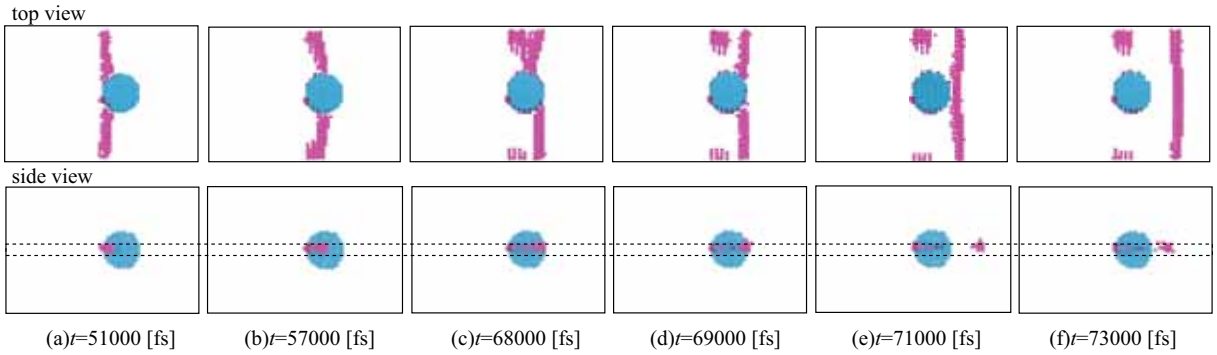

Figure 12: Motion of screw dislocation (L_x=10.4 nm, d = 3.0 nm).

(Fig. 12). Thus, it is difficult to obtain a clear tendency for the interaction between screw dislocation and YO precipitate. In addition, it also should be noted that the present model for screw dislocation has a large difference against the previous edge dislocation; that is, the simulation cell is not periodic in the glide direction and might be too small to mimic the dislocation motion in bulk. In this manner, more sophisticated model is so far needed for screw dislocation, and the present report could be a help for refinement.

5 CONCLUSIONS

We have performed various molecular dynamics simulations on the interaction between edge/screw dislocations and nanosphere of yttria oxide in bcc Iron, targetting the phenomena in oxide dispersion strengthened (ODS) steels. Since there is no all-round interatomic potential functions that can represent all the bonding state, i.e. metal, ion and covalent systems, we have adopted rough approximation that each atom in yttria oxide is not distinguished but treated as "monatomic" pseudo-atom, and its motion is represented with the simple pairwise potential function as same as Johnson potential for Fe. The potential parameters are fitted to the energy change in the hcp infinite crystal, by using the ab-

initio density functional theory (DFT) calculation against explicitly discriminated Y and O. We have observed various dislocation behavior by changing the diameter and periodic distance of the coherently precipitated YO cluster using a periodic slab cell. Although it is also clarified that we might need refinement of the simulation model for screw dislocation, still we have obtained many useful insight on the dislocation/yttria oxide interaction, *e.g.* (1) YO cluster larger than 0.9 nm strongly attracts and traps edge dislocation, (2) highly tensioned screw dislocation easily cut through the precipitate without resistance, and (3) loose screw dislocation shows complicated behavior by changing the slip plane, at the point far away from the precipitate.

REFERENCES

[1] T. Okuda, S. Nomura, S. Shikakura, K. Asabe, S. Tanoue and M. Fujiwara, Proc. Symp. Sponsored by the TMS Powder Metallurgy Committee, Indiana, p.195 (1989)

[2] S. Ukai, T. Nishida, H. Okada, T. Okuda, M. Fujiwara and K. Asabe, Development of Oxide Dispersion Strengthened Ferritic Steels for FBR Core Application, (1) Improvement of Machanical Properties by Recrystallization Processing, Journal of Nuclear Science and Technology, 34 (1997) 256–263.

[3] R. L. Klueh, P. J. Maziasz, I. S. Kim, L. Heatherly, D. T. Hoelzer, N. Hashimoto, E. A. Kenik and K. Miyahara, Tensile and Creep Properties of an Oxide Dispersion-Strengthened Ferritic Steel, Journal of Nuclear Materials, 307–311 (2002) 773–777.

[4] M. Ohnuma, J. Suzuki, S. Ohtsuka, S.-W. Kim, T. Kaito, M. Inoue and H. Kitazawa, A New Method for the Quantitative Analysis of the Scale and Composition of Nanosized Oxide in 9Cr-ODS steel, Acta Materialia, 57 (2009) 5571–5581.

[5] K. Yashiro, M. Naito and Y. Tomita, Molecular Dynamics Simulation of Dislocation Nucleation and Motion at γ/γ' Interface in Ni-Based Superalloy International Journal of Mechanical Sciences, 44 (2002) 1845–1860.

[6] K. Yashiro, F. Kurose, Y. Nakashima, K. Kubo, Y. Tomita and H. M. Zbib, Discrete Dislocation Dynamics Simulation of Cutting of γ' Precipitate and Interfacial Dislocation Network in Ni-Based Superalloys, International Journal of Plasticity, 22 (2006) 713–723.

[7] M. J. Alinger, B. D. Wirth,, H. J. Lee and G. R. Odette, Lattice Monte Carlo Simulations of Nanocluster Formation in Nanostructured Ferritic Alloys, Journal of Nuclear Materials, 367–370 (2007) 153–159.

[8] C. Hin, B. D. Wirth and J. B. Neaton, Formation of Y_2O_3 Nanoclusters in Nanostructured Ferritic Alloys during Isothermal and Anisothermal Heat Treatment: A Kinetic Monte Carlo Study, Physical Review B, 80 (2009) 134118.

[9] G. Kresse and J. Hafner, Ab Initio Molecular Dynamics for Liquid Metals, Physical Review B, 47 (1993) 558–561.

[10] E. N. Maslen, V. A. Streltsov, and N. Ishizawa, Acta Crystallographica B, 52 (1996) 414–422.

[11] D. Vanderbilt, Soft Self-Consistent Pseudopotentials in a Generalized Eigenvalue Formalism, Physical Review B, 41 (1990) 7892–7895.

[12] D. C. Langreth and J. P. Perdew, Theory of Nonuniform Electronic Systems. I. Analysis of the Gradient Approximation and a Generalization that Works, Physical Review B, 21 (1980) 5469–5493.

XI International Conference on Computational Plasticity. Fundamentals and Applications
COMPLAS XI
E. Oñate, D.R.J. Owen, D. Peric and B. Suárez (Eds)

MULTI-SCALE MODELLING FOR FERRITE-PEARLITE COMPOSITE STEEL

IKUMU WATANABE*, DAIGO SETOYAMA† AND NORITOSHI IWATA†

*National Institute for Materials Science (NIMS)
Sengen 1-2-1, Tsukuba, Ibaraki, 305-0047 Japan
e-mail: WATANABE.Ikumu@nims.go.jp, www.nims.go.jp/

†TOYOTA Central R&D Labs., Inc. (TCRDL)
Yokomichi 41-1, Nagakute, Aichi 480-1192 JAPAN

Key words: Microstructures, Multiscale Modeling, Finite Element Method

Abstract. The multiscale mechanical behaviors of Ferrite-Pearlite steel were predicted using Numerical Material Testing (NMT) based on the finite element method. The microstructure of Ferrite-Pearlite steel is regarded as a two-component aggregate of Ferrite crystal grains and Pearlite colonies. In the NMT, the macroscopic stress-strain curve and the deformation state of the microstructure were examined by means of a two-scale finite element analysis method based on the framework of the mathematical homogenization theory. For the NMT of Ferrite-Pearlite steel, constitutive models for Ferrite crystal grains and Pealite colonies were prepared to describe the anisotropic mechanical behavior at the micro-scale.

1 INTRODUCTION

The macroscopic material behavior is governed by the microstructure. The numerical homogenization approach was to evaluate the macroscopic material behavior from its microscopic information with a computational method, namely the finite element method. The feature of this methodology is that the morphology of the microstructure can be explicitly modeled with finite elements. Then the interaction between each component can be mechanically taken into consideration. In addition, the microscopic model undergoes the numerical examination under idealized macroscopic and microscopic states over and over again, which is almost impossible when carrying out actual experiments. In this study, the computational framework used to examine the material behavior is called *Numerical Material Testing* (NMT).

The key element to the success of such a numerical homogenization approach is to be able to describe the microscopic mechanism realistically in the form of a computational

model. Special attention has to be paid to constitutive models for each component of the microstructure in order to describe the microscopic material behavior. It should be noted that the microscopic material behavior is anisotropic even if the macroscopic material behavior is isotropic, making the standard constitutive models for macro-scale problem completely unsuitable to the microscopic components in general. The single crystal plasticity model is a well-known microscopic constitutive model for a metallic material, which expresses the crystallographically-defined plastic anisotropy.

Turning to the application of the computational approach based on the continuum mechanics into steel, various studies have been made on the numerical evaluation of the mechanical behavior because of the practical importance of steel as a structural material. General carbon steels are characterized with the precipitation of Cementite, which is an iron carbide, in various forms. A typical microstructure of Ferrite-Pearlite steel is depicted in Figure1, which is composed of several Ferrite crystal grains and Pearlite blocks. And a Pearlite block contains some Pearlite colonies characterized by the lamellar structures of Ferrite and Cementite phases. Such hierarchical heterogeneity is the dominant factor of the strength and the deformation characteristic.

In this study, we apply the framework of an NMT to evaluate and model the hierarchical mechanical behavior of Ferrite-Pearlite steel. Both anisotropic linear elasticity and single crystal plasticity models can be employed to describe the mechanical behavior of Ferrite crystal grains. However, the anisotropic constitutive model for Pearlite colonies has yet to be proposed. The constitutive model is newly formulated in reference to the results of the NMT for the microscopic lamellar structures composed of Ferrite and Cementite phases: that is, the NMT is carried out to produce mechanical behavior for the formulation of microscopic constitutive equations which can be substituted for the constitutive theory. In this sense, it is possible to approach the evaluation of mechanical behavior using physical computations as first principle calculations although the applicability of this approach is limited to elastic regions, given the limits we have.

2 HOMOGENIZATION METHOD AND CONSTITUTIVE MODEL FOR FERRITE CRYSTAL

2.1 Homogenization approach based on finite element method

In the two-scale finite element analysis method [1], a representative volume element (RVE) of the microstructure is discretized with finite elements and the microscopic boundary value problem (BVP) is simultaneously solved with the macroscopic BVP in the two-scale BVP. We here reduce the macroscopic BVP to a point-wise stress-strain relationship. Then the two-scale BVP turns into a problem to evaluate the material behavior of a numerical specimen represented as a microscopic finite element model under the control of the macroscopic stress or strain, i.e. this framework is regarded as *Numerical Material Testing* (NMT) based on the finite element method [2].

With this framework, we can evaluate both the macroscopic material response and

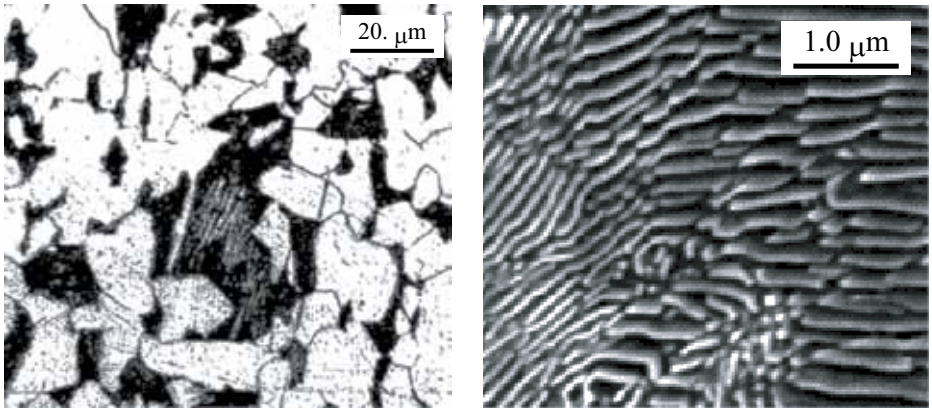

(a) Ferrite-Pearlite steel (b) Pearlite block

Figure 1: Microstructure of Ferrite-Pearlite steel. The Microstructure of Ferrite-Pearlite steel is composed of several Ferrite crystal grains and Pearlite blocks. Pearlite block contains some Pearlite colonies characterized with the lamellar structure of Ferrite and Cementite phases.

the deformation state of a microstructure. By conducting a series of numerical material tests, the macroscopic material response of the microstructure is examined in detail. In this study, we employ the computational approach to develop an anisotropic constitutive model depending on the morphology of the intended microstructure and identify the material constants of the constitutive model.

2.2 Elastic-plastic constitutive model for Ferrite single crystal

An anisotropic linear elasticity and a single crystal plasticity are introduced to capture the anisotropic mechanical behavior of a single crystal.

Here, we use the single crystal plasticity based on the representative characteristic length [3]. In this constitutive model, the critical resolved shear stress (CRSS) is characterized with the representative characteristic length, which in turn represents the dominant strengthening mechanics. In addition, the yield-point elongation and the hardening behavior can be described with the evolution of the dislocation density.

3 ELASTIC-PLASTIC CONSTITUTIVE MODEL FOR PEARLITE COLONY

3.1 Finite element model for Pearlite colony

The finite element model of the Pearlite colony is defined as shown in Figure2, where the white elements indicate the Ferrite phase and the others are Cementite phases. It is assumed that the Ferrite and Cementite lamellar structures are completely parallel with each other, the boundary between them does not slip, and this finite element model satisfies the geometrical periodicity boundary condition. Also, the normal vector, $\boldsymbol{m}_0$, of the lamella is set as heading in the direction of Y_3 at the initial configuration for the

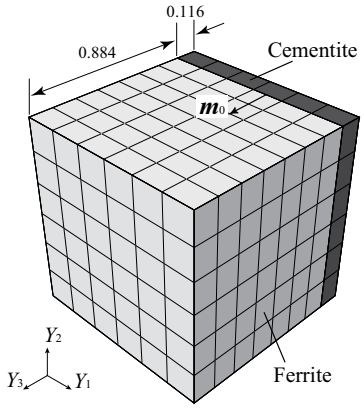

Figure 2: Finite element model of Pearlite colony. The white and shaded areas indicate the Ferrite and Cementite phases, respectively. The normal vector of the lamella indicates $\boldsymbol{m}_0$ at the initial state.

formulation of the constitutive model. Here we employ the crystallographic orientation relationships of Bagaryatskii [4] as below:

$$\begin{cases} (001)_{\text{Cementite}} \ // \ (211)_{\text{Ferrite}} \\ [100]_{\text{Cementite}} \ // \ [0-11]_{\text{Ferrite}} \\ [010]_{\text{Cementite}} \ // \ [-111]_{\text{Ferrite}} \end{cases} \tag{1}$$

In addition, the mechanical character of the Cementite phase is considered as an elastic material, whereas this does not seem to be true in the finite strain range as mentioned later.

3.2 Numerical Material Tests for Pearlite colony

The macroscopic elastic-plastic material behavior was investigated with an NMT for the microscopic finite element model of the Pearlite colony.

3.2.1 Elasticity

The components of the fourth order elastic tensor were estimated with finite element analyses of the RVE (Figure2). Before that, however, the elastic constants of both the Ferrite and Cementite phases must be prepared for computation. For the Ferrite phase, the values were taken from the experimental database. The metastability of Cementite, however, makes it extremely difficult to estimate the elasticity of Cementite phase. The first-principles calculations in this study were performed by the projector augmented wave method [5, 6] as implemented in the Vienna *ab-initio* simulation package (VASP) [7, 8]. The elastic constants estimated from the calculation are presented as below, where the

Table 1: Components of fourth order elastic tensor for Pearlite colony.

Component	$\hat{\mathbb{C}}^{e}_{1111}$	$\hat{\mathbb{C}}^{e}_{2222}$	$\hat{\mathbb{C}}^{e}_{3333}$	$\hat{\mathbb{C}}^{e}_{1122}$	$\hat{\mathbb{C}}^{e}_{2233}$	$\hat{\mathbb{C}}^{e}_{1133}$	$\hat{\mathbb{C}}^{e}_{1212}$	$\hat{\mathbb{C}}^{e}_{1313}$	$\hat{\mathbb{C}}^{e}_{2323}$
[GPa]	302.	313.	292.	98.	100.	115.	69.	94.	74.
Component	$\hat{\mathbb{C}}^{e}_{1112}$	$\hat{\mathbb{C}}^{e}_{1113}$	$\hat{\mathbb{C}}^{e}_{1123}$	$\hat{\mathbb{C}}^{e}_{2212}$	$\hat{\mathbb{C}}^{e}_{2213}$	$\hat{\mathbb{C}}^{e}_{2223}$	$\hat{\mathbb{C}}^{e}_{3312}$	$\hat{\mathbb{C}}^{e}_{3313}$	$\hat{\mathbb{C}}^{e}_{3323}$
[GPa]	0.	0.	-26	0.	-26	1.	0.	0.	27.

Component	$\hat{\mathbb{C}}^{e}_{1213}$	$\hat{\mathbb{C}}^{e}_{1223}$	$\hat{\mathbb{C}}^{e}_{1323}$
[GPa]	0.	0.	0.

anisotropy is orthotropic in type.

$$\begin{array}{lll} \hat{\mathbb{C}}^{e(Fe_3C)}_{1111} = 397.0\text{GPa} & \hat{\mathbb{C}}^{e(Fe_3C)}_{2222} = 364.0\text{GPa} & \hat{\mathbb{C}}^{e(Fe_3C)}_{3333} = 317.\text{GPa} \\ \hat{\mathbb{C}}^{e(Fe_3C)}_{1122} = 168.\text{GPa} & \hat{\mathbb{C}}^{e(Fe_3C)}_{2233} = 183.3\text{GPa} & \hat{\mathbb{C}}^{e(Fe_3C)}_{1133} = 154.\text{GPa} \\ \hat{\mathbb{C}}^{e(Fe_3C)}_{1212} = 66.\text{GPa} & \hat{\mathbb{C}}^{e(Fe_3C)}_{1313} = 138.\text{GPa} & \hat{\mathbb{C}}^{e(Fe_3C)}_{2323} = 142.\text{GPa} \end{array} \tag{2}$$

Using the finite element model presented in Figure2 and the elastic constants, the components of the elastic tensor of Pearlite colony were numerically evaluated, with the macroscopic deformation modes corresponding to each strain component imposed on the finite element model of the microstructure. The resulting values are give in Table1, where the anisotropy is described with twenty-one independent elastic constants.

3.2.2 Plasticity

After determining the elastic material behavior of the Pearlite colony, the next step was to evaluate its plasticity with an NMT based on the finite element method. Here it is assumed that the Cementite phase is elastic. Also, the elastic-plastic material behavior of the Ferrite phase was characterized with the constitutive model explained in Section 2.2. The material constants of the plasticity of the Ferrite phase were found after trial and error by comparing between a result of an experimental axial tensile test for a Ferrite single-phase steel and the macroscopic stress-strain curve of the corresponding NMT. Considering the rotational symmetry of the lamellar structure for the third coordinate axis, five macroscopic deformation modes, i.e. the five components of macroscopic displacement gradient listed below, were respectively imposed on the finite element model of the microstructure of Pearlite colony (Figure2) until there was sufficient large strain to describe the macroscopic plastic behavior:

$$\tilde{H}_{11}, \quad \tilde{H}_{12}, \quad \tilde{H}_{13}, \quad \tilde{H}_{31}, \quad \tilde{H}_{33}, \tag{3}$$

which are two types of uniaxial deformation mode and three types of simple shear deformation mode.

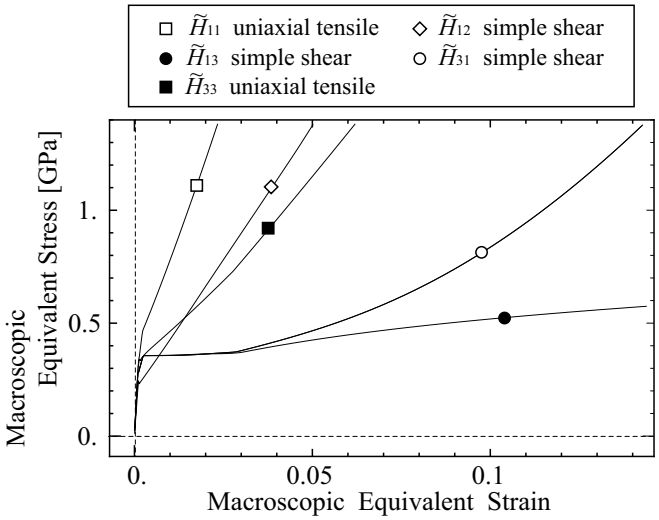

Figure 3: Macroscopic stress-strain curves of Pearlite colony.

The resulting macroscopic, or homogenized, equivalent stress-strain curves are illustrated in Figure3, where the equivalent stress is the Mises stress and the equivalent strain is defined with Henky strain $\boldsymbol{\epsilon} = \frac{1}{2}\ln\left[\boldsymbol{F}\boldsymbol{F}^{\mathrm{T}}\right]$ as

$$\epsilon^* := \sqrt{\frac{2}{3}\mathrm{dev}\left[\boldsymbol{\epsilon}\right] : \mathrm{dev}\left[\boldsymbol{\epsilon}\right]}. \tag{4}$$

As it can be seen, the results clearly indicate strong anisotropic plastic behavior, which is extremely stiff after yielding except in the case of the simple shear deformation modes $\tilde{H}_{13}$ and $\tilde{H}_{31}$. The response of $\tilde{H}_{13}$, the interlamellar shear deformation mode, is particularly close to the material behavior of the Ferrite phase.

With regard to the microscopic investigation, three representative deformation states and stress values at a macroscopic equivalent strain of 10 % are depicted in Figure4 with the equivalent stress values of each phases. It needs to be pointed out that the stress values of the Cementite phase are unrealistically high in these results except for the interlamellar shear deformation mode. It is quite likely that such a high stress state induces some dissipation mechanics, e.g. in the plastic behavior of the Cementite phase or debonding at the boundary between the Ferrite and Cementite phases. Although some studies have been carried out with the aim of observing such microscopic material behavior, the deformation mechanism of the Cementite phase at finite strain is still controversial. Regardless of the cause of the dissipation behavior, the plastic deformation of the Ferrite phase appears to be released from the constraint and also the macroscopic yielding stands out on the macroscopic, or homogenized, stress-strain curve of Pearlite colony.

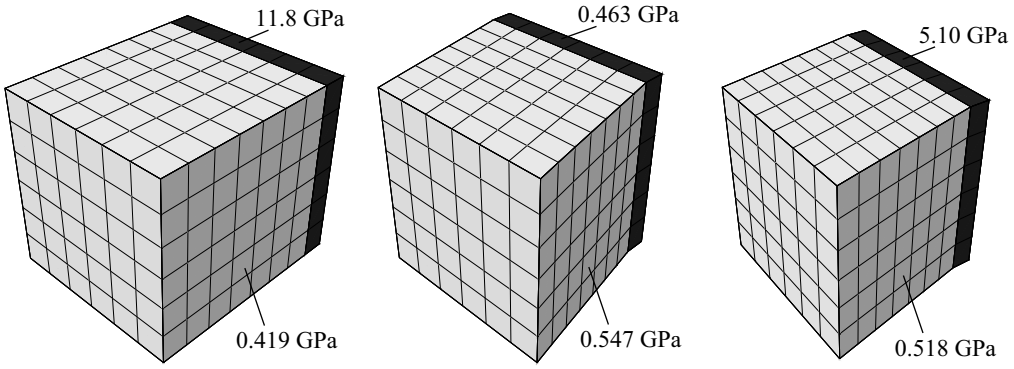

(a) $\tilde{H}_{33}$ (uniaxial tensile) (b) $\tilde{H}_{13}$ (simple shear) (c) $\tilde{H}_{31}$ (simple shear)

Figure 4: Microscopic deformation state of Pearlite colony. The stress states are homogeneous in each phase and the equivalent stress values are written in the Figure.

3.3 Plastic constitutive model for Pearlite colony

Based on the characterization of the anisotropic material behavior using the NMT, we propose the anisotropic plastic constitutive model for the Pearlite colony. In this study, the plastic behavior of the Pearlite colony is defined as two-stage yielding behavior; interlamellar shear yielding and the yielding of overall microstructure. That is, the plastic constitutive model for the Pearlite colony is described with two yield functions consisted of an anisotropic interlamellar shear plasticity and a standard isotropic metal plasticity. For the Kirchhoff stress $\boldsymbol{\tau}$ and the plastic internal variables $\zeta^{(\alpha)}$ ($\alpha = 1, 2$), the two yield functions are defined at current configuration as below:

$$\psi^{(1)} := |\boldsymbol{s} \cdot (\boldsymbol{\tau}\boldsymbol{m})| - \left(\tau_{\mathrm{Y}}^{(1)} + h_{11}\zeta^{(1)} + h_{12}\zeta^{(2)}\right) \leq 0 \tag{5}$$

$$\psi^{(2)} := \sqrt{\frac{3}{2}\mathrm{dev}[\boldsymbol{\tau}] : \mathrm{dev}[\boldsymbol{\tau}]} - \left(\tau_{\mathrm{Y}}^{(2)} + h_{21}\zeta^{(1)} + h_{22}\zeta^{(2)}\right) \leq 0 \tag{6}$$

where $\tau_{\mathrm{Y}}^{(\alpha)}$ is the initial yield stress for the α-th yield function ($\alpha = 1$ or 2) and $h_{\alpha\beta}$ ($\alpha, \beta =$ 1 or 2) is the hardening coefficient containing cross-hardening. The first yield function $\psi^{(1)}$ represents the slip behavior on the lamellar structure. The slip direction vector $\boldsymbol{s}$ and the normal vector $\boldsymbol{m}$ are pushed forward from the intermediate configuration with the elastic deformation gradient $\boldsymbol{F}^{\mathrm{e}}$ as

$$\boldsymbol{s} = \boldsymbol{F}^{\mathrm{e}}\boldsymbol{s}_0, \quad \boldsymbol{m} = \boldsymbol{F}^{\mathrm{e}-\mathrm{T}}\boldsymbol{m}_0, \tag{7}$$

where $\boldsymbol{s}_0$ and $\boldsymbol{m}_0$ are respectively the slip direction vector and the normal vector of the lamella at the intermediate configuration. With equation (7), the yield functions at the

intermediate configuration are given as below:

$$\psi^{(1)} := \left|\hat{\boldsymbol{T}} : (\boldsymbol{s}_0 \otimes \boldsymbol{m}_0)\right| - \left(\tau_{\mathrm{Y}}^{(1)} + h_{11}\zeta^{(1)} + h_{12}\zeta^{(2)}\right) \leq 0 \tag{8}$$

$$\psi^{(2)} := \sqrt{\frac{3}{2}\mathrm{dev}[\hat{\boldsymbol{T}}] : \left(\mathrm{dev}[\hat{\boldsymbol{T}}]\right)^{\mathrm{T}}} - \left(\tau_{\mathrm{Y}}^{(2)} + h_{21}\zeta^{(1)} + h_{22}\zeta^{(2)}\right) \leq 0 \tag{9}$$

The slip direction vector $\boldsymbol{s}_0$ is determined as the unit vector which indicates the direction of the innerlamellar component of the traction force vector $\hat{\boldsymbol{T}}\boldsymbol{m}_0$ on the lamella, i.e. it is defined with the normal vector $\boldsymbol{m}_0$ and the stress state $\hat{\boldsymbol{T}}$ as below:

$$\boldsymbol{s}_0 := \frac{\boldsymbol{t}}{\sqrt{\boldsymbol{t}\cdot\boldsymbol{t}}}, \qquad \boldsymbol{t} := \hat{\boldsymbol{T}}\boldsymbol{m}_0 - \left\{\boldsymbol{m}_0 \cdot \left(\hat{\boldsymbol{T}}\boldsymbol{m}_0\right)\right\}\boldsymbol{m}_0 \tag{10}$$

In equations (8) and (9), only h_{22} is defined as a non-linear function of $\zeta^{(1)}$ to express the non-linear hardening behavior:

$$h_{22} := \left(h_{22}^0 - h_{22}^\infty\right)\exp\left[-p\zeta^{(2)}\right] + h_{22}^\infty, \tag{11}$$

where p is a sensitivity of the exponential function, h_{22}^0 is the initial value of h_{22} and h_{22}^∞ is the corresponding convergent value. In this study, we are not concerned with the strengthening effect of lamellar spacing, but it is possible to introduce the effect on the material constants of the initial strength and the hardening behavior.

Finally, the proposed constitutive model was examined by making a comparison between its response and the results of the NMT of the Pearlite colony. The equivalent stress-strain curves are evaluated for three deformation modes corresponding to the components of the displacement gradient, H_{11}, H_{13} and H_{31}, where it is assumed that the vector $\boldsymbol{m}_0$ is directed to the coordinate axis direction Y_3 in the same way as the finite element model in Figure2. Here the plastic behavior of the interlamellar shear deformation mode is determined from NMT, and the constants of isotropic hardening were found by trial and error as they were for the Ferrite phase. The results are shown in Figure5.

4 NUMERICAL ANALYSIS FOR FERRITE-PEARLITE STEEL

The NMT based on finite element method was performed to predict the mechanical behavior of Ferrite-Pearlite steel with the constitutive models discussed in Section 2 and 3, and the computational results were compared with the experimental results.

4.1 Setting of finite element model of microstructure

We set the finite element models of the microstructure for Ferrite-Pearlite steel to carry out the following NMT.

The basic finite element model given in Figure6 is assumed to satisfy the geometrical periodicity condition and is composed of fifty-four blocks. In this finite element model, each block has an idealized geometry of truncated octahedrons and is discretized by eighty

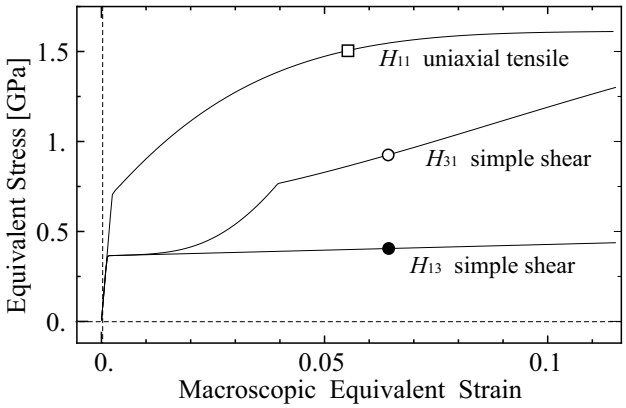

Figure 5: Stress-strain curves of constitutive model of Pearlite colony. The vector $\boldsymbol{m}_0$ is set up as an unit vector directed to third coordinate axis.

standard isoparametric hexahedron finite elements. In addition, each block is recognized as either Ferrite or Pearlite. The properties of the blocks are randomly arranged in accordance with the volume fraction of the Ferrite-Pearlite steel under consideration, where the discretely-distributed microstructure of Ferrite-Pearlite steel is supposed as Figure1(a); the finite element model shown in Figure6 is made of 33 percent Pearlite. If the property of a block is Ferrite, the block is recognized as a single grain. If it is Pearlite, the block is equally divided into eight colonies as illustrated in Figure6. That is, Pearlite always exists as an aggregate composed of some Pearlite colonies. Anisotropic elastic-plastic constitutive models for Ferrite single crystals and Pearlite colonies, which are presented in Section 2 and 3, are employed for the corresponding components. As mentioned before, some material constants of plasticity were determined to reproduce the stress-strain curves in experimental axial tensile tests as the results of the homogenization analyses. The orientations of each Ferrite crystal grain and Pearlite colony, i.e. the crystallographic orientations and the direction of the normal vector of the lamella, are provided in a random fashion.

4.2 Numerical results and validation

First, we investigate the elastic constants of Ferrite single-phase steel (Pearlite volume fraction 0 percent) and full Pearlite steel (Pearlite volume fraction 100 percent) with an NMT for the microstructure shown in Figure6, which is the same as the NMT used for the Pearlite colony. The almost isotropic material behaviors are evaluated in this computations. The results were acceptable values of the Young modulus and Poisson's ratio for each steel, as estimated as below:

$$\begin{aligned} E^{(\text{Ferrite})} &\simeq 200.\ \text{GPa} \qquad & \nu^{(\text{Ferrite})} &\simeq 0.296 \\ E^{(\text{Pearlite})} &\simeq 216.\ \text{GPa} \qquad & \nu^{(\text{Pearlite})} &\simeq 0.288 \end{aligned} \tag{12}$$

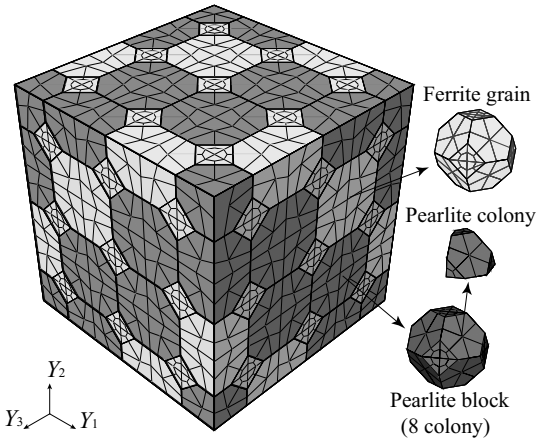

Figure 6: Finite element model of microstructure of Ferrite-Pearlite steel. The finite element model is composed of 54 blocks. Each block has an idealized geometry of a truncated octahedron and is recognized as a Ferrite crystal grain or a Pearlite block equally divided into eight colonies.

Obviously, the elasticity of Ferrite-Pearlite steel takes a value intermediate between these.

Next, we performed a series of numerical experiments in which the volume fraction of Ferrite/Pearlite was changed. Macroscopic uniaxial tensile deformation was imposed to the finite element model of Ferrite-Pearlite microstructure in the corresponding Y_1 direction, as illustrated in Figure6. The resulting macroscopic stress-strain curves are almost isotropic because Ferrite and Pearlite blocks are randomly arranged in the finite element model of the microstructures. The macroscopic, or homogenized, axial stress-strain curves of five cases are presented in Figure7, where the experimental results of three cases, Pearlite volume fraction 0 percent, 38 percent and 100 percent, are illustrated together by the dashed lines. Here we prepare a tensile test specimen of Ferrite-Pearlite steel which consists of almost the same scale of lamellar spacing with the corresponding specimen of full Pearlite steel to cut off a strengthening effect of the lamellar spacing.

The numerical results for Pearlite with a volume fraction of 0 percent and 100 percent is obiously similar since the material constants of the results of the NMTs reproduce the experimental results. Furthermore the experimental stress-strain curve of the Ferrite-Pearlite steel with a volume fraction of 38 percent is close to the numerical result with a 33 percent volume fraction. Therefore it is concluded that this NMT successfully predicted macroscopic mechanical behavior.

For the composite case (Pearlite volume fraction 33 percent, i.e. the finite element model Figure6), the distributions of equivalent stress and maximum principal strain are depicted in Figure8 at the point where the macroscopic axial strain is 15 percent. In this figure, the stress states are significantly different between Ferrite grains and Pearlite blocks. Compared to the arrangement of Ferrite grains and Pearlite blocks in Figure6, the Ferrite grains underwent more plastic deformation than the Pearlite blocks due to the

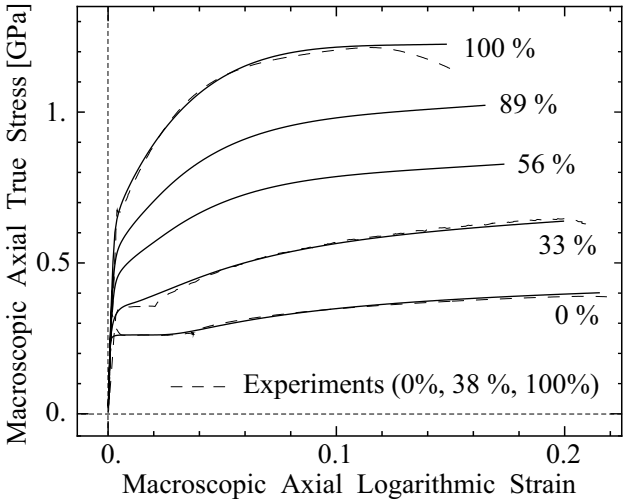

Figure 7: Macroscopic axial stress-strain curves of Ferrite-Pearlite steel. The solid and the dash lines indicate numerical and experimental results respectively.

higher yield strength of the Pearlite blocks.

5 CONCLUSIONS

We have predicted multiscale mechanical behavior of Ferrite-Pearlite steel with the hierarchical Numerical Material Testing using a deductive approach. A first principle calculation was performed to estimate the components of fourth order elastic tensor of the Cementite phase. With the elastic tensor, an NMT based on the finite element analysis was conducted to evaluate the anisotropic mechanical behavior of a Pearlite colony. Based on the resultant homogenized mechanical behavior of the Pearlite colony, an anisotropic plastic constitutive model for Pearlite colonies proposed to enable the NMT for Ferrite-Pearlite steel to be carried out. Finally, both the macroscopic and microscopic mechanical behavior of Ferrite-Pearlite steel was predicted with the NMT. We were thus able to demonstrate that this numerical approach provides acceptable results at both the macro- and micro-scale.

REFERENCES

[1] Terada K, Saiki I, Matsui K, Yamakawa Y. Two-scale kinematics and linearization for simultaneous two-scale analysis of periodic heterogeneous solids at finite strain. *Comput Meth Appl Mech Eng* (2003) **192** 3531–3563.

[2] Watanabe I, Terada K. A method of predicting macroscopic yield strength of polycrystalline metals subjected to plastic forming by micro-macro de-coupling scheme. *Int J Mech Sci* (2010) **52** 343–355.

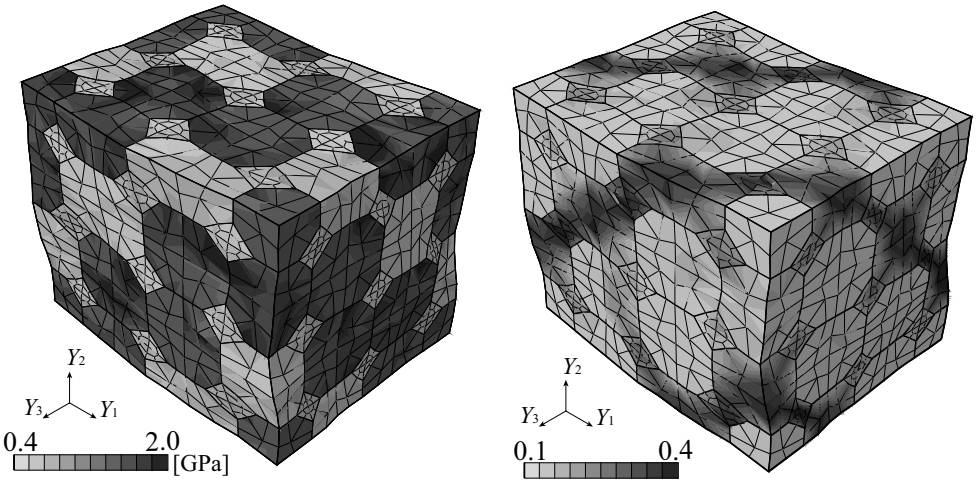

(a) Equivalent stress (b) Maximum principal strain

Figure 8: Microscopic stress and strain distributions for Ferrite-Pearlite steel. These figures show the results of the case of Pearlite volume fraction 33 % at a point of macroscopic axial strain 15 % on macroscopic axial stress-strain curve of Figure7.

[3] Watanabe I, Setoyama D, Iwata N, Nakanishi K. Characterization of yielding behavior of polycrystalline metals with single crystal plasticity based on representative characteristic length. *Int J Plasticity* (2010) **26** 570–585.

[4] Bagaryatskii YA. Possible mechanism of martensite decomposition. *Dokl Acad Nauk SSSR* (1950) **73** 1161–1164,.

[5] Blöchl PE. Projector augmented-wave method. *Phys Rev B* (1994) **50** 17953–17979.

[6] Kresse G, Joubert D. From ultrasoft pseudopotentials to the projector augmented-wave method. *Phys Rev B* (1999) **59** 1758–1775.

[7] Kresse G, Furthmuller J. Efficiency of ab-initio total energy calculations for metals and semiconductors using a plane-wave basis set. *Comput Mater Sci* (1996) **6** 15–50.

[8] Kresse G, Furthmuller J. Efficient iterative schemes for ab initio total-energy calculations using a plane-wave basis set. *Phys Rev B* (1996) **50** 11169–11186.

XI International Conference on Computational Plasticity. Fundamentals and Applications
COMPLAS XI
E. Oñate, D.R.J. Owen, D. Peric and B. Suárez (Eds)

NUMERICAL INVESTIGATIONS OF MECHANICAL STRESS CAUSED IN DENDRITE BY MELT CONVECTION AND GRAVITY

H. Kashima*, T. Takaki†, T. Fukui† and K. Morinishi†

* Mechanical and system Engineering
Kyoto Institute of Technology
Matsugasaki, Sakyo, Kyoto, 606-8585, Japan
e-mail: m0623012@kit.ac.jp

† Mechanical and system Engineering
Kyoto Institute of Technology
Matsugasaki, Sakyo, Kyoto, 606-8585, Japan
e-mail: takaki@kit.ac.jp, www.cis.kit.ac.jp/~takaki/

Key words: Dendrite, Fragmentation, Solidification, Melt Convection, Stress, Phase-Field Method, Navier-Stokes Equations, Finite Element Method.

Abstract. In order to investigate the effects of stress around dendrite neck cased by the convection and gravity on the dendrite fragmentation, the novel numerical model, where phase-field method, Navier-Stokes equations and finite element method are continuously and independently employed, has been developed. By applying the model to the dendritic solidification of Al-Si alloy, the maximum stress variations by melt convection and gravity with dendrite growth were evaluated.

1 INTRODUCTION

Dendrite plays especially important role for formation of solidification microstructure of metallic alloy, because it determines the size and shape of solidified grains. Therefore, it is essential for high quality casting to predict and control the dendritic morphology with high accuracy.

In casting, the final microstructure in the ingot is formed through two different dendritic growths. One is columnar structure, in which the dendrites grow preferentially oriented perpendicular to the mold walls, and the other is equiaxed structure, in which the dendrites grow in all space directions. In particular, the equiaxed grain structure has a dominant influence on the mechanical characteristics of casting product, because it controls the size of solidification microstructure. One of the sources of the equiaxed grains is thought to be the dendrite fragmentations caused in columnar region.

It is reported that the dendrite fragmentation occured by local remelting and the mechanical fragmentation due to the melt flow is not important for grain refinement [1] except for rapid solidification [2]. Recently, studies using in-situ and real-time observations reported that the mechanical stress caused by the melt convection and the gravity promotes the dendrite fragmentation [3]. However, its detail mechanism is not yet elucidated.

In this study, in order to reveal the effects of mechanical stress caused by the convection

and gravity on dendrite fragmentation, we developed a new simulation model and investigate the stress in dendrite neck. The coupling simulations by phase-field method, Navier-Stokes equations and finite element method are performed. In this simulation, first, realistic dendritic morphologies are simulated by phase-field method and, successively, the flow fields around the dendrite are simulated by Navier-Stokes equations. Lastly, the stresses in dendrite caused by melt convection and gravity are calculated by finite element method. The variations of maximum stress occurred at the dendrite neck with dendrite growth are discussed.

2 NUMERICAL PROCEDURE AND MODELS

2.1 Numerical procedure

The dendritic growth of Al-Si alloy and the flow field of solution around the dendrite in forced flow are simulated. And then, the stresses in dendrite caused by the flow and gravity are calculated. The calculations are performed in the order of phase-field method, Navier-Stokes equation and finite element method.

At first, the dendrite morphologies during solidification of Al-Si alloy are simulated by the phase-field method. Next, the fluid flow around the dendrite is simulated by using two-phase Navier-Stokes equations and the pressure distributions acting on the dendrite surface are calculated. Lastly, the stress distributions in the dendrite caused by the fluid flow and gravity are simulated by using finite element method. In the following, the phase-field model and the two-phase Navier-Stokes equation are explained in detail.

2.2 Phase-field model

The dendritic growth of Al-Si alloy in isothermal condition is simulated by the phase-field method. The evolution equation of phase field variable ϕ, which takes 1 in a solid and 0 in a liquid, is expressed by

$$\frac{\partial \phi}{\partial t} = M_\phi \left[\nabla (a^2 \nabla \phi) - \frac{\partial}{\partial x}\left(a \frac{\partial a}{\partial \theta} \frac{\partial \phi}{\partial y} \right) + \frac{\partial}{\partial y}\left(a \frac{\partial a}{\partial \theta} \frac{\partial \phi}{\partial x} \right) + 4W\phi(1-\phi)(\phi - 0.5 + \beta) \right], \quad (1)$$

where, τ is the time and a is the gradient coefficient considering interface anisotropy by the equation $a(\theta) = \bar{a}\{1 + \zeta \cos(k\theta)\}$, where θ is the angle between x-axis and interface normal, ζ is the strength of anisotropy and κ is the anisotropy mode of κ=4. β in the Eq. (1) is expressed by

$$\beta = -\frac{15}{2W}\phi(1-\phi)\Delta S(T - T_m(c)). \quad (2)$$

Here, ΔS is the transformation entropy, T is the temperature, Tm is the temperature on the linearized liquidus line expressed by $T_m = m_L c + T_r$, where mL is the liquidus slope, c is the

solute concentration, *Tr* is a reference temperature. In addition, $\bar{a}$, W and M_ϕ in Eq.(1) can be related to the material parameters by following equations:

$$\bar{a} = \sqrt{\frac{3\delta\gamma}{b}},\ W = \frac{6\gamma b}{\delta},\ M_\phi = \frac{\sqrt{2W}}{6a}M\ , \tag{3}$$

where, δ is the interface thickness, γ is the interface energy, M is the interface mobility, and $b = 2\tanh^{-1}(1-2\lambda)$ is a constant related to interface thickness, where $\lambda = 0.1$ is employed. The concentration *c* in Eq.(2) is calculated by the following diffusion equation

$$\frac{\partial c}{\partial t} = \nabla D\left[\nabla c + \frac{(1-k)c}{1-\phi+k\phi}\nabla\phi\right], \tag{4}$$

where, *k* is the partition coefficient given by $k = cs/c_L$, where *cs* and *cL* are the concentrations in solid and liquid, respectively. The concentration *c* is defined by

$$c = \phi c_S + (1-\phi)c_L\ . \tag{5}$$

Diffusion coefficint *D* in Eq.(4) is indicated by

$$D = D_s + (D_L - D_S)\frac{1-\phi}{1-\phi+k\phi}, \tag{6}$$

where, *Ds* and *DL* are diffusion coefficients of solid and liquid, respectively.

2.3 Two-phase Navier-Stokes model

The melt convection around dendrite in forced flow is simulated by the following two-phase Navier-Stokes equations using phase-field parameter [4, 5].

$$\frac{\partial(1-\phi)u}{\partial x} + \frac{\partial(1-\phi)v}{\partial y} = 0\ . \tag{7}$$

$$\frac{\partial(1-\phi)u}{\partial t} + u(1-\phi)\frac{\partial u}{\partial x} + v(1-\phi)\frac{\partial u}{\partial y} = -\frac{1}{\rho}(1-\phi)\frac{\partial p}{\partial x} + \nu\left(\frac{\partial^2(1-\phi)u}{\partial x^2} + \frac{\partial^2(1-\phi)u}{\partial y^2}\right) + F_{dx}\ . \tag{8}$$

$$\frac{\partial(1-\phi)v}{\partial t} + u(1-\phi)\frac{\partial v}{\partial x} + v(1-\phi)\frac{\partial v}{\partial y} = -\frac{1}{\rho}(1-\phi)\frac{\partial p}{\partial y} + \nu\left(\frac{\partial^2(1-\phi)v}{\partial x^2} + \frac{\partial^2(1-\phi)v}{\partial y^2}\right) + F_{dy}\ . \tag{9}$$

Here, u and v are velocities in x and y direction, respectively. ρ is the flow density, p is the pressure, and ν is the kinetic viscosity. Note that, in the liquid of $\phi = 0$, Eqs. (7) - (9) reduce to the normal single-phase Navier-Stokes equations for a Newtonian fluid with a constant density and viscosity. The last term on the right hand side of Eq.(8) and Eq.(9), or F_{dx} and F_{dy}, are employed to account for the dissipative viscous stress in the liquid due to interactions with the solid in the diffuse interface region and expressed by

$$F_{dx} = \mu_L \frac{h_d \phi^2 (1-\phi)}{\Delta^2} u \,, \tag{10}$$

$$F_{dy} = \mu_L \frac{h_d \phi^2 (1-\phi)}{\Delta^2} v \,, \tag{11}$$

where, μ_L is the kinetic coefficint, Δ is the thickness of interface which is expressed by $\Delta = \delta / \Delta x$, where Δx is the lattice size. The *hd* is a dimensionless constant which is determined by numerical experiment.

3 NUMRICAL RESULTS

3.1 Dendritic growth simulations by phase-field method

By coupling Eq.(1) and Eq.(4), dendritic growths of Al-Si alloy under isothermal condition are simulated. Figure 1 shows the computational domain and initial conditions.

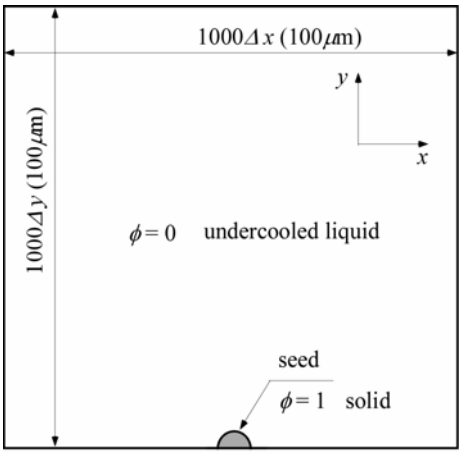

Figure 1 : Computational domain and boundary conditions
for dendritic growth simulation by phase-field method

Initially, all regions are filled with the undercooled liquid ($\phi = 0$), and temperature and concentration is set to be T = 886 K and c = 0.06, respectively. To simulate the dendritic growth from the bottom of computational domain which images the mold wall, one semicircle seed with radius $6\Delta x$ is putted on the bottom of the region. Computational domain with 100μm×100μm is divided into 1000×1000 finite different lattices. Therefore, the lattice size $\Delta x = \Delta y$ is to be 100 nm. The zero Neumann boundary conditions are employed on all boundaries for both ϕ and c. In the present simulations, we focus on the growth of first dendrite arm. Therefore, the concentration fluctuation which is usually used in the dendritic

growth simulation to form second arm is not taken into consideration. The employed material parameters for Al-Si alloy are shown in Table1.

Table 1 : Physical properties

Partition coefficient k	0.13
Reference temperature T_r [K]	933.47
Liquidus slope m_L [K/mol. fract.]	-600
Diffusion coefficient of liquid D_L [m^2/s]	1.0×10^{-12}
Diffusion coefficient of solid Ds [m^2/s]	3.0×10^{-9}
Interface energy γ [J/m^2]	0.16
Transformation entropy ΔS [JK/m^3]	8.0×10^{5}
Interface thickness δ [m]	$6\Delta x$
Interface mobility M [m^4/Js]	0.03

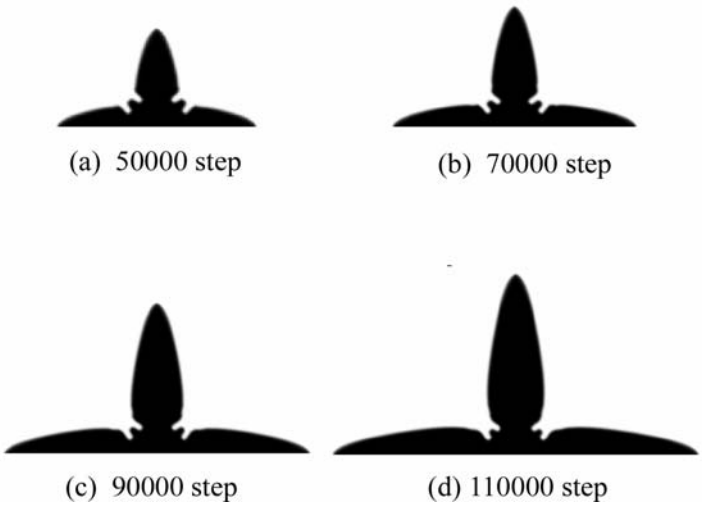

Figure 2 : Variations of dendrite morphologies

Figure 2 shows the numerical results of dendrite growth process during solidification simulation. It is observed that Al-Si alloy dendirte grows keeping the thin shape and the width of the thinest portion of dendrite neck is almost constant during growth. Therefore, it is concluded that the Al-Si dendrite has a shape which easily cause the stress concentration at the dendrite neck by the convection and gravity.

3.2 Fluid flow simulations around dendrite by two-phase Navier-Stokes equations

Next, the melt convection around the dendrite shown in Fig. 2 is calculated by using two-phase Navier-Stokes equations of Eqs.(7) - (9). Then, those equations are solved by artificial compressibility method [6], where the inertial term is discretized by third-order weighted ENO scheme and the viscous term is computed by using second-order accurate central-difference scheme.

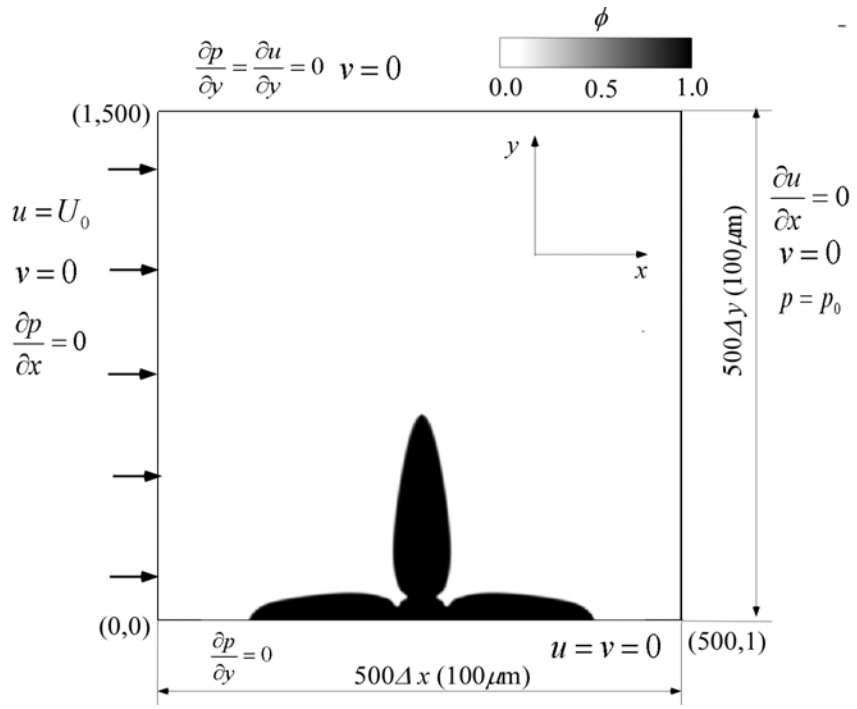

Figure 3 : Computational domain and initial conditions for simulation of melt convection around the dendrite

Figure 3 shows the computational domain and boundary conditions. The uniform forced flow *U0*= 0.01 m/s, which is normal melt flow velocity in casting [7], is applied on the left side of the domain and the pressure on the right side are fixed to $p_0 = \rho U02$ [Pa]. The other boundary conditions are shown in Fig.3. Reynolds number is set to be Re = 5. The dimensionless constant hd in Eq.(10) and Eq.(11) was determined as $hd = 5.0\times10^6$ by performing numerical experiments so as that the fluid velocity at $\phi = 0.5$ is to be zero. For reducing the computational cost, the coarse finite difference lattices of 500×500 (Δx = 200 nm) are employed.

Numerical results at steady-state condition are shown in Figs. 4 and 5. Figure 5 shows the fluid flow velocities by both color and vectors and Fig. 4 shows pressure distributions. In both figures, figures (a), (b), (c) and (d) correspond to those of Fig. 2. From Fig.4, the vortex occurred at the right side of dendrite becomes larger as the dendrite grows. Therefore, the negative pressure is generated at the right side of dendrite. On the left surface of dendrite, the compressive pressures are generated and its magnitude increases with growing the dendrite. The fluid pressures acting on the dendrite surface are transferred to the next stress simulation.

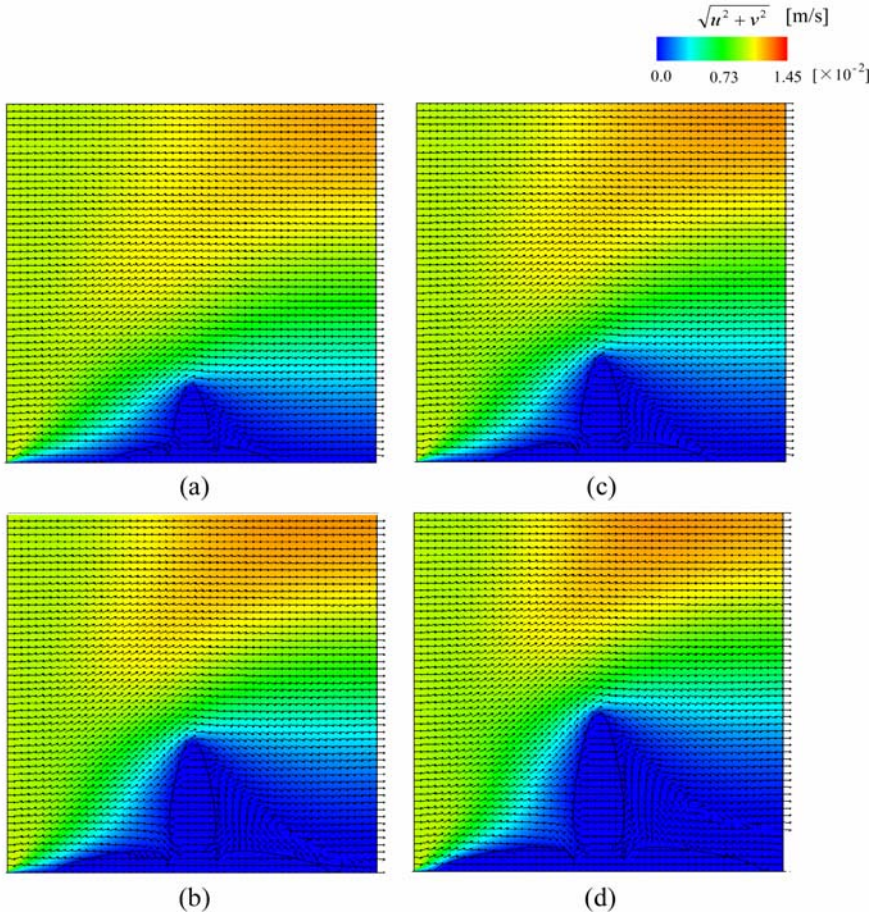

Figure 4 : Variations of fluid flow velocity with dendrite growth

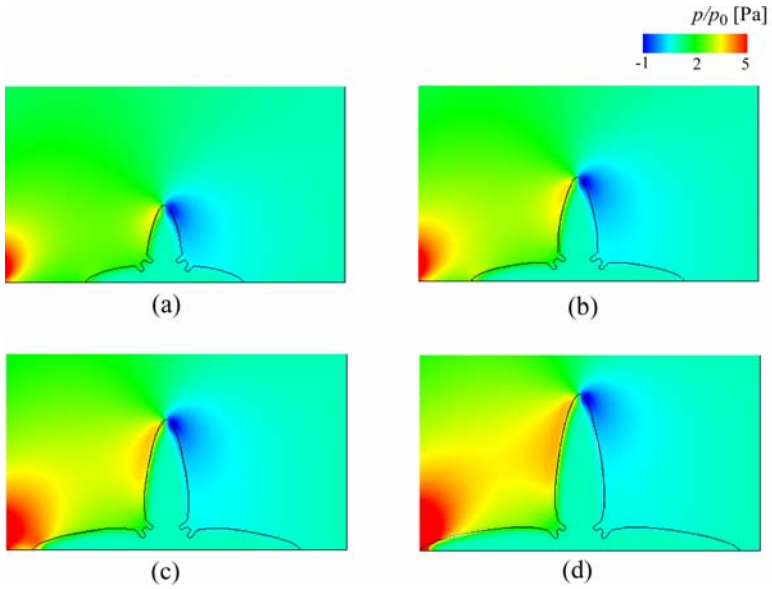

Figure 5 : Variations of pressure distribution with dendrite growth

3.3 Finite element simulations of stress in dendrite

The stresses in dendrite caused by the convection calculated in the previous section and the gravity which acts in vertical direction of dendrite first arm are simulated by finite element method using four node isoparametric elements as plane stress problem.

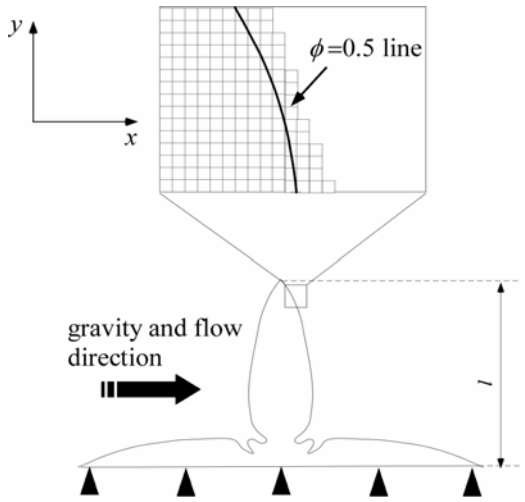

Figure 6 : Computational domain and boundary conditions for finite element simulation to calculate stress field in dendrite

Figure 6 shows the computational domain and boundary conditions. From the results of phase-field simulation shown in Fig. 2, the finite difference lattices with $\phi > 0.1$ are taken out and are used as elements for the stress evaluation by finite element method. In the interface, the Young's modulus is set to change smoothly as ϕE, where E is Young's modulus in solid phase. Both displacements in x and y directions on the bottom of the computational domain, which corresponds to the mold wall, are constrained. l shown in Fig.6 is the dendrite length. The pressure distributions on the dendrite surface caused by the convection are transformed to the nodal forces by following equations:

$$F_x = \phi(p - p_0)\Delta x \cos\theta, \tag{12}$$

$$F_y = \phi(p - p_0)\Delta y \sin\theta, \tag{13}$$

where, θ is the angle between x-axis and interface normal. Equations (12) and (13) are calculated in the range $0.1 < \phi < 0.5$ and the nodal forces are applied to the nodes having ϕ nearest to 0.5.

The body force due to gravity is introduced to all nodes by the nodal force calculated by

$$F_g = \phi\Delta x\Delta y(\rho_s - \rho_L)g, \tag{14}$$

where, ρ_s and ρ_L are the density in solid and liquid, respectively, and g is the gravitational acceleration. The employed material parameters using finite element method are as follows:

Young's modulus E = 4.5 GPa, Poisson's ratio ν = 0.3, the gravitational acceleration g = 9.8 m/s^2, the solid density $\rho_s = 2.68\times10^3$ kg/m^3 , and the liquid density $\rho_L = 2.4\times10^3$ kg/m^3 [8].

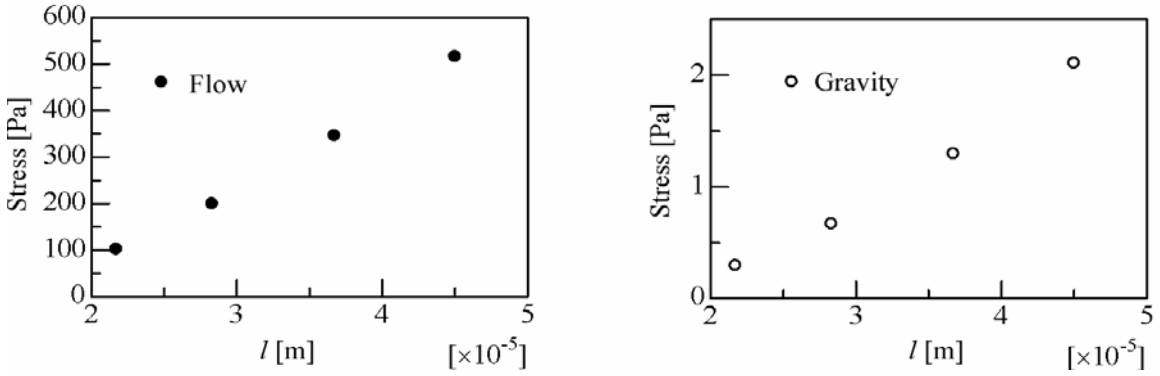

(a) Convection (b) Gravity

Figure 7 : Variations of maximum stress caused at dendrite neck by convection and gravity

Figure 7 shows the variations of maximum stress caused at dendrite neck by convection and gravity. The abscissa is the dendrite length l and the ordinate is the maximum equivalent stress. From Fig.7, the maximum stress by convection is much higher than that of gravity. In the present simulations, the forced flow is set to be 0.01 m/s which is normal melt flow velocity in casting. On the other hand, the most severe condition is set for the gravity, because the gravity acts in the perpendicular direction to the dendrite axis. Considering these points, it is concluded that the gravity has less influence on the fragmentation comparing to the melt convection. However, we need further investigations for larger dendrite with many secondary arms.

4 CONCLUSION

In order to investigate the effects of stress around dendrite neck cased by the convection and gravity on the dendrite fragmentation, the novel numerical model, where phase-field method, Navier-Stokes equations and finite element method are continuously and independently employed, has been developed. By applying the model to the dendritic solidification of Al-Si alloy, the maximum stress variations by melt convection and gravity with dendrite growth were evaluated. As a result, it was concluded that the convection is more important for the maximum stress in dendrite than the gravity.

REFERENCES

[1] J. Pilling and A. Hellawell, Mechanical deformation of dendrites by fluid flow, *Metal. Mater. Trans. A,* (1996) **27**:229-232.

[2] A. M. Mullis, D. J. Walkers, S.E. Battersby and R. F. Cochrane, Deformation of dendrites by fluid flow during rapid solidification, *Mater. Sci. Eng. A*, (2001) **304-306**:245-249.

[3] G. Reinhart, A. Buffet, H. Nguyen-Thi, B. Billia, H. Hung, N. Mangelick-Noël, N. Bergeon, T. Schenk, J. Härtwing and J. Baruchel, In-situ and real-time analysis of the formation of strains and

microstructure defects during solidification of Al-3.5 Wt Pct Ni alloys, *Metal. Mater. Trans. A*, (2008) **39**:865-874.

[4] J. Ni and C. Beckermann, A Volume-Averaged Two-Phase Model for Solidification Transport Phenomena, *Metall. Trans. B*, (1991) **22**:349-361.

[5] C. Beckermann, H.-J. Diepers, I. Steinbach, A. Karma and X. Tong, Modeling melt convection in phase-field simulations of solidification, *J. Compu. Phys*., (1999) **154**:468-496.

[6] T. Miyake, H. Tokunaga, N. Satofuka, Explicit time accurate pseudo-compressibility method for numerical solutions of unsteady incompressible viscous flows, *Eng. Mech. Soc. Jpn. Trans. B*, (1993) **59**:36-42. (in Japanese)

[7] H. Takatani, Ch.-A. Grandin and M. Rappaz, EBSD characterisation and modelling of columnar dendritic grains growing in the presence of fluid flow, *Acta. Mater.*, (2000) **59**:675-688. (in Japanese)

[8] The Japan institute of metals, *Kinnzoku deta bukku.* Maruzen, Vol. II., (1999) 67-68. (in Japanese)

XI International Conference on Computational Plasticity. Fundamentals and Applications
COMPLAS XI
E. Oñate, D.R.J. Owen, D. Peric and B. Suárez (Eds)

NUMERICAL PREDICTION OF MECHANICAL PROPERTIES OF DUAL-PHASE STEEL BY USING MULTI-PHASE-FIELD METHOD AND HOMOGENIZATION METHOD

A. YAMANAKA[*] AND T. TAKAKI[†]

[*] Graduate School of Mechanical and Control Engineering,
Tokyo Institute of Technology
2-12-1, O-okayama, Meguro-ku, Tokyo, 152-8552, Japan
e-mail: ayamanaka@mes.titech.ac.jp

[†] Graduate School of Science and Technology,
Kyoto Institute of Technology
Matsugasaki, Sakyo-ku, Kyoto, 606-8585, Japan
email: takaki@kit.ac.jp

Key words: Mullti-Phase-Field Method, Crystal Plasticity Finite Element Method, Homogenization Method, Dual-Phase Steel, Microstructure.

Abstract. In this study, a numerical prediction method by combining the crystal plasticity finite element method, the multi-phase-field method and the homogenization method is developed to predict microstructure formation and mechanical property of the dual-phase (DP) steel efficiently. With the developed method, the austenite – to – ferrite transformation from the deformed austenite phase is simulated and the mechanical properties of the DP steel which includes the predicted microstructure are investigated.

1 INTRODUCTION

The mechanical property of ferrite (α) + martensite (α') dual-phase (DP) steel is largely characterized by distribution of the microstructure. It is also well-known that the refinement of α grain size by thermo-mechanical controlled processing (TMCP) is quite essential to improve strength of the DP steel. Therefore, to understand the austenite-to-ferrite (γ - α) transformation behavior in deformed γ phase during the TMCP is quite important to control the mechanical property of the DP steel. However, since the γ - α transformation is influenced

by several factors, e.g. chemical composition, transformation temperature, γ grain size and strain applied by the TMCP, it is difficult to predict the transformation behavior only by experiments.

Recently, it has been well-recognized that the multi-phase-field method (MPFM) is a powerful simulation tool to predict microstructure evolutions in polycrystalline materials [1]. The most attractive advantage of the MPFM is to simulate morphological change of microstructures. Therefore, if we utilize digital data of the microstructure morphology simulated by the MPFM as input data for finite element (FE) simulation, systematic simulation model for steel design can be realized [2]. This will enable us to predict the microstructure formation and the mechanical property of the DP steel efficiently.

Therefore, the purpose of this study is to develop a numerical prediction method by combining the crystal plasticity FE method (CPFEM), the MPFM and the homogenization method. In this paper, we simulate the γ - α transformation from the deformed γ phase and evaluate the mechanical properties of the DP steel which includes the predicted microstructure. Then, the effects of the distribution of α phase on macro- and microscopic deformation behavior of the DP steel are studied.

2 SIMULATION METHOD

The procedures to simulate the γ - α transformation from the deformed γ phase and evaluate the mechanical property of the DP steel are as follows: First, to simulate the hot plastic forming of Fe-C alloy, simulation of compression deformation of polycrystalline γ phase is conducted by the CPFEM based on the strain gradient crystal plasticity theory. Second, nucleation rate and nucleation site of the α phase in the deformed γ phase are estimated based on the classical nucleation theory. Third, the γ - α transformation during continuous cooling process is simulated by the MPFM with the estimated nucleation condition. Finally, we perform numerical simulation of uniaxial tensile test of the DP steel by the CPFEM based on the homogenization method with the simulated microstructure.

2.1 Strain gradient crystal plasticity theory

In order to simulate plastic deformation behavior of polycrystalline γ phase during the hot plastic forming, we employ the following crystal plasticity constitutive equation [3],

$$\overset{\nabla}{S}_{ij} = D^{e}_{ijkl}\varepsilon_{kl} - \sum_{\alpha=1}^{2}\left(D^{e}_{ijkl}P^{(\alpha)}_{kl} + W^{(\alpha)}_{ik}\sigma_{kj} + \sigma_{ik}W^{(\alpha)}_{kj}\right)\dot{\gamma}^{(\alpha)} \tag{1}$$

Here, $\overset{\nabla}{S}_{ij}$, D^{e}_{ijkl}, ε_{ij}, σ_{ij} and $\dot{\gamma}^{(\alpha)}$ are the Jaumann rate of Kirchoff stress tensor, the elastic modulus tensor, the strain tensor, the Cauchy stress tensor and the plastic shear strain rate on the slip system α, respectively. Also, $P^{(\alpha)}_{ij}$ and $W^{(\alpha)}_{ij}$ are the schmid tensor and the plastic spin tensor, respectively.

Since we use the strain rate dependent crystal plasticity constitutive equation [4], the plastic shear strain rate is defined as follows:

$$\dot{\gamma}^{(\alpha)} = \dot{\gamma}^{(\alpha)}_{0} \frac{\tau^{(\alpha)}}{g^{(\alpha)}} \left(\frac{\tau^{(\alpha)}}{g^{(\alpha)}} \right)^{\frac{1}{m}-1} \tag{2}$$

where $\dot{\gamma}^{(\alpha)}_{0}$ is the reference shear strain rate and the resolved shear stress $\tau^{(\alpha)}$ is calculated by $\tau^{(\alpha)} = \sum_{\alpha=1}^{2} P^{(\alpha)}_{ij} \sigma_{ij}$. The evolution equation of the critical resolved shear stress (CRSS) $g^{(\alpha)}$ is chosen as,

$$g^{(\alpha)} = g^{(\alpha)}_{0} + a\mu\tilde{b} \sum_{\beta=1}^{2} \omega_{\alpha\beta} \sqrt{\rho^{(\alpha)}_{a}} \tag{3}$$

Here, $g^{(\alpha)}_{0}$, a, μ, $\tilde{b}$ and $\omega_{\alpha\beta}$ are the initial critical resolved shear stress, the shear elastic modulus, the magnitude of burgers vector and the dislocation interaction coefficient, respectively. The accumulated dislocation density is given as follows:

$$\rho^{(\alpha)}_{a} = \rho^{(\alpha)}_{SS} + \left\| \rho^{(\alpha)}_{GN} \right\| \tag{4}$$

where $\rho^{(\alpha)}_{SS}$ and $\rho^{(\alpha)}_{GN}$ are the statically stored dislocation (SSD) density and the geometrically necessary dislocation (GND) density, respectively. In this study, the following evolution equation for the SSD density is used.

$$\dot{\rho}^{(\alpha)}_{SS} = \frac{c\left|\dot{\gamma}^{(\alpha)}\right|}{\tilde{b}\sqrt{\sum_{\beta=1}^{2} \omega_{\alpha\beta}\left(\rho^{(\alpha)}_{SS} + \left\|\rho^{(\alpha)}_{GN}\right\|\right)}} \tag{5}$$

And, the GND density is evaluated as,

$$\left\|\rho^{(\alpha)}_{GN}\right\| = \sqrt{\left(-\frac{1}{\tilde{b}} \frac{\partial \gamma^{(\alpha)}}{\partial x_i} s^{(\alpha)}_{i}\right)^{2} + \left(\frac{1}{\tilde{b}} \frac{\partial \gamma^{(\alpha)}}{\partial x_i} e_{ijk} s^{(\alpha)}_{j} m^{(\alpha)}_{k}\right)^{2}} \tag{6}$$

where $\rho^{(\alpha)}_{GN,edge}$ and $\rho^{(\alpha)}_{GN,screw}$ are the edge and screw components of the GND density, respectively. With the accumulated dislocation density ρ_a, the stored energy E_{store} can be derived as

$$E_{store} = \frac{1}{2}\mu\tilde{b}^2 \sum_{\alpha=1}^{2} \rho_a^{(\alpha)} \tag{7}$$

2.2 Modeling of α nucleation behavior

In this study, the potential nucleation sites (i.e., grain boundary corner, grain boundary edge, grain boundary face and deformation band) and the nucleation rate at each nucleation site are estimated by using the results of the hot plastic forming simulation.

According to the classical nucleation theory, the nucleation rate of α phase J^i is described as,

$$J^i\left(C_\gamma, T, t\right) = d^i\left(t\right)\beta^* Z \exp\left(-\frac{1}{kT}\frac{\psi^i}{\Delta G_V^2\left(C_\gamma, T\right)}\right) \tag{8}$$

where $d^i(t)$ is density of the potential nucleation site, where upper subscription i means kind of the above mentioned nucleation sites (i = c, e, f and d). Since the nucleation site is consumed with progression of the transformation, $d^i(t)$ is defined as a function of time t. β^* is the frequency coefficient which is assumed to be related to the temperature-dependent carbon diffusion coefficient in the γ phase as $\beta^* = \lambda D_\gamma(T)$. Z, k, T and C_γ are the Zeldovich parameter, the Boltzmann constant, the temperature of the system and the carbon concentration in the γ phase, respectively. Also, Ψ^i is the geometry coefficient of nucleation site i. The chemical driving force for the nucleation $\Delta G_V(C\gamma, T)$ can be caluculated based on the CALPHAD method.

The density of the potential nucleation site $d^i(t)$ in Eqn.(8) is calculated by $d^i(t) = N^i(t) / S$ where $N^i(t)$ and S are number of potential nucleation site and area of the system, respectively. $N^i(t)$ is determined using the number of grain n which is explained in next section and the misorientation $\Delta\theta$. That is, a computational grid satisfying n = 4 is considered as a potential nucleation site on the grain boundary corner. Similarly, position of the potential nucleation sites on the grain boundary edge (n = 3) and the grain boundary face (n = 2) is determined. For the nucleation sites in the deformation band, we assume that high-angle grain boundary region which is given as n = 1 and $\Delta\theta > 15^\circ$ or the region in which the stored energy E_{store} is more than a critical value E_{cri} is possible site. As a result, time interval for the α nucleation at each nucleation site is given by inverse of Eqn. (8). For all nucleation sites, order of the α nucleation is determined by order of the magnitude of the stored energy.

2.3 Multi-Phase-Field method

The γ- α transformation during the continuous cooling is simulated by the generalized MPFM proposed by Steinbach et al [5]. In the MPFM, the total free energy of the system, G, is defined as the Ginzburg-Landau free energy functional which is given by the sum of the gradient energy, potential energy and bulk free energy as,

$$G = \int_V \left\{ \sum_{i=1}^{N} \sum_{k=i+1}^{N} \left(-\frac{a_{ik}^2}{2} \nabla \phi_i \cdot \nabla \phi_k \right) + \sum_{i=1}^{N} \sum_{k=i+1}^{N} \left(W_{ik} \phi_i \phi_k \right) + g_{bulk} \right\} dV \tag{9}$$

Here, we use N phase field variables, ϕ_i (i = 1,2,3, …, N). ϕ_i describes the fraction of the i th grain. The phase field variables vary smoothly across the interface from ϕ_i = 1 in the i ith grain to ϕ_i = 0 in other grain. All phase field variables satisfy the constant, $\sum_{i=1}^{N} \phi_j^i = 1$ at all points. a_{ij} and W_{ij} are the gradient coefficient and potential height, respectively. These parameters are related to the interfacial energy and interfacial thickness.

By assuming the total free energy decreases monotonically with time, the evolution equation of the phase field variable is written as,

$$\frac{\partial \phi_j^i}{\partial t} = -\frac{2}{n} \sum_{k=1}^{n} M_{ik}^{\phi} \left[\sum_{l=1}^{n} \left\{ \left(W_{il} - W_{kl} \right) \phi_j^l + \frac{1}{2} \left(a_{il} - a_{kl} \right) \nabla^2 \phi_j^l \right\} - \frac{8}{\pi} \sqrt{\phi_j^i \phi_j^k} \Delta E_{ik} \right] \tag{10}$$

where n is the number of phase fields in the arbitrary point and is given by $n = \sum_{i=1}^{N} \xi_i$. Here, ξ_i is a following step function, which is expressed as ξ_i =1 in a region $0 < \phi_i \leq 1$ and ξ_i = 0 in other region. The magnitude of the transformation driving force, ΔE_{ij}, is given by sum of the reduction of the chemical free energy and the stored energy obtained by the CPFEM simulation as $\Delta E_{ij} = \Delta E_{chem} + E_{store}$. The chemical driving force is described as $\Delta E_{chem} = \Delta S \, \Delta T$ at the α-γ interface, where ΔS and ΔT are the entropy difference between the α and γ grains and the undercooling, respectively.

To simulate the diffusion of carbon atoms during γ- α transformation, the total carbon concentration C is defined as a linear function of the local carbon concentration c_i weighted by the phase-field variables ϕ_i. The local carbon concentration is given by the $c_i = k_i c_i \Big/ \left(\sum_{j=1}^{n} k_j \phi_j \right)$. Here, k_i is the partition coefficient of carbon atoms. Hereafter, we consider an $\alpha + \gamma$ two-grain system (N = 2) for simple description. Therefore, when ϕ_1 and ϕ_2 correspond to the α and γ phases, respectively.

The diffusion equation for total carbon concentration is expressed by the sum of diffusion fluxes of carbon atoms in the i th grains J_i as,

$$\frac{\partial C}{\partial t} = \nabla \cdot \left\{ \sum_i \phi_i J_i \right\} = \nabla \cdot \left\{ \sum_i \phi_i D_i \nabla C_i \right\} = \nabla \cdot \{ \phi_1 D_1 \nabla c_1 + \phi_2 D_2 \nabla c_2 \} \tag{11}$$

Here, D_i is diffusion coefficient of carbon atom in the i the grain.

In this study, the undercooling ΔT and the partition coefficient k_i are evaluated by using a linearized phase diagram of Fe-C alloy.

2.4 Homogenization method

In this study, we employ the homogenization method proposed by Grudes et al to investigate the mechanical properties of the DP steel which contains the simulated α phase. By using the homogenization method, the micro- and macroscopic deformation behaviors of the steel depending on heterogeneous microstructure morphology can be simulated.

In the homogenization method, we consider the two-scale boundary value problem for the micro- and macroscopic scales as shown in Fig.1. The microstructure in the steel is assumed to be a periodic array of representative volume elements (RVEs). In this study, The RVE describes heterogeneous distribution of the microstructure obtained by the MPFM. x_i and y_i (i = 1 and 2) are macro- and microscopic coordinates, respectively. These scales are related to each other as $y_i = x_i / \eta$ with a parameter η. By using these two coordinates, the velocity can be described by the following asymptotic expansion with η :

$$\dot{u}_i(x,y) = \eta^0 \dot{u}_i^0(x,y) + \eta \dot{u}_i^1(x,y) + \eta^2 \dot{u}_i^2(x,y) + \cdots \tag{12}$$

Here, we use the first order approximation as,

$$\dot{u}_i(x,y) = \dot{u}_i^0(x) + \eta \dot{u}_i^1(x,y) = \dot{u}_i^0(x) + \eta \left(-\chi_i^{mn} \frac{\partial \dot{u}_m^0}{\partial x_n} + \phi \right) \tag{13}$$

where $\dot{u}_i^0(x,y)$ represents the homogenized macroscopic velocity. χ_i^{mn} and ϕ_i are the characteristic velocities which corresponds to components of macro-velocity gradient tensor, respectively. With Eqns.(12) and (13), the velocity gradient L_{ij} is given by,

$$L_{ij}(x,y) = \frac{\partial \dot{u}_i(x,y)}{\partial x_j} = \frac{\partial \dot{u}_i^0(x)}{\partial x_j} + \frac{\partial \dot{u}_i^1(x,y)}{\partial y_j} = \frac{\partial \dot{u}_i^0(x)}{\partial x_j} - \frac{\partial \chi_i^{mn}}{\partial y_j} \frac{\partial \dot{u}_m^0(x)}{\partial x_n} + \frac{\partial \phi_i(x)}{\partial y_j} \tag{14}$$

According to the updated Lagrange formulation and the strain gradient crystal plasticity theory explained in previous section, the principle of virtual work is written as,

$$\int_{\Omega}\left(C_{ijkl}-H_{ijkl}\right)L_{kl}\delta L_{ij}dV=\int_{S}\dot{P}_i\delta\dot{u}_i dS+\int_{V}\sum_{a=1}^{2}R_{ij}^{(a)}\dot{f}^{(a)}\delta L_{ij}dV \tag{15}$$

To accomplish the homogenization formulation, we take the limit of η to zero and employing the following integral formula,

$$\lim_{\eta\to 0}\int_{\Omega}\Phi\left(x,y=\frac{x}{\eta}\right)d\Omega=\frac{1}{|Y|}\int_{\Omega}\int_{Y}\Phi\left(x,y=\frac{x}{\eta}\right)dYd\Omega \tag{16}$$

where is Φ a so-called Y-periodic function. The integral sing $\frac{1}{|Y|}\int_{Y}\Phi(x,y)dY$ means the volume average of function Φ in a RVE. By substituting Eqn. (14) into Eqn.(15) and introduce Eqn.(16), we can derive the governing equations for the macro- and microscopic regions, respectively.

$$\int_{\Omega}\frac{1}{|Y|}\int_{Y}C'_{ijkl}\left(\frac{\partial\dot{u}_k^0}{\partial x_l}+\frac{\partial\dot{u}_l^1}{\partial y_k}\right)\frac{\partial\delta\dot{u}_k^0}{\partial x_l}dYd\Omega=\int_{S}\dot{P}_i\delta\dot{u}_i^0 dS+\frac{1}{|Y|}\int_{\Omega}\int_{Y}\sum_{a=1}^{2}R_{ij}^{(a)}\dot{f}^{(a)}\frac{\partial\delta\dot{u}_k^0}{\partial x_l}dYd\Omega \tag{17}$$

$$\int_{\Omega}\frac{1}{|Y|}\int_{Y}C'_{ijkl}\left(\frac{\partial\dot{u}_k^0}{\partial x_l}+\frac{\partial\dot{u}_l^1}{\partial y_k}\right)\frac{\partial\delta\dot{u}_l^1}{\partial y_k}dYd\Omega=\frac{1}{|Y|}\int_{\Omega}\int_{Y}\sum_{a=1}^{2}R_{ij}^{(a)}\dot{f}^{(a)}\frac{\partial\delta\dot{u}_l^1}{\partial y_k}dYd\Omega \tag{18}$$

Since we obtain the velocity of displacement in the micro- and macro scale by solving Eqns.(17) and (18) with the finite element method, the variation of strain and stress in the steel can be calculated.

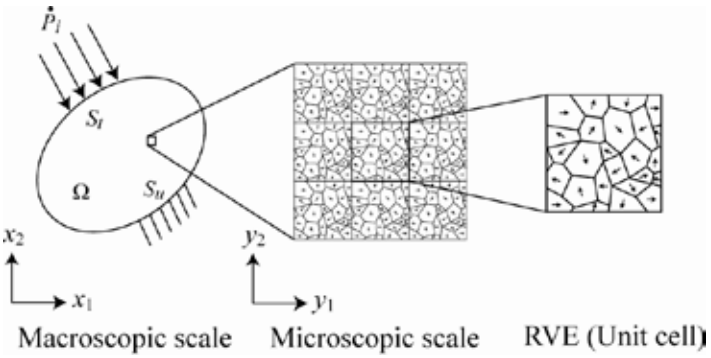

Figure 1: Schematic explanation of two-scale boundary value problem

3 SIMULATION RESULTS

Figure 2 shows the simulation model used in the hot plastic forming simulation. The computational region is meshed with 128 x 128 crossed-triangle elements. The size of a finite

element is set to be $\Delta X = \Delta Y = 0.5$ μm. Since a two-slip system is assumed for simplicity, the crystal orientation is defined by the rotation angle θ as shown in Fig.2(b). The initial polycrystalline structure of the γ phase consists twenty grains with random crystal orientations. These γ grains are compressed up to strain of $\varepsilon = 0.2$ at a strain rate of 10^{-3} s^{-1}. In this study, we assume the plain strain problem and the periodic boundary condition. The temperature is assumed to be 1150 K which is lower than the recrystallization temperature of steels, 1173 K.

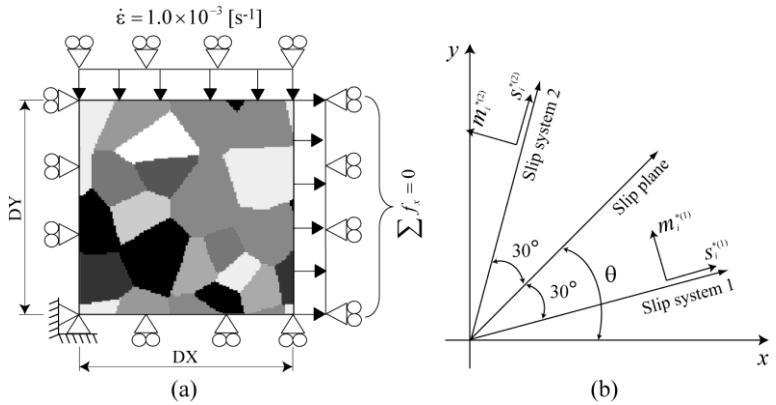

Figure 2: Simulation model for compression deformation of polycrystalline γ phase and definition of crystal orientation θ in a two-slip system

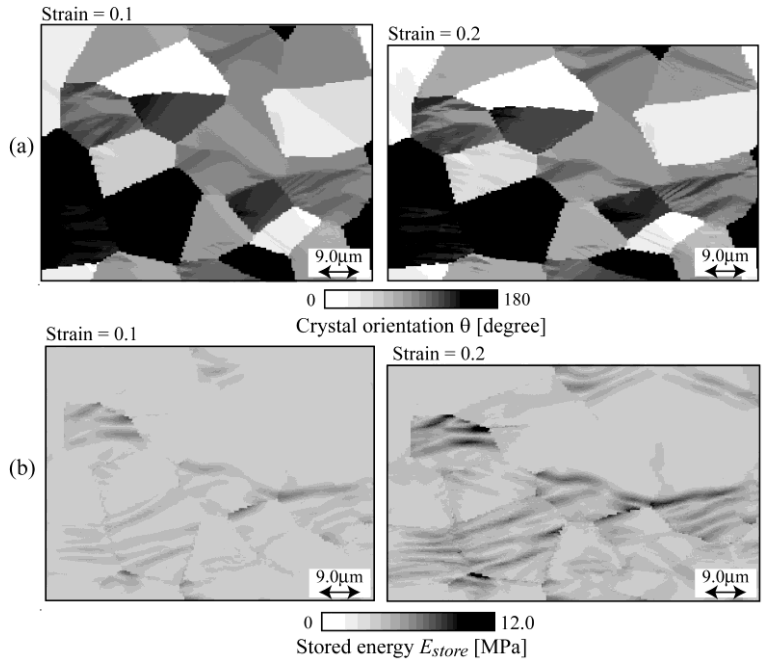

Figure 3: Distributions of (a) crystal orientation and (b) stored energy in deformed γ phase

Table 1: Parameters for α nucleation

Geometry coefficient, φ^c	1.30×10^{-6} [J^3/m^6]
Geometry coefficient, φ^e	5.00×10^{-8} [J^3/m^6]
Geometry coefficient, φ^f and φ^g	2.10×10^{-6} [J^3/m^6]
Zeldovich constant, Z	0.05
Parameter, λ	75

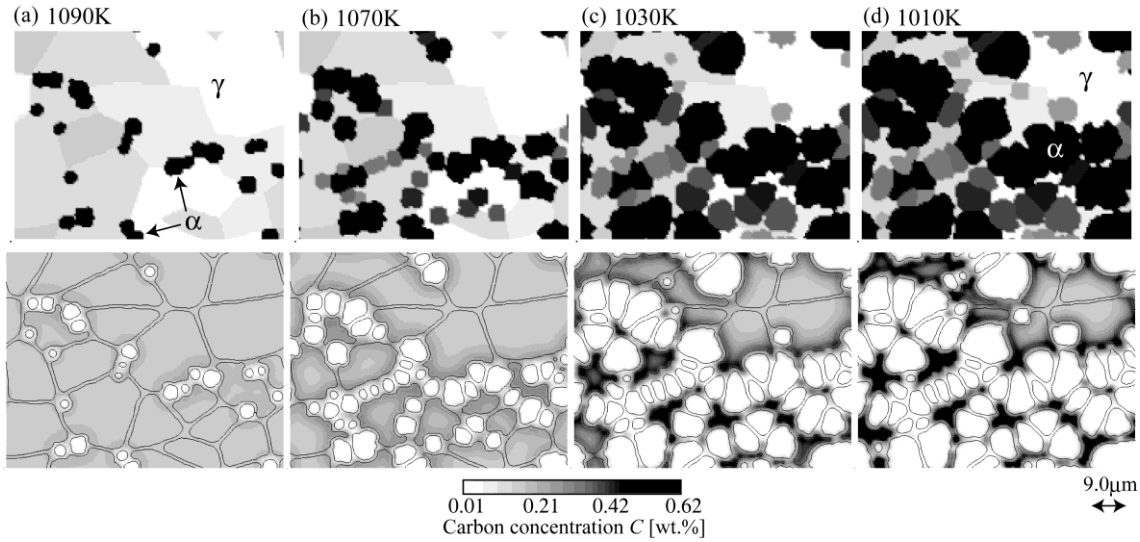

Figure 4: Distributions of (a) α and γ grains and (b) carbon concentration during γ-to-α transformation

Figure 3 shows the distributions of crystal orientation and stored energy in the deformed γ phase at different strains. As shown in Fig.3(b), the stored energy is increased with the increasing strain. In particular, the strain energy tends to concentrate near grain boundaries, because dislocations accumulate at the grain boundary. On the other hand, it is found that the region which exhibits high strain energy and large crystal rotation is formed with in some γ grain interiors. This indicates the deformation band is introduced in the γ phase by the plastic forming. Also, it is clearly shown that large crystal rotation is occurred in the deformed γ phase.

Based on the simulated deformed γ phase, the γ - α transformation is simulated. The distributions of crystal orientation and stored energy shown in Fig.3 are mapped on the computational region for the MPF simulation. The initial temperature and initial carbon concentration of γ phase are set to be 1110 K and 0.2 wt%, respectively. The parametes for the α nucleation are summarized in Table 1. The computational region is meshed with 144 x 112 finite difference grid. The size of the grid is set to be $\Delta x = \Delta y = 0.5$ μm. In this simulation,

Table 2: Material parameters for uniaxial tensile test

Elastic constants, C_{11} , C_{12}, C_{44}	C_{11} = 237 [GPa] C_{12} = 141 [GPa] C_{44} = 116 [GPa]
Poisson's ratio, ν	0.345
Reference shear strain, $\dot{\gamma}_0^{(\alpha)}$	0.001 [1/s]
Initial CRSS, $\tau_0^{(\alpha)}$	200 [MPa] (α phase) 380 [MPa] (α' phase)
Strain rate sensitivity constant, $1/m$	0.05
Parameter, a	0.4
Shear modulus, μ	80.7 [GPa]
Length of burgers vector, $\tilde{b}$	0.2624 [nm]
Initial dislocation density, ρ_0	10^{-10} [1/m]
Dislocation interaction matrix, ω_{ij}	1.0 (all componets)

we assume the critical value of stored energy E_{cri} for the α nucleation to be E_{cri} = 15 MPa, because it is difficult to determine this value from experiments.

Figure 4 shows the evolutions of α and γ grains and the variation of carbon concentration during γ–α transformation. The temperature is decreased from 1110 K to 1010 K with cooling rate of ΔT = 5 K/s. We can see that inhomogeneous nucleation of α phase is occurred during the continuous cooling. At 1090 K, it is found that some α grains are newly formed and these α grains tend to locate at grain boundary corner and edge. With decreasing temperature due to the cooling, more α grains are nucleated on the grain boundary face and the grain interior. According to the distribution of α phase at 1010 K, it is demonstrated that the formation of α phase is concentrated on the grain boundary of the γ grains with large stored energy.

The uniaxial tensile test of the DP steel is conducted with the CPFEM based on the homogenization method. In this study, the RVE is modeled with the simulated microstructure shown in Fig.4(d). Here, the untransformed γ phase after the continuous cooling is assumed to be transformed into uniform α' phase by quenching to room temperature. Size of the RVE is same as that of the computational domain for the MPFM simulation. In the tensile test, the system is deformed up to a true strain of 0.1 at a strain rate of 10^{-4} s^{-1}. Although the crystal structure of α and α' phases is body-centered cubic, we consider only 12 slip systems on {110} plane along <111> direction for simplicity. The material parameters and physical values for α and α' phases are listed in Table 2.

Figure 5 indicates the calculated macroscopic stress-strain (SS) curve of the DP steel. Similar to the experimental results, the obtained SS curve exhibits continuous yielding behavior and high strain hardening behavior.

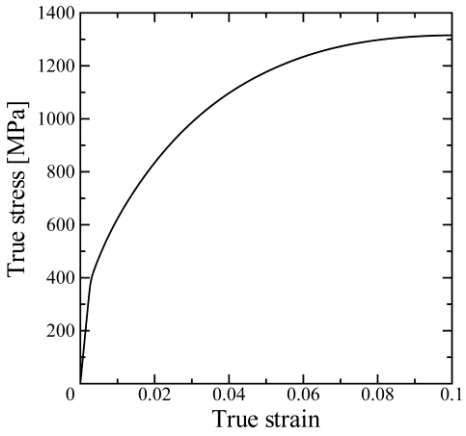

Figure 5: Macroscopic stress-strain curve of the DP steel

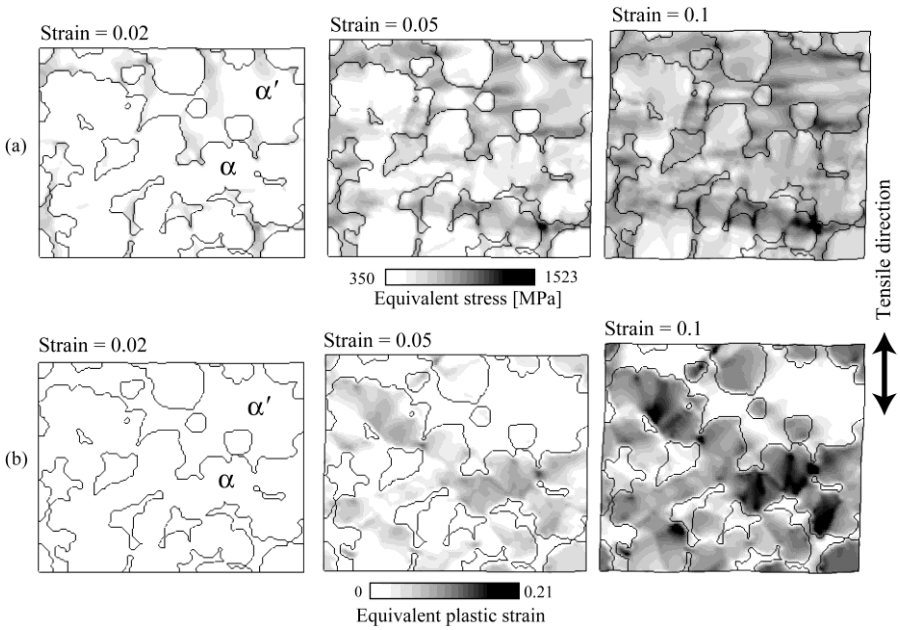

Figure 6: Distributions of (a) equivalent stress and (b) equivalent plastic strain for different strains

In this study, since we employ the homogenization method, not only the macroscopic mechanical response, but also the microscopic deformation behavior of the DP steel can be investigated. Figure 6 shows the distributions of the equivalent stress and equivalent plastic strain in the DP microstructure at different macroscopic strains (ε = 0.02, 0.05 and 0.10), respectively. As shown in Fig.6(a), the stress is increased with increasing macroscopic strain and concentrated in the harder α' phase near the α/α' interface. On the other hand, the plastic strain is generated along the aggregated softer α phase. The simulation results confirm that

the stress concentration at the α' phase is main mechanism of high strength and high strain hardening behavior of the DP steel.

4 CONCLUSIONS

- A numerical prediction method by combining the crystal plasticity finite element method, the multi-phase-field and the homogenization method is developed to predict the microstructure formation and the mechanical property of the DP steel efficiently.
- With a developed method, the γ - α transformation from the deformed γ phase is simulated by the MPFM and the uniaxial tensile test of the DP steel by the CPFEM based on the homogenization method with the simulated microstructure
- Through numerical simulations, the effects of the distribution of α phase on macro- and microscopic deformation behavior of the DP steel which includes the predicted microstructure are clarified.

REFERENCES

[1] A. Yamanaka, T. Takaki and Y. Tomita, Multi-phase-field modeling of diffusional solid phase transformation in carbon steel during continuous cooling transformation, *Mater. Sci. Eng. A* (2008) **310**: 1337-1342.

[2] A.Yamanaka, T. Takaki and Y. Tomita, Coupled simulation of microstructural formation and deformation behavior of ferrite-pearlite steel by phase-field method and homogenization method, *Mater. Sci. Eng. A* (2008) **480**: 244-252.

[3] J. Pan and J. R. Rive, Rate sensitivity of plastic flow and implications for yield-surfce vertices, *Int. J. Solid. Struct.* (1983) **19**: 973-987.

[4] T. Ohashi, Numerical modeling of plastic multislip in metal crystals of f.c.c type, *Philos. Mag. A* (1994) **70**: 793-803.

[5] I. Steinbach and F. Pezzolla, A generalized filed method for multiphase transformation using interface fields, *Physica D* (1999) **134**: 385-393.

XI International Conference on Computational Plasticity. Fundamentals and Applications
COMPLAS XI
E. Oñate, D.R.J. Owen, D. Peric and B. Suárez (Eds)

RELATIONSHIP BETWEEN DEFORMATION AND STABILITY SWITCHING IN AMORPHOUS METAL : LOCAL LATTICE INSTABILITY ANALYSIS

MASAOMI NISHIMURA*, KISARAGI YASHIRO† AND MASAHIRO ARAI‡

*,‡Department of Mechanical Systems Engineering, Shinsyu University
Wakasato 4-17-1, Nagano 380-8553, Japan
e-mail: nishimu@shinshu-u.ac.jp, http://str.shinshu-u.ac.jp
e-mail: arai@shinshu-u.ac.jp, http://str.shinshu-u.ac.jp

†Graduate School of Engineering, Kobe University
Rokkodai 1-1, Nadaku, Kobe 657-8501, Japan
e-mail: yashiro@mech.kobe-u.ac.jp, http://mm4.scitec.kobe-u.ac.jp

Key words: Molecular Dynamics Simulation, Amorphous Metals, Local Lattice Instability Analysis, Stability-Switching, Local Volume Change

Abstract. We have attempted to comprehend the deformation behavior of amorphous metals by the local lattice instability analysis that discusses the positiveness of atomic elastic stiffness coefficients, B_{ij}^{α}, or the second-order derivatives of atomic energy composition. In the present study, we discuss the stability-switching, or transitions between $\det B_{ij}^{\alpha} \geq 0$ and $\det B_{ij}^{\alpha} < 0$, by the "probabilistic" fluctuation and the "deterministic" mechanical load. No-load equilibrium, tension, compression and simple shear are performed on an amorphous nickel by molecular dynamics simulations. The positive and negative stability-switching, or "stabilization" and "destabilization", occur due to the "probabilistic" fluctuation even at the equilibrium state. The number of $\det B_{ij}^{\alpha} < 0$ atoms shows almost constant while the distribution of $\det B_{ij}^{\alpha} < 0$ atoms indicates different morphology at each observation time. Ratios of switched atoms with stability-switching under tension, compression and shear are larger than that under the equilibrium because the local structural relaxation produces simultaneously both positive and negative stability-switching. Atoms with negative and positive stability-switching show increases and decreases of atomic volume, respectively; while only positive switching shows the decreases in local volumes, evaluated with the atomic volumes of surrounding atoms within the cutoff radius, according to the incidence of "deterministic" structural changes.

1 INTRODUCTION

Amorphous metals have short and middle range order such as an icosahedral atomic-cluster [1, 2]. These atomic scale structures play important roles in the formability and deformability of amorphous metals. On the other hand, it is difficult to understand universally deformation behaviors of these in disordered or inhomogeneous structure. We have discussed the mechanical characteristic of local structure by local lattice instability analysis (LLIA) [3] in molecular dynamics (MD) simulations. LLIA is expected to extract the universal mechanism of deformation because the local stability on LLIA is consistently determined only by the positive definiteness of atomic elastic stiffness coefficients, B^{α}_{ij}.

We have so far shown that amorphous metals have many $\det B^{\alpha}_{ij} < 0$ atoms even at the equilibrium state [4, 5] by LLIA. In our previous report [5], we have discussed the changes in $\det B^{\alpha}_{ij} < 0$ atoms in monatomic amorphous metals during uniaxial tension. Under the tension, it is considered from the comparison of stress components on $\det B^{\alpha}_{ij} \geq 0$ and $\det B^{\alpha}_{ij} < 0$ atoms that the local stress reduction occurs by transitions between each other. Then we have picked up atoms that have actually switched between $\det B^{\alpha}_{ij} \geq 0$ and $\det B^{\alpha}_{ij} < 0$. As a result, we have concluded that the stress relaxation is not caused by a straightforward image of "stabilization" or "destabilization", but by "shuffle of atomic arrangement" which involves positive and negative stability-switching.

In the present study, we perform compression and simple shear in addition to tension. In order to explore further relationship between deformation and the stability-switching based on LLIA in amorphous metals, we discuss the stability-switching by the "probabilistic" fluctuation and the "deterministic" mechanical load, and evaluate the changes of atomic and local volume on the stability-switching.

2 LOCAL LATTICE INSTABILITY ANALYSIS

Wang et al. have proposed the evaluation of lattice stability at finite strain and temperature, on the basis of the positive definiteness of elastic stiffness coefficients [6, 7]. The elastic stiffness, or stress-strain, coefficients are written as [8]

$$B_{ijkl} \equiv \left(\frac{\partial \sigma_{ij}}{\partial \varepsilon_{kl}}\right) = C_{ijkl} + \frac{1}{2}(\sigma_{il}\delta_{jk} + \sigma_{jl}\delta_{ik} + \sigma_{ik}\delta_{jl} + \sigma_{jk}\delta_{il} - 2\sigma_{ij}\delta_{kl}), \tag{1}$$

where δ_{ij} is Kronecker's delta. The stress, σ_{ij}, and the elastic coefficients, C_{ijkl}, are defined as

$$\sigma_{ij} = \frac{1}{V}\left(\frac{\partial U}{\partial \eta_{ij}}\right), \; C_{ijkl} = \frac{1}{V}\left(\frac{\partial^2 U}{\partial \eta_{ij}\partial \eta_{kl}}\right). \tag{2}$$

Here U is the internal energy and V is the volume of crystal at the equilibrium. Note that the differentiation in Eq. (2) is for the infinitesimal virtual strain, η_{ij}, at the equilibrium state under the external load. The B_{ijkl} combines the stress and actual strain, ε_{ij}, from the load-free reference state. In the linear elasticity region, B_{ijkl} is identical to C_{ijkl}

but it is not equivalent in the nonlinear elasticity or finite strain region. That is, B_{ijkl} represents the gradient at the stress-strain surface in the six dimensional strain spaces, whether the system is in the linear or nonlinear elasticity. Thus we can easily imagine the physical meaning of the Wang's stability criteria; it is the point where the crystal loses the deformation resistance. The symmetric part of the tensor of Eq. (1), $B^{\mathrm{sym}}_{ijkl} \equiv (B_{ijkl} + B_{lkji})/2$, dominates the lattice stability [6, 7]. The symmetric tensor B^{sym}_{ijkl} is represented by the 6×6 matrix, B_{ij} $(i, j = 1 \sim 6)$, in the Voigt notation [8]. Thus the instability criterion could be written as $\det B_{ij} < 0$.

The system energy, E_{tot}, can be divided into the contribution of each atom, E_α, in the framework of the embedded atom method (EAM) [9]. The atomic stress, σ^α_{ij}, and the atomic elastic coefficient, C^α_{ijkl}, are defined as the 1st and 2nd order derivatives of E_α against local strain perturbation, respectively. Thus, we can calculate the atomic elastic stiffness coefficients, B^α_{ijkl}, at any time and configuration in the MD simulation, using Eq.(1). The symmetric part of B^α_{ijkl} is also used for stability analysis, so that we denote the local instability condition as $\det B^\alpha_{ij} < 0$ $(i, j = 1 \sim 6)$, according to the Voigt notation.

3 SIMULATION PROCEDURE

An amorphous nickel is made by usual melt-quench simulation under the periodic boundary condition in all directions. The interatomic potential adopted is the EAM by Voter and Chen [10]. The total number of atoms is 108,000. A nickel crystal is melted during 10ps MD calculation at the temperature of $T = 3000$K. The temperature is quenched to 10K with the cooling rate of -5×10^{13}K/s. The no-load calculation is performed during 200ps at $T = 10$K after the melt-quench simulation. Then, tension, compression and simple shear are applied on the amorphous nickel under the periodic boundary. The tension or compression is performed by uniform expansion or contraction of the distance of each atom in the z-direction. The strain rates of tension and compression are 1.0×10^8/s. The cell length in the transverse directions is also controlled to cancel the normal stress originated by the Poisson's contraction/expansion. On the other hand, simple shear is performed by transition from the cubic cell to the monoclinic one. The cell length of x and y direction are fixed; and the system volume is unchanged during the shear deformation. The strain rate is also set to 1.0×10^8/s in engineering strain. The temperature is kept at 10K by velocity scaling during all the deformations.

4 RESULTS AND DISCUSSION

4.1 No-load calculation

Figure 1 shows a change in a potential energy during no-load calculation after the melt-quench simulation. The potential energy drastically decreases on the initial stage of the calculation because the structural relaxation continues from the melt-quench simulation. The decrease stops at 50ps, while there is a slight plateau of energy from 20ps to 30ps.

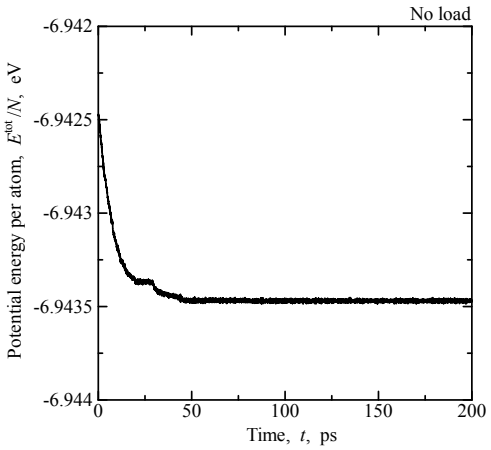

Figure 1: Change in the potential energy during the no-load calculation.

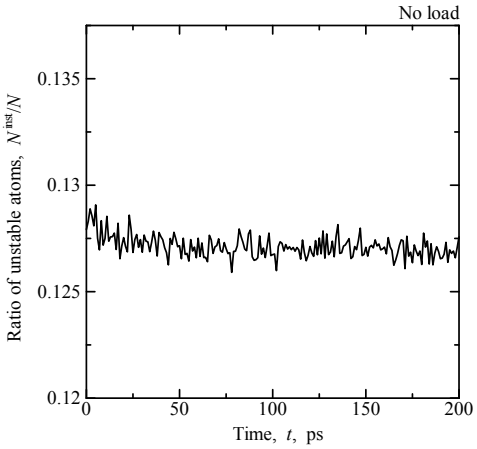

Figure 2: Change in the ratio of $\det B_{ij}^{\alpha} < 0$ atoms during the no-load calculation.

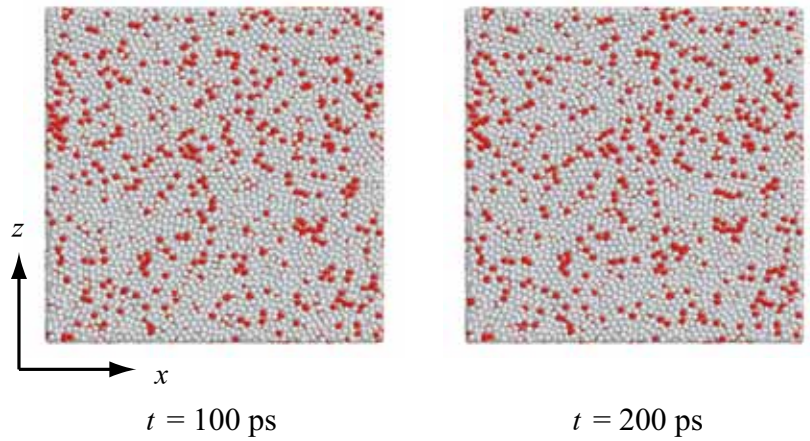

Figure 3: Distributions of $\det B_{ij}^{\alpha} < 0$ atoms at $t = 100$ps and 200ps in the no-load calculation.

This change is caused by the nucleation of a fractional crystalline structure; only 0.1% atoms are evaluated as "crystal" by this change. The potential energy remains unchanged after 50ps. Thus, the amorphous nickel has reached an equilibrium state.

Figure 2 shows a change in the ratio of $\det B_{ij}^{\alpha} < 0$ atoms during the no-load calculation. We have evaluated the elastic stiffness coefficient, B_{ij}^{α}, of all atoms on each 1ps. N^{inst}/N is "momentary" ratio of $\det B_{ij}^{\alpha} < 0$ atoms, where N^{inst} and N are a number of $\det B_{ij}^{\alpha} < 0$ atoms and a total number of atoms, respectively. N^{inst}/N slightly decreases from 0ps to 20ps on the initial stage, while there is no change of N^{inst}/N by the nucleation of a crystalline structure. The ratio of $\det B_{ij}^{\alpha} < 0$ atoms seems mostly unchanged and vibrates at around 12.7% during the energy equilibrium after 50ps. Thus, the amorphous nickel contains many "unstable" atoms of $\det B_{ij}^{\alpha} < 0$ even in the no-load equilibrium, and the ratio is almost constant. Figure 3 shows snapshots of the amorphous nickel at $t = 100$ps

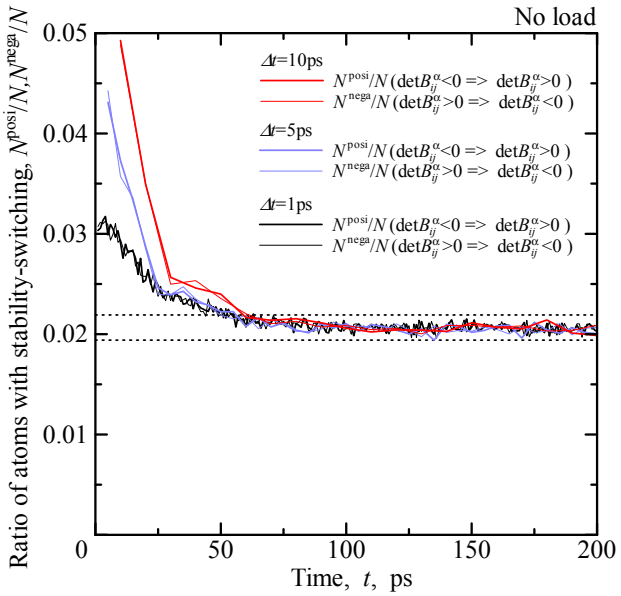

Figure 4: Changes in the ratio of atoms that have switched their stability for Δt in the no-load calculation.

and 200ps. Distributions of $\mathrm{det}B_{ij}^{\alpha} < 0$ atoms are indicated by red circles. There is no difference between atomic structure of Fig.3(a) and (b) because this amorphous metal has achieved equilibrium from $t = 50$ps. On the other hand, we can find a difference in the distribution of $\mathrm{det}B_{ij}^{\alpha} < 0$ or red atoms. That is, although the ratio of $\mathrm{det}B_{ij}^{\alpha} < 0$ atoms is almost constant in Fig.2, it is not always true that the distribution of $\mathrm{det}B_{ij}^{\alpha} < 0$ is same. We can understand that the stability-switching such as $\mathrm{det}B_{ij}^{\alpha} \geq 0 \leftrightarrow \mathrm{det}\ B_{ij}^{\alpha} < 0$ occurs even in the equilibrium state.

Then we have picked up atoms that have actually switched between $\mathrm{det}B_{ij}^{\alpha} \geq 0$ and $\mathrm{det}B_{ij}^{\alpha} < 0$ for each time interval of Δt. Figure 4 shows changes in ratios of these atoms, where N^{posi}/N and N^{nega}/N are the ratio of atoms with the positive change from $\mathrm{det}B_{ij}^{\alpha} < 0$ to $\mathrm{det}B_{ij}^{\alpha} \geq 0$ and the negative change from $\mathrm{det}B_{ij}^{\alpha} \geq 0$ to $\mathrm{det}B_{ij}^{\alpha} < 0$, respectively. We have evaluated the stability-switching by comparing of "momentary" values of $\mathrm{det}B_{ij}^{\alpha}$ before and after time intervals as Δt =1ps, 5ps or 10ps. N^{posi}/N shown with heavy lines and N^{nega}/N shown with thin lines are almost the same path. At the initial stage of relaxation before $t = 50$ps, ratios of N^{posi} and N^{nega} decrease and its decrease rate varies according to the evaluation time interval. This difference by the time interval disappears at 70ps. Moreover, all the ratios of N^{posi} and N^{nega} converges with 2.0% after 70ps. Two horizontal dotted lines describe upper and lower limits of the stability-switching after 70ps. We can understand that these ratios of stability-switching are caused by the "probabilistic" fluctuation such as the subtle change in local mechanical condition by the atomic perturbation or thermal vibration. Under the non-equilibrium state before 70ps, N^{posi}/N and N^{nega}/N show higher value than the upper limits under the equilibrium,

and vary according to the time interval because one-way stability-switching caused by "deterministic" nonequilibrium change is added to the ratio of the "probabilistic" changes.

4.2 Tension, compression and shear

Figure 5 shows stress-strain curves and changes in the ratio of $\det B_{ij}^{\alpha} < 0$ atoms under the tension, compression and shear. The scale of stress is indicated in the right axis. Stress and strain in the compression are shown by absolute value for comparison. Stresses show linear increases on the initial stage in every deformation. Gradients of stress-strain curves in the tension and compression are almost the same. After the linear increase, stress-strain curves become nonlinear, and alternate between increase and decrease showing zigzag response. We have evaluated $\det B_{ij}^{\alpha} < 0$ of all atoms at each 5ps, which correspond to the strain of 0.0005. Ratios of these atoms, N^{inst}/N, show the increasing tendency in every deformations. On the other hand, the ratio in tension shows a peak around $\varepsilon_{zz} = 0.037$ shown with a vertical broken line in Fig.5(a).

Figure 6 indicates the changes in the ratio of atoms that show stability-switching. As shown in Fig.4, we investigate the switching of positiveness of $\det B_{ij}^{\alpha}$ for several time intervals. In this figure, $\Delta t = 5$ps and 10ps, or $\Delta\varepsilon_{zz}, \Delta\gamma_{zx} = 0.0005$ and 0.001, are selected as intervals for comparison of $\det B_{ij}^{\alpha}$. Stress-strain curves are also shown. Horizontal dotted lines describe upper and lower limit of the stability-switching under the equilibrium state (Fig.4). Changes in N^{posi}/N and N^{nega}/N are shown by heavy lines and thin ones, respectively; while they are almost same just like in the no-load calculation of Fig.4. However, note that the accumulation of slight difference between them leads increase of $\det B_{ij}^{\alpha} < 0$ atoms under deformations (Fig.5). N^{posi}/N and N^{nega}/N stay in the upper and lower zone of equilibrium state in the initial stage. Then, they jump up from the upper limits around vertical dash-dotted lines shown with (A), and vary according to the time interval. These strains correspond with transition points from linear to nonlinear on stress-strain curves. After these strain, the tension and compression show larger ratios of stability-switching than the upper limit of equilibrium state. On the other hand, the ratios under the shear sometimes return to ratio zone of the equilibrium state. The N^{posi}/N and N^{nega}/N jump up again from the upper limits at vertical dash-dotted lines in Fig.6(c). The gradient of stress-strain curve also changes at these points. If we assume the ratio of "probabilistic" stability-switching is not changed under the deformation, the increase beyond the upper dotted line suggests the incidence of "deterministic" stability-switching by structural changes such as collapses of atomic cluster shown in our previous report [4]. In addition, occurrences of "deterministic" structural change induce differences of stability-switching according to time intervals, as shown in the non-equilibrium of Fig.4. In tension and compression of Figs. 6(a) and (b), the difference by time intervals after (A) almost disappear at vertical dash-dotted lines. Gradients of stress-strain curves also change at these lines. These suggest that the stress relaxation is caused by "shuffle of atomic arrangement" which involves positive and negative stability-switching simultaneously. Vertical dashed lines indicate the remarkable peak of N^{posi}/N and N^{nega}/N. These

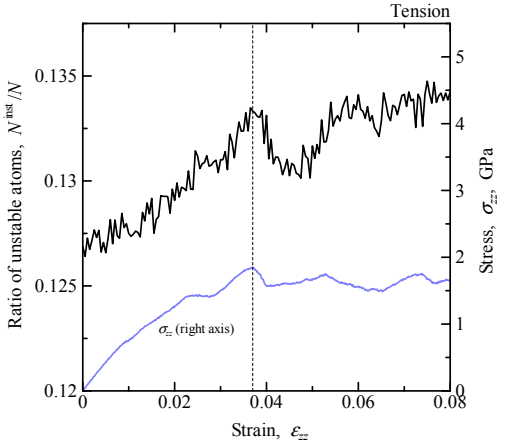

(a) Tension

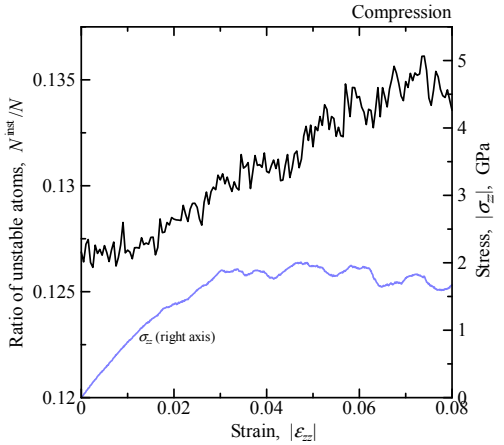

(b) Compression

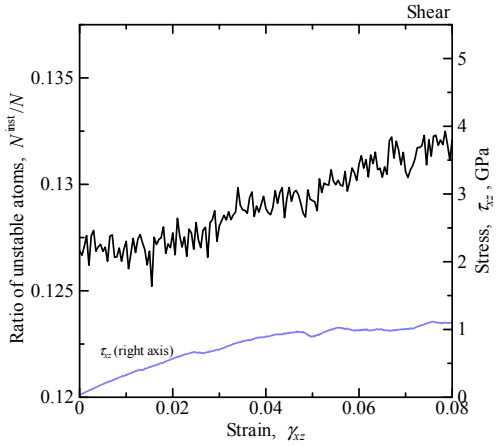

(c) Shear

Figure 5: Changes in the ratio of $\det B_{ij}^{\alpha} < 0$ atoms and stress-strain curves under the tension, compression and shear.

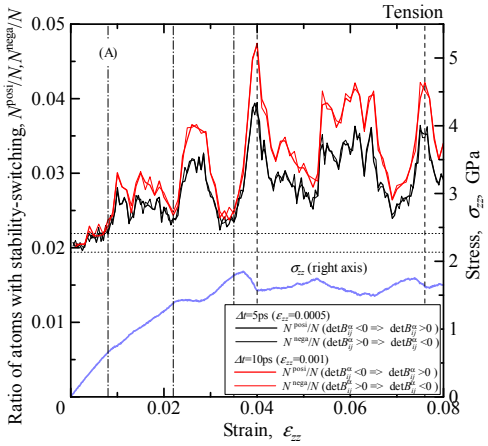

(a) Tension

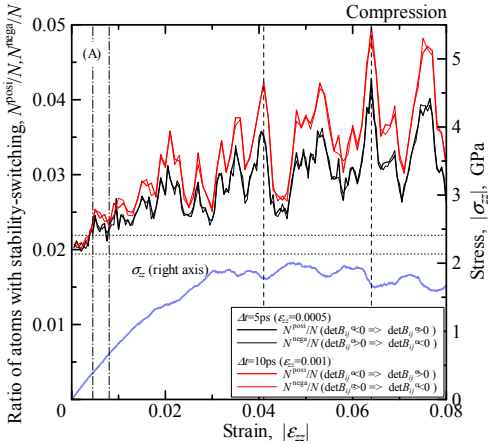

(b) Compression

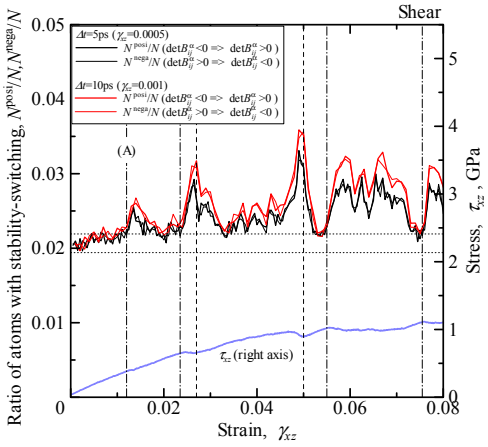

(c) Shear

Figure 6: Changes in the ratio of atoms that have switched their stability for Δt and stress-strain curves under the tension, compression and shear.

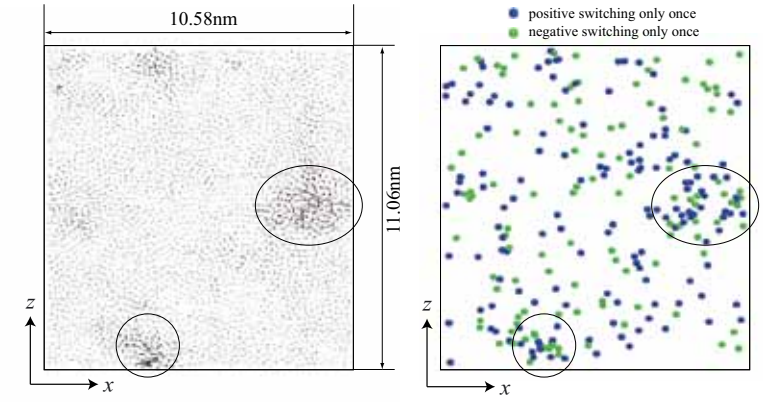

(a) Displacements of atoms (b) The distribution of atoms that have switched between stable and unstable

Figure 7: Comparison between atom motions and distribution of atoms that have switched their stability during $\varepsilon_{zz} = 0.035 \sim 0.037$ under tension.

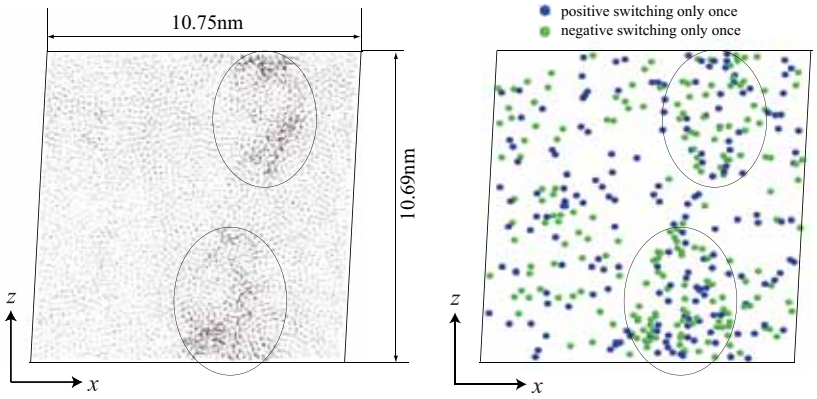

(a) Displacements of atoms (b) The distribution of atoms that have switched between stable and unstable

Figure 8: Comparison between atom motions and distribution of atoms that have switched their stability during $\gamma_{xz} = 0.05 \sim 0.052$ under shear.

correspond with the valley of stress-strain curves because stress relaxations weaken due to reduction of the shuffles.

We have considered a relationship between the local deformation and the stability-switching. Figures 7 and 8 show (a) the magnitude and direction of migration of each atoms with small vector and (b) the distribution of atoms that have switched between $\det B_{ij}^{\alpha} \geq 0$ and $\det B_{ij}^{\alpha} < 0$, during $\varepsilon_{zz} = 0.035 \sim 0.037$ in the tension and $\gamma_{xz} = 0.055 \sim 0.056$ in the shear, respectively. These periods just correspond to spans from the onset point of the increment of N^{posi} and N^{nega}, as shown with vertical dash-dotted lines in Fig.6, to the peak points of stress-strain curves. The trajectory and distribution

are shown only thin part in the simulation cell, in which the atoms show the largest migration during these periods. Colored circles in Figs.7(b) and 8(b) are atoms with stability-switching only once for each strain interval of 0.0005 during these observation periods; green atoms have negatively switched and blue ones have positively done. Some atoms switch their stabilities more than once, but these are mainly caused by probabilistic changes. Thus, these atoms are not shown in Figs.7(b) and 8(b) because we want to understand the relationship between the local deformation and the stability switching. We can find remarkable atom rearrangements as shown with ellipsoids in Figs.7(a) and 8(a). These regions have many atoms with stability-switching in Figs.7(b) and 8(b). This demonstrates that the "shuffle of atomic arrangement" simultaneously produce both positive and negative stability-switching. Note that these periods are before the peaks of stress-strain curves. The emergence of these local events leads to the global deformation. It is suggested the possibility that we can evaluate the origin of global deformation by the observation of the stability switching.

4.3 Volume changes by the stability-switching

In order to understand structural changes by the stability-switching, we evaluated a volume change of Voronoi polyhedron of each atom under tension, compression and shear. Voronoi polyhedra are determined by nearest neighbor atoms of center atom. Thus, we can regard the Voronoi volume, V_α, as an atomic volume of atom α. Variations of Voronoi volume by the stability-switching are determined as follows;

$$\Delta V_\alpha^{\mathrm{posi}} = \frac{1}{N^{\mathrm{posi}}} \sum_i^{N^{\mathrm{posi}}} \{V_i(t) - V_i(t-\Delta t) - \Delta V_\alpha^{\mathrm{all}}\},$$
$$\Delta V_\alpha^{\mathrm{nega}} = \frac{1}{N^{\mathrm{nega}}} \sum_i^{N^{\mathrm{nega}}} \{V_i(t) - V_i(t-\Delta t) - \Delta V_\alpha^{\mathrm{all}}\}, \tag{3}$$

where N^{posi} and N^{nega} are the number of atoms with positive and negative stability-switching for the time interval of Δt. $\Delta V_\alpha^{\mathrm{all}}$ is determined by a system volume, V, as

$$\Delta V_\alpha^{\mathrm{all}} = \frac{1}{N} \sum_i^N \{V_i(t) - V_i(t-\Delta t)\} = \frac{1}{N}\{V(t) - V(t-\Delta t)\}. \tag{4}$$

We uniformly remove the effect due to affine deformation from each atom because the system volume changes under the tension and compression. $\Delta V_\alpha^{\mathrm{all}}$ in the shear is zero, all of the time. Figure 9 shows changes in $\Delta V_\alpha^{\mathrm{posi}}$ and $\Delta V_\alpha^{\mathrm{nega}}$ under the tension, compression and shear. The interval for evaluation of stability-switching is $\Delta t = 10$ps, or $\varepsilon_{zz}, \gamma_{xz} = 0.001$. Vertical lines shown in Fig.6 are indicated again in this figure. Shapes of the changes in $\Delta V_\alpha^{\mathrm{nega}}$ are similar to those in the ratio of stability-switching previously shown in Fig.6, while $\Delta V_\alpha^{\mathrm{posi}}$ are opposite in sign to $\Delta V_\alpha^{\mathrm{nega}}$. So that, the volume increase and decrease are induced by the negative and positive stability-switching, respectively.

Magnitudes of $\Delta V_\alpha^{\rm posi}$ and $\Delta V_\alpha^{\rm nega}$ rise just behind vertical dash-dotted lines as shown by arrows, and peaks of these also correspond with dashed lines. It is suggested that the volume change by "deterministic" stability-switching are larger than that by "probabilistic" one. Volume changes of $\Delta V_\alpha^{\rm posi}$ and $\Delta V_\alpha^{\rm nega}$ almost get balanced out each other because ratios of $N^{\rm posi}$ and $N^{\rm nega}$ almost coincide with each other.

We can understand the volume change of an atom by the stability-switching. On the other hand, structural changes on the amorphous metal occur in dozens of atoms, as shown in Figs.7 and 8. We evaluate the changes in local volume around atoms with the stability-switching,

$$\Delta V_{\rm rc}^{\rm posi} = \frac{1}{N^{\rm posi}} \sum_i^{N^{\rm posi}} \sum_j^{N_i^{\rm rc}} \{V_j(t) - V_j(t-\Delta t) - \Delta V_\alpha^{\rm all}\}$$
$$\Delta V_{\rm rc}^{\rm nega} = \frac{1}{N^{\rm nega}} \sum_i^{N^{\rm nega}} \sum_j^{N_i^{\rm rc}} \{V_j(t) - V_j(t-\Delta t) - \Delta V_\alpha^{\rm all}\} \quad (5)$$

where $N_i^{\rm rc}$ is the number of atoms in a sphere centering on atom i at time of t. A radius of this sphere is 0.48nm, which correspond with a cutoff radius for calculation of EAM interaction. Thus, $\Delta V_{\rm rc}^{\rm posi}$ and $\Delta V_{\rm rc}^{\rm nega}$ mean volume changes of the spherical region around atoms with negative and positive stability-switching. Figure 10 shows changes in the $\Delta V_{\rm rc}^{\rm posi}$ and $\Delta V_{\rm rc}^{\rm nega}$ under the tension, compression and shear. $\Delta V_{\rm rc}^{\rm nega}$ has a tendency of volume increase, and $\Delta V_{\rm rc}^{\rm posi}$ do that of volume decrease; however, these are not symmetric about the x-axis. Values of $\Delta V_{\rm rc}^{\rm posi}$ exhibit a clear declining trend just behind vertical dash-dotted lines as shown by arrows, and almost peaks of these correspond with dashed lines. On the other hand, we cannot find clear correspondences between $\Delta V_\alpha^{\rm nega}$ and vertical lines. Here, these changes in $\Delta V_{\rm rc}^{\rm posi}$ are not caused by only an atomic volume change of the center atom. Note that scales of y-axis in Fig.10 are larger than those in Fig.9. Thus, the positive stability-switching, or "stabilization", produces a local volume decrease with surrounding neighbor atoms. Both positive and negative stability-switching under the deformations occur at the same region, as previously shown in Figs.7 and 8. Thus the negative stability-switching occurs in order to absorb the volume decrease by the stabilization.

5 CONCLUSIONS

In order to explore further relationship between deformation in amorphous metals and changes in the atomic stability determined by the positiveness of atomic elastic stiffness coefficients, B_{ij}^α, we have discussed stability-switching as $\det B_{ij}^\alpha < 0 \leftrightarrow \det B_{ij}^\alpha \geq 0$ in an amorphous nickel under several deformations. First, $\det B_{ij}^\alpha$ of all atoms are evaluated during the no-load calculation after the melt-quench simulation. The negative and positive stability-switching occur due to the "probabilistic" fluctuation even at the equilibrium state, and the number of $\det B_{ij}^\alpha < 0$ atoms shows almost constant while the distribution

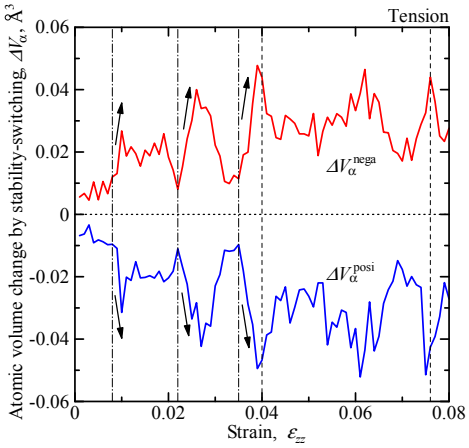

(a) Tension

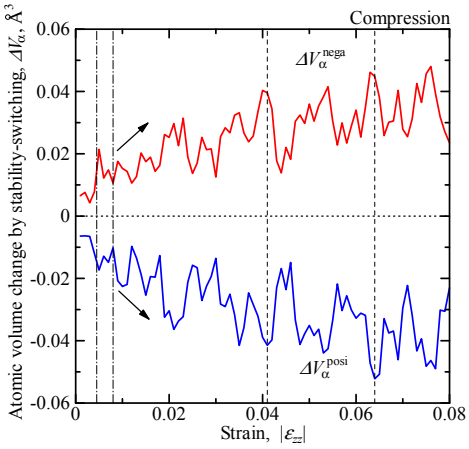

(b) Compression

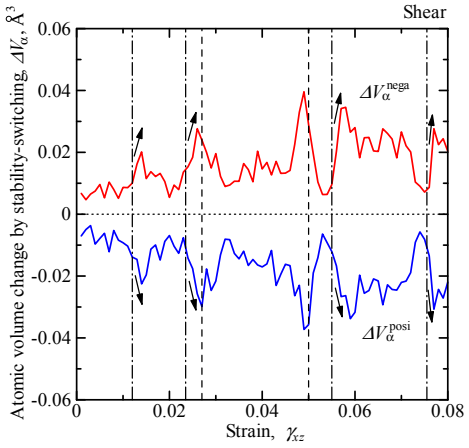

(c) Shear

Figure 9: Changes in variation of atomic volume by the stability-switching under the tension, compression and shear.

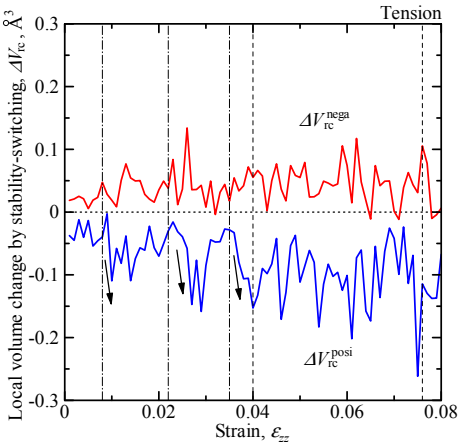

(a) Tension

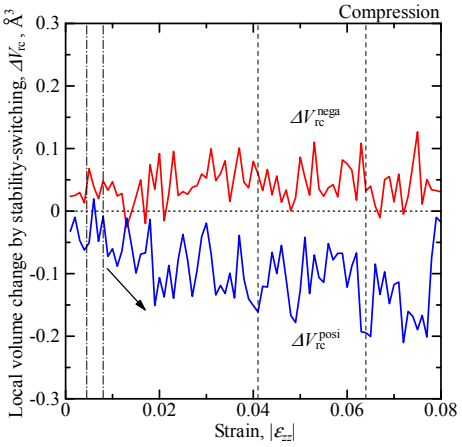

(b) Compression

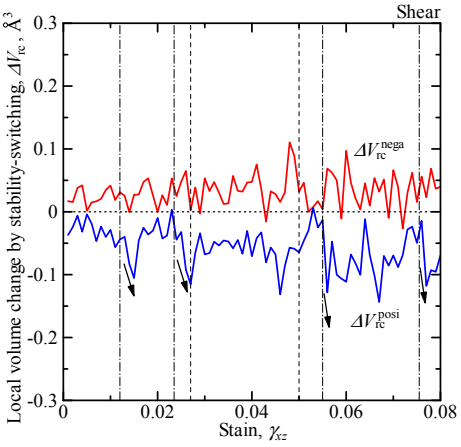

(c) Shear

Figure 10: Changes in variation of local volume by the stability-switching under the tension, compression and shear.

of $\det B_{ij}^{\alpha} < 0$ atoms changes from time to time. Then, tension, compression and simple shear are applied on the amorphous nickel in order to discuss the stability-switching by "deterministic" mechanical load. We have revealed the following facts : (1) The number of $\det B_{ij}^{\alpha} < 0$ atoms shows the increasing tendency under deformations. (2) Ratios of atoms with stability-switching under deformations is larger than that under the equilibrium because the local structural relaxation produces simultaneously both positive and negative stability-switching. (3) Atoms with negative and positive stability-switching show increases and decreases of atomic volume, respectively. Moreover, magnitude of both volume changes rise according to the incidence of "deterministic" stability-switching. (4) The negative and positive stability-switching also produce increases and decreases of local volume, evaluated with the atomic volumes of surrounding atoms within the cutoff radius, respectively; while only positive switching shows the correspondence between the change of local volume and the incidence of "deterministic" stability-switching.

REFERENCES

[1] M. Shimono and H. Onodera, Short-Range and Medium-Range Order in Supercooled Liquids of Alloys, *Mat. Sci. Eng. A* (2007) **449–451**:717–721.

[2] H. W. Sheng, W. K. Luo, F. M. Alamgir, J. M. Bai and E. Ma, Atomic Packing and Short-to-Medium-Range Order in Metallic Glasses, *Nature* (2006) **439**:419–425.

[3] K. Yashiro and Y. Tomita, Local lattice instability at a dislocation nucleation and motion, *J. de Phys. IV*(2001) **11**:Pr5-3-Pr5-10.

[4] K. Yashiro, M. Nishimura and Y. Tomita, Deformation analysis of amorphous metals based on atomic elastic stiffness coefficients, *Model. Sim. Mater. Sci. Eng.* (2006) **14**:597-605.

[5] M. Nishimura, K. Yashiro and M. Arai, Local lattice instability analysis on amorphous metals: switching between stable and unstable atoms, *J. Sol. Mech. Mater. Eng.* (2010) **4**:1550-1562.

[6] J. Wang, S. Yip, S. R. Phillpot and D. Wolf, Crystal instabilities at finite strain, *Phys. Rev. Lett.* (1993) **71**:4182–4185.

[7] J. Wang, J. Li, S. Yip, S. R. Phillpot and D. Wolf, Mechanical instabilities of homogeneous crystals, *Phys. Rev. B* (1995) **52**:12627–12635.

[8] P. C. Wallace, *Thermodynamics of Crystals*. Wiley, Newyork, (1972).

[9] M. S. Daw and M. I. Baskes, Embedded–Atom Method : Derivation and Application to Impurities, Surfaces and Other Defects in Metals, *Phys. Rev. B* (1984) **29**:6443–6453.

[10] A. F. Voter and S. P. Chen, Accurate Interatomic Potentials for Ni, Al and Ni_3Al, *Mater. Res. Soc. Sympo. Proc.* (1987) **82**:175-180.

XI International Conference on Computational Plasticity. Fundamentals and Applications
COMPLAS XI
E. Oñate, D.R.J. Owen, D. Peric and B. Suárez (Eds)

NEURAL NETWORK BASED MATERIAL DESCRIPTION OF UNCURED RUBBER FOR USE IN FINITE ELEMENT SIMULATION

C. ZOPF[*], S. FREITAG[*†] AND M. KALISKE[*]

[*]Institute for Structural Analysis (ISD)
Technische Universität Dresden
D-01062 Dresden, Germany
e-mail: christoph.zopf@tu-dresden.de, michael.kaliske@tu-dresden.de
web page: http://www.tu-dresden.de/isd

[†]School of Civil and Environmental Engineering
Georgia Institute of Technology
Savannah, GA 31407, USA
e-mail: steffen.freitag@tu-dresden.de

Key words: Non-Conventional Material Modeling, Uncured Rubber, Artificial Neural Network, Viscoelasticity, Irreversible Deformation, Forming Process

Abstract. The finite element method (FEM) is widely used for structural analysis in engineering. In order to predict the behaviour of structures realistically, it is important to understand and to describe the material behaviour. Therefore, extensive material tests have to be conducted. For highly inelastic materials, such as uncured rubber, the characterisation of the behaviour requires a quite complex rheology. Rheological models are used to describe time-dependent mechanical material behaviour (stress-strain-time dependencies). The mapping of the real material behaviour by such models is only possible with restrictions. However, the evaluation of these models at each integration point within the FEM needs time consuming internal iterations in most cases. In order to describe the material behaviour without model restrictions and to reduce computational cost, the aim of this work is the development of a procedure which enables structural analyses without a specific constitutive material model. In this paper, a neural network is used in order to describe uncured rubber behaviour as a model-free approach.

1 INTRODUCTION

Rubber products are essential components of technical systems for example in mobility. Tires, braking systems and engines are not imaginable without rubber parts. Elastomeric material mainly consists of natural or synthetic rubber. Other ingredients are e.g. sulphur,

carbon black, softener and antioxidants. All these components influence the properties and the behaviour of rubber material significantly. Rubber material is temperature dependent. For low temperature, the constitutive behaviour is nearly elastic whereas for rising temperature, rubber offers a viscoelastic feature. Irreversible deformation occurs for higher temperature or for large deformations. Beside, rubber material withstands large deformations with little damage effects. It is a thermal and electrical isolator and has a huge damping capacity. Hence, rubber material is a useful and flexible applicable material.

Rubber develops its intended properties after curing under high pressure and temperature. Before the curing process starts, the uncured rubber is formed into a mould in order to obtain the designated shape of the product. Mostly, this forming process of uncured rubber takes place in a curing press. A monitoring of this process is difficult and quite expensive.

Using simulation tools based on the finite element method (FEM) enables a visualisation of such forming processes. In order to predict the behaviour of forming procedures within the FE simulation realistically, it is important to understand and describe the behaviour of green rubber material. Uncured rubber is characterised by elastic, plastic and viscous constitutive response. The constitutive behaviour can be analysed by appropriate material tests. Viscoelasticity is characterised by time- and history-dependent behaviour (see [1, 2, 3, 4]). If a specimen of viscoelastic material is loaded by a constant stress, the strain within the specimen will grown over time (creep). The stress within the same specimen will decrease over time (relaxation) if it is loaded at a constant strain. For a realistic description of the elastomer, extensive compression, tensile and pure shear tests are conducted to generate different states of loading. The viscous effects are characterised by means of relaxation and cyclic tests. Furthermore, the irreversible part of the deformation is determined with the help of a special kind of tensile test.

Usually, specific material models are developed, which are able to represent the constitutive behaviour. The selection and validation of adequate material models as well as the development of new formulations is often time consuming. Highly inelastic materials, such as uncured rubber, are characterised by a quite complex rheology. The time-dependent mechanical behaviour (stress-strain-time dependencies) is described by rheological models. In most cases, these approaches require time consuming internal iterations at each integration point within the FE procedure. After the selection of a suitable model, its parameters have to be identified. The identification is realised by parameter fitting procedures which are in fact an optimisation process.

The selection and development of a material model as well as the identification of material parameters require a lot of computational cost and manpower. Furthermore, the material models are an idealisation of reality and, therefore, this representation is always a reduction of properties and information. Additionally, the computational cost due to internal iteration within the rheology of the material model slow down FE simulations significantly. Hence, the goal of the authors' work is the development of a procedure which

enables structural analyses without an explicit constitutive approach. Such a procedure can be used for different types of materials and, hence, the development of different models for different materials is no longer required. In this approach, the material behaviour is described by an artificial neural network (ANN). Commonly, ANN are used for different tasks in engineering [5], e.g. response surface approximation, parameter and system identification. Here, the representation of material behaviour by ANN and the implementation into the FEM are of interest (see e.g. [6]). For the description of time-dependent material behaviour, the authors' decided to use a recurrent neural network (RNN) [7]. The architecture of these ANN enable the consideration of inelastic time-dependent material features. The network parameters are identified using directly data (representing stresses and strains) obtained from tests. One benefit of this approach is the reduction of computational cost, because no internal iteration at the integration points is required. RNN can be adapted to different kinds of constitutive behaviour, which reduces the development time for material representations. Additionally, a higher accuracy is expected because of the direct implementation of material test results into the FE model with no reduction of information.

2 EXPERIMENTAL INVESTIGATIONS

The material properties of an uncured rubber can be observed by appropriate material tests. For an intensive study of the following material tests, it is referred to [8]. A realistic description of material properties requires extensive testing. Therefore, tensile, compression, and shear tests are carried out. In Figure 1, the specimens of the different material tests are shown. All types of specimen are punched and cut out of rubber plates

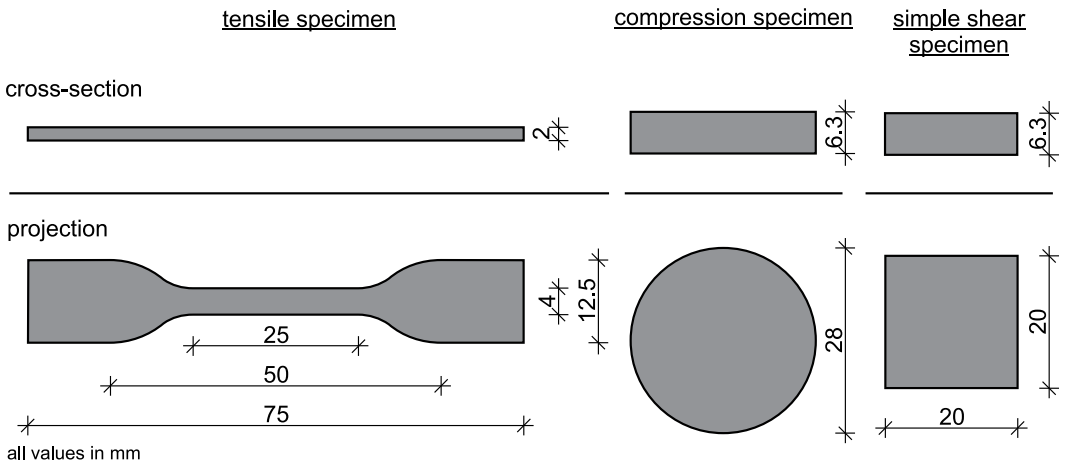

Figure 1: Cross-section and projection of the specimens

with a thickness of 2 mm and 6.3 mm, respectively.

The tensile tests are conducted using a standardised specimen [9]. In the middle of this

specimen, the cross-sectional area is smaller than at its edge, in order to preserve a uniaxial state of stress. The displacements of the undisturbed and uniform deformation region of the specimen are measured by an external displacement transducer. The reference length l_0 of the undisturbed region is 15 mm. The complete test equipment is shown in Figure 2a. In order to obtain the temperature dependency of the material, all tests are pursued at three different temperatures (T = 25°C, 65°C and 105°C). At first, single stage tensile tests are conducted until breaking elongation is achieved. Inelastic properties can be obtained under consideration of cyclic and relaxation tests. Every cyclic test consists of five load cycles. One load cycle consists of a loading phase and a following unloading period. The unloading is completed when the measured force is equal to zero. After every cycle, the strain is increased by 20%. Hence, the maximum strain of the specimen within the cyclic test is 100%. The relaxation tests take place in three load steps. At the beginning of every load step, the strain is increased by 30%. After achieving the current load level, the strain is kept constant for 900 s. Within that time, stress relaxation takes place. Finally, a cyclic test with a holding time after the unloading of every cycle is conducted. The holding time is 240 s. Within this time, the viscoelastic part of deformation is reversed and only the irreversible deformation is stored in the material. Under consideration of these material tests, the irreversible and viscoelastic part of deformation can be quantified.

The compression tests are carried out with cylindrical specimen. The diameter is 28 mm and the total height is 18.9 mm. The contact surface between the specimen and the testing machine is rough. By means of physical and numerical tests, it is shown that within the specimen a uniaxial state of stress exists for a strain up to −40%. The test equipment is presented in Figure 2b. Also for the compression tests, single stage and

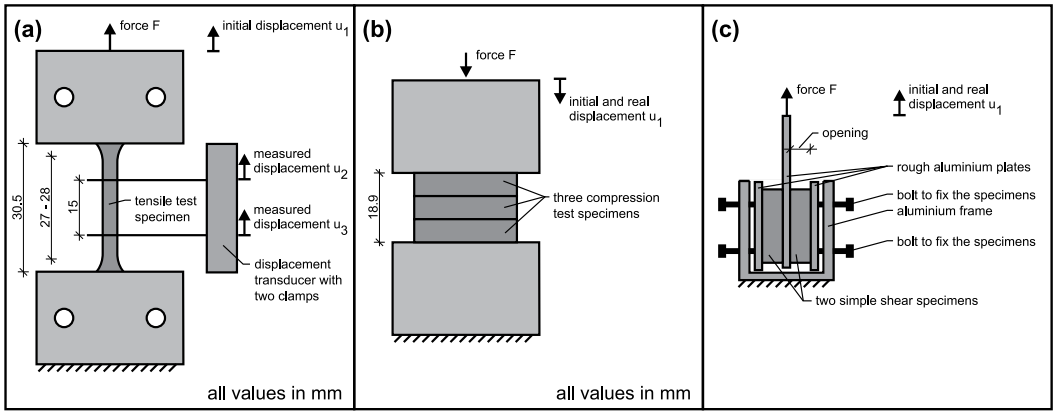

Figure 2: Test equipment for: (a) tensile test; (b) compression test; (c) simple shear test

cyclic tests are carried out. The single stage tests have a maximum strain of −75%. The cyclic tests consist of seven load cycles. In every load cycle, the strain increases by −10% and, hence, the maximum strain within this test series is −70%.

Finally, simple shear tests are developed in order to gain information on the uncured rubber material behaviour for a different state of stress. The used specimen is a cuboid with a square base area (20 mm × 20 mm) and a height of 6.3 mm. Two of these specimen are fixed in the frame of the test equipment (compare Figure 2c). Between the two specimen, a rough aluminum plate is placed. The frame is fixed and the aluminum plate is loaded. The distance between the frame and the aluminum plate is defined as the opening. During the different shear tests, the opening has a value of 4 mm and 5 mm, respectively. For this kind of material test, also single stage tests and a cyclic test are carried out. Within the single stage tests, the aluminum plate is driven by 5 mm and the total displacement of the plate within the cyclic test is 5.3 mm. The cyclic test consists of five load cycles and, hence, the displacement of the aluminum plate increases by 1.06 mm for every load cycle.

3 MATERIAL DESCRIPTION BY ARTIFICIAL NEURAL NETWORKS

3.1 Recurrent neural networks

Recurrent neural networks enable, among others time-dependent approximations of different classes of structural analysis. The computation is time efficient and, hence, it can be used especially for the approximation of time-dependent structural behaviour (see e.g. [10, 11]). Here, a RNN is used instead of a material model in a FEM code.

For the formulation of stress-strain-time dependencies, a network architecture according to [7] is used. These RNN consist of M layers (input, $M-2$ hidden and output layer). Each layer m has a number of neurons, which are linked by synaptic connections to the neurons of the following layer $m+1$. The number of input and output neurons is defined by the number of strain and stress tensor components. For 3D material formulations, six input and six output neurons are required. The experimentally obtained data series are discretised into equidistant time steps n. In each time step, the $j = 1, \ldots, 6$ strain components are transferred to input signals ${}^{[n]}x_j^{(1)}$ and the output signals ${}^{[n]}x_k^{(M)}$ of the network define the $k = 1, \ldots, 6$ stress components. The hidden and the output neurons are connected additionally to context neurons in order to capture time-dependent material behaviour. This approach enables to consider all $j = 1, \ldots, 6$ current strain components and the whole strain history for the computation of each stress component of time step n.

The signals of RNN are computed layer by layer. The output signal of neuron k in layer m is obtained by

$$ {}^{[n]}x_k^{(m)} = \varphi\left(\sum_{j=1}^{J}\left[{}^{[n]}x_j^{(m-1)} \cdot w_{kj}^{(m)}\right] + \sum_{i=1}^{I}\left[{}^{[n]}y_i^{(m)} \cdot c_{ki}^{(m)}\right] + b_k^{(m)}\right) . \tag{1} $$

The argument of the activation function φ contains the sum of all input signals ${}^{[n]}x_j^{(m-1)}$ of the previous layer multiplied by the weights $w_{kj}^{(m)}$, the sum of all context signals ${}^{[n]}y_i^{(m)}$

multiplied by the context weights $c_{ki}^{(m)}$ and the bias value $b_k^{(m)}$. Various types of activation functions can be used (see e.g. [12]). In this application, the area hyperbolic sine activates the hidden neurons and a linear function is selected for the output neurons.

The output signals of the context neurons are computed by the previous output signal of the hidden or output neuron i multiplied by the memory factors $\gamma_i^{(m)}$ and the previous context signal ${}^{[n-1]}y_i^{(m)}$ multiplied by the feedback factor $\lambda_i^{(m)}$ summarised by

$${}^{[n]}y_i^{(m)} = {}^{[n-1]}x_i^{(m)} \cdot \gamma_i^{(m)} + {}^{[n-1]}y_i^{(m)} \cdot \lambda_i^{(m)} \; . \tag{2}$$

The memory factors and the feedback factors are defined as values of the interval [0, 1]. A feed forward network is obtained as a special case of the presented RNN, if all memory factors are zero.

The analytical determination of the algorithmic tangential stiffness for the element stiffness matrix requires to evaluate the partial derivatives

$${}^{[n]}C_{kj} = \frac{z_k^{sc}}{x_j^{sc}} \cdot \frac{\partial {}^{[n]}x_k^{(M)}}{\partial {}^{[n]}x_j^{(1)}} \tag{3}$$

of the output signals ${}^{[n]}x_k^{(M)}$ with respect to the input signals ${}^{[n]}x_j^{(1)}$. The parameters x_j^{sc} and z_k^{sc} are scaling factors of the input and output signals, respectively. The partial derivatives are computed by multiple applications of the chain rule (see [12]). They can be computed layer by layer similar to the output signals.

3.2 Modification of neural network output quantities for application in FEM

Within the RNN approach, input quantities are mapped onto system responses (output quantities). For the introduced application of the RNN, the elements of the strain tensor (input quantities) are mapped onto the elements of the stress tensor (output quantities). The usage of a RNN instead of a material model requires a modified strain and stress tensor as input and output quantities. This adaptation of the strain and the stress tensor is necessary to ensure an interaction between FEM and RNN. In order to solve the nonlinear and inelastic FE problem, an incremental iterative solution is employed.

The used FE code needs the Cauchy stress tensor ${}^{[n]}\underline{\boldsymbol{\sigma}}$. All stress and strain tensors of the following derivation are tensors at the time step n. For simplification, the index of the time step ${}^{[n]}\bullet$ is omitted in the tensor notation.

In classical continuum mechanics, the Cauchy stress tensor $\underline{\boldsymbol{\sigma}}\,(\underline{\mathbf{b}})$ can be given in dependency on the Finger tensor $\underline{\mathbf{b}} = \underline{\mathbf{F}}\,\underline{\mathbf{F}}^T$. The dilatation $J = \det \underline{\mathbf{F}}$ is an indicator for the compressibility of the material. For $J \approx 1$, the material is nearly incompressible. The dilatation is given in dependency on the deformation gradient $\underline{\mathbf{F}}$. The Cauchy stress tensor $\underline{\boldsymbol{\sigma}}$ is mainly calculated by the Finger tensor $\underline{\mathbf{b}}$ and, therefore, the Finger tensor should be used as input of the RNN and the scaled output signals $z_k^{sc} \cdot {}^{[n]}x_k^{(M)}$ deliver Cauchy stresses $\underline{\boldsymbol{\sigma}}$. In order to preserve the functionality of the RNN, the inputs $x_j^{sc} \cdot {}^{[n]}x_j^{(1)}$ are substituted by the difference of Finger tensor and identity tensor $\underline{\mathbf{b}} - \underline{\mathbf{1}}$.

The tangent moduli

$$\underline{\underline{\mathfrak{C}}} = 2\,J^{-1}\underline{\mathbf{b}}\frac{\partial\underline{\boldsymbol{\sigma}}\,J\,\underline{\mathbf{b}}^{-1}}{\partial\underline{\mathbf{b}}}\underline{\mathbf{b}} \tag{4}$$

are defined as the derivatives of the Cauchy stress tensor $\underline{\boldsymbol{\sigma}}$ with respect to the Finger tensor $\underline{\mathbf{b}}$. Finally, the tangent moduli in the current configuration

$$\underline{\underline{\mathfrak{C}}} = 2\,J^{-1}\underline{\mathbf{b}}\cdot\left(J\,\underline{\mathbf{b}}^{-1}\cdot\frac{\partial\underline{\boldsymbol{\sigma}}}{\partial\left(\underline{\mathbf{b}}-\underline{\mathbf{1}}\right)}:\underline{\underline{\mathbb{I}}}+\underline{\boldsymbol{\sigma}}\cdot\left[\frac{J}{2}\left(\underline{\mathbf{b}}^{-1}\otimes\underline{\mathbf{b}}^{-1}\right)-J\,\underline{\mathbf{b}}^{-1}\cdot\underline{\underline{\mathbb{I}}}\cdot\underline{\mathbf{b}}^{-1}\right]\right)\cdot\underline{\mathbf{b}} \tag{5}$$

are derived in dependency on the partial derivatives of the network outputs with respect to the network inputs $\partial_{\underline{\mathbf{b}}-\underline{\mathbf{1}}}\,\underline{\boldsymbol{\sigma}}$, the Cauchy stress tensor, the Finger tensor and the forth order identity tensor $\underline{\underline{\mathbb{I}}}$. The derivative $\partial_{\underline{\mathbf{b}}-\underline{\mathbf{1}}}\,\underline{\boldsymbol{\sigma}}$ is equivalent to the tangential stiffness ${}^{[n]}C_{kj}$ of the RNN. The Cauchy stress tensor and the derivatives are obtained from the RNN algorithm. These output quantities can be used directly to calculate the tangent moduli $\underline{\underline{\mathfrak{C}}}$ in Eq. (5) which is consistent with the FEM.

3.3 Verification of approach by FE simulations

The described approach has to be verified via FE simulations. If the RNN is able to represent the behaviour of a real rubber material, then it has to represent also the behaviour of a non-linear elastic material model. Here, the Yeoh material description [13] is chosen as one typical model. The typical upturn at large strain can be represented by the Yeoh formulation.

Within a training procedure, the unknown network parameters, i.e. the weights, the bias values and the context weights, have to be determined. These unknowns are chosen by the comparison of training data and network responses. The aim of the training is to find network parameters which provide a minimised difference between training data and network response. A more detailed explanation of the training algorithm is given in Section 3.5.

In this example, 2000 different states of strain are randomly found. The corresponding stresses are calculated by the chosen Yeoh material model. Hence, 2000 different states of strain and corresponding stresses define the data set of 2000 strain-stress dependencies. Subsequently, the data set is divided into two parts. 1000 strain-stress dependencies are used for the training and the other 1000 are used in order to validate the quality of the identified network parameters. This kind of validation is a part of the training procedure.

After the implementation of the authors' approach, explained in Section 3.1 and 3.2, two different examples are carried out for verification. The conducted uniaxial tensile and shear test are pictured in Figure 3. The geometry of the uniaxial test sample is a cuboid with a square base area of 4 mm × 4 mm and a height of 20 mm. It is discretised by 40 solid elements with 8-nodes per element. The boundary conditions enable a uniaxial behaviour of the test sample. The load is applied in two steps. In the first step, the top of the test sample is driven by 20 mm in y-direction (see Figure 3) and, in the second step,

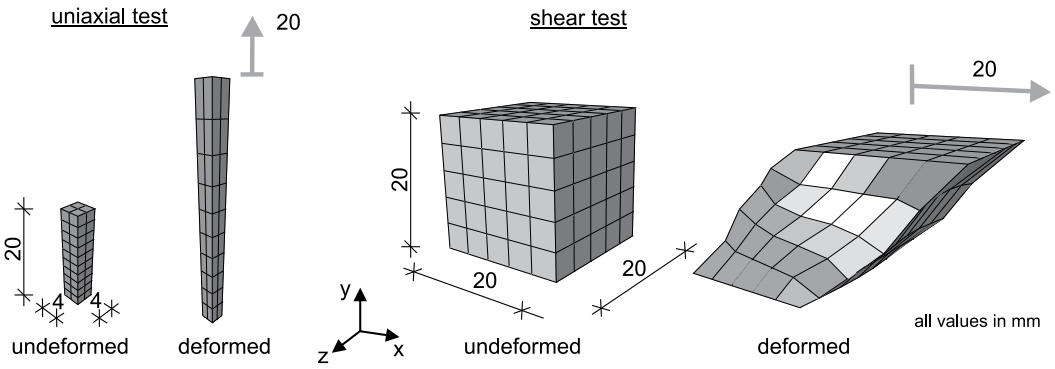

Figure 3: FE simulations: uniaxial and shear test

the top is deformed into the initial condition. The geometry of the shear test sample is a cube with an edge length of 20 mm. Here, likewise 8-node solid elements are used for discretisation. The shear test sample consists of 125 elements. The nodes at the top and at the bottom of the shear test sample are fixed in all three directions. The shear test also consists of two load steps. In the first step, the top of the test sample is deformed by 20 mm in x-direction (see Figure 3) and, in the second step, the top is driven back into the initial condition.

In Figure 4, results of the simulation using Yeoh material formulation and the RNN are shown for the tensile and shear test. The pictured stress-time dependencies represent the stresses in the middle of the test samples. For the uniaxial test, the stress σ_{22} in loading

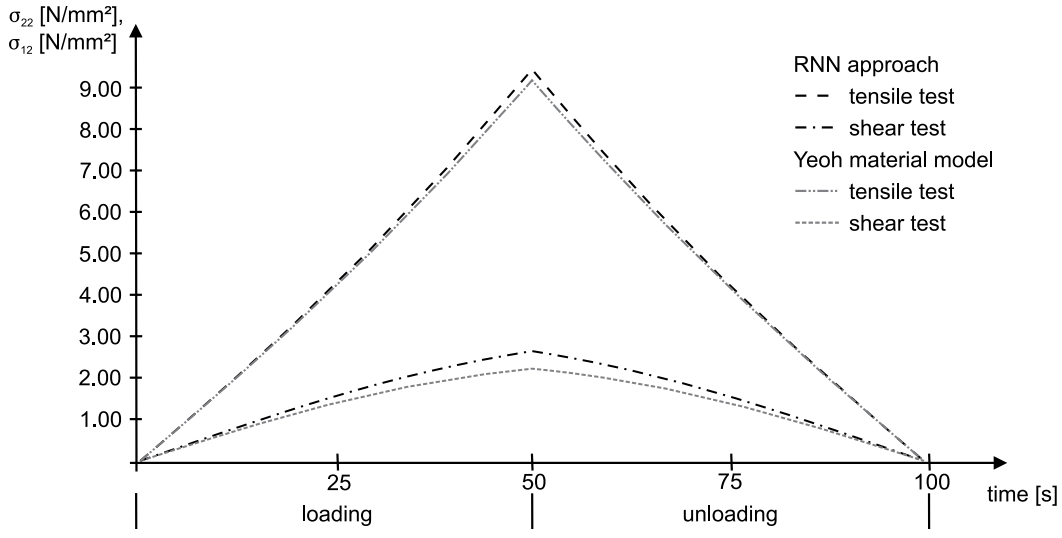

Figure 4: Comparison of Yeoh material model and RNN approach

direction is chosen for the comparison of the two approaches. The shear component σ_{12}

is used to compare both shear test results. The differences between the two formulations are marginal in both cases. The behaviour of the Yeoh model can be represented by the RNN.

The training of the RNN delivers quite good results. The consideration of additional state of strains, especially with a focus on shear strains, even would improve the training and, therefore, the simulation results. For this example, the quality of the RNN is acceptable. It could be shown, that the approach is ready for implementation into a FE code.

3.4 Preparation of material test results for training of neural network

The usage of the RNN instead of a material model for a real material requires the training of the network parameters in dependency on the material behaviour. All training data are based on the results of the material tests (compare with Section 2). Therefore, the material test results have to be prepared for training of the neural network.

The testing machines deliver time-dependent displacements u and forces F. For all uniaxial tests, the strain $\varepsilon = u/l_0$ is equal to the ratio of displacement and reference length. The stretch λ is equal to the sum of 1 and the strain ε. The stress component P_u is defined as the ratio of the force F and the reference cross-sectional area A_0 of the specimen. For the interpretation of shear tests, the shear angle and the shear stress are necessary. The required shear angle $\gamma = u/Sb$ is the ratio of the displacement u of the test machine and the opening Sb (see Figure 5). The shear stress P_s is calculated by dividing the measured force F by the square base area (20 mm $\times$ 20 mm) of the specimen.

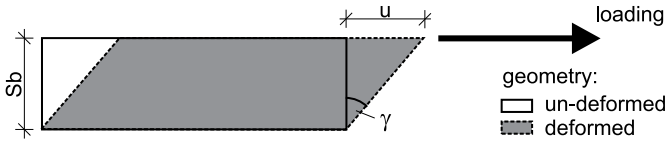

Figure 5: Shear angle in dependency of displacement u and opening Sb

Uncured rubber material is nearly incompressible. Hence, the deformation gradient is defined as

$$\underline{\mathbf{F}} = \begin{bmatrix} \lambda & \gamma & 0 \\ 0 & \lambda^{-1/2} & 0 \\ 0 & 0 & \lambda^{-1/2} \end{bmatrix}. \tag{6}$$

Based on this deformation gradient, the Finger tensor can be calculated. For the uniaxial tests, the shear angle γ is set to zero and for the shear tests, the stretch λ is equal 1. The required Cauchy stress tensor $\underline{\boldsymbol{\sigma}} = J^{-1}\,\underline{\mathbf{P}}\,\underline{\mathbf{F}}^T$ is a function of the deformation gradient $\underline{\mathbf{F}}$ and the first Piola-Kirchhoff stress tensor $\underline{\mathbf{P}}$. The component P_{11} of the first Piola-Kirchhoff stress tensor $\underline{\mathbf{P}}$ is equal to the force in uniaxial direction P_u and the component P_{12} is equal to the shear stress P_s.

3.5 Training and validation results

The determination of the unknown network parameters is achieved by a training procedure. This training procedure is an optimisation approach, comparable to identification tools for material parameter fitting. Therefore, the differences between test results and output values of the RNN are computed for all output neurons. The sum of these differences is equal to the objective function which has to be minimised by the optimisation procedure. Before the optimisation and training, respectively, starts, test data are divided into two parts. One part of data is used for the training and the other data set is used to validate the network quality.

In Figure 6, results of the network training and validation are shown for a uniaxial state of stress at a temperature of 25°C as an example. The stresses σ_{11} of the main

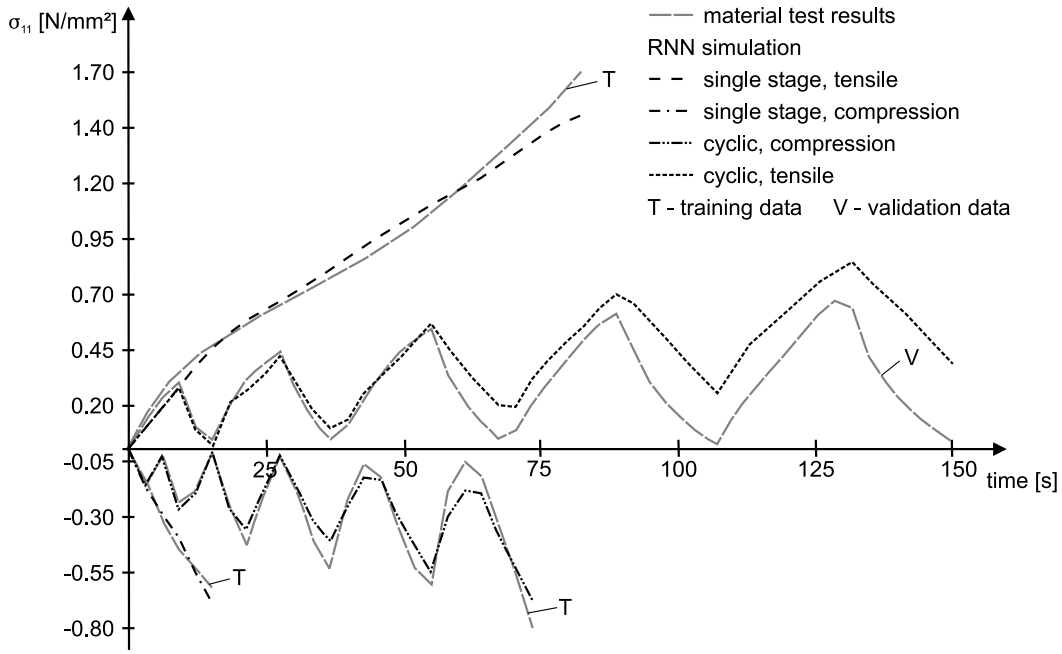

Figure 6: Stress-time dependency: material tests, training and validation results

loading direction versus time are plotted for four different tests. One single stage and one cyclic tensile test as well as single stage and one cyclic compression test are used. The cyclic tensile test has been used for validation. For the training, the other three test results are employed. The three tests which have been used for the training deliver quite good results. Especially, the time dependency of the cyclic tests can be represented by the RNN in an adequate way. Whereas the first three cycles of the validation curve match very well, it differs for the last two cycles.

The presented training and validation are first results. The improvement of the training results and the application of the RNN in complex FE simulations will be shown.

4 CONCLUSIONS

- The characterisation of material behaviour of uncured rubber requires an intensive study and extensive material tests. For each structural analysis (e.g. FE simulation), a realistic description of the material is fundamental in order to obtain realistic and consistent results.

- The feasibility of the usage of an RNN to substitute a classical continuum mechanical material model within the FEM is shown. A required modification in order to gain consistent tangent moduli and the appropriate preparation of the material test results for the training are explained. The application of the RNN instead of a material model could be shown by first FE simulations.

- Finally, first results of the functionality of the RNN are presented. Training and validation are shown for a representative state of strain.

- The neural network approach can be extended further to consider temperature dependencies of the uncured rubber.

ACKNOWLEDGEMENT

The realisation of the material tests conducted at the Leibniz Institute of Polymer Research in Dresden is gratefully acknowledged. Special thanks go to the Continental Reifen Deutschland GmbH for providing the rubber compounds and the financial support of the material tests. Additionally, the support of the authors research work by the Deutsche Forschungsgemeinschaft (DFG – German Research Foundation) within the framework of the Collaborative Research Centre 528 is acknowledged.

REFERENCES

[1] Kaliske, M. and Rothert, H. Formulation and implementation of three-dimensional viscoelasticity at small and finite strains *Comput. Mech.* (1997) **19**:228–239.

[2] Reese, S. and Govindjee, S. A theory of finite viscoelasticity and numerical aspects *Int. J. Solids Struct.* (1998) **35**:3455–3482.

[3] Miehe, C. and Göktepe, S. A micro-macro approach to rubber-like materials. Part II: The micro-sphere model of finite rubber viscoelasticity *J. Mech. Phys. Solids* (2005) **53**:2231–2258.

[4] Dal, H. and Kaliske, M. Bergström-Boyce model for non-linear finite rubber viscoelasticity *Comput. Mech.* (2009) **44**:809–823.

[5] Adeli, H. Neural Networks in Civil Engineering: 1989-2000 *Comput.-Aided Civ. Infrastruct. Engng.* (2001) **16**:126–142.

[6] Hashash, Y.M.A., Jung, S. and Ghaboussi, J. Numerical implementation of a neural network based material model in finite element analysis *Int. J. Num. Meth. Engng.* (2004) **59**:989–1005.

[7] Oeser, M. and Freitag, S. Modeling of materials with fading memory using neural networks *Int. J. Num. Meth. Engng.* (2009) **78**:843–862.

[8] Kaliske, M., Zopf, C. and Brüggemann, C. Experimental characterization and constitutive modelling of the mechanical properties of uncured rubber *Rubber Chem. Technol.* (2010) **83**:1–15.

[9] DIN 53504 *Bestimmung der Reißfestigkeit, Zugfestigkeit, Reißdehnung und Spannungswerten im Zugversuch*. Deutsches Institut für Normung, (1994).

[10] Graf, W., Freitag, S., Kaliske, M. and Sickert, J.-U. Recurrent neural networks for uncertain time-dependent structural behavior *Comput.-Aided Civ. Infrastruct. Engng.* (2010) **25**:322–333.

[11] Freitag, S., Graf, W., Kaliske, M. and Sickert, J.-U. Prediction of time-dependent structural behaviour with recurrent neural networks for fuzzy data *Comput. Struct.* (accepted), DOI: 10.1016/j.compstruc.2011.05.013

[12] Freitag, S. *Modellfreie numerische Prognosemethoden zur Tragwerksanalyse*. Dissertationsschrift (PhD Thesis), Veröffentlichungen – Institut für Statik und Dynamik der Tragwerke, Heft 19, Technische Universität Dresden, (2010).

[13] Yeoh, H. Characterization of elastic properties of carbon-black-filled rubber vulcanizates *Rubber Chem. Technol.* (1990) **63**:792–805.

XI International Conference on Computational Plasticity. Fundamentals and Applications
COMPLAS XI
E. Oñate, D.R.J. Owen, D. Peric and B. Suárez (Eds)

TOWARDS A NUMERICAL SIMULATION OF DIRECT MANUFACTURING OF THERMOPLASTIC PARTS BY POWDER LASER SINTERING
COMPLAS XI

D. DEFAUCHY[1], G. REGNIER[1], I. AMRAN[1], P. PEYRE[1]
A. AMMAR[2] AND F. CHINESTA[3]

[1] Arts et Métiers ParisTech, PIMM, CNRS
151 Boulevard de l'Hôpital, Paris France
e-mail: denis.defauchy@ensam.eu, http://pimm.paris.ensam.fr

[2] Arts et Métiers ParisTech, LAMPA
2 boulevard du Ronceray, Angers, France
e-mail: amine.ammar@ensam.eu

[3] EADS Corporate International Chair
Ecole Centrale de Nantes, 1 rue de la Noë, Nantes, France
e-mail: francisco.chinesta@ec-nantes.fr

Key words: Coalescence, Thermoplastic powder, C-NEM, Selective Laser Sintering (SLS), Simulation.

Abstract. Direct manufacturing technology using Selective Laser Sintering (SLS) on thermoplastic powders allows obtaining final parts in a short time, with classical polymer density and a high flexibility of shape and evolution of parts. The physical base of this process is the coalescence of grains, which initiates the densification of powder during SLS. This study presents a 2D C-NEM simulation of the whole process. We firstly focus on the chosen method and its advantages. We present the simulation details and validate the modeling through a 2D infinite cylinders coalescence simulation. The mesh of the grain interface is continuously adapted to the local curvature to better capture the coalescence phenomenon. We are able to simulate the sintering of twelve particles laying on a support within some hours.

1 INTRODUCTION

1.1 Selective laser sintering process

Polymer Parts obtained by direct manufacturing with laser sintering technology present porosities [1] which significantly reduce their mechanical resistance [2]. This porosity is due to the air between polymer powder grains which remains trapped into the material while polymer is melting. As the process needs to be performed with temperature variations, air

volume evolutions have to be taken into account, influencing directly the density of the material. It is also important to be able to predict the conditions in which porosity volume will be minimal.

The important material parameters acting in the process are the viscosity, the surface tension and the laser absortivity of the polymer.

Parts manufacturing by SLS is difficult for some reasons. Firstly, the polymer powder degrades while performed in the machines [3] maintained at high temperatures for some hours. It is also difficult to predict the polymer solidification, which depends on the cooling conditions as semicrystalline polymers are mainly used [4].

Among all articles cited here, it appears that the main controllable process parameters influencing the final material can be classed in order of importance [5]: layer thickness, laser speed, pre-heating powder bed temperature and laser power (most important). Some of these results have been confirmed through a finite element model [6]. Some other parameters are discussed as laser beam diameter, hatch distance and layering conditions. It seems clear that the use of a CO2 laser (10.6 μm) to melt the polymer powder is recommended.

All these parameters are often connected. For example, when particle size is decreased, the layering becomes difficult [4]. Among all articles cited here, studies concerning the influence of each process parameters and their relation on the final material can be found.

In parallel to the experiences, it is important to simulate the process for a better understanding of the parts characteristics. Simulating the process will enable to choose the best parameters for the manufacturing and predict the performances of SLS polymer parts, and as soon as the simulation is functional, have this information faster.

1.2 Physics of coalescence

The first coalescence model has been made by Frenkel [7] and improved a few years later by Eshelby [8]. Describing the evolution of the coalescence with three parameters (Figure 1), the neck radius y, the particles radius a, and the angle θ, they could quite well predict the evolution of the coalescence phenomenon in time (Equation 1) .

$$\frac{y}{a} = sin\left(\tau^{\frac{1}{2}}\right) \tag{1}$$

They could show that the coalescence is driven by the surface tension Γ while the viscosity η and the initial particles radius a_0 slow the phenomenon, introducing a dimensionless time τ (Equation 2).

$$\tau = \frac{t\Gamma}{\eta a_0} \tag{2}$$

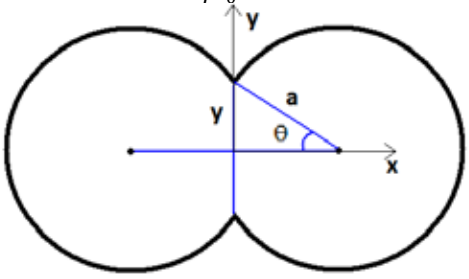

Figure 1: Shape of two cylinders during coalescence - Definition of parameters.

Other works have been done later [9,10] by taking into account a viscoelastic behaviour for

the polymer.

The presence of numerous necks on a particle induces effects in the kinetics of coalescence. It has been shown experimentally that the arrangement of particles has an effect on the coalescence rate [11].

1.3 Coalescence simulations

Finite element simulations of capillary driven flows have been done to evaluate the influence of grain sizes and several growing necks on particles.

One of the first finite element simulations [12] from 1995 is based on axisymmetric isothermal assumptions and shows the influence of multiples aligned particles in the coalescence phenomenon.

The first 3D finite element simulation of complicated initial geometries [13] confirmed the necessity to go further to understand the sintering of particles. In parallel to the previous study, authors presented [14] very well numerical difficulties like mesh distortions for large deformations (fluids) and front tracking methods. These methods are very useful in the cases of capillary flows to well describe the interface but can induce border inaccuracy and wrong surface tension evaluation. Furthermore, sintering problems seems to induce difficulties in convergence of iterative methods due to the matrix form and the mesh distortion increases these difficulties, then, it is necessary to remesh the domain. However, it is difficult to remesh a border which has no analytical definition.

Rotomolding process presents similarities to SLS. Main differences are the heating conditions, the polymer in SLS process melted by the laser action, from the free side of the powder layer. A study presents a isothermal simulation of the densification of spheres [15] trying to characterize the evolution of the air trapped into the material. The size of particles and rheology of material influence the bubbles size and the air trapped into cavities is supposed to diffuse through the polymer after the closure of cavities.

Finally, studies [16,17,18] show that the polymer viscoelasticity has an influence at the early stage of coalescence. Globally, the elasticity influence seems not to have a strong effect on the coalescence rate.

1.4 Objectives

The aim of this work is to simulate the SLS process in 2D to study the coalescence of a significant set of grains and to be able to know if the simulation can be extended to the 3D.

We first present all the details of our computation and results. To validate the modelling, we simulate the isothermal coalescence of two same size particles and compare it to a 2D coalescence model based on Frenkel-Eshelby 3D one. Then the coalescence of a set of grains is simulated in anisothermal conditions.

2 MODELLING LASER SINTERING

2.1 C-NEM Simulation

The C-NEM method [19,20] (Constrained Natural Element Method) is mainly based on usual Voronoï cells around nodes. The main advantage of this method is to take into account, in streams interpolations, the participation of all nearest neighbours around a point on the

domain. As a consequence, the mesh is not constrained as it is in a current finite element method (FEM). Performing FEM, it is important to have no distorted elements in the mesh. The remeshing of the whole domain is frequently needed, which is computer time consuming. In a C-NEM computation, the nodes can move without any problem and is also well adapted for process simulations, as the domains have often large deformations.

The C-NEM method used here is defined by the fact that the velocity is interpolated by constrained Sibson natural element shape functions φ while the pressure P is assumed constant by cell interpolated by the shape functions ψ. The weak formulation integration is done by nodal integration and the velocity gradient is done using the SCNI method (Stabilized Conform Modal Integration).

Taking this into account, the problem is discretized and the velocity u, pressure p and temperature T expressions are developed (Equations 3,4,5) with their nodal values.

$$u(x,y) = \sum_{i=1}^{Nd} \varphi_i \begin{pmatrix} Ui \\ Vi \end{pmatrix} = N^T U = \begin{pmatrix} \varphi_1 & 0 & \dots & \varphi_k & 0 & \dots & \varphi_N & 0 \\ 0 & \varphi_1 & \dots & 0 & \varphi_k & \dots & 0 & \varphi_N \end{pmatrix} \begin{pmatrix} U_1 \\ V_1 \\ \vdots \\ U_k \\ V_k \\ \vdots \\ U_N \\ V_N \end{pmatrix} \tag{3}$$

$$p(x,y) = \sum_{i=1}^{Nd} \psi_i P_i = \bar{N}^T P = \begin{pmatrix} \psi_1 & \dots & \psi_k & \dots & \psi_N \end{pmatrix} \begin{pmatrix} P_1 \\ \vdots \\ P_k \\ \vdots \\ P_N \end{pmatrix} \tag{4}$$

$$T(x,y) = \sum_{i=1}^{Nd} \varphi_i T_i = N^T \bar{T} = \begin{pmatrix} \varphi_1 & \dots & \varphi_k & \dots & \varphi_N \end{pmatrix} \begin{pmatrix} T_1 \\ \vdots \\ T_k \\ \vdots \\ T_N \end{pmatrix} \tag{5}$$

where x and y are the coordinates on the domain, U_i and V_i the nodal velocities on $\vec{x}$ and $\vec{y}$, T_i the nodal temperature, φ_i and ψ_i the nodal shape functions and Nd the number of nodes.

2.2 Basic equations

In high viscosities capillarity flows, velocities are very small, then inertial terms can be neglected and the polymer can be considered as a Newtonian viscous fluid.

The basic equations which drives the fluid movements are given (the local equilibrium - Equation 6) using the deformation tensor D (Equation 7).

$$\begin{cases} \nabla . \sigma + f_d = 0 \\ \sigma = -pI + 2\mu D \\ \nabla . V = 0 \end{cases} \tag{6}$$

where σ is the strain tensor, fd the volume force in the domain, D the deformation tensor and μ the viscosity.

$$D = \begin{pmatrix} \dfrac{\partial u}{\partial x} & \dfrac{1}{2}\left(\dfrac{\partial u}{\partial y} + \dfrac{\partial v}{\partial x}\right) \\ \dfrac{1}{2}\left(\dfrac{\partial u}{\partial y} + \dfrac{\partial v}{\partial x}\right) & \dfrac{\partial v}{\partial y} \end{pmatrix} \tag{7}$$

2.3 Computation of equations on the discretized domain

The basic equations are integrated on the domain introducing the variational formulation (Equation 8,9) depending on the vectors U and P.

$$U^{*T}\left[\int_{\Omega} 2\mu B^T B\, d\Omega\right]U - U^{*T}\left[\int_{\Omega} B^T \tilde{I}\overline{N}^T\, d\Omega\right]P - U^{*T}\left[\int_{\partial\Omega} N(\Gamma\kappa - P)n\, dS + \int_{\Omega} N f_d\, d\Omega\right] = 0$$

$$\tilde{I} = \begin{bmatrix}1\\1\\0\end{bmatrix}, B = \begin{pmatrix} \varphi_{1,x} & 0 & \cdots & \varphi_{k,x} & 0 & \cdots & \varphi_{N,x} & 0 \\ 0 & \varphi_{1,y} & \cdots & 0 & \varphi_{k,y} & \cdots & 0 & \varphi_{N,y} \\ \frac{\varphi_{1,y}}{\sqrt{2}} & \frac{\varphi_{1,x}}{\sqrt{2}} & \cdots & \frac{\varphi_{k,y}}{\sqrt{2}} & \frac{\varphi_{k,x}}{\sqrt{2}} & \cdots & \frac{\varphi_{N,y}}{\sqrt{2}} & \frac{\varphi_{N,x}}{\sqrt{2}} \end{pmatrix} \tag{8}$$

where κ is the local curvature and n the normal vector on the surface.

$$U^T\left[\int_{\Omega} B^T \tilde{I}\overline{N}^T\, d\Omega\right]P^* = 0 \tag{9}$$

By introducing the vector $\overline{U}$ (Equation 10) which enables to regroup all the degrees of freedom in one vector, the system can be defined with one matrix (Equation 11).

$$\overline{U} = \begin{pmatrix} U_1 \\ V_1 \\ P_1 \\ \vdots \\ U_N \\ V_N \\ P_N \end{pmatrix} \tag{10}$$

$$\overline{U}^{*T} K \overline{U} - \overline{U}^{*T} F = 0 \tag{11}$$

Details on the matrix K and the vector F are given in Equations 12 and 13.

$$K_{ij} = \int_{\Omega} \begin{pmatrix} 2\mu\left(\varphi_{i,x}\varphi_{j,x} + \frac{\varphi_{i,y}\varphi_{j,y}}{2}\right) & \mu\varphi_{i,y}\varphi_{j,x} & -\varphi_{i,x}\psi_j \\ \mu\varphi_{i,x}\varphi_{j,y} & 2\mu\left(\varphi_{i,y}\varphi_{j,y} + \frac{\varphi_{i,x}\varphi_{j,x}}{2}\right) & -\varphi_{i,y}\psi_j \\ -\varphi_{j,x}\psi_i & -\varphi_{j,y}\psi_i & 0 \end{pmatrix} \tag{12}$$

$$F = \int_{\Omega} \begin{pmatrix} \varphi_1 & 0 \\ 0 & \varphi_1 \\ 0 & 0 \\ \vdots & \vdots \\ \varphi_k & 0 \\ 0 & \varphi_k \\ 0 & 0 \\ \vdots & \vdots \\ \varphi_N & 0 \\ 0 & \varphi_N \\ 0 & 0 \end{pmatrix} \rho\begin{pmatrix} f_x \\ f_y \end{pmatrix} d\Omega + \int_{\partial\Omega} \left(\frac{\Gamma}{R} - P\right) \begin{pmatrix} \varphi_1 & 0 \\ 0 & \varphi_1 \\ 0 & 0 \\ \vdots & \vdots \\ \varphi_k & 0 \\ 0 & \varphi_k \\ 0 & 0 \\ \vdots & \vdots \\ \varphi_N & 0 \\ 0 & \varphi_N \\ 0 & 0 \end{pmatrix} \begin{pmatrix} n_x \\ n_y \end{pmatrix} dS \tag{13}$$

2.4 Displacement boundary limit conditions

During SLS simulation, the displacement boundary limit conditions will be set by representing the true limit conditions of the powder tray. The three rigid body displacements are blocked.

However, to be able to simulate the coalescence of particles with no displacement boundary limit conditions, three Lagrangian conditions (Equations 14,15,16) are added in the

system, Equation 11 is used to block the 3 rigid body movements.

The two translations on x and y are blocked through a global condition on the displacement of the domain, which has to be null (Equations 14,15).

$$\sum Vol_i U_i = 0 \tag{14}$$

$$\sum Vol_i V_i = 0 \tag{15}$$

where Vol_i is the Voronoï cell area in 2D, around node i.

The z rotation is blocked through a global condition on the rotation of the domain (Equation 16).

$$\sum_{i=1}^{Nd} \frac{\left|\underline{u_i}.(\underline{z}\Lambda\underline{GM_i})\right|}{\left\|\underline{GM_i}\right\|^2} = 0 \tag{16}$$

where G is the gravity center of the domain, which remains constant during the coalescence, u_i the velocity of the node M_i.

As fluids are considered, the global conditions on all nodes are needed to not deform the domain.

2.5 Time step calculation

While simulating coalescence, a too large time step induces small inaccurate local curvatures on the border. This induces bad movements which influence the rest of the simulation.

The time step is also constrained with movements, by limiting the local rotation of the two segments joining each node of the border to an angle value of some degrees.

2.6 Cavities (Volume, Pressure)

At the beginning, the pressure was set on the border of the domain. The air in the cavities was assumed compressible and cavities presented oscillating volume variations. To avoid these problems, the only solution was to strongly decrease the time step

Simulating the sintering of a Polyamide 12 of about 1000 Pa.s of viscosity, no significant pressure variations were observed in cavities. The pressure will also be assumed constant.

We decided to use the perfect gas law, calculating the cavities volumes at each time step according to the temperature variation.

Knowing the theoretical volume of the cavity, a Lagrangian condition is created in the system (Equation 17) for each cavity, imposing its derivative.

$$\frac{\mathrm{dVol}}{\mathrm{dt}} = \frac{1}{2}\sum_{\mathrm{i=1}}^{\mathrm{Nd}} \left[\begin{pmatrix}\mathrm{U_i}\\ \mathrm{V_i}\end{pmatrix}\Lambda\begin{pmatrix}\mathrm{x_{i+1}}\\ \mathrm{y_{i+1}}\end{pmatrix} - \begin{pmatrix}\mathrm{U_{i+1}}\\ \mathrm{V_{i+1}}\end{pmatrix}\Lambda\begin{pmatrix}\mathrm{x_i}\\ \mathrm{y_i}\end{pmatrix}\right] \tag{17}$$

$$i+1 = 1 \; if \; i = N$$

where x_i and y_i are the components of the velocity of the node i.

As the time step is linked to the velocity of the nodes, it is not determined before the resolution of the system and the time step is chosen as the maximum value on some precedent time steps to avoid node oscillations.

2.7 Mesh

Node density should not be important except on the border of the domain to well take into

account the surface tension. The initial mesh is indeed adapted to the curvature on the border, nodes are created and deleted depending on the local curvature during the simulation.

2.8 Surface tension modeling

The surface tension effect (Equation 18) has to be discretized.

$$F_{tension} = \int_{\partial\Omega} N \frac{\Gamma}{R} n \, dS \tag{18}$$

The nodal curvature is determined by the radius of the circle passing by the considered node and its two neighbors (Figure 2).

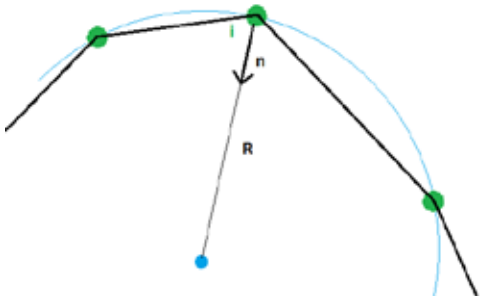

Figure 2: Surface tension calculation on discretized domain

2.9 Numerical details

The system to solve (Equation 19) presents three degrees of freedom per node (U,V,P).

$$KU = F, U = (U\ V\ P\ \dots) \tag{19}$$

The iterative methods GMRES and PCG were used but it was difficult to get the convergence. We separate the pressure and the velocity (Equation 20,21), and add a compressible coefficient of 10^6 Pa.s into the matrix C to keep the quasi-incompressible behavior of the polymer.

$$\begin{pmatrix} A & B \\ B^T & C \end{pmatrix} \begin{pmatrix} U \\ P \end{pmatrix} = \begin{pmatrix} F \\ G \end{pmatrix} \tag{20}$$

$$\begin{cases} AU + BP = F \\ B^T U + CP = G \end{cases} \rightarrow P = C^{-1}G - C^{-1}B^T U \rightarrow AU + BC^{-1}G - BC^{-1}B^T U = F \tag{21}$$

The system obtained has a length of 66% of the initial one (Equation 22) and iterative methods converge well to the solution.

$$(A - BC^{-1}B^T)U = F - BC^{-1}G \tag{22}$$

This method gives the same results than considering that the polymer is compressible in the local equilibrium equations.

The displacements of the nodes are calculated through a Taylor development at second order (Equation 23) by calculating the acceleration on two time steps (Equation 24).

$$X(t + dt) = x(t) + v(t)dt + \gamma(t)\frac{dt^2}{2} \tag{23}$$

$$\gamma(t) = \frac{v(t) - v(t - dt)}{dt} \tag{24}$$

2.10 Heating conditions

SLS process is performed in a complex transient thermal situation. The temperature is set on the stage and the vertical sides (Figure 3). Air convection at the upper surface of the polymer is modelled by a heat exchange coefficient. The laser heats the material during its

Laser

pass. The polymer coalescence is considered in the studied area.

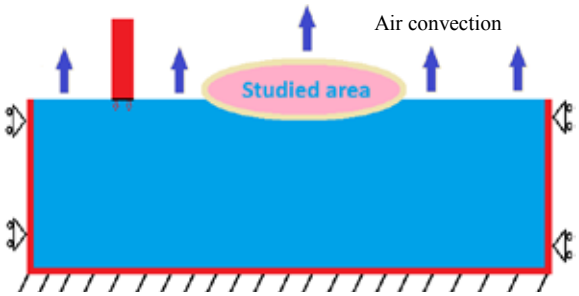

Figure 3: Thermal and displacement limit conditions of the simulation

The cavities are supposed not to exchange energy, and their temperatures are calculated by a mean calculation on their surface and nodal temperatures. Their temperature changes induce volume changes, pressure assumed constant (Section 2.6).

The viscosity, which is dependent on the temperature, is applied through an Arrhenius law (Equation 25), and its maximum value (solid material) is limited with a high viscosity of 10.000 Pa.s, which seems to be enough to limit coalescence.

$$\mu(T) = Ke^{\frac{E}{RT}} \tag{25}$$

As done for the mechanical behaviour of the polymer (U,V,P), a thermal numerical resolution of the temperature of the domain is performed beginning with the local equilibrium equation (Equation 26).

$$\lambda \Delta T + P = \rho c \frac{\partial T}{\partial t} \tag{26}$$

where λ is the thermal conductivity, P the heat source, ρ the volume mass and c the heat capacity

By introducing three parameters (Equation 27), and performing a variational formulation on the domain, the system to solve and its details are obtained (Equation 28 & 29):

$$\begin{aligned} b &= \frac{P}{\rho c} \\ k &= \frac{\lambda}{\rho c} \\ \varphi &= -\lambda \nabla \mathrm{T} \end{aligned} \tag{27}$$

$$\underline{\underline{M}}\dot{\bar{T}} = -\underline{\underline{K}}\,\bar{T} + \underline{B} \tag{28}$$

$$\begin{aligned} \underline{\underline{K}} &= k \int_{\Omega} \frac{\partial N}{\partial \underline{x}} \frac{\partial N^T}{\partial \underline{x}} \, d\Omega \\ \underline{B} &= -\frac{1}{\rho c} \int_{\partial\Omega} N\varphi.n \; d\Gamma + \int_{\Omega} Nb \, d\Omega \\ \underline{\underline{M}} &= \int_{\Omega} NN^T \, d\Omega \\ \dot{\bar{T}} &= \frac{\partial \bar{T}}{\partial t} \end{aligned} \tag{29}$$

Evaluating the derivative of temperature with time by a Taylor development at order 1 (Equation 30), the new nodal temperature (Equation 31) is calculated by an implicit method.

$$\dot{\bar{T}}^n = \frac{\bar{T}^{n+1} - \bar{T}^n}{\Delta t} \tag{30}$$

$$\bar{T}^{n+1} = \left[\frac{\underline{\underline{M}}}{\Delta t} + \underline{\underline{K}}\right]^{-1} \left(\frac{\underline{\underline{M}} T^n}{\Delta t} + B\right) \tag{31}$$

2.11 Laser action

The first test was to set a volume action into the whole height of the polymer to validate the principles, and then a more realistic model has been employed by applying a Gaussian repartition of the power flux on the surface [21].

It was necessary to find the nodes directly under laser beam (Figure 4).

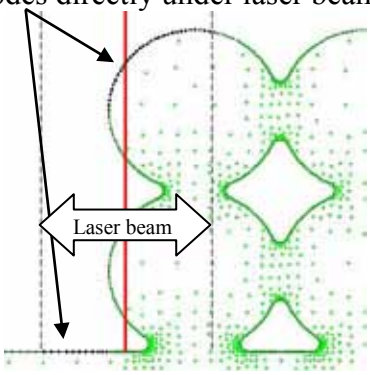

Figure 4: Nodes under laser action (Black)

The idea of the algorithm is the following. Working on the free surface of the domain, nodes are considered from the left to the right. Firstly cut the whole top surface exposed on one part to the laser, in different sections, depending on the x displacements changes (left to right and right to left) and under the edges of the laser field. Then identify all sections likely to be exposed to laser (surface whose direction is from left to right). Among these sections, determine which of the nodes under the laser is the highest, and begin the work from the section containing this node. All the nodes which will be considered here are under direct laser action. To the left (respectively to the right), and until crossing the laser beam boundary, identify whether the laser boundary is on the section or not. If not, proceed to the next section considering respectively the first node of next section as the first node of the section which is on the left (respectively right) of the last one of the studied section, and repeat the same work on the new section until crossing the laser demarcation. Finally, consolidate all the sections made by more than one node and manage some details on the sections extreme nodes, depending on whether the sections go up or down.

The laser time steps are adapted and the possibility to interpose movements during the laser pass is considered.

3 SIMULATION RESULTS

The simulation is computed on Matlab. The functions which have to be rapid (hydrodynamic and rigid matrix creation) are function written in C language called in Matlab.

3.1 Two cylinders coalescence

The first simulation is performed on the isotherm coalescence of two infinite cylinders in

order to validate the simulation [22]. A 2D model has been developed and the coalescence parameters *y* and *a* have been defined on the simulation to try to represent as well as possible the model. Good agreements were found between the model and the simulation.

3.2 Process simulation

We finally simulated the process taking into account the parameters exposed in Table 1 on a Polyamine 12. Applying the laser action on a non heated domain (Figure 5), it is seen that the laser/material interaction conduces to very high temperatures (15000°C) and it has been confirmed on COMSOL. The laser power has also been decreased from 5 W (normal SLS power) to 5.10^{-7} W to obtain a more realistic increase of temperature under laser action of about 100 °C to 200°C. This decrease of power induces the necessity to heat the domain from the sides to melt the polymer and see an evolution of the melting.

Figure 5 Laser action on polymer

Table 1: Process simulation parameters

Process parameters	Value	Material parameters	Value
Initial polymer temperature	150 °C	Cylinders diameter	100 µm
Border temperature	350 °C	Polymer Thermal conductivity	0.25 $W.m^{-1}.K^{-1}$
Air temperature	150 °C	Polymer density	1100 $Kg.m^{-3}$
Exchange convection coefficient	13 $W.m^{-1}.k^{-1}$	Air density	1.2 $Kg.m^{-3}$
Laser power	5.10^{-7} W	Gravity	9.81 $m.s^{-2}$
Laser beam diameter	200 µm	Surface Tension	0.03 $N.m^{-1}$
Laser velocity	1 $m.s^{-1}$	Polymer heat capacity	1700 $J.Kg^{-1}.K^{-1}$
Laser reflectivity	4 %	Arrhenius K (PA 12)	$3.5*10^{-6}$
		Arrhenius E (PA 12)	75647

Our results are presented simulating the sintering of 12 particles of Polyamide 12 lying on a support (Figure 6). The domain is heated from the bottom and the sides. The heat exchange with the air occurs. After 5 seconds, the laser is passing from the left to the right very rapidly (some ms), and symmetric displacements conditions are applied on both sides.

The principles are validated and the calculation specificities are exposed in table 2. Depending on the chosen parameters, mesh and time step conditions particularly, the calculation time can be much different, but results may be inaccurate. The best parameters are difficult to find at this time and work must be done to choose them.

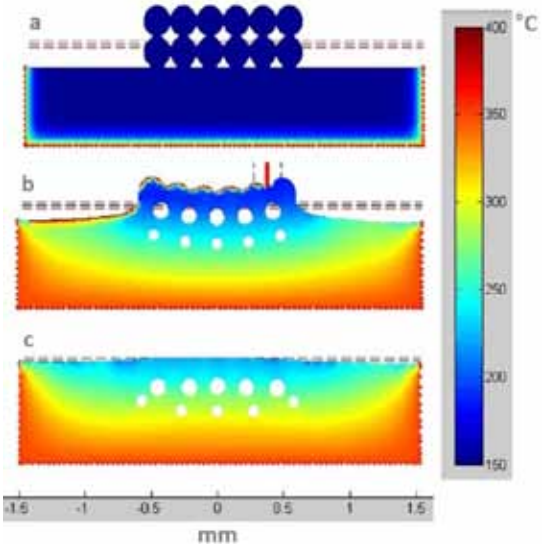

Figure 6: Captures of simulation evolution (a - solid polymer, b - laser pass, c - melted polymer) during the SLS process applied on 12 cylinders.

Furthermore, as the laser action is false and induces a high temperature on some local nodes, the movements become very high due to discontinuities and very low values of viscosities. This induces very small displacement time steps to limit local movements, which increase a lot the calculation time. The calculation presents 700 time step before laser pass (5s), 4500 time step during laser pass, and 2000 for the next 5 seconds. Without laser action, the same simulation gives a calculation time of 5.92 hours for 4362 time step.

Table 2: Calculation specificities for the presented simulation

Matlab	R2009B 64 bits	Nodes in final mesh	4381
Windows	7 64 bits	Number of movement time step	9067
RAM memory	DDR3 3*8 Go	Calculation duration	8.9 h
Processor	Intel Core i7-950	Laser pass calculation duration	0.57 h
Motherboard	ASUS P6T7	Volume conservation	100.0097 %

12 CONCLUSIONS

Selective laser sintering process is a complicated process in which thermal conditions are never the same for each layer. However, in chosen conditions, we are able to simulate the process in spite of the laser/material interaction, which has now to be improved.

At this time, the main difficulties consisted to obtain the iterative methods convergence, a well adapted mesh depending on the curvature, and the better choice on the time step to avoid to large mesh deformation inducing mesh distortions and next calculations.

After performing experiments with a CO_2 laser on polymer powder to characterize a Beer-Lambert law for the laser/material interaction, we will program it and begin simulations of multi grains conditions in 2D. In parallel, we will perform experiments on multi grains layers of polymer powders in a heat chamber to compare the simulation results with the experiments, and identify the multigrain influence on coalescence.

ACKNOWLEDGMENTS

This work is supported by the FUI Project FADIPLAST. The authors acknowledge all FADIPLAST partners for their enriching discussions.

REFERENCES

[1] G.V. Salmoria, J.L. Leite, R.A. Paggi, *Polymer Testing,* **28**, 746 (2009).
[2] M. Schmidt, D. Pohle, T. Rechtenwald, *CIRP Annals - Manufacturing Technology*, **56**, 205 (2007).
[3] D.T. Pham, K.D. Dotchev, W.A.Y. Yusoff, *Journal of Mechanical Engineering Science,* **222***,* 2163 (2008).
[4] V.E. Beal, R.A. Paggi, G.V. Salmoria, A. Lago, *Journal of Applied Polymer Science,* **113**, 2910 (2009).
[5] P. Wang, X. Li, J. Xiao, F. Zhu, Y. Yang, *ICALEO 2006 - 25th International Congress on Applications of Laser and Electro-Optics, Congress Proceedings*, art. 517 (2006).
[6] L. Dong, A. Makradi, S. Ahzi, Y. Remond, *Journal of Materials Processing Technology*, **209**, 700 (2009)
[7] Frenkel J., *J. PhysNature,* **9**, 385 (1945).
[8] Pokluda O., Bellehumeur C.T., Vlachopoulos J., *AIChE Journal*, **43**, 3253 (1997).
[9] Bellehumeur C.T., Kontopoulou M., Vlachopoulos J., *Rheologica Acta*, **37**, 270 (1998).
[10] Eshelby J. D., *Metallurgical Transactions*, **185**, 796 (1949).
[11] Asgapour M., Bakir F., Khelladi S., Khavandi A., Tcharkhtchi A., *Journal of Applied Polymer Science,* **119,** 2784
[12] Martinez-Herrera J. I., Derby J. J., *American Ceramic Society*, **78**, 645
[13] Zhou H., Derby J., *Theory and Modeling of Glasses and Ceramics*, **81**, 533
[14] Zhou H., Derby J., *International Journal for Numerical Methods in Fluids*, **36**, 841
[15] Bellehumeur C. T., Tiang J. S., *Polymer Engineering and Science*, **42**, 215 (2002).
[16] Lin Y. Y., Hui C. Y., Jagota A., *Journal of Colloid and Interface Science*, **237**, 267 (2001).
[17] Scribben E., Baird D., Wapperom P., *Rheological Acta*, **45**, 825 (2006).
[18] Hooper R., Macosko C. W., Derby J. J., *Chemical Engineering Science*, **55,** 5733 (2000).
[19] Yvonnet J., Ryckelynck D., Lorong P., Chinesta F., *International Journal for Numerical Methods in Engineering*, **60**, 1451 (2004).
[20] Alfaro I., Yvonnet J., Chinesta F., Cueto E., *International Journal for Numerical Methods in Engineering,* **71**, 1436 (2007).
[21] Dong L., Makradi A., Ahzi S., Remond Y., *Journal of Materials Processing Technology*, **209**, 700 (2009).
[22] Defauchy D., *27th Annual Meeting of the Polymer Processing Society*, Marrakech, Marrocco (2011).

XI International Conference on Computational Plasticity. Fundamentals and Applications
COMPLAS XI
E. Oñate, D.R.J. Owen, D. Peric and B. Suárez (Eds)

A MICROSTRUCTURAL APPROACH TO MODELLING INELASTIC EFFECTS IN FIBRED BIOLOGICAL TISSUES

Estefanía Peña[*†], Pablo Sáez[*†], Manuel Doblaré[*†] and Miguel A. Martínez[*†]

[*]Group of Structural Mechanics and Materials Modeling.
Aragón Institute of Engineering Research (I3A). University of Zaragoza.
María de Luna, 3. E-50018 Zaragoza, Spain.
e-mail: fany@unizar.es

[†]CIBER de Bioingeniería, Biomateriales y Nanomedicina (CIBER-BBN)

Key words: Soft tissue, Microsphere, Affine deformations, damage and blood vessels

Abstract. Enormous progress has been made during recent years in the phenomenological modelling of soft tissue. In general, three important softening phenomena associated with biological tissues may be distinguished. First, there is the dependence of the mechanical response on the previously attained maximum load level. This is quite similar to the well-known Mullins effect in rubber-like materials. Another typical phenomenon known as permanent set is characterized by residual strains after unloading. Finally, there is the softening behaviour resulting from fibre rupture and matrix disruption associated with material damage. There are several phenomenological constitutive models able to describe the failure of soft tissues from a macroscopic point of view. In this contribution a three-dimensional micro-sphere-based constitutive model for anisotropic fibrous soft biological tissue is presented, including elastic anisotropy as well as inelastic effects (softening, preconditioning and damage). The link between micro-structural inelastic contribution of the collagen fibers and macroscopic response is achieved by means of computational homogenization, involving numerical integration over the surface of the unit sphere. In order to deal with the random distribution of the fibrils within the fiber, a von Mises probability function is incorporated, and the mechanical behavior of the fibrils is defined by an exponential-type model. The inelastic effects in soft biological tissues were modeled by internal variables that characterize the structural state of the material.

1 INTRODUCTION

Enormous progress has been made during recent years in the phenomenological modelling of soft tissue. In general, three important softening phenomena associated with biological tissues may be distinguished. First, there is the dependence of the mechanical response on the previously attained maximum load level. This is quite similar to the

well-known Mullins effect in rubber-like materials. Another typical phenomenon known as permanent set is characterized by residual strains after unloading. Finally, there is the softening behaviour resulting from fibre rupture and matrix disruption associated with material damage [15, 3, 30].

There are several constitutive models able to describe the failure of soft tissues [17, 20, 25, 40, 5, 34, 37, 36, 38, 21, 11]. Balzani et al. [5] assumed that discontinuous damage occurs in arterial walls and mainly along the fiber direction. Rodríguez et al. [34, 33] introduced a stochastic-structurally based damage model for fibrous soft tissues. Only a few constitutive models have been derived to describe the loading-unloading softening behavior of soft tissues [15, 10, 33, 12, 29, 21, 31]. Franceschini et al. [15] and Horgan and Saccomandi [19] proposed an isotropic pseudoelastic model for soft tissues using isotropic and anisotropic elastic strain energy functions respectively. Calvo et al. [10] proposed an uncoupled directional damage model for fibred biological soft tissues that considers different damage evolutions for the matrix and for the different fiber families. In Li and Robertson [21] two damage mechanisms are coupled in a multiplicative manner. Peña et al. [31] showed that continuum damage mechanics models can reproduce the softening behavior during unloading or reloading only for low dissipative effects. Ehret and Itskov [12] presented a model that reproduces the softening behavior including all the tissue dissipative effects (permanent set also). However, the main drawback of this model is its use of non-standard invariants that leads to a very complicated approach. The model is not able to reproduce the damage process. Peña and Doblare [29] present a very simple pseudo-elastic anisotropic model to reproduce the softening behavior exhibited in soft biological tissues without permanent set. However the pseudo-elastic model is not able to reproduce the failure region as a result of the bond rupture and complete damage while Continuum Damage Mechanics (CDM) and other models can. Finally, Peña [27] developed a phenomenological model that includes all these phenomena in a macro-estructural approach.

The high complexity of biological tissues requires mechanical models that include information of the underlying constituents and look for the physics of the whole processes within the material. This behavior of the micro-constituents can be taken into macroscopic models by means of computational homogenization. It is in this context where the microsphere-based approach acquires high relevance. [24], [23] and [16] used the microsphere approach with emphasis on elastomers. Later [2] focus on the anisotropy of the soft biological tissues.

In this contribution a three-dimensional micro-sphere-based constitutive model for anisotropic fibrous soft biological tissue is presented, including elastic anisotropy as well as inelastic effects (softening, preconditioning and damage). The link between microstructural inelastic contribution of the collagen fibers and macroscopic response is achieved by means of computational homogenization, involving numerical integration over the surface of the unit sphere. In order to deal with the random distribution of the fibrils within the fiber, a von Mises probability function is incorporated, and the mechanical behavior of

the fibrils is defined by an exponential-type model. The inelastic effects in soft biological tissues were modelled by internal variables that characterize the structural state of the material.

2 MICROSTRUCTURAL APPROACH FOR HYPERELASTIC MEDIA

2.1 KINEMATICS

Let $\mathcal{B}_0 \subset \mathbb{E}^3$ be a reference or rather material configuration of a body B of interest. The notation $\boldsymbol{\varphi} : \mathcal{B}_0 \times \mathcal{T} \rightarrow \mathcal{B}_t$ represents the one to one mapping, continuously differentiable, transforming a material point $\mathbf{X} \in \mathcal{B}_0$ to a position $\mathbf{x} = \boldsymbol{\varphi}(\mathbf{X}, t) \in \mathcal{B}_t \subset \mathbb{E}^3$, where $\mathcal{B}_t$ represents the deformed configuration at time $t \in \mathcal{T} \subset \mathbb{R}$. The mapping $\boldsymbol{\varphi}$ represents a motion of the body B that establishes the trajectory of a given point when moving from its reference position $\mathbf{X}$ to $\mathbf{x}$. The two-point deformation gradient tensor is defined as $\mathbf{F}(\mathbf{X}, t) := \nabla_{\mathbf{X}} \boldsymbol{\varphi}(\mathbf{X}, t)$, with $J(\mathbf{X}) = \det(\mathbf{F}) > 0$ the local volume variation. It is sometimes useful to consider the multiplicative decomposition of $\mathbf{F}$

$$\mathbf{F} := J^{1/3}\mathbf{I} \cdot \bar{\mathbf{F}}. \tag{1}$$

Hence, deformation is split into a dilatational part, $J^{1/3}\mathbf{I}$, where $\mathbf{I}$ represents the second-order identity tensor, and an isochoric contribution, $\bar{\mathbf{F}}$, so that $\det(\bar{\mathbf{F}}) = 1$ [14]. With these quantities at hand, the isochoric counterparts of the right and left Cauchy-Green deformation tensors associated with $\bar{\mathbf{F}}$ are defined as $\bar{\mathbf{C}} := \bar{\mathbf{F}}^{\mathrm{T}} \cdot \bar{\mathbf{F}} = J^{-2/3}\mathbf{C}$.
Furthermore, let $\mathbf{r}$ be a vector in the reference configuration. The so called push-forward operator, associated to the motion, maps this vector field in $\bar{\mathbf{t}} \in \Omega$, in the deformed configuration. Assuming that $\mathbf{r}$ is affected only by the isochoric part of $\mathbf{F}$

$$\bar{\mathbf{t}} = \bar{\mathbf{F}} \cdot \mathbf{r} = J^{-1/3}\mathbf{t} \quad \text{with} \quad \|\bar{\mathbf{t}}\| = \bar{\lambda} = J^{-1/3} \|\mathbf{t}\|, \tag{2}$$

where $\bar{\mathbf{t}}$ represents the isochoric push-forward of the material vector $\mathbf{r}$ and $\bar{\lambda}$ the isochoric stretch in the direction of $\mathbf{r}$ [18].

2.2 HYPERELASTIC FRAMEWORK

The free energy density function is given by a scalar-valued function Ψ defined per unit reference volume in the reference configuration and for isothermal processes. [14] postulated the additive decoupled representation of this SEDF in volumetric and isochoric parts as

$$\Psi = \Psi_{\mathrm{vol}} + \Psi_{\mathrm{ich}}. \tag{3}$$

As discussed in the introduction, soft biological tissues are a highly non-linear anisotropic materials. To differentiate between the isotropic and the anisotropic parts, the free energy density function can be split up again as

$$\Psi = \Psi_{\mathrm{vol}} + \Psi_{\mathrm{iso}} + \Psi_{\mathrm{ani}}, \tag{4}$$

where Ψ_{vol} describes the free energy associated to changes of volume, Ψ_{iso} is the isotropic contribution of the free energy (usually associated to the ground matrix) and Ψ_{ani} takes into account the isochoric anisotropic contribution (associated to the fibers) [35]. This strain-energy density function must satisfy the principle material frame invariance

$$\Psi(\mathbf{C},\mathbf{M},\mathbf{N}) = \Psi(\mathbf{Q}\cdot\mathbf{C},\mathbf{Q}\cdot\mathbf{M},\mathbf{Q}\cdot\mathbf{N})\text{for all}[\mathbf{C},\mathbf{Q}] \in [\mathbb{S}^3_+ \times \mathbb{Q}^3_+]. \tag{5}$$

The second Piola-Kirchhoff stress tensor is obtained by derivation of (3) with respect to the right Cauchy-Green tensor [22]. Thus, the stress tensor consists of a purely volumetric and a purely isochoric contribution, i.e. $\mathbf{S}_{\text{vol}}$ and $\mathbf{S}_{\text{ich}}$, so the total stress is

$$\begin{aligned}\mathbf{S} =& \mathbf{S}_{\text{vol}} + \mathbf{S}_{\text{ich}} = 2\frac{\partial \Psi_{\text{vol}}(J)}{\partial \mathbf{C}} + 2\frac{\partial \Psi_{\text{ich}}(\bar{\mathbf{C}},\mathbf{M},\mathbf{N})}{\partial \mathbf{C}} \\ =& 2\left[\frac{\partial \Psi_{\text{vol}}(J)}{\partial J}\frac{\partial J}{\partial \mathbf{C}} + \frac{\partial \Psi_{\text{ich}}(\bar{\mathbf{C}},\mathbf{M},\mathbf{N})}{\partial \bar{\mathbf{C}}}\frac{\partial \bar{\mathbf{C}}}{\partial \mathbf{C}}\right] = J\,p\mathbf{C}^{-1} + 2\sum_{j=1,2,4,6}\mathbf{P} : \frac{\partial \Psi_{\text{ich}}}{\partial \bar{I}_j}\frac{\partial \bar{I}_j}{\partial \bar{\mathbf{C}}},\end{aligned} \tag{6}$$

where the second Piola-Kirchhoff stress $\mathbf{S}$ consists of a purely volumetric contribution and a purely isochoric one. Moreover, one obtains the following noticeable relations $\partial_{\mathbf{C}} J = \frac{1}{2}J\mathbf{C}^{-1}$ and $\mathbf{P} = \partial_{\mathbf{C}}\bar{\mathbf{C}} = J^{-2/3}[\mathbf{I} - \frac{1}{3}\mathbf{C}\otimes\mathbf{C}^{-1}]$. $\mathbf{P}$ is the fourth-order projection tensor and $\mathbf{I}$ denotes the fourth-order unit tensor, which, in index notation, has the form $\mathsf{I}_{IJKL} = \frac{1}{2}[\delta_{IK}\delta_{JL} + \delta_{IL}\delta_{JK}]$. Application of the fourth-order projection tensor $\mathbf{P}$ furnishes the physically correct deviatoric operator in the Lagrangian description, so that $[\mathbf{P} : (\cdot)] : \mathbf{C} = \mathbf{0}$ [13]. Note that it is possible to obtain the Cauchy stress tensor by applying the push-forward operation to (6) $\boldsymbol{\sigma} = J^{-1}\boldsymbol{\chi}_*(\mathbf{S})$ [22].
Based on the kinematic decomposition of the deformation gradient tensor, the tangent operator, also known as the elasticity tensor when dealing with elastic constitutive laws, is defined in the reference configuration as

$$\mathbf{C} = 2\frac{\partial \mathbf{S}(\mathbf{C},\mathbf{M},\mathbf{N})}{\partial \mathbf{C}} = \mathbf{C}_{\text{vol}} + \mathbf{C}_{\text{ich}} = 4\left[\frac{\partial^2 \Psi_{\text{vol}}(J)}{\partial \mathbf{C}\otimes\partial \mathbf{C}} + \frac{\partial^2 \Psi_{\text{ich}}(\bar{\mathbf{C}},\mathbf{M},\mathbf{N})}{\partial \mathbf{C}\otimes\partial \mathbf{C}}\right]. \tag{7}$$

Note that its spatial counterpart of (7) is obtained from the application of the push-forward operation to (7) $\mathbf{c} = J^{-1}\boldsymbol{\chi}_*(\mathbf{C})$[8].

2.3 MICROSPHERE BASED MODEL

During the last years the most widely used approach for modeling anisotropy in soft tissues has been representing fiber directions by means of an invariant formulation. Lately, the use of statistical distributions has increased, being this latter also adopted in the present work. Furthermore, a microsphere-based approach has been used at a micro scale level.
The microsphere approach tries to capture micro-structural information and transfer it into the macroscopic behavior via a homogenization scheme over the unit sphere $\mathbb{U}^2$. In this approach, $\mathbb{U}^2$ is discretized into m directions $\{\mathbf{r}^i\}_{i=1\ldots m}$ that are weighted by factors

$\{w^i\}_{i=1...m}$, where $\langle \mathbf{r} \rangle \approx \sum_{i=1}^{m} w^i \mathbf{r}^i = 0$ and $\langle \mathbf{r} \otimes \mathbf{r} \rangle \approx \sum_{i=1}^{m} w^i \mathbf{r}^i \otimes \mathbf{r}^i = \frac{1}{3}\mathbf{I}$. So an integral over the unit sphere $\mathbb{U}^2$ can be approximated by

$$\langle (\bullet) \rangle = \frac{1}{4\pi} \int_{\mathbb{U}^2} (\bullet) \mathrm{dA} \approx \sum_{i=1}^{m} w^i (\bullet)^i. \tag{8}$$

The term 4π is a normalization factor, result of the surface integral $\int_0^\theta \int_0^\phi \sin(\theta) \mathrm{d}\theta \mathrm{d}\phi$ over the unit sphere. The unit vectors can be expressed in terms of the spherical coordinates $\theta \in [0, \pi)$ and $\phi \in [0, 2\pi)$ as $\mathbf{r} = \sin(\theta)\cos(\phi)\mathbf{e}_x + \sin(\theta)\sin(\phi)\mathbf{e}_y + \cos(\phi)\mathbf{e}_z$ with $\{\mathbf{e}_x, \mathbf{e}_y, \mathbf{e}_z\}$ the reference Cartesian system. Previous works [6, 1, 2] have used and compared different number of integration directions for isotropic and anisotropic functions and, in view of the results therein, 368 directions will be used in all the problems simulated in this work that demonstrated to provide sufficiently accurate results for relatively highly anisotropic materials (see [1]).

As detailed above, the anisotropic part of the SEDF is related to the fibers in the material. In a general situation with N families of fibers the anisotropic part of the SEDF can be expressed as

$$\Psi_{\mathrm{ani}} = \sum_{j=1}^{N} \Psi_{\mathrm{f}}^j = \sum_{j=1}^{N} \left[\frac{1}{4\pi} \int_{\mathbb{U}^2} n \rho_{\mathrm{f}} \psi_{\mathrm{f}} dA \right]_{\mathrm{j}}, \tag{9}$$

where Ψ_{f}^j is the strain energy density function for the j-nth fiber family, n the chain density, ρ_{f} a statistical value associated with the fibrils dispersion and ψ_{f} the free energy density function of the fibril. We will adopt an affine assumption for the integration directions (compare [24]), in spite of the model used for the micro fibers, as for example a non-affine eight-chain model [4]. Since an analytical integration of (9) is not possible in general, a discretization of this equation is used

$$\Psi_{\mathrm{ani}} \approx \sum_{j=1}^{N} \left[\sum_{i=1}^{m} n \rho_i w^i \psi(\bar{\lambda}_i) \right], \tag{10}$$

where $\bar{\lambda}_i$ and $\psi(\bar{\lambda}_i)$ are the stretch ratio and the free energy density function associated to each integration direction.

In order to obtain the macroscopic contribution to the Kirchhoff stresses and the elasticity tensor for a family of fibers, the SEDF has been written in terms of stretches, rather than the classical invariant's function [26]. The equations for the Kirchhoff stress and the elasticity tensors in the spatial configuration are expressed as:

$$\boldsymbol{\tau}_f = \sum_{i=1}^{m} [n \rho_i \psi_i' \bar{\lambda}_i^{-1} \bar{\mathbf{t}} \otimes \bar{\mathbf{t}}] w^i \tag{11}$$

and

$$\mathbf{c}_f = \sum_{i=1}^{m} [n \rho_i [\psi_i'' - \psi_i' \bar{\lambda}_i^{-1}] \bar{\lambda}_i^{-2} \bar{\mathbf{t}} \otimes \bar{\mathbf{t}} \otimes \bar{\mathbf{t}} \otimes \bar{\mathbf{t}}] w^i \tag{12}$$

where ψ_i' and ψ_i'' are the first and second derivative of the fibril energy function with respect to λ_i. Additional details are given in Appendix A.

2.4 MATERIAL BEHAVIOR

The definition of a given material in the hyperelastic framework is associated therefore to establishing a free energy density function for each part of the above discussed splitting. Here, we have used

$$\Psi = \Psi_{\text{vol}}(J) + \Psi_{\text{iso}}(\bar{I}_1) + \Psi_{\text{ani}}(n, \rho, \bar{\lambda}), \tag{13}$$

$$\Psi_{\text{vol}}(J) = \frac{1}{D}\ln^2(\text{J}), \tag{14}$$

$$\Psi_{\text{iso}}(\bar{I}_1) = \mu[\bar{I}_1 - 3] \text{ and} \tag{15}$$

$$\Psi_{\text{ani}}(n, \rho, \bar{\lambda}) = \langle n\rho_f\psi_f\rangle\,. \tag{16}$$

The matrix is known to be composed of an important water content, which results in an almost incompressible behavior, so the volumetric part of the energy density function enforces the quasi-incompressibility constraint depending on the value of the penalty parameter D (14). The matrix contributes to the overall behavior through the volumetric and the isotropic parts of the energy density function (15).

The contribution of each single collagen fibril in the micro scale is here assumed as a first approach, to be defined by an exponential-type function, widely used in macroscopic approaches [18]. In [1] a comparison between this phenomenological function and the worm-like chain model in the microsphere framework is discussed. Note that, although the integration directions are mathematically identified with the homogenization directions, they can be physically associated to the contribution of a fibril. The free density energy associated to each fibril or, equivalently, to each integration direction, is assumed as

$$n\psi_i^j(\bar{\lambda}_i) = \begin{cases} 0, & \text{if } \bar{\lambda}_i < 1 \\ \dfrac{k_1}{2k_2}\left[\exp(k_2[\bar{\lambda}_i^2 - 1]^2)\right] & \text{if } \bar{\lambda}_i \geq 1 \end{cases} \tag{17}$$

2.5 THE VON MISES ORIENTATION DISTRIBUTION FUNCTION

Regarding the anisotropic part of the model (16), a statistical distributions of the fibrils around a preferential orientation is considered through a von Mises statistical function. This orientation distribution function is denoted by ρ and has some interesting properties such as symmetry $\rho(\mathbf{r};\mathbf{a}) = \rho(-\mathbf{r};\mathbf{a})$ and rotational symmetry with respect to the preferred orientation $\mathbf{a}$, which can be expressed as $\rho(\mathbf{Q}\cdot\mathbf{r};\mathbf{a}) = \rho(\mathbf{r};\mathbf{a})\ \forall\mathbf{Q}\in\mathbb{Q}_+^3$. Note that $\mathbf{a}$ could be oriented in any direction of the space leading to a mismatch angle $w = \arccos(\mathbf{r}\cdot\mathbf{a})$. A π-periodic von Mises orientation density function (ODF) (18) has been adopted in this work to take into account the fibrils dispersion [1]

$$\rho(\theta) = 4\sqrt{\frac{b}{2\pi}}\frac{\exp(b[\cos(2\theta)+1])}{\text{erfi}(\sqrt{2b})}, \tag{18}$$

where the concentration parameter $b \in \mathbb{R}^+$ is a measure of the anisotropy. $b \to 0$ represents an isotropic material, and $b \to \infty$ a transversally isotropic one. Erfi(x) is the imaginary error function approximated by a sufficiently large number of terms within its MacLaurin series expansion, which can be written as

$$\text{erfi}(x) \approx \pi^{-1/2} \left[2x + \frac{2x^3}{3} + \sum_{j=3}^{k} \frac{x^{2j-1}}{a(j)} \right], \tag{19}$$

with $a(j) = 0.5[2j-1][j-1]!$ [39] provides a 60 term expansion, sufficiently accurate for values of $b \leq 20$. Figure 1 shows the spherical representation of two distributions for different values of b.

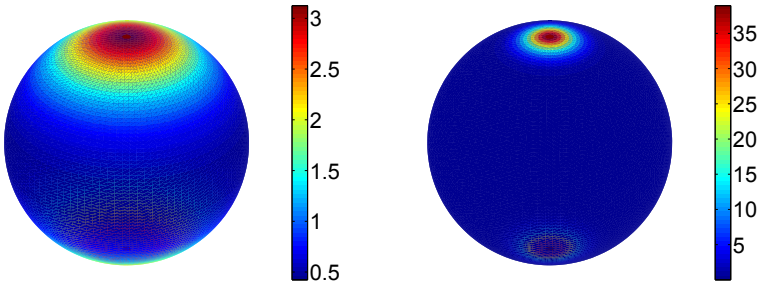

(a) b=1 (b) b=10

Figure 1: Shape of the von Mises ODF for b=1 and b=10.

3 INELASTIC CONSTITUTIVE MODEL

The experimental results suggest that just like the elastic properties, the inelastic behavior of soft tissues is also characterized by anisotropy [3, 31, 28, 30]. Accordingly, a suitable constitutive model should account for this directional dependence and take into account the different alteration mechanisms associated with this anisotropy. The phenomenological inelastic model should include the Mullins effect, the permanent set resulting from the residual strains after unloading, and the fibre and matrix disruption associated to supraphysiological loads or strains [9].

3.1 Hypothesis of the model

To model these inelastic processes, we apply the following considerations:

- We have modified the equation (17) by the parameter w_i

$$n\psi_i^j(\bar{\lambda}_i) = \begin{cases} 0, & \text{if } \bar{\lambda}_i < 1 \\ \dfrac{k_1}{2k_2}\left[\exp(k_2[\bar{\lambda}_i^2 - w_i]^2)\right] & \text{if } \bar{\lambda}_i \geq 1 \end{cases} \tag{20}$$

  that governs the anisotropic contribution to the global mechanical response of the tissue only when stretched, that is, $\bar{\lambda}_i^2 > w_i$ [27].

- Finally, we modified this parameter that changes independently from each direction to take into account structural alterations along the fiber direction. With this modification, we can reproduce at the same time the softening behavior and the permanent set presented in this kind of tissue.

The second law of thermodynamics asserts a non-negative rate of entropy production. Using standard arguments based on the Clausius-Duhem inequality [22]

$$\mathcal{D}_{int} = -\dot{\Psi} + \frac{1}{2}\mathbf{S} : \dot{\mathbf{C}} \geq 0 \tag{21}$$

yields

$$\mathcal{D}_{int} = -\sum_{j=1}^{N}\left[\sum_{i=1}^{m}\frac{\partial\psi_{j,0}^i(\overline{\lambda}^i)}{\partial w_i}\dot{w}_i\right] \geq 0 \tag{22}$$

where the thermodynamic forces are

$$f_{w_i} = -\frac{\partial\psi_{j,0}^i(\overline{\lambda}^i)}{\partial w_i} \tag{23}$$

The thermodynamic force f_{w_i} is conjugated to the internal variable w_i, so the process could be controlled by f_{w_i} instead of w_i (see e.g. [10]).

3.2 Evolution of the internal variables

For the softening variables w_i, we consider the following criteria

$$\Upsilon_i(\mathbf{C}(t), \Gamma_{i_t}) = \frac{\partial\psi_{j,0}^i(\overline{\lambda}^i)}{\partial\overline{\lambda}^i} - \Gamma_{i_t} = \Gamma_i - \Gamma_{i_t} \leq 0 \tag{24}$$

where $\Gamma_i = \frac{\partial\psi_{j,0}^i(\overline{\lambda}^i)}{\partial\overline{\lambda}^i}$ is the softening stress release rate at time $t \in \mathbb{R}_+$ and Γ_{i_t} signifies the softening threshold (stress barrier) at current time t for matrix and fibers

$$\Gamma_{i_t} = \max_{sr\in(-\infty,t)}\frac{\partial\psi_{j,0}^i(\overline{\lambda}^i)}{\partial\overline{\lambda}^i} \tag{25}$$

The equation $\Upsilon_i(\mathbf{C}(t), \Gamma_{i_t}) = 0$ defines a softening surface in the strain space. With these means at hand, we finally propose the following set of rate equations for an evolution of the softening variables

$$\dot{w}_i \doteq \begin{cases} \kappa_i \dot{\Gamma}_{i_t} & \text{if} \quad \Upsilon = 0 \quad \text{and} \quad \mathbf{N}_i : \dot{\mathbf{C}} > 0 \\ 0 & \text{otherwise} \end{cases} \tag{26}$$

Let us now consider softening functions of the simple form

$$w_i = \kappa_i \Gamma_{i_t} + 1 \tag{27}$$

where κ_i is the only parameter to define the softening mechanism in each fiber direction.

4 NUMERICAL EXAMPLE

The principal aim of this section is to illustrate the performance and the physical mechanics involved in the above presented model. With this purpose, a uniaxial test of an incompressible biological tissue is computed in this example. Only one family of fibres is defined along the X direction. The softening evolution is formulated in (27). The tissue was subjected to stepwise uniaxial loading in fiber direction with five stretch controlled cycles where the stretch was 1.4, 1.6, 1.8, 2.0, 2.2.

μ	k_1	k_2	w_i^0	κ_i
0.28	1.1226	1.5973	1.1	0.003

Table 1: Material, damage and softening parameters for uniaxial simple tension.μ and k_1 are in MPa, and other parameters are dimensionless

Figure 2 shows the results. It is possible to observe the softening phenomena during unloading that increases when the maximum load increases showing the typical Mullins' effect observed in soft biological tissues. Finally, the permanent set is presented in the model when the stress are null, and, again the residual stretch increases when the maximum load increases.

5 CONCLUSIONS

The aim of this work is to present the complete formulation of a softening model within an anisotropic microsphere-based approach in order to a better characterization of this phenomenon in biological soft tissues. We consider the weight factors w_i (as internal variables characterizing the structural state of the material with different evolution rule in each integration direction of the microsphere. The limitations of the study include: (1) the need for a suitable experimental plan to obtain the many parameters involved; (2) the softening behavior of biological tissues is also related to viscoelastic effects; (3) one numerical problem concerning the finite element implementation should be addressed.

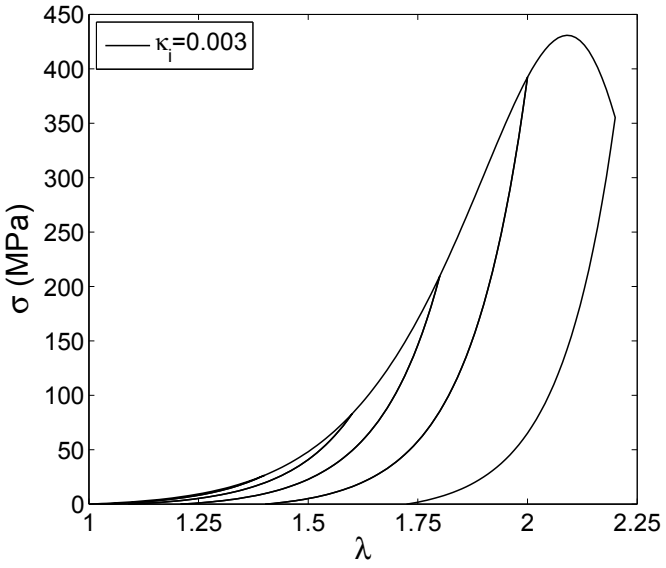

Figure 2: Uniaxial stress response under cyclic uniaxial tension in X direction.

This is related with the necessity of regularizing the ill-posed numerical problem [7] where the loss of ellipticity/hyperbolicity of the governing equations with softening can lead to pathological mesh-sensitivity [32]. In spite of these limitations, the one dimensional character of the constitutive equations applied at the micro-level offers huge possibilities, due to its simplicity and the possibility of incorporating other micro-structural variables.

6 ACKNOWLEDGEMENTS

Support of the Spanish Ministry of Research and Innovation through the research project DPI2010-20746-C03-01 and through the grant BES-2009-028593 to P. Sáez, as well as the support of the Instituto de Salud Carlos III through the CIBER are highly appreciated. CIBER-BBN is an initiative funded by the VI National R&D&i Plan 2008-2011, Iniciativa Ingenio 2010, Consolider Program, CIBER Actions and financed by the Instituto de Salud Carlos III with assistance from the European Regional Development Fund.

References

[1] Alastrué, V., Martinez, M. A., Menzel, A., and Doblare, M. (2009a). On the use of non-linear transformations for the evaluation of anisotropic rotationally symmetric directional integrals. application to the stress analysis in fibred soft tissues. *Int J Numer Meth Biom Eng*, 79:474–504.

[2] Alastrué, V., Martínez, M. A., Doblaré, M., and Menzel, A. (2009b). Anisotropic

micro-sphere-based finite elasticity applied to blood vessel modelling. *J Mech Phys Solids*, 57:178–203.

[3] Alastrué, V., Peña, E., Martínez, M. A., and Doblaré, M. (2008). Experimental study and constitutive modelling of the passive mechanical properties of the ovine infrarenal vena cava tissue. *J Biomech*, 41:3038–3045.

[4] Arruda, E. M. and Boyce, M. C. (1993). A three-Ddimensional constitutive model for the large stretch behavior of rubber elastic materials. *J Mech Phys Solids*, 41(2):389–412.

[5] Balzani, D., Schröder, J., and Gross, D. (2006). Simulation of discontinuous damage incorporating residual stress in circumferentially overstretched atherosclerotic arteries. *Acta Biomater*, 2:609–618.

[6] Bažant, P. and Oh, B. H. (1986). Efficient numerical integration on the surface of a sphere. *ZAMM-Z Angew Math Mech*, 66:37–49.

[7] Bazant, Z. P. and Jirasek, M. (2002). Nonlocal integral formulations of plasticity and damage: Survey of progress. *J Eng Mech*, 128:1119–1149.

[8] Bonet, J. and Wood, R. D. (2008). *Nonlinear Continuum Mechanics for Finite Element Analysis*. Cambridge University Press, Cambridge.

[9] Calvo, B., Peña, E., Martins, P., Mascarenhas, T., Doblare, M., Natal, R., and Ferreira, A. (2009). On modelling damage process in vaginal tissue. *J Biomech*, 42:642–651.

[10] Calvo, B., Peña, E., Martínez, M. A., and Doblaré, M. (2007). An uncoupled directional damage model for fibered biological soft tissues. Formulation and computational aspects. *Int J Numer Meth Engng*, 69:2036–2057.

[11] Ciarletta, P. and Ben-Amar, M. (2009). A finite dissipative theory of temporary interf ibrillar bridges in the extracellular matrix of ligaments and tendons. *J R Soc Interface*, 6:909–92.

[12] Ehret, A. E. and Itskov, M. (2009). Modeling of anisotropic softening phenomena: Application to soft biological tissues. *Int J Plasticity*, 25:901–919.

[13] Federico, S. (2010). Volumetric-distortional decomposition of deformation and elasticity tensor. *Math Mech Solids*, 15:672–690.

[14] Flory, P. J. (1961). Thermodynamic relations for high elastic materials. *Trans Faraday Soc*, 57:829–838.

[15] Franceschini, G., Bigoni, D., Regitnig, P., and Holzapfel, G. A. (2006). Brain tissue deforms similarly to filled elastomers and follows consolidation theory. *J Mech Phys Solids*, 54:2592–2620.

[16] Göktepe, S. and Miehe, C. (2005). A micro-macro approach to rubber-like materials–part iii: the micro-sphere model of finite rubber viscoelasticity. *J Mech Phys Solids*, 53:2259–2283.

[17] Hokanson, J. and Yazdami, S. (1997). A constitutive model of the artery with damage. *Mech Res Commun*, 24:151–159.

[18] Holzapfel, G. A. (2000). *Nonlinear Solid Mechanics*. Wiley, New York.

[19] Horgan, C. O. and Saccomandi, G. (2005). A new constitutive theory for fiber-reinforced incompressible nonlinearly elastic solids. *J Mech Phys Solids*, 53:1985–2025.

[20] Hurschler, C., Loitz-Ramage, B., and Vanderby, R. (1997). A structurally based stress-stretch relationship for tendon and ligament. *ASME J Biomech Eng*, 119:392–399.

[21] Li, D. and Robertson, A. M. (2009). A structural multi-mechanism damage model for cerebral arterial tissue. *ASME J Biomech Eng*, 131:101013 1–8.

[22] Marsden, J. E. and Hughes, T. J. R. (1994). *Mathematical Foundations of Elasticity*. Dover, New York.

[23] Miehe, C. and Göktepe, S. (2005). A micro-macro approach to rubber-like materials–part ii: the micro-sphere model of finite rubber viscoelasticity. *J Mech Phys Solids*, 53:2231–2258.

[24] Miehe, C., Göktepe, S., and Lulei, F. (2004). A micro-macro approach to rubber-like materials–part i: the non-affine micro-sphere model of rubber elasticity. *J Mech Phys Solids*, 52:2617–2660.

[25] Natali, A. N., Pavan, P. G., Carniel, E. L., Luisiano, M. E., and Taglialavoro, G. (2005). Anisotropic elasto-damage constitutive model for the biomechanical analysis of tendons. *Med Eng Phys*, 27:209–214.

[26] Ogden, R. W. (1996). *Non-linear Elastic Deformations*. Dover, New York.

[27] Peña, E. (2011). Prediction of the softening and damage effects with permanent set in fibrous biological materials. *J Mech Phys Solids*, page Accepted.

[28] Peña, E., Alastrue, V., Laborda, A., Martínez, M. A., and Doblare, M. (2010). A constitutive formulation of vascular tissue mechanics including viscoelasticity and softening behaviour. *J Biomech*, 43:984–989.

[29] Peña, E. and Doblare, M. (2009). An anisotropic pseudo-elastic approach for modelling Mullins effect in fibrous biological materials. *Mech Res Commun*, 36:784–790.

[30] Peña, E., Martins, P., Mascarenhas, T., Natal-Jorge, R. M., Ferreira, A., Doblaré, M., and Calvo, B. (2011a). Mechanical characterization of the softening behavior of human vaginal tissue. *J Mech Behav Biomed*, 4:275–283.

[31] Peña, E., Peña, J. A., and Doblaré, M. (2009). On the Mullins effect and hysteresis of fibered biological materials: A comparison between continuous and discontinuous damage models. *Int J Solids Struct*, 46:1727–1735.

[32] Peña, J. A., Martínez, M. A., and Peña, E. (2011b). A formulation to model the nonlinear viscoelastic properties of the vascular tissue. *Acta Mech*, 217:63–74.

[33] Rodríguez, J. F., Alastrue, V., and Doblaré, M. (2008). Finite element implementation of a stochastic three dimensional finite-strain damage model for fibrous soft tissue. *Comput Methods Appl Mech Engrg*, 197:946–958.

[34] Rodríguez, J. F., Cacho, F., Bea, J. A., and Doblaré, M. (2006). A stochastic-structurally based three dimensional finite-strain damage model for fibrous soft tissue. *J Mech Phys Solids*, 54:564–886.

[35] Spencer, A. J. M. (1971). Theory of Invariants. In *Continuum Physics*, pages 239–253. Academic Press, New York.

[36] Vita, R. D. and Slaughter, W. S. (2007). A constitutive law for the failure behavior of medial collateral ligaments. *Biomech Model Mechanbiol*, 6:189–197.

[37] Volokh, K. Y. (2007). Hyperelasticity with softening for modeling materials failure. *J Mech Phys Solids*, 55:2237–2264.

[38] Volokh, K. Y. and Vorp, D. A. (2008). A model of growth and rupture of abdominal aortic aneurysm. *J Biomech*, 41:1015–1021.

[39] Weisstein, E. W. (2004). "Erfi." From MathWorld–A Wolfram Web Resource. http://mathworld.wolfram.com/Erfi.html.

[40] Wulandana, R. and Robertson, A. M. (2005). An inelastic multi-mechanism constitutive equation for cerebral arterial tissue. *Biomech Model Mechanbiol*, 4:235–248.

XI International Conference on Computational Plasticity. Fundamentals and Applications
COMPLAS XI
E. Oñate, D.R.J. Owen, D. Peric and B. Suárez (Eds)

AN ANISOTROPIC PSEUDO-ELASTIC MODEL FOR THE MULLINS EFFECT IN ARTERIAL TISSUE

EVA GULTOVA*, LUKAS HORNY†, HYNEK CHLUP†, RUDOLF ZITNY†

*† Faculty of Mechanical Engineering
Czech Technical University in Prague
Technická 4, 16607 Prague, Czech Republic
Email: eva.gultova@fs.cvut.cz, web page: http://www.biomechanika.cz/departments/20

Key words: Aorta, Mullins effect, anisotropy, constitutive modeling, limiting fiber extensibility, pseudo-elasticity.

Summary. This paper is focused on developing the theory which describes the Mullins effect in human arterial tissue. Cyclic uni-axial tensile tests were performed to obtain data characterizing the Mullins effect in arterial tissue.

In order to account anisotropy of arterial tissue, longitudinally as well as circumferentially resected samples of human aorta were tested. Each sample underwent repeated (four times) loading and unloading to a certain value of maximum stretch. This limiting stretch increased in several consecutive steps.

The arterial wall is considered as hyperelastic, locally orthotropic, incompressible material. A strain energy function is adopted in the limiting fiber extensibility form. Description of primary material response, followed by material stress softening in the repeated cycles, is based on pseudo-elastic constitutive model proposed by Dorfmann and Ogden. This theory is developed using anisotropic form of the softening variable. The primary loading curve and the fourth unloading curve of each set of cycles are chosen for regression analysis. The model with thus estimated parameters successfully fits experimental data and is suitable for application in biomedicine.

1 INTRODUCTION

Due to cardiac cycle, arteries are subjected to cyclic loading and unloading in their physiological conditions. In vitro, mechanical response of arteries is mostly realized by cyclic inflation tests and tensile tests. Some irreversible effects are observed during these tests. One of them is known as the Mullins effect (Fig.1). This softening phenomenon is characterized by the following features: when a so called virgin material (previously undeformed) is loaded to a certain value of deformation (under uniaxial tension), stress–stretch curve follows so called primary loading curve (Fig.1 – green curve). Subsequent unloading (Fig.1 – yellow and red curve) exhibits stress softening. Next reloading follows the former unloading curve until the previous maximum stretch is reached. At this moment the loading path starts to trace the primary loading curve.

Purely elastic response of soft tissues is often modeled within the framework of hyperelasticity, see [1, 2] for examples. Concerning with the Mullins effect, soft tissue is most

frequently modeled within two conceptions. The first one is based on Continuum Damage Mechanics (CDM). The CDM describes the Mullins effect using a system of internal variables reflecting irreversible effects. See e.g. Peña et al. [3], who considered the internal variables corresponding to separated contribution of the matrix and the fibers in a model of arterial wall.

The second conception results from theory of pseudo-elasticity. Ogden and Roxburgh [4], Beatty and Krisnaswamy [5] and Dorfmann and Ogden [6] formulated pseudo-elastic models of the Mullins effect in rubber-like materials. Such a model describes irreversible behavior incorporating softening variable, which is included into the strain energy density function (SEDF). Peña and Doblaré [7] suggested an anisotropic extension of the pseudo-elastic model of Ogden and Roxburgh [4] with anisotropic form of softening variable. The variable is different for matrix and fibers, which are arranged in two preferred directions. This model successfully described the softening behavior of sheep vena cava under uniaxial tension.

The aim of this paper is to extend the theory of pseudo-elasticity developed by Dorfmann and Ogden [6]. The pseudo-energy function in limiting fiber extensibility form [8] is used. Contrary Dorfmann and Ogden, the anisotropic form of the softening variable is suggested.

2 METHODS

In order to illustrate the Mullins effect in human aorta, cyclic uniaxial tension tests were performed on MTS Mini Bionix testing machine (MTS, Eden Prairie, USA). Two samples of human thoracic aorta were resected from cadaveric donors with the approval of the Ethic Committee of the University Hospital Na Kralovskych Vinohradech in Prague. Respecting anisotropy of the aorta, samples were resected in the circumferential and longitudinal directions. The arteries were stored in physiological solution at a temperature of about 5°C till the beginning of the experiment. Post mortem interval was about 40–48 hours. The temperature during the test was 23°C.

An extension and loading force were measured by MTS testing machine. Five levels of maximum stretch were performed during the tests: $\lambda_m = 1.1$, $\lambda_m = 1.2$, $\lambda_m = 1.3$, $\lambda_m = 1.4$ and $\lambda_m = 1.5$, where λ_m is the maximum ratio between current length l and referential length L. Recorded data are shown in Fig. 1.

Each level represented four-cycle of loading. Considering the incompressibility of the tissue, loading stresses were obtained according to the following relation:

$$\sigma = \frac{F}{s} = \frac{F \cdot l}{L \cdot B \cdot H} \tag{1}$$

where F denotes applied force and s the current cross-section. B and H denote width and thickness of a sample in the reference configuration.

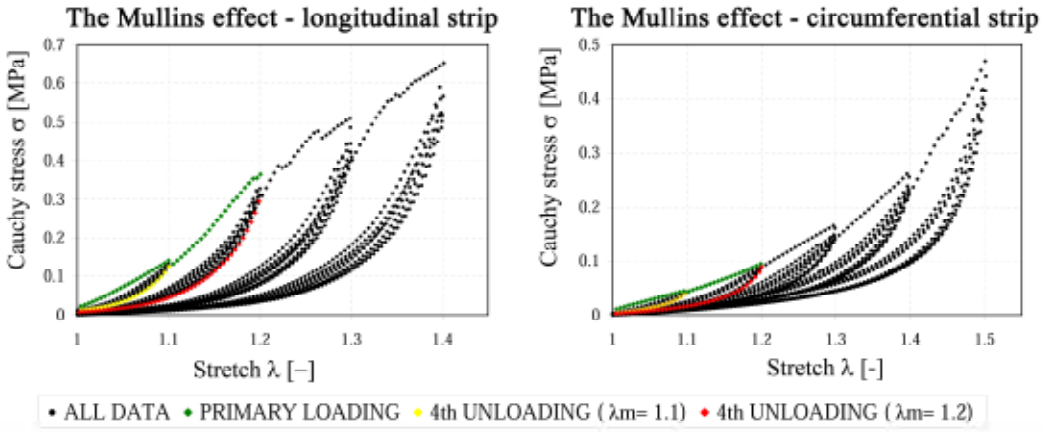

Figure 1: Stress–strain response of the human thoracic aorta under cyclic uniaxial tension . Maximum stretch has increased after 4 cycles due to stabilizing mechanical response of the aorta. Colored points correspond to cycles used within regression analysis

3 MODEL

Primary response of the artery was modeled as an incompressible, hyperelastic, locally orthotropic continuum. Deformation was described with the deformation gradient $\boldsymbol{F}$, which was assumed in the form of:

$$\boldsymbol{F} = diag\left[\lambda_1, \lambda_2, \frac{1}{\lambda_1 \lambda_2}\right] \tag{2}$$

where λ_i are principal stretches. Strain energy density function for incompressible rectangular sample embodied in x_1x_2 plane of Cartesian coordinate system $x_1x_2x_3$, is expressed in form:

$$W_0 = W_{0iso}(I_1) + W_{0aniso}(I_4) \tag{3}$$

which reflects the microstructure of an transversally isotropic material, composed of a ground isotropic matrix and fibrous network. I_i are the principal invariants of the right Cauchy-Green tensor.

SEDF is incorporated in limiting fiber extensibility form as follows [8]:

$$W_0 = \frac{c}{2}(\lambda_1^2 + \lambda_2^2 + \frac{1}{\lambda_1^2 \lambda_2^2} - 3) - \mu J_f \ln\left(1 - \frac{(\lambda_1^2 \cos^2 \beta + \lambda_2^2 \sin^2 \beta - 1)^2}{J_f^2}\right) \tag{4}$$

where μ and c are stress-like material parameters, J_f +1 is the limiting stretch of the reinforcing fibres, β is an angle of enforcing fibres with coordinate axis x_1.

Let us assume that sample is loaded in the direction of coordinate axis x_α (α = 1,2). Corresponding Cauchy stresses in the direction of (unidirectional) loading are:

$$\sigma_\alpha = \lambda_\alpha \frac{\partial W_0}{\partial \lambda_\alpha} - p_0, \quad \alpha = 1, 2, \tag{5}$$

where p_0 denotes a Lagrange multiplier associated with the incompressibility constrain $\lambda_1\lambda_2\lambda_3$=1. The Eq. (5) describes stresses at the "virgin" material (primary loading). Within unloading a stress softening occurs, and stresses should be reduced by a factor η_α:

$$\sigma_\alpha = \eta_\alpha \lambda_\alpha \frac{\partial W_0}{\partial \lambda_\alpha} - p, \quad \alpha = 1,2, \tag{6}$$

The softening variable η_α may be active or inactive and this change from inactive to active state is induced when unloading is initiated:

$$\begin{aligned} \lambda_\alpha &= \lambda_{\alpha\max} \rightarrow \eta_\alpha = 1 \\ \lambda_\alpha &< \lambda_{\alpha\max} \rightarrow \eta_\alpha = \eta_\alpha(\lambda_\alpha) \end{aligned} \tag{7}$$

The reduction of stresses (Mullins effect, $\eta_\alpha < 1$) occurs as soon as the actual energy W_0 is less than maximum value $W_{m\alpha}$ attained during the whole previous deformation history. The stress reduction increases with the increasing difference $W_{m\alpha}$ - W_0 and is approximated by the following empirical formula:

$$\eta_\alpha = 1 - \frac{1}{r} f\left(\frac{W_{m\alpha} - W_0(\lambda_1, \lambda_2)}{k_\alpha s}\right) \tag{8}$$

where $f(t)$ can be any monotonically increasing and bounded function, e.g. Error function $Erf(t)$ [4]. Resulting model has 6 parameters: c, μ, β, J_f, r, s that should be identified by experiments.

We suggest material parameter k_α in the form which incorporates material anisotropy, in the meaning of the Young modulus of the material in the initial (virgin) reference configuration. Its advantage is in not increasing number of material parameters:

$$k_\alpha = \left.\frac{\partial^2 W_0(\lambda_1, \lambda_2)}{\partial \lambda_\alpha^2}\right|_{\lambda_1=\lambda_2=1} \tag{9}$$

4 RESULTS

Due to the testing machine design, only displacements in loading directions (α =1 and α=2) were measured. Displacements in the transversal direction were eliminated using the boundary conditions of zero transversal stresses. Parameters p_0 and p were determined from Eq. (5, 6) considering $\sigma_3 = 0$.

Primary loading curve and fourth unloading curve for $\lambda_m = 1.1$ and $\lambda_m = 1.2$ were included in the regression analysis. Assuming the idealized Mullins effect, following reloading was identified with previous unloading. Primary material responses of loading with $\lambda_m > 1.2$ were not considered because of their non-convexity in longitudinal samples (see Fig. 1). Regression analysis was performed using weighted least square method in Maple (Maplesoft, Waterloo, Canada).

Using form of the softening variable expressed by Error function, we estimated parameters J_f, c, μ, $sin^2\beta$, r and s that are summarized in Table 1. Experimental and numerical results for loading and unloading of the thoracic aorta are shown in Fig. 2. Regression results were also checked on the condition $I_4 > 1$. Because I_4 models reinforcement with collagen fibers they may contribute to the stored energy only in tensile strains. It was found that this condition was satisfied in all data points.

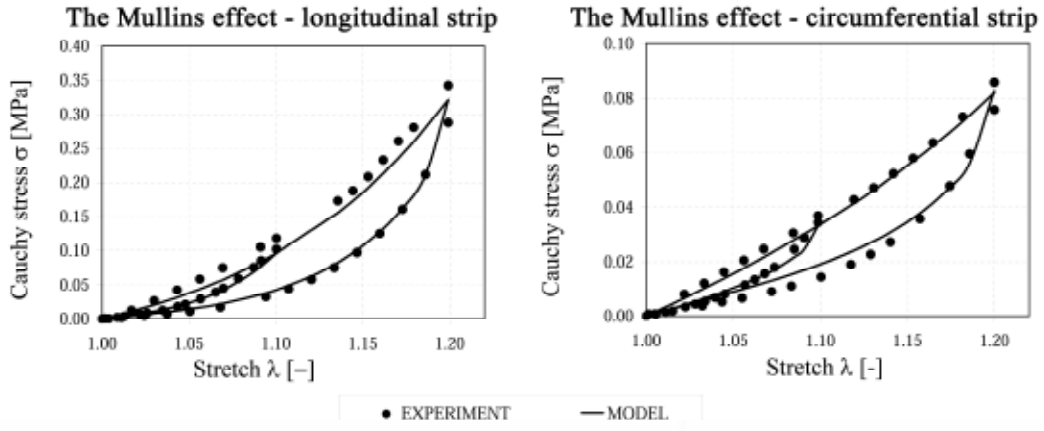

Figure 2: Comparison of the experiment and numerical model of loading and unloading curves in human thoracic aorta with maximum stretches of $\lambda_m = 1.1$ and $\lambda_m = 1.2$. Numerical simulations have been performed using the pseudo-elastic model with anisotropic form of the softening variable. The softening variable has been designed in form incorporating Error function.

Table 1: Material parameters of the pseudo-elastic model

sample	Material parameter	
Thoracic aorta	J_f [1]	0.0786
	c [Pa]	96401
	μ[Pa]	116744
	$sin^2\beta$ [1]	0.5863
	s[1]	2.47E-5
	r[1]	3.2058

5 DISCUSSION

The strain-induced stress softening in human aorta has been described by means of the stress reduction factor η. Particular mathematical form of η has been adopted from the pseudo-elasticity theory introduced by Dorfmann and Ogden [4] who successfully described the Mullins effect in particle-reinforced rubber. We used anisotropic form of the softening

variable in contrast of these authors. It means that model is able to reflect dependence of the stress softening on the direction in which the tension is applied.

The main advantage of the present model is a small number of material parameters. Only 2 of the proposed 6 parameters belong to the pseudo-elastic theory. The anisotropic model suggested by Peña and Doblaré [7] fits the data using 7 pseudo-elastic material parameters.

However present study has some limitations. The first one is due to the limited number of experimental data. Also the design of the experiment does not enable to measure transversal stretches. Finally, the model in the present form is not able to describe permanent strains usually observed during cyclic experiments.

In spite of all these limitations, experimental and numerical simulations show good agreement.

6 CONCLUSIONS

Under cyclic loading conditions, large strain-induced softening (known as the Mullins effect) was observed during uniaxial tension of human thoracic aorta. Purely elastic response of arterial tissue was successfully fitted using SEDF in limiting fiber extensibility form. The Mullins effect was modeled within the theory of pseudo-elasticity. The pseudo-elastic model of Ogden and Roxburgh [4] has been extended by applying anisotropic form of the softening variable. This has been suggested in the form incorporating Error function. The model described experimental data successfully and is applicable to model the Mullins effect in arterial tissue.

ACKNOWLEDGEMENTS

This work has been supported by the Czech Ministry of Education project MSM6840770012; Czech Science Foundation GA106/08/0557; and Grant Agency of the Czech Technical University in Prague SGS10/247/OHK2/3T/12.

REFERENCES

[1] Holzapfel, G.A.; Gasser, T.C. and Ogden, R.W. A new constitutive framework for arterial wall mechanics and a comparative study of material models. *J Elast* (2000) **61**:1–48.

[2] Humphrey, J.D. Continuum biomechanics of soft biological tissues. *Proc R Soc Lond A* (2003) **459**: 3-46.

[3] Pena, E.; Pena, J.A. and Doblare, M. On the Mullins effect and hysteresis of fibered biological materials: A comparison between continuous and discontinuous damage models. *Int J Solids Struct* (2009) **46**:1727–1735.

[4] Ogden, R.W. and Roxburgh, D.G. A pseudo-elastic model for the Mullins effect in filled rubber. *Proc R Soc London A* (1999) **455**:2861–2877.

[5] Beatty, M. and Krishnaswamy, S. The Mullins effect in equibiaxial deformation. *Z Angew Phys* (2000) **51**: 984 –1015.

[6] Dorfmann, A. and Ogden, R. A pseudo-elastic model for loading, partial unloading and reloading of particle-reinforced rubbers. *Int J Solids and Struct* (2003) **40**: 2699-2714.

[7] Pena, E. and Doblare, M. An anisotropic pseudo-elastic approach for modelling Mullins effect in fibrous biological materials. *Mech Res Commun* (2009) **36**:784–790.

[8] Horgan, C.O. and Saccomandi, G. A new constitutive theory for fiber-reinforced

incompressible nonlinearly elastic solids. *J Mech Phys Solids* (2005) **53**:1985–2015.

XI International Conference on Computational Plasticity. Fundamentals and Applications
COMPLAS XI
E. Oñate, D.R.J. Owen, D. Peric and B. Suárez (Eds)

COLLAGEN ORIENTATION AND WAVINESS WITHIN THE VEIN WALL

JAN VESELY*, LUKAS HORNY*, HYNEK CHLUP* AND RUDOLF ZITNY*

* Faculty of Mechanical Engineering
Czech Technical University in Prague
Technicka 4, 16607 Prague, Czech Republic
e-mail: Jan.Vesely1@fs.cvut.cz, www.biomechanika.cz/departments/20

Key words: Vena cava, Blood vessel architecture, Collagen, Fiber orientation distribution, Anisotropy

Summary. This paper presents the analysis of the internal structure and organization of components within the vein wall. Dominant directions and statistical distribution of collagen fibers undulation were investigated in digitalized histological sections from media and adventitia layer of human vena cava inferior.

Orientations of collagen fibers were analyzed by the in-house developed software Binary Directions. Digital images were converted to binary pixel maps with collagen fibers enhanced. The software employs an algorithm of the *Rotation Line Segment* to determine significant directions in digital images. It was found that collagen fibers are aligned in circumferential direction in media layer. Contrary to that in adventitia fibers are arranged in longitudinal direction. In contrast to elastic artery, no evidence of helically reinforced composite structure was found.

Second goal was to find out which statistical distribution, usually using in structural models (Gamma, Beta or Weibull), fits to the undulation distribution of collagen fibers. Collagen waviness was characterized by a probability density function for the strain necessary to straighten a crimped fiber. Computer analysis of the end-to-end and contour length was performed using Nis-Elements software. The statistical analysis suggests that the waviness of collagen fibers is identical in media and adventitia It was found that the average strain necessary for straightening collagen fibers is 0.24±0.11 (±SD) and that all three probability distributions fit straightening strains very well and can be used in structural models.

1 INTRODUCTION

In recent years a big increase in interest in constitutive models of biological tissues based on their microstructure was noticed. Biological tissues comprise a large number of different cells, matrix proteins and bonding elements. For effective development of structural constitutive models, good understanding of internal structure and organization of the material is necessary.

According to [3], the gross mechanical response of soft tissues is attributed to the mechanical properties and geometrical arrangement of the tissues components: fiber families (collagen and elastin) and ground substance. The fibers are oriented in different directions and

have different undulation (waviness) in the tissue. Upon loading, the fibers lose their waviness and start to carry a load [1]. It is assumed that gradual recruitment of collagen fibers under a deformation leads to a typical non-linear behavior of soft tissues.

A number of investigators have analyzed the fiber orientation and crimp distribution to implement them into structural mechanical models [1, 3, 6, 9]. This paper deals with histomorfometrical analysis of internal structure of the vein wall. Dominant directions and distribution of undulation of collagen fibers were investigated in histological sections from media and adventitia layer of human vena cava.

2 METHODS – COLLAGEN FIBERS ORIENTATION

Histological sections were obtained from abdominal vena cava inferior. The orientation of sections and the definition of collagen fiber angle β are shown in Fig. 1. Specimens were routinely fixed in 10% buffered formaldehyde, embedded in paraffin, cut, and stained with orcein. Digitalized images were evaluated by in house developed software BinaryDirections with implemented algorithm of the *Rotating Line Segment* (RoLS).

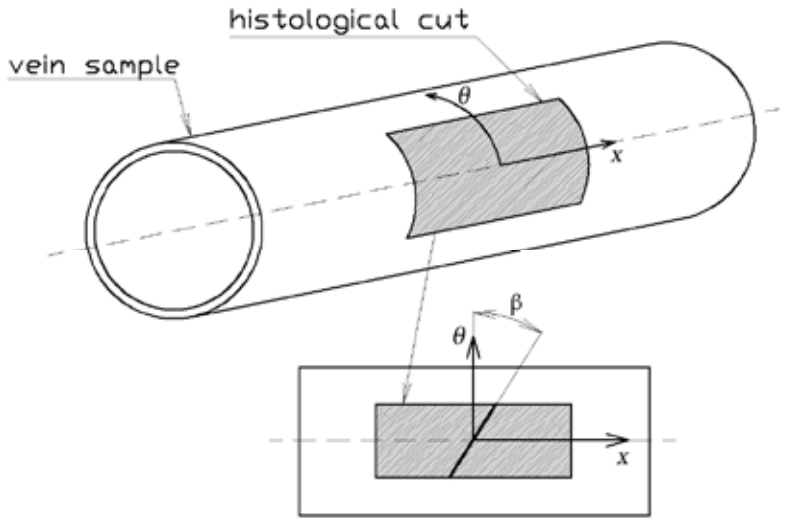

Figure 1: Definition of the angle β.

Digital images were converted to binary pixel maps by tresholding of RGB filter which transforms stained collagen to white (logical unity) pixels and non-collagen components to black (logical zero) pixels. Binary conversion was realized by software NIS-Elements (NIKON INSTRUMENTS INC., USA, New York). Final orientations were obtained by averaging results from 5 histological sections from each layer (media and adventitia).

2.1 ROLS Algorithm

Exact mathematical formulation of the *Rotating Line Segment* (RoLS) was described in details in [2]. Histological section converted to binary pixel map canbe viewed as the matrix with elements uniquely corresponding to pixels. Elements are equal to either zero or unity depending on the pixel color. The algorithm explores neighborhood of each non-zero pixel

(called target pixel) in the image using the rotating line segment. The neighborhood of the target pixel is a square represented by *N*x*N* submatrix **M**, where *N* is an odd integer. Now, imaginary line segment is rotated step by step around the midpoint of the neighborhood. Each rotating step, β, of the line segment is represented via additional *N*x*N* matrix, say $\mathbf{L}^{\beta}$. $\mathbf{L}^{\beta}$ has only non-zero elements in positions corresponding to the rotated line segment.

The aim of RoLS is to find dominant directions in an image. This procedure is based on so-called matching coefficient, $C(\beta)$. The matching coefficient is normalized number of non-zero pixels shared with the line segment and neighborhood of target pixel at given rotating step β:

$$C(\beta) = \frac{\sum_{i=1}^{N}\sum_{j=1}^{N} M_{ij} \cdot L_{ij}^{\beta}}{Nl} \tag{1}$$

$$l = \sum_{i=1}^{N}\sum_{j=1}^{N} L_{ij}^{\beta} \tag{2}$$

Normalization procedure is related to length of square neighborhood *N* and number of pixels creating the line segment, *l*.

There are two ways how to obtain relevant information about directional frequency of non-zero (collagen) pixels in the neighborhood of target pixel. First, one can reduce information from pixels neighborhood to the most frequent angle (rotation step with the greatest *C(β))* and create histogram over the entire image (all target pixels). The second way is to consider $C(\beta)$ as a function of β in each pixel and averaged these functions through all target pixels. Obtained results may depend on *N,* therefore analyses should be repeated with different values of *N* and the *N* should be chosen with respect to characteristic dimensions of structures observed in images (eyes of expert are the best optimization tool, as usually).

Image-based determination of tissue architecture may employ many kinds of algorithms and mathematical methods. Presented algorithm, RoLS, is similar to the so-called volume orientation (VO) method which operates with point grid and seeks for the longest intercept in target volume. VO was first described in Odgaard et al. [4]. It was found to be suitable within an analysis of bone architecture. Interested reader can track details in [5] or recent review [7].

2.2 Test images

Test binary images were evaluated by BinaryDirections before processing histological sections to verify that this software is a suitable instrument for fibers orientation analysis. Selected tested images and results are shown in Fig. 2.

Evaluating of testing images showed that software BinaryDirection is convenient for determining dominant directions in binary image.

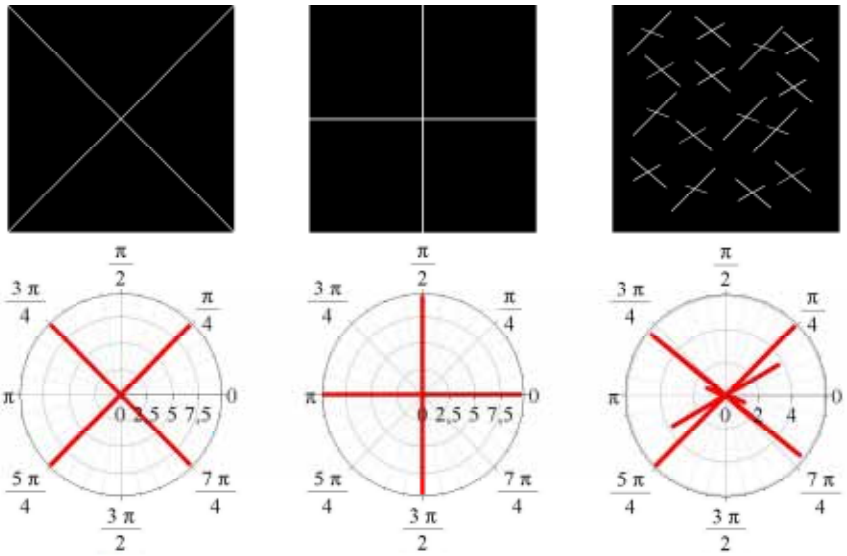

Figure 2: Tested binary images and empirical probability density for evaluated images.

3 METHODS – COLLAGEN FIBERS UNDULATION

The fiber waviness was characterized statistically by a probability density function for the strain ε_s necessary to straighten a crimped fiber, Fig. 3.

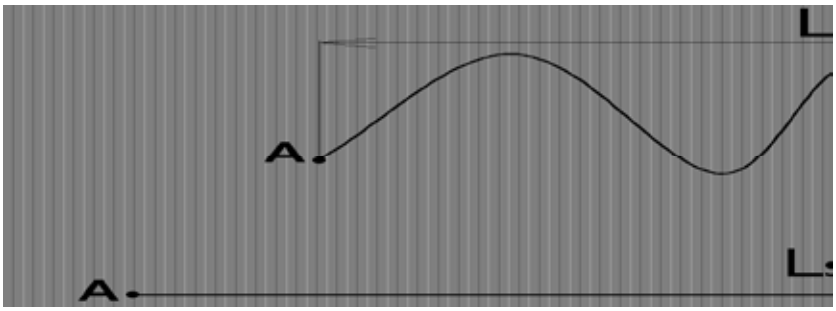

Figure 3: Axial fiber strain ε_S.

Strain ε_S is defined:

$$\varepsilon_s = \frac{L_s}{L_o} - 1, \tag{3}$$

where L_o is end-to-end length of the fiber, and L_s is the contour length of the fiber.

Computer analysis of the end-to-end and contour length was performed manually using NIS-Elements (NIKON INSTRUMENTS INC., USA, New York), Fig. 4.

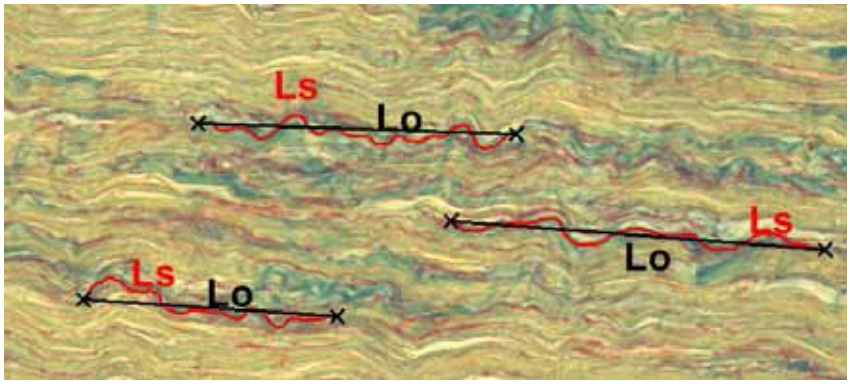

Figure 4: Digital image from media. Measuring of lengths *Lo* and *Ls* by Nis-Elements.

Statistical computations were performed in Maple 13 (Maplesoft, Canada, Waterloo). The aim was to find out suitable statistical model for ε_s probability distribution. Following distributions were considered:

Weibull distribution

$$f(\varepsilon_s;\lambda,k)=\frac{k}{\lambda}\left(\frac{\varepsilon_s}{\lambda}\right)^{k-1}e^{-\left(\frac{\varepsilon_s}{\lambda}\right)^k}, \tag{4}$$

where $k > 0$ is the shape parameter and $\lambda > 0$ is the scale parameter of the distribution.

Beta distribution

$$f\left(\varepsilon_s;\alpha,\beta\right)=\frac{\varepsilon_s^{\alpha-1}\left(1-\varepsilon_s\right)^{\beta-1}}{B\left(\alpha,\beta\right)}, \tag{5}$$

where B is Beta function and α, $\beta>0$ are shape parameters.

Gamma distribution

$$f\left(\varepsilon_s;k,\theta\right)=\varepsilon_s^{k-1}\frac{e^{\frac{\varepsilon_s}{\theta}}}{\theta^k\Gamma\left(k\right)}, \tag{6}$$

where Γ is Gamma function, $k>0$ is the shape parameter and $\theta>0$ is the scale parameter. In all distributions $\varepsilon_s > 0$.

4 RESULTS

4.1 Collagen fibers orientation

Fig. 5 – Left panel shows an example of digital image from media and definition of angle β. The same image converted to a binary pixel map is in Fig. 5 (Right panel). The sensitivity

of the results to the length of rotating line segment is shown in Fig. 6. It was found that the usage of different lengths of the rotating segment N∈{61 pix, 121 pix, 181 pix, 201 pix} have not significant effect on the distribution of angle β. Final results for images processed in BinaryDirections from media and adventitia are shown in Fig. 7.

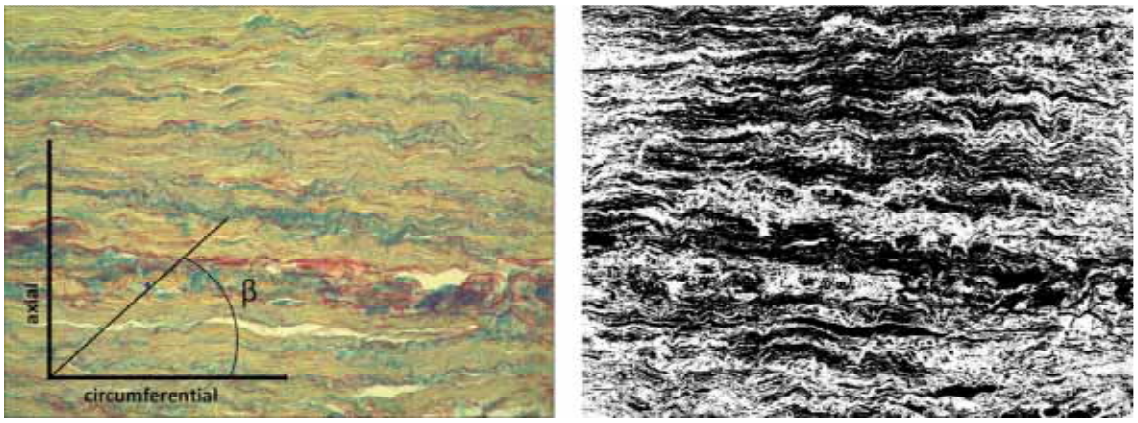

Figure 5: Left: Histological section from media layer stained with orcein. Collagen fibers are stained in blue. **Right:** Binary pixel map created from histological image in left panel. White color represents collagen fibers.

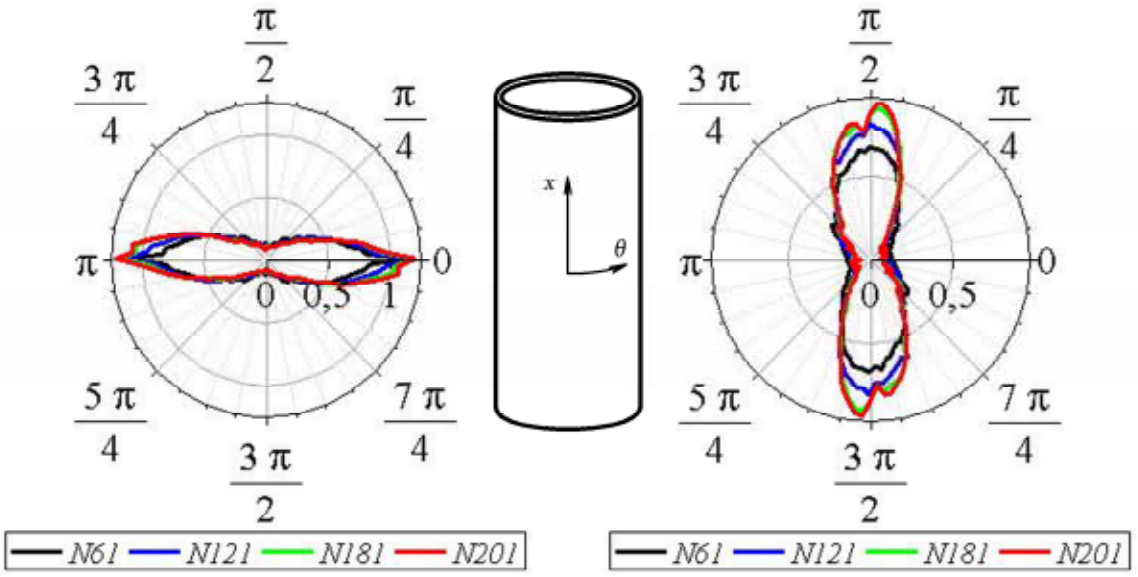

Figure 6: Left: Empirical probability density function for selected section from media for 4 lengths of line segment. **Right:** Empirical probability density function for selected section from adventitia for 4 lengths of line segment.

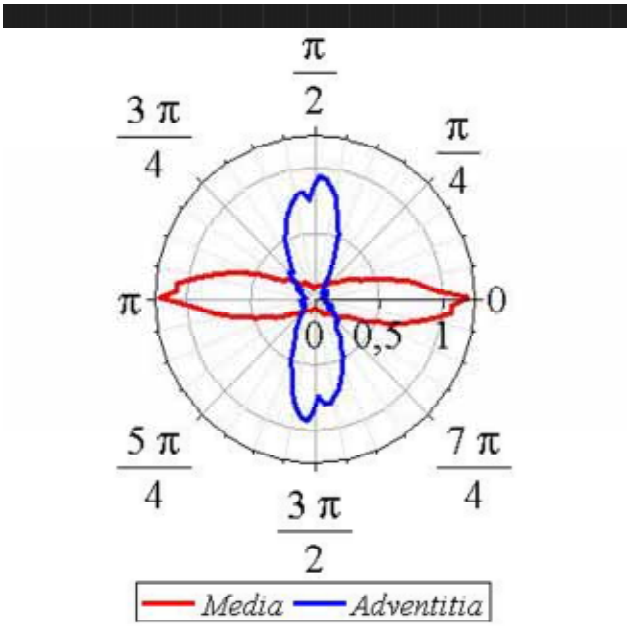

Figure 7: Resulting averaged empirical probability density function for axial cut from media (red) and adventitia (blue).

It was found that collagen fibers in media are aligned in circumferential direction. Contrary to that fibers in adventitia are oriented in longitudinal direction.

4.2 Collagen fibers undulation

Strains ε_s were evaluated for media and adventitia separately. The Chi-Square Goodness-of-fit test was performed to decide if the data may be considered as drawn from one statistical sample. The test suggested that it is possible to merge the data from media and adventitia together (*P-value = 0.74*).

The histogram of obtained strains necessary for the straightening and the fit of experimental data by the Weibull, Beta and Gamma probability distribution, Fig. 9. The average value of straightening strain is ε_s =0.24 ± 0.1 (±SD). It was found that all three probability distributions fit experimental strains very well. The best fit was achieved with the Beta distribution (α = 4.20, β = 12.58).

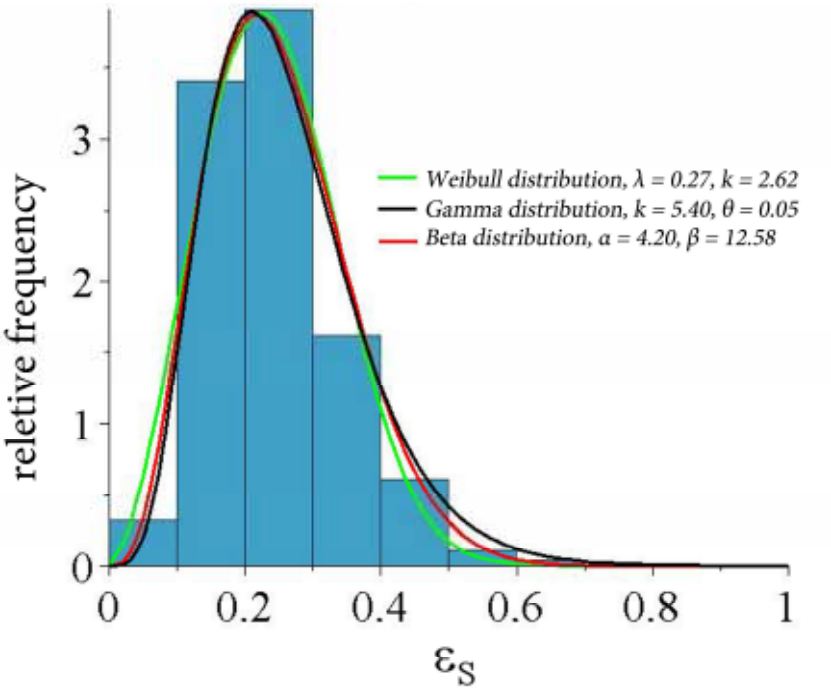

Figure 8: Fitting of obtained strains ε_s (from media and adventitia) by Weibull, Beta and Gamma probability distribution.

5 DISCUSSION

The analysis of the histological images from human abdominal vena cava showed that collagen fibers are in media oriented in the circumferential direction with very compact organization of the collagen. Conversely, in adventitia collagen is aligned with the longitudinal direction with sparse arrangement of fibers.

This arrangement of components within the vein wall differs from arrangement for example in aorta. This may be a consequence of another type of loading, where skeletal muscles are helping venous return mechanism. There is also lower blood pressure in veins than in arteries. Our results suggest that collagen fiber form unidirectional structure in each layer of the vein.

The distribution of undulation of collagen fibers in human vena cava can be fitted by all three considered statistical distributions. The Beta distribution fits the best. The statistical analysis suggests that the waviness of collagen fibers is identical in media and adventitia. It was found that the average strain necessary for straightening collagen fibers is 0.24. These results differ from findings by Sokolis [8], who investigated the waviness of medial collagen in vena cava inferior in New Zealand rabbits (averaged ε_s =0.57). It suggested species-dependent waviness.

ACKNOWLEDGEMENTS

This work has been supported by the Czech Ministry of Education project MSM6840770012; Czech Science Foundation GA106/08/0557; and Grant Agency of the Czech Technical University in Prague SGS10/247/OHK2/3T/12.

REFERENCES

[11] De Vita, R. Structural constitutive models for knee ligaments. Disertation thesis, University of Pittsburgh (2005)
[2] Horny, L., Hulan, M.; Zitny, R.; Chlup, H.; Konvickova, S.; Adamek, T. Computer-Aided Analysis of Arterial Wall Architecture. *IFMBE Proceedings*, vol. 25/4, World Congress on Med. Phys. & Biomed. Eng., Munich, Germany (2009) 1494–1497
[3] Lanir, Y. Constitutive equations for fibrous connective tissues. *Journal of Biomechanics* (1983) **16**:1–12
[4] Odgaard, A.; Jensen, E.B.; Gundersen, H.J.G. Estimation of structural anisotropy based on volume orientation. A new concept. *Journal of Microscopy* (1990) **157**:149-162
[5] Odgaard, A. Three-dimensional methods for quantification of cancellous bone architecture. *Bone* (1997) **20**:315-328
[6] Sachs, M.; Sun, W. Multiaxial Mechanical Behavior of Biological Materials. *Annual Review of Biomedical Engineering* (2003) **5**:251-284
[7] Sander, E.A.; Barocas, V.H. Comparison of 2D fiber network orientation measurement methods. *Journal of biomedical materials research. Part A* (2009) **88A**:322-331
[8] Sokolis, P. D. Passive mechanical properties and constitutive modeling of blood vessels in relation to microstructure. *Med Biol Eng Comput* (2008) **46**:1187–1199
[9] Zullinger, M.; Fridez, P.; Hayashi, K.; Stergiopulos, N. A strain energy function for arteries accounting for wall composition and structure. *Journal of Biomechanics* (2003) **37**:989-1000

XI International Conference on Computational Plasticity. Fundamentals and Applications
COMPLAS XI
E. Oñate, D.R.J. Owen, D. Peric and B. Suárez (Eds)

COMPUTATIONAL HOMOGENIZATION FOR TWO-SCALE MODELING OF PERFUSED TISSUES

EDUARD ROHAN AND VLADIMÍR LUKEŠ

Department of Mechanics, Faculty of Applied Sciences, University of West Bohemia,
Univerzitní 22, 306 14 Plzeň, Czech Republic, e-mail: rohan@kme.zcu.cz

Key words: Perfusion, Homogenization, Porous Media, Large Deformation

Abstract. We developed a two-scale approach for modeling large-deforming perfused media with the 3-compartment microstructure. An incremental formulation based on the updated Lagrangian configuration and the Biot-type continuum model is introduced. Equations of the model express mechanical equilibrium and the volume fluid redistribution (the Darcy law), assuming both the fluid and solid phases are incompressible. This linearized system was treated by the homogenization method assuming locally periodic structures. The local reference cell involving geometrical representations of the blood vessels evolves in time due to large deformation. The homogenized model is implemented using a finite element code and a numerical example is presented.

1 INTRODUCTION

Modeling of tissue perfusion is one of the most challenging issues in biomechanics. There are several hurdles originating in structural arrangement of the so-called perfusion tree, necessity of bridging several scales, the blood flow descriptions depending on the scale, and fluid-structure interactions. We focus on modeling the perfusion of deforming tissue parenchym. At the level of small vessels and microvessels, the perfusion can be described using the Darcy flow in a double-porous structure consisting of 3 compartments: two disconnected channels (small arteries and veins) and the matrix (microvessels and capillaries), represented as the dual porosity, where the permeability is decreasing with the scale parameter the size of the microstructure. In some kinds of tissues, the coupling between flow (fluid diffusion) and deformation is quite important, cf. [7] where the case of linear deformation is described. In this short communication we present a perfusion model of the homogenized large deforming medium whereby the incremental formulation based on the updated Lagrangian formulation is employed.

The computational algorithm can be characterized as the cycle comprising the following steps: 1) for given reference microstructure - the local configuration (LC) - compute the local response functions and the effective constitutive parameters, 2) compute the

macroscopic response (MR) for given external loads, 3) compute the deformation and stresses at each reference microstructure using MR and update the LC. This algorithm is now implemented in the Sfepy code [1] and tested on 2D examples.

2 LARGE DEFORMING MEDIA AND HOMOGENIZATION

Problems involving nonlinear partial differential equations are difficult to solve in general, therefore, their homogenization by asymptotic analysis with respect to the scale of heterogeneities is quite cumbersome, in general. We follow an approach which is based on homogenization of linear subproblems arising from an incremental formulation associated with the numerical treatment, see [8] and [3, 4, 5]. The homogenization procedure can be described by the following steps:

- A reference configuration at time t is considered. The configuration is defined by locally periodic structure and by the reference state in the form of bounded two-scale functions.
- The homogenization is applied to the linear subproblem: given the configuration at time t, compute the increments associated with time increment Δt, see Section 2.2. The locally periodic microstructure (see Section 2.1) and the reference state define the oscillating coefficients of the linearized equations. Then the standard homogenization [2] can be applied, such that on solving local microscopic problems, the characteristic responses are obtained and the homogenized coefficients can be evaluated at any "macroscopic position" x, as reported in Sections 3.1 and 3.2.
- The homogenized subproblem can be solved at the macroscopic level, thus the increments of the macroscopic response are obtained, see Section 3.3.
- In order to establish new microscopic configurations at time $t + \Delta t$ and at "any" macroscopic position, the macroscopic response is combined with the local microscopic characteristic responses to update the local microscopic states, see Section 3.4. Then the next time step can be considered and the whole procedure repeats.

In contrast with linear problems, where the microscopic responses are solved only once (even though they can depend on time [6, 7]), in nonlinear problems the local microscopic problems must be solved for any iteration (time step) and at "any" macroscopic point, [3, 4, 5]. In fact, the homogenization leads to a two-scale domain decomposition: the macroscopic domain is decomposed into locally representative cells where the microscopic problems must be solved. The data (i.e. the solutions) are passed between the two levels after any iteration (the time increment step), so that the problem remains fairly two-scale during the whole solution procedure. This is the major difficulty which affects directly the complexity of the numerical treatment.

2.1 Locally periodic microstructures and scale separation

Homogenization methods based on the asymptotic analysis of a system of partial differential equation employ the concept of locally almost periodic microstructures. Let ε be the scale which is the ratio between the "microscopic" and the "macroscopic" characteristic lengths. Later we shall need material parameters defined in the local microscopic cell Y^ε using the coordinate split

$$x = \xi^\varepsilon + \varepsilon y \ , \quad y \in Y^\varepsilon(x) \ ,$$

where ξ^ε is the lattice coordinate. The unfolding operation denoted by $\tilde{}$, which enables to rewrite any function of x as a function of two variables: $\phi^\varepsilon(x) = \tilde{\phi}^\varepsilon(\xi^\varepsilon, y)$. The assumption of the local periodicity means that for $\varepsilon \to 0$ the following holds:

(i) $Y^\varepsilon(x) \to Y(x)$,

(ii) $\phi^\varepsilon(x) \to \tilde{\phi}(x, y)$ for a.a. $x \in \Omega$ and $y \in Y(x)$,

where $Y(x)$ is the local reference cell. The scale separation is achieved in the limit $\varepsilon \to 0$. It means that the macroscopic position $x \in \Omega$ is associated with a local periodic microstructure — a periodic array of cells, which are defined by translations of $Y(x)$.

Obviously, a real problem is characterized by a given finite scale ε_0, so that the "absolute" scale separation does not hold. However, the limit problem obtained as $\varepsilon \to 0$ and its solution computed by solving the homogenized equations (see below) can be employed to construct an approximation of the original problem featured by ε_0. For this some postprocessing based on averaging operators can be used.

We shall introduce the following decomposition of Y into the sectors of primary and dual porosities, *cf.* [7]. Let Y_α, $\alpha = 1, 2$ be two disjoint subdomains of Y with Lipschitz boundary, such that $\partial_\alpha Y_\alpha := \overline{Y_\alpha} \cap \partial Y \neq \emptyset$ is formed by mutually homologous points of ∂Y, see Fig. 1 (right); this is necessary to have connected channels. The periodic array obtained by translating Y_α forms a connected domains.

Further by $Y_3 = Y \setminus (\overline{Y_1} \cup \overline{Y_2})$ we denote the "matrix", which thus separates the channels Y_1 and Y_2. Domain Y_3 is associated with the dual porosity, where the permeability is very small, see equation (4). By $\Gamma_\beta = \partial Y_\beta \cap \partial Y_3$ we denote the channel-matrix interface.

2.2 Updated Lagrangian formulation

In order to define the weak formulation for the linearized deformation-diffusion problem, we need some preliminaries. Let $\partial_D\Omega \subset \partial\Omega$ be the part of the boundary where the zero displacements are prescribed. Now we define $\boldsymbol{V}_0(\Omega) = \{\boldsymbol{v} \in W^{1,2}(\Omega)^3 \mid v_i = 0 \text{ on } \partial_D\Omega, i = 1, \ldots, 3\}$ for 3D problems.

In what follows we denote by superscript ε all the quantities which vary with heterogeneities. The micromodel incorporates the following material parameters. The elasticity tensor $D^{\text{eff}\,\varepsilon}_{ijkl}$ is the Truesdell rate of the effective Kirchhoff stress $\tau^{\text{eff},\varepsilon}_{ij}$, which is associated

with a given strain energy function. Denoting by F^ε_{ij} the deformation gradient, $J^\varepsilon = \det F^\varepsilon_{ij}$. Both $D^{\mathrm{eff}\,\varepsilon}_{ijkl}$ and $\tau^{\mathrm{eff}\,\varepsilon}_{ij}$ are functions of F^ε_{ij}, namely $\tau^{\mathrm{eff},\varepsilon}_{ij} = \mu^\varepsilon (J^\varepsilon)^{-2/3}\,\mathrm{dev}(F^\varepsilon_{ik}F^\varepsilon_{jk})$. The Green-Lagrange strain w.r.t. the updated configuration consists of the linear part $\boldsymbol{e} = (e_{ij})$ and the nonlinear part $\boldsymbol{\eta} = (\eta_{ij})$. The porous properties of the medium are described by the symmetric positive definite permeability tensor K^ε_{ij}.

The incremental "algorithmic" approach of time stepping is adhered to formulate the evolution problem for the porous medium. We consider the subproblem of computing the new configuration at time $t + \Delta t$, given a finite time step Δt and the configuration $\mathcal{C}^{\varepsilon,(t)}$ at time t, which is determined by the triplet $\{\Omega, F^\varepsilon_{ij}(x), p^\varepsilon(x)\}(t)$ for $x \in \Omega$.

Let $L^{\mathrm{new}}(\boldsymbol{v})$ be the functional involving the instantaneous boundary and volume forces at time $t + \Delta t$. The finite increments of displacement $\Delta\boldsymbol{u}^\varepsilon \in \boldsymbol{V}_0(\Omega)$ and hydrostatic pressure $\Delta p^\varepsilon \in L^2(\Omega)$ verify the variational equations (1)-(2) which express respectively the balance of stresses – quasi-static equilibrium equation (notation: $\boldsymbol{I} = \delta_{ij}$, $\mathbb{I} = 1/2(\delta_{ik}\delta_{jl} + \delta_{il}\delta_{jk})$, $\boldsymbol{\eta}(\boldsymbol{v}) = (\partial v_k/\partial x_i)(\partial v_k/\partial x_j)$, $\mathbb{D} = (D_{ijkl})$ and $\boldsymbol{\tau} = (\tau_{ij})$)

$$\begin{aligned}
&\int_\Omega [\mathbb{D}^{\mathrm{eff},\varepsilon} : \boldsymbol{e}(\Delta\boldsymbol{u}^\varepsilon)] : \boldsymbol{e}(\boldsymbol{v}^\varepsilon)(J^\varepsilon)^{-1}\mathrm{d}x + \int_\Omega \boldsymbol{\tau}^{\mathrm{eff},\varepsilon} : \delta\boldsymbol{\eta}(\Delta\boldsymbol{u}^\varepsilon;\boldsymbol{v}^\varepsilon)(J^\varepsilon)^{-1}\mathrm{d}x \\
&- \int_\Omega \Delta p^\varepsilon\,\mathrm{div}\boldsymbol{v}^\varepsilon\mathrm{d}x + \int_\Omega p^\varepsilon \nabla(\Delta\boldsymbol{u}^\varepsilon) : (\mathbb{I} - \boldsymbol{I}\otimes\boldsymbol{I}) : \nabla\boldsymbol{v}^\varepsilon\mathrm{d}x \qquad (1)\\
=&L(\boldsymbol{v}^\varepsilon) - \int_\Omega \boldsymbol{\tau}^\varepsilon : \boldsymbol{e}(\boldsymbol{v}^\varepsilon)(J^\varepsilon)^{-1}\mathrm{d}x \qquad\qquad \forall\boldsymbol{v}^\varepsilon \in V(\Omega)\ ,
\end{aligned}$$

where the total Kirchhoff stress is $\tau^\varepsilon_{ij} = -J^\varepsilon\delta_{ij}\ p^\varepsilon + \tau^{\mathrm{eff},\varepsilon}_{ij}$, and the Darcy flow in the dual-porous structure

$$\int_\Omega q^\varepsilon\,\mathrm{div}\Delta\boldsymbol{u}^\varepsilon\mathrm{d}x + \Delta t\int_\Omega \boldsymbol{K}^\varepsilon\cdot\nabla(p^\varepsilon + \Delta p^\varepsilon)\cdot\nabla q^\varepsilon\mathrm{d}x = 0\ , \quad \forall q^\varepsilon \in H^1(\Omega)\ . \qquad (2)$$

3 PERFUSION IN LARGE DEFORMING POROUS MEDIA

The material parameters in deformed configuration depend on the deformation gradient $F^\varepsilon_{ij}(x)$. Within the *updated Lagrangian formulation* we use the coordinates in the deformed reference configuration. At the microscopic scale, we establish the *local deformed configuration*: For $x \in \Omega$, let $\tilde{F}_{ij}(x,y)$, $y \in Y(x)$ be the two-scale limit of the deformation gradient associated with the mapping of the corresponding initial (undeformed) reference cell onto $Y(x)$. Then the local microscopic configuration at time t is the triplet

$$\mathcal{C}^{(t)}(x) = \{Y^{(t)}(x), \tilde{F}^{(t)}_{ij}(x,y), \tilde{p}^{(t)}(x,y) | y \in Y^{(t)}(x)\}\ . \qquad (3)$$

We assume that at any such configuration we may establish locally periodic material parameters. The permeability is defined using the dual porosity ansatz (for homogenization) characterized by ε^2 scaling of the permeability coefficients in the "matrix":

$$K^\varepsilon_{ij}(x) := \begin{cases} \tilde{K}^\alpha_{ij}(x,y) & y \in Y_\alpha,\ \alpha = 1,2\ , \\ \varepsilon^2\tilde{K}^3_{ij}(x,y) & y \in Y_3\ . \end{cases} \qquad (4)$$

Obviously, tensors $\tilde{K}_{ij}$ depend on the material deformation and should be modified from one time level to the next one using $\tilde{F}$, as will be discussed in Section 3.4.

Further we define tangent modulus $\tilde{\mathbb{A}} = (\tilde{A}_{ijkl})$ which depends on $\tilde{F}_{ij}$ (through $\tilde{D}^{\rm eff}_{ijkl}$ and $\tilde{\tau}^{\rm eff}_{jl}$) and on the interstitial fluid pressure $\tilde{p}$,

$$\tilde{A}_{ijkl}(x,y) = \left(\tilde{D}^{\rm eff}_{ijkl} + \tilde{\tau}^{\rm eff}_{jl}\delta_{ki} + \tilde{J}\tilde{p}\,(\delta_{jk}\delta_{il} - \delta_{ij}\delta_{kl})\right)\ , \tag{5}$$

where all quantities denoted by $\tilde{}$ are expressed for $x \in \Omega$ as locally periodic functions of $y \in Y(x)$.

3.1 Asymptotic expansions and corrector basis functions

The linearized problem can be treated using standard homogenization methods, such as the periodic unfolding, the two-scale convergence, or even the asymptotic expansion methods. The fluctuating fields $\Delta\boldsymbol{u}^\varepsilon$ and Δp^ε can be expressed by the following asymptotic expansions:

$$\begin{aligned}
\Delta\boldsymbol{u}^\varepsilon(x) &= \Delta\boldsymbol{u}^0(x) + \varepsilon\Delta\boldsymbol{u}^1(x,y) + O(\varepsilon^2)\ ,\\
\Delta p^\varepsilon(x) &= \sum_{\alpha=1,2}\chi_\alpha(y)\left(\Delta p^0_\alpha(x) + \varepsilon\Delta p^1_\alpha(x,y) + O(\varepsilon^2)\right) + \chi_3(y)\left(\Delta\tilde{p}_3(x,y) + O(\varepsilon)\right)\ ,
\end{aligned} \tag{6}$$

where $y \in Y(x)$, $\chi_s(y)$, $s = 1,2,3$ are characteristic functions of subdomains Y_s and all functions are Y-periodic in variable y. For this we established appropriate spaces:

$$\begin{aligned}
H^1_{\#}(Y_\alpha) &= \{v \in H^1(Y_\alpha)\ ,\ v \text{ is Y-periodic, } \int_{Y_\alpha} v = 0\}\ ,\\
H^1_{\#0}(Y_3) &= \{v \in H^1(Y_3)\ ,\ v \text{ is Y-periodic, } v = 0 \text{ on } \Gamma_\alpha\}\ .
\end{aligned} \tag{7}$$

The fluctuating parts of the displacements and pressures are expressed in terms of the corrector basis functions: we introduce Y-periodic functions $\boldsymbol{\omega}^{rs}, \boldsymbol{\omega}^\alpha, \boldsymbol{u}^P \in \mathbf{H}^1_{\#}(Y)$, $\pi^{rs}, p^P \in H^1_{\#0}(Y_3)$, $\pi^\alpha \in H^1_{\#}(Y_3)$, $\eta^k_\alpha \in H^1_{\#}(Y_\alpha)$,

$$\begin{aligned}
\Delta\boldsymbol{u}^1 &= \boldsymbol{\omega}^{rs}\partial^x_s\Delta u_r + \sum_{\alpha=1,2}\boldsymbol{\omega}^\alpha\Delta p^0_\alpha + \boldsymbol{u}^P\ ,\\
\Delta\tilde{p}_3 &= \pi^{rs}\partial^x_s\Delta u_r + \sum_{\alpha=1,2}\pi^\alpha\Delta p^0_\alpha + p^P\ ,\\
\Delta p^1_\alpha &= \eta^k_\alpha\partial^x_k\Delta p^0_\alpha\ ,\quad \alpha = 1,2\ ,
\end{aligned} \tag{8}$$

due to the "channel-matrix interface" conditions, $\pi^\alpha = \delta_{\alpha\beta}$ on Γ_β.

3.2 Local microscopic problems

We shall need the following notation to introduce the local microscopic problems:

$$a_Y(\boldsymbol{u},\,\boldsymbol{v}) = \int_Y \tilde{A}_{ijkl}\partial^y_l u_k\partial^y_j v_i\tilde{J}^{-1}{\rm d}y\ ,\qquad c_{Y_k}(p,\,q) = \int_{Y_k}(\tilde{\boldsymbol{K}}^k\cdot\nabla_y p)\cdot\nabla_y q\,{\rm d}y\ , \tag{9}$$

where $k = 1, 2, 3$. These bilinear forms depend on $\mathcal{C}^{(t)}(x)$ for $x \in \Omega$, see (3). The following microscopic problems must be solved:

1. Correctors w.r.t $\partial_s^x \Delta u_r$: find $(\boldsymbol{\omega}^{rs}, \pi^{rs}) \in \mathbf{H}^1_{\#}(Y) \times H^1_{\#0}(Y_3)$ satisfying

$$\begin{aligned} a_Y\left(\boldsymbol{\omega}^{rs} + \boldsymbol{\Pi}^{rs},\, \boldsymbol{v}\right) - \langle \pi^{rs},\, \mathrm{div}_y \boldsymbol{v}\rangle_{Y_3} = 0\,, \quad \forall \boldsymbol{v} \in \mathbf{H}^1_{\#}(Y) \\ \langle q,\, \mathrm{div}_y[\boldsymbol{\omega}^{rs} + \boldsymbol{\Pi}^{rs}]\rangle_{Y_3} + \Delta t\, c_{Y_3}\left(\pi^{rs},\, q\right) = 0\,, \quad \forall q \in H^1_{\#0}(Y_3)\,. \end{aligned} \tag{10}$$

2. Correctors w.r.t Δp_α: find $(\boldsymbol{\omega}^{\alpha}, \pi^{\alpha}) \in \mathbf{H}^1_{\#}(Y) \times H^1_{\#}(Y_3)$ satisfying

$$\begin{aligned} a_Y\left(\boldsymbol{\omega}^{\alpha},\, \boldsymbol{v}\right) - \langle \pi^{\alpha},\, \mathrm{div}_y \boldsymbol{v}\rangle_{Y_3} = \int_{\Gamma_\alpha} \boldsymbol{v}\cdot\boldsymbol{n}^{[\alpha]}\,\mathrm{dS}_y\,, \quad \forall \boldsymbol{v} \in \mathbf{H}^1_{\#}(Y) \\ \langle q,\, \mathrm{div}_y \boldsymbol{\omega}^{\alpha}\rangle_{Y_3} + \Delta t\, c_{Y_3}\left(\pi^{\alpha},\, q\right) = 0\,, \quad \forall q \in H^1_{\#0}(Y_3)\,, \\ \pi^{\alpha} = \delta_{\alpha\beta} \quad \text{a.e. on } \Gamma_\beta\,. \end{aligned} \tag{11}$$

3. Particular responses for given $\tilde{\boldsymbol{\tau}}$ and $\tilde{p}_3$: find $(\boldsymbol{u}^P, p^P) \in \mathbf{H}^1_{\#}(Y) \times H^1_{\#0}(Y_3)$ such that

$$\begin{aligned} a_Y\left(\boldsymbol{u}^P,\, \boldsymbol{v}\right) - \left\langle p^P,\, \mathrm{div}_y \boldsymbol{v}\right\rangle_{Y_3} = -\int_Y \tilde{\boldsymbol{\tau}} : e_y(\boldsymbol{v}) J^{-1}\mathrm{d}y\,, \quad \forall \boldsymbol{v} \in \mathbf{H}^1_{\#}(Y) \\ \left\langle q,\, \mathrm{div}_y \boldsymbol{u}^P\right\rangle_{Y_3} + \Delta t\, c_{Y_3}\left(p^P,\, q\right) = -\Delta t c_{Y_3}\left(\tilde{p}_3,\, q\right)\,, \quad \forall q \in H^1_{\#0}(Y_3)\,. \end{aligned} \tag{12}$$

4. In the channels $\alpha = 1, 2$ the corrector basis functions η^k_α, $k = 1, 2, 3$ satisfy:

$$c_{Y_\alpha}\left(\eta^k_\alpha + y_k,\, q\right) = 0\,, \quad \forall q \in H^1_{\#}(Y_\alpha)\,. \tag{13}$$

3.3 Macroscopic equations of the time increment

The microscopic responses introduced in (10)-(13) are employed to compute the homogenized coefficients $A_{ijkl}, B_{ij}, G^\beta_\alpha, C^\beta_{ij}, Q_{ij}$ and the stress S_{ij} which are now listed; they constitute the homogenized (macroscopic) equations:

- Effective visco-elastic modulus (involving time step Δt)

$$A_{ijkl} = \frac{1}{|Y|} a_Y\left(\boldsymbol{\omega}^{kl} + \boldsymbol{\Pi}^{kl},\, \boldsymbol{\omega}^{ij} + \boldsymbol{\Pi}^{ij}\right) + \Delta \frac{1}{|Y|} t c_{Y_3}\left(\pi^{kl},\, \pi^{ij}\right)\,. \tag{14}$$

- Effective Biot poroelasticity tensor

$$B^\alpha_{ij} = \frac{|Y_\alpha|}{|Y|}\delta_{ij} + \frac{1}{|Y|}\left\langle \pi^{\alpha},\, \mathrm{div}_y \boldsymbol{\Pi}^{ij}\right\rangle_{Y_3} - \frac{1}{|Y|} a_Y\left(\boldsymbol{\omega}^{\alpha},\, \boldsymbol{\Pi}^{ij}\right)\,, \tag{15}$$

- Averaged total Kirchhoff stress (in the updated reference configuration)

$$S_{ij} = \frac{1}{|Y|}\int_Y \boldsymbol{\tau}^{\rm tot} J^{-1}{\rm d}y \ . \tag{16}$$

- Effective retardation stress

$$Q_{ij} = \frac{1}{|Y|}\left[a_Y\left(\boldsymbol{u}^P,\, \boldsymbol{\Pi}^{ij}\right) - \left\langle p^P,\, {\rm div}_y \boldsymbol{\Pi}^{ij}\right\rangle_{Y_3}\right] \ , \tag{17}$$

- Effective channel permeability (of the sector β):

$$C^\beta_{ij} = \frac{1}{|Y|} c_{Y_\beta}\left(\pi^l + y_l,\, \pi^k + y_k\right) \ , \tag{18}$$

  where π^l solves the autonomous local problem (13).

- Perfusion coefficient – inter-sector permeability

$$G^\alpha_\beta = \frac{1}{|Y|}\int_{\Gamma_\alpha}\left(\boldsymbol{K}^3\cdot\nabla_y\pi^\beta\right)\cdot\boldsymbol{n}^{[3]}\,{\rm dS}_y + \frac{1}{\Delta t}\frac{1}{|Y|}\int_{\Gamma_\alpha}\boldsymbol{\omega}^\beta\cdot\boldsymbol{n}^{[\alpha]}\,{\rm dS}_y \ , \tag{19}$$

- Effective discharge due to deformation of the reference state (in the updated configuration)

$$g^{\rm eff}_\alpha = \frac{1}{|Y|}\int_{\Gamma_\alpha}\left(\boldsymbol{K}^3\cdot\nabla_y(p^P+\tilde{p}^3)\right)\cdot\boldsymbol{n}^{[3]}\,{\rm dS}_y + \frac{1}{\Delta t}\frac{1}{|Y|}\int_{\Gamma_\alpha}\boldsymbol{u}^P\cdot\boldsymbol{n}^{[\alpha]}\,{\rm dS}_y \ , \tag{20}$$

The macroscopic incremental problem is solved for displacements $\Delta\boldsymbol{u}^0 \in \boldsymbol{V}(\Omega)$ and pressures $\Delta p^0_\beta \in H^1(\Omega)$, $\beta = 1,2$ which satisfy the following equations:

Equilibrium equation:

$$\int_\Omega\left(A_{ijkl}\partial_l\Delta u^0_k - \sum_{\alpha=1,2}B^\alpha_{ij}\Delta p^0_\alpha\right)\partial_j v^0_i{\rm d}x = L(\boldsymbol{v}^0) - \int_\Omega\left(Q_{ij}+S_{ij}\right)\partial_j v^0_i{\rm d}x \tag{21}$$

for all $\boldsymbol{v}^0 \in \boldsymbol{V}_0(\Omega)$,

Diffusion equations: for $\beta = 1,2$,

$$\int_\Omega q^0_\beta\left(B^\beta_{ij}\partial_j\Delta u^0_i + \sum_{\alpha=1,2}G^\beta_\alpha\Delta p^0_\alpha\right){\rm d}x + \int_\Omega C^\beta_{kl}\partial_l(\Delta p^0_\beta + p^0_\beta)\,\partial_k q^0_\beta{\rm d}x = -\int_\Omega g^{\rm eff}_\beta q^0_\beta{\rm d}x \ , \tag{22}$$

for all $q^0_\beta \in H^1(\Omega)$. The homogenized problem involves two diffusion equations describing perfusions in the two compartments labeled by $\beta = 1,2$. This is the direct consequence of a) the dual porosity in Y_3 and b) topology of the decomposition of Y with Y_1 disconnected from Y_2.

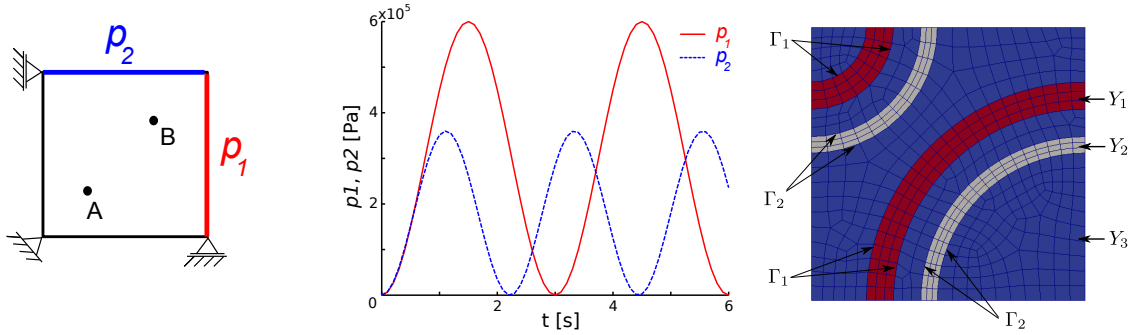

Figure 1: A macroscopic tissue 2D-sample with two labeled points (left), prescribed perfusion pressures $p_1(t)$, $p_2(t)$ as constant along two different faces (center) and the 2D microstructure (right).

3.4 Updating the local microstructures

We shall now explain the time stepping algorithm which is used to compute deformation of the medium and fluid redistribution in the pores at discrete time levels. At a certain time level (labeled by $^{(t)}$), the macroscopic configuration is represented by the triplet $\mathcal{M}^{(t)} \equiv \{\Omega^{(t)}, F_{ij}^{(t)}(x), p_\alpha^{(t)}(x) |\ x \in \Omega^{(t)}\}$ and the microscopic configurations are given by $\mathcal{C}^{(t)}(x)$, are given, see (3). The coupled micro-macro algorithm involves the following steps:

1. Given $\mathcal{M}^{(t)}$ and $\mathcal{C}^{(t)}(x)$ for $x \in \Omega^{(t)}$, solve the microscopic problems (10)-(13), then compute all the homogenized coefficients: $A_{ijkl}, B_{ij}, G_\alpha^\beta, C_{ij}^\beta, Q_{ij}$ and stress S_{ij}.
2. Compute Δu^0 and Δp_α^0 by solving (21)-(22).
3. Update macroscopic configuration $\mathcal{M}^{(t)} \to \mathcal{M}^{(t+\Delta t)}$, $\Omega^{(t+\Delta t)} := \Omega^{(t)} + \{\Delta u^0\}$.
4. For a.a. points $x \in \Omega^{(t)}$ update $\mathcal{C}^{(t)}(x) \to \mathcal{C}^{(t+\Delta t)}(\boldsymbol{x} + \Delta \boldsymbol{u}^0(x))$; this step consists in:

(a) Updating deformation and deformed domain

$$
\begin{aligned}
\Delta u_i^* &:= (\delta_{ir}\delta_{js} y_j + \omega_i^{rs})\ \partial_s^x \Delta u_r^0(x) + \sum_{\alpha=1,2} \omega_i^\alpha \Delta p_\alpha^0(x) + u_i^P\ , \\
f_{ij} &:= \delta_{ij} + \partial_j^y \Delta u_i^*\ , \\
F_{ij} &:= f_{ik} F_{kj}\ , \\
Y^{(t+\Delta t)}(x) &:= Y^{(t)}(x) + \{\Delta \boldsymbol{u}^*\}\ ,
\end{aligned}
\tag{23}
$$

where F_{ij} is the total deformation gradient at the microscopic level.

(b) Updating pressure fields for $x \in \Omega^{(t)}$:

- update the channel pressures:

$$
\begin{aligned}
\Delta \tilde{p}_\alpha &= \Delta p_\alpha^0 + \varepsilon_0 \eta_\alpha^k \partial_k^x \Delta p_\alpha^0\ , \\
\tilde{p}_\alpha^{(t+\Delta t)} &= \tilde{p}_\alpha^{(t)} + \Delta \tilde{p}_\alpha\ ,
\end{aligned}
\tag{24}
$$

where $\varepsilon_0 > 0$ is a given scale of the microstructure.

- update the dual porosity pressure:

$$\Delta\tilde{p}_3 = \pi^{rs}\partial_s^x \Delta u_r^0(x) + \sum_{\alpha=1,2} \pi^\alpha \Delta p_\alpha^0(x) + p^P \,, \qquad \tilde{p}_3^{(t+\Delta t)} = \tilde{p}_3^{(t)} + \Delta\tilde{p}_3 \,. \tag{25}$$

Now $\mathcal{C}^{(t+\Delta t)}(\boldsymbol{x} + \Delta\boldsymbol{u}^0(x))$ for $x \in \Omega^{(t)}$ is constituted by $(23)_{3,4}$ and $(25)_2$.

5. Stop, when maximum time is reached, or return to step 1 with $t := t + \Delta t$.

Material parameters depend on local strain and stress, in general, so they are defined in the updated local microscopic configuration $\mathcal{C}^{(t)}(x)$.

domain	shear modulus μ [Pa]	permeability coef. c_{perm} [m^2/(Pa·s)]
matrix Y_3	1×10^6	1×10^{-9}
channel Y_1	6×10^5	1×10^{-8}
channel Y_2	4×10^5	2×10^{-8}

Table 1: Material parameters at the microscale; the permeability is isotropic, $K_{ij}^k = c_{perm}^k \delta_{ij}$, in all subdomains Y_k, $k = 1, 2, 3$. Thus, for scale $\varepsilon_0 = 0.01$, the matrix permeability is $c_{perm}^{\varepsilon_0,3} = \varepsilon_0^2 c_{perm}^3 = 10^{-13}$.

4 EXAMPLE – PERFUSION IN 2D

The two-scale model of the perfusion is now implemented in the in-house developed FE code **SfePy** , [1] which was developed using some techniques already tested on problems of large deforming solids, as reported in papers [5, 3]. Here we report a simple simulation in 2D, see Tab. 1 for the material parameters used at the microscopic scale. The specimen is loaded just by two perfusion pressures varying in time and supported at three nodes as illustrated in Fig. 1. The microstructure is (initially) periodic with the reference cell Y containing two systems of curved channels. The material parameters defining the microscopic problems are listed in Tab. 1; note that the "real permeability" in the dual porosity Y_3 is 10^{-4} times smaller, being the ε_0^2-multiple, where $\varepsilon_0 = 0.01$ in our situation. (We used nonphysiological values for testing the model on "non-realistic" 2D examples; in this case the elasticity in the channels must be taken larger.)

The simulation was performed with the time increment $\Delta t = 0.2\,\mathrm{s}$, which is sufficiently large to use the Q1-Q1 finite element discretization for both the displacements and the pressures (note that too small step Δt induces "numerical incompressibility" and another mixed element would have to be used, like Q2-Q1). The microstructures are updated for each Gauss point of the macroscopic domain (discretized using 16 elements, i.e. $16\times4 = 64$ microstructures updated at each time level, in our example), 30 time levels were evaluated. The approximate wall-time of the simulation on one single-processor PC was ≈30 minutes.

Some numerical illustrations are displayed in Figs. 2-4. The tissue perfusion at a macroscopic position $x \in \Omega$ can be deduced form the pressure difference, see Fig. 3.

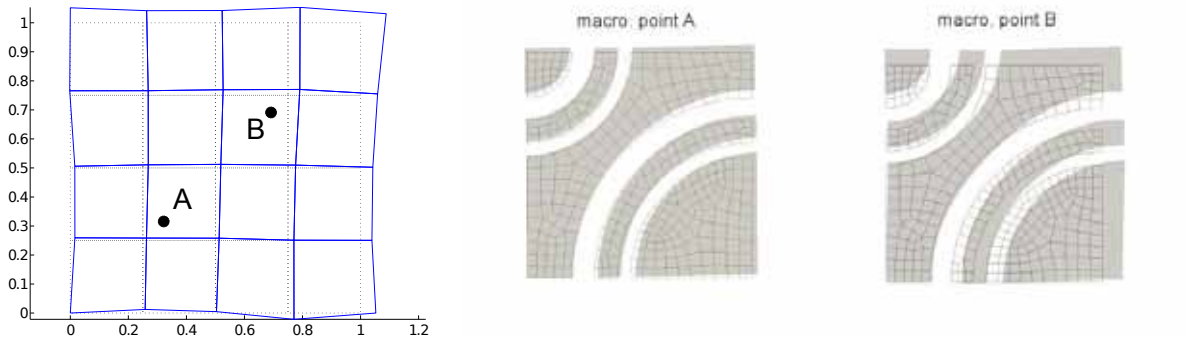

Figure 2: Deformation of the macroscopic specimen (left) and the local deformed configurations $Y(x^A)$ and $Y(x^B)$ for the labeled positions. We recall the fixed corner points of the specimen, see Fig. 1.

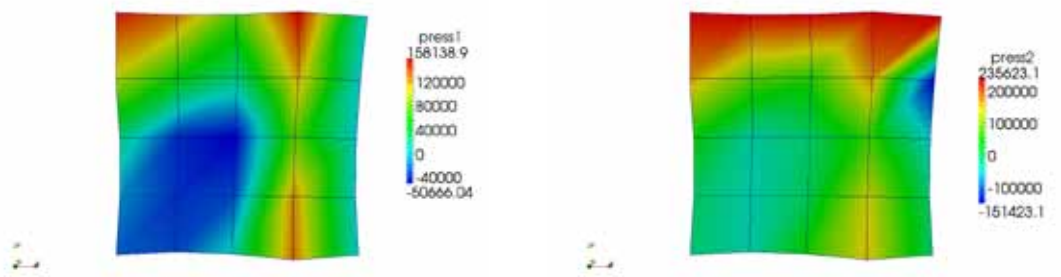

Figure 3: Macroscopic distribution of two perfusion pressures p_1 and p_2 in the deformed domain Ω (evaluated at the final time of the simulation).

5 CONCLUSIONS

We combined the double-porous media approach employed in homogenization of the linear models [6, 7] with the large deformation description defined using the updated Lagrangian formulation [5]. The fluid redistribution at the macroscopic scale between the two channel systems is proportional to the difference of these pressures. At the microscopic scale the fluid flows can be recovered using the corrector functions.

The fluid-solid interactions governed by the poroelasticity model of Biot are responsible for viscoelastic effects observed at the macroscopic scale, which are represented in the global macroscopic homogenized model by the retardation stress Q_{ij}. It is worth noting that apart of the homogenized permeabilities C_{ij}^{β}, all the other homogenized coefficients of the incremental problem depend on the time step Δt by virtue of the microscopic problems (10)-(12). In the linear case, the homogenized model involves the homogenized kernels of the time-convolution integrals, inducing the fading memory effects [6, 7].

Some effective strategy is required to tackle the number of the microscopic problems that have to be solved at each time step to recover the effective (homogenized) material constants. In [3] we have presented a parallel micro-macro algorithm, attempting to

address this issue.

The numerical simulations will be extended for 3D problems and some more realistic data will be used to validate the homogenized model. Since experimental results are unavailable, the model and the two-scale computational approach will be verified using a "non-homogenized" model (the reference model) based on a direct FE discretization of the system (1)-(2), whereby the geometry will be extremely complex (even for some higher scale parameters ε_0). To obtain a numerical solution for the reference model, some domain-decomposition techniques will be employed, including parallel algorithms.

Acknowledgment This research is supported by research projects GACR 106/09/0740 and MSM 4977751303 of the Czech Republic.

REFERENCES

[1] Cimrman, R. etal, "Software, finite element code and applications", SfePy home page, http://sfepy.kme.zcu.cz,http://sfepy.org, (2009).

[2] Cioranescu, D. and Donato, P. *An Introduction to Homogenization*, Oxford Lecture Series in Mathematics and its Applications 17, Oxford University Press, Oxford, (1999).

[3] Rohan, E., Cimrman, R. and Lukeš, V. Numerical modelling and homogenized constitutive law of large deforming fluid saturated heterogeneous solids. *Computers and Structures* 84 (2006), 1095-1114.

[4] Rohan, E. and Lukeš, V. Homogenization of perfusion in large-deforming medium using the Updated Lagrangean Formulation. *In Proc. 7th Int. Conf. ECT 2010*, Saxe-Coburg Publ., Edinburgh, Paper 83 (2010).

[5] Rohan, E. Modelling large deformation induced microflow in soft biological tissues. *Theor. and Comp. Fluid Dynamics* 20 (2006), 251–276.

[6] Rohan, E. and Cimrman, R. Multiscale FE simulation of diffusion-deformation processes in homogenized dual-porous media. *Math. and Comp. Simul.*, In Press (2011)

[7] Rohan, E. and Cimrman, R. Two-scale modelling of tissue perfusion problem using homogenization of dual prous media. *Int. Jour. Multiscale Comput. Eng.*, 8 (2010), 81-102.

[8] Takano, N., Ohnishi, Y., Zako, M. and Nishiyabu, N. The formulation of homogenization method applied to large deformation problem for composite materials, *International Journal of Solids and Structures* 37, (2000), 6517-6535.

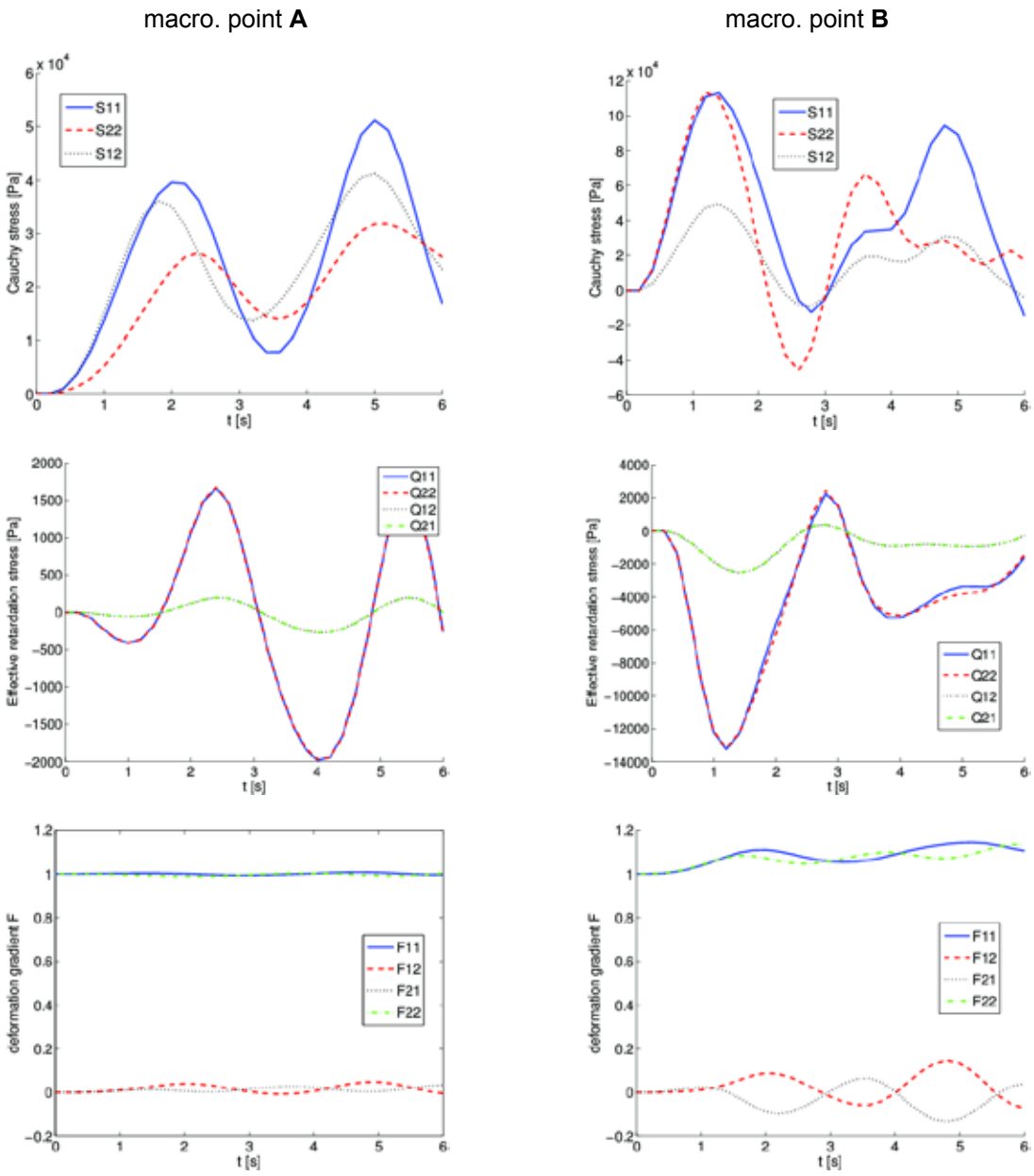

Figure 4: Macroscopic quantities S_{ij}, Q_{ij} and F_{ij} evaluated in time at points A (left column) and B (right column) of the macroscopic specimen.

XI International Conference on Computational Plasticity. Fundamentals and Applications
COMPLAS XI
E. Oñate, D.R.J. Owen, D. Peric and B. Suárez (Eds)

DETERMINING THE CONSTITUTIVE PARAMETERS OF THE HUMAN FEMORAL VEIN IN SPECIFIC PATIENTS

G. FORTUNY[*], B. HERRERA[*], F. MARIMÓN[+] AND J. MARCÉ[†]

[*] Department of Computer Engineering and Mathematics
Universitat Rovira i Virgili
Av/ Universitat 1, 43204 Reus, Spain
e-mail: gerard.fortuny@urv.cat, http://deim.urv.cat/~gerard.fortuny/

[+]Department of Medicine and Surgery
Universitat Rovira i Virgili
C/ Sant Llorenç 21, 43201 Reus, Spain

[†]Department of Strength of Materials and Structural Engineering,
Universitat Politècnica de Catalunya,
C/ Colom 11, 08222 Terrassa, Spain
e-mail: jordi.marce@upc.edu

Key words: Femoral vein; Constitutive equations; Venous live tissue; Human; Parameter identification.

Abstract. This study suggests a method for computing the constitutive model for veins in vivo from clinically registered ultrasound images. The vein is modelled as a hyperelastic, incompressible, thin-walled cylinder and the membrane stresses are computed using strain energy. The material parameters are determined by tuning the membrane stress to the stress obtained by enforcing global equilibrium.
In addition to the mechanical model, the study also suggests a preconditioning of the pressure-radius signal. The preconditioning computes an average pressure-radius cycle from all consecutive cycles in the registration and removes, or reduces undesirable disturbances. In order to overcome this problem, an approach is proposed that allows constitutive equations to be determined from clinical data by means of reasonable assumptions regarding in situ configurations and stress states of vein walls. The approach is based on a two-dimensional Fung-type stored-energy function that captures the characteristic nonlinear and anisotropic responses of veins.

1 INTRODUCTION

4.5% of the population is at risk of suffering a venous thromboembolism disease, with an approximate mortality rate of 11% ([2, 3]). Our general objective consists of studying a

serious pathology that has important consequences: deep vein thrombosis (DVT). The problems involved in modeling venous tissue have been largely ignored by biomechanics researchers, most of whose efforts have instead focused on determining constitutive models of the arterial tissue ([7, 11]). Venous and arterial walls have a similar structure and composition, the main difference between their respective walls being the thickness and fiber orientation of the medial zone.

In this study, we determine a constitutive model of the venous wall tissue in its real life location inside the human body. In the future, we intend to study diseased venous walls and their relation to the origins of DVP. Some studies have modulated the mechanical properties of venous walls ([1, 9]), although these studies have only looked at these properties in laboratory conditions and in non-live tissue.

Constitutive equations can be determined from experimental data regarding the diameter of a vessel segment that is subject to internal pressure and external axial force, and the load-free reference geometry of the vessel segment, including the wall thickness.
In the present study, if the membrane stresses are to be computed, two assumptions need to be made to overcome the limitations of the clinical data ([10]),
(i) The in vivo conditions, the axial stretch of the vessel and the axial external force are constant and independent from internal pressure
(ii) The ratio between the axial and circumferential stress is known at one internal pressure P.

2. METHODS

2.1. Original Data

To carry out the present study, we have used images captured by projecting ultrasound in real time, which is a typical method for clinically registering the pressure and radius. The ultrasound probe is lineal to 4.5 MHz and uses the MyLab Xview 70 high resolution image projection system (Esaote, Genoa, Italy). This new-generation ultrasound tool eliminates particles whilst preserving the information needed for diagnosis. We have used a time sequence of 10 seconds to register in a file of a healthy 40 year-old person. With this observation, we also obtain the internal pressure P.

2.2. Theoretical framework

In general, veins and arteries have similar walls and a structure in three distinct layers: the *intima*, the *media* and the *adventitia*. The media is the middle layer of the vein and consists of a complex three-dimensional network of smooth muscle cells, and elastin and collagen fibrils ([4]). The mechanical properties of venous and arterial walls are different; for example, the pulsating behaviour of the arterial walls is absent from the venous walls. In venous walls the media layer is thinner than the arterial wall. Also, the fibre orientation of venous walls is not clear. Consequently, we use a non-fibre oriented model to approximate the constitutive equation of the venous wall.

In the femoral vein, the variation range of the pressure–inner diameter and the wall thickness at mean pressure is taken from clinical data. A two-dimensional (membrane) model describing the biaxial (i.e. circumferential and axial) response is to be determined. Employing a least-squares approach this can be achieved by minimizing the sum of the squared errors W:

$$W = \sum_i \left[\left(\sigma_{\theta\theta}^{\mathrm{mod}} - \sigma_{\theta\theta} \right)_i^2 + \left(\sigma_{zz}^{\mathrm{mod}} - \sigma_{zz} \right)_i^2 \right] \tag{1}$$

In Eq.(1), the index i denotes the ith of the n data points, $\sigma_{\theta\theta}^{\mathrm{mod}}$ and $\sigma_{zz}^{\mathrm{mod}}$ are the circumferential and axial Cauchy stresses predicted by the model, and $\sigma_{\theta\theta}$ and σ_{zz} are the mean circumferential and axial Cauchy stresses of the wall computed directly from experimental data by enforcing equilibrium.

Following the theory of hyperelasticity ([6]) the principal model stresses:

$$\sigma_{\theta\theta}^{\mathrm{mod}} = \lambda_\theta \frac{\partial \psi}{\partial \lambda_\theta}; \qquad \sigma_{zz}^{\mathrm{mod}} = \lambda_z \frac{\partial \psi}{\partial \lambda_z} \tag{2}$$

may be derived from the two-dimensional SEF $\psi = \psi(\lambda_\theta, \lambda_z)$ and can be expressed in terms of the principal stretches λ_θ and λ_z associated with the circumferential and axial directions, respectively. The circumferential and axial stretches are defined as $\lambda_\theta = d_m / D_m$ and $\lambda_z = z / Z$; whereby d_m and D_m denote the actual and the referential (unloaded) mid-wall diameter of the vessel, and z and Z denote the actual and the referential length of a vessel segment. Note that Eq. (2) is only valid if the stress tensor and the strain tensor are coaxial. This is the case in the present study, which is restricted to axisymmetric geometry and boundary conditions. For ψ a two-dimensional Fung-type SEF proposed by Von Maltzahn et al.(1984) is used as follows:

$$\psi = \frac{C}{2}(e^Q - 1), \tag{3}$$

where

$$Q = c_{\theta\theta} E_{\theta\theta}^2 + 2c_{\theta z} E_{\theta\theta} E_{zz} + c_{zz} E_{zz}^2 \tag{4}$$

The SEF ψ incorporates four constitutive parameters, C, $c_{\theta\theta}$, $c_{\theta z}$ and c_{zz}. The circumferential and axial Green–Lagrange strains $E_{\theta\theta}$ and E_{zz} can be expressed in terms of the circumferential and axial stretches, that is, $E_{\theta\theta} = \frac{1}{2}(\lambda_\theta^2 - 1)$ and $E_{zz} = \frac{1}{2}(\lambda_z^2 - 1)$, respectively. Fung-type SEFs have been used successfully to model the mechanical responses of numerous veins from various species and anatomical sites. Substituting Eq.(4) for Eq.(2) leads to explicit expressions for $\sigma_{\theta\theta}^{\text{mod}}$ and σ_{zz}^{mod} as functions of the principal stretches λ_θ, λ_z and the constitutive parameters C, $c_{\theta\theta}$, $c_{\theta z}$ and c_{zz}. Note that ψ is convex if and only if $c_{\theta z}^2 < c_{\theta\theta} c_{zz}$, $c_{\theta\theta} > 0$ and $c_{zz} > 0$ (for a derivation see [6]).

The circumferential and axial mean wall stress $\sigma_{\theta\theta}$ and σ_{zz} can be determined by enforcing global equilibrium. Thus,

$$\sigma_{\theta\theta} = \frac{rP}{h},\ \sigma_{zz} = \frac{r^2 P\pi + F}{h(2r+h)\pi} \tag{5}$$

where h is the actual wall thickness, r is the actual inner radius, P is the transmural pressure and F is the external axial force. Substituting these expressions in $k = \sigma_{zz}/\sigma_{\theta\theta}$ the external axial force F can be determined explicitly as:

$$F = r^2 P\pi(2k-1) + APk \tag{6}$$

where, according to assumption (ii), the stress ratio k is known for a particular pressure P associated with the actual radio r and $A = rh\pi$.

2.3. Calculus

The constitutive parameters C, $c_{\theta\theta}$, $c_{\theta z}$ and c_{zz} have to be determined as variables from a nonlinear zero function in order to determine the minimum error function. We consider the function W as the function of error, we want to obtain the minimum of this function or the zero of this function's derivative. To do so we will use the Levenberg-Marquardt method for the non-linear least squares problems [8]. Thus, we will considerer C, $c_{\theta\theta}$, $c_{\theta z}$ and c_{zz} as variables in the function W, that is $W(C, c_{\theta\theta}, c_{\theta z}, c_{zz})$, so that its minimum will be found in values that verify that $\nabla W(C, c_{\theta\theta}, c_{\theta z}, c_{zz}) = 0$
that is:

$$\begin{aligned}
&\frac{\partial W}{\partial C}(C, c_{\theta\theta}, c_{\theta z}, c_{zz}) = 0 \\
&\frac{\partial W}{\partial c_{\theta\theta}}(C, c_{\theta\theta}, c_{\theta z}, c_{zz}) = 0 \\
&\frac{\partial W}{\partial c_{\theta z}}(C, c_{\theta\theta}, c_{\theta z}, c_{zz}) = 0 \\
&\frac{\partial W}{\partial c_{zz}}(C, c_{\theta\theta}, c_{\theta z}, c_{zz}) = 0
\end{aligned} \tag{7}$$

where $\partial W / \partial x$ are the partial derivative of function W by the variable x. Now we need to apply the Newton-Raphson method to the function ∇W in dimension 4:

$$\nabla W'(X^{(k)})(X^{(k+1)} - X^{(k)}) + \nabla W(X^{(k)}) = 0 \qquad k \geq 1 \tag{8}$$

where $\nabla W'$ is the Jacobian 4×4 matrix. We take $X^{(0)} = (C^0, c^0_{\theta\theta}, c^0_{\theta z}, c^0_{zz})$ where $(C^0, c^0_{\theta\theta}, c^0_{\theta z}, c^0_{zz})$ are the values obtained in [10] for arteries. This is a linear system of equations for $X^{(k+1)}$, and given that $\nabla W'$ is a non-singular matrix, it can be solved using a normal lineal system method.
A simple verification shows the local minimum property of the value obtained (we apply a small perturbation to our final value).

3. RESULTS

We obtain values for the constitutive parameters C, $c_{\theta\theta}$, $c_{\theta z}$ and c_{zz}; and (using the constitutive model) we can obtain information on the unloaded referential geometry (inner diameter *D*) and the in situ boundary force *F* for each observation (see Table 1).

Table 1: Computed inner diameter D; external axial force F; constitutive parameters C, $c_{\theta\theta}$, $c_{\theta z}$ and c_{zz}.

	D(mm)	**F(N)**	**C(kPa)**	$c_{\theta\theta}$	$c_{\theta z}$	c_{zz}
Femoral Vein	8.8	1.14	14.37	2.08	1.39	1.01

With the specified constitutive parameters summarized in Table 1, the SEFs turn out to be convex, which is a crucial property that ensures mechanically and mathematically reliable behaviour. Specific constitutive equations are obtained by substituting the constitutive parameters in Eq.(2). The relations between the pressure and the inner diameter computed from the constitutive models are approximately the same as the observed values (Fig.1). The biaxial response (Fig.2) shows the anisotropy and nonlinearity between the axial and circumferential stretches.

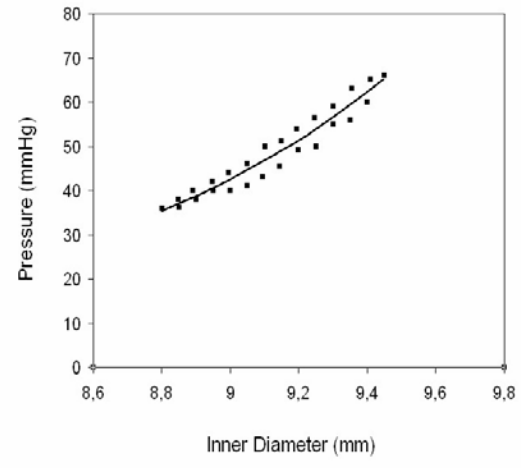

Figure 1: Pressure–inner diameter cycles (marked by squares) from the values for the femoral vein. The solid line indicates the pressure–inner diameter relation predicted by the constitutive model.

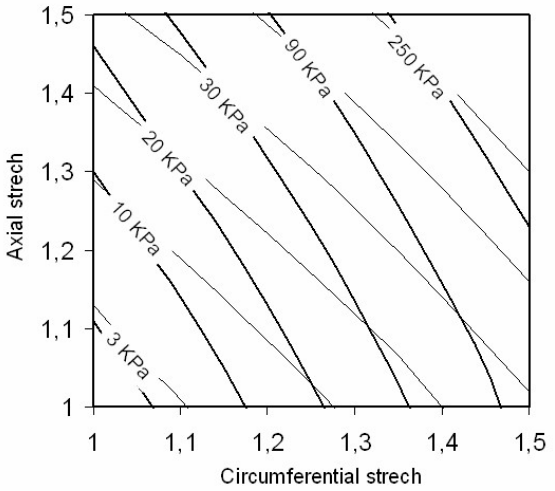

Figure 2: Circumferential (thick lines) and axial (thin lines) Cauchy stress contours in the (mid-wall) stretch plane for the femoral vein from a non pathologic subject.

4. CONCLUSIONS

This is the first attempt to provide constitutive equations for human veins and the femoral vein in particular. The mechanical behaviour of human arteries has already been described, but this is not the case for human veins. Consequently, we have used the results obtained in [9] to develop a new constitutive model for human veins.

In this study we have tried to show a simple method for determining constitutive parameters for the biaxial stretch states of human vein walls (Fig.2) in a specific subject (Fig.1).

The proposed approach is based on providing information about the axial values (axial stretch, external axial force and axial stress) that is not contained in clinical data. Evaluating the predictive capability of constitutive equations requires changes in the boundary conditions, that is, in the pressure and stretches. However, it is possible to alter the boundary conditions in a tolerable way. Obviously, future research in this area could compare several constitutive model approximations in various subjects, each one from a different risk population. Even so, the particular conditions for a specific patient can change; blood pressure can be elevated through exercise or diminished by pharmacological methods. The specificity of this method allows a specific model for each patient.

These models try to characterize the nonlinear anisotropic material responses and the in-situ boundary conditions, because the original data are measurements of stretches in-situ. This fact will promote future research into potential thrombosis risk factors and parameters for monitoring pharmacological therapies, etc. Despite inherent limitations the present approach demonstrates a reasonable way to determine constitutive equations for human veins that would otherwise not be available.

5. ACKNOWLEDGMENTS

Support was provided by Universitat Rovira i Virgili grant: AIRE2010-01

REFERENCES

[1] Ackroyd JS, Pattison M, Browse NL. 1985. A study of the mechanical properties of fresh and preserved human femoral vein wall and valve cusps. Br J Surg **72**, 117-19.

[2] Cohen AT, Agnelli G, Anderson FA, Arcelus JI, Bergqvist D, Brecht JG, Greer IA, Heit JA, Hutchinson JL, Kakkar AK, Mottier D, Oger E, Samama MM, Spannagl M 2007. Venous thromboembolism (VTE) in Europe. The number of VTE events and associated morbidity and mortality. Thromb Haemost **98(4)**, 756-64.

[3] Cushman M, Tsai AW, White RH, Heckbert SR, Rosamond WD, Enright P, Folsom AR. 2004. Deep vein thrombosis and pulmonary embolism in two cohorts: the longitudinal investigation of thromboembolism etiology. Am J Med **117(1)**,19-25.

[4] Fawcett D.W. (Bloom Fawcett), 1995, Tratado de Histologia. McGraw-Hill Interamericana, Madrid 438-443

[5] Fung, Y.C., Fronek, K., Patitucci, P., 1979. Pseudoelasticity of arteries and the choice of its mathematical expression.Am J Physiol **237 (5)**, H620–631.

[6] Holzapfel, G.A., 2000. Nonlinear Solid Mechanics, A Continuum Approach for Engineering.Wiley, Chichester.

[7] Holzapfel, G.A., Gasser, T.C., Ogden, R.W., 2000. A new constitutive framework for arterial wall mechanics and a comparative study of material models.J Elasticity **61**, 1–48.

[8] Marquardt D. 1963. An algorithm for least squares estimation on nonlinear parameters. SIAM. J.Appl. Math. **11**, 431-441

[9] Opgaard OS, Edvinsson L. 1997. Mechanical properties and effects of sympathetic co-transmitters on human coronary arteries and veins. Basic Res Cardiol **92**, 168-80.

[10] Schulze-Bauer C.A.J., Holzapfel G.A. 2003 Determination of constitutive equations for human arteries from clinical data. Journal of Biomechanics **36**, 165–169

[11] Stålhand J. 2009. Determination of human arterial wall parameters from clinical data. Biomech Model Mechanobiol **8**, 141–148

[12] von Maltzahn, W.W., Warriyar, R.G., Keitzer, W.F., 1984. Experimental measurements of elastic properties of media and adventitia of bovine carotid arteries. J Biomech **17 (11)**, 839–847.

XI International Conference on Computational Plasticity. Fundamentals and Applications
COMPLAS XI
E. Oñate, D.R.J. Owen, D. Peric and B. Suárez (Eds)

INTERACTIONS BETWEEN SELF PENETRATING NEURAL INTERFACES AND PERIPHERAL NERVES

PIER NICOLA SERGI[*], SILVESTRO MICERA [#,*]

[*]BioRobotics Institute, Scuola Superiore Sant'Anna Polo Sant'Anna Valdera, 56025 Pontedera,Italy
e-mail: p.sergi@sssup.it

[#] Institute for Automation, Swiss Federal Institute of Technology, 8092 Zürich, Switzerland
[*]BioRobotics Institute, Scuola Superiore Sant'Anna Polo Sant'Anna Valdera, 56025 Pontedera, Italy
e-mails: micera@control.ee.ethz.ch, micera@sssup.it

Key words: Biomechanics, neural interfaces, neuroprostheses, buckling, self penetrating electrodes.

Abstract: This work provides a simple framework to optimize the design of self penetrating neural interfaces. First, an assessment of interactions between electrodes and peripheral nerves is provided and related to the instantaneous elasticity of the tissue. Then, the elastic instability of electrodes is considered, because it is the main cause of failure of implants. The connection between the previous two sections, integrated with an assessment of a safety coefficient for in-vivo implants, allows to predict some important parameters of a reliable electrode: its maximum slenderness ratio (SR) and the minimum Young modulus of its main shaft.

1 INTRODUCTION

The use of neural interfaces with the peripheral nervous tissue (PNT) allows to develop neuroprosthetic devices and hybrid bionic systems [1]. These devices can create an intimate and selective contact with the PNT, recording and stimulating from different fascicles into the nerves to restore the efferent and afferent neural pathways in an effective way. Several research groups started investigating the possibility of develop neural interfaces characterized by self penetrating electrodes vertically or longitudinally inserted into the tissue [2,3]. This approach seems to be promising because a quite low invasiveness is combined with a quite good selectivity. Unfortunately, the high slenderness ratio of these structure can make difficult their insertion into the PNT: the success of this task is strongly dependent from the biomechanical properties of the tissue, the geometry and the mechanical characteristics of the neural interface. Indeed, while a stiff electrode is necessary to enter the tissue, it could increase both the invasiveness and the probability of provoking damages into the nerve. For this reason, the design of effective and low-invasive self penetrating interfaces is a crucial task which requires an integrate design accounting for the PNT biomechanics influencing the interactions with the electrode structures. In the first part of this work a macroscopic approach is used to study the interactions between peripheral nerves and structure with high slenderness ratio, in particular self penetrating electrodes. Simple mathematical models are used to quantify these interactions as explicitly depending from the tissue mechanics [4].

These models are able to account for experimental studies [5,6]. In the second part of this work, the previously achieved framework is used to improve and integrate the design of self penetrating [7] (e.g. needle-like and shaft) neural interfaces as far as the choice of structural materials, giving elements to optimize the geometry and to maximize the insertion ability.

2 METHODS

2.1 Simple assessment of superficial interactions between electrodes and peripheral nerves

Interactions between electrodes and external surface of the peripheral nerves are quite complex. In this work the attention will be focused only on the initial phase of contact between the electrode tip and the tissue. Moreover, the velocity of the local dimpling of the tissue under the electrode tip is assumed to have a characteristic time considerably shorter than the relaxation time of the tissue: this allows to neglect viscoelastic effects. With the previous assumptions, the tip force arising during the initial phase can be generally modelled using Equation (1):

$$F(z) = f(\alpha)M(E,z)\wp[n,z,g(\rho)] \tag{1}$$

where z is the dimpling of the tissue (which equals the electrode tip displacement), $f(\alpha)$ is a function of the half opening angle of the tip, $M(E,z)$ is a function of the Young modulus of nerve and z, $\wp[n,z,g(\rho)]$ is a polynomial of n degree in z and $g(\rho)$, finally $g(\rho)$ is a function the radius of curvature of the tip. To simplify the writing of Equation (1) some assumptions can be reasonably done. First, $f(\alpha)$ is constant for a selected type of electrode. Then, in spite of $M(E,z)$ could be non linear with z [4], it can be expanded in Taylor series around the point $z=0$ leading to $M(E,z)=E+o(E,z)$. Finally, $\wp[n,z,g(\rho)]=\wp[2,z,g(\rho)]=z^2+k_2 z$ [8], where $k_2 \in \Re$ is a constant accounting for the real geometry. As a consequence, Equation (1) can be approximated with:

$$F(z) \approx k_1 E(z^2 + k_2 z) \tag{1.2}$$

Equation (1.2) models the first phase of interaction as an indentation, and can assess the instantaneous elasticity of the external layer of peripheral nerves starting from experimental data [5,6].

2.2 Basic elements of rational design of self -penetrating electrodes

Self-penetrating electrodes has to bear compressive forces arising in dimpling of external layer of nerves. Since the main macroscopic cause of implantation failure is elastic instability, the investigation of buckling of needle-like and shaft structures is crucial to their effective design. To this aim, since both the approaching velocity is low (for careful

implantations ~ several mm/min), and the mass of the electrode is small, inertial effects can be neglected and the analysis can be performed in the quasi-static buckling framework. Moreover, since the main shaft is considerably longer than the tip high, the analysis will be focused on the first mode of buckling of the global structure. For slender electrodes the first buckling load can be generally written as [7]:

$$P_{cr} = \frac{\psi^2 E_n J}{(\omega L)^2} \tag{2}$$

where J is the minimum second area moment of the cross section, E_n is the Young modulus of the electrode material, ψ is the Legendre elliptic integral of the first kind, L the length of electrode, and ω the end-condition constant. In this case, since also small deflections result in a failure of implantation we have $\psi \to \pi$ and $\omega \to 0.7 \div 2$, depending from the boundary conditions (pin-fixed and free-fixed). In particular, introducing in Equation (2) the slenderness ratios $S_r = L/r$ for a circular shaft, and $S_h = L/h$ for a prismatic one (where h is the electrode depth), and dividing P_{cr} for the cross sectional area of the main shaft, it follows:

$$\sigma_{cr} = \frac{\pi^2 E_n}{\gamma_r S_r^2} \tag{2.1.1}$$

$$\sigma_{cr} = \frac{\pi^2 E_n}{\gamma_h S_h^2} \tag{2.1.2}$$

where Equations (2.1.1) and (2.1.2) holds respectively for circular and prismatic sections, and γ_r=1.96÷16 and γ_h=5.88÷48 respectively for pin-fixed and free-fixed boundary conditions. Therefore, the structural condition for which the main structure can bear the maximum dimpling force is:

$$P_{cr} \geq SF_{global} F(z_0) \tag{3}$$

where SF_{global} is the global safety factor that will be assessed in the next paragraph, and z_0 is the dimpling of the nerve when the piercing of the external layer happens. From Equations (1.2), (2.1), (2.1.1-2) and (3), an approximation of the maximum slenderness ratio for low z_0 can be written as:

$$S_r(m, k_2, k_1, z_0, X, SF_{global}, A, E, E_n) \approx \pi \frac{g(m, k_2, z_0)}{h\left(\frac{2m+1}{2}, k_2\right)} \sqrt{\frac{E_n A}{X SF_{global} k_1 E z_0}} \tag{4}$$

where X stands for γ_r or γ_h respectively for circular or shaft electrodes, $g(m,k_2,z_0)$ is a polynomial of m degree in k_2 and z_0, and $h\left(\frac{2m+1}{2},k_2\right)$ is a polynomial in k_2. The more m increases, the more S_r approximates the exact value of the minimum slenderness ratio for any value of local dimpling. As illustration of the case m=5, the values of $\wp(m,k_2,z_0)$ are listed and plotted below:

$$g(5,k_2,z_0) = 63z_0^5 - 70k_2z_0^4 + 80k_2^2z_0^3 - 96k_2^3z_0^2 + 128k_2^4z_0 - 256k_2^5$$
$$h(11/2,k_2) = 256k_2^{11/2} \tag{5.1}$$

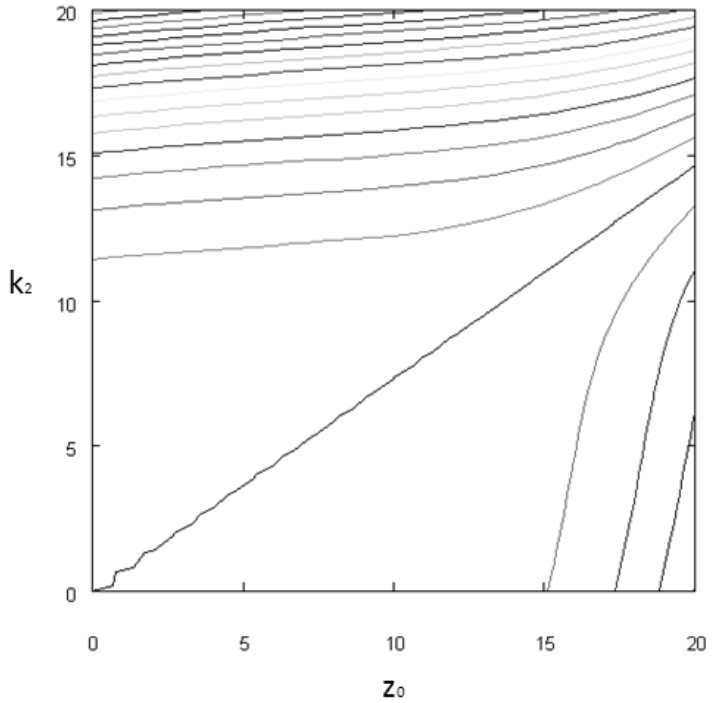

Figure 1: Contour plot of $g(5,k_2,z_0)$

2.3 Safety coefficient for in vivo insertions of self- penetrating electrodes

Self penetrating electrodes have to be implanted in living peripheral nerves. As a consequence, at least in this final phase, the implantation has to assure good performances and reliability in time without ethically unacceptable complications (sources of pain, need of several surgical operations, etc.). Moreover, the surgical procedure of insertion in living peripheral nerves has to be totally safe for the patients, but also without any risk of damages for the electrodes. Unfortunately, from a purely mechanical point of view, the in vivo

insertion procedure is less studied and all possible causes of overloads are difficult to assess. Moreover, the range of mechanical stresses on the electrodes can largely change with the surgical set up. All these issues lead to the use of safety coefficients (SF) to assure the success of the implant without any damages of the electrodes in uncertain conditions. To approximate this coefficient some different factors have to be considered: the material properties (e.g. mechanical properties of the main shaft of the electrode), the knowledge of the loading-overloading conditions, the knowledge of the surgical environment. A possible way to assess the SF is to use the Norton's approach [9], where all the previous factors are involved.

Table 1: Coefficient of safety [9] as function of the material properties, loading conditions and working environment.

Coefficient of safety	SF1 - Material properties (from tests)	SF2 - Loading conditions (knowledge)	SF3 - Working environment
1.3	Well known / characteristic	Verified by testing	Same as material testing conditions
2	Well approximated	Well approximated	Checked, room temperature
3	Fairly approximated	Fairly approximated	Slightly demanding
5+	Roughly approximated	Roughly approximated	Extremely demanding

In our case self penetrating electrodes derive from well-known microtechnological processes, with conventional material, then the coefficient SF1, due to the material properties can be set to 1.3 (see Table 1). On the contrary, the surgical environment is in general unknown. Even if, with the use of special supports the stability of the insertion can be improved, nevertheless the contact conditions between the nerve and the surrounding environment are still quite indeterminate. Furthermore, the pushing forces given by the surgeon during a manual insertion are difficult to achieve and liable to large changes related to its specific ability and experience. As a consequence, for SF2 (considering the knowledge of the loading conditions) the value of 5+ can be chosen. Finally, at least for preclinical trials, the working environment is directly the body of a human being, and every damage to the residual nerve stump can further compromise the condition of the patient. Then, as well as ethically unacceptable, every damage can have a legal and financial impact. So, also for SF3 the value of 5+ can be set. Following the standard approach the global safety coefficient can be obtained using Equation (6):

$$SF = \max\{SF1, SF2, SF3\} \tag{6}$$

Therefore in our case $SF=5+$ (that is, 5 or larger values).

3 RESULTS

The previous simple approach helps to rationalize the design of self penetrating electrodes: in this paragraph will be analyzed both the choice of the minimum Young's modulus of the electrode main shaft, once given its slenderness ratio, and the assessment of the maximum slenderness ratio for a given construction material. Figure (2) shows how the minimum Young modulus depends on the maximum slenderness ratio through experimental values of piercing forces. Indeed, σ_{cr} can be defined starting from both Equations (3) and (1.2). As a consequence, it is related to both the peripheral nerve biomechanics and the geometry of the electrode. Therefore, if technical constraints fix the electrode geometry (and then SR), the main shaft material can be chosen in order to ensure the bearing of the maximum dimpling force. In this way, the failure of the implantation procedure can be avoided.

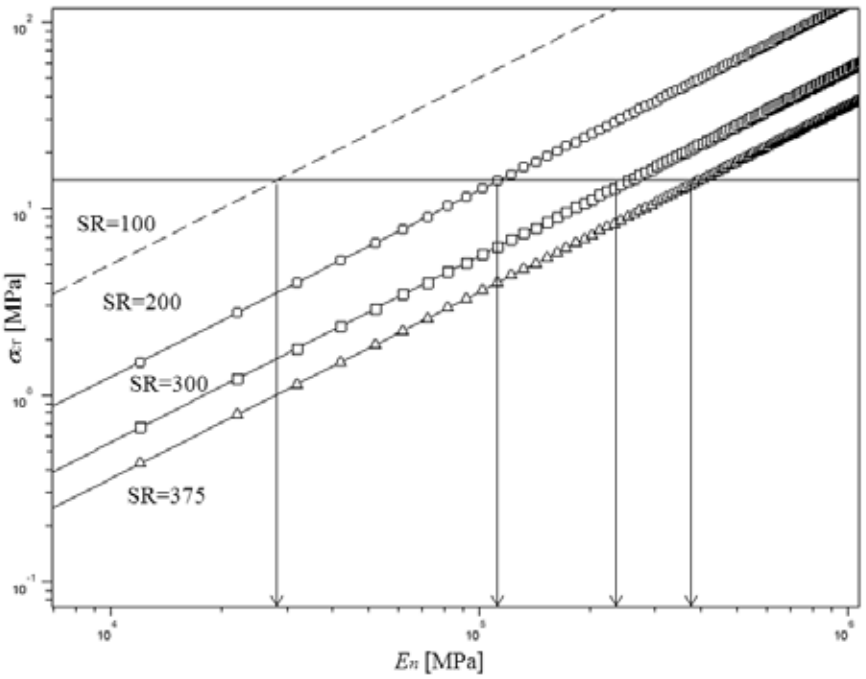

Figure 2: This log-log plot shows the usefulness of biomechanical inputs, deriving form the interaction phase (σ_{cr}), to rationally assess the minimum Young modulus providing a safe utilization with a given slenderness ratio. Figure (2) illustrates the case of electrodes with a circular cross sectional area and pin-fixed boundary conditions.

On the other hand, if biocompatibility issues constrain the choice of the material of electrodes, their SR can be chosen in order to avoid implantation failures. To this aim, Figure

(3) shows as starting from the Young modulus of a set material the maximum slenderness ratio can be found. Also in this case, the biomechanical input about the expected maximum forces (or dimpling) is crucial to univocally assess σ_{cr} and then the intersection points of interest. Both Figures (2) and (3) illustrate the procedure of choice for electrodes with circular section and pin-fixed boundary conditions.

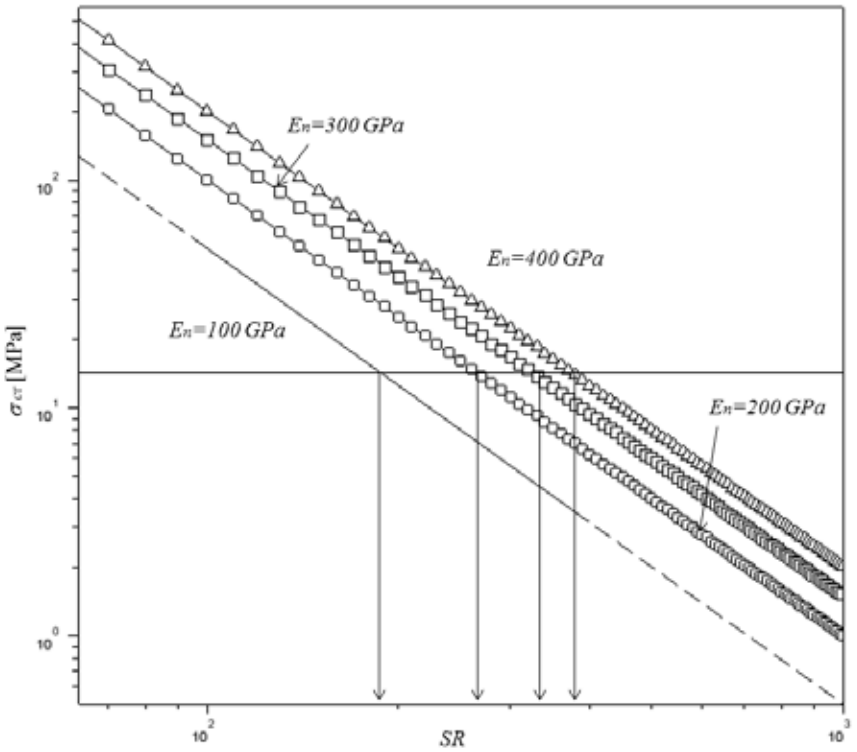

Figure 3: This log-log plot illustrates the importance of the biomechanical assessment of the interaction phase (σ_{cr}) to rationally found the maximum slenderness ratio providing a safe implant with a given material. Figure (3) shows how to choose parameters for electrodes with a circular cross sectional area and pin-fixed boundary conditions.

4 DISCUSSION

4.1 From biomechanics to design of self penetrating electrodes: a possible path for safe implantations

Several neural interfaces have been developed to control neuroprostheses and hybrid bionic systems . Among them, self penetrating electrodes seems to be promising because they represent an interesting trade-off between the needs for high selectivity and reduced invasiveness. However, no particular attention is usually paid to design their structures accounting for the biomechanical properties of the system to be interfaced. Furthermore, the

implantation of electrodes in the peripheral nerves is a complex surgical task: a great experience in insertion is required to avoid tissue damages (which could result in pain) and electrode breakage. The sum of these factors results in failure of implantations, also with already tested and commercialized products, in significant increases of surgical times and number of attempts, risks of damages for nerves and waste of expensive electrodes. Therefore, to rationally design self penetrating electrodes the knowledge of the surrounding environment is necessary. Indeed, the choice of structural materials, the geometry, and also the procedure of implantation depends on the magnitude of the reciprocal interactions between tissue and electrode. To quantify these forces appears to be "strategic" to provide useful information about the design process. To this aim, in section (2.1) a simple framework to assess these interactions was provided. However, it is an approximation and the more it is valid, the more the characteristic time of tissue local reaction are shorter than the relaxation one. In other words, this approximated framework only consider the local instantaneous elastic response of peripheral nerves. This is, of course, a limitation but for many real surgical procedures it provides a suitable approximation. Moreover, a problem to be solved in electrode design is to balance the minimum stiffness able to enter the tissue and minimize the internal damages. A possible suitable solution is to minimize the stiffness considering all different designs having the first buckling load greater than a given force accounting for the maximum piercing force and the right safety factor. To this aim in section (2.2) the basic elements leading to a rational design of a self penetrating interface were provided, and in section (2.3) an assessment of a possible safety factor was presented. The synergistic use of these two parts allows to assess some useful design parameters of electrodes, as the SR and the Young modulus. This approach seems to be effective and is able to predict the outcome of real trials of surgical implantation [6].

REFERENCES

[1] Navarro X., Krueger T. B., Lago N., Micera S., Dario P., and Stieglitz T., A critical review of interfaces with the peripheral nervous system for the control of neuroprostheses ad hybrid bionic systems. *J. Pher. Nerv. Syst.* (2005), **10**:229–258.

[2] Lawrence S. M., Dhillon G. S., Jensen W., Yoshida K., and Horch K.W., Acute peripheral nerve recording Characteristics of polymer-based longitudinal intrafascicular electrodes. *IEEE Trans. Neural Syst. Rehab. Eng*. (2004), **12**:345–348.

[3] McDonnall D., Clark G.A., and Normann R. A., Interleaved, multisite electrical stimulation of cat sciatic nerve produces fatigue-resistant, ripple-free motor responses. *IEEE Trans Neural Syst. Rehab. Eng*.(2004), **12**: 208–215.

[4] Ju M.S., Lin C.C.K., Fan J.L, and Chen R.J., Transverse elasticity and blood perfusion of sciatic nerves under in situ circular compression. *Journal of Biomechanics*,(2006), **39**: 97-102.

[5] Jensen W., Yoshida K., Hofmann U.G., In vivo implant mechanics of single-shaft microelectrodes in peripheral nervous tissue ", on In Proceedings of the 3rd International *IEEE/EMBS Conference on Neural Engineering* 1-4, (2007).

[6] Yoshida K., Lewinsky I., Nielsen M., and Hylleberg M., Implantation mechanics of tungsten microneedles into peripheral nerve trunks. *Med Biol Eng Comput*,(2007), **45**: 413-20.
[7] Sergi P.N., Carrozza M.C., Dario P., and Micera S., Biomechanical characterization of needle piercing into peripheral nervous tissue. *IEEE Trans Biomed Eng*,(2006), **53**: 2373-868.
[8] Okamura A. M., Simone C., and O'Leary M. D.,Force modeling for needle insertion into soft tissue. *IEEE Trans Biomed Eng*,(2004), **51**: 1707-1716.
[9] Norton, R.L., 1996, *Machine Design – An Integrated Approach*, Prentice-Hall, Upper Saddle River, New York.

XI International Conference on Computational Plasticity. Fundamentals and Applications
COMPLAS XI
E. Oñate, D.R.J. Owen, D. Peric and B. Suárez (Eds)

LONGITUDINAL PRESTRAIN IN MALE ABDOMINAL AORTA FROM PULSE WAVE VELOCITY VIEWPOINT

Lukáš Horný[*], Tomáš Adámek[†], Hynek Chlup[*], Rudolf Žitný[*], Eva Gultová[*] and Jan Veselý[*]

[*] Faculty of Mechanical Engineering
Czech Technical University in Prague
Technická 4, 16607 Prague, Czech Republic
e-mail: Lukas.Horny@fs.cvut.cz, http://www.biomechanika.cz/departments/20

[†] Third Faculty of Medicine
Charles University in Prague
Ruská 87, 10000 Prague, Czech Republic
email: adamek@fnkv.cz, http://www.lf3.cuni.cz/en

Key words: Abdominal Aorta, Adaptation, Aging, Prestrain, Pretension, Pulse wave velocity.

Summary. *Arteries in situ are subjected to the pretension developed upon the growth period. The magnitude of the pretension was shown to be age-dependent. Detailed statistics are, however, rare. This study was designed to expand our knowledge of the prestrain sustained by arteries during the lifespan. Age-related distribution of the longitudinal prestrain in the male abdominal aorta obtained within 93 regular autopsies is shown (age = 41.6±15.8 years; prestretch =1.174±0.099). Data indicate that the prestrain decreases nonlinearly during the aging. Bilinear regression function revealed the breakpoint in the prestrain–age dependency at age about 40. The comparison of this result with studies which document the nonlinearity in the pulse wave velocity–age dependency indicates that steep increase of the velocity is preceded by the loss of the pretension. It suggests that the pretension could play a compensation role within artery stiffening.*

1 INTRODUCTION

Computational methods of biomechanics become increasingly directed to the so-called patient-specific analyses[1-2]. They can help in customized therapy. Such an approach, however, necessitates patient-specific (and pathology-specific) constitutive models, loading conditions and geometries to be known during computer modeling.

Geometrical patient-specific models of tissues and organs can be obtained by modern computer imaging methods. It is well-known, however, that arteries in situ (under geometry observed with CT, MRI or IVUS in vivo) are not in the zero stress and strain state. Beside the blood pressure-induced loading there is significant residual stress acting in the circumferential direction[3-5]. In the longitudinal direction arteries exhibit significant pretension. This can be proved upon the excision of a sample. The sample will retract[6-9]. Hence direct incorporation of in situ geometry into the computational model can lead to nonrealistic results.

The existence of the longitudinal prestrain (pretension) is known more than a century[14]. Bergel[6] reported mean shrinkage of the excised samples of the canine arteries ranging between 32% - 42% (percentage of original length) depending on the position in the arterial tree. Han and Fung[7] confirmed this result. They reported monotonically increasing longitudinal prestretch (from 1.2 to 1.5) with the increasing distance from the heart. Learoyd and Taylor[8] measured 59 samples of arteries obtained from 12 human donors. Their results proved the position dependency of the prestrain. They also found negative correlation between the age and the prestrain[10].

The species and position dependency of the longitudinal prestrain seems to be explainable by means of the intramural collagen-to-elastin ratio[11]; the higher the ratio, the lower the prestrain. The key role of the elastin was proved by enzyme digestion and also in animal models with the elastin insufficiency[12,13,16].

Recent papers have shown that the longitudinal prestrain is involved in the artery remodeling and adaptation. Jackson at al. [16] shown that elevated axial prestrain in rabbit carotid arteries was normalized within 7 days after the surgery. It was accompanied by increased endothelial and smooth muscle cell replication rate[16,17]. Also increased extracellular matrix content was observed. In contrast to the elevated longitudinal load the culturing under infraphysiological axial strain resulted in a mass loss and decreased cell proliferation[18].

It is well known that arteries stiffen with increasing age. This process is called arteriosclerosis. Increased stiffness of conduit arteries results in the increase of the pressure pulse wave velocity (PWV)[19,22,23]. Elevated PWV, however, lead to early pressure wave reflections which contribute to the heart load. The artery wall exhibits nonlinear and anisotropic mechanical behavior. In such a material actual stiffness depends on actual strain/stress state[20,21]. Concerning these facts rather surprising hypothesis can be derived. Although the loss of the longitudinal strain is likely negative consequence of the aging, it reduces overall strain state of an artery. Reduced axial strain results in the reduction of actual stiffness. This mechanism could compensate for increased stiffness developed within arteriosclerosis.

To test the hypothesis of the compensation ability we compared the age-related distribution of the longitudinal prestrain with the distribution of the pulse wave velocity in human aorta. It will be shown that progressive decrease of the prestrain magnitude in male abdominal aorta is followed by only small change at age above 40 years. Our data indicate that rapid increase of PWV is preceded by the period of the progressive loss of the prestrain.

2 METHODS

The statistics of 93 abdominal aortic longitudinal prestrains was collected within regular autopsies of male Caucasian cadavers of known age in the University Hospital Na Kralovskych Vinohradech in Prague. The longitudinal prestrain was quantified by the stretch ratio λ defined in (1). l and L denote the length of the tubular sample (below renal arteries branching and above aortoiliac bifurcation) before and after the excision.

$$\lambda = \frac{l}{L} \tag{1}$$

It was hypothesized that the age-dependency of λ can be expressed by means of stepwise linear function with the breakpoint, t_k, corresponding to the loss of the compensation ability (2).

$$\lambda(t) = \begin{cases} at + b & \text{if } t \le t_k \\ ct + d & \text{if } t_k < t \end{cases} \tag{2}$$

Where a, b, c, d are real parameters and t denotes the age [years]. The condition of continuity has to be added, $at_k + b = ct_k + d$, to obtain meaningful results.

Constrained optimization problem was solved in Maple 13. It should be mentioned that besides parameters a, b, c and d, the position of the breakpoint, t_k, was also the subject of the optimization. The final model was evaluated with generalized F-test. The null hypothesis, $H_0 : [a,b] = [c,d]$, was tested against the alternative $H_A : [a,b] \neq [c,d]$.

The regression was accompanied with the correlation analysis exploring the link between the prestrain and additional cardiovascular indices. The correlations include carotid-femoral pulse wave velocity (cfPWV), distensibility of descending aorta (DDA), maximum strain of descending aorta (mS), central aortic systolic (SP), diastolic (DP) and pulse pressure (PP), and augmentation index (AI). Since there is no possibility to find out these quantities post mortem we had to incorporate data from the literature[23]. The data were obtained within MRI investigation and tonometry. Here we will not repeat details of the procedure. We only mention that mS was obtained as the relative change of the lumen area; DDA denotes the change in the lumen area with respect to minimal area and PP, and AI is the ratio between systolic pressure augmentation and PP. The simple correlation coefficients, R, were computed based on data averaged through decades of the life.

3 RESULTS

Data sample involved in our study consisted of 93 male subjects with age ~ 17—81 (41.6±15.8) and prestretch ~ 1.023—1.417 (1.174±0.099); minimum—maximum (mean±SD). The study proved significantly decreasing prestrain upon increasing age. It was found that the stepwise linear model (2) fits prestrain–age relationship with lower sum of squares than simple linear. The parameters estimating resulted in $a = -9.556 \cdot 10^{-3}$; $b = 1.520$; $c = -2.588 \cdot 10^{-3}$; $d = 1.241$; and $t_k = 40$ years. F-test proved that there are strong statistical evidences against the null hypothesis (the risk of true hypothesis rejection $p < 0.0001$). Results are depicted in Fig. 1. Fig. 2 shows the ratio between residual standard deviation (RSD) computed for optimal model and RSD obtained in models with t_k in different positions (and different valaues of the parameters).

Table 1 documents age-related mean values of the prestrain and data adopted from the literature[23]. Results suggest that especially non-dimensional indices are highly correlated. The correlation found for entire sample of the prestrain and age reached $R = -0.856$. It proves strong age-dependency of the prestrain. High correlation between the carotid-femoral pulse wave velocity and prestrain was also confirmed, $R = -0.884$.

4 DISCUSSION

We postulated the hypothesis that decreasing longitudinal prestrain could compensate artheriosclerosis-induced stiffening of an artery. This compensation ability would be, however, limited with the initiative value of the prestrain developed within the growth period. The analysis suggests that the process of the prestrain decrease is not linear. The stepwise linear model revealed the breakpoint at age about 40 years.

Table 1: Prestrain correlations. X denotes the number of our observations. Y denotes the number of observations involved in [23]. Used acronyms: cfPWV – carotid-femoral pulse wave velocity; DDA – distensibility of descending aorta; mS – maximum strain; AI – augmentation index; DP, SP and PP denote central diastolic, systolic and pulse pressure, respectively. *The correlation between age and prestrain was based on non-averaged data.

Number of samples X/Y	Age [years]	Prestretch [1]	cfPWV [ms^{-1}]	DDA [$10^{-3}\cdot kPa^{-1}$]	mS [%]	DP [mm Hg]	SP [mm Hg]	PP [mm Hg]	AI [%]
22/21	20-29	1.296	6.2	72	33	59	109	48	-10
19/15	30-39	1.199	6.7	70	27	66	113	46	-4
20/31	40-49	1.135	8.8	38	15	75	122	46	16
18/16	50-59	1.091	9.5	29	11	77	134	55	31
7/14	60-69	1.068	12.8	18	9	75	143	66	26
5/14	70-	1.061	13.8	17	8	69	135	66	32
Correlation	-0.856*	1	-0.884	0.949	0.985	-0.828	-0.932	-0.748	-0.958

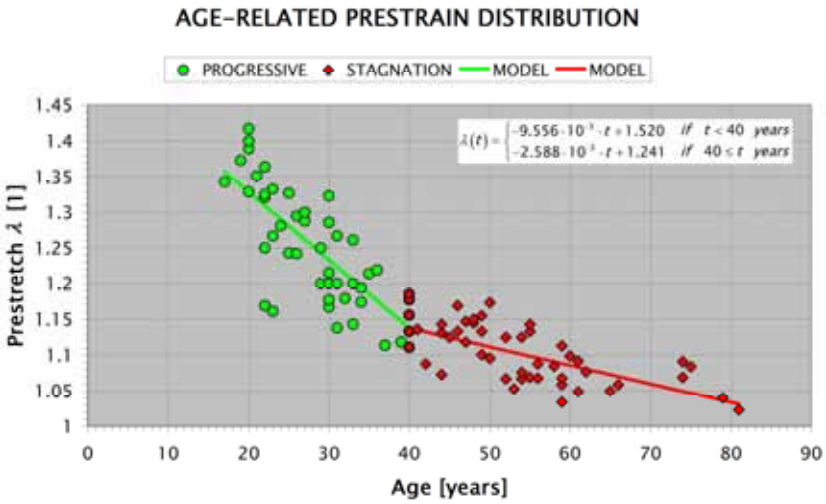

Figure 1: Optimal stepwise linear regression. We suggested the hypothesis that progressively decreasing prestrain could compensate for overall stiffening of an artery. It would mean that only small increase in pulse wave velocity should be expected before the breakpoint.

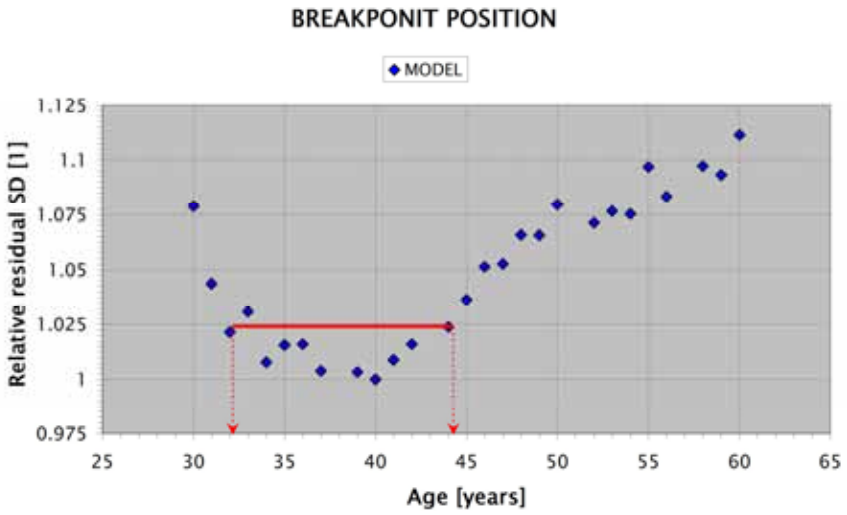

Figure 2: Uncertainty of the breakpoint position. Breakpoint position can be affected with the data sample character. The graph shows rather flat character of the extreme. Hypothetical variability of the breakpoint position is outlined with the interval of 2.5% difference from the optimum.

It has to be mentioned, however, that post mortem collected data may not correspond exactly to in vivo pretensions. There are some sources of differences: 1. influence of post mortem interval (PMI); 2. necessity of the removing tethering tissue during preparation; 3. absence of the blood pressure. Previous analysis proved that PMI does not correlate with the prestrain in our statistical sample[24]. Nevertheless, the removing of the tethering tissue and the absence of the blood pressure can cause that the in vivo prestrains are higher than herein reported. Bearing this in mind our data should only be considered as the estimations of the in vivo longitudinal prestrain.

Thus the position of the breakpoint, identified here at 40 years, can also move depending on the specific statistics. To emphasize this fact we included Fig. 2. It shows the character of the change in RSD with relation to the breakpoint position. The minimum is rather flat which indicates an uncertainty of the estimation.

Herein presented statistical analysis can not give evidences how much longitudinal prestrain affects PWV. It only proves that PWV and prestrain are correlated. The true link between the age, PWV and prestrain must be clarified by methods of the computational mechanics. They can incorporate constituent-based models to explain this link.

Strong correlations between the prestrain, PWV and other indices were found. They, however, can be overestimated due to averaging of the data which has a smoothing effect. Nevertheless, Redheuil et al.[23] shown the breakpoint in the PWV-age and ascending aortic distensibility-age dependency (see Fig. 2 in their study; http://hyper.ahajournals.org/cgi/reprint/55/2/319) at age 50 years. Our study shown the breakpoint in the prestrain at age about 40 years. The preceding loss of the prestrain before the increase of PWV is consistent with the hypothesis of the compensation ability.

ACKNOWLEDGEMENT

This work has been supported by the Czech Ministry of Education project MSM6840770012; Czech Science Foundation GA106/08/0557; and Grant Agency of the Czech Technical University in Prague SGS10/247/OHK2/3T/12.

REFERENCES

[1] Selimovic, A., Penrose, J., Bogunovic, H., Villa-Uriol, M-C., Holzapfel, G.A., Ventikos, Y. and Watton, P.N. A computational framework to explore the role of pulsatile haemodynamics on cerebral aneurysm development for patient-specific arterial geometries. (2010) IFMBE Proc. vol. 31, part 3, 6th World Congress of Biomechanics, Singapore, 2010, pp 759-762, DOI 10.1007/978-3-642-14515-5_193

[2] Pekkan, K., Whited, B., Kanter, K., Sharma, S., de Zelicourt, D., Sundareswaran, K., Frakes, D., Rossignac, J. and Yoganathan, A.P. Patient-specific surgical planning and hemodynamic computational fluid dynamics optimization through free-form haptic anatomy editing tool (SURGEM). *Med. Biol. Eng. Comput* (2008) **46**:1139-1152 DOI 10.1007/s11517-008-0377-0

[3] Rachev, A. and Greenwald, S.E. Residual strains in conduit arteries. *J. Biomech* (2003) **36**:661-670. DOI 10.1016/S0021-9290(02)00444-X

[4] Valenta, J., Vitek, K., Cihak, R., Konvickova, S., Sochor, M. and Horny, L. Age related constitutive laws and stress distribution in human main coronary arteries with reference to residual strain. *Bio-Med. Mater. Eng* (2002) **12**:121-134

[5] Takamizawa, K. and Hayashi, K. Strain energy density function and uniform strain hypothesis for arterial mechanics. *J. Biomech* (1987) **20**:7-17

[6] Bergel, D. The static elastic properties of the arterial wall. *J. Physiol* (1961) **156**:445-457

[7] Han, H.C. and Fung, Y.C. Longitudinal strain of canine and porcine aortas. *J. Biomech* (1995) **28**:637-641 DOI 10.1016/0021-9290(94)00091-H

[8] Learoyd, B.M. and Taylor, M.G. Alterations with age in the viscoelastic properties of human arterial walls. *Circ. Res* (1966) **18**:278-292

[9] Langewouters, G.J., Wesseling, K.H. and Goedhard, W.J.A. The static elastic properties of 45 human thoracic and 20 abdominal aortas in vitro and the parameters of a new model. *J. Biomech* (1984) **17**:425-435. DOI 10.1016/0021-9290(84)90034-4

[10] Schulze-Bauer, C.A., Mörth, C. and Holzapfel, G.A. Passive biaxial mechanical response of aged human iliac arteries. *J. Biomech. Eng* (2003) **125**:395-406

[11] Humphrey, J.D., Eberth, J.F., Dye, W.W. and Gleason, R.L. Fundamental role of axial stress in compensatory adaptations by arteries. *J. Biomech* (2009) **42**:1-8 DOI 10.1016/j.jbiomech.2008.11.011

[12] Dobrin, P.B., Schwarcz, T.H. and Mirkvicka, R. Longitudinal retractive force in pressurized dog and human arteries. *J. Surg. Res* (1990) **48**:116-120 DOI 10.1016/0022-4804(90)90202-D

[13] Wagenseil, J.E., Ciliberto, C.H., Knutsen, R.H., Levy, M.A., Kovacs, A. and Mecham, R.P. Reduced vessel elasticity alters cardiovascular structure and function in newborn mice. *Circ. Res* (2009) **104**:1217-1224 DOI 10.1161/CIRCRESAHA.108.192054

[14] Fuchs, R.F. Zur physiologie und wachstumsmechanik des blutgefass-systems. *Arch. Anat. Physiol* (1900) 102-154

[15] Zulliger, M.A. and Stergiopulos, N. Structural strain energy function applied to the ageing of the human aorta. *J. Biomech* (2007) **40**:3061-3069 DOI 10.1016/j.jbiomech.2007.03.011

[16] Jackson, Z.S., Gotlieb, A.I. and Langille, B.L. Wall tissue remodeling regulates longitudinal tension in arteries. *Circ. Res* (2002) **90**:918-925 DOI 10.1161/01.RES.0000016481.87703.CC

[17] Han, H-C., Ku, D.N. and Vito RP. Arterial wall adaptation under elevated longitudinal stretch in organ culture. *Ann. Biomed. Eng* (2003) **31**:403-411 DOI 10.1114/1.1561291

[18] Lawrence, A.R. and Gooch, K.J. Transmural pressure and axial loading interactively regulate arterial remodeling ex vivo. *Am. J. Physiol. Heart. Circ. Physiol* (2009) **297**:H475-H484 DOI 10.1152/ajpheart.00972.2008

[19] O'Rourke, M.F. and Hashimoto, J. Mechanical factors in arterial aging. *J. Am. Coll. Cardiol* (2007) **50**:1-13 DOI 10.1016/j.jacc.2006.12.050

[20] Holzapfel, G.A., Gasser, T.C. and Ogden R.W. A new constitutive framework for arterial wall mechanics and a comparative study of material models. *J. Elast* (2000) **61**:1-48 DOI 10.1023/A:1010835316564

[21] Holzapfel, G.A. and Ogden, R.W. Constitutive modelling of arteries. *Proc. R. Soc. A* (2010) **466**:1551-1597 DOI 10.1098/rspa.2010.0058

[22] McEniery, C.M., Yasmin, Hall, I.R., Qasem, A., Wilkinson, I.B. and Cockcroft, J.R. Normal vascular aging: differential effects on wave reflection and aortic pulse wave velocity. *J. Am. Coll. Cardiol* (2005) **46**:1753-1760 DOI 10.1016/j.jacc.2005.07.037

[23] Redheuil, A., Yu, W.-C., Wu, C.O., Mousseaux, E., de Cesare, A. et al. Reduced ascending aortic strain and distensibility: earliest manifestations of vascular aging in humans. *Hypertension* (2010) **55**:319-326 DOI 10.1161/hypertensionaha.109.141275

[24] Horny, L., Gultova, E., Adamek, T., Zitny, R. and Chlup, H. In situ longitudinal pretesnion in human aorta. Accepted for publication in *IFMBE Proceedings* within 5th European IFMBE MBEC conference in Budapest, Hungary, 14-18 September 2011.

XI International Conference on Computational Plasticity. Fundamentals and Applications
COMPLAS XI
E. Oñate, D.R.J. Owen, D. Peric and B. Suárez (Eds)

MODELING OF DAMAGE IN SOFT BIOLOGICAL TISSUES AND APPLICATION TO ARTERIAL WALLS

Daniel Balzani*, Gerhard A. Holzapfel† and Sarah Brinkhues*

*Institute of Mechanics, University of Duisburg-Essen, Faculty of Engineering,
Universitätsstr. 15, 45117 Essen, Germany
e-mail: daniel.balzani@uni-due.de, www.uni-due.de/mechanika

†Graz University of Technology, Institute of Biomechanics, Center of Biomedical Engineering,
Kronesgasse 5-I, 8010 Graz, Austria
e-mail: holzapfel@tu-graz.at, www.biomech.tugraz.at
and
Royal Institute of Technology, Department of Solid Mechanics, School of Engineering Sciences,
Osquars Backe 1, 100 44 Stockholm, Sweden

Key words: Computational biomechanics, damage mechanics, arterial walls, softening behavior, soft biological tissues

Abstract. A new material model is proposed for the description of stress-softening observed in cyclic tension tests performed on soft biological tissues. The modeling framework is based on the concept of internal variables introducing a scalar-valued variable for the representation of fiber damage. Remanent strains in fiber direction can be represented as a result of microscopic damage of the fiber crosslinks. Particular internal variables are defined able to capture the nature of soft biological tissues that no damage occurs in the physiological loading domain. A specific model is adjusted to experimental data taking into account the supra-physiological loading regime. For the description of the physiological domain polyconvex functions are used which also take into account fiber dispersion in a phenomenological approach. The applicability of the model in numerical simulations is shown by a representative example where the damage distribution in an arterial cross-section is analyzed.

1 INTRODUCTION

As a result of hypertension, overweight, rich alimentation, smoking, diabetes and stress, biochemical and mechanical degenerative processes in arterial walls are followed by a lumen reduction referred to as stenosis. In severe cases such stenosis may result in heart attacks, smoker's legs or in strokes. To prevent such complications one frequently used method of treatment is balloon dilatation accompanied by the implantation of a stent.

Thereby, a balloon catheter is inserted into the affected artery and dilated with an internal pressure increase. After removing the balloon the luminal area remains enlarged. During this procedure microscopic damage is induced in the vessel wall which is partly responsible for the treatment success since it results in increased strains when unloading to the state of physiological blood pressure again. Within the clinical context these effects are referred to as controlled vessel injury, see, e.g., [5]. In order to improve insight into the complex biomechanical processes during therapeutical interventions such as angioplasty and for the optimization of treatment methods, the modeling of arterial tissues and related computer simulations are subject of current research.

Most experimental approaches dealing with the measurement of mechanical properties of soft biological tissues are related to the analysis of loading within the physiological domain. With respect to degenerative processes occurring during angioplasty especially supra-physiological (therapeutical) loadings are required. These load levels are characterized by loading conditions significantly higher than those that occur under normal (physiological) conditions. In [19] first layer-specific experiments are performed under supra-physiological conditions. In such experiments a pronounced softening hysteresis is observed with respect to the stress-strain response. For the description of isotropic softening there exist various models. One of the first representations of damage at large strains is introduced in [20]. In order to describe damage, showing a saturating behavior during repeated un- and reloading cycles for fixed maximum load levels, [13] introduced a suitable model. An alternative phenomenological form of describing damage mechanisms is linked with the notion of pseudo-elasticity. Thereby, the main idea is that different loading branches are described by different strain-energy functions. As one of the first works in this context one should mention [15]. With respect to soft biological tissues a practical approach avoiding the usage of damage tensors is given in [17], where the anisotropic damage can be described by scalar-valued variables. The model by [16] uses scalar-valued variables as well and considers a stochastic framework on the basis of the wavy structure of the collagen fibers. A model for the preconditioning of soft biological tissues and the anisotropic Mullins effect is proposed in [7]. Another recent approach provides the description of remanent strains after overstretch in the framework of finite plasticity based on the assumption of remaining deformations at the micro-scale of the fibers, see [9]. A particular damage behavior for the matrix material is taken into account in e.g. [14] or [4]. These two contributions are formulated in terms of the continuum damage mechanics, where the existence of an effective (ficticiously undamaged) strain energy function is postulated. Since this function is associated to the physiological regime, where the response of soft biological tissues is hyperelastic, a polyconvex function should be used because then the existence of minimizers of underlying variational problems is guaranteed if additionally coercivity is ensured. In addition to that, quasiconvexity and material stability are automatically fulfilled, cf. [18], where the first transversely isotropic and orthotropic polyconvex functions are introduced. In [10] a first polyconvex model for arterial tissues is proposed as an exponential function of the fourth mixed invariant

of the right Cauchy-Green tensor and the structural tensor characterizing the material symmetries. Further polyconvex models able to describe soft biological tissues which are a priori stress-free in the (undeformed) reference configuration are proposed in, e.g., [1] or [6].
Here, we focus on the construction of a new model able to describe the complex softening hysteresis observed in experiments of soft biological tissues. The model is formulated in terms of the continuum damage mechanics and reflects the anisotropic character of the material. In addition to that, a rather low number of material parameters with physical interpretability is introduced keeping the proposed model applicable. Please note that full details regarding the model and numerical examples can be found in the original paper [3].

2 CONTINUUM MECHANICAL FRAMEWORK

In the reference configuration the body of interest is denoted by $\mathcal{B} \subset \mathbb{R}^3$ and parameterized in $\boldsymbol{X}$; in the deformed configuration it is denoted by $\mathcal{S} \subset \mathbb{R}^3$ and parameterized in $\boldsymbol{x}$. The nonlinear deformation map $\boldsymbol{\varphi}_t : \mathcal{B} \to \mathcal{S}$ at time $t \in \mathbb{R}_+$ maps points $\boldsymbol{X} \in \mathcal{B}$ onto points $\boldsymbol{x} \in \mathcal{S}$. The deformation gradient $\boldsymbol{F}$ and the right Cauchy–Green tensor $\boldsymbol{C}$ are defined by

$$\boldsymbol{F}(\boldsymbol{X}) := \nabla \boldsymbol{\varphi}_t(\boldsymbol{X}) \quad \text{and} \quad \boldsymbol{C} := \boldsymbol{F}^T \boldsymbol{F} \,, \tag{1}$$

with the Jacobian $J := \det \boldsymbol{F} > 0$. In case of hyperelastic materials we postulate the existence of a strain-energy function ψ, defined per unit reference volume. In order to obtain constitutive equations which satisfy *a priori* the principle of material objectivity, the functional dependency $\psi := \psi(\boldsymbol{C})$ is taken into account. Then we compute the second Piola–Kirchhoff stresses and the Cauchy stresses by

$$\boldsymbol{S} = 2\partial_C \psi \quad \text{and} \quad \boldsymbol{\sigma} = J^{-1} \boldsymbol{F} \boldsymbol{S} \boldsymbol{F}^T \,, \tag{2}$$

respectively. A suitable framework for the description of anisotropic materials is the concept of structural tensors. Therein, an additional argument tensor, the structural tensor, is defined such that it reflects the symmetry group of the considered material. We concentrate on fiber-reinforced materials, hence, we restrict ourselves to the cases of transverse isotropy and to materials which can be characterized by a given number of non-orthogonal preferred directions. In these cases we are able to express the material symmetry of the considered body by a set of second-order structural tensors

$$\boldsymbol{M}_{(a)} := \boldsymbol{A}_{(a)} \otimes \boldsymbol{A}_{(a)} \quad \text{with} \quad a = 1...n_a \,, \tag{3}$$

where n_a is the number of fiber directions. For the construction of specific constitutive equations we focus on a coordinate-invariant formulation, thus, the invariants of the deformation tensor and of the structural tensors are required. The explicit expressions for the principle invariants of the right Cauchy–Green tensor are given by

$$I_1 := \operatorname{trace} \boldsymbol{C}, \quad I_2 := \operatorname{trace}[\operatorname{Cof} \boldsymbol{C}], \quad I_3 := \det \boldsymbol{C} \,. \tag{4}$$

Let $\boldsymbol{M}_{(a)}$ be of rank one and let us assume the normalization condition $||\boldsymbol{M}_{(a)}|| = 1$ due to $|\boldsymbol{A}_{(a)}| = 1$, then the additional invariants, the mixed invariants, are

$$J_4^{(a)} := \text{trace}[\boldsymbol{C}\boldsymbol{M}_{(a)}], \quad J_5^{(a)} := \text{trace}[\boldsymbol{C}^2\boldsymbol{M}_{(a)}] \,. \tag{5}$$

For the construction of constitutive equations we obtain the possible polynominal basis $\mathcal{P}_1 := \{I_1, I_2, I_3, J_4^{(a)}, J_5^{(a)}\}$.

3 DAMAGE MODEL FOR SOFT BIOLOGICAL TISSUES

In arterial walls the tissues are basically composed of an isotropic ground substance and mainly two embedded fiber families, which are typically arranged cross-wise helically. This fiber-reinforcement can be taken into account by consideration of a strain energy function of the type

$$\psi(I_1, I_2, I_3, J_4^{(a)}, J_5^{(a)}) := \psi^{vol}(I_3) + \psi^{iso}(I_1, I_2, I_3) + \sum_{a=1}^{2} \psi_{(a)}^{ti}(I_1, I_3, J_4^{(a)}, J_5^{(a)}) \,. \tag{6}$$

The energy associated to the isotropic ground substance is represented by ψ^{iso} whereas the fiber energy is denoted by $\psi_{(a)}^{ti}$. A weak interaction between the individual fiber families is assumed and therefore the orthogonal response of the material is approximated by the superposition of two transversely isotropic energies. The energy ψ^{vol} is a penalty function accounting for the incompressibility constraint. Here, it is assumed that the ground-substance is able to undergo significantly higher deformations before a dissipative behavior is observed and therefore no damage is taken into account in the matrix. The associated strain energy function is chosen as

$$\psi^{iso} = c_1 \left(\frac{I_1}{I_3^{1/3}} - 3 \right) , \tag{7}$$

where $c_1 > 0$ is a stress-like material parameter. This function leads to an almost linear stress-strain relationship which can be experimentally substantiated.
For the description of the damage-induced softening observed in experiments the main damage evolution is assumed to be in the fibers since these are the main load-bearing elements. Therefore, the transversely isotropic part is decomposed into the effective (ficticiously undamaged) hyperelastic strain energy $\psi_{(a)}^0$ and a reduction term $(1 - D_{(a)})$ with $D \in [0, 1[$ accounting for the microscopic damage evolution. In order to consider remanent strains in the fibers when unloading the material a further decomposition into an external and an internal function m and P is taken into account, respectively. Then we obtain

$$\psi_{(a)}^{ti} := m(P(\boldsymbol{C}, D_{(a)})) \quad \text{with} \quad P = (1 - D_{(a)})\, \psi_{(a)}^{ti,0} - c \,, \tag{8}$$

wherein the constant value c represents the value of the effective energy in the reference configuration. For the external and effective strain energy function we choose

$$m(P_{(a)}) = \frac{k_1}{2k_2}\left\{\exp\left(k_2\langle P_{(a)}\rangle^2\right) - 1\right\}\,, \quad \psi_{(a)}^{ti,0} = \kappa\, I_1 + (1-3\,\kappa) J_4^{(a)}\,, \quad c = 1 \tag{9}$$

such that for the undamaged case ($D = 0$) the well-known strain energy function [10] together with the fiber dispersion approach introduced in [8] is obtained. This approach is incorporated in order to account for distributed fiber orientations, which is controlled by adjusting the parameter $\kappa \in [0, 1/3]$. If $\kappa = 0$ then a perfectly transversely isotropically distributed orientation is obtained. Please note that the Macauley bracket $\langle(\bullet)\rangle = \frac{1}{2}[(\bullet) + |(\bullet)|]$ in $(9)_1$ filters out positive values. Preliminary mechanical experiments of cyclically overstretched soft biological tissues show that if the maximum load level is fixed in a cyclic tension test, then the stress hysteresis converges to a "saturated" response curve. This behavior has to be modeled by an appropriate choice of the damage function D, which is assumed to depend on the fictitiously undamaged (effective) energy $\psi_{(a)}^{ti,0}$, cf. [2], such that evolution of damage is activated in the loading and reloading processes. This can be achieved by defining the internal variable

$$\beta_{(a)} := \left\langle \tilde{\beta}_{(a)} - \tilde{\beta}_{(a)}^{ini} \right\rangle \quad \text{with} \quad \tilde{\beta}_{(a)} = \int_0^t \left\langle \dot{\psi}_{(a)}^{ti,0}(s) \right\rangle ds\,, \tag{10}$$

with $\tilde{\beta}_{(a)}^{ini}$ being the internal variable at an initial damage state in order to make sure that the damage evolution starts when entering the supra-physiological domain. Clearly, $\tilde{\beta}_{(a)}^{ini}$ is the value of $\tilde{\beta}_{(a)}$ at each material point reached for the situation where the damage evolution starts. In arterial walls this should be the case when the upper edge of "normal" blood pressure is attained. The time associated to the loading history is denoted by $s \in \mathbb{R}^+$; $t \in \mathbb{R}^+$ defines the actual loading situation. Then the internal variable (10) enters the damage function

$$D_{(a)}(\beta) = D_{s,(a)}\left[1 - \exp\left(\frac{\ln(1-r_s)}{\beta_s}\,\beta_{(a)}\right)\right] \quad \text{with} \quad D_{s,(a)} \in [0,1[\,,\ r_s \in [0,1[\,,\ \beta_s > 0\,, \tag{11}$$

cf. [12]. Herein, the only material parameter β_s is the value of the internal variable β which is reached at a certain fraction r_s of the maximal damage value $D_{s,(a)}$ for a fixed maximum load level. We consider a fraction of $r_s = 0.99$ and thus, β_s represents the value of internal variable at a damage value which can be interpreted as saturated. The response of the damage function (11) converges to a maximum value of damage $D_{s,(a)}$, which is in turn not a specified number but rather a function increasing the maximally reachable damage value for increased maximum load levels. For convenience we consider the same type of function and define

$$D_{s,(a)}(\gamma_{(a)}) = D_\infty\left[1 - \exp\left(\frac{\ln(1-r_\infty)}{\gamma_\infty}\gamma_{(a)}\right)\right] \quad \text{with} \quad D_\infty \in [0,1[\,,\ r_\infty \in [0,1[\,,\ \gamma_\infty > 0\,. \tag{12}$$

The parameter γ_∞ represents the value of the internal variable γ reached at the fraction $r_\infty = 0.99$ of D_∞; D_∞ denotes a predefined converging limit for the overall damage value. In order to take into account that $D_{s,(a)}(\gamma)$ remains unaltered for cyclic processes under fixed maximum load levels we consider the internal variable

$$\gamma_{(a)} = \max_{s\in[0,t]} \left\langle \psi^{ti,0}_{(a)}(s) - \psi^{ti,0}_{(a),ini} \right\rangle , \tag{13}$$

which is defined as the maximum value of effective energy reached up to the actual state. Herein, $\psi^{ti,0}_{ini,(a)}$ denotes the effective strain energy at an initial damage state obtained at the limit of the physiological domain. This expression leads to the saturation criterion

$$\phi_{(a)} := \left\langle \psi^{ti,0}_{(a)} - \psi^{ti,0}_{(a),ini} \right\rangle - \gamma_{(a)} \leq 0 \, . \tag{14}$$

Since D_∞ will be usually a number close to 1, the proposed damage model gets along with the two material parameters β_s and γ_∞, which have to be adjusted to experimental data.
The second Piola-Kirchhoff stresses are then computed from

$$\boldsymbol{S} = 2\,\frac{\partial \psi}{\partial \boldsymbol{C}} = \boldsymbol{S}^{vol} + \boldsymbol{S}^{iso} + \sum_{a=1}^{2} \boldsymbol{S}^{ti}_{(a)} \, , \tag{15}$$

with the individual abbreviations

$$\boldsymbol{S}^{vol} = 2\,\frac{\partial \psi^{vol}}{\partial \boldsymbol{C}} \, , \; \boldsymbol{S}^{iso} = 2\,\frac{\partial \psi^{iso}}{\partial \boldsymbol{C}} \, , \; \boldsymbol{S}^{ti}_{(a)} = m'(1-D_{(a)})\,\boldsymbol{S}^{ti,0}_{(a)} \quad \text{and} \quad \boldsymbol{S}^{ti,0}_{(a)} = 2\,\frac{\partial \psi^{ti,0}_{(a)}}{\partial \boldsymbol{C}} \, . \tag{16}$$

It is emphasized that in the physiological (hyperelastic) regime where $D_{(a)} = 0$ the strain energy function is polyconvex and coercive and ensures therefore the existence of minimizers and material stability.

4 NUMERICAL EXAMPLES

In this section numerical examples are provided. First, the proposed model is adjusted to uniaxial tension tests performed with test stripes taken from the media of a human carotid artery in order to show that the model is able to capture the mechanical behavior of arterial tissues. Second, a circumferential overstretch of an atherosclerotic artery is simulated in order to analyze the distribution of damage through the arterial wall.

4.1 ADJUSTMENT TO EXPERIMENTAL DATA

Uniaxial tension tests are performed on two test stripes taken from the media of a human carotid artery, where one stripe is extended in circumferential and the other one

	c_1 [kPa]	k_1 [kPa]	k_2 [-]	α_1 [kPa]	α_2 [-]	κ [-]	β_f [°]	D_∞ [kPa]	γ_∞ [kPa]	β_s [-]
physiological	6.56	1482.38	564.81	-	-	0.16	37.03			
supra-physiological	7.50	1266.57	400.0	-	-	0.19	35.05	0.99	6.71	1e-8

Table 1: Material parameters of the proposed model for the media of a human carotid artery in the purely physiological and in the supra-physiological loading domain.

in axial direction. The proposed model is adjusted to the experimental data by minimizing the least-square function

$$\bar{r}(\boldsymbol{\alpha}) = \sum_{e=1}^{n_e} \sqrt{\frac{1}{n_{mp}} \sum_{m=1}^{n_{mp}} \left(\frac{\sigma_{exp}(\lambda_1^{(m)}) - \sigma_{comp}(\lambda_1^{(m)}, \boldsymbol{\alpha})}{\max[\sigma_{exp}]} \right)^2}, \tag{17}$$

wherein σ_{exp} and σ_{comp} denote the experimentally measured and modeled Cauchy-stresses, respectively; $\lambda_1 = F_{11}$ denotes the stretch in the tension direction which coincides with the x_1-direction. Two experiments, i.e. tension in circumferential and axial direction ($n_\mathrm{e} = 2$) are considered and a number of n_{mp} measuring points are taken into account. The material parameters are arranged in the vector $\boldsymbol{\alpha}$ and identified by minimizing $\bar{r}$. In order to incorporate incompressibility the penalty term $\psi^{vol} = p(I_3 - 1)$ is included in the strain energy function, where p can be interpreted as a pressure-like Lagrange multiplier. The angle between the fiber orientation and the circumferential direction is treated as a fitting parameter and is defined to be β_f. In order to weight the two experiments in a representative manner the differences are normalized by the maximal values of the experimental stresses reached for the actual loading cycle. For the minimization problem sequential quadratic programming is applied.

In the first instance, only the hyperelastic, physiological regime is considered. Here, the number of measuring points is $n_{mp} = 49$ for the axial and $n_{mp} = 43$ for the circumferential tension test. The resulting hyperelastic material parameters are listed in the first row of Table 1. Fig. 1a shows the corresponding hyperelastic stress-strain response of the model compared with experimental data. As can be seen in this figure the model lead to an accurate match of the experimental data. Furthermore, the model response is adjusted to experimental data for significantly increased loadings such that the supra-physiological domain can be analyzed. For this purpose cyclic uniaxial tension tests in circumferential and axial direction are considered. The results of the experiments are shown in Fig. 1b. A strong anisotropy as well as a pronounced softening hysteresis is observed.

For the least-squares fit the hyperelastic parameters given in Table 1 (physiological) serve as estimators for the definition of suitable bounds for the hyperelastic parameters. Then, the hyperelastic as well as the damage parameters are adjusted. Due to this procedure, the fit provides the parameters given in the second row of Table 1. Fig. 1c shows the resulting response of the proposed model. We observe a good qualitative and quantitative correlation with the experiments.

4.2 NUMERICAL SIMULATION OF ATHEROSCLEROTIC ARTERY

In the following a numerical example for the anisotropic damage model described above is given by a numerical simulation of an atherosclerotic arterial wall. A stenosis caused by atherosclerosis is mostly treated by a balloon-angioplasty in combination with stenting. In this context, a high internal (supra-physiological) pressure acts on the arterial wall during inflating an inserted dilatation-catheter. The purpose of this section is to simulate such an arterial overexpansion in a two-dimensional approximation which basically enables the investigation of the influence due to the circumferential overstretch.
Therefore, a two-dimensional geometrical model with an average diameter of approximately one centimeter is used and computed with 6048 triangular elements with quadratic ansatz functions. The model is constructed based on hrMRI (high resolution magnetic resonance imaging). The considered cross-section is shown in Fig. 2a, where the discretization and the particular components are depicted.

The components of the artery are identified by hrMRI examination and histological analysis, namely the nondiseased intima, fibrous cap (Ifc), i.e. the fibrotic part at the luminal border, fibrotic intima at the medial border, calcification (Ic), lipid pool (Ilp), nondiseased media, diseased fibrotic media and adventitia (Adv), cf. [11]. For the numerical investigation the nondiseased intima with its less significant mechanical behavior is neglected and the fibrotic intima at the medial border and the diseased fibrotic media are combined to fibrotic media (Mf). The parameters for the media originate from Section 4.1 and the parameters for the adventitia are adjusted analogously to cyclic experiments such that the parameters given in Table 2 (Adv) are obtained. Unfortunately, for the fibrous cap and the fibrotic media no data is available for the supra-physiological regime and therefore the model is adjusted to the physiological data given in [11] and the same damage parameter identified for the media are taken. The lipid pool is assumed to be a butterlike, incompressible fluid not able to sustain shear stress. For the nearly rigid calcificated regions an average Youngs Modulus of 12(+-4.7) MPa is regarded. No damage is considered within the calcification and the lipid regions, because here dam-

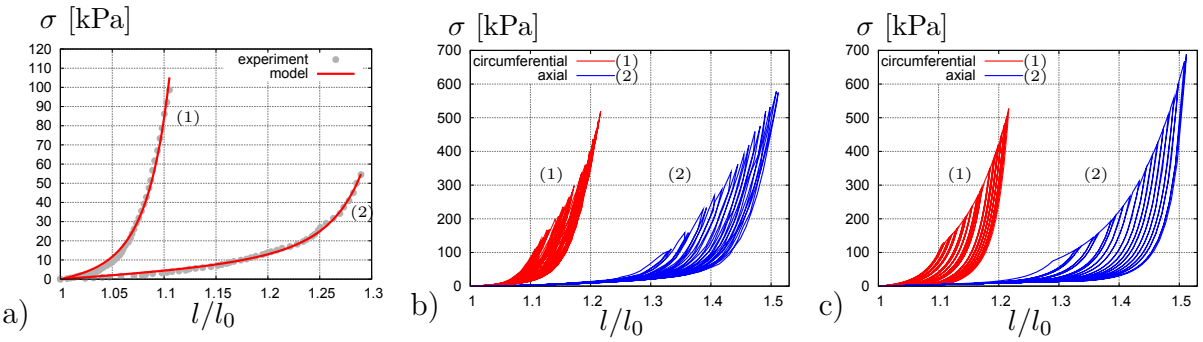

Figure 1: Uniaxial tension tests of the media of a human carotid artery in circumferential (1) and axial (2) directions: a) Comparison of the constitutive model response with experimental data in the physiological range; Cyclic uniaxial tension tests: b) experimental data and c) results of the constitutive model.

age plays a minor role. An overview of all parameters are listed in Table 2. For the nondiseaed and fibrotic media, the adventitia and the fibrous cap, which sustain damage evolution, the parameters $r_s = r_\infty = 0.99$ are taken into account. In order to enforce the incompressibility constraint, the penalty function $\psi^{vol} = \varepsilon_1 \left(I_3^{\varepsilon_2} + I_3^{-\varepsilon_2} - 2\right)$ is used, where the parameters ε_1 and ε_2 are chosen such that $\det \boldsymbol{F} = 1 \pm 1\%$ in the numerical simulation. For the simulation, first an internal pressure of 24.0 kPa ($\hat{=}$ 180.0 mmHg) representing the upper edge of the physiological regime and simultaneously an axial prestretch of 2% is applied. This situation is defined to be the initial damage state meaning that damage evolution starts after a pressure higher than 24.0 kPa. In a further step the internal pressure is increased up to 150.0 kPa ($\hat{=}$ 1125.0 mmHg) in order to simulate the overexpansion of the artery. After that the internal pressure is decreased till reaching a pressure of $p = 24.0$ kPa again, i.e. the natural state after a balloon-angioplasty. Here, no circumferential eigenstrains are considered because their order of magnitude is relatively small compared to the stresses resulting from the overstretch and their influence on the situation after the overstretch is assumed to be negligible. In Fig. 2b the distribution of the normalized damage variable $D_{(1)}/\max D_{(1)}$ is depicted at an internal blood pressure of 180 mmHg after the overstretch. A damage concentration in the healthy part of the media and the fibrous cap are observed. In addition to that the remaining strains under physiological blood pressure are significant by comparing the cross-section area A of the lumen before ($A_0 \approx 0.11$ cm^2) and after ($A \approx 0.17$ cm^2) the overexpansion. The resulting increase of the blood lumen due to the overstretch is $0.17/0.11 \approx 1.5$.
Remark: this simulation of an arterial wall can only be interpreted as an illustration that the proposed model provided in this contribution is able to be implemented in finite-element simulations. Although the qualitative distribution of damage may be reasonable the quantitative results are not necessarily realistic due to the lack of experimental data

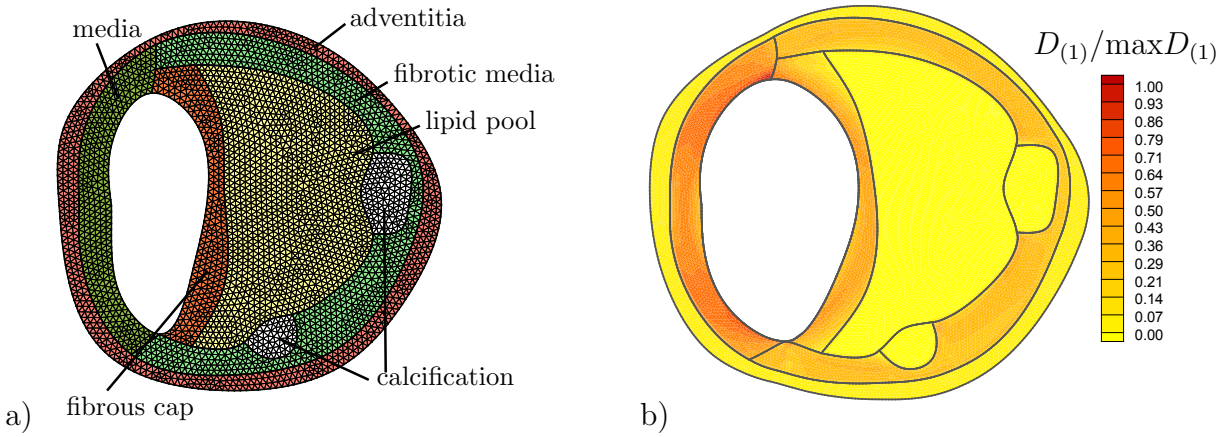

Figure 2: a) Cross section of the arterial model discretized with 6048 quadratic triangular finite elements; the components are: adventitia (Adv), nondiseased media, fibrotic media (Mf), fibrous cap (Ifc), lipid pool (Ilp), calcification (Ic); b) normalized damage variable $D_{(1)}/\max D_{(1)}$ with $\max D_{(1)} = 0.1048$ of a loaded artery after overexpansion at an internal pressure of $p = 24$ kPa (180 mmHg).

	c_1 [kPa]	k_1 [kPa]	k_2 [-]	κ [-]	β_f [°]	D_∞ [kPa]	γ_∞ [kPa]	β_s [-]
Adv	4.0	1640.23	115.63	0.097	45.60	0.99	10.84	7.36
Mf	21.12	1951.48	925.37	0.095	25.55	0.99	6.52	0.37
Ifc	24.12	4778.44	1023.59	0.12	53.18	0.99	6.52	0.37
Ic	2250.0	–	–	–	–	–	–	–
Ilp	2.5	–	–	–	–	–	–	–

Table 2: Hyperelastic and damage parameters of the other components.

and the two-dimensional approximation of the three-dimensional artery.

5 CONCLUSION

An anisotropic damage model for soft biological tissues was presented able to describe stress-softening hysteresis and remanent strains in the collagen fibers after unloading. A specific constitutive model was given and by defining suitable internal variables an undamaged physiological loading regime could be taken into account. The resulting strain energy function is polyconvex and coercive in the physiological (hyperelastic) regime and guarantees therefore the existence of minimizers of variational problems. The proposed model has been adjusted to cyclic uniaxial tension tests of the media and adventitia of a human carotid artery and an accurate matching was observed. Furthermore, a circumferential overstretch of an atherosclerotic artery was simulated in order to show the performance of the proposed model in finite element calculations.

ACKNOWLEDGEMENT: The authors greatly appreciate the Deutsche Forschungsgemeinschaft (DFG) for the financial support under the research grant BA 2823/5-1.

REFERENCES

[1] Balzani, D., Neff, P., Schröder, J. and Holzapfel, G.A., A polyconvex framework for soft biological tissues. Adjustment to experimental data, *International Journal of Solids and Structures* (2006) **43/20**:6052–6070.

[2] Balzani, D., Polyconvex anisotropic energies and modeling of damage applied to arterial walls, PhD-thesis, *Report No 2 of the Institute of Mechanics at the University of Duisburg-Essen* (2006), Verlag Glückauf Essen, ISBN 3-7739-6019-0.

[3] Balzani, D., Brinkhues, S. and Holzapfel, G.A., Constitutive framework for the modeling of damage in soft biological tissues (2011), submitted

[4] Calvo, B., Peña, E., Martínez, M.A. and Doblaré, M., An uncoupled directional damage model for fibered biological soft tissues, *International Journal for Numerical Methods in Engineering* (2007) **69**:2036–2057.

[5] Castaneda-Zuniga, W, Pathophysiology of transluminal angioplasty. *Improvement of myocardial perfusion* (Eds.: Meyer, J. and Erberl, R. and Rupprecht, H. J.), Martinus Nijhof (publisher), Boston (1985).

[6] Ehret, A. and Itskov, M., A Polyconvex Hyperelastic Model for Fiber-Reinforced Materials in Application to Soft Tisues, *Journal of the Mechanics and Physics of Solids* (2007) **42**:8853–9963.

[7] Ehret, A. and Itskov, M., Modeling of Anisotropic Softening Phenomena: Application to Soft Biological Tissues, *International Journal of Plasticity* (2009) **25**:901–919.

[8] Gasser, T.C., Ogden, R.W. and Holzapfel, G.A., Hyperelastic modelling of arterial layers with distributed collagen fibre orientations, *Journal of the Royal Society Interface* (2006) **3**:15–35.

[9] Gasser, T.C. and Holzapfel, G.A., Finite element modeling of balloon angioplasty by considering overstretch of remnant non-diseased tissues in lesions, *Computational Mechanics* (2007) **40**:47–60.

[10] Holzapfel, G. A., Gasser, T.C. and Ogden, R.W., A new constitutive framework for arterial wall mechanics and a comparative study of material models, *Journal of Elasticity* (2000) **61**:1–48.

[11] Holzapfel, G.A., Sommer, G. and Regitnig, P., Anisotropic Mechanical Properties of Tissue Components in Human Atherosclerotic Plaques, *Journal of Biomechanical Engineering* (2004) **126**:657–665.

[12] Miehe, C., Discontinuous and continuous damage evolution in Ogden-type large-strain elastic materials, *European Journal of Mechanics, A/Solids* (1995) **14**:697–720.

[13] Miehe, C. and Keck, J., Superimposed finite elasticviscoelasticplastoelastic stress response with damage in filled rubbery polymers. Experiments, modelling and algorithmic implementation, *Journal of the Mechanics and Physics of Solids* (2000) **48**:323–365.

[14] Natali, A.N., Pavan, P.G., Carniel, E.L. and Dorow, C., A transversally isotropic elasto-damage constitutive model for the periodontal ligament, *Computer Methods in Biomechanics and Biomedical Engineering* (2003) **6**:329–336.

[15] Ogden, R.W. and Roxburgh, D.G., An energy-based model of the Mullins effect, *Proceedings of the First European Conference on Constitutive Models*, (Eds.: Al Dorfmann and Alan Muhr), A. A. Balkema (publisher), Rotterdam, Brookfield (1999) 23–28.

[16] Rodríguez, J.F., Cacho, F., Bea, J.A., and Doblaré, M., A stochastic-structurally based three dimensional finite-strain damage model for fibrous soft tissue, *Journal of the Mechanics and Physics of Solids* (2006) **54**:864–886.

[17] Schröder, J., Balzani, D. and Gross, D., Aspects of modeling and computer simulation of soft tissues: applications to arterial walls, *Materialwissenschaft und Werkstofftechnik* (2005) **36/12**:795–801.

[18] Schröder, J. and Neff, P., Invariant formulation of hyperelastic transverse isotropy based on polyconvex free energy functions, *International Journal of Solids and Structures* (2003) **40**:401–445.

[19] Schulze-Bauer, C.A.J., Regitnig, P., and Holzapfel G.A., Mechanics of the human femoral adventitia including the high-pressure response, *American Journal of Physiology - Heart and Circulatory Physiology* (2002) **282**:H2427–H2440.

[20] Simo, J.C., On a fully three-dimensional finite-strain viscoelastic damage model: formulation and computational aspects, *Computer Methods in Applied Mechanics and Engineering* (1987) **60**:153–173.

XI International Conference on Computational Plasticity. Fundamentals and Applications
COMPLAS XI
E. Oñate, D.R.J. Owen, D. Peric and B. Suárez (Eds)

NUMERICAL ANALYSIS OF PULSATILE BLOOD FLOW IN REALISTIC CORONARY BYPASS MODELS

JAN VIMMR*, ALENA JONÁŠOVÁ* AND ONDŘEJ BUBLÍK*

*University of West Bohemia, Department of Mechanics
Univerzitni 22, CZ-306 14 Pilsen, Czech Republic
e-mail: jvimmr@kme.zcu.cz

Key words: Aorto-coronary Bypass, End-to-side Anastomosis, Side-to-side Anastomosis, Hemodynamics, Pulsatile Flow, FVM

Abstract. The paper's objective lies in numerical modelling of pulsatile blood flow in complete aorto-coronary bypass models reconstructed from CT data, especially in models with individual and sequential bypass grafts. Unsteady blood flow is described by the nonlinear system of the incompressible Navier-Stokes equations in 3D, which is numerically solved using developed computational algorithm based on the fully implicit projection method and on the cell-centred finite volume method for hybrid unstructured tetrahedral grids. Obtained numerical results are discussed with regard to distribution of velocity, wall shear stress and oscillatory shear index at proximal and distal anastomoses, i.e., in areas prone to development of intimal hyperplasia.

1 INTRODUCTION

According to the most recent European cardiovascular disease statistics[1] almost half of affected people had either brain stroke or heart infarction. Considering also the increasing number of patients and surgical treatments connected with stenosed or occluded arteries, the understanding of cardiovascular disease origin and development is crucial for its future prevention and treatment. In the case of ischemic heart disease, one of possible surgical interventions is the implantation of venous bypass grafts, often creating a detour between aorta and the damaged coronary artery branch. The failure rate of implanted bypass grafts is mostly related to the development of intimal hyperplasia, an abnormal healing process in the anastomosis region. It is typical for the thickening of tunica intima leading to decrease in the arterial lumen and consequently to graft failure[2]. Nowadays atherosclerosis and intimal hyperplasia alike are hypothesized to be triggered by non-uniform hemodynamics leading to morphological and metabolic changes within the vessel wall[3]. Recirculation zones and low and oscillating wall shear stress are some of the supposed triggering factors that are responsible for endothelium activation[4]. Beside

clinical research, numerical investigation of bypass hemodynamics represents a valuable insight into the problem and provide so better understanding of blood flow influence on cardiovascular disease occurrence and development.

The objective of this paper is the modelling of pulsatile blood flow in patient-specific aorto-coronary bypass models with emphasis placed on the hemodynamics study in individual and sequential types. We denote the individual type as the bypass with one proximal and one distal (end-to-side) anastomosis and the sequential type as the one with one proximal and two distal (side-to-side and end-to-side) anastomoses. As is apparent from the presence of multiple anastomoses, the sequential bypass technique is often employed to connect several coronary arteries by one graft. However, a major unknown of such bypasses lies in the resulting blood supply to each connected coronary artery and the possibility of intimal hyperplasia formation at one or both established anastomoses. In this regard, we perform a numerical analysis of pulsatile blood flow in two aorto-coronary bypass models reconstructed from CT data provided by the University Hospital Pilsen, Czech Republic. For results discussion, special emphasis is placed on the evaluation and analysis of main hemodynamic factors such as distribution of velocity, wall shear stress (WSS) and oscillatory shear index (OSI) in areas that may be prone to development of intimal hyperplasia.

2 PROBLEM FORMULATION AND BYPASS MODELS

In comparison to other published papers, which mostly dealt with distal bypass parts, especially the distal anastomosis[5], the present study considers complete aorto-coronary bypass models with realistic geometry, i.e., both proximal and distal anastomoses are modelled. In this way, the problem of boundary conditions may be adequately approached. In human vessels, blood behaves as an incompressible non-Newtonian fluid. As is shown in other studies[6], blood's shear-thinning behaviour may be neglected in selected cases such

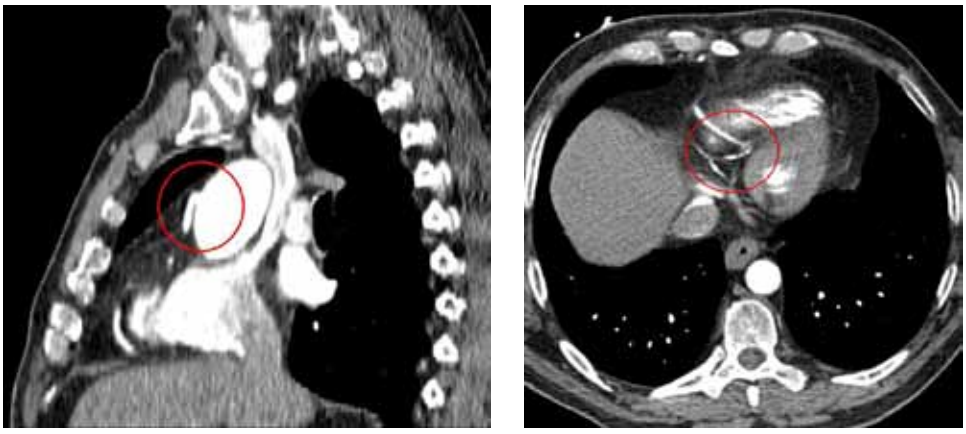

Figure 1: CT scans of individual aorto-coronary bypass model – position of the proximal end-to-side anastomosis (*left*) and the distal end-to-side anastomosis (*right*)

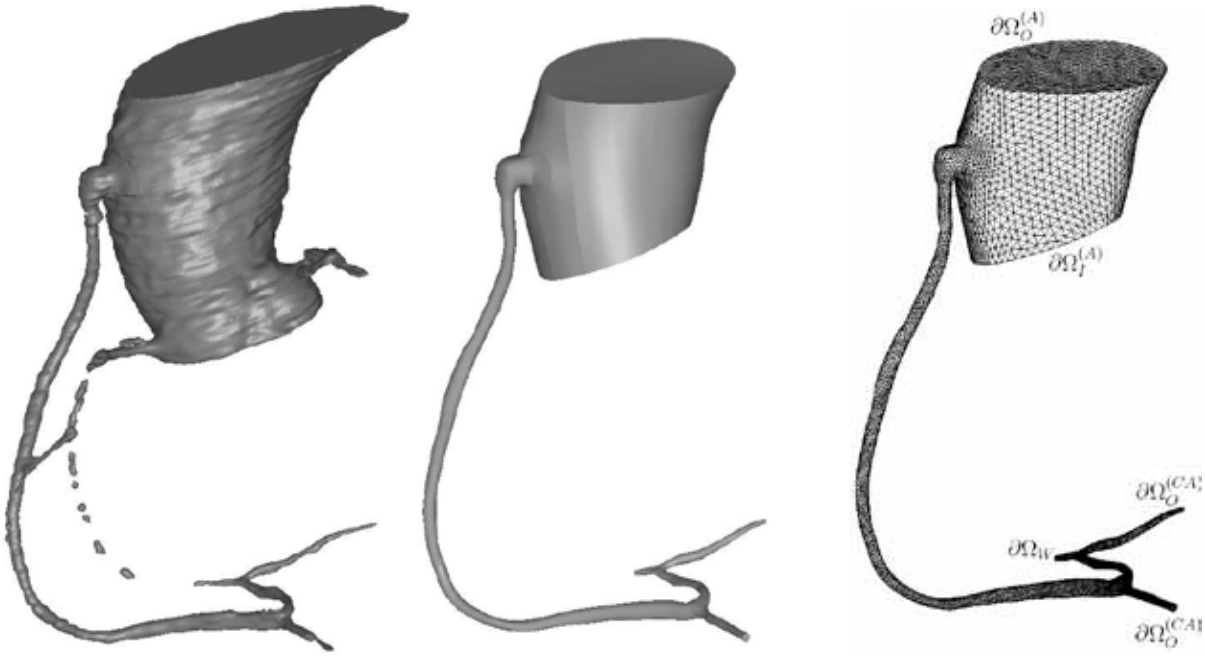

Figure 2: Individual aorto-coronary bypass model – (*from left to right*) primary reconstruction from CT data, model after smoothing, tetrahedral computational mesh with denoted computational domain boundaries

as in human aorta. Furthermore, previous numerical simulations of steady non-Newtonian blood flow performed by the authors of this paper in an idealized coronary bypass model[7] showed negligible non-Newtonian effects. Therefore, in the present study, blood's complex rheological properties are neglected and blood is assumed to be an Newtonian fluid. Further, all numerical simulations of pulsatile blood flow are carried out for bypass models with rigid and impermeable walls. The authors are aware that this assumption, especially in connection with the elastic aorta, represents a relevant limitation of the current mathematical model. However, an improvement in relation to vessel compliance is planned in one of their future studies.

For the purpose of the present study, two sets of CT data were provided by the University Hospital Pilsen, Czech Republic. The first data set contained the CT scans of an individual graft, Fig. 1, whose proximal end was attached to the aorta and the distal one was sewn to an occluded branch of coronary arteries. The corresponding primary model after reconstruction in software Amira is shown in Fig. 2 together with the final smoothed model and the unstructured tetrahedral computational mesh, which was generated in the system Altair Hypermesh. Fig. 3 gives a detailed view at the mesh in the distal anastomosis region and in the pre-anastomosis coronary bifurcation. For this bypass type, following inlet and outlet boundary conditions are prescribed, see boundaries denoted in Fig. 2,

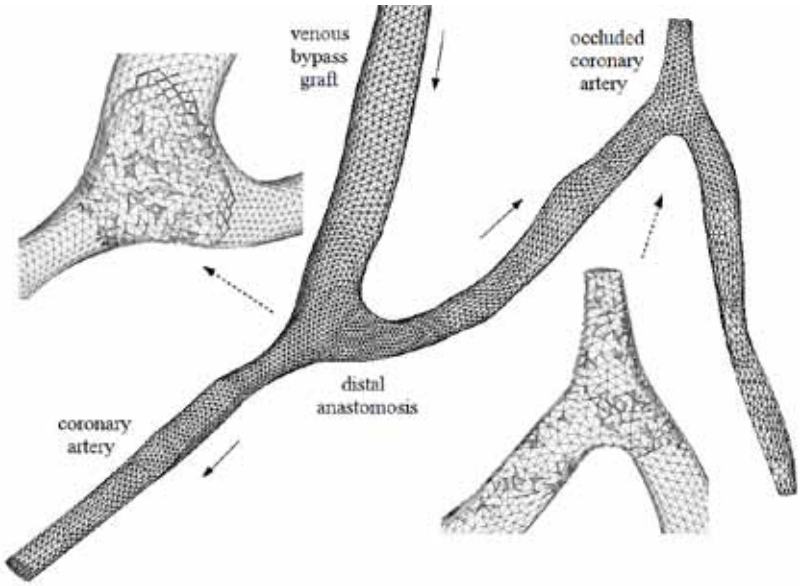

Figure 3: Individual aorto-coronary bypass model – view at the distal end-to-side anastomosis region with coronary bifurcation

- aorta inlet $\partial\Omega_I^{(A)}$ and aorta outlet $\partial\Omega_O^{(A)}$ – time-dependent flow rate $Q(t)$ and pressure $p(t)$, respectively, are applied. The values of flow rate and pressure are taken from literature[8], Fig. 4;
- coronary artery outlet $\partial\Omega_O^{(CA)}$ – constant pressure equal to average arterial pressure 12 000 Pa is given;
- occluded coronary artery is treated as a rigid wall boundary $\partial\Omega_W$.

In order to perform numerical computations with non-dimensional primitive variables, reference values have to be set. For the individual graft, the reference velocity $U_{ref}^{(1)}$ is

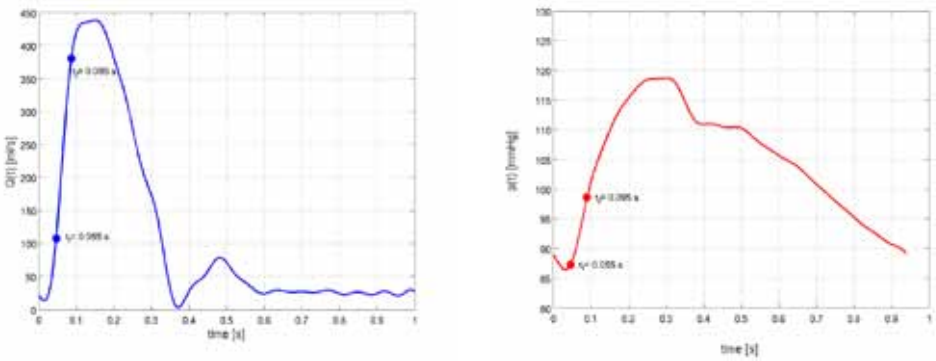

Figure 4: Individual aorto-coronary bypass model – time-dependent flow rate $Q(t)$ prescribed at the aorta inlet $\partial\Omega_I^{(A)}$ (*left*) and time-dependent pressure $p(t)$ prescribed at the aorta outlet $\partial\Omega_O^{(A)}$ (*right*)

chosen to be equal to $0.1592\,\mathrm{m}\cdot\mathrm{s}^{-1}$, corresponding to average aorta inlet flow rate, Fig. 4 (*left*), and the reference diameter is $D_{ref}^{(1)} = 0.036\,\mathrm{m}$, corresponding to average aorta diameter. According to prescribed boundary conditions[8], blood's density and viscosity are considered to be constant $\eta^{(1)} = 0.0049\,\mathrm{Pa}\cdot\mathrm{s}$ and $\varrho^{(1)} = 1055\,\mathrm{kg}\cdot\mathrm{m}^{-3}$, respectively.

The second set of provided CT scans contained data of a sequential aorto-coronary bypass with one side-to-side anastomosis and one end-to-side anastomosis, Fig. 5. The figure shows the reconstructed bypass model and the unstructured tetrahedral computational mesh as well. Detailed view at both the side-to-side and end-to-side anastomoses is given in Fig. 6. Since the authors of this paper have access to physiological data measured within a real side-to-side anastomosis[9], first numerical simulations of pulsatile blood flow in the sequential aorto-coronary bypass model are done for the side-to-side anastomosis

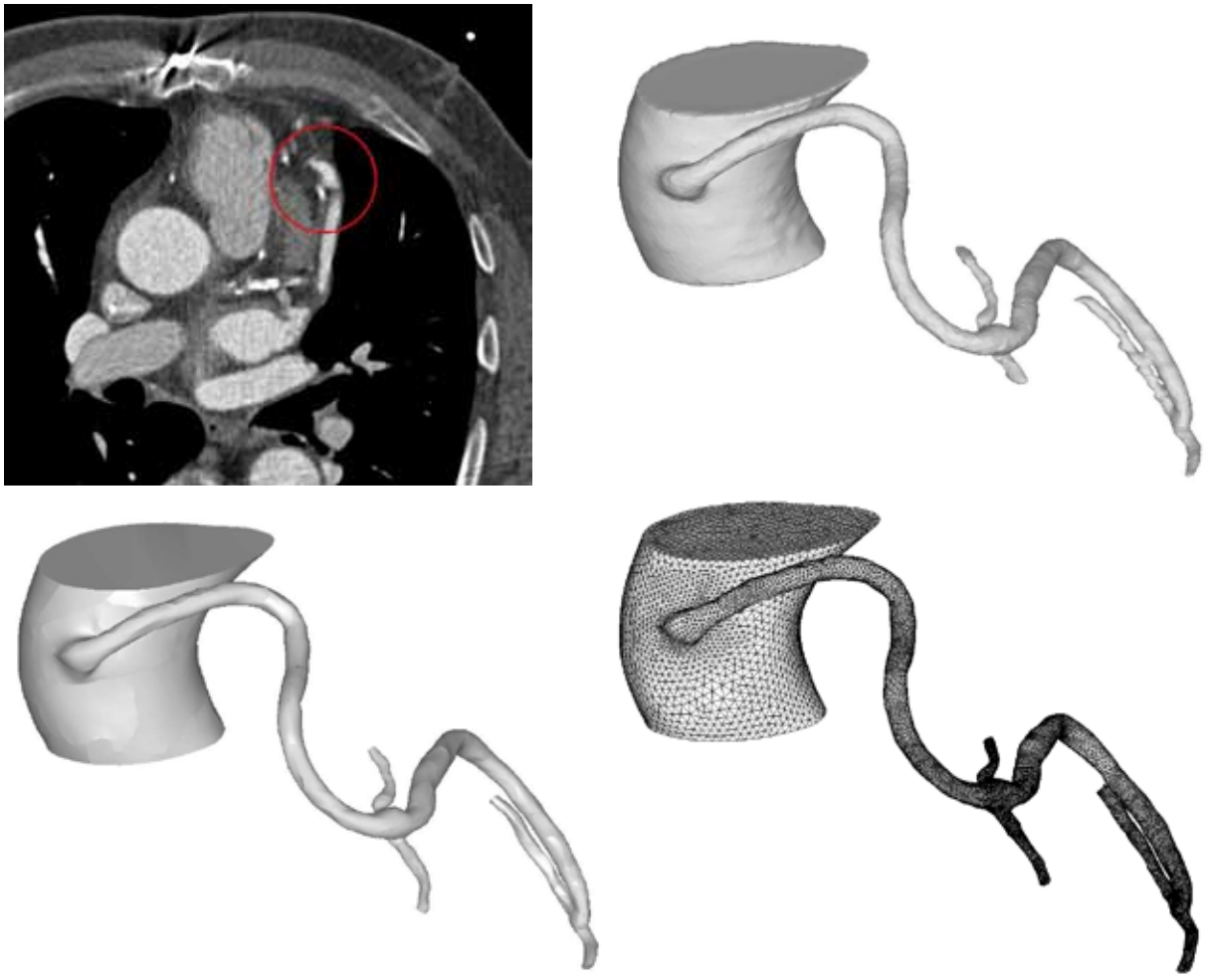

Figure 5: Sequential aorto-coronary bypass model – (*from left to right*) CT scan with denoted position of the side-to-side anastomosis, primary reconstruction from CT data, model after smoothing, tetrahedral computational mesh

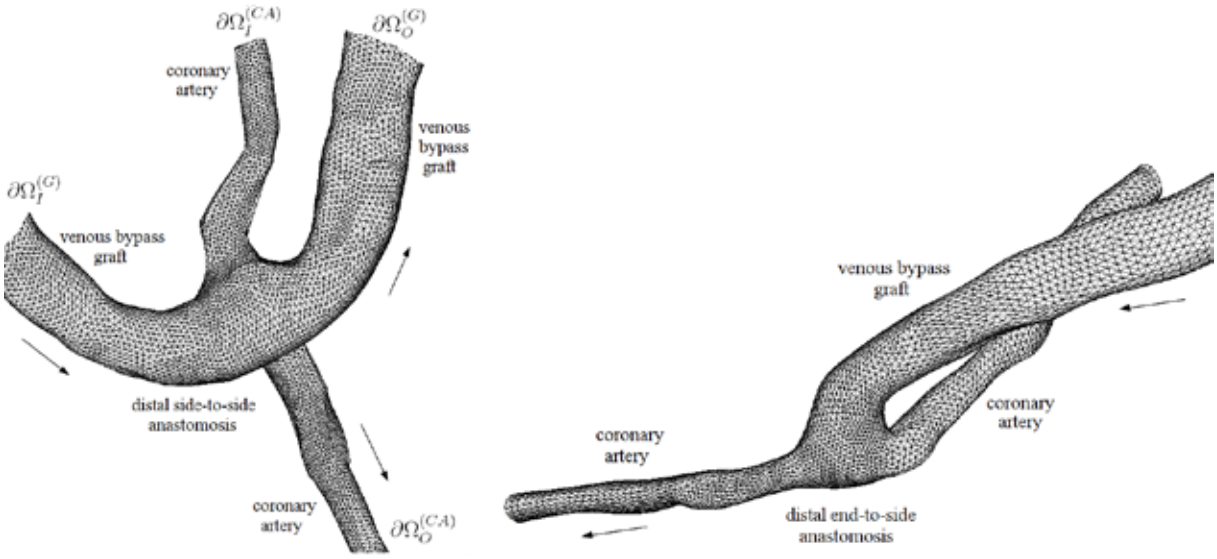

Figure 6: Sequential aorto-coronary bypass model – view at the distal side-to-side anastomosis (*left*) and at the distal end-to-side anastomosis (*right*)

with following inlet and outlet boundary conditions, Fig. 6 (*left*),

- graft inlet $\partial\Omega_I^{(G)}$ and coronary artery inlet $\partial\Omega_I^{(CA)}$ – time-dependent flow rates $Q(t)^{(G)}$ and $Q(t)^{(CA)}$, respectively, are applied according to literature[9], Fig. 7;
- graft outlet $\partial\Omega_O^{(G)}$ and coronary artery outlet $\partial\Omega_O^{(CA)}$ – constant pressure equal to average arterial pressure 12 000 Pa is given.

Similarly to the case of individual graft, reference values have to be chosen. The reference velocity $U_{ref}^{(2)} = 0.1193\,\mathrm{m}\cdot\mathrm{s}^{-1}$ is determined from average graft inlet flow rate, Fig. 7, and the reference diameter $D_{ref}^{(2)} = 0.0045\,\mathrm{m}$ set equal to average graft diameter. According to prescribed values of boundary conditions[9], blood's density and viscosity are $\eta^{(2)} = 0.0037\,\mathrm{Pa}\cdot\mathrm{s}$ and $\varrho^{(2)} = 1060\,\mathrm{kg}\cdot\mathrm{m}^{-3}$, respectively.

3 MATHEMATICAL MODELLING

3.1 Mathematical model

Let us consider a time interval $(0, \mathcal{T})$, $\mathcal{T} > 0$ and a bounded 3D computational domain $\Omega \subset \mathbf{R}^3$ with boundary $\partial\Omega$. According to assumptions established in the previous section, coronary blood flow in this computational domain may be modelled as unsteady laminar isothermal flow of incompressible Newtonian fluid that in the space-time cylinder $\Omega_T = \Omega \times (0, \mathcal{T})$ is mathematically described by the non-linear system of incompressible Navier-

Stokes (NS) equations written in the non-dimensional form as

$$\frac{\partial v_j}{\partial x_j} = 0\,, \tag{1}$$

$$\frac{\partial v_i}{\partial t} + \frac{\partial}{\partial x_j}(v_i v_j) + \frac{\partial p}{\partial x_i} = \frac{1}{\mathrm{Re}^{(s)}} \frac{\partial^2 v_i}{\partial x_j \partial x_j} \quad i,j = 1,2,3, \tag{2}$$

where t is the time, v_i is the i-th component of the velocity vector $\boldsymbol{v} = [v_1, v_2, v_3]^T$ corresponding to the Cartesian component x_i of the space variables vector $\boldsymbol{x} = [x_1, x_2, x_3]^T$, p is the pressure and $\mathrm{Re}^{(s)} = U_{ref}^{(s)} D_{ref}^{(s)} \varrho^{(s)} / \eta^{(s)}$, $s = 1, 2$ is the reference Reynolds number. For the individual aorto-coronary bypass model and for the side-to-side anastomosis model, we get $\mathrm{Re}^{(1)} = 1\,234.3$ and $\mathrm{Re}^{(2)} = 153.8$, respectively.

3.2 Numerical method

The numerical solution of the non-linear time-dependent system of the incompressible NS equations (1) – (2) is based on the fractional step method and the cell-centred finite volume method formulated for hybrid unstructured tetrahedral grids, whose control volume Ω_k is shown in Fig. 8. The principle of hybrid grid systems was proposed by Kim et al.[10] Time discretization of the incompressible NS equations (2) is performed using the implicit second order Crank-Nicolson scheme with linearization of the convective term.

Let us introduce a variable $\delta\hat{v}_i = \hat{v}_i - v_i^n$, where $\hat{v}_i$ is the intermediate velocity and v_i^n is the velocity computed at the time level n. Let us further introduce a pressure correction function Ψ defined as $\Psi = (p^{n+1} - p^n)\Delta t$, where p^{n+1} and p^n are the pressure values computed at the time levels n and $(n+1)$, respectively. After the discretization, we get

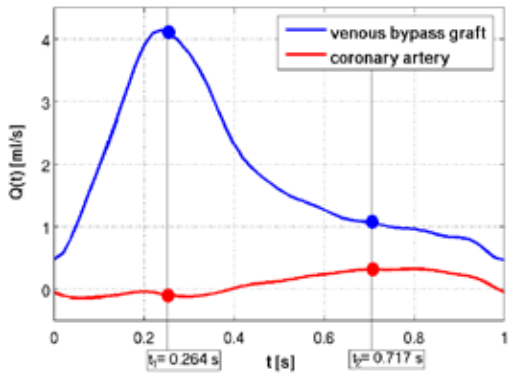

Figure 7: Time-dependent flow rates prescribed at the graft inlet $Q(t)^{(G)}$ and at the coronary artery inlet $Q(t)^{(CA)}$ of the side-to-side anastomosis model

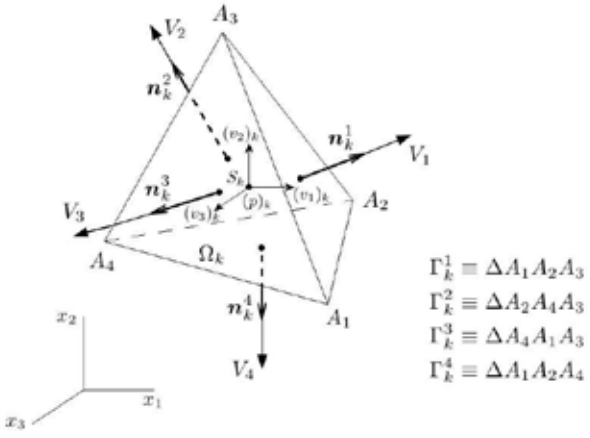

Figure 8: A tetrahedral control volume $\Omega_k = A_1A_2A_3A_4$ with boundary $\partial\Omega_k = \bigcup_{m=1}^{4} \Gamma_k^m$

following system of equations

$$(\delta\hat{v}_i)_k + \frac{\Delta t}{2|\Omega_k|}\sum_{m=1}^{4}\left(\delta\hat{v}_{i\,m}V_m^n + v_{i\,m}^n \cdot {}^j n_k^m \;\delta\hat{v}_{j\,m} + 2v_{i\,m}^n V_m^n\right)|\Gamma_k^m|$$

$$+\frac{\Delta t}{2|\Omega_k|}\sum_{m=1}^{4} p_m^n \cdot {}^i n_k^m\,|\Gamma_k^m| = \frac{\Delta t}{2\mathrm{Re}^{(s)}|\Omega_k|}\sum_{m=1}^{4}\frac{\partial}{\partial \boldsymbol{n}_k^m}\left(\delta\hat{v}_{i\,m} + 2v_{i\,m}^n\right)|\Gamma_k^m|\,, \tag{3}$$

$$(\hat{v}_i)_k = (v_i^n)_k + (\delta\hat{v}_i)_k, \tag{4}$$

$$\sum_{m=1}^{4}\frac{\partial\Psi}{\partial \boldsymbol{n}_k^m}|\Gamma_k^m| = \sum_{m=1}^{4}\hat{v}_{i\,m}\cdot {}^i n_k^m\,|\Gamma_k^m| \equiv \sum_{m=1}^{4}\hat{V}_m\,|\Gamma_k^m|, \tag{5}$$

$$(v_i^{n+1})_k = (\hat{v}_i)_k - \frac{1}{|\Omega_k|}\sum_{m=1}^{4}\Psi_m \cdot {}^i n_k^m\,|\Gamma_k^m|, \tag{6}$$

$$(p^{n+1})_k = (p^n)_k + \frac{1}{\Delta t}(\Psi)_k, \tag{7}$$

$$V_m^{n+1} = \hat{V}_m - \frac{\partial\Psi}{\partial \boldsymbol{n}_k^m}\,, \tag{8}$$

where Δt is the time step, $|\Omega_k|$ is the volume of the control volume Ω_k, $k = 1, \ldots, N_{CV}$, Fig. 8, $(\Phi)_k = \frac{1}{|\Omega_k|}\int_{\Omega_k}\Phi \mathrm{d}\Omega$ is the integral average for an arbitrary flow quantity Φ over control volume Ω_k, $|\Gamma_k^m|$, $m = 1, \ldots, 4$ is the area of the m-th face Γ_k^m of the control volume Ω_k, ${}^i n_k^m$ is the i-th component of the outward unit vector $\boldsymbol{n}_k^m = [{}^1 n_k^m, {}^2 n_k^m, {}^3 n_k^m]^T$ normal to the face Γ_k^m and $\hat{V}_m = \hat{v}_{im}\cdot {}^i n_k^m$ denotes the intermediate face-normal velocity at the face Γ_k^m. Note that the values of face-normal velocity V_m^{n+1} computed with the help of Eq. (8) are used as values of face-normal velocity V_m^n in Eq. (3) at the next time level. For the determination of values $\delta\hat{v}_{i\,m}$, $v_{i\,m}^n$, p_m^n, Ψ_m and derivatives $\frac{\partial\Psi}{\partial \boldsymbol{n}_k^m}$, $\frac{\partial}{\partial \boldsymbol{n}_k^m}\left(\delta\hat{v}_{i\,m} + 2v_{i\,m}^n\right)$ at the m-th face Γ_k^m of the control volume Ω_k, the application of an interpolation method is used. For more details on the described numerical method, see Vimmr et al.[11] In relation to paper's objectives to model pulsatile blood flow, boundary conditions are prescribed as

- inlet $\Gamma_k^m \subset \partial\Omega_I$: $v_{i\,m} = v_{i\,I}$, $\left.\frac{\partial v_{i\,m}}{\partial \boldsymbol{n}_k^m}\right|_{\Gamma_k^m} = 0$, $\left.\frac{\partial\Psi}{\partial \boldsymbol{n}_k^m}\right|_{\Gamma_k^m} = 0$, where the inlet velocity vector components $v_{i\,I}$ are given in non-dimensional form for corresponding inlet boundaries of both bypass models, see Sec. 2;
- outlet $\Gamma_k^m \subset \partial\Omega_O$: $p_m \boldsymbol{n}_k^m - \frac{1}{\mathrm{Re}^{(s)}}\frac{\partial \boldsymbol{v}_m}{\partial \boldsymbol{n}_k^m} = p_O \boldsymbol{n}_k^m$, $\Psi_m = 0$, where p_O is the prescribed non-dimensional value of outlet pressure, see Sec. 2;
- rigid wall $\Gamma_k^m \subset \partial\Omega_W$: $v_{i\,m} = 0$, $\left.\frac{\partial\Psi}{\partial \boldsymbol{n}_k^m}\right|_{\Gamma_k^m} = 0$.

The solution of Eq. (3) leads to a system of linear algebraic equations $\mathbf{A}_{NS} \cdot \mathbf{x}_{NS} = \mathbf{b}_{NS}$ for $3 \cdot N_{CV}$ unknown values $(\delta\hat{v}_i)_k$, $i = 1, 2, 3$, $k = 1, 2, \ldots N_{CV}$, where N_{CV} is the number of control volumes within the hybrid unstructured computational mesh. Similarly, the solution of Poisson equation (5) for the pressure correction function leads to a system of linear algebraic equations $\mathbf{A}_{Poi} \cdot \mathbf{x}_{Poi} = \mathbf{b}_{Poi}$ for N_{CV} unknown values $(\Psi)_k$, $k = 1, 2, \ldots N_{CV}$. Since both systems of equations contain large sparse matrices $\mathbf{A}_{NS}$ and $\mathbf{A}_{Poi}$, it is favourable to use an iterative solution. In our case, BICGSTAB method with incomplete LU preconditioner is applied. This kind of methods is a standard part of the MATLAB software. For the incomplete LU decomposition, the UMFPACK library is used.

4 NUMERICAL RESULTS, DISCUSSION AND CONCLUSIONS

Let us note that in this section all numerical results are presented in their dimensional form. For the case of individual aorto-coronary bypass, Fig. 9–10 show velocity vectors at both the proximal and distal anastomoses at two time instants $t_1 = 0.055\,\mathrm{s}$ and $t_2 = 0.095\,\mathrm{s}$, respectively. The position of both pre-systolic time instants within the the cardiac cycle at the aorta is denoted in Fig. 4 for the values of inlet flow rate and outlet pressure. In the case of proximal anastomosis, the presence of a 'bulge' filled with a weak recirculation zone seems to significantly affect velocity distribution and consequently the blood supply to the distal anastomosis. Moreover, the present shape of the proximal junction region and its close proximity to high-velocity aorta may enhance the risk of thrombus formation due to the possibility of blood cells accumulation and platelet activation. Regarding the distal anastomosis of the individual bypass model, the flow distribution between the pre- and

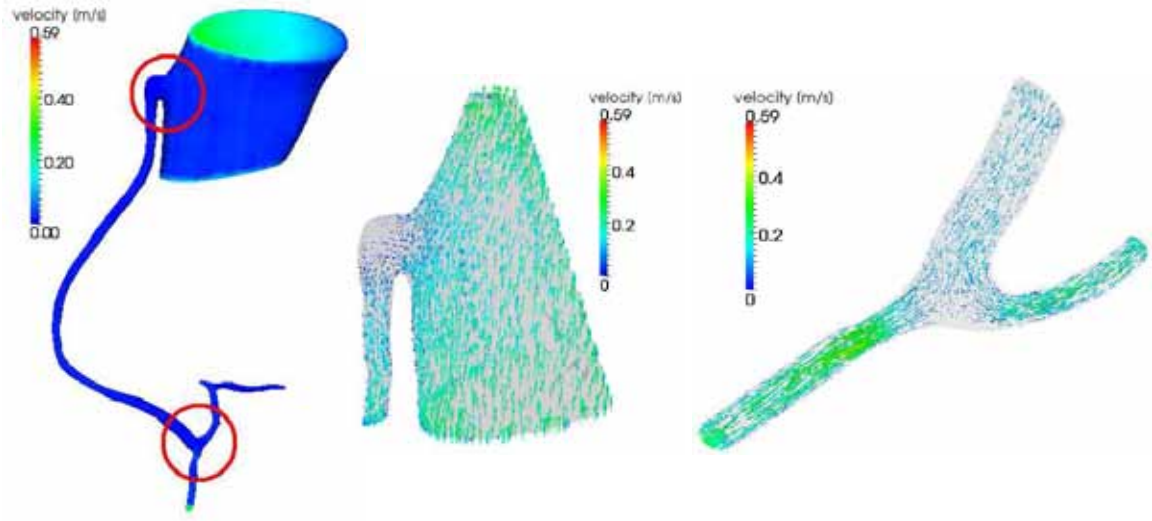

Figure 9: Velocity distribution within the individual aorto-coronary bypass model and velocity vectors at the proximal end-to-side and distal end-to-side anastomoses at the time $t_1 = 0.055\,\mathrm{s}$

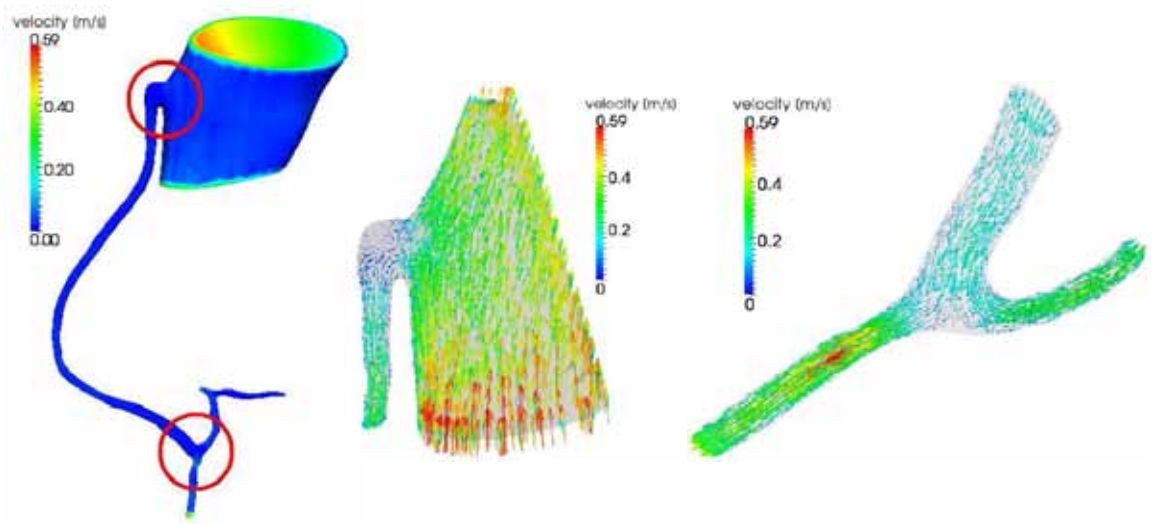

Figure 10: Velocity distribution within the individual aorto-coronary bypass model and velocity vectors at the proximal end-to-side and distal end-to-side anastomoses at the time $t_2 = 0.095\,\mathrm{s}$

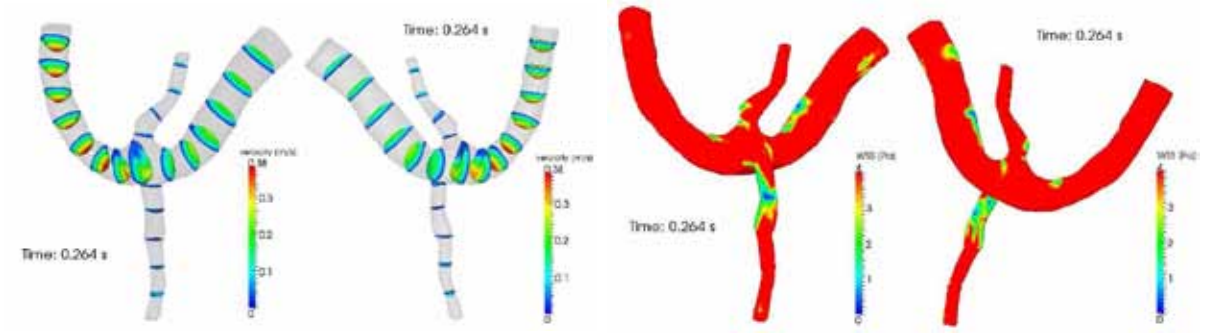

Figure 11: Side-to-side anastomosis – selected velocity profiles (*left*) and corresponding WSS distribution (*right*) at the time $t_1 = 0.264\,\mathrm{s}$

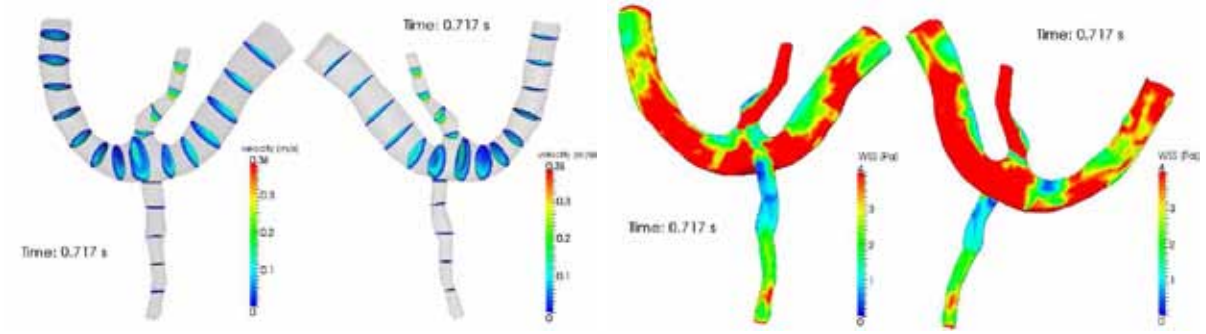

Figure 12: Side-to-side anastomosis – selected velocity profiles (*left*) and corresponding WSS distribution (*right*) at the time $t_2 = 0.717\,\mathrm{s}$

$$\mathrm{OSI} = \frac{1}{2}\left(1 - \frac{\left|\int_0^T \boldsymbol{\tau}_W \,\mathrm{d}t\right|}{\int_0^T |\boldsymbol{\tau}_W| \,\mathrm{d}t}\right)$$

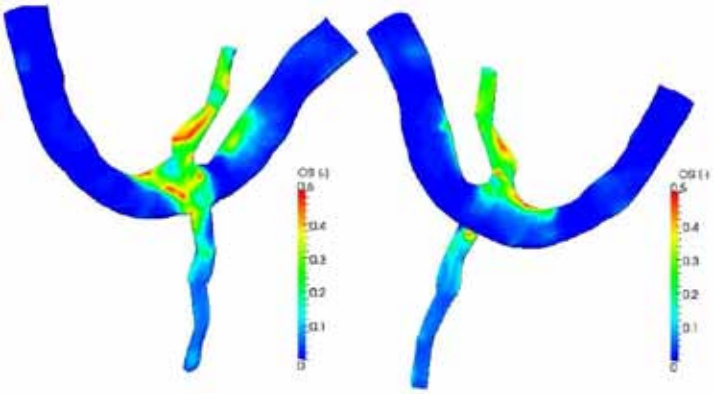

Figure 13: Formula used for the calculation of oscillatory shear index (OSI)[12] and OSI distribution at the side-to-side anastomosis

post-anastomosis branch of the coronary artery appears to be relatively uniform. However, due to this kind of stream division, blood remains almost motionless in a certain part of the anastomosis near the arterial floor, which may prove to be a significant trigger of intimal hyperplasia in this bypass model.

In relation to numerical simulation of pulsatile blood flow in the side-to-side anastomosis model, velocity profiles at selected cross-sections with corresponding WSS distributions are shown in Fig. 11–12 for two time instants $t_1 = 0.264\,\mathrm{s}$ and $t_2 = 0.717\,\mathrm{s}$, respectively. The time instants correspond either to systolic or diastolic phases of the cardiac cycle, see Fig. 7. Since low WSS values are of main interest when dealing with intimal hyperplasia, WSS distributions in Fig. 11–12 are displayed for a lowered range $(1 - 4\,\mathrm{Pa})$. The results indicate a considerably non-uniform WSS stimulation of all bypass walls, especially in the anastomosis region. This assumption is supported by the skewed shape of velocity profiles in this area during systole, Fig. 11. Moreover, according to calculated WSS values, blood supply to the coronary artery downstream from the anastomosis seems to be taking place only before diastole. The influence of pulsatile blood flow on arterial wall stimulation in relation to intimal hyperplasia development is usually recorded in the form of oscillatory shear index[12]. The formula for its calculation and corresponding distribution at the side-to-side anastomosis model is shown in Fig. 13, where OSI values equal to 0.5 indicate a highly oscillating WSS and at the same time denote a bypass area prone to intimal thickening.

ACKNOWLEDGMENTS

This investigation was supported by the European Regional Development Fund, project "NTIS – New Technologies for Information Society", European Centre of Excellence, CZ.1.05/1.1.00/02.0090 and by the research project MSM 4977751303 of the Ministry of Education, Youth and Sports of the Czech Republic.

REFERENCES

[1] *European Cardiovascular Disease Statistics - 2008 Edition*. European Heart Network, (2008), Oxford, UK.

[2] Haruguchi, H. and Teraoka, S. Intimal hyperplasia and hemodynamic factors in arterial bypass and arteriovenous grafts: A review. *J. Artif. Organs* (2003) **6**:227–235.

[3] Loth, F., Fischer, P.F. and Bassiouny, H.S. Blood flow in end-to-side anastomoses. *Annu. Rev. Fluid Mech.* (2008) **40**:367–393.

[4] Malek, A.M. and Izumo, S. Mechanism of endothelial cell shape change and cytoskeletal remodelling in response to fluid shear stress. *J. Cell Sci.* (1996) **109**:713–726.

[5] Bertolotti, C., Deplano, V., Fuseri, J. and Dupouy, P., Numerical and experimental model of post-operative realistic flows in stenosed coronary bypasses. *J. Biomech.* (2001) **34**:1049-1064.

[6] Friedman, M.H., Bargeron, C.B., Duncan, D.D., Hutchins, G.M. and Mark, F.F. Effects of arterial compliance and non-Newtonian rheology on correlations between intimal thickness and wall shear. *J. Biomech. Eng.* (1992) **114**:317–320.

[7] Vimmr, J. and Jonášová, A. Non-Newtonian effects of blood flow in complete coronary and femoral bypasses. *Math. Comput. Simulat.* (2010) **80**:1324–1336.

[8] Olufsen, M.S., Peskin, C.S., Kim, W.Y., Pedersen, E.M., Nadim, A. and Larsen, J. Numerical simulation and experimental validation of blood flow in arteries with structured-tree out?ow conditions. *Ann. Biomed. Eng.* (2000) **28**:1281–1299.

[9] Frauenfelder, T., Boutsianis, E., Schertler, T., Husmann, L., Leschka, S., Poulikakos, D., Marincek, B. and Alkadhi, H. Flow and wall shear stress in end-to-side and side-to-side anastomosis of venous coronary artery bypass grafts. *BioMedical Engineering OnLine* (2007) **6**:1–13. (doi:10.1186/1475-925X-6-35)

[10] Kim, D. and Choi, H. A second-order time-accurate finite volume method for unsteady incompressible flow on hybrid unstructured grids. *J. Comput. Phys.* (2000) **162**:411–428.

[11] Vimmr, J., Jonášová, A. and Bublík, O. Effects of three geometrical parameters on pulsatile blood flow in complete idealized coronary bypasses. *Comput. Fluids* (2011). (preprint submitted in March 2011)

[12] Ku, D.N., Giddens, D.P., Zarins, C.K. and Glagov, S. Pulsatile flow and atherosclerosis in the human carotid bifurcation - Positive correlation between plaque location and low oscillating shear stress. *Arterioscl. Throm. Vas.* (1985) **5**:293–302.

XI International Conference on Computational Plasticity. Fundamentals and Applications
COMPLAS XI
E. Oñate, D.R.J. Owen, D. Peric and B. Suárez (Eds)

A COMBINED FINITE-DISCRETE ELEMENT MODEL FOR REINFORCED CONCRETE UNDER SEISMIC LOAD

N. ŽIVALJIĆ*, Ž. NIKOLIĆ* AND A. MUNJIZA*

* Faculty of Civil Engineering and Architecture
University of Split
Matice hrvatske 15, 21000 Split, Croatia
e-mail: nikolina.zivaljic@gradst.hr, zeljana.nikolic@gradst.hr, ante.munjiza@gradst.hr
web page: http://www.gradst.hr

Key words: Reinforced concrete structures, Seismic load, Combined finite-discrete element method.

Abstract. In this work a numerical model for analysis of reinforced concrete structures under seismic load is presented. The model uses the combined finite-discrete element method; thus taking into account the discontinuous nature of the reinforced concrete at the failure stages. The application of the combined finite-discrete element method includes a number of deformable discrete elements that interact with each other, fracture, fragmentation and disjoint during the seismic load. To these a robust model for reinforcement bars has been added. Interaction solutions between bars and concrete have also been developed and implemented into the open source Y2D combined finite-discrete element code. This way it is possible to describe initiation of the cracks, crack propagation and fracture which are important mechanisms in the analysis of reinforced concrete structures under seismic load. Through numerical examples these have been demonstrated and tested using reinforced concrete structure under an experimentally recorded earthquake accelelogram.

1 INTRODUCTION

The development of the numerical models for simulation of the response of reinforced concrete structures under seismic load, taking into consideration non-linear behaviour of the concrete and reinforcement, makes possible the results of high accuracy almost equivalent to the results obtained by expensive laboratory experiments. One of the main causes of concrete non-linear behaviour is cracking. A reliable model for simulation of the opening and closing the cracks is especially important in the structures under seismic load because a significant part of seismic energy is lost in cracking. The most of the models described in literature is based on finite element method where the cracking is described with smeared crack models or with embedded models where the cracks are modelled as discontinuity within the elements by enriching interpolation function. In contrast to the finite elements, in discrete models cracks are simulated as discontinuities of displacement between two elements.

A numerical model for analysis of reinforced concrete structures under seismic load developed in this work is based on combined finite-discrete element method [1].

Transition from continua to discontinua in the combined finite discrete element method

occurs through fracture and fragmentation processes. A typical combined finite discrete element method based simulation may start with a few discrete elements and finished with very large number of discrete elements. Fracture occurs through alteration, damage, yielding or failure of microstructural elements of the material.

There has been a number of fracture models proposed in the context of both discrete element methods and combined finite discrete element method. Some of the models are based on a global approach applied to each individual body, while others used a local smeared crack approach or local single-crack approach. In this work a model for plane crack initiation and crack propagation in concrete is used [2]. The model combines standard finite element formulation for the hardening part of the constitutive law with the single-crack model for the softening part of stress-strain curve. Finite elements are used to model behaviour of the material up to the ultimate tensile strength while a discrete crack model is used for modelling of the crack opening and separation along edges of finite elements.

In this work an embedded model of reinforcing bars [3,4] is implemented in Y2D combined finite-discrete element code. The concrete structure is discretized on triangular finite elements, while the reinforcing bars are modelled with linear one-dimensional elements which can be placed in arbitrary position inside the concrete finite elements. The main assumption of the model is that the concrete tensile strength will be exceeded before the yield stress will achieved in steel. The behaviour of the structure is linear-elastic up to the opening of the crack. After that joint elements in concrete as well as in reinforcing bar are occurred. The concrete and reinforcing bars are analyzed separately, but they are connected by the relation between the size of the concrete crack and strain of the reinforcing bar [5,6]. Cyclic behaviour of the steel during the seismic load is modelled with improved Kato's model [7].

The formulation which has allowed the introducing of the seismic load modelled by an earthquake accelelogram is developed in this model.

2 MODELLING OF THE REINFORCED CONCRETE STRUCTURE

In this work an embedded model of reinforcing bars [3,4] is implemented in Y2D code based on combined finite-discrete element method. The concrete structure is discretized on triangular finite elements, while the reinforcing bars are modelled with linear one-dimensional elements which can be placed in arbitrary position inside the concrete finite elements. The model of the reinforced concrete structure with the embedded reinforcing bar is shown in Figure 1.

In the first step the reinforcement is modelled as bar AB (Figure 1.). Intersection between the sides of concrete finite elements and reinforcing bars gives the reinforcement finite elements. The behaviour of the structure is linear-elastic up to the opening of the crack. In that phase the triangular concrete element and line element of reinforcing bar behave as one body. The deformation of the triangular element influence to the deformation of the reinforcing bars. When the crack in concrete appears, joint element in concrete as well as joint element in reinforcing bars is occurred.

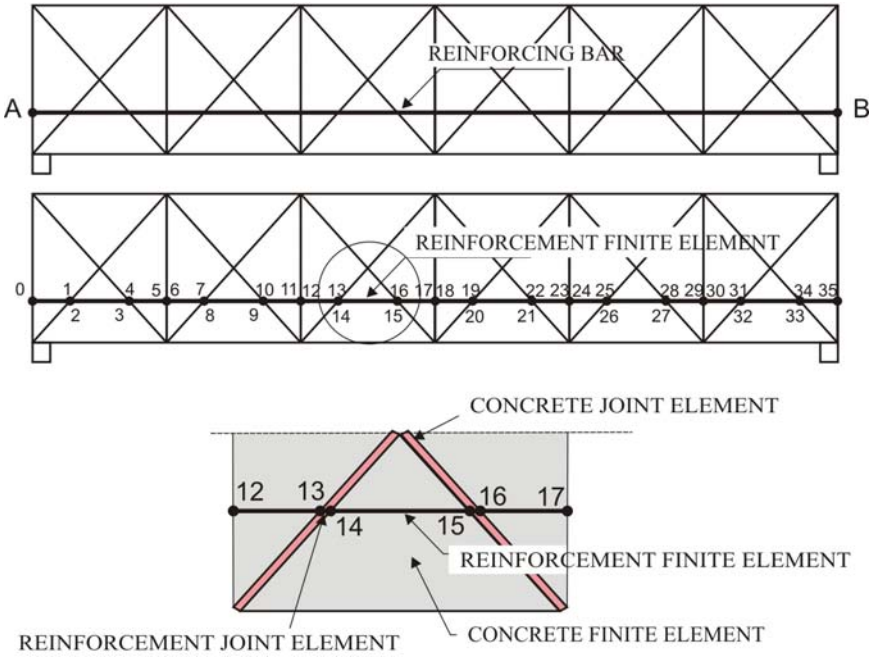

Figure 1: Discretization of reinforced concrete structure

3 NON-LINEAR MATERIAL MODEL IN JOINT ELEMENTS

3.1 Basic crack model

A model of discrete crack in reinforced concrete element with joint elements of concrete and reinforcing bar described in previous section is shown in Figure 2.

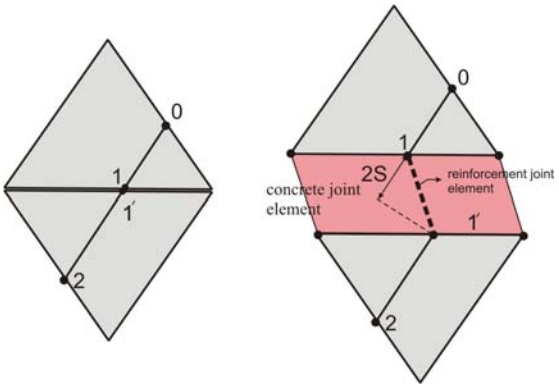

Figure 2: Discrete crack: crack initiation and crack development in concrete

3.2 Concrete model in joint element

In this work the combined finite-discrete element method uses the concrete model [2] which is based at crack initiation and crack propagation of mode I loaded cracks. The model is developed on the basis of experimental stress-strain curves for concrete in tension [8].

The area under the stress-strain curve consists of two parts (Figure 3). Part ″A″ is used for modelling of the concrete behaviour up to the crack opening while part ″B″ represents strain softening after the tensile strength is exceeded. The assumption of the discrete crack model is that the cracks coincide with the finite element edges. The total number of nodes for each of the finite element meshes is doubled and the continuity between elements is realized through the penalty method. Separation of the edges induces a bonding stress, which is a function of the size separation δ (Figure 3.).

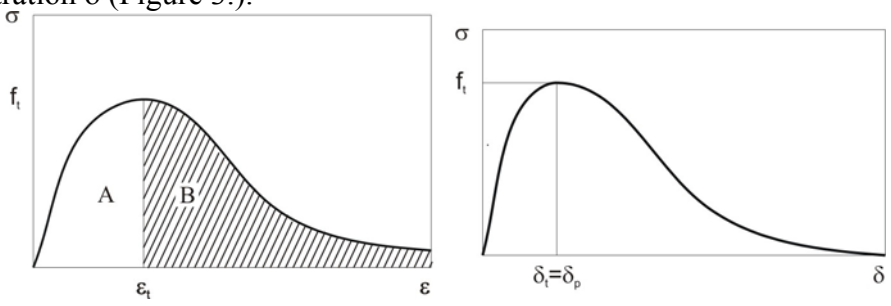

Figure 3: Strain softening stress-strain and stress-displacement curves

No separation of the adjacent elements occurs before the tensile strength is reached, i.e. $\delta_t = 0$. The edges of two adjacent elements are held together by normal and shear springs (Figure 4.) Procedure of the separation of the elements and complete relationship for the normal and shear bonding stress are given in [2].

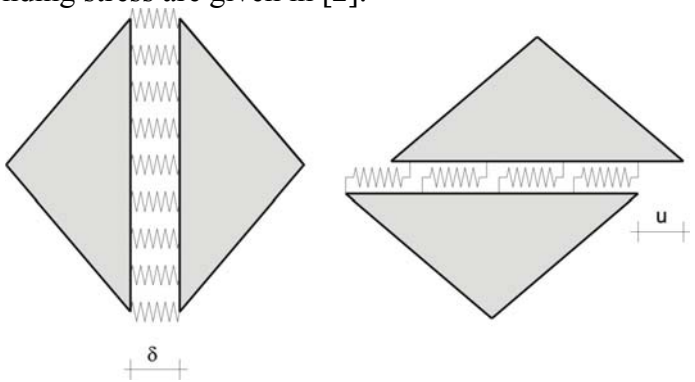

Figure 4: Normal and shear springs between the finite elements

3.3 Steel material model in reinforcement joint element

The main assumption of the model is that the concrete tensile strength will be exceeded before the yield stress will achieved in steel. The behaviour of the structure is linear-elastic up to the opening of the crack. After that joint elements in concrete as well as in reinforcing bar are occurred. The concrete and reinforcing bars are analyzed separately, but they are connected by the relationship between the size of the concrete crack and strain of the reinforcing bar.

In this work a model of the relationship between the concrete crack size and strain of the reinforcing bar developed by Shima [5] and Shin [6] is applied. The model is based on experimental strain-slip curves and represents well approximation of the behaviour of

reinforcing bar with the expressed plastic strain caused by cyclic loading.

The steel strain-slip relation before the yielding of reinforcing bar is given by expressions:

$$s = \varepsilon_s (6 + 3500\varepsilon_s) \tag{1}$$

$$s = \left(\frac{S}{D}\right) \cdot K_{fc}, \quad K_{fc} = \left(\frac{f_c'}{20}\right)^{2/3} \tag{2}$$

where $s = s(\varepsilon_s)$ is normalized steel slip, D is bar diameter and f_c' is concrete strength.

Normalized slip in the post-yield range is given by expression:

$$s = s_{pl} + s_e . \tag{3}$$

where s_e is slip in the elastic region and s_{pl} is slip in the yield region. A strain distribution along the reinforcing bar in the post-yield region is shown in Figure 5 where ε_{se} is a strain at the yield boundary point on the elastic region and ε_{sp} is a strain at the yield boundary point on the yield region.

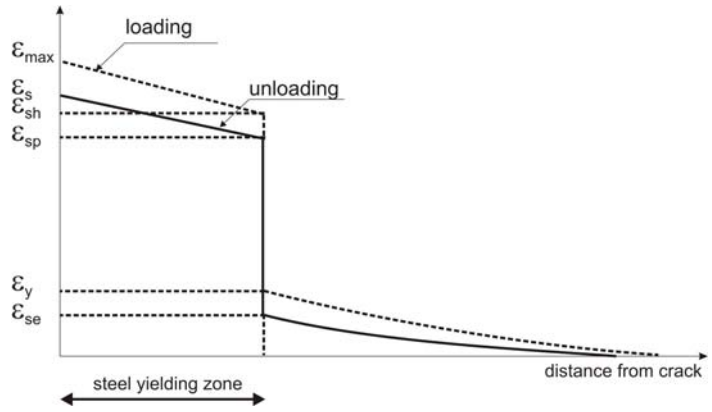

Figure 5: Strain distribution along the reinforcing bar in the post-yield range

If the deformation of concrete is ignored, the steel slip can be determined by integration of steel strain along the reinforcement axis. Normalized plastic steel slip in the yield region is given by an expression:

$$s_{pl} = \frac{(1+\beta)\varepsilon_s + \varepsilon_{sh} - \beta\varepsilon_{\max}}{\varepsilon_{\max} + \varepsilon_{sh}} \cdot (s_{\max} - s_y^*) \tag{4}$$

.

where $\beta = \sigma_{max} / \sigma_y$ represents the gradient of the line shown in Figure 5., σ_{max} is the maximum stress in reinforcing bar under tensile loads, s_{max} is a function of ε_{max} and $s_y^* = \varepsilon_s (2 + 3500\varepsilon_s)$.

In this paper non-linear material model for steel is based on experimental stress-strain curve and it is shown on Figure 6a. Cyclic behaviour of the steel during the seismic load is modelled with improved Kato's model [7] (Figure 6.b).

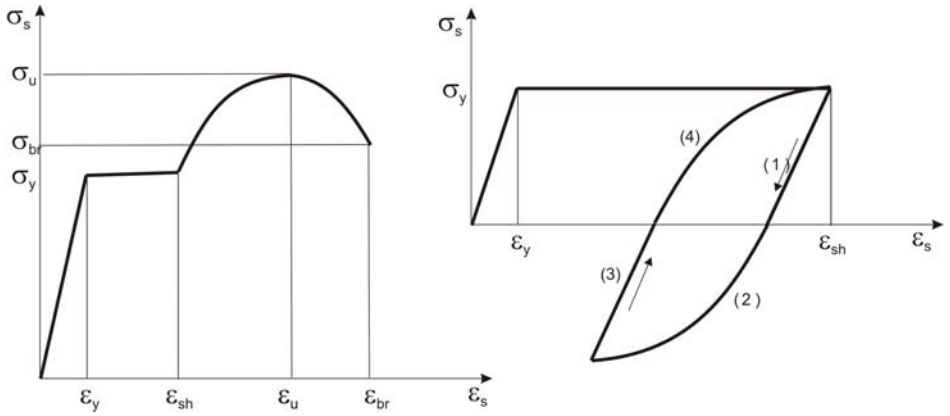

a) Stress-strain relation for steel b) Cyclic behaviour of steel

Figure 6: Material model for steel

4 EXAMPLES

4.1 Reinforced concrete beam

Reinforced concrete beam (Figure 7.) subjected to self weight is analyzed in order to verified implemented model of the reinforcing bars in static conditions. The span of the beam is 6.0 (m). Analysis is performed with two discretization presented in Figure 7. The midspan deflection, the stress in the concrete and the stress in the reinforcing bar in the marked point are analyzed. The results obtained by numerical model are compared with the analytical results in the Table 1.

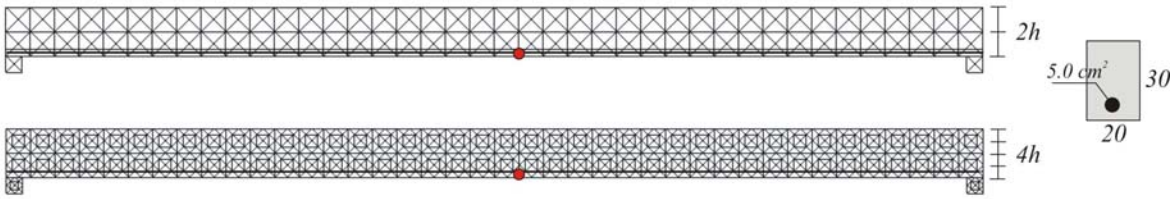

Figure 7: Reinforced concrete beam

Table 1: Comparison of numerical solutions with analytical ones

	Analytical	Numerical - 2h	Numerical - 4h
Midspan deflection (mm)	1.351	1.15	1.350
Concrete stress (N/m^2)	$1.65 \cdot 10^6$	$1.40 \cdot 10^6$	$1.65 \cdot 10^6$
Stress in reinforcing bar (N/m^2)	$11.60 \cdot 10^6$	$9.89 \cdot 10^6$	$11.56 \cdot 10^6$

Presented results show that the numerical solutions is very close to the analytical ones for the discretization 4h.

4.2 Analysis of steel behaviour in joint element of reinforcing bar

A simple example of reinforced concrete structure consists of 3 triangular finite elements with a reinforcing bar is analyzed. The length of triangular finite element side is 1.4 (m) and the cross-section area of reinforcing bar is 0.05 (m^2). Compressive concrete strength is 30 (MPa) while the characteristics of the steel are $\sigma_y=275\cdot10^6(N/m^2)$, $\sigma_u=430\cdot10^6(N/m^2)$, $\varepsilon_{sh}=0.005$, $\varepsilon_u=0.01$. The structure is subjected to initial velocity of 80 (m/s). The applied time interval is $\Delta t=0.3\cdot10^{-5}$s.

Figure 8 shows initial stage of the structure and stage of the structure after the cracking of reinforcing bar. Stress-strain relation in joint element of reinforcing bar, which is presented in Figure 9, shows cyclic behaviour of the steel.

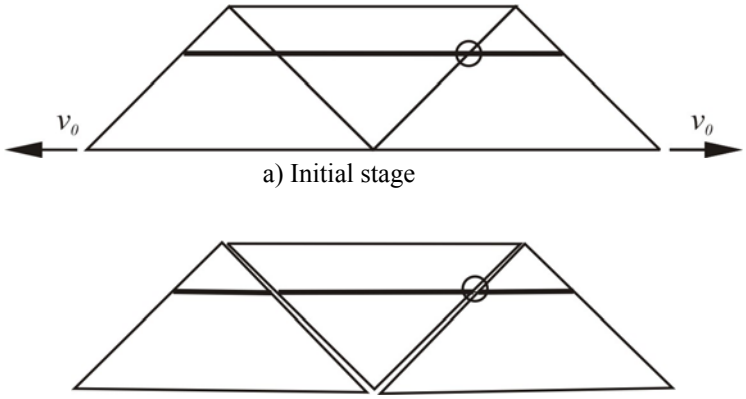

a) Initial stage

b) Stage after the cracking of reinforcing bar

Figure 8: Reinforced-concrete element subjected to initial velocity

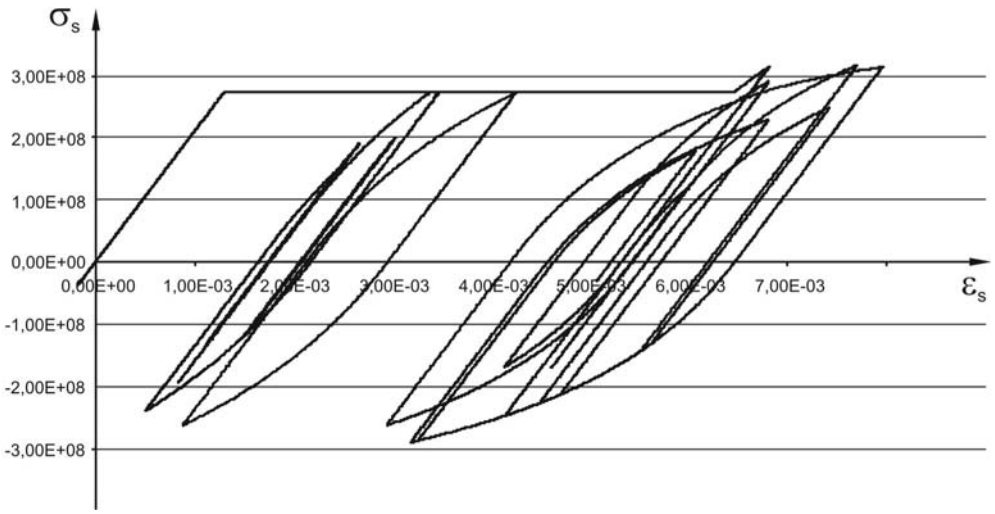

Figure 9: Stress-strain relation in reinforcing bar

5 CONCLUSIONS

- This paper presents a new numerical model for analysis of reinforced concrete structures under seismic load based on combined finite-discrete element method. The model combines standard finite element formulation for the hardening part of the constitutive law with the single-crack model for the softening part of stress-strain curve.
- An embedded model of reinforcing bars is implemented. The concrete structure is discretized on triangular finite elements, while the reinforcing bars are modelled with linear one-dimensional elements which can be placed in arbitrary position inside the concrete finite elements.
- The main assumption of the model is that the concrete tensile strength will be exceeded before the yield stress will achieved in the steel. The behaviour of the structure is linear-elastic up to the opening of the crack. After that joint elements in concrete as well as in reinforcing bar are occurred. Interaction solutions between bars and concrete have also been developed and implemented into the open source Y2D combined finite-discrete element code. Cyclic behaviour of the steel during the seismic load is modelled with improved Kato's model.

REFERENCES

[1] Munjiza, A. *The combined finite-discrete element method*, John Wiley & Sons, 2004.
[2] Munjiza, A., Andrews, K.R.F. and White, J.K. Combined single and smeared crack model in combined finite-discrete element analysis. *Int. J. for Numerical Methods in Engineering* (1999) **44**:41-57.
[3] Elwi, A.E. and Hrudey, M. Finite element model for curved embedded reinforcement. *Journal of Engineering Mechanics* (1989) **115**:740-754.
[4] Nikolić, Ž. And Mihanović, A. Non-linear Finite Element Analysis of Post-tensioned Concrete Structures, *Engineering Computations* (1997) **14**(5):509-528.
[5] Shima, H., Chou, L. and Okamura, H. Micro and macro model for bond behaviour in RC, *Journal of the Faculty of Engineering,* The University of Tokyo (1989) **39**(2): 133-94.
[6] Shin, H., Maekawa, K. and Okamura, H. Analytical approach of RC members subjected to reversed cyclic in plane loading, *Proceeding of JCI Colloquium on Ductility of Concrete Structures and its Evaluation* (1988): 245-256.
[7] Kato, B. Mechanical properties of steel under load cycles idealizing seismic action, *Bulletin D'Information* (1979), CEB, AICAP-CEB symposium, Rome: **131**:7-27.
[8] Evans, P.H. and Marthe, S. Microcracking and stress-strain curves for concrete in tension, *Materials and Structures* (1968) **1**:61-64.

XI International Conference on Computational Plasticity. Fundamentals and Applications
COMPLAS XI
E. Oñate, D.R.J. Owen, D. Peric and B. Suárez (Eds)

MICROPLANE MODEL M6F FOR FIBER REINFORCED CONCRETE

Ferhun C. Caner* **and Zdeněk P. Bažant†**

* Institute of Energy Technologies (INTE/ETSEIB)
Universitat Politecnica de Catalunya
Campus Sud, 08028 Barcelona, Spain
e-mail:ferhun.caner@upc.edu

†Dept. of Civil and Environmental Engineering
Northwestern University
2145 Sheridan Rd., Evanston, IL 60208, USA
e-mail:z-bazant@northwestern.edu

Key words: Microplane model, constitutive modeling, fracture, damage, fiber reinforced, concrete

Abstract. The new microplane model M6f for fiber reinforced concrete features several improvements over the earlier versions: (i) An explicit volumetric-deviatoric split to no split transition formulation in tension which eliminates spurious contraction under tension that the earlier models suffered; (ii) tension-compression load cycles are now correctly simulated using the loading/unloading rules prescribed in the transition function; (iii) a new micro- macro stress equilibrium equation in which the work of volumetric stresses on deviatoric strains and the work of deviatioric stresses on volumetric strains are explicitly accounted for is introduced to correctly model the pressure sensitive dilatant behavior of low to normal strength concretes; (iv) the volumetric boundary is made a function of the maximum principal strain difference in addition to the volumetric strains, so as to extend the data fitting capability to lower strength concretes; (v) the cohesion in the friction boundary now approaches zero linearly, instead of asymptotically with growing tensile volumetric strains, so as to generate an earlier decaying tail in the uniaxial tension and compression. The material behavior has been verified against various test data from the literature. The fits have been improved compared to the previous versions of the model.

1 INTRODUCTION

The microplane models, which range from M0 to M6 developed since 1984 primarily for the constitutive behavior of concrete, are hierarchically semi-multiscale models [1], because the angular interactions of inelastic phenomena are captured explicitly whereas

the interactions at a distance cannot be captured as a result of lumping the inelastic phenomena into a single material point. Consequently, the microplane models have already featured some of the properties of the now fashionable multiscale models. In certain important respect, the hierarchical multiscale models for quasibrittle fracture are no better than the microplane models [1] because both miss the microcrack interactions at a distance and fail to predict the size of the fracture process zone (or the localization limiter), while both can capture the angular interactions.

Microplane models have a number of advantages over the conventional tensorial models. Through the microplane concept, the constitutive model can be specified in terms of vectors instead of stress and strain tensor invariants [3] which removes the dependence on the invariants of stress and strain tensors. The principle of frame indifference is still satisfied, albeit approximately, by virtue of using microplanes that sample without bias all possible orientations in the three-dimensional space. The constitutive laws specified on the microplanes is activated by employing either the kinematic or the static constraints. It is well known that for quasi-brittle materials such as concrete, the softening behavior can only be captured if the kinematic constraint is employed [3]. A selective activation of the constitutive behavior on various microplanes results in a macroscopic constitutive behavior equivalent to multisurface plasticity, one or several surfaces on each microplane. Thus, the advantages of the multisurface plasticity, such as capturing the vertex effect and frictional shear with apparently non-associated dilatancy [4, 5], are also exhibited by the microplane models.

The latest of the microplane models for fiber reinforced concrete reported in this paper features several improvements over the earlier version [6]. To remove the spurious lateral contraction under tension, the traditional volumetric-deviatoric split formulation [4] gradually becomes the formulation without a split [3], in a form proposed by G. di Luzio as a function of increasing tensile strains. Thus, under tension, the new model predominantly behaves as a model without volumetric-deviatoric split. Also, with the new formulation, the model correctly features extensional damage as observed in the loading-unloading tensile-compressive tests reported in the literature.

Furthermore, the experimental data reported on specimens of low strength concretes [7], which could not be fitted well with the earlier versions of the model, can now be fitted well. To this end, the volumetric-deviatoric coupling is extended to the volumetric boundary. To account for the cross coupling of shear and dilatancy more accurately, the macro-micro stress equilibrium equation is also modified: The normal microplane stress is now treated directly as the sum of the volumetric and deviatoric parts without any additional constraints. Thus, the requirements of vanishing work of the deviatoric stresses on the volumetric strains, and of the volumetric stresses on the deviatoric strains, which was postulated in models M4, M5 and M5f, is now removed [4, 9, 10]. As a result, the predictive capabilities of the model have been drastically improved.

2 BASIC CONSTITUTIVE EQUATIONS OF MICROPLANE MODEL

Microplane models for concrete are defined using the kinematic constraint, which means that microplane strains are projections of the strain tensor on the microplanes [3, 4, 9, 10]:

$$\epsilon_N = n_i n_j \epsilon_{ij} = N_{ij} \epsilon_{ij} \tag{1}$$

where n_i are the components of the microplane normal vectors and $i, j = 1, 2, 3$ are the indices of the cartesian coordinate system. Alternatively, a static constraint in which the stress tensor is projected on the microplanes to yield the microplane stresses is also possible, but this approach is useful mainly for modeling hardening type inelastic behavior in which no softening can take place. For the modeling of softening, it is essential to use the kinematic constraint as given by Eq.1 [**?**, 3].

The projection of the strain tensor on the microplane system results in microplane shear strain vectors. However, to be able to fit some of the unconventional experimental data on concrete, it was found essential that the microplane shear strain vectors be represented with respect to in-plane orthogonal directions given by the randomly generated in-plane microplane vectors $\vec{m}$ and $\vec{l}$. Thus, the shear strains on the microplanes are defined as

$$\epsilon_M = \frac{1}{2}\left(n_i m_j + n_j m_i\right)\epsilon_{ij} = M_{ij}\epsilon_{ij};\ \epsilon_L = \frac{1}{2}\left(n_i l_j + n_j l_i\right)\epsilon_{ij} = L_{ij}\epsilon_{ij} \tag{2}$$

To separate the normal response into its volumetric and deviatoric parts, which is necessary for being able to model linear elasticity by means of the microplane model [4], we define the relations

$$\epsilon_N = \epsilon_V + \epsilon_D;\ \sigma_N = \sigma_V + \sigma_D \tag{3}$$

where $\epsilon_V = \epsilon_{kk}/3$ and $\epsilon_D = (N_{ij} - \delta_{ij}/3)\epsilon_{ij}$. The microplane volumetric and deviatoric stresses σ_V and σ_D as well as the microplane shear strains σ_M and σ_L must be prescribed as functions of the microplane strains. These relations are the microplane constitutive laws which must be determined through data fitting:

$$\sigma_V = \mathcal{F}_V\left(\epsilon_V, \sigma_I, \sigma_{III}\right);\ \sigma_D = \mathcal{F}_D\left(\epsilon_D, \epsilon_V\right);\ \sigma_L = \mathcal{F}_T\left(\epsilon_L, \epsilon_V, \sigma_N\right);\ \sigma_M = \mathcal{F}_T\left(\epsilon_M, \epsilon_V, \sigma_N\right) \tag{4}$$

Although the constitutive relation for the microplane shear strain components σ_L and σ_M are given by the same shear law in Eq.4, this is actually not strictly necessary; one may assume an in-plane orthotropy of microplanes and prescribe different shear laws for the two orthogonal shear components on the microplane as well.

When the microplane constitutive laws depend on some measure of stress, they become implicit. For the modeling of highly inelastic frictional behavior, it is desirable to achieve explicit microplane constitutive laws which would be free of iterations. Explicit constitutive laws are always sought in the development of microplane models. However, in some constitutive laws, it was inevitable to introduce stresses as the independent variables. For example, the shear behavior must involve the normal stresses because in the

inelastic range it is the friction that is modeled, which is by definition a function of the normal stresses. For volumetric behavior, it is simpler to define the deviatoric effects in terms of the principal stress difference.

2.1 Normal Boundaries

The normal boundary governs the tensile fracturing behavior of the model. It is expressed as:

$$\sigma_N^b = F_N(\epsilon_N) = Ek_1c_1 \exp\left(-\frac{\langle \epsilon_N - c_1c_2k_1 \rangle}{k_1c_3 + c_4 \langle -\sigma_V/E_V \rangle}\right) \tag{5}$$

2.2 Deviatoric Boundaries

The deviatoric boundaries simulate the spreading and splitting cracks under compression. They are given by:

$$\sigma_D^{b+} = F_D^+(\epsilon_D) = \frac{Ek_1\beta_1}{1 + \left(\langle \epsilon_D - \beta_1\beta_2k_1 \rangle / (k_1c_{17}\beta_3)\right)^2} \tag{6}$$

$$\sigma_D^{b-} = F_D^-(-\epsilon_D) = \frac{Ek_1\beta_4}{1 + \left(\langle -\epsilon_D - \beta_4\beta_5k_1 \rangle / (k_1\beta_3)\right)^2} \tag{7}$$

where

$$\beta_1 = c_{18} \exp\left(-\left(f_c'/E - f_{c0}'/E_0\right)\right) \tanh\left(c_{19} \langle -\epsilon_V \rangle / k_1\right)(1 + \chi_1) + \chi_1 + c_5 \tag{8}$$

where $\chi_1 = k_9 \tanh(c_{29}V_f)$;

$$\beta_2 = c_6 \exp\left(-\left(f_c'/E - f_{c0}'/E_0\right)\right) \min\left[\exp\left(c_{20} \langle -\epsilon_V/k_1 \rangle\right), c_{21}\right] \tag{9}$$

$$\beta_3 = c_{22} \exp\left(-\left(f_c'/E - f_{c0}'/E_0\right)\right) \tanh\left(c_{19} \langle -\epsilon_V \rangle / k_1\right)(1 + \chi_2) + \chi_2 + c_7 \tag{10}$$

where $\chi_2 = k_{10} \tanh(c_{29}V_f)$;

$$\beta_4 = c_{23} \exp\left(-\left(f_c'/E - f_{c0}'/E_0\right)\right) \tanh\left(c_{19} \langle -\epsilon_V \rangle / k_1\right)(1 + \chi_1) + \chi_1 + c_8 \tag{11}$$

$$\beta_5 = c_9 \exp\left(-\left(f_c'/E - f_{c0}'/E_0\right)\right) \min\left[\exp\left(c_{20} \langle -\epsilon_V/k_1 \rangle\right), c_{21}\right] \tag{12}$$

The functions χ_1, χ_2 represent the contribution of the fibers to resist the compressive splitting and slip cracks. The compressive strength may be calculated using the ACI formula in MPa $f_c' = (E/5150.226)^2$ if it is not given.

2.3 Frictional Yield Surface

The frictional yield surface simulates the shear behavior of the model. It is given by:

$$\sigma_T^b = F_T(-\sigma_N) = \frac{E_Tk_1k_2c_{10} \langle -\sigma_N + \sigma_N^0 \rangle}{E_Tk_1k_2 + c_{10} \langle -\sigma_N + \sigma_N^0 \rangle} \tag{13}$$

where

$$\sigma_N^0 = \langle E_T k_1 c_{11} - c_{12} \langle \epsilon_V \rangle \rangle \tag{14}$$

Under compression, the best data fits are obtained when the shear boundary is applied to the microplane shear components before the peak load is reached, especially in fitting the strength envelopes. In model M6f, a formulation that transits from application of the shear boundary to the microplane shear components to the microplane shear resultant is introduced. The formulation involves calculating the in-plane microplane shear components twice, once by applying the shear boundary to the microplane shear components, and once by applying it to the microplane shear resultant. Then, the transition formulation can be expressed as:

$$\sigma_L = \hat{\sigma_L}\tilde{\phi} + \bar{\sigma_L}\left(1 - \tilde{\phi})\right) ; \sigma_M = \hat{\sigma_M}\tilde{\phi} + \bar{\sigma_M}\left(1 - \tilde{\phi})\right) \tag{15}$$

where the quantities with $\hat{}$ are those obtained by applying the shear boundary to the microplane shear components, and the quantities with $\bar{}$ are those obtained by applying the shear boundary to the microplane shear resultant; the transition parameter is defined as:

$$\tilde{\phi} = \exp\left(c_{27} \langle \epsilon_V - c_{28} \rangle\right) \tag{16}$$

2.4 Volumetric Boundary

The volumetric boundary simulates the pore collapse and expansive breakup of the material. It is given by :

$$\sigma_V^b = F_V^- \left(-\epsilon_V\right) = -E k_1 k_3 \exp\left(\frac{-\epsilon_V}{k_1 \beta_6}\right) \tag{17}$$

where

$$\beta_6 = \frac{k_5 \left(\sigma_I - \sigma_{III}\right)}{k_1 \left(1 + \langle -\sigma_V / E_V \rangle\right)} + k_4 \tag{18}$$

and σ_I = maximum principal stress; σ_{III} = minimum principal stress.

2.5 Unloading and Stiffness Degradation

The unloading behaviors of concrete under tension and compression are radically different. Under tension the unloading slope is close to the secant modulus, and under compression, on the average it is close to the elastic slope. For $\sigma_I > c_{26}$, where c_{26} is a tensile stress threshold, the tension-tension and the tension-compression load cycles can be successfully obtained using the loading-unloading rules prescribed in terms of the

transition function ϕ as follows:

$$\phi(\epsilon_N) = \begin{cases} \exp\left(-c_{24}\sqrt{\left\langle \epsilon_N/k_1 - c_{25} + \min(\epsilon_I^{unl}, c_{25})\right\rangle}\right) & \text{if } \epsilon_N/k_1 < \epsilon_I^{unl} - \min(\epsilon_I^{unl}, c_{25}) \\ \exp\left(-c_{24}\sqrt{\left\langle \epsilon_I^{unl} - c_{25}\right\rangle}\right) & \text{if } \epsilon_I^{unl} - \min(\epsilon_I^{unl}, c_{25}) \le \epsilon_N/k_1 < \epsilon_I^{unl} \\ \exp\left(-c_{24}\sqrt{\left\langle \epsilon_N/k_1 - c_{25}\right\rangle}\right) & \text{if } \epsilon_N/k_1 \ge \epsilon_I^{unl} \end{cases} \tag{19}$$

where ϵ_I^{unl} is the value of the maximum principal strain at the initiation of unloading and it is a history parameter. When $\sigma_I \le c_{26}$, there is no tension and thus $\phi = 1$.

The loading with a transition from split to no split, along with the unloading, are depicted in Fig. 1(a). For the initial virgin loading, the load path with a transition to no split formulation is the path [ABDC]. At any given point where the unloading starts, for example at point D, the unloading path is given by [DEFA]. This results into a transition from the no split formulation into the split formulation. The subsequent loading passing into the tension zone follows the path [AFEDC]. The length $|DE| = c_{25}$.

As in model M4, the unloading under triaxial compression at high pressures is governed by the unloading rule of the volumetric boundary given by $C_V^u\left(-\epsilon_V, -\sigma_V\right) = E_V\left(c_{13}/(c_{13} - \epsilon_V) + \sigma_V/(c_{13}c_{14}E_V)\right)$. As in model M4, the unloading under compression at low confining pressures is governed by the unloading rules of the deviatoric and frictional boundaries. The unloading rule for the compressive deviatoric boundary is givenby $C_{-D}^u = (1 - c_{15})\, E_D + c_{15}E_D^s$ where $E_D^s = \min(\sigma_D/\epsilon_D, E_D)$ for $\sigma_D\epsilon_D > 0$ and $E_D^s = E_D$ for $\sigma_D\epsilon_D \le 0$. The unloading rule for the tensile deviatoric boundary is given by $C_{+D}^u = (1 - c_{16})\, E_D + c_{16}E_D^s$.

The unloading rule of the friction boundary is that the unloading slope is the same as the deviatoric unloading slope; thus

$$C_T^u = \begin{cases} C_{-D}^u & \text{if } C_D^u = C_{-D}^u \\ C_{+D}^u & \text{if } C_D^u = C_{+D}^u \end{cases} \tag{20}$$

2.6 Fiber Constitutive Relation

When the cracks are of the opening mode, the contribution of fiber to the crack bridging stress is given by a simplified form of Kholmyansky's equation [11]:

$$\frac{\sigma_N^f}{E} = \begin{cases} k_6k_1\left\langle \epsilon_N/k_1\right\rangle \exp\left(-k_7\left\langle \epsilon_N/k_1\right\rangle\right) & \text{if } \epsilon_N/k_1 < 1/k_7 \\ k_6k_1/k_7 \exp\left(-1\right) & \text{if } 1/k_7 \le \epsilon_N/k_1 < k_8 \\ k_6k_1\left\langle \epsilon_N/k_1 - k_8 + 1/k_7\right\rangle \exp\left(-k_7\left\langle \epsilon_N/k_1 - k_8 + 1/k_7\right\rangle\right) & \text{if } k_8 \le \epsilon_N/k_1 \end{cases} \tag{21}$$

and the fiber and the matrix are assumed to be coupled in parallel. Thus the result is

$$\sigma_N^{bf} = \sigma_N^b + \sigma_N^f \tag{22}$$

where σ_N^{bf} =total normal boundary for fiber reinforced concrete, σ_N^b =boundary for plain concrete matrix and σ_N^f =contribution of the fiber given by Eq.21.

2.7 Thermodynamic Dissipation

The thermodynamic dissipation can be formulated as the energy dissipated by deviatoric, volumetric and shear stresses in the case of formulation with a deviatoric-volumetric split. In the case of the formulation without a split, it can be formulated as the energy dissipated by the normal and shear stresses. Under isothermal conditions, the energy dissipated by a microplane stress is given by

$$Ts_{int} = \int_0^{\epsilon} \sigma d\epsilon - \frac{\sigma^2}{2C^u} \tag{23}$$

where $E_s \leq C^u \leq E$ with E_s = secant modulus. When the loading switches to unloading before reaching any of the boundaries, the response is elastic, and thus such the load cycles do not increase dissipation. When the boundaries are reached during loading, energy dissipation takes place as given by Eq.(23). The unloading slope is assumed to be constant although it has a slight curvature for the volumetric boundary. Thus, the energy dissipated by the deviatoric, volumetric, normal and shear stresses may be expressed as

$$\begin{aligned} Ts^D_{int} &= \int_0^{\epsilon_D} \sigma_D d\epsilon_D + \int_0^{\epsilon_v} \sigma_D d\epsilon_V - \frac{\sigma_D^2}{2C_D^u}; \; Ts^V_{int} = \int_0^{\epsilon_D} \sigma_V d\epsilon_D + \int_0^{\epsilon_v} \sigma_V d\epsilon_V - \frac{\sigma_V^2}{2C_V^u} \\ Ts^N_{int} &= \int_0^{\epsilon_N} \sigma_N^* d\epsilon_N - \frac{(\sigma_N^*)^2}{2C_N^u}; \; Ts^L_{int} = \int_0^{\epsilon_L} \sigma_L d\epsilon_L - \frac{\sigma_L^2}{2C_T^u}; \; Ts^M_{int} = \int_0^{\epsilon_M} \sigma_M d\epsilon_M - \frac{\sigma_M^2}{2C_T^u} \end{aligned}$$

Consequently, the total energy dissipation per unit volume of material is, in model M6f, approximately given by

$$T\tilde{s}_{int} = T\frac{3}{2\pi}\int_\Omega \left[(s^D_{int} + s^V_{int})\phi + s^N_{int}(1-\phi) + s^L_{int} + s^M_{int}\right] d\Omega \tag{24}$$

3 MICRO-MACRO STRESS EQUILIBRIUM

3.1 The model with volumetric-deviatoric split

The microplane model with volumetric-deviatoric split in the new microplane model M6 is defined as in the model M2:

$$\frac{2\pi}{3}\sigma_{ij}\delta\epsilon_{ij} = \int_\Omega \left[\sigma_D\delta\epsilon_D + \sigma_V\delta\epsilon_V + \sigma_M\delta\epsilon_M + \sigma_L\delta\epsilon_L\right] d\Omega + \int_\Omega \left[\sigma_D\delta\epsilon_V + \sigma_V\delta\epsilon_D\right] d\Omega \tag{25}$$

$$\frac{2\pi}{3}\sigma_{ij}\delta\epsilon_{ij} = \int_\Omega \left[(\sigma_D + \sigma_V)(\delta\epsilon_N - \delta\epsilon_V) + (\sigma_V + \sigma_D)\delta\epsilon_V + \sigma_M\delta\epsilon_M + \sigma_L\delta\epsilon_L\right] d\Omega \tag{26}$$

$$\frac{2\pi}{3}\sigma_{ij}\delta\epsilon_{ij} = \int_\Omega \left[\sigma_N\delta\epsilon_N + \sigma_M\delta\epsilon_M + \sigma_L\delta\epsilon_L\right] d\Omega \tag{27}$$

$$\Rightarrow \sigma_{ij} = \frac{3}{2\pi}\int_\Omega \left[\sigma_N N_{ij} + \sigma_M M_{ij} + \sigma_L L_{ij}\right] d\Omega \tag{28}$$

where $\sigma_N = \sigma_V + \sigma_D$. The last integral on the right hand side of Eq.(25) did not exist in the model M4, because it was postulated that the work of deviatoric stresses on the volumetric strains and the work of volumetric stresses on the deviatoric strains did not exist. Thus the volumetric stresses were work-conjugate to only the volumetric strains and the deviatoric stresses only to the deviatoric strains.

However, the triaxial compressive test data for low strength concretes, for which the behavior is more dissipative and ductile than the normal strength concretes, could not be fitted using the model M5f. It was found out that, these test data could be fitted easily if an explicit volumetric-deviatoric coupling could be assumed. Thus, the macro-micro stress equilibrium formula employed in model M5f has been replaced with that employed in M2 and M3, given by Eq.28. In general, it was found out that, as the strength of concrete increases, such a coupling must have lesser effect because the material becomes more brittle, with a progressively shrinking cohesive zone. For very high strength concretes, the size of the cohesive zone essentially becomes sub-millimeter, and the crack surfaces become smoother. This means that the frictional nature of the material becomes much less significant as the strength of the concrete increases compared to the normal strength concrete.

3.2 The model without volumetric-deviatoric split

The macro-micro stress equilibrium equation for the kinematically constrained microplane model without volumetric-deviatoric split can be written as $\frac{2\pi}{3}\sigma^*_{ij}\delta\epsilon^*_{ij} = \int_\Omega \left[\sigma^*_N\delta\epsilon^*_N + \sigma^*_M\delta\epsilon^*_M + \sigma^*_L\delta\epsilon^*_L\right] d\Omega$, leading to

$$\Rightarrow \sigma^*_{ij} \;=\; \frac{3}{2\pi}\int_\Omega \left[\sigma^*_N N_{ij} + \sigma^*_M M_{ij} + \sigma^*_L L_{ij}\right] d\Omega \tag{29}$$

where $\epsilon^*_N = N_{ij}\epsilon^*_{ij}$, $\epsilon^*_M = M_{ij}\epsilon^*_{ij}$, $\epsilon^*_L = L_{ij}\epsilon^*_{ij}$; $\sigma^*_N = \mathcal{F}^*_N(\epsilon^*_N)$, $\sigma_M = \mathcal{F}^*_T(\epsilon^*_M, \sigma^*_N)$ and $\sigma^*_L = \mathcal{F}^*_T(\epsilon^*_L, \sigma^*_N)$. In this model, the microplane normal stress is directly calculated as a function of the microplane normal strains.

3.3 The model with transition

The present model, model M6f, employs an explicit transition formulation, in which the model with a split given by Eq.28 gradually transits to the model without a split given by Eq.29;

$$\sigma_{ij} \;=\; \frac{3}{2\pi}\int_\Omega \left[\left\{\sigma^*_N\left(1-\phi\right) + \sigma_N\phi\right\} N_{ij} + \sigma_M M_{ij} + \sigma_L L_{ij}\right] d\Omega \tag{30}$$

where $\sigma_M = \sigma^*_M$ and $\sigma_L = \sigma^*_L$. The transition function ϕ for monotonic loading is defined as

$$\phi(\epsilon_N) = \begin{cases} \exp\left(-c_{24}\sqrt{\langle \epsilon_I/k_1 - c_{25}\rangle}\right) & \text{if } \sigma_I > c_{26} \\ 1 & \text{if } \sigma_I \le c_{26} \end{cases} \tag{31}$$

and thus is active only under tension.

4 RESULTS AND DISCUSSION

The simulations to predict experimental data for Harex and PVA fiber reinforced concretes under uniaxial tension are shown in Fig.1(b),(c) [8]; and those for steel fiber reinforced concretes under uniaxial compression and triaxial compression are shown in Figs.1(d)-(f) [7] respectively. The agreement between the data and the predictions is quite satisfactory. The model parameters, their values and their brief descriptions, are shown in Table 1. The "c" parameters are fixed parameters which do not change from one concrete to another; the "k" parameters may change from one concrete to another and thus they must be calibrated for each given concrete. Although there seem to be too many parameters, only 5 of them are free parameters for the concrete matrix and another 5 free parameters are for the fiber effect on the opening, splitting and slipping type fracture which must be supplied by the user of the model. For most low to normal strength concretes, the values provided in Table 1 should be sufficient. For others, identification of these free parameters (k_1 to k_5) using test data conducted on specimens of the concrete under consideration may be necessary. For various types of fibers, the values of free fiber parameters (k_6 to k_{10}) are already determined as shown in Table 1. If a new type of fiber used, these values should be recalibrated by fitting uniaxial tension and uniaxial compression test data.

Table 1: Parameters of the model M6f, their typical values and their meanings.

par.	**value**	**meaning**
f'_{c0}	15.08MPa	reference compressive strength
E_{c0}	20GPa	reference elastic modulus
c_1	0.46	controls the uniaxial tensile strength
c_2	2.76	controls the roundness of the peak in uniaxial tension
c_3	4	controls the slope of the postpeak in uniaxial tension
c_4	70	controls the slope of the postpeak tail in uniaxial compression
c_5	2.5	controls the vol. expansion under compression
c_6	1.3	controls the roundness of the peak in vol. expansion under compression
c_7	50	controls the slope of the initial postpeak in uniaxial compression
c_8	8	controls the peak strength in uniaxial compression
c_9	1.3	controls the peak roundness in uniaxial compression
c_{10}	0.73	controls the effective friction coefficient
c_{11}	0.2	initial cohesion in frictional response
c_{12}	$7 \cdot 10^3$	controls the change of cohesion with tensile vol. strains
c_{13}	0.02	controls the unloading slope at high hydrostatic compression
c_{14}	0.01	controls the unloading slope at low hydrostatic compression
c_{15}	0.4	controls the unloading slope of the compressive dev. boundary
c_{16}	0.99	controls the unloading slope of the tensile dev. boundary
c_{17}	0.082	controls the tensile cracking under compression

Table 1 – continued from previous page

par.	value	meaning
c_{18}	4	controls the vol. expansion for low strength concretes
c_{19}	0.012	controls the vol. expansion rate for low strength concretes
c_{20}	400	controls the roundness of vol. expansion for low strength concretes
c_{21}	13	controls the roundness of vol. expansion for low strength concretes
c_{22}	$3.5 \cdot 10^3$	controls the roundness of vol. expansion for low strength concretes
c_{23}	20	controls the roundness of vol. expansion for low strength concretes
c_{24}	0.12845	controls the rate of transition from split to no split
c_{25}	0.7576	controls unloading under tension
c_{26}	$1.7 \cdot 10^{-4}$	tensile stress treshold for initiation of split to no split transition
c_{27}	$1 \cdot 10^3$	rate of transition from shear boundary over shear components to over resultant
c_{28}	$5 \cdot 10^{-4}$	threshold of vol. strain to start the above transition
c_{29}	100	fiber contribution to resist splitting and slipping
k_1	$1.5 \cdot 10^{-4}$	radial scaling parameter
k_2	500	controls the horizontal asymptote value in the frictional boundary
k_3	15	controls the shape of the volumetric boundary
k_4	150	controls the shape of the volumetric boundary
k_5	2	controls the triaxial hardening for low strength concretes at low pressures
k_6	0.357	fiber law vertical scaling
k_7	0.2345	fiber law softening rate
k_8	5.09	controls the length of fiber law horizontal plateau
k_9	0.25	fiber contribution to resist splitting and slipping
k_{10}	240	fiber contribution to resist splitting and slipping
V_f	0.02	fiber volume fraction

5 CONCLUSIONS

A new, improved microplane model, called M6f, for mechanical behavior of fiber reinforced concretes has been reported. The new model improves upon its predecessors (i) by eliminating the spurious contraction under tension that the earlier models suffered, (ii) by predicting the tension-compression load cycles correctly, unlike the earlier versions, (iii) by extending range of experimental data fitted to lower strength concretes. The model performance has been calibrated and verified against numerous test data from the literature.

Acknowledgment: The work of the second author was supported by Grant W911NF-09-1-0043 from ARO Durham, monitored by James O'Daniel, Kent Danielson and Marc Adley of ERDC, Vicksburg, and partly also by the U.S. DoT through NU Infrastructure Technology Institute Grant 60027740.

REFERENCES

[1] Bažant, Z.P. Can Multiscale-Multiphysics Methods Predict Softening Damage and Structural Failure?, *Mechanics of the American Academy of Mechanics (AAM)* (2007) 36(5-6):5-12.

[2] Bažant, Z.P. Microplane model for strain-controlled inelastic behavior. Chapter 3 in *"Mechanics of Engineering Materials."* ed. by C. S. Desai and R. H. Gallagher, J. Wiley, London (1984) 45-59.

[3] Bažant, Z. P., and Oh, B.-H. Microplane model for progressive fracture of concrete and rock. *ASCE J. of Engrg. Mechanics* (1985) 111:559-582.

[4] Bažant, Z. P., Caner, F. C., Carol, I., Adley, M. D., and Akers, S. A. Microplane model M4 for concrete: I. Formulation with work-conjugate deviatoric stress. *ASCE J. Eng. Mech.* (2000) 126(9): 944-953.

[5] Caner, F. C., Bažant, Z. P., and Červenka, J. Vertex effect in strain-softening concrete at rotating principal axes. *ASCE J. Eng. Mech.* (2002) 128(1): 24-33.

[6] Beghini, A., Bažant, Z.P., Zhou, Y., Gouirand, O. and Caner, F. C. Microplane Model M5f for Multiaxial Behavior and Fracture of Fiber-Reinforced Concrete. *ASCE J. of Eng. Mech.* (2007) 133(1):66-75

[7] Chern, J.-C., Yang, H.-J., and Chen, H.-W. Behavior of steel fiber-reinforced concrete in multiaxial loading. *ACI Mater. J.* (1992) 891:32-40.

[8] Li, F., and Li, Z. Continuum damage mechanics based modeling of fiber-reinforced concrete in tension. *Int. J. Solids Struct.* (2001) 38:777-793.

[9] Bažant, Z. P., and Caner, F. C. Microplane model M5 with kinematic and static constraints for concrete fracture and anelasticity. I. Theory. *J. Eng. Mech.* (2005) 131(1):31-40.

[10] Bažant, Z. P., and Caner, F. C. Microplane model M5 with kinematic and static constraints for concrete fracture and anelasticity. II. Computation. *J. Eng. Mech.* (2005) 131(1):41-47.

[11] Kholmyansky, M. M. Mechanical resistance of steel fiber reinforced concrete to axial load. *J. Mater. Civ. Eng.* (2002)144:311-319.

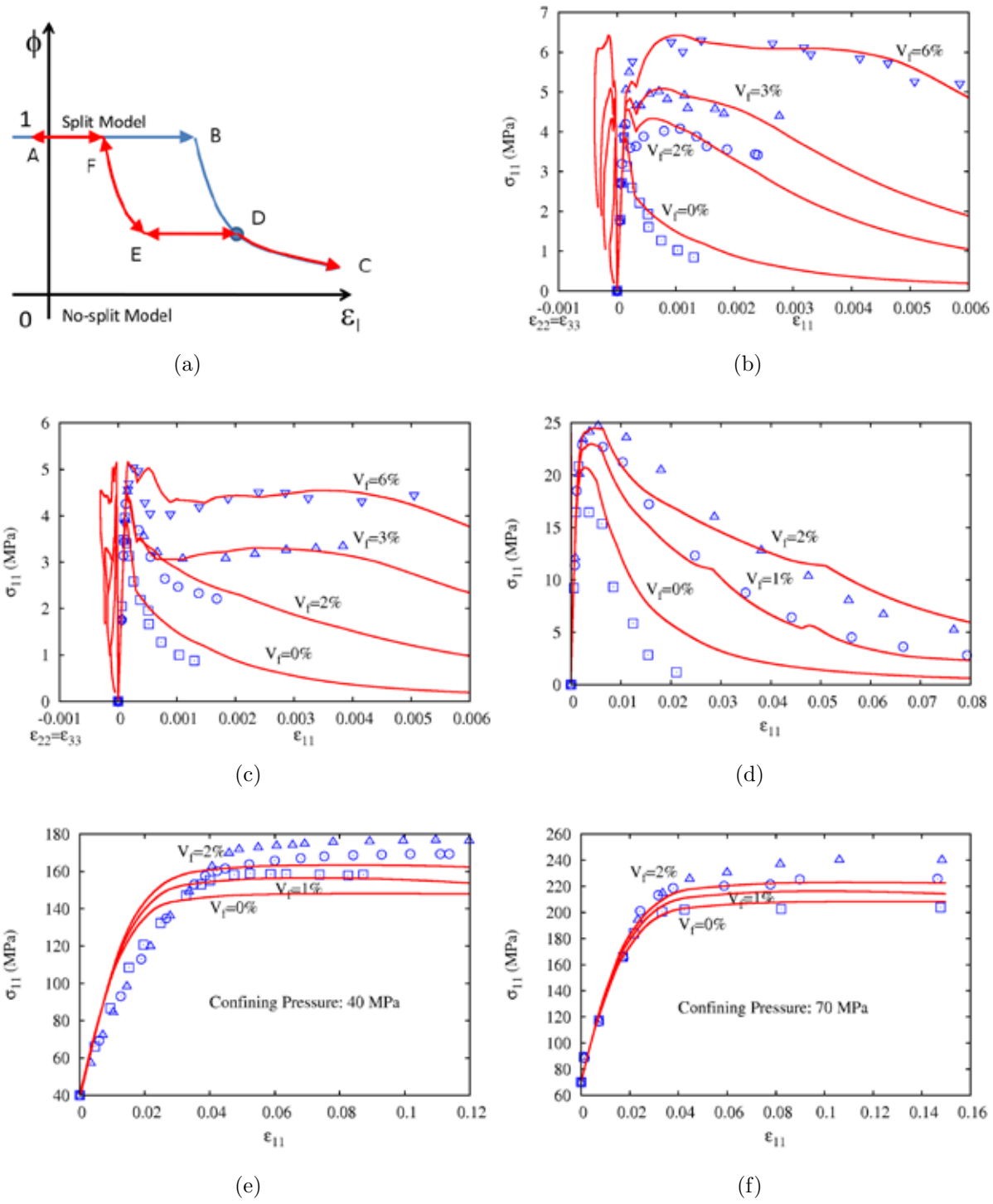

Figure 1: (a) the loading/unloading rule under tension; test data with its prediction by the model M6f for (b) Harex [8], (c) PVA [8], (d),(e) and (f) carbon steel fiber [7] reinforced concrete.

XI International Conference on Computational Plasticity. Fundamentals and Applications
COMPLAS XI
E. Oñate, D.R.J. Owen, D. Peric and B. Suárez (Eds)

NUMERICAL MODELLING OF A RC BEAM-COLUMN CONNECTION SUBJECTED TO CYCLIC LOADING BY COUPLING DIFFERENT NON LINEAR MATERIAL MODELS

JESÚS PÉREZ-MOTA* **AND NORBERTO DOMINGUEZ***

* Sección de Estudios de Posgrado e Investigación (SEPI)
Escuela Superior de Ingeniería y Arquitectura Unidad Zacatenco
Instituto Politécnico Nacional of Mexico
Edificio de Posgrado e Investigación, Av. Miguel Bernard s/n 07300 Mexico D.F., Mexico
e-mail: ndominguez@ipn.mx , www.sepi.esiaz.ipn.mx

Key words: Reinforced Concrete, Beam-Column Connection, Non-Linear Behaviour.

Abstract. The aim of this work is to study the effects of steel reinforcement array inside the RC beam-column connection as it is subjected to cyclic loading, through the numerical simulation of the joint adopting different stirrup's arrays: in order to simulate a real case of study, two specimens extracted from an experimental test of 12 RC beam-column connections reported in literature are modelled in the FEAP code. About numerical simulations based on the Finite Element Method (FEM), the non linear response of the RC beam-column connection is evaluated taking into account the non linear thermodynamic behaviour of each component: for concrete, it is used a damage model; for steel reinforcement, a classical plasticity model is adopted; for steel-concrete bonding, a plasticity-damage model is applied. At the end, the experimental structural response is compared to the numerical results, as well as the distribution of shear stresses and damage inside the concrete core of the beam-column connection, which are analyzed for a low and high confinement.

1 INTRODUCTION

Nowadays, Reinforced Concrete (RC) is one of the most important hybrid materials used in the construction industry and consequently its efficient behaviour depends on different aspects basically related to structural design and constructive techniques. Both of them must fulfil with local regulatory requirements for structural security which, given the complex nature of RC, adopt a lot of technical simplifications in design rules and construction codes in order to reduce the effects of uncertainties. In the case of structural design, the accomplishment is done by specifying the geometrical dimensions of the structural element as well as the quantification and location of the respective steel reinforcement. Theoretically, the respect of these specifications must assure the loading capacity of the structural element, or in other words, a good transference of internal efforts and stress between concrete and steel bars. However, in some occasions a blind application of these design specifications complicates unnecessarily the construction work of the structural elements, in particular the beam-column connections, which are at the same time, the key-points for the structural stability of the whole

system. In the other hand, the unreasoned removing of steel bars might reduce dramatically the resistance of the joint, particularly in the event of an earthquake.

Being the beam-column connection the main point of transmission of forces between horizontal elements (beams) and vertical elements (columns), it should provide enough stiffness to the structural system and because of this, there is a high concentration of stresses that potentially might produce any damage in concrete and/or plastic deformations on steel bars. That is the reason why beam-column connection is one of the most risky points of failure in RC structures.

By the way, modern design is strongly dependent of the numerical method adopted for structural analysis –typically a standard finite element code- and the better prediction of the real response (efforts and displacements) is directly derived from the computational capabilities of the code. Modelling of any mechanical problem should include not only the definition of a set of load combinations, but also the selection of a proper finite element associated to efficient material models as well as a good representation of the real boundary conditions. Perhaps due to the complexity of a complete modelling, the local study of any RC connection is practically disregarded by structural engineers, while steel reinforcement array is basically proposed from practical recommendations extracted from limited experimental tests. In consequence, the quantity of steel reinforcement inside the connection might be overestimated or simply poor distributed.

The aim of this work is to study the effects of steel reinforcement array inside the RC beam-column connection as it is subjected to cyclic loading, through the numerical simulation of the joint adopting different stirrup's arrays and quantities. About numerical simulations based on the Finite Element Method (FEM), we evaluated the non linear response of the RC beam-column connection taking into account the non linear thermodynamic behaviour of each component: for concrete, we adopted the concrete damage model proposed by Mazars [1]; for steel reinforcement, we used a classical plasticity model with Von Mises criterion; for steel-concrete bonding, an elastic-plastic-damage model [2,10] is applied. In order to calibrate the modelling, we adopted as an experimental reference the results reported by [3] for a RC beam-column connection.

1.1 Basic concepts about beam-column connections

According to [4], the beam-column connections may be classified following two criteria:

- by the geometrical configuration of reinforcement,
- by the local behaviour of the whole joint.

In the first case, there are internal joints (if the steel bars of beams pass across the joint) and external joints (when the steel bars of beams are anchored into the joint). For the second case, there are elastic joints (if plastic articulations appear into the structural element –beam or column-) and inelastic joints (if any non linearity appears into the connection). The mechanisms of failure of the beam-column connection identified by different authors [5, 6, 7, 8, 9] are the following:

- Beam reinforcement anchorage is not enough inside the joint and the bar slips,
- Shear forces developed into the joint activate the inelastic response of the core of concrete.
- A poor transference of shear forces may produce a failure plan between the joint and the beam, or between the joint and the column.

In general, the most accepted criteria of failure out of the connection is the SC-WB (Strong Column – Weak Beam), which means that any plastic articulation should appear on the beam instead of on the column.

2 ESSENTIAL COMPONENTS FOR THE NON-LINEAR MODELLING

2.1 The experimental test of reference

The experimental work carried out by Alameddine and Ehsani [3] consisted in reproducing the structural response of an external beam-column joint subjected to cyclic loading in order to verify the recommendations of the ACI-ASCE-352 code. The tests were classified in three groups of four specimens (see figure 1-a), each group with a specific concrete high resistance. Each specimen was designated by two letters and a number, indicating the level of the maximal joint shear stress (first letter), the level of confinement induced by the number of stirrups (second letter) and the value of the compressive strength. For example, the LH11 denomination designates a specimen with a Low shear stress, High confinement level, and a compressive strength of 11 ksi. In other words, these three variables were observed and studied:

a) The compression strength of concrete (55.8 MPa (8 ksi), 73.8 MPa(11 ksi) and 93.8 MPa (14ksi) respectively);
b) The maximal value of the shear stress into the connection, with a minimal value of 7.6 MPa (1100 psi) and a maximum of 9.7 MPa (1400 psi); and
c) The contribution of the stirrups by improving the confinement of the core of concrete (see Table 1 for stirrup characteristics).

Table 1: Reinforcement on the transversal section of specimen's elements

Specimen	LL	LH	HL	HH
A_{s1c}	2 # 8, 1 # 7	2 # 8, 1 # 7	3 # 8	3 # 8
A_{s2c}	2 # 7	2 # 7	2 # 8	2 # 8
A_{s3c}	2 # 8, 1 # 7	2 # 8, 1 # 7	3 # 8	3 # 8
A_{s1b}	4 # 8	4 # 8	4 # 9	4 # 9
A_{s2b}	4 # 8	4 # 8	4 # 9	4 # 9
Number of stirrups	4	6	4	6
ρ_t	1.2	1.8	1.2	1.8
$h_s/d_{b,col}$	20	20	20	20
Development length l_{dh} (inches) required for $f'c$=8,000 (psi) (Recommendations 1985)	8.9	8.9	10.0	10.0
Development length l_{dh} (inches)	10.5	10.5	10.5	10.5

Notes:
1 psi = 6.89 kPa; 1 inch = 25.4 mm; L: Low; H: High; the first letter indicates the level of shear stress; the second letter indicates the level of confinement.

Based on a cyclic controlled displacement test (see figure 1-b), the initial displacement in the free edge of the beam was of ± ½ inches (13 mm), being increased in ± ½ inches (13 mm) in each cycle of loading; during the test a small axial load was applied in the top of the column.

At the end of the test, they reached distortions up to 7% corresponding to a maximum displacement of 4 ½ inches (114 mm), concluding that:

- Elevated shear stresses reduce significantly the load capacity of the connection.
- The value of the ultimate shear stress recommended by the ACI-ASCE-352 for the joint was lower than the value observed in the experimental tests for high resistance concrete.
- The increment of transversal reinforcement reduces the deterioration into the connection, avoiding the failure of the reinforcement anchorage.

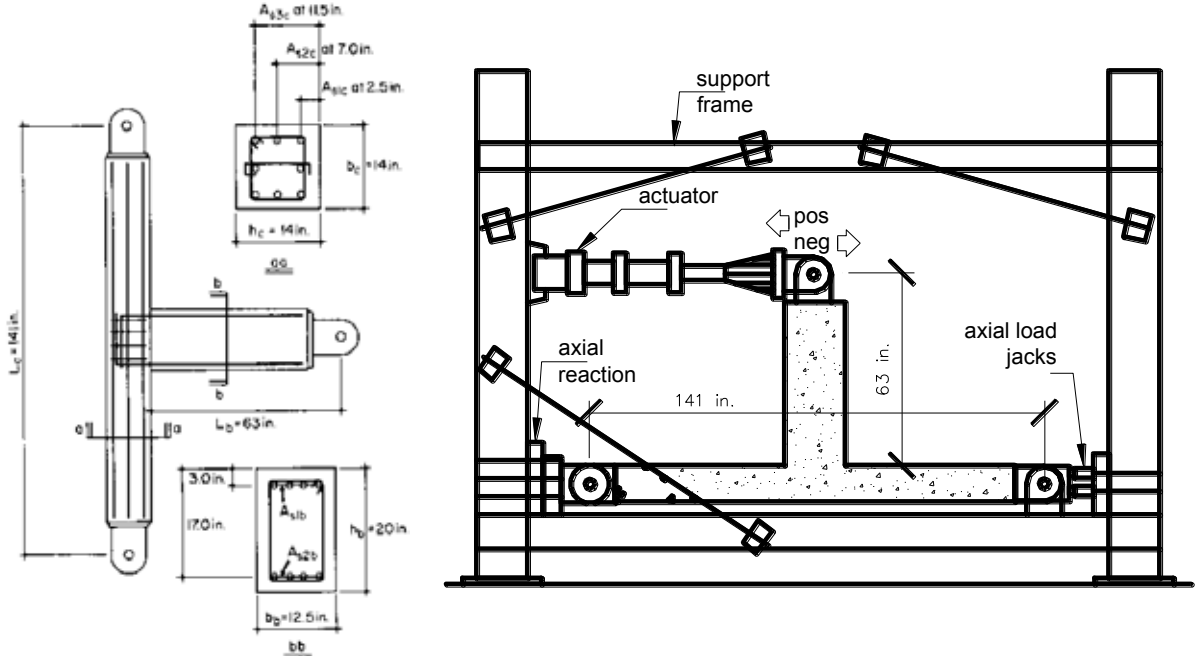

Figure 1: Description of the experimental test: (a) dimensions of the specimen, in inches; (b) Mounting of the experimental test

2.2 Brief description of the non linear models adopted for different material behaviours

One of the main ideas of this research was to adopt and combine different non linear models based on a thermodynamic formulation, in order to include in the structural response the effects of the different dissipative phenomena associated to each inelastic material behaviour.

Concrete behaviour: the non linear damage model of Mazars.

The model of Mazars [1] was specially conceived for the particular behaviour of concrete, which is different in compression compared to traction. As any other model of damage, this model is based on the calculation of an effective stress (equation 1) which is function of two scalar damage variables, $\boldsymbol{D_t}$ and $\boldsymbol{D_c}$ -traction and compression damage respectively- (equations 2,3). Nevertheless, instead of building the surface of failure in the space of stresses, this one is built in the space of strains, needing the calculation of an equivalent strain (equation 4).

$$\boldsymbol{\sigma = (1 - D)E^e : \varepsilon^e} \tag{1}$$

$$\boldsymbol{D = \alpha_t D_t + \alpha_c D_c} \tag{2}$$

$$\boldsymbol{D_i(\tilde{\varepsilon}) = 1 - \frac{(1 - A_i)\varepsilon_{do}}{\tilde{\varepsilon}} - \frac{A_i}{exp[B_i(\tilde{\varepsilon} - \varepsilon_{do})]} \qquad (i = t, c)} \tag{3}$$

$$\boldsymbol{\tilde{\varepsilon} = \sqrt{\sum_i (\varepsilon_i^+)^2} \qquad \varepsilon_i^+ = max(0, \varepsilon_i)} \tag{4}$$

In the last equations, $\boldsymbol{\alpha_t, \alpha_c, A_i, B_i, \varepsilon_{do}}$ are model parameters which can be determined from experimental tests; for this work, their values are presented in Table 2.

Table 2: Material parameters for the damage model of Mazars

A_c	1.446
B_c	1570
ε_{do}	7.428E-05
A_t	0.97
B_t	8000
f'c (*PSI*)	81
Confinement index	1.06
ft (*PSI*)	407.49

Steel behaviour: a classical non linear plasticity model with hardening.

For the steel bars, a classical elasto-plastic model based on Von Mises Criterion was chosen, which includes isotropic hardening.

Bond behaviour: a non linear plasticity-damage model based on a non-width finite element.

An elastic-plastic-damage model for bonding [10] was adopted in the formulation due to its various advantages: a) thermodynamics formulation, written in stress-strain terms; b) capacity of coupling between: "cracking and frictional sliding", and "tangential and normal stresses"; c) able to take account of confinement influence and lateral pressure; d) great stability for monotonic and cyclic loading. This model was already used in the prediction of the structural response of tie tests [2], and its robustness is supported by a 2D non-width interface element, which is fully described in [11].

3 NUMERICAL ANALYSIS OF THE BEAM-COLUMN CONNECTION

3.1 Hypothesis, limitations and strategy of the proposed modelling

In order to make our simulations, we have chosen the finite element code FEAP v.7.4 [12], an open-source code with license in which is possible to implement user material models and user finite elements. The models of Mazars and bonding were specifically integrated into the code, but the last one is only available for a 2D formulation. For this reason and due to the limitations in memory capacity, we have decided to model in a 2D-space the beam-column connection, which may provide acceptable results –in comparison with 3D models- if some simplifications are made. For example, in a real RC structural element, the steel reinforcement forms a cage embedded into the concrete, inducing a particular concentration of stresses in the concrete around each bar; however, taking into account that bending is acting only in one plane, and assuming that the most important shear stresses might be developed in the same plane, it is possible to "homogenize" the steel reinforcement in layers for a 2D simulation. In the case of the stirrups, only the branches parallel to the bending plane are taken into account, modelled with one truss element whose transversal section corresponds to the total area of the stirrups. Because the concrete cannot develop large rotations, any possible geometrical non linearity was not considered into the model.

In which concerns to the adopted strategy, we followed the next steps:

a) Selection of the experimental reference
b) Definition of the cases to simulate:
    - only longitudinal steel without stirrups;
    - with minimal quantity of stirrups;
    - with the quantity of stirrups indicated in experimental test,
c) Cases with bond material model (still in progress):
    - Bonding included only in the flexural steel
    - Bonding included in all of the reinforcement
d) Comparison of results

3.2 Construction of the model

According to the proposed strategy, among the 12 corner-reinforced concrete beam-column subassemblies reported in the experimental reference, we selected the LL11 and LH11 specimens, having both of them the same geometrical and material properties, except for the number of stirrups inside the core of concrete (four stirrups for "Low confinement", and six stirrups for "High confinement").

The basic model was constructed in a 2D space based on a plane strain formulation, using QUAD4 elements (4-node quadrangular element with 4 integration points) for the concrete body and TRUSS2 elements (2-node bar element) for the steel reinforcement. Initially, the reinforcement was modelled with QUAD4 elements as well, but due to their minimal dimensions, there were some numerical problems by a non-realistic excessive concentration

of stresses around the union between longitudinal steel and the stirrups. In which concerns to the bonding, two non-width interface elements were initially placed between the concrete QUAD4 element and the steel QUAD4 element –one on each side of the steel-, but due to the numerical instabilities mentioned previously, they were replaced by a unique interface element linking the steel rebar to the concrete elements: this numerical solution is still in progress.

About boundary conditions, bottom face of the column is fully-restrained, while the top face was constrained only in the transversal direction because a constant axial load was applied and distributed at the same face. By the way, the free edge of the beam is restrained in the axial direction, with a cyclic displacement imposed in its transversal direction (see figure 2-a).

In the experimental test, at least eight displacement transducers were positioned in order to follow the evolution of displacements over the concrete face of the joint (see figure 2-b). In the same way, we followed the numerical evolution of these points, in order to construct the corresponding load-displacement response.

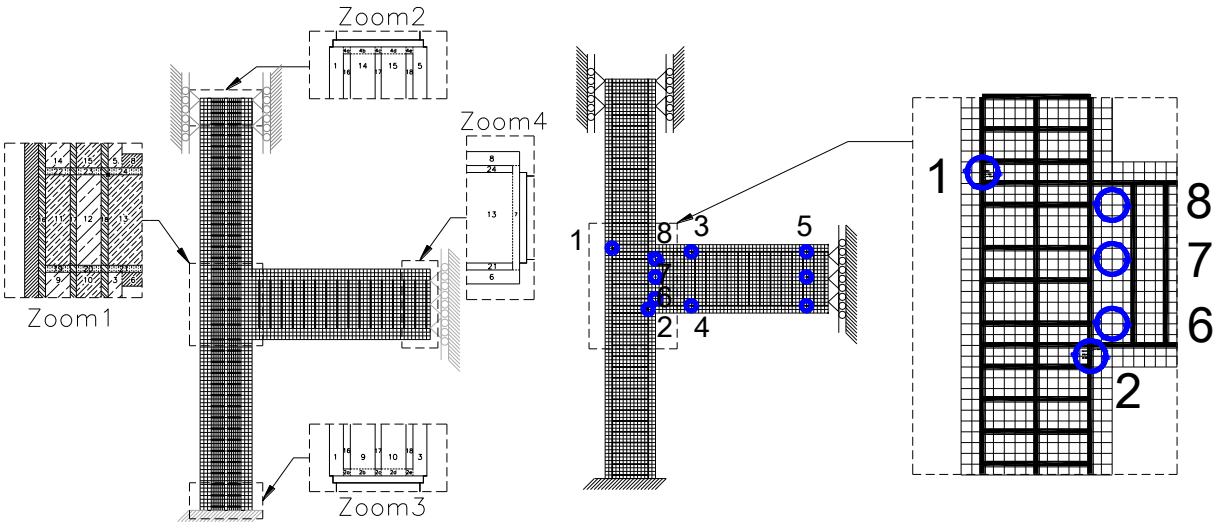

(a) (b)

Figure 2: Meshing of the beam-column connection: (a) boundary conditions and reinforcement array; (b) points of observation of the stress-strain relationship according to the experimental tests.

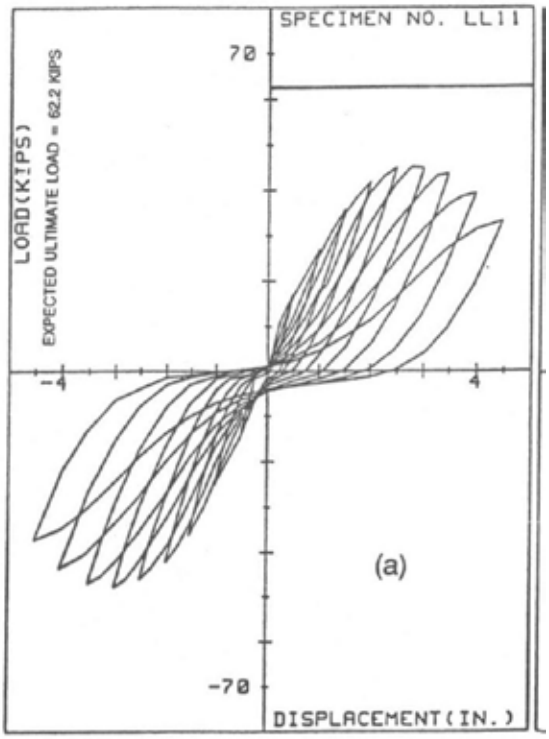

(a)

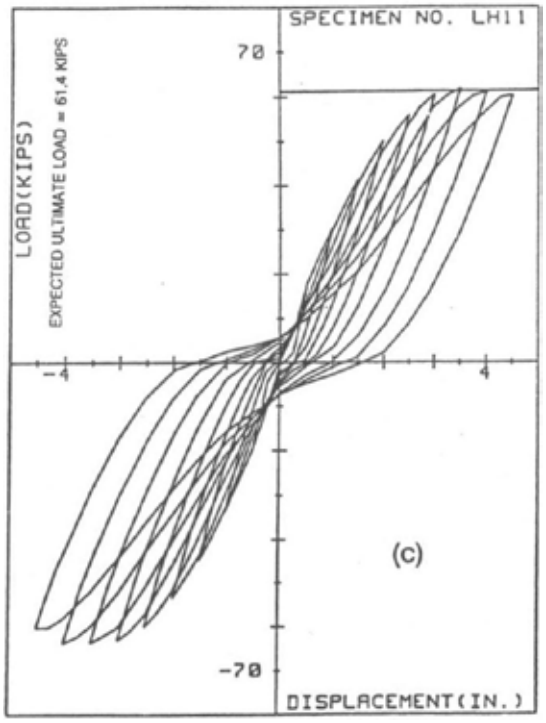

(b)

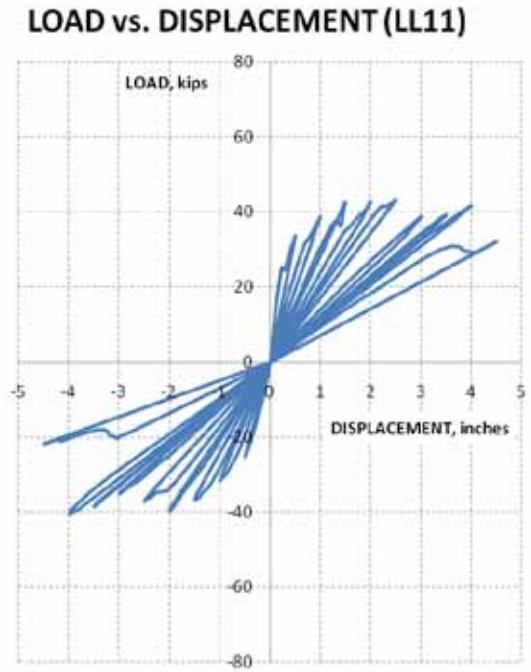

(c)

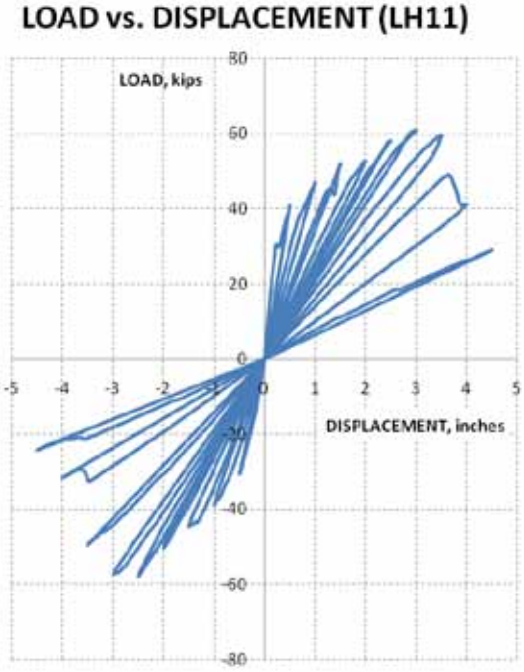

(d)

Figure 3: Load-displacement structural response of the beam-column connection: (a) experimental curve for specimen LL11; (b) experimental curve for specimen LH11; (c) numerical curve for specimen LL11; (d) numerical curve for specimen LH11.

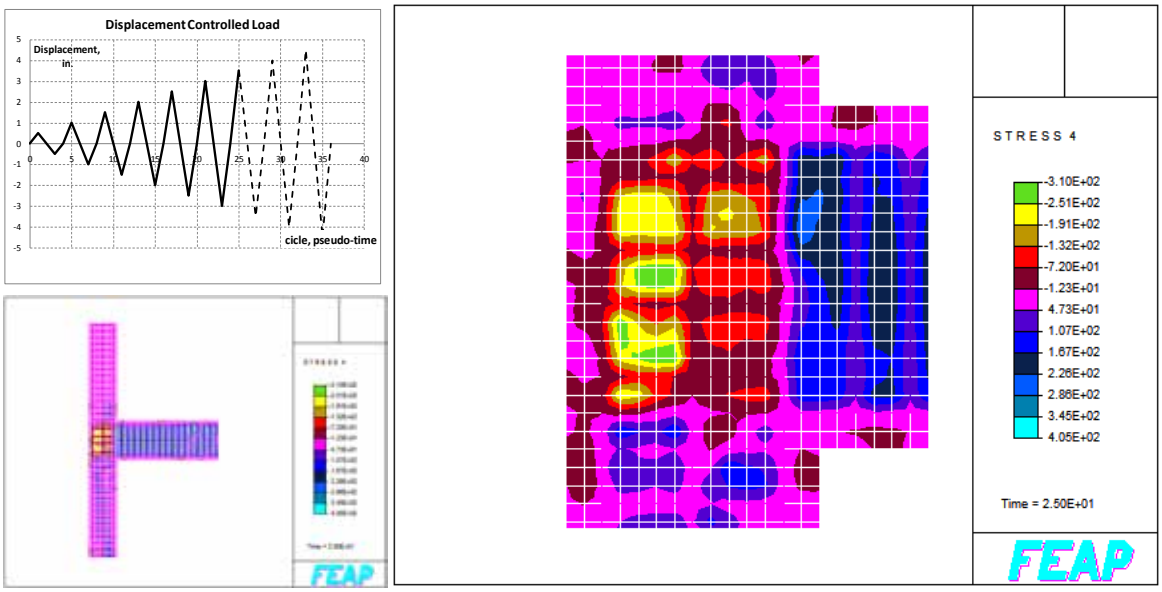

Figure 4: Shear stress distribution on specimen LL11 (low confinement) for a displacement of 3.5 inches.

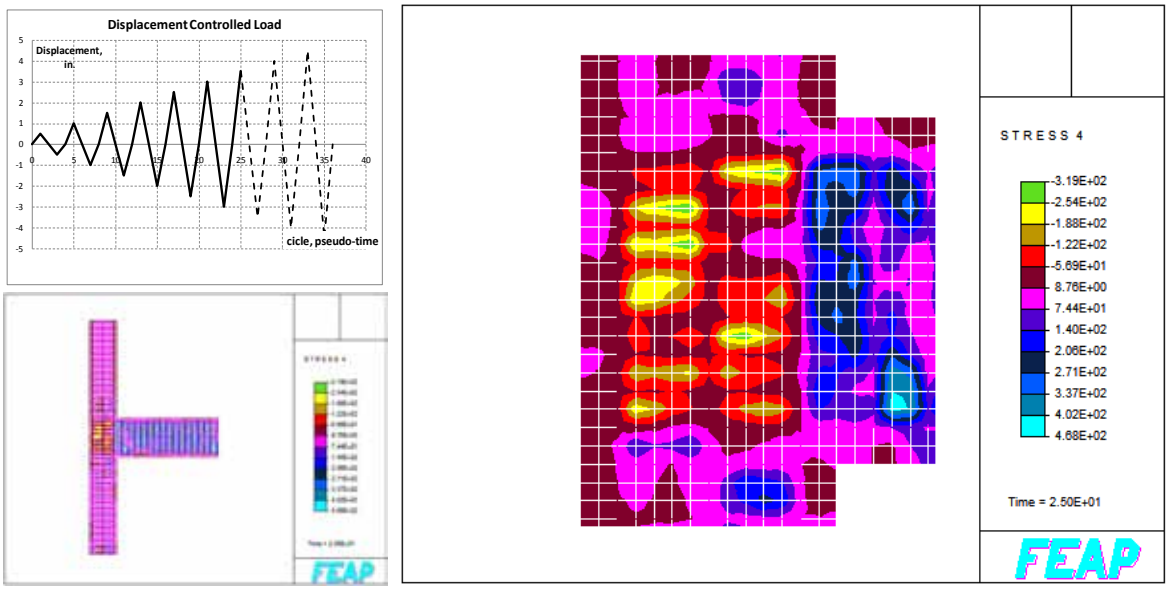

Figure 5: Shear stress distribution on specimen LH11 (high confinement) for a displacement of 3.5 inches.

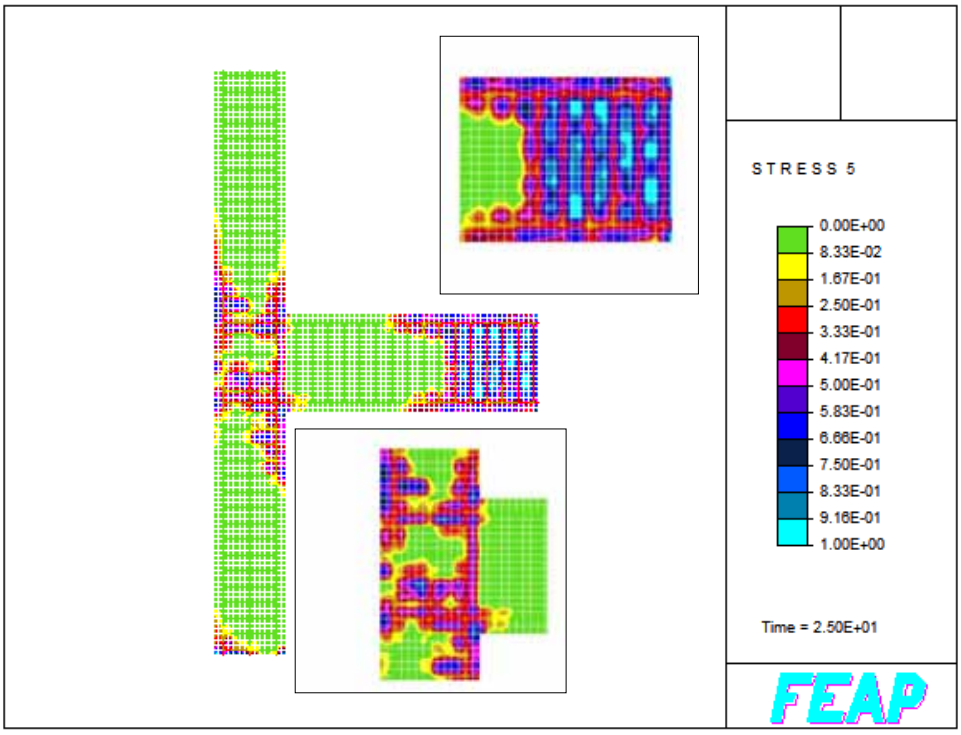

Figure 6: Damage distribution on specimen LL11 (low confinement) for a displacement of 3.5 inches.

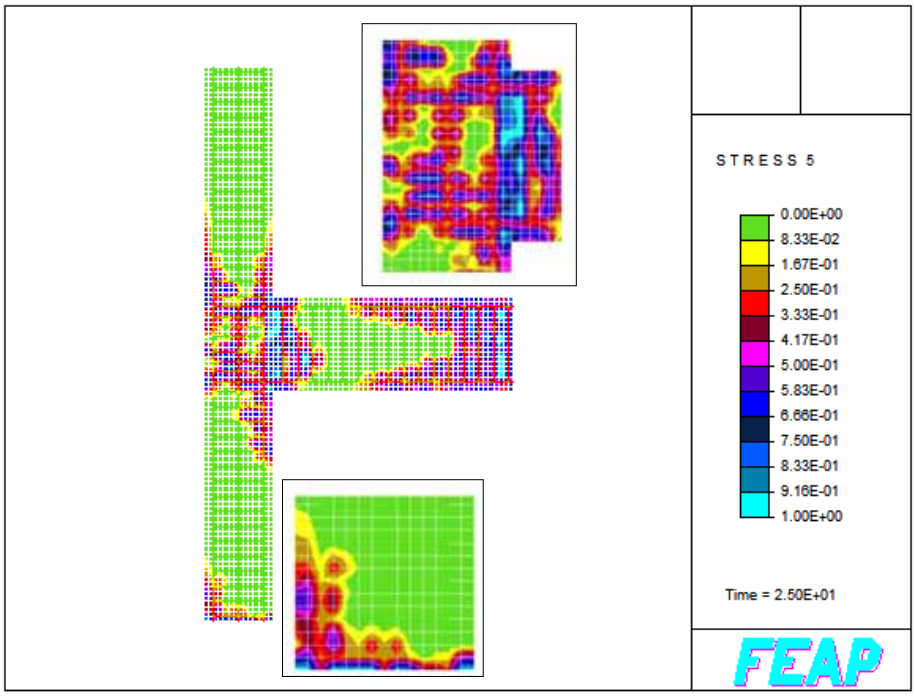

Figure 7: Damage distribution on specimen LH11 (high confinement) for a displacement of 3.5 inches.

4 DISCUSSION OF RESULTS

In the next paragraphs, we will discuss the numerical results of the modelling coupling the nonlinear behaviour of steel and concrete. It should be mentioned that they do not include the bonding cases, which are still in progress. So on, first at all we compare the structural response of the two specimens, both experimental and numerical, in figure (3). Figures (3-a) and (3-c) correspond to the LL11 specimen, in which the maximal load capacity was reached between 40 and 45 kips for a displacement near to two inches. For the LH11 specimen, figures (3-b) and (3-d) show a maximal load capacity near to 60 kips, very close to three inches of displacement. By comparing experimental curves with numerical results, it can be appreciated that some key-values are very similar (maximal load capacity associated to the lateral displacement), but their shapes are far away from any similitude. In numerical curves, all the unloading branches go directly to the origin, without any accumulated permanent displacement as it is observed in the experiments. Typically, the origin of these permanent displacements is associated to the crack friction on concrete. For cyclic loads, the damage model of Mazars includes only the slope variation of the elastic unloading, since cracks on concrete are closed as soon as there is a reversibility of loading, assuming no friction on cracks. Because of this, it is not possible to reproduce numerically any dissipative boucle or permanent deformation. This was already explained by Ragueneau et al. [13], who presented a modified version of Mazars model which includes these effects.

Figures (4) and (5) show the distribution of shear stresses inside the specimens. In both of them, the concentration of stresses is determined by the disposition of the stirrups, being greater the affected area when the reinforcement is lower inside the core. In fact, when no stirrups are placed inside the core, the damage is reached almost immediately, even if the longitudinal bars of the column and beams pass through the joint. Other relevant points observed in numerical simulations are the following: (a) in both cases, the highest value of shear stress was reached on the beam, and not in the column or in the connection; (b) when the number of stirrups is increased inside the core, the principal damage is placed out of the core, exactly in the plane of connectivity between the beam and the core of the connection (see figure 7); and (c) if the constant axial load on the column is not included in the modelling, the resistance of the beam-column connection decreases substantially (according to [14]).

In general, all the simulations stopped as soon as a non convergence condition was reached. Sometimes this problem was solved by reducing the time step, in particular in the picks of the displacement when unloading started. From a physical point of view, this non convergence corresponds to the instant when a set of concrete elements reaches a high level of damage. Figures (6) and (7) show the level and distribution of damage in concrete for both specimens respectively. Apparently, damage is higher in LH11 specimen, but in reality is better distributed along the stirrups, although the numerical value seems to be elevated. The implementation of bond elements must reduce this effect on the concrete body, as it was demonstrated in [2], due to the redistribution of stresses induced by bonding, which allows a small slip between steel bars and concrete, avoiding a false premature degradation of concrete as it is observed in these simulations.

5 CONCLUSIONS

In this work, we have focused in modelling the non linear structural response of a beam-column connection subjected to cyclic loading. Thus, we have: (a) modelled different cases of beam-column connection and reproduced their experimental structural response, including different material models for steel and concrete (elasto-plastic and damage models respectively); (b) corroborated the influence of the stirrups in the resistance of the connection; and (c) analyzed the damage distribution inside the core of the connection.

REFERENCES

[1] Mazars J., A description of micro- and macroscale damage of concrete structures, *Journal of Engineering Fracture Mechanics* (1986) **25**(5/6):729-737.

[2] Dominguez N., Brancherie D., Davenne L. and Ibrahimbegovic A., Prediction of crack pattern distribution in reinforced concrete by coupling a strong discontinuity model of concrete cracking and a bond-slip of reinforcement model, *Engineering Computations* (2004) **22** (5/6):558-582.

[3] Alamedinne F. and Ehsani M. R., High-strength RC connections subjected to inelastic cycling loading, *ASCE Journal of Structural Engineering* (1991) **117** (3):829-850.

[4] Alcocer, S. *Comportamiento y diseño de estructuras de concreto reforzado. Uniones de elementos*. CENAPRED/Instituto de Ingeniería-UNAM (1991).

[5] Ma, S-Y. M., Bertero V. V. and Popov E. P., *Experimental and Analytical Studies of the Hysteretic Behavior of Reinforced Concrete Rectangular and T-Beams.* Report No. EERC-76-2. Berkeley: EERC, University of California, USA (1976).

[6] Meinheit, D. F. and Jirsa, J. O., *The shear strength of reinforced concrete beam-column joints*. CESRL Report No. 77-1. Austin: University of Texas (1977).

[7] Lowes, L. N. and Moehle J. P., Evaluation and retrofit of beam-column T-joints in older reinforced concrete bridge structures, *ACI Structural Journal* (1995) **96** (4):519-532.

[8] Lowes, L. N., *Finite element modeling of reinforced concrete beam-column bridge connections*. Ph. D. Thesis, Civil Engineering Graduated Division, University of California, Berkeley, USA (1999).

[9] Lowes, L. N., Mitra, N. and Altoontash A, *A beam-column joint model for simulating the earthquake response of reinforced concrete frames*. Pacific Earthquake Engineering Research Center, PEER Report 2003/10, University of California, Berkeley, USA (2004).

[10] Dominguez N. and Ibrahimbegovic A., A non-linear thermodynamical model for steel-concrete bonding – Part I: Theoretical formulation and numerical implementation, *Submitted to Computers and Structures* (2011).

[11] Ragueneau F., Dominguez N. and Ibrahimbegovic A., Thermodynamic-based interface model for cohesive brittle materials: application to bond-slip in RC structures. *Computer Methods in Applied Mechanics and Engineering*. (2006) **195** (52):7249-7263.

[12] Taylor, R. L., *FEAP- A finite element analysis program version 7.4. User manual*. See: http://www.ce.berkeley.edu/~rlt/feap/ .

[13] Ragueneau F., La Borderie Ch. and Mazars J., Damage model for concrete like materials coupling cracking and friction, contribution towards structural damping: first uniaxial application. *Mechanics of Cohesive-frictional Materials*. (2000) **5**:607-625.

[14] Park, R. and Paulay T. *Estructuras de concreto reforzado*. Limusa, México (1997).

XI International Conference on Computational Plasticity. Fundamentals and Applications
COMPLAS XI
E. Oñate, D.R.J. Owen, D. Peric and B. Suárez (Eds)

THERMOMECHANICAL SIMULATION OF SHAPE MEMORY ALLOYS STRUCTURES: VARIATIONAL METHODS AND ASSOCIATED NUMERICAL TOOLS

M.PEIGNEY

Université Paris-Est/IFSTTAR
58 boulevard Lefebvre
75732, Paris cedex 15, France
e-mail: michael.peigney@ifsttar.fr

Key words: Computational Plasticity, Shape memory alloys, Thermomechanical coupling, Linear complementarity problem

Abstract. Shape Memory Alloys (SMA) offer new perspectives in various fields such as aeronautics, robotics, biomedicals, or civil engineering. Efficient design of such innovative systems requires both adequate material models and numerical methods for simulating the response of SMA structures. Whereas much effort has been devoted to developing constitutive laws for describing the behaviour of SMAs, the structural problem (i.e. the simulation of a three-dimensional SMA structure) has received far less attention, in spite of substantial difficulties notably due to the strong thermomechanical coupling and the presence of physical constraints on the internal variables. The time-discretization of the evolution problem obtained is not obvious, and special care must be taken to avoid convergence difficulties and ensure robustness of the numerical schemes. Computation time and ease of implementation (for instance in an existing finite element code) also are major issues that need to be addressed. In this communication are presented some recent results in that direction. A central result is a recent time-discretization scheme for the thermomechanical problem. A variational formulation is attached to the corresponding incremental problem, allowing one to prove the existence of solutions for a large class of usual SMA models. The variational nature of the problem at hand also calls for an easy implementation in an existing finite element code, building on well-established descend algorithms. Using that approach, the solution of the thermomechanical incremental problem is typically obtained by solving a sequence of linear thermal problems and purely mechanical (i.e. at prescribed temperature) nonlinear problems. That approach is fairly general and applies for a wide range of SMA models. The numerical scheme for solving the purely mechanical problem, however, strongly depends on the particular model that is used. In a micromechanical modelling of SMAs, the phase transformation is described locally by an internal vectorial variable which is physically constrained to satisfy a set of inequalities at each point. We show that the corresponding incremental problem can

be recast as a linear complementarity problem, for which efficient algorithms (such as interior-point methods) are available. That reformulation essentially consists in a change of variables. In terms of variational formulation, that approach amounts to replace a convex but non-quadratic minimization problem with an equivalent quadratic minimization problem.

1 COUPLED THERMOMECHANICAL EVOLUTIONS

We consider the evolution problem of an arbitrary SMA structure, in quasi-statics and under the assumption of small strains. The structure occupies a domain Ω and is submitted to body forces $\boldsymbol{f}^d$ and tractions $\boldsymbol{T}^d$, the latter being applied on a portion Γ^T of the boundary. Prescribed displacements $\boldsymbol{u}^d$ are imposed on $\Gamma^U = \partial\Omega - \Gamma^T$. The temperature θ is set equal to θ^d on a portion Γ_θ of $\partial\Omega$, and the heat flux q^d is imposed on a portion Γ_q such that $\Gamma_q \cap \Gamma_\theta = \emptyset$. On the remaining part $\Gamma_r = \partial\Omega - \Gamma_q - \Gamma_\theta$ of the boundary, the heat flux is given by $K'(\theta - \theta_R)$ where K' is a (positive) heat transfer coefficient between the system and its environment. The functions $\boldsymbol{f}^d$, $\boldsymbol{T}^d$, $\boldsymbol{u}^d$, θ^d, q^d describing the thermomechanical loading depend on the position $\boldsymbol{x}$ and on the time t. In the domain Ω, the heat flux $\boldsymbol{q}$ is supposed to satisfy the Fourier's law with a thermal conductivity K. The displacement, stress and temperature are denoted by $\boldsymbol{u}$, $\boldsymbol{\sigma}$ and θ respectively.

In a mesoscopic modelling of SMAs, the local state of the material is described by the variables ($\boldsymbol{\varepsilon}$, $\boldsymbol{\xi}$, θ) where $\boldsymbol{\varepsilon}$ is a strain and $\boldsymbol{\xi}$ is a (possibly vectorial) internal variable tracking the phase transformation. That variable $\boldsymbol{\xi}$ must generally satisfy a condition of the form $\boldsymbol{\xi} \in \mathcal{T}$ where $\mathcal{T}$ is a given bounded set (see Section 3 for an explicit example). Denoting the free energy of the material by w and the dissipation potential by ϕ, the evolution of the system is governed by the following system (see [2] and references therein for more details) :

$$\boldsymbol{\sigma} = \frac{\partial w}{\partial \boldsymbol{\varepsilon}} \ , \ \boldsymbol{B} = -\frac{\partial w}{\partial \boldsymbol{\xi}} \ , \ s = -\frac{\partial w}{\partial \theta} \tag{1.1}$$

$$\boldsymbol{\varepsilon} = (\nabla \boldsymbol{u} + {}^t\nabla \boldsymbol{u})/2 \tag{1.2}$$

$$-K\nabla\theta.\boldsymbol{n} = q^d \text{ on } \Gamma_q, \ -K\nabla\theta.\boldsymbol{n} = K'(\theta - \theta_R) \text{ on } \Gamma_r \tag{1.3}$$

$$\boldsymbol{u} \in \mathcal{K}_u \ , \boldsymbol{\sigma} \in \mathcal{K}_\sigma \ , \ \boldsymbol{\xi} \in \mathcal{K}_\xi \ , \ \theta \in \mathcal{K}_\theta \tag{1.4}$$

$$\boldsymbol{B} = \boldsymbol{B}^r + \boldsymbol{B}^d \tag{1.5}$$

$$\boldsymbol{B}^r \in \partial I_{\mathcal{T}}(\boldsymbol{\xi}) \ , \ \boldsymbol{B}^d \in \partial\phi(\dot{\boldsymbol{\xi}}) \tag{1.6}$$

$$K\Delta\theta + \boldsymbol{B}^d.\dot{\boldsymbol{\xi}} - \theta\dot{s} = 0 \tag{1.7}$$

where the sets $\mathcal{K}_u$, $\mathcal{K}_\sigma$, $\mathcal{K}_\xi$, $\mathcal{K}_\theta$ are defined by

$$\begin{array}{lcl} \mathcal{K}_u & = & \{\boldsymbol{u} | \boldsymbol{u} = \boldsymbol{u}^d \text{ on } \Gamma^u\} \\ \mathcal{K}_\sigma & = & \{\boldsymbol{\sigma} | \operatorname{div} \boldsymbol{\sigma} + \boldsymbol{f}^d = 0 \text{ in } \Omega; \boldsymbol{\sigma}.\boldsymbol{n} = \boldsymbol{T}^d \text{ on } \Gamma^T\} \\ \mathcal{K}_\xi & = & \{\boldsymbol{\xi} | \boldsymbol{\xi} \in \mathcal{T} \text{ in } \Omega\} \\ \mathcal{K}_\theta & = & \{\theta | \theta = \theta^d \text{ on } \Gamma_\theta\} \end{array} \tag{2}$$

In (1), $I_\mathcal{T}$ is the indicator function of the set $\mathcal{T}$ (equal to 0 in and infinite outside) et ∂ denotes the subdifferential [1]. In the heat equation (1.7), the thermomechanical coupling is embedded both in the entropy-related term $\theta \dot{s}$ (which contains the latent heat effect) and in the dissipative term $\boldsymbol{B}^d.\dot{\boldsymbol{\xi}}$.

2 TIME-DISCRETIZATION OF THE EVOLUTION PROBLEM

2.1 Incremental problem

To solve a system such (1), one generally resorts to a space- and time-discretization strategy. The space discretization is generally supplied by a finite element method. The time discretization consists in introducing a finite time-step problem for estimating the solution $(\boldsymbol{u}, \boldsymbol{\sigma}, \theta)$ at a given time $t^0 + \delta t$, supposing that $(\boldsymbol{u}^0, \boldsymbol{\sigma}^0, \theta^0)$ at time t^0 are known. For the system considered, a common finite time-step problem is supplied by the backwards Euler scheme, which can be formulated as follows:

$$(\boldsymbol{u}, \boldsymbol{\xi}, \theta) \text{ verifies (1.1)-(1.4) at } t^0 + \delta t \tag{3.1}$$

$$\boldsymbol{B} = \boldsymbol{B}^r + \boldsymbol{B}^d \tag{3.2}$$

$$\boldsymbol{B}^r \in \partial I_\mathcal{T}(\boldsymbol{\xi}) \ , \ \boldsymbol{B}^d \in \partial \phi\big((\boldsymbol{\xi} - \boldsymbol{\xi}^0)/\delta t\big) \tag{3.3}$$

$$K \delta t \Delta\theta - \theta^0 (s - s^0) + \boldsymbol{B}^d.(\boldsymbol{\xi} - \boldsymbol{\xi}^0) = 0 \tag{3.4}$$

where $s^0 = s(\boldsymbol{\varepsilon}^0, \boldsymbol{\xi}^0, \theta^0)$. A major drawback of this scheme is that the existence of a solution to (3) is not guaranteed. Let us develop this point: if θ is known, then the purely mechanical finite-step problem (3.1-3) has a solution. Similarly, if $(\boldsymbol{u}, \boldsymbol{\xi})$ is fixed, then the thermal problem (3.4) also has a solution. However, one cannot ensure the existence of a solution $(\boldsymbol{u}, \boldsymbol{\sigma}, \theta)$ to the *coupled* thermomechanical problem (3.1-4). This is intimately connected to the non-existence of a variational formulation corresponding to (3).

Such difficulties can be avoided by using the following finite time-step problem:

$$(\boldsymbol{u}, \boldsymbol{\xi}, \theta) \text{ verifies (1.1)-(1.4) at } t^0 + \delta t \tag{4.1}$$

$$\boldsymbol{B} = \boldsymbol{B}^r + \frac{\theta}{\theta^0} \boldsymbol{B}^d \tag{4.2}$$

$$\boldsymbol{B}^r \in \partial I_\mathcal{T}(\boldsymbol{\xi}) \ , \ \boldsymbol{B}^d \in \partial \phi\big((\boldsymbol{\xi} - \boldsymbol{\xi}^0)/\delta t\big) \tag{4.3}$$

$$K \delta t [\Delta\theta + \frac{\nabla\theta^0}{\theta^0}.\nabla(\theta^0 - \theta)] - \theta^0 (s - s^0) + \boldsymbol{B}^d.(\boldsymbol{\xi} - \boldsymbol{\xi}^0) = 0 \tag{4.4}$$

It can be verified that - just as the more intuitive scheme (3) - the incremental problem (4) is a consistent time-discretization of (1), in the sense that (3) coincides with (1) in the limit $\delta t \to 0$ [3, 4]. Motivation of the scheme (3) is that a variational formulation can be given, allowing one to study the existence of solutions. More precisely, it can be proved that solutions of (3) are solutions of the following variational problem

$$\begin{array}{c} find\ (\boldsymbol{u},\boldsymbol{\xi},\theta) \in \mathcal{K}_u \times \mathcal{K}_\xi \times \mathcal{K}_\theta\ such\ that\ for\ all\ (\boldsymbol{u}^*,\boldsymbol{\xi}^*,\theta^*) \in \mathcal{K}_u \times \mathcal{K}_\xi \times \mathcal{K}_\theta : \\ 0 \leq \partial \mathcal{F}[\boldsymbol{u},\boldsymbol{\xi},\theta].(\boldsymbol{u}^*-\boldsymbol{u},\boldsymbol{\xi}^*-\boldsymbol{\xi},\theta^*-\theta) \end{array} \tag{5}$$

where $\mathcal{F}(\boldsymbol{u},\boldsymbol{\xi},\theta) = \mathcal{F}^e(\boldsymbol{u},\boldsymbol{\xi},\theta) + \mathcal{F}^d(\boldsymbol{\xi},\theta) + \mathcal{F}^\theta(\theta)$ and

$$\begin{aligned} \mathcal{F}^e(\boldsymbol{u},\boldsymbol{\xi},\theta) = \quad & \int_\Omega w(\boldsymbol{\varepsilon}(\boldsymbol{u}),\boldsymbol{\xi},\theta)\, d\omega - \int_\Omega \boldsymbol{f}^d.\boldsymbol{u}\, d\omega - \int_{\Gamma^T} \boldsymbol{T}^d.\boldsymbol{u}\, da \\ \mathcal{F}^d(\boldsymbol{\xi},\theta) = \quad & \delta t \int_\Omega \phi\big(\frac{\theta}{\theta^0}\frac{\boldsymbol{\xi}-\boldsymbol{\xi}^0}{\delta t}\big)\, d\omega \\ \mathcal{F}^\theta(\theta) = \quad & \int_\Omega \theta s^0\, d\omega + \delta t \int_\Omega K(-\frac{1}{2}\frac{1}{\theta^0}\|\nabla\theta\|^2 + (\frac{\|\nabla\theta^0\|}{\theta^0})^2\theta)\, d\omega \\ & -\delta t \int_{\Gamma_q} \frac{q^d}{\theta^0}\theta\, da - K'\frac{\delta t}{2}\int_{\Gamma_r}\frac{(\theta-\theta_R)^2}{\theta^0}\, da \end{aligned} \tag{6}$$

Assume in particular that (i) the free energy w is convex in $(\boldsymbol{u},\boldsymbol{\xi})$ and concave in θ, (ii) the dissipation potential ϕ is positively homogeneous of degree 1 (which corresponds to a rate-independent dissipative behaviour). Note that those assumptions are satisfied by a wide range of SMA models (see Section 3 for some examples). In such a situation, the problem (5) can be rewritten as

$$\max_{\theta\in\mathcal{K}_\theta} J(\theta) \tag{7}$$

where

$$J(\theta) = \mathcal{F}^\theta(\theta) + \min_{(\boldsymbol{u},\boldsymbol{\xi})\in\mathcal{K}_u\times\mathcal{K}_\xi} \{\mathcal{F}^e(\boldsymbol{u},\boldsymbol{\xi},\theta) + \mathcal{F}^d(\boldsymbol{\xi},\theta)\} \tag{8}$$

Moreover, the maximization problem (7) admits some solutions (provided adequate functional spaces are chosen for $\mathcal{K}_u$, $\mathcal{K}_\xi$, $\mathcal{K}_\theta$), which ensure existence of solutions to the thermomechanical incremental problem (4) .

2.2 A maximization approach

To solve a problem such as (3) or (4), a general strategy is to solve directly the local equations using a Newton-Raphson algorithm. In such a framework, a partitioning approach is often used: the mechanical and the thermal subproblems are decoupled and solved successively until convergence. The global convergence of such methods is not ensured, and in practice one can face difficulties of convergence when for instance the initial guess is not close enough to the solution. Observe that, in the case of (4), such strategies ignore the variational nature of the problem at hand. As an alternative, using

the variational formulation of the problem, the solution of (4) can notably be found by solving the maximisation problem (7). A lot of well-known methods can be used to solve such a problem, some of them being built-in functions of scientific calculation softwares. Such methods (such as BFGS for instance) are iterative and require the computation of J and its gradient J' (or at least of an ascend direction). In this regard, note from (8) that the calculation of $J(\theta)$ amounts to solve the minimization problem

$$\min_{(\boldsymbol{u},\boldsymbol{\xi})\in\mathcal{K}_u\times\mathcal{K}_\xi} \mathcal{F}^e(\boldsymbol{u},\boldsymbol{\xi},\theta)+\mathcal{F}^d(\boldsymbol{\xi},\theta) \tag{9}$$

for which the local equations (expressing the stationarity of the functional) read as

$$\begin{gathered} \boldsymbol{u}\in\mathcal{K}_u\ ,\boldsymbol{\sigma}\in\mathcal{K}_\sigma\ ,\ \boldsymbol{\xi}\in\mathcal{K}_\xi \\ \boldsymbol{B}^d\in\frac{\theta}{\theta^0}\partial\phi(\frac{\boldsymbol{\xi}-\boldsymbol{\xi}^0}{\delta t})\ ,\ \boldsymbol{B}^r\in\partial I_{\mathcal{T}}(\boldsymbol{\xi}) \\ \boldsymbol{\sigma}=\frac{\partial w}{\partial\boldsymbol{\varepsilon}}\ ,\ \boldsymbol{B}=-\frac{\partial w}{\partial\boldsymbol{\xi}} \\ \boldsymbol{B}=\boldsymbol{B}^d+\boldsymbol{B}^r \end{gathered} \tag{10}$$

Those equations correspond to the backwards Euler scheme for an isothermal problem, with a dissipation potential set equal to $(\theta/\theta_0)\phi$. The calculation of $J(\theta)$ is thus equivalent to solving a incremental problem at a fixed temperature field. It can be proved that the calculation of the gradient $J'(\theta)$ is equivalent to solving a linear thermal problem. As a conclusion, using the variational framework described so far, the solution of the thermomechanical incremental problem can be obtained by solving a sequence of mechanical problems at a fixed temperature field (for evaluating $J(\theta)$) and linear scalar problems (for evaluating $J'(\theta)$). Therefore, that methods allows for a simple implementation of the thermomechanical problem, provided a solver for the isothermal problem is available. That last point is the focus of the next section.

3 CASE OF MICROMECHANICAL SMA MODELS

3.1 Micromechanical modelling

In most of micromechanical models of monocrystalline shape memory alloys, the internal variable $\boldsymbol{\xi}$ is taken as $(\xi_1,\cdots,\xi_n)$ where n is the number of martensitic variants and ξ_i denotes the volume fraction of martensitic variant i. The volume fraction ξ_0 of austenite is given by $\xi_0=1-\sum_{i=1}^n\xi_i$. Since each volume fraction ξ_i $(i=0,\cdots,n)$ must be positive, the variable $\boldsymbol{\xi}$ is required to take values in the convex and closed subset $\mathcal{T}$ of $\mathbb{R}^n$ defined as

$$\mathcal{T}=\{\boldsymbol{\xi}\in\mathbb{R}^n|\xi_i\geq 0\ \forall i;\boldsymbol{\xi}.\mathbf{1}_n\leq 1\} \tag{11}$$

where $\mathbf{1}_n$ is the vector of $\mathbb{R}^n$ with all its components equal to 1. Most of micromechanical SMA models are based on free energy functions of the form

$$w(\boldsymbol{\varepsilon},\boldsymbol{\xi},\theta)=\sum_{i=0}^n\xi_i w_i(\boldsymbol{\varepsilon},\theta)+h^{mix}(\boldsymbol{\xi}) \tag{12}$$

where $w_0(\boldsymbol{\varepsilon}, \theta) = (1/2)\boldsymbol{\varepsilon} : \boldsymbol{L} : \boldsymbol{\varepsilon}$ is the free energy of the austenite (with $\boldsymbol{L}$ symmetric positive definite) and

$$w_i(\boldsymbol{\varepsilon}, \theta) = \frac{1}{2}(\boldsymbol{\varepsilon} - \boldsymbol{\varepsilon}_i^{tr}) : \boldsymbol{L} : (\boldsymbol{\varepsilon} - \boldsymbol{\varepsilon}_i^{tr}) + c(1 - \log\frac{\theta}{\theta_0}) + \lambda_T \frac{(\theta - \theta_T)}{\theta_T} \tag{13}$$

is the free energy of the martensitic variant i. In (13), $\boldsymbol{\varepsilon}_i^{tr}$ is the transformation strain of martensitic variant i, c is the heat capacity, θ_T is the transformation temperature, and λ_T is the latent heat of the austenite $\rightarrow$ martensite transformation at temperature θ_T. The term h^{mix} in (12) is the interaction energy between the different variants. In the following, we will consider interaction energy h^{mix} of the form

$$h^{mix}(\boldsymbol{\xi}) = \frac{1}{2}(\underline{\boldsymbol{\varepsilon}}^{tr}.\boldsymbol{\xi}) : \boldsymbol{L} : (\underline{\boldsymbol{\varepsilon}}^{tr}.\boldsymbol{\xi}) + (\boldsymbol{J} - \boldsymbol{J}^{tr}).\boldsymbol{\xi} + \frac{1}{2}\boldsymbol{\xi}.\boldsymbol{H}.\boldsymbol{\xi} \tag{14}$$

where $\boldsymbol{H} \in \mathbb{R}^{n\times n}$ is symmetric positive and $\boldsymbol{J}$ is a given vector of $\mathbb{R}^n$. In such case, w is convex in $(\boldsymbol{u}, \boldsymbol{\xi})$. Functions of the form (14) have notably been used in [5, 6] with $\boldsymbol{H}$ and $\boldsymbol{J}$ equal to 0, in which case the obtained expression of w can be proved to be a rigorous lower bound on the effective free energy that would be obtained from relaxation [5, 7]. Concerning the dissipation potential, a classical choice, directly inspired from crystalline plasticity, is to take ϕ as

$$\phi(\dot{\boldsymbol{\xi}}) = \boldsymbol{G}^+.\langle\dot{\boldsymbol{\xi}}\rangle_+ + \boldsymbol{G}^-.\langle\dot{\boldsymbol{\xi}}\rangle_- \tag{15}$$

where $\langle\boldsymbol{x}\rangle_+$ is the positive vector whose component i is $\max(0, x_i)$. Similarly, for any vector $\boldsymbol{x}$, $\langle\boldsymbol{x}\rangle_-$ is the positive vector with components $\max(0, -x_i)$. In (15), $\boldsymbol{G}^+$ and $\boldsymbol{G}^-$ are two given positive vectors of $\mathbb{R}^n$.

3.2 Space discretization

In the following, we discuss the implementation of the general approach presented in Section 2 for the class of micromechanical SMA models introduced in the preceeding subsection. We focus on the problem (9), for which the temperature field θ is fixed. As explained in Section 2, that purely mechanical problem is indeed the central building block for solving the thermomechanical incremental problem.

The problem (9) is solved by a Galerking approach, i.e. (9) is replaced by

$$\min_{(\boldsymbol{u},\boldsymbol{\xi})\in\tilde{\mathcal{K}}_u\times\tilde{\mathcal{K}}_\xi} \mathcal{F}^e(\boldsymbol{u}, \boldsymbol{\xi}, \theta) + \mathcal{F}^d(\boldsymbol{\xi}, \theta) \tag{16}$$

where $\tilde{\mathcal{K}}_u$ and $\tilde{\mathcal{K}}_\xi$ are finite-dimensional subsets of $\mathcal{K}_u$ and $\mathcal{K}_\xi$, respectively. Any $\boldsymbol{u} \in \tilde{\mathcal{K}}_u$ admits a representation of the form

$$\boldsymbol{u}(\boldsymbol{x}) = \boldsymbol{M}_u(\boldsymbol{x}).\underline{\boldsymbol{v}} \tag{17}$$

where $\underline{\boldsymbol{v}} \in \mathbb{R}^M$ and $\boldsymbol{M}_u : \Omega \mapsto \mathbb{R}^{3\times M}$ is a given function. The vector $\underline{\boldsymbol{v}}$ would typically correspond to the nodal displacement vector if the finite element method is used. The

admissibility conditions $\boldsymbol{u} = \boldsymbol{u}^d$ on Γ_u might set restrictions on the admissible values of the vector $\underline{\boldsymbol{v}}$. However, to simplify the presentation, we assume that $\boldsymbol{u}^d = 0$, so that the vector $\underline{\boldsymbol{v}}$ can be considered as free from any constraint. Concerning the space discretization of $\boldsymbol{\xi}$, we assume here that functions in $\tilde{\mathcal{K}}_\xi$ are piecewise constant. More precisely, we assume the existence of a decomposition $\Omega = \bigcup_{i=1}^N \Omega_i$ such that any $\boldsymbol{\xi} \in \tilde{\mathcal{K}}_\xi$ takes a constant value (denoted by $\boldsymbol{\xi}_i$) on Ω_i. In such case, functions $\boldsymbol{\xi}$ in $\tilde{\mathcal{K}}_\xi$ can be written as

$$\boldsymbol{\xi}(\boldsymbol{x}) = \sum_{i=1}^{N} \chi_i(\boldsymbol{x}) \boldsymbol{\xi}_i \tag{18}$$

where χ_i is the characteristic function of Ω_i and $\boldsymbol{\xi}_i \in \mathcal{T}$. The vector $(\boldsymbol{\xi}_1, \cdots, \boldsymbol{\xi}_N)$ is denoted by $\underline{\boldsymbol{\xi}}$.

Substituting (17) and (18) in the expression of $\mathcal{F}^e + \mathcal{F}^d$, the problem (16) takes the form

$$\min_{\underline{\boldsymbol{v}} \in \mathbb{R}^M, \underline{\boldsymbol{\xi}} \in \mathcal{T}^N} \frac{1}{2} \underline{\boldsymbol{v}}.\mathbb{K}.\underline{\boldsymbol{v}} + \frac{1}{2} \underline{\boldsymbol{\xi}}.\mathbb{B}.\underline{\boldsymbol{\xi}} - \underline{\boldsymbol{v}}.\mathbb{C}.\underline{\boldsymbol{\xi}} - \underline{\boldsymbol{v}}.\boldsymbol{F}_u + \underline{\boldsymbol{\xi}}.\boldsymbol{F}_\xi + \Phi(\underline{\boldsymbol{\xi}} - \underline{\boldsymbol{\xi}}^0) \tag{19}$$

where the matrices $\mathbb{K}$ and $\mathbb{B}$ are both symmetric positive definite, the former corresponding to the standard stiffness matrix (see [10] for more details). The function Φ that appears in (19) is the convex function defined by

$$\Phi(\underline{\boldsymbol{\xi}}) = \int_\Omega \frac{\theta}{\theta^0} \phi(\sum_{i=1}^{N} \chi_i(\boldsymbol{x}) \boldsymbol{\xi}_i) d\omega = \sum_{i=1}^{N} p_i \phi(\boldsymbol{\xi}_i) \text{ with } p_i = \int_{\Omega_i} \frac{\theta}{\theta^0} \, d\omega \tag{20}$$

The function in (19) being quadratic with respect to $\boldsymbol{v}$, the minimization with respect to $\boldsymbol{v}$ in (19) can be performed in closed form. The problem (19) is found to reduce to

$$\min_{\underline{\boldsymbol{\xi}} \in \mathcal{T}^N} \frac{1}{2} \underline{\boldsymbol{\xi}}.\mathbb{K}'.\underline{\boldsymbol{\xi}} - \underline{\boldsymbol{\xi}}.\boldsymbol{F}' + \Phi(\underline{\boldsymbol{\xi}} - \underline{\boldsymbol{\xi}}^0) \tag{21}$$

with

$$\mathbb{K}' = \mathbb{B} - \mathbb{C}^T.\mathbb{K}^{-1}.\mathbb{C} \ , \ \boldsymbol{F}' = \mathbb{C}^T.\mathbb{K}^{-1}.\boldsymbol{F}_u + \boldsymbol{F}_\xi \tag{22}$$

It can be verified that the symmetric matrix $\mathbb{K}'$ is positive [10]. Consequently, the function to minimize in (21) is convex (but not quadratic) with respect to $\underline{\boldsymbol{\xi}}$. Using standard results from convex analysis [1], the problem (19) can be rewritten as

$$-\mathbb{K}' \left\{ \begin{array}{c} \boldsymbol{\xi}_1 \\ \vdots \\ \boldsymbol{\xi}_N \end{array} \right\} + \boldsymbol{F}' = \left\{ \begin{array}{c} \boldsymbol{B}_1^r \\ \vdots \\ \boldsymbol{B}_N^r \end{array} \right\} + \left\{ \begin{array}{c} \boldsymbol{B}_1^d \\ \vdots \\ \boldsymbol{B}_N^d \end{array} \right\} \tag{23}$$

$$\boldsymbol{\xi}_i \in \mathcal{T} \ , \boldsymbol{B}_i^r \in \partial I_{\mathcal{T}}(\boldsymbol{\xi}_i) \ , \ \boldsymbol{B}_i^d \in p_i \partial \phi(\boldsymbol{\xi}_i - \boldsymbol{\xi}_i^0) \text{ for } i = 1, \cdots, N$$

The issue of practically solving that problem is the focus of the next subsection.

3.3 Formulation of a linear complementarity problem

The identity matrix of $\mathbb{R}^{n\times n}$ is denoted by $\mathbb{I}_n$, and $\mathbb{E}$ denotes the $nN \times N$ matrix with the following block structure

$$\mathbb{E} = \begin{pmatrix} \mathbf{1}_n & \mathbf{0} & \mathbf{0} \\ \mathbf{0} & \ddots & \mathbf{0} \\ \mathbf{0} & \mathbf{0} & \mathbf{1}_n \end{pmatrix} \tag{24}$$

For latter reference, we also introduce the two vectors $\tilde{\boldsymbol{G}}^+$ and $\tilde{\boldsymbol{G}}^-$ of $\mathbb{R}^{nN}$ defined by

$$\tilde{\boldsymbol{G}}^+ = \left\{ \begin{array}{c} p_1\boldsymbol{G}^+ \\ \vdots \\ p_N\boldsymbol{G}^+ \end{array} \right\} \ , \ \tilde{\boldsymbol{G}}^- = \left\{ \begin{array}{c} p_1\boldsymbol{G}^- \\ \vdots \\ p_N\boldsymbol{G}^- \end{array} \right\} \tag{25}$$

Consider now a solution $(\boldsymbol{\xi}_j, \boldsymbol{B}^r_j, \boldsymbol{B}^d_j)_{1\leq j\leq N}$ of (23) and define

$$\begin{array}{l} \boldsymbol{\alpha}^+_j = p_j\boldsymbol{G}^+ - \boldsymbol{B}^d_j \quad , \quad \boldsymbol{\mu}^+_j = \langle \boldsymbol{\xi}_j - \boldsymbol{\xi}^0_j \rangle_+ \\ \boldsymbol{\alpha}^-_j = p_j\boldsymbol{G}^- + \boldsymbol{B}^d_j \quad , \quad \boldsymbol{\mu}^-_j = \langle \boldsymbol{\xi}_j - \boldsymbol{\xi}^0_j \rangle_- \\ \gamma_j = 1 - \mathbf{1}_n.\boldsymbol{\xi}_j \end{array} \tag{26}$$

Since $\mathcal{T}$ takes the form (11) and $\boldsymbol{B}^r_j \in \partial I_{\mathcal{T}}(\boldsymbol{\xi}_j)$, there exists $z_j \in \mathbb{R}$ and $\boldsymbol{a}_j \in \mathbb{R}^n$ [10] such that

$$\boldsymbol{B}^r_j = z_j\mathbf{1}_n - \boldsymbol{a}_j \ , z_j \geq 0 \ , \ \boldsymbol{a}_j \geq 0 \ , \ \boldsymbol{a}_j.\boldsymbol{\xi}_j = z_j(1 - \boldsymbol{\xi}_j.\mathbf{1}_n) = 0 \tag{27}$$

Define

$$\boldsymbol{\alpha}^\pm = \left(\begin{array}{c} \boldsymbol{\alpha}^\pm_1 \\ \vdots \\ \boldsymbol{\alpha}^\pm_N \end{array} \right) \ , \ \boldsymbol{\mu}^\pm = \left(\begin{array}{c} \boldsymbol{\mu}^\pm_1 \\ \vdots \\ \boldsymbol{\mu}^\pm_N \end{array} \right) \ , \ \boldsymbol{a} = \left(\begin{array}{c} \boldsymbol{a}_1 \\ \vdots \\ \boldsymbol{a}_N \end{array} \right) \ , \ \boldsymbol{\gamma} = \left(\begin{array}{c} \gamma_1 \\ \vdots \\ \gamma_N \end{array} \right) \ , \ \boldsymbol{z} = \left(\begin{array}{c} z_1 \\ \vdots \\ z_N \end{array} \right) \tag{28}$$

Setting $k = (3n + 1)$, we consider the two following vectors of $\mathbb{R}^k$:

$$\boldsymbol{s} = \left(\begin{array}{c} \boldsymbol{\alpha}^+ \\ \boldsymbol{\alpha}^- \\ \underline{\boldsymbol{\xi}} \\ \boldsymbol{\gamma} \end{array} \right) \ , \ \boldsymbol{x} = \left(\begin{array}{c} \boldsymbol{\mu}^+ \\ \boldsymbol{\mu}^- \\ \boldsymbol{a} \\ \boldsymbol{z} \end{array} \right) \tag{29}$$

Using the relations (23), it can be verified that $(\boldsymbol{x}, \boldsymbol{s})$ are solution of the problem

$$\textit{Find } \boldsymbol{x} \in \mathbb{R}^k \textit{ and } \boldsymbol{s} \in \mathbb{R}^k \textit{ such that } \boldsymbol{s} = \mathbb{M}.\boldsymbol{x} + \boldsymbol{q} \ , \ \boldsymbol{s} \geq 0 \ , \ \boldsymbol{x} \geq 0, \boldsymbol{s}.\boldsymbol{x} = 0 \tag{30}$$

where $\mathbb{M} \in \mathbb{R}^{k\times k}$ and $\boldsymbol{q} \in \mathbb{R}^k$ are defined by

$$\mathbb{M} = \begin{pmatrix} \mathbb{K}' & -\mathbb{K}' & -\mathbb{I}_{nN} & \mathbb{E} \\ -\mathbb{K}' & \mathbb{K}' & \mathbb{I}_{nN} & -\mathbb{E} \\ \mathbb{I}_{nN} & -\mathbb{I}_{nN} & \mathbf{0} & \mathbf{0} \\ -\mathbb{E}^T & \mathbb{E}^T & \mathbf{0} & \mathbf{0} \end{pmatrix} \ , \ \boldsymbol{q} = \begin{pmatrix} \tilde{\boldsymbol{G}}^+ - \boldsymbol{F}' + \mathbb{K}'.\underline{\boldsymbol{\xi}^0} \\ \tilde{\boldsymbol{G}}^- + \boldsymbol{F}' - \mathbb{K}'.\underline{\boldsymbol{\xi}^0} \\ \underline{\boldsymbol{\xi}^0} \\ \mathbf{1}_N - \mathbb{E}^T.\underline{\boldsymbol{\xi}^0} \end{pmatrix} \tag{31}$$

Conversely, it can easily be verified that any solution of (30) generates a solution of the incremental problem (23), so that the two problems (23) and (30) are equivalent. The motivation of that reformulation is that (30) is a standard problem in mathematical programming. It is known as a Linear Complementarity Problem (LCP) and has been extensively studied [8, 9]. In particular, efficient numerical algorithms, such as interior-point methods, have been developed and are now available in various toolboxes. That reformulation thus allows for an easy and efficient way of solving the incremental problem, building on existing algorithms suited to large-scale problems. Is should be mentionned that solving a LCP amounts to solve a quadratic minimization problem (with linear constraints). As a consequence, the change of variables (26) allows us to turn the convex but non quadratic problem (23) into an equivalent quadratic problem, easier to solve. Some examples of numerical simulations are presented in [10].

It would be interesting to study if the proposed method could be extended to more sophisticated micromechanical models, in order to account for crystalline texture [7] or large strain effects [11].

REFERENCES

[1] Brézis, H. *Opérateurs maximum monotones et semigroupes de contractions dans les espaces de Hilbert*. North-Holland, Amsterdam, (1972).

[2] Peigney, M., Shakedown theorems and asymptotic behaviour of solids in non-smooth mechanics. *Eur.J.Mechanics A* (2010) **29**:785-793.

[3] Yang, Q., Stainier, L. and Ortiz, M., A variational formulation of the coupled thermo-mechanical boundary-value problem for general dissipative solids. *J. Mech. Phys. Solids* (2006) **54**:401-424.

[4] Peigney, M., A time-integration scheme for thermomechanical evolutions of shape-memory alloys. *C.R.Mécanique* (2006) **334**:266-271.

[5] Govindjee, S. and Miehe, C., A multi-variant martensitic phase transformation model : formulation and numerical implementation. *Comput. Mech. Appli. Mech. Eng.* (2001) **191**:215-238.

[6] Anand, L. and Gurtin, M.E., Thermal effects in the superelasticity of crystalline shape-memory materials. *J. Mech. Phys. Solids* (2003) **51**:1015-1058.

[7] Peigney, M., A non-convex lower bound on the effective free energy of polycrystalline shape memory alloys. *J. Mech. Phys. Solids* (2009) **57**:970-986.

[8] Ye, Y. *Interior Point Algorithms : theory and analysis*. Wiley Interscience (1997).

[9] Wright, S.J. *Primal-dual interior-point methods*. Society for Industrial and Applied Mathematics (1997).

[10] Peigney, M., Seguin, J.P. and Herve-Luanco, E., Numerical simulation of shape memory alloys structures using interior-point methods. *Int.J.Sol.Struct.* (2011) doi:10.1016/j.ijsolstr.2011.05.017.

[11] Peigney, M., Recoverable strains in composite shape memory alloys. *J. Mech. Phys. Solids* (2008) **56**:360-275.

XI International Conference on Computational Plasticity. Fundamentals and Applications
COMPLAS XI
E. Oñate, D.R.J. Owen, D. Peric and B. Suárez (Eds)

3D MODELLING OF THE ELASTO-PLASTIC BEHAVIOUR OF ADHESIVELY BONDED JOINTS SUITED FOR A WIDE RANGE OF TENSILE-SHEAR LOADS

Julien Maurice [1,2,*], Jean-Yves Cognard [2], Romain Créac'hcadec [2], Laurent Sohier [2], Peter Davies [3], Georges Meirinhos [1], Stéphane Mahdi [1]

[1] Airbus Operations S.A.S
316 Route de Bayonne, 31060 Toulouse Cedex 9, France
E-mail: julien.maurice@airbus.com, stephane.mahdi@airbus.com

[2] Brest Laboratory of Mechanics and Systems (LBMS), ENSTA Bretagne / UBO / ENIB,
LBMS, 2 rue François Verny, 29806 Brest Cedex 9, France.
E-mail: julien.maurice@ensta-bretagne.fr, jean-yves.cognard@ensta-bretagne.fr,
romain.creachcadec@ensta-bretagne.fr, laurent.sohier@univ-brest.fr - Web page: http://www.lbms.fr

[3] IFREMER, Materials & Structure Group
IFREMER, Centre de Brest, BP70 29280 Plouzané
E-mail: peter.davies@ifremer.fr - Web page: http://wwz.ifremer.fr/rd_technologiques

Key words: elasto-plastic behaviour, adhesives, modified Arcan test

Abstract.

Airframe developments use composite components extensively; bonding, as a rivetless assembly solution, is thus gaining in importance, leading to the need for accurate characterization of adhesive behaviour and the development of adapted models.

Structural adhesives often show large inelastic behaviour before failure [1]; however the modelling of the 3D elasto-plastic behaviour of adhesives is not straightforward. Indeed, advanced models taking into account the hydrostatic pressure dependency and defined under a non-associated formalism ([1- 4]) are needed for an accurate description of adhesive materials under a wide range of loads covering tension, shear, mixed tension/compression-shear loads.

This study presents the assessment of two non-associated elasto-plastic models: the Exponent Drucker-Prager model, and the Mahnken-Schlimmer model [3], using a large experimental database obtained with a modified Arcan apparatus [5] on a structural adhesive. The aim is to develop a reliable numerical model in order to obtain good numerical predictions of the real behaviour of complex industrial type bonded assemblies.

1 INTRODUCTION

In a context of the growing importance of composite in modern commercial aircrafts, bonding has kept gaining in importance in the design of airframe components over the last 40 years, and is now to be used extensively [6].

In order to model the local behaviour of a bonded assembly and to achieve a good prediction of crack onset within the adhesive, it is necessary to develop non-linear constitutive laws well-suited for adhesive materials.

It is well known that the yielding and the plastic flow behaviour of epoxy adhesives depend on the hydrostatic stress component ([1-4], [7-12]). Besides, recent studies tend to prove that non-associated formalism ([3,4,11,12]) is also needed for a good description of the high ratio between the normal and the tangential non-linear deformations of adhesives subjected to mixed tensile/compression-shear loads. This makes the characterization and the 3D modelling of such behaviour under a wide range of loads all but straightforward, since several parameters have to be identified, which involves using several load test configurations.

The aim of this paper is to present the identification and the validation of two elasto-plastic models using experimental results obtained by means of a modified Arcan test [5]. This test presents the advantages of requiring a unique apparatus mounted on a tension machine and only one type of bonded specimen design, while offering a wide range of proportional loads from tension, shear, mixed tension-shear and compression-shear with different ratios.
Using these characterization results, a simplified inverse identification approach using FEA is proposed for two models: the Exponent Drucker-Prager model and the Mahnken-Schlimmer model [3]. Both of these models have been shown recently to be well suited for the modelling of adhesive materials ([3,11,12]) in a tension-shear domain.

The particularity of this study lies in the fact that a whole wide range of proportional loads, including mixed compression-shear, are covered and that only experimental results obtained using a modified Arcan apparatus test results are used for the identification of the models and a first validation.

2. EXPERIMENTAL RESULTS

2.1 Presentation of the modified Arcan test used

The adhesive considered for this study is the Redux 420 A/B of Huntsman [13], a bi-component epoxy-based paste.

The device used is the modified Arcan test presented in figure 1. It aims to load with different ratios of shear and tension or compression (given by γ the angle of load defined in figure 1-a) a single configuration of bonded assemblies loaded with a standard tensile testing machine. The bonded specimens (figure 1-b) are made of substrates in 2017 aluminium designed with

beaks all around the surfaces to be bonded according to the geometry presented in figure 1-c. A rounded shape is also applied to the adhesive layer at the edges by "cleaning" immediately after the application of the adhesive. This specific design enables us to significantly limit the influence of edge effects (i.e. stress concentrations) that can lead to premature crack onset and thus misunderstanding of the results. More details on the design and advantages of the system can be found in [4] and [5].

The measurements were made using 3D video correlation [14]. This enables the displacement field to be recorded against the applied load at the centre of the bonded joint. Relative displacements between the two substrates in the two directions, called DT for the tangential one and DN for the normal one, at a given length from the adhesive layer are then post-processed respectively against the tangential (FT) and normal (FN) transmitted load components.

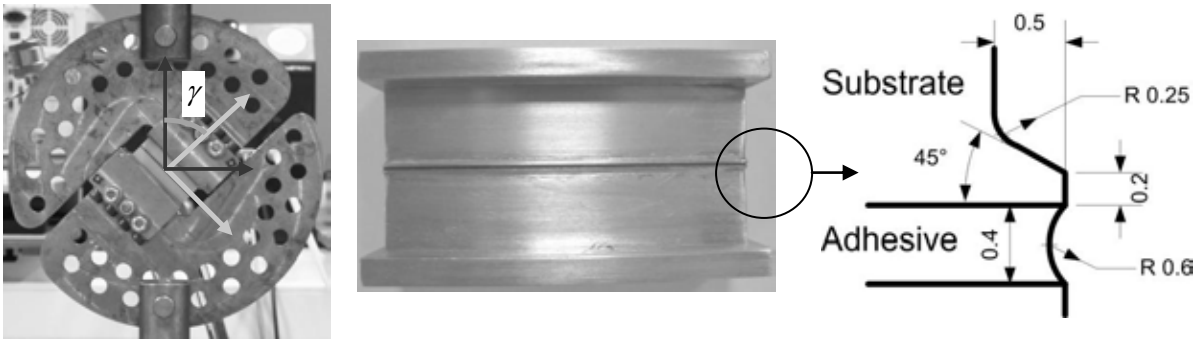

Figure 1: Modified Arcan apparatus with the definition of the angle of load ratio: γ Bonded assembly (a) and specific design of the beaks (b) to limit edge effects within the adhesive layer (c) geometry of the beaks.

2.2 Experimental results

The adhesive layer for all the specimens considered in this study was 0.4 mm thick and the load was imposed by a constant velocity of the crosshead of the tensile testing machine of 0.5 mm/min.

The results obtained are presented by the dotted lines in figure 4 for $\gamma = 0°$ (tension load) and 90° (shear) and in figures 5-a, 5-b and 5-c for $\gamma = 30°$, 45° (mixed tension-shear) and 135° (compression-shear) respectively. In figure 5, N and T represent respectively the results obtained in the normal and the tangential directions.

For mixed loads (30°, 45°, 135°) an important ratio between DN and DT can be noted. Indeed, when failure is reached, |DT/DN| is equal to 3.2 at 30° and 7 at 45°.
The response of the bonded assembly also exhibits large inelastic behaviour and the relative tangential displacements at failure are in the order of the adhesive thickness. Because the substrates remain in their elastic domain, and assuming a constant strain rate between the

different load ratios, the behaviour can be first approximated as elasto-plastic for the adhesive considered here (under such conditions viscous effects can be neglected).
The aim is thus to propose a 3D elasto-plastic model that enables the most accurate description of the adhesive material over the whole range of load ratios considered.

3. INVERSE IDENTIFICATION OF THE EDP AND THE MS MODELS

Two models were considered: the Exponent Drucker-Prager (EDP) model, as implemented in Abaqus FE code [15] and the Mahnken-Schlimmer (MS) model that has been implemented as a user subroutine in Abaqus as proposed by [3]. Both of them take into account the dependence of the yield surface and the flow rule on the hydrostatic stress component. They have been proved to be well-suited for the modelling of structural adhesive behaviour [1-3, 11, 12] under tension-shear loads.

3.1 Description of the constitutive laws

The Yield functions of the EDP and the MS models are respectively given by $F_0^{EDP} = 0$ and $F_0^{MS} = 0$ with:

$$F_0^{EDP} = a\sigma_{VM}^b + p - p_{t0} \quad (1)$$

$$F_0^{MS} = \sqrt{\sigma_{VM}^2 + a_1 Y_0 p + a_2 p^2} - Y_0 \quad (2)$$

where: p is the hydrostatic stress component, σ_{VM} is the von Mises stress, and (a,b, p_{t0}) and (a_1, a_2, Y_0) are material parameters to be identified.

They both have a quadratic form in the Mises stress- hydrostatic stress plane. However, the MS model is an ellipse-like surface whereas the EDP is an open parabola in the direction of negative hydrostatic stress component: hence, the yielding limit is never reached under a pure compressive hydrostatic load for the latter criteria.

For the MS model, the hardening is given by the three parameters q, b and H, with:

$$Y = Y_0 + q(1 - e^{-be_v}) + He_v \text{ where } \dot{e}_v Y_0 = \underline{\underline{\sigma}} : \underline{\underline{\dot{\varepsilon}}}^{pl} \quad (3)$$

For the EDP model, it is given by:

$$p_t = a\,(\sigma_t)^b + \frac{\sigma_t}{3} \text{ where : } \sigma_t = \tilde{\sigma}\big|_0 + Ke_p \quad (4)$$

There are thus only two parameters, K and $\tilde{\sigma}\big|_0$, to be identified.

Considering the flow rule, the formalism proposed by the two models differs. For the EDP, the flow rule is always non-associated with the yield function.

$$G^{EDP} = \sqrt{(e\tilde{\sigma}|_0 \tan\psi)^2 + \sigma_{VM}^2} + p\tan\psi \tag{5}$$

The only parameter to identify is ψ, called the dilatation angle; e has a default value of 0.1 that will be kept unchanged in the following.

For the MS model, both associated and non-associated formalisms are possible. However as demonstrated in [3], it is more convenient for thermodynamic consistency to choose the non-associated one, reducing to a_2^* the only parameter to be defined:

$$G^{MS} = \sqrt{\sigma_{VM}^2 + a_2^* p^2} \tag{6}$$

Because the stress and strain states are multi-axial within the bonded layer, inverse identification of the models using 3D finite element analysis (FEA) is more appropriate. It consists of an optimization loop that enables the best parameter set to be found for a given model considering the experimental results obtained.

The bonded specimens were modelled with appropriate geometry, loads and symmetry as presented in figure 2. A relatively coarse mesh was used within the adhesive layer since refining the mesh near the edges has no effect on the global response considered for the identification (relative displacement vs. applied load). Substrates were modelled assuming an elastic behaviour with a Young's modulus of 70 GPa and a Poisson's coefficient of 0.3.

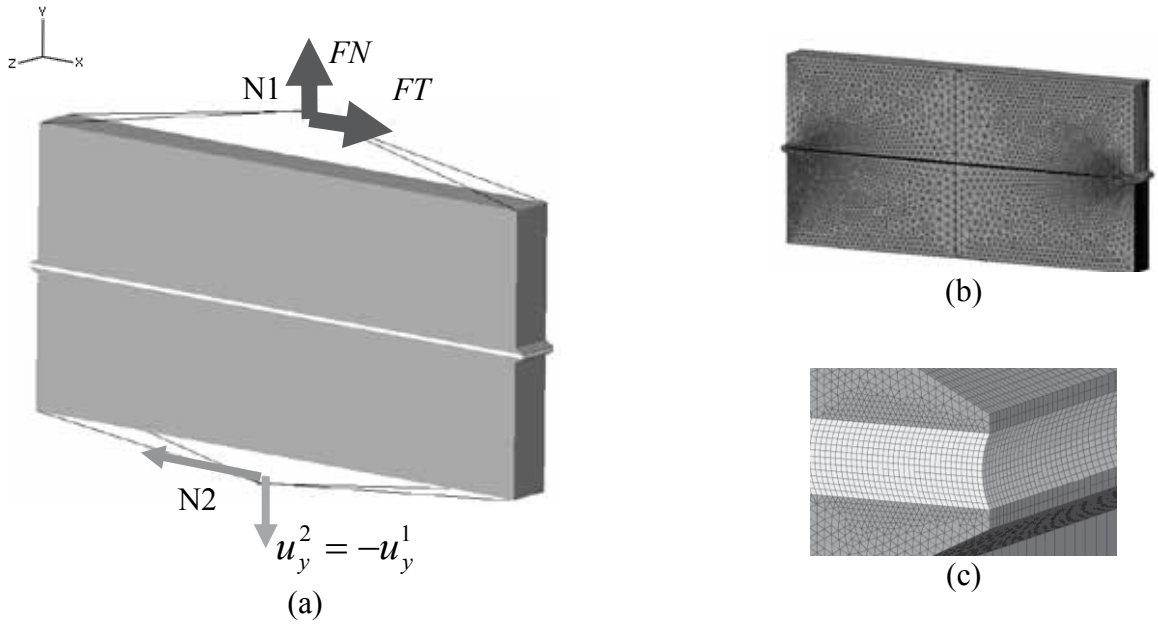

Figure 2 : Mesh of the Arcan bonded assembly : (a) Loads and boundary conditions (b) Global mesh (c) Beak's mesh

3.2 Identification of the models

Due to the large number of parameters to be identified, 7 for the MS and 5 for the EDP plus the elastic constants, and considering that only inverse identification based on FEA is appropriate, a sequential and simplified approach, summmarized as follows, has been chosen:

- Step 1: Identification of the elastic parameters of the adhesive: E (Young's modulus) and ν (Poisson's coefficient) using modified Arcan test results at 0° and 90°.

- Step 2: Identification of the yield surfaces based on experimental yield points obtained at 0°, 90° and 135°.

- Step 3: Identification of the hardening functions and the flow rule parameters using 0° and 90°.

Since only 90° (shear) and 0° (tension) results were completely used for the identification of the two parameters sets, a validation could be performed using experimental results at 45°, 135° and 30°.

- Identification of the Elastic parameters and the Yield surface (Steps 1 and 2)

Young's modulus and Poisson's coefficient of the adhesive have been identified using a parametric study on the domain respectively covering: 1700 to 2200 MPa with increments of 100 MPa and 0.3 to 0.45 with increments of 0.05. By comparing FE and experimental results at 0° and 90°, the set minimising a least-square type error has been found to be: E = 2100 MPa and Nu= 0.35.

It has been demonstrated that, once the elastic parameters are known, the Modified Arcan test results enable the experimental yield surface to be determined in the Mises stress- hydrostatic stress plane [11]. Using this result, the yield functions were fitted using the ratio loads of 0°, 90° and 135°. Figure 3 presents the comparison of this identification for the two models in the Mises stress- hydrostatic stress plane.

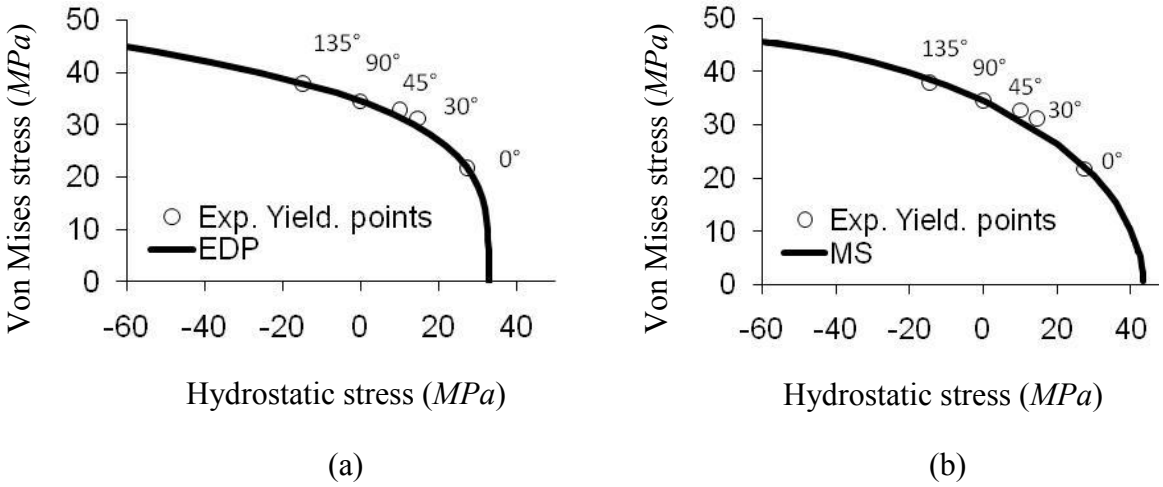

Figure 3: Comparison of the identification of the yield surfaces using Arcan test results at angles loads of 0°, 45° and 135° and the experimental yield surface: (a) EDP model, (b) MS model

Both of the criteria provide a good correlation over the wide range of loads considered: the yield points at 30° and 45°, which were not used for the identification, are slightly underestimated.
The main difference is in the predicted yield point under pure hydrostatic tension (for such tests we have no experimental results). For the EDP model yielding occurs at 33 MPa compared with 42 MPa for the MS model. The identified EDP yield criterion has a higher sensitivity to peel loads than the MS yield criterion; this sensitivity being emphasized for von Mises stresses below 20 MPa for which the slope is almost vertical.

- Identification of the hardening function and the flow rule (step 3)

The third step consists of the identification of the complete response at 0° and 90° by optimizing the hardening and flow function parameters.

Results are presented in figure 4-a and 4-b respectively for the EDP and the MS models.

Both of the models enabled the experimental results to be fitted correctly. The rounded shape at 90° and the linear asymptotic part are described well, and the fact that the non-linear response is reduced to a small part of the curve at 0° whereas it is predominant in shear is well represented.

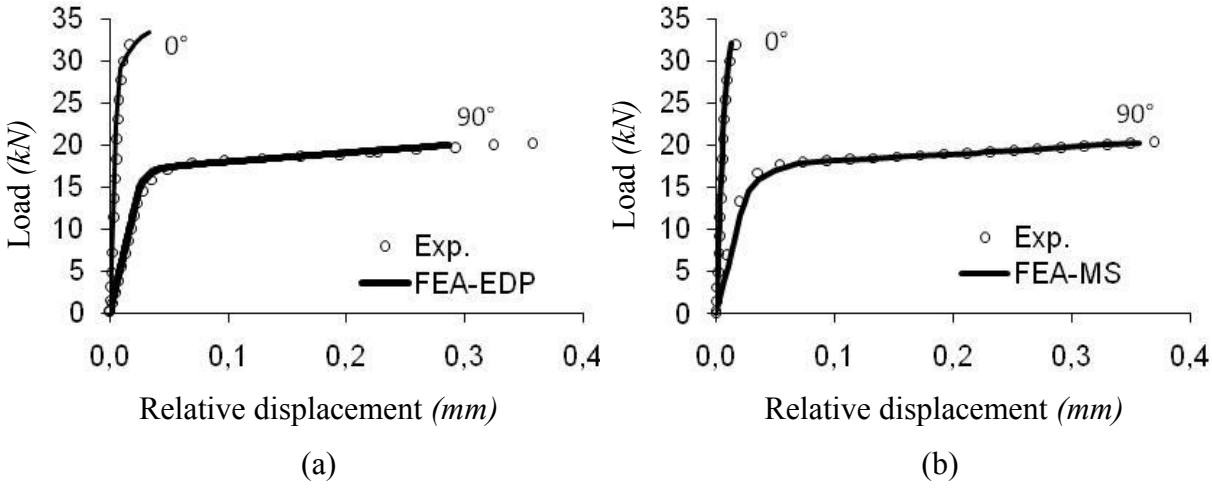

Figure 4: Comparison of FE and experimental results at 0° and 90°: (a) EDP model; (b) MS model

Table I: Parameter sets with the simplified identification approach for the Mahnken-Schlimmer and the EDP models

Mahnken-Schlimmer							Exponent Drucker-Prager					
a_1	a_2	Y_0	a_2^*	H	q	b	p_{t0}	a	b	K	$\tilde{\sigma}\|_0$	ψ
(-)	(-)	MPA	(-)	MPa	MPa	(-)	MPa	SI	SI	MPa	MPa	°
0.29	0.015	33.5	0.06	20	10	100	31.7	1.10^{-6}	4.87	29.3	37.2	25

4. VALIDATION AND DISCUSSION

Using the previous parameter sets identified using only 0° and 90° results (Table I.), a comparison, acting as a first validation of this previous identification, has been conducted.

Comparisons of FE and experimental results obtained considering the force vs. relative displacements in the normal and tangential directions are presented in figure 5. At 30° and 45° the precision of the two models regarding the experimental results are similar. As noticed for the identification of the yield surface, the yield points are underestimated leading to a poor estimation of the rounded shape. This is particularly emphasized at 45° for both of the models.
Indeed, the stress-state is not uniform within the adhesive layer [5] and maximum stresses are encountered in the middle of the adhesive layer. Thus plasticity occurs progressively from the centre to the edges of the adhesive joint. An underestimation of the yielding thus leads to an underestimation of the transmitted load for a given relative displacement, since yielding spreads prematurely along the adhesive layer.

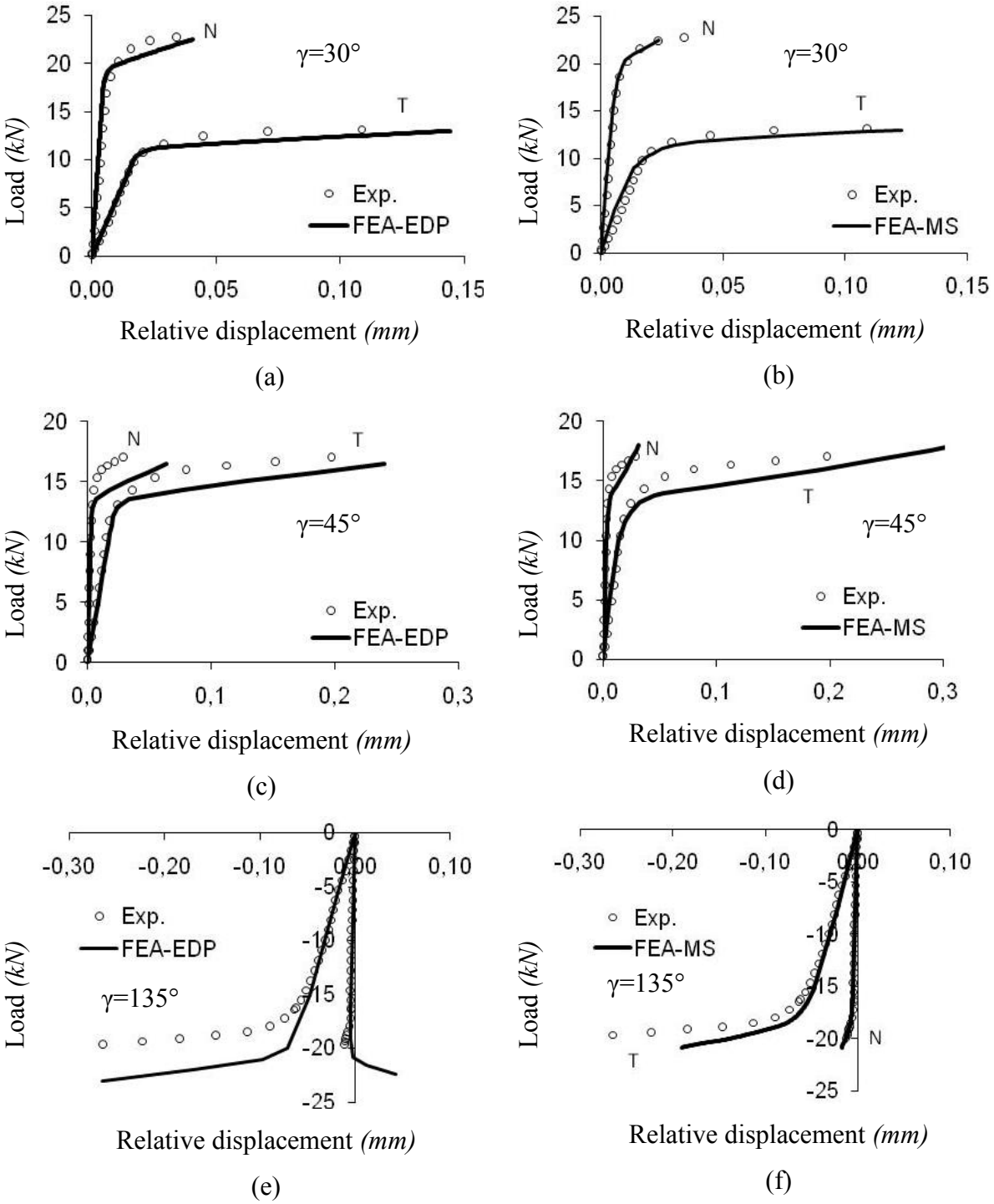

Figure 5: Comparisons of the identifications at 30° (a) & (b) , 45° (c) & (d) and 135° (e) & (f) for the EDP (left) and the MS (right) models. Experimental (Exp.) vs. FE results (FEA-EDP or FEA-MS).

It could be interesting to perform an identification of the flow rule and hardening based on mixed tension-shear loads, using 0° and 90° results for validation. Indeed, because plasticity is not very developed at 0°, the identification domain remains limited and could be insufficient for an accurate identification.

The main difference in the predicted results concerns the normal behaviour for a compression-shear load (135°, Figure 5-e and 5-f). On the one hand, both models reach almost the same level of accuracy in the tangential behaviour: the EDP model gives a more over-estimated load compared to the MS model. But, on the other hand, only the MS model gives a good representation of the FN vs. DN behaviour whereas the EDP model predicts a plastic dilatation that starts with plasticity and that does not correspond to the experimental observations.

Such behaviour can be explained by the overall shape of the EDP flow rule given by ψ (the "dilatation angle"). Indeed, the EDP model only permits the flow direction to be towards positive hydrostatic stress whatever the position in the Mises stress - hydrostatic plane. On the contrary, the MS model, as identified in the previous section, gives flow directions that are symmetrical about the Mises axis for two points that are also symmetrical. This radically changes the behaviour in the normal direction when considering compression-shear loads which are load cases that are rarely taken into account for the characterization of structural adhesives since they are relatively difficult to obtain and are not considered as the most detrimental. However, as the stress-state in the adhesive spew fillet, which is often the location of crack onset, is multi-axial, a poor estimation of the behaviour over the whole domain of hydrostatic stresses can lead to inaccurate modelling of the stress state within this region, and misunderstanding when comparing different stress criteria for example.

5. CONCLUSIONS

This study aims to characterize and identify the 3D elasto-plastic behaviour of structural adhesive materials. Two models, taking into account the hydrostatic stress dependency and non-associated formalism, have been identified using experimental results obtained with a modified Arcan test and a simplified inverse identification approach. The main conclusions that can be drawn are the following:

- The modified Arcan test is very efficient to characterize the behaviour of adhesive materials since it enables several load configurations to be applied to a bonded assembly using a unique specimen design and single test apparatus. In particular it allows the hydrostatic stress dependency to be highlighted.

- Applied to the case of the Redux 420 A/B epoxy adhesive, it is very useful in the discrimination between different elasto-plastic models.

- When considering structural adhesive elasto-plastic behaviour, characterization and validation on both the tension-shear and compression-shear domain are needed and particular care has to be taken in the choice of the flow rule.

- Optimisation of the identification procedure and study of the robustness of the inverse identification could lead to a better fitting of the experimental results.

Application of a similar procedure for the case of adhesives films, that also show hydrostatic stress dependency [1] and are used in aircraft manufacturing, is in progress. Next, a validation on non-proportional cases will constitute a natural extension to this work in order to validate a Mahnken-Schlimmer type model. Finally, a damage and failure approach, based on the typical requirements of a design office will be implemented.

REFERENCES

[1] Wang C-H, Chalkley P., Plastic yielding of a film adhesive under multiaxial stresses, Int. J. of Adh.& Adh., (2000) **20**:155-164.
[2] Dean G., Crocker L., Read B., Wright L., Prediction of deformation and failure of rubber-toughened adhesive joints, Int. J. of Adh. & Adh., (2004) **24**:295-306.
[3] Mahnken R, Schlimmer M, Simulation of strength difference in elasto-plasticity for adhesive materials, Int. J. for Num. Meth. in Eng., (2005) **63**:1461-1477.
[4] Créac'hcadec R., Cognard J.Y, 2-D Modeling of the behavior of an adhesive in an assembly using a non-associated elasto-visco-plastic model, J. of Adh., (2009) **85**:239-260.
[5] Cognard J.Y ,Davies P., Sohier L. and Créac'hcadec R., A study of the non-linear behavior of adhesively-bonded composite assemblies, Compos. Str., (2006) **76**:34-46
[6] Bishopp J., *Handbook of Adhesives and Sealants*, *Volume 1*, *Chapter 5 Aerospace: A pioneer in structural adhesive* bonding, (2005), Pages 215-347
[7] Adams R.D, Comyn J.,Wake W.C, *Structural Adhesive Joints in Enginnering*, 2nd ed (1997), Chapman & Hall
[8] Dolev G., Ishai O., Mechanical characterization of adhesive layer in-situ and as bulk Material, J. Adhesion, (1981) **12**:283-294.
[9] Malvade I., Deb A., Biswas P., Kumar A., Numerical prediction of load displacement behaviors of adhesively bonded joints at different extension rates and temperatures, Comp. Mat. Sc., (2009) **44**:1208-1217.
[10] Duncan B., Dean G., Measurements and models for design with modern adhesives, Int. J. of Adh. & Adh., (2003) **23**:141-149.
[11] Cognard J.Y, Créac'hcadec R., Maurice J., Davies P., Peleau M and da Silva L.F.M, Analysis of the influence of hydrostatic stress on the behaviour of an adhesive in a bonded assembly, J. of Adh. Sc. and Tech, (2010) **24**: 1977-1994
[12] Jousset P., Rachik M., Pressure-Dependent Plasticity for Structural Adhesive Constitutive Modeling, J. of Adh. Sc. and Tech, (2010) **24**:1995–2010
[13] Huntsman™ Structural Adhesives – Araldite® 420 A/B, Publication No A161, UK 2004.
[14] www.gom.com/metrology-systems/system-overview/aramis.html
[15] Abaqus reference manuals version 6.8. Simulia, Providence, RI, USA (2008).

XI International Conference on Computational Plasticity. Fundamentals and Applications
COMPLAS XI
E. Oñate, D.R.J. Owen, D. Peric and B. Suárez (Eds)

AN EFFICIENT NUMERICAL INTEGRATION ALGORITHM FOR THE SINGLE MODE COMPRESSIBLE LEONOV MODEL – COMPLAS XI

M. MIRKHALAF[*], F. PIRES[†] AND R. SIMÕES[†]

[*] Department of Mechanical Engineering (DEMec)
Faculty of Engineering
University of Porto, Porto, Portugal
email: mohsen.mirkhalaf@fe.up.pt

[†] Department of Mechanical Engineering (DEMec)
Faculty of Engineering
University of Porto, Porto, Portugal
email: fpires@fe.up.pt

[†] Institute for Polymers and Composites - IPC / I3N,
University of Minho, 4800-058 Guimarães, Portugal
email: rsimoes@dep.uminho.pt

Key words: Numerical integration, Leonov model, Return mapping.

Abstract. In this contribution, an algorithm for numerical integration of the Leonov elasto-viscoplastic model is proposed. The operator split methodology and the Newton-Raphson method are used to derive the state update algorithm and obtain the numerical solution of the discretized evolution equations. Particular effort is devoted to the reduction of the number of required residual equations in order to have a more efficient numerical implementation. The consistent tangent module is expressed in a closed form as a result of the exact linearization of the discretized evolution equations. The performance of the algorithm is validated through comparison with existing experimental data.

1 INTRODUCTION

As polymeric based materials can have a considerable role in structural applications, it is important to understand how their mechanical performance is affected by the molecular structure, the processing conditions and the geometry of the micro constituents. In order to have an optimal design, optimization of all aforementioned parameters would be highly desireable. Such an optimization would be impossible using only experiments. Consequently, other methods should be used for that goal.

During the last few decades, many researchers have devoted their work to the development of constitutive models for different materials such as metals and polymers. Among others, Haward and Tackray [6] developed one of the earliest one dimensional constitutive models to

predict the behavior of polymeric materials. The model takes into account the strain rate dependency of the yield point and strain hardening. The three dimensional version of Haward and Tackray model was proposed by Boyce et al. [2]. A modified version of this model was later formulated by Wu and van der Giessen [13]. The other constitutive model which is able to predict the typical deformation behavior of polymeric materials is the generalised compressible Leonov model, which has been proposed by Baaijens [1] and extended by Tervoort et al. [9] and Govaert et al. [5].
In order to analyze real problems, an efficient numerical integration algorithm of the constitutive relations, within the finite element framework, is necessary. Since the numerical treatment of the Leonov constitutive relations has not been, to the authors' knowledge, presented in the open literature, an attempt is made to introduce an efficient numerical integration algorithm for the model. Therefore, in the next section, the constitutive relations of the Leonov model are presented. Section 3 deals with the numerical treatment of the constitutive relations. In the subsequent section, two numerical examples and their corresponding results are provided. Finally and based on the obtained results, section 5 presents some conclusions made from this work.

2 CONSTITUTIVE RELATIONS

In this section, the constitutive relations of the Leonov model, used in this work, are presented. In the Leonov model, the total stress is composed of driving and hardening stresses.

$$\boldsymbol{\sigma}^{total} = \boldsymbol{\sigma}^{hardening} + \boldsymbol{\sigma}^{driving} \tag{1}$$

The hardening stress is computed by the following relation:

$$\boldsymbol{\sigma}^{hardening} = \boldsymbol{s}^{hardening} = H\mathbf{e}, \tag{2}$$

where **e** is the total deviatoric strain and H is the hardening modulus.

2.1 Elastic part of the constitutive relations

The relation between stress and strain in the elastic domain is given by:

$$\boldsymbol{\sigma} = \boldsymbol{D}\colon \boldsymbol{\varepsilon}^{e}. \tag{3}$$

Here $\boldsymbol{\varepsilon}^{e}$ is the elastic strain and $\boldsymbol{D}$ is the fourth order elasticity tensor (fourth order elastic constitutive isotropic tensor) that is defined as follows:

$$\boldsymbol{D} = 2\mu \mathrm{I_s} + \lambda(\boldsymbol{I} \otimes \boldsymbol{I}), \tag{4}$$

where $\boldsymbol{I}$ is the second order identity tensor, $\mathrm{I_s}$ is a fourth order symmetric identity tensor and μ and λ are the Lame´s elastic material constants. The Cartesian components of $\mathrm{I_s}$ are given by:

$$\mathrm{I_s}_{\,ijkl} \coloneqq \frac{1}{2}\left(\delta_{ik}\delta_{jl} + \delta_{il}\delta_{jk}\right). \tag{5}$$

In the case of separated deviatoric and volumetric stresses, the stress strain relations are given by:

$$\boldsymbol{s} = 2G\mathbf{e}^{e} \quad , \quad p = -K\boldsymbol{I}\colon \boldsymbol{\varepsilon}\,, \tag{6}$$

where $\boldsymbol{\varepsilon}$ is the total strain and $\mathbf{e}^e$ is the elastic deviatoric strain:

$$\mathbf{e}^e = dev[\boldsymbol{\varepsilon}^e] = \left[\mathrm{I_s} - \frac{1}{3}(\boldsymbol{I} \otimes \boldsymbol{I})\right] : \boldsymbol{\varepsilon}^e = \mathrm{I_d} : \boldsymbol{\varepsilon}^e \tag{7}$$

where $\mathrm{I_d}$ is the deviatoric projection tensor.

2.2 Yield criterion

The yield function for the Leonov model is defined as follows:

$$\phi \coloneqq \overline{\sigma} - \overline{\sigma}_y \leq 0, \tag{8}$$

where $\overline{\sigma}$ is the effective stress and $\overline{\sigma}_y$ is the uniaxial initial yield stress defined by:

$$\overline{\sigma} = \sqrt{\frac{3}{2}\boldsymbol{s} : \boldsymbol{s}}\,, \tag{9}$$

$$\overline{\sigma}_y = \frac{3}{\sqrt{3}+\mu}\left(\tau_0 \ln\left(2\sqrt{3}A_0\dot{\overline{e}}\right) + \mu p_0 + \frac{\Delta H \tau_0}{R\theta}\right), \tag{10}$$

where $\dot{\overline{e}}$ is the total equivalent strain rate, p_0 is the superimposed pressure of the analysis, R is the universal gas constant and θ is the absolute temperature. The other parameters $(\mu, \tau_0, \Delta H, A_0)$ in relation (10) are material properties.

2.3 Viscoplastic part of the constitutive relations

The rate of the viscoplastic strain is obtained by the following relation:

$$\dot{\boldsymbol{\varepsilon}}^{vp} = \frac{\boldsymbol{s}}{2\eta}, \tag{11}$$

where $\boldsymbol{\varepsilon}^{vp}$ is the viscoplastic strain; the second order tensor $\boldsymbol{s}$ is the deviatoric stress and η is the viscosity. The deviatoric stress is defined as:

$$\boldsymbol{s} \coloneqq dev\,[\boldsymbol{\sigma}] = \boldsymbol{\sigma} + p\boldsymbol{I}, \tag{12}$$

where $\boldsymbol{I}$ is second order identity (unit tensor of order 2, $\boldsymbol{I}_{ij} = \delta_{ij}$) and p is the hydrostatic pressure defined by the following equation:

$$p = -\frac{1}{3}\,tr\,[\boldsymbol{\sigma}] = -\frac{1}{3}\,\boldsymbol{I} : \boldsymbol{\sigma}. \tag{13}$$

The viscoplastic flow rule in the Leonov model is characterized by the generalized Eyring equation. The viscosity is defined based on the Eyring flow relation and is defined as follows:

$$\eta = A_0 \exp\left[\frac{\Delta H}{R\theta} + \frac{\mu p}{\tau_0} - Q_\infty + Q_\infty \exp\left(\frac{-h}{Q_\infty}\sqrt{3}\overline{e}^{vp}\right)\right] \frac{\sqrt{\frac{1}{3}}\overline{\sigma}}{\sinh\left(\frac{\sqrt{\frac{1}{3}}\overline{\sigma}}{\tau_0}\right)}, \tag{14}$$

where $\overline{\sigma}$ is effective stress, $\overline{e}^{vp}$ is equivalent viscoplastic strain, p is hydrostatic pressure, R is the universal gas constant, θ is absolute temperature and the other parameters $(A_0, \Delta H, \mu, \tau_0, Q_\infty, h)$ are material properties.

3 NUMERICAL IMPLEMENTATION

Operator split algorithms are widely used for numerical integration of constitutive equations in the context of elasto-plasticity and elasto-viscoplasticity. Numerical implementation of constitutive models through finite element codes basically includes a state update procedure and the computation of the consistent tangent operator.

3.1 State update

Let us consider a typical time interval $[t_n, t_{n+1}]$. The set of variables $\{\boldsymbol{\sigma}_n, \boldsymbol{\varepsilon}_n^e, \boldsymbol{\varepsilon}_n^{vp}, \overline{e}_n^{vp}\}$ is known at time t_n and the main problem is to determine the same set $\{\boldsymbol{\sigma}_{n+1}, \boldsymbol{\varepsilon}_{n+1}^e, \boldsymbol{\varepsilon}_{n+1}^{vp}, \overline{e}_{n+1}^{vp}\}$ at time t_{n+1}. The operator split algorithm comprises an *Elastic predictor* and a *Return mapping* algorithm which are described in this subsection.

Elastic predictor
In this stage, we assume that the material behaves purely elastically. The elastic trial strain at time step t_{n+1} is assumed to be given by:

$$\boldsymbol{\varepsilon}_{n+1}^{e\,trial} = \boldsymbol{\varepsilon}_{n+1} = \boldsymbol{\varepsilon}_n^e + \Delta\boldsymbol{\varepsilon}. \tag{15}$$

The deviatoric part of the total strain is given by

$$\boldsymbol{\varepsilon}_{d\,n+1}^{e\,trial} = dev\left(\boldsymbol{\varepsilon}_{n+1}^{e\,trial}\right) = \left[\mathrm{I_s} - \frac{1}{3}(\boldsymbol{I} \otimes \boldsymbol{I})\right] : \boldsymbol{\varepsilon}_{n+1}^{e\,trial} = \mathrm{I_d} : \boldsymbol{\varepsilon}_{n+1}^{e\,trial}. \tag{16}$$

The trial deviatoric stress is given by:

$$\boldsymbol{s}_{n+1}^{trial} = 2G\boldsymbol{\varepsilon}_{d\,n+1}^{e\,trial}, \tag{17}$$

where G is shear modulus. The hydrostatic pressure is computed by:

$$p_{n+1}^{trial} = -K\varepsilon_{v\,n+1}^{e\,trial} \tag{18}$$

where K is bulk modulus and $\varepsilon_{v\,n+1}^{e\,trial}$ is

$$\varepsilon_{v\,n+1}^{e\,trial} = tr\left(\boldsymbol{\varepsilon}_{n+1}^{e\,trial}\right). \tag{19}$$

The trial accumulated viscoplastic strain is assumed to be frozen:

$$\overline{\varepsilon}_{n+1}^{vp\,trial} = \overline{\varepsilon}_n^{vp}. \tag{20}$$

After computing the aforementioned variables, checking the yield criterion determines whether the initial assumption based on being in the elastic domain is correct or not. If the yield function is satisfied, we are in the elastic domain, then we update the variables as

$$(\blacksquare)_{n+1} = (\blacksquare)_{n+1}^{trial} \tag{21}$$

If the yield criterion is not satisfied, we are in the viscoplastic domain which needs a return mapping scheme to update the state variables.

Return mapping
By manipulating the constitutive relations, two residual equations are obtained.

$$R_1\left(\overline{e}^{vp}_{n+1}, \overline{\sigma}_{n+1}\right) := \overline{e}^{vp}_{n+1} - \overline{e}^{vp}_{n} - \frac{\Delta t}{3\eta_{n+1}}\overline{\sigma}_{n+1} = 0 \tag{22}$$

$$R_2\left(\overline{e}^{vp}_{n+1}, \overline{\sigma}_{n+1}\right) := 3G\left(\overline{e}^{vp}_{n+1} - \overline{e}^{vp}_{n}\right) - \overline{\sigma}^{trial}_{n+1} + \overline{\sigma}_{n+1} = 0. \tag{23}$$

Where Δt is the time interval between two consecutive time steps. We will use the well-known Newton-Raphson iterative procedure to solve our system of residual equations. To do so, the following matrix representation is presented:

$$\boldsymbol{A\delta} = \boldsymbol{B} \tag{24}$$

where $\boldsymbol{A}$ is matrix of coefficients, $\boldsymbol{\delta}$ is the array of unknowns and finally $\boldsymbol{B}$ is the array of constants. The components of the aforementioned matrix and arrays are represented in the following form:

$$\begin{bmatrix} \dfrac{\partial R_1\left(\overline{e}^{vp}_{n+1}, \overline{\sigma}_{n+1}\right)}{\partial \overline{e}^{vp}_{n+1}} & \dfrac{\partial R_1\left(\overline{e}^{vp}_{n+1}, \overline{\sigma}_{n+1}\right)}{\partial \overline{\sigma}_{n+1}} \\ \dfrac{\partial R_2\left(\overline{e}^{vp}_{n+1}, \overline{\sigma}_{n+1}\right)}{\partial \overline{e}^{vp}_{n+1}} & \dfrac{\partial R_2\left(\overline{e}^{vp}_{n+1}, \overline{\sigma}_{n+1}\right)}{\partial \overline{\sigma}_{n+1}} \end{bmatrix} \begin{bmatrix} \Delta \overline{e}^{vp}_{n+1} \\ \Delta \overline{\sigma}_{n+1} \end{bmatrix} = \begin{bmatrix} -R_1\left(\overline{e}^{vp}_{n+1}, \overline{\sigma}_{n+1}\right) \\ -R_2\left(\overline{e}^{vp}_{n+1}, \overline{\sigma}_{n+1}\right) \end{bmatrix}. \tag{25}$$

After computing the accumulated viscoplastic strain, $\overline{e}^{vp}_{n+1}$, and the effective stress, $\overline{\sigma}_{n+1}$, the following variables should be updated as follows:

$$\boldsymbol{\varepsilon}^{vp}_{n+1} = \boldsymbol{\varepsilon}^{vp}_{n} + \frac{3\left(\overline{e}^{vp}_{n+1} - \overline{e}^{vp}_{n}\right)\Delta t}{2\left(\overline{\sigma}_{n+1}\Delta t + 3\left(\overline{e}^{vp}_{n+1} - \overline{e}^{vp}_{n}\right)\Delta t G\right)}\boldsymbol{s}^{trial}_{n+1}, \tag{26}$$

$$\boldsymbol{s}_{n+1} = \frac{1}{1 + \dfrac{3G}{\overline{\sigma}_{n+1}}\left(\overline{e}^{vp}_{n+1} - \overline{e}^{vp}_{n}\right)}\boldsymbol{s}^{trial}_{n+1}, \tag{27}$$

$$\boldsymbol{\varepsilon}^{e}_{d\,n+1} = \frac{1}{1 + \dfrac{3G}{\overline{\sigma}_{n+1}}\left(\overline{e}^{vp}_{n+1} - \overline{e}^{vp}_{n}\right)}\frac{\boldsymbol{s}^{trial}_{n+1}}{2G}. \tag{28}$$

It must be emphasized here that after implementing the aforementioned relations for the state update, it was observed that due to the behavior of the first residual equation, convergence was not achieved in many problems. Therefore, in order to achieve convergence, the first residual equation was transformed into a logarithmic version. The new residual equation has the following form:

$$R_1\left(\overline{e}^{vp}_{n+1}, \overline{\sigma}_{n+1}\right) := \ln\left(\overline{e}^{vp}_{n+1} - \overline{e}^{vp}_{n}\right) - \ln(\Delta t) - \ln(\overline{\sigma}_{n+1}) + \ln(3) + \ln(\eta_{n+1}) = 0. \tag{29}$$

Using the new residual led us to a remarkable improvement in the convergence rate of the state update procedure.

3.2 Consistent tangent operator

In order to complete the numerical implementation of the compressible Leonov model within an implicit quasi-static integration scheme, we need to obtain the consistent tangent operator. In other words, since the full Newton-Raphson scheme will be used within an implicit finite element implementation of the Leonov model, the tangent stiffness matrix must be computed. The tangent stiffness matrix is assembled using the tangent operators which are derived by consistently linearizing the state update relations. The tangent operator has the following definition:

$$\mathbf{D} \coloneqq \frac{d\boldsymbol{\sigma}_{n+1}}{d\boldsymbol{\varepsilon}_{n+1}}. \tag{30}$$

In the elastic domain, the tangent operator is the following:

$$\mathbf{D}_e = (2G + H)\left[\mathrm{I}_s - \frac{1}{3}(\boldsymbol{I} \otimes \boldsymbol{I})\right] + K(\boldsymbol{I} \otimes \boldsymbol{I}). \tag{31}$$

Exact linearization of the constitutive telations and performing some algebraic manipulations result in the following closed form relation for viscoplastic tangent operator.

$$\mathbf{D}_{vp} = \left(\frac{2G\eta_{n+1}}{\eta_{n+1} + \Delta t\, G} + H\right)\left[\mathrm{I}_s - \frac{1}{3}(\boldsymbol{I} \otimes \boldsymbol{I})\right] + K(\boldsymbol{I} \otimes \boldsymbol{I}) + \frac{3G^2\Delta t}{\overline{\sigma}_{n+1}^{trial}\,\Omega\,\eta_{n+1}}\left[\frac{\Delta t C_1}{3\eta_{n+1}} + C_2\right]\boldsymbol{s}_{n+1} \otimes \boldsymbol{s}_{n+1} - \frac{GK\Delta t\,\mu}{\eta_{n+1}\Omega\tau_0}\,\boldsymbol{s}_{n+1} \otimes \boldsymbol{I} \tag{32}$$

Where

$$C_1 = -\sqrt{3}h\exp\left(\frac{-h}{Q_\infty}\sqrt{3}\overline{e}_{n+1}^{vp}\right), \tag{33}$$

$$C_2 = \left[\frac{\tau_0 \sinh\left(\dfrac{\sqrt{\frac{1}{3}}\overline{\sigma}_{n+1}}{\tau_0}\right) - \sqrt{\frac{1}{3}}\overline{\sigma}_{n+1}\cosh\left(\dfrac{\sqrt{\frac{1}{3}}\overline{\sigma}_{n+1}}{\tau_0}\right)}{\tau_0\,\overline{\sigma}_{n+1}\sinh\left(\dfrac{\sqrt{\frac{1}{3}}\overline{\sigma}_{n+1}}{\tau_0}\right)}\right], \tag{34}$$

$$\Omega = 1 + \frac{\Delta t\ G}{\eta_{n+1}} + \frac{\Delta t\ \overline{\sigma}_{n+1}}{3\eta_{n+1}}(C_1 - 3GC_2). \tag{35}$$

4 NUMERICAL EXAMPLES

In order to check the performance of the numerical implementation, two examples are considered. In the single element compression test, it is shown that the implementation can capture the effects of superimposed hydrostatic pressure and strain rate on the deformation behavior. Furthermore, it is illustrated that by changing the first residual to a logarithmic

function, the convergence rate of the implementation is considerably improved. In addition to the single element test, a compression test is numerically performed on a standard specimen and the results are compared with available experimental results.

4.1 Single element test

A single element under compression is analyzed and true stress-strain curves are provided. A four node quadratic element with four Gauss points is used for the analysis. The dimensions of the element are (1×1 *mm*) and the displacement applied to the element is (*0.5 mm*). The material is assumed to be PET Copolyester 9921W (referred to as PET) and the material properties, taken from [12], are listed in Table 1.

Table 1: Material properties for PET

E(MPa)	ν	ΔH	A_0	τ_0(MPa)	Q_∞	h	μ	R	H(MPa)
2211	0.4	2.3E+5	8.1E-26	0.9	27.3	205	0.047	8.3143	26

The test is performed at room temperature, under different hydrostatic pressures and with different strain rates. Figures 1 and 2 show the effects of strain rate and hydrostatic pressure on deformation behavior, respectively.

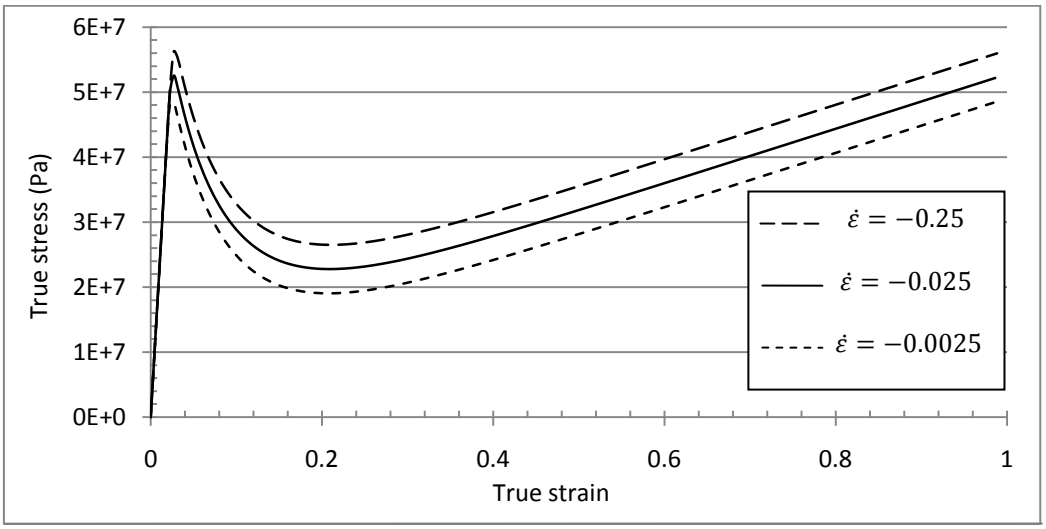

Figure 1: Stress strain curves for the single element compression test using PET at different strain rates under atmospheric condition ($P_0 = 0.1\ MPa$)

Table 2 shows the number of required iterations for a typical increment and corresponding residuals for the two different approaches. It can be clearly observed that the logarithmic transformation (indicated as the second approach) has been extremely effective to improve the convergence rate of the state update algorithm.

4.2 Standard specimen

The compression of a standard specimen is shown in Figure 3. In order to simulate the problem and due to symmetry , the simulation has been performed as a two-dimensional axisymmetric problem.

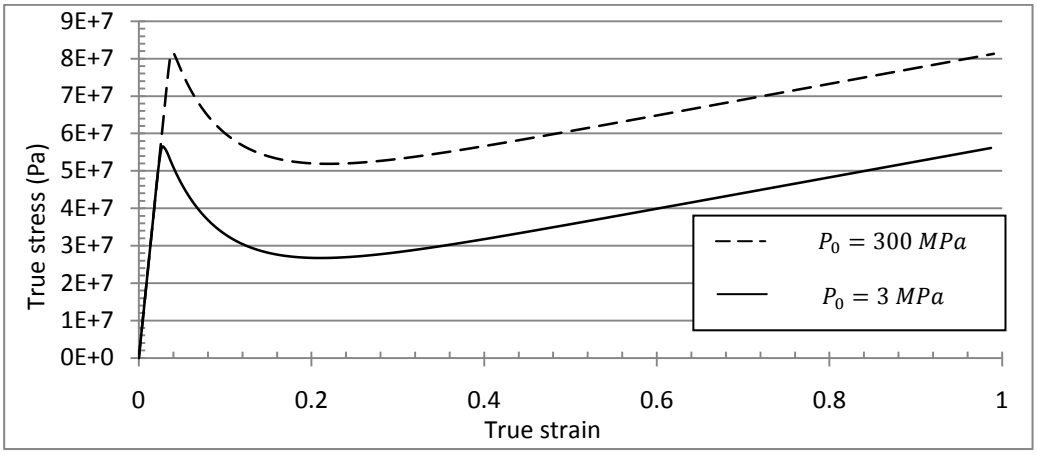

Figure 2: Stress strain curves for the single element compression test using PET at strain rate of ($\dot{\varepsilon} = -0.25$) under different superimposed pressures

In fact, a rectangular with dimensions (*4mm*× *2mm*) has been analyzed with 8 quadratic elements with dimensions (*1*×*1 mm*). The applied displacement is (*3 mm*). It must be noted that the hydrostatic pressure for this test is assumed to be $P_0 = 300\ MPa$, and the simulations have been performed assuming room temperature.

Figure 4 shows results obtained from both simulations and experiments for the compressed cylinder made from PET at the strain rate of $\dot{\varepsilon} = -0.25\ s^{-1}$. The experimental results are taken form [12].

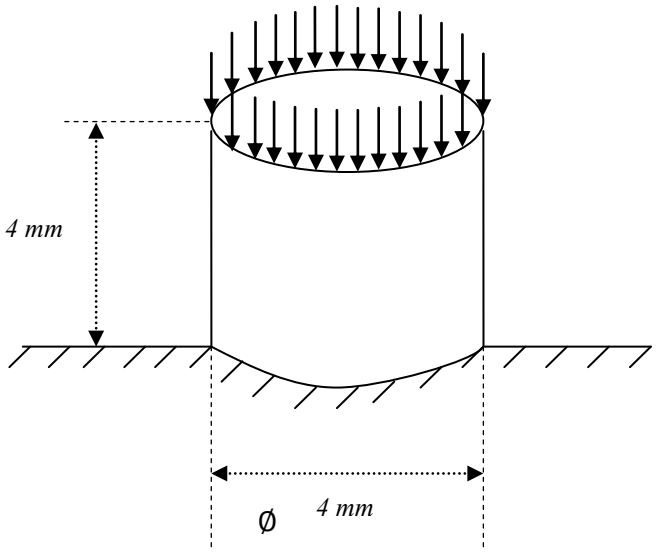

Figure 3: Schematic representation of the compressed cylinder (geometry, boundary conditions and loading)

A reasonable qualitative and quantitative agreement between numerical and experimental results can be observed.

Table 2: Convergence table for two approaches

Iteration no.	*1st approach residual*	*2nd approach residual*
1	*0.636690*	*9.231974*
2	*2.435265E-2*	*0.135657*
3	*2.486794 E-2*	*7.634257E-4*
4	*2.540770 E-2*	*1.854449E-8*
5	*2.597371 E-2*	
6	*2.656790 E-2*	
7	*2.719243 E-2*	
8	*2.784967 E-2*	
9	*2.854220 E-2*	
10	*2.927289 E-2*	
11	*3.004483 E-2*	
12	*3.086112 E-2*	
13	*3.172435 E-2*	
14	*3.263460 E-2*	
15	*3.358365 E-2*	
16	*3.435756 E-2*	
17	*3.538555 E-2*	
18	*3.579642 E-2*	
19	*3.485924 E-2*	
20	*3.049617 E-2*	
21	*2.015115 E-2*	
22	*6.934124 E-3*	
23	*6.409727 E-4*	
24	*4.919388 E-6*	
25	*2.867187 E-10*	

5 CONCLUSIONS

According to the results presented, it can be concluded that the numerical implementation is able to capture the effect of different parameters on the deformation behavior of polymeric based materials. Moreover, due to the considerable improvement on the convergence rate obtained by converting the first residual to a logarithmic function, it can be claimed that the transformation has been absolutely necessary. Finally, in view of the reasonable agreement

between simulations and experimental results, it seems that the Leonov model is able to predict the polymeric based materials behavior in compressive conditions adequately.

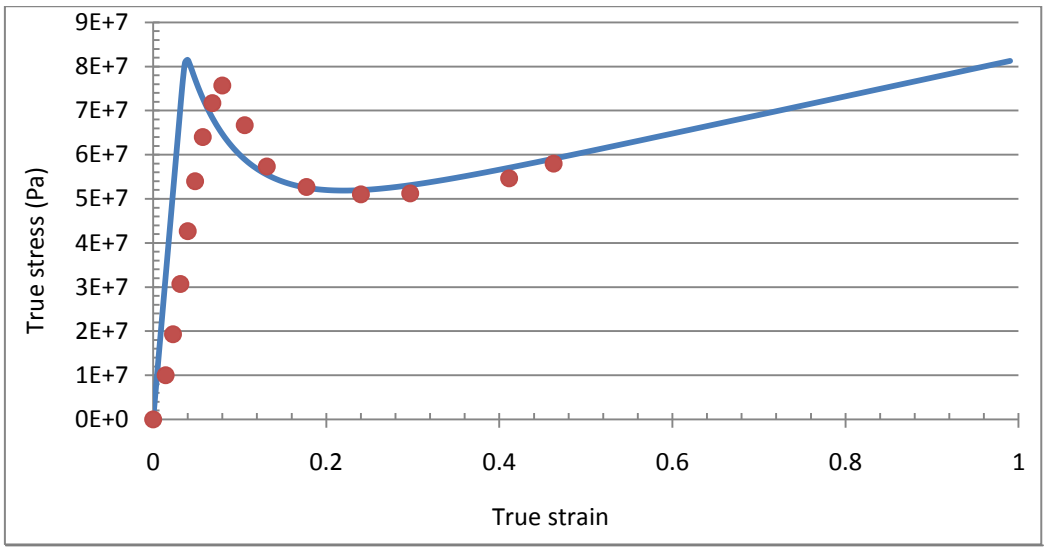

Figure 4: Stress strain curve for the compressed cylinder at the strain rate ($\dot{\varepsilon} = -0.25$). Solid line shows numerical simulations and circles show experimental results.

ACKNOWLEDGEMENTS

The authors acknowledge financial support from IDMEC under project PTDC/EME-PME/108859/2008 and scholarship provided by FCT (Foundation for Science and Technology) under SFRH/ BD/74027/2010 grant.

REFERENCES

[1] Baaijens, F.P.T. Calculation of residual stresses in injection molded products. *Rheol. Acta* (1991) **30**: 284–299.

[2] Boyce, M.C., Parks, D.M. and Argon, A.S. Large inelastic deformation of glassy polymers, Part I: Rate dependent constitutive model. *Mech. Mat* (1988) **7**: 15–33.

[3] De Souza Neto, E. A. A simple robust numerical integration algorithm for a power-law visco-plastic model under both high and low rate sensitivity. *Commun. Numer. Meth. Engng* (2004) **20**: 1-17.

[4] De Souza Neto, E. A., Peric, D., Owen, DRJ. *Computational methods for plasticity: Theory and applications*. Wiley (2008).

[5] Govaert, L., Timmermans, P., Brekelmans, W. The influence of intrinsic strain softening on strain localization in polycarbonate: modeling and experimental validation. *J. Engng. Mater. Tech* (2000) **122**: 177–185.

[6] Haward, R.N. and Thackray, G. The use of mathematical model to describe isothermal stress-strain curves in glassy polymers, *Proc. Roy. Soc. A* (1968) **302**: 453–472.

[7] Leonov, A. Non-equilibrium thermodynamics and rheology of viscoelastic polymer media. *Rheol. Acta* (1976) **15**: 85–98.

[8] Masud, A. and Chudnovsky A. A constitutive model of cold drawing in polycarbonates. *Int. J. Plasticity* (1999) **15**: 1139-1157.
[9] Tervoort, T., Smit, R., Brekelmans, W., Govaert, L. A constitutive equation for the elasto-viscoplastic deformation of glassy polymers. *Mech. Time Dep. Mater* (1998) **1**: 269–291.
[10] Tervoort, T. Constitutive Modelling of Polymer Glasses: Finite, Nonlinear Viscoelastic Behaviour of Polycarbonate. *Ph.D. thesis*, Eindhoven University of Technology, Eindhoven, The Netherlands (1996).
[11] Timmermans, P.H.M. Evaluation of a constitutive model for solid polymeric materials: model selection and parameter quantification. *Ph.D. thesis*, Eindhoven University of Technology, Eindhoven, The Netherlands (1997).
[12] Van der Aa. Michiel A.H. Wall ironing of polymer coated sheet metal. *PhD. thesis*, Eindhoven University of Technology, Eindhoven, The Netherlands (1999).
[13] Wu, P., van der Giessen, E. Analysis of shear band propagation in amorphous glassy polymers. *Int. J. Solids Structures* (1994) **31**: 1493–1517

XI International Conference on Computational Plasticity. Fundamentals and Applications
COMPLAS XI
E. Oñate, D.R.J. Owen, D. Peric and B. Suárez (Eds)

COMPUTATIONAL MODELLING OF A MULTIFIELD SINGLE-CRYSTAL GRADIENT PLASTICITY FORMULATION

C. B. HIRSCHBERGER*, B. D. REDDY†

*Institute of Continuum Mechanics
Leibniz Universität Hannover
Appelstr. 11, 30167 Hannover, Germany
e-mail: hirschberger@ikm.uni-hannover.de,

† Centre of Research in Applied Mechanics (CERECAM)
University of Cape Town, South Africa
7701 Rondebosch, South Africa
e-mail: daya.reddy@uct.ac.za, www.cerecam.uct.ac.za

Key words: Crystal plasticity, dislocations, finite deformation, size effects, finite elements.

Abstract. A model of higher-order single crystal plasticity is presented and reviewed in order to develop a corresponding finite-element framework. Contrary to the underlying model of Gurtin [Int. J. Plast. 24:702-725, 2008], here rather than the slip rate, the slip and its gradient constitute primary micro state variables. The resulting rate-dependent formulation accounts for size effects through the free energy depending on density of geometrically necessary dislocations. The relationship to multifield theories of continua with microstructure is pointed out. With the presented finite-element approach, the corresponding fully coupled initial-boundary value problem is solved monolithically, and features of the model are illustrated in two preliminary numerical examples.

1 INTRODUCTION

The size-dependent behaviour of polycrystalline materials such as metals at grain sizes of the order of tens to hundreds of microns is well documented. Such behaviour stems from heterogeneities in crystallites and arise, for example, due to the existence of grain boundaries, as well as due to impurities, inclusions, and other imperfections in the crystal lattices. The appropriate modelling of behaviour at the microstructural level requires a knowledge of the underlying dynamics of dislocations, and proper incorporation of such dynamics and associated length scales into the model. Dislocation-based crystal plasticity formulations capture size effects largely by including dislocation behaviour through an

averaged field description of dislocation populations in crystals. Some representative works in an extensive literature include [17, 9, 13, 6, 10, 12, 18]. Typically, the mutual interaction of dislocations are captured in a back-stress term that counteracts the resolved shear stress driving the flow of dislocations on the lattice glide planes.

The objective of this contribution is to develop finite element approximations of a model of single-crystal higher-order plasticity due to Gurtin [10]. The model is based on the use of geometrically necessary dislocation (GND) densities as a field variable. However, in contrast to the treatment in [10], instead of the slip rate, the slip constitutes a micro state variable. The relationship between gradient of slip and GND density is nevertheless constructed in a way that is consistent with the dissipation inequality. The slip together with macroscopic displacements are the primary unknown variables of the problem. It is shown that the formulation has a relationship to multifield theories [3, 4]. Conforming finite element approximations are based on a fully coupled, monolithic approach to solving the governing equations of the rate-dependent initial-boundary value problems. The article closes with two preliminary numerical examples.

2 A MULTIFIELD CRYSTAL PLASTICITY FRAMEWORK

The model of higher-order crystal plasticity largely follows that due to Gurtin [10].

2.1 Kinematics

The starting point for the description of kinematical relations is the standard multiplicative decomposition

$$\boldsymbol{F} = \boldsymbol{F}_{\mathrm{e}} \cdot \boldsymbol{F}_{\mathrm{p}} \tag{1}$$

of the deformation gradient $\boldsymbol{F} = \boldsymbol{\nabla}_{\boldsymbol{X}} \boldsymbol{\varphi}$ into elastic and plastic parts $\boldsymbol{F}_{\mathrm{e}}$ and $\boldsymbol{F}_{\mathrm{p}}$ respectively. Here $\boldsymbol{x} = \boldsymbol{\varphi}(\boldsymbol{X}, t)$ describes the motion from the material to the spatial configuration and $\boldsymbol{\nabla}_{\boldsymbol{X}}$ is the material gradient. The plastic deformation is assumed to be isochoric implying $\det \boldsymbol{F}_{\mathrm{p}} = 1$. It follows that $J := \det(\boldsymbol{F}) = \det \boldsymbol{F}_{\mathrm{e}} > 0$.

The spatial velocity gradient $\boldsymbol{l} = \boldsymbol{\nabla}_{\boldsymbol{x}} \boldsymbol{v}$ may be decomposed additively according to

$$\boldsymbol{l} = \dot{\boldsymbol{F}} \cdot \boldsymbol{F}^{-1} = \boldsymbol{l}_{\mathrm{e}} + \boldsymbol{F}_{\mathrm{e}} \cdot \widehat{\boldsymbol{L}}_{\mathrm{p}} \cdot \boldsymbol{F}_{\mathrm{e}}^{-1} \tag{2}$$

in which

$$\widehat{\boldsymbol{L}}_{\mathrm{p}} = \dot{\boldsymbol{F}}_{p} \boldsymbol{F}_{\mathrm{p}}^{-1} \,. \tag{3}$$

The elastic Cauchy–Green tensor

$$\widehat{\boldsymbol{C}}_{\mathrm{e}} = \boldsymbol{F}_{\mathrm{e}}^{\mathrm{t}} \cdot \boldsymbol{F}_{\mathrm{e}} = \boldsymbol{F}_{\mathrm{p}}^{-\mathrm{t}} \cdot \boldsymbol{C} \cdot \boldsymbol{F}_{\mathrm{p}}^{-1} \tag{4}$$

characterizes the deformation of the intermediate configuration, quantities in which are denoted here and henceforth by $\widehat{\square}$.

The motion of dislocations in a single crystal takes place on a set of n_S defined slip systems, whereby an orthonormal pair comprising a slip direction $\widehat{\boldsymbol{s}}^\alpha$ and slip-plane normal vector $\widehat{\boldsymbol{m}}^\alpha$ ($\alpha = 1, \dots, N$) in the intermediate configuration precisely defines the α-th system. It is useful also to introduce the Schmid (projection) tensor $\widehat{\boldsymbol{Z}}^\alpha = \widehat{\boldsymbol{s}}^\alpha \otimes \widehat{\boldsymbol{m}}^\alpha$, which is trace-free. For edge dislocations, the slip line direction $\widehat{\boldsymbol{l}}^\alpha$ is defined by $\widehat{\boldsymbol{l}}^\alpha = \widehat{\boldsymbol{m}}^\alpha \times \widehat{\boldsymbol{s}}^\alpha$, so that $\{\widehat{\boldsymbol{m}}^\alpha, \widehat{\boldsymbol{s}}^\alpha, \widehat{\boldsymbol{l}}^\alpha\}$ form a local orthonormal basis. In case of screw dislocations, the slip line and the slip direction coincide to $\widehat{\boldsymbol{s}}^\alpha$.

The plastic distortion-rate tensor $\widehat{\boldsymbol{L}}_\mathrm{p}$ is determined by the slip rates acting on each of the slip systems according to

$$\widehat{\boldsymbol{L}}_\mathrm{p} = \sum_{\alpha=1}^{n_\mathrm{S}} \dot{\gamma}^\alpha \, \widehat{\boldsymbol{s}}^\alpha \otimes \widehat{\boldsymbol{m}}^\alpha =: \sum_{\alpha=1}^{n_\mathrm{S}} \dot{\gamma}^\alpha \, \widehat{\boldsymbol{Z}}^\alpha \,. \tag{5}$$

The slip direction $\widehat{\boldsymbol{s}}^\alpha$, slip plane normal $\widehat{\boldsymbol{m}}^\alpha$ and dislocation line direction $\widehat{\boldsymbol{l}}^\alpha$ may be mapped to their counterparts $\boldsymbol{s}^\alpha$, $\boldsymbol{m}^\alpha$ and $\boldsymbol{l}^\alpha$ in the current configuration by setting

$$\boldsymbol{s}^\alpha = \boldsymbol{F}_\mathrm{e} \cdot \widehat{\boldsymbol{s}}^\alpha \,, \qquad \boldsymbol{m}^\alpha = (\boldsymbol{F}_\mathrm{e})^{-\mathrm{t}} \cdot \widehat{\boldsymbol{m}}^\alpha \,, \qquad \boldsymbol{l}^\alpha = \boldsymbol{F}_\mathrm{e} \cdot \widehat{\boldsymbol{l}}^\alpha \,. \tag{6}$$

2.1.1 Dislocation densities

The dislocations and their interactions are accounted for by fields of spatial densities of dislocations. In the spirit of Gurtin [10] we define both the total density of dislocations, $\rho^\alpha_\square$, and the – polar – density of geometrically necessary dislocations (GND), $\kappa^\alpha_\square$, per unit length, i. e.,, normalized by the Burgers vector length.

According to Nye [14], only the geometrically necessary dislocations are relevant to the occurrence of size effects. Following [2], the GND relates to the gradient of slip as

$$\dot{\kappa}^\alpha_\square = \boldsymbol{\nabla}_{\boldsymbol{x}} \dot{\gamma}^\alpha \cdot \boldsymbol{p}^\alpha = \boldsymbol{\nabla}_{\boldsymbol{X}} \dot{\gamma}^\alpha \cdot \boldsymbol{F}_\mathrm{p}^{-1} \cdot \widehat{\boldsymbol{p}}^\alpha \quad \text{with} \quad \widehat{\boldsymbol{p}}^\alpha = \begin{cases} -\widehat{\boldsymbol{s}}^\alpha & \text{for edge dislocations } (\square = \perp) \\ \widehat{\boldsymbol{l}}^\alpha & \text{for screw dislocations } (\square = \odot) \,. \end{cases} \tag{7}$$

Here a pullback from the spatial form to the intermediate configuration has been carried out. The respective subscript $\square \in \{\perp, \odot\}$ identifies either edge or screw dislocations.

Remark 1. *The formulation by Gurtin [10] bases on the slip rate ν^α as the primary micro state variable, the gradient of which corresponds to the* GND *rate. Contrarily, we assume the slip itself and its gradient as primary micro quantities, for which we develop the governing equations, the variational formulation and computational algorithm. Our choice is particularly beneficial as it reduces the complexity of the computational treatment.*

Remark 2. *In [7] the relationship between GND density and slip gradient is assumed to take the form*

$$\kappa^\alpha_\square = \widehat{\nabla} \gamma^\alpha \cdot \widehat{\boldsymbol{p}}^\alpha$$

in which $\widehat{\nabla}$ denotes the gradient with respect to the intermediate configuration. In the absence of the notion of a placement vector in the intermediate configuration, the nature of the gradient term is not clear. Likewise, a spatial relation of the form

$$\kappa_{\square}^{\alpha} = \boldsymbol{\nabla}_{\boldsymbol{x}} \gamma^{\alpha} \cdot \boldsymbol{p}^{\alpha} \,,$$

which is used by some authors, does not imply nor is implied by (7).

2.2 Free energy, dissipation inequality, stresses and microstresses

Dissipation inequality. The spatial form of the local dissipation inequality is

$$\mathcal{D} = \boldsymbol{\sigma} : \boldsymbol{l}_{\mathrm{e}} + \sum_{\alpha=1}^{n_{\mathrm{S}}} (\boldsymbol{\xi}^{\alpha} \cdot \boldsymbol{\nabla}_{\boldsymbol{x}} \dot{\gamma}^{\alpha} + \pi^{\alpha} \dot{\gamma}^{\alpha}) - J^{-1} \dot{\Psi} \geq 0 \qquad \text{in} \quad \mathcal{B}_t \,. \tag{8}$$

In the material configuration this inequality reads

$$\mathcal{D}_0 = \tfrac{1}{2} \widehat{\boldsymbol{S}}_{\mathrm{e}} : \mathcal{L}_{\boldsymbol{v}}^{\mathrm{p}}(\widehat{\boldsymbol{C}}_{\mathrm{e}}) + \sum_{\alpha=1}^{n_{\mathrm{S}}} (\boldsymbol{\xi}_0^{\alpha} \cdot \boldsymbol{\nabla}_{\boldsymbol{X}} \dot{\gamma}^{\alpha} + \pi_0^{\alpha} \dot{\gamma}^{\alpha}) - \dot{\Psi} \geq 0 \qquad \text{in} \quad \mathcal{B}_0 \tag{9}$$

with the Lie derivative $\mathcal{L}_{\boldsymbol{v}}^{\mathrm{p}}(\widehat{\boldsymbol{C}}_{\mathrm{e}}) = \boldsymbol{F}_{\mathrm{p}}{}^{-\mathrm{t}} \cdot \dot{\boldsymbol{C}} \cdot \boldsymbol{F}_{\mathrm{p}}^{-1} = \dot{\widehat{\boldsymbol{C}}}_{\mathrm{e}} + 2[\widehat{\boldsymbol{C}}_{\mathrm{e}} \cdot \widehat{\boldsymbol{L}}_{\mathrm{p}}]^{\mathrm{sym}}$ [16] and $\boldsymbol{\xi}_0^{\alpha} = \boldsymbol{F}^{-1} \cdot \boldsymbol{\xi}^{\alpha}$.

The free energy $\widehat{\Psi}$ is assumed to depend on the elastic tensor $\widehat{\boldsymbol{C}}_{\mathrm{e}}$ and the set $\vec{\kappa}$ of dislocation densities. This motivates the definition of a macrostress $\widehat{\boldsymbol{S}}_{\mathrm{e}}$ and vector microstress $\boldsymbol{\xi}_{\mathrm{en}}^{\alpha}$ according to

$$\widehat{\boldsymbol{S}}_{\mathrm{e}} = 2 \frac{\partial \widehat{\Psi}}{\partial \widehat{\boldsymbol{C}}_{\mathrm{e}}} \,, \qquad\qquad \boldsymbol{\xi}_{\mathrm{en}}^{\alpha} := J^{-1} \frac{\partial \widehat{\Psi}}{\partial \kappa_{\square}^{\alpha}} \boldsymbol{p}^{\alpha} \,. \tag{10}$$

By assuming that the microstress is purely energetic (that is, $\boldsymbol{\xi}^{\alpha} = \boldsymbol{\xi}_{\mathrm{en}}^{\alpha}$: see also [15]), the dissipation inequality (9) reduces to

$$\mathcal{D}^{\mathrm{red}} = \sum_{\alpha=1}^{n_{\mathrm{S}}} \pi^{\alpha} \dot{\gamma}^{\alpha} \geq 0 \,, \tag{11}$$

A flow rule for π^{α} will be specified later.

Macro- and micro-force balances. Balance equations are derived from a principle of virtual power [10]. The macroforce balance or equilibrium equation is expressed in terms of the first Piola-Kirchhoff stress and the referential body force $\mathbf{0}$ as

$$\mathrm{Div}\, \boldsymbol{P} + \boldsymbol{f}_0 = \mathbf{0} \quad \text{in } \mathcal{B}_0 \,. \tag{12}$$

This equation is supplemented by the boundary conditions $\boldsymbol{u} = \boldsymbol{u}^{\mathrm{p}}$ on $\partial \mathcal{B}_t^u$ and $\boldsymbol{P} \cdot \boldsymbol{N} = \boldsymbol{t}_0^{\mathrm{p}}$ on $\partial \mathcal{B}_0^p$, in which $\partial \mathcal{B}_t^u$ and $\partial \mathcal{B}_0^p$ are non-overlapping parts that cover the boundary $\partial \mathcal{B}_0$.

The microforce balance is given for each slip system α in the spatial configuration by

$$\operatorname{div} \boldsymbol{\xi}^\alpha - \pi^\alpha + \sigma^\alpha = 0 \quad \text{on } \alpha \text{ in } \mathcal{B}_t \tag{13}$$

In the material configuration this reads

$$\operatorname{Div} \boldsymbol{\xi}_0^\alpha - \pi_0^\alpha + \sigma_0^\alpha = 0 \quad \text{on } \alpha \text{ in } \mathcal{B}_0 \,. \tag{14}$$

Here σ_0^α is the resolved shear stress defined by

$$\sigma_0^\alpha = \left[\widehat{\boldsymbol{C}}_\mathrm{e} \cdot \widehat{\boldsymbol{S}}_\mathrm{e}\right] : \boldsymbol{Z}^\alpha \tag{15}$$

and $\operatorname{Div} = \boldsymbol{F}^{-1} : \boldsymbol{\nabla}_{\boldsymbol{X}}$.

Dirichlet and Neumann boundary conditions are assumed to be $\gamma^\alpha = \gamma_\mathrm{p}$ on $\partial\mathcal{B}_0^\nu$ and $\boldsymbol{\xi}_0^\alpha \cdot \boldsymbol{N} = t_0^{\xi\alpha}$ on $\partial\mathcal{B}_0^\xi$. For an overview on the choice of micro-hard and micro-free boundary conditions, see e. g., [7] and references cited in this work.

Remark 3. *The macro- and microforce balance equations may also be derived by adopting a micromorphic or microfield continuum approach [11, 3], in which the energy functional corresponding to the incremental problem is written as the sum of the free energy $\widehat{\Psi}$ and the dissipative flow potential Υ, which generates the dissipative microforce through the incremental form of the relation [15]*

$$\pi^\alpha = \frac{\partial \Upsilon}{\partial \dot{\gamma}^\alpha} \,. \tag{16}$$

2.3 Constitutive relations

Based on an underlying hyperelastic material, the crystal plasticity constitutive framework relies on the choice of a free energy and the definition of a flow rule or dissipation function.

2.3.1 Free energy

The free energy per reference volume is assumed to comprise an elastic or macro-energy $\widehat{\Psi}^\mathrm{macro}$ and a defect or micro-energy $\widehat{\Psi}^\mathrm{micro}$:

$$\widehat{\Psi} = \widehat{\Psi}^\mathrm{macro}(\widehat{\boldsymbol{C}}_\mathrm{e}) + \sum_{\alpha=1}^{n_\mathrm{S}} \widehat{\Psi}^\mathrm{micro}(\kappa_\square^\alpha) \,. \tag{17}$$

This yields the stress and energetic microstress via the definitions (10). For the sake of simplicity, latent hardening effects are neglected in the energetic part, and will instead be captured in the dissipative microforce via the flow rule .

Due to the relatively small elastic deformations in crystal plasticity, it suffices to choose for the macro-energy a St. Venant–Kirchhoff relation

$$\widehat{\Psi}^{\text{macro}} = \frac{\lambda}{8}\text{tr}^2(\widehat{\boldsymbol{C}}_{\text{e}} - \boldsymbol{I}) + \frac{1}{4}\mu[\widehat{\boldsymbol{C}}_{\text{e}} - \boldsymbol{I}]^2 \,. \tag{18}$$

However, following Gurtin [10], the micro-energy is formulated for both edge and screw dislocations as

$$\widehat{\Psi}^{\text{micro}}(\kappa^\alpha_\square) = \tfrac{1}{2}\sum_{\alpha=1}^{N_s} (C_1\kappa^\alpha_\perp)^2 + \left(C_2\kappa^\alpha_\odot\right)^2 \,. \tag{19}$$

With the choices $C_1 = \frac{\mu R^2}{8[1-\nu]}$ and $C_2 = \frac{\mu R^2}{4}$, the relation of [8] is retrieved (see [7] for the relationship between the two approaches).

2.3.2 Flow rule and slip resistance

Due to the physically well-established assumption that all dislocations are mobile all the time, hence we choose a viscoplastic flow rule. Various options are available: for example,

$$\pi^\alpha = S^\alpha \left(\frac{|\dot{\gamma^\alpha}|}{\dot{\gamma}^\alpha_0}\right)^m \text{sgn}(\pi^\alpha) \,. \tag{20}$$

The slip resistance S^α is given in [10] by the evolution equation

$$\dot{S}^\alpha = \sum_\beta h^{\alpha\beta}(\boldsymbol{S})|\dot{\gamma}^\beta| \tag{21}$$

in which $h^{\alpha\beta}$ is a matrix of hardening moduli and $\boldsymbol{S}$ denotes the array $[S_1, \ldots, S_{n_{\text{S}}}]^{\text{t}}$ for n_{S} slip systems. See also [1] for further details.

3 NUMERICAL FRAMEWORK FOR CRYSTAL PLASTICITY

A conforming finite element approximation is used to solve the initial-boundary value problem, with the displacement $\boldsymbol{u}$ and slips γ^α being the unknown variables.

Finite-element approximations. In a standard Bubnov–Galerkin approximation, the test and trial functions of both unknowns are discretized with the same shape functions: thus

$$\boldsymbol{u}^h = \sum_{J=1}^{n^u_{en}} N^u_J \boldsymbol{u}_J \,, \quad \delta\boldsymbol{u}^h = \sum_{I=1}^{n^u_{en}} N^u_I \delta\boldsymbol{u}_I \,, \quad \boldsymbol{\gamma}^h = \sum_{L=1}^{n^\gamma_{en}} N^\gamma_L \boldsymbol{\gamma}_L \,, \quad \delta\boldsymbol{\gamma}^h = \sum_{K=1}^{n^\gamma_{en}} N^\gamma_K \delta\boldsymbol{\gamma}_K \,, \tag{22}$$

with provision for different orders of interpolation of the displacement and slips.

Table 1: Algorithm for the crystal plasticity material routine

1. The approximate exponential map with a backward Euler approximations gives

$$\boldsymbol{F}_{\mathrm{p}}^{n+1} = [\boldsymbol{I} - \boldsymbol{\Lambda}^{n+1}]^{-1} \boldsymbol{F}_{\mathrm{p}}^{n} \qquad \text{where} \quad \boldsymbol{\Lambda}^{n+1} = \sum_{\alpha=1}^{n_{\mathrm{S}}} \Delta\gamma^{\alpha}\, \widehat{\boldsymbol{Z}}^{\alpha}$$

2. Obtain elastic right Cauchy–Green deformation tensor $\widehat{\boldsymbol{C}}_{\mathrm{e}}$ from

$$\boldsymbol{F}_{\mathrm{e}}^{n+1} = \boldsymbol{F}^{n+1} \cdot (\boldsymbol{F}_{\mathrm{p}}^{n+1})^{-1} \qquad \widehat{\boldsymbol{C}}_{\mathrm{e}}^{n+1} = (\boldsymbol{F}_{\mathrm{e}}^{n+1})^{\mathrm{t}} \cdot \boldsymbol{F}_{\mathrm{e}}^{n+1}$$

3. Obtain the GND density from

$$\kappa^{\alpha\, n+1} = \kappa^{\alpha n} + [\boldsymbol{\nabla}_{\boldsymbol{X}} \Delta\gamma^{\alpha} \cdot \boldsymbol{F}_{\mathrm{p}}^{-1} \cdot \widehat{\boldsymbol{s}}^{\alpha}]^{n+1}$$

4. Obtain the stress, microstress and resolved shear stress from

$$\widehat{\boldsymbol{S}}_{\mathrm{e}}^{n+1} = 2\frac{\partial \Psi}{\partial \widehat{\boldsymbol{C}}_{\mathrm{e}}^{n+1}}, \quad \boldsymbol{\xi}_0^{\alpha\, n+1} = (J^{n+1})^{-1} (\boldsymbol{F}^{n+1})^{-1} \left(\frac{\partial \Psi}{\partial \kappa^{\alpha}}\right)^{n+1}, \quad \sigma_0^{\alpha\, n+1} = \left[\widehat{\boldsymbol{C}}_{\mathrm{e}}^{n+1} \cdot \widehat{\boldsymbol{S}}_{\mathrm{e}}^{n+1}\right] : \widehat{\boldsymbol{Z}}^{\alpha}$$

3. Obtain the microforce π_0^{α} from the evolution

$$\pi^{\alpha\, n+1} = S^{\alpha} \left(\frac{|\Delta\gamma^{\alpha}|}{\Delta t\, \dot{\gamma}_0^{\alpha}}\right)^{m} \operatorname{sgn} \pi^{\alpha}$$

Finite-element residual and iterative solution. A spatial discretization of the weak form of the macro and micro balance (12) and (14) yields the element residuals

$$\mathbf{r}_{0I}^{u\,h}(\boldsymbol{u}^h) = \mathbf{f}_{0\mathrm{int}I}^{u\,h} - \mathbf{f}_{0\mathrm{sur}I}^{u\,h} - \mathbf{f}_{0\mathrm{vol}I}^{u\,h} \doteq \mathbf{0} \tag{23}$$

$$\mathbf{r}_{0K}^{\gamma\alpha\,h}(\gamma^{\alpha h}) = \mathbf{f}_{0\mathrm{int}K}^{\gamma\alpha\,h} - \mathbf{f}_{0\mathrm{sur}K}^{\gamma\alpha\,h} \doteq \mathbf{0} \tag{24}$$

that have to vanish at equilibrium. The internal and external macro forces at nodes I are assembled from the element contributions, which from the weak form of (12) are

$$\mathbf{f}_{\mathrm{int}I}^{u\,h} = \operatorname*{\mathbf{A}}_{e=1}^{n_{\mathrm{el}}} \int_{\mathcal{B}_0} \boldsymbol{P} \cdot \boldsymbol{\nabla}_{\boldsymbol{X}} N_I^u \,\mathrm{d}V, \quad \mathbf{f}_{\mathrm{sur}I}^{u\,h} = \operatorname*{\mathbf{A}}_{e=1}^{n_{\mathrm{el}}} \int_{\partial\mathcal{B}_0} \boldsymbol{t}_0\, N_I^u \,\mathrm{d}A, \quad \mathbf{f}_{\mathrm{vol}I}^{u\,h} = \operatorname*{\mathbf{A}}_{e=1}^{n_{\mathrm{el}}} \int_{\mathcal{B}_0} \boldsymbol{f}_0\, N_I^u \,\mathrm{d}V \tag{25}$$

Likewise, the internal and external micro forces stemming from (14) for each slip system α are determined at nodes K as

$$\mathbf{f}_{\mathrm{int}K}^{\gamma\alpha\,h} = \operatorname*{\mathbf{A}}_{e=1}^{n_{\mathrm{el}}} \int_{\mathcal{B}_0} \boldsymbol{\xi}_0^{\alpha} \cdot \boldsymbol{\nabla}_{\boldsymbol{X}} N_K^{\gamma} + [\pi_0^{\alpha} - \sigma_0^{\alpha}]\, N_K^{\gamma} \,\mathrm{d}V \qquad \alpha = 1, \ldots, n_S \tag{26}$$

$$\mathbf{f}_{\mathrm{sur}K}^{\gamma\alpha\,h} = \operatorname*{\mathbf{A}}_{e=1}^{n_{\mathrm{el}}} \int_{\partial\mathcal{B}_0} \boldsymbol{t}_0^{\xi}\, N_K^{\gamma} \,\mathrm{d}A \qquad \alpha = 1, \ldots, n_S \tag{27}$$

The energetic stresses $\boldsymbol{P}$ and $\boldsymbol{\xi}_0^{\alpha}$ are obtained from the free energy (10). The Schmid stress (15) and the dissipative micro force (20) follow from an Euler-backward time integration for the update on the plastic deformation, as summarized in Table 1.

With these ingredients, the time-dependent problem is solved incrementally for the unknown $\boldsymbol{u}$ and γ^α using an iterative global Newton-Raphson iterative solution procedure

$$\begin{bmatrix} \mathrm{D}_{\boldsymbol{u}_J}\mathbf{r}_{0I}^{u\,h} & \mathrm{D}_{\boldsymbol{\gamma}_L}\mathbf{r}_{0I}^{u\,h} \\ \mathrm{D}_{\boldsymbol{u}_J}\mathbf{r}_{0K}^{\gamma\alpha\,h} & \mathrm{D}_{\boldsymbol{\gamma}_L}\mathbf{r}_{0K}^{\gamma\alpha\,h} \end{bmatrix} \cdot \begin{bmatrix} \Delta\boldsymbol{u}_J \\ \Delta\boldsymbol{\gamma}_L \end{bmatrix} = - \begin{bmatrix} \mathbf{r}_I^u \\ \mathbf{r}_K^\gamma \end{bmatrix} \tag{28}$$

with tangent stiffness matrices $\mathrm{D}_\bullet\mathbf{r}_0^\circ$ quantifying the sensitivity of the nodal residua $\circ \in \{u, \gamma^\alpha\}$ with respect to the nodal unknowns $\bullet \in \{\boldsymbol{u}, \gamma^\alpha\}$.

4 NUMERICAL EXAMPLES

The numerical algorithm for the present crystal plasticity framework is demontrated in two benchmark-type problems. At this stage, the simulations are restricted to single slip, with a extension to multiple slip as part of future work.

4.1 Single slip in a shear layer

We first study a shear layer with one slip system under an angle of $\theta = \pi/3$, similar to the problem studied for example in [12]. Omitting periodic boundary conditions, a slip profile with little boundary influences is produced by choosing a relative broad shear layer. Unit values are used for material parameters in these preliminary computations.

Macroscopically, a lateral displacement u_1 is prescribed at top and bottom in opposite directions, and homogeneous Neumann boundary conditions are prescribed on the other two sides. To mimic the dislocation distribution within the shear layer, homogeneous micro Dirichlet, i. e.,*"micro-hard"* boundary conditions, $\gamma = 0$, are chosen at the top and bottom boundary. On the other hand the left and right boundaries obey homogenous micro Neumann boundary conditions, $t^{\xi\alpha} = 0$, often referred to as *"micro free"*.

Neglecting the lateral boundary region, we concentrate on the central region of the boundary value problem. Within the shear layer with approximately homogeneous macro deformation, the shear problem correctly reflects the zero slip at the boundaries and a non zero slip over the height profile of the shear layer. Moreover, the GND density is larger near the boundaries which reflects the pile-up of positive and negative dislocations against a dislocation-impenetrable boundary.

4.2 Single slip in a micro composite

The typical example of a model composite presented in [5] comprises a composite material with rectangular elastic particles embedded in a plastically deforming matrix. Such a double-symmetric problem can be reduced to the symmetric unit cell shown in 2(a). The elastic inclusions are modelled by prescribing zero slip within these subdomains, and the cell is subjected to simple shear loading.

While the macroscopic displacement exhibits a slightly heterogeneous deformation, the slip is, naturally, zero within the elastic inclusions and strongly heterogenous in the plastic matrix material. The slip particularly localizes horizontally just above and below

the inclusion. Due to the limitation to single slip and the modelling of gliding mechanisms only, dislocations from the left bottom cannot propagate to the top right region (Fig. 2(e)). Instead dislocations pile up against the elastic inclusions with different signs, as shown in 2(f).

5 CONCLUSION

In this short contribution, we present a multifield-type single crystal plasticity theory at finite strain, similar to the formulation of [10]. The presented governing equations stem from the choice of the the displacement, the plastic slip (rather than its rate [10]) and its gradient as the primary macro and micro state variables. With a thermodynamically consistent relationship between dislocation density rate and slip rate, the free energy, however, is formulated in terms of the GND density, which is directly related to the gradient of slip. For this framework we provide a corresponding finite-element framework that employs both the displacement and the plastic slip as primary nodal degrees of freedom and hence is a strongly coupled problem. Results based on initial computations indicate that the fully coupled algorithm based on a conforming finite element framework is robust. Current work is concerned with the extension to multiple slip, and the use of alternative forms of the hardening law based on total dislocation densities.

References

[1] R. J. Asaro and A. Needleman. Texture development and strain hardening in rate dependent polycrystals. *Acta Metall.*, 33:923–953, 1985.

[2] M. F. Ashby. The deformation of plastically non-homogeneous materials. *Phil. Mag.*, 21:399–424, 1970.

[3] G. Capriz. Continua with latent microstructure. *Arch. Rat. Mech. Anal.*, 90:43–56, 1985.

[4] G. Capriz. *Continua with Microstructure*. Springer, 1989.

[5] H. H. M. Cleveringa, E. van der Giessen, and A. Needleman. Comparison of discrete dislocation and continuum plasticity predictions for a composite material. *Acta Mater.*, 45:3163–3179, 1997.

[6] M. Ekh, M. Grymer, K. Runesson, and T. Svedberg. Gradient crystal plasticity as part of the computational modelling of polycrystals. *Int. J. Numer. Meth. Engng*, 72:197–220, 2007.

[7] I. Ertürk, J. A. W. Dommelen, and M. G. D. Geers. Energetic dislocation interactions and thermodynamical aspects of strain gradient crystal plasticity theories. *J. Mech. Phys. Solids*, 57:1801–1814, 2009.

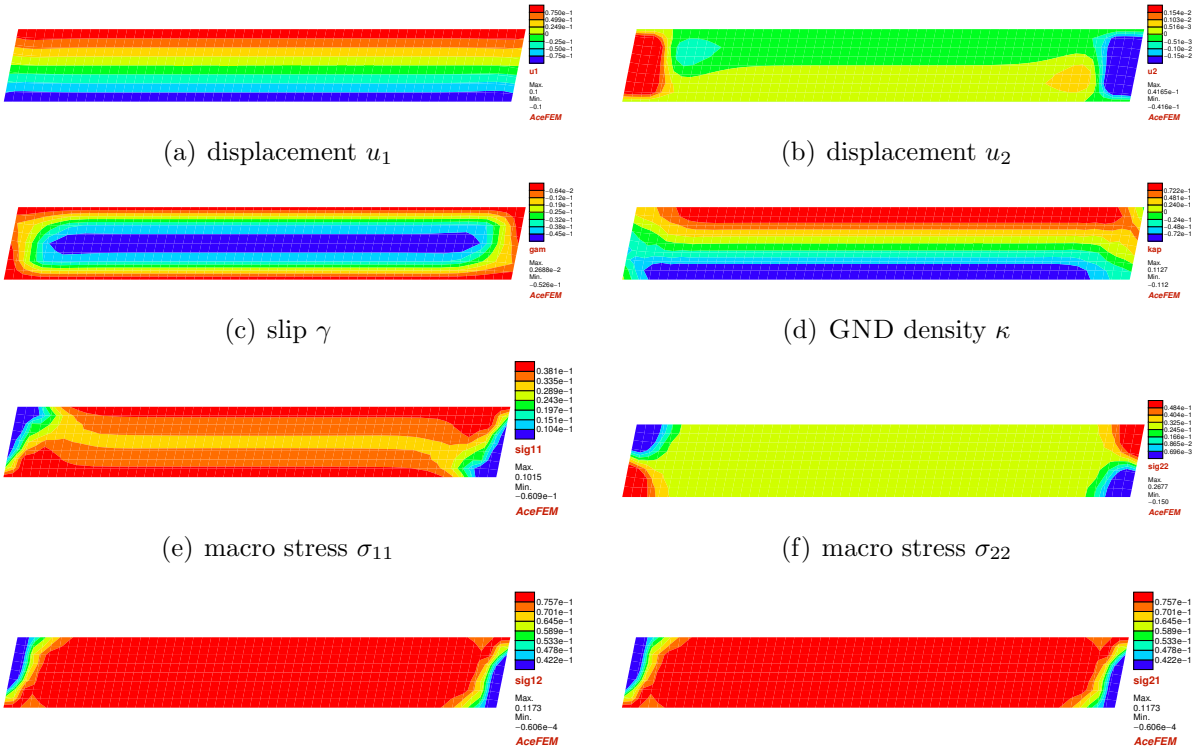

(a) displacement u_1 (b) displacement u_2

(c) slip γ (d) GND density κ

(e) macro stress σ_{11} (f) macro stress σ_{22}

(g) macro stress σ_{12} (h) macro stress σ_{21}

Figure 1: Shear layer with single slip at $\theta = 60$ and micro-hard boundary conditions for the slip.

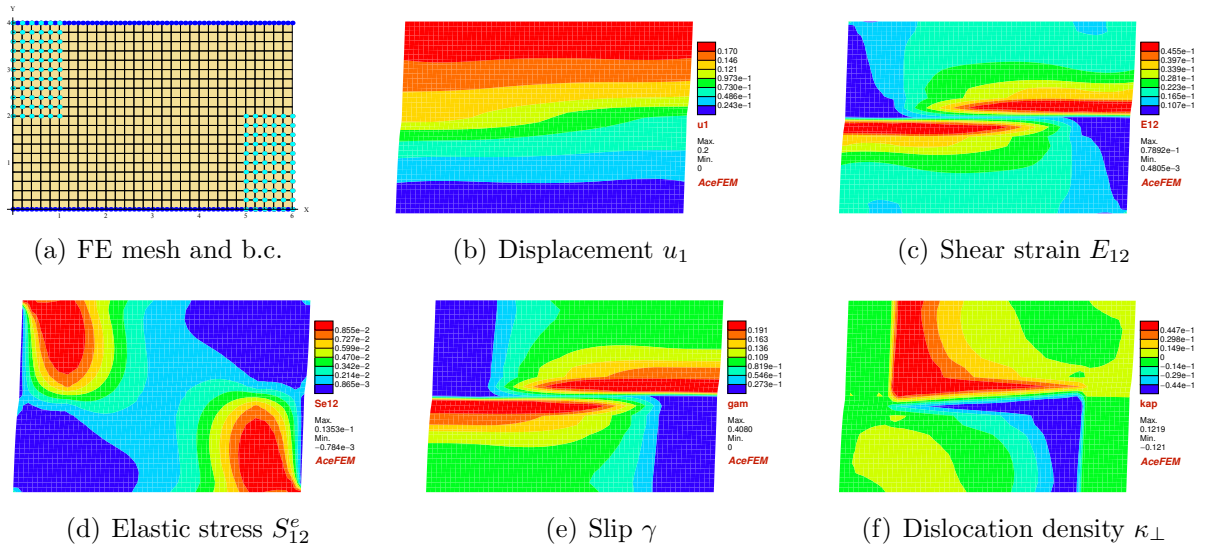

(a) FE mesh and b.c. (b) Displacement u_1 (c) Shear strain E_{12}

(d) Elastic stress S^e_{12} (e) Slip γ (f) Dislocation density $\kappa_\perp$

Figure 2: Micro composite unit cell with elastic inclusions and single slip at $\theta = 0$.

[8] L. P. Evers, W. A. M. Brekelmans, and M. G. D. Geers. Scale dependent crystal plasticity framework with dislocation density and grain boundary effects. *Int. J. Solid Struct.*, 41:5209–5230, 2004.

[9] L. P. Evers, W. A. M. Brekelmans, and M. G. D. Geers. Non-local crystal plasticity model with intrinsic SSD and GND effects. *J. Mech. Phys. Solids*, 52:2379–2401, 2004.

[10] M. E. Gurtin. A finite-deformation, gradient theory of single-crystal plasticity with free energy dependent on densities of geometrically necessary dislocations. *Int. J. Plast.*, 24:702–725, 2008.

[11] C. B. Hirschberger and P. Steinmann. Classification of concepts in thermodynamically consistent generalised plasticity. *J. Eng. Mechanics*, 135:156–170, 2009.

[12] M. Kuroda and V. Tvergaard. On the formulations of higher-order strain gradient crystal plasticity models. *J. Mech. Phys. Solids*, 56:1591–1608, 2008.

[13] A. Ma, F. Roters, and D. Raabe. A dislocation density based constitutive model for crystal plasticity fem including geometrically necessary dislocations. *Acta Mater.*, 54:2169–2179, 2006.

[14] J. F. Nye. Some geometrical relations in dislocated crystals. *Acta Metall.*, 1:153–162, 1953.

[15] B. D. Reddy. The role of dissipation and defect energy in variational formulations. Part 2: Single-crystal plasticity. *In review.*

[16] P. Steinmann and E. Stein. On the numerical treatment and analysis of finite deformation ductile single crystal plasticity. *Comput. Methods Appl. Mech. Engrg.*, 129: 235–254, 1996.

[17] B. Svendsen. On the modelling of anisotropic elastic and inelastic material behaviour at large deformation. *Int. J. Solid Struct.*, 38:9579–9599, 2001.

[18] T. Yalcinkaya, W. A. M. Brekelmans, and M. G. D. Geers. Deformation patterning driven by rate dependent non-convex strain gradient plasticity. *J. Mech. Phys. Solids*, 59:1–17, 2011.

XI International Conference on Computational Plasticity. Fundamentals and Applications
COMPLAS XI
E. Oñate, D.R.J. Owen, D. Peric and B. Suárez (Eds)

COMPRESSION BEHAVIORS OF LOW-DENSITY POROUS MATERIALS UNDER MULTIAXIAL STRESS CONDITIONS

ATSUSHI SAKUMA[*] AND SHIGERU NAGAKI[†]

[*] Institute of Technology
Tokyo Univeristy of Agriculture and Technology
2-24-16 Nakacho, Koganei, Tokyo, Japan
e-mail: asakuma@cc.tuat.ac.jp

[†]Institute of Technology
Tokyo Univeristy of Agriculture and Technology
2-24-16 Nakacho, Koganei, Tokyo, Japan
e-mail: nagaki@cc.tuat.ac.jp

Key words: Stress-strain Measurement, Material Testing, Nonlinear Problem, Constitutive Equation, Inelasticity, Poromechanics, Low-density Porous Material, Phase Transformation, Compression Testing, Polystyrene foam

Abstract. In this study, uniaxial and multiaxial compression tests are conducted for studying the nonlinear deformation behaviors of a porous material during compression. In the results of uniaxial compression tests, the stress level in the plateau region is varied by the difference of direction but it is shown that this material has the character of transverse isotropicity. The multiaxial behavior of the material is also observed in this study. Equibiaxial pre-strained compression tests are adopted for the observation of the characteristics of the material. The results of these tests show that the pre-strain causes the porous material to harden, and the extent of the hardening depends on the difference of the amount of pre-strain.

1 INTRODUCTION

Low-density porous materials are useful to design the shock absorbing parts of various machines. The deformation analysis of the materials is needed in the design but it is difficult because of the nonlinearity caused by the crush of cellular structure in the materials.

Then, the multiaxial behavior of compression process of the porous materials is evaluated by using equibiaxial compression testing in addition to the fundamental uniaxial compression testing for the formulation of FEM. Polystyrene foam is adopted to study the behavior and it is revealed that there is complex relationship between the compression direction.

2 FUNDAMENTAT COMPRESSON

Uniaxtial compression test is adopted to reveal the fundamental characteristics of the porous materials. The specimens are made by using the polystyrene foam “STYROFOAM” of Dow Chemical, Co. Ltd. The dimensions of specimens are 30mm x 30mm x 10mm and talcum powder is sprinkled at their surfaces for lubrication in the testing. The three type of

direction is defined as shown in Figure 1. Every type of the specimens are compressed in their direction of height, and observed response is indicated in Figure 2.

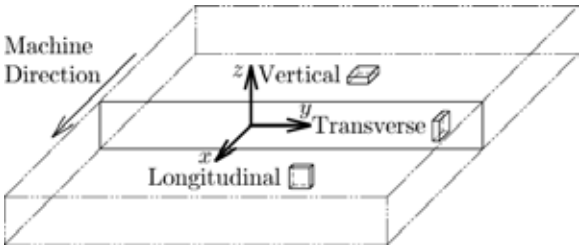

Figure 1: The three type of direction is defined by depending on machine direction of polystyrene form.

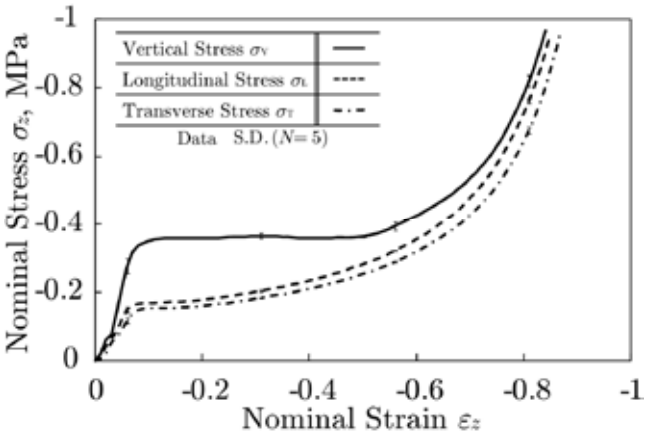

Figure 2: Transverse isotropicity is observed in uniaxial compression test. Here,

Uniaxtial compression test is adopted to reveal the fundamental characteristics of the porous materials. The specimens are made by using the polystyrene foam “STYROFOAM” of Dow Chemical, Co. Ltd. The dimensions of specimens are 30mm x 30mm x 10mm and talcum powder is sprinkled at their surfaces for lubrication in the testing. The three type of direction is defined as shown in Figure 1. Every type of the specimens is compressed in this test and transverse isotropicity is observed as shown in Figure 2. Here, highest level of plateau stress is observed in the vertical direction of the foam. The stress responses are similar between longitudinal and transverse directions.

3 MULTIAXIAL COMPRESSION

3.1 Procedure of compression

Multiaxial compression testing indicated in Figure 3 is proceeded to investigate the complicated behavior of the materials [1]. Here, the polystyrene form adopted in former section is also applied for the investigation.

The equibiaxial compression system indicated in Figure 3 can give pre-strain to the specimen. Here, Fig. (a)-(c) are the procedure of the multiaxial compression testing. In this Figure 3, settled specimen (a) is pre-strained at procedure (b), and compressed as shown at procedure (c).

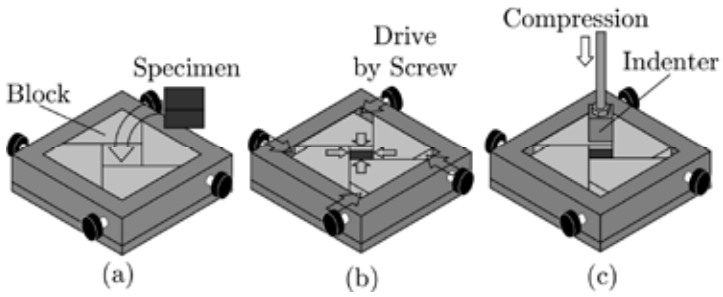

Figure 3: Multiaxial compression can be devied to three procedures (a)-(c).

3.2 Measurement of Stress Response

The stress response of the specimen is measured in the every direction of x, y and z of testing system by using load cell and pressure sensors as shown in Figure 4. The load cell is used to measure the stress response in the final compression procedure of Figure 3 (c). On the other hand, pressure sensors are settled at pre-straining surface of the block in equibiaxial compressor as shown in Figure 4, and used to measure the response in pre-straining and final compression procedures of Figure 3 (b)-(c).

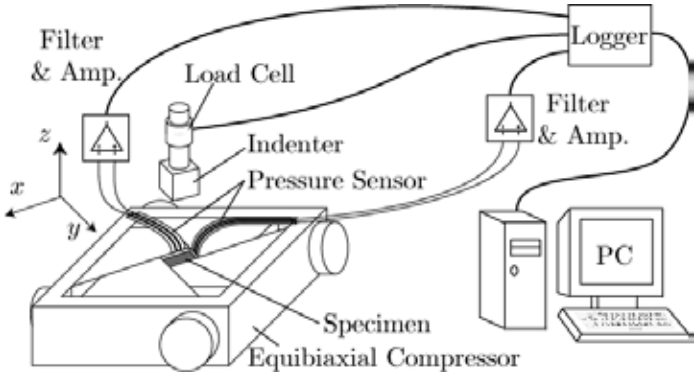

Figure 4: Measurement system of stress responce.

3.3 Muliaxial Response

3.3.1 Response in Pre-Straining

The result measured in pre-straining procedure is shown in Figure 5. This stress response is taken by using the pressure sensor on the block in equibiaxial compressor. The plateau stresses are observed in every direction of longitudinal and transverse even if little difference is also observed between them. This result indicates that the phenomena of plateau stress is occurred in the biaxial pre-straining process, and it is similar to the result of uniaxial compression which is shown in Figure 2.

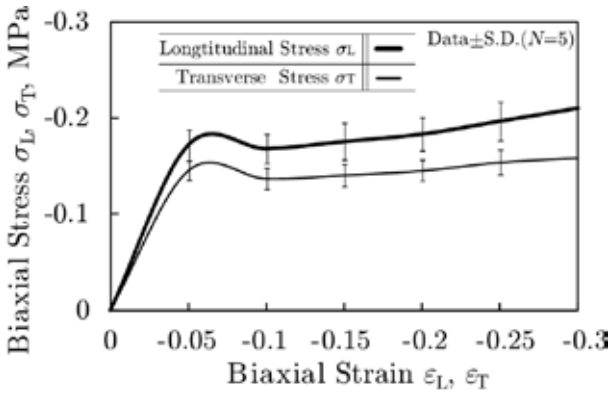

Figure 5: Stress response measured in pre-straining procedure.

3.3.2 Response in Final Compression

In the final compression procedure, the response of compression stress is measured with the response of equibiaxial stress.

Figure 6 shows the responses of compression stress observed in this procedure, and the variation caused by the difference of the amount of pre-strain can be observed here. Especially, the level of plateau stress is rise by pre-strain and the soften effect induced by the pre-strain is not observed in this direction.

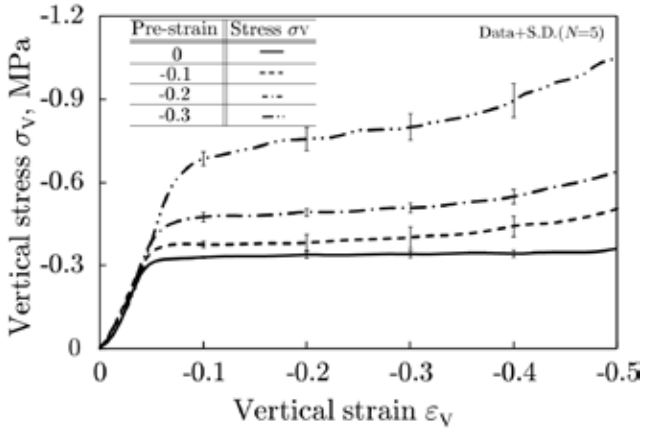

Figure 6: The stress responses of compression observed in final procedure.

The response of equibiaxial stress in final procedure is shown Figure 7. The variation induced by the difference of the amount of pre-strain is observed here, and it is shown that much pre-strain causes the stable level of plateau stress. On the other hand, the soften effects of this material are observed in the lower pre-strain conditions. This means that less pre-strain causes the instability of compression process of the porous materials even if the stable compression of the material can be observed in the condition of much pre-strain. Then, the maltiaxial condition of the low-density porous materials should be considered in the compression process with complex conditions of stresses.

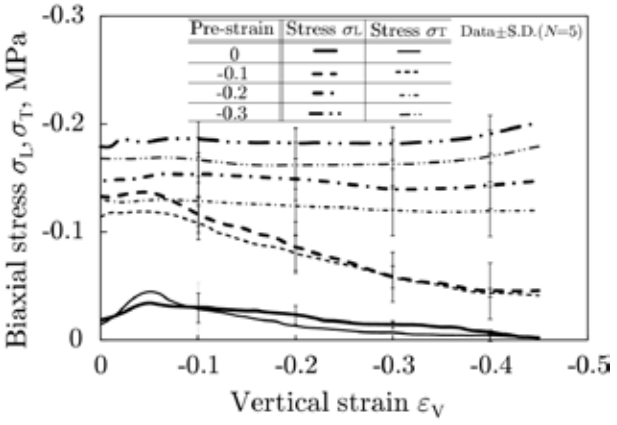

Figure 7: Equibiaxial stress response in final procedure of compression.

12 CONCLUSIONS

In order to study the behavior of multiaxial stress response of low-density porous materials, the compression test with multiaxial stress condition is conducted by developing the equibiaxial compressor [1]. Especially, the equibiaxial stress responses in the compression procedures are observed by the pressure sensor in the compressor. Then the instable phenomenon of the materials in multiaxial stress condition is observed by the conduction of the compression test of the materials.

By considering the results of this result, the constitutive equations of the porous materials will be formulated to simulate the compression of them for the machine design which uses the materials.

REFERENCES

[1] Sakuma, A., Azusawa, N., Shinomiya, M., Abe, K. and Nagaki, S., Multiaxial and Dynamic Compression Behavior of Low-Deisnty Porous Materials and their Constitutive Representation, *Proc. 10th Int. Conf. Comp. Plast. (COMPLAS X)*, (2009), CD-ROM.

XI International Conference on Computational Plasticity. Fundamentals and Applications
COMPLAS XI
E. Oñate, D.R.J. Owen, D. Peric and B. Suárez (Eds)

IMPLEMENTATION OF A MATERIAL MODEL FOR A CAST TRIP-STEEL

Stefan Prüger*, Meinhard Kuna*, Kai Nagel† and Horst Biermann†

*TU Bergakademie Freiberg
Institute for Mechanics and Fluid Dynamics
Lampadiusstrasse 4, 09599 Freiberg, Germany
email: Stefan.Prueger@imfd.tu-freiberg.de

†TU Bergakademie Freiberg
Institute of Materials Engineering
Gustav-Zeuner-Strasse 5, 09599 Freiberg, Germany

Key words: TRIP-steel, finite element implementation, affine trust-region method, notched tensile test

Abstract. The implementation of a phenomenological, macroscopic model for TRIP-steels in the finite element code ABAQUS is presented. The model takes into account both the strain-rate dependent flow behaviour of the two phases, austenite (γ) and martensite (α'), and the temperature and stress state dependent $\gamma \rightarrow \alpha'$ phase transformation. In order to solve the system of nonlinear equations, which results from the implicit integration of the constitutive model, the application of an affine trust-region approach is proposed to compute strictly feasible solutions. Furthermore, model predictions are compared with experimental results obtained from tensile tests on notched specimens.

1 INTRODUCTION

A common feature of many TRIP-steels is their favourable combination of high strength and pronounced ductility. These properties also apply to a newly developed as cast TRIP-steel [1] and are attributed to the inelastic deformation of the two phases austenite (γ) and martensite (α') and the strain-induced $\gamma \rightarrow \alpha'$ phase transformation, which accompanies the deformation. The cast TRIP-steel possesses a fully austenitic, coarse grain initial microstructure and the transformation proceeds by the formation of shear bands within the grains and subsequent nucleation of martensite within these bands [2]. It has been found that the transformation behaviour is rather sensitive to temperature and strain rate [3]. Therefore, an adequate material model is required to describe the complex material behaviour of the TRIP-steel.
An approach, which has been successfully applied to develop macroscopic models for

TRIP-steels relies on the computation of effective properties of composites. Herein, TRIP-steels are considered as composites with evolving microstructure [4], [5], [6]. In the current paper, we also follow this approach and give an extension of the model proposed in [6]. The composite approach is advantageous, because it allows insight into the stress and strain levels in the single phases of the TRIP-steel as their constitutive response is explicitly taken into account. However, the burden of such a procedure is the increased complexity and possibly additional nonlinearity of the model due to the required homogenisation process. Therefore, more elaborated numerical methods might be required to solve the nonlinear equations, associated with the implicit integration of the constitutive model. Besides the required starting point, the physical nature of the independent variables or numerical considerations impose certain restrictions on these variables in order to exclude infeasible solutions. In case of viscoplastic models, it has been shown by de Souza Neto [7] that the commonly applied Newton's method is not appropriate to handle such bounds. In this paper an affine trust-region method [8] is applied to solve the bound constrained nonlinear equations, which arise from the implicit integration procedure.
Throughout this paper symbolic notation is employed, where $\mathbb{A}$ and $\mathbf{A}$ denote fourth order and second order tensors, respectively. The norm of $\mathbf{A}$ is defined as $\|\mathbf{A}\| = \sqrt{\mathbf{A} : \mathbf{A}}$. Vectors are given in matrix notation, i.e. the norm of a vector is described as $\|\mathrm{A}\| = \sqrt{\mathrm{A}^{\mathrm{T}}\mathrm{A}}$. The Jacobian of a vector function $\mathrm{F(x)}$ is introduced as $\mathrm{F}' = \frac{\partial F_i}{\partial x_j}$. The fourth order isotropic tensor and the Kronecker symbol are given as $\mathbb{I} = \frac{1}{2}(\delta_{ik}\delta_{jl} + \delta_{il}\delta_{jk})e_i \otimes e_j \otimes e_k \otimes e_l$ and $\mathbf{I} = \delta_{ij}e_i \otimes e_j$, respectively. The material time derivative is expressed as $\dot{(\ )} = \frac{\mathrm{d}(\ )}{\mathrm{d}t}$.

2 MATERIAL MODEL

In order to describe the response of the TRIP-steel under arbitrary large deformations, the finite deformation theory is employed to formulate the corresponding constitutive equations. An additive split of the rate of deformation tensor according to

$$\mathbf{D} = \mathbf{D}^{\mathrm{e}} + \mathbf{D}^{\mathrm{vp}} + \mathbf{D}^{\mathrm{trip}} \tag{1}$$

is carried out. The elastic and the viscoplastic rates of deformation are denoted by $\mathbf{D}^{\mathrm{e}}$ and $\mathbf{D}^{\mathrm{vp}}$, respectively, whereas the rate of deformation associated with the phase transformation is termed $\mathbf{D}^{\mathrm{trip}}$. The assumption of small elastic strains, generally valid in metal plasticity, allows to formulate the constitutive law as a linear, hypoelastic relation

$$\overset{\triangledown}{\mathbf{\Sigma}} = \mathbb{C} : \mathbf{D}^{\mathrm{e}} \tag{2}$$

that connects the Jaumann rate of the Cauchy stress and the elastic rate of deformation tensor [9]. In the case of isotropic elasticity the elastic modulus tensor

$$\mathbb{C} = 2G\mathbb{I} + (K - \frac{2}{3}G)\mathbf{I} \otimes \mathbf{I} \tag{3}$$

is described in terms of the shear modulus G and the bulk modulus K. This approach assumes identical elastic properties of the two phases austenite and martensite. The viscoplastic rate of deformation is defined as

$$\mathbf{D}^{\mathrm{vp}} = \frac{1}{2}\Theta^{\mathrm{hom}}\mathbf{S}, \tag{4}$$

where $\mathbf{S}$ denotes the deviator of the Cauchy stress and Θ^{hom} the viscoplastic compliance of the two-phase composite, which is determined by homogenising the viscoplastic response of the single phases. During phase transformation both volumetric and deviatoric deformations occur. Therefore, the rate of deformation associated with the phase transformation takes the form

$$\mathbf{D}^{\mathrm{trip}} = \dot{f}_m \left(R\mathbf{N} + \frac{1}{3}\Delta_v \mathbf{I} \right) \ . \tag{5}$$

Herein, the volumetric transformation strain is denoted by Δ_v, while

$$R = R_0 + R_1 \frac{\bar{\Sigma}}{\sigma_a^*} \tag{6}$$

is the stress dependent magnitude of the deviatoric transformation strain, whose direction is given in terms of the normalized stress deviator $\mathbf{N} = \mathbf{S}/\|\mathbf{S}\|$. The von Mises equivalent stress is computed as $\bar{\Sigma} = \sqrt{\frac{3}{2}}\|\mathbf{S}\|$. The transformation strain is controlled by the rate of the martensite volume fraction $\dot{f}_m$.

Due to the significant difference in the flow behaviour of the two phases, their rate dependent flow behaviour is modeled separately. Therefore, each phase is described by a unified viscoplastic model of the von Mises type, i.e. the viscoplastic deformation is strictly deviatoric. The viscoplastic equivalent strain rate is defined as

$$\dot{\bar{\varepsilon}}^{\mathrm{vp}}_{(r)} = \dot{\varepsilon}^{0}_{(r)} \left(\frac{\tilde{\sigma}_{(r)}}{\sigma^{\mathrm{y}}_{(r)}} \right)^{m_{(r)}} \ , \tag{7}$$

where $\tilde{\sigma}_{(r)}$, $\sigma^{\mathrm{y}}_{(r)}$ and $\dot{\varepsilon}^{0}_{(r)}$ denote the equivalent stress, the yield stress and the reference strain rate of the phase r, which can be either austenite (a) or martensite (m). The isotropic strain hardening of each phase is considered by using the power law

$$\sigma^{\mathrm{y}}_{(r)} = A_{(r)} + B_{(r)} (\bar{\varepsilon}^{\mathrm{vp}}_{(r)})^{q_{(r)}} \ . \tag{8}$$

According to the variational principle for the homogenisation of nonlinear composites, described in [10], the equivalent stresses $\tilde{\sigma}_{(r)}$ can be related to macroscopic equivalent stress $\bar{\Sigma}$ as

$$\tilde{\sigma}_{(r)} = \bar{\Sigma} \sqrt{\frac{1}{f_{(r)}} \frac{\partial \Theta^{\mathrm{hom}}}{\partial \Theta_{(r)}}} \ . \tag{9}$$

This relation holds, if the composite consists of isotropic phases arranged in a statistically uniform and isotropic manner. In order to evaluate this expression, a description of the homogenised compliance Θ^{hom} in terms of the compliances of the single phases $\Theta_{(r)}$ is required. Here the bound

$$\Theta^{\mathrm{hom}} = \frac{f_m(\frac{2}{\Theta_a} + \frac{3}{\Theta}) + f_a(\frac{2}{\Theta_m} + \frac{3}{\Theta})}{\frac{f_m}{\Theta_m}(\frac{2}{\Theta_a} + \frac{3}{\Theta}) + \frac{f_a}{\Theta_a}(\frac{2}{\Theta_m} + \frac{3}{\Theta})} \,, \tag{10}$$

as proposed by Hashin Shtrikman [11], is used. It should be noted that $\Theta = \max(\Theta_a, \Theta_m)$ and the volume fraction of austenite is defined as $f_a = 1 - f_m$. The viscoplastic compliances of the single phases

$$\Theta_{(r)} = \frac{3}{\tilde{\sigma}_{(r)}} \dot{\bar{\varepsilon}}^{\mathrm{vp}}_{(r)} = \frac{3\dot{\varepsilon}^0_{(r)}}{\tilde{\sigma}_{(r)}} \left(\frac{\tilde{\sigma}_{(r)}}{\sigma^{\mathrm{y}}_{(r)}} \right)^{m_{(r)}} \tag{11}$$

correspond to a linearized form of Eq. (7).
In order to describe the phase transformation behaviour of the cast TRIP-steel, the macroscopic transformation model by Stringfellow [5] is extended. This model is inspired by the experimental observation that martensite nucleates predominantly at shear band intersection, which have been formed prior to the nucleation event. Following the derivation in [5], an evolution equation for the martensite volume fraction of the form

$$\dot{f}_m = (1 - f_m)(A\dot{\bar{\varepsilon}}^{\mathrm{vp}}_a + B(\dot{g} - \dot{\bar{g}})) \tag{12}$$

is proposed. Herein, the thermodynamical driving force g for the martensite evolution

$$g = g_0 - g_1\vartheta + g_2\vartheta^2 + g_3(\Delta_v p + \sqrt{\frac{2}{3}} R\bar{\Sigma}) \tag{13}$$

is taken as a function of the hydrostatic stress $p = \frac{1}{3}\boldsymbol{\Sigma} : \mathbf{I}$, the von Mises equivalent stress $\bar{\Sigma}$ and the normalized temperature ϑ

$$\vartheta = \frac{T - M^\sigma_{\mathrm{s}}}{M_{\mathrm{d}} - M^\sigma_{\mathrm{s}}}, \tag{14}$$

where T and M^σ_{s} correspond to the temperature and the start temperature for stress-induced martensite formation, respectively. M_{d} is the highest temperature, at which martensite can be mechanically induced [12]. The mean transformation barrier $\bar{g}$ is assumed to depend on the viscoplastic equivalent strain in the austenite in the form

$$\bar{g} = \bar{g}_0 + \bar{g}_1 \bar{\varepsilon}^{\mathrm{vp}}_a \,. \tag{15}$$

This approach incorporates the effect that the energy required for the accommodation of the martensite nuclei in the surrounding matrix material depends on the viscoplastic

deformation of the austenite prior to the nucleation [13]. The parameter A that controls the martensite formation due to an increase in nucleation sites is given as

$$A = a\beta n (f_{SB})^{n-1}(1 - f_{SB})P \ . \tag{16}$$

The formation of shear bands in austenite is modeled via the volume fraction of shear bands f_{SB}, whose evolution is described according to

$$\dot{f}_{SB} = (1 - f_{SB})a\dot{\bar{\varepsilon}}_a^{\mathrm{vp}} \ . \tag{17}$$

The rate of shear band formation a is taken as function of the temperature T and the stress triaxiality $h = p/\bar{\Sigma}$ in the form

$$a = a_1 + a_2 T + a_3 T^2 - a_4 \arctan(h) \ . \tag{18}$$

To account for the observation that under given values of the driving force and the transformation barrier martensite is formed only at a certain fraction of potential nucleation sites, the following function P is introduced.

$$P = \frac{1}{\sqrt{2\pi}s_g} \int_{-\infty}^{g} \exp\left[-\frac{1}{2}\left(\frac{g' - \bar{g}}{s_g}\right)^2\right] \mathrm{d}g' \tag{19}$$

The parameter B, which incorporates the change in martensite volume fraction due to a change in the driving force and the transformation barrier is given as

$$B = \beta (f_{SB})^n \frac{\mathrm{d}P}{\mathrm{d}g} H(\dot{P}) \ . \tag{20}$$

It should be noted that β, n and $H(\dot{P})$ in equation (16) and (20) describe two geometrical constants and the unit step function, respectively.

3 IMPLEMENTATION

3.1 Integration of the material model

The constitutive model, described in Sect. 2, is implemented in the finite element program ABAQUS using the user subroutine interface UMAT. The applied incremental, iterative solution strategy requires the integration of the rate form of the constitutive equations in the context of finite deformations over a finite time increment $\Delta t = t|_{n+1} - t|_n$. In the following, quantities at the beginning and the end of the increment are indicated by $()|_n$ and $()|_{n+1}$, respectively, while the increments of these quantities are defined as $\Delta = ()|_{n+1} - ()|_n$. The integration is carried using the algorithm proposed by Hughes and Winget [14], because it preserves the objectivity incrementally. When applied to a second order tensor $\mathbf{A}$, it takes the form

$$\mathbf{A}|_{n+1} = \Delta\mathbf{R} \cdot \mathbf{A}|_n \cdot \Delta\mathbf{R}^{\mathbf{T}} + \Delta\mathbf{A}(\Delta\mathbf{E}), \tag{21}$$

where $\Delta\mathbf{R}$ and $\Delta\mathbf{E}$ denote the increment in rotation and an approximation of the strain increment, respectively. The last term of the right hand side corresponds to the change in $\mathbf{A}$ as a result of the strain increment $\Delta\mathbf{E}$ associated with Δt. Under suitable assumptions regarding the rotation of the principle axis of the strain, the time integration of Eq. (1) yields the incremental relation

$$\Delta\mathbf{E} = \Delta\mathbf{E}^{\mathrm{e}} + \Delta\mathbf{E}^{\mathrm{vp}} + \Delta\mathbf{E}^{\mathrm{trip}}. \tag{22}$$

Due to its unconditional stability, the integration is carried out using a one-step implicit integration scheme. Therefore, the inelastic strain increments are calculated by

$$\Delta\mathbf{E}^{\mathrm{vp}} = \frac{\Delta t}{2}\Theta^{\mathrm{hom}}|_{n+1}\mathbf{S}|_{n+1} \tag{23}$$

and

$$\Delta\mathbf{E}^{\mathrm{trip}} = \Delta f_m \left(R|_{n+1}\mathbf{N}|_{n+1} + \frac{1}{3}\Delta_v\mathbf{I} \right) \ . \tag{24}$$

The stress increment is computed according to

$$\Delta\boldsymbol{\Sigma} = \mathbb{C} : (\Delta\mathbf{E} - \Delta\mathbf{E}^{\mathrm{vp}} - \Delta\mathbf{E}^{\mathrm{trip}}) \tag{25}$$

after the stress at the beginning of the increment is rotated as described in Eq. (21). The constitutive description of the viscoplastic behaviour of the single phases, which has been introduced in Eq. (7),(8) and (11), is given in the discretized form as

$$\dot{\bar{\varepsilon}}^{\mathrm{vp}}_{(r)}|_{n+1} = \dot{\varepsilon}^{0}_{(r)} \left(\frac{\tilde{\sigma}_{(r)}|_{n+1}}{\sigma^{\mathrm{y}}_{(r)}|_{n+1}} \right)^{m_{(r)}} \tag{26}$$

$$\Theta_{(r)}|_{n+1} = \frac{3\dot{\varepsilon}^{0}_{(r)}}{\tilde{\sigma}_{(r)}|_{n+1}} \left(\frac{\tilde{\sigma}_{(r)}|_{n+1}}{\sigma^{\mathrm{y}}_{(r)}|_{n+1}} \right)^{m_{(r)}} \tag{27}$$

$$\sigma^{\mathrm{y}}_{(r)}|_{n+1} = A_{(r)} + B_{(r)}(\bar{\varepsilon}^{\mathrm{vp}}_{(r)}|_{n} + \dot{\bar{\varepsilon}}^{\mathrm{vp}}_{(r)}|_{n+1}\Delta t)^{q_{(r)}} \ , \tag{28}$$

while the equivalent stresses are computed as

$$\tilde{\sigma}_{(r)}|_{n+1} = \bar{\Sigma}|_{n+1}\sqrt{\frac{1}{f_{(r)}|_{n+1}}\frac{\partial\Theta^{\mathrm{hom}}}{\partial\Theta_{(r)}}\bigg|_{n+1}} \ . \tag{29}$$

The evolution of the martensite volume fraction over the time increment Δt is approximated with

$$\Delta f_m = (1 - f_m|_{n+1})(A|_{n+1}\dot{\bar{\varepsilon}}^{\mathrm{vp}}_{a}|_{n+1} + B|_{n+1}(\dot{g}|_{n+1} - \dot{\bar{g}}|_{n+1}))\Delta t \ . \tag{30}$$

The incremental change in the volume fraction of shear bands is obtained from

$$\Delta f_{SB} = (1 - f_{SB}|_{n+1}) a|_{n+1} \dot{\bar{\varepsilon}}_a^{\mathrm{vp}}|_{n+1} \Delta t \ . \tag{31}$$

Using Eq. (13) and (15) the rate of the driving force and the transformation barrier are given at the end of the increment as

$$\dot{g}|_{n+1} = -g_1 \dot{\vartheta}|_{n+1} + 2 g_2 \vartheta|_{n+1} \dot{\vartheta}|_{n+1} + g_3 \left(\Delta_v \dot{p}|_{n+1} + \sqrt{\frac{2}{3}} \left(R + \bar{\Sigma} \frac{\partial R}{\partial \bar{\Sigma}} \right) \Big|_{n+1} \dot{\bar{\Sigma}}|_{n+1} \right) \tag{32}$$

$$\dot{\bar{g}}|_{n+1} = \bar{g}_1 \dot{\bar{\varepsilon}}_a^{\mathrm{vp}}|_{n+1} \ , \tag{33}$$

respectively.
According to Papatriantafillou [6], the nonlinear, implicit tensor equation (25) can be efficiently solved by applying the integration algorithm proposed by Aravas [15] in the case of pressure dependent plasticity models. We follow this approach and state the resulting two nonlinear equation for the stress invariants.

$$p|_{n+1} = p^{\mathrm{trial}}|_{n+1} - K \Delta E^{\mathrm{in}} \tag{34}$$

$$\bar{\Sigma}|_{n+1} = \bar{\Sigma}^{\mathrm{trial}}|_{n+1} - 3G \Delta \bar{G}^{\mathrm{in}} \tag{35}$$

The trial stress $\boldsymbol{\Sigma}^{\mathrm{trial}}$ is obtained from Eq. (25) by

$$\boldsymbol{\Sigma}^{\mathrm{trial}}|_{n+1} = \boldsymbol{\Sigma}|_n + \mathbb{C} : \Delta \mathbf{E} \ . \tag{36}$$

The quantities ΔE^{in} and $\Delta \bar{G}^{\mathrm{in}}$ are defined as

$$\Delta E^{\mathrm{in}} = (\Delta \mathbf{E}^{\mathrm{vp}} + \Delta \mathbf{E}^{\mathrm{trip}}) : \mathbf{I} = \Delta_v \Delta f_m \tag{37}$$

$$\begin{aligned} \Delta \bar{G}^{\mathrm{in}} &= \sqrt{\frac{2}{3} \left(\Delta \mathbf{E}^{\mathrm{vp}} + \Delta \mathbf{E}^{\mathrm{trip}} - \frac{1}{3} \mathbf{I} \Delta E^{\mathrm{in}} \right) : \left(\Delta \mathbf{E}^{\mathrm{vp}} + \Delta \mathbf{E}^{\mathrm{trip}} - \frac{1}{3} \mathbf{I} \Delta E^{\mathrm{in}} \right)} \\ &= \Delta f_m \sqrt{\frac{2}{3}} R|_{n+1} + \frac{\Delta t}{3} \Theta^{\mathrm{hom}}|_{n+1} \bar{\Sigma}|_{n+1} \ . \end{aligned} \tag{38}$$

In order to compute the stress at the end of the increment, $\Delta \bar{G}^{\mathrm{in}}$ and $f_m|_{n+1}$ are taken as the primary unknowns and the Eq. (30) and (38) are reformulated as residuals.
The determination of the quantities at level of the single phases, namely $\dot{\bar{\varepsilon}}^{\mathrm{vp}}_{(r)}|_{n+1}$, $\Theta_{(r)}|_{n+1}$, $\sigma^{\mathrm{y}}_{(r)}|_{n+1}$ and $\tilde{\sigma}_{(r)}|_{n+1}$ requires the solution of the system of equations defined by (26) to (29). According to the proposal in [6], the introduction of the ratio of the viscoplastic compliance $X_m = \frac{\Theta_m}{\Theta_a}$ allows for a reduction of the two nonlinear equations (27) to a single equation. In contrast to [6] the yield stresses in both phases are evaluated at the end of

the increment. Therefore, equation (26) and (29) are included in (28), which leads to the following system of equations

$$X_m|_{n+1} = \frac{\dot{\varepsilon}_m^0}{\dot{\varepsilon}_a^0} \frac{(\sigma_a^{\mathrm{y}}|_{n+1})^{m_a}}{(\sigma_m^{\mathrm{y}}|_{n+1})^{m_m}} \frac{\left(\sqrt{\frac{1}{f_m|_{n+1}} \frac{\partial \Theta^{\mathrm{hom}}}{\partial \Theta_m}\Big|_{n+1}}\right)^{m_m-1}}{\left(\sqrt{\frac{1}{f_a|_{n+1}} \frac{\partial \Theta^{\mathrm{hom}}}{\partial \Theta_a}\Big|_{n+1}}\right)^{m_a-1}} (\bar{\Sigma}|_{n+1})^{m_m-m_a} \tag{39}$$

$$\sigma_a^{\mathrm{y}}|_{n+1} = A_a + B_a \left(\bar{\varepsilon}_a^{\mathrm{vp}}|_n + \Delta t \dot{\varepsilon}_a^0 \left(\frac{\bar{\Sigma}|_{n+1} \sqrt{\frac{1}{f_a|_{n+1}} \frac{\partial \Theta^{\mathrm{hom}}}{\partial \Theta_a}\Big|_{n+1}}}{\sigma_a^{\mathrm{y}}|_{n+1}} \right)^{m_a} \right)^{q_a} \tag{40}$$

$$\sigma_m^{\mathrm{y}}|_{n+1} = A_m + B_m \left(\bar{\varepsilon}_m^{\mathrm{vp}}|_n + \Delta t \dot{\varepsilon}_m^0 \left(\frac{\bar{\Sigma}|_{n+1} \sqrt{\frac{1}{f_m|_{n+1}} \frac{\partial \Theta^{\mathrm{hom}}}{\partial \Theta_m}\Big|_{n+1}}}{\sigma_m^{\mathrm{y}}|_{n+1}} \right)^{m_m} \right)^{q_m} . \tag{41}$$

Note that the derivatives $\frac{\partial \Theta^{\mathrm{hom}}}{\partial \Theta_a}$ and $\frac{\partial \Theta^{\mathrm{hom}}}{\partial \Theta_m}$ also dependent on X_m and the solution of the system of implicit equations requires iterative methods, which are described in Sect. 3.2. Once the above equations are solved together with Eq. (30) and (38), the viscoplastic and the transformation strain can be updated based on the trial stress and determined quantities according to Eq. (23) and (24).
The use of an implicit integration scheme for the constitutive equations necessitates the computation of the consistent material tangent, which is defined as

$$\mathbb{C}^{\mathrm{t}}|_{n+1} = \left.\frac{\partial \boldsymbol{\Sigma}}{\partial \mathbf{E}}\right|_{n+1} = \mathbb{C} - \mathbb{C} : \mathbb{M}|_{n+1} : \mathbb{C} \, . \tag{42}$$

The tensor $\mathbb{M}|_{n+1}$ takes the form

$$\mathbb{M}|_{n+1} = \frac{1}{3} \Delta_v \left.\frac{\partial f_m}{\partial \boldsymbol{\Sigma}^{\mathrm{trial}}}\right|_{n+1} \otimes \mathbf{I} + \frac{3}{2} \left(\left.\frac{\partial \Delta \bar{G}^{\mathrm{in}}}{\partial \boldsymbol{\Sigma}^{\mathrm{trial}}}\right|_{n+1} \otimes \mathbf{M}|_{n+1} + \Delta \bar{G}^{\mathrm{in}} \left.\frac{\partial \mathbf{M}}{\partial \boldsymbol{\Sigma}^{\mathrm{trial}}}\right|_{n+1} \right) . \tag{43}$$

The derivatives of f_m and $\Delta \bar{G}^{\mathrm{in}}$ with respect to the trial stress tensor are obtained by implicit differentiation of the residual form of Eq. (30) and (38). The differentiation of the normalized stress deviator $\mathbf{M} = \mathbf{S}/\bar{\Sigma}$ is carried out consistent with [16]. Note that the resulting consistent material tangent is unsymmetric due to the mutual coupling between f_m and $\Delta \bar{G}^{\mathrm{in}}$.

3.2 Numerical solution of the nonlinear systems of equations

As mentioned in Sect. 3.1, iterative methods are required the solve the two systems of equations $(\mathrm{r_I}, \mathrm{r_{II}})$, which are given by Eqs. (39) to (41) and Eq. (30) and (38), respectively. Due to the choice of independent variables in the corresponding systems, the staggered

solution procedure shown in Fig. 1 is proposed. In order to avoid iterates that are unphysical due to the irreversible nature of the inelastic processes and may lead to numerical difficulties, the following bounds are introduced (see Tab. 1).

Table 1: Bounds on variables

$0 \leq \Delta\bar{G}^{\text{in}}$	$f_m\|_n \leq f_m\|_{n+1}$
$0 \leq X_m\|_{n+1}$	$\sigma_a^{\text{y}}\|_n \leq \sigma_a^{\text{y}}\|_{n+1}$
$\sigma_m^{\text{y}}\|_n \leq \sigma_m^{\text{y}}\|_{n+1}$	

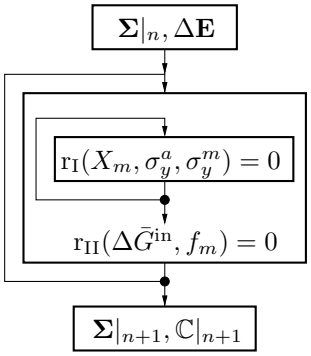

Figure 1: Staggered solution algorithm

As Newton's method is not intended for handling such bounds and truncating the Newton step may result in poor convergence when approaching a bound, an interior global method proposed by Bellavia et al. [8] is used. This method belongs to the group of affine trust-region methods and is able to solve problems of the kind

$$\mathrm{F(x)} = 0 \ , \quad \mathrm{l} \leq \mathrm{x} \leq \mathrm{u} \ , \tag{44}$$

where F is a system of nonlinear equations and x is the vector of independent variables, while l and u denote given lower and upper bounds. As the use of such a method is not commonly employed in the context of constitutive modelling, the method is briefly described. When applying this method to solve Eq. (44), the computed steps are guaranteed to sufficiently reduce the norm $\|\mathrm{F(x)}\|$ and to stay strictly inside the feasible region. This requires the solution of an elliptical trust-region problem

$$\min_{\mathrm{q}} \{ m_k(\mathrm{q}) : \|\mathrm{D}_k \mathrm{q}\| \leq \Delta_k \} \tag{45}$$

at every iteration k, where

$$m_k(\mathrm{q}) = \frac{1}{2}\|\mathrm{F}_k\| + \mathrm{F}_k^{\mathrm{T}}\mathrm{F}'_k\mathrm{q} + \frac{1}{2}\mathrm{q}^{\mathrm{T}}\mathrm{F}'^{\mathrm{T}}_k\mathrm{F}'_k\mathrm{q} \ . \tag{46}$$

The sufficient reduction is ensured by adjusting the step size of q via the trust-region radius Δ_k, while the scaling matrix D_k, which measures the distance of the current iterate to the bound, is used to adapt the current step q in order to generate feasible iterates. According to [8] the method shows quadratic convergence even to solutions on the boundary of the feasible region and is not much more computational expensive than a conventional Newton iteration. Due to these favourable properties, the affine trust-region method is employed in the solution of both systems of equations $(\mathrm{r_I}, \mathrm{r_{II}})$ that arise from the implicit integration of the material model. The interested reader is referred to [8] for convergence proofs and implementation issues.

Table 2: Material parameters

A_a [MPa]	B_a [MPa]	q_a	A_m [MPa]	B_m [MPa]	q_m	a_1	a_4
180	1564	0.83	1429	276	0.86	4.61	0.13
$\bar{g}_0$ $[\frac{mJ}{mm^3}]$	$\bar{g}_1$ $[\frac{mJ}{mm^3}]$	s_g $[\frac{mJ}{mm^3}]$	R_0	R_1	n	β	Δ_v
207	20	178	0.0284	0.0574	2.61	1.4	0.04
M_{s}^{σ} $[°C]$	M_{d} $[°C]$	K [MPa]	G [MPa]	g_0 $[\frac{mJ}{mm^3}]$	g_1 $[\frac{mJ}{mm^3}]$	g_2 $[\frac{mJ}{mm^3}]$	g_3
20	100	123077	77419	330	71.6	0.56	1
σ_a^*	m_a	$\dot{\varepsilon}_a^0$ $[s^{-1}]$	m_m	$\dot{\varepsilon}_a^0$ $[s^{-1}]$	a_2	a_3	
387	30	0.001	40	0.001	0	0	

4 RESULTS

The material model presented in Sect. 2 is applied to describe the deformation behaviour of a newly developed CrMnNi cast TRIP-steel [1]. The model has been calibrated using data from both tensile and compression tests to account for the tension-compression asymmetry included in the model. The mechanical tests were carried out at room temperature under quasistatic loading conditions. Details of the employed parameter identification strategy are given in [17]. The identified parameters are included in the upper half of Tab. 2. Furthermore, the constant parameters listed in the lower half of Tab. 2 are used, which were obtained either by thermodynamical calculation (g_0, g_1, g_2), direct measurement (K, G) or have been assumed as in case of temperature and strain rate dependent material behaviour. In order to evaluate the capabilities of the calibrated model to predict the deformation behaviour under different inhomogeneous triaxial stress states, a series of notched tensile tests has been conducted. The corresponding specimens were manufactured with notch radii $R = \{1, 2, 4, 8\mathrm{mm}\}$. The measurements were accomplished under displacement control at a constant rate of 0.5mm/min employing a servohydraulic test machine MTS Landmark 100. During the test, force and displacement were recorded utilizing the built-in load cell of the test machine and a MTS extensiometer. Additionally, the notch radius and the diameter reduction at the notch root were measured during deformation by an optical extensiometer. Consistent with the experiment, a gauge length $L = 35\mathrm{mm}$, an outer diameter $D = 12\mathrm{mm}$ and a diameter $d = 6\mathrm{mm}$ of the minimum section of the notched tensile specimen were used in the finite element model to simulate the notched tensile tests with the finite element code ABAQUS. Due to the symmetries intrinsic to the problem, only the upper half of the specimen is modeled, employing linear axisymmetrical elements (CAX4). The boundary value problem is depicted in Fig. 2. The displacement in positive z-direction is uniformly prescribed at the top of the specimen according to the experimental procedure. The experimentally determined force displacement curves for different notch radii are shown in Fig. 3 together with the corresponding

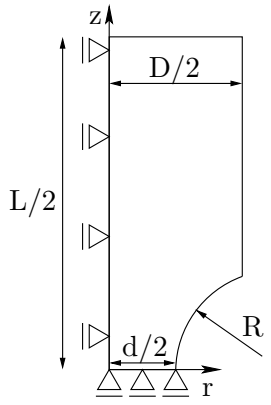

Figure 2: Notched tensile specimen

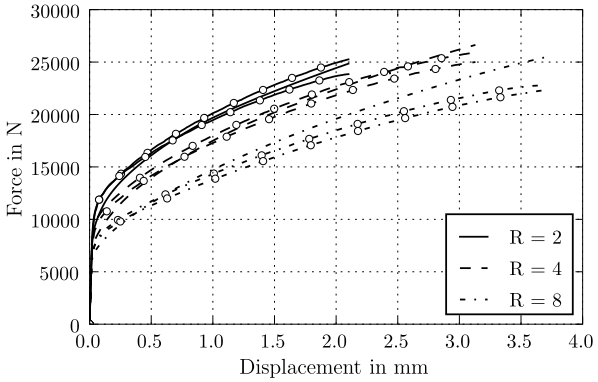

Figure 3: Comparison between experiments (○) and simulation

results of the simulation. Reasonable good agreement between the results from the simulation and the experimental measurements is observed, although the model overestimates the force displacement curve in case of low stress triaxialities. It can be concluded that the model is able to capture the effect of stress triaxiality on the force displacement curve.

5 CONCLUSIONS

In the current paper the implementation of a macroscopic material model for TRIP-steels into the finite element code ABAQUS has been presented. A staggered solution procedure is used to solve the coupled systems of nonlinear equations, which result from the implicit integration of the constitutive model. The computation of infeasible solutions is avoided by applying an affine trust-region approach. The calibrated model is employed to predict the force displacement curve of notched tensile tests. Reasonable good agreement can be observed, if model predictions are compared to experimental results.

ACKNOWLEDGEMENTS

The authors gratefully acknowledge the Deutsche Forschungsgemeinschaft (DFG) for supporting this work carried out in the framework of the Collaborative Research Center TRIP-Matrix composites (SFB 799, C5 and B4).

REFERENCES

[1] Jahn, A. et al., Mechanical properties of high alloyed cast and rolled CrMnNi TRIP steels with varying Ni contents. 05013 (2009), DOI: 10.1051/esomat/200905013.

[2] Martin, S. et al., Investigations on martensite formation in CrMnNi-TRIP steels. 05022 (2009), DOI: 10.1051/esomat/200905022.

[3] Krüger, L. et al., Strain rate and temperature effects on stress-strain behaviour of cast high alloyed CrMnNi-steel. *DYMAT 2009* (2009) 1069-1074 DOI: 10.1051/dy-

mat/2009149.

[4] Cherkaoui, M et al., A phenomenological dislocation theory for martensitic transformation in ductile materials: From micro- to macroscopic description. *Philosophical Magazine* (2008) **88**:3479–3512.

[5] Stringfellow, R. G. et al., A Constitutive Model For Transformation Plasticity Accompanying Strain-Induced Martensitic Transformations In Metastable Austenitic Steels. *Acta Metall. Mater.* (1992) **40**:1703–1716.

[6] Papatriantafillou, I. et al., Constitutive modeling and finite element methods for TRIP steels. *Comput. Method Appl. M.* (2006) **195**:5094–5114.

[7] de Souza Neto, E. A., A simple robust numerical integration algorithm for a power-law visco-plastic model under both high and low rate-sensitivity. *Commun. Numer. Meth. En.* (2004) **20**:1–17.

[8] Bellavia, S. and Morini, B., An interior global method for nonlinear systems with simple bounds. *Optim. Method Softw.* (2005) **20**:453–474.

[9] Needleman, A., On Finite-Element Formulations For Large Elastic Plastic-Deformations. *Comput. Struct.* (1985) **20**:247–257.

[10] Ponte Castañeda, P. and Suquet, P., Nonlinear Composites. *Adv. Appl. Mech.* (1998) **34**:172–302.

[11] Hashin, Z. and Shtrikman, S., Note on a variational approach to the theory of composite elastic materials. *J. Franklin I.* (1961) **271**:336–341.

[12] Olson, G. B. and Cohen, M., Mechanism For Strain-Induced Nucleation Of Martensitic Transformations. *J. Less-Common Met.* (1972) **28**:107–118

[13] Lani, F. et al., Multiscale mechanics of TRIP-assisted multiphase steels: II. Micromechanical modelling. *Acta Mater.* (2007) **55**:3695–3705.

[14] Hughes, T. J. R. and Winget, J., Finite Rotation Effects In Numerical-Integration Of Rate Constitutive-Equations Arising In Large-Deformation Analysis. *Int. J. Numer. Methods Eng.* (1980) **15**:1862–1867.

[15] Aravas, N., On the numerical integration of a class of pressure-dependent plasticity models. *Int. J. Numer. Methods Eng.* (1987) **24**:1395–1416.

[16] Simo, J. C. and Taylor, R. L., Consistent tangent operators for rate-independent elastoplasticity. *Comput. Method Appl. M.* (1985) **48**:101–118.

[17] Prüger S. et al., A material model for TRIP-steels and its application to a CrMnNi cast alloy. *Steel Res. Int.* (2011) accepted for publication.

XI International Conference on Computational Plasticity. Fundamentals and Applications
COMPLAS XI
E. Oñate, D.R.J. Owen, D. Peric and B. Suárez (Eds)

INFLUENCE OF THE PLASTIC POTENTIAL ON THE MECHANICAL RESPONSE OF THERMOPLASTIC COMPONENTS

MARIO A. POLANCO-LORIA[*] AND EINAR L. HINRICHSEN[†]

[*] SINTEF Materials and Chemistry, NO-7465 Trondheim, Norway
email: mario.polanco@sintef.no , http://www.sintef.no

[†] SINTEF Materials and Chemistry
Polymers and Composites Materials, NO-0314, Oslo, Norway
email: einar.hinrichsen@sintef.no , http://www.sintef.no

Key words: Thermoplastics, Computational Plasticity, Plastic potential.

Summary. This paper presents the influence of the plastic potential in the mechanical response of thermoplastic components. This study is based on a recently hyperelastic-viscoplastic constitutive model developed for polymeric materials. Assuming a non-associative plasticity framework different plastic potentials are considered in this study (e.g. isochoric, quasi-linear, parabolic and elliptic). The present model is intended to be used to characterize closer the matrix behavior of polymeric based composite materials under a micro-mechanics framework.

1 THE MBR CONSTITUTIVE MODEL

Polymers are increasingly being used in the transport industry, specially, in structural components related to passengers or pedestrian safety. In this direction, a new hyperelastic-viscoplastic constitutive model for thermoplastics (under isothermal conditions) has been developed by Polanco-Loria et al.[1] (see Fig. 1). The model is a physically-based constitutive model, involving the typical mechanisms of the elastic behavior of polymers, i.e. relative rotation around backbone carbon-carbon bonds and entropy change by un-coiling molecule chains. In addition, viscoplastic flow associated with relative movement between molecules is included. Historically, the development of this model goes back to the work by Haward and Thackray[2] and further developed by Boyce[3] and Boyce et al.[4], who assumed that the total stress was the sum of an inter-molecular and intra-molecular contribution denoted Part A and Part B, respectively.

Shortly, the elastic response of part A is described by a compressible Neo-Hookean material where the Cauchy stress tensor reads:

$$\boldsymbol{\sigma}_A = \frac{1}{J_A^e}\left[\lambda \ln J_A^e \,\mathbf{I} + \mu(\mathbf{B}_A^e - \mathbf{I})\right] \tag{1}$$

In addition, yield condition assumes a pressure-sensitivity criterion based on the work of Raghava et al.[5]

$$\bar{\sigma}_A = \frac{(\alpha-1)I_{1A} + \sqrt{(\alpha-1)^2 I_{1A}^2 + 12\alpha J_{2A}}}{2\alpha} \tag{2}$$

In order to control the plastic dilatation, a non-associative flow rule is introduced where a Raghava-like plastic potential is defined as

$$g_A = \frac{(\beta-1)I_{1A} + \sqrt{(\beta-1)^2 I_{1A}^2 + 12\beta J_{2A}}}{2\beta} \geq 0 \tag{3}$$

With respect to the plasticity response of Part A (see Fig.1) the model was enhanced to include isotropic hardening/softening behavior according to Voce's saturation model[6]:

$$R = \left(\sigma^{sat} - \sigma_T\right)\left[1 - \exp^{-H\bar{\varepsilon}^p}\right] \tag{4}$$

where, R is the stress hardening level. The hardening/softening modulus is represented by H, the saturation and yield tensile stress by σ^{sat} and σ_T, respectively. Hence, for the hardening case $\sigma^{sat} > \sigma_T$ while for the softening case $\sigma^{sat} < \sigma_T$.

The part B includes the deformation gradient $\mathbf{F}_B = \mathbf{F}_A = \mathbf{F}$, representing the network orientation. The network resistance is assumed to be hyperelastic. The Cauchy stress-stretch relation is used as the original definition of Boyce et al. [4]:

$$\boldsymbol{\sigma}_B = \frac{1}{J}\left[\frac{C_R}{3}\frac{\sqrt{N}}{\bar{\lambda}}\mathcal{L}^{-1}\left(\frac{\bar{\lambda}}{\sqrt{N}}\right)(\mathbf{B}_B^* - \bar{\lambda}^2\mathbf{I})\right] \tag{5}$$

The constitutive model requires 11 parameters to be identified:

- **Spring A** represents the initial elastic stiffness with a Neo-Hookean formulation. There are two elastic coefficients E (Young's modulus) and ν (Poisson's ratio).
- **Friction element A** models the yielding process with pressure dependency and a non-associative flow rule. Three parameters in this friction element are needed: the uniaxial yield tensile stress σ_T, the pressure sensitive parameter α and the volumetric

plastic strain control parameter β. The hardening/softening behaviour necessitates two additional terms (see Eqn. 1): H and σ^{sat}.

- **Dashpot A** is included to represent the rate dependence of the material. The visco-plastic multiplier uses a linear (log scale) strain rate law characterized by two parameters: the reference strain rate $\dot{\varepsilon}_0$ and the strain rate coefficient C.
- **Spring B** represents the elongation of the molecule chains, here modeled with a hyperelastic law. Only the distortional stress-stretch relation is used here where two hardening coefficients C_R and N need to be identified.

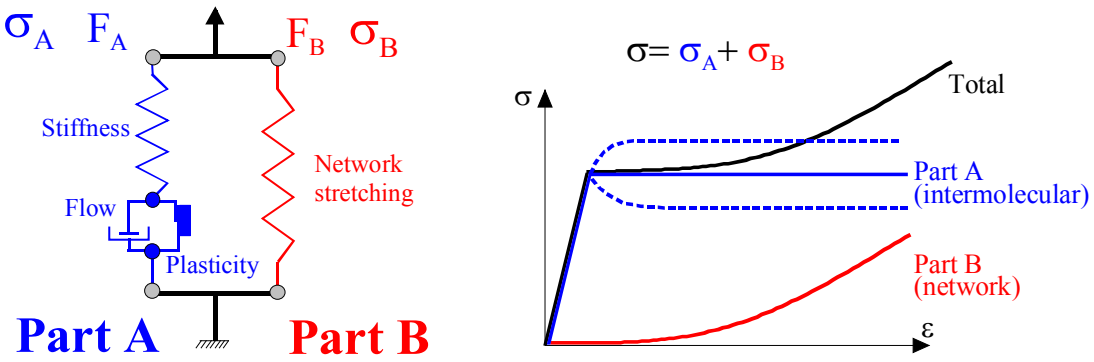

Figure 1: Constitutive model with inter-molecular (A) and network (B) contributions

A complete description of the parameter identification process has been proposed elsewhere[7]. The model will be referred here as the modified Boyce-Raghava (MBR) model.

2 INFLUENCE OF THE PLASTIC POTENTIAL

The original work[1] proposes a non-associative plastic potential (see Eqn. 3) to handle the volumetric plastic flow, commonly observed in polymers. The apparently drawback of such proposal is the dilation behavior under compressive stresses. For this reason, a closer study on the importance of such plastic potential is considered here. In addition to the classical isochoric assumption three different potentials, all of them giving the *same volumetric* plastic contribution, have been considered: quasi-linear, parabolic (Eqn. 3) and elliptic. All of them can be calibrated to give the same plastic volumetric response in uniaxial tension. Qualitatively the quasi-linear model predicts less volumetric plastic strain than the parabolic and elliptic in the high triaxial state of stress. Only the elliptic model is capable of predicting compaction for negative pressures. This model however, requires an additional parameter. An illustration of the plastic potentials studied is indicated in Figure 2.

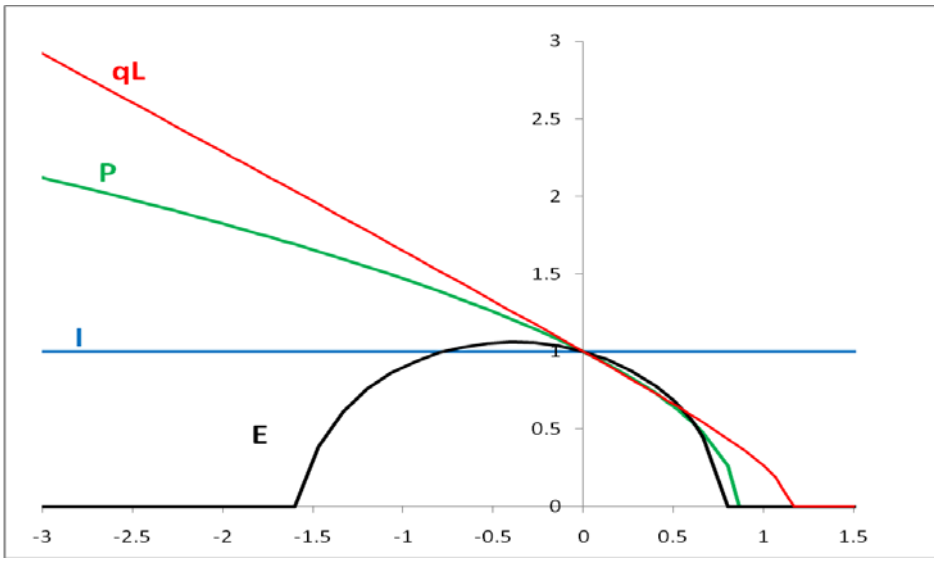

Figure 2: Different plastic potentials considered

3 EXPERIMENTAL DATA USING A PP COPOLYMER MATERIAL

3.1 Introduction

The experimental results of a commercial impact-modified PP used for injection molded automotive exterior parts are used for illustration purposes[7]. This PP compound is a 20 % mineral filled and rubber modified. A complete description of the parameter identification process was proposed by Polanco-Loria et al.[7] and the predictions of the constitutive model (assuming the original parabolic law) are presented in Figure 3. The material parameters assumed for the PP copolymer are indicated in Table 1.

Table 1: Material parametrs for the PP copolymer

E MPa	ν	C	$\dot{\varepsilon}_0$ 1/s	σ_T MPa	σ_{Sat} MPa	H MPa	C_R MPa	N	β	α
1500	0.4	0.08	$2\text{x}10^{-4}$	14.0	11.5	8.0	1.60	5.0	1.47	1.17

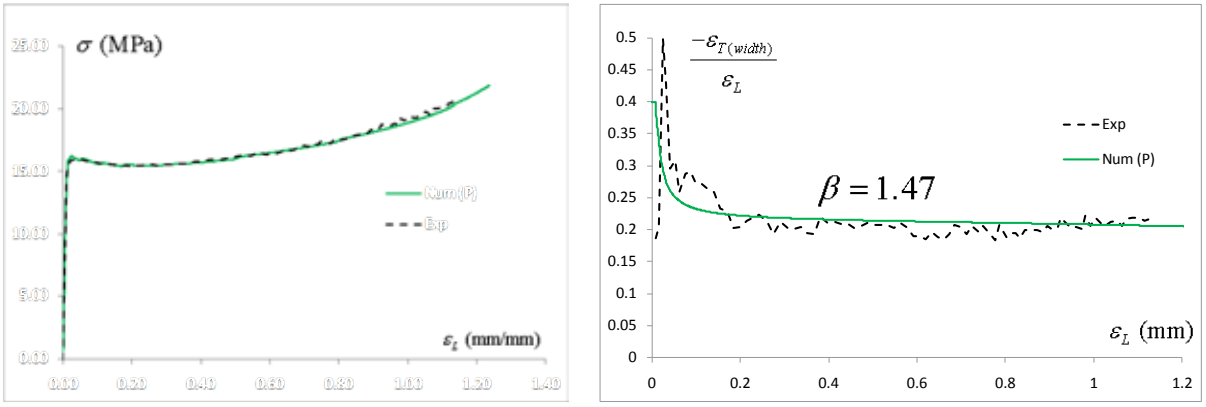

Figure 3: Uniaxial tensile stress-strain response and prediction of the "Poisson" ratio variation

3.2 Material calibration for the quasi-linear, elliptic and isochoric plastic flow rules

The material identification procedure was applied to the quasi-linear, elliptic and isochoric assumptions based on the experimental tension test results of Fig. 3. As one can expect, the stress-strain response of these three models are similar, as illustrated in Fig 4. In this figure we included the numerical and experimental response of the isochoric model. The differences between these responses clearly indicates damage activity in form of void grow and crazes formation.

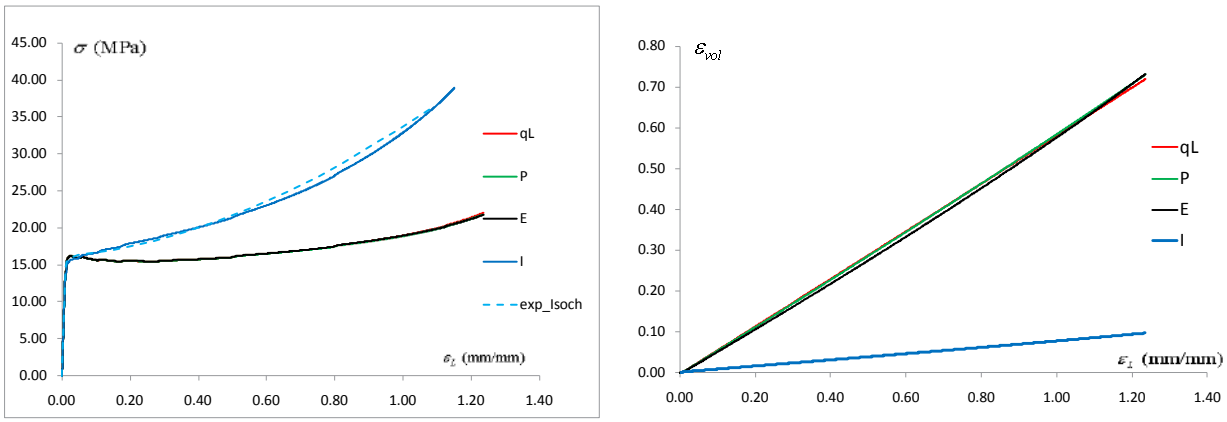

Figure 4: Uniaxial tensile stress-strain response and prediction of the volumetric strains

The total volumetric strain response predicted by the models is also indicated in figure 4. Once again, the volumetric response of the parabolic, quasi-linear and elliptic is similar. Large differences in the volumetric strain response between these models and the isochoric one (e.g. only predicts elastic strains) are observed (bleu line).

Now, a more reliable comparison can be performed to assess the influence of the plastic potential in the mechanical behavior of thermoplastic components.

4 CONCLUSIONS

- The study of the plastic potential on the mechanical response of thermoplastic components has been proposed.
- In addition to the isochoric assumption three potentials were considered: quasi-linear, parabolic and elliptic. With proper calibration all of them give the same response under uniaxial tension loading.
- Several examples of thermoplastic components will be given at the oral presentation (e.g. beam and plates)
- The present model is part of a new development to characterize closer the matrix behavior of polymeric based composite materials under a micro-mechanics framework.

REFERENCES

[1] M. Polanco-Loria, A.H. Clausen, T. Berstad, and O.S Hopperstad "Constitutive model for thermoplastics with structural applications" International Journal of Impact Engineering, 37, 12 (2010).

[2] R.N. Haward and G. Thackray, "The Use of a Mathematical Model to Describe Isothermal Stress-Strain Curves in Glassy Thermoplastics". Proceedings of the Royal Society of London. Series A. Mathematical and Physical Sciences, 302, 1471 (1968).

[3] M.C. Boyce, "Large inelastic deformation of glassy polymers", in Department of Mechanical Engineering. Massachusetts Institute of Technology: Boston, USA (1986).

[4] M.C. Boyce, S. Socrate, and P.G. Llana, "Constitutive model for the finite deformation stress-strain behavior of poly(ethylene terephthalate) above the glass transition". Polymer, 41, 6 (2000).

[5] R. Raghava, R.M. Caddell, and G.S.Y. Yeh, "The macroscopic yield behaviour of polymers". Journal of Materials Science, 8, 2 (1973).

[6] Polanco-Loria M. and Clausen A.H., "An inverse modelling methodology for parameters identification of thermoplastic materials" Keynote Lecture. Proceedings of 23th Nordic Seminar on Computational Mechanics, NSCM-23, Editors: A. Eriksson and G. Tibert. KTH, Royal Institute of Thechnology. ISSN 0348-467X; Stockholm, Sweden, 21-22 October, (2010).

[7] M. Polanco-Loria, H. Dayan and F. Grytten "Material parameters identification: An inverse modelling procedure applicable for thermoplastic materials" accepted for publication in Polymer Engineering Science (2011).

XI International Conference on Computational Plasticity. Fundamentals and Applications
COMPLAS XI
E. Oñate, D.R.J. Owen, D. Peric and B. Suárez (Eds)

JOHNSON-COOK PARAMETER IDENTIFICATION FROM MACHINING SIMULATIONS USING AN INVERSE METHOD

AVIRAL SHROT* AND MARTIN BÄKER†

*Technische Universität Braunschweig
Institut für Werkstoffe
Langer Kamp 8, 38106 Braunschweig, Germany
e-mail: a.shrot@tu-bs.de

†Technische Universität Braunschweig
Institut für Werkstoffe
Langer Kamp 8, 38106 Braunschweig, Germany
e-mail: martin.baeker@tu-bs.de

Key words: Machining simulation, Johnson-Cook, Inverse determination

Abstract. The Johnson-Cook model is a material model which has been widely used for simulating the chip formation processes. It is a simple 5 parameter material model which predicts the flow stress at large strains, strain-rates and at high temperatures. These parameters are usually identified by determining the flow stress curves experimentally, and then using curve fitting techniques to find the optimal parameters to describe the material behaviour. However the state-of-the-art experimental methods can only rely on data obtained from strains of up to 50% and strain-rates of the order of 10^3 per second, whereas in machining processes strains of more than 200% are reached at strain-rates of the order of 10^6 or more. Therefore, the parameters obtained at much milder conditions have limited applicability when simulating machining.

In this paper an inverse method of material parameter identification from machining simulations is described. It is shown that by using the observables of a machining process such as the chip shape and cutting forces, the underlying material parameters can be identified. In order to achieve this, a finite element model of the machining process is created and simulation is carried out using a known standard parameter set from literature. The objective of the inverse method is to reidentify this set by using the chip shape and cutting forces. An error function is created using the non-overlap area of the chip shapes and the difference in the cutting forces. The Levenberg-Marquardt algorithm is used to minimise the error function.

It has been shown before that multiple sets of Johnson-Cook parameter sets exist which might give rise to indistinguishable chip shapes and cutting forces. In order to identify the

parameter set uniquely, simulations are performed at widely varying cutting conditions such as differing rake angles, cutting speeds and non-adiabatic conditions. Thus, material parameters which represent the material behaviour over a wide range can be identified.

1 INTRODUCTION

In a conventional machining process the material from a workpiece is removed using a harder tool material. Simulation of the material removal process by machining has been extremely challenging due to the complex character of the process. The removed material undergoes large plastic deformation (strains of more than 200%), at very high strain rates ($\sim 10^6$ s^{-1} or more) and is accompanied by a temperature rise of hundreds of degrees in the deformation zone. A number of material models have been suggested which take into account the before mentioned issues. Identification of material parameters for such models is usually done by material tests at varying strains, strain rates and temperatures. Split Hopkinson Bar tests are widely used for conducting high strain rate tests. The data obtained from such tests are used for parameter identification using curve fitting techniques. However due to physical constraints the material is usually deformed only upto 50% of plastic strain and at strain rates of the order of $\sim 10^3$ - 10^4 s^{-1}. Therefore when simulating the chip formation process, strains and strain rates are extrapolated over several orders of magnitudes leading to erroneous simulation results.

The issue of material parameter determination for machining process has been addressed by different researchers. Jaspers and Dautzenberg [1] had proposed using Split Hopkinson Bar data for determining material parameters. However, the shortcomings of this method have been discussed in the previous paragraph. The approach of Tounsi et al.[2] and Shatla et al. [3] depends on using a theoretical model for estimating the material parameters. Howeve,r the problem with this approach is that theoretical models are difficult to verify under the extreme conditions of large strains, strain rates and high temperatures. Another problem in such an approach is that material parameters can be varied to obtain a good match between the simulation results and experiments for a particular set of cutting conditions. However, when the cutting conditions are varied widely, the results fail to match outside the domain where they have been explicitly matched.

In this paper a method for inverse determination of material parameters is proposed. In Section 2 the Johnson-Cook material model is briefly described. In Section 3 the inverse identification problem is explained along with the description of the error function to be minimised and the finite element model that is used. The results are presented in Section 4. Finally conclusions are drawn in Section 5 and the line of future work is also suggested.

2 JOHNSON-COOK MATERIAL MODEL

The Johnson-Cook Model [4] is a five parameter material model which is used to describe material behaviour over a large range of strains, strain rates and temperatures.

Due to its simplicity and the low number of free parameters, this model is widely used in machining simulations. The flow stress σ is expressed as

$$\sigma = \underbrace{(A + B\varepsilon^n)}_{Elasto-Plastic\,term} \underbrace{\left[1 + C \ln\left(\frac{\dot{\varepsilon}}{\dot{\varepsilon}_0}\right)\right]}_{Viscosity\,term} \underbrace{\left[1 - \left(\frac{T - T_{room}}{T_{melt} - T_{room}}\right)^m\right]}_{Thermal\,softening\,term} \tag{1}$$

where ε is the plastic strain, $\dot{\varepsilon}$ is the strain rate, $\dot{\varepsilon}_0$ is the reference strain rate. T is the temperature of the material, T_{melt} is the melting point of the material and T_{room} is the room temperature. The empirical constants are as follows: A is the yield stress, B is the pre-exponential factor, C is the strain rate factor, n is the work-hardening exponent and m is the thermal-softening exponent.

3 INVERSE IDENTIFICATION PROBLEM

The cutting force, chip shape, chip temperature etc are observables in a machining process. These quantities are a function of the material behaviour and the cutting conditions. Using finite element simulations and keeping the cutting conditions identical to the machining experiment, it might be possible to inversely determine the material parameters. In order to test this hypothesis, a standard material parameter set is inversely reidentified using machining simulations. A standard simulation is done using a material parameter set from literature and while keeping the cutting conditions constant, test simulations are carried out in order to identify the standard parameter set. This methodology was also adopted because this way it was possible to keep the cutting conditions the same in case of standard simulations and the test simulations.

The material parameters for the test simulations were systematically varied during the inverse identification process. The inverse identification was conducted in two stages where the goal is to minimise the error function which is expressed as a sum of squares of non-linear functions. In the first optimisation stage the Levenberg-Marquardt algorithm was used and the converged set from this stage is used as the starting set during the second stage for which the Simplex algorithm is used. In a Levenberg-Marquardt algorithm, the parameters are changed in the direction of the steepest descent which is determined by evaluating a Jacobian. The amount of variation in this direction is determined by a damping parameter which is reduced during the course of the optimisation process so as to have a faster convergence and is increased when close to the minimum so that the steps become smaller and the minimum is not overstepped. In case of the Simplex algorithm, a simplex crawls towards the minimum using a set of reflection, expansion, contraction and reduction steps. An exhaustive explanation of the two algorithms can be found in literature [5, 6, 7].

3.1 Error Function

The aggregate error function takes into account the chip shape and the cutting force. The area of non-overlap between two chips is used as a measure of the chip shape error. The difference in the cutting force between the standard case and the test case is the measure of the cutting force error. In order to find the chip shape error, the standard chip and the test chip are superimposed and the region of interest where non-overlap is to be found is bound by a window. This region is then discretised by a number of horizontal lines. The intersection of the horizontal lines with the chip outlines is found out which gives the length of the line intercepted between the chip outlines. Using the distance between the discretising lines and the intercepted length, the elemental area of non-overlap is found which is summed over all the elemental areas to give the chip overlap error (Figure 1). The chip overlap error and the cutting force error are combined using a weighting factor w, which is used to balance the contribution of the two factors in the overall optimisation, to give an aggregate error function $\phi_i(\mathbf{x})$ (Equation 2). The value of w used in this paper is $1/500$ mm^2 N^{-1}. The error function $\chi^2(\mathbf{x})$ is obtained by summing the square of the aggregate error functions over all the observations (Equation 3).

$$\phi_i(\mathbf{x}) = \left|e_i^A(\mathbf{x})\right| + w.\left|e_i^F(\mathbf{x})\right| \tag{2}$$

$$\chi^2(\mathbf{x}) = \frac{1}{2}\sum_{i=1}^{N}\phi_i^2(\mathbf{x}) = \frac{1}{2}\sum_{i=1}^{N}\left(\left|e_i^A(\mathbf{x})\right| + w.\left|e_i^F(\mathbf{x})\right|\right)^2 \tag{3}$$

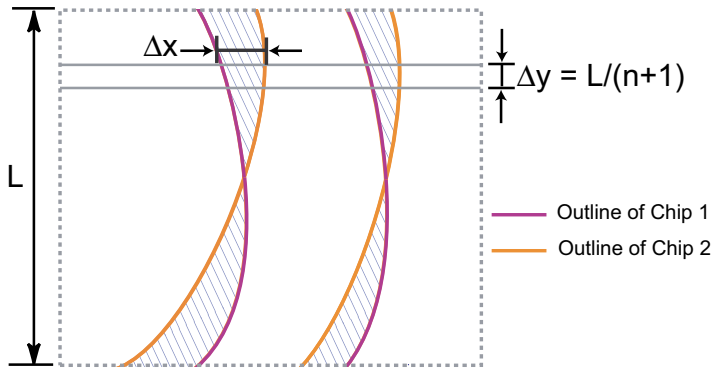

Figure 1: Estimation of chip overlap error. The region of interest is discretised by n lines.

3.2 Finite Element Model

The two-dimensional adiabatic finite element model for machining simulation was made using the commercial finite element software ABAQUS 6.9-1 and consisted of a rigid tool meshed with R2D2 elements and a workpiece meshed with four node CPE4R elements

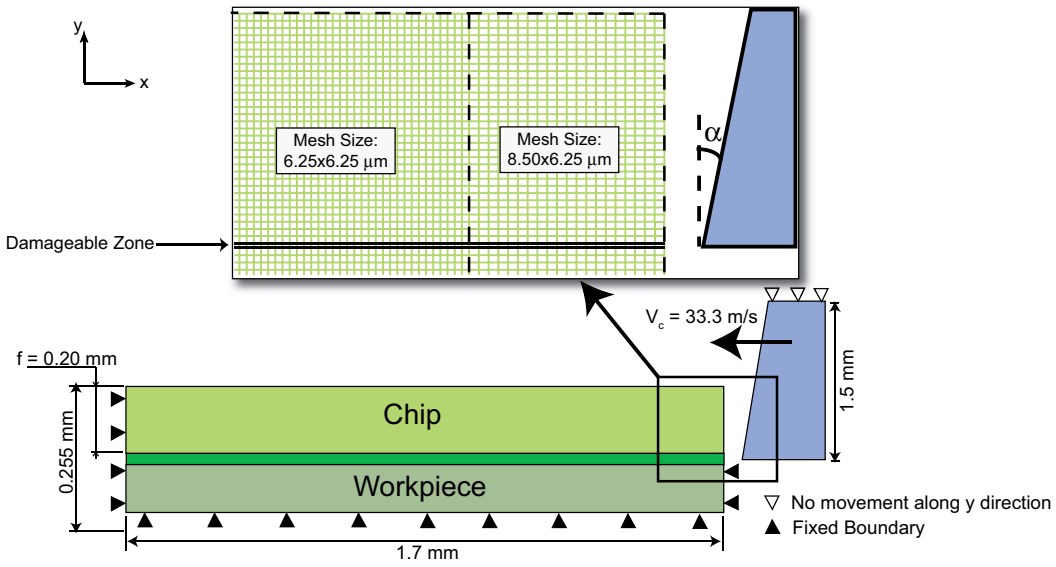

Figure 2: Finite Element Model showing the boundary conditions and the non uniform meshing

(Figure 2). The workpiece was partitioned into three regions such that the top region formed the chip, the bottom region the machined workpiece and the intermediate region comprised of damageable elements which were removed from the simulation after a critical shear strain of 2.0 is exceeded. The cutting speed is fixed at 33.3 m/s and the simulation is conducted for 0.040 ms during which 500 frames are recorded. Friction is neglected throughout the simulation. In order to ensure that the optimisation takes into account a wider range of cutting conditions, two different values of rake angles were used, viz. 1° and 10°. The material properties used for the simulation have been shown in Table 1 and Table 2. The thermal properties of the material have been taken from [8].

$$C_P = 92.78 + 0.7454T + \frac{12404 \times 10^3}{T^2} \mathrm{J\,kg^{-1}\,K^{-1}} \tag{4}$$

Table 1: Material properties for HY 100 steel [9, 10, 11]

Density [$\mathrm{kg\,m^{-3}}$]	7860
Young's Modulus [GPa]	205
Poisson's Ratio	0.28

Table 2: Johnson-Cook parameters for HY 100 steel [9, 10, 11] used in the standard simulation

A [MPa]	B [MPa]	C	m	n	T_{melt} [K]	T_{room} [K]	$\dot{\varepsilon}_0$ [$\mathrm{s^{-1}}$]
316	1067	0.0277	0.7	0.107	1500	300	3300

The elements on the workpiece after coming in contact initially with the tool get badly crushed thereby reducing the characteristic length of such elements. This in turn reduces the stable time increment and thus increases the total simulation time. As a solution to this problem, the first 10% length of the workpiece is meshed with rectangular elements of dimensions 8.5 × 6.25 µm. The rest of the workpiece is meshed with square elements of dimensions 6.25 × 6.25 µm. The workpiece is finely meshed with 32 elements across the uncut chip thickness. A C++ code is written to read the deformed chip shape coordinates and the cutting force values. The values thus obtained are used with the minimisation algorithms which are available in the GNU Scientific Library [12]. From the two simulations which are conducted for the different rake angle values 15 observations, from frames 486 to 500, are taken from each to evaluate the error function.

4 RESULTS AND DISCUSSIONS

In order to keep the problem moderately difficult, only 3 Johnson-Cook parameters, viz. A, B and n, are reidentified. Three different starting parameter sets are chosen for inverse identification. The first set is reasonably close to the standard parameter set, the second and the third sets are far from the standard parameter set (refer Table 3).

Table 3: Standard and Starting parameter sets

	A	B	n
Standard Set	316	1067	0.107
Starting Set Case 1	250	900	0.020
Starting Set Case 2	800	50	0.400
Starting Set Case 3	50	50	0.400

For the first stage of optimisation the Levenberg-Marquardt algorithm is chosen as it gives faster convergence towards the standard set. Transformed optimisation parameters are used as they were found to give better convergence [13].

4.1 Optimisation parameters

During a high speed machining process the material heats up due to the plastic work done. Since the process is very fast, the heat cannot be conducted away from the shear zone sufficiently quickly. The effective material behaviour due to the continuous heating of the material can be expressed by using adiabatic stress-strain curves, which can be drawn after taking into account the adiabatic heating of the material. The adiabatic stress-strain curves can be used to explain the chip formation process [14] and therefore they can also aid in determining the optimisation parameters for inverse determination.

Johnson-Cook parameters A and B can be varied from the standard values A_s and B_s in order to estimate the deviations between the corresponding adiabatic stress-strain

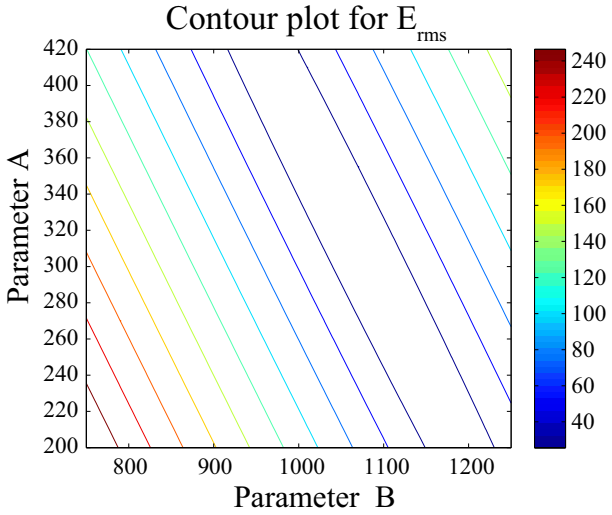

Figure 3: Contour plot for E_{rms}

curves. The root mean squared error (Equation 5) between the curves expressed as

$$E_{rms}(A,B) = \frac{||\sigma_{adia}(A,B) - \sigma_{adia}(A_s,B_s)||}{\sqrt{M}} \tag{5}$$

is a measure of such deviations. Here $\sigma_{adia}(A,B)$ is the set of points lying on the adiabatic stress-strain curve from parameters A and B, A_s and B_s are the target Johnson-Cook parameters and M is the total number of points. $||\bullet||$ is the Euclidean norm.

On plotting E_{rms} w.r.t parameters A and B, a valley containing the minimum is seen to run in the direction of $(A-B)$ (Figure 3). Consequently the direction $(A+B)$ is the direction of steepest ascent. New parameters K and L are defined such that

$$K = A + B \tag{6a}$$

$$L = A - B \tag{6b}$$

Using the transformed parameters (Equations 6a and 6b), the Johnson-Cook equation can be rewritten as

$$\sigma = \left(\frac{K+L}{2} + \frac{K-L}{2}\varepsilon^n\right) f(\dot{\varepsilon},T) \tag{7}$$

where

$$f(\dot{\varepsilon},T) = \left[1 + C\ln\left(\frac{\dot{\varepsilon}}{\dot{\varepsilon}_0}\right)\right]\left[1 - \left(\frac{T-T_{room}}{T_{melt}-T_{room}}\right)^m\right] \tag{8}$$

The effectiveness of using such modified optimisation parameters has been shown in earlier papers [13, 15].

4.2 Simulation results

The starting parameter sets for the inverse identification have been shown in Table 3. In the first stage of optimisation Levenberg-Marquardt algorithm was used. The initial chip shapes and cutting forces are different from the standard chip shapes and cutting forces (specially in Case 3). The chip shapes at the end of each optimisation stage has been shown in Figure 4 and Figure 5. The standard chip is represented in green and the test chip in red. At the end of the first stage the chip shapes (Figure 4(a), 4(b) and 5(a), 5(b)) and cutting forces (Figure 6(a) and 6(b)) show substantial improvement. This was found to work consistently well with all the three cases. The test adiabatic stress-strain curves are also seen to come closer towards the standard adiabatic stress-strain curve (Figure 7(a), 7(b) and 7(c)). At the end of the first stage the solution could not be further improved by using the Levenberg-Marquardt algorithm.

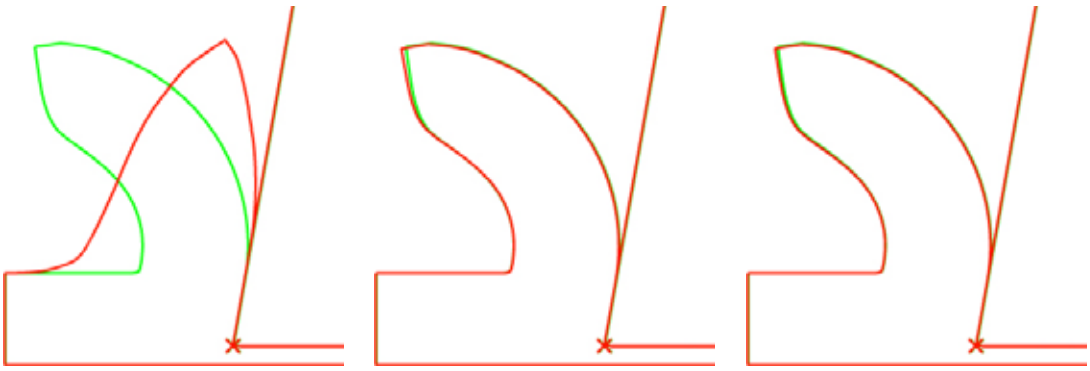

(a) Starting set (b) Stage 1 (c) Stage 2

Figure 4: Chip shapes (rake +10°) at different stages of optimisation for Case 3

In order to further improve the solution and checking the feasibility of reidentifying the parameters robustly, a second stage of optimisation was carried out using the downhill simplex algorithm. At the end of the optimisation, the chip shapes (refer Figure 4(c) and 5(c)), the cutting forces and the adiabatic stress-strain curves were found to match exactly (Figure 7(a), 7(b), 7(c)). Despite having a near perfect match of chip shapes, cutting forces and adiabatic stress-strain curves, the converged Johnson-Cook parameter sets are not unique [16]. Some non-unique parameter sets can be eliminated by using wide ranges of cutting conditions.

5 CONCLUSION

In this paper a two stage inverse material parameter determination method was discussed. An error function was defined by taking into account the chip shape and the cutting force. Levenberg-Marquardt and Downhill Simplex methods were used for the minimisation of the error function. The two stage optimisation process is found to be

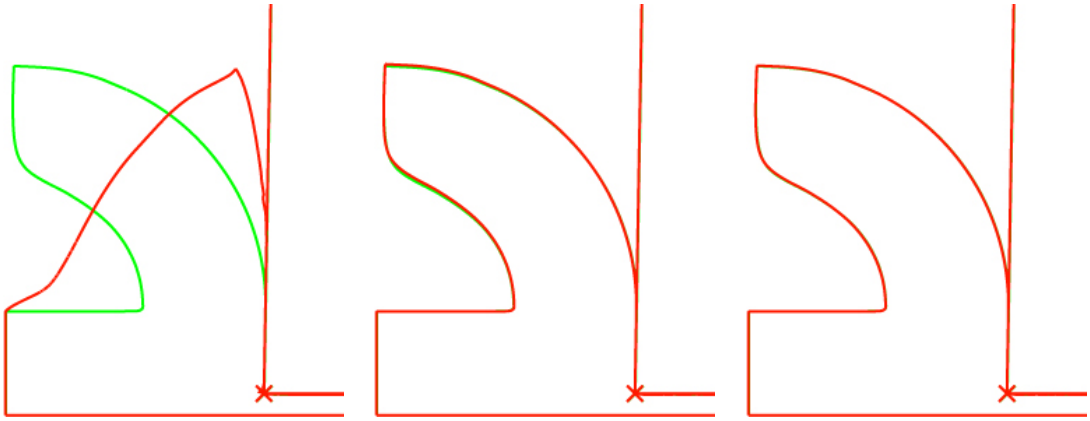

(a) Starting set (b) Stage 1 (c) Stage 2

Figure 5: Chip shapes (rake 0°) at different stages of optimisation for Case 3

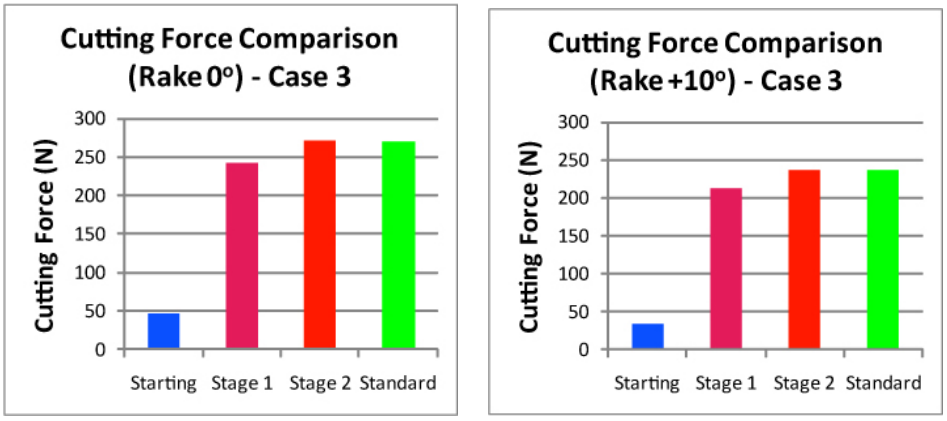

(a) Rake angle = 0° (b) Rake angle = 10°

Figure 6: Cutting force at the end of different stages of optimisation

Table 4: Converged parameter sets at the end of stage 1 and stage 2

	Case 1			Case 2			Case 3		
	A	B	n	A	B	n	A	B	n
Stage 1	287.11	935.36	0.080	943.6	435.6	0.306	650.6	549.3	0.151
Stage 2	449.4	943.9	0.126	942.4	445.3	0.309	707.7	684.4	0.180

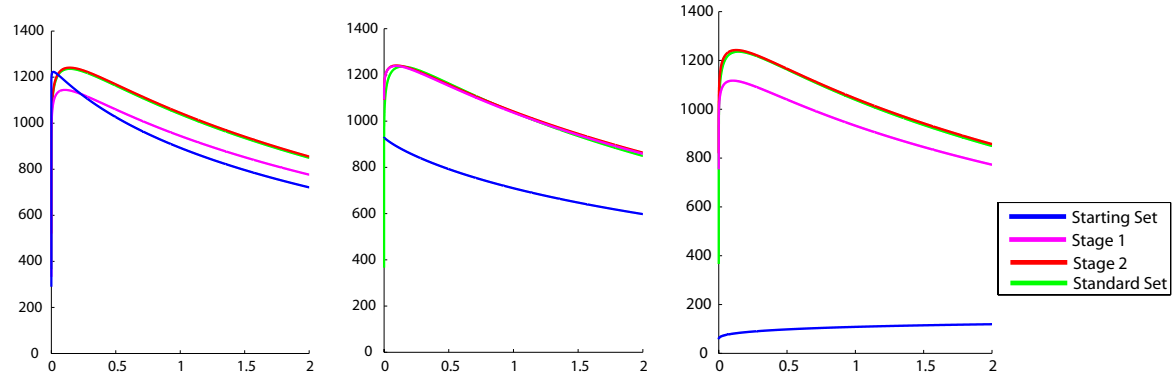

(a) Case 1 (b) Case 2 (c) Case 3

Figure 7: Adiabatic stress-strain curves at different stages of optimisation

robust as the original chip shape and cutting force can be reidentified after starting from substantially different initial parameter sets. It is also observed that after optimisation, the adiabatic stress-strain curve of the converged parameter set matches that of the standard parameter set. It was also observed that the converged parameter sets were not unique.

Thus using inverse identification techniques, it is possible to identify material parameters. In order to eliminate some of the non-unique parameter sets, the cutting conditions must be varied widely. Further work must be done in order to find the good search directions which lead to quicker identification of material parameters. Such improved optimisation strategies can substantially reduce the computational costs.

6 ACKNOWLEDGEMENTS

The research leading to these results has received funding from the European Union Seventh Framework Programme (FP7/2007-2013) under grant agreement No. PITN-GA-2008-211536, project MaMiNa.

REFERENCES

[1] Jaspers, S. P. F. C., Dautzenberg, J. H., Material behaviour in conditions similar to metal cutting: flow stress in the primary shear zone, *Journal of Materials Processing Technology*, (2002), **122**, Issues 2-3, pp 322-330.

[2] Tounsi, N., Vincenti, J., Otho, A., Elbestawi, M. A., From the basic mechanics of orthogonal metal cutting toward the identification of the constitutive equation, *International Journal of Machine Tools and Manufacture*, (2002), **42**, Issue 12, September 2002, pp. 1373-1383.

[3] Shatla, M., Kerk, C., Altan, T., Process modeling in machining. Part I: determination of flow stress data, *International Journal of Machine Tools and Manufacture*, (2001),

41, Issue 10, Pages 1511-1534.

[4] Johnson, G.R., Cook, W.H., A constitutive model and data for metals subjected to large strains, high strain rates and high temperatures, *In: 7th International Symposium on Ballistics* (1983), p. 514.

[5] Levenberg, K., A method for the solution of certain nonlinear problems in least squares, *The Quarterly of Applied Mathematics*, (1944), **2**, p. 164.

[6] Marquardt, D., An algorithm for least-squares estimation of nonlinear parameters,*Journal of the Society for Industrial and Applied Mathematics*, (1963),**11**, No. 2., p. 431.

[7] Nelder, J. A. and Mead, R., A Simplex Method for Function Minimization, *The Computer Journal*, (1965), **7**, pp. 308-313.

[8] Taljat, B.,Radhakrishnan, B., Zacharia, T., Numerical Analysis of GTA Welding Process with Emphasis on Post-Solidification Phase Transformation Effects on Residual Stresses *Materials Science and Engineering A*, (1998) **246**, Issues 1-2, p. 45.

[9] Batra, R.C., Kim, C.H., Effect of viscoplastic flow rules on the initiation and growth of shear bands at high strain rates, *Journal of the Mechanics and Physics of Solids*, (1990) **38**, Issue 6, p. 859.

[10] Goto, D.M., Bingert, J.F., Chen, S.R., Gray, G.T., Garrett, R.K., The Mechanical Threshold Stress Constitutive-Strength. Model Description of HY-100 Steel, *Metallurgical and Materials Transactions A*, (2000), **31**, issue 8, p. 1985.

[11] Durrenberger, L., Molinari, A., The Mechanical Threshold Stress Constitutive-Strength. Model Description of HY-100 Steel, *Experimental Mechanics*, (2009), **49**, Issue 2 , p. 247.

[12] Press, W.H., Teukolsky, S.A., Vetterling, W.T., Flannery, B. P., *Numerical recipes in C (2nd ed.): the art of scientific computing* (1992), Cambridge University Press, New York, USA.

[13] Shrot, A. and Bäker, M., How To Identify Johnson-Cook Parameters From Machining Simulations, *AIP Conference Proceedings*, (2011), **1353**, pp. 29-34.

[14] Bäker, M. *Finite Element Simulation of Chip Formation*, (2004), Shaker Verlag, Aachen.

[15] Shrot, A. and Bäker, M., Inverse Identification of Johnson-Cook Material Parameters from Machining Simulations, *Advanced Materials Research*, (2011),**223**, pp. 277-285.

[16] Shrot, A. and Bäker, M., Is it possible to identify Johnson-Cook law parameters from machining simulations?,*International Journal of Material Forming*, (2010),**3**, No. 0., p. 443.

XI International Conference on Computational Plasticity. Fundamentals and Applications
COMPLAS XI
E. Oñate, D.R.J. Owen, D. Peric and B. Suárez (Eds)

PLASTIC TORSIONAL ANALYSIS OF STEEL MEMBERS

YONG-LIN PI[*] AND MARK ANDREW BRADFORD[†]

[*]Centre for Built Infrastructure Research
School of Civil and Environmental Engineering
University of Technology, Sydney
City Campus 2007, NSW, Australia
e-mail: YongLin.Pi@uts.edu.au, web page: http://www.uts.edu.au

[†]Centre for Infrastructure Engineering and Safety
The University of New South Wales
UNSW Sydney 2052, NSW, Australia
e-mail: m.bradford@unsw.edu.au, web page: http://www.unsw.edu.au

Key words: Plastic Torsion, Steel, Collapse, Analysis.

Summary. A plastic torsional analysis of structural steel I-section members subject to torsion is presented in this paper. A method of plastic torsional analysis that is much simpler than elastic analysis is proposed, and it is validated against results obtained from advanced computational plastic models. The load factor at plastic collapse is obtained from the sum of the independent load factors for uniform-torsion plastic collapse and warping-torsion plastic collapse. The proposed plastic torsional analysis allows a method of plastic design to be used for torsion that is much simpler and more economical than first yield design. The use of plastic analysis and design will facilitate the design of steel torsion members and lead to more economical structures.

1 INTRODUCTION

Despite their importance, torsional actions are rarely considered in the design of steel structures, because of the difficulty in analysing them. Torsion in a thin-walled steel member is resisted by a combination of the resistance to uniform torsion developed by shear stresses, and the resistance to warping torsion developed by equal and opposite flange bending and shear actions. While an elastic theory for combining these two torsional actions is well developed, its solutions are sufficiently difficult to discourage its use in routine design.

Elastic analysis can be used for first-yield designs. However, this is likely to be extremely conservative, not only because of the significant difference between first yield in a cross-section and its full plasticity, but also because of the unaccounted for but significant reserve of strength. This situation contrasts strongly with that in the design braced steel beams, where the use of plastic analysis not only simplifies the analysis of redundant beams, but also allows due account to be taken of both the difference between first yield and full plasticity, and of the plastic redistribution as the collapse mechanism forms.

The results of advanced computational elastic-plastic analyses reported by Pi and Trahair[1, 2] and Pi et al.[3] have validated a simple method of predicting plastic torsional collapse. In this

method, the full plastic collapse capacities of a member in torsion are evaluated separately for uniform and warping torsion, and then added together. This method allows a direct transfer of the methods of analysis for the plastic collapse of beams in bending to the plastic collapse of members under non-uniform torsion.

This paper explains and demonstrates the use of this method of analysing the plastic collapse of members in torsion. The method is simple to use, and comparisons with experimental results and computational non-linear elastic-plastic analysis[1-3] have demonstrated that it is conservative. The use of plastic analysis avoids the conservatism of first-yield analysis and design, because it accounts for the spread of plasticity across the critical sections and the redistribution of torsional actions. Design that is based on plastic analysis of torsion will lead to significant economies over first yield designs based on elastic analysis, and is much needed in design codes of practice for steel structures.

2 TORSIONAL BEHAVIOUR

2.1 Linear elastic behaviour

For the linear elastic torsional analysis of steel beams, the steel is assumed to be linear and the twist rotations are assumed to be small, so that the twists are proportional to the applied torques as shown in Fig. 1.

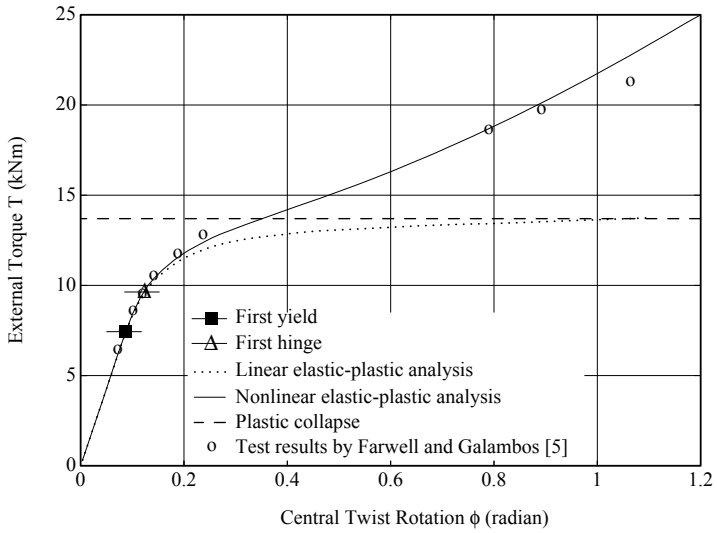

Figure 1: Torsional behaviour

The elastic methods of linear torsion analysis are well established[4]. The engineering method consists of two parts: cross-section analysis that relates the stresses to the stress resultants; and linear member analysis that relates the twist rotations and stress resultants to the applied torsional loading. The combination of these two parts allows the twist rotations and stresses to be predicted. The linear elastic method of torsion analysis is most logically used for serviceability design. Under service loading, most of the member remains elastic, and the linear elastic analysis closely predicts twist rotations. These and any related deflections

can then be assessed by comparing them with what are considered to be limiting values. Linear elastic torsion analysis is used less logically for strength design, because yielding usually takes place well before the ultimate torsion capacity is reached. Nevertheless, the absence of accepted methods of failure prediction has forced designers to use the linear elastic method to predict the stresses caused by the strength design loads and to compare them with limiting values that are usually related to the yield stress. This method generally gives very conservative strength predictions.

When a member is subjected to a toque m_z distributed uniformly along its length, the differential equation of equilibrium for linear analysis can be written as[4]

$$GJ(\mathrm{d}^2\phi/\mathrm{d}z^2) - EI_w(\mathrm{d}^4\phi/\mathrm{d}z^4) = m_z\,, \tag{1}$$

where E and G are the Young's modulus and shear modulus of elasticity, J is the section torsional constant, I_w is the section warping constant, ϕ is the angle of twist rotation of the cross-section, and z is the coordinate along the member.

Eq. (1) can be solved for different boundary conditions, which may include the kinematic boundary conditions such as twist rotation prevented ($\phi = 0$), warping prevented ($\mathrm{d}\phi/\mathrm{d}z = 0$), warping free ($\mathrm{d}^2\phi/\mathrm{d}z^2 = 0$), and the static boundary condition given by

$$GJ(\mathrm{d}\phi/\mathrm{d}z) - EI_w(\mathrm{d}^3\phi/\mathrm{d}z^3) = M_z \tag{2}$$

where M_z is the toque acting at the beam ends.

The linear elastic behaviour of a member in torsion is terminated by the occurrence of first yield at a point in the member as indicated in Fig. 1. First yield in ductile materials under combined normal and shear stresses is usually modelled using the von Mises (circular) interaction equation. When applied to combinations at a point of warping normal stresses f_w due to warping torsion with shear stresses τ_u due to uniform torsion and warping shear stress τ_w due to warping torsion, this becomes

$$(f_w/f_y)^2 + [(\tau_u + \tau_w)/\tau_y]^2 = 1 \quad \text{with} \quad \tau_y = f_y/\sqrt{3} \tag{3}$$

where f_y is the normal yield stress and τ_y is the shear yield stress.

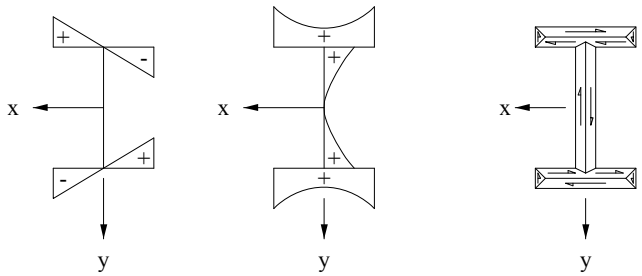

(a) Warping Streeses $f_w = -\omega\,\phi''$ (b) Wagner Streeses $f_Q = \frac{1}{2}(x^2 + y^2)\phi'^2$ (c) Uniform Torsion Shear Streeses $\tau_u = -G\Omega\,\phi'$

Figure 2: Elastic-torsion

The stresses f_w and τ_u vary in different ways around the cross-section (Fig. 2(a) and 2(c)) and along the member, and so the point at which first yield occurs may be quite difficult to determine. However, the different locations of the maximum values of f_w and τ_u often lead to a low value of one of these coinciding with the maximum value of the other. Consequently, a good approximation for first yield is often obtained by considering the separate conditions $f_w = f_y$ and $\tau_u = \tau_y$.

Numerical methods such as finite element methods can be developed based on Eq. (1) and material nonlinearity such as shown in Fig. 3 for the linear elastic-plastic torsional analysis (i.e. the geometrically linear and material nonlinear analysis). When strain hardening is neglected, the finite element result[2] of the linear elastic-plastic torsional analysis is shown in Fig.1 by the dotted line, which indicates that the torque approaches a limiting value (the broken line) as shown in Fig. 1, which corresponds to plastic collapse of the cross-section.

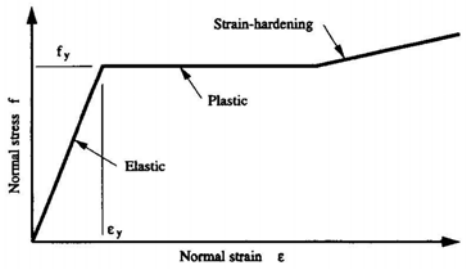

Figure 3: Stress-strain relationship for structural steel

2.2 Nonlinear Elastic-Plastic Behaviour and Large Twists and Failure

The normal stress/normal strain curve of structural steel is usually modelled as being elastic-plastic-strain hardening, as shown in Fig. 3. After first yield occurs, the torque-twist rotation relationship becomes nonlinear, as indicated in Fig. 1. The differential equations of equilibrium for nonlinear elastic-plastic torsion of I-section members are given by[2]

$$\mathrm{d}[AE(\mathrm{d}w/\mathrm{d}z) + EI_P(\mathrm{d}\phi/\mathrm{d}z)^2/2]/\mathrm{d}z = 0 \tag{4}$$

and

$$GJ(\mathrm{d}^2\phi/\mathrm{d}z^2) + \mathrm{d}\{[AE(\mathrm{d}w/\mathrm{d}z) + EI_P(\mathrm{d}\phi/\mathrm{d}z)^2/2)](\mathrm{d}\phi/\mathrm{d}z)\}/\mathrm{d}z - EI_w(\mathrm{d}^4\phi/\mathrm{d}z^4) = m_z \tag{5}$$

where A is the area of the cross-section and I_P is defined by $I_P = \int_A (x^2 + y^2)\mathrm{d}A$.

The corresponding static boundary conditions are given by

$$AE(\mathrm{d}w/\mathrm{d}z) + EI_P(\mathrm{d}\phi/\mathrm{d}z)^2/2 = 0\,, \tag{6}$$

and

$$GJ(\mathrm{d}\phi/\mathrm{d}z) + [AE(\mathrm{d}w/\mathrm{d}z) + EI_P(\mathrm{d}\phi/\mathrm{d}z)^2/2)](\mathrm{d}\phi/\mathrm{d}z) - EI_w(\mathrm{d}^3\phi/\mathrm{d}z^3) = M_z\,. \tag{7}$$

The finite element result based the differential equations of equilibrium for the nonlinear elastic-plastic analysis given by Eqs. (4) and (5) is shown in Fig. 1 by the solid line, which is much higher than the limiting value (the broken line). Hence, it is conservative to use the limiting value of the toque as the plastic collapse toque.

The assumption of linear twist rotation analysis ignores the secondary longitudinal Wagner stresses[5] f_Q associated with the relative extensions of the fibres of the cross-section away from the axis of twist (Fig. 3(b)). At small twist rotations these stresses are secondary and have little effect as shown in Fig. 1. However, at large twist rotations, they lead to significant longitudinal tensions in the regions of the flange tips, which increases the resistance of the member to torsion, as shown in Fig. 1. Final failure of the member is by tensile rupture at the flange tips[5] and at a torque that is significantly higher than the plastic collapse torque[2]. The plastic-collapse torque provides a quite conservative estimate of the strength of a member in torsion. Although this is not unlike the conservatism of bending plastic-collapse mechanisms of beams under moment gradient caused by strain-hardening effects, the degree of conservatism of torsion plastic-collapse mechanisms is significantly greater.

3 PLASTIC-COLLAPSE ANALYSIS OF TORSION

3.1 General

In the simple method described here of analysing the plastic collapse of a member in torsion, independent analyses are made for the plastic collapse in uniform torsion and in warping torsion to determine their collapse load factors λ_{up} and λ_{wp} and the actual plastic collapse load factor λ_p is approximated using

$$\lambda_p = \lambda_{up} + \lambda_{wp} . \tag{8}$$

This very simple approximation assumes no interaction at plastic collapse between uniform and warping torsion, and assumes that the separate plastic collapse capacities are additive. The errors due to these assumptions are on the unsafe side when compared with more accurate linear elastic-plastic analyses[2], but are very small and on the safe side when compared with accurate nonlinear elastic-plastic analyses[2], because (1) the warping torsion shear strains are small; (2) the yielding and plasticity interactions between normal and shear stresses, which are described by circular interaction equations given by Eq. (3), are small; (3) sections that are fully plastic due to warping torsion often occur at different locations along the member than those that are fully plastic due to uniform torsion. The unsafe errors caused by these assumptions are more than compensated for by the conservatism of ignoring the strengthening effects of strain hardening, and the strengthening effects of the Wagner stresses at large rotations.

3.2 Uniform-Torsion Plastic Collapse

When uniform torsion provides the only method of resisting applied torques, a collapse mechanism develops when a sufficient number of cross-sections of the member become fully plastic in uniform torsion, as shown for example, in Fig. 4.

These fully plastic sections are usually located at the supports where the reaction torques act. The sand-heap analogy[2, 4] can be used to analyse a thin-walled open section to approximate the uniform-torsion plastic torque

$$M_{up} \approx \tau_y \sum (bt^2 / 2) \tag{9}$$

in which b and t are the width and thickness of each rectangular element of the cross-section. For an I-section, the uniform torsion plastic torque is given by

$$M_{up} = \tau_y \left[b_f t_f^2 \left(1 - t_f / 3b_f\right) + b_w t_w^2 / 2 + t_w^3 / 6 \right], \tag{10}$$

in which b_f is the flange width; t_f is the flange thickness; b_w is the web depth between flanges; and t_w is the web thickness.

An example of a uniform-torsion plastic-collapse mechanism is shown in Fig. 4. In this case, a general rigid-body twist rotation occurs when a uniform-torsion plastic hinge has formed at each end. In general, plastic hinges will develop progressively until the collapse mechanism forms. For the example shown in Fig. 4, the uniform-torsion plastic-collapse load factor is

$$\lambda_{up} = 2M_{up} / T \,. \tag{11}$$

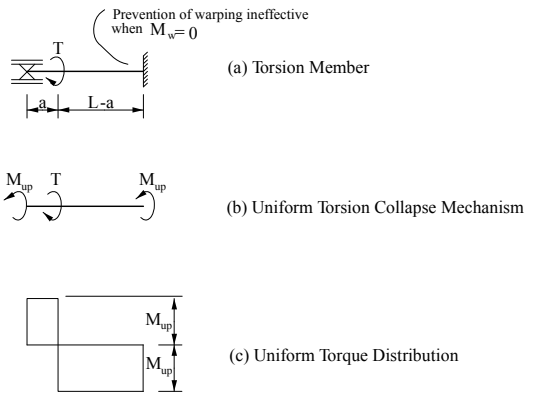

Figure 4: Uniform torsion plastic collapse

It is noted in Fig. 4 that preventing warping at the ends is ineffective in uniform torsion, because warping torsion is not accounted for. Other examples of uniform-torsion plastic-collapse mechanisms are shown in Fig. 5.

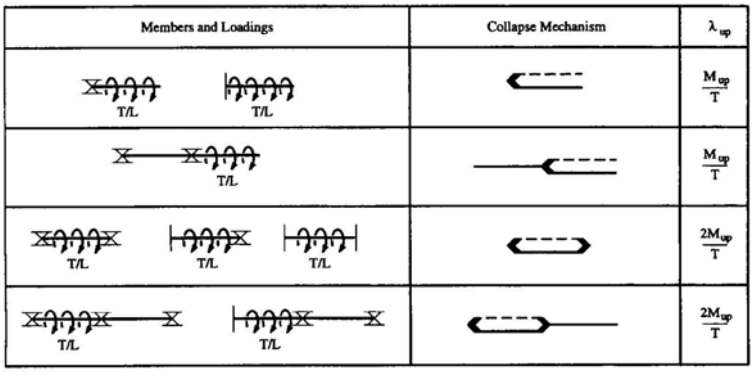

Figure 5: Uniform-torsion plastic-collapse mechanism

3.3 Warping Torsion Plastic Collapse

When warping torsion provides the only method of resisting applied torques, a collapse mechanism develops when there are a sufficient number of warping hinges (frictionless or plastic) to transform the member into a mechanism. In the case of an equal-flanged I-section member, these warping hinges transform each flange into a flexural collapse mechanism, as shown in Fig. 6. Warping hinges often occur at supports or at points of concentrated torque. When there are distributed torques, then the location of the warping hinges may lie between points of concentrated torque, and may not be conspicuous. In this case, the location may be guessed, and the upper- and lower-bound techniques of plastic analysis[4] are used to determine a sufficiently accurate collapse load factor.

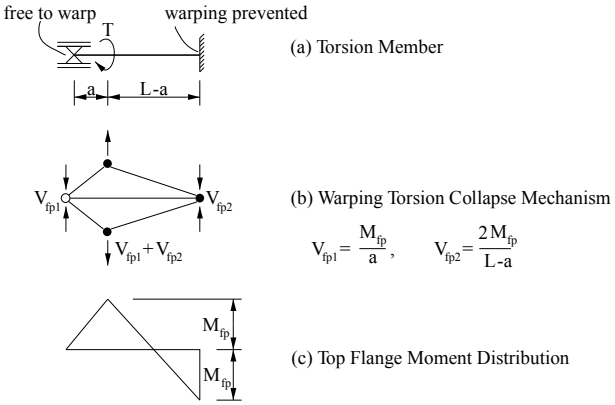

Figure 6: Warping torsion plastic collapse

Members and Loadings	Collapse Mechanism	λ_{wp}
T/L		0
T/L		$\frac{2M_{fp}h}{TL}$
T/L		$\frac{2M_{fp}h}{TL}$
T/L		$\frac{8M_{fp}h}{TL}$
T/L		$\frac{11.66M_{fp}h}{TL}$
T/L		$\frac{16M_{fp}h}{TL}$
T/L		$\frac{11.66M_{fp}h}{TL}$
T/L		$\frac{16M_{fp}h}{TL}$

Figure 7: Warping torsion plastic collapse mechanism

The fully plastic bimoment B_p at which warping hinges form in an equal-flanged I-section is given as[4]

$$B_p = M_{fp} h \quad \text{with} \quad M_{fp} = f_y b_f^2 t_f / 4 \quad \text{and} \quad h = b_w + t_f \tag{12}$$

in which M_{fp} is the flange plastic moment and h is the distance between the flange centroids.

The warping-torsion plastic-collapse load factor λ_{wp} of an equal-flanged I-section torsion member can be found from the flexural plastic collapse loads for the flanges, which can be analysed by the methods of analysing plastic collapse in flexural structures[4]. An example of a warping-torsion plastic-collapse mechanism is shown in Fig. 6. In this case, there are frictionless hinges at the end that is free to warp, and general twist rotation occurs when each flange forms a collapse mechanism with plastic hinges at the other end and within the member length. In general, plastic hinges will develop progressively until the flange collapse mechanisms form. The warping plastic torque for the example in Fig. 6 is given by

$$M_{wp} = V_{fp} h \quad \text{with} \quad V_{fp} = \frac{\mathrm{d}M_f}{\mathrm{d}z} \tag{13}$$

with the gradient of the flange moment $\mathrm{d}M_f/\mathrm{d}z$ being given by M_{fp}/a and $2M_{fp}/(L\text{-}a)$ (Fig. 6(b)). Thus the warping torsion collapse load factor is given by

$$\lambda_{wp} = \frac{M_{wp}}{T} = \frac{M_{fp} h}{T}\left(\frac{1}{a} + \frac{2}{L-a}\right). \tag{14}$$

Other examples of warping-torsion plastic-collapse mechanisms are shown in Fig. 7.

4 A NUMERICAL EXAMPLE

A 4,500 mm long torsion member and its torsional loading are shown in Fig. 8. The I-section dimensions are b_f =420 mm; t_f =30 mm; b_w =400 mm; and t_w = 22 mm. The normal yield stress is f_y = 250 N/mm^2; and the uniformly distributed torque is 150 kNm/m.

From Eq. (3), the shear yield stress is obtained as $\tau_y = f_y / \sqrt{3} = 250/\sqrt{3} = 114.34$ N/mm^2.

The uniform torsion collapse toque can be obtained from Eq. (10), as

$$\begin{aligned} M_{up} &= \tau_y \left[b_f t_f^2 \left(1 - t_f / 3b_f\right) + b_w t_w^2 / 2 + t_w^3 / 6 \right] \\ &= 114.34 \times \{420 \times 30^2 \times [1 - 20/(3 \times 420)] + 400 \times 22^2 / 2 + 22^3 / 6\} = 53.81 \text{KNm} \end{aligned} \tag{15}$$

while the warping torsion collapse toque can be obtained from Eq. (12) as

$$M_{fp} = f_y b_f^2 t_f / 4 = 250 \times 420^2 \times 30 / 4 = 330.75 \text{KNm}. \tag{16}$$

The uniform torsion collapse factor is the obtained from Eq. (11) as

$$\lambda_{up} = 2M_{up} / T = 2 \times 53.81 \times 10^6 / (150 \times 10^3 \times 4500) = 0.1594. \tag{17}$$

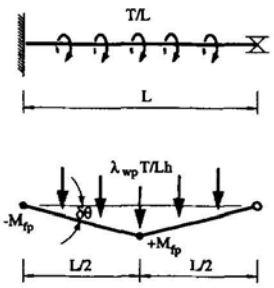

Figure 8: Worked example

The warping-torsion flange plastic-collapse mechanism is not obvious, but an upper-bound solution can be obtained by assuming that plastic flange hinges occur at mid-span, as shown in Fig. 8. In this case, a virtual work analysis of each flange mechanism leads to

$$\delta W = (\lambda_{wp} T / Lh)(L^2 \delta\theta / 4) \tag{18}$$

for the external work done by the distributed flange loads T/Lh , and

$$\delta U = 3M_{fp}\delta\theta \tag{19}$$

for the internal work absorbed at the plastic hinges, in which $\delta\theta$ is the virtual rotation of each half flange.[4] An upper bound is obtained from the inequality $\delta W \leq \delta U$, so that

$$\lambda_{wp} \leq 12M_{wp}h / TL^2 . \tag{20}$$

A lower bound is found by determining that at this load factor, the maximum flange moment is $25M_{fp}/24$, so that

$$\lambda_{wp} \leq 12M_{wp}h / TL^2 \times (24/25) = 11.52M_{wp}h / TL^2 , \tag{21}$$

which is very close to the exact solution[4]

$$\lambda_{wp} = \frac{(6+4\sqrt{2})M_{fp}h}{TL^2} \approx 11.66M_{fp}h / TL^2 . \tag{22}$$

The warping torsion collapse factor can then be obtained as

$$\lambda_{wp} = \frac{11.66M_{fp}h}{TL^2} = \frac{11.66 \times 330.75 \times 10^6 \times 430}{150 \times 10^3 \times 4500^2} = 0.546 . \tag{23}$$

Finally, the torsion collapse factor is obtained from Eq. (8) as

$$\lambda_p = \lambda_{up} + \lambda_{wp} = 0.1594 + 0.546 = 0.7054 . \tag{24}$$

5 CONCLUSIONS

- Hand methods for the linear elastic analysis of the non-uniform torsion of thin-walled

steel members are difficult to carry out, but first-yield methods of design based on elastic analyses are unnecessarily conservative.

- This paper presents and demonstrates a very simple method of analyzing the plastic collapse of equal-flanged I-section members in torsion. The method can be used manually, and is no more difficult than the plastic-collapse analysis of beams in bending. Comparisons have demonstrated that the method produces predictions that are very close to those of more accurate linear elastic-plastic analyses, and substantially less than test results and predictions of nonlinear large-rotation elastic-plastic analyses.
- The use of plastic analysis avoids the conservatism of first yield analysis and design, because it accounts for the spread of plasticity across the critical sections and the redistribution of torque that occurs in redundant members after the first hinge forms. Designs based on plastic analyses of torsion will lead to significant economies over first yield designs based on elastic analysis.

ACKNOWLEDGMENTS

This work has been supported by the Australian Research Council through Discovery Projects (DP1097096 and DP1096454) awarded to the authors and a Laureate Fellowship (FL100100063) awarded to the second author.

REFERENCES

[1] Y.-L. Pi and N. S. Trahair, "Nonlinear inelastic analysis of steel beam-columns. I: Theory", *J. Struc. Engng. ASCE*, **120**(7), 2041-2061 (1994).

[2] Y.-L. Pi and N. S. Trahair, "Inelastic torsion of steel I-beams", *J. Struc. Engng. ASCE,* **121**(4), 609-620 (1995).

[3] Y.-L. Pi, M.A. Bradford, and B. Uy, "A rational elasto-plastic spatially curved thin-walled beam element", *Int. J. Num. Meth. Engng*, **70**(3), 253-290 (2007).

[4] N.S Trahair, M.A. Bradford, D.A. Nethercot, and L Gardner, *The behaviour and design of steel structures to EC3*, 4th Edition, Taylor & Francis, London (2008).

[5] C.R Farwell Jr. and T.V. Galamhos, "Nonuniform torsion of steel beams in inelastic range", *J. Struct. Div. ASCE*, **95**(12), 2813-2829 (1969).

XI International Conference on Computational Plasticity. Fundamentals and Applications
COMPLAS XI
E. Oñate, D.R.J. Owen, D. Peric and B. Suárez (Eds)

RHEOLOGICAL METHOD FOR CONSTRUCTING CONSTITUTIVE EQUATIONS OF ONE-PHASE GRANULAR AND POROUS MATERIALS

VLADIMIR M. SADOVSKIY

Institute of Computational Modeling SB RAS
Akademgorodok 50/44, 660036 Krasnoyarsk, Russia
e-mail: sadov@icm.krasn.ru, http://icm.krasn.ru

Key words: Microstructure, Granular Material, Porous Metal, Variational Inequality

Abstract. To make possible the description of deformation of materials with different resistance to tension and compression, the rheological method is supplemented by a new element, a rigid contact, which serves for imitation of a perfectly granular material with rigid particles. By using a rigid contact in combination with conventional rheological elements the constitutive equations of granular materials and soils with elastic-plastic particles and of porous materials, like metal foams, are constructed.

1 INTRODUCTION

The theory of granular materials is among the most intensively developing fields of mechanics because the area of its application is very wide. In spite of the fact that the foundations of this theory have been laid even at the dawn of the development of continuum mechanics in the classical works by Coulomb and Reynolds, by now the theory is still far from completion. The main difficulties are caused by drastic difference in behaviour of granular materials in tension and compression experiments. Essentially all of known natural and artificial materials possess this property of heteroresistance (heterostrength) to some extent. For some of them, differences in modulus of elasticity, yield point, or creep diagram obtained with tension and compression are small to an extent that they should be neglected. However, in the studies of alternating-sign strains in granular materials, these differences may not be neglected. In addition, mechanical properties of granular materials, as a rule, depend on a number of side factors such as inhomogeneity in size of particles and in composition, anisotropy, fissuring, moisture etc. This results in low accuracy of experimental measurements of phenomenological parameters of models.

At the present time, two classes of mathematical models corresponding to two different conditions of deformation of a granular material (quasistatic conditions and fast motion

ones) have been formed [1]. The first class describes behaviour of a closely packed medium at compression load on the basis of the theory of plastic flow. In the space of stress tensors conical domains of admissible stresses rather than cylindrical ones, as in the perfect plasticity theory, satisfy these conditions. In the second class, a loosened medium modeled as an ensemble of a large number of particles in the context of the kinetic gas theory is considered.

To study quasistatic conditions of deformation, the stress theory in statically determinate problems which is applied in soil mechanics is developed. The case of plane strain is best studied by Sokolovskii [2], and the axially symmetric case – by Ishlinskii [3]. Velocity fields in these problems are defined according to the associated flow rule considered by Drucker and Prager [4]. Mróz and Szymanski [5] showed that the special nonassociated rule provides more accurate results in the problem on penetration of a rigid stamp into sand. A common disadvantage of these approaches lies in the fact that, when unloading, in the kinematic laws of the plastic flow theory a strain rate tensor is assumed to be zero, hence, deformation of a material is possible only as stresses achieve a limiting surface. From this it follows, for example, that a loosened granular material whose stressed state corresponds to a vertex of admissible cone can not be compressed by hydrostatic pressure since to any state of hydrostatic compression there corresponds an interior point on the axis of the cone. This is in contradiction with a qualitative pattern.

Kinematic laws turn out to be applicable in practice in the case of monotone loading only. Constitutive equations of the hypoplasticity in application to soil mechanics have a similar disadvantage [6, 7], because tension and compression states in them differ from one another in sign of instantaneous strain rate rather than in sign of total strain.

The equations of uniaxial dynamic deformation of a granular material, correct from the mechanical point of view, being a limiting case of the equations of heteromodular elastic medium [8], were studied by Maslov and Mosolov [9]. Phenomenological models of a spatial stressed-strained state of a cohesive soil for finite strains were proposed by Grigoryan [10] and Nikolaevskii [11]. The works [12, 13] are devoted to generalization of fundamentals of the plasticity theory for description of dynamics and statics of granular materials.

A spatial model of fast motions was proposed by Savage [14], who compared the solution of the problem on channel flow with experimental results, in particular, with those of Bagnold. Goodman and Cowin [15] developed a model for the analysis of gravity flow of a granular material. Nedderman and Tüzün [16] constructed a simple kinematic model which allows one to simulate an experimental pattern of steady-state outflow from funnel-shaped bunkers.

Nevertheless there is no a simple mathematical model which can be applicable both in the case of quasistatics and in the case of fast motions to describe the stagnant zones in a granular flow. The efforts to construct such model give only some limited applications for one-dimensional shear motions.

Porous metals are new artificial materials that can find wide application in engineering, thanks to the low density and good damping properties. The ability of porous metals effectively absorb energy during plastic deformation opens up the prospects of their use for production of the car bumpers and elements of the car body, so called "crushed" zones. They can be also used in reducers and drives as destructible fuses which dissipate the energy of dynamic impact, preventing the destruction of all mechanical system.

Similar to granular materials, their deformation properties significantly differ in tension and compression, which is typical virtually for all porous materials. Under tension, the stages of elastic deformation of the skeleton and plastic flow up to fracture are distinguished. Under compression, the stages of elastic and plastic deformation of the skeleton up to the collapse of pores, and the subsequent stage of elastic or elastic-plastic deformation of a solid, non-porous material are distinguished. In the case of small pore sizes, the collapse may occur in the elastic stage with the appearance of plasticity only at sufficiently high levels of loading at the last stage.

Currently the technology of production of metal foams on the basis of aluminum, copper, nickel, tin, zinc and other metals is worked out. Extensive experimental researches of mechanical properties of such materials are carried out. The diagrams of uniaxial tension and uniaxial compression on an example of aluminum foam and porous copper were obtained in [17, 18]. The paper [19] deals with problems of the wear resistance and the cyclic fatigue of porous metals.

Theoretical results related to the construction of constitutive equations and to the analysis on this basis of a spatial stressed-strained state of structural elements of a metal foam, according to available publications, are practically not studied. Still more difficult to construct a universal model for the description of a spatial stressed-strained state. Performing of adequate computations based on discrete models of a metal foam as a structurally inhomogeneous material is possible only with using the multiprocessor systems which have high speed and large amounts of RAM.

In this paper a simple method for constructing constitutive equations of granular and porous materials based on the rheological approach is suggested.

2 GRANULAR MATERIALS

Rheology is the basis of the phenomenological approach to the description of a stressed-strained state of materials with complex mechanical properties. As a rule, for the models obtained with the help of rheological method, solvability of main boundary-value problems can be analyzed and efficient algorithms for numerical implementation can be easily constructed. At the same time, with the use of conventional rheological elements (a spring simulating elastic properties of a material, a viscous damper, and a plastic hinge) only, it is impossible to construct a rheological scheme for a medium with different resistance to tension and compression or for a medium with different ultimate strengths under tension and compression. To make it possible, the rheological method is supplemented by a new element, a rigid contact (see Fig. 1*a*), which serves for imitation of a perfectly granular

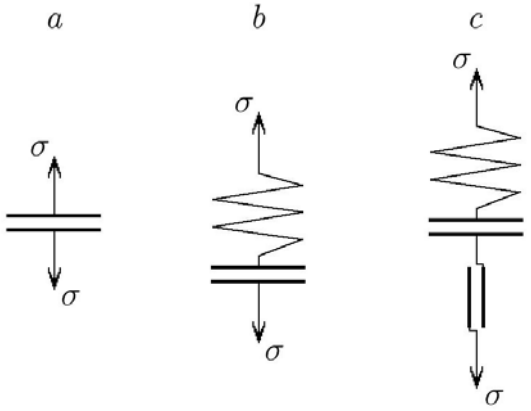

Figure 1: Rheological models of a granular material: rigid (a), elastic (b) and elastic-plastic (c)

material with rigid particles [20]. Under compressive stresses this element doesn't deformed. If stress is equal to zero then strain may be arbitrary positive value. Tensile stresses aren't admissible. Rheological models of perfectly elastic and elastic-plastic granular media are represented in Figs. 1b and 1c. In the case of compression such media are either in elastic state or in plastic one, but in the case of tension the stresses are equal to zero. By different combining these elements with viscous element, one can construct rheological models of more complex media.

Mathematical model of a rigid contact (perfectly granular medium with rigid particles) is reduced to the system of relationships

$$\sigma \le 0, \qquad \varepsilon \ge 0, \qquad \sigma\,\varepsilon = 0.$$

It is possible to represent it in the form of variational inequalities

$$(\tilde{\varepsilon} - \varepsilon)\,\sigma \le 0, \quad \varepsilon,\ \tilde{\varepsilon} \ge 0, \qquad (\tilde{\sigma} - \sigma)\,\varepsilon \le 0, \quad \sigma,\ \tilde{\sigma} \le 0,$$

each of which assumes the potential representation

$$\sigma \in \partial\varphi(\varepsilon), \qquad \varepsilon \in \partial\psi(\sigma). \tag{1}$$

Here φ and ψ – the potentials of stresses and strains – are the indicator functions, equal to zero on cones $C = \{\varepsilon \ge 0\}$ and $K = \{\sigma \le 0\}$ respectively, and equal to infinity outside of these cones. These functions are denoted as $\delta_C(\varepsilon)$ and $\delta_K(\sigma)$. The symbol ∂ serves for designation of a subdifferential, the arbitrary variable values are denoted by a wave.

Generalization of the model, schematically represented in Fig. 1a, on the case of a spatial stressed-strained state is easily constructed on the basis of inclusions (1). For that it is necessary to set the convex cone C in the space of strain tensors or the cone K in

the space of stress tensors. If one of these cones is known then another one is found as conjugate:

$$K = \Big\{\sigma \,\Big|\; \sigma : \varepsilon \le 0 \quad \forall\, \varepsilon \in C\Big\}, \qquad C = \Big\{\varepsilon \,\Big|\; \sigma : \varepsilon \le 0 \quad \forall\, \sigma \in K\Big\}$$

(the colon denotes the convolution of tensors). Corresponding potentials – the indicator functions of cones C and K – are dual, i.e. they are determined one by another with the help of the Young transformation

$$\varphi(\varepsilon) = \sup_{\sigma}\Big\{\sigma : \varepsilon - \psi(\sigma)\Big\}, \qquad \psi(\sigma) = \sup_{\varepsilon}\Big\{\sigma : \varepsilon - \varphi(\varepsilon)\Big\}.$$

Known experimental results on the deformation properties of compact sands confirm the hypothesis about elastic state of a medium under stresses, close to hydrostatic compression. Such stresses are interior points of the cone K. For an elastic granular medium (Fig. 1*b*) $\psi = \sigma : a : \sigma/2 + \delta_K(\sigma)$, where a is the tensor of moduli of elastic compliance of fourth rank, corresponding to the model of an elastic element. The constitutive relationships (1) are reduced to the Haar–Karman inequality [20]

$$(\tilde{\sigma} - \sigma) : (a : \sigma - \varepsilon) \ge 0, \qquad \sigma,\ \tilde{\sigma} \in K. \tag{2}$$

Taking into account the symmetry and the positive definiteness of the tensor a, it is possible to show that the solution of inequality (2) is the tensor of stresses $\sigma = s^{\pi}$, equals to the projection of the conditional stress tensor s, determined from the linear Hooke law $a : s = \varepsilon$, onto K with respect to the norm $|\sigma|_a = \sqrt{\sigma : a : \sigma}$.

For a medium possessing plastic properties, rheological scheme of which is represented in Fig. 1*c*, the strain tensor is decomposed into the sum of elastic and plastic components: $\varepsilon = \varepsilon^e + \varepsilon^p$. The tensor of elastic strain satisfies the inequality (2), taking into account the property of granularity of a medium. For the plastic strain rate tensor the constitutive relationships of the flow theory

$$\sigma \in \partial\eta(\dot{\varepsilon}^p) \tag{3}$$

are correct. Here η is the dissipative potential of stresses being a convex positive homogeneous function of the strain rates, the dot over a symbol serves to indicate the time derivative. Homogeneity of this potential is the consequence of independence of the process of plastic deformation on time scale. By virtue of this property, the dual potential $\chi(\sigma)$ – the Young transformation of the function $\eta(\dot{\varepsilon})$ – is equal to the indicator function of the convex closed set

$$F = \Big\{\sigma \,\Big|\; \sigma : \dot{\varepsilon} \le \eta(\dot{\varepsilon}) \quad \forall\, \dot{\varepsilon}\Big\}.$$

The boundary of F in the stress space defines the yield surface of a material. If the set F is a cylinder with the axis of hydrostatic stresses then the volume strain of a medium obeys the linearly elastic law. In the opposite case the model, being under consideration, describes irreversible volumetric contraction.

The inclusion (3) in the equivalent form $\dot{\varepsilon}^p \in \partial\chi(\sigma)$ is reduced to the Mises inequality

$$(\tilde{\sigma} - \sigma) : \dot{\varepsilon}^p \leq 0, \qquad \sigma,\ \tilde{\sigma} \in F. \tag{4}$$

The variational inequality (2) for elastic part of the strain tensor and the inequality (4) for its plastic part together with the equations of motion and the kinematic equations

$$\rho\,\dot{v} = \nabla \cdot \sigma, \qquad 2\,(\dot{\varepsilon}^e + \dot{\varepsilon}^p) = \nabla v + (\nabla v)^* \tag{5}$$

form a closed model describing the dynamics of a granular medium. Here ρ is the density, v is the velocity vector, ∇ is the gradient, an asterisk denotes the operation of transposition.

3 POROUS METALS

The porosity of a metal foam is determined as the ratio of the pore volume to the volume of a porous material: $\varepsilon_0 = V_0/V$. If ρ is the density of initial (solid) metal, then, ignoring the presence of gas in the pores, the density of a porous metal can be calculated by formula: $\rho_0 = \rho\,(V - V_0)/V$. Consequently, $\varepsilon_0 = (\rho - \rho_0)/\rho$. For highly porous materials the volume strain caused by the collapse of pores is much higher than the concomitant strain of volume compression of the skeleton, therefore the pores disappear when the volume strain is approximately equal to $\theta_0 \approx ((V - V_0) - V)/V = -\varepsilon_0$.

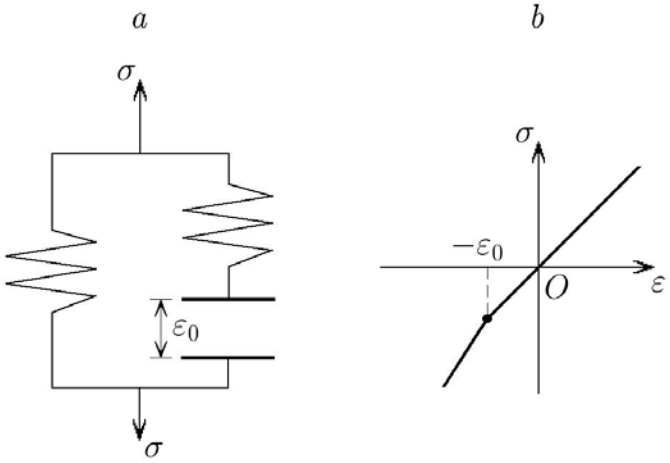

Figure 2: Rheological scheme (a) and diagram of uniaxial elastic deformation of a porous metal (b)

The simplest rheological scheme taking into account the main qualitative features of deformation of porous metals is represented in Fig. 2*a*. In this scheme the behaviour of a material under tension and under compression up to the moment of pores collapse is simulated by an elastic spring with the compliance modulus a, and the increasing of rigidity as the collapse of pores is simulated by a spring with the compliance modulus b. Segments of the diagram of uniaxial deformation with a break at the point $\varepsilon = -\varepsilon_0$ (see Fig. 2*b*) are defined by the equations: $\sigma = \varepsilon/a$ and $\sigma = \varepsilon/a + (\varepsilon + \varepsilon_0)/b$. This scheme describes an elastic process that occurs without the dissipation of mechanical energy.

Fig. 3*a* shows a more general rheological scheme with a plastic hinge. It is assumed that under tensile stress σ_s^+ the skeleton goes into the yield state, and under compressive stress $-\sigma_s^-$ the plastic loss of stability takes place. The corresponding diagram of uniaxial deformation is a four-segment broken line (see Fig. 3*b*). Elastic stage is described by the equation $\sigma = \varepsilon/a$, and the stage of elastic-plastic deformation of a solid material after collapse of the pores is described by the equation $\sigma = (\varepsilon + \varepsilon_0)/b - \sigma_s^-$. Transitions of a material in the unloading state are shown by arrows. The unloading of a porous material occurs by the law $d\sigma = d\varepsilon/a$, and the unloading of a solid material occurs by the law $d\sigma = d\varepsilon\,(1/a + 1/b)$. Specific dissipative energy, which is released during the collapse of the pores, is estimated by the product $\sigma_s^-\varepsilon_0$ in this model. The plastic flow, which occurs in a solid material at higher level of compressive stresses, is not considered.

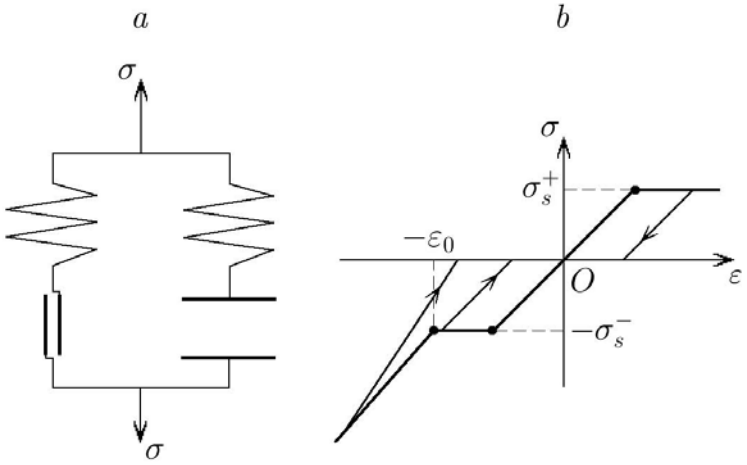

Figure 3: Rheological scheme (a) and diagram of elastic-plastic deformation of a skeleton (b)

In the general case of a spatial stressed-strained state, in accordance with the rheological scheme in Fig. 3*b*, the stress tensor σ is equal to the sum of the tensors σ^p of plastic stresses and σ^c of additional stresses acting after collapse of the pores. It is assumed that these tensors are symmetric. Elastic compliance of a material at small strains is characterized by the fourth-rank tensors a and b, satisfying the usual conditions of symmetry and positive definiteness. The series connection of an elastic spring and a plastic hinge in

the scheme corresponds to the theory of elastic-plastic flow of Prandtl–Reuss. Within the framework of this flow theory the constitutive relationships are postulated in the form of principle of maximum of the energy dissipation rate:

$$(\tilde{\sigma} - \sigma^p) : (a : \dot{\sigma}^p - \dot{\varepsilon}) \geq 0, \qquad \tilde{\sigma},\ \sigma^p \in F. \tag{6}$$

Here ε is the actual strain tensor, F is the convex set in the stress space, bounded by the yield surface of a material. Assuming that the deformation of the jumpers of porous skeleton, distributed randomly on macrovolume of a material, can be described with satisfactory accuracy as a bar model, let us define concretely the set of admissible stresses:

$$F = \left\{ \tilde{\sigma} \,\middle|\, -\sigma_s^- \leq \tilde{\sigma}_k \leq \sigma_s^+, \quad k = 1, 2, 3 \right\},$$

where $\tilde{\sigma}_k$ are the principal values of σ.

Constitutive relationships of a rigid contact are formulated as the variational inequality

$$(\tilde{\sigma} - \sigma^c) : (\varepsilon^c + \varepsilon^0) \leq 0, \qquad \tilde{\sigma},\ \sigma^c \in K. \tag{7}$$

Here $\varepsilon^c = \varepsilon - b : \sigma^c$ is the strain tensor of porous skeleton, $\varepsilon^0 = \varepsilon_0\, \delta/3$ is the spherical tensor of initial porosity of a material, δ is the Kronecker delta. The transition of a material from porous state to continuous one is modeled by the convex cone K. As a simple variant of K one can use the Mises–Schleicher circular cone:

$$K = \left\{ \tilde{\sigma} \,\middle|\, \tau(\tilde{\sigma}) \leq æ\, p(\tilde{\sigma}) \right\},$$

where æ is the phenomenological parameter of a dilatancy, $p(\sigma) = -\sigma : \delta/3$ is the hydrostatic pressure, $\tau(\sigma)$ is the intensity of tangential stresses determined via the deviator of the stress tensor $\sigma' = \sigma + p(\sigma)\, \delta$ by means of the formula: $\tau^2(\sigma) = \sigma' : \sigma'/2$.

Taking into account these notations, the inequality (7) is converted to the form

$$(\tilde{\sigma} - \sigma^c) : b : (\sigma^c - s) \geq 0, \qquad \tilde{\sigma},\ \sigma^c \in K. \tag{8}$$

Here s is a tensor of conditional stresses, which is calculated by the law of linear elasticity with initial strains: $b : s = \varepsilon + \varepsilon^0$. If this tensor is admissible, i.e. if the inclusion $s \in K$ is fulfilled, then by (8) $\sigma^c = s$. If $s \notin K$ and for any $\tilde{\sigma} \in K$ the inequality $\tilde{\sigma} : b : s \leq 0$ is valid, which means precisely that the sum of tensors $\varepsilon + \varepsilon^0$ belongs to the cone $C = \left\{ \tilde{\varepsilon} \,\middle|\, \tilde{\sigma} : \tilde{\varepsilon} \leq 0, \quad \tilde{\sigma} \in K \right\}$ of admissible strains, dual to the cone K, then as follows from (8) $\sigma^c = 0$. In the general case, the variational inequality (8) allows to

determine the tensor $\sigma^c = s^\pi$ as a projection of the tensor s onto K with respect to the norm $|s| = \sqrt{s : b : s}$, and the above two variants for setting s are special cases when the projection coincides with the original tensor and the projection is a vertex of cone. If the projection belongs to a conical surface, then the formulas for calculating the projection take the next form [20]:

$$p(\sigma) = \frac{\mu\, p(s) + æ\, k\, \tau(s)}{\mu + æ^2 k}, \qquad \sigma' = æ\, p(s)\, \frac{s'}{\tau(s)} \tag{9}$$

(for an isotropic medium the tensor b of elastic compliance is characterized by two independent parameters – the volume compression modulus k and the shear modulus μ). This variant is realized when both of the conditions $s \notin K$ and $\varepsilon + \varepsilon^0 \notin C$ are fulfilled. The cone C, dual to the Mises–Schleicher cone, is defined as

$$C = \Big\{ \tilde{\varepsilon} \,\Big|\; æ\, \gamma(\tilde{\varepsilon}) \le \theta(\tilde{\varepsilon}) \Big\},$$

where $\gamma(\tilde{\varepsilon}) = \sqrt{2\, \tilde{\varepsilon}' : \tilde{\varepsilon}'}$ is the shear intensity, and $\theta(\tilde{\varepsilon}) = \tilde{\varepsilon} : \delta$ is the volume strain.

The inclusion $\varepsilon + \varepsilon^0 \in C$ means that the rigid contact in rheological scheme is opened, i.e. the pores are in the open state. When the collapse of pores take place, the limit condition $æ\, \gamma(\varepsilon) = \varepsilon_0 + \theta(\varepsilon)$ is satisfied, which describes the dilatational volume increasing of a material due to the shear strain.

Note that in the simulation of real porous metals it is necessary to take into account a random character of distribution of a pore size, therefore the value ε_0 can vary randomly at each elementary portion of a sample (at each mesh of the grid domain). In principle, the law of distribution of pores by size is completely determined by technology of the production of metal foams, however in numerical computations (in order to describe qualitatively the effect of random distribution of pores on the stressed-strained state of a material) can be used, for example, the formula

$$\varepsilon_0 = \varepsilon_0^- + (\varepsilon_0^+ - \varepsilon_0^-)\, rand,$$

where $\varepsilon_0^\pm$ are the boundaries of porosity, *rand* is a built-in function of the uniform distribution on the segment $[0, 1]$.

4 UNIVERSAL FORM OF MODELS

Mathematical model describing the dynamic deformation of porous metal under small strains and rotations of elements can be written in the next form:

$$\begin{aligned} &\rho_0\, \dot{v} = \nabla \cdot \sigma, \\ &(\tilde{\sigma} - \sigma^p) : (a : \dot{\sigma}^p - \nabla v) \ge 0, \qquad \tilde{\sigma},\ \sigma^p \in F, \\ &b : \dot{s} = (\nabla v + \nabla v^*)/2, \qquad \sigma = \sigma^p + \pi_K(s). \end{aligned} \tag{10}$$

Unknown functions are the velocity vector v and the tensors of plastic stresses σ^p and of conditional stresses s. The initial conditions, describing the natural (stress-free) state of a material, are formulated for the system (10) as

$$v\big|_{t=0}= 0, \qquad \sigma^p\big|_{t=0}= 0, \qquad s\big|_{t=0}= b^{-1} : \varepsilon^0.$$

The boundary conditions can be given in the terms of velocities: $v\big|_\Gamma= v^0(x)$, as well as in stresses: $\sigma\big|_\Gamma \cdot \nu(x) = q(x)$, where ν is the outward normal vector, v^0 and q are given functions.

It turns out that the relationships (10) and the relationships (2), (4), (5) of mathematical model of an elastic-plastic granular material can be represented in the universal matrix form

$$\big(\tilde{U} - U\big)\left(A\,\dot{U} - \sum_{i=1}^{n} B^i\,U^{\pi}_{,i}\right) \geq 0, \qquad \tilde{U},\ U \in F. \tag{11}$$

Here U is the unknown m-dimensional vector–function, A and B^i are the given matrices whose coefficients are the density and the mechanical coefficients of a material, subscripts after a comma denote partial derivatives with respect to spatial variables, superscript π denotes the projection of vector U onto the cone K of admissible variations with respect to the energy norm $|U| = \sqrt{UAU}$, $n = 1, 2,$ or 3 is the spatial dimension of the model.

The difference is that the vector–function U in the model of an elastic-plastic granular material consists of the projections of the velocity vector v and the components of the conditional stress tensor s. In the model of a porous metal it consists of the velocities and the components of two stress tensors – the plastic stress tensor σ^p, which is constrained by the plasticity condition, and the conditional stress tensor s.

The inequality (11) is very useful in constructing the numerical algorithms for the solution of initial-boundary problems. A variant of such algorithm is considered in our monograph [20]. In this monograph one can find the examples of numerical modeling of the processes of an elastic-plastic waves propagation in a loosened granular medium.

5 CONCLUSIONS

- Rheological method is supplemented by a new element, a rigid contact, which make it possible to describe mechanical properties of materials having different resistance to compression and tension.

- By means of this method constitutive relationships of granular materials with rigid, elastic and elastic-plastic particles are considered.

- Constitutive equations of metal foams of low porosity are obtained describing the phases of elastic deformation and plastic loss of stability of a skeleton and the phase of elastic deformation of a compact material after the pores collapse.

Acknowledgements

This work was supported by the Russian Foundation for Basic Research (grant no. 11–01–00053), the Complex Fundamental Research Program no. 2 of the Presidium of the Russian Academy of Sciences, and the Interdisciplinary Integration Project no. 40 of the Siberian Branch of the Russian Academy of Sciences.

REFERENCES

[1] Golovanov, Yu.V, Shirko, I.V. Review of current state of the mechanics of fast motions of granular materials. *Mechanics of granular media: Theory of fast motions, Ser. New in Foreign Science*, **36**: 271–279. Mir, Moscow (1985).

[2] Sokolovskii, V.V. *Statics of granular media*. Nauka, Moscow (1990).

[3] Ishlinskii, A.Yu. and Ivlev, D.D. *Mathematical theory of plasticity*. Fizmatlit, Moscow (2003).

[4] Drucker, D.C. and Prager, W. Soil mechanics and plastic analysis or limit design. *Quart. Appl. Math.* (1952) **10**:157–165.

[5] Mróz, Z. and Szymanski, Cz. Non-associated flow rules in description of plastic flow of granular materials. *Limit analysis and rheological approach in soil mechanics*, No. 217. Springer–Verlag, Wien – New–York (1979).

[6] Gudehus, G. A comprehensive constitutive equations for granular materials. *Solids Found* (1996) **36**:1–12.

[7] Wu, W., Bauer, E. and Kolymbas, D. Hypoplastic constitutive model with critical state for granular materials. *Mech. Materials* (1996) **23**:45–69.

[8] Ambartsumyan, S.A. *Heteromodular elasticity theory*. Nauka, Moscow (1982).

[9] Maslov, V.P. and Mosolov, P.P. General theory of the solution of equations of motion for heteromodular elastic medium. *Prikl. Mat. Mekh.* (1985) **49**:419–437.

[10] Grigoryan, S.S. On basic concepts of the dynamics of soils. *Prikl. Mat. Mekh.* (1960) **24**:1057–1072.

[11] Nikolaevskii, V.N. Constitutive relationships of plastic deformation of granular medium. *Prikl. Mat. Mekh.* (1971) **35**:1070–1082.

[12] Geniev, G.A. and Estrin, M.I. *Dynamics of plastic and granular medium*. Stroiizdat, Moscow (1972).

[13] Berezhnoy, I.A., Ivlev, D.D. and Chadov, V.B. On the construction of the model of granular media, based on the definition of the dissipative function. *DAN SSSR* (1973) **213**:1270–1273.

[14] Savage, S.B. Gravity flow of cohesionless granular materials in chutes and channels. *J. Fluid Mech.* (1979) **92**:53–96.

[15] Goodman, M.A. and Cowin, S.C. Two problems in the gravity flow of granular materials. *J. Fluid Mech.* (1971) **45**:321–339.

[16] Nedderman, R.M. and Tüzün, U. A kinematic model for the flow of granular materials. *Powder Technology* (1979) **22**:243–253.

[17] Badiche, X., Fores, S., Guibert, T., Bienvenu, Y., Bartout, J.-D., Ienny, P., Croset, M. and Bernet, H. Mechanical properties and non-homogeneous deformation of open-cell nickel foams application of the mechanics of cellular solid and of porous metals. *Mater. Sci. Eng.* (2000) **A289**:276–288.

[18] Banhart, J. and Baumeister, J. Deformation characteristics of metal foams. *J. Mater. Sci.* (1998) **33**:1431–1440.

[19] Ashby, M.F. Plastic deformation of cellular materials. *Encyclopedia of Materials: Science and Technology* (2008) 7068–7071.

[20] Sadovskaya, O.V. and Sadovskii, V.M. *Mathematical modeling in the problems of mechanics of granular materials*. Fizmatlit, Moscow (2008).

XI International Conference on Computational Plasticity. Fundamentals and Applications
COMPLAS XI
E. Oñate, D.R.J. Owen, D. Peric and B. Suárez (Eds)

SMOOTHING OF YIELD SURFACES AND A REFORMULATION OF MULTI-SURFACE PLASTICITY

JOSE M. GESTO*, ANTONIO GENS* AND JEAN VAUNAT*

* Department of Geotechnical Engineering and Geosciences
Universitat Politècnica de Catalunya
Jordi Girona 1-3, Edifici D-2, 08034 Barcelona, Spain
e-mail: jose.manuel.gesto@upc.edu, antonio.gens@upc.edu, jean.vaunat@upc.edu
web page: http://www.upc.edu

Key words: Corners, Yield Surface, Plastic Potential, Multi-Surface Plasticity.

Abstract. In this work we describe a procedure for the smoothing of non-regular yield surfaces and plastic potential functions. We also present several application examples corresponding to different well-known cases. Moreover, we show that a multi-surface plasticity model can be reduced to a model with a single yield surface by using the same smoothing procedure.

1 INTRODUCTION

Yield Surfaces and Plastic Potential functions are two essential ingredients in Plasticity Theory; the former are defined as surfaces in the stress space that bound the elastic domain; the latter fix the direction of the vector of incremental plastic strains that appears under plastic loading. Many equations have been proposed to fit the shape of different yield surfaces and plastic potential functions and improving the performance of material modeling. Some of these equations produce geometrical singularities that imply the appearance of different conceptual and numerical problems due basically to that for certain loading states the vector of incremental plastic strains cannot be properly defined as the product of a plastic multiplier times the gradient of a yield function or a plastic potential function.

A celebrated theoretical solution due to Koiter [1] consists in writing the plastic strain rate vector at a singular point as a linear combination of the gradients of the concurrent plastic potential functions; the coefficients of the linear combination can be determined by solving a linear system of equations which is obtained by imposing the consistency conditions associated to each one of the involved yield surfaces. Further developments can be found, for instance, in [2,3,4] and the references therein.

Regarding the numerical implementation of models with singularities, often *ad hoc* corner rounding techniques are employed, though the programming may be laborious and the problem of the singularities may remain if higher-order derivatives of the involved functions

are needed. In some particular cases closed-form expressions for smooth yield surfaces and plastic potential functions have been derived. Occasionally, the smooth approximations fit the experimental data better than the original singular model; this is the case, for instance, of Mohr-Coulomb's (MC) surface, for which some smooth variations are available in the literature [5,6,7].

Here we describe a smoothing technique based on the algebraic composition of several implicit equations corresponding to different yield surfaces or plastic potential functions in order to produce a single implicit equation corresponding to a family of regular surfaces. The presented procedures have a wide range of application and their versatility allow us to tackle different variants of the smoothing problem. For instance, the non-regular points may appear due to the symmetries of the stress tensor, as it is the case of the MC model. In other cases, the singularities appear because the elastic domain is defined by means of different surface equations that correspond to different plastic mechanisms; this is the case of the so-called multi-surface models. With the proposed method, the reduction of a given multi-surface model to a model with a single regular yield surface is straightforward, which can be viewed as a reformulation of multi-surface plasticity.

In the following Sections we describe and illustrate the application of the presented approach to the smoothing of different yield surfaces; nevertheless, the presented procedures are applicable to yield surfaces and to plastic potential functions indistinctly, and they can be used both in the frameworks of associated and non-associated plasticity.

2 BRIEF DESCRIPTION OF THE SMOOTHING TECHNIQUE

Let us start with the simple case of the approximation of the boundary of a square by a smooth curve. We can draw the family of curves defined by the implicit equations $x^{2n} + y^{2n} = 1$ and study its behavior. In Figure 1 we can observe that, as n increases, the corresponding curve, which is a circumference in the beginning, becomes a square. Nevertheless, the obtained curves are perfectly regular in all cases.

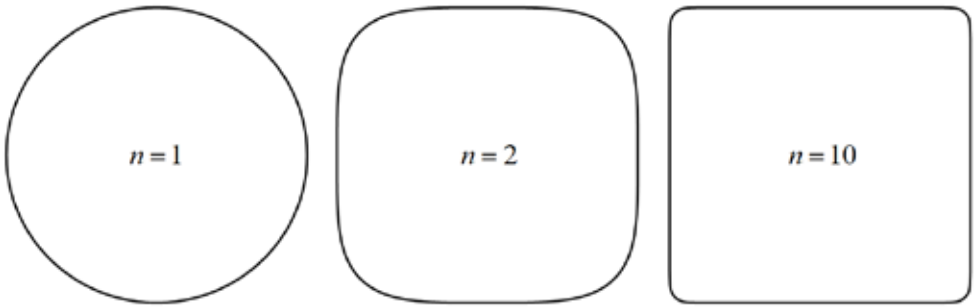

Figure 1: Evolution from a circumference to a square.

Let us note that the interior of the square can be described with the set $\left\{(x,y) \in \mathbb{R}^2 \,\middle|\, F_1(x,y) < 1,\ F_2(x,y) < 1\right\}$, where functions $F_1(x,y) = x^2$ and $F_2(x,y) = y^2$ are non-negative.

2.1 Foundations of the method

If Ω is a region of $\mathbb{R}^m$ which can be described in the form

$$\Omega = \left\{ \mathbf{x} \in \mathbb{R}^m \,\middle|\, F_i(\mathbf{x}) < 1,\ i = 1,...,k \right\}$$

for some k non-negative functions $F_i : \mathbb{R}^m \to \mathbb{R}^+$, $\mathbb{R}^+ = [0, \infty)$, then the sequence of sets $\{A_n\}_{n=1}^{\infty}$ defined by

$$A_n = \left\{ \mathbf{x} \in \mathbb{R}^m \,\middle|\, \sum_{i=1}^{k} \left(F_i(\mathbf{x}) \right)^n < 1 \right\}$$

grows up to Ω -*i.e.*, in terms of the Theory of Sets, $A_n \uparrow \Omega$-.

This result can be easily proved: if $\mathbf{x} \in A_n$, then $\left(F_i(\mathbf{x}) \right)^{n+1} \le \left(F_i(\mathbf{x}) \right)^n$, and, therefore, $\mathbf{x} \in A_{(n+1)}$. Moreover, if $\mathbf{x} \in \Omega$, then some $n_x \in \mathbf{N}$ there exists such that $\mathbf{x} \in A_{n_x}$; to see this, it is enough to see that $\sum_{i=1}^{k} \left(F_i(\mathbf{x}) \right)^n \le k \left(\max\{ F_i(\mathbf{x}) \} \right)^n$; thus, one can choose $n_x > \dfrac{\ln(1/k)}{\ln \max\{ F_i(\mathbf{x}) \}}$ if $\max\{ F_i(\mathbf{x}) \} > 0$ and $n_x = 1$ if $\max\{ F_i(\mathbf{x}) \} = 0$.

As a consequence of that, if F_i are regular functions, then the surface implicitly defined as $F(\mathbf{x}) = \sum_{i=1}^{k} \left(F_i(\mathbf{x}) \right)^n = 1$ -that is, ∂A_n- is also regular and can be used as a smooth approximation of $\partial\Omega$.

The above reasoning can be easily adapted to a more general expression like $F(\mathbf{x}) = \sum_{i=1}^{k} \left(F_i(\mathbf{x}) \right)^{\alpha_i} = 1$, where the exponents α_i are different and not necessarily integers. Moreover, if Ω is described by $\Omega = \left\{ \mathbf{x} \in \mathbb{R}^n \,\middle|\, \widetilde{F}_i(\mathbf{x}) < a_i,\ i = 1,...,k \right\}$, where $\widetilde{F}_i$ are not positive functions, it is always possible to obtain an equivalent description of Ω in the form $\Omega = \left\{ \mathbf{x} \in \mathbb{R}^m \,\middle|\, F_i(\mathbf{x}) < 1,\ i = 1,...,k \right\}$, where F_i are positive functions, just by taking, for example, $F_i(\mathbf{x}) = e^{\widetilde{F}_i(\mathbf{x}) - a_i}$.

This smoothing procedure is well-known, especially in the field of Computer Graphics. As a reference, the work [8] can be mentioned. A more detailed description of the technique can be found in [9], where it is applied to obtain numerical solutions for non-linear optimization problems on non-regular domains.

2.2 A general application example

Let us consider the functions

$$F_1(x, y, z) = x^2 + y^2 + z^2 - 1 \qquad F_2(x, y, z) = (x - 1.1)^2 + y^2 + z^2 - 0.35^2$$

$$F_3(x,y,z)=\frac{1}{2}\left(\frac{x-z}{1.2}\right)^2+\left(\frac{y-1.3}{0.6}\right)^2+\frac{1}{2}\left(\frac{x+z}{0.6}\right)^2-1$$

$$F_4(x,y,z)=\left(\frac{\sqrt{(y+0.6)^2+(z-0.6)^2}-1}{0.3}\right)^2+\left(\frac{x}{0.3}\right)^2-1,$$

and the domain $\Omega=\left\{x\in\mathbb{R}^3:\min\left\{F_1,F_2,F_3,F_4\right\}>0\right\}$. Equations $F_1=F_2=F_3=F_4=0$ describe two spheres, an ellipsoid and a torus, respectively, and Ω is the intersection of the exterior of these surfaces. Figure 2 displays $\partial\Omega$, which is a piecewise regular surface.

Figure 2: The boundary of Ω (left) and two perspectives of a smooth approximating surface (center and right).

We have $\Omega=\left\{x\in\mathbb{R}^3:\min\left\{e^{F_1},e^{F_2},e^{F_3},e^{F_4}\right\}>1\right\}=\left\{x\in\mathbb{R}^3:\max\left\{e^{-F_1},e^{-F_2},e^{-F_3},e^{-F_4}\right\}<1\right\}$, which allows us to define the implicit equations of smooth surfaces that tend to $\partial\Omega$ as, for instance, $S_p=\left\{x\in\mathbb{R}^3:F(x,y,z,p)=e^{-pF_1}+e^{-pF_2}+e^{-pF_3}+e^{-pF_4}=1\right\}$. Figure 2 shows two perspectives of the surface S_3.

2.3 The derivatives of the approximating smooth functions

With regards to the derivatives of *F,* note that $\frac{\partial F}{\partial x_i}=\sum_{j=1}^{k}\alpha_j\left(F_j(\mathbf{x})\right)^{\alpha_j-1}\frac{\partial F_j}{\partial x_i}$, and, therefore, the derivative $\frac{\partial F}{\partial x_i}$ is simply a linear combination of the derivatives $\frac{\partial F_j}{\partial x_i}$. The coefficients or weights $w_i=\alpha_i\left(F_i(\mathbf{x})\right)^{\alpha_i-1}$ of the linear combination describe the 'proximity' of $\mathbf{x}$ to each one of the different hyper-surfaces implicitly defined by $F_i(\mathbf{x})=1$. Let us finish by observing that if $\Omega=\left\{\mathbf{x}\in\mathbb{R}^m\,\middle|\,\widetilde{F}_i(\mathbf{x})<a_i,\ i=1,...,k\right\}$, then the surface $\widetilde{F}(\mathbf{x})=\sum_{i=1}^{k}e^{\alpha\left(\widetilde{F}_i(\mathbf{x})-a_i\right)}=1$, where we have supposed that all the exponents α_i are equal, is equivalent to the surface

$F(\mathbf{x}) = \ln\left(\sum_{i=1}^{k} e^{\alpha\left(\widetilde{F}_i(\mathbf{x})-a_i\right)}\right)^{\frac{1}{\alpha}} = 0$, and that this yield function satisfies $\frac{\partial F}{\partial x_i} = \sum_{j=1}^{n} w_j \frac{\partial F_j}{\partial x_i}$, where the weights $w_i = \frac{e^{\alpha\left(\widetilde{F}_i(\mathbf{x})-a_i\right)}}{\sum_{j=1}^{n} e^{\alpha\left(\widetilde{F}_j(\mathbf{x})-a_j\right)}}$ take values between 0 and 1.

3 PRIMARY SMOOTHING

If the material is isotropic, then the yield functions are commonly written in terms of invariants of the stress tensor. We will work here with three classical invariants: $p = \frac{\sigma_1+\sigma_2+\sigma_3}{3}$, the average stress, $J = \sqrt{\frac{1}{6}\left((\sigma_1-\sigma_2)^2+(\sigma_1-\sigma_3)^2+(\sigma_2-\sigma_3)^2\right)}$, a deviatoric stress, and $\theta = \arctan\left(-\frac{1}{\sqrt{3}}\frac{\sigma_1-2\sigma_2+\sigma_3}{\sigma_1-\sigma_3}\right)$, Lode's angle. We can suppose now that an expression for a yield surface of the model is $F(p,J,\theta,\boldsymbol{\chi}) = 1$, where $F(p,J,\theta,\boldsymbol{\chi}) \geq 0$ and F is a regular function. This yield surface defines an elastic domain in the first sextant $S = \left\{(\sigma_1,\sigma_2,\sigma_3) \in \mathbb{R}^3 \,|\, \sigma_1 \geq \sigma_2 \geq \sigma_3\right\}$. By using symmetries, we can obtain the corresponding elastic domain Ω in the stress space.

In this context, we distinguish two categories of smoothing: the first one, that we will call *primary smoothing*, corresponds to the fact that each one of the yield functions involved in the definition of a given model could need to be smoothed because of the apparition of corners after the application of the symmetries; if it would occur, this primary smoothing should be made even with a single-surface model. On the other hand, if the model requires different yield surfaces, a *multi-surface smoothing* could be needed to have a regular transition between all of them. In this Section we focus on the case of primary smoothing; multi-surface smoothing will be dealt with in Section 4.

3.1 Drucker-Prager's (DP) surface

Let us consider a yield function of the form $\widetilde{F}(p,J,a,b) = -ap + J - b$ for some $a > 0$, $b \geq 0$. The function is independent of the third invariant θ, and the surface $\widetilde{F}(p,J,a,b) = 0$ is a half cone in the stress space.

The surface $-ap + J - b = 0$ can be represented in the two-dimensional auxiliary space $p - J$, and also the surface $\widetilde{F}(p,-J,a,b) = -ap - J - b = 0$. Then, a smooth surface that approximates the cone is $F(p,J,a,b) = e^{\alpha(-ap+J-b)} + e^{-\alpha(ap+J+b)} = 2e^{-\alpha(ap+b)} ch\alpha J = 1$. Figure 3 shows the shape of the approximation in a generic case. The relationship between the power

α and the maximum absolute error ε is $\alpha = \frac{\ln 2}{a\varepsilon}$, and an alternative expression for the equation of the smoothed half cone is $2^{-\left(\frac{ap+b}{a\varepsilon}-1\right)} \cosh\frac{J\ln 2}{a\varepsilon} = 1$.

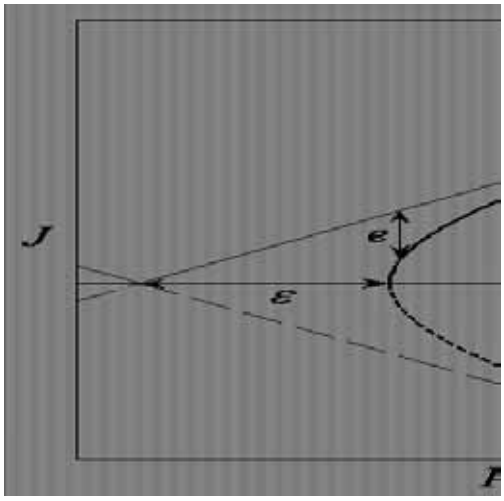

Figure 3: a smooth approximation of a DP surface.

On the other hand, it is frequent to describe the yield surfaces by means of dimensionless implicit equations. In that case, we can consider for instance the expression $\widetilde{F}(p,J,a,b) = \frac{J}{ap+b} = 1$. A smooth approximation of the half cone can be obtained by combining the yield function $\left|\frac{J}{ap+b}\right|$ with the plane $p = -\frac{b}{a} + \varepsilon$, $\varepsilon > 0$, in the form $\left|\frac{J}{ap+b}\right|^{\alpha} + e^{-\beta\left(\frac{ap+b}{a\varepsilon}-1\right)} = 1$, where $\alpha > 1$ -this restriction is necessary for guarantying the differentiability of the yield surface in the hydrostatic axis $J = 0$- and $\beta > 0$. As can be seen, in this case we have two independent parameters for controlling the shape of the approximation. It is necessary to choose carefully the values of these parameters in order to guaranty that the shape of the smooth surface is acceptable; in particular, we recommend to use $\beta \geq 1$.

3.2 Mohr-Coulomb's (MC) surface

In this case we can choose for the yield surface the dimensionless expression $\widetilde{F}(p,J,\theta,c',\varphi') = g(\theta) - \frac{p+a}{J} = 0$, where $g(\theta) = \frac{\cos\theta}{\sin\varphi'} + \frac{1}{\sqrt{3}}\sin\theta$, $a = c'\cot\varphi'$ and c', φ' are the cohesion and the internal friction angle of the material, respectively. The above yield surface is a straight line in the π-plane; if we apply the symmetries with respect to the axis of principal strains, we obtain the following six functions

$$F_1(p,J,\theta,c',\varphi') = \widetilde{F}(p,J,\theta,c',\varphi'), F_2(p,J,\theta,c',\varphi') = F_1\left(p,J,\frac{\pi}{3}-\theta,c',\varphi'\right)$$

$$F_3(p,J,\theta,c',\varphi') = F_1\left(p,J,-\frac{\pi}{3}-\theta,c',\varphi'\right), F_4(p,J,\theta,c',\varphi') = F_1(p,J,\pi-\theta,c',\varphi'),$$

$$F_5(p,J,\theta,c',\varphi') = F_1\left(p,J,\frac{2\pi}{3}+\theta,c',\varphi'\right),\ F_6(p,J,\theta,c',\varphi') = F_1\left(p,J,\frac{4\pi}{3}+\theta,c',\varphi'\right).$$

Now we can combine these functions by using the procedure described in Section 2. This gives the expression $F(p,J,\theta,c',\varphi') = e^{\alpha\left(g_{\varphi'}(\theta,\alpha)-\frac{p+a}{J}\right)} = 1$, or, equivalently, $J = \dfrac{p+a}{g_{\varphi'}(\theta,\alpha)}$, where the function $g_{\varphi'}(\theta,\alpha)$ is defined by

$$g_{\varphi'}(\theta,\alpha) = \frac{1}{\alpha}\ln\left(e^{\alpha g(\theta)} + e^{\alpha g\left(\frac{\pi}{3}-\theta\right)} + e^{\alpha g\left(-\frac{\pi}{3}-\theta\right)} + e^{\alpha g(\pi-\theta)} + e^{\alpha g\left(\frac{2\pi}{3}+\theta\right)} + e^{\alpha g\left(\frac{4\pi}{3}+\theta\right)}\right).$$

Fig. 7 shows the shape of the approximation for $\varphi' = 15^o$ and for $\varphi' = 40^o$.

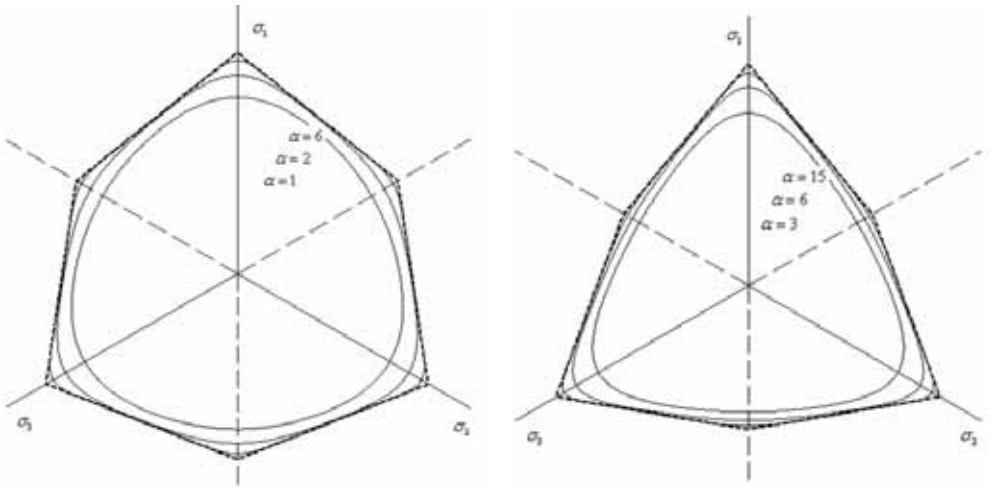

Figure 7: smooth approximations of MC surfaces for $\varphi' = 15^o$ and for $\varphi' = 40^o$.

Now, it is easy to modify this expression in order to smooth the vertex. By analogy with Subsection 3.1, we can construct the explicit equation $J = \dfrac{p+a}{g_{\varphi'}(\theta,\alpha)}\left(1-e^{-\beta\left(\frac{p+a}{\varepsilon}-1\right)}\right)^{\frac{1}{\delta}}$, $\delta > 1$, which corresponds to the implicit equation $\left|\dfrac{Jg_{\varphi'}(\theta,\alpha)}{p+a}\right|^{\delta} + e^{-\beta\left(\frac{p+a}{\varepsilon}-1\right)} = 1$. Other interesting choice for this case could be $2^{-\left(\frac{p+a}{\varepsilon}-1\right)}\cosh\dfrac{Jg_{\varphi'}(\theta,\alpha)\ln 2}{\varepsilon} = 1$.

3.3 Original Cam-Clay (OCC) surface

If we consider the general expression $\frac{JG_{\varphi'}(\theta)}{p_0+a}+\frac{p+a}{p_0+a}\ln\frac{p+a}{p_0+a}=0$, where $a=c'\cot\varphi'$ and $G_{\varphi'}(\theta)$ is a function that contains the influence of Lode's angle θ, then we can construct the smoothed surface $2e^{\alpha\frac{p+a}{p_0+a}\ln\frac{p+a}{p_0+a}}\cosh\frac{\alpha JH_{\varphi'}(\theta,\beta)}{p_0+a}=1$, where, for instance, $H_{\varphi'}(\theta,\beta)=C$ if $G_{\varphi'}(\theta)=C$ and $H_{\varphi'}(\theta,\beta)=g_{\varphi'}(\theta,\beta)$ if $G_{\varphi'}(\theta)=g(\theta)$. For a given absolute error ε_1 (Figure 4) we can define the dimensionless variable $c_1=1-\frac{\varepsilon_1}{p_0+a}$. Then, it holds that $\alpha=\frac{\ln 2}{c_1\ln\frac{1}{c_1}}$, which leads to the expression $2^{-\left(\frac{\frac{p+a}{p_0+a}\ln\frac{p+a}{p_0+a}}{c_1\ln c_1}-1\right)}\cosh\frac{JH^2_{\varphi'}(\theta,\beta_2)\ln 2}{(p_0+a)c_1\ln\frac{1}{c_1}}=1$ for the smoothed yield surface. It must been taken into account that this procedure also generates an absolute error ε_2 (Fig. 4) at point $p=-a$, $J=0$, though the original load surface is smooth there. If we define $c_2=\frac{\varepsilon_2}{p_0+a}$, then we have that, for a given $\alpha\geq e\ln 2$, c_1, c_2 are the two solutions of the equation $c\ln\frac{1}{c}=\frac{\ln 2}{\alpha}$.

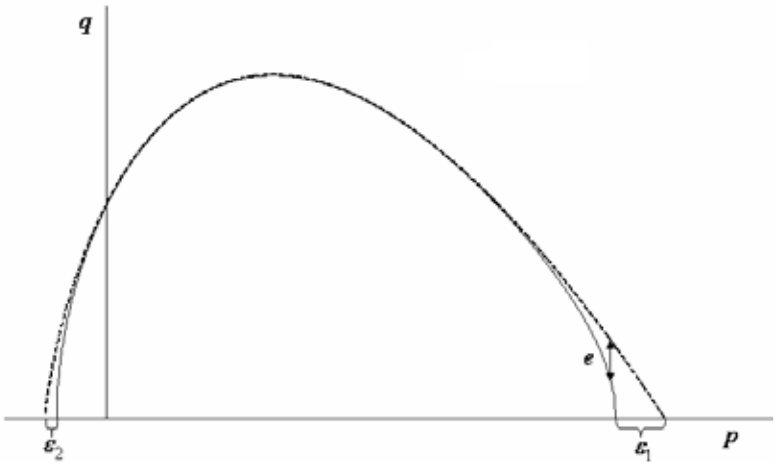

Figure 4: smooth approximation of the OCC surface.

4 MULTI-SURFACE SMOOTHING

The presented smoothing procedure allows us to reduce a multi-surface elasto-plastic model to an 'equivalent' single-surface elasto-plastic model. Let us consider for a multi-surface model all its *k* yield functions $F_1(\boldsymbol{\sigma},\boldsymbol{\chi}_1)$, ..., $F_k(\boldsymbol{\sigma},\boldsymbol{\chi}_k)$ and their corresponding plastic

potential functions and hardening functions, $G_1(\boldsymbol{\sigma},\xi_1)$, ..., $G_k(\boldsymbol{\sigma},\xi_k)$ and $\boldsymbol{\chi}_1\left(\boldsymbol{\varepsilon}^p\right)$, ..., $\boldsymbol{\chi}_k\left(\boldsymbol{\varepsilon}^p\right)$, respectively. Then, $d\boldsymbol{\varepsilon}^p=\sum_{i=1}^{n}\frac{\partial G_i}{\partial\boldsymbol{\sigma}}d\lambda_i$ and $d\boldsymbol{\chi}_i=\sum_{j=1}^{n}h_{ij}d\lambda_j$ are two general expressions for the flow rule and for the hardening rules, respectively. If we suppose that the equations of the plastic surfaces are $F_1(\boldsymbol{\sigma},\boldsymbol{\chi}_1)=1$, ..., $F_k(\boldsymbol{\sigma},\boldsymbol{\chi}_k)=1$, where $F_1(\boldsymbol{\sigma},\boldsymbol{\chi}_1)\geq 0$, ..., $F_k(\boldsymbol{\sigma},\boldsymbol{\chi}_k)\geq 0$, then, when all the yield functions are regular, we can construct the yield function $F\left(\boldsymbol{\sigma},\boldsymbol{\chi}_1,...,\boldsymbol{\chi}_k\right)=\sum_{i=1}^{k}\left(F_i(\boldsymbol{\sigma},\boldsymbol{\chi}_i)\right)^{\alpha_i}$ and the corresponding smooth single yield surface $F\left(\boldsymbol{\sigma},\boldsymbol{\chi}_1,...,\boldsymbol{\chi}_k\right)=1$. The flow rule $d\boldsymbol{\varepsilon}^p=d\lambda\sum_{i=1}^{k}w_i\frac{\partial G_i}{\partial\boldsymbol{\sigma}}$ can be used, where weights w_i are defined as in Subsection 2.3. This choice is motivated by the need of recovering the expression $d\boldsymbol{\varepsilon}^p=d\lambda\frac{\partial F}{\partial\boldsymbol{\sigma}}$ in associated plasticity. Let us observe that if we take $d\lambda_i=w_i d\lambda$, then we have $d\boldsymbol{\varepsilon}^p=\sum_{i=1}^{k}d\lambda_i\frac{\partial G_i}{\partial\boldsymbol{\sigma}}$. This expression is formally equal to the classical Koiter's one, but with this approach only an independent plastic multiplier there exists. In the same way, we can write $d\boldsymbol{\chi}_i=d\lambda\sum_{j=1}^{n}w_j h_{ij}$. The value of the plastic multiplier $d\lambda$ is obtained by means of the usual single-surface consistency condition $dF=0$.

4.1 MC with a MC-OCC cap model

Consider a bi-surface shear-volumetric plastic model with an OCC cap. The elastic domain corresponding to such a model is in general bounded (in the first sextant) by the yield surfaces $G^1_{\varphi'}(\theta)-\frac{p+a}{J}=0$ (shear surface) and $\frac{G^2_{\varphi'}(\theta)}{\ln\frac{p_0+a}{p+a}}-\frac{p+a}{J}=0$ (OCC cap). In these equations, the expression of the functions $G^1_{\varphi'}$ and $G^2_{\varphi'}$ can correspond to a DP model, a MC model or other models.

A first step towards the smooth 'equivalent' single-surface could consist in substituting functions $G^1_{\varphi'},G^2_{\varphi'}$ by other functions $H^1_{\varphi'},H^2_{\varphi'}$ -which can be obtained like it has been shown in previous Sections- and making the composition $e^{\alpha\left(H^1_{\varphi'}(\theta,\beta_1)-\frac{p+a}{J}\right)}+e^{\alpha\left(\frac{H^2_{\varphi'}(\theta,\beta_2)}{\ln\frac{p_0+a}{p+a}}-\frac{p+a}{J}\right)}=1$, which leads to the explicit expression

$$J=\frac{p+a}{h_{\varphi'}\left(p,\theta,\alpha,\beta_1,\beta_2\right)},\ \text{where}\ h_{\varphi'}\left(p,\theta,\alpha,\beta_1,\beta_2\right)=\frac{1}{\alpha}\ln\left(e^{\alpha H^1_{\varphi'}(\theta,\beta_1)}+e^{\alpha\frac{H^2_{\varphi'}(\theta,\beta_2)}{\ln\frac{p_0+a}{p+a}}}\right).$$

After that, there are still two singular points on the hydrostatic axis at $p=-a$ and at $p=p_0$. They can be eliminated, for instance, by taking the new explicit expression $J=\frac{p+a}{h_{\varphi'}(p,\theta,\alpha,\beta_1,\beta_2)}\left[\left(1-e^{-\beta\left(\frac{1}{c_2}\frac{p+a}{p_0+a}-1\right)}\right)\left(1-e^{\beta\left(\frac{1}{c_1}\frac{p+a}{p_0+a}-1\right)}\right)\right]^{\frac{1}{\delta}}$, where $\delta>1$, $\beta>0$ and c_1, $c_2>0$; in these conditions, J nulls at $p_1=-a+c_2(p_0+a)$ and at $p_2=-a+c_1(p_0+a)$. The implicit equation that corresponds to this smoothed surface is $\left|\frac{Jh_{\varphi'}(p,\theta,\alpha,\beta_1,\beta_2)}{p+a}\right|^{\delta}+e^{-\beta\left(\frac{1}{c_2}\frac{p+a}{p_0+a}-1\right)}+e^{\beta\left(\frac{1}{c_1}\frac{p+a}{p_0+a}-1\right)}-e^{-\beta\frac{p+a}{p_0+a}\frac{c_1-c_2}{c_1c_2}}=1$.

Figure 9 shows, for instance, a smoothed MC & MC-OCC surface.

Figure 9: 3D representation of a regular approximation of a MC model with a MC-OCC cap.

4 CONCLUSIONS

We have described a smoothing technique based on the algebraic combination of different functions and we have showed how this technique can be used in the framework of isotropic plasticity to obtain smooth approximations for yield surfaces with corners. Moreover, the introduced procedures have been used to propose a reformulation of multi-surface plasticity. We have presented several application examples that illustrate the versatility of the presented approach.

REFERENCES

[1] Koiter, W.T. Stress-strain relations, uniqueness and variational theorems for elasto-plastic materials with a singular yield surface. *Quart. Appl. Math.* (1953) **11**: 350-354.

[2] De Borst, R. Integration of Plasticity Equations for singular Yield Functions, *Computers & Structures* (1987) **5**: 823-829.

[3] Ottosen, N.S. and Ristinmaa, M. Corners in Plasticity-Koiter's Theory revisited, *Int. J. Solids Structures* (1996) **25**: 3697-3721.

[4] Clausen, J. M. *Efficient non-Linear Finite Element Implementation of Elasto-Plasticity for Geotechnical Problems* (2007), Ph.D. Thesis, Esbjerg Institute of Technology, Aalborg University, Denmark.

[5] Lade, P.V. and Duncan, J.M. Elasto-plastic stress-strain theory for cohesionless soil, *Jour. Geot. Eng. Div*. (1975) **101**: 1037-1053.
[6] Matsuoka, H & Nakai, T. Stress-deformation and strength characteristics of soil under three different principal stresses, *Proc. JSCE* (1974) **232**: 59-70.
[7] Van Eekelen, H.A.M. Isotropic yield surfaces in three dimensions for use in soil mechanics. *Int. J. Nume. Anal. Meth. Geomech.* (1980) **4**: 89-101.
[8] Blinn, J.F. A generalization of algebraic surface drawing, *ACM Trans. Graph.* (1982), **1**: 235-256.
[9] Bendito, E., Carmona, A., Encinas, A.M. & Gesto, J.M. Estimation of Fekete points, *J. Comput. Phys*. (2007) **225**: 2354-2376.

XI International Conference on Computational Plasticity. Fundamentals and Applications
COMPLAS XI
E. Oñate, D.R.J. Owen, D. Peric and B. Suárez (Eds)

THE TIKHONOV REGULARIZATION METHOD IN ELASTOPLASTICITY

HILBETH P. AZIKRI DE DEUS†, CLAUDIO R. ÁVILA DA SILVA Jr.†, IVAN M. BELO† AND JOÃO CARLOS A. COSTA Jr.††

†Nucleus of Applied and Theoretical Mechanics (NuMAT - UTFPR/PPGEM/DAMEC)
UTFPR/DAMEC: Av. Sete de Setembro, 3165, CEP 80230-901, Curitiba-PR, Brazil
e-mail: numat-ct@utfpr.edu.br, http://www.numat.ct.utfpr.edu.br/
(supported by Araucaria Fundation, PR, Brazil, grant 249/2010-17670)

†† Federal University of Rio Grande do Norte (UFRN/DEM)
Email: arantes@ufrnet.br, http://www.dem.ufrn.br

Key words: Elastoplasticity, regularization method, Galerkin method

Abstract. The numeric simulation of the mechanical behaviour of industrial materials is widely used in the companies for viability verification, improvement and optimization of designs. The eslastoplastic models have been used for forecast of the mechanical behaviour of materials of the most several natures (see [1]). The numerical analysis from this models come across ill-conditioning matrix problems, as for the case to finite or infinitesimal deformations. A complete investigation of the non linear behaviour of structures it follows from the equilibrium path of the body, in which come the singular (limit) points and/or bifurcation points. Several techniques to solve the numerical problems associated to these points have been disposed in the specialized literature, as for instance the call Load controlled Newton-Raphson method and displacement controlled techniques. Although most of these methods fail (due to problems convergence for ill-conditioning) in the neighbour of the limit points, mainly in the structures analysis that possess a snap-through or snap-back equilibrium path shape (see [2]). This work presents the main ideas formalities of Tikhonov Regularization Method (for example see [12]) applied to dynamic elastoplasticity problems (J2 model with damage and isotropic-kinetic hardening) for the treatment of these limit points, besides some mathematical rigour associated to the formulation (well-posed/existence and uniqueness) of the dynamic elastoplasticity problem. The numeric problems of this approach are discussed and some strategies are suggested to solve these misfortunes satisfactorily. The numerical technique for the physical problem is by classical Gelerkin method.

1 INTRODUCTION

Elastoplastic models have been widely used to forecast the behaviour of rate independent (in deformation sense) materials (see [1]). The numerical solution of these models involves handling of ill-conditioned matrices, for finite or infinitesimal deformations (see [**?**]). Such instabilities are due to the tangent operator being close to an identically null forth order tensor operator at the neibourhood of critical or limit points.

A complete investigation of non linear structural behaviour involves following the bodies equilibrium path through singular (limit) points and/or bifurcation points. In order to solve the numerical problems associated to these points several techniques have been considered in the specialized literature, for instance the so-called load controled Newton-Raphson method and displacement controled techniques. Due to ill-conditioning convergence problems, most of these methods fail, specially in the case of structures which present (λ-load factor,u-displacement) snap-through or snap-back equilibrium paths ([2]), as shown in figure (Fig.1).

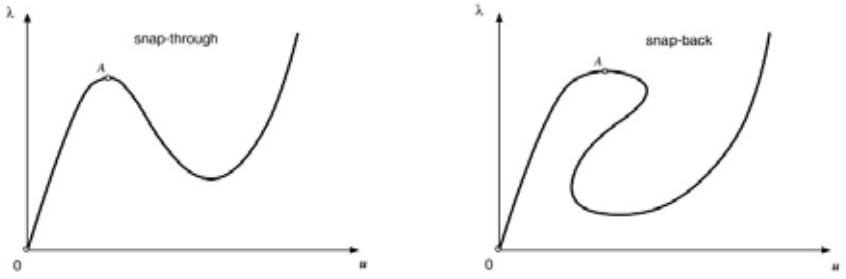

Figure 1: Snap-through and snap-back behaviour

Aiming at transposing these difficulties, this study proposes use of the L-curve Tikhonov regularization method ([14], [15], [6] and [12]). One of the objectives of the study is to investigate the potential of this approach in the solution of elastoplastic problems of infinitesimal strain. An overview of elastoplastic contitutive model is shown in section 2. Details about incremental approach are presented in section 3. In sections 4 and 5, it is presented the L-curve Thikhonov regularization method and main properties are shown. In section 6, a numerical problem case are presented to verify the efficacy of this proposed approch and concluding remarks are made in section 7.

2 YIELDING AND HARDENING LAWS (THE ELASTOPLASTIC CONSTITUTIVE MODEL)

A complete characterization of general elastoplastic model request definition of evolutionary laws of internal variables, i. e., variables associated to dissipative phenomena (ε^p and α_k - associated with the kinematic hardening mechanism). The first point in this

analysis is determination of the plastic multiplier $\dot{\lambda}$ which is computed from consistence condition ($\mathcal{F} = 0$ and $\dot{\lambda} > 0$). Hence, from definition of α_k, we obtain

$$\dot{\lambda} = \frac{\frac{\partial \mathcal{F}}{\partial \sigma} : \mathbb{D}\dot{\varepsilon}}{\left\{ \frac{\partial \mathcal{F}}{\partial \sigma} : \mathbb{D}\mathbf{N} - \rho \frac{\partial \mathcal{F}}{\partial \alpha_k} . \left[\frac{\partial^2 \Psi^p}{\partial \beta_k^2} \right] \mathbf{H} \right\}}. \tag{1}$$

More details about constitutive Lemaitre's elastoplastic-damage simplified model with isotropic hardening can be found in [4] and [3]. In this sense, the elastoplastic constitutive model is described in following steps

Elastoplastic Constitutive Model

1. **Strain Tensor Additive Decomposition**
$$\varepsilon = \varepsilon^e + \varepsilon^p.$$
2. **Free Energy Potential Definition**
$$\Psi\left(\varepsilon^e, r, \alpha^D, D\right) = \Psi^e\left(\varepsilon^e, D\right) + \Psi^p\left(r, \alpha^D\right)$$
where α^D is the deviator part of α (backstrain tensor), r is the accumulated plastic strain, D is the isotropic damage variable.
3. **Constitutive equation for σ and thermodynamics forces β_k**
$$\sigma = \rho \frac{\partial \Psi^e}{\partial \varepsilon^e} \qquad \text{and} \qquad \beta_k = \rho \frac{\partial \Psi^p}{\partial \alpha_k}.$$
4. **Elastic-damage Coupling** $\sigma = (1 - D)\mathbb{D}\varepsilon^e$.
5. **Yield Function/Dissipation Potential(Associative Approach)**

$\mathcal{F}_p = \|\tilde{\sigma}^D - \chi^D\| - (R + \sigma_y)$ where $\tilde{\sigma}^D_{eq} = \left\{ \frac{3}{2} \tilde{\sigma}^D : \tilde{\sigma}^D \right\}^{\frac{1}{2}}$;
$\tilde{\sigma}^D = \frac{1}{(1-D)} \{\sigma - \sigma_H I\}$ and $\sigma_H = \frac{1}{3} tr(\sigma)$.

6. **Hardening and Evolutionary Plastic Laws**

$\dot{\varepsilon}^p = \dot{\lambda} \frac{\partial \mathcal{F}_p}{\partial \sigma}$, $\dot{r} = -\dot{\lambda} \frac{\partial \mathcal{F}_p}{\partial R}$ and $\dot{D} = \dot{\lambda} \frac{\partial \mathcal{F}_D}{\partial Y}$
where
$\mathcal{F} = \mathcal{F}_p + \mathcal{F}_D$ with $\mathcal{F}_p = \|\tilde{\sigma}^D - \chi^D\| - (R + \sigma_y)$ and $\mathcal{F}_D = \frac{Y^2}{2S(1-D)} H(p - p_d)$.

From these potentials it follows that
$\dot{\varepsilon}^p = \frac{3}{2} \frac{\dot{\lambda}}{(1-D)} \frac{\sigma^D}{\sigma^D_{eq}}$, $\dot{\chi} = \gamma(\chi_\infty \dot{\varepsilon}^p - \chi \dot{\lambda})$, $\dot{R} = b(R_\infty - R)\dot{\lambda}$ and $\dot{D} = \frac{Y}{S}\, \dot{p}\, H(p - p_d)$.
Then
$\dot{p} = \frac{\dot{\lambda}}{(1-D)}$ and $Y = \frac{\left(\tilde{\sigma}^D\right)^2}{2E} \left\{ \frac{2}{3}(1 + \nu) + 3(1 - 2\nu) \left(\frac{\sigma_H}{\sigma^D_{eq}} \right)^2 \right\}$.

7. **Consistence Condition under Plastic Yielding** $\left(\dot{\lambda} \neq 0\right)$
$$\mathcal{F}(\sigma, \alpha_k) \leq 0, \qquad \dot{\lambda} \geq 0, \qquad \mathcal{F}(\sigma, \alpha_k)\, \dot{\lambda} = 0$$
and $\dot{\lambda}\, \dot{\mathcal{F}}(\sigma, \alpha_k) = 0$.

3 INCREMENTAL FORMULATION

In this section we describe the incremental formulation of the problem between t_n and t_{n+1} instants. We consider that all state variables are known on Ω_n and equilibrium equations are imposed in Ω_{n+1}. In this way, on t_{n+1}, the weak formulation of the problem can be written as:

Problem 1. *Determine* $u_{n+1} \in Kin_o^u$ *such that*

$$\digamma\left(u_{n+1};\hat{\mathbf{v}}\right)=0, \qquad \forall \;\; \hat{v} \in Var_o^u, \tag{2}$$

where

$$\digamma\left(u_{n+1};\hat{\mathbf{v}}\right)=\int_{\Omega_o}\mathbf{P}\left(u_{n+1}\right):\nabla\hat{\mathbf{v}}d\Omega_o-\int_{\Omega_o}\rho_o\left(\bar{\mathbf{b}}-\ddot{u}_n\right)\cdot\hat{\mathbf{v}}d\Omega_o-\int_{\Gamma_o^t}\mathbf{t}\cdot\hat{\mathbf{v}}dA_o. \tag{3}$$

To solve above non linear problem in terms of u_{n+1} is used the Newton method. Hence, taking

$$u_{n+1}^0=u_n, \qquad k=0 \tag{4}$$

where k denotes the Newton method iteration step. Supposing the initial condition is given by last increment step converged solution u_n, then on k-th iteration we have

$$u_{n+1}^{k+1}=u_{n+1}^k+\Delta u_{n+1}^k. \tag{5}$$

To determine $\Delta\mathbf{u}_{n+1}^k$, one has

$$D\digamma\left(u_{n+1}^k;\hat{\mathbf{v}}\right)\left[\Delta u_{n+1}^k\right]=-\digamma\left(u_{n+1}^k;\hat{\mathbf{v}}\right), \tag{6}$$

with

$$D\digamma\left(u_{n+1}^k;\hat{\mathbf{v}}\right)\left[\Delta u_{n+1}^k\right]=\int_{\Omega_o}\frac{d}{d\epsilon}\left[\mathbf{P}\left(u_{n+1}^k+\epsilon\Delta u_{n+1}^k\right)\right]_{\epsilon=0}:\nabla\hat{\mathbf{v}}\;d\Omega_o, \tag{7}$$

where Ω_o is fixed in space and it is supposing that $\mathbf{t}_{o_{n+1}}$ and $\bar{\mathbf{b}}_{n+1}$ are non depended of u. After some algebraic manipulations, we obtain

$$D\digamma\left(u_{n+1}^k;\hat{\mathbf{v}}\right)\left[\Delta u_{n+1}^k\right]=\int_{\Omega_o}\left[\mathbb{A}\left(u_{n+1}^k\right)\right]\nabla\left(\Delta u_{n+1}^k\right):\nabla\hat{\mathbf{v}}\;d\Omega_o, \tag{8}$$

where $\mathbb{A}$ (fourth order tensor) is the global tangent modulus, that is given by

$$\left[\mathbb{A}\left(\mathbf{u}_{n+1}^k\right)\right]_{ijkl}=\left.\frac{\partial P_{ij}}{\partial F_{kl}}\right|_{\mathbf{u}_{n+1}^k}. \tag{9}$$

On the other hand,observing the problem from an Eulerian approach, it is defined a couple of sets for each $t \in S$

$$Kin_u(\Omega) = \left\{u_i:\Omega\to\mathbb{R}\mid u_i\in H^1(\Omega),u\left(\mathbf{x},t\right)=\bar{u}\left(\mathbf{x},t\right),\forall\mathbf{x}\in\Gamma^u\right\}; \tag{10}$$

$$Var_u(\Omega) = \left\{\hat{v}_i:\Omega\to\mathbb{R}\mid \hat{v}_i\;\in H^1(\Omega_t),\hat{v}_i\left(\mathbf{x}\right)=0,\forall\mathbf{x}\in\Gamma^u\right\}. \tag{11}$$

Hence, the weak formulation of the problem can be written as

Problem 2. *Determine* $u(\mathbf{x},t) \in Kin_u(\Omega)$*, for each* $t \in S$*, such that*

$$\int_\Omega \sigma \colon \nabla\hat{\mathbf{v}} d\Omega = \int_\Omega \rho\,(\mathbf{b} - \ddot{u}) \cdot \hat{\mathbf{v}} d\Omega + \int_{\Gamma^t} \mathbf{t} \cdot \hat{\mathbf{v}} dA, \qquad \forall \;\; \hat{\mathbf{v}} \in Var_u(\Omega), \tag{12}$$

and in this case the tangent operator (or the global tangent modulus) can be described as

$$\left[\mathbb{A}\left(u^k_{n+1}\right)\right]_{ijkl} = \left.\frac{\partial \sigma_{ij}}{\partial \epsilon_{kl}}\right|_{\mathbf{u}^k_{n+1}}. \tag{13}$$

It is important to comment that in bouth cases (Lagrangian or Eulerian approach) the global tangent modulus is defined by a rate of conjugated pairs.

4 THE TIKHONOV REGULARIZATION METHOD

After the Galerkin method discretization the problem described above belongs

$$\min_{\mathbf{f}\in\mathbb{R}^n} \|\mathbf{A}\mathbf{f} - \mathbf{g}\|_2, \quad \mathbf{A} \in \mathbb{R}^{n\times n} \quad \mathbf{g} \in \mathbb{R}^n, \tag{14}$$

where $\mathbf{A}$ (matrix representation for discretized tangent operator $\left[\mathbb{A}\left(\mathbf{u}^k_{n+1}\right)\right]_{ijkl}$) has high condition number (ill-conditioned and singular values decreasing to zero without a gap on spectrum) on limit points neighbourhood ($\partial\sigma_{ij}/\partial\epsilon_{kl} \approx$ null fourth order tensor) due to the shape of the equilibrium path response. The $\mathbf{g}$ consists to discretized vectorial representation of $-\digamma\left(\mathbf{u}^k_{n+1}; \hat{\mathbf{v}}\right)$. Unfortunately for the standard least square (LS) the solution can be presented as $\mathbf{f}_{\text{ls}} = \mathbf{A}^\dagger\mathbf{g}$ (where $\mathbf{A}^\dagger$ denotes the pseudoinverse of $\mathbf{A}$) has serious numerical spurious error. In this sense, the Tikhonov regularization method is a natural way to computate a solution less susceptible to numerical errors. The classical Tikhonov method ([5] and [6]) consists in

$$\min_{\mathbf{f}\in\mathbf{R}^n} \beth(\mathbf{f}) \tag{15}$$

where $\beth(\mathbf{f}) = \|\mathbf{A}\mathbf{f} - \mathbf{g}\|^2 + \tilde{\lambda}\|\mathbf{f}\|^2$ and $\tilde{\lambda} > 0$ is the regularization parameter. This problem (15) is equivalent to research solution of the regularized normal equation

$$(\mathbf{A}^T\mathbf{A} + \tilde{\lambda}\mathbf{I}_n)\mathbf{f} = \mathbf{A}^T\mathbf{g}, \tag{16}$$

whose solution is $\mathbf{f}_{\tilde{\lambda}} = (\mathbf{A}^T\mathbf{A} + \tilde{\lambda}\mathbf{I}_n)^{-1}\mathbf{A}^T\mathbf{g}$, and $\mathbf{I}_n$ is the identity matrix $n \times n$. Now the problem is how to determine $\tilde{\lambda}$ parameter such that $\mathbf{f}_{\tilde{\lambda}}$ be the nearest solution of the solution without numeric errors. A lot of techniques for the regularization parameter choice were developed and they are presented in the specialized literature. hese techniques can be organized in two classes: techniques that involves the pre-known (or estimative) of the norm error e behaviour, as discrepancy principle (DP) evidenced in Morozov [8], and techniques that do not explore this information. In this second class it can be cited the L-curved method (see [9]), generalized cross-validation (GCV) (see [10]), weighted-GCV

(W-GCV) (see [11]), and a fixed point method (FP-method) (see [12]). For an overview of parameter-choice techniques for Tikhonov regularization method see [6] and recently [12].

Considering SVD of $\mathbf{A}$, $\mathbf{A} = \hat{\mathbf{S}}_1\hat{\mathbf{S}}_2\hat{\mathbf{S}}_3^T$, where $\hat{\mathbf{S}}_2 \in \mathbb{R}^{n\times n}$ is a singular value diagonal matrix, and $\hat{\mathbf{S}}_1, \hat{\mathbf{S}}_3 \in \mathbb{R}^{n\times n}$ are unitary matrixes, with $\hat{\mathbf{S}}_3$ non sigular matrix, the Thikhonov problem (15) can be written as

$$(\mathbf{A}^T\mathbf{A} + \tilde{\lambda}\mathbf{I}_n)\mathbf{f}_{\tilde{\lambda}} = \mathbf{A}^T\mathbf{g} \therefore \mathbf{f}_{\tilde{\lambda}} = \hat{\mathbf{S}}_3(\hat{\mathbf{S}}_2^2 + \tilde{\lambda}\mathbf{I}_n)^{-1}\hat{\mathbf{S}}_2\hat{\mathbf{S}}_1^T\mathbf{g}, \tag{17}$$

or $\mathbf{f}_{\tilde{\lambda}} = \sum_{i=1}^{n} \frac{\hat{S}_{2_i}^2}{\hat{S}_{2_i}^2+\tilde{\lambda}^2}\frac{\hat{\mathbf{S}}_{1_i}^T\mathbf{g}}{\hat{S}_{2_i}}\hat{\mathbf{S}}_{3_i}$ with $\hat{S}_{2_i}^2$ representing the i-th singular value, $\hat{\mathbf{S}}_{1_i}$ is the i-th colum vector of $\hat{\mathbf{S}}_1$ and $\hat{\mathbf{S}}_{3_i}$ is the i-th colum vector of $\hat{\mathbf{S}}_3$.

Observing the problem (15), it is expected that the solution of this optimization problem converges to the solution of the equation $\mathbf{Af} = \mathbf{g}$ as $\tilde{\lambda}$ tends to zero. In this sense, some properties of Tikhonov regularization method are shown in following theorem

Theorem 1. *Let $\mathbf{A} : \mathbb{R}^n \to \mathbb{R}^n$ be bounded. For every $\tilde{\lambda} > 0$ there exists a unique minimum $\mathbf{f}_{\tilde{\lambda}}$ of (15). Furthermore, $\mathbf{f}_{\tilde{\lambda}}$ satisfies the normal equation*

$$\tilde{\lambda}\langle\mathbf{f}_{\tilde{\lambda}}, \omega\rangle + \langle\mathbf{Af}_{\tilde{\lambda}} - \mathbf{g}, \mathbf{A}\omega\rangle = 0, \forall\omega \in \mathbb{R}^n, \tag{18}$$

or, using the adjoint $\mathbf{A}^* = \mathbf{A}^T : \mathbb{R}^n \to \mathbb{R}^n$ of $\mathbf{A}$,

$$(\mathbf{A}^T\mathbf{A} + \tilde{\lambda}\mathbf{I}_n)\mathbf{f}_{\tilde{\lambda}} = \mathbf{A}^T\mathbf{g}. \tag{19}$$

If, in addition, $\mathbf{A}$ is one-to-one and $\mathbf{f} \in \mathbb{R}^n$ is the (unique) solution of the equation $\mathbf{Af} = \mathbf{g}$ then $\mathbf{f}_{\tilde{\lambda}} \to \mathbf{f}$ as $\tilde{\lambda}$ tends to zero. Finally, if $\mathbf{f} \in \mathbf{A}^T(\mathbb{R}^n)$ or $\mathbf{f} \in \mathbf{A}^T\mathbf{A}(\mathbb{R}^n)$, then $\exists c > 0$ with $\|\mathbf{f}_{\tilde{\lambda}} - \mathbf{f}\| = c\sqrt{\tilde{\lambda}}$ or $\|\mathbf{f}_{\tilde{\lambda}} - \mathbf{f}\| = c\tilde{\lambda}$, respectively.

5 THE L-CURVE TECHNIQUE

In this section it is presented some ideas about the L-curve thechnique for choosing the regularization parameter. In this sense, let $\mathbf{f}_{\tilde{\lambda}}$ for be the family of solutions of the method of Tikhonov problem (15) and set

$$\vartheta_{1\tilde{\lambda}} := \|\mathbf{Af}_{\tilde{\lambda}} - \mathbf{g}\|^2 \text{ and } \vartheta_{2\tilde{\lambda}} := \|\mathbf{f}_{\tilde{\lambda}}\|^2. \tag{20}$$

It can be verified that $\mathbf{f}_{\tilde{\lambda}}$ is a solution of the method of residuals ($e_{1\tilde{\lambda}} := \sqrt{\vartheta_{1\tilde{\lambda}}}$) and quasisolutions ($e_{2\tilde{\lambda}} := \sqrt{\vartheta_{2\tilde{\lambda}}}$). Defining the bounded set

$$C := \left\{(c_1, c_2) \in \mathbb{R}^2 | \exists\mathbf{f} \in \mathbb{R}^n \text{ with } \|\mathbf{Af} - \mathbf{g}\| \le c_1 \text{ and } \|\mathbf{f}\| \le c_2\right\}, \tag{21}$$

it can be shown that the function $\tilde{\lambda} \mapsto e_{1\tilde{\lambda}}$ is increasing, $\tilde{\lambda} \mapsto e_{2\tilde{\lambda}}$ is decreasing and C is a convex set with boundary given by the curve $\tilde{\lambda} \mapsto (e_{1\tilde{\lambda}}, e_{2\tilde{\lambda}})$. Although if it cannot

determine the rate $\frac{e_{1\tilde{\lambda}}}{e_{2\tilde{\lambda}}}$, it must be have to specify a method/technique to determine $\tilde{\lambda}$ in an optimal sense with using $\vartheta_{1\tilde{\lambda}}$ and $\vartheta_{2\tilde{\lambda}}$. In this way, the L−curve criterion consists in determine $\tilde{\lambda}$ which maximizes the curvature in the typical L-shaped curve $\ell : \tilde{\lambda} \in (0,\infty) \mapsto (\ln(e_1), \ln(e_2)) \in \mathbb{R}^2$. The main motivation comes from the fact that in almost vertical portion of $\ell-$graph for very small changes of $\tilde{\lambda}$ values corresponds to rapidly varying to regularized solutions norm with very little change in $\vartheta_{1\tilde{\lambda}}$, while on horizontal part of the graphic for larger values of $\tilde{\lambda}$ corresponds to regularized solutions norm where the plot is flat or slowly decreasing, for more detail see [9]. From these arguments, the L-curve corner is located in a natural transition point that links these two regions, for more details and substantial results see [6].

The evaluation of second derivatives shows that curve is convex and steeper as $\tilde{\lambda}$ approaches to the smallest singular value. The L−curve consists of a vertical part where e_2 is near of the maximum value and adjacent part with smaller slope and the more horizontal part corresponds to solutions dominated by regularization errors where the regularization parameter is too large. In this sense, the problem is to seek the L−curve point where the maximum curvature is reached.

Supposing L−curve is sufficiently smooth (in continuous sense) curvature $\kappa\left(\tilde{\lambda}\right)$ can be computed as

$$\kappa\left(\tilde{\lambda}\right) = \frac{e_1^{'} e_2^{''} - e_1^{''} e_2^{'}}{\left(\left(e_1^{'}\right)^2 + \left(e_2^{'}\right)^2\right)^{\frac{3}{2}}}, \tag{22}$$

where $(')$ denotes a derivative with respect to $\tilde{\lambda}$ regularization parameter and any one dimensional optimization method can be used to solve $\tilde{\lambda}$ for the maximum curvature problem. It must be to point out that numerical effort involved in minimization is smaller than SVD computation. Although, in many cases it is limited a finite set of points on L−curve, hence the curvature $\kappa\left(\tilde{\lambda}\right)$ cannot be computed as (22) . In a numerical sense the L−curve consists of a number of discrete points corresponding to different regularization parameter $(\tilde{\lambda})$ values at which we have evaluated e_1 and e_2. Thus, it is defined a sufficiently smooth curve associated to the set of discrete points in such way that the overall shape of L−curve is maintained. This procedure consists in determine an approximating smooth curve for L−curve. A reasonable approach for this is a cubic spline pair fitting for e_1 and e_2. Such a curve has some interesting properties as twice differentiable, numerically differentiable in stable way and local shape preserving features. It is important to comment that computational implementation of Tikhonov L−curve regularization technique is based on criteria described in [7] and [9]. In the next section we will point out the performance of proposed Tikhonov L−curve regularization method for dynamic elastoplasticity problem.

6 NUMERICAL EXAMPLE

The objective of presented numerical examples are to attest efficiency of the numerical regularization technique proposed for the time evolutionary analysis in elastoplasticity problems. Our implementation was made in MATLAB and results analysis are given by a comparative response between regularized (Tikhonov L−curve parameter choice) numerical solution and non-regularized numerical solution. The numerical examples presented here consists of 1-D low cycle fatigue applications and a monotonic load test. The body initial length is 100 mm, its elasticity modulus is $E = 2 \times 10^5\ MPa$, Poisson ratio is $\nu = 0.3$, yielding limit is $\sigma_y = 260\ MPa$, kinematic hardening constants is $\chi_\infty = 200\ MPa$ (kinematic hardening amplitude) and $\gamma = 2.0$ (controls the kinematic hardening increase rate), isotropic hardening constants is $R_\infty = 300\ MPa$ (isotropic hardening amplitude) and $b = 1$ (controls the isotropic hardening increase rate), and damage constants are $P_d = 0.0005$ and $D_c = 0.2$ (critical value of damage). This last value depends upon the material and the loading conditions. D_c represents the final decohesion of atoms is characterized by a critical value of effective stress acting on the resisting area. It is important to cite that D_c gives the critical value of the damage at a mesocrack initiation occurring for unidimensional stress, usually $D_c \in [0.2, 0.5]$. A sketch of the problem cases may be seen in figure below (see Fig.2).

Figure 2: Problem Case Domain Sketch

The load, in this example, is given by $\bar{u}\,(x,t) = 0.8\sin^2(2\pi t)$ where t is in cycles. The regularized numerical solution (rns) and the non-regularized numerical solution (nrns) for analysis over $t \in [0, 4]$ are computed under 10^{-4} tolerance value. A fictitious exact solution (fes) was too construct for this application. A important fact that must be noted is bouth numerical solution didn't get to realize entire analysis over range $t \in [0, 4]$. The "nrns" was capable to continue the analysis until $t = 2.787$ cycles. The "rns-analysis", that use the Tikhonov regularization technique, can be cover range $t \in [0, 3.137]$ cycles with a excellent agreement with the "fes" as presented in figure (Fig. 3) below.

The nrns-analysis failed due to ill-condition problems. At point $t = 2.787$ cycles the condition number associated to the linearised system on Newton method iteration is 2.4×10^8. For this case the number of iteration extrapolated a lot allowed limit (500 iterations) with residual norm value oscillating in one belittles strip around 10^{-3}. If we grow up the allowed limit of iteration same pattern is the reached until 624710 iterations. In following figure (4) it can be seen a good agreement between "fes" and "rns". Note that the rns-response was capable to reproduce the beginning of softening behaviour.

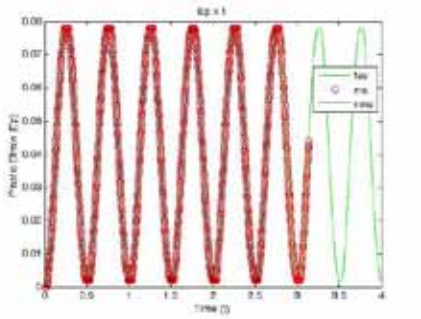

Figure 3: Plastic Strain vs. Time

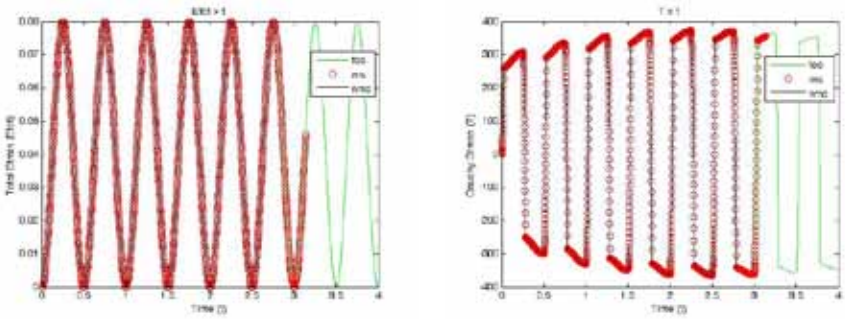

Figure 4: Total Strain vs. Time / Cauchy Stress vs. Time

In next figure (5) the hardening behaviour during analyzed time can be seen. Again, a good agreement among the numerical results ("fes" and "rns") can be noted.

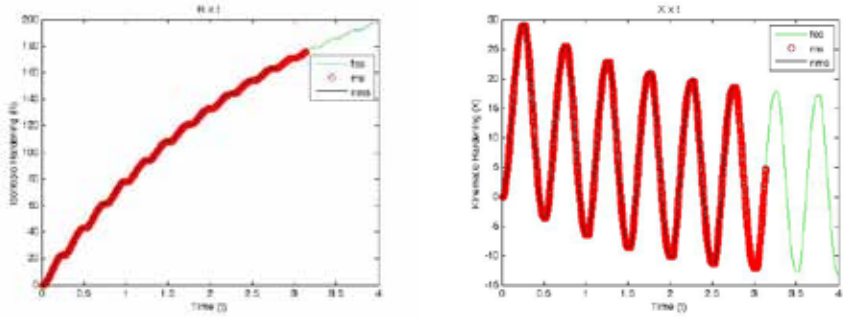

Figure 5: Isotropic Hardening vs. Time / Kinematic Hardening vs. Time

At this point, it is presented the responses about damage variable and storage plastic strain (see Fig. 6). A perfect "fes-rns" agreement has been noted in storage plastic

strain behaviour. The damage variable evolutionary profile shows a little bit discrepancy between "fes" and "rns" at $t = 2.75$ cycles (maximum difference) with 1.2% as relative error. It is important to stand that there is a tendency to both graphs ("fes" and "rns") coincides. The Tikhonov regularization process is setting to start when condition number is equal or greater than 2.4×10^8. Other settings are tested but the same unexpected pattern on rns-response was observed and non significant changes are noted.

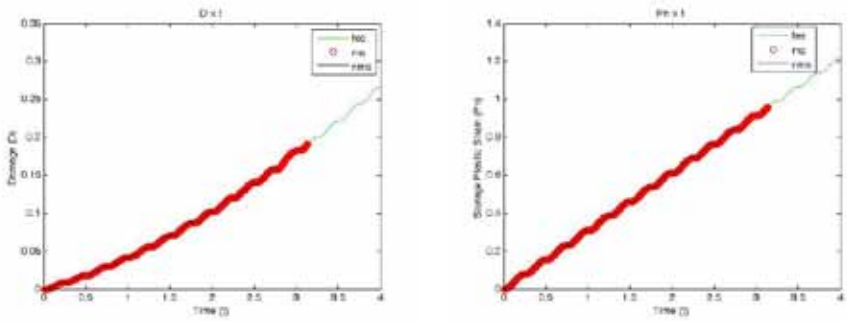

Figure 6: Damage vs. Time / Storage Plastic Strain vs. Time

The Tikhonov regularization method allowed that the numerical analysis continues until 3.06×10^8 as condition number. The regularization parameter computed for last Newton's iteration was $\tilde{\lambda} \approx 0.0525$ (see Fig. 7).

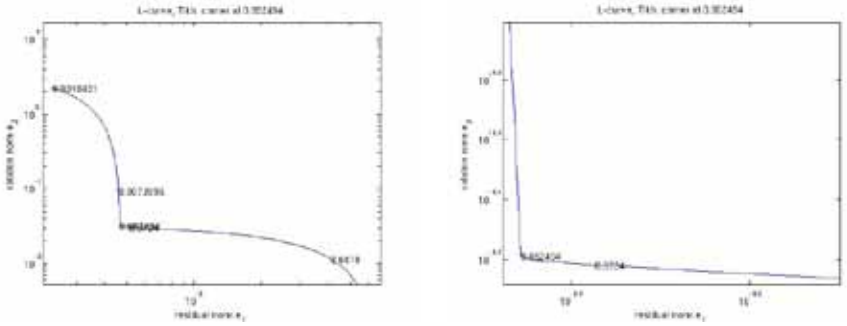

Figure 7: L−curve: e_2 vs. e_1/ L−curve (zoom): e_2 vs. e_1

7 CONCLUSION

In this work, it has discussed/analyzed the computational implementation of elasto-plsticity problem. As mentioned above to treat the critical points on equilibrium-path it was proposed a Thikhonov L-cruve regularization approach over Newton method. In this sense it has prsented some theoretical results from Thikonov regularization method

and your application over numerical dynamic elastoplastic problem as an efficient form of transposing the numerical problems associated to ill-conditioning happened in neighbourhoods of critical points.

It is important comment that the Thikonov L-curve regularization method approach in elastoplastcity numerical analysis showed robustness, efficiency and potential as it can be seen in the comparative numerical example here presented. The used tolerance convergence criterion (10^{-4}) was obtained after tests with larger and smaller tolerance values, in that none differences in the pattern of the responses was noticed. In this numerical example it was verified the consistency, performance and computational accuracy of the approach proposed. In fact, there was an excellent agreement between the regularized numerical response and fictitious exact solution, adding numerical stability and possibiliting advances in the time of analysis over permanent deformation computational modelling. Although, it is clear that new numerical experiments in terms of applications to explore as problems involving time rate dependences (viscoplasticity) over permanent/plastic deformations.

Additionally it is important to point out that besides new applications, other choosing parameters techniques (see [13] and [12]) must be investigated in terms of computational efforts, accuracy and performance in relation to L-curve approach. In particular, some experience is needed with large problems from distinct application requiring the use of general-form Tikhonov regularization. These are the subject of a research that should be continued.

REFERENCES

[1] C. S. Desai, Mechanics of materials and interfaces : the disturbed state concept, New York, CRC Press, 2001.

[2] Memon Bashir-Ahmed, SU Xiao-zu, Arc-length technique for nonlinear finite element analysis, J Zhejiang Univ SCI 2004 5(5):618-628, 2004.

[3] J. A. Lemaitre, J. L. Chaboche, Mechanics of Solid Materials, Cambridge University Press, Cambridge, UK, 1990.

[4] J. A. Lemaitre, Course on Damage Mechanics, Springer, Berlin, Germany, 1996.

[5] A. N. Tikhonov, Solution of incorrectly formulated problems and the regularization method, Soviet Math. Dokl., **4**(1963), pp. 1035-1038.

[6] P. C. Hansen, Rank-deficient and discrete ill-posed problems, SIAM Philadelphia, PA, 1998.

[7] P. C. Hansen, Regularization tools: a MATLAB package for analysis and solution of discrete ill-posed problems, Numer. Algorithms **6** (1994), pp. 1–35.

[8] V. A. Morozov, Regularization methods for solving incorrectly posed problems, Springer-Verlag, New York, 1984.

[9] P. C. Hansen and D. P. O'Leary, The use of the L-curve in the regularization of discrete ill-posed problems, SIAM J. Sci. Comput., **14**(1993), pp. 1487-1503.

[10] G. H. Golub, M. Heath, amd G. Wahba, Generalized cross-validation as a method for choosing a good ridge parameter, Technometrics, **21**(1979), pp. 215-222.

[11] J. Chung, J. G. Nagy, and D. P. O'Leary, A Weighted-GCV Method for Lanczos-Hybrid Regularization, Electronic Transaction on Numerical Analysis, Vol. 28, pp 149-167, 2008.

[12] F. S. Viloche Bazán, Fixed-point iterations in determining the Tikhonov regularization parameter, Inverse Problems **24** (2008) 035001.

[13] M. V. W. Zibetti, F. S. V. Bazán, and J. Mayer, Determining the regularization parameters for super-resolution problems, Signal Process. **88**(2008), 2890-2901.

[14] D. Calvettia, S. Morigib, L. Reichelc and F. Sgallarid, Tikhonov regularization and the L-curve for large discrete ill-posed problems, Journal of Computational and Applied Mathematics 123 (2000), pp. 423-446.

[15] F. Bloom, Ill-posed problems for integrodifferential equations in mechanics and electromagnetic theory, SIAM Studies in Applied Mathematics, Philadelphia, PA, 1991.

XI International Conference on Computational Plasticity. Fundamentals and Applications
COMPLAS XI
E. Oñate, D.R.J. Owen, D. Peric and B. Suárez (Eds)

DISCRETE MESO-MODELING OF STEEL FIBER REINFORCED CONCRETE: SIMULTATION OF FLEXURAL BEHAVIOR

ALBA PROS*, PEDRO DÍEZ* AND CLIMENT MOLINS†

*Laboratori de Càlcul Numèric (LaCàn)
Escolta Tècnica Superior d'Enginyers de Camins, Canals i Ports
Universitat Politècnica de Catalunya
Campus Nort UPC, 08034 Barcelona, Spain
e-mail: alba.pros,pedro.diez@.upc.es, www-lacan.upc.edu/

†Departament d'Enginyeria de la Construcció
Escolta Tècnica Superior d'Enginyers de Camins, Canals i Ports
Universitat Politècnica de Catalunya
Campus Nort UPC, 08034 Barcelona, Spain
e-mail: climent.molins@.upc.es

Key words: Plain Concrete, Steel Fiber Reinforced Concrete, Numerical model, Flexural Behavior, Three point bending test

Abstract. Concrete provides with a variety of innovative designs, but two characteristics have limited its use: it is brittle and weak under tension. One way to overcome this problem is to add steel fibers into the concrete matrix, a technique introduced in the 70's called Steel Fiber Reinforced Concrete (SFRC). Fibers shape, length and slenderness characterize its behavior. It is also necessary to take into account the orientation and the distribution of the fibers in the concrete matrix. Different flexural tests are reproduced considering SFRC in order to characterize and analyze the influence of the fibers. In the present work, a numerical tool for including fibers into plain concrete is presented. The numerical approach considered is based on the idea of the Immersed Boundary (IB) methods which were designed for solving problems of a solid structure immersed on a fluid. Herein, the IB method is applied for SFRC considering the concrete accounting for fluid and the steel fibers playing the role of the solid structure. Thus, the philosophy of the IB methodology is used to couple the behavior of the two systems, the concrete bulk and the fiber cloud, precluding the need of matching finite element meshes. Note that, considering the different size scales and the intricate geometry of the fiber cloud, the conformal matching of the meshes would be a restriction resulting in a practically unaffordable mesh. Concrete is modeled considering a nonlinear model and to take into account the whole process between fibers and concrete, the constitutive equations of the fibers are based on analytical expressions available in the literature describing the pullout

test behavior. The constitutive expressions depend on (1) the angle between each fiber and the crack of the concrete specimen and (2) the shape of the fiber.

1 INTRODUCTION

The most used techniques to overcome the main drawbacks of plain concrete are the reinforced concrete and the prestressed concrete. Another alternative which appeared in the 70's is the Steel Fiber Reinforced Concrete (SFRC) and consists of adding steel fibers into the concrete matrix. The length, the shape and the slenderness of the steel fibers characterize the behavior of the SFRC as well as the orientation and the distribution of the fibers into the concrete matrix.

SFRC has a large range of applications in civil engineering (bridges, pipes, airport runways, tunnel linings, pavements,...). The fracture energy and the residual strength increase due to the presence of steel fibers into plain concrete, particularly, in tension.

Several tests have been carried out in order to study the tensile behavior of SFRC: (a) direct tension tests ([1]), (b) indirect tension tests (splitting test ([2]) and Barcelona test ([3], UNE 83515)) and (c) bending tests of prismatic beam specimens, which are the most used to characterize the post-cracking response of SFRC. These can be either based on three point tests ([4], [5]) or four point tests ([6]).

Although experimental tests are usefull for characterizing the SFRC, a numerical tool is needed for studying the behavior in more complex setups.

In the present work, a numerical approach for simulating the SFRC is presented avoiding conformal meshes (too expensive and not affordable for large number of steel fibers) and homogenized models (not accounting for the actual geometry of the fibers). Thus, the proposed approach allows defining a mesh for the concrete bulk and another one for the fiber cloud accounting for the actual geometry of the fibers. Moreover, the materials for the concrete bulk and the fiber cloud are independent, but coupled following the ideas of the Immersed Boundary (IB) methods ([9, 10, 11]).

In the proposed approach, the model for the concrete bulk can be any nonlinear material which describes precisely the behavior of the plain concrete. However, for the example presented in the current work a nonlocal Mazars damage model is chosen.

The constitutive equations of the steel fibers are defined accounting for the interaction between the concrete and the fiber cloud. Therefore, they are different for each fiber depending on the angle with the fracture pattern and their shape.

The application of the proposed approach is the simulation of the three point bending test considering SFRC.

2 NUMERICAL APPROACH FOR COUPLING STEEL FIBERS AND PLAIN CONCRETE

The proposed approach for coupling the fiber cloud and the concrete bulk (introduced in [8]) is based on the IB methods which were introduced for solving problems of a solid immersed on a fluid (here, concrete is thought as the fluid and the fibers are like the solid structure immersed in the fluid). The main idea of these methods is to neglect the space occupied by the solid structure. The fluid is considered to occupy the whole domain and the velocities of both solid and fluid are made compatible in the coinciding points. Then, the effect of the solid in the fluid is accounted for by adding an interaction force. The two systems (fluid and solid structure) are considered separately and compatibility is enforced by adding the corresponding interaction forces. The discretization of the problem is therefore simplified because the mesh of the whole domain (the fluid) may be very simple (eventually a cartesian mesh) and the mesh for the solid body does not require to be conformal with it. The models corresponding to the fluid and the solid are defined independently.

Therefore, the problem of SFRC is discretized defining independently one mesh for the concrete bulk and one mesh for the fiber cloud. The mesh for the concrete bulk is kept simple while preserving the geometrical features of the sample. The discretization of the fiber cloud is a series of straight bar elements (in the examples included in this work each fiber is discretized with five elements). No conformity or geometrical matching is enforced between the discretizations of the concrete bulk and the fiber cloud.

For a given discretization, the two materials of the concrete bulk and the fiber cloud are defined independently and the equilibrium in both materials must be ensured.

The displacement compatibility between the displacement fields in the concrete bulk and the fiber cloud, u_c and u_s is expressed in algebraic form via the projection operator Π: $u_s = \Pi u_c$. This linear restriction is enforced via the Lagrange multipliers method.

3 MATERIAL MODELS

3.1 Concrete bulk

For modeling plain concrete, both continuous and discontinuous nonlinear models can be considered (in [7] two different possibilities are considered for modeling the plain concrete for the Double Punch Test). In the current work, a nonlinear continuous model is chosen: the nonlocal Mazars damage model.

The material parameters considered for characterizing the plain concrete are presented in table 1.

3.2 Fiber cloud

The model considered for steel fibers accounts for the whole process of slipping and debonding of the fiber into plain concrete and, precisely, allows capturing the whole behavior between the fibers and plain concrete bulk. Therefore, an elasto-plastic angle

Table 1: Material parameters for the nonlocal Mazars damage model

parameter	value
Young Modulus	$E = 30 \cdot 10^9$Pa
Poisson coefficient	$\mu = 0$
Characteristic length	$l_{car} = 10^{-3}$m
A_t	1.2
A_c	1
B_t	2500
B_c	266
β	1.06

dependent model with softening is adopted for the steel fibers, described in [8].

The mesomodel expected for the steel fibers must define inside the whole interaction process between concrete and fibers and characterize the behavior of the steel fibers. Thus, the constitutive equations of steel fibers are deduced from experimental results and analytical descriptions of pullout tests.

Pullout tests describes all the phenomena of the SFRC not only for straight fibers (fiber debonding, matrix spalling, frictional sliding and fiber removal), but also for hooked fibers (which are the same for the case of straight fibers but, with plastic deformations, magnifying the matrix spalling effects).

Fortunately, there is a recent analytical phenomenological description of pullout tests is available based on experimental results ([12] and [13]). These analytical expressions depend on the angle between the fiber and the load direction and on the shape of the fiber, which can be straight or hooked.

As mentioned in [8], the analytical expression of the pullout tests are translated into the constitutive equations of the fibers. Thus, for each fiber, the angle between the fiber and the fracture pattern is computed and depending on its shape, the constitutive equation is defined.

For the most common cases (when the volumetric proportion of steel fibers into plain concrete is $\leq 1\%$), the behavior described by one single fiber into plain concrete is enough for describing the behavior of all the fibers in SFRC, without taking into account the interaction between them. However, when the volumetric proportion of fibers is higher than 1%, it could not be realistic.

4 3D EXAMPLE: THREE POINT BENDING TEST

Once the numerical tool is presented, a 3D example is presented: the three point bending test. Figure 1 represents the scheme of the test.

The three point bending test is simulated considering plain concrete and hooked SFRC.

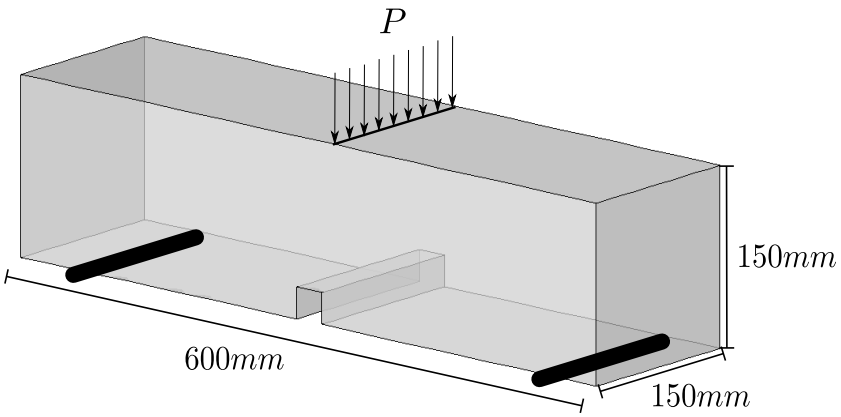

Figure 1: Three point bending test scheme.

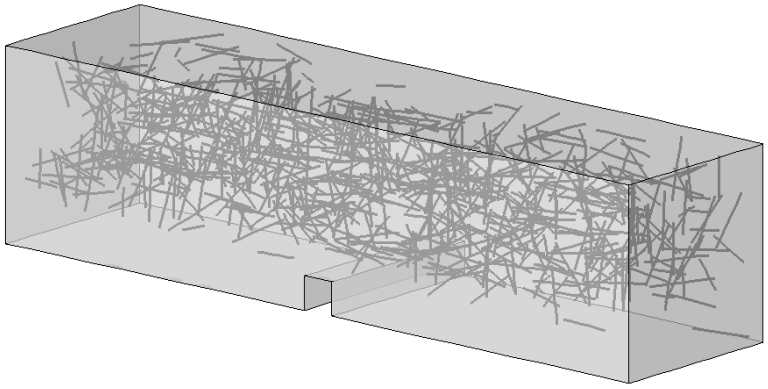

Figure 2: Fiber distribution into the specimen.

The distribution and orientation of the fibers is computed randomly. In figure 2, the fibers distribution into the plain concrete specimen is represented. The properties of the fibers are presented in table 2.

Table 2: Hooked fiber properties

length	$50 \cdot 10^{-3}$m
diameter	0.510^{-3}m

In order to study the influence of the volumetric proportion of steel fibers, two different volumetric proportions are considered: (a) 0.04% and (b) 0.3%.

The results are presented in figure 3 considering plain concrete and SFRC with hooked

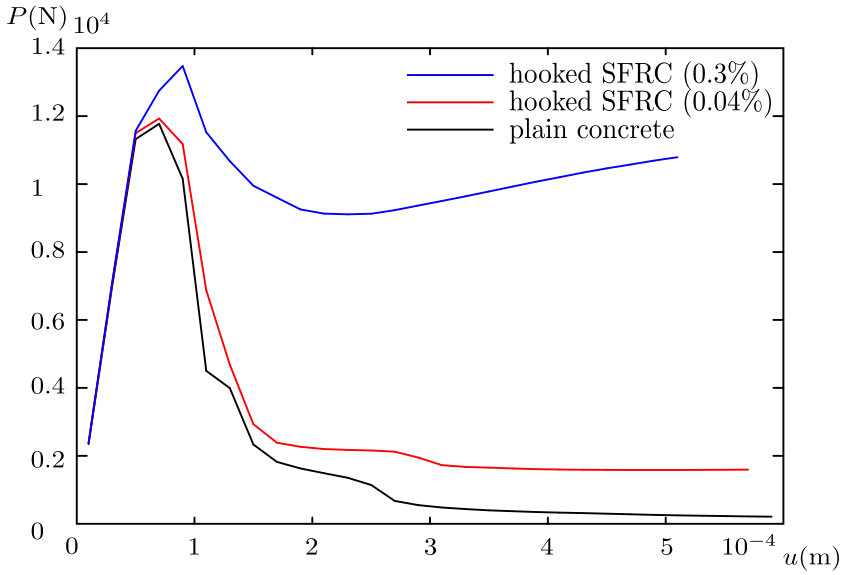

Figure 3: Three point bending test results considering (a) plain concrete, (b) SFRC (0.04%) and (c) SFRC (0.3%).

fibers. The vertical load is represented depending on the vertical displacement.

With the presence of the steel fibers, the energy dissipation and the residual strength increase, as expected. Moreover, the increase is higher when more fibers are considered. For the case when the volumetric proportions is 0.3%, after the peak, some hardening is observed, as it was expected observing the experimental results.

5 CONCLUDING REMARKS

Finally, the most important points are listed in order to conclude:

- A numerical tool for modeling SFRC is presented.
- It is possible to account for the actual geometry, distribution and orientation of the fibers because the mesh of the concrete bulk and the mesh of the fiber cloud are nonconformal.
- The materials corresponding to the concrete bulk and fiber cloud are independent, but coupled imposing displacement compatibility.
- The constitutive model of the steel fibers accounts for the interaction between concrete and fibers.
- The three point bending test is reproduced considering both plain concrete and SFRC. Moreover, different volumetric proportions of the steel fibers are considered

- The influence of the steel fibers is observed in the example: the increase of the energy dissipation and residual strength.

REFERENCES

[1] Recommendations of RILEM TC 162-TDF: Test and design methods for steel fibre reinforced concrete Uni-axial tension test for steel fibre reinforced concrete, *Materials and Structures*, (2001) **34**, No. **235**, 3–6.

[2] E. K. Tschegg and H. N. Linsbauer. Test Method for the Determination of Fracture Mechanics Properties. *Patent specification* (1986) **No. A-233/86 390 328**, Austrian Patent Office.

[3] C. Molins, A. Aguado and S. Saludes. Double Punch Test to control the energy dissipation in tension of FRC (Barcelona test). *Materials and Structures*, (2009) **42**, No. **4**, 415–425.

[4] EN 14651. Test method for metallic fibred concrete. Measuring the flexural tensile strength (limit of proportionality (LOP), residual), European Committee for Standardization, Brussels, 2005.

[5] RILEM TC 162-TDF. Test and design methods for steel fibre reinforced concrete: uniaxial tension test for steel fibre reinforced concrete. Final recommendations, *Materials and Structures*, (2003), **36**, 560–567.

[6] NBN B 15-238. Test on fibre reinforced concrete bending test on prismatic samples, Norme Belge, Institut Belge de Normalisation, Brussels, 1992.

[7] A. Pros, P. Diez and C. Molins. Numerical modeling of Double Punch Test for plain concrete. *International Journal of solids and structures*, (2011) **4**, Issues 7-8, 1229–1238.

[8] A. Pros, P. Diez and C. Molins. Modeling Steel Fiber Reinforced Concrete: numerical Immersed Boundary approach and a phenomenological mesomodel for concrete-fiber interaction. Submitted in the *International Journal of Numerical Methods in Engineering* (2011).

[9] Boffi, D. and Gastaldi, L. A finite approach of the Immersed boundary Method. *Computers and Structures* (2003) **81**: 491–501.

[10] Boffi, D., Gastaldi, L. and Heltai L. On the CFL condition for the finite element immersed boundary method. *Computers and Structures* (2003) **85**: 775–783.

[11] Iaccarino, G. and Mittal, R. Immersed Boundary Method. *Annu. Rev. Mech.* (2003) **37**: 239–261.

[12] F. Lagranjeira, A. Aguado and C. Molins. Predicting the pullout response of inclined straight steel fibers. *Materials and structures* (2010) **43**, 875–89.

[13] F. Lagranjeira, C. Molins and A. Aguado. Predicting the pullout response of inclined hooked steel fibers. *Cement and Concrete Research* (2010) **40**, Issue 10, 1471–1487.

XI International Conference on Computational Plasticity. Fundamentals and Applications
COMPLAS XI
E. Oñate, D.R.J. Owen, D. Peric and B. Suárez (Eds)

NUMERICAL MODELLING OF BEHAVIOUR OF CARBON NANOTUBE-REINFORCED COMPOSITES

F. OTERO*, S. OLLER*, X. MARTÍNEZ* AND O. SALOMON*

* International Center for Numerical Methods in Engineering (CIMNE)
Universidad Politécnica de Cataluña
Campus Norte UPC, 08034 Barcelona, Spain
e-mail: fotero@cimne.upc.edu, oller@cimne.upc.edu, x.martinez@upc.edu, salomon@cimne.upc.edu

Key words: Carbon nanotubes, Composites, Nano-mechanics.

1 INTRODUCTION

Since their discovery by Lijima in 1991[1], carbon nanotubes (CNTs), are considered a new generation of reinforcement [2]. Their "nano" size structure makes them potentially free of defects, which provides them with excellent physical properties [3,4]. There are two main nanotube types: single wall nanotubes (SWNT) and multi wall nanotubes (MWNT). These last ones consist in several concentric walls, one inside the other.

In a composite, one the most important factors that condition their mechanical performance is the interfacial tension between matrix and reinforcement. In general, the loads in a composite structure are introduced to the matrix and then are transferred to the reinforcement through the interface [5]. Therefore, the interface can be defined as the region, surrounding the reinforcement, where this stress transfer takes place. The properties of the composite depend on the properties of this region and its ability to transfer the load efficiently.

This work proposes a new formulation to predict the mechanical properties and mechanical behaviour of nanotube-reinforced composites. The formulation is based on the mixing theory [6]. It obtains the behaviour of the composite from the mechanical performance of its constitutive materials: matrix, carbon-nanotube and the interface that bonds both of them.

2 DESCRIPTION OF CONSTITUTIVE MODEL

The theory presented in this work obtains the mechanical performance of the composite from the behaviour of the composite constituents, each one simulated with its own constitutive equation [7]. As it is written, the theory can be understood as a constitutive equation manager. This approach increases the versatility and simulation capability of the formulation.

The model assumes that the composite is the combination of three different materials: matrix, CNTs and interface zone [8]. The interface corresponds to the matrix surrounding the CNTs. It is considered an independent component, with its own constitutive law. The function of the interface material in the model is to define the capacity of the matrix to transfer the loads to the reinforcement.

Although the phenomenological performance of the composite completely justifies the definition of an interface material, its existence also justified by measurements performed on

CNTs reinforced composites. Differential Scanning Calorimetry (DSC) measurements, carried out in composites with semi-crystalline polymer as matrix material, show a linear increase of crystalline matrix as the nanotube volume fraction increases. This result suggests that each nanotube has a crystalline coating [9]. This phenomenon can be also seen in Scanning Electron Microscope (SEM) images such the ones shown in Figure 1. Such images revealed that the structures protruding from the fracture surface seemed to have larger diameters than the original MWCNTs used in the sample preparation [10].

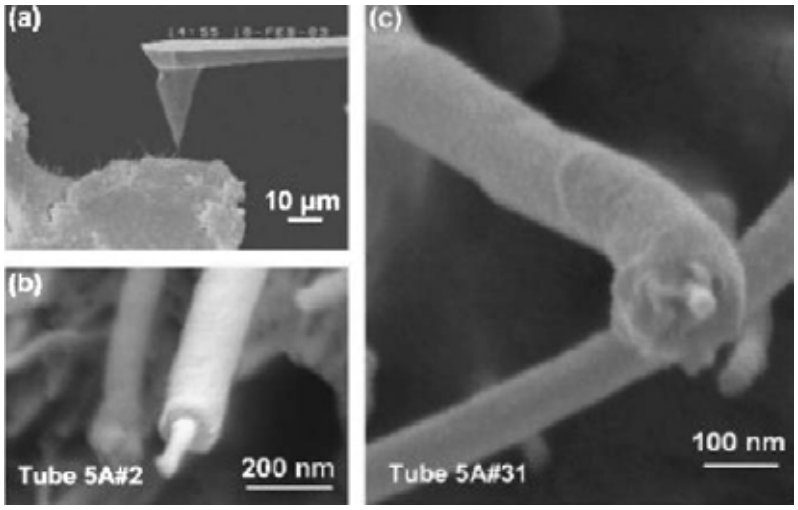

Figure 1: SEM image of nanomanipulation and fracture surface of composites [10].

A general description of the proposed procedure to simulate CNTs reinforced composites is shown in Figure 2. This figure shows that the composite is divided in several layers, each one containing nanotubes with a different orientation. All layers are coupled together using the parallel mixing theory. This division into layers allows taking into account the different orientations that may have the nanotubes in the composite. And, eventually, allows defining a composite with different materials in each layer (i.e. a foam core in a sandwich laminate).

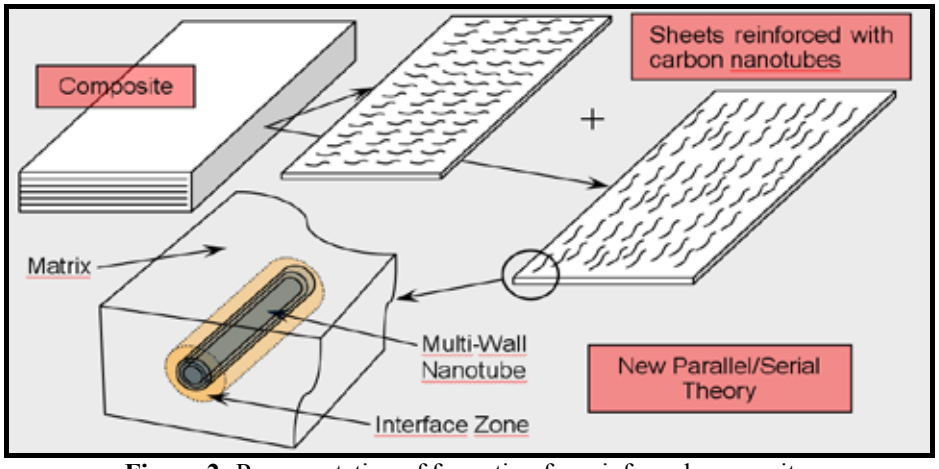

Figure 2: Representation of formation for reinforced composite.

Each layer is defined by the volume content of matrix, interface and carbon nanotubes. The mechanical performance of each layer is obtained with a new mixing theory formulation, which consists in combining the mechanical performance of the three co-existing materials.

First, the layer is split into matrix and a new material result of coupling the CNTs with the interface. The relation between the matrix and the CNTs-interface is established in terms of the parallel mixing theory; this is, they are assumed to have an iso-strain behaviour. On the other hand, CNTs and the interface zone are bonded together with a combination of parallel and serial mixing theories. The serial mixing theory states that all composite constituents have the same stresses.

The formulation used to characterize the CNTs-interface material is based in the short fibre model developed by Car [12]. Figure 3 shows the scheme used to obtain the performance of the CNTs-interface material. According to this model, the load transfer from the interface to the nanotube is produced at both the ends of the reinforcement, through shear stresses. At the centre of the reinforcement there is no load transfer and, therefore, shear stresses are null. A simplified model can be defined in which the CNT-interface performance is defined with a serial mixing theory at the ends of the reinforcement (iso-stress behaviour) and with a parallel mixing theory at the centre of it (iso-strain behaviour).

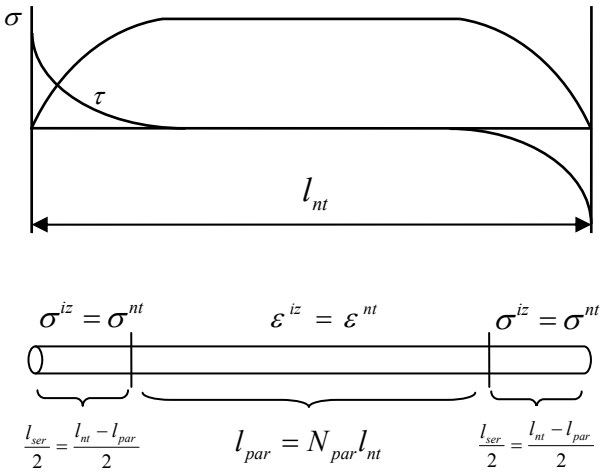

Figure 3: Different regions in the new material CNTs-interface.

A parallel factor named N^{par} is defined to differentiate the two regions. This parameter, multiplied by the nanotube length, provides the length of the nanotube-interface element with a parallel behaviour. The length with a serial performance is defined by the complementary factor.

3 FORMULATION OF CONSTITUTIVE MODEL

The Helmholtz free energy [13] of a material point subjected to small deformations can be described with the following thermodynamic formulation [14, 15]:

$$\Psi = \Psi\left(\boldsymbol{\varepsilon};\theta,\boldsymbol{\alpha}\right) \tag{1}$$

where $\boldsymbol{\varepsilon}$ is the deformation tensor, θ the temperature and $\boldsymbol{\alpha} = \{\boldsymbol{\varepsilon}^p; d; \boldsymbol{s}\}$ a set of inner variables, for example: $\boldsymbol{\varepsilon}^p$ is the plastic deformation, d damage inner variable and $\boldsymbol{s}$ any other material internal variables.

The model proposed to simulate the composite material consists on a combination of the different components of the composite, using the parallel and the serial mixing theories, as has been described in previous section. The expression of the Helmholtz free energy for the composite material may be written as:

$$\Psi = k_m \Psi_m + \left(k_{nt} + k_{iz}\right)\left[\underbrace{N^{par}\left(\bar{k}_{nt}\Psi_{nt} + \bar{k}_{iz}\Psi_{iz}\right)}_{\widetilde{\Psi}^{par}_{ntiz}} + \underbrace{\left(1 - N^{par}\right)\left(\bar{k}_{nt}\Psi_{nt} + \bar{k}_{iz}\Psi_{iz}\right)}_{\widetilde{\Psi}^{ser}_{ntiz}}\right] \tag{2}$$

where Ψ_m, Ψ_{nt} and Ψ_{iz} are the specific Helmholtz free energy for the matrix, the nanotube and the interface components, respectively; $\widetilde{\Psi}^{par}_{ntiz}$ and $\widetilde{\Psi}^{ser}_{ntiz}$ states parallel and serial Helmholtz free energy of the news CNTs-interface material, k_m, k_{nt} and k_{iz} are the volume fraction of each component, and N^{par} is a parallel factor and:

$$\bar{k}_{nt} = \frac{k_{nt}}{k_{nt} + k_{iz}} \qquad \bar{k}_{iz} = \frac{k_{iz}}{k_{nt} + k_{iz}} \tag{3}$$

are the volume fractions of the composite components. These must verify:

$$k_m + k_{nt} + k_{iz} = 1 \qquad \bar{k}_{nt} + \bar{k}_{iz} = 1 \tag{4}$$

The relation among the strain tensors of the different components is:

$$\boldsymbol{\varepsilon} = \boldsymbol{\varepsilon}_m = \boldsymbol{\varepsilon}^{par}_{ntiz} = \boldsymbol{\varepsilon}^{ser}_{ntiz} \tag{5}$$

where $\boldsymbol{\varepsilon}$ and $\boldsymbol{\varepsilon}_{\mathrm{m}}$ are the composite and matrix deformations, respectively; $\boldsymbol{\varepsilon}^{par}_{ntiz}$ is the deformation of a new material, result of the combination of nanotubes with the interface, that has a parallel behaviour; and $\boldsymbol{\varepsilon}^{ser}_{ntiz}$ is deformation of a nanotube-interface material that has a serial behaviour.

The tangent constitutive tensor of the composite material may be derived from Eq. (2):

$$\boldsymbol{C} = \frac{\partial^2 \boldsymbol{\Psi}}{\partial \boldsymbol{\varepsilon} \otimes \partial \boldsymbol{\varepsilon}} = k_m \frac{\partial^2 \boldsymbol{\Psi}_m}{\partial \boldsymbol{\varepsilon}_m \otimes \partial \boldsymbol{\varepsilon}_m} + \frac{\partial^2 \widetilde{\boldsymbol{\Psi}}^{par}_{ntiz}}{\partial \boldsymbol{\varepsilon}^{par}_{ntiz} \otimes \partial \boldsymbol{\varepsilon}^{par}_{ntiz}} + \frac{\partial^2 \widetilde{\boldsymbol{\Psi}}^{ser}_{ntiz}}{\partial \boldsymbol{\varepsilon}^{ser}_{ntiz} \otimes \partial \boldsymbol{\varepsilon}^{ser}_{ntiz}} \tag{6}$$

A parallel behaviour means that all composite constituents have the same value for this strain component and therefore:

$$\varepsilon^{par}_{ntiz} = \varepsilon_{nt} = \varepsilon_{iz} \quad \Rightarrow \quad \frac{\partial^2 \widetilde{\Psi}^{par}_{ntiz}}{\partial \varepsilon^{par}_{ntiz} \otimes \partial \varepsilon^{par}_{ntiz}} = N^{par}\left[\bar{k}_{nt}\boldsymbol{C}_{nt} + \bar{k}_{iz}\boldsymbol{C}_{iz}\right] = N^{par}\boldsymbol{C}^{par}_{ntiz} \tag{7}$$

A serial behaviour means that all composite constituents have the same value for this stress

component and therefore:

$$\sigma_{ntiz}^{ser} = \sigma_{nt} = \sigma_{iz} \quad \Rightarrow \quad \varepsilon_{nt} = \mathbf{C}_{nt}^{-1} : \mathbf{C}_{ntiz}^{ser} : \varepsilon_{ntiz}^{ser} \quad ; \quad \varepsilon_{iz} = \mathbf{C}_{iz}^{-1} : \mathbf{C}_{ntiz}^{ser} : \varepsilon_{ntiz}^{ser} \tag{8}$$

$$\frac{\partial^2 \widetilde{\Psi}_{ntiz}^{ser}}{\partial \varepsilon_{ntiz}^{ser} \otimes \partial \varepsilon_{ntiz}^{ser}} = \left(1 - N^{par}\right)\left[\bar{k}_{nt}\mathbf{C}_{nt}^{-1} + \bar{k}_{iz}\mathbf{C}_{iz}^{-1}\right]^{-1} = \left(1 - N^{par}\right)\mathbf{C}_{ntiz}^{ser} \tag{9}$$

Replacing Eq. (7) and Eq (9) in Eq (6) it is possible to obtain a simplified expression of the tangent constitutive tensor:

$$\mathbf{C} = k_m \mathbf{C}_m + \left(k_{nt} + k_{iz}\right)\left[N^{par}\mathbf{C}_{ntiz}^{par} + \left(1 - N^{par}\right)\mathbf{C}_{ntiz}^{ser}\right] \tag{10}$$

3.1 Definition of the parallel factor N^{par}

The parallel factor is defined as:

$$N^{par} := \frac{l_{par}}{l_{nt}} \qquad , \quad 0 \le N^{par} \le 1 \tag{11}$$

where l_{nt} is the length of the nanotube and l_{par} is function of geometry and mechanical properties of the nanotube and the interface.

Based on the short fiber formulation defined in [5], the equation of tension distribution in a reinforcement considering perfect bond with the matrix is:

$$\sigma_{nt}(x) = E_{nt}\left[1 - \frac{\cosh\left(\beta\left(l_{nt} - 2x\right)\right)}{\cosh\left(\beta l_{nt}\right)}\right]\varepsilon_m \qquad \beta = \sqrt{\frac{2G_{iz}}{E_{nt}\, d_{nt}^2 \ln\left(1 + b/r_{nt}\right)}} \tag{12}$$

where x represents the longitudinal positions in the reinforcement, the subscript "nt" and "iz" refers to the properties of nanotube and interface zone, respectively, and b is the thickness of interface.

Considering that $l_{par} = l_{nt} - 2x$ and finding the positions "x" which verifies that the effective modulus obtained of integrate the tension distributions is equal to:

$$\bar{E}_{nt} = \frac{l_{par}}{l_{nt}} E_{ntiz}^{par} + \left(1 - \frac{l_{par}}{l_{nt}}\right) E_{ntiz}^{ser} \tag{13}$$

The parallel longitudinal can be written as:

$$l_{par} = \frac{1}{\beta}\cosh^{-1}\left[\tfrac{1}{3}\cosh\left(\beta l_{nt}\right)\right] \tag{14}$$

4 CONSTITUTIVE MODEL FOR A SINGLE MATERIAL

All models used in the formulation depart from Eq. (1). Therefore it is possible to use any constitutive law to describe the behaviour of the constituent materials defined: matrix, interface and CNTs. However, for the sake of clarity, in the following are defined three

specific models that will be used afterwards.

4.1 Constitutive model for matrix material

Matrix material is defined with an elastoplastic law. Therefore, the specific Helmholtz free energy for this material, considering uncoupled elasticity is:

$$\Psi\left(\boldsymbol{\varepsilon}^e, \boldsymbol{p}\right) = \Psi^e\left(\boldsymbol{\varepsilon}^e\right) + \Psi^p\left(\boldsymbol{p}\right) = \frac{1}{2}\boldsymbol{\varepsilon}^e : \boldsymbol{C} : \boldsymbol{\varepsilon}^e + \Psi^p\left(\boldsymbol{p}\right) \tag{15}$$

where the total deformation of the material tensor is split into its elastic, $\boldsymbol{\varepsilon}^e$ and plastic, $\boldsymbol{\varepsilon}^p$ parts. This is:

$$\boldsymbol{\varepsilon} = \boldsymbol{\varepsilon}^e + \boldsymbol{\varepsilon}^p \tag{16}$$

The local form of the Clausius-Duhem inequality for this material can be expressed as:

$$\Xi = \boldsymbol{\sigma} : \dot{\boldsymbol{\varepsilon}} - \eta\dot{\theta} - \dot{\Psi} - \frac{1}{\theta}\boldsymbol{q}.\frac{\partial\theta}{\partial\boldsymbol{x}} \geq 0 \tag{17}$$

$$\boldsymbol{\sigma} : \left(\dot{\boldsymbol{\varepsilon}}^e + \dot{\boldsymbol{\varepsilon}}^p\right) - \eta\dot{\theta} - \left[\frac{\partial\Psi^e}{\partial\boldsymbol{\varepsilon}^e} : \dot{\boldsymbol{\varepsilon}}^e + \frac{\partial\Psi^p}{\partial\boldsymbol{p}}.\dot{\boldsymbol{p}} + \frac{\partial\Psi}{\partial\theta} : \dot{\theta}\right] - \frac{1}{\theta}\boldsymbol{q}.\frac{\partial\theta}{\partial\boldsymbol{x}} \geq 0 \tag{18}$$

$$\left(\boldsymbol{\sigma} - \frac{\partial\Psi^e}{\partial\boldsymbol{\varepsilon}^e}\right) : \dot{\boldsymbol{\varepsilon}}^e - \left(\eta + \frac{\partial\Psi}{\partial\boldsymbol{\theta}}\right)\dot{\theta} + \boldsymbol{\sigma} : \dot{\boldsymbol{\varepsilon}}^p - \frac{\partial\Psi^p}{\partial\boldsymbol{p}}.\dot{\boldsymbol{p}} - \frac{1}{\theta}\boldsymbol{q}.\frac{\partial\theta}{\partial\boldsymbol{x}} \geq 0 \tag{19}$$

where $\boldsymbol{\sigma}$ is the stress tensor, η the entropy, and $\boldsymbol{q}$ the vector field of heat flow.

To ensure compliance with the second thermodynamic law it must be defined:

$$\boldsymbol{\sigma} := \frac{\partial\Psi^e}{\partial\boldsymbol{\varepsilon}^e} \qquad \eta := -\frac{\partial\Psi}{\partial\boldsymbol{\theta}} \qquad \boldsymbol{P} := -\frac{\partial\Psi^p}{\partial\boldsymbol{p}} \tag{20}$$

where $\boldsymbol{P}$ is the thermodynamic tensor associated with the internal variable tensor $\boldsymbol{p}$.

Finally, the mechanical dissipation for a material point is:

$$\Xi_m = \Xi_p = \boldsymbol{\sigma} : \dot{\boldsymbol{\varepsilon}}^p + \boldsymbol{P}.\dot{\boldsymbol{p}} \geq 0 \tag{21}$$

4.2 Constitutive model for interface material

The interface region will be simulated with a damage material. In this case, the expression of the Helmholtz free energy is:

$$\Psi\left(\boldsymbol{\varepsilon}^e, d\right) = \Psi^e\left(\boldsymbol{\varepsilon}^e, d\right) = \left(1-d\right)\Psi_o^e\left(\boldsymbol{\varepsilon}^e\right) = \left(1-d\right)\frac{1}{2}\boldsymbol{\varepsilon}^e : \boldsymbol{C} : \boldsymbol{\varepsilon}^e \tag{22}$$

The local form of the Clausius-Duhem inequality for this material can be expressed as:

$$\Xi = \boldsymbol{\sigma} : \dot{\boldsymbol{\varepsilon}} - \eta\dot{\theta} - \dot{\Psi} - \frac{1}{\theta}\boldsymbol{q}.\frac{\partial\theta}{\partial\boldsymbol{x}} \geq 0 \tag{23}$$

$$\boldsymbol{\sigma} : \dot{\boldsymbol{\varepsilon}} - \eta\dot{\theta} - \left[\frac{\partial\Psi^e}{\partial\boldsymbol{\varepsilon}} : \dot{\boldsymbol{\varepsilon}} + \frac{\partial\Psi^e}{\partial d} : \dot{d}\right] - \frac{1}{\theta}\boldsymbol{q}.\frac{\partial\theta}{\partial\boldsymbol{x}} \geq 0 \tag{24}$$

$$\left(\boldsymbol{\sigma} - \frac{\partial\Psi^e}{\partial\boldsymbol{\varepsilon}}\right) : \dot{\boldsymbol{\varepsilon}} - \left(\eta + \frac{\partial\Psi}{\partial\boldsymbol{\theta}}\right)\dot{\theta} - \frac{\partial\Psi^e}{\partial d}\dot{d} - \frac{1}{\theta}\boldsymbol{q}.\frac{\partial\theta}{\partial\boldsymbol{x}} \geq 0 \tag{25}$$

To ensure compliance with the second thermodynamic law it must be defined:

$$\boldsymbol{\sigma} := \frac{\partial\Psi^e}{\partial\boldsymbol{\varepsilon}} \qquad \eta := -\frac{\partial\Psi}{\partial\boldsymbol{\theta}} \qquad D := \frac{\partial\Psi^e}{\partial d} \tag{26}$$

where D is the thermodynamic scalar associated with the internal scalar variable d.

And, the mechanical dissipation for a material point is:

$$\Xi_m = \Xi_d = D\,\dot{d} \geq 0 \tag{27}$$

4.3 Constitutive model for nanotubes

Nanotubes are considered elastic, therefore the Helmholtz free energy is:

$$\Psi\left(\boldsymbol{\varepsilon}^e\right) = \Psi^e\left(\boldsymbol{\varepsilon}^e\right) = \frac{1}{2}\boldsymbol{\varepsilon}^e : \boldsymbol{C} : \boldsymbol{\varepsilon}^e \tag{28}$$

And the local form of the Clausius-Duhem inequality can be expressed as:

$$\Xi = \boldsymbol{\sigma} : \dot{\boldsymbol{\varepsilon}} - \eta\dot{\theta} - \dot{\Psi} - \frac{1}{\theta}\boldsymbol{q}.\frac{\partial\theta}{\partial\boldsymbol{x}} \geq 0 \tag{29}$$

$$\boldsymbol{\sigma} : \dot{\boldsymbol{\varepsilon}} - \eta\dot{\theta} - \frac{\partial\Psi^e}{\partial\boldsymbol{\varepsilon}} : \dot{\boldsymbol{\varepsilon}} - \frac{1}{\theta}\boldsymbol{q}.\frac{\partial\theta}{\partial\boldsymbol{x}} \geq 0 \tag{30}$$

$$\left(\boldsymbol{\sigma} - \frac{\partial\Psi^e}{\partial\boldsymbol{\varepsilon}}\right) : \dot{\boldsymbol{\varepsilon}} - \left(\eta + \frac{\partial\Psi}{\partial\boldsymbol{\theta}}\right)\dot{\theta} - \frac{1}{\theta}\boldsymbol{q}.\frac{\partial\theta}{\partial\boldsymbol{x}} \geq 0 \tag{31}$$

To ensure compliance with the second thermodynamic, $\boldsymbol{\sigma}$ and η are defined as:

$$\boldsymbol{\sigma} := \frac{\partial\Psi^e}{\partial\boldsymbol{\varepsilon}} \qquad \eta := -\frac{\partial\Psi}{\partial\boldsymbol{\theta}} \tag{32}$$

5 NON-LINEARITY OF THE PROPOSED MODEL

In the proposed model, the composite performance is obtained from the mechanical

performance of its constituent materials. Therefore, if a constituent (i.e. the interface) is simulated with a non-linear law and the strains applied to it lead to a non-linear state, the whole composite will become non-linear.

However, beyond the non-linear performance provided by the constitutive law used to simulate each constituent, the load transfer capacity in the interface region is also affected if the interface is damaged. This effect must be included in the formulation.

According to Figure 3, the load transfer from the interface to the reinforcement is produced at the ends of the reinforcement. Therefore, initial interface damage will occur at the ends of the reinforcement, where there is larger stress concentrations, reducing the effective length of the nanotube. In other words, the parallel length of the nanotube is reduced based on the damage of the interface material. The new parallel length can be computed as:

$$l_{par} = l^{o}_{par}\left(1 - d\right) \tag{33}$$

where l^{o}_{par} is the initial length of the nanotube working in parallel and d is the interface damage.

The addition of this new length, depending on the non-linear performance of the interface material, provides a non-linear response of the composite (see equation 10), even when matrix and the carbon nantotube reinforcement are in their linear range.

6 NUMERICAL IMPLEMENTATION

The proposed model has been implemented in PLCd [16] a finite element code that works with 3D solid geometries. The algorithm developed has been implemented as a new composite equation manager in the FEM code [17]. PLCd has already implemented the constitutive laws that will be used to predict the performance of the composite components (elastoplastic, damage and elastic). The formulation proposed has been written so that the constitutive laws of the constituents are seen as “black boxes”, that will compute the material stresses for a given strain.

7 RESULTS

The elastic performance of the model presented in this work has been already validated, proving that it provides good results. The validation performed consisted in comparing the prediction made by the model, of different elastic parameters (Young modulus and shear modulus) for several CNTs reinforced polymers, with the data existing in literature for these same composites. A detailed description of this comparison is reported in [18].

The non-linear behaviour of the numerical model is validated hereafter, comparing the results provided by the model with experimental data obtained from M-Rect project (see acknowledgements). The matrix used is PEEK; Young’s modulus and shear modulus were measured: *3.9* [GPa] and *1.9* [GPa], respectively. The composite has a 3% weight of MWNT (Baytubes® C 70 P). However, measurements with X-ray showed an apparent 5% weight, this means that the nanotubes have a higher apparent diameter than the pristine one. Therefore, the b/r_{nt} is calculated assuming that 2% weight extra is the coating polymer around the nanotubes. The Young’s modulus of the interface zone was estimated using the procedure proposed by Coleman et al. [19]. The data used for the estimation of the modulus is the one

defined by Díez-Pascual et al. [20,21], obtaining a final value of *5* [GPa].

The properties used in the model for the CNTs were obtained considering them as solid cylinders with the same external diameter. To do so it is necessary to reduce their elastic modulus in order to have an equivalent material. The values used as effective Young's modulus and effective shear modulus are $E_{nt} = 4.t/d_{nt}.E_g$ and $G_{nt} = [1- (1-2.t/d_{nt})4].G_g$, respectively [22]. The value of the properties used to get the effective properties were $E_g = 1$ [TPa], $G_g = 0.44$ [TPa] (the Young' modulus and the shear modulus of graphite sheet), its thickness was considered to be $t = 0.34$ [nm].

Table 1: Project data for implementation of numerical model

Type	d_{nt} [nm]	l_{nt} [μm]	l_{nt}/d_{nt}	b/r_{nt}	E_{nt} [GPa]	G_{nt} [GPa]	N^{par}
MWNT	13	1	44	0.3	105	85	0.97

The composite is defined with different layers in order to assign different CNTs orientations. Each layer contains a volume fraction of CNTs with a specific orientation. The constitutive model used for PEEK material is an elasto-plastic model, for the interface zone is an explicit scalar elasto-damage, and for the nanotube is an elastic model. The parameters that control the no-lineal behaviour on the interface zone were calibrated with the experimental data of project.

Figure 4 shows the mechanical performance of the model when the composite is loaded with a shear load. The simulation has been performed applying a controlled displacement load. The figure shows the strain-stress graph obtained for the composite (red line) and these same graphs for the interface material of the different layers in which the composite is divided. These last graphs show that the maximum stress in all interface materials do not exceed the defined threshold value of 15 MPa.

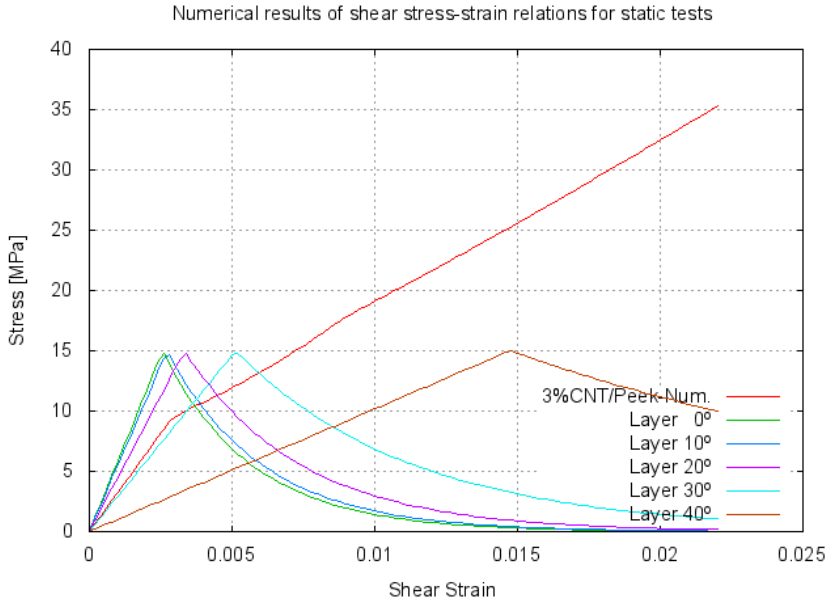

Figure 4: Numerical behaviour for the model proposed in shear load.

Figure 4 shows that once the first interface material reaches its threshold value, the composite modifies its mechanical performance reducing its stiffness. This occurs because the interface itself reduces its stiffness due to damage, but also because damage in the interface reduces the parallel fraction of the CNTs-interface material (equation 33); hence, the participation of the CNTs in the composite is less significant. When all interfaces (in all layers) are completely damaged, the CNTs contribution to the composite stiffness and strength becomes null and the composite behavior is such as having just matrix material with some voids in it.

The mechanical performance just described is better shown in figure 5, in which is represented the behaviour of the numerical model calibrated in a load-unload test. The PEEK curve shows the plastic behaviour of the numerical model. When it is unloaded, the composite curve shows not only plastic deformation, but also a variation in its stiffness produced by interface damage.

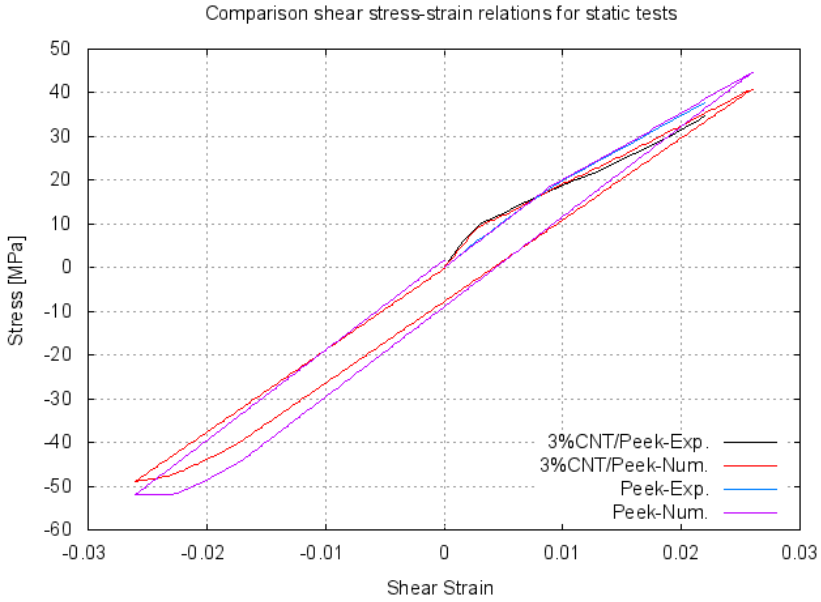

Figure 5: Comparison of numerical and experimental results, load and unload curves.

8 CONCLUSIONS

- A new formulation has been presented, which is based on the mixing theory, developed to predict the mechanical performance of composites reinforced with carbon nanotubes. The model presented has the advantage of relating the CNTs and the matrix with an interface material. This makes possible to simulate the composite material by using constitutive laws defined for each composite component and the interaction between them.
- The model was calibrate and compared with experimental data. The elastic properties predicted by the model, as well as the nonlinear behaviour estimated are in good agreement with experimental values.

REFERENCES

[1] Lijima S., Helical microtubules of graphitic carbon, Nature, vol. 354, pp. 56-8, Japan, (1991).
[2] Coleman J. N., et al, Small but strong: A review of the mechanical properties of carbon nanotube-polymer composites, Carbon, vol. 44, no. 9, pp. 1624-52, ISSN 0008-6223, (2006).
[3] Ruoff R. S. and Lorents D. C., Mechanical and thermal properties of carbon nanotube, Carbon, vol. 33, no. 7, pp. 925-930, ISSN 0008-6223, (1995).
[4] , Salvetat J. P., et al, Mechanical properties of carbon nanotubes, Appl. Phys. A., vol. 69, no. 3, pp. 255-260, ISSN 0947-8396, (1999).
[5] Jayatilaka A. S., Fracture of engineering brittle materials, Applied Science Publishers LTD, London, (1979).
[6] Trusdell C., Toupin R., The classical Field Theories, Handbuck der Physik III/I, Springer, Berlin, (1960).
[7] Car E., Oller S. and Oñate E., An Anisotropic Elastoplastic Constitutive Model for Large Strain Analysis of Fiber Reinforced Composite Materials, Computer Methods in Applied Mechanics and Engineering, vol. 185, no. 2-4, pp. 245-277, ISSN 0045-7825, (2000).
[8] Coleman J. N., et al., Reinforcement of Polymers with Carbon Nanotubes. the Role of an ordered polymer Interfacial Region. Experiment and Modeling, Polymer, vol. 47, no. 26, pp. 8556-8561, ISSN 0032-3861,(2006).
[9] Cadek M., et al., Morphological and Mechanical Properties of Carbon-Nanotube-Reinforced Semicrystalline and Amorphous Polymer Composites, Applied Physics Letters, vol. 81, no. 27, pp. 5123-5125, (2002).
[10] Ding W., et al., Direct Observation of Polymer Sheathing in Carbon Nanotube-Polycarbonate Composites, Nano Letters, vol. 3, no. 11, pp. 1593-1597, (2003).
[11] Rastellini F., et al., Composite materials non-linear modelling for long fibre-reinforced laminates continuum basis, computational aspects and validations, Computers and Structures, vol. 86, pp. 879-896, ISSN 0045-7949, (2008).
[12] Car E., A Continuum Constitutive Model to Simulate the Mechanical Behaviour of Composite Materials, PhD Thesis, Technical University of Catalonia, 2000.
[13] Malvern L. E., Introduction to the Mechanics of a Continuous Medium, ISBN 134876032, (1969).
[14] Lubliner J., et al., A Plastic-Damage Model for Concrete, International Journal of Solids and Structures, vol. 25, no. 3, pp. 299-326, ISSN 0020-7683, (1989).
[15] Oller S., et al., A Plastic Damage Constitutive Model for Composite Materials, International Journal of Solids and Structures, vol. 33, no. 17, pp. 2501-2518, ISSN 0020-7683, (1996).
[16] PLCd Manual. Non-linear thermomechanic finite element code oriented to PhD student education, code developed at CIMNE, 1991 - to present.
[17] Martinez X., et al., A numerical procedure simulating RC structures reinforced with FRP using the serial/parallel mixing theory, Computers and Structures, vol. 86, pp. 1604-1618, ISSN 0045-7949, (2008).

[18] Otero, F., et al, Modelling of behaviour of carbon nanotube-reinforced composites, IX Congreso Nacional de Materiales Compuestos, pp. 545-550. ISBN 978-84-8458-352-3, (2011)
[19] Coleman J. N., et al., Reinforcement of Polymers with Carbon Nanotubes. The Role of an ordered polymer Interfacial Region. Experiment and Modelling, Polymer, vol. 47, no. 26, pp. 8556-8561, ISSN 0032-3861, (2006).
[20] Díez-Pascual A. M., et al., High performance PEEK/carbon nanotube composites compatibilized with polysulfones-I. Structure and thermal properties, Carbon, vol. 48, pp. 3485-3499, ISSN 0008-6223, (2010).
[21] Díez-Pascual A. M., et al., High performance PEEK/carbon nanotube composites compatibilized with polysulfones-II. Mechanical and electrical properties, Carbon, vol. 48, pp. 3500-3511, ISSN 0008-6223, (2010).
[22] Zhou X., et al., Interfacial damping characteristics of carbon nanotube-based composites, Composites Science and Technology, vol. 64, pp. 2425-2437, ISSN 0266-3538, (2004).

ACKNOWLEDGEMENTS

This work has been supported by the European community under grant 246067, Multiscale Reinforcement of Semi-crystalline Thermoplastic Sheets and Honeycombs (M-RECT), NMP-2009-2.5-1.

XI International Conference on Computational Plasticity. Fundamentals and Applications
COMPLAS XI
E. Oñate, D.R.J. Owen, D. Peric and B. Suárez (Eds)

A DUAL MORTAR-BASED CONTACT FORMULATION APPLIED TO FINITE PLASTIC STRAINS – COMPLAS XI

T. Doca, F.M. Andrade Pires and J.M.A. César de Sá

Department of Mechanical Engineering (DEMec)
Faculty of Engineering
University of Porto, Porto, Portugal
e-mail: thiago.doca@fe.up.pt

Key words: Dual mortar method, active set strategy, finite plastic deformation.

Abstract. Significant progress has been made on computational contact mechanics over the past decade. Many of the drawbacks that were inherent to the standard node-to-segment element strategy, such as locking/over-constraint and non-physical jumps in the contact forces due to the discontinuity of the contact surface, have been systematically overcome. In particular, the formulation of the mortar finite element method [1], which has allowed the establishment of efficient segment-to-segment approaches [2, 3] when applied to the discretization of a contact surface, has promoted significant advance. However, the regularization schemes used with the mortar element (e.g. the Penalty method, the Lagrange multipliers method or combination of them) still cause unwanted side-effects such as: ill-conditioning, additional equations in the global system or a significant increase in the computational time for solution. In order to circumvent these shortcomings, Wohlmuth [4] has proposed the use of dual spaces for the Lagrange multipliers allowing the local elimination of the contact constraints. As a consequence, the Lagrangian multipliers can be conveniently condensed and no additional equations are needed for the solution of the global system of equations. H́ueber et al. [5], Hartmann et al. [6], Popp et al.[7] and Gitterle et al [8]. have later combined this methodology with an active set strategy and obtained improved results in terms of convergence rate. Despite the successful application of the dual mortar formulation to contact problems, the advances presented in the literature have, to the authors knowledge, only been employed for the simulation of elastic problems. However, contact between bodies has a strong influence in many applications (e.g., metal forming and cutting) where finite inelastic strains play a crucial role. Therefore, the main goal of the present work is both the application and assessment of the dual mortar method in problems where contact takes place coupled with finite plastic strains.

1 INTRODUCTION

The great majority of industrial processes involve plastic deformation of metallic bodies. There are several manufacturing procedures to modify the shape (i.e. Extrusion, U-Shaping, L-Shaping, Upsetting, etc) and they all share a common mechanism: the frictional contact. The correct prediction of frictional forces is intimately related to the precise computation of the normal contact forces. One of the most common methods to solve a non-conforming contact contact problem is the standard node-to-segment Lagrangian method. However the drawbacks inherent to the node-to-segment (NTS) approach, such as locking/over-constraint and non-physical jumps in the contact forces due to the discontinuity of the contact surface, use to compromise the method's results. Therefore, it is possible to replace the strong pointwise non-penetration function by a weaker integral condition through the use of dual spaces for the Lagrange multiplier [4]. This provides a very efficient discretization approach for non-conforming meshes, and therefore, a more accurate evaluation of the normal contact forces. The main goal in this work is to assess how the Dual Mortar method behaves when the deformation field along the contact surface evolves to the plastic zone. This paper is organized as follows: in Section 2, the contact problem is presented by stating the boundary conditions, the contact kinematics and the material model employed. In Section 3, the final equation system of the Dual Mortar method is presented. Numerical examples comparing the Dual Mortar method and the lagrangian method, are given in Section 4. Conclusion remarks are presented in Section 5.

2 PROBLEM DEFINITION

Considering two solid bodies in the reference configuration, we denote them by Ω^s and Ω_m, $\{\Omega_s \cup \Omega_m = \Omega : \Omega \subset \mathbb{R}^2\}$. The boundaries of subset Ω are divided in a contact zone Γ_c, a Neumann part Γ_N and a Dirichlet part Γ_D, $\{\Gamma_c \cup \Gamma_N \cup \Gamma_D = \Gamma : \Gamma \subset \mathbb{R}\}$. It is assumed that Γ_D has a non-zero measure. The boundary value problem, in terms of the displacement vector $\mathbf{u}$, is given as follows:

$$-\nabla \cdot (\sigma(\mathbf{u})) = f \ in \ \Omega, \tag{1}$$

$$\mathbf{u} = 0 \ on \ \Gamma_D \tag{2}$$

$$\sigma(\mathbf{u})\,\mathbf{n} = \mathbf{t}, \tag{3}$$

where f is the body forces over Ω and $\mathbf{t}$ are the prescribed tractions on the Neumann boundary. The outward unit normal vector $\mathbf{n}$ on Γ_c is defined with respect to the slave body Ω_s. The stress tensor σ is obtained using the classical von Mises nonlinear model. The yield function for the von Mises criterion can be defined as:

$$\Phi(\sigma) = \sqrt{J_2\left(\mathcal{S}\left(\sigma\right)\right)} - \tau_y, \tag{4}$$

with J_2 as the second principal invariant of the deviatoric stress tensor $\mathcal{S} = \sigma - p\mathbf{I}$, where p is hydrostatic pressure, and τ_y as the shear stress tensor. The gap function $g(\mathbf{X}, t)$ is

defined as the normal distance between a point $\mathbf{x}^{(1)}$ over the slave surface (Γ_s) and a point $\mathbf{x}^{(2)}$ over the master surface (Γ_m) in the current configuration as

$$g(\mathbf{X},t) = -\mathbf{n}[\mathbf{x}^{(1)}(\mathbf{X}^{(1)},t)] \cdot [\mathbf{x}^{(1)}(\mathbf{X}^{(1)},t) - \hat{\mathbf{x}}^{(2)}(\mathbf{X}^{(2)},t)]. \tag{5}$$

Together with the normal contact pressure, $\lambda_n(\mathbf{X},t)$, the gap function creates a set of conditions known as the Kuhn-Karush-Tucker (KKT) conditions, which enforce a non-penetration relation on the normal direction of Γ_c,

$$g(\mathbf{X},t) \geq 0,\ \lambda_n \leq 0,\ \lambda_n g(\mathbf{X},t) = 0. \tag{6}$$

In the tangential direction, the frictional conditions are given by the Coulomb's law:

$$\psi := |t_\tau| - \mu|\lambda_n| \leq 0. \tag{7}$$

Having stated these definitions, let $\mathbf{v}$ be virtual displacement vector and $\mathbf{V}$ the space of test functions fulfilling the condition $\mathbf{v} = 0$ on the Dirichlet boundary Γ_D. Then, applying the principle of virtual work to the boundary value problem and using the KKT conditions (6), the energy problem is reduced to finding $\mathbf{u} \subset \{\mathbf{u}_s, \mathbf{u}_m\} \in V$ such that,

$$\partial\Pi(\mathbf{u},\delta\mathbf{u}) = \partial\Pi_{int,ext}(\mathbf{u},\delta\mathbf{u}) + \partial\Pi_c(\mathbf{u},\delta\mathbf{u}) = 0, \tag{8}$$

where $\partial\Pi_{int,ext}(\mathbf{u},\delta\mathbf{u})$ represents the virtual work from the internal and external forces. The contact virtual work, $\partial\Pi_c(\mathbf{u},\delta\mathbf{u})$, is obtained by the integration – over the *slave side* – of the work done by the contact traction $\mathbf{t}_c^{(1)}$,

$$\partial\Pi_c(\mathbf{u},\delta\mathbf{u}) = -\int_{\Gamma_s} \mathbf{t}_c^{(1)} \cdot \left(\delta\mathbf{u}^{(1)} - \delta\mathbf{u}^{(2)}\right) d\Gamma_s. \tag{9}$$

The next section presents the discretization procedures adopted for solving the contact virtual work equation (9).

3 DISCRETIZATION

Since the lagrangian method has been extensively treated in the literature, the discretization procedure adopted for this method may be found in references such as Laursen [9] and Wriggers [10]. The discretization using a dual basis for the lagrangian multipliers adopted in this work is strongly based in the works of Hüeber et al. [5], Popp et al. [7] and Gitterle et al. [8], however a remark – concerning the final equation system used – must be made. Introducing the Lagrange multiplier, on the slave side, as the negative of the contact traction $\boldsymbol{\lambda} = -\mathbf{t}_c^{(1)}$ it is possible to rewrite equation (9) as,

$$\delta\Pi_c(\mathbf{u},\delta\mathbf{u},\boldsymbol{\lambda}) = \int_{\gamma_c^{(1)}} \boldsymbol{\lambda} \cdot \left(\delta\mathbf{u}^{(1)} - \delta\mathbf{u}^{(2)}\right) d\gamma \tag{10}$$

which represents a weak integral replacement of the strong pointwise non-penetration condition. The matrix form of equation (8) was reduced to the following pure displacement problem,

$$\begin{bmatrix} \mathbf{K}_{\mathcal{NN}} & \mathbf{K}_{\mathcal{NM}} & \mathbf{K}_{\mathcal{NI}} & \mathbf{K}_{\mathcal{NI}} \\ \mathbf{K}_{\mathcal{MN}} + \hat{\mathbf{M}}_{\mathcal{A}}^{T}\tilde{\mathbf{K}}_{\mathcal{AN}} & \tilde{\mathbf{K}}_{\mathcal{MM}} + \hat{\mathbf{M}}_{\mathcal{A}}^{T}\tilde{\mathbf{K}}_{\mathcal{AM}} & \tilde{\mathbf{K}}_{\mathcal{MI}} + \hat{\mathbf{M}}_{\mathcal{A}}^{T}\tilde{\mathbf{K}}_{\mathcal{AI}} & \tilde{\mathbf{K}}_{\mathcal{MA}} + \hat{\mathbf{M}}_{\mathcal{A}}^{T}\tilde{\mathbf{K}}_{\mathcal{AA}} \\ \mathbf{K}_{\mathcal{MA}} & \tilde{\mathbf{K}}_{\mathcal{IM}} & \tilde{\mathbf{K}}_{\mathcal{II}} & \tilde{\mathbf{K}}_{\mathcal{IA}} \\ \mathbf{0} & \hat{\mathbf{M}}_{\mathcal{A}} & \tilde{\mathbf{S}}_{\mathcal{AI}} & \tilde{\mathbf{S}}_{\mathcal{AA}} \\ \hat{\mathbf{T}}_{\mathcal{A}}\mathbf{K}_{\mathcal{AN}} & \hat{\mathbf{T}}_{\mathcal{A}}\tilde{\mathbf{K}}_{\mathcal{AN}} & \hat{\mathbf{T}}_{\mathcal{A}}\tilde{\mathbf{K}}_{\mathcal{AN}} - \tilde{\mathbf{F}}_{\mathcal{AI}} & \hat{\mathbf{T}}_{\mathcal{A}}\tilde{\mathbf{K}}_{\mathcal{AN}} - \tilde{\mathbf{F}}_{\mathcal{AI}} \end{bmatrix} \begin{bmatrix} \Delta\mathbf{d}_{\mathcal{N}} \\ \Delta\mathbf{d}_{\mathcal{M}} \\ \Delta\mathbf{d}_{\mathcal{I}} \\ \Delta\mathbf{d}_{\mathcal{A}} \end{bmatrix} = \begin{bmatrix} \mathbf{r}_{\mathcal{N}} \\ \mathbf{r}_{\mathcal{M}} + \hat{\mathbf{M}}_{\mathcal{A}}^{T}\mathbf{r}_{\mathcal{A}} \\ \mathbf{r}_{\mathcal{I}} \\ \tilde{\mathbf{g}}_{\mathcal{A}} \\ \hat{\mathbf{T}}_{\mathcal{A}}\mathbf{r}_{\mathcal{A}} \end{bmatrix} \quad (11)$$

here, indexes $\mathcal{N}$, $\mathcal{M}$, $\mathcal{I}$, $\mathcal{A}$ stands for the set of internal nodes, nodes on the mortar side, inactive non-mortar nodes and active non-mortar nodes, respectively. The matrix $\tilde{\mathbf{K}}$ corresponds to the summation of the standard tangent stiffness matrix $\mathbf{K}$ and the matrix $\tilde{\mathbf{C}}$, which contains the directional derivatives of both mortar matrices $\mathbf{D}$ and $\mathbf{M}$. Matrix $\tilde{\mathbf{S}}$ contains the directional derivatives of the gap functions vector $\tilde{\mathbf{g}}$, while the matrix $\tilde{\mathbf{F}}$ is obtained by assembling the tangent vector linearizations together with the current values of the Lagrange multipliers. The matrices $\hat{\mathbf{T}}$ and $\hat{\mathbf{M}}$ are defined as, $\hat{\mathbf{T}} = \mathbf{D}^{-1}\mathbf{T}$ and $\hat{\mathbf{M}} = \mathbf{D}^{-1}\mathbf{M}$, respectively. Since friction is taken into account, the terms related to stick and slip must be considered in the tangent matrix $\mathbf{T}$. Finally, the residual force vector is computed in terms of the vector of internal forces, $\mathbf{f}_{int}$, the vector of external forces, $\mathbf{f}_{ext}$, and the contact forces, $\mathbf{f}_c$, as follows,

$$\mathbf{r} = \mathbf{f}_{int}(\mathbf{d}) + \mathbf{f}_c(\mathbf{d}, \mathbf{z}) - \mathbf{f}_{ext} = \mathbf{0}, \quad (12)$$

where $\mathbf{d}$ represents the nodal displacements and the nodal values of the lagrangian multipliers, $\mathbf{z}$, are recovered using the following relation,

$$\mathbf{z} = \mathbf{D}^{-1}\left(-\mathbf{r}_{\mathcal{I}} - \mathbf{K}_{\mathcal{IN}}\Delta\mathbf{d}_N - \tilde{\mathbf{K}}_{\mathcal{IM}}\Delta\mathbf{d}_M - \tilde{\mathbf{K}}_{\mathcal{II}}\Delta\mathbf{d}_I\right). \quad (13)$$

The solution is undertaken using a sparse equation solver with the Newton-Raphson method, were the residual forces are indirectly used as a control parameter. The outcome is a fast and memory-optimized solver.

4 NUMERICAL EXAMPLES

In this section a set of three numerical problems is presented. The objective of those analyzes is to compare the standard Lagrange method and the Dual Mortar method, when plastic strain comes to play. Two normal contact problems are considered first to evaluate which formulation provides better load transfer. The second example is a classical Hertzian contact problem. Lastly, a conical extrusion problem is considered. Three materials were employed in the simulations and their properties are detailed in Table 1. All the examples employ the four node quadrilateral F-BAR finite element [11] and two node linear mortar elements.

Table 1: Material properties.

Material	E	G	ν	σ_y	Hardening law
Steel ANSI 9000	210 GPa	76 GPa	0.33	830 MPa	$\sigma = \sigma_y + 600\,(\epsilon)^{0.21}$
Al ANSI 201.0(†)	71.15 GPa	26 GPa	0.30	370 MPa	$\sigma = \sigma_y + 550\,(\epsilon)^{0.223}$
Al ANSI 771.0(‡)	69.8 GPa	26.12 GPa	0.32	31 MPa	$\sigma = \sigma_y + (\epsilon)\,(G/100)$

4.1 Normal contact problems

This first case study is mainly concerned with the correct prediction of strains/stresses in the normal direction, and therefore no friction is considered. Two contact problems are chosen: the classical contact patch test (Fig. 1) and the block pile problem (Fig. 2). The contact patch test [12] is the most commonly used benchmark to evaluate the load transfer from the contacting surface (master surface) to the target surface (slave surface). Here, a point load $F = 7.2kN$ is applied on each node at the top of the structure. The objective is to generate a constant uniaxial stress field in both contact bodies. By doing this, the Ladyzhenskaya-Babuska-Brezzi (LBB) criteria (discrete version of the inf-sub condition) should be satisfied.

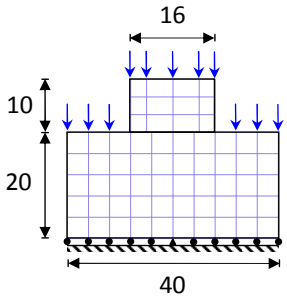

Figure 1: Contact patch test.

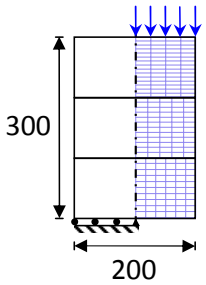

Figure 2: Block pile problem.

Another example typically employed to verify if the normal contact forces are correctly computed, is solving the block pile problem [13]. It consists of an arrangement of several blocks – with the same geometry – where a prescribed displacement (or distributed load) over the top surface of the last block on the pile is applied. The structure is meant to behave as an axisymmetric bar. Here, a prescribed displacement of $\delta_y = -15mm$ is applied to the top surface of the upper block. Since no friction is considered, the contacting surfaces should slide over each other, making the blocks deform alike. The ANSI 9000 Steel (Table 1) was employed for both problems. Applying the Lagrange Method to enforce the contact constraints in the first problem and using a single pass NTS detection to create the contact pairs will produce the results shown in Fig. 3. The displacement field, despite the excessive penetration of the contacting nodes at the corner of the slave body, have a quite smooth pattern. However, the effective stresses are not equally distributed over the structure and the formulation fails the test. The use of a double pass NTS detection approach to reduce penetration leads to the locking of the contacting surfaces. On the other hand, solving the contact constraints using the Dual Mortar Method provides an exact displacement pattern and the stress field is constant, see Fig. 4. The use of a non-linear material did not affect the quadratic convergence rate of the relative residual force.

The solution of the block pile problem also emphasized the limitations of the NTS approach, see Fig. 5. The pointwise nature of the contact enforcement, especially at the block's corner, made it very difficult to maintain the correct contact pairs. Eventually,

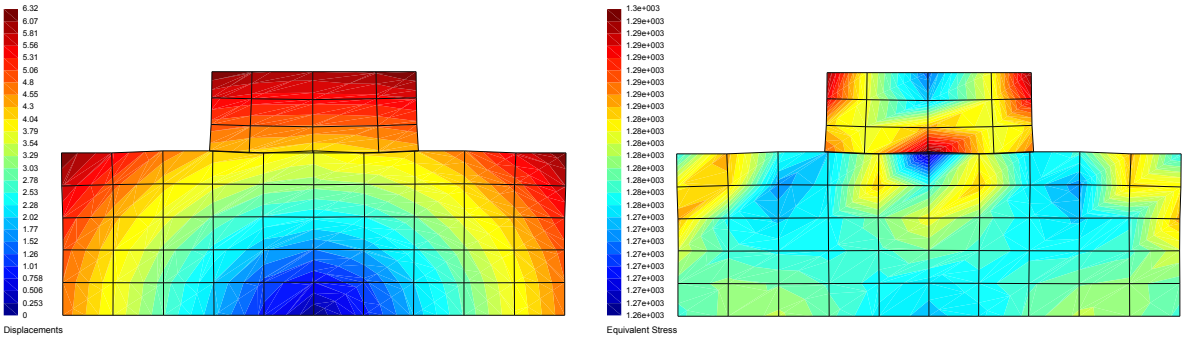

Figure 3: Contact patch test - Lagrange.

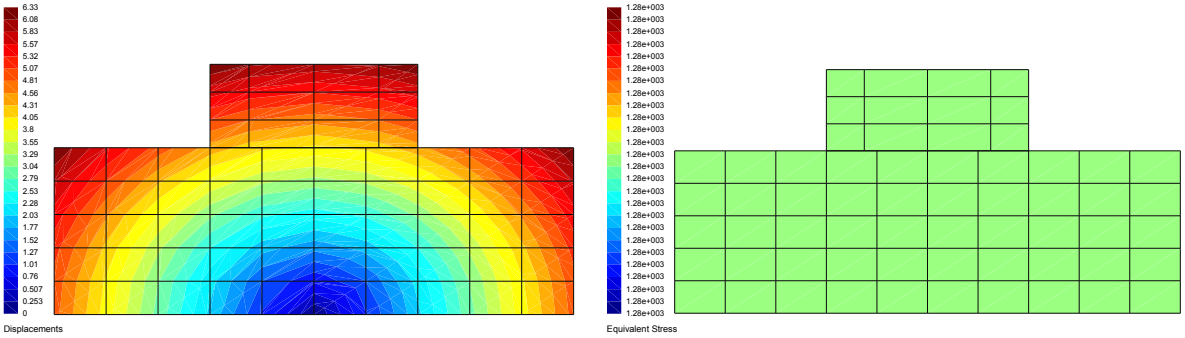

Figure 4: Contact patch test - Dual Mortar.

the corner nodes on the slave side went outside the limits of the master side domain. When this happens, the slave node is no longer enforced. High levels of penetration are reached, which also compromises the enforcement of the neighborings nodes. The results obtained by the Dual Mortar method are shown in Fig. 6. The segment-to-segment pairing, provided by the dual functions, compel the corner nodes to remain in contact. The outcome is a smooth deformation of the entire structure and a uniform uniaxial stress field.

4.2 Hertizian problem

The classical problem of Hertz is the second case of study. In this problem, a steel cylinder is pressed into an aluminium[†] block. The initial contact area is very small (non-conforming point contact) and a curved contact surface is present. The simulation is conducted as a two-dimensional plane-strain analysis. Geometry of the problem and finite element mesh are depicted in Fig. 7. Due to the symmetry, only half mesh is analyzed. The block's bottom surface is fixed. A friction coefficient of 0.1 was adopted in this analysis. The great asset of this case study relies on the existence of an analytical solution in the elastic domain. It is obtained from the Hertizian contact formulae for two

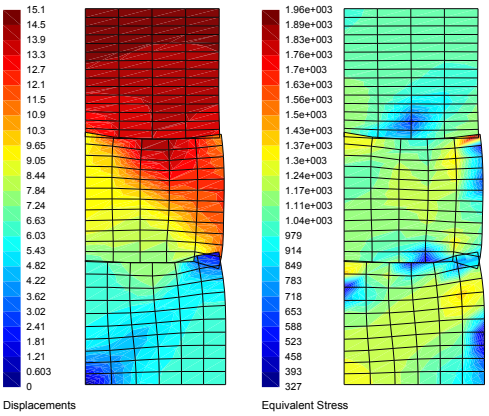

Figure 5: Block pile problem - Lagrange.

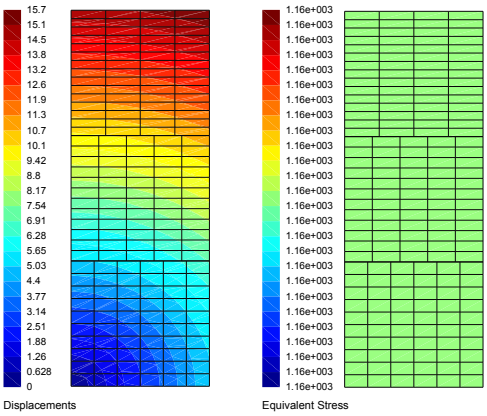

Figure 6: Block pile problem - Dual Mortar.

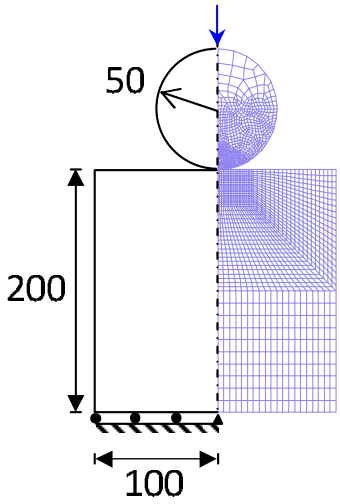

Figure 7: Hertizian problem.

cylinders, which defines the maximum contact pressure, P_{max}, the contact width, a, and the contact pressure along x-coordinate P as:

$$P_{max} = \sqrt{\frac{FE^*}{2\pi R^*}} \ , \ a = \sqrt{\frac{8FR^*}{\pi E^*}} \ , \ P = P_{max}\sqrt{1 - \left(\frac{x}{a}\right)} \tag{14}$$

where the combined elasticity modulus, E^*, is obtained from the material parameters of the punch (E_p) and the block (E_b) as follows:

$$E^* = \frac{2E_pE_b}{E_p\left(1-\nu_b^2\right) + E_b\left(1-\nu_p^2\right)} . \tag{15}$$

and the combined radius, R^*, is evaluated from the radius of the cylinder, R_1, and block, R_2, in a similar way, but since $\Rightarrow R_2 \rightarrow \infty$, the combined radius is reduced to the cylinder's radius,

$$R^* = \lim_{R_2 \to \infty} \frac{R_1 R_2}{R_1 + R_2} = \lim_{R_2 \to \infty} \frac{R_1}{R_1/R_2 + 1} = R_1. \tag{16}$$

In order to compare the numerical results and analytical solution, the analysis was divided in two phases. In a first moment, a compressive point load $F = 5kN$ is applied to the top of the cylinder. Under this load, only elastic strains will manifest, which allows a direct comparison with the analytical solution. For the given numerical parameters, the expected results are: $P_{max} = 1577.32N/mm^2$; $a = 2.018mm$; and $P = 1577.32\sqrt{1 - \left(\frac{x}{a}\right)^2}$.

In the second phase of the analysis, the point load is raised to $F = 12.5kN$, which leads to the appearance of plastic strains on both sides of the contact surface. The frictional forces becomes more significant, making the limitations of the NTS discretization more evident.

4.2.1 Elastic strains

In the first phase of the case study, the applied load yields a maximal Equivalent Stress at $x = 0$ equal to $327kN/mm^2$. This pressure is below the yield stress of both material employed, which assures that no plastic strains are in place. Also at this point, frictional forces are negligible. The load is well transfered and a Relative Residual Norm of E-10 is quadratically achieved after 4 iterations for the Lagrange method and 3 iteration for the Dual Mortar method. A comparison between the analytical solution and the results provided by the numerical simulations is depicted in Fig. 8. Despite the oscillation of the normal forces both results have a reasonable agreement.

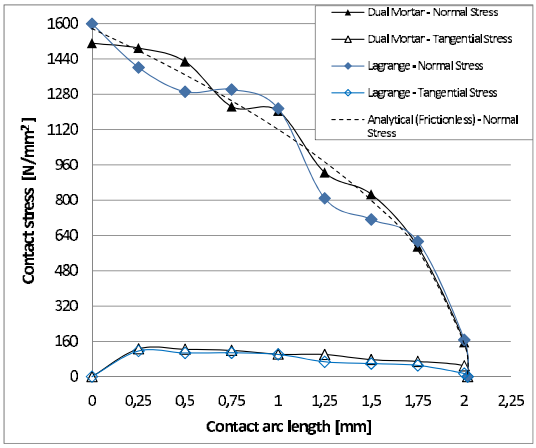

Figure 8: Contact stress - Elastic strains.

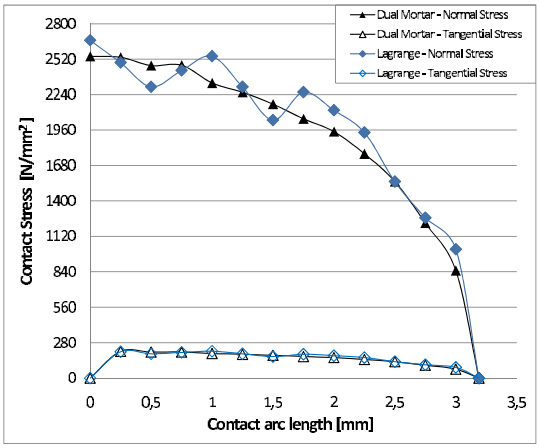

Figure 9: Contact stress - Plastic strains.

4.2.2 Plastic strains

On to the second phase, under the action of a vertical force of 12.5kN, the contact surface includes plastic deformation and the friction forces becomes considerably higher. Results are shown in Fig. 9 and Table 2. The stress distribution predicted by the NTS-

Table 2: Results of Hertizian problem - Plastic strains.

		Lagrange	Dual Mortar
TOTAL DISPLACEMENT [mm]	Cylinder	0.433	0.431
	Block	0.432	0.431
AVERAGE DEFORMATION	Cylinder	0.184	0.182
	Block	0.416	0.431
CONTACT LENGTH [mm]		3.178	3.198
Increment	Iteration	Relative residual norm (%)	
1	1	0.575085E-01	0.836091E-02
	2	0.140132E-04	0.739726E-06
	3	0.212436E-06	0.922262E-10
	4	0.172358E-10	
100	1	0.213476E-01	0.223108E-03
	2	0.510660E-04	0.198341E-07
	3	0.399832E-09	0.135704E-11
	4	0.340939E-12	
200	1	0.354716E-01	0.754524E-04
	2	0.485938E-03	0.917062E-08
	3	0.337746E-06	0.896271E-12
	4	0.852251E-11	

Lagrange method is no longer liable. Oscillations of normal forces reduced the results accuracy. The convergence rate is also decreased. On the other hand, since the number of contacting nodes increased, the results obtained using the Dual Mortar method have a better distribution of loads over the contact surface. Normal and tangential forces follow a relatively smoother pattern and convergence rate remained faster.

4.3 Conical extrusion

The problem undertaken in this example is an elasto-plastic stress analysis of an aluminium[‡] cylindrical billet. The billet is pushed a total distance of 177.8mm through a rigid conical die which has a wall angle of 5 degrees, see Fig. 10. The objectives are to predict the displacement of the billet material, the forces generated during the extrusion process and also the effective plastic strain distribution of the deformed billet. By analyzing the evolution of these variables it is also possible to assess the performance of

the Lagrangian Method and the Dual Mortar method when the contacting body is in the presence of frictional forces and plastic strains.

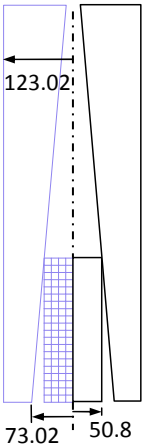

Figure 10: Conical extrusion - Geometry.

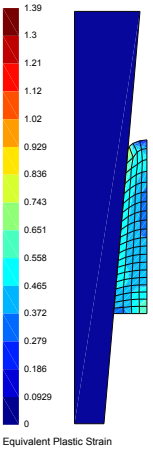

Figure 11: Conical extrusion - Plastic Strain.

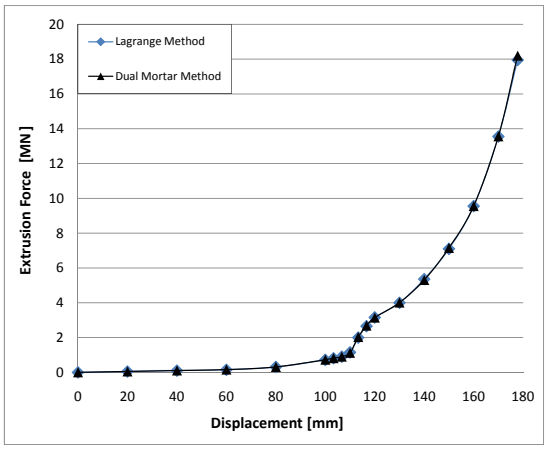

Figure 12: Extrusion forces.

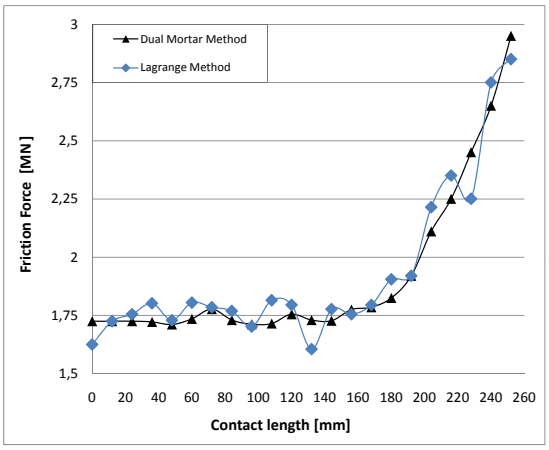

Figure 13: Frictional forces.

The Equivalent Plastic Strain obtained by the Dual Mortar method is shown in Fig. 11. The higher plastic deformation is found at the upper left side of the billet with a maximal value of 1.39. The final contact surface length is 257.33mm. A graphical representation of the extrusion force (measured from the reaction at the billet bottom) is shown in Fig. 12, the deviation between the two methods is very small. The convergence rate achieved was similar to the one obtained in section 4.2.2. Nevertheless, the evolution of the friction forces obtained by the Lagrangian method, see Fig. 13, shows the typical oscilation, which is due to the finite element discontinuities along the contact surface. This

drawback is mitigated by the segment-to-segment approach of the Dual Mortar method, which performs better.

5 CONCLUDING REMARKS

The results presented emphasize the benefits of using a dual basis for the lagrangian multipliers. The evaluation of the gap function as a semi-continuous weak integral yields a much better enforcement of constraints in the normal direction. This advantage leads to a more accurate evaluation of the contact forces, not only in the normal direction but also the reactions in the tangential direction as well. Additionally, it contributes to the correct fulfillment of the additional nonlinearity sources, i.e. sharp contact, friction plastic strain and friction forces. Furthermore, the superior correlation between the contacting bodies will promote a smaller initial value for the residual forces which will lead to a faster solution. The results suggest that the use of a higher order finite element/mortar element would also improve the effectiveness of the method, especially when dealing with sharp contact surfaces and curved surfaces. Such an improvement is necessary for solving contact problems between solids with irregular surfaces and with a higher friction coefficient, which may be a topic for future work.

REFERENCES

[1] C. Bernardi, Y. Maday, A. Patera, "*A new nonconforming approach to domain decomposition: the mortar element method*", in: H. Brezia, J. Lions (Eds.), Nonlinear Partial Differential Equations and their Applications, Pitman and Wiley, 1992, pp. 13-51.

[2] M.A. Puso, T.A. Laursen and J. Solberg, "*A segment-to-segment mortar contact method for quadratic elements and large deformations*", Comput. Methods. Appl. Mech. Engrg. (2008); 197: 555-566.

[3] M. Tur, F.J. Fuenmayor and P. Wriggers, "*A mortar-based frictional contact formulation for large deformations using Lagrange multipliers*". Comput. Methods Appl. Mech. Engrg, (2009); 198: 2860-2873.

[4] B. Wohlmuth. "*A mortar finite element method using dual spaces for the Lagrange multiplier*". SIAM Journal on Numerical Analysis (2000); 38: 989-1012.

[5] S. Hüeber and B.I. Wohlmuth. "*A primal-dual active set strategy for non-linear multibody contact problems*". Comput. Methods Appl. Mech. Engrg(2005); 194: 3147-3166

[6] S. Hartmann, S. Brunssen, E. Ramm and B. Wohlmuth. "*Unilateral non-linear dynamic contact of thin-walled structures using a primal-dual active set strategy*". Int. J. Numer. Meth. Engng. (2007); 70: 883-912.

[7] A. Popp, M.W. Gee and W.A. Wall. "*A finite deformation mortar contact formulation using a primal-dual active set strategy*". Int. J. Numer. Meth. Engng. (2009); 79: 1354-1391.

[8] M. Gitterle, A. Popp, M.W. Gee and W.A. Wall. "*Finite deformation frictional mortar contact using a semi-smooth Newton method with consistent linearization*". Int. J. Numer. Meth. Engng (2010); 84: 543-571.

[9] T.A. Laursen, "*Computational Contact and Impact Mechanics: Fundamentals of Modeling Interfacial Phenomena in Nonlinear Finite Element Analysis*", Springer-Verlag, Heidelberg (2002).

[10] P. Wriggers, "*Computational Contact Mechanics*", John Wiley & Sons, 2002.

[11] E.A. de Souza Neto, D. Perić, M. Dutko, and D.R.J. Owen, "*Design of Simple Low Order Finite Elements for Large Strain Analysis of Nearly Incompressible Solids*". Int. J. Solids Structs (1996); 33, 3277-3296.

[12] R.L. Taylor and P. Papadopoulos. "*On a patch test for contact problems in two dimensions. Computational Methods in Nonlinear Mechanics*", Wriggers, P. and Wagner, W., Springer-Verlag, pages 670-702, 1991.

[13] T.A. Laursen et al., "*Mortar contact formulations for deformable-deformable contact: Past contributions and new extensions for enriched and embedded interface formulations*", Comput. Methods Appl. Mech. Engrg. (2010), doi:10.1016/j.cma.2010.09.006

XI International Conference on Computational Plasticity. Fundamentals and Applications
COMPLAS XI
E. Oñate, D.R.J. Owen, D. Peric and B. Suárez (Eds)

HALFSPACE MODELING OF ELASTIC-PLASTIC CONTACT OF ROUGH SURFACES

F. HAUER AND K. WILLNER

Chair of Applied Mechanics (LTM)
University of Erlangen-Nuremberg
Egerlandstraße 5, 91058 Erlangen, Germany
e-mail: franz.hauer@ltm.uni-erlangen.de, www.ltm.uni-erlangen.de

Key words: Halfspace, Computational Plasticity, Contact, Metal forming

Abstract. Friction has a significant influence on the tool lifetime and the quality of products in manufacturing processes. Real surfaces are always rough, so that for moderate loads contact occurs only at surface roughness peaks. Thus the real contact area A_{real} is smaller than the apparent contact area A_0. Adhesive forces, which are an important contribution to friction, can only be transferred within A_{real}. Consequently A_{real} has to be determined in order to analyse the tribological behaviour of technical surfaces. The halfspace approach is used because of its advantage in numerical effort compared to the Finite-Element-Method. Due to the fact that contact pressures can be very large the plastic deformation of roughness peaks has to be taken into account. Therefore a three-dimensional plasticity algorithm is implemented into the halfspace model.

1 INTRODUCTION

Friction forces in dry metal contact are primarily caused by adhesion and ploughing [2]. Ploughing is the plastic deformation of a soft surface by a hard contact partner. It occurs between contact partners of different hardness or in the presence of hard particles. Adhesive forces can only be transferred in the real contact area A_{real} where material contact occurs. The real contact area is usually smaller than the apparent contact area A_0 because technical surfaces are always rough and consequently only the peaks of surface roughness are in contact. Therefore many researchers investigated the size of A_{real}. Archard [1] found a linear relation between normal load and A_{real} for a hierarchy of elastic Hertzian contacts. But the assumption of hierarchically Hertzian contacts is only an approximation of real surface shape. Therefore a model based on halfspace theory, which can handle arbitrary surfaces, has been introduced by Kalker [8]. However there is still the assumption of purely elastic surface deformation which is not true for primal contact, where surfaces are very rough. High roughness leads to a small real contact area, which leads to huge

contact pressures, which in turn causes the plastic deformation of the surface. For run-in surfaces the plastic behaviour is not significant, but for initial contact of rough surfaces it determines the contact behaviour. Therefore the elastic halfspace model was enhanced to an elastic-plastic model with a simple non volume conservative plasticity algorithm [11, 12]. In this algorithm the maximum pressure is limited to the surface hardness which is often set to three times the yield stress of the weaker contact partner, as observed experimentally by Bowden and Tabor [2]. The use of the Finite-Element-Method for the investigation of three-dimensional rough contact is impeded by its huge numerical cost. In order to provide a fast and accurate elastic-plastic contact code the halfspace model was extended to three-dimensional plasticity by Jacq et al. [6] and was applied to investigate the contact in bearings. The same approach will be used here in the context of the contact of rough surfaces in metal forming.

2 ELASTIC HALFSPACE MODEL

In order to account for the roughness of both contact partners the surface height $h(x, y)$ of the rough surface in the numerical model is the superposition of the surface roughness of both contact partners $z_1(x, y)$ and $z_2(x, y)$.

$$h(x, y) = z_1(x, y) + z_2(x, y) \tag{1}$$

The prescribed surface displacement in A_{real} is defined by the surface height, the maximum surface height h_{max} and the normal approach d.

$$\bar{u}_z = h(x, y) - h_{max} + d \tag{2}$$

The normal displacement of the halfspace surface $u_z(x, y)$ due to a pressure $p(\xi, \eta)$ on a surface segment is calculated with the Boussinesq solution:

$$u_z(x, y) = \frac{1}{\pi E^*} \int_\Gamma \frac{p(\xi, \eta)}{\rho} d\Gamma \tag{3}$$

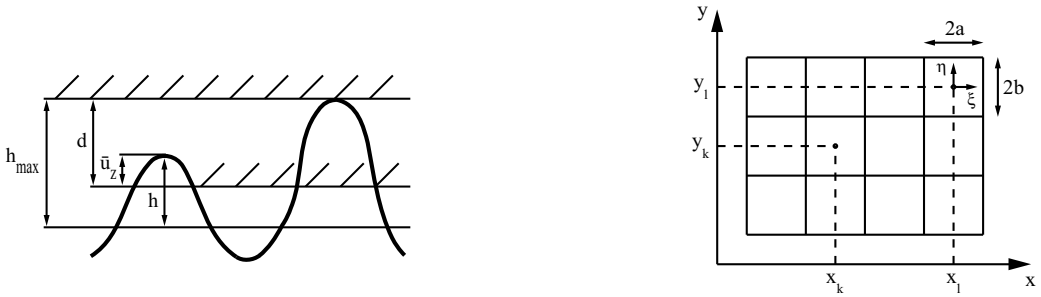

a) b)

Figure 1: Surface displacement (a) and discretisation (b) in the halfspace model

$$\rho = \sqrt{(x_k - x_l)^2 + (y_k - y_l)^2} \tag{4}$$

The compliance of both contact partners is considered by using the composite elastic modulus E^*:

$$\frac{1}{E^*} = \frac{1 - \nu_1^2}{E_1} + \frac{1 - \nu_2^2}{E_2} \tag{5}$$

The variational approach states that both total elastic strain energy and total complementary potential energy have a minimum for the true solution of a mechanical problem. In the halfspace model the principle of total complementary potential energy is preferred, because of its simplicity for the contact problem. The total complementary potential energy V^* is given by [11]:

$$V^* = \int_\Omega U^*(\sigma_{ij}) d\Omega - \int_\Gamma t_i \bar{u}_i d\Gamma \tag{6}$$

The integral of the internal complementary energy density $U^*(\sigma_{ij})$ over the bulk volume Ω equates the internal complementary energy U_E^*, which equals the internal energy U_E for linear elastic materials. The second term is the integral of the surface tractions t_i times the prescribed surface displacements $\bar{u}_i$ over the surface Γ. This term simplifies to the surface integral over the surface pressure p times the surface normal displacement u_z for the case of pure normal loading.

$$V^* = U_E - \int_\Gamma p \bar{u}_z d\Gamma \tag{7}$$

The internal energy can be expressed as:

$$U_E = \frac{1}{2} \int_\Gamma p u_z d\Gamma \tag{8}$$

This leads to the following expression for the total complementary potential energy:

$$V^* = \frac{1}{2} \int_\Gamma p u_z d\Gamma - \int_\Gamma p \bar{u}_z d\Gamma \tag{9}$$

The halfspace surface is discretised into M rectangular segments. The surface deformation due to several segments in contact is calculated by summation over the contact pressure times the compliance $C_{kl}^{(zz)}$:

$$u_{zk} = \sum_{l=1}^{M} C_{kl}^{(zz)} p_l \tag{10}$$

$$C_{kl}^{(zz)} = \frac{1}{2\pi G} \int_{-a}^{a} \int_{-b}^{b} \frac{1 - \nu}{\rho_{kl}} d\eta \, d\xi \tag{11}$$

with

$$\rho_{kl} = \sqrt{(x_k - x_l - \xi)^2 + (y_k - y_l - \eta)^2} \tag{12}$$

Using this discretisation the total complementary potential energy can be expressed as:

$$V^* = \frac{1}{2}\sum_{k=1}^{M} p_k \left(\sum_{l=1}^{M} C_{kl}^{(zz)} p_l \right) - \sum_{k=1}^{M} p_k \bar{u}_z \tag{13}$$

The derivative of this functional is set to zero in order find its minimum:

$$\sum_{l=1}^{M} C_{kl}^{(zz)} p_l - \bar{u}_z = 0 \quad \Longrightarrow \quad C^{(zz)} p = u_z \tag{14}$$

To solve the contact problem the system of equations compliance matrix $C^{(zz)}$ times pressure field p equals the surface displacement field u_z is solved by the Gauss-Seidel method. The resulting pressure field has to be free from negative entries. This is enforced by applying the following condition:

$$p_l \geq 0 \quad \forall \quad l \in 1, \ldots, M \tag{15}$$

3 ELASTIC-PLASTIC HALFSPACE MODEL

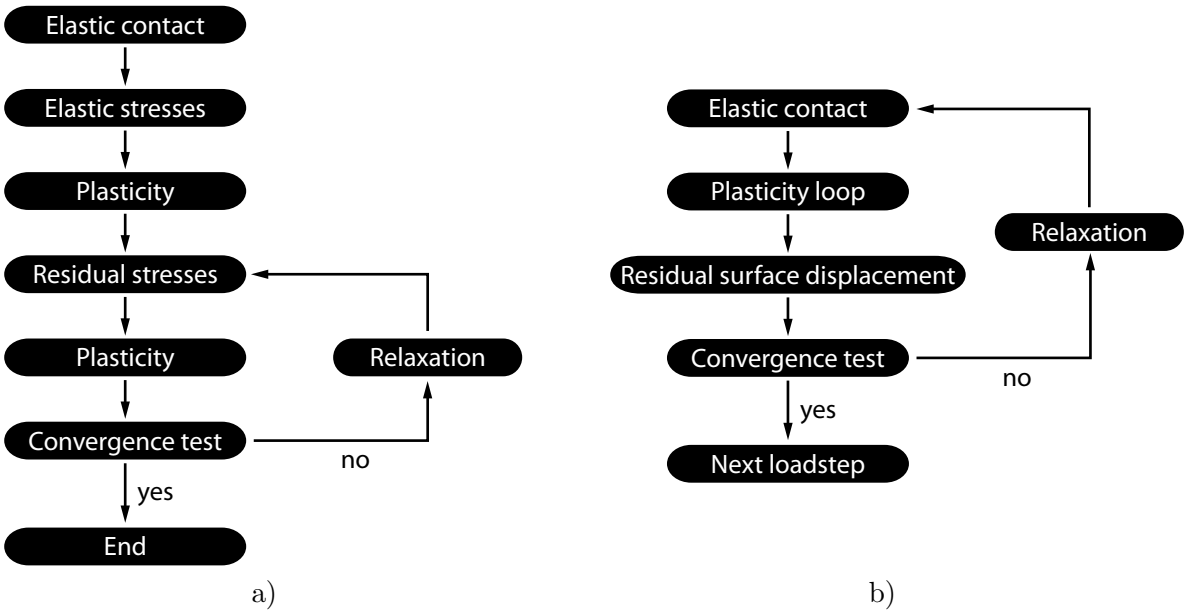

Figure 2: Plasticity loop (a) and contact loop (b)

The elastic-plastic halfspace model was first introduced by Jacq [6] and starts with a elastic contact simulation. The bulk underneath the contact is discretised into cuboids. The stresses within the cuboids due to pressure on surface segments are calculated via influence functions. If the equivalent stress in a cuboid exceeds the yield strength of

the material plastic strains are calculated based on von Mises plasticity. These plastic strains lead to residual stresses within the bulk, which are as well calculated by means of influence functions. The residual stresses and the elastic stresses are superpositioned and the calculation of plastic strains is repeated with the superpositioned stresses. If there is no convergence in plastic strains the plasticity loop is reentered at the calculation of residual stresses with relaxed plastic strains. Plastic strains in the bulk cause a deformation of the surface which changes the geometry and pressure distribution of the contact. When the plasticity loop, which is the inner loop, has converged the surface shape is updated with the residual surface displacements. In the contact loop, which is the outer loop, the final surface shape and contact distribution are found iteratively.

3.1 Elastic stresses

The elastic strains in the bulk due to a surface segment under uniform normal pressure can be expressed by derivatives of the Boussinesq potential functions [7]. The stress components due to the surface load are obtained by inserting derivatives of the strains into Hooke's law.
Boussinesq potential functions:

$$H_1 = \int_\Gamma \int p \left[z \log \left(\rho + z \right) - \rho \right] \, d\xi \, d\eta \tag{16}$$

$$H = \frac{\partial H_1}{\partial z} = \int_\Gamma \int p \log \left(\rho + z \right) d\xi \, d\eta \tag{17}$$

$$\rho = \sqrt{(\xi - x)^2 + (\eta - y)^2 + z^2} \tag{18}$$

Displacements:

$$u_x = \frac{1}{4\pi G} \left\{ \left(2\nu - 1 \right) \frac{\partial H}{\partial x} - z \frac{\partial^2 H}{\partial x \partial z} \right\} \tag{19}$$

$$u_y = \frac{1}{4\pi G} \left\{ \left(2\nu - 1 \right) \frac{\partial H}{\partial y} - z \frac{\partial^2 H}{\partial y \partial z} \right\} \tag{20}$$

$$u_z = \frac{1}{4\pi G} \left\{ 2 \left(1 - \nu \right) \frac{\partial H}{\partial z} - z \frac{\partial^2 H}{\partial z^2} \right\} \tag{21}$$

Stresses (Hooke's law):

$$\sigma_{xx} = \frac{2\nu G}{1 - 2\nu} \left(\frac{\partial u_x}{\partial x} + \frac{\partial u_y}{\partial y} + \frac{\partial u_z}{\partial z} \right) + 2G \frac{\partial u_x}{\partial x} \tag{22}$$

Finally the stresses in the bulk can be expressed as combinations of derivatives of the Boussinesq potential functions:

$$\sigma_{xx} = \frac{1}{2\pi} \left\{ 2\nu \frac{\partial^2 H}{\partial z^2} - z \frac{\partial^3 H}{\partial x^2 \partial z} + (2\nu - 1) \frac{\partial^2 H}{\partial x^2} \right\} \tag{23}$$

$$\sigma_{yy} = \frac{1}{2\pi}\left\{2\nu\frac{\partial^2 H}{\partial z^2} - z\frac{\partial^3 H}{\partial y^2 \partial z} + (2\nu - 1)\frac{\partial^2 H}{\partial y^2}\right\} \tag{24}$$

$$\sigma_{zz} = \frac{1}{2\pi}\left\{2\nu\frac{\partial^2 H}{\partial z^2} - z\frac{\partial^3 H}{\partial z^3}\right\} \tag{25}$$

$$\tau_{xy} = -\frac{1}{2\pi}\left\{(1 - 2\nu)\,\frac{\partial^2 H}{\partial x \partial y} + z\frac{\partial^3 H}{\partial x \partial y \partial z}\right\} \tag{26}$$

$$\tau_{yz} = -\frac{1}{2\pi} z \frac{\partial^3 H}{\partial y \partial z^2} \tag{27}$$

$$\tau_{zx} = -\frac{1}{2\pi} z \frac{\partial^3 H}{\partial x \partial z^2} \tag{28}$$

3.2 Plasticity algorithm

The plastic deformation is calculated using a return mapping algorithm with an elastic predictor step and a plastic corrector step. The utilised method was developed by Fotiu and Nemat-Nasser [5] and is described nicely by Nélias [10]. The plastic deformation rate is given by

$$\dot{\epsilon}_p = \dot{\gamma}\,\mu \tag{29}$$

with the normalised tensor μ giving the direction of plastic strain and the effective plastic strain rate $\dot{\gamma}$

$$\mu = \frac{3\,\sigma'}{2\,\sigma_{vm}} \tag{30}$$

$$\mu : \mu = \frac{3}{2} \tag{31}$$

The von Mises equivalent stress is defined as

$$\sigma_{vm} = \sqrt{\frac{3}{2}\,\sigma' : \sigma'} \tag{32}$$

and σ' is the deviatoric part of the stress tensor. The equivalent total strain rate is similarly defined by

$$\dot{e} = \sqrt{\frac{2}{3}\,\dot{e}' : \dot{e}'} \tag{33}$$

Using (33) the deviatoric part of the total strain rate can be expressed as

$$\dot{\epsilon}' = \dot{e}\,\eta \tag{34}$$

$$\eta : \eta = \frac{3}{2} \tag{35}$$

With the yield stress σ_y the yield function f can be given by

$$f = \sigma_{vm} - \sigma_y(\gamma) \tag{36}$$

The Kuhn-Tucker conditions, which have to be fulfilled at all times, are defined as

$$f \leq 0, \qquad \dot{\gamma} \geq 0, \qquad f\,\dot{\gamma} = 0 \tag{37}$$

Under the assumption of isotropic behaviour in the elastic regime the following condition applies

$$\sigma' = 2G\,(\epsilon' - \epsilon_p) \tag{38}$$

G is the shear modulus of the material. If μ and η are considered to be collinear it can be shown that

$$\dot{\sigma}_{vm} = \dot{\sigma}' : \mu = 3G\dot{\epsilon} - 3G\dot{\gamma} \tag{39}$$

It follows directly

$$\Delta\sigma_{vm} = 3G\dot{\epsilon}\Delta t - 3G\Delta\gamma \tag{40}$$

The computation of plastic strains starts with the calculation of the elastic predictor, the equivalent stress and the direction tensor μ of the deviatoric stress σ'. Then the yield function f is calculated

$$f^{(n)} = \sigma_{vm}^{(n)} - \sigma_y^{(n)} \tag{41}$$

The Newton's method is performed in order to execute the return mapping to the yield surface. Therefore f is linearised along the plastic corrector direction.

$$f_L^{(n)} = f^{(n)} + f_{,\sigma_{vm}}^{(n)} \cdot \Delta\sigma_{vm}^{(n)} + f_{,\gamma}^{(n)} \cdot \Delta\gamma^{(n)} = 0 \tag{42}$$

$$f_{,\sigma_{vm}}^{(n)} = 0 \qquad f_{,\gamma}^{(n)} = -\sigma_{y,\gamma}^{(n)} \tag{43}$$

Using the plastic corrector increment

$$\Delta\sigma_{vm}^{(n)} = -3G \cdot \Delta\gamma^{(n)} \tag{44}$$

we can calculate the effective plastic strain increment

$$\Delta\gamma^{(n)} = \frac{f^{(n)}}{3G + \sigma_{y,\gamma}^{(n)}} \tag{45}$$

Then the stresses and effective strain are updated and the yield stress is recalculated

$$\sigma_{vm}^{(n+1)} = \sigma_{vm}^{(n)} - 3G \cdot \Delta\gamma^{(n)} \tag{46}$$

$$\gamma^{(n+1)} = \gamma^{(n)} + \Delta\gamma^{(n)} \tag{47}$$

$$\sigma_y^{(n+1)} = \sigma_y(\gamma^{(n+1)}) \tag{48}$$

The yield function is checked in order to ensure convergence

$$|f^{(n+1)}| = |\sigma_{vm}^{(n+1)} - \sigma_y^{(n+1)}| < \text{tol} \tag{49}$$

If if the convergence test fails the Newton-iteration is repeated, otherwise the plastic strains are calculated

$$\Delta\epsilon_p = \Delta\gamma \cdot \mu \tag{50}$$

3.3 Residual stresses and surface displacement

Plastically strained cuboids in the halfspace lead to residual stresses. Chiu [3] solved the problem of stresses due to uniform strains in cuboids in infinite space. The solution for a halfspace is obtained by superposition of the stresses due to a cuboid in infinite space, a mirror cuboid in infinite space and the elastic stresses due to a surface load [4]. The position of the cuboid relative to the halfspace surface corresponds to the position of the strained cuboid. The mirror cuboid is situated at the mirror position to the halfspace surface. Its strains in xz- and yz-direction are inverted. This superposition leaves the halfspace surface free from shear stresses in the mentioned directions, which is a necessary condition of a free surface. However there remains a normal stress on the surface. This normal stress is removed by subtracting the elastic stresses due to this fictitious normal pressure from the total stress field. Benchmarks for the influence functions for residual stresses are found in Chiu's papers and in [13].

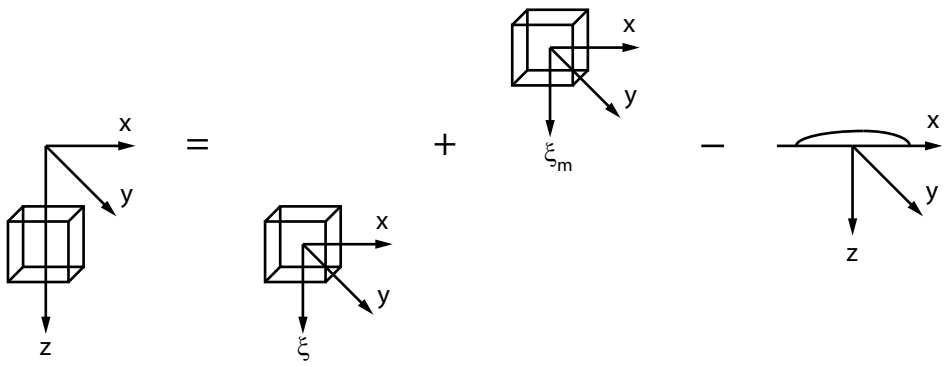

Figure 3: Superposition of stresses

Influence functions for the residual surface displacement can be found in [6] and [9].

4 RESULTS

4.1 Hertzian contact

Figure 4a shows the pressure distribution underneath the Hertzian contact of a rigid ball of radius 40 mm with an deformable plane. The analytical solution and the result of the elastic halfspace simulation are in good agreement. The elastic-plastic result exhibits a much smaller maximum contact pressure value and a larger contact radius due to the plastic surface deformation. Figure 4b shows the radial distribution of the residual surface deformation in the elastic-plastic simulation. There is a large indent at the centre of contact. Due to plastic flow material builds up at the border of contact. The yield stress in the plastic simulation is defined by the following relation: The material in the elastic-plastic simulation has a Young's modulus of 205 000 MPa and Poisson's number of 0.34.

The yield stress depends on the equivalent plastic strain γ and is defined as:

$$\sigma_y = 200\,MPa + 1550\,MPa \cdot \gamma \tag{51}$$

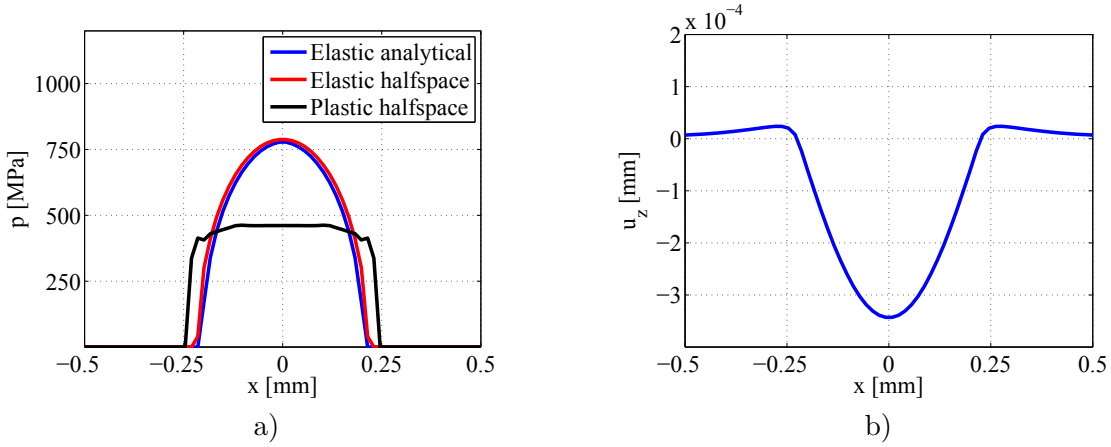

a) b)

Figure 4: Pressure distribution (a) and residual surface displacement (b)

4.2 Contact of rough surfaces

An example of a simulation of a real rough surface is presented here. Figure 5a shows the rough surface before contact, whereas figure 5b shows the same surface after plastic deformation due to contact loads. It can be seen that the highest surface peaks are reduced in height and the surface shape is less rough after contact. Figure 6 shows the dependency between the average normal pressure and the real contact area. For low contact pressures there is no plastic deformation of the surface. Above approximately $100\,MPa$ plastic surface deformation occurs and the real contact area in the elastic-plastic simulation is higher than in the purely elastic calculation. The difference in A_{real} increases with the contact pressure. The same material parameters as in the elastic-plastic simulation of the Hertzian contact were used.

5 CONCLUSIONS

An elastic-plastic contact algorithm for the simulation of rough surfaces based on the ideas of Jacq [6] was set up and tested with an analytical example and a simulation of a rough surface. The present model has to be validated with a comparison to Finite-Element-Method simulations. Then results of the real contact area for different surfaces and pressures will be compared to the results of the simple non volume conservative plasticity algorithm. The final aim of this research work is the simulation of friction in metal forming. Metal forming is always done with lubrication, so that the modelling of lubricant effects is necessary. The total contact area can be classified into the real contact

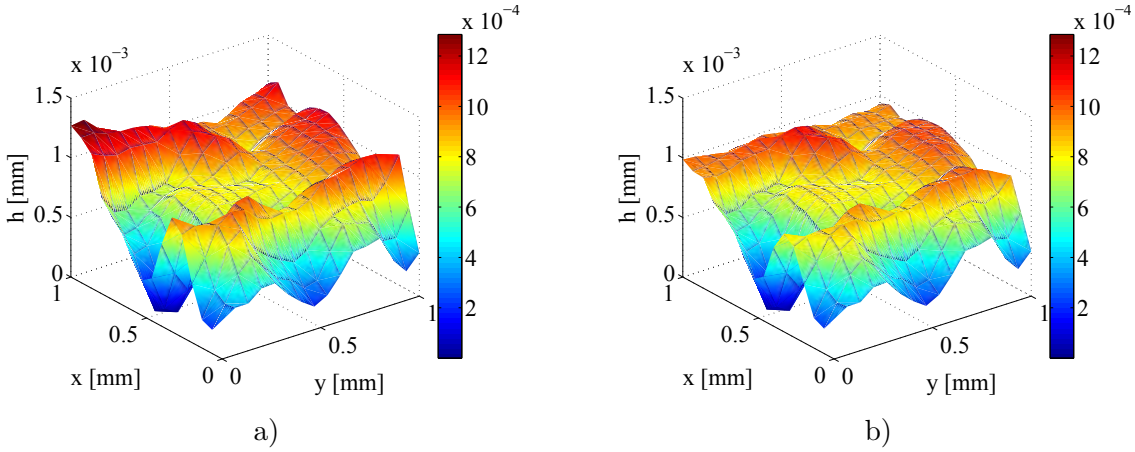

Figure 5: Rough surface before (a) and after contact (b)

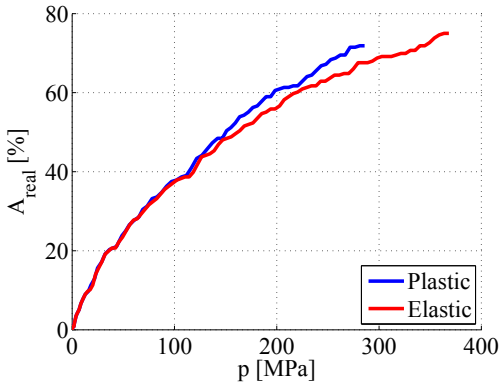

Figure 6: Load-area curve in elastic-plastic and purely elastic contact

area, open lubricant pockets and closed lubricant pockets. A fist approach towards this challenge will be the modelling of hydrostatic pressure in closed lubricant pockets.

6 ACKNOWLEDGEMENT

This research project is supported by the German Research Foundation (DFG) within the Transregional Collaborative Research Centre on sheet-bulk metal forming (SFB/TR 73).

REFERENCES

[1] J. F. Archard, *Elastic deformation and the laws of friction*. Proceedings of the Royal Society of London, Series A, Vol. 243, pp. 190-205, 1957.

[2] F. P. Bowden, D. Tabor, *The friction and lubrication of solids*. Oxford University Press, 1986.

[3] Y. P. Chiu, *On the Stress Field Due to Initial Strains in a Cuboid Surrounded by an Infinite Elastic Space*. Journal of Applied Mechanics, Vol. 44, pp 587-590, 1977.

[4] Y. P. Chiu, *On the Stress Field and Surface Deformation in a Half Space With a Cuboidal Zone in Which Initial Strains Are Uniform*. Journal of Applied Mechanics, Vol. 45, pp 302-306, 1978.

[5] P. A. Fotiu, S. Nemat-Nasser, *A Universal Integration Algorithm for Rate-Dependent Elastoplasticity*. Computers & Structures, Vol. 59, pp. 1173-1184, 1996.

[6] C. Jacq, D. Nélias, G. Lormand, D. Girodin, *Development of a Three-Dimensional Semi-Analytical Elastic-Plastic Contact Code*. Journal of Tribology, Vol. 124, pp. 653-667, 2002.

[7] K. L. Johnson, *Contact mechanics*. Cambridge University Press, 1985.

[8] J. J. Kalker. Y. van Randen, *A Minimum Principle for Frictionless Elastic Contact with Application to Non-Hertzian Half-Space Contact Problems*. Journal of Engineering Mathematics, Vol. 6, pp. 193-206, 1972.

[9] S. Liu, Q. Wang, *Elastic Fields due to Eigenstrains in a Half-Space*. Journal of Applied Mechanics, Vol. 72, pp. 871-878, 2005.

[10] D. Nélias, V. Boucly, M. Brunet, *Elastic-Plastic Contact Between Rough Surfaces: Proposal for a Wear or Running-in Model*. Journal of Tribology, Vol. 128, pp. 236-244, 2006.

[11] X. Tian, B. Bhushan, *A Numerical Three-Dimensional Model for the Contact of Rough Surfaces by Variational Principle*. Journal of Tribology, Vol. 118, pp. 33-42, 1996.

[12] K. Willner, *Elasto-Plastic Normal Contact of Three-Dimensional Fractal Surfaces Using Halfspace Theory*. Journal of Tribology, Vol. 126, pp. 28-33, 2004.

[13] K. Zhou, W. W. Chen, L. M. Keer, Q. J. Wang, *A fast method for solving three-dimensional arbitrarily shaped inclusions in half space*. Computational Methods in Applied Mechanical Engineering, Vol. 198, pp. 885-892, 2009.

XI International Conference on Computational Plasticity. Fundamentals and Applications
COMPLAS XI
E. Oñate, D.R.J. Owen, D. Peric and B. Suárez (Eds)

NUMERICAL ANALYSIS OF ELASTIC-PLASTIC CONTACT PROBLEMS

OXANA V. SADOVSKAYA

Institute of Computational Modeling SB RAS
Akademgorodok 50/44, 660036 Krasnoyarsk, Russia
e-mail: o_sadov@icm.krasn.ru, http://icm.krasn.ru

Key words: Contact Interaction, Elastic-plastic Material, Parallel Computations

Abstract. The algorithm for numerical realization of boundary conditions of contact interaction of deformable bodies taking into account a friction is worked out. Contact conditions are formulated in the form of quasivariational inequality with one-sided constraint. This constraint corresponds to the condition of nonpenetration of deformable bodies into each other. Dynamic interaction of elastic-plastic materials with beforehand unknown, time-dependent zone of contact is described by the model taking into account small strains and finite rotations. This model consists of the system of equations of motion, the Hooke law for elastic constituents of the strain tensor, the equation for the rotation angle and the principle of maximum of the energy dissipation rate describing the process of plastic flow. The transition of material from elastic state to plastic one is determined by the Mises yield condition. Parallel shock-capturing algorithm is proposed for implementation of the model on multiprocessor computer systems. It is based on a combination of splitting methods with respect to physical processes and spatial variables. The results of computations of an oblique impact of two deformable plates are represented.

1 INTRODUCTION

Dynamic contact problems of the theory of elasticity and plasticity with beforehand unknown, time-dependent zone of contact have a wide field of applications connected with the analysis of processes of impact and punching of obstacles, mechanical processing of materials, etc. As a rule, explicit in time procedures of the contact boundaries computation are applied for numerical solution of such problems. But the use of these procedures results either in intersection of deformable bodies or in violation of discrete dynamic conditions in a contact zone. One of possible approaches to the modeling of dynamic contact interaction is based on the formulation of boundary conditions of contact in the form of variational and quasivariational inequalities [1, 2]. Such approach makes possible to construct implicit iterative procedures, ensuring the fulfilment of geometric

constraints in a contact zone, condition of non-negativity of normal contact pressure, and condition of opposite directivity of the vectors of tangential velocity and tangential stress at sliding.

2 BOUNDARY CONDITIONS OF CONTACT INTERACTION

2.1 Variational formulation of contact conditions

Let S_c^+ and S_c^- be the parts of boundaries of two deformable bodies in the Lagrange variables which include the whole contact zones

$$S_t^{\pm} = \left\{ x^{\pm} \in S_c^{\pm} \mid \; x^+ + u^+(t, x^+) = x^- + u^-(t, x^-) \right\}$$

at each fixed instant t. Here u is the displacement vector, the superscripts $\pm$ denote quantities related to different bodies. Under S_c^+ and S_c^- are assumed such parts of boundaries of interacting bodies in an initial undeformed state, material points of which are in contact or are free of stresses at each following instant of time, whereas on the remaining part of boundary the conditions of a rather general form are fulfilled but the contact is impossible. In Fig. 1 the position of the boundaries of bodies at the initial instant of time is shown by dashed lines and that of at the instant $t - \Delta t$ is shown by solid lines (Δt is a small time interval). An approximate constraint on velocities $v^{\pm}$ of the points $x^+ \in S_c^+$ and $x^- \in S_c^-$ can be written in the following way:

$$(\tilde{v}^- - \tilde{v}^+)\,\hat{n} \le \frac{1}{\Delta t} \left| x^+ + u^+_{|\,t-\Delta t} - x^- - u^-_{|\,t-\Delta t} \right|. \tag{1}$$

This constraint is a condition of nonpenetration of deformable bodies into each other. The boundary points involved in (1) are assumed to be related by a one-to-one correspondence that depends on time as on a parameter. With this correspondence, the point x^+ of the

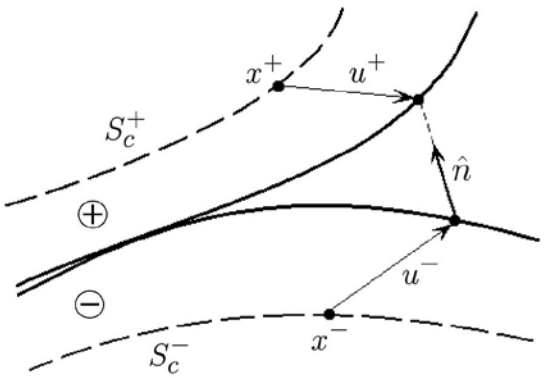

Figure 1: Constraint in a contact zone of two deformable bodies

contact zone S_t^+ is related to the point x^- of S_t^-, determined by equality of positions at an actual instant of time:

$$x^+ + u^+(t, x^+) = x^- + u^-(t, x^-).$$

In the noncontact domains $S_c^\pm \setminus S_t^\pm$ the correspondence may be arbitrary. The unit vector $\hat{n}$, indicating a local direction of convergence of bodies, is given by

$$\hat{n} = \begin{cases} n^- = -\,n^+, & \text{if } \ x^\pm \in S_{t-\Delta t}^\pm\,, \\ \dfrac{x^+ + u^+_{|\,t-\Delta t} - x^- - u^-_{|\,t-\Delta t}}{\left| x^+ + u^+_{|\,t-\Delta t} - x^- - u^-_{|\,t-\Delta t} \right|}, & \text{if } \ x^\pm \notin S_{t-\Delta t}^\pm\,. \end{cases}$$

The right-hand side of (1), which is proportional to the distance between points at the instant $t - \Delta t$, has the sense of maximal possible velocity of convergence. When solving contact problems, the choice of a one-to-one correspondence for the approximate constraint (1) is one of the stages of constructing a computational algorithm.

The exact constraint on the velocity vectors is obtained from (1) by going to the limit with respect to Δt as $\Delta t \to 0$:

$$\tilde{v}^{\,-} n^- + \tilde{v}^{\,+} n^+ \le \begin{cases} 0, & \text{if } \ x^\pm \in S_t^\pm, \\ +\infty, & \text{if } \ x^\pm \notin S_t^\pm. \end{cases} \tag{2}$$

Boundary conditions of contact interaction in the presence of a friction can be formulated as follows [2]:

$$(\tilde{v}^- - v^-)\,\sigma_n^- + (\tilde{v}^+ - v^+)\,\sigma_n^+ + F\left(\frac{\sigma^+_{n\hat{n}} - \sigma^-_{n\hat{n}}}{2}\right)\left(\left|\tilde{v}^+_{\hat{\tau}} - \tilde{v}^-_{\hat{\tau}}\right| - \left|v^+_{\hat{\tau}} - v^-_{\hat{\tau}}\right|\right) \ge 0. \tag{3}$$

Here $\sigma_n^\pm(t, x^\pm)$ is the stress vector acting on an area element of a deformed surface with the normal $n^\pm$, $F(\sigma_{nn}) = \min\left\{ f|\sigma_{nn}|,\, \tau_s^+,\, \tau_s^- \right\}$ is a function that determines the limit tangential stress of sliding friction, f is the friction coefficient, $\tau_s^\pm$ are the yield points of materials, the vectors $\hat{\tau}$ and $\hat{n}$ are orthogonal to each other. The arbitrary variable vectors $\tilde{v}^\pm$ as well as the vectors $v^\pm$ of actual velocities satisfy the constraint (1) at the contact zones $S_c^\pm$. The inequality (3) is quasivariational, since the constraints (1), (2) depend on an unknown solution $u^\pm$. It can be interpreted as the minimum principle for power of normal stress in a contact zone. Equivalence between the inequality (3) and a generalized friction law is established in [3].

2.2 Velocities correction algorithm

Conditions of contact of deformable bodies can be represented in a form, convenient for numerical realization:

$$(\tilde{w} - w)A(w - \bar{w}) + F\Big(b(w - \bar{w})\Big)\Big(\omega(\tilde{w}) - \omega(w)\Big) \geq 0. \tag{4}$$

The approximate constraint (1) for velocities is reduced to the general form:

$$\tilde{w}\, n \leq h, \quad w\, n \leq h. \tag{5}$$

Here the vector w consists of components of the velocity vectors v^+ and v^-, $\tilde{w}$ is an arbitrary admissible variation of w, A is a positive-definite square matrix which relates velocities and stresses, $\bar{w}$ is the velocity vector corresponding to setting the conditions of a free surface in a contact zone, n is the vector consisting of components of outward normals to contacting surfaces, $b = n\,A$. In (4) $\omega(w)$ denotes the modulus of the difference between the tangential components of velocities. This function can be represented in the form $\omega(w) = \max\limits_{\tilde{l} \in L}\Big\{w\,\tilde{l}\Big\} = w\,l$, where the bounded closed convex set L consists of vectors which are orthogonal to a normal vector and whose length does not exceed unity: $L = \Big\{\tilde{l} \mid \ \tilde{l} \perp n, |\,\tilde{l}\,| \leq 1\Big\}$. The vectors w and $\tilde{w}$, involved in the inequality (4), satisfy the one-sided constraint (5): they belong to the convex and closed set of admissible variations $K = \Big\{\tilde{w} \mid \ \tilde{w}\, n \leq h\Big\}$. The scalar quantity h is defined by the distance between corresponding points of contacting surfaces at an actual instant of time.

For numerical solution of the variational inequality (4) in boundary meshes of the finite-difference grid the velocities correction algorithm is proposed [3]. The idea of this algorithm is that in such boundary meshes of a grid, where contact is possible, a convergent iterative process is constructed, on each step of which the projections of velocity vectors and auxiliary vectors, determining the sliding direction, onto convex and closed sets of a special form are successively calculated. If the friction forces are not taken into account under the realization of contact conditions, then the iterations are not required.

Specifying the vector $w = \hat{w}$ in the inequality (4), we fix the value of the function F: $\hat{F} = F\Big(b(\hat{w} - \bar{w})\Big) \geq 0$. We obtain the more simple inequality

$$(\tilde{w} - w)A(w - \bar{w}) + \hat{F}\Big(\omega(\tilde{w}) - \omega(w)\Big) \geq 0. \tag{6}$$

The matrix A is positive-definite, the function $\omega(w)$ and the set K are convex, hence, this inequality has a unique solution. So, one can construct a mapping $Q : \hat{w} \mapsto \hat{F} \mapsto w$, such that the solution of (4) is its fixed point: $w = Q(w)$. The fact that the mapping Q

is contractive for a sufficiently small friction coefficient $f < a/|b|$ $\left(a = \min\limits_{|w|=1}\{wAw\}\right)$ is proved in [3]. Thus, the solution of (4) can be determined by the method of successive approximations, where at each step it is necessary to solve the inequality (6) with the coefficient $\hat{F}$ calculated from the previous approximation. To construct the solution of (6), let us consider the following auxiliary inequality:

$$(\tilde{w} - w)\Big(A(w - \bar{w}) + \hat{F}\, l\Big) \geq 0. \tag{7}$$

For given vector $l \in L$ there exists a unique solution $w \in K$. A mapping $R : l \mapsto w \mapsto$ $\mapsto P_L(l + \alpha\, w) = \tilde{l}$ ($\alpha > 0$ is a constant, P_L is a projector onto the set L with respect to the Euclidean norm) is continuous, the set L is convex and compact. Hence, the Brouwer theorem is valid, according to which R has a fixed point $l \in L$. The inequality (7) has a solution which satisfies the condition $l = P_L(l + \alpha\, w)$. One can show that this solution satisfies (6) independently of α.

When constructing a solution of (6), an algorithm of the Uzawa type is applied. At the m-th step of this algorithm the vector w^m is determined as a projection of the vector $\bar{w}^{\,m} = \bar{w} - \hat{F}\, A^{-1} l^m$ onto the set K: $w^m = P_K(\bar{w}^{\,m})$. In an explicit form

$$w^m = \begin{cases} \bar{w}^{\,m}, & \text{if } \ \bar{w}^{\,m} n \leq h, \\ \bar{w}^{\,m} + \dfrac{h - \bar{w}^{\,m} n}{n\, A^{-1} n}\, A^{-1} n, & \text{if } \ \bar{w}^{\,m} n > h. \end{cases} \tag{8}$$

Then the vector l is recalculated by the formula $l^{m+1} = P_L(\bar{l}^{\,m})$ where $\bar{l}^{\,m} = l^m + \alpha\, w^m$, or in an explicit form

$$l^{m+1} = \begin{cases} \bar{l}^{\,m} - \beta^m n, & \text{if } \ |\bar{l}^{\,m} - \beta^m n| \leq 1, \\ \dfrac{\bar{l}^{\,m} - \beta^m n}{|\bar{l}^{\,m} - \beta^m n|}, & \text{if } \ |\bar{l}^{\,m} - \beta^m n| > 1, \end{cases} \qquad \beta^m = \frac{\bar{l}^{\,m} n}{|n|^2}. \tag{9}$$

An initial approximation l^0 is arbitrary. It is proved that the sequence of vectors w^m converges to the vector w as $m \to \infty$ provided that $\alpha < 2\, a/\hat{F}$.

It should be noticed that recurrent calculation of iterations in the described algorithm is performed on the basis of the contractive mapping Q and two nonexpanding operators P_K and P_L. Such algorithm is stable with respect to round-off errors, i.e. going to the next iteration step does not lead to increasing of computational errors. When implementing this algorithm, it is sufficient to restrict oneself to the construction of the so-called diagonal sequence, calculating at the m-th step of the method of successive approximations only m iteration steps of the Uzawa algorithm.

3 DYNAMIC DEFORMATION OF ELASTIC-PLASTIC BODIES

3.1 Mathematical model

To describe the process of dynamic deformation of elastic-plastic bodies, let us consider geometrically nonlinear mathematical model taking into account finite rotations of elements at small strains [4]. This model is based on the decomposition of the deformation gradients tensor into a product of orthogonal tensor of finite rotation and symmetric strain tensor, which is identified with unit tensor. Under such assumptions in 2D case the model can be represented in the form of the system of equations of motion

$$\rho\,\dot{v}_i = \tau_{ij,\,j} + \rho\,g_i, \tag{10}$$

the constitutive relationships of elastic-plastic deformation in the form of the principle of maximum of the energy dissipation rate

$$(\tilde{\sigma}_{ij} - \sigma_{ij})(\dot{\sigma}_{ij} - \lambda\,e\,\delta_{ij} - 2\,\mu\,e_{ij}) \geq 0 \tag{11}$$

and the equation for the rotation angle

$$\dot{\varphi} = \frac{1}{2}\Big((v_{2,\,1} - v_{1,\,2})\cos\varphi - (v_{1,\,1} + v_{2,\,2})\sin\varphi\Big). \tag{12}$$

Here ρ is the density of a material, v_i are the components of velocity vector, τ_{ij} and σ_{ij} are the components of nonsymmetric and symmetric stress tensors, g_i are the components of vector of mass forces, λ and μ are the Lame parameters, $e = e_{11}+e_{22}+e_{33}$ is the velocity of volume deformation, δ_{ij} is the Kronecker delta, $i, j = 1, 2$. Dot over a symbol denotes the time derivative, subscripts after comma denote partial derivatives with respect to spatial variables, summation over repeated indices takes place. Components of the strain rate tensor have the form

$$\begin{gathered} e_{11} = v_{1,1}\cos\varphi + v_{2,1}\sin\varphi, \quad e_{22} = v_{2,2}\cos\varphi - v_{1,2}\sin\varphi, \quad e_{33} = 0, \\ e_{12} = e_{21} = \frac{1}{2}\Big((v_{2,1} + v_{1,2})\cos\varphi - (v_{1,1} - v_{2,2})\sin\varphi\Big). \end{gathered} \tag{13}$$

The nonsymmetric stress tensor τ and the symmetric stress tensor σ are connected as follows

$$\begin{pmatrix} \tau_{11} & \tau_{12} & 0 \\ \tau_{21} & \tau_{22} & 0 \\ 0 & 0 & \tau_{33} \end{pmatrix} = R \begin{pmatrix} \sigma_{11} & \sigma_{12} & 0 \\ \sigma_{12} & \sigma_{22} & 0 \\ 0 & 0 & \sigma_{33} \end{pmatrix}, \quad R = \begin{pmatrix} \cos\varphi & -\sin\varphi & 0 \\ \sin\varphi & \cos\varphi & 0 \\ 0 & 0 & 1 \end{pmatrix}. \tag{14}$$

The variational inequality (11) is fulfilled for all possible variations of the stress tensor $\tilde{\sigma}$ satisfying, as well as the tensor σ of actual stresses, the Mises yield condition

$$f_s(\sigma_{ij}) \le \tau_s, \tag{15}$$

where $f_s(\sigma_{ij}) = \sqrt{\sigma'_{ij}\sigma'_{ij}\,/\,2}$ is the convex symmetric yield function dependent on the deviator components σ'_{ij} of stress tensor.

The system of basic equations and inequalities (10)–(14) can be represented in a uniform vector form [3]:

$$(\widetilde{U} - U)\left(A\,\dot{U} - \sum_{i=1}^{n} B^i\,U_{,i} - G\right) \ge 0, \quad U,\,\widetilde{U} \in W. \tag{16}$$

Here $U(t,x)$ is the m-dimensional vector–function composed of nonzero components of the velocity vector v, the nonsymmetric stress tensor τ and the rotation angle φ. The symmetric $(m \times m)$-dimensional matrix–coefficients A and B^i, included in the variational inequality, contain the parameters of elasticity of a material, the vector G is nonzero when the mass forces are taken into account, $\widetilde{U}$ is a varied vector, n is the spatial dimension of the problem, W is the convex and closed set determined by the criterion of plasticity (15). In the 2D case, being under consideration, $U = \Big(v_1, v_2, \tau_{11}, \tau_{22}, \tau_{33}, \tau_{12}, \tau_{21}, \varphi\Big)$. In the 3D case $U = \Big(v_1, v_2, v_3, \tau_{11}, \tau_{22}, \tau_{33}, \tau_{23}, \tau_{32}, \tau_{31}, \tau_{13}, \tau_{12}, \tau_{21}, \varphi\Big)$.

3.2 Shock-capturing algorithm

The algorithm used for the numerical implementation of (16) is explicit in time and is constructed as follows (see [3]). First, the problem of deformation of an elastic material is solved at each time step. Next, the obtained solution is corrected to take into account plastic properties of a material. The initial data $U(0,x) = U_0(x)$ are specified at $t = 0$. The boundary conditions can be given in the terms of velocities as well as in stresses.

For the solution of elastic problem the two-cyclic splitting method with respect to the spatial variables is used [5]. In the 2D case this method on the time interval $(t, t + \Delta t)$ consists of 4 stages: the solution of a one-dimensional problem in the x_1-direction on $(t, t + \Delta t/2)$, the similar stage in the x_2-direction, repeated recalculation of the problem in the x_2-direction on $(t + \Delta t/2, t + \Delta t)$, and repeated recalculation in the x_1-direction. The x_3-direction is added and the splitting method includes 6 stages in the 3D case. This structure of the splitting method ensures the stability of numerical solution in the multi-dimensional case under implementation of the one-dimensional Courant condition. One-dimensional systems of equations of the form

$$A\,\dot{U}^k = B^i\,U^k_{,i} + G^i \tag{17}$$

($k = \overline{1, 2\,n}$ is the number of the splitting stage, $i = \overline{1, n}$ is the direction of splitting) in spatial directions are solved by means of the explicit monotone difference ENO scheme of the "predictor–corrector" type. Piecewise-linear splines, discontinuous at the boundaries of meshes, are constructed by means of a special procedure of limit reconstruction, which enables one to improve an accuracy of a numerical solution.

Plasticity of materials is taken into account by the splitting method with respect to physical processes. Variational inequality (16) is solved at each mesh of a spatial grid with using special algorithms for the correction of stresses [4]. After approximation of (16) we obtain the inequality

$$\big(\widetilde{U} - U\big) A \big(U - \bar{U}\big) \geq 0, \tag{18}$$

where $U, \widetilde{U} \in W$, and $\bar{U}$ is such that $A\,\dot{\bar{U}} = \sum\limits_{i=1}^{n} B^i\, U_{,i} + G$. In terms of stresses the correction procedure can be reduced to the form

$$\sigma_{ij} = \frac{2}{1+\eta}\,\sigma^*_{ij} - \frac{1-\eta}{1+\eta}\,\bar{\sigma}_{ij}, \quad \sigma^*_{ij} = \begin{cases} \bar{\sigma}_{ij}, & \text{if } \ f_s \leq \tau_s, \\ \bar{\sigma}'_{ij}\,\dfrac{\tau_s}{f_s} + \sigma\,\delta_{ij}, & \text{if } \ f_s > \tau_s. \end{cases} \tag{19}$$

For $\eta = 0$ it is non-dissipative correction of the second order of accuracy, and for $\eta = 1$ this procedure coincides with the well-known Wilkins procedure of the correction of stresses.

3.3 Parallel program system

Described computational algorithm is implemented as a parallel program system for the solution of problems of the dynamics of elastic-plastic media on multiprocessor computers [3]. This program system consists of a preprocessor program, a main program for computation of velocities and stresses, subroutines for realization of boundary conditions, including the conditions of contact interaction with friction, and a postprocessor program. The programming was carried out in Fortran using the MPI (Message Passing Interface) library and the SPMD (Single Program – Multiple Data) technology. The universality of programs is achieved by a special packing of the variables used at each of computational nodes of a cluster into large one-dimensional arrays. Computational domain is distributed between the cluster nodes by means of 1D, 2D or 3D decomposition so as to load the nodes uniformly and to minimize the number of passing data.

The parallelization is performed at the stage of splitting the problem with respect to the spatial variables. Under the solution of one-dimensional systems of equations, the data exchange between processors occurs at step "predictor" of the finite-difference scheme with the help of shadow edges. At first each processor exchanges with neighboring processors the boundary values of their data by means of the MPI_Sendrecv function, and

then calculates the required quantities in accordance with the difference scheme. Under numerical realization of contact conditions, the correspondence between boundary meshes of independent grids of interacting bodies is established and variational inequality (4) is solved on a grid refinement, common for two contacting surfaces. Computation of the whole contact boundary is produced by a separate processor, other processors send to him data about their part of boundary and then they receive the final result.

For the organization of the control points, each processor generates binary files of direct access, the total size of the files on the same time step can considerably exceed the size of RAM of a single processor. The procedure of compressing of files, containing the results of computations, is worked out, since the file size can be very large and for their transportation along network the significant resources are required. Graphical output of results is carried out with the help of special programs for usual personal computer.

4 OBLIQUE IMPACT OF PLATES

Numerical computations for the problem of an oblique impact of two deformable plates were performed on a cluster. The problem of an oblique impact has great importance in connection with an analysis of the process of explosion welding of metals. As a rule, this process is accompanied by generation of the periodic strain waves at the contact boundary of plates [6]. On the basis of computations the interconnection of wave formation in explosion welding and mechanical loss of stability of the surface layer in the neighbourhood of the contact point was established.

4.1 Problem statement

Let us consider an oblique impact of plates, situated at some angle γ to each other (Fig. 2). One of plates is stationary and fixed from below, another plate falls on it with a constant velocity $V = (V_1, V_2)$. The lower boundary of the projectile plate and the upper boundary of the fixed one are zones of possible contact, the remaining parts of the boundaries are free of stresses. Lengths of both plates are equal to h_1, thicknesses of the

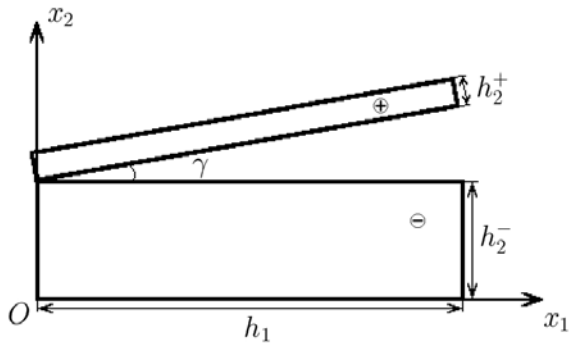

Figure 2: Problem statement

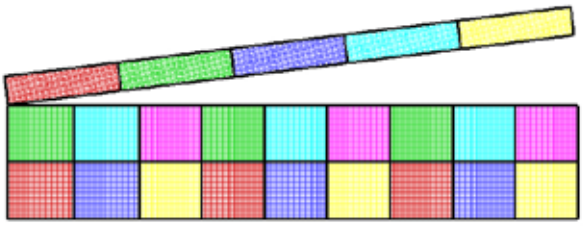

Figure 3: Distribution of computational load

projectile plate and the fixed plate are h_2^+ and h_2^-, respectively. The problem is considered in a two-dimensional formulation. An example of the distribution of computational domain between 23 processors is shown in Fig. 3.

4.2 Results of two-dimensional computations

In Fig. 4 one can see numerical results obtained by means of described computational technique for the problem of an oblique impact of elastic-plastic plates. The collision angle γ and the velocity V_c of a contact point are varied ($V_c = V_1 - V_2 \operatorname{ctg}\gamma$). Computations were performed on 25 processors for steel plates of the length $h_1 = 10\,\text{cm}$ and of the thicknesses $h_2^+ = 0.5\,\text{cm}$ and $h_2^- = 2\,\text{cm}$. Finite-difference grids consist of 2000×100 and 2000×400 meshes for upper and lower plates, respectively.

The analysis of results shows, in particular, that the configuration of the plastic zone depends essentially on the velocity V_c of a contact point: if this velocity exceeds the velocity of the plastic shock waves c_f, then this zone lies behind of a contact point (Fig. 4*a*), otherwise the plastic zone is running ahead in relation to a contact point (Fig. 4*b*). In the case of $V_c < c_f$ the elastic-plastic loss of stability of a surface layer may take place, realizing as a hill of positive strain, which leads to the wave formation under an oblique impact.

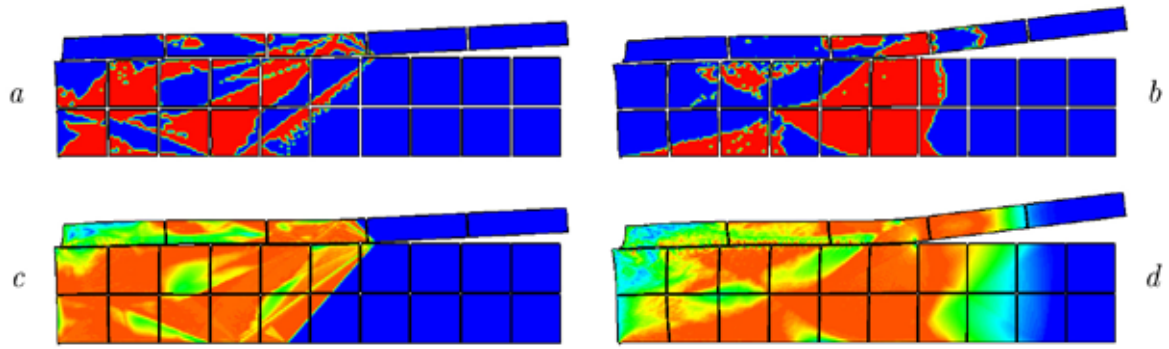

Figure 4: Configurations of plastic zones (a, b), level curves of the intensity of tangential stresses (c, d)
a), c) $\gamma = 3^0$, $V_c = 4\,\text{km/s}$, b), d) $\gamma = 7^0$, $V_c = 2\,\text{km/s}$

Figs. 5 – 7 illustrate the loss of stability under an oblique impact of two elastic plates. Velocity of a contact point and thicknesses of plates are varied. Plates are the same length $h_1 = 10\,\text{cm}$, the collision angle $\gamma = 13^0$ everywhere. Material of both plates is steel. The upper plate is 3 times thinner than the lower plate in Figs. 5*a*, 6*a*, and 7*b*; both plates are thick (with the same thickness $h_2^\pm = 3\,\text{mm}$) in Figs. 5*b*, 6*b*, and 7*c*; both plates are thin (with the same thickness $h_2^\pm = 1\,\text{mm}$) in Fig. 7*a*.

If the velocity V_c of a contact point is less than the velocity c_R of the Rayleigh waves, then the loss of stability of the upper plate ahead of a contact point takes place (Fig. 5). If $V_c > c_R$, then the lower plate loses its stability behind of a point of contact (Fig. 6).

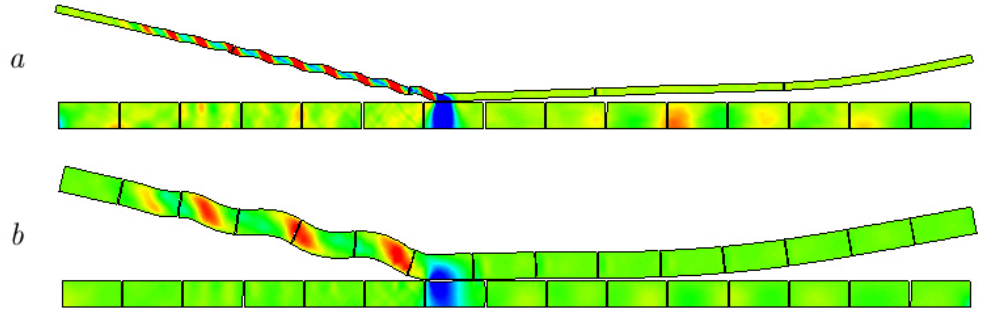

Figure 5: Level curves of the stress τ_{22} ($\gamma = 13^0$, $V_c = 1\,\text{km/s}$)
a) thicknesses of plates $h_2^+ = 1\,\text{mm}$, $h_2^- = 3\,\text{mm}$, *b*) plates of uniform thickness $h_2^+ = h_2^- = 3\,\text{mm}$

Region of the loss of stability increases with time. Characteristic wavelengths and their amplitude depend on the thicknesses of upper and lower plates, respectively. In both cases, the adhesion of plates behind of a contact point is not taken into account. The projectile plate moves from right to left, with time the right edge of this plate is reflected from a contact surface and flies up. In the case of $V_c < c_R$, the number of waves decreases and the amplitude of waves increases with increasing the thickness of the upper plate, besides the number of waves decreases with decreasing the velocity V_c. In the case of $V_c > c_R$, conversely, the number of waves decreases with increasing the velocity V_c.

In computations, the results of which are represented in Fig. 7, the contact surfaces of plates are pasted together behind a point of contact. One can see that in this case ($V_c > c_R$) the number of waves decreases with increasing the thickness of the lower plate and the amplitude of waves increases with increasing the thickness of the upper plate.

The results, presented in Figs. 5*a*, 6*a*, 7*a*, and 7*b*, were obtained on 20 processors, and the results, presented in Figs. 5*b*, 6*b*, and 7*c*, were obtained on 30 processors. The dimensions of grids in the plates are 5000×50 or 5000×150 meshes, depending on the thickness of the plate.

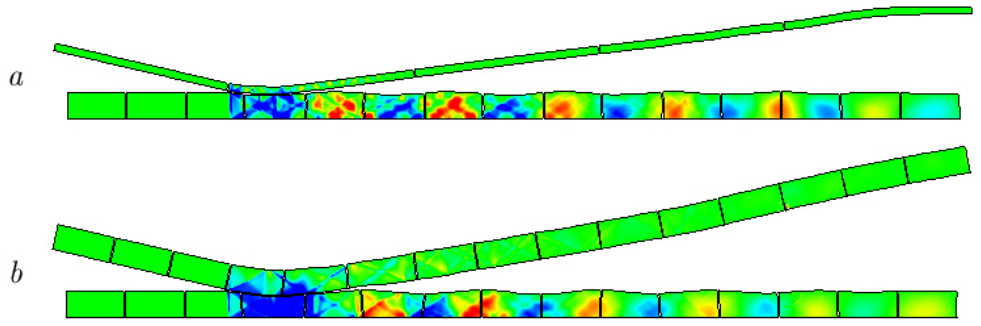

Figure 6: Level curves of the stress τ_{22} ($\gamma = 13^0$, $V_c = 3\,\text{km/s}$)
a) thicknesses of plates $h_2^+ = 1\,\text{mm}$, $h_2^- = 3\,\text{mm}$, *b*) plates of uniform thickness $h_2^+ = h_2^- = 3\,\text{mm}$

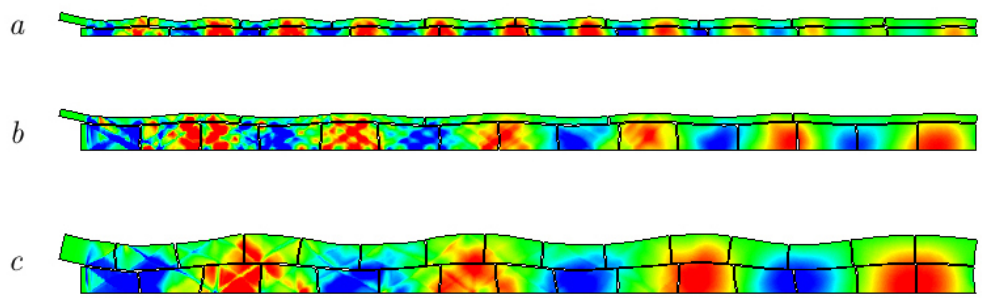

Figure 7: Level curves of the stress τ_{22} ($\gamma = 13^0$, $V_c = 3\,\text{km/s}$, pasting together of plates)
a) $h_2^+ = h_2^- = 1\,\text{mm}$, *b*) $h_2^+ = 1\,\text{mm}$, $h_2^- = 3\,\text{mm}$, *c*) $h_2^+ = h_2^- = 3\,\text{mm}$

The computations were performed on the clusters MVS–1000/96 of the Institute of Computational Modeling of SB RAS (Krasnoyarsk) and MVS–100k of the Joint Supercomputer Center of RAS (Moscow).

Acknowledgements

This work was supported by the Russian Foundation for Basic Research (grant no. 11–01–00053), the Complex Fundamental Research Program no. 2 of the Presidium of the Russian Academy of Sciences, and the Interdisciplinary Integration Project no. 40 of the Siberian Branch of the Russian Academy of Sciences.

REFERENCES

[1] Duvaut, G. and Lions, J.-L. *Les inéquations en mécanique et physique*. Dunod, Paris (1972).

[2] Kravchuk, A.S. *Variational and quasivariational inequalities in mechanics*. MGAPI, Moscow (1997).

[3] Sadovskaya, O.V. and Sadovskii, V.M. *Mathematical modeling in the problems of mechanics of granular materials*. Fizmatlit, Moscow (2008).

[4] Sadovskii, V.M. *Discontinuous solutions in dynamic elastic-plastic problems*. Fizmatlit, Moscow (1997).

[5] Kulikovskii, A.G., Pogorelov, N.V. and Semenov, A.Yu. *Mathematical aspects of the numerical solution of hyperbolic systems of equations*. Fizmatlit, Moscow (2001).

[6] *Wave formation in oblique impacts: Col. of articles*. Ed. by Yakovlev, I.V. et al. Publishing house of the Institute of Discrete Mathematics and Informatics SB RAS, Novosibirsk (2000).

XI International Conference on Computational Plasticity. Fundamentals and Applications
COMPLAS XI
E. Oñate, D.R.J. Owen, D. Peric and B. Suárez (Eds)

THE CONTACT TEMPERATURE AND DEFORMATION AREA OF ASPERITIES ON ROUGH SURFACE FOR THREE- BODY CONTACT SITUATION

Jeng-Haur Horng *, Chin-Chung Wei *, Yang-Yuan Chen † and Shin-Yuh Chern*

* Department of Power Mechanical Engineering,
National Formosa University, Yunlin, Taiwan
e-mail: jhhorng@gmail.com, ccwei@nfu.edu.tw, kevindga@nfu.edu.tw

† Department of Systems and Naval Mechatronic Engineering,
National Cheng Kung University, Tainan, Taiwan
Email: td7211@gmail.com

Key words: Micro-Machine, Contact Temperature, Three-Body Microcontact, Friction Coefficient, Plasticity Index.

Abstract. In the micro-machine or precision machine, particles are often presented at contact interfaces. And these particles will affect the variation of plastic deformation of asperities and the contact temperature between the contact surfaces. In this paper, we used three-body microcontact model and contact temperature theory to evaluate elastic contact area, plastic contact area, elastic-plastically deformed contact area and contact temperature under the different particle sizes, velocities and applied loads conditions. The friction force is one of the main heat resources of contact temperature. Because friction coefficient is variable parameter in this work, the contact temperature rise between the contact surfaces is larger than that of assuming the constant friction coefficient conditions of CrMo steel for the different loads. The contact temperatures of particles and asperity increase when the velocity and applied load increase. The increases of particle size will give rise to the increase of particle temperature and decrease of asperity temperature on rough surface. The plastic deformed contact area increases when the particle size and particle density increase.

1 INTRODUCTION

When the precision machine or the micro machine operate and the two surfaces make contact, will cause the asperity and particles has the elastic, elasto-plastic, or plastic contact deformation between surface roughness. The practical contact area is the sum of the areas of the contact surface summits and only a small part of the vision area [1, 2]. The most widely used stochastic model to predict the real contact area is that proposed by Greenwood and Williamson (GWmodel) [3]. The experimental observations of Pullen and Williamson (PW model) [4] showed that, in the plastic deformation state, volume is conserved by a rise in the non-contacting surface under extremely high loading. Chang et al. [5] proposed an elastic–plastic microcontact model (CEB model) to study the contact properties of rough surfaces. Research using this model has shown that the GW model of fully elastic surface microgeometry and the PW model of fully plastic surface microgeometry have two limiting cases of the general elastic–plastic contact. Horng [6] proposed a generalized elliptic elastic–plastic microcontact model (H model) that takes into account the directional nature of surface roughness for elliptic contact spots between anisotropic rough surfaces. This model can be simplified to become the GW, PW, on CEB model. Kogut and Etsion [7] (KE model) presented elastic–plastic asperity models to modify the shortcomings of the transition from elastic deformation to fully plastic deformation in other models.

When two bodies slide relative to each other, the friction heat is expened at a restuiced number of contact spots between two surfaces or surface and particle. The maximum local temperature generated at the contact spot, called the flash temperature, is higher than that at the surrounding area. The flash temperature is one of the reasons causing fatigue, high wear and failure of material. It produced at rubbing contact are of shot duration (say 10^{-3}s or less) and occur only over small dimensions (say10^{-4}m or less). They are therefore difficult to measure and, in the interpretation of almost all experiments, recourse is generally made to estimating their magnitude using the theory originally formulated by Blok [8] and Jaeger [9]. Geeim and Winer [10] considered the transient temperature rise in the vicinity of a microcontact. Tian and Kennedy [11] used the green function method to obtain Peclet numbers of the approximation of flash temperatures. Compared to isolated contact, there are selective few contributions in the literature on flash temperature in multiple contact conditions. Ling [12] develops a method for studying two comparably rough surfaces and generating the statistics of their interaction. Results show that, with time, the interaction between contacts mitigates the effects of velocity somewhat. Knothe and Liebelt [13] studied contact temperature and temperature fields of components by Laplace transforms and the Green's functions. The results show that different kind of topography causes different rise of the maximum contact temperature for wheel-rail system. Up to now, very few work discuss the contact temperature for three-body contact situations. This work study a more generalized three-body contact temperature model and discusses the effect of each operating parameter on contact temperatures.

2 ANALYSIS

2.1 Microcontact model

In the contact model, we made the following assumptions: 1. All surface asperities are far

apart and there is no interaction between them. 2. There is no bulk deformation, only the surface asperities deform during contact. 3. The diameter of spherical particles is D and much harder than the upper and lower contact surfaces, which deform plastically during contact with particles. 4. Slopes of surface asperities are negligibly small. Figure 1 shows the geometry of the three contacting bodies : surface 1, surface 2, and the particles. Here, z and d denote the asperity height and separation of surfaces, respectively.

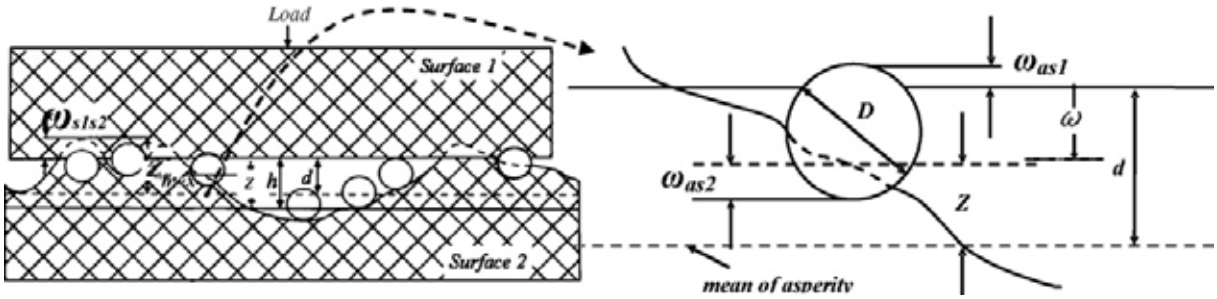

Figure 1: Geometry of three contacting bodies

According to the paper [2], the tree-body microcontact model becomes:

$$F_{total} = F_{as1} + F_{s1s2-as1} = \frac{\pi H_{s1} H_{s2} \eta_a A_n}{H_{s1} + H_{s2}} \left[\frac{9\pi^2}{4} \left(\frac{H_{s1}^2}{E_{as1}^2} + \frac{H_{s2}^2}{E_{s1s2}^2} \right) \int_{d-h_e}^{d} x^2 \phi_a(x) dx + \int_{d}^{x_{max}} x^2 \phi_a(x) dx \right] + \left(1 - \frac{\pi H_{s1} \eta_a}{H_{s1} + H_{s2}} \int_{X_{min}}^{X_{max}} x^2 \phi_a(x) dx \right) \cdot F_{s1s2} \quad (1)$$

$$A_{total} = A_{as1} + A_{s1s2-as1} = \frac{\pi H_{s2} \eta_a A_n}{H_{s2} + H_{s1}} \left[\frac{9\pi^2}{4} \left(\frac{H_{s1}^2}{E_{as1}^2} + \frac{H_{s2}^2}{E_{s1s2}^2} \right) \int_{d-h_e}^{d} x^2 \phi_a(x) dx + \int_{d}^{X\max} x^2 \phi_a(x) dx + A_{s1s2} \right] \cdot \left\{ 1 - \frac{\pi H_{s1} \eta_a}{H_{s1} + H_{s2}} \int_{d}^{X_{max}} x^2 \phi_a(x) dx \right\} \quad (2)$$

where A_{s1s2} is the real total contact area of the two-body microcontact models. The total contact areas A_t, and the total contact load F_t of the three bodies can be obtained from Eq. (1) and (2).

2.2 Friction model

Our friction analysis model is based on the analyses of Komvopoulos et al. [14] and Bhushan et al.[15-16]. The friction is expressed as the sum of four components: surface asperity deformation (μ_d), plowing deformation by particles entrapped between contact surface (μ_a), adhesive friction (μ_s), and ratchet friction (μ_r) at the contact region. The total friction force and friction components become:

$$\mu = \mu_d + \mu_a + \mu_s + \mu_r = A_r \tau_a + A_{s1s2\text{-}s1a} \tau_{s1s2} + A_{s1a} \tau_{s1a} + A_{s1s2\text{-}s1a} \tau_{s1s2} \times tan^2\theta \quad (3)$$

where A_r, $A_{s1s2\text{-}s1a}$, and A_{s1a} are the real areas of contact during adhesion, two surface

deformation, and particle-surface 1 deformation, respectively. They are calculated from Eq(1). τ_a, τ_{s1s2}, and τ_{s1a}, are the shear strengths during adhesion, two surface deformation, and particle-surface deformation [16],respectively.

2.3 Flash temperature model

Frictions were made when the surface 1, surface 2, and particles made contact, and the energy consumed was mostly converted to heat. This caused an increase in surface temperature, and heat generated was determined using the following equation,

$$Q=\mu FV \tag{4}$$

Where μ is the friction coefficient, V is the relative speed, and F is the normal load. The heat conductance quantity of a unit area was used to express the magnitude heat conductance.

$$q=\frac{Q}{A}=\frac{\mu FV}{\pi a^2}=\mu P_m V \tag{5}$$

A is the practical contact area and a is the contact radius.

The Peclet Number (P_e) is a nondimensional speed parameter used to evaluate the movement rate of contact heat. It is defined as：

$$P_e=\frac{Va}{2\alpha}=\frac{Va\rho C}{2K} \tag{6}$$

Where a is contact heat, α is the rate of heat diffusion ($\alpha=K/\rho C$), K is the heat conductance coefficient, ρ is the density, and C is the specific heat. Different Peclet Numbers exist at different velocities. Tian and Kennedy [8] proposed a model whose maximum temperature could be applied to all Peclet Numbers. The average temperature increase of its spherical contact heat as expressed as

$$T=\frac{1.22qa}{K\sqrt{\pi(0.6575+P_e)}} \tag{7}$$

When $F_{ai}=F_{as1,max}$, the maximum temperature when the abrasive particles made contact with the workpiece is

$$T_{as1,\max}=\frac{1.22\mu_a V\sqrt{F_{as1,\max}H_{s1}}}{\pi\left[K_{s1}\sqrt{(0.6575+P_{e,s1})}+K_a\sqrt{(0.6575+P_{e,a})}\right]} \tag{8}$$

Therefore, the increase of relative velocity will result in the increase of contact temperature. and the average temperature between the abrasive particle and workpiece is

$$T_{as1,ave}=\frac{\int_{x_{\min}}^{x_{\max}}T_{as1}\phi_a(x)dx}{\int_{x_{\min}}^{x_{\max}}\phi_a(x)dx} \tag{9}$$

3 RESULTS AND DISCUSSION

This paper study three-body contact temperature for the different particle sizes, particle densities and the relative velocities. The maximum contact temperature, average contact temperature and deformation area between particle and asperity were calculated. The material used in the analysis was CrMo steel.

Fig.2 (a) shows the maximum contact temperature $T_{as1,max}$, average contact temperature $T_{as1,ave}$, and total friction coefficient μ_{total} versus applied loads. It is interesting to note that the maximum contact temperature and average contact temperature increased linearly with increasing applied loads. The maximum contact temperature was higher than the average contact temperature for the different loads. Fig.2 (b) shows the surface and particle friction coefficients versus applied loads for the different particle size when Ψ = 1.5, Rq = 100 nm, and v = 0.2 m/s. The total friction coefficient is the sum of surface friction coefficient and particle friction coefficient. When particle size is 500 nm, and the intersection pressure of the particle and the surface friction coefficient is about 2 MPa; but when the particle size decreases to 300nm and 100nm, the intersection pressure of the particle and the surface friction coefficient increase to 5 MPa and 50 MPa. The bigger the size of particle, the larger the total friction coefficient. Fig.2 (c) shows the elastic, elastic-plastic and plastic deformed

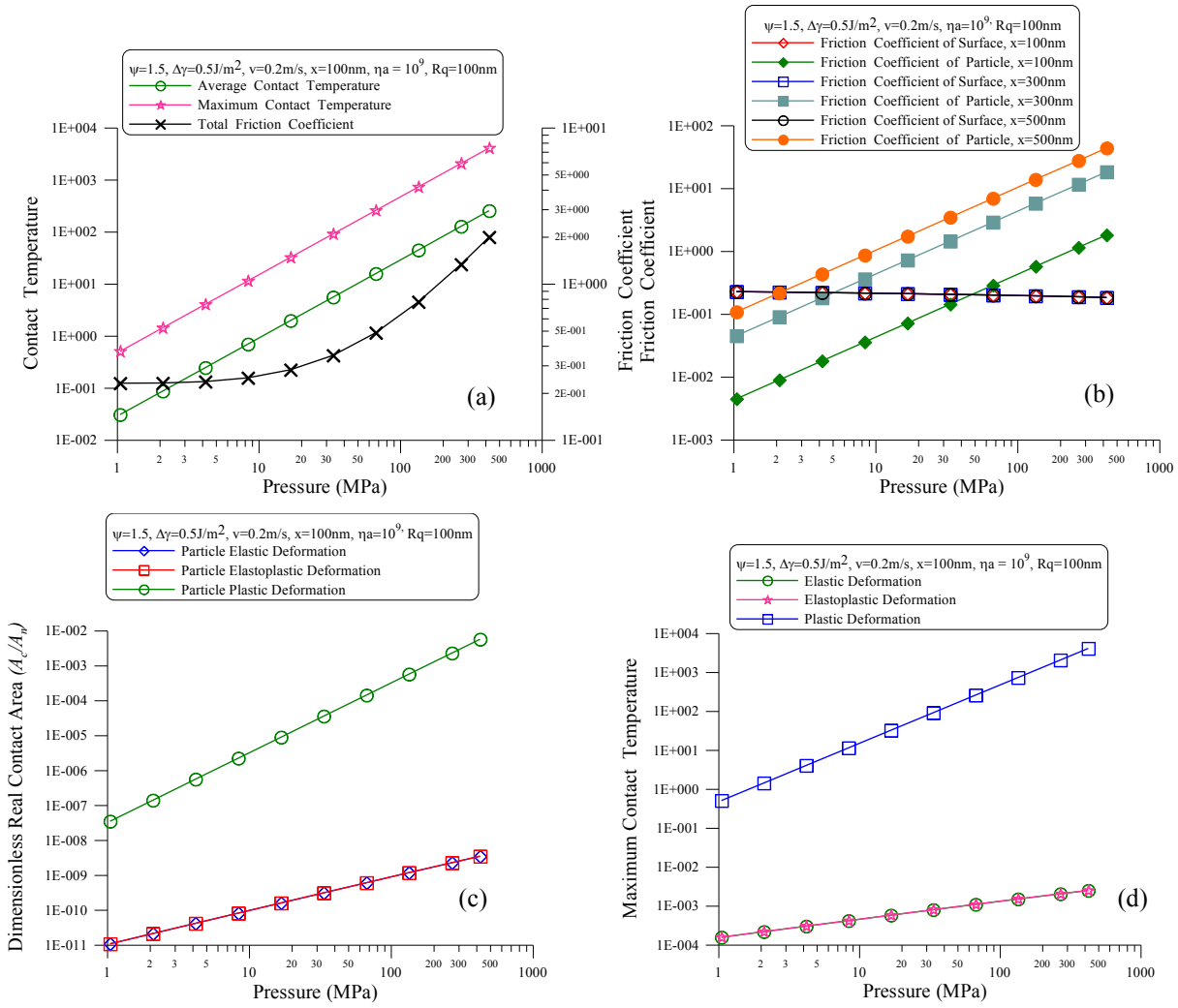

Figure 2: (a) Contact temperature and total friction coefficient varying with applied loads;(b) The surface and particle friction coefficients varying with applied loads when different particle size;(c) The dimensionless real contact area components varying with applied loads; (d) The maximum contact temperature components varying with applied loads

real contact area of particles. the real contact area increased with increasing applied loads. The plastic deformed real contact area is larger than the elastic and elastic-plastic deformed real contact area. Results indicate that the real deformation contact area of particle is mainly affected by the plastic deformation. Fig.2 (d) shows three kinds of maximum contact temperature of particles for the different deformed areas. The maximum contact temperature of plastic deforming controls the maximum contact temperature. The trend of the maximum contact temperature is the similar with the deformation area in Fig.2 (c). It indicates that the particle plastic deformation area has a significant effect on the maximum contact temperature between two sliding surfaces.

Fig.3 (a) and Fig.3 (b) are the different relative velocity's relationship with average and maximum contact temperature for the particle density $\eta_a=10^9 m^{-2}$, surface roughness Rq=100nm, relative velocity v=0.2 m/s. The average contact temperature and the maximum contact temperature increase with increasing pressure and particle size. Because the increase of particle size will result in the increase of particle load and then increase the contact temperature of particle. It indicates that effectively control of the particle size between the contact interface of mechanical elements can reduce the contact temperature.

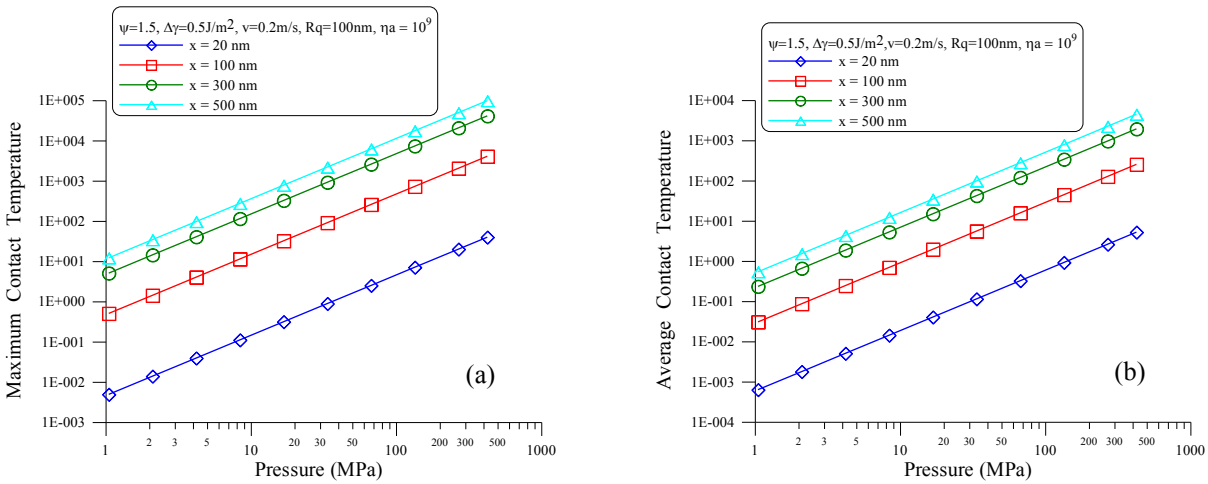

Figure 3: Relationship between particle contact temperature and applied loads of different particles size

Fig.4 (a) and Fig.4 (b) are the different relative velocity's relationship with average and maximum contact temperature for the particle size x=100nm, surface roughness Rq=100nm, relative velocity v=0.2 m/s. The average contact temperature and the maximum contact temperature increase with increasing pressure. Because the increase of particle density will result in the increase of particle load and then increase the contact temperature of particle. It indicates that decrease the wear debris between the contact interface of mechanical elements can reduce the contact temperature.

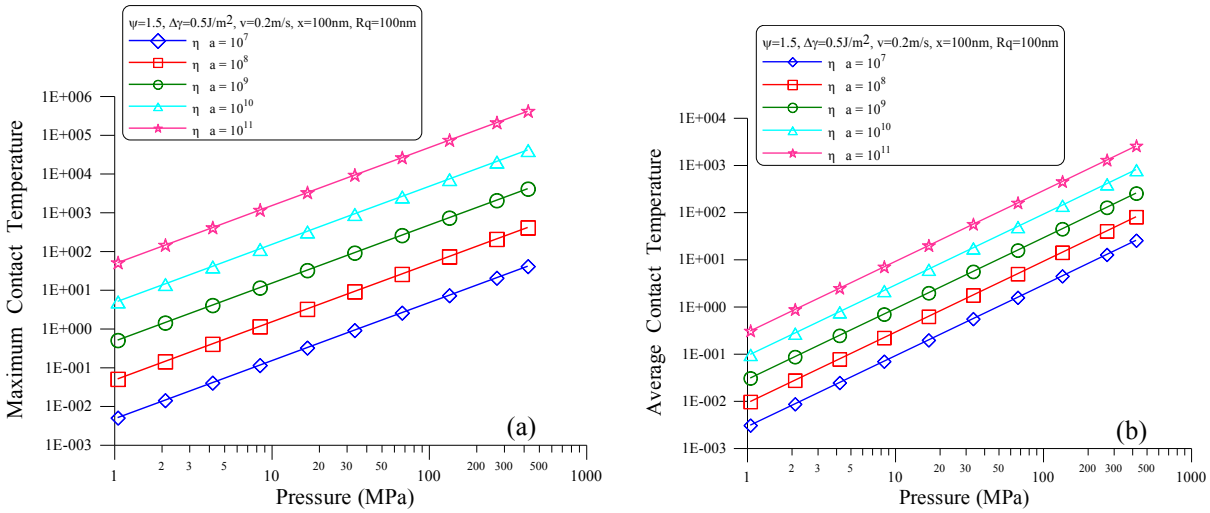

Figure 4: Relationship between particle contact temperature and applied loads of different particles density

4 CONCLUSIONS

- The trend of the maximum contact temperature of two surfaces is the similar with the particle plastic deformation area. It indicates that the particle plastic deformation area has a significant effect on the maximum contact temperature between two sliding surfaces.
- In contact interface, the contact temperatures of particles and asperity increase when the velocity and applied load increase
- The increase of particle size and density will result in the increase of particle load for three-body contact condition. It indicates that decrease the particle size or wear debris between the contact interface of mechanical elements can reduce the contact temperature.

REFERENCES

[1] Kikuchi, N. and Oden, J. T. *Contact problems in elasticity.* SIAM, in Press, (1988).
[2] Horng, J. H. and Wei C. C. A study of surface friction and particle friction between rough surfaces. *Wear* (2009) **267**:1257-1263.
[3] Greenwood, J. A. and Williamson, J. B. P. Contact of nominal flat surface. *Proc. R. Soc. London, Ser. A.*(1996) **295**:300-319.
[4] Pullen, J. and Williamson, J. B. P. On the plastic contact of rough surface.*Proc. R. Soc. London* (1972) **327**:157-173.
[5] Chang, W. R., Etsion, I. and Bogy, D. B. An elastic-plastic model for the contact of rough Surface. *ASME Journal of Tribology* (1987) **110**:50-56.
[6] Homg, J. H. An elliptic elastic-plastic asperity microcontact model for rough surface. *ASME Journal of Tribology* (1988) **120**:82-88.
[7] Kogut, L. and Etsion, I. Elastic-plastic contact analysis of a sphere and a rigid flat. *ASME Journal of Applied Mechanics* (2002) **69**:657-662.
[8] Blok, H. Theoretical study of temperature rise at surfaces of actual contact under oiliness lubricating conditions. General discussion on lubrication, *Proc. Inst. Mech. Eng.*

London (1937) **2**: 222-235.

[9] Jaeger, J. C. Moving sources of heat and the temperature at sliding surfaces. *Proc. R.Soc. NSW* (1942) **66**: 203-224.

[10] Geeim, B. and Winer, W. O. Transient temperatures in the vicinity of asperity contact. *ASME J. Tribology* (1985) **107**: 333-342.

[11] Tian, X., and Kennedy, F.E., " Maximum and Average Flash Temperatures in Sliding Contacts, " ASME journal of Tribology (1994) **116 NO.1**:167-174.

[12] Ling, F. F. On temperature transients at sliding interface. *ASME J. Lubrication Technology* (1969) **91** : 397-405.

[13] Knothe, K. and Liebelt, S. Determination of temperatures for sliding contact with applications for wheel-rail system. *Wear* (1995) **189** : 91-99.

[14] Komvopoulos, K., Saka, N. and Suh, N. P. Plowing friction in dry and lubricated metal sliding. *ASME Journal of Tribology* (1986) **108**:301-313.

[15] Bhushan, B. and Nosonovsky, M. Scale effects in friction using strain gradient plasticity and dislocation-assisted sliding (microslip). *Acta Mater* (2003) **51**:4331–4345.

[16] Bhushan, B. and Nosonovsky, M. Comprehensive model for scale effects in friction due to adhesion and two- and three-body deformation (plowing). *Acta Mater* (2004) **52**:2461-2474.

[17] Chen, W. W. and Wang, Q. Thermo-mechanical analysis of elasto-plastic bodies in a sliding spherical contact and the effect of sliding speed, heat partition, and thermal softening. *ASME J. Tribology* (2008) **130**:041402-1~041402-10.

[18] Horng, J. H., Lee, J. S., Ku, M. Y. and Chen, C. H. Fractal contact model between rough surfaces in considering elastoplastic deformation and adhesion force. *Key Engineering Material, March* (2008) **364~366**:442~448.

XI International Conference on Computational Plasticity. Fundamentals and Applications
COMPLAS XI
E. Oñate, D.R.J. Owen, D. Peric and B. Suárez (Eds)

3D MODELING OF DAMAGE GROWTH AND DUCTILE CRACK PROPAGATION USING ADAPTIVE FEM TECHNIQUE

HAMID MOSLEMI[*] AND AMIR R. KHOEI[†]

[*] Department of Civil Engineering, Engineering Faculty
Shahed University
P.O. Box .18155/159, Tehran, Iran
e-mail: h.moslemi@shahed.ac.ir

[†] Center of Excellence in Structures and Earthquake Engineering
Department of Civil Engineering, Sharif University of Technology,
P.O. Box. 11365-9313, Tehran, Iran
e-mail: arkhoei@sharif.edu

Key words: Damage Mechanics, Crack Initiation, Crack Closure, Adaptive Mesh Refinement, Weighted SPR Technique.

Abstract. In this paper, the continuum damage mechanics model originally proposed by Lemaitre [1] is presented through an adaptive finite element method for three-dimensional ductile materials. The macro-crack initiation–propagation criterion is used based on the distribution of damage variable in the continuum damage model. The micro-crack closure effect is incorporated to simulate the damage evolution more realistic. The Zienkiewicz-Zhu posteriori error estimator is employed in conjunction with a weighted superconvergence patch recovery (SPR) technique at each patch to improve the accuracy of error estimation and data transfer process. Finally, the robustness and accuracy of proposed computational algorithm is demonstrated by a 3D numerical example.

1 INTRODUCTION

The fracture of ductile materials is the consequence of a progressive damaging process and considerable plastic deformation usually precedes the ultimate failure. The numerical prediction of damage evolution and crack initiation–propagation can be described by the means of continuum damage approach. The continuum damage mechanics was originally developed to describe the creep rupture. It was first introduced by Kachanov [2] to describe the effects of an isotropic distribution of spherical voids on plastic flow. Gurson [3] proposed a model based on the theory of elasto-plasticity for ductile damage where the (scalar) damage variable was obtained from the consideration of microscopic spherical voids embedded in an elasto-plastic matrix. It was shown that the theory is particularly suitable for representation of the behavior of porous metals. Lemaitre [1] proposed a micro-mechanical damage model to simulate the physical process of void nucleation, growth and coalescence using continuum mechanics. Lemaitre and Chaboche [4] pointed out the fracture as the ultimate consequence

of material degradation process. The superconvergent patch recovery (SPR) method was first introduced by Zienkiewicz and Zhu [5] in linear elastic problems. The technique was applied in nonlinear analysis by Boroomand and Zienkiewicz [6], in which the strain was recovered by SPR in elasto-plasticity problems. An extension of SPR technique to 3D plasticity problems was presented by Khoei and Gharehbaghi [7]. A modified–SPR technique was applied by Khoei et al. [8] for simulation of crack propagation, in which the polynomial function was replaced by singular terms of analytical solution of crack problems in the process of recovery solution. The technique was improved by Moslemi and Khoei [9] and Khoei et al. [10] to estimate a more realistic error in LEFM problems and cohesive zone models by applying the weighting function for various sampling points. In the present paper, an adaptive finite element method is presented based on the weighted–SPR technique to model the damage of ductile material in 3D problems.

2 NONLINEAR DAMAGE MODEL

Damage in materials is mainly the process of initiation and growth of micro-cracks and cavities. Continuum damage mechanics discusses systematically the effects of damage on the mechanical properties of materials and structures as well as the influence of external conditions and damage itself on the subsequent development of damage. In this study, this nonlinear interaction is investigated via the Lemaitre damage constitutive model. In order to describe the internal degradation of solids within the framework of the continuum mechanics theory, new variables intrinsically connected with the internal damage process need to be introduced in addition to the standard variables. Variables of different mathematical nature possessing different physical meaning have been employed in the description of damage under various circumstances. The damage variable used here is the relative area of micro-cracks and intersections of cavities in any plane oriented by its normal n as

$$D_{(\mathrm{n})} = \frac{S_{\Phi}}{S} \tag{1}$$

where S_{Φ} is the area of micro-cracks and intersections and S is the total area of the cross section. It is assumed that micro-cracks and cavities are distributed uniformly in all directions. In the isotropic case, the damage variable is adopted as a scalar. The behavior of damaged material is governed by the principle of strain equivalence which states that the strain behavior of a damaged material is represented by constitutive equations of the virgin material (without damage) in the potential of which the stress is simply replaced by the effective stress. By this assumption the effective stress tensor is related to the true stress tensor by

$$\boldsymbol{\sigma}_{eff} = \frac{1}{1-D}\boldsymbol{\sigma} \tag{2}$$

In Lemaitre damage model the evolution of damage variable is assumed to be given by

$$\dot{D} = \begin{cases} 0 & \varepsilon^p_{eq} \le \varepsilon^p_D \\ \dot{\gamma}\dfrac{1}{1-D}\left(\dfrac{-Y}{r}\right)^s & \varepsilon^p_{eq} > \varepsilon^p_D \end{cases} \tag{3}$$

where r and s are material and temperature-dependant properties, $\varepsilon_{eq}^{p} = \sqrt{2/3\left\|\varepsilon^{p}\right\|}$ is equivalent plastic strain, $\dot{\gamma}$ is the plastic multiplier and is equal to the rate of equivalent plastic strain and ε_{D}^{p} is threshold damage where damage growth starts only at this critical value. Y is called damage energy release rate and is expanded by using the inverse of the elastic stress-strain law as

$$\begin{aligned} Y &= -\frac{1}{2(1-D)^2}\boldsymbol{\sigma}:[\mathbf{D}^{e}]^{-1}:\boldsymbol{\sigma} \quad = -\frac{1}{2E(1-D)^2}[(1+\nu)\boldsymbol{\sigma}:\boldsymbol{\sigma}-\nu(tr\,\boldsymbol{\sigma})^2] \\ &= -\frac{q^2}{2E(1-D)^2}\left[\frac{2}{3}(1+\nu)+3(1-2\nu)\left(\frac{p}{q}\right)^2\right] \end{aligned} \tag{4}$$

where p is the hydrostatic stress and q is the equivalent von–Mises stress.As can be seen in above equation the damage rate depends on the stress state, plastic strain growth and instantaneous damage variable. The effect of damage variable on mechanical behavior of material is accounted in degradation of elastic modulus of material and its yield surface. Based on the equivalent strain principle this modification can be expressed as

$$\mathbf{D}_{eff} = (1-D)\mathbf{D}^{e} \tag{5}$$

$$\Phi = \sqrt{\frac{3}{2}}\frac{\left\|\mathbf{s}\right\|}{(1-D)} - [\sigma_{Y}^{0} + R(\varepsilon_{eq}^{p})] \tag{6}$$

where $\mathbf{D}^{e}$ and $\mathbf{D}_{eff}$ are the elastic modulus of material before damage and after damage, respectively, $\boldsymbol{\Phi}$ is the modified yield surface, $\mathbf{s}$ is the deviatoric stress tensor and R is the isotropic plastic growth function.

2.1 Finite element implementation

The accuracy of the overall finite element scheme depends crucially on the accuracy of particular numerical algorithm adopted. This section describes a numerical procedure for integration of the Lemaitre damage elasto-plastic model presented in preceding section, based on the well-known two-step elastic predictor–plastic corrector method. At each Gauss point, the values of state variables including the stress tensor $\boldsymbol{\sigma}_{n}$, plastic strain tensor $\boldsymbol{\varepsilon}_{n}^{p}$, equivalent plastic strain $(\varepsilon_{eq}^{p})_{n}$ and damage variable D_{n} are known at the start of interval, and for a given strain increment $\Delta\boldsymbol{\varepsilon}$, the value of variables are desired at the end of interval. At the first stage of computational algorithm the material behavior is assumed to be elastic, the yield surface at the end of interval can be then evaluated as

$$\Phi = \sqrt{\frac{3}{2}}\frac{\left\|\mathrm{s}_{n+1}\right\|}{(1-D_{n})} - [\sigma_{Y}^{0} + R(\varepsilon_{eq}^{p})_{n}] \tag{7}$$

If $\boldsymbol{\Phi} \le 0$, the assumed elastic behavior is correct and the damage variable and plastic strain remain unchanged. If $\boldsymbol{\Phi} > 0$, the plastic corrector step must be applied to obtain the updated

state variables by simultaneously establishing four equations consisting of the plastic flow equation, equivalent plastic strain growth equation, damage growth equation, and the yield surface equation as

$$\varepsilon_{n+1}^{p} = \varepsilon_{n}^{p} + \frac{\Delta\gamma}{1-D_{n+1}}\sqrt{\frac{3}{2}}\frac{\mathrm{s}_{n+1}}{\left\|\mathrm{s}_{n+1}\right\|} \tag{8}$$

$$(\varepsilon_{eq}^{p})_{n+1} = (\varepsilon_{eq}^{p})_{n} + \Delta\gamma \tag{9}$$

$$D_{n+1} = D_{n} + \Delta\gamma\frac{1}{1-D_{n+1}}\left(\frac{-Y_{n+1}}{r}\right)^{s} \tag{10}$$

$$\Phi = \sqrt{\frac{3}{2}}\frac{\left\|\mathrm{s}_{n+1}\right\|}{(1-D_{n+1})} - \left[\sigma_{Y}^{0} + R\,(\varepsilon_{eq}^{p})_{n+1}\right] = 0 \tag{11}$$

The solution of these four nonlinear coupled equations simultaneously is a costly computational task. By performing relatively straightforward algebraic manipulations, the above system can be reduced to a single nonlinear algebraic equation for the plastic multiplier $\Delta\gamma$ expressed as

$$\omega(\Delta\gamma) - \omega_{n} + \frac{\Delta\gamma}{\omega(\Delta\gamma)}\left(\frac{-Y(\Delta\gamma)}{r}\right)^{s} = 0 \tag{12}$$

where ω is the integrity variable in contrast to damage variable and is evaluated by

$$\omega_{n+1} = 1 - D_{n+1} = \omega(\Delta\gamma) = \frac{3G\Delta\gamma}{\bar{q}_{n+1}^{trial} - \sigma_{Y}(R_{n} + \Delta\gamma)} \tag{13}$$

where $\bar{q}_{n+1}^{trial}$ is the von–Mises equivalent stress obtained in the elastic predictor step. The damage energy release rate is a function of $\Delta\gamma$ calculated by

$$Y(\Delta\gamma) = \frac{\left[\sigma_{Y}(R_{n} + \Delta\gamma)\right]^{2}}{6G} + \frac{\bar{p}_{n+1}^{2}}{2K} \tag{14}$$

where $\bar{p}_{n+1}$ is the elastic predicted hydrostatic pressure without damage effect. Equation (12) can be solved by an iterative method such as Newton-Raphson method. By computing the plastic multiplier, the updated state variables can be obtained using four basic equations.

2.2 Micro-crack closure effect

From the micromechanical view, the damage can be considered as the degradation of material properties due to the evolution of voids and micro-cracks. The Lemaitre damage model discussed in previous section, suffers from an important drawback, since the effect of hydrostatic stress is captured by the damage energy release rate Y with equal response in tension and compression. On the other hand, the micro-cracks which open in tensile stresses may partially close at a compression stress state. Hence, after having been damaged in

tension, the material recovers its stiffness partially under compression. In this study, the stress tensor is decomposed into the positive and negative parts and the effect of compressive stress tensor is considered as a fraction of the effect of tensile stress tensor. In the process of decomposition, the stress tensor is first mapped to the principle directions to form a diagonal matrix with the principle stresses. This matrix is then decomposed to tensile and compressive stress tensors as

$$\boldsymbol{\sigma} = \boldsymbol{\sigma}^{+} + \boldsymbol{\sigma}^{-} \tag{15}$$

This decomposition is defined mathematically using the Macaulay bracket $\langle\ \rangle$ as

$$\boldsymbol{\sigma}^{+} = \begin{bmatrix} \langle\sigma_1\rangle & 0 & 0 \\ 0 & \langle\sigma_2\rangle & 0 \\ 0 & 0 & \langle\sigma_3\rangle \end{bmatrix} \qquad \boldsymbol{\sigma}^{-} = -\begin{bmatrix} \langle-\sigma_1\rangle & 0 & 0 \\ 0 & \langle-\sigma_2\rangle & 0 \\ 0 & 0 & \langle-\sigma_3\rangle \end{bmatrix} \tag{16}$$

The Macaulay bracket is a scalar function defined as

$$\langle a\rangle = \begin{cases} a & \text{if } a \geq 0 \\ 0 & \text{if } a < 0 \end{cases} \tag{17}$$

By decomposition of stress tensor, each component affects the damage energy release rate separately. The effect of tensile component given in Section 2 remains valid, but the compression component has a more moderate effect with an experimental reduction factor of h. This value is called as the crack closure effect constant and has the value in the range of $[0-1]$. Thus, the effect of compressive component of stress tensor can be superposed with the effect of tensile component of stress tensor by modifying equation (4) as

$$Y = -\frac{1}{2E(1-D)^2}\left[(1+\nu)\boldsymbol{\sigma}^{+}:\boldsymbol{\sigma}^{+} - \nu\langle tr\,\boldsymbol{\sigma}\rangle^2\right] - \frac{h}{2E(1-hD)^2}\left[(1+\nu)\boldsymbol{\sigma}^{-}:\boldsymbol{\sigma}^{-} - \nu\langle -tr\,\boldsymbol{\sigma}\rangle^2\right] \tag{18}$$

By modifying the value of damage energy release rate, the remaining parts of the procedure of original Lemaitre model will not be changed.

3 ADAPTIVE FINITE ELEMENT STRATEGY

In numerical analysis of FE solution, it is essential to introduce some measures of error and use adaptive mesh refinement to keep this error within prescribed bounds to ensure that the finite element method is effectively used for practical analysis. To automate this process, several adaptive finite elements have been implemented to obtain an optimal mesh. Due to the localized material deterioration in the damaged body problems, many elements will be severely distorted producing unacceptably inaccurate solutions and this optimization takes a more important and necessary role. In order to obtain an optimal mesh, in the sense of an equal solution quality, it is desirable to design the mesh such that the error contributions of the elements are equally distributed over the mesh. This criterion illustrates what parts of the discretized domain have to be refined/de-refined and what degree of mesh fineness is needed to maintain the solution error within the prescribed bounds. The plastic deformation of problem necessitates transferring all relevant variables from the old mesh to new one. In

general, the procedure described above can be executed in four parts; an error estimation, an adaptive mesh refinement, an adaptive mesh generator, and the mapping of variables.

3.1 Error estimation using weighted SPR technique

In the error estimation process two main aims are followed: firstly, to determine the error for the chosen mesh and secondly, to reduce this error to a permissible value by an automatic adaptive remeshing. The discretization error for a state variable represents the difference between its exact and the finite element solutions. Thus, the error of typical state variable α can be defined by $e_\alpha = \alpha - \hat{\alpha}$, with α denoting the exact value of state variable and $\hat{\alpha}$ the value of state variable derived by a finite element solution. Since the exact value of state variables for nonlinear problems is not available, we use a recovered solution instead of exact ones and then approximate the error as the difference between the recovered values and those given directly by the finite element solution, i.e. $e_\alpha \approx \alpha^* - \hat{\alpha}$, where α^* denotes the recovered value of state variable α.

Since the damage variable plays an important role in predicting the crack initiation and crack growth, its accuracy is very crucial in this process. Thus, the error is estimated based on the damage variable D. In order to obtain an improved solution, the nodal smoothing procedure is performed using the weighted superconvergent patch recovery (WSPR) technique, which was originally proposed by Moslemi and Khoei [9] to simulate the crack growth in linear fracture mechanics. The objective of recovery of the finite element solution is to obtain the nodal values of damage variable D such that the smoothed continues field defined by the shape functions and nodal values is more accurate than that of the finite element solution. A procedure for utilizing the Gauss quadrature values is based on the smoothing of such values by a polynomial of order p in which the number of sample points can be taken as greater than the number of parameters in the polynomial. In this case, if we accept the superconvergence at certain points of each element, the computed values of damage variable have the superconvergent accuracy at all points within the element. Thus, the recovered solution of damage variable D^* can be obtained as

$$D^* = \mathbf{P}\mathbf{a} \tag{19}$$

where $\mathbf{a}$ is a vector of unknown parameters and $\mathbf{P}$ the polynomial base functions. Depending on the order of polynomial the technique is called as C0-SPR, C1-SPR, etc. It was shown by Khoei et al. [8] in crack growth problems that if the singular elements are used near the crack tip the modified–SPR technique, in which the polynomial function is replaced by the singular terms of analytical solution of crack problems leads to better results in the process of recovery solution. Since the isoparametric elements are employed here over the domain, the linear base functions are used for the recovery process. Hence, the vectors $\mathbf{P}$ and $\mathbf{a}$ are represented in their simplest form as

$$\mathbf{P} = \langle 1, x, y, z \rangle \qquad \mathbf{a} = \langle a_1, a_2, a_3, a_4 \rangle^T \tag{20}$$

The determination of the unknown parameters $\mathbf{a}$ can be made by performing a least square

fit to the values of superconvergent, or sampling points. After finite element analysis, a patch is defined for each vertex node inside the domain by the union of elements sharing the node. At each node of interior patch center, the connected tetrahedral elements along with their nodes and Gauss points are obtained. The number of sampling points must be at least equal to number of parameters in the polynomial. In the standard SPR technique, all sampling points have similar properties in the patch, which may produce significant errors in the boundaries, particularly the edges of crack. In fact, for elements located on the boundaries, constraints and crack edges, which do not have enough sampling points, we need to use the sampling points of nearest patch. These new sampling points induce unreal value of damage variables in the patch and overestimate the value of error, which results in unreasonable mesh refinement in the boundaries of domain. Moslemi and Khoei [9] proposed the weighted–SPR technique by using different weighting parameters for sampling points of the patch. It results in more realistic recovered values at the nodal points, particularly near the crack tip and boundaries. Hence, if we have n sampling points in the patch with the coordinates (x_k, y_k, z_k), the function F needs to be minimized in this patch as

$$\begin{aligned} F(\mathbf{a}) &= \sum_{k=1}^{n} w_k \left[D_i^*(x_k, y_k, z_k) - \hat{D}_i(x_k, y_k, z_k) \right]^2 \\ &= \sum_{k=1}^{n} w_k \left[\mathbf{P}(x_k, y_k, z_k)\mathbf{a} - \hat{D}_i(x_k, y_k, z_k) \right]^2 \end{aligned} \tag{21}$$

In order to incorporate the effects of nearest sampling points in the recovery process, the weighting parameter is defined as $w_k = 1/r_k$, with r_k denoting the distance of sampling point from the vertex node which is under recovery. The minimization of function F with respect to $\mathbf{a}$ results in the unknown parameters $\mathbf{a}$ as

$$\mathbf{a} = \left(\sum_{k=1}^{n} w_k^2 \, \mathbf{P}_k^T \, \mathbf{P}_k \right)^{-1} \sum_{k=1}^{n} \left[w_k^2 \, \mathbf{P}_k^T \, \hat{D}_i(x_k, y_k) \right] \tag{22}$$

It must be noted that the implementation of global coordinates may result in ill-conditioned coefficient matrix, hence it is preferred to use a local coordinate system in the patch. Once the components of the vector of unknown parameters $\mathbf{a}$ are determined, the damage variables at nodal points inside the patch are computed by substituting their coordinates in equation (19). These nodal values $\bar{\boldsymbol{D}}^*$ can be used to construct a continuous damage field over the entire domain at the next step, that is, for each element, the recovered damage variable is represented as an interpolation of nodal values using the standard shape functions $\mathbf{N}$ in finite element analysis as

$$D^* = \mathbf{N} \, \bar{\boldsymbol{D}}^* \tag{23}$$

The recovered damage variable obtained by above equation can be used to obtain a pointwise error in the domain. Since the pointwise error becomes locally infinite in critical points, such as crack tip, point constraint and point loads, the error estimator can be replaced by a global parameter using the norm of error defined as

$$\left\|e_D\right\| = \left\|D^* - \hat{D}\right\| = \left(\int_\Omega (D^* - \hat{D})^T (D^* - \hat{D})\, d\Omega\right)^{\frac{1}{2}} \tag{24}$$

The above *L2* norm is defined over the whole domain Ω. The overall error can be related to each element error by

$$\left\|e_D\right\|^2 = \sum_{i=1}^{m} \left\|e_D\right\|_i^2 \tag{25}$$

with *i* denoting an element contribution and m the total number of elements. The distribution of error norm across the domain indicates which portions need refinement and which other parts need de-refinement, or coarsening elements.

3.2 Adaptive mesh refinement

Once the error estimator process has been achieved it needs to implement a technique by which the solution can be improved. Since the total error permissible must be less than a certain value, it is a simple matter to search the design field for a new solution in which the total error satisfies this requirement. The simplest process is based on an equal error distribution among all elements as with such equal error distribution the results are most economical. In fact, after remeshing each element must obtain the same error and the overall percentage error must be less than the target percentage error, i.e.

$$\theta = \frac{\left\|e_D\right\|}{\left\|\hat{D}\right\|} \le \theta_{\text{aim}} = \frac{\left\|e_D\right\|_{\text{aim}}}{\left\|\hat{D}\right\|} \tag{26}$$

where θ_{aim} is the prescribed target percentage error. Hence, the aim error at each element can be obtained as

$$\left(\left\|e_D\right\|_i\right)_{\text{aim}} = \frac{1}{\sqrt{m}} \left\|\hat{D}\right\| \ \theta_{\text{aim}} \tag{27}$$

The rate of convergence of local error depends on the order of elements. The higher-order elements show faster convergence to the aim error. Thus, such elements need less refinement and new element size depend on its error norm and its order. Thus, the new element size can be evaluated as

$$(h_i)_{\text{new}} = \left[\frac{\left(\left\|e_D\right\|_i\right)_{\text{aim}}}{\left(\left\|e_D\right\|_i\right)_{\text{old}}}\right]^{1/p} (h_i)_{\text{old}} \tag{28}$$

where *h* is the average element size and p is the order of element. To obtain the nodal element size, a simple averaging between elements joining a node is used. As the mesh tends progressively to be optimal with the error uniformly distributed between elements this theoretical rate of convergence appears very effective. The above technique can be coupled with an efficient mesh generator which allows the new mesh to be constructed according to a predetermined size distribution.

3.3 Data transfer operator

In the nonlinear FE analysis, the new mesh must be used starting from the end of previous load step since the solution is history-dependent in nonlinear problems. Thus, the state and internal variables need to be mapped from the old finite element mesh to the new one. The state variables consist of the nodal displacements and the internal variables, including the Cauchy stress tensor, the strain tensor, the plastic strain tensor and damage variable. Since these variables are transferred separately, it is important that the transfer of information from the old to new meshes is achieved with minimum discrepancy in equilibrium and constitutive relations. Hence, a minimum number of internal variables must be transferred and remaining variables are calculated by equilibrium and constitutive equations. In the case of internal variables which their values evaluated at the Gauss points of the old mesh, corresponding values at the Gauss points of the new mesh are desired.

The direct mapping of variables may lead to inconsistency between transferred variables and shape functions of the elements. In this case the process of data transfer can be carried out in three steps. In the first step the continuous internal variables are obtained by projecting the Gauss point components to the nodal values. In order to project the values of Gauss points to nodal points, the 3D weighted–SPR method is applied here, as described in previous section. In the second step, the nodal values of internal variables of old mesh are transferred to the nodes of new mesh. For this purpose, we must first determine which element in the old mesh contains the nodal point in the new finite element mesh. The nodal components in the old mesh are then transferred to the nodes of new mesh by applying the old shape functions of old elements and the global coordinates of the new nodes. The components of internal variables at the Gauss points of new mesh are finally obtained by interpolation using the shape functions of elements of the new mesh. These three steps are illustrated schematically in Figure 1. In addition, a transfer operator is employed that transfers the state variables, i.e. displacement field, from the old to a new mesh. This operator includes only the second step of the first operator where the nodal components in the old mesh are transferred to the nodes of new mesh.

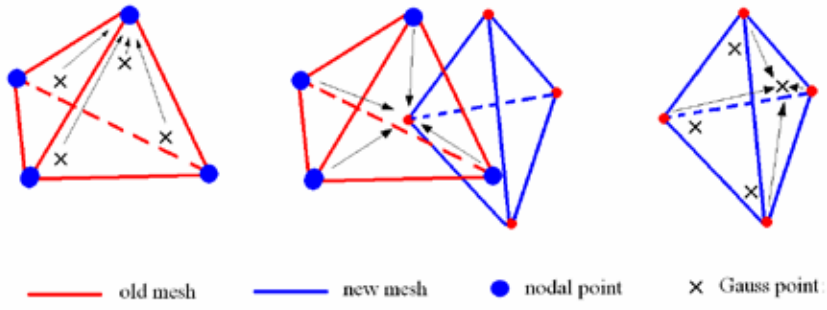

Figure 1: Three-step procedure of the transfer operator

4 NUMERICAL SIMULATION RESULTS

In order to illustrate the accuracy and robustness of the proposed adaptive finite element method in three-dimensional damage mechanics, a classical tensile test of a cylindrical pre-

notched bar is simulated numerically. The geometry and boundary conditions of the specimen are shown in Figure 2. On the virtue of symmetry, only one-eighth of the problem is modeled. The specimen is subjected to the tensile prescribed displacement at the top edge. The bar is constructed by a low carbon steel in a rolled state with the following material properties; $E = 210$ GPa and $\nu = 0.3$. The strain hardening is considered to be isotropic. The parameters of Lemaitre model for this specimen is taken as $s = 1.0$ and $r = 3.5$ MPa. This specimen was also simulated by de Souza Neto et al. [11] using 2D FE modeling to validate the performance of their constitutive model in damage mechanics. The vertical displacement is applied incrementally in 600 increments of 0.001 mm. The damage evolution is predicted by Lemaitre model until its value reaches to the critical damage value of $D_C = 0.99$.

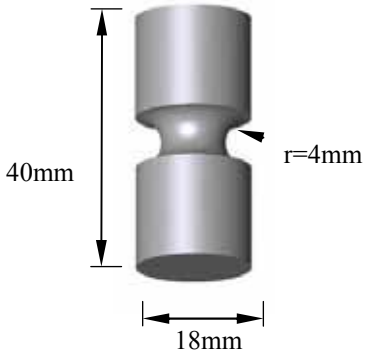

Figure 2: The cylindrical notched specimen; The geometry

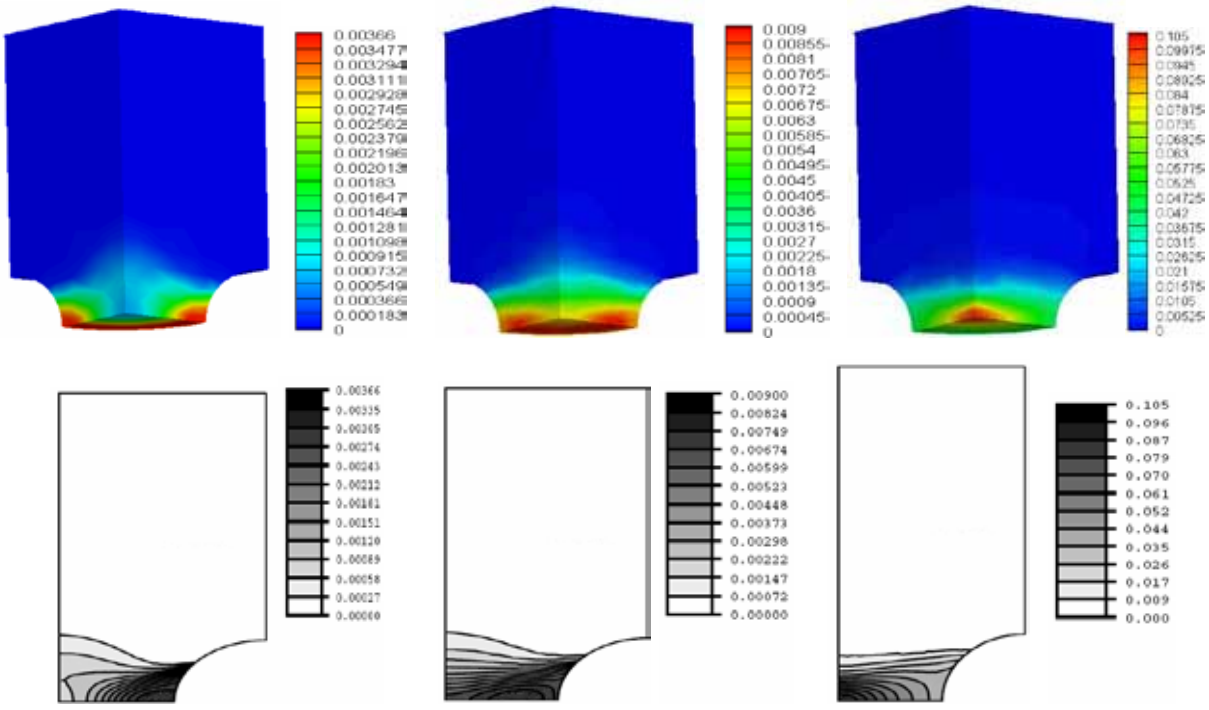

Figure 3: The distribution of damage contours at various load steps; A comparison between the present 3D model and result reported by de Souza Neto et al.[11]; a) $u = 0.051$ mm , b) $u = 0.076$ mm , c) $u = 0.246$ mm

In Figure 3, the distribution of damage contours are shown at three stages and compared wit h those reported by de Souza Neto et al. [11] in two dimensional modeling. It can be seen that the predicted damage contours are in good agreement with those obtained in reference [11]. It is interesting to note that the location of maximum damage is not fixed in the model and moves at different stages of loading. It can be observed that the maximum damage occurs in the outer part of the specimen at the first stages of loading, however – it moves toward the center of the bar by increasing the load. This can be justified by the fact that at early stages of loading the hydrostatic stress is low and the damage evolution is affected by the plastic flow. Thus, the damage grows in outer layers, where the maximum equivalent plastic strain occurs. However, by increasing the load, the hydrostatic stress increases and its effect becomes dominant. Hence, the damage critical point moves toward the center of the bar where the maximum value of hydrostatic stress occurs. In order to control the error of the solution, an adaptive FE mesh refinement is carried out to generate the optimal mesh. The weighted superconvergent patch recovery technique is used with the aim error of 5%. This process is carried out at two steps of 50 and 360, as shown in Figure 4. This figure clearly presents the distribution of elements on the specimen with the growth of damage. In Figure 5, the effect of adaptive strategy can be observed on the estimated error. Obviously, the adaptive mesh refinements result in a reduced estimated error and converge to the prescribed target error.

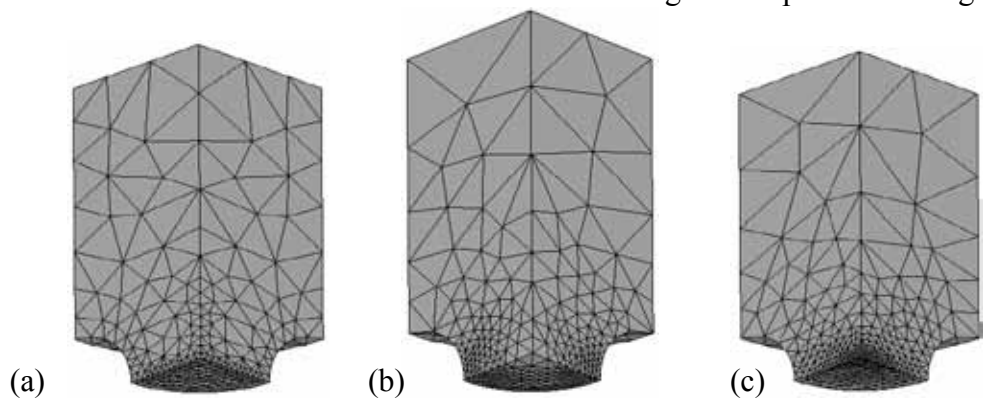

Figure 4: Adaptive mesh refinement technique for the cylindrical notched specimen; a) Initial FE mesh, b) Adapted mesh at $u = 0.05$ mm , c) Adapted mesh at $u = 0.36$ mm

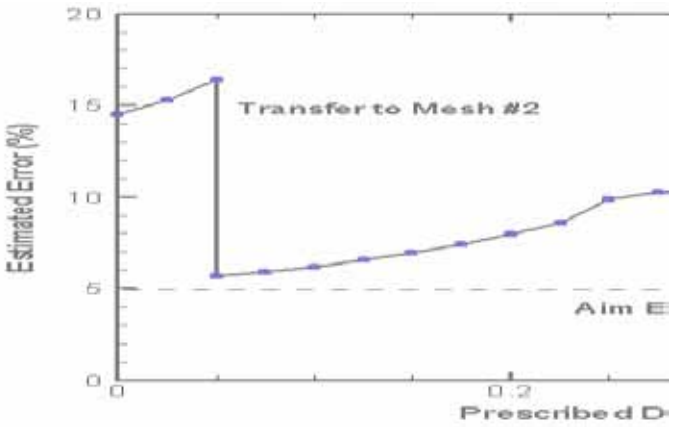

Figure 5: The variation of estimated error with prescribed displacement during adaptive mesh refinement

5 CONCLUSIONS

In the present paper, an adaptive finite element method was presented for the three-dimensional analysis of damage growth and crack initiation. The constitutive modeling was implemented within the framework of continuum damage mechanics. A simplified version of Lemaitre damage model was employed to estimate the damage evolution. The adaptive finite element technique was implemented through the following three stages; an error estimation, adaptive mesh refinement, and data transferring. The error estimation procedure was used based on the Zienkiewicz–Zhu error estimator and a weighted superconvergent patch recovery technique was employed. The accuracy and robustness of proposed computational algorithm in 3D damage mechanics were presented by a numerical example. The results clearly show the ability of the model in capturing the damage growth and crack initiation in complex 3D problem. In a later work, we will show how the proposed technique can be used in a 3D automatic simulation of crack propagation in the fracture of ductile materials.

REFERENCES

[1] Lemaitre, J. A continuous damage mechanics model for ductile fracture, *Journal of Engineering Materials and Technology.* (1985) **107**:83–89.

[2] Kachanov, L.M. Time of the rupture process under creep condition, *Izvestiya Akademii Nauk SSSR*, Otdeleniya Tekhnika Nauk. (1958) **8**:26–31.

[3] Gurson, A.L. Continuum theory of ductile rupture by void nucleation and growth – Part I: Yield criteria and flow rule for porous media, *Journal of Engineering Materials and Technology.* (1977) **99**:2–15.

[4] Lemaitre, J. and Chaboche, J.L. *Mechanics of Solid Materials,* Cambridge University Press, (1990).

[5] Zienkiewicz, O.Z. and Zhu, J.Z. The superconvergent patch recovery and a posteriori error estimates. Part I: The recovery technique, *International Journal for Numerical Methods in Engineering.* (1992) **33**:1331-1364.

[6] Boroomand, B. and Zienkiewicz, O.C. Recovery procedures in error estimation and adaptivity, part II: adaptivity in nonlinear problems of elasto-plasticity behaviour, *Computer Methods in Applied Mechanics and Engineering.* (1999) **176**:127–146.

[7] Khoei, A.R. and Gharehbaghi, S.A. The superconvergence patch recovery and data transfer operators in 3D plasticity problems, *Finite Elements in Analysis and Design.* (2007) **43**: 630–648.

[8] Khoei, A.R., Azadi, H. and Moslemi, H. Modeling of crack propagation via an automatic adaptive mesh refinement based on modified superconvergent patch recovery technique, *Engineering Fracture Mechanics.* (2008) **75**:2921–2945.

[9] Moslemi, H. and Khoei, A.R. 3D adaptive finite element modeling of non-planar curved crack growth using the weighted superconvergent patch recovery method. *Engineering Fracture Mechanics.* (2009) **76**:1703–1728.

[10] Khoei, A.R., Moslemi, H., Majd Ardakany, K., Barani, O.R. and Azadi, H. Modeling of cohesive crack growth using an adaptive mesh refinement via the modified-SPR technique, *International Journal of Fracture.* (2009) **159**:21–41.

[11] de Souza Neto, E.A., Peric and Owen, D.R.J. *Computational Methods for Plasticity: Theory and Applications*, Wiley, UK. (2008).

XI International Conference on Computational Plasticity. Fundamentals and Applications
COMPLAS XI
E. Oñate, D.R.J. Owen, D. Peric and B. Suárez (Eds)

CYCLIC VISCOELASTOPLASTICITY AND FATIGUE FRACTURE OF POLYMER COMPOSITES

ALEKSEY D. DROZDOV*

*Department of Plastics Technology
Danish Technological Institute
Gregersensvej 1, 2630 Taastrup, Denmark
e-mail: Aleksey.Drozdov@teknologisk.dk

Key words: Viscoelastoplasticity, Polymer/clay hybrids, Ratcheting, Fatigue

Abstract. Observations are reported on isotactic polypropylene/nanoclay hybrids with various concentrations of filler ranging from 0 to 5 wt.% in cyclic tensile tests with a stress–controlled program (ratcheting between minimum stresses $\sigma^{\min}$ and maximum stresses $\sigma^{\max}$). A pronounced effect of filler is demonstrated: reinforcement of polypropylene with 1 wt.% of nanoclay results in reduction of maximum and minimum strains per cycle by several times and growth of number of cycles to failure by an order of magnitude. To rationalize these findings, a constitutive model is developed in cyclic viscoelastoplasticity of polymer nanocomposites. Adjustable parameters in the stress–strain relations are found by fitting experimental data in relaxation tests and cyclic tests. It is demonstrated that the model correctly predicts growth of maximum and minimum strains per cycle with number of cycles and can be applied for evaluation of fatigue failure of nanocomposites.

1 INTRODUCTION

This paper is concerned with experimental investigation and constitutive modeling of the viscoelastic and viscoplastic responses of polymer/clay nanocomposites in tensile cyclic tests with stress-controlled programs.

A number of studies on the mechanical behavior of polymer/clay hybrids reveal noticeable improvement of their properties due to the presence of nanoparticles [1, 2, 3]. This enhancement remains, however, rather modest compared with what has been expected from the effect of reinforcement a decade ago [3]. Keeping in mind these discrepancies between expected and real mechanical properties of nanohybrids in conventional tensile tests, it seems natural to focus on more sophisticated deformation programs, where the effect of nanofiller becomes significant for applications. This approach was initiated in [4, 5, 6] by demonstrating that reinforcement of polymers with nanoparticles dramatically enhanced creep resistance and in [7, 8] by revealing a similar effect for ratcheting strain in cyclic tests.

The objective of this study is threefold: (i) to demonstrate that reinforcement of polypropylene with nanoclay results in a strong decrease in maximum and minimum strains per cycle observed in uniaxial tensile cyclic tests with a stress-controlled program, (ii) to develop a constitutive model in cyclic viscoelastoplasticity of polymer nanocomposites that describes this phenomenon, and (iii) to rationalize physical mechanisms responsible for the improvement of fatigue resistance by comparison of material parameters in the stress–strain relations.

2 EXPERIMENTAL RESULTS

Nanocomposites with isotactic polypropylene as a matrix [Moplen HP 400R (Albis Plastic Scandinavia AB, Sweden)], maleic anhydride grafted polypropylene as a compatibilizer [Eastman G 3015 (Eastman Chemical Company, USA)], and organically modified montmorillonite nanoclay as a filler [Delitte 67G (Laviosa Chimica Mineraria S.p.A., Italy)] were manufactured in a two-step process described in [6]. Nanohybrids with clay/compabilizer proportion 1:2 and clay contents $\chi = 0$, 1, 3, and 5 wt.% were prepared by means of twin-screw extruder Brabender PL2000. Dumbbell specimens for tensile tests (ASTM standard D638) were molded by using injection-molding machine Arburg 320C.

Uniaxial tensile tests were performed at room temperature by means of universal testing machine Instron–5569 equipped with an electro-mechanical sensor for control of longitudinal strains. The engineering stress σ was determined as the ratio of axial force to cross-sectional area of undeformed specimens.

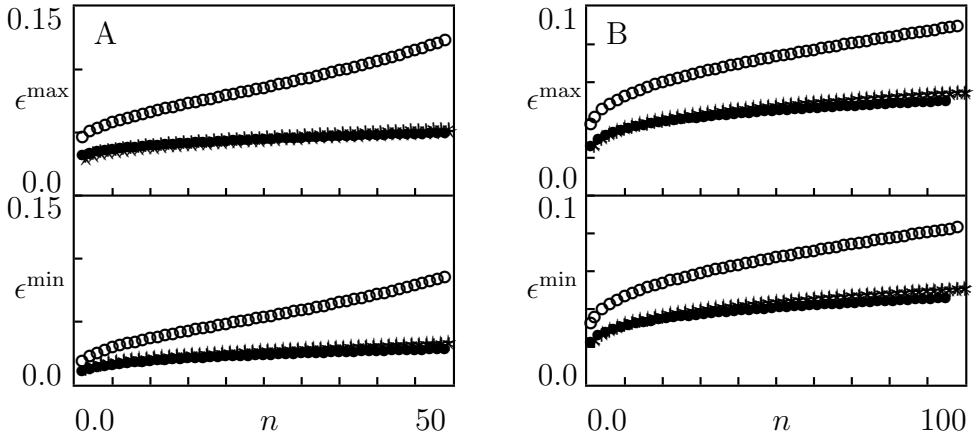

Figure 1: Maximum $\epsilon^{\max}$ and minimum $\epsilon^{\min}$ strains per cycle versus number of cycles n. Symbols: experimental data in cyclic tests with $\dot{d} = 10$ mm/min, $\sigma^{\max} = 25$ MPa, $\sigma^{\min} = 20$ MPa (A) and $\dot{d} = 100$ mm/min, $\sigma^{\max} = 30$ MPa, $\sigma^{\min} = 10$ MPa (B) on nanocomposites with clay content χ wt.% ($\circ$ $\chi = 0$, $\bullet$ $\chi = 1$, $*$ $\chi = 3$, $\star$ $\chi = 5$).

Two series of experiments were conducted at room temperature. The first was aimed to choose deformation programs that ensure the most pronounced effect of reinforcement. It involved five ratcheting tests with various maximum stresses $\sigma^{\max}$, minimum stresses

$\sigma^{\min}$ and strain rates $\dot{\epsilon}$. In each test, a specimen was stretched with a fixed cross-head speed $\dot{d}$ up to a maximum stress $\sigma^{\max}$, retracted down to a minimum stress $\sigma^{\min}$ with the same cross-head speed, reloaded up to the maximum stress $\sigma^{\max}$ with the cross-head speed $\dot{d}$, unloaded down to the minimum stress $\sigma^{\min}$ with the same cross-head speed, etc. Some experimental data in cyclic tests are reported in Figure 1, where maximum strain per cycle $\epsilon^{\max}$ and minimum strain per cycle $\epsilon^{\min}$ are plotted versus number of cycles n. Observations show that for all experimental conditions, reinforcement of polypropylene with nanoclay results in noticeable reduction in $\epsilon^{\max}$ and $\epsilon^{\min}$. The strongest improvement of fatigue resistance is reached when concentration of filler equals 1 wt.%.

The other series of tests was carried out for identification of parameters in constitutive equations. It involved cyclic tests with a stress-controlled program and relaxation tests. Each test was carried out on a new sample and repeated by twice to confirm reproducibility of measurements. Based on observations in the first series of tests, we confine ourselves to the analysis of nanocomposites with $\chi = 0$ and 1 wt.%.

Ratcheting tests were performed with $\dot{d} = 100$ mm/min, $\sigma^{\max} = 30$ MPa, and $\sigma^{\min} = 20$ MPa. Experimental stress–strain curves (16 cycles of loading–retraction) and diagrams $\epsilon^{\max}(n)$, $\epsilon^{\min}(n)$ are depicted in Figure 2.

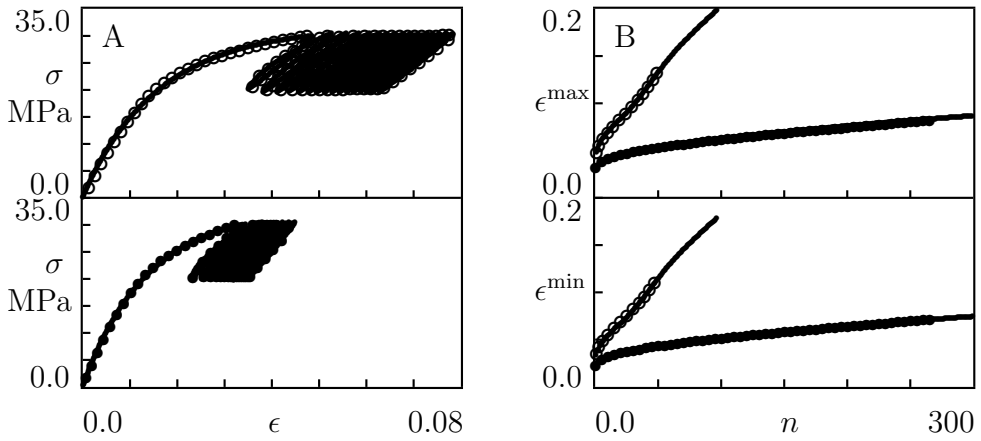

Figure 2: A—Stress σ versus strain ϵ. B—Maximum $\epsilon^{\max}$ and minimum $\epsilon^{\min}$ strains versus number of cycles n. Circles: experimental data in cyclic tests on nanocomposites with $\chi = 0$ ($\circ$) and $\chi = 1$ ($\bullet$) wt.%. Solid lines: results of numerical simulation.

Relaxation tests were conducted with a fixed strain $\epsilon = 0.1$. In each test, a specimen was stretched with $\dot{d} = 100$ mm/min up to the required strain. Afterwards, ϵ was preserved constant, and a decrease in stress σ was monitored as a function of time t. Following the ASTM protocol E–328 for short-term relaxation tests, duration of relaxation tests $t_{\rm rel} = 20$ min was chosen.

Observations in relaxation tests are reported in Figure 3, where engineering stress σ is depicted versus relaxation time $t' = t - t_0$ (t_0 stands for the instant when relaxation starts). Following common practice, the semi-logarithmic plot is chosen with $\log = \log_{10}$.

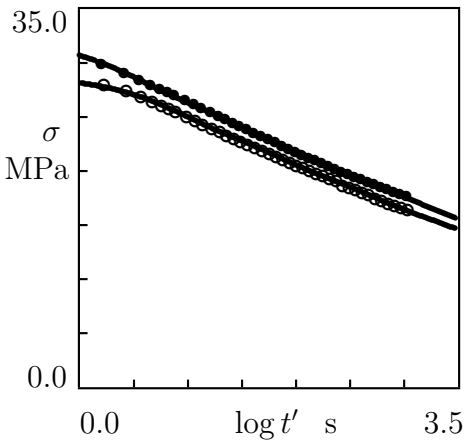

Figure 3: Stress σ versus relaxation time t'. Symbols: experimental data in relaxation tests on nanocomposites with $\chi = 0$ ($\circ$) and $\chi = 1$ ($\bullet$) wt.%. Solid lines: results of numerical simulation.

Figure 3 shows that the viscoelastic response of nanocomposites is weakly affected by clay content.

3 CONSTITUTIVE MODEL

With reference to the homogenization concept [9], a nanocomposite with a complicated microstructure (a semicrystalline matrix reinforced with randomly distributed clay platelets and their stacks) is replaced with an equivalent isotropic medium, whose mechanical response resembles that of the composite. An incompressible, inhomogeneous, transient, non-affine network of polymer chains bridged by junctions is chosen as the equivalent continuum. The incompressibility hypothesis is confirmed by observations in uniaxial tensile tests with cross-head speed 200 mm/min, where longitudinal and transverse strains were measured simultaneously. Poisson's ratios of nanocomposites with $\chi = 0$ and 1 wt.% read 0.498 and 0.476, respectively.

3.1 Kinematics of plastic deformations

To describe plastic flow in the equivalent medium at small strains, the strain tensor for macro-deformation $\hat{\epsilon}$ is presented as the sum of elastic strain tensor $\hat{\epsilon}_{\rm e}$ and plastic strain tensor $\hat{\epsilon}_{\rm p}$

$$\hat{\epsilon} = \hat{\epsilon}_{\rm e} + \hat{\epsilon}_{\rm p}. \tag{1}$$

With reference to conventional phenomenological models with two plastic elements connected in series, the plastic strain tensor $\hat{\epsilon}_{\rm p}$ is split into the sum of two components

$$\hat{\epsilon}_{\rm p} = \hat{\epsilon}_{\rm p}^{(1)} + \hat{\epsilon}_{\rm p}^{(2)}. \tag{2}$$

The tensors $\hat{\epsilon}_{\rm p}^{(1)}$ and $\hat{\epsilon}_{\rm p}^{(2)}$ are presumed to describe inelastic deformations in the matrix and inclusions, respectively.

The strain rate for plastic deformation in the matrix is proportional to strain rate for macro-deformation

$$\frac{\mathrm{d}\hat{\epsilon}_{\mathrm{p}}^{(1)}}{\mathrm{d}t} = \phi \frac{\mathrm{d}\hat{\epsilon}}{\mathrm{d}t}, \tag{3}$$

where the non-negative function ϕ (i) vanishes in the undeformed state (which means that no plastic deformation occurs at very small strains), (ii) monotonically grows under active loading and decreases under retraction (which reflects stress-induced acceleration of plastic flow), and (iii) reaches its ultimate value $\phi_\infty = 1$ at large strains (when the rates of plastic deformation and macro-deformation coincide). Changes in ϕ with time are governed by the differential equation

$$\frac{\mathrm{d}\phi}{\mathrm{d}t} = \pm a(1-\phi)^2 \dot{\epsilon}, \qquad \phi(0) = 0, \tag{4}$$

where the signs "+" and "−" correspond to loading and retraction, respectively, $\dot{\epsilon} = \left(\frac{2}{3}\frac{\mathrm{d}\hat{\epsilon}}{\mathrm{d}t} : \frac{\mathrm{d}\hat{\epsilon}}{\mathrm{d}t}\right)^{\frac{1}{2}}$ stands for the equivalent strain rate for macro-deformation, and the coefficient a adopts different values a_1 and a_2 under active deformation and unloading. For uniaxial tension, loading and unloading are determined unambiguously. For an arbitrary three-dimensional deformation, these processes are defined following [10, 11].

3.2 Heterogeneity of the network

An inhomogeneous transient polymer network is composed of meso-domains with various activation energies for rearrangement of chains. The rate of separation of active chains from their junctions in a meso-domain with activation energy u is governed by the Eyring equation $\Gamma = \gamma \exp[-u/(k_B T)]$, where γ is an attempt rate, k_B denotes Boltzmann's constant, and T stands for absolute temperature. Introducing dimensionless activation energy $v = u/(k_B T)$, we obtain

$$\Gamma(v) = \gamma \exp(-v). \tag{5}$$

Denote by N concentration of active chains in the equivalent network [12]. The number of active chains $n_0(v)$ in meso-domains with activation energy v (per unit volume) reads

$$n_0(v) = N f(v), \tag{6}$$

where $f(v)$ stands for a distribution function of meso-domains. With reference to the random energy model [13], the quasi-Gaussian expression is accepted for this function

$$f(v) = f_0 \exp\Big[-\frac{1}{2}\Big(\frac{v}{\Sigma}\Big)^2\Big] \qquad (v \geq 0), \qquad f(v) = 0 \qquad (v < 0). \tag{7}$$

Parameters N, γ, and Σ are assumed to be independent of mechanical factors. The pre-factor f_0 is determined from the normalization condition $\int_0^\infty f(v)\mathrm{d}v = 1$.

3.3 Rearrangement of chains

Rearrangement of a temporary network is described by a function $n(t,\tau,v)$ which equals the number (per unit volume) of temporary chains at time $t \geq 0$ that have returned into the active state before instant $\tau \leq t$ and belong to a meso-domain with energy v. The number of active chains in meso-domains with energy v at time t reads

$$n(t,t,v) = n_0(v). \tag{8}$$

The number of chains that were active at the initial instant $t = 0$ and have not separated from their junctions until time t is $n(t,0,v)$. The number of chains that were active at the initial instant and detach from their junctions within the interval $[t, t+\mathrm{d}t]$ equals $-\partial n/\partial t(t,0,v)\,\mathrm{d}t$, the number of dangling chains that return into the active state within the interval $[\tau, \tau+\mathrm{d}\tau]$ is given by $P(\tau,v)\mathrm{d}\tau$ with

$$P(\tau,v) = \frac{\partial n}{\partial \tau}(t,\tau,v)\Big|_{t=\tau}, \tag{9}$$

and the number of chains that merged (for the last time) with the network within the interval $[\tau, \tau+\mathrm{d}\tau]$ and detach from their junctions within the interval $[t, t+\mathrm{d}t]$ reads $-\partial^2 n/\partial t\partial\tau(t,\tau,v)\,\mathrm{d}t\mathrm{d}\tau$. Detachment of chains from their junctions is described by the kinetic equations

$$\frac{\partial n}{\partial t}(t,0,v) = -\Gamma(v)n(t,0,v), \qquad \frac{\partial^2 n}{\partial t\partial\tau}(t,\tau,v) = -\Gamma(v)\frac{\partial n}{\partial\tau}(t,\tau,v), \tag{10}$$

which mean that the number of active chains separating from their junctions per unit time is proportional to the total number of active chains in an appropriate meso-domain. Integration of Eq. (10) with initial conditions (6), (8), and (9) implies that

$$n(t,0,v) = Nf(v)\exp[-\Gamma(v)t], \qquad \frac{\partial n}{\partial\tau}(t,\tau,v) = Nf(v)\Gamma(v)\exp[-\Gamma(v)(t-\tau)]. \tag{11}$$

3.4 Stress–strain relations

The strain energy of an active chain reads

$$w = \frac{1}{2}\bar{\mu}\hat{\epsilon}_{\mathrm{e}} : \hat{\epsilon}_{\mathrm{e}}, \tag{12}$$

where $\bar{\mu}$ stands for rigidity of a chain, and the colon denotes convolution of tensors. The strain energy of a chain that has last returned into the active state at instant $\tau < t$ is determined by Eq. (12), where $\hat{\epsilon}_{\mathrm{e}}(t)$ is replaced with $\hat{\epsilon}_{\mathrm{e}}(t) - \hat{\epsilon}_{\mathrm{e}}(\tau)$. The strain energy density (per unit volume) of individual chains in a transient polymer network is given by

$$\begin{aligned} W_1(t) \;=\; & \frac{1}{2}\bar{\mu}\Big[\int_0^\infty n(t,0,v)\,\mathrm{d}v\;\hat{\epsilon}_{\mathrm{e}}(t) : \hat{\epsilon}_{\mathrm{e}}(t) \\ & + \int_0^\infty \mathrm{d}v \int_0^t \frac{\partial n}{\partial\tau}(t,\tau,v)\Big(\hat{\epsilon}_{\mathrm{e}}(t) - \hat{\epsilon}_{\mathrm{e}}(\tau)\Big) : \Big(\hat{\epsilon}_{\mathrm{e}}(t) - \hat{\epsilon}_{\mathrm{e}}(\tau)\Big)\,\mathrm{d}\tau\Big]. \end{aligned} \tag{13}$$

The first term in Eq. (13) equals the energy of active chains that have not been rearranged within the interval $[0,t]$. The other term expresses the energy of chains that have last merged with the network at various instants $\tau \in [0,t]$ and remained active until instant t.

At the nth cycle of cyclic deformation, the energy of interaction between chains and nanofiller is described by the analog of Eq. (12)

$$W_2 = \frac{1}{2}\tilde{\mu}\Bigl(\hat{\epsilon}_{\rm p}^{(2)} : \hat{\epsilon}_{\rm p}^{(2)} - \hat{\epsilon}_{\rm p}^{(2)0} : \hat{\epsilon}_{\rm p}^{(2)0}\Bigr), \tag{14}$$

where the tensor $\hat{\epsilon}_{\rm p}^{(2)}$ describes irreversible deformation in stacks of clay platelets, $\hat{\epsilon}_{\rm p}^{(2)0}$ coincides with $\hat{\epsilon}_{\rm p}^{(2)}$ at the instant when the strain rate for macro-deformation changes its sign, and $\tilde{\mu} > 0$ accepts different values $\tilde{\mu}_1$ and $\tilde{\mu}_2$ under loading and unloading, respectively. It is worth noting that the last term in Eq. (14) does not affect constitutive equations as the strain energy is determined up to an arbitrary additive constant.

The strain energy density of the equivalent network equals the sum of strain energies of individual chains and the energy of their interaction

$$W = W_1 + W_2. \tag{15}$$

For isothermal volume-preserving deformation, the Clausius–Duhem inequality reads

$$\frac{{\rm d}Q}{{\rm d}t} = -\frac{{\rm d}W}{{\rm d}t} + \hat{\sigma}' : \frac{{\rm d}\hat{\epsilon}}{{\rm d}t} \geq 0, \tag{16}$$

where Q stands for internal dissipation per unit volume, and $\hat{\sigma}'$ denotes deviatoric part of the stress tensor $\hat{\sigma}$. Combining Eqs. (12)–(16) and using Eq. (11), we arrive at the stress–strain relation

$$\hat{\sigma}(t) = -p(t)\hat{I} + \mu\Bigl(1-\phi(t)\Bigr)\Bigl[\hat{\epsilon}_{\rm e}(t) - \int_0^\infty f(v){\rm d}v \int_0^t \Gamma(v)\exp\Bigl(-\Gamma(v)(t-\tau)\Bigr)\hat{\epsilon}_{\rm e}(\tau){\rm d}\tau\Bigr], \tag{17}$$

where $\mu = \bar{\mu}N$, p is an unknown pressure, and $\hat{I}$ stands for the unit tensor. Inequality (16) is satisfied provided that

$$\frac{{\rm d}\hat{\epsilon}_{\rm p}^{(2)}}{{\rm d}t}(t) = S\dot{\epsilon}\Bigl[\hat{\epsilon}_{\rm e}(t) - R\hat{\epsilon}_{\rm p}^{(2)}(t) - \int_0^\infty f(v)\hat{Z}(t,v){\rm d}v\Bigr], \tag{18}$$

where the coefficients $R = \tilde{\mu}/\mu$ and S adopts different (but constant) values R_1, S_1 and R_2, S_2 under loading and unloading, respectively. The function $\hat{Z}(t,v) = \int_0^t \Gamma(v)\exp[-\Gamma(v)(t-\tau)]\hat{\epsilon}_{\rm e}(\tau){\rm d}\tau$ is governed by the differential equation

$$\frac{\partial \hat{Z}}{\partial t}(t,v) = \Gamma(v)[\hat{\epsilon}_{\rm e}(t) - \hat{Z}(t,v)], \qquad \hat{Z}(0,v) = 0. \tag{19}$$

Stress–strain relation (17) together with kinematic equations (1), (2) and kinetic equations (3), (4), (18), and (19) provide constitutive equations for the viscoelastoplastic behavior of

polymer nanocomposites under cyclic deformation. These relations involve three material constants, μ, γ, Σ, and six adjustable functions, a_1, a_2, R_1, R_2, S_1, S_2, with the following meaning: (i) μ stands for an elastic modulus of a polymer nanocomposite, (ii) γ and Σ characterize its linear viscoelastic behavior, (iii) a_1 and a_2 describe irreversible deformation in the matrix under loading and unloading, (iv) R_1, S_1 and R_2, S_2 characterize plastic flow in stacks of clay platelets under active deformation and retraction.

3.5 Adjustable functions

Evolution of material functions under cyclic deformation is described by the following scenario.

The coefficients S_1 and S_2 reach their ultimate values within the first two cycles. For active loading of a virgin specimen, $S_1 = 0$, while for subsequent reloadings, $S_1 = S_{1\infty}$. Similarly, S_2 adopts some value S_{20} for the first retraction, whereas for subsequent unloadings, $S_2 = S_{2\infty}$. The entire set of these coefficients is determined by three constants: S_{20}, $S_{1\infty}$, and $S_{2\infty}$.

The coefficients a_1 and a_2 are equilibrated within first 5–6 cycles. In subsequent cycles of loading–retraction, they adopt their ultimate values $a_{1\infty} = a_{2\infty} = a_\infty$.

The coefficient R_2 is a decreasing function of intensity of plastic strain $\epsilon_{\rm p} = \left(\frac{2}{3}\hat{\epsilon}_{\rm p} : \hat{\epsilon}_{\rm p}\right)^{\frac{1}{2}}$ at instants when transition occurs from active loading to unloading ($\epsilon_{\rm p} = \epsilon_{\rm p}^{\max}$). This function obeys the differential equation

$$\frac{{\rm d}R_2}{{\rm d}\epsilon_{\rm p}^{\max}} = -A_2 R_2^2, \tag{20}$$

where A_2 is a positive coefficient.

The coefficient R_1 is split into the sum of two components

$$R_1 = r + R, \tag{21}$$

where evolution of r is induced by damage accumulation in stacks of clay platelets, and R characterizes changes in energy of inter-particle interaction driven by plastic flow.

For a stress-controlled deformation program with fixed maximum and minimum stresses, number of cycles n serves as a measure of damage accumulation. The effect of this measure on r is described by the phenomenological equation

$$r = r_0 \exp(-\alpha n), \tag{22}$$

where r_0 and α are positive constants. The decay in r with n occurs rather rapidly, which implies that r vanishes after a transition period (about 10 cycles).

A decrease in R with plastic strain is governed by the differential equation

$$\frac{{\rm d}R}{{\rm d}\epsilon_{\rm p}^{\min}} = A_1(R_\infty - R), \tag{23}$$

where A_1 and R_∞ are adjustable parameters, and $\epsilon_{\rm p}^{\rm min}$ stands for intensity of plastic strain $\epsilon_{\rm p}$ at instants when transition occurs from retraction to reloading.

After an initial transition period, the viscoelastoplastic response of a nanocomposite is determined by 10 material constants: μ, γ, Σ, A_1, A_2, a_∞, r_∞, R_∞, $S_{1\infty}$, and $S_{2\infty}$. Although this number is not small, it is substantially lower than the number of adjustable parameters in conventional constitutive models for multi-cycle loading [15, 16, 17]. An important advantage of the present approach is that the material constants are found by fitting loading and unloading paths of stress–strain diagrams step by step, which implies that not more than 3 parameters are determined by matching each set of observations.

4 FITTING OF OBSERVATIONS

Adjustable parameters in the constitutive equations are found by approximation of the experimental data in Figures 2 and 3 following the algorithm described in [14]. Each set of observations is matched separately. Material constants in the stress–strain relations are listed in Table 1.

Table 1: Adjustable parameters for polypropylene/nanoclay hybrids

Parameter	$\chi = 0$	$\chi = 1$	Parameter	$\chi = 0$	$\chi = 1$
E (GPa)	2.04	2.48	γ ($\rm s^{-1}$)	0.10	0.34
Σ	10.9	11.7	$S_{1\infty}$	4.70	14.4
S_{20}	12.9	12.7	$S_{2\infty}$	19.6	26.5
a_∞	9.13	9.56	A_1	51.5	73.0
R_∞	6.84	2.53	A_2	58.0	44.1

Figure 2 demonstrates good agreement between the observations in cyclic tests (cycles) and the results of numerical analysis (solid lines). To reveal the quality of fitting, the experimental stress–strain curves for the first two cycles and the 16th cycle are reported in Figure 4 together with results of simulation. This figure confirms that accuracy of approximation is not reduced with number of cycles.

5 DISCUSSION

To understand physical mechanisms responsible for substantial reduction in ratcheting strain due to reinforcement of polypropylene, we compare adjustable parameters listed in Table 1.

Reinforcement of polypropylene with 1 wt.% of nanoclay results in an increase in Young's modulus E by 22%, which reflects improvement of its elastic properties.

The effect of filler on viscoelastic properties appears to be of secondary importance. It is observed as a weak broadening of the relaxation spectrum (Σ grows by 7%) and an increase in the rate of rearrangement γ (by 3 times). The growth of relaxation rate

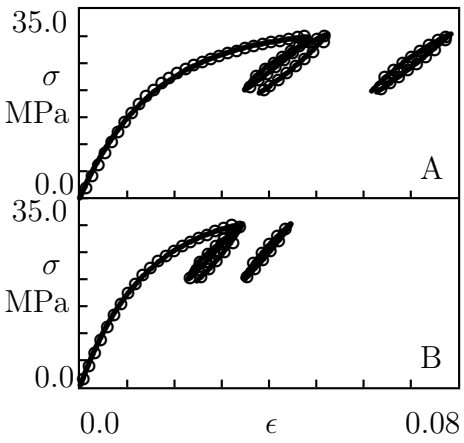

Figure 4: Stress σ versus strain ϵ. Circles: experimental data in cyclic tests (the first two cycles and the 16th cycle) with $\sigma^{\max} = 30$ MPa and $\sigma^{\min} = 20$ MPa on nanocomposites with $\chi = 0$ (A) and $\chi = 1$ (B) wt.%. Solid lines: results of numerical simulation.

does not seem dramatic, as $\log \gamma$ is conventionally employed in the Eyring or Arrhenius relations.

The equilibrium rate of viscoplastic flow in the polymer matrix a_∞ remains practically unaffected by clay content (it increases by less than 5% due to the presence of nanoclay).

Rather substantial changes are observed in coefficients $S_{1\infty}$ and $S_{2\infty}$ that reflect evolution of plastic strain tensor $\hat{\epsilon}_{\rm p}^{(2)}$ (which serves as a measure of irreversible deformations in stacks of clay platelets). Reinforcement of polypropylene with 1 wt.% of nanoclay results in an increase in $S_{1\infty}$ by 3 times and in $S_{2\infty}$ by 35%. Keeping in mind that S_1 and S_2 are proportional to rates of plastic flow under loading and unloading, respectively, one can conclude that the effect of filler is stronger at loading than at retraction.

This result is confirmed by comparison of ultimate values R_∞ of parameter R_1 (which provides a measure of energy of interaction between polymer chains and inclusions under loading). A pronounced decay in R_∞ (R_∞ at $\chi = 0$ exceeds that at $\chi = 1$ wt.% by a factor of 2.7) may reflect damage of stacks of clay platelets under cyclic deformation.

The coefficients A_1 and A_2 that describe reduction in R_1 and R_2 with plastic strain adopt similar values (A_1 at $\chi = 1$ exceeds that at $\chi = 0$ wt.% by 42%, while A_2 at $\chi = 0$ is higher than A_2 at $\chi = 1$ wt.% by 32%). However, if the decrease in R_1 and R_2 is analyzed as functions of n, the situation changes dramatically: after 16 cycles of loading–retraction, R_1 at $\chi = 0$ exceeds that at $\chi = 1$ wt.% by a factor of 3.3, whereas R_2 at $\chi = 1$ exceeds that at $\chi = 0$ wt.% by a factor of 2.5.

These estimates lead to the conclusion that strong enhancement of fatigue resistance due to reinforcement may be ascribed to (i) a substantial growth of rates of plastic flow in stacks of platelets which induces (ii) noticeable reduction in the energy of interaction between polymer chains and inclusions.

6 CONCLUDING REMARKS

Observations have been reported on polypropylene/nanoclay hybrids with various concentrations of filler in tensile cyclic tests with a stress–controlled program. Reinforcement of polypropylene with nanoclay resulted in strong (by several times) reduction in ratcheting strain. Although substantial enhancement of fatigue resistance was observed at all experimental conditions, the most pronounced improvement of mechanical properties was reached when concentration of nanoclay equaled 1 wt.% at the highest value of maximum stress $\sigma^{\max} = 30$ MPa.

A constitutive model has been developed in cyclic viscoelastoplasticity of polymer nanocomposites. With reference to the homogenization concept, a nanocomposite is treated as an equivalent polymer network with two characteristic features: (i) the plastic strain tensor is split into the sum of two components that obey different flow rules, and (ii) the strain energy density equals the sum of strain energies of individual chains and the energy of interaction between chains and stacks of clay platelets.

Stress–strain relations are derived by using the Clausius–Duhem inequality. Adjustable parameters in the constitutive equations are found by fitting the experimental data (16 cycles of loading–unloading for each set of observations). The model correctly describes the stress–strain diagrams and evolution of maximum $\epsilon^{\max}$ and minimum $\epsilon^{\min}$ strains per cycle with number of cycles n.

Comparison of material constants for polymer/clay hybrids leads to a conclusion that enhancement of fatigue resistance may be attributed to acceleration of plastic flow in clusters of nanoclay which induces noticeable reduction in the energy of interaction between polymer chains and inclusions.

Acknowledgment

Financial support by the European Commission through project Nanotough–213436 is gratefully acknowledged.

REFERENCES

[1] Tjong, S.C. Structural and mechanical properties of polymer nanocomposites. *Mater. Sci. Eng. R* (2006) **53**: 73–197.

[2] Pavlidou, S. and Papaspyrides, C.D. A review on polymer–layered silicate nanocomposites. *Progr. Polym. Sci.* (2008) **33**: 1119–1198.

[3] Jancar, J., Douglas, J.F., Starr, F.W., Kumar, S.K., Cassagnau, P., Lesser, A.J., Sternstein, S.S., and Buehler, M.J. Current issues in research on structure-property relationships in polymer nanocomposites. *Polymer* (2010) **51**: 3321–3343.

[4] Yang, J.-L., Zhang, Z., Schlarb, A.K., and Friedrich, K. On the characterization of tensile creep resistance of polyamide 66 nanocomposites. Part I. Experimental results and general discussions. *Polymer* (2006) **47**: 2791–2801.

[5] Lietz, S., Yang, J.-L., Bosch, E., Sandler, J.K.W., Zhang, Z., and Altstadt, V. Improvement of the mechanical properties and creep resistance of SBS block copolymers by nanoclay filler. *Macromol. Mater. Eng.* (2007) **292**: 23–32.

[6] Drozdov, A.D., Hog Lejre, A.-L., and Christiansen, J.deC. Viscoelasticity, viscoplasticity, and creep failure of polypropylene/clay nanocomposites. *Compos. Sci. Technol.* (2009) **69**: 2596–2603.

[7] Wang, Z.D. and Zhao, X.X. Modeling and characterization of viscoelasticity of PI/SiO_2 nanocomposite films under constant and fatigue loading. *Mater. Sci. Eng. A* (2008) **486**: 517–527.

[8] Wang, Z.D. and Zhao, X.X. Creep resistance of PI/SiO_2 hybrid thin films under constant and fatigue loading. *Composites A* (2008) **39**: 439–447.

[9] Drozdov, A.D. and Christiansen, J.deC. Cyclic viscoplasticity of high-density polyethylene: Experiments and modeling. *Comput. Mater. Sci.* (2007) **39**: 465–480.

[10] Bari, S. and Hassan, T. An advancement in cyclic plasticity modeling for multiaxial ratcheting simulation. *Int. J. Plasticity* (2002) **18**: 873–894.

[11] Xia, Z., Shen, X., and Ellyin, F. An assessment of nonlinearly viscoelastic constitutive models for cyclic loading: The effect of a general loading/unloading rule. *Mech. Time-Dependent Mater.* (2005) **9**: 281–300.

[12] Tanaka, F. and Edwards, S.F. Viscoelastic properties of physically cross-linked networks. Transient network theory. *Macromolecules* (1992) **25**: 1516–1523.

[13] Derrida, B. Random-energy model: limit of a family of disordered models. *Phys. Rev. Lett.* (1980) **45**: 79–92.

[14] Drozdov, A.D. Cyclic viscoelastoplasticity and low-cycle fatigue of polymer composites. *Int. J. Solids Struct.* (2011) **48**: 2026–2040.

[15] Chaboche, J.L. A review of some plasticity and viscoplasticity constitutive theories. *Int. J. Plasticity* (2008) **24**: 1642–1693,

[16] Kang, G. Ratchetting: Recent progresses in phenomenon observation, constitutive modeling and application. *Int. J. Fatigue* (2008) **30**: 1448–1472.

[17] Sai, K. Multi-mechanism models: Present state and future trends. *Int. J. Plasticity* (2011) **27**: 250–281.

XI International Conference on Computational Plasticity. Fundamentals and Applications
COMPLAS XI
E. Oñate, D.R.J. Owen, D. Peric and B. Suárez (Eds)

NON INTRUSIVE TECHNIQUE BASED ON DISCRETE ELEMENT APPROACH TO EXTRACT CRACK OPENING FROM 3D FINITE ELEMENT COMPUTATIONS

B. RICHARD, C. OLIVER, A. DELAPLACE AND F. RAGUENEAU

Laboratoire de Mcanique et Technologie (LMT)
ENS-Cachan/CNRS/Universit Paris 6/PRES UniverSud
61 Avenue du Prsident Wilson 94230 Cachan, France
e-mail: Benjamin.Richard@lmt.ens-cachan.fr
e-mail: Cecile.Oliver@lmt.ens-cachan.fr
e-mail: Arnaud.Delaplace@lmt.ens-cachan.fr
e-mail: Frederic.Ragueneau@lmt.ens-cachan.fr

Key words: Crack opening, discrete element, continuum damage mechanics, non-linear finite element, quasi-brittle material

Abstract. Closing the gap between damage and cracking is still nowadays an opened-question. This study aims at proposing a post-process technique to extract local information (crack openings) from continuous computations. In this paper, the approach is exposed and first results are discussed.

1 INTRODUCTION

When dealing with the behavior of plain concrete or reinforced concrete structures, the prediction of cracking remains a major issue. The effects of a crack on the durability of a structure are a major concern as long as the predictivity improvement for the numerical analysis is required. Not only the crack pattern but also crack features such as spacing, openings, rugosity or tortuosity have to be assessed at a member scale [1]. Two levels of analysis appear: the structure level and the crack level. Different approaches concerning structural modeling accounting for local nonlinear behaviors can be used to tackle the problems related to reinforced concrete structures subject to complex loading based on plasticity theories [2] or damage mechanics [3]. The use of such models needs the introduction of characteristic lengths to prevent the occurrence of spurious mesh dependency related to strain softening. Based on differential or integral nonlocal theories for example [4] or using viscosity approach [5], such characteristic lengths aim to smooth the discontinuity over a certain vicinity. The identification of the characteristic lengths is a major drawback when crack openings have to be quantified. Only a numerical post-treatment allows recovering the discontinuity features of a crack in terms of displacements jump [6].

Nevertheless, the problem remains unsolved in the case of multiple cracks as well as for composite materials such as reinforced concrete. An explicit description of a crack can be achieved using the discrete element methods [7]. The main physical mechanisms of quasi-brittle materials failure are recovered such as spatial correlation, crack tortuosity or scale effects. The mesh density needed for such modeling is nevertheless prohibitive to treat the case of industrial structures. More recent advances in numerical analysis of concrete structures have promoted the enhancement of finite element discretization by directly introducing material discontinuities in the finite element formulations. Based on shape functions finite elements kinematics enrichments [9] or nodal enhancements [10], such frameworks allow to deal with displacement jumps and singular stress fields close to the crack tip in case of strong discontinuity approach. For an industrial reinforced concrete structure such as nuclear power plant containment vessels for which hundreds of cracks may initiate and propagate, such numerical procedures would lead to excessive and prohibitive CPU time consumptions. The cyclic loadings including crack closing are also difficult to handle. The multiscale analysis introduces explicitly the two levels of interest: the structure level and the crack level. If a general agreement for employing finite element discretization at the macroscale is observed, the models employed at the local scale describing strong nonlinearities and discontinuities can be numerous. One can use refined meshing but homogeneous and continuous models [11], or introduce heterogeneities based on a continuous or a discrete approach. Such methods need coupling operators based on side-to-side modeling or overlapping domain [12]. An alternative procedure lies in the direct geographic coupling of two models based on a finite element discretization far from the zone of interest and a discrete modeling in the critical zone [13]. This kind of method needs to previously anticipate the localization of the part of the structure which will need a refine analysis with no possibility to extend the analysis without a complete remeshing. The purpose of the present study is therefore to propose a technique allowing the use of finite element models at a structural scale and a decoupled local analysis for some interesting zones for which a local information is needed. In this paper, first numerical results are shown and seem to be very encouraging for further works. In the first part, the theoretical framework of the proposed non-intrusive approach is exposed and, in a second part, numerical case studies are shown.

2 Combining finite and discrete element methods

The proposed decoupled strategy is obtained after a first analysis at macroscale, using here a finite element approach. Then, depending on the problem, a Region Of Interest (ROI) is defined, usually corresponding to the zones where the damage is developed. Note that if a sequential analysis is performed, the size of the ROI could evolve with the increasing of the loading. This ROI is then analyzed at the mesoscale, using here a discrete element approach, with the boundary conditions extracted from the macroscale computation applied on the non free surface of the ROI. The successive steps of the strategy are summarized in the following: (i) computation of the whole domain at the

macroscale, (ii) definition of the ROI to be analyzed at the mesoscale, (iii) definition of the coupling operators between both scales along the non free surface of the ROI and (iv) computation of the ROI at the mesoscale.

2.1 Definition of the Region OF Interest

The ROI that is reanalyzed at the mesoscale is a region where nonlinearities appear. In this contribution, we choose a fixed ROI (although we could have considered an evolving size of the region with respect to the evolution of the non linear region). Then, all the nonlinear domain obtained at the last step of the macroscale computation must be included in the ROI. This consideration allows avoiding any tricky coupling due to the nonlinear behavior through the ROI boundary. The boundary ∂R of the ROI is split into two parts: the free boundary ∂R_f and the boundary ∂R_u, where the boundary conditions obtained at macroscale will be applied. As soon as the ROI is defined, the coupling operators along ∂R_u between the two different scales are defined.

2.2 Coupling operators

The Dirichlet boundary conditions of the mesoscale computation are obtained from the macroscale computation, all along the non-free surfaces ∂R_u of the ROI. The natural way to transfer the displacement field from the macroscale to the mesoscale is to use the shape functions of the finite elements used at the macroscale. Then, the displacement $\bar{\mathbf{u}}_D(\mathbf{x}_D^0)$ at each nuclei $\mathbf{x}_D^0$ of the cells related to the discrete model along the ROI boundary are directly obtained with:

$$\bar{\mathbf{u}}_D(\mathbf{x}_D^0) = \sum_j \mathbf{N}_j(\mathbf{x}_D^0)\mathbf{u}_j \tag{1}$$

where $\mathbf{N}_j$ are the shape functions of the finite element model, $\mathbf{u}_j$ is the displacement vector computed at macroscale. The equilibrium of the ROI is naturally fulfilled if the same model is considered at macroscale and mesoscale. For two different models, one can obtain a slight gap from equilibrium, that should be estimated a posteriori. Next, we introduce an estimator of the gap between the continuous model and the discrete one.

2.3 Gap estimator

The advantage of this strategy, where the computation is performed twice (first at macroscale and second at mesoscale), is that an estimator of the gap between the two models is not limited to the ROI boundary but can be extended over the whole region. Then, one can distinguish the different areas where the models are more or less in agreement with each other. We propose a gap estimator based on the displacement fields obtained with the two models. As the displacement field at the mesoscale is only computed at the cells nuclei, we compute the gap estimator field at the cells nuclei, using the shape functions of the finite elements in order to compute the macroscale displacement.

The gap at the point $\mathbf{x}_D^0$ is:

$$\mathcal{E}(\mathbf{x}_D^0) = \frac{||\mathbf{u}_D(\mathbf{x}_D^0) - \sum_j \mathbf{N}_j(\mathbf{x}_D^0)\mathbf{u}_j||_2}{||\mathbf{u}_D(\mathbf{x}_D^0)||_2} \tag{2}$$

where $\mathbf{u}_D$ is the displacement field obtained at mesoscale. Note that:

$$\forall \mathbf{x}_D^0 \in \partial R_u, \qquad \mathcal{E}(\mathbf{x}_D^0) = 0$$

3 Continuum damage modeling for concrete

This section aims at giving an overview of the main features related to the concrete model used. A detailed description can be found in [14]. Formulating a constitutive model within the rigorous and consistent framework of the thermodynamically irreversible processes requires the definition of a state potential. This functional must be positive, convex and differentiable with respect to each variable. Moreover, this potential must lead to a satisfying description of the local mechanisms related to quasi-brittle materials such as the strong dissymmetry between the behaviors in tension and in compression, the inelastic strains and the unilateral effect. To split the difficulties, the cracked behavior will be assumed to be separated into two independent behaviors [15]: the hydro-static strain mechanisms and the frictional sliding. For the hydro-static strain mechanisms, only cracks opening and closing are considered. The frictional sliding is only treated on the deviatoric part of the strain and stress tensors. These considerations lead to a decomposition of the strain energy into two different parts, respectively due to the spherical and the deviatoric components. This feature is one of the key points for taking into account damage and sliding properly. A admissible state potential can be found (see [14]) and the positivity of the corresponding intrinsic dissipation can be shown (see [16]).

4 Discrete modeling

A particle-based discrete model is used for the fine crack description. With this approach, the material is described as a particle assembly. A crack is naturally obtained if a bond linking two particles breaks. A Voronoi tessellation is used, allowing an efficient and easy mesh generation. The particle nuclei are randomly generated on a grid [17] in order to control the boundary conditions. Cohesion forces can be equally represented either by springs at the interface of neighboring particles or by beams linking the nuclei of the particles. Euler-Bernoulli beams are chosen in the model used in this study. Then, four parameters have to be identified: the length ℓ_b, the cross section area A_b, the inertia I_b (or the adimensional parameter $\alpha = I_b/I_0$ where I_0 is the inertia of the equivalent circular section) and the elastic modulus E_b of the beam [18]. The first two parameters are prescribed by the mesh geometry and are different for each beam. The last two parameters are supposed equal for all beams and are identified in order to obtain the elastic properties of the material, E and ν, respectively the Young's modulus and the Poisson's ratio [19]. Note that if necessary, one can compute contact forces between unlinked particles, for

example for cyclic loading with crack opening and closing. The nonlinear behavior of the material is obtained by considering brittle behavior for the beams. The simplicity of this behavior is allowed because the model represents the material at a mesoscale, where just a simple phenomenon, a crack opening in mode I, is represented. The breaking threshold P_{ij} depends not only on the beam strain but also on the rotations of the particles (respectively i and j) linked by the beam. It is written as:

$$P_{ij}\left(\frac{\varepsilon_{ij}}{\varepsilon^{cr}}, \frac{\theta_{ij}}{\theta^{cr}}\right) > 1 \tag{3}$$

The critical strain ε^{cr} is identified by fitting the material tensile strength coming from basic mechanical tests. Then, the critical rotation θ^{cr} is identified by fitting the material compressive strength. Note that if the threshold depends only on the beam strains, the material compressive strength is overestimated by the model. With this simple beam behavior, one can obtain a reliable description of the material behavior, either for uniaxial loadings or biaxial ones [20]. Our study focuses (i) on a fine description of the crack pattern, and (ii) on the measurement of the crack opening. The crack pattern is defined as the common side of the particles initially linked by the breaking beams. The opening of the crack is computed by considering the relative displacement $(\mathbf{u}_j - \mathbf{u}_i)$ of the unlinked particles i and j. This approximation is justified by considering that the particles are rigid bodies and that the material is unloaded close to the crack lips. The measure of the opening between two particles i and j is projected on the normal $\mathbf{n}_{ij}$ of the local discontinuity, and is expressed as:

$$e_{ij} =< (\mathbf{u}_j - \mathbf{u}_i).\mathbf{n}_{ij} >_+ \tag{4}$$

where the dot stands for the scalar product.

5 Two-dimensional problem

We propose to test the proposed combining strategy on the single edge notched beam experimentally and numerically analyzed by [21, 22]. This test is particularly interesting because the loading ensures the rotation of the principal axes. Therefore, the main crack rotates with the principal directions making their propagation interesting to study. Such a crack pattern remains a major challenge for modeling assessments. We first focus on describing the finite element modeling realized. Second, the elastic response and the influence of the ROI size are analyzed and discussed. Last, we consider the crack propagation problem that requires a robust management of nonlinearities.

5.1 Finite element computation

The beam is 440 mm long, 100 mm height and 50 mm thick. A 5 mm notch is created on the top face, and a dissymmetric four-point bending test is carried out on the beam in order to ensure the rotation of the principal axes. To control the ratio between the loads,

a rigid trimmer has been modeled. A vertical displacement has been prescribed in such a way that the ratios $\frac{10}{11}$ and $\frac{1}{11}$ are ensured. The domain occupied by the concrete beam has been meshed by 394 three-node triangular elements. A coarse mesh has been chosen allowing to capture the global nonlinear phenomenon (damage field) with a reasonable computational cost. The local quantities of interest, such as stress singularities at the notch tip guiding the crack initiation and propagation, should be accounted for in the ROI using discrete modeling. The loading is controlled by displacement in order to improve the numerical robustness of the finite elements computations (in the nonlinear regime, in the following section). The concrete model used requires height material parameters: two related to the elasticity mechanism, four related to the isotropic damage mechanism and two related to the internal sliding. They have been identified with respect to the available experimental information (see [14]). They have been deduced from the experimental knowledge of the Young's modulus (40000 MPa), the compressive stress (37.5 MPa) and the tensile stress (2.70 MPa). The Poisson's ratio has been assumed to be equal to 0.2. Since the loading is purely monotonic, the material parameters related to the internal sliding mechanism do not play an important role. Therefore, no specific attention has been paid to identify them accurately. The characteristic length related to the non-local approach has been chosen equal to 5 mm, which ensures that two or three finite elements are included in the vicinity $\Omega(\mathbf{x}, l_c)$.

5.2 Elastic analysis

The proposed strategy is applied on the two following meshes. The first one is the mesh we use at the macroscale. The second one is the mesh we use at the mesoscale. 26 000 particules (78 000 dofs) are used. The meso model parameters are identified by ensuring the best force equilibrium when applying the boundary conditions computed from the macro computation. The gap estimator is shown on figure 1. The maximum is 60%, seemingly quite disappointing. The reason is obviously that a voluntary coarse mesh is used at the macroscale, that leads to a poor approximation of the displacement field at the macroscale. This effect is seen on the right hand side of figure 1, where a zoom is done around the notch, showing the 2000× amplified deformed shape of the macro- and meso-models. Local stress singularities due to cracks or notches conditioning crack initiation and propagation will be catched thanks to the meso discrete model. Using threshold on the gap estimator helps going deeper in the understanding of the numerical results. The first step is a lower thresholding at a level of 15% (figure 2-left). It is clear that the important gap is localized around the left side of the notch, where just one column of triangular elements are used. On the other hand, a upper thresholding at a level of 5% (figure 2-right) shows that the gap is lower almost everywhere on the ROI.

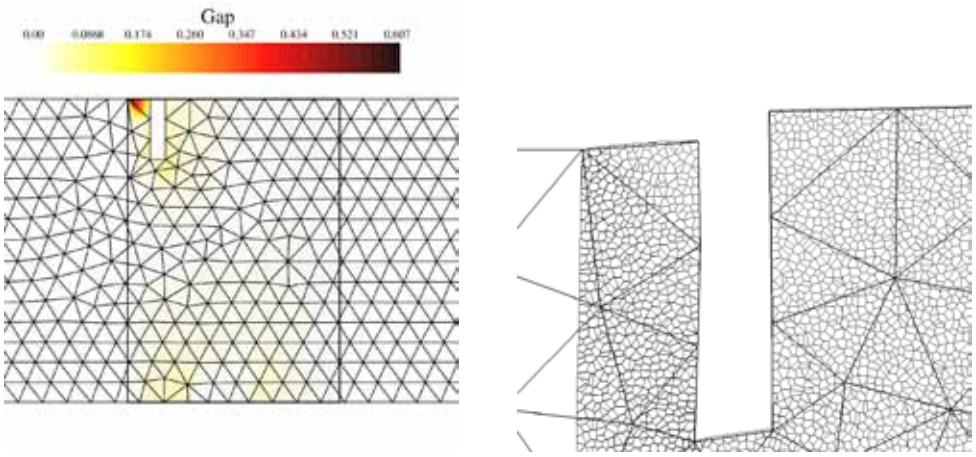

Figure 1: The gap estimator for the elastic loading on the Geers beam (left) and a zoom on the deformation (right).

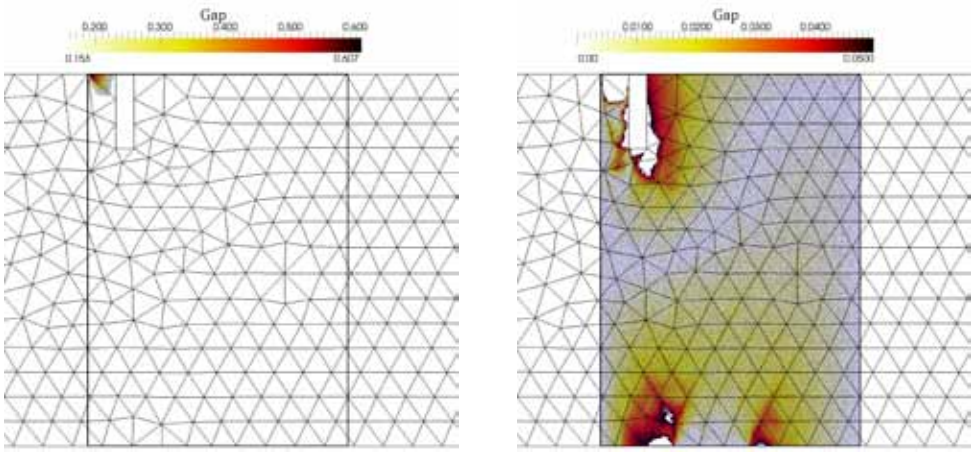

Figure 2: The gap with a lower threshold (15% left) and a upper one (5% right).

5.3 Nonlinear analysis

The nonlinear analysis is performed using the R_0-ROI. The main difference with the elastic analysis is that the macroscale resolution is now carried out by an incremental-iterative procedure, and different analyses at mesoscale should be done. An important point is that it is not necessary to perform mesoscale reanalysis for each macroscale computation step. The connectivity table between particles is initialized from the last discrete computation, and the boundary conditions are derived from the corresponding macroscale computation. For the 2D example considered in this paper, only three damage states (figure 3-top) for a total of 40 steps have been reanalyzed at mesoscale, leading to

the fine description of the cracking pattern in the center of the Geer's beam (figure 3-bottom). One can note the good agreement between the macroscale computation and the mesoscale one. As expected, it can be noticed that the mesoscale analysis obviously offers a finer description of the crack. In the final cracking pattern, one can distinguish a macrocrack starting from the notch as well as microcracks starting from the lower loading plate. It can be observed that the description of microcracking is not allowed only using macroscale analysis. Finally, the deformed configurations at the mesoscale and at the macroscale are presented in figure 4. Again a good agreement between both descriptions is obtained, but the crack opening is directly obtained only with the mesocale analysis.

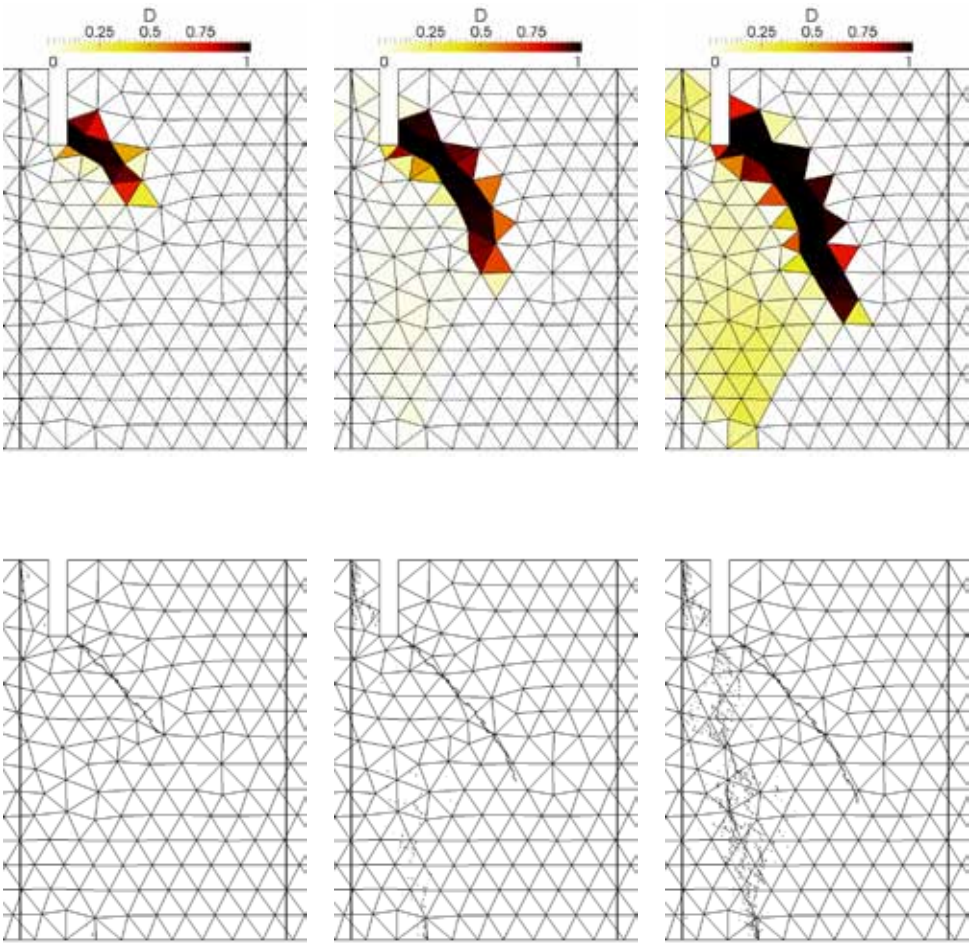

Figure 3: Damage maps and crack description obtained with discrete modeling.

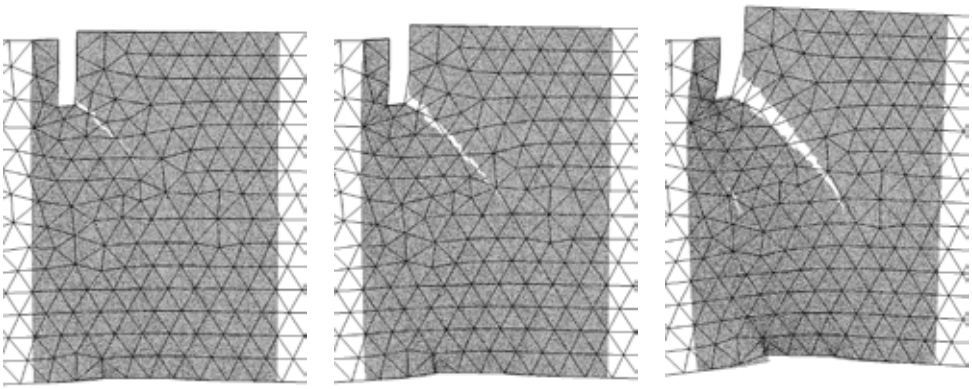

Figure 4: Deformation maps (×200).

6 Three-dimensional perpectives

We propose to apply the numerical strategy on a 3D problem. The protocol is strictly identical to the one used for the 2D problem. The only difference is that ∂R_u is now a surface compared to the line of the 2D case. We chose the PCT3D test proposed by Feist et al [23]. The feature of this test is a real 3D crack propagation, due to the asymmetry of the loading setup. The sample is a beam of 600 mm length, with a 180x180 mm square section, supported by two horizontal sleeves. A triangular notch is done in an angle of the mid section. The curves crack is obtained through an eccentric load.

Three damage states have been considered for the mesoscale reanalysis. These states are shown in figure 5 for the front face and in figure 6 in 3D, with the corresponding meso-scale results. Again, one can note the good agreement of the two analyses and the more realistic description of the crack at meso-scale. The value of the crack opening is given on the mesoscale cracking pattern (figure 6-right). Although the experimental values are not known all along the crack, one can note the satisfactory agreement of the numerical value (6.8×10^{-4} mm) with respect to the maximum experimental value (8×10^{-4} mm [23]) of the crack mouth opening displacement.

7 Conclusion

In this paper, an uncoupled numerical strategy dealing with a macroscale model and a mesoscale one is presented. The aim is to obtain a fine description of cracking (opening, length, tortuosity...) in certain regions of interest. The main concept is that a complete computation at macroscale is done, and a reanalysis at mesoscale using the boundary conditions computed at macroscale is carried out. The main features of the approach are the following: (i) the strategy is non intrusive and therefore does not require any

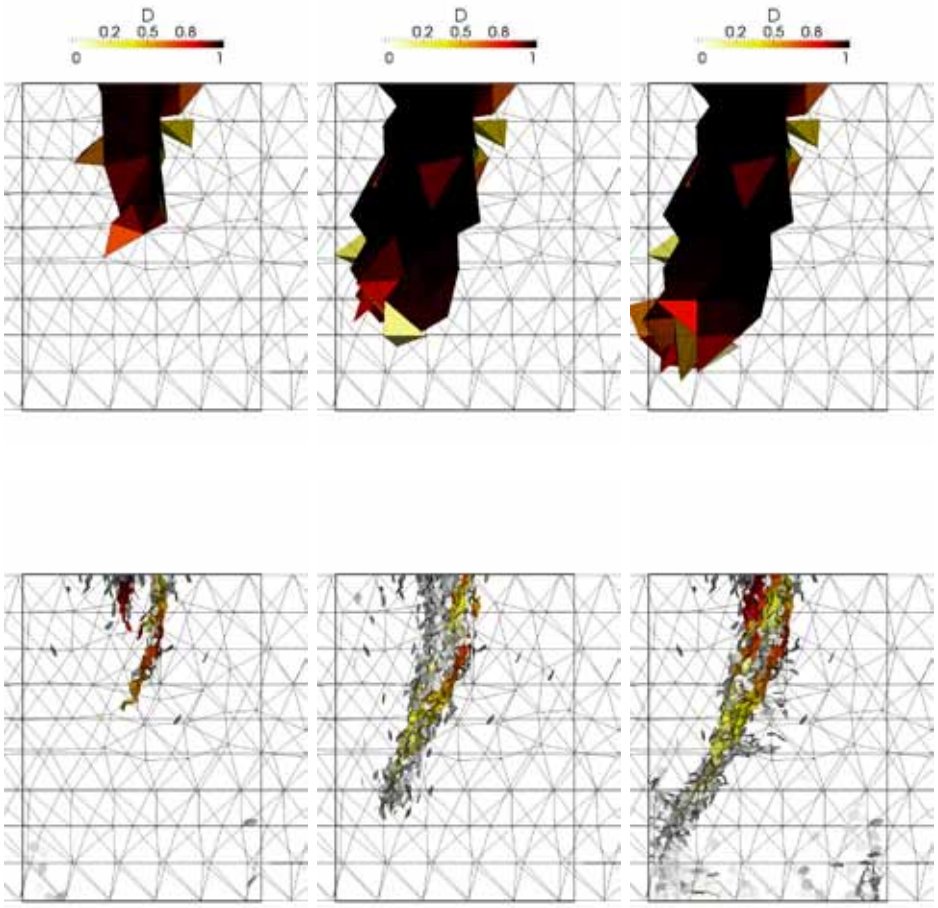

Figure 5: The damage patterns (top) obtained at macroscale and the correponding cracking pattern (bottom) obtained at mesoscale after the reanalyses.

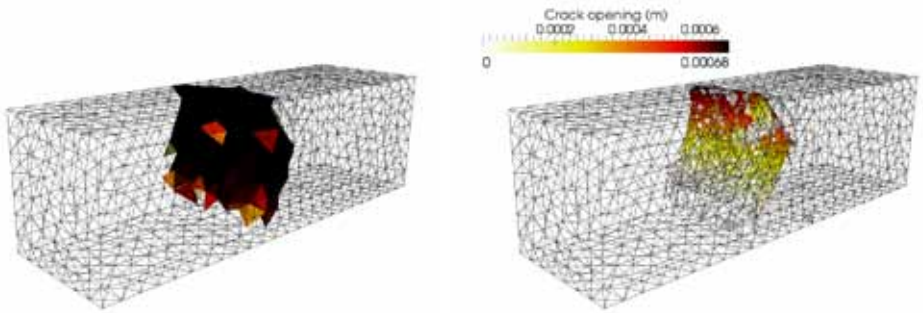

Figure 6: The 3D damage and cracking pattern obtained at the end of the loading.

modification of the computational codes, (ii) a gap estimator between both approaches can be estimated over the whole reanalyzed region and is not limited to the boundaries and (iii) because of the uncoupled resolution, the computations at the different scales can be naturally parallelized. The major drawback of the method is of course that the force equilibrium between the two levels is not verified since the a displacement based compatibility is used. Nevertheless, the different numerical results presented herein show that the obtained results are satisfactory. A further study dealing with this point is still under progress and will give quantitative results and discussions on this aspect.

REFERENCES

[1] Kozicki, J. and Tejchman, J. *Modeling of fracture processes using a novel lattice model. Granular Mat.* (2008) **10**(5):377–388.

[2] Dragon, A. and Mroz, Z. A continuum model for plastic-brittle behaviour of rock and concrete. *Int. J. Engn. Sci.* (1979) **17**:121–137.

[3] Mazars, J. Application de la mcanique de l'endommagement au comportement non linaire et la rupture du bton de structure, Universit Paris 6 (1984).

[4] Pijaudier-Cabot, G. and Bazant, Z. Nonlocal damage theory. *J. Eng. Mech. ASCE* (1987) **113**:1512–1533.

[5] Needleman, A. Material rate dependance and mesh sensitivity in localization problems. *Computer Methods in applied Mechanics and Engineering* (1988) **67**:69–85.

[6] Matallah, M. and La Borderie, C. and Maurel, O. A practical method to estimate crack openings in concrete structures. *International Journal for Numerical and Analytical Methods in Geomechanics* (2010) **34**:1615–1633.

[7] Cundall, P. A. and Strack, O. D. L. A discrete numerical model for granular assemblies. *Géotechnique* (1979) **29**:47–65.

[8] Bazant, Z.P. and Tabbara, M.R. and Kazemi, M.T. and Pijaudier-Cabot, G. Random particle model for fracture of aggregate and fibre composites. *Journal of Engineering Mechanics, ASCE* (1990) **116**(8):1686–1705.

[9] Belytschko, T. and Fish, J. and Engelman, B.E. A finite element with embedded localisation zones. *Computer Methods in applied Mechanics and Engineering* (1988) **70**:59–89.

[10] Moes, N. and Dolbow, J. and Belytschko, T. A Finite Element Method for Crack Growth Without Remeshing. *International Journal for Numerical Methods in Engineering* (1999) **46**:131–150.

[11] Feyel, F. and Chaboche, J.L. FE2 multiscale approach for modelling the elastoviscoplactic behaviour of long fibre SiC/Ti composite materials. *Computer Methods in applied Mechanics and Engineering* (2000) **183**:309–330.

[12] Gosselet, P. and Rey, C. Non-overlapping domain decomposition methods in structural mechanics. *Archives of Computational Methods in engeneering* (2006) **13**(4):515–572.

[13] Rousseau, J. and Frangin, E. and Marin, P. and Daudeville, L. Damage prediction in the vicinity of an impact on a concrete structure: a combined FEM/DEM approach. *Computers and Concrete* (2008) **5**(4):343–358.

[14] Richard, B. and Ragueneau, F. and Cremona, C. and Adelaide, L. Isotropic continuum damage mechanics for concrete under cyclic loading: stiffness recovery, inelastic strains and frictional sliding. *Engineering Fracture Mechanics* (2010) **77**:1203-1223.

[15] Pensée, V. and Kondo, D. and Dormieux, L. Micromechanical analysis of anisotropic damage in brittle materials. *J. Eng. Mech. ASCE* (2002) **128**:889–897.

[16] Adelaide, L. and Richard, B. and Ragueneau, F. and Cremona, C. Thermodynamical admissibility of a class of constitutive equation coupling elasticity, isotropic damage and internal sliding. *Comptes Rendu Mécanique* (2010) **338**:158–163.

[17] Moukarzel, C. and Herrmann, H. J. A vectorizable random lattice. *J. Stat. Phys.* (1992) **68**:911–923.

[18] Schlangen, E. and Garboczi, E. J Fracture Simulations of Concrete Using Lattice Models: Computational Aspects. *Eng. Fracture Mech.* (1997) **57**(2/3):319–332.

[19] Delaplace, A. and Desmorat, R. Discrete 3D model as complimentary numerical testing for anisotropic damage. *International Journal of Fracture* (2007) **148**:115–128.

[20] Delaplace, A. Tensile damage response from discrete element virtual testing. *Geomechanics and Geoengineering* (2009) **4**:79–89.

[21] Schlangen, E. Experimental and numerical analysis of fracture processes in concrete. *PhD thesis, Delft University of Technology, The Netherlands* (1993).

[22] Geers, M.G.D. and de Borst, F. and Peerlings, R.H.J. Damage and crack modeling in single-edge and double-edge notched concrete beams. *Engineering Fracture Mechanics* (2009) **65**(2/3):247–261.

[23] Feist, C. and Hostetter, G. Validation of 3D crack propagation in plain concrete. Part I: Experimental investigation - the PCT3D test. *Computers and Concrete* (2007) **4**(1):49–96.

XI International Conference on Computational Plasticity. Fundamentals and Applications
COMPLAS XI
E. Oñate, D.R.J. Owen, D. Peric and B. Suárez (Eds)

NUMERICAL STUDY ON INTERFACIAL DAMAGE OF SPRAYED COATINGS DUE TO THERMO-MECHANICAL FATIGUE

STEPHAN ROTH* **AND MEINHARD KUNA***

*TU Bergakademie Freiberg (TUBAF)
Institut für Mechanik und Fluiddynamik
Lampadiusstraße 4, 09596 Freiberg, Germany
e-mail: Stephan.Roth@imfd.tu-freiberg.de, http://tu-freiberg.de/fakult4/imfd/

Key words: Low Cycle Fatigue, Thermo-Mechanical Fatigue, Cohesive Zone Model, Damage Mechanics, Thermal Spraying

Abstract. In order to protect materials, thermally sprayed metallic coatings are applied to the surface of structural components operating at high temperatures and in corrosive media. The mesostructure of these coatings mainly consist of deformed flattened particles partially separated by small oxide interface layers. In this study, the FEM implementation of a representative volume element of a coating is presented focussing on the modelling of interfaces. The structure is approximated as a hardcore VORONOI mosaic, based on randomised seeds. While the particles are meshed with standard volume elements, cohesive elements are used for the interfaces. A cyclic traction-separation law is implemented to account for damage initiation and evolution under cyclic loading until failure. Compared with experimental observations, the results of the FEM computation demonstrate the applicability of the model to predict static and cyclic damage evolution as well as delamination.

1 INTRODUCTION

Flame spraying is a widely used technology to apply metallic corrosion protection coatings to components subjected to high temperature conditions. In particular, the technology of high-velocity oxy-fuel flame spraying (HVOF) allows to produce coatings with high-quality resistance properties in combination with high strength and low porosity. The main bonding mechanism of thermally sprayed coatings is mechanical locking of the initially globular particles after impact and deformation [1]. The flattened particles separated from each other by thin oxide layers form the characteristic "pan cake" structure depicted in Fig. 1 a). Experimental observation [1] shows that crack initiation and propagation occurs at the oxides when the coating is subjected to mechanical loading (s. Fig. 1 b)).

In operation, thermal and mechanical loading cause thermo-mechanical fatigue (TMF) which is amongst others a consequence of different coefficients of thermal expansion between substrate and coating. Since the fatigue life of the coating influences substrate crack initiation as well as the corrosion resistance properties, the prediction of damage and delamination is of high interest. The challenge of modelling the thermo-mechanical behaviour including TMF is to characterise both coating particles and interface properties.

a) 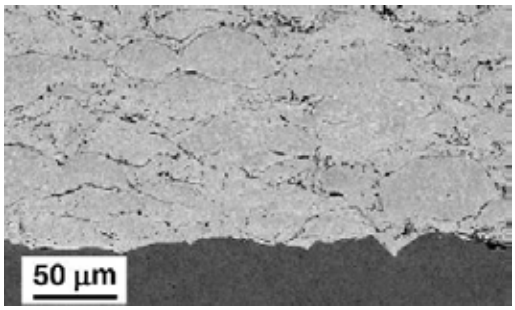

b) 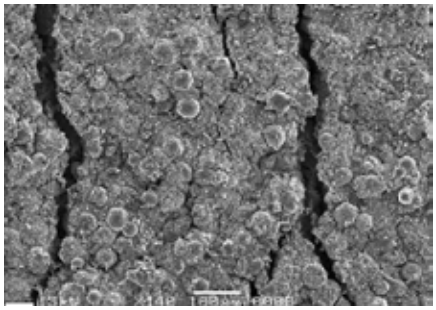

Figure 1: SEM micrographs of HVOF-sprayed INC625 coatings a) cross-section (taken from [2]); b) cracked surface after mechanical loading (taken from [1])

Throughout this study, we presume that damage initiation and evolution is restricted to the interfaces either between substrate and particles or between several particles yielding delamination and coating separation, respectively. Therefore, the theory of cohesive zones enables a capable modelling approach. Cohesive zone models allow to describe separation phenomena with the help of constitutive equations. By means of a traction-separation law (TSL), the surface tractions of an opening crack are determined as function of the separation vector and the local damage state, while the latter characterises the softening behaviour. The position of the physical crack front and thus crack propagation is associated with vanishing tractions. The formulation of the TSL which constitutes the core of a cohesive model is explained in more detail in section 3.

Cohesive zone models are denoted as monotonic if there is no distinction between unloading and reloading paths under constant amplitude cyclic loading. In contrast, cyclic cohesive zone models exhibit a pronounced hysteresis behaviour associated with energy dissipation. Recently several cyclic cohesive models [3, 4, 5, 6, 7] have been developed, based on the work of Roe and Siegmund [8, 9]. They introduce an explicit evolution equation for the internal damage variable. History effects are accounted for as well as the decrease of maximum attainable traction with ongoing cycling. The cohesive zone model presented in section 3 adopts these features.

2 GEOMETRICAL REPRESENTATION

In this study the qualitative behaviour of the interfaces in sprayed coatings is analysed through a representative volume element (RVE) comprising a substrate and a coating section. Here we focus on the finite element model of the latter, which is obtained in

three steps: (i) the geometric modelling of the sprayed particles; (ii) the generation of the finite element mesh with standard continuum elements; (iii) the modelling of the interfaces with cohesive zone elements.

Presuming that the formation of particles is well represented by a VORONOI-tessellation, a number of seeding points is distributed randomly in a cube ranging in each direction between -1 and 1 (s. Fig. 2 a)). To prevent large differences in particle size, a minimum distance between the seeding points is enforced by an additional hardcore VORONOI condition. Periodical continuation is established according to [10]. Therefore, a supercube, ranging in each direction between -3 and 3, is filled with 27 units of the previously identically seeded cubes. After the VORONOI-tessellation of the supercube has been generated using MATLAB toolboxes, the centre cube with its pairwise identical lateral faces is cut out (s. Fig. 2 b)).

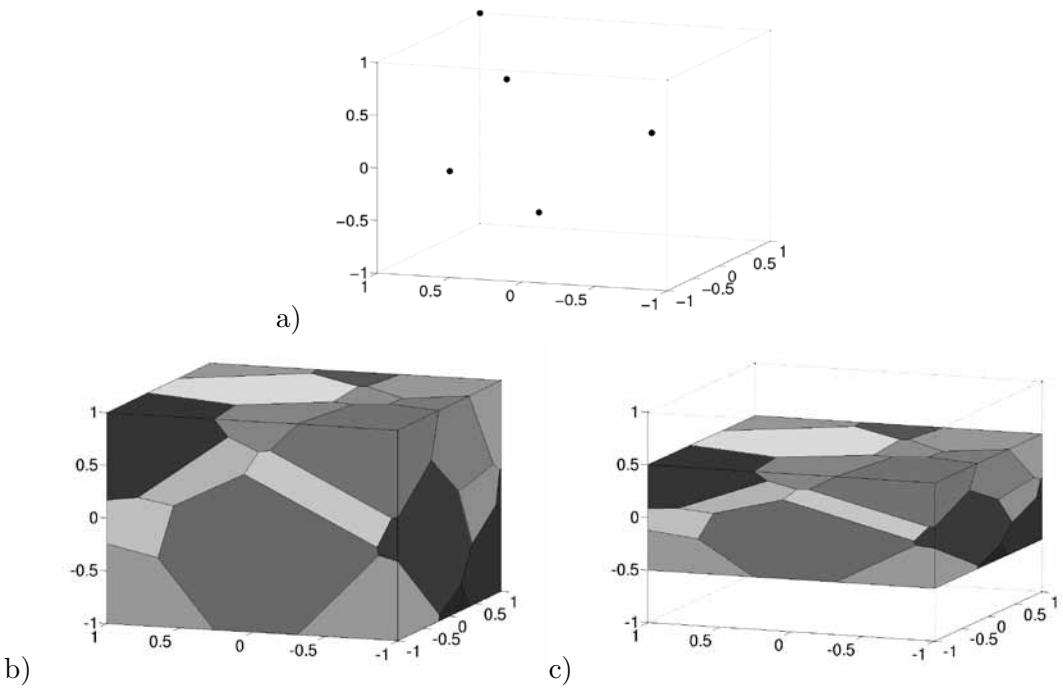

Figure 2: a) Distribution of five seeding points; b) VORONOI-tessellation; c) VORONOI-tessellation after compression with a ratio of 0.5

As stated above, thermal spraying produces coatings composed of flattened particles with a preferential direction perpendicular to the substrate surface. Unfortunately, the procedure described above does not capture this feature, since the random distribution of the seeding points is not constrained and the VORONOI-tessellation exhibits an isotropic growth rule. Instead of affecting the tessellation algorithm, here the flat shape of the particles is achieved by scaling the thickness of the tessellated cube. For this purpose, a model parameter is introduced, which describes the flatness of the particles and the

compression ratio of the former cube, respectively (s. Fig. 2 c)).

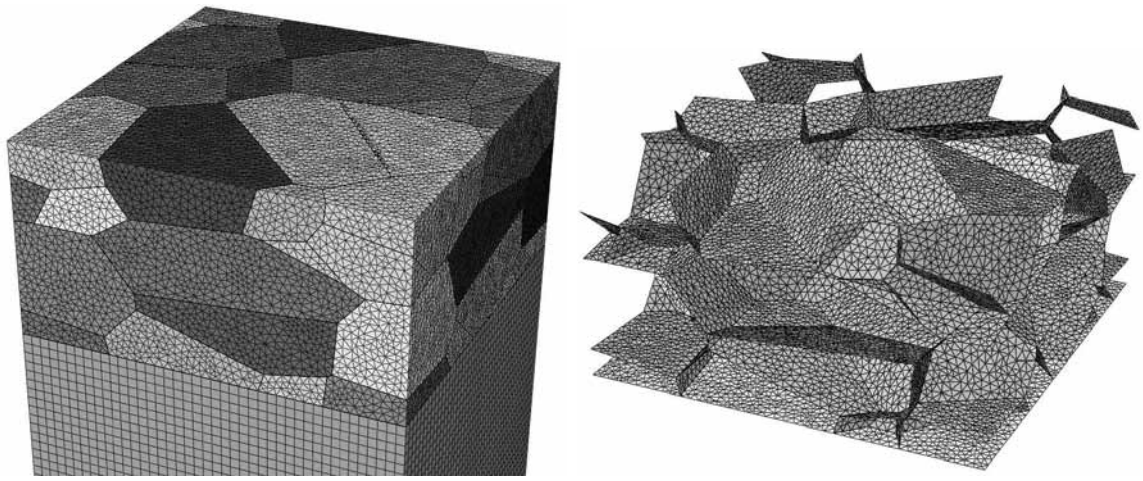

Figure 3: a) RVE; b) Honeycomb structure of the cohesive zone elements within the RVE

The finite element discretisation is performed by a bottom-up procedure with the help of the free libraries TRIANGLE [1] and TETGEN [2]. Each particle is meshed separately whereby edges and facets adjacent to each other get the same topology. Exemplarily, the finite element model of a RVE is depicted in Fig. 3 a). The interfaces between particles and between particles and substrate are meshed with cohesive zone elements (CZE). Thereby, the single particles are connected to each other. Figure 3 b) shows the resulting honeycomb structure of the cohesive zone elements within the RVE. It is worth mentioning that the CZE are of zero-thickness type. The theory of cohesive zone elements will be explained in more detail in the following section.

The modelling just presented is performed with a MATLAB-Script which organises both the geometrical description and the finite element discretisation. It requires four input parameters: (i) an averaged diameter of the initially globular particles to define the number and the minimum distance of the seeding points, (ii) the compression ratio to determine the flatness of the particles; (iii) the intrinsic length of the cohesive law which limits the characteristic element length; (iv) the order of shape functions (linear or quadratic) in both continuum and cohesive zone elements.

3 THE COHESIVE ZONE MODEL

The simulation of fracture processes with the help of cohesive zone models relies on the hypotheses that damage evolution and progressive separation is limited to a distinct internal surface called cohesive zone. Cracks are constrained to propagate within this zone,

[1] http://www.cs.cmu.edu/~quake/triangle.html
[2] http://tetgen.berlios.de/index.html

while in the surrounding bulk material undamaged deformation is postulated to occur. In this context fracture or delamination are the result of a continuous damage evolution towards physical separation. The corresponding constitutive law relates the traction vector, t_i, to the separation vector, δ_j, also known as displacement jump vector. Considering the principle of virtual work, the cohesive zone contributes $\delta W^{\mathrm{c}} = \int_{A^{\mathrm{c}}} t_i \, \delta\delta_i \mathrm{d}A^{\mathrm{c}}$ to the internal work. Following the formulation given by [11] within the framework of finite elements, cohesive zone elements are implemented as ABAQUS UEL subroutine.

3.1 Monotonic cohesive zone model

The key element of a cohesive zone model is the traction-separation law (TSL). It relates the normalized effective traction τ to the normalized effective separation λ,

$$\tau = \sqrt{t_{\mathrm{n}}^2 + t_{\mathrm{r}}^2 + t_{\mathrm{s}}^2}/t_0 \tag{1}$$

$$\lambda = \sqrt{\langle\delta_{\mathrm{n}}\rangle^2 + \delta_{\mathrm{r}}^2 + \delta_{\mathrm{s}}^2}/\delta_0 \quad , \tag{2}$$

whereby the indices n, r, and s denote the normal and the two tangential directions, respectively. By using the MacAulay brackets, $\langle x\rangle = \frac{1}{2}(x + |x|)$, any contribution to separation is prevented in pure compression mode.

Under monotonic displacement driven loading, the TSL describes a specific traction-separation curve (TSC). The TSC consists of a monotonically increasing branch followed by a monotonically decreasing one. The critical point at maximum is characterised by the intrinsic model parameters cohesive strength, t_0, and critical length, δ_0. Loading above δ_0 results in initiation and evolution of irreversible damage. In the softening zone the stiffness of the TSC decreases with increasing damage until the traction vanishes which goes along with physical separation and advancing failure. Therefore, this branch of the TSC is called "damage locus". It forms an envelope of all admissible states. The damage state at the damage locus is characterised by a damage variable D ranging between zero at the apex of the TSC and one for infinite separation. The integral of the TSC equals the specific fracture energy per unit area [12].

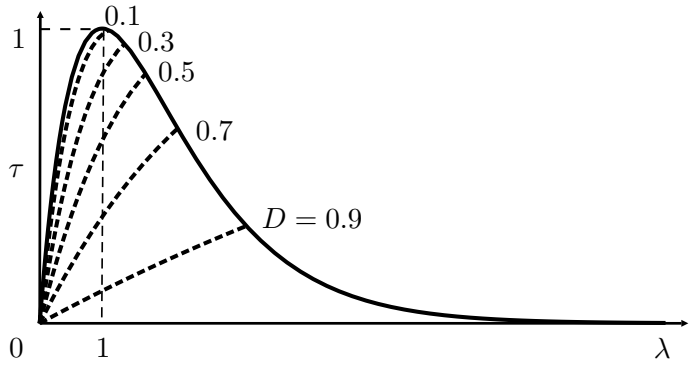

Figure 4: Monotonic TSL: damage locus (solid) and unloading paths for different damage states (dashed)

Usually, unloading is assumed to occur towards the origin of the TSC with unchanged damage [13, 8, 6]. In contrast, here a weak non-linearity is admitted to reconcile the unloading curve at zero damage and the first branch of the TSC, since below the critical point reversible material behaviour is postulated. With ongoing damage evolution the non-linearity is supposed to vanish (s. Fig. 4).

Throughout this paper we restrict to an exponential form of the TSC depicted in Fig. 4. This approach was firstly proposed by NEEDLEMAN and is well establish in the literature. Motivated by interatomic potentials [14, 8, 6, 15, 16], a cohesive zone potential function,

$$\Gamma(\lambda, D) = \frac{t_0 \delta_0}{F(D)} \left[\mathrm{e} - [1 + \lambda F(D)] \, \mathrm{e}^{1-\lambda F(D)} \right] \tag{3}$$

is assumed depending on the effective normalized separation and the damage variable D. Inside Γ, the damage variable is embedded in a function, F, comprising all effects of the non-linear unloading,

$$F(D) = \frac{\mathrm{W}((1-D)(\ln(1-D)-1)\mathrm{e}^{-1})}{\ln(1-D)-1} \quad , \tag{4}$$

wherein the LAMBERT W function implicitly defined by $\mathrm{W}(x)\mathrm{e}^{\mathrm{W}(x)} = x$ is used. It can easily be determined numerically using the iterative NEWTON algorithm ($\mathrm{w} = \mathrm{W}(x)$, iteration number i, EULER's number e),

$$\mathrm{w}_{(\mathrm{i}+1)} = \mathrm{w}_{(\mathrm{i})} - \frac{\mathrm{w}_{(\mathrm{i})} \, \mathrm{e}^{\mathrm{w}_{(\mathrm{i})}} - x}{\mathrm{e}^{\mathrm{w}_{(\mathrm{i})}} (1 + \mathrm{w}_{(\mathrm{i})})} \quad . \tag{5}$$

According to [8, 6], the components of the traction vector are obtained by taking the derivative of Γ with respect to the components of the separation vector,

$$t_\mathrm{n} = \frac{\partial \Gamma}{\partial \delta_\mathrm{n}} = \frac{t_0}{\delta_0} \langle \delta_\mathrm{n} \rangle F \mathrm{e}^{1-\lambda F} \, , \quad t_\mathrm{r} = \frac{\partial \Gamma}{\partial \delta_\mathrm{r}} = \frac{t_0}{\delta_0} \delta_\mathrm{r} F \mathrm{e}^{1-\lambda F} \, , \quad t_\mathrm{s} = \frac{\partial \Gamma}{\partial \delta_\mathrm{s}} = \frac{t_0}{\delta_0} \delta_\mathrm{s} F \mathrm{e}^{1-\lambda F} \quad . \tag{6}$$

Consequently, the normalized effective traction (1) and thus the TSL are found as

$$\tau = \lambda F \mathrm{e}^{1-\lambda F} \quad . \tag{7}$$

It is worth noting that the somewhat complicated looking function $F(D)$ does not cause any (numerical) problems when deriving the tangent stiffness for finite element analysis. To complete the monotonic cohesive model, the relation between damage variable and maximum effective separation, λ_max, has to be given,

$$D = \begin{cases} 0 & , \forall \ \lambda_\mathrm{max} \leq 1 \\ 1 - \mathrm{e}^{1-\lambda_\mathrm{max}} & , \forall \ \lambda_\mathrm{max} > 1 \end{cases} = 1 - \mathrm{e}^{-\langle \lambda_\mathrm{max} - 1 \rangle} \tag{8}$$

incorporating reversible and damaged states. Moreover, compressive loading has to be considered. Here we assume that there is no frictional sliding. A simple contact model

prevents interpenetration by magnifying the contact forces and stiffnesses with a high penalty factor.

Figure 4 illustrates the loading and unloading behaviour of the monotonic TSL. It is seen that the non-linearity of the unloading paths decreases with increasing damage. Furthermore, considering cyclic loading with constant amplitude it is clear that this model cannot predict fatigue crack growth, since damage accumulation arrests after the first cycle. A capable extension of the model to allow damage accumulation even beyond the damage locus is proposed in the following.

3.2 Cyclic cohesive zone model

In order to extend the monotonic cohesive model by cyclic damage accumulation, (8) is replaced by an evolution law. The proposed power law approach, formulated again in terms of effective cohesive zone quantities,

$$\dot{D} = (1 - D) \left(\frac{\lambda}{1 - \ln (1 - D)} \right)^r \langle \dot{\lambda} \rangle \tag{9}$$

incorporates the following assumptions and characteristics:

- Thermodynamics requirements $\dot{D} \geq 0$.
- Damage accumulation is restricted to the (re)loading portion of a load cycle.
- The damage locus remains an envelope of all admissible states. It forms a limit for each loading path.
- The maximum attainable effective traction decreases as the damage increases.

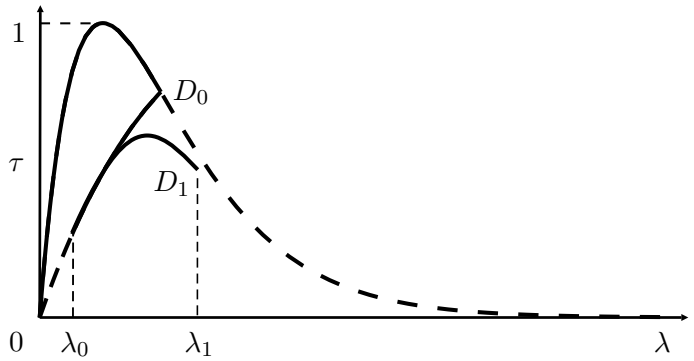

Figure 5: Cyclic TSL: unloading with $\dot{D} = 0$, $D = D_0 = \text{const.}$ and reloading with $\dot{D} > 0$

The evolution equation described above allows to get a solution in closed form for a displacement driven reloading stage starting at $D = D_0$ and $\lambda = \lambda_0$ after unloading

with $D = D_0 = \text{const.}$ (s. Fig. 5). The resulting damage, D_1, at an arbitrary effective separation, λ_1, reads as follows

$$D(\lambda_1) = D_1 = 1 - \exp\left(1 - \sqrt[r+1]{\lambda_1^{r+1} + [1 - \ln(1 - D_0)]^{r+1} - \lambda_0^{r+1}}\right) \quad . \tag{10}$$

A smooth transition from the cyclic to the monotonic CZE is realised by introducing an endurance limit, which is the maximum effective traction for an infinite number of cycles,

$$\tau_\mathrm{e} = (1 - D)^\alpha [1 - \ln(1 - D)] \quad . \tag{11}$$

Obviously, for an undamaged state the endurance limit equals the maximum effective cohesive strength again indicating the reversible portion of the TSC. In contrast, for D approaching one the endurance limit vanishes. In order to achieve a compact evolution equation, the endurance limit is converted into an endurance separation with the help of (7),

$$\lambda_\mathrm{e} = -\frac{1}{F(D)} \mathrm{W}((1 - D)^\alpha (\ln(1 - D) - 1)\mathrm{e}^{-1}) \quad . \tag{12}$$

For $\alpha = 1$ the model reduces to the monotonic TSL. The complete evolution equation augmented by the endurance limit becomes

$$\dot{D} = (1 - D)\left(\frac{\lambda}{1 - \ln(1 - D)}\right)^r \left\langle \dot{\lambda}\, \mathrm{sign}\,(\lambda - \lambda_\mathrm{e}(D))\right\rangle \quad . \tag{13}$$

Besides the loading direction, now the comparison between current effective separation and endurance separation, referring to the current damage state, decides about the occurrence of further damage evolution. Effective separations below λ_e enforce $\dot{D} = 0$. The analytical solution (10) is applicable when replacing λ_0 by λ_e for $\lambda_0 < \lambda_\mathrm{e}$.

4 APPLICATION TO THERMO-MECHANICAL FATIGUE

In the following, the capability of the cyclic cohesive model to predict thermo-mechanical fatigue of sprayed coatings is considered. For simplicity, both substrate and particles are assumed to be of linear elastic materials. Damage is restricted to the cohesive zones according to the cohesive model presented in section 3. For the purpose of qualitative analyses, the computations are limited to one set of parameters, shown in Table 1. For the material parameters of substrate and particles, the elastic properties of steel and the NI-base alloy INC625 are assumed. The cohesive parameters are not available. Estimated values are chosen in this way that there is a pronounced damage evolution even in the first few cycles of a TMF analysis. The amount of damage growth during one cycle mainly depends on the exponent r which is set here to a very low value, $r = 2$. By setting $\alpha = 50$, it is assumed that there is almost no endurance limit once the material is damaged. This reduces cyclic damage arrest.

Table 1: Parameters of the linear-elastic materials (substrate and coating particles) and cohesive law

substrate	particles	interface
$E_\mathrm{S} = 210\,\mathrm{GPa}$	$E_\mathrm{P} = 180\,\mathrm{GPa}$	$t_0 = 50\,\mathrm{MPa}$
$\nu_\mathrm{S} = 0.3$	$\nu_\mathrm{P} = 0.3$	$\delta_0 = 1 \cdot 10^{-4}\,\mathrm{mm}$
$\alpha_\mathrm{S}^\mathrm{th} = 12 \cdot 10^{-6}\,\mathrm{K}^{-1}$	$\alpha_\mathrm{P}^\mathrm{th} = 13 \cdot 10^{-6}\,\mathrm{K}^{-1}$	$r = 2$
		$\alpha = 50$

In order to account for the periodic continuation of the RVE, the normal displacement components with respect to the lateral faces are coupled between coating and substrate (s. Fig. 6). A coupling of the in-plane displacement components at corresponding lateral faces is not implemented so far.

For cyclic loading, the model is subjected to a homogeneous oscillating temperature load with constant amplitude of 400 K. Due to the slight misfit of the thermal expansion coefficients and the Young's moduli, cohesive zones develop depending on the specific interface density and orientation. The distribution of the damage variable is depicted in Fig. 7 after various cycles. After two cycles, damage initiation is observable at distinct positions. With ongoing cycling, these damaged areas increase, while the damage level evolves towards one. This indicates that in this areas physical interface debonding happens. Figures 7 d) and f) show crack branching and coalescence of the cracks with progressing cycling. In summary, it can be stated that these numerical results match the experimental observations qualitatively very well (compare Fig. 1 b)).

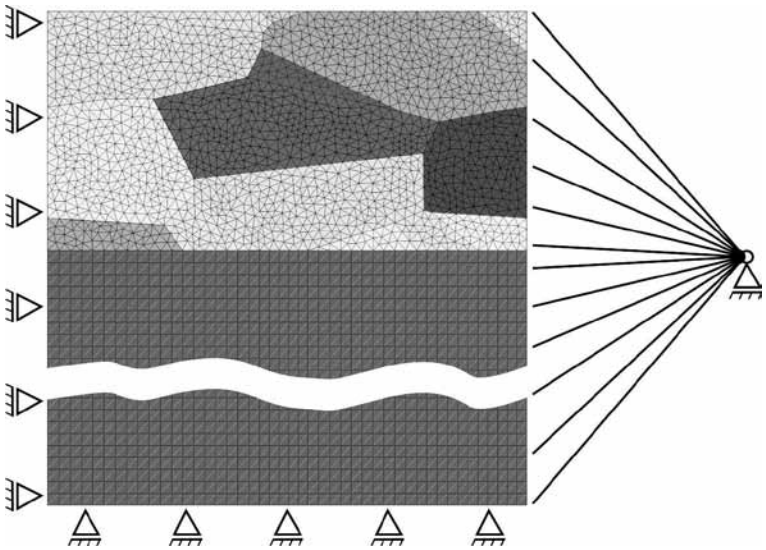

Figure 6: Finite element model of the RVE with boundary conditions

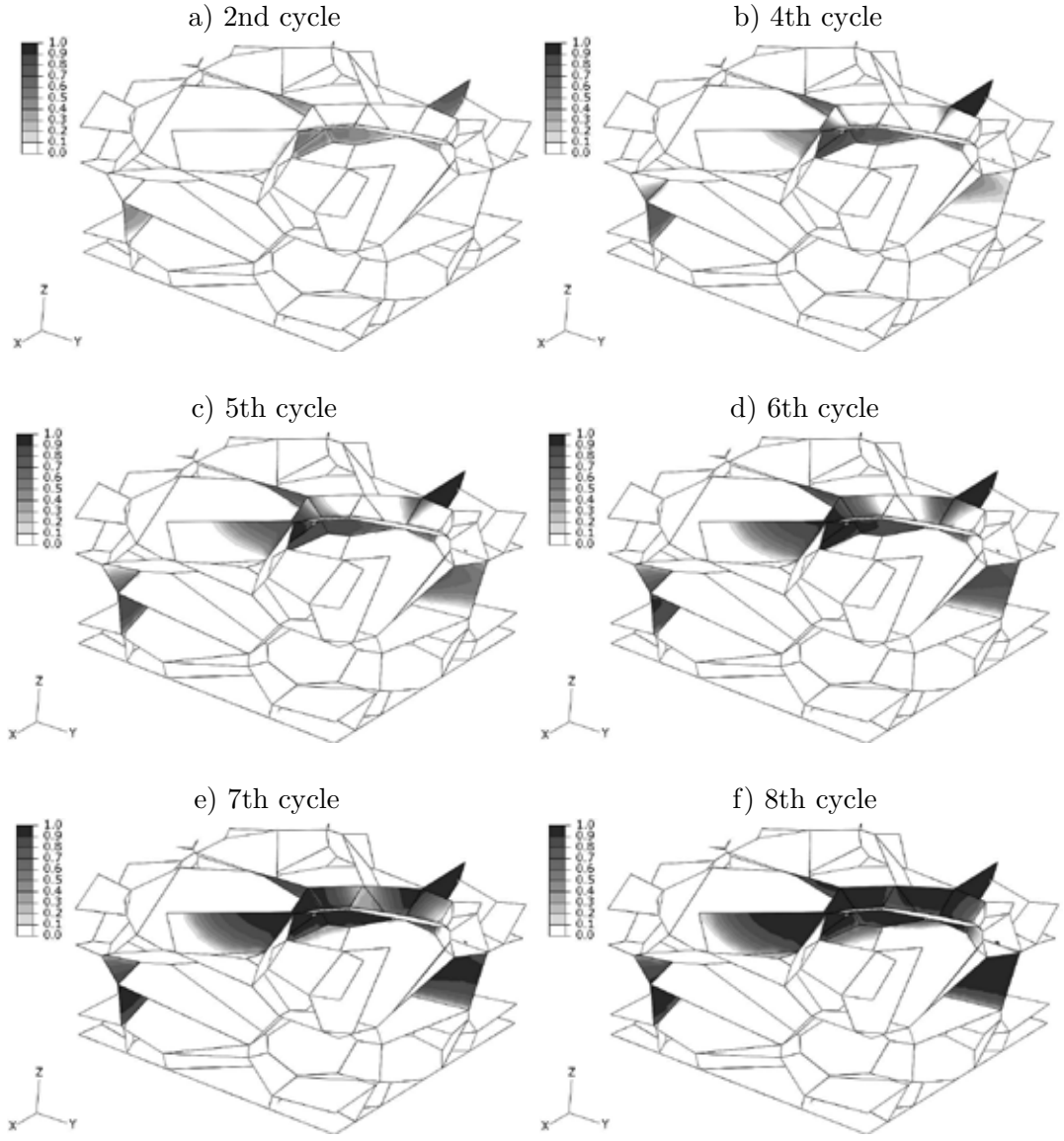

Figure 7: Damage distribution at the cohesive zone of the RVE under cyclic thermal loading

5 SUMMARY AND CONCLUSIONS

In this feasibility study, we investigate the use of a cyclic cohesive model to predict initiation and evolution of fracture and delamination of sprayed coatings in the framework of finite element analyses. The specific mesostructure of sprayed coatings is regarded at the geometric modelling. Coating particles are represented by a randomly seeded VORONOI-tessellation. Cohesive zone elements are used at the interfaces between coating and substrate and between the coating particles, since damage initiation and evolution are presumed to occur there. A cyclic cohesive model with four material parameters is presented featuring an exponential damage locus and slight non-linear unloading. The numerical simulations of a thermo-mechanical fatigue test demonstrate that this modelling including a combination of geometrical issues and interfacial properties is able to reproduce experimental observations.

Since throughout this qualitative study the cohesive parameters have been estimated, future work has to be done concerning their identification. This implies a deeper investigation of the intrinsic length scales of the model.

ACKNOWLEDGEMENT

This work was performed within the Cluster of Excellence "Structure Design of Novel High-Performance Materials via Atomic Design and Defect Engineering (ADDE)" that is financially supported by the European Union (European regional development fund) and by the Ministry of Science and Art of Saxony (SMWK).

REFERENCES

[1] Yilbas, B., Arif, A. and Gondal, M. Hvof coating and laser treatment: Three-point bending tests. *Journal of Materials Processing Technology* (2005) **164-165**:954–957.

[2] Bolelli, G., Lusvarghi, L. and Giovanardi, R. A comparison between the corrosion resistances of some hvof-sprayed metal alloy coatings. *Surface and Coatings Technology* (2008) **202**(19):4793–4809.

[3] Abdul-Baqi, A., Schreurs, P. and Geers, M. Fatigue damage modeling in solder interconnects using a cohesive zone approach. *International Journal of Solids and Structures* (2005) **42**(3-4):927–942.

[4] Geers, M., Ubachs, R., Erinc, M., Matin, M., Schreurs, P. and Vellinga, W. Multiscale analysis of microstructural evolution and degradation in solder alloys. *International Journal for Multiscale Computational Engineering* (2007) **5**(2):93–103.

[5] Xu, Y. and Yuan, H. On damage accumulations in the cyclic cohesive zone model for xfem analysis of mixed-mode fatigue crack growth. *Computational Materials Science* (2009) **46**(3):579–585.

[6] Bouvard, J., Chaboche, J., Feyel, F. and Gallerneau, F. A cohesive zone model for fatigue and creep-fatigue crack growth in single crystal superalloys. *International Journal of Fatigue* (2009) **31**(5):868–879.

[7] Liu, J., Yuan, H. and Liao, R. Prediction of fatigue crack growth and residual stress relaxations in shot-peened material. *Materials Science and Engineering: A* (2010) **527**(21-22):5962–5968.

[8] Roe, K. and Siegmund, T. An irreversible cohesive zone model for interface fatigue crack growth simulation. *Engineering Fracture Mechanics* (2003) **70**(2):209–232.

[9] Siegmund, T. A numerical study of transient fatigue crack growth by use of an irreversible cohesive zone model. *International Journal of Fatigue* (2004) **26**(9):929–939.

[10] Fritzen, F., Böhlke, T. and Schnack, E. Periodic three-dimensional mesh generation for crystalline aggregates based on voronoi tessellations. *Computational Mechanics* (2009) **43**(5):701–713.

[11] Geißler, G. *The Cohesive Crack Tip Model within the Finite Element Method Implementations, Enhancements, Applications*. Ph.D. thesis, Technische Universität Dresden, Inst. für Statik und Dynamik der Tragwerke (2009).

[12] Harper, P.W. and Hallett, S.R. A fatigue degradation law for cohesive interface elements - development and application to composite materials. *International Journal of Fatigue* (2010) **32**(11):1774–1787.

[13] Nguyen, O., Repetto, E., Ortiz, M. and Radovitzky, R. A cohesive model of fatigue crack growth. *International Journal of Fracture* (2001) **110**(4):351–369.

[14] Needleman, A. An analysis of decohesion along an imperfect interface. *International Journal of Fracture* (1990) **42**:21–40.

[15] Goyal, V.K., Johnson, E.R. and Davila, C.G. Irreversible constitutive law for modeling the delamination process using interfacial surface discontinuities. *Composite Structures* (2004) **65**(3-4):289–305.

[16] Krull, H. and Yuan, H. Suggestions to the cohesive traction-separation law from atomistic simulations. *Engineering Fracture Mechanics* (2011) **78**(3):525–533.

XI International Conference on Computational Plasticity. Fundamentals and Applications
COMPLAS XI
E. Oñate, D.R.J. Owen, D. Peric and B. Suárez (Eds)

PLASTIC DEFORMATION OF HETEROGENEOUS MATERIALS: NUMERICAL SIMULATION STUDY

R.M. BRANCO, P.A. PRATES, M.C. OLIVEIRA, N.A. SAKHAROVA AND J.V. FERNANDES

CEMUC – Department of Mechanical Engineering, University of Coimbra,
Rua Luís Reis Santos
Pinhal de Marrocos, 3030-788 Coimbra, Portugal
email: {pedro.prates, marta.oliveira, nataliya.sakharova, valdemar.fernandes}@dem.uc.pt
https://cemuc.dem.uc.pt/cemuc/

Keywords: Plastic Deformation, Heterogeneous material, Numerical Simulation

Abstract. A methodology for determining the local stress-strain curves of heterogeneous specimens is proposed. This methodology resorts to the same type of variables usually obtained in the experimental tensile test with the aid of the digital image correlation technique. This approach was successfully tested for heterogeneous specimens composed by several materials with dissimilar plastic properties.

1 INTRODUCTION

Describing the plastic deformation behaviour of heterogeneous materials is important for various applications where mismatch of material properties is involved, such as welding joints [1, 2], where the local variation in material properties has an impact on the overall mechanical response of the welded joints.

In order to experimentally analyse the material response of heterogeneous samples, the digital image correlation (DIC) technique can be used for measuring the local material properties dissimilarities along the sample [4]. In recent years, several investigations have been performed on the application of the DIC technique to characterize the local mechanical behaviour in heterogeneous materials [2 - 4].

The analysis of the DIC experimental results can be difficult and questionable, especially when the objective is to determine the local tensile stress-strain curve of the material. In this context, the finite element method is a very interesting tool to study this theme because it provides detailed data for a suitable description of the local mechanical behaviour which allows the development of approaches for its local characterization, including error estimation.

The aim of this work is to study the mechanical behaviour of heterogeneous samples under uniaxial tensile test conditions, resorting to finite element analysis.

2 NUMERICAL SIMULATION AND MATERIALS

The three-dimensional numerical simulation in-house code, DD3IMP, was used .This code has been specifically developed to simulate sheet metal forming processes [5]. The model adopted considers only one eighth part of the 1 mm thick sheet tensile specimen due to

geometrical and material symmetries, as shown in Fig 1a. Five regions, accountable for different mechanical behaviours, were pre-defined in the sample with the respective boundaries distant from its centre 2, 4, 6 and 8mm (see Fig. 1a). Such configuration allows considering a sample with up to five different mechanical behaviours. In the present study, only two regions with different stress-strain curves were considered, and the results were analysed in the points (nodes) distant 0, 2, 4, 6, 8 and 18 mm from the centre of the specimen (in the next figures designated by: N 0mm, N 2mm, N 4mm, N 6mm, N 8mm and N 18mm, respectively), as it is shown on Fig. 1a. The tensile sample was discretized with 3D 8-node elements with an average in-plane size of 0.5 mm. The finite element mesh used in the numerical simulations was composed of 20 elements along Oy axis and 8 elements along Ox axis for each of the four zones A, B, C and D. The finite element mesh between the beginning of zone D and the end of the specimen was composed of 20 elements along Oy axis and 58 elements along Ox axis. The specimen has two elements in half thickness. The finite element mesh considered for the tensile specimen is shown on Fig. 1b.

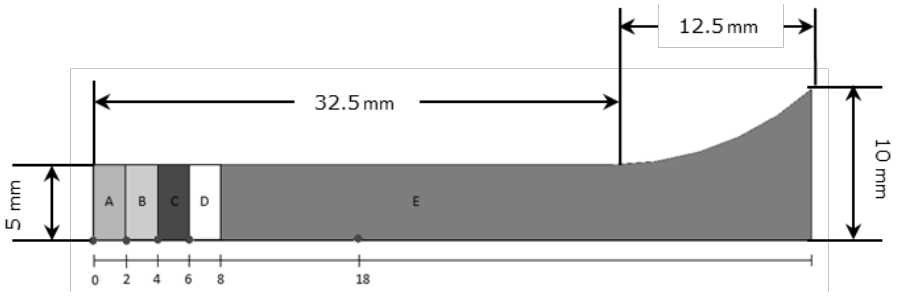

(a)

(b)

Fig.1. (a) Tensile specimen model with five possible regions accountable for different mechanical properties; the points considered in the results analysis are identified; (b) finite element mesh of the specimen.

The plastic behaviour of the material is described by the von Mises isotropic yield criterion and the flow stress in tension described by the Swift equation: $\bar{\sigma} = K(\varepsilon_0 + \bar{\varepsilon}_p)^n$, where $\bar{\sigma}$ and $\bar{\varepsilon}_p$ are the equivalent stress and plastic strain, respectively, and K , ε_0 and n (work-hardening coefficient) are constants for a particular material. After the Swift equation, the yield stress value is: $\sigma_0 = K\varepsilon_0{}^n$; the constant ε_0 was considered equal to 0.005, for all simulations.

The mechanical properties of the materials composing the specimen are shown in Table 1, highlighting the change of only the yield stress, σ_0, value. M1 is the material used for the central region and materials M2, M3, M4, M5 and M6 are used alternatively for the exterior

region of the specimen. Specimens with different central region size, equal to 2, 4, 6 and 8 mm, were considered in numerical simulations. The elastic behaviour is assumed as isotropic and it is described by the Young modulus E and the Poisson coefficient ν.

Table 1: Mechanical properties of the heterogeneous samples analysed.

Materials	σ_0 (MPa)	n	E (GPa)	ν
M1	100	0.25	72	0.33
M2	150			
M3	200			
M4	250			
M5	300			
M6	350			

3 RESULTS AND DISCUSSION

3.1 Methodology for Determination of Local Stress-Strain Curves

The methodology for determining the local stress-strain curves consists of using the values of longitudinal deformation ε_1 (deformation in the axis direction of the specimen), in each node and their evolution during deformation, as a function of the applied force. In these conditions, it is possible to retrieve the value of the area of the cross section of the sample in each point and to determine the respective value of the normal true stress, σ_1, according to the following equations:

$$A = \frac{A_0}{e^{\varepsilon_1}} \tag{1}$$

$$\sigma_1 = \frac{F}{A} \tag{2}$$

where A_0 is initial area of the cross section of the specimen; A and F are the area and the applied load on the cross section of the specimen, at each moment of the deformation. The variable ε_1 can be experimentally obtained and correlated with F, using DIC results.

The methodology was tested numerically on a homogeneous specimen, i.e. composed by a unique material [6]. The local stress-strain curves obtained in different points of the specimen, using the proposed methodology, follows the local input curves described by the Swift law.

3.2 Local Stress-Strain Curves: Influence of the Size of the Central Region

Fig. 2 shows examples of the evolution of the load as a function of the displacement during the numerical simulation of the tensile test, with different central region sizes, equal to 2, 4, 6 and 8 mm, for the case of the heterogeneous specimens considering the combination of materials M1-M3. The value of the maximum load decreases and the corresponding displacement value increases for increasing lengths values of the central region.

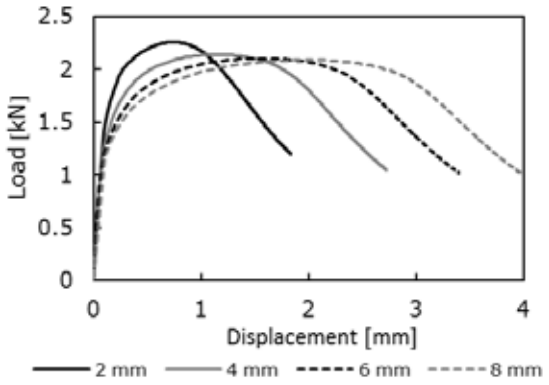

Fig. 2. Load *vs.*displacement evolution for heterogeneous specimens considering the combination M1-M3 with different central region sizes, equal to 2, 4, 6 and 8 mm.

First of all, the strain paths and their evolution during plastic deformation of the heterogeneous specimens with different length of the central region were analysed. For this, the ratio $\varepsilon_2/\varepsilon_1$ between transverse deformation, ε_2, and deformation along the axis of the specimen, ε_1, as a function of ε_1 was plotted, as shown in the examples of Fig. 3, for two specimens considering the M1-M3 materials combination. After the initial part of the curves, not all of the strain paths tend to plastic deformation in pure tension ($\varepsilon_2/\varepsilon_1$= -0.5). This is due to the fact that the heterogeneity of the plastic properties introduces constraints, which alter the strain path. In fact, these constraints cause the strain paths to tend to values of $\varepsilon_2/\varepsilon_1$ superior to -0.5, in case of the softer (central) region, and inferior to -0.5, in the case of the harder (exterior) region. When the points are away from the boundary between both materials, this effect decreases. Fig. 3 also shows that, in the exterior region of the specimen, the deformations attained are extremely low (inferior to 1%).

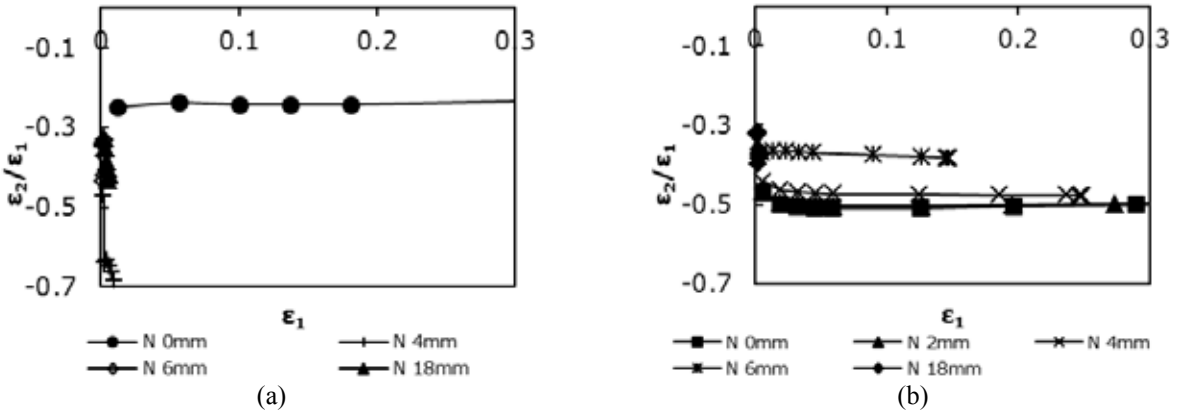

Fig. 3. Strain paths ($\varepsilon_2/\varepsilon_1$) along the specimen axis as a function of respective longitudinal deformations, ε_1, for the specimens M1-M3. Boundary of the central region is distant from the specimen centre: (a) 2 mm and (b) 8 mm.

The distribution of the longitudinal deformation, ε_1, in the surface of the specimen, immediately before the maximum load, was also studied for the cases where the boundary between two regions is distant from the centre of the specimen of 2 and 8 mm, as shown in

Fig. 4. Near the boundary between the two regions, the value of ε_1 tends to decrease, in the central region, and tends to increase in the exterior region. Moreover, the study of the $\varepsilon_2/\varepsilon_1$ ratio distribution in the surface of the specimen showed that its value is close to -0.5 (pure tension) near the periphery border and can drastically increase along its axis.

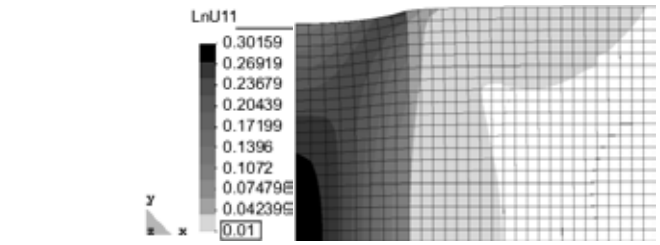

(a)

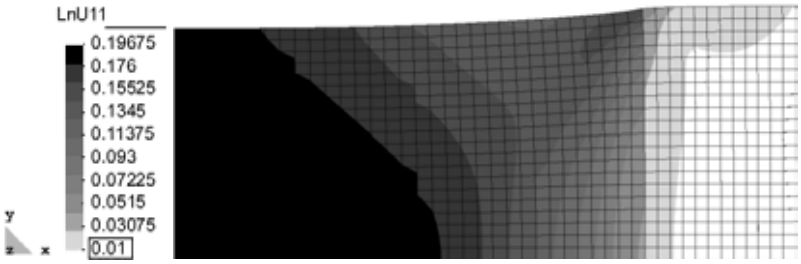

(b)

Fig. 4. Distribution of the longitudinal deformation, ε_1, in the heterogeneous specimens, immediately before the maximum load, for specimens M1-M3. Boundary between materials is distant from the specimen centre: (a) 2 mm and (b) 8 mm.

Fig. 5 compares the local stress-strain curves, determined by the procedure described in the previous section, with the local input curves described by the Swift law. Examples, for the specimens combining the materials M1-M2 and M1-M3, are shown. In general, the results show that the methodology proposed in the present work allows the suitable determination of the local stress-strain curves. However, in some cases, the coincidence between the two curves is not conveniently obtained, as for the example in Fig. 5 (c), for the central point of the specimen. This is due to the strong constraint in this point which is more important for smaller sizes of the central region of the specimen (see Fig. 3).

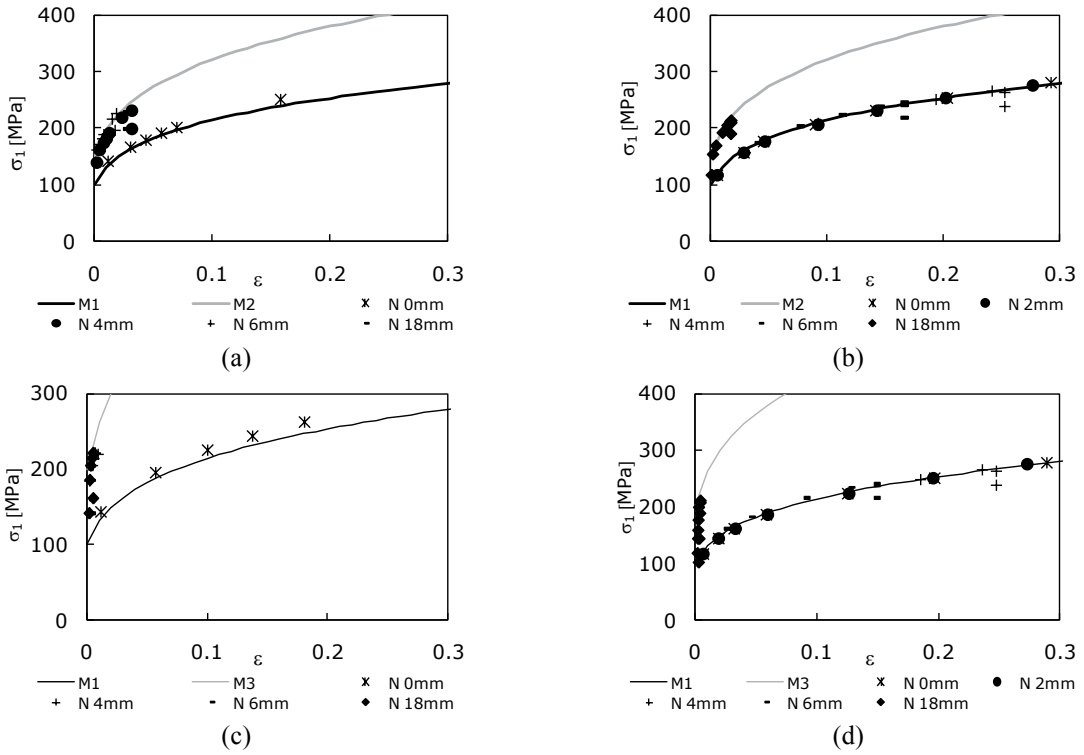

Fig. 5. Local stress-strain curves in points of the heterogeneous specimens and corresponding local input curves for specimens: (a) and (b) M1-M2; and (c) and (d) M1-M3. Boundary of the central region is distant from the specimen centre: (a) and (c) 2 mm; and (b) and (d) 8 mm.

3.4 Local Stress-Strain Curves: Influence of the Yield Stress Value

Fig. 6 shows examples of the strain paths and their evolution during plastic deformation of the heterogeneous specimens, for all the material combinations studied, with two different central region lengths. The strain paths were determined in the points situated in the central region: in the centre of the specimen, for the case of the central region length equal 2 mm, and in the point distant 2 mm from the centre, for the case of the central region length equal to 4 mm. The results are qualitatively similar for all cases: the ratio $\varepsilon_2/\varepsilon_1$ is always higher than -0.5 (corresponding to pure tension; see also previous section). Fig. 7 summarises the results of $\varepsilon_2/\varepsilon_1$, as a function of the difference between the yield stress values of the materials selected for the exterior and central regions of the specimen, $\Delta\sigma_0$ (results from Fig. 6, for high strain value: ε_1 at about 0.20). The value of the ratio $\varepsilon_2/\varepsilon_1$ is higher for specimens with central region length equal to 2 mm than for the case of 4 mm length, due to the higher constraints in the first case. Also, for both specimens, the change of strain path, i.e. the withdrawal from the value $\varepsilon_2/\varepsilon_1 = -0.5$ (pure tension), increases with the increase of the $\Delta\sigma_0$ value. Moreover, this withdrawal seems to be saturated when the values of $\Delta\sigma_0$ approaches 200 MPa (σ_0 =300 MPa). Fig. 8 compares the local stress-strain curves, determined by the procedure described in the present work, with the local input curves described by the Swift law, in the central region of the materials studied. The local curves were determined in the centre of the specimen for the case of the specimen with a central region length equal to 2 mm, and in the point distant 2

mm from the centre for the case of specimen with a central region length equal to 4 mm. The withdrawal of the local stress-strain curves from the respective input curve is visible after a deformation value $\varepsilon \approx 0.10$, for specimens with central region length equal to 2 mm. Again, this is due to the strong constraint induced by plastic deformation heterogeneity in these specimens.

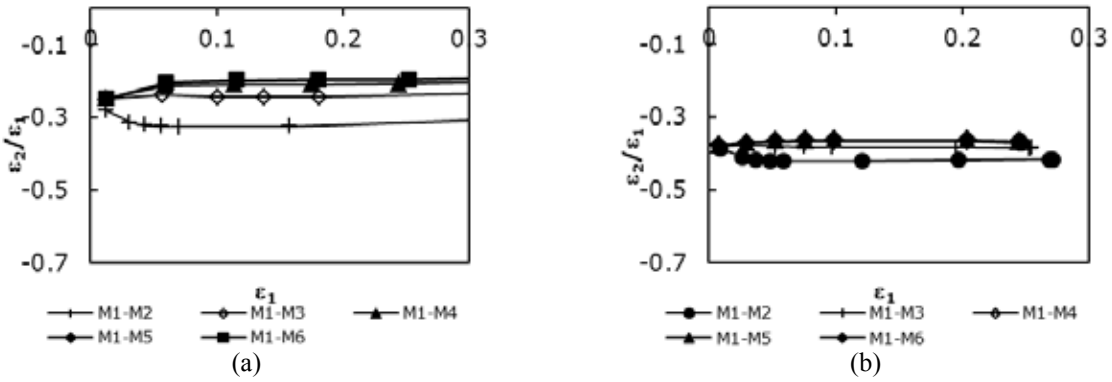

Fig. 6. Strain paths ($\varepsilon_2/\varepsilon_1$) as a function of respective longitudinal deformations, ε_1. Boundary of the central region is distant from the specimen centre: (a) 2 mm and (b) 4 mm.

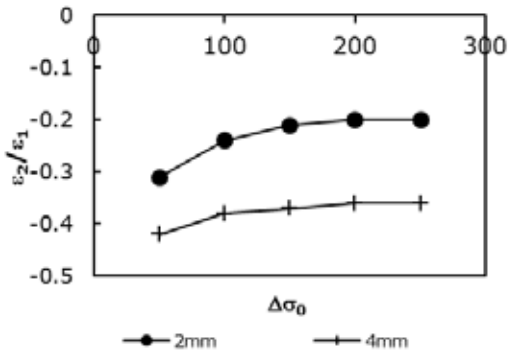

Fig. 7. Strain path $\varepsilon_2/\varepsilon_1$ evolution as a function of the difference between σ_0 for the materials in the central and exterior regions of the specimen, $\Delta\sigma_0$.

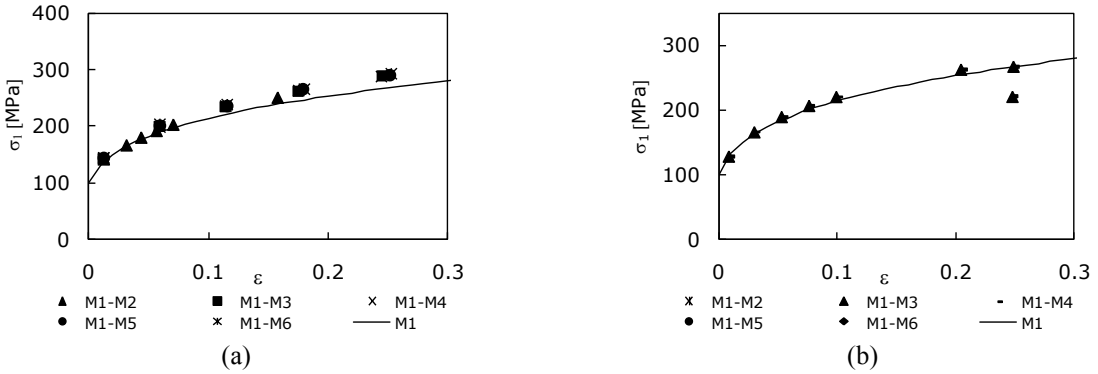

Fig. 8. Local stress-strain curves in points of the heterogeneous specimens and the stress-strain curves for materials M1. Boundary between materials is distant from the centre of specimen: (a) 2 mm and (b) 4 mm.

These results prove that the methodology proposed in the present work, for determining the local stress-strain curves, is appropriate. Small inaccuracies are observed, for cases with drastic changes of material yield stress between adjacent regions.

4 CONCLUSIONS

- This is an exploratory study concerning the possibility of determining local stress-strain curves of heterogeneous materials, using the technique of digital image correlation;
- Dissimilarity of the mechanical properties in the heterogeneous tensile specimen creates constraints which modify the strain path in relation to pure tension;
- The intensity of constraints, defined by withdrawal of the strain path ($\varepsilon_2/\varepsilon_1$) relatively to pure tension ($\varepsilon_2/\varepsilon_1$=-0.5) increased near the boundary between regions with different plastic properties and decreases from the symmetry axis to the specimen border;
- The methodology proposed for determining the local tensile stress-strain curves was numerically tested on heterogeneous samples. In some cases, the withdrawal between local curves and the ones of the material is visible due to the drastic variation of mechanical properties of adjacent regions of heterogeneous specimen.
- This methodology uses the same type of results than the ones that can be experimentally obtained by DIC technique.

REFERENCES

[1] D.M. Rodrigues, A. Loureiro, C. Leitão, R.M. Leal, B.M. Chaparro and P. Vilaça, Influence of friction stir welding parameters on the microstructural and mechanical properties of AA 6016-T4 thin welds. *Mater. Design* (2009) **30**:1913-1921.

[2] M.A. Sutton, J.H. Yan, S. Avril, F. Peirron and S.M. Adeeb, Identification of heterogeneous parameters in a weld specimen: uniform stress and virtual fields methods for material properity estimation. *Exp. Mech.* (2008) **48**:451-464.

[3] S.-H. Tung, M.-H. Shih and J.-C. Kuo, Application of digital image correlation for anisotropic plastic deformation tension testing. *Opt. Lasers Eng.* (2010) **48**:636-641.

[4] S. Belhabib, H. Haddadi, M. Gasperini and P. Vacher, Heterogeneous tensile test on elastoplastic metallic sheets: Comparison between FEM simulations and full-field strain measurements. *Int. J. Mech. Sci.* (2008) **50**:14–21.

[5] M.C. Oliveira, J.L. Alves and L.F. Menezes, Algorithms and strategies for treatment of large deformation frictional contact in the numerical simulation of deep drawing process. *Arch. Comput Method* (2008) **E15**:113-162.

[6] R.M. Branco, P.A. Prates, M.C. Oliveira, N.A. Sakharova and J.V. Fernandes, Numerical study of mechanical behaviour of heterogeneous Materials. *Mater. Sci. Forum (VI International Materials Symposium MATERIAIS 2011, XV meeting of SPM - Sociedade Portuguesa de Materiais)* (submitted).

XI International Conference on Computational Plasticity. Fundamentals and Applications
COMPLAS XI
E. Oñate, D.R.J. Owen, D. Peric and B. Suárez (Eds)

PREDICTION OF DAMAGE INTENSITY IN MOMENT FRAMES BY USING WAVELET ANALYSIS

Raufi, F. [*], **Bahar, O.** [†]

[*] Ph.D. Candidate, Science and Research Branch, Islamic Azad University, Tehran, Iran
e-mail: fardin_raufi@yahoo.com

[†] International Institute of Earthquake Engineering and Seismology (IIEES), Structural Engineering Research Centre, Tehran, Iran, e-mail: omidbahar@iiees.ac.ir

Key words: damage detection, wavelet transform, plastic hinge, moment frame

Abstract. After occurrence of an earthquake, one of the most important applications of recorded information in instrumented buildings is using these data in observation and estimation of damage in the structural systems of the building. A method using plastic hinge formation and wavelet analysis has been presented which directly makes use of rotational response history of frame nodes (rotation, angular velocity, angular acceleration) for extracting information of damage.

1 INTRODUCTION

The estimation of severity of the damage has two main goals: (a) determining the stability and serviceability of structures after the earthquake, (b) getting timetable and its priority scheme for the damaged parts repairing. Topic of intensity of damage in structures subject to earthquake is a matter of major interest in most papers. The reason for this interest is that estimating the severity of damage with respect to onset and its position is difficult. One of the problems is that estimation of damage is a relative issue. In other words, although the damage severity of a member can be judged relative to the other members, but the damage influence and its severity, for example in a section of the structure cannot be estimated, correctly. Also, as these estimates are often based on vibration responses of system, substantive changes in response - for example, frequency of the lower modes - is the basis for damage detection. These changes are functions of intensity and distance of damaged part to the measured position. This means that small damage at the closer distance may have similar effects as a large damage at farther away which makes the detection more complicated. In some cases, relative damage estimation is also useful because it can be a basis for choosing a strategy to repair damaged areas. For calculating structural damage in members we can use Joint plastic rotation in beams and columns of a frame. First of all moment-curvature diagram is determined, and then the level of plastic rotation capacity is calculated. Campbell has presented a similar damage index [1].

2 WAVELET

Wavelet is now a well known tool to detect damages. It defines a group of mathematical functions that are used to break down a signal to its frequency components. Wavelet functions have a limited bandwidth in time domain and frequency domain. Wavelets are transferred and scaled samples obtained by affecting a wavelet mother function on the main signal.

Wavelet coefficients contain much information about the contents of the signal. Eqs. 1 to 4 show main equations of wavelet transform method. Using a selected analyzing or mother wavelet function ψ(t), the continuous wavelet transform of a signal f(t) is defined as (M. Misti et al., 2007) [2]:

$$C(a,b) = \int_{-\infty}^{+\infty} f(t)\psi_{a,b}(t)dt \tag{1}$$

$$\psi_{a,b}(t) = a^{-\frac{1}{2}}\psi\left(\frac{t-b}{a}\right) \tag{2}$$

Discrete wavelet transform is similarly defined as follows:

$$C(a,b) = c(j,k) = \sum_{n\in z} f(n)\psi_{j,k}(n) \tag{3}$$

in which $\psi_{j,k}$ is a discrete mother wavelet, which is defined as follows and sometimes also called binary analysis:

$$\psi_{j,k}(n) = 2^{-j/2}\psi(2^{-j}n - k) \tag{4}$$

Selection of proper mother wavelet function is the first step in the wavelet analysis. The choice depends on the desired issue and can have a considerable effect on the results. In this study, discrete wavelet transform (DWT) employing "Bior 6.8" [3], is used. In DWT, scale parameter 'a' is chosen as $a= 2^J$ where J is an integer values J ϵ Z. For a function f(t) ϵ L2-space with a Fourier transform F(ω), a change in scale factor J is followed by a change in scale of frequency domain given by $a= 2^J$. Signal decomposition in wavelet analysis is carried out by projecting the signal into a subspace of scaling and wavelets basis functions at different scales and their transmission.

3 METHODOLOGY

Based on the definition of the Federal Emergency Management Agency (FEMA 356) [4] plastic formation at a joint of a steel frame in a Moment-Rotation curve has a clear transition point, "point A" in Fig. 1, that the member's elastic behavior ends and its inelastic behavior starts. After that, there is "point B", in which the member cannot carry more loads. In this situation the member has been sustained severe damages. In other words, there are two clear stages: (a) Passing from point "A" and (b) Passing from point "B". Transition from point A is considered as the beginning of the plastic behavior and actually is the criterion for determining starting time of damage, while passing from point B can be considered as a criterion for determining severity changes, which leads to destructive damages.

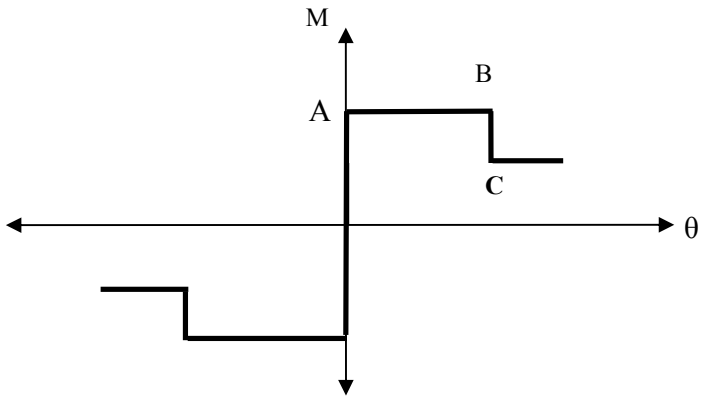

Fig.1. Moment - rotation behavior

Moving from point A to C can be estimated from response history of the nodes adjacent to the hinge. These changes cause permanent alteration in the responses of the joint and it would lead to a shift in the response base line of the adjacent node. For determining the value of this shift, using wavelet analysis, details can be removed from the response and an approximation can be achieved. Details will contain information for computing time of damage [5] and approximation will have information about the severity of damage. Details demonstrate passing from point A and approximation demonstrates if the response falls between A and B or it has passed B.

To further clarify the above mentioned method, consider the frame shown in Fig. 2 under the loading shown in Fig. 3. Two cases are assumed: First, all members behaves within their elastic ranges such that no plastic hinges would be formed by increasing external load, F(t). In this case, the rotation time history response of node P, such as loading, has a linear gradient and increases constantly. Second, it is permitted that by increasing external load a plastic hinge initiates to form at a member. Again we analyzed the rotation response of node P. As it can be seen in Fig. 4, after plastic hinge formation, slope of the response function increases clearly. Also for this frame the occurrence time and their related values of the rotation for the end section of member AP in each states: A, B and C are speciifed in Fig. 4.

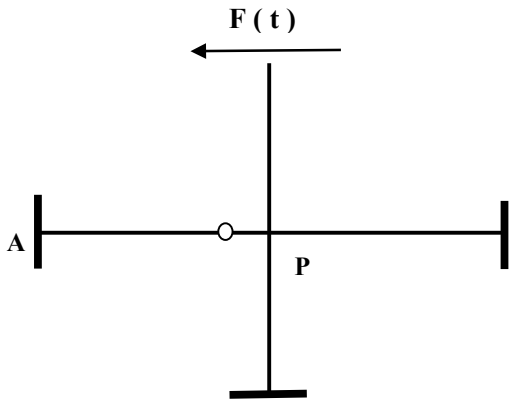

Fig. 2. Simplified model of Plastic hinge formation (on the frame subjected to a horizontal load)

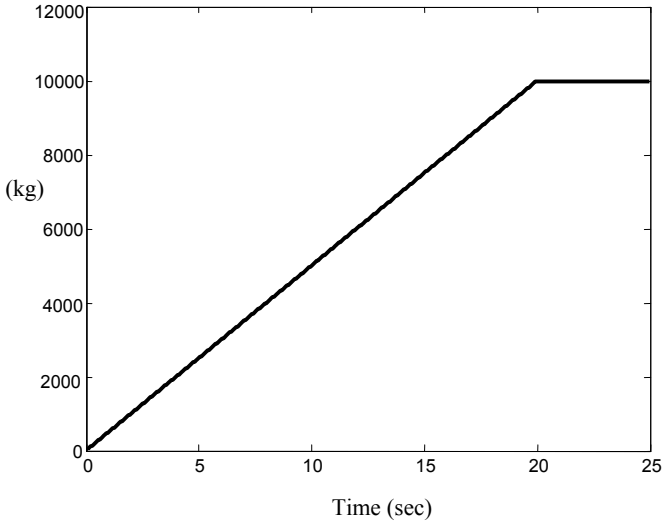

Fig. 3. Monotonic loading

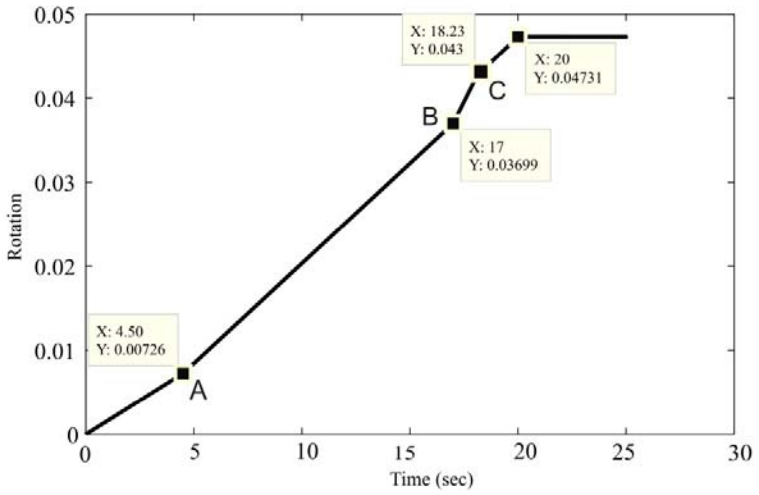

Fig. 4. Time history response of node B in case of plastic hinge formation in a member

4 NUMERICAL ANALYSIS AND RESULTS

Now, we aim to examine this procedure to a moment steel frame, Fig. 5, subjected to a random support excitation like an earthquake. This frame is a 5 meter length, 3 meter height simple frame with fixed bases and a uniform dead load about 2000 kg/m. Fig. 6 shows the strong ground motion recorded at Tabas, Iran. This earthquake was a huge earthquake measuring 7.8 on the Richter scale, which struck on September 16, 1978 in central Iran.

Fig. 5. Schematic representation of main damage in the studied frame subject to Tabas excitation

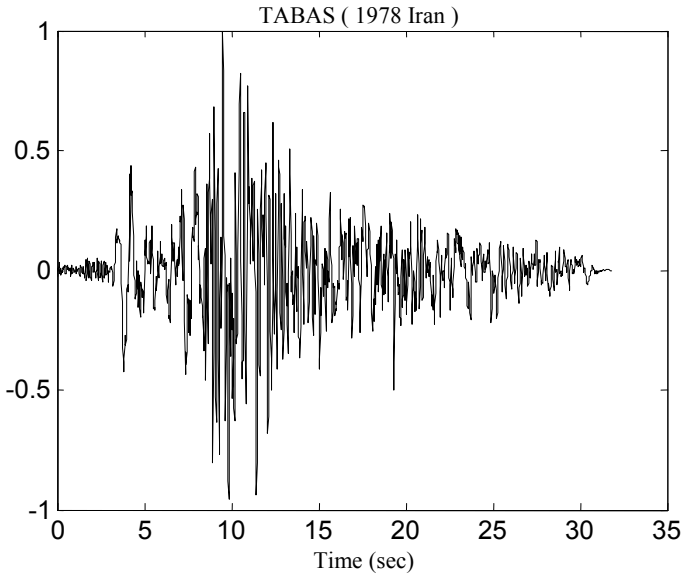

Fig. 6. Normalized Tabas record with respect to its peak ground acceleration (PGA)

As can be seen in Fig.7 changes in the difference of two nodes is similar to the rotational response history of the plastic hinge formed between them.

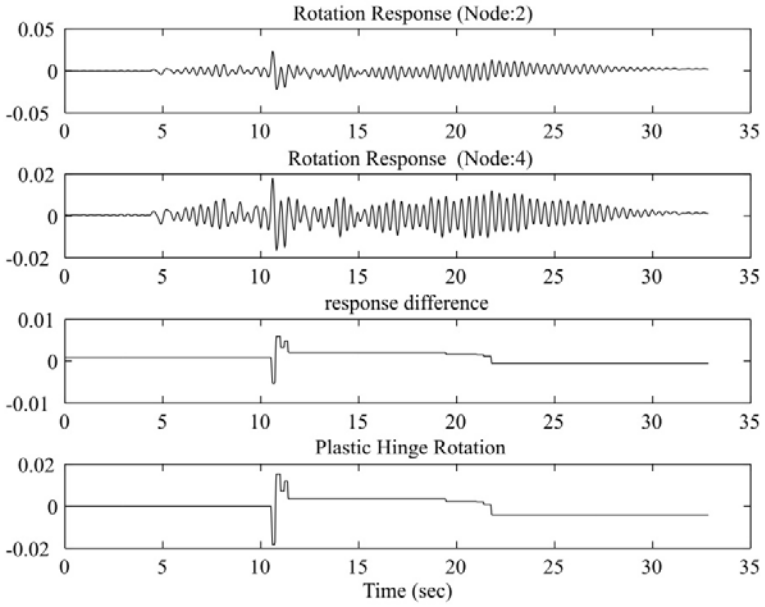

Fig. 7. Response difference and hinge rotation history

Hence having behavioral curve and rotational response history of the plastic hinge the current place on the behavior curve can be determined. Where the intensity of damage does not reach the point B, in other words if it lies between points A and B, there will also be a shift in the base line which demonstrates plastic deformation and can be captured by "approximate signal", Fig.8.

In the case of intense damage, point B on the behavioral curve in Fig. 9, a total shift will occur in the base line which is visible in the wavelet approximation as well as the response itself. Also there will be an increase in the period of the structure which can be a criterion for determining intensity of damage.

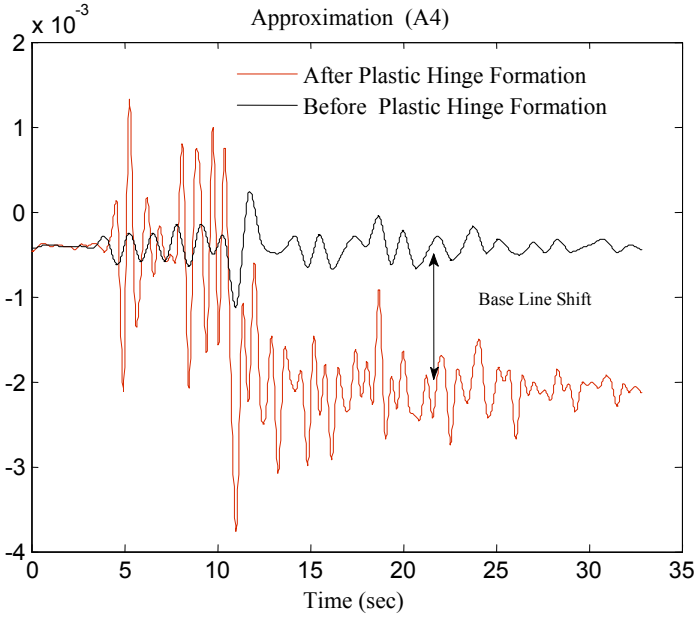

Fig. 8. 4th approximation obtained from wavelet transformation of point 2 rotational response (intensity corresponding to points A to B)

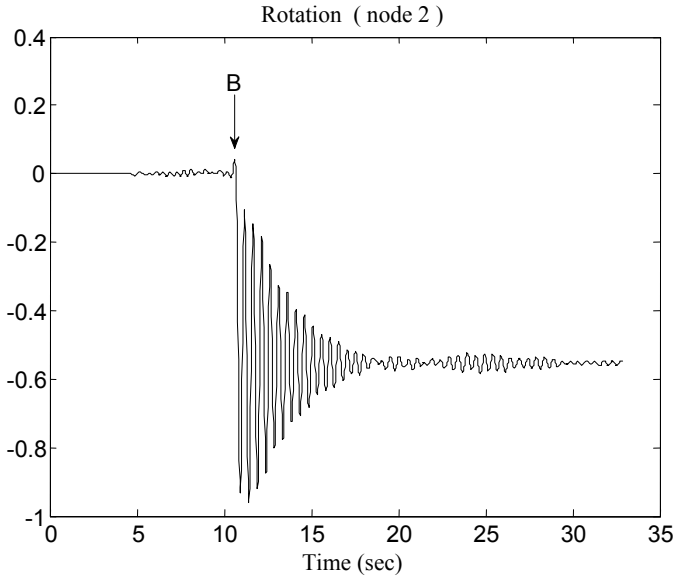

Fig. 9. Base line shift corresponding to point B

5 CONCLUSION

Plastic deformation causes permanent shift in response time history. In moment frames this shift is well represented in the rotational response time histories of nodes which mean plastic rotation in adjacent hinges. Recognizing any change in differences of the rotational response histories of the two adjacent nodes has a similar pattern to the rotational response history of the plastic hinge forming between them.

Shift in the base line is apparent in the "approximate" obtained from wavelet transform of the response. "Details" obtained from wavelet transform of the response could be used to determine damage onset while information on the severity of the damage can be estimated from "approximate"

REFERENCES

[1] Campbell, S.D., Richard, R.M., Partridge, J.E. Steel Moment Frame Damage Predictions Using Low-Cycle Fatigue. *14th World Conference on Earthquake Engineering, China* (2008).

[2] Misisti, M., Misiti, Y.,Oppenheim, G., Poggi, J. *Wavelets and Their Application*, ISTE Ltd, UK (2007).

[3] Ovanesova, A.V., Sua´rez, L.E. Applications of Wavelet Transforms to Damage Detection in Frame Structures. *Engineering Structures* (2004) **26**:39–49.

[4] *FEMA-356 Prestandard and commentary for the seismic rehabilitation of buildings*, Federal Emergency Management Agency, Washington, DC (2000).

[5] Raufi, F. and Bahar, O. Damage Detection in 3-Story Moment Frame Building by Wavelet Analysis , *14th ECEE* (2010).

XI International Conference on Computational Plasticity. Fundamentals and Applications
COMPLAS XI
E. Oñate, D.R.J. Owen, D. Peric and B. Suárez (Eds)

PREDICTION OF STRAIN LOCALIZATION DURING SHEET METAL FORMING USING BIFURCATION ANALYSIS AND GURSON-TYPE DAMAGE - COMPLAS XI

L. Z. MANSOURI, H. CHALAL, F. ABED-MERAIM, T. BALAN

LEM3, UMR CNRS 7239
Arts et Métiers ParisTech
4, rue Augustin Fresnel, 57078 Metz Cedex 03, France
email: Lotfi-Zoher.MANSOURI-7@etudiants.ensam.eu, www.ensam.eu

Key words: Finite Elasto-Plasticity, Damage, Strain Localization, Sheet Metal Forming, Forming Limit Diagram.

Abstract. The strain localization phenomenon that may occur during sheet metal forming represents a major cause of defective parts produced in the industry. Several instability criteria have been developed in the literature to predict the occurrence of these instabilities. The proposed work aims to couple a Gurson-type model to the Rice's localization criterion. The implementation of the modeling is achieved via a user subroutine (Umat) in Abaqus/std using a Runge-Kutta explicit integration scheme. Finally, we show the effectiveness of the proposed coupling for the prediction of the formability of stretched metal sheets.

1 INTRODUCTION

Material instabilities in the form of shear bands represent one of the main phenomena that limit sheet metal formability. This instability in the plastic flow is still an issue for industry, since it is responsible for most of the defective parts after forming operations. Consequently, it is important to provide reliable and validated numerical tools able to predict the appearance of these plastic instabilities. The occurrence of localization through shear bands is often due to concentrations of deformation where damage is in excess. Thus, taking into account damage development during metal forming operations is essential to obtain reliable results.

Two main approaches for damage descriptions were developed in the literature during these last four decades. The first one is known as the continuum damage mechanics approach (Lemaitre [1]) and is based on the introduction of a damage variable that can be scalar or tonsorial describing the surface density of defects. The second approach, physically motivated by micromechanics concepts, accounts for the effect of the hydrostatic pressure on the material behavior through the void volume fraction. In this contribution, the second approach for damage will be used, i.e., the so-called Gurson-Tvergaard-Needleman model (GTN) [2-4].

In order to predict the onset of strain localization, it is necessary to couple the constitutive model with a localization criterion. Several localization criteria have been developed in the literature, which differ in their theoretical foundations. Brunet *et al.* [5] used the GTN model coupled with the Modified Maximum Force Criterion (MMFC) (Hora *et al*. [6]) to predict

forming limit curves for different steel grades. The obtained numerical results were compared to experimental data showing good agreements. Besson *et al.* [7] have coupled the Rice localization criterion with the GTN model for the prediction of ductile fracture in notched bars. It was shown that the introduction of the effective porosity (f^*) favors flat fracture under plane strain conditions. In the current work, the formability limits of metal sheets are investigated by means of the GTN-Rice modeling.

The paper is organized as follows: the main equations that govern the GTN model are first reviewed; then the expression of the acoustic tensor is derived within a finite strain framework. In the results and discussion section, we show the effectiveness of the proposed modeling for the prediction of forming limit diagrams (FLDs). Finally, some concluding remarks are drawn as well as some directions for future work.

2 PRESENTATION OF THE GTN MODEL

The GTN model originally proposed by Gurson [2] and phenomenologically extended by Tvergaard [3], Tvergaard and Needleman [4] is perhaps one of the most popular damage models for the prediction of the ductile fracture (Sànchez *et al.*, [8]). This damage model has shown its efficiency in particular for the prediction of the cup-cone fracture that usually appears during tensile tests of notched cylindrical bars. The approximate macroscopic yield criterion proposed by Gurson and driven from a limit analysis is given by the following relation:

$$\Phi = \left(\frac{\Sigma_{eq}}{\bar{\sigma}} \right)^2 + 2q_1 f^* ch\left(\frac{3}{2} \frac{q_2 \Sigma_m}{\bar{\sigma}} \right) - \left(1 + q_3 f^{*2} \right) \leq 0 \tag{1}$$

where $\Sigma_{eq} = \left(3/2 \boldsymbol{\Sigma}' : \boldsymbol{\Sigma}' \right)^{1/2}$ and $\Sigma_m = 1/3 tr\left(\boldsymbol{\Sigma} \right)$ represent, respectively, the macroscopic equivalent stress and the macroscopic average stress. $\bar{\sigma}$ is the yield stress of the fully dense matrix, here only isotropic hardening is considered using a Swift law defined as follows:

$$\bar{\sigma} = k(\varepsilon_0 + \bar{\varepsilon}^p)^n \tag{2}$$

where k , ε_0 and n are parameters of the Swift hardening law and $\bar{\varepsilon}^p$ is the equivalent plastic strain of the matrix material. The parameters q_1, q_2 and q_3 were introduced by Tvergaard [9] in order to take into account the effect of interaction between cavities, and f^* represents the effective porosity, which will be defined hereafter. For the isotropic GTN model, the plastic part of the macroscopic strain rate $\mathbf{D}^p$ and the rate of equivalent plastic strain $\dot{\bar{\varepsilon}}^p$ are assumed to be related by the equivalent plastic work expression as follows:

$$\left(1 - f \right) \bar{\sigma} \dot{\bar{\varepsilon}}^p = \boldsymbol{\Sigma} : \mathbf{D}^p \tag{3}$$

where f represents the void volume fraction and $\boldsymbol{\Sigma}$ the macroscopic Cauchy stress tensor. This relation is exact for $f=0$ and is a reasonable assumption for porous materials with low hardening exponents [9]. The plastic strain rate is defined by the normality law as follows:

$$\mathbf{D}^p = \dot{\lambda}\mathbf{V}_\Sigma \tag{4}$$

such as $\dot{\lambda}$ represents the plastic multiplier, and $\mathbf{V}_\Sigma = \partial\Phi/\partial\boldsymbol{\Sigma}$ is the flow direction tensor. By injecting relation (4) into (3), one obtains the rate of equivalent microscopic stress given by the following relation:

$$\dot{\bar{\sigma}} = \frac{d\bar{\sigma}}{d\bar{\varepsilon}^p}\dot{\bar{\varepsilon}}^p = H_{\bar{\sigma}}\frac{\boldsymbol{\Sigma}:\mathbf{V}_\Sigma}{(1-f)\bar{\sigma}}\dot{\lambda} \tag{5}$$

Before coalescence, the evolution of porosity is mainly due to two phenomena: nucleation and growth. It is thus possible to express the porosity rate as follows:

$$\dot{f} = \dot{f}_n + \dot{f}_g \tag{6}$$

where $\dot{f}_n$ and $\dot{f}_g$ represent the porosity rate due to nucleation and growth, respectively. In this work, it is considered that nucleation is strain controlled; in this case the evolution law of f_n due to particle fracture or particle-matrix debonding is given by the following relation [10]:

$$\dot{f}_n = \frac{f_N}{s_N\sqrt{2\pi}}\exp\left[-\frac{1}{2}\left(\frac{\bar{\varepsilon}^p - \varepsilon_N}{s_N}\right)^2\right]\dot{\bar{\varepsilon}}^p \tag{7}$$

where f_N represents the volume fraction of inclusions likely to nucleate, ε_N the equivalent plastic strain for which half of inclusions have nucleate and s_N the standard deviation on ε_N. The porosity rate due to growth depends strongly on the stress triaxiality and is given by the following relation [9]:

$$\dot{f}_g = (1-f)tr(\mathbf{D}^p) \tag{8}$$

The detection of the coalescence stage uses the phenomenological criterion introduced by Tvergaard and Needleman [7] by means of the effective porosity such as:

$$f^* = f_{cr} + \delta_{GTN}(f - f_{cr}) \tag{9}$$

with

$$\delta_{GTN} = \begin{cases} 1 & \text{if } f < f_{cr} \\ \dfrac{1/q_1 - f_{cr}}{f_R - f_{cr}} & \text{if } f > f_{cr} \end{cases} \tag{10}$$

where f_{cr} represents the critical porosity and f_R the void volume fraction at final fracture. Thus, when the material enters the coalescence phase, the introduction of effective porosity results in an accelerated degradation of its mechanical properties.

3 ELASTO-PLASTIC TANGENT MODULUS

In order to determine the expression of the elasto-plastic tangent modulus in the case of the GTN model, we apply the consistency condition given by the following relation:

$$\dot{\Phi} = \mathbf{V}_\Sigma : \dot{\boldsymbol{\Sigma}} + V_{\bar{\sigma}} \dot{\bar{\sigma}} + V_{f^*} \dot{f}^* = 0 \tag{11}$$

where $V_{\bar{\sigma}} = \partial\Phi / \partial\bar{\sigma}$ and $V_{f^*} = \partial\Phi / \partial f^*$. The terms involved in equation (11) are given by the following relations:

$$\mathbf{V}_\Sigma : \dot{\boldsymbol{\Sigma}} = \left[\frac{3}{\bar{\sigma}^2} \boldsymbol{\Sigma}' + \frac{q_1 q_2 f^*}{\bar{\sigma}} \mathrm{sh}\left(\frac{3}{2} q_2 \frac{\Sigma_m}{\bar{\sigma}} \right) \mathbf{I} \right] : \dot{\boldsymbol{\Sigma}} \tag{12}$$

$$V_{\bar{\sigma}} \dot{\bar{\sigma}} = -\frac{1}{\bar{\sigma}^2} \left[\frac{2\Sigma_{eq}^2}{\bar{\sigma}} + 3 q_1 q_2 f^* \Sigma_m \mathrm{sh}\left(\frac{3}{2} q_2 \frac{\Sigma_m}{\bar{\sigma}} \right) \right] H_{\bar{\sigma}} \frac{\boldsymbol{\Sigma} : \mathbf{V}_\Sigma}{(1-f)\bar{\sigma}} \dot{\lambda} \tag{13}$$

$$V_{f^*} \dot{f}^* = \left[2 q_1 \mathrm{ch}\left(\frac{3}{2} q_2 \frac{\Sigma_m}{\bar{\sigma}} \right) - 2 q_3 f^* \right] \dot{f}^* \tag{14}$$

Let us now introduce the hypo-elastic law, which reduces in the co-rotational (material) frame to a simple material derivative:

$$\dot{\boldsymbol{\Sigma}} = \mathbf{C}^e : \left(\mathbf{D} - \dot{\lambda} \mathbf{V}_\Sigma \right) = \mathbf{C}^{ep} : \mathbf{D} \tag{15}$$

where $\mathbf{C}^e$ represents the isotropic elasticity tensor, and $\mathbf{D}$ the strain rate tensor. Substituting equations (12) to (15) in the consistency condition, one can derive the expression of the plastic multiplier, which is given by the following relation:

$$\dot{\lambda} = \frac{\mathbf{V}_\Sigma : \mathbf{C}^e : \mathbf{D}}{H_\lambda} \tag{16}$$

where H_λ is a scalar variable such as:

$$H_\lambda = \mathbf{V}_\Sigma : \mathbf{C}^e : \mathbf{V}_\Sigma - \left(V_{\bar{\sigma}} H_{\bar{\sigma}} + V_{f^*} \delta_{GTN} A_n \right) \frac{\boldsymbol{\Sigma} : \mathbf{V}_\Sigma}{(1-f)\bar{\sigma}} - (1-f) V_{f^*} \delta_{GTN} \mathbf{V}_\Sigma : \mathbf{I} \tag{17}$$

substituting relation (16) in (15) gives the expression of the elasto-plastic tangent modulus as follows:

$$\mathbf{C}^{ep} = \mathbf{C}^e - \alpha \frac{\left(\mathbf{C}^e : \mathbf{V}_\Sigma \right) \otimes \left(\mathbf{V}_\Sigma : \mathbf{C}^e \right)}{H_\lambda} \tag{18}$$

where $\alpha = 0$ for elastic loading or unloading and $\alpha = 1$ in case of strict elasto-plastic loading.

4 INSTABILITY CRITERION

In addition to the behavior model, prediction of forming limits requires the use of an instability criterion allowing detection of the onset of localization. The instability criterion selected in this work is the Rice localization criterion [11-12], based on the singularity of the acoustic tensor. As discussed in the introduction, the coupling of the GTN model with the Rice instability criterion has been considered in the literature mainly for the prediction of ductile fracture in cylindrical bars under plane strain conditions. However, to the authors' knowledge, no attempt has been made for the prediction of FLDs within this constitutive and material instability framework. Thus, the originality of the present work is to demonstrate the

efficiency of such modeling in the prediction of forming limit diagrams. Then, the sensitivity of FLDs to the material parameters is investigated. The condition of localization, which can be derived from the Hadamard compatibility condition and the static equilibrium equation is given by the following relation:

$$\det(\mathbf{Q}) = \det(\boldsymbol{n}\cdot\mathbf{L}\cdot\boldsymbol{n}) = 0 \tag{19}$$

where $\mathbf{Q}$ represents the acoustic tensor, $\boldsymbol{n}$ the normal to the localization band and $\mathbf{L}$ the tangent modulus which relates the nominal stress tensor to the velocity gradient (see Haddag *et al.* [13]). Its expression is given by the following relation:

$$\mathbf{L} = \mathbf{C}^{ep} + \mathbf{L}_1 - \mathbf{L}_2 - \mathbf{L}_3 \tag{20}$$

where $\mathbf{L}_1$, $\mathbf{L}_2$ and $\mathbf{L}_3$ are fourth-order tensors induced by the large strain framework, and given by the following relations [13]:

$$\begin{aligned} L_{1ijkl} &= \sigma_{ij}\delta_{kl} \\ L_{2ijkl} &= \frac{1}{2}\left[\delta_{ik}\sigma_{lj} + \delta_{il}\sigma_{kj}\right] \\ L_{3ijkl} &= \frac{1}{2}\left[\sigma_{ik}\delta_{lj} - \sigma_{il}\delta_{jk}\right] \end{aligned} \tag{21}$$

The implementation of the above-described behavior model is carried out via a user material routine UMAT in Abaqus/standard, by means of a Runge-Kutta explicit integration scheme. This time integration scheme offers a reasonable compromise between simplicity and computational efficiency. Another reason behind the choice of an explicit scheme is that localization occurs in the softening range, and often at small stress values where implicit integration schemes (Aravas [14]) may experience difficulties at this stage of the analysis. Indeed, in the softening regime, positive definiteness of the consistent tangent modulus might not be guaranteed by classical implicit schemes (Oliver *et al.*, [15], Sànchez *et al.*, [8]). Because our main objective in this work is to show the effectiveness of the proposed framework in predicting forming limit diagrams of sheet metals, the choice of the Runge-Kutta time integration scheme is justified, despite the relatively higher computation times compared to implicit algorithms.

5 RESULTS AND DISCUSSION

In what precedes, the coupling of the GTN model with the Rice localization criterion was described. In this section, some results obtained by means of this coupling are shown. The material studied corresponds to a mild steel, mainly because of its widespread use in industry. The parameters related to this material were drawn from literature (see Brunet *et al.* [5]) and are reported in the following tables:

Table 1: Mechanical properties and strain hardening parameters

Material	E (MPa)	ν	k (MPa)	ε_0	n

Mild steel	198000	0.3	551.1	$9.54\ 10^{-3}$	0.279

Table 2: Parameters of the damage model

Material	f_0	s_N	ε_N	f_N	f_{cr}	f_R	q_1	q_2	q_3
Mild steel	10^{-3}	0.1	0.21	0.039	0.03	0.15	1.52	1.0	2.15

Figure 1-a represents the evolution of the Cauchy stress versus the true strain up to the localization point for three strain paths, namely uniaxial tension (UT), plane strain tension (PST) and balanced biaxial tension (BBT). In the case of PST, localization occurs very early, as soon as the stress-strain curve starts to soften, whereas for the BBT loading path, localization occurs for very low stress values at the end of coalescence.

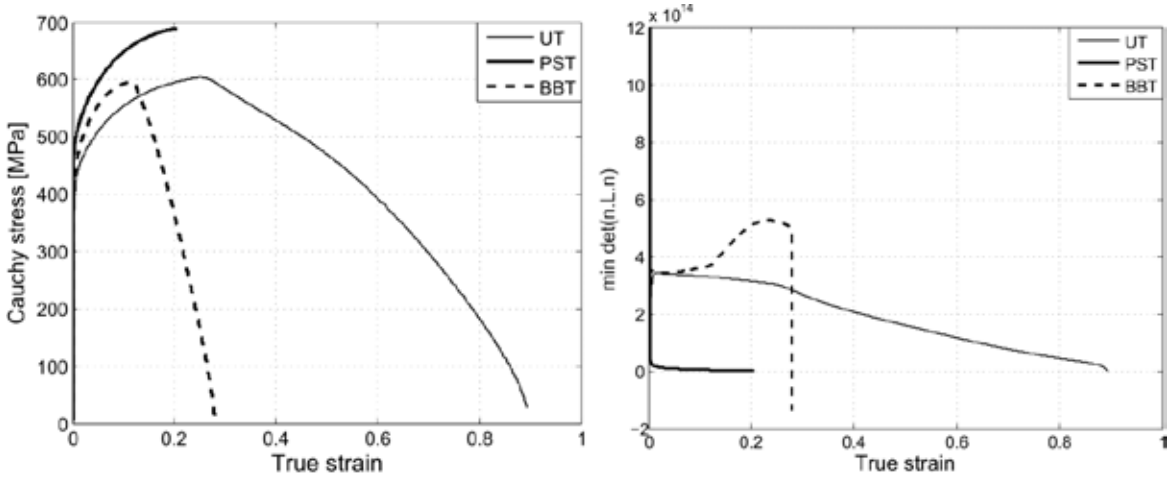

(a) (b)

Figure 1: (a) Simulation of three loading paths up to localization; (b) Evolution of the minimum of the determinant of the acoustic tensor as a function of the deformation.

Furthermore, localization takes place when the minimum of the determinant of the acoustic tensor is equal to zero (see equation (19)). In practice, during numerical computations this condition is not exactly met, and the value of det(**Q**) changes from positive to slightly negative (see Figure 1-b) during one loading increment (see also Besson et al. [7]).Figures 2-a to 2-d illustrate the effect of the coalescence parameters (f_{cr} and f_R) on the moment of detection of localization in BBT strain path. One can notice that decreasing parameter f_R results in an increase of δ_{GTN}, which makes it possible to detect localization in a premature way. On the other hand, increasing parameter f_{cr} will delay the mechanism of coalescence and in some way the occurrence of strain localization.

The modeling of coalescence phase is a major point when dealing with the proposed coupling. Indeed, Rudnicki and Rice [12] showed that for associative plasticity models (which

is our case); localization criterion can detect bifurcation only in the presence of softening behavior. Consequently, it is important to take into account the mechanism of coalescence.

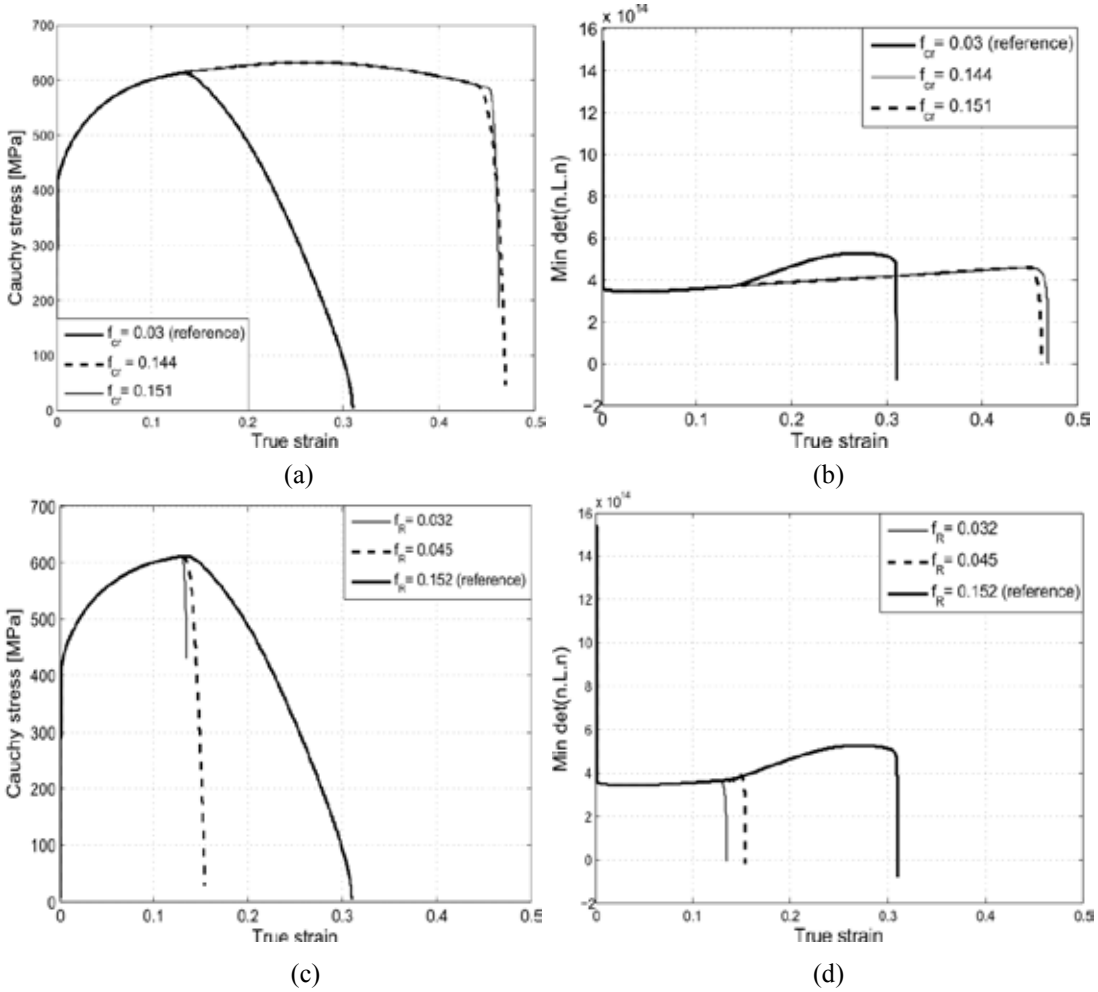

Figure 2: Effect of the coalescence parameters on the prediction of localization.

This phenomenon has a considerable effect on the obtained forming limit diagrams, since no localization can occur with the proposed modeling during positive hardening behavior. Note that several authors [16-18] suggested that parameter δ_{GTN} should not be constant, but should rather depend on other parameters, such as the stress triaxiality, initial porosity, etc. Although the coalescence model taken in the current work is kept in its simplest form (i.e., with constant parameter δ_{GTN}), the extension of this modeling framework to more physically-based descriptions can be readily done in future investigations of sheet metal formability.

5.1 Effect of the GTN parameters on the prediction of forming limits

In this section, the effect of the GTN model parameters on the prediction of FLDs is investigated. These parameters are divided into three families; each family reproducing one of the three mechanisms leading to ductile fracture (i.e. nucleation, growth and coalescence).

The results of this parametric study will be shown by varying one parameter at the same time and the reference curve will be that obtained by the parameters given in Tables 1 and 2. Thus, we will analyze the effect of initial porosity and the parameters associated with nucleation and coalescence mechanisms. Figures 4-a, 4-b and 4-c represent, respectively, the sensitivity of the FLDs to parameters f_N, s_N and ε_N.

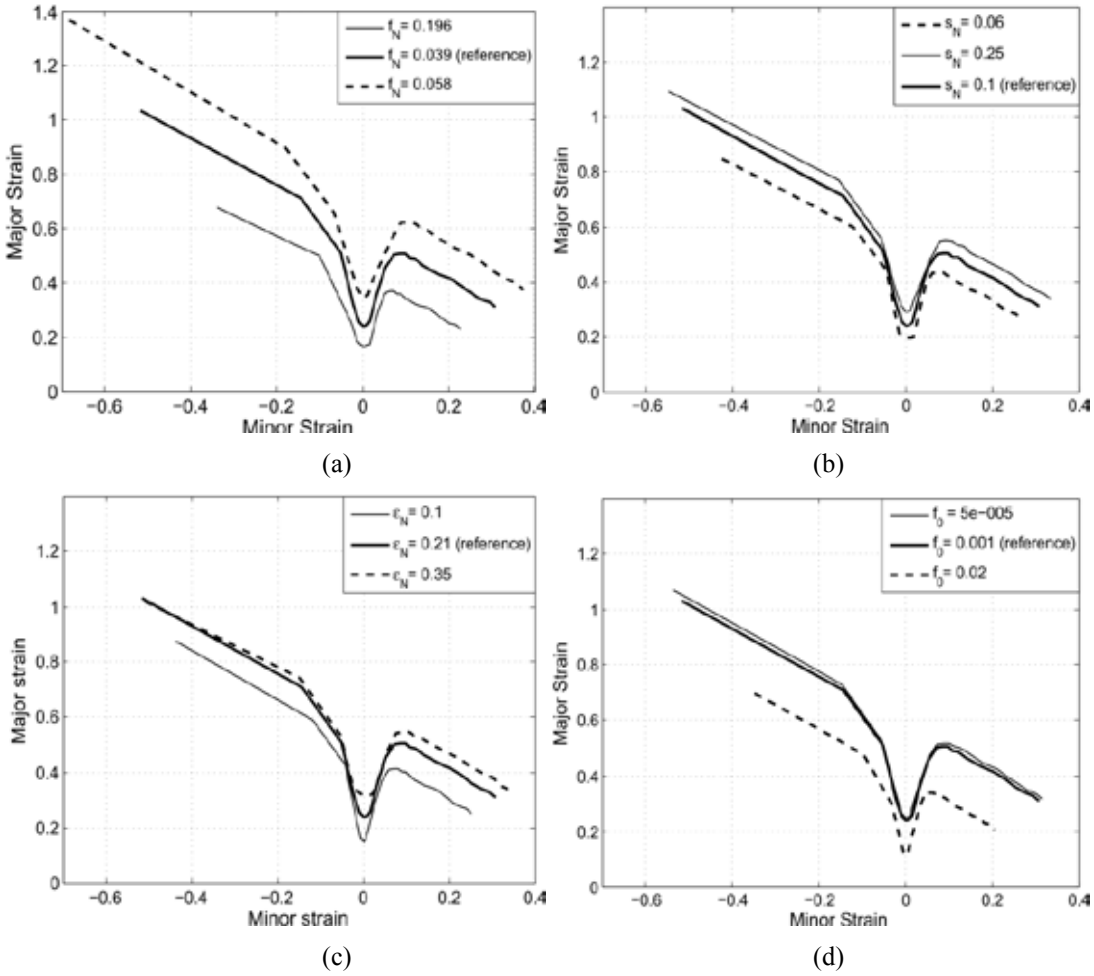

Figure 3: Effect of nucleation parameters and initial porosity on the prediction of FLDs.

The increase of f_N (decrease in s_N or ε_N) seems to have the same effect on the obtained FLD; indeed, the increase in f_N (reduction in s_N or ε_N) translates each point of the FLD downward, thus reducing the formability limits. The initial porosity is one of the most influential parameters of the GTN model, and many authors agree with its major importance (Pardoen and Hutchinson [18]). Figure 4.d represents the sensitivity of an FLD to the initial porosity; one can observe that the increase in initial porosity reduces the overall level of the FLD, and consequently reduces the material ductility.

It was shown in the previous section that the effect of coalescence parameters on the moment of occurrence of localization is crucial. In what follows, we propose to study the

sensitivity of an FLD to these parameters. One notices on Figures 5-a and 5-b that variation of parameters f_{cr} and f_R strongly affects the shape of the FLDs. Indeed, this is mainly due to the role of each parameter in the coalescence modeling, since f_{cr} indicates the onset of coalescence, whereas f_R indicates the complete loss of carrying capacity.

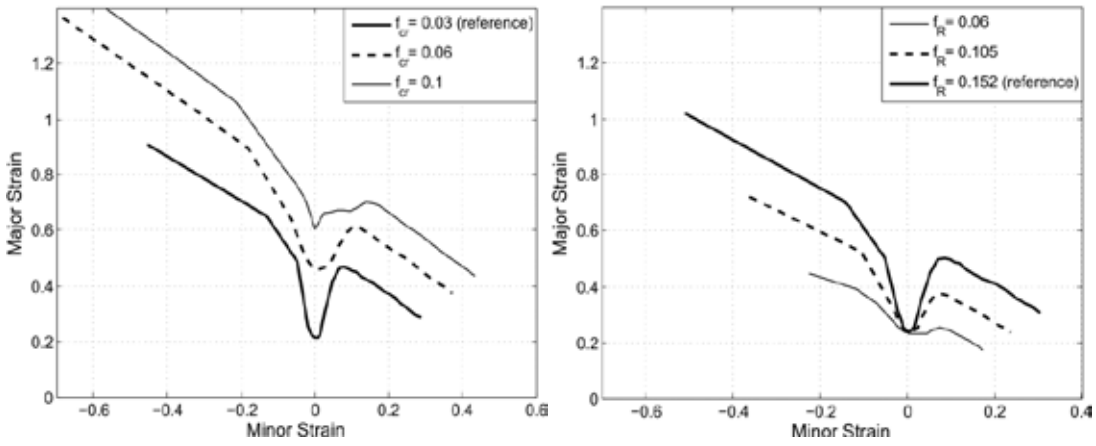

(a) (b)

Figure 4: Effect of coalescence parameters on the prediction of FLDs.

6 CONCLUSIONS

In this work, the combination of the GTN damage model and the Rice's localization criterion, which is based on the singularity of the acoustic tensor, has been proposed for application to sheet metal forming. A preliminary parametric study was conducted for different loading paths, which leads to the following observations: Concerning the nucleation parameters, it seems that the increase of f_N (decrease in s_N or ε_N) tends to lower each point of the forming limit curve. An increase of δ_{GTN} parameter accentuates the softening slope during the coalescence stage, which leads to an earlier detection of localization. It was shown that the choice of the coalescence parameters is particularly crucial in the prediction of localization. For the coalescence parameters, the increase of f_{cr} produces an upward translation of the FLD, while for f_R we notice that its decrease will lower the overall level of the FLDs.

REFERENCES

[1] Lemaitre, J.. A course on damage mechanics. (1992).
[2] Gurson, A.L.. Continuum theory of ductile rupture by void nucleation and growth: Part I-yield criteria and flow rules for porous ductile media. *Journal of Engineering Materials and Technology*, **99**(1):2–15, (1977).
[3] Tvergaard, V. Influence of voids on shear bands instabilities under plain strain conditions. *International Journal of Fracture* (1981) **32**:57-169.
[4] Tvergaard, V. and Needleman, A.. Analysis of the cup-cone fracture in a round tensile bar. *Acta Metallurgica*, (1984) **32**:57.

[5] Brunet, M., Mguil, S. and Morestin, F.. Analytical and experimental studies of necking in sheet metal forming processes. *Journal of Material Processing Technology*, (1998) **80-81**:40-46.
[6] Hora, P., Tong, L. and Reissner, J.. A prediction method of ductile sheet metal faillure in FE simulation. *Numisheet* (1996) 252-256.
[7] Besson, J., Steglich, D. and Brocks, W.. Modeling of crack growth in round bars and plane strain specimens. *International Journal of Solids and Structures* (2001) **38**:8259-8284.
[8] Sànchez, P. J., Huespe, A. E. and Oliver, J.. On some topics for the numerical simulation of ductile fracture. *International Journal of Plasticity* (2008) 24:1008-1038.
[9] Tvergaard, V.. Effect of yield surface curvature and void nucleation on plastic flow localization. *Journal of the Mechanics and Physics of Solids* (1987) **35**:43-60 .
[10] Chu, C. C. and Needleman, A.. Void nucleation effects in biaxially stretched sheets. *Journal of Engineering Material and Technology* (1980) 102:249.
[11] Rice, J. R.. The localization of plastic deformation. *Theorical and applied mechanics. Koiter ed.* (1976) 207-227.
[12] Rudnicki, J. W. and Rice, J. R. Conditions for the localization of deformation in pressure sensitive dilatant materials. *Journal of the Mechanics and Physics of Solids* (1975) **23**:71-394.
[13] Haddag, B., Abed-Meraim, F. and Balan, T.. Strain localization analysis using a large deformation anisotropic elastic-plastic model coupled with damage. *International journal of Plasticity* (2009) **25**:1970-1996.
[14] Aravas, N.. On the numerical integration of a class of pressure dependant plasticity models. *International Journal of Numerical Methods* (1987) 1395-1416.
[15] Oliver, J., Huespe, A., Blanco, S. and Linero, D. Stability and robustness issues in numerical modeling of material faillure with stong discontinuty approach. *Computer Methods in Applied Mechanical Engineering* (2005) **195:**7093-7114.
[16] Benzerga, A. A.. Micromechanics of coalescence in ductile fracture. *Journal of the Mechanics and Physics of Solids* (2002) 1331-1362.
[17] Zhang, Z. L., Thaulow, C. and Ødegård, J. A complete Gurson model approach for ductile fracture. *Engineering Fracture Mechanics* (2000) 155-168.
[18] Pardoen, T. and & Hutchinson, J. W. An extended model for void growth and coalescence. *Journal of the Mechanics and Physics of Solids* (2000) 2467–2512.

XI International Conference on Computational Plasticity. Fundamentals and Applications
COMPLAS XI
E. Oñate, D.R.J. Owen, D. Peric and B. Suárez (Eds)

STIFFNESS AND STRENGTH OF HIERARCHICAL POLYCRYSTALLINE MATERIALS WITH IMPERFECT INTERFACES

MARCO PAGGI[1] AND PETER WRIGGERS

Leibniz University Hannover
Institute of Continuum Mechanics
Appelstraße 11, 30167 Hannover, Germany
e-mail: paggi@ikm.uni-hannover.de, wriggers@ikm.uni-hannover.de

Key words: Hierarchical materials; Polycrystalline materials; Imperfect interfaces; Cohesive zone models; Finite element method.

Abstract. In this paper, considering a cohesive zone model (CZM) for finite thickness interfaces recently proposed by the authors, the stiffness of polycrystalline materials with imperfect interfaces is characterized. Generalized expressions for the Voigt and Reuss estimates of the effective elastic modulus of the composite are derived to interpret the numerical results. Considering a polycrystalline material with a hierarchical microstructure, the interaction between interfaces at the different hierarchical levels is numerically investigated. A condition for scale separation, which suggests how to design the optimal microstructure to maximize the material tensile strength is determined. An original interpretation of this phenomenon based on the concept of flaw tolerance is finally proposed.

1 INTRODUCTION

The upper and lower bounds to the effective stiffness of a composite material have long been the subject of research (see [1] for an overview). Bounds to the effective properties of heterogeneous solids were put forward by Voigt [2] and Reuss [3]. Eshelby [4] obtained a compact solution that has been the basis for many approximation methods. Based on variational principles, Hashin and Shtrikman [5] developed a refined model for the computation of the effective properties. Several other models have been proposed to estimate the effective properties and their bounds, including computational homogenization [6] for linear and also nonlinear elasticity [7, 8]. Recent progress in this field regards the analysis of random components, coupling homogenization methods with a statistical description of randomness [9].

[1]On leave from Dept. of Structural and Geotechnical Engineering, Politecnico di Torino, Torino, Italy.

Based on Hill's work [10], the effective elastic modulus of a polycrystalline material with perfectly bonded interfaces, E_{eff}, is bounded as follows:

$$E_{\text{R}} \leq E_{\text{eff}} \leq E_{\text{V}}, \tag{1}$$

where the indices R and V stand for Reuss and Voigt estimates. The Reuss estimate corresponds to *isostress* conditions, whereas the Voigt estimate is related to *isostrain* conditions and are given by:

$$E_{\text{R}} = \left(\sum_{i=1}^{n} \frac{v_i}{E_i} \right)^{-1}, \tag{2a}$$

$$E_{\text{V}} = \sum_{i=1}^{n} v_i E_i, \tag{2b}$$

where the summation is extended to all the n material components and v_i denotes the volumetric fraction of the i-th component ($\sum_{i=1}^{n} v_i = 1$). However, these estimates apply in case of perfectly bonded interfaces, a situation which is often violated in engineering applications.

In this paper, finite element simulations of polycrystalline materials with imperfect interfaces governed by the cohesive zone model (CZM) are carried out. To interpret the numerical results, a generalization of the Voigt and Reuss estimates in case of imperfect cohesive interfaces is proposed. In the second part of the paper, considering a polycrystalline material with a hierarchical microstructure, the effect of interfaces at the different hierarchical levels on the material tensile strength is investigated. The condition for scale separation, often put forward in homogenization methods, is carefully checked and it is found that it is not always fulfilled. When scale separation holds, the material microstructure becomes flaw tolerant and the material tensile strength is maximized, for given interface characteristics at the upper level. These results are useful for a better understanding of the mechanisms leading to the superior mechanical properties of hierarchical polycrystalline materials with respect to their conventional counterpart [11].

2 GENERALIZED VOIGT AND REUSS ESTIMATES OF THE EFFECTIVE ELASTIC MODULUS IN CASE OF IMPERFECT INTERFACES

To understand how imperfect interfaces modify the bounds to the effective elastic modulus of a heterogeneous material, let us consider the composite layouts shown in Fig. 1. We assume that m material layers behave linear elastically and the remaining $q = n - m$ layers are finite thickness interfaces undergoing damage. Damage is related to the deformation of the interface layer as proposed in [12]. Hence, an effective damage D_i is introduced for a generic interface layer i:

$$D_i = \left[\left(\frac{w_i}{w_{c,i}} \right)^2 + \left(\frac{u_i}{u_{c,i}} \right)^2 \right]^{\alpha_i/2}, \quad 0 \leq D_i \leq 1, \tag{3}$$

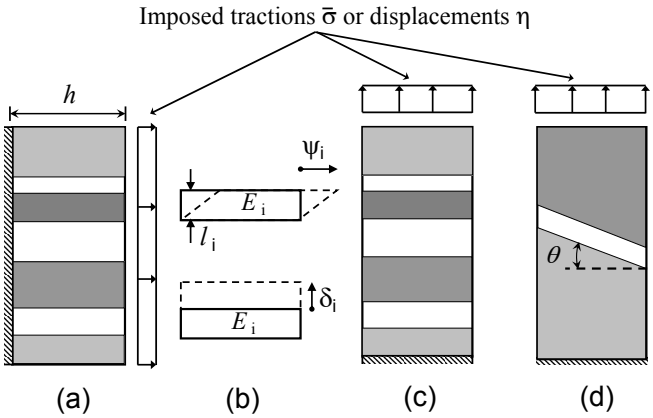

Figure 1: A composite system subjected to imposed tractions or displacements with different orientations of the interfaces with respect to the load direction.

where $w_i = \delta_i - \delta_{e,i} > 0$ is the difference between the displacement of the i-th layer in the direction perpendicular to the interfaces (Fig. 1(b))and a threshold value $\delta_{e,i}$ corresponding to the onset of damage. The variable $u_i = \psi_i - \psi_{e,i} > 0$ is the difference between the displacement of the i-th layer in the direction parallel to the material interfaces (Fig. 1(b)) and its threshold value $\psi_{e,i}$. The parameters $w_{c,i}$ and $u_{c,i}$ are critical values of the separations in the two orthogonal directions. For more details about the effect of the parameter α_i to the evolution of damage, the reader is referred to [12].

Considering the system in Fig. 1(a), isostrain conditions are simulated by imposing uniform horizontal displacements η on the vertical boundary on the right and fully restraining the opposite boundary. The horizontal boundaries are traction-free. The horizontal axial strain in each layer equals the average strain $\overline{\epsilon} = \eta/h$, where the distance h is quoted in Fig. 1(a). The stresses are different in the material regions and the average stress is:

$$\overline{\sigma} = \sum_{i=1}^{n} v_i \sigma_i = \left(\sum_{i=1}^{n} v_i E_i \right) \overline{\epsilon} = \left(\sum_{i=1}^{n} v_i E_i - \sum_{i=1}^{q} v_i D_i E_i \right) \overline{\epsilon}, \tag{4}$$

where the elastic modulus of the damaged interfaces is $E_i^D = (1 - D_i)E_1$. A generalized Voigt estimate considering damage in the finite thickness interfaces is therefore derived:

$$E_{\mathrm{V}}^{\mathrm{G}} = \sum_{i=1}^{n} v_i E_i - \sum_{i=1}^{q} v_i D_i E_i. \tag{5}$$

For $D_i = 0$, the classical Voigt estimate for the elastic modulus is recovered. However, neglecting Poisson's effects, it is interesting to note that the boundary conditions for this problem lead to $\delta_i = 0$ and $\psi_i = 0$. Consequently, no damage develops and the classical Voigt estimate holds without any modification.

Let us now consider the same problem but subjected to isostress conditions. They are obtained by imposing a constant horizontal traction $\sigma = \overline{\sigma}$ on the vertical boundary on the right (see Fig. 1(a)). The axial strain is different in the layers and its average is:

$$\overline{\epsilon} = \left(\sum_{i=1}^{n} \frac{v_i}{E_i} + \sum_{i=1}^{q} \frac{v_i D_i}{E_i(1-D_i)} \right) \overline{\sigma}. \tag{6}$$

The effective elastic modulus gives the generalized Reuss estimate considering damage in the finite thickness interfaces:

$$E_{\mathrm{R}}^{\mathrm{G}} = \left(\sum_{i=1}^{n} \frac{v_i}{E_i} + \sum_{i=1}^{q} \frac{v_i D_i}{E_i(1-D_i)} \right)^{-1}. \tag{7}$$

The classical Reuss estimate is recovered when $D_i = 0$. In this case, however, we cannot exclude a positive relative tangential displacement u_i and therefore $D_i > 0$ in some finite thickness interface.

A different direction of loading with respect to the layer assembly can also be analyzed (see Fig. 1(c)). Vertical displacements or tensile tractions are imposed on the top horizontal boundary. The opposite boundary is fully constrained and the lateral sides are traction free. It is easy to verify that in this case both imposed displacement and imposed traction boundary conditions lead to an isostress state. The mechanical system can be idealized as a set of elastic springs (with damage) in series, whose effective stiffness can be estimated using the generalized Reuss formula (7). In this case, damage is related to a positive displacement w_i.

The generalized Reuss estimate derived in this study can also be applied to the case of zero-thickness interfaces governed by a standard cohesive zone model (CZM). The additional contribution of the interfaces to the Reuss estimate is due to the displacement discontinuities g_T and g_N in the tangential and normal directions, respectively. In case of Fig. 1(a) with isostress boundary conditions, the displacement discontinuity (gap) is g_T and we have:

$$\overline{E} = \left(\sum_{i=1}^{n} \frac{v_i}{E_i} + \sum_{i=1}^{q} \frac{g_{T,i}}{h} \right)^{-1}. \tag{8}$$

For the case in Fig. 1(c), the displacement discontinuity is represented by g_N:

$$\overline{E} = \left(\sum_{i=1}^{n} \frac{v_i}{E_i} + \sum_{i=1}^{q} \frac{g_{N,i}}{h} \right)^{-1}. \tag{9}$$

For an interface inclined by a generic angle $\theta_i \neq 90^\circ$ with respect to the direction of loading (see Fig. 1(d)), mixed mode deformation occurs and both w_i and u_i contribute to D_i. For a standard CZM, Eq.(9) should be used, with $g_{N,i}$ determined in correspondence of a given angle of mode mixity, $\theta_i = \arctan(g_{T,i}/g_{N,i})$.

3 STIFFNESS OF HIERARCHICAL POLYCRYSTALLINE MATERIALS

In this section, the stiffness of a cellular polycrystalline material with imperfect interfaces is numerically analyzed using the finite element method. One forth of a representative volume element (RVE) of the hexagonal microstructure is shown in Fig. 2(a). Zero-thickness interface elements are introduced between the linear elastic constant strain triangular elements used to discretize the continuum. The constitutive response of the interfaces is governed by the nonlocal CZM for finite thickness interfaces proposed in [12]. An implicit solution scheme is adopted, which requires the computation of the tangent stiffness matrix and the residual vector of the interface elements to be used in a Newton-Raphson iterative scheme. Moreover, the treatment of the CZM requires a nested Newton-Raphson loop to compute the cohesive tractions, see [13]. The RVE is tested in uniaxial tension, imposing the displacements on the nodes belonging to the vertical boundary on right.

Different bulk moduli E_{B} for the grains are considered. For infinitely stiff grains, $E_{\mathrm{B}} \to \infty$, the deformability is only due to the cohesive interfaces. The obtained dimensionless stress-strain curve is therefore that of the CZM of the inclined interface with a rescaled abscissa g_N/h, where h is the horizontal lateral size of the sample (see Fig. 2(b)). Reducing E_{B}, the deformability of the continuum increases and the effect of the interfaces is mitigated. The nonlinear CZM is responsible for the deviation from linearity in the stress-strain diagram, as it can be quantified by comparing the solid lines with the corresponding dashed lines in Fig. 2(b).

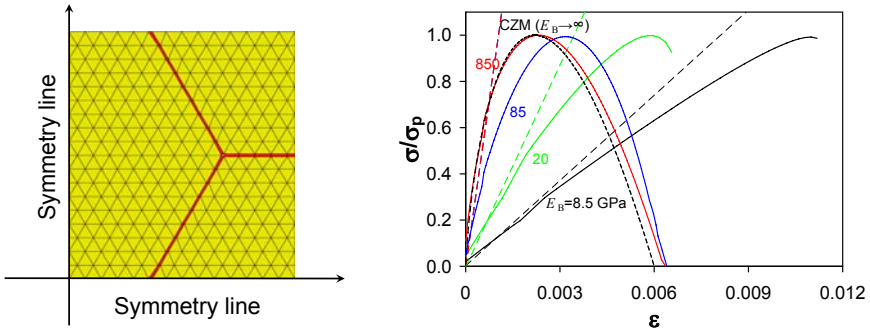

(a) 1/4 of the RVE. (b) Average stress vs. strain response.

Figure 2: The effect of the bulk modulus E_{B} on the average stress-strain response.

The computed tangent effective elastic modulus vs. σ/σ_p, where σ_p is the peak stress, is shown in Fig. 3(a). The CZM response is the upper limit for E_{eff}, obtained for infinitely stiff grains. The curves become progressively independent of σ/σ_p by reducing E_{B}. Since the specimen is subjected to isostress conditions, the obtained trend can be interpreted according to Eq.(7) with $n = 1$ and $q = 1$. Using the shape of the CZM corresponding to the angle of mode mixity induced by the hexagonal geometry ($\theta = 30°$), the analytical

predictions are shown in Fig. 3(b). The perfect agreement with the numerically computed curves in Fig. 3(a) is achieved.

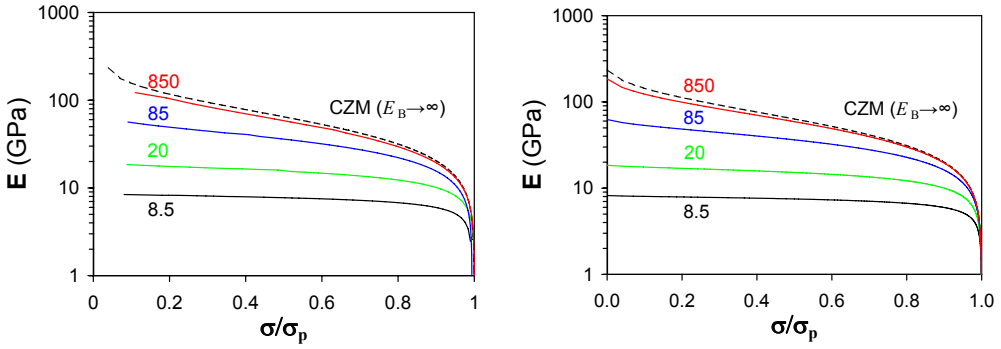

(a) Numerical results. (b) Analytical predictions.

Figure 3: Tangent effective elastic modulus E vs. σ/σ_p

Two further levels of hierarchy are now considered. The macroscopic level ($l = 1$) is the same as that analyzed in Fig. 2. Each grain is then partitioned into other cellular grains, generating the material mesostructure ($l = 2$). This procedure is repeated once more to obtain the material microstructure ($l = 3$) inside the mesogranules, see Fig. 4(a). For the sake of simplicity, and without any loss of generality, the CZM parameters are assumed to be the same at each level. The refinement of the material microstructure leads to a decrease of the dimensionless effective elastic modulus E/E_B for a given stress level, see Fig. 4(b). The numerical predictions using Eq.(7) with a constant angle of mode mixity equal to 30° are still a good approximation of the numerical results. More accurate predictions can be obtained by considering the actual angle of mode mixity of the various interfaces.

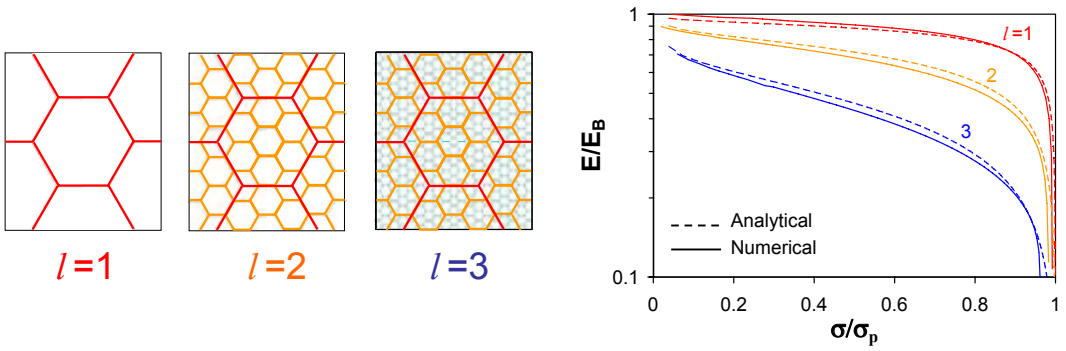

(a) Sketches of the hierarchical levels. (b) Numerical–analytical comparison.

Figure 4: Tangent effective elastic modulus E/E_B vs. σ/σ_p for a system with l hierarchical levels.

4 STRENGTH OF HIERARCHICAL POLYCRYSTALLINE MATERIALS

In this section we study focus on the effect of interfaces with different properties on the tensile strength of hierarchical polycrystalline materials. Let us consider the finest microstructure with hexagonal grains examined in the previous section as the level 1 (blue interfaces in Fig. 5(a)). A two-level hierarchical microstructure is realized by considering geometrically self-similar hexagonal mesogranules (level 2, red interfaces in Fig. 5(a)) embedding the hexagonal micrograins of the level 1. To do so, the interface characteristics at the level 2 are modified in order to make them tougher than those at the level 1. This condition alone is not sufficient to modify the crack pattern at failure and improve the material response. In fact, it is still possible to find a subvertical crack path involving only interfaces of level 1, as it happens without hierarchy. To involve the interfaces of the level 2, all the properties of the interfaces of the hexagons containing a triple junction have to be modified. This leads to the final configuration shown in Fig. 5(a).

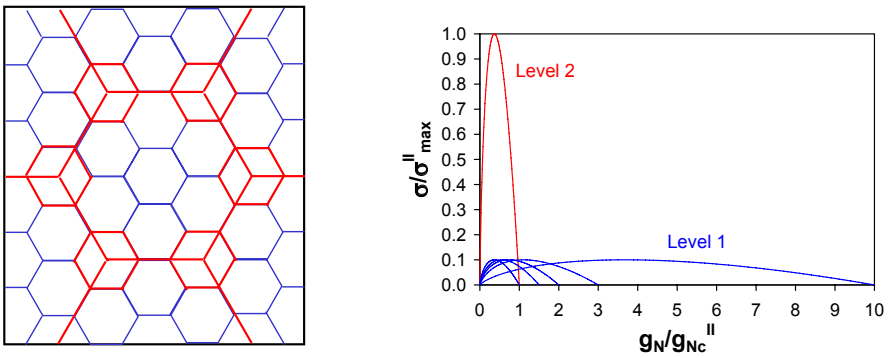

(a) Interfaces at the 2 levels. (b) Shape of the CZMs.

Figure 5: CZMs of the interfaces at the different levels: level 1 (blue), level 2 (red).

The material response is now investigated by performing virtual tensile tests in the horizontal directions and computing the peak stress σ_p of the average stress-strain curve. The shapes of the Mode I CZMs of the interfaces at the levels 1 and 2 are shown in Fig. 5(b). The ratio between the peak cohesive tractions of the CZMs at the two levels is constant and equal to $\sigma^{\rm I}_{\rm max}/\sigma^{\rm II}_{\rm max} = 0.1$. Different Mode I fracture energies (evaluated as the area between the Mode I CZM curve) for the level 1 are considered, exploring a range $G^{\rm I}_{\rm IC}/G^{\rm II}_{\rm IC}$ from 0.1 to 0.5 (see the different shapes of the CZM of the level 1 in Fig. 5(b)).

Dimensional analysis considerations suggest the following dependency for the tensile strength σ_p on the variables of the parametric analysis:

$$\sigma_p = \sigma_p \left(\sigma^{\rm I}_{\rm max}, G^{\rm I}_{IC}, d^{\rm II}, E_{\rm B}\right), \tag{10}$$

where $\sigma^{\rm I}_{\rm max}$ is the peak cohesive traction at the level 1, $G^{\rm I}_{\rm IC}$ is the Mode I fracture energy of the interfaces at the same level, $d^{\rm II}$ is the diameter of the mesogranules and $E_{\rm B}$ is the

bulk elastic modulus. Considering $G_{\rm IC}^{\rm I}$ and $d^{\rm II}$ as the variables with independent physical dimensions, the application of the Buckingham's theorem of dimensional analysis yields:

$$\frac{\sigma_p d^{\rm II}}{G_{\rm IC}^{\rm I}} = \Phi\left(\frac{\sigma_{\rm max}^{\rm I} d^{\rm II}}{G_{\rm IC}^{\rm I}}, \frac{E_{\rm B} d^{\rm II}}{G_{\rm IC}^{\rm I}}\right) = \Phi(s_1, s_2). \tag{11}$$

Changing $G_{\rm IC}^{\rm I}$, the dimensionless numbers s_1 and s_2 vary at the same time. It is therefore convenient to introduce a combination of these dimensionless numbers and plot the results of the parametric analysis as a function of it. Considering $s = s_2/s_1^2$, we have:

$$s = \frac{s_2}{s_1^2} = \frac{G_{\rm IC}^{\rm I} E_{\rm B}}{(\sigma_{\rm max}^{\rm I})^2 d^{\rm II}} = \frac{l_{\rm CZM}^{\rm I}}{d^{\rm II}}. \tag{12}$$

This dimensionless number is proportional to the ratio between the critical process zone size at the level 1, $l_{\rm CZM}^{\rm I}$, and the grain size of the mesograin, $d^{\rm II}$.

From numerical results (Fig. 6), the computed dimensionless tensile strength is an increasing function of $l_{\rm CZM}^{\rm I}/d^{\rm II}$ up to $l_{\rm CZM}^{\rm I}/d^{\rm II} = 1$, when a plateau is reached. A further increase of the interface fracture energy of the level 1 does not permit us to increase the tensile strength. This result can be explained according to a consideration of *flaw tolerance*, as also proposed by Gao [14] for defects in bone-like materials. When the interface cracks inside the mesogranule (having a size $a \leq d^{\rm II}$) are such that $l_{\rm CZM}^{\rm I} > d^{\rm II}$, their maximum opening displacement lies within the range of cohesive interactions. Therefore, no stress-free cracks develop in the mesogranule, which is able to tolerate the intrinsic defects of any size. Fracture has to involve the upper scale interfaces at the level 2 and the strength is maximized. Similar considerations have been put forward by Carpinteri [15] for the problem of tension collapse that precedes brittle crack propagation in a strip. These results are important for the application of homogenization techniques. In fact, a separation of scales, leading to no interaction between the interfaces at the different hierarchical levels is fulfilled only for $l_{\rm CZM}^{\rm I}/d^{\rm II} > 1$.

The diagram in Fig. 6 can also be interpreted in a different way. For given material interface properties at the level 1 ($l_{\rm CZM}^{\rm I}$ is fixed), the optimal geometry of the mesostructure corresponds to $d^{\rm II} = l_{\rm CZM}^{\rm I}$. In this way, the interfaces at the upper level act as *crack arresters* for the microcracks at the lower level. When this flaw tolerance condition is achieved at a given level, the same reasoning can be repeated for the higher hierarchical levels in order to obtain the optimal response for a given set of material properties.

5 CONCLUSION

In the present paper, the role of imperfect interfaces on the stiffness and strength of hierarchical polycrystalline materials has been numerically investigated using finite elements. The constitutive behavior of finite thickness interfaces has been modelled using the nonlocal CZM recently proposed in [12, 13].

Numerical simulations show that the effective elastic modulus depends on the debonding process occurring at the interfaces. Generalized Voigt and Reuss estimates accounting

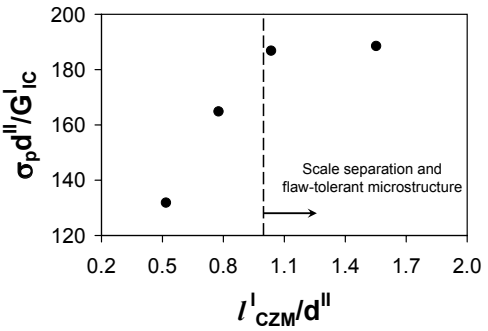

Figure 6: Dimensionless tensile strength vs. ratio between the critical process zone size and the diameter of the mesogranules.

for such a form of nonlinearity are proposed for the computation of the bounds to the tangent effective elastic modulus. The interplay between the interface deformability and the elasticity of the bulk material has been numerically characterized.

Finally, the effect of interfaces at different hierarchical levels on the strength of a two-level hierarchical material has been numerically investigated. The results show that the condition for scale separation applies only for certain properties of the interfaces at the lower level. If such a condition, represented by the inequality $l^{\mathrm{I}}_{\mathrm{CZM}} > d^{\mathrm{II}}$, is fulfilled, then the microstructure becomes flaw tolerant and the strength is ruled by the interfaces characteristics at the upper level.

ACKNOWLEDGEMENTS

MP would like to thank the Alexander von Humboldt Foundation for supporting his research stay at the Leibniz Universität Hannover during the year 2010.

REFERENCES

[1] Nemat-Nasser, S. and Hori, M. *Micromechanics: Overall Properties of Heterogeneous Solids*. Elsevier, Amsterdam (1999).

[2] Voigt, W. Über die Beziehung zwischen den beiden Elastizitätskonstanten isotroper Körper. *Wied. Ann.* (1889) **38**:573-587.

[3] Reuss, A. Berechnung der Fliessgrenz von Mischkristallen auf Grund der Plastizitätsbedingung fur Einkristalle. *Z. Angew. Math. Mech.* (1929) **9**:49-58.

[4] Eshelby, J.D. The elastic field of an ellipsoidal inclusion, and related problems. *Proc. Royal Soc. A* (1957) **241**:376-396.

[5] Hashin, Z., Shtrikman, S. On some variational principles in anisotropic and nonhomogeneous elasticity. *J. Mech. Phys. Solids* (1962) **10**:335-342.

[6] Zohdi, I.I., Wriggers, P. *Introduction to Computational Micromechanics*. Springer, Berlin, Heidelberg, New York (2005).

[7] Temizer, İ., Zohdi, T.I. A numerical method for homogenization in non-linear elasticity. *Comp. Mechanics* (2006) **40**:281–298.

[8] Temizer, İ., Wriggers, P. An adaptive method for homogenization in orthotropic nonlinear elasticity. *Comp. Meth. Appl. Mech. Engng.* (2007) **196**:3409–3423.

[9] Ma, J., Temizer, İ., Wriggers, P. Random homogenization analysis in linear elasticity based on analytical bounds and estimates. *Int. J. Solids and Struct.* (2011) **48**:280–291.

[10] Hill, R. The elastic behavior of a crystalline aggregate. *Proc. Phys. Soc. London A* (1952) **65**:349–354.

[11] Fang, Z.K. et al. Fracture resistant super hard materials and hardmetals composite with func-tionally graded microstructure. *Int. J. Refr. Met. & Hard Mat.* (2001) **19**:453–459.

[12] Paggi, M., Wriggers, P. A nonlocal cohesive zone model for finite thickness interfaces Part I: mathematical formulation and validation with molecular dynamics. *Comp. Materials Science* (2011) **50**:1625–1633.

[13] Paggi, M., Wriggers, P. A nonlocal cohesive zone model for finite thickness interfaces Part II: FE implementation and application to polycrystalline materials. *Comp. Materials Science* (2011) **50**:1634–1643.

[14] Gao H. Application of fracture mechanics concepts to hierarchical biomechanics of bone and bon-like materials. *Int. J. Fract.* (2006) **138**:101–137.

[15] Carpinteri A. Notch sensitivity in fracture testing of aggregative materials. *Engng. Fract. Mech.* (1982) **16**:467-481.

XI International Conference on Computational Plasticity. Fundamentals and Applications
COMPLAS XI
E. Oñate, D.R.J. Owen, D. Peric and B. Suárez (Eds)

AN ARBITRARY LAGRANGIAN-EULERIAN (ALE) APPROACH FOR THE MODELING OF TENSION LEVELING PROCESSES

LORENZ STEINWENDER*, ALEXANDER KAINZ*, KONRAD KRIMPELSTÄTTER† AND KLAUS ZEMAN*

*Institute of Computer-Aided Methods in Mechanical Engineering
Johannes Kepler University Linz
Altenbergerstraße 69, 4040 Linz, Austria
e-mail: lorenz.steinwender@jku.at, web page: http://came.mechatronik.uni-linz.ac.at

†Siemens VAI Metals Technologies GmbH
Turmstraße 44, 4031 Linz, Austria
e-mail: konrad.krimpelstaetter@siemens.com, web page: http://www.siemens-vai.com

Key words: Metal Forming, Tension Leveling, Arbitrary Lagrangian-Eulerian (ALE), Principle of Virtual Work

Abstract. Strip flatness and surface quality are crucial factors for the production of high-quality cold-rolled metal strip. Tension leveling (employed as one of the final steps in continuous galvanizing and finishing lines) improves strip flatness and minimizes residual stresses by inducing small elasto-plastic strip deformations, while the strip is bent under high tension stresses around multiple rolls with small diameters.

Simulations of tension leveling processes employing commercial Finite Element software packages yield unacceptable computational costs: The small and coupled elasto-plastic deformations occur simultaneously at concentrated regions along the strip bending line and steady-state solutions cannot be reached before at least one strip cross-section has passed through the entire process unit of the tension leveler.

In order to overcome these critical aspects, a new and alternative modeling approach, based on the principle of virtual work and on a specialized "Arbitrary Lagrangian-Eulerian" (ALE) formulation was elaborated. This novel concept utilizes "Parametric Shape Functions" (PSF) that describe both geometry and strain distribution of the deformed strip. The decoupling of the mesh movement from the material movement in the ALE description allows for the implementation of highly efficient contact algorithms, while the strip length under consideration can be minimized. Compared to (already) optimized commercial FEM-models, the PSF-model exhibits a drastic reduction of degrees of freedom and computational costs (by a factor of 100 and more in typical test cases) while high agreement of the key results is simultaneously maintained.

1 INTRODUCTION

As the demand for perfect flatness and outstanding surface properties both of hot- and cold-rolled strips rises continuously, tension leveling becomes an increasingly important process step in the production of high-class metal strip. Tension levelers are typically located at the exit of strip processing lines (for example continuous galvanizing or finishing lines) to reduce flatness deficiencies like center and edge buckles or strip camber as well as to minimize residual stresses of the finished strip. These often unacceptable quality deficiencies are the result of an inappropriate material flow inside the roll gap during hot- or cold-rolling operations or may occur due to plastic deformations after rolling (e.g. during coiling or uncoiling).

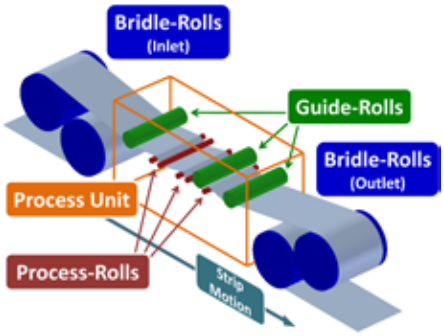

Figure 1: Typical Tension Leveler Setup.

Figure 2: Industrial Tension Leveler.

As depicted in Figure 1, a tension leveler typically consists of a set of *bridle-rolls* at the inlet and outlet (large black & yellow rolls in Figure 2) and a *process unit* (green machine block in Figure 2), which is located in-between the bridle-rolls. In this process unit the metal strip is bent alternately under high tension stresses (in the range of 5-70% of the yield strength, cp. [5]) around *guide-rolls* and *process-rolls* with particularly small diameters (both roll types are typically undriven). The combined bending and tensile stresses yield elasto-plastic strip deformations, which are comparatively small at the strip centerline (where plastic strip elongations typically do not exceed a value of about five percent), but may be locally considerably large (at the strip surfaces) due to the superimposed bending strains.

The cumulative amount of the elasto-plastic centerline strain depends strongly on the *curvature peaks* of the strip, which occur at the strip/roll contact points in typical tension leveling setups. Observations at industrial tension levelers prove that the strip will not approach the roll radii in many typical tension leveling cases – in particular when thick strip, small rolls, low strip tension, small roll adjustments, high-strength materials or high strip velocities (leading to pronounced inertial effects) are involved. In these cases, the strip will exhibit *line contact* as opposed to *surface contact* and the curvature of the strip will be smaller than the curvature of the roll in this point. The fast and precise prediction

of the actual strip curvature distribution is therefore of high relevance to a reliable design of tension leveling machines.

2 STATE OF THE ART & PROBLEM STATEMENT

First works dealing with aspects of the tension leveling process date back to the 1950s and 1960s. At that time it was common in the scientific community to assume that the strip would approach the curvature of the process-rolls in all strip/roll contact points (cp. e.g. [2]). In the early 1970s, Sheppard and Roberts [3] were among the first researchers to state that the actual bending radius of the strip in the contact point can be significantly larger than the radius of the roll. In the mid 1970s, first attempts were made to empirically predict the strip curvature at those rolls, where line contact occurs [4].

Hoffmann [5] proposed in his PhD thesis a basic, iterative model for the geometrical fitting of the strip curvature distribution in a given roll system. Applying certain simplifications and restrictions, a prediction for the shape of the strip bending line could be made for different strip dimensions, materials and roll settings.

With the emergence of sufficiently fast mainframes in the late 1990s, the Finite Element Method (FEM) allowed for the numerical determination of the strip curvature distribution. However, due to their excessive calculation times, most FEM analyses presented in the literature still require problematic trade-offs between the model's significance and the computational cost efficiency and can therefore only be used to simulate few selected tension leveling scenarios.

Nowadays, in many cases, tension leveling designs and roll adjustment strategies are based on computationally expensive but still rough offline calculation models, which have to be supplemented by trial and error procedures during the operation. In order to improve the design of tension leveling machines, precise numerical methods are essential. Key objectives of adequate models are the determination of the strip bending line, the analysis of the reaction forces at the bending rolls, the required level of tension, the tension losses due to plastic deformation as well as the power requirements of the drives (which was elaborately analyzed by the authors in an associated research project, cp. [6]).

3 CHALLENGES USING COMMERCIAL FINITE ELEMENT PACKAGES

Finite Element Models yield all key results, but require unacceptable computational costs. It could be shown in detailed analyses that both 3-D and 2-D (plane strain) simulations, and both continuum and structural modeling concepts yield comparable and reliable simulation results [7].

The numerical simulation of the tension leveling process utilizing commercial FEM packages is particularly challenging, as the strip is deformed simultaneously at different small regions along its bending line. This sequence of small elasto-plastic deformations has to be treated as a coupled whole. Hence, in a Lagrangian formulation (where mesh and material are coupled throughout the deformation process), the simulated strip has to

be several times longer than the length of the leveler's process-unit and the mesh needs to be finely discretized along this entire strip length.

Large numbers of nodes and degrees of freedom, severely non-linear contact characteristics (hard and frictionless, with frequent contact updates), a non-linear constitutive law (elasto-viscoplastic, path-dependent, including the Bauschinger effect) and large strip rotations cause unacceptable simulation runtimes (in the range of a few days for already optimized, but still significant FEM models on modern mainframes) – making such models inappropriate as efficient dimensioning tools for industrial applications.

4 PARAMETRIC SHAPE FUNCTION (PSF) MODEL

To reduce the unacceptable computational costs of FEM simulation models, a novel modeling approach was pursued. On account of an in-depth analysis of the physical correlations relevant for the tension leveling process, appropriate parametric shape functions (PSF) could be identified, which describe both the strip's geometry (i.e. its curvature) and the strain state of the centerline along the Eulerian (i.e. actual) arc length of the strip. The bending line is determined in 2-D (plane strain) employing a drastically reduced number of degrees of freedom as compared to concepts based on commercial FEM software packages (as discussed above).

5 PROPOSED ARBITRARY LAGRANGIAN-EULERIAN FORMALISM

When handling the investigated problem, the application of the Arbitrary Lagrangian-Eulerian (ALE) theory is very advantageous. In the ALE referential formulation, the mesh speed $\hat{v}$ can be chosen arbitrarily, which is a fundamental difference to both the Lagrangian material formulation (where the mesh speed equals the material speed $\rightarrow\ \hat{v} = v$) and the Eulerian spatial formulation (where the mesh speed is zero $\rightarrow\ \hat{v} = 0$).

Any arbitrary position along the bending line of a strip can be denoted in the ALE, the Lagrangian and in the Eulerian formulation. In the Lagrangian material-based formulation, the reference is the *undeformed* centerline of the strip, denoted as the material-fixed arc length coordinate S. In the Eulerian space-based formulation, the arc length is measured along the actual *deformed* centerline of the strip, which is represented as the space-fixed arc length coordinate s. The "axial stretch" $\lambda_{11,CL}$ follows as differential mapping from the Lagrangian to the Eulerian domain at time t

$$ds = \lambda_{11,CL} \cdot dS = (1 + \varepsilon_{11,CL}) \cdot dS \tag{1}$$

and depends on the tangential centerline strain $\varepsilon_{11,CL}$. Let us now introduce a special ALE reference system with an ALE referential coordinate χ along the undeformed centerline of the strip (cp. Figure 3). The referential coordinate χ of a certain material point (described by S in the Lagrangian material-based reference system) is expressed as "particle name difference"

$$\chi(S,t) = S - S_Q(t), \tag{2}$$

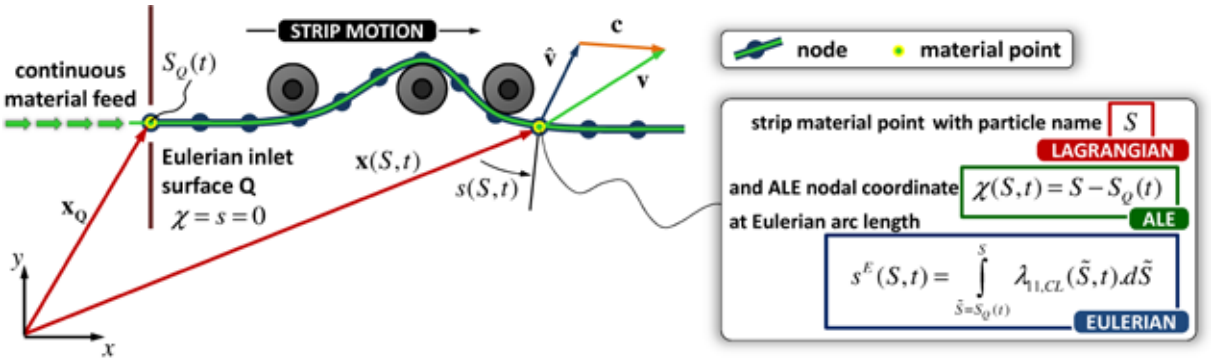

Figure 3: Correlations between Lagrangian, Eulerian and ALE referential domains.

Figure 4: Mapping between Lagrangian, Eulerian and ALE referential domains.

therefore,

$$d\chi = dS \quad \text{and} \quad \left.\frac{\partial}{\partial \chi}\right|_t = \left.\frac{\partial}{\partial S}\right|_t . \tag{3}$$

The actual position of this point along the Eulerian space-based arc length s follows from the integration of Equation 1 as

$$s(S,t) = \int_{S_Q(t)}^{S} \lambda_{11,CL}(\tilde{S},t) \cdot d\tilde{S}. \tag{4}$$

In Equations 2 and 4, $S_Q(t)$ refers to the time-dependent material-based "particle name", which – at time t – enters the system at the Eulerian (hence, space-fixed) inlet surface Q.

According to the correlations presented in [1], the function $\boldsymbol{\varphi}$ denotes the nonlinear mapping from the Lagrangian material domain to the Eulerian spatial domain, the function $\boldsymbol{\Phi}$ represents the nonlinear mapping from the ALE referential domain to the Eulerian spatial domain and the function $\boldsymbol{\Psi}$ designates the linear mapping from the ALE referential domain to the Lagrangian spatial domain (cp. Figure 4).

$$\begin{aligned} \text{Lagrangian} \rightarrow \text{Eulerian:} \quad & \boldsymbol{\varphi} : (S,t) \longmapsto \boldsymbol{\varphi}(S,t) = (s,t) \\ \text{ALE} \rightarrow \text{Eulerian:} \quad & \boldsymbol{\Phi} : (\chi,t) \longmapsto \boldsymbol{\Phi}(\chi,t) = (s,t) \\ \text{ALE} \rightarrow \text{Lagrangian:} \quad & \boldsymbol{\Psi} : (\chi,t) \longmapsto \boldsymbol{\Psi}(\chi,t) = (S,t), \end{aligned} \tag{5}$$

then the mapping $\boldsymbol{\varphi}$ can be expressed by $\boldsymbol{\Phi}$ and $\boldsymbol{\Psi}$ as

$$(s,t) = \boldsymbol{\varphi}(S,t) = \boldsymbol{\Phi}(\chi,t) = \boldsymbol{\Phi}\left(\boldsymbol{\Psi}^{-1}(S,t)\right), \tag{6}$$

with

$$\boldsymbol{\varphi}(S,t) = \begin{pmatrix} \int_{S_Q}^{S} \lambda_{11,CL}(\tilde{S},t)\cdot d\tilde{S} \\ t \end{pmatrix}, \boldsymbol{\Phi}(\chi,t) = \begin{pmatrix} \int_{0}^{\chi} \lambda_{11,CL}(\tilde{\chi},t)\cdot d\tilde{\chi} \\ t \end{pmatrix} \tag{7}$$

$$\text{and } \boldsymbol{\Psi}^{-1}(S,t) = \begin{pmatrix} S - S_Q(t) \\ t \end{pmatrix}.$$

The derivatives of $\boldsymbol{\varphi}$ with respect to the Lagrangian material based arc-length S and time t follow from Equation 6 as

$$\frac{\partial \boldsymbol{\varphi}(S,t)}{\partial(S,t)} = \frac{\partial \boldsymbol{\Phi}}{\partial(\chi,t)} \cdot \frac{\partial \boldsymbol{\Psi^{-1}}}{\partial(S,t)}, \tag{8}$$

which can be re-written in matrix notation as

$$\begin{pmatrix} \left.\frac{\partial s}{\partial S}\right|_t & v \\ 0 & 1 \end{pmatrix} = \begin{pmatrix} \frac{\partial s}{\partial \chi} & \hat{v} \\ 0 & 1 \end{pmatrix} \cdot \begin{pmatrix} \left.\frac{\partial \chi}{\partial S}\right|_t & w \\ 0 & 1 \end{pmatrix}, \tag{9}$$

with

$$\hat{v} = \left.\frac{\partial s}{\partial t}\right|_{\chi} = \int_{0}^{\chi} \left.\frac{\partial \lambda_{11,CL}}{\partial t}\right|_{\tilde{\chi}} \cdot d\tilde{\chi} \text{ and } w = \left.\frac{d\chi}{dt}\right|_{S} = -\frac{dS_Q}{dt}, \tag{10}$$

where v denotes the material speed, $\hat{v}$ represents the nodal speed and w describes the referential material velocity (i.e. the change rate of the "position" of a certain material particle S in the ALE referential coordinate system χ).

Block multiplication of Equation 9 using Equation 10 leads to

$$v = \left.\frac{\partial s}{\partial t}\right|_{S} = \hat{v} + \frac{\partial s}{\partial \chi}\cdot w = \underbrace{\int_{0}^{\chi} \left.\frac{\partial \lambda_{11,CL}}{\partial t}\right|_{\tilde{\chi}} \cdot d\tilde{\chi}}_{\substack{\text{nodal movement:} \\ \text{transient phase only}}} + \underbrace{\lambda_{11,CL}\cdot w}_{\substack{\text{transient} \\ \text{phase \&} \\ \text{steady} \\ \text{state}}}, \tag{11}$$

which can be transformed into the definition of the convective velocity c (cp. again [1]), which follows as

$$c = v - \hat{v} = \frac{\partial s}{\partial \chi} \cdot w = \lambda_{11,CL} \cdot w. \tag{12}$$

Note that the convective speed c will only coincide with w if $ds/dS = 1$, implying that the mapping is purely translational, i.e. not exhibiting any axial stretches. Furthermore, the nodal speed $\hat{v}$ will vanish under steady state conditions for this special ALE formulation, as $\partial\lambda_{11,CL}/\partial t|_{\chi\in[0,\chi_{END}]} = 0$ in a steady state. Hence, in the considered steady state, the material speed and the convective speed coincide ($v = c$). The material time derivative of a physical distribution $f = f^{LAG}(S,t) = f^{EUL}(s,t) = f^{ALE}(\chi,t)$ along the strip's bendingline can be written as

$$\frac{df}{dt} = \left(\left.\frac{\partial}{\partial t}\right|_S\right) f^{LAG} = \left(\left.\frac{\partial}{\partial t}\right|_s + v \cdot \frac{\partial}{\partial s}\right) f^{EUL} = \left(\left.\frac{\partial}{\partial t}\right|_\chi + w \cdot \frac{\partial}{\partial \chi}\right) f^{ALE}. \tag{13}$$

The ALE steady state condition follows as

$$\left.\frac{\partial f}{\partial t}\right|_\chi = \underbrace{\left(\frac{1}{\lambda_{11,CL}} \cdot v - w\right)}_{\substack{=0 \text{ in the steady state} \\ \text{for this special ALE formulation}}} \cdot \frac{\partial f}{\partial \chi}, \tag{14}$$

which illustrates that the time derivatives at any ALE reference coordinate χ must vanish in the considered steady state employing the presented special ALE description.

In special physical scenarios, the presented ALE formulation may be directly transformed either into a purely Lagrangian or into a purely Eulerian formulation.

For the *Lagrangian formulation*, $S_Q(t) = const.$ In this case, the derivative $\partial\boldsymbol{\Psi}^{-1}/\partial(S,t)$ reduces to the identity matrix $\boldsymbol{I}$ and Equation 8 turns into $\partial\boldsymbol{\varphi}/\partial(S,t) = \partial\boldsymbol{\Phi}/\partial(\chi,t)$, which requires that $\chi \equiv S - const.$ The ALE domain changes into a purely Lagrangian formulation, where the material referential velocity as well as the convective velocity are zero ($w = c = 0$), and the material speed and the mesh speed coincide ($v = \hat{v}$).

In the *Eulerian formulation*, $ds/d\chi = \lambda_{11,CL} = 1$ and $\chi \equiv s$. Analogously to above, the derivative $\partial\boldsymbol{\Phi}/\partial(S,t)$ reduces to the identity matrix $\boldsymbol{I}$ and Equation 8 turns into $\partial\boldsymbol{\varphi}/\partial(S,t) = \partial\boldsymbol{\Psi}^{-1}/\partial(S,t)$. For this special case, the ALE domain changes into a purely Eulerian formulation, where the actual material speed v equals both the convective speed c and the material referential velocity w ($v = c = w$), and where the mesh speed $\hat{v}$ is zero ($\hat{v} = 0$) even in the transient phase of the simulation.

6 PARAMETERIZATION

Appropriate *Parametric Shape Functions* are essential both for the strip curvature κ and the centerline strain $\varepsilon_{11,CL}$ distributions

$$\kappa = \frac{d\theta}{ds} \quad \text{and} \quad \varepsilon_{11,CL} = \lambda_{11,CL} - 1 = \left\| \frac{d\boldsymbol{x}}{d\chi} \right\| - 1, \tag{15}$$

where θ denotes the strip section angle and $\boldsymbol{x}(\chi)$ the strip centerline in real space. The section angle θ determines the direction of the strip's tangential unit vector $\hat{\boldsymbol{t}} = (cos\theta, sin\theta)^T$ as well as of the strip's normal vector $\hat{\boldsymbol{n}} = (-sin\theta, cos\theta)^T$. The Bernoulli-Euler beam theory is applied here, which requires that plane strip cross-sections remain plane and normal to the strip centerline throughout the deformation.

The nodal interpolation scheme (i.e. the order of the shape functions used in-between the parametric sampling points at the nodes) must be chosen carefully to comply with the fundamental correlations of the local equilibrium conditions in curved rods. As outlined in [8], the distribution of the bending moment $M(s)$ along the actual Eulerian arc length s must be continuous within the process unit of a tension leveler, however, the first derivative dM/ds of the bending moment with respect to the arc length, as well as the shear force distribution $F_{12}(s)$ are typically discontinuous at the contact areas. The distribution of the concentrated tangential strip force $F_{11}(s)$ is typically continuous, if the rolls are not driven.

Presuming a continuous, path-dependent, elasto-viscoplastic constitutive law (excluding special phenomena like a pronounced yield strength, recrystallization processes, crack formations, etc.), then arbitrarily small tangential strip force and bending moment variations are the result of arbitrarily small cross-section strain variations. In this case, the continuity condition of the bending moment distribution $M(s)$ can be extended to the strip curvature distribution $\kappa(s)$, and the continuity condition of the tangential force distribution $F_{11,CL}(s)$ also applies to the strip centerline strain distribution $\varepsilon_{11,CL}$.

7 PRINCIPLE OF VIRTUAL WORK

The *principle of virtual work* is employed in order to identify the parameter set that matches the solution. Only for this parameter set, the virtual internal strain energy δU equals the virtual work of the external forces δW, hence, the principle of virtual work can be written as

$$\delta U - \delta W = 0 = \sum_{i=1}^{n} \delta P_i \cdot \Bigg(\underbrace{\int_0^{l_0} \left(F_{11} \cdot \frac{\partial \varepsilon_{11,CL}}{\partial P_i} + M \cdot \frac{\partial \kappa}{\partial P_i} \right) \cdot d\tilde{\chi}}_{\text{virt. internal strain energy}} - \tag{16}$$

$$- \underbrace{\sum_{j=1}^{k} \mathbf{F}_{\mathbf{EXT},j} \cdot \frac{\partial \mathbf{x}_{\mathbf{EXT},j}}{\partial P_i}}_{\text{virt. work of external forces}} - \underbrace{\int_0^{l_0} \left(\mathbf{q} \cdot \frac{\partial \mathbf{x}}{\partial P_i} \right) \cdot d\tilde{\chi}}_{\text{virt. work of distr. loads}} \Bigg),$$

where P_i denote the shape function parameters ($i \in [1, n]$, with n parameters in total), l_0 represents the modeled, undeformed strip length ($\chi \in [0, l_0]$), $\boldsymbol{F_{EXT,j}}$ (with $j \in [1, k]$) designate the concentrated external forces at the material points $\boldsymbol{x_{EXT,j}}$ and $\boldsymbol{q}(\chi)$ represents the distributed loads along the bending line $\boldsymbol{x}(\chi)$. Distributed loads may arise from inertial and gravitational effects and can be computed as

$$\boldsymbol{q}(\chi) = -\varrho^*(\chi) \cdot \left(\hat{\boldsymbol{e}}_y \cdot g + \hat{\boldsymbol{n}}(\chi) \cdot v(\chi)^2 \cdot \kappa(\chi)\right), \tag{17}$$

where ϱ^* denotes the local mass per unit of strip length ($\varrho^*(\chi) = \varrho \cdot b \cdot h(\chi)$ – with strip width b and strip thickness h), where $\hat{\boldsymbol{e}}_y$ represents the unit vector in the global y-direction, and where g stands for the gravitational constant.

8 CONTACT FORMULATION

In order to include nodal contact into the principle of virtual work, the undisturbed system is extended by a contact term δW_C (hence, $\delta U - \delta W - \delta W_C = 0$).

Strip/roll contact is established at selected nodes by employing the Lagrange Multiplier method. A contact identification algorithm detects those nodes that penetrate one of the rolls. At these nodes, contact forces are determined by the additional Lagrangian parameter $\lambda_{C,a}$ ($a \in [1, c]$ for c contact nodes).

The contribution to the virtual work can be written as

$$\delta W_C = \sum_{i=1}^{n} \delta P_i \cdot \left(\sum_{a=1}^{c} \left(\boldsymbol{F_{C,a}} \cdot \frac{\partial \boldsymbol{x_C}(\chi_a)}{\partial P_i} + \frac{\partial \boldsymbol{F_{C,a}}}{\partial P_i} \cdot \boldsymbol{c}_a \right) \right), \tag{18}$$

where the nodal contact force $\boldsymbol{F_{C,a}}$ must be normal to the strip centerline, as frictionless strip/roll contact is assumed

$$\boldsymbol{F_{C,a}} = \lambda_{C,a} \cdot \hat{\boldsymbol{n}}(\chi_a) \text{ and } \frac{\partial \boldsymbol{F_{C,a}}}{\partial P_i} = \frac{\partial \lambda_{C,a}}{\partial P_i} \cdot \hat{\boldsymbol{n}}(\chi_a) - \lambda_{C,a} \cdot \frac{\partial \theta}{\partial P_i} \cdot \hat{\boldsymbol{t}}(\chi_a). \tag{19}$$

The contact condition $\boldsymbol{c}_a$ (i.e. the side condition for the geometric distance, which vanishes when the contact is established) can be written as the following kinematic constraint

$$\boldsymbol{c}_a = \boldsymbol{x_{C,a}} - \boldsymbol{x_{R,a}} - \varpi_a \cdot r_a \cdot \hat{\boldsymbol{n}}(\chi_a), \tag{20}$$

where $\boldsymbol{x_{C,a}}$ denotes the position of the node in contact, $\boldsymbol{x_{R,a}}$ the center of the respective roll in contact, $\varpi_{,a}$ the contact orientation ($\varpi_a = 1$ if the strip normal vector $\hat{\boldsymbol{n}}(\chi_a)$ points in the direction of the respective roll's center point, and $\varpi_a = -1$ if $\hat{\boldsymbol{n}}(\chi_a)$ points into the opposite direction) and where r_a represents the respective roll radius.

9 PRESENTATION OF SELECTED RESULTS

A self-developed and customized simulation prototype (implemented in MATLAB$^{\text{TM}}$) can now be used instead of computationally expensive FEM simulations (based on commercial Finite Element packages). The CPU times for typical tension leveling scenarios

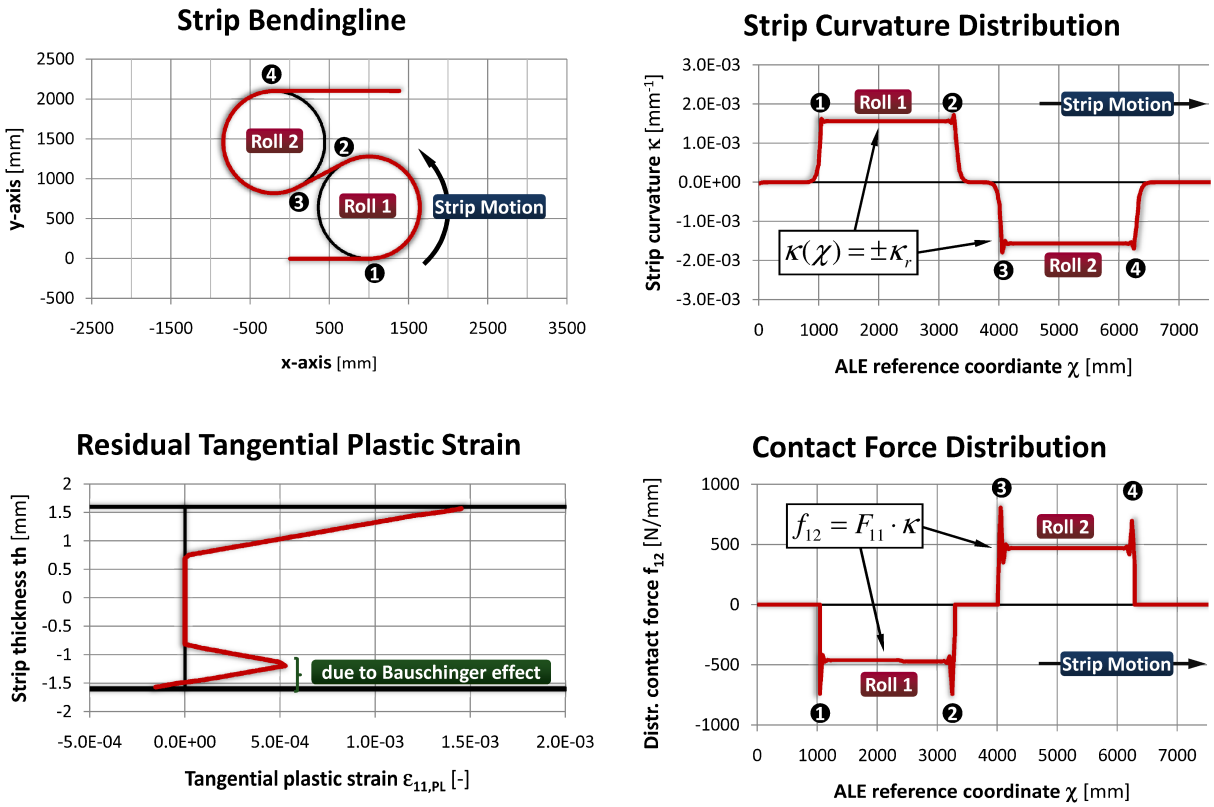

Figure 5: Selected results for surface contact scenarios, in which strip exhibits surface contact.

could be reduced from some days (using commercial Finite Element packages) to a few minutes (employing the self-developed PSF model).

Due to the advantageous parameterization along the referential ALE arc length of the bending line, large strip rotations (of more than 180°) can be handled without any problem. Both *line contact* (where the peak curvature of the strip is smaller than the curvature of the respective roll and therefore has to follow from the simulation) and *surface contact* (where the strip's curvature adopts the curvature of the respective roll) can be handled by the implemented contact algorithm.

Figure 5 depicts the simulation results of a roll unit, where metal strip is deflected under high tension around two undriven rolls of large diameters. From the strip bending line (top left image in Figure 5) it follows that the strip is deflected twice by more than 180° as it runs around the rolls. The strip curvature distribution diagram (top right image in Figure 5) exhibits the typical plateaus, where the strip's curvature is restricted by the curvature of the roll as upper bound (the roll radius is 640 mm in this case, hence the strip's curvature cannot exceed $1.6 \cdot 10^{-3}$ mm^{-1}). The bottom left diagram in Figure 5 depicts the residual strain distribution across the strip thickness, after the strip was bent twice around both rolls. Note that the plastic compression at the bottom strip surface

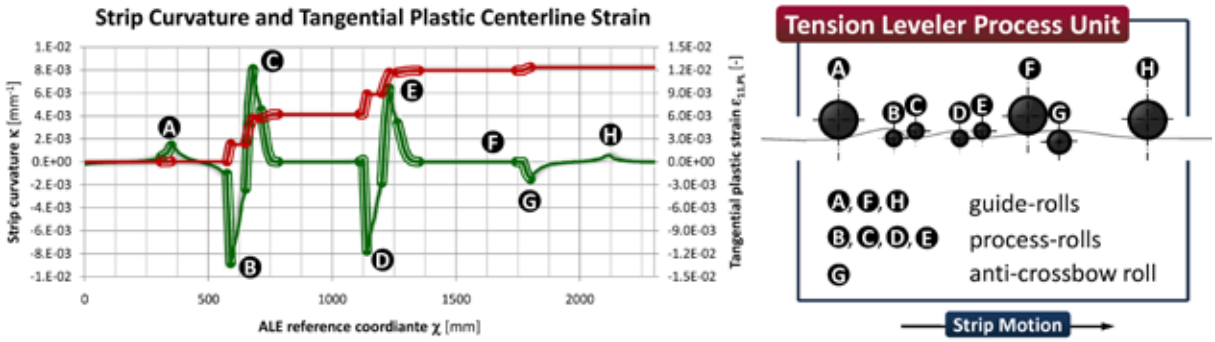

Figure 6: Strip curvature and tangential plastic centerline strain for a typical tension leveling scenario.

is due to the consideration of the material's Bauschinger effect: after first elasto-plastic strains have occurred at the strip bottom surface fibers (near the contact point with roll 1), the yield strength of the material is reduced when the direction of the deformation is inverted from tension to compression (at roll 2). The contact force distribution diagram (bottom right image in Figure 5) clearly displays the single contact force peaks at the beginning and at the end of each strip/roll contact (labels 1 - 4) as well as the evenly distributed sectional shear force f_{12} (proportional to the roll radius and the tangential strip force F_{11} – cp. [8]) within the surface contact zone.

Figure 6 illustrates some simulation results of typical strip deformations within the process unit of an industrial tension leveler. The red line illustrates the tangential strip strain distribution, the green line shows the strip curvature distribution. Those strip segments along the bending line, which exhibit plastic deformation, are highlighted as bold lines. It becomes obvious that the largest tangential plastic strains occur within the curved strip segments before the process-rolls (labels "B", "C", "D" and "E" in Figure 6). Minor plastifications can be observed after process-rolls "C" and "E" as well as near guide-roll "A" and anti-crossbow roll "G". From Figure 6 it becomes obvious, that less than 20 % of the strip length in the process unit are deformed plastically in typical steady state scenarios of the tension leveling process.

10 CONCLUSIONS

A thorough analysis of the physical correlations and mechanical aspects of tension leveling scenarios is essential for the reliable and accurate design of the tension leveling processes, machines and controls. The presented self-developed simulation prototype is based on a special Arbitrary Lagrangian-Eulerian formulation and employs the Principle of Virtual Work. Due to its optimized simulation algorithms and the decoupling of the nodal from the material movement, it allows for short simulation runtimes (within the range of a few minutes).

The model is currently used in large-scale parametric studies in the design phase of industrial tension levelers. The direct benefits gained from the model are minimized plant

investments, better plant performance as well as a reduction of energy costs.

ACKNOWLEDGEMENT

This research project was carried out within the framework of the "Austrian Center of Competence in Mechatronics" (ACCM), a K2 center of the COMET program, which is carried out by FFG and is supported by the Austrian Federal Government (the Federal Ministry for Transport, Innovation and Technology and the Federal Ministry of Economy, Family and Youth), by the Province of Upper Austria, as well as by the Company Partners and Scientific Partners of ACCM.

The authors gratefully acknowledge the continuous and comprehensive support of Siemens VAI in this research project.

REFERENCES

[1] Donea, J., Huerta, A., Ponthot, J.Ph. and Rodríguez-Ferran, A., Arbitrary Lagrangian-Eulerian methods. *Encyclopedia of Computational Mechanics.* (2004).

[2] Kulbatschny, I.G., *Maschinelle Ausrüstung von Walzwerken (German).* VEB Verlag Technik Berlin, (1954).

[3] Sheppard, T. and Roberts, J.M. On the Strip-to-Roll Conformity in the Tension-Leveling Process. *Journal of the Institute of Metals* (1972): 130–135.

[4] Misaka, Y. and Masui T., Shape Correction of Steel Strip by Tension Leveler. *Transaction ISIJ* (1977) **18**:475-484.

[5] Hoffmann, J., *Simulationsmodell für das Streckbiegerichten (German).* PhD-thesis, Magdeburg, (1996).

[6] Steinwender, L., Salzmann, C., Kainz, A., Krimpelstätter, K. and Zeman, K., A Holistic Modeling Approach for the Design of Tension Leveling Processes and Equipment. *Proceedings SHEMET Leuven/Belgium. Key Engineering Materials* (2011) **473**:757-764.

[7] Steinwender, L., Kainz, A., Krimpelstätter, K. and Zeman, K., Computational Analysis of the Curvature Distribution and Power Losses of Metal Strip in Tension Levellers. *Proceedings WCCM/APCOM Sydney/Australia. IOP Conf. Ser.: Mater. Sci. Eng.* (2010) **10**.

[8] Steinwender, L., Kainz, A., Krimpelstätter, K. and Zeman, K., A Novel Approach for Modeling of the Tension Leveling Process by Employing Parametric Shape Functions. *Proceedings STEELSIM Düsseldorf/Germany* (2011).

XI International Conference on Computational Plasticity. Fundamentals and Applications
COMPLAS XI
E. Oñate, D.R.J. Owen, D. Peric and B. Suárez (Eds)

ANALYSIS OF PROFILE AND FLATNESS IN FLAT HOT ROLLING BASED ON NON LINEARLY COUPLED MODELS FOR ELASTIC ROLL STACK DEFLECTION AND PSEUDO-STEADY-STATE ELASTO-VISCOPLASTIC STRIP

ALEXANDER KAINZ*, MARKUS WIDDER†, ERIK PARTEDER‡, GERALD HEIN♦, KARL SCHÖRKHUBER♦, KLAUS ZEMAN*

* Institute of Computer Aided Methods in Mechanical Engineering, Johannes Kepler University of Linz, Altenbergerstr. 69, A - 4040 Linz, Austria.
E-mail: alexander.kainz@jku.at - Web page: http://came.mechatronik.uni-linz.ac.at

† Siemens VAI Metals Technologies GmbH & Co, Turmstr. 44, A-4031 Linz, Austria
E-mail: markus.widder@siemens.com - Web page: http://www.siemens-vai.com

‡ voestalpine Grobblech GmbH, voestalpine-Str. 3, A-4020 Linz, Austria.
E-mail: erik.parteder@voestalpine.com - Web page: http://www.voestalpine.com/grobblech/en.html

♦ voestalpine Stahl GmbH, voestalpine-Str. 3, A-4020 Linz, Austria
E-mail: gerald.hein@voestalpine.com - Web page: http://www.voestalpine.com/stahl/en.html

Key words: Flat Hot Rolling, Bulk Forming, Profile and Flatness, Elastic Roll Stack, Strip Profile Transfer, Incompatible Residual Strains.

ABSTRACT. An enhanced iterative concept for the effective numerical simulation of flat hot rolling processes is presented. The underlying physical process is the forming of metal within a flat rolling stand, i.e. between a lower and an upper roll set, each of them consisting of one or more rolls. The strip material is described elasto-viscoplastically, whereas the roll stack is deformed elastically. The accurate coupling of the strip model with the routines for the elastic roll stack deflection is a precondition to get reliable results concerning profile transfer and incompatible residual strains inside the strip, which allows the prediction of flatness defects, such as buckling. Especially for thin, wide strips and heavy plates, where the aspect ratio width over thickness is extremely unfavourable, the determination of profile transfer and flatness obviously leads to extremely high calculation times with commercial FEM-programs. Therefore, a tailor-made FEM-code for the efficient simulation of the elasto-viscoplastic material flow inside the roll gap was developed and programmed in C++. It is based on pseudo-steady-state, fully implicit stress-update approaches, where the incremental material objectivity is satisfied exactly. The developed model is well suited for systematic parameter studies to investigate flatness defects in more detail and to develop enhanced flatness criteria for thin hot and cold strips and plates.

1 INTRODUCTION AND SURVEY

For optimization and control, the development of highly sophisticated mathematical offline and online models in both hot and cold flat rolling is a vital precondition for manufacturing high quality products satisfying even the most challenging tolerance demands. Control of strip crown and shape can be considered to be among the most important technologies in flat rolling of strip and plate. Although the analysis of transient and steady-state rigid-viscoplastic and elasto-viscoplastic forming processes is not new (cf. e.g. [1–7], 13, 14), the high customer demands concerning productivity and product quality are the reason, why it is of utmost importance to attain a better understanding of the underlying process details, which requires highly sophisticated formalisms and optimized numerical simulation concepts and their application to process optimization and control purposes. During the last three decades, great efforts have been paid to competitive developments of new technologies to reduce or avoid profile errors and shape defects [11, 12]. The theoretical understanding of the underlying material flow behavior is the crucial foundation for the development of improved calculation tools for strip crown and shape evaluation in order to better meet the "offline task" of designing new machines including actuators and the "online challenge" of guiding and controlling flat rolling processes.

The accurate and reliable prediction of lateral flow and strip spread can be considered to be one of the essential objectives of (steady-state) flat hot rolling simulations. It enables the pre-calculation of strip profile (thickness over width), of profile transfer functions, and relative strip crown changes [11, 12]. For the prediction of the material flow behavior of wide strips and plates in hot and cold rolling, highly sophisticated procedures are essential, which are able to couple the deformation of the rolled stock with the elastic response of the rolls. Especially for thin, wide strips, where the aspect ratio width over thickness is extremely unfavorable, the determination of profile transfer and flatness obviously leads to extremely high calculation times of several days with commercial FEM-programs, in particular, when the elasto-plastic strip models have to be coupled with elastic roll stack deflection models. Some critical details concerning the underlying formalism of the self-developed customized simulation models will be outlined in this paper.

The tailor-made FEM-code for the efficient simulation of the elasto-viscoplastic material flow inside the roll gap is based on pseudo-steady-state and fully implicit stress-update approaches (cf. e.g. [6, 7]), where the incremental material objectivity is satisfied exactly. Special emphasis was put on the coupling of strip models with routines for the elastic roll stack deflection [8], which is a precondition to get reliable results concerning strip profile transfer and residual strain and stress distributions inside the strip [9, 10]. Such data allow the evaluation of strip-flatness based on buckling analysis and of the effectivity and adjustment ranges of profile and flatness actuators [11, 12]. The model is well suited for systematic parameter studies to investigate flatness of strips and plates in more detail and to develop enhanced flatness criteria for thin hot and cold strips. Of particular interest is the dependence of the longitudinal stress and strain distributions and of the corresponding specific rolling force-distributions across the strip width on the underlying constitutive elasto-viscoplastic laws including work hardening and softening between consecutive passes.

The basic geometry of the rolling process under consideration consists of two rotating work rolls, which are supported by backup rolls (i.e. quarto flat rolling stand) and reduce the

thickness of the incoming steel strip or plate. During the rolling process, a considerable amount of force is exerted on the roll assembly, which deforms the rolls accordingly. Of particular interest is the pressure distribution between strip and work roll and also between backup roll and work roll to determine the actual elastic deformation of the roll assembly. The total elastic deformation of the roll stack can be determined very effectively and accurately by solving the 3D elastic Lame equations according to the method developed and patented by Siemens-VAI [8]. The determination is performed in cylindrical coordinates and utilizes systematic Fourier series expansions [16, 17]. As is well known [18] it suffices for hot rolling scenarios to take into account merely the radial surface displacement function u_r to describe the deformed work roll surface adequately.

2 DISCUSSION OF THE UNDERLYING COUPLING CONCEPT

Due to the high non-linearity of the whole problem, the coupling between roll stack and rolled stock has to be performed iteratively. The contact stress distribution resulting from the strip model serves as input for the determination of the deformed work roll surface, which can be performed very accurately and effectively by applying appropriate analytical and numerical methods. The new deformed work roll surface represents the *"flow channel"* for the next calculation step of the strip model. The routines for the elastic roll stack deflection have to be coupled with the modules for the strip-behavior via the a priori unknown deformed contact surface between the strip and work roll. Both the deformed contact surface and the corresponding 2D contact stress distribution have to be determined consistently and result from the coupling between the models for the strip and the roll-stack. The accurate coupling of the strip models with the routines for the elastic roll stack deflection is a precondition to get reliable results concerning profile transfer and residual stresses (cf. [9-12]) inside the strip, which allows the prediction of flatness defects, such as strip buckling.

A systematic, iterative calculation concept is taken into consideration to treat the highly non-linear coupling between deformable bodies in metal forming in an efficient and accurate manner. For prescribed contact surface geometry, the strip-model determines the contact stress distribution in real space, which serves as input distribution for the roll stack deflection model. The resulting new work roll surface contour serves as new contact surface geometry, thus, enabling the strip model to perform the next iteration step. As the roll stack model is based on the theory of linear elasticity [16, 17] (but includes the non-linear contact between work- and backup-rolls), the load is applied onto the undeformed reference configuration. This necessitates a back-transformation of the real-space contact stress distribution onto an undeformed cylindrical surface, which will be performed systematically in the next section. The transformation concept is based on the postulation that infinitesimal surface traction vectors transform covariantly, analogously to the coordinate differentials. Therefore, it suffices to determine the underlying deformation gradient [1-5], which essentially generates this highly non-linear transformation. To actually perform the contact stress transformation, the knowledge of the radial surface displacement function u_r does not suffice to determine the full deformation gradient, as the partial derivatives $\partial u_r/\partial r$ evaluated at the surface $r = R$ are required as well. The determination of both u_r and the corresponding radial strain $\partial u_r/\partial r$

at the cylindrical work roll surface is accomplished by a combination of analytical and numerical methods, the details of which will be published in a subsequent paper.

3 NON-LINEAR CONTACT MAPPING CONCEPT

The two-dimensional contact pressure distribution (both normal contact stress and tangential shear stresses) between strip and work roll, which can be calculated by an adequate strip-FE model for a given *"flow-channel"* (i.e. the deformed work roll contour), serves as input quantity for the determination of the corresponding elastic roll stack deformation. As pointed out above, a non-linear mapping of the contact stress distribution onto non-deformed (i.e. cylindrical) work roll boundaries has to be performed. This transformation of stress distributions between an Eulerian configuration (actually deformed real space scenario) and a corresponding Lagrangian (i.e. undeformed scenario) can be performed systematically by the transformation concept outlined in this section.

The undeformed reference configuration corresponding to an undeformed cylindrical work roll, which serves as Lagrangian (upper index *L*) reference configuration here, can be represented in adequate cylindrical coordinates as

$$\vec{x}^{(L)}\left(r,\vartheta,y\right)=\left(\left[x_C-r\sin\vartheta\right],\quad y,\quad \left[z_C-r\cos\vartheta\right]\right)\,, \tag{1}$$

where $r=\sqrt{(x-x_C)^2+(z-z_C)^2}$ is the distance from the axis of the cylinder, y designates the lateral coordinate (direction of the axis of the undeformed cylinder) and ϑ is the angular coordinate in azimuthal direction. Surface evaluations are performed at the value $r=R$, where R denotes the undeformed work-roll radius. Obviously, the undeformed centre-line of the cylinder is represented by $y\rightarrow(x_C,y,z_C)$.

A suitable parameterization of the actually deformed configuration, i.e. the Eulerian (upper index *E*) representation reads

$$\vec{x}^{(E)}\left(r,\vartheta,y\right)=\begin{pmatrix}x_C-\left[r+u_r\left(r,\vartheta,y\right)\right]\sin\vartheta\\ y\\ z_C-\left[r+u_r\left(r,\vartheta,y\right)\right]\cos\vartheta\end{pmatrix}\,, \tag{2}$$

where only the radial displacement field $u_r\left(r,\vartheta,y\right)$ will be taken into account to describe the deviation from the undeformed reference configuration, which suffices for hot rolling scenarios. The transformation rule between the Eulerian *(E)* and Lagrangian *(L)* coordinates is given by the deformation gradient $\vec{\vec{F}}$ (3 x 3 - matrix), which is defined by utilizing coordinate differentials as follows

$$d\vec{x}^{(E)}=\vec{\vec{F}}\,d\vec{x}^{(L)}\,. \tag{3}$$

Taking into account that the cylindrical coordinate differentials $(dr,d\vartheta,dy)$ can be represented in terms of the Cartesian Lagrangian coordinates according to

$$\begin{pmatrix}dr\\ d\vartheta\\ dy\end{pmatrix}=\begin{pmatrix}-\sin\vartheta & 0 & -\cos\vartheta\\ -\cos\vartheta/r & 0 & \sin\vartheta/r\\ 0 & 1 & 0\end{pmatrix}\begin{pmatrix}dx^{(L)}\\ dy^{(L)}\\ dz^{(L)}\end{pmatrix} \tag{4}$$

leads directly to the explicit representation of the deformation gradient $\ddot{F}$ as a function of the cylindrical coordinates

$$\begin{pmatrix} \left\{(-\sin\vartheta)\left(\frac{\partial x^{(E)}}{\partial r}\right)-\frac{\cos\vartheta}{r}\left(\frac{\partial x^{(E)}}{\partial \vartheta}\right)\right\} & \left\{\left(\frac{\partial x^{(E)}}{\partial y}\right)\right\} & \left\{(-\cos\vartheta)\left(\frac{\partial x^{(E)}}{\partial r}\right)+\left(\frac{\sin\vartheta}{r}\right)\left(\frac{\partial x^{(E)}}{\partial \vartheta}\right)\right\} \\ 0 & 1 & 0 \\ \left\{(-\sin\vartheta)\left(\frac{\partial z^{(E)}}{\partial r}\right)-\frac{\cos\vartheta}{r}\left(\frac{\partial z^{(E)}}{\partial \vartheta}\right)\right\} & \left\{\left(\frac{\partial z^{(E)}}{\partial y}\right)\right\} & \left\{(-\cos\vartheta)\left(\frac{\partial z^{(E)}}{\partial r}\right)+\left(\frac{\sin\vartheta}{r}\right)\left(\frac{\partial z^{(E)}}{\partial \vartheta}\right)\right\} \end{pmatrix}, \tag{5}$$

where the involved partial derivatives of Eulerian coordinates in Equation 5 can be represented in terms of the radial displacement field $u_r(r,\vartheta,y)$, e.g.

$$\left(\frac{\partial x^{(E)}}{\partial r}\right)=\left\{-\left[1+\left(\frac{\partial u_r}{\partial r}\right)\right](\sin\vartheta)\right\}. \tag{6}$$

The deformation gradient $\ddot{F}$ directly serves as basic operator to determine the transformation behaviour of covariant vector differentials, such as Eulerian and Lagrangian surface traction vectors, denoted by $\vec{p}^{(E)}$ and $\vec{p}^{(L)}$, respectively. As covariant vectors transform analogously to coordinate differentials represented in Equation 4, the underlying transformation rule reads

$$d\vec{P}^{(E)}=\ddot{F}\,d\vec{P}^{(L)} \;\rightarrow\; d\vec{P}^{(L)}=\ddot{F}^{(-1)}\,d\vec{P}^{(E)}, \tag{7}$$

where the infinitesimal Eulerian and Lagrangian force vectors are given by

$$d\vec{P}^{(E)}=dS^{(E)}\vec{p}^{(E)}=dS^{(E)}\left\{\sigma_N^{(E)}\hat{N}^{(E)}+\vec{\sigma}_T^{(E)}\right\} \tag{8}$$

$$d\vec{P}^{(L)}=dS^{(L)}\vec{p}^{(L)}=dS^{(L)}\left\{\sigma_N^{(L)}\hat{N}^{(L)}+\vec{\sigma}_T^{(L)}\right\}, \tag{9}$$

where $dS^{(L)}$ and $dS^{(E)}$ denote the infinitesimal surface elements, on which $\vec{p}^{(L)}$ and $\vec{p}^{(E)}$ are acting. The vectors $\hat{N}^{(L)},\hat{N}^{(E)}$ are normal vectors to these surface elements, hence, $\hat{N}^{(E)}\cdot\vec{\sigma}_T^{(E)}=0$ and $\hat{N}^{(L)}\cdot\vec{\sigma}_T^{(L)}=0$.

Note that the infinitesimal surface vectors transform in a contravariant manner leading to

$$d\vec{S}^{(E)}=J\;\ddot{F}^{(-T)}\,d\vec{S}^{(L)} \tag{10}$$

with the functional determinant of the deformation gradient $J=\det\left(\ddot{F}\right)$.

By taking the scalar product between covariant and contravariant vector differentials, one is immediately led to the representation

$$\left(d\vec{P}^{(E)}\cdot d\vec{S}^{(E)}\right)=J\left(d\vec{P}^{(L)}\cdot d\vec{S}^{(L)}\right) \tag{11}$$

directly yielding the following scalar relation between the Eulerian and Lagrangian contact stress values

$$\sigma_N^{(E)}\left(dS^{(E)}\right)^2=J\;\sigma_N^{(L)}\left(dS^{(L)}\right)^2. \tag{12}$$

Equation 12 enables the determination of the Lagrangian normal contact stress distribution, provided that the corresponding Eulerian values are known. Note that the knowledge of the Eulerian normal contact stress distribution $\sigma_N^{(E)}$ suffices to determine the Lagrangian counterpart $\sigma_N^{(L)}$, i.e. this quantity is not directly influenced by the Eulerian shear stress distribution $\vec{\sigma}_T^{(E)}$. A more detailed analysis based on Equation 12, yields the following explicit representation in terms of the (inverse and transposed) deformation gradient

$$\sigma_N^{(L)}(\vartheta, y) = \left\{ J \left\| \vec{F}^{(-T)} \hat{N}^{(L)} \right\|^2 \right\} \sigma_N^{(E)}(\vartheta, y) \cdot \tag{13}$$

The partial derivatives $\partial u_r / \partial r$ evaluated at the surface $r=R$ (i.e. the radial surface strains) are required explicitly to determine the deformation gradient $\vec{F}$. By utilizing sophisticated mathematical methods, essential details of which will be published in a subsequent paper, an analytical formula could be derived, which is valid exactly for planar surfaces and still a highly satisfactory approximation for cylindrical (i.e. curved) surfaces, at least for localized normalized contact stress distributions $\sigma_N(\vartheta, y)$, as is the case for flat rolling of metal strip:

$$\frac{\partial u_r}{\partial r}(r = R, \vartheta, y) \cong \frac{(1+\nu)(1-2\nu)}{E} \sigma_N(\vartheta, y) \cdot \tag{14}$$

This formula for the determination of the radial surface strain is applied directly in numerical calculations and enables the correct non-linear mapping of the Eulerian contact stress distribution onto the Lagrangian frame of reference.

4 ELASTO-VISCOPLASTIC STRIP MODELING CONCEPT

For the numerical simulation of steady-state elasto-viscoplastic rolling processes, especially for thin wide strips, standard incremental approaches based on updated Lagrangian concepts are not very efficient and lead to very high calculation times. Therefore, an effective customized pseudo-steady-state algorithm was implemented, some basic ideas of which were proposed some years ago by Hacquin et al. [7]. The global algorithm is based on an iterative calculation of the stress and velocity fields inside the strip. The strip model is coupled with a consistent determination of the flow channel geometry (i.e. work roll surface) resulting from the deformation of the work roll surface loaded by the 2D-contact stress distribution obtained from the preceding strip calculation step.

The elasto-viscoplastic constitutive law is based on the Prandtl-Reuss decomposition of the total rate of deformation tensor $\vec{D}^{(tot)} = \left[\vec{D}^{(el)} + \vec{D}^{(pl)}\right]$ into elastic and plastic parts, where the plastic part behaves incompressible for metal forming processes (at least in very good approximation), i.e. $tr\left(\vec{D}^{(pl)}\right) = 0$. For elastic parts, isotropic linear behaviour is assumed, whereas the plastic parts are treated according to Levy-Mises. For incremental constitutive laws, the stress-update has to be performed along material streamlines. For fixed velocity-field and steady-state particle run-time values $\Delta t_{(n \to n+1)}$ between successive Gauss-integration points, denoted by n and $(n+1)$, the new Cauchy stress-values can be determined according to the fully implicit prescription in Equation 15, which satisfies exactly the required incremental material objectivity (i.e. corotational stress formulation) even for large local rotations:

$$\vec{\sigma}_{n+1} \cong \exp\left\{\vec{W}_{n+1}\,\Delta t\right\}\vec{\sigma}_n \exp\left\{-\vec{W}_{n+1}\,\Delta t\right\} + \Delta t\,\overset{\odot}{\vec{\sigma}}_{(n\to n+1)} \,. \tag{15}$$

The materially objective part of the Cauchy stress-rate (according to Jaumann-Kirchhoff) is denoted by the symbol $\odot$. For the case of isotropic elasticity, this constitutive law in rate representation reads

$$\overset{\odot}{\vec{\sigma}}_{(n\to n+1)} = \left[\, 2G\,\vec{D}'^{(el)}_{n+1} + K\,tr\left(\vec{D}_{n+1}\right)\vec{I}\,\right] . \tag{16}$$

The local rotation-tensor $\vec{R} = \exp\left\{\vec{W}\,\Delta t\right\}$ with $\vec{R}\,\vec{R}^T = \vec{I}$ and $\dot{\vec{R}}\,\vec{R}^T = \vec{W}$ (anti-symmetric spin-tensor $\vec{W}$) ensures the physically correct stress-update behaviour and avoids erroneous results, which occur when the infinitesimal rotation-tensor $\vec{R} \cong \left\{\vec{I} + \vec{W}\,\Delta t\right\}$ is used in Equation 15. To determine the elasto-viscoplastic stress-increments along the material streamlines, operator splitting concepts (cf. Belytschko et al. [1]) are beneficial. The radial return method (cf. Simo and Hughes [2], Montmitonnet [6]) is based on the application of an elastic predictor, followed by a plastic corrector. Although the real local material rotations inside the strip forming zone (located inside the roll-gap) remain very small for flat rolling, the rotations corresponding to the elastic predictor may become pretty large when plasticity occurs, afterwards, an orthogonal back-projection onto the yield-surface is performed.

$$\begin{aligned} 0 \overset{!!}{=} & \iiint_V tr\left[\vec{\sigma}\,\delta\vec{D}\right] dV - \iint_{S_C}\left[\delta\left(\sigma_N \mathrm{v}_N\right) + \vec{\sigma}_T \cdot \delta\vec{\mathrm{v}}_T\right] dS \\ & -\left[\bar{\sigma}_F\, A_{out}\,\delta\mathrm{v}_{out} - \bar{\sigma}_B\, A_{in}\,\delta\mathrm{v}_{in}\right] + \left\{\delta\lambda_{OUT}\left[\left(\bar{\sigma}_{xx}\right)_{|x_{out}} - \bar{\sigma}_F\right] + \lambda_{OUT}\,\delta\left(\bar{\sigma}_{xx}\right)_{|x_{out}}\right\} . \end{aligned} \tag{17}$$

An extended variant of the principle of virtual power, Equation 17 serves as underlying weak representation for FE-discretization. For fixed geometry, both the velocity field $\vec{\mathrm{v}}$ as well as the contact stress distribution σ_N (treated as independent Lagrange-parameter-field to ensure the impenetrability condition between strip and work-roll) are determined numerically. Concerning the tangential surface traction vector $\vec{\sigma}_T$ in Equation 17, a velocity-regularized Coulomb frictional law (Kobayashi et al. [15]), in most cases truncated by the shear-yield stress, is employed. The prescribed mean back and front tensile stress values $\bar{\sigma}_B$ and $\bar{\sigma}_F$, respectively, are applied at the strip inlet (A_{in}) and outlet (A_{out}) cross sections far enough outside the roll gap. It turned out to be beneficial to apply an additional stabilization concept to match the prescribed front-tension value $\bar{\sigma}_F$ at the strip exit cross section exactly. This task was accomplished by supplementing an additional Lagrange-parameter λ_{OUT} in Equation 17.

5 CONSISTENT DETERMINATION OF RESIDUAL STRIP STRAINS

A systematic evaluation of the intrinsic (i.e. incompatible) residual strains (and stresses) is performed by employing the logarithmic strain tensor $\vec{H}$ (Hencky strain-tensor), which is defined by

$$\vec{H} = \ln\vec{V} \quad \text{with} \quad \vec{F} = \vec{V}\,\vec{R} \tag{18}$$

(multiplicative decomposition of the deformation gradient $\vec{\vec{F}}$ into a stretch tensor $\vec{\vec{V}}$ and a rotation-tensor $\vec{\vec{R}}$). It can be decomposed exactly into elastic and incompressible plastic contributions even for large strains

$$\vec{\vec{H}} = \left[\vec{\vec{H}}^{(el)} + \vec{\vec{H}}^{(pl)} \right] \quad \text{with} \quad tr\left(\vec{\vec{H}}^{(pl)} \right) = 0 \ . \tag{19}$$

This tensor quantity can be determined by a materially objective streamline update concept similar to that for the Cauchy-stress tensor, as the Jaumann time derivative of the Hencky strain tensor equals the rate of deformation tensor

$$\overset{\odot}{\vec{\vec{H}}} = \vec{\vec{D}} \quad \text{with} \quad \overset{\odot}{\vec{\vec{H}}} \equiv \left\{ \dot{\vec{\vec{H}}} + \vec{\vec{H}}\vec{\vec{W}} - \vec{\vec{W}}\vec{\vec{H}} \right\} \ . \tag{20}$$

For numerical purposes, discrete (i.e. finite) time increments Δt appear. Therefore, it is essential to utilize a streamline-update prescription, exactly fulfilling incremental material objectivity

$$\vec{\vec{H}}_{n+1} \cong \Delta t \vec{\vec{D}}_{n+1} + \exp\left(\vec{\vec{W}}_{n+1} \Delta t \right) \vec{\vec{H}}_n \exp\left(-\vec{\vec{W}}_{n+1} \Delta t \right) \ . \tag{21}$$

The knowledge of the Hencky-strains enables a systematic decomposition of the inhomogeneous deformation during rolling into thickness reduction, longitudinal and lateral contributions, which establishes the material flow basis for the determination of "suitably defined" transfer functions. Taking into account the plastic parts of the logarithmic Hencky-strain distributions at the strip inlet and outlet cross-sections, denoted by upper indices *(IN)* and *(OUT)*, respectively, the deviations from the respective cross-sectional mean values read

$$\delta H_{ij}^{(IN)}(y,z) \equiv \left[H_{ij}^{(pl)}(x = x_{IN}, y, z) - \left\langle H_{ij}^{(pl)} \right\rangle^{(IN)} \right] \tag{22}$$

$$\delta H_{ij}^{(OUT)}(y,z) \equiv \left[H_{ij}^{(pl)}(x = x_{OUT}, y, z) - \left\langle H_{ij}^{(pl)} \right\rangle^{(OUT)} \right] . \tag{23}$$

The strip transfer-distributions (averaged in strip-thickness direction) describing the non-uniform plastic strain-redistributions during a rolling pass can be represented as

Length transfer function:
$$L_T(y) \equiv \left\{ \delta \bar{H}_{xx}^{(OUT)}(y) - \delta \bar{H}_{xx}^{(IN)}(y) \right\} \tag{24}$$

Width transfer function:
$$W_T(y) \equiv \left\{ \delta \bar{H}_{yy}^{(OUT)}(y) - \delta \bar{H}_{yy}^{(IN)}(y) \right\} \tag{25}$$

Thickness transfer function:
$$T_T(y) \equiv \left\{ \delta \bar{H}_{zz}^{(OUT)}(y) - \delta \bar{H}_{zz}^{(IN)}(y) \right\} . \tag{26}$$

Note that due to the incompressibility constraint in Equation 19 one is led to the relation

$$\left[L_T(y) + W_T(y) + T_T(y) \right] \equiv 0 \ , \tag{27}$$

i.e. only two of these three strip transfer-functions are actually independent of each other. Further details concerning a systematic decomposition of the non-uniform thickness reduction across the strip-width into corresponding width- and length-contributions is scheduled for a subsequent paper.

6 SELECTED RESULTS FOR THE COUPLED PROBLEM

By utilizing the iterative coupling concept and formalism as outlined above, essential information concerning the actual elasto-viscoplastic material flow behavior inside the strip can be determined. In this context, special emphasis was put on the convergence properties of the coupled system, which has to be solved iteratively. The initial contact surface chosen here refers to a uniform contact pressure distribution, which suffices to obtain convergency, although the final results deviate considerably from this simple initial choice.

Iteration	*Rolling Force [MN]*	*Spread [mm]*	*C25 [µm]*	*C40 [µm]*	*C150 [µm]*
1	20.646	8.140	281.471	216.515	78.722
2	21.502	6.188	264.367	194.884	67.160
3	21.818	6.367	243.890	165.660	44.577
4	22.272	6.141	227.249	144.718	33.312
5	22.353	6.099	214.098	127.141	20.231
6	22.601	6.011	204.366	115.003	16.643
7	22.631	6.054	198.078	106.360	11.284
8	22.752	6.054	194.893	102.429	11.372
9	22.779	6.083	192.558	99.068	9.314
10	22.837	6.089	191.504	97.845	9.756
11	22.871	6.092	190.385	96.342	8.777
12	22.901	6.097	191.341	97.357	9.765

Table 1: Convergence properties of the iterative coupling loop between strip and elastic roll stack.

After each coupling iteration, a modified contact surface and a corresponding contact stress distribution (i.e. both normal and shear stresses) are determined. By systematic numerical investigations it could be shown that the initially considerable differences between results from consecutive iteration steps decrease very fast, as can be seen exemplarily from Table 1. After about nine to twelve iteration loops both the calculated geometric, velocity- and stress-distributions, and also the corresponding integral properties have converged satisfactorily in most cases considered. Beside the roll separating force, the resulting strip spread after the roll pass and the corresponding absolute strip-crown values *Cxx* (measured a distance *xx* away from the strip edge) are summarized in Table 1 for a typical test-case.

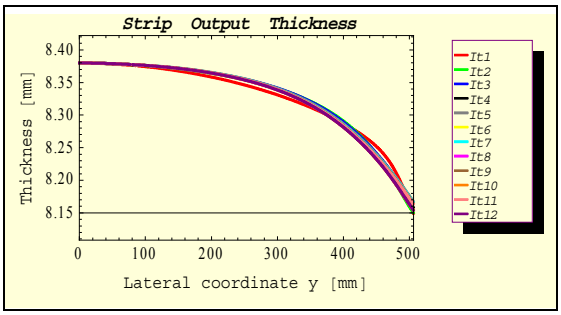

Figure 1: Deformed strip output thickness across the strip width after coupling iterations 1 to 12 (only the upper right quarter is depicted).

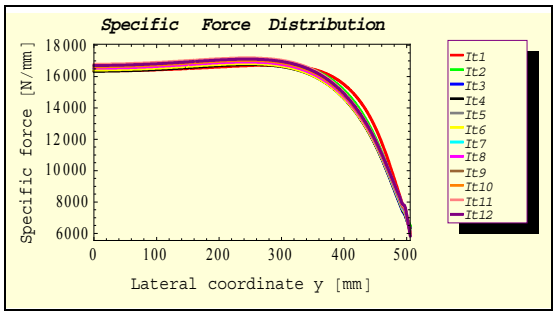

Figure 2: Specific rolling force distribution across the strip width after coupling iterations 1 to 12.

The exemplary results as represented in Figures 1 - 4 refer to a flat hot rolling test-case, where a steel strip with initial width of 1000 mm and rectangular strip entry cross section is

reduced from 35 mm to 16.76 mm at the first stand of a hot finishing mill. Note that on account of assumed horizontal and vertical mid-plane symmetry properties only the upper work roll and the upper right half of the strip need to be simulated, i.e. only a quarter of the whole problem is represented here.

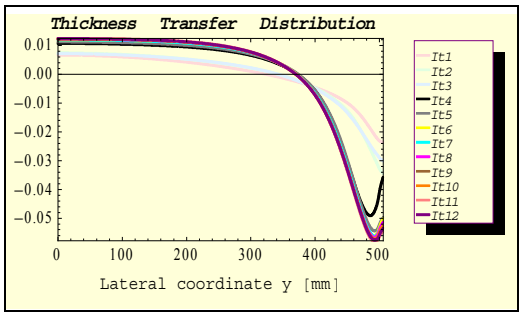

Figure 3: Intrinsic thickness transfer function, as defined by Equation (26).

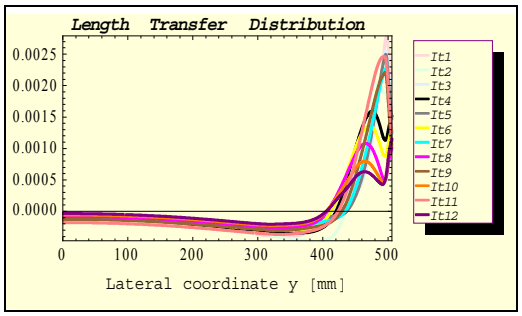

Figure 4: Corresponding length transfer function (i.e. incompatible longitudinal residual strains), as defined by Equation (24).

Of particular interest is the resulting deformed strip thickness distribution in lateral (i.e. strip-width) direction in combination with the specific rolling force distribution, the latter of which follows immediately from the two-dimensional contact stress distribution by integrating it in azimuthal work roll direction. It can be seen from the data depicted in Figure 1 and Figure 2, that the results for the strip output cross-section and the specific rolling force, respectively, meet the expectations and converge satisfactorily. Additionally, the resulting residual thickness- and length-transfer distributions, averaged over the strip thickness and determined by evaluating the logarithmic plastic Hencky strain-tensor (as outlined in section 5) about five contact lengths downstream the roll-gap, and normalized to zero mean-value, are represented in Figures 3 and 4, respectively.

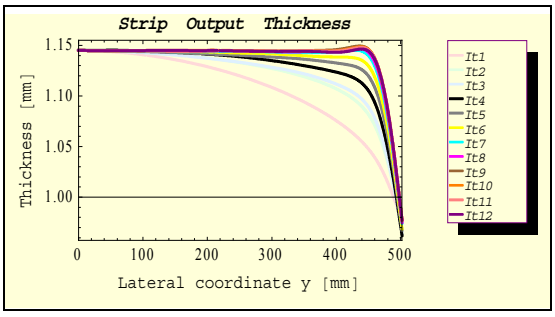

Figure 5: Deformed strip output thickness for test case 2.

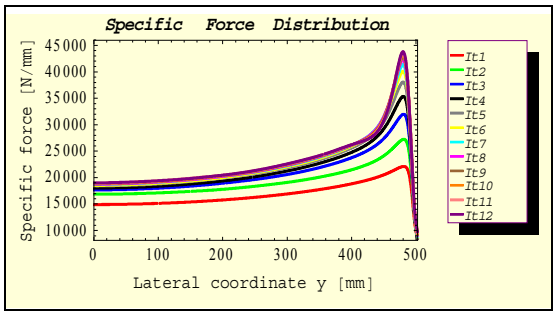

Figure 6: Specific rolling force distribution for test case 2.

The same quantities as in Figures 1 - 4 are depicted in Figures 5 – 8 for an additional finishing mill test case, where the strip is rolled from 3.26 mm to 2.29 mm, i.e. the strip aspect ratio (output width versus thickness) is now significantly higher than in the former test case. Therefore, for test case 2 the lateral material flow inside the roll gap is significantly inhibited, resulting in a drastic increase of the specific rolling force towards the strip edges, as can be seen in Figure 6. Due to the reduced support near the strip edge, the specific force sharply

drops only there, which is significantly different from the long range dropping effect, as depicted in Figure 2 for the first test-case.

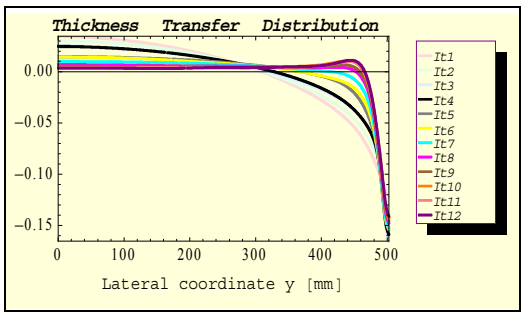

Figure 7: Intrinsic thickness transfer function, as defined by Equation (26), for test case 2.

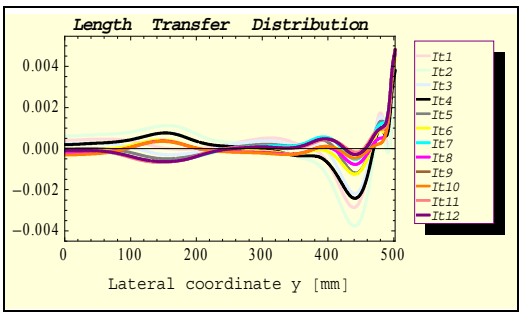

Figure 8: Corresponding length transfer function, as defined by Equation (24), for test case 2.

Note that for regions with high relative thickness reduction increased longitudinal strains are induced (corresponding to compressive residual stresses), as can be seen in Figure 4 and Figure 8. The convergence behaviour of the longitudinal strains is extremely critical due to the high sensitivity with respect to small local changes of geometric properties.

7 CONCLUSIONS

In the present study, a systematic iterative calculation concept was presented to treat the highly non-linear coupling between deformable bodies in metal forming in an efficient and accurate manner. Based on the underlying theoretical modeling concepts, as outlined in this paper, effective numerical simulation models, algorithms and tools were developed and programmed in C++. Special emphasis was put on the coupling of the strip models with the routines for the elastic roll stack deflection, which is a precondition to get reliable results concerning strip profile transfer and residual stress and strain distributions inside the strip. Such data allow the evaluation of strip-flatness and of profile adjustment ranges. The results, attained by utilizing this physically based and mechanically consistent model, were compared to data attained by commercial FEM-calculations (based on standard incremental formulations) and will be validated and calibrated against practical data from an industrial hot finishing mill. Currently, the model is already in practical use by the industrial partners to attain deeper insight into the evolution of profile and flatness in hot rolling processes. Currently, the model is used for systematic parameter studies to investigate flatness properties in more detail and to develop enhanced flatness criteria for thin hot and cold strips as well as hot rolled heavy plates. In future, the model will constitute an essential basis for enhanced metallurgical process investigations.

ACKNOWLEDGEMENT

This research project was carried out within the framework of the “Austrian Center of Competence in Mechatronics” (ACCM), a K2 center of the COMET program, which is carried out by FFG and is supported by the Austrian Federal Government (the Federal Ministry for Transport, Innovation and Technology and the Federal Ministry of Economy, Family and Youth), by the Province of Upper Austria and by the Company Partners and

Scientific Partners of ACCM. The authors gratefully acknowledge the continuous and comprehensive support of voestalpine Stahl, voestalpine Grobblech and of Siemens-VAI Metals Technologies within the frame of this research project.

REFERENCES

[1] Belytschko, T, Liu, W.K. and Moran, B. *Nonlinear Finite Elements for Continua and Structures*. John Wiley & Sons, Chichester, New York, (2002).

[2] Simo, J.C. and Hughes, T.J.R. *Computational Inelasticity*. Springer, New York, (1998).

[3] Hosford, W.F., Cadell, R.M. *Metal Forming (Mechanics and Metallurgy).* Cambridge University Press, Cambridge, New York, (2007).

[4] Dunne, F. and Petrinic, N. *Introduction to Computational Plasticity.* Oxford University Press, New York, (2005).

[5] Neto, E.S, Peric, D. and Owen, D.R.J. *Computational Methods for Plasticity (Theory and Applications)*. John Wiley & Sons Ltd., Chichester, United Kingdom, (2008).

[6] Montmitonnet, P. Hot and cold strip rolling processes. *Comput. Methods Appl. Mech. Engrg* (2006) **195**:6604-6625.

[7] Hacquin, A., Montmitonnet, P. and Guillerault, J.Ph.,. A steady state thermo-elasto-viscoplastic finite element model of rolling with coupled thermo-elastic roll deformation. *J. Mater. Process. Technol* (1996) **60**:109-116.

[8] Widder, M. Method and apparatus for calculating the roll gap contour. *Patent No. EP1240955*, S-VAI, (2002).

[9] Totten, G., Howes, M. and Inoue, T. *Handbook of Residual Stress and Deformation of Steel,* ASM International, Materials Park, Ohio, USA, (2002).

[10] Wiklund, O., Nilsson, A. and Sidestam, P. Flatness and residual stresses during and after rolling. In: *Simulation of Materials processing*: Theory, Methods and Applications, ed. by Mori et al. (2001): 507-512.

[11] Finstermann, G. and Zeman, K. *Profile and flatness control in hot strip mills.* VAI Technical report, (1995).

[12] Matsumoto, H., Nakajima, K. and Yanai, T. Comparison of various crown-control mills in hot rolling. In: *METEC Congress* 94, Düsseldorf, (1994).

[13] Lenard, J.G., Pietrzyk, M. and Cser, L. *Mathematical and physical simulation of the properties of hot rolled products*. Elsevier, Amsterdam, (1999).

[14] Osakada, K. History of plasticity and metal forming analysis. *Journal of Materials Processing Technology* (2010) **210**:1436-1454.

[15] Kobayashi, S., Oh, S. and Altan, T. *Metal forming and the finite-element method.* Oxford University Press, New York, (1989).

[16] Love, A.E.H. *A Treatise on the Mathematical Theory of Elasticity.* Dover Publications, New York, (1944).

[17] Muskhelishvili, N.I. *Some basic problems of the mathematical theory of elasticity.* P. Noordhoff Ltd, Groningen, The Netherlands, (1953).

[18] Krimpelstätter, K., Zeman, K. and Kainz, A. Non circular arc temper rolling model considering radial and circumferential work roll displacements. In: *Proceedings of the 8th Int. Conference on Numerical Methods in Industrial Forming Processes (Numiform),* Columbus, Ohio, USA, (2004).

XI International Conference on Computational Plasticity. Fundamentals and Applications
COMPLAS XI
E. Oñate, D.R.J. Owen, D. Peric and B. Suárez (Eds)

NUMERICAL AND EXPERIMENTAL STUDY OF SANDWICH PLATES WITH METALLIC FOAM CORES

H. MATA[*], M.P.L. PARENTE[†], A.A. FERNANDES[†], R. NATAL JORGE[†], R. VALENTE[†] AND A. SANTOS[†]

[*] IDMEC – Faculty of Engineering, University of Porto
Rua Dr. Roberto Frias, 4200-465 Porto, Portugal
e-mail: {dem09005, mparente, aaf, rnatal}@fe.up.pt

[†] University of Aveiro
Campus Universitário de Santiago 3810-193 Aveiro, Portugal
e-mail: robertt@ua.pt

[†] INEGI - Faculty of Engineering, University of Porto
Rua Dr. Roberto Frias, 4200-465 Porto, Portugal
e-mail: abel@fe.up.pt

Key words: Computational Plasticity, Metal Foam, Sandwich Structures.

Abstract. World-wide vehicles safety experts agree that significant further reductions in fatalities and injuries can be achieved as a result of the use of new energy absorbing materials. In this field, passive safety systems still have great potential to reduce fatalities and injuries, as in the case of using new lightweight energy-absorbing materials. On this work, the authors present the development of a procedure able to perform reliable panels of sandwich sheets with metallic foam cores for industrial applications. The mathematical model used to describe the behavior of sandwich shells with metal cores form is presented and some numerical examples are included. The numerical results are validated using the experimental results obtained from the mechanical experiments. Using the crushable foam constitutive model, available on ABAQUS, a set of different mechanical tests were simulated.

1 INTRODUCTION

Despite significant improvements in car safety in the last 25 years, the actual number of deaths and wounded arising from automobile accidents, in addition to all social and economic costs, remains unacceptable. Here, the passive safety systems still have great potential for development as a way to reduce deaths and injuries. On the other hand, from an environmental point of view, the use of materials optimized in terms of energy absorption, with a reduced weight, has a direct impact on the thermal efficiency, and consumption of the engines, thus emitting less greenhouse gases for the atmosphere. Within this framework, it makes sense the study and development of this new composite material, formed by two sheets of aluminium separated by a foam core of aluminium [1-2].

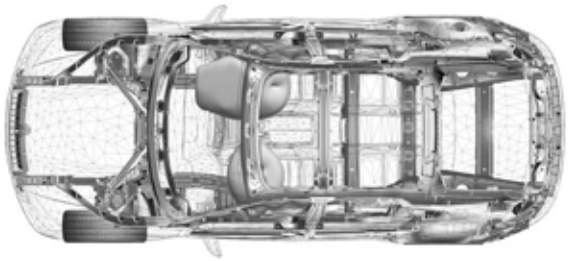

Figure 1: Example the study of passive safety systems [3].

The composite structure used on this work is formed by two sheets of aluminium with 1mm thickness, separated by a aluminium foam core with a thickness of 8mm. Since the specific characteristics of this composite material are mainly due to the behaviour of its core, namely the energy absorbing during impact and vibration isolation properties [4-5], the foam will be studied in detail on this work.

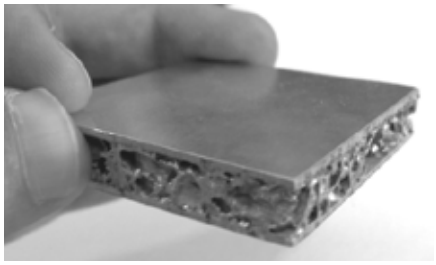

Figure 2: Panels with aluminum foam core.

The structure of the foam corresponds to a three-dimensional arrangement of cells, which can be divided into two groups: open and closed cells. On metal foam with open cells, the individual pores are open. When the individual pores are closed, the metal foam belongs to the closed cells group [6-7].

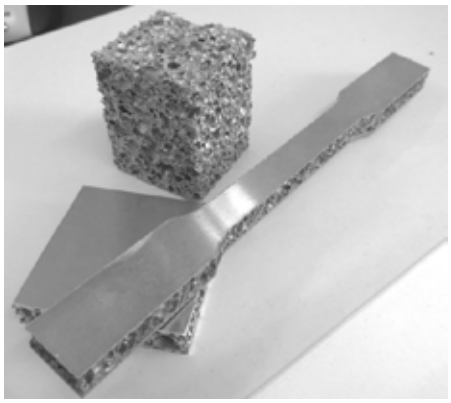

Figure 3: Specimens with aluminum foam core and metal foam.

2 CONSTITUTIVE MODEL

To describe the plastic behavior of the metal foam in this work, the constitutive model proposed by Deshpande was used [8]. This model was chosen due to its capability to describe the behavior of porous metals and due to fact that the yield surface used on this model depends only on the plastic Poisson's ratio.

2.1 Yield Surface

Metal foams have an approximately linear elastic behavior for small strains. Metallic foams plastic deformation occurs when there is a change in volume, unlike solid metals. For metal foams the yield criterion can be formulated as follows:

$$\hat{\sigma} \geq \sigma_y \text{ with} \tag{1}$$

$$\hat{\sigma}^2 = \frac{1}{(1+(\alpha/3)^2)}[(\sigma_e{}^2 + \alpha^2 \sigma_m{}^2] \tag{2}$$

$$\sigma_m = -\frac{1}{3}(\sigma_1 + \sigma_2 + \sigma_3) \tag{3}$$

$$\sigma_e \equiv \sqrt{\frac{3}{2}\sigma_{ij}' : \sigma_{ij}'} \tag{4}$$

Where the equivalent stress is given by $\hat{\sigma}$, and σ_e is the von Mises equivalent stress. σ_m is the mean stress and is defined as $\sigma_m = \frac{1}{3}\sigma_{kk}$. The shape of the yield surface is defined by α and σ_y is the yield stress of the material [1].

Considering the stress plane σ_m, versus stress equivalent σ_e, from Figure 2 is possible to obtain the points 1, 3, 6, 8 that define the yield surface. These points were obtained by varying the pressure *p*, and the uniaxial load [8-9].

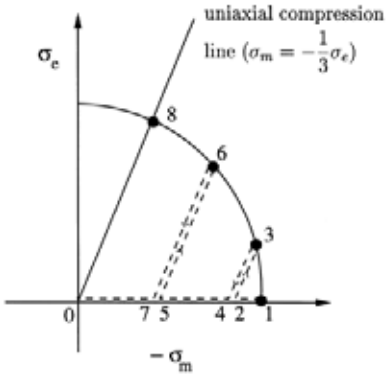

Figure 4: Definition of the yield surface Deshpande model.

2.1 Deshpande Model

Based on the experimental results of the definition of the yield surface previously presented, but now considering a reference $\sigma_m \rightarrow p$, $\sigma_e \rightarrow q$, the model of Deshpande [10] can be summarized as follows:

Elastic law:

$$\boldsymbol{\sigma} = \mathbf{D}^e : \boldsymbol{\varepsilon}^e$$

Yield Surface:

$$\phi = \sqrt{\frac{1}{1+\left(\frac{\alpha}{3}\right)^2}\left[q^2 + \alpha^2 p^2\right]} - \sigma_y(\bar{\varepsilon}^p) = 0$$

Plastic evolution law:

$$\dot{\boldsymbol{\varepsilon}}^p = \dot{\gamma}\boldsymbol{N}$$

Elastic evolution law:

$$\dot{\boldsymbol{\varepsilon}}^e = \dot{\boldsymbol{\varepsilon}} - \dot{\gamma}\boldsymbol{N}$$

Evolution of the equivalent plastic strain:

$$\dot{\bar{\varepsilon}}^p = \dot{\gamma}\sqrt{\frac{2}{3}\boldsymbol{N} : \boldsymbol{N}}$$

3 EXPERIMENTAL TESTS

To validate the numerical model previously presented, uniaxial compression tests of samples obtained from the panels were performed. Figure 5 illustrates the experimental procedure, from which it was possible to record force/displacement values for this material, which are then compared with the numerical values. This mechanical test is one of the tests commonly used to characterize the mechanical behavior of metallic foams.

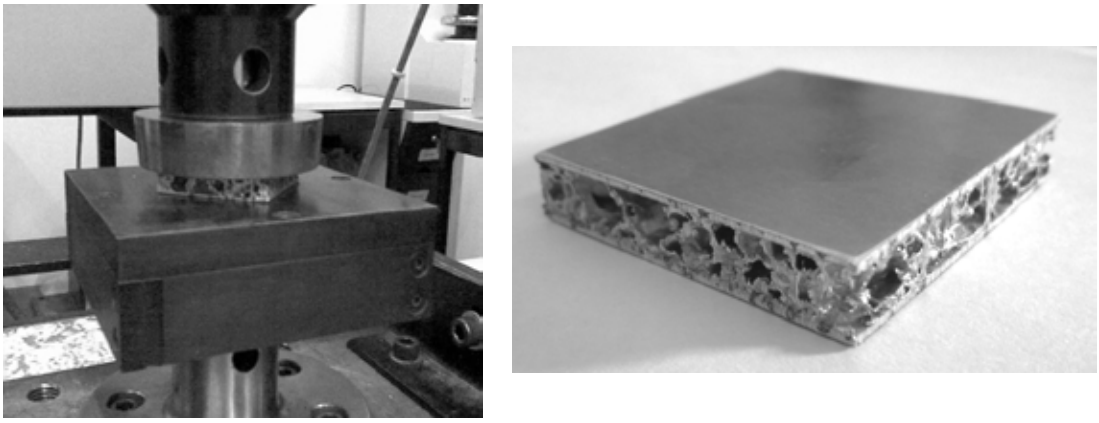

Figure 5: Uniaxial compression test.

Tensile tests were also performed in order to evaluate the mechanical behavior of this composite material under traction. To this end specimens were cut from the panel with the dimension shown on Figure 6.

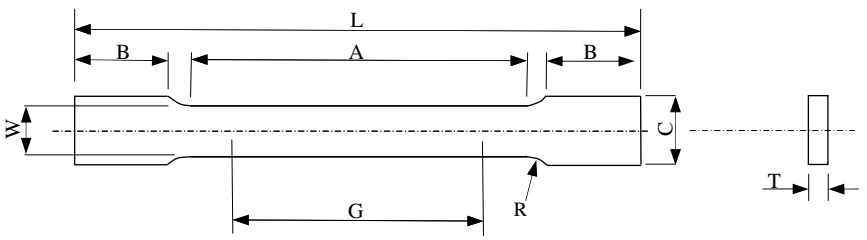

G=50 mm,
W=12.5 mm,
R=20 mm,
L=200 mm,
A=75 mm,
B=50 mm,
C≈20 mm,
T- Thickness [mm]

Figure 6: Specimens used on the tensile test, according to ASTM E 8M-04.

The following Figure shows de experimental setup used to conduct the tensile tests.

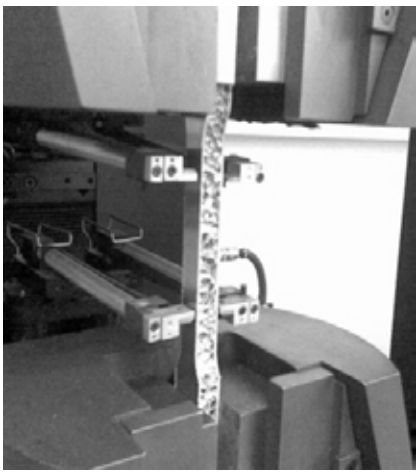

Figure 7: Experimental tensile test.

4 NUMERICAL SIMULATIONS

Numerical simulations of the same experimental tests were performed. For the aluminum sheet an elasto-plastic behavior was assumed with Young module: 70 GPa, Poisson ratio: 0.33 and points from the yield stress/plastic strain curve. For the metallic foam core an elasto-plastic behavior was also assumed, based on the model previously defined. The properties used to describe the metal foam behavior are the Young module: 0.354 GPa, Poisson ratio: 0.33, Compression Yield Stress Ratio: 1.71, plastic Poisson ratio: 0.013 and points from the yield stress/plastic strain curve. The stress-strain curve obtained by the uniaxial compression test is also used to describe the metallic foam behavior [8, 11-12].

The numerical simulations were conduct using the software ABAQUS. Only 1/8 of each specimen was represented numerically in order to minimize the computational effort, and improve the quality of the approximation given by the finite element method.

5 PRESENTATION AND DISCUSSION OF RESULTS

Figure 8a shows the spciments before and after the compression test. It can be observed the high volume change by compression, suffered by the foam.

Figure 8b shows the deformed mesh obtained for the numerical simulation of the compression test.

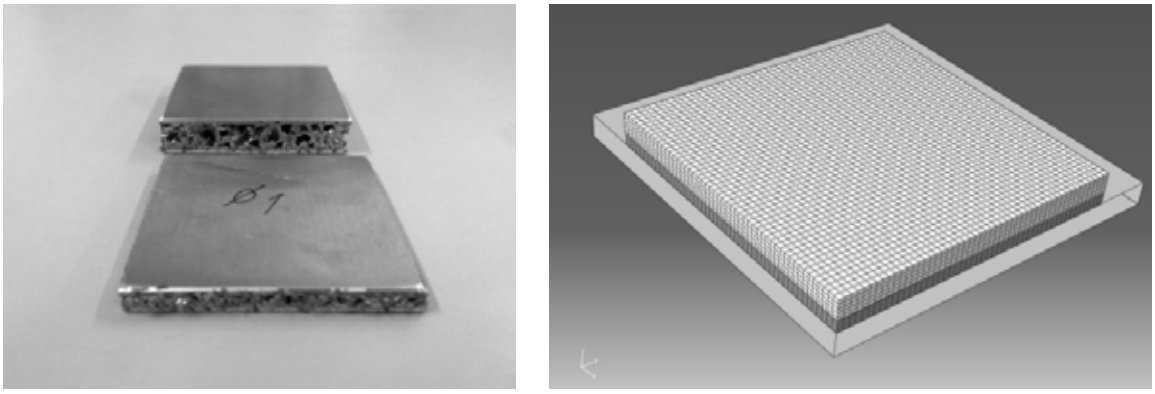

a) Final result of experimental compression test. b) Final numerical result.

Figure 8: Compression test.

Comparison of the results in terms of force-displacements graph shows a good agreement between the numerical results obtained using the Deshpande model and experimental results.

For the numerical test, the metal foam core assumes an important role. After a small domain of elastic behavior, the foam quickly reaches its yield value. This can be physically interpreted as the beginning of the collapse of the cells that constitute the foam. This process is almost constant with some small variations in strength. After all the cells

have collapsed, the numerical specimen starts behaving as a solid, resulting on a rapid increase on the applied force for small increments of displacements.

A good agreement was obtained between the numerical results and the experimental results. This validates the use of the Deshpande constitutive model, used to describe the difficult behavior of plastic porous materials.

Figure 9 shows the speciments after the tensile tests experiments. The obtained numerical and experimental results for the tensile tests are shown in Figure 10. Observing the force/displacement curves of Figure 10, they appear to be similar to a typical curve of a tensile test for an homogeneous solid metal, with an initial elastic behaviour and a second plastic behaviour. The high forces that leads to the rupture of the speciments are mainlly supported by the two aluminum sheets, since the rupture of the metal foam core occurs for much lower forces than those achieved during the experimental tensile tests.

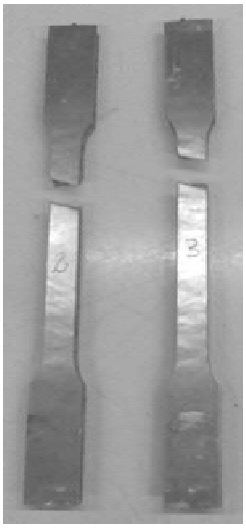

Figure 9: Specimens after the tensile test.

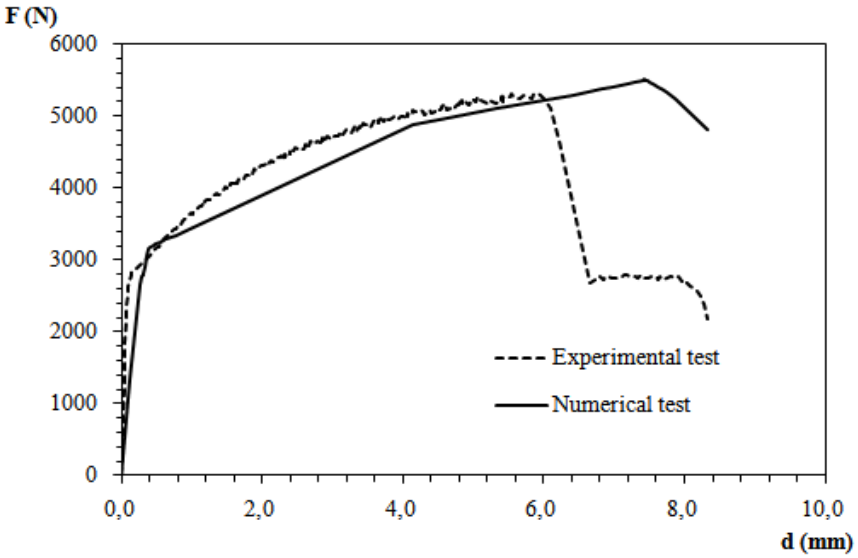

Figure 10: Force/displacement curve for the experimental and numerical tensile test.

6 CONCULUSIONS

A good agreement was verified between the numerical and experimental results for the uniaxial compression test. It is possible to conclude that the model of Deshpande can be used to describe the plastic behavior associated with the metal foam cores.

For the tensile test a good agreement between the numerical and experimental results was obtained. It is also still possible to conclude that the aluminum sheets are the main responsible for the high force achieved experimentally, due to the foam's low ability to withstand tensile forces.

Finally, and as a way to improve the numerical results, additional experimental studies would be needed in order to obtain the properties of the sheets separated from the foam, and an approach to study the anisotropy associated with both materials that constitute these panels.

ACKNOWLEDGEMENT

The authors gratefully acknowledge the funding provided by Ministério da Ciência, Tecnologia e Ensino Superior - Fundação para a Ciência e a Tecnologia (Portugal) and by FEDER/FSE, under grant PTDC / EME – TME / 098050 /2008.

REFERENCES

[1] MF Ashby et al.; *Metal foams: a design guide*, Oxford, Butterworth-Heinemann; 2000.

[2] Baumeister et al.; *Aluminium foams for transport industry*; Mat and Design; 18:217-220; 1997.

[3] http://www.bmw.com/com/en/newvehicles/x6/x6/2007/allfacts/ergonomics/passive_safety.html

[4] Topin, F., et al., *Experimental Analysis of Multiphase Flow in Metallic foam: Flow Laws, Heat Transfer and Convective Boiling*; Advanced material Engineering; 8(9): p. 890-899; 2006

[5] Banhart, J., Manufacture; *Characterization and application of cellular metals and metal foams*; Progress in materials Science; 2001. 46: p. 559-632.

[6] Mata H. et al, *Study of sandwich shells with metallic foam cores;* Int J Mater Form Vol. 3 Suppl 1:903– 906 DOI 10.1007/s12289-010-0914-x, Springer-Verlag France, 2010;

[7] Mata H. et al, *FEM analysis of Sandwich Shells with Metallic Foam Cores*, Key Engineering Materials Vol. 473, Trans Tech Publications, Switzerland, 2011;

[8] Deshpande, V. S., and N. A. Fleck; Isotropic *Constitutive Model for Metallic Foams*; Journal of the Mechanics and Physics of Solids; pp. 1253–1276; 2000.

[9] A.G. Hanssen et al., *Validation of constitutive models applicable to aluminium foams*; International Journal of Mechanical Sciences 44 (2002) 359–406; 2001.

[10] Neves M. P. Rui, *Modelação Constitutiva do Comportamento Mecânico de Espumas Metálicas*, 2009.

[11] R.E. Miller / International Journal of Mechanical Sciences 42 (2000) 729}754.

[12] T.M McCormack et al., *Failure of sandwich beams with metallic foam cores*, International Journal of Solids and Structures; 38 (2001) 4901-4920; 2000.

XI International Conference on Computational Plasticity. Fundamentals and Applications
COMPLAS XI
E. Oñate, D.R.J. Owen, D. Peric and B. Suárez (Eds)

ON STANDARD PREDICTIONS OF REFORMABILITY AND COLLAPSE RESISTANCE FOR EXPANDABLE TUBULARS BASED ON ELASTO-PLASTICITY MODEL

T. SRISUPATTARAWANIT*, G.-P. OSTERMEYER†

Institute of Dynamics and Vibrations

Technische Universität Braunschweig

Schleinitzstraße 20, 38106 Braunschweig, Germany

E-Mail : * t.srisupattarawanit@tu-bs.de, † gp.ostermeyer@tu-bs.de

Web page: http://www.ids.tu-bs.de/

Key words: Elasto-Plasticity, Forming Process, Expandable Tubulars, FEM.

Abstract. The exploitation of geothermal power is an innovative energy source with great potential. However the exploration for deep geothermal sources is still costly and high risk operations. Recently, an expandable tubulars technology for casing is proposed with the potential to construct monobore completions. These lead to a smaller borehole and significantly reduce the cost of drilling process. Technically the expandable tubulars will be initially reduced by a folded plasticity condition and be expanded again downhole. In our studies, the performances of using them were studied in terms of reformability (foldability and expandability) and collapse resistance based on numerical approach. Elasto--plasticity models were investigated, conventional finite element method (FEM) was used for dicretizations combined with other necessary numerical algorithms. The standard predictions of expandable tubular performance were finally proposed, the numerical results were also presented at the final part of this paper.

1 INTRODUCTION

An innovative energy source such as geothermal is exploitation with very high potential. In deep geothermal source, the operations include high cost and risk. The major cost come from a part of drilling bore completion. Recently, a new technology is being developed, namely expandable tubulars technology, the diameter of tubulars will be initially reduced by a folded plasticity condition and could be expanded again downhole. This technology offered the expandable tubulars on using with maximizing through bore, reducing cost and improving productivity.

The fundamentals of mechanical reforming process involved an application of sufficient forces to overcome the yields strength of tubular material and taking the advantages of plastics deformation to reform a new geometry of tubular. The reforming process consists of folding and expansion process. The method of folding process is typically using contact with hard material. The methods of expansion process have been established alternatively [6],

such as hydraulic pressure, cone expansion, rotary expansion or combination between them. With hydraulics pressure, the high pressure may require in some cases and the capacity of machine has to be considered. It could be used for initial expansion process for other methods. Cone expansion method is an extrusion process in which a tubular is subjected to the expansion forces acting around entire inner circumference. The tubulars will be radially expanded when the cone move in axial direction. The rotary expansion consist of a roller set which is discrete the position of expansion force in circumference. To apply acting expansion force to entire inner circumference, the roller set will be moved in longitudinal axis. The cone expansion and rotary expansion require minimizing frictions and vibrations of reforming system.

The concepts of productions are two possibilities of producing expandable tubulars. The first may produce expandable tubulars directly from tube in which available in market. This reforming process will include both folded reforming and expanded reforming. For the second concept, tubulars may be completely formed with expected geometry from factory directly, using them just complete only the expansion process.

As we have mentioned with some different of producing expandable tubulars or different of reforming methods. With this expandable tubulars technology, drilling operation can now using smaller hole for drilling deeper vertical wells or it can be used for extending the holes horizontally to reach untapped reservoir. In such a case, these expandable tubulars can provide very effective cost solutions and significantly save the drilling cost.

However to use expandable tubulars there still have some difficulties remaining. There is plastics flow deformation during the reforming process. Tubular structure will be reformed repeatly as folding and expansion, plastic behavior could be complicated. The Bauschinger effect [2] occurs during plastics deformation process. Tubular might be collapsed before the reforming process has completed. Furthermore, after completing reforming process the high pressure resistance, namely collapse pressure must be examined. This collapse pressure occurs due to different of pressure between inside and outside tubing. The different of pressure could be very high pressure and making catastrophically deform to tubular, especially in the area of salt at downhole.

In this research work, we studied the reformability and collapse resistance of expandable tubular by using modeling of elasto-plasticity [4,5], combined with conventional finite element method (FEM) and necessary numerical algorithms. The different geometries of expandable tubulars have been tested numerically combined with different types of steel, e.g. mild steel, TRIP steel and TWIP steel. Note that TRIP is stand for Transformation Induced Plasticity and TWIP is stand for Twinning Induced Plasticity.

2 REFORMING PROCESS FOR EXPANDABLE TUBULARS

The expandable tubulars includes plastic deformation due to reforming process (folding and expansion), also bending and straightening during transportations and installation process. After reforming process this tubular must satisfy the resistance of collapse pressure at downhole. In Fig.(1) shown the overview of reforming process and collapse pressure resistance. The tubulars begin with an initial geometry (G1), tubulars are perfectly round. These tubulars will be folded with plastic deformation at the folding process, typically this process could be done by pressing with hard material. After folding process the tubulars have

reformed one time, the geometry is shown in (G2). Now the diameters of tubulars are significantly reduced with no round geometry. This will make the transportations more efficiently economically. The tubulars may be deformed again by bending on reeling and unreeling process. In order to prepare the tubulars for installation into drilling hole, the straightening is required. These tubulars must be reversely deform again by bending until the straight tubulars have found or atleast having possibility to install into drilling hole, this is shown in (G3).

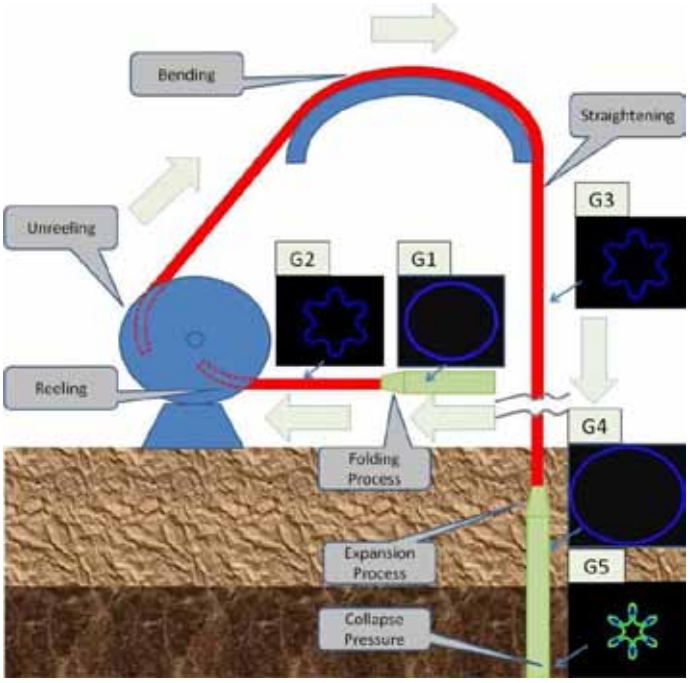

Figure 1: Overview of reforming process and collapse pressure resistance for expandable tubulars

After the folded tubulars are installed into drilling hole, the expansion processes can be now started, may be with different methods as we have mentioned before. The expansion process will make the tubular round with plastic deformation. After installation the tubulars will be applied by namely collapsed pressure. This pressure in some condition could make the tubulars catastrophically deform as in (G5). There are clearly shown that the reforming process and collapse pressure resistance will make tubulars repeatly plastically deform. The analysis of these tubulars requires the suitable model, especially plastic flow deformation. This elasto-plastic deformation model will be discussed in the next section.

3 MODEL THEORY OF ELASTO-PLASTICITY

According to applied forces, material deforms with elastic properties until some magnitude of this force, stress may not increase but strain is significantly increased. This is the physical phenomena for typical elasto-plastic model. The strain rate ($\dot{\boldsymbol{\varepsilon}}$) which describe the total deformation is divided into strain rate of elastic deformation ($\dot{\boldsymbol{\varepsilon}}^{el}$) and strain rate of plastic deformation($\dot{\boldsymbol{\varepsilon}}^{pl}$), given by the following function.

$$\dot{\boldsymbol{\varepsilon}} = \dot{\boldsymbol{\varepsilon}}^{el} + \dot{\boldsymbol{\varepsilon}}^{pl} \ . \tag{1}$$

On elastic deformation, the structural response is assumed to be derivable from strain energy ($\boldsymbol{U}$), so that stress fields can be directly defined by gradient of strain energy respect to the elastics strain $\boldsymbol{\sigma} = \partial \boldsymbol{U}/\partial \dot{\boldsymbol{\varepsilon}}^{el}$. In order to implement hardening law, it is a proper combinations of isotropic and kinematics hardening model. The particular yield surface condition is described by

$$f(\boldsymbol{\sigma} - \boldsymbol{\alpha}) - \boldsymbol{\sigma}^{\boldsymbol{o}} = 0 \ , \tag{2}$$

combine with the equivalent Mises stress $f(\boldsymbol{\sigma} - \boldsymbol{\alpha}) = \sqrt{3/2(\boldsymbol{S} - \boldsymbol{\alpha}^{dev}) : (\boldsymbol{S} - \boldsymbol{\alpha}^{dev})}$, where **(:)** denotes the tensor operator**,** $\boldsymbol{S}$ denotes the deviatoric stress tensor and $\boldsymbol{\alpha}^{dev}$ is the deviatoric part of back stress tensor and $\boldsymbol{\sigma}^{\boldsymbol{o}}$ denotes current yield stress.

During the plastic deformation, material behaves as flow plastically. The plastics deformation can be obtain by namely the flow rule, it is given by

$$\dot{\boldsymbol{\varepsilon}}^{pl} = \dot{\boldsymbol{\lambda}} \frac{\partial \boldsymbol{\Psi}}{\partial \boldsymbol{\sigma}} \ , \tag{3}$$

where $\boldsymbol{\Psi}$ denotes flow potential and $\dot{\boldsymbol{\lambda}}$ is time rate parameter here the equivalent plastics strain rate is used.

Considering the hardening law, the nonlinear isotropic /kinematics hardening model is used to describe the stress evolution. This consists of two components: one is the nonlinear kinematics hardening which describe the translation of yield surface in stress space through backstress [3]; another is an isotropic hardening in which describe the size of yield surface. The formulation is given by

$$\dot{\boldsymbol{\alpha}} = C \frac{1}{\boldsymbol{\sigma}^{\boldsymbol{o}}} (\boldsymbol{\sigma} - \boldsymbol{\alpha}) \dot{\boldsymbol{\lambda}} + \gamma \boldsymbol{\alpha} \dot{\boldsymbol{\lambda}} \, , \tag{4}$$

where C and γ are material constant, when γ is zero become the linear kinematics model and when C and γ are zero so become the isotropic hardening model.

The model has been implemented in material property subroutine in Abaqus/CAE [1], combination with nonlinear finite element and some other numerical necessary algorithms in the computation. The tool for standard prediction of plastic behavior for expandable tubular can be performed and simulated the mechanism of expandable tubular, which will be discussed in the next section.

4 NUMERICAL RESULS OF REFOMABILITY AND COLLAPSE RESISTANCE

4.1 Expandability of folded tubulars

In this computation, we deal with expandability of folded tubulars. The hydraulics pressure is used for expansion process. The folded geometry may already be obtained by tubulars production manufacturing. We start with the geometry G2 (see in Fig.(1)) and concerning only on expansions process The analysis of plastic deformation are performed with different tubular geometry and different material. The main objective of this computation is to find out the mechanism of plastics deformation with different optimized geometry and different tubular material.

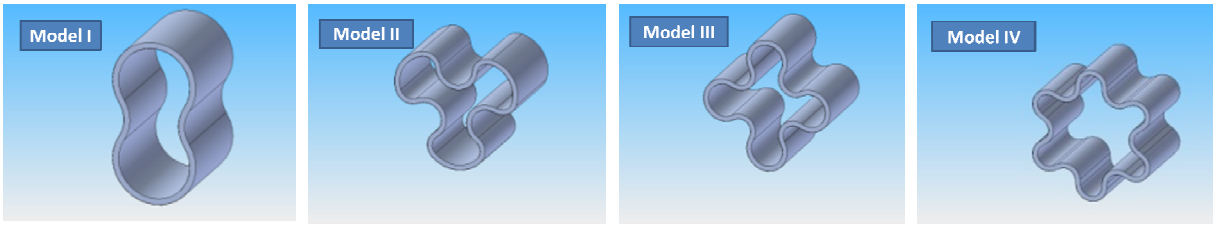

Figure 2: Geometry of tubulars

The optimized geometries are obtained by our project partner [5] at Institute of Production Engineering and Machine Tools, University of Hannover. The different geometries are shown in Fig. (2). The parameters shown in Table (1) with the maximum outer diameter (*OD*), thickness (*t*) and maximum ovalidity (*OD/t*). Tubular geometry is analyzed with different kind of tubular material.

Table 1: Geometry parameters of Tubulars

Max. OD (mm.)	Thickness (mm.)	Max. OD/t
165.0	6.0	27.5

Table 2: Material properties

Descriptions	Modulus of Elasticity *(N/mm^2)*	Poison's ratio	Yields stress *(N/mm^2)*	Rupture stress *(N/mm^2)*	Max. Strain %
Mild steel	2.10E+05	3.00E-01	4.00E+02	5.00E+02	8.20E+00
TRIP steel	2.10E+05	3.00E-01	4.80E+02	1.10E+03	5.00E+01
TWIP steel	2.10E+05	3.00E-01	4.50E+02	6.99E+02	9.00E+01

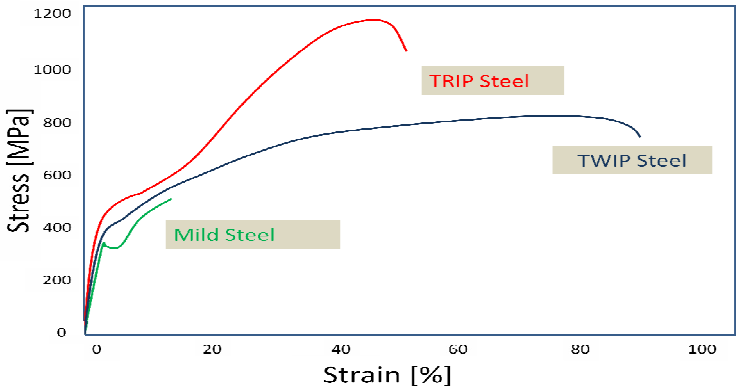

Figure 3: Stress-strain curve for different steel materials

There are mild steel, TRIP steel and TWIP steel, the mechanical properties can be found in Fig. (3) and Table (2). Mild steel represents the steel which is normally used for tube and available in market, typically rupture strain is less than 20 %. TRIP steel is used for representing high strength steel, the strength is higher than 1000 N/mm^2 and rupture strain can reach 50 % approximately. The TWIP steel is used for representing high deformation which is 90 % approximately.

For TRIP steel, the plastic flow process occurs with phase transformation from austenite to martensite. The molecule builds the new structure during the plastics flow process, which is the reason why strength can be increased significantly. Also the strain can be increased but only depending on new form of molecular structure. For TWIP steel, the strength can be increased but smaller amount compare to TRIP, while rupture strain increase significantly due to the so-called Twinning effect. TRIP and TWIP are now widely used in auto-industry.

Table 3: Summary results.

Descriptions	Material	Max. Stress *(N/mm^2)*	Pressure *(N/mm^2)*	Evaluation deformation	Expansion Ratio %
Model 1 Set # I	Mild steel	5.00E+02	5.71E+00	*Rupture*	-
Model 1 Set # II	TRIP steel	6.05E+02	3.00E+01	*Plastic*	-1,41E+01
Model 1 Set # III	TWIP steel	5.89E+02	3.00E+01	*Plastic*	-1,41E+01
Model 2 Set # I	Mild steel	5.00E+02	8.16E+00	*Rupture*	-
Model 2 Set # II	TRIP steel	7.23E+02	2.98E+01	*Plastic*	2,01E+01
Model 2 Set # III	TWIP steel	6.18E+02	3.00E+01	*Plastic*	1,96E+01
Model 3 Set # I	Mild steel	5.00E+02	6.61E+00	*Rupture*	-
Model 3 Set # II	TRIP steel	8.46E+02	3.00E+01	*Plastic*	2,15E+01
Model 3 Set # III	TWIP steel	6.28E+02	3.00E+01	*Plastic*	2,06E+01
Model 4 Set # I	Mild steel	5.00E+02	4.33E+00	*Rupture*	-
Model 4 Set # II	TRIP st eel	7,46E+02	3.00E+01	*Plastic*	2,27E+01
Model 4 Set # III	TWIP steel	6,30E+02	3.00E+01	*Plastic*	2,29E+01

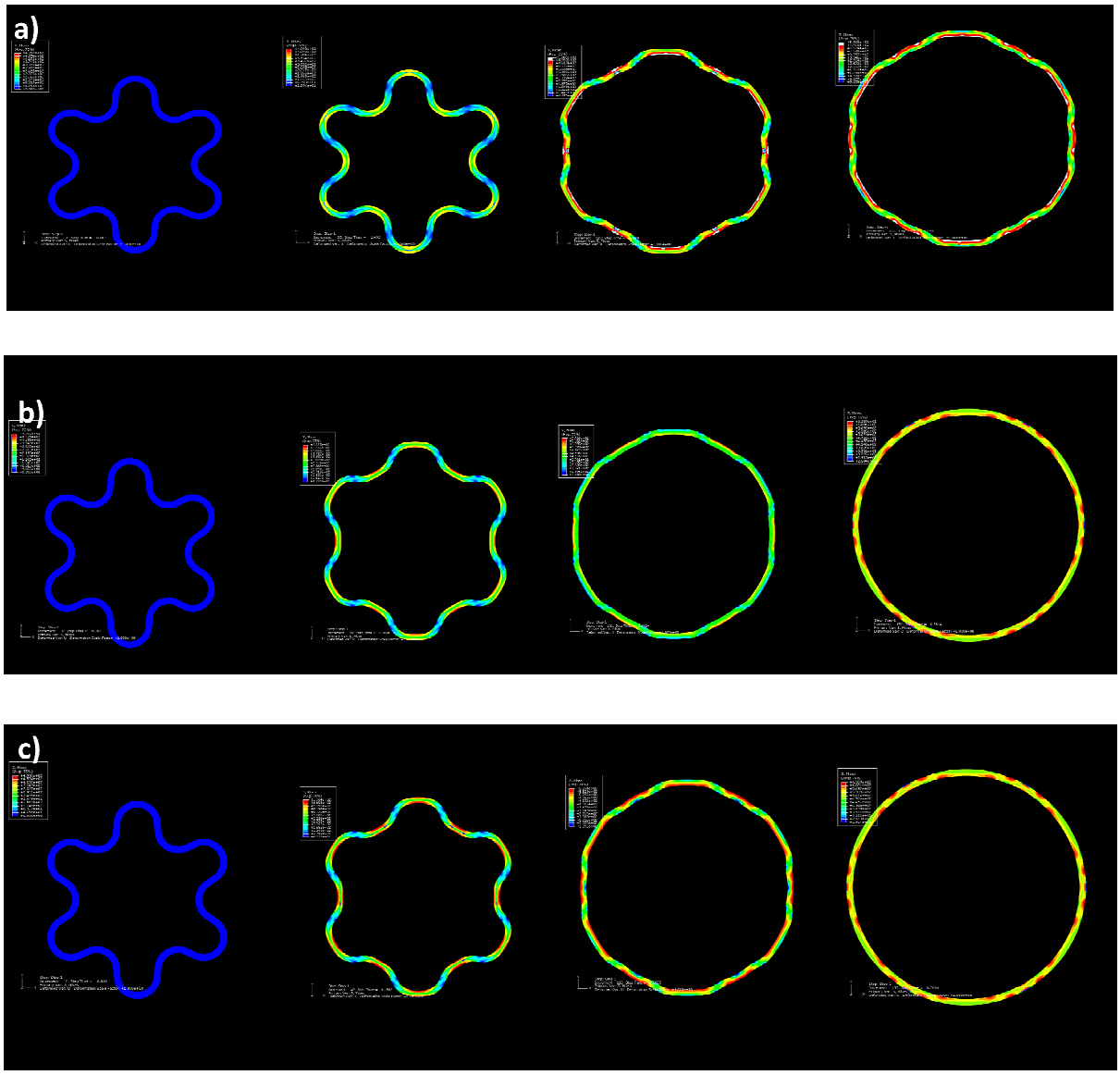

Figure 4: Mechanism of expansion process for model 4; a) mild steel; b) TRIP steel; c) TWIP steel.

To obtain reasonable solutions with acceptable accuracy, high requirements towards the modeling technique and the numerical treatment are necessary. The nonlinearity in this computation includes geometrical nonlinearity due to the large deformations and the material nonlinearity which describes the nonlinearity of the material laws. The iterative Newton method is used to obtain the nonlinear solution, while the system equation solver is the direct method. The element meshes are implemented with rectangular element type. The resolutions are obtained with global mesh refinement, beginning with course mesh and then refine until convergence occur.

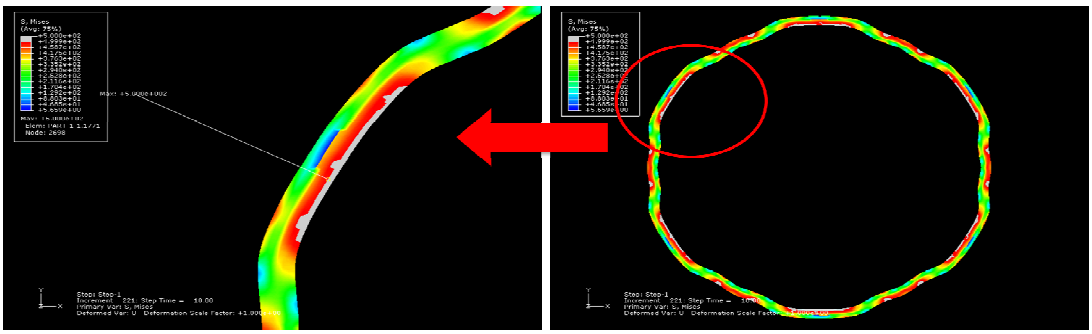

Figure 5: Expansion process at critical part of structure.

Concerning numerical results, the plastic strain occurred after the pressure was increased. At some pressure the tubular were reformed. Theoretically, if materials do not arrive at the rupture point when increasing the internal pressure; they should be reformed until the round geometry occurs. If they arrive rupture point, they will be damaged before the round geometries have formed.

Three different types of steel (mild steel, TRIP steel and TWIP steel) are considered. The results showed very clearly that, for all model geometry of mild steel is damaged before round geometry could be formed. Oppositely, TRIP and TWIP steel can be formed until round geometry occur without any damages. Concerning again maximum stress, the TRIP steel has higher magnitudes compared with TWIP steel at the same internal pressure. These came from the nonlinearity of the material, or TRIP steel is harder and TWIP steel can be reformed easier than TRIP steel. The results of the expansion process with different geometries and different materials are presented in Table (3). The expansion mechanisms can be found in Fig.(4) and in Fig.(5), where the critical part of the structure in the expansion process is shown.

4.2 Testing of resistance collapse pressure

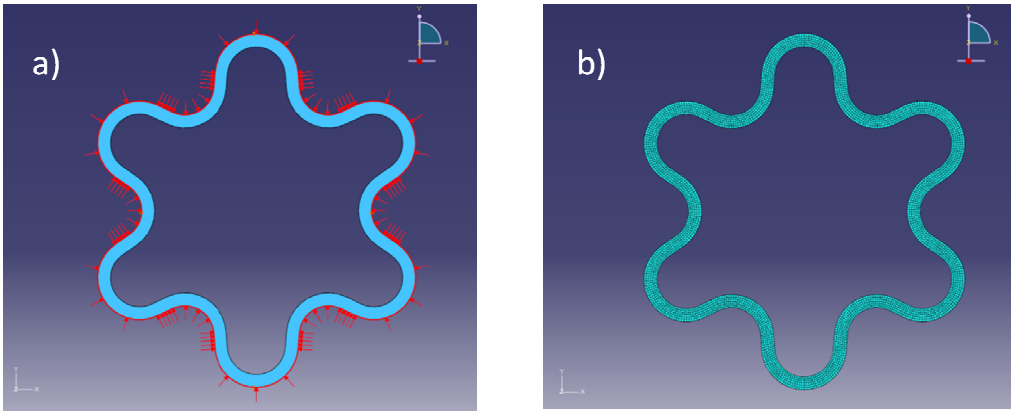

Figure 6: Setting problem for collapse pressure test; a) collapse pressure; b) 3456 rectangular meshes

Extension from previous example (4.1) the numerical testing of collapse pressure resistance is investigated. The main objective for this computation is to study the deformed mechanism of resistance collapse pressure and the influence of geometry imperfection on the capacity of resistance collapse pressure. As we have mentioned when using expandable tubular downhole, it has a possibility to get high pressure due to movement of salt. In this computation, the collapse pressure is applied directly from outside with perfectly uniform distribution, see in Fig.(6). The tubular geometries are the same as in example (4.1). For material properties, TWIP steel is used for this testing. The expansive pressures are varied from lower magnitude (10 N/mm^2) to higher magnitude (40 N/mm^2), while the collapse pressure is linearly increased from zero to 40 N/mm^2.

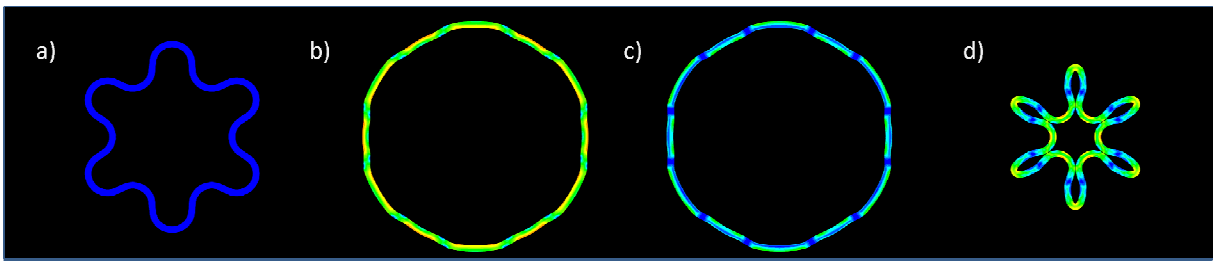

Figure 7: Mechanism of expansion and collapse pressure; a) Initial geometry; b) Expansive pressure; c) Unloading expansive pressure and d) Collapse pressure.

The results shown that, model 1 can be expanded with increasing expansive pressure until 40 N/mm^2 without damaged while others model were collapsed at expansive pressure about 32 N/mm^2 approximately. In expansion mechanism the tubulars are expanded and slowly deform until plastic deformation occurred as shown in Fig.(7 b). After that the expansive pressure is linearly unloaded the elastic deformation part can be reversely deformed, while the plastic deformation does not reverse as shown in Fig.(7 c). Thus this geometry is the beginning form for analysis of resistance collapse pressure. The different expansive pressure will give different final geometry, some of them are completely round some of them are not depending on the expansive pressure itself, in Fig.(9) shown the different final geometry of tubular with varying expansive pressure. In Fig.(8) shown the results of collapse pressure when the expansive pressures are varied. There is an interested observation that when the expansive pressure is increased the collapsed pressure is increased as well. There could be explained that, when expansive pressure increase tubular is reformed and giving more a round geometrical property as shown in Fig.(9), until at some expansive pressure the tubular become completely round. At this point tubular begin namely perfection geometry, this kind of geometry is completely round and it has more capacity for resistance collapse pressure. Oppositely, before arriving this perfection point the geometry has some geometrical imperfection, the geometry is not completely round. Also it reduce the capacity of resistance collapse pressure as shown in Fig.(8).

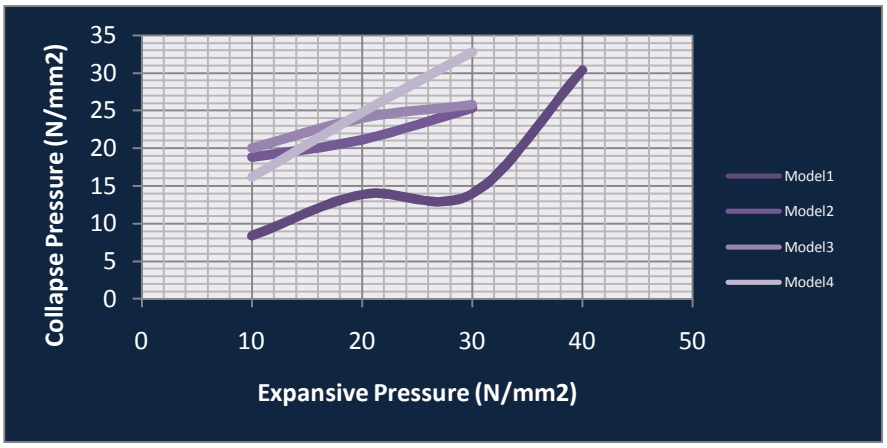

Figure 8: The relations of expansive pressure and collapse pressure

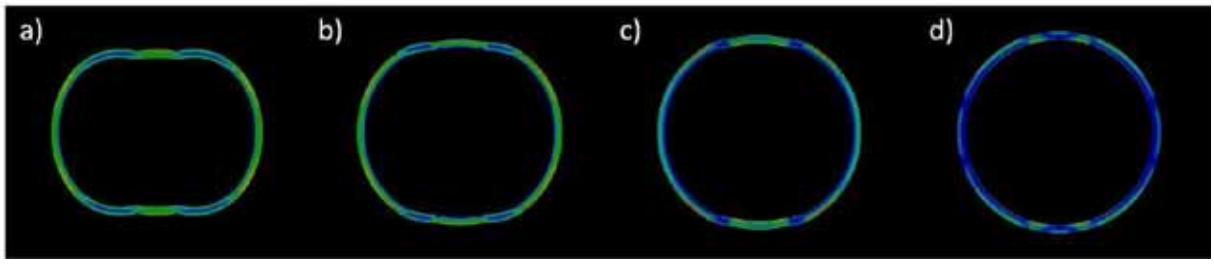

Figure 9: Tubular geometry after unloading expansive pressure of model 1 ; a) Expansive pressure 10 (N/mm^2) ; b) Expansive pressure 20 (N/mm^2) ; c) Expansive pressure 30 (N/mm^2) ; d) Expansive pressure 40 (N/mm^2)

4.3 Expandability of folded tubulars with cone expansion

As we mentioned in examples (4.1) and (4.2) the expansion process have involved with hydraulics pressure. In this example, we interested in cone expansion method. Tubulars will be expanded by contact forces between cone expander and tubular, the cone expander has to be moved inside through tubing with the expected diameter. The 10 % expansion rate is considered in these cases. We interested on mechanism of model 1 with different material (mild steel, TRIP and TWIP). The main questions are these 3 materials could be used with cone expansion method and what are the magnitudes of driving force for cone expander. As the contact between cone expander and tubular are main consideration, the model of contact mechanics is included by penalty methods [3] with the Coulomb's friction coefficient 0.1.

The results shown that mild steel damaged before cone expander has completely drived through the tubular, oppositely for TRIP and TWIP, did not damage and the cone expander can drive through the tubular. Considering mechanism of expansion process, the expander is moved forward by driving force. Due to the geometry of the cone, the tubular will be automatically expanded when the cone pass through. The plastic deformation occurred and

reforming the round geometry while the elastic deformations did some reversely reform after the cone expander has already pass through.

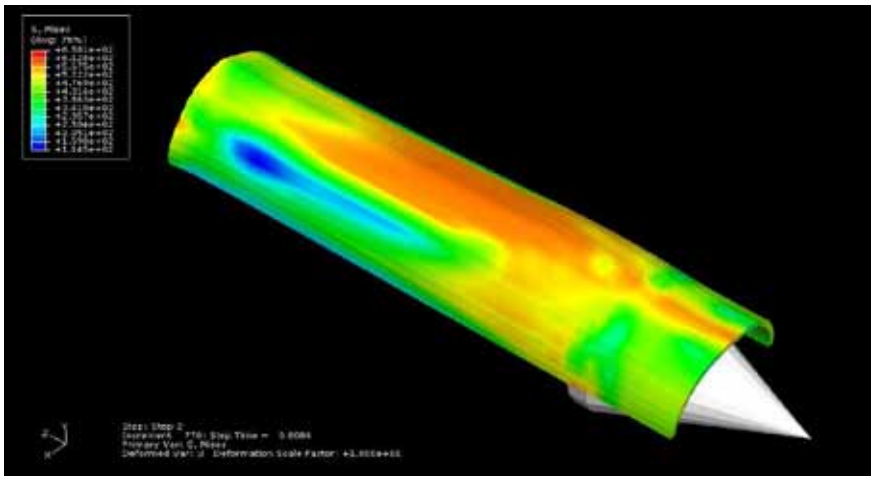

Figure 10 : Expansion process with cone expander for model 1

In Fig.(10) shown the result of expansion process for model 1 with TWIP steel, the high plastic deformation occurred at red part. Concerning the driving force in different material, the mild steel required low magnitude of driving force as this material is already damaged and cannot resist the force due to contact of the expander. TRIP steel requires higher magnitude of driving force compare to TWIP steel. This could be explained that TRIP steel has higher strength property compare to TWIP steel which has extremely high deformation property. This high strength property could make the cone expander difficult to drive forward and required driving force too high. The comparison of driving force for different materials are shown in Fig.(11).

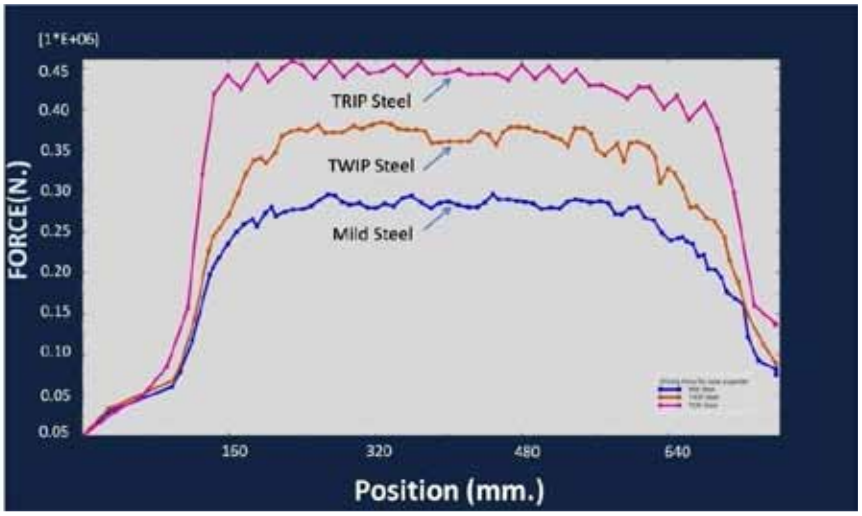

Figure 11: Driving force for moving cone expander forward with different material.

5 CONCLUSIONS

The performance of using an innovaive expandable tubular technology was studied interm of reformability which including foldability and expandability, and collapse resistance based on numerical approaches. Typical models of elasto-plasticity were investigated espcieally with the combined isotropic and kinematics model, in which the Bauschinger's effect [2] can be taken into account. The conventional nonlinear finite element method was used combined with the necesary numerical algorithm in order to solve the model and perform the standard tool for prediction of the expandable tubular performance. According to the numerical results, there are some interested observation as :

- In term of material the high strength such as TRIP and TWIP steel are recommended to use for expandable tubular later than mild steel.
- In term of geometry, imperfection geometry of expansion has significantly influence to the capacity of collapse pressure resistance. The perfectly round geometry has significantly more capacity for resistance collapse pressure than the imperfection.
- The imperfection of collapse pressure itself is also interested in term of the distribution pattern and the magnitude, it is still an open question in this field.
- For the cone expansion type, the influence of friction is also interested; it will be investigated and published later.

ACKNOWNLEDGEMENT

This contribution was made possible by financial support of "Ministerium für Wissenschaft und Kultur", Niedersachsen (MWK) and Bayker Hughes, Celle with the collaborative research program "gebo" (Geothermal Energy and High Performance Drilling).

REFERENCES

[1] Abaqus/CAE User's Manual (2007).
[2] Bausching, J., Über die Veränderung der Elastizitätsgrenze und Elastizitätsmodul verschiedener, Metal Civil Ing N.F., 27, (1881) 289-348.
[3] Belystschko, T., Liu, W.K. and Moran, B*., Nonlinear Finite Elements for Continua and Structures*, John Wiley & Sons (2002), New York.
[4] Ostermeyer, G.-P., Srisupattarawanit, T., Schiefer, F., Numerical Analysis of 'Expandable Tubulars based on Elasto-Plasticity Model. Technical Report, Institute of Dynamics and Vibrations, Technical University Braunschweig. Braunschweig 2010.
[5] Reinicke, K. M., et.al, Geothermal Energy and High Performance Drilling Collaborative Research Program (gebo). Technical Report, Niedersachsen, Germany, 2011.
[6] Mack, R.D., The Effect of Tubular Expansion on the Mechanical Properties and Performance of Selected OCTG-Results of Laboratory Studies. *In Proceeding of Offshore Technology Conference*. OCTG 17622, (2005).

XI International Conference on Computational Plasticity. Fundamentals and Applications
COMPLAS XI
E. Oñate, D.R.J. Owen, D. Peric and B. Suárez (Eds)

ON THE PREDICTION OF THE CURVATURE OF CROSS ROLL STRAIGHTENED BARS

A. MUTRUX, B. BERISHA AND P. HORA

Institute of Virtual Manufacturing
ETH Zurich
Tannenstr. 3, 8092 Zurich, Switzerland
e-mail: mutrux@ivp.mavt.ethz.ch

Key words: Cross roll straightening, cyclic softening

Abstract. A recently proposed procedure for the simulation of cross roll straightening allows to predict successfully the residual stress distribution in straightened bars as well as their yield stress. Although the procedure allows also to make predictions about the curvature of straightened bars, large discrepancies appear between predictions and experiments. The present study aims at understanding the causes of these deviations. The standard experimental setup for the measurement of curvature provides values on the assumption of a constant in-plane curvature. Using a modified procedure for the prediction of the curvature, this study shows that, according to the model, the curvature of straightened bars is not constant and not in-plane. The reason for the deviation observed between predictions and measurements is then obvious.

1 INTRODUCTION

Cross roll straightening is the last mechanical operation in the production process of bright steel bars and aims principally at reducing: (1) the curvature and (2) the detrimental residual tensile stresses on, and close to, the surface of round bars. On the downside, the operation may lead to a decrease of the yield stress of the bars. Modelling approaches to describe the process can be grouped into two main categories: analytical procedures and FE based procedures. The former ones (see e.g. [1, 2]) relie on the assumption of straightening under pure alternate bending and cannot take into account such influences as the lateral stamping applied by the rolls on the bar. The latter ones (see e.g. [3, 4]) are CPU cost intensive and, therefore, require the use of relatively rough meshes, making them unable to predict subtle differences in e.g. the yield stress of straightened bars.

During cross roll straightening, the bar is bent and stamped between two rotating rolls, a convex and a concave one, as shown in Figure 1. Apart from the geometry of the

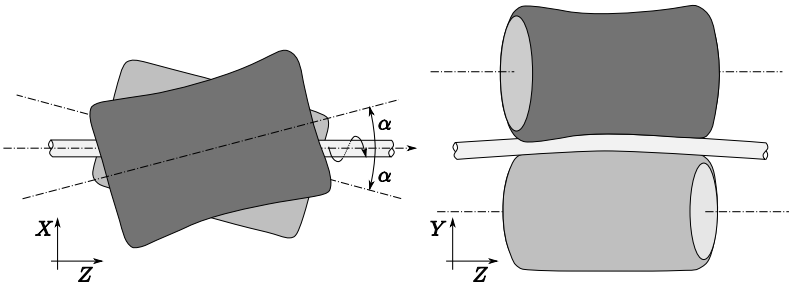

Figure 1: Sketch of the cross roll straightening process. The two main process parameters are the angle α and stamping δ. XYZ are the principal axes of the global coordinate system.

rolls, the main process parameters are the angle α between the rolls and the bar and the stamping δ, defined as the diameter of the bar minus the minimum distance between the rolls. During straightening, the rolls rotate, inducing a forward motion of the bar and a rotation about its main axis.

A mixed analytical-numerical modelling approach to cross roll straightening, based on similar assumptions as the one introduced in [5], is presented in [6]. The procedure allows to predict quantitatively the influence of the straightening parameters α and δ on the yield stress of straightened bars. The predicted residual stress distribution is in qualitative agreement with the measurements presented in [7].

In [6], only intermediate results about the prediction of the curvature of straightened bars are presented. The predictions lie about an order of magnitude higher than the experimental values and no satisfying explanation of this discrepancy is provided. The present study aims at shedding light on the capabilities of the procedure regarding the prediction of the curvature of bars after straightening.

2 PROCESS MODELLING

This section presents a summary of the modelling approach. A more detailed explanation can be found in [6]. The main assumptions on which the procedure rely are the following:

- a *closing* simulation, in which the bar is simply bent and stamped between two static rolls (without rotation or forward feed), provides a decent approximation of the total strain distribution in a bar during cross roll straightening. For example, the influence of the rolling contact between the bar and the rolls can be neglected

- the total strain distribution in the bar depends marginally on the behaviour of the material

- the path of a material point of the bar during straightening can be computed analytically

The first step of the procedure is a *closing* simulation. This simulation is conducted using a dynamic implicit scheme and the material behaviour is described using a linear isotropic model. The results are the total strain distribution within the bar and the bending line $b(t)$. $b(t)$, with $t \in [0,1]$, is a parameterised curve in the ZY plane passing through the nodes lying on the neutral axis of the bar in the deformed configuration. A coordinate system $\{\xi(t), \eta(t), \zeta(t)\}$ is associated to $b(t)$

$$\begin{aligned} e_\xi(t) &= \begin{pmatrix} 1 \\ 0 \\ 0 \end{pmatrix} \\ e_\eta(t) &= \frac{1}{\|b'(t)\|} \begin{pmatrix} 0 \\ b'_z(t) \\ -b'_y(t) \end{pmatrix} \\ e_\zeta(t) &= \frac{1}{\|b'(t)\|} \begin{pmatrix} 0 \\ b'_y(t) \\ b'_z(t) \end{pmatrix} \end{aligned} \tag{1}$$

where $b'(t)$ is the directional derivative of $b(t)$.

A sufficient number of points P_i are chosen over a cross section of the bar. Their helical paths $p_i(t)$, having $b(t)$ as neutral axis and a pitch $\varkappa = 2\pi r_{rod} \tan(\alpha)$, are computed. The solids lying on each path are identified. The sequence of the total strain tensors associated to these elements builds the total strain history of each material point considered. Total strain increments are defined as the differences between consecutive states along a given path. Those strain increments are then integrated according to the constitutive equations presented in Section 3.2. To compensate for eventual deviations from the state of equilibrium, the internal variables obtained for each P_i are mapped to a corresponding layer of solid elements and, applying adequate boundary conditions, the equilibrium is sought using a one-step static implicit solution scheme.

For predictions regarding the evolution of the curvature of the bar, axis asymmetric axial initial stresses are considered. An initial curvature $\kappa^{bs} < \sigma_y / (E r_{rod})$ of a bar can be reduced to a stress distribution over its cross section according to relation

$$\sigma^{in}_{\zeta\zeta}(\eta) = E\kappa^{bs}\eta \tag{2}$$

Considering $\sigma^{in}_{\zeta\zeta}$ as initial stresses, the corresponding $\sigma^{out}_{\zeta\zeta}$ stresses after straightening are computed using the procedure described above. This stress distribution generates a moment $M_{\tilde{\xi}}$ about an axis $\tilde{\xi}$

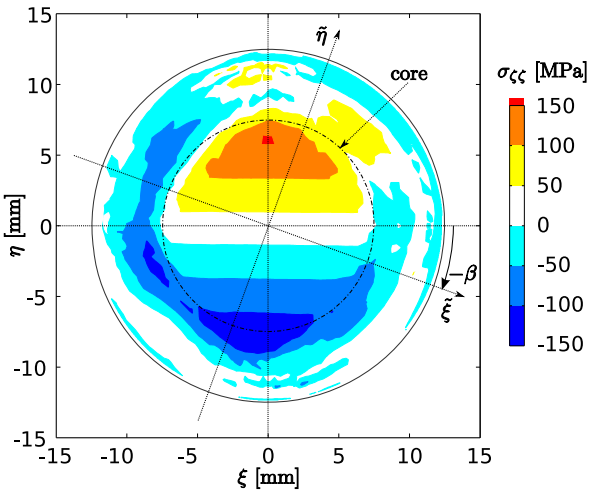

Figure 2: $\sigma_{\zeta\zeta}^{out}$ stress distribution in a bar with an initial curvature $\kappa^{bs} = 10^{-4}$ straightened with $\alpha = 18°$ and $\delta = 0.50$ mm. The angle β is highlighted ($\beta = -20°$ in the present case). The linear initial stress distribution in the core of the bar is not affected by the plastification that takes place in the peripheral layers.

$$M_{\tilde{\xi}} = \int_A \sigma_{\zeta\zeta}^{out} \tilde{\eta} dA \tag{3}$$

where $\tilde{\xi}\tilde{\eta}$ is obtained by a rotation of $\xi\eta$ by an angle β around the axis ζ, as shown in Figure 2. The moment $M_{\tilde{\xi}}^{max}$ is

$$M_{\tilde{\xi}}^{max} = \max\left(M_{\tilde{\xi}}\left(\beta\right)\right) \tag{4}$$

The curvature after straightening is $\kappa^{as} = M_{\tilde{\xi}}^{max} / \left(EI\right)$.

3 MATERIAL MODELLING

3.1 Tension-compression tests

The material investigated in the context of this study is a SAE 1144 medium carbon steel ($\varnothing$25 mm). As mentionned above, cross roll straightening induces a cyclic deformation in the bar. The cyclic behaviour of the material is investigated by carrying out tension-compression tests under total strain control with an amplitude $\Delta\varepsilon/2 = 1.5{\cdot}10^{-2}$ at a strain rate of approximately $5 \cdot 10^{-3}$ 1/s. The material exhibits a strong Bauschinger effect, cyclic softening and a small apparent tension-compression asymmetry. The term *apparent* is used to highlight the fact that the phenomenon is more likely due to a Bauschinger effect from the previous drawing operation than to a *real* (according to the definition given in [8]) strength differential effect.

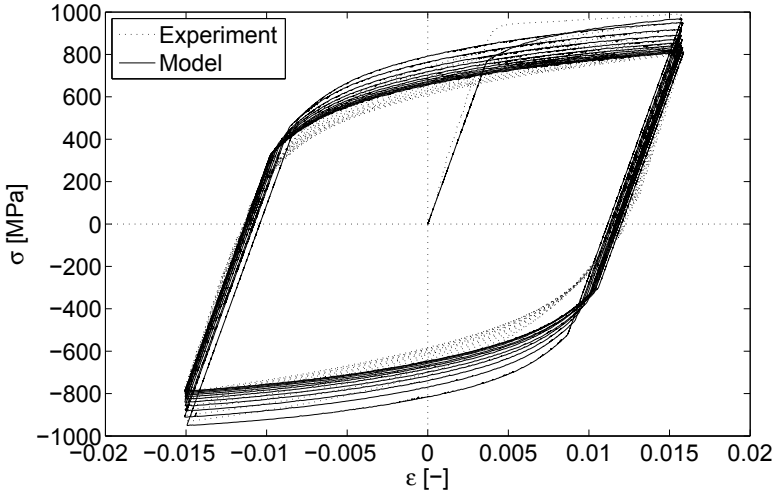

Figure 3: Stress-strain curve obtained from a tension-compression test and corresponding values according to the Chaboche model.

3.2 Constitutive equations

The total strain tensor is additively decomposed in an elastic strain and a plastic strain. The elastic part of the strain tensor obeys Hooke's law. The plastic strain components are governed by the associated flow rule. The yield function is expressed as

$$F = \frac{3}{2}(\boldsymbol{s} - \boldsymbol{a}) : (\boldsymbol{s} - \boldsymbol{a}) - Y^2 \tag{5}$$

where $\boldsymbol{s}$ is the deviatoric stress tensor and $\boldsymbol{a}$ is the backstress tensor. Y, the isotropic hardening (or softening) part, is

$$Y = Q(1 - \exp(-bp)) + \sigma_0 \tag{6}$$

where p is the accumulated plastic strain. $\boldsymbol{a}$ (i.e. its evolution equation) is decomposed according to [9] as

$$\boldsymbol{a} = \sum_{i=1}^{M} \boldsymbol{a}^{(i)} + \boldsymbol{a}_0 \tag{7}$$

where $\boldsymbol{a}_0$ allows to take into account the initial asymmetry between tension and compression in a non-evanescent manner. $\boldsymbol{a}^{(i)}$ is defined through the (Armstrong-Frederick) differential equation

$$\mathrm{d}\boldsymbol{a}^{(i)} = \frac{2}{3} C_i \mathrm{d}\boldsymbol{\varepsilon}^p - \gamma_i \boldsymbol{a}^{(i)} \mathrm{d}p \tag{8}$$

Figure 3 shows the fitted model on the experimental stress-strain curve; the corresponding values of the parameters are given in Table 1. The material model is implemented according to the radial return algorithm presented in [10]. For the *closing* simulation mentionned in Section 2, a linear isotropic model is fitted on the first tension branch ($\sigma_y = 935$ MPa and $E_{tan} = 3000$ MPa).

Table 1: Fitted parameters for the Chaboche model ($E = 210$ GPa and $M = 3$)

C_1	C_2	C_3	γ_1	γ_2	γ_3	Q	b	σ_0	$\boldsymbol{a}_{33}$
44400	18100	1430	665	87	0	-214	5.5	757	7.7

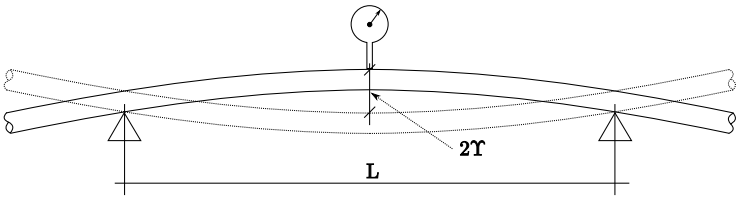

Figure 4: Experimental setup used to measure the curvature of bars ($L = 1$ m).

4 PREDICTION OF RESULTING STRAIGHTNESS

The curvatures of 40 bars before and after straightening with $\alpha = 18°$ and $\delta = 0.50$ mm are measured using the setup sketched in Figure 4. The setup is a common means of assessing the curvature of bars in the industry and [11] presents measurements obtained using a similar device, the dial gauge being replaced by a laser one. The maximum dial gauge amplitude 2Υ is recorded and is converted into a curvature $\kappa = 8\Upsilon/L^2$ assuming that the bar has a constant radius of curvature in a single plane. Experimental results and corresponding predictions are plotted in Figure 5.

It appears from Figure 5 that the curvatures predicted by the model are about an order of magnitude higher than the experimental values. A straightening effect can be predicted when relatively large values of curvature before straightening are considered. When bars with a small initial curvature are considered, such as the ones investigated in this study, the predicted curvatures after straightening are larger than the ones before straightening.

In [11], the roller leveller straightening of coiled medium carbon steel wire (⌀6 mm) is investigated both experimentally and numerically. In a roller leveller, the bar is repeatedly bent in a single plane. Considering a bar initially curved in a single plane and straightening it in its plane of curvature leads to (1) a reduction of its main curvature and (2) the appearance of a small out-of-plane curvature. In this case, the assumption that straightened bars are curved in a single plane does not hold.

In order to verify the hypothesis of the constant in-plane curvature of the bars after straightening for the present case, κ^{as} is computed for different sections over a distance $\varkappa$ of the bar ($\varkappa = 25.52$ mm for $r_{rod} = 12.5$ mm and $\alpha = 18°$). The computations are made with $\alpha = 18°$ and $\delta = 0.50$ mm and two initial curvatures are considered: (1) $\kappa^{bs} = 0$ and

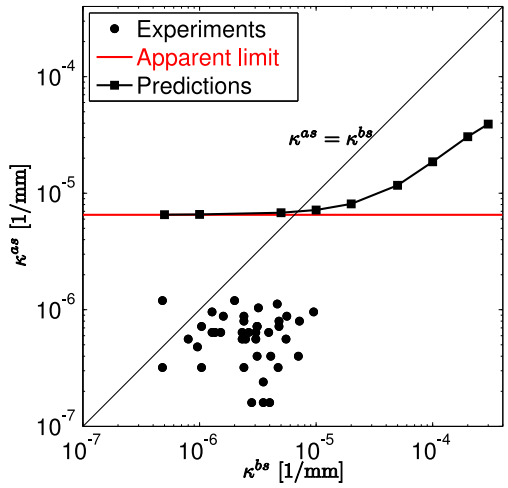

Figure 5: The curvatures before (κ^{bs}) and after (κ^{as}) straightening (with $\alpha = 18°$ and $\delta = 0.50$ mm) of 40 bars are measured. The values predicted by the model are also plotted. The model cannot, apparently, predict curvatures below $\kappa^{as} = 6.5 \cdot 10^{-6}$ 1/mm.

(2) $\kappa^{bs} = 10^{-4}$ 1/mm. The predicted curvatures as well as the corresponding angles β are plotted in Figure 6.

It appears from the results obtained for $\kappa^{bs} = 0$ (Figure 6 (top)) that:

- the curvature of the bar after straightening is approximately constant ($\kappa^{as} \approx 6.6 \cdot 10^{-6}$ 1/mm, which corresponds to the *apparent limit* highlighted in Figure 5)
- the angle β between the axis of principal curvature and the axis ζ completes a whole rotation over a distance $\varkappa$

According to the model, the shape after straightening of an initially perfectly straight bar is hence a helix whose main axis is a straight line. Random numerical errors lead to variations $2\Delta\kappa^{as} < 5 \cdot 10^{-7}$ 1/mm, which are acceptable considering the scattering of the experimental data.

It appears from the results obtained for $\kappa^{bs} = 10^{-4}$ 1/mm (Figure 6 (bottom)) that:

- the curvature of the bar after straightening varies over a length $\varkappa$
- the angle β varies in a $\pm 30°$ strip

These results highlight the fact that the comparison made in Figure 5 between experimental (global) values of curvature and predicted (local) curvatures is not relevant. The assumption of a constant in-plane curvature after straightening does not hold. The experimental setup pictured in Figure 4 is not sufficient to assess the curvature of straightened bars.

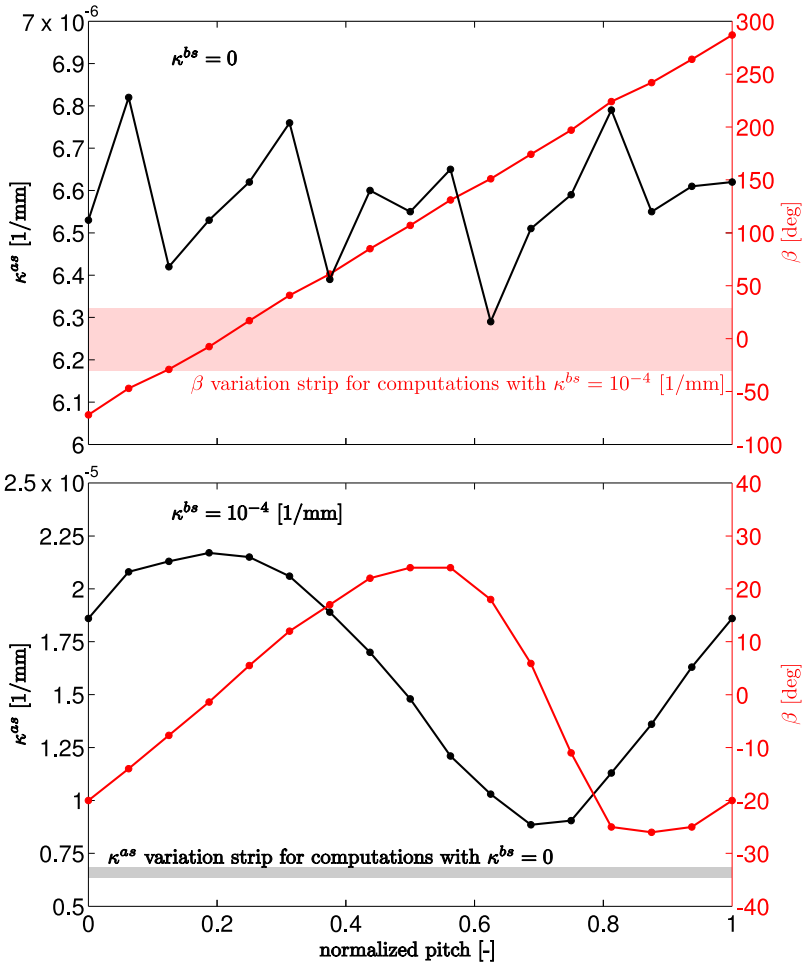

Figure 6: Predicted curvatures after straightening (κ^{as}) and the corresponding angles to the axis ξ for two different curvatures before straightening: $\kappa^{bs} = 0$ (top) and $\kappa = 10^{-4}$ 1/mm (bottom).

5 CONCLUSIONS

The present study sheds light on the causes of the large discrepancy observed between measurements and experiments in [6]. Using a standard experimental setup, the curvature of bars is measured on the assumption of a constant in-plane curvature. Although drawn bars may exhibit such curvatures, it is shown numerically that the assumption does not hold for straightened bars. A meaningful link, if any, between predicted (local) and measured (global) values is still to be established.

REFERENCES

[1] Das Talukder, N.K. and Johnson, W. On the arrangement of rolls in cross-roll straighteners. *Int. J. Mech. Sci.* (1981) **23**:213–220.

[2] Wu, B.J., Chan, L.C., Lee, L.C and Ao, L.W. A study on the precision modeling of the bars produced in two cross-roll straightening. *J. Mater. Proc. Technol.* (2000) **99**:202–206.

[3] Mutrux, A., Berisha, B., Hochholdinger, B. and Hora, P. Numerical modelling of cross roll straightening. *Proc. 7th LS-Dyna Anwederforum* (2008).

[4] Kuboki, K., Huang, H., Murata, M., Yamaguchi, Y. and Kuroda, K. FEM analysis of tube straightener adopting implicit scheme. *Steel Res. Int.* (2010) **9**:584–587.

[5] Furugen, M. and Hayashi, C. Theory of tube deformation on cross roll straightening. *Proc. 3rd Int. Conf. Steel Rolling* (1985) 717–724.

[6] Mutrux, A., Berisha, B., Hora, P. Prediction of cyclic softening in a medium carbon steel during cross roll straightening. *J. Mater. Proc. Technol.* (2011) DOI 10.1016/j.jmatprotec.2011.03.019.

[7] Davis, J.R. and Mills, K.M (eds.). *Metals Handbook, vol. 1: Properties and Selection: Irons, Steels, and High-Performance Alloys*. ASM International, p. 258, (1990).

[8] Banabic, B. (ed.) *Advanced Methods in Material Forming*. Springer, p. 3, (2007).

[9] Chaboche, J.L. Time-independent constitutive theories for cyclic plasticity. *Int. J. Plast.* (1986) **2**:149–188.

[10] Kobayashi, M. and Ohno, N. Implementation of cyclic plasticity models based on a general form of kinematic hardening. *Int. J. Num. Methods Engng.* (2002) **53**:2217–2238.

[11] Asakawa, M., Urabe, M., Nishimura, K., Hamada, R., Aizawa, S. and Amari, M. Theoretical and experimental analysis of roller leveller straightening for coiled bar. *Steel Res. Int.* (2010) **81(9)**:242–245.

XI International Conference on Computational Plasticity. Fundamentals and Applications
COMPLAS XI
E. Oñate, D.R.J. Owen, D. Peric and B. Suárez (Eds)

REPRODUCE DIAMETER REDUCTION PROCESS OF A POWDER FILLED TUBE IN FINITE ELEMENT ANALYSIS

B. BÖCK*, B. BUCHMAYR[1], S. WALLNER[1] AND G. POSCH[2]

*,1 Chair of Metalforming
Montanuniversitaet Leoben
Franz Josef Straße 18, 8700 Leoben, Austria
e-mail: barbara.boeck@unileoben.ac.at, web page: http://www.metalforming.at

[2] Böhler Schweißtechnik Austria GmbH
Böhler-Welding-Straße 1, 8605 Kapfenberg
e-mail: gerhard.posch@bsga.at, web page: http://www.boehler-welding.at

Key words: Roll Drawing, Reduction of a tube with powder filling, Powder Compaction,

Abstract. Aim of the present work is to improve the production of laserwelded flux cored wires with the help of Finite Element Analysis in Abaqus. This flux cored wires are used as welding consumables. To simulate the whole production process for every variety of input parameters is far too time-consuming particularly with regard to the filling. The production process is as following: after roll forming of a strip to a U-shape it is filled continuously with flux. This powder consists of up to 20 different substances. Afterwards the profile is closed to a tube and the edge is laserwelded. At last the diameter of the tube is reduced to 1.2 mm. The reduction step is investigated and subject of the present work. Observations have shown the most abrasion of the working dies in reduction steps where it is not expected due to the calculated true strain sequence. Therefore, the influence of the filling on the roll drawing process has to be taken into account. This is not easy because the process starts with loose multicomponent powder and ends with high compaction. It is hard to cover these demands with a single model for powder behaviour. So a phenomenological approach is established to solve the problem. The influence of the powder is described as a load which only appears in the projected contact area. Consequently, it becomes possible to study parameters on the reduction like different quantities of the multicomponent powder, the reduction sequence of the roll drawing process and the geometry of the rolls.

1 INTRODUCTION

Different powder models were studied to characterise the influence of the powder in the process. Soil mechanic models like Drucker-Prager/Cap describe lower compaction [1]. Many models exists which handle the powder as a metal matrix with porosity, like Shima and Oyane or Gurson [2]. These models are right at higher compaction [3]. At last there are models which calculate the behaviour of spheres under pressure [4,5]. This is far to time consuming for this kind of simulation. The production process leads to a high range in the compaction. Therefore one model could hardly reproduce the whole process. But it is impossible to fix a crossover

between two models. Furthermore all of them focus on the strength of the compacted powder and the density distribution during production to predict cracks in the finished parts. This is not relevant in this case. At least the experiments to characterise the powder are mostly very complex and expensive [6,7]. This is the reason why a phenomenological approach is added to the finite element analysis. A lot of investigational work has been done on characterisation of drawing process with axially symmetric dies [8,9,10]. The roll drawing process using roller dies is less studied [11,12,13]. All the researchers concentrate in their work on the reduction of rods or tubes with or without mandrel. The problem in the present work is that at the beginning loose powder is added. During the reduction process the multicomponent powder (flux) is compacted and acts as some kind of mandrel to the process. This is tightening up the investigation of the production process. Beside the pass schedule and the filling, the geometry of the rolls plays an important role. Also the strain-hardening of the tube has to be considered. These parameters are interacting in the roll drawing process that's why it is difficult to handle in the finite element analysis.

2 ROLL DRAWING

Metallographic specimens show the influence of the used amount of multicomponent powder. Due to varying bulk volumes the wall thickness in the final cross section differs. If there is no powder added the inner diameter vanish. Three examples are shown in Figure 1. The outer diameter stays the same.

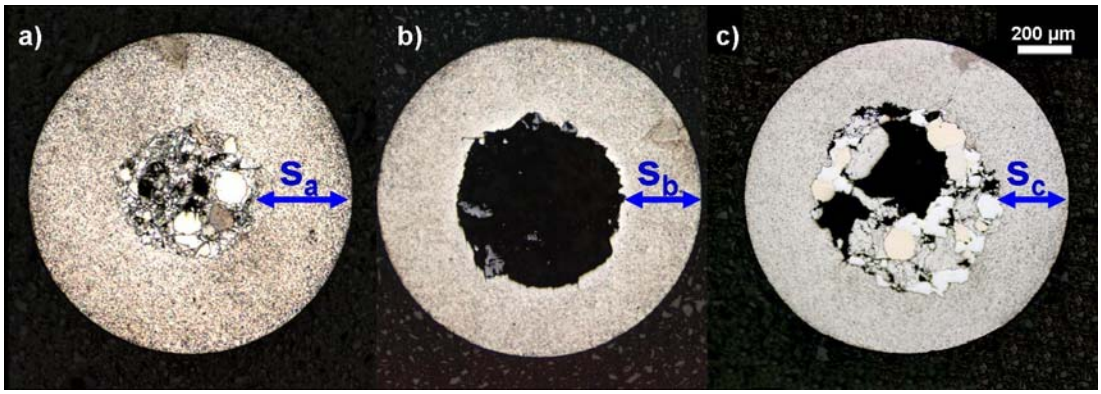

Figure 1: Cross section through the final product for three different filling volumes (increasing from a to c), outer diameter 1.2 mm

The wall thickness is measured in three different positions, because the inner outline is very rough. The mean is build as schown in Table 1.

Table 1: Measured and Mean Wall Thickness

Sample ID	Measured Value [µm]			Mean [µm]
s_a	232	339	338	333
s_b	264	289	233	262
s_c	225	251	245	240

For the shown cross sections an axial elongation can be calculated, which reaches from 12 up to 15. This leads to the assumption of an equlibrium between the compaction of the multicomponent powder, the reduction of the roll drawing process and the strain-hardening of the strip metal. These parameters influence the outcoming wall thickness.

The strain-hardening of the outer strip material was determined with tensile tests. The extended formula of Ludwik [14] is used to calculate the flow stress (k_f) for the deformed outer tube in every specific sequence of the reduction process.

$$k_f = k_{fA} + B\varphi^n \tag{1}$$

The function is defined as following: k_f is the true stress, k_{fA} is the yield strength at $\varphi=0$, B is the yield strength at $\varphi=1$, n is the strain hardening exponent, φ is the true strain. An ideal plastic strain is defined by the sequence of the process. This is set as initial condition to the model to consider the hardening of the outer strip metal.

3 INFLUENCE OF THE POWDER COMPACTION

The compaction behaviour is studied with an isostatic press. Different equiaxed loads are applied on a weighted mass of the multicomponent powder in a rubber mould and the volume is detected. From the results the relative density under pressure is recorded. The compaction behaviour depends on many parameters like chemical composition, additives, particle size, particle shape and the mechanical properties of the full material [15,16,17]. Therefore the graph shown in Figure 2 is only valid for this special composition.

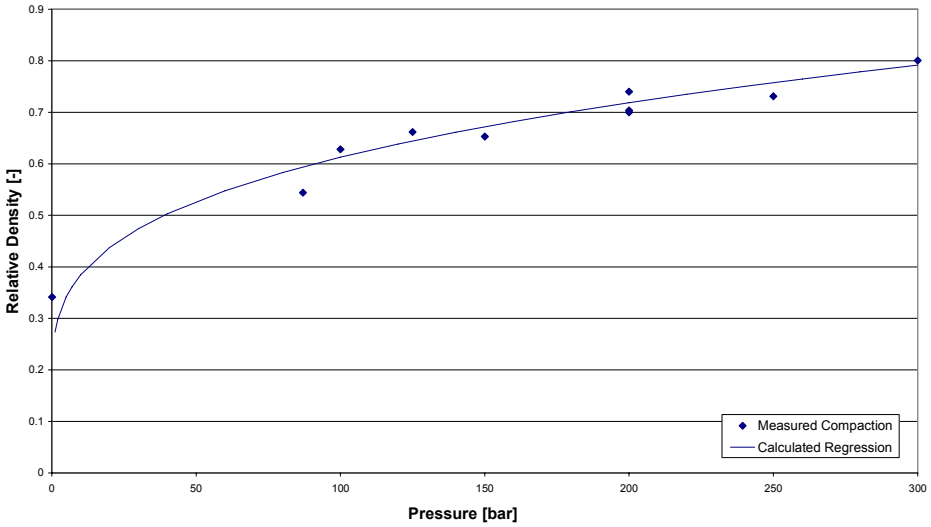

Figure 2: Measured Compaction and the Calculated Regression of the powder filling

The compaction behaviour of the multicomponent powder is expressed mathematically. Literature gives correlations between powder compaction and surrounding pressure. For example Schatt [15] defines the pressure which is needed to compact the powder until no porosity is left (p_{max}).

$$p_{\max} = p\left(\frac{1}{\rho_{rel}}\right)^m \tag{2}$$

For cylindrical specimen can be calculated [16]

$$F = \int_0^{r_i} 2r\pi\sigma_z dr \tag{3}$$

where σ_z is

$$\sigma_z = \overline{\sigma}\exp^{\left[\frac{2\mu_i}{L}(r_f - r)\right]} \tag{4}$$

$$\overline{\sigma} = k_f\left(\frac{1+\mu_i}{1-\mu_i}\right)$$

μ_i is set for the inner friction between the particles. r is the specimen radius. p stands for the pressure. ρ_{rel} is the relative density. σ are stress components (z direction and mean stress). k_f is the yield strength of the powder as full material. m is the compaction exponent. A potential function is used to express the compaction of the powder. So it is valid to use a similar function to calculate the regression for the powder compaction (Figure 2).

$$\rho_{rel} = \rho_b + B\varphi^m \tag{5}$$

ρb stands for the bulk density of the powder. B is a factor which is adjusted to the compaction behaviour. This formula is used to calculate different quantities of the filling. From this the behaviour of any bulk volume under pressure can be calculated. The limits are given by the production process. Figure 3 shows an example for the correlation between volume and pressure for three different quantities of the multicomponent powder.

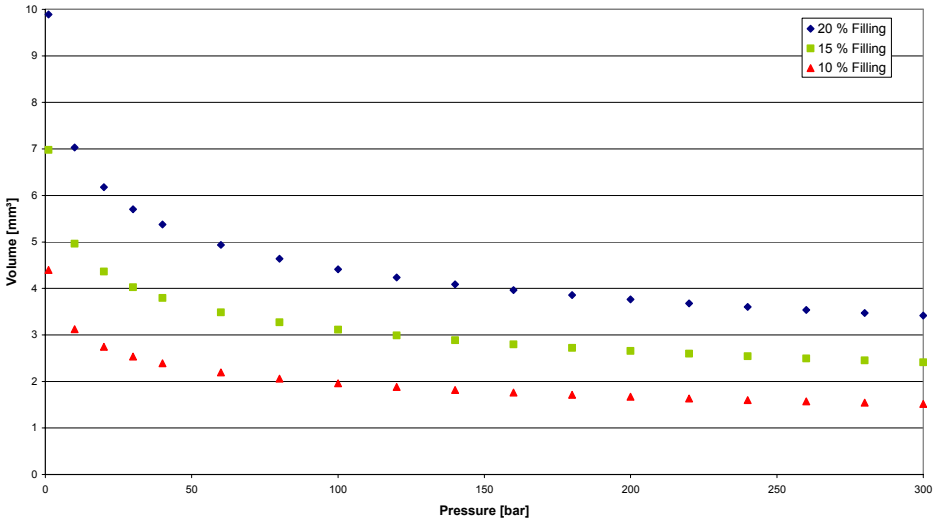

Figure 3: Different quantities of powder under pressure

After each roller die package a cross section was taken to measure the inner and outer diameter of the tube. The area is calculated and multiplied with the elongation of the tube. This leads to the actual volume. Now a pressure which is needed to compact the multicomponent powder to this level can be assigned to the inner volume. So, a value for the inner pressure as a result of the powder compaction is found and added to the finite element analysis. Of course, the relationship of the inner and outer diameter is influenced by the quantity of the powder and its compaction. But as a compromise this is neglected and the inner volume is taken absolut.

To fix the region in which the compaction of the powder lead to a pressure on the inner wall a finite element analysis has been started. The projected contact area is a far to rough estimate. A very soft material is taken instead of powder. The geometry is authentic to the production process. A region could be fixed following the stress distribution in a cut of the finite element analysis shown in Figure 4.

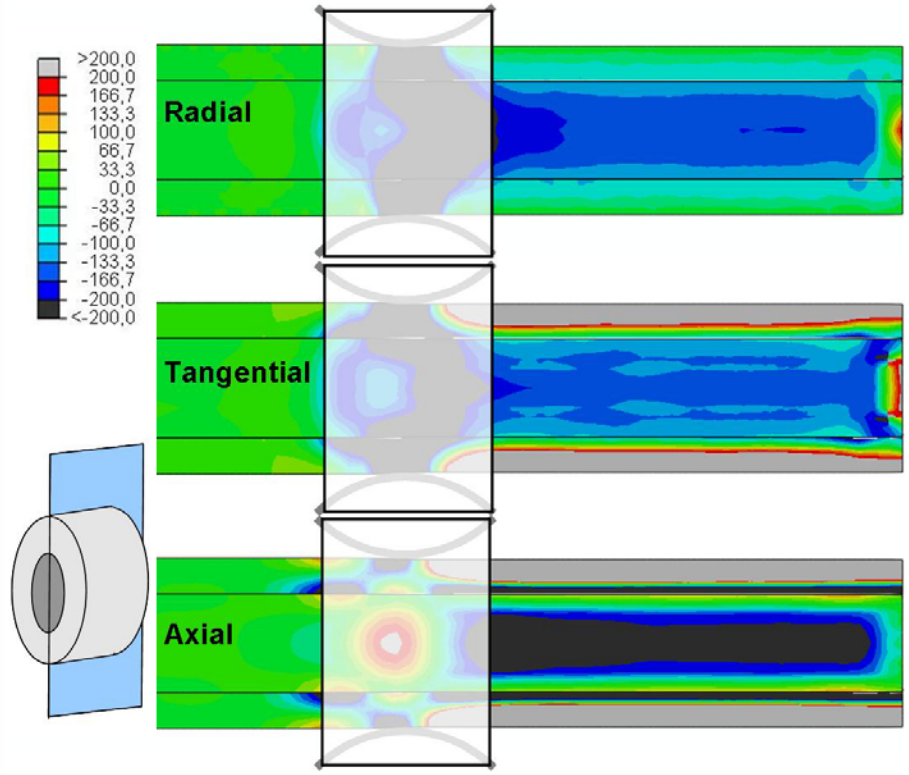

Figure 4: Cut through the tube in the FEA with the stress distribution for the principal directions

A few differences have to be considered between deformation of a soft full material and a powder. At first no tension can occur in powders like the axial stress distribution shows. A far smaller elastic springback appears in compacted powder. The contact area for friction is much higher between a rod and a surrounding tube. The powder does not compact under shear stresses, whereas full materials can yield. This is why this analysis is only valid for finding the region for backpressure and could not be a simplification for the whole process.

4 FEA MODEL

For the first simulated roller die the tube is considered as a stress and strain free material. On later roller dies a strain-hardening is added. The influence of the multicomponent powder is included through a user defined subroutine. The load only appears in the roller dies. The tube between the roller dies is unaffected which agrees with reality. The welding seam is included in the tube geometry and carries a separate material property due to the laser welding process. A package with twelve roller dies is always simulated at once. Two dies have always the same geometry. They alternate between horizontal and vertical positions. Abaqus Explicit is used, with C3D8 elements. The outer strip is made out of a soft steel with low strength. In the welding seam a modified material property is installed, due to the rapid cooling in the laser welding process. Roll drawing is a cold forming process. Between the roller dies and the tube rolling friction appears. As a result not much heat occurs. That's why the heat is neglected in the finite element analysis. Figure 5 show the start of the finite element analysis with the tube in front and the alternating roller dies in the back.

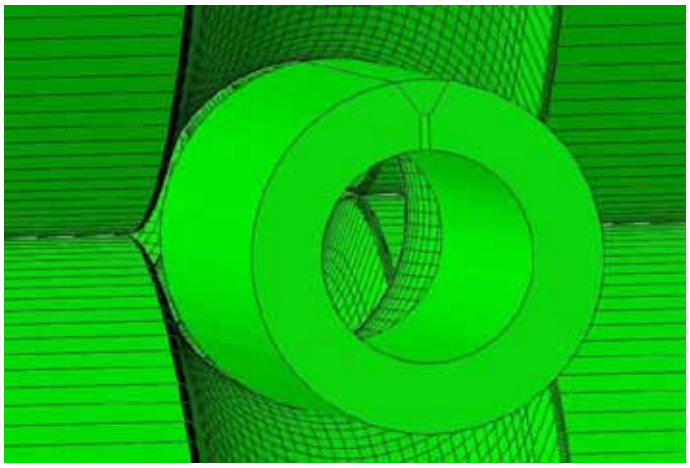

Figure 5: FEA model of the roll drawing process

Figure 6 shows the radial stresses due to the load of the powder defined in the user defined subroutine. This picture is taken from an analysis with no rolls to control the input.

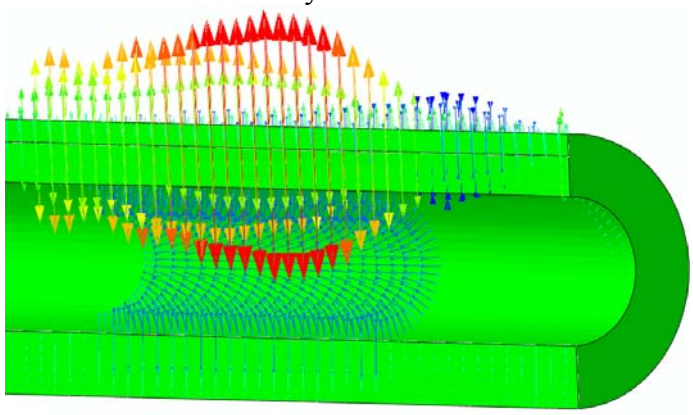

Figure 6: Stresses due to VDLoad

5 RESULTS

Figure 7 shows the equivalent stress and the principal stresses for the first roller die. The upper roll which is identical to the lower is hidden to get a free view on the welding seam. The ovality occurs due to the spread. The geometry of the rolls itself is round and ends in 40° tangents. Between 40° and 50° is common for pass design.

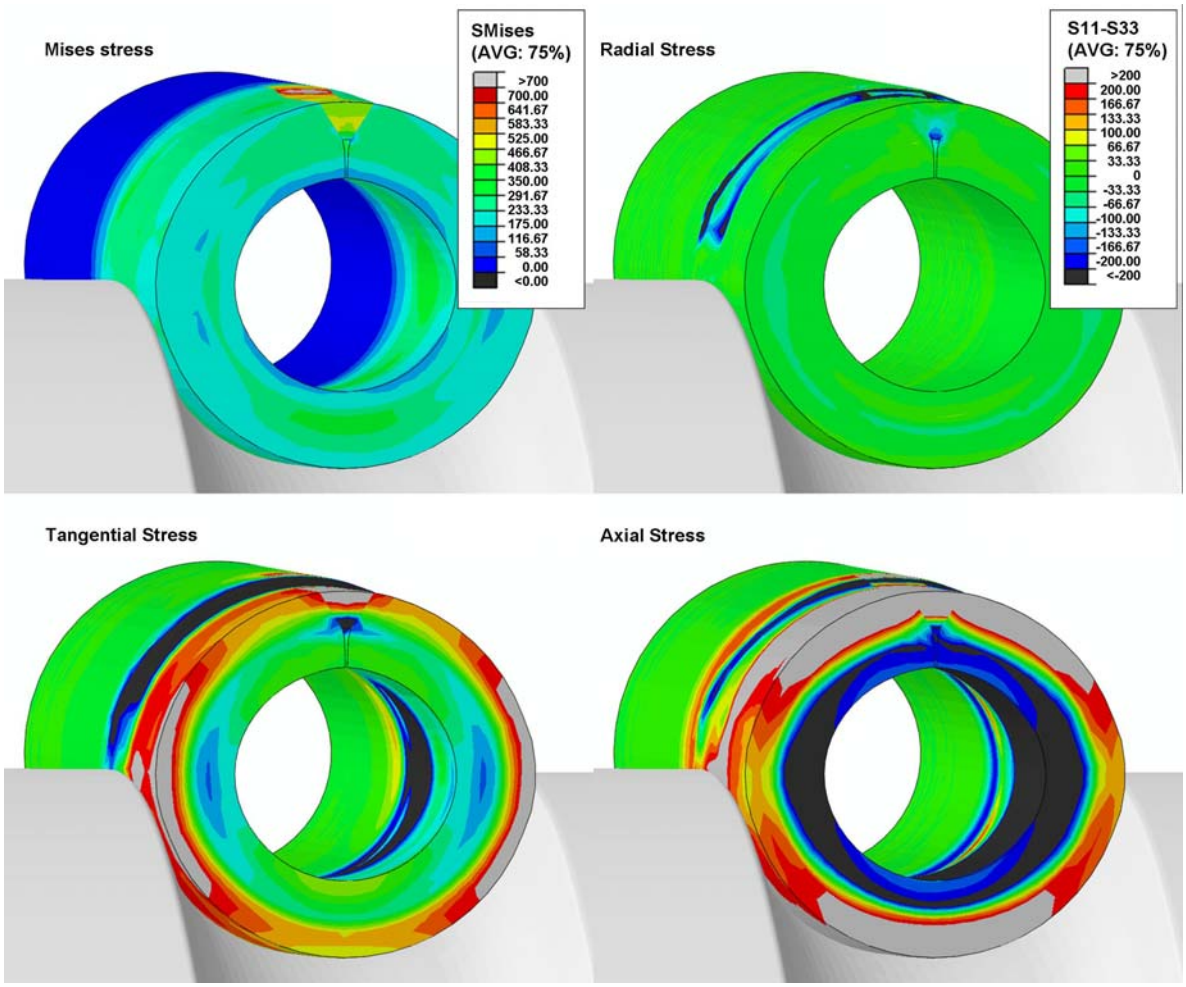

Figure 7: First Roller Die with inner pressure, upper roll is removed, Mises and principal stresses

6 CONCLUSION

The discussed procedures allows to simulate the complex relationship in this production. The model show good correlation to reality which proves its validity. Specific sequences can picked out to study the parameters like roll geometry, process variables and the reduction sequence. The reactions of the system as there are out-of-roundness, stress and strain distribution and twisting can be determined. Furthermore the Finite Element Analysis runs at reasonable computing times.

ACKNOWLEDGEMENT

Financial support by the Austrian Federal Government (in particular from the Bundesministerium für Verkehr, Innovation und Technologie and the Bundesministerium für Wirtschaft und Arbeit) and the Styrian Provincial Government, represented by Österreichische Forschungsförderungsgesellschaft mbH and by Steirische Wirtschaftsförderungsgesellschaft mbH, within the research activities of the K2 Competence Centre on "Integrated Research in Materials, Processing and Product Engineering", operated by the Materials Center Leoben Forschung GmbH in the framework of the Austrian COMET Competence Centre Programme, is gratefully acknowledged.

REFERENCES

[1] Coube, O. Modellierung von Verdichtung und Rißbildung beim Trockenpressen von Metallpulvern, *Symposium 14:* Simulation Metalle, Werkstoffwoche 98, Wiley-VCH, Weinheim, 1999

[2] Parteder E. *Ein Modell zur Simulation von Umformprozessen pulvermetallurgisch hergestellter hochschmelzender Metalle*, Umformt. Schriften V. 94, Shaker Verlag, 2000

[3] Lorenz B. *Ein Beitrag zur Theorie der Umformung pulvermetallurgischer Anfangsformen,* Habilitation, TU Freiberg, 1996

[4] Martin, C.L. Elasticity, fracture and yielding of cold compacted metal powders, *Journal of Mechanics and Physics of Solids* (2004) **52** 1691-1717,

[5] Sinka I.C., Cocks, A.C.F. Constitutive modeling of powder compaction I+II, *Mechanics of Materials* (2007) **39** 392-403

[6] Rottmann G. Mechanisches Verhalten beim Trockenpressen, *Doctoral thesis*, University of Karlsruhe (2001)

[7] Chtourou H., Guillot M., Gakwaya A. Modeling of the metal powder compaction process using the cap model. Part I, *Int. Journal of Solids and Structures* (2002) **39** 1059-1075

[8] Kröff A. Numerische Untersuchung und Optimierung des Ziehens von hoch kohlenstoffhaltigen Stahldrähten, *Doctoral thesis*, University of Hannover (2001)

[9] Gummert H.-J. *Ziehen*, (2005), F&S Druck, Hundsmühlen, ISBN 3-00-016406-5

[10] Funke P. *Ziehen von Drähten, Stangen und Rohren* (1987), ISBN 3-88355-124-4

[11] Jaschke D. Untersuchung zum Ziehwalzen von Drähten und Profilen aus metallischen Werkstoffen, *Doctoral thesis*, University of Clausthal (1976)

[12] Överstam H. The influence of bearing geometry on the residual stress state in cold drawn wire, *Journal of Material Processing Technology* (2006) **171** 446-450

[13] Murakawa M. Masahiko J. Hayashi M., Study on semidry/dry wire drawing using DLC coated dies*, Surface and Coating Technology* (2004) **177** 631-637

[14] Hensel A., Spittel T. *Kraft und Arbeitsbedarf bildsamer Formgebungsverfahren* (1978) VEB, Leipzig ISBN 152-915/74/78

[15] Schatt W., Wieters K.-P., Kieback B. Pulvermetallurgie (2007), Springer Verlag, Berlin ISBN 3-540-23652-X

[16] Al-Qureshi H.A., Galiotto A., Klein A.N. On the mechanics of cold die compaction for powder metallurgy, *Journal of Materials Processing Technology* (2005) **166** 135-146

[17] Lee S.C., Kim K.T. A densification model for powder materials under cold isostatic pressing*, Materials Science and Engineering* (2008) **A 498**, 359-368

XI International Conference on Computational Plasticity. Fundamentals and Applications
COMPLAS XI
E. Oñate, D.R.J. Owen, D. Peric and B. Suárez (Eds)

VALIDATION OF THERMAL-MECHANICAL MODELING OF STAINLESS STEEL FORGINGS[1]

ARTHUR A. BROWN[*], TIMOTHY D. KOSTKA[*], BONNIE R. ANTOUN[*], MICHAEL L. CHIESA[*], DOUGLAS J. BAMMANN[†], STEPHANIE A. PITTS[#], STEPHEN B. MARGOLIS[*], DEVIN O'CONNOR[+], NANCY Y.C. YANG[*]

[*] Sandia National Laboratories
7011 East Ave. MS9042, Livermore, CA 94550, USA
e-mail: aabrown@sandia.gov, www.ca.sandia.gov

[†] Computational Manufacturing and Design
Mississippi State University, MS 39762, USA
e-mail: bammann@cavs.msstate.edu, www.cavs.msstate.edu

[#] Mechanical Engineering Department
Washington State University, Pullman, WA 99164, USA
e-mail: sapitts@wsu.edu, www.wsu.edu

[+] Mechanical Engineering Department
Northwestern University, Evanston, IL 60208, USA
e-mail: dtoconno@northwestern.edu, northwestern.edu

Key words: Recrystallization, Forging, Thermal-Mechanical, Validation, Plasticity.

Abstract. A constitutive model for recrystallization has been developed within the framework of an existing dislocation-based rate and temperature-dependent plasticity model. The theory has been implemented and tested in a finite element code. Material parameters were fit to data from monotonic compression tests on 304L steel for a wide range of temperatures and strain rates. The model is then validated by using the same parameter set in predictive thermal-mechanical simulations of experiments in which wedge forgings were produced at elevated temperatures. Model predictions of the final yield strengths compare well to the experimental results.

1 INTRODUCTION

During high temperature manufacturing processes, metals undergo microstructural changes that can greatly affect material properties and residual stresses. Some of the physical mechanisms that influence the strength of a material are strain hardening, recovery,

[1] This work was performed at Sandia National Laboratories. Sandia is a multiprogram laboratory operated by Sandia Corporation, a Lockheed Martin Company, for the United States Department of Energy under contract DEAC04-94AL85000.

recrystallization, and grain growth [1,2]. If the deformation conditions such as temperature and strain rate are not controlled properly during forging, welding, rolling, or other processes, the final part may have inadequate strength or residual stresses that could be detrimental to the life of the part [3]. In order to be able to optimize manufacturing processes using computational capabilities, it is necessary to have a physically-based constitutive model that captures the dominant strengthening and softening mechanisms. Such a model with predictive capabilities can be used in an optimization scheme to reduce the number of design iterations required to produce a part that meets all strength and microstructural requirements.

Recrystallization is a complex, inhomogeneous process in which nucleation and growth of new strain-free grains replace the worked microstructure of a strained material [4,5]. Recrystallization is due to the motion of grain and subgrain boundaries. As the boundaries move, they sweep away the dislocation structure, leaving a strain-free material with a very low dislocation density. The nucleation of a new recrystallized grain is believed to be due to the growth of an existing deformation-induced subgrain [6]. At elevated temperatures, a subgrain with a lower level of stored energy will preferentially expand at the expense of neighboring subgrains. The driving force for recrystallization is the difference in energy between the deformed and recrystallized state [7]. If the expanding subgrain reaches a critical size, it becomes a stable recrystallized grain.

In [8], a constitutive model for static and dynamic recrystallization was developed in which no critical criterion was utilized to initiate recrystallization. Rather, the kinetics of recrystallization are modeled based on the mobility of grain and subgrain boundaries under the driving force provided by the stored energy in the dislocation structure. The theory is capable of modeling single and multiple-peak dynamic recrystallization.

In this paper, coupled thermal-mechanical simulations are performed, including the effects of die chill, heat generated due to plastic dissipation, and conduction and strength evolution that occurs after compression but before quenching. Uncertainties in processing conditions were considered and propagated through the simulations to determine uncertainties in final predicted strengths.

A simplified version of the model is presented in the next section since we are primarily concerned with static recrystallization for high-rate forgings. Parameter optimization is then discussed. Finally, a comparison between model predictions and experimental results is provided.

2 CONSTITUTIVE MODEL

A treatment of the kinematics and thermodynamics of the model is documented in a full-length manuscript under review [9]. The constitutive model is explained in detail in [8]. Here, as in [10], a condensed treatment of the constitutive model is given for the simplified case of uniaxial stress and at most only once cycle of recrystallization.

For uniaxial stress, let σ represent the only non-vanishing component of the Cauchy stress tensor and ε represent the axial component of the Eulerian strain tensor. After making approximations for small elastic strains, it can be shown that the model reduces to the following set of equations, written here in the current configuration:

$$\dot{\sigma} = E(\dot{\varepsilon} - \dot{\varepsilon}^p) \tag{1}$$

$$\dot{\varepsilon}^p = c\left(\sinh\left[\left\langle \frac{\sigma}{\kappa + Y(\theta)} - 1 \right\rangle\right]\right)^{n(\theta)} \tag{2}$$

$$\kappa = \kappa_{1-X}(1-X) \tag{3}$$

$$\dot{\kappa}_{1-X} = \left[H(\theta)\left(1 + \frac{\bar{\zeta}_{1-X}}{\bar{\kappa}_{1-X}}\right) - R_d(\theta)\kappa_{1-X} \right]\left|\dot{\varepsilon}^p\right| \tag{4}$$

$$\dot{\zeta}_{1-X} = h_\zeta \zeta_{1-X}^{1-1/r}\left|\dot{\varepsilon}^p\right| \tag{5}$$

$$\dot{X} = \frac{1}{\mu\theta} e^{-\frac{c_\theta}{\theta}}\left(1 - e^{-B\bar{\zeta}_{1-X}^m}\right)\left[c_{\bar{\kappa}}\bar{\kappa}_{1-X}^2 + c_{\bar{\zeta}}\bar{\zeta}_{1-X}^2\right] X^a (1-X)^b \tag{6}$$

$$\dot{\theta} = \frac{\beta}{\rho c_p}\sigma\dot{\varepsilon}^p \tag{7}$$

Equations (1) and (2) provide the elasticity relation and the flow rule for the plastic strain rate. Equation (3) averages the isotropic hardening variable, κ, between the unrecrystallized and recrystallized volume fractions, where the isotropic hardening variable in the recrystallized volume fraction is assumed to be zero. Equation (4) is the evolution equation for the isotropic hardening variable in the unrecrystallized volume fraction, which has a hardening minus recovery format based on [11]. The hardening rate increases as the subgrain boundary spacing, represented by the misorientation variable ζ, decreases. Equation (5), based on [12], tracks the misorientation variable, ζ_{1-X}, in the unrecrystallized volume fraction. ζ_{1-X} is inversely related to the average spacing between geometrically necessary boundaries. Equation (6) describes the kinetics of recrystallization through a variable representing the volume fraction of recrystallized material, *X*. The stored energy due to the dislocation structure, represented by κ_{1-X} and ζ_{1-X}, drives the recrystallization kinetics. The mobility of subgrain boundary motion increases with misorientation angle, which increases as the spacing between geometrically necessary boundaries decreases. The last equation tracks the evolution of temperature due to adiabatic heating. Here, it is assumed that $\beta = 0.95$, i.e. 95% of the plastic work is dissipated as heat. In this work, coupled thermal-mechanical simulations are performed in which the constitutive model calculates the heat generated due to plastic work, which is passed to the thermal code for use as a source term in the energy equation. Thus the temperature will also change due to conduction, radiation, and convection.

The model in this form is only valid for static recrystallization, where the isotropic hardening variable in the recrystallized volume fraction is assumed to be zero. For dynamic recrystallization, the recrystallized material will continue to harden with increased strain. For a treatment of the model form capable of both static and dynamic recrystallization, see [8].

3 MODEL PERFORMANCE

Material parameters were fit to data from monotonic compression tests on 304L steel for a wide range of temperatures and strain rates. Three types of test data were included in the set used for parameter optimization. Stress-strain data from single-stage compression at constant strain rate is shown in Figure 1. The plot legends show the initial specimen temperature.

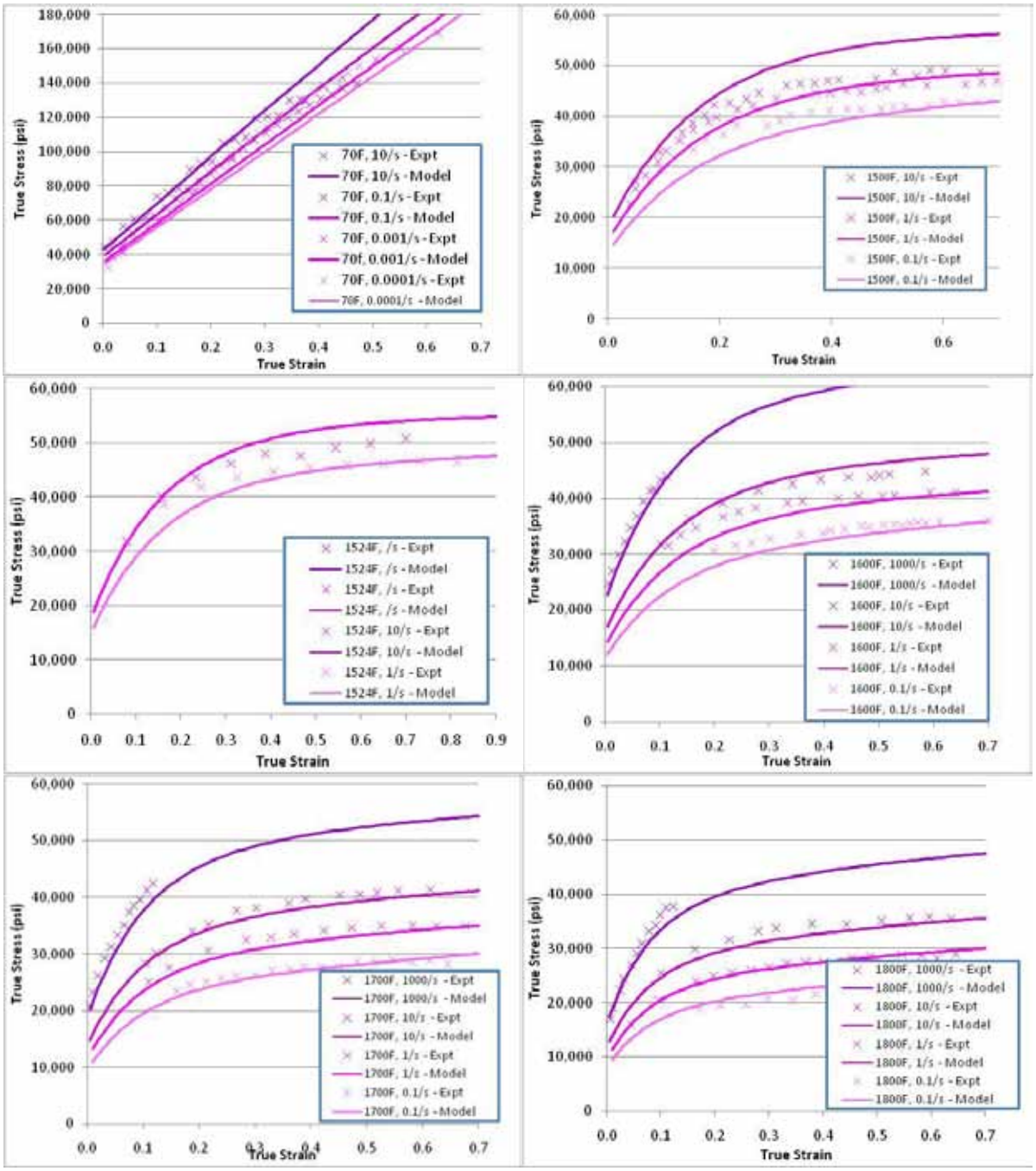

Figure 1: Stress-strain data from single-stage compression tests

During straining at high rates, the temperature increases somewhat due to plastic dissipation. Figure 2 shows stress-strain data from two-stage compression tests. For each specimen, the first stage of compression was performed at elevated temperature, followed by a quench after approximately five seconds. The second compression stage was conducted at room temperature. Figure 3 contains recrystallized volume fraction data from single-stage

compressions tests followed by various hold times before quenching. The data was determined from microstructure from etched samples of the compression specimens.

Model parameters were optimized using the three types of data discussed above (see Appendix). The results are shown in Figures 1 through 3. The model captures the material response quite well over the full range of temperatures and strain rates.

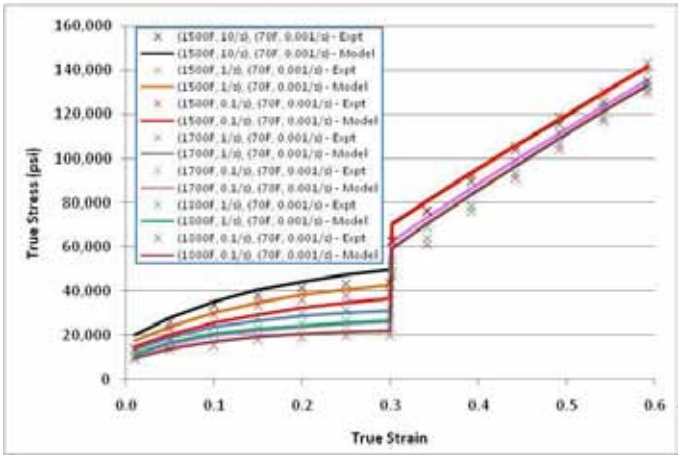

Figure 2: Stress-strain data from two-stage compression tests

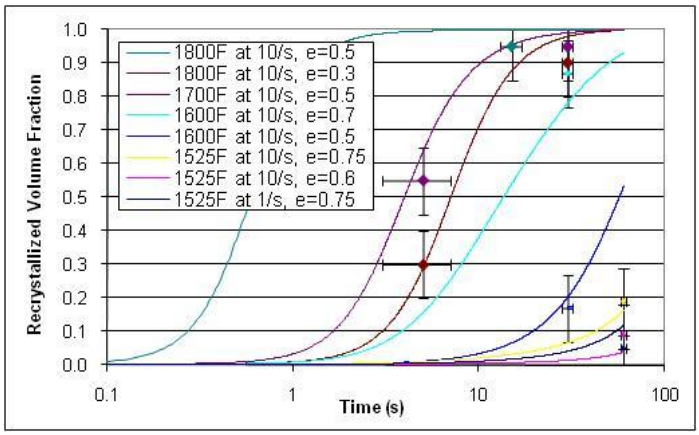

Figure 3: Recrystallized volume fraction data from compress-and-hold tests

4 VALIDATION

The theory has been implemented and tested in Arpeggio, Sandia's code coupling of an implicit quasistatics code, Adagio [13], with a thermal code, Aria [14]. The model is then validated by using the same parameter set in predictive simulations of experiments in which 304L stainless steel wedges were forged with a HERF machine at Precision Metal Products, Inc. (PMP). Two wedge geometries, shown in Figure 4, were forged at 1500F and 1600F. For each forging, the wedge heated in a furnace to the nominal temperature, then transferred to a flat die, and compressed to a final height of one inch by a platen traveling at a rate of approximately 20 ft/s. The forging was then transferred to a quench bath. From the flattened forgings, tensile specimens were machined and tested. Figure 5 shows the locations of the

tensile specimens. For all wedges, specimen A was taken one inch to the right of the initially-tapered edge. The spacing between each specimen location was 0.52" for the short wedges and 0.64" for the tall wedges.

A set of simulations were performed to account for uncertainties in the input parameters. Due to time constraints, for each nominal case, simulations were done to provide upper and lower bounds on the expected final yield strengths at the six specimen locations. The uncertainties were based on measurements taken at PMP during forgings of different geometries. The ingot temperature when transferred from the furnace is assumed to be within +-20F of nominal. Radiation and convection were modeled for the estimated transfer time of 1.7 to 3.7 seconds. Conduction to the die was also modeled for 2.8 to 4.9 seconds before compression began. After the wedge is flattened at 20 ft/s, conduction occurs for 0.5 to 2 seconds before the wedge is removed for transfer to the quench bath, which takes between 3 to 4.8 seconds. To account for the uncertainty in the coefficient of friction, we ran the suite of simulations once with a coefficient of friction of 0.1 and once with frictionless contact.

The plastic strain contours for a typical run (in this case, 1580F for the tall wedge with a coefficient of friction of 0.1) are plotted in Figure 6. The plastic strain increases as one moves from position "A" to position "F". Figure 7 shows the temperature distribution immediately after the wedge is forged (t~4.5s) and immediately before it is quenched (t~8s). Due to adiabatic heating, the temperature after forging is highest in the locations that see the highest strains, although the bottom of the wedge is somewhat cooler due to the die chill before forging, and further conduction after forging. The dislocation density increases with plastic strain, as does the average misorientation angle across deformation-induced subgrain boundaries. The rate of recrystallization increases with dislocation density and misorientation angle, so the recrystallized volume fraction increases from position "A" to position "F" in a trend similar to that of the plastic strain (see Figure 7). The bottom of the wedge recrystallizes less due the lower temperature there.

Figure 8 shows how the yield strength drops during recrystallization. The room-temperature yield strength distribution is calculated at two times, both under the assumption that the wedge is quenched instantaneously, i.e. as if the temperature drops immediately to room temperature. The left plot in Figure 8 shows what the final strength would be if quenched immediately after forging, before recrystallization has a chance to evolve. This is obviously not physically possible, but is shown for purposes of illustration. The right plot shows the strength after 3.5s of post-forge conduction and recrystallization. A comparison shows the importance that the amount of time it takes to quench a forging has when recrystallization is evolving.

The final room-temperature, quasistatic yield strength predictions for the short and tall wedges are plotted in Figures 9 and 10, respectively. The range of yield strengths predicted by the simulations based on the uncertainties in the input parameters are depicted by error bars; the experimental measurements are represented by "x" symbols. Since recovery and recrystallization are thermally activated processes, the final strengths of 1500F forgings are higher than the 1600F forgings. As strain increases (e.g. over positions A, B, and C), strength increases due to additional work hardening. However, if the temperature is high enough, the additional work hardening can induce recrystallization, which causes the strength to drop at higher strains (e.g. over positions D, E, and F). The simulations capture the general trends in the data very well. The error in final yield strength predictions is plotted in Figure 11. For

cases in which the experimental value lies within the prediction bounds, the error is zero. Otherwise, the error is calculated as the difference between the closest prediction bound and the experimental value, normalized by the experimental value.

The uncertainties in the yield strength predictions are largest for higher temperature and higher strains because those conditions induce a higher rate of recrystallization. When the rate of recrystallization is high, uncertainty in time before quenching causes uncertainty in the amount of recrystallization that occurs (see Figure 3) and hence in the final strength.

5 CONCLUSIONS

Coupled thermal-mechanical simulations were performed to predict the final yield strength in two wedge forging geometries for two nominal temperatures. Uncertainty quantification is performed to account for unknown input parameters in the simulations. The predictions match the experimental results fairly well for all combinations of temperature and geometry.

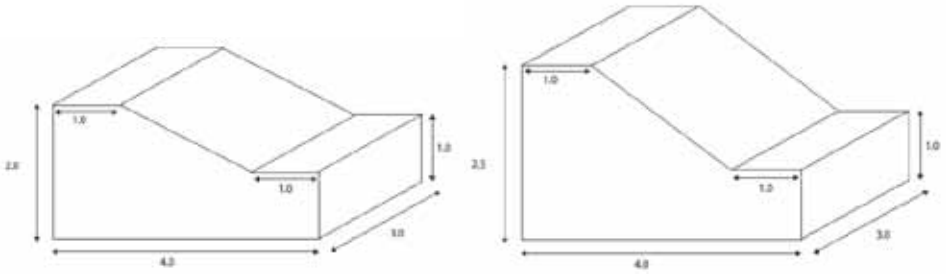

Figure 4: Dimensions of the short and tall wedge designs

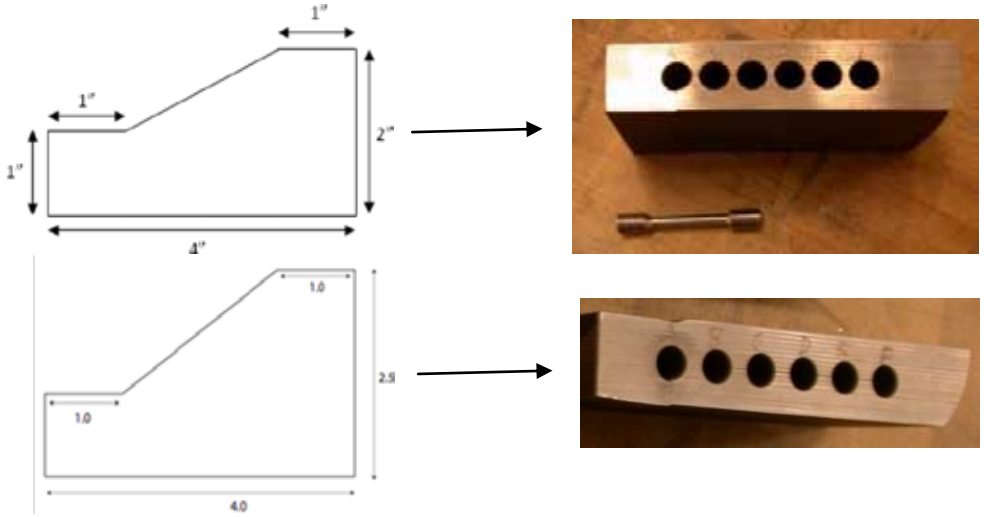

Figure 5: Locations of the tensile specimens for the short and tall wedge designs

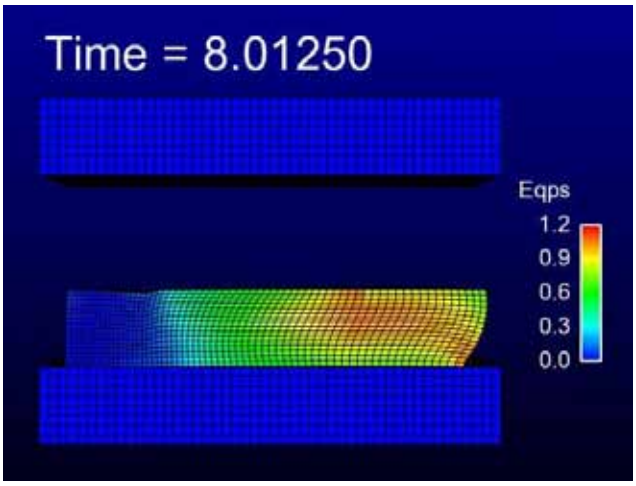

Figure 6: Plastic strain contour plot for the tall wedge for a tall wedge initially at 1580°F

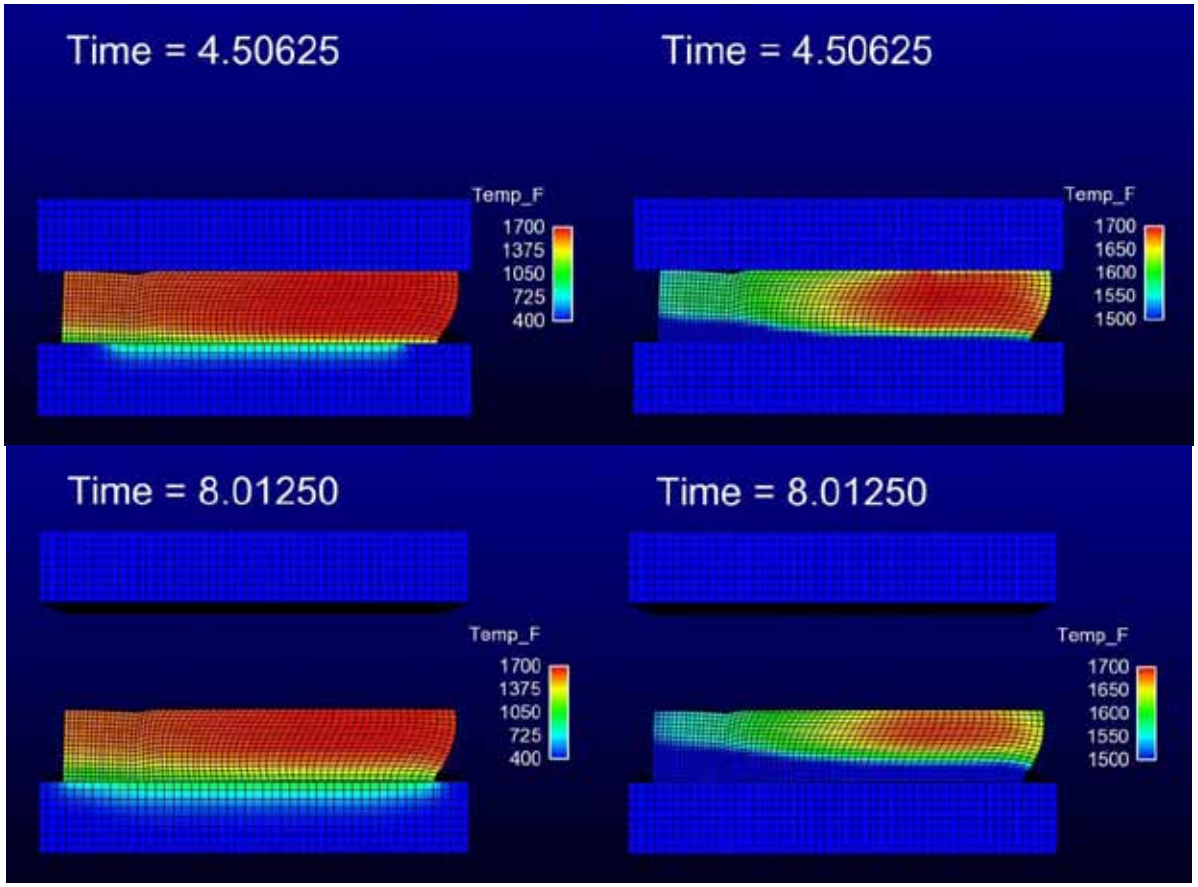

Figure 7: Contour plots of the temperature immediately after forging and immediately before quenching

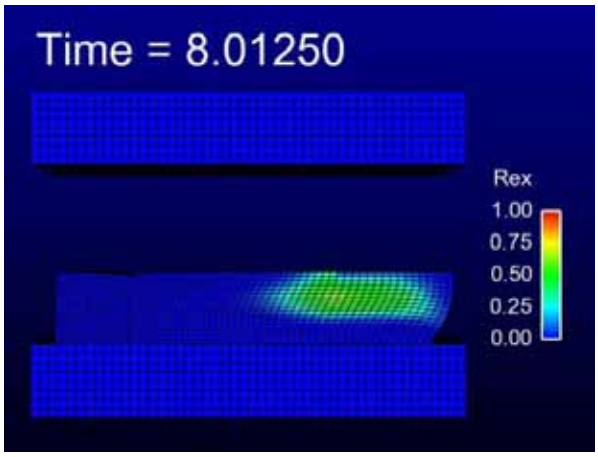

Figure 8: Contour plot of the recrystallized volume fraction for a tall wedge initially at 1580°F

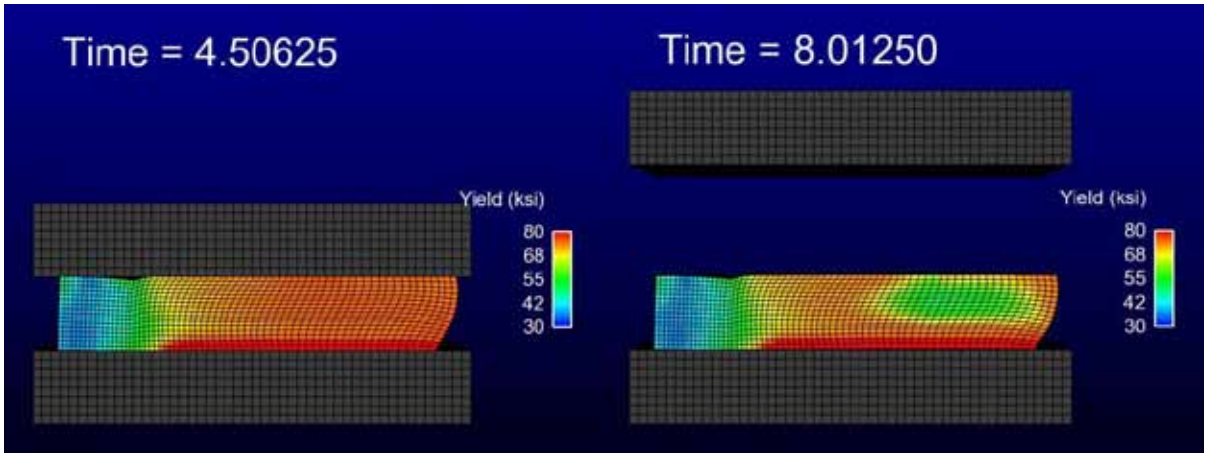

Figure 9: Contour plots showing the evolution of the room-temperature yield strength after forging

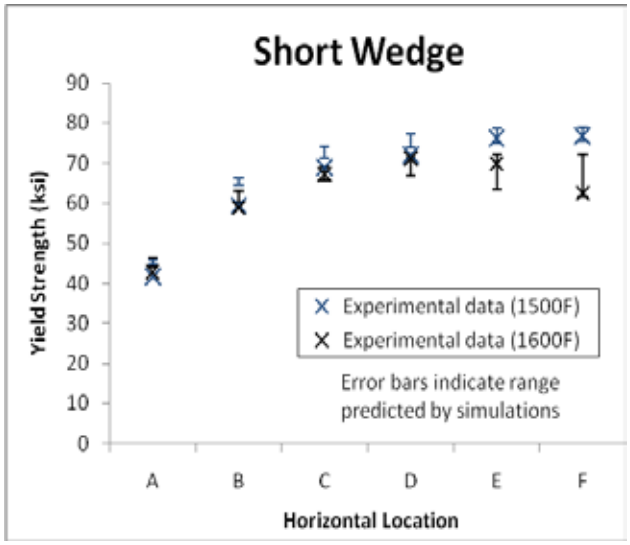

Figure 9: Final yield strengths from simulation predictions and experiments for the short wedge

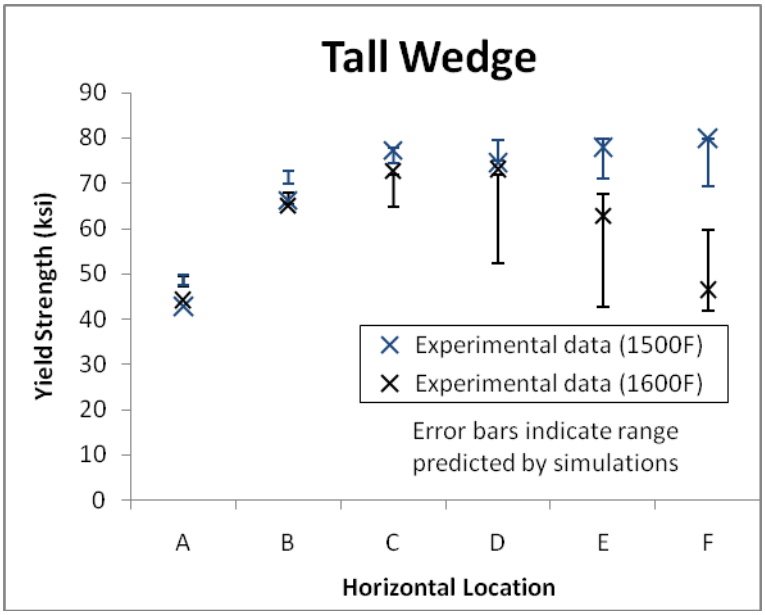

Figure 10: Final yield strengths from simulation predictions and experiments for the tall wedge

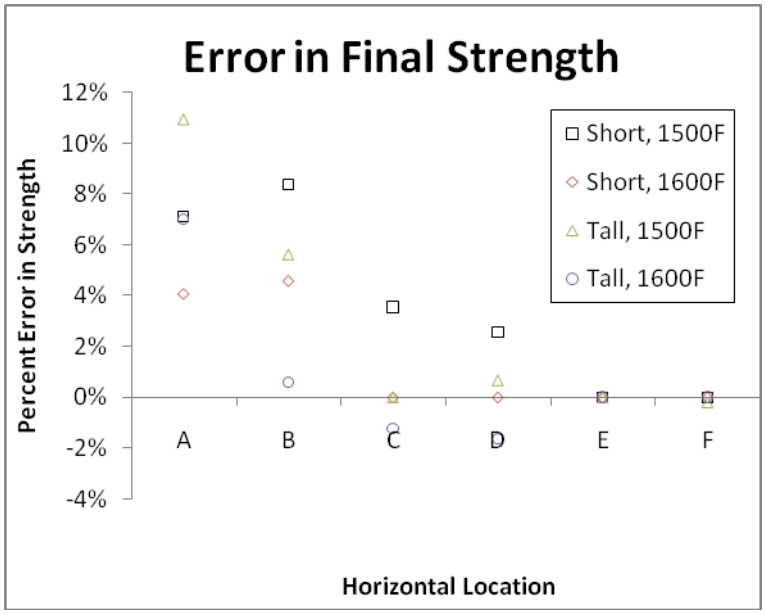

Figure 11: The error in final yield strength predictions

APPENDIX

The set of parameters used in all the results presented here are as follows in SI units:

$$E = 2.00e11 - 8.70e7(\theta - 292) \text{ Pa} \tag{8}$$
$$\mu = 8.01e10 - 3.70e7(\theta - 292) \text{ Pa}$$
$$c = 0.0918$$

$$n(\theta) = \frac{5700}{\theta}$$

$$Y(\theta) = \frac{5.27e9}{33.2 + \exp\left(-2.69e5/\theta\right)} \frac{1}{2} \tanh\left[0.00187\left(868 - \theta\right)\right]$$

$$H(\theta) = 0.01\mu$$

$$R_d(\theta) = 857 \exp\left(-5420/\theta\right) \text{ Pa/K}$$

$$h_{\zeta^-} = 0.00167$$

$$r = 1$$

$$c_\theta = 5.53e4$$

$$c_{\bar{\kappa}} = 0$$

$$c_{\bar{\zeta}} = 9.73e17$$

$$a = 0.667$$

$$b = 1.33$$

$$\rho = 8.00e3$$

$$c_p = 667$$

$$\beta = 0.95$$

REFERENCES

[1] Kocks,U. F., Argon, A. S., Ashby, M. F. The Thermodynamics and Kinetics of Slip. Prog. Mater. Sci. 19, 1-291, 1975.

[2] Doherty, R.D., Hughes, D.A., Humphreys, F.J., Jonas, J.J., Jensen, D.J., Kassner, M.E., King, W.E., McNelley, T.R., McQueen, H.J., Rollett, A.D. Current issues in recrystallization: a review. Mater. Sci. Eng. A238, 219–274, 1997.

[3] Chiesa, M. L., Brown, A. A., Antoun, B. R., Ostien, J. T., Regueiro, R. A., Bammann, D. J., Yang, N. Y. Prediction of final material state in multi-stage forging processes. *AIP Conference Proceedings,* no.712, pt.1, 510-515, 2004.

[4] Haessner, F. (Ed.), Recrystallization of Metallic Materials, 2nd ed., Rieder-Verlag, Stuttgart, 1978.

[5] Humphreys, F. J., Hatherly, M. Recrystallization and Related Annealing Phenomena, Pergamon Press, Oxford, 1995.

[6] Holm, E. A., Miodownik, M. A., Rollett, A. D. On abnormal subgrain growth and the origin of recrystallization nuclei. Acta Mater. 51, 2701–2716, 2003.

[7] Doherty, R. D. Primary recrystallization. In: Cahn, R.W. et al., (Eds.), Encyclopedia of Materials: Science and Technology. Elsevier, pp. 7847–7850, 2005.

[8] Brown, A.A., Bammann, D. J., Chiesa, M. L., Winters, W.S., Ortega, A.R., Antoun, B. R., Yang, N.Y. Modeling static and dynamic recrystallization in FCC metals. In Anisotropy, Texture, Dislocations and Multiscale Modeling in Finite Plasticity & Viscoplasticity, and Metal Forming - Proceedings of PLASTICITY '06: The Twelfth International Symposium on Plasticity and its Current Applications, 2006.

[9] Brown, A.A., Bammann, D. J. A model for static and dynamic recrystallization in metals. Manuscript under revision for International Journal of Plasticity.

[10] Brown, A.A., Kostka, T.D., Antoun, B.R., Chiesa, M. L., Bammann, D. J., Pitts, S.A.,

Margolis, S.B., O'Connor, D., Yang, N.Y. Thermal-mechanical modeling of stainless steel forgings. In Proceedings of the 28th Forging Industry Technical Conference, 2011.

[11] Kocks, U. F., Mecking, H. A Mechanism for static and dynamic recovery. In: Haasen, P., Gerold, V., Kostorz, G. (Eds.), Strength of Metals and Alloys. Pergamon Press, Oxford, pp. 345–350, 1979.

[12] Kok, S., Beaudoin, A. J., Tortorelli, D. A. On the development of stage IV hardening using a model based on the mechanical threshold. Acta Mater. 50 (7), 1653-1667, 2001.

[13] SIERRA Solid Mechanics Team. Adagio 4.14 User's Guide. Sandia Report 2009-7410, 2009.

[14] Patrick K. Notz, Samuel R. Subia, Matthew M. Hopkins, Harry K. Moffat, David R. Noble. Aria 1.5 User Manual. Sandia Report 2007-2734, 2007.

XI International Conference on Computational Plasticity. Fundamentals and Applications
COMPLAS XI
E. Oñate, D.R.J. Owen, D. Peric and B. Suárez (Eds)

3D MODELLING OF GEOMATERIALS ACCOUNTING FOR AN UNCONVENTIONAL PLASTICITY APPROACH

VALENTINA A. SALOMONI*, RICCARDO FINCATO*

* Department of Structural and Transportation Engineering
Faculty of Engineering, University of Padua
Via F.Marzolo, 9 – 35131 Padua, Italy
e-mail: salomoni@dic.unipd.it, fincato@dic.unipd.it, www.dic.unipd.it

Key words: Coupled problems, Compaction, Subsidence, Plasticity, Subloading surface.

Abstract. The coupled hydro-mechanical state in geomaterials undergoing plasticity phenomena is here evaluated by means of the subloading surface model . The most important feature of this theory is the abolition of the distinction between the elastic and plastic domain, as it happens in conventional elastoplastic models. This means that plastic deformations are generated whenever there is a change in stress and a smoother elasto-plastic transition is produced. The subloading surface takes the role of a loading surface which always passes through the current stress point $\boldsymbol{\sigma}$ and keeps a shape similar to that of the normal yield surface and a similar orientation with respect to the origin of stress space. Additionally, the model allows for giving a smooth response in a smooth monotonic loading process and the stress is automatically drawn back to the normal-yield surface even if it goes out from that surface, leading to a more stable and robust calculation even for large loading steps. The plasticity algorithm has been implemented within the FE PLASCON3D research code, coupling hydro-(thermo)-mechanical fields within a saturated porous medium (locally partially saturated) subjected to external loads. Applications to soils allow e.g. for assessing subsidence evolution at regional scale.

1 INTRODUCTION

The three-dimensional behaviour of geomaterials is here analysed making specifically reference to soils undergoing compaction and ensuing surface subsidence due to gas withdrawal from a typical deep reservoir.

Surface subsidence due to withdrawal of underground fluids occurs in many parts of the world, see for instance the case book of Poland [1]. Such surface settlement is a particular threat if it is experienced in low lying areas, close to the sea. Surface subsidence of this kind is almost exclusively understood in terms of drop of pressure in the aquifers or in the reservoir: i.e. withdrawal of these underground fluids results in a reduction of their pressure downhole; this in turn increases the part of the overburden carried by the skeleton of the reservoir rocks causing compaction. The compaction manifests itself, through deformation of the overlying strata, as surface settlement.

In case of a single fluid (water) involved, compaction can easily be explained by the principle of Terzaghi [2] which states that the compression of a porous medium is controlled by changes of effective stresses, i.e. variations of the difference between total stresses and the pressure of the fluid in the pores. However, when more fluids are involved or more phases of the same fluid, the Terzaghi traditional expression of effective stress alone is not sufficient to completely justify measured compaction and the concepts of unsaturated soil mechanics with appropriate stress measures and elastoplasticity concepts are needed. Drop of reservoir pressure is not the only mechanism leading to reservoir compaction and suction effects must also be accounted for at least for some types of extracted fluids and some reservoir rocks.

Capillary effects and structural collapse are treated in [3]-[5] and seem to provide sound explanations for continuing surface settlements when reservoir pore pressures stabilise and for additional settlements occurring even after the end of gas production. However, it is to be said that for the investigated area here considered, undergoing subsidence, there is no direct experimental evidence on samples from the field to show the key effect of capillarity on subsidence itself and hence any additional consideration could be largely speculative with many assumptions that are not justified enough.

Again, the discussion about the contribution of capillary effects when performing reservoir compaction and subsidence analyses at regional scale is out of scope for the present paper. The idea is to make use of unconventional plasticity [6] by means of the subloading surface model [7]-[11] for predicting softening behaviour of soil as well as reducing computational efforts when performing fully coupled hydro-mechanical subsidence analyses in three-dimensional domains [12], as demonstrated below.

It is to be said that, from a computational point of view, strain-softening may be associated to numerical procedures affected by a lack of convergence and the solution may depend strongly on the mesh adopted. Several techniques have been reported in literature, essentially when dealing with shear band formation and strain localization [13], [14], employed to obtain mesh size-independent shear banding (e.g. [15]). Mesh size-dependent hardening modulus procedures have been proposed by Pietruszczak and Mroz [16] and employed by a number of authors (e.g. Willam [17], Grammatikopoulou et al. [18]); enrichments or enhancements of the continuum models can be alternatively found [19]-[26] which include the non-local

formulation proposed by Eringen [27] and Kroner [28] and developed extensively by Bažant and Cedolin [29]. A complete review of softening plasticity models with internal variables regularized by non-local averaging of integral type can be found in Marotti de Sciarra [30], where it is stated that the appropriate choice of the regularization operator and of the internal variables to model a non-local continuum need to be dealt with a combination of micromechanical analysis and experimental investigations; probably only experimental investigations can provide the validation of one choice or of the other.

However, as evidenced in Yamakawa et al. [31], the accuracy and the convergence property of the subloading surface model (even if there incorporated into a stress-update algorithm for the Cam-Clay one), when e.g. used to reproduce over-consolidated soils experiencing softening, has been demonstrated for a single finite element and a plane mesh of 2460 8-node quadratic elements as well; in the latter situation different mesh sizes have not been considered. The robustness of the model has been there proved by increasing the number of loading steps only, even when considering dilation with a decrease in deviatoric stress.

Hence at present, essentially considering the main objectives of this paper as outlined before and in line with [31], it seems reasonable to prove the accuracy of the calculations presented here by comparing the numerical solutions for different mesh sizes and time steps as well; such a comparison is developed in the last Section, referring to the 3D subsidence analysis on regional scale.

2 FLOW FIELD ANALYSIS

It is here made reference to the coupled solution proposed in [32]-[36] to obtain the flow data necessary for a compaction analysis. This solution considers the mass balance equation in integral form for the fluids in the reservoir, which is then solved together with the state equation of gas via a three-dimensional consolidation analyzer, which uses an (a) equilibrium equation for the multiphase medium (solid + water or solid + gas) and a (b) mass balance equation for the water; the code has been upgraded to take into account possible plastic strain evolutions, following an unconventional plasticity approach, as exposed in the next Section.

The material balance equation referring to the reservoir and the state equation of gas yield at each time step the average reservoir pressure p_g when gas production and water inflow are known; this gas pressure is applied to the reservoir volume and the whole subsiding volume is then analysed by using the fully coupled equations (a) and (b). These equations give the flow of water across the reservoir boundary which is required in the material balance equation at reservoir level, and also its deformation, as well as of the overburden and underburden.

The reader is referred to [36]-[37] for additional details.

3 MODELLING PLASTICITY VIA THE SUBLOADING SURFACE MODEL

The subloading surface model is a particular elasto-plastic model falling within the framework of unconventional elastoplasticity [6], an extended elastoplasticity theory such that the interior of the yield surface is not a purely elastic domain, but rather a plastic deformation is induced by the rate of stress inside the yield surface [7]-[11]. Its main features are briefly

recalled here.

In the subloading surface model the conventional yield surface is renamed the *normal yield surface*, since its interior is not regarded as a purely elastic domain. The plastic deformation develops gradually as the stress approaches the normal yield surface, exhibiting a smooth elastic-plastic transition. Thus the subloading surface model fulfils the *smoothness condition* [11], [39]-[41], which is defined as the stress rate-strain rate relation (or the stiffness tensor) changing continuously for a continuous change of stress rate. Strain accumulation is predicted for a cyclic loading with an arbitrary stress amplitude, where the magnitude of accumulated strain depends continuously on the stress amplitude because of the fulfillment of the smoothness condition. Inelastic deformation occurs immediately when the stress point once again moves outward the current yield surface. Zero diameter yield surface bounding surface models, nested surface models, and subloading models have this attribute, but do not display any purely elastic response [6].

A *subloading surface* is also introduced, which always passes through the current stress point $\boldsymbol{\sigma}$ and keeps a shape similar to that of the normal yield surface and a similar orientation with respect to the origin of stress space, i.e. $\boldsymbol{\sigma} = \mathbf{0}$.

The ratio of similarity R is named *normal yield ratio* and governs the approach of the subloading surface to the normal one, i.e. if R = 0 the subloading surface is a point coinciding with the origin of the stress space, whereas $0 < R < 1$ represents the subyield state and with R = 1 the stress lies directly on the normal surface.

The subloading surface can be described by the scalar-valued tensor function

$$f(\boldsymbol{\sigma}) = RF(H) \tag{1}$$

where the scalar H is the isotropic hardening/softening variable; in agreement with [10] the normal yield surface takes e.g. the form

$$F = F_0 \exp\left(\frac{H}{\rho' - \gamma}\right) \tag{2}$$

in which F_0 is the initial value of F, ρ' and γ the slopes of the normal consolidation and swelling curves respectively in $\ln\upsilon$-$\ln p$ space (υ being the specific volume and $p = -\mathrm{tr}(\boldsymbol{\sigma})/3$).

The extended consistency condition for the subloading surface is obtained by differentiating Eq. (1), which leads to

$$\mathrm{tr}\left(\frac{\partial f(\boldsymbol{\sigma})}{\partial \boldsymbol{\sigma}} \dot{\boldsymbol{\sigma}}\right) = \dot{R}F + RF'\dot{H} \tag{3}$$

together with considering the evolution rule of the normal yield ratio, given by

$$\dot{R} = U\left\|\dot{\boldsymbol{\varepsilon}}^{p}\right\| \quad \text{for} \quad \dot{\boldsymbol{\varepsilon}}^{p} \neq \mathbf{0} \tag{4}$$

where $\dot{\boldsymbol{\sigma}}$ is the proper objective co-rotational stress rate, $\dot{\boldsymbol{\varepsilon}}^{e} = \mathbf{E}^{-1}\dot{\boldsymbol{\sigma}}$, $\dot{\boldsymbol{\varepsilon}}^{p}$ is the plastic strain rate

and U is a monotonically decreasing function of R satisfying the condition

$$\begin{cases} U = +\infty \quad \text{for} \quad R = 0 \\ U = 0 \quad \text{for} \quad R = 1 \\ (U < 0 \quad \text{for} \quad R > 1) \end{cases} \tag{5}$$

The associated flow rule is assumed as

$$\dot{\boldsymbol{\varepsilon}}^{\mathrm{p}} = \overline{\lambda}\,\overline{\mathbf{N}} \tag{6}$$

where $\overline{\lambda}$ is the positive proportional factor representing the increment of plastic deformation along the direction given by the normalized outward normal of the subloading surface $\overline{\mathbf{N}}$ (expressed as a second order tensor)

$$\overline{\lambda} = \frac{\mathrm{tr}\,(\overline{\mathbf{N}}\dot{\boldsymbol{\sigma}})}{\overline{\mathrm{M}}^{\mathrm{p}}} \tag{7}$$

$$\overline{\mathbf{N}} \equiv \frac{\partial \mathrm{f}(\boldsymbol{\sigma})}{\partial \boldsymbol{\sigma}} \Bigg/ \left\| \frac{\partial \mathrm{f}(\boldsymbol{\sigma})}{\partial \boldsymbol{\sigma}} \right\| \tag{8}$$

being $\overline{\mathrm{M}}^{\mathrm{p}}$ the plastic modulus.

The loading criterion is finally given [41], [42]

$$\begin{cases} \dot{\boldsymbol{\varepsilon}}^{\mathrm{p}} \neq \mathbf{0}: \quad \mathrm{tr}\,(\overline{\mathbf{N}}\mathbf{E}\dot{\boldsymbol{\varepsilon}}) > 0 \\ \dot{\boldsymbol{\varepsilon}}^{\mathrm{p}} = \mathbf{0}: \quad \mathrm{tr}\,(\overline{\mathbf{N}}\mathbf{E}\dot{\boldsymbol{\varepsilon}}) \leq 0 \end{cases} \tag{9}$$

For additional details, see [37], [38].

4 APPLICATION CASE: 3D SUBSIDENCE ANALYSIS ON REGIONAL SCALE

The numerical model has been first calibrated and subsequently validated against the results obtained by Siriwardane and Desai [43], the first dealing with the consolidation of a column of soil under a uniformly distributed load, the second with the consolidation of a soil strip in plane strain. For brevity reasons, the procedures and their results are not reported here; they have anyway allowed for defining a value for the plastic variables necessary to the subloading surface model (see below) so to reproduce the same behaviour as the one evidenced in [43] accounting for conventional plasticity.

It is additionally to be said, as previously stated, that the main objective here is not to compare the material response by assuming conventional or unconventional plasticity models (about which it has been largely discussed in e.g. [40], [41]) but, on one side, to numerically confirm the capability of the subloading surface model in predicting softening behaviours and, on the other side, to be able to explain, via such a model, ongoing surface subsidence

(observed in reality) after shutdown of the wells. In fact, it has already been proved in [4] that conventional plasticity alone is not fully able to reproduce such a phenomenon.

A typical subsidence problem of regional scale is here investigated, referring to a pools' depth of burial ranging between 900 and 4000 m and an horizontal area involved of about 19000 Km^2 (**Figure 1**). In addition, the different pools are not scheduled to be put in production at the same time, which complicates the situation further.

Figure 1: Location of gas pools in the Northern Adriatic Sea [44].

Particularly, the effects of the exploitation of four of the gas reservoirs shown in **Figure 1**, located at three different depths and undergoing different production histories [45], are here analysed; the region covers an area of 40×40 km^2 and has a depth of 1300 m; it is discretized by about 500 20-node isoparametric elements (additional analyses, as reported below, refer to 980 and 2940 elements as well). Free flux on the horizontal and vertical boundaries of the investigated area is considered. The main material parameters are shown in **Table 1** [35], [45]; the grains are assumed to be incompressible and the clayey layers to behave in agreement with the subloading surface model when accounting for plasticity effects. The geomechanical data have been obtained through analysis of master-logs at our disposal, which are representative of the investigated area, whereas the plastic variables have been taken from the calibration and validation tests, appropriately scaled to take into account the effect of depth.

As evidenced by **Table 1** and **Figure 2**, some planimetric variability for the soil strata has been additionally introduced just to be closer to the real configuration of the subsoil, e.g. considering the available seismic section of [45]; so 7 *macro-levels* are present, including 15 different soil strata. The exploitation points (wells) are assumed to be equally distributed above each reservoir such as to allow for the assumption of a constant drop of pressure inside them.

The analysis has been pushed up to 30 years from the beginning of exploitations, when a general pressure recovery has already been attained; the results in terms of surface subsidence above each reservoir are shown in **Figure 3**, accounting for elasticity and unconventional elasto-plasticity as well. The effect of interaction among the different reservoirs can be seen from the shifting in time of the maximum subsidence value as compared with the minimum of reservoir pressure: this phenomenon is also to be partly ascribed to the presence of clay layers

confining the pools, but it is particularly evident when plasticity is introduced: as an extreme situation, maximum subsidence can not be reached even after 30 years; a "residual" delayed land subsidence has clearly appeared, so confirming the usefulness of the proposed unconventional plasticity model for modelling continuing surface settlements when reservoir pore pressures stabilize and for additional settlements occurring even after the end of gas production.

Table 1: Material data for subsidence analyses

Soil stratum #	**E** [MPa]	ν	$\mathbf{k_i}$ [m/day]	**Depths [m]**
1	$1.13 \cdot 10^4$	0.17	0.2208	1300÷1254
2	$1.00 \cdot 10^4$	0.17	$0.865 \cdot 10^{-4}$	1300÷1254
3 & Reservoir # 1	$1.13 \cdot 10^4$	0.17	0.2208	1300÷1254
4	$1.00 \cdot 10^4$	0.17	$0.865 \cdot 10^{-4}$	1300÷1254 & 1300÷1070
5, 7, 9	$1.14 \cdot 10^4$	0.30	0.7985	1254÷1070
6, 8, 10	$0.322 \cdot 10^4$	0.38	$0.865 \cdot 10^{-4}$	1254÷1070
11 & Reservoir # 4	$1.14 \cdot 10^4$	0.30	0.7985	1070÷1027
12	$0.322 \cdot 10^4$	0.38	$0.865 \cdot 10^{-4}$	1027÷860
13 & Reservoirs # 2, 3	$0.898 \cdot 10^4$	0.15	0.9752	860÷848
14	$0.555 \cdot 10^4$	0.37	$0.865 \cdot 10^{-4}$	848÷600
15	$0.224 \cdot 10^4$	0.39	$0.865 \cdot 10^{-4}$	600÷0

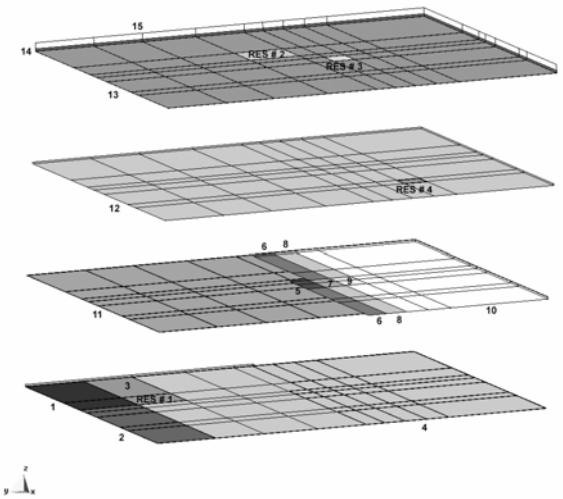

Figure 2: Schematic representation of the soil strata distribution: macro-levels are superimposed from surface (top) to bottom (see **Table 1**).

The subsidence bowl is depicted in **Figure 4**, referring to the evolution of surface subsidence for a fixed domain section when unconventional plasticity is accounted for. The time scales involved, as well as the orders of magnitude for the resulting subsidence, agree well with what evidenced by [45] and [46] (the former referring to linear elasticity only), with similar (or equal, as in the latter case) cumulative gas production histories and geological/geomechanical subsoil configurations.

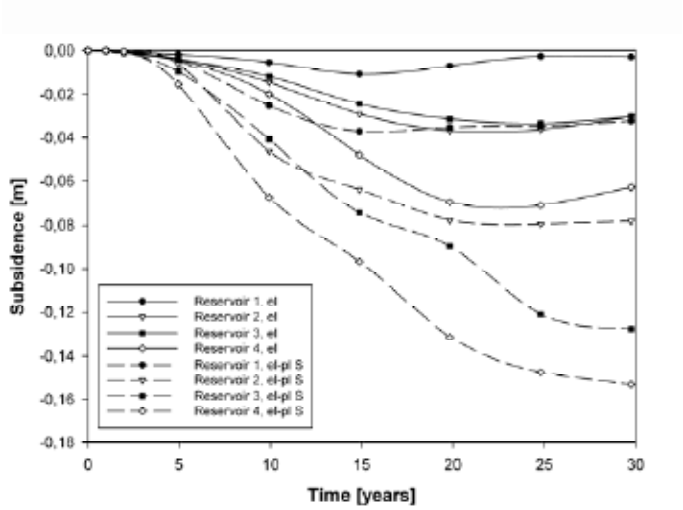

Figure 3: History of surface subsidence above the reservoirs.

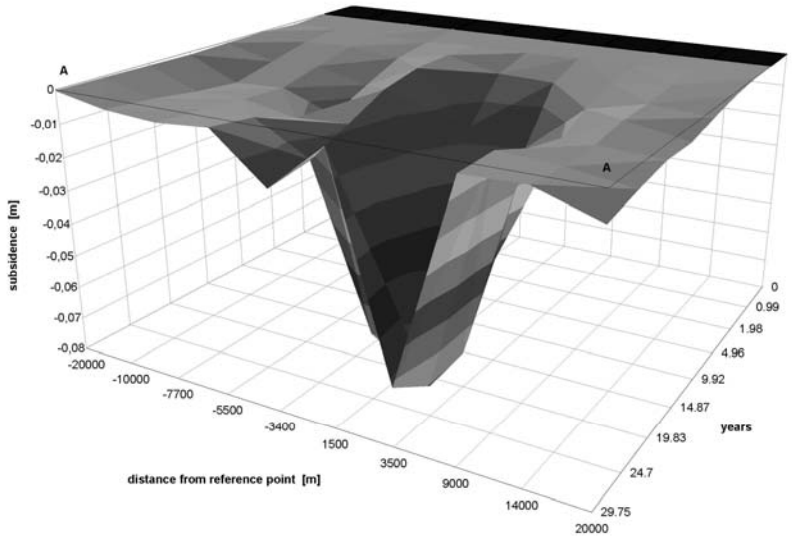

Figure 4: Subsidence bowl, elasto-plastic case.

In order to check the robustness of the model, a series of additional numerical analyses has been performed, by assuming a) different time (loading) steps, and b) different mesh sizes; the results refer to unconventional plasticity analyses only. In the former situation, three reference time-steps have been accounted for, i.e. 362 (load-case LS1), 181 (LS2) and 90.5 days (LS3) respectively (for additional details the reader is referred to [38]): an independence of the computations on loading steps has been clearly evidenced. Two reference points (RP1 close to the deepest rigid underburden, belonging to layer 4 -see **Table 1-**, and RP2, at about 1100 m depth and at the conjunction of layers 6-9 and under layer 12, both in proximity of Reservoir

1) have been considered for representing stress-strain curves (**Figure 5**) taking into account LS1 and LS2 only (being the results of LS3 superimposed to those of LS2): after a short expansion phase, the soils evidence or hardening or softening, depending on material characteristics and depth; the smoothness and shape of the elasto-plastic curves (subloading model) recalls the one reported in [10]. Elastic responses have been added for comparison purposes only. It is to be noticed that the unloading phases do not occur simultaneously with pressure recovery (of e.g. Reservoir # 1) but they are delayed in time. The mechanisms are strongly differentiated depending on the considered points, but they can give a general estimate of the complexity of the subsoil behaviour and they can provide for a first explanation of observed delayed surface settlements.

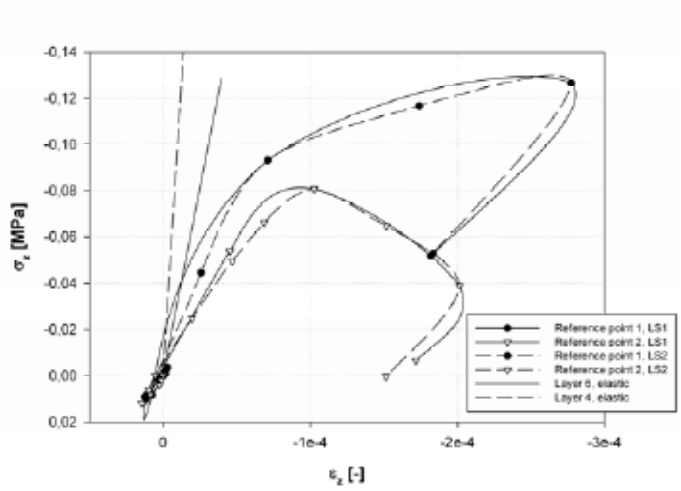

Figure 5: Stress-strain curves for RP1 and RP2.

To complete the check of the plasticity model, two additional meshes have been considered [38]: 4907 nodes and 980 20-node isoparametric elements (M1) and 13978 nodes and 2940 20-node isoparametric elements (M2), with 5 d.o.f. (u_i, i = 1-3, p, T) per node as for the first mesh (M0) of **Figure 1**. The results are depicted in **Figure 6** in terms only of surface subsidence for sake of brevity, referring to the elasto-plastic results from the load-case LS1: mesh independency is evidenced, with a maximum error (taking as reference the values from M2) of about 10%: the error tends to decrease with time, suggesting the ability of the model to perform long-term predictive subsidence analyses.

5 CONCLUSIONS

The coupled hydro-mechanical state in soils coming from consolidation/subsidence processes and undergoing plasticity phenomena has been evaluated by means of the subloading surface model, allowing for predicting a smooth response for smooth monotonic loading, considering the sign of $\mathrm{tr}(\overline{\mathbf{N}}\mathbf{E}\mathbf{D})$ only in the loading criterion, automatically drawing back of a stress to the normal yield surface even if it goes out from the surface itself. Hence a

rough numerical calculation with a large loading step is allowed and return-mapping iterative techniques can subsequently be skipped, so enhancing speedup and efficiency of large scale coupled analyses, as required when modelling subsidence in 3D domains and for long-term scenarios. The plasticity algorithm has been implemented in the PLASCON3D FE code, coupling hydro-thermo-mechanical fields within a saturated (locally partially saturated) porous medium subjected to external loads and water/gas withdrawals from deep layers (aquifers/reservoirs).

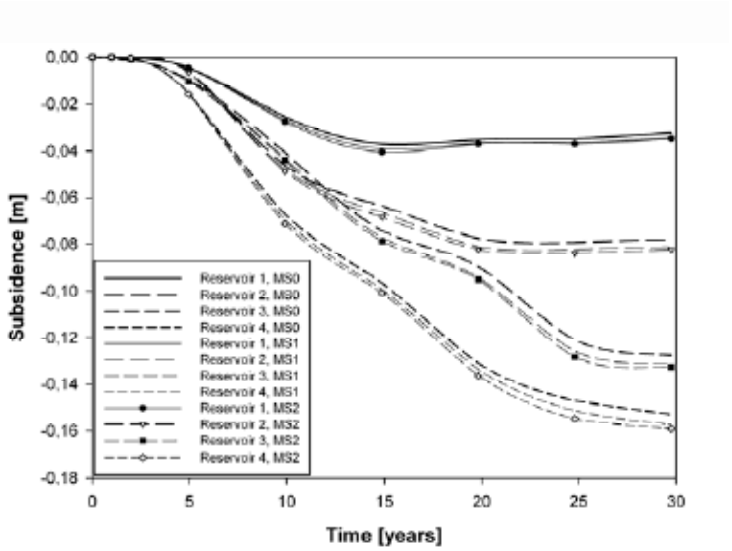

Figure 6: Surface subsidence above the reservoirs, unconventional elasto-plasticity analyses; mesh sizes M0, M1, M2.

The plastic deformation due to the change of stress inside the yield surface exhibiting a smooth elastic-plastic transition has been described, as well as a first ability of describing softening behaviours has been shown.

The robustness of the model has been tested by comparing numerical solutions for different mesh sizes and different time steps.

Regional subsidence analyses due to gas extractions have been possible with reduced computational efforts when introducing unconventional elasto-plasticity in the code. It has been demonstrated that the time scales involved, as well as the orders of magnitude for the resulting subsidence, agree well with what evidenced by [45] and [46] (the former referring to linear elasticity only), with similar (or equal, as in the latter case) cumulative gas production histories and geological/geomechanical subsoil configurations. Particularly, the effects of interaction among exploitations have been estimated, as well as the phenomenon of residual land subsidence near abandoned gas fields has been successfully modelled: the estimation of this delayed environmental cost of gas pumping is generally neglected, whereas it clearly appears of being fundamental for an increased awareness of the consequence that gas production may have on future coastline stability relatively far from the gas field [46].

REFERENCES

[1] Poland, J. (Ed.). *Guidebook to Studies of Land Subsidence due to Groundwater withdrawal*. UNESCO, Paris (1984).

[2] Terzaghi, K. Die Berechnung der Durchlassigkeitsziffer des Tones aus dem Verlauf der hydrodynamischen Spannungserscheinungen. *Akademie der Wissenchaften in Wien, Sitzungsberichte, Mathematisch-naturwissenschaftliche Klasse*, Part Iia (1923) **132**(3/4): 125-138.

[3] Schrefler, B.A., Bolzon, G., Salomoni, V., Simoni, L. On compaction in gas reservoirs. *Atti dell'Accademia Nazionale dei Lincei - Rendiconti Lincei: Scienze Fisiche e Naturali*, s. IX (1997) **VIII**(4): 235-248.

[4] Simoni, L., Salomoni, V., Schrefler, B.A. Elastoplastic subsidence models with and without capillary effects. *Comp. Meth. Appl. Mech. Engrg*. (1999) **171**(3-4): 491-502.

[5] Menin, A., Salomoni, V.A., Santagiuliana, R., Simoni, L., Gens A, Schrefler BA. A mechanism contributing to subsidence above gas reservoirs. *Int. J. Comp. Meth. Engrg. Sci. Mech*. (2008) **9**(5): 270-287.

[6] Drucker, D.C. Conventional and unconventional plastic response and representation. *J. Appl. Mech. Rev.* ASME (1988) **41**(4):151-167.

[7] Hashiguchi, K., Ueno, M. Elastoplastic constitutive laws of granular materials. *Proc. 9th Int. Conf. Soil Mech. Found. Engrg*. Special Session 9, Tokyo, Japan (1977): 73-82.

[8] Hashiguchi, K. Constitutive equations of elastoplastic materials with elastic-plastic transitions. *ASME J. Appl. Mech*. (1980) **47**(2): 266-272.

[9] Hashiguchi, K. Subloading surface model in unconventional plasticity. *Int. J. Solids Struct.* (1989) **25**(8): 917-945.

[10] Hashiguchi, K., Saitoh K, Okayasu T, Tsutsumi S. Evaluation of typical conventional and unconventional plasticity models for prediction of softening behaviour of soils. *Geotech*. (2002) **52**(8): 561-578.

[11] Hashiguchi, K. *Elastoplasticity theory*. In: F Pfeiffer, P Wriggers (Eds.), Lecture notes in applied and computational mechanics. Springer: Berlin (2009) **42**: 393 p.

[12] Yale, D.P. Coupled geomechanics-fluid flow modelling: effects of plasticity and permeability alteration. *SPE/ISRM Rock Mech. Conf*. Irving, TX, USA, Oct. 20-23 (2002) **SPE/ISRM 78202**: 10 p.

[13] Needleman, A. Material rate dependence and mesh sensitivity in localization problems. *Com. Meth. Appl. Mech. Engrg.* (1988) **67**: 69-86.

[14] Garikipati, K., Hughes, T.J.R. A study of strain localization in a multiple scale framework - the one dimensional problem. *Com. Meth. Appl. Mech. Engrg.* (1998) **159**: 193-222.

[15] Zhou, H., Randolph, M.F. Computational Techniques and Shear Band Development for Cylindrical and Spherical Penetrometers in Strain-Softening Clay. *Int. J. Geomech.* (2007) **7**(4): 287-295.

[16] Pietruszczak, S., Mroz, Z. Finite element analysis of deformation of strain softening materials. *Int. J. Num. Meth. Engrg.* (1981) **17**: 327-334.

[17] Willam, K. *Experimental and computational aspects of concrete failure*. In: F. Damjanic (Ed.), Computer Aided Analysis and Design of Concrete Failure. Pineridge Press: Swansea (1984): 33-70.

[18] Grammatikopoulou, A., Zdravkovic, L., Potts, D.M. General Formulation of Two Kinematic Hardening Constitutive Models with a Smooth Elastoplastic Transition. *Int. J. Geomech.* (2006) **6**(5): 291-302.

[19] Aifantis, E.C. On the microstructural origin of certain inelastic models. *J. Engrg. Mat. Tech.* (1984) **106**: 326-334.

[20] Pijaudier-Cabot, G., Bažant, Z.P. Nonlocal damage theory. *ASCE J. Engrg. Mech.* (1987) **113**(10): 1521-1533.

[21] Mühlhaus, H.B., Vardoulakis, I. The thickness of shear bands in granular materials. *Geotech.* (1987) **37**: 271-283.

[22] Bažant, Z.P., Lin, F.B. Non-local yield limit degradation. *Int. J. Num. Meth. Engrg.* (1988) **26**: 1805-1823.

[23] Mühlhaus, H.B., Aifantis, E.C. A variational principle for gradient plasticity. *Int. J. Solids Struct.* (1991) **28**: 845-857.

[24] De Borst, R., Mühlhaus, H.B. Gradient dependent plasticity: formulation and algorithmic aspects. *Int. J. Num. Meth. Engrg.* (1992) **35**: 521-539.
[25] De Borst, R., Sluys, L.J., Mühlhaus, H.B., Pamin, J. Fundamental issues in finite element analyses of localization of deformation. *Engrg. Comp.* (1993) **10**: 99-121.
[26] Galavi, V., Schweiger, H.F. Nonlocal Multilaminate Model for Strain Softening Analysis. *Int. J. Geomech.* (2010) **10**(1): 30-44.
[27] Eringen, A.C. Theory of micropolar continuum. *Proc. 9th Midwestern Mechanical Conference*. University of Wisconsin, Madison, Wisconsin (1965): 23-40.
[28] Kroner, E. Elasticity theory of material with long-range cohesive forces. *Int. J. Solids Struct.* (1967) **3**:731-742.
[29] Bažant, Z.P., Cedolin, L. *Stability of Structures*. Oxford University Press: NY (1991).
[30] Marotti de Sciarra, F. A general theory for nonlocal softening plasticity of integral-type. *Int. J. Plasticity* (2008) **24**: 1411-1439.
[31] Yamakawa, Y., Hashiguchi, K., Ikeda, K. Implicit stress-update algorithm for isotropic Cam-clay model based on the subloading surface concept at finite strains. *Int. J. Plasticity* (2010) **26**(5): 634-658.
[32] Lewis, R.W., Schrefler, B.A. *A finite element simulation of the subsidence of gas reservoirs undergoing a waterdrive*. In: RH Gallagher, DH Norrie, JT Oden, OC Zienkiewicz (Eds.), Finite Element in Fluids. Wiley: Chichester (1982) **4**: 179-199.
[33] Schrefler, B.A., Lewis, R.W., Majorana, C.E. Subsidence above volumetric and waterdrive gas reservoirs. *Int. J. Num. Meth. Fluids* (1981) **1**(2): 101-15.
[34] Lewis, R.W., Schrefler, B.A. *The finite element method in the deformation and consolidation of porous media*. Wiley: Chichester (1987).
[35] Lewis, R.W., Schrefler, B.A. *The finite element method in the static and dynamic deformation and consolidation of porous media*. Wiley: Chichester (1998).
[36] Schrefler, B.A., Wang, X., Salomoni, V., Zuccolo, G. An efficient parallel algorithm for three-dimensional analysis of subsidence above gas reservoirs. *Int. J. Num. Meth. Fluids* (1999) **31**(1): 247-60.
[37] Salomoni, V.A., Fincato, R. 3D subsidence analyses above gas reservoirs accounting for an unconventional plasticity model. *Int. J. Num. Anal. Meth. Geomech*. (2011) (in press).
[38] Salomoni, V.A., Fincato, R. Subloading surface plasticity model algorithm for 3D subsidence analyses above gas reservoirs. *Int. J. Geomech*. (2011) (in press).
[39] Hashiguchi, K. Mechanical requirements and structures of cyclic plasticity models. *Int. J. Plasticity* (1993) **9**(6): 721-748.
[40] Hashiguchi, K. The extended flow rule in plasticity. *Int. J. Plasticity* (1997) **13**(1): 37-58.
[41] Hashiguchi, K. Fundamentals in constitutive equation: continuity and smoothness conditions and loading criterion. *Soils Found*. (2000) **40**(3): 155-161.
[42] Hashiguchi, K. On the loading criterion. *Int. J. Plasticity* (1994) **10**(8): 871-878.
[43] Siriwardane, H.J., Desai, C.S. Two numerical schemes for non linear consolidation, *Int. J. Num Meth. Engrg.* (1981) **17**: 405-426.
[44] *Il Sole 24 Ore*, July 16 (2008) **195** (in Italian).
[45] AGIP, *Progetto Alto Adriatico – Studio di impatto ambientale*. AGIP, San Donato, Italy (1996) (in Italian).
[46] Baù, D., Gambolati, G., Teatini, P. Residual land subsidence near abandoned gas fields raises concern over Northern Adriatic coastland. *Eos* (2000) **81**(22): 245-249.

XI International Conference on Computational Plasticity. Fundamentals and Applications
COMPLAS XI
E. Oñate, D.R.J. Owen, D. Peric and B. Suárez (Eds)

A STRUCTURED CONSTITUTIVE MODEL FOR SIMULATING THE BEHAVIOUR OF AN OVERCONSOLIDATED BONDED CLAY

NUBIA A. GONZÁLEZ[*], ANTONIO GENS[*], MARCOS ARROYO[*] AND MOHAMED ROUAINIA[†]

[*] Department of Geotechnical Engineering and Geosciences
Universitat Politècnica de Catalunya
Jordi Girona 1-3, Edifici D-2, 08034 Barcelona, Spain
e-mail: antonio.gens@upc.edu, nubia.aurora.gonzalez@upc.edu, marcos.arroyo@upc.edu
web page: http://www.upc.edu

[†] School of Civil Engineering and Geosciences
Newcastle University
6 Kensington Terrace, Newcastle upon Tyne, UK
e-mail: m.rouainia@newcastle.ac.uk web page: www.ncl.ac.uk

Key words: Structure, London clay, Kinematic Hardening, Stiffness.

Abstract. The paper presents some improvements in the formulation of a kinematic hardening constitutive soil model incorporating structure initially proposed for soft clays. For the modelling of overconsolidated bonded clay the elastic formulation was deemed more important. Two different alternatives, one purely empirically based the other with a background in thermodynamics were implemented. It was also found that a smooth elasto-plastic transition was required to avoid a spurious stiffness degradation response. Consequently, the hardening modulus formulation of the model was modified. The paper presents some results from a parametric analysis of the triaxial drained response of a material tailored to mimic London clay. The results chosen do not show a major difference between the chosen alternative elastic formulations, although both do improve the original model response. On the other hand the importance of ensuring a smooth elasto-plastic transition is clearly highlighted.

1 INTRODUCTION

Critical state soil mechanics led to a significant improvement of predictions of soil behaviour by introducing specific volume as an additional state variable. The essential features of the classical critical state models are that on a primary loading large plastic strains occur, but on subsequent unload - reload cycles within the yield surface only elastic strains are predicted. Later research on the behaviour of soil in the small strain and very small strain range [1] revealed that the assumption of elastic behaviour inside the state boundary surface is not acceptable due to the non–linearity of soil behaviour in the small strain range. Models based on the concepts of kinematic hardening [2] and bounding surface [3] plasticity seem to provide and improvement, over simple elasto-plastic constitutive models, in modelling the

highly nonlinear and inelastic behaviour of soils. These models allows for plasticity and nonlinearity to be invoked within the conventionally defined yield surface. A kinematic hardening extension of a Cam clay-like model was proposed by [4]. Later, [5] extended this model to simulate the behaviour of natural clays damaged only by plastic straining.

This chapter describes a kinematic hardening soil model for structured soils, its numerical implementation and validation. The kinematic hardening constitutive model (KHSM) used is based on [5] here modified to improve the model response in the small strain region and to predict a smooth variation in stiffness. The chapter starts with a brief description of the KHSM formulated in the general stress space. Modifications to the original model are presented in section 3. Section 4 presents some parametric studies of the performance of the model for the simulation of drained triaxial test on London clay.

2 MODEL FORMULATION

3.1 Original KHSM

The model contains three surfaces in stress space: a kinematic yield surface (f_b), a structure surface (F) and a reference surface (f_r) as shown in Figure 1. The bubble surface separates the elastic response from the elasto-plastic response while the structure surface position defines the current structure magnitude and anisotropy of the structure. The size of the structure surface reduces, due to plastic strain, towards the reference surface which defines the behaviour of the non-structured or remoulded material.

$$f_r = \frac{3}{2M_\theta^2}\boldsymbol{s}:\boldsymbol{s} + \left(p' - P_c\right)^2 - \left(P_c\right)^2 = 0$$

$$f_b = \frac{3}{2M_\theta^2}\left(\boldsymbol{s}-\boldsymbol{s}_\alpha\right):\left(\boldsymbol{s}-\boldsymbol{s}_\alpha\right) + \left(p' - p_\alpha'\right)^2 - \left(RP_c\right)^2 = 0 \tag{1}$$

$$F = \frac{3}{2M_\theta^2}\left(\boldsymbol{s}\right):\left(\boldsymbol{s}\right) + \left(p' - rP_c\right)^2 - \left(rP_c\right)^2 = 0$$

where p and $\boldsymbol{s}$ are the mean pressure and the deviatoric stress tensor, $\left\{p_\alpha' \boldsymbol{I}, \boldsymbol{s}_\alpha\right\}^T = \bar{\boldsymbol{\alpha}}$ denotes the location of the centre of the bubble and $\left\{rP_c\boldsymbol{I}\right\}^T = \hat{\boldsymbol{\alpha}}$ denotes the centre of the structure surface. R is a model parameter and M_θ the slope of the critical state line. This is a function of the Lode angle θ following a proposal in [6]

$$M_\theta = M\left(\frac{2\alpha^4}{1+\alpha^4+\left(1-\alpha^4\right)\sin\left(3\theta\right)}\right)^{1/4} \tag{2}$$

where M is the slope of the CSL under triaxial compression (θ=-30º).

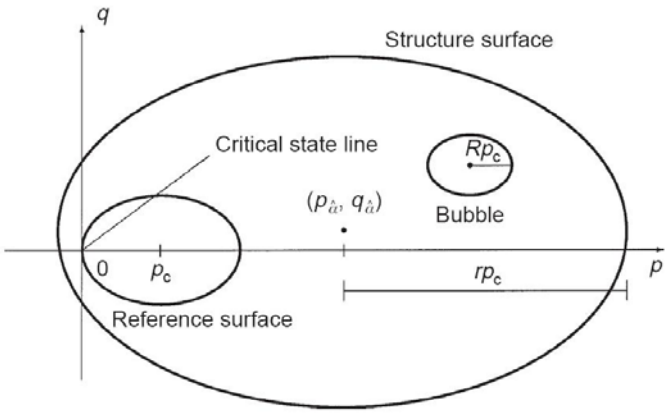

Figure 1: KHSM constitutive model [5]

The scalar variable r, is assumed to be a monotonically decreasing function of the plastic strains and represents the progressive degradation of the material. The incremental form of the destructuration law is written as,

$$\dot{r} = -\frac{k}{\left(\lambda^* - \kappa^*\right)}\left(r-1\right)\dot{e}_d$$
$$\dot{e}_d = \left[\left(1-A\right)\left(\dot{\varepsilon}_v^p\right)^2 + A\left(\dot{\varepsilon}_q^p\right)^2\right]^{1/2} \tag{3}$$

A is a non-dimensional scaling parameter, $\dot{\varepsilon}_v^p$ is the plastic volumetric strain rate, $\dot{\varepsilon}_q^p$ is the equivalent plastic shear strain rate and $\dot{e}_d$ is the destructuration strain rate.

In line with Cam-clay, a volumetric hardening rule is adopted, whereby the change in size of the reference surface, P_c, is controlled only by plastic volumetric strain rate, $\dot{\varepsilon}_v^p$,

$$\frac{\dot{P}_c}{P_c} = \frac{\dot{\varepsilon}_v^p}{\lambda^* - \kappa^*} \tag{4}$$

It can be shown that the plastic multiplier, $\dot{\gamma}$, can be computed as:

$$\dot{\gamma} = \frac{1}{H}\left(\boldsymbol{n} : \dot{\boldsymbol{\sigma}}'\right) = \frac{1}{H_c}\left(\boldsymbol{n} : \dot{\boldsymbol{\sigma}}_c'\right) \tag{5}$$

where the plastic scalar moduli H and H_c are functions of state associated with $\dot{\boldsymbol{\sigma}}'$ and $\dot{\boldsymbol{\sigma}}_c'$, respectively. $\boldsymbol{\sigma}_c'$ is the conjugate stress tensor, defined as the point on the structure surface having the same outward normal as the current stress point $\boldsymbol{\sigma}'$ on the bubble. The conjugate hardening modulus H_c is derived from the consistency condition on the structure surface for the case where the bubble and the structure surface are in contact. The explicit expression is,

$$H_c = \frac{2rP_c}{\lambda^* - \kappa^*}\left[\left(2\left(p - p_\alpha\right) + \frac{k\left(1-r\right)}{r}\frac{\dot{e}_d}{\dot{\gamma}}\right)\left(\left(p - p_\alpha\right) + RP_c\right)\right] \tag{6}$$

The variation of the hardening modulus within the structure surface is described by an interpolation rule along the distance b, which connects the current stress state on the yield surface with its conjugate point on the structure surface. Hence,

$$H = H_c + \frac{BP_c^3}{\lambda^* - \kappa^*}\left(\frac{b}{b_{\max}}\right)^{\Psi} \tag{7}$$

Where Ψ and B are model parameters, b is the distance between current stress and conjugate stress, and b_{max} its maximum as defined below

$$b = \mathbf{n} : \left(\boldsymbol{\sigma}_c^{'} - \boldsymbol{\sigma}^{'}\right) \tag{8}$$

$$b_{\max} = 2\left(\frac{r}{R} - 1\right)\mathbf{n} : \left(\boldsymbol{\sigma}^{'} - \bar{\boldsymbol{\alpha}}\right)$$

If a stress increment requires movement of the bubble relative to the structure surface, a geometric kinematic hardening rule is invoked to describe this movement. The translation rule of the centre of the bubble $\bar{\boldsymbol{\alpha}}$ is,

$$\dot{\bar{\boldsymbol{\alpha}}} = \bar{\boldsymbol{\alpha}}\left(\frac{\dot{P}_c}{P_c} + \frac{\dot{r}}{r}\right) + \frac{\dot{\gamma}H - \boldsymbol{n} : \left[\frac{\dot{P}_c}{P_c}\boldsymbol{\sigma} + \frac{\dot{r}}{r}\bar{\boldsymbol{\alpha}}\right]}{\boldsymbol{n} : \left(\boldsymbol{\sigma}_c - \boldsymbol{\sigma}\right)}\left[\frac{\boldsymbol{\sigma} - \bar{\boldsymbol{\alpha}}}{R} - \frac{\boldsymbol{\sigma} - \hat{\boldsymbol{\alpha}}}{r}\right] \tag{9}$$

3.2 Modified elastic behaviour

The original elastic formulation in KHSM was

$$K = \frac{p^{'}}{\kappa^*} \tag{10a}$$

$$G = \frac{3p^{'}}{2\kappa^*}\frac{\left(1+2\upsilon\right)}{\left(1+\upsilon\right)} \tag{10b}$$

As an alternative to the equation (8b) the shear modulus can be described by an empirically based equation proposed in [7]

$$\frac{G}{p_r} = A_g\left(\frac{p^{'}}{p_r}\right)^{n_g} R_o^{m_g} \tag{11}$$

Where A_g, n_g and m_g are dimensionless parameters p_r, is a reference pressure (1 kPa) and

$R_o = 2P_c / p'$, is the isotropic overconsolidation. Correlations of all the parameters entering the equation with plasticity index are given in [7].

According to [8] simplistic models in which tangent moduli are arbitrarily defined as functions of stress can lead to a non-conservative response, in violation of the laws of thermodynamics. In contrast, an hyper-elastic approach guarantees thermodynamic acceptability. Based on considerations of a free energy (or elastic strain energy) potential, [8] derive the following stiffness matrix, which can be used directly in, for instance, a finite element program for general stress states, ensuring fully conservative elastic behaviour when the moduli are functions of pressure,

$$D_{ijkl} = p_a \left(\frac{p_o}{p_a} \right)^{n_h} \left[n_h K_h \frac{\sigma'_{ij}\sigma'_{ikl}}{p_o^2} + K_h \left(1 - n_h\right) \delta_{ij}\delta_{kl} + 2G_h \left(\delta_{ik}\delta_{jl} - \frac{1}{3}\delta_{kl}\delta_{ij} \right) \right] \tag{12}$$

where, p_o, is a function of stresses defined in (11); p_a, is the atmosferic pressure taken equal to 100 kPa; K_h, is a dimensionless bulk stiffness factor;G_h, is a dimensionless shear stiffness factor and n_h, is a dimensionless pressure exponent.

$$p_o^2 = \frac{\sigma'_{mm}\sigma'_{nn}}{9} + \frac{K_h \left(1 - n_h\right) s_{mn} s_{mn}}{2G_h} \tag{13}$$

The form of the stiffness matrix in equation (10) has two important consequences: i) the moduli depend on all the stress invariants (not just the mean stress) ii) the elastic response is anisotropic.

3.2 Modified plastic hardening

The kinematic hardening embedded in KHSM does not predict a smooth transition from elastic to elasto-plastic behaviour. To do so, [9], the value of hardening modulus should be infinite when the stress state engaged the yield surface. This is because when the stress state is within the yield surface the strains predicted are elastic and the plastic strains are equal to zero. When the stress state touches the yield surface, both elastic and plastic strains are predicted, so in order to have a smooth transition the plastic strains should be initially equal to zero and hence the hardening modulus equal to infinite. Inspection of equation (7) shows that, when the stress state engages the yield surface, a finite value of the hardening modulus is calculated.

As an alternative to (7) for this the formulation proposed in [9] is therefore adopted as an alternative to compute the hardening modulus,

$$H = H_c + \frac{BP_c^3}{\lambda^* - \kappa^*} \left(\frac{b}{b^*_{\max} - b} \right) R^2 \tag{13}$$

Where, H_c and b were defined in equations (6) and (8) respectively. B is a parameter. The value of $b^*_{\max}$ is set equal to the value of b each time the stress state becomes elasto-plastic (i.e., engages the yield surface). Details of the necessary incremental updating procedure are

given in [10], where the numerical implementation of the model in a FE program is also discussed.

3 PARAMETRIC ANALYSIS IN DRAINED TRIAXIAL TESTS

A parametric analysis of the influence of some parameters of the KHSM was done by the simulation of drained compression triaxial test. Here only some results for the influence of structure parameters or elasticity formulation are shown, more details are presented in [10].

Soils parameters are chose to represent the behavior of intact London Clay and the initial stress conditions before shearing are close to the initial state for triaxial tests of at 12 m of depth given by [11]. Some parameters are fixed (Table 1) and the influence of others is explored (Table 2, with base values in bold characters). Fixed parameters correspond with parameters for reconstituted London Clay given by [12]. The base values of Viggiani's elastic parameters Ag=300, ng=0.87 and mg=0.28 were selected based on the plasticity index of 50, representative of London Clay [13] Initial stress state is shown in Table 3, the initial position for the reference surface is derived from the preconsolidation pressure (P_0) value (in the model $Pc = P_0/2$) estimated from oedometer tests reported by [11].

Table 1: Fixed parameters for the sensitivity analysis

λ^*	κ^*	M	ϕ_{cs} [°]	R	B	$\psi^{(a)}$	A
0.097	0.046	0.85	22	0.02	4	7	0.75

a) Only required for the original Plastic modulus (eq. 7)

Table 2: Exploratory parameters for the sensitivity analysis

Parameter	Values explored
k	0, **0.5**, 1, 2
r_0	1, **4**, 8
A_g	100, **300**, 700
n_g	0.5, 0.7, **0.87**
m_g	0.2, **0.28,** 0.4
n_h	0.5, 0.75, 0.9
K_h	100, 300, 700
G_h	100, 300, 700

Table 3: Initial stress state for the sensitivity analysis

p' [kPa]	q [kPa]	P_c [kPa]
260	-90	400

Results of the sensitivity analysis are shown in terms of stress-strain and stiffness-strain curves. The stiffness plotted is the octahedral shear stiffness $3G_{oct} = dq/d\varepsilon_s$, where $q = \left[3/2(\boldsymbol{s}:\boldsymbol{s})\right]^{0.5}$ is the generalized shear stress and $\varepsilon_s = \left[2/3(\boldsymbol{e}_s:\boldsymbol{e}_s)\right]^{0.5}$ is the generalized shear

strain; $\boldsymbol{e}_s$ is the deviatoric component of the strain tensor. The superscript "tan" in the figures is used to denote tangent stiffness. The stiffness is further normalized by p_i', which is the value of p' at the start of shearing.

3.1 Influence of structure parameters

In all the analyses in this section a comparison is made between results obtained using the original plastic modulus formulation (7) and the modified one (eq.13). The influence of structure parameters: r0 and k is shown in Figure 2. Figure 2 shows a strong influence of the plastic modulus formulation in the stiffness degradation curves. The original plastic modulus predicts a drop in stiffness, faster when r0 increases, while the modified plastic modulus results in a smoother stiffness degradation. This behaviour is attributed to the non-smooth elasto-plastic transition when the stress state engaged the yield surface (bubble) as was discussed previously. The variation of the plastic modulus (H) with axial strain for the two formulations is shown in Figure 3. A consistent behavior is observed for the modified plastic modulus. A higher initial structure results in slower the decay of the plastic modulus. Then, for given axial strain, higher values of H are observed when r_0 increases and the generation of plastic strains is reduced, this behaviour is consistent with the structure increasing both stiffness and strength. An opposite effect is observed for the original plastic modulus formulation which is reflected in decreasing stiffness in the small strain region when r_0 increases.

The effect of the rate of destructuration (k) can be seen in Figure 4. In general a higher destructuration rate induces lower strength values. The destructuration effect on stiffness is negligible. When the original plastic modulus is employed (Figure 4b) a marked peak strength appears as the rate of destructuration increases. Also a non-smooth stiffness degradation and a non-physical effect in the small strain region of increase in stiffness as the degradation rate increases.

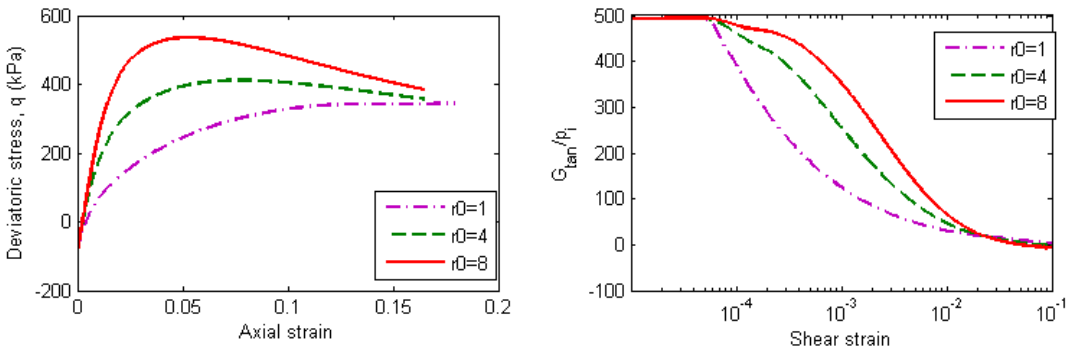

(a)

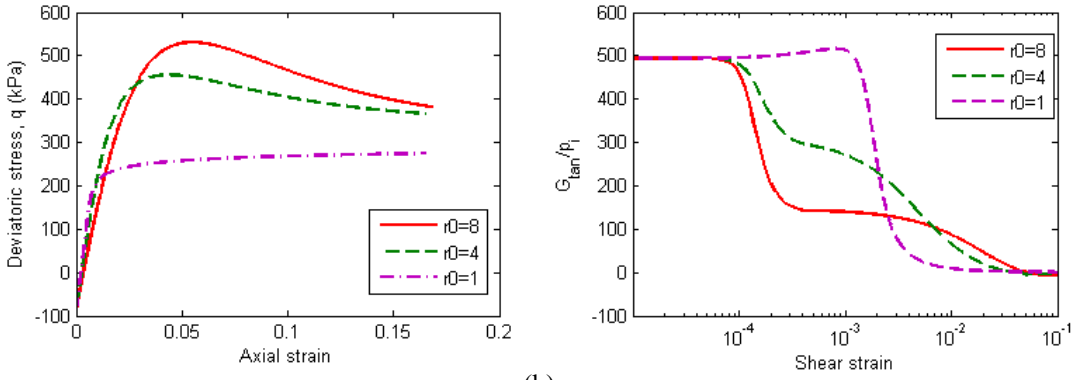

(b)

Figure 2: Influence of initial structure. (a) Modified *H*, (b) Original *H*

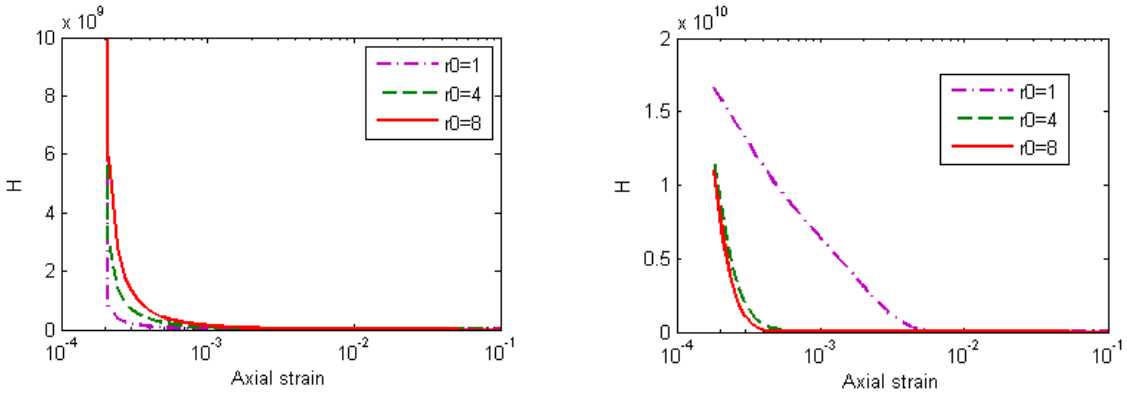

(a) (b)

Figure 3: Comparison of plastic modulus (*H*) evolution. (a) Modified *H*, (b) Original *H*

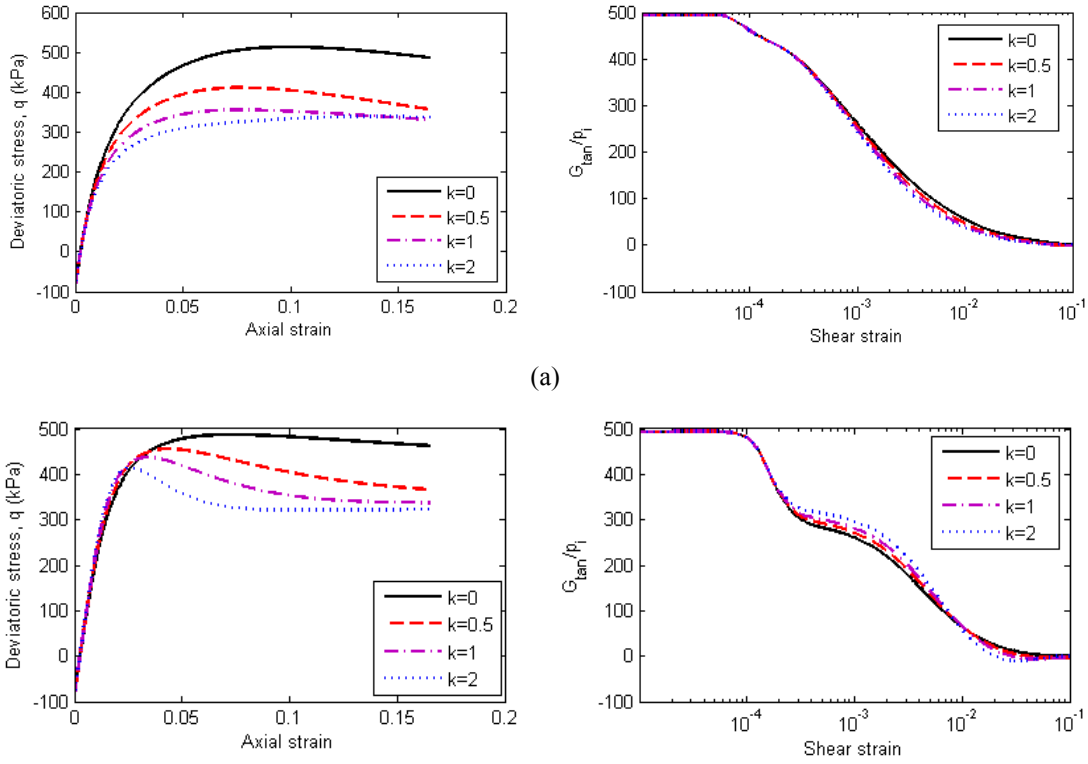

(a)

(b)

Figure 4: Influence of the rate of destructuration. (a) Modified *H*, (b) Original *H*

3.2 Influence of elasticity laws

We examine the influence of the parameters in the different elasticity formulations. Simulations using Viggiani's and Hyper-elasticity are shown in Figure 5 and Figure 6, respectively. The set of constant parameters selected is: R=0.02, B=4 and r0=1, hence a non-structured case is examined. The modified plastic modulus equation was used for all the analysis in this section. The traditional formulation (10) was also employed, for comparison, using a constant Poisson's ratio of υ=0.2.

Figure 5 shows that parameters A_g and n_g of Viggiani elasticity law have large influence on soil stiffness at very small strains, while the influence of m_g is almost negligible. At large strains (γ>0.1%) n_g still shows an influence on stiffness when n_g<0.7. Following [7] the value of n_g is in the region of 0.5-0.9 depending on the plasticity index. Low values of n_g are applied to soils with low plasticity index which is not the case of London Clay.

For the triaxial compression test, bulk stiffness factor (K_h) of Hyper-elasticity law shows a negligible influence on initial shear stiffness and stiffness degradation curves as is shown in Figure 6(a). Shear stiffness factor (G_h) and n_h have a significant influence on initial stiffness in a similar way to the effects of A_g and n_g, respectively, of Viggiani's elasticity law.

It is also observed in Figures 5 and 6 that traditional elasticity law reaches very low shear stiffness at small strains which is reflected in the shape of stress-strain curve. Only at shear

strains greater than 1% traditional elasticity shows similar stiffness values than the others elasticity laws. Regardless of the elasticity law used the same ultimate stress level is reached at large strains.

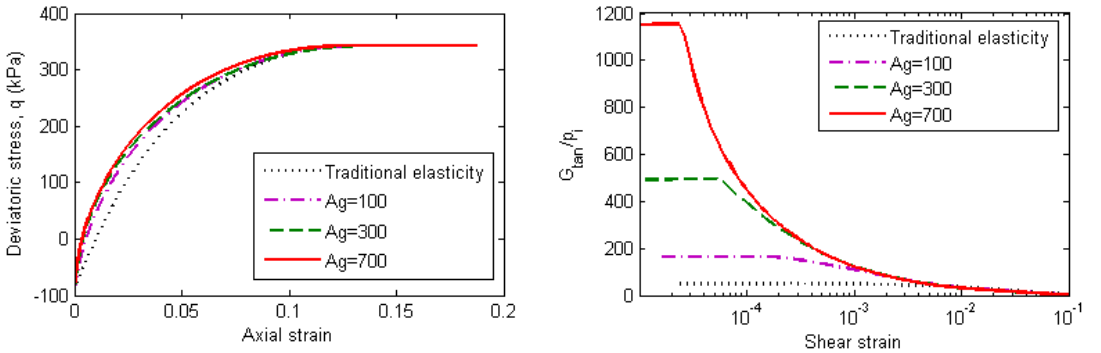

(a) Constants: ng=0.87, mg=0.28

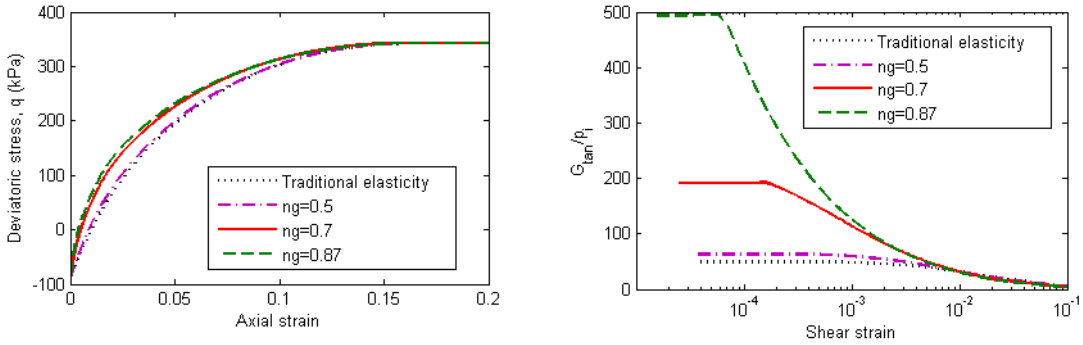

(b) Constants: A_g=300, m_g=0.28

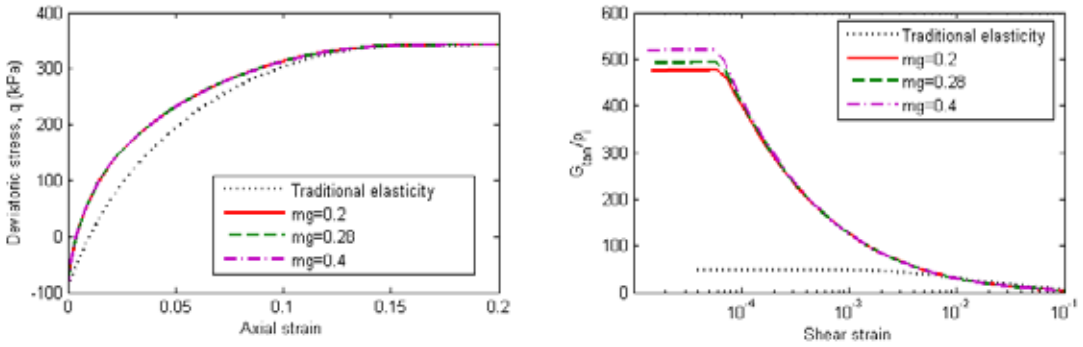

(c) Constants: A_g=300, n_g=0.87

Figure 5: Influence of Viggiani's elasticity law. (a) A_g, (b) n_g, (c) m_g

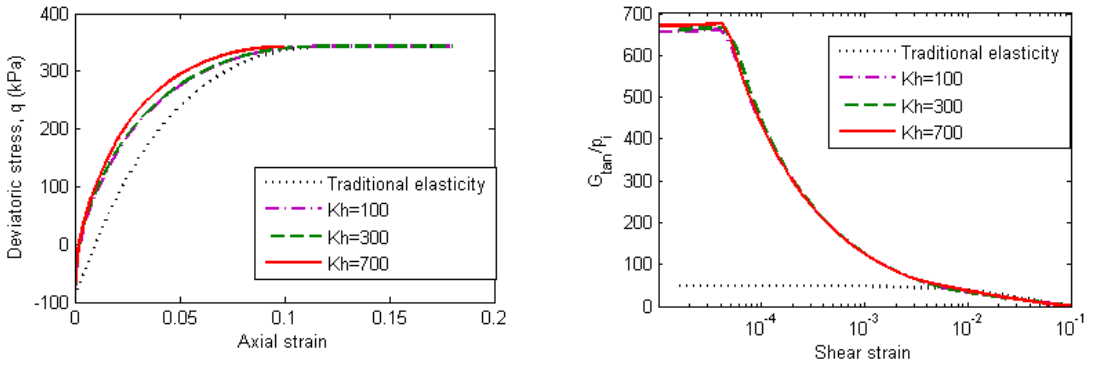

(a) Constants: Gh=300, nh=0.75

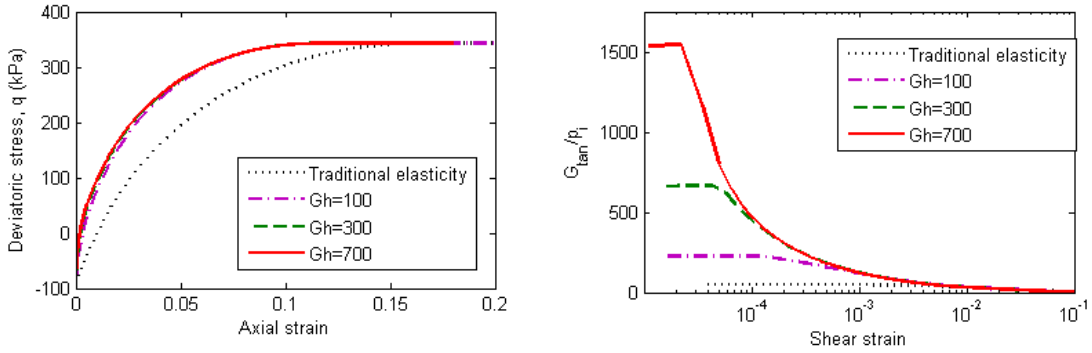

(b) Constants: K_h=300, n_h=0.75

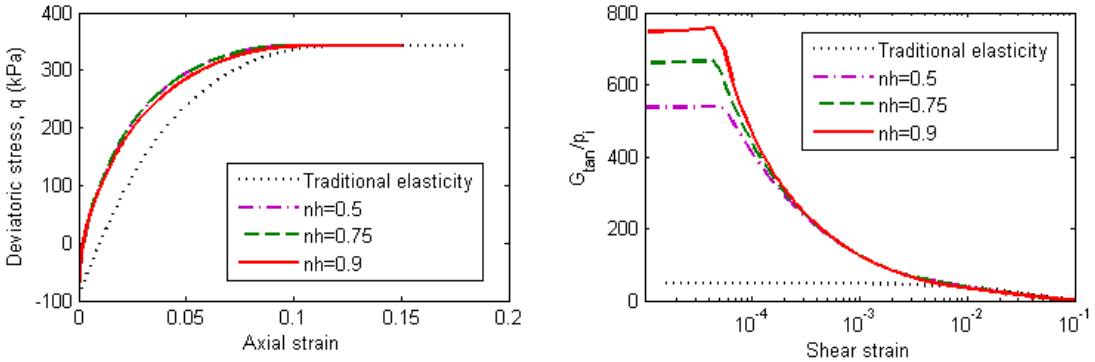

(c) Constants: K_h=300, G_h=300

Figure 6: Influence of Hyper-elasticity law parameters. (a) K_h, (b) G_h, (c) n_h

4 CONCLUSIONS

Initial structure of the soil is a state variable which modified both strength and stiffness of the soil. If the original plastic modulus is used, an anomalous stiffness degradation will be observed due to the abrupt drop in stiffness observed when structure increases. The structure parameter k shows a negligible influence on stiffness, but not on strength. In case of modified

plastic modulus, k affects both peak strength and residual strength, while only residual strength is affected when original plastic modulus is used. In addition, modified plastic modulus seems to result in a less brittle response than the original one.Two alternative formulations have been used to describe the elastic behaviour of the soil. It has been shown that both formulations give equivalent results for the chosen parameters. In contrast, the traditional elastic formulation does not attain high initial stiffness at small strains.

ACKNOWLEDGMENT

The support of the Spanish Ministry of Science through research grant BIA2008-06537 is grate-fully acknowledged.

REFERENCES

[1] Jardine, R.J., Symes, M.J.& Burland, J.B. (1984). The measurement of soil stiffness in the triaxial apparatus. Géotechnique, 34(3), 323-340.
[2] Mroz, Z., Norris, V.A. & Zienkiewicz, O.C. (1978). An anisotropic hardening model for soils and its application to cyclic loading. Int. J. N. A. Meth. Geomech., 2(3), 203-221.
[3] Dafalias, Y.F. & Herrmann, L.R. (1980). A bounding surface soil plasticity model. Proc. Int. Symp. on Soils under Cyclic and Transient Loading, Vol. 1, G.N. Pande & O.C.Zienkiewicz, eds., Swansea, U.K., 335–345.
[4] Al-Tabbaa, A. & Wood, D.M. (1989). An experimentally based 'bubble' model for clay. Proceedings of “Numerical models in geomechanics” NUMOG 3 (eds S. Pietruszczak & G.N. Pande), pp. 91_99. London: Elsevier Applied Science.
[5] Rouainia, M. & Muir Wood, D. (2000). A kinematic hardening constitutive model for natural clays with loss of structure. Géotechnique 50 (2), 153–164.
[6] Sheng D., Sloan S.W. & Yu, H.S. (2000). Aspects of finite element implementation of critical state models. Computational Mechanics 26, 185-196.
[7] Viggiani, G. & Atkinson, J.H. (1995). Stiffness of fine-grained soil at very small strains. Géotechnique 42 (2), 249-265.
[8] Houlsby, G.T., Amorosi, A. & Rojas, E. (2005). Elastic moduli of soils dependent on pressure: a Hyperelastic formulation. Géotechnique 55 (5), 383-392.
[9] Grammatikopoulou, A., Zdravkovic, L. & Potts, D.M. (2006). General formulation of two kinematic hardening constitutive models with a smooth elastoplastic transition.International Journal of Geomechanics, Int. J. Geomech. Vol 6 (5), 291-302.
[10] González, N.A (2011). Development of a hierarchical suite of constitutive models for geotechnical applications. Ph.D. Thesis, Universitat Politécnica de Catalunya, Barcelona, Spain
[11] Gasparre, A.(2005). Advanced laboratory characterisation of London Clay. PhD thesis, Imperial College, London. http://www.imperial.ac.uk/geotechnics/Publications/PhDs/phdsonline.htm.
[12] Hight D.W., McMillan, F., Powell, J.J.M., Jardine, R.J. & Allenou, C.P. (2003). Some characteristics of London Clay. Characterisation and Engineering Properties of Natural Soils-Tan et al. (eds). Volume 2, 851-907. Rotterdam: Balkema.

XI International Conference on Computational Plasticity. Fundamentals and Applications
COMPLAS XI
E. Oñate, D.R.J. Owen, D. Peric and B. Suárez (Eds)

A THEORITICAL APPROACH TO THE STUDY OF COMPACTION BANDS IN POROUS ROCKS

ARGHYA DAS, GIANG D. NGUYEN, ITAI EINAV

School of Civil Engineering
The University of sydney
Sydney NSW 2006, Australia
email: arghya.das@sydney.edu.au, giang.nguyen@sydney.edu.au, itai.einav@sydney.edu.au,
Web page: http://sydney.edu.au/

Key words: Compaction band, Breakage mechanics, Localization analysis, Grain crushing, Rate dependency, Boundary value problem.

Summary. *The formation and propagation of compaction bands in high porosity sandstones is theoretically investigated in this paper using a new constitutive model based on the recently developed continuum breakage mechanics theory* [1,2]. *This model possesses a micromechanics-based link between the evolving grain size distribution (gsd) and the macroscopic stress strain relationship, through an internal variable called Breakage. This is an advanced feature over many existing plasticity based models in the literature, helping to faithfully track the evolving gsd and its related physics (e.g. permeability reduction). A localization analysis based on the acoustic tensor* [3] *is performed to determine both the onset and orientation of compaction bands due to grain crushing. It is shown that the model used is able to capture well both the material behaviour and formation of compaction band experimentally observed. An enhancement using rate-dependent regularization is applied to the model to deal with instability issues in the analysis of Boundary Value Problems. Based on the regularised model, the formation and propagation of compaction bands due to grain crushing is analysed through a numerical experiment on a porous rock specimen under triaxial loading condition. Good agreement between numerical predictions and experimental observations demonstrates the capability of the new model.*

1 INTRODUCTION

The formation of localization bands in high porosity sandstones involves several micromechanical processes such as grain crushing, grain sliding, bond breaking and pore collapse [4,5]. Shearing at low confining pressures facilitates the fracture of grain bonding cement, allowing the grains to rotate and slip, which could be followed by the flow of granulated material. This bond breaking also reduces the mobilized shear strength, observed through the shear stress drop in experiments. In contrast, shearing at high confining pressures leads to grain crushing followed by pore collapse. During this process, the contacting grains tend to crush under the pressure, leading to the rearrangement of fragments, which further reduces the porosity and consequently hardens the material [4,6]. In this sense, pore collapse acts as a passive mechanism facilitated by a grain-crushing event. At a macroscopic level,

these failure mechanisms can be classified as brittle failure under low pressure and cataclastic flow with shear-enhanced compaction in high-pressure regimes [6]. Although these physical insights on the failure of porous sandstones are well understood, their theoretical modeling is still a challenging task.

Continuum approach based on plasticity theory has been widely used for the prediction of compaction localization in porous rocks [7-12]. In these continuum approaches a bifurcation condition [3], as a material instability condition, is usually employed for the detection of both the onset and orientation of localization bands. It is however unclear whether the parameters giving a good prediction of compaction localization in these models correspond to an experimentally observed response. In other words, the capability of the model to capture the observed material responses is usually left untouched in these studies, while much attention is paid to adjusting model parameters for the prediction of compaction localization. In addition, the underlying evolving microstructures (e.g. grain size distribution) are not fully reflected in those models. It has been showed that these plasticity-based models can lead to erroneous predictions of the permeability changes due to grain crushing [15]. Consequently, despite their good theoretical predictions, lack of a sound physical basis seems to impair the usefulness of these models.

A new continuum model based on the breakage mechanics theory [1,2] has shown its capability in capturing the compaction band formation in porous rocks [13]. The main feature of this theory is that it can take into account the grain crushing effects on the constitutive behavior through an internal variable (called Breakage, B) of the continuum model. This internal variable is explicitly linked with the evolving grain size distribution (*gsd*), helping to continuously track the *gsd* during the crushing induced deformation process. The effects of pore collapse on the macroscopic behavior of the material are also accounted in this models based on breakage mechanics theory. A recent study [13] showed that this breakage mechanics model predicts well both the formation and orientation of compaction bands, besides its capability to capture the behavior of porous rocks under high confining pressures [15].

In this paper, the formation and propagation of compaction bands in high porosity sandstones is studied using the above model. An enhancement employing rate dependent regularization is incorporated in this constitutive model to deal with instability issues due to softening and strain localization. Numerical analyses of a porous rock sample under drain triaxial condition are carried out to study the formation and propagation of compaction band. The obtained numerical results are validated against experimental observations.

2 A CONSTITUTIVE MODEL BASED ON BREAKAGE MECHANICS

A brief outline of a model based on breakage mechanics theory is presented in this section. The details of the theory and the development of several constitutive models based on this theory can be found in the papers by Einav [1,2,14] and Nguyen and Einav [15]. Due to grain crushing, the *gsd* evolves during the deformation of crushable granular materials. In breakage mechanics theory [1,2] this evolution of the current *gsd* $p(d)$ is directly tracked through an internal variable, called Breakage (B) by the following relationship:

$$p\left(B,d\right)=\left(1-B\right)p_0\left(d\right)+Bp_u\left(d\right) \tag{1}$$

where d is the grain diameter, $p_0(d)$ is the initial *gsd* and $p_u(d)$ is the ultimate *gsd*, which can be conveniently assumed to be of fractal type.

The stress-strain relationship is:

$$\boldsymbol{\sigma} = \left(1 - \vartheta B\right)\mathbf{D} : \left(\boldsymbol{\varepsilon} - \boldsymbol{\varepsilon}^{p}\right) \tag{2}$$

where $\boldsymbol{\sigma}$ is Cauchy stress tensor; $\boldsymbol{\varepsilon}$ and $\boldsymbol{\varepsilon}^{p}$ are the total and plastic strain tensors respectively; $\mathbf{D}$ is the linear (isotropic) elastic tangent stiffness tensor; the grading index ϑ which is a result of the statistical homogenization, can be obtained from the initial and ultimate *gsd*'s as

$$\vartheta = 1 - J_{2u}/J_{20} \tag{3}$$

where J_{20} and J_{2u} are second order moments of initial and final *gsd* [1]. Einav [14] derived the following elastic-plastic-breakage yield criterion in mixed stress-energy space considering the energy balance driving particle breakage.

$$y = \frac{(1-B)^2 E_B}{E_c} + \left(\frac{q}{Mp}\right)^2 - 1 \le 0 \tag{4}$$

where E_c is the critical breakage energy which can be determined directly from the isotropic crushing pressure through the relationship $E_C = P_{cr}^2 \vartheta / 2K$ [2]; $p = -\left(1/3\right)\boldsymbol{\sigma} : \boldsymbol{\delta}$ is the mean stress (positive in compression); $q = \sqrt{\left(3/2\right)\mathbf{s} : \mathbf{s}}$ is the distortional stress ($\mathbf{s} = \boldsymbol{\sigma} + p.\boldsymbol{\delta}$ is the deviatoric stress; $\boldsymbol{\delta}$ is Kronecker delta); M is the slope of the critical state line in $p - q$ space; and E_B is the energy thermodynamically conjugated to the breakage internal variable.

$$E_B = \frac{2}{\left(1 - \vartheta B\right)^2}\left(\frac{p^2}{K} + \frac{q^2}{3G}\right) \tag{5}$$

A typical evolving yield envelope in *p-q-B* space is plotted in Fig. 1.

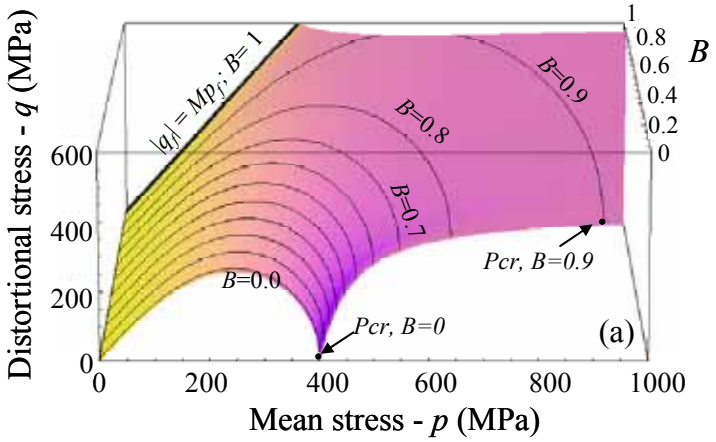

Figure 1: Typical yield surface in *q-p-B* space

The evolution rules for breakage and plastic strain are respectively,

$$\mathrm{d}B = 2\mathrm{d}\lambda\left(1-B\right)^2\cos^2\omega\big/E_c \text{ and} \tag{6}$$

$$\mathrm{d}\boldsymbol{\varepsilon}^p = \mathrm{d}\lambda\left(-2\frac{\left(1-B\right)^2 E_B\sin^2\omega}{pE_c}\frac{\boldsymbol{\delta}}{3}+\frac{3\mathbf{s}}{M^2p^2}\right). \tag{7}$$

In the above expression, ω is the parameter that couples the plastic volumetric deformation with grain crushing [2]. Physically, ω represents the pore collapse of the material, which is a consequence of grain crushing and grain/fragment reorganization. Further details on ω and pore collapse can be found in Einav [1, 2] and Das et al. [13].

3 ANALYSIS OF COMPACTION LOCALIZATION

3.1 Model behavior

The model behavior is presented in this section. The model parameters for a typical high porosity (23%) sandstone, the *Bentheim* sandstone are determined from experimental data. In particular, the stiffness (G, K), critical state parameter (M) and critical breakage energy (E_c) are obtained from published experimental stress-strain responses [16,17]. The grading index ϑ is determined from basic *gsd* [18] information and the assumption of power law distribution for both initial and final *gsd*. The coupling angle (ω) is chosen by matching the inelastic stress-strain response with experimental results. Details on the model calibration can be found in Das et al. [13] and corresponding model parameters are listed in table 1.

Table 1: Model parameters

Parameters	Value
G	7588 MPa
K	13833 MPa
M	1.7
E_c	4.67 MPa
ϑ	0.85
ω	70°

Fig. 2 presents the model behavior based on the model parameters in Table 1. The predicted stress-strain responses are found to be in good agreement with experimental observations.

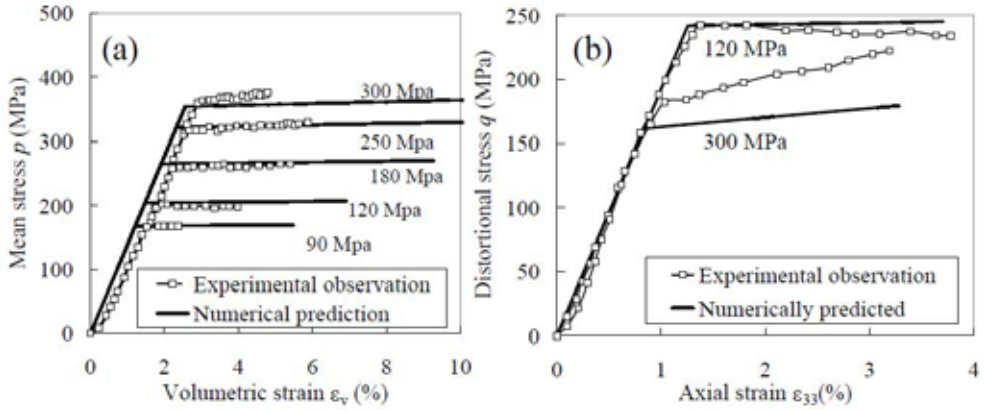

Figure 2: Numerical and experimental [19] comparisons of stress-strain responses of Bentheim sandstone under drained triaxial loading at different confining pressures; (a) mean stress vs. volumetric strain; (b) differential stress vs. axial strain.

3.2 Numerical prediction of compaction localization

We use the discontinuous bifurcation condition described in Rudnicki and Rice [3] to detect the formation of compaction band. Eq. 8 represents the simplified form of discontinuous bifurcation condition, considering the fact that the tangent stiffnesses of the material inside and outside the band are different in the case of breakage model [3,20].

$$\left|\mathbf{n}\cdot\mathbf{L}^{\mathrm{i}}\cdot\mathbf{n}\right| = \left|\mathbf{A}\right| \le 0\,. \tag{8}$$

In the above equation $\mathbf{n}$ is the band orientation vector; $\mathbf{L}^{\mathbf{i}}$ is the tangent stiffness tensor inside the localization zone (eq. 9); $\mathbf{A}$ is the strain localization tensor, also termed the acoustic tensor. The following tangent stiffness tensor is obtained using the model described in section 2. The details on the formulation of this forth order stiffness tensor were already given in Das et al. [13].

$$\mathbf{L}^{\mathrm{i}} = \left(1-\vartheta B\right)\mathbf{D} - \frac{\left(1-\vartheta B\right)\left[\left(1-\vartheta B\right)\mathbf{D}:\dfrac{\mathrm{d}\boldsymbol{\varepsilon}^{p}}{\mathrm{d}B}+\dfrac{\vartheta\boldsymbol{\sigma}}{\left(1-\vartheta B\right)}\right]\otimes\left[\mathbf{D}:\left(\dfrac{\partial y}{\partial p}\dfrac{\partial p}{\partial\boldsymbol{\sigma}}+\dfrac{\partial y}{\partial q}\dfrac{\partial q}{\partial\boldsymbol{\sigma}}\right)\right]}{\left(\dfrac{\partial y}{\partial p}\dfrac{\partial p}{\partial\boldsymbol{\sigma}}+\dfrac{\partial y}{\partial q}\dfrac{\partial q}{\partial\boldsymbol{\sigma}}\right):\left[\left(1-\vartheta B\right)\mathbf{D}:\dfrac{\mathrm{d}\boldsymbol{\varepsilon}^{p}}{\mathrm{d}B}+\dfrac{\vartheta\boldsymbol{\sigma}}{\left(1-\vartheta B\right)}\right]-\dfrac{\partial y}{\partial B}} \tag{9}$$

We show that the model described in the previous sections is capable of capturing the experimentally observed localization features of porous rocks, besides its capability in describing the material behavior (section 3.1). Fig. 3a highlights (the thick black line) the set of favorable stress states for the formation of localization band at the onset of yielding. The results are compared with their experimental counterpart [19]. At much higher-pressure regime, no localization failure is observed at the onset of inelastic deformation. As also numerically experienced, the closer to the isotropic compression line the stress path is, the easier the deformation would evolve into cataclastic flow without any compaction localization. However, shearing beyond elastic limit also eventually induces compaction

localization.

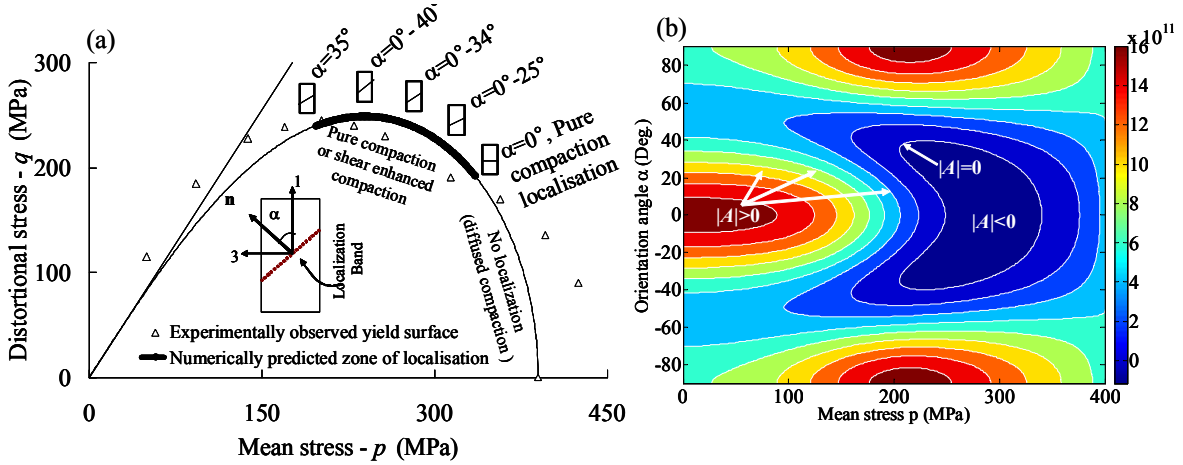

Figure 3: (a) Initial yield envelope and predicted stress states at the formation of compaction localization for Bentheim sandstone. (b) Corresponding contour of determinant of the acoustic tensor.

Fig. 3b shows the contours of the determinants of the acoustic tensor against the band orientation angle (α) and the mean stress (p). In this figure the inner most zone, where the determinant of the acoustic tensor is negative ($|\mathbf{A}| < 0$), indicates localization failure. It can be seen from Eq. 8 and Fig. 3b that for a given confining pressure p, there is a set of possible orientation angles for the localization band. From the experimental point of view, localization bands having orientation angle $0°\leq\alpha\leq10°$ can be classified as pure compaction band whereas those with $10°\leq\alpha\leq45°$ are treated as shear enhanced compaction bands [19]. Our analysis predicts that the band orientation for a wide range of confining pressure falls within the range of 0° to 40° that is close to the experimental observations in [19].

4 RATE DEPENDENT REGULARIZATION

4.1 Perzyna type rate dependent regularization

Due to the localization characteristics of the model, the boundary value problems (BVP) become ill-posed and hence treatment for this instability is needed. Introduction of material rate dependency, which implicitly introduces a length scale in to the governing constitutive equation [21], is one of the ways to make the BVPs well-posed. Here we incorporate rate effect in the breakage constitutive model presented in the preceding section using Perzyna type overstressed function. The model enhancement is carried out by modifying the evolution laws of breakage and plastic strain in the following manner.

$$\mathrm{d}B = \frac{\left\langle y^N \right\rangle}{\eta} \frac{2\left(1-B\right)^2 \cos^2\omega}{E_c} \mathrm{d}t \text{ , and} \tag{10}$$

$$\mathrm{d}\boldsymbol{\varepsilon}^{vp} = \frac{\left\langle y^N \right\rangle}{\eta}\left(-2\frac{(1-B)^2 E_B \sin^2\omega}{pE_c}\frac{\boldsymbol{\delta}}{3} + \frac{3\mathbf{s}}{M^2 p^2} \right)\mathrm{d}t\,. \tag{11}$$

It is noted that the viscosity parameter η is a dimensional quantity ($M^{-1}LT^3$) when used with this breakage model. Comparing the rate dependent flow condition with conventional rate independent evolution law, we can express the non-negative multiplier or consistency parameter as,

$$\mathrm{d}\lambda = \frac{\left\langle y^N \right\rangle}{\eta}\mathrm{d}t\,. \tag{12}$$

As can be seen, the Perzyna-type rate dependent breakage model provides an explicit form for the non-negative multiplier.

4.2 Rate effect on constitutive response

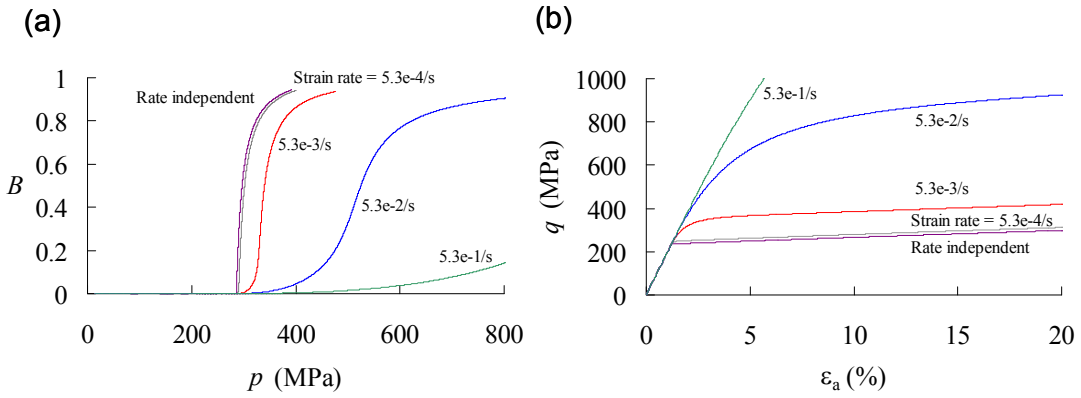

Figure 4: Effect of strain rate on the model response in drained triaxial loading - (a) breakage against mean stress; (b) distortional stress against axial strain.

Numerical drained triaxial tests are carried out to observe the effect of increasing strain rate on the material behavior. The same model parameters listed in Table 1 are used. Other parameters related to the rate dependency are, N = 1.0; and viscosity parameter η = 1.0 sec/kPa. In the numerical tests, the strain rate is increased via controlling the time increment (e.g. dt = 1s, 0.1s, 0.001s, and 0.0001s, corresponding to the strain rates indicated in Fig. 4). Fig. 4b indicates that with increasing strain rates the ultimate stress is also increasing. The transition from elastic to inelastic zone is smoother with increasing strain rate. On the other hand, at slow strain rates the model response approaches rate independent behavior. Besides the stress-strain response, the rate of breakage growth reduces with the increase in strain (Fig. 4a). From the microscopic point of view, high strain rate does not allow sufficient time to break or rearrange the grains [22]. Thus, the material becomes stronger and this feature is also reflected in the macroscopic stress-strain response of the proposed model.

4.3 Mesh independency of finite element solutions

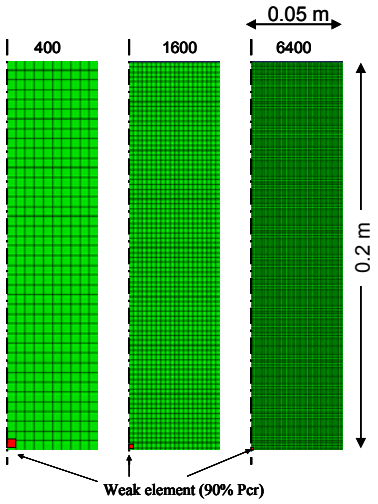

Figure 5: FE meshing for triaxial drained test

The stability of the above rate dependent breakage constitutive model is illustrated through the numerical analysis of a rock specimen under drained triaxial loading condition. The commercial package Abaqus (version - 6.8) is used for the entire finite element analysis. We construct the model (0.1 x 0.2 m) using linear quadrilateral finite elements (Fig. 4). Due to symmetry in geometry and loading, only half of specimen is modelled. The analysis is performed considering axisymmetric 2D plane strain condition with strain controlled loading. The entire loading arrangement is a two stage process where initially we apply a confining pressure and allow the material to deform isotropically. Thereafter axial load, through prescribed vertical displacement producing a constant axial strain rate of $5.3*10^{-4}$/s, is applied to the specimen, while the confining stress is kept constant. The boundary conditions are: restricted vertical movement of the bottom boundary; and (fixed) incremental vertical displacement at the top boundary. To trigger off the localization we introduce local anisotropy via a weak element having lower crushing pressure (90% of P_{cr}) (Fig. 5).

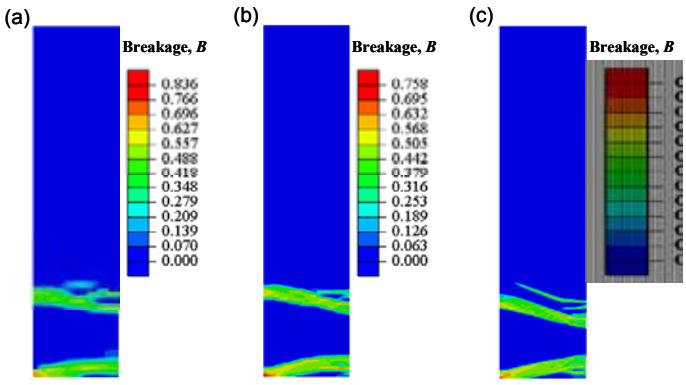

Figure 6: Breakage contours showing the formation of shear enhanced compaction band under drained triaxial test at 3% axial strain (a) 400 elements; (b) 1600 elements; (c) 6400 elements.

The effect of the spatial discretization on the numerical solutions is presented in Fig. 5. We use three different finite element meshes employing 400 elements, 1600 elements and 6400 elements, respectively. The contours in Fig. 5 indicate the growth of breakage during the deformation of the specimen. As can be seen, the localization zones and their widths are almost identical for all three cases of discretization The regularization effect of the rate dependent enhancement is clearly visible from the global load-deflection curves (Fig. 7), in which the trends of the curves and their periods of oscillation are almost identical.

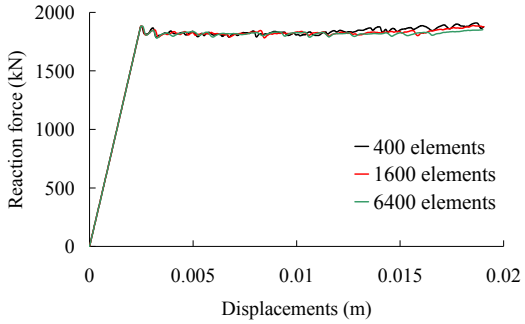

Figure 7: Reaction force against displacement plot for drained triaxial test

5 COMPACTION BAND PROPAGATION IN POROUS ROCKS

It is clear from the previous analysis that the use of rate effect eliminates the pathological mesh sensitivity of the numerical solutions. The propagation of compaction bands is studied in this section using the FE mesh consists of 1600 elements. We start the numerical drained shear test with an initial isotropic pressure of 300 MPa. The same axial strain rate of $5.3*10^{-4}$ /s, as used in section 4.3, is applied to the top of the specimen in the second stage of loading.

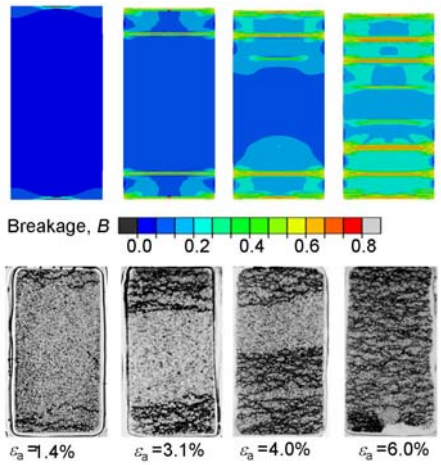

Figure 8: Breakage contours showing pure compaction band formation in drained triaxial test at different axial strains, (a) Numerical simulation; (b) Experimental observation [19].

From laboratory experiments it has been observed and reported [23,24] that compaction band initiates from the two ends of the sample due to the stiffness mismatch between the material

and the cap of testing device. To simulate similar band initiation we introduce two weaker finite elements at both ends of the numerical sample.

The breakage contours in Fig. 8 show the propagation of compaction bands during the shearing process. The colour code indicates intense grain crushing via breakage growth that takes place inside the compaction bands. As expected, compaction localization occurs at the two ends of the specimen and propagates towards its centre (Fig. 8). Baud et al. [19] also reported similar band propagation in their experimental results. This is manifested because of simultanous loading and unloading process during shearing at high confining pressure.

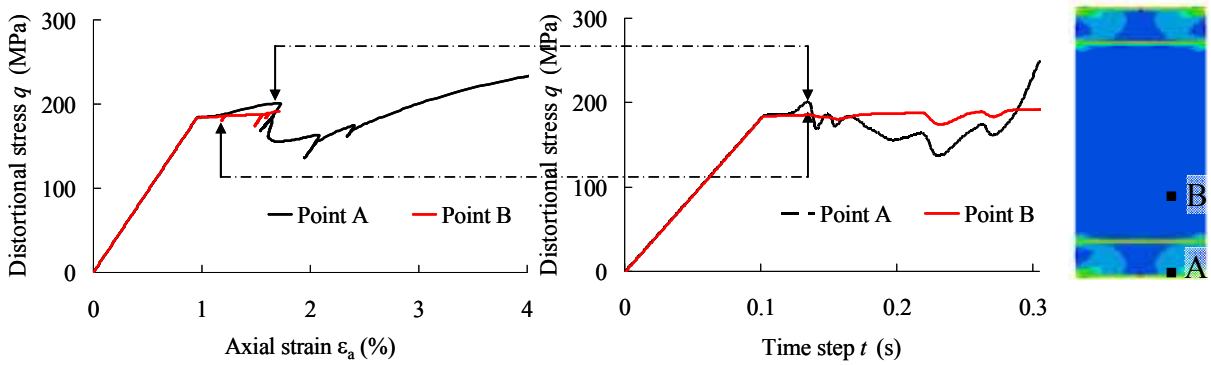

Figure 9: Stress responses at integration points (A and B) of numerical sample, (a) against axial strain; (b) against time, for a fixed time span.

The variation of distortional stress against time and axial strain is plotted in Fig. 9a,b for two integration points *A* and *B*. Due to the confinement and the varying inhomogeneous state (of stress, strains and breakage), the behavior of material points along the specimen height switches among hardening, softening, and elastic unloading. These material points take turn in the crushing process. Due to this process of simultaneous loading and unloading, compaction bands propagate from the two ends of the sample towards its centre, at discrete locations along the specimen height. This effect is also visible through the oscillating nature of the global stress strain response during shearing (Fig. 10).

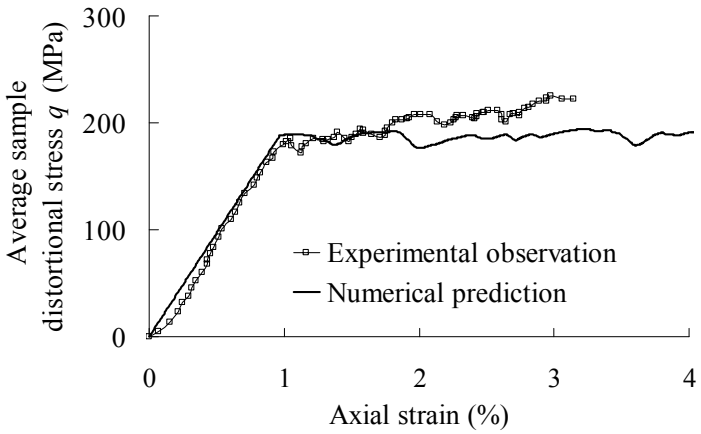

Figure 10 Global stress-strain response from numerical prediction and experimental observation [19]

The predicted average distortional stress-strain response and experimental observations [19] are plotted in Fig.10. These macroscopic model responses can be seen to be in good agreement with its experimental counterpart.

6 CONCLUSIONS

We show in this study a micromechanics-based constitutive model capable of capturing both the material behavior and the formation of compaction bands. The enhancement of this model to deal with material instability issues, using rate dependent regularization, allows us to to numerically explore the propagation of compaction bands in a porous rock specimen. The obtained numerical results are in good agreement with experimental observations, thus demonstrating the capability of the proposed model. This is an important starting point for a deeper study on the initiation and propagation of compaction bands in porous rocks.

REFERENCES

[1] Einav, I., Breakage mechanics—Part I: theory. *Journal of the Mechanics and Physics of Solids* (2007) **55**:1274-1297.
[2] Einav, I., Breakage mechanics—Part II: modelling granular materials. *Journal of the Mechanics and Physics of Solids* (2007) **55**:1298-1320.
[3] Rudnicki, J.W. and Rice, J.R., Conditions for the localization of deformation in pressure-sensitive dilatant materials. *Journal of the Mechanics and Physics of Solids* (1975) **23**:371-394.
[4] Menéndez, B., Zhu, W., and Wong, T.-f, Micromechanics of brittle faulting and cataclastic flow in berea sandstone. *Journal of Structural Geology* (1996) **18**:1-16.
[5] Wu, X.Y., Baud, P., and Wong, T.-f, Micromechanics of compressive failure and spatial evolution of anisotropic damage in darley dale sandstone. *International Journal of Rock Mechanics and Mining Sciences* (2000) **37**:143-160.
[6] Wong, T.-f, David, C., and Zhu, W., The transition from brittle faulting to cataclasic flow in porous sandstones:mechanical deformation. *Journal of Geophysical Research* (1997) **102**:3009-3025.
[7] Olsson, W.A., Theoretical and experimental investigation of compaction bands in porous rock. *Journal of Geophysical Research* (1999) **104**:7219-7228.
[8] Issen, K.A. and Rudnicki, J.W., Conditions for compaction bands in porous rock. *Journal of Geophysical Research* (2000) **105**:21529-21536.
[9] Rudnicki, J.W., Shear and compaction band formation on an elliptic yield cap. *Journal of Geophysical Research* (2004) **109**:1-10.
[10] Challa, V. and Issen, K.A., Conditions for compaction band formation in porous rock using a two-yield surface model. *Journal of Engineering Mechanics* (2004) **130**:1089-1097.
[11] Chemenda, A.I., The formation of tabular compaction-band arrays: theoretical and numerical analysis. *Journal of the Mechanics and Physics of Solids* (2009) **57**:851–868.
[12] Sternlof, K.R., Rudnicki, J.W., and Pollard, D.D., Anticrack inclusion model for compaction bands in sandstone. *Journal of Geophysical Research* (2005) **110**:1-16.

[13] Das, A., Nguyen, G.D., and Einav, I., Compaction bands due to grain crushing in porous rocks : a theoretical approach based on breakage mechanics. *Journal of Geophysical Research* (2011):(accepted in press).
[14] Einav, I., Soil mechanics: breaking ground. *Philosophical transactions. Series A, Mathematical, physical, and engineering sciences* (2007) **365**:2985-3002.
[15] Nguyen, G.D. and Einav, I., The energetics of cataclasis based on breakage mechanics. *Pure and Applied Geophysics* (2009) **166**:1693–1724.
[16] Wong, T.-f, Baud, P., and Klein, E., Localized failure modes in a compactant porous rock. *Geophysical Research Letters* (2001) **28**:2521-2524.
[17] Baud, P., Vajdova, V., and Wong, T.-f, Shear-enhanced compaction and strain localization: inelastic deformation and constitutive modeling of four porous sandstones. *Journal of Geophysical Research* (2006) **111**:1-17.
[18] Schutjens, P.M.T.M., Hausenblas, M., Dijkshoorn, M., and Munster, J.G.V., The influenec of intergranular microcracks on the petrophysical properties of sandstone - experiments to quantify effects of core damage. , *International Society of the Society of Core Analysts*, 1995, :1-12.
[19] Baud, P., Klein, E., and Wong, T.-f, Compaction localization in porous sandstones: spatial evolution of damage and acoustic emission activity. *Journal of Structural Geology* (2004) **26**:603-624.
[20] Chambon, R., Crochepeyre, S., and Desrues, J., Localization criteria for non-linear constitutive equations of geomaterials. *Mechanics of Cohesive-frictional Materials* (2000) **5**:61-82.
[21] Needleman, A., Material rate dependence and mesh sensitivity in localization problems. *Computer Methods in Applied Mechanics and Engineering* (1988) **67**:69-85.
[22] Yamamuro, J.A. and Lade, P.V., Effects of strain rate on instability of granular soils. *Geotechnical Testing Journal* (1993) **16**:304.
[23] Olsson, W.A., Quasistatic propagation of compaction fronts in porous rock. *Mechanics of Materials* (2001) **33**:659-668.
[24] Katsman, R., Aharonov, E., and Scher, H., Numerical simulation of compaction bands in high-porosity sedimentary rock. *Mechanics of Materials* (2005) **37**:143-162.

XI International Conference on Computational Plasticity. Fundamentals and Applications
COMPLAS XI
E. Oñate, D.R.J. Owen, D. Peric and B. Suárez (Eds)

AN ELASTOPLASTIC-VISCOPLASTIC SOIL MODEL FOR CYCLIC LOADING

J. R. MARANHA*, ANA VIEIRA†

* Laboratório Nacional de Engenharia Civil (LNEC)
Av. do Brasil, 101, 1700 066, Lisbon, Portugal
e-mail: jmaranha@lnec.pt, www.lnec.pt

† Laboratório Nacional de Engenharia Civil (LNEC)
Av. do Brasil, 101, 1700 066, Lisbon, Portugal
e-mail: avieira@lnec.pt, www.lnec.pt

Key words: Computational Plasticity, Soil Mechanics, Cyclic Loading

Abstract. A mobile projection centre extension to an existing elastoplastic-viscoplastic soil model is presented in this work. In this formulation, the projection centre evolves according to the stress path experienced by the soil, approaching it during the loading process [1]. In this way, the elastic (within which the behaviour is elastic) and the viscous (within which the behaviour is non-viscous) nuclei, will move with the projection centre. These nuclei may have reduced dimensions and reproduce more realistically the inelastic and time dependent soil response under a larger set of stress paths. The proposed formulation is based on the continuous plasticity model with a viscous mechanism proposed by Kaliakin and Dafalias [2, 3]. The observed occurrence of creep deformation in stiff clays at small levels of deviatoric stress was one of the motivations for this work. It is important to note that the majority of numerical and laboratory studies of the effect of strain rate on the behaviour of soils usually refers to normally consolidated soils, and, as already reported by Hashiguchi and Okayasu [4], further theoretical and experimental studies on the time dependent behaviour of overconsolidated soils are needed.

In order to validate the proposed formulation a cyclic undrained triaxial test with unloading and reloading stages with creep was performed on a sample of a stiff Lisbon clay. The test was simulated using the described soil model and the results of both compared. This formulation significantly improves the reproduction of viscous strains associated with unloading stress paths such as those occurring, for example, in excavation works.

1 INTRODUCTION

Laboratory tests performed on a stiff clay from the Lisbon region (*Formação de Benfica* clays) showed the occurrence of creep strains at small deviatoric stress levels. These results were confirmed by local displacement transducers LVDTs [5], and motivated the study here presented. It is interesting to note that the vast majority of laboratory and numerical studies of

strain rate effects on soil behaviour refers to normally or lightly overconsolidated soils, with further studies of these effects on overconsolidated soils being necessary, as noted by Hashiguchi e Okayasu [4], both from the experimental and theoretical standpoints. The study presented below aims to contribute to overcome this shortcoming, highlighting some important aspects.

There are on the literature various types of models conceived to reproduce the time-dependent behaviour of soils. These models can be divided into two main groups, those that allow and those that do not allow the occurrence of viscous deformation inside the yield surface. Since, in the case of overconsolidated soils, stress paths can develop to a large extent within the yield surface, the later type of model is clearly limited in its applicability. Instead, continuous plasticity models, with an added viscous mechanism, such as the model proposed by Kaliakin and Dafalias [2,3], by enabling the occurrence of inelastic deformations inside the yield surface (called bounding surface), improve the reproduction of soil behaviour.

2 THE KALIAKIN AND DAFALIAS BOUNDING SURFACE ELASTOPLASTIC VISCOPLASTIC MODEL

2.1 Brief model description

The elastoplastic-viscoplastic soil model proposed by Kaliakin and Dafalias [2] is based on the existence of a bounding surface, with an elliptical shape in the space of the stress invariants *(p,q,θ)*, shown in Figure 1. The stress state $\boldsymbol{\sigma}$ is always inside or on the bounding surface, having an image on it, $\bar{\boldsymbol{\sigma}}$, defined by a radial projection from a centre **a**. In this particular model, the projection centre is fixed and located on the hydrostatic axis. The bounding surface only undergoes isotropic hardening. The position of the stress state on the line segment joining the projection centre to the image point on the bounding surface defines the variable $b = \|\bar{\boldsymbol{\sigma}} - \mathbf{a}\| / \|\boldsymbol{\sigma} - \mathbf{a}\|$. This varies between $b=\infty$, when the stress state matches the projection centre, and $b=1$, on the bounding surface.

A basic assumption of this model is the additive decomposition of the inelastic deformation rate into a plastic component and a viscoplastic component. The directions of the plastic and viscoplastic deformation rates are given by derivative of the yield function relatively to the stress state on the image point, $\bar{\boldsymbol{\sigma}}$. There are two surfaces implicitly defined associated to each of the inelastic mechanisms. The first one defines the boundary beyond which plastic deformations can occur (if the loading condition is also verified) represented by the constant s_p, such that $b \le s_p/(s_p - 1)$. The second surface defines the boundary outside which viscous deformation occur and is defined by the constant s_v. That means that viscoplastic deformations occur only if $b \le s_v/(s_v - 1)$. Both surfaces are homothetic relatively to the bounding surface. The overstress defined as $\hat{\delta} = \|\boldsymbol{\sigma} - \hat{\boldsymbol{\sigma}}\|$ controls the magnitude of viscoplastic strain rate. $\hat{\boldsymbol{\sigma}}$ is the in intersection point between the line joining the projection centre and the stress point, and the viscous nucleus.

The plastic modulus, that determines incremental elastoplastic stifness is interpolated from its value on the image point, by means of variable *b*, so that a continuous monotonic transition

from an infinite value (elastic incremental stiffness) on the surface $b = s_p/(s_p - 1)$ to a corresponding value on the bounding surface (conventional elastoplastic stiffness).

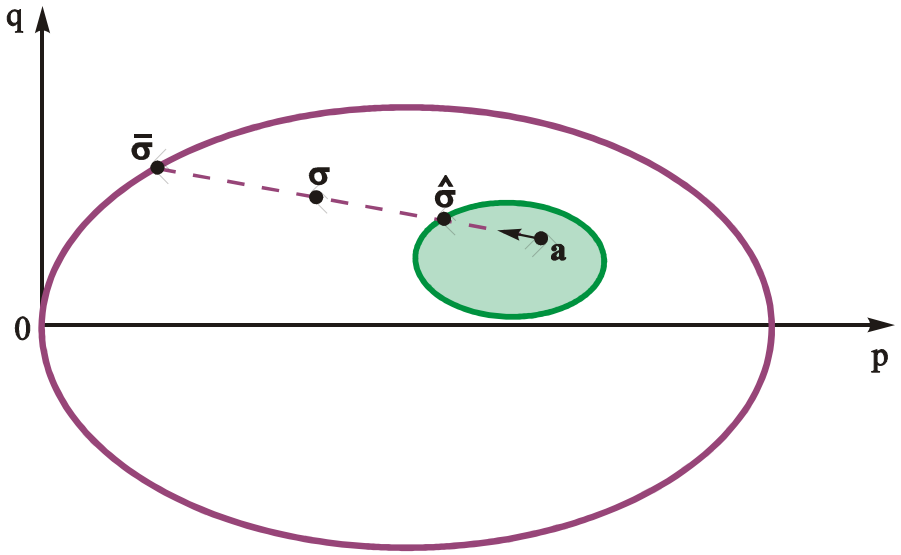

Figura 1: Bounding surface model.

The model was implemented in the explicit finite difference software FLAC. Details of this implementation can be found in [5,6].

2.2 Laboratory tests numerical modelling

The described model has enabled the reproduction of a set of three creep tests performed on *Formação de Benfica* stiff clays. The tests were triaxial undrained under constant mean stress after being isotropically consolidated to different effective mean stresses. The imposed loading sequence alternated steps of relatively high strain rate with 24 hours creep stages. This adjustment was initially achieved with a different set of model constants for each test, and, after a modification of the overstress function, by introducing a new parameter related with the viscous behaviour, the whole set of tests were adjusted using a single set of parameters [7]. The modified overstress function defining the magnitude of the viscous strain rates is given by

$$\phi = \frac{1}{V}\exp\left(\alpha\frac{J}{IN}\right)\left(\frac{\hat{\delta}}{r\left(\frac{s_v - 1}{s_v}\right)}\right)^n . \tag{1}$$

2.3 Limitations of the model

Although this model has been able to reproduce many of the relevant aspects of the viscous behaviour of soils, it still has some shortcomings. Figures 2 and 3 illustrate some of these

shortcomings. In the case of an overconsolidated clay, after the sedimentation process and associated creep, the stress state is at point A (apparent overconsolidation), soil undergoes unloading due to the erosion of the superficial layers (process which corresponds to a genuine overconsolidation process), and the final stress state point is B. Stress states A and B correspond to equilibrium situations, on which the creep strains have already occurred, and as such, are on the boundary of the viscous nucleus represented in Figures 2 and 3 as green shaded ellipses. The unloading stage from A to B, in the original model with the fixed projection centre over the hydrostatic axis, does not produce any creep (viscous) strains, because the corresponding stress path is now entirely included in the viscous nucleus (Figure 2). On the other hand, in the formulation now proposed, which admits the existence of a mobile projection centre (which implies a mobile viscous nucleus), creep strains will take place as long as the stress path AB is sufficiently long to cross the viscous nucleus.

Assuming the sample is sheared undrained from a state of isotropic consolidation, as was shown above, no creep deformations would occur within the surface s_v, according to the original model. However, it was observed that creep strains occurred from the earliest stress stages (low deviatoric stress), which is inconsistent with this model. This inconsistency can be eliminated by assuming that the projection centre (and the corresponding viscous nucleus) can move, as illustrated in Figure 3. The concept is equivalent to that proposed in two surface elastoplastic models. These, however, do not take into account the viscous behaviour. As long as the size of the viscous nucleus is sufficiently small, creep strains may occur at any point, inside the bounding surface.

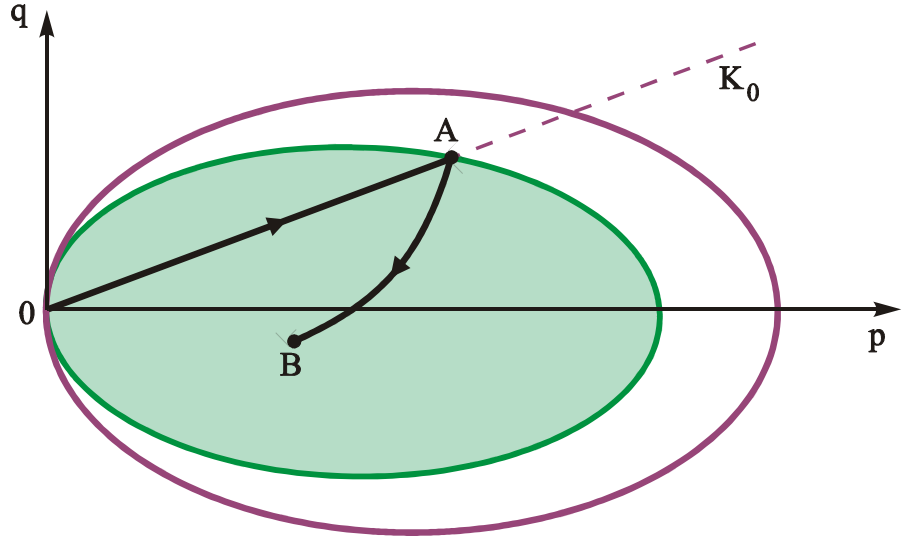

Figure 2 : Overconsolidation process in the original model (fixed projection centre).

In overconsolidated soils which have been stabilized in terms of creep, it would be necessary, according to the original model, to use a viscous nucleus large enough to accommodate the *in situ* stress states. Because, inside this nucleus no viscous strains may occur, this contradicts the results of the described tests. This contradiction may be eliminated by adopting a mobile projection centre defining a viscous nucleus of reduced dimension.

In the same way that the two surface models incorporate a mobile elastic domain in order to better represent the variation of the elastoplastic stiffness with the loading direction, it may

be assumed that the same principle applies to the viscous behaviour. The use of mobile viscoplastic potentials in metal models is well known [8].

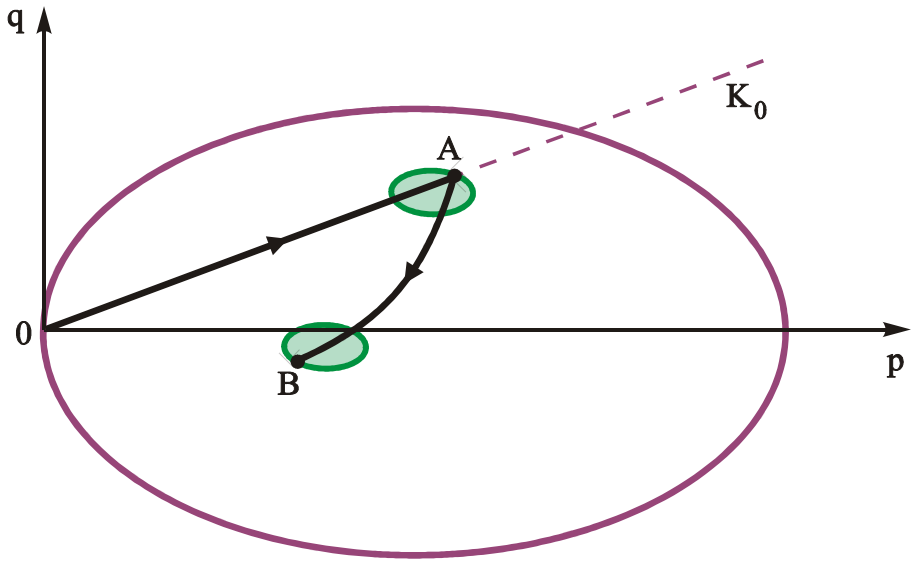

Figura 3: Overconsolidation process in the modified model (mobile projection centre).

3 MODEL WITH MOBILE PROJECTION CENTER

Although the initial general formulation of the bounding surface model was based on the assumption the existence of a mobile projection centre [9], the various specific formulations presented use a fixed projection centre located on the isotropic axis [10]. Here, it is proposed that the projection centre is able to move, pursuing the stress state, according to:

$$\dot{\mathbf{a}} = c_a \left\| \dot{\boldsymbol{\varepsilon}}^i \right\| (\boldsymbol{\sigma} - \mathbf{a}) \tag{2}$$

where $\dot{\boldsymbol{\varepsilon}}^i$ is the inelastic strain rate (plastic plus viscoplastic) and c_a is a model constant that controls the velocity of translation. This change implies several modifications in the model's formulation. Namely, the expressions for the plastic multiplier, the hardening function, the projection of the stress state into the bounding surface and the plastic modulus. The proposed changes have been implemented and confronted with experimental results, as will be shown in the next section.

Some numerical experiments simulating a conventional drained triaxial test on virtual soil with an unloading/reloading cycle were carried out in [1] and are shown in Figures 4 and 5. Figure 4 shows the stress-strain curves for different strain rates. In Figure 5, the first loading phase takes place at a strain rate equal in all tests (2×10^{-6} s^{-1}), with the unloading and reloading stages taking place at different strain rates. In both cases, the loading and reloading stages exhibit an expected increase in stress with the strain rate, with the upper limit being the elastoplastic behaviour. During unloading the stress decreases with increasing strain rate. Theses examples illustrate that, unlike the formulation with a fixed projection centre, this model can reproduce closed loops for relatively small variations of deviatoric stress, which

remains positive, as observed experimentally.

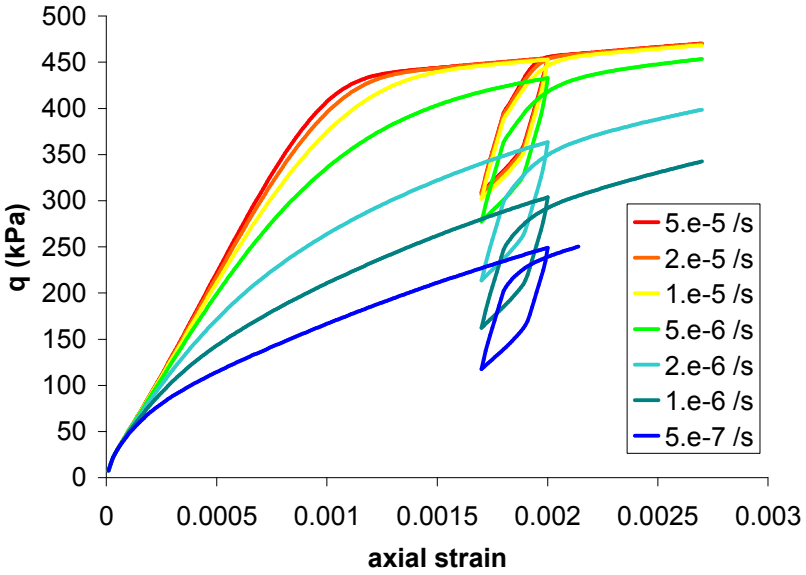

Figure 4: Drained triaxial tests for different strain rates (models with mobile projection centre).

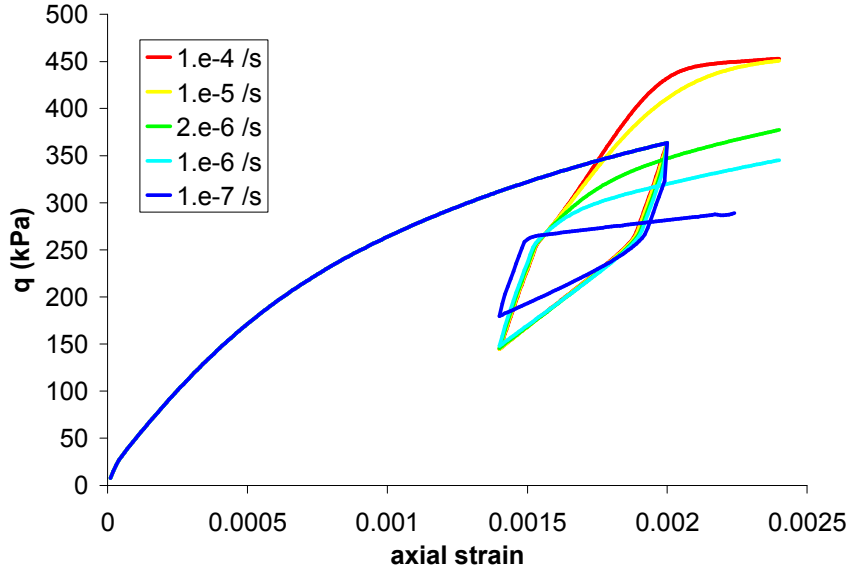

Figure 5: Drained triaxial tests with different strain rates in the unloading-reloading stages (model with mobile projection centre).

4 CYCLIC CREEP TEST. RESULTS AND NUMERICAL SIMULATION

4.1 Main characteristics of *Formação de Benfica* clay

The test carried out to study the model proposed in this work was carried out in the *Formação de Benfica* overconsolidated stiff clays, a significant geological formation within

the Lisbon region. This tested sample is a structured soil with an ASTM classification of SC with an IP of 35.4% and LL of 61.4% and low permeability (2×10^{-10} m/s).

4.2 Loading sequence

The imposed loading sequence involved a series of unloading steps followed by a series of reloading steps, with each step consisting first in a relatively fast change in deviatoric stress (aprox. 6×10^{-6} s^{-1} strain rate) followed by 24h creep at constant deviatoric stress and constant total mean stress. The loading sequence was carried out in undrained conditions.

After the monotonic deviatoric loading up to q=250kPa, during the unloading sequence, the creep strains increased in the reverse direction (Figure 6), *i.e.*, for the highest q values, the creep strains are lower and progressively increase with decreasing q. When the deviatoric stress attains zero, significant creep strains are observed. Conversely, during the reloading sequence, with q increasing from 0 to 250kPa, the creep strains increase with increasing q values with significant large creep strains for q=250kPa. It is however important to note that during initial loading sequence a situation corresponding to tertiary creep (failure) was not achieved.

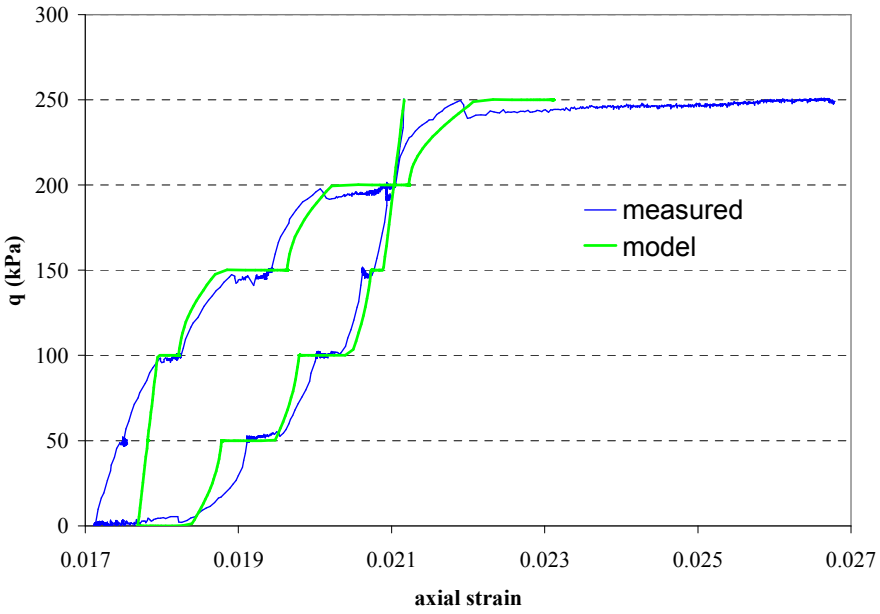

Figure 6: Unloading-reloading steps with creep stages in undrained triaxial test with constant p (measured – blue line, model with mobile projection centre – green line).

4.3 Numerical simulation

Some elements already available from previous studies on samples of this formation were used in the calibration of the model. This calibration was performed for a single unloading-reloading cycle and its aim was to reproduce qualitatively the most significant aspects observed in the experiment. A set of material constants was chosen from a large series of analyses made by randomly varying a set of five parameters affecting viscous behaviour that

produced a best fit to the measured stress-strain curve. The adjustment shown in Figure 6 has been achieved for the following material constant values: V=5×10^9 , s_v=1.12 , c_a=652 , n=2.1 and α=0.

It is important to note that a constitutive model with a fixed projection centre cannot even qualitatively reproduce the type of behaviour exhibited in this test.

The effective stress path and snapshots of the projection centre (whose speed can be controlled by the constant c_a) with the corresponding viscous nucleus at different instants are shown in Figure 7. The instants represented are the end of the isotropic consolidation stage, the end of the first unloading step and after the following creep stage, the end of the last unloading step and after the following creep stage, and the end of the last reloading step as well as the end of the next creep stage. The projection centre (and the viscous nucleus) follows the stress state. During the loading steps, due to the high rate of loading, the projection centre lags behind the stress state and consequently the stress moves outward from the viscous nucleus boundary. During the creep stages the projection centre approaches the stress state until the viscous nucleus's boundary catches the latter at which point the creep strains cease. In the case of the first unloading step, the stress moves to the inside of the viscous nucleus, the response is entirely elastic and the projection centre doesn't move. It should be mentioned that some viscous strains may also occur during the loading stages.

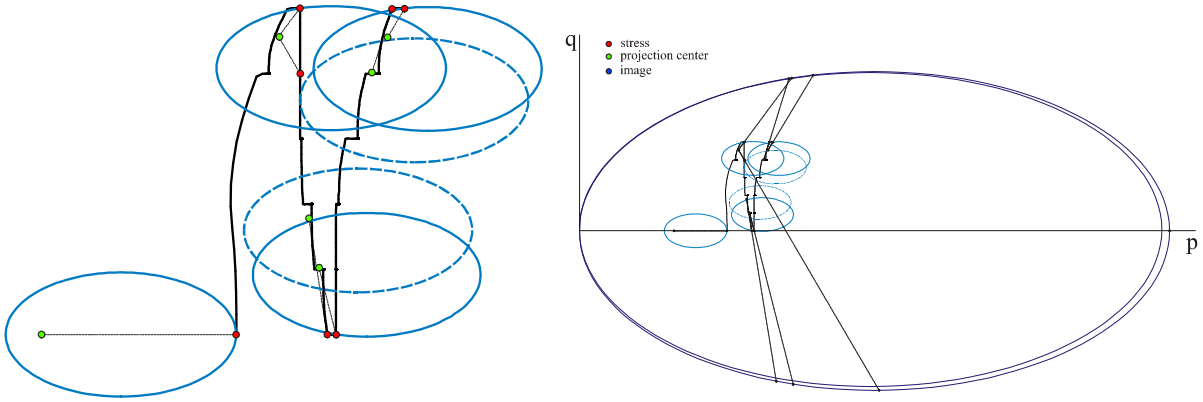

Figure 7: Computed effective stress path. Viscous nuclei at the end of isotropic consolidation, first unloading step, last unloading step and last reloading step. At the beginning (broken line) and the end of the creep stage (full line). Stress points (red). Projection centres (green). The global view on the right side includes image points (blue) on the bounding surface.

Results of the measured and computed pore pressures histories are shown in Figure 8. The model, as it stands, is not able to reproduce, even qualitatively, the observed pore pressure response. The model predicts pore pressure decreases during unloading, in contradiction with the measurements that show a pore pressure increase. This is one aspect of the model that needs to be improved. During reloading the model predicts decreasing pore pressures whose magnitude increases with the deviatoric stress level. This is in qualitative agreement with the measurements.

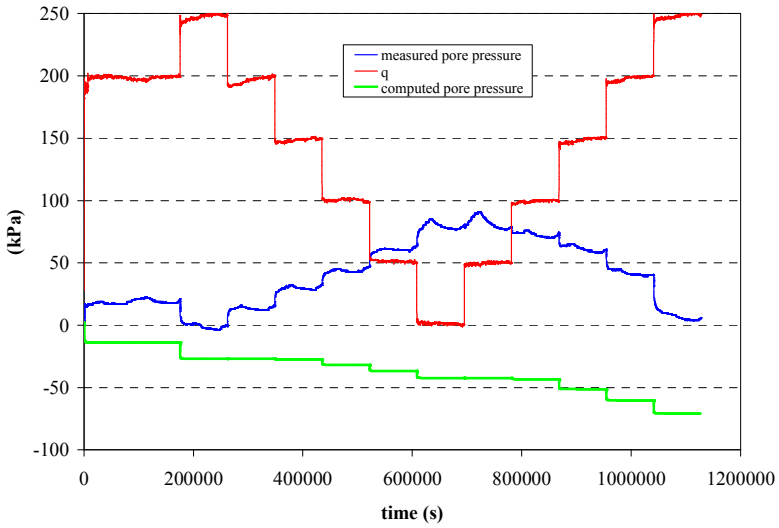

Figure 8: History of measured (blue line) and computed (green line) pore pressures. Applied deviatoric stress history (red line).

As the pore pressure variations reflect the inelastic volumetric strains, and assuming an associated flow rule, the inability of the model to reproduce the pore pressure changes with loading might be an indication that the shape of the bounding surface is not suitable. A sheared elliptical shape such as used to model anisotropic plastic response in soils [11] would produce, at least qualitatively, correct pore pressure variations as illustrated in Figure 9.

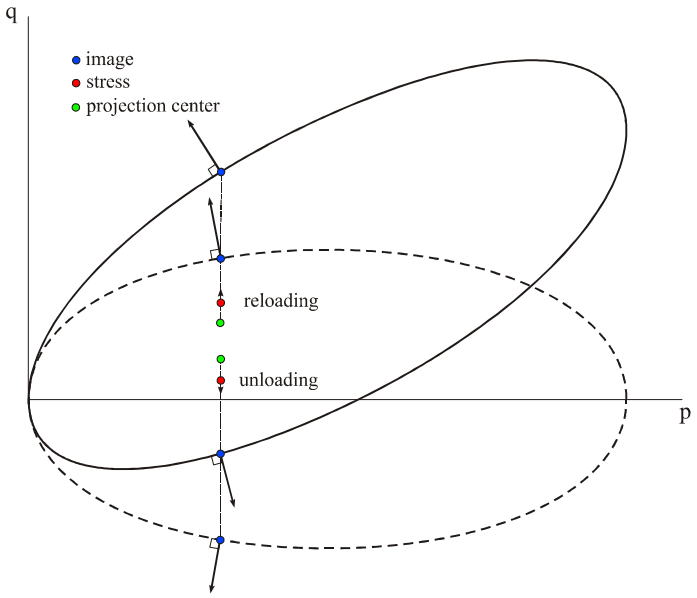

Figure 9: Isotropic (broken line) and anisotropic (full line) bounding surfaces with associated flow rule during unloading and reloading.

In the case of the sheared ellipse there is a region, from slightly to medium

overconsolidated states, inside which the sign of the pore pressure change response agrees with the measured. As can be seen in Figure 9 for the unloading situation, the projection of the normal to the anisotropic bounding surface on the isotropic axis has opposite direction to the one given by the isotropic bounding surface. This suggests that the anisotropic nature of the soil cannot be ignored if the correct volumetric response is to be achieved by the model.

5 CONCLUSIONS

In this work, a new model that takes into account the cyclic time behaviour of soils has been proposed. Some inconsistencies between observed soil behaviour and the response given by models for rate dependent soils have been described. These inconsistencies have been solved with a mobile projection centre that approaches the stress state with some delay and as such is able to develop viscous (including creep) strains.

The response of the improved model has been compared with that of a triaxial undrained test during an unloading/reloading deviatoric stress cycle at constant total mean stress that incorporated a series of staggered fast loading steps and creep stages. A reasonable agreement with the measured response has been obtained. The model has clearly been able to qualitatively reproduce the main observed aspects of the stress-strain response of a stiff overconsolidated clay under a stress loading cycle with creep stages.

One aspect that the model has not been able to reproduce is the observed pore pressure evolution. It has been suggested that the adoption of an anisotropic bounding surface with an associated flow can improve the model in this respect.

Another aspect that might improve the model concerning this type of soils is the incorporation of destructuring.

REFERENCES

[1] Maranha, J. R. and Vieira, A. (2010). Formulação de um centro de projecção móvel num modelo elastoplástico-viscoplástico para solos. *12º Congresso Nacional de Geotecnia*, Guimarães, Portugal.

[2] Kaliakin, V. N. and Dafalias, Y. F. (1990). Theoretical Aspects of the Elastoplastic-Viscoplastic Bounding Surface Model for Cohesive Soils. *Soils and Foundations*, Vol. 30, No. 3, 11-24

[3] Kaliakin, V. N. and Dafalias, Y. F. (1990a). Verification of the Elastoplastic-Viscoplastic Bounding Surface Model for Cohesive Soils. *Soils and Foundations*, Vol. 30, No. 3, 25-36.

[4] Hashiguchi, K. and Okayasu, T. (2000). Time-Dependent Elastoplastic Constitutive Equation Based on the Subloading Surface Model and Its Application to Soils. *Soils and Foundations*, Vol. 40, No. 4, 19-36.

[5] Vieira, A.M. (2006*). Estudo do Comportamento Diferido no Tempo de Túneis em Argilas Sobreconsolidadas.* Tese de Doutoramento, Faculdade de Ciências e Tecnologia da Universidade de Coimbra.

[6] Maranha, J. and Vieira, A. (2005). Modelling the time dependent behaviour of a tunnel using a elastoplastic-viscoplastic model. *Proceedings of the 8th International Conference on Computational Plasticity, COMPLAS VIII, Barcelona.*

[7] Vieira, A., Maranha, J., Bilé Serra, J. and Correia, R. (2007). Modelling the undrained creep behaviour of a hard clay in the super-critical region. (Eds. E. Oñate, D.R.J. Owen and B. Suárez), *Proceedings of the 9th International Conference on Computational Plasticity, COMPLAS IX, Barcelona*, pp. 836 – 839.
[8] Chaboche, J. L. (1977). Viscoplastic Constitutive Equations for the Description of Cyclic and Anisotropic Behaviour of Metals. *Bulletin de L'Academie Polonaise des Sciences*, Vol. 25-1, 33-39.
[9] Dafalias, Y. F. (1986). Bounding Surface Plasticity. I: Mathematical Foundation and Hypoplasticity. *Journal of Engineering Mechanics*, Vol. 112, No. 9, 966-987.
[10] Dafalias, Y. F. and Herrmann, L. R. (1986). Bounding Surface Plasticity. II: Application to Isotropic Cohesive Soils. *Journal of Engineering Mechanics*, Vol. 112, No. 12, 1263-1261.
[11] Whittle A. J. and Kavvadas M. J. (1994). Formulation of MIT-E3 constitutive model for overconsolidated clays. *Journal of Geotechnical Engineering*, ASCE, 120:173-198.

XI International Conference on Computational Plasticity. Fundamentals and Applications
COMPLAS XI
E. Oñate, D.R.J. Owen, D. Peric and B. Suárez (Eds)

EFFECT OF LARGE DISPLACEMENTS ON THE NUMERICAL ANALYSIS OF AN EMBANKMENT ON SOFT SOILS

PAULO J. VENDA OLIVEIRA[*] AND LUÍS J. L. LEMOS[†]

[*] Department of Civil Engineering
University of Coimbra,
Rua Luís Reis Santos, 3030-788 Coimbra, Portugal
e-mail: pjvo@dec.uc.pt, www.dec.uc.pt

[†] Department of Civil Engineering
University of Coimbra,
Rua Luís Reis Santos, 3030-788 Coimbra, Portugal
email: llemos@dec.uc.pt, www.dec.uc.pt

Key words: Large Displacements, Geometric Non-linearity, Consolidation, Embankments, Soft Soils.

Abstract. This paper intends to clarify the influence of geometric nonlinearity on the behaviour of an embankment built on soft soils, considering the material non-linearity associated with a coupled soil-water formulation. The numerical predictions are compared with the field data in terms of settlements, horizontal displacements and excess pore water pressures. The repercussions of including the large displacements formulation are also studied in terms of the increments of vertical and horizontal effective stresses and of the yield area. It is found that the analysis considering large displacements results in a decrease in settlements and a slight increase in the rate of excess pore pressure dissipation, both of which are related to the reduction of the thickness of a deformable layer.

1 INTRODUCTION

The analysis of most geotechnical problems assumes that the strains are infinitesimal, presuming that the geometry of the elements remains unchanged during the calculation process. However, for structures built on very deformable ground, like very compressible clays and organic soils, this assumption is not completely realistic since these soils are subject to high displacements. The lower permeability and high compressibility of these soils, which are nearly always saturated, means that the analysis should also consider the coupled formulation of the interstitial fluid flow and the deformation of the solid skeleton (Biot's theory).

Several studies about implementations of coupled consolidation theories with finite deformations have been published, considering either linear elastic materials [1-5] or non-linear material behaviour [6-9]. But only a few included applications to real situations, namely to embankments built on very compressive soils, i.e., where the consideration of geometric non-linearity is essential to the improvement in the numerical predictions.

This paper intends to clearly show the importance of considering geometric non-linearity

in the numerical analysis of coupled consolidation problems, particularly in problems of embankments on soft soils. In this way, a Lagrangian formulation is used, updating the nodal coordinates at the end of each step of time and/or load; this formulation was described by Zienkiewick [10].

Thus, the case of an embankment built on Portuguese soft soil is studied. The results of the numerical simulation, which considers a non-linear constitutive law (Modified Cam Clay model), with and without the geometric non-linearity phenomenon are compared with the results observed *in situ* in terms of settlements, horizontal displacements and excess pore water pressures. In addition, the influence of the large displacements analysis on the state of stress is studied in terms of vertical and horizontal effective stresses, and in terms of the yield area.

All the numerical analyses used the 2D finite element (FE) code, developed at the University of Coimbra [11], which can perform elastoplastic analyses with coupled consolidation.

2 CHARACTERISTICS OF THE EMBANKMENT

The site studied is located in Portugal, at km 7.775 on the A14 motorway. Three boreholes were performed (S_1, S_2 and S_3) to define the geotechnical profile presented in Figure 1.

The behaviour of the embankment was observed during its construction, with the following instrumentation (Figure 1): (i) a sub-vertical inclinometer tube placed on the vertical of the foot of the main embankment's slope to measure horizontal displacements with depth, (ii) a settlement plate (T) and a electrical piezometer (P) to measure pore pressure [11]. Under the embankment and the additional berm, vertical drains were installed down to the bottom of the soft deposit.

The time history of the construction of the embankment is described with elevations of 1.1, 1.85, 3.45, 4.7, 7.55 and 8.1 metres, applied at times 0, 80, 240, 290, 385 and 420 days, respectively.

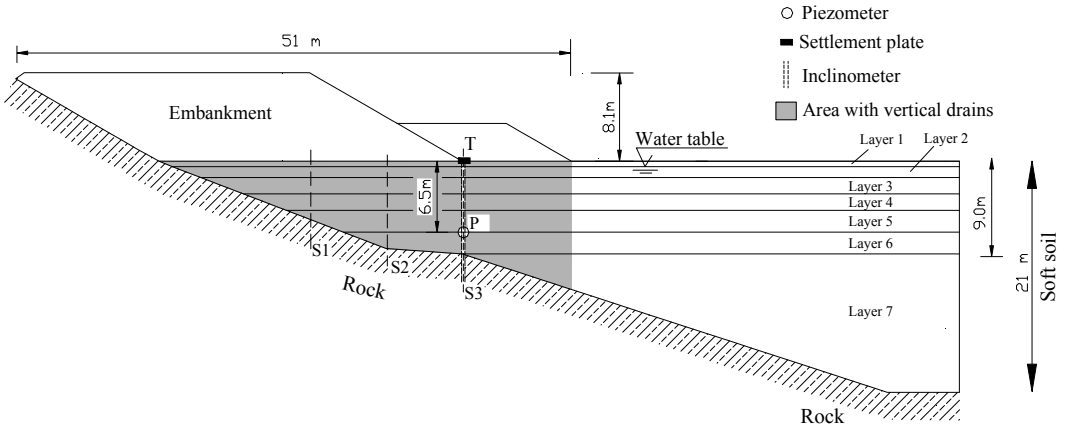

Figure 1: Geotechnical profile of the A14 motorway embankment (Portugal).

The geotechnical characterisation of these soils, carried out by Coelho [12], allowed the foundation soil to be zoned, as shown in Table 1, where the physical and mechanical characteristics of the layers are set forth. The behaviour of the foundation soil is simulated by

the Modified Cam Clay (MCC) model. The behaviour of the embankment is simulated by a linear elastic law, with ν' = 0.3 and the deformability modulus varying between 30 MPa (bottom layer) and 2 MPa (top layer), thereby reproducing the reduced containment of the upper layers.

Table 1: Physical and mechanical characteristics of soil layers.

Layer	Depth (m)	γ (kN/m^3)	OCR	K_o	e_o	Parameters of MCC model				$k_{y(eq)}$* (m/day) [x 10^{-4}]	k_x/k_y
						$e_{\lambda o}$	λ	κ	M		
1	0.0 - 0.5	15.0	7.0	0.87	2.0	2.58	0.226	0.028		-----	
2	0.5 - 1.5	15.0	5.0	0.76	2.0	2.76	0.226	0.028		15.6	
3	1.5 – 3.0	14.8	3.0	0.62	2.1	3.02	0.282	0.035		62.4	
4	3.0 - 4.5	14.5	1.5	0.47	2.3	3.41	0.374	0.05	1.48	103.6	3.0
5	4.5 - 6.5	14.5	1.0	0.40	2.1	3.10	0.343	0.063		20.8	
6	6.5 - 8.5	15.2	1.0	0.40	1.8	2.37	0.178	0.025		5.1	
7	8.5 - 21.0	15.0	1.0	0.40	1.9	2.76	0.217	0.026		6.2	
Embank.	------	22.0	----	----	-----	-----	-----	-----	-----	-----	-----

* $k_{y(eq)} = 12.\ k_{y(soil)}$

The vertical coefficients of permeability, given in Table 1, correspond to the global equivalent values, thus expressing the drainage conditions of the '*soil-vertical drains'* system [11, 13]. The relationship between the horizontal and vertical coefficients of permeability of the soil is three.

During the calculation, the coefficients of permeability change with the void ratio, in accordance with Taylor [14]:

$$k = k_0 x 10^{\frac{e-e_0}{C_k}} \qquad (12)$$

where e_0 represents the initial void ratio, k_0 the coefficient of permeability related to e_0, k the corrected coefficient of permeability related to the current void ratio e, and C_k is a constant equal to $0.5e_0$ [14].

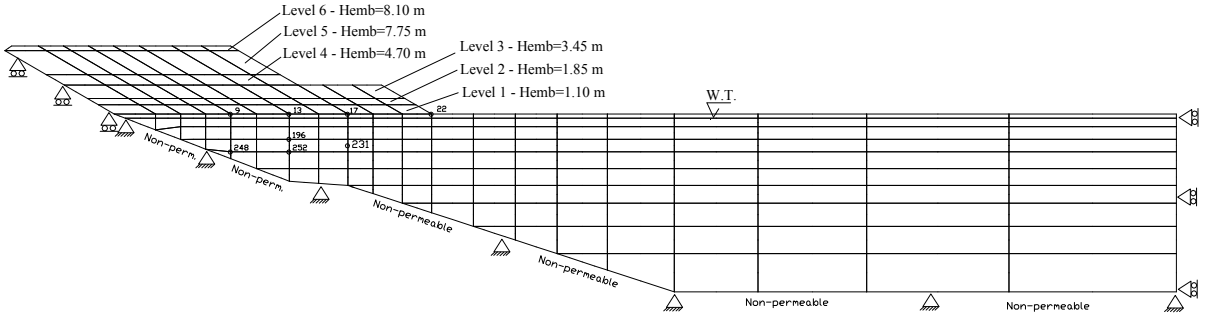

Figure 2: FE mesh.

The FE mesh for the plane-strain analysis is presented in Figure 2. It consists of 679 nodal points and 202 eight-noded isoparametric quadrilateral elements. Elements with twenty nodal degrees of freedom are used below the water table, allowing a coupled analysis of fluid flow and deformation in order to simulate the consolidation phenomenon in the soft soil. These

elements provide quadratic interpolation of displacements and linear interpolation of pore pressures; these elements therefore allow the calculation of the displacements in eight nodes and the excess pore pressure in four corner nodes.

The boundary conditions applied to the mesh are such that the right vertical side is restrained from moving in the horizontal direction, while the bottom boundaries are restrained from moving in both directions [12]. In terms of hydraulic conditions, only the top boundary, located at the same level of the water table, is permeable. Above the water table, no water flow was considered in the numerical analyses.

3 ANALYSIS OF RESULTS

The study of the behaviour of this embankment aims to clearly demonstrate the factors inherent in an analysis that involves large displacements. Thus, the results obtained by the two numerical analyses (infinitesimal and large displacements) are compared and also with the behaviour observed *in situ*. The study is carried out with respect to settlements, lateral displacements, excess pore pressures and effective stress state.

3.1 Displacements

The observed and computed time-settlement behaviour measured by plate T is shown in Figure 3. It can be seen that the consideration of geometrical non-linearity (large displacements) tends to reduce the settlements in relation to the infinitesimal analysis (small displacements), with this effect growing with time. This behaviour is consistent with soil mechanics theory, since with large displacements analysis the dependence of the settlements with respect to the real thickness of the compressible layers is considered. Thus, the decrease of the thickness of the soil layer is naturally linked to smaller settlements.

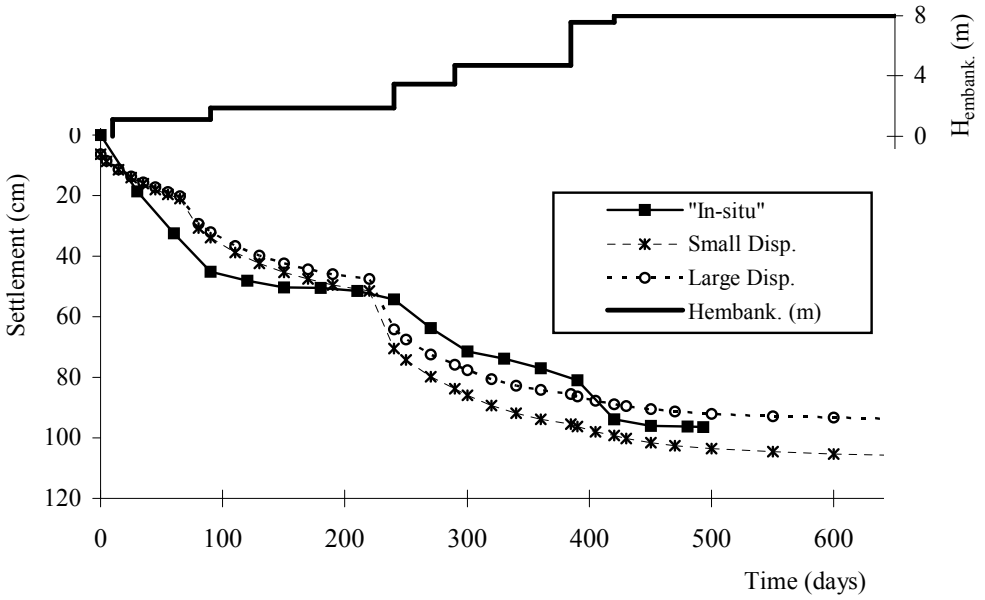

Figure 3: Observed and predicted settlements (plate T).

The comparison of the computed settlements and the field data shows that the

consideration of geometric non-linearity improves the numerical prediction. The differences between the numerical analyses and the measured settlements for 100 and 250 days are probably due to the consideration of equivalent coefficients of permeability, which are not the most appropriate to simulate the "real" flow conditions in the soil foundation.

Figure 4 shows the computed settlements under the foot of the embankment, for three times (240, 420 and 2000 days). In line with expected behaviour, it is in the surface area with greater settlements that the greatest discrepancies between the two numerical analyses are found, and these increase from 240 days to 420 days, i.e., with the increment of the settlements. Thus, it was found that the consideration of large displacements has more impact the greater the deformation of the soils involved is.

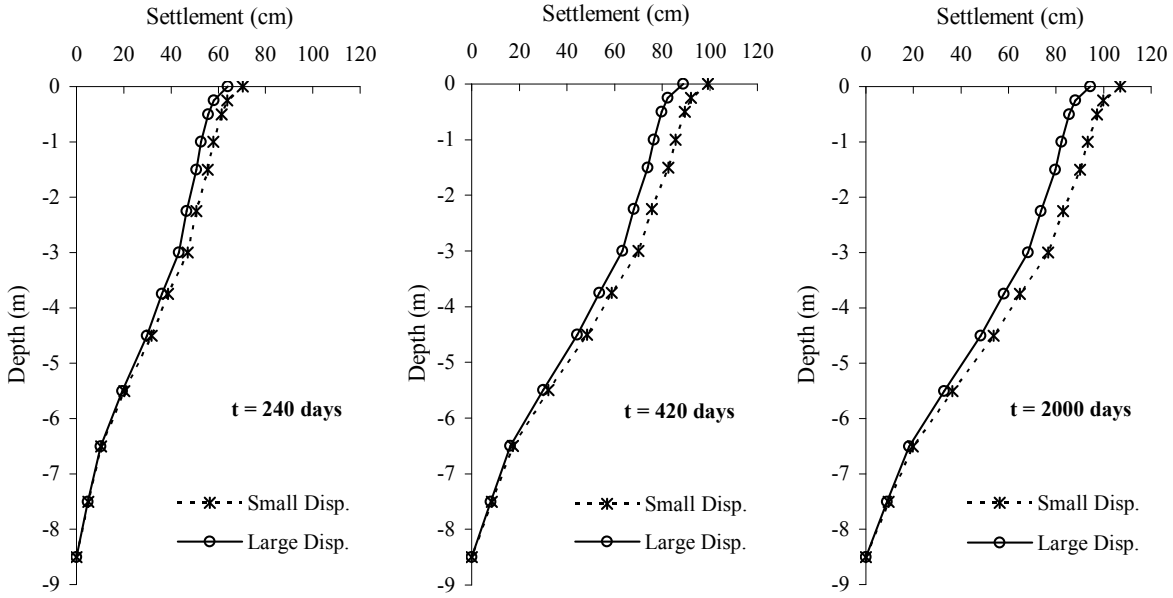

a) Evolution at 240 days. b) Evolution at 420 days. c) Evolution at 2000 days.

Figure 4: Computed settlements under the foot of the embankment.

Figure 5 illustrates the observed and predicted horizontal displacements under the foot of the main embankment at 290 and 500 days. According to the finding for the settlements, the consideration of geometrical non-linearity induces small horizontal displacements relatively to the infinitesimal analysis, and this difference naturally increases with time. The figure also shows that the behaviour of the embankment is qualitatively simulated by both the numerical analyses, albeit with some discrepancies. Thus, at 290 days a better simulation of the behaviour may be observed with the non-linear analysis, while at 500 days, a better agreement is obtained with the infinitesimal analysis.

3.2 Excess pore water pressures

The time evolution of excess pore pressures in piezometer P is given in Figure 6. The consideration of geometrical non-linearity leads to slightly faster dissipation of the excess pore pressure, being this fact linked to the shortening the drainage path length which results from the decreasing of soil thickness. Otherwise, for a time longer than 500 days, the large

displacement analysis induces slightly higher u-u_o than the infinitesimal analysis, a fact that is apparently inconsistent. However, these results are due to the fact that the large displacements analysis considers the real nodal coordinates, corrected with the deformations obtained. As the level of the water table does not change and the nodal points are displaced in the vertical, thus, the distance between the nodal points and the water table increases, therefore giving greater equilibrium pore pressure [15].

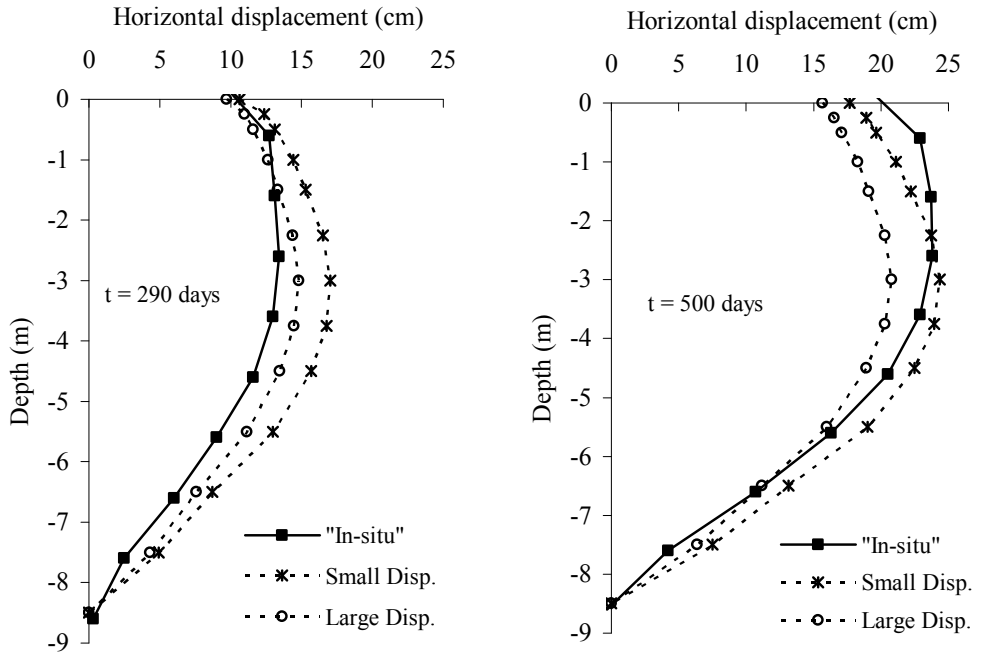

a) Evolution at 290 days. b) Evolution at 500 days.

Figure 5: Observed and predicted horizontal displacement under the foot of the embankment.

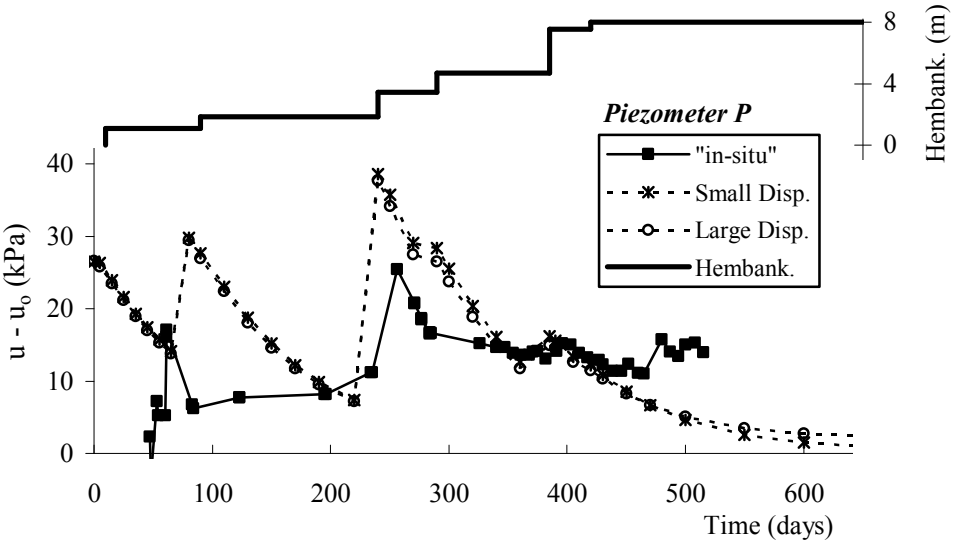

Figure 6: Observed and predicted excess pore pressure in piezometer P.

The contours of the excess pore pressure, shown in Figure 7, illustrate this clearly. At 420 days it can be seen that the non-linear analysis gives rise to an increase in the excess pore pressure close to the surface, reflecting the greatest settlement of the surface points and the corresponding increase in the equilibrium pore pressure. The reduction of the drainage path length associated with the large displacements analysis can also be seen in this figure, since this type of analysis generates smaller excess pore pressure near the bottom boundary.

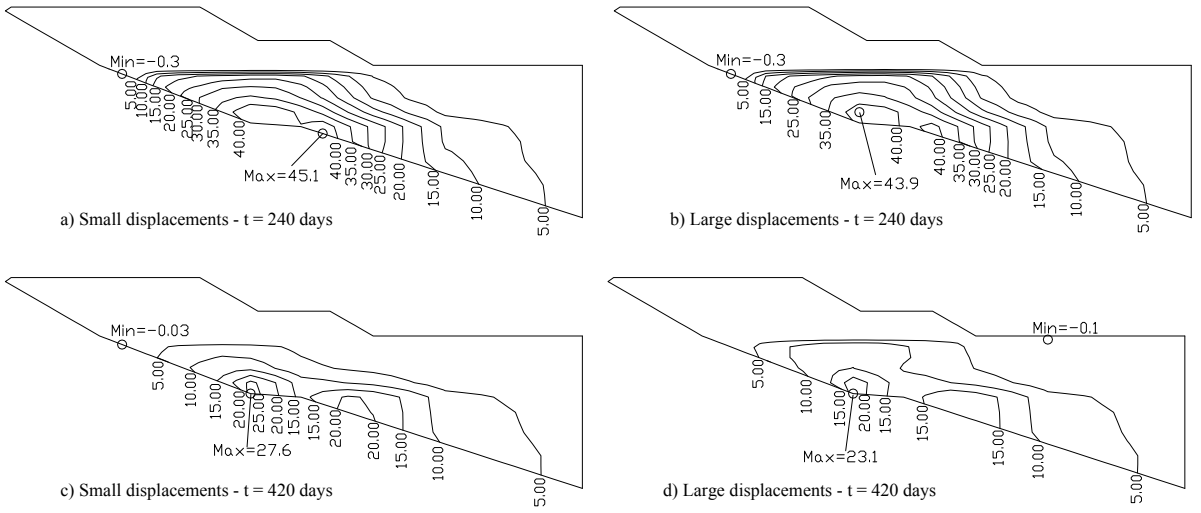

Figure 7: Contours of excess pore pressures at 240 and 420 days.

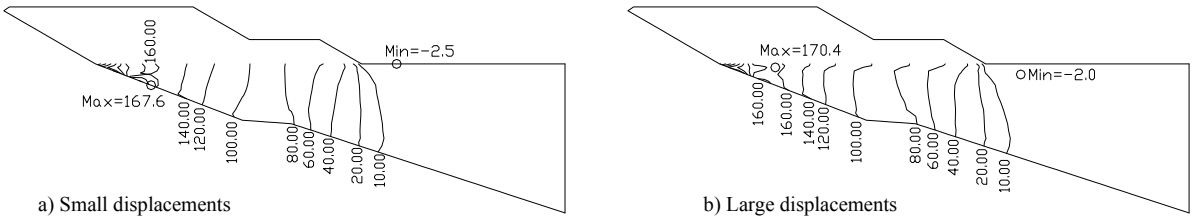

Figure 8: Contours of vertical effective stresses incremernts at 2000 days.

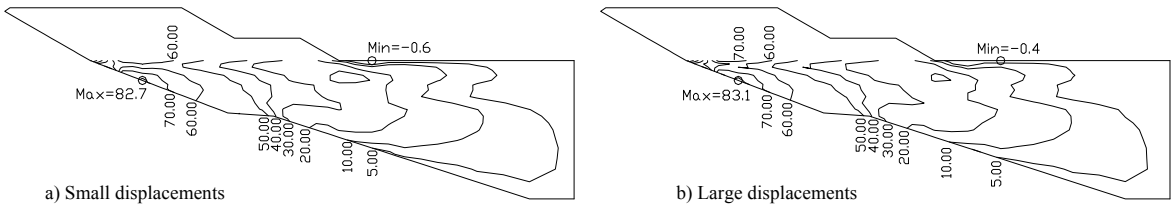

Figure 9: Contours of horizontal effective stresses increments at 2000 days.

3.3 Stress state

The contours of the effective vertical and horizontal stress increments at 2000 days, found with both numerical analyses, are presented in Figures 8 and 9, respectively. In general, it can be seen that the consideration of geometrical non-linearity does not generate qualitative

changes in the effective stress state. Figure 10 compares the results of the two analyses in terms of vertical effective stress increments along the embankment section for two depths (Figure 10a) and horizontal effective stress increments under the foot of the additional berm (Figure 10b). The results show that including the large displacement phenomenon in the calculation tends to reduce both the vertical and the horizontal stresses in relation to the infinitesimal analysis, obtaining differences that could be almost 10%. These results are consistent with the fact that the non-linear analysis induces greater equilibrium pore pressure, which naturally corresponds to smaller effective stresses, since the total stresses are unchangeable.

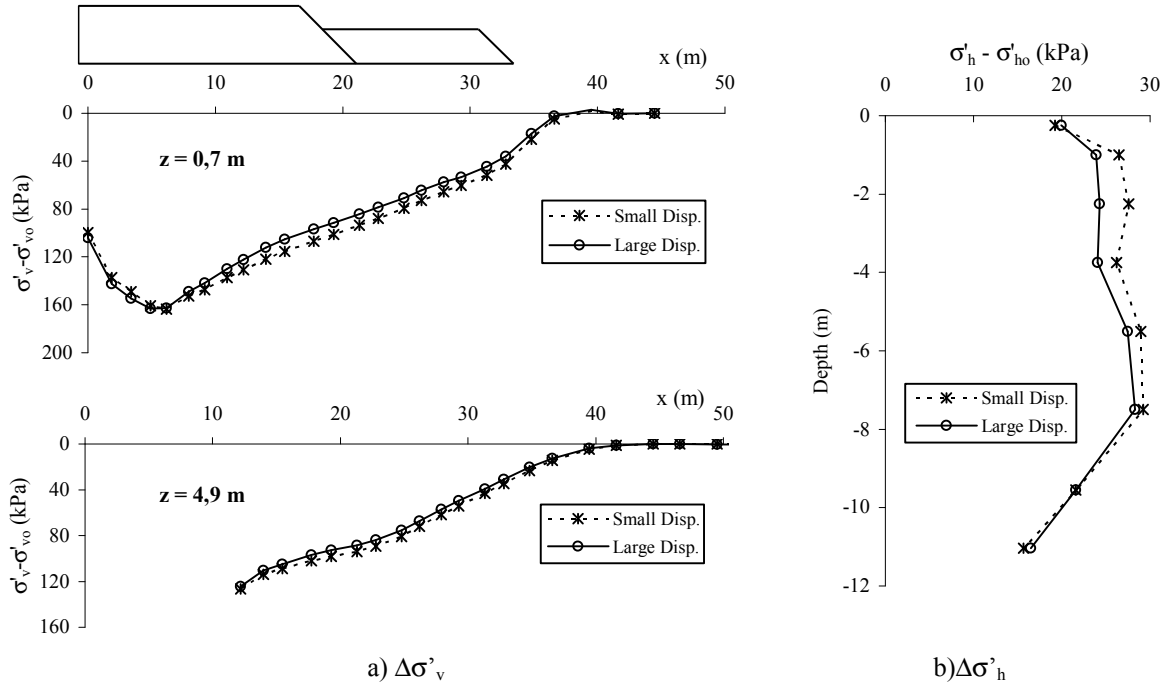

Figure 10: Increment of effective stresses at 2000 days.

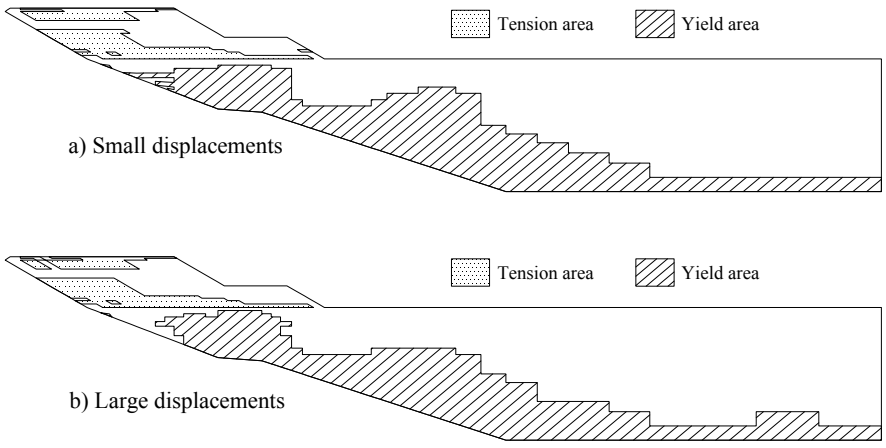

Figure 11: Yield areas at 2000 days.

The reduction of effective stresses indicated by the non-linear analysis, relative to the infinitesimal analysis, results in the shrinkage in the yield area (Figure 11) with special relevance in the layers nearer the surface and under the main embankment, which are initially overconsolidated. This smaller propagation of the yield zones is related to smaller vertical and horizontal displacements.

4 CONCLUSIONS

The analyses performed for this work revealed the following aspects:

- the large displacement analysis leads to a reduction of settlements in relation to the infinitesimal analysis. This fact can be explained by the proportion of the settlements in relation to the thickness of the deformable soil, i.e., when the soil settles, the thickness of the soil layer decreases, which induces the reduction of the settlements in the subsequent phases of the calculation.
- The geometrical non-linearity tends to reduce the horizontal displacements on the side of the embankment, which is also naturally associated with the reduction of settlements.
- The evolution of pore pressure is not particularly affected by the kind of analysis, although the pore pressure dissipates slightly faster as time passes when geometrical non-linearity is considered. This is because the progressive decrease of the soil layer thickness leads to a shorter drainage path length. However, the results do not show this clearly enough, since it can be masked by the increase in equilibrium pore pressure, due to the greater elevation difference between the nodal points and the water table, which is unchanged.
- The increase of equilibrium pore pressure in the points nearer the surface, due to the adjustment of the coordinates (obtained from the inclusion of geometrical non-linearity), contributes to the decrease of effective stress increments, since the total stress is independent of these kinds of analysis. This reduction of effective stresses gives rise to the shrinkage of the yield area. This fact is naturally linked to lesser displacements generated.

ACKNOWLEDGMENTS

The authors would like to express their gratitude to the institutions that financially supported the research: CIEC and FCT (PTDC/ECM/101875/2008).

REFERENCES

[1] Carter J.P., Small J.C. and Booker J.R. A theory of finite elastic consolidation. *International Journal Solids Structures* (1977) **13**:467-478.

[2] Gibson R.E., Gobert A. and Schiffman R.L. On Cryer's problem with large displacements. *International Journal for Numerical and Analytical Methods in Geomechanics* (1989) **13**:251-262.

[3] Gibson R.E., Gobert A. and Schiffman R.L. On Cryer's problem with large displacements and variable permeability. *Géotechnique* (1990) **40**:627-631.

[4] Asaoka A., Noda T. and Fernando G.S.K. Effects of changes in geometry on deformation behaviour under embankment loading. *Numerical Models in Geomechanics – NUMOG V*, Pand and Pietruszczak (eds), Balkema, Rotterdam (1995):545-550.

[5] Asaoka A., Noda T. and Fernando G.S.K. Effects of changes in geometry on the linear elastic consolidation deformation. *Soils and Foundations* (1997) **37**(1):29-39.

[6] Carter J.P., Booker J.R. and Small J.C. The analysis of finite elasto-plastic consolidation. *International for Numerical and Analytical Methods in Geomechanics* (1979) **3**:107-129.

[7] Prevost J.H. Non-linear transient phenomena in saturated porous media. *Computer Methods in Applied Mechanics and Engineering* (1982) **20**:3-18.

[8] Meroi E.A. and Schrefler B.A. Large strain static and dynamic semisaturated soil behaviour. *International for Numerical and Analytical Methods in Geomechanics* (1995) **19**:81-106.

[9] Nazem M., Sheng D., Carter J.P. and Sloan S.W. Arbitrary Lagrangian-Eulerian method for large-strain consolidation problems. *International for Numerical and Analytical Methods in Geomechanics* (2008) **32**:1023-1050.

[10] Zienkiewick O.C. *The Finite Element Method*. 3th edition, McGraw-Hill Book Company (UK) Limited, England, (1977).

[11] Venda Oliveira P.J. *Embankments on soft clays - Numeric analysis*. Ph.D. Dissertation, University of Coimbra, Portugal (in Portuguese), (2000).

[12] Coelho P.A.L.F. *Geotechnical characterization of soft soils. Study of the experimental site of Quinta do Foja*. MSc Dissertation, University of Coimbra, Portugal (in Portuguese), (2000).

[13] Venda Oliveira P.J., Lemos L.J.L. and Coelho P.A.LP. Behavior of an atypical embankment on soft soil: field observations and numerical simulation. *Journal of Geotechnical and Geoenvironmental Engineering* (2010) **136**(1):35-47.

[14] Taylor, D.W. *Fundamentals of Soil Mechanics*. John Wiley and Sons, Inc., New York, (1948).

[15] Venda Oliveira P.J. and Lemos L.J.L. Numerical analysis of an embankment on soft soils considering large displacements. *Computers and Geotechnics* (2011) **38**:88-93.

XI International Conference on Computational Plasticity. Fundamentals and Applications
COMPLAS XI
E. Oñate, D.R.J. Owen, D. Peric and B. Suárez (Eds)

EXPLICIT INTEGRATION SCHEME FOR GENERALIZED PLASTICITY CONSTITUTIVE MODELS WITH AUTOMATIC ERROR CONTROL

MIGUEL M. STICKLE[1]*, PABLO DE LA FUENTE[2] AND CARLOS OTEO[3]

1*: Applied Mathematics and Computer Science Department
ETSI Caminos, Canales y Puertos
Universidad Politécnica de Madrid
Avd. Profesor Aranguren s/n, 28040 Madrid, Spain
e-mail: miguelstickle@caminos.upm.es

2: Continuum Mechanics and Structures Department
ETSI Caminos, Canales y Puertos
Universidad Politécnica de Madrid
Avd. Profesor Aranguren s/n, 28040 Madrid, Spain
e-mail: pdelaf@caminos.upm.es

3: Professor on Ground Eng.
C / Torpedero Tucumán 26, 28016 Madrid, Spain
e-mail: carlosoteo@telefonica.net

Key words: Generalized Plasticity, explicit integration.

Abstract. *An explicit algorithm for integrating Generalized Plasticity constitutive models is presented. This automatically divides the applied strain increment into subincrements using an estimate of the local error controlling the global integration error in the stress. The algorithm modifies the well known S. W. Sloan substepping scheme to account for Generalized Plasticity constitutive models, in which, unlike Classical Elastoplasticity, the yield surface is not explicitly defined. The integration scheme is described and results are presented for a rigid footing resting on a layer of specific Generalized Plasticity model for sands, in which a hyperelastic formulation is introduced to describe the reversible component of the soil response instead of the hypoelastic approach originally proposed. The explicit algorithm with automatic substepping and error control is shown to be reliable and efficient for these complex constitutive laws.*

1 INTRODUCTION

Nowadays it is well recognized that the selection of an adequate constitutive model, together with the use of accurate, efficient and robust integration algorithms of the elastoplastic equations, is a key point in finite element analysis of geotechnical problems.

As observed by Hughes [1], the integration of the constitutive equations at the local level plays a crucial part in computational plasticity, since it strongly affects the performance of the constitutive equation in actual computations.

Implementation of an advanced elastoplastic constitutive model into a finite element

program requires the development of a robust and efficient numerical procedure in order to perform the integration of the constitutive equations along a given loading path.

In the context of classical plasticity formulations, in which a yield function is defined in an explicit manner and the enforcement of the consistency condition is a key feature of the integration algorithm, a variety of implicit and explicit integration schemes might be used [2, 3].

On the other hand, based on the assumption that explicit integration schemes for highly non-linear models may potentially lead to inaccuracy and unstable behavior [4], implicit integration algorithms have been considered mostly in the context of non-standard elastoplastic models. The aforementioned assumption cannot be further supported, in the context of classical plasticity formulations, if explicit schemes are endowed with error control techniques [5, 6]. The same situation is observed for Generalized Plasticity based models [7].

The outline of the paper is as follows. We first present the fundamentals of Generalized Plasticity, with particular attention paid to the SandPZ constitutive equations including the modifications in the elastic component introduced by Mira and coworkers in 2009 paper. A novel explicit algorithm for integrating Generalized Plasticity constitutive models is presented in the following section. Finally, Results and conclusions are presented for a rigid footing resting on a sand layer modeled by a SandPZ constitutive relation.

2 GENERALIZED PLASTICITY FRAME WORK. MODIFIED SAND PZ MODEL.

The Generalized Plasticity basic idea, introduced by Zienkiewicz and Mroz [8] later extended by Pastor and coworkers [9, 10] and also by Mira and coworkers [4], is that no yield neither plastic potential surface are explicitly defined, but the gradients to the functions themselves. The elastoplastic behavior of the material within the Generalized Plasticity theory is described by the general incremental relationship,

$$d\sigma'_{ij} = D^{ep}_{ijkl} \cdot d\varepsilon_{kl} \left(d\boldsymbol{\sigma}' = \mathbf{D}^{ep} : d\boldsymbol{\varepsilon} \right) \tag{1}$$

In which the tangent elastoplastic stiffness four order tensor $\mathbf{D}^{ep}$ depends not only on the internal state variables but also on the current effective stress state $\boldsymbol{\sigma}'$, on the strain-stress history and the direction of the effective stress increments $d\boldsymbol{\sigma}'$.

The dependence of $\mathbf{D}^{ep}$ on the direction of $d\boldsymbol{\sigma}'$ is expressed by simply distinguishing between two different loading classes, namely Loading (L) and Unloading (U). Therefore a normalized direction $\mathbf{n}$ is defined in the effective stress space for any given $\boldsymbol{\sigma}'$, determining loading/unloading/neutral loading condition.

There are two possibilities for the tangent elastoplastic stiffness tensor in (1) depending on whether loading, $\mathbf{D}^{ep}_{L}$ or unloading $\mathbf{D}^{ep}_{U}$ is occurring. To guarantee continuity between loading and unloading, $\mathbf{D}^{ep}_{L}$ and $\mathbf{D}^{ep}_{U}$ are defined as

$$\begin{aligned} \left(\mathbf{D}^{ep}_{L}\right)^{-1} &= \left(\mathbf{D}^{e}\right)^{-1} + \frac{1}{H_L} \cdot \left[\mathbf{m}_L \otimes \mathbf{n}\right] \\ \left(\mathbf{D}^{ep}_{U}\right)^{-1} &= \left(\mathbf{D}^{e}\right)^{-1} + \frac{1}{H_U} \cdot \left[\mathbf{m}_U \otimes \mathbf{n}\right] \end{aligned} \tag{2}$$

In expression (2), $\mathbf{m}_L$ and $\mathbf{m}_U$ are directions of unit norm representing the plastic flow direction in loading (L) and unloading (U) conditions respectively, H_L and H_U are two scalar functions defined as plastic moduli while $\mathbf{D}^e$ is the tangent elastic stiffness tensor. By suitable manipulation of (2), $\mathbf{D}_L^{ep}$ and $\mathbf{D}_U^{ep}$ can be obtained giving:

$$\begin{aligned}\mathbf{D}_L^{ep} &= \mathbf{D}^e - \frac{\mathbf{D}^e : \mathbf{m}_L \otimes \mathbf{n} : \mathbf{D}^e}{H_L + \mathbf{n} : \mathbf{D}^e : \mathbf{m}_L} \\ \mathbf{D}_U^{ep} &= \mathbf{D}^e - \frac{\mathbf{D}^e : \mathbf{m}_U \otimes \mathbf{n} : \mathbf{D}^e}{H_U + \mathbf{n} : \mathbf{D}^e : \mathbf{m}_U}\end{aligned} \tag{3}$$

The strain increment $d\boldsymbol{\varepsilon}$ can be decomposed into elastic and plastic parts as $d\boldsymbol{\varepsilon} = d\boldsymbol{\varepsilon}^e + d\boldsymbol{\varepsilon}^p$ where

$$\begin{aligned}d\boldsymbol{\varepsilon}^e &= \left(\mathbf{D}^e\right)^{-1} : d\boldsymbol{\sigma}' \\ d\boldsymbol{\varepsilon}^p &= \left(\frac{1}{H_L} \cdot \mathbf{m}_L \otimes \mathbf{n}\right) : d\boldsymbol{\sigma}' \text{ for loading} \\ d\boldsymbol{\varepsilon}^p &= \left(\frac{1}{H_U} \cdot \mathbf{m}_U \otimes \mathbf{n}\right) : d\boldsymbol{\sigma}' \text{ for unloading}\end{aligned} \tag{4}$$

Therefore, in a Generalized Plasticity approach, the non-linear irreversible behavior of soils can be fully described by simply specifying three directions, $\mathbf{n}, \mathbf{m}_L$ and $\mathbf{m}_U$, two scalars, H_L and H_U and a fourth order tensor $\mathbf{D}^e$.

Since the hardening moduli H_L and H_U as well as the plastic flow directions $\mathbf{m}_L$ and $\mathbf{m}_U$ are fully determined without reference to any yield surface nor plastic potential, different expressions can be selected for them whether the stress increment implies loading or unloading. Moreover consistency cannot be enforced and the consistency parameter $d\lambda$ is simply defined as:

$$d\lambda = \frac{\mathbf{n} : \mathbf{D}^e : d\boldsymbol{\varepsilon}}{H_{L/U} + \mathbf{n} : \mathbf{D}^e : \mathbf{m}_{L/U}} \tag{5}$$

Although not explicitly defined, plastic potential and yield surface can be established a posteriori, by integrating $\mathbf{m}_{L/U}$ and $\mathbf{n}$, respectively.

SandPZ model was developed by Pastor and coworkers [9] as a particular type of Generalized Plasticity formulation with the aim of predicting granular soil behavior under both monotonic and cyclic loading.

The model assumes an isotropic material response. As a result, the plastic flow direction $\mathbf{m}$, as well as the loading direction $\mathbf{n}$, is expressed in the invariant space defined by p', q, θ as

$$\mathbf{m} = \mathrm{m}_v \frac{\partial p'}{\partial \sigma'_{ij}} + \mathrm{m}_s \frac{\partial q}{\partial \sigma'_{ij}} + \mathrm{m}_\theta \frac{\partial \theta}{\partial \sigma'_{ij}} \tag{6}$$

The value of the coefficients $\mathrm{m}_v, \mathrm{m}_s, \mathrm{m}_\theta$ are loading class (loading or unloading) dependent. In order to take into account the main features of sand response, i.e. the existence of a critical state condition, dilative response after peak, liquefaction in loose sands, memory of previous stress path, Pastor and coworkers [9] proposed for the plastic modulus H_L the following relationship:

$$H_L = H_0 \cdot p' \cdot H_f \cdot \left(H_v + H_s\right) \cdot H_{DM} \tag{7}$$

Together with

$$H_f = \left(1 - \frac{\eta}{M_f} \cdot \frac{\alpha_f}{1+\alpha_f}\right)^4;\ H_v = 1 - \frac{\eta}{M_g};\ H_s = \beta_0 \beta_1 \exp\left(-\beta_0 \xi\right)$$

$$H_{Dm} = \left(\frac{\zeta_{\max}}{\zeta}\right)^\gamma;\ \xi = \int \left|d\varepsilon_s^p\right| = \int d\xi;\ \zeta = p' \left[1 - \left(\frac{\alpha_f}{1+\alpha_f}\right) \cdot \frac{\eta}{M_f}\right]^{-\frac{1}{\alpha_f}}$$

In these expressions $H_0, \beta_0, \beta_1, \gamma$ are constitutive parameters, ξ is the accumulated deviatoric plastic strain and $\zeta_{\max}$ stands as the maximum value of the mobilized stress function ζ accounting for the soil stress history.

In the case of unloading the plastic modulus H_U is given by:

$$H_U = H_{u0} \left(\frac{M_g}{\eta_u}\right)^{\gamma_u} \quad \text{for} \quad \left|\frac{M_g}{\eta_u}\right| > 1$$
$$H_U = H_{u0} \quad \text{for} \quad \left|\frac{M_g}{\eta_u}\right| < 1 \tag{8}$$

For where H_{u0} is a constitutive parameter and η_u, referred as unloading stress ratio, is the stress ratio q/p' from which unloading takes place.

Finally, the PZ model assumes a non-linear elastic response of the soils. As in a large number of constitutive models, the non-linear reversible behavior is described through a hypoelastic approach, in which the tangent bulk modulus K and shear modulus G only depend on the hydrostatic part of the effective stress tensor, according to the following relationships

$$K = K_0 \cdot \frac{p'}{p'_0},\ G = G_0 \cdot \frac{p'}{p'_0} \tag{9}$$

Although widely used, one of the major shortcomings of such hypoelastic formulation is that it results in a non-conservative elastic response and energy dissipation over closed stress

paths [11].

An alternative is to describe the elastic response of soils within a conservative framework adopting the hyperelastic approach based on the existence of an energy potential from which the reversible response can be derived. This naturally leads to a conservative elastic response, guaranteed to obey the First Law of Thermodynamics, and thus avoiding the problems on cycling described above [12, 13]

Among the different formulations recently proposed in the geotechnical literature, in this work the hyperelastic approach described by Houslby and coworkers in 2005 (from now on referred as HAR according to authors' initials) has been adopted to describe the reversible component of the soil response. This Generalized Plasticity PZ model for granular soils has been proposed firstly by Mira and coworkers [4] under its triaxial formulation, extending the model in the present work to deal with a general stress formulation.

The stored energy function Υ of the HAR model in general stress formulation has two different expressions depending on the value assigned to the dimensionless pressure exponent n_{HAR}, which governs the amount of nonlinearity involved in the formulation. For $n_{HAR} \neq 1$, Υ takes the following form:

$$\Upsilon\left(\varepsilon_{ij}^{e}\right)=\frac{p_a}{k_{HAR}\cdot\left(2-n_{HAR}\right)}\cdot\left[k_{HAR}\cdot\left(1-n_{HAR}\right)\cdot\upsilon_0\right]^{(2-n_{HAR})/(1-n_{HAR})} \tag{10}$$

Where $\upsilon_0^2=\left[\varepsilon_{ii}^{e}+\frac{1}{k_{HAR}\cdot\left(1-n_{HAR}\right)}\right]\cdot\left[\varepsilon_{jj}^{e}+\frac{1}{k_{HAR}\cdot\left(1-n_{HAR}\right)}\right]+\frac{2g_{HAR}e_{ij}^{e}e_{ij}^{e}}{k_{HAR}\left(1-n_{HAR}\right)}$, while the asymptotic expression for $n_{HAR}=1$ is $\Upsilon\left(\varepsilon_{ij}^{e}\right)=\left(p_a/k_{HAR}\right)\cdot e^{\left(k_{HAR}\cdot\varepsilon_{ii}^{e}+g_{HAR}\cdot k_{HAR}\cdot e_{ij}^{e}e_{ij}^{e}\right)}$. k_{HAR}, g_{HAR} are dimensionless constants representing the shear and bulk stiffness factors, respectively, while p_a is the atmospheric pressure, adopted as reference stress.

The effective stress tensor $\boldsymbol{\sigma}'$ and the tangent elastic tensor $\mathbf{D}^e$ can be unambiguously determined by taking the first and second order derivatives of (10), obtaining the following expression

$$D_{ijkl}^{e}=p_a\cdot\left(\frac{p_0}{p_a}\right)^{n_{HAR}}\cdot\left[n_{HAR}k_{HAR}\cdot\frac{\sigma'_{ij}\sigma'_{kl}}{p_0^2}+k_{HAR}\left(1-n_{HAR}\right)\delta_{ij}\delta_{kl}+2g_{HAR}\left(\delta_{ik}\delta_{jl}-\frac{1}{3}\delta_{kl}\delta_{ij}\right)\right] \tag{11}$$

Where $\left(p_0\right)^2=\frac{\sigma'_{mm}\sigma'_{nn}}{9}+\frac{k_{HAR}\cdot\left(1-n_{HAR}\right)\cdot s_{mn}s_{mn}}{2g_{HAR}}$

For the present model there are 12 material parameters requiring definition. Generally, all parameters are identified from monotonic and cyclic triaxial tests, though in certain cases some parameters are adopted from previous experiences if full test records are unavailable.

3 EXPLICIT INTEGRATION OF GENERALIZED PLASTICITY MODELS.

During a typical step or iteration of an elastoplastic finite element analysis, the forces are applied in increments and the corresponding displacement increments are found from the

global stiffness equations. Once the nodal displacement increments $d\overline{\boldsymbol{u}}$ are known, the strain increments at a discrete number of integration points within each element are determined using the strain-displacement relation $d\boldsymbol{\varepsilon} = \boldsymbol{B} d\overline{\boldsymbol{u}}$. If the stresses associated with an imposed strain increment cause plastic yielding, it is necessary to solve the system of firs order ordinary differential equations (12)-(13):

$$\dot{\boldsymbol{\sigma}}' = \mathbf{D}^{ep} : \left(\frac{\Delta \boldsymbol{\varepsilon}}{\Delta t} \right) = \mathbf{D}^{ep} : \dot{\boldsymbol{\varepsilon}} \tag{12}$$

$$\dot{\boldsymbol{\varepsilon}}^{p} = d\lambda \cdot \mathbf{m}_{L/U} \tag{13}$$

Where

$$\mathbf{D}^{ep} = \mathbf{D}^{e} - \frac{\mathbf{D}^{e} : \mathbf{m}_{L/U} \otimes \mathbf{n} : \mathbf{D}^{e}}{H_{L/U} + \mathbf{n} : \mathbf{D}^{e} : \mathbf{m}_{L/U}} \tag{14}$$

$$d\lambda = \frac{\mathbf{n} : \mathbf{D}^{e} : d\boldsymbol{\varepsilon}}{H_{L/U} + \mathbf{n} : \mathbf{D}^{e} : \mathbf{m}_{L/U}} \tag{15}$$

In these expressions, $\boldsymbol{\sigma}'$ denotes the effective stress tensor, $\boldsymbol{\varepsilon}$ the small strain tensor and $\boldsymbol{\varepsilon}^{p}$ the plastic strain tensor. The superior dot represents a derivative with respect to time while Δt is the time interval over which the external forces have been applied. Since the effective stress and the plastic strains are kwon at the beginning of the time interval, and the known strain rates may be assumed to be constant through the time interval with value $\Delta\boldsymbol{\varepsilon}/\Delta t$, the equations (12) and (13) define an initial value problem.

In order to integrate these equations numerically, it is convenient [14] to introduce a pseudotime, T, defined by $T = (t - t_0)/\Delta t$, where t_0 is the time at the start of the load increment, while $t_0 + \Delta t$ is the time at the end of the load increment, with $0 \le T \le 1$. Since $dT/dt = 1/\Delta t$ application of the chain rule to $\dot{\boldsymbol{\sigma}}'$ and $\dot{\boldsymbol{\varepsilon}}^{p}$ in (12) and (13) gives

$$\frac{d\boldsymbol{\sigma}'}{dT} = \mathbf{D}^{ep} : \Delta\boldsymbol{\varepsilon} = \left(\mathbf{D}^{e} - \frac{\mathbf{D}^{e} : \mathbf{m}_{L/U} \otimes \mathbf{n} : \mathbf{D}^{e}}{H_{L/U} + \mathbf{n} : \mathbf{D}^{e} : \mathbf{m}_{L/U}} \right) : \Delta\boldsymbol{\varepsilon} = \Delta\boldsymbol{\sigma}'^{e} - \Delta\lambda \mathbf{D}^{e} : \mathbf{m}_{L/U} \tag{16}$$

$$\frac{d\boldsymbol{\varepsilon}^{p}}{dT} = \Delta\lambda \cdot \mathbf{m}_{L/U} \tag{17}$$

Where

$$\Delta\lambda = \frac{\mathbf{n} : \mathbf{D}^{e} : \Delta\boldsymbol{\varepsilon}}{H_{L/U} + \mathbf{n} : \mathbf{D}^{e} : \mathbf{m}_{L/U}} \tag{18}$$

Equations (16) and (17) define a classical initial value problem which needs to be

integrated over the pseudo time interval from $T = 0$ to $T = 1$, where the known values known values in these relations are the imposed strain increments, $\Delta\boldsymbol{\varepsilon}$, together with the effective stresses and plastic strain at the start of the pseudo time increment. The quantities $\mathbf{m}_{L/U}$ and $\mathbf{n}$ are effective stress functions, while parameter $H_{L/U}$ is a function of both the effective stress and the plastic strain.

In order to solve the system of first order ordinary differential equations (16)-(17) Sloan developed a substepping algorithm [5] where the constitutive law is integrated by automatically dividing the strain increment into a number of substeps. An appropriate size for each substep is found through the use of modified Euler or Runge-Kutta-Dormand-Prince formulae, which are specially constructed to provide an estimate of the local error. Later, Sloan and coworkers [6] generalized the 1987 scheme, incorporating new algorithms for handling elastoplastic unloading, computing the yield intersection point, and restoring the stress to the yield surface.

Sloan and coworkers schemes were developed exclusively for classical plasticity based models, including classical and generalized critical state models, where non-linear elastic behavior inside the yield surface is exhibited. In all these models the admissible states in the stress space are constrained to lie within the interior or the boundary of the domain explicitly defined by the yield surface. As this is not the case for generalized plasticity based models, Sloan substepping algorithm should be adjusted in order to be able to integrate this kind of models.

The proposed integration scheme starts with the known strain increment, $\Delta\boldsymbol{\varepsilon}$, the initial stress $\boldsymbol{\sigma}_0$ and initial plastic strain $\boldsymbol{\varepsilon}_0^p$ at the start of the increment where $T = 0$ and $t = t_0$. At the end of the integration process the stresses and plastic strains are obtained at the end of the increment where $T = 0$ and $t = t_0$.

Consider a pseudo time subincrement in the range $0 \le \Delta T_n \le 1$ and let the subscripts $n-1$ and n, denote quantities evaluated at the pseudo times T_{n-1} and $T_n = T_{n-1} + \Delta T_n$, respectively.

Plastic modulus and plastic flow direction in expressions (16)-(17) are dependent on the direction of the effective stress increments therefore differentiation between the two loading classes should be performed before the proper integration process starts. By means of the strain subincrement $\Delta\boldsymbol{\varepsilon}_n = \Delta T_n \Delta\boldsymbol{\varepsilon}$ the loading class is firstly established through the following expression

$$\mathbf{n}\left(\boldsymbol{\sigma}'_n\right) : \mathbf{D}^e\left(\boldsymbol{\sigma}'_n\right) : \Delta\boldsymbol{\varepsilon}_n \tag{19}$$

If expression (19) is positive an elastoplastic loading process is performed, if negative an elastoplasctic unloading process is implied, while an elastic process comes from a zero value.

In the explicit Euler method, the solution for $\boldsymbol{\sigma}'$, $\boldsymbol{\varepsilon}^p$ at the end of the pseudo time step ΔT_n is found from

$$\begin{aligned} \boldsymbol{\sigma}'_n &= \boldsymbol{\sigma}'_{n-1} + \Delta\boldsymbol{\sigma}'_1 \\ \boldsymbol{\varepsilon}^p_n &= \boldsymbol{\varepsilon}^p_{n-1} + \Delta\boldsymbol{\varepsilon}^p_1 \end{aligned} \tag{20}$$

Where

$$\begin{aligned}\Delta\boldsymbol{\sigma}'_1 &= \mathbf{D}^{ep}\left(\boldsymbol{\sigma}'_{n-1}, \boldsymbol{\varepsilon}^p_{n-1}\right) : \Delta\boldsymbol{\varepsilon}_n \\ \Delta\boldsymbol{\varepsilon}^p_1 &= \Delta\lambda\left(\boldsymbol{\sigma}'_{n-1}, \boldsymbol{\varepsilon}^p_{n-1}, \Delta\boldsymbol{\varepsilon}_n\right)\cdot\mathbf{m}_{L/U}\left(\boldsymbol{\sigma}_{n-1}\right)\end{aligned} \tag{21}$$

A more accurate estimate of the stress and plastic strains at the end of the interval ΔT_n can be found using the modified Euler procedure, which is given by

$$\begin{aligned}\widehat{\boldsymbol{\sigma}}'_n &= \boldsymbol{\sigma}'_{n-1} + \frac{1}{2}\left(\Delta\sigma'_1 + \Delta\sigma'_2\right) \\ \widehat{\boldsymbol{\varepsilon}}^p_n &= \boldsymbol{\varepsilon}^p_{n-1} + \frac{1}{2}\left(\Delta\varepsilon^p_1 + \Delta\varepsilon^p_2\right)\end{aligned} \tag{22}$$

Where $\Delta\boldsymbol{\sigma}'_1$ and $\Delta\boldsymbol{\varepsilon}^p_1$ are obtained from Euler scheme and

$$\begin{aligned}\Delta\boldsymbol{\sigma}'_2 &= \mathbf{D}^{ep}\left(\boldsymbol{\sigma}'_{n-1} + \Delta\boldsymbol{\sigma}'_1, \boldsymbol{\varepsilon}^p_{n-1} + \Delta\boldsymbol{\varepsilon}^p_1\right) : \Delta\boldsymbol{\varepsilon}_n \\ \Delta\boldsymbol{\varepsilon}^p_2 &= \Delta\lambda\left(\boldsymbol{\sigma}'_{n-1} + \Delta\boldsymbol{\sigma}'_1, \boldsymbol{\varepsilon}^p_{n-1} + \Delta\boldsymbol{\varepsilon}^p_1, \Delta\boldsymbol{\varepsilon}_n\right)\cdot\mathbf{m}_{L/U}\left(\boldsymbol{\sigma}'_{n-1} + \Delta\boldsymbol{\sigma}'_1\right)\end{aligned} \tag{23}$$

Since the local truncation error [15] in the Euler and modified Euler solutions is $O\left(\Delta T^2\right)$ and $O\left(\Delta T^3\right)$, respectively, the error in $\boldsymbol{\sigma}_n$ and $\boldsymbol{\varepsilon}^p_n$ can be estimated from

$$\begin{pmatrix}\widehat{\boldsymbol{\sigma}}'_n \\ \widehat{\boldsymbol{\varepsilon}}^p_n\end{pmatrix} - \begin{pmatrix}\boldsymbol{\sigma}'_n \\ \boldsymbol{\varepsilon}^p_n\end{pmatrix} = \begin{pmatrix}\frac{1}{2}\left(\Delta\boldsymbol{\sigma}'_2 - \Delta\boldsymbol{\sigma}'_1\right) \\ \frac{1}{2}\left(\Delta\boldsymbol{\varepsilon}^p_2 - \Delta\boldsymbol{\varepsilon}^p_1\right)\end{pmatrix} \tag{24}$$

Using any convenient norm, this quantity can be used to compute the relative error measure

$$R_n = \frac{1}{2}\max\left\{\frac{\left\|\Delta\boldsymbol{\sigma}'_2 - \Delta\boldsymbol{\sigma}'_1\right\|}{\left\|\overline{\boldsymbol{\sigma}}_n\right\|}, \frac{\left\|\Delta\boldsymbol{\varepsilon}^p_2 - \Delta\boldsymbol{\varepsilon}^p_1\right\|}{\left\|\overline{\boldsymbol{\varepsilon}}^p_n\right\|}\right\} \tag{25}$$

Following 1987 Sloan work, the current strain subincrement is accepted if R_n is not greater than some prescribed tolerance, $STOL$, and rejected otherwise. Regardless of whether the subincrement is accepted or rejected, the next pseudo time step is found from the simple relation

$$\Delta T_{n+1} = q\cdot\Delta T_n \tag{26}$$

where q is chosen so that R_{n+1} satisfies the constraint

$$q \le 0.8\sqrt{STOL/R_n}, \quad 0.1 \le q \le 1.1 \tag{27}$$

Two typical controls are finally incorporated. A minimum absolute step size, $\Delta T_{\min}$, and a step size is not allowed to grow immediately after a failed subincrement.

4 RESULTS AND CONCLUSIONS.

The behavior of a smooth rigid strip footing resting on an elastoplastic soil mass, governed by the modified SandPZ model presented above, is consider in order to analyze the performance of the proposed integration scheme. Due to the singularity at the edge of the footing and the strong rotation of the principal stresses, this example is a good test for assessing the integration strategy. As loading is prescribed in the form of displacements, an equivalent uniform pressure is found by summing the appropriate nodal reactions.

To assess the accuracy of the scheme, an estimate of the stress integration error is found directly from

$$\sigma_{error} = \frac{\left\| \boldsymbol{\sigma}'_{ref} - \boldsymbol{\sigma}' \right\|_2}{\left\| \boldsymbol{\sigma}'_{ref} \right\|_2} \tag{28}$$

Where $\boldsymbol{\sigma}'$ are the effective stresses obtained by the proposed integration scheme, $\boldsymbol{\sigma}'_{ref}$ are the reference effective stresses while $\left\| \bullet \right\|_2$ is the Euclidean norm. The reference effective stresses are obtained by the explicit Dormand-Prince integration scheme with a stress tolerance of $STOL = 10^{-9}$. Note that the reference stresses provide a very accurate set of stresses for the given mesh and loading sequence and all values are computed at the end of the last load increment.

The results for the analyses with 10 load increments of equal size are presented in Table 1. It can be observed how the uniform pressure over the footing after applying 4mm of vertical displacement is similar for all of the specified stress tolerances with values varying by less than 0.6% of the reference pressure.

Table 1: Smooth rigid strip footing on SandPZ layer. 10 load steps.

Stress Tolerance	Equivalent uniform pressure after a vertical displacement of 4mm [N/m^2]	% of the equivalent pressure obtained under Dormand-Prince integration scheme	σ_{error}
$STOL = 10^{-2}$	115320	0.14%	$1.7 \cdot 10^{-3}$
$STOL = 10^{-4}$	115450	0.02%	$1.7 \cdot 10^{-4}$

The error in the computed stresses for the proposed scheme, as defined by equation (28), is less than the integration tolerance for $STOL = 10^{-2}$ and within the order of magnitude for $STOL = 10^{-4}$. Therefore the tolerance $STOL$ thus gives a required error control.

Figure 1 shows the error spatial distribution induced by the proposed local integration

scheme with $STOL = 10^{-2}$ stress tolerance.

Figure 1: Error spatial distribution for $STOL=10^{-2}$ after a vertical displacement of 4mm

As expected, the errors derived by the local integration process under the proposed method are almost uniform in the computational domain. An exception can be observed under the edge of the footing where a maximum value of the error is attained. This error distribution is consistent with the boundary value problem considered as the edge of the footing represents a singularity.

REFERENCES

[1] Hughes, T.J.R., 1984, "Numerical implementation of constitutive models: rate independent deviatoric plasticity". *Theoretical Foundations for Large Scale Computations of Nonlinear Behavior*, Martinius Nijhoff Publisher, Dordrecht, pp. 29-57.

[2] Potts, D., Axelsson, K., Grande, L., 2002, "Guidelines for the use of advanced numerical analysis", Thomas Telford, London, pp. 177.

[3] Potts, D., and Ganendra, D., 1992, "A comparison of solution strategies for non-linear finite element analysis of Geotechnical Problems", Proccedings of the Third International Conference on Computational Plasticity, Anonymous CIMNE, Barcelona, pp. 803-814.

[4] Mira, P., Tonni, L., Pastor, M., 2009, "A Generalized Midpoint Algorithm for the Integration of a Generalized Plasticity Model for Sands", Int. J. Numer. Methods Eng., **77**(9) pp. 1201-1223.

[5] Sloan, W., 1987, "Substepping Schemes for the Numerical Integration of Elastoplastic Stress-Strain Relations", Int. J. Numer. Methods Eng., **24**(5) pp. 893-911.

[6] Sloan, W., Abbo, A. J., and Sheng, D. C., 2001, "Refined Explicit Integration of Elastoplastic Models with Automatic Error Control", Engineering Computations, **18**(1/2) pp. 121-154.

[7] Stickle, M. M., 2010, "Sobre La Respuesta Dinámica Del Terreno Bajo La Acción Del Olaje En Cajones Fondeados En Suelos Arcillosos", PhD Thesis, Universidad Politécnica de Madrid.

[8] Zienkiewicz, O.C., and Mroz, Z., 1984, "Mechanics of Engineering Materials" Wiley, pp. 655-679, Chap. 33.

[9] Pastor, M., Zienkiewicz, O. C., and Chan, A. H. C., 1990, "Generalized Plasticity and the Modelling of Soil Behaviour", Int. J. Numer. Analyt. Meth. Geomech., **14**pp. 151-190.

[10] Pastor, M., Zienkiewicz, O.C., and Chan, A.H.C., 1987, "Numerical Methods in Engineering: Theory and Applications", Martinus Nijhoff Publ., .

[11] Zytynski, M., Randolph, M., Nova, R., 1978, "On Modelling the Unloading-Reloading Behaviour of Soils", Int. J. Numer. Analyt. Meth. Geomech., **2**pp. 87-93.

[12] Houlsby, G. T., Amorosi, A., and Rojas, E., 2005, "Elastic Moduli of Soils Dependent on Pressure: A Hyperelastic Formulation", Géotechnique, **55**(5) pp. 383-392.

[13] Borja, R. I., Tamagnini, C., and Amorosi, A., 1997, "Coupling Plasticity and Energy-Conserving Elasticity Models for Clays", Journal of Geotechnical and Geoenvironmental Engineering, **123**(10) pp. 948-957.

[14] Abbo, A. J., 1997, "Finite Element Algorithms for Elastoplasticity and Consolidation", PhD Thesis, University of Newcastle.

[15] Butcher, J.C., 2003, "Numerical Methods for Ordinary Differential Equations", Wiley, Chichester.

XI International Conference on Computational Plasticity. Fundamentals and Applications
COMPLAS XI
E. Oñate, D.R.J. Owen, D. Peric and B. Suárez (Eds)

MICROMECHANICAL ANALYSIS OF DAMAGE AND FRACTURE IN SANDSTONE ROCK SPECIMENS, USING ZERO-THICKNESS INTERFACE ELEMENTS

D. GAROLERA, I. CAROL AND C.M. LÓPEZ

Dept. of Geotechnical Engineering and Geo-Sciences
Universitat Politècnica de Catalunya. BarcelonaTech (UPC)
Campus Nord UPC, 08034 Barcelona, Spain
e-mail: daniel.garolera@upc.edu, Ignacio.carol@upc.edu

Key words: Rock mechanics, fracture, zero-thickness interface.

Abstract. This numerical study deals with the analysis of rock specimens from a micro-mechanical point of view. The analysis is based on the Finite Element Method (FEM) with fracture-based zero-thickness interface elements, and numerically generated micromechanical geometries. In previous studies this approach has been used very successfully to represent the mechanical behaviour of concrete and other quasi-brittle materials under a variety of loading scenarios. The current study, motivated by longer-term research on rock sanding in oil wells, is focused on the capability of the model to represent the type of failure observed near the walls of tunnels or holes bored in a medium subject to initial compressive stresses. In this context, the microstructure of sandstone rock is generated *via* Voronoi tessellation. Interface elements are inserted along all polygon contacts, and, for some calculations also within the polygons themselves. The two main loading scenarios explored are direct uniaxial compression, and uniaxial extension after hydrostatic loading. Besides a general good capability to represent the desired behaviour, the results show that direct uniaxial compression requires intra-granular cracks in the model in order to reach failure. However, if the same final loading state is reached via initial hydrostatic loading followed by uniaxial extension, (as typical in tunnel or borehole walls), then failure kinematics changes and failure may take place with the inter-granular interfaces exclusively (i.e. no need to consider intra-granular cracks to represent failure).

1 INTRODUCTION

In this paper, a micromechanical approach based on FEM with zero-thickness interface elements is described for the analysis of cemented granular materials such as sandstone rock, including the effects of inter-granular and intra-granular cracking and fracture. Instead of the phenomenological parameters used in the traditional continuum-based formulation of the FEM, the proposed methodology is capable of reproducing complex behaviour using only a few physical parameters, although this is at the expense of discretizing the grain microstructure explicitly. In previous studies this approach has been used very successfully to represent the mechanical behaviour of concrete and other quasi-brittle materials under a

variety of loading scenarios ([1], [2] and [3]).

2 MICROSTRUCTURAL MODELLING

2.1 Microstructure

In the current study, individual grains of the sandstone rock material are represented explicitly in the FE mesh. The geometry of the grains is generated numerically *via* Voronoi tessellation over a grid of points, which are randomly perturbed from their original regularly-spaced positions. Zero-thickness fracture-based interface elements [4] inserted between adjacent grains represent the behaviour of the inter-granular contact including the cementing material. With regard to the grains themselves, two different options have been explored: (1) the grains are considered as linear elastic and therefore they cannot crack, only inter-granular cracks are allowed in this first option; and (2) additional interface elements are inserted within each grain, along all radial lines connecting each grain corner to its center, so that intra-granular cracking becomes also possible (Fig.1).

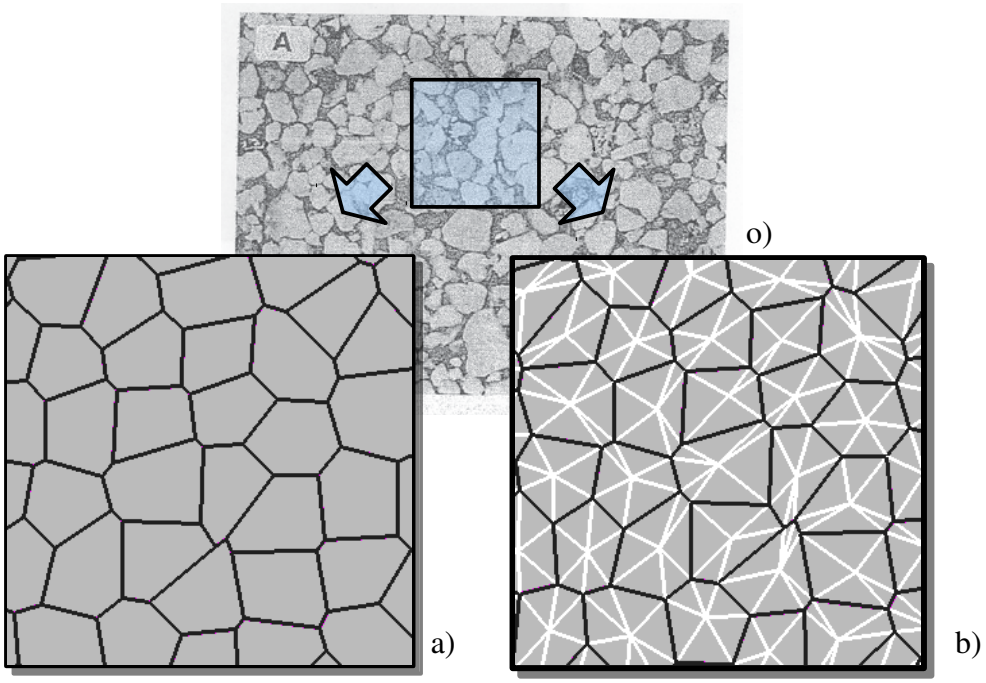

Figure 1: Microstructure representation. o) Micro-photograph from a sandstone sample; a) interface layout considering linear elastic grains (dark lines); and b) interface layout considering also the possibility of intra-granular cracks (pale lines).

2.2 Interface constitutive law

An essential ingredient of the approach described is the constitutive equation of the interface elements, which must be formulated in terms of normal and shear stress tractions (σ,τ) and the corresponding relative displacements (u,v). It consists of an elasto-plastic formulation incorporating some concepts of fracture mechanics. The model is defined by a hyperbolic fracture surface (yield surface) described by three parameters: c (cohesion),

χ (tensile strength) and ϕ (friction angle) (Eq. 1).

$$F\left(\sigma,p\left(W^{cr}\right)\right)=\tau^2-\left(c-\sigma\tan\phi\right)^2-\left(c-\chi\tan\phi\right)^2 \tag{1}$$

The evolution of the model parameters is controlled by an energy-based history variable W^{cr} (energy spent in fracture processes per unit area of the interface), the increments of which are calculated for each increment of the loading process using different expressions in tension and compression (case in which basic friction is substracted) (eq. 2):

$$dW^{cr}=\sigma\delta u_N^{cr}+\tau\delta u_T^{cr}\quad\left(\sigma\geq 0\right) \tag{2}$$

$$dW^{cr}=\tau\delta u_T^{cr}+\left(1-\left|\sigma\tan\phi/\tau\right|\right)\quad\left(\sigma<0\right)$$

The hardening/softening laws then define the evolution of the surface parameters in terms of the history variable W^{cr}, incorporating as parameters G_f^I (fracture energy in mode I) and G_f^{IIa} (fracture energy in mode IIa) [4].

The numerical integration of the constitutive law is implemented using an algorithm based on an implicit procedure (backward-Euler) with sub-incrementation [5]. One of the features of this procedure is that it provides an always consistent tangent matrix, even in the case of sub-increments.

3 RESULTS FOR THE HOLLOW CYLINDER TEST UNDER EXTERNAL PRESSURE

The study of this test is motivated by long-term research on sand production in oil wells [6]. In that context, the hollow cylinder test under increasing external pressure is widely used to understand wellbore stability problems. [7] and [8].

For simplicity, the numerical model was reduced to the analysis of a 2D transversal cross-section of the cylinder, under the assumptions of small deformation and plane strain (Figure 2). The darker inner corona of the domain was discretized using Voronoi polygons and interfaces, and the external pressure was applied on the outer boundary, while the prescribed nodes are reduced to a minimum of four (see Fig 2) in order to not to restrain the corresponding deformation. Given the material non-linearity provided by the interface elements, the external pressure was applied in small increments.

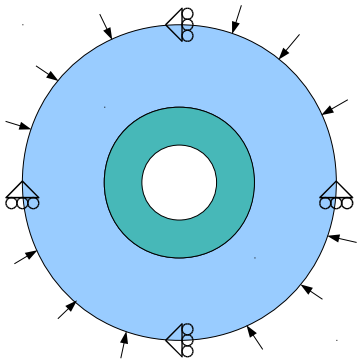

Figure 2: Schematic hollow cylinder test section with boundary conditions.

Some preliminary analyses of this case led to unexpected results. Using a friction angle of 30 degrees for the interfaces, under the level of expected failure pressure, the calculation was practically in elastic regime with hardly a few interfaces opening near the inner boundary. In order to get a failure pattern similar to experiments with the same mesh, the friction angle of the interfaces had to be lowered to unphysical values near 5 degrees.

A couple of images of the opened cracks and deformed mesh of the numerical solution in this case are shown in figure3. As it can be seen in the figure, in spite of the unrealistic friction value, the main failure patterns reported in the experimentation literature [7] are well captured: spalling (tensile break-offs) and shear-bands (breaks in shear compression mode that produce some typical spirals).

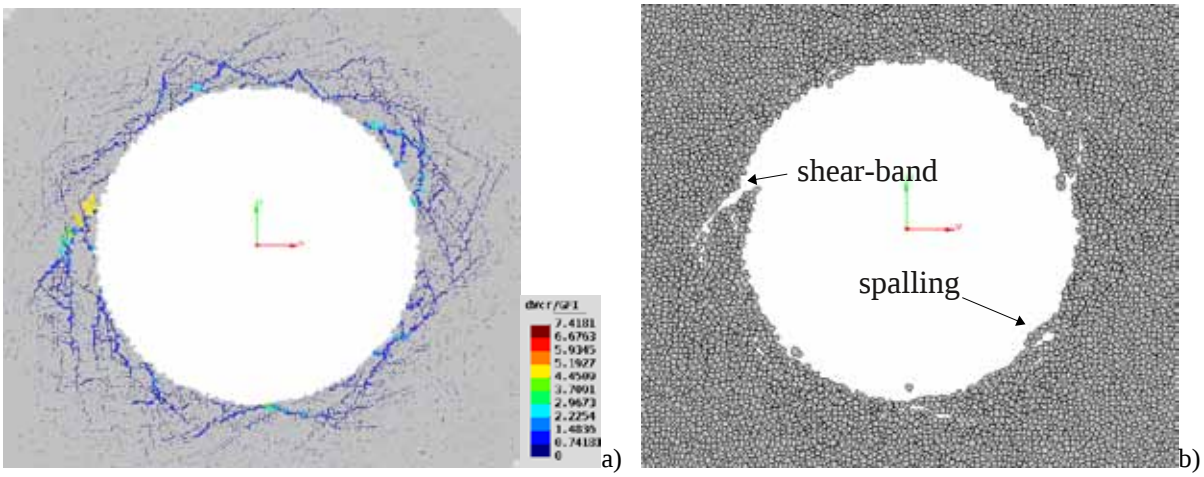

Figure 3: numerical results for tan(5); left, energy spent of fracture at the end of the load application; right, final deformation mesh (x25).

However, unrealistic friction angles were considered unacceptable and attention was turned onto a different option: introducing interface elements across grains, in order to allow for the development of intra-granular cracks. However, introducing intra-granular interface elements in the previous FE mesh, in the way shown in figure 1b, increases considerably the number of degrees of freedom. For this reason the study of this new approach to the problem was first studied on smaller specimens.

4 UNIAXIAL COMPRESSION AND EXTENSION TESTS OF 1X1CM SPECIMENS

The specimens considered for introducing inter-granular interfaces are square specimens with dimensions 1x1cm^2 and grain size of about 0,25 mm, which leads to approximately 40x40 grains over the specimen as represented in figure 4a. In order to open the possibility of intra-granular cracking, zero-thickness interface elements have been inserted, not only along the inter-granular boundaries, but also across grains, as depicted in figure 1b. This specimen has been analysed under uniaxial compression, and under hydrostatic pressured followed by uniaxial extension scenarios.

In order to evaluate the influence of intra-granular cracking, three different assumptions

have been considered regarding the strength parameters of intra-granular interfaces:

a. They are assumed as linear-elastic (and very high stiffness K_N and K_T); in this case these interfaces, even if present, cannot crack.
b. They are allowed to crack, but strength parameters have double values than those of inter-granular interfaces.
c. They are allowed to crack, with same strength parameters as inter-granular interfaces.

Table 1 contains the list of parameters used in the calculations.

Table 1: Material properties used in simulations.

Grain (cont.)	**Inter-grain interface**	**Intra-grain interface**	
		Fracture-grain	**Fracture-grain (double)**
E = 34.0e3 MPa	Kn = 1.0Ee9 MPa/m	Kn = 1.0Ee9 MPa/m	Kn = 1.0Ee9 MPa/m
ν = 0.27	Kt = 1.0Ee9 MPa/m	Kt = 1.0Ee9 MPa/m	Kt = 1.0Ee9 MPa/m
	Tan(ϕ) = 0.5773	Tan(ϕ) = 0.5773	Tan(ϕ) = 0.8389
	χ = 1.0 MPa	χ = 1.0 MPa	χ = 2.0 MPa
	C = 4.0 MPa	C = 4.0 MPa	C = 8.0 MPa
	GfI = 1.0E-5 MPa*m	GfI = 1.0E-5 MPa*m	GfI = 2.0E-5 MPa*m
	GfI = 1.0E-4 MPa*m	GfI = 1.0E-4 MPa*m	GfI = 2.0E-4 MPa*m
	σ_{dil} = 10.0 MPa	σ_{dil} = 10.0 MPa	σ_{dil} = 20.0 MPa

4.1 Uniaxial compression test

Figure 4 depicts the geometry of the mesh and the boundary conditions used in this case. Load application is performed by means of a prescribed displacement on the upper side of the specimen. Due to the expected softening behaviour, an arc-length strategy was employed to control post-peak response.

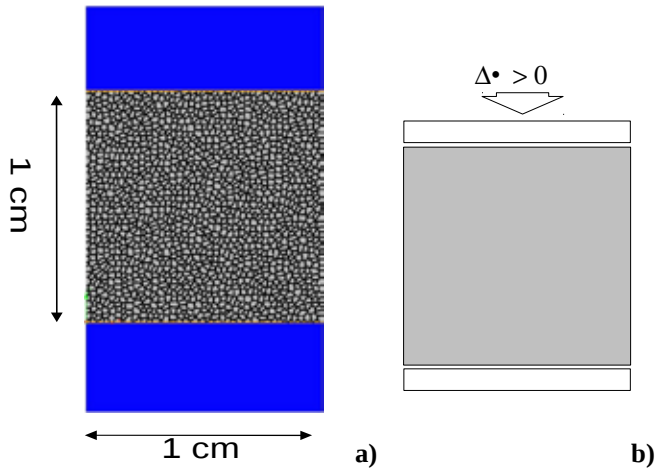

Figure 4: Uniaxial compression test. a) geometry; b) boundary conditions.

Figure 5 shows the average strain-stress curves obtained for the three scenarios of intra-

granular strength. It can be observed that intra-granular strength values influence dramatically the resulting behaviour of the overall material. Not allowing intra-granular cracking leads to an upper bound of the mechanical behaviour for which failure under uniaxial compression is never reached. On the other end, case c) approaches the behaviour of a quasi-brittle material without the granular structure considered (since cracks can develop equally through grains as in between grains), which leads to a lower bound of the overall strength; and finally option b) with the right parameters should represent a more realistic intermediate case.

As it can be also seen in Fig 5, the material post-peak response is also greatly influenced by grain resistance; as intra-grain resistance is increased, the model behaviour becomes more brittle.

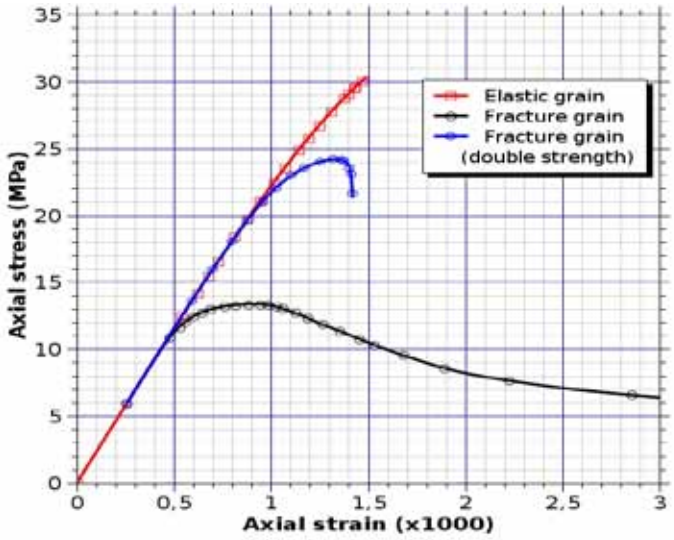

Figure 5: Average strain-stress curves for the uniaxial compression simulations, with the three different assumptions for intra-granular cracking.

In figure 6, the general crack pattern obtained and some enlarged detail of a section of a main macro-crack, are depicted for the three assumptions of intra-granular strength. For case b) with double strength, it may be clearly observed that cracks are basically opening/sliding around grains except at certain very specific points where grains crack due to the high stress concentration, while for case c) this happens systematically, and for case a) this does not happen at all. These details of micromechanical cracking may help understanding the resulting overall stress-strain curves of figure6. A first conclusion of these results is that the direct uniaxial compression test is very sensitive to grain strength, and that some form of intra-granular cracking must be allowed for a realistic description of the direct uniaxial compression test of a granular material using Voronoi-generated grain geometry.

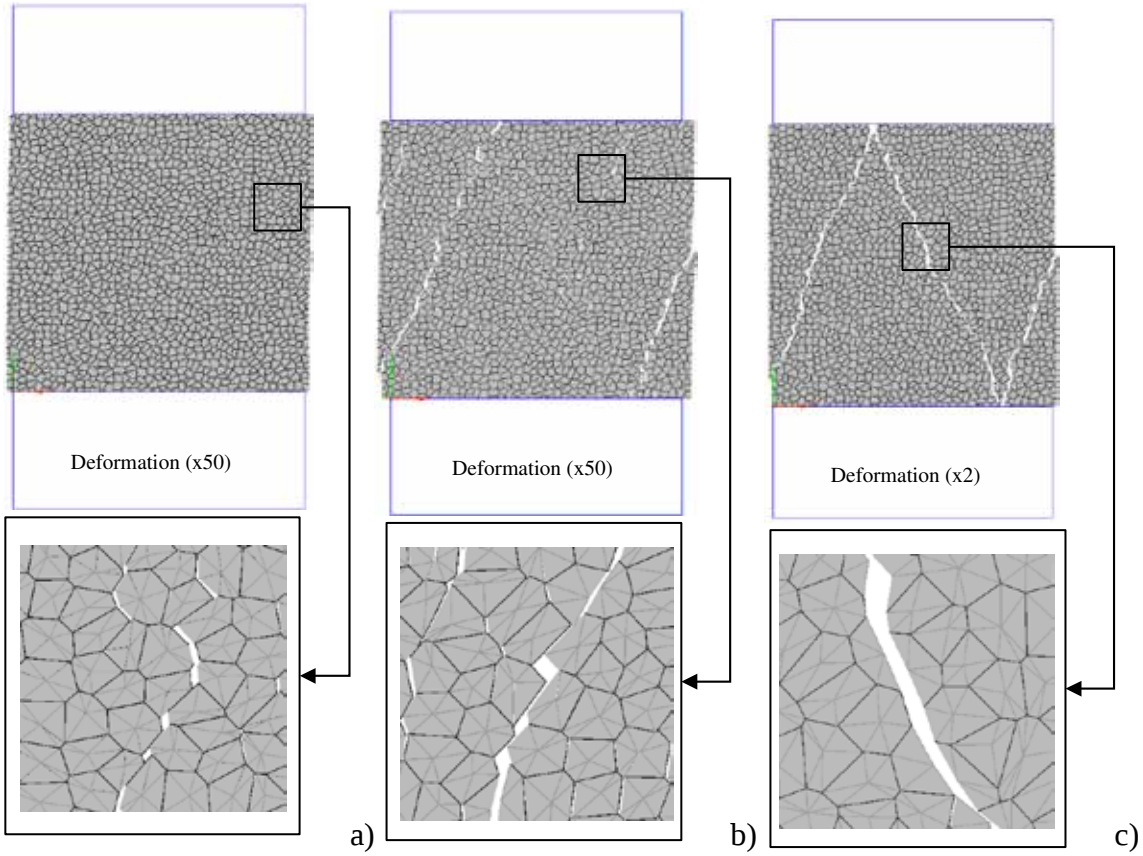

Figure 6: Mesh deformations for UCT at different values of grain resistance: a) elastic grains; b) fracture grains (double resistance) and c) fracture grains (single resistance).

4.2 Uniaxial extension test

The micro-structural grain geometry and meshes for this analysis are the same used for the uniaxial compression test in the precedent Sect 4.1. The first set of calculations is obtained without allowing intra-granular cracks, i.e. the grains are considered linear elastic. The loading and boundary conditions are represented in figure 7, and are applied in two steps: first, a hydrostatic stress is applied as a distributed load over top and right sides of specimen, while left and lower sides sit on rigid frictionless platens. And second, a progressively increasing horizontal displacement (extension) is prescribed to the right platen, while load is maintained constant in the vertical direction. In this way, the horizontal stress will be progressively decreased, therefore in the limit approaching a uniaxial compression. Note that this is the same final state as applied in the previous section, although in this case this is achieved following a totally different stress path, and that will make a significant difference.

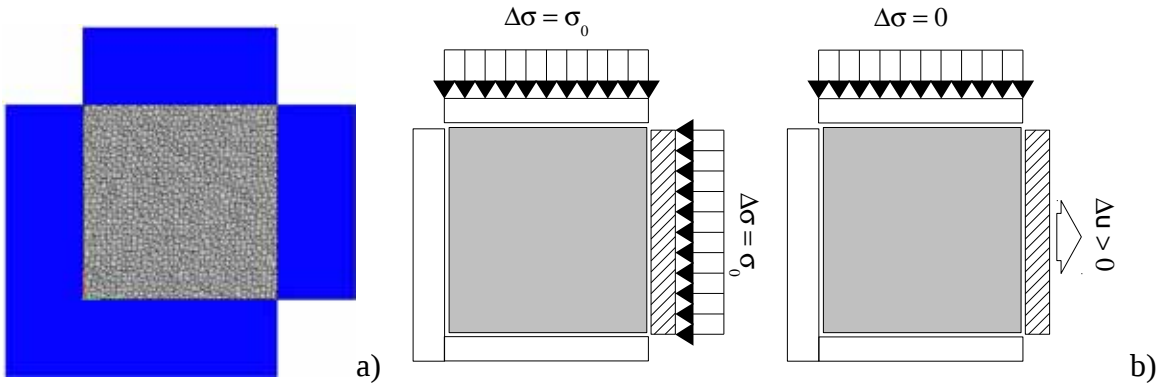

Figure 7: Extension test. a) geometry; b) boundary conditions.

This analysis (with elastic grains) has been repeated for different values of the initial hydrostatic load, and the results obtained are shown in figures 8 and 9. In figure 8, the average stress-strain curves for the specimen are represented, with the (computed) horizontal average stress on the vertical axis, and the corresponding average strains on the left horizontal axis. On the right horizontal axis, the transversal (in this case vertical) average strain is represented. Note that in this direction load is maintained constant. In the curves it is shown that as the initial confinement is higher, the material behaviour becomes more ductile, with a progressively more reduced tensile response, which, eventually (for a sufficiently high initial confinement) disappears altogether.

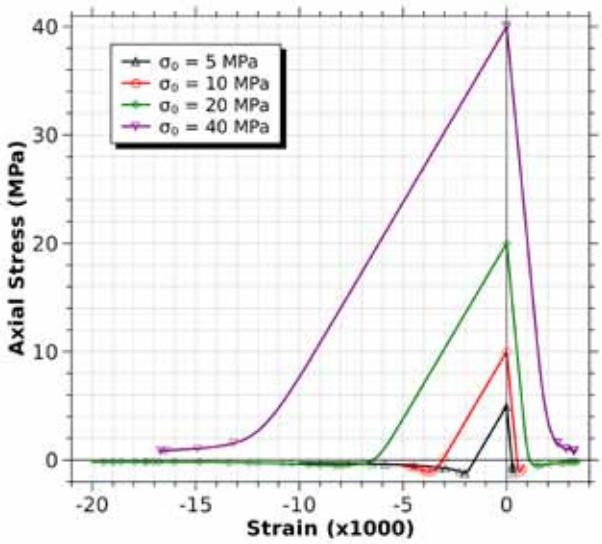

Figure 8: Strain-stress relationship for the extension test. The graph shows, for the intra-grain elastic case, results at different confinement levels.

In figure 9, the horizontal displacement field obtained at the end of the same calculations is shown via deformed meshes with a superimposed gray scale. The diagrams clearly show that the lower the initial confinement stress, the more brittle failure becomes. Likewise, the lower

the initial confinement, the more pronounced the cracking is, and the more clearly localized into macro-cracks the displacement jumps become, in contrast to the almost uniformly distributed cracking observed for the case of highest confinement σ = 40 MPa (lower right diagram).

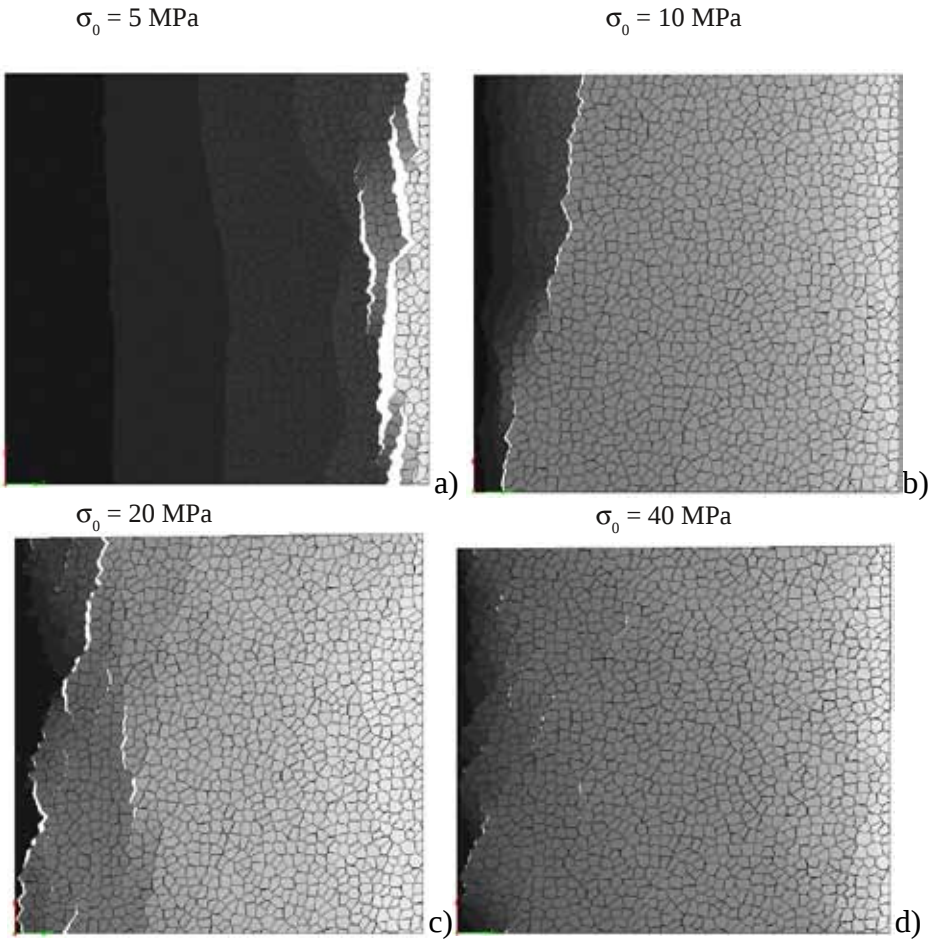

Figure 9: Deformation meshes (x5) for extension test for different initial confining pressures with elastic grains. a) σ_0 = 5 MPa; b) σ_0 = 10 MPa; c) σ_0 = 20 MPa and d) σ_0 = 40 MPa.

The effect of intra-granular cracking is also studied for this uniaxial extension test, by carrying out two additional calculations in which intra-granular interfaces are allowed to crack, one of them with same strength parameters as the inter-granular cracks, and the other with roughly double strength (same sets of parameters already used for the uniaxial compression test, see Table 1). Both calculations were performed for the same initial confinement pressure of 10 MPa, and the results can be compared to the results for this level of initial confinement and elastic grains already shown in previous figures 8 and 9.

In figure 10, the average stress-strain curves along the horizontal direction are represented for the two new cases with intra-granular cracking, together with the previous curve of elastic grains. In figure 11 the fields of horizontal deformation obtained in these calculations are depicted. It can be seen that the curves for elastic grains and for fracturing grains with higher

strength (that, from the material perspective, is a definitely more realistic assumption than that of equal strength) look very much alike. This, on the other hand, seems consistent with a kinematics of extension, cracks being opened predominantly in tensile mode I rather than the shear mode observed in the direct compression test (Sec. 4.1).

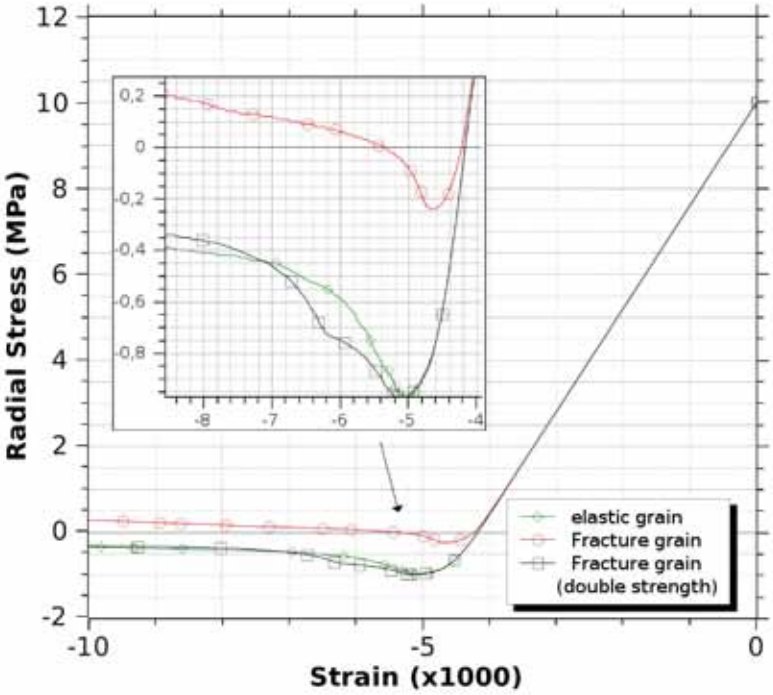

Figure 10: Average strain-stress curves for the extension test, assuming: a) elastic grains; b) fracturing grains (double strength) and c) fracturing grains (same parameters as inter-granular cracks).

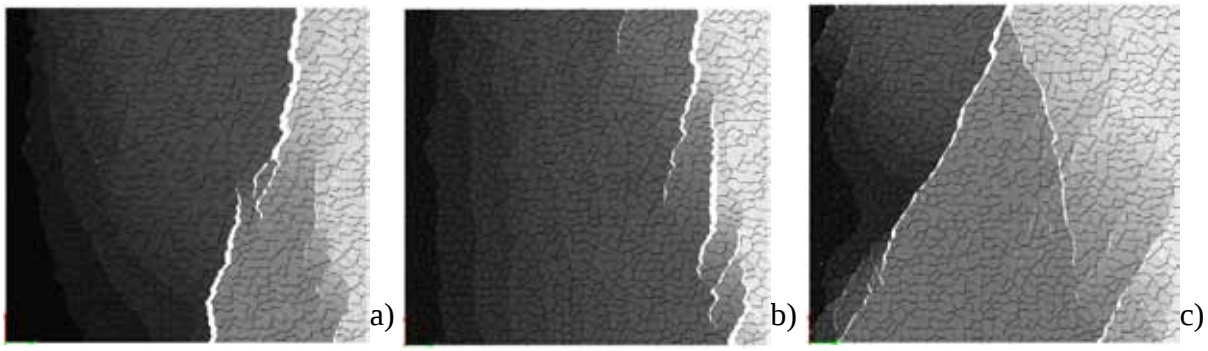

Figure 11: Horizontal deformation field for the uniaxial extension test for 10 MPa of initial confining pressure, assuming: a) elastic grains; b) fracturing grains (double strength) and c) fracturing grains (same parameters as inter-granular cracks).

5 CONCLUSIONS REMARKS

Micromechanical analysis via FEM with zero-thickness interface elements and Voronoi-

generated geometries seems capable of reproducing fracture propagation in cemented granular rock materials. In particular, the results presented show that, for direct uniaxial compression, intra-granular failure must be considered in the analysis in order to capture the overall failure kinematics and realistic peak loads. However, if the same uniaxial compressive stress failure state is reached via a more complex loading paths such as uniaxial extension in the transverse direction after an initial hydrostatic state, the kinematics of failure changes significantly from sliding to opening, and similar meshes without intra-granular interfaces seem sufficient to realistically represent failure.

4 ACKNOWLEDGEMENTS

This research is supported by grant BIA2009-10491, funded by MICINN (Madrid, Spain). The first author also wishes to acknowledge his current support from project 2009SGR-180 funded by AGAUR-Generalitat de Catalunya (Barcelona).

REFERENCES

[1] Carol, I., López, C. M. and Roa, O., "Micromechanical analysis of quasi-brittle materials using fracture-based interface elements". International Journal for Numerical Methods in Engineering, 52, p. 193-215 (2001).

[2] López, C. M., Carol I. and Aguado, A., "Meso-structural study of concrete fracture using interface elements. I: numerical model and tensile behavior". Materials and Structures, Vol. 41(3), p. 583-599 (2008).

[3] Caballero, A., Carol, I. and López, C. M., "A meso-level approach to the 3D numerical analysis of cracking and fracture of concrete materials". Fatigue and Fracture of Engineering Materials and Structures, Vol. 29(12), p. 979-991 (2006).

[4] Carol, I., Prat, P. and López, C.M., "A normal/shear cracking model. Application to discrete crack analysis" ASCE J. Engrg. Mech., Vol 123(8), p. 765-773 (1997).

[5] Caballero, A., Willam, K. and Carol, I., "Consistent tangent formulation for 3D interface modeling of cracking/fracture in quasi-brittle materials". Computer Methods In Applied Mechanics And Engineering, Vol. 197, p. 2804-2822 (2008).

[6] Garolera, D., López, C.M., Carol, I. and Papanastasiou, P., "Micromechanical analysis of the rock sanding problem". Journal of the Mechanical Behaviour of Materials. Vol. 16(1-2), p. 45-53. (2006).

[7] Cook, J.M., Bradford, I.D. and Plumb, R.A., "A study of the physical mechanisms of sanding and application to sand production prediction". Presented in European Petroleum Conference in London, UK, October 1994. SPE paper No. 28852, (1994).

[8] Papamichos, E., Tronvoll, J., Vardoulakis, I., Labuz, J.F., Skjærstein, A., Unander, T.-E. and Sulem, J., "Constitutive testing of Red Wildmoor sandstone". Mech. Cohes.-Frict. Mater. 5(1), p. 1-40 (2000).

XI International Conference on Computational Plasticity. Fundamentals and Applications
COMPLAS XI
E. Oñate, D.R.J. Owen, D. Peric and B. Suárez (Eds)

NUMERICAL ANALYSIS AND SAFETY EVALUATION OF A LARGE ARCH DAM FOUNDED ON FRACTURED ROCK, USING ZERO-THICKNESS INTERFACE ELEMENTS AND A c-ϕ REDUCTION METHOD

I. ALIGUER*, I. CAROL* AND E.E. ALONSO*

* Geotechnical Engineering and Geo-Sciences Department (DETCG)
ETSECCPB (School of Civil Engineering)
UPC (Universitat Politécnica de Catalunya), 08034 Barcelona
e-mail: ignasi.aliguer@upc.edu, ignacio.carol@upc.edu, eduardo.alonso@upc.edu

Key words: FEM, Rock Mechanics, Strength Reduction, Slope Stability

Abstract. A 140m high arch dam in the Pyrenees, built in the 50s, is founded on fractured limestone rock. Since the beginning of the design process, two main families of discontinuities were identified. The dam was built very close to the end of the narrow part of the valley, which raised stability concerns early on. In the late 80s - early 90s, a numerical study of the dam was developed at the Dept of Geotechnical Engineering and Geo-Sciences UPC (School of Civil Engineering) UPC, using a progressively more realistic series of models and approaches, culminating with a 3D discretization of the dam plus rock mass, in which discontinuities were explicitly represented using zero-thickness interface elements with frictional constitutive laws in terms of stress tractions and the corresponding normal and shear relative displacements. In the present study, that dam and its foundation are revisited and reanalyzed with current, more advanced numerical tools and a third family of rock joints which has been identified more recently. The same mesh is used as a departure point, although a much more detailed description is now possible. The analysis is also approached in a different way, now using the traditional $c-\phi$ reduction method developed and implemented specifically for non-linear zero-thickness interfaces.

1 INTRODUCTION

Canelles dam is a 151m high arch dam loacted in the Pyrennes (Catalunya, Spain), which was completed in April 1958. Since this date, different kinds of analyses have been carried out. Monitoring systems, model tests and numerical analyses have been combined to provide engineering evaluations of the dam safety [3, 4]. The most important one,

concerning the stability of the dam and both abutments, was performed during the 90s decade. The results and analysis procedures are reported in several references. [1, 2, 9, 13]

The non-linear calculation was carried out for real values of the gravity and water pressure loads, and safety was evaluated a posteriori by post-processing the stresses obtained along all interface families. A number of potential failure mechanisms were selected, and for each of them resisting forces and acting forces were evaluated, and safety coefficients were obtained by assuming a proportional increase of stress tractions with increasing water pressure or a decreasing resistance given by lower friction angle. That first study led to the conclusion that the dam was basically safe and the worst scenario corresponded to a safety coefficient between 2 and 3.

The dam is founded on cretaceous massive limestone that is fractured by two sets of discontinuities (Fig. 1). A main set of vertical joints is oriented parallel to the valley. The other family is a set of N-S planes which dip an average of 55° towards the West (nearly downstream). A Laser-Scanner field campaign in 2009 led to the identification of a third set of discontinuities. In addition, bedding planes dip 45° upstream. Due to the spatial arrengement of the three rock discontinuity families, several rock blocks have fallen down to the canyon, which keeps the facilities and people in danger. That has motivated to consider a new retaining wall in the left abutment. As a consequence, an analysis, this time focused only on the left abutment, has been recently started to evaluate the safety improvement that could be achieved with the construction of the wall.

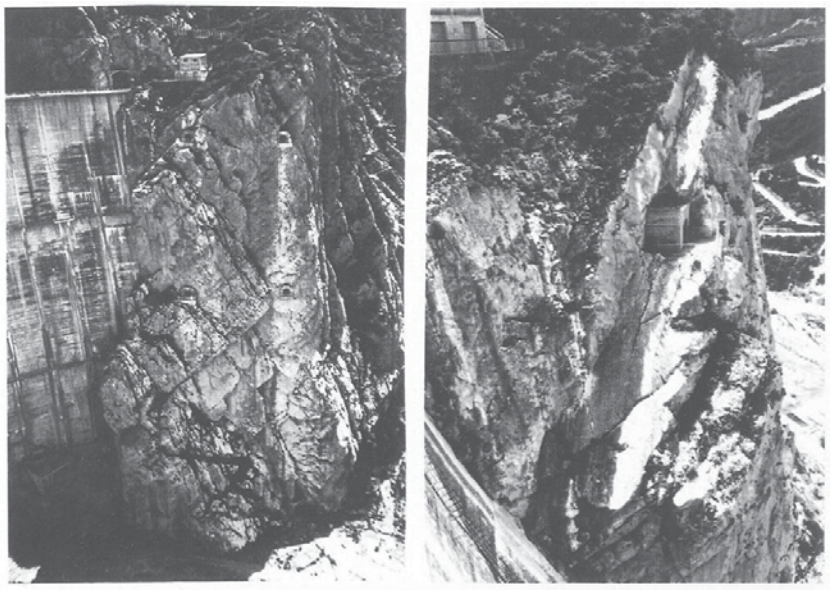

Figure 1: General view of the left abutment and anchorage tunnels

According to the 3D geometry of the canyon and the arch dam, the Finite Element Method is required to reach the analysis purpose. Considering the new set of joints and

other constructive details such as the new wall and four existing anchorage tunnels, the former model has been rebuilt. Moreover, block equilibrium analysis has been performed as a first simplified evaluation of the safety factor, which involves the retaining wall.

Safety analysis in engineering practice often requires simplifications such as the concept of safety factor, which tries to provide a single scalar simplified mesure of the distance between the failure state and service conditions.

2 MODELING THE LEFT ABUTMENT

2.1 Geometric model

As described in [1], a safety 3D FEM analysis has a number of requirements, including sufficient number of elements across the dam thickness in order to capture bending, and a sufficient number of joints of each family in the rock mass in order to include the most relevant failure mechanisms.

For the current analysis, the previous discretization has been verified with digital satellite topodata, and has been used as a basis fot the new geometric model, including: dam geometry, rock mass surface topography, right abutment retaining wall, grouted curtain and bedding and vertical joint sets. Additionally, left abutment retaining wall, reinforced concrete anchorage tunnel and 4 new family planes have been introduced only in the left abutment. The new family of discontinuities discovered, has been introduced in the geometric model through a total of four planes strategically located so that they cover the most significant mechanisms without generating an excessive number o geometric intersections with the previous existing planes and surfaces. The four selected planes are:

1. Plane defining a mechanism that does not involve the wall projected.
2. Plane intersecting the dam's top.
3. Plane crossing the new wall's base.
4. Plane defining a mechanism that is not supported by the anchorage tunnels.

Finally, in terms of rock discontionuities the model includes: 12 vertical joints (jV 1-12), 5 bedding planes (jS 1-5) and 4 new family planes -N-S orientation- (jN 1-4). (Fig. 2)

2.2 Material Parameters

The shear strength parameters were obtained from the existing information form large scale in situ shear tests on vertical joints ($c = 0.124MPa$ and $\phi' = 18.7°$) and bedding planes ($c = 0.135MPa$ and $\phi' = 35.2°$) [1]. For the new family planes, an anular shear test of the infill clay was performed yielding a residual strength value of $\phi'_{res} = 27°$.

Normal and shear stiffness moduli of all joints have been taken high as usual in numerical analysis with zero-thickness interfaces, in order to ensure the continuity of both sides of the joint if the shear stress does not reach the shear strength values ($K_n = K_t = 10^5 MPa$).

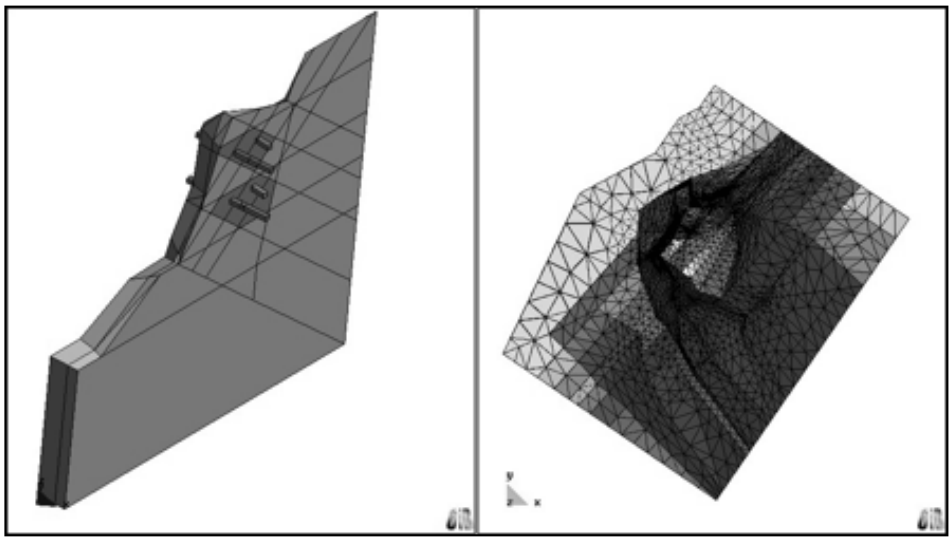

Figure 2: Vertical joint section (left). FEM mesh for the left abutment (right)

3 FINITE ELEMENT ANALYSIS

3.1 FEM Code

FEM computations have been performed using code DRAC [5, 14]. This is an in-house developed code which was first applied to rock mechanics problems considering zero-thickness interface elements, and later also used for fracture mechanics and a variety of other material and structural analysis applications. Its main flow diagram consists of 4 nested loops which correspond to:

Stage loop In each stage new geometry can be added (construction) or removed (excavation).

Step loop Load systems can be applied to each geometry.

Increment loop Each load can be applied in increments.

Iteration loop In non-linear analysis, this loop controles the number of iterations to convergence.

3.2 Interface constitutive model

The constitutive model which was implemented in the code and it is the most widely used for geotechnical analysis. It is a general elastoplasticity law which was formulated in terms of normal and shear stress and normal and tangential relative displacements [7]. However, a simplified version exists that permits an explicit integration [8]. The main simplifying assumptions are:

1. Perfect plasticity.
2. No dilatancy.
3. Linear elastic relationship between the normal stress and the normal relative displacement in compression (zero normal stress in tension).

The yield surface in the $\sigma - \tau$ plane, where $\tau = \sqrt{\tau_1^2 + \tau_2^2}$, is defined by (Fig. 3):

$$F = \tau^2 + \tan^2\phi(\sigma^2 + 2a\sigma) \equiv 0 \tag{1}$$

Due to the expression of the yield surface and the elastic relationship between the normal stress and the normal relative displacement, once the normal stress is known, the ratio between τ_1 and τ_2 is the only unknown in the integration of the constitutive law. The θ angle, which represents this ratio can be obtained by solving the following differential equation:

$$\frac{d\theta}{\sin(\beta - \theta)} = \frac{K_t}{K_n}\frac{\Delta v}{\Delta u}\frac{d\sigma}{\tan\phi\sqrt{\sigma^2 + 2a\sigma}} \tag{2}$$

Integrating between two instants leads to:

$$\tan\left(\frac{\beta - \theta}{2}\right) = \tan\left(\frac{\beta - \theta_0}{2}\right)\left(\frac{\tau + \sqrt{\tau^2 + a^2\tan^2\phi}}{\tau_0 + \sqrt{\tau_0^2 + a^2\tan^2\phi}}\right)^{-\frac{K_t}{K_n}\frac{\Delta v}{\Delta u\tan\phi}} \tag{3}$$

where β relates the imposed tangential relative displacements increments $\Delta v_1, \Delta v_2$.

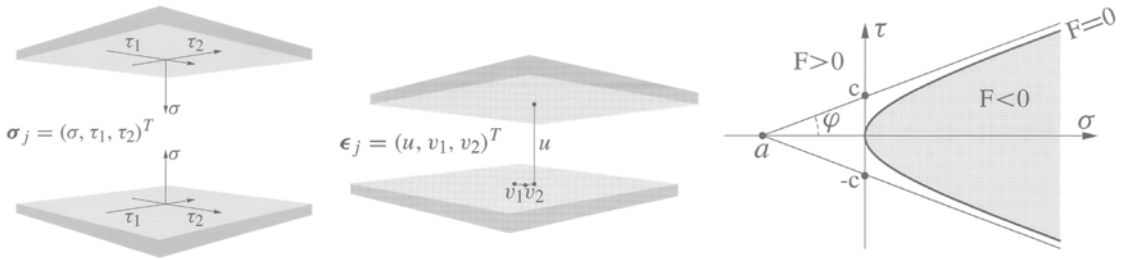

Figure 3: Constitutive model stress and displcement variables definition (left, center). Yield surface (right)

3.3 $c - \phi$ reduction

The first reference mentioning the idea of reducing the strength parameters of the material to evaluate the Safety Factor seems to be that of Zienkiewicz et al., 1975 [15], for a slope stability problem in soil. Later, various authors have used this method for other soil mechanics problems [6,10,12] Generally speaking, the Safety Factor (SF) is defined as

the scalar factor by which one has to reduce strength parametres in order to reach failure. Hence, at failure, the following relationships can be stablished:

$$c'_{mob} = \frac{c'}{SF} \qquad \phi'_{mob} = \arctan\left(\frac{\tan\phi'}{SF}\right) \tag{4}$$

In the numerical analysis of geotechnical problems using the FEM there are a few ways to define failure, but the most common (also used in this case) is the lack of convergence of the iterative calculation. In this study, the $c-\phi$ reduction method has been implemented as a modification of the constitutive model of section 3.2 with evolving c and ϕ. In this new implementation c and ϕ are being progressively reduced (softening) in connection to some fictitious time α:

$$\tan\phi \equiv \Phi = \Phi_0 - \frac{\Delta\Phi}{\Delta\alpha}(\alpha - \alpha_0) \tag{5}$$

Therefore, the right hand side of the ecuation (2) can be reformulated using this variable:

$$\frac{K_t \Delta v}{\Delta\alpha} \frac{d\alpha}{(-f\alpha + g)\sqrt{A\alpha^2 + B\alpha + C}} \tag{6}$$

where:

$$f = \frac{\Delta\Phi}{\Delta\alpha}$$

$$g = \Phi_0 + \frac{\Delta\Phi}{\Delta\alpha}\alpha_0$$

$$A = \left(\frac{\Delta\sigma}{\Delta\alpha}\right)^2$$

$$B = 2\left(\sigma_0\frac{\Delta\sigma}{\Delta\alpha} + a\frac{\Delta\sigma}{\Delta\alpha} - \alpha_0\left(\frac{\Delta\sigma}{\Delta\alpha}\right)^2\right)$$

$$C = \sigma_0^2 + 2a\sigma_0 - 2\sigma_0\alpha_0\frac{\Delta\sigma}{\Delta\alpha} - 2a\alpha_0\frac{\Delta\sigma}{\Delta\alpha} + \alpha_0^2\left(\frac{\Delta\sigma}{\Delta\alpha}\right)^2$$

In the same way as the previous section an analytical integration can be done to obtain the angle θ.

3.4 Verification examples

As a first example, a classic rock slope stability problem has been considered [11]. The geometry is represented in Fig.4. For this case, using the Limit Equilibrium Method the Safety Factor can be easily determined using a Mohr-Coulomb type failure criteria:

$$SF = \frac{T_{res}}{T_{mob}} = \frac{2c}{\gamma H \sin\beta\cos\beta} + \frac{\tan\phi}{\tan\beta} \tag{7}$$

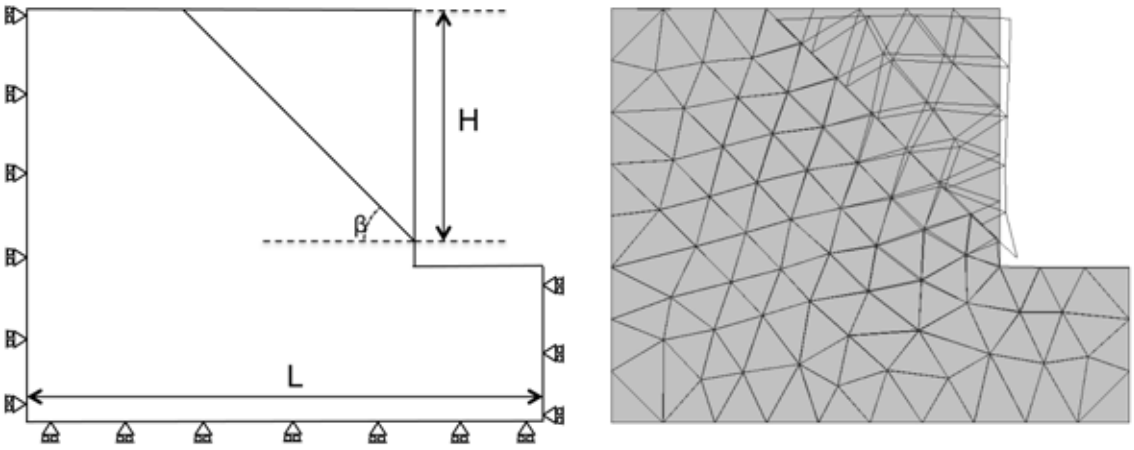

Figure 4: Geometric definition of the rock slope, FEM mesh original and deformed at failure.

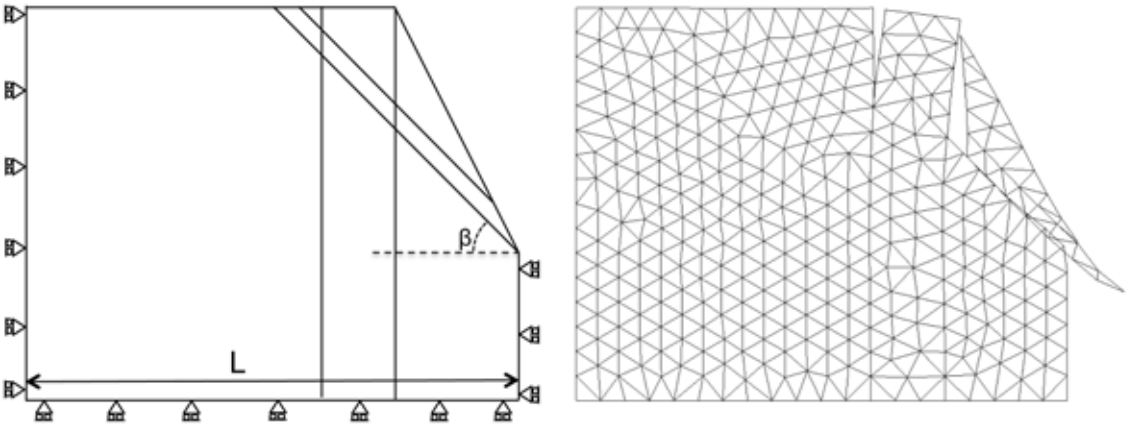

Figure 5: Geometric definition of the rock slope, FEM mesh deformed at failure.

The numerical example is with the following dimensions and parameters: L=100m, H=45m, $\beta = 45°$, $\tan\phi_{res} = 1.4$, c=10kPa (for both Mohr-Coulomb Limit Equilibrium and hyperbolic model). Introducing all these values into (7) a Safety Factor of 1.43864 results.

In the FEM computation a reference increment of $\Delta \tan\phi/\Delta t = -0.05$ was imposed, and the failure occured for a value of $\tan\phi_{mob} = 1.065$. Hence, a Safety Factor of 1.315 can be obtained using the $c - \phi$ reduction method.

In this case, as the rock matrix was considered linear elastic, the failure could only happen by sliding along the one single rock joint considered. Nevertheless, when more discontinuities are considered the failure mechanism turns out not so obvious.

The second example is also a 2D rock slope stability, but for the case of four joints intersecting each other. As a result, failure mechanisms that involve more than one joint can arise and no simplified formula such as (7) can be used. As can be observed in Fig.5,

two dipping and two vertical joints are considered. The deformed mesh at the end of the calculation reveals that the failure mechanism involves the lower inclined plane and the first vertical.

For that second example the same geometry was taken: L=100m and $\beta = 45°$ and the initial strength parameters were: c=10 kPa and $\tan\phi_{res} = 1.5$. Also a reference variation of $\Delta\tan\phi/\Delta t = -0.05$ was imposed, and the failure occured when the $\tan\phi$ had a value of 1.118.

3.5 Application to the left abutment of Canelles Dam. Preliminary 2D results

The last example presented in this paper consists of the application of the c-phi reduction method to the stability of the left abutment of Canelles Dam. As a first step in this direction, a 2D vertical cross-section of the rock mass has been extracted from the new 3D geometric model described in section 2. The aim of this preliminary analysis is two-fold: (1) to verify the method performance in a real case and (2) to evaluate the increase of the Safety Factor provided by the construction of the new wall. The vertical cross-section considered is oriented along the maximum dipping direction of the new joint family and intersects the new wall approximately at its gravity center (Fig.6).

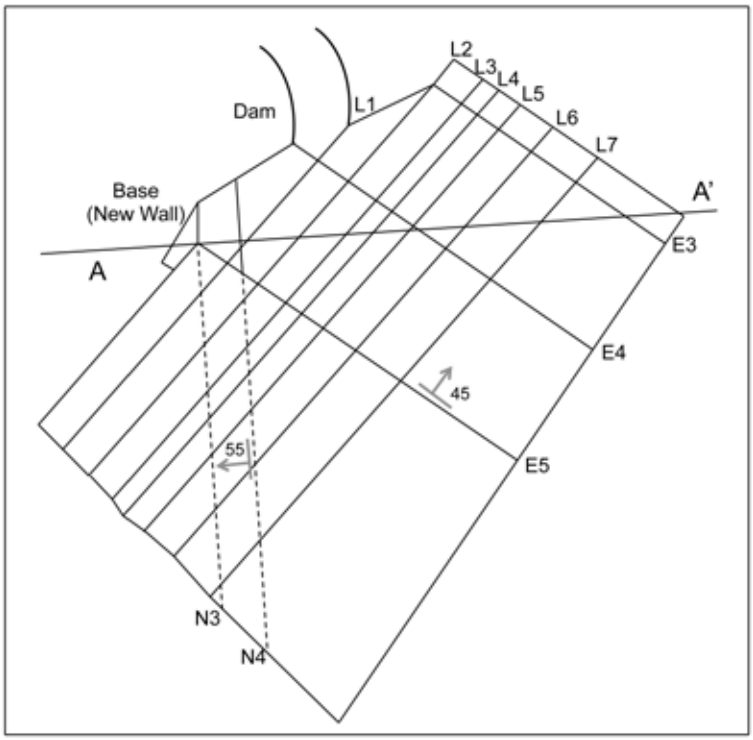

Figure 6: Horizontal cross-section at 375m. Bedding planes (E-planes), vertical principal joints family (L-planes) and new joints family (N-planes) are represented.

As it can be observed in Fig.7, three joints have been included in the discretisation: one representing the new joint family dipping 55°, and two more representing the rock-concrete contact joints (at the base and vertical side of the wall).

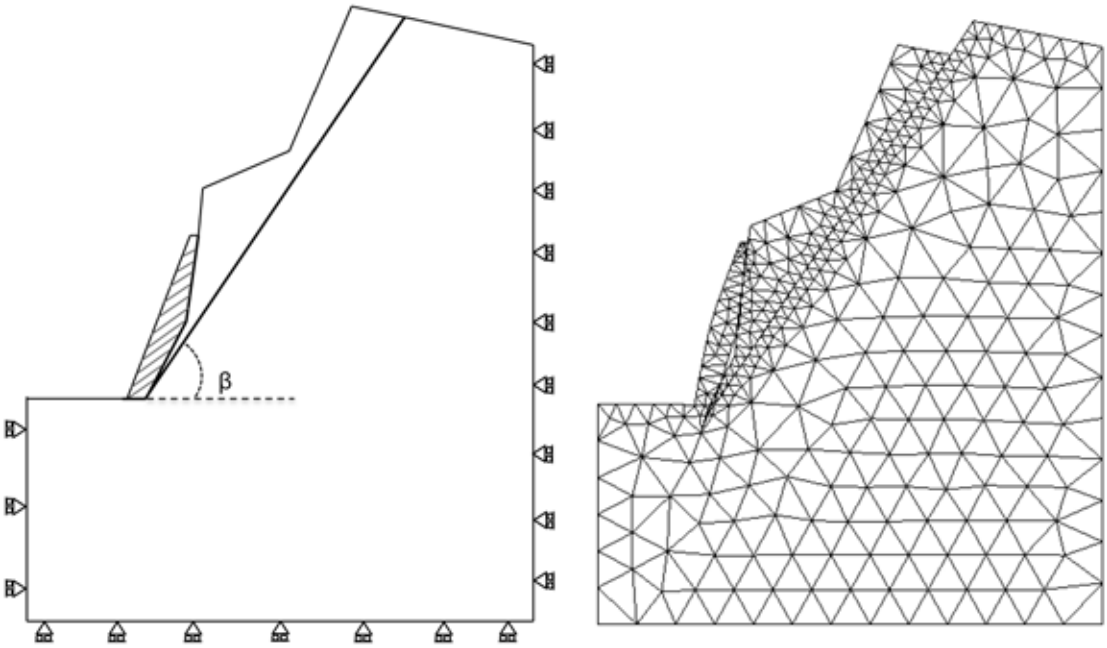

Figure 7: Geometric definition of the rock slope, FEM mesh deformed at failure.

For this example, the initial strength parameters used are: $c = 475$ kPa and $\tan\phi_{res} = 0.7$ (rock-rock), and $c = 10$ kPa and $\tan\phi_{res} = 1.0$ for the rock-concrete contacts. During the $c - \phi$ reduction process, only the rock-rock interface parameters were reduced (that is, those of the new joint family), while those of rock-concrete contact were assumed to remain constant. The failure occured when the $\tan\phi$ had a value of 0.4845, which corresponds to $\phi = 25.85°$.

4 ON-GOING WORK AND CONCLUDING REMARKS

The results presented show that the procedure implemented is capable of leading to reasonable results of failure analysis in rock masses, via $c - \phi$ reduction method in 2D vertical cross-sections.

Current on-going effort is devoted is devoted to (1) analysing new 2D cross-sections incorporating more joints of various families, and (2) carrying out the full 3D calculations of the left abutment of Canelles Dam including the three joint families and anchorage tunnels, with and without the new retaining wall. The latter case might require the improvement in the efficency and robustness of the numerical techniques employed.

5 ACKNOWLEDGMENTS

This research is supported partially by grants BIA2009-10491, from MICINN (Madrid,Spain), 2009SGR-180 from AGAUR-Generalitat de Catalunya (Barcelona) and by ENDESA (Madrid, Spain). The first author also wishes to acknowledge his current FPU doctoral fellowship from MICINN.

REFERENCES

[1] E.E. Alonso, I. Carol, C. Delahaye, A. Gens, and P. Prat. Evaluation of safety factors in discontinuous rock. *Int. J. Rock Mech. Min. Sci. and Geomech.*, 33:513–537, 1996.

[2] E.E. Alonso, A. Gens, I. Carol, P. Prat, and E. Herrero. Three-dimensional failure mechanisms in arch dam abutments. a safety study. In *XVIII Congres des Grands BArrages*, Durban, 1994.

[3] A. Alvarez, E. Herrero, and J.M. Buil. Some considerations concerning the effect on overall safety of interface problems between arch dams and their foundation. In *XIII Congres des Grands BArrages*, pages 1169–1185, N. Delhi, 1979.

[4] A. Alvarez, E. Herrero, and M. Vizcaino. Dams in karstified zones. three different solutions. In *XV Congres des Grands Barrages*, pages 1225–1246, Lausanne, 1985.

[5] I. Carol and P. Prat. Drac, finite element code. Technical report, Dept. of Geotechnical engineering, ETSECCPB-UPC, Barcelona, 2005.

[6] Y.M. Cheng, T. Lansivaara, and W.B. Wei. Two-dimensional slope stability analysis by limit equilibrium and strength reduction methods. *Computers and Geotechnics*, 34:137–150, 2007.

[7] A. Gens, I. Carol, and E.E. Alonso. An interface element formulation for the analysis of soil-reinforcement interaction. *Computers and Geotechnics*, 7:133–151, 1989.

[8] A. Gens, I. Carol, and E.E. Alonso. Rock joints: Finite element method, implementation and applications. In A.P.S. Selvadurai and M.J. Boulon, editors, *Mechanics of Geomaterial Interfaces*, pages 395–420. Elsevier, 1995.

[9] A. Gens, P. Prat, E.E. Alonso, and C. Delahaye. Finite element analysis for the safety evaluation of a dam on a fractured rock foundation. In *Beyond 2000 in Computational Geotechnics-10 Years of Plaxis International*, Balkema, Rotterdam, 1999.

[10] D.V. Griffiths and P.A. Lane. Slope stability analysis by finite elements. *Geotechnique*, 49(3):387–403, 1999.

[11] E. Hoek and J.W. Bray. *Rock Slope Engineering*. Taylor and Francis, 1974.

[12] T. Matsui and K.C. San. Finite element slope stability analysis by shear strength reduction technique. *Soil and Foundation*, 32(1):59–70, 1992.

[13] P. Prat, C. Delahaye, A. Gens, I. Carol, and E.E. Alonso. Safety evaluation of an arch dam founded on fractured rock based on a 3d nonlinear analysis with joint elements. In *International Conference on Dam Fracture and Damage*, chambery, France, 1994.

[14] P.C. Prat, A. Gens, I. Carol, A. Ledesma, and J.A. Gili. Drac: A computer software for the analysis of rock mechanics problems. In *Aplicatioms of Computer Methos in Rock Mechanics*, pages 1361–1369, Xian, China, 1993.

[15] O.C. Zienkiewicz, C. Humpheson, and R.W. Lewis. Associated and non-associated visco plasticity and plasticity in soil mechanics. *Geotechnique*, 25:671–689, 1975.

XI International Conference on Computational Plasticity. Fundamentals and Applications
COMPLAS XI
E. Oñate, D.R.J. Owen, D. Peric and B. Suárez (Eds)

NUMERICAL IMPLEMENTATION OF AN ELASTOPLASTIC MODEL FOR UNSATURATED SOILS

NUBIA A. GONZALEZ* AND ANTONIO GENS*

* Department of Geotechnical Engineering and Geosciences
Universitat Politècnica de Catalunya
Jordi Girona 1-3, Edifici D-2, 08034 Barcelona, Spain
e-mail: Nubia.Aurora.Gonzalez@upc.edu, antonio.gens@upc.edu web page: http://www.upc.edu

Key words: Unsaturated soils, constitutive model, integration algorithm, elastoplasticity, stress variables.

Abstract. This paper describes some issues related to the numerical implementation of a constitutive model for unsaturated soils based on the BBM [1]. The focus of the paper is on the stress variables used and on the numerical algorithms adopted. Conventional stress variable approach (net stress and suction) as well as the approach that takes into account the degree of saturation (Bishop's stress and suction) are examined. To solve the constitutive stress–strain equations, two stress integration procedures have been implemented, an explicit stress integration scheme with automatic substepping and error control techniques [2] and a fully implicit stress integration scheme based on the Backward-Euler algorithm with substepping [3]. Their performances during the integration of the constitutive laws are compared.

1 INTRODUCTION

There is agreement that at least two constitutive variables are generally required to represent adequately the full range of unsaturated soil behaviour, that is, including strength and deformation. Several review articles on the subject are available [4-6]. Conventional constitutive stress variable, namely net stress ($\bar{\sigma}_{ij} = \sigma_{ij} - u_a \delta_{ij}$) as well as the constitutive stress variable that takes into account the degree of saturation, commonly called Bishop's stress or average stress ($\sigma'_{ij} = \sigma_{ij} - u_a \delta_{ij} + S_r (u_a - u_w) \delta_{ij}$) are examined in this paper. In both formulations the second constitutive variable is the suction (s=u_a-u_w). σ_{ij} are total stresses, u_a the air pressure, u_w the water pressure and δ_{ij} the Kroneckers's delta. The selection of net stress or Bishop's stress or other alternative as the constitutive variable remains at present a matter of convenience [6].

Incremental stress-strain equations for unsaturated soils can be solved by a wide range of explicit and implicit integration algorithms. Explicit algorithms, use the gradients of the yield surface and plastic potential at the start of the strain increment, and their accuracy can only be controlled by breaking up the strain increment into sub-increments, special automatic

substepping and error control techniques have been proposed [2,7]. In implicit algorithms, all gradients are estimated at an advanced stress state (which is unknown) and then the resulting non-linear constitutive equations are solved by iteration [3,8]. The relative performance of implicit and explicit methods is strongly dependent on the precise form of the constitutive model. For unsaturated constitutive models, the problem of the non-convexity of the yield surface at the transition between saturated and unsaturated states can significantly complicate the implementation of these models into finite element codes [2,4]. In this paper both stress integration procedures are evaluated.

2 INTEGRATION ALGORITHMS

2.1 General

Integration algorithms will be applied to the elastoplastic BBM model for unsaturated soils [1] defined in terms of either net stresses or Bishop's stresses. In this model, suction is an additional independent variable. The constitutive equations that characterize the elasto-plastic material can be written in this particular case as:

$$\begin{aligned} &\mathrm{d}\boldsymbol{\varepsilon} = \mathrm{d}\boldsymbol{\varepsilon}^{e} + \mathrm{d}\boldsymbol{\varepsilon}^{p} + \mathrm{d}\boldsymbol{\varepsilon}^{e,s} \\ &\mathrm{d}\boldsymbol{\sigma} = \mathbf{D}^{\mathrm{e}}\left(\mathrm{d}\boldsymbol{\varepsilon} - \mathrm{d}\boldsymbol{\varepsilon}^{p} - \mathrm{d}\boldsymbol{\varepsilon}^{e,s}\right) \\ &\mathrm{d}\boldsymbol{\varepsilon}^{p} = \mathrm{d}\lambda\frac{\partial G(\boldsymbol{\sigma},k,s)}{\partial\boldsymbol{\sigma}} = \mathrm{d}\lambda\mathbf{m} \\ &\mathrm{d}k = \mathrm{d}P_o = \frac{\partial P_o}{\partial\boldsymbol{\varepsilon}^{\mathrm{p}}}\mathrm{d}\boldsymbol{\varepsilon}^{\mathrm{p}} \end{aligned} \tag{1}$$

where, $\mathrm{d}\boldsymbol{\varepsilon}$, $\mathrm{d}\boldsymbol{\varepsilon}^{e}$ and $\mathrm{d}\boldsymbol{\varepsilon}^{p}$ are increments of the total, elastic and plastic strain tensors respectively and $\mathrm{d}\boldsymbol{\varepsilon}^{e,s}$ is the contribution of suction to increment of elastic strain tensor (only necessary in the net stress formulation). **m** is the flow vector, $\mathrm{d}k$ represents the increment of hardening parameters (in this case P_0) and $\mathrm{d}\lambda$ is the plastic multiplier. Note that in above equations, $\boldsymbol{\sigma}$ vector can be either net stress ($\bar{\boldsymbol{\sigma}}$) or Bishop's stress ($\boldsymbol{\sigma}'$).

Satisfying the consistency condition,

$$\mathrm{d}F = \left(\frac{\partial F}{\partial\boldsymbol{\sigma}}\right)^{\mathrm{T}}\mathrm{d}\sigma + \frac{\partial F}{\partial s}\mathrm{d}s + \frac{\partial F}{\partial k}\mathrm{d}k = 0 \tag{2}$$

gives

$$\mathrm{d}\lambda = \frac{\mathbf{n}^{\mathrm{T}}\mathbf{D}^{e}\mathrm{d}\boldsymbol{\varepsilon} + \left(\mathrm{n}_s - \mathbf{n}^{\mathrm{T}}\mathbf{D}^{e}\mathbf{b}\right)\mathrm{d}s}{H + \mathbf{n}^{\mathrm{T}}\mathbf{D}^{e}\mathbf{m}} \tag{3}$$

$$\mathbf{n} = \frac{\partial F}{\partial\boldsymbol{\sigma}};\ \mathrm{n}_s = \frac{\partial F}{\partial s};\ \mathbf{m} = \frac{\partial G}{\partial\boldsymbol{\sigma}};\ \mathbf{b} = \frac{1}{3K_s}\boldsymbol{\delta};\ H = -\frac{\partial\mathrm{F}}{\partial P_o}\frac{\partial P_o}{\partial\varepsilon_v^{p}}\delta^{T}\mathbf{m};\ \boldsymbol{\delta}^{\mathrm{T}} = \{1,1,1,0,0,0\}$$

Note that for Bishop's stress formulation vector **b**=0. Combining equations (1) and (3), the constitutive equation integration is expressed as,

$$\begin{aligned} &\mathrm{d}\boldsymbol{\sigma} = \mathbf{D}^{\mathrm{ep}}\mathrm{d}\boldsymbol{\varepsilon} + \mathbf{W}^{\mathrm{ep}}\mathrm{d}s \\ &\mathrm{d}k = \mathbf{R}^{\mathrm{ep}}\mathrm{d}\boldsymbol{\varepsilon} + Q\mathrm{d}s \end{aligned} \tag{4}$$

where

$$\mathbf{D}^{ep} = \mathbf{D}^{e} - \frac{\mathbf{D}^{e}\mathbf{m}\mathbf{n}^{T}\mathbf{D}^{e}}{\mathrm{H} + \mathbf{n}^{T}\mathbf{D}^{e}\mathbf{m}} \quad \mathbf{W}^{ep} = -\frac{\mathbf{D}^{e}\mathbf{m}\left(\mathrm{n}_{s} - \mathbf{n}^{T}\mathbf{D}^{e}\mathbf{b}\right)}{\mathrm{H} + \mathbf{n}^{T}\mathbf{D}^{e}\mathbf{m}}$$
$$\mathbf{R}^{ep} = B\frac{\mathbf{n}^{T}\mathbf{D}^{e}}{\mathrm{H} + \mathbf{n}^{T}\mathbf{D}^{e}\mathbf{m}} \quad B = \frac{\partial P_{o}}{\partial \varepsilon_{v}^{p}}\delta^{T}\mathbf{m} \quad \mathrm{Q} = \frac{B\left(\mathrm{n}_{s} - \mathbf{n}^{T}\mathbf{D}^{e}\mathbf{b}\right)}{\mathrm{H} + \mathbf{n}^{T}\mathbf{D}^{e}\mathbf{m}} \tag{5}$$

In the integration the infinitesimal increments in the above equations (denoted by "d") are approximated with finite increments (denoted by "Δ").

2.2 Explicit algorithm

The more refined versions of the explicit algorithms [2,7] combine sub-stepping techniques with automatic sub-stepping control, error control and yield surface drift correction. An algorithm of this type has been implementedl. In this algorithm suction variable is treated as an additional strain component and it is assumed that it may be subincremented at the same rate as the other strain components.

The substepping procedure automatically divides the increment of strain and suction into a number of substeps small enough to ensure that the desired integration accuracy is enforced. The scheme involves splitting the elasto-plastic strain step $(1-\alpha)\Delta\boldsymbol{\varepsilon}$ and suction step $(1-\alpha)\Delta s$ into a series of smaller substeps, ${}^{s}\Delta\boldsymbol{\varepsilon} = \Delta T_{n}(1-\alpha)\Delta\boldsymbol{\varepsilon}$ and ${}^{s}\Delta s = \Delta T_{n}(1-\alpha)\Delta s$ (where $0 < \Delta T_{n} \le 1$), and using a modified Euler approximation for each substep. $(1-\alpha)\Delta\boldsymbol{\varepsilon}$ and $(1-\alpha)\Delta s$ are the portions of the strain increment and suction increment, respectively, that are outside of the yield surface. The size of each substep is determined by estimating the error in the stress changes and comparing it to a user-defined tolerance, *STOL*. The procedure begins assuming that only one substep is necessary. Consequently ΔT_{n} is set to unity and T_{n} is set to zero.

A first estimation of the changes in stresses and hardening parameters at the end of the pseudo-time step ΔT_{n} are evaluated using a first order Euler approximation, as,

$$\begin{aligned}\Delta\boldsymbol{\sigma}_{1} &= \mathbf{D}^{ep}\left(\boldsymbol{\sigma},k\right){}^{s}\Delta\boldsymbol{\varepsilon} + \mathbf{W}^{ep}\left(\boldsymbol{\sigma},k,s\right){}^{s}\Delta s\\ \Delta k_{1} &= \mathbf{R}^{ep}\left(\boldsymbol{\sigma},k\right){}^{s}\Delta\boldsymbol{\varepsilon} + \mathrm{Q}\left(\boldsymbol{\sigma},k,s\right){}^{s}\Delta s\end{aligned} \tag{6}$$

where, $\mathbf{D}^{ep}$, $\mathbf{W}^{ep}$, $\mathbf{R}^{ep}$ and Q are computed using equations (5). Using the above quantities, the stresses and hardening parameters at the end of the substep are $\boldsymbol{\sigma} + \Delta\boldsymbol{\sigma}_{1}$ and $k + \Delta k_{1}$, respectively. These are then used to calculate a second estimate of the changes in stress and hardening parameters over the substep, namely,

$$\begin{aligned}\Delta\boldsymbol{\sigma}_{2} &= \mathbf{D}^{ep}\left(\boldsymbol{\sigma} + \Delta\boldsymbol{\sigma}_{1}, k + \Delta k_{1}\right){}^{s}\Delta\boldsymbol{\varepsilon} + \mathbf{W}^{ep}\left(\boldsymbol{\sigma} + \Delta\boldsymbol{\sigma}_{1}, s + {}^{s}\Delta s, k + \Delta k_{1}\right){}^{s}\Delta s\\ \Delta k_{2} &= \mathbf{R}^{ep}\left(\boldsymbol{\sigma} + \Delta\boldsymbol{\sigma}_{1}, k + \Delta k_{1}\right){}^{s}\Delta\boldsymbol{\varepsilon} + \mathrm{Q}\left(\boldsymbol{\sigma} + \Delta\boldsymbol{\sigma}_{1}, s + {}^{s}\Delta s, k + \Delta k_{1}\right){}^{s}\Delta s\end{aligned} \tag{7}$$

A more accurate estimate and the end of interval ΔT_{n} is founded using the modified Euler procedure,

$$\begin{aligned}\boldsymbol{\sigma} &= \boldsymbol{\sigma} + \tfrac{1}{2}\left(\Delta\boldsymbol{\sigma}_{1} + \Delta\boldsymbol{\sigma}_{2}\right)\\ k &= k + \tfrac{1}{2}\left(\Delta k_{1} + \Delta k_{2}\right)\end{aligned} \tag{8}$$

A relative error measure is computed as,

$$R_n = \frac{1}{2}\text{máx}\left\{\frac{\left\|\Delta\boldsymbol{\sigma}_2 - \Delta\boldsymbol{\sigma}_1\right\|}{\left\|\boldsymbol{\sigma}\right\|}, \frac{\left|\Delta k_2 - \Delta k_1\right|}{k}\right\} \tag{9}$$

The current strain subincrement is accepted if R_n is not greater than *STOL*. If R_n>*STOL* then the solution is rejected and a smaller step size is computed. After accepting or rejecting the current substep, the size of the next substep is calculated based on the estimated error and the set tolerance. The next pseudo-time step is found from the relation, $\Delta T_{n+1} = q\Delta T_n$ where q is chosen so that, $R_{n+1} \le STOL$. A conservative choice for q is, $q = 0.9\sqrt{STOL / R_n}$ and it is also constrained to lie within the limits, $0.1 \le q \le 1.1$, so that, $0.1\Delta T_{n-1} \le \Delta T_n \le 1.1\Delta T_{n-1}$. The end of the integration procedure is reached when the entire increment of strain and suction is applied so that $\sum \Delta T_n = T_n = 1$.

After a successful substep the yield surface consistency condition is verified. If it is violated a drift correction procedure [9] is activated, which must ensure that the current state lies on the yield surface with a certain tolerance (*YTOL*). This correction changes both stress and internal variables but keeps the strain and suction increments unchanged.

2.3 Implicit algorithm

A fully implicit stress integration scheme based on the Backward-Euler (BE) algorithm with substepping [3] extended to unsaturated soil has been implemented. Integrating the constitutive equations with the BE methods, leads to an incremental algebraic format which is followed by a plastic corrector of the elastic trial stress violating the current yield surface. In this algorithm the plastic multiplier calculation is integrated with the internal variables updates and the incremental stress-strain relationship in a monolithic fashion.

Time-integration equation with BE scheme yields the following non-linear local problem of the type **R**=0:

$$\mathbf{R}\left\{\boldsymbol{\sigma}, k, \Delta\lambda\right\}^{(n+1)} = \begin{cases} \boldsymbol{\sigma}^{(n+1)} + \Delta\lambda \mathbf{D}^{e}\mathbf{m}^{(n+1)} - \boldsymbol{\sigma}^{(n)} - \mathbf{D}^{e\,s}\Delta\boldsymbol{\varepsilon} + \mathbf{D}^{e}\Delta\boldsymbol{\varepsilon}^{e,s} = 0 \\ k^{(n+1)} - \left(\dfrac{\partial k}{\partial \boldsymbol{\varepsilon}^{p}}\right)^{(n+1)} \boldsymbol{\delta}^{T}\mathbf{m}^{(n+1)}\Delta\lambda - k^{(n)} = 0 \\ F\left(\boldsymbol{\sigma}^{(n+1)}, k^{(n+1)}, s^{(n+1)}\right) = 0 \end{cases} \tag{10}$$

The unknowns of this local problem are the stresses $\boldsymbol{\sigma}^{(n+1)}$ and the hardening parameters $k^{(n+1)}$ at time $t^{(n+1)}$, and the plastic multiplier $\Delta\lambda$. $\Delta\boldsymbol{\varepsilon}^{e,s}$ is required only for net stress formulation and is a known variable. As in the explicit algorithm, the elasto-plastic strain step and suction step will be subdivided in smaller steps, as, ${}^{s}\Delta\boldsymbol{\varepsilon} = \Delta T_n(1-\alpha)\Delta\boldsymbol{\varepsilon}$ and ${}^{s}\Delta s = \Delta T_n(1-\alpha)\Delta s$ (where $0 < \Delta T_n \le 1$), in case that no convergence is reached in the iterative process of residual minimisation.

The non-linear system of equation (10) is solved by linearizing the residual and expanding it into a Taylor series, obtaining the following expression,

$$\mathbf{0} = \mathbf{R}\left\{\boldsymbol{\sigma}, k, \Delta\lambda\right\} + \frac{\partial \mathbf{R}\left\{\boldsymbol{\sigma}, k, \Delta\lambda\right\}}{\partial\left(\boldsymbol{\sigma}, k, \Delta\lambda\right)}\begin{bmatrix}\delta\boldsymbol{\sigma} \\ \delta k \\ \delta\lambda\end{bmatrix} + O\left[\delta^2\right] \tag{11}$$

The gradient expression $\partial_{(\boldsymbol{\sigma},k,\Delta\lambda)}\mathbf{R}\{\boldsymbol{\sigma},k,\Delta\lambda\}$ is the Jacobian matrix **J** (12). Truncating after

the first order terms, O[δ^2], and solving the linearized system of equations the new iterative update of the eight variables is obtained, as in (13)

$$\mathbf{J}\{\boldsymbol{\sigma},k,\Delta\lambda\}^{(n+1)}=\left\{\begin{array}{ccc}\mathbf{I}_{n\sigma}+\Delta\lambda\mathbf{D}^{\mathrm{e}}\dfrac{\partial\mathbf{m}}{\partial\boldsymbol{\sigma}} & \Delta\lambda\mathbf{D}^{\mathrm{e}}\dfrac{\partial\mathbf{m}}{\partial k} & \mathbf{D}^{\mathrm{e}}\mathbf{m}\\ -\Delta\lambda\dfrac{\partial k}{\partial\boldsymbol{\varepsilon}^{\mathrm{p}}}\dfrac{\partial\mathbf{m}}{\partial\boldsymbol{\sigma}} & 1-\Delta\lambda\dfrac{\partial k}{\partial\boldsymbol{\varepsilon}^{\mathrm{p}}}\dfrac{\partial\mathbf{m}}{\partial k} & -\dfrac{\partial k}{\partial\boldsymbol{\varepsilon}^{\mathrm{p}}}\mathbf{m}\\ \mathbf{n}^{T} & \dfrac{\partial F}{\partial k} & 0\end{array}\right\}_{t=t^{(n+1)}} \tag{12}$$

$$\begin{bmatrix}\delta\boldsymbol{\sigma}^{(n+1)}\\ \delta k^{(n+1)}\\ \delta\lambda^{(n+1)}\end{bmatrix}=-\left[\mathbf{J}\left\{\boldsymbol{\sigma}^{(n+1)},k^{(n+1)},\Delta\lambda^{(n+1)}\right\}\right]^{-1}\mathbf{R}\left\{\boldsymbol{\sigma}^{(n+1)},k^{(n+1)},\Delta\lambda^{(n+1)}\right\} \tag{13}$$

Adding the iterative corrector to the old values of the independent variables yields the eight updates:

$$\begin{bmatrix}\boldsymbol{\sigma}^{(n+1)}\\ k^{(n+1)}\\ \Delta\lambda^{(n+1)}\end{bmatrix}=\begin{bmatrix}\boldsymbol{\sigma}^{(n+1)}\\ k^{(n+1)}\\ \Delta\lambda^{(n+1)}\end{bmatrix}+\begin{bmatrix}\delta\boldsymbol{\sigma}^{(n+1)}\\ \delta k^{(n+1)}\\ \delta\lambda^{(n+1)}\end{bmatrix} \tag{14}$$

In some cases, when large strain increments are prescribed, the minimization of residual equations (11) is not possible after a given number of iterations. In this case, the strain and suction increments are reduced by $\Delta T_n = q\Delta T_n$, where q is chosen as 0.5. The end of the integration procedure is reached when the entire increment of strain and suction is applied so that $\sum\Delta T_n = T_n = 1$.

In order to start the iteration process, the elastic solution at the contact point with the yield surface is chosen:

$$\begin{aligned}&\boldsymbol{\sigma}_0^{(n+1)}=\boldsymbol{\sigma}^{(n)}+(1-\alpha)\mathbf{D}^{\mathrm{e}}\Delta\boldsymbol{\varepsilon}\quad;\quad k_0^{(n+1)}=k^{(n)}\\ &s_0^{(n+1)}=s^{(n)}+(1-\alpha)\Delta s\quad;\quad\Delta\lambda_0=0\end{aligned} \tag{15}$$

To solve the global problem with quadratic convergence it is necessary to use a consistent tangent matrix,

$$\frac{\partial^{n+1}\boldsymbol{\sigma}}{\partial^{n+1}\Delta\boldsymbol{\varepsilon}}=\mathbf{P}^{T}\left(\mathbf{J}^{n+1}\right)^{-1}\mathbf{P}\mathbf{D}^{\mathrm{e}} \tag{16}$$

$\mathbf{P}^{T}=(\mathbf{I}_{n\sigma}\,0\,0)$ is the projection matrix on stress space.

3 APPLICATION AND PERFORMANCE

The triaxial test on compacted Barcelona clayey silt presented in **Error! Reference source not found.** [10] was selected to examine the performance of the integration algorithms. The tests includes different types of stress paths typically performed on unsaturated soils: A1-A2, loading at constant suction, A2-A3, wetting path at constant net stress, A3-A4 drying path at constant net stress, A4-A4 shear to failure under constant suction.

Performance of numerical integration algorithms (explicit and implicit) is evaluated in terms of CPU time and the number of sub-increments required in each scheme. In all runs the yield surface tolerance is fixed at YTOL = 10^{-8}; this parameters is also used to control the

convergence of the residual in the implicit algorithm. Control error tolerance of explicit algorithm varies from STOL=10^{-2} to 10^{-6}. All CPU times presented are for an Intel Core Duo (2GHz) with 2GB of RAM. Results are presented in bar graphs where average values of the variables evaluated were computed for each stress path.

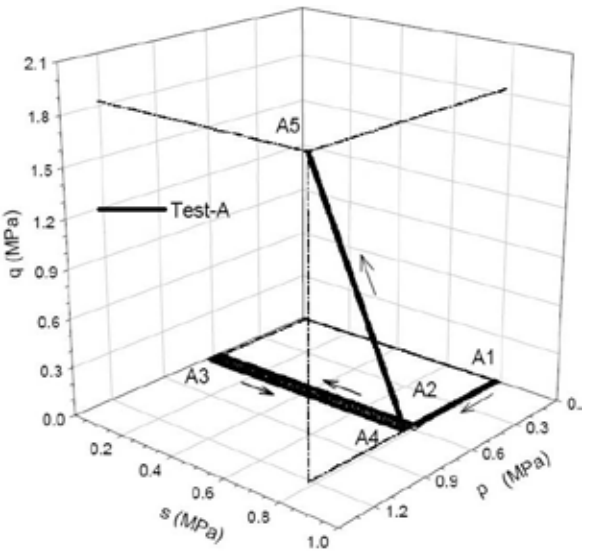

Figure 1: Stress paths followed by the test used in the evaluation of integration algorithms

Figure 2 shows a comparison between implicit and explicit algorithms for net stress and Bishop's stress. It is observed that the wetting path (A2-A3) requires both a higher computational cost and higher mean number of sub-increments when Bishop's stress and the implicit scheme are employed. This is because Bishop's stress induces a high curvature in this particular stress path. As a consequence, the plastic corrector of implicit scheme has difficulties in returning to the yield surface and the requirement for sub-increments increases. Explicit algorithm is more efficient in this case because proceeds in an incremental fashion where all gradients are estimated at known stress states. Also, it is noted for path A2-A3 that the computational cost of net stress formulation is considerably lower than that of Bishop's stress and differences between implicit and explicit schemes are minimised. Figure 2 also indicates that during stress path A1-A2 of isotropic load at constant suction, no significant differences are observed between implicit and explicit schemes. During drying path A3-A4, behaviour is elastic and no strain sub-incrementation is needed. Finally, during shearing path A4-A5, the explicit scheme demands a higher number of sub-increments than the implicit one. However, this tendency is not reflected in the CPU time, as the explicit scheme spends slightly less CPU time than implicit one. This may be explained by the fact that the implicit scheme requires second derivatives of yield function and plastic potential and the inversion of the Jacobian matrix.

Figure 3 shows the influence of the error control tolerance (*STOL*) on mean number of sub-increments and drift corrections of the explicit algorithm. As expected, the number of sub-increments and drift corrections increases as *STOL* is decreased. Due to the fact that the stress

error controls the strain sub-increments in proportion to the square root of *STOL*, their number increases by a factor of roughly $\sqrt{10}$ if *STOL* is reduced by an order of magnitude.

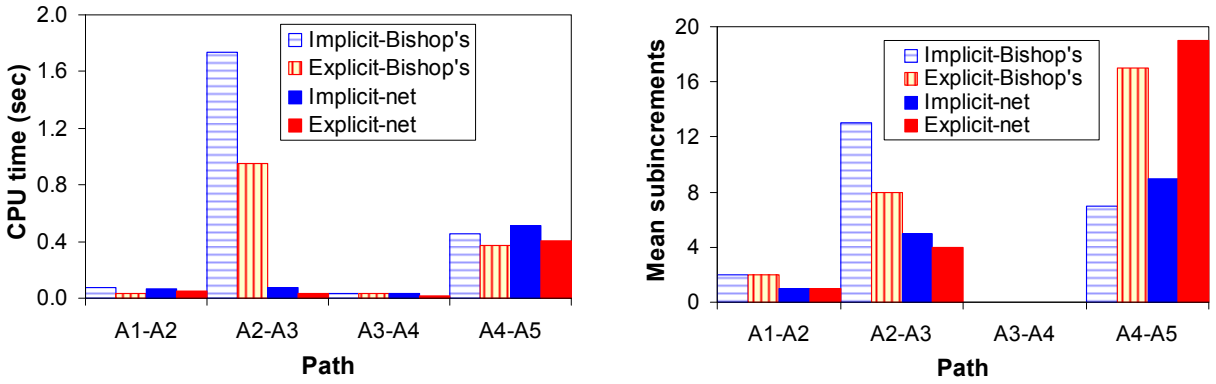

Figure 2: Comparison of integration algorithms (STOL=10^{-4} for explicit scheme)

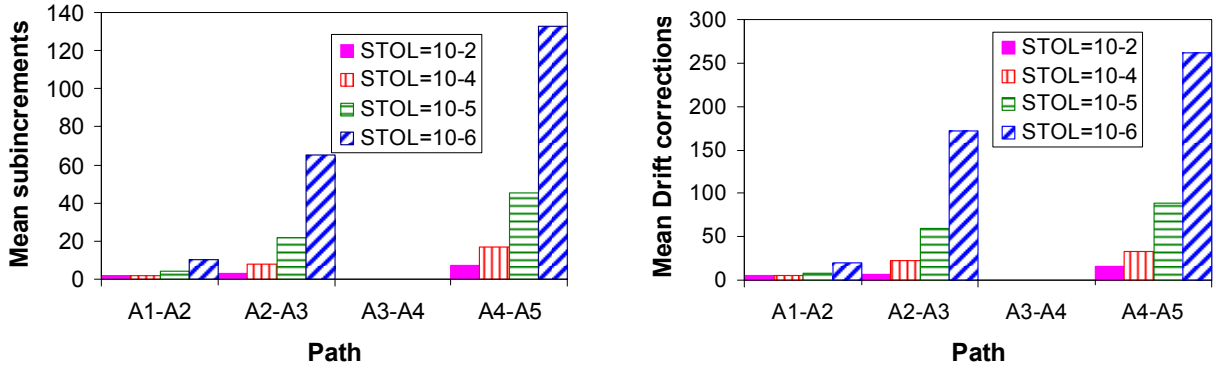

Figure 3: Influence of *STOL* on sub-increments and drift corrections of explicit algorithm. Constituive model

4 CONCLUSIONS

- Net stress is a more simple and practical choice in terms of stress path representation than Bishop's stress. However, it requires additional assumptions to take into account the shear strength increase with suction and the elastic volumetric strain due to changes in suction. Using Bishop's stresses this features derive directly from the definition of the constitutive stress. However, the performance of the model using Bishop's stress is more sensitive to the adopted soil water characteristic curve.
- In terms of the efficiency of numerical algorithms, the explicit scheme is likely to be more robust than implicit scheme to solve the kind of complex stress involved in unsaturated soil behaviour. The use of explicit scheme, however, does not yield quadratic convergence of the full problem.

ACKNOWLEDGEMENTS

The work reported has been partially funded by the European through project TUNCONSTRUCT. The support of the Spanish Ministry of Science and Innovation trough

grant BIA 2008-06537 is also gratefully acknowledged.

REFERENCES

[1] Alonso E, Gens A. and Josa A. A constitutive model for partially saturated soils. *Géotechnique* (1990) **40**:405-430.

[2] Sheng D., Sloan S.W., Gens A. and Smith D.W. Finite element formulation and algorithms for unsaturated soils. Part I: Theory. Part II: Verification and application. *Int. J. Numer. Anal. Methods Geomech.* (2003) **27**:745-790.

[3] Pérez A., Rodríguez A. and Huerta A. Consistent tangent matrices for substepping schemes. *Comput. Methods Appl. Mech. Engrg*. (2001) **190**:4627–4647.

[4] Sheng D., Gens A., Fredlund D.G. and Sloan S.W. Unsaturated soils: From constitutive modeling to numerical algorithms. *Computers and Geotechnics* (2008) **35**:810-824.

[5] Nuth M. and Laloui L. Effective stress concept in unsaturated soils: Clarification and validation of a unified framework. *Int. J. Numer. Anal. Geomech*. (2008) **32**:771-801.

[6] Gens A. Soil–environment interactions in geotechnical engineering. *Géotechnique* (2010) **60**:3–74.

[7] Sloan S.W., Abbo A.J. and Sheng D. Refined explicit integration of elasto-plastic models with automatic error control. *Engineering Computations* (2001) **18**:121–154.

[8] Vaunat J., Cante J.C., Ledesma A. and Gens A. A stress point algorithm for an elastoplastic model in unsaturated soils. *Int. J. Plasticity* (2000) **16**:121–141.

[9] Potts D. and Gens A. A critical assessment of methods of correcting for drift from the yield surface in elastoplastic finite element analysis. *Int. J. Numer. Anal. Methods Geomech*., (1985) **9**:149-159.

[10] Barrera M., Romero E., Sánchez M. and Lloret A. Laboratory tests to validate and determine parameters of an elastoplastic model for unsaturated soils. *Int. Symp. on identification and determination of soil and rock parameters for geotechnical design*. (J.P. Magna, ed.) 351-358 (2002).

XI International Conference on Computational Plasticity. Fundamentals and Applications
COMPLAS XI
E. Oñate, D.R.J. Owen, D. Peric and B. Suárez (Eds)

NUMERICAL SIMULATION OF DYNAMIC PORE FLUID-SOLID INTERACTION IN FULLY SATURATED NON-LINEAR POROUS MEDIA

H. SABETAMAL[†*], M.NAZEM [†], S.W. SLOAN[†] AND J.P.CARTER[†]

[†] Centre for Geotechnical and Materials Modelling
The University of Newcastle
Callaghan 2308, NSW, Australia
www.newcastle.edu.au/research-centre/cgmm/
[*]e-mail: Hassan.Sabetamal@uon.edu.au

Key words: Large strain, ALE method, Saturated soils, Dynamic consolidation.

Abstract. In this paper, a large deformation formulation for dynamic analysis of the pore fluid-solid interaction in a fully saturated non-linear medium is presented in the framework of the Arbitrary Lagrangian-Eulerian method. This formulation is based on Biot's theory of consolidation extended to include the momentum equations of the solid and fluid phases, large deformations and non-linear material behaviour. By including the displacements of the solid skeleton, **u**, and the pore fluid pressure, **p**, a (**u-p**) formulation is obtained, which is then discretised using finite elements. Time integration of the resulting highly nonlinear equations is accomplished by the generalized–α method, which assures second order accuracy as well as unconditional stability of the solution. Details of the formulation and its practical implementation in a finite element code are discussed. The formulation and its implementation are validated by solving some classical examples in geomechanics.

1 INTRODUCTION

In quasi-static analysis it is common to assume that soil behaves as either a drained or an undrained medium. Under these conditions a single phase description of the porous medium may provide reasonable and acceptable results. However, in many cases the fully drained or undrained assumptions may lead to inaccurate results due to partial consolidation occurring in the soil, which generally depends on the hydraulic conductivity of the soil as well as the rate of applied loading. By using an analytical solution for dynamic consolidation problems in a **u-p** formulation, Zienkiewicz *et al* [1] investigated the conditions under which the undrained or quasi-static assumptions can be safely used. For conditions that are intermediate between fully drained and undrained, in which consolidation of the soil will take place, there is an interaction between the solid soil skeleton and the pore fluid flow. Consequently, the equations of motion for the individual constituents involve interaction terms and the stresses, both total and effective, depend on the kinematics of both phases.

Biot[2] presented one of the first theories governing the behaviour of saturated porous media. Later, Small *et al*.[3] and Prevost [4] extended Biot's theory into the material and geometrically non-linear regimes, respectively. Zienkiewicz and Shiomi [5] conducted a comprehensive study

on solutions of the Biot-type formulation and summarised different analysing methods in three categories namely the (a) **u**-**p**, (b) **u**-**U** and (c) **u**-**p**-**U** formulations. Here **u**, **p**, and **U** represent the soil skeleton displacements, the pore fluid (water) pressure and the pore fluid (water) displacements, respectively. The finite element method (FEM) facilitates the discretisation of the governing differential equations in the space domain and makes it possible to extend the theory to employ elastoplastic nonlinear constitutive models in order to obtain reliable solutions for displacements and pore water pressures. This study presents an application of the FEM to solve dynamic coupled consolidation problems involving material nonlinearity as well as large deformations. Such an analysis requires a robust time marching scheme. The generalized-α algorithm (CH) developed by Chung and Hulbert [6] is an implicit integration scheme that possesses the necessary conditions of a standard time integration algorithm such as unconditional stability, second order accuracy and numerical damping capability. Kontoe *et al*.[7] used this scheme to solve coupled problems of geomechanics. The ability of this method in solving dynamic consolidation problems in geomechanics, particularly in an Arbitrary Lagrangian-Eulerian framework, is investigated in this paper.

Among others, two main sources of nonlinearity, namely material nonlinearity and geometric nonlinearity, can arise in the analysis of porous continua. Geometric nonlinearity is important in many cases such as the analysis of liquefaction, deep penetration of objects into soil layers, and any situation where the strain level is relatively high. This kind of analysis usually involves severe mesh distortion and, therefore, the Lagrangian finite element methods normally fail to provide a complete solution, usually due to the eventual development of a negative Jacobian in some elements. On the other hand, the Arbitrary Lagrangian-Eulerian (ALE) method has been developed to eliminate mesh distortion. In this study the ALE method presented by Nazem *et al*.[8, 9] is employed to solve dynamic consolidation problems of geomechanics in which the pore fluid interacts with the solid soil skeleton. The first part of this paper briefly describes the governing equations of the saturated porous medium. Time discretization of the governing equations is then presented using the CH method, followed by implementation of the approach in a finite element code. Finally, some numerical examples are presented in order to validate the implementation of the theoretical framework and to demonstrate its application in practice.

2 FINITE ELEMENT FORMULATION

The global equations governing the dynamic consolidation of a porous medium can be obtained by combining the overall momentum balance equation of the solid-fluid phase, the momentum balance equation for the pore fluid and the continuity of mass through the principle of effective stresses and the Darcy's law resulting in the following set of equations (e.g., Zienkiewicz *et al*.[5])

$$\mathbf{M}\ddot{\mathbf{u}} + \mathbf{C}\dot{\mathbf{u}} + \mathbf{K}_{ep}\mathbf{u} + \mathbf{L}\mathbf{p} = \mathbf{f}^{u} \tag{1}$$

$$\mathbf{L}^{T}\dot{\mathbf{u}} + \mathbf{S}\dot{\mathbf{p}} - \mathbf{H}\mathbf{p} = \mathbf{f}^{p} \tag{2}$$

where **M**, **C** and $\mathbf{K}_{ep}$ are, respectively, the mass matrix, the damping matrix, and the elastoplastic stiffness matrix of the solid soil skeleton. **L**, **H**, and **S** represent, respectively, the coupling matrix, the flow matrix, and the compressibility matrix. $\mathbf{f}^{u}$ is the vector of external nodal forces and $\mathbf{f}^{p}$ is a fluid supply vector. Classical finite-element algorithms used

in geomechanics usually assume that only small strains occur in the soil. However, this assumption is no longer valid for large deformation problems. Finite element approaches often use an Updated-Lagrangian (UL) formulation to incorporate the effects of finite deformations as well as the volume changes in a large-deformation analysis. However, the UL method fails to provide a solution in problems with relatively large displacements due to mesh distortion. Nonetheless, this method is the main engine of the ALE operator split technique presented in Section 4 of this paper, and thus a brief description of the time-stepping scheme employed to solve the governing equations in an UL framework is given in next section.

3 TIME INTEGRATION

Finite element discretisation of the global equations leads to a system of second-order ordinary differential equations in which time is a continuous variable. In a direct time-integration scheme, Equation (1) is integrated by a numerical step-by-step procedure. Newmark's scheme is one of the most popular methods in the family of direct time integration techniques. In this method, the displacements and velocities at time t_{n+1} can be approximated by

$$\mathbf{u}_{n+1} = \mathbf{u}_n + \Delta t \dot{\mathbf{u}}_{\boldsymbol{n}} + \frac{\Delta t^2}{2}[(1-2\beta)\ddot{\mathbf{u}}_n + 2\beta\ddot{\mathbf{u}}_{n+1}] \tag{3}$$

$$\dot{\mathbf{u}}_{n+1} = \dot{\mathbf{u}}_n + \Delta t[(1-\gamma)\ddot{\mathbf{u}}_n + \gamma\ddot{\mathbf{u}}_{n+1}] \tag{4}$$

where β and γ are integration parameters. However, Newmark's method cannot predict high-frequency modes accurately. Thus, numerical damping is introduced to eliminate spurious high frequency oscillations whilst preserving the important low frequency modes. Algorithmic damping can be introduced to Newmark's scheme by increasing the value of γ (larger than 0.5) and selecting the smallest value of β compatible with the stability requirements[10]. However, algorithmic damping influences the low-frequency behaviour, corresponding to a reduction of the accuracy to first order. By using averages with different degrees of forward weighting on the different terms in the equation of motion, the low-frequency properties can be improved, while retaining high-frequency damping. Three different schemes have been investigated in detail: forward weighing of the stiffness and load terms by Hilbert *et al.*[11], forward weighting of the inertial term by Wood *et al.*[12] and different forward weighting of the stiffness and the inertial terms by Chung and Hulbert [6]. In the last of these methods, which is known as the generalized-α or CH method, the inertia terms are evaluated at time $t = t_{n+1-\alpha_m}$ of the considered interval Δt, whereas all other terms are evaluated at some earlier time $t = t_{n+1-\alpha_f}$ $(\alpha_f \geq \alpha_m)$. Therefore, using this method equation (1) can be written as

$$\mathbf{M}\ddot{\mathbf{u}}_{n+1-\alpha_m} + \mathbf{C}\dot{\mathbf{u}}_{n+1-\alpha_f} + \mathbf{K}\mathbf{u}_{n+1-\alpha_f} + \mathbf{L}\mathbf{p}_{n+1-\alpha_f} = \mathbf{f}_{n+1-\alpha_f} \tag{5}$$

where

$$\ddot{\mathbf{u}}_{n+1-\alpha_m} = (1-\alpha_m)\ddot{\mathbf{u}}_{n+1} + \alpha_m\ddot{\mathbf{u}}_n \tag{6}$$

$$\dot{\mathbf{u}}_{n+1-\alpha_f} = (1-\alpha_f)\dot{\mathbf{u}}_{n+1} + \alpha_f\dot{\mathbf{u}}_n \tag{7}$$

$$\mathbf{u}_{n+1-\alpha_f} = (1-\alpha_f)\mathbf{u}_{n+1} + \alpha_f\,\mathbf{u}_n \tag{8}$$

$$\mathbf{p}_{n+1-\alpha_f} = (1-\alpha_f)\mathbf{p}_{n+1} + \alpha_f\, \mathbf{p}_n \tag{9}$$

$$\mathbf{f}_{n+1-\alpha_f} = (1-\alpha_f)\mathbf{f}_{n+1} + \alpha_f\, \mathbf{f}_n \tag{10}$$

The governing equations of the **u-p** formulation, defined here as equations (1) and (2), can now be discretised. Equation (1) can be written in incremental form at time $t = t_{n+1}$ as

$$\mathbf{M}\Delta\ddot{\mathbf{u}} + \mathbf{C}\Delta\dot{\mathbf{u}} + \mathbf{K}_{ep}\Delta\mathbf{u} + \mathbf{L}\Delta\mathbf{p} = \mathbf{f}^u - {}^t\mathbf{f}_{int} - \mathbf{M}\ddot{\mathbf{u}}_n - \mathbf{C}\dot{\mathbf{u}}_n \tag{11}$$

and according to the CH method

$$\mathbf{M}\Delta\ddot{\mathbf{u}}_{n+1-\alpha_m} + \mathbf{C}\Delta\dot{\mathbf{u}}_{n+1-\alpha_f} + \mathbf{K}\Delta\mathbf{u}_{n+1-\alpha_f} + \mathbf{L}\Delta\mathbf{p}_{n+1-\alpha_f} = \mathbf{f}^u_{n+1-\alpha_f} - {}^t\mathbf{f}_{int} - \mathbf{M}\ddot{\mathbf{u}}_n - \mathbf{C}\dot{\mathbf{u}}_n \tag{12}$$

where ${}^t\mathrm{f}_{\mathrm{int}}$ denotes the internal forces at the previous time step (t=$\mathrm{t_n}$).
Expressing Equations (6~9) in incremental form and substituting them in Equation (12) yields:

$$\frac{(1-\alpha_m)}{(1-\alpha_f)}\mathbf{M}\Delta\ddot{\mathbf{u}} + \mathbf{C}\Delta\dot{\mathbf{u}} + \mathbf{K}\Delta\mathbf{u} + \mathbf{L}\Delta\mathbf{p} = \frac{1}{(1-\alpha_f)}\left[\mathbf{f}^u_{n+1-\alpha_f} - {}^t\mathbf{f}_{int} - \mathbf{M}\ddot{\mathbf{u}}_n - \mathbf{C}\dot{\mathbf{u}}_n\right] \tag{13}$$

Similarly, Equation (2) may be written as

$$\mathbf{L}^T\dot{\mathbf{u}}_{n+1} + \mathbf{S}\dot{\mathbf{p}}_{n+1} - \mathbf{H}\mathbf{p}_{n+1} = \frac{1}{(1-\alpha_f)}\left[\mathbf{f}^p_{n+1-\alpha_f} - \alpha_f\mathbf{L}^T\dot{\mathbf{u}}_n - \alpha_f\mathbf{S}\dot{\mathbf{p}}_n + \alpha_f\mathbf{H}\mathbf{p}_n\right] \tag{14}$$

Newmark's recurrence relations in (3) and (4) can be written in incremental form as

$$\Delta\ddot{\mathbf{u}} = \frac{\Delta\mathbf{u} - \mathbf{u}^l}{\beta\Delta t^2} - \ddot{\mathbf{u}}_n \tag{15}$$

$$\Delta\dot{\mathbf{u}} = \dot{\mathbf{u}}^l - \frac{\gamma}{\beta\Delta t}(\mathbf{u}^l - \Delta\mathbf{u}) - \dot{\mathbf{u}}_n \tag{16}$$

Moreover, the pore water pressure at $t = t_{n+1}$ can be estimated by a first order approximation as[13]

$$\Delta\mathbf{p} = \mathbf{p}^l + \theta\Delta t\dot{\mathbf{p}}_{n+1} \tag{17}$$

Note that $\mathbf{u}^l$, $\dot{\mathbf{u}}^l$ and $\mathbf{p}^l$ appearing in the above Equations are considered as auxiliary variables to simplify the formulation, and they contain the known variables from the previous time step as

$$\mathbf{u}^l = \Delta t\dot{\mathbf{u}}_n + \frac{\Delta t^2}{2}(1-2\beta)\ddot{\mathbf{u}}_n \tag{18}$$

$$\dot{\mathbf{u}}^l = \dot{\mathbf{u}}_n + \Delta t(1-\gamma)\ddot{\mathbf{u}}_n \tag{19}$$

$$\mathbf{p}^l = \Delta t(1-\theta)\dot{\mathbf{p}}_n \tag{20}$$

Finally, introducing Equations (15) and (16) into Equations (13) and (14), the system of equations governing the dynamic consolidation of the continuum is obtained:

$$\begin{bmatrix} \dfrac{(1-\alpha_m)}{\beta\Delta t^2(1-\alpha_f)}\mathbf{M} + \dfrac{\gamma}{\beta\Delta t}\mathbf{C} + \mathbf{K}_{ep} & \mathbf{L} \\ \mathbf{L}^{\mathrm{T}} & \dfrac{\beta\Delta t}{\gamma}\left(\dfrac{\mathbf{S}}{\theta\Delta t} - \mathbf{H}\right) \end{bmatrix} \begin{bmatrix} \Delta\mathbf{u} \\ \Delta\mathbf{p} \end{bmatrix} = \begin{bmatrix} \mathbf{F}^u \\ \mathbf{F}^p \end{bmatrix} \tag{21}$$

where

$$\mathbf{F}^u = \frac{1}{(1-\alpha_f)}\left\{\mathbf{f}^u{}_{n+1-\alpha_f} + \mathbf{M}\left[\frac{(1-\alpha_m)}{\beta\Delta t^2}\mathbf{u}^l - \alpha_m\ddot{\mathbf{u}}_n\right] + \mathbf{C}\left[\left(1-\alpha_f\right)\left(\frac{\gamma}{\beta\Delta t}\mathbf{u}^l - \dot{\mathbf{u}}^l\right) - \alpha_f\dot{\mathbf{u}}_n\right] - {}^t\mathbf{f}_{int}\right\} \tag{22}$$

$$\mathbf{F}^p = \frac{\beta\Delta t}{\gamma(1-\alpha_f)}\left\{\mathbf{f}^p{}_{n+1-\alpha_f} + \mathbf{L}^{\mathrm{T}}\left[\left(1-\alpha_f\right)\left(\frac{\gamma}{\beta\Delta t}\mathbf{u}^l - \dot{\mathbf{u}}^l\right) - \alpha_f\dot{\mathbf{u}}_n\right] + \mathbf{S}\left[\frac{(1-\alpha_f)}{\theta\Delta t}\mathbf{p}^l - \alpha_f\dot{\mathbf{p}}_n\right] + \mathbf{H}\mathbf{p}_n\right\} \tag{23}$$

The unconditional stability of the scheme is guaranteed when

$$\alpha_m \le \alpha_f \le 0.5\ ,\ \ \beta \ge \frac{1+2(\alpha_f-\alpha_m)}{4}\ ,\theta > 0.5 \tag{24}$$

and second order accuracy is attained when

$$\gamma = 0.5 - \alpha_m + \alpha_f \tag{25}$$

4 ARBITRARY LAGRANGIAN-EULERIAN METHOD

In an Updated Lagrangian description of the motion of a body the mesh follows the material points. Consequently, the mesh can become excessively distorted in problems with relatively large deformations. In contrast, in an Eulerian description the mesh is fixed in space and the grid nodes are no longer coincident with material particles during the analysis. This may avoid mesh distortion but makes it difficult to describe the material boundaries. The ALE method attempts to combine the advantages of the Lagrangian and the Eulerian meshes. In this method, the computational grid does not necessarily adhere to the material points, and it can move arbitrarily. A common form of the ALE method is the operator split technique during which the analysis is performed in two steps: an Updated-Lagrangian step followed by an Eulerian step. In the first (Lagrangian) step the governing equations are solved to fulfil equilibrium and to obtain the material displacements. In the second (Eulerian) step the mesh is refined to eliminate the possible distortion. After refining the mesh, all kinematic and static variables must be transferred between the two meshes. In a coupled displacement-pore water pressure ALE analysis, the state parameters to be transformed at integration points include the effective stresses, hardening parameters, voids ratios and coefficients of permeability, while the pore-water pressures are transformed from old nodes to new nodes. The ALE operator split technique and the mesh refinement strategy used in this study were first presented by Nazem *et al*.[8] for the analysis of geotechnical problems. Nazem *et al*. [9] and Nazem *et al*.[14] applied the method to solve static consolidation problems and dynamic problems involving large deformations, respectively.

5 NUMERICAL EXAMPLES

The numerical time-integration scheme explained in Section 3 has been implemented into SNAC, a finite element code developed by the geomechanics group at the University of Newcastle, Australia. SNAC was used to analyse the two numerical examples presented in this section.

5.1 One-dimensional finite elastic consolidation

In order to validate the coupled formulation presented here, we study a 10 m deep column

of fully saturated soil and we compare the results with available analytical and numerical solutions. Figure 1 shows the geometry of the problem as well as the boundary conditions and applied load types. To simulate one-dimensional behaviour all nodes are restrained in the horizontal direction. Drainage can only take place through the top boundary of the model.

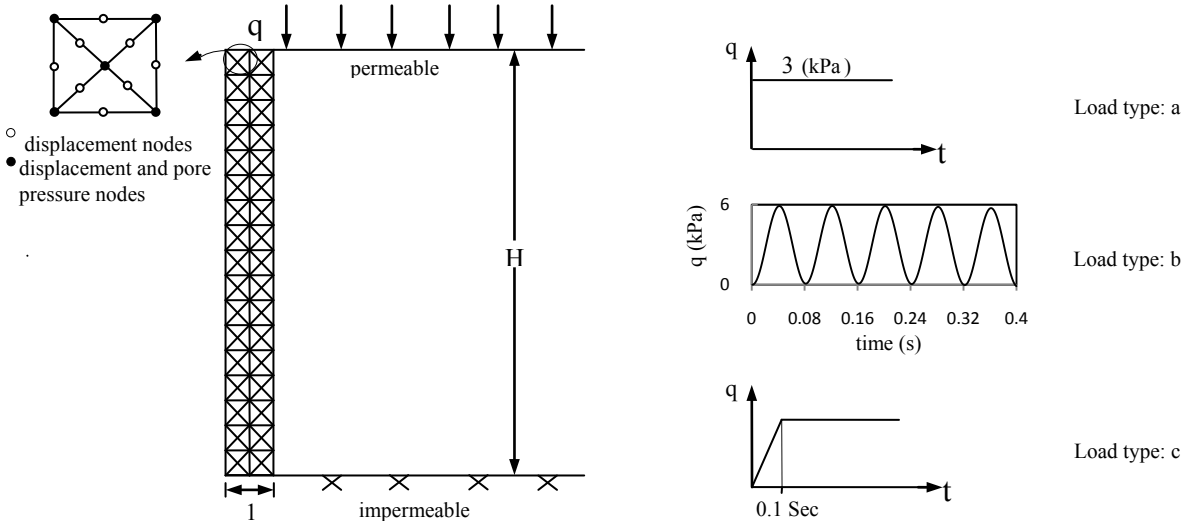

Figure 1: One-dimensional dynamic consolidation problem

de Boer[15] presented an analytical solution for a one dimensional transient wave propagation problem under a time-dependent load assuming small strains, an elastic material model and an incompressible pore fluid. The response of the soil column to step loading (type a) as well as a sinusoidal loading (type b) is investigated here. The material parameters are in accordance with de Boer[15], i.e., the Young's modulus of the soil is $E = 30$MPa, Poisson's ratio $\upsilon = 0.2$, the soil porosity $n = 0.33$ and the permeability $k = 0.01$m/s. Figure 2a shows the vertical displacement of the soil column versus time due to load type (a) and at depths 0.0 and 1.0m, whereas Figure 2b depicts the response of the pore water pressure at different depths and times. Figure 2 shows that the results obtained in this study are in good agreement with the analytical solution. For the case of a sinusoidal load, the pore water pressure response is plotted versus time in Figure 3, which indicates negative values (suction) in the vicinity of the loading surface. According to de Boer[15] this result is due to the recovery of the elastic skeleton matrix close to the surface during the sinusoidal loading, where the pore water does not squeeze out but is absorbed into the pores accompanied by fluid suction.

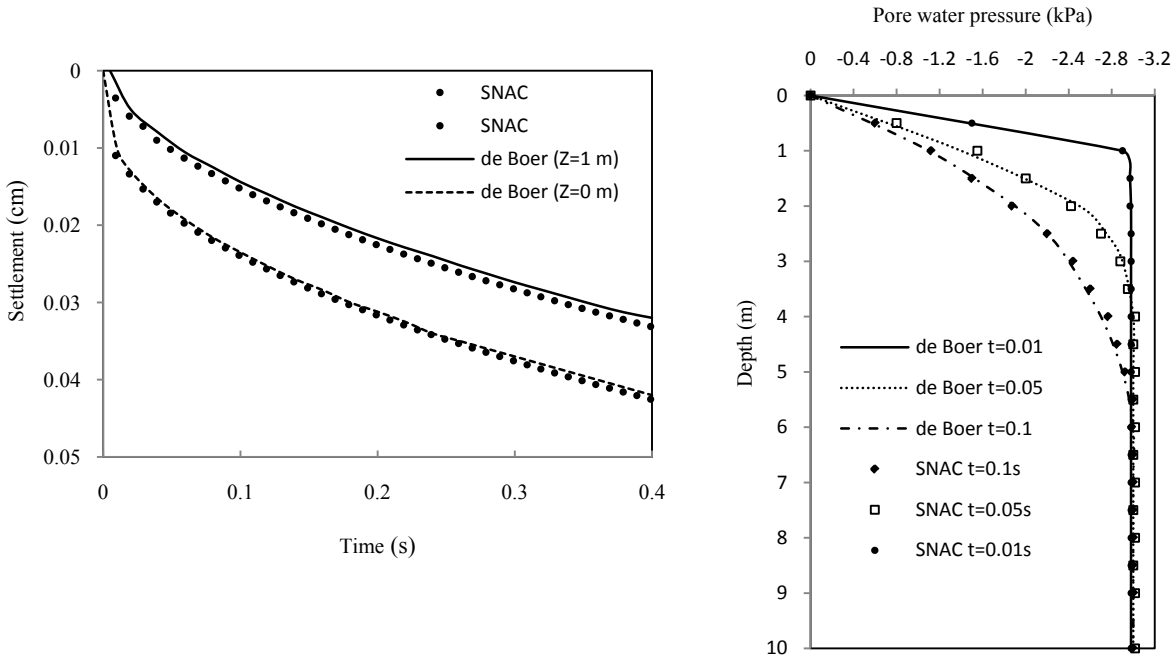

(a) (b)

Figure 2: (a) Vertical settlement under step loading vs. time. (b) pore pressure profile of the soil column at different times.

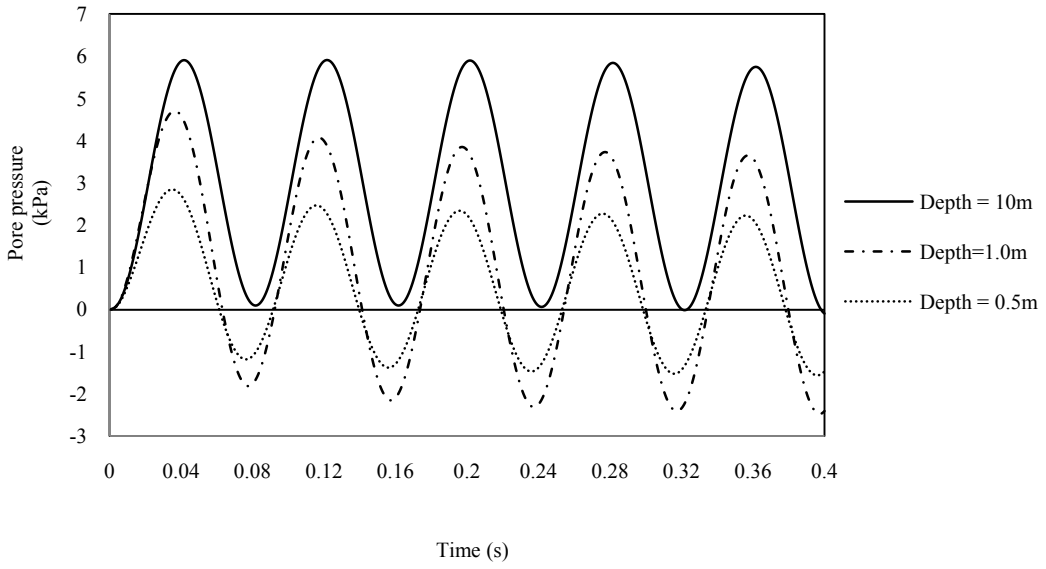

Figure 3: Response of pore water pressure vs. time to sinusoidal loading

To assess the large deformation capability of the code, the soil column was subjected to a uniformly distributed step load q at the free surface according to the load type (c) illustrated in Figure 1. Five load levels of $0.2E$, $0.4E$, $0.6E$, $0.8E$, and $1.0E$ were applied on the column, and the predicted results are compared with those reported by Meroi *et al*[16]. We assume $E = 1$GPa, $\upsilon = 0.0$, $n = 0.3$ and $k = 0.01$m/s. The applied pressure normalised by E is plotted versus the total consolidation settlements (at large time) normalized by the column depth (H) in Figure 4. The results obtained by SNAC are compared to those reported by Meroi *et al*.[16]

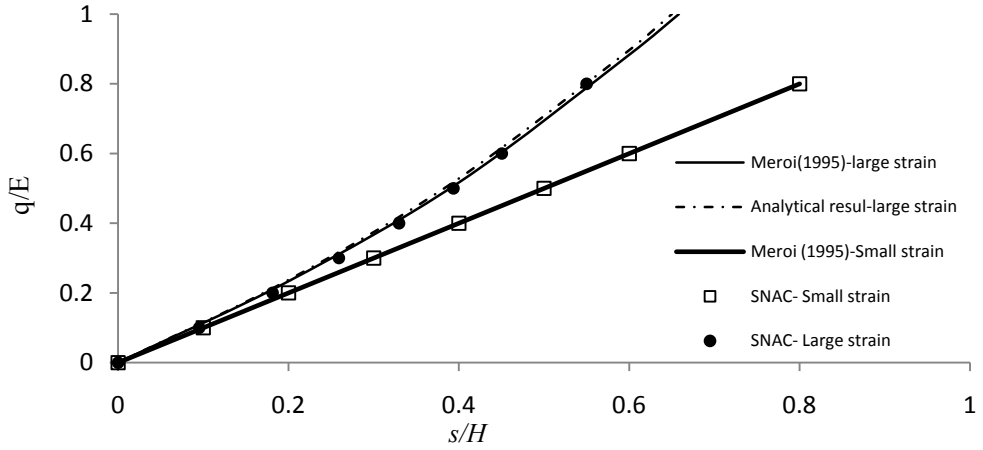

Figure 4: Normalised vertical settlement s versus load level.

5.2 Undrained analysis of a strip footing

In the second example an undrained soil layer under a rough rigid footing is considered. The mesh for the right half of the problem and the boundary conditions are shown in Figure 5. The mesh consists of 872 6-node plane strain triangular elements and 1817 nodal points. In this example we investigate the ability of the dynamic consolidation formulation to predict the undrained deformation response of the soil undergoing a dynamic load and large deformations. First we assume that the soil behaves as a Tresca material model under undrained conditions and we only consider the displacement degrees-of-freedom in the analysis. A non-associated Mohr-Coulomb material model is then used to predict the soil response by conducting a coupled consolidation analysis. Assuming zero initial geostatic stresses, the drained and undrained material properties of the soil must satisfy the following equations [17]

$$E_u = \frac{3E'}{2(1+\vartheta')} \tag{26}$$

$$\frac{c_u}{c'} = \frac{2\sqrt{N_\emptyset}}{1+N_\emptyset} \tag{27}$$

where the subscript u and the superscript ' denote an undrained and a drained quantity, respectively, c represents the cohesion of the soil, ϕ is the friction angle, E is the Young's modulus of the soil, ϑ is Poisson's ratio and N_ϕ is obtained according to

$$N_{\emptyset} = \frac{1 + sin\emptyset}{1 - sin\emptyset} \tag{28}$$

The material parameters used here are E'/c'=200, ϑ'=0.3, ϕ' =20 and hence E_u/c_u=245, φ_u=0 (the angle of dilation), with ϑ=0.49 to simulate elastic incompressibility. A unit mass density is assumed for the soil. In the undrained analysis the load is applied at a rate of $15c_u$/s, i.e., a total uniform pressure $15c_u$ is applied on the footing in 1 second. The settlement of the footing, normalised by its half width, is plotted versus the applied pressure, normalised by c_u, in Figure 6. A clear collapse load, similar to the Prandtl's undrained collapse load at small strain, $q = 5.14c_u$, is not identifiable in this analysis. The higher soil stiffness predicted by the dynamic analysis results from inertia effects alone since material rate effects have not been considered in this analysis.

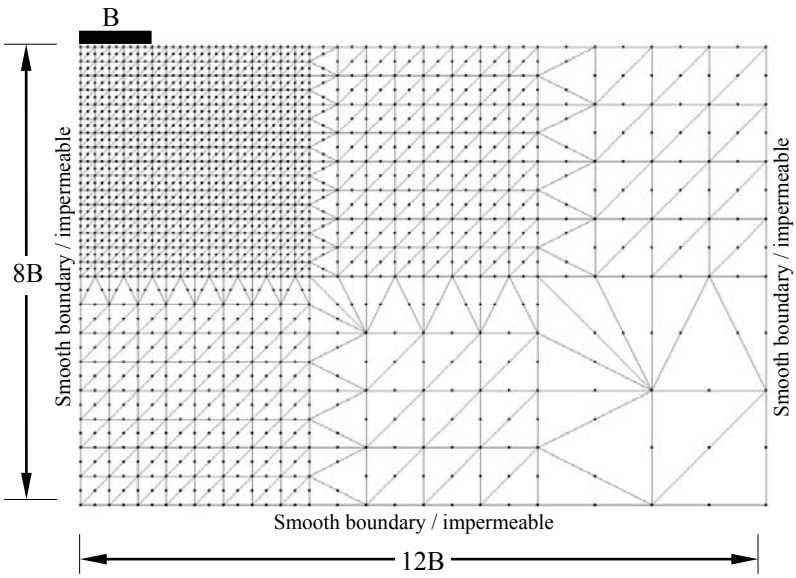

Figure 5: Rigid rough footing on a cohesive soil layer.

Similar analysis was performed utilizing the dynamic coupled consolidation algorithm with drained Mohr-Coulomb parameters, including a dilatancy angle of zero, to represent the behaviour of the soil skeleton. The soil response obtained from the dynamic consolidation analysis is also depicted in Figure 6. The results obtained from both analyses are in excellent agreement. It is worth noting that the large deformation results presented in Figure 6 were obtained by the ALE method and the UL method could not simulate the dynamic response under rapid loading due to the severe mesh distortion.

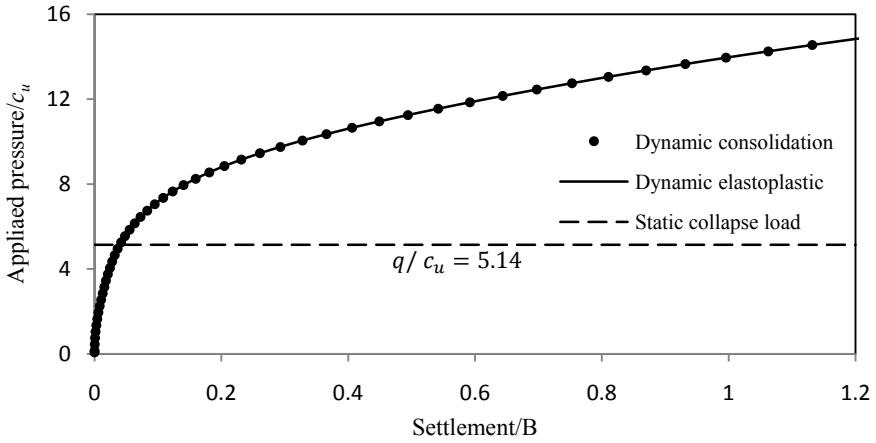

Figure 6: Load-displacement curves

6 CONCLUSIONS

A numerical procedure for the analysis of dynamic consolidation problems involving material nonlinearity as well as geometrical nonlinearity was presented in this study. Dynamic coupled equations were discretised in the time domain by using the generalized-α method, and the numerical algorithm was implemented in a finite element code. For the problems solved, the numerical results are in a good agreement with results available in the literature and analytical solutions. Also, it was shown that the generalised-α method can be used in large deformation analysis of consolidation problems with dynamic loads.

REFERENCES

[1] Zienkiewicz, O.C., Chang, T. and Bettess, P. Drained, undrained, consolidating and dynamic behaviour assumptions in soils. *Géotechnique* (1980) **30**(4):385-395.

[2] Biot M.A. General theory of three dimensional consolidation. *Journal of Applied Physics* (1941) **12**:155–164.

[3] Small, J.C., Booker, J.R and Davis, E.H. Elastoplastic consolidation of soils. *International Journal of Solids and Structures*, (1976), **12**:431-448.

[4] Prevost, J.H. Nonlinear transient phenomena in saturated porous media. *Computer Methods in Applied Mechanics and Engineering* (1982) **20**:3-18.

[5] Zienkiewicz, O.C. and Shiomi, T. Dynamic behaviour of saturated porous media; The generalized Biot formulation and its numerical solution. *International Journal for Numerical and Analytical Methods in Geomechanics*. (1984) **8**:71-96.

[6] Chung, J. and Hulbert, G.M. A time integration algorithm for structural dynamics with improved numerical dissipation: the generalized-α method. *Journal of Applied Mechanics.* (1993) **60**:371–375.

[7] Kontoe, S. Development of time integration schemes and advanced boundary conditions for dynamic geotechnical analysis. *Ph.D. Thesis, University of London.* (2006)

[8] Nazem, M. Sheng, D. and Carter, J.P. Stress integration and mesh refinement in numerical solutions to large deformations in geomechanics. *International Journal for Numerical Methods in Engineering*. (2006) **65**:1002-1027.

[9] Nazem, M. Sheng, D. Carter, J.P. and Sloan, S.W. Arbitrary-Lagrangian-Eulerian method for large-deformation consolidation problems in geomechanics. *International Journal for Analytical and Numerical Methods in Geomechanics*. (2008) **32**:1023-1050.
[10] Hughes T.J.R. Analysis of transient algorithms with particular reference to stability behavior. *In Computational Methods for Transient Analysis,* T. Belytschko and T.J.R. Hughes, Editors, North-Holland, Amsterdam,The Netherlands (1983): 67-155
[11] Hilbert, H.M. Hughes T.J.R. and Taylor R.L. Improved numerical dissipation for time integration algorithms in structural dynamics. *Earthquake Engineering and Structural Dynamics* (1977) **5**:283-292
[12] Wood, W.L. Bossak, M. Zienkiewicz, O.C. An alpha modification of Newmark's method. *International Journal for Numerical Methods in Engineering* (1981) **15**:1562-1566.
[13] Zienkiewicz, O.C. Taylor, R.L. and Zhu. J.Z. *The finite element method, its basis and fundamentals.* Elsevier, Vol. I., (2005)
[14] Nazem, M. Carter, J.P. and Airey, D. Arbitrary Lagrangian-Eulerian Method for dynamic analysis of Geotechnical Problems. *Computers and Geotechnics* (2009) **36**:549-557.
[15] de Boer, R. *Theory of porous media*. Springer, (2000)
[16] Meroi, E.A. Schrefler, B.A. Zienkiewicz, O.C. Large strain static and dynamic semi saturated soil behavior. *International Journal for Numerical and Analytical Methods in Geomechanics* (1995) **19**:81–106.
[17] Small, J.C. Elasto-plastic consolidation of soils. *Ph.D. Thesis, University of Sydney.* (1977)

XI International Conference on Computational Plasticity. Fundamentals and Applications
COMPLAS XI
E. Oñate, D.R.J. Owen, D. Peric and B. Suárez (Eds)

SOLDIER PILE WALLS – 3D NUMERICAL ANALYSIS OF SOLDIER PILE EMBEDMENT

CHALMOVSKY, J., FIALA, R. AND MICA, L*

* Faculty of Civil Engineering, Department Geotechnics
Brno University of Technology
Veveri 95, 602 00 Brno, Czech Republic
e-mail: chalmovsky.j@fce.vutbr.cz

Key words: 3D Passive Earth Pressure, Soldier Pile, Numerical Modeling.

Abstract. The paper is focused to a determination of spatial passive earth pressure (soil resistance) in the embedded part of the soldier pile. The analysis of 3D passive earth pressure is done numerically in software Plaxis 3D Tunnel v 2.2. The analysis of 3D passive earth pressure (soil resistance) is done for cantilever soldier pile walls in sand. The parameters for constitutive models were calibrated based on laboratory tests (triaxial – CD and oedometric tests). Hardening soil model is used in analysis. Outputs of the numerical analysis present a comparison for the resulting passive earth force in case of different *b/d* ratios and different angles of internal friction, parameter ω_R which is used in approach by Weissenbach and finally the magnitude of 3D passive earth pressure coefficients ($K_{P,3D}$) for different soldier pile distance (L), embedment depth (d) and angles of internal friction (φ'). Numerical analysis showed that the 3D passive earth pressure is higher than currently presented approach by Weissenbach. The other present theories don't take to account the behaviour for higher slenderness ratio and influence adjacent soldier pile no way.

1 INTRODUCTION

Passive earth pressure analysis plays an important role in geotechnical design process. Primarily, it is a spatial effect which is significant for local structural elements analysis (for example soldier pile, piles with long axial distances etc.) and therefore it might be important for designers and engineers to gain new knowledge and information about this problem. The topic of spatial passive earth pressure has been analysed by various authors who used three different methods: the limit equilibrium method, the slipe-line method and the limit analysis method. The first mentioned method is used by Blum [2] for analysing the 3D passive earth pressure. The resulting force of passive earth pressure is defined by

$$E_{Ph,Blum} = \frac{1}{2}\gamma d^2 btg^2\left(\frac{\pi}{4}+\frac{\phi}{2}\right)+\gamma\frac{d^3}{6}tg^2\left(\frac{\pi}{4}+\frac{\phi}{2}\right) \quad (1)$$

The disadvantage of Blum solution was, that interface between soil and structural element

was neglected and also the shape of 3D wedge was simplified. The author who firstly analysed the soldier pile wall was Weissenbach [10]. Weissenbach divided relation for determination of 3D earth passive pressure to two components. The first component includes the unit soil weight and the second equation member includes the cohesion of soil. He defined parameters ω_R and ω_K, which depend on the embedment depth (d) and width (b) of structure element and angle of internal friction of soil. In 1964 Ovesen [3] performed number of test on using dense sand. He found out that 3D passive earth pressure is significantly influenced by the structure element thickness. He also found out that structural members with smaller width give significantly higher passive earth pressures than it has ever been considered.

Another theory, limit analysis applying upper bound limit theorem, is widely used for determination of 3D earth passive earth pressure in the present. This theory was firstly applied by Soubra and Regenass [6]. Their calculations were based on determination of kinematically admissible multi-block failure mechanism, which consisted of one ore more rigid blocks. The blocks were labeled as „one-block, multiblock a truncated multiblock". The last-mentioned block is based on reduction of „multiblock" mechanism. The upper bound theorem within the framework of limit analysis theory is also considered in research works done by authors Škrabl, Macuh [7], Vrecl-Kojc, Škrabl [9] and Škrabl [8]. First mentioned authors took into account rotational failure mechanism. This mechanism is bounded by logarithmic spiral in vertical section and by hyperbolic shape in plan. On the contrary, Vrecl-Kojc, Škrabl [9] continued the work of Soubra a Regennas [6], who used translational failure mechanism, and they slightly modified it. The results of this analysis showed that the passive earth pressure coefficient is lower in comparison with Soubra and Regennas. These results were also confirmed by Škrabl [8] who updated his previous model using non-linear passive earth pressure distribution on non-rigid structural element.

Previously mentioned procedures used the change of structural element width to determinate the passive earth pressure coefficients for different d/b ratio. However, this procedure is not appropriate for soldier pile walls, where the change of embedment depth is more dominant than structural element width change.

The article is focused on the analysis of passive earth pressure for geotechnical structures where 3D effect is predominant (for example: soldier beam wall – Fig. 1). The above mentioned authors determined the 3D passive earth pressure for ratio $b/d > 0{,}25$. Benmebarek *et al.* [1] used minimal *b/d* ration 0,1. In our study, ration $b/d < 0{,}14$ has been taken into account. This range of b/d ratio is more common in case of using soldier pile walls, where a soldier pile is actually a slender structural element (usually I, IPE or HEB profile). For these small rations comparison of the resulting passive earth pressure force is done. It is compared with theory of Weissenbach [10] - (2) and Blum [2] - (1).

$$E_{Ph,Weissenbach} = \frac{1}{2}\gamma\omega_R d^3 + 2\alpha\omega_K d^2 \tag{2}$$

The resulting passive earth pressure force in our study is determined from 3D numerical analysis, which is briefly described in the next chapter.

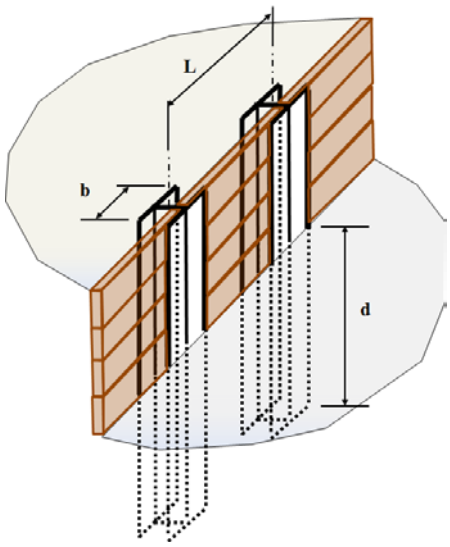

Figure 1: Scheme of soldier beam wall

2 NUMERICAL MODELS

The numerical calculations were done in software Plaxis 3D Tunel V2.4. The only one soldier pile is modelled and horizontal distance between them is done the width of model (Fig. 4). The width of soldier pile is 275 mm and it is supposed as very stiff. The soldier pile is installed in sand. The variable parameters are horizontal distance between soldier pile *L* (1; 1,5; 2; 2,5 and 3 m), embedment depth *d* (1;2;3m) and angle of internal friction φ (30°;35°;40°). The numerical analysis .The interface between soldier pile and soil is neglected in our analysis ($\delta/\varphi = 0$). The movement of soldier pile was the same longwise of embedment depth and the movement was done by function horizontal incremental. The output was resulting force of passive earth pressure which corresponded to stabilization of activation force during increasing movement of soldier pile.

2.1 Input parameters

Numerical modelling has been carried out in sand and for the description of the soil the Hardening soil model – HS (Fig. 2) has been used. The sand was classified according to EN ISO 14688-1 as "Sa". The void ratio was e = 0.524 in the natural state [11]. The sample was taken to conduct an extensive and complex laboratory tests to determine the input parameters for selected constitutive models. Oedometer, shear box and triaxial (CD test) test were performed on the samples. Oedometer test was used to determination of modulus E_{oed}^{ref} for HS model with the reference stress p_{ref} = 100 kPa. The result from oedometer and its calibration of HS model is shown in Fig. 3a. Angle of friction φ_{ef} and the cohesion c_{ef} were determined from shear box test. Triaxial CD test was used to determination of reference modulus E_{50}^{ref} and E_{ur}^{ref} for HS model with the reference stress p_{ref} = 100 kPa. In order to determine E_{ur}^{ref} parameter, unloading of the sample was carried out. Figure 3b shows stress-strain diagram from experiment (blue line) and calibrated stress – strain diagram with usage HS model. The laboratory tests were done in the geotechnical laboratory of the Faculty of Civil Engineering, Brno University of Technology.

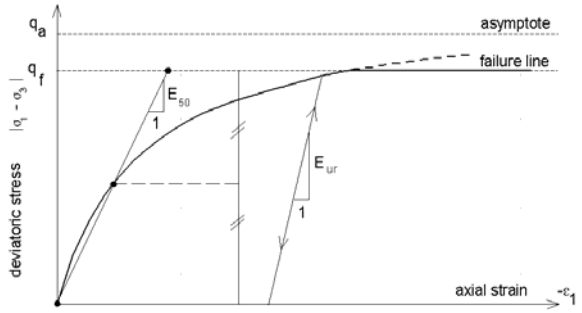

a) Hyperbolic stress-strain relation

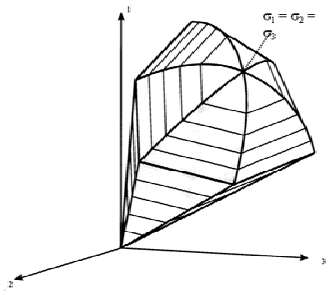

b) Soil plasticity surface for cohesionless soil

Figure 2: Hardening soil model [4]

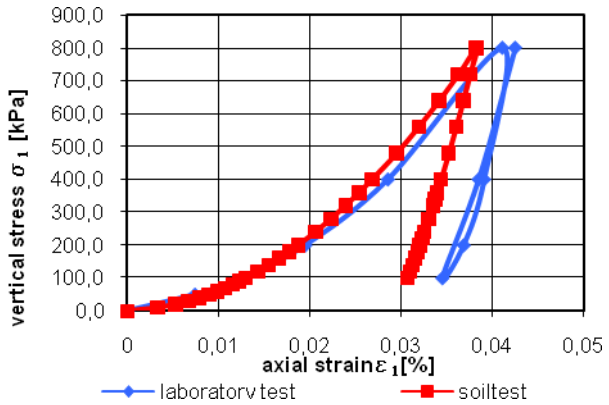

a) Oedometer test - stress-strain diagram

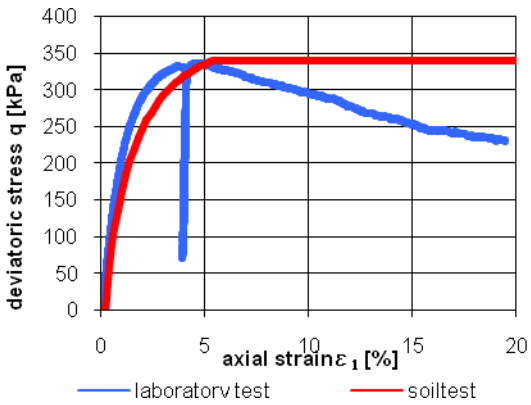

b) Triaxial test - stress-strain diagram

Figure 3: Laboratory test and calibration

The input parameters for Hs model are summarized in Table 1.

Table 1: Input parameters for sand

γ_{unsat}	E_{50}^{ref}	E_{oed}^{ref}	E_{ur}^{ref}	m	c´	φ´	ν_{ur}	R_f	p_{ref}
[kN/m^3]	[MPa]	[MPa]	[MPa]	[-]	[kPa]	[°]	[-]	[-]	[kPa]
17,6	22,567	11,22	59,14	0,50	0,1	40	0,2	0,8	100

2.2 Description of numerical calculations

For 2D calculations the plane strain condition is considered. General tensor of proportional deformations consists of 6 terms (3) in plane by equitation (4) reduce to triple tensor (5).

$$\underline{\varepsilon}_{3D}^{T} = \left\{ \varepsilon_{xx}; \varepsilon_{yy}; \varepsilon_{zz}; \gamma_{xy}; \gamma_{yz}; \gamma_{xz} \right\} \tag{3}$$

$$\varepsilon_{zz} = -\frac{\partial w}{\partial z} = 0\,;\ \gamma_{yz} = -\frac{\partial w}{\partial y} - \frac{\partial v}{\partial z} = 0\,;\ \gamma_{xz} = -\frac{\partial w}{\partial x} - \frac{\partial u}{\partial z} = 0 \tag{4}$$

$$\underline{\varepsilon}_{2D}^{T} = \left\{ \varepsilon_{xx}; \varepsilon_{yy}; \gamma_{xy} \right\} \tag{5}$$

The restrction of the deformation in the plane of retaining system cannot take into account

spatial character of the earth pressure under the bottom of the excavation with limited effective width. It leads to the conservative calculation of the passive earth pressure which can flow into non-economic design of such a retaining structure. For the purpose of examination of the passive earth pressure redistribution under the bottom of the excavation, the software Plaxis 3D Tunel v 2.2 has been used. For the example analysis the cut-out from the excavation pit with the high of 4m has been modelled. The example has been modelled as symmetrical with the axis in the middle distance between the soldier piles. The soldier piles have been embedded 2m, 3m and 4m under the bottom of the excavation. The distance of the soldier piles in the spatial analysis has been 1,0m; 1,5m; 2,0m; 2,5m and 3,0m. The soldier pile has been modelled as stiff element with the plan dimensions 275x275mm. The dimensions of 3D models are 10,25m (high), 13,5m (depth) and width is variable. The number of elements varies from 6030 to 7596. In the calculations only a part under the bottom of the excavation has been modelled mainly because of the time savings. The part above the bottom of the excavation has been substituted by equivalent geostatic stress. When considering the excavation pit 4m high and the bulk density 20kN/m^3 of the soil above the bottom, the upper edge of the models has been loaded by the distributed load of 80kPa. Figure 4 represent 3D model with the distance of the soldier piles 3,0m and the embedded depth of 4,0m.

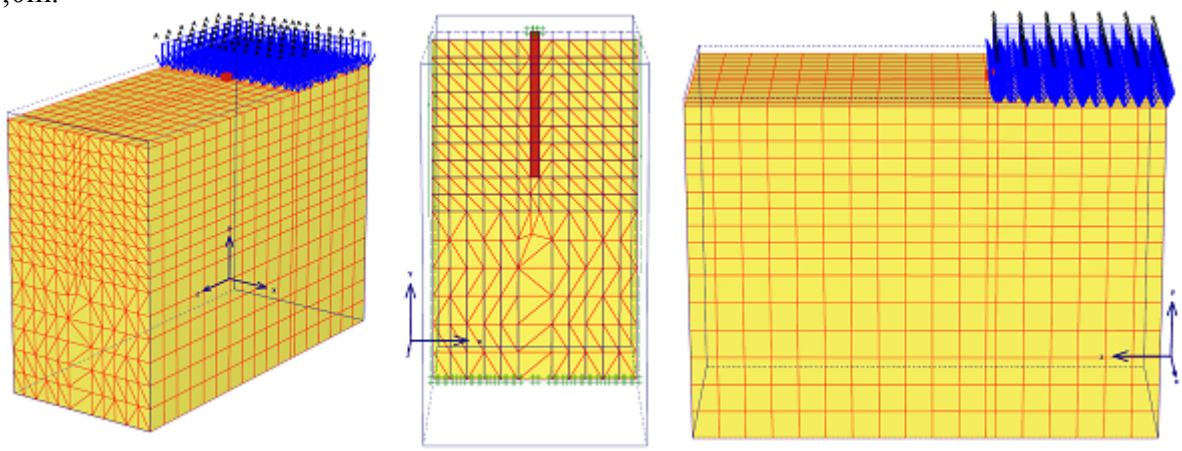

Figure 4: Different views on numerical models

In order to mobilise passive earth pressure the soldier pile has been subjected to prescribe deformation. This prescribe load has been increasing until the steady state of the passive force. The construction staged are summarised in Table 2.

Table 2: Construction sequences

ID	Name of Stage	Note
1	Initial conditions	For simulation of geostatic stress above the bottom of excavation POP=80kPa
2	Soldier Pile Construction	Staged construction
3	Primary prescribe deformation – 5mm	Staged construction
4	Increasing of prescribe deformation	Staged construction - incremental multipliers, M_{disp}=2,0

The variations of the calculations in the parametrical studies are summarised in the Tab. 3.

Table 3: Description of performed calculations

ID-3D	φ´ (°)	*L* (m)	*t* (m)
1a; 1b; 1c	30,35,40	1,00	2,00
2a; 2b; 2c	30,35,40	1,00	3,00
3a; 3b; 3c	30,35,40	1,00	4,00
4a; 4b; 4c	30,35,40	1,50	2,00
5a; 5b; 5c	30,35,40	1,50	3,00
6a; 6b; 6c	30,35,40	1,50	4,00
7a; 7b; 7c	30,35,40	2,00	2,00
8a; 8b; 8c	30,35,40	2,00	3,00
9a; 9b; 9c	30,35,40	2,00	4,00
10a; 10b; 10c	30,35,40	2,50	2,00
11a; 11b; 11c	30,35,40	2,50	3,00
12a; 12b; 12c	30,35,40	2,50	4,00
13a; 13b; 13c	30,35,40	3,00	2,00
14a; 14b; 14c	30,35,40	3,00	3,00
15a; 15b; 15c	30,35,40	3,00	4,00

3 RESULTS AND DISCUSSION

In the previous studies and analysis, primarily, small slenderness ratios were taken into account and the interaction between the adjacent structural elements was not considered (Fig. 5). The objective of the performed numerical analysis in this study was to investigate just the range of higher slenderness. Blum approach [2], Weissenbach approach [10] and partially Benmebarek *et al.* [1] should be used for comparisons because their researches partially covers the range of higher slenderness, but still without taking into account the interaction between the adjacent passive wedges. Only exception is the theory derived by Weissenbach which is used in German standard in order to design the soldier beam walls.

In the first step, the comparisons for the resulting passive earth force E_{ph} in case of different *b/d* ratios and different angles of internal friction were done (Fig. 6÷8). The numerically determined values of E_{ph} forces are then compared with resulting passive forces calculated by Weissenbach approach [10]. The values of E_{ph} forces are calculated for two cases. Firstly, the adjacent passive wedges overlap each other (6a). Secondly, the adjacent passive wedges do not overlap each other (6b). The value of E_{ph} (1) force calculated by Blum [2] is also shown in the graphs.

$$\mathrm{L} < 0{,}5\mathrm{d} \ \wedge \ \delta = 0 \Rightarrow E_{ph} = \frac{1}{2} \cdot \gamma \cdot \omega_{ph} \cdot L \cdot d^2 \quad \wedge \quad c = 0 \quad \Rightarrow \quad \omega_{ph} = K_{ph} \tag{6a}$$

$$\mathrm{L} \geq 0{,}5\mathrm{d} \ \wedge \ \delta = 0 \Rightarrow E_{ph} = \frac{1}{2} \cdot \gamma \cdot \omega_{r} \cdot d^3 \quad \wedge \quad c = 0 \quad \wedge \quad \omega_R [5] \tag{6b}$$

The analysis confirmed that the effect of adjacent elements is not negligible. It is apparent from the results that the increase of soldier pile distance for constant *b/d* ratio causes also the passive earth force increase. This tendency is related to the overlapping of passive wedges for the case of small soldier pile distances *L*. The results also showed rapid rise in passive force for lower *b/d* ratio. There is a reasonable consistency in resulting forces between computed results and results according to Weissenbach [10]. Blum [2] indicates lower forces values in contrary to the numerical results. It is probably caused by the fact that the simplified passive

wedge geometry is used in Blum solution.

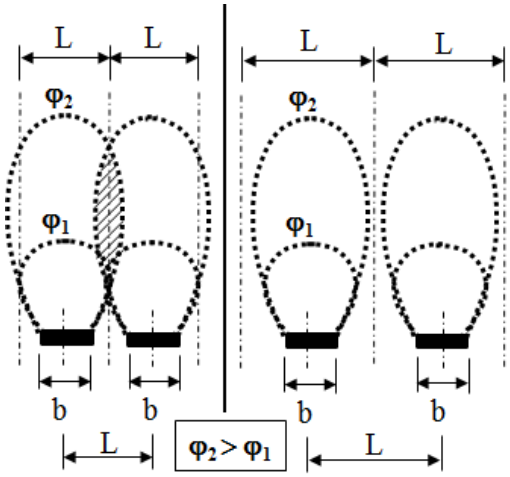

Figure 5: Scheme - influence of adjacent passive wedges

In the second step we focused on the parameter ω_R determination which used Weissenbach in his approach in order to affect spatial character of the passive earth pressure in case of analysing the constructions with limited width. This parameter was derived from (6a and 6b) where numerically calculated value of E_{ph} was substitute to the left part of the equation. Zero cohesion was assumed in soil parameters; the second equation member is therefore equals to zero. The numerically determined values of ω_R coefficient were compared again with values according to Weissenbach (Fig. 9÷11). It is apparent form the results that the ω_R values are directly proportional to the soldier pile distance, which confirms previous statement that the passive earth force is directly proportional to the soldier pile distance. The numerically determined values of ω_R are higher in comparisons with values by Weissenbach. These difference results in higher passive earth forces in case of FEM analysis. This tendency is even more evident for higher *b/d* ratio.

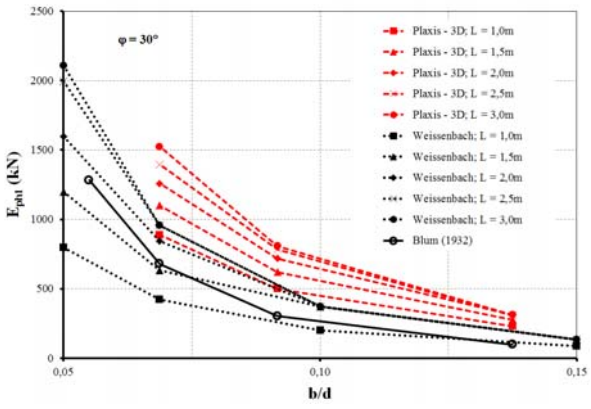

Figure 6: Comparison of E_{ph} with Weissenbach and Blum for φ = 30° and δ/φ = 0° for different values of b/d ratio.

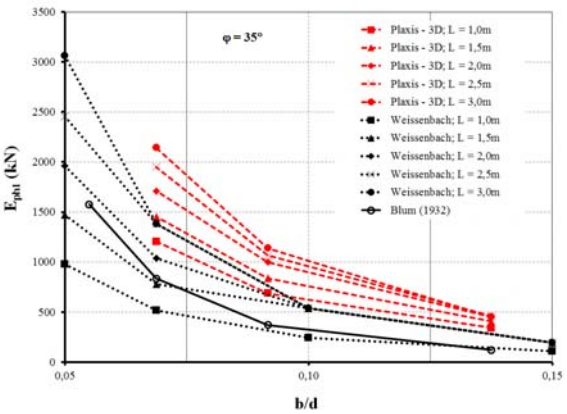

Figure 7: Comparison of E_{ph} with Weissenbach and Blum for φ = 35° and δ/φ = 0° for different values of b/d ratio.

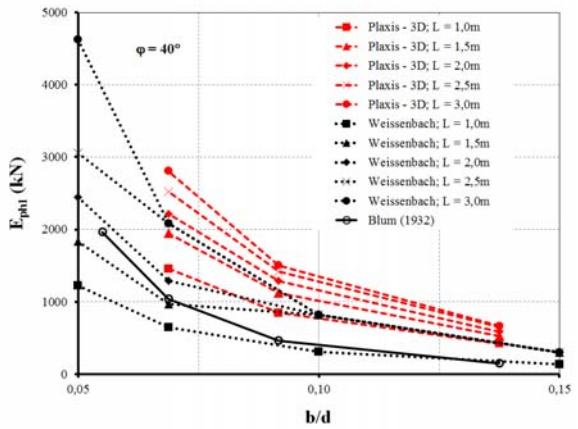

Figure 8: Comparison of E_{ph} with Weissenbach and Blum for φ = 40° and δ/φ = 0° for different values of b/d ratio.

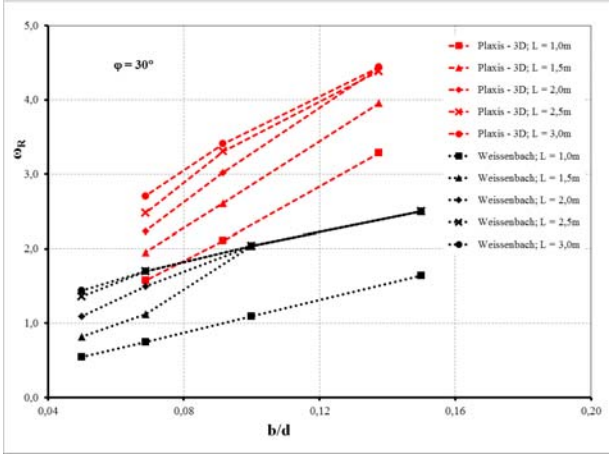

Figure 9: Comparison of ω_R with Weissenbach and Blum for φ = 30° and δ/φ = 0° for different values of b/d ratio.

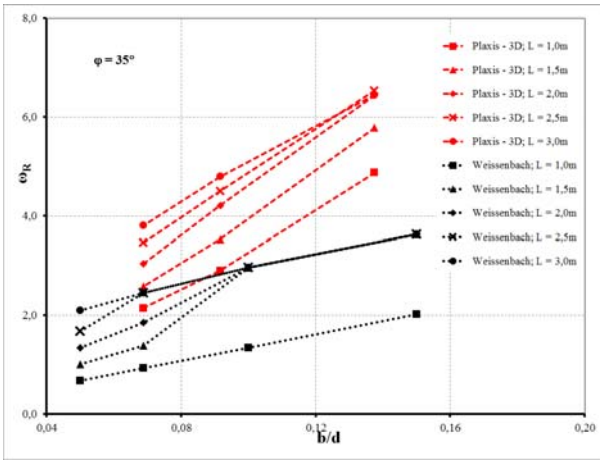

Figure 20: Comparison of ω_R with Weissenbach and Blum for φ = 35° and δ/φ = 0° for different values of b/d ratio.

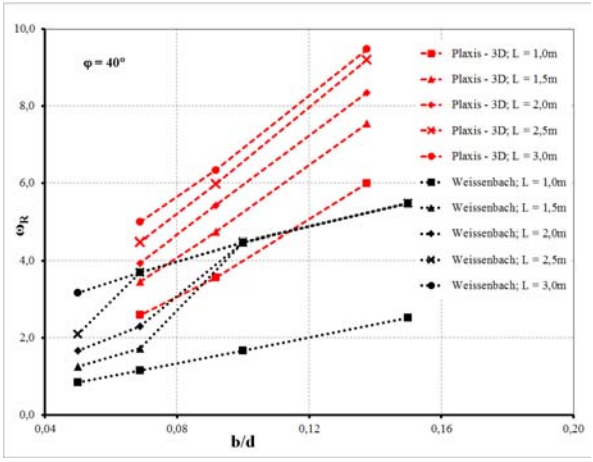

Figure 31: Comparison of ω_R with Weissenbach and Blum for φ = 40° and δ/φ = 0° for different values of b/d ratio.

The last step of the analysis was determination of 3D passive earth pressure coefficients ($K_{P,3D}$) for different soldier pile distance (L), embedment depth (d) and angles of internal friction (φ'). Using $K_{P,3D}$ (7) coefficients instead of ω_r might by also the way how to involve the spatial effect in 2D solution.

$$E_{ph} = \frac{1}{2} \times \gamma \times d^2 \times b \times K_{p,3D}$$
$$K_{p,3D} = \frac{2 \times E_{ph}}{\gamma \times d^2 \times b} \quad (7)$$

The computed values of passive earth coefficient $K_{P,3D}$ are listed in Table 4. The table shows that the passive earth pressure coefficient value are not only depended on distance L and angle of internal friction φ', but also on the embedment depth d. For large values of embedment

length *d*, the 3D effect decrease the value of $K_{P,3D}$ for small distances *L*. The rate of decreasing is also affected by angle of internal frictionφ. Note: In all presented analysis is values of soil-wall interface friction $\delta/\varphi = 0°$.

Table 4: $K_{p,3D}$ coefficient

b/d	φ	L				
		1	1,5	2	2,5	3
0,07	30°	22,92	28,41	32,52	36,04	39,34
	35°	31,18	37,57	44,18	50,33	55,35
	40°	37,64	50,33	57,24	65,10	72,51
0,09	30°	22,99	28,48	32,96	36,07	37,15
	35°	31,58	38,54	45,93	49,04	52,30
	40°	38,86	51,67	59,11	65,15	69,10
0,14	30°	23,90	28,76	32,21	31,90	32,28
	35°	35,43	42,02	46,79	47,49	46,86
	40°	43,61	54,88	60,72	66,94	68,93

4 SUMMARY AND CONCLUSIONS

Set of 3D numerical models were created in order to analyse the distribution of passive earth pressures behind the soldier pile wall, which is a truly spatial phenomenon. Parallel horizontal prescribed displacement with no rotation was applied on the soldier pile. Soldier pile was modelled as a rigid member. The interface elements were not used. The FEM calculation results are presented in form of passive earth forces.

The passive earth pressure increase with increasing soldier pile distance. This is due to the passive wedges overlapping. Passive earth force also grows exponentially with increasing slenderness. Calculated forces are in reasonable match with Weissenbach [10]. Blum [2] indicates lower forces values in contrary to the numerical results.

Numerical analysis have showed, that the coefficients ω_R respectively ω_{ph} are directly proportional to the soldier pile distance, which is in agreement with Weissenbach, however Weissenbach underestimates the ω_R respectively ω_{ph} values in comparisons to the numerical results. The differences are bigger for higher values of slenderness.

Final part of the article was focused on comparison of passive earth pressure coefficients K_{p3D} for different soldier pile distances and embedment length. It is obvious from the result that coefficient K_{p3D} is directly proportional to the soldier pile distance. The differences are, however, smaller for bigger soldier pile distances, because of the fact, that passive wedges doesn´t influence each other for bigger distances and they start to be independent on soldier pile distance.

For further research, parametric study with non-zero soil-wall friction angles, with another type of deformation (rotation) and also with considering non-rigid soldier pile will be undertaken. Spatial passive earth pressure for cohesive soils will be also analysed.

AKNOWLEDGMENT

This contribution was financially supported by the project of the Czech Science Foundation (GA ČR) No. GA103/09/1262, by the research project of The Ministry of

Education, Youth and Sports (MŠMT ČR) No. MSM0021630519 and by the project FAST-S-11-39. Authors appreciate this support.

REFERENCES

[1] Benmebarek, S., Khelifa, T., Benmebarek, N. and Kastner, R. Numerical evaluation of 3D passive earth pressure coefficients for retaining wall subjected to translation. *Computers and Geotechnice* (2008) **35**:47-60.

[2] Blum, H. Wirtschaftliche Dalbenformen und deren Berechnung. *Bautechnik* (1932) **10(5)**:122-135.

[3] Ovesen, N. K. *Anchor slabs, calculation method, and model tests*. Danish Geotechnical Institute, Kopenhagen (1964).

[4] Schanz, T., Vermeer, P.A., Bonnier, P.G. *The hardening soil model: Formulation and Verification*, Beyond 2000 in Computional Geotechnics – 10 Years of Plaxis, Rotterdam (1999)

[5] Smoltczyk, U. *Grundbau-Taschenbuch, Teil3: Gründungen*. Ernst & Son, (2001).

[6] Soubra, A.-H. and Regennas, P. Three-dimensional passive earth pressures by kinematical approach. *Journal of Geotechnical and Geoenvironmental Engineering*. ASCE, (2000) **126**(11):969-978.

[7] Škrabl, S. and Macuh, B. (2005). Upper-bound solution of three-dimensional passive earth pressures. *Canadian Geotechnical Journal* (2005) **42**:1449-1460.

[8] Škrabl, S. The limit values and the distribution of three-dimensional passive earth pressure. *Acta geotechnica Slovenika* (2008) **1**:21-34.

[9] Vrecl-Kojc, H. and Škrabl, S. (2007). Determination of passive earth pressure usány three-dimensional failure mechanism. *Acta Geotechnica Slovenika* (2007) **4**(1):11-23.

[10] Weissenbach, A. *Der erdwiderstand vor schmalen druckflechen*. PhD thesis, Franzius Institut für Grund und Wasserbau der Technischen Hoschule, Hannover (1961).

[11] Zedník, J. Zajištení stavební jámy v píscích. *Master thesis*, VUT Brno: 2010. (in Czech)

SYMBOLS

b ...	Width of soldier pile (m)
c ...	Cohesion, effective (kPa)
d ...	Eembedment depth (m)
E_{oed}^{ref} ...	Tangent stiffness for primary oedometer loading (kPa)
E_{50}^{ref} ...	Secant stiffness in standard drained triaxial test (kPa)
E_{ur}^{ref} ...	Unloading/reloading stiffness (kPa)
E_{ph} ...	Resulting passive earth pressure force (kN)
$K_{P,3D}$ ...	3D passive earth pressure coefficients
L ...	Horizontal distance of soldier pile (m)
m ...	Power for stress-level dependency of stiffness (-)
R_f ...	Failure ratio (-)
γ ...	Unit weight of soil (kNm^{-3})
φ ...	Angle of internal friction, effective (°)
ν_{ur} ...	Poisson´s ratio for unloading-reloading (-)
ω_R/ω_{ph}...	Coefficient by Weissenbach

XI International Conference on Computational Plasticity. Fundamentals and Applications
COMPLAS XI
E. Oñate, D.R.J. Owen, D. Peric and B. Suárez (Eds)

A COMPUTATIONAL STUDY ON THE OVERLOAD CHARACTERISTIC CURVES OF PROJECTILE PENETRATING METAL OBJECT

DENG QIONG*, FENG LONG, QI WEI

School of Aeronautics, Northwestern Polytechnical University, Xi'an 710072, P.R. China
e-mail: dengqiong24@nwpu.edu.cn

Keywords: Penetration, target plates, over load curve, Lagrange method, Lagrangian-Eulerian coupling algorithm

Abstract: The paper, based on ANSYS/LS-DYNA software, made a computational study on the overload characteristic curves of projectile penetrating metal objects. Adopting Lagrange method, Lagrangian-Eulerian coupling algorithm and SPH method, respectively, simulated the over-load characteristics of projectiles penetrating single-layer steel plates and multi-layer steel and aluminum alloy plates. The results affirmed that the curves agreed well with each other. The curves reached its peak during every penetrating layer and the accelerator peak declined with layers increasing. And the overload value fluctuated around zero during the penetrating interval. The fact, gained from the velocity curves, was that it dropped gradually, however, reached a plateau during the interval, suggesting that the velocity kept constant, and overload value came to zero. The simulation and the experimental results of penetrating the multi-layer aluminum alloy plates were in well accord. Besides, the overload curves shared the same trends with penetrating the multi-layer steel plates.

1 INTRODUCTION

As for studies about penetrating, consulting the references available, no matter experimental and simulation study, mechanism study gained the major focus. Nesterenko et al [1], using the steel-made columned and conical projectiles to penetrate into the targets of Ti–6Al–4V alloy, study the microstructure, and analyzed its effect on the anti-penetration property. Bøvik et al [2-6] and Dey et al [7-9], made a series of computational simulations and experiments to penetrate the Weldox 460 E steel plates systemically, to investigate the size effect. And Bøvik et al [10-11] also made some studies about penetrating the AA5083-H116 and AA6005-T6 plates. Besides, Gupta et al [12-13] focused on the penetrating mechanism changes ascribed from the projectiles' figure, plates' thickness, by using the penetrating experiments of 1100-H12 aluminum alloy plates with thickness below 3mm. The studies concentrated on the distortion mechanism of the targets and the projectile velocities after penetrating, but it would be difficult to get the overload characteristic curves

from the results, especially, the projectile overload curves could be seldom offered in the simulation study.

Based on the actualities, the paper, based on the ANSYS/LS-DYNA code, made studies about the overload characteristic curves by simulating the penetrating steel, aluminum alloy plates with different layers.

2. THE SELECTION OF CONSTITUTIVE MODELS

(1) Projectile

In order to get fine comparisons with experimental results[14], projectiles, which were made of 35CrMnSiA, with weight 3.2 kg，diameter 62 mm, length 215 mm，and its head arc semi-diameter 70 mm，impacted the target plates with the speed 800 m/s.

(2) Target plates

The target plates, were made of 45# steel, with the size of 10 mm×1200mm×1200mm.

(3) Ascertaining material model and parameters

The plastic Kinematic Model in the LS-DYNA code was adopted, with rate enhancement Cowper-Symonds model [15]. Table.1 showed the materials parameters after consulting Hu Changming et al [15].

Table.1: The materials parameters of projectiles and the target plates [15]

Materil	Density /（kg/m3）	Modula /GPa	Yield strength /MPa	Plastical harding modula/GPa	Passion ratio
35CrMnSiA	8.0×103	206	1 275	2.0	0.284
45#steel	7.85×103	200	496	0.5	0.28

3 OVERLOAD CURVES SIMULATIONS DURING PENETRATING

3.1 penetrating the single steel plate with the thickness 10mm

Adopting Lagrange method, Lagrangian-Eulerian coupling algorithm and SPH method in LS-DYNA code, simulated penetrating and got the over-load characteristic curves, in consequence

(1) Lagrange method

Considering the ratio of the target plate to the projectile diameter, and for optimal computation, a relevant axial symmetry model was built with the adoption of 4-node-2D axial symmetry mesh. And the section along the thick direction of the target plate model was divided into 24 meshes, which adopted single point integrals and sandglass control. The chart.1 showed the penetrating model and the local meshes schematically. And plastic

Kinematic model were selected for the projectile and target plate material.

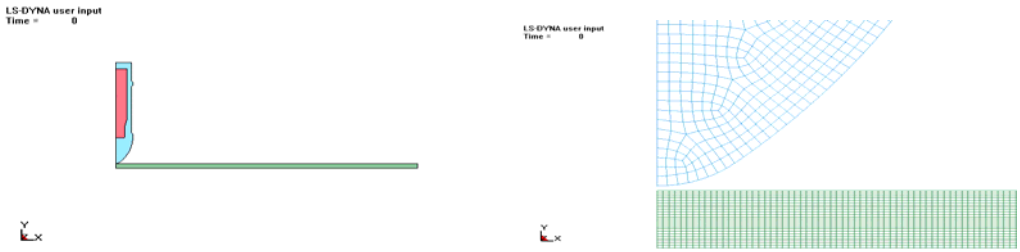

(a) Sketch map of penetrating steel plate (b) Local meshes

Chart 1: Penetrating model and the local meshes of Lagrange method axial symmetry model

The over load curves, gained from computational simulation, was showed in Chart.2, displaying that over load peak reached about 93,000g, and the length of the pulse came to about 60 μs.

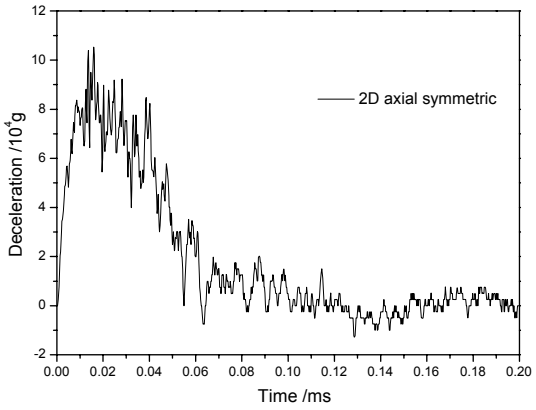

Chart 2 : Overload curves got from Lagrange method axial symmetry model

(2) Lagrangian-Eulerian coupling algorithm

The whole model was divided into single-node integration hex meshes, and a quarter was used to make computing simulation, just for optimal computation. The center section of the target plate was compartmentalized densely into Eulerian finite meshes. Chart.3 gave the schematic of the whole projectile mesh, and the diagram of penetrating the target plate at 120 seconds, respectively.

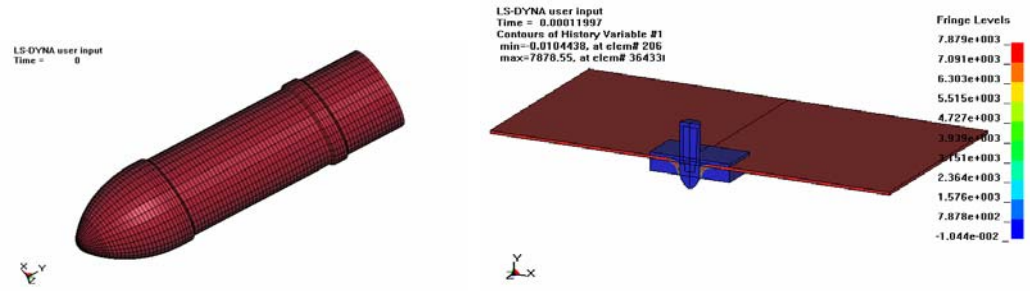

(a) The whole projectile mesh (b) Penetrating the target plate at 120s

Chart 3 : Schematics of penetrating the steel plate using Lagrangian-Eulerian coupling algorithm

And the result of the computational simulations, showed in Chart.4, told that, the overload peak came to 92,000g around, with about 60μs' pulse length.

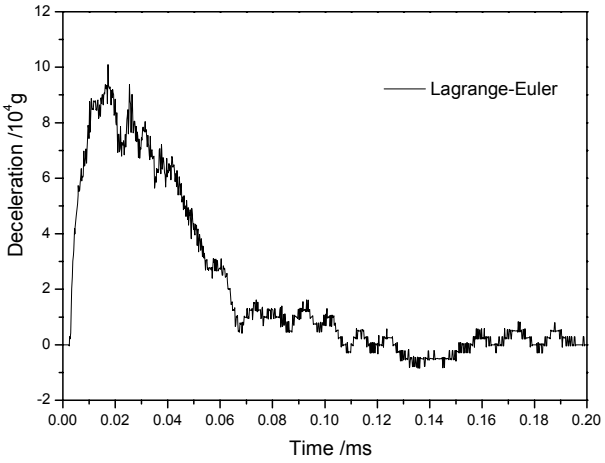

Chart 4 : Overload curve from Lagrangian-Eulerian coupling algorithm

(3) SPH method

The center section of the target plate with the dimension of 100mm×100mm×10mm was defined as SPH particles, with the number of 100×100×10 respectively. The rest were divided by Lagrangian hexahedron mesh. The contact between particles and lagrangian mesh was defined as boundary contact, whereas the contact between particles and projectile was defined as the contact of node to face. The chart 5 showed the schematic of the penetrating process.

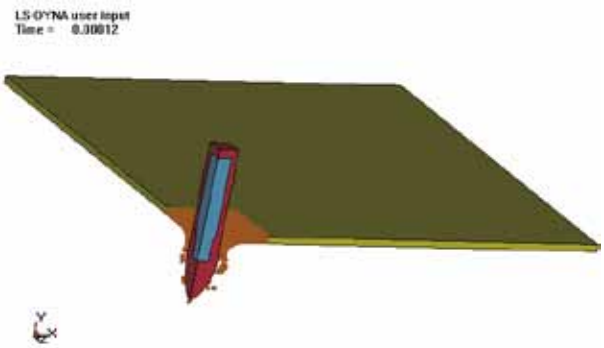

Chart 5 : the penetrating process by SPH method

The overload curve of the simulation, shown as chart 6, revealed the maximum of the acceleration can reached about 90 000, with the pulse length of 60μs around.

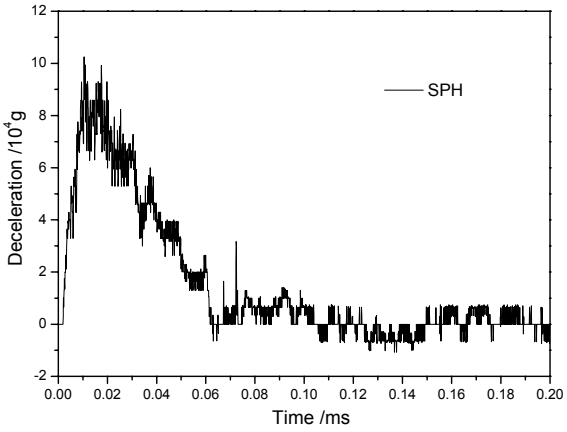

Chart 6 : the overload curve by the SPH method

Comparing with the over-mentioned results, rather difference could be found between the 3 methods. The axial symmetry model have predominated for its rather small computational amount and enough complexity. Thus, the axial symmetry model would be elected in the following simulations.

3.2 The investigation into the overload curves of penetrating multi-layer steel plates

Same to the above-mentioned conditions, over load curves were simulated to investigate into the penetrating into the multi-layer steel plates. The model diagram were shown as Chart 7, with the gap 250 mm, the thickness of 14 mm、10 mm for two layers、three layers steel plates respectively.

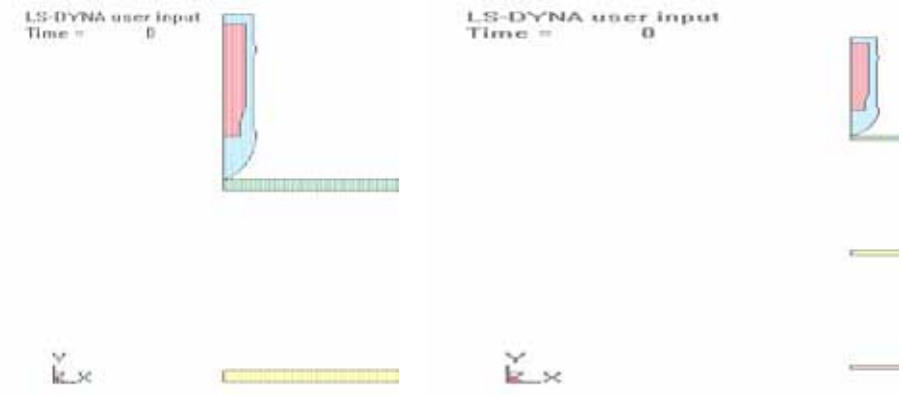

(a) 2 layers steel plates (b) 2 layers steel plates

Cahrt 7 : The model diagram of penetrating multi-layer steel plates

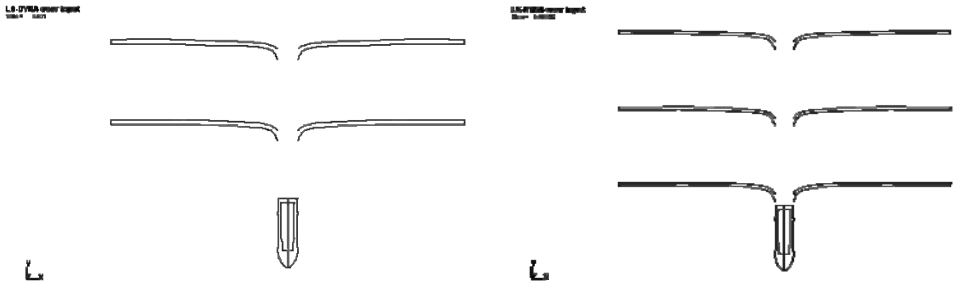

(a) 2 layers steel plates (b) 3 layers steel plates

Chart 8 : The distortion schematic after penetrating multi-layer steel plates

Chart.9 and 10 displayed the overload curves and velocity curves after penetrating two typical plates shown as the above charts.

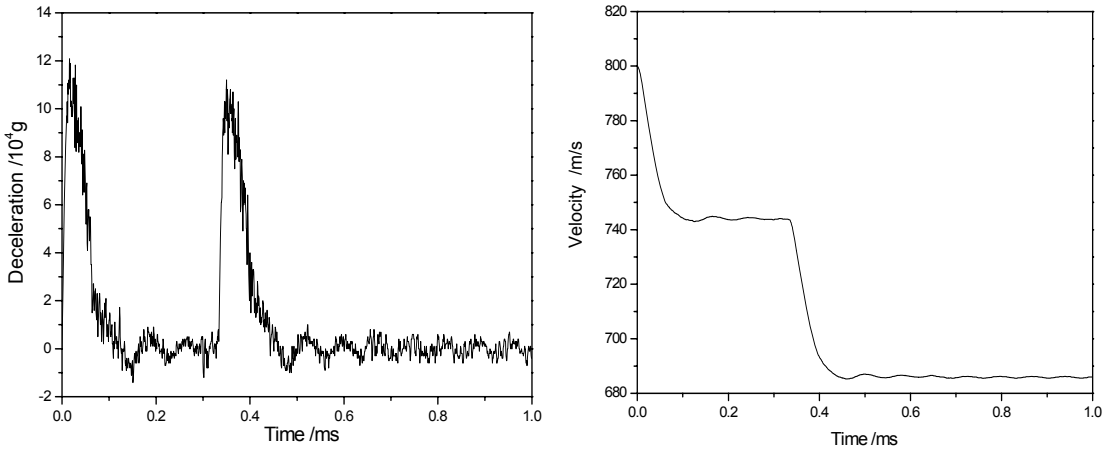

(a) Over load curve (b) Velocity curve

Chart 9 : The over load and velocity curves of penetrating two layers steel plate

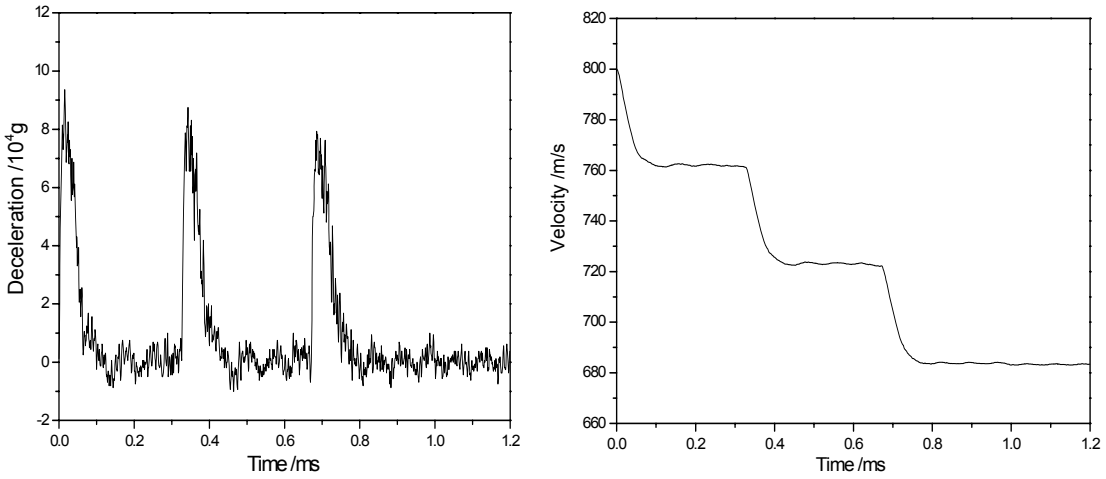

(a) Over load curve (b) Velocity curve

Chart 10 : The over load and velocity curves of penetrating three layers steel plate

The chart.9 and 10 displayed that three distinct peaks could be gained during the penetrating each layer (shown as (a)), and the accelerator sharply descend as the layer increased. During the penetrating interval, the over load fluctuated around zero. Besides, the velocity curve revealed that, during the penetrating each layer, the curve value dropped linearly, whereas during the interval, the value came to a plateau which explained the values kept about constant and the over load value went down towards zero.

3.3 The simulation of penetrating the multi-layer aluminium alloy plates

(1) Establishing model

45# mild steel was elected as the projectile material, and the projectile was modeled with the diameter of 12.7mm, length of 51mm, the mass of 48.5g, and the half ball head. The target plate was modeled as a sandwiched structure, made of the two layers (LY12-CZ, and 2mm in thickness), and foam core (10mm in thickness) sandwiched within the layers. The dimension of the target plate is 300 mm×300 mm×(2 mm+10 mm+2 mm). The Plastic Kinematic Model was elected as the material model for the projectile and the target plate. LY12-CZ was adopted as no strain rate effect. The table 2 showed the material parameters.

Table. 2: Materials parameters

Material	Density / kg/m^3	Modula /GPa	Yield strength /MPa	Plastical harding modula/GPa	Passion ratio
LY12-CZ	2 780	72	345	0.69	0.3
foam	200	0.9	8.3		0.33
45$^{\#}$ steel	7 850	200	496	0.5	0.28

(2) Computational model

As shown as the chart 11, a quarter of the whole model was used for simulation, and the impact section (within the three times of the projectile diameter) was compartmentalized densely in order to ensure the enough accuracy. The rest was divided normally for proper computational amount.

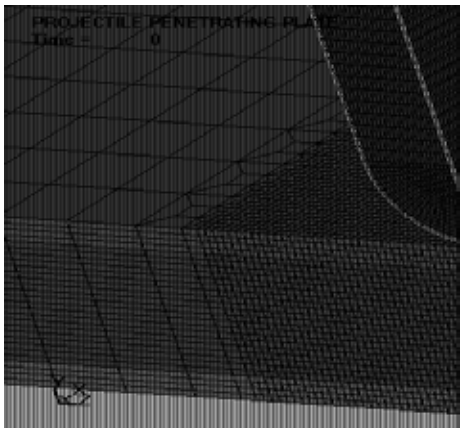

Chart 11 : finite element model of penetrating the aluminum alloy plate

(2) Computational results

The table 3 showed the experimental initial velocity, residual velocity and the computational residual velocity.

Table.3: Comparisons between experimental and\ simulation results of penetrating sandwiched plate/ (m/s)

	Initial velocity	Residual velocity（Exp.）	Residual velocity（Com..）
Sandwiched plate	191.3	169.8	155
	93.4		
	104.5		
	109.2	26.4	32
	73.0		

Abstracted from the table 3, the conclusion was that the simulation velocity went to the experimental velocity very nearly, thus the computational simulation could captured the experiments well.

The accelerator curves and velocity curves were shown as chart 12, gain from the simulation with the initial projectile velocity from 109 m/s, 191 m/s and 250 m/s.

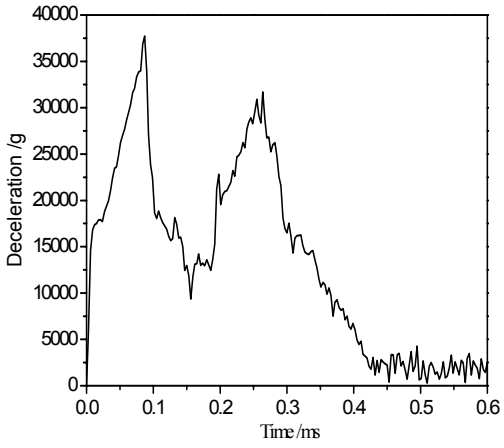

(a) Accelerator curve （v=109m/s）

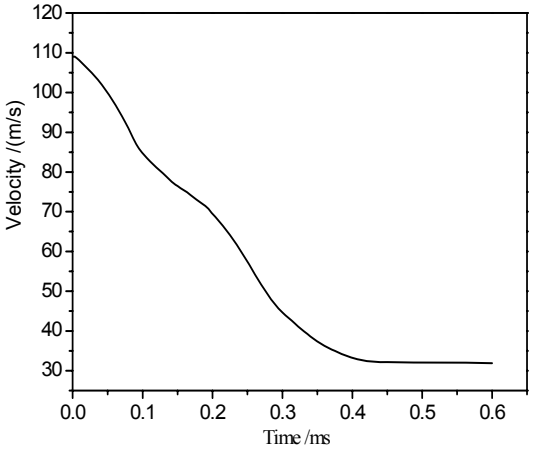

(b) Velocity curve（v=109m/s）

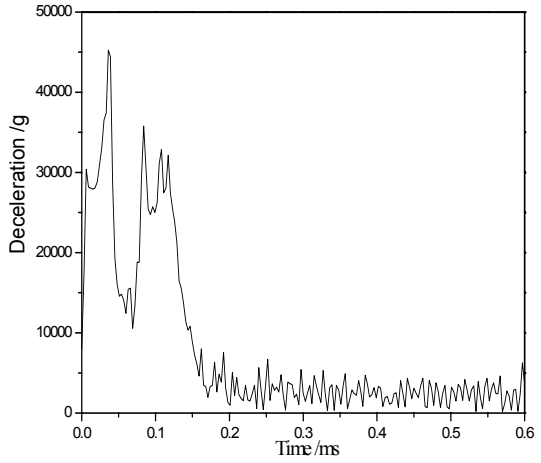

(c) Accelerator curve （v=191m/s）

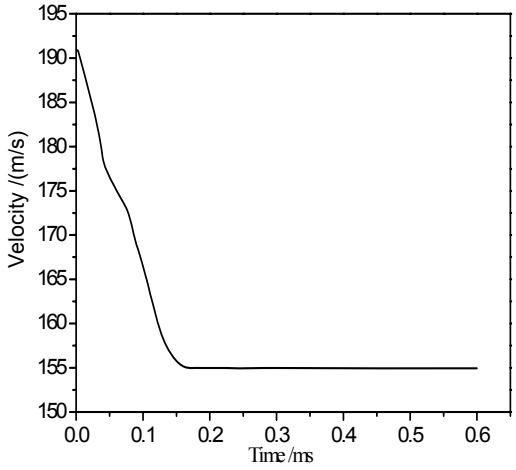

(d) Velocity curve（v=191m/s）

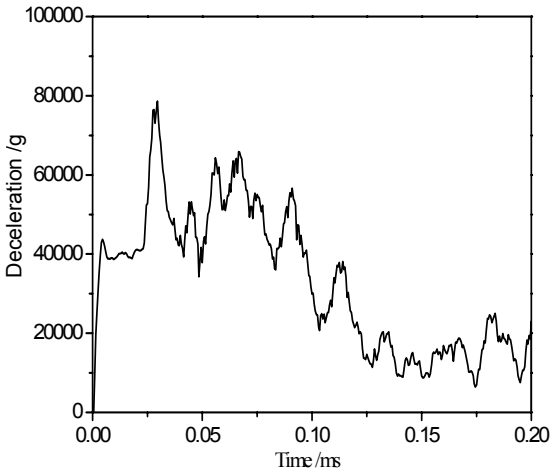

(e) Accelerator curve（v=250m/s）

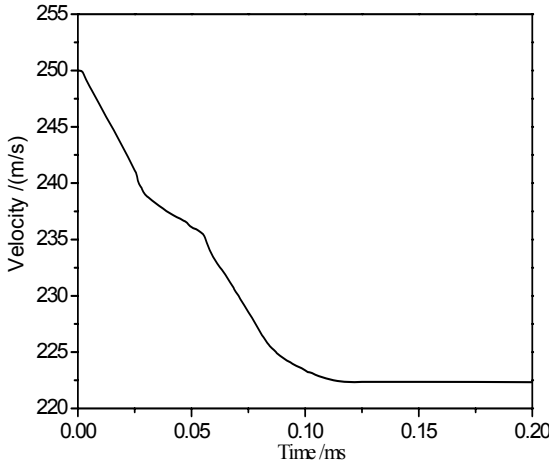

(f) Velocity curve（v=250m/s）

Chart 12 : Model I simulation results

The chart 12 displayed that the over load peaks increased sharply with the initial velocity gaining, resulting in the penetrating time shortening. During the penetrating with the initial velocity of 109 m/s, the accelerator value could reach 38,000g around for the first peak, the second could drop to about 30,000g, and the whole penetrating time could span about 0.44ms. As for the initial velocity of 191 m/s, the accelerator value could reach 45,000g around for the first peak, the second could drop to about 35 000g, and the whole penetrating time could span about 0.18ms. For the initial velocity of 250 m/s, the accelerator value could reach 78,000g around for the first peak, the second could drop to about 62,000g, and the whole penetrating time could span about 0.12ms.

4. CONCLUSION

(1) Based on the Lagrange method, Lagrangian-Eulerian coupling algorithm and SPH method, the computational results were in satisfactorily agreement among them.
(2) Simulating penetrating the multi-layer steel with certain distance, the results explained that the over load value reached its peak within penetrating the each layer, and the accelerator value dropped with the layer increasing. But during the interval, the over load values fluctuated about zero. Abstracted from the velocity curves of penetrating each steel plate, the curve descended linearly, whereas, the curve reached a plateau within the interval, meaning the velocity kept constant, and the over load value went to zero.
(3) Comparing with the experimental and simulation results from penetrating the foam core sandwiched with two layers, the results were in well agreement. The computational overload curve shared the same trend with the penetrating the multi-layer steel plate.

ACKNOWLEDGEMENT

This work was supported by the National Science Foundation of China (grant No. 10872174/A020602).

REFERENCES

[1] Nesterenko V F, Goldsmith W, Indrakanti S S, *et al*. Response of hot isostatically pressed Ti–6Al–4V targets to normal impact by conical and blunt projectiles [J]. International Journal of Impact Engineering, 2003, 28(2): 137–160.

[2] Bøvik T, Langseth M, Hopperstad O S, *et al*. Ballistic penetration of steel plates [J]. Int J Impact Eng, 1999, 22(9-10): 855–886.

[3] Bøvik T, Langseth M, Hopperstad O S, *et al*. Perforation of 12mm thick steel plates by 20mm diameter projectiles with blunt, hemispherical and conical noses, Part I: experimental study [J]. Int J Impact Eng, 2002, 27(1): 19–35.

[4] Bøvik T, Hopperstad O S, Langseth M, *et al*. Effect of target thickness in blunt projectile penetration of Weldox 460 E steel plates [J]. Int J Impact Eng, 2003, 28(4): 413–464.

[5] Bøvik T, Hopperstad O S, Berstad T, *et al*. Numerical simulation of plugging failure in ballistic penetration [J]. Int J Solids Struct, 2001, 38(34–35): 6241–64.

[6] Bøvik T, Hopperstad O S, Berstad T, *et al*. Perforation of 12mm thick steel plates by 20mm diameter projectiles with blunt, hemispherical and conical noses, Part II: numerical simulations [J]. Int J Impact Eng, 2002, 27(1): 37–64.

[7] Dey S, Bøvik T, Hopperstad O S, *et al*. The effect of target strength on the perforation of steel plates using three different projectile nose shapes [J]. International Journal of Impact Engineering, 2004, 30(8-9): 1005–1038.

[8] Dey S, Bøvik T, Hopperstad O S, *et al*. On the influence of fracture criterion in projectile impact of steel plates [J]. Computational Materials Science, 2006, 38(1): 176-191.

[9] Dey S, Bøvik T, Hopperstad O S, *et al*. On the influence of constitutive relation in projectile impact of steel plates [J]. International Journal of Impact Engineering, 2007, 34(3): 464–486.

[10] Bøvik T, Clausen A H, Hopperstad O S, *et al*. Perforation of AA5083-H116 aluminum plates with conical nose steel projectiles—experimental study [J]. Int J Impact Eng, 2004, 30(4): 367–384.

[11] Bøvik T, Clausen A H, Eriksson M, et al. Experimental and numerical study on the perforation of AA6005-T6 panels [J]. International Journal of Impact Engineering, 2005, 32(1-4): 35–64.

[12] Gupta N K, Iqbal M A, Sekhon G S. Experimental and numerical studies on the behavior of thin aluminum plates subjected to impact by blunt- and hemispherical-nosed projectiles [J]. International Journal of Impact Engineering, 2006, 32(12): 1921–1944.

[13] Gupta N K, Iqbal M A, Sekhon G S. Effect of projectile nose shape, impact velocity and target thickness on deformation behavior of aluminum plates [J]. Int. J. Solids. Struct., 2007, 44(10): 3411-3439.

XI International Conference on Computational Plasticity. Fundamentals and Applications
COMPLAS XI
E. Oñate, D.R.J. Owen, D. Peric and B. Suárez (Eds)

Dynamic Localizations in Structural Steel at High Strain Rates and Temperatures – COMPLAS XI

FARID H. ABED[*] AND FADI S. MAKAREM[*]

[*]Department of Civil Engineering
American University of Sharjah
Sharjah, P.O.Box 26666, United Arab Emirates
E-mail: fabed@aus.edu, web page: http://www.aus.edu

Key words: HSLA-65, DH-36, Flow stress, Shear band, Hat-shaped specimen.

Abstract. The proposed paper presents a numerical study on the formation of shear bands at localized regions in two ferrite steel alloys, HSLA-65 and DH-36, subjected to certain range of velocity impact. Constitutive relations developed by the author [1] for ferritic steels is utilized in simulating the thermal and athermal parts of the flow stress over a wide range of temperatures and strain rates. The proposed plasticity model is implemented into the commercially well-known finite element software ABAQUS through VUMAT user subroutine. This implementation enables studying the shear band formation over a wide range of initial temperatures and strain rates in a cylindrical hat-shaped specimen with certain dimensions where the location of shear localization preceding shear band formation is forced to be between the hat and the brim. Sensitivity analysis is performed on different mesh configurations in order to select the optimum mesh. Another sensitivity analysis is also performed on the constitutive plasticity model material parameters to study their effect on the shear bands formation. Several conclusions related to the width of the shear bands considering the velocity load and initial temperatures will be discussed throughout this work.

1 INTRODUCTION

Numerous studies on the formation of shear bands (shear localization) were conducted due to their importance as deformation mechanism especially during high speed loading (i.e. impact loading). The high concentration of strains in a particular location of a steel structure is a physical phenomenon that can be observed in reality and in laboratory testing. Areas of high strain concentrations can be developed in specimens prepared in the lab and tested under wide range of strain rates and temperatures. Even when the strain rate is low, the increase of plastic strains in the areas of strain concentration is fast and associated with higher than average dissipation of energy. Studying the development of shear bands is very important because they dominate the deformation and fracture modes in many metals. It is usual to observe strain localization in ductile materials like metals, but also can be observed in composite structures made of brittle and ductile components. The newly developed physically based constitutive viscoplastic model by the author [1] is utilized in investigating shear localization in ferrite steel over wide range of temperatures and strain rates. This proposed model is implemented in the well-known commercial finite element software ABAQUS

through the material subroutine VUMAT. This implementation is utilized in this study to investigate the dynamic simulation of adiabatic shear localization in a cylindrical hat-shaped sample where large shear strains are generated in a small region during compression mode [2].

Two high strength steels were considered in the proposed comparisons: DH-36 and HSLA-65 that are used in naval and other structural applications. They may be subjected, in their naval use, to high-rate loading due to collision or impact which, in turn, requires high toughness and high strength under variable conditions including various temperatures and strain rates. High strength low alloy (HSLA) steels were first used in 1960s by developing alloy of low-carbon steels with Niobium (Nb), Vanadium (V) and Titanium (Ti). HSLA-65 was recently developed with 65 ksi (450MPa) yield strength allowing the use of thinner plates to reduce the weight of the structure. DH-36 is commonly used in the manufacture of vessels and submarines. As ship hull steel, especially in high-speed sealift vessels, it may be subjected to high-rate loading due to collision, impact, or explosion. The major alloy content of the two investigated steels is given by Nemat-Nasser and Guo [3-4]. In addition to more than 97% of iron, the microstructure of HSLA-65 and DH-36 is mainly composed, of 1.4% and 1.37% of Manganese (Mn), 0.24% and 0.22% of Silicon (Si), and 0.08% and 0.14% of Carbon (C), respectively. Moreover, the alloy content of HSLA-65 contains very small portion of copper (<0.01%) as compared to DH-36 (0.14%).

2 MICROSTRUCTURE-BASED VISCOPLASTICITY IN FERRITIC STEEL

Accurate determination of plasticity models capable of predicting the flow stress of metals in general and steel in particular is not easy because of the coupling effects of strain, strain rate and temperature. The flow stress dependency of the above-mentioned three parameters becomes very significant at higher temperatures and strain rates. It was observed experimentally by different authors that the variation of stress strain curves at a certain strain rate and different temperatures or at certain temperature and different strain rates appear at yielding point and almost no variation was noticed in the hardening curves. The proposed model additively decomposes the flow stress into athermal and thermal components which coincides with the experimental observation. The athermal component is independent of strain rate and related to strain hardening, *R(p)*, and small portion of the yield stress, Y_a. The thermal component is mainly controlled by yield stress and shows a coupled effect of temperature and strain rate. The static definition of the yield function represented by the athermal flow stress is shown in Eq. (1):

$$f = \sigma_{eq} - Y_a - R(p) \tag{1}$$

The thermal component represents the dynamic stress that exceeds the static yield surface. This stress is related to the reference viscosity, η_o^{vp}, and threshold yield stress, $\hat{Y}$. The reference viscosity is the minimum value that can be achieved at very high temperature. The viscosity parameter (known as relaxation time), η^{vp}, is very important when it comes to finite element implementation of viscoplasticity because it helps in introducing a physical length

scale that is used in regularizing some problems encountered in finite elements computation. It also allows the spatial difference operator in the governing equations to retain its ellipticity. The dynamic stress is presented by Eq. (2) and viscoplastic multiplier is shown in Eq. (3) by rearranging Eq. (2).

$$\sigma_{th}^{v} = \hat{Y}(1-(-\beta_2 T \ln(\eta_o^{vp}\dot{\lambda}^{vp}))^{\frac{1}{q_1}})^{\frac{1}{q_2}} \tag{2}$$

$$\dot{\lambda}^{vp} = \frac{1}{\eta^{vp}(T)}\varphi(\sigma_{th}^{v}, T, \hat{Y}) \tag{3}$$

The overstress function presented in Eq. (4) and the viscosity parameter shown in Eq. (5) are explicitly temperature related variables. $\hat{Y}$ is chosen in normalizing the overstress function.

$$\varphi(\sigma_{th}^{v}, T, \hat{Y}) = \exp(1-\frac{\left(1-\left(\frac{\sigma_{th}^{v}}{\hat{Y}}\right)^{q_2}\right)^{q_1}}{\beta_2 T}) \tag{4}$$

$$\eta^{vp} = \eta_o^{vp}\exp(\frac{1}{\beta_2 T}) \tag{5}$$

The hardening *R(p)* which is strain dependent component of flow stress is defined in Eq. (6).

$$R(p) = \bar{B}(1-e^{-kp})^{\frac{1}{2}} \tag{6}$$

where the reference viscosity parameter, the threshold yield stress, the athermal yield stress and the parameter β_2, $\bar{B}$ are related to the microstructure physical quantities as follows:

$$\bar{B} = m\alpha\mu b\left(\frac{m}{k}\right)^{\frac{1}{2}};\ \eta_o^{vp} = (\bar{m}\, b\rho_i d)^{-1} t_{wo}$$

$$\hat{Y} = m\alpha_0\mu_o\frac{b^2}{A_0};\ Y_a = \alpha\mu\left(\frac{b}{D_g}\right)^{\frac{1}{2}};\ \beta_2 = \frac{K}{G_o} \tag{7}$$

Where *b* is the magnitude of the Burger vector, *m* is the orientation factor that relates the shear stress to the normal stress $\sigma = m\tau$ where $m = \sqrt{3}$ for the case of the von Mises flow rule, μ is the shear modulus; α is an empirical coefficient, *K* is the Boltzmann's constant, G_o is the Gibbs energy at zero Kelvin temperature, *M* represents the dislocation multiplication factor, *k* is the annihilation factor, D_g is the grain size, t_w is the time that a dislocation wait at

an obstacle and t_{wo} is the lowest value, $\bar{m} = \sqrt{M_{ij}M_{ij}}$ where M_{ij} is the Schmidt orientation tensor, d is average distance the dislocation moves between the obstacles, $\rho_i = l_i^{-2}$ is the initial dislocation density and l_i is the initial dislocation distance. An explicit definition of the length scale parameter l which is taken as initial value of dislocation distance can be derived in terms of microstructure physical quantities by rearranging the definition of the viscosity parameter in Eq. (7) as follows:

$$l = \left(ac\eta_o^{vp}\right)^{\frac{1}{2}}, \quad \text{where: } a = \bar{m}b\,; \quad c = d/t_w \tag{8}$$

The c parameter in Eq. (8) is actually the elastic wave propagation velocity in the material whereas a parameter is a proportional factor that depends on the particular initial boundary value problem under consideration. Once the viscosity parameter is calculated, the viscoplastic strain tensor is obtained by the following relation:

$$\hat{d}^{vp} = \dot{\lambda}^{vp} N = \dot{\lambda}^{vp} \frac{\partial f}{\partial \tau} = \dot{\lambda}^{vp} \frac{\partial \sigma^{eq}}{\partial \tau} \tag{9}$$

Where: $\partial\sigma^{eq} = (3\tau_{ij}\tau_{ij}/2)^{1/2}$ represents the equivalent stress, which is defined based on von Mises yield criterion in terms of the deviatoric stress, $\tau_{ij} = \sigma_{ij} - \sigma_{mm}\delta_{ij}/3$. The evolution equation for the dislocation density utilized in deriving the proposed ferrite steel model resulted in an exponential relation for the strain hardening as shown in Eq.(10) which shows the combined athermal and thermal stresses.

$$\sigma = c_1 + c_2\sqrt{1 - e^{-c_3\varepsilon_p}} + c_4(1 - (c_5T - c_6T\ln\dot{\varepsilon}_p)^{1/q_1})^{1/q_2} \tag{10}$$

The material parameters c_1–c_6 appeared in the above constitutive relations are related to the microstructure physical quantities as explained before in Eq. (7) as follows:

$$c_1 = Y_a\,;\ c_2 = \bar{B}\,;\ c_3 = k\,;\ c_4 = \hat{Y}\,;\ c_5 = \beta_2 \ln\left(\frac{1}{\eta_o^{vp}}\right);\ c_6 = \beta_2 \tag{11}$$

The above relation clearly shows the coupling effect of strain rate and temperature on the yield stress where σ is the equivalent stress, ε_p is the equivalent plastic strain, $\dot{\varepsilon}_p$ is the equivalent plastic strain rate, T is the temperature in Kelvin, and q_1 & q_2 are constants defining the shape of the short-range barriers. The material constants c_2 *and* c_3 define the strain dependent athermal component of the flow stress, c_1 represents an additional athermal stress, c_4 represents the threshold yield stress at which the dislocation can overcome the barriers without the assistance of thermal activation, c_5 and c_6 are two thermal activation parameters characterizing the thermal component of the flow stress and are related to the reference Gibbs energy at zero absolute temperature, Boltzmann's constant, reference dislocation velocity, and initial dislocation density [1]. In Eq. (10), the thermal component of

the flow stress is non-negative, thus, the term $(c_5 T - c_6 T \ln \dot{\varepsilon}_p)$ should be set equal to zero when the temperature exceeds the critical value. The critical temperature defines the stage of deformation at which the thermal stress is completely vanished. This critical value; however, is strain rate dependent and can be defined as follows:

$$T_{cr} = (c_5 - c_6 \ln \dot{\varepsilon}_p)^{-1} \tag{12}$$

3 SHEAR LOCALIZATION IN CLYNDYRICAL HAT-SHAPED SAMPLES

The developed constitutive model is implemented in ABAQUS via user's material subroutine VUMAT. ABAQUS/Explicit version is used to perform finite element simulation on hat-shaped modeled specimens and to investigate the formation of shear bands in ferrite steel such as HSLA-65 and DH-36. Experimental investigation of the dynamic deformation response of hat-shaped specimen shown schematically in Figure 1(a) was adopted by different authors. The dimensions of the specimens used in these studies differ from one author to another. The dimensions of the hat-shaped sample used in this study are presented in Table 1 and correspond to a study done by Perez-Prado [6]. The geometry was chosen in such a way that the inner diameter of the brim is shorter than the inner diameter of the hat by approximately 4.5% in order to sustain large amount of shear strain.

Table 1: Dimensions (mm) for ferrite steel hat-shaped sample

r_1	r_2	r_3	h_1	h_2	h_3
9.53	4.85	5.08	15	7.0	6.97

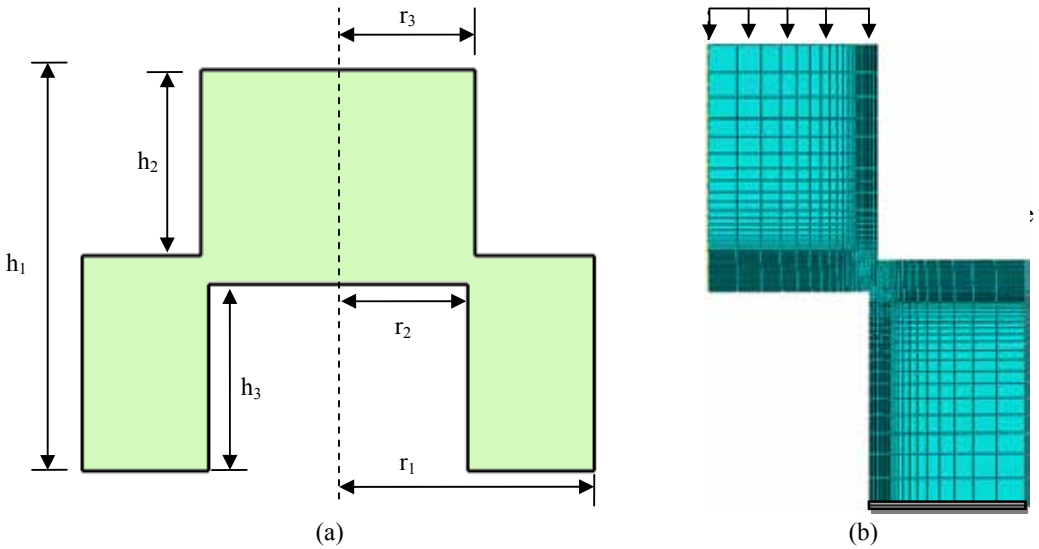

Figure 1: (a) geometric description of the cylindrical hat-shaped specimen (b) FE model for a quarter portion of the hat-shaped specimen using axisymmetric mesh elements.

The geometry of the hat-shaped specimen enables modeling it using four-node axisymmetric elements of CAX4R ABAQUS type with shear region zone limited between the upper hat and lower brim portions. The advantage of the hat-shaped specimen is that the location of shear localization preceding shear band formation is forced to be between the hat and the brim. This is because the dimensions of the specimen were chosen in this study so that there is mismatching between inner radius of the brim (r_2) and the hat radius (r_3) to create an overlapping region. A region of high strain concentration is created as a consequence. The axisymmetric specimen is subjected to compression dynamic velocity load from the top at the hat and movement is restrained at the bottom as illustrated in Figure 1(b).

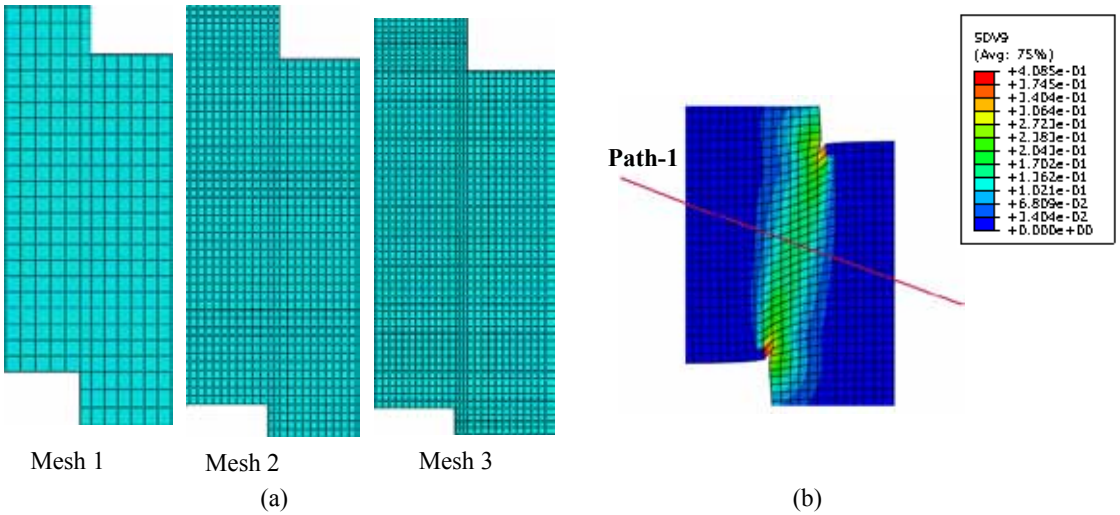

Figure 2: (a) Mesh refinements in the shear zone (b) Path 1 through the shear zone of the hat-shaped specimen

Three different mesh configurations were used to mesh the model geometry and the region of shear deformation as shown in Figure 2 (a). Mesh 1 represents a coarse mesh whereas Meshes 2 and 3 are of higher resolution. Figure 2(b) shows true path distance (Path-1) passing through the shear zone and perpendicular to the shear band. Simulations were carried out with the three mesh configurations to study the sensitivity of the results to mesh refinement. It was found out that shear stress-displacement curve presented in Figure 3(a) and plotted for an element located in the middle of the shear zone is not varying much when comparing with meshes 2 and 3. The same observation regarding mesh sensitivity was noticed when plotting the equivalent plastic strain along path1 as presented in Figure 3(b). It is obvious that the coarse mesh 1 is not able to capture a reasonable value for the equivalent plastic strain along the same true path and is of no match to the results obtained from meshes 2 and 3. Mesh 2 was chosen to carry out the rest of the dynamic simulations since it achieved balance between the accuracy of the results and reducing the computational time especially when it comes to dynamic explicit integration computational scheme.

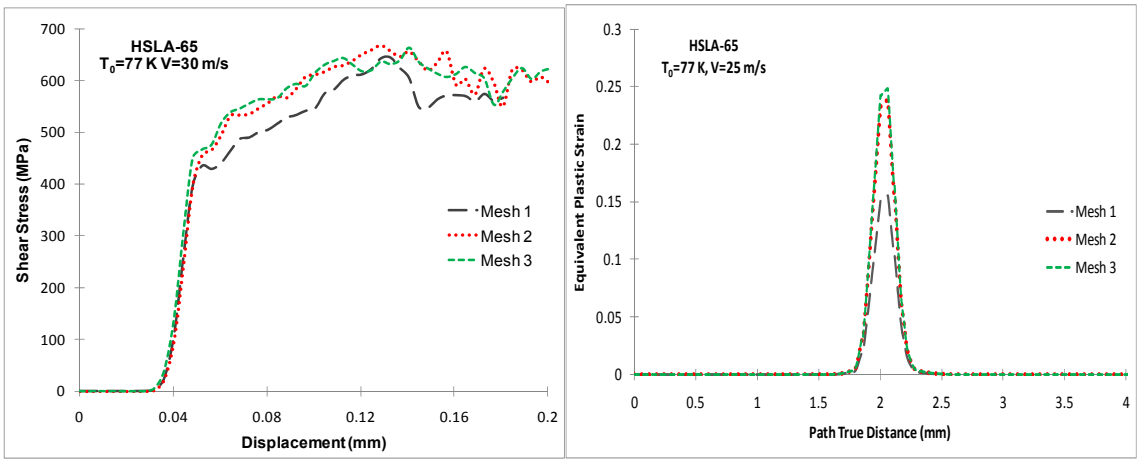

(a) (b)

Figure 3: (a) Shear stress for three different meshes configuration; (b) Distribution of the equivalent plastic strain for HSLA-65 across path 1for different meshes configuration.

4 NUMERICAL SIMULATIONS RESULTS

The axisymmetric model was subjected to wide range of velocities and initial temperatures. The velocities applied were 0.5 m/s, 1 m/s 10 m/s, 20 m/s and 30 m/s whereas the temperatures were 77 K, 200 K, 296 K, 400 K and 500 K. The modeled specimen was dynamically compressed up to a total displacement of 0.20 mm. It was observed that the shear stress first reaches a peak value before it decreases with increasing displacement which means that the hardening mechanism of ferrite steel prevails at the initial stage during plastic deformation. When the plastic deformation evolves, the softening mechanism becomes dominant as heat is accumulating in the shear zone especially when the specimen is subjected to high rate adiabatic deformation. Figure 4 shows contour plot of the equivalent plastic strain (shear bands) in three-dimensional shape corresponding to three fourths of the hat-shaped specimen. The plastic strain concentration is obvious in the shear zone region.

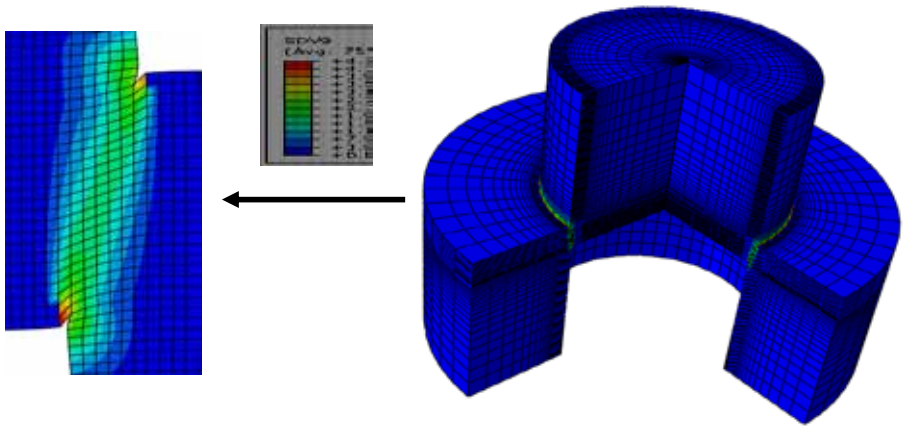

Figure 4: Contour plot of the equivalent plastic strain (shear bands) at velocity =25m/s and T_o = 296 K

A comparison between shear bands corresponding to simulation at different temperatures at the same velocity load is presented in Figures 5 and 6 for both HSLA-65 and DH-36 steels. It was observed that widths of the shear bands increase with temperature increasing. Figure 7 presents the distribution of the equivalent plastic strain in both steels at the end of the applied displacement along Path-1 passing through the center of the shear zone (shear band) at 25 m/s velocity and different temperatures. The distribution of the equivalent plastic strain is interpreted as the shear band width. The figures show that that the plastic strain peak is greatest when the temperature is lowest. For instance, the largest plastic strain is achieved at lowest temperature = 77 K. They also show the shear band width variation with respect to each initial temperature at the same compression velocity load. The widths of the shear zones range approximately from 0.5 to 1.0 mm in both steels depending on the initial temperatures and applied velocities. It can be concluded that the width of the shear band (localization) varies considerably with different initial temperatures.

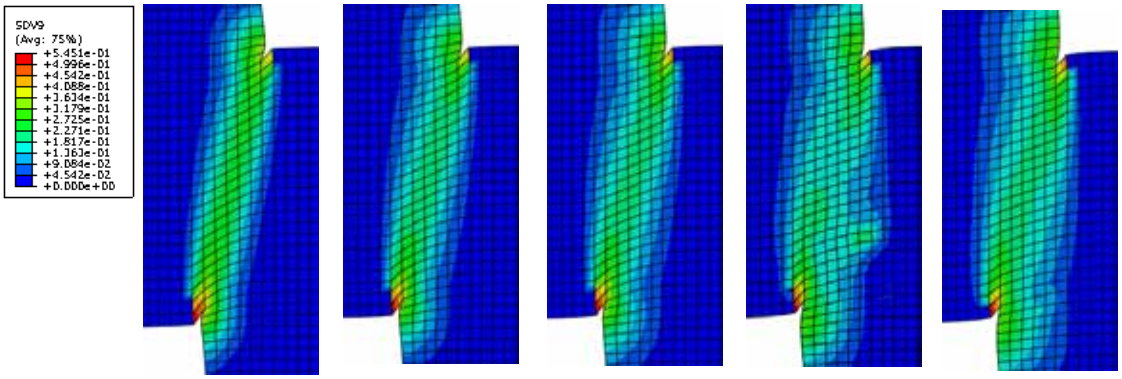

Figure 5: Contours of the equivalent plastic strain (shear bands) at 0.2 mm axial displacement and different temperatures, HSLA-65 Steel at V = 25m/s

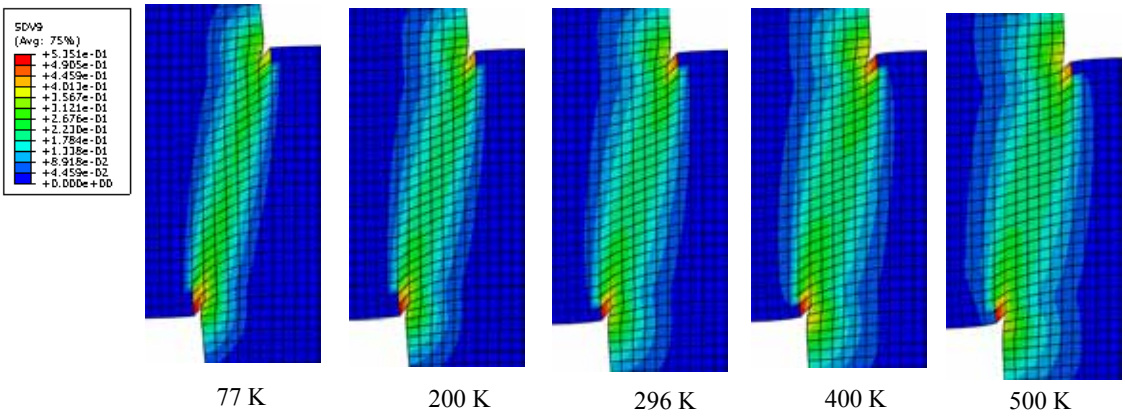

Figure 6: Contours of the equivalent plastic strain (shear bands) at 0.2 mm axial displacement and different temperatures, DH-36 steel at V = 25m/s

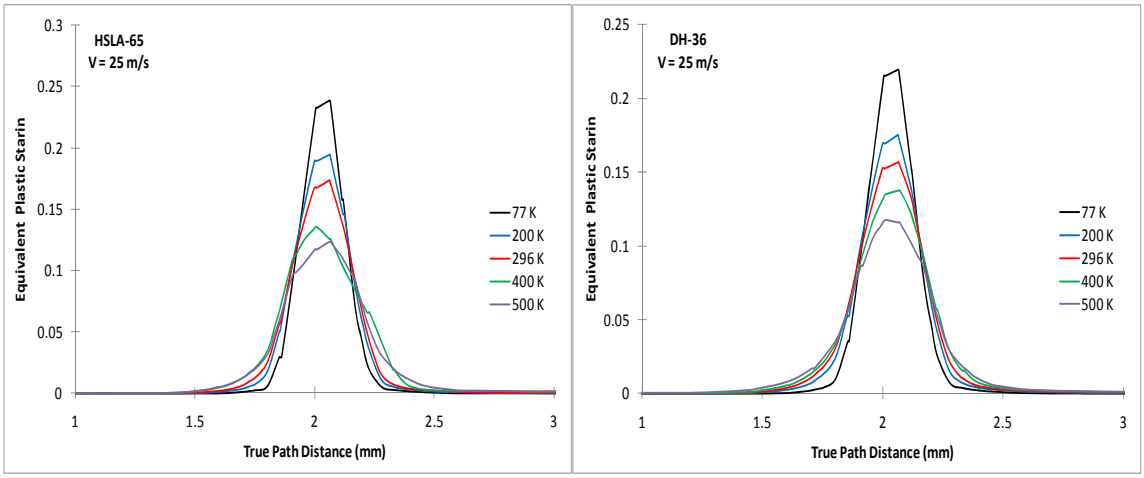

(a) (b)

Figure 7: Equivalent plastic strain at V=25 m/s, 0.2 mm axial displacement and different temperatures along path-1: (a) HSLA-65, (b) DH-36

On the other hand, less variation in the shear bands widths was noticed at different velocities at the same initial temperature as illustrated in Figure 8 which show the equivalent plastic strain distribution along Path-1 at initial temperature of T_o=77 K and different velocities for both steels.

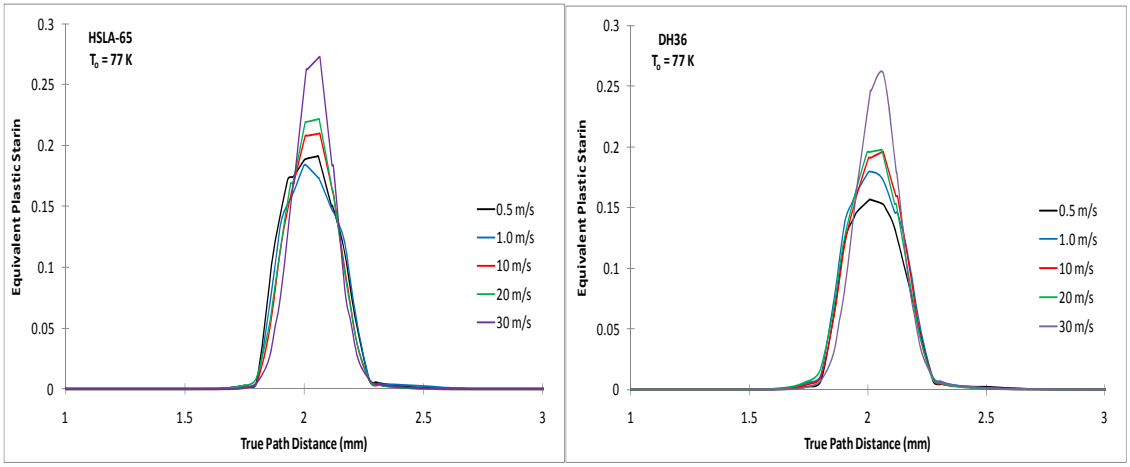

(a) (b)

Figure 8: Equivalent plastic strain at initial T=77K, 0.2mm axial displacement and different velocities: (a) HSLA-65, (b) DH-36

4 MODEL PARAMETERS SENSETIVITY ANALYSIS

Simulating the effect of impact load on steel structures requires choosing a robust plasticity finite element constitutive model. Some of these models are empirically, semi-physical or physically based. In other words, the material parameters of some models are obtained empirically whereas the material parameters in some other models are related to the micro-structure quantities of the material such as the proposed model. Complex statistics methods could be applied on a set of experimental data to determine the material parameters of plasticity model. Certain inaccuracy in the value of the determined material parameter might be encountered during the process of obtaining them which also depends on the accuracy and amount of the experimental data. Hence, it is recommended to study the sensitivity of a certain output to a change in one or more of the material constants. In this study, sensitivity analysis on the six constants of the developed model is performed, c_1,c_2, c_3, c_4, c_5 and c_6. It is expected to detect a change in the shear band width at certain velocity and temperature when changing one of the model parameters while keeping all others constant.

Comparisons between formed shear bands corresponding to simulations at the same conditions (velocity = 10 m/s and temperature = 77K) are conducted for all constants. For better quantification for the shear band width sensitivity to changes in the material parameters, the equivalent plastic strains were plotted along Path-1 which is perpendicular to the shear band. Figure 9 shows a sample of these comparisons for the effect of constant c_5 on the the width of the localized region at the shear zone at 10m/s velocity and 77K initial temperature for both HSLA-65 and DH-36 steels. It is clearly shown that increasing the material constants c_5 which is related to the thermal stress component of the VA model leads to increasing the value of the equivalent plastic strain. The width of the shear zone is increased consequently.

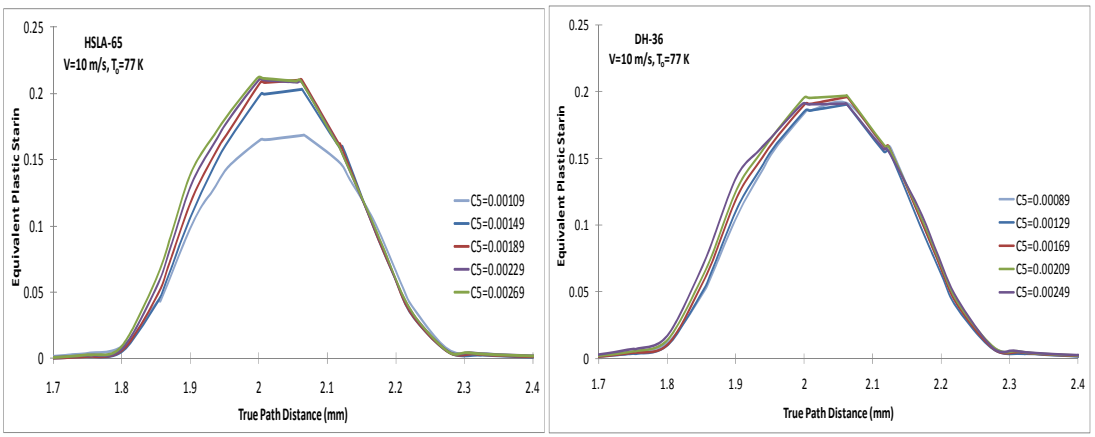

(a) (b)

Figure 9: Equivalent plastic strain when changing the model parameters c_5, at 0.2mm axial displacement for (a) HSLA-65 steel and (b) DH-36 steel.

CONCLUSIONS

In this work, the shear band formation in hat-shaped specimen were studied under different dynamic velocities (0.5, 1.0, 10, 20, 30 m/s) and initial temperatures (77, 200, 296, 400, 500K). The simulations were carried out using the new developed constitute model for ferrite steel after being implemented in ABAQUS via VUMAT user subroutine. It was observed that the width of the shear band increases with increasing the initial temperature in both HSLA-65 and DH-36 steels. The width of the shear band doesn't vary considerably when comparing at several applied dynamic velocities and at the same initial temperature. Sensitivity analysis was also performed on the model constants, by studying their variation effect on the width of the shear band. It was observed that increasing the value of material parameter c_5 increases the width of the shear band.

REFERENCES

[1] Abed, F.H. Constitutive modeling of the mechanical behavior of high strength ferritic steels for static and dynamic applications, *Mech Time-Depend Mater* (2010) **14**: 329-345.

[2] Abed, F.H. and Voyiadjis, G.Z. Adiabatic shear band localizations in BCC metals at high strain rates and various initial temperatures. *International Journal of Multiscale Computational Engineering* (2007) **5:** 325-349.

[3] Nemat Nasser, S. and Guo, W.G. Thermomechanical response of DH-36 structural steel over a wide range of strain rates and temperatures. *Mech Mater* (2003) **35**: 1023-1047.

[4] Nemat Nasser, S. and Guo, W.G. Thermomechanical response of HSLA-65 steel plates: experiments and modeling. *Mech Mater* (2005) **37**: 379-4057.

[5] Voyiadjis, G., and Abed, F., Microstructural Based Models for BCC and FCC Metal with Temperature and Strain Rate Dependency, *Mech Mater* (2005) **37**: 355-378.

[6] Perez-Prado, M.T., Hines, J.A., and Vecchio, K.S. Microstructural evolution in adiabatic shear bands in Ta and Ta-W alloys. *Acta Materialia* (2001) **49**: 2905-2917.

XI International Conference on Computational Plasticity. Fundamentals and Applications
COMPLAS XI
E. Oñate, D.R.J. Owen, D. Peric and B. Suárez (Eds)

A COMPUTATIONAL PROCEDURE FOR THE CYCLIC STEADY STATE ELASTOPLASTIC ANALYSIS OF STRUCTURES - COMPLAS XI

KONSTANTINOS V. SPILIOPOULOS*, KONSTANTINOS D. PANAGIOTOU†

* Institute of Structural Analysis and Antiseismic Research
National Technical University of Athens (NTUA)
Zografou Campus, 157 80 Athens, Greece
e-mail: kvspilio@central.ntua.gr; web page: http://users.ntua.gr/kvspilio/

† Institute of Structural Analysis and Antiseismic Research
National Technical University of Athens (NTUA)
Zografou Campus, 157 80 Athens, Greece
e-mail: dinoscivil@hotmail.com

Key words: Computational Plasticity, Cyclic Plasticity, Direct Method, Cyclic Loading, Elastic Adaptation, Alternating Plasticity, Incremental Collapse.

Abstract. A new computational procedure for the steady state elastoplastic analysis of structures under cyclic loading is presented. The procedure is based on the decomposition of the unknown steady state residual stress distribution into Fourier series. The coefficients of the series are evaluated in an iterative way by satisfying equilibrium and compatibility at some preselected time points inside the cycle. The procedure in the present work is applied to a simple 1-D three bar structure and to a 2-D plate. Various load cases are examined which may lead to elastic adaptation, alternating plasticity or incremental collapse.

1 INTRODUCTION

Structures such as nuclear reactors, aircraft gas turbine propulsion engines, etc. operate in high levels of loads and temperature. High levels of loading exist also in civil engineering structures like heavy traffic on bridges and pavements, earthquake loading etc.

The complete response of a structure, which is subjected to a given thermo-mechanical loading and exhibits inelastic time independent plastic strains, is quite complex. The reason of the complexity is the need to perform calculations over the lifetime history of the structure. The computation of the whole loading history, however, leads to lengthy and expensive incremental calculations, especially for structures with large number of degrees of freedom. Therefore, it is very useful to develop computational approaches for straightforward calculations of the possible stabilized state under repeated thermo-mechanical loading.

Direct cyclic methods offer this alternative. The ingredient of these methods is the existence of a steady state at the end of the loading procedure for structures made of ductile material [1].

The advantage that direct methods offer with respect to time-stepping ones has been

exploited by many researchers. Most of these methods aim at the evaluation of the limit or the shakedown loading of a structure. This is normally done using the framework of linear or nonlinear mathematical programming and most of these approaches are reduced to efficiently solve this problem with the means of algorithms like the simplex method or more recently by the interior point methods([2]-[4]).

A different direct method of an incremental-iterative type has been presented in [5]. A more "physical" approach which is based on spatially varying of the elastic modulus is the Linear Matching Method. This method has been extended up to the ratchet limits ([6]-[8]).

A direct method has been proposed by Spiliopoulos [9] in the context of the cyclic loading analysis of creeping structures. The irreversibility of the nonlinear material dictates the existence of residual stresses together with the elastic stresses. It is the distribution of the residual stresses that is sought at the cyclic stress state. The method is based first on decomposing the unknown residual stress in Fourier series and then trying to find the coefficients of this series in an iterative way by satisfying equilibrium and compatibility at some preselected time points inside the cycle.

In the present work a computational procedure is proposed, that has the same foundations and may be applied to structures made of elastic perfectly plastic material. The whole procedure is formulated within the framework of the finite element method and examples of application to 1- and 2- dimensional structures are presented.

2 RESIDUAL STRESS DECOMPOSITION

The main ingredient of the method is the time decomposition of the unknown residual stress distribution $\boldsymbol{\rho}(t)$ into Fourier series. Since in the steady state this stress also becomes periodic, it may be decomposed in its Fourier series over the period of loading, as this can be done for any periodic function:

$$\boldsymbol{\rho}(t) = \frac{\boldsymbol{a}_0}{2} + \sum_{k=1}^{\infty}\left(\boldsymbol{a}_k \cos\frac{2k\pi t}{T} + \boldsymbol{b}_k \sin\frac{2k\pi t}{T} \right) \tag{1}$$

where the coefficients $\boldsymbol{a}_0$, $\boldsymbol{a}_k$ and $\boldsymbol{b}_k$, $k = 1,2,...$ are the Fourier coefficients of the Fourier series. Vectors and matrices are denoted by bold letters.

Thus the problem is converted to a problem of evaluating the Fourier coefficients of the various terms of the series. Following, in short, the procedure developed in [9] we may get

$$\dot{\boldsymbol{\rho}}(t) = \frac{2\pi}{T}\sum_{k=1}^{\infty}\left\{ \left(-k\boldsymbol{a}_k\right) \sin\frac{2k\pi t}{T} + k\boldsymbol{b}_k \cos\frac{2k\pi t}{T} \right\} \tag{2}$$

Making use of the orthogonality properties of the trigonometric functions we can get expressions that may be used to evaluate these coefficients in terms of the time derivative $\dot{\boldsymbol{\rho}}(t)$:

$$\boldsymbol{a}_k = -\frac{1}{k\pi}\int_0^T \dot{\boldsymbol{\rho}}(t) \sin\frac{2k\pi t}{T} dt \tag{3}$$

$$\boldsymbol{b}_k = \frac{1}{k\pi}\int_0^T \dot{\boldsymbol{\rho}}(t) \cos\frac{2k\pi t}{T} dt \tag{4}$$

On the other hand, if we integrate $\dot{\boldsymbol{\rho}}(t)$ over the period T, we get

$$\int_0^T \dot{\boldsymbol{\rho}}(t)\,dt = \boldsymbol{\rho}(T) - \boldsymbol{\rho}(0) = \left(\frac{\boldsymbol{\alpha}_0(T)}{2} + \sum_{k=1}^{\infty} \boldsymbol{\alpha}_k(T)\right) - \left(\frac{\boldsymbol{\alpha}_0(0)}{2} + \sum_{k=1}^{\infty} \boldsymbol{\alpha}_k(0)\right) \tag{5}$$

where use of the expression (1) was made at the beginning and at the end of the cycle period. Equation (5) may be used to evaluate the coefficient $\boldsymbol{\alpha}_0$.

If one satisfies equilibrium and compatibility at some discrete preselected time points inside the cycle, the time derivatives of the residual stresses themselves may be expressed in terms of the Fourier coefficients we seek to find.

3 FINITE ELEMENT FORMULATION

In order to evaluate the time derivatives of the residual stresses we may discretize our structure with the aid of the finite element method.

Let us denote by $\dot{\boldsymbol{r}}$ the vector of the time rates of the time displacement of the nodal points of the discretized structure at some time t.

The total strain rates $\dot{\boldsymbol{\varepsilon}}$ at the Gauss integration points are given in term of $\dot{\boldsymbol{r}}$ by

$$\dot{\boldsymbol{\varepsilon}} = \boldsymbol{B}\dot{\boldsymbol{r}} \tag{6}$$

Decomposing $\dot{\boldsymbol{\varepsilon}}$ into two terms $\dot{\boldsymbol{e}}^{el}$ and $\dot{\boldsymbol{\varepsilon}}_r$

$$\dot{\boldsymbol{\varepsilon}} = \dot{\boldsymbol{e}}^{el} + \dot{\boldsymbol{\varepsilon}}_r = \dot{\boldsymbol{e}}^{el} + \dot{\boldsymbol{\varepsilon}}_r^{el} + \dot{\boldsymbol{\varepsilon}}_r^{pl} \tag{7}$$

In the above equation the residual strain rate term has been itself decomposed into elastic and plastic parts.

At the same time the stress also can be decomposed into two terms an elastic one and a residual stress part

$$\boldsymbol{\sigma}(t) = \boldsymbol{\sigma}^{el}(t) + \boldsymbol{\rho}(t) \tag{8}$$

The elastic strain rates are related to their corresponding stress rates by

$$\begin{aligned} \dot{\boldsymbol{e}}^{el} &= \boldsymbol{C}\dot{\boldsymbol{\sigma}}^{el} \\ \dot{\boldsymbol{\varepsilon}}_r^{el} &= \boldsymbol{C}\dot{\boldsymbol{\rho}} \end{aligned} \tag{9}$$

where $\boldsymbol{C}$ is the tensor of the elastic constants.

For the plastic component the associate flow rule gives

$$\dot{\boldsymbol{\varepsilon}}_r^{pl} = \lambda \frac{\partial \Phi}{\partial \boldsymbol{\sigma}} \tag{10}$$

where Φ is a strictly convex yield surface.

Combining the above equations (7) and (9) we may write

$$\dot{\boldsymbol{\rho}} = \boldsymbol{D}\left(\dot{\boldsymbol{\varepsilon}} - \dot{\boldsymbol{e}}^{el} - \dot{\boldsymbol{\varepsilon}}_r^{pl}\right) \tag{11}$$

where $\boldsymbol{D}$ is the elasticity matrix (inverse of $\boldsymbol{C}$).

Since the strain rates are compatible and the residual stress rates are self-equilibrated, from the principle of virtual work (P.V.W.) we may obtain

$$\int_V \dot{\boldsymbol{\varepsilon}}' \dot{\boldsymbol{\rho}} dV = 0 \tag{12}$$

where "′" denotes the transpose of a vector or a matrix.

After the substitution of (6) and (11), in (12) we get

$$\dot{\boldsymbol{r}}' \int_V \boldsymbol{B}' \boldsymbol{D} \left(\boldsymbol{B}\dot{\boldsymbol{r}} - \dot{\boldsymbol{e}}^{el} - \dot{\boldsymbol{\varepsilon}}_r^{pl} \right) dV = 0 \tag{13}$$

and since this equation must hold for any $\dot{\boldsymbol{r}}$

$$\left(\int_V \boldsymbol{B}' \boldsymbol{D} \boldsymbol{B} dV \right) \dot{\boldsymbol{r}} = \int_V \boldsymbol{B}' \dot{\boldsymbol{\sigma}}^{el} dV + \int_V \boldsymbol{B}' \boldsymbol{D} \dot{\boldsymbol{\varepsilon}}_r^{pl} dV \tag{14}$$

or

$$\boldsymbol{K}\dot{\boldsymbol{r}} = \dot{\boldsymbol{R}}^{ext} + \int_V \boldsymbol{B}' \boldsymbol{D} \dot{\boldsymbol{\varepsilon}}_r^{pl} dV \tag{15}$$

where $\boldsymbol{K}$ is the stiffness matrix of the structure and $\dot{\boldsymbol{R}}^{ext}$ is the nodal vector of the time rate of the given loading.

4 ITERATIVE PROCEDURE

The form of the expressions (3), (4) and (5) allow us to evaluate the Fourier series (1) in an iterative procedure. The proposed numerical procedure has the following steps during a current iteration μ :

1. Calculation of the total stresses $\boldsymbol{\sigma}^{(\mu)}(t) = \boldsymbol{\sigma}^{el}(t) + \boldsymbol{\rho}^{(\mu)}(t)$ at some preselected time points inside the cycle; $\boldsymbol{\sigma}^{el}(t)$ is the cyclic elastic stress and $\boldsymbol{\rho}^{(\mu)}(t)$ is a self equilibrating stress system due to plasticity.

2. Checking for every Gauss point if $\overline{\sigma}^{(\mu)}(t) > \sigma_Y$ and calculation of the amount $\Delta\boldsymbol{\sigma}^{(\mu)}(t) = \xi * \boldsymbol{\sigma}^{(\mu)}(t)$ where $\xi = \dfrac{\overline{\sigma}^{(\mu)}(t) - \sigma_Y}{\overline{\sigma}^{(\mu)}(t) - \overline{\rho}^{(\mu)}(t)}$. $\overline{\sigma}^{(\mu)}(t)$ and $\overline{\rho}^{(\mu)}(t)$ are the corresponding effective total and residual stresses, σ_Y is the yield stress. If $\overline{\sigma}^{(\mu)}(t) \le \sigma_Y$ we set $\xi = 0$ and continue to the next step.

3. Solving the expanded rate equilibrium equation $\boldsymbol{K}\dot{\boldsymbol{r}}^{(\mu)}(t) = \dot{\boldsymbol{R}}^{ext}(t) + \int_V \boldsymbol{B}^T \Delta\boldsymbol{\sigma}^{(\mu)}(t) dV$ where $\boldsymbol{B}$ is the compatibility matrix and $\dot{\boldsymbol{R}}^{ext}(t) \,\&\, \dot{\boldsymbol{r}}(t)$ are the corresponding vectors of the time rates of the external loads and displacements of the nodal points of the discretized structure at some time t. In this step we get the new vector $\dot{\boldsymbol{r}}(t)$

4. Calculation of $\dot{\boldsymbol{\rho}}^{(\mu)}(t) = \boldsymbol{D}\boldsymbol{B}\dot{\boldsymbol{r}}^{(\mu)}(t) - \dot{\boldsymbol{\sigma}}^{el}(t) - \Delta\boldsymbol{\sigma}^{(\mu)}(t)$.

5. Perform numerical time integration over all the time points and update the Fourier coefficients for the next iteration:

$$\begin{aligned}
\boldsymbol{a}_k^{(\mu+1)} &= -\frac{1}{k\pi}\int_0^T \left\{\left[\dot{\boldsymbol{\rho}}^{(\mu)}(t)\right]\left[sin\frac{2k\pi t}{T}\right]\right\}dt \\
\boldsymbol{b}_k^{(\mu+1)} &= \frac{1}{k\pi}\int_0^T \left\{\left[\dot{\boldsymbol{\rho}}^{(\mu)}(t)\right]\left[cos\frac{2k\pi t}{T}\right]\right\}dt \\
\boldsymbol{a}_0^{(\mu+1)} &= -\sum_{k=1}^{\infty}\boldsymbol{a}_k^{(\mu+1)} + \frac{\boldsymbol{a}_0^{(\mu)}}{2} + \sum_{k=1}^{\infty}\boldsymbol{a}_k^{(\mu)} + \int_0^T\left[\dot{\boldsymbol{\rho}}^{(\mu)}(t)\right]dt
\end{aligned} \tag{16}$$

6. Checking the convergence between two successive iterations using the Euclidian norm of the residual stress vector according to the following criterion:

$$\frac{\left\|\boldsymbol{\rho}^{(\mu+1)}\right\|_2 - \left\|\boldsymbol{\rho}^{(\mu)}\right\|_2}{\left\|\boldsymbol{\rho}^{(\mu+1)}\right\|_2} \le tol \tag{17}$$

where tol is a pre-specified tolerance. If convergence occurs we get the final stresses $\boldsymbol{\rho}^{(\mu)} = \boldsymbol{\rho}^{(\mu+1)} = \boldsymbol{\rho}^{(final)}$ and continue to the next step. Otherwise we go to the next iteration and return to the step 1.

7. In order to predict the cyclic behaviour of the structure we calculate the value $a = \left\|\int_0^T \Delta\boldsymbol{\sigma}^{(\mu)}(t)dt\right\|$.

If $a \neq 0$, the considered loading case leads the structure to *incremental collapse*.

If $a = 0$, we check if $\left\|\Delta\boldsymbol{\sigma}^{(\mu)}(t)\right\| = 0$ for every time point *t* inside the cycle. If this is the case we have *elastic adaptation*; otherwise we have *alternating plasticity*.

5 EXAMPLES

5.1 Three bar truss

A first example of application of the methodology presented above is the three bar structure which is shown in Fig. 1. The structure is subjected to cyclic loads $V(t), H(t)$ which are applied at node 4. All the members of the truss have equal cross section A and are made of steel. The following geometrical, material data were used: $L = 300cm$, Young's modulus $E = .21\times10^5 kN/cm^2$ and yield stress $\sigma_y = 40kN/cm^2$. All the elements of the truss have an equal cross-sectional area of $A = 5cm^2$. Three cases of loading have been considered to test the procedure. Each of these cases leads to different cyclic behaviour. The results for the elements *1*, *3* are equal to the ones of element *2*, but with opposite sign.

a) The first cyclic loading case has the following variation with time:

$$V(t) = 300\,sin^2(\pi t/T), H(t/T) = 0$$

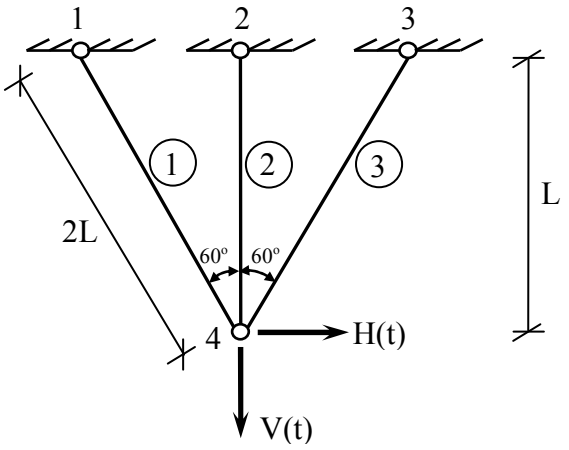

Figure 1: Three bar truss example

The analysis shows that bar *2* yields in tension and bars *1*, *3* remain elastic. As it may be observed, the residual stress remains constant inside the cycle (Fig. 2), therefore this load case leads to elastic adaptation. The cyclic steady state residual stress distribution for the element *2* inside a cycle may be seen in Fig. 2.

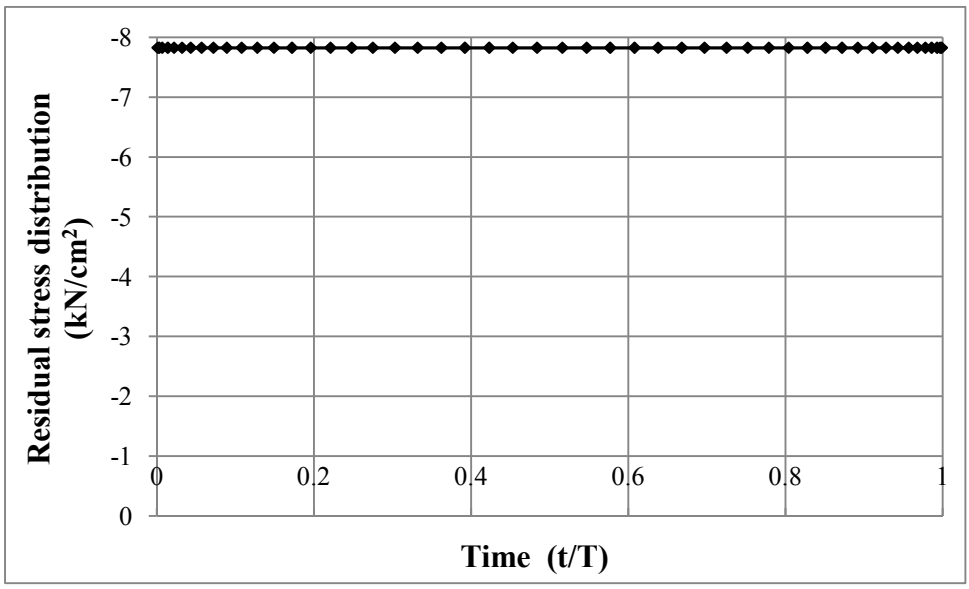

Figure 2: Cyclic state residual stress distribution inside a cycle for load case a (element 2)

b) The second cyclic loading case has the following variation with the time:

$$V(t) = 300\sin(2\pi t / T), H(t / T) = 0$$

The analysis shows that during the first half of the cycle bar *2* yields in tension and during the second half, bar *2* yields in compression. We also see that the plastic strain rates for the bar *2* are equal and of opposite sign in the first and second half of the cycle. Therefore this load case leads the structure to alternating plasticity. The cyclic steady state residual stress

distribution for the element *2* inside a cycle may be seen in Fig. 3.

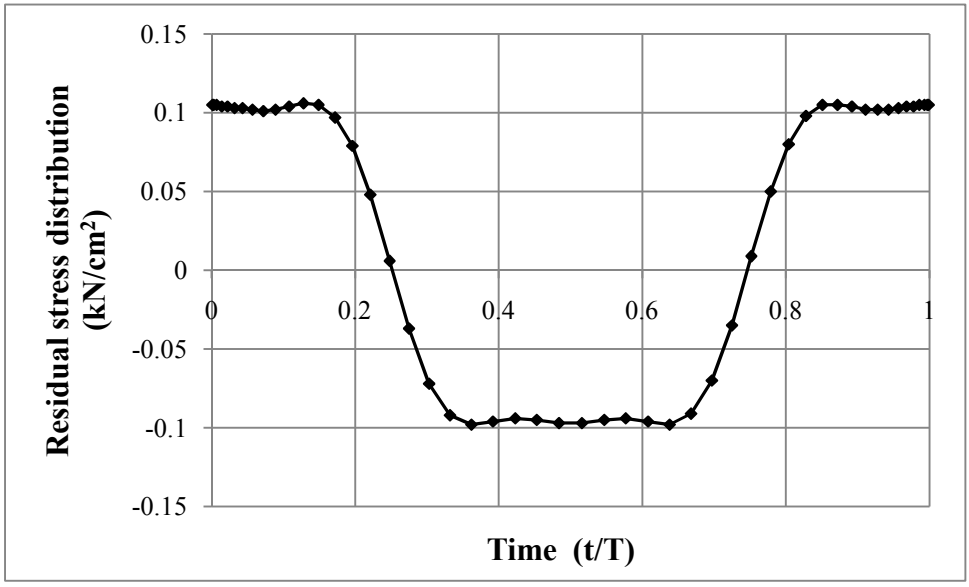

Figure 3: Cyclic state residual stress distribution inside a cycle for load case b (element 2)

c) The third cyclic loading case includes a variation with time of both the vertical and the horizontal load:

$$V(t) = 350\sin^2(\pi t / T),\ H(t) = 220\sin(2\pi t / T)$$

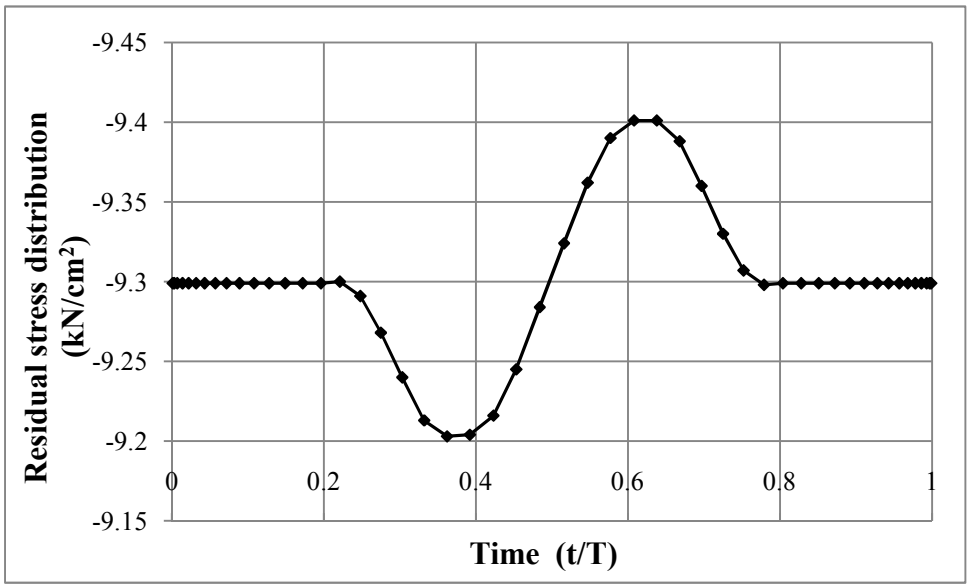

Figure 4: Cyclic state residual stress distribution inside a cycle for load case c (element 2)

The results obtained by the analysis show that during the first half of the cycle bar *2* yields in tension and during the second half bar *3* yields also in tension. Also the value

$a = \left\| \int_0^T \Delta\boldsymbol{\sigma}^{(\mu)}(t)dt \right\|$ referred to in the numerical procedure which is an indirect measure of the total change in plastic strains over the cycle is non zero; therefore this load case leads the structure to incremental collapse. The cyclic steady state residual stress distribution inside a cycle for the element *2* may be seen in Fig. 4.

5.2 Square plate with a hole

The second example of application is a plane stress concentration problem of a square plate with dimensions $20 \times 20cm$ and having a circular hole in its middle of a diameter of $2cm$. The loading is applied in equal pairs along the two vertical edges of the plate. Due to the symmetry of the structure and the loading we only analyze one quarter of the structure with $a = 10cm$ and $b = 1cm$. Ninety-eight 8-noded isoparametric elements with 3×3 Gauss integration points were used for the finite element discretization (Fig. 5).

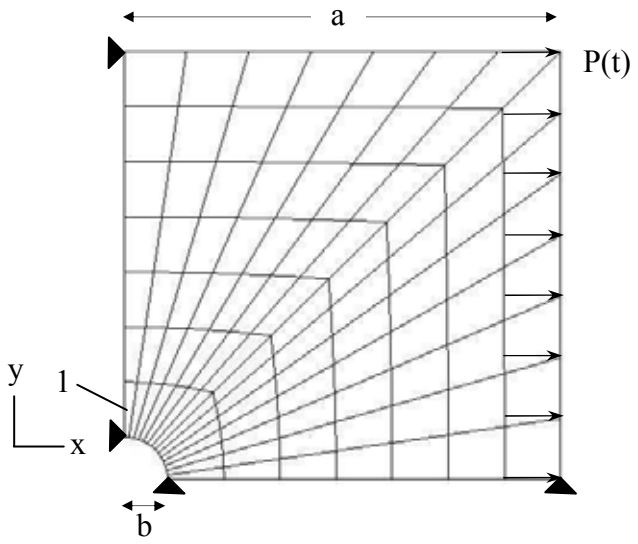

Figure 5: Finite element discretization of a quarter of a plate

The following material data was used: Young's modulus $E = .21 \times 10^5 kN/cm^2$ and yield stress $\sigma_y = 24kN/cm^2$. Two cases of loading have been considered that leads the plate to either elastic shakedown or alternating plasticity. The cyclic steady state residual stress distribution inside a cycle for the Gauss point *1* may be seen in Fig. 6, 7. This point is the nearest integration point to the corner where the longitudinal elastic stress is maximum.

a) The first cyclic loading case has the following variation with time where the maximum value of the cyclic loading is $P_0 = 20kN$:

$$P(t) = P_0 * sin^2\left(\pi \frac{t}{T}\right)$$

The cyclic steady-state residual stress distribution inside a cycle for Gauss point *1* may be seen in Fig. 6. As it may be observed, the residual stress remains constant inside the cycle. Therefore this load case leads to elastic adaptation.

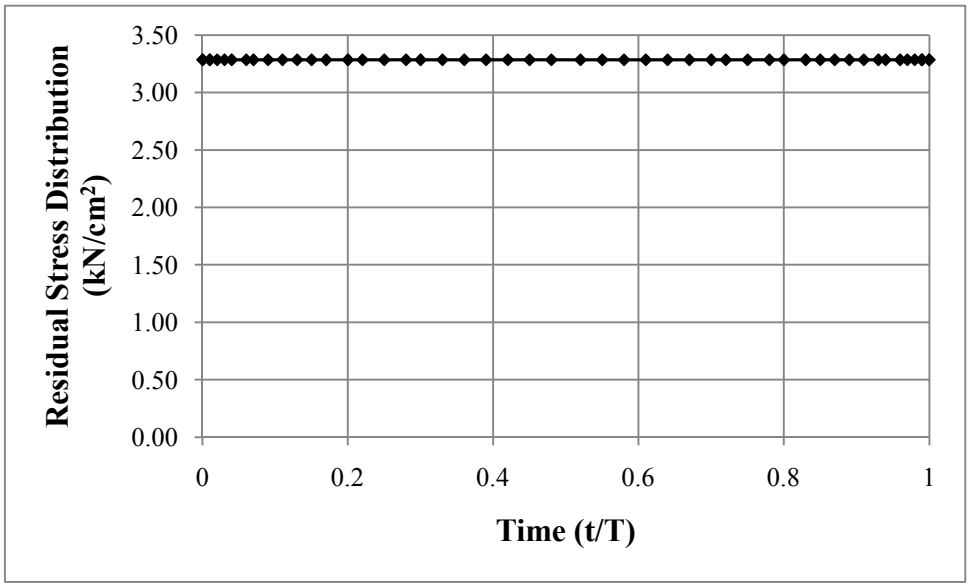

Figure 6: Cyclic state residual stress distribution inside a cycle for load case b (Gauss point 1)

b) The second cyclic loading case has the above variation with time while the maximum value of the cyclic loading being $P_0 = 20kN$:

$$P(t) = P_0 * sin\left(2\pi \frac{t}{T}\right)$$

The cyclic steady-state residual stress distribution inside a cycle for Gauss point *1* may be seen in Fig. 7. We also see that the plastic strain rates for the Gauss point *1* are equal and of opposite sign in the first and second half of the cycle. Therefore this load case leads the structure to alternating plasticity.

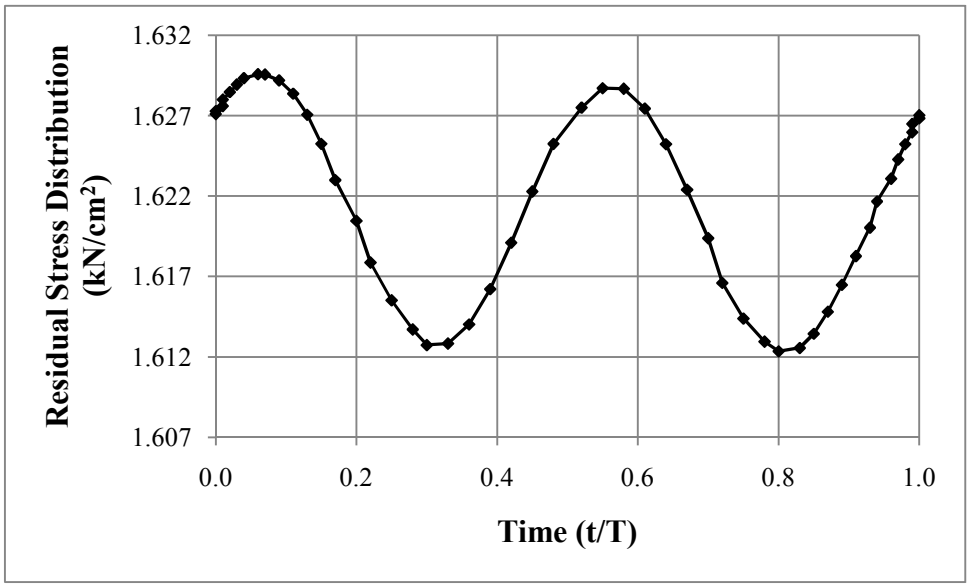

Figure 7: Cyclic state residual stress distribution inside a cycle for load case b (Gauss point 1)

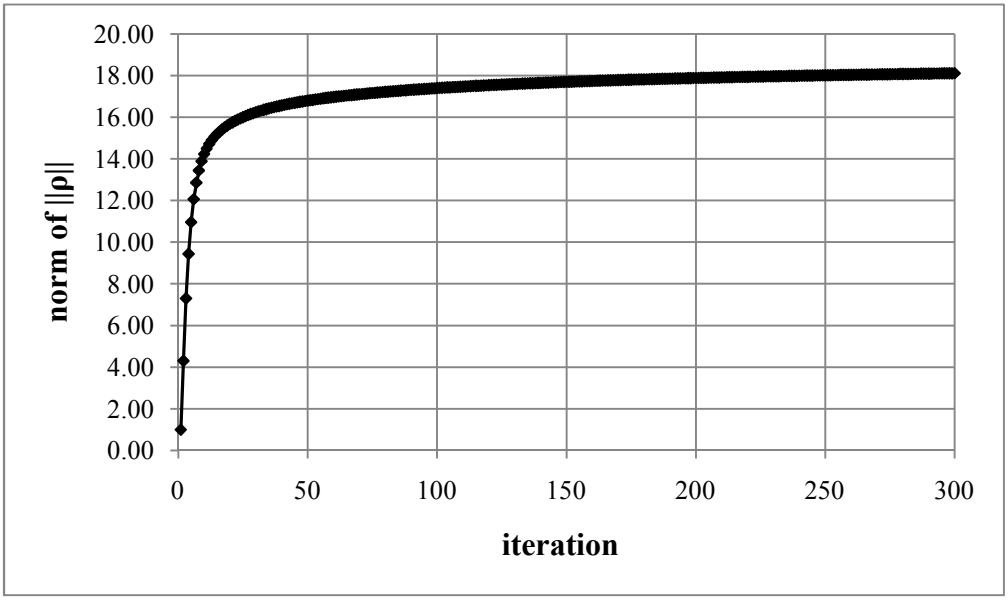

Figure 8: Norm variation with iterations (second example – incremental collapse case)

In Fig.8 one can see the convergence characteristics of the proposed method. It may be realized that the approach is very stable and with uniform convergence.

The observed behaviour of elastic shakedown, alternating plasticity or incremental collapse for both the one and two dimensional examples was found to coincide with the one obtained by a time-stepping finite element program, (ABAQUS [10]). Within [10] an explicit time integration scheme was considered and in order to get higher accuracy this time stepping program had to go through many time increments to get the steady-state solution and to predict the cyclic behavior of the structure, especially for the second example.

6 CONCLUSIONS

- In the present work a direct method is proposed that may be used for the cyclic steady state elastoplastic analysis of structures under cyclic loading.
- It is based on the decomposition of the residual stress distribution into Fourier series whose coefficients are calculated by iterations.
- The method allows approaching directly the long-term effects on the structure without following laborious time-stepping calculations.
- A very few number of terms of the Fourier series generally proved sufficient.
- A limited number of time points inside the cycle are needed, mainly to properly describe the time variation of the cyclic load.
- For all the examples that were presented above the cyclic steady-state was reached in a few iterations.
- The stiffness matrix needs to be formulated and decomposed only once.
- The procedure is stable and has uniform convergence.

REFERENCES

[1] Frederic C.O. and Armstrong P.J. Convergent internal stresses and steady cyclic states of stress. *J. Strain. Anal*. (1966) **1**: 154-169.

[2] Andersen E.D., Roos C., Terlaky T. On implementing a primal-dual interior-point method for conic quadratic optimization. *Math. Program. Ser. B* (2003) **95**: 249–277.

[3] Weichert D. and Hachemi A. Progress in the application of lower bound direct methods in structural design. *Int. J. Appl. Mech*. (2010) **2**: 145-160.

[4] Tran T.N., Liu G.R., Nguyen-Xuan H., Nguyen-Toi T. An edge-based smoothed finite element method for primal–dual shakedown analysis of structures. *Int. J. Numer. Meth. Engng.* (2010) **82**:917–938.

[5] Casciaro R. and Garcea G. An iterative method for shakedown analysis. *Comput. Methods Appl. Mech. Engrg.* (2002) **191**: 5761–5792.

[6] Ponter A.R.S. and Chen H. A minimum theorem for cyclic load in excess of shakedown, with application to the evaluation of a ratchet limit. *Eur. J. Mech. A/Solids* (2001) **20**: 539-553.

[7] Chen H. and Ponter A.R.S. A method for the evaluation of a ratchet limit and the amplitude of plastic strain for bodies subjected to cyclic loading. *Eur. J. Mech. A/Solids* (2001) **20**: 555–571.

[8] Ponter A.R.S. The linear matching method for limit loads, shakedown limits and ratchet limits. In Weichert D. and Ponter A. (eds.) *Limit states of materials and structures*. Springer (2009).

[9] Spiliopoulos K.V. A simplified method to predict the steady cyclic stress state of creeping structures. *ASME J. Appl. Mech*. (2002) **69**:148-153.

[10] ABAQUS 6.10. *User's Manual*. Dassault Systèmes Simulia Corp., Providence, RI, USA (2010)

XI International Conference on Computational Plasticity. Fundamentals and Applications
COMPLAS XI
E. Oñate, D.R.J. Owen, D. Peric and B. Suárez (Eds)

A GENERALIZED FINITE ELEMENT METHOD FOR MODELING ARBITRARY INTERFACES IN LARGE DEFORMATION PROBLEMS

S. OMID R. BIABANAKI[*] AND A.R. KHOEI [†]

[*] PhD Candidate of Civil Engineering, Sharif University of Technology, Tehran, Iran
O.biabanaki@gmail.com, http://mehr.sharif.ir/~sorbiabanaki/
[†] Professor of Civil Engineering, Center of Excellence in Structures and Earthquake Engineering, Sharif University of Technology, P.O. Box 11365-9313, Tehran, Iran
arkhoei@sharif.edu, http://civil.sharif.ir/

Key words: Generalized–FEM; Arbitrary interfaces; Large deformations; Conforming polygonal FEM; Pentagonal elements.

Abstract. In this paper, a generalized–FEM technique is presented in modeling of arbitrary interfaces in large deformations. The method is used to model the internal interfaces and arbitrary geometries using a uniform non-conformal mesh. The technique is applied to capture independent deformations at both sides of separated element cut by the interface in a uniform regular mesh. In this approach, a uniform non-conformal mesh is decomposed into sub-elements that conform to the internal interfaces. The geometry of interface is used to produce various triangular, quadrilateral and pentagonal elements at the intersection of interface with regular FE mesh, in which the extra degrees-of-freedom are defined along the interface. The level set method is employed to describe the material geometry on the background mesh. The technique is used to extrude any arbitrary geometry from an initial background mesh and model under different external effects. The most feature of the technique is to introduce the conformal decomposition finite element method, in which the new conforming elements are produced in the uniform structured mesh by decomposing the uniform mesh into elements that is conformed to the material interfaces. Finally, several numerical examples are analyzed to demonstrate the efficiency of proposed technique in modeling arbitrary interfaces in large deformations.

1 INTRODUCTION

In computational mechanics, modeling the internal interfaces and arbitrary geometries using a non-conformal uniform mesh is of great importance. Adaptive mesh strategy and conforming mesh generation for preserving the mesh to the shape of geometry at various stages of solution may consume high expenses of capacity and time. Thus, it is necessary to perform an innovative procedure to alleviate these difficulties by allowing the internal interfaces and arbitrary geometries to be mesh-independent. In fact, an approach that avoids the remeshing is preferable not only in the cost of creating a new mesh, but the tremendous overhead associated with adapting post-processing techniques, such as time histories of specified points, to sequences of meshes in evolution problems. The major appeal of such technique for incorporating discontinuities in finite elements is that it does not require the mesh to conform to discontinuities in the approximation function, or its derivatives.

There are several approaches proposed by researchers over past few decades to model discontinuity problems based on the mesh-free methods [1–3], the moving mesh technique [4], the incorporation of a discontinuous mode on an element level [5] and etc. Among various techniques, the generalized finite element method (G-FEM) [6, 7] and the extended finite element method (X-FEM) [8, 9] have been successfully employed for the weak and strong discontinuities. The capability of X-FEM has been shown in various problems, including: fracture mechanics problems [10–14], large plastic deformations [15–17], and contact friction problems [18–20]. A technique was proposed by Ventura et al. [21] based on a local enrichment of FE space by closed form solutions for dislocations in infinite media via the local partition of unity. Fries and Belytschko [22] proposed a method for arbitrary discontinuities without additional unknowns. A technique was introduced by Gracie et al. [23] in modeling of multiple dislocations based on interior discontinuities.

The X-FEM technique has been extensively employed to minimize the requirement of mesh generation in the problem with internal interfaces. In this method, the enrichment functions are defined to deal with the discontinuity of displacement inside the enriched element. In fact, the X-FEM method addresses the arbitrary interfaces without generating a boundary-fitted mesh by defining the extra degrees-of-freedom in the elements cut by the interfaces. Additional unknowns may be assigned to the mesh entities, such as: elements, nodes, or edges, by introducing additional equations for these unknowns based on the quadrature techniques for the resulting discontinuous interpolation [24, 25]. In this study, an alternative approach is presented, in which a uniform non-conformal mesh is decomposed into triangular, quadrilateral and pentagonal elements that conform to the internal interfaces and arbitrary geometries. The geometry of interface is used to define the extra degrees-of-freedom by adding nodal points that lie on the interfaces. The technique may be considered as a generalized finite element method introduced by Li et al. [26] using a Cartesian Grid with Added Nodes into the unstructured finite elements. In the FE based Cartesian Grid with Added Nodes method, the added nodes increase the size of the linear system of equations and significantly affect the structure of the matrix, which makes it undesirable compared to other generalized FEM techniques, such as Immersed FE methods. However, in the conformal decomposition finite element method proposed here, the new conforming elements are produced in the uniform structured mesh by decomposing the uniform mesh into elements that is conformed to the material interfaces. This method can be used for the multi-material problems, in which the mesh does not necessary to be conformed to the geometry of the materials. In order to describe the material geometry on the background mesh, the level set method is employed to represent the decomposition of non-conformal elements into the conformal sub-elements [27, 28]. The level set technique is used to extrude any arbitrary geometry from an initial background mesh and model under different external effects.

The construction of conforming finite elements based on polygonal meshes was proposed by Sukumar and Tabarraei [27]. The method provides a great flexibility in mesh generation of solid mechanics problems, which involve a significant change in the domain of material. The trial and test functions of polygonal finite elements have been generally constructed based on the approximation functions of mesh-free methods and computational geometry. A particular and notable contribution is based on the mesh-free, or natural–neighbor, basis functions on a canonical element combined with an affine map to construct conforming approximations on convex polygons. This numerical formulation enables the construction of conforming

approximation on any polygons, and hence extends the potential applications of finite elements to convex polygons of arbitrary order [28]. The present study illustrates the presentation of the conformal decomposition finite element method in large deformations, in which the new conforming elements are generated in the uniform structured mesh by decomposing the uniform mesh into sub-elements that is conformed to the material interfaces.

The plan of the paper is as follows; Section 2 is devoted to the concept of conforming polygonal finite elements. The implementation of conforming–FEM technique based on the polygonal elements is demonstrated in section 3. The procedure, in which the new conforming elements are produced in the uniform structured mesh by decomposing the uniform mesh into sub-elements, is described in this section. In section 4, several numerical examples are analyzed to demonstrate the efficiency of proposed technique in modeling arbitrary interfaces in large deformations. Finally, some concluding remarks are given in section 5.

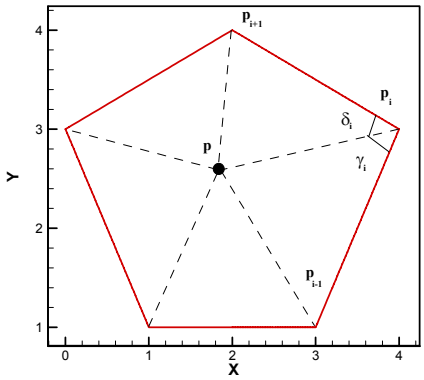

Figure 1. :A pentagon element; Element definition

2 CONFORMING POLYGONAL FEM

The construction of barycentric co-ordinates and the evaluation of shape functions on irregular polygons were originally proposed by Wachspress [29] based on the rational basis functions on polygonal elements. Wachspress [29] employed the principles of perspective geometry [30] to validate the nodal interpolation and linearity on the boundaries. Various aspects of the Wachspress basis function were presented in literature, including: the implementation in numerical analysis by Gout [31], the generalization to convex polytopes by Warren [32], the implementation to construct surface patches by Dahmen et al. [33], etc. The Wachspress basis function was employed into the finite element method by Dasgupta and Malsch [34, 35] to construct the shape functions for concave elements. Rashid and Gullett [36] proposed the technique to construct the shape functions for convex and non-convex elements using a constrained minimization procedure. The construction of conforming finite elements based on polygonal meshes was performed by Sukumar and Tabarraei [27].

An expression for the Wachspress shape functions was given by Meyer et al. [37] as

$$\varphi_i^w(\boldsymbol{x}) = \frac{w_i(\boldsymbol{x})}{\sum_{j=1}^{5} w_j(\boldsymbol{x})} \tag{1}$$

Where

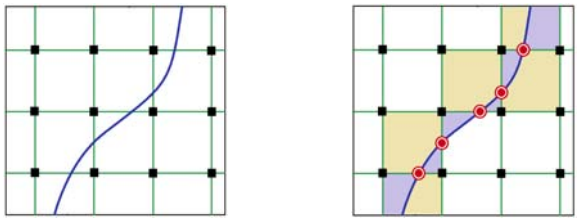

Figure 2. Decomposition of non-conformal elements cut by the interface into conformal sub-elements; ■ Original nodal points, ● New degrees-of-freedom along the interface

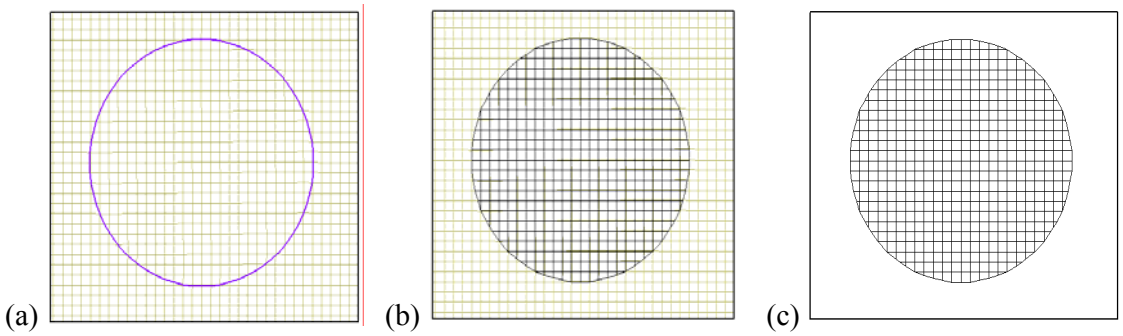

Figure 3. a) Definition of an interface in the uniform non-conformal mesh, b) Determination of standard elements and conformal sub-elements within the material zone, c) Elimination of elements not within the material zone

$$w_i(\boldsymbol{x}) = \frac{A(p_{i-1}, p_i, p_{i+1})}{A(p_{i-1}, p_i, p)\,A(p_i, p_{i+1}, p)} = \frac{\cot\gamma_i + \cot\delta_i}{\|\boldsymbol{x} - \boldsymbol{x}_i\|^2} \tag{2}$$

where $A(a,b,c)$ is the signed area of triangle $[a,b,c]$, and γ_i and δ_i are shown in Figure 1. Since $\cot\gamma_i + \cot\delta_i \equiv \sin(\gamma_i + \delta_i)/(\sin\gamma_i \sin\delta_i)$, the shape functions $\varphi_i^w(\boldsymbol{x})$ have non-negative values and the polygon must be convex, i.e. $\gamma_i + \delta_i < \pi$. The evaluation of the Wachspress basis function can be carried out using the elementary vector calculus operations, as demonstrated by Meyer et al. [37]. Considering the coordinates of the vertices of triangle (p_i, p_{i+1}, p) as (a_1,a_2), (b_1,b_2) and (x_1,x_2), respectively, the value of $\cot\delta_i$ can be computed by

$$\cot\delta_i = \frac{(\mathbf{p}_{i+1} - \mathbf{p}_i).(\mathbf{p} - \mathbf{p}_i)}{|(\mathbf{p}_{i+1} - \mathbf{p}_i) \times (\mathbf{p} - \mathbf{p}_i)|} = \frac{(b_1 - a_1)(x_1 - a_1) + (b_2 - a_2)(x_2 - a_2)}{(b_1 - a_1)(x_2 - a_2) - (x_1 - a_1)(b_2 - a_2)} \equiv \frac{C}{S} \tag{3}$$

and its derivatives can be evaluated as

$$\frac{\partial(\cot\delta_i)}{\partial x_1} = \frac{(b_1 - a_1) - \cot\delta_i\,(a_2 - b_2)}{S}$$
$$\frac{\partial(\cot\delta_i)}{\partial x_2} = \frac{(b_2 - a_2) - \cot\delta_i\,(b_1 - a_1)}{S} \tag{4}$$

The value of $\cot\gamma_i$ and its derivatives can be computed in a similar manner. Finally, the Wachspress shape function $\varphi_i^w(\boldsymbol{x})$ can be obtained according to relation (1).

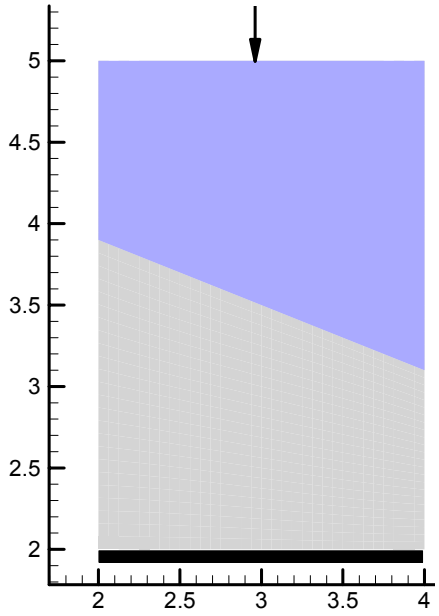

Figure 4: problem view for error analysis

3 GENERALIZED FEM WITH POLYGONAL ELEMENTS

In order to model arbitrary interfaces in a uniform mesh, the regular non-conformal mesh is decomposed into sub-elements that conform to the internal interfaces. In this approach, the concept of conformal decomposition finite element method is used to produce the conforming polygonal elements in the uniform structured mesh by decomposition of the uniform mesh into sub-elements that is conformed to the material interfaces. The geometry of interface is used to produce various polygonal elements at the intersection of interface, as shown in Figure 2, in which the extra degrees-of-freedom are defined along the interface. The position of material interface is determined according to the initial uniform mesh by using the level set method.

The level set method is employed to describe the material interface by extruding arbitrary geometry from the initial background mesh. The technique is used to represent the geometry of interface on the structured, non-conformal mesh. The level set method performs the decomposition of non-conformal elements into conformal sub-elements by introducing the material interface based on the sign of level set function. The performance of this conformal decomposition affects the quality of conformal sub-elements. In general, the conformal decomposition must be robustly handled for unacceptable and degenerate cases. These situations can be occurred whenever the interface passes through a nodal point. In such case, a robust scheme is needed for handling nearly degenerate cases. If nearly degenerate elements are not addressed, the resulting matrix system may be numerically singular.

A general procedure for handling the conformal decomposition can be performed by determination of the edges of non-conformal elements cut by the material interface. An edge is assumed to be cut by the interface if the level set values of two nodal points supported by the edge have different signs. The procedure to handle the nodal points with zero level set values, or nearly zero level set values is optional, but they must be handled consistently. For

the edge of element cut by the interface, new degrees-of-freedom are introduced at the edge of non-conformal element, as shown in Figure 2. The coordinates of this point can be obtained by linear interpolation on the edge of element. For an edge with nodal level set values of φ_1 and φ_2, the coordinates of new point can be obtained as

$$\boldsymbol{x}_i = \boldsymbol{x}_1 + \alpha(\boldsymbol{x}_2 - \boldsymbol{x}_1) \tag{5}$$

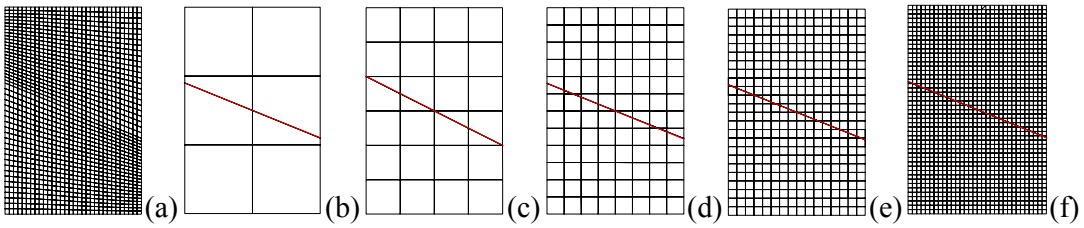

Figure 5: different mesh sizes used for error analysis

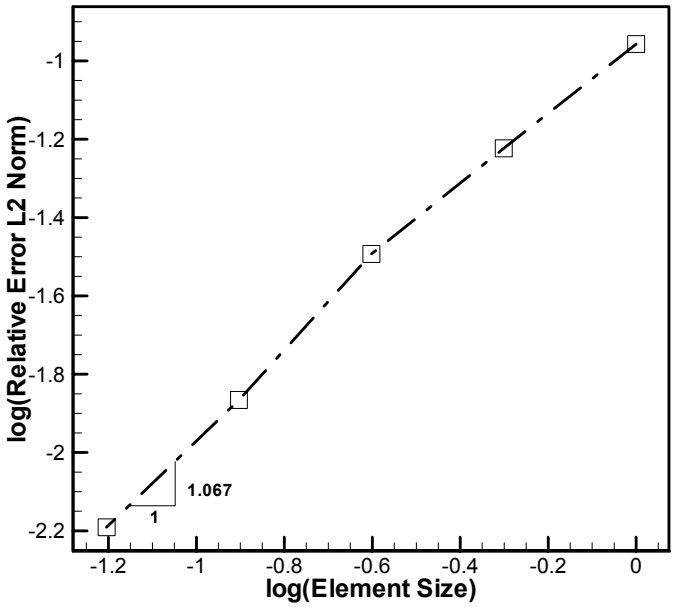

Figure 6: Displacement relative error L2 norm versus Mesh size

where $\boldsymbol{x}_1$ and $\boldsymbol{x}_2$ are the coordinates of new point and the value of α is defined by a linear interpolation as $\alpha = \|\varphi_1\|/h$,with h denoting the size of element. However, if $\alpha < \varepsilon$, or $\alpha > 1-\varepsilon$, in which the parameter ε is assumed to be 0.05, the new point is not generated. In this case, the interface passes through the nearest nodal point of the edge, and the level set value is set to zero at the nearest node. A detailed study of the sensitivity analysis to this decomposition parameter has not been performed here. However, it is obvious that a large value of parameter ε may cause significant errors due to deficiency between the prescribed geometry and the decomposed geometry. In addition, a small value of parameter ε results in multiple nodal points that is numerically coincident.

For the conformal sub-elements, the new point along the interface is added to the original vertex nodal points. Since the new point may be coincident with the vertex nodal points, different cases can be occurred for the conformal sub-elements.Various polygonal elements can be generated according to the position of interface in the regular uniform mesh, including the triangular, quadrilateral and pentagonal elements. If the interface passes through a nodal point, or nearest nodal point ($\alpha < \varepsilon$ or $\alpha > 1-\varepsilon$), it results in the triangular–quadrilateral sub-elements. If the interface cuts two edges of non-conformal element, the conformal decomposition results in two quadrilateral sub-elements, or the triangular–pentagonal sub-elements. The conformal decomposition strategy of degenerate cases depends on the path of interface across the edge and nodal points of the element. The conformal decomposition may result in two triangular sub-elements with no new degrees-of-freedom. If the interface passes through the edge of an element, or nearest nodal points of the edge, there is no conformal decomposition and no new degrees-of-freedom. By defining the material interface in the uniform non-conformal mesh and performing the conformal decomposition to generate various polygonal sub-elements, the standard elements and conformal sub-elements within the material zone must be first determined; those elements or sub-elements which are not within the material zone must be then removed, as shown in Figure 3, and the generalized finite element model is finally analyzed under the external loading.

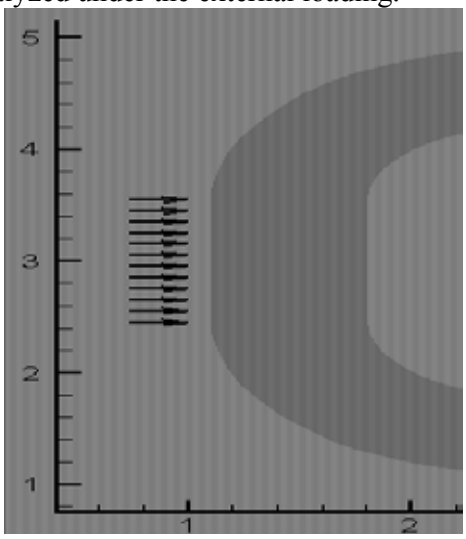

Figure 7. Pressing of an elastic ring; Problem definition

3 NUMERICAL RESULTS

In order to illustrate the accuracy and versatility of the generalized-FEM technique several numerical examples with curve interfaces are presented. The examples are solved using both the G-FEM and FEM techniques, and the results are compared. In order to perform a real comparison, the same number of elements are assumed for both the ‘coarse’ and ‘fine’ meshes independent of the shape of discontinuity to assess the accuracy of discretization. All numerical examples are modeled by a plain strain representation and the convergence tolerance is set to 10^{-14}.

3.1 DISPLACEMENT RELATIVE ERROR L2 NORM ANALYSIS

For determining accuracy of the method, we investigate the accuracy of the problem using error analysis of the method. We consider a simple problem as depicted in Figure 4. The problem is a general rectangular specimen with an inclined internal interface which have two different materials in each side of the interface. We constrained bottom edge of specimen and apply a uniform displacement on the top edge.for error analysis we use a dens standard FEM mesh as reference depicted in Figure 5a. For determining the sensitivity of the GFEM to mesh size we use 5 mesh with different sizes as depicted in Figure 5b to 5f. The result of displacement relative L2 error norm is depicted in figure 6, which shows the GFEM converges to FEM result by reducing the mesh size with a reasonable rate.

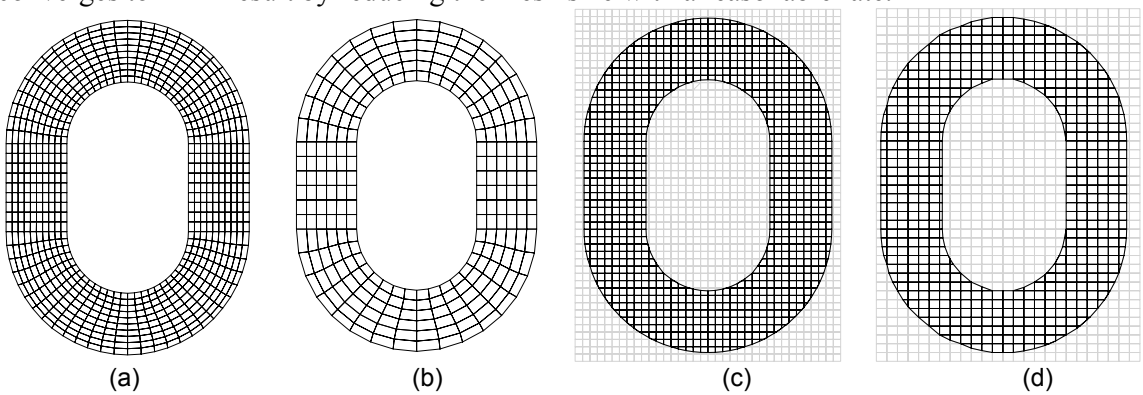

Figure 8. Pressing of an elastic ring; a) FEM mesh of 740 elements, b) FEM mesh of 264 elements, c) Generalized–FEM mesh of 1813 elements, d) Generalized–FEM mesh of 1000 elements

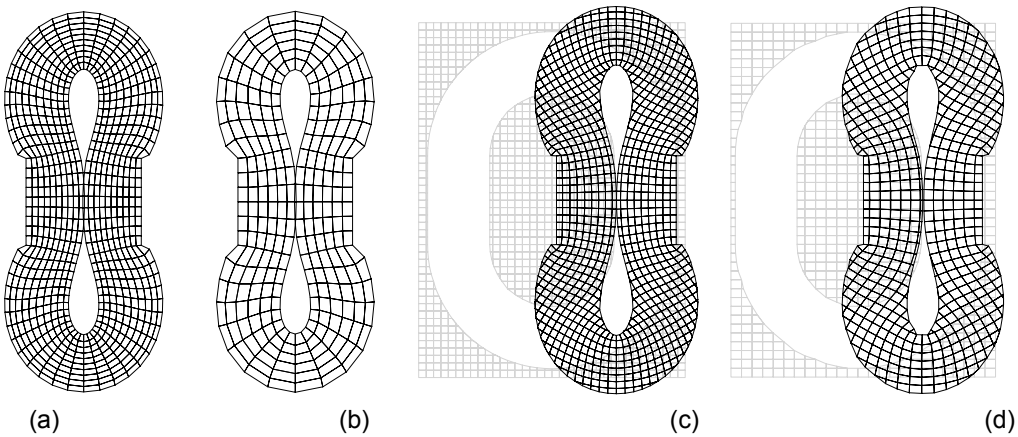

Figure 9. Deformed configurations at 1.4 cm; a) FEM mesh of 740 elements, b) FEM mesh of 264 elements, c) Generalized–FEM mesh of 1813 elements, d) Generalized–FEM mesh of 1000 elements

3.2 PRESSING OF AN ELASTIC RING

The last example refers to the pressing of an elastic ring, as shown in Figure 7. The ring is restrained at the right edge, and a uniform deformation of 1.48 cm is imposed at the left edge.

The ring is assumed to be elastic with the Young modulus of 2.1×10^6 Kg/cm^2 and Poisson ratio of 0.35. Two conformal meshes of 740 and 264 quadrilateral elements are employed in the FEM analysis and two uniform non-conformal meshes of 1000 and 1813 quadrilateral elements in the G-FEM analysis, as shown in Figure 8. In G-FEM, the non-conformal grid is decomposed into sub-elements, in which the geometry of interface is used to produce various polygonal elements at the intersection of interface together with the extra degrees-of-freedom defined along the interface. As can be observed from Figures 8(c–d), the elements and sub-elements that are not within the material zone are removed, and the G-FEM model is analyzed under the prescribed displacement. The deformed configurations of the G-FEM and FEM models are shown in Figure 9 at the deformation of 1.48 cm. In Figure 10, the distribution of normal stress σ_x contours are presented for both techniques at the final stages of pressing. A good agreement can be seen between the G-FEM and FEM approaches. Finally, a comparison of the reaction force versus vertical displacements is performed between the G-FEM and FEM in Figure 11.

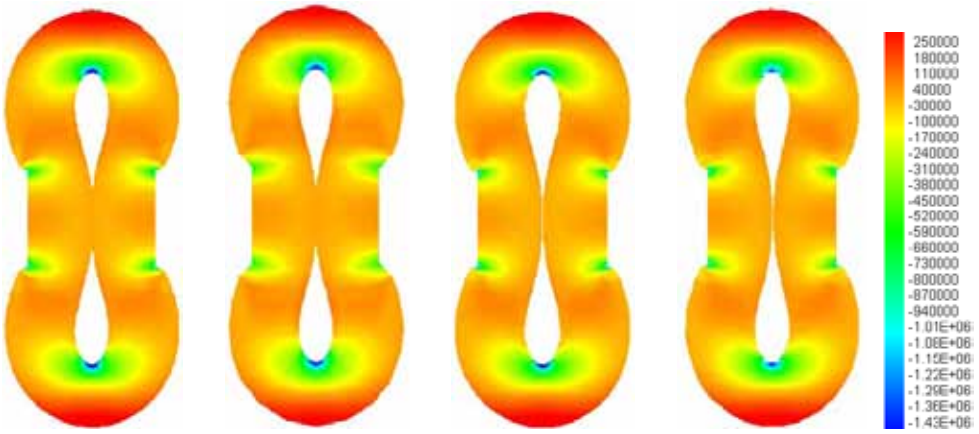

Figure 10. The distribution of normal stress contours at 1.4 cm; a) FEM mesh of 740 elements, b) FEM mesh of 264 elements, c) Generalized–FEM mesh of 1813 elements, d) Generalized–FEM mesh of 1000 elements

4 CONSLUSION

In the present paper, a generalized–FEM technique was presented in modeling of arbitrary interfaces in large deformation problems. A technique was proposed by conformal decomposition of FEM, in which the new conforming sub-elements were generated in the uniform structured mesh that conform to the internal interfaces. The method was used to model the arbitrary geometries using a uniform non-conformal mesh. The geometry of interface was used to produce various triangular, quadrilateral and pentagonal elements at the intersection of interface with regular FE mesh, in which the extra degrees-of-freedom were defined along the interface. The level set method was employed to describe the material geometry on the background mesh by extruding arbitrary geometry from an initial background mesh. By defining the material interface in the non-conformal mesh and performing the conformal decomposition to generate various polygonal sub-elements, the standard elements and conformal sub-elements within the material zone were determined, and

those elements or sub-elements which are not within the material zone were removed. Finally, the proposed generalized FE model was performed to demonstrate the efficiency of technique in modeling of arbitrary interfaces in large deformations by several numerical examples. Numerical simulations of problems with rewrelatively complex geometry were presented. The examples were solved using both the G-FEM and FEM techniques and the results were compared. The numerical results clearly demonstrate the capability of proposed technique in modeling large elastic deformations with multiple material interfaces.

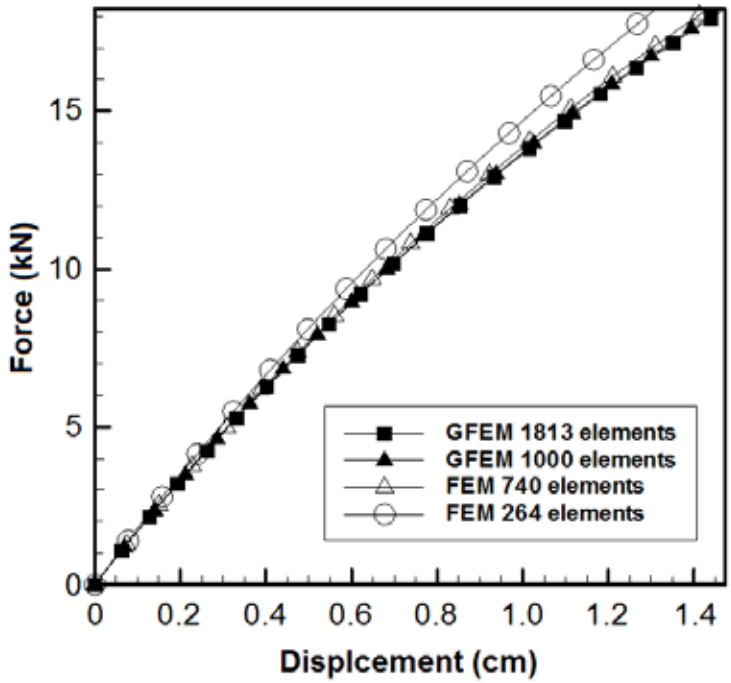

Figure 11. The variations of reaction force with horizontal displacement; A comparison between the FEM and generalized–FEM techniques

REFERENCES

[1] Belytschko T, Lu Y, Gu L. Element-free Galerkin methods. *Computer Methods in Applied Mechanics and Engineering*. 1994; **37**: 229–256.

[2] Belytschko T, Krongauz Y, Organ D, Fleming M, Krysl P. Mesh less methods: an overview and recent developments. *Computer Methods in Applied Mechanics and Engineering*. 1996; **139**: 3–47.

[3] Fleming M, Chu YA, Moran B, Belytschko T. Enriched element free Galerkin methods for crack tip fields. *International Journal for Numerical Methods in Engineering*. 1997; **40**: 1483–1504.

[4] Rashid M. The arbitrary local mesh refinement method: an alternative to remeshing for crack propagation analysis. *Computer Methods in Applied Mechanics and Engineering*. 1998; **154**: 133–150.

[5] Oliver J. Continuum modeling of strong discontinuities in solid mechanics using damage models. *Computational Mechanics*. 1995; **17**: 49–61.

[6] Strouboulis T, Copps K, Babuska I. The Generalized Finite element method, *Computer Methods in Applied Mechanics and Engineering*. 2001; **190**: 4081–4193.
[7] Duarte CA, Hamzeh ON, Liszka TJ, Tworzydlo WW. A generalized finite element method for the simulation of three-dimensional dynamic crack propagation, *Computer Methods in Applied Mechanics and Engineering*. 2001; **190**: 2227–2262.
[8] Belytschko T, Black T. Elastic crack growth in finite elements with minimal remeshing, *International Journal for Numerical Methods in Engineering*. 1999; **45**: 601–620.
[9] Daux C, Moës N, Dolbow J, Sukumar N, Belytschko T. Arbitrary branched and intersecting cracks with the extended finite element method, *International Journal for Numerical Methods in Engineering*. 2000; **48**: 1741–1760.
[10] Belytschko T, Moës N, Usui S, Parimi C. Arbitrary discontinuities in finite elements, *International Journal for Numerical Methods in Engineering*. 2001; **50**: 993–1013.
[11] Moës N, Belytschko T. Extended finite element method for cohesive crack growth, Engineering *Fracture Mechanics*. 2002; **69**: 813–833.
[12] Ventura G, Budyn E, Belytschko T. Vector level sets for description of propagating cracks in finite elements. *International Journal for Numerical Methods in Engineering*. 2003; **58**: 1571–1592.
[13] Lee SH, Song JH, Yoon YC, Zi G, Belytschko T. Combined extended and superimposed finite element method for cracks. *International Journal for Numerical Methods in Engineering*. 2004; **59**: 1119–1136.
[14] Areias PMA, Belytschko T. Analysis of three-dimensional crack initiation and propagation using the extended finite element method. International *Journal for Numerical Methods in Engineering*. 2005; **63**: 760–788.
[15] Khoei AR, Shamloo A, Azami AR. Extended finite element method in plasticity forming of powder compaction with contact friction. *International Journal of Solids and Structures*. 2006; *43*: 5421–5448.
[16] Khoei AR, Biabanaki SOR, Anahid M. Extended finite element method for three-dimensional large plasticity deformations. *Computer Methods in Applied Mechanics and Engineering*. 2008; **197**: 1100–1114.
[17] Khoei AR, Anahid M, Shahim K. An extended arbitrary Lagrangian–Eulerian finite element method for large deformation of solid mechanics. *Finite Elements in Analysis and Design*. 2008; **44**: 401–416.
[18] Khoei AR, Nikbakht M. An enriched finite element algorithm for numerical computation of contact friction problems. *International Journal of Mechanical Sciences*. 2007; **49**: 183–*199*.
[19] Khoei AR, Biabanaki SOR, Anahid M. A Lagrangian – extended finite element method in modeling large plasticity deformations and contact problems. International Journal of *Mechanical Sciences*. 2009; **51**: 384–401.
[20] Khoei AR, Taheri-Mousavi SM. Modeling of large deformation – large sliding contact via the penalty X-FEM technique. *Computational Materials Science*. 2010; doi:10.1016/j.*commatsci*.2010.02.008, in press.
[21] Ventura G, Moran B, Belytschko T. Dislocations by partition of unity. *International Journal for Numerical Methods in Engineering*. 2005; **62**: 1463–1487.

[22] Fries TP, Belytschko T. The intrinsic XFEM: a method for arbitrary discontinuities without additional unknowns. *International Journal for Numerical Methods in Engineering.* 2006; **68**: 1358–1385.
[23] Gracie R, Ventura G, Belytschko T. A new fast finite element method for dislocations based on interior discontinuities. *International Journal for Numerical Methods in Engineering*. 2007; **69**: 423–441.
[24] Ventura G. On the elimination of quadrature subcells for discontinuous functions in the extended finite-element method. *International Journal for Numerical Methods in Engineering*. 2006; **66**: 761–795.
[25] Holdych DJ, Noble DR, Secor RB. Quadrature rules for triangular and tetrahedral elements with generalized functions. *International Journal for Numerical Methods in Engineering*. *2008*; **73**: 1310–1327.
[26] Li Z, Lin T, Wu X. New Cartesian grid methods for interface problems using the finite element *formulation*. *Numerische Mathematik* 2003; 96:61–98.
[27] Sukumar N, Tabarraei A. Conforming polygonal finite elements. *International Journal for Numerical Methods in Engineering*. 2004; **61**: 2045–2066.
[28] Noble DR, Newren EP, Lechman JB. A conformal decomposition finite element method for modeling stationary fluid interface problems. *International Journal for Numerical Methods in Fluids*. 2010; **63**: 725–742.
[29] Wachspress EL. *A Rational Finite Element Basis*. Academic Press, New York. 1975.
[30] Coxeter HSM. *Introduction to Geometry.* Wiley, New York. 1961.
[31] Gout JL. Rational Wachspress-type finite elements on regular hexagons. *IMA Journal of Numerical Analysis*. 1985; **5**: 59 –77.
[32] Warren J. Barycentric coordinates for convex polytopes. *Advances in Computational Mathematics.* 1996; **6**: 97 –108.
[33] Dahmen W, Dikshit HP, Ojha A. On Wachspress quadrilateral patches. *Computer Aided Geometric Design*. 2000; **17**: 879–890.
[34] Dasgupta G. Interpolants within convex polygons: Wachspress' shape functions. *Journal of Aerospace Engineering.* 2003; **16**: 1– 8.
[35] Dasgupta G. Integration within polygonal finite elements. *Journal of Aerospace Engineering*. 2003; **16**: 9–18.
[36] Rashid MM, Gullett PM. On a finite element method with variable element topology. *Computer Methods in Applied Mechanics and Engineering*. 2000; **190**: 1509 –1527.
[37] Meyer M, Lee H, Barr A, Desbrun M. Generalized barycentric coordinates for irregular polygons. *Journal of Graphics Tools*. 2002; **7**: 13–22.

XI International Conference on Computational Plasticity. Fundamentals and Applications
COMPLAS XI
E. Oñate, D.R.J. Owen, D. Peric and B. Suárez (Eds)

A MIXED ALGORITHM FOR INCREMENTAL ELASTOPLASTIC ANALYSIS

A. BILOTTA, L. LEONETTI AND G. GARCEA

Department of Engineering Modeling
Universitá della Calabria
Rende, 87036 Cosenza, Italy
e-mail: giovanni.garcea@unical.it, www.labmec.unical.it

Key words: Computational Plasticity, finite element; convex optimization methods.

Abstract. A new method for the incremental analysis of elastoplastic associated materials is presented. The method fully retains all the equations and variables of the problems at the same level and uses a sequential quadratic programming with equality constraints to solve in an efficient and robust fashion the elastoplastic step equations derived by means of a suitable mathematical programming formulation of the problem. The new proposal is compared with standard strain driven formulations which use a return mapping by closest point projection schemes. The numerical tests performed show a good performance and a great robustness of the proposed formulation also in the case of multi–surface elastoplasticity.

1 INTRODUCTION

The finite element incremental elastoplastic analysis is commonly performed by means of a strain driven (SD) step by step procedure in which each step implements a return mapping strategy. The latter is based on the formulation of a finite step holonomic equation obtained from the irreversible incremental elastoplastic laws by using an integration process which evaluates all the quantities at the end of the step starting from the known values at the beginning of the step and from a prescribed value of the displacement field (strain driven). Among the available integration processes the backward–Euler scheme is the most used.

In standard FEM implementations, the plastic flow rule and consistency conditions are solved exactly and, for an assigned value of the displacements, the return mapping process imposes these equations for each Gauss point of the element. The major advantage of this approach is that the inequality constraints arising from the constitutive laws are eliminated from the step equations using the closest point projection scheme which solves a small optimization problem on each Gauss point of the finite element, so defining the

stress parameters in terms of the displacement ones. The finite step equations are so transformed into a nonlinear system of equations, without inequalities, easily solved by means of standard arc–length strategies. The global description of the algorithm is always performed in terms of displacement variables alone.

The use of descriptions based on displacement variables alone would not be the best choice and potentially more efficient and robust analysis algorithms could be obtained by directly solving the finite step equations, maintaining all the variables of the problems at the same level. Few attempts in this direction have been made and, among these we recall the use of nonsmooth Newton methods proposed by Cristiansen [1] or the use of interior point methods to solve an optimization problem exactly equivalent to the elastoplastic step of Krabbenhoft et al. [2].

In this work a new algorithm for the FEM elastoplastic analysis of structures is presented. The proposed algorithm uses the stress, displacement and plastic multiplier parameters introduced in the discretized form of the problem as primary variables. Adopting the mathematical programming point of view, which allows the use of a theoretically robust environment now endowed with several efficient solution algorithms, a sequential quadratic programming (SQP) formulation is proposed to solve the problem. All the equations describing the finite step are solved at the same level using an equality constraints sequential quadratic programming (EC-SQP) [3] which exploits the particular structure of the equations of the elastoplastic step in order to improve efficiency also for large dimensional problems. In particular an equality constrained sequential quadratic programming (EQ-SQP) is employed. The algorithm is subdivided in two phases: i) a suitable estimate of the active constraints at the current iteration is performed employing the closest point projection scheme; ii) the solution of a quadratic programming that retains only the active constraints is performed. In this way the solution of each QP problem is far easier than the general case and it also makes it possible to deal with very large dimension problems. In particular the solution of the QP subproblem can be performed after condensation of the locally defined quantities (stresses and plastic multipliers) so maintaining, at the global level of analysis, a pseudo compatible system that has the same structure used in standard elastoplastic analysis. The overall algorithm has then the same organization as standard SD-CPP ones and only a few modifications of the existing codes are required to implement the present proposal.

The finite elements used are of mixed type, see [4], but plastically enriched in order to work well also in the elastoplastic field. They are based on a three field interpolation and are so well suited for the application of the proposed algorithm. They also allow the new formulation to be tested in a more severe multi-surface case. The numerical results show how a great improvement in terms of robustness is achieved with respect to the standard SD-CPP algorithms. The proposed algorithms can painlessly undergo large steps sizes or singular yield conditions while the SD-CPP approach shows serious convergence difficulties or, also with respect to small step sizes, line search addiction is mandatory to obtain convergence.

2 THE DISCRETE EQUATIONS FOR THE ELASTOPLASTIC STEP

In the following, the elastoplastic step equations are derived by a backward Euler integration process and then are rewritten in terms of discrete algebraic expressions by introducing the finite element description. The chosen FEM format is based on the general three field interpolation presented in [4] but any other more usual finite element format could be considered by assigning the appropriate meaning to the discrete parameters used in the following.

2.1 The elastoplastic step equations for the continuum body

The nonlinear response of an elastoplastic body Ω subjected to bulk load $\boldsymbol{b}$ and tractions $\boldsymbol{t}$, increasing proportionally to a scalar multiplier λ, can be evaluated by using a standard step-by-step strategy based on the incremental computation of a sequence of discrete points along a time/loading process. In the following we will denote with a superscript $(n-1)$ the quantities relative to the current instant/load in which the solution is known and with a superscript (n) the unknown quantities at the new instant. The stress $\boldsymbol{\sigma}^{(n)}$ and the plastic multiplier $\gamma^{(n)}$ are evaluated by performing a time integration of the constitutive laws once the displacement field $\boldsymbol{u}^{(n)}$ at the end of the step is assigned. In this way the path–dependent elastoplastic behavior is transformed into a sequence of finite holonomic steps. In particular using a backward-Euler time integration scheme and omitting from now on the dependence of quantities on $\boldsymbol{x}$ for an easier reading, the n-th finite step equations can be written, using a standard vector notation, as follows:

$$\begin{aligned}
&\text{Compatibility:}\\
&\begin{cases} \boldsymbol{D}\Delta\boldsymbol{u} = \boldsymbol{\mathcal{C}}^{-1}\Delta\boldsymbol{\sigma} + \Delta\gamma \left.\dfrac{\partial\phi}{\partial\boldsymbol{\sigma}}\right|_n & \text{in } \Omega,\\ \boldsymbol{u}^{(n)} = \bar{\boldsymbol{u}} & \text{on } \partial\Omega_u; \end{cases}\\
&\text{Admissibility and consistency:}\\
&\phi[\boldsymbol{\sigma}^{(n)}] \le 0 \;\;,\;\; \Delta\gamma \ge 0 \;\;,\;\; \Delta\gamma\phi[\boldsymbol{\sigma}^{(n)}] = 0.
\end{aligned} \tag{1a}$$

The symbol $\Delta(\cdot) = (\cdot)^n - (\cdot)^{n-1}$ will denote, from now on, the difference between quantities in (n) and $(n-1)$, $\boldsymbol{\mathcal{C}}^{-1}$ the elastic compliance operator, $\boldsymbol{D}$ the compatibility operator, ϕ the convex yield function and $\bar{\boldsymbol{u}}$ the prescribed displacement on $\in \partial\Omega_u$. In the previous equations and from now on the finite increment of plastic strain is evaluated using an associated flow rule.

The holonomic finite step is then completed with the equilibrium equations:

$$\begin{cases} \boldsymbol{D}^T\boldsymbol{\sigma}^{(n)} + \lambda^{(n)}\boldsymbol{b} = \boldsymbol{0} & \text{in } \Omega,\\ \boldsymbol{n}\boldsymbol{\sigma}^{(n)} = \lambda^{(n)}\boldsymbol{t} & \text{on } \partial\Omega_t \end{cases} \tag{1b}$$

where $\boldsymbol{n}$ is the matrix collecting the normal to the loaded boundary $\partial\Omega_t$.

2.2 The weak form of the finite step equations

Following [5], the finite step equations (1a) can be rewritten in a weak form as

$$\int_\Omega \delta\boldsymbol{\sigma}^T \left(\boldsymbol{\mathcal{C}}^{-1}\Delta\boldsymbol{\sigma} - \boldsymbol{D}\Delta\boldsymbol{u} + \Delta\gamma \left.\frac{\partial\phi}{\partial\boldsymbol{\sigma}}\right|_n \right) = 0 \quad \forall\delta\boldsymbol{\sigma}, \tag{2a}$$

$$\int_\Omega \delta\gamma\phi[\boldsymbol{\sigma}^{(n)}] = 0 \quad \forall\delta\gamma \geq 0, \tag{2b}$$

where Eq. (2b) expresses, in a weak sense, the plastic admissibility condition for the material. In a similar fashion the weak statement of the equilibrium condition (1b) becomes

$$\int_\Omega (\boldsymbol{D}\delta\boldsymbol{u})^T \boldsymbol{\sigma}^{(n)} - \lambda^{(n)} \left(\int_\Omega \delta\boldsymbol{u}^T\boldsymbol{b} + \int_{\partial\Omega_t} \delta\boldsymbol{u}^T\boldsymbol{t} \right) = 0 \quad \forall\delta\boldsymbol{u}. \tag{2c}$$

Finally, the use of a path–following Riks algorithm to solve the step equations, requires the introduction of the arc–length parameters $\Delta\xi^{(n)}$. The following definition can be exploited

$$\delta\lambda \left(\int_\Omega \Delta\boldsymbol{u}^T\boldsymbol{b} + \int_{\partial\Omega_t} \Delta\boldsymbol{u}^T\boldsymbol{t} - \Delta\xi^{(n)} \right) = 0 \quad \forall\delta\lambda. \tag{2d}$$

2.3 The FE finite step equations

Following [4] where more details can be found, we adopt a finite element formulation based on the interpolation of three fields: displacement, stress and plastic multiplier. These interpolations can be expressed as:

$$\boldsymbol{u} := \boldsymbol{N}\boldsymbol{d}_e \qquad \boldsymbol{\sigma} := \boldsymbol{S}\boldsymbol{\beta}_e \qquad \gamma := \boldsymbol{G}\boldsymbol{\kappa}_e, \tag{3}$$

where $\boldsymbol{N}$, $\boldsymbol{S}$ and $\boldsymbol{G}$ are the matrices containing the interpolation functions and $\boldsymbol{d}_e$, $\boldsymbol{\beta}_e$ and $\boldsymbol{\kappa}_e$ are the vectors collecting the finite element parameters. The non–negativeness of the interpolation functions $\boldsymbol{G}$ allows the condition $\gamma \geq 0$ to be easily expressed by making $\boldsymbol{\kappa}_e \geq \boldsymbol{0}$, where, from now on, vector inequality will be considered in a componentwise fashion. Moreover an important aspect which will allow the nonlinear algorithm to be casted in the format described in the following regards the continuity order of the assumed interpolations, in particular the displacement field has to be capable of assuring the inter-element continuity while $\boldsymbol{\sigma}$ and γ can be defined locally inside the element.

From now on we omit reporting the superscript $()^{(n)}$ that defines the step.

2.3.1 Local equations

On the basis of the interpolations we obtain the discrete counterpart of the flow rule, plastic admissibility and consistency condition

$$\begin{cases} \boldsymbol{r}_\sigma \equiv \boldsymbol{H}_e\Delta\boldsymbol{\beta}_e - \boldsymbol{Q}_e\Delta\boldsymbol{d}_e + \boldsymbol{A}_e[\boldsymbol{\beta}_e]\Delta\boldsymbol{\kappa}_e = \boldsymbol{0} \\ \boldsymbol{r}_\mu \equiv \boldsymbol{\Phi}_e[\boldsymbol{\beta}_e^{(n)}] \leq 0, \quad \Delta\boldsymbol{\kappa}_e \geq 0, \quad \Delta\boldsymbol{\kappa}_e^T\boldsymbol{\Phi}_e[\boldsymbol{\beta}_e^{(n)}] = 0, \end{cases} \tag{4}$$

where $\boldsymbol{A}_e[\boldsymbol{\beta}_e]$ represents the discrete form of the plastic flux direction and is defined by

$$\boldsymbol{A}_e[\boldsymbol{\beta}_e] := \int_{\Omega_e} \boldsymbol{S}^T \frac{\partial \phi}{\partial \boldsymbol{\sigma}}[\boldsymbol{\beta}_e]\boldsymbol{G}$$

while the discrete operators

$$\boldsymbol{Q}_e := \int_{\Omega_e} \boldsymbol{S}^T \boldsymbol{D}\boldsymbol{N} \qquad \boldsymbol{H}_e := \int_{\Omega_e} \boldsymbol{S}^T \boldsymbol{\mathcal{C}}^{-1} \boldsymbol{S} \tag{5}$$

are the usual compatibility/equilibrium and elastic flexibility matrices respectively and

$$\boldsymbol{\Phi}_e[\boldsymbol{\beta}_e] := \int_{\Omega_e} \boldsymbol{G}^T \phi[\boldsymbol{\beta}_e], \tag{6}$$

corresponds to the element representation of the yield function and it depends on the final value of the stress parameters. As Eqs. (4) are expressed in terms of quantities locally defined on the element, or at the Gauss points for standard finite element interpolations, they will be denoted from now on as *local equations*.

2.3.2 Global equations

The discrete form of the equilibrium equations and the arc length condition to be used in the numerical solution of the problem are:

$$\mathcal{A}_e \left\{ \boldsymbol{Q}_e^T \boldsymbol{\beta}_e - \lambda \boldsymbol{p}_e \right\} = 0, \quad , \quad \mathcal{A}_e \left\{ \Delta \boldsymbol{d}_e^T \boldsymbol{p}_e \right\} = \Delta\xi, \tag{7}$$

$\mathcal{A}_e$ being the standard assembling operator which takes into account the inter–element continuity conditions on the displacement field and

$$\boldsymbol{p}_e := \int_{\Omega_e} \boldsymbol{N}^T \boldsymbol{b} + \int_{\partial\Omega_e} \boldsymbol{N}^T \boldsymbol{t} \tag{8}$$

is the element load vector. For the sake of the following discussion eqs.(7) can be rewritten as

$$\begin{cases} \boldsymbol{r}_u \equiv \boldsymbol{Q}^T \boldsymbol{\beta} - \lambda \boldsymbol{p} = \boldsymbol{0} \\ r_\lambda \equiv \Delta \boldsymbol{d}^T \boldsymbol{p} - \Delta\xi = 0, \end{cases} \tag{9}$$

where $\boldsymbol{\beta}$, $\boldsymbol{d}$ and $\boldsymbol{p}$ denote the global vectors collecting all the stress parameters $\boldsymbol{\beta}_e$, the displacement parameters $\boldsymbol{d}_e$ and the applied loads $\boldsymbol{p}_e$.

2.4 The mathematical programming point of view

Noting that

$$\boldsymbol{A}_e[\boldsymbol{\beta}_e] := \left(\frac{\partial \boldsymbol{\Phi}_e[\boldsymbol{\beta}_e]}{\partial \boldsymbol{\beta}_e} \right)^T$$

each finite step is characterized by the set of nonlinear equalities and inequalities defined by Eqs. (4) and (9) which represent the first order conditions of the following nonlinear convex optimization problem:

$$\begin{aligned} \text{maximize} \quad & \Delta\xi^{(n)}\lambda^{(n)} - \frac{1}{2}\sum_e (\Delta\boldsymbol{\beta}_e)^T \boldsymbol{H}_e \Delta\boldsymbol{\beta}_e, \\ \text{subject to} \quad & \boldsymbol{Q}^T\boldsymbol{\beta}^{(n)} = \lambda^{(n)}\boldsymbol{p} \\ & \boldsymbol{\Phi}_e[\boldsymbol{\beta}_e^{(n)}] \leq \boldsymbol{0} \qquad\qquad \forall \boldsymbol{\beta}_e. \end{aligned} \tag{10}$$

Assuming this point of view the actual solution strategy can be implemented on the basis of a nonlinear programming technique suitable for solving (10).

Note how more standard finite element formulations based on the numerical integration on the Gauss points could be easily framed inside the optimization problem defined by Eq. (10), by considering the quadratic terms of the objective function as the result of the sum of the contributions of the Gauss points of each element while the admissibility condition is imposed on each Gauss point.

3 A NEW SOLUTION SCHEME FOR ELASTOPLASTIC ANALYSIS

In the following section we will present an application of the SQP method to solve Eq. (10). The algorithm exploits the problem structure allowing its solution at the global level by means of a Newton (Riks) scheme which is characterized by minimal implementational differences with respect to standard SD-CPP formulations.

3.1 The linearized equations for the elastoplastic step and the sequential quadratic programming (SQP) formulation

The estimate of the unknowns relative to the new step, $\boldsymbol{z}^{(n)} = \{\lambda^{(n)}, \boldsymbol{\beta}^{(n)}, \boldsymbol{d}^{(n)}, \boldsymbol{\kappa}^{(n)}, \}$, will be denoted by $\boldsymbol{z}^{j+1} = \boldsymbol{z}^j + \dot{\boldsymbol{z}}$ where, in order to make the notation simpler, the superscript relative to the step number has been dropped leaving only the indication for the current j–th iteration. The starting point for the new algorithm is the linearization of the finite step equation (10) which yields the local equations (4) again, i.e.

$$\begin{cases} -\boldsymbol{H}_{et}\dot{\boldsymbol{\beta}}^j + \boldsymbol{Q}_e\dot{\boldsymbol{d}} - \boldsymbol{A}_e^j\dot{\boldsymbol{\kappa}}_e = -\boldsymbol{r}_\sigma^j, \\ \boldsymbol{\Phi}_e^{j+1} \leq \boldsymbol{0}\ ,\ \boldsymbol{\kappa}_e^{j+1} \geq \boldsymbol{0}\ ,\ (\boldsymbol{\kappa}_e^{j+1})^T\boldsymbol{\Phi}_e^{j+1} = 0. \end{cases} \quad \forall e \tag{11a}$$

Where

$$\boldsymbol{H}_{et} \equiv \boldsymbol{H}_e + \sum_k \kappa_{ek}^j \left.\frac{\partial^2 \Phi_{ek}}{\partial \boldsymbol{\beta}_e^2}\right|_{\boldsymbol{\beta}_e = \boldsymbol{\beta}_e^j} \quad , \quad \boldsymbol{A}_j = \left.\frac{\partial \boldsymbol{\Phi}_e}{\partial \boldsymbol{\beta}_e}\right|_{\boldsymbol{\beta}_e = \boldsymbol{\beta}_e^j},$$

κ_{ek}^j and Φ_{ek} are the kth components of $\boldsymbol{\kappa}_e^j$ and $\boldsymbol{\Phi}_e[\boldsymbol{\beta}_e^j]$ respectively, and

$$\boldsymbol{\Phi}_e^{j+1} \equiv \boldsymbol{\Phi}_e[\boldsymbol{\beta}_e^j] + (\boldsymbol{A}_e^j)^T(\boldsymbol{\beta}_e^{j+1} - \boldsymbol{\beta}_e^j) = \boldsymbol{\Phi}_e[\boldsymbol{\beta}_e^j] + (\boldsymbol{A}_e^j)^T\dot{\boldsymbol{\beta}}_e.$$

Moreover, the linearization of the global finite step equations (9) gives:

$$\begin{cases} \boldsymbol{Q}^T\dot{\boldsymbol{\beta}} - \dot{\lambda}\boldsymbol{p} = -\boldsymbol{r}_{uj}, \\ -\dot{\boldsymbol{d}}^T\boldsymbol{p} = -\boldsymbol{r}_{\lambda j}. \end{cases} \tag{11b}$$

Eq. (11) could also be obtained by applying a sequential quadratic programming (SQP) approach to (10) obtaining

$$\begin{aligned} \text{maximize} \quad & \Delta\xi\ \dot{\lambda} - \sum_e \left(\dot{\boldsymbol{\beta}}_e^{\,T}\boldsymbol{H}_e\Delta\boldsymbol{\beta}_e^j - \frac{1}{2}\dot{\boldsymbol{\beta}}_e^T\boldsymbol{H}_{et}\dot{\boldsymbol{\beta}}_e \right) \\ \text{subject to} \quad & \boldsymbol{Q}^T\dot{\boldsymbol{\beta}} - \dot{\lambda}\boldsymbol{p} + \boldsymbol{r}_u^j = \boldsymbol{0}, \\ & (\boldsymbol{A}^j)^T\dot{\boldsymbol{\beta}} + \boldsymbol{\Phi}_e[\boldsymbol{\beta}^j] \leq \boldsymbol{0}, \end{aligned} \tag{12a}$$

whose solution gives the new estimate $\boldsymbol{z}^{j+1}$ in the form

$$\boldsymbol{z}^{j+1} = \{\lambda^j + \dot{\lambda}, \boldsymbol{\beta}^j + \dot{\boldsymbol{\beta}}, \boldsymbol{d}^j + \dot{\boldsymbol{d}}, \boldsymbol{\kappa}^{j+1}\}. \tag{12b}$$

However the solution of the QP sub-problems (12a) with a standard SQP algorithm requires however a great computational effort due to the coupling action exerted by the equilibrium constraints. A method to efficiently solve Eq. (11) or problem in (12a) will now be examined.

3.2 The EC-SQP formulation

First the SQP problem in (12) is solved by using an equality constraint sequential quadratic programming (EC-SQP) approach [3]. Each iteration of the EC-SQP approach consists of two phases: i) estimation of the active set of constraints; ii) solution of an equality constrained quadratic program that imposes the apparently active constraints and ignores the apparently inactive ones. The idea is to identify the active constraints for the actual estimate of the solution using information available at a point near to $\mathbf{z}^{j+1}$, a point which in the sequel will be denoted by $\bar{\mathbf{z}}^{j+1}$.

3.2.1 The detection of the active set of constraints

The estimation of the active constraints is performed by advocating the decomposition point of view, i. e. solving an optimization problem obtained by the original ones (11a) for a fixed, properly assumed, value of the displacements $\bar{\boldsymbol{d}}^{j+1} = \boldsymbol{d}^j$. The series of decoupled problems obtained in this way have the same form as a standard CPP scheme and it can

be easily solved at the local element level in a way as efficient as, or also more, than the standard SD-CPP approach.

At the iteration $j+1$ then the active set of constraints is obtained by solving (11a) assuming $\bar{\boldsymbol{d}}_{j+1} \approx \boldsymbol{d}_j$ and so $\dot{\boldsymbol{d}} = \boldsymbol{0}$. The result is a problem that is now decoupled at the local level, i. e.

$$\begin{cases} -\boldsymbol{H}_{et}\dot{\bar{\boldsymbol{\beta}}}_e^j - \boldsymbol{A}_e^j\dot{\bar{\boldsymbol{\kappa}}}_e = -\boldsymbol{r}_\sigma^j, \\ \boldsymbol{\Phi}_e^{j+1} \le \boldsymbol{0}\ ,\ \bar{\boldsymbol{\kappa}}_e^{j+1} \ge \boldsymbol{0}\ ,\ (\bar{\boldsymbol{\kappa}}_e^{j+1})^T\boldsymbol{\Phi}_e^{j+1} = 0, \end{cases} \quad \forall e \tag{13}$$

where the symbols with a bar denote the estimates of the new quantities. In particular Eqs.(13) are the first order conditions of the following QP problem:

$$\begin{cases} \min\limits_{(\dot{\boldsymbol{\beta}}_e)} : \dfrac{1}{2}(\dot{\bar{\boldsymbol{\beta}}}_e^j)^T\boldsymbol{H}_{et}\dot{\bar{\boldsymbol{\beta}}}_e^j + (\dot{\bar{\boldsymbol{\beta}}}_e^j)^T\mathbf{g}^j, \\ \text{subj.: } \boldsymbol{A}_j^T\dot{\bar{\boldsymbol{\beta}}}_e^j + \boldsymbol{\Phi}_e^j \le \boldsymbol{0}, \end{cases} \quad \forall e \tag{14}$$

where $\boldsymbol{\Phi}_e^j = \boldsymbol{\Phi}_e[\boldsymbol{\beta}_e^j]$, $\mathbf{g}^j = \boldsymbol{H}_e(\boldsymbol{\beta}_e^j - \boldsymbol{\beta}_e^*)$. The solution of Eqs (14), which can be seen as the quadratic problems arising from an SQP approximation of the CPP projection scheme, gives the actual estimate of the stress and plastic multiplier parameters, $\bar{\boldsymbol{\beta}}_e^{\,j+1} = \boldsymbol{\beta}_e^j + \dot{\bar{\boldsymbol{\beta}}}_e$, $\bar{\boldsymbol{\kappa}}^{j+1}$. In particular the QP problem (14) is efficiently solved by using the Goldfarb-Idnani active set method, see [6] for further details.

3.2.2 The solution of the QP equality constraint scheme

After the detection of the set of active constraints, and assuming that this set is not void, we have to solve Eqs. (11) by means of the following system of equations in which only the residuals of the active constraints are considered:

$$\begin{bmatrix} \cdot & \boldsymbol{A}_e^{jT} & \cdot & \cdot \\ -\boldsymbol{A}_e^j & -\boldsymbol{H}_{et} & \boldsymbol{Q}_e & \cdot \\ \cdot & \boldsymbol{Q}_e^T & \cdot & -\boldsymbol{p}_e \\ \cdot & \cdot & -\boldsymbol{p}_e^T & \cdot \end{bmatrix} \begin{bmatrix} \dot{\boldsymbol{\kappa}}_e \\ \dot{\boldsymbol{\beta}}_e \\ \dot{\boldsymbol{d}}_e \\ \dot{\lambda} \end{bmatrix} = - \begin{bmatrix} \boldsymbol{r}_\mu^j \\ \boldsymbol{r}_\sigma^j \\ \boldsymbol{r}_u^j \\ r_\lambda^j \end{bmatrix} \quad , \quad \boldsymbol{z}^{j+1} = \boldsymbol{z}^j + \dot{\boldsymbol{z}}, \tag{15}$$

where the further condition $\boldsymbol{\kappa}_{j+1} \ge 0$ needs to be imposed.

System (15) is easily solved by static condensation of the local defined quantities. In particular, recalling that the QP scheme in (14) solves the first two equations of (11a) zeroing the displacements $\dot{\boldsymbol{d}}_e$, we obtain

$$\begin{cases} \dot{\boldsymbol{\beta}}_e = \boldsymbol{H}_{et}^{-1}\left(\boldsymbol{r}_\sigma^j + \boldsymbol{Q}_e\dot{\boldsymbol{d}}_e - \boldsymbol{A}_j\dot{\boldsymbol{\kappa}}_e\right) & = \dot{\bar{\boldsymbol{\beta}}}_e + \boldsymbol{H}_{et}^{-1}\boldsymbol{Q}_e\dot{\boldsymbol{d}}_e, \\ \dot{\boldsymbol{\kappa}}_e = \boldsymbol{W}\left(\boldsymbol{r}_\mu^j + \boldsymbol{A}_j^T\boldsymbol{H}_{et}^{-1}\boldsymbol{r}_\sigma^j + \boldsymbol{A}_j^T\boldsymbol{H}_{et}^{-1}\boldsymbol{Q}_e\dot{\boldsymbol{d}}_e\right) & = \dot{\bar{\boldsymbol{\kappa}}}_e + \boldsymbol{W}\boldsymbol{A}_j^T\boldsymbol{H}_{et}^{-1}\boldsymbol{Q}_e\dot{\boldsymbol{d}}_e, \end{cases} \tag{16}$$

where $\boldsymbol{W} = \left[\boldsymbol{A}_j^T\boldsymbol{H}_{et}^{-1}\boldsymbol{A}_j\right]^{-1}$.

At the global level then we have to assemble the condensed element contribution as

$$\mathcal{A}_e \left(\boldsymbol{Q}_e^T \boldsymbol{E}_t \boldsymbol{Q}_e \right) \dot{\boldsymbol{d}} - \dot{\lambda} \boldsymbol{p} = -\mathcal{A}_e \left(\tilde{\boldsymbol{r}}_u^j \right) \quad , \quad -\boldsymbol{p}^T \dot{\boldsymbol{d}}_e = -r_\lambda^j, \tag{17}$$

where

$$\tilde{\boldsymbol{r}}_u^j = \boldsymbol{r}_u^j + \boldsymbol{Q}_e^T (\boldsymbol{E}_t \boldsymbol{r}_\sigma^j - \boldsymbol{H}_{et}^{-1} \boldsymbol{A}_j \boldsymbol{W} \boldsymbol{r}_\mu^j) \quad \text{and} \quad \boldsymbol{E}_t = \boldsymbol{H}_{et}^{-1} - \boldsymbol{H}_{et}^{-1} \boldsymbol{A}_j \boldsymbol{W} \boldsymbol{A}_j^T \boldsymbol{H}_{et}^{-1}.$$

$\boldsymbol{E}_t$ has the same expression as the algorithmic tangent matrix evaluated by standard SD-CPP formulation.

System (17) is coincident with a standard SD-CPP iteration scheme except for the new definition of quantities $\tilde{\boldsymbol{r}}_u^j$. Note that $\boldsymbol{E}_t$ and $\boldsymbol{H}_{et}^{-1} \boldsymbol{A}_j \boldsymbol{W}$ are evaluated at each step of the QP problem, by the optimization algorithm used, so only the evaluation of $\tilde{\boldsymbol{r}}_u^j$ is required. In the case of an element with zero active constraints the solution is obtained from previous scheme by deleting the first row and column from system (15).

4 NUMERICAL RESULTS

A series of numerical tests, in plane stress/strain conditions has been performed in order to evaluate the performance of the proposed algorithm in the elastoplastic analysis of 2D problems under the action of various kinds of loads (traction tests characterized by stress concentration, in-plane bending actions) and for different materials (Von Mises and Drucker-Prager materials). The finite elements adopted are those proposed in [4] where the interpolation of the displacement, stress and plastic multiplier fields is adopted. In particular, among the elements proposed in the cited work, only the FC_4 element, with a piecewise-constant interpolation over 4 subareas into which the internal area of the element is divided, has been used. This choice allows to test the robustness of the proposed algorithm with respect to more severe and more nonlinear cases. Further details of the finite elements used can be found in [4].

The convergence to a new equilibrium point will be considered as achieved when the norm of residuals is less than a given tolerance, i.e. $\|\boldsymbol{r_u}\| + \|\boldsymbol{r_\sigma}\| + \|\boldsymbol{r}_\mu\| \leq$ toll, while the analysis is stopped when the displacement component of a specified point reaches a prescribed value. The number of points required by the Riks strategy to evaluate the equilibrium path will be denoted with steps while the iterations required for each step will be denoted with loops. The arc–length scheme adopted does not use any globalization technique, such as line search. In the case of convergence failure the algorithm simply restarts from the last point evaluated but with a reduced arc–length increment. A line search is performed in the return mapping process of the SD-CPP algorithm to allow the possibility of handling with large step sizes. Moreover, in order to test the robustness of the proposed EC-SQP algorithm, that is the possibility of convergence to an equilibrium point also starting very far from it, the analyses were repeated by increasing the value of the first step length $\Delta\xi^{(1)}$ selected in order to force the value of the observed component of the displacement to a prescribed amplitude. In this way the analysis works with larger

step sizes, this last one being controlled through an extrapolation parameter calculated by the formula $\left(1-\frac{1}{2}\frac{lps-lps_d}{lps+lps_d}\right)$, where lps is the number of loops required by the last step and lps_d the desired number of loops. However if the step is not closed within the maximum number of loops the analysis is restarted with a smaller initial step size. Then, for each test, a report is presented which shows the evaluated collapse load multiplier and the relative error, the number of steps, the total number of loops and the number of step failures (i. e. the steps not closed within lps_m). In this way a deep comparison of the SD-CPP and EC-SQP algorithm is performed. In the following only one test, representing well the behavior of the algorithm, will be presented.

4.1 Square plate with circular hole

This test is depicted in Fig. 1 and is known as square plate with circular hole. The analyses were performed in plane stress conditions on the basis of four different meshes of $(2^n \times 2^n)$ elements each denoted as mesh n and was stopped when the vertical component of node A reaches the value $5e-3$.

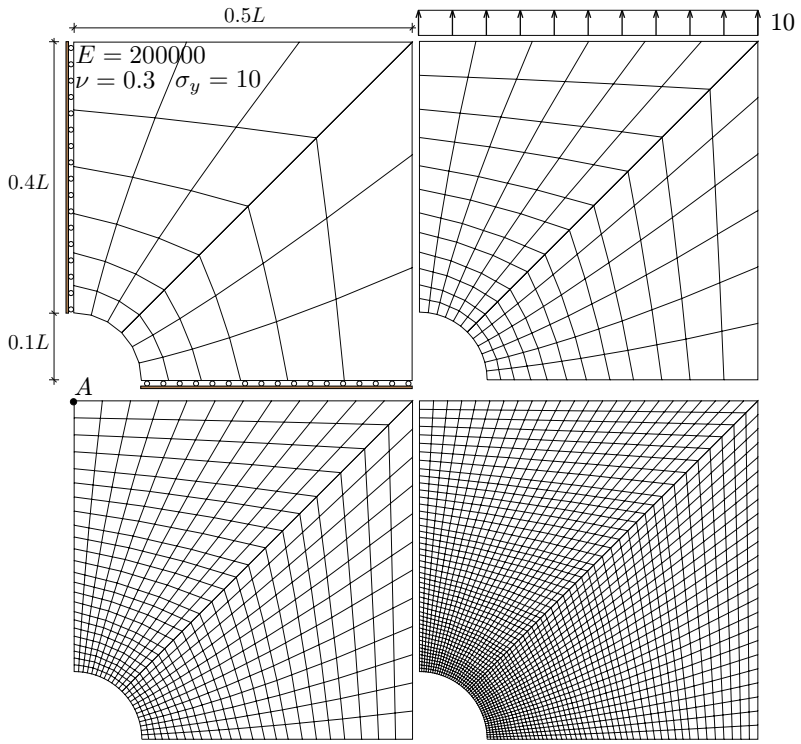

Figure 1: Plate with circular hole. Problem description and discretization meshes.

The results obtained on all the meshes using both the standard SD-CPP algorithm and the new EC-SQP algorithm are summarized in Tab. 4.1. The capability of the proposed algorithm to sustain even very large step sizes without affecting the computed

collapse load, regardless of the mesh considered, is clear. In contrast the standard SD-CPP algorithm has no particular problem for the first values of the assigned initial increment of the monitored displacement component, i.e. $5e-5$ and $1e-4$. Afterward, for the bigger increments, the algorithm makes some false steps until the step size is not reduced to a value that can be sustained.

	Mesh 1 (dofs 98)					*Mesh 2 (dofs 338)*				
	λ_c	stps	lps	flrs	incr.	λ_c	stps	lps	flrs	incr.
SD-CPP	0.8100	20	58	0	5e-5	0.8030	23	77	0	5e-5
	0.8100	18	55	0	1e-4	0.8030	20	73	1	1e-4
	0.8100	19	55	4	1e-3	0.8030	21	72	4	1e-3
	0.8100	21	57	7	5e-3	0.8030	25	84	7	5e-3
	0.8100	22	65	8	1e-2	0.8030	25	86	8	1e-2
EC-SQP	0.8100	20	58	0	1e-5	0.8030	24	87	0	5e-5
	0.8100	18	58	0	1e-4	0.8030	21	83	0	1e-4
	0.8100	6	32	0	1e-3	0.8030	9	72	0	1e-3
	0.8100	2	37	0	5e-3	0.8030	2	54	0	5e-3
	0.8100	1	20	0	1e-2	0.8030	1	28	0	1e-2
	Mesh 3 (dofs 1250)					*Mesh 4 (dofs 4802)*				
	λ_c	stps	lps	flrs	incr.	λ_c	stps	lps	flrs	incr.
SD-CPP	0.8015	27	105	0	5e-5	0.8006	28	113	1	5e-5
	0.8015	22	91	0	1e-4	0.8006	24	109	1	1e-4
	0.8015	25	97	4	1e-3	0.8006	27	118	6	1e-3
	0.8015	28	106	7	5e-3	0.8006	32	136	8	5e-3
	0.8015	27	100	8	1e-2	0.8006	31	128	8	1e-2
EC-SQP	0.8015	27	111	0	5e-5	0.8006	34	157	0	5e-5
	0.8015	25	112	0	1e-4	0.8006	29	143	0	1e-4
	0.8015	9	91	0	1e-3	0.8006	10	103	0	1e-3
	0.8015	2	86	0	5e-3	0.8005	2	77	1	5e-3
	0.8015	1	37	0	1e-2	0.8005	1	43	1	1e-2

Table 1: Plate with circular hole. Analysis report, $v_{Amax} = 5e-3$, $toll = 1e-4$, $desired = 6$, $max = 50$.

5 CONCLUSIONS

In this paper a new method for the incremental elastoplastic analysis of structures has been presented. The method is based on a SQP approximation of the finite element representation of the holonomic step equations that retains as primary variables, and at each iteration, all the variables of the problems. In the solution process, based on the equality constrained approach, the set of active constraints is obtained by solving a simple

quadratic programming problem which has the same structure and variables of a standard return mapping by closest point projection scheme, i.e. it is decoupled and it can be solved at a local level (finite element, Gauss point). The solution of the equality constraint problems is performed by means of a static condensation of the locally defined variables, that is stress and plastic multiplier parameters, for which the inter element continuity is not required so obtaining at the global level a nonlinear pseudo-compatible scheme of analysis that has the same structure as classic path following arc-length methods.

The numerical results are performed for plane stress/strain problems using both von Mises and Drucker-Pragher yield functions and adopting the finite element interpolation proposed in [4]. This finite element uses a three field interpolation and requires a multi-surface return mapping solution in the SD-CPP case, representing a good test for the robustness and efficiency of the incremental elastoplastic algorithm proposed here. A large number of numerical results performed for both single or multi–surface elastoplastic cases shows the great improvement in robustness and efficiency with respect to standard return mapping strain driven formulations.

The presentation and the application are limited to the perfect plasticity case but its extension to other more complex associated cases would be simple.

REFERENCES

[1] Peter W. Christensen, “A nonsmooth Newton method for elastoplastic problems ”, Computer Methods in Applied Mechanics and Engineering, 191, 1189 - 1219, 2002.

[2] K. Krabbenhoft and A.V. Lyamin and S.W. Sloan and P. Wriggers, “An interior-point algorithm for elastoplasticity”, Int. J. Num. Methods Engrg., 69, 592-626, 2007.

[3] Christina Oberlin and Stephen and J. Wright, “Active set identification in Nonlinear Programming”, SIAM Journal on Optimization, 17, 577-605, 2006.

[4] Bilotta, A. and Leonardo, L. and Garcea, G., “Three field finite elements for the elastoplastic analysis of 2D continua ”, Finite elements in analysis and design, in press, 2011.

[5] A. Bilotta and R. Casciaro, “A high performance element for the analysis of 2D elastoplastic continua”, Comput. Methods Appl. Mech. Engrg., 196, 818-828, 2007.

[6] D. Goldfarb and A. Idnani, “A numerically stable dual method for solving strictly convex quadratic programs”, Mathematical Programming, 27,1-33, 1983.

XI International Conference on Computational Plasticity. Fundamentals and Applications
COMPLAS XI
E. Oñate, D.R.J. Owen, D. Peric and B. Suárez (Eds)

AN EFFICIENT FETI BASED SOLVER FOR ELASTO-PLASTIC PROBLEMS OF MECHANICS

M. ČERMAK, T. KOZUBEK AND A. MARKOPOULOS

Department of Applied Mathematics
Faculty of Electrical Engineering and Computer Science
VSB-Technical University of Ostrava
Tr. 17. listopadu 15, CZ 708 33 Ostrava-Poruba, Czech Republic
e-mail: martin.cermak@vsb.cz, http://am.vsb.cz/

Key words: Computational Elasto-Plasticity, TFETI, Domain Decomposition, MatSol

Abstract. This paper illustrates how to implement effectively solvers for elasto-plastic problems. We consider the time step problems formulated by nonlinear variational equations in terms of displacements. To treat nonlinearity and nonsmoothnes we use semismooth Newton method. In each Newton iteration we have to solve linear system of algebraic equations and for the numerical solution of the linear systems we use TFETI algorithm. In our benchmark we compute von Misses plasticity with isotropic hardening and use return mapping concept.

1 INTRODUCTION

The goal of paper is to show how to implement effectively solvers for elasto-plastic problems. Such problems with hardening lead to quasi-static initial-boundary value problems, so the history of loading is taken into account. The problems are often solved by an incremental finite element method, see e.g [1]. For the time-discretisation we can use the explicit or implicit Euler methods or the return mapping concept. Each time-step problem may be formulated in different ways by variational equalities or inequalities described in terms of stress, plastic strain, hardening parameter, and displacements. In this paper, we consider the time-step problems formulated by nonlinear variational equations in terms of displacements. To treat nonlinearity and non-smoothness we use the semismooth Newton method introduced in [2] and used in [3] for elasto-plastic problems.

In each Newton iteration we have to solve an auxiliary (possibly of large size) linear system of algebraic equations. The key idea of our approach is to use for the numerical solution of the linear systems arising in each Newton step the FETI method with optimal convergence properties proposed by Farhat et al. [4] for parallel solution of linear problems. Using this approach, a body is partitioned into non-overlapping subdomains, an

elliptic problem with Neumann boundary conditions is defined for each subdomain, and intersubdomain field continuity is enforced via Lagrange multipliers. The Lagrange multipliers are evaluated by solving a relatively well conditioned dual problem of small size that may be efficiently solved by a suitable variant of the conjugate gradient algorithm. The first practical implementations exploited only the favorable distribution of the spectrum of the matrix of the smaller problem, known also as the dual Schur complement matrix, but such algorithm was efficient only with a small number of subdomains. Later, Farhat, Mandel, and Roux introduced a "natural coarse problem" whose solution was implemented by auxiliary projectors so that the resulting algorithm became in a sense optimal [4]. In our approach, we use the Total-FETI [5] variant of FETI domain decomposition method, where also the Dirichlet boundary conditions are enforced by Lagrange multipliers. Hence all subdomain stiffness matrices are singular with a-priori known kernels which is a great advantage in the numerical solution and also in the theory.

The paper is organized as follows. After introducing a model problem, we briefly review the TFETI methodology that transforms the large primal problem in terms of displacements into the smaller and better conditioned dual one in terms of the Lagrange multipliers whose conditioning is further improved by using the projectors defined by the natural coarse grid. Then we introduce a modification of the conjugate gradient algorithm for the solution of the resulting quadratic programming problem with equality constraints enforced by the orthogonal projector onto the subspace defined by the constraints. Futher we briefly review the elasto-plasticity methodology for von Mises plasticity with isotropic hardening. We illustrate the efficiency of our algorithm on the solution of 3D elasto-plastic model benchmark and give encouraging results of numerical experiments.

2 PROBLEM OF ELASTOSTATICS

Let us consider an isotropic elastic body represented in a reference configuration by a domain Ω in $\mathbb{R}^d, d = 2, 3$, with the sufficiently smooth boundary Γ as in Fig. 1. Suppose that Γ consists of two disjoint parts Γ_U and Γ_F, $\Gamma = \overline{\Gamma}_U \cup \overline{\Gamma}_F$, and that the displacements $\mathbf{U} : \Gamma_U \to \mathbb{R}^d$ and forces $\mathbf{F} : \Gamma_F \to \mathbb{R}^d$ are given. The mechanical properties of Ω are defined by the Young modulus E and the Poisson ratio ν.

Let $c_{ijk\ell} : \Omega \to \mathbb{R}^d$ and $\mathbf{g} : \Omega \to \mathbb{R}^d$ denote the entries of the elasticity tensor and a vector of body forces, respectively. For any sufficiently smooth displacement $\mathbf{u} : \overline{\Omega} \to \mathbb{R}^d$, the total potential energy is defined by

$$J(\mathbf{u}) = \frac{1}{2}a(\mathbf{u}, \mathbf{u}) - \int_\Omega \mathbf{g}^\top \mathbf{u} \, d\Omega - \int_{\Gamma_F} \mathbf{F}^\top \mathbf{u} \, d\Gamma, \tag{1}$$

where

$$a(\mathbf{u}, \mathbf{v}) = \int_\Omega c_{ijk\ell} e_{ij}(\mathbf{u}) e_{k\ell}(\mathbf{v}) d\Omega, \quad e_{k\ell}(\mathbf{u}) = \frac{1}{2}\left(\frac{\partial u_k}{\partial x_\ell} + \frac{\partial u_\ell}{\partial x_k}\right).$$

We suppose that the elasticity tensor satisfies natural physical restrictions so that

$$a(\mathbf{u}, \mathbf{v}) = a(\mathbf{v}, \mathbf{u}) \quad \text{and} \quad a(\mathbf{u}, \mathbf{u}) \geq 0. \tag{2}$$

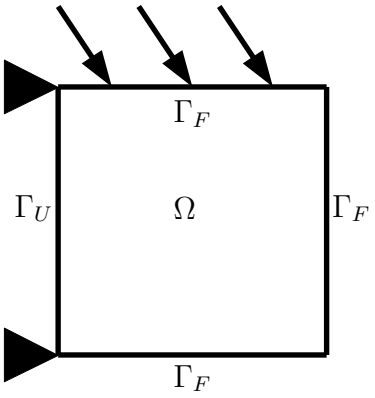

Figure 1: Model problem

Now let us introduce the Sobolev space $V = H^1(\Omega)^d$ and let K denote the set of all kinematically admissible displacements, where $K = \{\mathbf{v} \in V : \ \mathbf{v} = \mathbf{U} \ \text{ on } \ \Gamma_U\}$. The displacement $\mathbf{u} \in K$ of body in equilibrium satisfies

$$J(\mathbf{u}) \leq J(\mathbf{v}) \ \text{ for any } \ \mathbf{v} \in K. \tag{3}$$

Conditions that guarantee existence and uniqueness may be expressed in terms of coercivity of J. More general boundary conditions, such as prescribed normal displacements and periodicity, may be considered without any conceptual difficulties.

3 TFETI DOMAIN DECOMPOSITION

To apply the TFETI domain decomposition, we tear body from the part of the boundary with the Dirichlet boundary condition, decompose body into subdomains, assign each subdomain a unique number, and introduce new "gluing" conditions on the artificial intersubdomain boundaries and on the boundaries with imposed Dirichlet condition.

More specifically, the body Ω is decomposed into a system of s homogeneous isotropic elastic subdomains, each of which occupies, in a reference configuration, a subdomain Ω^p in $\mathbb{R}^d, d = 2, 3$. After decomposition each boundary Γ^p of Ω^p consists of three disjoint parts Γ^p_U, Γ^p_F, and Γ^p_G, $\Gamma^p = \overline{\Gamma}^p_U \cup \overline{\Gamma}^p_F \cup \overline{\Gamma}^p_G$, with the corresponding displacements $\mathbf{U}^p$ and forces $\mathbf{F}^p$ inherited from the originally imposed boundary conditions on Γ. For the artificial intersubdomain boundaries, we use the following notation: Γ^{pq}_G denotes the part of Γ^p that is glued to Ω^q and Γ^p_G denotes the part of Γ^p that is glued to the other subdomains. Obviously $\Gamma^{pq}_G = \Gamma^{qp}_G$. An auxiliary decomposition of the problem of Fig. 1 with renumbered subdomains and artificial intersubdomain boundaries is in Fig. 2. The gluing conditions require continuity of the displacements and of their normal derivatives across the intersubdomain boundaries. The mechanical properties of Ω^p are defined by the Young modulus E^p and the Poisson ratio ν^p.

Let $c^p_{ijk\ell}$ and $\mathbf{g}^p$ denote again the entries of the elasticity tensor and a vector of body forces, respectively. For any sufficiently smooth displacement $\mathbf{u} : \overline{\Omega}^1 \times \ldots \times \overline{\Omega}^s \to \mathbb{R}^d$, the

total potential energy is defined by

$$\mathcal{J}(\mathbf{u}) = \sum_{p=1}^{s} \left\{ \frac{1}{2} a^p(\mathbf{u}^p, \mathbf{u}^p) - \int_{\Omega^p} (\mathbf{g}^p)^\top \mathbf{u}^p d\Omega - \int_{\Gamma_F^p} (\mathbf{F}^p)^\top \mathbf{u}^p d\Gamma \right\}, \tag{4}$$

where

$$a^p(\mathbf{u}^p, \mathbf{v}^p) = \int_{\Omega^p} c_{ijk\ell}^p e_{ij}^p(\mathbf{u}^p) e_{k\ell}^p(\mathbf{v}^p) d\Omega, \qquad e_{k\ell}^p(\mathbf{u}^p) = \frac{1}{2}\left(\frac{\partial u_k^p}{\partial x_\ell^p} + \frac{\partial u_\ell^p}{\partial x_k^p} \right).$$

We suppose that the bilinear forms a^p satisfy (2) and let us introduce the product Sobolev space $\mathcal{V} = H^1(\Omega^1)^d \times \ldots \times H^1(\Omega^s)^d$, and let $\mathcal{K}$ denote the set of all kinematically admissible displacements, where $\mathcal{K} = \{\mathbf{v} \in \mathcal{V} : \ \mathbf{v}^p = \mathbf{U}^p \ \text{ on } \ \Gamma_U^p, \ \ \mathbf{v}^p = \mathbf{v}_{|\overline{\Omega}^p}\}$. The displacement $\mathbf{u} \in \mathcal{K}$ of the system of subdomains in equilibrium satisfies

$$\mathcal{J}(\mathbf{u}) \leq \mathcal{J}(\mathbf{v}) \ \text{ for any } \ \mathbf{v} \in \mathcal{K}. \tag{5}$$

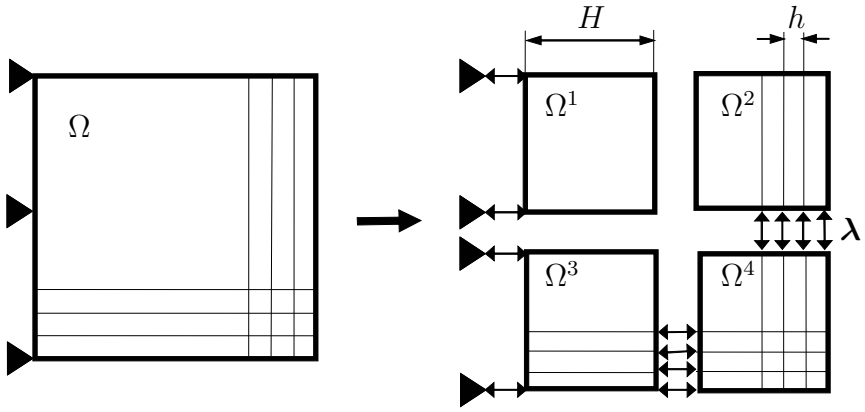

Figure 2: TFETI domain decomposition with subdomain renumbering

The finite element discretization of $\overline{\Omega} = \overline{\Omega}^1 \cup \ldots \cup \overline{\Omega}^s$ with a suitable numbering of nodes results in the quadratic programming (QP) problem

$$\frac{1}{2}\mathbf{u}^\top \mathbf{K}\mathbf{u} - \mathbf{f}^\top \mathbf{u} \to \min \ \ \text{subject to} \ \ \mathbf{B}\mathbf{u} = \mathbf{c}, \tag{6}$$

where $\mathbf{K} = \operatorname{diag}(\mathbf{K}_1, \ldots, \mathbf{K}_s)$ denotes a symmetric positive semidefinite block-diagonal matrix of order n, $\mathbf{B}$ denotes an $m \times n$ full rank matrix, $\mathbf{f} \in \mathbb{R}^n$, and $\mathbf{c} \in \mathbb{R}^m$.

The diagonal blocks $\mathbf{K}_p$ that correspond to the subdomains Ω^p are positive semidefinite sparse matrices with known kernels, the rigid body modes. The blocks can be effectively decomposed using the Choleski factorization [6]. The vector $\mathbf{f}$ describes the nodal forces arising from the volume forces and/or some other imposed traction.

The matrix $\mathbf{B}$ with the rows $\mathbf{b}_i$ and the vector $\mathbf{c}$ with the entries c_i enforce the prescribed displacements on the part of the boundary with imposed Dirichlet condition and the continuity of the displacements across the auxiliary interfaces. The continuity requires that $\mathbf{b}_i\mathbf{u} = c_i = 0$, where $\mathbf{b}_i$ are vectors of the order n with zero entries except 1 and -1 at appropriate positions. Typically m is much smaller than n.

Even though (6) is a standard convex quadratic programming problem, its formulation is not suitable for numerical solution. The reasons are that $\mathbf{K}$ is typically ill-conditioned, singular, and very large.

The complications mentioned above may be essentially reduced by applying the duality theory of convex programming (see, e.g., Dostál [7]), where all the constraints are enforced by the Lagrange multipliers $\boldsymbol{\lambda}$. The Lagrangian associated with problem (6) is

$$L(\mathbf{u}, \boldsymbol{\lambda}) = \frac{1}{2}\mathbf{u}^\top \mathbf{K}\mathbf{u} - \mathbf{f}^\top \mathbf{u} + \boldsymbol{\lambda}^\top(\mathbf{B}\mathbf{u} - \mathbf{c}). \tag{7}$$

It is well known [7] that (6) is equivalent to the saddle point problem

$$L(\overline{\mathbf{u}}, \overline{\boldsymbol{\lambda}}) = \sup_{\boldsymbol{\lambda}} \inf_{\mathbf{u}} L(\mathbf{u}, \boldsymbol{\lambda}). \tag{8}$$

4 OPTIMAL SOLVERS TO EQUALITY CONSTRAINED PROBLEMS

The solution of (8) leads to equivalent problem to find $(\bar{\mathbf{u}}, \bar{\boldsymbol{\lambda}}) \in \mathbb{R}^n \times \mathbb{R}^m$ satisfying:

$$\mathcal{A}\begin{pmatrix} \mathbf{u} \\ \boldsymbol{\lambda} \end{pmatrix} = \begin{pmatrix} \mathbf{f} \\ \mathbf{c} \end{pmatrix} \tag{9}$$

with the saddle-point matrix

$$\mathcal{A} := \begin{pmatrix} \mathbf{K} & \mathbf{B}^\top \\ \mathbf{B} & \mathbf{0} \end{pmatrix}.$$

We suppose that (9) is uniquely solvable which is guaranteed by the following necessary and sufficient conditions [8]:

$$Ker\mathbf{B}^\top = \{0\}, \tag{10}$$

$$Ker\mathbf{K} \cap Ker\mathbf{B} = \{0\}. \tag{11}$$

Notice that (10) is the condition on the full row-rank of $\mathbf{B}$. Let us mention that an orthonormal basis of $Ker\mathbf{K}$ is known à-priori and that its vectors are columns of $\mathbf{R} \in \mathbb{R}^{n\times l}$, $l = n - rank(\mathbf{K})$.

The first equation in (9) is satisfied iff

$$\mathbf{f} - \mathbf{B}^\top \bar{\boldsymbol{\lambda}} \in Im\mathbf{K} \tag{12}$$

and

$$\bar{\mathbf{u}} = \mathbf{K}^\dagger(\mathbf{f} - \mathbf{B}^\top \bar{\boldsymbol{\lambda}}) + \mathbf{R}\bar{\boldsymbol{\alpha}} \tag{13}$$

for an appropriate $\bar{\boldsymbol{\alpha}} \in \mathbb{R}^l$ and arbitrary generalized inverse $\mathbf{K}^\dagger$ satisfying $\mathbf{K}\mathbf{K}^\dagger\mathbf{K} = \mathbf{K}$. Moreover, (12) can be equivalently written as

$$\mathbf{R}^\top(\mathbf{f} - \mathbf{B}^\top\bar{\boldsymbol{\lambda}}) = 0. \tag{14}$$

Further substituting (13) into the second equation in (9) we arrive at

$$-\mathbf{B}\mathbf{K}^\dagger\mathbf{B}^\top\bar{\boldsymbol{\lambda}} + \mathbf{B}\mathbf{R}\bar{\boldsymbol{\alpha}} = \mathbf{c} - \mathbf{B}\mathbf{K}^\dagger\mathbf{f}. \tag{15}$$

Summarizing (15) and (14) we find that the pair $(\bar{\boldsymbol{\lambda}}, \bar{\boldsymbol{\alpha}}) \in \mathbb{R}^m \times \mathbb{R}^l$ satisfies:

$$\mathcal{S}\begin{pmatrix} \boldsymbol{\lambda} \\ \boldsymbol{\alpha} \end{pmatrix} = \begin{pmatrix} \mathbf{d} \\ \mathbf{e} \end{pmatrix}, \tag{16}$$

where

$$\mathcal{S} := \begin{pmatrix} \mathbf{B}\mathbf{K}^\dagger\mathbf{B}^\top & -\mathbf{B}\mathbf{R} \\ -\mathbf{R}^\top\mathbf{B}^\top & \mathbf{0} \end{pmatrix}$$

is the (negative) *Schur complement* of $\mathbf{K}$ in $\mathcal{A}$, $\mathbf{d} := \mathbf{B}\mathbf{K}^\dagger\mathbf{f} - \mathbf{c}$, and $\mathbf{e} := -\mathbf{R}^\top\mathbf{f}$. As both $\mathcal{S}$ and $\mathcal{A}$ are simultaneously invertible [8], we can compute first $(\bar{\boldsymbol{\lambda}}, \bar{\boldsymbol{\alpha}})$ by solving (16) and then we obtain $\bar{\mathbf{u}}$ from (13). Let us note that (16) has formally the same saddle-point structure as that of (9), however, its size is considerably smaller.

Before discussing the solution method for (16) we introduce new notation

$$\mathbf{F} := \mathbf{B}\mathbf{K}^\dagger\mathbf{B}^\top, \quad \mathbf{G} := -\mathbf{R}^\top\mathbf{B}^\top$$

which changes (16) into

$$\begin{pmatrix} \mathbf{F} & \mathbf{G}^\top \\ \mathbf{G} & \mathbf{0} \end{pmatrix}\begin{pmatrix} \boldsymbol{\lambda} \\ \boldsymbol{\alpha} \end{pmatrix} = \begin{pmatrix} \mathbf{d} \\ \mathbf{e} \end{pmatrix}. \tag{17}$$

Now we shall split (17) using the orthogonal projector $\mathbf{P}_\mathbf{G}$ onto $Ker\,\mathbf{G}$. As (11) implies that $\mathbf{G}$ is of full row-rank, we can identify $\mathbf{P}_\mathbf{G}$ with the following matrix:

$$\mathbf{P}_\mathbf{G} := \mathbf{I} - \mathbf{G}^\top(\mathbf{G}\mathbf{G}^\top)^{-1}\mathbf{G}.$$

Applying $\mathbf{P}_\mathbf{G}$ on the first equation in (17) we obtain that $\bar{\boldsymbol{\lambda}}$ satisfies:

$$\mathbf{P}_\mathbf{G}\mathbf{F}\boldsymbol{\lambda} = \mathbf{P}_\mathbf{G}\mathbf{d}, \quad \mathbf{G}\boldsymbol{\lambda} = \mathbf{e}. \tag{18}$$

In order to arrange (18) as one equation on the vector space $Ker\,\mathbf{G}$ we decompose the solution $\bar{\boldsymbol{\lambda}}$ into $\bar{\boldsymbol{\lambda}}_{Im} \in Im\,\mathbf{G}^\top$ and $\bar{\boldsymbol{\lambda}}_{Ker} \in Ker\,\mathbf{G}$ as

$$\bar{\boldsymbol{\lambda}} = \bar{\boldsymbol{\lambda}}_{Im} + \bar{\boldsymbol{\lambda}}_{Ker}. \tag{19}$$

Since $\bar{\boldsymbol{\lambda}}_{Im}$ is easily available via

$$\bar{\boldsymbol{\lambda}}_{Im} = \mathbf{G}^\top(\mathbf{G}\mathbf{G}^\top)^{-1}\mathbf{e},$$

it remains to show how to get $\bar{\boldsymbol{\lambda}}_{Ker}$. Substituting (19) into (18) we can see that $\bar{\boldsymbol{\lambda}}_{Ker}$ satisfies:

$$\mathbf{P_G F}\lambda_{Ker} = \mathbf{P_G}(\mathbf{d} - \mathbf{F}\bar{\boldsymbol{\lambda}}_{Im}), \quad \boldsymbol{\lambda}_{Ker} \in Ker\mathbf{G}. \tag{20}$$

Let us note that this equation is uniquely solvable, as $\mathbf{P_G F} : Ker\mathbf{G} \mapsto Ker\mathbf{G}$ is invertible if $\mathcal{A}$ is invertible [8]. Finally note that, if $\bar{\boldsymbol{\lambda}}$ is known, the solution component $\bar{\boldsymbol{\alpha}}$ is given by

$$\bar{\boldsymbol{\alpha}} = (\mathbf{G}\mathbf{G}^\top)^{-1}\mathbf{G}(\mathbf{d} - \mathbf{F}\bar{\boldsymbol{\lambda}}). \tag{21}$$

Let us algorithmically summarize the previous results. It turns out to be reasonable to form and store the $l \times m$ matrix $\mathbf{G}$ and the $l \times l$ matrix $\mathbf{H} := (\mathbf{G}\mathbf{G}^\top)^{-1}$ because l is usually small (the Cholesky factor of $\mathbf{G}\mathbf{G}^\top$ may be used instead of $\mathbf{H}$). On the other hand, the $m \times m$ matrices $\mathbf{F}$ and $\mathbf{P_G}$ are not assembled explicitly, since only their matrix-vector products are needed. Finally note that the actions of $\mathbf{B}$ are inexpensive in our problems due to sparsity of $\mathbf{B}$ and the actions of $\mathbf{K}^\dagger$ are computed effectively by the Cholesky factorization of $\mathbf{K}^p$, $p = 1, ..., s$ ([6]). All the above steps are summarized in the following algorithmic scheme.

Algorithmic scheme

Step 1.a: Compute $\mathbf{G} := -\mathbf{R}^\top\mathbf{B}^\top$, $\mathbf{H} := (\mathbf{G}\mathbf{G}^\top)^{-1}$, $\mathbf{d} := \mathbf{B}\mathbf{K}^\dagger\mathbf{f} - \mathbf{c}$, and $\mathbf{e} := -\mathbf{R}^\top\mathbf{f}$.
Step 1.b: Compute $\bar{\boldsymbol{\lambda}}_{Im} := \mathbf{G}^\top\mathbf{H}\mathbf{e}$.
Step 1.c: Compute $\tilde{\mathbf{d}} := \mathbf{d} - \mathbf{F}\bar{\boldsymbol{\lambda}}_{Im}$.
Step 1.d: Compute $\bar{\boldsymbol{\lambda}}_{Ker}$ by solving $\mathbf{P_G F}\boldsymbol{\lambda}_{Ker} = \mathbf{P_G}\tilde{\mathbf{d}}$ on $Ker\mathbf{G}$.
Step 1.e: Compute $\bar{\boldsymbol{\lambda}} := \bar{\boldsymbol{\lambda}}_{Im} + \bar{\boldsymbol{\lambda}}_{Ker}$.
Step 2: Compute $\bar{\boldsymbol{\alpha}} := \mathbf{H}\mathbf{G}(\mathbf{d} - \mathbf{F}\bar{\boldsymbol{\lambda}})$.
Step 3: Compute $\bar{\mathbf{u}} := \mathbf{K}^\dagger(\mathbf{f} - \mathbf{B}^\top\bar{\boldsymbol{\lambda}}) + \mathbf{R}\bar{\boldsymbol{\alpha}}$.

Finally, we introduce the projected conjugate gradient method with preconditioning (ProjCGM) [4] that we use for computing $\bar{\boldsymbol{\lambda}}_{Ker}$ in Step 1.d of Algorithmic scheme. Thus we want to compute $\bar{\boldsymbol{\lambda}}_{Ker}$ by solving the system $\mathbf{P_G F}\boldsymbol{\lambda}_{Ker} = \mathbf{P_G}\tilde{\mathbf{d}}$ on $Ker\mathbf{G}$ with the lumped preconditioner $\overline{\mathbf{F}^{-1}}$ [4] to $\mathbf{F}$.

Algorithm ProjCGM

1. Initialize
   $\mathbf{r}^0 = \tilde{\mathbf{d}}$, $\boldsymbol{\lambda}^0_{Ker} = \mathbf{o}$.
2. Iterate k =1, 2, ..., until convergence
   Project $\mathbf{w}^{k-1} = \mathbf{P_G}\mathbf{r}^{k-1}$.
   Precondition $\mathbf{z}^{k-1} = \overline{\mathbf{F}^{-1}}\mathbf{w}^{k-1}$.
   Project $\mathbf{y}^{k-1} = \mathbf{P_G}\mathbf{z}^{k-1}$.

$\boldsymbol{\beta}^k = (\mathbf{y}^{k-1})^\top \mathbf{w}^{k-1} / (\mathbf{y}^{k-2})^\top \mathbf{w}^{k-2}; \qquad (\boldsymbol{\beta}^1 = 0).$
$\mathbf{p}^k = \mathbf{y}^{k-1} + \boldsymbol{\beta}^k \mathbf{p}^{k-1}; \qquad (\mathbf{p}^1 = \mathbf{y}^0).$
$\boldsymbol{\alpha}^k = (\mathbf{y}^{k-1})^\top \mathbf{w}^{k-1} / (\mathbf{p}^k)^\top \mathbf{F}\mathbf{p}_k.$
$\boldsymbol{\lambda}_{Ker}^k = \boldsymbol{\lambda}_{Ker}^{k-1} + \boldsymbol{\alpha}^k \mathbf{p}^k.$
$\mathbf{r}^k = \mathbf{r}^{k-1} - \boldsymbol{\alpha}^k \mathbf{F}\mathbf{p}_k.$

3. $\bar{\boldsymbol{\lambda}}_{Ker} = \boldsymbol{\lambda}_{Ker}^k.$

Using TFETI in combination with ProjCGM algorithm we are able to find the solution of the original elasto-plastic problem in O(1) matrix-vector multiplications independently of the problem size provided the ratio between the decomposition step H and the discretization step h is kept bounded. For more details about optimality see [4].

5 ELASTO-PLASTICITY

Elasto-plastic problems are the so-called quasi-static problems where the history of loading is taken into account. We consider the von Mises elasto-plasticity with the strain isotropic hardening and incremental finite element method with the return mapping concept [1].

The elasto-plastic deformation of an body Ω after loading is descibed by the Cauchy stress tensor $\boldsymbol{\sigma}$, the small strain tensor $\boldsymbol{\varepsilon}$, the displacement $\mathbf{u}$, and the nonnegative hardening parameter $\boldsymbol{\kappa}$. Symmetric tensor is represented by the vector and its deviatoric part is denoted by the symbol *dev*.

Let us denote the space of continuous and piecewise linear functions constructed over a regular triangulation of Ω with the discretization norm h by $V_h \subset V$, where $V = \left\{\mathbf{v} \in H^1(\Omega)^d : \quad \mathbf{v} = 0 \text{ on } \Gamma_U\right\}$. Let

$$0 = t_0 < t_1 < \ldots t_k < \ldots < t_N = t^* \tag{22}$$

be a partition of the time interval $[0, t^*]$. Then the solution algorithm after time and space discretizations has the form:

Algorithm 3.

1. Initial step: $\mathbf{u}_h^0 = 0,\ \boldsymbol{\sigma}_h^0 = 0,\ \boldsymbol{\kappa}_h^0 = 0,$
2. **for** $k = 0,\ \ldots, N-1$ **do** (load step)
3. From previous step we know: $\mathbf{u}_h^k,\ \boldsymbol{\sigma}_h^k,\ \boldsymbol{\kappa}_h^k$ and compute $\triangle\mathbf{u}_h,\ \triangle\boldsymbol{\sigma}_h,\ \triangle\boldsymbol{\kappa}_h$

$$\triangle\boldsymbol{\varepsilon}_h = \varepsilon(\triangle\mathbf{u}_h), \quad \triangle\mathbf{u}_h \in V_h, \tag{23}$$

$$\triangle\boldsymbol{\sigma}_h = T_\sigma(\boldsymbol{\sigma}_h^k,\ \boldsymbol{\kappa}_h^k,\ \triangle\boldsymbol{\varepsilon}_h), \tag{24}$$

$$\triangle\boldsymbol{\kappa}_h = T_\kappa(\boldsymbol{\sigma}_h^k,\ \boldsymbol{\kappa}_h^k,\ \triangle\boldsymbol{\varepsilon}_h). \tag{25}$$

4. Solution $\triangle\boldsymbol{\sigma}_h(\boldsymbol{\sigma}_h^k,\ \boldsymbol{\kappa}_h^k, \varepsilon(\triangle\mathbf{u}_h))$ is substituted into equation of equilibrium:

$$\int_\Omega \triangle\boldsymbol{\sigma}_h^T(\boldsymbol{\sigma}_h^k,\ \boldsymbol{\kappa}_h^k, \varepsilon(\triangle\mathbf{u}_h))\varepsilon(\mathbf{v}_h)dx = \langle\triangle\mathbf{f}_h^k,\ \mathbf{v}_h\rangle, \quad \forall\mathbf{v}_h \in V_h. \tag{26}$$

This leads to a nonlinear system of equations with unknown $\triangle\mathbf{u}_h$ which is solved using the Newton method. The linearized problem arising in each Newton step is solved by TFETI algorithmic scheme proposed above.

5. Then we compute values for the next step: $\mathbf{u}_h^{k+1} = \mathbf{u}_h^k + \triangle\mathbf{u}_h$, $\boldsymbol{\sigma}_h^{k+1} = \boldsymbol{\sigma}_h^k + \triangle\boldsymbol{\sigma}_h$, $\boldsymbol{\kappa}_h^{k+1} = \boldsymbol{\kappa}_h^k + \triangle\boldsymbol{\kappa}_h$.

6. **enddo**

Above we consider the following notation. Let $\mathbf{C}$ denote the Hook's matrix, $\mathbf{E}$ represent linear operator *dev*, μ, λ be the Lamé coefficients, $\triangle\mathbf{f}_h^k$ be the increment of the right hand side and $\boldsymbol{\sigma}_h^t = \boldsymbol{\sigma}_h^k + \mathbf{C}\triangle\boldsymbol{\varepsilon}_h$. For return mapping concept we define

$$\begin{aligned} \triangle\boldsymbol{\sigma}_h &= T_\sigma(\boldsymbol{\sigma}_h^k, \boldsymbol{\kappa}_h^k, \triangle\boldsymbol{\varepsilon}_h) = T_\sigma^{RM}(\boldsymbol{\sigma}_h^k, \boldsymbol{\kappa}_h^k, \triangle\boldsymbol{\varepsilon}_h) = \\ &= \begin{cases} \mathbf{C}\triangle\boldsymbol{\varepsilon}_h & \text{if } P(\boldsymbol{\sigma}_h^t, \boldsymbol{\kappa}_h^k) \le 0, \\ \mathbf{C}\triangle\boldsymbol{\varepsilon}_h - \gamma_R\widehat{\mathbf{n}} & \text{if } P(\boldsymbol{\sigma}_h^t, \boldsymbol{\kappa}_h^k) > 0, \end{cases} \end{aligned} \tag{27}$$

$$\begin{aligned} \triangle\boldsymbol{\kappa}_h &= T_\kappa(\boldsymbol{\sigma}_h^k, \boldsymbol{\kappa}_h^k, \triangle\boldsymbol{\varepsilon}_h) = T_\kappa^{RM}(\boldsymbol{\sigma}_h^k, \boldsymbol{\kappa}_h^k, \triangle\boldsymbol{\varepsilon}_h) = \\ &= \begin{cases} 0 & \text{if } P(\boldsymbol{\sigma}_h^t, \boldsymbol{\kappa}_h^k) \le 0, \\ \gamma z = \gamma_R\|\mathbf{Cp}\|^{-1}z & \text{if } P(\boldsymbol{\sigma}_h^t, \boldsymbol{\kappa}_h^k) > 0, \end{cases} \end{aligned} \tag{28}$$

where

$$\begin{aligned} \gamma_R &= \tfrac{3\mu}{3\mu+H_m}\sqrt{\tfrac{2}{3}}\left(\sqrt{\tfrac{3}{2}}\|dev(\boldsymbol{\sigma}_h^t)\| - (Y_0 + H_m\boldsymbol{\kappa}_h^k)\right) = \\ &= \tfrac{3\mu}{3\mu+H_m}\sqrt{\tfrac{2}{3}}P(\boldsymbol{\sigma}_h^t, \boldsymbol{\kappa}_h^k), \end{aligned} \tag{29}$$

$$\widehat{\mathbf{n}} = \frac{dev(\boldsymbol{\sigma}_h^t)}{\|dev(\boldsymbol{\sigma}_h^t)\|}, \quad \|\mathbf{Cp}\| = 2\mu\sqrt{\frac{3}{2}}, \quad z = 1, \tag{30}$$

and plasticity function

$$P(\boldsymbol{\sigma}_h^t, \boldsymbol{\kappa}_h^k) = \sqrt{\frac{3}{2}}\|dev(\boldsymbol{\sigma}_h^t)\| - (Y + H_m\boldsymbol{\kappa}_h^k), \qquad Y, H_m > 0. \tag{31}$$

The function $\gamma_R\widehat{\mathbf{n}}$ is semismooth and potential. The derivative of T_σ^{RM} is

$$\begin{aligned} (T_\sigma^{RM})'(\triangle\boldsymbol{\varepsilon}) &= \mathbf{C} - 2\mu\tfrac{3\mu}{3\mu+H_m}\left[\mathbf{E} + \right. \\ &+ \left. \sqrt{\tfrac{2}{3}}\tfrac{Y_0+H_m\boldsymbol{\kappa}_h^k}{\|dev(\boldsymbol{\sigma}_h^k+\mathbf{C}\triangle\boldsymbol{\varepsilon})\|}\left(\tfrac{dev(\boldsymbol{\sigma}_h^k+\mathbf{C}\triangle\boldsymbol{\varepsilon})(dev(\boldsymbol{\sigma}_h^k+\mathbf{C}\triangle\boldsymbol{\varepsilon}))^T}{\|dev(\boldsymbol{\sigma}_h^k+\mathbf{C}\triangle\boldsymbol{\varepsilon})\|^2} - \mathbf{E}\right)\right]. \end{aligned} \tag{32}$$

If we represent a function $\mathbf{v}_h \in V_h$ by the vector $\mathbf{v} \in \mathbb{R}^n$ and omit index k then (26) can be rewritten as the system of nonlinear equations

$$F(\triangle \mathbf{u}) = \triangle \mathbf{f}, \tag{33}$$

where

$$\begin{array}{rcll} \langle F(\mathbf{v}), \mathbf{w} \rangle & = & \int_\Omega \langle T_\sigma^{RM}(\varepsilon(\mathbf{v}_h)), \varepsilon(\mathbf{w}_h) \rangle dx, & \forall \mathbf{v}, \mathbf{w} \in \mathbb{R}^n \\ \langle \triangle \mathbf{f}, \mathbf{w} \rangle & = & \triangle \mathbf{f}_h(v_h), \quad \forall \mathbf{w} \in \mathbb{R}^n. & \end{array} \tag{34}$$

6 NUMERICAL EXPERIMENTS

Described algorithms were implemented in `MatSol` library [9] developed in Matlab environment and tested on solution of 3D problems.

Let us consider a 3D plate with a hole in the center (due to symmetry only a quatre of the whole structure is used) with the geometry depicted in Fig. 3. Boundary conditions are specified in Fig. 4. Symmetry conditions are prescribed on the left and lower sides of Ω. The surface load $g(t) = 450 \sin(2\pi t)$ [MPa], $t \in [0, \frac{1}{4}]$ [sec], is applied to the upper side of Ω. The elasto-plastic material parameters are $E = 206900$ [MPa], $\nu = 0.29$, $Y = 450$, $H_m = 100$ and the time interval $[0, \frac{1}{4}]$ [sec] is divided into 50 steps. We consider a mesh with 5489 nodes and 19008 tetrahedrons. The body Ω is decomposed into 20 subdomains.

In the nth Newton iteration we compute an approximation $\triangle \mathbf{u}^n$ by solving the constrained linear problem of the form

$$\min_{\mathbf{B}\triangle \mathbf{u}^n = \mathbf{o}} \frac{1}{2} (\triangle \mathbf{u}^n)^\top \mathbf{K}^n \triangle \mathbf{u}^n - (\triangle \mathbf{u}^n)^\top \triangle \mathbf{f}^n$$

using the TFETI algorithmic scheme proposed above. We stop the Newton method in every time step if $\|\triangle \mathbf{u}^{n+1} - \triangle \mathbf{u}^n\| / \left(\|\triangle \mathbf{u}^{n+1}\| + \|\triangle \mathbf{u}^n\|\right)$ is less than 10^{-6}.

Notice that the maximum number of the Newton iterations is small for all time steps (less than 7), therefore the method is suitable for the problem. In the following figures, we depict plastic and elastic elements, graph of maximum value of hardenining at each time step and von Mises stress in the xy plane cross-section with the z coordinate 0 [mm] corresponding to the surface of Ω. In Figs. 5, 6, we see which elements are plastic (gray color) and which are elastic (white color) in chosen time steps. Particularly, in time steps 1-12 we observe only elastic behavior, and in time steps 13-50 plastic behavior of some elements. The maximum value of hardenining at each time step is depicted in Fig. 7. The von Mises stress distribution on deformed mesh is showed in Fig. 8.

7 CONCLUSIONS AND GOALS

We have presented an efficient algorithm for the numerical solution of elasto-plastic problems. These problems lead to the quasi-static problems, where each nonlinear and nonsmooth time step problem is solved by the semismooth Newton method. In each Newton iteration we solve an auxiliary (possibly of large size) linear system of algebraic

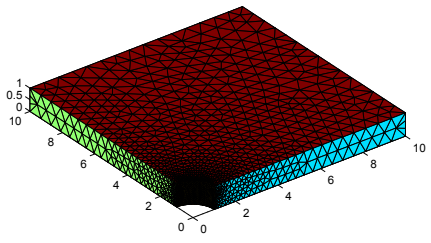

Figure 3: 3D plate geometry in [mm]

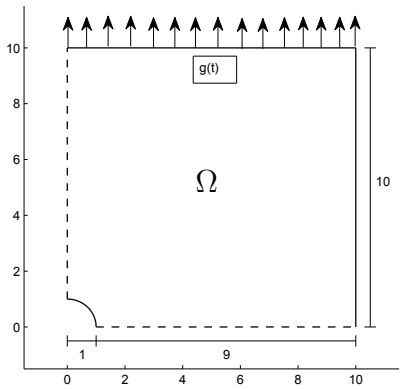

Figure 4: 2D plate geometry in [mm] and boundary conditions

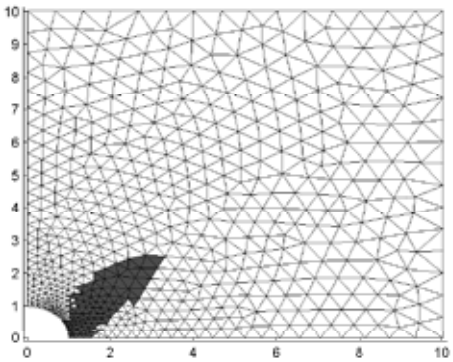

Figure 5: Plastic and elastic elements after 35 time steps

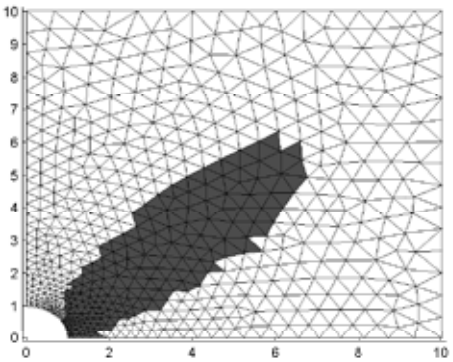

Figure 6: Plastic and elastic elements after 50 time steps

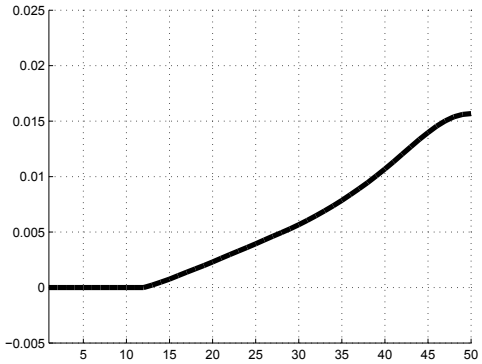

Figure 7: Maximum values of hardening in time iterations

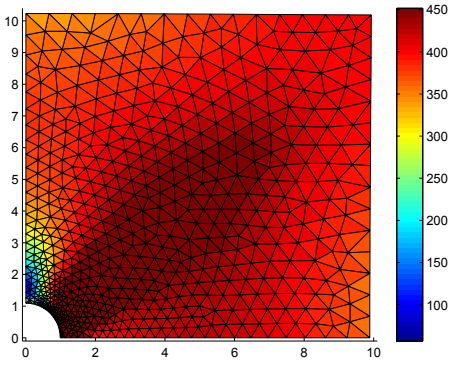

Figure 8: Von Mises stress distribution on the deformed mesh (scaled 10x)

equations using in a sense optimal algorithm based on our Total-FETI variant of FETI domain decomposition method. We illustrated the efficiency of our algorithm on the solution of 3D elasto-plastic model benchmark and gave results of numerical experiments. The results indicate that the algorithm may be efficient. In the future we would like to adapt this approach to the solution of contact problems.

REFERENCES

[1] Blaheta, R. *Numerical methods in elasto-plasticity*, Documenta Geonica 1998, PERES Publishers, Prague, (1999).

[2] Gruber, P. G. and Valdman, J. *Solution of One-Time Step Problems in Elastoplasticity by a Slant Newton Method*, SIAM J. Sci. Comp. **31** (2009) 1558-1580.

[3] Qi, L. and Sun, J. *A nonsmooth version of Newtons method*, Mathematical Programming **58** (1993) 353-367.

[4] Farhat, C., Mandel, J. and Roux, F-X. *Optimal convergence properties of the FETI domain decomposition method*, Comput. Methods Appl. Mech. Eng. **115**, (1994); 365–385.

[5] Dostál, Z., Horák, D. and Kučera, R. *Total FETI - an easier implementable variant of the FETI method for numerical solution of elliptic PDE*, Communications in Numerical Methods in Engineering, 22(2006), 12, pp. 1155-1162

[6] Brzobohatý, T., Dostál, Z., Kovář, P., Kozubek, T. and Markopoulos, A. *Cholesky decomposition with fixing nodes to stable evaluation of a generalized inverse of the stiffness matrix of a floating structure*, IJNME, DOI: 10.1002/nme.3187

[7] Dostál, Z. *Optimal Quadratic Programming Algorithms, with Applications to Variational Inequalities*, 1st edition, SOIA 23, Springer US, New York, (2009)

[8] Haslinger, J., Kozubek, T., Kučera, R. and Peichl, G. *Projected Schur complement method for solving non-symmetric saddle-point systems arising from fictitious domain approach*, Numerical Linear Algebra with Applications (2007); **14**(9):713–739.

[9] Kozubek, T., Markopoulos, A., Brzobohatý, T., Kučera, R., Vondrák, V. and Dostál, Z. *MatSol - MATLAB efficient solvers for problems in engineering*, http://matsol.vsb.cz/.

[10] Dostl, Z., Kozubek, T., Markopoulos, A., Brzobohat, T., Vondrk, V., Horyl, P *.: Theoretically supported scalable TFETI algorithm for the solution of multibody 3D contact problems with fiction*, (2011) doi:10.1016/j.cma.2011.02.015

XI International Conference on Computational Plasticity. Fundamentals and Applications
COMPLAS XI
E. Oñate, D.R.J. Owen, D. Peric and B. Suárez (Eds)

AN IMPROVED ACCURACY ANALYSIS OF ELASTOPLASTIC INTEGRATION ALGORITHMS

FOTIOS E. KARAOULANIS*

*Department of Civil Engineering
Aristotle University of Thessaloniki
Box 424, GR-54124, Thessaloniki, Greece
e-mail: fkar@civi.auth.gr, http://users.auth.gr/fkar/

Key words: Accuracy Assessment, Isoerror Maps, Plasticity, Implicit Integration Algorithm, Mohr–Coulomb

Abstract. An improved accuracy analysis of elastoplastic integration algorithms is presented and proposed in this paper. The notion of the well–established isoerror maps is extended and polar plots are constructed for a wide range of stress points, algorithmically selected in the principal stress space. The selection of the stress points is independent of the yield surface and therefore a general procedure is obtained. The individual maps are then joined together to produce a complete view of the accuracy assessment of the stress update algorithm. The proposed procedure is validated in a characteristic multisurface yield criterion.

1 INTRODUCTION

Within the context of computational plasticity it is desirable that the stress update algorithms employed at the Gauss point level should be sufficiently accurate for strain increments as large as possible in order to ensure that the global finite element solution remains within reasonable bounds of accuracy for large load increments. Therefore, accuracy assessment of elastoplastic integration algorithms under finite steps becomes crucial.

A systematic approach to accuracy analyses of elastoplastic algorithms have been first developed by Krieg and Krieg [1] who constructed isoerror maps on a strain controlled homogeneous problem investigating the behaviour of integration algorithms for the Huber–von Mises perfectly plastic model. Although this technique should not be regarded as a replacement of a rigorous accuracy and stability analysis, it have been proved very effective and is generally accepted as a reliable tool for the accuracy assessment of integration algorithms [2].

Standard accuracy assessment employing isoerror maps follows a typical pattern. For a given yield surface, a range of possible stress points that reside on the surface and

correspond to different stress states (eg. uniaxial loading, biaxial loading, pure shear stress etc.) must be identified. A sequence of yield surface and position dependant, normalized strain increments is then applied at each individual stress point and the error between the computed and the exact solution is obtained and plotted [3].

Clearly the accuracy assessment following the above procedure is a rather tedious work, which depends on the correct identification of all possible states, is limited only in the vicinity of these states and differs considerably in each yield surface.

In this paper an improved accuracy analysis of elastoplastic integration algorithms is presented and proposed. The isoerror maps are constructed for a wide range of stress points, algorithmically selected in the principal stress space. The selection of the stress points is independent of the yield surface and therefore a general procedure is obtained. The individual maps are then used together to produce a complete view of the accuracy assessment of the stress update algorithm. The proposed procedure is validated in the Mohr–Coulomb yield criterion.

2 METHODOLOGY

Let $P(\rho, \theta, z)$ denote a point in a cylindrical coordinate system and assume a tranformation that maps P to the Haigh–Westergaard stress space [4] as shown in **Fig. 1**, i.e.

$$\mathbf{T} : (\rho, \theta, z) \rightarrow (\sigma_1, \sigma_2, \sigma_3) \tag{1}$$

where σ_i are the principal stresses.

Now assume that the stress state corresponding to point P defines a *trial* stress state, i.e. $P \equiv \boldsymbol{\sigma}^{trial}$. Within the context of perfect plasticity, a scalar function $f : \mathbb{S} \rightarrow \Re$ is defined, which goes by the name *yield function* and constrains the admissible stresses to lie in the so called *elastic domain*, such as:

$$\mathbb{E}_{\boldsymbol{\sigma}} := \{\boldsymbol{\sigma} \in \mathbb{S} | f(\boldsymbol{\sigma}) \leq 0\} \tag{2}$$

If $\boldsymbol{\sigma}^{trial}$ violates the constraint defined by the yield function then a plastic correction is needed in order to bring back the trial state in the boundary of $\mathbb{E}_{\boldsymbol{\sigma}}$, namely $\partial\mathbb{E}_{\boldsymbol{\sigma}}$. From a numerical standpoint, a typical choice would be a fully–implicit integration algorithm, which will approximate the solution, yielding a stress state $\boldsymbol{\sigma}^{approx}$ on $\partial\mathbb{E}_{\boldsymbol{\sigma}}$.

However, it has been proved [5, 6] that a fully–implicit scheme tends to provide the exact solution $\boldsymbol{\sigma}^{exact}$ of the problem when $\boldsymbol{\sigma}^{trial}$ is divided into a sufficiently large number n of subincrements. Thus an error estimate can be defined as:

$$\epsilon(\%) = 100 \times \frac{\sqrt{(\boldsymbol{\sigma}^{exact} - \boldsymbol{\sigma}^{approx}) : (\boldsymbol{\sigma}^{exact} - \boldsymbol{\sigma}^{approx})}}{\sqrt{\boldsymbol{\sigma}^{exact} : \boldsymbol{\sigma}^{exact}}} \tag{3}$$

Therefore, one has to define a suitable search space $\mathcal{V}$ for (ρ, θ, z) and apply the error estimate for sufficiently large value of n, as described in algorithm **1**.

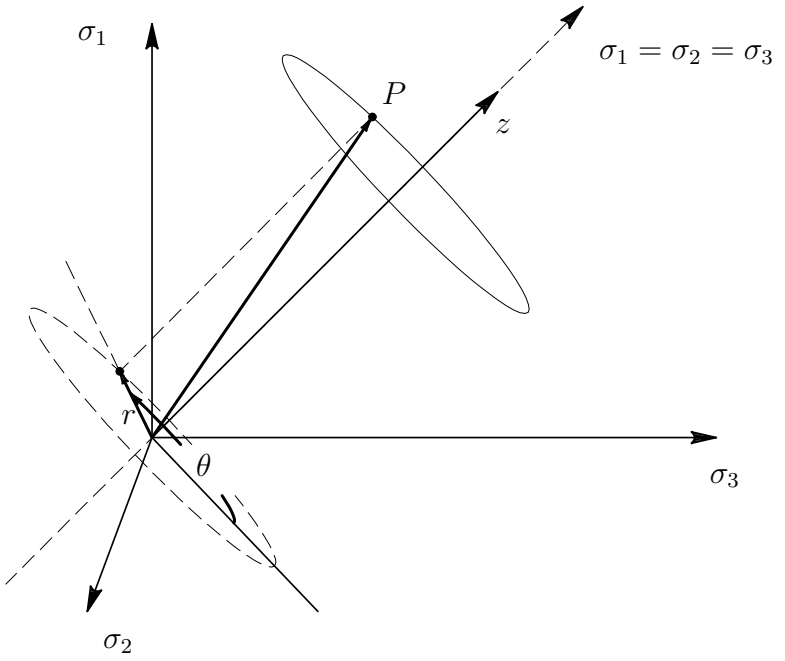

Figure 1: An arbitrary stress state P.

3 APPLICATION

The above proposed methodology is applied in what follows to the Mohr–Coulomb yield criterion.

3.1 The Mohr–Coulomb yield criterion

The Mohr–Coulomb yield criterion is frequently acknowledged as one of the first and most important criteria, widely used to describe the yield behavior of a wide range of materials. It is defined by six linear surfaces in the principal stress space (Fig. **2(a)**), assuming however and without any loss of generality that $\sigma_1 \geq \sigma_2 \geq \sigma_3$, only the following

Algorithm 1 Construction of improved isoerror maps.

```
for z ∈ [z_0, z_1, ...] do
  for θ ∈ [−π/6, π/6] with step dθ do
    for r ∈ [r_1, r_2] with step dr do
      transform (z, r, θ) to (σ_1, σ_2, σ_3)
      Find σ^approx
      Find σ^exact using n subincrements
      Find error ϵ
    end for
  end for
end for
```

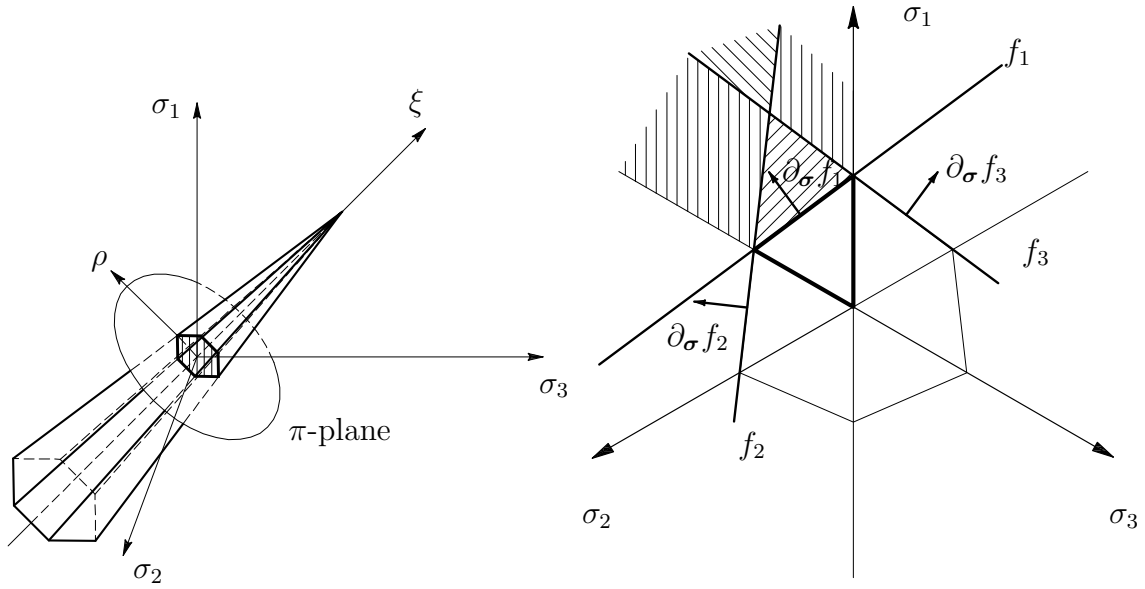

(a) Haigh–Westergaard space. (b) Projection in the π–plane.

Figure 2: The Mohr–Coulomb yield criterion.

three surfaces (Fig. **2(b)**) can describe the elastic domain:

$$f_1(\sigma_1, \sigma_2, \sigma_3) = (\sigma_1 - \sigma_3) + (\sigma_1 + \sigma_3)\sin(\phi) - 2c\cos(\phi) \tag{4}$$
$$f_2(\sigma_1, \sigma_2, \sigma_3) = (\sigma_2 - \sigma_3) + (\sigma_2 + \sigma_3)\sin(\phi) - 2c\cos(\phi) \tag{5}$$
$$f_3(\sigma_1, \sigma_2, \sigma_3) = (\sigma_1 - \sigma_2) + (\sigma_1 + \sigma_2)\sin(\phi) - 2c\cos(\phi) \tag{6}$$

For the problem examined next an associative flow rule is assumed. The elastic properties are characterized by $E = 1000$, $\nu = 0.25$ while cohesion and internal friction angle are given as $c = 15$ and $\phi = 20^\circ$.

3.2 The return mapping scheme

The return mapping scheme used here is thoroughly examined in [7, 8] and implemented in [9]. It is based on a spectral representation of stresses and strains and a return mapping scheme in principal stress directions. Because of the linearity of the yield surfaces in the principal stress space the return mapping reduces to a one step closest–point projection.

3.3 Accuracy assessment

For the accuracy assessment of the above implementation, it is chosen that $z = [0., -10., \ldots, -50.]$, $\rho = [0.01, 0.02, \ldots, 100.]$ and $\theta = [30^\circ, 40^\circ, \ldots, 90^\circ]$. As described in the algorithm **1**, for a fixed z and θ both the $\boldsymbol{\sigma}^{approx}$ and $\boldsymbol{\sigma}^{exact}$ are recovered, the latter assuming a division into 1000 subincementations.

The results, along with the corresponding elastic domains for the given deviatoric plane, are plotted in **Fig.3.3**.

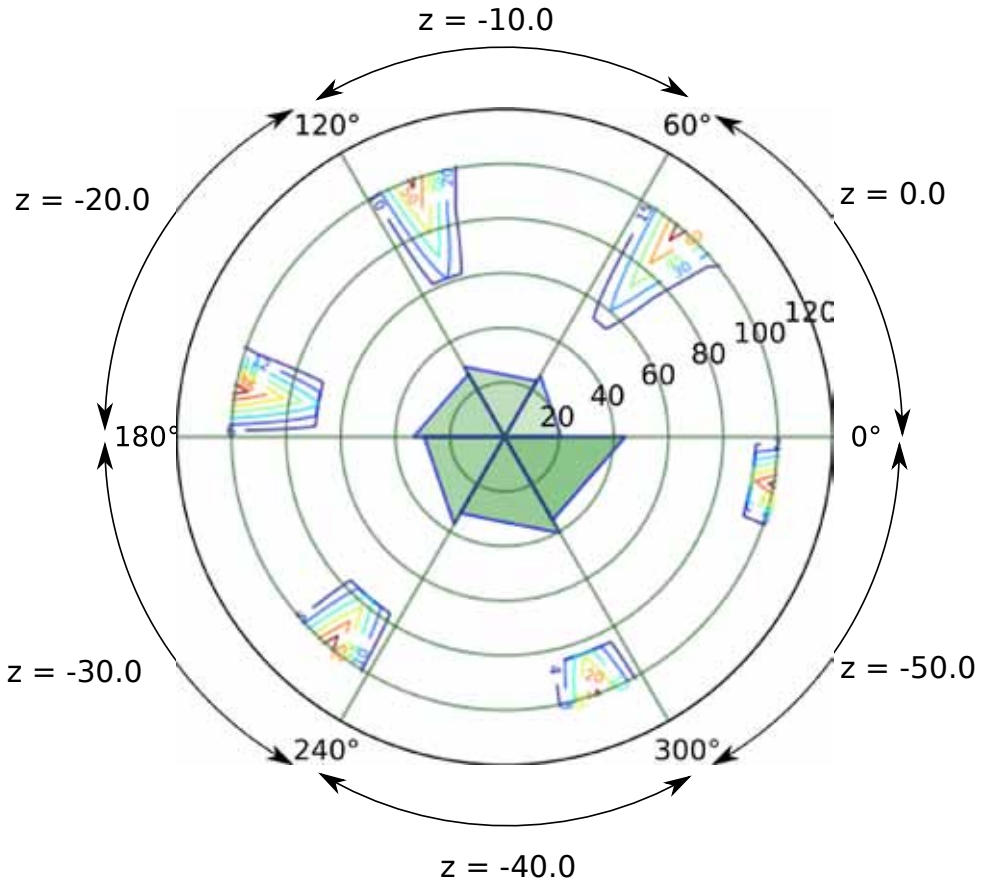

Figure 3: Isoerror maps for the Mohr–Coulomb yield criterion.

4 CONCLUSIONS

An improved accuracy analysis of elastoplastic integration algorithms is presented and proposed in this paper. The notion of the well–established isoerror maps is extended and polar plots are constructed for a wide range of stress states spreading over the principal stress space. The main advantages of this approach is that the selection of the stress states leads to a procedure that:

- is yield surface–agnostic,
- does not depend on the integration algorithm and
- is able to cover the entire range of possible stress states.

Contrary to typical isoerror maps, the individual equipotential diagrams produced are joined together and plotted in polar coordinates as to generate a complete picture of the accuracy assessment of the stress update algorithm. The proposed procedure is validated in a characteristic multisurface yield criterion, namely the Mohr–Coulomb yield criterion, composing an intuitive view of the selected integration scheme's accuracy.

REFERENCES

[1] Krieg, R.D and Krieg, D.B. Accuracies of Numerical Solution Methods for the Elastic–Perfectly Plastic Model. *Journal of Pressure Vessel Technology* (1977) **99**:510–515.

[2] Simo, J.C. and Hughes T.J.R *Computational Inelasticity*. Springer Verlag (1998).

[3] De Souza Neto, Perić, D. and Owen D.J.R. *Computational Methods for Plasticity: Theory and Applications*. John Wiley & Sons (2008).

[4] Ottosen, N.S. and Ristinmaa, M. *The Mechanics of Constitutive Modeling*. Elsevier Science Ltd, (2005).

[5] Ortiz, M. and Popov, E.P. Accuracy and stability of integration algorithms for elastoplastic constitutive relations. *International Journal for Numerical Methods in Engineering* (1985) **21**:1561–1576.

[6] Simo J.C. and Govindjee S. Non–linear B–stability and symmetry preserving return mapping algorithms for plasticity and viscoplasticity. *International Journal for Numerical Methods in Engineering* (1991) **31**:151–176.

[7] Karaoulanis, F.E. and Chatzigogos, T.N. Implicit Numerical Integration of the Mohr–Coulomb Surface in Principal Stress Space. *2nd South-East European Conference on Computational Mechanics (SEECCM 2009)*, M. Papadrakakis, M. Kojic, V. Papadopoulos (eds.), Rhodes, Greece, 22–24 June 2009.

[8] Karaoulanis, F.E. *Multisurface elastoplastic yield criteria. Numerical implementation in principal stress space and application in Geotechnical Engineering problems*. PhD Thesis *(in Greek)*, Aristotle University of Thessaloniki (2010).

[9] Karaoulanis, F.E. *nemesis, an experimental finite element code*, `http://www.nemesis-project.org`, retrieved on May 2011.

XI International Conference on Computational Plasticity. Fundamentals and Applications
COMPLAS XI
E. Oñate, D.R.J. Owen, D. Peric and B. Suárez (Eds)

APPLICATION OF SENSITIVITY ANALYSIS – PRELIMINARY STEP OF THE PROCESS PARAMETERS ESTIMATION

D. SZELIGA

Department of Applied Computer Science and Modelling
Faculty of Metals Engineering and Industrial Computer Science
Akademia Górniczo-Hutnicza
Al. Mickiewicza 30
30-059 Kraków, Poland
e-mail: szeliga@agh.edu.pl

Key words: Sensitivity analysis, inverse problem, parameter identification, *hp*-adaptivity, electrical resistivity

Abstract. Simulation of any physical process requires definition of the physical model, method – analytical or numerical, to solve the set of equations describing the physical model and the parameters expressing the body properties and boundary conditions. This paper focus on two latter aspects of the numerical simulation process. Precise determination of the model quantities are crucial for high quality of the model predictions and accurate reflection of real system. Determination of the process parameters is defined as an inverse problem. Following this the sensitivity analysis is applied as the preliminary step of the inverse analysis to reduce the number of model evaluations and to increase the inverse calculations robustness and efficiency. Sensitivity analysis techniques show how "sensitive" is a model to its input parameters variations and to changes of the model structure. As the example the sensitivity analysis was applied to the 2D DC borehole resistivity measurements simulation problem solved with *hp*-Finite Element Method.

1 INTRODUCTION

Modeling of any physical problem requires precise quantitative information of the model parameters. Some of them are derived from physical laws, others are of phenomenological nature. Proper physical and mathematical description of the problem as well as selection of the solution method and accurate estimation of the model parameters are crucial for the high quality of the modeling results. The paper focuses on the problem of model parameters estimation and the efficient methods to determine the parameters.

Most problems describing physical phenomena related to identification of some quantities are defined as inverse problems [1],[2]. Those problems are hard to solve due to non-unique solution and the lack of the model output stability with respect the identified parameters. Another aspect is efficiency of the identification. Models of physical phenomena are based on differential equations and solved with time consuming numerical methods (e.g. finite element method, finite volume method, particles method). All those features motivate to develop the robust parameter identification method of high efficiency with respect to the calculation time. Classical inverse method was developed and applied by the Author to identify rheological

material properties [3]–[5]. One of the main disadvantages of that approach is calculation time. The idea of the modified inverse method is to supply the classical algorithm with sensitivity analysis as the preliminary step of the solution to decrease the calculation time. As the application example problem of DC (direct current) borehole resistivity measurements is analyzed.

2 PROBLEM FORMULATION

2.1 Direct and inverse problem

Integral or differential equations describing any physical phenomena are set out in terms of functional analysis as:

$$K : X \to Y \tag{1}$$

where X and Y are normed spaces and K is a mapping (linear or nonlinear).

The direct problem is formulated as evaluating $y = K(x) \in Y$ for given $x \in X$ and an operator K that is equivalent to solve a boundary value problem for differential equation or to evaluate an integral. The inverse problem is defined as evaluating the $x \in X$ value for given K and $y \in Y$ [1],[2].

It could be shown that inverse problems described as the integral/differential equations are ill-posed in the sense of Hadamard [6]. Those problems require regularization procedure and one of the solution is transforming them to the following, well-posed, problems:

$$x \mapsto \left\| Kx - y \right\|^2 \tag{2}$$

The form (2) leads to minimization with respect to the parameters, which are identified: boundary conditions parameters or material parameters. In terms of optimization terminology, the inverse problem is to find the minimum of the objective function:

$$\Phi(x) := \left\| Kx - y^{\delta} \right\|^2 \tag{3}$$

where y^{δ} is the perturbated (measured) data such that $\| y^{\delta} - y \| \leq \delta$, $y \in K(X)$ – exact solution of equation (1).

The objective function (3) depends on the norm in the Y space, if it is supplied with Euclid's norm, the objective function is defined as an average square root error (the Euclidean distance) between calculated and measured quantities.

Equation (1) can be expressed as:

$$x = \left(I - aK^* K \right) x + aK^* y \tag{4}$$

where K^* is adjoint operator and $a>0$ is the a number.

For equation (4) the iteration procedure scheme :

$$\begin{aligned} & x^0 := 0 \\ & x^m = \left(I - aK^* K \right) x^{m-1} + aK^* y, \qquad m = 1, 2, \ldots \end{aligned} \tag{5}$$

leads to the solution of the inverse problem described by (2). The general flow chart of the inverse analysis algorithm is presented in figure 1. Regardless of the process type inverse problem and independently of the applied method of the solution, the algorithm consists of three parts:

- The set of process outputs measured in the experiments (real or virtual).
- Solver of the direct problem (in most cases of high computation cost).
- Optimization procedure of objective function. The objective function is defined as a distance between measured and calculated model outputs in the selected space norm or it can be Pareto set. Either gradient and non-gradient or bio-inspired optimization algorithms are applied to determine the minimum of the objective function.

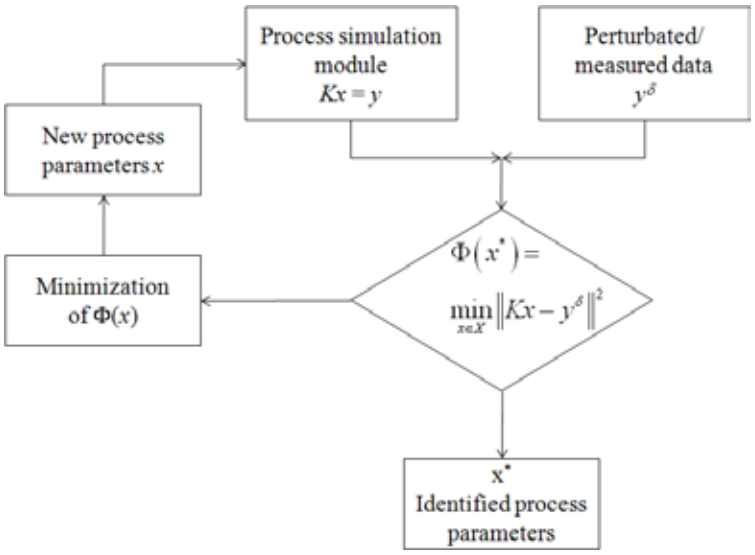

Figure 1: Inverse analysis flow chart.

2.2 Sensitivity analysis

Sensitivity analysis allows to assess the accuracy of the model of the analyzed system or process, determine the parameters which contribute the most to the output variability, indicate the parameters which are insignificant and may be eliminated from the model, evaluate these parameters which interact with each other, determine the input parameters region for subsequent calibration space [7],[8].

The steps of the sensitivity analysis are as following:

- Sensitivity measure. The measure expresses the model solution (model output) changes to the model parameter variation.
- Selection of the parameter domain points. Design of experiment techniques are commonly used to select the lower number of points guaranteed searching whole the domain.
- Method of sensitivities calculation. The sensitivities are estimated by global indices or by local ones.

The information obtained from sensitivity analysis is applied to the inverse method:

- To verify if the objective function is well defined – it means if it is possible to estimate the

parameters, which are looked for, based on the information included in the objective function. In case of no sensitivity or low sensitivity of the objective function to the parameter changes, the parameter identification cannot be performed and the objective function hast to be transformed to another form including verification of the model output space norm.

- As the preliminary step – to select the starting point/the first region of interest or the first population for optimization algorithm.
- Optimization process – to construct the hybrid algorithms (e.g. the combination of a genetic algorithm to select local minima and a gradient method to explore those minima) or modified algorithms (e.g. the particle swarm procedure enriched with the local sensitivities information [9]) to increase the procedure efficiency.

In this work the model output was defined as the Euclidean distance to exact logging curve. To points selection Latin hypercube sampling (LHS) was used. The sensitivities were defined as the first order local sensitivities estimated using partial derivatives.

2.3 2D DC borehole resistivity measurements problem

Computational domain. The problem geometry was described as 2D problem of plane coordinates (*x*,*y*). The following materials were used (figure 2a):

- borehole: a subdomain Ω_0 of width 10 cm $\Omega_0 = \{(x,y): 0\text{cm} \le x \le 10\,\text{cm}\}$ with resistivity $\rho_0 = 0.1\,\Omega\cdot\text{m}$,
- upper and lower formations (no. 1 and 4): a subdomains Ω_1, Ω_5 defined by $\Omega_1 = \{(x,y): 10\,\text{cm} < x,\ 3\text{m} \le y\}$, $\Omega_5 = \{(x,y): 10\,\text{cm} < x,\ y < -2\text{m}\}$ with resistivity $\rho_{1,4} = 1000\,\Omega\cdot\text{m}$,
- formation no. 2: a subdomain Ω_2 defined by $\Omega_1 = \{(x,y): 10\,\text{cm} < x,\ 2\text{m} \le y < 3\text{m}\}$ with resistivity $\rho_2 = 5\,\Omega\cdot\text{m}$,
- formation no. 3: a subdomain Ω_3 defined by $\Omega_3 = \{(x,y): 10\,\text{cm} < x,\ 0\text{m} \le y < 2\text{m}\}$ with resistivity ρ_3,
- formation no. 4: a subdomain Ω_4 defined by $\Omega_4 = \{(x,y): 10\,\text{cm} < x,\ -2\text{m} \le y < 0\text{m}\}$ with resistivity $\rho_4 = 1\,\Omega\text{m}$.

Variational problem formulation. Find $u \in V$ the electrostatic scalar potential such that:

$$b(u,v) = l(v) \quad \forall v \in V \tag{6}$$

$$b(u,v) = \int_\Omega \sum_{i=1}^{2} \sigma \frac{\partial u}{\partial x_i}\frac{\partial v}{\partial x_i} dx$$

$$l(v) = \int_\Omega \sum_{i=1}^{2} \frac{\partial J}{\partial x_i} v\, dS + \int_{\Gamma_N} g\, v\, dS$$

where

$$V = \left\{ v \in L^2(\Omega) : \int_\Omega \|v\|^2 + \|\nabla v\|^2 \, dx < \infty : \mathrm{tr}(v) = 0 \text{ on } \Gamma_D \right\} \tag{7}$$

and J denotes a prescribed, impressed current source, σ is the conductivity, and the electrostatic scalar potential u is related to the electric field E by $E = -\nabla u$. More information of DC borehole resistivity measurements problem is presented in [10].
The direct problem formulated by equations (6) is solved using automatic *hp*-Finite Element Method software (for detail description see [11],[12]). An example of the *hp* adaptive computations is presented in figure 2b.

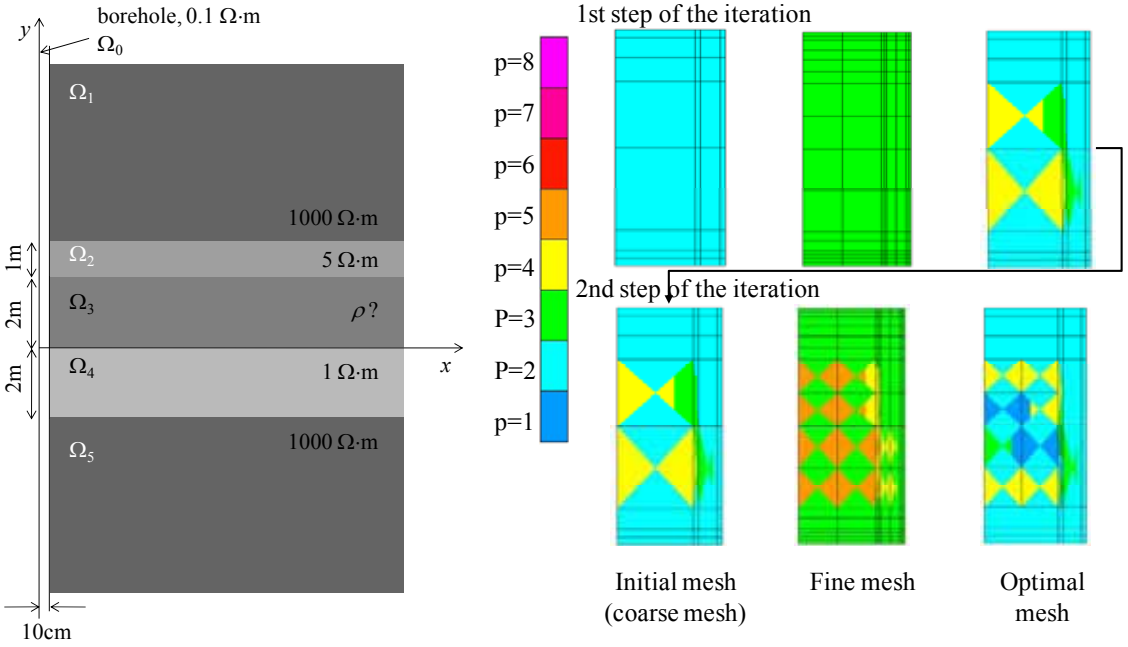

Figure 2: a) The 2D geometry of 3D DC borehole resistivity measurements problem. The rock formation is composed of five different layers of various resistivities, b) Automatic *hp*-adaptive solver – a solution example.

3 CALCULATIONS

Inverse calculations. The objective function in the inverse method for DC borehole logging curve measurements was defined as the Euclidean distance between measured and calculated values:

$$\Phi(\mathbf{a}) = \sqrt{\frac{1}{N}\sum_{i=1}^{N}\left(\frac{u_i(\mathbf{a}) - u_i^m}{u_i^m}\right)^2} \tag{8}$$

where u is the potential of electrical field, $\mathbf{a}$ – vector of identified parameters, N – number of measured points along the logging curve, m index – measured value.
The measurement values of electrical field potential u^m were generated for the problem

described in the chapter 2.3 and the resistivity ρ_3 = 200 Ω·m for Ω_3 layer and next randomly perturbated.
In general case vector **a** is of the form:

$$\mathbf{a} = \left\{ \rho_j, h_j, \alpha \right\} \tag{9}$$

where ρ_j, h_j – resistivity and height of the j^{th} layer, respectively, α – deviation angel of the well from perpendicular, $j = 1 \ldots nf$, nf – the number of formation layers.

As yet inverse calculations were performed using hierarchical genetic searching [13],[14] with respect to some resistivities and the angel. Since the results of estimation were sufficient, the computations have been very time-consuming. The idea was to performed sensitivity analysis to investigate the parameters domain and to develop more efficient searching algorithm.

Calculation time depends on the assumed accuracy of *hp*-FEM solver. The accuracy of *hp*-FEM modeling is defined as the difference between coarse-grid and fine-grid solution in the quantity of interest. To increase the efficiency of the calculations some simulations of the process were performed with various accuracies. The calculations were carried out with the computer of two 3 GHz processors and 8 GB RAM, the times are shown in table 1. The accuracy of 10^{-2} was taken for further investigations.

Table 1: Relation between hp-FEM accuracy and the execution time of the solution.

hp-FEM accuracy	Execution time
10^{-5}	5h 21min 40s
10^{-4}	3h 30min
10^{-3}	1h 4min 15s
10^{-2}	20min 24s
10^{-1}	9min 40s
1	3min 52s
10	2min 26s
100	2min 17s
1000	2min 19s

Sensitivity analysis. The sensitivity measure was expressed as derivatives of the objective function (8) and estimated though Taylor series expansion:

$$\Phi\left(\mathbf{a} + \Delta\mathbf{a}\right) = \Phi\left(\mathbf{a}\right) + \sum_{i=1}^{2nf+1} \frac{\partial \Phi}{\partial a_i} \Delta a_i + \mathrm{O}\left(\mathbf{a}^2\right) \tag{10}$$

where $\mathrm{O}\left(\mathbf{a}^2\right)$ residue is neglected.

As the result the first-order local sensitivities are obtained $\mathbf{S} = \left\{ s_i \right\} = \left\{ \partial\Phi / \partial a_i \right\}$.

Current investigations were focus on the resistivity coefficient ρ and the sensitivity analysis was performed with respect to that parameter: $\partial\Phi / \partial\rho$.

The domain for the resistivity was specified as $\rho \in \left[0.1, 1000\right]$ Ω·m. To provide uniform but random covering of the interval, points were generated by LHS with equal probability for

each subinterval. To evaluate numerical computations of $\partial\Phi/\partial\rho$ the value of $\Delta\rho$ was assumed as 5% and 10% of ρ resistivity.

In figure 3 the logging curves calculated for various values of resistivity are presented. The changes of the goal function are shown in figure 4a and the results of sensitivities estimations – in figure 4b.

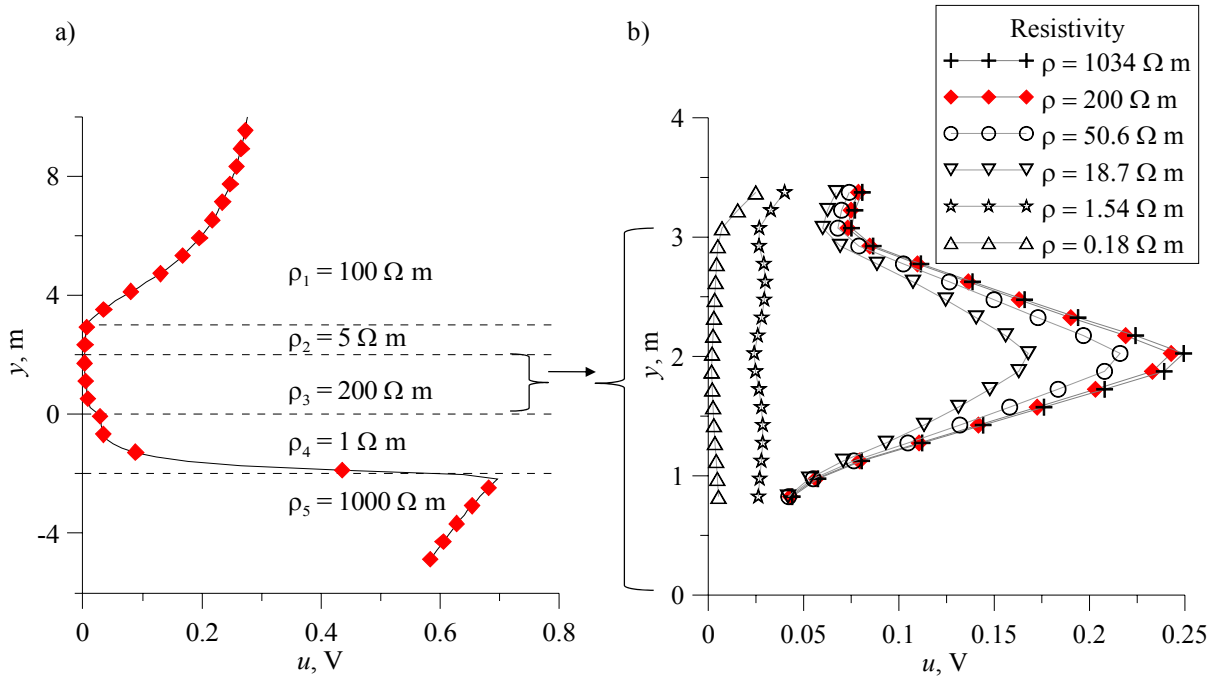

Figure 3: Logging curves of DC borehole resistivity problem: a) all formers layers, b) focus of one of the layer with curves obtained for various resistivity parameters.

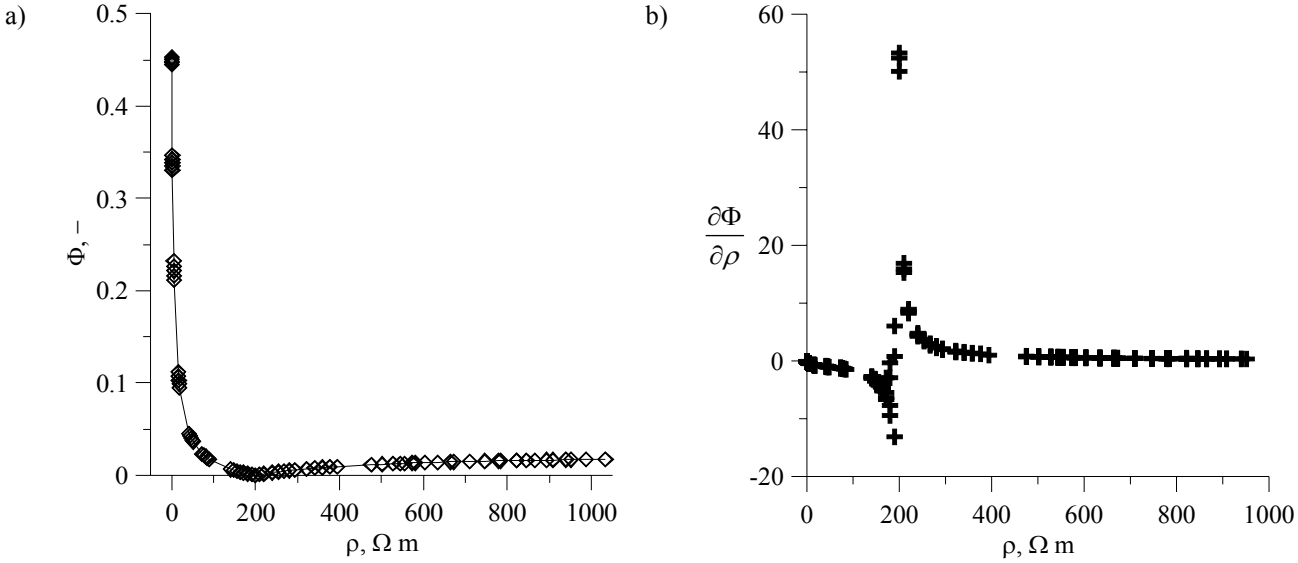

Figure 4: a) Objective function computed for various resistivities, b) Sensitivity of the objective function with

respect to the resistivity parameter.

4 DISCUSSION

Computations of the inverse calculations objective function sensitivities were performed for the resistivity screening the parameter domain. For resistivity values higher than 50 Ω·m the electrical field potential changes are not significant (see figure 3b). Similar behavior is observed for the objective function (figure 4a): the values are high for small resisitivties, close to zero for exact solution (200 Ω·m) and next they a little increase but are still low. The sensitivities are close to zero all over the interval except narrow interval of the exact solution (figure 4b). Such distribution of the objective function and the sensitivities effect the optimization procedure hard to performed using conventional optimization algorithms.

The investigations were performed for the resistivity of the one layer. In real systems the identification consists of several resistivities and the heights of the layers (vector **a**, equation (9)), consequently the objective function (8) is multimodal function of high sensitivities with respect to the resistivities close to the problem solution, remaining area is of low sensitivities.

The results of current investigations are guidelines for two optimization strategies:

- Hierarchical genetic searching (or another bio-inspired optimization algorithm) to select local minima and next application of the gradient method to explore the local minima,
- Application of design of experiment method (LHS or screening design) to select a set of points, for which objective function is computed with *hp*-FEM model and next, based on the those accurate results, generating fast metamodel using one of the approximation method (e.g. response surface algorithm) or neural network, and performing inverse calculations with investigated, fast model.

Both the strategies are expected to increase the efficiency of the inverse calculations in terms of computation time.

5 CONCLUSIONS

In that work application of the sensitivity analysis to the hard inverse problem as the preliminary step of the computations was proposed. As the example inverse problem of DC borehole resistivity measurements was formulated. The sensitivities were defined locally and expressed using Taylor series expansion. The set of the points that sensitivities were estimated for, was generated with design of experiment algorithm. The guidelines for the inverse optimization procedure were developed. The accuracy of the *hp*-FEM solution of the direct model in relation to the inverse problem objective function was analyzed as well.

The obtained results of calculations, as the first attempt, are the basis to develop efficient optimization procedures with sensitivity analysis application to solve hard inverse problem: hybrid methods or algorithms with metamodels. Another way to decrease the number of the solver evaluations is to modify the objective function by including the information of the sensitivities. All above aspects will have been investigated.

Acknowledgements. The work on sensitivity analysis has been supported by Polish MNiSW, project no. N N508 629 740. The *hp*-Finite Element Method calculations have been supported by Polish MNiSW, project no. NN519 447 739.

REFERENCES

[1] Kirsch A., *An Intoduction to the Mathematical Theory of Inverse Problems*. Springer-Verlag, New York (1996).

[2] Engl H.W., Hanke M., Neubauer A., *Regularization of Inverse Problems*. Kluwer Academic Publishers (1996).

[3] Szeliga, D., Pietrzyk, M., Identification of rheological models and boundary conditions in metal forming, *International Journal of Materials & Product Technology* (2010), **39**: 388–405.

[4] Gawąd, J., Kuziak, R., Madej, Ł., Szeliga, D., Pietrzyk, M., Identification of rheological parameters on the basis of various types of compression and tension tests, *Steel Research International* (2005), **76**: 131–137.

[5] Szeliga, D., Gawąd, J., Pietrzyk, M., Inverse analysis for identification of rheological and friction models in metal forming, *Computer Methods in Applied Mechanics and Engineering* (2006), **195**: 6778–6798.

[6] Hadamard, J., *Lectures on the Cauchy Problem in Linear Partial Differential Equations*. Yale University Press, New Haven (1923).

[7] Kleiber, M., Antunez, H., Hien, T.D., Kowalczyk, P., *Parameter Sensitivity in Nonlinear Mechanics*. Wiley (1997).

[8] Saltelli, A., Chan, K., Scott, E.M., *Sensitivity Analysis*. Wiley (2000).

[9] Sztangret, Ł., Szeliga, D., Kusiak, J., Sensitivity analysis as a supporting procedure in optimization of metallurgical processes, *Hutnik Wiadomości Hutnicze* (2010) **76**(12): 721–725 (in Polish)

[10] Pardo, D., and Torres-Verdin, C., Paszyński, M., Simulation of 3D DC borehole resistivity measurements with a goal-oriented hp-Finite Element Method, Part II: Through Casing Resistivity Instruments, *Computational Geosciences* (2008) **12**(1): 83-89.

[11] Demkowicz, L., *Computing with hp-Adaptive Finite Elements*. Vol. I, Chapman & Hall /CRC (2006).

[12] Demkowicz, L., Kurtz, J., Pardo, D., Paszyński, M., Rachowicz, W., Zdunek, A., *Computing with hp-Adaptive Finite Elements*. Vol. II, Chapman & Hall/CRC (2007).

[13] Barabasz, B., Migórski, S., Schaefer, R., Paszyński, *M.,* Multi-deme, twin adaptive strategy *hp*-HGS, *Inverse Problems in Science and Engineering* (2011), **19**: 3–16.

[14] Schaefer, R., and Kołodziej, J., Genetic search reinforced by the population hierarchy, *Foundation of Genetic Algorithm 7*, De Jong, K., A., Poli, R., Rowe, J., E., Ed., Morgan Kaufman Publisher (2003): 383-399.

XI International Conference on Computational Plasticity. Fundamentals and Applications
COMPLAS XI
E. Oñate, D.R.J. Owen, D. Peric and B. Suárez (Eds)

ASSESSMENT OF THE ENHANCED ASSUMED STRAIN (EAS) AND THE ASSUMED NATURAL STRAIN (ANS) TECHNIQUES IN THE MECHANICAL BEHAVIOR OF THE SSH3D SOLID-SHELL ELEMENT

LAURENT DUCHÊNE, AMINE BEN BETTAIEB AND ANNE MARIE HABRAKEN

ARGENCO Department, MS^{2}F Division
University of Liège
Chemin des Chevreuils 1, 4000 Liège, Belgium
e-mails: {l.duchene; amine.benbettaieb; anne.habraken}@ulg.ac.be, www.argenco.ulg.ac.be

Key words: Solid-Shell finite element, Enhanced Assumed Strain technique, Assumed Natural Strain technique, Patch Test, Volumetric Locking.

1 INTRODUCTION

This paper presents the recently developed SSH3D Solid-Shell element implemented in the home-made LAGAMINE finite element code. This element is based on the Enhanced Assumed Strain (EAS) technique and the Assumed Natural Strain (ANS) technique. These techniques permit to avoid locking problems even in very bad conditions (nearly incompressible materials, very thin elements conducting to large aspect ratios, distorted element geometry…). The EAS technique artificially introduces additional degrees of freedom (DOFs) to the element. In the current configuration of the SSH3D element, up to 30 independent DOFs can be added to the 24 classical displacement DOFs (corresponding to the 3 displacements of the 8 element nodes). Contrarily to the nodal displacements, these additional DOFs are not linked between adjacent elements, so that they can be eliminated at the element level during the computation of the solution (before the assembling procedure). Nevertheless, they permit to increase the flexibility of the element which is very efficient for several locking issues. On the other hand, the ANS technique modifies the interpolation scheme for particular strain components. This technique is useful when shear and curvature locking problems are encountered. The ANS technique proved to eliminate the transverse shear locking from the element in bending dominated situations. In the current configuration of the element, four different versions of the ANS technique were implemented in the SSH3D element. Besides, a numerical integration scheme dedicated to Solid-Shell elements was implemented. It uses a user-defined number of integration points along the thickness direction, which permits to increase the element accuracy with a mesh containing a reduced number of elements along the thickness direction.

In Sections 2, 3 and 4, the main features of the SSH3D element, i.e. the EAS technique, the ANS technique and the integration scheme are briefly described. Then, in this study, the quality of the element results is assessed in different applications. The effects of the EAS technique and the integration scheme on the volumetric locking and the effects of the ANS technique on the bending behavior of the element are analyzed in Sections 5 and 6.

2 ENHANCED ASSUMED STRAIN TECHNIQUE

This section summarizes the formulation of the SSH3D Solid-Shell element. It is an 8 node hexahedral element using the Enhanced Assumed Strain (EAS) method to avoid different locking issues. The formulation of the SSH3D element departs from the Hu-Washizu variational principle:

$$\int_{\mathcal{B}} \nabla^s \underline{\eta}.\underline{\sigma} dv - G_{ext}(\underline{\eta}) = 0 \tag{1}$$

$$\int_{\mathcal{B}} \underline{\tau}.\left[\nabla^s \underline{\eta} - \underline{\varepsilon}\right] dv = 0$$

$$\int_{\mathcal{B}} \underline{\gamma}.[-\underline{\sigma} + \underline{\sigma}^m(\underline{x},\underline{q},\underline{\varepsilon})] dv = 0$$

for all variations $\underline{\eta}$, $\underline{\gamma}$, $\underline{\tau}$ of the displacement $\underline{u}$, strain $\underline{\varepsilon}$ and stress $\underline{\sigma}$ fields, respectively.

In Equation (1), the symbol ∇^s represents the symmetric gradient operator, $G_{ext}(\underline{\eta})$ is the virtual work of the external loading and $\underline{\sigma}^m(\underline{x},\underline{q},\underline{\varepsilon})$ is the stress computed by the material constitutive law at point $\underline{x}$ for the strain value $\underline{\varepsilon}$ and the current material state being represented by the vector of history variables $\underline{q}$. Note that in Equation (1), the tensors are expressed as 6 component vectors.

The main idea behind the EAS technique is the enhancement of the strain field as originally proposed by [1]:

$$\underline{\varepsilon} = \underline{\varepsilon}^{com} + \underline{\tilde{\varepsilon}} \tag{2}$$

The classical compatible part of the strain field $\underline{\varepsilon}^{com}$ is modified with the enhanced part of the strain field $\underline{\tilde{\varepsilon}}$. Note that a similar enhancement is achieved on the variation of the strain $\underline{\gamma}$. The compatible part of the strain is computed from the displacement field according to Equation (3), where the vector $\underline{U}$ contains the 24 nodal displacement DOFs and $\underline{\underline{B}}(r,s,t)$ is the classical strain-displacement operator whose components are derivatives of the shape function with respect to the spatial coordinates x, y and z. For convenience, in a finite element approach, the $\underline{\underline{B}}(r,s,t)$ matrix is expressed as a function of the intrinsic coordinates of the element r, s and t.

$$\underline{\varepsilon}^{com} = \nabla^s \underline{u} = \underline{\underline{B}}(r,s,t) \cdot \underline{U} \tag{3}$$

The enhanced part of the strain field is constructed in a similar way (see Equation (4)) using the $\underline{\underline{G}}(r,s,t)$ matrix. The additional DOFs related to the EAS techniques are included in the vector $\underline{\alpha}$.

$$\underline{\tilde{\varepsilon}} = \underline{\underline{G}}(r,s,t).\underline{\alpha} \tag{4}$$

As proposed by [1], the enhancing matrix $\underline{\underline{G}}(r,s,t)$ is build according to Equation (5) with the help of the transformation from the spatial coordinates to the intrinsic coordinates. $j(r,s,t)$ is the determinant of the Jacobian at point *(r,s,t)*, j_0 is the same at the centre of the element (defined by *r*=*s*=*t*=0). The 6 by 6 matrix $\underline{\underline{F}}_0^{-T}$ is detailed in [2]. It permits to transform a 6-component strain vector from the intrinsic coordinates to the spatial coordinates; it is computed at the centre of the element.

$$\underline{\underline{G}}(r,s,t) = \frac{j_0}{j(r,s,t)}.\underline{\underline{F}}_0^{-T}.\underline{\underline{M}}(r,s,t) \tag{5}$$

The enhancing modes of the EAS technique are included in the $\underline{\underline{M}}(r,s,t)$ matrix. Thanks to the transformation shown in Equation (5), the EAS modes are expressed in the intrinsic coordinate system in a form which is independent of the element spatial configuration, i.e., in accordance with the notation and the numbering of [3]:

$$\underline{\underline{M}}(r,s,t) = \tag{6}$$

r	0	0	0	0	0	0	0	0	0	0	0	0	0	0	*rs*	*rt*	0	0	0	0	0	0	0	*rst*	0	0	0	0	0
0	*s*	0	0	0	0	0	0	0	0	0	0	0	0	0	0	0	*rs*	*st*	0	0	0	0	0	0	*rst*	0	0	0	0
0	0	*t*	0	0	0	0	0	0	0	0	0	0	0	0	0	0	0	0	*rt*	*st*	0	0	0	0	0	*rst*	0	0	0
0	0	0	*r*	*s*	0	0	0	0	*rt*	*st*	0	0	0	0	0	0	0	0	0	0	*rs*	0	0	0	0	0	*rst*	0	0
0	0	0	0	0	*r*	*t*	0	0	0	0	*rs*	*st*	0	0	0	0	0	0	0	0	0	*rt*	0	0	0	0	0	*rst*	0
0	0	0	0	0	0	0	*s*	*t*	0	0	0	0	*rs*	*rt*	0	0	0	0	0	0	0	0	*st*	0	0	0	0	0	*rst*
1	2	3	4	5	6	7	8	9	10	11	12	13	14	15	16	17	18	19	20	21	22	23	24	25	26	27	28	29	30

This $\underline{\underline{M}}(r,s,t)$ matrix contains 30 potential EAS modes (the columns of $\underline{\underline{M}}(r,s,t)$ numbered form 1 to 30), which correspond to 30 additional DOFs. They are grouped by 3 or 6 modes corresponding to similar modes along different directions (the light and dark gray zones). The six lines of the $\underline{\underline{M}}(r,s,t)$ matrix correspond to the six components (respectively 11, 22, 33, 12, 13, 23) of the strain tensor expressed as a vector. Each EAS mode permits to increase the flexibility of the element thanks to an additional deformation mode not included in the standard 24 displacement modes (the 3 displacements of the 8 element nodes). For instance, the first mode corresponds to a linear variation along the *r*-axis of the ε_{rr} component of the strain.

An important characteristic of the EAS technique is that the additional DOFs (the $\underline{\alpha}$ values) are eliminated at the element level by static condensation before the assembling procedure of the FE code. Therefore, they do not contribute to the size of the global stiffness

matrix of the finite element technique but they improve its quality by bringing their effect on the enhanced flexibility of each SSH3D element (see [1] for further details).

In the SSH3D element, the number and the choice of the EAS modes is left to the finite element code user. The effect of the number of EAS modes on the mechanical behavior of the element is presented in Section 5.

3 THE ASSUMED NATURAL STRAIN TECHNIQUE

The Assumed Natural Strain (ANS) technique permits to avoid several locking issues by modifying the interpolation of the strain components in the element as briefly explained hereafter. Classically, the strain is computed at the integration point or at any location inside the finite element from the nodal displacements with the $\underline{\underline{B}}(r,s,t)$ matrix according to Equation (3). For some particular cases, this usual technique yields to inadequate strain values for some components depending on the location where the strain is computed. The ANS technique, originally proposed by [4] for shell elements, suggests to achieve the interpolation of the problematic strain components in two steps. First, these strain components are evaluated by the classical interpolation method at the so-called 'sampling points', where the erroneous values are not likely to be encountered. In a second step, these strain components are interpolated linearly from the sampling points to the integration points (or any location in the element).

In order to assess the efficiency of the ANS technique on the mechanical behavior of the SSH3D element, four different versions of the ANS interpolation have been implemented to date. These versions are detailed below.

For the first version [4-6], the location of the sampling points are shown in Figure 1 (a) for the 13-component (with respect to the *r*, *s*, *t* reference frame) and in Figure 1 (b) for the 23-component. The corresponding interpolation scheme is expressed by Equations (7) and (8) for the 13 and 23-components respectively. For this first version, the four other components of the strain tensor (namely 11, 22, 33, 12) are not altered by the ANS technique.

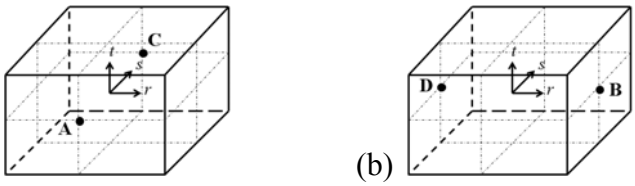

Figure 1: ANS method in the SSH3D element, version 1. Sampling points for the components 13 (a) and 23 (b).

$$E_{13}^{ANS1} = \frac{1}{2}.(1-s).E_{13}^{com}\Big|_A + \frac{1}{2}.(1+s).E_{13}^{com}\Big|_C \tag{7}$$

$$E_{23}^{ANS1} = \frac{1}{2}.(1-r).E_{23}^{com}\Big|_D + \frac{1}{2}.(1+r).E_{23}^{com}\Big|_B \tag{8}$$

It must be noted here that the ANS technique must be applied to the components of the strain expressed in the *r*, *s*, *t* reference frame and not the *x*, *y*, *z* frame of the finite element code. This is emphasized by the use of E for the strain components instead of ε in Equations

(7) and (8). The transformation tools already used for the EAS technique (see for instance Equation (5)) are adapted for the transformation of the strain tensors from the intrinsic reference frame to the global reference frame according to Equation (9).

$$\underline{\varepsilon} = \frac{j_0}{j(r,s,t)} . \underline{\underline{F}}_0^{-T} . \underline{E} \tag{9}$$

For the second ANS version of the SSH3D element [7, 8], the 33-component is also taken into consideration as shown by Figure 2 and Equations (10), (11) and (12).

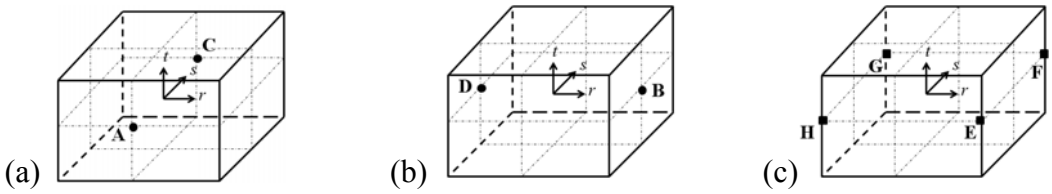

Figure 2: ANS method in the SSH3D element, version 2. Sampling points for the components 13 (a), 23 (b) and 33 (c).

$$E_{13}^{ANS2} = \frac{1}{2}.(1-s).E_{13}^{com}\Big|_A + \frac{1}{2}.(1+s).E_{13}^{com}\Big|_C \tag{10}$$

$$E_{23}^{ANS2} = \frac{1}{2}.(1-r).E_{23}^{com}\Big|_D + \frac{1}{2}.(1+r).E_{23}^{com}\Big|_B \tag{11}$$

$$E_{33}^{ANS2} = \frac{1}{4}.(1-r).(1-s).E_{33}^{com}\Big|_H + \frac{1}{4}.(1+r).(1-s).E_{33}^{com}\Big|_E + \frac{1}{4}.(1+r).(1+s).E_{33}^{com}\Big|_F + \frac{1}{4}.(1-r).(1+s).E_{33}^{com}\Big|_G \tag{12}$$

For the third version of the ANS [9, 10], the 13 and 23-component interpolation schemes are modified from the previous case by using four sampling points instead of two, as shown in Figure 3 and Equations (13), (14) and (15).

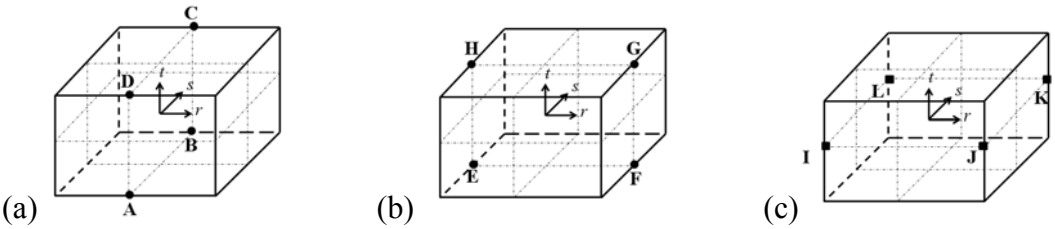

Figure 3: ANS method in the SSH3D element, version 3. Sampling points for the components 13 (a), 23 (b) and 33 (c).

$$E_{13}^{ANS3} = \frac{1}{4}.(1-s).(1-t).E_{13}^{com}\Big|_A + \frac{1}{4}.(1+s).(1-t).E_{13}^{com}\Big|_B + \frac{1}{4}.(1+s).(1+t).E_{13}^{com}\Big|_C + \frac{1}{4}.(1-s).(1+t).E_{13}^{com}\Big|_D \tag{13}$$

$$E_{23}^{ANS3} = \frac{1}{4}.(1-r).(1-t).E_{23}^{com}\Big|_E + \frac{1}{4}.(1+r).(1-t).E_{23}^{com}\Big|_F + \frac{1}{4}.(1+r).(1+t).E_{23}^{com}\Big|_G + \frac{1}{4}.(1-r).(1+t).E_{23}^{com}\Big|_H \tag{14}$$

$$E_{33}^{ANS3} = \frac{1}{4}.(1-r).(1-s).E_{33}^{com}\Big|_I + \frac{1}{4}.(1+r).(1-s).E_{33}^{com}\Big|_J + \frac{1}{4}.(1+r).(1+s).E_{33}^{com}\Big|_K + \frac{1}{4}.(1-r).(1+s).E_{33}^{com}\Big|_L \tag{15}$$

Finally, the fourth ANS version, originally proposed in this paper, uses four common sampling points for the three strain components as illustrated in Figure 4 and Equations (16), (17) and (18).

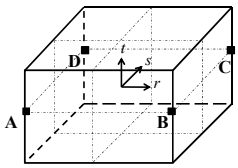

Figure 4: ANS method in the SSH3D element, version 4. Sampling points for the components 13, 23 and 33.

$$E_{13}^{ANS4} = \frac{1}{4}.(1-r).(1-s).E_{13}^{com}\Big|_A + \frac{1}{4}.(1+r).(1-s).E_{13}^{com}\Big|_B + \frac{1}{4}.(1+r).(1+s).E_{13}^{com}\Big|_C + \frac{1}{4}.(1-r).(1+s).E_{13}^{com}\Big|_D \quad (16)$$

$$E_{23}^{ANS4} = \frac{1}{4}.(1-r).(1-s).E_{23}^{com}\Big|_A + \frac{1}{4}.(1+r).(1-s).E_{23}^{com}\Big|_B + \frac{1}{4}.(1+r).(1+s).E_{23}^{com}\Big|_C + \frac{1}{4}.(1-r).(1+s).E_{23}^{com}\Big|_D \quad (17)$$

$$E_{33}^{ANS4} = \frac{1}{4}.(1-r).(1-s).E_{33}^{com}\Big|_A + \frac{1}{4}.(1+r).(1-s).E_{33}^{com}\Big|_B + \frac{1}{4}.(1+r).(1+s).E_{33}^{com}\Big|_C + \frac{1}{4}.(1-r).(1+s).E_{33}^{com}\Big|_D \quad (18)$$

4 THE INTEGRATION SCHEME OF THE SSH3D ELEMENT

An important characteristic of a finite element is the numerical integration scheme. The number and the location of the Gauss points inside the element can have a significant influence on its mechanical behavior. For instance, the reduced integration or the selective reduced integration schemes are often used to avoid volumetric locking issues for hexahedral elements with an isochoric or nearly isochoric material behavior.

In the development of a Solid-Shell element dedicated to the modeling of thin-walled structures, an improved integration scheme with a large number of integration points along the thickness direction was considered. It is indeed expected that a high gradient of stress and strain along the thickness direction is present during the deformation of thin materials (during e.g. a bending deformation mode). The classical full integration of brick elements (with two integration points along each direction) is not able to accurately capture such large gradients. In this respect, in the SSH3D element, the stress is computed along a user-defined number (ranging from 2 to 10) of integration points along the thickness direction (*t* axis), as shown in Figure 5.

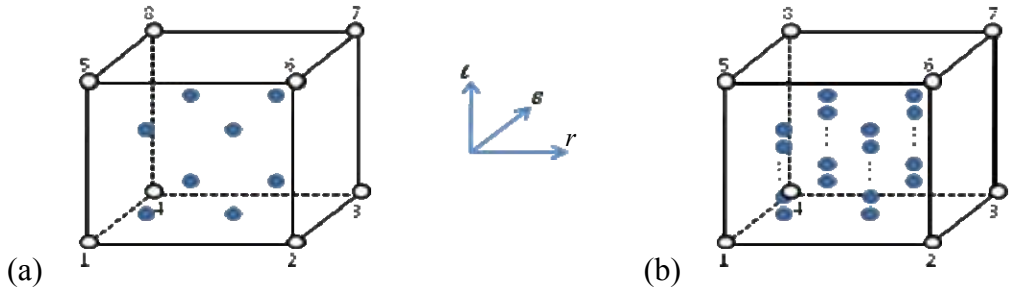

Figure 5: Integration scheme: (a) Classical full integration, (b) SSH3D integration scheme with *n* Gauss points along the thickness direction.

5 EFFECT OF EAS ON THE VOLUMETRIC LOCKING

The volumetric locking is an important issue in finite element approaches. It is likely to appear when incompressibility or nearly incompressibility is imposed by the material model (e.g. in elasticity when the Poisson's ratio approaches 0.5 or in elasto-plastic simulations where the classical assumption of plastic incompressibility is employed). Thanks to a subspace analysis, it has been shown in [11] that any deformation mode with an incompressibility constraint can be obtained as a combination of 23 linearly independent deformation modes. Consequently, an hexahedral element should be able to reproduce (without locking) these 23 modes in order to avoid volumetric locking for any deformation mode (see also [2]). As illustrated in Figure 6, these 23 modes can be divided into four groups: 12 modes corresponding to the translation of one edge of the element (Figure 6 (a)), 5 modes representing the contraction-expansion of one face (Figure 6 (b)), 3 modes related to the so-called hourglass deformation modes, where the element gets a trapezoidal shape (Figure 6 (c)) and 3 warp modes (Figure 6 (d)).

In this respect, in order to check volumetric locking issues with the SSH3D element, the deformation modes of Figure 6 are analyzed in this section for different numbers of EAS modes and different numbers of integration points along the thickness. In this study, the influence of the EAS modes is assessed by increasing successively their number according to the groups defined by the light and dark gray zones of Equation (6). Therefore, in the results, 'SSH3D - 3' means the SSH3D element with the three first EAS modes, 'SSH3D - 9' corresponds to the nine first EAS modes and so on up to 'SSH3D - 30'. The ANS technique was turned off in this section and three different integration schemes were tested with 2 (classical full integration), 5 and 8 Gauss points along the thickness direction. The incompressibility constraint was imposed by an elastic material with a Poisson's ratio close to 0.5, i.e. 0.499.

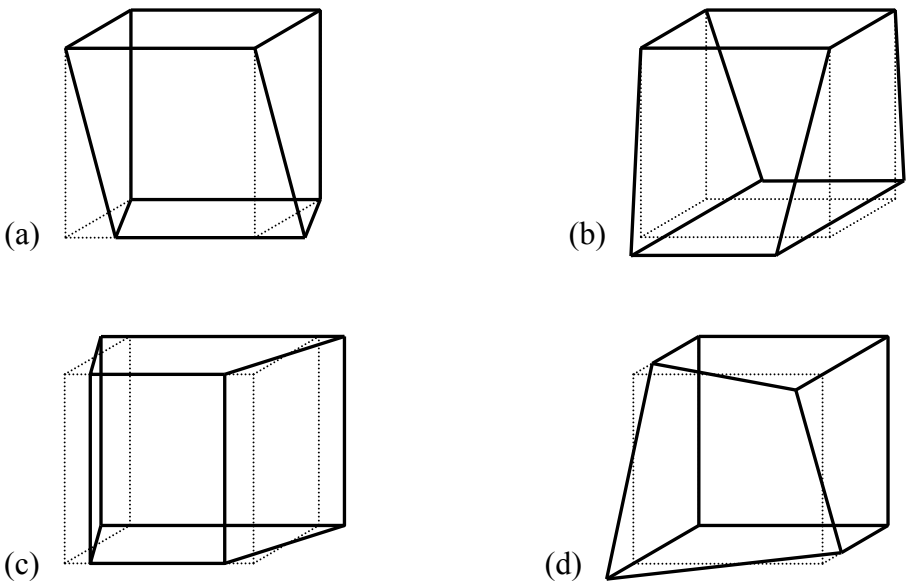

Figure 6: Groups of isochoric deformation modes: (a) Edge translation, (b) Contraction-expansion of one face, (c) Hourglass mode, (d) Warp mode.

The nodal forces required to enforce the deformation modes of Figure 6 are plotted in Figure 7, Figure 8, Figure 9 and Figure 10 for the four groups of deformation modes respectively (the nodes with non zero imposed displacement are analyzed). As they depend on the geometry of the element, the stiffness of the selected material constitutive law, the nodal forces should be regarded as arbitrary values. The purpose of the following figures is only to compare the results according to the number of EAS modes and the selected integration scheme in order to detect volumetric locking issues.

The first group of deformation modes of Figure 6 (a) is analyzed in Figure 7, where it appears that the EAS technique has almost no effect on the nodal forces. In fact, it is expected that even a classical displacement based hexahedral element with a full integration scheme will not show volumetric locking problems in this case. Indeed, this mode induces shear type deformation in the whole finite element corresponding to no volume variation, which is in accordance with the isochoric material model. Therefore, no volumetric locking is detected in this case. Anyway, a small effect of the integration scheme can be noticed.

The second group, corresponding to the contraction-expansion of one face, is treated in Figure 8. For the integration scheme with 2 Gauss points along the thickness direction (classical full integration), as in the previous case, the number of EAS modes do not influence the results. Contrarily, for the integration schemes with 5 and especially with 8 Gauss points along the thickness direction, a stiffer behavior is observed for the lowest numbers of EAS modes. For these integration schemes, volumetric locking, with a rather limited effect, is then observed when the number of EAS modes is lower than or equal to 21. The effect of the number of Gauss points on the element response is related to the fact that the volumetric constraints are applied at the Gauss points through the nearly isochoric material model.

In Figure 9, a non-zero but limited effect of the number of EAS modes can be observed. The influence of the integration scheme for the case 'SSH3D - 24' was not expected and remains unexplained.

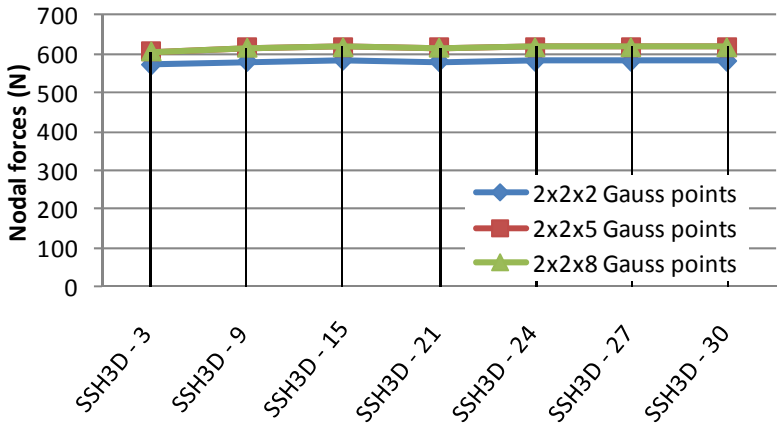

Figure 7: Nodal forces for the isochoric deformation mode of Figure 6 (a) (edge translation) versus the number of EAS modes in the SSH3D element for three different integration schemes.

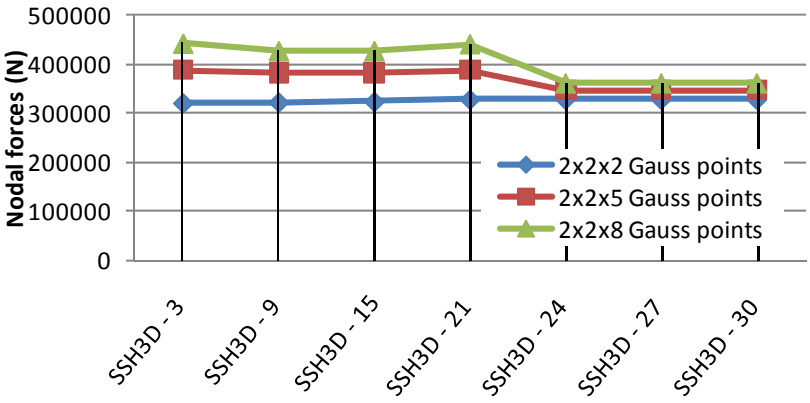

Figure 8: Nodal forces for the isochoric deformation mode of Figure 6 (b) (contraction-expansion of one face) versus the number of EAS modes in the SSH3D element for three different integration schemes.

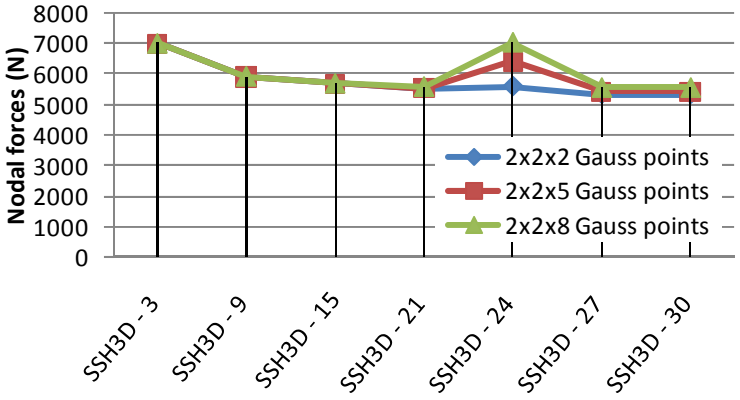

Figure 9: Nodal forces for the isochoric deformation mode of Figure 6 (c) (hourglass mode) versus the number of EAS modes in the SSH3D element for three different integration schemes.

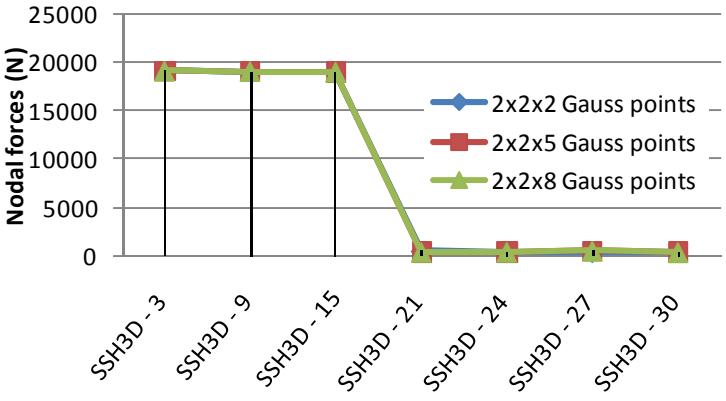

Figure 10: Nodal forces for the isochoric deformation mode of Figure 6 (d) (warp mode) versus the number of EAS modes in the SSH3D element for three different integration schemes.

The fourth group of deformation modes (Figure 6 (d)) related to the warp element shape clearly proves the occurrence of volumetric locking (see Figure 10). When the number of EAS modes is lower than or equal to 15, the computed nodal forces are much too large due to an erroneously overestimated stiffness of the element. When 21 or more EAS modes are used, the volumetric locking is avoided and the stiffness of the element abruptly drops to an accurate value. In this case, no noticeable effect of the integration scheme was observed.

6 EFFECT OF ANS ON THE BENDING BEHAVIOR OF SSH3D

In order to assess the effect of the ANS technique on the mechanical behavior of the SSH3D element, a cylindrical bending patch was investigated. The thin plate submitted to bending had the dimensions 3 x 3 x 0.02 (without units) as shown in Figure 11. The plate was fixed along the X and Z directions on its left face defined by the equation *x=0* (nodes 1, 4, 5 and 8). It was submitted to a bending loading on its right face defined by *x=3* (nodes 13, 14, 15 and 16). The imposed displacements on the right face was such that the plate was deformed into a part of a cylinder whose axis was parallel to the Y-axis and whose radius was 1000.

The accuracy of the element bending behavior is assessed by analyzing the agreement of the displacements of the free interior nodes (2, 3, 6, 7, 9, 10, 11 and 12) with the imposed cylindrical shape. In this respect, the irregular mesh presented in Figure 11 was used. The four versions of the ANS technique implemented in the SSH3D element (see Section 3) as well as the element without the ANS technique were tested.

The results are shown in Table 1, where the nodal displacements along the X and the Z axes are compared with the theoretical displacements required to obtain a perfectly cylindrical deformed geometry. It appears that the bending behavior of the SSH3D element without the ANS technique is not satisfactory (relative error of the nodal displacements up to 49%). The ANS technique with the versions 1, 2 and 3 provides even worse results with relative errors around 96%. Fortunately, the fourth version of ANS seems to be well adapted to the modeling of this bending situation. The maximum relative error on the nodal displacements is limited to 2.9% with the ANS 4, which is acceptable.

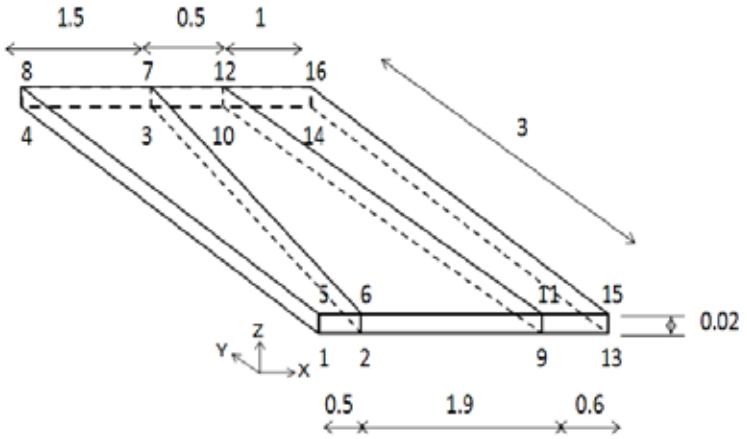

Figure 11: Geometry and irregular mesh used for the cylindrical bending patch test.

Table 1: Cylindrical bending patch test: errors from theoretical values (the largest values among the different nodes are in bold).

	Relative error on nodal displacements along X-axis (%)					Relative error on nodal displacements along Z-axis (%)				
Node	No ANS	ANS 1	ANS 2	ANS 3	ANS 4	No ANS	ANS 1	ANS 2	ANS 3	ANS 4
2	16	73	73	73	2.1	**49**	74	74	74	0.21
3	6.7	77	77	77	**2.9**	1.7	**83**	**83**	**83**	**2.3**
6	**18**	73	73	73	1.7	**49**	74	74	74	0.20
7	4.7	88	88	88	1.6	1.7	**83**	**83**	**83**	**2.3**
9	3.7	17	17	17	0.24	0.35	3.6	3.6	3.6	0.010
10	6.3	**97**	**96**	**96**	2.3	2.0	41	41	41	1.1
11	3.1	13	13	13	0.13	0.35	3.6	3.6	3.6	0.011
12	4.8	71	71	71	2.2	2.0	41	41	41	1.1

7 CONCLUSIONS

This paper presents the main features of the recently developed SSH3D Solid-Shell element. They have been implemented in order to improve the mechanical behavior of the element in various applications dedicated to Solid-Shell or shell elements, e.g. thin-walled structures submitted to large strains and large displacements. These features are:

- The EAS technique which improves the flexibility of the element thanks to additional degrees of freedom. In the SSH3D element, the finite element user can choose which EAS modes (from 1 to 30) he wants to employ according to its particular application.
- The ANS technique which modifies the interpolation of the strain tensor in order to circumvent several locking issues, e.g. transverse shear locking in bending dominated problems or curvature locking. Four different versions of the ANS technique have been implemented in the SSH3D element. Among them, three have been extracted from the literature and the fourth one is an original contribution of the SSH3D element.
- An integration scheme dedicated to Solid-Shell elements. A classical full integration scheme (2 x 2 Gauss points) is employed in the plane of the element, while a user-defined number (from 2 to 10) integration points can be used along the thickness direction. This permits to capture the through-thickness stress and strain gradients with a limited number of element layers.

In this study, the influence of the EAS technique and the integration scheme on the volumetric locking and the influence of the ANS technique on the bending behavior were analyzed. The following comments were attained:

- The volumetric locking can be avoided by using at least 21 EAS modes if a 2 x 2 x 2 integration scheme is used. If 5 or 8 integration points along the thickness direction are used, 24 EAS modes are required.
- An accurate bending behavior is obtained during the cylindrical bending patch test with the fourth version of the ANS technique. The other versions as well as the element without ANS conducted to an erroneous bending behavior of the SSH3D element.

Further applications will be investigated in order to confirm or adapt the conclusions drawn in this paper.

ACKNOWLEDGEMENTS

The authors acknowledge the Interuniversity Attraction Poles Program - Belgian State – Belgian Science Policy (Contract P6/24). L.D. and A.M.H. also thank the Belgian Fund for Scientific Research FRS-FNRS for its financial support.

REFERENCES

[1] Simo, J.C. and Rifai M.S. A Class of Mixed Assumed Strain Methods and the Method of Incompatible Modes. *Int. J. Num. Meth. Engng.* (1990) **29**: 1595-1638.

[2] Alves de Sousa, R.J., Yoon, J.W., Cardoso, R.P.R., Fontes Valente, R.A., Gracio, J.J. On the use of a reduced enhanced solid-shell (RESS) element for sheet forming simulations. *Int. J. Plast.* (2007) **23**: 490-515.

[3] Andelfinger, U. and Ramm, E. EAS-elements for two-dimensional, three-dimensional, plate and shell structures and their equivalence to HR-elements. *Int. J. Num. Meth. Engng.* (1993) **36**: 1311-1337.

[4] Dvorkin, E.N. and Bathe K.-J. A continuum mechanics based four-node shell element for general nonlinear analysis. *Engineering computations* (1984) **1**: 77-88.

[5] Hauptmann, R., Schweizerhof, K. and Doll, S. Extension of the 'solid-shell' concept for application to large elastic and large elastoplastic deformations. *Int. J. Num. Meth. Engng.* (2000) **49**: 1121-1141.

[6] Nguyen, N.H. Development of solid-shell elements for large deformation simulation and springback prediction. Ph.D. Thesis (2009), University of Liège, Belgium. Available from http://bictel.ulg.ac.be/ETD-db/collection/available/ULgetd-11012009-164626/

[7] Vu-Quoc, L. and Tan, X.G. Optimal solid shells for non-linear analyses of multilayer composites. I. Statics. *Comput. Meth. Appl. Mech. Eng.* (2003) **192**: 975-1016.

[8] Klinkel, S., Gruttmann, F. and Wagner, W. A robust non-linear solid shell element based on a mixed variational formulation. *Comput. Meth. Appl. Mech. Eng.* (2006) **195**: 179-201.

[9] Schwarze, M. and Reese, S. A reduced integration solid-shell finite element based on the EAS and the ANS concept-Geometrically linear problems. *Int. J. Num. Meth. Engng.* (2009) **80**: 1322-1355.

[10] Cardoso, R.P.R., Yoon, J.W., Mahardika, M., Choudhry, S., de Sousa, R.J.A. and Fontes Valente, R.A. Enhanced assumed strain (EAS) and assumed natural strain (ANS) methods for one-point quadrature solid-shell elements. *Int. J. Num. Meth. Engng.* (2008) **75**: 156-187.

[11] Alves de Sousa, R.J., Natal Jorge, R.M., Fontes Valente, R.A., César Sá, J.M.A. A new volumetric and shear locking-free EAS element. *Engineering Computations* (2003) **20**:896-925.

XI International Conference on Computational Plasticity. Fundamentals and Applications
COMPLAS XI
E. Oñate, D.R.J. Owen, D. Peric and B. Suárez (Eds)

ELASTIC-PLASTIC ANALYSES USING THE SOLID-SHELL FINITE ELEMENT SHB8PS AND EVALUATION ON SHEET FORMING APPLICATIONS - COMPLAS XI

A. SALAHOUELHADJ[*], H. CHALAL[†], F. ABED-MERAIM[†] AND T. BALAN[†]

Laboratoire d'Etude des Microstructures et de Mécanique des Matériaux (LEM3)
[*] Université Paul Verlaine
Ile du saulcy, 57045 Metz Cedex 01, France
e-mail: abdellah.salahouelhadj@univ-metz.fr, www.univ-metz.fr

[†] Arts et Métiers ParisTech
4, rue Augustin Fresnel, 57078 Metz Cedex 03, France
email: hocine.chalal@ensam.eu, www.ensam.eu

Key words: Solid–Shell Element, Reduced Integration, Physical Stabilization, Assumed Strain Method, Elastic–Plastic Behavior, Sheet Metal Forming.

Abstract. In this contribution, the formulation of the SHB8PS continuum shell finite element is extended to anisotropic elastic–plastic behavior models with combined isotropic-kinematic hardening at large deformations. The resulting element is then implemented into the commercial implicit finite element code Abaqus/Standard via the UEL subroutine. The SHB8PS element is an eight-node, three-dimensional brick with displacements as the only degrees of freedom and a preferential direction called the thickness. A reduced integration scheme is adopted using an arbitrary number of integration points along the thickness direction and only one integration point in the other directions. The hourglass modes due to this reduced integration are controlled using a physical stabilization technique together with an assumed strain method for the elimination of locking. Therefore, the element can be used to model thin structures while providing an accurate description of the various through-thickness phenomena. Its performance is assessed through several applications involving different types of non-linearities: geometric, material and that induced by contact. Particular attention is given to springback prediction for a Numisheet benchmark problem.

1 INTRODUCTION

During the last decade, considerable effort has been devoted to the development of eight-node solid–shell elements for modeling of thin structures (e.g. [1-4]). As they use linear interpolation for efficiency reasons, these elements exhibit various locking phenomena which need to be cured in order to preserve the desired accuracy. Nevertheless, compared to conventional shell elements they have many advantages: the use of full three-dimensional constitutive laws, direct calculation of thickness variations, easy treatment to update configurations (no rotational degrees of freedom used), and simple connection with three-

dimensional elements since displacements are the only degrees of freedom. For sheet forming applications, key features like double-sided contact and increased accuracy with only one layer of elements through the thickness make these elements particularly attractive.

The reduced integration technique, initiated by the works of Zienkiewicz et al. [5] and Hughes et al. [6], was the first successful solution to alleviate some locking pathologies. Finite elements using this method are very efficient due to their low numerical cost. However, stabilization techniques are needed in order to control the spurious zero-energy deformation modes (or hourglass modes) induced by this reduced integration.

In order to circumvent locking phenomena for three-dimensional low-order elements, several authors have used the enhanced assumed strain (EAS) method, based on Simo and Rifai's pioneer work [7]. The basis of such element formulations is given by the mixed variational principle in which the so-called incompatible strain and stress act as additional independent variables. Recent investigations have combined EAS and reduced integration techniques to derive efficient and accurate elements. As examples, some authors used a fixed number of Gauss points in the thickness direction [1-4].

The SHB8PS is one such element that has been recently developed [1, 2], based on in-plane one-point numerical quadrature with eight physical nodes and using an arbitrary number of integration points through the thickness direction. This avoids the use of several layers of elements in order to increase the number of integration points in the thickness, e.g. for metal forming problems. The hourglass modes caused by this reduced integration are efficiently controlled by a physical stabilization technique based on the assumed strain method [8].

In the current contribution, the formulation of the SHB8PS solid–shell finite element is extended to anisotropic elastic–plastic behavior models with combined isotropic-kinematic hardening at large deformations. The resulting element is then implemented into the commercial implicit finite element code Abaqus/Standard via the UEL subroutine. Its good performance is demonstrated through non-linear benchmark problems involving large strains, plasticity and contact. Particular attention is given to springback prediction for a NUMISHEET benchmark problem.

2 FORMULATON OF THE SHB8PS ELEMENT

2.1 Finite element interpolation

SHB8PS is an eight-node, isoparametric hexahedral element with linear interpolation. It has a set of nint integration points chosen along the thickness direction ζ in the local coordinate frame (see Fig. 1).

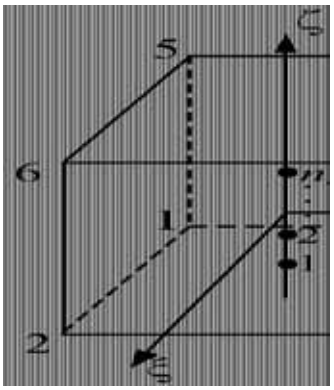

Figure 1: SHP8PS reference geometry

The spatial coordinates x_i and displacements u_i of any point in the element are related to the nodal coordinates and nodal displacements x_{iI} and u_{iI}, respectively, using the classic linear isoparametric shape functions N_I:

$$x_i = x_{iI} N_I(\xi,\eta,\zeta) = \sum_{I=1}^{8} x_{iI} N_I(\xi,\eta,\zeta) \tag{1}$$

$$u_i = u_{iI} N_I(\xi,\eta,\zeta) = \sum_{I=1}^{8} u_{iI} N_I(\xi,\eta,\zeta) \tag{2}$$

Subscript *i* varies from 1 to 3 and represents the direction of the spatial coordinates. Subscript *I* varies from 1 to 8.

2.2 Discretized gradient operator

First, we introduce the $\underline{b}_i$ (i = 1,..., 3) vectors, representing the derivatives of the shape functions at the origin of the reference coordinate system, defined by Hallquist [9] as

$$\underline{b}_i^T = \underline{N}_{,i}(0,0,0) \qquad i = 1,2,3 \tag{3}$$

The displacement gradient can then be written as follows (see Belytschko and Bindeman [8]):

$$u_{i,j} = \left(\underline{b}_j^T + \sum_{\alpha=1}^{4} h_{\alpha,j} \underline{\gamma}_\alpha^T \right) \cdot \underline{d}_i = \left(\underline{b}_j^T + h_{\alpha,j} \underline{\gamma}_\alpha^T \right) \cdot \underline{d}_i \tag{4}$$

where $\underline{d}_i$ are the nodal displacement vectors. The functions h_α and vectors $\underline{\gamma}_\alpha$ (α=1,...,4) are given by

$$h_1 = \eta\zeta,\ h_2 = \zeta\xi,\ h_3 = \xi\eta,\ h_4 = \xi\eta\zeta \tag{5}$$

$$\underline{\gamma}_{\alpha} = \frac{1}{8}\left[\underline{h}_{\alpha} - \sum_{j=1}^{3} (\underline{h}_{\alpha}^{T} \cdot \underline{x}_{j}) \underline{b}_{j} \right] \tag{6}$$

The discretized gradient operator can be written as

$$\underline{\underline{B}} = \begin{bmatrix} \underline{b}_x^T + h_{\alpha,x}\underline{\gamma}_{\alpha}^T & \underline{0} & \underline{0} \\ \underline{0} & \underline{b}_y^T + h_{\alpha,y}\underline{\gamma}_{\alpha}^T & \underline{0} \\ \underline{0} & \underline{0} & \underline{b}_z^T + h_{\alpha,z}\underline{\gamma}_{\alpha}^T \\ \underline{b}_y^T + h_{\alpha,y}\underline{\gamma}_{\alpha}^T & \underline{b}_x^T + h_{\alpha,x}\underline{\gamma}_{\alpha}^T & \underline{0} \\ \underline{0} & \underline{b}_z^T + h_{\alpha,z}\underline{\gamma}_{\alpha}^T & \underline{b}_y^T + h_{\alpha,y}\underline{\gamma}_{\alpha}^T \\ \underline{b}_z^T + h_{\alpha,z}\underline{\gamma}_{\alpha}^T & \underline{0} & \underline{b}_x^T + h_{\alpha,x}\underline{\gamma}_{\alpha}^T \end{bmatrix} \tag{7}$$

2.3 Stabilization and assumed strain method

The particular location of the integration points along a line generates six so-called hourglass modes. The control of the hourglass modes of the SHB8PS element is achieved by adding a stabilization component $\underline{\underline{K}}_{STAB}$ to the element stiffness matrix $\underline{\underline{K}}_{e}$. This part is drawn from the work of Belytschko and Bindeman [8], who applied an efficient stabilization technique together with an assumed strain method. The stabilization forces are consistently derived in the same way. Moreover, the discretized gradient operator is projected onto an appropriate sub-space in order to eliminate shear and membrane locking.

In this approach, the $\underline{b}_i$ vectors (Eq. (3)) are replaced by the mean value of the derivatives of the shape functions over the element, denoted by $\underline{\hat{b}}_i$, as proposed by Flanagan and Belytschko [10]:

$$\underline{\hat{b}}_i^T = \frac{1}{\Omega_e} \int_{\Omega_e} \underline{N}_{,i}(\xi,\eta,\zeta) d\Omega, \quad i = 1,2,3 \tag{8}$$

Then, vectors $\underline{\gamma}_{\alpha}$ are replaced by vectors $\underline{\hat{\gamma}}_{\alpha}$ where the $\underline{b}_i$ vectors are simply substituted by $\underline{\hat{b}}_i$. A modified discretized gradient operator $\underline{\underline{\hat{B}}}$ can be constructed in the same way. It can be shown that the terms of the $\underline{\underline{\hat{B}}}$ operator vanish for $\alpha = 3,4$. In other words, the $\underline{\underline{\hat{B}}}$ operator reduces to its $\underline{\underline{\hat{B}}}_{12}$ part defined identically but where α varies only from 1 to 2. Then, the remaining part $\underline{\underline{\hat{B}}}_{34}$ of $\underline{\underline{\hat{B}}}$, which vanishes at the integration points, is further projected as $\underline{\underline{\hat{B}}}_{34}$. One can project the $\underline{\underline{\hat{B}}}$ operator onto a $\underline{\underline{\overline{\hat{B}}}}$ operator as:

$$\underline{\underline{\overline{\hat{B}}}} = \underline{\underline{\hat{B}}}_{12} + \underline{\underline{\overline{\hat{B}}}}_{34} \tag{9}$$

where $\underline{\underline{\hat{B}}}_{34}$ is given by:

$$\underline{\underline{\overline{\hat{B}}}}_{34} = \begin{bmatrix} \sum_{\alpha=3}^{4} h_{\alpha,x}\underline{\hat{\gamma}}_{\alpha}^{T} & \underline{0} & \underline{0} \\ \underline{0} & \sum_{\alpha=3}^{4} h_{\alpha,y}\underline{\hat{\gamma}}_{\alpha}^{T} & \underline{0} \\ \underline{0} & \underline{0} & h_{3,z}\underline{\hat{\gamma}}_{3}^{T} \\ \underline{0} & \underline{0} & \underline{0} \\ \underline{0} & \underline{0} & \underline{0} \\ \underline{0} & \underline{0} & h_{4,x}\underline{\hat{\gamma}}_{4}^{T} \end{bmatrix} \tag{10}$$

The stiffness matrix $\underline{\underline{K}}_{e}$ takes the form:

$$\underline{\underline{K}}_{e} = \int_{\Omega_e} \underline{\underline{\overline{\hat{B}}}}^{T} \cdot \underline{\underline{C}}^{ep} \cdot \underline{\underline{\overline{\hat{B}}}}\; d\Omega + \underline{\underline{K}}_{Geom} = \underline{\underline{K}}_{12} + \underline{\underline{K}}_{STAB} + \underline{\underline{K}}_{Geom} \tag{11}$$

where the first term $\underline{\underline{K}}_{12}$ is evaluated at the integration points as

$$\underline{\underline{K}}_{12} = \int_{\Omega_e} \underline{\underline{\hat{B}}}_{12}^{T} \cdot \underline{\underline{C}}^{ep} \cdot \underline{\underline{\hat{B}}}_{12}\; d\Omega = \sum_{I=1}^{5} \omega(\zeta_I) J(\zeta_I) \underline{\underline{\hat{B}}}_{12}^{\;T}(\zeta_I) \cdot \underline{\underline{C}}^{ep} \cdot \underline{\underline{\hat{B}}}_{12}(\zeta_I) \tag{12}$$

In this equation, $J(\zeta_I)$ is the Jacobian of the transformation between the reference and the current configurations; $\omega(\zeta_I)$ is the corresponding weight, while $\underline{\underline{C}}^{ep} = \dfrac{\partial \Delta \underline{\sigma}}{\partial \Delta \underline{\varepsilon}}$ is the elastic–plastic tangent modulus. The geometric stiffness matrix $\underline{\underline{K}}_{Geom}$ is due to the non-linear (quadratic) part of the strain tensor and $\underline{\underline{K}}_{STAB}$ represents the stabilization stiffness given by equation:

$$\underline{\underline{K}}_{STAB} = \int_{\Omega_e} \underline{\underline{\hat{B}}}_{12}^{T} \cdot \underline{\underline{C}}^{ep} \cdot \underline{\underline{\overline{\hat{B}}}}_{34}\; d\Omega + \int_{\Omega_e} \underline{\underline{\overline{\hat{B}}}}_{34}^{T} \cdot \underline{\underline{C}}^{ep} \cdot \underline{\underline{\hat{B}}}_{12}\; d\Omega + \int_{\Omega_e} \underline{\underline{\overline{\hat{B}}}}_{34}^{T} \cdot \underline{\underline{C}}^{ep} \cdot \underline{\underline{\overline{\hat{B}}}}_{34}\; d\Omega \tag{13}$$

In a similar way, the internal forces of the element can be written as

$$\underline{f}^{int} = \sum_{I=1}^{5} \omega(\zeta_I) J(\zeta_I) \underline{\underline{\hat{B}}}_{12}^{T}(\zeta_I) \cdot \underline{\sigma}(\zeta_I) + \underline{f}^{STAB} \tag{14}$$

where $\underline{f}^{STAB}$ represents the stabilization forces.

The stabilization terms are calculated in a co-rotational coordinate system [8].

3 NUMERICAL EXAMPLES

3.1 Pinched cylinder

In this example, the elastic-plastic deformation of a cylinder subjected to two opposite concentrated loads in the middle of the structure and bounded by rigid diaphragms on its extremities is considered. This problem has been investigated by a number of authors like [2, 11-15].

The undeformed mesh and boundary conditions are shown in Figure 2. The geometry is characterized by the length L=600 mm, the radius R =300 mm and thickness t = 3 mm. Due to symmetry, only one eighth of the cylinder is discretized. At the ends of the cylinder, the rigid diaphragms prevent any displacement in the radial directions. Material properties are the elasticity modulus E = 3000 MPa, Poisson's coefficient ν = 0.3 and initial yield stress σ_0 = 24.3 MPa. A linear isotropic hardening law is adopted and can be written as:

$$\sigma_Y = \sigma_0 + H\varepsilon_{eq}^P \tag{15}$$

Where ε_{eq}^P is the equivalent plastic strain and H the linear hardening coefficient taken equal to 300 MPa.

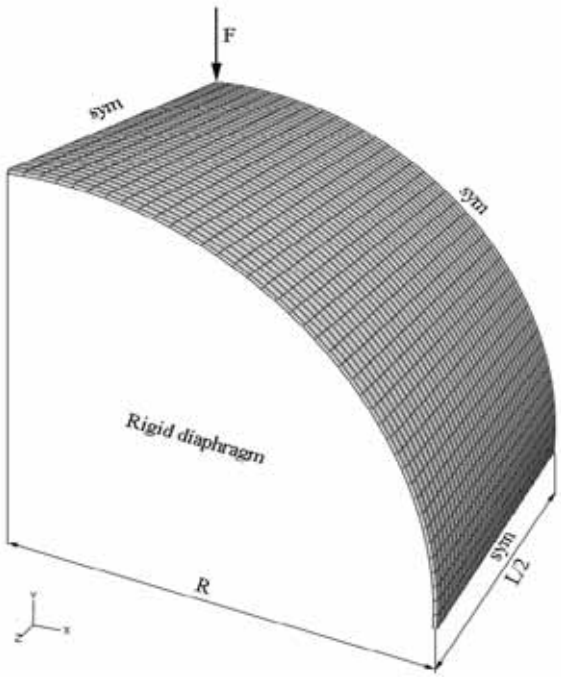

Figure 2: Geometry and boundary conditions for the pinched cylinder

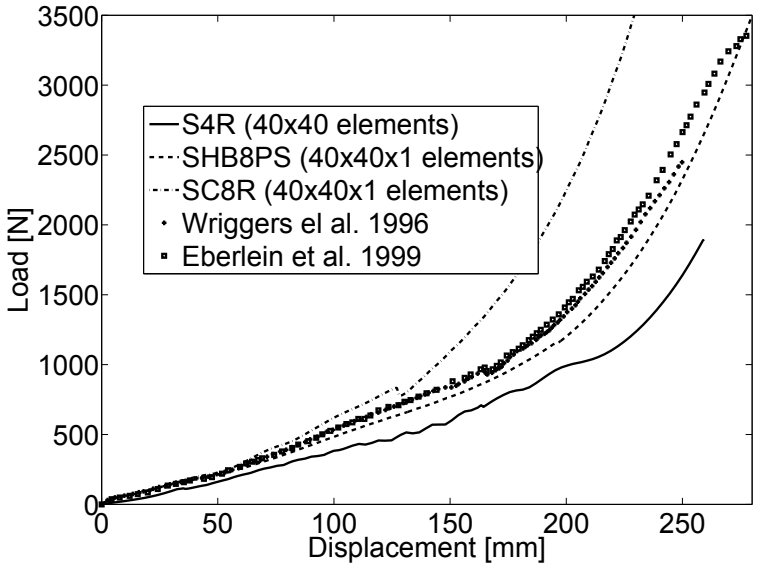

Figure 3: Load deflection curves for elastic-plastic pinched cylinder

Figure 3 shows the load versus the vertical deflection. For the same mesh (40×40×1 elements), the results of the SHB8PS solid-shell element are compared to those of the SC8R solid-shell element and the S4R shell element, along with the reference solutions obtained by [12] and [16]. The calculations using the S4R element failed at a certain loading level, while the SC8R element is too stiff in this test problem and also converges more slowly. For this particularly discriminating test, the curve using SHB8PS element is clearly in better agreement with the 3D investigations of [12] and [16].

3.2 Unconstrained cylindrical bending

The example of the unconstrained cylindrical bending test proposed as springback benchmark in NUMISHEET 2002 is studied [17]. This application allows us to evaluate the performance of the SHB8PS element, implemented in Abaqus/Standard, in presence of geometric, material and contact non-linearities. This benchmark involves a bending-dominated deformation since there is no blank holder. The problem has complex contact boundary conditions during the forming process and the springback after forming is severe. The geometry of the problem is illustrated in Figure 4 and the geometric parameters are summarized in Table 1.

The material under investigation is a High Strength Steel, which is supposed elastic–plastic with isotropic hardening following Swift law:

$$\sigma_Y = K\left(\varepsilon_0 + \varepsilon_{eq}^P\right)^n \tag{16}$$

where K, ε_0 and n represent the hardening parameters of the material. The Young modulus E = 2.175 × 10^5 MPa and the Poisson ration ν = 0.3. Further K = 645.24 MPa, n = 0.25177 and ε_0 = 0.0102. The friction coefficient of the interaction between surfaces punch-sheet and die-sheet is μ = 0.14812.

The amount of springback is quantified by the angle θ as defined in Figure 5. This angle is measured after forming at the maximum punch displacement and after springback. The tools are defined as analytical rigid surfaces.

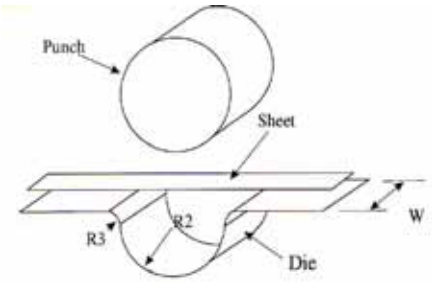

Figure 4: Tool geometry for the unconstrained bending problem

Table 1: Geometric parameters of the unconstrained cylindrical bending problem

Geometric parameter	[mm]	Geometric parameter	[mm]
Punch radius	23.5	Length of the sheet	120.0
Die radius (R2)	25.0	Thickness of the sheet	1.0
Die shoulder (R3)	4.0	Width of the sheet	30.0
Width of tools (W)	50.0	Punch stroke	28.5

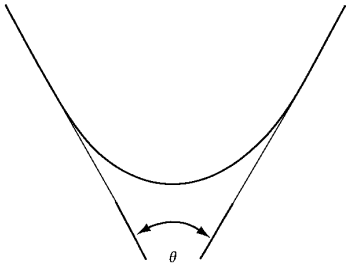

Figure 5: Definition of the angle to measure springback for the unconstrained cylindrical bending problem

The SHB8PS element is compared with both solid and shell elements. Indeed, it is well-known that in applications of sheet metal forming, shell elements have difficulties in dealing with double-sided contact – while conventional solid elements require several element layers to capture bending effects. In the present work, the simulations carried out with the SHB8PS element use only one element layer through the thickness. For symmetry reasons, only one quarter of the blank is discretized by means of 150 SHB8PS elements in the length and only one element over the width of the sheet. The analysis with the SHB8PS element is carried out using five Gauss points in the thickness direction because elastic–plastic applications require, in general, five integration points in minimum to describe the strongly non-linear through-thickness stress distribution [2].

In order to validate the proposed solid–shell element, its predictions are compared to the experimental results of the Numisheet 2002 benchmarks. Two elements from the element library of the Abaqus code are also used in the comparison: the shell element S4R and the 3D

continuum element C3D8I. Again, 150 uniformly distributed elements are used in the length direction for these two elements. However, two layers of C3D8I elements are required in the thickness direction in order to represent the stress distribution due to bending with sufficient accuracy. Also, ten C3D8I elements are used along the width direction in order to keep their aspect ratio in acceptable limits. Figure 4 displays the punch force versus punch displacement curves predicted by the three elements, along with the experimental results (BE-1 to BE-4) from Meinders et al. [17].

Figure 6 shows that the numerical results obtained with SHB8PS element are the closest to the experimental results and they lay close to the solid element predictions. The slight differences between the two may be due to the different number and distribution of integration points along the thickness direction. The S4R element has too soft behavior with respect to SHB8PS and C3D8I elements.

The springback angles are also investigated, as they were also experimentally measured [17]. The springback phenomenon is particularly exacerbated in this unconstrained bending application, as illustrated in Figure 7. Table 2 summarizes the opening angles before and after springback for elements SHB8PS, C3D8I and S4R, compared to experiments. The simulated values with SHB8PS and C3D8I elements are close to each other and the closest to experiments. Comparing the numerical results to the experimental ones, the good performance of the SHB8PS solid–shell element is confirmed.

Table 2: Measured and simulated opening angles before and after springback

	Experimental				**Simulated**		
	BE-01	BE-02	BE-03	BE-04	SHB8PS	C3D8I	S4R
Forming	22.7707	22.0064	23.0255	20.8599	23.0692	22.5820	33.3078
Springback	37.4212	35.6787	30.9036	35.3636	36.3952	32.0832	43.9071

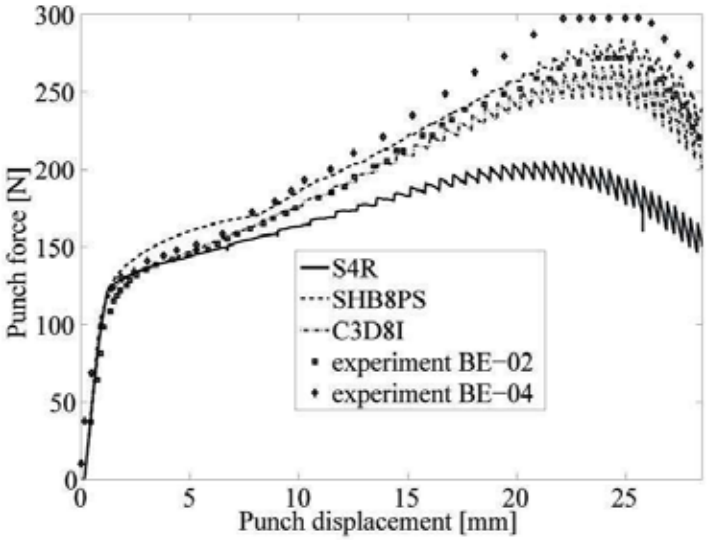

Figure 6: Punch force vs. punch displacement curves for High Strength Steel

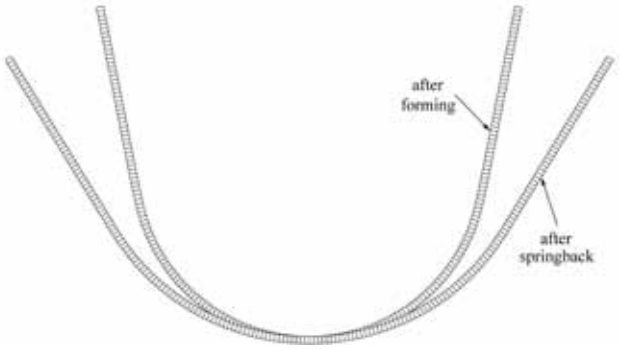

Figure 7: Deformed shape of the sheet in the unconstrained bending problem

4 CONCLUSIONS

An extended version of the solid--shell finite element SHB8PS has been implemented into the implicit finite element code Abaqus/Standard via the UEL subroutine. The formulation of this element employs a combination of the reduced integration scheme with the assumed strain method and a specific projection to eliminate locking phenomena. The resulting hourglass modes are controlled using a physical self-adapting stabilization procedure. This version of the SHB8PS element can deal with problems involving anisotropic elastic-plastic behavior at large deformations and double-sided contact between sheet and tools, which are typical in sheet metal forming applications.

The performance of SHB8PS element has been shown through two numerical examples involving various types of non-linearities: geometric, material and contact. Indeed, at equivalent mesh density, SHB8PS performs at least as well as the most accurate (and expensive) solid elements. However, this accuracy is achieved at a lower cost by using one single layer of SHB8PS elements and simply adjusting the number of integration points through the thickness. This feature makes the element very competitive for sheet metal forming.

REFERENCES

[1] Abed-Meraim, F. and Combescure, A. *International Journal for Numerical Methods in Engineering* (2009) **80**:1640-1686.

[2] Legay, A. and Combescure, A. *International Journal for Numerical Methods in Engineering* (2003) **57**:1299-1322.

[3] Alves de Sousa, R.J., Cardoso, R.P.R., Fontes Valente, R.A., Yoon, J.W., Grácio, J.J. and Natal Jorge, R.M. *International Journal for Numerical Methods in Engineering* (2006) **67**:160-188.

[4] Reese, S. *Computer Methods in Applied Mechanics and Engineering* (2005) **194**:4685-4715.

[5] Zienkiewicz, O., Taylor, R. and Too, J. *International Journal for Numerical Methods in Engineering* (1971) **3**:275–290.

[6] Hughes, T., Cohen, M. and Haroun, M. *Nuclear Engineering Design* (1978) **4**6:203–222.

[7] J. Simo and M. Rifai, *International Journal for Numerical Methods in Engineering* (1990) **29**:1595–1638.
[8] Belytschko, T., and Bindeman, L. *Computer Methods in Applied Mechanics and Engineering* (1993) **105**:225-260.
[9] Hallquist, J. Theoretical manual for DYNA3D. *Tech. Rep. Report UC1D-19401* (1983) Lawrence Livermore National Laboratory, Livermore, CA.
[10] Flanagan, D. and Belytschko, T. *International Journal for Numerical Methods in Engineering* (1981) **17**:679-706.
[11] Simo, J.C. and Kennedy, J.G. *Computer Methods in Applied Mechanics and Engineering* (1992) **96**:133-171.
[12] Wriggers, P. and Eberlein, R. and Reese, S. *International Journal of Solids and Structures* (1996) **33**:3309-3326.
[13] Sori\'{c}, J. and Montag, U. and Kr\"{a}tzig, WB. Computer Methods in Applied Mechanics and Engineering (1997) **148**:315-328.
[14] Brank, B. and Peri\'{c}, D. and Damjani\'{c}, FB. International Journal for Numerical Methods in Engineering (1997) **40**: 689-726.
[15] Miehe, C. Computer Methods in Applied Mechanics and Engineering (1998) **155**:193-233.
[16] Eberlein, R. and Wriggers, P. *Computer Methods in Applied Mechanics and Engineering* (1999) **171**: 243-279.
[17] Meinders, T., Konter, A., Meijers, S., Atzema, E. and Kappert H. *NUMISHEET 2005, 6th international conference and workshop on numerical simulation of 3D sheet metal forming processes* (2005) Detroit, Michigan, USA.

XI International Conference on Computational Plasticity. Fundamentals and Applications
COMPLAS XI
E. Oñate, D.R.J. Owen, D. Peric and B. Suárez (Eds)

ELASTOPLASTIC ANALYSIS OF PLANE STEEL FRAMES UNDER DYNAMIC LOADING

ANDRÉA R.D. SILVA[*], WILLIAM L. FERNANDES[†], RICARDO A.M. SILVEIRA[*] AND PAULO B. GONÇALVES[†]

[*] Department of Civil Engineering, School of Mines, Federal University of Ouro Preto
Campus Universitário s/n, Morro do Cruzeiro, 35400-000 Ouro Preto, MG, Brazil
emails: andreadiassilva@yahoo.com.br, ricardo@em.ufop.br

[†] Department of Civil Engineering, Catholic University (PUC-Rio)
Rua Marquês de São Vicente, 225, Gávea, 22453-900 Rio de Janeiro, RJ, Brazil
emails: wlfernandes13@gmail.com, paulo@puc-rio.br

Key words: Nonlinear Dynamic Behavior, Elastoplastic Analysis, Plastic Hinge Method, Steel Frames, Finite Element Method.

1 INTRODUCTION

Knowledge of structural behavior is essential for designing lighter constructions without affecting their safety and quality standards. Lack of levels and characteristics of dynamic response, for example, can lead to system failure during repetitive loading application, due to the accumulation of structural damage. Thus, it becomes necessary to use more complex theories, such as nonlinear formulations, avoiding simplifications in the process of analysis/design.

Plastic analysis of steel structures enhances several benefits compared to the elastic's, because one of the most important characteristics of this material, the ductility — ability to withstand large deformations before breaking — is fully considered. This allows for force redistribution after the yielding limit of some structural member's cross section has been achieved. This property also promotes the absorption of energy, which becomes extremely important in structures subjected to seismic excitations [1].

Most studies on inelastic analysis rely on the plastic-zone method (or plasticity distributed) or the plastic hinge method (concentrated plasticity or lumped model). The basic difference between them is the refinement degree used to represent the structural member plastification. In the plastic-zone method, the structure is discretized into finite elements and the cross-sections of these elements are subdivided into many fibers. The second-order effects and residual stresses can be considered directly in the analysis. Due to the high degree of refinement, the analyses made with this method are treated as close-to-accurate solutions. However, as it has a high computational cost, the plastic-zone approach is used more for simulation of simple structures that can serve as a calibration for other models and numerical formulations. Few works are found in this line of research directly related to dynamic analysis. Among these are: Kant and Marur [2], Mamaghani et al. [3], and Thai and Kim [4].

In contrast, the plastic hinge approach, which assumes the effects of plasticity concentrated at hinge points located at the ends of the elements, can be classified as an elastic-plastic hinge model or a refined-plastic hinge model. The first one, used in this work, is the simplest way to consider the inelastic effects in structural analysis. The element remains in an elastic regime until the plastic resistance of the cross-section is achieved by forming a plastic hinge. The residual stress effects are not considered. In the refined-plastic hinge model, on the contrary, the process of cross-section plastification can be accompanied and the residual stresses can be considered. By providing an approximate representation of the member behavior in relation to the plastic-zone approach, computationally, the plastic hinge models become significantly less expensive and more applied ([5] – [10]).

The computational system for advanced structural analysis CS-ASA [10] is used in this work. The main characteristic of this computational tool is the accomplishment of the nonlinear static and dynamic analyses of steel plane framed structures. In these analyses, the geometric nonlinearity or second-order effects can be simulated, as well as those introduced by considering semi-rigid connections, and steel inelasticity. The introduction of all these nonlinear effects in the numerical models and formulations makes it possible to establish the stability and strength limit of the structural system in a direct manner, without the necessity to separately verify each member's capacity [11]. For this article, a routine able to simulate the nonlinear cyclic behavior of the material was implemented in the CS-ASA system. Basically, this model is a natural extension of those already implemented in CS-ASA for the static case and can be found in detail in Silva [10]. Therefore, the numerical formulation adopted considers two sources of nonlinearities: the geometric, which includes structural displacement effects, and the physical, caused by the steel's inelasticity. The methods of Newmark (integration process) and Newton-Raphson (iteration process) are used for solving the nonlinear equations of motion. This numerical methodology is discussed throughout the work. Some examples considering the nonlinear inelastic time-history response of planar steel frames will be discussed at the end of the work.

2 FINITE ELEMENT FORMULATION

This section presents the finite element formulation used in the study of the inelastic behavior of steel structures. This formulation, as already highlighted, follows the plastic hinge approach, and the effect of the material yielding is considered in the finite element force-displacement constitutive relationship. Initially, some assumptions should be made. The inelastic behavior is restricted to the ends of the element (nodal points) that will simulate the plastic hinges. The length of these plastic hinges will be null and its deformation is constituted only by inelastic rotation. Once the plastic hinge is formed, the inner forces in cross-section must respect the plastic resistance surface (full yield surface of the section).

Consider then the finite element shown in Figure 1. The beam-column element presented has fictitious section springs attached at its ends. These springs are imagined to have a bending stiffness S_s, which can be defined based on a state parameter ψ (this state parameter monitors the cross-section yielding process and will be discussed in the next subsection). The element force-displacement relationship on the co-rotational local system, considering the cross-section material yielding effect, can be written as [10]:

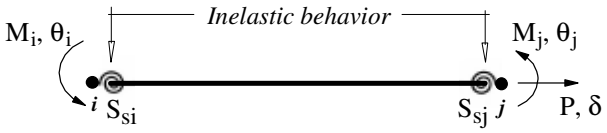

Figure 1: Beam-column finite element with fictitious section springs

$$\begin{Bmatrix} \Delta P \\ \Delta M_i \\ \Delta M_j \end{Bmatrix} = \begin{bmatrix} EA/L & 0 & 0 \\ 0 & S_{si} - S_{si}^2\left(k_{jj} + S_{sj}\right)/\beta & S_{si}S_{sj}k_{ij}/\beta \\ 0 & S_{si}S_{sj}k_{ji}/\beta & S_{sj} - S_{sj}^2\left(k_{ii} + S_{si}\right)/\beta \end{bmatrix} \begin{Bmatrix} \Delta\delta \\ \Delta\theta_i \\ \Delta\theta_j \end{Bmatrix}, \text{ or, } \Delta\mathbf{f}_c = \mathbf{K}_c\Delta\mathbf{u}_c \qquad (1)$$

with $\beta = \left(S_{si} + k_{ii}\right)\left(S_{sj} + k_{jj}\right) - k_{ij}k_{ji}$.

In Eq. (1), the subscribes *i* and *j* are related to the element ends, and the subscript *c* indicates the coordinate system used; *E* is the Young's modulus; *A* is the cross-section area; *L* is the element length; ΔP, ΔM, $\Delta\delta$ and $\Delta\theta$ are, respectively, the axial force, the bending moment, the nodal axial deformation and nodal rotation increments, and are represented in Figure 1. The coefficients of the matrix $\mathbf{K}_c$, besides simulating the section's material plastification at each end of the element, also considers the second-order effects — for relatively large displacements, the lateral deflection of a member can generate additional bending moments because of the presence of axial force. In this case, the terms k_{ii}, k_{jj}, k_{ij} and k_{ji} involved in the simulation are:

$$k_{ii} = k_{jj} = 4EI/L + 2PL/15 + 4PI/(AL) \text{ and } k_{ij} = k_{ji} = 2EI/L - PL/30 + 2PI/(AL) \qquad (2)$$

where *I* represents the moment of inertia.

With the increase of axial force on a section with a plastic hinge already formed, the section resistance may become smaller than the internal forces acting on it. Then, a change in the force-displacement relationship of the element (Eq. 1) will be required so that the section's plastic resistance is not violated. This change can be expressed by the following equation:

$$\begin{Bmatrix} \Delta P \\ \Delta M_i \\ \Delta M_j \end{Bmatrix} = \begin{bmatrix} EA/L & 0 & 0 \\ 0 & C_1K_1 & 0 \\ 0 & 0 & C_2K_2 \end{bmatrix} \begin{Bmatrix} \Delta\delta \\ \Delta\theta_i \\ \Delta\theta_j \end{Bmatrix} + \begin{Bmatrix} 0 \\ \zeta_i \\ \zeta_j \end{Bmatrix}, \text{ or, } \Delta\mathbf{f}_c = \mathbf{K}_{ch}\Delta\mathbf{u}_c + \Delta\mathbf{f}_{ps} \qquad (3)$$

where the parameter vector $\Delta\mathbf{f}_{ps}$ defines the correction of the internal forces. The other matrix $\mathbf{K}_{ch}$ coefficients are presented in Table 1 according to the element end where the plastic hinge is formed. In this table, δM_{pr} is the modification to translate the section moment *M* to the interaction surface (resistance or full yield surface), maintaining the axial force *P* fixed. Details of this change and the process to transform Eqs. (1) and (3) into the global coordinate system, later obtaining the structural system internal forces vector $\mathbf{F}_i$ and stiffness matrix $\mathbf{K}$, can be found in Silva [10].

The section resistance surface adopted here will be presented in the following subsection, which also discusses the numerical procedure used to simulate the material's nonlinear behavior.

Table 1: Parameters in Eq. (3)

Plastic hinge	Parameters			
	C_1	C_2	ζ_1	ζ_2
End *i*	0	1	δM_{pr_i}	$\delta M_{pr_i}(k_{c(3,2)}/k_{c(2,2)})$
End *i*	1	0	$\delta M_{pr_j}(k_{c(2,3)}/k_{c(3,3)})$	δM_{pr_j}
Ends *i* and *j*	0	0	δM_{pr_i}	δM_{pr_j}

$K_1 = k_{c(2,2)} - k_{c(2,3)}k_{c(3,2)}/k_{c(3,3)}$ and $K_2 = k_{c(3,3)} - k_{c(2,3)}k_{c(3,2)}/k_{c(2,2)}$

$k_{c(m,n)}$ is the term corresponding to the row *m* and the column *n* in $\mathbf{K}_c$ (see Eq. 1)

2.1 Cyclic plasticity model

Steel inelasticity is the yielding process of the fibers causing changes in cross-section stress distribution when acting forces increase. Under loading/unloading conditions, the steel can be idealized as an elastic-perfectly plastic material and its constitutive tension-deformation relationship in this case is illustrated graphically in Figure 2a. It is assumed that the plastification occurs when the stress reaches the yield stress σ_y. After that, an increase in loading causes increase in axial deformation without, however, increasing the stress. In this model, the material's permanent deformation appears after the unloading. Load relief makes the material return to the elastic state, remaining, however, with a residual deformation. Models that directly simulate the stress-strain relationship are usually applied in methodologies based on the plastic-zone method. In this work, the cross-section plasticity state, in the same situation, is characterized by the elastic-perfectly plastic model expressed, however, in the moment-curvature relationship as shown in Figure 2b. It is worth clarifying that the potential benefits from the material hardening (strain-hardening) and the Bauschinger effect [6] are ignored in this model.

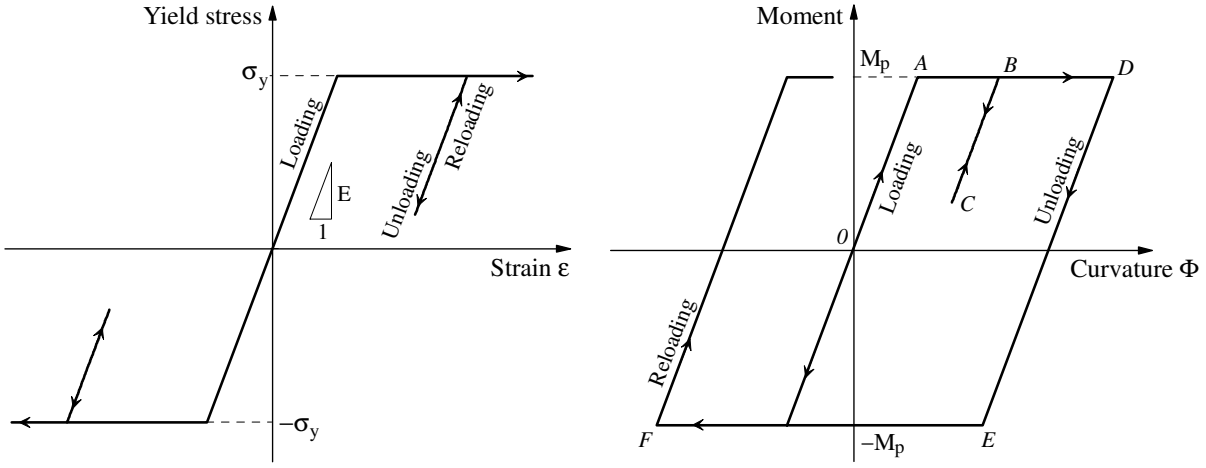

(a) Tension-deformation relation (b) Moment-curvature relation

Figure 2: Elastic-perfectly plastic constitutive material hysteretic model

Figure 2b illustrates the section's behavior during the loading-unloading process through its moment-curvature relationship. The section's material remains elastic along the line *0A*

under loading conditions. When the plastic moment is reached, $M_p = Z\sigma_y$, Z being the module plastic, a plastic hinge is formed and no additional moment can be resisted. So, with the increase in loading, and this section already yielded, the exceeded moment will be redistributed to adjacent members. As a result, the path continues along the horizontal line *AB*. When unloading occurs at *B*, the direction of rotation is reversed and the section returns to the elastic state, but with a residual deformation. In this case, the curve follows the line *BC* parallel to the virgin slope *0A*. If reloaded at point *C*, the path will move along *CB* up to reach again the plastic moment M_p, and continue along the line BD. With the unloading at point *D*, the path *DEF* will be followed where the line *EF* indicates that the negative plastic moment ($-M_p$) has been reached.

The full yield surface, defining the boundary where the material ceases to behave elastically and becomes plastic, will be evaluated from internal acting forces and geometrical characteristics of the finite element cross-section. The structure's resistance limit can be achieved with the development of a plastic mechanism, which is the consequence of a number of plastic hinges formed. If a structural element is subjected to the combined action of bending moment and axial force, its moment capacity M_p is reduced [10]. This influence is seen through the full yield surface defined by equations:

$$M_{pr} = \left[B_f t_f \left(D - t_f \right) + \left((d/2)^2 - \eta^2 \right) t_w \right] \sigma_y \text{, para } \eta \le d/2 \tag{4a}$$

$$M_{pr} = \left[(D/2)^2 - \eta^2 \right] B_f \sigma_y \text{, para } d/2 < \eta \le d/2 + t_f \tag{4b}$$

with:

$$\eta = P / \left(2\sigma_y t_w \right) \text{, para } \eta \le d/2 \tag{5a}$$

$$\eta = \left(P - \sigma_y t_w d \right) / \left(2\sigma_y B_f \right) + d/2 \text{, para } d/2 < \eta \le d/2 + t_f \tag{5b}$$

The interaction equations between the axial force and bending moment follow the requirements of BS 5950 [12] and are valid for the I or H profiles. The full yield surface for the profile W470x74 is exemplified in Figure 3. The axial force and bending moment are parameterized, respectively, by axial yield limit, $P_y = A\sigma_y$, and the plastic moment M_p. Figure 3 shows how the terms B_f, t_f, D, t_w and d are defined, which characterize the profile's web and flange dimensions and appear in Eqs. (4) and (5).

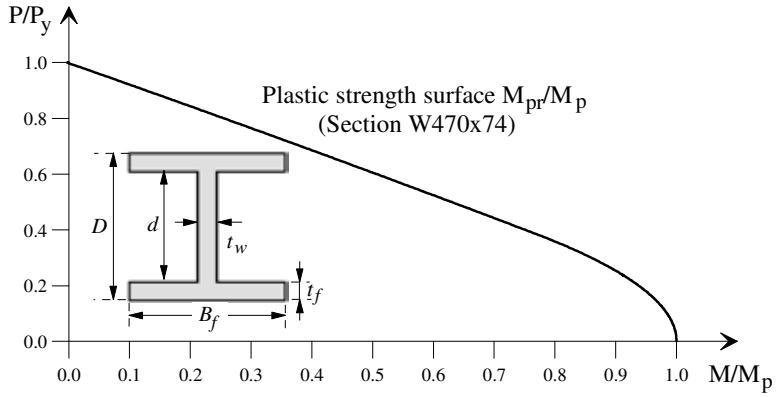

Figure 3: Reduced plastic moment capacity of I-shaped cross-section under axial load

Admitting the material to have elastic-perfectly plastic behavior, it is assumed that a given cross-section remains in elastic regime until its plastic resistance is reached. To accompany the stiffness loss of the cross-section during the loading/unloading process, a dimensionless parameter ψ is adopted. Thus, the development of plasticity in the structure's cross-section members is reflected in the section spring stiffness at the edge of the element, which when using ψ, is defined by equation:

$$S_s = \frac{6EI}{L}\frac{\psi}{1-\psi} \tag{6}$$

It is considered that ψ has the value "1" when the material is in elastic regime, i.e., while the section bending moment does not reach the reduced plastic moment M_{pr}. In this case, using (6), the section remains rigid ($S_s \to \infty$), with the plastic rotation null. On the other hand, with the section yielding ($M = M_{pr}$), ψ reduces to "0" and the section stiffness becomes null ($S_s \to 0$), simulating the plastic hinge formation.

3 SOLUTION PROCEDURE FOR THE TRANSIENT INELASTIC PROBLEM

The equilibrium equation that governs the nonlinear dynamic response of a structural system can be obtained using the Virtual Displacement Principle (VDP). Considering that, besides the restoration tensions provoked by structural deformation and external forces, the structural system is also submitted to inertial and dissipated forces. The equation to obtain the equilibrium of the elements in this system, at time $t + \Delta t$, can be expressed as [13]:

$$\int_{{}^{t}V} \tau_{ij}\delta\varepsilon_{ij}dV + \int_{{}^{t}V} \rho\ddot{d}_k\delta\ddot{d}_k dV + \int_{{}^{t}V} \mu\dot{d}_k\delta\dot{d}_k dV = \delta d_k{}^{T} f_{ek} \tag{7}$$

where τ_{ij} represents the Cauchy tensor in equilibrium with external excitation f_{ek}; $\delta\varepsilon_{ij}$ are the virtual Green-Lagrange deformation components corresponding to random arbitrary displacements δd_k, which are cinematically compatible with the boundary conditions; ρ is the density or the volumetric mass (mass per volume unit), and μ is the viscous damping coefficient of the material. To determine the equilibrium configuration of the structure in $t + \Delta t$, the updated Lagrangian referential is used. In this case, the configuration in instant t is used as the reference for analysis.

According to the usual finite element procedures, establishing the deformation field and displacement of the elements in function of the nodal displacements and using Eq. (7), it is possible to obtain, in a discretized form, the following matrix equation:

$$\mathbf{M}\ddot{\mathbf{U}} + \mathbf{C}\dot{\mathbf{U}} + \mathbf{F}_i = \lambda(t)\mathbf{F}_r \tag{8}$$

in which $\mathbf{M}$ and $\mathbf{C}$ are the mass and damping matrices, respectively; $\mathbf{U}$, $\dot{\mathbf{U}}$ and $\ddot{\mathbf{U}}$, represent the displacement, velocity and acceleration vectors, respectively, of the structural system; $\mathbf{F}_i$ is the internal force vector; $\mathbf{F}_r$ is the vector that defines the direction of the external excitation; and λ establishes the intensity and direction of the load in a determined instant t.

In a nonlinear structural study, as is done herein, the stiffness matrix should be constantly updated to capture the state of equilibrium influenced by second order effects (P-Δ and P–δ) and inelasticity of the material. Afterwards, it becomes necessary to use an incremental-

iterative solver strategy. For this, a numerical procedure, which combines the methods of Newmark and Newton-Raphson, is used here to obtain a nonlinear dynamic response of the structural system. The computational steps necessary to achieve this objective are detailed in Table 2. Analyzing the numerical procedures adopted, see that the members' plasticity is assessed at the end of each iterative cycle; and the technique described in Section 2 is used for simulating the material nonlinear behavior when the structure is subjected to a cyclic loading. The computational algorithm is summarized in Table 3.

Table 2: Numerical strategy for nonlinear transient analysis

1. Input the material and geometric properties of the frame, and obtain the force vector $\mathbf{F}_r$

2. Start the initial displacement, velocity and acceleration vectors ${}^0\mathbf{U}$, ${}^0\dot{\mathbf{U}}$ and ${}^0\ddot{\mathbf{U}}$

3. Select the time step Δt

4. FOR EACH TIME STEP $t+\Delta t$

4a. Derive the tangent stiffness, mass and damping matrices: **K**, **M**, and **C**

4b. Using Newmark parameters β and γ, calculate the constants:

$a_0 = 1/(\beta\Delta t^2)$; $a_1 = \gamma/(\beta\Delta t)$; $a_2 = 1/(\beta\Delta t)$; $a_3 = 1/(2\beta)-1$; $a_4 = \gamma/\beta-1$;

$a_5 = \Delta t\left(\gamma/(2\beta)-1\right)$; $a_6 = a_0$; $a_7 = -a_2$; $a_8 = -a_3$; $a_9 = \Delta t(1-\gamma)$; $a_{10} = \alpha\Delta t$

4c. Form the effective stiffness matrix: $\hat{\mathbf{K}} = \mathbf{K} + a_0\mathbf{M} + a_1\mathbf{C}$

4d. Calculate: $\hat{\mathbf{F}} = {}^{(t+\Delta t)}\lambda\mathbf{F}_r + \mathbf{M}\left(a_2\,{}^t\dot{\mathbf{U}} + a_3\,{}^t\ddot{\mathbf{U}}\right) + \mathbf{C}\left(a_4\,{}^t\dot{\mathbf{U}} + a_5\,{}^t\ddot{\mathbf{U}}\right) - {}^t\mathbf{F}_i$

4e. Solve for displacement increments: $\hat{\mathbf{K}}\Delta\mathbf{U}^0 = \hat{\mathbf{F}}$

5. NEWTON-RAPHSON ITERATION: k = 1, 2, 3,...

5a. Evaluate the approximation of the acceleration, velocities and displacements:

${}^{(t+\Delta t)}\ddot{\mathbf{U}}^{(k-1)} = a_0\Delta\mathbf{U}^{(k-1)} - a_2\,{}^t\dot{\mathbf{U}} - a_3\,{}^t\ddot{\mathbf{U}}$, ${}^{(t+\Delta t)}\dot{\mathbf{U}}^{(k-1)} = a_1\Delta\mathbf{U}^{(k-1)} - a_4\,{}^t\dot{\mathbf{U}} - a_5\,{}^t\ddot{\mathbf{U}}$, and

${}^{(t+\Delta t)}\mathbf{U}^k = {}^t\mathbf{U} + \Delta\mathbf{U}^{(k-1)}$

5b. Update the geometry of the frame

5c. Evaluate the internal forces vector: ${}^{(t+\Delta t)}\mathbf{F}_i^{(k-1)} = {}^t\mathbf{F}_i + \mathbf{K}\Delta\mathbf{U}^{(k-1)}$

5d. Form: ${}^{(t+\Delta t)}\mathbf{R}^k = {}^{(t+\Delta t)}\lambda\mathbf{F}_r - \left(\mathbf{M}\,{}^{(t+\Delta t)}\ddot{\mathbf{U}}^{(k-1)} + \mathbf{C}\,{}^{(t+\Delta t)}\dot{\mathbf{U}}^{(k-1)} + {}^{(t+\Delta t)}\mathbf{F}_i^{(k-1)} - {}^{(t+\Delta t)}\mathbf{F}_{ps}^{(k-1)}\right)$

5e. Solve for the corrected displacement increments $\hat{\mathbf{K}}\delta\mathbf{U}^k = {}^{(t+\Delta t)}\mathbf{R}^k$

5f. Evaluate the corrected displacement increments: $\Delta\mathbf{U}^k = \Delta\mathbf{U}^{(k-1)} + \delta\mathbf{U}^k$

5g. Check the convergence of the iteration process:

$\|\Delta\mathbf{U}^k\| / \|{}^t\mathbf{U} + \Delta\mathbf{U}^k\| \le \xi$, where ξ is a tolerance factor **NO**: Go to 5

5h. Calculate the acceleration, velocities and displacements at time $t+\Delta t$

${}^{(t+\Delta t)}\ddot{\mathbf{U}}^k = a_0\Delta\mathbf{U}^k - a_2\,{}^t\dot{\mathbf{U}} - a_3\,{}^t\ddot{\mathbf{U}}$, ${}^{(t+\Delta t)}\dot{\mathbf{U}}^k = a_1\Delta\mathbf{U}^k - a_4\,{}^t\dot{\mathbf{U}} - a_5\,{}^t\ddot{\mathbf{U}}$ and

${}^{(t+\Delta t)}\mathbf{U}^k = {}^t\mathbf{U} + \Delta\mathbf{U}^k$

6. FOR THE NEXT TIME STEP

6a. Evaluate the internal forces vector: ${}^{(t+\Delta t)}\mathbf{F}_i = {}^t\mathbf{F}_i + \mathbf{K}\Delta\mathbf{U}^k$

6b. Evaluate the plastification at the ends of the finite elements (see Table 4)

Table 3: Algorithm for modeling of section behavior under cyclic loading

1. Consider the internal forces vectors ${}^{(t+\Delta t)}\mathbf{F}_i$ and ${}^{t}\mathbf{F}_i$

2. FOR EACH FINITE ELEMENT

3. FOR EACH NODAL POINT OF THE ELEMENT

4. Consider the moments ${}^{(t+\Delta t)}M$ and ${}^{t}M$, and the axial force ${}^{(t+\Delta t)}P$ at section

5. Evaluate the incremental moment in this section: $\Delta M = {}^{(t+\Delta t)}M - {}^{t}M$

6. Consider the reduced plastic yield moment M_{pr} (see Eq. 4)

7. If $(M \cdot \Delta M \geq 0)$ then ⇨ LOADING CONDITION

If $(|M| < |M_{pr}|)$: $\psi = 1$ and $S_s = 10^{10}\ EI/L$ (rigid section – elastic behavior)

If $(|M| \geq |M_{pr}|)$: $\psi = 0$ and $S_s = 10^{-10}\ EI/L$ (plastic hinge – plastic behavior)

8. If $(M \cdot \Delta M < 0)$ then ⇨ UNLOADING CONDITION

$\psi = 1$ and $S_s = 10^{10}\ EI/L$ (rigid section – elastic behavior)

9. Go to step 4 in Table 2

4 NUMERICAL APPLICATIONS

In this section, the methodology presented for nonlinear dynamic analysis is used to obtain the response of three planar structural systems with elastic-perfectly plastic material. All structures were also investigated by Chan and Chui [6] and their results are used for validation of the numerical strategy proposed. No viscous damping was considered and time increments of 10^{-3}s were adopted in the numerical integration process.

4.1 Toridis-Khozeimeh portal frame

The simple portal frame with fixed ends shown in Figure 4, initially studied by Toridis and Khozeimeh [14] and subsequently by Marur and Kant [2], is the first example of this section. The steel profile masses of the structure members were multiplied by 625 and considered concentrated in the elements nodal points following the modeling made by the aforementioned authors. Three finite elements were used in the modeling of each of the three structural members.

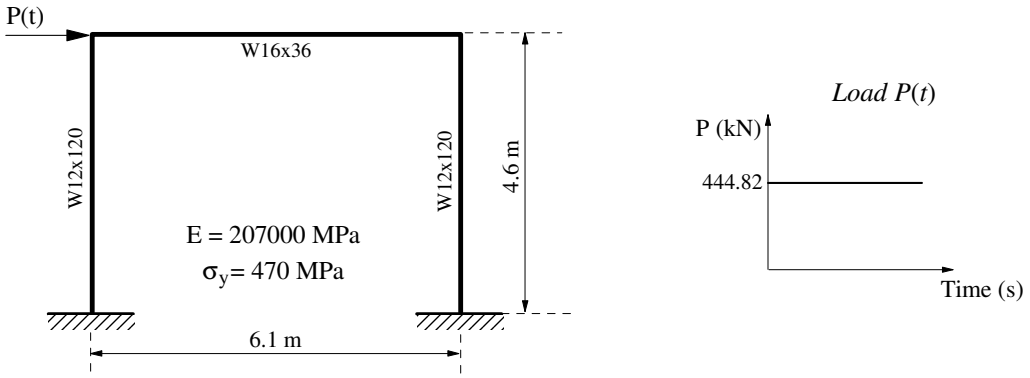

Figure 4: Toridis-Khozeimeh portal frame: geometry and loading

A constant impact load equal to 444.82 kN is applied on top of the column on the left side of the frame, and the transient responses of this structure are presented in Figure 5. Figure 5a shows the horizontal displacement time-history at the point of application of the load for the perfectly elastic material; and Figure 5b presents the dynamic response considering the elastic-perfectly plastic material. Figure 5a also indicates the displacement obtained from the static elastic analysis, u = 3.97 cm, which represents half of the maximum amplitude obtained in dynamic analysis. Comparing the displacement time-histories for these studies, according to Figure 5b, it can be seen that the amplitudes begin diverting more significantly from 0.55s, due to the increase of plastic deformations. There is, moreover, a constant movement response. In this case, the material exhibits an elastic behavior but with a residual deformation. This is a feature of elastic-perfectly plastic model used on this work, and just as in the elastic model, it does not allow the dissipation of energy.

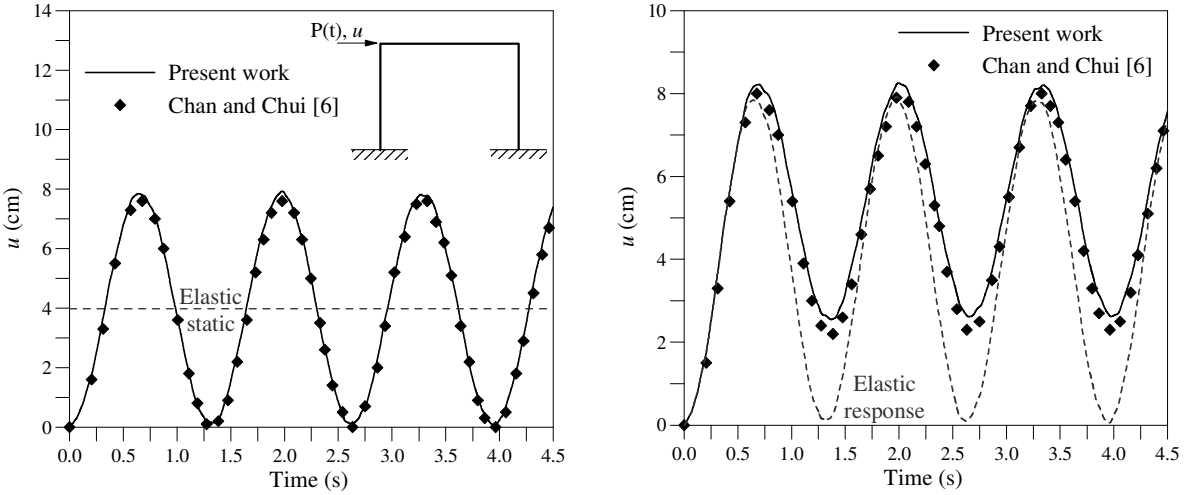

(a) Elastic response (b) Elastoplastic response

Figure 5: Time history of the horizontal displacement, u, on top of the frame

4.2 Steel arch-shaped frame

The structure shown in Figure 6 is now studied. The curved shape of this structure was obtained modeling it with six pieces of steel profile UB305x165x40 kg/m. Besides Chan and Chui [6], Lee et al. [5] also investigated the transient elastic-perfectly plastic response of the arch but using a bilinear plastic resistance surface.

Six finite elements, each modeling of the steel parts, were adopted on discretization. The steel arch, which has fixed supports, is subjected to an vertical impact load $P(t)$ applied at its top (the triangular decaying over time of this vertical load is showed in Figure 6). Gravitational loads of intensity 10 kN statically applied and a lumped mass of 0.5 kNs^2/m attached to each node were also considered. The time histories of the vertical deflection at the arch top are illustrated in Figure 7. A permanent plastic deformation is observed, and the amplitude of displacement becomes virtually constant indicating that the structure remains in the elastic regime after 0.012s.

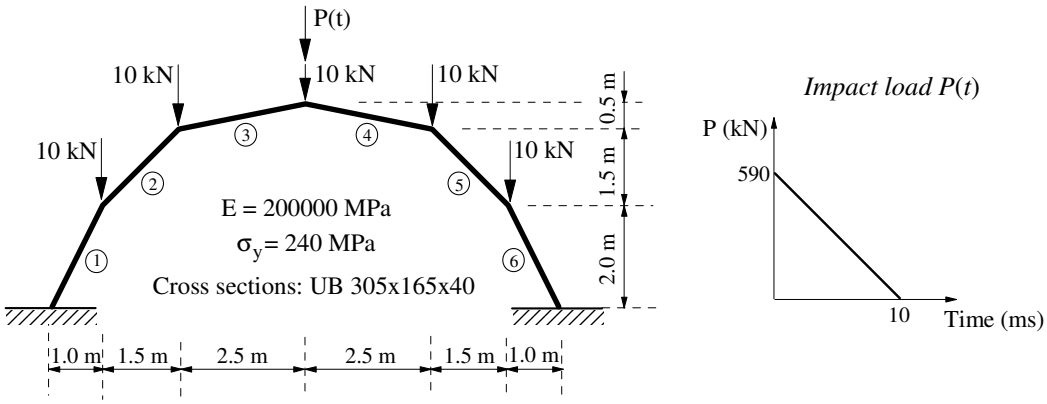

Figure 6: Arch-shaped frame: geometry and loading

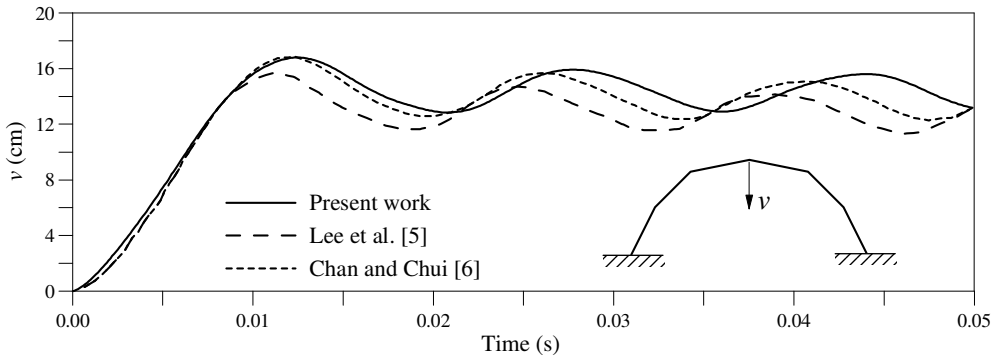

Figure 7: Dynamic elastoplastic response of the arch under impact load

4.3 Simple portal frame with initial geometric imperfection

In the last analysis, attention is given to the yield stress effect on the structural response of a simple portal frame with pinned supports illustrated in Figure 8. An initial geometric imperfection Δ_0 in columns was assumed. To predict a more realistic behavior of this structure, two heavy gravitational loads of 200 kN acting at the ends of the beam (or at the top of the columns) were considered. These loads induce axial forces in columns, and as a consequence, additional bending moments appear, reducing the stiffness of these members and structural system (P-Delta effect in the analysis). The beam and columns of the frame are made by hot-rolled steel profiles W8x48.

The nonlinear transient frame responses considering the elastic and inelastic (elastoplastic) material behavior are illustrated in Figure 8. Yield stress equal to 235 MPa and 260 MPa were adopted in the elastoplastic analysis. Figure 8b shows the members' sections plastic resistance surface considered. In Figures 8c and 8d can be observed that the magnitude of plastic deformation decreases with the increasing of the material yield stress. In the limit, i.e., for $\sigma_y \to \infty$, the material would tend to present the elastic behavior, whose results are plotted in Figure 8a.

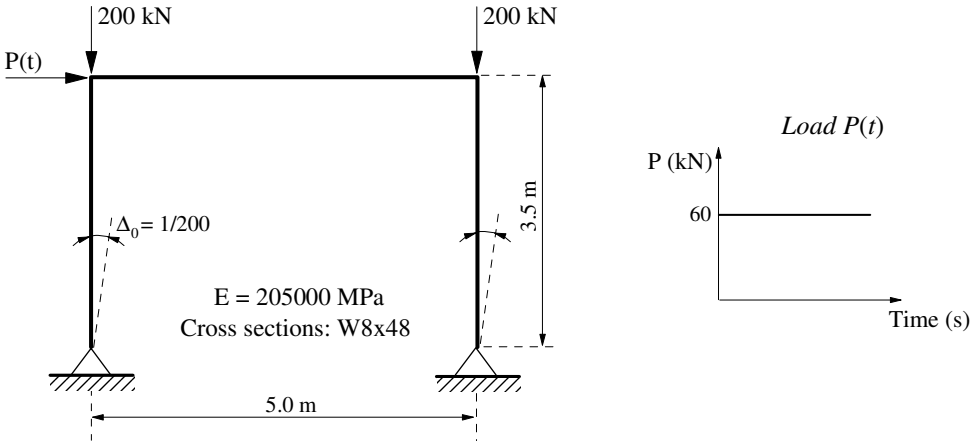

Figure 8: Simple portal frame with initial geometric imperfection: geometry and loading pattern

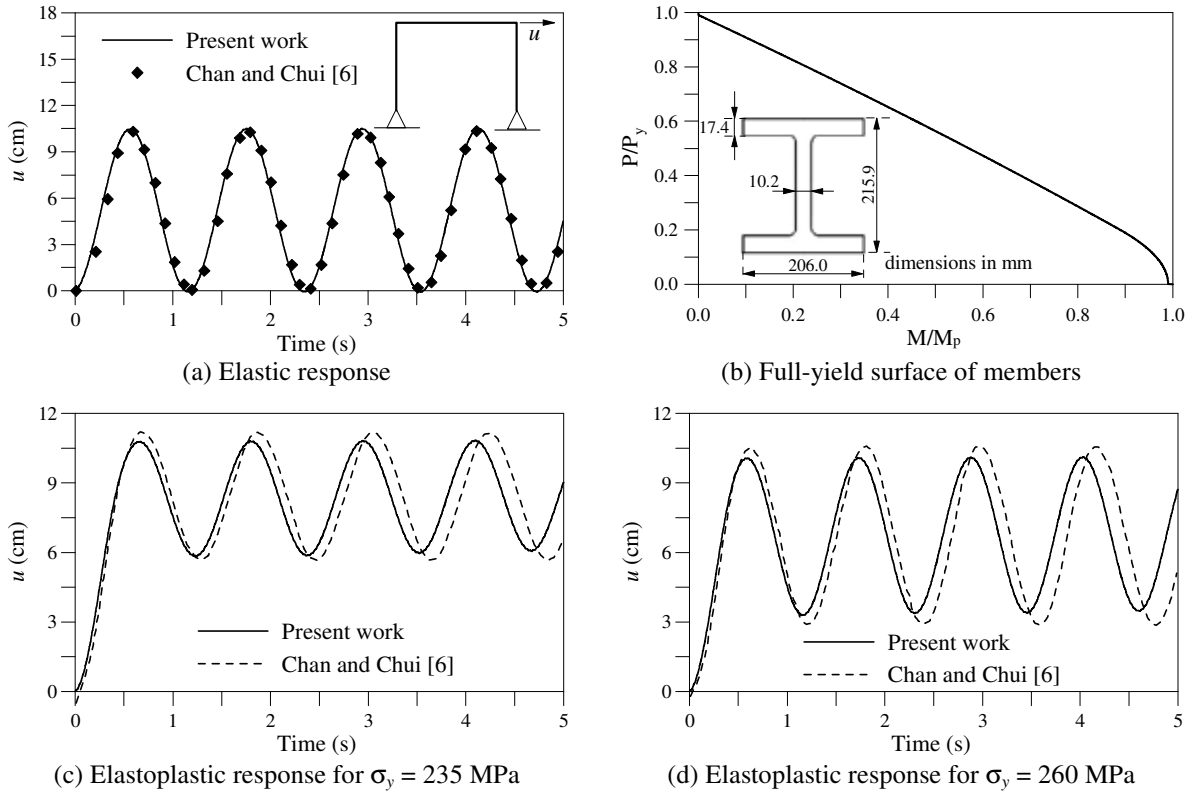

(a) Elastic response

(b) Full-yield surface of members

(c) Elastoplastic response for σ_y = 235 MPa

(d) Elastoplastic response for σ_y = 260 MPa

Figure 9: Dynamic elastic and inelastic responses of the simple portal frame

5 FINAL REMARKS AND FUTURE RESEARCH

This article described a numerical methodology for nonlinear dynamic analysis of steel frames. The main feature of the finite element formulation adopted is the consideration of the geometric nonlinear effects and the material elastic-perfectly plastic behavior. The plastic hinge model was used to evaluate the members' section yielding. The steel section gradual yielding and residual stresses were not considered. Numerical examples presented

demonstrated the applicability of the numerical strategy proposed, and the good agreement between the results here obtained and those found in literature have validated such strategy.

It is worth informing that future authors' research should address the influence of the combined effects of geometric nonlinearity, steel inelasticity and semi-rigid connections on the nonlinear static and dynamic behavior of steel structures. In these studies, the refined plastic hinge model (with steel section gradual yielding), which enables the energy dissipation through the plastic hinges, will be adopted.

ACKNOWLEDGMENTS

The authors are grateful to CAPES, CNPq and FAPEMIG for the financial supports received for this research.

REFERENCES

[1] Lui, E.M. *Structural Steel Design*. In Structural Engineering Handbook, Ed. W.F. Chen, CRC Press LLC, (1999).

[2] Marur, S.R. and Kant, T. A stress correction procedure for the analysis of inelastic frames under transient dynamic loads. *Computers & Structures* (1994) **50**(5) 603-613.

[3] Mamaghani, I. H.P., Usami T. and Mizuno E. Inelastic large structural steel cyclic loading. *Engineering Structures* (1996) **18**(9) 659-668.

[4] Thai, H.-T. and Kim, S.-E. Second-order inelastic dynamic analysis of steel frames using fiber hinge method. *Journal of Constr. Steel Re* (2011) doi:10.1016/j.jcsr.2011.03.022.

[5] Lee, S.L., Swaddiwudhipong, S. and Alwis, W.A.M. Elasto-plastic dynamic analysis of plane frames and deep arches. *Computational Mechanics* (1988) **3** 39-48.

[6] Chan, S.L. and Chui, P.P.T. *Non-linear Static and Cyclic Analysis of Steel Frames with Semi-Rigid Connections*. Elsevier, Oxford, (2000).

[7] Kim, S.-E., Cuong N.-H. and Lee D.-H. Second-order inelastic dynamic analysis of 3-D steel frames. *International Journal of Solids and Structures* (2006) **43**: 1693–1709.

[8] Au, F.T.K. and Yan Z.H. Dynamic analysis of frames with material and geometric nonlinearities based on the semirigid technique. *International Journal of Structural Stability and Dynamics* (2008) **8**(3): 415–438.

[9] Sekulovic, M. and Nefovska-Danilovic, M. Contribution to transient analysis of inelastic steel frames with semi-rigid connections. *Engineering Structures* (2008) **30**: 976–989.

[10] Silva, A.R.D. *Computational System for Static and Dynamic Advanced Analysis of Steel Frames,* D.Sc. Dissertation, PROPEC/Deciv/UFOP, Ouro Preto/MG, Brazil, (2009) (in Portuguese).

[11] Chen, W.F and Toma, S. *Advanced Analysis of Steel Frames*, CRC Press, Boca Raton, Flórida, (1994).

[12] BS 5950. *Structural Use of Steelwork in Buildings. Part 1*. British Standards Institution, London, England, (1990).

[13] Zienkiewicz, O.C. and Taylor, R.L. *The finite element method*. McGraw Hill, Vol. I., (1989), Vol. II, (1991).

[14] Toridis, T.G. and Khozeimeh, K. Inelastic response of frames to dynamic loads. *Journal of Engineering Mechanics* (1971) **97**(3), 847-863.

XI International Conference on Computational Plasticity. Fundamentals and Applications
COMPLAS XI
E. Oñate, D.R.J. Owen, D. Peric and B. Suárez (Eds)

GLOBAL EQUILIBRIUM TRIANGULAR ELEMENT FOR LOWER BOUND LIMIT ANALYSIS XI INTERNATIONAL CONFERENCE ON COMPUTATIONAL PLASTICITY. FUNDAMENTALS AND APPLICATIONS – COMPLAS XI

DENILSON J. R. SODRÉ* AND ELISEU LUCENA NETO†

*Universidade Federal do Pará
Faculdade de Engenharia Civil
66075-900 Belém, PA, Brasil
e-mail: dsodre@ufpa.br, www.ufpa.br

†Instituto Tecnológico de Aeronaútica
12228-900 São José dos Campos, SP, Brazil
e-mail: eliseu@ita.br, www.ita.br

Key words: Finite Elements, Limit Analysis, Lower Bound, Computational Plasticity

Abstract. A three-node triangular finite element developed for the static theorem of limit analysis is evaluated considering the Mohr-Coulomb material in plane strain condition. This element, named *GET* (*Global Equilibrium Triangle*), satisfies the equilibrium equations in the integral sense, global sense, according to the principle of virtual displacements. The equilibrium equations and the yield criterion inequalities, expressed in terms of nodal stresses, are dealt with as constraints of a large-scale optimization problem whose objective function is defined by the loading which is maximized until a limit value is reached. Numerical predictions are performed for purely cohesive and cohesive-frictional thick cylinder expansion under internal pressure. The results demonstrate that not satisfying the equilibrium equations rigorously is far from being a severe handicap for the *GET*.

1 INTRODUCTION

The plasticity theory allows to estimate ultimate limit states by means of limit analysis. This technique, based on the static and kinematic theorems, gives in a theoretically rigorous way lower and upper bounds on the collapse load, respectively [1].

Analytical solution obtained with limit analysis is restricted in scope and, depending on the complexity of the problem, it may not be available or there may be a big gap between the bounds. This restriction is overcome by coupling the limit theorems with

the finite element method. The emphasis here is on numerical formulation for the static theorem.

Formulations of the lower bound method by finite elements lead to a convex optimization problem with a large number of variables and constraints. It is originally formulated as a nonlinear programming (NLP) due to the yield function nonlinearity (e.g. Mohr-Coulomb, Tresca, Drucker-Prager, von Mises, Gurson, Nielsen, Ilyushin), but it can also be dealt with as a linear programming (LP) by using a yield function linearization procedure. Early implementations of linear and nonlinear finite element limit analysis were proposed by Lysmer [2] and Belytschko and Hodge [3], respectively. Since then, an extensive research into numerical implementations of the lower bound approach using finite elements has been carried out [4–16].

In this work, a three-node triangular finite element, named *GET* (*Global Equilibrium Triangle*) in short, is developed for performing lower bound limit analysis considering the Mohr-Coulomb material in plane strain condition.

The *GET* is evaluated with respect to convergence, accuracy and efficiency by taking into account the effects of discretization (domain selection, element distortion, mesh arrangement and refinement), yield surface approximation, strength parameters and mathematical programming technique employed. Numerical predictions of lower bound limit load are performed for thick cylinder expansion under internal pressure.

2 GLOBAL EQUILIBRIUM TRIANGLE - GET

The finite-element *GET* was developed based on the formulation originally proposed by Anderheggen and Knöpfel [4] concerning with a four-node quadrilateral element for limit analysis.

The *GET* will be derived within the framework of the discrete formulation of the lower bound method. The static theorem states that the applied load corresponding to a statically and plastically admissible stress field is a lower bound to the true collapse load. A statically admissible stress field satisfies the equilibrium equations into the volume and the mechanical boundary conditions, and a plastically admissible stress field does not violate the yielding condition of the material.

2.1 Static admissibility

By considering a body under plane strain conditions parallel to the xy-plane, the equilibrium in the domain and the mechanical boundary conditions are expressed in the sense of the principle of virtual displacements given by

$$\int_{S_\sigma} \{T\}^T \{\delta u\}\, dS + \int_V \{F\}^T \{\delta u\}\, dV - \int_V \{\sigma\}^T \{\delta \epsilon\}\, dV = 0 \tag{1}$$

where $\{T\} = \lfloor\ T_x \quad T_y\ \rfloor^T$ are the surface forces, $\{F\} = \lfloor\ F_x \quad F_y\ \rfloor^T$ are the body forces, $\{\sigma\} = \lfloor\ \sigma_x \quad \sigma_y \quad \tau_{xy}\ \rfloor^T$ is the stress field, $\{\delta u\} = \lfloor\ \delta u \quad \delta v\ \rfloor^T$ is the virtual displacement

field, $\{\delta\epsilon\} = \lfloor\ \delta\epsilon_x \quad \delta\epsilon_y \quad \delta\gamma_{xy}\ \rfloor^T$ is the virtual strain field, S_σ is the surface where $\{T\}$ is prescribed and V is the body volume. The virtual displacement field $\{\delta u\}$ is zero on the surface S_u, where the real displacement $\{u\}$ is known, and relates to the virtual strain field $\{\delta\epsilon\}$ by

$$\delta\epsilon_x = \frac{\partial\delta u}{\partial x} \qquad \delta\epsilon_y = \frac{\partial\delta v}{\partial y} \qquad \delta\gamma_{xy} = \frac{\partial\delta u}{\partial y} + \frac{\partial\delta v}{\partial x}. \tag{2}$$

Unknown surface forces $\{T\}$ correspond to reactions on S_u ($S_u \cup S_\sigma = S$; $S_u \cap S_\sigma = \emptyset$).

In doing so, the finite element method requires interpolation functions for $\{\delta u\}$ and $\{\sigma\}$ with continuity C^1 and C^0 into the elements and C^0 and C^{-1} at the interelement boundaries, respectively. Linear virtual displacement and stress fields are adopted.

The virtual displacement is expressed by

$$\begin{aligned}\{\delta u\} &= \left\{ \begin{array}{c} \delta u \\ \delta v \end{array} \right\} = \left[\begin{array}{cccccc} N_1 & 0 & N_2 & 0 & N_3 & 0 \\ 0 & N_1 & 0 & N_2 & 0 & N_3 \end{array} \right] \left\{\delta\bar{d}\right\} \\ &= [N_u] \left\{\delta\bar{d}\right\} \end{aligned} \tag{3}$$

where $\left\{\delta\bar{d}\right\} = \lfloor\ \delta u_1 \quad \delta v_1 \quad \delta u_2 \quad \delta v_2 \quad \delta u_3 \quad \delta v_3\ \rfloor^T$ refers to the components of $\{\delta u\}$ at each triangle vertex and $[N_u]$ is a linear shape function matrix. Substituting (3) into $\{\delta\epsilon\}$ given in (2) yields

$$\begin{aligned}\{\delta\epsilon\} &= \left\{ \begin{array}{c} \delta\epsilon_x \\ \delta\epsilon_y \\ \delta\gamma_{xy} \end{array} \right\} = \frac{1}{2A} \left[\begin{array}{cccccc} y_{23} & 0 & y_{31} & 0 & y_{12} & 0 \\ 0 & x_{32} & 0 & x_{13} & 0 & x_{21} \\ x_{32} & y_{23} & x_{13} & y_{31} & x_{21} & y_{12} \end{array} \right] \left\{\delta\bar{d}\right\} \\ &= [B] \left\{\delta\bar{d}\right\}. \end{aligned} \tag{4}$$

The stress field is approximated by

$$\{\sigma\} = [N_\sigma] \{\bar{\sigma}\} \tag{5}$$

where $\{\bar{\sigma}\}$ is a nodal stress vector and $[N_\sigma]$ is a linear shape function matrix. Due to the stress approximation, the equilibrium equations are only satisfied in the integral sense.

For a domain divided into E elements, the substitution of (3), (4) and (5) into (1) leads to

$$\sum_{i=1}^{E} \left\{\delta\bar{d}\right\}^T \left(\int_{S_{\sigma i}} [N_u]^T \{T\}\, dS + \int_{V_i} [N_u]^T \{F\}\, dV - \int_{V_i} [B]^T [N_\sigma] \{\bar{\sigma}\}\, dV \right) = 0 \tag{6}$$

or

$$\sum_{i=1}^{E} \left\{\delta\bar{d}\right\}^T \left(\left\{\bar{f}\right\} - \left[\bar{l}\right] \{\bar{\sigma}\} \right) = 0 \tag{7}$$

where $\left\{\bar{f}\right\}$ and $\left[\bar{l}\right]\{\bar{\sigma}\}$ are the external and internal nodal forces at the element i, respectively, with

$$\left[\bar{l}\right] = \int_{V_i} [B]^T [N_\sigma]\, dV \tag{8}$$

$$= \frac{1}{6}\begin{bmatrix} y_{23} & 0 & x_{32} & y_{23} & 0 & x_{32} & y_{23} & 0 & x_{32} \\ 0 & x_{32} & y_{23} & 0 & x_{32} & y_{23} & 0 & x_{32} & y_{23} \\ y_{31} & 0 & x_{13} & y_{31} & 0 & x_{13} & y_{31} & 0 & x_{13} \\ 0 & x_{13} & y_{31} & 0 & x_{13} & y_{31} & 0 & x_{13} & y_{31} \\ y_{12} & 0 & x_{21} & y_{12} & 0 & x_{21} & y_{12} & 0 & x_{21} \\ 0 & x_{21} & y_{12} & 0 & x_{21} & y_{12} & 0 & x_{21} & y_{12} \end{bmatrix}. \tag{9}$$

Introducting the contribution of all the elements into (7) it follows that

$$\{\delta d'\}^T \left(\{f'\} - [l']\{\sigma'\}\right) = 0, \tag{10}$$

where the global quantities $\{\delta d'\}$, $\{f'\}$, $[l']$, $\{\sigma'\}$ correspond to the scattering of the local quantities $\left\{\delta\bar{d}\right\}$, $\left\{\bar{f}\right\}$, $\left[\bar{l}\right]$, $\{\bar{\sigma}\}$, respectively. As $\{\delta d'\}$ is arbitrary,

$$\{f'\} - [l']\{\sigma'\} = 0. \tag{11}$$

There will be $2N$ equilibrium equations with $3N$ unknowns for a discretization with N nodes.

2.2 Plastic admissibility

The Mohr-Coulomb yield function is adopted as yield criterion. In plane strain condition parallel to the xy-plane, it reduces to

$$f = (\sigma_x - \sigma_y)^2 + 4\tau_{xy}^2 - [2c\cos\phi - (\sigma_x + \sigma_y)\sin\phi]^2 = 0 \tag{12}$$

where c is the cohesion and ϕ is the angle of internal friction.

To enforce plastic admissibility, the yielding condition is now expressed by

$$f = (\sigma_x - \sigma_y)^2 + 4\tau_{xy}^2 - [2c\cos\phi - (\sigma_x + \sigma_y)\sin\phi]^2 \leq 0. \tag{13}$$

The yield function introduces nonlinearity. However, a piecewise linearization of the Mohr-Coulomb yield function can be performed so that the problem can locally be treated as linear [17].

To proceed with the linearization of (12) it is first necessary a change of variables as follows

$$X = \sigma_x - \sigma_y \qquad Y = 2\tau_{xy} \qquad R = 2c\cos\phi - (\sigma_x + \sigma_y)\sin\phi. \tag{14}$$

In this new XY-space the equation (12) becomes

$$X^2 + Y^2 = R^2, \tag{15}$$

which represents a circumference of radius R.

The circumference is approximated by an inscribed regular polygon of p sides and p vertices in the XY-space (see Sloan [9]). The polygon side k defined in terms of stresses is

$$A_k\sigma_x + B_k\sigma_y + C_k\tau_{xy} = D \qquad k = 1, 2, \ldots, p \tag{16}$$

where

$$\begin{aligned} A_k &= \cos\frac{2k\pi}{p} + \sin\phi\cos\frac{\pi}{p} & B_k &= \sin\phi\cos\frac{\pi}{p} - \cos\frac{2k\pi}{p} \\ C_k &= 2\sin\frac{2k\pi}{p} & D &= 2c\cos\phi\cos\frac{\pi}{p}. \end{aligned} \tag{17}$$

From plastic admissibility it follows that

$$A_k\sigma_x + B_k\sigma_y + C_k\tau_{xy} \leq D \qquad k = 1, 2, \ldots, p. \tag{18}$$

Therefore, the constraints imposed on the nodal stresses by the linearized form of the Mohr-Coulomb yield surface can be expressed by

$$[a_i]\,\{\sigma_i\} \leq \{b_i\} \tag{19}$$

where

$$[a_i] = \begin{bmatrix} A_1 & B_1 & C_1 \\ A_2 & B_2 & C_2 \\ \vdots & \vdots & \vdots \\ A_p & B_p & C_p \end{bmatrix} \tag{20}$$

$$\{\sigma_i\} = \lfloor\ \sigma_{xi} \quad \sigma_{yi} \quad \tau_{xyi}\ \rfloor^T \tag{21}$$

$$\{b_i\} = 2c_i\cos\phi\cos\frac{\pi}{p}\lfloor\ 1 \quad 1 \quad \cdots \quad 1\ \rfloor^T.$$

The static theorem requires plastic admissibility ($f \leq 0$) everywhere in the continuum media. It can be shown that if the plastic admissibility is satisfied at the element nodes it will also be satisfied at any point in the domain. This is verified for both linearized (Sloan [9]) and original yield surface (Sodré [15]).

2.3 Optimization procedure

For lower bound computations the equilibrium equations $[l]\{\bar{\sigma}\} = \{f\}$ and the yield criterion inequalities $f(\bar{\sigma}) \leq 0$, expressed in terms of nodal stresses $\{\bar{\sigma}\}$, are dealt with as constraints of an optimization problem whose objective function is defined by the loading. The load multiplier λ, associated to unknown external loads $\{f\}$, is maximized toward a limit value λ^* that the body can sustain without collapsing. Thus, the discretized lower bound limit analysis may then be concisely formulated as

$$\lambda^* = \{\max \lambda \mid [l]\{\bar{\sigma}\} = \lambda\{f\},\ f(\bar{\sigma}) \leq 0\}. \tag{22}$$

The discrete lower bound limit analysis may be stated for the finite element *GET* as a nonlinear programming problem by

$$\begin{aligned} &\textbf{Maximize} && \lambda \\ &\textbf{Subjected to} && [l']\{\sigma'\} = \{f_1'\} + \lambda\{f_2'\} \\ & && f\{\sigma\} \leq 0 \end{aligned} \tag{23}$$

and as a linear programming problem by

$$\begin{aligned} &\textbf{Maximize} && \lambda \\ &\textbf{Subjected to} && [l']\{\sigma'\} = \{f_1'\} + \lambda\{f_2'\} \\ & && [a]\{\sigma\} \leq \{b\} \end{aligned} \tag{24}$$

where $\{f_1'\}$ and $\lambda\{f_2'\}$ are the fixed and variable external nodal loads, respectively.

The linear approach has the advantage of presenting a consistent mathematical structure with stable and global solution. For this reason, the LP-based limit analysis was the preferred choice for assessing the *GET* performance.

3 THICK CYLINDER EXPANSION

Predictions of lower bound limit load are carried out for cylinder expansion under internal pressure. This test case was performed using the LP-based interior-point optimizer of the code *XpressMP* from DASH Optimization and the NLP solver based on the modified method of feasible directions of the code *DOT* from Vanderplaats R&D, Inc.

The analytical solution for the collapse load of a purely cohesive thick cylinder subjected to uniform internal pressure is given according to Kachanov [18] by

$$P = 2c \ln \frac{r_o}{r_i} \tag{25}$$

and of a cohesive-frictional thick cylinder according to Nadai [19] by

$$P = c \cot \phi \left[\left(\frac{r_o}{r_i} \right)^{(\xi-1)/\xi} - 1 \right]. \tag{26}$$

The parameter P is the collapse pressure, r_i and r_o are the inner and outer radii of the cylinder, c is the cohesion, ϕ is the angle of internal friction and $\xi = \tan^2(\pi/4 + \phi/2)$ is a material constant (Figure 1).

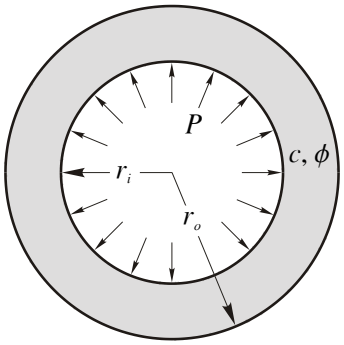

Figure 1: Cylinder under uniform internal pressure P.

The limit loads are estimated for a cylinder with $r_o/r_i = 1.5$, purely cohesive ($\phi = 0°$) and cohesive with friction ($\phi = 30°$). The axi-symmetry of the cylinder allows that only an angular sector is discretized. The adopted discrete arrangements are shown in Figure 2.

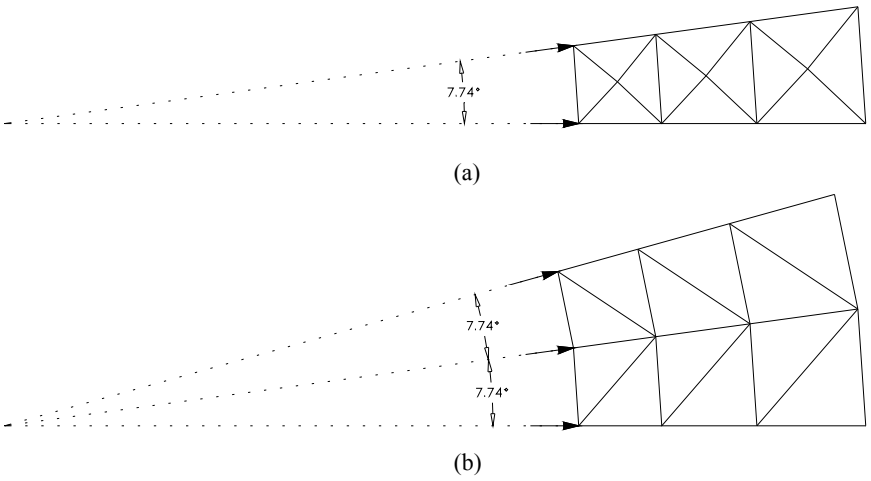

Figure 2: Cylinder discretization ($n = 3$): (a) C_1M_3; (b) C_2M_3.

In the configuration C_1 only one angular sector θ is considered and in C_2 the angular sector is divided into two other sectors, each with an angle θ, therefore symmetrical with respect to an intermediary radial axis. For each configuration C_1 or C_2, a mesh is identified by the number n of elements in the radial direction. Thus, the discretization C_1M_3, for

example, corresponds to the configuration C_1 with $n = 3$, that is, mesh M_3. The elements are defined by a logarithmic spiral progression to avoid element distortion,

$$\theta = \frac{1}{n} \ln \left(\frac{r_o}{r_i} \right), \tag{27}$$

and all elements are similar triangles. The boundary conditions are set by nullifying the nodal virtual displacements in the circumferential direction at all nodes.

The results from the mesh refinement and the number of sides p of the piecewise linearization of the yield surface, considering angles of friction $\phi = 0°$ and $\phi = 30°$, are shown in Figures 3 e 4. The exact solution is soon reached regardless of the angle of friction values.

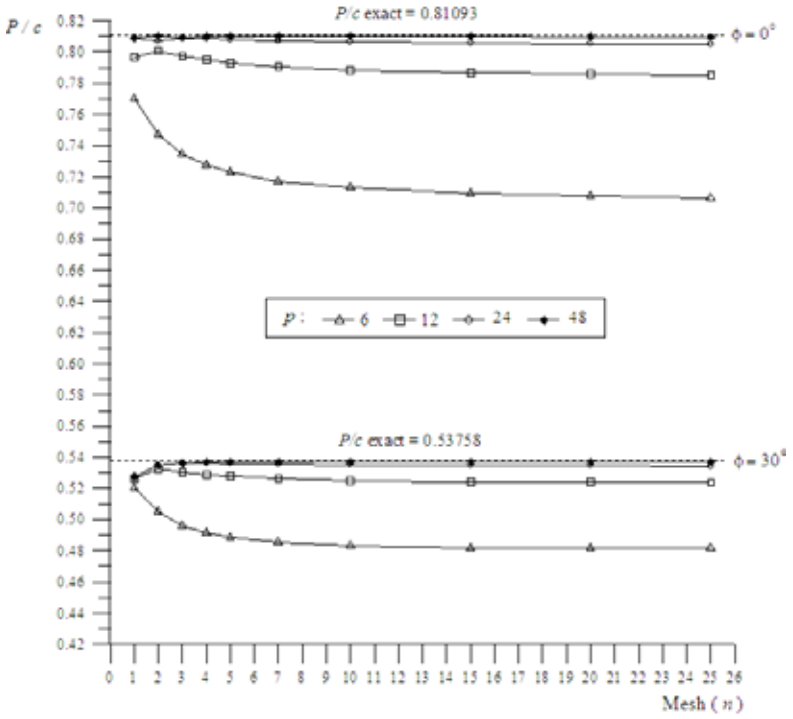

Figure 3: Results for configuration C_1.

Since there is no stress gradient in the circumferential direction, it does not make sense, in principle, to discretize the domain in that direction. Thus, it is assumed that an effective discretization can be achieved by refining the mesh only in the radial direction.

Lyamin and Sloan [11] analyzed the cylinder with arrangement similar to the C_1M_5 with $\phi = 30°$ whose exact solution is $P/c = 0.53758$. One-quarter of the cylinder was discretized into 300 elements utilizing double symmetry rather than the major advantage given by the axi-symmetry. The limit value $P/c = 0.5269$ was obtained for $p = 36$. Under

the same conditions, by adopting an angular sector of 4.65° and the mesh C_1M_5 with 20 elements, the *GET* yields the limit value $P/c = 0.5369$.

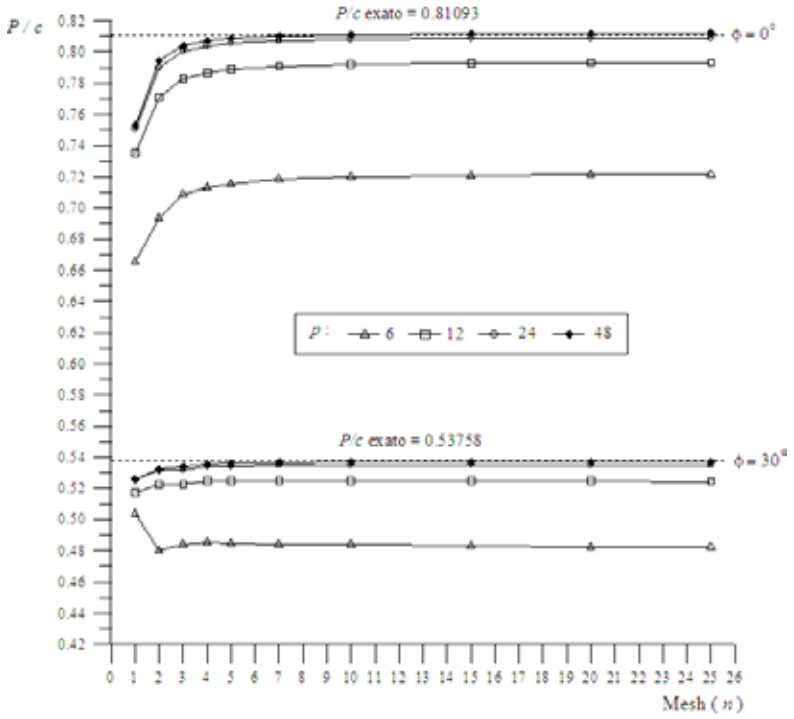

Figure 4: Results for configuration C_2.

The variation of the relative error,

$$\varepsilon_r = \frac{P_{\text{obtained}} - P_{\text{exact}}}{P_{\text{exact}}} 100\%, \tag{28}$$

with p values are performed for the mesh M_{15} (Figura 5). At least 48 sides are necessary to model the original yield function accurately. For $p \geq 96$ the error is of the order of hundredths or even thousandths.

The angle θ in (27) is associated to a mesh with elements almost without distortion. Distorted elements are generated by keeping the radial dimension and decreasing the angular sector. The mesh quality is evaluated, according to Bhatia and Lawrence [20], by

$$q_f = \frac{4\sqrt{3}A}{\sum_{i=1}^{3} l_i^2} \qquad 0 \leq q_f \leq 1 \tag{29}$$

where A and l_i are the area and sides of the element, respectively. The expression of q_f is obtained dividing A by the area of an equilateral triangle with side $\left[\left(l_1^2 + l_2^2 + l_3^2\right)/3\right]^{1/2}$.

An element without distortion has $q_f = 1$. The *GET* is more sensitive to distortion when the material is purely cohesive, as shown in Table 1.

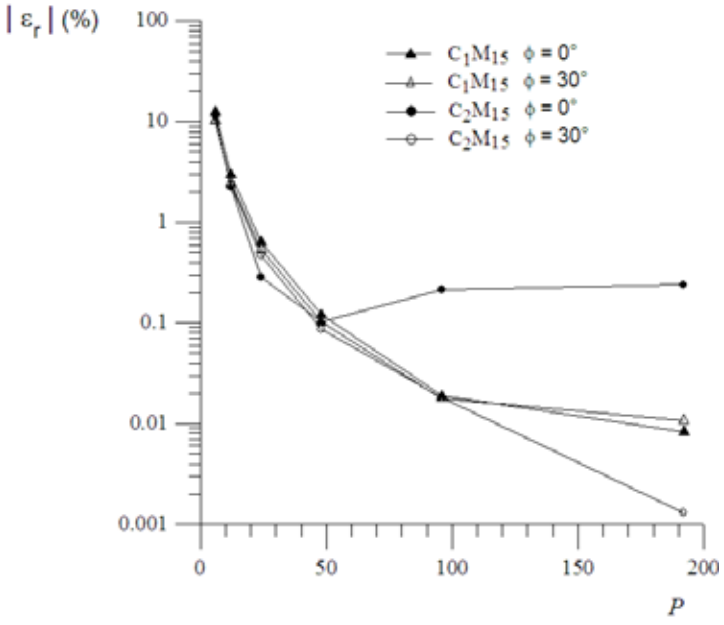

Figure 5: Variation of the relative error with p for the mesh M_{15}.

Table 1: Limit value of P/c normalized in relation to the exact value considering $r_e/r_i = 1.5$, mesh C_2M_{10} and p=*48*.

ϕ	P/c exact		θ=2.32°	$\theta/2$	$\theta/4$
0°	0.81093		1.0003 (0.1)*	1.0102 (0.1)	1.0446 (0.1)
30°	0.53758		0.9988 (0.1)	1.0005 (0.1)	1.0020 (0.1)
Mesh Quality	**min**	**max**			
q_f	0	1	0.875	0.704	0.415

** CPU time (sec)

The performances of the mathematical programming techniques adopted are compared in Table 2.

Table 2: Limit value of P/c normalized in relation to the exact value considering $r_e/r_i = 1.5$, mesh C_1M_{10} and p=*100*.

ϕ	*P/c* **exact**	**Xpress**^{MP}	**CPU time** (sec)	**DOT**	**CPU time** (sec)
0°	0.81093	0.9998	0.2	0.9989	0.53
15°	0.67713	0.9998	0.2	0.9992	0.48
30°	0.53758	0.9998	0.3	0.9995	0.56

4 CONCLUDING REMARKS

The *GET* does not lead to strict lower bound solution, but this seems irrelevant in view of its accuracy and little storage requirement. It presents low computational cost and insensitivity to strength parameters, but it shows some susceptibility to element distortion which, although insignificant, should be kept under control anyway. The increase of the domain and the discretization in the circumferential direction, increases the cost and decreases the accuracy of the solution.

REFERENCES

[1] Drucker, D.C.; Prager, W. and Greenberg, H.J. Extended limit design theorems for continuous media. *Quarterly Journal of Applied Mathematics* (1952) **9**:381–389.

[2] Lysmer, J. Limit analysis of plane problems in soil mechanics. *Journal of the Soil Mechanics and Foundations Division, A.S.C.E.* (1970) **96**(SM4):1311–1334.

[3] Belytschko, T. and Hodge, P.G. Plane stress limit analysis by finite elements. *Journal of the Engineering Mechanics Division* (ASCE) (1970) **96**:931–944.

[4] Anderheggen, E. and Knöpfel, H. Finite element limit analysis using linear programming. *International Journal of Solids and Structures* (1972) **8**:1413–1431.

[5] Pastor, J. Analyse limite: détermination de solutions statiques complètes - application au talus vertical. *Journal de Mécanique Appliquée*, *European Journal of Mechanics*, *A/Solids* (1978) **2**(2):176–196.

[6] Bashudar, P.K.; Valsangkar, A.J. and Madhav, M.R. Optimal lower bound of passive earth pressure using finite elements and nonlinear programming. *International Journal for Numerical and Analytical Methods in Geomechanics* (1979) **3**:367–379.

[7] Bottero, A.; Negre, R.; Pastor, J. and Turgeman, S. Finite element method and limit analysis theory for soil mechanics problems. *Computer Methods in Applied Mechanics and Engineering* (1980) **22**(1):131–149.

[8] Arai, K. and Tagyo, K. Limit analysis of geotechnical problems by applying lower bound theorem. *Soils and Foundations* (1985) **25**(4):37–48.

[9] Sloan, S.W. Lower bound limit analysis using finite elements and linear programming. *International Journal for Numerical and Analytical Methods in Geomechanics* (1988) **12**(1):61–77.

[10] Krabbenhoft, K. and Damkilde, L. Lower bound limit analysis of slabs with nonlinear yield criteria. *Computers and Structures* (2002) **80**:2043–2057.

[11] Lyamin, A.V. and Sloan, S.W. Lower bound limit analysis using non-linear programming. *International Journal for Numerical Methods in Engineering* (2002) **55**:573–611.

[12] Tin-Loi, F. and Ngo, N.S. Performance of the p-version finite element method for limit analysis. *International Journal of Mechanical Sciences* (2003) **45**:1149–1166.

[13] Ciria, H. Computation of upper and lower bounds in limit analysis using second-order cone programming and mesh adaptivity. *Master Thesis in Aeronautics and Astronautics at the Massachusetts Institute of Technology, MIT, USA* (2004).

[14] Makrodimopoulos, A. and Martin, C.M. Lower bound limit analysis of cohesive-frictional materials using second-order cone programming. *International Journal for Numerical Methods in Engineering* (2006) **66**(4):604–634.

[15] Sodré, D.J.R. Plastic limit analysis by finite elements and mathematical programming. *Doctoral Thesis in Aeronautics and Mechanics at the Technological Institute of Aeronautics, ITA, Brazil*, in portuguese, (2007).

[16] Martin, C.M. and Makrodimopoulos, A. finite-element limit analysis of Mohr–Coulomb materials in 3D using semidefinite programming. *Journal of Engineering Mechanics ASCE* (2008) **134**(4):339–347.

[17] Maier, G. A matrix structural theory of piecewise-linear plasticity with interacting yield planes. *Meccanica* (1970) **5**:55–66.

[18] Kachanov, L.M. *Foundations of the Theory of Plasticity*. North-Holland Publishing Company (1971).

[19] Nadai, A. *Theory of Flow and Fracture of Solids*. McGraw-Hill: New York (1963).

[20] Bhatia, R.P. and Lawrence, K.L. Two-dimensional finite element mesh generation based on stripwise automatic triangulation. *Computers and Structures* (1990) **36**(2):309–319.

XI International Conference on Computational Plasticity. Fundamentals and Applications
COMPLAS XI
E. Oñate, D.R.J. Owen, D. Peric and B. Suárez (Eds)

INTERIOR-POINT ALGORITHM FOR SHAKEDOWN ANALYSIS ACCOUNTING FOR LIMITED KINEMATICAL HARDENING

JAAN-W. SIMON AND DIETER WEICHERT

Institute of General Mechanics, RWTH Aachen University
Templergraben 64, 52062 Aachen, Germany
e-mail: simon@iam.rwth-aachen.de, weichert@iam.rwth-aachen.de

Key words: Shakedown Analysis, Direct Methods, Interior-Point Algorithm, Limited Kinematical Hardening, Nonlinear Programming

Abstract. We present a numerical method for the computation of shakedown loads of structures under thermo-mechanical loading accounting for limited kinematical hardening. The method is based on the lower bound approach by Melan extended to the hardening using a two-surface model. Both the yield and the bounding surface are defined by the von Mises condition. Melan's shakedown theorem leads to a nonlinear convex optimization problem. This is solved by the interior-point algorithm IPSA recently developed by the authors. In this paper, theoretical and numerical aspects will be presented as well as numerical examples from mechanical engineering.

1 INTRODUCTION

We consider engineering structures subjected to varying thermo-mechanical loading beyond the elastic limit. For these, we determine the shakedown factor α_{SD}, which is the maximum loading factor α such that the structure does neither fail due to spontaneous or incremental collapse nor due to alternating plasticity. In this paper, this is done by means of direct methods, comprising limit and shakedown analysis. In particular, we follow the statical approach of MELAN [7], who formulated a shakedown theorem for elastic-perfectly plastic and unlimited kinematical hardening continua.

Consideration of kinematical hardening is crucial for most engineering problems and thus has been addressed by several authors in the field of shakedown analysis. Notably, accounting for only unlimited kinematical hardening does not cover incremental collapse but solely alternating plasticity, see e.g. [6, 12, 18]. Thus, it is important to take into account limited kinematical hardening for obtaining realistic results. The first explicit formulation for this was given by WEICHERT and GROSS-WEEGE [3, 17], who developed

a two-surface model, which allows an easy introduction of this phenomenon to the statical shakedown theorem [3, 10, 11, 16, 17].

Using the statical shakedown theorem leads to nonlinear convex optimization problems, which are typically characterized by large numbers of unknowns and constraints. In this work, these will be solved by the interior-point algorithm IPSA recently developed by the authors [13–15], which is extended for limited kinematical hardening.

2 STATICAL APPROACH OF SHAKEDOWN ANALYSIS

The current formulation is based on the statical shakedown theorem by MELAN [7]. This states that a structure will shake down, if there exists a time-independent residual stress field $\bar{\boldsymbol{\rho}}(\boldsymbol{x})$, such that the yield condition $f[\boldsymbol{\sigma}(\boldsymbol{x},t)] \leq 0$ is satisfied for any loading path in the considered loading domain at any time t and in any point $\boldsymbol{x}$ of the structure. For the mathematical formulation, the total stress $\boldsymbol{\sigma}(\boldsymbol{x},t)$ is decomposed into an elastic stress $\boldsymbol{\sigma}^E(\boldsymbol{x},t)$ and a residual stress $\boldsymbol{\rho}(\boldsymbol{x},t)$ induced by the evolution of plastic strains.

$$\boldsymbol{\sigma}(\boldsymbol{x},t) = \boldsymbol{\sigma}^E(\boldsymbol{x},t) + \boldsymbol{\rho}(\boldsymbol{x},t) \tag{1}$$

Here, $\boldsymbol{\sigma}^E(\boldsymbol{x},t)$ denotes the stress state, which would occur in a fictitious purely elastic reference body under the same conditions as the original one. Clearly, the residual stresses satisfy the equilibrium condition, which can be transferred to a system of linear equations using the principle of virtual work, as shown e.g. in [2].

$$\sum_{r=1}^{NG} \mathbb{C}_r \cdot \bar{\boldsymbol{\rho}}_r = \mathbf{0} \tag{2}$$

Hereby, the system has been discretized using the finite element method (FEM) and thus the stresses are approximately evaluated in the GAUSS points $r \in [1, NG]$. The equilibrium matrixes $\mathbb{C}_r$ depend on the geometry and the elementation. The kinematical boundary conditions are taken into account considering the virtual displacements to be kinematical admissible.

Let the considered body be subjected to NL varying loads. Then, the according loading domain is polyhedral with $NC = 2^{NL}$ corners. As shown in [6], it is sufficient to only consider these corners to ensure shakedown for all possible loading paths inside of the loading domain. Then, introducing the loading factor $\alpha > 0$, Melan's statical shakedown theorem can be formulated as an optimization problem:

$$(\mathcal{P}_{Melan}) \qquad \alpha_{SD} = \max \alpha$$

$$\sum_{r=1}^{NG} \mathbb{C}_r \cdot \bar{\boldsymbol{\rho}}_r = \mathbf{0} \tag{3a}$$

$$f\left(\alpha\, \boldsymbol{\sigma}_r^{E,j} + \bar{\boldsymbol{\rho}}_r, \sigma_{Y,r}\right) \leq 0\,, \quad \forall j \in [1, NC],\ \forall r \in [1, NG] \tag{3b}$$

3 CONSIDERATION OF LIMITED KINEMATICAL HARDENING

In order to take into account the limited kinematical hardening we use the two-surface model proposed by Weichert and Gross-Weege [17]. The kinematical hardening is considered as a rigid body motion of the yield surface in stress space, which is described by the six-dimensional vector of back-stresses $\boldsymbol{\pi}$ representing the translation of the yield surface's center, Fig. 1. Through the introduction of a second surfaces corresponding to the ultimate stress σ_H, the motion of the yield surface is bounded.

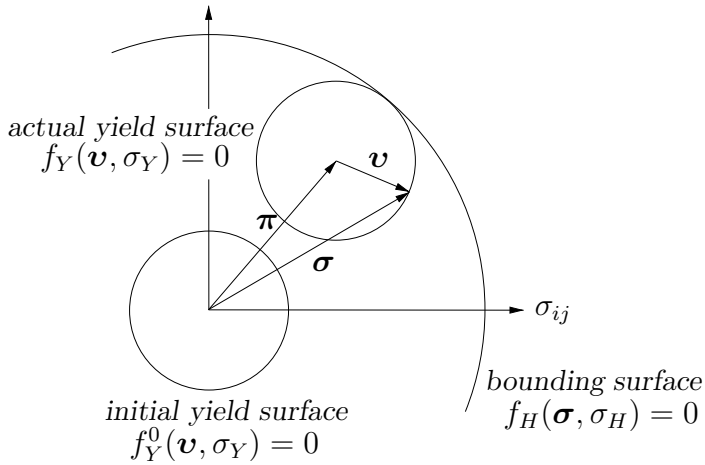

Figure 1: Kinematic hardening considered as translation of the yield surface in stress space

Thereby, the total stresses are divided into the back stresses $\boldsymbol{\pi}$ and the reduced stresses $\boldsymbol{\upsilon}$, which are responsible for the occurrence of plastic strains.

$$\boldsymbol{\sigma}(\boldsymbol{x}, t) = \boldsymbol{\pi}(\boldsymbol{x}, t) + \boldsymbol{\upsilon}(\boldsymbol{x}, t) \tag{4}$$

As before, the total stresses are decomposed, $\boldsymbol{\sigma}_r^j = \alpha\, \boldsymbol{\sigma}_r^{E,j} + \bar{\boldsymbol{\rho}}_r$. In an analogous manner, the reduced stresses $\boldsymbol{\upsilon}_r^j$ can be formulated, keeping in mind that the back stresses are time-independent and thus not dependent on the considered corner j of the loading domain, because the bounding surface is fixed in stress space.

$$\boldsymbol{\upsilon}_r^j = \boldsymbol{\sigma}_r^j - \bar{\boldsymbol{\pi}}_r = \alpha\, \boldsymbol{\sigma}_r^{E,j} + \bar{\boldsymbol{\rho}}_r - \bar{\boldsymbol{\pi}}_r \tag{5}$$

Thereby, Melan's theorem accounting for limited kinematical hardening reads as follows.

$(\mathcal{P}^H_{Melan})$ $\quad \alpha_{SD} = \max \alpha$

$$\sum_{r=1}^{NG} \mathbb{C}_r \cdot \bar{\boldsymbol{\rho}}_r = \mathbf{0} \tag{6a}$$

$$f_H\left(\alpha\, \boldsymbol{\sigma}_r^{E,j} + \bar{\boldsymbol{\rho}}_r, \sigma_{H,r}\right) \leq 0\,, \quad \forall j \in [1, NC],\ \forall r \in [1, NG] \tag{6b}$$

$$f_Y\left(\alpha\, \boldsymbol{\sigma}_r^{E,j} + \bar{\boldsymbol{\rho}}_r - \bar{\boldsymbol{\pi}}_r, \sigma_{Y,r}\right) \leq 0\,, \quad \forall j \in [1, NC],\ \forall r \in [1, NG] \tag{6c}$$

4 SOLUTION WITH INTERIOR-POINT METHOD

For a clear presentation, the problem is rewritten in the following form. To achieve this, several transformations are necessary, which are not in the scope of this paper but can be followed in [13, 15].

$$
\begin{aligned}
(\mathcal{P}_{IP}^{H}) \qquad & \min f(\boldsymbol{x}) = -\alpha \\
& \boldsymbol{A}_H \cdot \boldsymbol{x} = \boldsymbol{0} && \text{(7a)} \\
& \boldsymbol{c}_H(\boldsymbol{x}) \geq \boldsymbol{0} && \text{(7b)} \\
& \boldsymbol{c}_Y(\boldsymbol{x}) \geq \boldsymbol{0} && \text{(7c)} \\
& \boldsymbol{x} \in \mathbb{R}^n \,, && \text{(7d)}
\end{aligned}
$$

The problem $(\mathcal{P}_{IP}^{H})$ consists of n variables, merged to the solution vector $\boldsymbol{x}$, m_E equality constraints, represented by the affine linear system (7a), and $2\,m_I$ nonlinear concave inequality constraints (7b) and (7c). The equality constraints can be interpreted as equilibrium condition for the residual stresses (2), whereas the inequality constraints represent the yield and the bounding condition (6b) and (6c), respectively. The inequality constraints are converted into equality constraints by introducing slack variables $\boldsymbol{w}_H \in \mathbb{R}^{m_I}$ and $\boldsymbol{w}_Y \in \mathbb{R}^{m_I}$. Moreover, we use split variables $\boldsymbol{y} \in \mathbb{R}^n$ and $\boldsymbol{z} \in \mathbb{R}^n$ in order to avoid numerical instabilities due to the unboundedness of the solution vector (7d). Then, we use the interior-point method perturbing the objective function by logarithmic barrier terms, which penalize directions leading outside of the feasible region. Thereby, the barrier parameter μ is introduced, which is tending to zero during the iteration.

$$
f_\mu(\boldsymbol{x}, \boldsymbol{y}, \boldsymbol{z}, \boldsymbol{w}_H, \boldsymbol{w}_Y) = f(\boldsymbol{x}) - \mu \left[\sum_{i=1}^{n} \log(y_i) + \sum_{i=1}^{n} \log(z_i) + \sum_{j=1}^{m_I} \log(w_{H,j}) + \sum_{j=1}^{m_I} \log(w_{Y,j}) \right] \tag{8}
$$

The resulting optimization problem can then be expressed as follows.

$$
\begin{aligned}
(\mathcal{P}_{\mu}^{H}) \qquad & \min f_\mu(\boldsymbol{x}, \boldsymbol{y}, \boldsymbol{z}, \boldsymbol{w}_H, \boldsymbol{w}_Y) \\
& \boldsymbol{A}_H \cdot \boldsymbol{x} = \boldsymbol{0} && \text{(9a)} \\
& \boldsymbol{c}_H(\boldsymbol{x}) - \boldsymbol{w}_H = \boldsymbol{0} && \text{(9b)} \\
& \boldsymbol{c}_Y(\boldsymbol{x}) - \boldsymbol{w}_Y = \boldsymbol{0} && \text{(9c)} \\
& \boldsymbol{x} - \boldsymbol{y} + \boldsymbol{z} = \boldsymbol{0} && \text{(9d)} \\
& \boldsymbol{w}_H > \boldsymbol{0},\ \boldsymbol{w}_Y > \boldsymbol{0},\ \boldsymbol{y} > \boldsymbol{0},\ \boldsymbol{z} > \boldsymbol{0} && \text{(9e)}
\end{aligned}
$$

Since the underlying optimization problem $(\mathcal{P}_{IP}^{H})$ is convex and regular, the Karush-Kuhn-Tucker condition is both necessary and sufficient, which states that the solution is optimal if the Lagrangian $\mathcal{L}_H$ of the problem possesses a saddle point.

$$
\begin{aligned}
\mathcal{L}_H = & f_\mu(\boldsymbol{x}, \boldsymbol{y}, \boldsymbol{z}, \boldsymbol{w}_H, \boldsymbol{w}_Y) - \boldsymbol{\lambda}_E \cdot (\boldsymbol{A}_H \cdot \boldsymbol{x}) - \boldsymbol{\lambda}_H \cdot (\boldsymbol{c}_H(\boldsymbol{x}) - \boldsymbol{w}_H) \\
& - \boldsymbol{\lambda}_Y \cdot (\boldsymbol{c}_Y(\boldsymbol{x}) - \boldsymbol{w}_Y) - \boldsymbol{s} \cdot (\boldsymbol{x} - \boldsymbol{y} + \boldsymbol{z}) \,,
\end{aligned} \tag{10}
$$

where $\boldsymbol{\lambda}_E \in \mathbb{R}^{m_E}$, $\boldsymbol{\lambda}_H \in \mathbb{R}_+^{m_I}$, $\boldsymbol{\lambda}_Y \in \mathbb{R}_+^{m_I}$ and $\boldsymbol{s} \in \mathbb{R}_+^n$ are appropriate Lagrange multipliers. Thereby, the saddle point conditions reads as follows:

$$\begin{aligned}
\boldsymbol{\nabla}_x \mathcal{L}_H =& \boldsymbol{\nabla}_x f(\boldsymbol{x}) - \boldsymbol{A}_H^T \cdot \boldsymbol{\lambda}_E - \boldsymbol{C}_H^T(\boldsymbol{x}) \cdot \boldsymbol{\lambda}_H - \boldsymbol{C}_Y^T(\boldsymbol{x}) \cdot \boldsymbol{\lambda}_Y - \boldsymbol{s} = \boldsymbol{0} && \text{(11a)}\\
\boldsymbol{\nabla}_y \mathcal{L}_H =& -\mu\, \boldsymbol{Y}^{-1} \cdot \boldsymbol{e} + \boldsymbol{s} = \boldsymbol{0} && \text{(11b)}\\
\boldsymbol{\nabla}_z \mathcal{L}_H =& -\mu\, \boldsymbol{Z}^{-1} \cdot \boldsymbol{e} - \boldsymbol{s} = \boldsymbol{0} && \text{(11c)}\\
\boldsymbol{\nabla}_{w_H} \mathcal{L}_H =& -\mu\, \boldsymbol{W}_H^{-1} \cdot \boldsymbol{e} + \boldsymbol{\lambda}_H = \boldsymbol{0} && \text{(11d)}\\
\boldsymbol{\nabla}_{w_Y} \mathcal{L}_H =& -\mu\, \boldsymbol{W}_Y^{-1} \cdot \boldsymbol{e} + \boldsymbol{\lambda}_Y = \boldsymbol{0} && \text{(11e)}\\
\boldsymbol{\nabla}_{\lambda_E} \mathcal{L}_H =& -(\boldsymbol{A}_H \cdot \boldsymbol{x}) = \boldsymbol{0} && \text{(11f)}\\
\boldsymbol{\nabla}_{\lambda_H} \mathcal{L}_H =& -(\boldsymbol{c}_H(\boldsymbol{x}) - \boldsymbol{w}_H) = \boldsymbol{0} && \text{(11g)}\\
\boldsymbol{\nabla}_{\lambda_Y} \mathcal{L}_H =& -(\boldsymbol{c}_Y(\boldsymbol{x}) - \boldsymbol{w}_Y) = \boldsymbol{0} && \text{(11h)}\\
\boldsymbol{\nabla}_s \mathcal{L}_H =& -(\boldsymbol{x} - \boldsymbol{y} + \boldsymbol{z}) = \boldsymbol{0} && \text{(11i)}
\end{aligned}$$

where: $\boldsymbol{C}_H(\boldsymbol{x}) = \boldsymbol{c}_H(\boldsymbol{x})\boldsymbol{\nabla}_x \in \mathbb{R}^{m_I \times n}$ and $\boldsymbol{C}_Y(\boldsymbol{x}) = \boldsymbol{c}_Y(\boldsymbol{x})\boldsymbol{\nabla}_x \in \mathbb{R}^{m_I \times n}$

For consistency during the iteration, we introduce the new variable $\boldsymbol{r} = -\boldsymbol{s}$ into (11c). Both of these variables are tending to zero during the iteration. In addition, the equations (11b)–(11e) are multiplied by the matrixes $\boldsymbol{Y}$, $\boldsymbol{Z}$, $\boldsymbol{W}_H$ and $\boldsymbol{W}_Y$, respectively. Merging all variables of the problem to the vector $\boldsymbol{\Pi}$), the resulting system of optimality conditions can be expressed by the function $\boldsymbol{F}_\mu^H(\boldsymbol{\Pi})$:

$$\boldsymbol{F}_\mu^H(\boldsymbol{\Pi}) = -\begin{pmatrix}
-\boldsymbol{\nabla}_x f(\boldsymbol{x}) + \boldsymbol{A}_H^T \cdot \boldsymbol{\lambda}_E + \boldsymbol{C}_H^T(\boldsymbol{x}) \cdot \boldsymbol{\lambda}_H + \boldsymbol{C}_Y^T(\boldsymbol{x}) \cdot \boldsymbol{\lambda}_Y + \boldsymbol{s} \\
\mu\, \boldsymbol{e} - \boldsymbol{Y} \cdot \boldsymbol{S} \cdot \boldsymbol{e} \\
\mu\, \boldsymbol{e} - \boldsymbol{Z} \cdot \boldsymbol{R} \cdot \boldsymbol{e} \\
\mu\, \boldsymbol{e} - \boldsymbol{W}_H \cdot \boldsymbol{\Lambda}_H \cdot \boldsymbol{e} \\
\mu\, \boldsymbol{e} - \boldsymbol{W}_Y \cdot \boldsymbol{\Lambda}_Y \cdot \boldsymbol{e} \\
\boldsymbol{A}_H \cdot \boldsymbol{x} \\
\boldsymbol{c}_H(\boldsymbol{x}) - \boldsymbol{w}_H \\
\boldsymbol{c}_Y(\boldsymbol{x}) - \boldsymbol{w}_Y \\
\boldsymbol{x} - \boldsymbol{y} + \boldsymbol{z} \\
\boldsymbol{r} + \boldsymbol{s}
\end{pmatrix} = \boldsymbol{0} \qquad (12)$$

Equation (12) constitutes a system of nonlinear equations, which will be linearized using the Newton method. The variables $\boldsymbol{\Pi}_{k+1}$ of the subsequent iteration step $k+1$ are computed from the variables $\boldsymbol{\Pi}_k$ of the previous one k and the step values $\Delta\boldsymbol{\Pi}_k$:

$$\boldsymbol{\Pi}_{k+1} = \boldsymbol{\Pi}_k + \Upsilon_k\, \Delta\boldsymbol{\Pi}_k\,, \qquad (13)$$

where Υ_k denotes a matrix of damping factors, which is introduced for numerical reasons. The step values $\Delta\boldsymbol{\Pi}_k$ are determined from the following linearized system of equations.

$$\boldsymbol{J}(\boldsymbol{\Pi}_k) \cdot \Delta\boldsymbol{\Pi}_k = -\boldsymbol{\nabla}_{\Pi}\mathcal{L}_H(\boldsymbol{\Pi}_k) \tag{14}$$

$$\text{where:} \quad \boldsymbol{J}(\boldsymbol{\Pi}_k) = \boldsymbol{\nabla}_{\Pi}\mathcal{L}_H(\boldsymbol{\Pi})\,\boldsymbol{\nabla}_{\Pi}\Big|_{\boldsymbol{\Pi}=\boldsymbol{\Pi}_k}$$

The Jacobian $\boldsymbol{J}(\boldsymbol{\Pi})$ of the function $\boldsymbol{F}_{\mu}^{H}(\boldsymbol{\Pi})$ can be expressed as follows:

$$\boldsymbol{J}(\boldsymbol{\Pi}) = \begin{pmatrix} \boldsymbol{\nabla}_x^2\mathcal{L}_H & \mathbf{0} & \mathbf{0} & \mathbf{0} & \mathbf{0} & -\boldsymbol{A}_H^T & -\boldsymbol{C}_H^T(\boldsymbol{x}) & -\boldsymbol{C}_Y^T(\boldsymbol{x}) & -\boldsymbol{I}_n & \mathbf{0} \\ \mathbf{0} & \boldsymbol{S} & \mathbf{0} & \mathbf{0} & \mathbf{0} & \mathbf{0} & \mathbf{0} & \mathbf{0} & \boldsymbol{Y} & \mathbf{0} \\ \mathbf{0} & \mathbf{0} & \boldsymbol{R} & \mathbf{0} & \mathbf{0} & \mathbf{0} & \mathbf{0} & \mathbf{0} & \mathbf{0} & \boldsymbol{Z} \\ \mathbf{0} & \mathbf{0} & \mathbf{0} & \boldsymbol{\Lambda}_H & \mathbf{0} & \mathbf{0} & \boldsymbol{W}_H & \mathbf{0} & \mathbf{0} & \mathbf{0} \\ \mathbf{0} & \mathbf{0} & \mathbf{0} & \mathbf{0} & \boldsymbol{\Lambda}_Y & \mathbf{0} & \mathbf{0} & \boldsymbol{W}_Y & \mathbf{0} & \mathbf{0} \\ -\boldsymbol{A}_H & \mathbf{0} & \mathbf{0} & \mathbf{0} & \mathbf{0} & \mathbf{0} & \mathbf{0} & \mathbf{0} & \mathbf{0} & \mathbf{0} \\ -\boldsymbol{C}_H(\boldsymbol{x}) & \mathbf{0} & \mathbf{0} & \boldsymbol{I}_{m_I} & \mathbf{0} & \mathbf{0} & \mathbf{0} & \mathbf{0} & \mathbf{0} & \mathbf{0} \\ -\boldsymbol{C}_Y(\boldsymbol{x}) & \mathbf{0} & \mathbf{0} & \mathbf{0} & \boldsymbol{I}_{m_I} & \mathbf{0} & \mathbf{0} & \mathbf{0} & \mathbf{0} & \mathbf{0} \\ -\boldsymbol{I}_n & \boldsymbol{I}_n & -\boldsymbol{I}_n & \mathbf{0} & \mathbf{0} & \mathbf{0} & \mathbf{0} & \mathbf{0} & \mathbf{0} & \mathbf{0} \\ \mathbf{0} & \mathbf{0} & \mathbf{0} & \mathbf{0} & \mathbf{0} & \mathbf{0} & \mathbf{0} & \mathbf{0} & -\boldsymbol{I}_n & -\boldsymbol{I}_n \end{pmatrix} \tag{15}$$

The system (14) is reduced by successive elimination of those equations, which involve diagonal matrixes. After substituting the variables $\Delta\boldsymbol{s}$, $\Delta\boldsymbol{r}$, $\Delta\boldsymbol{y}$, $\Delta\boldsymbol{z}$, $\Delta\boldsymbol{w}_H$ and $\Delta\boldsymbol{w}_Y$, the following system remains:

$$\begin{pmatrix} -\left(\boldsymbol{\nabla}_x^2\mathcal{L}_H + \boldsymbol{E}_1\right) & \boldsymbol{A}_H^T & \boldsymbol{C}_H^T(\boldsymbol{x}) & \boldsymbol{C}_Y^T(\boldsymbol{x}) \\ \boldsymbol{A}_H & \mathbf{0} & \mathbf{0} & \mathbf{0} \\ \boldsymbol{C}_H(\boldsymbol{x}) & \mathbf{0} & \boldsymbol{E}_H & \mathbf{0} \\ \boldsymbol{C}_Y(\boldsymbol{x}) & \mathbf{0} & \mathbf{0} & \boldsymbol{E}_Y \end{pmatrix} \cdot \begin{pmatrix} \Delta\boldsymbol{x} \\ \Delta\boldsymbol{\lambda}_E \\ \Delta\boldsymbol{\lambda}_H \\ \Delta\boldsymbol{\lambda}_Y \end{pmatrix} = \begin{pmatrix} \boldsymbol{d}_1 \\ \boldsymbol{d}_2 \\ \boldsymbol{d}_3^H \\ \boldsymbol{d}_3^Y \end{pmatrix} \tag{16}$$

The right-hand side values are as follows

$$\boldsymbol{d}_1 = \boldsymbol{\nabla}_x f(\boldsymbol{x}) - \boldsymbol{A}_H^T \cdot \boldsymbol{\lambda}_E - \boldsymbol{C}_H^T(\boldsymbol{x}) \cdot \boldsymbol{\lambda}_H - \boldsymbol{C}_Y^T(\boldsymbol{x}) \cdot \boldsymbol{\lambda}_Y - \boldsymbol{s} + \boldsymbol{E}_1 \cdot \boldsymbol{b}_1 \tag{17a}$$

$$\boldsymbol{d}_2 = -\boldsymbol{A}_H \cdot \boldsymbol{x} \tag{17b}$$

$$\boldsymbol{d}_3^H = -\boldsymbol{c}_H(\boldsymbol{x}) + \mu\,\boldsymbol{\Lambda}_H^{-1} \cdot \boldsymbol{e} \tag{17c}$$

$$\boldsymbol{d}_3^Y = -\boldsymbol{c}_Y(\boldsymbol{x}) + \mu\,\boldsymbol{\Lambda}_Y^{-1} \cdot \boldsymbol{e} \tag{17d}$$

$$\text{where:} \quad \boldsymbol{b}_1 = \boldsymbol{x} + \boldsymbol{z} + \mu\left(\boldsymbol{R}^{-1} - \boldsymbol{S}^{-1}\right) \cdot \boldsymbol{e} + \boldsymbol{R}^{-1} \cdot \boldsymbol{Z} \cdot \boldsymbol{s} \tag{17e}$$

$$\boldsymbol{E}_1 = \left(\boldsymbol{S}^{-1} \cdot \boldsymbol{Y} + \boldsymbol{R}^{-1} \cdot \boldsymbol{Z}\right)^{-1} \tag{17f}$$

$$\boldsymbol{E}_H = \boldsymbol{W}_H \cdot \boldsymbol{\Lambda}_H^{-1} \tag{17g}$$

$$\boldsymbol{E}_Y = \boldsymbol{W}_Y \cdot \boldsymbol{\Lambda}_Y^{-1} \tag{17h}$$

5 NUMERICAL EXAMPLES

5.1 Open-ended pipe subjected to thermo-mechanical loading

The proposed method is applied to a thin pipe subjected to an internal pressure p and a temperature load $\Delta T = T_1 - T_0$, which vary independently of each other, Fig. 2. The pipe is assumed to be long, open-ended and thin with a ratio of radius to thickness $R/h = 10$. The material parameters are assumed to be temperature-independent. Furthermore, we only consider steady-state processes assuming that the temperature is applied sufficiently slow, and no transient thermal effects are taken into account. In addition, creep due to high temperature is not considered.

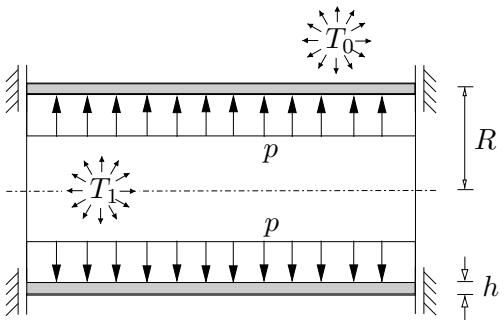

Figure 2: System of the open-ended pipe

The pipe is made of steel X6CrNiNb 18-10 and assumed to be homogeneous isotropic. The material parameters are given in Tab. 1.

Table 1: Thermal and mechanical characteristics

Young's modulus [MPa]	2.0×10^5
Yield stress [MPa]	205
Poisson's ratio	0.3
Density [kg/m^3]	7.9×10^3
Thermal conductivity [W/(m·K)]	15
Specific heat capacity [J/(kg·K)]	500
Coefficient of thermal expansion [1/K]	1.6×10^{-5}

Taking into account the symmetry of the system, the mesh consists of 984 nodes and 600 elements, where five elements over the thickness are used, Fig. 3(a). The FEM-analyses has been carried out with the software package ANSYS using isoparametric solid elements with 8 nodes. In particular, we use the element *solid45* for the structural analysis and

solid70 for the thermal one. The resulting distributions of equivalent elastic stresses are presented in Fig. 3, where the arbitrarily chosen values $p = 10$ MPa and $\Delta T = 100$ K have been used.

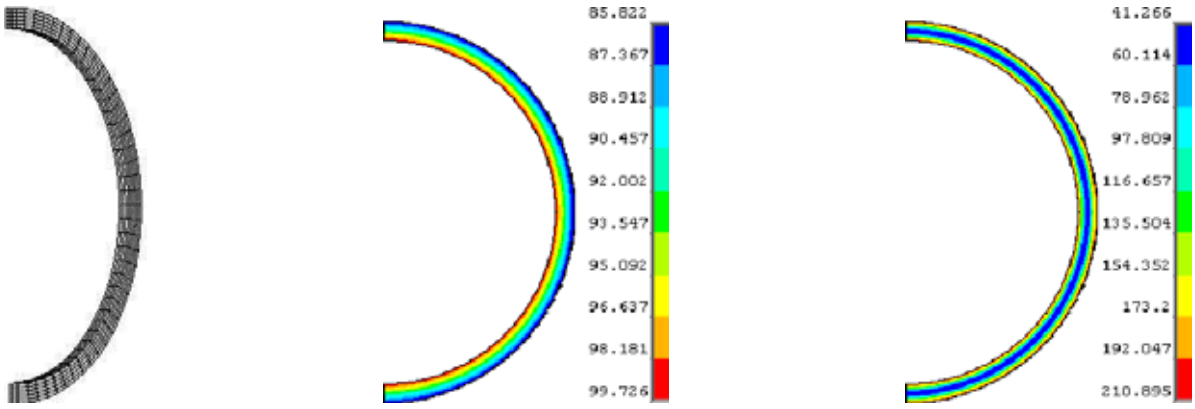

(a) FEM model

(b) Equivalent stresses due to internal pressure

(c) Equivalent stresses due to temperature loading

Figure 3: Model and elastic equivalent stresses of the open-ended pipe

The results of the shakedown analysis are presented in Fig. 4(a). There, the elastic domain (dotted line) and the shakedown curves for perfectly plastic materials as well as for limited kinematic hardening ones with different ratios $\sigma_{H,1} = 1.2\,\sigma_Y$, $\sigma_{H,2} = 1.35\,\sigma_Y$ and $\sigma_{H,3} = 1.5\,\sigma_Y$ are plotted. Both axes are scaled to the value in the perfectly plastic case p_0 and ΔT_0, respectively.

In both the perfectly plastic and the hardening case, one can clearly identify the two mechanisms of alternating plasticity and incremental collapse. In case of predominating temperature, all shakedown curves coincide with the one for unlimited hardening, which represents alternating plasticity. Here, no influence of hardening can be observed. On the other hand, failure is due to incremental collapse in the regime of predominating pressure. The limited kinematical hardening influences the shakedown curves such that the according domains increase in direct proportion with the ratio σ_H/σ_Y.

To validate the presented results, we compare them in Fig. 4 to the ones given by Mouhtamid [9], Hachemi [4] and Heitzer et al. [5]. These works are based on the static approach as well, but differ in the chosen solution strategies. Heitzer et al. applied the basis reduction technique, whereas Mouhtamid used the program Lancelot [1], which is based on the augmented Lagrangian method, and Hachemi used the bfgs algorithm, see [8]. The computed shakedown domains of Hachemi are above our ones, Fig. 4(c). The shakedown loads are overestimated in both cases with and without considering hardening. Nevertheless, the curves are qualitatively similar as well as the inclinations at the intercept points. Also, our results are in agreement with the ones of Heitzer, Fig. 4(d), which are slightly lower in the case of hardening. Furthermore, the comparison with Mouhtamid

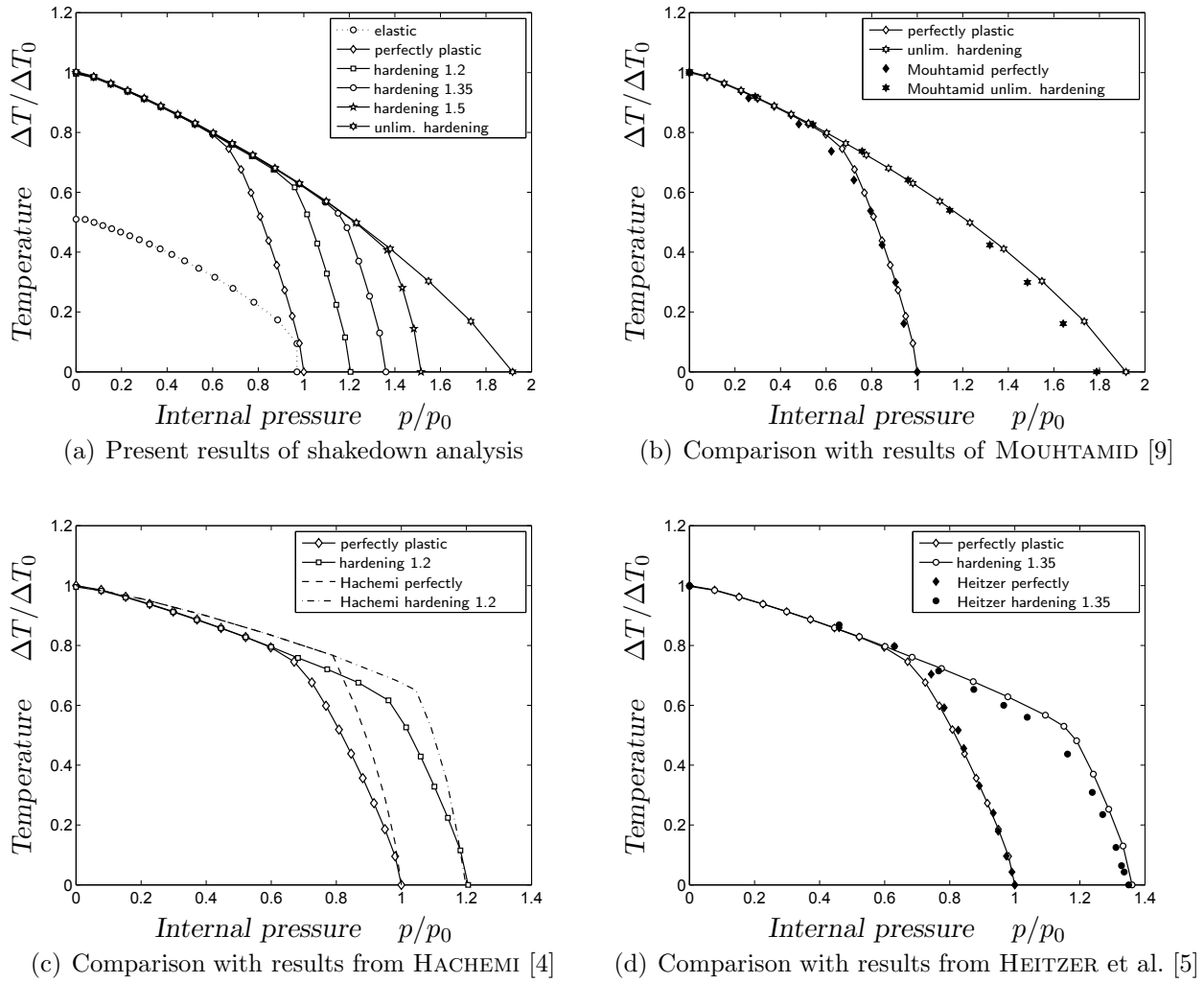

(a) Present results of shakedown analysis

(b) Comparison with results of MOUHTAMID [9]

(c) Comparison with results from HACHEMI [4]

(d) Comparison with results from HEITZER et al. [5]

Figure 4: Results of shakedown analysis and comparison to reference solutions of the open-ended pipe

shows a good agreement, too. However, a discrepancy can be observed in the regime of predominating pressure, which can be explained by different elastic solutions due to different meshes.

5.2 Closed pipe subjected to thermo-mechanical loading

For further validation, the pipe is considered now as closed, Fig. 5(a). We focus on a part of the pipe, which is far away of the closure such that local stress concentrations can be neglected. Then, the difference compared to the above calculation is the additional

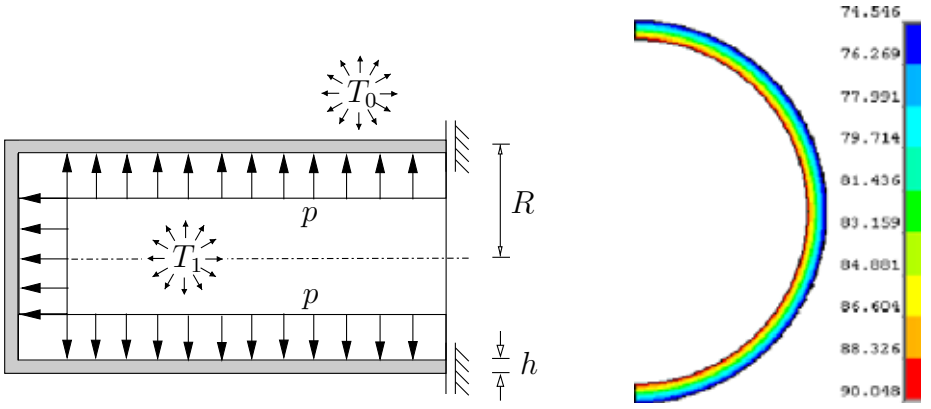

(a) System and loading conditions

(b) Equivalent stresses due to internal pressure

Figure 5: System and equivalent elastic stresses of the closed pipe

axial stress σ_{ax}, which is induced by the internal pressure acting on the cover plate.

$$\sigma_{ax} = p\,\frac{(R-h)^2}{(2\,R\,h - h^2)} \tag{18}$$

Through this additional axial stress the elastic stresses are changed in case of internal pressure, as shown in Fig. 5(b). As above, the value $p = 10$ MPa has been used. The elastic stresses due to the temperature loading remain as in Fig. 3(c).

The results of the shakedown analysis are presented in Fig. 4(a). There, the elastic domain (dotted line) and the shakedown curves for perfectly plastic materials as well as for limited kinematic hardening ones with different ratios $\sigma_{H,1} = 1.2\,\sigma_Y$, $\sigma_{H,2} = 1.35\,\sigma_Y$ and $\sigma_{H,3} = 1.5\,\sigma_Y$ are plotted. Both axes are scaled to the value in the perfectly plastic case p_0 and ΔT_0, respectively. Again, the two different mechanisms of alternating plasticity and incremental collapse can be clearly identified.

Finally, we compare the presented results with the ones obtained by Gross-Weege [2] using the basis reduction technique, which is based on the statical shakedown approach, too. The results are in agreement, even though in the range of incremental collapse one can observe a slight difference, Fig. 6(b).

6 CONCLUSIONS

We have presented a numerical method for shakedown analysis of engineering structures with limited kinematic hardening. The method has been implemented into the interior-point algorithm IPSA and applied to numerical examples. The validation with reference solutions is satisfying.

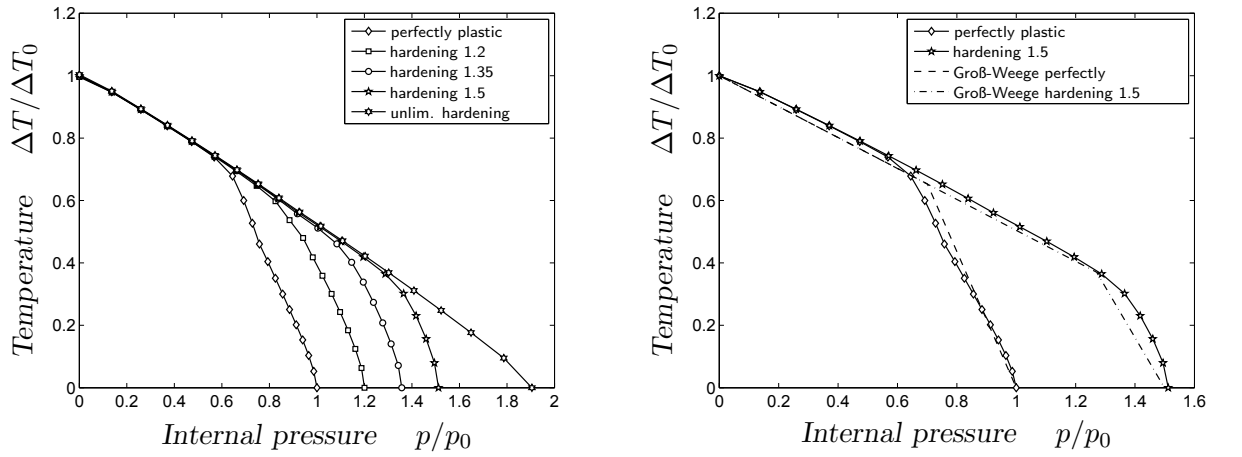

(a) Present results of shakedown analysis (b) Comparison with results of GROSS-WEEGE [2]

Figure 6: Results of shakedown analysis and comparison to reference solution of the closed pipe

REFERENCES

[1] A.R. Conn, N.I.M. Gould, and P.L. Toint. *LANCELOT: a Fortran package for large-scale nonlinear optimization (Release A)*, volume 17. Springer Series in Computational Mathematics, Springer, Heidelberg/New York, 1992.

[2] J. Groß-Weege. On the numerical assessment of the safety factor of elastic-plastic structures under variable loading. *Int J Mech Sci*, 39(4):417–433, 1997.

[3] J. Groß-Weege and D. Weichert. Elastic-plastic shells under variable mechanical and thermal loads. *Int J Mech Sci*, 34:863–880, 1992.

[4] A. Hachemi. Sur les méthodes directes et leurs applications, Habilitation, Université des Sciences et Technologies de Lille, France, 2005.

[5] M. Heitzer, G. Pop, and M. Staat. Basis reduction for the shakedown problem for bounded kinematical hardening material. *J Glob Opt*, 17:185–200, 2000.

[6] J.A. König. *Shakedown of elastic-plastic structures*. Elsevier, Amsterdam, 1987.

[7] E. Melan. Zur Plastizität des räumlichen Kontinuums. *Ing-Arch*, 9:116–126, 1938.

[8] A.J. Morris. *Foundation of Structural Optimization: A unified approach*. John Wiley, 1982.

[9] S. Mouhtamid. *Anwendung direkter Methoden zur industriellen Berechnung von Grenzlasten mechanischer Komponenten*. PhD thesis, Institute of General Mechanics, RWTH Aachen University, Germany, 2007.

[10] Q.-S. Nguyen. On shakedown analysis in hardening plasticity. *J Mech Phys Solids*, 51:101–125, 2003.

[11] P.T. Pham, D.K. Vu, T.N. Tran, and M. Staat. An upper bound algorithm for shakedown analysis of elastic-plastic bounded linearly kinematic hardening bodies. In *Proc ECCM 2010*, 2010.

[12] A.R.S. Ponter. A general shakedown theorem for elastic plastic bodies with work hardening. In *Proc SMIRT–3, paper L5/2*, 1975.

[13] J.-W. Simon, M. Chen, and D. Weichert. Shakedown analysis combined with the problem of heat conduction. In *ASME Conf Proc PVP2010*, volume 2, pages 133–142, 2010.

[14] J.-W. Simon and D. Weichert. An improved interior-point algorithm for large-scale shakedown analysis. In *PAMM – Proc Appl Math Mech*, volume 10, pages 223–224, 2010.

[15] J.-W. Simon and D. Weichert. Interior-point method for the computation of shakedown loads for engineering systems. In *ASME Conf Proc ESDA2010*, volume 4, pages 253–262, 2010.

[16] M. Staat and M. Heitzer. The restricted influence of kinematical hardening on shakedown loads. In *Proc WCCM V*, 2002.

[17] D. Weichert and J. Groß-Weege. The numerical assessment of elastic-plastic sheets under variable mechanical and thermal loads using a simplified two-surface yield condition. *Int J Mech Sci*, 30(10):757–767, 1988.

[18] J. Zarka and J. Casier. Elastic-plastic response of a structure to cyclic loading: practical rule. In S. Nemat-Nasser, editor, *Mechanics today*, volume 6. Pergamon, 1981.

XI International Conference on Computational Plasticity. Fundamentals and Applications
COMPLAS XI
E. Oñate, D.R.J. Owen, D. Peric and B. Suárez (Eds)

NON-LINEAR ANALYSIS WITH THE BOUNDARY ELEMENT METHOD

ERNESTO PINEDA*, IGNACIO VILLASEÑOR† AND JANIS ZAPATA†

* Instituto Politécnico Nacional (IPN), ESIA-UZ, Unidad Profesional Adolfo López Mateos s/n, 07320, México D.F.
e-mail: epinedal@ipn.mx

† Instituto Politécnico Nacional (IPN), ESIA-UZ, Unidad Profesional Adolfo López Mateos s/n, 07320,México D.F
email: janis_zapata@hotmail.com

KEY WORDS: *Boundary Element, Visco-plasticity.*

Abstract. This paper presents a new formulation of the Boundary Element Method to visco-plastic problems in a two-dimensional analysis. Visco-plastic stresses and strains are obtained until the visco-plastic strain rate reaches the steady state condition. A perfect visco-plastic analysis is also carried out in linear strain hardening (H'=0) materials. Part of the domain, the part that is susceptible to yield is discretized into quadratic, quadrilateral continuous cells. The loads are used to demonstrate time effects in the analysis carried out. Numerical results are compared with solution obtained from the Finite Element Method (FEM).

1 INTRODUCTION

In the case of inelastic fracture mechanic problems and in problems with high temperature gradients where inelastic strain rates are proportional to high power of stress, regions with strain rate concentration provide nearly all the inelastic contribution to the stress rates [1]. The main reason for the success of the BEM (boundary element method) in fracture mechanics applications is the ability to model high stress concentration fields accurately and efficiently. A comprehensive review of the historic development of the BEM for fracture mechanics can be found in the work of Aliabadi [2]. One of the early efforts in solving non-elastic fracture mechanics problems by using BEM was made by Morjaria and Mukherjee [3] and Banthia and Mukherjee [4] where they used a crack Green's function to model the crack and obtain solution for the time-dependent stress field which was developed near the crack tip in finite plates. An alternative methodology based on the use of the Kelvin fundamental solutions was presented in [5], [6] and [7]. Recently, the DBEM (dual boundary element method) has been developed as a very effective numerical tool to model general fracture problems with numerous applications to linear elastic and non-elastic fracture problems [8].

BEM has been applied to elasto-plastic problems since the early seventies with the work of Swedlow and Cruse [9] and Richardella [10] who implemented the von Mises criterion for 2D

problems using piecewise constant interpolation for the plastic strains. Later, Telles and Brebbia [11] and others had, by the beginning of the eighties, developed and implemented BEM formulations for 2D and 3D inelastic, viscoplastic and elastoplastic problems (see [12] for further details).

In recent years, Aliabadi and co-workers [13] have introduced a new generation of boundary element method for solution of fracture mechanics problems. The method which was originally proposed for linear elastic problems [14],[15] and [16] has since been extended to many other fields including problems involving nonlinear material and geometric behaviour [17].

In the present paper applications of the DBEM to visco-plasticity are presented. The specimens analyzed are a square plate and a plate with a hole, both of them with different crack length. The boundary was discretized with quadratic continuous and semi-discontinuous elements, but the domain with nine nodes internal cells. In visco-plasticity only the part susceptible to yielding was discretized. The von Mises yield criterion was applied so the material used for these sort of analysis were metals.

2 BASIC CONCEPTS OF VISCO-PLASTICITY

In order to explain the theory of visco-plasticity it is convenient to analyze the one-dimensional rheological model see [22] for more details. A uniaxial yield stress σ_y governs the onset of the visco-plastic deformation. Once visco-plasticty begins the stress level for continuing visco-plastic flow depends on the strain hardening characteristics of the material ($H' \neq 0$).
After applying Hook's law and boundary conditions, see Pineda [22] for further details, it is possible to obtain:

$$\dot{\varepsilon}^{vp} = \gamma\left[\sigma - \left(\sigma_y + H'\varepsilon^{vp}\right)\right] \tag{11}$$

Expression (11) is the visco-plastic strain rate in terms of the stresses for the uniaxial case in which (.) denotes the derivative with respect to the time, t.
From the visco-plastic model see [22] the strain response with time can be represented by two cases. The first case is the perfectly visco-plastic material in which $H' = 0$. In this case the visco-plastic deformation continues at a constant strain rate.
The second case is the linear hardening case ($H' \neq 0$), where after the initial elastic response, the *visco-plastic strain rate* is exponential and reaches the *steady state condition* when this value becomes zero. On the other hand, for a perfectly visco-plastic material there is always an imbalance of stress $\sigma_a - \sigma_y$ in the system which does not reduce and consequently the steady state condition can not be achieved.

3 BOUNDARY INTEGRAL EQUATIONS

The boundary conditions in terms of rates are; for displacements $\dot{u}_i = \dot{\bar{u}}_i$ and for tractions $\dot{t}_i = \dot{\bar{t}}_i$ and the equation representing the traction boundary conditions is,

$$\dot{t}_i + 2\mu\left(\dot{\varepsilon}_{ij}^{\ a} + \frac{\nu}{1-2\nu}\dot{e}\right)n_j = \frac{2\mu\nu}{1-2\nu}\dot{u}_{l,l}n_i + \mu\left(\dot{u}_{i,j} + \dot{u}_{j,i}\right)n_j \tag{2}$$

Equation (2) is for three dimensional problems. In order to work with two dimensional problems for the plane stress state it is necessary to remove the strain in z direction, so $\dot{\varepsilon}^a{}_{33} = 0$.

The solution of the equation (1) leads to the following boundary Integral representation of the *boundary displacements* when the *initial strain approach* for the solution of visco-plastic problems is used

$$c_{ij}\dot{u}_i + \oint_\Gamma \dot{t}'_{ij}\,\dot{u}_j d\Gamma = \int_\Gamma \dot{u}'_{ij}\,\dot{t}_j d\Gamma + \int_\Omega \dot{\sigma}'_{ijk}\,\dot{\varepsilon}^{vp}{}_{jk} d\Omega \tag{3}$$

In a similar way the boundary integral equation of the internal stresses is expressed by

$$\dot{\sigma}_{ij} = \int_\Gamma D_{ijk}\dot{t}_j d\Gamma - \int_\Gamma S_{ijk}\dot{u}_j d\Gamma + \oint_\Omega \Sigma_{ijk}\dot{\varepsilon}^a{}_{jk} d\Omega + f_{ij}\dot{\varepsilon}^{vp}{}_{jk} \tag{4}$$

Where $\oint$ is a Cauchy integral, D_{ijk} and S_{ijk} are terms containing the derivative of the displacements and tractions, f_{ij} is the free term and Σ_{ij} is the fundamental solution for the domain.

3.1 Boundary Integral Formulation for Visco-plasticity

In the visco-plastic analysis like plasticity, the initial strain approach will be applied and the integral equation to calculate the displacement on the boundary is basically the same, the only difference is that the plastic strain is replaced with the visco-plastic strain rate. So the displacement equation can be rewritten as:

$$c_{ij}(x')\dot{u}_j(x') + \int_\Gamma t'_{ij}(x',x)\dot{u}_i(x')d\Gamma = \int_\Gamma u'_{ij}(x',x)\dot{t}_j(x')d\Gamma + \int_\Omega \sigma'_{ij}(x',z)\dot{\varepsilon}^{vp}{}_{ij}(z)d\Omega \tag{5}$$

Where $\dot{u}_i$, $\dot{t}_i$ and $\dot{\varepsilon}^{vp}{}_{ij}$ are the displacement, traction and visco-plastic strain rates respectively. t'_{ij}, u'_{ij} and σ'_{ij} are the displacement, traction and third order fundamental

solutions, respectively, which are functions of the positions of the collocation point x′ and the field point x which belong to the boundary, or the internal point z and the material properties.

4 EXAMPLES

An aluminum plate with a notch and geometry as illustrated in figure 1 is considered in this case. The plate is constrained in X and Y direction on the edge of the notch and it is assumed to have the following material properties: Young's modulus, E =70000 MPa; Poisson's ratio, ν= 0.2; Applied stress σ_a =140 Mpa., σ_y = 243 Mpa. with γ=0.01 and $\Delta t = 0.01$

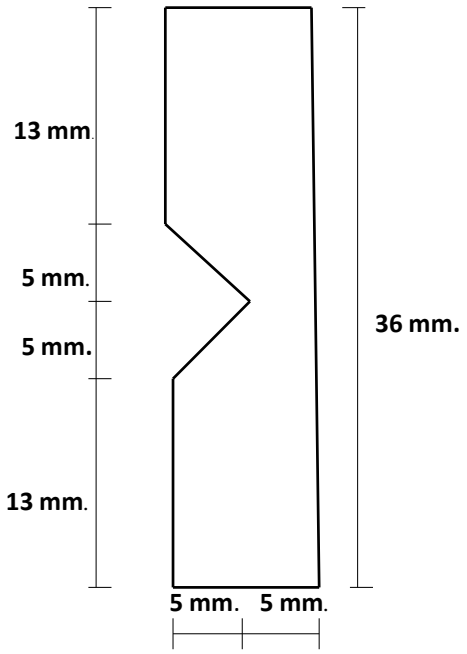

Figure 1 Geometry in a plate with a notch

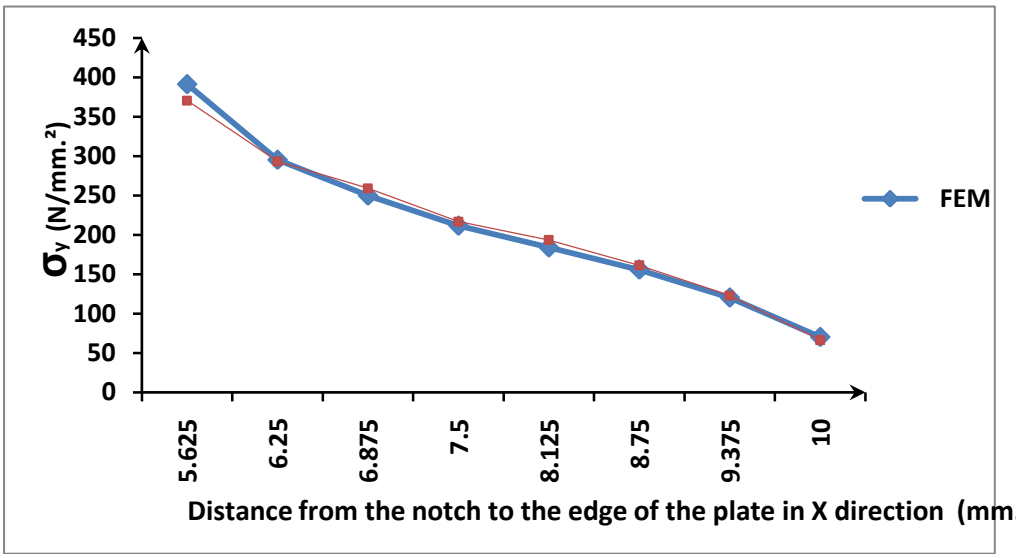

Figure 2. Stresses in Y direction for a notched plate.

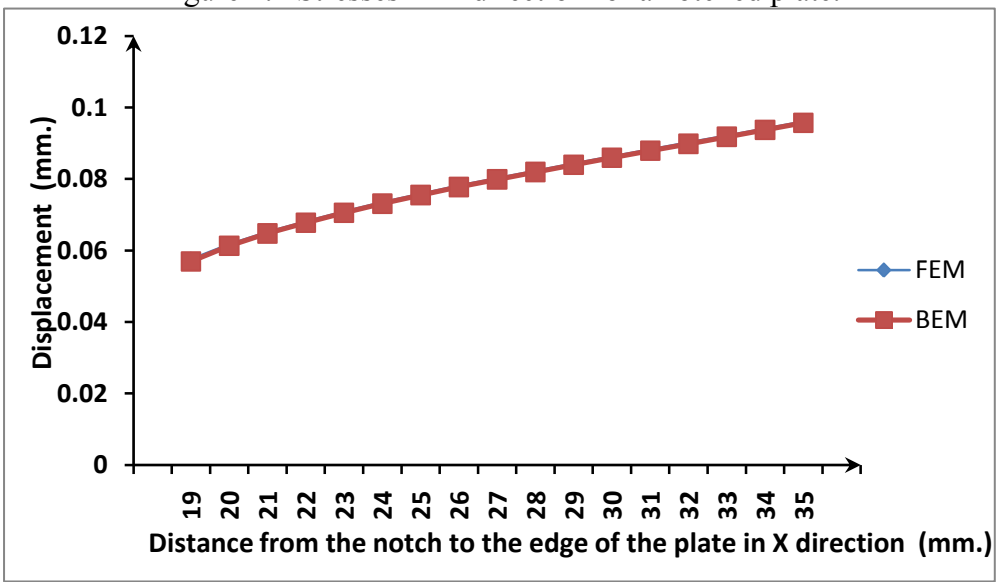

Figure 3. Displacements in Y direction for a notched plate.

Plate with a hole

A perforated tension specimen with geometry and boundary conditions as illustrated in figure 4, was analyzed in this example.

PLACA DE ALUMINIO DE 10 mm. DE ANCHO POR 36 mm. DE ALTO CON UNA CON UNA PERFORACION SEMICIRCULAR EN UNO DE SUS LADOS. DEL LADO DERECHO DE LA PERFORACION LA PLACA SE ENCUENTRA RESTRINGIDA AL DEZPLAZAMIENTO TANTO EN LA DIRECCION x COMO EN y. LA PLACA ES

SOMETIDA A UN ESTADO DE ESFUERZO DE TENSION DE 140 N/mm.² Y TIENE LAS SIGUIENTES CONSTANTES.E=70 000 N/mm.², ν=0.2, σ_a 140 N/mm.², σ_y =243 N/mm.², γ =0.01, Δt =0.01

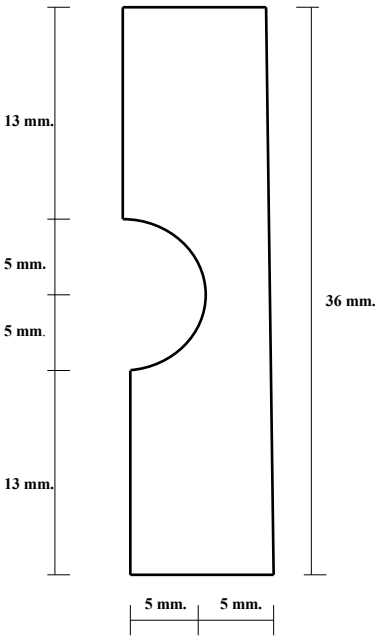

Figure 4 Geometry for a plate with a hole

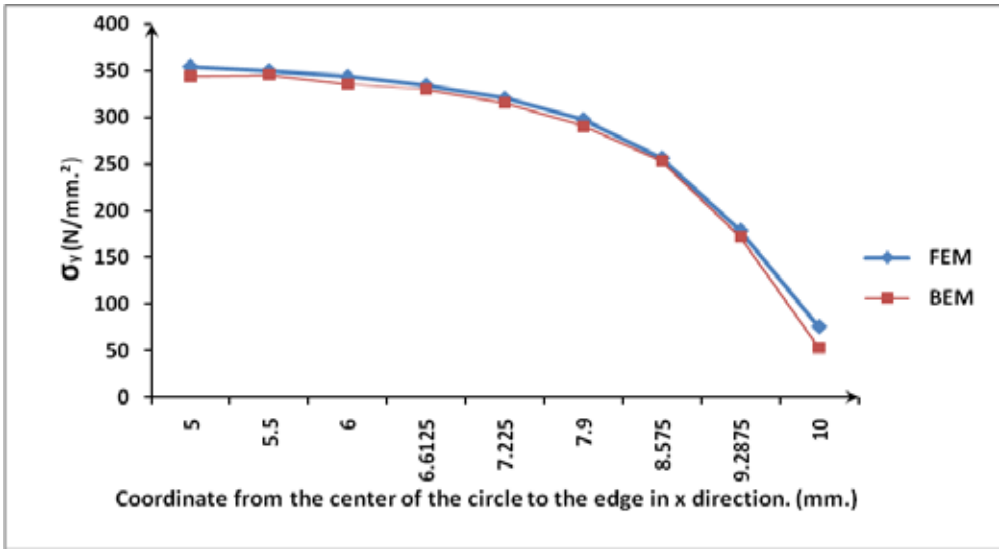

Figure 5 Stresses in the center of the plate in Y direction from the center of the hole.

PLACA DE ALUMINIO CON 10 mm. DE ANCHO Y UNA ALTURA DE 36 MILIMETROS LIMITADA EN SUS LADOS POR DOS SEMICIRCULOS Y SE SOMETE A UN ESTADO DE ESFUERZOS DE TENSION DE 140 N/mm.² Y CUENTA CON LAS SIGUIENTES CONSTANTES.

E=70 000 N/mm.², ν=0.2, σ_a 140 N/mm.², σ_y=243 N/mm.², γ=0.01, Δt=0.01

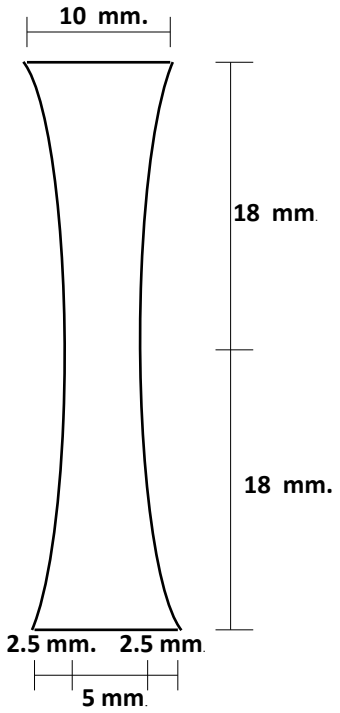

Figure 6 Geometry of a narrow plate with stresses in Y direction.

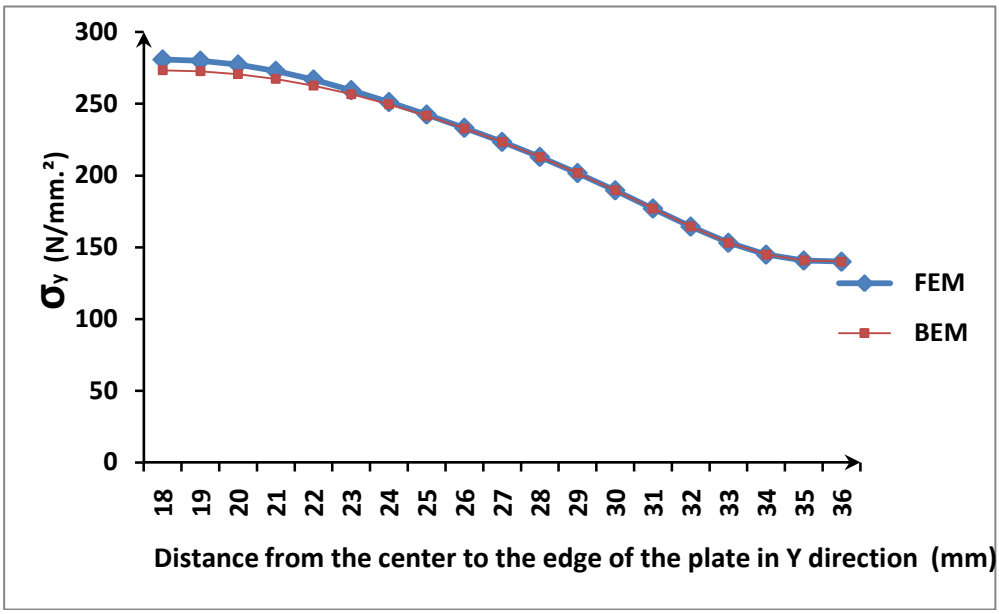

Figure 7 Stresses in Y direction from the center of the plate until the upper part.

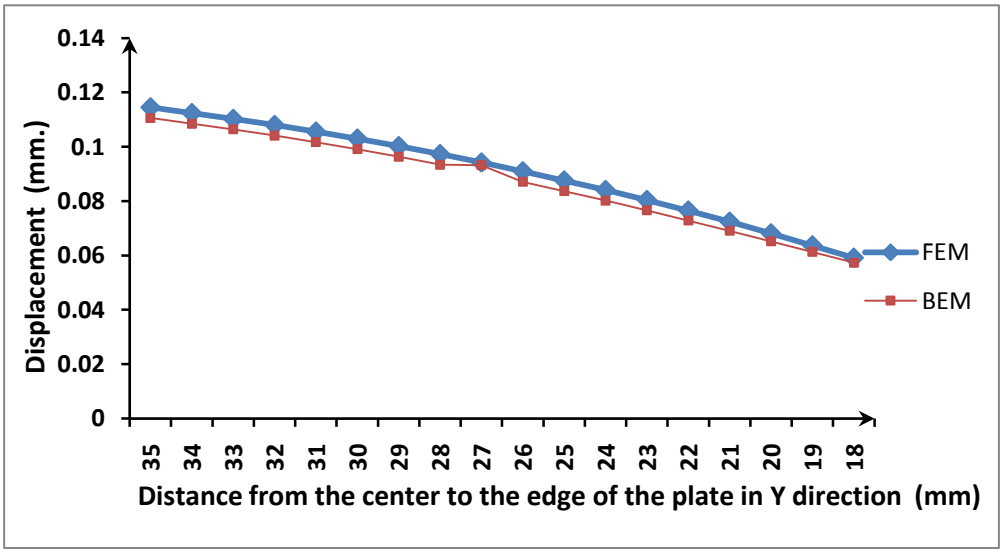

Fig. 6 Displacements in Y direction from the center of the plate until the upper part

5 CONCLUSIONS

In this paper the BEM was applied to the analysis of non-elastic problems. It has been demonstrated here that this method is an accurate and efficient method for analyzing and modeling visco-plastic problems. The analysis is general and can be applied to mixed mode cracks in non-linear fracture mechanics problems. The displacement and traction boundary integral equation used are independent. In the case of the traction equation continuity of strains is required at the collocation node to guarantee the existence of the finite part integrals.

Since this discontinuous boundary elements have to be used on the crack faces. The visco-plastic behaviour is represented by a plastic strain field over a region, susceptible to yield, discretized with quadrilateral quadratic continuous and discontinuous internal cells.

REFERENCES

[1] Providakis, C.P., Viscoplastic BEM Fracture Analysis of Creeping Metallic Cracked Structures in Plane Stress using Complex Variable Technique. *Engineering Fracture Mechanics,* 70, 707-720, (2003).

[2] Aliabadi, M.H., Boundary Element Methods in Fracture Mechanics. Appl Mech Rev, 50, 83-96, (1997).

[3] Morjaria, M., and Mukherjee, S., Numerical Analysis of Planar, Time-Dependent inelastic Deformation of Plates with Cracks by the Boundary Element Method, *Int. J. Solids Structures,* 17, 127-143, (1981).

[4] Banthia V., and Mukherjee, S., On Stress and Line Integrals in the Presence of Cracks, *Research Mechanica,* 15, 151-158, (1982).

[5] Tan, C.L., Lee, K.H. Elastic-Plastic Stress Analysis of a Cracked thick-walled Cylinder, *Journal of Strain Analysis,* 50-57, (1983).

[6] Yong, L., and Guo, W.G., The calculation of J_1 Integrals of Thick-Walled Tubes with One and Two Symmetrick Cracks by Elastoplastic BEM, *Int. J. Pres. Ves. & Pipping,* 51, 143-154, (1992).

[7] Hantschel T., Busch, M., Kuna, M., and Maschke, H.G., Solution of Elastic-Plastic Crack Problems by an Advanced Boundary Element Method, *in Proceedings of the 5th. International Conference on Numerical Methods in Fracture Mechanics,* A.R.. Luxmoore and D.R.J. Owen, Eds., pp. 29-40, (1990).

[8] Leitão, V., An Improved Bounadry Element Formulation for Nonlinear Fracture Mechanics I, PhD *Thesis,* Wessex Institute of Technology, University of Porsmouth, (1993).

[9] Swedlow, J. L. and Cruse, T. A. Formulation of the boundary integral equation for three-dimensional elastoplastic flow, *International Journal of Solids and Structures,* 7, 1673-1681 (1971).

[10] Riccardella, P. *An Implementation of the Boundary Integral Technique for plane problems of Elasticity and Elastoplasticity,* PhD Thesis, Carnegie Mellon University, Pitsburg, PA (1973).

[11] Telles, J. C. F., and Brebbia,C.A. Elastic/viscoplastic Problems using Boundary Elements,International Journal of Mechanical Sciences, 24, 605-618, (1982).

[12] Aliabadi, M.H., The Boundary Element Method. Applications in Solids and Structures. Vol. 2. John Wiley & Sons, Ltd, West Sussex, England (2002).

[13] Aliabadi,M.H. A new generation of boundary element methods in fracture mechanics,International Journal of Fracture, 86, 91-125, (1997).

[14] Aliabadi,M.H. and Portela,A. Dual boundary element incremental analysis of crack growth in rotating disc. Boundary Element Technology VII, Computational Mechanics Publica-tions, Southampton, 607-616, (1992).

[15] Portela, A. Aliabadi, M.H., and Rooke, D.P., Dual Boundary Element Incremental Analysis of Crack propagation. *Computers & Structures,* 46, 237-247, (1993).

[16] Mi, Y., Aliabadi, M.H., Dual Boundary Element Method for Three-Dimensional Fracture Mechanics Analysis, *Engng. Anal. with Bound. Elem.,* 10, 161-171, (1992).

[17] Chao Y.J., Zhu, X.K., and Zhang, L., Higher-Order Asymptotic Crack-Tip .elds in a power-lawCreeping material, International Journal of Solids and Structures, 38, (2001).

[18] Cisilino, A.P. and Aliabadi, M.H., Three-dimensional BEM Analysis for Fatigue Crack Growth in Welded Components, International Journal for Pressure Vessel and Piping, 70,135-144, (1997).

[19] Cisilino, A.P., Aliabadi, M.H. and Otegui, J.L., A Three-dimensional Element Formulation for the Elasto-Plastic analysis of Cracked Bodies, International Journal for Numerical Methods in Engineering, 42, 237-256, (1998).

[20] Hutchinson, J.W., Singular behaviour at the end of a tensile crack in a hardening material, *J. Mech. Phys. Solids*, 16, 13-31, (1968).

[21] Zienkiewicz, O.C., and Cormeau, I.C., Visco-Plasticity and Creep in Elastic-Solids A Unified Numerical Solution Approach, *International Journal for Numerical Methods in Engineering,* vol. 8, 821-845, (1974).

[22] Pineda, E., Dual Boundary Element Analysis for Creep Fracture, *Ph. D. Thesis*, Queen Mary College, University of London, (2005).

XI International Conference on Computational Plasticity. Fundamentals and Applications
COMPLAS XI
E. Oñate, D.R.J. Owen, D. Peric and B. Suárez (Eds)

NONLINEAR DYNAMIC MODEL FOR ELASTIC STRUCTURES – A NEW APPROACH

S. A. DAVID*, C. OLIVEIRA†

* Departamento de Ciências Básicas (ZAB)
Universidade de São Paulo
Av. Duque de Caxias Norte 225, 13635-900 Pirassununga, Brazil
e-mail: sergiodavid@usp.br

† Faculdade de Engenharia de Energia (FAEN)
Universidade Federal da Grande Dourados
Rodovia Dourados – Itahum Km 12, 79804-970 Dourados, Brazil
e-mail : ClivaldoOliveira@ufgd.edu.br

Key words: Flexible structures, lightweight elements, Lagrangian dynamics, nonlinear systems.

Abstract. In this paper the Lagrangian dynamics in conjunction with the assumed modes method is utilized in order to obtain the non-linear equations of motion for a flexible structure with all non-linearities taken into account, without the usage of any simplifying linearization procedure, as found in most of the works presented in the literature. The non-linear model is composed of six coupled and strongly non-linear ordinary differential equations.

1 INTRODUCTION

The use of the lightweight structural elements in space applications, underwater interventions as well as in robotic manipulators under the requirement for precise positioning, easier transportation, less power consumption, has increased the interest in having a precise model that closely represents such mechanical systems for all their conditions. The position and velocity vector obtained, after imposing the inextensibility conditions, are used in kinetic energy expression while the curvature is used in the potential energy. The Lagrangian dynamics in conjunction with the assumed modes method is utilized in order to obtain the non-linear equations of motion that are treated with all non-linearities taken into account, without the usage of any simplifying linearization procedure, as found in most of the works found in the literature. The resulting non-linear model is composed of six coupled and strongly non-linear ordinary differential equations is discussed, simulated and some results of this simulation are presented. The effects of the flexibility are explored by comparing the resulting simulation results. Besides, the way in which the motion equations are treated in this paper allows the monitoring of each contributing factor for the system elasticity. The main goal of this work is to treat the motion equations according to a general approach, without simplifying linearizations, and to assess the system behavior through controlled simulations.

2 PROBLEM DESCRIPTION

In this work the dynamic modeling is performed for a system that contains two flexible links and two rotational joints. For the sake of comparison a rigid structure with two links and two rotational joints is also analyzed. In this case two degrees of freedom are defined.

A convenient parametrization of the terms of the motion equations, which makes it easier to compare the simulation results for the rigid and for the flexible system is also developed.

The studied flexible system is assumed to have a planar movement. Even with this assumption, the complexity of the resulting dynamic equations for this system is large when compared to the equations for rigid manipulators.

The Lagrange equations and the assumed mode method are applicable in this model. The model is established basically by the superposition of the flexible movement with the movement of an hypothetical rigid body. A convenient mathematical set of equations is developed for this purpose The elastic movement of the links is truncated in the second mode, that is, it is considered that the amplitudes of all higher order vibration modes are much smaller than the amplitude of vibration of the first mode. In such a case, a non-linear model with six degrees of freedom is obtained.

We outline the fact that the motion equations are treated with all non-linearities taken into account, without the usage of any simplifying linearization procedure, as found in most of the works present in the literature. This linearization procedure may not to consider small contributions of physical effects that are summed or superimposed and that may significantly influence the system behavior.

For this reason, one of the tasks of this work is to treat the motion equations according to a general approach, without simplifying linearizations, and to assess the system behavior through controlled simulations.

3 THE MODEL

The physical model for the flexible system is established in accordance to the schematic drawing shown in the Figure 1.

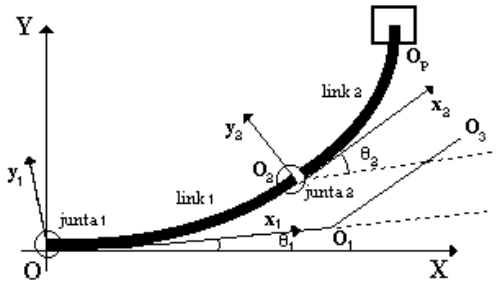

Figure 1: Physical model

The following assumptions are made: the system has planar movement and the relative movement between the two links is resulting from the torques applied in each joint of the system.

At the terminal of the link 1, a concentrated mass represents both the servo-motor and the joint masses. At the terminal of the link 2, a discrete mass is used to represent the load to be handled between two points of the plane.

In order to describe the movement, three reference systems are defined:
[O,X,Y] - inertial referential system with origin in joint 1;
[O,x_1,y_1] - referential system with origin in O and the x_1 axis tangent to link 1 at point O;
[O_2,x_2,y_2] - referential system with origin in joint 2 and with the x_2 axis tangent to link 2 at point O_2. Two angles are defined:
$\theta_1(t)$ is the angle between the x_1 and x axis;
$\theta_2(t)$ is the angle between the x_1 and x_2 axis.

It is also defined a new system that is formed by the two segments OO_1 and O_1O_3, with angle θ_2 in O_1. The global (total) movement may be understood as being the movement of an hypothetical rigid system OO_1O_3 and a flexible movement of the links 1 and 2 with respect to this mobile system.

3.1 Kinematics Description

The position of any point in the system may be described by a convenient description of a set of coordinates. Any point P_i may be specified if a new variable u_i (x_i , t) is defined as being the coordinate of the flexible movement with respect to the reference system [O x_i y_i].

The position vector for point P_i will be:

$$\vec{R}_{dii} = \left\{\vec{U}_i\right\}^T \begin{Bmatrix} x_i \\ y_i \end{Bmatrix} = x_i\,\vec{u}_{xi} + y_i\,\vec{u}_{yi} \tag{1}$$

With the aid of this definition, it is possible to express the position vectors - and consequently the velocity vectors - for the links 1 and 2, both for the mass concentrated in joint 2 as well as for the load at the terminal of link 2.

3.2 Kinetic Energy

By means of the velocity vectors previously mentioned, the total kinetic energy of the system may be expressed by the following equation:

$$\begin{aligned} T = {} & \frac{1}{2}\int_{m_1} \dot{\vec{R}}_{d1}\cdot\dot{\vec{R}}_{d1}\,dm + \frac{1}{2}\int_{m_2} \dot{\vec{R}}_{d2}\cdot\dot{\vec{R}}_{d2}\,dm \\ & + \frac{1}{2}\,m_j\,\dot{\vec{R}}_j\cdot\dot{\vec{R}}_j + \frac{1}{2}\,m_p\,\dot{\vec{R}}_p\cdot\dot{\vec{R}}_p + \frac{1}{2}\,J_p\,\dot{u}_{2E}^{|2} \end{aligned} \tag{2}$$

Where:

$\frac{1}{2}\int_{m_1} \dot{\bar{R}}_{d1} \cdot \dot{\bar{R}}_{d1}\, dm$ is the kinetic energy of link 1;

$\frac{1}{2}\int_{m_2} \dot{\bar{R}}_{d2} \cdot \dot{\bar{R}}_{d2}\, dm$ is the kinetic energy of link 2;

$\frac{1}{2} m_j\ \dot{\bar{R}}_j \cdot \dot{\bar{R}}_j$ is the kinetic energy related to the concentrated mass that represents the servo-motor and the joint. The mass is located at point O_2, in joint 2;

$\frac{1}{2} m_p\ \dot{\bar{R}}_p \cdot \dot{\bar{R}}_p$ is the kinetic energy related to the mass of the load. This mass is located at the terminal of link 2;

$\frac{1}{2} J_p\ \dot{u}_{2E}^{|2}$ is the rotational kinetic energy of the load due to its movement around the axis that passes through point O_2 and that is perpendicular to the plane shown in Figure 1.

3.3 Potential Energy

In the calculation of the total potential energy of the system it is assumed an energy associated to the rigid movement (gravitational potential energy), plus the elastic potential energy of the links.

Ox is taken as reference and the potential energy of the system (assuming u_1 and u_2 sufficiently small) is given by:

$$\begin{aligned} V = {} & m_1 g \frac{L_1}{2} s\theta_1 + m_j g L_1 s\theta_1 + \\ & + m_2 g\left[L_1 s\theta_1 + \frac{L_2}{2} s(\theta_1 + \theta_2) \right] + \\ & + m_p g\left[L_1 s\theta_1 + L_2 s(\theta_1 + \theta_2) \right] \\ & - \frac{1}{2}\int_0^{L_1} E I_1 \left(\frac{\partial^2 u_1}{\partial x_1^2} \right)^2 dx_1 - \frac{1}{2}\int_0^{L_2} E I_2 \left(\frac{\partial^2 u_2}{\partial x_2^2} \right)^2 dx_2 \end{aligned} \tag{3}$$

where:

g is the gravitational acceleration constant;
L_1 and L_2 are the lengths of the links 1 and 2, respectively;
EI_1 and EI_2 are the rigidity of the links 1 and 2, respectively, which in this model are assumed to be constants, and
$s\,\theta_1 = \sin\theta_1$; $s\,(\theta_1 + \theta_2) = \sin(\theta_1 + \theta_2)$.

3.4 Motion Equations

In order to write down the motion equations of the system it will be used the assumed modes method. This method consists in considering a solution for the flexible movements in the form of a series composed by a linear combination of admissible functions in the spatial coordinates, multiplied by the time dependent function $q_i(t)$.

In the case of the flexible displacements of the links 1 and 2, it is possible to asume that

$$u_1 = \sum_{i=1}^{n} \phi_{1i}(x_1)\ q_{1i}(t) \tag{4}$$

and

$$u_2 = \sum_{i=1}^{n} \phi_{2i}(x_2)\, q_{2i}(t) \tag{5}$$

where the admissible functions $\phi_{ji}(x)$ must satisfy the geometrical boundary conditions with respect to the representation of the links in the reference systems $[Ox_1y_1]$ and $[O_2x_2y_2]$.

Hence the system becomes represented by (2n + 2) degrees of freedom.

If it is assumed that the amplitudes of the higher order vibration modes are very small when compared to the first vibration mode, the system may be truncated with *n* equal to 2, resulting in a problem involving six degrees of freedom.

Besides this, if it is assumed that $\phi_{ji}(x)$ are eigenfunctions of the problem of a clamped free beam, that is, clamped in one end and free at the other end, the geometrical boundary conditions will be fulfilled and due to the ortogonality of this functions we will have:

$$\int_0^{L_4} \phi_r(x)\ \ \phi_s\ (x)\, dx = \begin{cases} 0 & se \quad r \neq s \\ 1 & se \quad r = s \end{cases} \tag{6}$$

With this equation, one can assess each one of the integrals in the equations for both the kinetic and the potential energy considering $\theta_1, \theta_2, q_{11}, q_{12}, q_{21}, q_{22}$ the generalized coordinates and Γ_1, Γ_2 the non-conservative torques acting at the joint of the system, it is possible to write down the equations of the movement - with convenient parametrization of the terms and without the usage linearization procedure- using the Lagrange equations for non-conservative systems,

$$\frac{d}{dt}\left[\frac{\partial T}{\partial \dot{q}_r}\right] - \frac{\partial T}{\partial q_r} + \frac{\partial V}{\partial q_r} = Q_r \tag{7}$$

r = 1(1)6

where:

Q_r are the time dependent generalized non-conservative forces (or torques).

The equations assume the final form,

$$J_1\ \ddot{\theta}_1 + F_1\ \dot{\theta}_1 + \ \Gamma_{perturb\ 1} = \tau_1 \tag{8}$$

$$J_2\ \ddot{\theta}_2 + F_2\ \dot{\theta}_2 + \ \Gamma_{perturb\ 2} = \tau_2 \tag{9}$$

$$J_3\ \ddot{q}_{11} + F_3\ \dot{q}_{11} + \ \Gamma_{perturb\ 3} = 0 \tag{10}$$

$$J_4\ \ddot{q}_{12} + F_4\ \dot{q}_{12} + \ \Gamma_{perturb\ 4} = 0 \tag{11}$$

$$J_5\ \ddot{q}_{21} + F_5\ \dot{q}_{21} + \ \Gamma_{perturb\ 5} = 0 \tag{12}$$

$$J_6\ \ddot{q}_{22} + F_6\ \dot{q}_{22} + \ \Gamma_{perturb\ 6} = 0 \tag{13}$$

where

$$J_1 = A_1 + B_1 + C_1 s\theta_2 + D_1 c\theta_2 + E_1 \tag{14}$$

$$F_1 = H_1 + I_1 s\theta_2 + M_1 c\theta_2 \tag{15}$$

$$\Gamma_{perturb.1} = P_1 \ddot{\theta}_2 + R_{111}\ddot{q}_{11} + R_{112}\ddot{q}_{12} + R_{121}\ddot{q}_{21} + R_{122}\ddot{q}_{22} + S_1\dot{\theta}_2 - T_1\dot{\theta}_2^2 + U_1 c\theta_1 + V_1 c(\theta_1+\theta_2) - Y_1 + \left[a_1\ddot{\theta}_2 - b_1\dot{\theta}_2 - c_1\dot{\theta}_2^2 + e_1\right] s\theta_2 \tag{16}$$

$$J_2 = A_2 + B_2 \tag{17}$$

$$F_2 = H_2 \tag{18}$$

$$\Gamma_{perturb.2} = P_2\ddot{\theta}_1 + R_{21}\ddot{q}_{21} + R_{222}\ddot{q}_{22} + S_2\dot{\theta}_1 + V_2 c(\theta_1+\theta_2) + Y_2 \left[a_2\ddot{\theta}_1 + b_2\dot{\theta}_1 + c_2\dot{\theta}_1^2 - e_2\right] s\theta_2 + \left[p_2\ddot{\theta}_1 - r_2\dot{\theta}_1^2 + s_2\dot{\theta}_1 + v_2\right] c\theta_2 \tag{19}$$

$$J_3 = A_{311} \tag{20}$$

$$F_3 = 0 \tag{21}$$

$$\Gamma_{perturb.3} = P_{311}\ddot{\theta}_1 + R_{312}\ddot{q}_{12} - T_{312}\dot{\theta}_1^2 - 2\,Kw_{311} - \phi_{11E}\left[a_3(\ddot{\theta}_1+\ddot{\theta}_2) + b_3\dot{\theta}_1 + c_3\dot{\theta}_2 + e_3\right] s\theta_2 + \phi_{11E}\left[p_3(\ddot{\theta}_1+\ddot{\theta}_2) + 2a_3(\dot{\theta}_1\dot{\theta}_2 + \tfrac{1}{2}\dot{\theta}_1^2 + \tfrac{1}{2}\dot{\theta}_2^2) + v_3\right] c\theta_2 \tag{22}$$

$$J_4 = A_{412} \tag{23}$$

$$F_4 = 0 \tag{24}$$

$$\Gamma_{perturb.4} = P_{412}\ddot{\theta}_1 + R_{411}\ddot{q}_{11} - T_{411}\dot{\theta}_1^2 - 2\,Kw_{412} - \phi_{12E}\left[a_4(\ddot{\theta}_1+\ddot{\theta}_2) + b_4\dot{\theta}_1 + c_4\dot{\theta}_2 + e_4\right] s\theta_2 + \phi_{12E}\left[p_4(\ddot{\theta}_1+\ddot{\theta}_2) - 2a_4(\dot{\theta}_1\dot{\theta}_2 + \tfrac{1}{2}\dot{\theta}_1^2 + \tfrac{1}{2}\dot{\theta}_2^2) + v_4\right] c\theta_2 \tag{25}$$

$$J_5 = A_{521} \tag{26}$$

$$F_5 = 0 \tag{27}$$

$$\begin{aligned}\Gamma_{perturb.5} &= P_{521}(\ddot{\theta}_1+\ddot{\theta}_2) + R_{522}\,\ddot{q}_{22} - Z_{521} - 2\,Kw_{521} \\ &+ \left[a_{521}\,\ddot{\theta}_1 + b_{521}\,\dot{\theta}_1 - c_{521}\,\dot{\theta}_2 + d_{521}(\dot{\theta}_1\dot{\theta}_2 + \dot{\theta}_1^2)\right] s\theta_2 \\ &- \left[p_{521}\,\ddot{\theta}_1 + r_{521}\,\dot{\theta}_1^2 + s_{521}\,\dot{\theta}_1\dot{\theta}_2 - v_{521}\right] c\theta_2\end{aligned} \tag{28}$$

$$J_6 = A_{622} \tag{29}$$

$$F_6 = 0 \tag{30}$$

$$\begin{aligned}\Gamma_{perturb.6} &= P_{622}(\ddot{\theta}_1+\ddot{\theta}_2) + R_{621}\,\ddot{q}_{21} - Z_{622} - 2\,Kw_{622} \\ &+ \left[a_{622}\,\ddot{\theta}_1 + b_{622}\,\dot{\theta}_1 - c_{622}\,\dot{\theta}_2 + d_{622}(\dot{\theta}_1\dot{\theta}_2 + \dot{\theta}_1^2)\right] s\theta_2 \\ &- \left[p_{622}\,\ddot{\theta}_1 + r_{622}\,\dot{\theta}_1^2 + s_{622}\,\dot{\theta}_1\dot{\theta}_2 - v_{622}\right] c\theta_2\end{aligned}$$

4 SIMULATIONS RESULTS

This flexible system may be mathematically reduced to the rigid one by vanishing the terms related to system flexibility, which characterizes the possibility of finding a frontier between both systems.

With this fact in mind, mathematical simulations are performed according to the following methodology:

* initially the rigid system is simulated in a separate manner;

* following, the flexible system is simulated with all its contributions taken into account;

* after that, the effects are individually and cumulatively subtracted and the system behavior is analyzed;

* the effects are subtracted until the limit condition in which the flexible system is reduced to a rigid one and the system response converges - as expected - for the case of the rigid system modeled separately.

Some results obtained correspond to simulations realized for the angular position θ_1 and θ_2 in the following cases:

Flexible system reduced to a rigid one (Fig.2) ;

Flexible system, subtracted flexibility in the $T_{perturb.}$ Term (Fig.3);

Flexible system, subtracted flexibility in the J term (Fig.4);

Flexible system reduced to a rigid one (Fig.5).

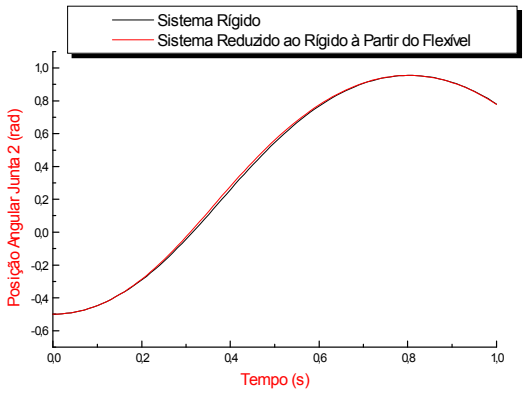

Fig.2:Flexible system reduced to a rigid one

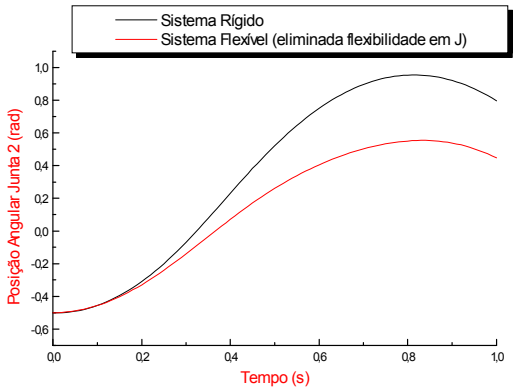

Fig.4:Flexible system, subtracted flexibility in J term

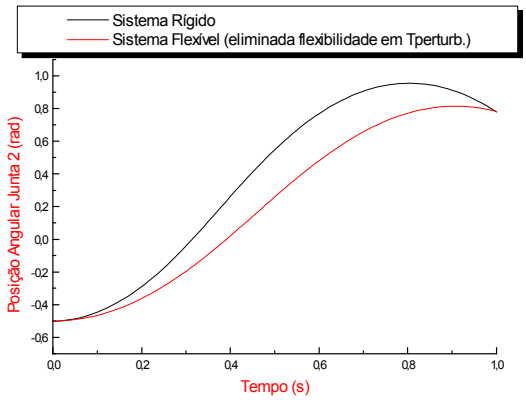

Fig.3:Flexible system, subtracted flexibility in $T_{perturb.}$

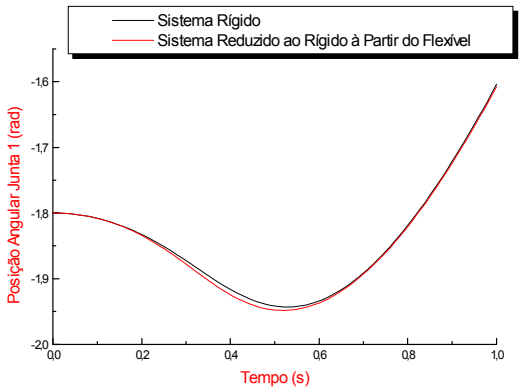

Fig.5: Flexible system reduced to a rigid one.

The way in which the motion equations are treated in this paper may allow the monitoring of each contributing factor for the system flexibility. The Table 1 provides a qualitative analysis of the systems.

TABLE 1. Qualitative Analysis.

Systems	Rigid	Flexible
J (Term)	Very much relevant	Very much relevant
F (Term)	Irrelevant	Not much relevant
Tperturb (Term)	Relevant	Relevant

5 CONCLUSIONS

The Lagrangian dynamics in conjunction with the assumed modes method were utilized in order to obtain the non-linear equations of motion that are treated with all non-linearities taken into account, without the usage of any simplifying linearization procedure.

A convenient parametrization of the terms of the motion equations, which makes it easier to compare the simulation results for the rigid and for the flexible system was also developed.

The flexible structure may be mathematically reduced to a rigid one by means of vanishing the flexibility related terms. The same procedure may be extended to the simulations, which makes it possible to find a mathematical frontier between both systems.

The effects of the flexibility are explored by comparing the resulting simulation results.

Besides, the way in which the motion equations are treated in this paper allows the monitoring of each contributing factor for the system elasticity.

REFERENCES

[1]J. M. Balthazar, A. Fenili, "*Some remarks on nonlinear vibrations of ideal and nonideal slewing flexible structures"*, Journal of Sound and vibration, Holanda, v. 282, n 1-2, pp. 543-552, 920050 (2009).

[2]S. A. David, J. M. Rosario, ; J. Machado, "*Investigation about chaos in a magneto-elastic dynamical system"*. Computational Fluid and Solid Mechanics - Solids and Structures[JCR], Multi-Physics, vol.2, K.J.Bathe editor, pp. 1120-1123, Elsevier Science Ltd., England,ISBN 0-08-043944-6. (2001).

[3]C. Oliveira, S. A. David, "*A control platform based on dynamic modeling of structures*". In Proc: 8º Congresso Nacional de Mecânica Experimental- CNME2010, Guimarães, Portugal (2010).

[4] H.Goldstein*,"Classical Mechanics",* Reading Mass., Addison Wesley Publishing Company, Second Edition (1981).

[5] P. Hagedorn, *"Oscilações Não Lineares"*, São Paulo: Editora Edgard Blucher LTDA, (1984) (In Portuguese).

[6] A. Nayfeh , D. T. Mook, *"Nonlinear Oscillations",* Wiley & Sons - New York (1979).

XI International Conference on Computational Plasticity. Fundamentals and Applications
COMPLAS XI
E. Oñate, D.R.J. Owen, D. Peric and B. Suárez (Eds)

NON-LINEAR FINITE ELEMENT ASSESSMENT ANALYSIS OF A MODERN HERITAGE STRUCTURE

STEFANO SORACE[*] AND GLORIA TERENZI[†]

[*] Department of Civil Engineering and Architecture
University of Udine
Via delle Scienze 208, 33100 Udine, Italy
e-mail: stefano.sorace@uniud.it

[†] Department of Civil and Environmental Engineering
University of Florence
Via di S. Marta 3, 50139 Florence, Italy
e-mail: terenzi@dicea.unifi.it

Key words: Non-linear Finite Elements, Structural Assessment, Steel, Reinforced Concrete, Buckling, Smeared Cracking.

Abstract. A synthesis of a non-linear finite element structural assessment enquiry carried out on a monumental modern heritage building is reported in this paper. The study includes a buckling analysis of the slender steel beams constituting a mushroom-type roof, and an "integral" seismic pushover analysis of the supporting R/C columns. The computational solutions obtained for the steel roof beams are compared to the results derived from a calculation of the critical stress of beam panels, and the global lateral-torsional buckling resistance of members developed according to the Technical Standards adopted for structural verifications. The unconventional "full-cracking" pushover application to the R/C columns offers detailed simulation of the evolution of their non-linear response, which is discussed in the paper, along with the most significant parameter and procedure choices made in the analysis.

1 INTRODUCTION

Non-linear finite element approaches are suggested in the latest generation of international Technical Standards as preferential analysis methods for the static and seismic assessment of existing structures. This prompts an extension of the use of non-linear models and calculus programs, which are typically conceived, developed and implemented in the academic community for research aims, to the professional community of structural engineers. An important role can be played by academicians also at this challenging phase, where a critical review of the theoretical options and of the limits of available models, as well as an expert guidance to their practical application, are urged by professional users.

A study in this field is currently being carried out by the authors within a National Research Project, financed by the Italian Ministry of Education and University and dedicated to the historical and structural analysis of Italian modern heritage architecture built in the

1950s and in the 1960s. Special care is devoted in this paper to a representative masterpiece building, the "Palazzo del Lavoro" in Turin, designed in 1959 by the world-famous Italian engineer Pier Luigi Nervi, and completed in 1961. The main structural elements of the building consist of sixteen monumental reinforced concrete (R/C) columns, 20 m high, and sixteen supported steel mushroom roof panels, each covering an area of 40×40 m×m. The building includes other monumental structural members, and namely the R/C ribbed slabs typical of Nervi's style, which constitute the two perimeter gallery floors, and the continuous gallery-to-roof glass façades. External views of the building at the time of its opening and in its current conditions; the plans of the roof and upper gallery floors; the elevation design drawing and a view of a mushroom steel roof panel and relevant R/C column, are shown in Figures 1, 2 and 3, respectively.

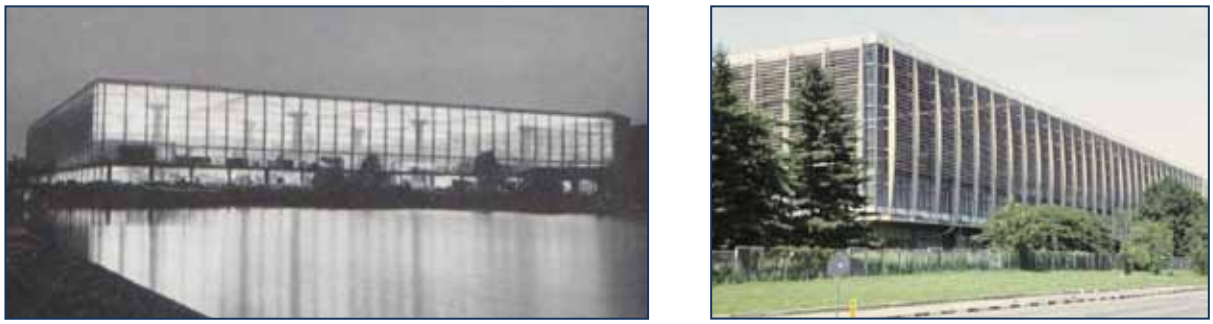

Figure 1: External views of the building at the time of its opening and in its current conditions

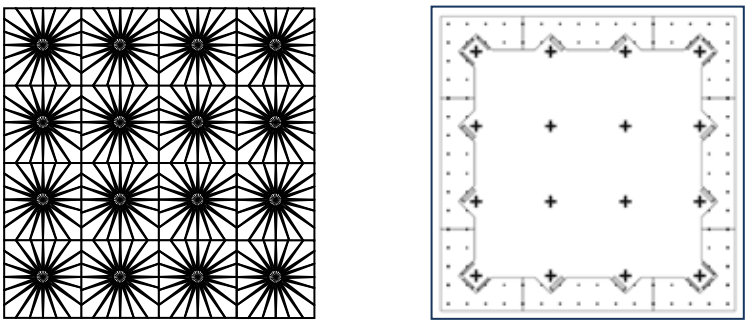

Figure 2: Plans of the roof and the upper gallery

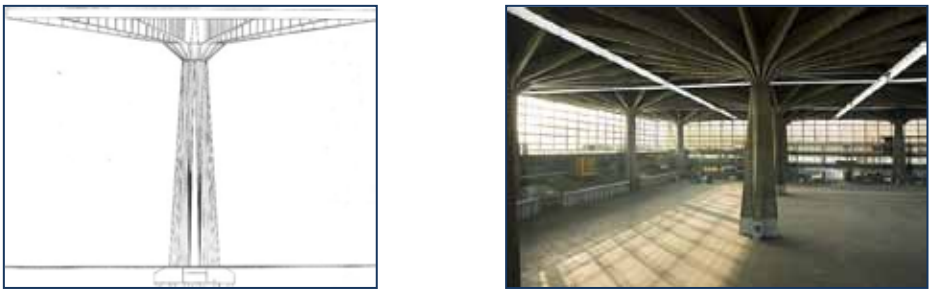

Figure 3: Elevation design drawing and view of a mushroom steel roof panel and the supporting R/C column

Linear elastic finite element analyses of these structural elements taken separately, as well as of the entire building, were initially carried out to evaluate their static and dynamic characteristics, and to check their current nominal safety conditions [1]. Based on the results of this first-level assessment analyses, a second-level step was then undertaken, aimed at carefully evaluating the structural performance of the two most important types of members, i.e., the steel roof beams and the R/C monumental columns. This new section of the numerical study posed two representative problems of non-linear geometrical—steel beams—and material—R/C columns—type, respectively.

A local and global buckling analysis was developed for the roof beams, in order to investigate the instability effects arising from their very slender sections. Similarly to many other finite element commercial codes, the SAP2000NL [2] program used for this analysis produces a not plainly understandable buckling mode calculation, which leaves uncertainties both on the non-linear geometrical formulation of the problem and the final results. These aspects were investigated by comparing the computational solutions with the results derived from the expressions of the critical stress of panels and the global lateral-torsional buckling resistance of beams provided by the reference Technical Standards on steel structures adopted for the structural verifications [3-6].

The R/C columns were evaluated with an "integral" seismic pushover analysis of the numerical model constituted by a full mesh of solid octahedral smeared cracking "concrete" elements with embedded steel reinforcements, generated by the ANSYS non-linear calculus program [7]. No reductions to simplified models were considered in this enquiry, as the "uniform resistance" columns designed by Nervi should ideally reach the first significant cracked configurations, and then the plasticization of vertical reinforcements, simultaneously in several sections along the height. This "full-cracking" application offers a more direct and realistic simulation of the evolution of the non-linear response of columns as compared to models including lumped plastic hinges or fiber-composed plastic zones, but it requires a much greater computational effort, more careful choices of the mechanical and algorithmic parameters, and proper checks on the stability and accuracy of the solution.

A synthesis of the analyses carried out on the roof steel beams and the R/C columns is presented in the following two sections.

2 ANALYSIS OF STEEL ROOF BEAMS

The 20 cantilever steel radial beams forming the corolla of each one of the 16 mushroom panels of the roof have fixed-end bolted connections to a circular drum, constituted by 20 rectangular steel frames, whose height is 2800 mm and whose base is 1900 mm. Each frame is supported by a triangular steel plate—with a 1500 mm-long vertical side and a 1900 mm-long horizontal side—placed over a 200 mm-deep groove on the upper section of the R/C column (Figure 4). The I-section welded beams, which are joined on their free end to a continuous C-shaped steel edge beam outlining the square perimeter of the mushroom panel, are 2800 mm to 700 mm high, and their top and bottom flanges are 690 mm to 200 mm wide. The beams have three different spans, ranging from 15,750 mm (type 1 beams, orthogonal to the C edge profile) to 20,250 mm (type 3 beams, close to the diagonal of the square). The constituting steel is equivalent to the current S235JR type, with yielding and ultimate nominal stress values f_y=235 MPa and f_u=355 MPa, respectively. The web of the beams is very thin (5

mm—type 1 through 7 mm—type 3); this determines a high slenderness of cross sections, especially in the areas close to the fixed end. The web is subdivided in 13 (type 1 beam) through 17 (type 3) panels by a set of vertical stiffening plates welded to the web and to the top and bottom flanges. The different web thickness and stiffener spacing values determine a very similar resistance of the three types of beams to bending and shear stresses, as well as to local and global buckling, as planned in the original design of the metallic roof (carried out by engineer Gino Covre, who worked with Pier Luigi Nervi for this part of the building structure). In view of this, the finite element and verification analyses are synthesized below for type 1 beams, whose dimensions are reported in Figure 4, as they are also representative of the remaining two beam types.

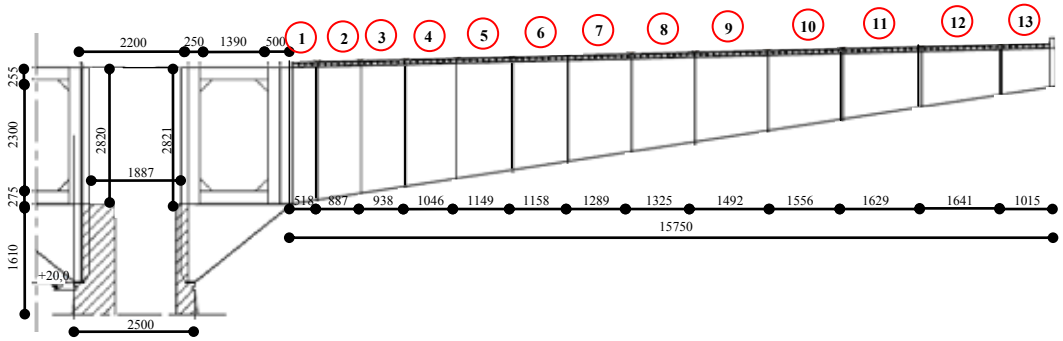

Figure 4: Upper section of a R/C column and relevant steel drum, and view of a triangular bearing plate and a type 1 cantilever beam (dimensions in millimeters)

2.1 Bending and shear resistance and lateral-torsional buckling verifications

The resistance verification to the in-plane bending moment at the ultimate limit states—carried out by referring to the effective properties of Class 4 cross-sections, to which the considered members belong according to Eurocode 3 Part 1-1 rules [3]—is not met. Indeed, the ratio of the design value of bending moment to the corresponding design resistance is significantly greater than 1 (and it reaches 1.57 for the fixed-end section) along over 3/4 of beam span. The resistance verification to shear stress is met for all sections. The verification at the serviceability limit states concerning vertical deflection, developed according to the current Italian Technical Standards [5] (as Eurocode 3 devolves this specification to the National Annexes), is widely met too.

The verification of the beams to lateral-torsional buckling was carried out by considering the only effect of the major axis bending, since the compression axial force induced by the slope of the center-line of the beams is very low (with a maximum of 22 kN at the fixed-end section). The relevant verification formula is:

$$\frac{M_{Ed}}{M_{b,Rd}} < 1 \tag{1}$$

where M_{Ed}, $M_{b,Rd}$ are the design value of the moment and the design buckling resistance moment, respectively, with $M_{b,Rd}$ expressed as:

$$M_{b,Rd} = \chi_{LT} W_y \frac{f_y}{\gamma_{M1}} \tag{2}$$

being $W_y=W_{eff,y}$ for Class 4 sections ($W_{eff,y}$ is computed by determining the effective section as a function of the reduction factor ρ for the compressed portion of the web and the compressed flange), f_y=235 MPa, as noted above, and γ_{M1}=1.05; χ_{LT} is given by the following relation:

$$\chi_{LT} = \frac{1}{\Phi_{LT} + \sqrt{\Phi_{LT}^2 - \bar{\lambda}_{LT}^2}} \tag{3}$$

where $\Phi_{LT} = 0.5\left[1 + \alpha_{LT}\left(\bar{\lambda}_{LT} - 0.2\right) + \bar{\lambda}_{LT}^2\right]$, α_{LT} is an imperfection factor, equal to 0.76 for welded I-sections with height-to-base ratio greater than 2, $\bar{\lambda}_{LT} = \sqrt{\frac{W_y f_y}{M_{cr}}}$, and M_{cr} is the elastic critical moment for lateral-torsional buckling evaluated according to the expression in Annex F of [3]. By applying the relations above, the ratio of M_{Ed} (equal to 2414 kNm) to $M_{b,Rd}$ (1415 kNm) results to be equal to 1.706, and thus the verification inequality (1) is definitely not met. The unsafety factor is obtained by inverting the ratio between the two moments ($M_{b,Rd}$/ M_{Ed}=1/1.706), i.e. 0.586.

2.2 Web panel buckling verifications

The web panels are much more sensitive to buckling than the flange plates are, as a consequence of the high slenderness of the web determined by the geometrical characteristics of the beams. The verification analysis is carried out in this case by referring to the criterion proposed in a previous edition of the Italian Standards for steel structures [6], where the effects of normal and shear stresses are jointly considered, assuming an ideal critical stress $\sigma_{cr,id}$ to be compared to the design ideal stress computed according to the von Mises rule. The expression of $\sigma_{cr,id}$ is derived from the Massonnet normal critical stress–shear critical stress domain [8] as follows:

$$\sigma_{cr,id} = \frac{\sqrt{\sigma_1^2 + 3\tau^2}}{\frac{1+\psi}{4}\cdot\frac{\sigma_1}{\sigma_{cr}} + \sqrt{\left(\frac{3-\psi}{4}\cdot\frac{\sigma_1}{\sigma_{cr}}\right)^2 + \left(\frac{\tau}{\tau_{cr}}\right)^2}} \tag{4}$$

where σ_1=130.9 MPa, τ=20.1 MPa are the design normal and shear stress values; $\sigma_{cr} = k_\sigma \cdot \sigma_{cr,0}$, $\tau_{cr} = k_\tau \cdot \sigma_{cr,0}$, being k_σ, k_τ the normal and shear stress buckling factors, and $\sigma_{cr,0}$ the elastic critical plate buckling stress of the equivalent orthotropic plate, expressed as $\sigma_{cr,0} = \frac{\pi^2 E}{12(1-\nu)}\left(\frac{t}{h}\right)^2$, with t=plate thickness and h=plate width (or mean width in case of variable section); and ψ is a coefficient that defines the linear variation of normal stress over the section, which can be set as equal to -1 in this case, by neglecting the very little contribution of the axial force to σ_1, quantified by a normal stress of 1.6 MPa. Panel 4 (Figure

5) results to be the most critical among the 13 web panels of type 1 beams. Considering its geometrical characteristics (base=b=1050 mm, h=2445 mm, t=5 mm), k_σ=27.6, k_τ=33 and $\sigma_{cr,0}$=0.78 MPa values come out, from which σ_{cr}=21.6 MPa and τ_{cr}=25.9 MPa are derived. By applying formula (4), $\sigma_{cr,id}$ results to be equal to 22.2 MPa.

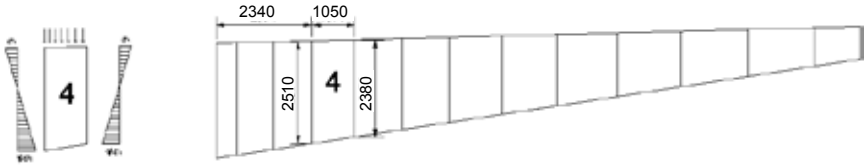

Figure 5: Geometry of panel 4 of type 1 beam (dimensions in millimeters)

The values of the normal and shear stress buckling factors are computed in [6] as a function of the aspect ratio α=b/h (whose average value is equal to 0.427 for panel 4) according to the expressions

$$k_\sigma = 15.87 + \frac{1.87}{\alpha^2} + 8.6\alpha^2 \quad \alpha < \frac{2}{3} \tag{5}$$

$$k_\tau = 4 + \frac{5.34}{\alpha^2} \quad \alpha < 1 \tag{6}$$

which provide good analytical approximations of the Timoshenko-Gere [9] original instability curves for linearly varying (with $\psi \leq 1$) normal stress, and uniform shear stress distributions, respectively. The difference between the $\sigma_{cr,id}$ and σ_{cr} values above is so little because of the great prevalence of σ_1 over τ, which produces a scarce influence of shear stress on the critical stress interaction domain. A second observation concerns σ_{cr}, which is greater than the value of 19.1 MPa derived by the Eurocode 3 – Part 1-5 [4] formula

$$\bar{\lambda}_p = \sqrt{\frac{f_y}{\sigma_{cr}}} = \frac{\bar{b}/t}{28.4\varepsilon\sqrt{k_\sigma}} \tag{7}$$

where $\bar{b}$ is the web width, $\varepsilon = \sqrt{\frac{235}{f_y}}$, and k_σ=23.9 for ψ=-1. The difference between the two σ_{cr} estimates is caused by the two k_σ values adopted (27.6 against 23.9). Indeed, unlike Standards [6], Eurocode 3 Part 1-5 [4] prudentially assumes the minimal theoretical value of 23.9—corresponding to α=2/3—for any aspect ratio of panels, when ψ=1.

2.3 Finite element buckling analysis

The finite element model of type 1 beams generated for the buckling analysis is constituted by a mesh of quadrilateral isoparametric shell elements with an average side of 150 mm. This dimension determines a number of constituting elements of each beam panel varying from around 80 to around 120, which is generally deemed appropriate for an accurate simulation of local buckling effects in laterally loaded stiffened or unstiffened plates [10-11]. Fixed end restraints are imposed to the end section of beams connected to the steel drum, whereas only

the lateral displacements are blocked on the tip end section, so as to reproduce exactly the restraint offered by the perimeter C-shaped edge beam of each mushroom roof panel.

The buckling analysis is developed in SAP2000NL by a classical eigenvalue formulation:

$$([K_E]+\lambda[K_G])\{v\}=\{0\} \tag{8}$$

where $[K_E]$ and $[K_G]$ are the elastic and geometric stiffness matrixes of the structural element or system, λ is the generic eigenvalue, and $\{v\}$ is the corresponding eigenvector. The solution of equation (8) provides the instability factors λ_i and the instability modal vectors $\{v_i\}$. The minimum among the λ_i multipliers computed by the program represents the first (or critical) eigenvalue λ_1. If λ_1 is greater than 1, no buckling occurs under the imposed loads.

The first mode buckling configuration of type 1 beams resulting from the analysis, displayed in Figure 6, highlights that the maximum lateral deformation is achieved in panel 4, consistently with the analytical assessment predictions.

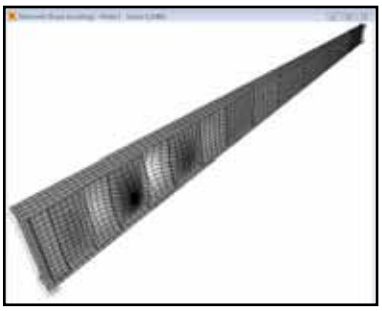

Figure 6: Deformed shape of type 1 beams obtained for the first buckling mode

The λ_1 factor is equal to 0.259. By multiplying this value by the maximum von Mises ideal stress obtained in the central zone of the panel for the first buckling mode deformed configuration, equal to 90 MPa, the following finite element critical ideal stress estimate $\sigma_{cr,id,FE}$ is deducted: $\sigma_{cr,id,FE}$=23.3 MPa. This value is very close to the $\sigma_{cr,id}$ normative estimate of 22.2 MPa given by formula (4), with a percent difference limited within 5%. Similar correlations are obtained for the subsequent local buckling modes too (the second mode achieves the maximum lateral displacements in panel 5, the third mode in panel 3, etc) as the differences between $\sigma_{cr,id}$ and $\sigma_{cr,id,FE}$ never exceed 5%.

The seventh and eighth buckling modes are the first two involving a global (lateral-torsional) instability deformed shape. The maximum lateral displacements and stresses are reached in the eighth mode, visualized in Figure 7 with an amplification factor of 5000. The horizontal projection is also plotted in this drawing, showing that the deformed shape corresponds, as for the seventh mode, to the first theoretical global buckling mode of the beams. The λ_8 eigenvalue is equal to 0.524, which must be compared to the unsafety factor $M_{b,Rd}/M_{Ed}$=0.586 resulting from the lateral/torsional buckling verification discussed in section 2.1. The difference between the two values is around 12%, and the numerical result in this case is more conservative than the normative factor estimate.

The data obtained from a computational analysis are always a function of the geometrical dimensions of the mesh. Mesh-sensitivity was investigated by varying the sides of the shell

elements by factors 2, 1.5, 0.75 and 0.5 with respect to the reference average dimensions of 150 mm.

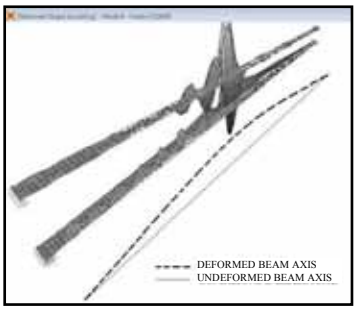

Figure 7: 5000-times magnified deformed shape of type 1 beams obtained for the eighth buckling mode

As a general result of this enquiry, no appreciable influence on eigenvalues and eigenvectors was observed when passing to the most refined meshes. A trend to a progressive increase of the eigenvalues emerges when increasing the sides (e.g., $\sigma_{cr,id,FE}$ in panel 4 becomes equal to 24.1 and 25.3 MPa for mesh factors 1.5 and 2, respectively), even if the shapes and the hierarchy of buckling modes are kept unchanged. Based on these observations, the average dimensions assumed for this analysis appear to be the maximum compatible with the accuracy of the solution, and thus they can represent a credible balance point between the need to reach accurate results and to constrain the computational effort. Limitedly to this case study, it can be concluded that the buckling analysis performed by SAP2000NL allows acceptably estimating the local and global critical buckling conditions of steel beams.

3 ANALYSIS OF R/C COLUMNS

A view of a monumental column during the construction phases of the building, and the sequence of geometrical sections along its height, are reproduced in Figure 8. As illustrated in these images, the shape of columns constantly varies from the base (cross-type section with 6 m-long and 1 m-wide sides) to the top (circular-type section, 2.5 m wide). The top section, reduced to a diameter of 2 m, is prolonged for further 1.6 m to form the groove where the triangular steel plates supporting the circular drum of the mushroom roof are positioned, as described in section 2.

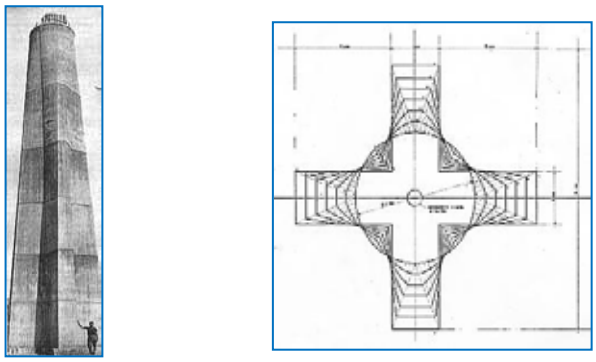

Figure 8: View of a column during the construction phases, and sequence of its geometrical sections

The drawings of the R/C sections at the base, at an intermediate height and on top, displayed in Figure 9, show an inner hole, where a spiral steel staircase to access the roof, and a conductor pipe are housed.

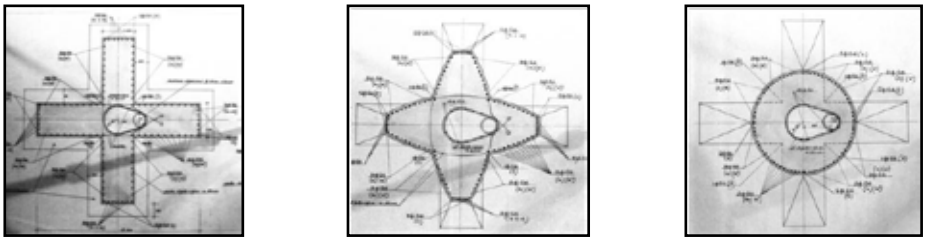

Figure 9: R/C sections at the base, an intermediate height and the top

As observed in the introductory section, an "integral" seismic pushover assessment analysis of the columns was carried out in view of their "uniform resistance" design conception. The model was generated with ANSYS [7] and is made of a full mesh of solid octahedral "concrete" elements, with embedded steel reinforcing bars that can be freely oriented with respect to the global coordinate system. A sketch of the geometry of a "concrete" element is shown in Figure 10.

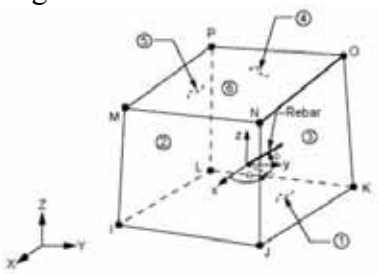

Figure 10: Geometrical representation of an octahedral "concrete" element with embedded reinforcing bars

The Willam-Warnke triaxial failure domain [12]—a three-dimensional view of which in the space of the principal stresses (σ_{xp}, σ_{yp}, σ_{zp}) normalized to the compressive strength f_c, and a projection of which on the σ_{xp}–σ_{yp} plane are displayed in Figure 11—is adopted to model the ultimate compressive, tensile and mixed compressive-tensile triaxial ultimate response of the concrete material. The classical Drucker-Prager yield criterion [13] is assumed by the program for plastic deformations. A bilinear strain-hardening elasto-plastic behaviour is assigned to reinforcing steel.

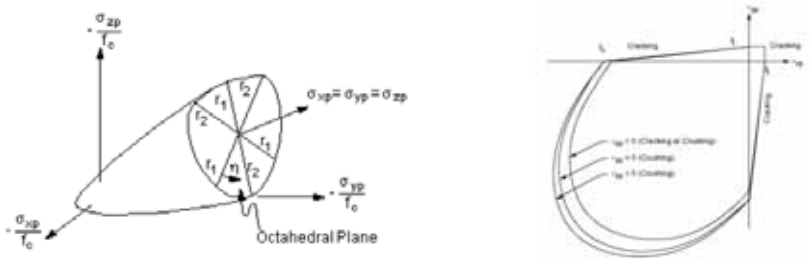

Figure 11: Representations of the Willam-Warnke failure domain

The main mechanical parameters of the "concrete" model are as follows: σ_o=shear transfer coefficient for an open crack, σ_c=shear transfer coefficient for a closed crack, f_t=uniaxial tensile cracking stress, f_c=uniaxial crushing stress, f_{cb}=biaxial crushing stress, E_c=Young modulus, and ν_c=Poisson ratio. The parameters of reinforcing steel are: f_y=yielding stress, s_h=kinematic strain hardening ratio, E_s=Young modulus, and ν_s=Poisson ratio. The parameters that define the surface of the Drucker-Prager domain are: c=cohesion, ϕ=friction angle, and ψ= dilatancy angle. The following values of these quantities were adopted in the analysis: σ_o=0.3, σ_c=0.85, f_t=1.7 MPa, f_c=23.8 MPa, f_{cb}=1.2 f_c, E_c=35600 MPa, ν_c=0.2; f_y=321.6 MPa, s_h=0.015, E_s=206000 MPa, ν_s=0.3, according to the characteristics of the materials; and c=2.12 MPa, ϕ=30º, ψ=0º (associated flow rule), from literature suggestions concerning the plasticity domain for concrete elements [7], [14-15].

The horizontal load for the development of the pushover process was applied to the top of the column. P-delta effects were taken into account, in view of the expected high maximum displacements. As for all types of incremental analysis, the critical parameter for the convergence and the accuracy of the numerical solution was represented by the number of sub-steps to be developed in the ramped loading process within any single load step, with the latter fixed at 10 mm. A displacement-based criterion for convergence control was adopted, with a tolerance of 5%. The following numbers of sub-steps were finally selected, after several tentative choices: 50 (corresponding to 0.2 mm) for steps 1 through 13, characterized by moderate cracking effects in the concrete elements; 200 (0.05 mm) for steps 14-27—extensive cracking in the tension zones; 300 (0.033 mm) for steps 28-70—softening response phase. These data confirm general suggestions [14] about the preferable values (ranging from 0.1 mm to 0.01 mm) of the displacement increments in full-cracking/crushing problems when the non-linear behaviour of a significant portion of the model is activated. Further increases of the number of sub-steps in the more accentuated non-linear response phases did not show any practical influence on the accuracy of the solution. Indeed, by amplifying the number of sub-steps by a factor up to 10, that is, by assuming up to 2000 sub-steps for steps 14-27, and up to 3000 sub-steps for steps 28-70, differences no greater than 0.1% on base shear were found.

For the assumed set of mechanical parameters, derived from the original design documentation of the building, the pushover analysis was concluded at the end of step 70, corresponding to a top displacement of 700 mm (drift ratio of 3.5%). At the current level of refinement of the model, this was assumed as the numerically determined structural collapse condition. The only two parameters not related to the specific characteristics of the constituting materials—σ_o and σ_c—were varied in their technical ranges of interest (σ_o from 0.2 to 0.4, σ_c from 0.65 to 0.9) to check their influence on response, which resulted to be negligible.

The base shear-top displacement capacity curve obtained from the analysis is plotted in Figure 12. A median vertical section reproducing the cracked configuration of the model at the end of the last step of the pushover analysis, and two views orthogonal to the loading direction showing the distributions of the vertical component of normal stress and the axial stress in reinforcing bars, are displayed in Figure 13. The following observations can be drawn from Figures 12 and 13.

- A remarkably smooth shape of the capacity curve emerges, as a consequence of the high number of sub-steps adopted in the analysis;

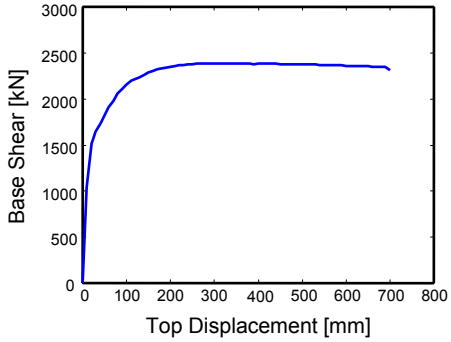

Figure 12: Response curve obtained from the pushover analysis

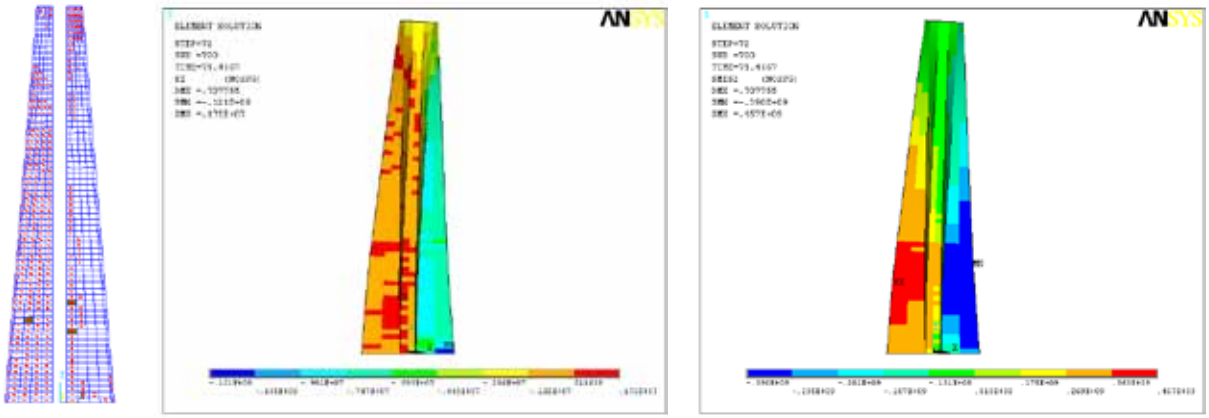

Figure 13: Cracked configuration of the model, vertical normal stress distribution, and stress distribution in reinforcing bars at the end of the last step of the pushover analysis

- The curve is rather linear up to around 1500 kN (with top displacement of 20 mm and drift ratio of 0.1%), that is up to around 60% the maximum base shear, equal to 2390 kN; then, cracking begins to develop significantly in the elements situated on the tension side, and the curve visibly gets non-linear elastic;
- This second response phase goes on up to a force of 2200 kN, with corresponding top displacement of 110 mm (drift ratio of 0.55%), when the first plasticization of reinforcing bars occurs;
- The plasticization then increases, determining nearly a plateau zone extended from around 250 mm to around 450 mm; the maximum shear force is reached for a displacement of 300 mm (drift ratio of 1.5%);
- A softening branch follows, featuring a strength degradation of around 0.2 kN/mm up to the last two steps, where the degradation reaches accentuated values of 0.5 kN/mm (step 69) and 2kN/mm (step 70), while it does not mean a sudden drop of strength in proximity to the numerical solution divergence point;
- Cracking extends rather uniformly over the tension side, whereas crushing is attained only in very few local elements situated around the inner hole (dark-coloured elements in the vertical section in Figure 13). This indicates that concrete is far from ultimate strength conditions on the compression side of the column at the last step of the analysis;

- This is confirmed by the distribution of the vertical components of normal stress, which shows maximum values no greater than 0.5 f_c, in the external fiber of base section;
- Plasticization of reinforcing bars is spread over 2/3 of the height of the column.

These observations highlight that numerical collapse is not determined by the failure of the constituting materials, but by the excessive deformation of the octahedral elements in various portions of the mesh. Deformation is not sensitive to the number of sub-steps, which was increased further to a value of 10000 in the 70th step to check its possible influence, without any practical consequences.

The response curve highlights acceptable behavioural capacities of columns, with no damage for rather high base shear values, and reasonably good ductility resources. A complete interpretation of the results of the pushover enquiry, based on a formal seismic assessment analysis, will be presented in forthcoming communications about this research.

ACKNOWLEDGMENTS

The study reported in this paper was financed by the Italian Ministry of Education, University and Research within the PRIN 2008 Project (Research Programme "Conceiving structures: engineering and architecture in Italy in the 1950s and 1960s. A multi-disciplinary research"). The authors gratefully acknowledge this financial support.

REFERENCES

[1] Sorace, S. and Terenzi, G. Structural and historical assessment of a modern heritage masterpiece: the "Palazzo del Lavoro" in Turin. Proc. STREMAH 2011, C. Brebbia and L. Binda, Eds., Chianciano Terme, Italy, WIT Press, Southampton (2011).

[2] Computers & Structures, Inc. *SAP2000NL, Structural Analysis Programs – Theoretical and users' manual*, Version No. 14.03, Berkeley, CA (2010).

[3] Eurocode 3. *Design of steel structures. Part 1-1: General rules and rules for buildings*. EN 1993-1-1, Bruxelles (2005).

[4] Eurocode 3. *Design of steel structures. Part 1-5: Design of plated structures*. EN 1993-1-5, Bruxelles (2006).

[5] NTC 2008. *New Technical Standards for constructions [in Italian]*. G.U., Rome, Italy (2008).

[6] CNR 10011. *Steel structures – Instructions for design, construction, testing and maintenance* [in Italian]. UNI, Milan, Italy (1997).

[7] Swanson Analysis System, Inc. *ANSYS, Engineering Analysis System – Theory/users' manual.* Release 10.0, Canonsburg, PA (2010).

[8] Massonnet, C. Rapport sur le theme II C: Poutres de grandes dimensions à âme mince. Proc. 8th AIPC Congress, New York, pp. 157-208 (1968).

[9] Timoshenko, S.P. and Gere, J.M. *Theory of elastic stability*. 2nd edition. Mc-Graw Hill, New York (1961).

[10] Mukhopadhay, M. and Mukherjee, A. Finite element buckling analysis of stiffened plates. *Computer & Structures* (1990) **34**:795-803.

[11] Chin, C.-K., Al-Bermani, F.G. and Kitipornchai S. Finite element for buckling analysis of plate structures, *Journal of Structural Engineering (ASCE)* (1993) **119**: 1048-1068.

[12] Willam, K.J. and Warnke, E.P. Constitutive model for the triaxial behaviour of concrete. Proc. IABSE Seminar on Concrete structures subjected to triaxial stresses, Bergamo, Italy, Vol. 19, pp. 1- 30 (1974).

[13] Drucker, D.C. and Prager, W. Soil mechanics and plastic analysis for limit design. *Quarterly of Applied Mathematics* (1952) **10**:157–165.

[14] Chen, W.F. *Plasticity in reinforced concrete*. Mc-Graw Hill, New York (1982).

[15] Borri, A., and Sorace, S. FE analysis strategies for structural materials with small tensile strength. *Journal of Pressure Vessel Technology (ASME)* (1993) **115**:156-163.

XI International Conference on Computational Plasticity. Fundamentals and Applications
COMPLAS XI
E. Oñate, D.R.J. Owen, D. Peric and B. Suárez (Eds)

NUMERICAL IMPLEMENTATION OF A GENERALIZED PLASTICITY MODEL AT FINITE STRAINS

FABIO DE ANGELIS*, ROBERT L. TAYLOR†

*Department of Structural Engineering
University of Naples Federico II
Naples, Italy
e-mail: fabio.deangelis@unina.it

†Department of Civil and Environmental Engineering
University of California, Berkeley
Berkeley, CA 94720-1710, USA
e-mail: rlt@ce.berkeley.edu

Key words: Generalized Plasticity, Finite Element Method, Computational Algorithms

Abstract. In the present paper an algorithmic implementation of a generalized plasticity model is presented with reference to a material behaviour at finite strains. A return mapping algorithm is implemented for an elastoplastic material behaviour in large deformations. A computationally efficient algorithmic scheme is described and the performance of a generalized plasticity model at finite deformations is illustrated. Numerical results and examples are finally reported.

1 INTRODUCTION

The simulation and numerical treatment of the evolutive problem in elastoplasticity has become nowadays an important topic in the literature. Significant progress has been achieved over the last decades both in the mathematical comprehension of the problem and in the related computational treatment. At present, the algorithmic procedures have acquired significant improvements in the integration of the boundary value problem in elastoplasticity, see among others Simo and Hughes [1] and Zienkiewicz and Taylor [2]. However, in order to describe the observed behaviour of solids which are plastically loaded, unloaded, and then reloaded, it is necessary for the model to exhibit renewed plasticity prior to the state at which unloading initially occurred. With this perspective a generalized plasticity model was originally developed by Lubliner [3] [4]. Subsequently, a new model of generalized plasticity was proposed by Lubliner et al. [5] with the aim of including refinements for improved numerical implementation performances. An analysis of the numerical properties of the generalized plasticity model was illustrated by Auricchio

and Taylor [6] for the case of elastoplasticity at infinitesimal strains. In the mentioned paper a comparative analysis is also reported with respect to other types of plasticity models which are classically adopted in the literature.

In the present paper a generalized plasticity model is described in a finite deformation setting and the characteristics of the generalized plasticity model at finite deformations are illustrated. An algorithmic scheme is presented for the numerical integration of the generalized plasticity model in the context of elastoplasticity at finite strains. A return mapping algorithm is described for an elastoplastic material behaviour in large deformations. The computational performance of the algorithmic scheme and its numerical integration features are reported. Numerical results and examples are finally presented in order to illustrate the effectiveness of the proposed solution scheme for the numerical integration of the generalized plasticity model in the simulation of inelastic processes at finite deformations.

2 CONTINUUM PROBLEM AND CONSTITUTIVE EQUATIONS

A local multiplicative decomposition of the deformation gradient $\mathbf{F}$ is considered in the form (Lee [7], Mandel [8])

$$\mathbf{F} = \mathbf{F}^e \mathbf{F}^p \tag{1}$$

where $\mathbf{F}^e$ and $\mathbf{F}^p$ respectively represent the elastic and plastic part of the deformation gradient. The elastic right Cauchy-Green tensor $\mathbf{C}^e$ and the elastic left Cauchy-Green tensor $\mathbf{b}^e$ are defined as

$$\begin{aligned} \mathbf{C}^e &= \mathbf{F}^{e,T}\,\mathbf{F}^e \\ \mathbf{b}^e &= \mathbf{F}^e\,\mathbf{F}^{e,T} \end{aligned} \tag{2}$$

where the superscript T indicates the transpose. We also consider $\mathbf{b}^e$ as expressed by (Simo and Hughes [1])

$$\mathbf{b}^e = \mathbf{F}\mathbf{C}^{p-1}\mathbf{F}^T, \tag{3}$$

where the plastic right Cauchy-Green tensor $\mathbf{C}^p$ is defined as

$$\mathbf{C}^p = \mathbf{F}^{p,T}\mathbf{F}^p. \tag{4}$$

The free energy ψ is expressed as an isotropic function

$$\psi = \hat{\psi}(\mathbf{b}^e, \boldsymbol{\xi}), \tag{5}$$

where $\boldsymbol{\xi}$ is a kinematic internal variable, and the Kirchhoff stress $\boldsymbol{\tau}$ is given by

$$\boldsymbol{\tau} = 2\frac{\partial \psi}{\partial \mathbf{b}^e}\mathbf{b}^e. \tag{6}$$

As a result of the restriction to isotropy the principal directions of the Kirchhoff stress and of the elastic left Cauchy-Green tensor coincide and therefore, by indicating with $\mathbf{n}_A$ such principal directions, a spectral decomposition is introduced as

$$\begin{aligned}\boldsymbol{\tau} &= \sum_{A=1}^{3} \tau_A \, \mathbf{n}_A \otimes \mathbf{n}_A, \\ \mathbf{b}^e &= \sum_{A=1}^{3} (\lambda_A^e)^2 \, \mathbf{n}_A \otimes \mathbf{n}_A.\end{aligned} \tag{7}$$

Equation (6) therefore reduces to

$$\tau_A = 2 \frac{\partial \psi}{\partial [(\lambda_A^e)^2]} (\lambda_A^e)^2. \tag{8}$$

The Kirchhoff stress is split into its volumetric and deviatoric parts as

$$\boldsymbol{\tau} = p\mathbf{1} + \mathbf{t} \tag{9}$$

where $\mathbf{1}$ is the second order identity tensor, $p \stackrel{\text{def}}{=} (\boldsymbol{\tau} : \mathbf{1})/3$ is the pressure and $\mathbf{t} \stackrel{\text{def}}{=} \boldsymbol{\tau} - p\mathbf{1}$ is the deviatoric part of $\boldsymbol{\tau}$, with spectral representation

$$\mathbf{t} = \sum_{A=1}^{3} t_A \, \mathbf{n}_A \otimes \mathbf{n}_A. \tag{10}$$

An isotropic yield function is considered and expressed as

$$F(J_2) = f(J_2) - \sigma_y \tag{11}$$

where J_2 is the second invariant of the deviatoric Kirchhoff stress and σ_y is a material parameter. We also consider the evolutive equation in the form (Simo and Hughes [1], Simo [9])

$$-\frac{1}{2} \mathcal{L}_v \mathbf{b}^e = \dot{\gamma} \mathbf{N} \mathbf{b}^e, \tag{12}$$

where

$$\mathcal{L}_v \mathbf{b}^e = \mathbf{F} \frac{\partial}{\partial t} [(\mathbf{C}^{p-1})] \mathbf{F}^T \tag{13}$$

is the Lie derivative of $\mathbf{b}^e$, $\dot{\gamma}$ is the plastic consistency parameter, and $\mathbf{N} = \partial_{\boldsymbol{\tau}} F$ is the normal to the yield surface with spectral representation

$$\mathbf{N} = \sum_{A=1}^{3} N_A \, \mathbf{n}_A \otimes \mathbf{n}_A. \tag{14}$$

In generalized plasticity at finite strains a limit equation is introduced and expressed as (Auricchio and Taylor [6])

$$h(F)[\mathbf{N} : \dot{\boldsymbol{\tau}}] - \dot{\gamma} = 0, \tag{15}$$

where

$$h(F) = \frac{F}{\delta(\beta - F) + H\beta}, \tag{16}$$

with β and δ being two positive constants with dimensions of stress and $H = H_{iso} + H_{kin}$.

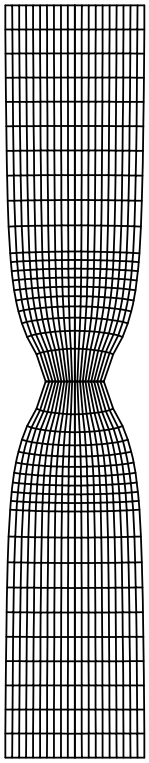

Figure 1: Deformed configuration of the circular bar at an elongation of 26.25 per cent

3 TIME DISCRETE SOLUTION ALGORITHM

A product formula algorithm is considered via an operator split approach for the local problem of evolution. A relative deformation gradient $\mathbf{f}$ is introduced such that

$$\mathbf{F} = \mathbf{f}\,\mathbf{F}_n. \tag{17}$$

Consequently, the operator split approach leads to a trial elastic state in which

$$\mathbf{b}^{e,TR} = \mathbf{f}\,\mathbf{b}_n^e\mathbf{f}^T, \tag{18}$$

and subsequently, via an exponential approximation for the rate equation, a return mapping state in which

$$\mathbf{b}^e = \exp\left[-2\Delta\gamma\mathbf{N}\right]\mathbf{b}^{e,TR}. \tag{19}$$

In the above equation we observe that $\mathbf{b}^e$ and $\mathbf{N}$ have the same spectral decomposition, which implies that also $\mathbf{b}^e$ and $\mathbf{b}^{e,TR}$ have the same spectral decomposition. Consequently $\mathbf{n}_A^{TR} = \mathbf{n}_A$ and equation (19) can be expressed as three scalar equations relative to the space of principal directions

$$\lambda_A^e = \exp\left[-\Delta\gamma\mathbf{N}_A\right]\lambda_A^{e,TR} \tag{20}$$

where $(\lambda_A^{e,TR})^2$ and $\mathbf{n}_A^{TR}$ are the eigenvalues and the eigenvectors of $\mathbf{b}^{e,TR}$. By taking the logarithm of both sides of equation (20) we get

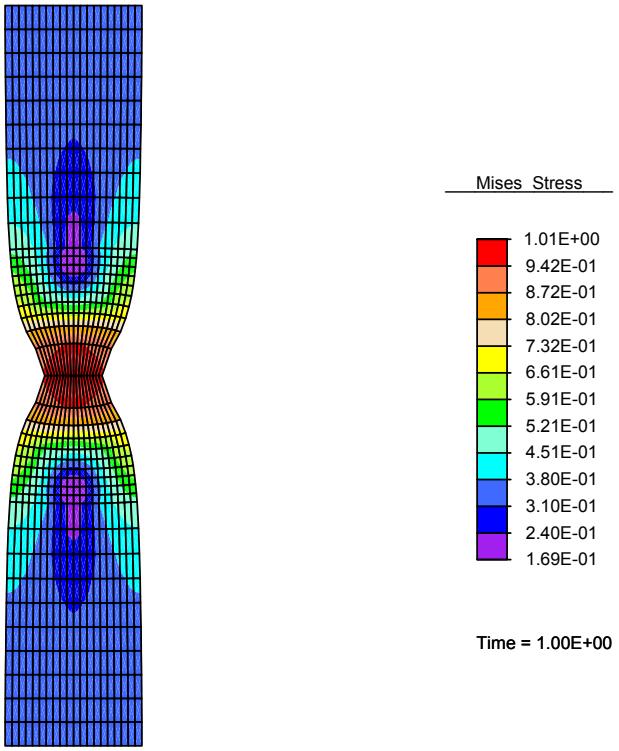

Figure 2: Contour plot of the second invariant of the deviator stress

$$\log\left[\lambda_A^e\right] = -\Delta\gamma \mathbf{N}_A + \log\left[\lambda_A^{e,TR}\right], \tag{21}$$

and introducing the principal elastic logarithmic strains

$$\varepsilon_A^e = \log\left[\lambda_A^e\right], \qquad \varepsilon_A^{e,TR} = \log\left[\lambda_A^{e,TR}\right], \tag{22}$$

equation (21) is expressed as

$$\varepsilon_A^e = \varepsilon_A^{e,TR} - \Delta\gamma \mathbf{N}_A, \tag{23}$$

which represents a return mapping algorithm in strain space. For a more detailed description of the algorithmic procedure we refer to De Angelis and Taylor [10].

4 NUMERICAL EXAMPLE

In this example we consider the three-dimensional behaviour of a circular bar subjected to tension. This well-documented problem has been studied by several authors, see e.g. Simo and Hughes [1] and Simo [9]. Due to symmetry only 1/4 of the cylindrical specimen is considered for the discretization with finite elements. Isoparametric 4-node mixed elements are employed in the numerical simulation and implemented in the general purpose finite element program FEAP documented in [11]. An axisymmetric analysis with finite deformations is performed. The mesh consists of 200 elements and 242 nodal points. The

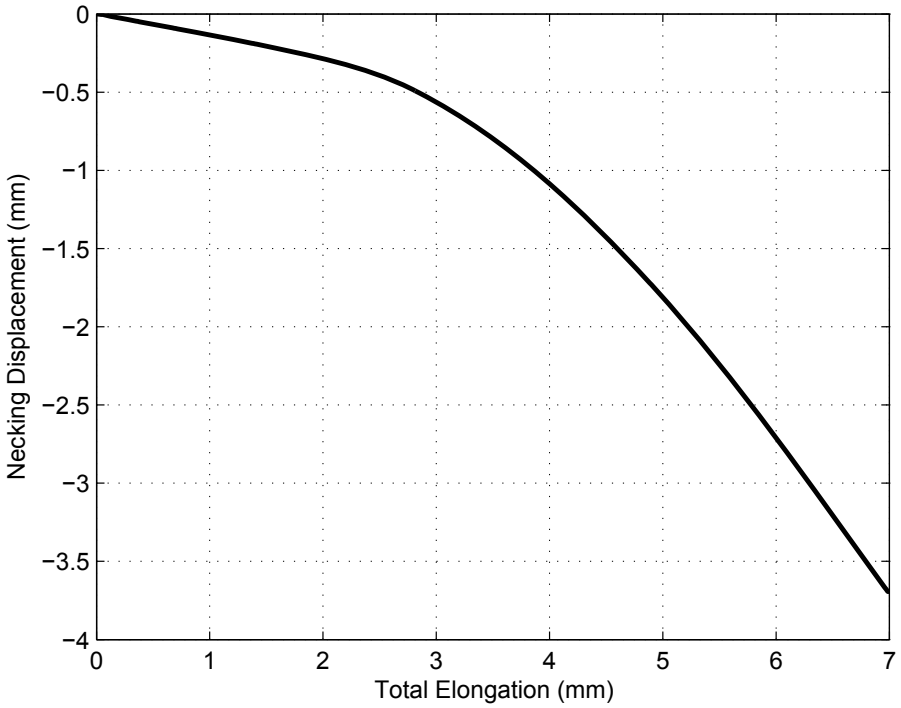

Figure 3: Plot of the necking displacement at the symmetry section versus the elongation of the bar

radius of the cylinder is R = 6.413 mm and the total length of the bar is L = 53.334 mm. The specimen tapers by a small amount to a central location to ensure that the necking will occur in a specified location. In the example a uniform taper to a central radius of $R_c = 0.982$ R is used. A fit of the hardening data reported in [12] leads to the following material hardening properties for a generalized plasticity model: elastic modulus E = 206.9 GPa, Poisson ratio $\nu = 0.29$, initial flow stress $\sigma_{yo} = 0.45$ GPa, residual flow stress $\sigma_{y\infty} = 0.76$ GPa, $\beta = 0.31$ GPa, $\delta = 0.004$ E, isotropic hardening $H_{iso} = 0.12924$ GPa. A total axial elongation of 14 mm is prescribed, corresponding to an an elongation of 26.25 per cent. This example is quite sensitive to solve as the response involves an unstable behavior of the necking process. In Fig. 1 the deformed configuration of the bar is illustrated at an elongation of 26.25 per cent. The contour plot of the second invariant of the deviator stress is shown in Fig. 2. The necking displacement at the symmetry section versus the elongation of the bar is plotted in Fig. 3.

5 CONCLUSIONS

In the existing literature the model of generalized plasticity has been adopted for the description of material behaviour experiencing inelastic processes in a small strain formulation. In the present paper the model of generalized plasticity has been considered

and analyzed with reference to inelastic processes at finite deformations. Accordingly, an effective algorithmic procedure has been proposed for a generalized plasticity model in finite strains elastoplasticity. A product formula algorithm via an operator split approach has been illustrated. A return mapping algorithm has been adopted which has led to a computationally effective solution scheme. The numerical implementation has shown a robust performance in the integration of the model problem. Numerical applications and computational results have been reported with reference to the three-dimensional necking problem of a circular bar subjected to tension.

REFERENCES

[1] Simo, J.C., and Hughes, T.J.R., *Computational Inelasticity*. Springer-Verlag, Berlin, (1998).

[2] Zienkiewicz, O.C., and Taylor, R.L., *The Finite Element Method for Solid and Structural Mechanics*. Elsevier, Oxford, 6th ed., (2005).

[3] Lubliner, J., A simple model of generalized plasticity. *Int. J. Solids Structures* (1991) **28**:769–778.

[4] Lubliner, J., *Plasticity theory*. Macmillan, New York, (1990).

[5] Lubliner, J., Taylor, R.L., and Auricchio, F., A new model of generalized plasticity and its numerical implementation. *Int. J. Solids Structures* (1993) **30**:3171–3184.

[6] Auricchio, F., and Taylor, R.L., Two material models for cyclic plasticity: nonlinear kinematic hardening and generalized plasticity. *Int. J. Plasticity* (1995) **11**:65–98.

[7] Lee, E.H., Elastic-plastic deformation at finite strains. *J. of Applied Mechanics* (1969) **36**:1–6.

[8] Mandel, J., Thermodynamics and plasticity. In: Delgado Dominger, J.J., Nina, M.N.R., Whitelaw, J.H., (Eds.), *Foundations of Continuum Thermodynamics*, pages 283-304. Macmillan, London, (1974).

[9] Simo, J.C., A framework for finite strain elastoplasticity based on maximum plastic dissipation. Part II: Computational aspects. *Comput. Methods Applied Mechanics and Engineerins* (1988) **68**:1–31.

[10] De Angelis, F., and Taylor, R.L., Computational procedures for a generalized plasticity model at finite deformations, *in preparation*.

[11] Taylor, R.L., A finite-element analysis program, *User Manual, Vers: 8.3*, University of California, Berkeley, CA, (2011).

[12] Engelmann, B.E., and Hallquist, J.O., NIKE 2D: A Nonlinear, Implicit, Two-Dimensional Finite Element Code for Solid Mechanics, *Lawrence Livermore National Laboratory*, pages 1-208. University of California, Livermore, CA, (1991).

XI International Conference on Computational Plasticity. Fundamentals and Applications
COMPLAS XI
E. Oñate, D.R.J. Owen, D. Peric and B. Suárez (Eds)

ON THE PERFORMANCES OF DIFFERENT NODAL INTEGRATION TECHNIQUES AND THEIR STABILIZATION

F.GRECO[*], L.FILICE[*], I.ALFARO[†] AND E.CUETO[†]

[*] Dept. of Mechanical Engineering, University of Calabria, Italy
e-mail: francesco.greco@unical.it
l.filice@unical.it

[†] Aragon Institute of Engineering Research, Universidad de Zaragoza, Spain
e-mail: iciar@unizar.es
ecueto@unizar.es

Key words: Nodal Integration, stabilization.
Abstract. Finite element method was successfully applied in the simulation of several forming processes; however, it does not represent an absolute reference point. In fact, large deformation corresponds to a heavy mesh distortion. Powerful rezoning-remeshing algorithms strongly reduce the effects of such a limitation but the computational time significantly increases and additional errors occur. Nodal Integration is a recently introduced technique that allows finite element method to provide reliable results also when meshes becomes distorted in traditional FEMs. Furthermore, volumetric locking problems seem to be avoided using this integration technique instead of other methods such as coupled formulations. Nevertheless, spurious low-energy modes appear due to the nodal averaging of strain. For this reason stabilizing methods application seems to be suitable. What is more, different nodal integration techniques have been proposed, although spurious modes are a common problem. In this paper the performances of three different nodal integration techniques and the effects of a recently introduced stabilization methodology are studied simulating a classical forming process.

1 INTRODUCTION

Finite element method is surely the referential numerical technique in the analysis of solid mechanics problems. It has been successfully used in the simulation of several phenomena, providing excellent results.

Nevertheless, FEM requires an adequate discretization of the computational domain in terms of node and elements since the final results are sensible to the distribution and regularity of this decomposition [1]. In small deformation problems, such as linear elasticity, it is quite easy to obtain a reliable discretization and very accurate solutions, also with a low computational cost. The situation suddenly changes in problems characterised by large deformations, such as the material forming processes. In this case, if a Lagrangian formulation is used, the mesh moves with material and elements become so distorted that numerical results lose their validity.

Different techniques have been developed across the last years to overcome this problem.

Among them, Eulerian formulations, arbitrary Lagrangian-Eulerian (ALE) and remeshing techniques are the most known. In any case, additional drawbacks appeared especially when the remeshing techniques are applied. Remeshing-rezoning approach avoids the results worsening but, at the same time, the computational time increases and supplementary errors are introduced.

A possible alternative is the use of meshless methods [2] but in many cases the improvement of the results quality, with the same number of degrees of freedom, is vanished by the very high computational time for the shape functions calculation.

In the FEM environment the performances of the analysis depend on the used element. The constant strain elements (triangle with 3 nodes or tetrahedrons with 4 nodes in the 3D case) would be preferable for different reasons, especially when non-linear problems are investigated. Nevertheless their poor performances force the researchers to use high-order elements, such as 8 nodes tetrahedral or hexahedral. However, these formulations are not free from the results worsening due to the mesh deterioration and, besides, the remeshing procedure is very costly to be implemented, particularly for the hexahedral elements.

A great drawback of conforming FEM is that the numerical model is always more stiff than the studied material. What is more, any mesh distortion gives a further spurious stiffness to the model. Introducing a Nodal Integration scheme the FEM model is not necessarily stiffer than the real material; on the contrary, in many applications the initial model is less stiff and a distorted mesh could paradoxically have a beneficial effect on the performances.

The basics of nodal integration in FE analysis were firstly introduced by Dohrmann et al. [3]. They showed that applying the new technique the performances of the constant strain elements are significantly improved in the study of acute bending problems. Moreover the method was shown to be free from volumetric locking in the simulation of quasi-incompressible materials.

The nodal integration (NI) has been introduced also in the meshless environment [4-5], as an alternative to the standard integration, due to its efficiency and applicability in large deformations problems.

Puso and Solberg [6] noted that the formulation proposed in [3] was prone to spurious low energy modes and introduced a new stabilized nodal integrated tetrahedral element. They also analytically showed that their new element was stable and consistent for linear elasticity.

In [7] the stabilizing technique proposed in [6] was further analyzed and extended to the meshless methods, since spurious modes were detected also in this case.

In this work a comparison was done between the two nodal integration schemes proposed in [3] and the scheme proposed in [4], whose usage is suitable also in the FEM. The three techniques will be applied to the simulation of extrusion, as a typical example of a forming process where significant deformations are present.

Moreover the effect of the stabilization technique presented in [6] was studied.

2 THE NODAL INTEGRATION FORMULTIONS

Let Ω be a 2D computational domain, discretized by a cloud of nodes, from 1 to N_N denoted by I and a mesh of triangular elements, from 1 to N_E, denoted by J. In a traditional finite element code, the strain is calculated using the gradient matrix $\boldsymbol{B}$, that, if $\varphi_1, \varphi_2 \ldots . \varphi_{N_N}$ are the shape functions, is defined as:

$$\boldsymbol{B} = \begin{bmatrix} \frac{\partial \varphi_1}{\partial x} & 0 & \cdots & \frac{\partial \varphi_{N_N}}{\partial x} & 0 \\ 0 & \frac{\partial \varphi_1}{\partial y} & \cdots & 0 & \frac{\partial \varphi_{N_N}}{\partial y} \\ \frac{\partial \varphi_1}{\partial y} & \frac{\partial \varphi_1}{\partial x} & \cdots & \frac{\partial \varphi_{N_N}}{\partial y} & \frac{\partial \varphi_{N_N}}{\partial x} \end{bmatrix} \tag{1}$$

Thus, if $\boldsymbol{d}$ is the vector containing the (unknown) nodal displacements, the strain is given by:

$$\boldsymbol{\varepsilon}(\boldsymbol{x}) = \boldsymbol{B}(\boldsymbol{x})\boldsymbol{d} \tag{2}$$

If three-node triangular elements are used, the shape functions derivates are constant in every element, and also the matrix $\boldsymbol{B}$. Thus element strain could be expressed as:

$$\boldsymbol{\varepsilon}_J = \boldsymbol{B}_J \boldsymbol{d} \tag{3}$$

and, if $\boldsymbol{E}$ is the matrix that relates strain and stress vectors, a stiffness matrix $\boldsymbol{K}$ is assembled, in order to solve the approximated problem:

$$\boldsymbol{K} = \int_{\Omega} \boldsymbol{B}^T \boldsymbol{E} \boldsymbol{B} d\Omega = \sum_{J=1}^{N_E} \boldsymbol{B}_J^T \boldsymbol{E} \boldsymbol{B}_J \times A_J \tag{4}$$

Where A_J is the area of each element.

When the nodal integration is applied to FEM a constant strain field $\tilde{\boldsymbol{\varepsilon}}_I$ is assumed within a particular volume $\tilde{V}_I$, associated to each node.

The easiest to interpret NI scheme is the one proposed in [4], that is based on the Voronoi diagram [8]. As it is shown in Figure 1, the Voronoi diagram is a subdivision of the computational domain in regions Ω_I, where each region is associated with a node I, so that any point in Ω_I is closer to the node I than to any other node in the domain.

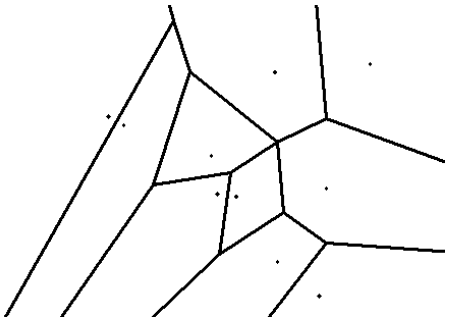

Figure 1: An example of Voronoi Diagram

In this case the nodal volume $\tilde{V}_I$ is, for each node, the area A_I of the corresponding cell in the diagram and the assumed strain is the average strain in this cell:

$$\tilde{\boldsymbol{\varepsilon}}_I = \frac{1}{A_I} \int_{\Omega_I} \boldsymbol{\varepsilon}(\boldsymbol{x}) d\Omega \tag{5}$$

Since constant strain elements are used, equation 5 could be rewritten as:

$$\tilde{\boldsymbol{\varepsilon}}_I = \frac{1}{A_I}\sum_{J=1}^{N_E} \boldsymbol{\varepsilon}_J \times Area(\Omega_I \cap T_J) \tag{6}$$

We will call this scheme Global Voronoi Integration (GV). Observing that $\sum_{J=1}^{N_E} Area(\Omega_I \cap T_J) = A_I$, the strain $\tilde{\boldsymbol{\varepsilon}}_I$ is a weighted average of the strain of the elements. The two NI schemes proposed in [3] provide also a strain averaging, but the weights are different. In particular it is imposed that the strain $\tilde{\boldsymbol{\varepsilon}}_I$ depends only on the strain of the set of elements S_I that contain the node I. According to this constraint, one of the two schemes is also based on the Voronoi Diagram, but in this case the Diagram is locally calculated in each triangle. In particular each triangle T_J is divided in three zones t_{JI}, associated to its nodes, so that every point in t_{JI} is closer to the node I than to any other node in T_J. Then the nodal volume and the assumed strain are calculated as:

$$\tilde{V}_I = \sum_{J\in S_I} Area(t_{JI}) \tag{7}$$

$$\tilde{\boldsymbol{\varepsilon}}_I = \frac{1}{\tilde{V}_I}\sum_{J\in S_I} \boldsymbol{\varepsilon}_J \times Area(\, t_{JI}) \tag{8}$$

We will refer to this scheme as Local Voronoi Integration (LV). The other technique proposed in [3] is not based on geometrical considerations but provides a heuristic calculation of the assumed strain, imposing that the area of the triangles is divided in three equal parts, associated to its nodes. Hence:

$$\tilde{V}_I = \sum_{J\in S_I} \frac{Area(T_J)}{3} \tag{9}$$

$$\tilde{\boldsymbol{\varepsilon}}_I = \frac{1}{\tilde{V}_I}\sum_{J\in S_I} \boldsymbol{\varepsilon}_J \times \frac{Area(T_J)}{3} \tag{10}$$

The latter scheme is called Direct Averaging Integration (DA).

3 IMPLEMENTATION OF THE METHOD AND COMPUTATIONAL TIMES

Similarly to a traditional FE interpolation the assumed strain could be related to the displacement field using an equivalent gradient matrix:

$$\boldsymbol{\varepsilon}_I = \tilde{\boldsymbol{B}}_I \boldsymbol{d} \tag{11}$$

It is easy to demonstrate that the matrixes $\tilde{\boldsymbol{B}}_I$ will be a weighted average of the element matrixes $\boldsymbol{B}_J$, calculated using the same weight coefficients of the strain case, depending on the specific NI scheme. Thus, in the implementation of the method, the matrixes $\tilde{\boldsymbol{B}}_I$ are calculated and the global stiffness matrix is assembled as:

$$\widetilde{\boldsymbol{K}} = \sum_{I=1}^{N_N} \widetilde{\boldsymbol{B}}_I^T \boldsymbol{E} \widetilde{\boldsymbol{B}}_I \times \tilde{V}_I \tag{12}$$

This last calculation takes an additional computational time that is negligible respect to a traditional FEM code when DA scheme is used. In fact, only the volume of the elements has to be calculated and the equivalent gradient matrixes are directly calculated as a linear combination of the element gradient matrixes.

The situation changes in the Voronoi-based (GV and LV) techniques. In particular in the GV case all the areas of the intersections between a given Voronoi cell and the elements have to be calculated. In this work this operation has been carried out describing both the cells and the elements as convex polygons and then applying the Lasserre algorithm [9]. Although the computational complexity is linear with the number of nodes this is a significant time consuming operation that could take a computational time of the same order or slightly higher than the total time consumed for the analysis by a traditional FEM code. Anyway, the asymptotical linear complexity ensures that for clouds composed by a high enough number of nodes this time tends to be smaller than the time requested for the resolution of the equations.

The LV scheme could be also implemented describing the geometrical entities by convex inequalities and applying the Lasserre algorithm or other similar. Nevertheless in order to advantage the rapidity of the simulation other more efficient strategies are possible. In particular, after determining the coordinates of the circumcenters of the triangular elements, the intersections areas could be find out calculating the areas of particular triangles. This operation takes a practically negligible time, as in the DA case.

Concerning the computational times of a NI code two more aspects have to be taken into account. The first is that the assembled stuffiness matrix is denser that the matrix that would be assembled using a traditional procedure. This increases the resolution time about the 30%.

On the contrary the second aspect advantages the new technique. In fact the use of Nodal Integration seems to avoid the volumetric locking problems typical of FEM when incompressibility is imposed. Thus, unlike in a traditional code where coupled pressure-velocity formulations has to be used to overcome to this problem, only the velocities could be taken as unknowns, reducing significantly the resolution time. This second recovery offsets the precedent augment.

4 THE CASE STUDY

According to the introduction, an extrusion process has been analyzed as a typical example of forming process in which the large deformation stresses the classical FE formulation. A plain strain 2D model has been used, with the geometrical characteristics and the boundary conditions illustrated in figure 2. As far as the material behavior is considered, in the forming processes and in particular in extrusion, strains are very large as compared to elastic ones. Thus, it is a common practice for this kind of processes to assimilate the material behavior to a viscoplastic one, in which the stress depends on the strain rate [10].

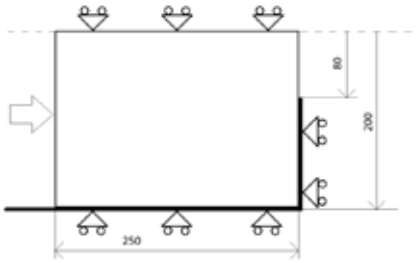

Figure 2: Sketch of the used model

In particular, a Northon-Hoff model has been used; it relates the effective stress to the equivalent strain rate in the following form:

$$S_f = C\bar{\dot{\varepsilon}}^n \tag{13}$$

Together with this global relation the stress components assembled in the vector $\boldsymbol{\sigma} = |\sigma_x \quad \sigma_y \quad \tau_{xy}|^T$ has to be related to the strain rate components, $\dot{\boldsymbol{\varepsilon}} = |\dot{\varepsilon}_x \quad \dot{\varepsilon}_y \quad \dot{\gamma}_{xy}|^T$. In the used model this corresponds to define a viscosity μ in the following form:

$$\mu = \frac{C}{3}\bar{\dot{\varepsilon}}^{n-1} = \mu_0\bar{\dot{\varepsilon}}^{n-1} \tag{14}$$

and to use it in the assembling of the constitutive matrix $\boldsymbol{E}$, whose expression, in plain strain, is given by:

$$\boldsymbol{E} = \frac{2\mu}{1-2\nu}\begin{vmatrix} 1-\nu & \nu & 0 \\ \nu & 1-\nu & 0 \\ 0 & 0 & \dfrac{1-2\nu}{2} \end{vmatrix} \tag{15}$$

In this work a value of the Poisson's coefficient $\nu = 0.49999$ has been employed in order to impose incompressibility.

The used values of the Northon-Hoff coefficients have been:

$$\mu_0 = 150, \qquad n = 0.2 \tag{16}$$

that, according to [11], correspond to some common Aluminum alloys.

Due to the non-linear character of the constitutive equations an iterative scheme has to be applied for their resolution. In particular, taking into account the strong nonlinearities given from the value of n, the Direct Iteration Method [12] has been preferred to the Newton-Raphson scheme, whose convergence is not ever straightforward in this type of problems. This iterative procedure has been combined with the stabilization technique, as it is discussed in the following chapter.

5 THE STABILIZATION TECHNIQUE

According to [6], a stabilized stiffness matrix $\boldsymbol{K_{STAB}}$ has to be assembled using the stabilization parameter α and the modified behavior matrix $\widetilde{\boldsymbol{E}}$ that, when a linear problem is studied, leads to:

$$\boldsymbol{K_{STAB}} = \boldsymbol{K_{NOD}} + \boldsymbol{K_{ELEM}} = \sum_{I=1}^{N_N} \widetilde{\boldsymbol{B}}_I^T (\boldsymbol{E} - \alpha \widetilde{\boldsymbol{E}}) \widetilde{\boldsymbol{B}}_I \tilde{V}_I + \alpha \sum_{J=1}^{N_E} \boldsymbol{B}_J^T \widetilde{\boldsymbol{E}} \boldsymbol{B}_J A_J \tag{17}$$

The influence of α on the results will be discussed in the relative section; the matrix $\widetilde{\boldsymbol{E}}$ differs from $\boldsymbol{E}$ because it is assembled using a different Poisson's coefficient, since locking problems would be present in the elementary term. A value of $\tilde{\nu} = 0.4$ has been used.

In the resolution of the non-linear equations the stabilized stiffness matrix is then assembled in the form:

$$\boldsymbol{K}_{\boldsymbol{STAB}}^{n} = \sum_{I=1}^{N_N} \widetilde{\boldsymbol{B}}_I^T [\boldsymbol{E}_{(\mu^{n-1})} - \alpha \widetilde{\boldsymbol{E}}_{(\mu^{n-1})}] \widetilde{\boldsymbol{B}}_I \tilde{V}_I + \alpha \sum_{J=1}^{N_E} \boldsymbol{B}_J^T \widetilde{\boldsymbol{E}}_{(\mu^{n-1})} \boldsymbol{B}_J A_J \tag{18}$$

where the superscript n indicates the iteration within a time increment as well as μ^{n-1} is the viscosity calculated from the previous velocity field. The iteration method is initialized with $\mu = \mu_0$ and obviously terminates when $\boldsymbol{v}^n = \boldsymbol{v}^{n-1}$. Obtained the velocity values the geometry is updated and the following time step could be studied.

6 RESULTS

The investigated process was simulated using a punch speed $v_p = 1mm/s$ and considering 50 time steps ($1s/step$). In figure 3 are reported the pressure and velocity field, using the LV scheme, with a regular mesh and an irregular one of about 1000 nodes. No stabilization has been considered. Looking at the velocity field of the regular mesh the presence of the spurious modes is clearly observable; what it is more the pressure field is completely wrong since it presents strong oscillation in the direction of the mesh. The situation is quite different when the irregular mesh is used; in this case the velocity field is quite more regular as well as the pressure field has a satisfactory trend, considering the reduced number of nodes. This confirms the well-known phenomenon that the regularity of the mesh favors the spurious deformations.

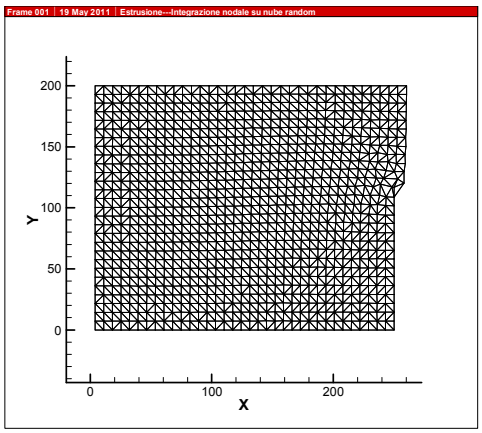

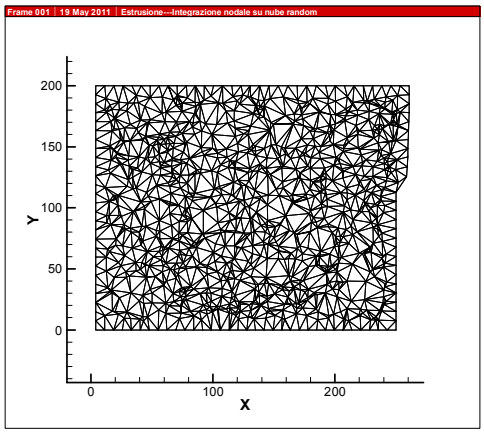

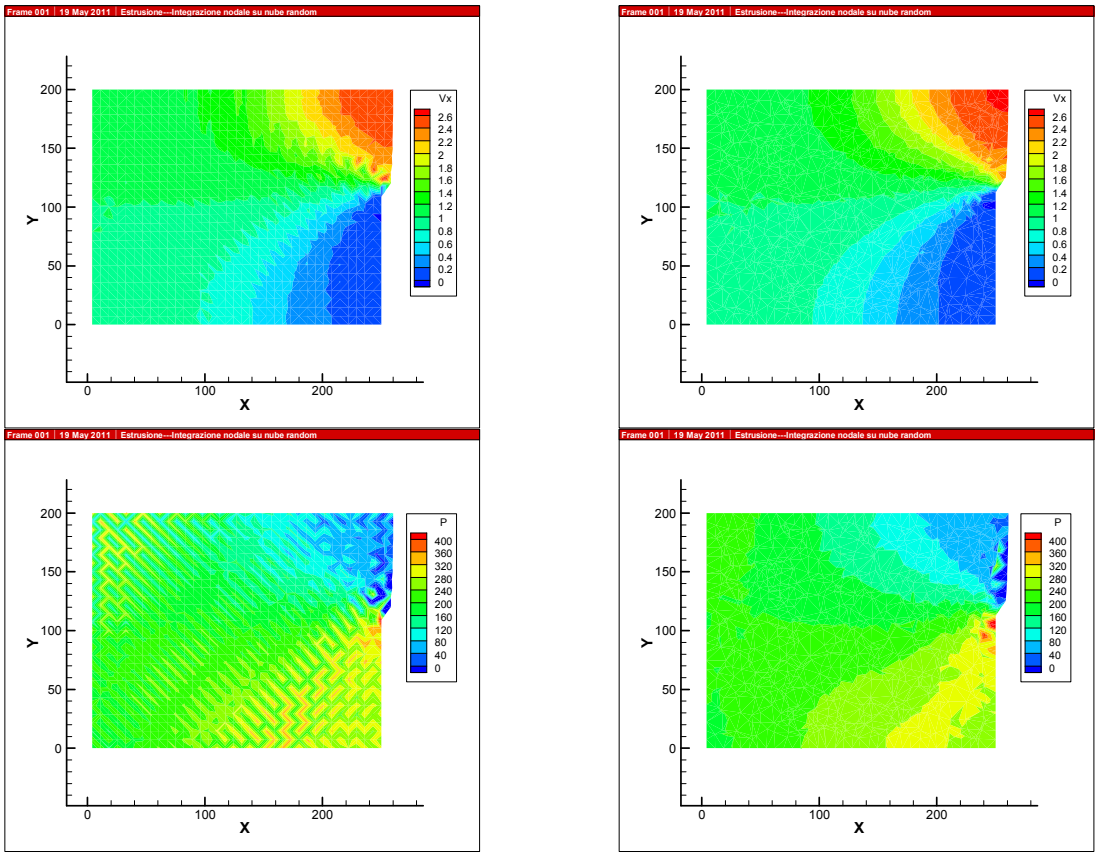

Figure 3: The regular and the irregular mesh and their respective pressure and velocity fieldsp

Since a first stabilizing effect is given only by using an irregular mesh the three NI schemes has been preliminarily compared without introduce the stabilization technique, but using only the benefic effects of the irregularity of the mesh.

In figure 4 has been reported the punch load during the process predicted with the three techniques, using two meshes, of 2000 and 5000 nodes respectively.

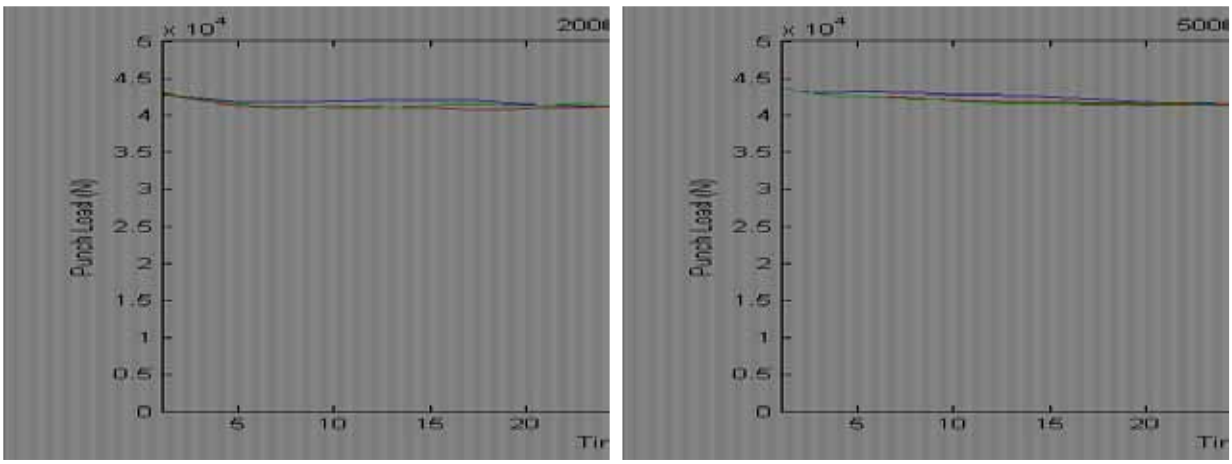

Figure 4: Extrusion load for the three scemes with different types of mesh

Looking at the graphs a very slightly difference is observed between the different schemes. Anyway the extrusion force is a global variable whose prevision does not heavily depends on local phenomena that could condition the specific code prediction; for this reason a better comparison could be done looking at the flow stress distribution at the last step, in figure 4.

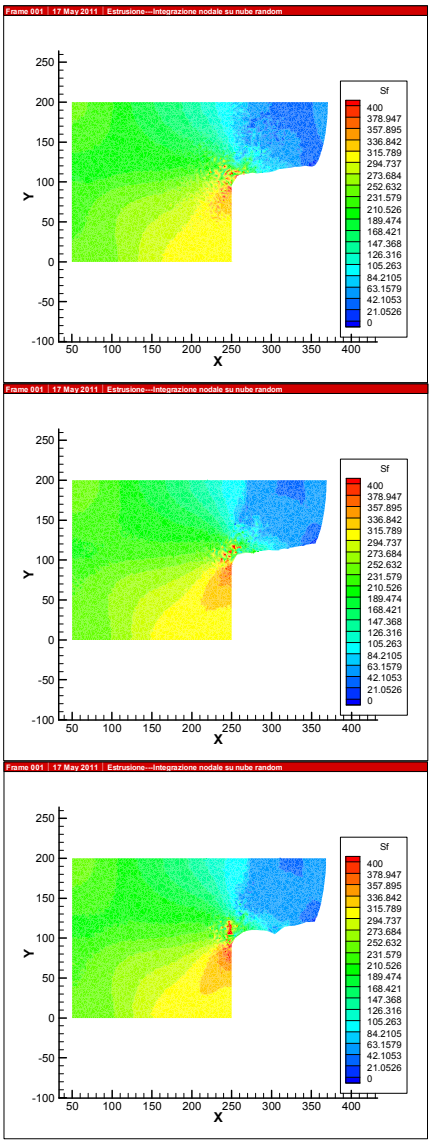

Figure 5: The flow stress distribution for the three nodal integration schemes

In this case the Voronoi-based schemes are quite similar, while the DA presents a slightly lower and more irregular field. Since, according to session 3, the DA and LV schemes would be preferable for the computational times and considering the more regular trend of LV results, that are in excellent agreement with GV ones, the Local Voronoi integration scheme appears to be the most convenient choice.

Concerning the stabilization in figure 6 the velocity field at the 4th step is reported for the two types of mesh (again using the LV scheme with 1000 nodes) and for different values of α.

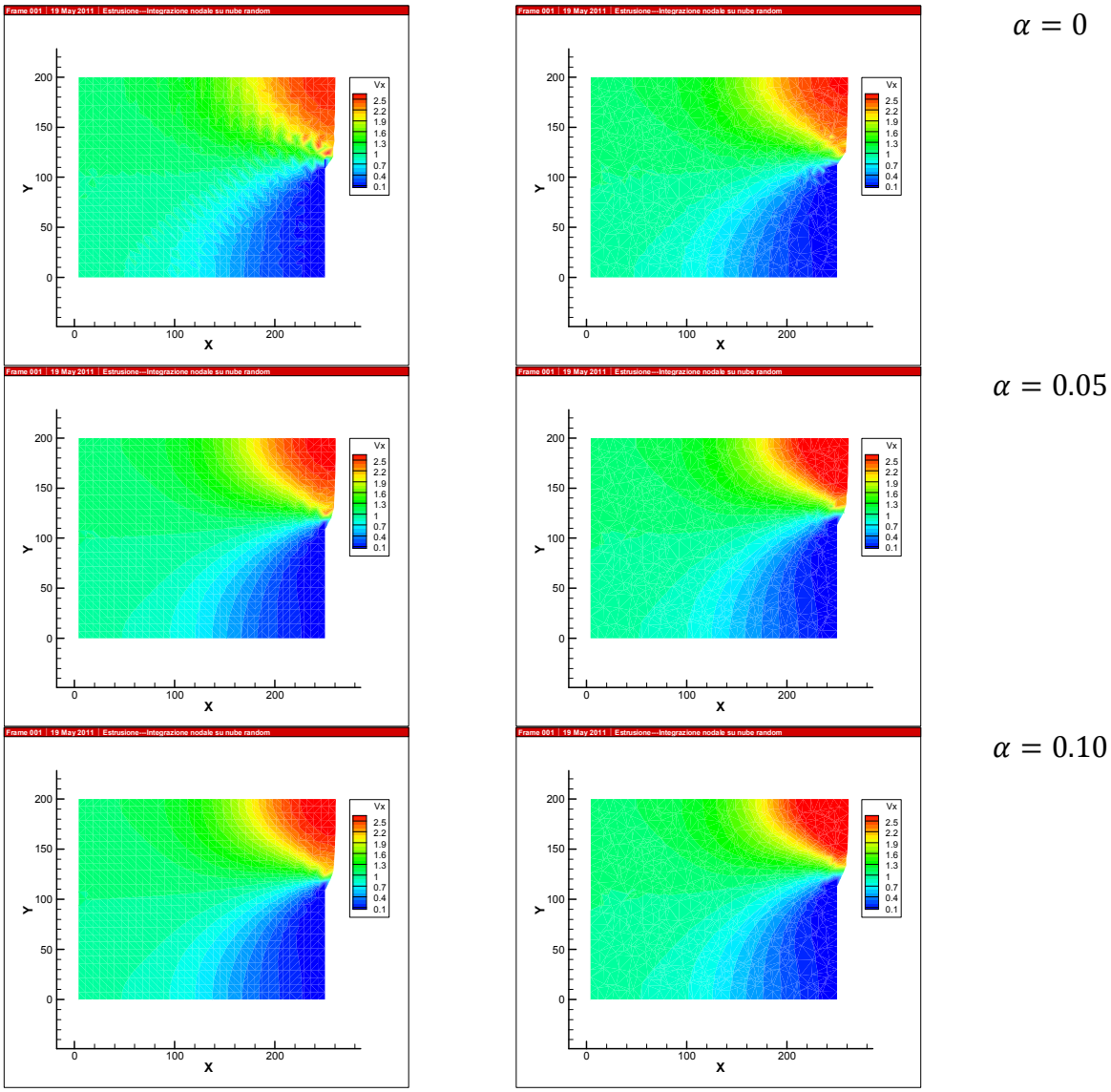

Figure 6: Influence of the stabilization parameter on the velocity field, for the regular mesh (left) and the irregular one (right)

It is very interesting to note that already a value of $\alpha = 0.05$ has a significant stabilizing effect and that imposing $\alpha = 0.10$ even the regular mesh simulation has a very regular velocity field, as in a traditional FEM.

Even more interesting are the effects of α on the punch load. In order to compare the prediction capabilities of the NI techniques with a reference result, the investigated case study has been also simulated with the commercial FEM code DEFORM, that demonstrated in the last years an excellent accuracy in 2D models such as the one considered in this work; moreover, a very refined mesh has been used in this simulation so that the DEFORM solution

could be considered to be very close to the analytical one. Observing the figure 7, obtained for the LV scheme with an irregular mesh of 5000 nodes, two evidences are remarkable:

- all the stabilized curves are close to the DEFORM solution, while the non-stabilized one presents a significant lower load prediction.
- increasing the value of α the stabilized curves cover a range that includes the DEFORM and presumably also the effective solution.

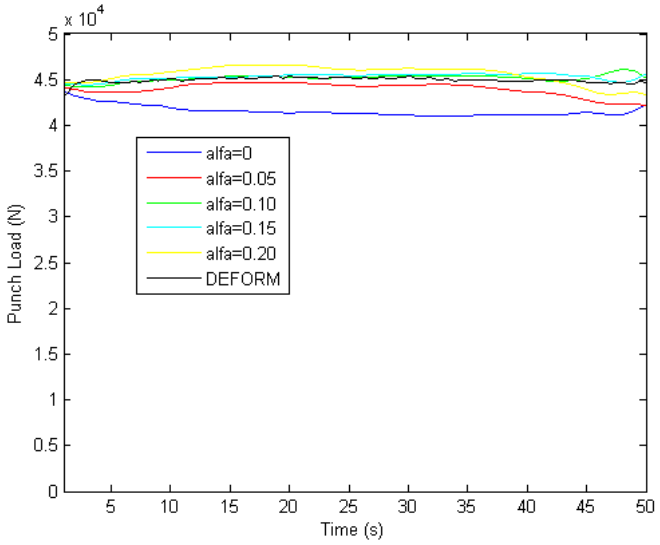

Figure 7: Punch load for different values of the stabilization parameter

The first aspect is due to the more irregular velocity field that leads to a different shape of the extruded material. In figure 8 a comparison is done between the shape of the non-stabilized simulation and stabilized one with α=0.10.

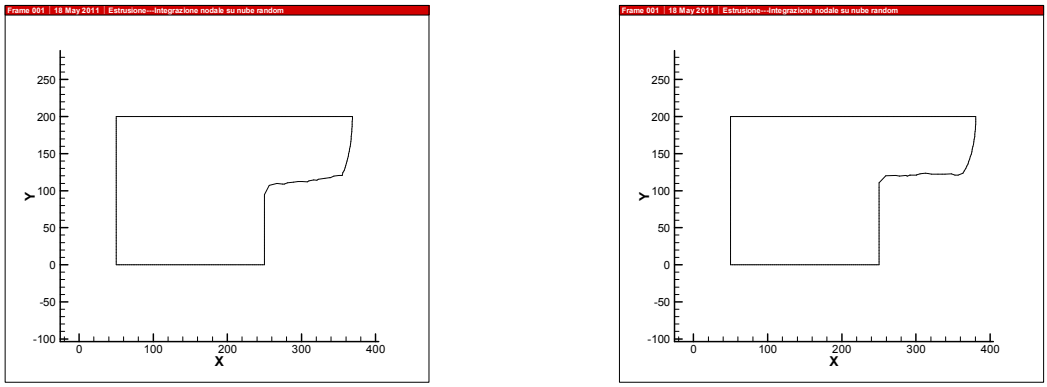

Figure 5: The predicted shape for the non-stabilized code (left) and the stabilized (right)

In particular, when the stabilization is not applied, the extruded material has a larger shape and, for this reason, the requested load results to be slower.

Concerning the second consideration, the influence of α on the load could be explained observing that the traditional FEM matrix $\boldsymbol{K_{ELEM}}$ in equation 17 gives additional stiffness to the model with the increase of α. Analyzing the curves in figure the optimal value of α, in this

application, is about 0.10. Anyway, in general, the most favorable choice of its value depends on several aspects, such as the mesh characteristics, and could be also a lower value, since as it has been shown it is already sufficient to stabilize the model.

7 CONCLUSIONS

In this paper three nodal integration techniques have been compared in the simulation of an extrusion process. The Voronoi-based formulations have shown a slightly better quality of predictions; in particular the LV scheme appears to be the most favorable choice since it requires only a negligible computational time for the geometrical part.

Furthermore the stabilization of this method has been discussed. In particular it has been shown that even if satisfactory results are obtainable using an irregular mesh, their quality is significantly improved if a stabilization is introduced; moreover varying the stabilization parameter the stiffness of the model can be properly tuned.

REFERENCES

[1] Babuška, I. and Aziz A. On the angle condition in the Finite Element Method. *SIAM Journal of Numerical Analysis* (1976) **13**:214-227.

[2] Belytschko, T., Krongauz, Y., Organ, D. and Krysl, P. Meshless Methods: An Overview and recent developments. *Computer Methods in Applied Mechanics and Engineering* (1996) **139(1-4)**:3-47.

[3] Dohrmann, C.R., Heinstein, M.W., Jung, J., Key, S.W. and Witkowski, W.R. Node-based uniform strain elements for three-node triangular and four-node tetrahedral meshes. *International Journal for Numerical Methods in Engineering* (2000) **47**:1549–1568.

[4] Jiun-Shyan Chen, Cheng-Tang Wu, Sangpil Yoon and Yang You. A stabilized conforming nodal integration for Galerkin mesh-free methods. *International Journal for Numerical Methods in Engineering* (2001) **50(2)**:435-466.

[5] Beissel, S. and Belytschko, T. Nodal Integration of the element-free Galerkin method. *Computer Methods in Applied Mechanics and Engineering* (1996) **139**:49-74.

[6] Puso, M.A. and Solberg, J. A stabilized nodally integrated tethaedral. *International Journal for Numerical Methods in Engineering* (2006) **67**:841-867.

[7] Puso, M.A., Chen, J.S., Zywicz, E. and Elmer, W. Meshfeee and finite elements nodal integration methods. *International Journal for Numerical Methods in Engineering* (2007) **74**:416-446.

[8] Preparata, F.P. and Shamos, MI. *Computational Geometry: An Introduction* (1985). Springer: New York.

[9] Lasserre, J.B. An analytical expression and an algorithm for the volume of a convex polyhedron. Optimization Theory Application (1983) **39**:363-377.

[10] Zienkiewicz, O.C. and Godbolet, P.N. Flow of plastic and visco-plastic solids with special reference to extrusion and forming processes. *International Journal for Numerical Methods in Engineering* (1974) **8**:3–16.

[11] Kalpakjian, S. and Schmid, S.R. *Manufacturing processes for engineering materials. IV Ed* (2003). Pearson Education, Inc.

[12] Kobayashi, S., Soo-ik Oh and Altan, T. *Metal forming and the finite element method* (1989). Oxford University press.

XI International Conference on Computational Plasticity. Fundamentals and Applications
COMPLAS XI
E. Oñate, D.R.J. Owen, D. Peric and B. Suárez (Eds)

PREDICTIVE MODELS FOR BOLTED T-STUB CONNECTIONS COMBINING FEM WITH INTELLIGENT ARTIFICIAL TECHNIQUES

JULIO FERNÁNDEZ-CENICEROS*, RUBÉN LOSTADO-LORZA, ROBERTO FERNÁNDEZ-MARTÍNEZ, ANDRÉS SANZ-GARCÍA AND FCO. JAVIER MARTÍNEZ-DE-PISÓN

* EDMANS Research Group, Department of Mechanical Engineering
Universidad de La Rioja
C/Luis de Ulloa 20, Logroño 26004, Spain
e-mail: julio.fernandezc@unirioja.es, web page: http://www.mineriadatos.com

Key words: T-stub connection, Nonlinearity, Finite Element Method, Artificial Intelligent, Component Method, Eurocode 3.

Abstract. The behavior of bolted connections is inherently nonlinear because of geometric discontinuities, stress concentrations, contacts or local yielding. In structural field, component method adopted by Eurocode 3 separates the joint in individual elements that are called T-stub. Each component should be defined at least by three parameters: initial stiffness, strength and deformation capacity. In this paper, a new methodology based on a combination of Finite Element Method (FEM) and Artificial Intelligence (AI) techniques is presented in order to predict force-deformation response of bolted T-stub connection.

An advanced finite element model is generated and validated by comparison with experimental tests in the literature. Parametric study combining bolt diameters, hot-rolled profile geometry and steel class is carried out for generating training database with output variables of T-stub characterization. Several AI algorithms as regression trees, neural artificial networks or radial basis function networks are training so as to find the best generalizing model of the problem. The results show a high correlation between FEM and the predictive model, which replaces the first one. Test errors for output variables of the T-stub model prediction are lower than 5%.

Finally, this methodology provides an alternative to analytical models which includes the Eurocode 3 for the determination of T-stub parameters. This alternative includes the advantages of FEM (realistic simulation validated against experimental tests or the ability to obtain stress and strain values) but minimizes the complexity and computing time by using AI techniques.

1 INTRODUCTION

Bolted connections are complex elements of the utmost importance in buildings' structural design and they should be carefully assessed. Their behavior is inherently nonlinear due to contacts, geometrical discontinuities, stress concentrations or material plasticity, among

others. That behavior is a handicap to establish an analytical method to describe the connection response.

Among different analytical procedures, Annex J of Eurocode 3 [1] includes the component method which is suitable in beam-to-column connections. In this procedure, the connection is divided into isolated joints which represent the sources of deformability. Each component is characterized by a force-deformation response and then, a mechanical model make up springs (components) and rigid links are assembled. Finally, the moment-rotation response for the whole connection can be obtained from the behavior of the individual components. This overall connection response is mostly governed by the end plate and the bolt under tension. The tension component is the outstanding issue in a beam-to-column connection, which is called *equivalent T-stub* (Figure 1). During the last decades, this component has been widely studied by researchers in order to develop a realistic and reliable procedure to obtain force-deformation response of this connection. The equivalent bolted T-stub was originally introduced by Zoetemeijer [2] in 1974 and, since that time, a great number of studies have been carried out. These researches can be divided into analytical [3-10] or mechanical models [11, 12], experimental tests [13-15] and numerical finite element (FE) simulations [16-20]. The last ones are capable to reproduce the connection behavior fairly accurately. Nevertheless, in spite of the advances in computational field, attempts to achieve more realistic simulations have resulted as a longer model calculation times due to nonlinearities, making these models uncompetitive compared to analytical models [21].

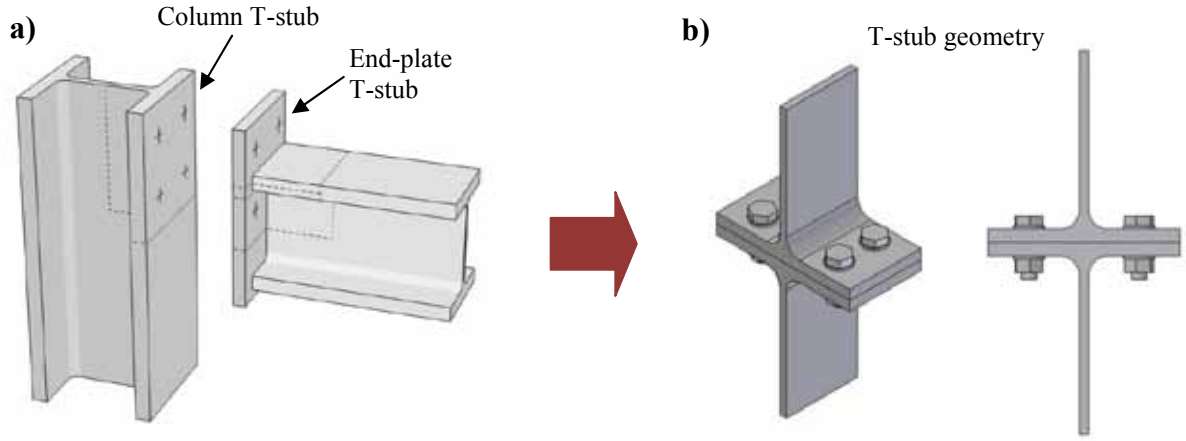

Figure 1: a) Beam-to-column connection ; b) Tension component model (T-stub)

In this paper, it is drawn a methodology [21] to obtain force-deformation response in a T-stub connection. In section 2, an advanced FE model is developed and, in section 3, the results are validated against experimental test in the literature. Parametric study is carried out in section 4 for generating training database with output variables which defines force-deformation response in the T-stub. Finally, several AI algorithms as regression trees, neural artificial networks or radial basis function networks are training so as to find the best generalizing model of the problem.

2 NUMERICAL MODEL

The force-deformation response in the T-stub is carried out by an advanced three dimensional FE model. This numerical model is developed using ABAQUS® finite element software [22]. The T-stub geometry is composed of two T-shape hot rolled profiles connected by means of one or more rows of bolts, as indicated in Figure 1b. This type of joint may fail according to three failure modes (Figure 2) depending mainly on the hot rolled profiles and bolts geometry. The first failure mode occurs when the ratio flange thickness/bolt diameter is low and four plastic hinges in the flange plates are located at the bolt holes and near the web plate. The second one is a combination between the development of two plastic hinges and the tension failure of the bolts. Finally, the third failure mode occurs with tension failure of the bolts.

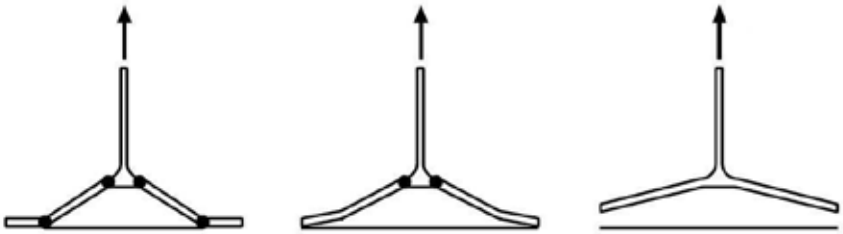

Figure 2: Failure modes in a T-stub

2.1 Material modeling

The constitutive material laws of hot rolled profiles and bolts are according to the experimental validation carried out by Bursi and Jaspart [11]. In that work, the authors reproduced the material behavior with a piecewise linear model (Figure 3) and different laws for flange and web were considered in order to improve the model accuracy. The properties of these materials are entered the software as a set of points on the stress-strain curve.

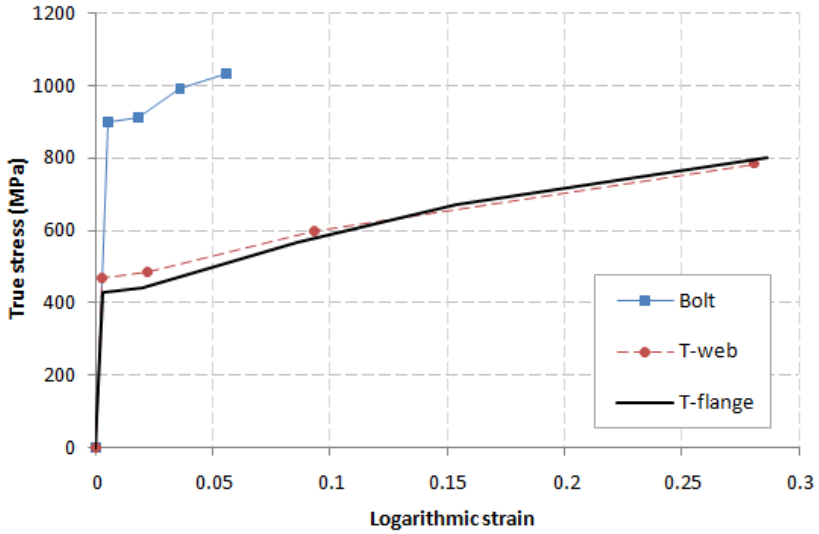

Figure 3: True stress-logarithmic strain material laws

2.2 FE Meshing

Continuous hexahedral solids elements are used because they are suitable for linear and nonlinear stress/displacement analysis, including contacts, plasticity and major strains. They are first-order (linear) interpolation elements, with nodes only at the corners.

Partitions are established in the hot rolled profile to create a more refined mesh in the area surrounding the bolt hole (Figure 4).

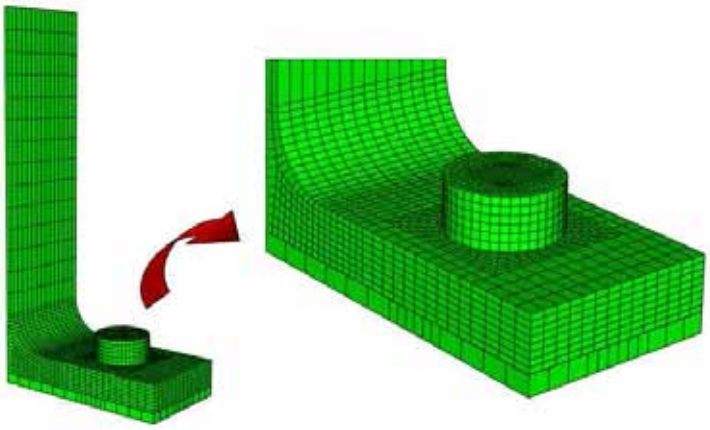

Figure 4: Finite element mesh of the T-stub connection

2.3 Contact

In ABAQUS/Explicit, the definition of *General Contact* is used for the simulation of contacts between plates and bolts. This definition automatically establishes the interactions between contact surfaces and allocates *master* and *slave* characteristics to each pair of surfaces. The general contact algorithm uses a formula known as *finite sliding*, which allows arbitrary separation between sliding and rotation of surfaces. It is designed to simulate highly non-linear processes.

The normal behavior of the bolt shank with regard to the walls of the hole is modeled by the hard contact property. When the surfaces are in contact, any pressure between them can be transmitted, with the surfaces separated if the pressure drops to zero.

Tangential behavior is modeled by Coulomb's basic friction model, in which two surfaces in contact can withstand shearing stresses of a certain magnitude at their interface before one starts to slide over the other. In this case, the friction coefficient adopted for the model is 0.25.

2.4 Boundary conditions and loads

Only one eighth of the model is simulated, so major savings in computation costs are made. In order to simulate the contact between two T-elements, one element is substituted by a rigid plate according to the symmetry conditions.

The tensile load over the T-element is entered the software as a load evenly distributed. It is applied as a linear ramp divided into 100 steps, so that it is possible to obtain a force-deformation response of the joint.

2.5 Type of analysis

ABAQUS® provides two analysis options: *Standard* and *Explicit*, which they correspond with two solution procedures: *Implicit* and *Explicit*. Implicit method is based on static equilibrium and simultaneous resolution of a linear equations set. The most relevant characteristic of this method is the assembly of the global stiffness matrix. On the other hand, in the explicit analysis, the state of the model at the end of an increment (time t+Δt) is based on the displacements, velocities and accelerations at the beginning of the increment (time t) [23]; this method lacks a global stiffness matrix.

Explicit method is used in this work because it is suitable for nonlinearities, such as contacts or geometrical discontinuities and it shows a good convergence. Nevertheless, explicit analysis should be checked because it may yield results significantly affected by dynamic effects. In this case, kinematic/internal energy ratio is below 5% during loading process, so dynamics effects can be neglected.

3 FE MODEL VALIDATION

FE model is validated against experimental test program carried out by Bursi and Jaspart in 1997 [11]. The authors created a reference model (specimen T1) which was obtained from an IPE300 hot rolled profile and it was attached with four bolts M12. The material properties for bolts and steel were published in the original work and they have been adopted in this paper (Figure 3).

In Figure 5, von Mises stresses in the T-stub are shown. According to the experimental test [11], the failure occurs by bolt fracture after significant flange yielding. Two plastic hinges are developed in the bolt holes and near the web plate, according to the failure mode 2 (Figure 6).

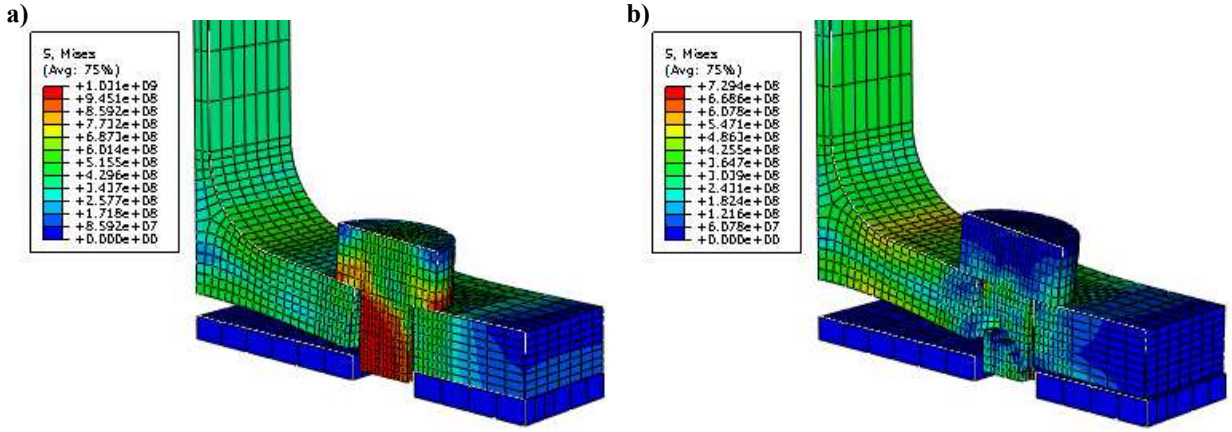

Figure 5: Von Mises stress; a) maximum strength; b) axial failure in the bolt.

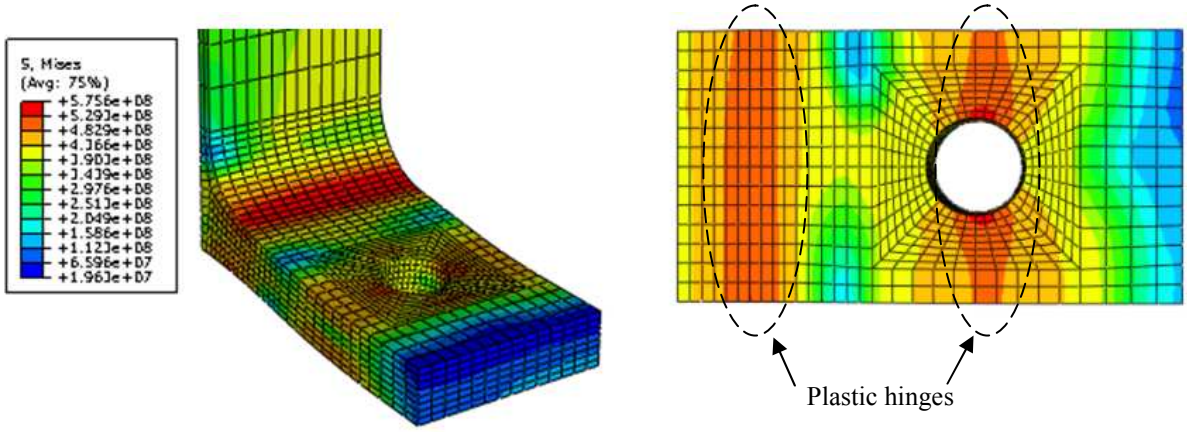

Figure 6: Von Mises stress in the flange. Plastic hinges are located at the bolt holes and near the web plate.

In order to validate the accuracy of the model, force-deformation characteristic response for FE numerical analysis is compared to experimental test (Figure 7). The numerical results are very close to the experimental response, so the advanced FE model is rather accurate.

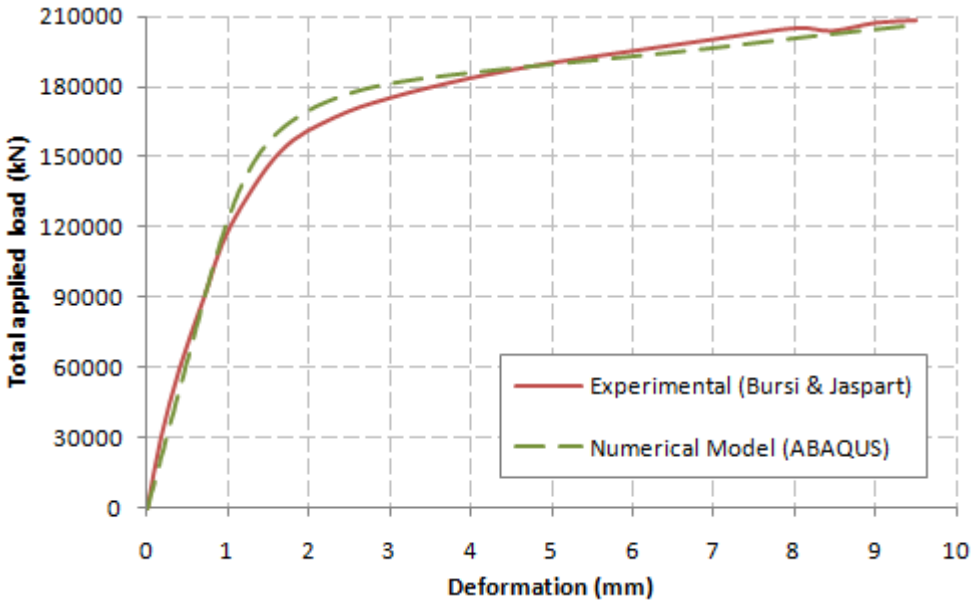

Figure 7: Force-deformation response in the T-stub. Experimental vs. Numerical model

4 PREDICTIVE MODELS

Once that numerical model has been performed and validated by experimental test, a parametric study is carried out in order to study the influence of several geometric parameters. The results obtained in the parametric study form a database useful to training predictive models.

4.1 Parametric study

81 numerical FE simulations have been fulfill by varying the following parameters (Figure 8):

- *Effective width (b)*. This parameter varies between 68 and 100 mm.
- *Edge distance (m)*. This parameter varies between 25 and 35 mm.
- *Bolt diameter (d)*. This parameter varies between 8 and 14 mm.

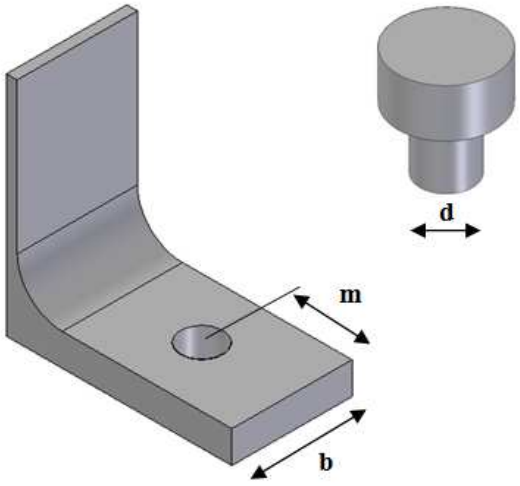

Figure 8: Input parameters

For each simulation, force-deformation response is obtained and it is simplified by a bilinear model. This simplified model is defined by means of four output parameters (Figure 9).

- *Initial stiffness (k_{ini}).*
- *Elastic strength (F_{el}).*
- *Maximum strength (F_{max}).*
- *Maximum displacement (U_{max}).*

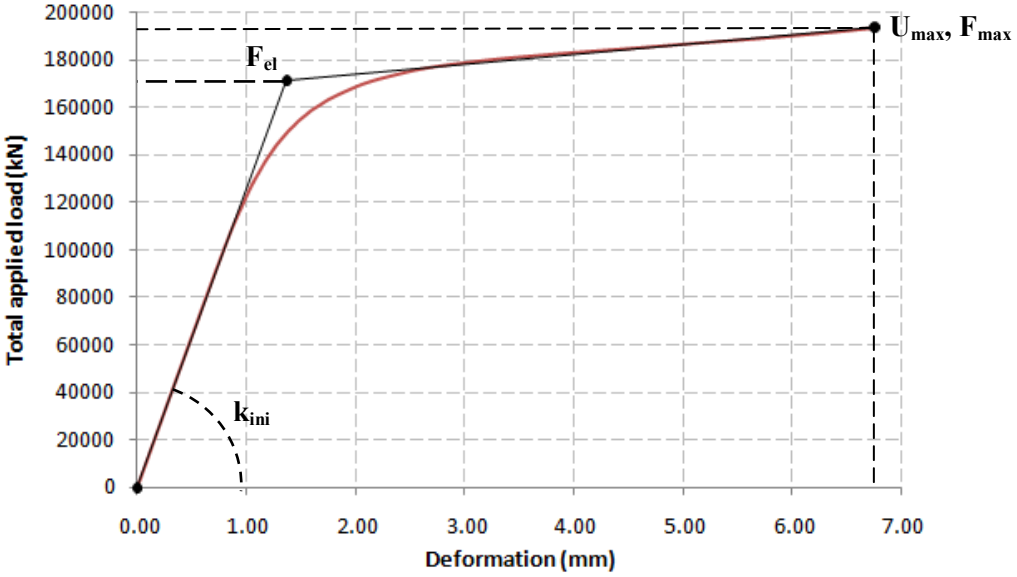

Figure 9: Output variables in parametric study

The outcome results of the whole simulation make up the database for the training of the different predictive models.

4.2 Selection of the best data mining technique

Several data mining techniques are training in order to find the best generalizing model of the problem. These techniques are: *multilayer perceptron artificial neural network (ANN), M5P regression trees, radial basis function network (RBFN) and support vector regression model (SVRM).* Among them, ANN provides the lowest root mean square error (RMSE) and mean absolute error (MAE), according to the following formulae:

$$RMSE = \sqrt{\frac{1}{n}\sum_{k=1}^{n}\left(y(k)-\bar{y}(k)\right)^2} \tag{1}$$

$$MAE = \frac{1}{n}\sum_{k=1}^{n}\left|y(k)-\bar{y}(k)\right| \tag{2}$$

Multilayer Perceptron (MLP) is a typology of ANN which it is used in this work. It is a classifier and predictor that uses back propagation to classify instances. All nodes in this network are sigmoid, except when the class is numeric. In the latter case, the output nodes become unthresholded linear units [24].

Several parameters such the number of neurons in the hidden layer or the learning rate are varying during MLP's training process in order to reduce the errors.

4.3 Results of the predictive models

Table 1 shows the results of the training and cross-validation process for the four output variables *(k_{ini}, F_{el}, F_{max}* and *U_{max})*. The mean values are shown for the cross-validation errors 10, CORR, RMSE and MAE for each group of 10 models created for each type of configuration and algorithm. Training and validating 10 models of each type reduces errors due to local minimum levels and improves the actual estimation of the level of accuracy achieved by each algorithm in each configuration. The number of neurons in the hidden layer is shown in brackets.

As it can be seen in Table 1, MLP's with a low number of neurons in the hidden layer are capable to predict output variables with RMSE errors below 5%. The best results are obtained for prediction the initial stiffness (k_{ini}) and the maximum strength (F_{max}), which are the most important parameters in the T-stub prediction. In these cases, mean absolute error (MAE) is close to 1%. On the other hand, maximum displacement (U_{max}) prediction presents errors next to 5%.

Table 1: Results of the training process for output variables. Validation errors for each model's configuration

Output variable	Algorithm	CORR_MEAN	MAE_MEAN	RMSE_MEAN
k_{ini}	MLP (5)	0.9988	0.0112	0.0133
F_{el}	MLP (6)	0.9963	0.0165	0.0245
F_{max}	MLP (6)	0.9989	0.0106	0.0134
U_{max}	MLP (4)	0.9754	0.0501	0.0647

Finally, in order to check the generality of the created models, 12 more FE simulations are performed with parameter values not used in the training phase, and the results are compared with those of the predictive models. In Figure 10, the force-deformation responses are performed with output variables predictions and, it can be seen, the results are close to FE simulations. The number below graphs represents *"b_m_d"* (effective width, edge distance and bolt diameter, respectively).

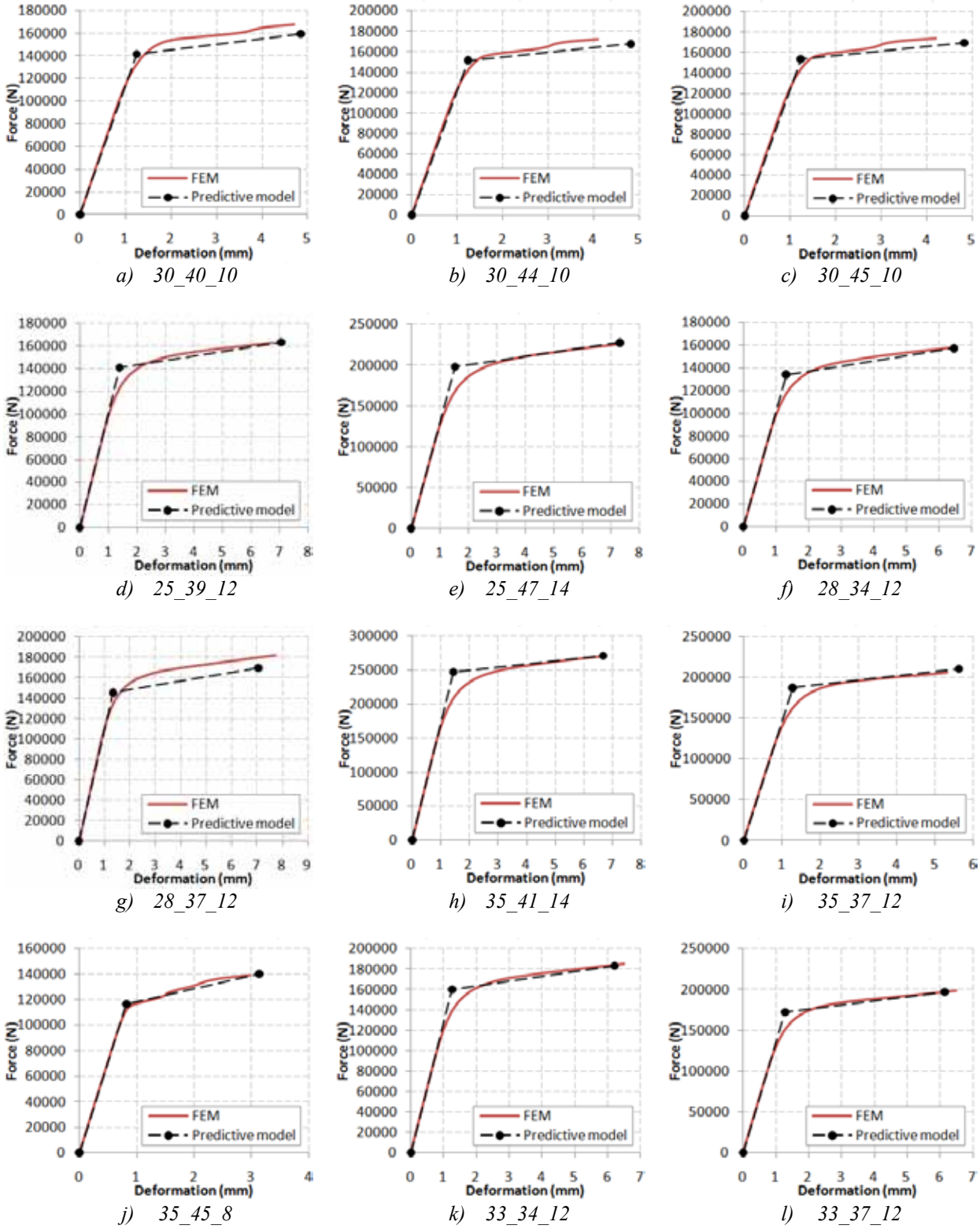

Figure 10: Force-deformation response. Numerical simulation *vs.* predictive model

5 CONCLUSIONS

A methodology based on predictive models for calculating the force-deformations response in T-stub joints has been presented in this work. In the mechanical model established by the Eurocode 3 in Annex J (Component Method), these joints represent the tension component in beam-to-column connections and it is very important to know their behavior in order to obtain a reliable connection design.

FE simulations provide a powerful tool due to its ability to reproduce the nonlinearities involved in the T-stub design, such as contacts, material plasticity or stress concentration. However, the complexity of this numerical method needs a great amount of time, resources and high computational cost. Thus, this method is not efficient for repetitive tasks such as the case of joints.

In this paper, predictive models have been developed from an advanced finite element model validated by experimental tests. The creation of 81 FE simulations varying characteristic parameters of joint has been used to generate a training database. Using this database, MPL's have been training and prediction errors below 5% have been achieved in each output variable. Finally, the generated models have been validated with new test data and the results have been compared with numerical simulations finding a good accuracy between them. In conclusion, the use of predictive models could replace the implementation of FE simulations saving time and avoiding a high computational cost.

REFERENCES

[1] European Committee for Standardization CEN. EN 1993-1-8. Eurocode 3 - Design of steel structures - Part 1-8: Design of joints.

[2] Zoetemeijer, P. A design method for the tension side of statically loaded bolted beam-to-column connections. *Heron* (1974) **20**(1): 1-59.

[3] Agerskov, H. High-strength bolted connections subject to prying. *J Struct Div, ASCE* (1976) **102**: 162–175.

[4] Agerskov, H. Analysis of bolted connections subject to prying. *J Struct Div, ASCE* (1977) **103**: 2145–2163.

[5] Swanson, J.A. and Leon, R.T. Stiffness modeling of bolted T-stub connection components. *J Struct Eng, ASCE* (2001) **127**(5): 498–505.

[6] Piluso, V., Faella, C. and Rizzano, G. Ultimate behavior of bolted T-stubs. I: theoretical model. *J Struct Eng, ASCE* (2001) **127**(6): 686–693.

[7] Piluso, V., Faella, C. and Rizzano, G. Ultimate behavior of bolted T-stubs. II: model validation. *J Struct Eng, ASCE* (2001) **127**(6): 694–704.

[8] Girao Coelho, A.M., Simoes da Silva, L. and Bijlaard, F.S.K. Characterization of the nonlinear behavior of single bolted T-stub connections. *Connections in Steel Structures V* (2004).

[9] Lemonis, M.E. and Gantes, C.J. Incremental modeling of T-stub connections. *Journal of Mechanics of Materials and Structures* (2006) **7**: 1135-1159.

[10] Loureiro, A., Gutiérrez, R., Reinosa J.M. and Moreno, A. Axial stiffness prediction of non-preloaded T-stubs: an analytical frame approach. *Journal of Constructional Steel Research,* (2010) **66**: 1516–1522.

[11] Lemonis, M.E. and Gantes, C.J. Mechanical modeling of the nonlinear response of beam-to-column joints. *Journal of Constructional Steel Research* (2009) **65**: 879-890.
[12] Wang, Z.Y., Tizani, W. and Wang, Q.Y. Strength and initial stiffness of a blind-bolt connection based on the T-stub model. *Eng Struct* (2010) **32**(9): 2505–2517.
[13] Bursi, O.S. and Jaspart, J.P. Benchmarks for finite element modelling of bolted steel connections. *Journal of Constructional Steel Research* (1997) **43**:17-42.
[14] Swanson, J.A. and Leon, R.T. Bolted steel connections: Tests on T-stub components. *J Struct Eng, ASCE* (2000) **126**(1): 50–56.
[15] Clemente, I., Noé, S. and Rassati, G.A. Experimental behavior of T-stub connection components for the mechanical modeling of bare-steel and composite partially-restrained beam-to-column connections. *Connections in Steel Structures V* (2004).
[16] Krishnamurthy, N. and Graddy, D.E. Correlation between 2-and-3-dimensional finite element analyses of steel bolted endplate connections. *Computers & Structures* (1976) **6**:381-389.
[17] Bursi, O.S. and Jaspart, J.P. Basic issues in the finite element simulation of extended end plate connections. *Computers & Structures* (1998) **69**:361-382.
[18] Swanson, J.A., Kokan, D.S. and Leon, R.T. Advanced Finite element modeling of bolted T-stub connection components. *Journal of Constructional Steel Research* (2002) **58**:1015-1031.
[19] Girao Coelho, A.M., Simoes da Silva, L. and Bijlaard, F.S.K. Finite element modeling of the nonlinear behaviour of bolted T-stub connections. *Journal of the Structural Engineering* (2006) **132**: 918-929.
[20] Loureiro, A., Reinosa J.M., Gutiérrez, R. and Moreno, A. New proposals on the calculation of the flexural resistance in angle connections. *Journal of Constructional Steel Research* (2011) **67**: 613-622.
[21] Fernández, J., Pernía, A., Martínez-de-Pisón, F.J. and Lostado, R. Prediction models for calculating bolted connections using data mining techniques and the finite element method. *Engineering Structures* (2010) **32**(10): 3018-3027.
[22] ABAQUS, Inc. ABAQUS. Ver. 6.7. Analysis user's manual. 2007.
[23] Vegte van der, G.J. and Makino, Y. Numerical simulations of bolted connections: the implicit versus the explicit approach. *Connections in Steel Structures V* (2004).
[24] Haykin, S. *Neural networks, a comprehensive foundation*. New Jersey: Prentice Hall, (1999).

XI International Conference on Computational Plasticity. Fundamentals and Applications
COMPLAS XI
E. Oñate, D.R.J. Owen, D. Peric and B. Suárez (Eds)

SHAPE OPTIMIZATION FOR ANISOTROPIC ELASTOPLASTICITY IN LOGARITHMIC STRAIN SPACE

S. GERMAIN* AND P. STEINMANN

Chair of Applied Mechanics
University of Erlangen-Nuremberg
Egerlandstr.5, 91058 Erlangen, Germany
www.ltm.uni-erlangen.de
*e-mail: sandrine.germain@ltm.uni-erlangen.de

Key words: Shape Optimization, Elastoplasticity, Anisotropy

Abstract. This paper deals with shape optimization for anisotropic elastoplasticity in logarithmic strain space. We aim to find an appropriate undeformed configuration of a workpiece knowing in advance its deformed configuration, the boundary conditions and the applied loads. The node coordinates of the finite element (FE) domain are chosen as design variables. A discrete sensitivity analysis is presented and analytical gradients are performed. A numerical example illustrates the theoretical aspects.

1 INTRODUCTION

A challenge in the design of functional parts is the determination of the initial, undeformed shape such that under a given load a part will obtain the desired deformed shape. This problem is inverse to the standard (direct) static analysis in which the undeformed shape is known and the deformed unknown. [1] extended the method originally proposed in [2] to anisotropic hyperelasticity that is based on logarithmic (Hencky) strains. [3] extended the method proposed in [1] to anisotropic elastoplastic materials. It was shown that the inverse form finding model in elastoplasticity can be used under the condition that the plastic strains are previously given. This is the case when a desired hardening state is prescribed. Basics on shape optimization can be found in [4]. In [5] a continuum sensitivity analysis is presented for the computation of shape sensitivity for finite hyperelastic-viscoplastic deformations. This method involves contact with friction using a direct differentiation method in 2D. [6] extented the work in [5] to thermoplasticity combined with ductile damage at finite strains. A gradient-based optimization framework for the computational design of metal forming processes for porous materials is introduced. [7] extented the work in [5] and [6] to 3D and defined the surface of the die by Bezier curves. This work focuses on the review of sensitivity contact. An alternative method

to continuum sensitivity analysis is a discrete formulation. This substitute has been applied in [8] for finite deformations in elastoplasticity in principal directions to parameter identification, which can be formulated as an optimization problem. [9] introduced a new regularization technique to avoid convergence problems and problems with jagged shapes. An artificial inequality constraint added to the optimization problems limits a fictitious total strain energy that measures the shape change of the design with respect to a reference design. The coordinates of boundary nodes of the FE-domain are chosen as design variables. The analytical gradients are derived using the adjoint method. The presented applications are restricted to linear elastostatic problems. [10, 11] proposed a shape optimization method for non-steady-state metal forming processes. The initial shape of a part as well as the shape of the preform tool during a two-step forging operation was optimized. Shapes are described using spline functions. The FE-method and remeshing operations are used during the simulation. Contact during the process are taken into account.
In this contribution we present a classical numerical shape optimization method for anisotropic elastoplastic materials that is based on logarithmic strains. A Limited–Broyden–Flechter–Goldfarb–Shanno (gradient-based descent method) algorithm from [12] is used. The objective function that needs to be minimized in order to obtain the optimal undeformed workpiece is the quadratic difference between the node positions in the targeted and computed deformed shape, i.e. the node coordinates of the FE-domain are chosen as design variables. A discrete sensitivity analysis is presented. Analytical gradients are performed. A remeshing of the shape is not applied during the computation.
This paper is organized as follows: In section 2 we briefly present the kinematics of the direct and the inverse problems. Section 3 summarizes anisotropic elastoplasticity in the logarithmic strain space. Section 4 presents the dissipation and the plastic flow response. In section 5 we review the Piola and Cauchy formulation to determine the deformed shape based on the knowledge of the undeformed shape. The finite element discretization is described in section 6. Section 7 presents the formulation of the sensitivity analysis. In section 8 a numerical example for the shape optimization in anisotropic elastoplasticity illustrates the theoritical aspects.

2 KINEMATICS OF GEOMETRICALLY NONLINEAR CONTINUUM MECHANICS

Let $\mathcal{B}_0$ denote the reference configuration of a continuum body with the boundary surface $\partial\mathcal{B}_0$ at time $t = 0$ parameterized by material coordinates $\boldsymbol{X}$. $\mathcal{B}_t$ is the current configuration with the boundary surface $\partial\mathcal{B}_t$ at time t parameterized by spatial coordinates $\boldsymbol{x}$, as depicted in Figure 1. The deformation map $\boldsymbol{\varphi}$ is defined as

$$\boldsymbol{x} = \boldsymbol{\varphi}(\boldsymbol{X}) : \mathcal{B}_0 \longrightarrow \mathcal{B}_t. \tag{1}$$

The corresponding deformation gradient together with its Jacobian determinant are given by

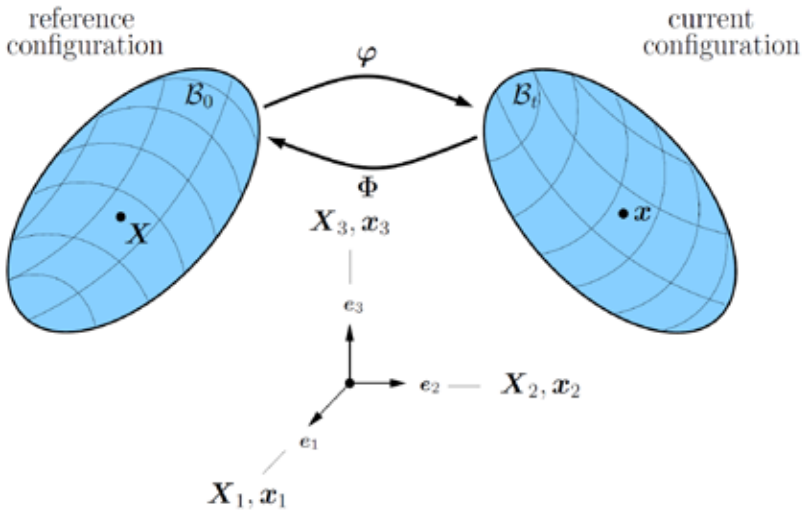

Figure 1: Nonlinear continuum mechanics.

$$\boldsymbol{F} = \nabla_{\boldsymbol{X}} \boldsymbol{\varphi}, \qquad J = \det \boldsymbol{F}. \tag{2}$$

$\nabla_{\boldsymbol{X}}$ denotes the gradient operator with respect to the material coordinates $\boldsymbol{X}$. The deformation map $\boldsymbol{\Phi}$ is defined as

$$\boldsymbol{X} = \boldsymbol{\Phi}(\boldsymbol{x}) : \mathcal{B}_t \longrightarrow \mathcal{B}_0. \tag{3}$$

The corresponding deformation gradient together with its Jacobian determinant are given by

$$\boldsymbol{f} = \nabla_{\boldsymbol{x}} \boldsymbol{\Phi}, \qquad j = \det \boldsymbol{f}. \tag{4}$$

$\nabla_{\boldsymbol{x}}$ denotes the gradient operator with respect to the spatial coordinates $\boldsymbol{x}$. It follows from the above definitions that

$$\boldsymbol{\Phi} = \boldsymbol{\varphi}^{-1}, \qquad \boldsymbol{f} = \boldsymbol{F}^{-1}, \qquad j = J^{-1}. \tag{5}$$

3 ANISOTROPIC ELASTOPLASTICITY IN LOGARITHMIC STRAIN SPACE

In this section we summarize the exposition in [13]. A valid model option for anisotropic finite strain elastoplasticity is a decomposition of the free energy into an elastic and a plastic part

$$\Psi = \psi^e + \psi^p. \tag{6}$$

The elastic part is a quadratic free energy density per unit volume in $\mathcal{B}_0$

$$\psi^e(\boldsymbol{E}^e) = \frac{1}{2}\boldsymbol{E}^e : \mathbb{E}^e : \boldsymbol{E}^e \tag{7}$$

in terms of the second-order elastic strain tensor $\boldsymbol{E}^e$ and a constant anisotropic elastic fourth-order stiffness tensor $\mathbb{E}^e$. For cubic materials, $\mathbb{E}^e$ can be decomposed into Kelvin modes [14] as

$$\mathbb{E}^e = 3\kappa\mathbb{P}_1 + 2\mu\mathbb{P}_2 + 2E_{55} \tag{8}$$

where κ is the bulk modulus, μ is the shear modulus and E_{55} is a constant material parameter. $\mathbb{P}_1$, $\mathbb{P}_2$ and $\mathbb{P}_3$ are fourth-order projection tensors. They can be expressed in terms of the volumetric and symmetric devatoric part of the fourth-order identity tensor as

$$\begin{aligned} \mathbb{P}_1 &= \mathbb{I}_{vol}, \\ \mathbb{P}_2 + \mathbb{P}_3 &= \mathbb{I}^{sym}_{dev}. \end{aligned} \tag{9}$$

An additive decomposition of the plastic strains into an elastic and a plastic part in terms of the second-order logarithmic (Hencky) strain tensor is assumed as

$$\boldsymbol{E} = \boldsymbol{E}^e + \boldsymbol{E}^p = \frac{1}{2}\ln \boldsymbol{C}. \tag{10}$$

Futhermore the plastic free energy part can be decomposed into parts which describe isotropic and kinematic hardening

$$\psi^p = \psi^{iso} + \psi^{kin}. \tag{11}$$

In the following only nonlinear isotropic hardening is considered. It follows

$$\psi^p = \psi^{iso} = \frac{1}{2}h\alpha + (\sigma_\infty - \sigma_0)(\alpha + \exp(\frac{-w\alpha}{w})) \tag{12}$$

where α is a scalar that models isotropic hardening. The spectral decomposition of the right Cauchy–Green strain tensor $\boldsymbol{C}$ reads

$$\boldsymbol{C} = \boldsymbol{F}^t \cdot \boldsymbol{F} = \sum_{i=1}^{3} \lambda_i \boldsymbol{M}_i \tag{13}$$

with $\{\lambda_i\}_{i=1,2,3}$ the real eigenvalues of $\boldsymbol{C}$ and $\{\boldsymbol{M}_i\}_{i=1,2,3}$ the associated eigenbases [15]. The spectral representation facilitates the computation of the logarithmic strain

$$\boldsymbol{E} = \frac{1}{2}\sum_{i=1}^{3} \ln \lambda_i \boldsymbol{M}_i \tag{14}$$

and allows a closed form expression for the (first and second) derivatives of the logarithmic strain with respect to the right Cauchy–Green strain

$$\mathbb{P} = 2\frac{\partial \boldsymbol{E}}{\partial \boldsymbol{C}} \quad \text{and} \quad \mathbb{L} = 2\frac{\partial \mathbb{P}}{\partial \boldsymbol{C}} = 4\frac{\partial^2 \boldsymbol{E}}{\partial \boldsymbol{C} \partial \boldsymbol{C}}. \tag{15}$$

For further details regarding the computation of these derivatives the interested reader is referred to [16]. Using (15), the Piola–Kirchhoff stress may be represented as

$$\boldsymbol{S} = 2\frac{\partial \Psi}{\partial \boldsymbol{C}} = \boldsymbol{T} : \mathbb{P} \quad \text{with} \quad \boldsymbol{T} = \frac{\partial \Psi}{\partial \boldsymbol{E}^e} = \mathbb{E}^e : \boldsymbol{E}^e. \tag{16}$$

Considering this expression, the linearization of the Piola–Kirchhoff stress (tangent operator needed in a Newton type solution scheme) reads

$$\mathbb{C} = 4\frac{\partial^2 \Psi}{\partial \boldsymbol{C} \partial \boldsymbol{C}} = \mathbb{P}^T : \mathbb{E}^* : \mathbb{P} + \boldsymbol{T} : \mathbb{L} \quad \text{with} \quad \mathbb{E}^* = \frac{\partial^2 \Psi}{\partial \boldsymbol{E} \partial \boldsymbol{E}}. \tag{17}$$

The transposition symbol $[\bullet]^T$ refers to an exchange of the first and last pairs of indices. The fourth-order tensor $\mathbb{E}^*$ is the fourth-order elasticity tensor $\mathbb{E}^e$ in the case of an elastic loading and the elastoplasticity tensor $\mathbb{E}^{ep}$ in the case of a plastic loading [13], respectively.

4 DISSIPATION AND PLASTIC FLOW RESPONSE

In the logarithmic strain space the dissipation inequality can be written as

$$\boldsymbol{T} : \overset{\circ}{\boldsymbol{E}}{}^p - \frac{\partial \Psi}{\partial \alpha} \cdot \overset{\circ}{\alpha} \geq 0, \tag{18}$$

where $[\overset{\circ}{\bullet}]$ denotes the time derivative and $\{\boldsymbol{E}^p, \alpha\}$ is the set of internal variables. We consider the following quadratic yield function

$$\Upsilon = \|\mathrm{dev}\boldsymbol{T}\| - \sqrt{\frac{2}{3}} B \quad \text{with} \quad B = h\alpha + (\sigma_\infty - \sigma_0)(1 - \exp(-w\alpha)). \tag{19}$$

Using the principle of maximum plastic dissipation and the definition of the Lagrange function $\mathcal{L}$,

$$\mathcal{L}(\boldsymbol{T}, \frac{\partial \Psi}{\partial \alpha}, \gamma) = -\boldsymbol{T} : \overset{\circ}{\boldsymbol{E}}{}^p - \frac{\partial \Psi}{\partial \alpha} \cdot \overset{\circ}{\alpha} + \gamma(\Upsilon - \sqrt{\frac{2}{3}}\sigma_0), \tag{20}$$

we obtain the Karush-Kuhn-Tucker equations

$$\left\{ \begin{array}{c} \overset{\circ}{\boldsymbol{E}}{}^p = \gamma \dfrac{\partial \Upsilon}{\partial \boldsymbol{T}}, \quad \overset{\circ}{\alpha} = \gamma \dfrac{\partial \Upsilon}{\partial B} = \sqrt{\dfrac{2}{3}}\gamma, \\ \gamma \geq 0, \quad \Upsilon - \sqrt{\dfrac{2}{3}}\sigma_0 \leq 0 \quad \text{and} \quad \gamma \Upsilon = 0, \end{array} \right. \tag{21}$$

where $\gamma \geq 0$.

5 DETERMINING THE DEFORMED SHAPE FROM EQUILIBRIUM

In this contribution we omit distributed body forces and inertia henceforth.

5.1 Piola formulation

The Piola formulation for the equilibrium is determined by the following boundary value problem

$$\begin{aligned} \mathrm{Div}\boldsymbol{P} &= \boldsymbol{0} \quad \text{in} \quad \mathcal{B}_0, \\ [\boldsymbol{F}\cdot\boldsymbol{S}]\cdot\boldsymbol{N} &= \boldsymbol{t}_0 \quad \text{on} \quad \partial\mathcal{B}_0^t, \\ \boldsymbol{\varphi} &= \overline{\boldsymbol{\varphi}} \quad \text{on} \quad \partial\mathcal{B}_0^{\varphi} \end{aligned} \tag{22}$$

where $\partial\mathcal{B}_0^t$ corresponds to the part of the boundary surface where the Direchlet boundary conditions hold, $\partial\mathcal{B}_0^{\varphi}$ corresponds to the part of the boundary surface where the Neumann boundary conditions hold and we set

$$\partial\mathcal{B}_0 = \mathcal{B}_0^t \bigcup \mathcal{B}_0^{\varphi} \quad \text{with} \quad \mathcal{B}_0^t \bigcap \mathcal{B}_0^{\varphi} = \varnothing. \tag{23}$$

$\boldsymbol{N}$ is defined as a unit vector at $\boldsymbol{X}$ directed along the outward normal to an material surface element $\mathrm{d}A \in \partial\mathcal{B}_0^t$. $\boldsymbol{t}_0$ is the first Piola-Kirchhoff traction vector exerted on $\mathrm{d}A$ with normal $\boldsymbol{N}$. Div denotes the material divergence operator with respect to the material coordinates $\boldsymbol{X}$. Accordingly, the weak form of the given boundary value problem reads, with the test function $\boldsymbol{\eta} = \boldsymbol{0}$ on the boundary surface $\partial\mathcal{B}_0^{\varphi}$,

$$G(\boldsymbol{\varphi}, \boldsymbol{\eta}; \boldsymbol{X}) = \int_{\mathcal{B}_0} [\boldsymbol{F}^t \cdot \nabla_{\boldsymbol{X}}\boldsymbol{\eta}] : \boldsymbol{S}\,\mathrm{d}V - \int_{\partial\mathcal{B}_0} \boldsymbol{\eta}\cdot\boldsymbol{t}_0\,\mathrm{d}A = 0. \tag{24}$$

The above expression is the common virtual work statement with a parameterization of all quantities in the material coordinates $\boldsymbol{X}$. The (symmetric) Piola–Kirchhoff stress is expressed as a functional of $\boldsymbol{\varphi} = \boldsymbol{\varphi}(\boldsymbol{X})$ as

$$\boldsymbol{S} = \boldsymbol{S}(\nabla_{\boldsymbol{X}}\boldsymbol{\varphi}(\boldsymbol{X})). \tag{25}$$

The corresponding linearization (directional derivative) of the weak form in the direction $\Delta\boldsymbol{\varphi}$ at fixed material coordinates $\boldsymbol{X}$, as needed in a Newton type solution scheme, is finally expressed as

$$\frac{d}{d\epsilon} G(\boldsymbol{\varphi} + \epsilon\Delta\boldsymbol{\varphi}, \boldsymbol{\eta}; \boldsymbol{X})|_{\epsilon=0} = \int_{\mathcal{B}_0} \nabla_{\boldsymbol{X}}\boldsymbol{\eta} : \mathbb{A} : \Delta\boldsymbol{F}\,\mathrm{d}V. \tag{26}$$

The fourth-order tangent operator $\mathbb{A}$ decomposes into the material tangent operator $\mathbb{C}$ (see (17)) and a geometrical contribution

$$\mathbb{A} := \frac{\partial[\boldsymbol{F}\cdot\boldsymbol{S}]}{\partial\boldsymbol{F}} = [\boldsymbol{F}\overline{\otimes}\boldsymbol{I}] : \mathbb{C} : [\boldsymbol{F}^t\overline{\otimes}\boldsymbol{I}] + \boldsymbol{i}\overline{\otimes}\boldsymbol{S}. \tag{27}$$

In the above expression $\boldsymbol{I}$ and $\boldsymbol{i}$ denote the material and spatial unit tensors with coefficients δ_{IJ} and δ_{ij}, respectively, $\overline{\otimes}$ denotes a non-standard dyadic product with $[\boldsymbol{A}\overline{\otimes}\boldsymbol{B}]_{IJKL} = A_{IK}B_{JL}$ and $I, J, K, L, i, j = 1\ldots3$.

5.2 Cauchy stress formulation

The equilibrium statement may alternatively be expressed by the following variant of the boundary value problem (Cauchy stress formulation) in terms of spatial description quantities

$$\begin{aligned} \operatorname{div}\boldsymbol{\sigma} &= \mathbf{0} \quad \text{in} \quad \mathcal{B}_t, \\ \boldsymbol{\sigma}\cdot\boldsymbol{n} &= \boldsymbol{t} \quad \text{on} \quad \partial\mathcal{B}_t^t, \\ \boldsymbol{\varphi} &= \overline{\boldsymbol{\varphi}} \quad \text{on} \quad \partial\mathcal{B}_t^{\varphi} \end{aligned} \tag{28}$$

where $\partial\mathcal{B}_t^t$ corresponds to the part of the boundary surface where the Direchlet boundary conditions hold, $\partial\mathcal{B}_t^{\varphi}$ corresponds to the part of the boundary surface where the Neumann boundary conditions hold and we set

$$\partial\mathcal{B}_t = \mathcal{B}_t^t \bigcup \mathcal{B}_t^{\varphi} \quad \text{with} \quad \mathcal{B}_t^t \bigcap \mathcal{B}_t^{\varphi} = \varnothing. \tag{29}$$

div denotes the divergence operator with respect to the spatial coordinates $\boldsymbol{x}$. $\boldsymbol{n}$ is defined as a unit vector at $\boldsymbol{x}$ directed along the outward normal to an spatial surface element $\mathrm{d}a \in \partial\mathcal{B}_t$ and $\boldsymbol{t}$ represents the Cauchy traction vector exerted on $\mathrm{d}a$ with normal $\boldsymbol{n}$. The (symmetric) Cauchy stress $\boldsymbol{\sigma}$ is obtained from the Piola–Kirchhoff stress by a push-forward according to

$$J\boldsymbol{\sigma} = \boldsymbol{F}\cdot\boldsymbol{S}\cdot\boldsymbol{F}^t. \tag{30}$$

Accordingly, the weak form of the given boundary value problem, corresponding to the equilibrium requirement for the spatial configuration, reads with the test function $\boldsymbol{\eta} = \mathbf{0}$ on the boundary surface $\partial\mathcal{B}_t^{\varphi}$

$$g(\boldsymbol{\Phi}, \boldsymbol{\eta}; \boldsymbol{x}) = \int_{\mathcal{B}_t} \nabla_{\boldsymbol{x}}\boldsymbol{\eta} : \boldsymbol{\sigma}\, \mathrm{d}v - \int_{\partial\mathcal{B}_t^t} \boldsymbol{\eta}\cdot\boldsymbol{t}\, \mathrm{d}a = 0. \tag{31}$$

The corresponding linearization (directional derivative) of the weak form in the direction $\Delta\boldsymbol{\Phi}$ at fixed spatial coordinates $\boldsymbol{x}$, as needed in a Newton type solution scheme, is finally expressed as

$$\frac{d}{d\epsilon} g(\boldsymbol{\Phi} + \epsilon\Delta\boldsymbol{\Phi}, \boldsymbol{\eta}; \boldsymbol{x})|_{\epsilon=0} = \int_{\mathcal{B}_t} \nabla_{\boldsymbol{x}}\boldsymbol{\eta} : \mathbb{a} : \Delta\boldsymbol{f}\, \mathrm{d}v. \tag{32}$$

The fourth-order tangent operator $\mathbb{a}$ is depicted as

$$\mathbb{a} := \frac{\partial[j\boldsymbol{F}\cdot\boldsymbol{S}\cdot\boldsymbol{F}^t]}{\partial\boldsymbol{f}} = \boldsymbol{\sigma}\otimes\boldsymbol{F}^t - \boldsymbol{F}\overline{\otimes}\boldsymbol{\sigma} + j\boldsymbol{F}\cdot\left[\frac{1}{2}\mathbb{C} : \frac{\partial\boldsymbol{C}}{\partial\boldsymbol{f}}\right]\cdot\boldsymbol{F}^t - \boldsymbol{\sigma}\underline{\otimes}\boldsymbol{F}. \tag{33}$$

The derivative of the right Cauchy–Green strain is expressed as

$$\frac{\partial\boldsymbol{C}}{\partial\boldsymbol{f}} = -\boldsymbol{F}^t\underline{\otimes}\boldsymbol{C} - \boldsymbol{C}\overline{\otimes}\boldsymbol{F}^t. \tag{34}$$

In the above equations, the non-standard dyadic product $\underline{\otimes}$ is defined by $[\boldsymbol{A}\underline{\otimes}\boldsymbol{B}]_{IJKL} = A_{IL}B_{JK}$ and $I, J, K, L = 1\ldots 3$.

6 DISCRETIZATION

For the finite element solution of the two problems ((24) and (31)) the material solution domain $\mathcal{B}_0$ is discretized into n_{el} elements

$$\mathcal{B}_0 \approx \mathcal{B}_0^h = \bigcup_{e=1}^{n_{el}} \mathcal{B}_0^e. \tag{35}$$

Following the standard isoparametric approach, the geometry is approximated on each element by the following shape functions

$$\boldsymbol{X}^e(\boldsymbol{\xi}) = \sum_{i=1}^{n_{en}} \boldsymbol{X}^{(i)} N^{(i)}(\boldsymbol{\xi}), \qquad \boldsymbol{x}^e(\boldsymbol{\xi}) = \sum_{i=1}^{n_{en}} \boldsymbol{x}^{(i)} N^{(i)}(\boldsymbol{\xi}). \tag{36}$$

Thereby the shape functions $N^{(i)}$ are parameterized by isoparametric coordinates $\boldsymbol{\xi}$ defined on the isoparametric cube $\mathcal{B}^\xi = [-1,1]^3$, whereas n_{en} is the total number of nodes per element, and $\boldsymbol{X}^{(i)}$ and $\boldsymbol{x}^{(i)}$ denote nodal values. Finally, following the Bubnov–Galerkin method the test function is again approximated by the same shape functions $N^{(i)}$

$$\boldsymbol{\eta}^e(\boldsymbol{\xi}) = \sum_{i=1}^{n_{en}} \boldsymbol{\eta}^{(i)} N^{(i)}(\boldsymbol{\xi}). \tag{37}$$

Substituting the finite element approximations into the weak form, we obtain the discrete equilibrium condition as a residual that is expressed at each node (i) (n_{np} is the total number of node points) as

$$\boldsymbol{r}^{(i)} = \boldsymbol{r}^{(i)}_{ext} - \boldsymbol{r}^{(i)}_{int} \qquad \text{with} \qquad i = 1 \dots n_{np}. \tag{38}$$

The contributions to the internal and external nodal forces read

$$\begin{aligned} \boldsymbol{r}^{(i)}_{int} &= \mathop{\mathsf{A}}_{e=1}^{n_{el}} \int_{\mathcal{B}_0^e} [\boldsymbol{F}\cdot\boldsymbol{S}]\cdot\nabla_{\boldsymbol{X}} N^{(i)}\,\mathrm{d}V = \mathop{\mathsf{A}}_{e=1}^{n_{el}} \int_{\mathcal{B}_t^e} \boldsymbol{\sigma}\cdot\nabla_{\boldsymbol{x}} N^{(i)}\,\mathrm{d}v, \\ \boldsymbol{r}^{(i)}_{ext} &= \mathop{\mathsf{A}}_{e=1}^{n_{el}} \int_{\partial\mathcal{B}_0^{e,t}} \boldsymbol{t}_0^e N^{(i)}\,\mathrm{d}A = \mathop{\mathsf{A}}_{e=1}^{n_{el}} \int_{\partial\mathcal{B}_t^{e,t}} \boldsymbol{t}_t^e N^{(i)}\,\mathrm{d}a. \end{aligned} \tag{39}$$

The tangent stiffness matrix $\boldsymbol{k}$ is defined as the Jacobian matrix of the residual (Piola formulation) with respect to the spatial coordinates as

$$\boldsymbol{k}^{(ij)} := -\frac{\partial \boldsymbol{r}^{(i)}}{\partial \boldsymbol{x}^{(j)}} = \mathop{\mathsf{A}}_{e=1}^{n_{el}} \int_{\mathcal{B}_0^e} \nabla_{\boldsymbol{X}} N^{(i)} \overset{2}{\cdot} \mathbb{A}\cdot\nabla_{\boldsymbol{X}} N^{(j)}\,\mathrm{d}V. \tag{40}$$

The tangent stiffness matrix $\boldsymbol{K}$ is defined as the Jacobian matrix of the residual (Cauchy stress formulation) with respect to the material coordinates as

$$\boldsymbol{K}^{(ij)} := -\frac{\partial \boldsymbol{r}^{(i)}}{\partial \boldsymbol{X}^{(j)}} = \mathop{\mathsf{A}}_{e=1}^{n_{el}} \int_{\mathcal{B}_t^e} \nabla_{\boldsymbol{x}} N^{(i)} \overset{2}{\cdot} \mathfrak{a}\cdot\nabla_{\boldsymbol{x}} N^{(j)}\,\mathrm{d}v. \tag{41}$$

In the above expressions $\overset{2}{\cdot}$ denotes contraction with the second index of the corresponding tangent operator.

7 SENSITIVITY ANALYSIS

The aim of the sensitivity analysis is to supply the gradients of the objective function and the constraints with respect to the design variables, which are necessary for the use of gradient-based optimization algorithms [9]. In the following we restrict ourself to unconstraint problems. The objective function is defined as

$$f(\boldsymbol{X}) = \frac{1}{2}[\boldsymbol{x}^{\text{target}} - \boldsymbol{x}^{\text{current}}(\boldsymbol{X})]^2 \rightarrow \min_{\boldsymbol{X}} \tag{42}$$

where the material coordinates $\boldsymbol{X}$ are the design variables. By applying the chain rule, we obtain

$$\frac{\mathrm{d}f(\boldsymbol{X})}{\mathrm{d}\boldsymbol{X}} = \frac{\partial f^{\text{explicite}}}{\partial \boldsymbol{X}} + \frac{\partial f}{\partial \boldsymbol{x}^{\text{current}}} \frac{\mathrm{d}\boldsymbol{x}^{\text{current}}}{\mathrm{d}\boldsymbol{X}}. \tag{43}$$

According to the implicite dependency of the objective function to $\boldsymbol{X}$ we have

$$\frac{\partial f^{\text{explicite}}}{\partial \boldsymbol{X}} = 0 \qquad \text{and then} \qquad \frac{\mathrm{d}f(\boldsymbol{X})}{\mathrm{d}\boldsymbol{X}} = \frac{\partial f}{\partial \boldsymbol{x}^{\text{current}}} \frac{\mathrm{d}\boldsymbol{x}^{\text{current}}}{\mathrm{d}\boldsymbol{X}}. \tag{44}$$

The key for the computation of the Jacobian matrix $\dfrac{\mathrm{d}\boldsymbol{x}^{\text{current}}}{\mathrm{d}\boldsymbol{X}}$ in (44) is the mechanical equilibrium condition [9]

$$\boldsymbol{r}^{\text{current}}(\boldsymbol{X}) = \boldsymbol{r}(\boldsymbol{x}^{\text{current}}(\boldsymbol{X}), \boldsymbol{X}) = \boldsymbol{r}_{ext} - \boldsymbol{r}_{int}(\boldsymbol{x}^{\text{current}}(\boldsymbol{X}), \boldsymbol{X}) = 0. \tag{45}$$

Applying the total differential on the above equation we obtain

$$\frac{\mathrm{d}\boldsymbol{r}^{\text{current}}}{\mathrm{d}\boldsymbol{X}} = \frac{\partial \boldsymbol{r}}{\partial \boldsymbol{X}} + \frac{\partial \boldsymbol{r}}{\partial \boldsymbol{x}^{\text{current}}} \frac{\mathrm{d}\boldsymbol{x}^{\text{current}}}{\mathrm{d}\boldsymbol{X}} = 0. \tag{46}$$

After a rearrangement we deduce

$$\frac{\mathrm{d}\boldsymbol{x}^{\text{current}}}{\mathrm{d}\boldsymbol{X}} = -[\frac{\partial \boldsymbol{r}}{\partial \boldsymbol{x}^{\text{current}}}]^{-1} \frac{\partial \boldsymbol{r}}{\partial \boldsymbol{X}}. \tag{47}$$

Substituting (47) in (44) we obtain

$$\frac{\mathrm{d}f(\boldsymbol{X})}{\mathrm{d}\boldsymbol{X}} = -\frac{\partial f}{\partial \boldsymbol{x}^{\text{current}}}[\frac{\partial \boldsymbol{r}}{\partial \boldsymbol{x}^{\text{current}}}]^{-1} \frac{\partial \boldsymbol{r}}{\partial \boldsymbol{X}} = (\boldsymbol{x}^{\text{target}} - \boldsymbol{x}^{\text{current}})[\frac{\partial \boldsymbol{r}}{\partial \boldsymbol{x}^{\text{current}}}]^{-1} \frac{\partial \boldsymbol{r}}{\partial \boldsymbol{X}}. \tag{48}$$

Considering the form of (40) and (41) we finally obtain

$$\frac{\mathrm{d}f(\boldsymbol{X})}{\mathrm{d}\boldsymbol{X}} = (\boldsymbol{x}^{\text{target}} - \boldsymbol{x}^{\text{current}})[\boldsymbol{k}]^{-1}\boldsymbol{K}.$$

8 NUMERICAL EXAMPLE

As an example we simulate a tension test on a cylinder with an internal hole in 3D. The outer diameter of the cylinder is 20mm, the inner diameter is 10mm and the thickness is 30mm. The base of the cylinder is clamped (red squares on Figure 3). A distributed load F=110kN is applied on the top of the cylinder (red arrows on Figure 3). We consider an anisotropic elastoplastic material with a cubic symmetry and the following properties: E=210000MPa, μ=0.3, E_{55}=60000MPa, h=305MPa, σ_0=180MPa, σ_∞=305MPa and w=15. The domain is discretized using trilinear hexahedral finite elements (50 elements and 120 nodes). Figure 2 shows the deformed shape on which the obtained von Mises stresses are plotted after applying loads and boundary conditions on the computed undeformed sheet (Figure 3). As expected the top outer diameter of the computed undeformed cylinder (Figure 3) became larger and the thickness of the undeformed cylinder has been reduced. The convergence time to the solution is 4 hours 49 min 32s. The L-BFGS algorithm needs 23 iterations to find a minimum less than 10^{-14}.

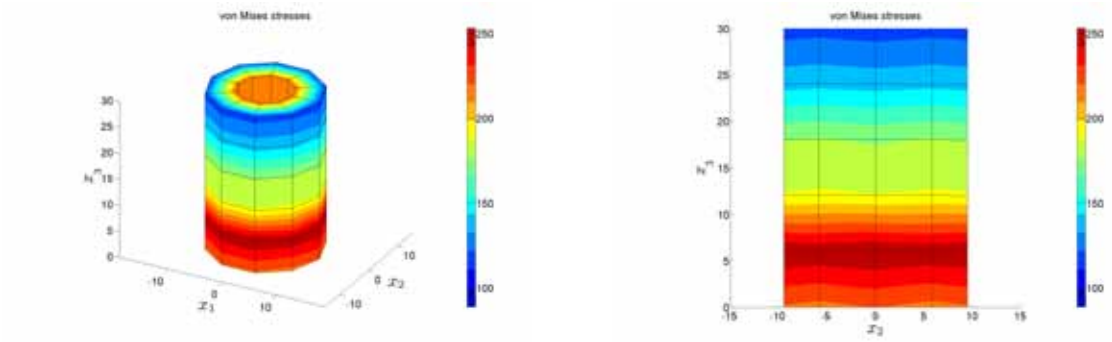

Figure 2: Deformed sheet with von Mises stresses in the final configuration $\mathcal{B}_t$.

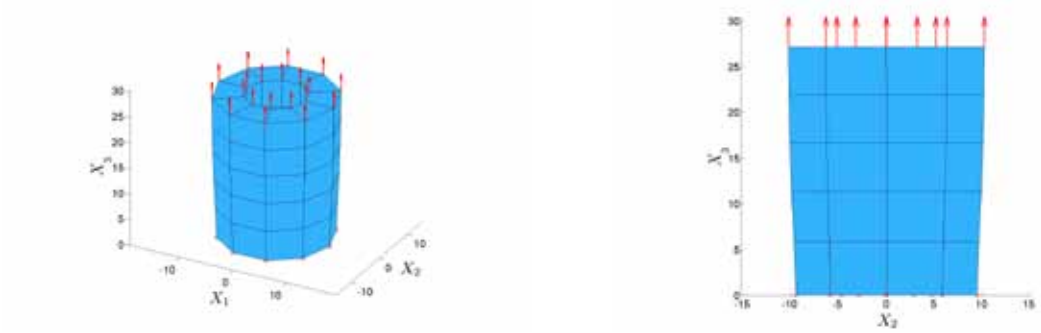

Figure 3: Undeformed sheet in the reference configuration $\mathcal{B}_0$.

9 CONCLUSION

This work presents a three dimensional procedure for anisotropic elastoplastic materials based on shape optimization theory. The aim is the determination of the undeformed shape of a workpiece when knowing its desired deformed shape, the boundary conditions and the loads. A logarithmic strain space formulation is used. A spectral decomposition of the right Cauchy–Green tensor allows a simple evaluation and linearization of the logarithmic strain measure. The node coordinates of the finite element domain, excluding the boundary conditions, are chosen as design variables. The gradient of the objective function needed by the L-BFGS algorithm is computed analytically using a discrete sensitivity analysis approach. A numerical example in nonlinear cubic elastoplasticity illustrates the ability to numerically approximate the undeformed shape. Future research will be conducted on the remeshing of the workpiece during the computation and a regularization will be considered in order to avoid mesh distorsions.

ACKNOWLEDGEMENT

This work was supported by the German Research Foundation (DFG) under the Transregional Collaborative Research Center SFB/TR73: "Manufacturing of Complex Functional Components with Variants by Using a New Sheet Metal Forming Process - Sheet-Bulk Metal Forming".

REFERENCES

[1] S. Germain, M. Scherer and P. Steinmann, *On Inverse Form Finding for Anisotropic Hyperelasticity in Logarithmic Strain Space*. Int. J. of Structural Changes in Solids - Mechanics and Applications, Vol. 2. No.2, pp.1–16 (November 2010).

[2] S. Govindjee and P.A. Mihalic, *Computational methods for inverse finite elastostatics*, Comput. Methods Appl. Mech. Engrg., Vol. 136, pp.47–57 (1996).

[3] S. Germain and P. Steinmann, *On Inverse Form Finding for Anisotropic Elastoplastic Materials*, The 14th International ESAFORM Conference on Material Forming, AIP Conf. Proc., Vol. 1353, pp.1169–1174 (2011).

[4] D.G. Luenberger, *Linear and nonlinear programming*, Addison-Wesley Publishing Company, Second Edition (1984).

[5] A. Srikanth and N. Zabaras, *Shape optimization and preform design in metal forming processes*, Comput. Methods Appl. Mech. Engrg., Vol. 190, pp.1859–1901 (2000).

[6] S. Ganapathysubramanian and N. Zabaras, *Computational design of deformation processes for materials with ductile damage*, Comput. Methods Appl. Mech. Engrg., Vol. 192, pp.147–183 (2003).

[7] S. Acharjee and N. Zabaras, *The continuum sensitivity method for computational design of three-dimensional deformation processes*, Comput. Methods Appl. Mech. Engrg., Vol. 195, pp.6822–6842 (2006).

[8] R. Mahnken and E. Stein, *A unified approach for parameter identification of inelastic material models in the frame of the finite element method*, Comput. Methods. Appl. Mech. Engrg., Vol.136, pp.225-258 (1996).

[9] M. Scherer, R. Denzer and P. Steinmann, *A fictitious energy approach for shape optimization*, Int. J. Numer. Meth. Engng., Vol. 82, pp.269–302 (2010).

[10] L. Fourment and J. L. Chenot, *Optimal design for non-steady-state metal forming processes - I. Shape optimization method*, Int. J. Numer. Meth. Engng., Vol. 39, pp.33–50 (1996).

[11] L. Fourment and J. L. Chenot, *Optimal design for non-steady-state metal forming processes - II. Application of shape optimization in forging*, Int. J. Numer. Meth. Engng., Vol. 39, pp.51–65 (1996).

[12] M. Schmidt, http://www.cs.ubc.ca/schmidtm/Software/minFunc.html (2005).

[13] N. Apel, *Approaches to the Description of Anisotropic Material Behaviour at Finite Elastic and Plastic Deformations - Theory and Numerics*, In: Prof. Dr.-Ing. C. Miehe (Hrsg.): Institut fuer Mechanik (Bauwesen), Lehrsthul I, Universitaet Stuttgart, Dissertation, Bericht Nr.: I-12 (2004).

[14] S. Sutcliffe, *Spectral Decomposition of the Elasticity Tensor*, J. of Applied Mechanics, Vol. 59, 1992, pp.762–773 (1992).

[15] C. Miehe, *Computation of isotropic tensor functions*, Communications in numerical methods in engineering, Vol. 9, pp.889–896 (1993).

[16] C. Miehe and M. Lambrecht, *Algorithms for computation of stresses and elasticity moduli in terms of Seth-Hill's family of generalized strain tensors*, Communications in numerical methods in engineering, Vol. 17, pp.337–353 (2001).

XI International Conference on Computational Plasticity. Fundamentals and Applications
COMPLAS XI
E. Oñate, D.R.J. Owen, D. Peric and B. Suárez (Eds)

A COMPARISON BETWEEN THE TOTAL LAGRANGIAN SCHEME (TLS) AND THE PREDOMINAT TWIN REORIENTATION (PTR) METHODS TO ANALYZE THE TWINNING DEFORMATIONS IN A RATE DEPENDENT CRYSTAL PLASTICITY MODEL

KOHSHIROH KITAYAMA[1,2], RUI P. R. CARDOSO[2] , JEONG WHAN YOON[2,4], TAKESHI UEMOR[3] AND FUSAHITO YOSHIDA[1]

[1]Department of Engineering Mechanics, Hiroshima University, 1-4-1 Kagamiyama, Higashi-Hiroshima, 739-8527, Japan

[2] Centre for Mechanical Technology and Automation, University of Aveiro, 3810-193, Aveiro, Portugal

[3] Faculty of Engineering, Kindai University, 1 Takaya Umenobe, Higashi-Hiroshima, 739-2116, Japan

[4] Faculty of Engineering & Industrial Science, Swinburne University of Technology, Hawthorn, 3122, Australia

Key words: Crystal Plasticity, Predominant Twinning Reorientation, Total Lagrangian Scheme.

Abstract. Materials with Hexagonal-Closed Pack (HCP) crystal structures, as for example the magnesium and titanium alloys, have a small number of active slip systems at room temperature. This fact makes twinning as a predominant deformation mechanism and thus essential for the accurate prediction of plastic deformations and texture evolution. Also, because of the directional property of the twinning mechanism, different responses are obtained for tension and compression, explaining the asymmetric behaviour of HCP metals. As reported by Van Houtte [1], the twinning mechanism is also important for low stacking fault energy Face Centred Cubic (FCC) metals.

In this work, we developed two types of a finite element analysis code, based on the crystal plasticity theory, including twinning as a dominant deformation mechanism. The first twinning model is based on the Predominat Twin Reorientation (PTR) scheme, suggested initially by Van Houtte [1], and the second one is based on the Total Lagragian Scheme (TLS), suggested by Kalidindi [2]. The PTR model has the advantage of being simple and computationally efficient. On the other hand, the TLS model has some advantages when compared with the PTR model that are: i) the possibility of continuously consider the texture's evolution from both slip and twinning deformations; ii) the consideration of slip in the twinned regions.

In the present paper, the two models are compared for a tension and a compression simulation for a FCC material.

1 INTRODUCTION

Materials with Hexagonal-Closed Packed (HCP) crystal structures, as for example the magnesium and titanium alloys, have a small number of active slip systems at room temperature. This fact makes twinning a predominant deformation mechanism, essential for the accurate prediction of plastic deformations and texture evolution. Also, because of the directional property of the twinning mechanism, different responses are obtained for tension and compression, explaining in this way the asymmetric behaviour of HCP materials. As reported by Van Houtte [1], the twinning mechanism is also important for low stacking fault energy Face Centred Cubic (FCC) metals.

To predict the elasto-plastic behaviour of HCP materials, several material models were suggested in the last years. As an example, the Predominant Twin Reorientation (PTR) method was initially proposed by van Houtte [1]. This innovative model evaluates the twinning deformation from the crystal plasticity theory. After reaching a threshold value for the twinning volume fraction, the deformation by twinning causes reorientation of the grains almost instantaneously. This is in contrast with the TLS method that considers twinning reorientation continuously.

To treat both slip, twinning and slip in the twined regions, Kalidindi[2] suggested the Total Lagragian Scheme (TLS). This work is based on the decomposition of the deformation gradient into components related with slip, twinning and slip deformations in the twined regions. The set of nonlinear constitutive equations for slip, twinning and slip-twinning deformation modes are fully linearized for a single Crystal. In this way, a fully implicit time integration schemes can be obtained.

2 KINEMATICS AND CONSTITUTIVE RELATIONS

2.1 Total Lagragian Scheme (TLS)

To consider twinning and slip deformations in the twined area, the decomposition of the velocity gradient tensor should be defined as follows,

$$\mathbf{L}^p = \left(1 - \int \sum_{\beta} \dot{f}^{(\beta)} dt\right) \sum_{\alpha} \dot{\gamma}_s^{(\alpha)} \left(\mathbf{s}_s^{(\alpha)} \otimes \mathbf{m}_s^{(\alpha)}\right) + \sum_{\beta} \dot{f}^{(\beta)} \gamma_{twc}^{(\beta)} \left(\mathbf{s}_t^{(\beta)} \otimes \mathbf{m}_t^{(\beta)}\right) + \sum_{\beta} \int \dot{f}^{(\beta)} dt \sum_{\alpha} \dot{\gamma}_{st}^{(\alpha,\beta)} \left(\mathbf{s}_{st}^{(\alpha,\beta)} \otimes \mathbf{m}_{st}^{(\alpha,\beta)}\right) \tag{1}$$

where,

$\mathbf{L}^p$: plastic velocity gradient

$\dot{f}^{(\square)}$: rate of the volume fraction of the $\square$ twin system

$\dot{\gamma}_s^{(\square)}$: Slip rate of $\square$ slip system

$\mathbf{s}_s^{(\square)}, \mathbf{m}_s^{(\square)}$: Normalized vector of slip direction and normal to slip plane of $\square$ slip system

$\gamma_{twc}^{(\square)}$: Characteristic shear strain of $\square$ twinning system

$\mathbf{s}_t^{(\square)}, \mathbf{m}_t^{(\square)}$: Normalized vector of twinning direction and normal to twinning plane of $\square$ twinning system

$\dot{\gamma}_{st}^{(\square,\square)}$: Slip rate of $\square$ slip system in $\square$ twinning system

$\mathbf{s}_{st}^{(\square,\square)}, \mathbf{m}_{st}^{(\square,\square)}$: Normalized vector of slip direction and normal to slip plane of $\square$ slip system in $\square$ twined area

The first term on the right hand side of eq. (1) means pure slip deformation in the non-twined area. The second term means twinning deformation and the last term means slip deformation in the twined area (Fig.1). The shear slip rate and the volume fraction rate are obtained from the Pan-Rice formula as follows,

$$\dot{\gamma}_s^{(\alpha)} = \dot{\gamma}_0 \,\mathrm{sgn}\left(\tau_s^{(\alpha)}\right)\left|\frac{\tau_s^{(\alpha)}}{g_s^{(\alpha)}}\right|^{\frac{1}{m}} \quad , \quad \dot{f}^{(\beta)} = \frac{\dot{f}_0}{\gamma_{twc}^{(\beta)}}\left(\frac{\tau_t^{(\beta)}}{g_t^{(\beta)}}\right)^{\frac{1}{m}} \tag{2}$$

where $\square, g, \square_0, \dot{f}_0$ and m are the resolved shear stress, the critical resolved shear stress, the reference shear slip rate, the reference twinning rate and the rate sensitivity coefficient, respectively. Because of the asymmetry or polarity of the twinning mechanism, the following constraints should be applied,

$$\dot{f}^{(\beta)} = 0 \quad if\ \tau_t^{(\beta)} \le 0\ or\ \int \sum_{\beta} \dot{f}^{(\beta)} dt \ge f^{threshold} \tag{3}$$

The threshold value for the TLS model means that twinning is finished after the accumulated volume fraction overcomes this value. These constraints for twinning are validated experimental and they explain the asymmetrical stress behavior between tension and compression deformation modes.

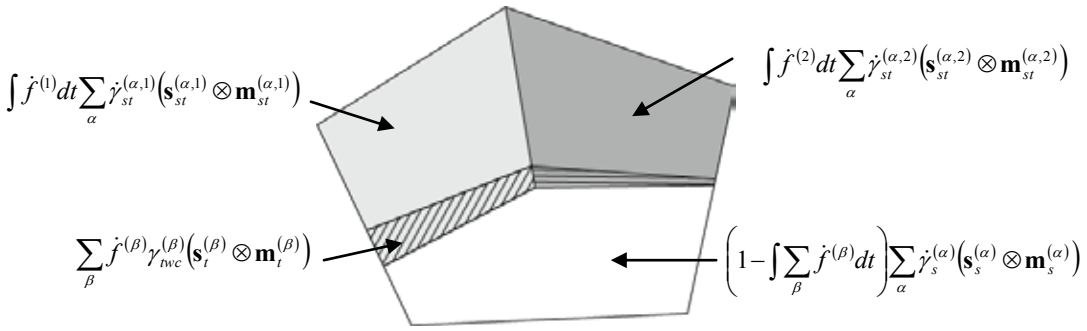

Figure 1: Schematic illustration of decomposition of velocity gradient

In order to obtain the slip shear strain rate at each slip system and the rate of volume fraction for twinning, the rate dependent crystal plasticity approach of Yoon et al. [3] is considered in this work. According to Yoon et al. [3], the Jaumann rate of Kirchhoff stress is defined as,

$$\overset{\nabla^{kirch}}{\tau} = \mathbf{C} : \mathbf{D} - \sum_{\alpha}(1-f)\dot{\gamma}_s^{(\alpha)}\mathbf{R}_s^{(\alpha)} - \sum_{\beta}\dot{f}^{(\beta)}\gamma_{twc}^{(\beta)}\mathbf{R}_t^{(\beta)} - \sum_{\beta} f^{(\beta)} \sum_{\alpha} \dot{\gamma}_{st}^{(\alpha,\beta)}\mathbf{R}_{st}^{(\alpha,\beta)} \tag{4}$$

As can be seen from equation (4), the Jaumann rate of Kirchhoff stress includes contributions from slip, twin and slip deformations in the twinned regions allowing in this way a more accurate prediction for metals with dominant twinning deformation mechanisms.

2.2 Predominat Twin Reorientation (PTR) method

In the Total Lagragian Scheme, the number of deformation systems is very high and, as a result, the CPU cost increases considerably. The PTR model doesn't include slip deformations in the twinned areas. Also, the twinning mechanisms are only effective after a threshold value for the twinning volume fraction is achieved. These facts make the Predominat Twin Reorientation method computationally more effective than TLS method.

In the Predominat Twin Reorientation method, the velocity gradient is decomposed as follows,

$$\mathbf{L}^{p} = \sum_{\alpha} \dot{\gamma}_{s}^{(\alpha)} \left(\mathbf{s}_{s}^{(\alpha)} \otimes \mathbf{m}_{s}^{(\alpha)} \right) + \sum_{\beta} \dot{f}^{(\beta)} \gamma_{twc}^{(\beta)} \left(\mathbf{s}_{t}^{(\beta)} \otimes \mathbf{m}_{t}^{(\beta)} \right) \tag{5}$$

which means that only the deformation by slip and twinning are included in the velocity gradient. In the PTR method, the accumulated volume fraction for twinning is tracked carefully. However, before the accumulated volume fraction reaches a threshold value, the grain is reoriented only by slip deformations. The threshold value is a parameter that can be fitted experimentally. According to Choi et al. [4], this threshold value can be defined as

$$f^{threshold} = C_{th1} + C_{th2} f^{accumulated} \tag{6}$$

where Cth1 and Cth2 are material constants. The accumulated twined volume fractions from all of the twinning systems are compared with this threshold value at each time step. After the accumulated volume fraction reaches the threshold value, the grain is reoriented with respect to the dominant twinning deformation system.

3 RESULTS AND DISCUSSION

3.1 Analysis conditons

We have developed an analysis code based on both PTR and TLS methods for ABAQUS/Standard 6.10-1 user material routine (UMAT). Table 1 shows the material parameters used in the analysis. In the simulations, we used the same material parameters for both slip and twinning deformations. Also, we employed 12 slip systems, {111}<110>, and 12 twinning systems, {111}<112>, for a FCC material. We implemented the hardening rule for both slip and twinning systems described in the below equation,

$$g = H_1 \left(H_2 + \sum_{\alpha} \left| \gamma^{(\alpha)} \right| dt \right)^{H_3} \tag{7}$$

$$\Delta g^{(\alpha)} = \frac{\partial g}{\partial \dot{\gamma}^{(\alpha)}} \sum_{\phi} H_{\alpha\phi} \left| \dot{\gamma}^{(\alpha)} \right|$$

For the TLS model, the threshold value for the twined volume fraction was set to 0.8. For the PTR model, we set the same material parameters Cth1=0.8 and Cth2=0 as for the TLS model for comparison purposes.

Table 1: Material parameters for both PTR and TLS

Elastic component	C_{11}	91538.5 MPa
	C_{12}	39230.8 MPa
	C_{44}	26153.8 MPa
Slip deformation	$H_1.H_2.H_3$	33 MPa, 0.0005,0.285
	Reference slip rate	0.005
	Rate sensitivity component	0.3
Twinning deformation	$H_1.H_2.H_3$	33 MPa, 0.0005,0.285
	Reference twinning rate	0.005
	Rate sensitivity component	0.3

In the TLS model, the number of active deformation systems is very high. To avoid it, we employed another threshold value for the activation of slip deformations in the twined region. If the twined volume fraction doesn't reach the threshold value, we ignore the contribution of the slip deformation in the twined region to the total deformation.

3.2 Results

Fig.2 shows the stress-strain response of both PTR and TLS simulations. According to this result, there is no clear difference between both methods in tension and compression tests for low values of strain. But, for higher values of strain, the difference is more significative, specially for the compression test. Fig.3 shows the total accumulated twined volume fraction obtained from both methods. According to this result, the twined region's evolution is almost the same for both TLS and PTR methods at low strains. In the compression test at high strain, the PTR method's total accumulated twinning volume fraction is clearly higher than the one obtained from the TLS method. Fig. 4 shows the activation ratio of each system. According to this result, the slip deformation in the twined region was activated in the compression test at high strain. This result demonstrates that the slip deformation in the twined region plays an important role if twinning deformation mechanisms occur extensively.

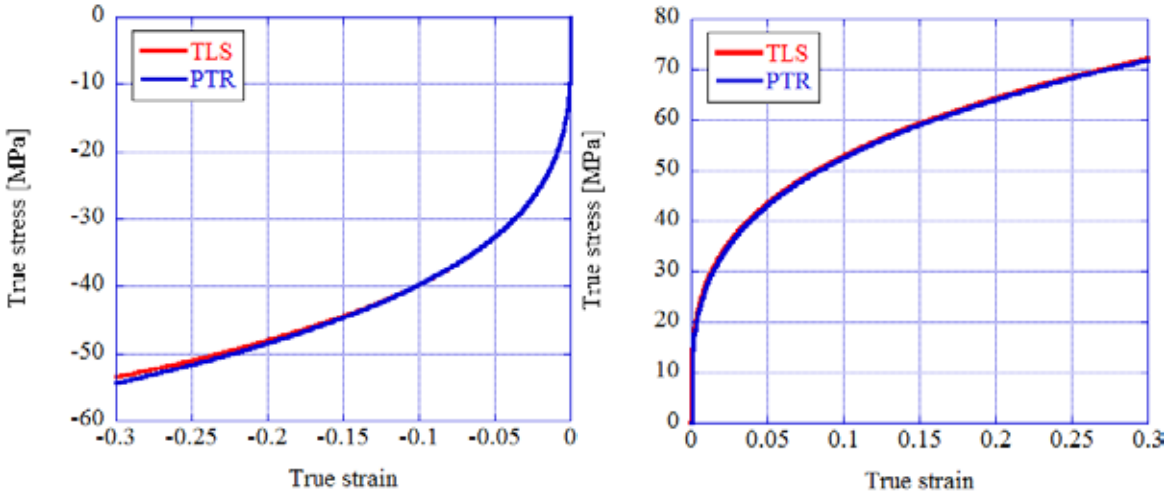

Figure 2: Stress strain reponse of PTR method and TLS

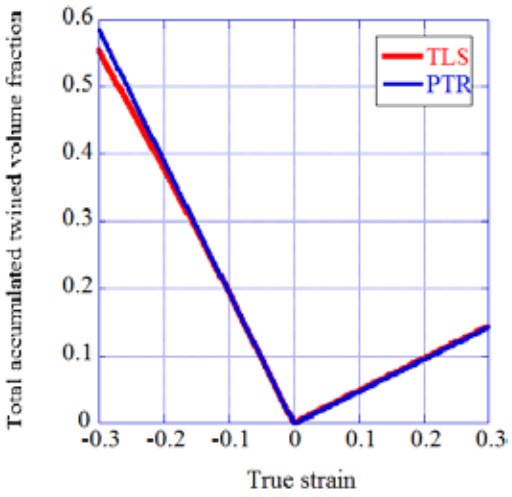

Figure 3: Total accumulated twined volume fraction

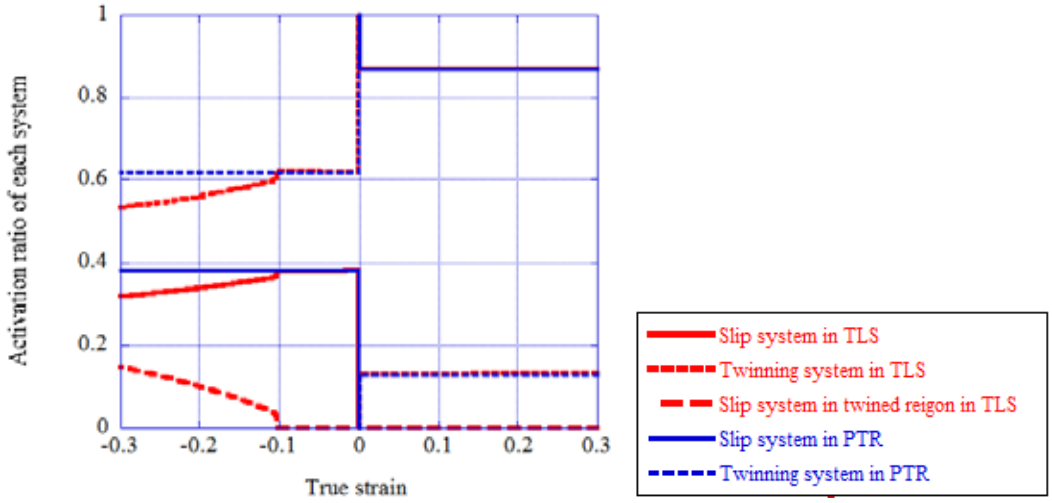

Figure 4: Activation ratio of eash system of PTR method and TLS

4 CONCLUSIONS

- From the crystal plasticity simulations with PTR and TLS twinning models, it can be observed that the TLS compression stress is lower than the one predicted by the PTR model. The main reason for this difference is because the TLS twinning model considers additional slip deformation in the twinned regions.
- The PTR model is simpler, computationally more efficient but less accurate, essentially because of the assumption that twinning mechanism is only active after the twinning volume fraction overcomes a pre-defined threshold value. On the contrary, the TLS model considers twinning effects continuously with more active slip systems, resulting thus in a more accurate prediction for materials with dominant twinning deformation modes.

5 ACKNOWLEDEMENTS

The financial support from Ministério da Ciência e Ensino Superior (FCT- Portugal) under PTDC/EME-TME/109119/2008 and PTDC/EME-TME/105688/2008 is gratefully acknowledged.

REFERENCES

[1] P. Van Houtte, “SIMULATION OF THE ROLLING AND SHEAR TEXTURE OF BRASS BY THE TAYLOR THEORY ADAPTED FOR MECHANICSL TWINNING”, Acta metal., 26, 591-604 (1978).

[2] S. R. Kalidindi, “INCORPORATION OF DEFORMATION TWINNING IN CRYSTAL PLASTICITY MODELS”, J. Mech. Phys. Solids, 46, 267-290 (1998).

[3] J.W. Yoon, F. Barlat, J.J. Gracio and E. Rauch. “Anisotropic strain hardening behavior in simple shear for cube textured aluminum alloy sheets”, Int. J. of Plasticity, 21, 2426-2447 (2005)

[4] S.-H. Choi, D.H. Kim, H.W. Lee and E.J. Shin. “Simulation of texture evolution and macroscopic properties in Mg alloys using the crystal plasticity finite element method”, Mat. Sci. and Eng. A, 527, 1151-1159(2010)

XI International Conference on Computational Plasticity. Fundamentals and Applications
COMPLAS XI
E. Oñate, D.R.J. Owen, D. Peric and B. Suárez (Eds)

DISCONTINUITY LAYOUT OPTIMIZATION IN UPSCALING OF EFFECTIVE STRENGTH PROPERTIES IN MATRIX-INCLUSION MATERIALS

SEBASTIAN BAUER AND ROMAN LACKNER

Material Technology Innsbruck (MTI)
University of Innsbruck
Technikerstraße 13, 6020 Innsbruck, Austria
e-mail: {Sebastian.Bauer,Roman.Lackner}@uibk.ac.at, www.uibk.ac.at/mti/

Key words: Discontinuity layout optimization, limit-analysis, upscaling, homogenisation of strength

Abstract. The prediction of strength properties of engineering materials, which in general are time dependent due to chemical reactions and deterioration processes, plays an important role during manufacturing and construction as well as with regard to durability aspects of materials and structures. On the one hand, the speed of production processes and the quality of products may be significantly increased by improved material performance at early ages. On the other hand, the life time of materials and structures can be enlarged and means of repair and maintenance can be optimized.
For determination of strength properties of composite materials, a multiscale approach is proposed in this paper. For upscaling of strength properties, numerical limit analysis considering discontinuity layout optimization (DLO) is employed. In a first step, DLO is applied to two-phase material systems, with the matrix being represented by node clouds. In this paper, adaptive techniques regarding the spatial distribution of nodes thus the discontinuity generation are introduced in DLO, improving the computational performance of DLO within upscaling of strength properties.

1 MOTIVATION

The prediction of strength properties of engineering materials, which in general are time dependent due to chemical reactions and deterioration processes, plays an important role during manufacturing and construction as well as with regard to durability aspects of materials and structures. On the one hand, the speed of production processes and the quality of products may be significantly increased by improved material performance at early ages. On the other hand, the life time of materials and structures can be enlarged and means of repair and maintenance can be optimized.

For determination of strength properties of composite materials, multiscale approaches are often employed. Several methods for prediction of strength of materials can be found in the literature, among these are e.g. continuum micromechanics [8], the finite-element method (FEM) [9], and numerical limit analysis (LA) [6].
In this work, a two-phase composite material exhibiting a matrix-inclusion morphology is considered. For upscaling of strength properties of these two-phase material systems, numerical limit analysis [1] considering discontinuity layout optimization (DLO) [2] is employed and extended towards adaptive discontinuity layout optimization (ADLO).
First, the methodology of the employed approach is discussed which is followed by the presentation of first results obtained from ADLO. Finally, concluding remarks and an outlook on future work are given.

2 METHODOLOGY

2.1 Fundamental principle of DLO

DLO is a limit-analysis methodology for determining strength properties of materials or collapse loads of structures. Recently, this method was applied to steel frames [3], geotechnical engineering [2], concrete slabs [4] as well as masonry structures [5].
DLO requires the generation of discontinuities, of which every one may be a potential failure discontinuity and, thus, contribute to the failure mode of the material or structure. With (i) the aid of linear programming (LP), (ii) assigning of material properties to every discontinuity (Mohr-Coulomb-type material), and (iii) the definition of boundary conditions, the discontinuities contributing to the failure mechanism are obtained, when the system reaches a total internal energy minimum. This leads to an upper bound (UB) formulation with the following LP problem (see [2]):

$$min\ \lambda \mathbf{f}_L^T \mathbf{d} = -\mathbf{f}_D^T \mathbf{d} + \mathbf{g}^T \mathbf{p},$$

subject to

$$\begin{aligned} \mathbf{B}\mathbf{d} &= \mathbf{0}, \\ \mathbf{f}_L^T \mathbf{d} &= 1, \\ \mathbf{N}\mathbf{p} - \mathbf{d} &= \mathbf{0}, \\ \mathbf{p} &\geq \mathbf{0}. \end{aligned} \tag{1}$$

In Equation (1), $\mathbf{f}_L$ and $\mathbf{f}_D$ are the vector for live and dead load, respectively, $\mathbf{g}$ is a matrix containing length and cohesive shear strength of the discontinuities, $\mathbf{d}$ is the vector of discontinuity displacements, $\mathbf{B}$ is the compatibility matrix, $\mathbf{N}$ is the plastic-flow matrix, and $\mathbf{p}$ is the vector of plastic multipliers.
In the present application, DLO is used to determine the strength properties of matrix-inclusion materials. For this purpose, the dead load will be disregarded.

2.2 Current methodology and limitations

So far, a constant set of regularly distributed nodes serves as basis for the definition of discontinuities. The size of the underlying LP problem increases rapidly for larger number of nodes and discontinuities, which cannot be solved on currently available personal computers with efficiency. Instead of generating all possible discontinuities among the nodes in the model, only discontinuities existing length lower than a certain threshold length are generated within the first step. Within an stepwise calculation, additional discontinuities are gradually added to the model in zones of plastic failure of the structure (see [2]).
For the application of DLO to matrix-inclusion materials, this procedure has certain drawbacks. First, a constant (regular) set of nodes limits the number of possible failure modes to the orientation of the discontinuities. Second, in regions of the material where no discontinuities will fail, the density of the nodes remains constant, thus considering discontinuities not contributing to the failure mechanism. Third, in contrast to homogeneous materials, the node distribution at the boundary between matrix and inclusion is crucial for determination of strength properties, taking into account the influence of interface properties and the strength properties of materials.

2.3 Adaptive discontinuity layout optimization (ADLO)

With the mentioned limitations in mind, a random cloud of nodes giving the layout of the discontinuities is proposed in this paper. Hereby, the generation of discontinuities is performed with a delaundray triangulation [7]. The iterative adaptation of nodes in regions of plastic failure is illustrated in Figure 1 considering additional nodes in triangles and boundary discontinuities adjacent to discontinuities contributing to the failure mechanism. The ADLO algorithm involves the following steps:

- Preprocessing:
  - Node generation
  - Relaxation of nodes
  - Triangulation (discontinuity layout)
  - Discontinuity generation
  - Generation of compatibility matrix $\mathbf{B}$
  - Generation of vector of plastic multipliers $\mathbf{p}$
  - Application of external loads $\mathbf{f}_L$
- Solving LP:
  - Solving LP problem (Equation (1))
- Postprocessing:
  - Location of failed discontinuities
  - Consideration of additional nodes in zones of material failure (see Figure 1)

Figure 2 illustrates the difference between regular (203 nodes, 738 discontinuities) and random node (288 nodes, 738 discontinuities) generation. While the regular node dis-

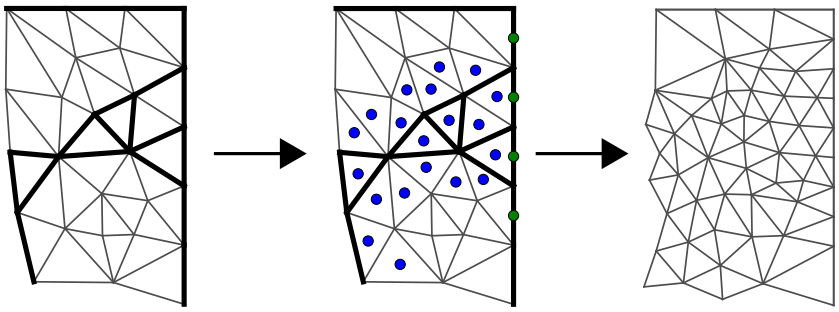

(a) (b) (c)

Figure 1: Illustration of node adaptation in zones of plastic failure: (a) failure mechanism obtained from current layout of discontinuities; (b) introducing additional nodes at the centroid of triangles and at the center of boundary discontinuities adjacent to this failure mechanism; (c) new layout of discontinuities

tribution leads to similar angles, the random layout of discontinuities, with subsequent adaptive refinement steps, yields a larger variety of angles and therefore a larger variety of possible failure modes.

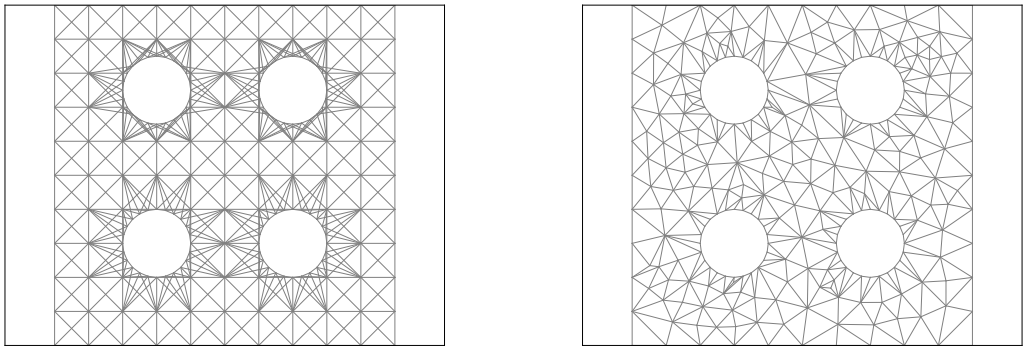

(a) regular distribution of nodes (b) random distribution of nodes

Figure 2: Effect of node arrangement on discontinuity layout

3 Results and Discussion

Process of adaptive node generation

For the demonstration of the adaptive node generation, a porous material with a single circular pore subjected to uniaxial loading is considered. Hereby, symmetry in horizontal and vertical direction are exploited. At the right boundary of the model, the load is applied. In Figure 3, thick lines indicate discontinuities which experience plastic defor-

mation and thereby contribute to material failure. The absolute value of the velocity is illustrated by the width of the lines.

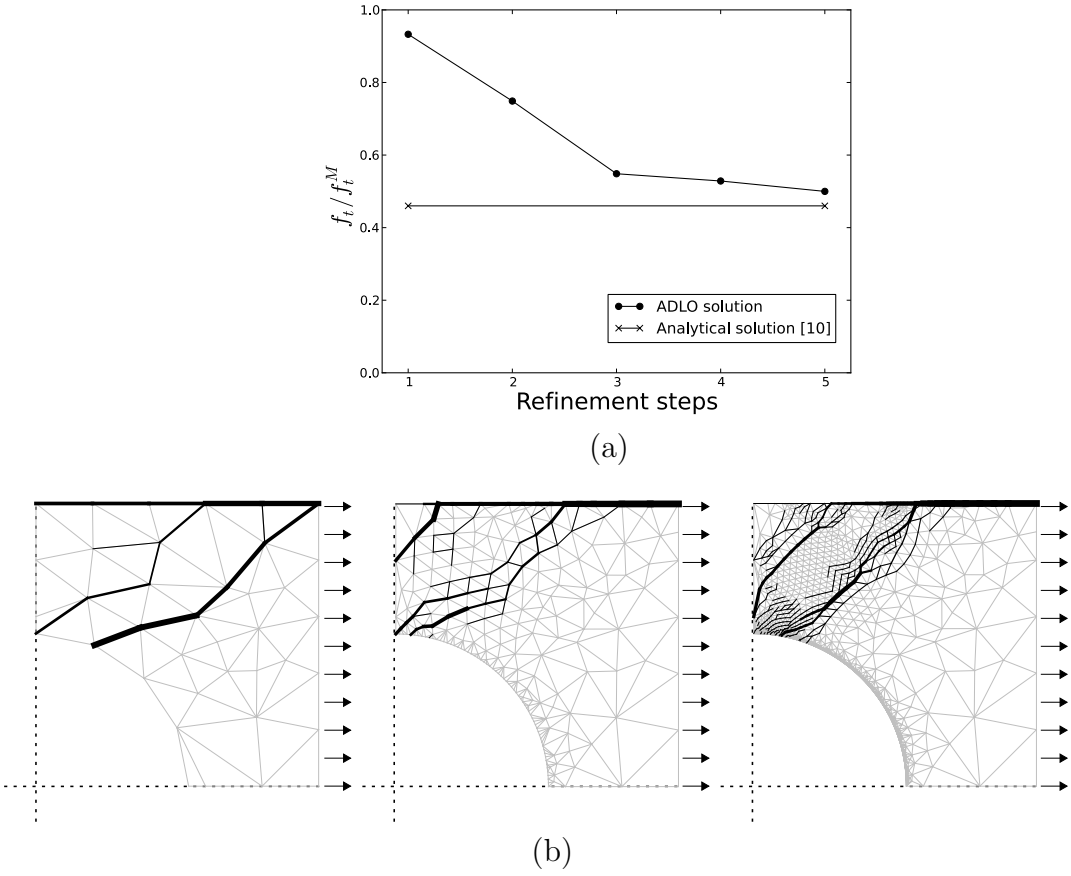

Figure 3: ADLO results obtained for porous material with one single circular pore: (a) material strength related to matrix strength as a function of refinement steps; (b) layout of discontinuities for different refinement steps

The underlying material properties of the matrix phase are chosen as: cohesion = 1, angle of friction = 0, giving an angle of the failure mode of $\pi/4$ and a failure load of $f_t/f_t^M = 0.46$ (see [10]), were f_t^M refers to the tensile strength of the matrix and f_t to the tensile strength of the porous material. Both f_t/f_t^M of 0.49 (obtained for refinement step 5) and the failure mode obtained from ADLO correlate well with the analytical solution.

Porous material with two inclusions

In the second example, a porous material with two circular pores subjected to uniaxial tensile loading is considered. By means of ADLO, the upper bound of the uniaxial tensile

strength is calculated. Hereby, the two pores are rotated with respect to the loading direction from $\beta = 0°$ to $90°$ [6]. Figure 4 illustrates, the effect of β on the results obtained from different sets of nodal distributions. The different results corresponding to one angle in Figure 4(a) reflect the influence of the nodal distribution on the predicted material strength.

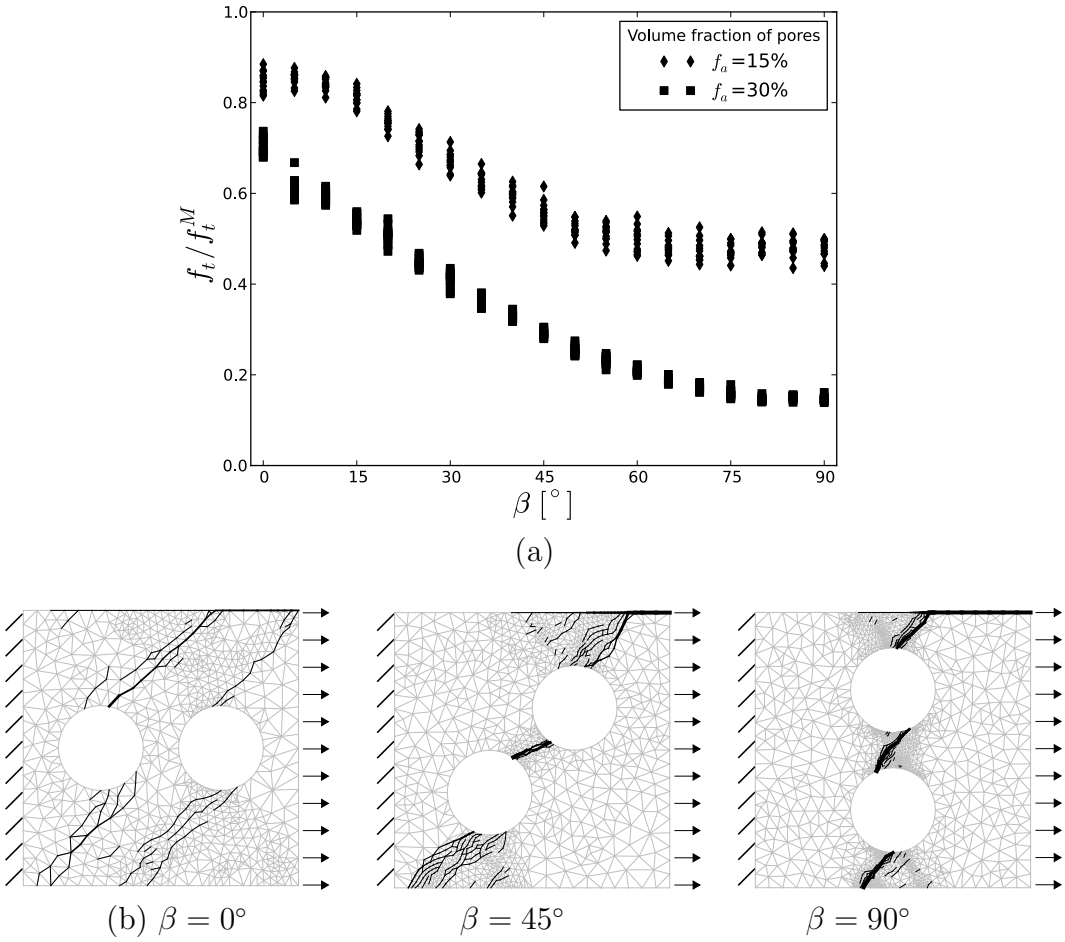

Figure 4: ADLO results obtained for porous material with two circular pores: (a) effect of β on tensile strength and (b) discontinuity layout for three different angles of β (f_a volume fraction of air voids)

3.1 Conclusion and outlook

In this work, an adaptive mode of the discontinuity layout optimization (DLO) for upscaling of strength properties is proposed. Hereby the regular generation of nodes is replaced by random nodal distribution, which is enhanced in an step-wise manner in zones

of plastic failure.
First results showed a good performance of the proposed node adaptation in plastic zones by ADLO. Also the improvement of the solution within increasing number of iteration step was illustrated. An example of a material with two inclusion showed the influence of the arrangement of the pores on the strength properties of the porous material.
Future work will focus on the refinement of the nodal enhancement in plastic zones. Moreover, removal of nodes in regions were no failure occurred shall be included.

3.2 Acknowledgement

The presented results were obtained within the research project "Numerical model for predicting the strength evolution in cemented soil", financially supported by the Austrian Research Promotion Agency (FFG). This support is gratefully acknowledged! The authors thank Klaus Meinhard (Porr Technobau und Umwelt) and Markus Astner (Geosystems Spezialbaustoffe GmbH) for fruitfull discussions and helpful comments throughout the research work.

REFERENCES

[1] Sloan, S.W. *Lower bound limit analysis using finite elements and linear programming.* Journal for Numerical and Analytical Methods in Geomechanics, 12(1), 61-67 (1988).

[2] Smith, C.C. and Gilbert, M. *Application of discontinuity layout optimization to plane plasticity problems.* Proc. Royal Society A, 463(2086), 2461-2484 (2007).

[3] Gilbert, M. and Tyas, A. *Layout optimization of large-scale pin-jointed frames.* Engineering Computations, 20(8), 1044-1064 (2003).

[4] Le, C.V., Gilbert, M. and Askes H. *Limit analysis of plates and slabs using a meshless equilibrium formulation.* International Journal for Numerical Methods in Engineering, 83(13), 1739-1758 (2010).

[5] Gilbert, M., Smith, C.C., and Pritchard, T.J. *Masonry arch analysis using discontinuity layout optimisation.* Proceedings of the Institution of Civil Engineers - Engineering and Computational Mechanics, 163(3), 155-166 (2010).

[6] Füssl, J., Lackner, R. and Mang, H.A. *Failure Modes and Effective Strength of Two-Phase Materials Determined by Means of Numerical Limit Analysis* . Acta Mechanica, 195, 185-202 (2008).

[7] Dale, D., Droettboom, M., Firing, E. and Hunter, J. *Matplotlib Documentation.* Release 1.0.1 (2011).

[8] Maghousa, S. , Dormieux, L. and Barthlmyb, J.F. *Micromechanical approach to the strength properties of frictional geomaterials.* European Journal of Mechanics - A/Solids 28, 179-188 (2009).

[9] Warner, D.H. and Molinari, J.F. *Micromechanical finite element modeling of compressive fracture in confined alumina ceramic.* Acta Materialia 54, 5135-5145 (2006).

[10] Mang, H. and Hofstetter, G. *Festigkeitslehre.* Springer Verlag (2004).

[11] Jones, E., Oliphant, T., Peterson, P. and others *SciPy: Open source scientific tools for Python.* http://www.scipy.org/ (2001-2011).

[12] Makhorin, A. *GPLK: GNU Linear Programming Kit.* http://www.gnu.org/software/glpk/ (2008).

[13] Kroshko, D.L. *OpenOpt* http://openopt.org/ (2011).

XI International Conference on Computational Plasticity. Fundamentals and Applications
COMPLAS XI
E. Oñate, D.R.J. Owen, D. Peric and B. Suárez (Eds)

FINITE-TEMPERATURE NANOVOID DEFORMATION IN COPPER UNDER TENSION

M.P. ARIZA*, M. PONGA*, I. ROMERO† AND M. ORTIZ‡

*Escuela Técnica Superior de Ingeniería
Universidad de Sevilla
Camino de los descubrimientos, s.n. 41092-Sevilla, Spain
e-mail: mpariza@us.es, mponga@us.es, http://grupo.us.es/gingest/

†Escuela Técnica Superior Ingenieros Industriales
Universidad Politécnica de Madrid
José Gutiérrez Abascal, 2, 28006 Madrid, Spain
e-mail: ignacio.romero@upm.es

‡Engineering and Applied Sciences Division
California Institute of Technology
1200 E. California Blvd. Pasadena, 91125 CA, USA
e-mail: ortiz@aero.caltech.edu, http://aero.caltech.edu/ ortiz/index.html

Key words: Quasicontinuum method, Plasticity, Nanovoids, Multiscale modeling

Abstract. Tensile failure of metals often occurs through void nucleation, growth and coalescence. In high-purity metals, void nucleation often operates at the nanoscale and is followed by plastic cavitation when the void attains the critical size for dislocation emission. This work is concerned with the study of plastic nanovoid cavitation in face-centered cubic (fcc) crystals at finite temperature. In particular, the Quasicontinuum (QC) method, suitably extended to finite temperatures (HotQC), is taken as the basis for the analysis. The Quasicontinuum method is a multiscale modeling scheme that seamlessly links continuum and atomistic descriptions. HotQC is a method for systematically coarse-graining atomistic models at finite temperature. We specifically focus on nanovoids in copper single crystals deforming in uniaxial and triaxial tension. The results of the calculations provide a detailed characterization of the cavitation mechanism, including the geometry of the emitted dislocations, the dislocation reaction paths and attendant macroscopic quantities of interest such as the cavitation pressure as a function of triaxiality.

1 INTRODUCTION

In order to understand the mechanical response of materials subject to dynamical loads, the knowledge of the physical and thermodynamical properties of materials is required.Tensile failure of metals often occurs through void nucleation, growth and coalescence. This process, known as spallation, has been the subject of extensive metallurgical investigation [1]. In high purity metals, void nucleation often operates at the nanoscale and is followed by plastic cavitation when the void attains the pressure and temperature dependent critical size for dislocation emission. The voids grow through nucleation and motion of dislocations.

Molecular dynamics (MD) techniques have been used by many authors to understand the mechanical response of materials based on the mechanisms controlling the growth and evolution of nanovoids [2, 14]. However, a correct simulation of plastic phenomena requires the use of very large systems and appropriate boundary conditions, which may result in complex MD models. Computed plastic work during void growth indicate that there is a growth threshold controlled by the stress required to nucleate dislocation activity. The time-scale for complete dynamic fracture ($0.1-1\ \mu s$) is several orders of magnitude beyond the current limitations of molecular dynamics simulations. The study of slower strain rates, in the experimental range, requires much larger system sizes or a special continuum boundary condition. In this sense, multiscale modelling provides an alternative to MD simulation, especially for this type of problems.

The Quasicontinuum method (QC) is a multiscale modelling scheme that seamlessly links continuum and atomistic descriptions. In this paper we are going to use an extension of the static QC theory developed by [4] and subsequently adapted by [5], to systems in thermodynamic equilibrium and non-equilibrium (HotQC) established in [6]. Previous to this work, a number of finite-temperature extensions of QC were proposed within the framework of equilibrium statistical mechanics and thermodynamics [7, 8]. Whereas these formulations are effective for equilibrium problems, systems at uniform temperature, they cannot be applied to systems away from equilibrium. In [6] the probability density function of finding the system in a certain state is directly approximate by recourse to variational mean-filed theory and the *maximum-entropy* formalism. Every atom within the system has its own local statistical parameters, temperature and entropy. Therefore, the net result of the procedure is to define a *non-equilibrium free energy* depending on the positions and temperatures of all atoms. Conveniently, for several interatomic potentials of interest, including Lennard-Jones (LJ) and Embedded-Atom Method (EAM), the non-equilibrium free energy can be computed explicitly up to numerical quadratures, and the result may be regarded as a *temperature-dependent interatomic potential*. This structure greatly facilitates implementation, which is reduced to replacing ordinary interatomic potentials by temperature-dependent ones. It is worth emphasis that at no time in this procedure equilibrium statistical mechanics is invoked to define temperature and entropy or to determine the probability density function of the system. Thus, unlike the conven-

tional temperature and entropy defined in equilibrium thermodynamics and statistical mechanics, the local temperatures and entropies that arise in this theory are parameters that the mean-field probability density function is endowed with. For non-interacting atoms, the local temperatures and entropies do indeed coincide with the equilibrium values of each one of the atoms regarded as an isolated system in thermodynamic equilibrium, which justifies the use of terminology. Likewise, the non-equilibrium free energy is defined formally from the mean-field probability density function and reduces to the equilibrium free energy of the system when the temperature field is uniform.

Although experimental investigations [9, 10] indicate the existence of strong void size effects in plastic deformation of ductile materials with the growth of nanovoids, its experimental quantification remains an open problem. This size effect has been studied by [11] for periodic single crystals under different load conditions using discrete dislocation plasticity combined with a continuum strain gradient crystal plasticity theory. Similar techniques were applied by [12] to simulate the effect of lattice orientation on an isolated crystal with a cylindrical void.

Within the framework of MD, nanosized void growth in single crystal copper at finite temperature and high strain rates have been analyzed extensively. MD simulations of void growth at high strain-rate and room temperature [13], effect of stress triaxiality [14], void coalescence [15] have been carried out using the copper embedded atom method (EAM) potential due to [16]. More recently, [19] have studied the effect of loading orientation and initial void size at finite temperature using LAMMPS code and the EAM potential by [22].

Results are shown for numerical tests according to a non-equilibrium finite temperature problem using QC method. This problem has been studied by many authors, but none of them have included systems outside equilibrium. Also, the purpose of these tests is to understand the nucleation of particular arrangement of atoms around a nanovoid and the evolution of the temperature field in this process.

2 METHODOLOGY

2.1 The Quasicontinuum method (QC)

QC is a method for systematically coarse-graining lattice statics models. The method starts with a small and complete atomistic system around a core defect. Then the rest of the crystal is modelled in the geometry and reducing the configuration space of the crystal trough a judicious application of a finite element-based kinematic constraints. To avoid full lattice sums, only atoms in small clusters, surrounding the representative atoms must be visited for computing the effective out-of-balance forces. Additionally, the selection of representative atoms is performed adaptively based on the local strain of the elements. The tolerance governing the adaptation process is set so that the full atomistic resolution is attained only in the presence of dislocations.

The force among atoms is directly computed by empirical potentials. As in conventional

continuum mechanics, QC permits the direct simulation of systems controlled through the application of remote boundary conditions. Details of the implementation of QC used in the present study and an analysis of convergence of the method may be found in [4].

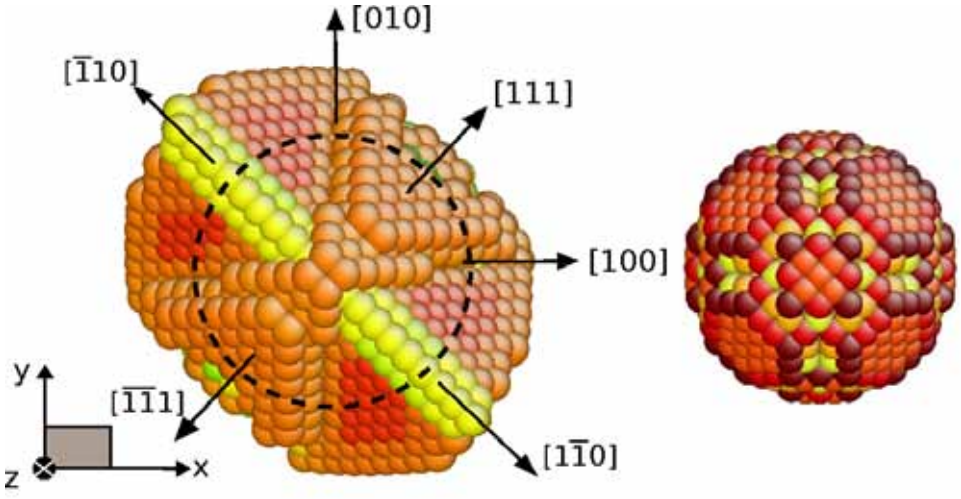

Figure 1: Initial void and incipient dislocation structures for the uniaxial loading simulation (load is applied in the [110] direction).

2.2 Equilibrium and Non-Equilibrium (HotQC)

The QC extension to systems in thermodynamic equilibrium and non-equilibrium (HotQC) was developed in [6] and extended to the study of nanovoids in single crystals for the first time in [20]. This extension is possible by the application of a variational mean-field theory and the maximum-entropy (*max-ent*) formalism. Using this formalism, we can directly approximate the probability density function to find the system in a certain state, not necessarily an equilibrium state. In this model, every representative atom has local state variables akin to temperature, entropy in addition to position, as parameters that determine the local statistics of the atom. Then, the *max-ent* variational principle provides the most likely probability density function within the assumed mean-field class and consistent with all constraints on the systems.

Attention to macroscopic processes that are quasi-static is performed. Under these conditions, the net result of the *max-ent* procedure is to define a non-equilibrium free energy depending on the positions and temperatures of all the atoms. The non-equilibrium free energy is computed explicitly by numerical quadratures and the result may be regarded as a temperature-dependent interatomic potential. The stable configuration of the system is found by minimization of the free energy for a given temperature field.

The next step in the development of the method therefore concerns the computations

of the evolving temperature field. We accomplish this by coupling the free-energy minimization problem to a diffusion form of the energy-balance equation. The proper form of the coupling is suggested by the variational formulation of coupled thermo-mechanics problems proposed in [21].

3 NUMERICAL TEST

We have carried out simulations under uniaxial and triaxial loading, using the empirical embedded-atom (EAM) potential due to Johnson [16]. For the uniaxial case, we consider a computational cell of size $432a_0 \times 432a_0 \times 432a_0$ ($a_o = 0.3615$nm) of copper, containing a total of 120×10^6 atoms. A spherical void of $7.5a_0$ radius is created in the center of the cell with initial full atomistic resolution within a $16a_0 \times 16a_0 \times 16a_0$ region surrounding the void. The initial mesh contains 4052 nodes after removing the atoms from the void. The external load consists of a uniaxial expansion in the [110] direction which provides the simplest dislocation configuration. We prescribe pure dilatational displacements on the external boundary (deformation is increased by steps of 0.2% increments) with the strain rate of $5 \times 10^7\ s^{-1}$. In every step of deformation a new stable equilibrium configuration is obtained by using the Polak-Ribière variant of the non-linear conjugate gradient algorithm. Previously to loading process the sample is allowed to expand isothermally at uniform temperature $T_0 = 300K$. In order to capture all the defects surrounding the void, we implement a routine that automatically remeshes the sample using the second invariant of the deviatoric part of the Lagrangian strain tensor as adaptivity indicator.

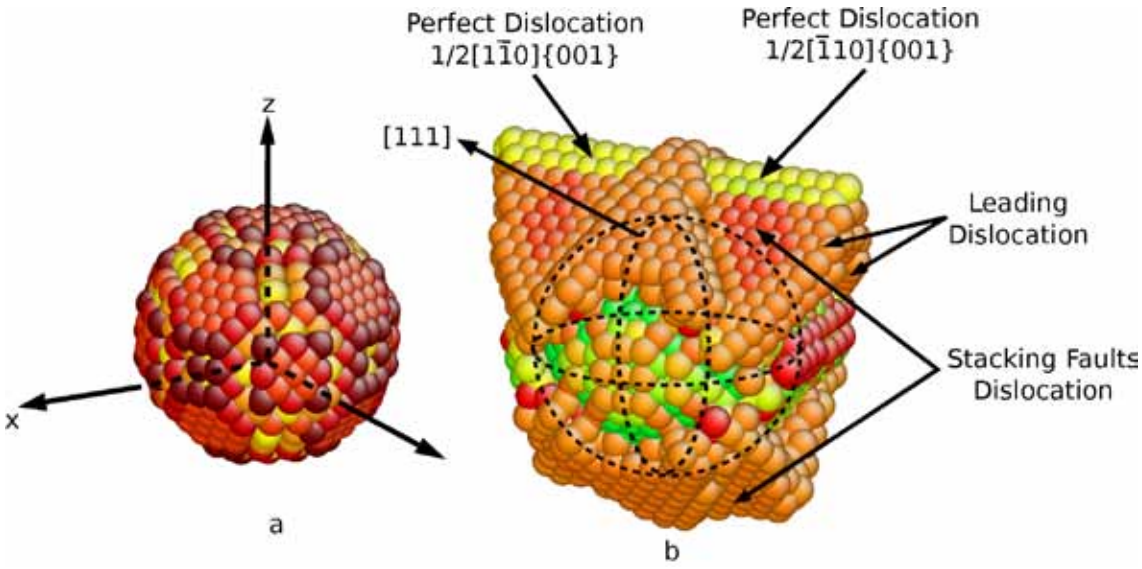

Figure 2: Isometric view of initial void and incipient dislocation structures. Stacking faults in {111} planes, perfect dislocations 1/2[110] in {001} planes and leading dislocations are observed.

During this uniaxial simulation, the void first becomes elongated in the direction of the

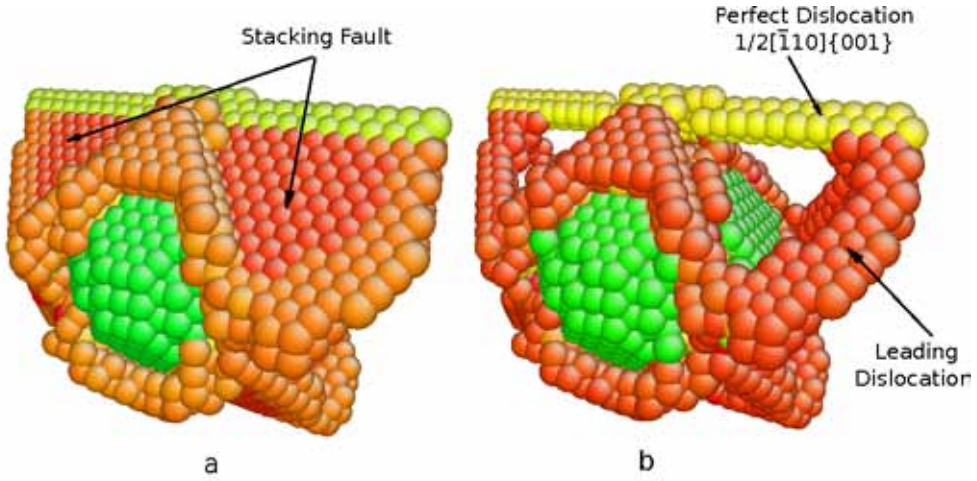

Figure 3: Initial stage of prismatic loop. This emission of dislocations is on the intersecting {111} planes have been predicted by [17]. a) Red atoms belong to stacking faults. b) Prismatic loop initiation (red) and perfect dislocation (yellow).

expansion without dislocation emission. In a second phase, dislocations grow around the surface of the void. The structures of the incipient dislocations are shown in Figs. 1 and 2. The vectors [111] and [$\bar{1}\bar{1}$1] indicate the plane of the stacking fault for FCC crystals. In Fig. 2 it is clearly seen the presence of stacking faults in {111} planes. On the intersection of these {111} planes, perfect dislocations labeled with 1/2[1$\bar{1}$0]{001} and 1/2[$\bar{1}$10]{001} appear. This first result agrees with the simulations presented in [17] and is the first step of the prismatic loop formation described in Fig. 1 in [18].

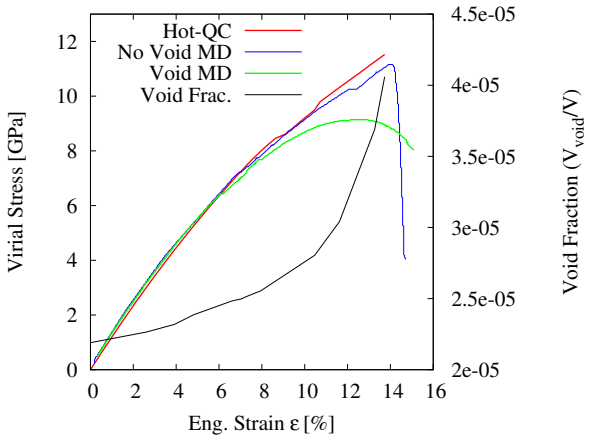

Figure 4: Computed virial stress for the uniaxial loading case compared with molecular dynamics simulations results [14] and normalized void volume expansion V_{void}/V vs deformation ε of the sample.

Once the prismatic loop is formed (Fig. 3), the loop emerges and moves away from

the void and is stopped when it reaches the limit of the atomistic region. This situation is obviously due to the computational mesh used in our simulations. Fig. 4 shows the stress-strain curve for the uniaxial loading simulation. We must note that the plotted strains and stresses are in the loading direction [110]. A comparison has been made with previous MD simulations of uniaxial loading in cooper [14] with loading direction [001] (see Fig. 4). It is noteworthy that the elastic moduli are in good agreement, and the linear regime is approximately up to 8% of deformation for both cases. In the plastic region, there is a difference probably due to the differences in the void size, the potential used and the loading direction, that activates different slip systems. The void fraction is also plotted in Fig. 4. At low deformations, the void grows approximately linearly up to 8% of deformation. Next, the void changes the rate of growth, and the behavior is approximately exponential as indicated by continuum theories.

In order to study the thermoplastic behavior of the material at high strain rates the triaxial loading case is simulated. The void dislocation emission analysis requires more attention, for this reason this study is out of the scope of this work. Additionally, the temperature of the atoms around the void when the fracture occurs is also studied.

Fig. 5 shows the stress-strain curves for the triaxial case. In this curve, a linear regime is observed up to 4% of deformation, followed by a non-linear regime representing the plastic work around the void. At this stage, the fracture mechanism is initiated and dislocations are emitted away from the void. When the deformation reaches the 6%, the void has a drastically change in shape and volume. This process is called *cavitation*. After this point, the stiffness of the sample decreases and the fracture extends all over the sample. The temperature evolution of this process is shown in Fig. 6. In this figure a first linear stage up to 4% of deformation is observed and is identified with the linear stage in the stress-strain curve. Then, up to 6% of deformation, a change in the slope occurs, corresponding to the non-linear stage. When the deformation reaches the cavitation point, and due to the breakage of atomic bounds the temperature increases. Atoms belonging to the void surface and near to the void show a higher increase rate of temperature. As the deformation increases, the temperature oscillates due to the successive breakage of bounds. The temperature of the atoms on the void surface to the void surface is approximately constant after cavitation. In contrast, the temperature of the atoms away from the void increases during the cavitation process.

4 CONCLUSIONS

In this work we have applied an extension of the QC method to study the thermomechanical behavior of a nanovoid under tension in copper. The extension of the Quasicontinuum method to non-equilibrium systems has provided a detailed solution of the forces, deformation, and temperature at every point of the sample, with atomistic resolution close to the defect. In this region, both adiabatic as well as isothermal simulations indicate that a fragile fracture occurs in the material shortly after dislocation structures appear. The multiscale resolution of the Quasicontinuum approach then serves to com-

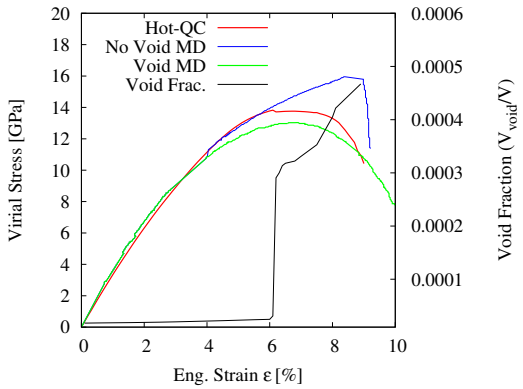

Figure 5: Virial stress for the triaxial loading case compared with MD results [14]. Note that at 6% of deformation the cavitation is reached and the material loss stiffness.

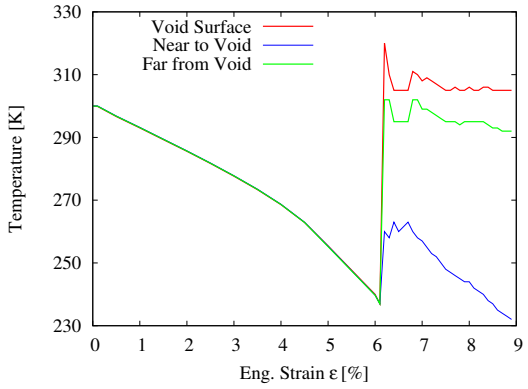

Figure 6: Temperature evolution during void growth process at different positions. Three temperatures are shows: a) void surface b) position close to the void surface and c) position away from the void surface.

pute a macroscopic response of the whole crystal, where fracture is clearly identified.

5 ACKNOWLEDGMENT

We gratefully acknowledge the support of the Ministerio de Ciencia e Innovación of Spain (DPI2009-14305-C02-01/02), the support of the Consejería de Innovación of Junta de Andalucía (P09-TEP-4493) and the support of the Department of Energy National Nuclear Security Administration under Award Number DE-FC52-08NA28613 through Caltechs ASC/PSAAP Center for the Predictive Modeling and Simulation of High Energy Density Dynamic Response of Materials.

REFERENCES

[1] Meyers, M. A. and Aimone, C. T. Dynamic fracture (spalling) of metals. *Progress in Materials Science* (1983) **28**(1):1–96.

[2] Strachan, A., Cagin, T. and Goddard, W.A. Critical behavior in spallation failure of metals. *Physical Review B* (2001) **63**(6).

[3] Seppälä, E.T., Belak, J. and Rudd, R.E. Effect of stress triaxiality on void growth in dynamic fracture of metals: A molecular dynamics study. *Physical Review B* (2004) **69** (13):134101.

[4] Tadmor, E.B., Ortiz, M. and Phillips, R. Quasicontinuum analysis of defects in solids. *Philos. Mag.* (1996) **73**: 1529–1563.

[5] Knap, J. and Ortiz, M. An analysis of the quasicontinuum method. *Journal of the Mechanics and Physics of Solids* (2001) **49**:1899–1923.

[6] Kulkarni, Y., Knap, J. and Ortiz, M. A variational approach to coarse graining of equilibrium and non-equilibrium atomistic description at finite temperature. *Journal of the Mechanics and Physics of Solids* (2008) **56**:1417–1449.

[7] Dupuy, L. M., Tadmor, E. B., Miller, R. E. and Phillips, R. Finite-temperature quasicontinuum: Molecular dynamics without all the atoms. *Physical Review Letters* (2005) **95**:060202–1–060202–4.

[8] Tang, Z., Zhao, H., Li, G. and Aluru, N. R. Finite-temperature quasicontinuum method for multiscale analysis of silicon nanostructures. *Physical Review B* (2006) **74**(6).

[9] Schluter, N., Grimpe, F., Bleck, W. and Dahl, W. Modelling of the damage in ductile steels. *Computational Materials Science* (1996) 7(1-2):27–33.

[10] Khraishi, T.A., Khaleel, M.A. and Zbib, H.M. A parametric-experimental study of void growth in superplastic deformation. *International Journal of Plasticity* (2001) **17**(3):297–315.

[11] Hussein, M. I., Borg, U., Niordson, C. F. and Deshpande, V. S. Plasticity size effects in voided crystals. *Journal of the Mechanics and Physics of Solids* (2008) **56**(1):114–131.

[12] Segurado, J. and LLorca, J. Discrete dislocation dynamics analysis of the effect of lattice orientation on void growth in single crystals. *International Journal of Plasticity* (2010) **26**(6):806–819.

[13] Belak, J. Multi-scale applications to high strain-rate dynamic fracture *Journal of Computer-Aided Materials Design* (2002) **9**: 165-172.

[14] Seppala, E.T., Belak, J. and Rudd, R.E. Effect of stress triaxiality on void growth in dynamic fracture of metals: A molecular dynamics study *Physical Review B* (2004) **69**(13):134101.

[15] Seppala, E.T., Belak, J. and Rudd, R.E. Three-dimensional molecular dynamics simulations of void coalescence during dynamic fracture of ductile metals *Physical Review B* (2005) **71**(6):064112.

[16] Johnson R.A. , Analytic nearest-neighbor model for fcc metals. *Physical Review B* (1988) **37**, 3924-3931.

[17] Traiviratana S., Bringa E.M., Benson D.J. Void growth in metals: Atomistic calculations. *Acta Materialia* **56**:3874-3886.

[18] Bulatov V.V., Wolfer W.G., Kumar M., Shear impossibility: Comments on "Void growth by dislocation emission" and "Void growth in metals: Atomistic calculations". *Scripta Materialia* (2010) **63**:144-147.

[19] Bringa, E.M., Traiviratana, S. and Meyers, M. A. Void initiation in fcc metals: Effect of loading orientation and nanocrystalline effects *Acta Materialia* (2010) **58**(13):4458-4477.

[20] Arevalo, C., Kulkarni, Y., Ariza, M. P., Ortiz, M., Knap, J. and Marian, J. Quasicontinuum method at finite temperature applied to the study of nanovoids evolution in fcc crystals. *Progress in industrial mathematics at ECMI 2008* (2010) **15**:709-714.

[21] Yang, Q., Stainier, L., Ortiz, M., A variational formulation of the coupled thermomechanical boundary-value problem for general dissipative solids. *J. Mech. Phys. Solids* (2006) **54**:401-424.

[22] Mishin, Y., Mehl, M.J., Papaconstantopoulos, D.A., Voter, A.F. and Kress, J.D. Structural stability and lattice defects in copper: Ab initio, tight-binding, and embedded-atom calculations *Physical Review B* (2001) **63**(22).

XI International Conference on Computational Plasticity. Fundamentals and Applications
COMPLAS XI
E. Oñate, D.R.J. Owen, D. Peric and B. Suárez (Eds)

HYDRO-MECHANICAL MODELING OF TWO-PHASE FLUID FLOW IN DEFORMING, PARTIALLY SATURATED POROUS MEDIA WITH PROPAGATING COHESIVE CRACKS USING THE EXTENDED FINITE ELEMENT METHOD

TOKTAM MOHAMMADNEJAD[*] AND AMIR REZA KHOEI[†]

[*]Center of Excellence in Structural and Earthquake Engineering, Department of Civil Engineering
Sharif University of Technology
P.O. Box. 11365-9313, Tehran, Iran
email: toktammd@yahoo.com

[†] Center of Excellence in Structural and Earthquake Engineering, Department of Civil Engineering
Sharif University of Technology
P.O. Box. 11365-9313, Tehran, Iran
email: arkhoei@sharif.edu

Key words: Deformable, fracturing and partially saturated porous medium, Two-phase fluid flow, Cohesive crack propagation, Extended finite element method (XFEM), Fully coupled model.

Abstract. In the present paper, a fully coupled numerical model is developed for the hydro-mechanical analysis of deforming, progressively fracturing porous media interacting with the flow of two immiscible, compressible wetting and non-wetting pore fluids. The governing equations involving the coupled two-phase fluid flow and deformation processes in partially saturated porous media containing cohesive cracks are derived within the framework of the generalized Biot theory. The displacement of the solid phase, the pressure of the wetting phase and the capillary pressure are taken as the primary unknowns of the three-phase formulation. A softening cohesive law is employed to describe the nonlinear behavior of the material in the fracture process zone. In order to account for the flux of the two fluid phases through the fracture faces, the mass balance equation for each flowing fluid inside the fully damaged zone and the cohesive zone is averaged over its cross section. The resulting equations provide mass couplings to the standard equations of the multiphase system. The effect of cracking and therefore change of porosity on the permeability of the damaged zone is also taken into account. To arrive at the discrete equations, the extended finite element method (XFEM) is utilized to discretize the weak form of the balance equations of mass and linear momentum in spatial domain along with the Generalized Newmark scheme for time domain discretization. By exploiting the partition of unity property of finite element shape functions, the evolving cohesive crack is simulated independently of the underlying finite element mesh and without continuous remeshing of the domain as the crack grows by adding enriched degrees of freedom to nodes whose support is bisected by the crack. For the numerical solution, the unconditionally stable direct time-stepping procedure is applied to solve the resulting system of strongly coupled non-linear algebraic equations using a Newton-Raphson iterative procedure. Finally, numerical simulations are presented to demonstrate the capability of the proposed method and the significant influence of the hydro-mechanical coupling between the continuum porous medium and the discontinuity on the results.

1 INTRODUCTION

The present paper focuses on the hydro-mechanical modeling of two-phase fluid flow in deforming, partially saturated porous media containing propagating cohesive cracks, which has practical applications in a broad range of engineering areas. In the literature, the topic of fluid flow in fractured/fracturing porous media has been dealt with in different ways: in [1] a numerical procedure for the simulation of hydraulically-driven fracture propagation in poroelastic materials has been presented combining the finite element method with the finite difference method, in [2] the problem of hydraulic cohesive crack growth in fully saturated porous media has been solved using the finite element method with mesh adaptation, in [3] a hydro-mechanical formulation for fully saturated geomaterials with pre-existing discontinuities has been presented based on the finite element method with zero-thickness interface elements, and the subject of fluid flow in fractured fully saturated systems and in fracturing unsaturated systems with passive gas phase has been treated in [4] and [5], respectively, using the extended finite element method, which is now extended to three-phase porous media. The three-phase numerical model developed here is based upon the mechanics of deformable porous media on the basis of the generalization of the Biot theory in conjunction with the cohesive fracture mechanics, which provides a suitable framework to describe the coupled hydro-mechanical and fracture mechanisms occurring in fracturing, multiphase porous media. In such multiphase systems, the coupling between the flow of the wetting and non-wetting phases in the pore spaces of the continuous porous medium and the discontinuity, the deformation of the solid phase, the fluid exchange between the discontinuity and the surrounding porous medium and the possible development of the discontinuity across which the cohesive tractions are transmitted is usually strong, which demands the fully coupled treatment of the problem. In the formulation presented herein, all these components are brought together to thoroughly simulate the deforming, partially saturated porous medium behavior in the presence of geomechanical discontinuities, thus exhibiting fluid flow, deformation and fracture processes properly.

The extended finite element method combined with the cohesive crack model yields an efficient approach to simulate the cohesive crack propagation [6-8]. In fracturing, partially saturated porous media, the crack growth occurs as the progressive decay of the cohesive tractions transferred across the fracture process zone and the imposition of the mean pore pressure onto the crack faces by means of the pore fluids within the crack. The tractions acting on the fracture faces give rise to the mechanical coupling between the fracture and the medium surrounding the fracture. Besides, the flux of the two fluid phases through the fracture borders leads to the mass transfer coupling, which is a subject of great interest in hydraulic fracturing.

2 THE PHYSICAL MODEL

The pores of the solid skeleton in the partially saturated porous medium are assumed to be filled up partly with water (w) and partly with gas (g). Thus, degrees of saturation of the liquid phase S_w and the gaseous phase S_g always sum to unity, i.e. $S_w + S_g = 1$. The capillary pressure between the two fluid phases is defined as $p_c = p_g - p_w$.

The stress relation is expressed by introducing the concept of the modified effective stress

$$\boldsymbol{\sigma}'' = \boldsymbol{\sigma} + \alpha \mathbf{m} p \tag{1}$$

in which $\boldsymbol{\sigma}$ is the total stress vector, $\boldsymbol{\sigma}''$ is the modified effective stress vector, $\mathbf{m}$ is the identity vector, p denotes the mean pore pressure applied by the porous fluids on the solid skeleton, which

is given by the averaging technique $p = S_w p_w + S_g p_g$, and α is the Biot constant. The constitutive equation of the solid phase in the continuum medium surrounding the crack is expressed by an incrementally linear modified effective stress-strain relationship

$$\mathrm{d}\boldsymbol{\sigma}'' = \mathbf{D}\,\mathrm{d}\boldsymbol{\varepsilon} \tag{2}$$

where **D** represents the tangential constitutive matrix of the continuum.

The non-linear behavior of the fracturing material in the cohesive zone is governed by a traction-separation law relating the cohesive tractions to the relative displacements

$$\mathbf{t}_d = \mathbf{t}_d(\llbracket \mathbf{u} \rrbracket) \tag{3}$$

where $\mathbf{t}_d$ is the cohesive traction transmitted across the fracture process zone and $\llbracket \mathbf{u} \rrbracket$ is defined as the relative displacement vector at the discontinuity. In quasi-brittle materials, as soon as the failure limit of the material is exceeded, the cohesive zone develops in which the material exhibits a softening behavior. Linearization of the cohesive relation (3) results in

$$\mathrm{d}\mathbf{t}_d = \mathbf{T}\,\mathrm{d}\llbracket \mathbf{u} \rrbracket \tag{4}$$

in which **T** represents the tangential modulus matrix of the discontinuity to be used in the iterative solution procedure, obtained from the relation $\mathbf{T} = \partial \mathbf{t}_d / \partial \llbracket \mathbf{u} \rrbracket$.

3 GOVERNING EQUATIONS

3.1 Strong form

In what follows, the equations specifying the problem are written in terms of the displacement of the solid phase, the pressure of the wetting phase and the capillary pressure. For a more detailed presentation of the governing equations see Ref. [9].

The linear momentum balance equation for the porous medium can be written as

$$\boldsymbol{\nabla} . \boldsymbol{\sigma} + \rho \mathbf{b} - \rho \ddot{\mathbf{u}} = \mathbf{0} \tag{5}$$

where $\ddot{\mathbf{u}}$ is the acceleration vector of the solid phase, **b** is the body force vector, ρ is the average density of the multiphase system defined as $\rho = (1-n)\rho_s + n\left(S_w \rho_w + S_g \rho_g\right)$, in which n stands for the porosity of the porous medium.

The continuity equations for the flow of wetting and non-wetting phase fluids through the deforming, isothermal porous medium can be written as

$$\begin{aligned} \frac{1}{Q_{ww}}\,\dot{p}_w + \frac{1}{Q_{wc}}\,\dot{p}_c + \alpha\,\boldsymbol{\nabla}.\dot{\mathbf{u}} + \boldsymbol{\nabla}.\dot{\mathbf{w}}_w + \boldsymbol{\nabla}.\dot{\mathbf{w}}_g = 0 \\ \frac{1}{Q_{cw}}\,\dot{p}_w + \frac{1}{Q_{cc}}\,\dot{p}_c + \alpha\,S_g\boldsymbol{\nabla}.\dot{\mathbf{u}} + \boldsymbol{\nabla}.\dot{\mathbf{w}}_g = 0 \end{aligned} \tag{6}$$

where $\dot{\mathbf{u}}$ is the solid velocity vector, and $\dot{\mathbf{w}}_w$ and $\dot{\mathbf{w}}_g$ are the Darcy velocity vectors of the two flowing fluids. The compressibility coefficients are defined as

$$\begin{aligned} \frac{1}{Q_{ww}} &= \frac{\alpha - n}{K_s} + \frac{nS_w}{K_w} + \frac{nS_g}{K_g} \\ \frac{1}{Q_{wc}} &= \frac{\alpha - n}{K_s}\left((1 - S_w) - p_c \frac{\partial S_w}{\partial p_c}\right) + \frac{nS_g}{K_g} \end{aligned} \tag{7}$$

$$\frac{1}{Q_{cw}} = \frac{(\alpha - n)S_g}{K_s} + \frac{nS_g}{K_g}$$

$$\frac{1}{Q_{cc}} = \frac{(\alpha - n)S_g}{K_s}\left((1 - S_w) - p_c\frac{\partial S_w}{\partial p_c}\right) - n\frac{\partial S_w}{\partial p_c} + \frac{nS_g}{K_g}$$

in which K_w and K_g are the bulk moduli of the porous fluids.

The Darcy relation for pore fluid flow can be written as

$$\dot{\mathbf{w}}_\alpha = \mathbf{k}_\alpha[-\boldsymbol{\nabla} p_\alpha + \rho_\alpha(\mathbf{b} - \ddot{\mathbf{u}})] \qquad \alpha = w, g \tag{8}$$

where $\mathbf{k}_w$ and $\mathbf{k}_g$ are the permeability matrices of the porous medium to the pore fluids, which are generally evaluated by the following expression

$$\mathbf{k}_\alpha = \mathbf{k}\frac{k_{r\alpha}}{\mu_\alpha} \qquad \alpha = w, g \tag{9}$$

in which $\mathbf{k}$ denotes the intrinsic permeability matrix of the porous medium, which is simply replaced by a scalar value k for the isotropic medium, $k_{r\alpha}$ is the relative permeability coefficient of the fluid, and μ_α denotes the dynamic viscosity of the fluid.

The permeability inside the fracture, i.e. the fully damaged zone and the micro-cracked zone, is strongly influenced by the change in the pore spaces of the solid skeleton as a result of cracking and micro-cracking processes. To this end, the pore fluid flow within the fracture is modeled by means of Darcy law with porosity dependent permeability, in which the dependence of the fracture permeability on the porosity is incorporated into the formulation via the coefficient k_{n_d}

$$\mathbf{k}_{\alpha d} = \mathbf{k}\frac{k_{n_d}k_{r\alpha}}{\mu_\alpha} \qquad \alpha = w, g \tag{10}$$

The following relation based on Ref. [10] is assigned to k_{n_d}

$$k_{n_d}(n_d) = 10^{\delta_{n_d}}, \qquad \delta_{n_d} = \frac{6(n_d - n)}{0.3 - 0.4n} \tag{11}$$

where n_d and n are the current and the initial porosity of the fracture material, respectively.

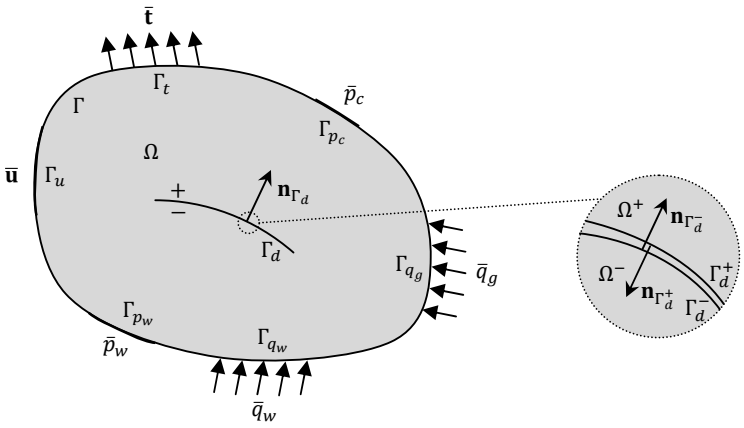

Figure 1: Boundary conditions of the body Ω involving the geomechanical discontinuity Γ_d

3.2 Weak form

To develop the equations, the two-dimensional domain Ω bounded by the boundary Γ is considered. As depicted in Fig. 1, the domain contains the geomechanical discontinuity Γ_d.

The weak form of the equilibrium equation for the multiphase system is given by

$$\int_{\Omega} \boldsymbol{\nabla}^{s}\boldsymbol{\eta} : \boldsymbol{\sigma}\, d\Omega + \int_{\Omega} \rho\boldsymbol{\eta}.\ddot{\mathbf{u}}\, d\Omega + \int_{\Gamma_d} [\![\boldsymbol{\eta}]\!].\left(\mathbf{t}_d - \alpha p\mathbf{n}_{\Gamma_d}\right) d\Gamma = \int_{\Gamma_t} \boldsymbol{\eta}.\bar{\mathbf{t}}\, d\Gamma + \int_{\Omega} \rho\boldsymbol{\eta}.\mathbf{b}\, d\Omega \tag{12}$$

which must hold for any kinematically admissible test function for the solid phase displacement $\boldsymbol{\eta}$, satisfying the homogenized essential boundary condition.

Incorporating Darcy law, the weak form of the continuity equation of flow for each of the fluid phases is given by

$$\begin{aligned}
&\int_{\Omega} \zeta_w \frac{1}{Q_{ww}}\dot{p}_w\, d\Omega + \int_{\Omega} \zeta_w \frac{1}{Q_{wc}}\dot{p}_c\, d\Omega + \int_{\Omega} \zeta_w \alpha\, \boldsymbol{\nabla}.\dot{\mathbf{u}}\, d\Omega + \int_{\Omega} \left(\mathrm{k}_w + \mathrm{k}_g\right)\boldsymbol{\nabla}\zeta_w\,.\boldsymbol{\nabla}p_w\, d\Omega \\
&\quad + \int_{\Omega} \mathrm{k}_g\, \boldsymbol{\nabla}\zeta_w\,.\boldsymbol{\nabla}p_c\, d\Omega + \int_{\Omega} \left(\mathrm{k}_w\rho_w + \mathrm{k}_g\rho_g\right)\boldsymbol{\nabla}\zeta_w\,.\ddot{\mathbf{u}}\, d\Omega - \int_{\Gamma_d} \zeta_w\left(q_{wd} + q_{gd}\right) d\Gamma \\
&\quad = \int_{\Omega} \left(\mathrm{k}_w\rho_w + \mathrm{k}_g\rho_g\right)\boldsymbol{\nabla}\zeta_w.\mathbf{b}\, d\Omega - \int_{\Gamma_{q_w}} \zeta_w\, \bar{q}_w\, d\Gamma - \int_{\Gamma_{q_g}\cap\,\Gamma_{q_w}} \zeta_w\, \bar{q}_g\, d\Gamma \\
&\quad - \int_{\Gamma_{p_c}\cap\,\Gamma_{q_w}} \zeta_w\, \dot{\mathbf{w}}_g.\mathbf{n}_{\Gamma}\, d\Gamma \\
&\int_{\Omega} \zeta_c \frac{1}{Q_{cw}}\dot{p}_w\, d\Omega + \int_{\Omega} \zeta_c \frac{1}{Q_{cc}}\dot{p}_c\, d\Omega + \int_{\Omega} \zeta_c \alpha\,(1 - S_w)\,\boldsymbol{\nabla}.\dot{\mathbf{u}}\, d\Omega + \int_{\Omega} \mathrm{k}_g\, \boldsymbol{\nabla}\zeta_c\,.\boldsymbol{\nabla}p_w\, d\Omega \\
&\quad + \int_{\Omega} \mathrm{k}_g\, \boldsymbol{\nabla}\zeta_c\,.\boldsymbol{\nabla}p_c\, d\Omega + \int_{\Omega} \mathrm{k}_g\rho_g\, \boldsymbol{\nabla}\zeta_c\,.\ddot{\mathbf{u}}\, d\Omega - \int_{\Gamma_d} \zeta_c\, q_{gd}\, d\Gamma \\
&\quad = \int_{\Omega} \mathrm{k}_g\rho_g\, \boldsymbol{\nabla}\zeta_c.\mathbf{b}\, d\Omega - \int_{\Gamma_{q_g}} \zeta_c\, \bar{q}_g\, d\Gamma
\end{aligned} \tag{13}$$

which must hold for any kinematically admissible test function for the wetting phase pressure ζ_w and the capillary pressure ζ_c, respectively, each disappearing on the boundary portion where the corresponding essential boundary condition is imposed. q_{wd} and q_{gd} are the leakage fluxes of the two pore fluids along the fracture toward the surrounding porous medium, which implies that there exists a discontinuity in the normal flow of the pore fluids across Γ_d. In order to arrive at a relation for the leakage flux of the pore fluids into the medium surrounding the discontinuity, the flow continuity equation for each flowing fluid inside the fracture is averaged over its cross section. Following this, the leakage terms appearing in the weak form of the wetting and non-wetting fluid flow continuity equations of the continuum medium are respectively obtained as

$$\begin{aligned}
q_{wd} + q_{gd} = &-2h\frac{1}{Q_{ww}}\,\dot{p}_w - 2h\frac{1}{Q_{wc}}\,\dot{p}_c - 2h\alpha\,\langle\frac{\partial \dot{u}_{x'}}{\partial x'}\rangle - \alpha\,[\![\dot{u}_{y'}]\!] \\
&-2h\,\frac{\partial}{\partial x'}\left(k_{wd}\left[-\frac{\partial p_w}{\partial x'} + \rho_w(b_{x'} - \langle\ddot{u}_{x'}\rangle)\right]\right)
\end{aligned} \tag{14}$$

$$-2h\ \frac{\partial}{\partial x'}\left(k_{gd}\left[-\frac{\partial p_w}{\partial x'}-\frac{\partial p_c}{\partial x'}+\rho_g(b_{x'}-\langle\ddot{u}_{x'}\rangle)\right]\right)$$

$$q_{gd}=-2h\frac{1}{Q_{cw}}\ \dot{p}_w-2h\frac{1}{Q_{cc}}\ \dot{p}_c-2h\alpha(1-S_w)\left\langle\frac{\partial \dot{u}_{x'}}{\partial x'}\right\rangle-\alpha(1-S_w)\left[\!\left[\dot{u}_{y'}\right]\!\right] \tag{15}$$
$$-2h\ \frac{\partial}{\partial x'}\left(k_{gd}\left[-\frac{\partial p_w}{\partial x'}-\frac{\partial p_c}{\partial x'}+\rho_g(b_{x'}-\langle\ddot{u}_{x'}\rangle)\right]\right)$$

in which the notation $[\![*]\!]=*^{+}-*^{-}$ represents the difference between the corresponding values at the two fracture faces and $\langle*\rangle=(*^{+}+*^{-})/2$ is specified as the average of the corresponding values at the discontinuity faces.

4 DISCRETIZATION OF THE GOVERNING EQUATIONS AND SOLUTION PROCEDURE FOR THE DISCRETIZED SYSTEM

In order to account for the displacement jump across the fracture, the displacement field should be discontinuous. In addition, to take into account each fluid flow jump normal to the fracture, it is required that the water pressure and also the capillary pressure field be continuous, while their corresponding gradient normal to the fracture be discontinuous.

Thus, the extended finite element approximation of the displacement field is written as

$$\mathbf{u}^h(\mathbf{x},t)=\sum_{I\in\mathcal{N}}N_{uI}(\mathbf{x})\,\mathbf{u}_I(t)+\sum_{I\in\mathcal{N}^{enr}}N_{uI}(\mathbf{x})\frac{1}{2}\left(H_{\Gamma_d}(\mathbf{x})-H_{\Gamma_d}(\mathbf{x}_I)\right)\,\tilde{\mathbf{u}}_I(t) \tag{16}$$

where $N_{uI}(\mathbf{x})$ is the standard finite element shape function of node I, $\mathcal{N}$ is the set of all nodes in the mesh, and $\mathcal{N}^{enr}$ is the set of enriched nodes defined as the set of nodes in the mesh whose support is bisected by the discontinuity. To ensure that the displacement jump is zero at the discontinuity tip, the nodes belonging to the element edge on which the discontinuity tip lies are not enriched. $\mathbf{u}_I(t)$ and $\tilde{\mathbf{u}}_I(\mathrm{t})$ are the standard and enriched degrees of freedom, respectively. The discontinuous function $H_{\Gamma_d}(\mathbf{x})$ is taken as the sign function centered on the line of the discontinuity Γ_d, i.e. $H_{\Gamma_d}(\mathbf{x})=\mathrm{sign}\big(\emptyset(\mathbf{x})\big)$, in which $\emptyset(\mathbf{x})$ is the level set function.

Symbolically, the enriched finite element approximation of the displacement field in Eq. (16) can be written in the following form

$$\mathbf{u}^h(\mathbf{x},t)=\mathbf{N}_u(\mathbf{x})\,\mathbf{U}(t)+\mathbf{N}_u^{enr}(\mathbf{x})\,\tilde{\mathbf{U}}(t) \tag{17}$$

in which $\mathbf{N}_u(\mathbf{x})$ is the matrix of the standard shape functions, and $\mathbf{N}_u^{enr}(\mathbf{x})$ is referred to as the matrix of the enriched shape functions. $\mathbf{U}(t)$ is the vector of the standard displacement degrees of freedom, and $\tilde{\mathbf{U}}(t)$ is the vector of the enriched displacement degrees of freedom.

The water pressure as well as the capillary pressure is approximated as

$$p_\alpha^h(\mathbf{x},t)=\sum_{I\in\mathcal{N}}N_{p_\alpha I}(\mathbf{x})\,p_{\alpha I}(t)+\sum_{I\in\mathcal{N}^{enr}}N_{p_\alpha I}(\mathbf{x})\left(D_{\Gamma_d}(\mathbf{x})-D_{\Gamma_d}(\mathbf{x}_I)\right)R(\mathbf{x})\,\tilde{p}_{\alpha I}(t) \tag{18}$$

where $N_{p_\alpha I}(\mathbf{x})$ are the standard finite element shape functions. Nodes in $\mathcal{N}^{enr}$ have their support bisected by the discontinuity. It is essential that the leakage flux vanish at the discontinuity tip. This is assured by requiring that the nodes on the element edge with which the discontinuity tip coincides not be enriched. $p_{\alpha I}(t)$ and $\tilde{p}_{\alpha I}(t)$ are the standard and enriched pressure degrees of freedom, respectively. $D_{\Gamma_d}(\mathbf{x})$ is the distance function, i.e. $D_{\Gamma_d}(\mathbf{x})=|\emptyset(\mathbf{x})|$. $R(\mathbf{x})$ is a weight

function with compact support given by

$$R(\mathbf{x}) = \sum_{I \in \mathcal{N}^{enr}} N_{p_\alpha I}(\mathbf{x}) \quad \alpha = w, c \tag{19}$$

It is noted that the multiplication with $R(\mathbf{x})$ causes the weighted enrichment function to vary continuously between the standard enrichment function and zero in the elements whose some nodes are in the enriched nodal set, reproducing the standard enrichment function in the elements whose all nodes are in the enriched nodal set. The enriched formulation in Eq. (18) has the form of the enrichment function in common with the modified formulation in [11,12], but the nodes chosen for enrichment conform with those of the standard one.

Likewise, the enriched finite element approximation of the water pressure and capillary pressure fields in Eq. (18) can be rewritten as

$$p_\alpha^h(\mathbf{x}, t) = \mathbf{N}_{p_\alpha}(\mathbf{x})\, \mathbf{P}_\alpha(t) + \mathbf{N}_{p_\alpha}^{enr}(\mathbf{x})\, \widetilde{\mathbf{P}}_\alpha(t) \qquad \alpha = w, c \tag{20}$$

Following Bubnov–Galerkin, the discretized form of the equations defining the multiphase problem is reached

$$\begin{aligned}
&\mathbf{M}_{uu}\ddot{\mathbf{U}} + \mathbf{M}_{u\tilde{u}}\ddot{\widetilde{\mathbf{U}}} + \int_\Omega \mathbf{B}^{\mathrm{T}}\boldsymbol{\sigma}'' \mathrm{d}\Omega - \mathbf{Q}_{uw}\mathbf{P}_w - \mathbf{Q}_{u\tilde{w}}\widetilde{\mathbf{P}}_w - \mathbf{Q}_{uc}\mathbf{P}_c - \mathbf{Q}_{u\tilde{c}}\widetilde{\mathbf{P}}_c = \mathbf{F}_u^{ext} \\
&\mathbf{M}_{u\tilde{u}}^{\mathrm{T}}\ddot{\mathbf{U}} + \mathbf{M}_{\tilde{u}\tilde{u}}\ddot{\widetilde{\mathbf{U}}} + \int_{\Omega^{enr}} (\mathbf{B}^{enr})^{\mathrm{T}}\boldsymbol{\sigma}'' \mathrm{d}\Omega - \mathbf{Q}_{\tilde{u}w}\mathbf{P}_w - \mathbf{Q}_{\tilde{u}\tilde{w}}\widetilde{\mathbf{P}}_w - \mathbf{Q}_{\tilde{u}c}\mathbf{P}_c - \mathbf{Q}_{\tilde{u}\tilde{c}}\widetilde{\mathbf{P}}_c \\
&\qquad + \mathbf{F}_{\tilde{u}}^{int} = \mathbf{F}_{\tilde{u}}^{ext} \\
&\mathbf{M}_{wu}\ddot{\mathbf{U}} + \mathbf{M}_{w\tilde{u}}\ddot{\widetilde{\mathbf{U}}} + \mathbf{Q}_{uw}^{\mathrm{T}}\dot{\mathbf{U}} + \mathbf{Q}_{\tilde{u}w}^{\mathrm{T}}\dot{\widetilde{\mathbf{U}}} + \mathbf{C}_{ww}\dot{\mathbf{P}}_w + \mathbf{C}_{w\tilde{w}}\dot{\widetilde{\mathbf{P}}}_w + \mathbf{C}_{wc}\dot{\mathbf{P}}_c + \mathbf{C}_{w\tilde{c}}\dot{\widetilde{\mathbf{P}}}_c \\
&\qquad + \mathbf{H}_{ww}\mathbf{P}_w + \mathbf{H}_{w\tilde{w}}\widetilde{\mathbf{P}}_w + \mathbf{H}_{wc}\mathbf{P}_c + \mathbf{H}_{w\tilde{c}}\widetilde{\mathbf{P}}_c - \mathbf{F}_w^{int} = \mathbf{F}_w^{ext} \\
&\mathbf{M}_{\tilde{w}u}\ddot{\mathbf{U}} + \mathbf{M}_{\tilde{w}\tilde{u}}\ddot{\widetilde{\mathbf{U}}} + \mathbf{Q}_{u\tilde{w}}^{\mathrm{T}}\dot{\mathbf{U}} + \mathbf{Q}_{\tilde{u}\tilde{w}}^{\mathrm{T}}\dot{\widetilde{\mathbf{U}}} + \mathbf{C}_{w\tilde{w}}^{\mathrm{T}}\dot{\mathbf{P}}_w + \mathbf{C}_{\tilde{w}\tilde{w}}\dot{\widetilde{\mathbf{P}}}_w + \mathbf{C}_{\tilde{w}c}\dot{\mathbf{P}}_c + \mathbf{C}_{\tilde{w}\tilde{c}}\dot{\widetilde{\mathbf{P}}}_c \\
&\qquad + \mathbf{H}_{w\tilde{w}}^{\mathrm{T}}\mathbf{P}_w + \mathbf{H}_{\tilde{w}\tilde{w}}\widetilde{\mathbf{P}}_w + \mathbf{H}_{\tilde{w}c}\mathbf{P}_c + \mathbf{H}_{\tilde{w}\tilde{c}}\widetilde{\mathbf{P}}_c - \mathbf{F}_{\tilde{w}}^{int} = \mathbf{F}_{\tilde{w}}^{ext} \\
&\mathbf{M}_{cu}\ddot{\mathbf{U}} + \mathbf{M}_{c\tilde{u}}\ddot{\widetilde{\mathbf{U}}} + \mathbf{Q}_{uc}^{\mathrm{T}}\dot{\mathbf{U}} + \mathbf{Q}_{\tilde{u}c}^{\mathrm{T}}\dot{\widetilde{\mathbf{U}}} + \mathbf{C}_{cw}\dot{\mathbf{P}}_w + \mathbf{C}_{c\tilde{w}}\dot{\widetilde{\mathbf{P}}}_w + \mathbf{C}_{cc}\dot{\mathbf{P}}_c + \mathbf{C}_{c\tilde{c}}\dot{\widetilde{\mathbf{P}}}_c \\
&\qquad + \mathbf{H}_{wc}^{\mathrm{T}}\mathbf{P}_w + \mathbf{H}_{\tilde{w}c}^{\mathrm{T}}\widetilde{\mathbf{P}}_w + \mathbf{H}_{cc}\mathbf{P}_c + \mathbf{H}_{c\tilde{c}}\widetilde{\mathbf{P}}_c - \mathbf{F}_c^{int} = \mathbf{F}_c^{ext} \\
&\mathbf{M}_{\tilde{c}u}\ddot{\mathbf{U}} + \mathbf{M}_{\tilde{c}\tilde{u}}\ddot{\widetilde{\mathbf{U}}} + \mathbf{Q}_{u\tilde{c}}^{\mathrm{T}}\dot{\mathbf{U}} + \mathbf{Q}_{\tilde{u}\tilde{c}}^{\mathrm{T}}\dot{\widetilde{\mathbf{U}}} + \mathbf{C}_{\tilde{c}w}\dot{\mathbf{P}}_w + \mathbf{C}_{\tilde{c}\tilde{w}}\dot{\widetilde{\mathbf{P}}}_w + \mathbf{C}_{c\tilde{c}}^{\mathrm{T}}\dot{\mathbf{P}}_c + \mathbf{C}_{\tilde{c}\tilde{c}}\dot{\widetilde{\mathbf{P}}}_c \\
&\qquad + \mathbf{H}_{w\tilde{c}}^{\mathrm{T}}\mathbf{P}_w + \mathbf{H}_{\tilde{w}\tilde{c}}^{\mathrm{T}}\widetilde{\mathbf{P}}_w + \mathbf{H}_{c\tilde{c}}^{\mathrm{T}}\mathbf{P}_c + \mathbf{H}_{\tilde{c}\tilde{c}}\widetilde{\mathbf{P}}_c - \mathbf{F}_{\tilde{c}}^{int} = \mathbf{F}_{\tilde{c}}^{ext}
\end{aligned} \tag{21}$$

The above equation system is then discretized in time domain following the line of the well-known Newmark scheme. To advance the solution in time, the link between the successive values of the unknown field variables at time t_{n+1} and the known field variables at time t_n is established by applying GN22 and GN11 to the displacement and pressure variables, respectively, as

$$\begin{aligned}
\ddot{\mathbf{U}}^{n+1} &= a_0\,(\mathbf{U}^{n+1} - \mathbf{U}^n) - a_2\,\dot{\mathbf{U}}^n - a_4\,\ddot{\mathbf{U}}^n \\
\dot{\mathbf{U}}^{n+1} &= a_1\,(\mathbf{U}^{n+1} - \mathbf{U}^n) - a_3\,\dot{\mathbf{U}}^n - a_5\,\ddot{\mathbf{U}}^n \\
\ddot{\widetilde{\mathbf{U}}}^{n+1} &= a_0\left(\widetilde{\mathbf{U}}^{n+1} - \widetilde{\mathbf{U}}^n\right) - a_2\,\dot{\widetilde{\mathbf{U}}}^n - a_4\,\ddot{\widetilde{\mathbf{U}}}^n \\
\dot{\widetilde{\mathbf{U}}}^{n+1} &= a_1\left(\widetilde{\mathbf{U}}^{n+1} - \widetilde{\mathbf{U}}^n\right) - a_3\,\dot{\widetilde{\mathbf{U}}}^n - a_5\,\ddot{\widetilde{\mathbf{U}}}^n \\
\dot{\mathbf{P}}_\alpha^{n+1} &= a_1'\,(\mathbf{P}_\alpha^{n+1} - \mathbf{P}_\alpha^n) - a_3'\,\dot{\mathbf{P}}_\alpha^n \qquad \alpha = w, c \\
\dot{\widetilde{\mathbf{P}}}_\alpha^{n+1} &= a_1'\left(\widetilde{\mathbf{P}}_\alpha^{n+1} - \widetilde{\mathbf{P}}_\alpha^n\right) - a_3'\,\dot{\widetilde{\mathbf{P}}}_\alpha^n \qquad \alpha = w, c
\end{aligned} \tag{22}$$

in which $a_0 = 1/\beta\Delta t^2$, $a_1 = \gamma/\beta\Delta t$, $a_2 = 1/\beta\Delta t$, $a_3 = \gamma/\beta - 1$, $a_4 = 1/2\beta - 1$, $a_5 = \Delta t(\gamma/2\beta - 1)$, $a_1' = 1/\theta\Delta t$ and $a_3' = 1/\theta - 1$. In these relations, $\Delta t = t_{n+1} - t_n$ is the time increment, and β, γ and θ are the Newmark parameters. To guarantee the unconditional stability of the time integration procedure, the Newmark parameters must be chosen such that $\gamma \geq 0.5$, $\beta \geq 0.25(0.5 + \gamma)^2$, and $\theta \geq 0.5$.

In order to resolve the system of fully coupled non-linear algebraic equations at each time step, the direct solution procedure is employed. In this numerical strategy, the discrete system of equations is solved at any specified time t_{n+1} applying the Newton–Raphson iterative algorithm to its residual form, $\boldsymbol{\Psi}^{n+1} = \mathbf{0}$. By expanding the residual equations with the first-order truncated Taylor series, the following linear approximation for the non-linear system to be solved is reached

$$\boldsymbol{\Psi}^{i+1,n+1} = \begin{Bmatrix} \boldsymbol{\Psi}_u^{i+1,n+1} \\ \boldsymbol{\Psi}_{\tilde{u}}^{i+1,n+1} \\ \boldsymbol{\Psi}_w^{i+1,n+1} \\ \boldsymbol{\Psi}_{\tilde{w}}^{i+1,n+1} \\ \boldsymbol{\Psi}_c^{i+1,n+1} \\ \boldsymbol{\Psi}_{\tilde{c}}^{i+1,n+1} \end{Bmatrix} = \begin{Bmatrix} \boldsymbol{\Psi}_u^{i,n+1} \\ \boldsymbol{\Psi}_{\tilde{u}}^{i,n+1} \\ \boldsymbol{\Psi}_w^{i,n+1} \\ \boldsymbol{\Psi}_{\tilde{w}}^{i,n+1} \\ \boldsymbol{\Psi}_c^{i,n+1} \\ \boldsymbol{\Psi}_{\tilde{c}}^{i,n+1} \end{Bmatrix} + \mathbf{J} \begin{Bmatrix} \mathrm{d}\mathbf{U}^{i+1,n+1} \\ \mathrm{d}\widetilde{\mathbf{U}}^{i+1,n+1} \\ \mathrm{d}\mathbf{P}_w^{i+1,n+1} \\ \mathrm{d}\widetilde{\mathbf{P}}_w^{i+1,n+1} \\ \mathrm{d}\mathbf{P}_c^{i+1,n+1} \\ \mathrm{d}\widetilde{\mathbf{P}}_c^{i+1,n+1} \end{Bmatrix} = \mathbf{0} \tag{23}$$

where $\mathbf{J}$ is the well-known Jacobian matrix, defined as $\partial\boldsymbol{\Psi}^{i,n+1}/\partial\mathbf{X}^{i,n+1}$ in which $\mathbf{X}$ represents the vector of nodal unknowns, $\mathbf{X} = [\mathbf{U}^{\mathrm{T}} \quad \widetilde{\mathbf{U}}^{\mathrm{T}} \quad \mathbf{P}_w^{\mathrm{T}} \quad \widetilde{\mathbf{P}}_w^{\mathrm{T}} \quad \mathbf{P}_c^{\mathrm{T}} \quad \widetilde{\mathbf{P}}_c^{\mathrm{T}}]^{\mathrm{T}}$. By finding the solution of the linearized system of equations (23), i.e. the increment of the standard and enriched nodal degrees of freedom, the corresponding nodal unknowns are subsequently attained through the incremental relation $\mathbf{X}^{i+1,n+1} = \mathbf{X}^{i,n+1} + \mathrm{d}\mathbf{X}^{i+1,n+1}$.

5 NUMERICAL SIMULATION RESULTS

The square plate with the edge crack of length $0.05\,m$ lying along its symmetry axis is simulated. The length sides of the plate is $0.25\,m$. The plate is loaded in tension by two uniform vertical velocities with magnitude $\bar{\dot{u}} = 2.35 \times 10^{-2}\ \mu m/s$ applied in opposite directions to the top and bottom edges of the plate. It is assumed that the plate has impervious boundaries to both fluids. Initially, the fully saturated condition is supposed. In the cohesive zone, the linear softening cohesive law is applied The material properties of the partially saturated porous medium are listed in Table 1. For fracture analysis, the cohesive fracture parameters of the material are set as follows: the cohesive strength $\sigma_c = 2.7$ MPa and the cohesive fracture energy $G_c = 95$ N/m.

The constitutive relations for the water saturation as well as the water and gas relative permeabilities are assumed on the basis of the van Genuchten-Mualem (VGM) model

$$\begin{aligned} S_w &= S_{rw} + (1 - S_{rw})\left[1 + \left(\frac{p_c}{p_{ref}}\right)^{1/(1-m)}\right]^{-m} \\ k_{rw} &= {S_e}^{1/2}\left[1 - \left(1 - {S_e}^{1/m}\right)^m\right]^2 \\ k_{rg} &= (1 - S_e)^{1/2}\left[1 - {S_e}^{1/m}\right]^{2m} \end{aligned} \tag{24}$$

in which the residual water saturation $S_{rw} = 0$, the empirical curve-fitting parameter $m = 0.4396$, the reference pressure $p_{ref} = 18.6$ MPa, and the effective water saturation S_e is defined as $S_e = (S_w - S_{rw})/(1 - S_{rw})$.

The numerical analysis of the plate is performed employing the three-phase model as well as the passive gas phase assumption. In these modelings, a comparison is made between the numerical results obtained considering the full coupling, i.e. the mechanical and the mass transfer coupling between the crack and the surrounding porous medium, and disregarding the mass transfer coupling. In the latter case, the interfacial flux vectors in the system of equations to be solved are omitted. Subsequently, the water pressure and capillary pressure fields need not be enriched any longer. Thus, the crack is not identified as a discontinuity in the fluid flow normal to the crack. That is, in the case without the mass transfer coupling term, no distinction is made between the flow of the pore fluids in the crack and in the porous medium surrounding the crack.

The numerical analysis continues until the crack tip gets to the right-hand side of the plate. The simulation results are presented for the time step before the crack propagates through the whole plate. Fig. 2 exhibits the contours of the water pressure for different simulations. As can be seen, incorporating the mass transfer coupling term into the simulation results in high negative water pressures concentrated in the vicinity of the crack, which implies that the pore water is drawn into the crack. These effects can also be distinguished in the contours of the gas pressure shown in Fig. 3, which result from the three-phase model. As observed in this figure, the negative pressures are greater in the case with full coupling than those without the mass transfer coupling. Moreover, it can be noticed that allowing for the interfacial flux along the crack leads to the considerable decrease of the gas pressure in the area surrounding the crack. This causes the pore gas to flow toward the crack. The gas pressure contours reveal that the values of the gas pressure, ignored in the model based on the assumption of the passive gas phase, can be as large as those of the water pressure. The impact of the incorporation of the mass transfer coupling on the results can further be evidenced by comparing the contours given in Figs. 4 and 5 representing the norm of the water pressure and gas pressure gradients, respectively. In accordance with what was observed before, pressure gradients with high values develop in the zone around the crack due to the mass transfer coupling. It also appears that the simulation in which all primary variables are enriched results in much higher values of the pressure gradient compared with those obtained without the water pressure and the capillary pressure enrichment. The results obtained with the passive gas phase assumption qualitatively correspond to those reported in Ref. [5].

Table 1: Material properties

Young's modulus	$E = 25.85$ GPa
Poisson's ratio	$\nu = 0.18$
Biot's constant	$\alpha = 1$
Initial porosity	$n = 0.2$
Solid phase density	$\rho_s = 2000$ kg/m^3
Water density	$\rho_w = 1000$ kg/m^3
Air density	$\rho_g = 1.2$ kg/m^3
Bulk modulus of solid phase	$K_s = 13.46$ GPa
Bulk modulus of water	$K_w = 0.2$ GPa
Bulk modulus of air	$K_g = 0.1 \times 10^{-3}$ GPa
Intrinsic permeability	$k = 2.78 \times 10^{-21}$ m^2
Dynamic viscosity of water	$\mu_w = 5 \times 10^{-4}$ Pa s
Dynamic viscosity of air	$\mu_g = 5 \times 10^{-6}$ Pa s
Atmospheric pressure	$p_{atm} = 0$ Pa

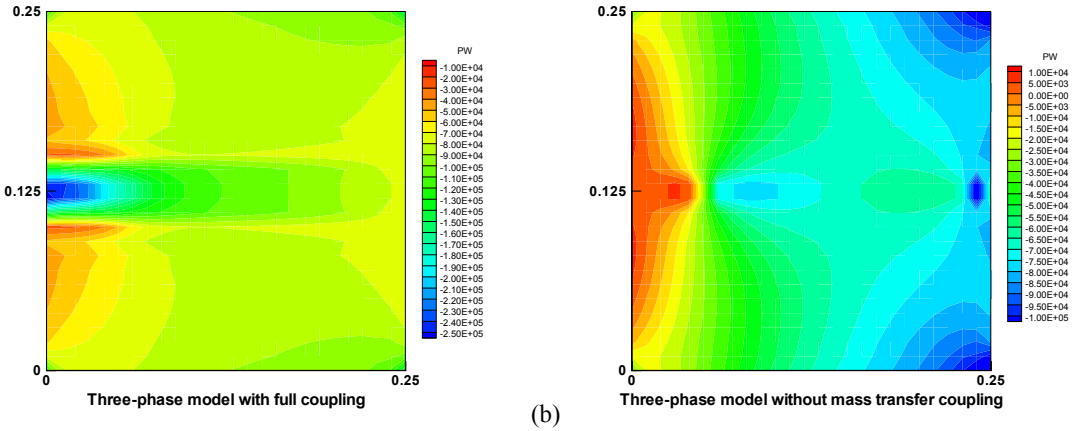

(a) (b)

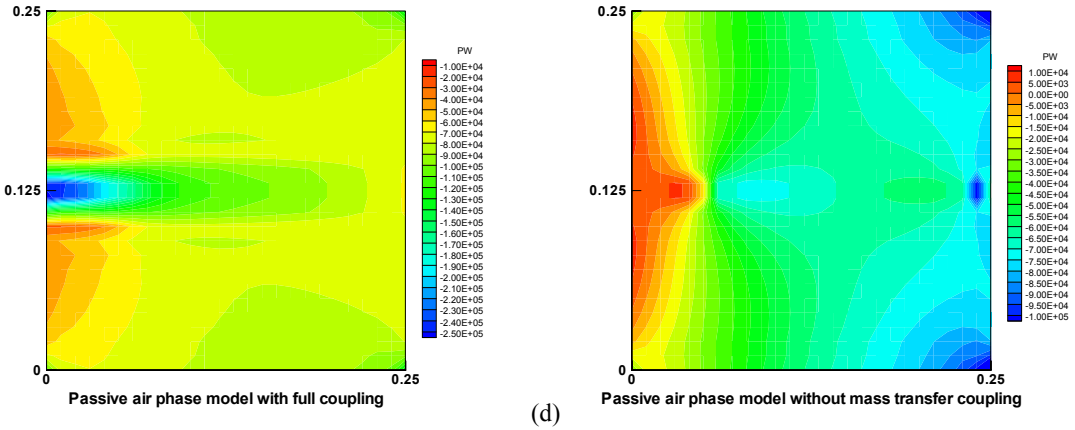

(c) (d)

Figure 2: Water pressure (Pa) contours: (a) three-phase model with full coupling, (b) three-phase model without mass transfer coupling, (c) passive air phase model with full coupling and (d) passive air phase model without mass transfer coupling

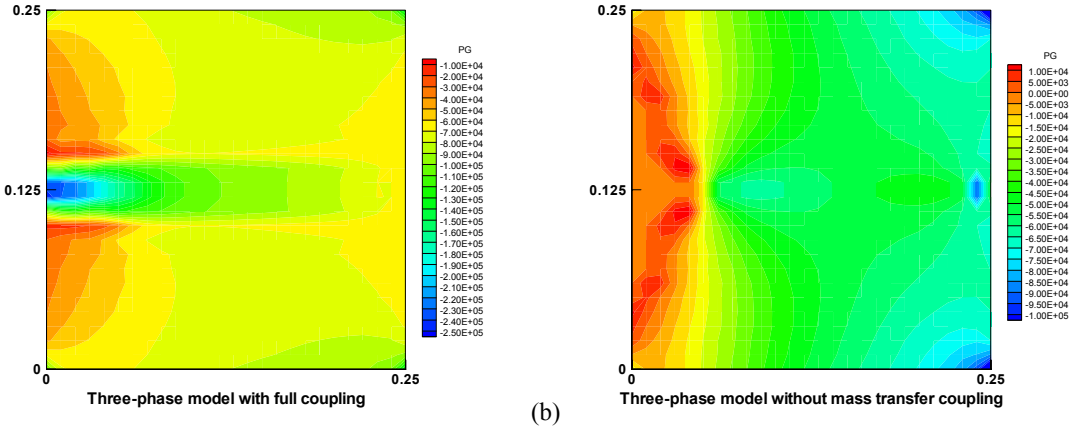

(a) (b)

Figure 3: Gas pressure (Pa) contours: (a) three-phase model with full coupling and (b) three-phase model without mass transfer coupling

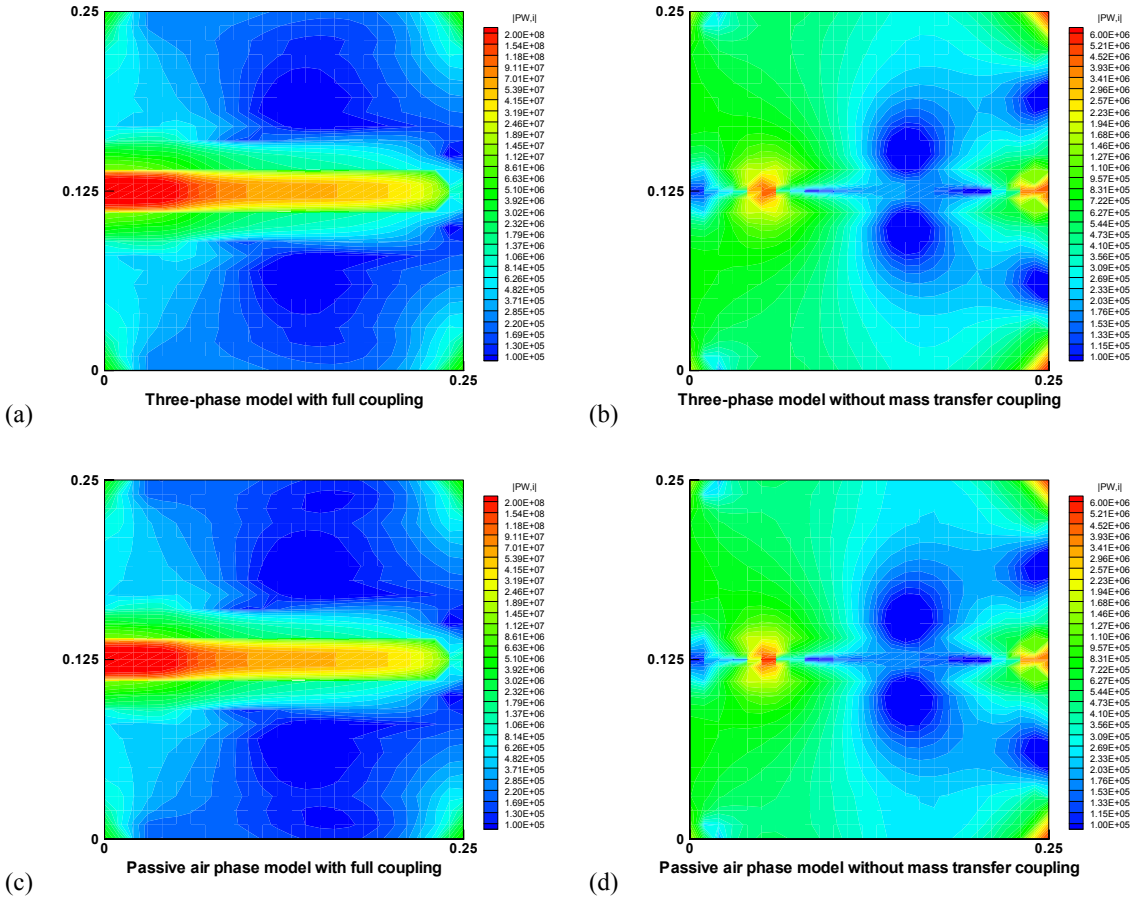

Figure 4: Norm of the water pressure gradient (Pa/m) contours (logarithmic scale): (a) three-phase model with full coupling, (b) three-phase model without mass transfer coupling, (c) passive air phase model with full coupling and (d) passive air phase model without mass transfer coupling

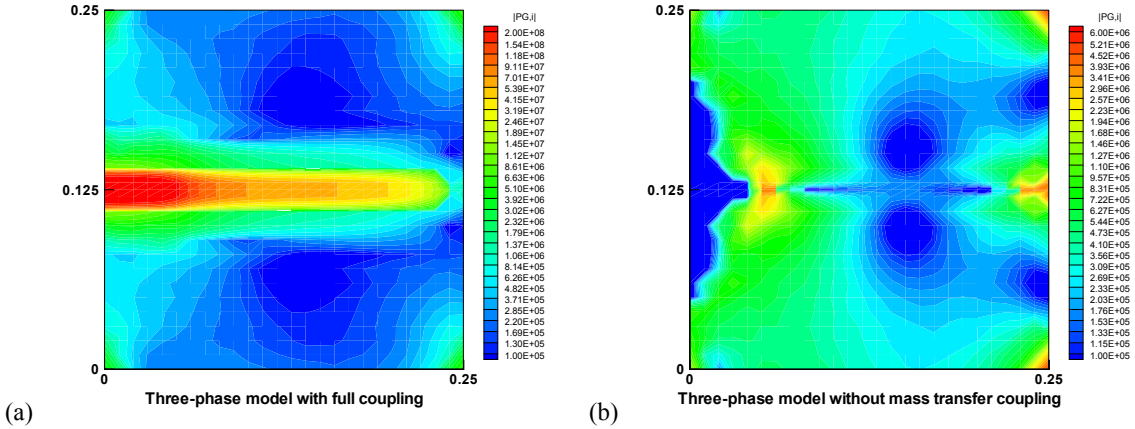

Figure 5: Norm of the gas pressure gradient (Pa/m) contours (logarithmic scale): (a) three-phase model with full coupling and (b) three-phase model without mass transfer coupling

6 CONCLUSIONS

In this paper, a numerical model was developed to simulate the flow of wetting and non-wetting pore fluids in progressively fracturing, partially saturated porous media in which the mechanical and the mass transfer coupling between the crack and the porous medium surrounding the crack were taken into account. For numerical simulation, the multiphase formulation was established based upon the linear momentum balance equation for the multiphase system and the flow continuity equation for each fluid phase. The cohesive crack concept was introduced, which gives the possibility to describe the non-linear behavior of the quasi-brittle material in the fracture process zone. In numerical modeling, the partition of unity property of finite element shape functions was exploited, which allows the local characteristic to be incorporated into the standard finite element approximation. The proposed method was successfully applied to the example involving a plate with a propagating cohesive crack, which puts in evidence the performance and applicability of the method. As illustrated in this example, the results are highly affected by inserting the discontinuity in the pressure normal derivative and thus considering the mass transfer coupling through the enrichment of the pressure field. In addition, it was verified that for a complete analysis of the problem the three-phase model is needed to be employed.

REFERENCES

[1] Boone, T.J. and Ingraffea, A.R. A numerical procedure for simulation of hydraulically-driven fracture propagation in poroelastic media. *Int. J. Numer. Anal. Meth. Geomech.* (1990) **14**:27-47.

[2] Schrefler, B.A., Secchi, S., Simoni, L. On adaptive refinement techniques in multi-field problems including cohesive fracture. *Comput. Methods Appl. Mech. Engrg.* (2006) **195**:444-461.

[3] Segura, J.M. and Carol, I. Coupled HM analysis using zero-thickness interface elements with double nodes. Part I: Theoretical model. *Int. J. Numer. Anal. Meth. Geomech*. (2008) **32**:2083-2101.

[4] Rethore, J., de Borst, R. and Abellan, M.A. A two-scale approach for fluid flow in fractured porous media. *Int. J. Numer. Meth. Engng*. (2007) **71**:780-800.

[5] Rethore, J., de Borst, R. and Abellan, M.A. A two-scale model for fluid flow in an unsaturated porous medium with cohesive cracks. *Comput. Mech*. (2008) **42**:227-238.

[6] Wells, G.N. and Sluys, L.J. A new method for modelling cohesive cracks using finite elements. *Int. J. Numer. Meth. Engng*. (2001) **50**:2667-2682.

[7] Moes, N., Belytschko, T. Extended finite element method for cohesive crack growth. *Engng. Fract. Mech.* (2002) **69**:813-833.

[8] Remmers, J.J.C., de Borst, R. and Needleman, A. The simulation of dynamic crack propagation using the cohesive segments method. J. *Mech. Phys. Solids* (2008) **56**:70-92.

[9] Khoei, A.R. and Mohammadnejad, T. Numerical modeling of multiphase fluid flow in deforming porous media: A comparison between two- and three-phase models for seismic analysis of earth and rockfill dams. *Comput. Geotech.* (2011) **38**:142-166.

[10] Meschke, G. and Grasberger, S. Numerical modeling of coupled hygromechanical degradation of cementitious materials. *J. Eng. Mech.* (2003) **129**:383-392.

[11] Fries, T-P. A corrected XFEM approximation without problems in blending elements. *Int. J. Numer. Meth. Engng*. (2008) **75**:503-532.

[12] Ventura, G., Gracie, R. and Belytschko, T. Fast integration and weight function blending in the extended finite element method. *Int. J. Numer. Meth. Engng*. (2009) **77**:1-29.

XI International Conference on Computational Plasticity. Fundamentals and Applications
COMPLAS XI
E. Oñate, D.R.J. Owen, D. Peric and B. Suárez (Eds)

MULTI-SCALE FAILURE FOR HETEROGENEOUS MATERIALS: LINK WITH MORPHOLOGICAL MODELING – COMPLAS XI

E. Roubin, M. Bogdan and J.B. Colliat

LMT-Cachan
ENS-Cachan, Paris 6 University, CNRS, UniverSud Paris PRES
61 avenue du Président Wilson, 94230 Cachan Cedex, France
e-mail: {roubin,colliat}@lmt.ens-cachan.fr, http://www.lmt.ens-cachan.fr/

Key words: Heterogeneous materials, FE method, Random fields, Excursion set, Embedded discontinuity

Abstract. A 3D meso-scale model for failure of heterogeneous quasi-brittle materials is presented. At such scale, concrete can be represented as an heterogenous material with two phases, where aggregates are included within the concrete. The model problem of heterogeneous materials that is adressed in detail here is based, on the one hand, on FE models with embedded discontinuities and, on the other hand, on a morphological representation using Gaussian or Gaussian related random field excursion sets.

1 Introduction

In view of the growing complexity of macroscopic models of concrete like materials, the question of multi-scale observation became relevant. It clearly appears that macroscopic behaviours of such material (cracking, creep...) take their origin at smaller scales (mesoscopic, microscopic...). The framework presented here is to be seen in this context, and especially in a sequenced way (as opposed to integrated one [1]) where the macroscopic behaviour comes from a mesoscopic description of the material. At this particular scale, concrete must be represented as heterogenous materials. Therefore, both mechanical and geometrical properties have to be represented by the framework.

This communication first present a morphological modeling framework for heterogenous materials. A concrete like material described as a two-phase material is considered here, where inclusions (aggregates) are included within a matrix (cement past and sand). The idea behind this morphological model is to yield the phases from random field excursion sets. Moreover, adding more phases in order to extend possibilities of representation is possible by adding excursion sets. If the framework deals with correlated Gaussian or Gaussian related random field (such as the chi-square distribution - χ^2), an analytic

formulae links the random field characteristics with geometrical and topological quantities (volume, surface area, Euler Characteristic...) of the underlying excursion set. This link has been recently made in [2] giving the possibility of controlling the excursion set characteristics and applying it to represent material phase with chosen characteristics. For a realistic modeling of a concrete like material, both in term of geometrical and topological quantities, due the Gaussian case limitation, an application of the χ^2 random field is made. Both unidimensional Karhunen-Loève decomposition and turning-bands projectional method are used to simulate three dimensional discrete correlated Gaussian random fields.

Efforts of morphological modeling are here made within a multi-scale linear framework using a FE model with embedded discondinuities [3]. In order to represent these heterogeneities, those excursions are projected onto the FE mesh, thus defining a set of discontinuities within the strain field interpolation (weak discontinuities [4]). These kinematics enhancements lead to "non-adapted" meshes in the sense of independence between heterogeneities morphology and the underlying FE mesh. Application of this linear implementation is made for a simple hydration process model presented here.

Considering the non linear failure behaviour, weak discontinuities are completed with a set of strong (displacement field) discontinuities within the framework of local enhancement [5]. Those discontinuities allow for a simple and accurate representation of the meso-scale cracks. The macroscopic response of this model is shown for a simple tension test.

2 Random field generation

As the whole morphological framework is based on Gaussian (or Gaussian related) correlated random field, efforts have to be made in the numerical implementation of their generation. This part explains two methods used to generate realisations of such fields. First the Karhunen-Loève decomposition [6] and then the turning bands projection [7]. Through this paper, we shall call $\gamma(x, w)$ a Gaussian random field over a parameter space M (which shall always be taken here to be a bounded region of $\mathbb{R}^N$) which takes values in $\mathbb{R}$. It is assumed that γ has mean zero, variance σ^2 and is isotropic and stationnary with a Gaussian covariance function defined as $C(x, y) = C(\|x - y\|) = \mathbb{E}\{\gamma(x)\gamma(y)\} = \sigma^2 e^{-\|x-y\|/L_c}$ where L_c is the correlation length.

The orthogonal decomposition of Gaussian correlated random fields theory stipulates [8] that mean zero Gaussian field with continuous covariance function (such as C) can be written as follows

$$\gamma(x, w) = \sum_{n=1}^{\infty} \varphi_n(x)\xi_n(w), \tag{1}$$

where $\xi_n(w)$ are zero mean, unit variance Gaussian random variables, and $\varphi_n(x)$ are functions on M determined by the covariance function C. It is worth noting that eq.(1)

allows for stochastic - w - and spatial -x - variables separation. Therefore, implementing this framework comes to put the effort in the determination of the spatial functions $\varphi_n(x)$.

The Karhunen-Loève decomposition is based on the previous orthogonal decomposition. It allows us to determine these spatial functions $\varphi_n(x)$ for simple compact M in $\mathbb{R}^N$. Demonstration can be found in [9] that they can be determined by first solving the following eigenvalues problem (known as Fredholm problem):

$$\int_M C(x,y)\psi(y)dy = \lambda\psi(x) \tag{2}$$

where λ and ψ are respectively the eigenvalues and eigenvector and then by setting $\varphi_n(x) = \sqrt{\lambda_n}\psi_n(x)$. Theoretically, an infinite sum is needed to define the exact random field in eq.(1). For the numerical implementation made here, a Finite Element Method is used to solve a discretized Fredholm problem. Therefore, using a finite set of eigenvalues and eigenvectors, the following troncated Karhunen-Loève decomposition eq.(3) defines an approximative realization of the underlying random field.

$$\gamma(x,w) = \sum_{n=1}^{m} \sqrt{\lambda_n}\xi_n(w)\psi_n(x). \tag{3}$$

The fact that stochastic and spatial variables are still separated is an essential result for any numerical implementation. Indeed, once the m couples $\{\lambda_n;\psi_n\}$ of a certain correlated random field are determined, the generation of a realization comes to generate a set of independent Gaussian variables (which only requires a random number generator). Moreover, the same couples can be used to produce any other realizations of the same field.

The precision of this method, involving full squared matrix eigenvalues problem, is quickly limitated by the memory storage when one deals with multi-dimensional random fields of large size. The turning bands projectional method has been developped by Matheron [7] in order to reduce the amount of numerical ressources. The idea is to generate several one-dimensional realizations of random fields to produce a multi-dimensional one. The algorithm below explains this projectional method with details.

Let M be the discreted multi-dimensional bounded region where the final realization will be created. Several lines have to be generated (we shall call L their number) with one arbitrary intersection point 0 and an uniform distribution of directions over the unit ball (see Fig.1).

Let $z(\zeta, w_i)$, $i = 1..L$ be the L realizations of a one-dimensional correlated random field generated over the L lines. For each point N on M, the value of the multi-dimensional realization is the average of the one-dimensional realization values at the projection of N on each line i:

$$\gamma(N,w) = \frac{1}{\sqrt{L}} \sum_{i=1}^{L} z(\zeta_{N_i}, w_i) \tag{4}$$

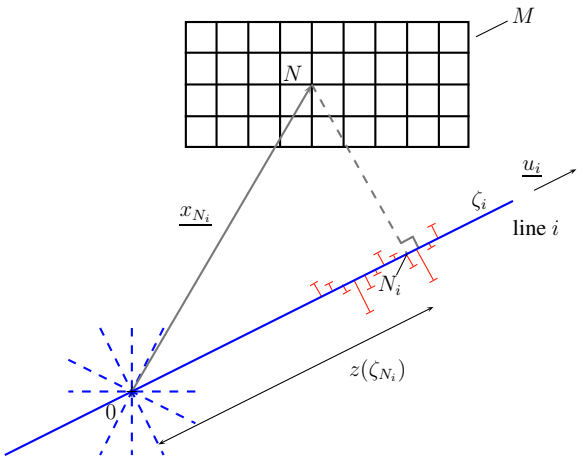

Figure 1: Schematic representation of the turning band method (from [10])

In this paper, the application of the method is made for three-dimensional random fields. The key of this method is the link between the three-dimensional covariance function C and the equivalent one-dimensional covariance function C_1 we need to generate the L realizations. Let $C(r)$ be as above (with $r = \|x - y\|$). Following [7] we have

$$C_1(r) = \frac{d}{dr}\left(rC(r)\right) = \sigma^2 \left(1 - \frac{2r^2}{L_c^2}\right) e^{-r^2/L_c^2} \tag{5}$$

3 Excursion Set

We call an excursion set the morphology of a subset of a bounded region defined by thresholding a realization of a random field. It allows us to create a set of random shapes. Let γ be a realization of $\gamma(x, w) : M \subset \mathbb{R}^N \to \mathbb{R}$ define as above and $u \in \mathbb{R}$ a chosen threshold. The underlying excursion set A_u is defined by the points of M where the values of γ are above u (eq.(6)).

$$A_u \equiv A_u(\gamma, M) \triangleq \{x \in M : \gamma(x) \geq u\} \tag{6}$$

This principle, applied for $M \in \mathbb{R}$ is shown on Fig.2.

In our case, random fields will be yield in a three dimensional space ($M \subset \mathbb{R}^3$) and therefore define three-dimensional excursion sets. The two excursions represented in Fig.3 are made from the same realization with two different threshold values. It is clear that, by changing this value, a large range of varied morphologies can be generated. This exemple shows that "low" values of u produce excursions mainly made of handles with high volume fraction, giving a "sponge" like topology (Fig.3(a)), whereas "high" values of u produce excursion made of several connected components with a lower volume fraction (Fig.3(b)).

In order to provide a global description of the resulting morphology, the Lipschitz-Killing curvatures, hereafter LKCs, are choosen. In a N-dimensional space $N + 1$ LKCs can be defined where each can be thought of measures of the "j-dimensional sizes" of

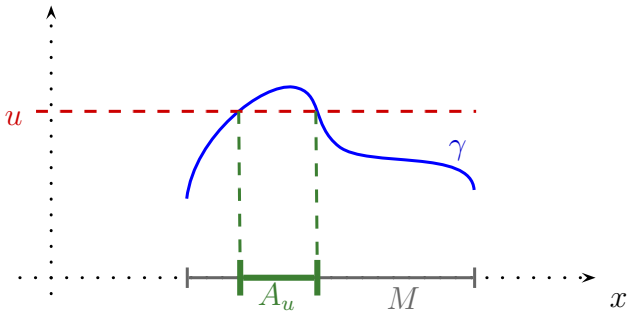

Figure 2: Schematic representation of a one-dimensional excursion set A_u

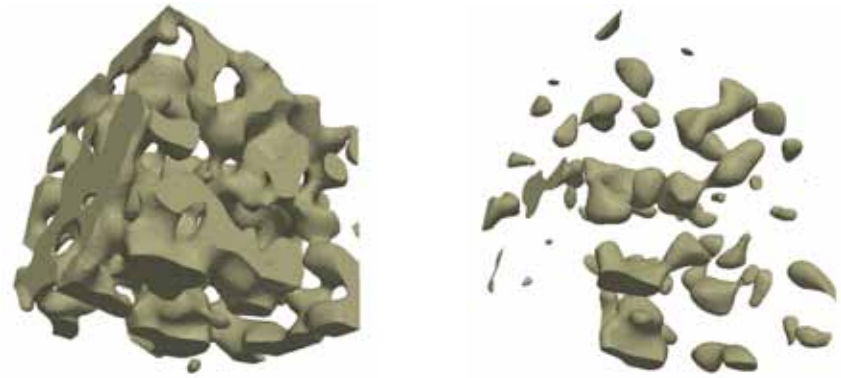

(a) "Low" threshold - sponge topology

(b) "High" threshold - meatball topology

Figure 3: Effect of threshold value on tri-dimensional excursion topology

A_u. In our three-dimensional case, the four LKCs, denoted by $\mathcal{L}_j$, $j = 0..3$, provide both geometrical - $\mathcal{L}_1$, $\mathcal{L}_2$, $\mathcal{L}_3$ - and topological - $\mathcal{L}_0$ - descriptions of the morphology A_u. They are defined by:

- $\mathcal{L}_3(A_u)$ is the three dimensional volume of A_u.
- $\mathcal{L}_2(A_u)$ is half the surface area of A_u.
- $\mathcal{L}_1(A_u)$ is twice the caliper diameter of A_u.
- $\mathcal{L}_0(A_u)$ is the Euler characteristic of A_u, which contrary to the other LKCs is a topological measure. In three-dimension, it can be calculated by:

  $\mathcal{L}_0(A_u) = \#\{\text{connected components in } A_u\} - \#\{\text{"handles" in } A_u\} + \#\{\text{"holes" in } A_u\}$

  For exemple, a ball or a cube are topologicaly identical (Euler characteristic $\mathcal{L}_0 = 1$) but differ from a hollow ball ($\mathcal{L}_0 = 2$) or a ring torus ($\mathcal{L}_0 = 0$).

Following [2], a probabilistic link has been made between excursion set properties and random field thresholding parameters giving an explicit formulae for the expectation of the LKCs - $\mathbb{E}\left\{\mathcal{L}_i\left(A_u\left(\gamma, M\right)\right)\right\}$. It is not the purpose of this paper to give details on these formulae, however, full proof and details can be found in [9]. The only idea one need to remember to go through this paper is that this theory gives a new tool helping us to predict all the geometrical and topological properties of an excursion set from the random field characteristics and the threshold - σ, L_c, u -. These relations have been made explicit for $\gamma(x, w)$ as above on a cube $M = \prod_{i=1}^{3}[0; T]$:

$$\left\{\begin{array}{lcl} \mathbb{E}\{\mathcal{L}_0\}(A_u) & = & \left(\frac{\sqrt{2}}{2\pi^2}\frac{T^3}{L_c^3}\left(\frac{u^2}{\sigma^2}-1\right)+\frac{3\sqrt{2}}{2\pi^{3/2}}\frac{T^2}{L_c^2}\frac{u}{\sigma}+\frac{3\sqrt{2}}{2\pi}\frac{T}{L_c}\right)e^{-u^2/2L_c^2}+\Psi\left(\frac{u}{\sigma}\right) \\ \mathbb{E}\{\mathcal{L}_1\}(A_u) & = & \left(\frac{\sqrt{2}}{\pi^{3/2}}\frac{T^3}{L_c^2}\frac{u}{\sigma}+\frac{3\sqrt{2}}{4}\frac{T^2}{L_c}\right)e^{-u^2/2L_c^2}+3T\Psi\left(\frac{u}{\sigma}\right) \\ \mathbb{E}\{\mathcal{L}_2\}(A_u) & = & \frac{\sqrt{2}}{\pi}\frac{T^3}{L_c}e^{-u^2/2L_c^2}+3T^2\Psi\left(\frac{u}{\sigma}\right) \\ \mathbb{E}\{\mathcal{L}_3\}(A_u) & = & T^3\Psi\left(\frac{u}{\sigma}\right) \end{array}\right. \tag{7}$$

Fig.4(a) and Fig.4(b) represent respectively the Euler characteristic and the volume fraction - directly linked with the fourth LKC by $\mathbb{E}\{\mathcal{L}_3\}(A_u)/T^3$ - of excursion sets of $\gamma(x, w)$ for u from -20 to 20.

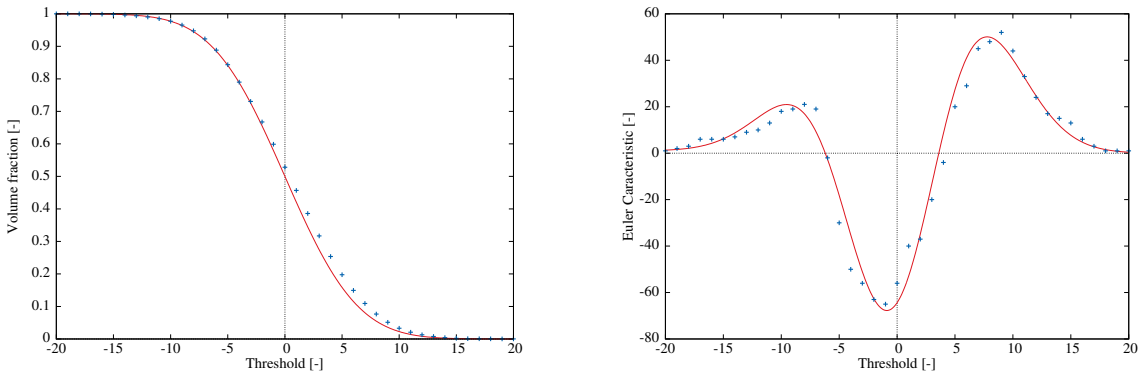

(a) (b)

Figure 4: LKCs of excursion sets of Gaussian random field in term of threshold values.

— Expected values of LKCs provided by (7), + Numerical values calculated from one realization of $\gamma(x, w)$.

The constant decreasing shape of the volume fraction curve in term of u clearly reflects the effect of the threshold level on the "size" of A_u. Even if more peculiar, the Euler characteristic curve shape reflects also easily the effect of the threshold on excursion sets topology. For values of u lower than the lowest value of γ, the Euler characteristic is the one of the full cube ($\mathcal{L}_0 = 1$). By increasing u, several holes appear, counting in positive for the Euler characteristic ($\mathcal{L}_0 > 1$). Then, the expansion of the holes starts to form handles which lead to a sponge like topology ($\mathcal{L}_0 < 0$). By increasing u even more,

handles disappear forming a "meatball" like topology of connected components ($\mathcal{L}_0 > 0$). Finally, the Euler characteristic decreases to $\mathcal{L}_0 = 0$ when no more connected components remain.

From the comparison between theorical values and measures on one realization, we can point out that the variability of the numerical generation is very low. Therefore, although eq.(7) gives only expectations of LKCs, for this range of excursion sets we can assume that $\mathbb{V}\{\mathcal{L}_i(A_u)\} \ll 1$.

So far, we have seen the effect of the threshold value on excursion sets. But one needs to remember that, according to eq.(7), both variance and covariance length of $\gamma(x, w)$ affect the morphology as well. Understanding the full behaviour of these equations is a key point for anyone who wants to make excursion set modeling.

4 Application of the modeling framework on concrete like material

The material is represented as an heterogeneous material with two phases. One phase (aggregates) is represented by an excursion set of a correlated random field while its second phase (concrete) is represented by its complementary. Therefore in this part, the effort will be put in a "realistic" representation of the aggregates phase. We keep only three relevant characteristics from the four LKCs: the volume fraction V_v, the volumic surface area $\mathcal{S}$ and the number of agregates $\mathcal{N}$ which are respetively linked with $\mathcal{L}_3$, $\mathcal{L}_2$ and $\mathcal{L}_0$. Thought V_v and $\mathcal{S}$ can be directly estimated, attention must be taken when it comes to $\mathcal{N}$. Indeed the Euler characteristic does not indicate the number of aggregates for every topology. In our case, the "meatball" topology has to be targeted and it is only once we assume that the excursion set is free from holes and handles that $\mathcal{N}$ can be estimated by $\mathcal{L}_0$. In this specific kind of topology: $\mathcal{N} \triangleq \#\{\text{connected components}\} = \mathcal{L}_0$.

Once the three characteristics $(\mathcal{N}, \mathcal{S}, V_v)$ of the phase are set, the generation of the underlying excursion set rely on finding a solution for (u, σ, L_c) that satisfy the following system:

$$\left\{ \begin{array}{lcl} \mathbb{E}\{\mathcal{L}_3\}(u,\sigma) & = & V_v T^3 \\ \mathbb{E}\{\mathcal{L}_2\}(u,\sigma,L_c) & = & \frac{1}{2}\mathcal{S}T^3 \\ \mathbb{E}\{\mathcal{L}_0\}(u,\sigma,L_c) & = & \mathcal{N} \end{array} \right. \tag{8}$$

Due to the intrinsic non linearity of eq.(7), depending on the different values of $(\mathcal{N}, \mathcal{S}, V_v)$ (especially for "meatball" topology - $\mathcal{N} \gg 1$) the problem eq.(8) do not always have a solution. For exemple, we can clearly see on Fig.4 that we can not expect $\mathcal{N}$ to be upper than 40 while keeping a "high" volume fraction ($V_v > 40\%$). Which in our case of concrete like material modeling leads to a major issue. So far, the more realistic solution for "meatball" topology we get with this framework allows us to represent an aggregate phase with a maximum of 15% volume fraction.

Until now, the framewok has been presented considering Gaussian random fields. But estimation of LKCs for excursion set can also be worked out considering Gaussian related fields. The application of this paper is made using a chi-square distribution with k degrees

of freedom - χ^2_k -. Realizations of such fields can be seen as sum of k independent squared realizations of a correlated Gaussian random field. Let δ be a realization of such field and γ_i, $i = 1..k$ be k realizations of the Gaussian field $\gamma(x, w)$ described above. We have :

$$\delta = \sum_{i=1}^{k} \gamma_i^2 \tag{9}$$

Although similar to eq.(7), the use of a χ^2_k distribution add the parameter k to the system eq.(8). With such field, the nearest solution is found for $k = 1$ and enable us to double the previous volume fraction $V_{v_{max}} \approx 30\%$. Fig.5 shows a two-dimensional slice of excursions from a Gaussian realization and a χ^2_1 made from the same realization. Fig.5(b), being the excursion from the squared realization of the excursion Fig.5(a), shows clearly that, for the same threshold, it is natural to expect the volume fraction to double between excursions of Gaussian and χ^2_1 random fields.

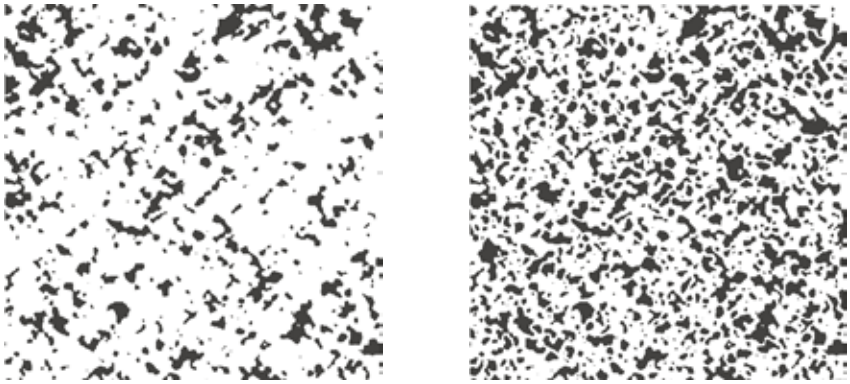

(a) Gaussian realization - γ (b) χ^2_1 realization - $\delta = \gamma^2$

Figure 5: Comparison between Gaussian and χ^2_1 excursion sets for the same threshold value.

The χ^2_1 distribution remains the more suitable solution for meatball topology and high volume fraction morphology we found.

5 FE model for heterogeneous material - Application to hydration process modeling

The approach made here relies on a spatial truss, to model pattern of heterogeneities. The choice of a not adapted meshing process is made here thus, the spatial positions of nodes are not constrained by the morphology. Therefore, both gemetrical and mechanical properties have to be handle inside some interface elements. These cut elements are split into two parts, each having different elastic properties by enhancing them with strain (weak) discontinuities [11]. An elementary enhancements method (E-FEM) method for kinematic enhancement of Finite Element using the Hu-Washizu variational formulation is used here. For example, if we consider a two-phase material (inclusions within a matrix),

three sets of elements are needed: those entirely in the matrix, those entirely in the inclusions, and those which are split between both (cut elements). To calculate these elements repartition, a projection of the previous excursion set is made onto the truss. In order to illustrate this linear framework, a simple hydration process of concrete like material modeling has been implemented. Considering a simplistic version of the Powers and Brownyard hydration model [12], with only three phases: unreacted cement, hydration products (including gel water) and free water, the volume fraction of each one of them can be calculated according to the following equations:

$$\begin{cases} p = \frac{w/c}{w/c+\rho_w/\rho_c} \\ V_{anh} = (1-p)(1-\alpha) \\ V_h = 2.12(1-p)\alpha \\ V_w = 1 - V_h - V_{anh} \end{cases} \tag{10}$$

where p is the initial porosity, α the hydration degree and V_{anh} , V_h, V_w respectively the volume fractions of anhydrous cement, hydration products and water.

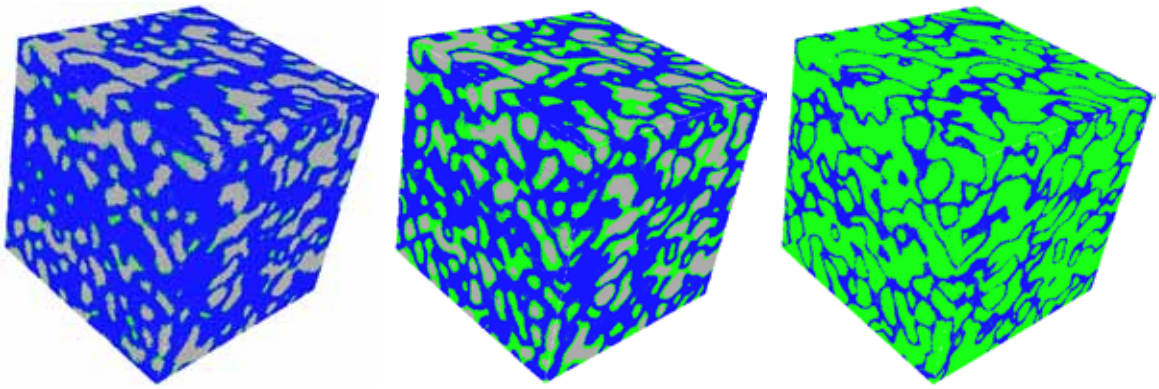

(a) $\alpha = 0.1$ (b) $\alpha = 0.5$ (c) $\alpha = 1$

Figure 6: Projection of excusion set shapes on FE truss for different hydration degrees.

■ water, ■ hydration products, ■ anydrous cement

As explained previously, thresholding a random field with a scalar allows to create a two phase material. One can easily imagine, that a second threshold, with a different value, will allow to create an additional phase, concentrical to the first one. Therefore, setting two thresholds will allow us to create a three phase material. Thus, for different hydration degrees, each phase's volume fraction is known and can be linked to the random field's thresholds u_i (equation eq.(7)). Eventually, the initial morphology is set up by one threshold (two phases: water and unhydrated cement), and then, for a growing hydration degree, two thresholds are calculated and applied to the random field, creating a three phase material (water, unhydrated cement and hydration products).

Within this framework, macroscopic material characteristics like Young modulus can be estimated over a given hydration degree with simple tension tests. The following

characteristics have been chosen $E_{anh} = 135\,000\ MPa$, $E_h = 25\,000\ MPa$ and $E_w = 1\ MPa$.

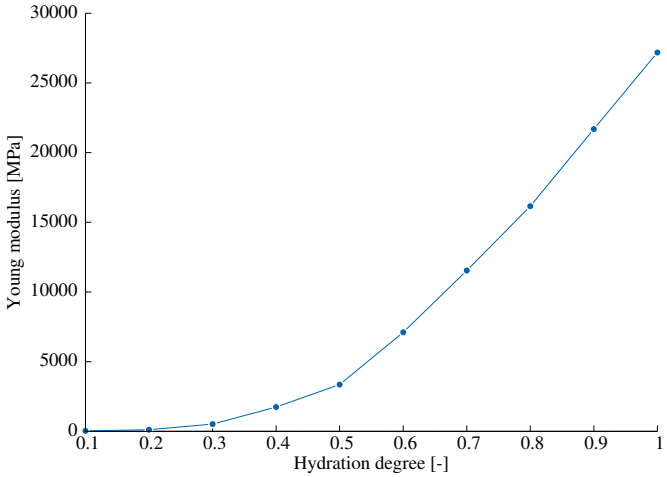

Figure 7: Young modulus of a concrete like material for different hydration degrees.

Fig.7 shows that the continuous growing of the macroscopic Young modulus over hydration degree is well handled by this FE representation. A slight raising of the slope can be seen after $\alpha = 0.4$.

6 FE models with embedded discontinuities

In addition to the geometrical representation of heterogeneities, displacement (strong) discontinuities are also introduced in the elements, in order to model a non-linear softening response based on failure quasi-brittle. These discontinuities represent micro-cracks that can occurs in both phases as well as at the interfaces (debonding). Details of this FE numerical implementation can be found in [3].

A other simple tension test is presented here. Material properties are defined according to Tab.1.

Table 1: Material properties

Matrix	Inclusions	Interface
$E = 10GPa$	$70GPa$	–
$\sigma_u = 3MPa$	–	$3MPa$
$Gf = 11J/m^2$	–	$11J/m^2$

Two remarks are worthy of attention. The first is that the interface is of rigid-brittle type. The second is that we choosed for inclusions to remains in the linear elastic regime.

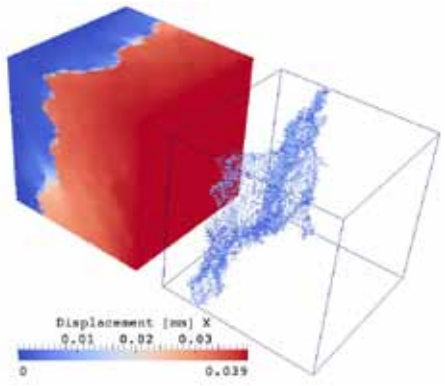

(a) Displacement field and crack pattern at last time step

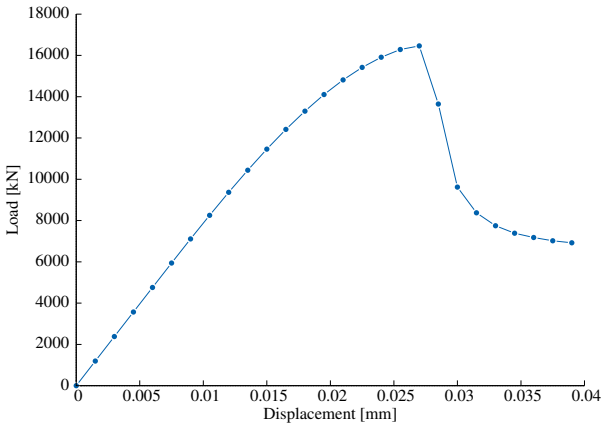

(b) Load vs imposed displacement

Figure 8: Results for simple tension

The cracking pattern is shown on Fig.8(a) where two zones are splited by a macroscopic crack (represented by means of the broken elements). Fig.8(b) shows the macroscopic load vs imposed displacement curve where three steps can be seen. First, a linear part where no failure occurs. Then, with the apparition of several microscopic cracks, we can observe a yield behaviour. Finaly, the softening part begin when the localisation of these microscopic cracks creates a macrosopic one.

7 Concluding remarks

This communication presents a first attempt to create a sequential multi-scale framework where morphology of heterogeneous material is defined by excursion sets of correlated random fields. Though, efforts still have to be made in order to generate more realistic morphologies, advantages have been shown through two examples. We can also add that this framework is well adapted to other problematics related with concrete like materials such as the effect of morphological variability on macroscopic behaviour. Indeed, the use of both Karhunen-Loève decomposition and non-adapted meshes allows fast computations, limiting the growing amount of numerical ressources needed when dealing with large sets of morphologies. Futhermore, being able to represent broken elements by means of a strong discontinuity in the FE method allows calculations of permeability or diffusion in such damaged materials [13].

REFERENCES

[1] Feyel, F. and Chaboche, J.-L. Multi-scale non-linear FE analysis of composite structure: damage and fiber size effects. *Revue européenne des Éléments Finis : NUMDAM'00 isues* (2001) **10**:449–472

[2] Adler, R.J. Some new random field tools for spatial analysis. *Stochastic Environmental Research and Risk Assessment* (2008) **22**:809–822

[3] Benkemoun, N., Hautefeuille, M., Colliat, J.-B., Ibrahimbegovic, A. Failure of heterogeneous materials: 3D meso-scale FR models with embedded discontinuities. *Int J. Num. Meth. in Engng.* (2010) **82**:1671–1688

[4] Sukumar, N., Chapp, D.L., Moës, N. and Belytshcko, T. Modeling holes and inclusions by level sets in the extended finite element method. *Computer Methods in Applied Mechanics and Engineering* (2001) **190**:6183–6200

[5] Oliver J. Modelling strong discontinuities in solid mechanics via strain softening constitutive equations. *International Journal for Numerical Methods in Engineering* (1996) **39**:3575–3623

[6] Loeve, M. Probability Theory. *Graduated Texts in Mathematics* (1978) Vol. II, 4th ed..

[7] Matheron, G. The intrinsic random functions and their applications. *Advances in Applied Probability* (1973) **5**:439–468

[8] Karhunen, K. Über lineare Methoden in der Wahrscheinlichkeitsrechnung. *Ann. Acad. Sci. Fennicae. Ser. A. I. Math.-Phys* (1947) **37**:1–79

[9] Adler, R.J. and Taylor, J.E. *Random Fields and Geometry* (2007) Springer, Boston

[10] Mantoglou, A. and Wilson, J.L The Turning Bands Method for Simulation of Random Fields using Line Generation with a Spectral Method *Water Resources Research* (1982) Vol.II, **2**:129–149

[11] Ortiz, M., Leroy, Y. and Needleman, A. A Finite Element method for localized failure analysis *Computer Methods in Applied Mechanics and Enginnering* (1987) **61**:189–214

[12] Powers, T.C. and Brownyard, T.L. Studies of the physical properties of hardened Portland cement paste. *J. Am. Concr. Inst.*, (1947). **43**101–132, 249–336, 469–505, 549–602, 669–712, 845–880, 933–992.

[13] Jourdain, X., Colliat, J.-B., De Sa, C., Benboudjema, F. and Gatuingt, F. Upscaling permeability for fractured concrete : meso-macro numerical approach within a sequential framework *submitted*

XI International Conference on Computational Plasticity. Fundamentals and Applications
COMPLAS XI
E. Oñate, D.R.J. Owen, D. Peric and B. Suárez (Eds)

PORE-SPACE CONTROLLED HARDENING MODEL IN PLASTICITY OF POROUS MATERIALS: APPLICATION TO THE ANALYSIS OF INDENTATION EXPERIMENTS

ROLAND TRAXL AND ROMAN LACKNER

Material Technology Innsbruck (MTI)
University of Innsbruck
Technikerstraße 13, A-6020 Innsbruck, Austria
e-mail: {Roland.Traxl, Roman.Lackner}@uibk.ac.at, www.uibk.ac.at/mti

Key words: Computational Plasticity, Indentation Analysis, Hardness, Porous Materials, Strength Homogenization

Abstract. Based on a multi-scale approach comprising a multi-scale material model and a respective finite-element (FE) analysis tool, the indentation response of porous materials is examined in this paper. The considered material is assumed to consist of a homogeneous Drucker-Prager-type matrix-phase and spherical pores. Non-linear homogenization is employed to derive both a strength criterion and a hardening rule at the macroscopic scale without the need of any additional non-physical material parameters. Hereby, the underlying macroscopic hardening is exclusively controlled by the evolution of the pore-space during loading. The material model is implemented in a FE program within the framework of elastoplasticity. The so-obtained analysis tool is applied to the analysis of indentation experiments commonly used for characterization and performance-based optimization of materials.

1 INTRODUCTION

Indentation experiments are commonly employed for determination of strength properties (hardness) of materials. Nowadays indentation analysis is applied on a great variety of materials and at various length scales, ranging from nanoindentation (e.g. Constantinides et al. [6]) to classical hardness measurements according to Tabor [15]. This gives scientists and engineers access to material properties even if ordinary test specimens for mechanical (compressive/tensile) testing are not available.

Meanwhile there are a number of publications treating indentation analysis for monolithic solids, focusing on the phenomenological aspect at the macro-scale (see e.g. Cheng et al. [5] for elastoplasticity, and Pichler et al. [14] for viscous material behaviour). In order to obtain a better understanding of indentation experiments, micro-mechanical changes

taking place in course of the indentation process are considered. E.g., application of limit analysis to porous material as presented in Cariou et al. [3] gives access to characteristic hardness-packing relations. Still, there are some underlying assumptions and restrictions: The change of material properties caused by the load history (hardening or softening) is neglected as well as piling-up or sinking-in effects. Besides, the so-obtained relations are only valid for virtually rigid materials and associated yielding.

Departing from the work presented in [3], a micromechanics-based material model based on nonlinear homogenization is developed and implemented in a FE program within the framework of non-associated hardening/softening elastoplasticity. Based on numerical simulations, the significance of the involved physical mechanism is investigated in regard to material characterization in indentation tests.

2 MATERIAL MODEL

The underlying material is assumed to consist of two phases: a solid phase and a pore phase. In the sequel, the existence of a representative elementary volume (REV) is assumed, which is equivalent with the requirement

$$d \ll L \ll h \ , \tag{1}$$

where d represents the characteristic size of pores, L the size of the REV, and h the indentation depth.

2.1 Elastic and plastic material properties

The pore phase of the considered two-phase material is characterized by its volume fraction φ and the shape of the pores. In the following, the pores are assumed to be spherical. The solid (matrix) phase is modeled as an elastoplastic material. Hereby, the domain of strength compatible stress states, E_M, is defined by a yield function according to the Drucker-Prager criterion, given by the cohesion c and the friction coefficient α of the material:

$$\boldsymbol{\sigma} \in E_M \ \Leftrightarrow \ f_M(\boldsymbol{\sigma}) = \sigma_d(\boldsymbol{\sigma}) + \alpha\sigma_m(\boldsymbol{\sigma}) - c \leq 0 \ , \tag{2}$$

where σ_m is the hydrostatic pressure, and σ_d the equivalent deviatoric stress:

$$\sigma_m = \frac{1}{3}\mathrm{tr}\boldsymbol{\sigma}, \quad \sigma_d = \sqrt{\frac{1}{2}\mathbf{s} : \mathbf{s}}, \quad \mathbf{s} = \boldsymbol{\sigma} - \mathbf{I}\sigma_m \ . \tag{3}$$

Within the elastic domain, the material is supposed to exhibit linear-elastic behavior, represented by the fourth-order tensor $\mathbb{C}_M$.

The domain E_M remains unchanged during loading (ideal plasticity). While an associated flow rule implies dilatation, a non-associated flow rule is adopted in order to describe volume-preserving yielding of the solid (matrix) phase, giving a plastic potential in the form:

$$g(\boldsymbol{\sigma}) = \sigma_d(\boldsymbol{\sigma}) \ . \tag{4}$$

2.2 Homogenization of elastic properties

Let V be the domain of the REV and V_M the domain of the solid (matrix) phase. In case of absence of pore pressure as supposed in the following, the homogenization problem of elastic properties is given in the framework of uniform strain boundary conditions by

$$\begin{aligned} \mathrm{div}\boldsymbol{\sigma} &= \mathbf{0} \qquad \text{in } V \\ \boldsymbol{\sigma} &= \mathbb{C}_M : \boldsymbol{\epsilon} \quad \text{in } V_M \\ \boldsymbol{\xi} &= \mathbf{E} \cdot \mathbf{x} \qquad \text{in } \partial V \end{aligned} \tag{5}$$

Therein, $\mathbf{x}$ is the position vector, $\mathbf{E}$ the macroscopic strain tensor, and $\boldsymbol{\xi}$ the displacement vector at the boundary of the REV. A macroscopic stress tensor $\boldsymbol{\Sigma}$ is defined as the average of the local stress $\boldsymbol{\sigma}$:

$$\boldsymbol{\Sigma} = \frac{1}{V}\int_V \boldsymbol{\sigma} dV = \langle \boldsymbol{\sigma} \rangle_V \ . \tag{6}$$

The homogenized stiffness tensor $\mathbb{C}_{hom}$ sought-after relates the macroscopic strain to the macroscopic stress:

$$\boldsymbol{\Sigma} = \mathbb{C}_{hom} : \mathbf{E} \tag{7}$$

For homogenization, the Mori-Tanaka scheme is applied, which yields the homogenized bulk and shear modulus as (see, for instance, [7] for details):

$$k_{hom} = \frac{4k_M\mu_M(1-\varphi)}{3k_M\varphi + 4\mu_M}, \quad \mu_{hom} = \mu_M \frac{(1-\varphi)(9k_M + 8\mu_M)}{9k_M(1+\frac{2}{3}\varphi) + 8\mu_M(1+\frac{3}{2}\varphi)} \tag{8}$$

Accordingly, the macroscopic stiffness tensor is obtained by:

$$\mathbb{C}_{hom} = 3k_{hom}\mathbb{J} + 2\mu_{hom}\mathbb{K}, \tag{9}$$

with

$$J_{ijkl} = \frac{1}{3}\delta_{ij}\delta_{kl}, \quad \mathbb{K} = \mathbb{I} - \mathbb{J} \ , \tag{10}$$

where δ is the Kronecker delta and $\mathbb{I}$ is the fourth-order unit tensor.

2.3 Homogenization of strength properties

While application of homogenization schemes to elastic properties is widely spread, most developments concerning non-linear behavior of composite material are relatively recent. An early and widely accepted criterion for porous Mises-type material was established by Gurson [8]. Since then, a number of contributions dealt with purely cohesive matrix phases, describing the material as fictitious non-linear elastic (see [16] for a survey). In [10], this approach was adopted for frictional solid phases with rigid inclusions

and in [7] for porous media, respectively. While these contributions derived the macroscopic yield criterion analytically, Pastor et al. [12] made use of simulation tools based on limit analysis.

An analytical formulation based on non-associated yielding was reported in [11]. Therein, the non-associated plasticity problem is interpreted as a nonlinear-viscoplastic problem with a pre-stress depending on the strain rate field $\dot{\boldsymbol{\epsilon}}$ to account for non-associated yielding. By introducing a representative strain rate (see [7]), this problem can be further simplified to a problem yielding an analogous structure as the problem of homogenization of elastic properties with pre-stress. Using the Mori-Tanaka scheme, the macroscopic yield function reads [11]:

$$F_{hom}(\boldsymbol{\Sigma}, \varphi) = \left(\frac{3}{4}\varphi - \alpha^2\right)\Sigma_m^2 + 2\alpha c(1-\varphi)\Sigma_m + \left(\frac{2}{3}\varphi + 1\right)\Sigma_d^2 - c^2(1-\varphi)^2 \ , \tag{11}$$

where φ represents the porosity of the material. For volume preserving yielding, the corresponding plastic potential is given by [11]:

$$G_{hom}(\boldsymbol{\Sigma}, \varphi) = \frac{3}{4}\varphi\Sigma_m^2 + \left(\frac{2}{3}\varphi + 1\right)\Sigma_d^2 \ . \tag{12}$$

In contrast to the model proposed in [11], φ is considered as hardening variable in this paper, depending on the volumetric change of the material. The total change of volume, ΔV, reads:

$$\Delta V = \Delta V_I + \Delta V_M \ . \tag{13}$$

ΔV_I and ΔV_M refer to the volume change in the inclusions (pores) and the matrix phase, respectively. ΔV_M, resulting only from elastic material response, is neglected (plastic deformation was assumed to be volume preserving). Thus, the macroscopic volumetric strain is given by:

$$E^{vol} = \frac{\Delta V}{V} \approx \frac{\Delta V_I}{V} = \frac{V_I + \Delta V_I}{V} - \frac{V_I}{V} = \varphi - \varphi_0 \ . \tag{14}$$

Since the initial φ_0 is a constant, expression (14) becomes in rate form:

$$\dot{\varphi} = \dot{E}^{vol} = \mathrm{tr}(\dot{\mathbf{E}}) \ . \tag{15}$$

2.4 Finite-element implementation

In the numerical simulation of indentation tests, geometric nonlinearities are taken into account. In large-strain elastoplasticity, a common concept is the multiplicative decomposition of the deformation gradient into an elastic and plastic part ($\mathbf{F} = \mathbf{F}^e\mathbf{F}^p$), as originally proposed in [9]. In case of isotropy, this is equivalent to the additive decomposition of the logarithmic strain measure (see, for instance, [13]). Thus, the measures used in the following refer to the logarithmic strain measure.

The material model is defined by

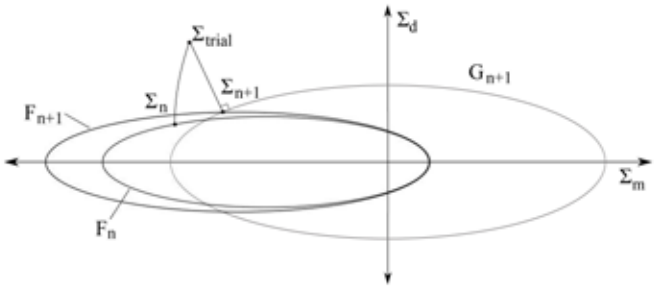

Figure 1: Illustration of the return mapping algorithm.

$$
\begin{aligned}
&\text{decomposition of strain:} && \mathbf{E} = \mathbf{E}^e + \mathbf{E}^p \\
&\text{elastic relation:} && \dot{\boldsymbol{\Sigma}} = \mathbb{C}_{hom} : \dot{\mathbf{E}}^e \\
&\text{flow rule:} && \dot{\mathbf{E}}^p = \dot{\gamma}\mathbf{r}(\boldsymbol{\Sigma}, \varphi) \\
&\text{hardening rule:} && \dot{\varphi} = \dot{\gamma} h(\boldsymbol{\Sigma}, \varphi) \\
&\text{Kuhn-Tucker condition:} && \dot{\gamma} F_{hom}(\boldsymbol{\Sigma}, \varphi) = 0 \ ,
\end{aligned}
$$

where

$$
\mathbf{r}(\boldsymbol{\Sigma}, \varphi) = \frac{\partial G_{hom}(\boldsymbol{\Sigma}, \varphi)}{\partial \boldsymbol{\Sigma}} \qquad \text{and} \qquad h(\boldsymbol{\Sigma}, \varphi) = \text{tr } \mathbf{r}(\boldsymbol{\Sigma}, \varphi) \ . \tag{16}
$$

Herein, $\dot{\gamma}$ denotes the plastic multiplier. For numerical implementation, these equations are discretized with respect to the time, reading for time increment $n+1$:

$$
\begin{aligned}
\boldsymbol{\Sigma}_{n+1} &= \mathbb{C}_{hom} : \mathbf{E}^e_{n+1} \\
\mathbf{E}^e_{n+1} &= \mathbf{E}^e_n + \Delta\mathbf{E}_{n+1} - \Delta\gamma\mathbf{r}(\boldsymbol{\Sigma}_{n+1}, \varphi_{n+1}) \\
\varphi_{n+1} &= \varphi_n + \Delta\gamma h(\boldsymbol{\Sigma}_{n+1}, \varphi_{n+1}) \\
\Delta\gamma F_{hom}(\boldsymbol{\Sigma}_{n+1}, \varphi_{n+1}) &= 0 \ .
\end{aligned} \tag{17}
$$

This non-linear system of equations is solved with a Newton scheme (return mapping) as illustrated in Figure 1. The trial stress is projected normally to the corresponding contour line of the plastic potential onto the updated yield surface. The incremental evolution of the yield surface is governed by the hydrostatic stress change within the correction step. If the hydrostatic stress of $\boldsymbol{\Sigma}_{trial}$ is smaller than that of $\boldsymbol{\Sigma}_{n+1}$ as in Figure 1, negative plastic volumetric strain and consequentially compaction occurs. The resulting decrease of porosity leads to an expansion of the yield surface (hardening).

3 INDENTATION ANALYSIS

3.1 Indentation

During indentation experiments, an indenter with a well-defined geometry is impressed into the surface of the material, while recording the applied force P and the penetration history. In general, the total deformation of the solid comprises a reversible and an

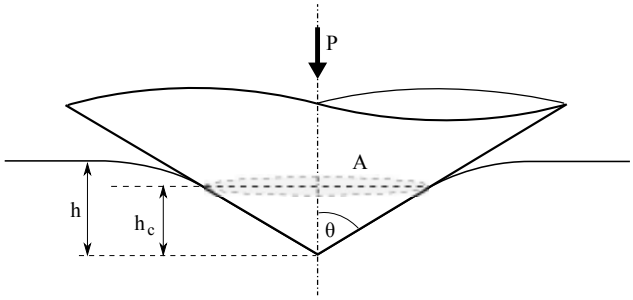

Figure 2: Conical indentation (h: indentation depth, h_c: penetration depth considering pile-up/sink-in, θ: half-angle of the cone, A: projected area of indent, P: applied force.

irreversible part. As a result, permanent deformation remains after unloading, giving access to the hardness of the material usually defined by the ratio of the applied force P and the projected area A of the residual imprint ($H = P/A$).

In this paper, the indentation of the three-sided pyramidal-shaped Berkovic indenter is treated. As this indenter belongs to the class of geometric self-similar indenter, it does not posses a characteristic length scale (unlike, e.g., the radius of spherical indenters). The geometry is completely described by the angle of inclination θ of the pyramid. Consequentially, the applied force P can be expressed in case of porous materials treated in the previous section as

$$P = f_P(E, \nu, c, \alpha, \varphi_0, d_i, h, \theta) \ . \tag{18}$$

Therein, the first four variables are the elastic and plastic properties of the matrix phase and φ_0 is the initial void ratio. The set of variables d_i represents the size of the pores. Applying the Π-theorem according to Cheng [4] yields:

$$\frac{P}{Eh^2} = \Pi_P \left(\frac{E}{c}, \nu, \alpha, \varphi_0, \frac{d_i}{h}, \theta \right) \ . \tag{19}$$

As the sizes of the pores are assumed to be very small in relation to the indentation depth (i.e., $d_i/h \to 0$), the function Π_P can be regarded as independent of the specific values of h and d_i. Thus, the resulting indentation problem is given by

$$\frac{P}{Eh^2} = \Pi_P \left(\frac{E}{c}, \nu, \alpha, \varphi_0, \theta \right) \ . \tag{20}$$

For describing the sink-in and pile-up effect, the variable h_c is introduced (see Figure 2). It defines the vertical distance between the tip of the indenter and the highest point of the material which is in contact with the indenter. Analogously to P, the following relations can be established:

$$h_c = f_h(E, \nu, c, \alpha, \varphi_0, d_i, h, \theta) \ , \tag{21}$$

which yields

$$\frac{h_c}{h} = \Pi_h \left(\frac{E}{c}, \nu, \alpha, \varphi_0, \theta \right) \ . \tag{22}$$

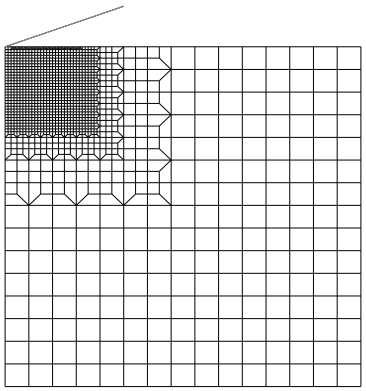

Figure 3: FE model.

3.2 Results

The indentation experiment was simulated with the FE program Abaqus using the user material subroutine and considering geometric nonlinearities. At large strain analysis, Abaqus delivers approximations of logarithmic strains to the user subroutine (c.f. [1]). Thus, the model given in Equation (17) can be employed without modifications.

Instead of using the real geometry of the Berkovic-Indenter, the indentation was simulated by means of a cone with an accordant A/h^2 ratio, giving a half-angle of the cone of 70.32°. Hence, the problem becomes axisymmetric and is modeled in two dimensions (see FE model in Figure 3). Through varying the parameters E/c, α, and φ_0, the yet unknown functions Π_P and Π_h are numerically evaluated.

Π_P and Π_h are evaluated for three different friction coefficients α (0.0, 0.25, and 0.5, see Figure 4). Note, that φ_0 denotes the initial porosity while the current porosity φ depends on the loading history and varies in space.

Low values for the E/c-ratios represent purely elastic material behavior while increasing E/c leads to an increasing influence induced by plasticity. In the elastic range, Π_h apparently does not depend on the porosity φ_0, while this influence increases for larger values for E/c. For materials with porosities larger than about 0.3, Π_h approaches 1.0 for large E/c-ratios. As expected, a higher friction coefficient α causes more stiffness (i.e., higher Π_P) in the elastoplastic domain.

Using Π_P and Π_h, the hardness of the material related to the cohesion is obtained by

$$\frac{H}{c} = \frac{E}{c} \frac{\Pi_P}{\Pi_h^2 \, \pi \, \tan^2\theta} \, . \tag{23}$$

In Figure 5, H/c is displayed and compared with results of Cariou et al.[3]. In [3], extensive parameter studies were performed, examining the material response for a number of different indenters and material properties. Therein, the material model is based on the same yield criterion as in the present work but restricted to associated yielding. As the analysis in [3] is based on limit analysis, neither the loading history and thus sink-in/pile-

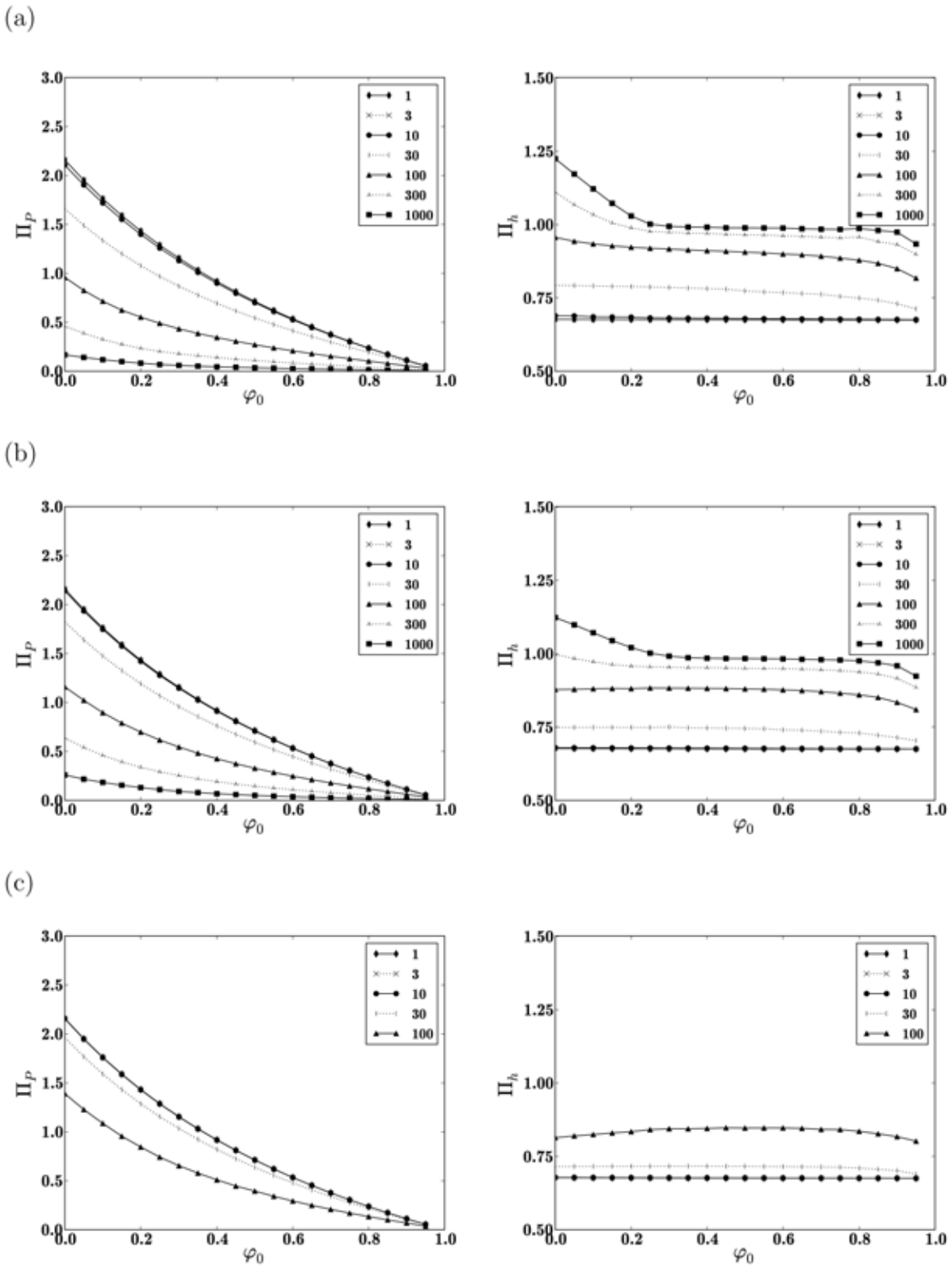

Figure 4: Functions Π_P and Π_h for different E/c-ratios: (a) $\alpha = 0$, (b) $\alpha = 0.25$, and (c) $\alpha = 0.50$.

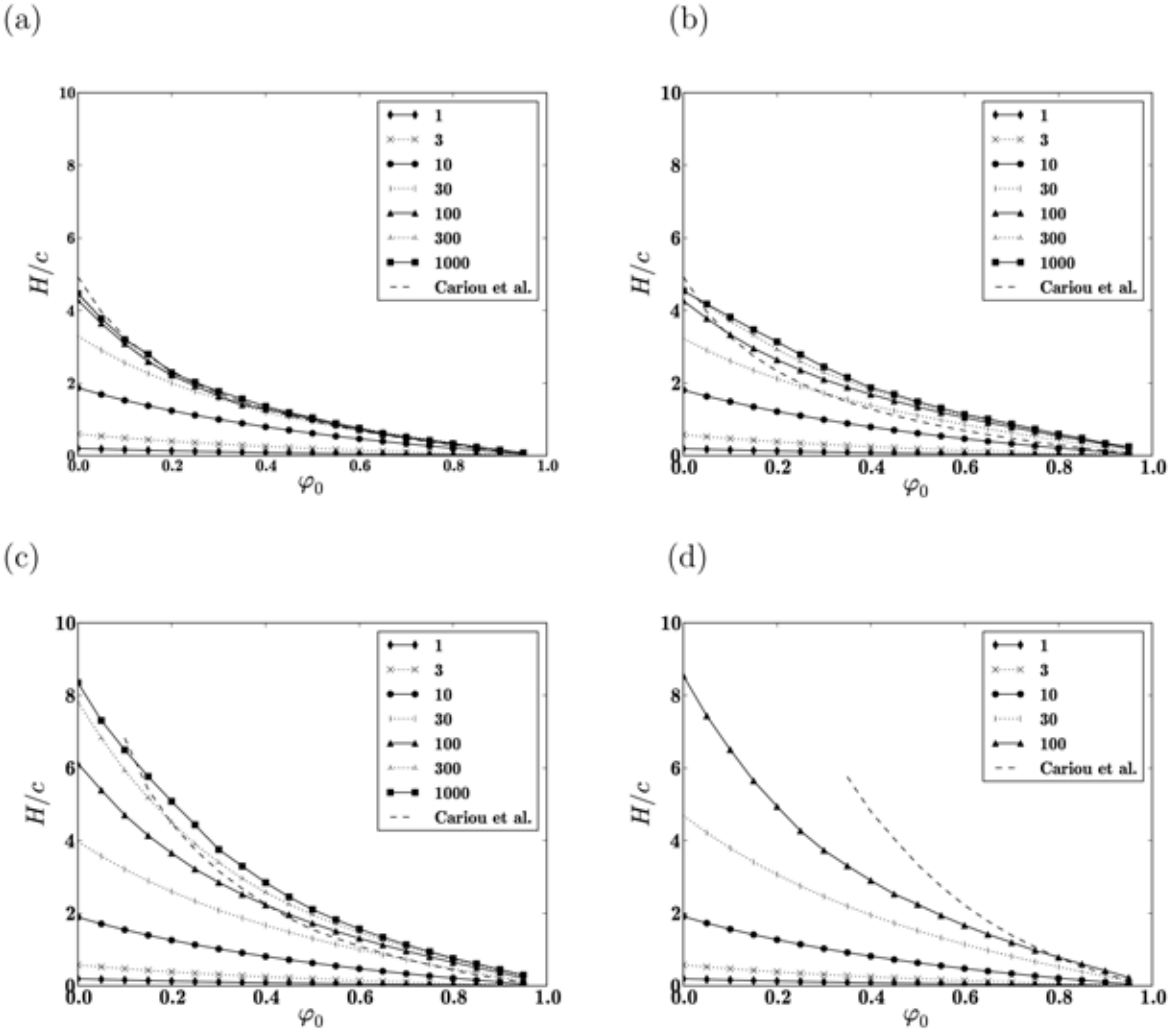

Figure 5: Related hardness H/c for different E/c-ratios: (a) $\alpha = 0$ without hardening, (b) $\alpha = 0$, (c) $\alpha = 0.25$, and (d) $\alpha = 0.50$.

up nor hardening effects were taken into account. Whereas a porosity range from $\varphi = 1.0$ to $\varphi_{crit} = 4/3\alpha^2$ was considered in [3] - for porosities below φ_{crit}, $F_{hom}(\boldsymbol{\Sigma}, \varphi)$ becomes a hyperbolic function - the porosity was varied between 0.0 and 1.0 in the present paper.

To highlight the possible influence of the loading history, Figure 5(a) shows simulation results where hardening, as proposed in this work, is neglected and associated yielding occurs. In this case, the plasticity model coincides with that in [3] while only the analysis methods differ. Since the reference solution from Cariou et al. [3] is valid for rigid materials, it represents an upper bound for the elastoplastic solutions. For large porosities, the solutions for different E/c are indeed bounded by this reference solution. For dense materials, the reference solution shows higher values for H/c which can be explained by the pile-up effect, which occurs at lower porosities and is neglected in Cariou et al. [3].

Figure 5(b) contains simulation results with pore-space controlled hardening, where

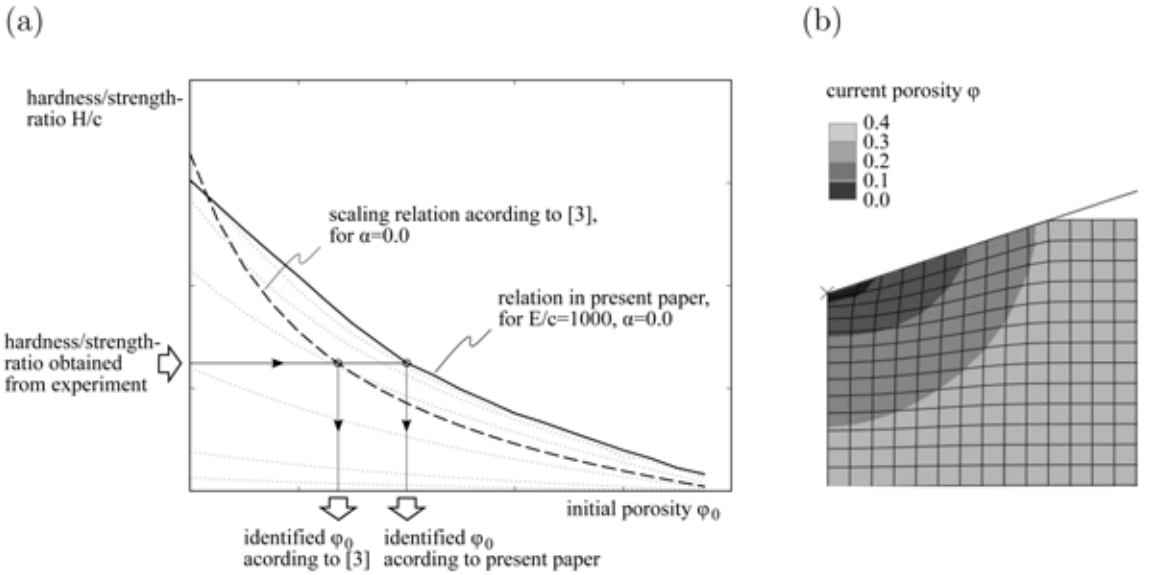

Figure 6: (a) Illustration of parameter identification where matrix material properties are known ($\alpha = 0.0$, $E/c = 1000$) and the initial porosity is looked after. (b) Contour plot of distribution of current porosity from FE analysis ($\varphi_0 = 0.4$, $\alpha = 0.0$, $E/c = 1000$).

the same material parameters were used as in Figure 5(a). Since no hardening occurs at absence of pore space, results for $\varphi = 0$ coincide in Figures 5(a) and (b). For $\varphi > 0$ however, an increase of the hardness as a consequence of hardening is clearly visible.

In case of $\alpha \neq 0$, the flow rule of the present material model becomes non-associated (see Equations (11) and (12)). While in [3] plastic dilation as well as plastic contraction are observed, only plastic contraction takes place in the present case since there are no distinct zones of hydrostatic tension. The absence of dilation reduces the hardness. A comparison of Figures 5(a) to (c) indicates, that the overall influence of the flow and hardening rule become larger for decreasing friction coefficients, providing improved estimates for the hardness when non-associated flow and hardening are taken into account.

4 CONCLUSION

Based on a continuum micro-mechanical approach described in Maghous et al. [11] a formulation of a material model was presented considering hardening controlled by change of porosity. By means of FE simulations, the indentation response of porous materials was evaluated for different materials, characterized by varying initial porosity, friction, and stiffness/strength-ratio. The so-obtained relations serve as a basis for identification of parameters of porous materials, giving insight into strength properties of material phase and/or into the composition of the material (porosity).

First results indicate that consideration of loading history and hardening may significantly improve the model performance, especially for high porosities and low friction angles, where the hardness may be clearly underestimated otherwise. For illustration

purpose, one application in parameter identification, shown in Figure 6(a), is considered where the properties of the matrix phase are known (E, ν, c, and α) and the initial porosity φ_0 should be determined. For an experimentally-determined hardness/strength-ratio H/c of 1.95, the scaling relation presented in this paper yields an initial porosity of $\varphi_0 \approx 0.4$ for $\alpha = 0$ and $\varphi_0 \approx 0.53$ for $\alpha = 0.25$, whereas the scaling relations in [3] underestimate the initial porosity with $\varphi_0 \approx 0.26$ and $\varphi_0 \approx 0.45$, respectively, representing somehow the spatial distribution of the porosity below the indenter tip (see Figure 6(b)) in an average manner.

ACKNOWLEDGMENT

The results reported in this paper were obtained within the research project "Model-based optimization of recycling building materials for the use as unbounded base-layer material", financially supported by the Austrian Research Promotion Agency (FFG). The authors gratefully acknowledge this support!

REFERENCES

[1] Abaqus Version 6.10 Documentation. Dassault Systèmes (2010).

[2] Barthélémy, J.F. and Dormieux, L. Détermination du critère de rupture macroscopique d'un milieu poreux par homogénéisation non linéaire. *Comptes Rendes Mecanique* (2003) **331**:271–276.

[3] Cariou, S., Ulm, F.J. and Dormieux, L. Hardness-packing density relation for cohesive-frictional porous materials. *Journal of the Mechanic and Physics of Solids* (2008) **56**:924–952.

[4] Cheng, Y.-T. and Cheng, C.-M. Scaling, dimensional analysis, and indentation measurements. *Material, Science and Engineering* (2004) **R44**:91–149.

[5] Cheng, Y.-T. and Cheng, C.-M. Scaling relationships in conical indentation of elastic - perfectly plastic solids. *Inernational Journal of Solids and Structures* (1999) **36**:1231–1243.

[6] Constantinides, G. , Ravi Chandran, K.S., Ulm F.-J. and Van Vliet K.J. Grid indentation analysis of composite microstructure and mechanics: Principles and validation. *Materials Science and Engineering A* (2006) **430**:189–202.

[7] Dormieux, L., Kondo, D. and Ulm, F.J. *Microporomechanics*. Wiley, Chichester, UK, (2006).

[8] Gurson, A.L. Continuum theory of ductile rupture by void nucleation and growth: part I - yield criteria and flow rules for porous ductile media. *ASME Journal of Engineering Materials and Technology* (1977) **99**:2–15.

[9] Lee, E.H. and Liu, D.T. Finite strain elastic-plastic theory with application to plane-wave analysis. *Journal of Applied Physics* (1967) **36**:1–6.

[10] Lemarchand, E., Ulm, F.J. and Dormieux, L. The effect of inclusions on the friction coefficient of highly-filled composite materials. *Journal of Engineering Mechanics* (2002) **128** (8):876–884.

[11] Maghous, S., Dormieux, L. and Barthélémy, J.F. Micromechanical approach to the strength properties of frictional geomaterials. *European Journal of Mechanics A/Solids* (2009) **28**:179–188.

[12] Pastor, J., Thoré, Ph. and Pastor, F. Limit analysis and numerical modeling of spherically porous solids with Coulomb and Drucker-Prager matrices. *Journal of Computational and Applied Mathematics* (2010) **234**:2162–2174.

[13] Perić, D., de Souza Neto, E.A. and Owen, D.R.J. *Computational Methodes for Plasticity* . John Wiley & Sons, Chichester, (2008).

[14] Pichler, C., Lackner, R. and Ulm, F.J. Scaling relations for viscoelasticcohesive conical indentation. *International Journal of Materials Research* (2008) **99**:836–846.

[15] Tabor, D. A simple theory of static and dynamic hardness. *Proceedings of the Royal Society, Series A* (1948) **192**:247–274.

[16] Zaoui, A., Continuum micromechanics: survey. *Journal of Engineering Mechanics* (2002) **128** (8):808–816.

XI International Conference on Computational Plasticity. Fundamentals and Applications
COMPLAS XI
E. Oñate, D.R.J. Owen, D. Peric and B. Suárez (Eds)

SIMULATION OF DP-STEELS BASED ON STATISTICALLY SIMILAR REPRESENTATIVE VOLUME ELEMENTS AND 3D EBSD DATA

D. BRANDS*, D. BALZANI*, J. SCHRÖDER* AND D. RAABE†

*Institute of Mechanics, Faculty of Engineering, Department of Civil Engineering,
University of Duisburg-Essen,
Universitätsstraße 15, 45141 Essen, Germany
e-mail: dominik.brands@uni-due.de

† Max-Planck-Institut für Eisenforschung GmbH
Dept. Microstructure Physics and Metal Forming
Max-Planck-Straße 1, 40237 Düsseldorf, Germany

Key words: multiscale problems, homogenization, material properties, finite plasticity, microstructures, statistically similar RVE, EBSD

Abstract. Micrographs of a dual-phase steel obtained from a EBSD-FIB imaging are analyzed with respect to a set of statistical measures. Then the applicability of this data to the construction of statistically similar representative volume elements (SSRVEs) is discussed. These SSRVEs are obtained by minimizing a least-square functional taking into account differences of statistical measures computed for a given reference microstructure and the SSRVE, cf. [11]. For an analysis of the mechanical response the FE^2-method is used and a series of virtual experiments shows the accordance of the response of the SSRVE to the one of the reference microstructure. In order to demonstrate the performance of the proposed procedure some representative numerical examples are given.

1 Introduction

To achieve the demands for high strength and good formability modern steels as e.g. dual-phase steels make use of multi-phase microstructures, see e.g. [4], [5]. Since the micromechanics of these micro-heterogeneous materials mainly govern the overall material behavior they need to be taken into account when computer simulations of deep-drawing processes are performed. For this purpose the FE^2-method provides a suitable numerical tool, see e.g. [12], [7], [10]. There a microscopic boundary value problem, which is based on the definition of a representative volume element (RVE), is solved at each macroscopic integration point. However, this method is computationally expensive if substructures of real micrographs are used as an RVE since these are typically too complex for efficient

discretizations at the microscale. For that reason the estimation of a suitable RVE is a challenging task. Thus, we analyze in a first step several micrographs obtained from a 3D EBSD imaging. Afterwards we construct statistically similar RVEs (SSRVEs) which are characterized by a strongly reduced complexity than usual RVEs and which therefore lead to procedures of significantly improved efficiency.
The paper is organized as follows. In the first section we introduce several statistical measures for the characterization of microstructural morphology and afterwards analyze them for micrographs from a three-dimensional EBSD-FIB imaging. Section 3 describes the construction method of SSRVEs and the application to a dual-phase steel microstructure. This paper is closed with numerical examples and a conclusion.

2 Characterization of the Morphology

In this section we are interested in the analysis of the morphology of dual-phase steels, which are characterized by a martensitic inclusion phase embedded in a ferritic matrix phase. In addition to the individual mechanical properties of both constituents, the macroscopic mechanical behavior is also significantly governed by the morphology of the inclusion phase at the microscale. Therefore we introduce in the following subsections several statistical measures characterizing the inclusion morphology and analyze a stack of two-dimensional micrographs obtained from a 3D EBSD-FIB imaging with respect to these measures.

2.1 Statistical Measures

A well-known fundamental measure for the characterization of the morphology is the volume fraction, also referred to as phase fraction. This measure is defined for the inclusion phase i by

$$\mathcal{P}_V^{(i)} := \frac{V_{(i)}}{V} \,, \tag{1}$$

where $V_{(i)}$ denotes the volume of the phase i. In [8] additional basic parameters for the description are given, e. g. surface density and integrals of curvature. Since typically also direction-dependend information regarding e.g. laminate-like arranged inclusions leading to a macroscopically anisotropic behavior, these measures are not sufficient for the characterization of complex microstructures, see [2]. Thus, we consider statistical measures of higher order to capture microscopic information regarding periodic and directional characteristics in the microstructure.
As a first measure of higher order we consider the (discrete) spectral density (SD) for the inclusion phase computed from the binary image of the micrograph. The SD is computed by the multiplication of the (discrete) Fourier transform with its conjugate complex. The discrete SD is defined by

$$\mathcal{P}_{SD}(m,k) := \frac{1}{2\pi\, N_x\, N_y} \left|\mathcal{F}(m,k)\right|^2 \tag{2}$$

with the Fourier transform given by

$$\mathcal{F}^I(m,k) = \sum_{p=1}^{N_x}\sum_{q=1}^{N_y} \exp\left(\frac{2\,i\,\pi\,m\,p}{N_x}\right) \exp\left(\frac{2\,i\,\pi\,k\,q}{N_y}\right) \chi^I_{SD}(p,q)\,. \tag{3}$$

The maximal numbers of pixels in the considered binary image are given by N_x and N_y; the indicator function is defined as

$$\chi_{SD} := \begin{cases} 1, & \text{if } (p,q) \text{ is in the inclusion phase} \\ 0, & \text{else}\,. \end{cases} \tag{4}$$

A further statistical measure is provided by the lineal-path function, which describes the probability that a complete line segment $\overrightarrow{\boldsymbol{x_1 x_2}}$ is located in the same phase, see [13]. For its mathematical description we consider the modified indicator function

$$\chi_{LP}(\overrightarrow{\boldsymbol{x}_1\boldsymbol{x}_2}) := \begin{cases} 1, & \text{if} \quad \overrightarrow{\boldsymbol{x}_1\boldsymbol{x}_2} \quad \text{is in the inclusion phase} \\ 0, & \text{else}\,. \end{cases} \tag{5}$$

For two-dimensional binary images of statistically homogeneous and ergodic inclusion-matrix microstructures the lineal-path function is computed by

$$\mathcal{P}^I_{LP}(m,k) = \frac{1}{N_x N_y} \sum_{p=1}^{N_x}\sum_{q=1}^{N_y} \chi^I_{LP}(\overline{\boldsymbol{x}_m \boldsymbol{x}_k})\,, \tag{6}$$

for a periodic unitcell. Herein, $N_x \times N_y$ defines the number of pixels of the binary microstructure image to be analyzed. Efficient procedures for the calculation of the lineal-path function can be obtained by defining suitable templates, cf. [15].

2.2 Analysis of Ensemble Average

In this section we analyze several micrographs with respect to the statistical measures introduced in the previous subsection. They are obtained from a metallographic characterization using the 3D electron backscatter diffraction (3D EBSD) method. Thereby a joint high-resolution field emission SEM/EBSD set-up is coupled with a focused ion beam system (FIB) and provides a set of cross-sectional planes of the considered dual-phase steel. The equipment and the geometric arrangement is shown in Fig. 1a,b

The sample of the considered dual-phase steel is mounted on a tiltable holder inside the equipment, cf. Fig. 1b. During the investigation the sample is tilt between two positions: the cutting and the EBSD position. In the cutting position the FIB system milling thin layers (10 nm - 1 μm thick) from the investigated surface of the sample. The other position is used for the EBSD analysis, where an electron beam is focussed onto the milled surface and the back scatter diffraction patterns are monitored by the EBSD camera. Due to different diffraction patterns several properties of the sample can be analyzed, e. g. crystal orientations and grain size. Additionally a reconstruction of the in-plane morphology

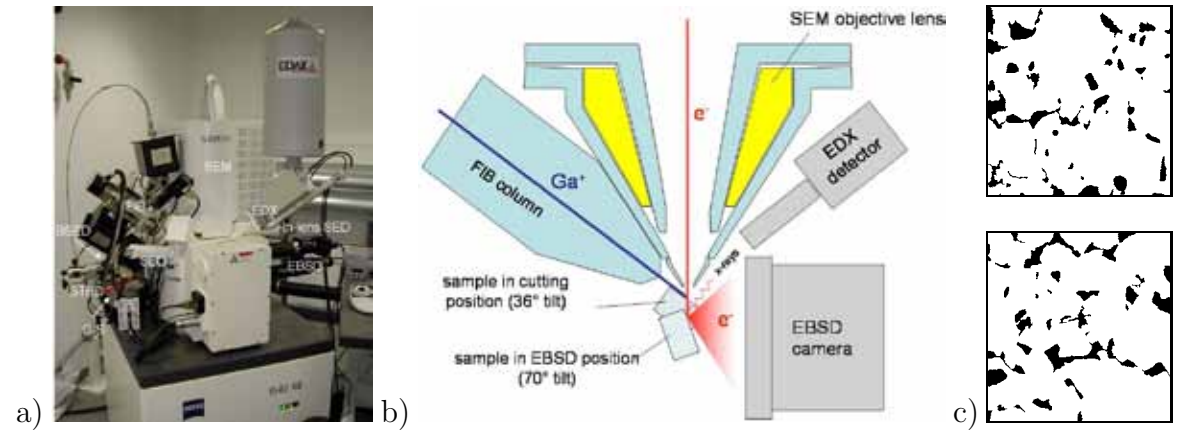

Figure 1: 3D EBSD: a) equipment, b) technical setup, cf. [6], and c) two examples of obtained cross-sections of the considered dual-phase. The micrographs are color-coded with respect to the phases (white: ferrite, black: martensite) and with an approximate dimension of $15 \times 15\,\mu\mathrm{m}^2$.

of the ferritic matrix and the martensitic inclusion phase are possible based on this back scatter diffraction patterns. Such micrographs are exemplarily depicted in Fig. 1c. For more details concerning the 3D EBSD method we refer to [6, 3, 14].
In this contribution we use a set of 50 micrographs obtained by the aforementioned technique. The volume fraction, the spectral density and the lineal-path function of all slices are calculated from the binary images. Considering a constant distribution density for the individual samples (micrographs) the ensemble average $\overline{\mathcal{P}_{SM}}$ of the particular statistical measures $\mathcal{P}_{SM}$ can be computed by

$$\overline{\mathcal{P}_{SM}} = \frac{1}{n_\alpha} \sum_{\alpha=1}^{n_\alpha} \mathcal{P}_{SM} \quad \text{with } n_\alpha \text{ samples}\,, \tag{7}$$

where n_α denotes the number of samples. The relative standard deviation is given by

$$\hat{S}_{SM} = S_{SM} \big/ \overline{\mathcal{P}_{SM}} \quad \text{with} \quad S_{SM} = \sqrt{\frac{\sum_{n=1}^{n_\alpha} (\mathcal{P}_{SM}(\alpha) - \overline{\mathcal{P}_{SM}})}{n_\alpha (n_\alpha - 1)}}\,, \tag{8}$$

where S_{SM} denotes the absolute standard deviation and $\mathcal{P}_{SM}(\alpha)$ the individual value of the statistical measure computed from the sample α. Note, that due to the two-dimensional character of the spectral density and lineal-path function we apply the latter equations to each point in the image space. The results are represented by two-dimensional arrays $\hat{S}_{SM}(p,q)$ with the dimension $N_x^{SM} \times N_y^{SM}$. To achieve a scalar-valued comparative measure we introduce the mean relative standard deviation

$$\hat{S}_{SM}^{\varnothing} = \sqrt{\frac{1}{N_X N_y} \sum_{p=1}^{N_X^{SM}} \sum_{q=1}^{N_y^{SM}} \left[\hat{S}_{SM}(p,q)\right]^2}\,. \tag{9}$$

Finally, we obtain the values of the relative standard deviation and the mean relative standard deviations

$$\hat{S}_V = 0.45{\cdot}10^{-1}\,, \quad \hat{S}^{\varnothing}_{SD} = 1.57{\cdot}10^{-1}\,, \quad \text{and} \quad \hat{S}^{\varnothing}_{LP} = 2.36{\cdot}10^{-1} \tag{10}$$

of the volume fraction (V), spectral density (SD) and the lineal-path function (LP), respectively. From the relatively low values we conclude, that the distribution of the considered statistical measures along the thickness direction is relatively homogeneous. This leads to the conclusion that two-dimensional micrograph data might be suffient for the construction of two-dimensional SSRVEs, which in turn may enter numerical calculations of two-dimensional boundary value problems. Thus, in the following section we use one micrograph taking into account a larger region as the reference microstructure for the construction of the SSRVEs, cf. Fig. 2a.

3 Statistically Similar RVEs

The choice of the representative volume elements (RVE) is an essential task in the context of direct micro-macro approaches. In general, the RVE is determined by the smallest possible sub-domain reflecting the macroscopic behavior of the target material in an adequate manner. However, these RVEs are typically too complex for efficient calculations. Therefore, the construction of statistically similar RVEs (SSRVEs) which are characterized by a significantly lower complexity are to be constructed in this section, cf. [1], where the method is introduced taking into account the volume fraction and the spectral density. The main effort of such SSRVEs is that due to the reduced complexity a significantly reduced number of finite elements is required for the discretization of the microscopic boundary value problem in the context of FE^2-calculations. As a result, a decreased computational cost is obtained.

3.1 Method for Construction

The main idea for the construction of SSRVEs is to minimize a least-square functional taking into account differences of statistical measures computed for the real target microstructure and the SSRVE. Thereby, it is assumed that the inclusion phase morphology mainly influences the overall behavior provided that the material properties of the individual phases are known. The minimization problem is formulated by

$$\mathcal{L}(\boldsymbol{\gamma}) = \sum_{L=1}^{n_{sm}} \omega_i \, \mathcal{L}^{(L)}_{SM}(\boldsymbol{\gamma}) \quad \rightarrow \quad \min\,, \tag{11}$$

where the individual least-square functionals $\mathcal{L}^{(L)}_{SM}$ are based on the difference of suitable statistical measures. The weighting factor ω levels the influence of the individual measures. The vector $\boldsymbol{\gamma}$ describes the parameterization of the inclusion phase morphology. Here, splines are used for the parameterization and thus, the sampling point coordinates enter

the generalized vector $\boldsymbol{\gamma}$ of the degrees of freedom of the minimization problem given in (11). In this contribution five different types of SSRVEs are considered: Type I taking into account one inclusion with three sampling points (leading to an inclusion with a convex shape), Type II with one inclusion and four sampling points, Type III with two inclusions and three sampling points each, Type IV with two inclusions and four sampling points each and Type V with three inclusions and three sampling points each. Due to the discrete character of the statistical measures used in the minimization problem (11) the energy surface is not smooth and therefore, no gradient-based optimization method can be applied. Therefore, the moving-frame algorithm proposed in [2] is used. In [11] we showed that the combination of the volume fraction (V), the spectral density (SD) and the lineal-path function (LP) as statistical measures leads to promising results in the context of two-phase materials, whose macroscopic mechanical response is mainly governed by the microstructural morpohology. From this we define the three individual least-square functionals

$$\begin{aligned}
\mathcal{L}_V(\boldsymbol{\gamma}) &:= \left(1 - \frac{\mathcal{P}_V^{SSRVE}(\boldsymbol{\gamma})}{\mathcal{P}_V^{real}}\right)^2 , \\
\mathcal{L}_{SD}(\boldsymbol{\gamma}) &:= \frac{1}{N_x\, N_y} \sum_{m=1}^{N_x} \sum_{k=1}^{N_y} \left(\mathcal{P}_{SD}^{real}(m,k) - \mathcal{P}_{SD}^{SSRVE}(m,k,\boldsymbol{\gamma})\right)^2 , \\
\mathcal{L}_{LP}(\boldsymbol{\gamma}) &:= \frac{1}{N_x\, N_y} \sum_{m=1}^{N_x} \sum_{k=1}^{N_y} \left(\mathcal{P}_{LP}^{real}(m,k) - \mathcal{P}_{LP}^{SSRVE}(m,k,\boldsymbol{\gamma})\right)^2 .
\end{aligned} \tag{12}$$

It is remarked that for the computation of the statistical measures $\mathcal{P}_{SD}$ and $\mathcal{P}_{LP}$ periodic expansions of the SSRVE are considered by placing as much SSRVEs as needed at each other periodically. Following equation (11) we end up with the objetive function

$$\mathcal{L}(\boldsymbol{\gamma}) = \omega_V \mathcal{L}_V(\boldsymbol{\gamma}) + \omega_{SD} \mathcal{L}_{SD}(\boldsymbol{\gamma}) + \omega_{LP} \mathcal{L}_{LP}(\boldsymbol{\gamma}) , \tag{13}$$

which is minimized using the aforementioned optimization algorithm.

3.2 Two-Dimensional SSRVEs

Now we apply the method for the construction of SSRVEs to a real dual-phase steel microstructure and consider the micrograph shown in Fig. 2 as target structure. Considering the objective function (13) and the five different types of inclusion parameterization we receive from minimizing (11) five realizations of SSRVEs. The finite element discretization of these SSRVEs required for the following mechanical error analysis are shown in Fig. 3. After the SSRVE construction we have to analyze the capability of the resulting structures to represent the macroscopic mechanical response of the target structure. Thus, we consider three different simple macroscopic virtual experiments: horizontal tension, vertical tension and simple shear. FE^2-simulations taking into account the target structure at the microscale are compared with FE^2-calculations focussing on the constructed SSRVEs.

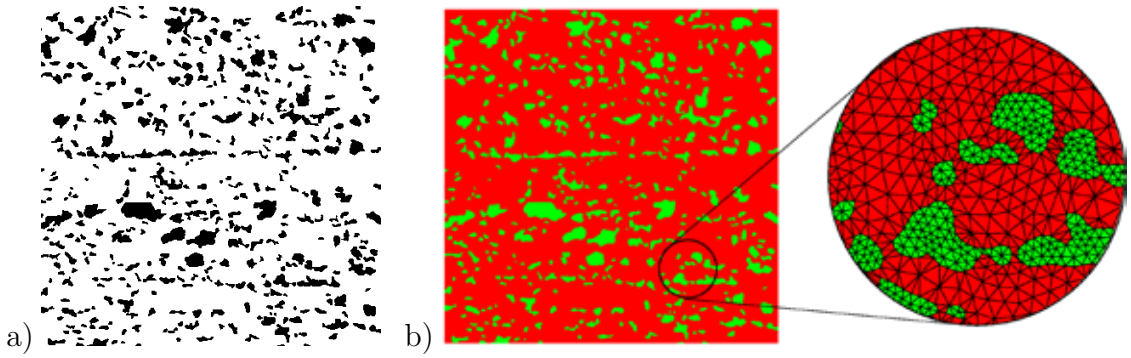

Figure 2: Target Structure: a) real micrograph with a dimension of approximately $100 \times 100\,\mu\text{m}^2$ and b) discretization by 6-noded triangular finite elements resulting in approximately 150,000 degrees of freedom.

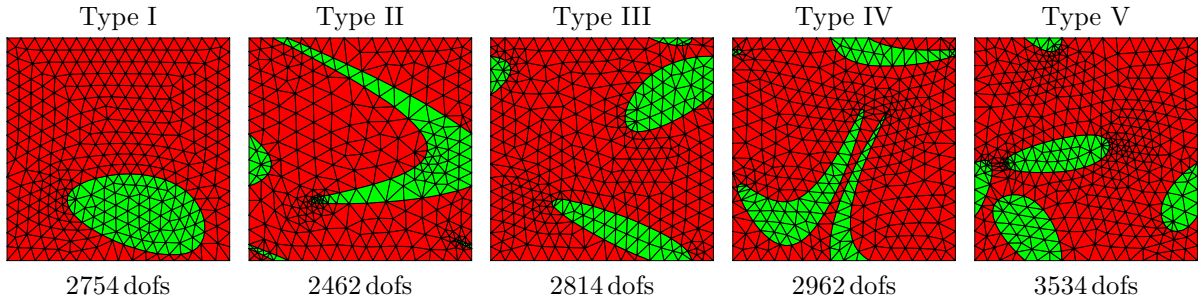

Figure 3: Discretization of the resulting SSRVEs with the associated number of degrees of freedom (dofs).

For this purpose microscopic boundary value problems where a discretization by triangular Finite Elements with quadratic ansatz functions for the displacements are considered. Furthermore, plain stress conditions and periodic boundary conditions are applied. The individual constituents at the microscale are modeled by a standard J_2-finite plasticity model, for details see e. g. [9]. An exponential von Mises hardening law is used, i.e.

$$\beta = y_\infty + (y_0 - y_\infty)\exp(-\eta\alpha) + h\,\alpha\,, \tag{14}$$

with $\beta = \partial_\alpha \psi^p$ and ψ^p denoting the strain energy function associated to the hardening; α are the equivalent plastic strains. The material parameters are adjusted to experiments performed on purely ferritic and purely martensitic test specimens and given in Table 1.

Table 1: Material parameters of the single phases

phase	λ [MPa]	μ [MPa]	y_0 [MPa]	y_∞ [MPa]	η [-]	h [-]
matrix	118,846.2	79,230.77	260.0	580.0	9.0	70.0
inclusion	118,846.2	79,230.77	1000.0	2750.0	35.0	10.0

Table 2: Values of the objective functions $\mathcal{L}$ and the mechanical errors $\widetilde{r}$. n_{ele} denotes the number of finite elements in the discretization.

SSRVE	$\mathcal{L}$ $[10^{-3}]$	$\mathcal{L}_V$ $[10^{-5}]$	$\mathcal{L}_{SD}$ $[10^{-4}]$	$\mathcal{L}_{LP}$ $[10^{-5}]$	n_{ele}	$\widetilde{r}_x$ [%]	$\widetilde{r}_y$ [%]	$\widetilde{r}_{xy}$ [%]	$\widetilde{r}$ [%]
I	39.41	238.05	230.96	139.38	656	1.16 ± 0.29	1.58 ± 0.39	3.34 ± 0.91	2.24
III	8.66	8.82	62.87	22.81	670	0.26 ± 0.20	2.24 ± 0.52	0.41 ± 0.22	1.32
V	4.22	1.42	36.62	5.41	850	1.12 ± 0.35	0.92 ± 0.26	1.10 ± 0.23	1.05
II	9.29	14.90	71.31	20.08	582	8.24 ± 2.10	2.10 ± 0.31	7.45 ± 2.87	6.53
IV	3.70	4.33	33.88	2.73	708	2.22 ± 0.80	4.89 ± 1.24	2.43 ± 1.22	3.40

As comparative mechanical measures we consider the relative errors r_x, r_y and r_{xy} defined as the deviation of the resulting macroscopic SSRVE stress response from the target structure response at each evaluation point i for the three virtual experiments:

$$r_x^{(i)} = \frac{\overline{\sigma}_{x,i}^{\text{real}} - \overline{\sigma}_{x,i}^{\text{SSRVE}}}{\overline{\sigma}_{x,i}^{\text{real}}}, \qquad r_y^{(i)} = \frac{\overline{\sigma}_{y,i}^{\text{real}} - \overline{\sigma}_{y,i}^{\text{SSRVE}}}{\overline{\sigma}_{y,i}^{\text{real}}}, \qquad r_{xy}^{(i)} = \frac{\overline{\sigma}_{xy,i}^{\text{real}} - \overline{\sigma}_{xy,i}^{\text{SSRVE}}}{\overline{\sigma}_{xy,i}^{\text{real}}}, \tag{15}$$

where only values with non-vanishing denominators are taken into account. In addition to that, the average errors for each experiment

$$\widetilde{r}_{x,y,xy} = \sqrt{\frac{1}{n_{ep}} \sum_{i=1}^{n_{ep}} [r_{x,y,xy}^{(i)}]^2} \quad \text{with} \quad r_{x,y,xy}^{(i)} := r\left(\tfrac{i}{n} \triangle l_{\max}/l_0\right) \tag{16}$$

and the overall comparative measure

$$\widetilde{r}_{\varnothing} = \sqrt{\frac{1}{3}\left(\widetilde{r}_x^2 + \widetilde{r}_y^2 + \widetilde{r}_{xy}^2\right)} \tag{17}$$

are taken into account for quantitative statements with respect to the performance of the individual SSRVEs. The total number of evaluation points i is denoted by n_{ep}. The mechanical response of the five SSRVEs in the three virtual experiments are calculated using the FE^2-scheme. The results of the construction of the SSRVEs are summarized in Tab. 2. Therein we order the results of the SSRVE types seperately with respect to the number of sampling points. First, it can be observed that with increasing complexity, i.e. higher numbers of inclusions, the value of the objective function $\mathcal{L}$ decreases. Second, it turns out that Type V is showing satisfying results in all virtual experiments and has consequently the lowest value of the overall error $\widetilde{r}$. Thus, we consider Type V as the "best" SSRVE in this analysis and use it in a numerical example in the next chapter.

4 Numerical Example

Now we consider a macroscopically inhomogeneous FE^2-simulation to show the capability of the SSRVE. Therefore, we consider a radially loaded circular disk with a hole,

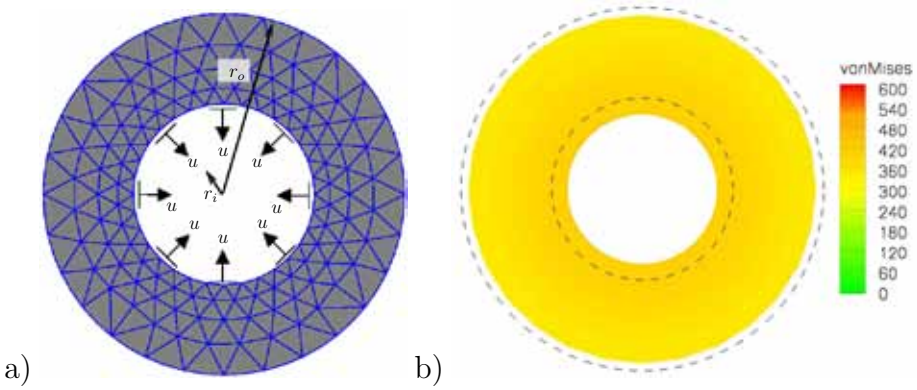

Figure 4: Radially loaded circular disk: a)Macroscopic boundary value problem, b)von Mises stress distribution of the computation using a phenomenological material law (finite J_2 plasticity) at the macroscale.

discretized by 252 triangular elements with quadratic ansatz functions and plain strain conditions. The outer radius of the disk is $r_o = 4\,\text{cm}$ and the inner one is $r_i = 2\,\text{cm}$, see Fig. 4a. The load is applied on the inner radius of the disk and pulls the inner border radially inwards up to a displacement of $u = 0.35\,\text{cm}$. This boundary value problem is known to be an approximation for a deep-drawing process of a cup if the outer part of the plate is to be analyzed.

Firstly, we use a phenomenological material law to describe the mechanical behavior in each macroscopic integration point and consequently it represents a purely macroscopic computation. We apply the same finite J_2 plasticity model as for the individual phases of the microstructures. The material parameters are adjusted such that the mechanical behavior matches the response of the target structure in the three virtual experiments as similarly as possible. Here we already observe that only the tensions tests can be represented accurately in contrast to the simple shear test. In Fig. 4b the results of the purely macroscopic computation of the circular disk are shown. A slightly graded stress distribution with a range about 350 MPa at the outer radius to 430 MPa at the inner one is observed. These results are now compared with the FE^{2}simulation using the SSRVE Type V at the microscale, which shows the "best" accuracy regarding the mechanical behavior of the real microstructure in the aforementioned virtual experiments. In Fig. 5 the results of this FE^2-simulation are depicted, where we show the macroscopic response top left. For the analysis of the microscopic results we select three integration points at the macroscale and place the associated microstructures also in Fig. 5, where contour plots of the von Mises stresses are shown. At the macroscale the stress ranges from about 400 MPa at the outer radius to 630 MPa at the inner one. The maximum stress level at the microscale is significantly higher as at the macroscale, up to a factor of two. Compared to the purely macroscopic simulation this is a higher maximum stress and has a stronger gradient in radial direction. These aspects show the advantages of a FE^{2}simulation because it offers a more critical view on the stress levels at the macro- and microscale and consequently provides information which might be important for failure initialization analysis.

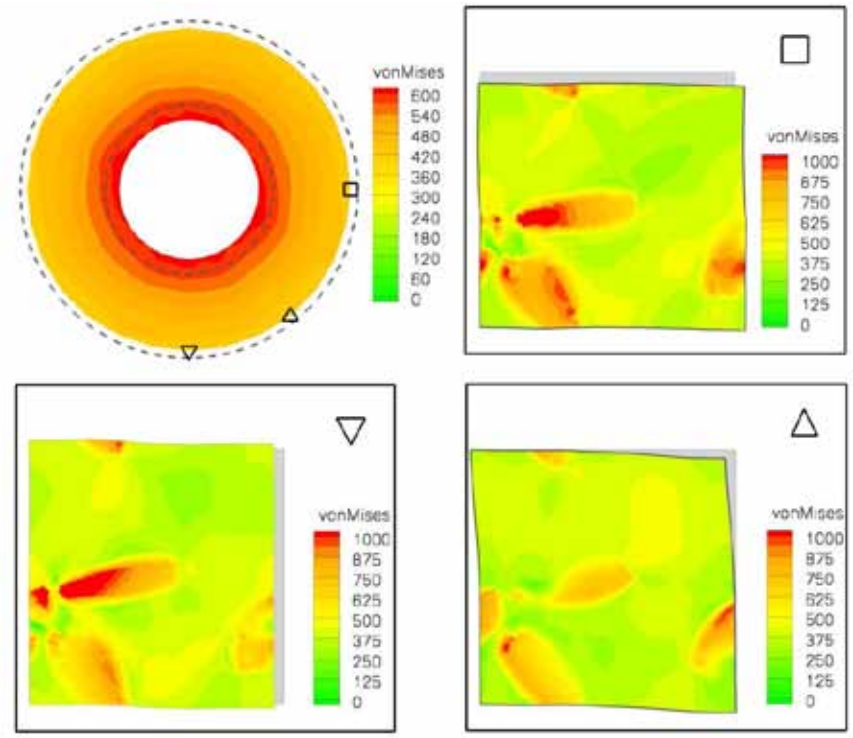

Figure 5: Results of the FE^2-simulations based on SSRVE Type V with the von Mises stress distributions in the deformed microstructures for three selected positions. The symboles in the upper right corner of the images for the microscopic response represent the link to the macroscopic position; the grey area behind the microstructure indicates the undeformed configuration.

5 Conclusions

A stack of micrographs of a dual-phase steel, which was obtained from a 3D EBSD imaging, was analyzed with respect to the distribution of three statistical measures: the volume fraction, the spectral density and the lineal-path function. From this it was observed that the measures show a relatively low variance along the thickness direction. Thus, based on these results only one micrograph was considered for the construction of statistically similar RVEs. Then, it was shown in several virtual experiments that the constructed SSRVEs are able to represent the mechanical behavior of the real microstructure, while the number of degrees of freedom is significantly decreased. By comparing the mechanical response observed in three different virtual experiments of different types of SSRVEs with the mechanical behavior of the target microstructure a number of three convex inclusions (Type V) turned out to be sufficient for the representation of the original microstructure. As an example this SSRVE was used in a macroscopically inhomogeneous boundary value problem and compared with the response obtained from a purely macroscopic computation.

Acknowledgement: The financial support of the "Deutsche Forschungsgemeinschaft" (DFG), research group MICROPLAST (FG 797) on "Analysis and Computation of Microstructures in Finite Plasticity", projects TP7 "High resolution scanning electron back scatter diffaction experiments of local crystallographic orientation patterning during plastic deformation" and TP8 "Statistically similar representative microstructures in elasto-plasticity" (SCHR 570/8-2) is gratefully acknowledged.

REFERENCES

[1] D. Balzani, J. Schröder, and D. Brands, FE^2-Simulation of Microheterogeneous Steels based on Statistically Similar RVE's, *IUTAM Bookseries, 1, Vol. 21, IUTAM Symposium on Variational Concepts with applications to the mechanics of materials, Bochum, September 22-26, 2008*, 15–28, 2010.

[2] D. Balzani, D. Brands, J. Schröder, and C. Carstensen, Sensitivity Analysis of Statistical Measures for the Reconstruction of Microstructures Based on the Minimization of Generalized Least-Square Functionals, *Technische Mechanik*, **30**, 297–315, 2010.

[3] A. Bastos, S. Zaefferer, D. Raabe, C. Schuh, Characterization of the Microstructure and Texture of Nanostructured Electrodeposited NiCo by use of Electron Backscatter Diffraction (EBSD), *Acta Materialia*, **54**, 2451– 2462, 2006.

[4] M. Calcagnotto, D. Ponge, D. Raabe, Orientation gradients and geometrically necessary dislocations in ultrafine grained dual-phase steels studied by 2D and 3D EBSD, *Mater. Sc. Engin. A*, **527**, 2738-2746, 2010.

[5] M. Calcagnotto, Y. Adachi, D. Ponge, D. Raabe, Deformation and fracture mechanisms in fine- and ultrafine-grained ferrite/martensite dual-phase steels and the effect of aging, *Acta Materialia*, **59**, 658-670, 2011.

[6] J. Konrad, S. Zaefferer, D. Raabe, Investigation of Orientation Gradients Around a Hard Laves Particle in a Warm Rolled Fe3Al-Based Alloy by a 3D EBSD-FIB Technique, *Acta Materialia*, **54**, 1369–1380, 2006.

[7] C. Miehe, J. Schröder, and J. Schotte, Computational homogenization analysis in finite plasticity. Simulation of texture development in polycrystalline materials, *Computer Methods in Applied Mechanics and Engineering*, **171**, 387–418, 1999.

[8] J. Ohser and F. Mücklich, *Statistical analysis of microstructures in materials science.* J Wiley & Sons, 2000.

[9] J.C. Simo, A framework for finite strain elastoplasticity based on maximum plastic dissipation and the multiplicative decomposition: Part I. Continuum formulation. *Computer Methods in Applied Mechanics and Engineering*, **66**, 199-219, 1988.

[10] J. Schröder, *Homogenisierungsmethoden der nichtlinearen Kontinuumsmechanik unter Beachtung von Stabilitätsproblemen*, Bericht aus der Forschungsreihe des Institut für Mechanik (Bauwesen), Lehrstuhl I, Habilitationsschrift, 2000.

[11] J. Schröder, D. Balzani, and D. Brands, Approximation of Random Microstructures by Periodic Statistically Similar Representative Volume Elements Based on Lineal-Path Functions, *Archive of Applied Mechanics*, DOI 10.1007/s00419-010-0462-3, 2010.

[12] R.J.M. Smit, W.A.M. Brekelmans, and H.E.H. Meijer, Prediction of the mechanical behavior of nonlinear heterogeneous systems by multi-level finite element modeling, *Computer Methods in Applied Mechanics and Engineering*, **155**, 181–192, 1998.

[13] T. Torquato, *Random heterogeneous materials. Microstructure and macroscopic properties*, Springer, 2002.

[14] S. Zaefferer, S. I. Wright, D. Raabe. Three-dimensional orientation microscopy in a focused ion beam-scanning electron microscope: A new dimension of microstructure characterization, *Metallurgica and Material Transactions A*, **39A**, 374–389, 2008.

[15] J. Zeman, *Analysis of Composite Materials with Random Microstructure*, University of Prague, Dissertation, 2003.

XI International Conference on Computational Plasticity. Fundamentals and Applications
COMPLAS XI
E. Oñate, D.R.J. Owen, D. Peric and B. Suárez (Eds)

TIME-DEPENDENT MESOSCOPIC MODELLING OF MASONRY USING EMBEDDED WEAK DISCONTINUITIES

B. VANDOREN*†, K. HEYENS* AND K. DE PROFT†

*XIOS Hogeschool Limburg
Departement TIW, Vakgroep Bouwkunde
Agoralaan Gebouw H, 3590 Diepenbeek, Belgium
e-mail: bram.vandoren@xios.be

†Hasselt University
Faculteit WET, Vakgroep FYS
Agoralaan Gebouw D, 3590 Diepenbeek, Belgium

Key words: masonry, mesoscopic modelling, weak discontinuities, partition of unity

Abstract. In this contribution, a rate-dependent mesoscopic masonry model is presented in which the mortar joints are incorporated by embedded weak discontinuities based on partitions of unity. Within the discontinuities, both an isotropic damage and a Perzyna viscoplastic model are used to describe joint degradation. The elastic domain of the joint behaviour is bounded by a modified Drucker-Prager yield function. The performance of the developed masonry model is demonstrated by the simulation of a three-point bending test and a shear wall test.

1 INTRODUCTION

The modelling of masonry has been a popular topic within computational mechanics for some years now. Two major groups of modelling approaches can be distinguished: macroscopic and mesoscopic [1]. In the macroscopic approach the joints and bricks are homogenized to one orthotropic material. The main advantage of this method is that not much computational effort is needed to calculate large structures. However, the obtained crack path is less detailed. This drawback can be alleviated by the use of mesoscopic models. In this approach, joints and bricks are modelled by separate entities. Classically, the joints are incorporated by interface elements, situated on the boundaries of the continuum brick elements [1, 2]. When a critical state is reached in a joint, a strong discontinuity (i.e. a jump in the displacement field) is introduced in the interface.

An alternative way to incorporate strong discontinuities is the partition of unity method [3, 4, 5]. Within this method, nodes are locally enhanced to enrich the solution with discontinuous modes. This concept was applied to masonry by De Proft et al. [6] and will be extended in this paper by the incorporation of weak discontinuities. A weak discontinuity introduces a jump in the strain field, allowing for failure to localise in a zone with finite width [7, 8, 9]. The thickness of this failure is in this case linked to the joint thickness.

2 PARTITION OF UNITY CONCEPT FOR WEAK DISCONTINUITIES

2.1 Displacement decomposition

The displacement field of a body crossed by a weak discontinuity (Figure 1) is obtained by:

$$\mathbf{u} = \hat{\mathbf{u}} + H_{\Omega^w}\tilde{\mathbf{u}} \tag{1}$$

in which $\hat{\mathbf{u}}$ and $\tilde{\mathbf{u}}$ denote the regular and enhanced displacement field, respectively. H_{Ω^w} is a unit ramp function [10], defined by:

$$H_{\Omega^w} = \begin{cases} 0 & \text{if } \mathbf{x} \in \Omega^- \\ \frac{\xi-\xi^-}{\xi^+-\xi^-} & \text{if } \mathbf{x} \in \Omega^w \\ 1 & \text{if } \mathbf{x} \in \Omega^+ \end{cases} \tag{2}$$

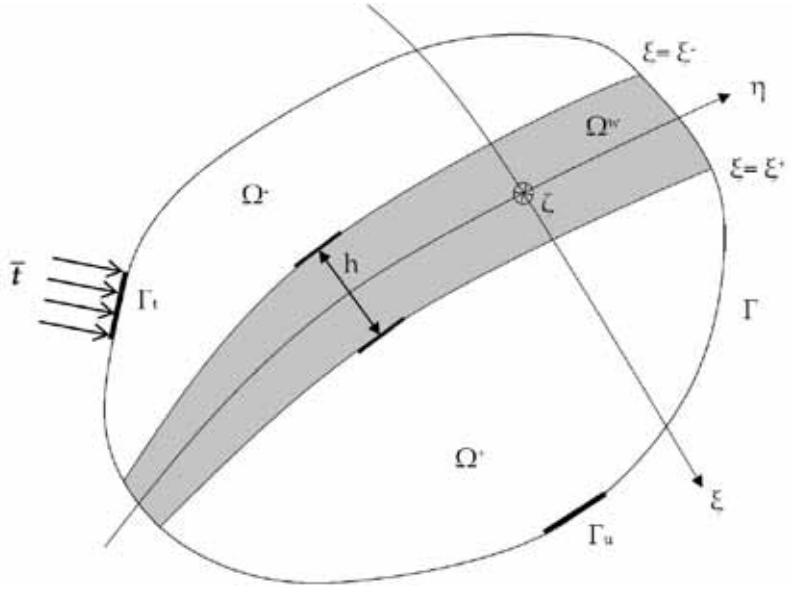

Figure 1: Body crossed by a weak discontinuity

2.2 GFEM discretisation

In this work, the Generalized Finite Element method has been adopted to model the discontinuities [11]. The unit ramp function (Equation (2)) is used as an enhanced basis: its value equals unity for a point inside a masonry brick. When a support of a node is crossed by a weak discontinuity (i.e. joint), an enhanced set of degrees of freedom is added to the solution field of that node. Consequently, each brick possesses its own set of enhanced degree of freedom. Special care has to been taken in the implementation of a meshgenerator, to prevent linear dependancy of the enhanced basis functions [11]. In the current model, two linear quadrilateral elements are used to model one brick.

3 MATERIAL MODELS

Two material laws have been implemented to model the nonlinear joint behaviour: an isotropic damage model and a viscoplastic model. The stone behaviour remains linear elastic throughout the simulations. Consequently, cracks cannot run through bricks.

3.1 Damage model

The nonlinear joint behaviour is governed by an exponential damage evolution law [12]:

$$\begin{cases} \omega = 0 & \text{if } \kappa < \kappa_0 \\ \omega = 1 - \frac{\kappa_0}{\kappa} \exp\left[-\frac{(\kappa-\kappa_0)}{\gamma}\right] & \text{if } \kappa \geq \kappa_0 \end{cases} \tag{3}$$

where $\kappa_0 = \frac{f_{t0}}{E}$ in which E represents the Young's modulus of the mortar joints. The loading function κ, expressed in terms of strain invariants, is derived from the Drucker-Prager model [13]:

$$\kappa = \alpha \frac{I_{1,\varepsilon}}{1-2\nu} + \beta \frac{\sqrt{J_{2,\varepsilon}}}{1+\nu} \tag{4}$$

The material parameters α and β are chosen to fit the uniaxial tensile strength f_{t0} and uniaxial compressive strength f_{c0}:

$$\alpha = \frac{1}{2} \frac{f_{c0} - f_{t0}}{f_{c0}} \tag{5}$$

$$\beta = \frac{\sqrt{3}}{2} \frac{f_{c0} + f_{t0}}{f_{c0}} \tag{6}$$

Finally, the brittleness of response is governed by γ:

$$\gamma = \frac{G_{fI}}{l_c f_{t0}} - \frac{1}{2}\kappa_0 \tag{7}$$

where G_{fI} denotes the mode I fracture energy and l_c is a regularising equivalent length parameter.

3.2 Viscoplastic model

An alternative way to model the softening and failure behaviour of masonry is the use of a viscoplastic model. The incorporation of this type of model is twofold: time-dependent behaviour can be modelled (e.g. the creep phenomenon [14]) and the model has a regularising effect [15, 16]. In this work, the Perzyna overstress model has been adopted [17]. Classically, the strain rate is decomposed into an elastic and a viscoplastic strain rate:

$$\dot{\boldsymbol{\varepsilon}} = \dot{\boldsymbol{\varepsilon}}^{e} + \dot{\boldsymbol{\varepsilon}}^{vp} \tag{8}$$

in which the viscoplastic strain rate for non-associative flow is expressed by:

$$\dot{\boldsymbol{\varepsilon}}^{vp} = \frac{1}{\eta}\langle\phi(f)\rangle\mathbf{m} \tag{9}$$

where η represents the viscosity parameter, f is a yield function and $\mathbf{m} = \frac{\partial g}{\partial \boldsymbol{\sigma}}$ in which g is a viscoplastic potential. $\langle\phi(f)\rangle$ is defined as:

$$\langle\phi(f)\rangle = \begin{cases} \left(\frac{f}{\bar{\sigma}_0}\right)^N & \text{if } f \geq 0 \\ 0 & \text{if } f < 0 \end{cases} \tag{10}$$

in which $\bar{\sigma}_0$ is the initial yield stress and scalar N is a material parameter which equals 1 in the present study. The rate-independent and elastic cases can be recovered when η approaches 0 and ∞, respectively. The elastic domain is bounded by a modified Drucker-Prager yield surface, expressed in terms of stress invariants $I_{1,\sigma}$ and $\sqrt{J_{2,\sigma}}$:

$$f = aI_{1,\sigma} + \sqrt{\chi^2 + J_{2,\sigma}} - b \tag{11}$$

where χ controls the hyperboloid character of the yield surface (Figure 2). The original Drucker-Prager cone is recovered by setting $\chi = 0$. If $\chi \neq 0$, the apex is smoothened and no special stress return-mapping algorithms are required [16]. The material parameters a and b are chosen to fit the uniaxial tensile and compressive strenghts:

$$a = \frac{1}{\sqrt{3}}\frac{f_c - f_t}{f_c + f_t} \tag{12}$$

$$b = \frac{2}{\sqrt{3}}\frac{f_c f_t}{f_c + f_t} \tag{13}$$

The viscoplastic potential used in this paper is given by:

$$g = a' I_{1,\sigma} + \sqrt{\chi^2 + J_{2,\sigma}} \tag{14}$$

in which a' is expressed in terms of the dilatancy angle ψ [14]:

$$a' = \frac{\tan\psi}{\sqrt{9 + 12\tan^2\psi}} \tag{15}$$

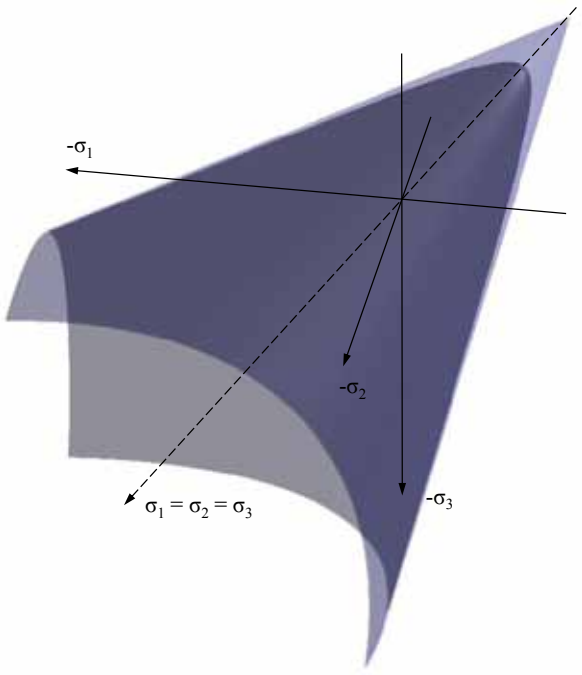

Figure 2: Drucker-Prager hyperboloid yield surface in principal stress space

Isotropic softening of the material model is determined by an exponential law:

$$f_t = f_{t0} \exp\left[-f_{t0}\frac{\kappa_w}{G_{fI}}\right] \tag{16}$$

where f_{t0} represents the initial uniaxial tensile strength and G_{fI} is the mode I fracture energy. In the present study, the compressive strength is assumed to remain constant during the simulations. The work softening parameter κ_w is calculated by:

$$\kappa_w = \Delta t \boldsymbol{\sigma}^T \dot{\boldsymbol{\varepsilon}}^{vp} \tag{17}$$

in which Δt is the time increment. The viscoplastic rate equations are integrated with a fully implicit Euler backward scheme:

$$\begin{bmatrix} \mathbf{I} + \Delta\lambda \mathbf{D}^{el}\frac{\partial \mathbf{m}}{\partial \boldsymbol{\sigma}} & \mathbf{D}^{el}\bar{\mathbf{m}} \\ -\frac{\Delta t}{\eta}\frac{\partial \phi}{\partial f}\mathbf{n} & 1 - \frac{\Delta t}{\eta}\frac{\partial \phi}{\partial f}\frac{\partial f}{\partial \kappa_w}\frac{\partial \kappa_w}{\partial \lambda} \end{bmatrix} \begin{Bmatrix} d\boldsymbol{\sigma} \\ d\lambda \end{Bmatrix} = \begin{Bmatrix} \boldsymbol{\sigma}_{trial} - \boldsymbol{\sigma} - \Delta\lambda \mathbf{D}^{el}\mathbf{m} \\ \frac{\Delta t}{\eta}\langle \phi(f) \rangle - \Delta\lambda \end{Bmatrix} \tag{18}$$

where $\mathbf{D}^{el}$ represents the elastic material stiffness matrix, $\mathbf{n} = \frac{\partial f}{\partial \boldsymbol{\sigma}}$, $\boldsymbol{\sigma}_{trial}$ denotes the elastic predictor stress and:

$$\bar{\mathbf{m}} = \mathbf{m} + \Delta\lambda \frac{\partial \kappa_w}{\partial \lambda}\frac{\partial \mathbf{m}}{\partial \kappa_w} \tag{19}$$

Since plane stress conditions are assumed in this paper, the return mapping procedure is performed in an expanded stress space ($\boldsymbol{\sigma} = \{\sigma_{xx}\ \sigma_{yy}\ \sigma_{xy}\ \sigma_{zz}\}^T$) and the zero out-of-plane stress condition $\sigma_{zz} = 0$ is enforced at integration point level [14, 18]. After the return mapping procedure, the algorithmic consistent tangent stiffness matrix is retrieved by:

$$\mathbf{D}^t = \mathbf{H} - \frac{\mathbf{H}\bar{\mathbf{m}}\mathbf{n}^T\mathbf{H}}{-\frac{\partial f}{\partial \kappa_w}\frac{\partial \kappa_w}{\partial \lambda} + \mathbf{n}^T\mathbf{H}\bar{\mathbf{m}} + \frac{\eta}{\Delta t \frac{\partial \phi}{\partial f}}} \tag{20}$$

in which:

$$\mathbf{H} = \left(\left(\mathbf{D}^{el}\right)^{-1} + \Delta\lambda\frac{\partial \mathbf{m}}{\partial \boldsymbol{\sigma}}\right)^{-1} \tag{21}$$

4 NUMERICAL EXAMPLES

4.1 Three-point bending test

In order to demonstrate the potential of the developed mesoscopic masonry model, a three-point bending test has been carried out using the isotropic damage model. The material parameters are given by Tables 1-2. The results show a good agreement with the experimental data obtained from [19] (dotted curve).

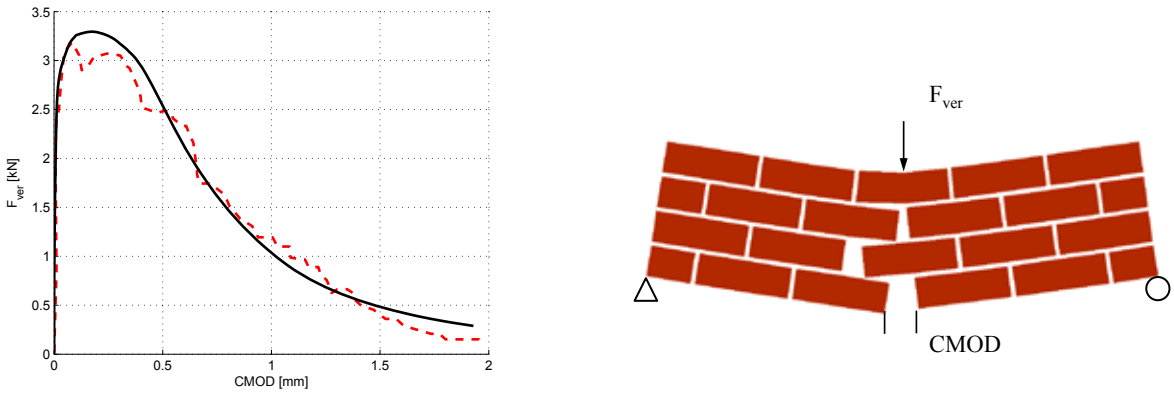

Figure 3: Load-CMOD curve and deformed mesh for a three-point bending test

Table 1: Elastic material parameters for the three-point bending test

	dimensions	$E\ [N/mm^2]$	ν
joints	$10\,mm$	3369	0,20
bricks	$76 \times 230 \times 110\,mm^3$	16700	0,15

Table 2: Inelastic material parameters for the three-point bending test

	f_{t0} $[N/mm^2]$	f_{c0} $[N/mm^2]$	G_{fI} $[N/mm]$	l_c $[mm]$
joints	0,086	3,52	0,002	1

4.2 Shear wall test

The second example is a shear wall with opening [20]. Tables 3-4 summarise the employed material parameters. A confining stress of $0,30\,N/mm^2$ is applied on top of the wall. The average horizontal loading rate at the top equals $0,01\,mm/s$.

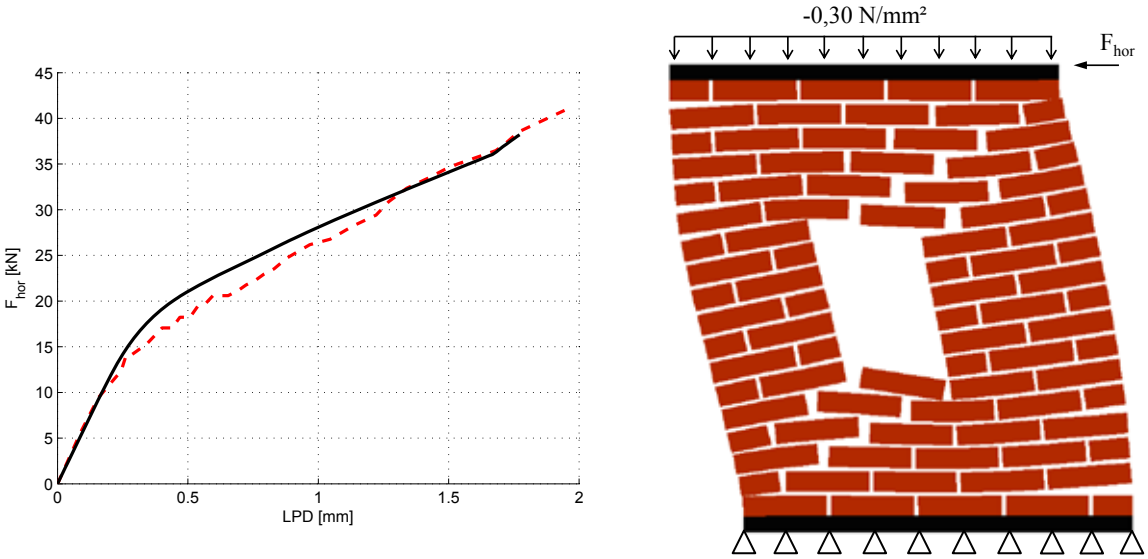

Figure 4: Load-displacement curve and deformed mesh for a shear wall test

The results show a good agreement with those from previous research work (dotted curve), in which a sequentially linear approach has been used [6]. Since no compressive cap is implemented, no compressive failure takes place and the load-displacement curve keeps increasing. The typical stair-step crack pattern, found in experimental tests [20], is recovered.

Table 3: Elastic material parameters for the shear wall test

	dimensions	E $[N/mm^2]$	ν
joints	$10\,mm$	782	0,14
bricks	$52 \times 210 \times 100\,mm^3$	16700	0,15

Table 4: Inelastic material parameters for the shear wall test

	f_{t0} $[N/mm^2]$	G_{fI} $[N/mm]$	f_{c0} $[N/mm^2]$	G_{fc} $[N/mm]$	ψ $[^\circ]$	η $[s]$	χ
joints	0,25	0,018	10,5	∞	0	30	0,01

5 CONCLUSIONS

In this paper, a mesoscopic masonry model is developed in which joints are modelled by weak discontinuities. The discontinuities are incorporated using the Generalized Finite Element Method. A modified Drucker-Prager model is used to describe the failure of the mortar joints, whereas the stone behaviour remains linear elastic. A Perzyna viscoplastic model is employed as a regularisation technique. Special attention was given to the algorithmic aspects of the model. A three-point bending test and a shear wall test showed that the presented method leads to realistic load capacities and failure patterns. In the example of the shear wall test, the results showed good agreement with those of previous research work, although the modelling approaches differ.

ACKNOWLEDGMENT

The support of this research by the Bijzonder Onderzoeksfonds Doctoral Funding program of Hasselt University (BOF-DOC) is gratefully acknowledged.

REFERENCES

[1] Lourenço, P.B. *Computational Strategies for Masonry Structures*. PhD Thesis, (1996). Technische Universiteit Delft.

[2] Alfaïte, J.V. and de Almeida, J.R. Modelling Discrete Cracking on Masonry Walls. *Masonry International* (2004) **17**(2): 83–93.

[3] Belytschko, T. and Black, T. Elastic Crack Growth in Finite Elements with Minimal Remeshing. *Int. J. Num. Meth. Engng.* (1999) **45**(5): 601–620.

[4] Wells, G.N. and Sluys, L.J. A New Method for Modelling Cohesive Cracks Using Finite Elements. *Int. J. Num. Meth. Engng.* (2001) **50**(12): 2667–2682.

[5] De Proft, K. *A Combined Experimental-Computational Study to Discrete Fracture of Brittle Materials*. PhD Thesis, (2003). Vrije Universiteit Brussel.

[6] De Proft, K., Heyens, K. and Sluys, L.J. Mesoscopic Modelling of Masonry Failure. *Proceedings of the ICE - Engineering and Computational Mechanics* (2010) **164**(EM1): 41–46.

[7] Belytschko, T., Fish, J. and Engelmann, B.E. A Finite-Element with Embedded Localization Zones. *Comput. Meth. Appl. Mech. Eng.* (1988) **70**(1): 59–89.

[8] Sluys, L.J. and Berends, A.H. Discontinuous Failure Analysis for Mode-I and Mode-II Localization Problems. *Int. J. Solids Structures* (1998) **35**(31-32): 4257–4274.

[9] Jirásek, M. Comparative Study on Finite Elements with Embedded Discontinuities. *Comput. Meth. Appl. Mech. Eng.* (2000) **188**(1-3): 307–330.

[10] Oliver, J., Cervera, M. and Manzoli, O. Strong Discontinuities and Continuum Plasticity Models: the Strong Discontinuity Approach. *Int. J. Plast.* (1999) **15**(3): 319–351.

[11] Simone, A., Duarte, C.A. and Van der Giessen, E. A Generalized Finite Element Method for Polycrystals with Discontinuous Grain Boundaries. *Int. J. Num. Meth. Engng.* (2006) **67**(8): 1122–1145.

[12] Feenstra, P.H. Implementing an isotropic damage model in Diana. Use-case for the user-supplied subroutine usrmat. *Proceeding of the Third DIANA World Conference* (2002).

[13] Massart, T.J., Peerlings, R.H.J. and Geers, M.G.D. Mesoscopic Modeling of Failure and Damage-induced Anisotropy in Brick Masonry. *European Journal of Mechanics a-Solids* (2004) **23**(5): 719–735.

[14] de Souza Neto, E.A., Perić, D. and Owen, D.R.J. *Computational Methods For Plasticity, Theory and Applications*. John Wiley & Sons Ltd, Chichester, (2008).

[15] Wells, G.N. *Discontinuous Modelling of Strain Localisation and Failure*. PhD Thesis, (2001). Technische Universiteit Delft.

[16] Sluys, L.J. *Wave Propagation, Localisation and Dispersion is Softening Solids*. PhD Thesis, (1992). Technische Universiteit Delft.

[17] Perzyna, P. Fundamental Problems in Viscoplasticity. *Recent Advances in Applied Mechanics*. Academic Press, New York, (1966) **9**: 243–377.

[18] de Borst, R. The Zero-Normal-Stress Condition in Plane-Stress and Shell Elastoplasticity. *Comm. Appl. Numer. Meth.* (1991) **7**(1): 29–33.

[19] Chaimoon, K. and Attard, M.N. Experimental and Numerical Investigation of Masonry under Three-Point Bending (In-Plane). *Eng. Struct.* (2009) **31**(1): 103–112.

[20] Raijmakers, T.M.J. and Vermeltvoort, A.T. *Deformation Controlled Tests in Masonry Shear Walls*. Report B-92-1156, (1992). TNO Bouw, Delft.

XI International Conference on Computational Plasticity. Fundamentals and Applications
COMPLAS XI
E. Oñate, D.R.J. Owen, D. Peric and B. Suárez (Eds)

TOWARDS THE EFFECTIVE BEHAVIOUR OF POLYCRYSTALLINE MICROSTRUCTURES AT FINITE STRAINS

EVA LEHMANN[*†], STEFAN LOEHNERT[*♯] AND PETER WRIGGERS[*◇]

[*]Institute of Continuum Mechanics
Leibniz Universität Hannover
Appelstraße 11, 30167 Hannover, Germany

[†] e-mail: lehmann@ikm.uni-hannover.de,
web page: http://www.ikm.uni-hannover.de/

[♯] e-mail: loehnert@ikm.uni-hannover.de
[◇] e-mail: wriggers@ikm.uni-hannover.de

Key words: Finite Crystal Plasticity, Sheet Bulk Metal Forming, Homogenisation

Summary. It is well known that metals behave anisotropically on their microstructure due to their crystalline nature. FE-simulations in the metal forming field however sometimes lack the right macroscopic anisotropies as their type can be unspecific.

In order to find a suitable effective elastoplastic material model, a finite crystal plasticity model is used to model the behaviour of polycrystalline materials in representative volume elements (RVEs) representing the microstructure, taking into account the plastic anisotropy due to dislocations occurring within considered slip systems. A multiplicative decomposition of the deformation gradient into elastic and plastic parts is performed, as well as the split of the elastic free energy into volumetric and deviatoric parts resulting in a compact expression of the resolved SCHMID stress depending on the slip system vectors. In order to preserve the plastic incompressibility condition, the elastic deformation gradient is updated via an exponential map scheme. To further circumvent singularities stemming from the linear dependency of the slip system vectors, a viscoplastic power-law is introduced providing the evolution of the plastic slips and slip resistances.

The model is validated with experimental microstructural data under deformation. Through homogenisation and optimisation techniques, effective stress-strain curves are determined and can be compared to results from real manufacturing and fabrication processes leading to an effective elastoplastic material model which is suitable for metal forming processes at finite strains.

1 INTRODUCTION

Phenomenological macroscopic observations of metals do not acknowledge actual heterogeneities in the microstructure at once. For some time, the mechanics of heterogeneous and polycrystalline materials have been limited to the formulation of simplified models taking into account some aspects of the microstructural characteristics. However, the proceeding increase of computational capabilites enables a more elaborated approach towards the development of a suitable material model for specific requirements and numerical simulations in the forming field. At the same time, modeling the microstructure is already a complex task as certain microstructural properties have to be considered. On the microscopic level of metals, anisotropies have to be taken into account stemming from dislocations occurring on the atomic lattice within considered slip systems. Such mechanisms are macroscopically observed as plastic anisotropic yielding.

In order to take into account the microstructural complexity on the one hand and aiming at the ability to compute real manufacturing and forming processes on the other hand, a macroscopic effective material model which sufficiently represents the microstructure has to be developed. Due to the various different boundary conditions the material can be constrained to during fabrication stages, it has to be validated for these applications. A huge challenge appears in the attempt to fulfil the requirements of both sheet and bulk metal forming processes. In doing so, the model approach has naturally to be performed in a three-dimensional way, as the structure can certainly be constrained to any geometrical limit or constitution. However, the dislocation movement on the microstructure evolves in three required directions.

2 CONSTITUTIVE FRAMEWORK: MULTIPLICATIVE MULTISURFACE ELASTOPLASTICITY

The deformation gradient $\boldsymbol{F} = \frac{\partial \boldsymbol{x}}{\partial \boldsymbol{X}}$ with Jacobian $\mathrm{J} = \det \boldsymbol{F} > 0$ maps tangent vectors of material lines in the reference configuration $\mathcal{B} \in \mathbb{R}^3$ onto tangent vectors of deformed lines in the current configuration $\mathcal{B}_\mathrm{t} \in \mathbb{R}^3$ and is decomposed into an elastic and a plastic part. The elastic part $\boldsymbol{F}^e$ contributes to stretching and rigid body rotation of the crystal lattice, the plastic part $\boldsymbol{F}^p$ characterises plastic flow caused by dislocations on defined slip systems

$$\boldsymbol{F} = \boldsymbol{F}^e \boldsymbol{F}^p. \tag{1}$$

The multiplicative split assumes a local unstressed intermediate configuration defined by the plastic deformation gradient, see Fig. 1, which can be determined through an evolution assumption and whose initial condition is assumed to be $\boldsymbol{F}^p_0 = \boldsymbol{1}$.

Further, a volumetric-deviatoric split of the deformation gradient and its constituents is performed

$$\boldsymbol{F}_\mathrm{iso} = \mathrm{J}^{-1/3} \boldsymbol{F}, \quad \boldsymbol{F}^e_\mathrm{iso} = \mathrm{J}^{e\,-1/3} \boldsymbol{F}^e, \quad \boldsymbol{F}^p_\mathrm{iso} = \mathrm{J}^{p\,-1/3} \boldsymbol{F}^p, \tag{2}$$

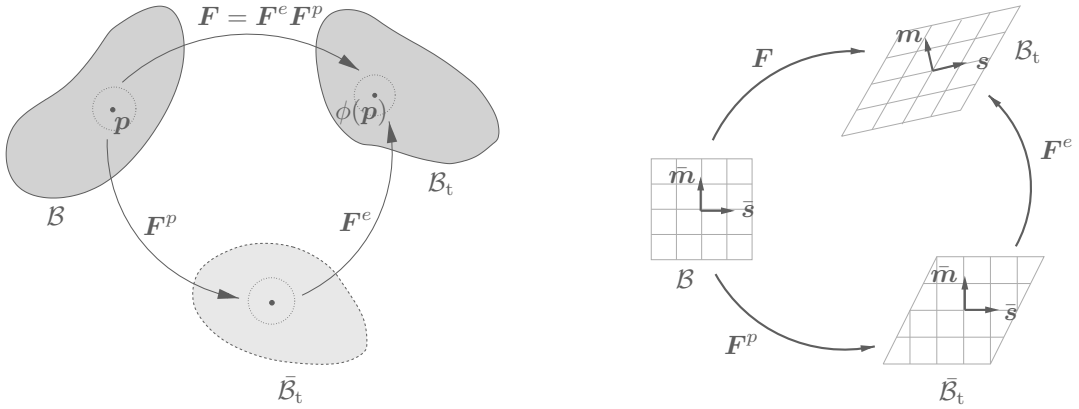

(a) Continuum mechanical framework (b) Crystallographic conception

Figure 1: Multiplicative elasto-plastic decomposition of the deformation gradient $\boldsymbol{F}$

with $\mathrm{J} = \mathrm{J}^e$ due to fulfilling the requirement of present plastic incompressibility expressed through $\mathrm{J}^p = 1$.

2.1 Thermodynamical considerations

The deformation power per unit undeformed volume can be written as

$$\boldsymbol{P} : \dot{\boldsymbol{F}} = \bar{\boldsymbol{P}} : \dot{\boldsymbol{F}}^e + \bar{\boldsymbol{\Sigma}} : \bar{\boldsymbol{L}}^p, \tag{3}$$

where $\bar{\boldsymbol{P}} = \boldsymbol{P}\boldsymbol{F}^{p\,T}$ is the 1st PIOLA-KIRCHHOFF stress tensor relative to the intermediate configuration $\bar{\mathcal{B}}_\mathrm{t}$ and $\bar{\boldsymbol{\Sigma}} = \boldsymbol{F}^{e\,T}\boldsymbol{P}\boldsymbol{F}^{p\,T} = \boldsymbol{F}^{e\,T}\boldsymbol{\tau}\boldsymbol{F}^{e\,-T}$ a stress measure conjugate to the plastic velocity gradient $\bar{\boldsymbol{L}}^p = \dot{\boldsymbol{F}}^p\boldsymbol{F}^{p\,-1}$ on $\bar{\mathcal{B}}_\mathrm{t}$, $\boldsymbol{\tau}$ being the KIRCHHOFF stress tensor on $\mathcal{B}_\mathrm{t}$. Further, it is

$$\bar{\boldsymbol{P}} = \boldsymbol{F}^e\bar{\boldsymbol{S}}, \quad \bar{\boldsymbol{S}} = \bar{\boldsymbol{C}}^{e\,-1}\bar{\boldsymbol{\Sigma}}, \quad \bar{\boldsymbol{C}}^e = \boldsymbol{F}^{e\,T}\boldsymbol{F}^e, \tag{4}$$

where $\bar{\boldsymbol{S}}$ is the 2nd PIOLA-KIRCHHOFF stress tensor relative to the intermediate configuration $\bar{\mathcal{B}}_\mathrm{t}$ which is symmetric, $\bar{\boldsymbol{C}}^e$ is further the elastic right CAUCHY-GREEN tensor on $\bar{\mathcal{B}}_\mathrm{t}$.

The evolution of the plastic deformation gradient $\boldsymbol{F}^p$ is defined by the plastic flow equation, resulting from the plastic rate of deformation $\bar{\boldsymbol{L}}^p$. In the presence of n_syst systems undergoing plastic slip, represented by the plastic shear rates $\dot{\gamma}^\alpha$, the plastic flow equation is further generalised

$$\bar{\boldsymbol{L}}^p = \dot{\boldsymbol{F}}^p\boldsymbol{F}^{p\,-1}, \quad \bar{\boldsymbol{L}}^p = \sum_{\alpha=1}^{n_\mathrm{syst}} \dot{\gamma}^\alpha \bar{\boldsymbol{s}}^\alpha \otimes \bar{\boldsymbol{m}}^\alpha, \tag{5}$$

$\bar{\boldsymbol{s}}^\alpha$ being the slip direction vector and $\bar{\boldsymbol{m}}^\alpha$ being the slip plane normal vector of the α-th slip system $\{\bar{\boldsymbol{s}}^\alpha, \bar{\boldsymbol{m}}^\alpha\}$. The slip system vectors have the properties $\bar{\boldsymbol{s}} \cdot \bar{\boldsymbol{m}} = 0$ and

thus $(\bar{\boldsymbol{s}}^\alpha \otimes \bar{\boldsymbol{m}}^\alpha)(\bar{\boldsymbol{s}}^\alpha \otimes \bar{\boldsymbol{m}}^\alpha) = \boldsymbol{0}$. The generalisation in (5) leads to the modified evolution equation of the plastic deformation gradient depending on the plastic slips

$$\dot{\boldsymbol{F}}^p = \left[\sum_\alpha \dot{\gamma}^\alpha \, \bar{\boldsymbol{s}}^\alpha \otimes \bar{\boldsymbol{m}}^\alpha\right] \boldsymbol{F}^p. \tag{6}$$

2.2 The resolved Schmid stress

The SCHMID stress τ^α is the projection of $\bar{\boldsymbol{\Sigma}}$ onto the slip system $\bar{\boldsymbol{s}}^\alpha \otimes \bar{\boldsymbol{m}}^\alpha$

$$\tau^\alpha = (\mathrm{dev}[\bar{\boldsymbol{\Sigma}}] \cdot \bar{\boldsymbol{m}}^\alpha) \cdot \bar{\boldsymbol{s}}^\alpha = \mathrm{dev}[\bar{\boldsymbol{\Sigma}}] : \bar{\boldsymbol{s}}^\alpha \otimes \bar{\boldsymbol{m}}^\alpha. \tag{7}$$

As the slip system tensor $\bar{\boldsymbol{s}}^\alpha \otimes \bar{\boldsymbol{m}}^\alpha$ is purely deviatoric, only the deviator of the stress tensor contributes to the resolved stress. With the relations in (4) and some straightforward recast, it is

$$\tau^\alpha = \boldsymbol{R}^{e\,T} \boldsymbol{\tau} \boldsymbol{R}^e : \bar{\boldsymbol{s}}^\alpha \otimes \bar{\boldsymbol{m}}^\alpha. \tag{8}$$

2.3 Elastic response

The elastic part of the deformation is gained from a NEO-HOOKEean strain energy function. Due to assumed isotropy within the elastic contribution, the description is given in terms of the elastic left CAUCHY-GREEN tensor $\boldsymbol{b}^e$. Applying a volumetric-deviatoric split yields

$$\rho\psi(\boldsymbol{b}^e_{\mathrm{iso}},\, \mathrm{J}^e) = \frac{\mu}{2}\,(\mathrm{tr}\,\boldsymbol{b}^e_{\mathrm{iso}} - 3) + \frac{\kappa}{2}\,(\ln \mathrm{J}^e)^2 \tag{9}$$

$$\boldsymbol{\tau} = 2\,\rho\,\frac{\partial \psi}{\partial \boldsymbol{b}^e}\,\boldsymbol{b}^e = \mu\,\mathrm{dev}(\boldsymbol{b}^e_{\mathrm{iso}}) + \kappa\,\ln \mathrm{J}^e\,\boldsymbol{1}, \quad \mathrm{dev}(\boldsymbol{\tau}) = \mu\,\mathrm{dev}(\boldsymbol{b}^e_{\mathrm{iso}}),\ \mathrm{vol}(\boldsymbol{\tau}) = \kappa\,\ln \mathrm{J}^e\,\boldsymbol{1}. \tag{10}$$

Because slip-system tensors are deviatoric by construction, their internal product by the hydrostatic KIRCHHOFF stress components vanishes and the SCHMID stress in (8) remains

$$\tau^\alpha = \mu\,\bar{\boldsymbol{s}}^\alpha_{\mathrm{iso}} \cdot \bar{\boldsymbol{m}}^\alpha_{\mathrm{iso}}, \quad \bar{\boldsymbol{s}}^\alpha_{\mathrm{iso}} = \boldsymbol{F}^e_{\mathrm{iso}} \cdot \bar{\boldsymbol{s}}^\alpha, \quad \bar{\boldsymbol{m}}^\alpha_{\mathrm{iso}} = \boldsymbol{F}^e_{\mathrm{iso}} \cdot \bar{\boldsymbol{m}}^\alpha. \tag{11}$$

2.4 A rate-dependent formulation via a viscoplastic power-law

A rate-dependent theory enables the modeling of creep in single crystals and is performed by the introduction of a power law-type constitutive equation for the rates $\dot{\gamma}^\alpha$ of inelastic deformation in the slip systems

$$\dot{\gamma}^\alpha = \dot{\gamma}_0\,\frac{\tau^\alpha}{\tau_y}\left(\frac{|\tau^\alpha|}{\tau_y}\right)^{m-1} = \dot{\gamma}_0\,\tau^\alpha\,|\tau^\alpha|^{m-1}\,\tau_y^{-m}, \tag{12}$$

$\dot{\gamma}_0$ and τ_y being the reference shear rate and slip resistance, and m being a rate-sensivity parameter. Within an isotropic TAYLOR hardening model, the evolution for the slip resistance τ_y is considered

$$\dot{\tau}_y = \sum_\alpha H \cdot |\dot{\gamma}^\alpha|, \quad \gamma = \int_0^t \dot{\gamma}\,dt, \quad \dot{\gamma} = \sum_\alpha \dot{\gamma}^\alpha. \tag{13}$$

3 INCREMENTAL KINEMATICS

The slip rate is discretised with a standard backward EULER integration in order to obtain incremental evolution equations for the update of the evolving quantities

$$\Delta\gamma^\alpha = \Delta t\, \dot{\gamma}^\alpha\,(\boldsymbol{F}^e)\,. \tag{14}$$

The implicit exponential integrator is then used to discretise the plastic flow equation (6)

$$\boldsymbol{F}^p_{n+1} = \exp\left[\sum_\alpha \Delta\gamma^\alpha \bar{\boldsymbol{s}}^\alpha \otimes \bar{\boldsymbol{m}}^\alpha\right] \cdot \boldsymbol{F}^p_n. \tag{15}$$

Due to the property $\det[\exp(\bar{\boldsymbol{s}}^\alpha \otimes \bar{\boldsymbol{m}}^\alpha)] = \exp[\mathrm{tr}\,(\bar{\boldsymbol{s}}^\alpha \otimes \bar{\boldsymbol{m}}^\alpha)] = \exp(0) = 1$, it preserves the plastic volume. Here, $\boldsymbol{F}^{e\,\mathrm{trial}}_{n+1} = \boldsymbol{f}_{n+1}\,\boldsymbol{F}^e_n$, is the *trial* elastic deformation gradient with $\boldsymbol{f}_{n+1} = \boldsymbol{F}_{n+1}\,\boldsymbol{F}^{-1}_n = \boldsymbol{1} + \mathrm{grad}_n\,(\Delta\boldsymbol{u})$ and $\mathrm{J}_{n+1} = \det\boldsymbol{F}_{n+1}$, $\boldsymbol{F}^{e\,\mathrm{trial}}_{\mathrm{iso}} = \mathrm{J}^{-1/3}_{n+1}\,\boldsymbol{F}^{e\,\mathrm{trial}}_{n+1}$, so that an exponential update for the new elastic deformation gradient can be obtained

$$\boldsymbol{F}^e_{n+1} = \boldsymbol{F}^{e\,\mathrm{trial}}_{n+1} \cdot \exp\left[\sum_\alpha -\Delta\gamma^\alpha \bar{\boldsymbol{s}}^\alpha \otimes \bar{\boldsymbol{m}}^\alpha\right]. \tag{16}$$

The current *trial* resolved shear stress $\tau^{\alpha\,\mathrm{trial}}_{n+1}$, cf. (11), is obtained with the current orientation of the crystal through rotation of the slip system with the trial elastic deformation gradient

$$\tau^{\alpha\,\mathrm{trial}}_{n+1} = \mu\,\bar{\boldsymbol{s}}^{\alpha\,\mathrm{trial}}_{\mathrm{iso}} \cdot \bar{\boldsymbol{m}}^{\alpha\,\mathrm{trial}}_{\mathrm{iso}}, \quad \bar{\boldsymbol{s}}^{\alpha\,\mathrm{trial}}_{\mathrm{iso}} = \boldsymbol{F}^{e\,\mathrm{trial}}_{\mathrm{iso}} \cdot \bar{\boldsymbol{s}}^\alpha, \quad \bar{\boldsymbol{m}}^{\alpha\,\mathrm{trial}}_{\mathrm{iso}} = \boldsymbol{F}^{e\,\mathrm{trial}}_{\mathrm{iso}} \cdot \bar{\boldsymbol{m}}^\alpha. \tag{17}$$

3.1 Equilibrating the plastic state

Omitting the subscript $n+1$, a residual based on the exponential map is defined to equilibrate the plastic state, leading to a local NEWTON-RAPHSON algorithm through a TAYLOR expansion about the reached point $\boldsymbol{F}^e_k$

$$\boldsymbol{R}(\boldsymbol{F}^e) := \boldsymbol{F}^e - \boldsymbol{F}^{e\,\mathrm{trial}} \cdot \exp\left[\sum_\alpha -\Delta\gamma^\alpha \bar{\boldsymbol{s}}^\alpha \otimes \bar{\boldsymbol{m}}^\alpha\right] = \boldsymbol{0}, \tag{18}$$

and

$$\boldsymbol{R}_k + \partial_{\boldsymbol{F}^e_k}\boldsymbol{R}(\boldsymbol{F}^e_k) : \Delta\boldsymbol{F}^e_k = \boldsymbol{0}, \tag{19}$$

$$\Delta\boldsymbol{F}^e_k = -\left[\partial_{\boldsymbol{F}^e_k}\boldsymbol{R}(\boldsymbol{F}^e_k)\right]^{-1} : \boldsymbol{R}_k, \quad \boldsymbol{F}^e_{k+1} = \boldsymbol{F}^e_k + \Delta\boldsymbol{F}^e_k, \tag{20}$$

with the important derivatives

$$\left[\partial_{\boldsymbol{F}^e}\boldsymbol{R}(\boldsymbol{F}^e)\right]_{ijkl} = \delta_{ik}\delta_{jl} + F^{e\,\mathrm{trial}}_{im}\,\mathbb{E}_{mjpq}\left[\sum_\alpha \bar{\boldsymbol{s}}^\alpha \otimes \bar{\boldsymbol{m}}^\alpha \otimes \partial_{\boldsymbol{F}^e}\Delta\gamma^\alpha\right]_{pqkl} \tag{21}$$

$$\mathbb{E}_{mjpq} = \frac{\partial \exp\left(\left[-\sum_\alpha \Delta\gamma^\alpha(\boldsymbol{F}^e)\,\bar{\boldsymbol{s}}^\alpha \otimes \bar{\boldsymbol{m}}^\alpha\right]_{mj}\right)}{\partial\left[-\sum_\alpha \Delta\gamma^\alpha(\boldsymbol{F}^e)\,\bar{\boldsymbol{s}}^\alpha \otimes \bar{\boldsymbol{m}}^\alpha\right]_{pq}}, \tag{22}$$

and

$$\partial_{\boldsymbol{F}^e} \Delta\gamma^\beta = \Delta t\, \dot{\gamma}_0\; m\; |\tau^\alpha|^{m-1}\; \tau_y^{-m}\; \left[\Xi^{\alpha\,\beta}\right]^{-1}\; \partial_{\boldsymbol{F}^e}\, \tau^\alpha \tag{23}$$

$$\partial_{\boldsymbol{F}^e}\, \tau^\alpha = -\frac{2}{3}\, \tau^\alpha\, \boldsymbol{F}^{e\,-T} + \mu\, \mathrm{J}^{-1/3}\, [\bar{\boldsymbol{m}}^\alpha_{\mathrm{iso}} \otimes \bar{\boldsymbol{s}}^\alpha + \bar{\boldsymbol{s}}^\alpha_{\mathrm{iso}} \otimes \bar{\boldsymbol{m}}^\alpha] \tag{24}$$

$$\Xi^{\alpha\,\beta} = \delta^{\alpha\,\beta} + \Delta t\, \dot{\gamma}_0\, m\, \tau^\alpha\; |\tau^\alpha|^{m-1}\, \tau_y^{-m-1} \sum\nolimits_\beta H\, \mathrm{sign}(\Delta\gamma^\beta). \tag{25}$$

4 MODEL OF THE POLYCRYSTAL

4.1 Voronoi cell grains

The polycrystal is modelled with three-dimensional VORONOI cell shaped grains. Through the DELAUNAY triangulation of a given random point seed, a polycrystal of arbitrary size can be obtained through stating the size of the bounding box.

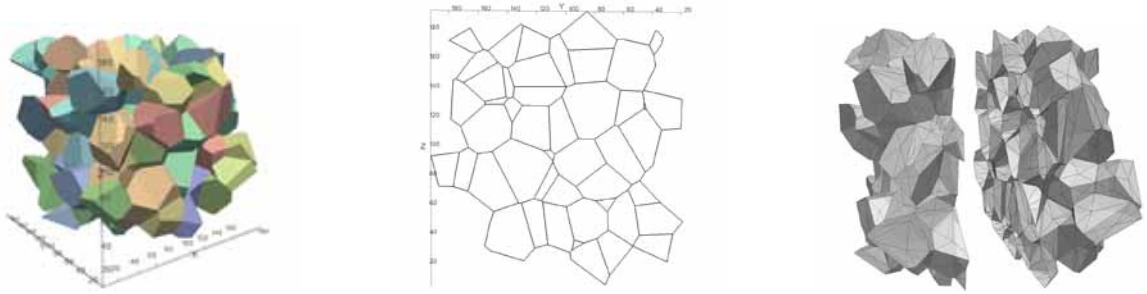

(a) Polycrystal consisting of VORONOI cell grains.

(b) Cut through polcrystalline structure.

(c) Three-dimensional view into the cutted polycrystal.

Figure 2: Polycrystalline model within bounding box $200 \times 200 \times 200\,\mu$m. The VORONOI cell shaped crystal grains are obtained through DELAUNAY triangulation of a random point seed.

4.2 Euler angle rotation of the grains

In order to realise randomly orientated slip systems in each grain of the undeformed polycrystalline structure, the slip system vectors are rotated around the cartesian axes about three EULER angles Φ, Θ and Ψ according to a y-convention, see Fig. 3; Performed is a rotation about the z-axis, the y-axis and the new z-axis, successively,

$$\boldsymbol{R}_\Psi = \begin{bmatrix} \cos\Psi & -\sin\Psi & 0 \\ \sin\Psi & \cos\Psi & 0 \\ 0 & 0 & 1 \end{bmatrix} \quad \boldsymbol{R}_\Theta = \begin{bmatrix} \cos\Theta & 0 & \sin\Theta \\ 0 & 1 & 0 \\ -\sin\Theta & 0 & \cos\Theta \end{bmatrix} \quad \boldsymbol{R}_\Phi = \begin{bmatrix} \cos\Phi & -\sin\Phi & 0 \\ \sin\Phi & \cos\Phi & 0 \\ 0 & 0 & 1 \end{bmatrix}, \tag{26}$$

$$\boldsymbol{R} = \boldsymbol{R}_\Psi \cdot \boldsymbol{R}_\Theta \cdot \boldsymbol{R}_\Phi. \tag{27}$$

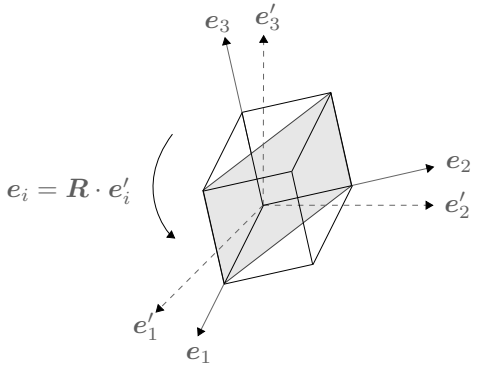

Figure 3: Rotation of the axes around random EULER angles

5 NUMERICAL HOMOGENISATION

5.1 Boundary conditions

Based on the construction of polycrystalline structures according to Sec. 4, polycrystals of several sizes are modelled, representing the microstructure of the polycrystalline material, see Fig. 2. The displacement field $\boldsymbol{u}$ is given through a constant displacement gradient $\boldsymbol{H}$ on the entire boundary of the polycrystal

$$\boldsymbol{u}|_{\mathrm{d}\Omega} = \boldsymbol{H} \cdot \boldsymbol{X}|_{\mathrm{d}\Omega}\,, \quad \boldsymbol{H} = \text{const.} \tag{28}$$

5.2 Volume average

In order to approach the prediction of an overall material behaviour of the representative volume element and hence of the macroscopic material, the volume averages of the deformation gradient $\boldsymbol{F}$ and the 1st PIOLA-KIRCHHOFF stress tensor $\boldsymbol{P}$ over the volume $V = \int_\Omega \mathrm{d}\Omega$ are defined as

$$\langle \boldsymbol{F} \rangle_\Omega := \frac{1}{V} \int_\Omega \boldsymbol{F} \; \mathrm{d}\Omega \tag{29}$$

$$\langle \boldsymbol{P} \rangle_\Omega := \frac{1}{V} \int_\Omega \boldsymbol{P} \; \mathrm{d}\Omega. \tag{30}$$

5.3 Overall polycrystalline behaviour

Differently sized polycrystals, from a size edge range between 100 and 200 μm, see Fig. 4, are subjected to pure shear loading through the displacement gradient $\boldsymbol{H} = \boldsymbol{e}_1 \otimes \boldsymbol{e}_2$. The number of crystal grains depend on the size and are shown in Tab. 1. The material parameters for all the microstructures are equal; it is the bulk modulus $\kappa = 152.2$ GPa, the shear modulus $\mu = 79.3$ GPa, and the parameters for the viscoplastic range amount to $H = 1.0$ GPa, $\tau_{y0} = 180$ MPa, $\dot{\gamma}_0 = 0.0005$ and $m = 3.0$. In order to obtain a statistically admissible response, 200 tests are computed for each size with body-centered cubic crystals with 24 slip system vectors of Tab. 2.

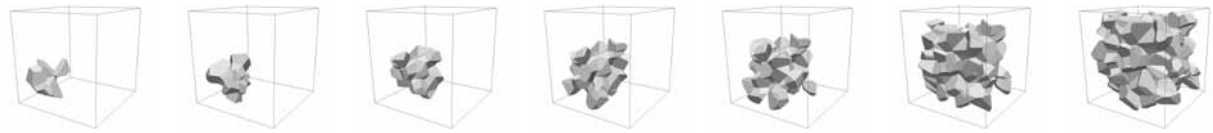

(a) 100 μm (b) 110 μm (c) 130 μm (d) 140 μm (e) 150 μm (f) 180 μm (g) 200 μm

Figure 4: Polycrystals of different sizes. The shown cube represents a bounding box of size $200 \times 200 \times 200$ μm.

Table 1: Number of grains for polycrystal edge sizes

bounding box size edge [μm]	100	110	130	140	150	180	200
number of grains	6	13	20	32	45	107	157

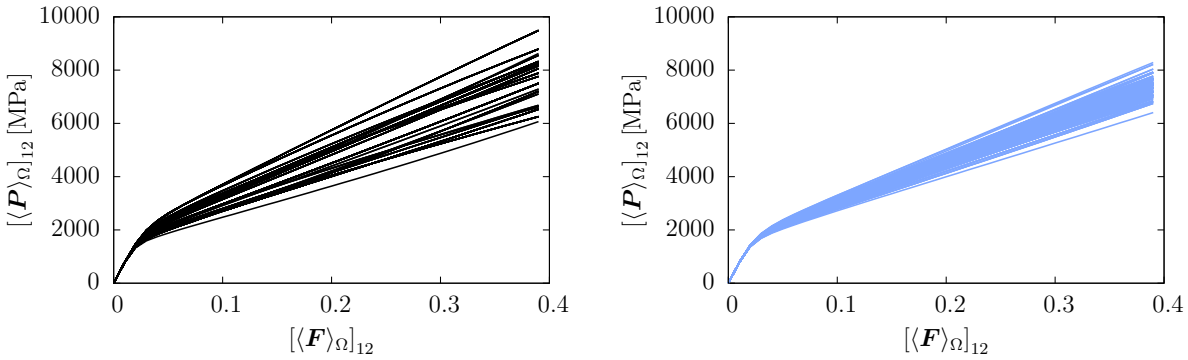

(a) Polycrystal within the bounding box $100 \times 100 \times 100$ μm.

(b) Polycrystal within the bounding box $150 \times 150 \times 150$ μm.

Figure 5: Stress-strain relations of the polycrystals of different sizes.

Table 2: 24 slip system vectors for body-centered cubic crystals

$\bar{\boldsymbol{s}}^\alpha$	$\bar{\boldsymbol{m}}^\alpha$	$\bar{\boldsymbol{s}}^\alpha$	$\bar{\boldsymbol{m}}^\alpha$	$\bar{\boldsymbol{s}}^\alpha$	$\bar{\boldsymbol{m}}^\alpha$	$\bar{\boldsymbol{s}}^\alpha$	$\bar{\boldsymbol{m}}^\alpha$
$[\bar{1}11]$	$(0\bar{1}1)$	$[111]$	$(0\bar{1}1)$	$[11\bar{1}]$	(011)	$[1\bar{1}1]$	(011)
$[\bar{1}11]$	(101)	$[111]$	$(\bar{1}01)$	$[11\bar{1}]$	(101)	$[1\bar{1}1]$	$(\bar{1}01)$
$[\bar{1}11]$	(110)	$[111]$	$(\bar{1}10)$	$[11\bar{1}]$	$(\bar{1}10)$	$[1\bar{1}1]$	(110)
$[\bar{1}11]$	(211)	$[111]$	$(\bar{2}11)$	$[11\bar{1}]$	$(2\bar{1}1)$	$[1\bar{1}1]$	$(21\bar{1})$
$[\bar{1}11]$	$(12\bar{1})$	$[111]$	$(1\bar{2}1)$	$[11\bar{1}]$	$(\bar{1}21)$	$[1\bar{1}1]$	(121)
$[\bar{1}11]$	$(1\bar{1}2)$	$[111]$	$(11\bar{2})$	$[11\bar{1}]$	(112)	$[1\bar{1}1]$	$(\bar{1}12)$

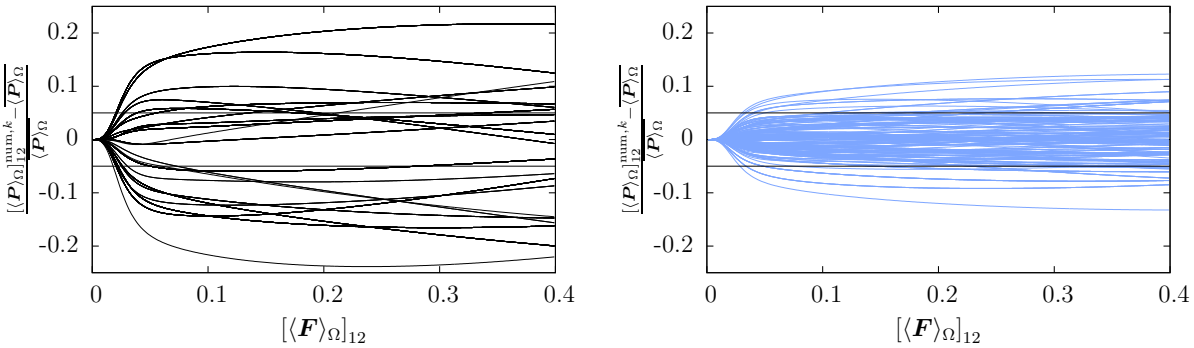

(a) Polycrystal within the bounding box $100 \times 100 \times 100$ μm.

(b) Polycrystal within the bounding box $150 \times 150 \times 150$ μm.

Figure 6: Relative errors with respect to mean value of the computations.

As an example, the overall stress-strain relations for 200 polycrystalline structures of edge size 100 and 150 μm, respectively, are shown in Fig. 5. Whereas the response of the smaller polycrystal shows a rather scattering stress-strain behaviour due to the remaining high influence of the boundary loading, the larger polycrystal presents a more representative behaviour of the microstructure. Expressed this in terms of the relative error in the homogenised 1st PIOLA-KIRCHHOFF stresses $\langle \boldsymbol{P} \rangle_\Omega$, the error reaches a level of 20 % and more over the whole deformation, see Fig. 6. Increasing the size of the polycrystal results in a decrease of the relative error. In order to restrict the error to 5 %, error lines at ± 5 % are included.
The same effect applies for the normalised standard deviation $\sigma(\langle P_{ij} \rangle_\Omega) / \overline{||\langle P_{ij} \rangle_\Omega||}$ with

$$\sigma(\langle P_{ij} \rangle_\Omega) = \sqrt{\frac{1}{n} \sum_{k=1}^{n} \left(\langle P_{ij} \rangle_\Omega^k - \overline{\langle P_{ij} \rangle_\Omega} \right)^2} \tag{31}$$

$$\overline{\langle P_{ij} \rangle_\Omega} = \frac{1}{n} \sum_{k=1}^{n} \langle P_{ij} \rangle_\Omega^k \tag{32}$$

$$\overline{||\langle P_{ij} \rangle_\Omega||} = \frac{1}{n} \sum_{k=1}^{n} \left|| \langle P_{ij} \rangle_\Omega^k \right|| \tag{33}$$

Fig. 7(a) shows the normalised standard deviation of the component $[\langle \boldsymbol{P} \rangle_\Omega]_{12}$ for different polycrystals over the deformation, Fig. 7(b) represents it over the polycrystal size in terms of the crystal grain quantity. From a grain number of about 20 on, the standard deviation does not decrease significantly anymore, whereas the ± 5 % error measure requires polycrystalline structures of 100 grains and more.

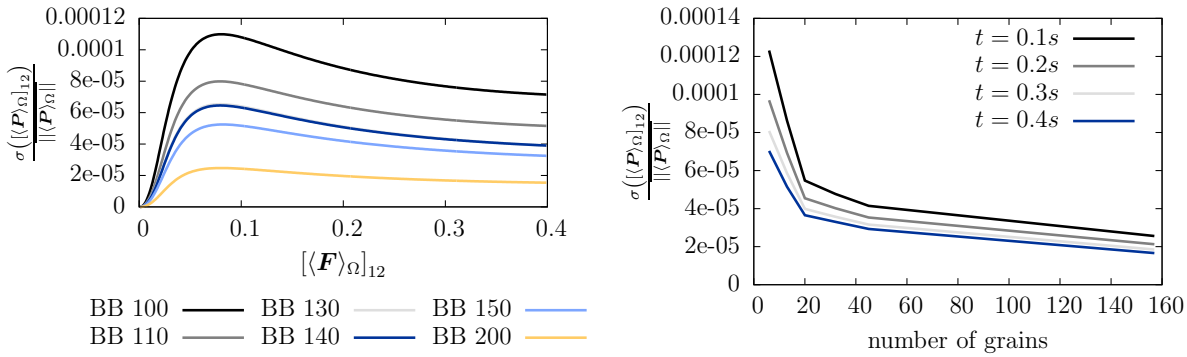

(a) Standard deviation over time.

(b) Standard deviation over grain number.

Figure 7: Normalised standard deviation of the polycrystals of different sizes for a population of 200 computations.

6 CONCLUDING REMARKS AND OUTLOOK

6.1 Effective material properties

Assuming that the stresses from the volume averaging procedure are the same as from an effective material assumption

$$\langle \boldsymbol{P} \rangle_\Omega = \boldsymbol{P}^{\text{eff}} = \boldsymbol{P}(\langle \boldsymbol{F} \rangle_\Omega) = \boldsymbol{P}(\boldsymbol{F}^{\text{eff}}), \tag{34}$$

the determination of the effective material parameters can be performed based on a least square fit between the mean stresses out of n performed computations and the stresses from an effective constitutive assumption

$$\Pi := \left[\frac{1}{n} \sum_{k=1}^{n} \left(\langle \boldsymbol{P} \rangle_\Omega^k \right) - \boldsymbol{P}(\boldsymbol{F}^{\text{eff}}(\boldsymbol{\kappa}^{\text{eff}})) \right]^2 \rightarrow \text{minimum} \tag{35}$$

$$\boldsymbol{\kappa}^{\text{eff}} := \left[\boldsymbol{\kappa}_{el}^{\text{eff}}, \boldsymbol{\kappa}_{pl}^{\text{eff}} \right]^T . \tag{36}$$

Due to the volumetric-deviatoric split of the constitution, see (10), both parts of the deformation can be separated and reveals quite an easy way to determine first the isotropic elastic material parameters $\boldsymbol{\kappa}_{el}^{\text{eff}}$ by remaining in the elastic range of the deformation. Having determined the parameters with (35), also for varying elastic parameters within the crystal grains, the assignment of the plastic parameters $\boldsymbol{\kappa}_{pl}^{\text{eff}}$ can be done. Eventually, the gained effective material model representing the microstructural behaviour has to be validated for different kinds of boundary conditions and constraints of real forming processes.

7 ACKNOWLEDGEMENTS

Financial support for this research was provided by the Deutsche Forschungsgemeinschaft (DFG) under grant SFB TR 73. This is gratefully acknowledged.

REFERENCES

[1] Anand, L. Single-crystal elasto-viscoplasticity: application to texture evolution in polycrystalline metals at large strains. *Comput. Meth. Appl. Mech. Eng.* (2004) **193**:5359–5383.

[2] Asaro, R.J. Crystal plasticity. *J. Appl. Mech.* (1983) **50**:921–934.

[3] Cuitiño, A.M. and Ortiz, M. Computational modelling of single crystals. *Modelling Simul. Mater. Sci. Eng.* (1992) **1**:225–263.

[4] De Souza, E.A. The exact derivative of the exponential of an unsymmetric tensor. *Comput. Meth. Appl. Mech. Eng.* (2001) **190**:2377–2383.

[5] De Souza, E.A. and Perić, D. and Owen, D.R.J. *Computational methods for plasticity. Theory and applications*. John Wiley and Sons Ltd Publication, (2008).

[6] Hosford, W.F. *The mechanics of crystals and textured polycrystals*. Oxford Engineering Science Series (1993).

[7] Itskov, M. Computation of the exponential and other isotropic tensor functions and their derivatives. *Comput. Meth. Appl. Mech. Eng.* (2003) **192**:3985–3999.

[8] Mandel, J. *Plasticité classique et viscoplasticité*. CISM Lecture Notes No. 97, International center for mechanical sciences, Springer Verlag, New York (1972).

[9] Miehe, C. Exponential map algorithm for stress updates in anisotropic multiplicative elastoplasticity for single crystals. *Int. J. Numer. Methods Eng.* (1996) **50**:273–298.

[10] Needleman, A. and Asaro, R.J. and Lemonds, J. and Peirce, D. Finite element analysis of crystalline solids. *Comput. Meth. Appl. Mech. Eng.* (1985) **52**:689–708.

[11] Steinmann, P. and Stein, E. On the numerical treatment and analysis of finite deformation ductile single crystal plasticity. *Comput. Meth. Appl. Mech. Eng.* (1996) **129**:235–254.

XI International Conference on Computational Plasticity. Fundamentals and Applications
COMPLAS XI
E. Oñate, D.R.J. Owen, D. Peric and B. Suárez (Eds)

AN ELASTO-PLASTIC DAMAGE MODEL FOR CONCRETE

E. Lale*, M. Aydoğan†

* Civil Engineering Faculty
Istanbul Technical University
Ayazaga, 34469 Istanbul, Turkey
e-mail: lale@itu.edu.tr

† Civil Engineering Faculty
Istanbul Technical University
Ayazaga, 34469 Istanbul, Turkey
e-mail: aydoganm@itu.edu.tr

Key words: Computational Plasticity, Constitutive modeling, Concrete, Damage mechanics.

Abstract. Constitutive modeling of concrete using continuum damage mechanics and plasticity theory is presented in this work. In order to derive the constitutive equations the strain equivalence hypothesis is adopted. Menetrey-William type yield function (in the effective stress space) with multiple hardening functions is used to define plastic loading of the material. Non-associated plastic flow rule is used to control inelastic dilatancy. Drucker-Prager type function is chosen as a plastic potential. Damage is assumed to be isotropic and two damage variables are used to represent tensile and compressive damage independently. Damage parameter is driven based on the plastic strain. Fully implicit integration scheme is employed and the consistent elastic-plastic-damage tangent operator is also derived. The overall performance of the proposed model is verified by comparing the model predictions to various numerical simulations, cyclic uniaxial tensile and compressive tests, monotonic biaxial compression test and reinforced concrete beam test.

1 INTRODUCTION

Concrete is widely used material due to its ability to be cast on site and to be formed in different shapes. Therefore its mechanical behaviour under different loading conditions must be better understood and it can be simulated by numerical methods. Several concrete constitutive equations have been developed based on nonlinear elasticity, plasticity theory, continuum damage mechanics (CDM), fracture mechanics and microplane model.

Concrete is a highly nonlinear material. Most prominent characteristic of concrete is its low tensile strength compared with its compressive strength. This causes micro-cracking of concrete even under very low loads which reduces the stiffness of concrete element. This leads to use of damage mechanics to model constitutive equations of concrete. On the other hand concrete exhibits some irreversible strain under compressive loads which can be simulated by using plasticity theory. Therefore accurate modeling of concrete behaviour needs to use plasticity theory and damage mechanics simultaneously.

Plasticity theory has been used successfully in modeling behavior of concrete by many researchers such as Grassl 2002, Papanikolaou and Kappos 2007, Kang and William, Imran and Pantazopoulou 2001, Etse and William 1994, Menetrey and William 1995. The main feature of these models is a pressure sensitive yield surface with parabolic meridians, non-associated flow and nonlinear hardening rule. However these models cannot take into account the degradation of material stiffness due to micro-cracking. On the other hand some researchers used continuum damage mechanics alone to simulate concrete behaviour Mazar and Cabot 1989, Simo and Ju 1987, Ortiz and Popov 1982, Tao and Phillips 2005.

Since both micro-cracking and irreversible deformations are two main distinct aspects of nonlinear response of concrete, several combined plasticity and CDM models have been developed in recent years. Combinations of plasticity and CDM are usually based on isotropic hardening plasticity with isotropic damage model. However some researchers use anisotropic damage model such as Çiçekli and Voyiadjis (2007), Carol et al (2001), Abu Al-Rub and Voyiadjis (2009). Most popular combination type is stress-based plasticity in effective space with damage because coupled plastic-damage models formulated in the effective space are more stable and attractive [2].

In this study concrete constitutive model is developed based on scalar damage with plasticity in effective stress space. Damage is modeled as the functions of plastic strain following Lee and Fenves (1998).

2 PLASTICITY FORMULATION

Three parameter Menetrey-William type yield function (in the effective stress space) with multiple hardening parameters is chosen to define plastic loading of the material. This criterion has been successfully used in simulating the concrete behaviour under uniaxial, biaxial and multiaxial loadings by many researchers [7,16]. It is smooth and convex, except the point where parabolic meridians intersect the hydrostatic axis. The yield function is formulated as follows:

$$f = 1.5\frac{\rho^2}{k\,f_c} + m\frac{\rho\, r(\theta)}{\sqrt{6}} + m\frac{\xi}{\sqrt{3}} - k\,f_c = 0 \tag{1}$$

in terms of Haigh-Westergaard coordinates in the effective stress space. Here ξ, ρ and θ is hydrostatic length, deviatoric length and Lode angle respectively and they are the functions of stress invariants according to following equations:

$$\xi = \frac{I_1}{\sqrt{3}} \tag{2}$$

$$\rho = \sqrt{2J_2}$$

$$\theta = \frac{1}{3}\cos^{-1}\left(\frac{3\sqrt{3}}{2}\frac{J_3}{J_2^{3/2}}\right)$$

where I_1 is first invariant of stress tensor and J_2, J_3 are second and third invariant of deviatoric stress tensor respectively.

Given yield surface possess parabolic meridians and triangular sections at low confinement to almost circular sections at high confinement on deviatoric plane shown in Figure 1. Deviatoric sections shape is controlled by the function:

$$r(\theta, e) = \frac{4\left(1-e^2\right)\cos^2\theta + \left(2e-1\right)^2}{2\left(1-e\right)^2\cos\theta + \left(2e-1\right)\left[4\left(1-e^2\right)\cos^2\theta + 5e^2 - 4e\right]^{1/2}} \tag{3}$$

which is proposed by Willam and Warnke (1974). Here e is eccentricity parameter and it must be calibrated according to the uniaxial tensile and compressive strength and biaxial compressive strength.

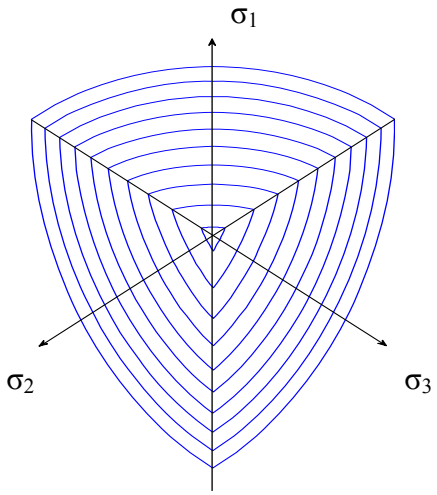

Figure 1. Deviatoric sections of yield functions

In yield surface equation f_c is the uniaxial compressive strength and m is friction parameter respectively. Friction parameter formulated in terms of compressive and tensile strength as

following equations:

$$m = 3\frac{(k\,f_c)^2 - (c\,f_t)^2}{k\,c\,f_c\,f_t}\frac{e}{e+1} \tag{4}$$

where k and c is compressive and tensile hardening-softening parameter respectively.

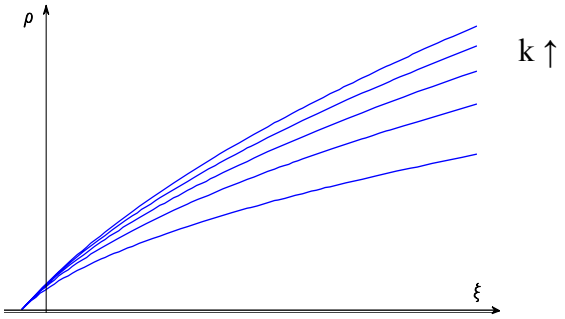

Figure 2. Evolution of Loading Surfaces

2.1 Flow Rule

In this study non-associated flow rule is adopted due to control excessive dilatancy. Non-associated means yield function and plastic potential are different each other and, therefore, plastic flow direction is not normal to the yield surface. This is important for realistic modelling of cohesive frictional material such as concrete and rock. The plastic strain rate obtained as:

$$\dot{\varepsilon}^p = \dot{\lambda}\frac{\partial g}{\partial \bar{\sigma}} \tag{5}$$

Where $\dot{\lambda}$ is plastic multiplier which can be obtained from plastic consistency condition and g is plastic potential. Drucker-Prager type potential function is chosen as follows

$$g = \alpha\, I_1 + \sqrt{3J_2} \tag{6}$$

such that;

$$\frac{\partial g}{\partial \bar{\sigma}} = \alpha\,\delta_{ij} + \frac{3}{2}\frac{s_{ij}}{\sqrt{3J_2}} \tag{7}$$

Here α is dilatation parameter and it controls inelastic volume expansion. Plastic consistency condition is obtained by taking the time derivative of yield function and satisfying Kuhn-Tucker conditions:

$$f < 0 \quad \rightarrow \quad \dot{\lambda} = 0 \quad (Elastic)$$

$$f = 0 \; and \; \dot{f} < 0 \quad \rightarrow \quad \dot{\lambda} = 0 \quad (unloading) \tag{8}$$

$$f = 0 \; and \; \dot{f} = 0 \quad \rightarrow \quad \dot{\lambda} > 0 \quad (plasticity)$$

$$f \le 0, \dot{\lambda} \ge 0 \quad \rightarrow \quad \dot{\lambda} \; f = 0 \;\; Kuhn\,Tucker$$

2.2 Hardening and Softening Rule

The nonlinear behaviour of concrete in the pre-peak and post-peak region is described by isotropic hardening/softening rule. Hardening/softening and damage states are defined independently by two variables, κ_c and κ_t due to different behaviour under compressive and tensile loading. For uniaxial loading κ_c and κ_t is defined as axial plastic strain under compression and tension respectively [12].

$$\kappa = \begin{bmatrix} \kappa_t \\ \kappa_c \end{bmatrix} \tag{9}$$

$$\dot{\kappa}_t = \dot{\varepsilon}_1^p \qquad \kappa_t = \int_0^t \dot{\kappa}_t \, dt$$

$$\dot{\kappa}_c = -\dot{\varepsilon}_3^p \qquad \kappa_c = \int_0^t \dot{\kappa}_c \, dt$$

Under multiaxial loading the evolution of hardening variables is given as follows (Lee and Fenves 1998):

$$\Delta\kappa = h\left(\bar{\sigma}, \varepsilon^p\right) \Delta\hat{\varepsilon}^p \tag{10}$$

where $\hat{\varepsilon}^p$ represents eigenvalues of strain tensor

$$\Delta\hat{\varepsilon}^p = \begin{bmatrix} \Delta\hat{\varepsilon}_1^p & \Delta\hat{\varepsilon}_2^p & \Delta\hat{\varepsilon}_3^p \end{bmatrix}^T \tag{11}$$

and

$$h\left(\hat{\bar{\sigma}}, \tilde{\varepsilon}^p\right) = \begin{bmatrix} r\left(\hat{\bar{\sigma}}\right) & 0 & 0 \\ 0 & 0 & -\left(1 - r\left(\hat{\bar{\sigma}}\right)\right) \end{bmatrix} \tag{12}$$

The scalar $0 \le r\left(\hat{\bar{\sigma}}\right) \le 1$ is a weight factor and defined as

$$r\left(\hat{\bar{\sigma}}\right)=\frac{\sum_{i=1}^{3}\left\langle\hat{\bar{\sigma}}_i\right\rangle}{\sum_{i=1}^{3}\left|\hat{\bar{\sigma}}_i\right|} \tag{13}$$

Where $\langle x\rangle=\left(|x|+x\right)/2$ denotes the Macaulay bracket function and $\hat{\bar{\sigma}}$ is effective principal stress.

Under Tension

Concrete assumed linear elastic up to tensile strength. After that concrete exhibits strain softening. Descending part of tensile stress-strain curve is formulated by stress-crack opening relations given by Hordjik(1991).

$$\sigma_t=f_t\left[\left(1+\left(c_1\frac{w}{w_c}\right)^3\right)\exp\left(-c_2\frac{w}{w_c}\right)-\frac{w}{w_c}\left(1+c_1^3\right)\exp\left(-c_2\right)\right] \tag{14}$$

Where f_t tensile strength, w crack opening, w_c critical crack opening and c_1, c_2 are material constants. Hordjik gives material constants values as c_1=3, c_2=6.93. To prevent mesh dependent result Hordjik stress-crack opening equation formulated in terms of inelastic strain and stress by incorporating fracture energy and characteristic length as follows:

$$G_f=\int\sigma_t\cdot dw \tag{15}$$

$$w=l_c\cdot\varepsilon^{cr}$$

$$G_f=l_c\int_0^{\kappa_{tu}}\sigma_t\,d\varepsilon^{cr}$$

$$\kappa_{tu}=5.14\frac{G_f}{l_c\,f_t}$$

Where G_f, l_c, σ_t are crushing energy, characteristic length and stress in the direction of crack normal, respectively.

Under Compression:

Strength parameter k, which controls the evolution of the yield surface under compression, is defined in terms of hardening variable κ_c as follows [5,9]:

$$k = k_0 + \frac{\left(2\sqrt{\kappa_c\,\kappa_{c\max}} - \kappa_c\right)}{\kappa_{c\max}}\left(1-k_0\right) \qquad 0 \le \kappa_c \le \kappa_{c\max} \tag{16}$$

$$k = 1 - \left(\frac{\kappa_c - \kappa_{c\max}}{\kappa_{cu} - \kappa_{c\max}}\right)^2 \qquad \kappa_c > \kappa_{c\max}$$

Where $k_0=f_{c0}/f_c$ and κ_{cmax} and κ_{cu} is equivalent plastic strain at peak stress and ultimate equivalent plastic strain respectively. Second part gives compressive softening which also causes mesh dependent results. To prevent mesh dependency same procedure is followed as tension softening.

$$\kappa_{cu} = \kappa_{c\max} + 1.5\frac{G_c}{l_c\, f_c} \tag{17}$$

Where G_c is crushing energy.

3 DAMAGE MODEL

Isotropic damage is responsible for the degradation in elastic stiffness in this work. Two damage variables, one for tensile damage ω_t and one for compressive damage ω_c, are defined independently following Lee and Fenves (1998). It is assumed that damage variables are increasing functions of the equivalent plastic strains and they can take values ranging from zero, for the undamaged material, to one, for the fully damaged material.

It is assumed that the degradation takes the following exponential form [12,13]:

$$\omega_t = 1 - e^{-a_t \kappa} \tag{18}$$

$$\omega_c = 1 - e^{-a_c \kappa}$$

Where a_t and a_c are material constant for uniaxial tension and compression respectively and they must be calibrated from uniaxial tests. When uniaxial tensile and compressive damage variables are obtained then total damage variables calculated as the following form [1,12]:

$$1 - \omega = 1 - \left(1 - s_c\,\omega_t\right)\left(1 - s_t\,\omega_c\right) \tag{19}$$

Here s_t and s_c are used for to take into account closing and reopening of cracks.

4 NUMERICAL INTEGRATION

The implemented integration scheme is divided into two sequential steps, corresponding to the plastic and damage parts. In the plastic part, the plastic strain ε_p and the effective stress $\bar{\sigma}$ at the end of the step are determined by using the implicit backward-Euler return-mapping scheme. In the damage part, damage variable ω and nominal stress σ at the end of the step are determined.

Implementation of return-mapping algorithm requires integrating the rate form of constitutive relations in finite time step $\Delta t = t^{n+1} - t^n$ to obtain the stress changes $\Delta\sigma$ and the state variables corresponding to a total change of displacement $\Delta\varepsilon$ within the load increment.

$$\bar{\sigma}_{n+1} = \bar{\sigma}^t - D\,\Delta\varepsilon^p_{n+1} = \bar{\sigma}^t - \Delta\lambda_{n+1} D \frac{\partial g}{\partial \bar{\sigma}_{n+1}} \tag{20}$$

Where $\bar{\sigma}^{tr}$ is the effective trial stress which is evaluated from given strain increment assuming that plastic strain increment is zero. If trial stress is not outside the yield stress, $f \leq 0$, then step is elastic and plastic strain increment is zero. On the other hand if the trial stress is outside the yield surface then $\bar{\sigma}_{n+1}, \varepsilon^p_{n+1}, \kappa^p_{n+1}$ are determined according to calculated $\Delta\lambda$.

At the end of the loading step following four equations must be satisfied:

$$\bar{\sigma}_{n+1} = D\left(\varepsilon_{n+1} - \varepsilon^p_{n+1}\right) \tag{21}$$

$$\varepsilon^p_{n+1} = \varepsilon^p_n + \Delta\varepsilon^p_{n+1}$$

$$\kappa_{n+1} = \kappa_n + \Delta\kappa_{n+1}$$

$$f \leq 0$$

If one defines the residuals for the equations (4.17), (4.18) and (4.19) as follows:

$$R_{n+1} = \begin{Bmatrix} R_{\varepsilon,n+1} \\ R_{\kappa,n+1} \\ R_{f,n+1} \end{Bmatrix} = \begin{Bmatrix} \varepsilon^p_{n+1} - \varepsilon^p_n - \Delta\lambda_{n+1} \dfrac{\partial g}{\partial \bar{\sigma}_{n+1}} \\ \kappa_{n+1} - \kappa_n - \Delta\lambda_{n+1} H_{n+1} \\ f_{n+1} \end{Bmatrix} \tag{22}$$

and linearizates these according to Taylor expansion following equations are obtained:

$$\begin{aligned} &R_{\varepsilon,n+1} + \Delta\varepsilon^p_{n+1} - \Delta\lambda_{n+1}\,\Delta b_{n+1} - \delta\lambda_{n+1}\, b_{n+1} = 0 \\ &R_{\kappa,n+1} + \Delta\kappa_{n+1} - \Delta\lambda_{n+1}\,\Delta H_{n+1} - \delta\lambda_{n+1}\, H_{n+1} = 0 \\ &f + \frac{\partial f_{n+1}}{\partial \bar{\sigma}_{n+1}} \Delta\bar{\sigma}_{n+1} + \frac{\partial f_{n+1}}{\partial \kappa_{n+1}} \Delta\kappa_{n+1} = 0 \end{aligned} \tag{23}$$

After few manipulations, $\Delta\lambda$ can be determined as follows:

$$\delta\lambda_{n+1} = \frac{f - \begin{bmatrix} \dfrac{\partial f_{n+1}}{\partial \bar{\sigma}_{n+1}} & \dfrac{\partial f_{n+1}}{\partial \kappa} \end{bmatrix}^T [A] \begin{Bmatrix} R_{\varepsilon,n+1} \\ R_{\kappa,n+1} \end{Bmatrix}}{\begin{bmatrix} \dfrac{\partial f_{n+1}}{\partial \bar{\sigma}_{n+1}} & \dfrac{\partial f_{n+1}}{\partial \kappa} \end{bmatrix}^T [A] \begin{Bmatrix} b_{n+1} \\ H_{n+1} \end{Bmatrix}} \tag{24}$$

Where

$$[A]^{-1} = \begin{bmatrix} I + D\,\Delta\lambda_{n+1} \dfrac{\partial b_{n+1}}{\partial \bar{\sigma}_{n+1}} & -\Delta\lambda_{n+1} \dfrac{\partial b_{n+1}}{\partial \kappa_{n+1}} \\ D\,\Delta\lambda_{n+1} \dfrac{\partial H_{n+1}}{\partial \bar{\sigma}_{n+1}} & I - \Delta\lambda_{n+1} \dfrac{\partial H_{n+1}}{\partial \kappa_{n+1}} \end{bmatrix} \tag{25}$$

and $b = \dfrac{\partial g}{\partial \bar{\sigma}}$ is the gradient of the plastic potential.

Once the effective stress $\bar{\sigma}_{n+1}$ is computed in the elastic predictor/plastic corrector steps, the damage parameter is then calculated from equation (3.10):

$$1 - \omega = 1 - \left(1 - s_c\,\omega_t\right)\left(1 - s_t\,\omega_c\right) \tag{26}$$

and the stress is updated as:

$$\sigma_{n+1} = \left(1 - \omega\right)\bar{\sigma}_{n+1} \tag{27}$$

5 NUMERICAL EXAMPLES

The present concrete model is implemented in Abaqus 6.8 by user element subroutine Umat. Its performance is denoted by comparing with uniaxial tensile and compressive, biaxial compressive and cyclic experimental test from literature.

In Figure 3 the cyclic uniaxial tensile test of Taylor (1992) and the cyclic compressive test of Karson and Jirsa (1969) are evaluated numerically to demonstrate the capability of the proposed model under cyclic load conditions. The following properties are adopted: for Taylor's simulation, E_c=3.1×10^4 MPa, f_t= 3.5 MPa, G_f=100 N/m; and for Karsan and Jirsa's one, E = 3.17×10^4 MPa, f_t= 3.0 MPa and f_{c0}=10.2 MPa. As shown in Figure 3, the experimentally observed strain softening, stiffness degrading, and irreversible strains, are agree well with the proposed results under both tension and compression.

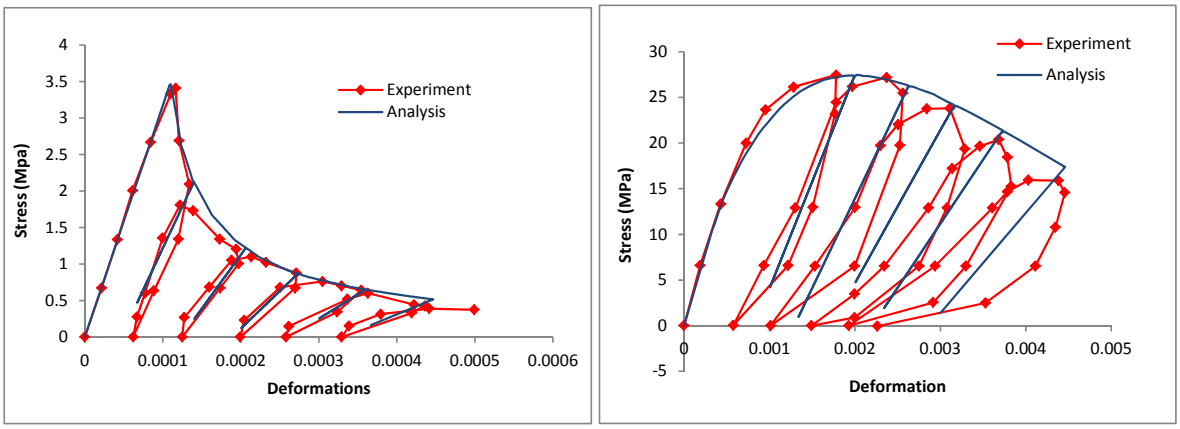

Figure 3 Uniaxial Cyclic Tensile (Taylor, 1992) and Compressive test (Karsan and Jirsa, 1969)

The proposed model is also validated with the results of biaxial compression test reported in Kupfer et al. (1969). The material properties adopted in the analysis are: $E_c=3.1\times10^4$ MPa f_t=3.0 Mpa and G_f=75 N/m. For specimens under load conditions $\sigma_2/\sigma_1=1/0$, $\sigma_2/\sigma_1=1/1$ and $\sigma_2/\sigma_1=1/0.5$, the predicted stress–strain curves given in Figure 4a–c agree well with the experimental results.

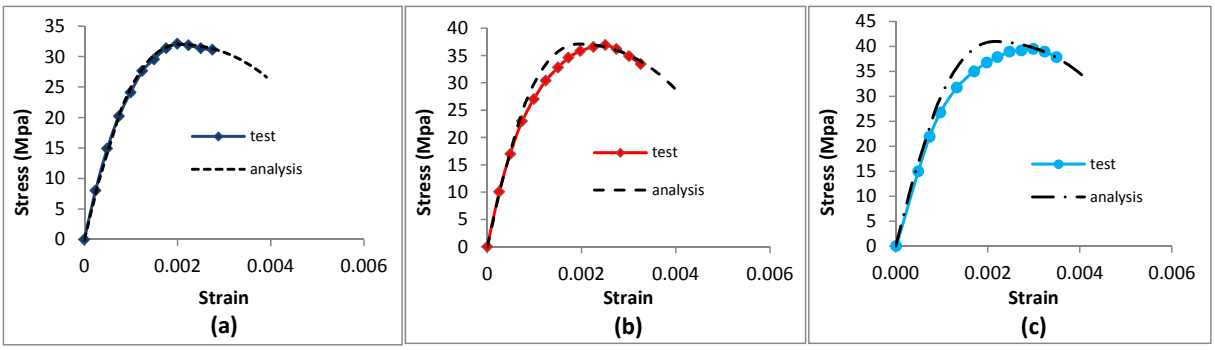

Figure 4 Monotonic Biaxial Compressive test (Kupfer et al, 1969)

Finally Bresler–Scordelis beam is used to validate the model performance for RC element. It is simply supported beam with 3.7m long span and subjected to concentrated load at midspan. The longitudinal reinforcement consists of four steel bars with total area of 2580 mm^2. The concrete has a compressive strength of 24.5 MPa and elastic modulus of 21300 MPa. The elastic modulus and yield stress of steel bars is 191.4 GPa and 444 Mpa respectively. In the finite element modeling, 4-noded rectangular plane stress element is used for concrete and truss elements for steel bars. Perfect bond between concrete and reinforcement is assumed. Load-displacement curve given in Figure 5 shows that analysis results is agree well with test results.

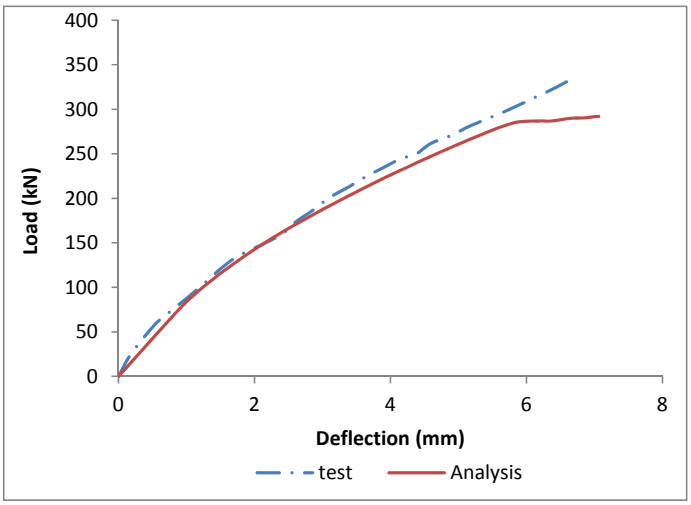

Figure 5 Reinforced Concrete Simply Supported Beam (Bresler-Scordelis,1963)

6 CONCLUSIONS

A constitutive model for concrete using continuum damage mechanics and plasticity theory is presented. The plastic part formulated in effective stress space and isotropic damage is formulated in terms of plastic strain. Multiple hardening and damage parameter are used due to different behaviour under tensile and compressive loading. The model predictions are found to be in good agreements with experimental results in uniaxial and biaxial loadings. Localization of deformations is considered by the fracture/crushing energy approach. This model may be enhanced by taking into account lateral confinement.

REFERENCES

[1] ABAQUS standard User's Manual. Hibbitt, Karlson and Sorenson, Inc. vol. 1,2 and 3, Version 6.4, USA, 2004.

[2] Abu Al-Rub, R.K. and Sun-Myung, K., Computational applications of a coupled plasticity-damage constitutive model for simulating plain concrete fracture, *Engineering Fracture Mechanics* (2010), **77**:1577-1603.

[3] Bresler, B. and Scordelis, A.C. Shear Strength of Reinforced Concrete Beams, *Journal of ACI* (1963), **60**:51-72.

[4] Etse, G. and William, K., Fracture energy formulation for inelastic behaviour of plain concrete, *Journal of Engineering Mechanics*, *ASCE* (1994), **120**:1983-2011.

[5] Feenstra, P.H. and de Borst, R. A composite plasticity model for concrete, *Int. J. Solids Struct.* (1996), 33:707-730.

[6] Gopalaratnam, V.S. and Shah, S.P. Softening response of plain concrete in direct tension, *ACI Journal* (1985), **85**:310-323.

[7] Grassl, P., Lundgren, K., Kent, G. Concrete in compression: a plasticity theory with a novel hardening law, *Int. J. Solids and Structures* (2002), **39**:5205-5223.

[8] Grassl, P. and Jirasek, M. Damage-plastic model for concrete failure, *Int. J. Solid and Structures* (2006), **43**:7166-7196.

[9] Imran, I. and Pantazopoulou, and S.J. Plasticity Model for Concrete under Triaxial Compression, *ASCE J. Engng. Mech* (2001), **127**: 281-290.

[10] Kang, H.D. *Triaxial constitutive model for plain and reinforced concrete behavior*, Phd Thesis, University of Colorado at Boulder, 1997.

[11] Kupfer, H.B., Hildorf, H.K. and Rusch, H. Behavior of concrete under biaxial stresses, ACI Journal (1969), **66**:656-666.

[12] Lee, J. and Fenves, G.L. Plastic-damage model for cycling loading of concrete structures, *Journal of Engineering Mechanics* (1998), **124**:892-900.

[13] Lubliner, J., Oliver, J., Oller, S. and Onate, E. A plastic-damage model for concrete, *Int. J. Solids Struct*. (1989), **25**:299-326.

[14] Mazars, J. and Cabot, G.P. Continuum damage theory-application to concrete, *Journal of Engineering Mechanics* (1989), **115**:345-365.

[15] Nguyen, G. D. and Houlsby, G.T. A coupled damage-plasticity model for concrete based on thermodynamic principles: Part I: model formulation and parameter identification, Int. J. Numer. Anal. Meth. Geomec. (2008), **32**:353-389.

[16] Papanikolaou, V.K. and Kappos, A.J. Confinement-sensitive plasticity constitutive model for concrete in triaxial compression, *Int. J. Solids and Structures* (2007), **44**:7021-7048.

[17] Salari, M.R., Saeb, S., Willam, K.J., Patchet, S.J. and Carrasco R.C. A coupled elastoplastic damage model for geomaterials, *Comput. Methods Appl. Mech. Engrg* (2004), **193**:2625-2643.

[18] Simo, J.C., and Ju, J.W. Strain and stress based continuum damage models, Part I: Formulation*, Int. J. Solids and Structures* (1987), 23: 821—840.

[19] Tao, X. and Phillips, D. V. A simplified isotropic damage model for concrete under bi-axial stress states, *Cement and Concrete Composites* (2005), **27**:716-726.

[20] Voyiadjis, G.Z. and Taqieddin, Z.N. Elastic Plastic and Damage Model for Concrete Materials: Part I – Theoretical Formulation, *Int. J. Struct. Chan. in Solids* (2009) **1**: 31-59.

[21] Wu, J.Y., Li, J., Faria, R. An energy release rate-based plastic-damage model for concrete, *Int. J. Solids and Structures* (2007), **43**:583-612.

XI International Conference on Computational Plasticity. Fundamentals and Applications
COMPLAS XI
E. Oñate, D.R.J. Owen, D. Peric and B. Suárez (Eds)

HIGH TEMPERATURE EFFECTS IN MORTAR AND CONCRETE SPECIMENS USING A MESO-MECHANICAL MODEL WITH FRACTURE BASED ZERO-THICKNESS INTERFACE ELEMENTS

M. RODRÍGUEZ[1], C.M. LÓPEZ[1], I. CAROL[1], J. MURCIA[2]

[1] Department of Geotechnical Engineering and Geo-Sciences
ETSECCPB (School of Civil Engineering)-UPC (Technical Univ. of Catalonia), 08034 Barcelona
[2]Instituto Eduardo Torroja CSIC, 28033 Madrid, Spain.
E-mail: carlos.maria.lopez@upc.edu, ignacio.carol@upc.edu

Key words: High temperature effects in mortar and concrete, Meso-mechanics, Finite element method, Interface elements.

Abstract. This paper describes recent numerical simulation results of a purely mechanical study of the effects of high temperature in mortar and concrete. The material has been considered as a two-phase composite, with different thermal expansion laws of matrix and particles taken from the literature. The numerical simulation is based on a meso-mechanical model developed in the group of Mechanics of Materials UPC, which represents the largest aggregate particles explicitly, and represent cracks in a discrete manner by inserting zero-thickness interface elements in all potential crack trajectories a priori of the analysis. The differential expansions create tensile stresses and therefore cracking, that eventually may close, reopen and lead to non-trivial overall material behavior. The results are discussed and compared to the experimental information available, and lead to a general good agreement, capturing the essential mechanisms described in the literature.

1 INTRODUCTION

Under high temperature variations, heterogeneous materials such as concrete may develop internal stresses and complex behavior including cracking and degradation as the result of the expansion mismatch between components. Cruz and Gillen [1] show experimental results of thermal expansion of concrete specimens, as well as of individual ingredients: cement paste, mortar and dolomite rock. In their tests, temperature ranged between 27 and 871ºC. The experimental test was carried out on cylindrical samples of 13mm in diameter and 76 mm in length. Experimental results show a variable coefficient of thermal expansion for cement paste, first expanding (until approximate 180ºC) and then contracting. In contrast, Dolomite rock shows, between 93 and 871ºC, an almost linear expansion as temperature is increased. Figure 1 shows the experimental results that were taken as the basic input information for the numerical study of Sect. 3.1, which deals with the free expansion of mortar specimens. Additional results also reported in the paper, deal with the influence of pre-imposed vertical stresses or prescribed deformations on the expanding specimen, as reported from Anderberg and Thelandersson [2], Thelandersson [3] and Willam et al. [4].

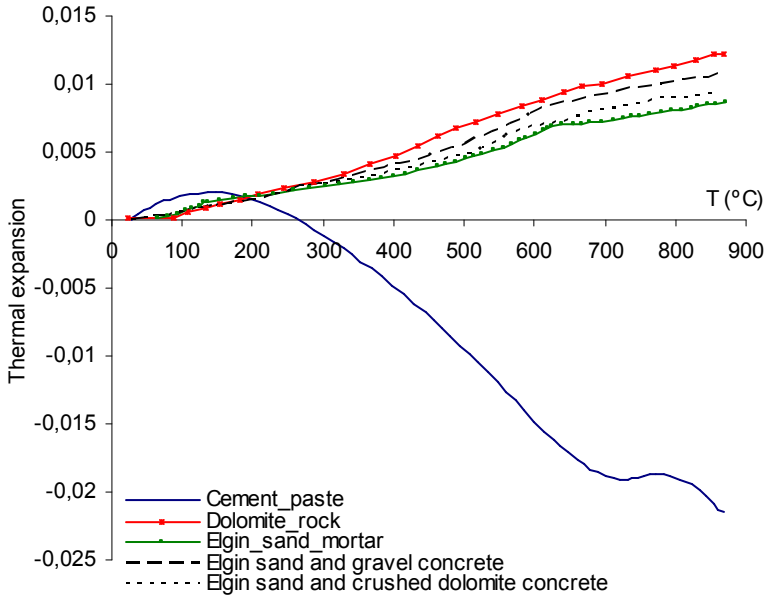

Figure 1: Experimental results for cement paste, dolomite rock, mortar and concrete (from Cruz and Gillen [1]).

2 MESOMECHANICAL MODEL

The numerical simulation is based on a meso-structural model in which the largest aggregate particles are represented explicitly, surrounded by a homogeneous matrix representing the average behavior of mortar plus the smaller aggregates. In order to capture the main potential crack trajectories, zero-thickness interface elements are inserted *a priori* of the analysis, along all the aggregate-mortar and some of the mortar-mortar mesh lines. These interface elements are equipped with a nonlinear constitutive law based on elasto-plasticity and concepts of fracture mechanics, which is formulated in terms of normal and shear components of the stress on the interface plane and the corresponding relative displacement variables. The initial loading (failure) surface F = 0 is given as three-parameters hyperbola (tensile strength χ, asymptotic cohesion c and asymptotic friction angle tanϕ). The evolution of F (hardening-softening laws), is based on the internal variable W^{cr} (work spent in fracture processes), with the two material parameters G_F^I and G_F^{IIa} that represent the classical fracture energy in Mode I, plus a second fracture energy for an "asymptotic" Mode IIa under shear and high confinement. A more detailed description of this elasto-plastic constitutive law can be found in the literature [5,6]. Results of the meso-mechanical model for normal concrete specimens subject to a variety of loading cases in 2D and 3D can also be found elsewhere [6-9].

For the current study, some of the FE meshes used previously have been modified in the sense of adding some interface elements along mesh lines perpendicular to the aggregate surfaces at mid-distance between aggregate corners. In this way, the medium surrounding the expanding aggregate particle can crack in the direction that is more physical, and possible spurious tensile stresses in the surrounding material are minimized.

3 RESULTS AND DISCUSSION

3.1 Thermal expansion of mortar specimens

The first numerical analysis is a mortar specimens composed by small aggregate particles of dolomite embedded in a cement paste matrix. For the cement paste the expansion vs. temperature law is extracted directly from the experimental curve above (in figure 1). Since the curve shows first expansion and then contraction, the thermal coefficient, which corresponds to the secant line from the origin to the desired point on the curve, changes sign from positive to negative as temperature increases. For dolomite rock, which constitutes the sand, experimental results show an almost linear expansion as temperature is increased. For this reason a constant coefficient of thermal expansion has been used in the calculations, with a value of 0.0000125/ºC.

In the experiment, thermal expansions were also measured for the overall mortar specimens, these values have been used to compare the results from the numerical calculations. For the numerical simulation, a 12x12 mm^2 square specimen was considered with volume fraction of sand aggregates 39% and maximum size 1.7mm (average aggregates size 1.02mm). These values were adopted based on available data from the lab specimens. The resulting meso-geometry and FE mesh are shown in figure 4.

3.1.1 Elastic analysis

The first analysis run for the mortar specimen has been under the assumption of linear-elastic interfaces (figure 2). Note that in this case interfaces are not allowed to open (crack) or slide. Therefore, the change from expansion to contraction of the cement paste for high temperature, forces the overall initial mortar expansion (with tensioned sand aggregates) to turn later into overall contraction (with compressed sand aggregates), and all materials and interface are assumed to withstand tensile stresses without limit.

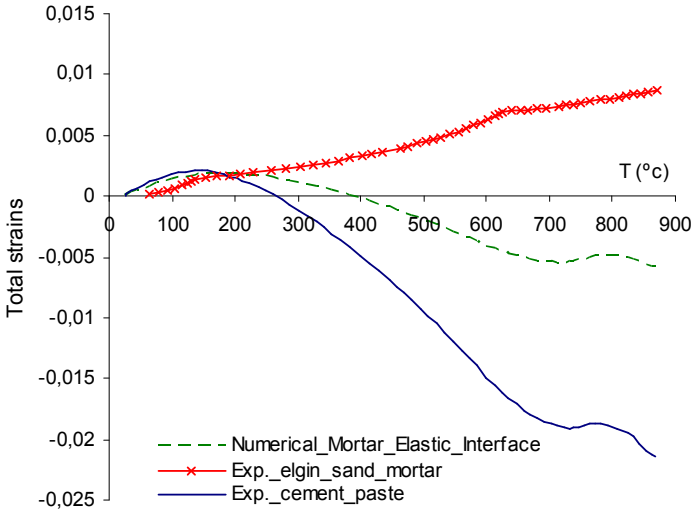

Figure 2: Experimental curves for mortar and cement paste expansion, together with numerical results of a heterogeneous mortar specimen assuming linear elasticity (linear elastic interfaces).

3.1.2 Non-linear analysis with cracking

In this case the interface elements are assumed to follow a fracture-based non-linear constitutive law with softening that simulates cracking [5]. The material parameters used are: for the continuum medium: E = 70000 MPa (dolomite rock), E = 25000 MPa (cement paste) and υ = 0.2 (both); for all interfaces (along both dolomite sand-cement and cement-cement contacts): $K_N = K_T = 500000$ MPa/mm, $\tan\phi_0 = 0.90$, $\chi_0 = 6$ MPa, $c_0 = 15$MPa, $G^F_I = 0.025$ N·mm, $G^F_{II} = 10\ G^F_I$, $\sigma_{dil} = 40$ MPa, $\alpha_d = -2$.

Figure 3 shows the numerical and experimental results obtained for mortar specimens, together with the experimental results for dolomite rock and cement paste.

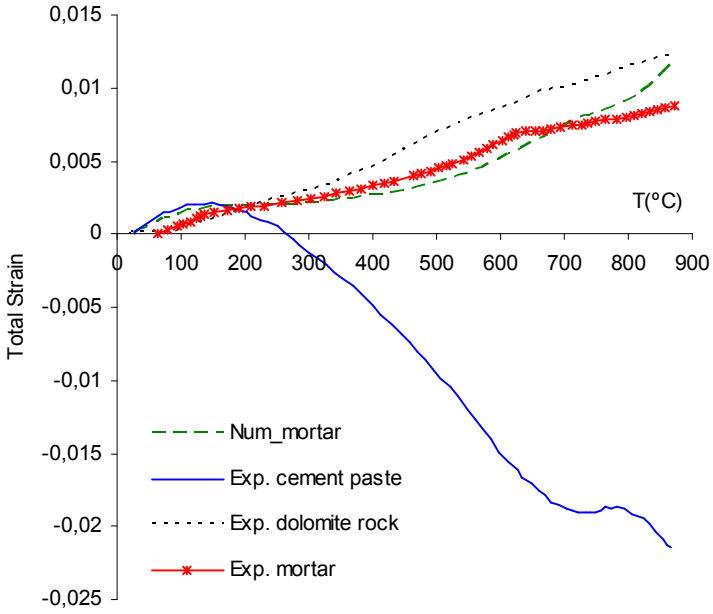

Figure 3: Numerical versus experimental specimen expansion curves for the mortar specimen with cracking, together with the curves obtained for sand and for cement paste.

3.1.3 Crack evolution and final deformation

Figures 4 and 5 show the details of crack evolution for eleven different prescribed temperature values (54, 110, 148, 180, 192, 286, 547, 612, 711, 806 and 867ºC), as well as the final deformation mesh (in the last diagram for 867 ºC, the red mesh overlapped represents the undeformed mesh). In the figures, cracking is represented in term of the magnitude of the relative displacement vector (square root of normal plus tangential relative displacements squared). The graphic scale factor is not the same in all figures because for temperatures below 201ºC displacement magnitudes are significantly lower than for temperatures above that value. The maximum values of the relative displacement norm obtained through the entire mesh for each temperature are indicated in the figure captions.

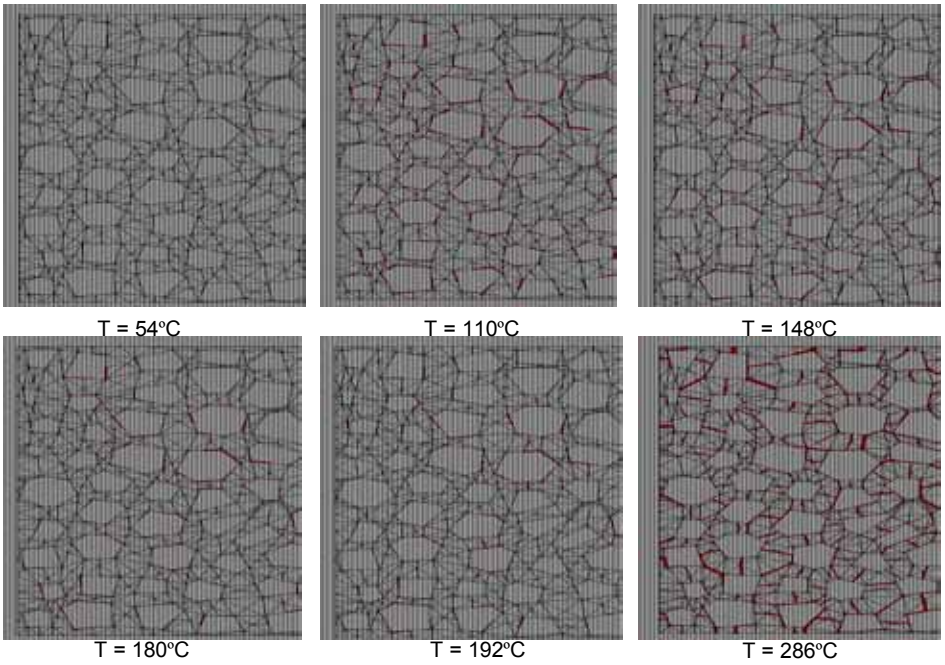

Figure 4: Crack pattern evolution of mortar in terms of the magnitude of the relative displacement vector, for increasing prescribed temperature (same graphic scale factor for the six diagrams, but not the same as in figure 5; maximum value for each diagram (x10-4): 0.131, 0.204, 0.193, 0.169, 0.158 and 4.24).

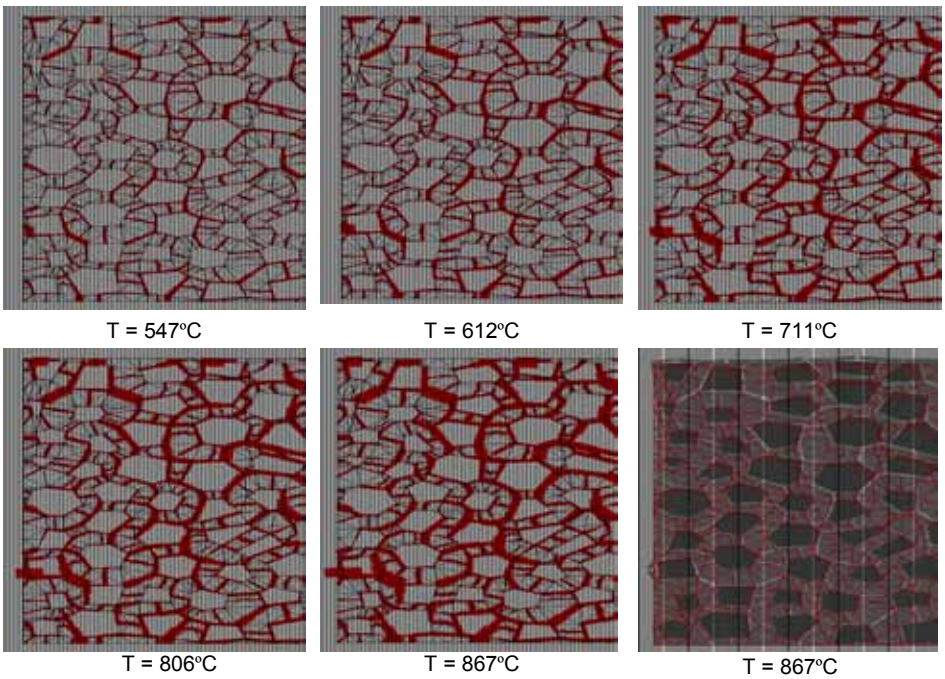

Figure 5: Crack pattern evolution of mortar in terms of the magnitude of the relative displacement vector, for increasing prescribed temperature (same graphic scale factor for the five diagrams, but not the same as in figure 4; maximum value for each diagram(x10-4): 33.9, 46.1, 60.3, 65.1 and 78.8).

In figures 4 and 5 it is shown that initially only the interface elements between aggregate and matrix develop cracks (three first pictures in figure 4), while for higher temperature practically all interface elements become activated. This is related to the fact that for temperature below 180ºC the aggregates are basically in tension and the matrix is in compression, while for higher temperature this situation is inverted.

3.1.4 Evolution of the stresses of the continuous medium

Figure 6 shows the evolution of the stresses within the cement paste and sand grains (continuous medium), red color representing tensile stresses and blue color compressive stresses. For temperatures below 180ºC, cement paste expands more that the aggregates (see figure 1), causing the aggregates to be subject to tension and the matrix to compression. Above that temperature, however, this trend is inverted: the aggregates expand more that the cement paste and the stresses change sign. In figure 6 we can see both states:

- Below 180ºC the aggregates are in tension and the matrix is in compression. Stress values increase until 110ºC, then start decreasing.
- Above 180ºC the stress state changes and aggregates turn into compression while the matrix turns into tension. Once signs have changed, stress values increase until approximately 286ºC, and beyond that temperature they decrease again.

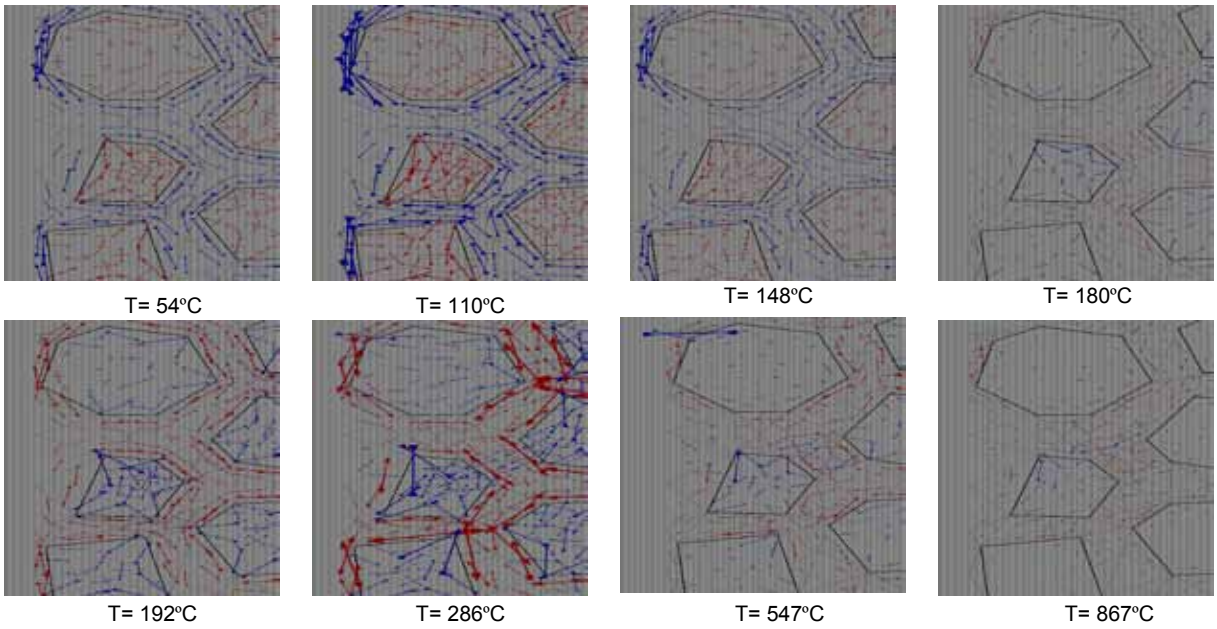

Figure 6: Evolution of stresses in the continuous medium of aggregates and matrix for the following temperature values: T = 54ºC, 110ºC, 148ºC, 180ºC, 192ºC, 286ºC, 547ºC and 867ºC, same scale factor for stresses in all graphs in this figure.

3.1.5 Numerical estimate of the influence of pre-existing vertical compressive stress

The fact that thermal action without confinement generates cracking, motivates the investigation of the effects of simultaneous loading and temperatures. Intuitive understanding tells us that under initial compression, cracking caused by tensile stress increments generated by temperature action might be postponed or prevented altogether. Therefore the combined effects of compression and temperatures might differ significantly from the superposition of the individual effects. These aspects are investigated in this section, by means of some additional calculations, using the same mortar mesh of the previous section with the parameters already calibrated for the mortar of Cruz and Guillen [1], which is subject to simultaneous thermal action and vertical confining stress. Because Cruz and Guillen [1] did not perform any such test under compressive load, the numerical results obtained are compared in a pure qualitative manner with some existing experimental results of Anderberg and Thelandersson [2], which were carried out in concrete specimens with different properties and geometric characteristic of the mortar used in the simulation.

In the numerical simulations, the specimens were loaded to a certain vertical stress level and then heated to 800ºC. The load level is given as a percentage of the compressive strength of the material. Ten specific cases were analyzed with the nine compressive vertical stresses over f'_c values of: 0, 0.01, 0.03, 0.05, 0.112, 0.225, 0.450, 0.675 and 1. The results obtained in terms of overall vertical strain (positive = expansion, negative = contraction) against temperature are shown in figure 7.

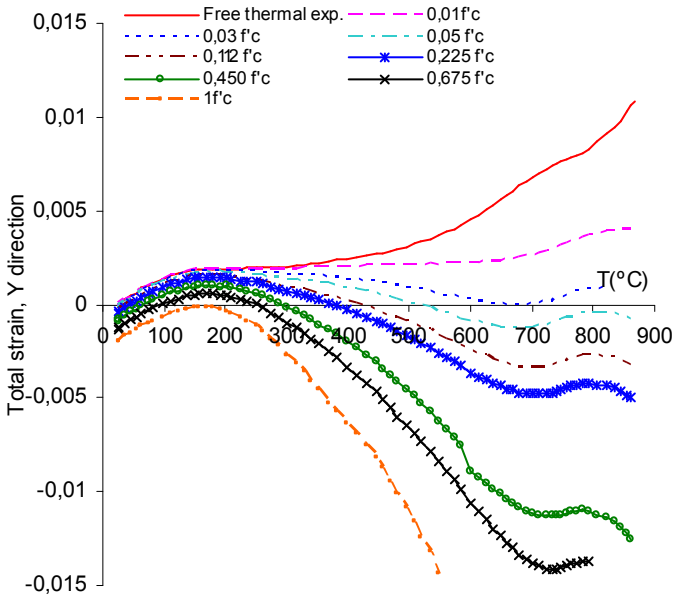

Figure 7: Total strain vs. temperature for different stress levels (numerical study).

In the figure, the upper continuous curve corresponds to free expansion (no compression), and coincides with the mortar curve in figure 3. For low temperatures, the effect of compression on the thermal expansion is reflected by the shift downwards of each curve,

which remains approximately constant until the temperature of 200-300^{0}C. In this range the effects of compression and temperatures could be simply superimposed. Beyond that temperature, however, the (upper) uncompressed curve shows an inflection point corresponding to the beginning of internal cracking when the contracting matrix gets detached from the expanding aggregates, while the pre-compressed curves tend to turn downwards following the matrix contraction. Tensile stresses due to thermal mismatch have to overcome existing compressions, with the result that cracking and overall expansions are delayed to higher and higher temperatures, or even suppressed altogether for high compression values approaching the compressive strength.

The main trends observed in the computations are similar qualitatively to those observed in the experiments A5, A6, A8 and A9 of Anderberg and Thelandersson [2], results that are shown in section 3.2.2 (figure 10).

3.2 Thermal expansion of concrete specimens

Experimental tests of thermal expansion at high temperature of concrete specimens with and without compression stress were reported, among others, by Anderberg and Thelandersson [2]. The calculations in this section try to reproduce those material characteristics and results, but due to the lack of basic material information (those authors did not report details of thermal expansions of the individual components cement, aggregate, mortar), the missing information is taken from the experiments from Cruz and Guillen [1] already mentioned in previous sections.

In the numerical analysis, concrete is represented by large aggregates particles of dolomite rock surrounded by a matrix that represents mortar and smaller aggregates. The specimen considered has dimensions 10x10cm^2, volume fraction of large aggregates 28% and maximum aggregate size 14mm (average aggregate size 10.4mm). The material parameters are: E = 70000 MPa (dolomite rock), E = 29000 MPa (mortar) and υ = 0.2 (both); for dolomite aggregate-mortar interfaces $K_N = K_T$ = 500000 MPa/mm, $tan\phi_0$ = 0.90, χ_0 =4 MPa, c_0 = 15MPa, G^F_I = 0.025 N·mm, G^F_{II} = 10 G^F_I, σ_{dil} = 40 MPa, α_d = -2, and for mortar-mortar interfaces: $K_N = K_T$ = 500000 MPa/mm, $tan\phi_0$ = 0.90, χ_0 =6 MPa, c_0 = 20MPa, G^F_I = 0.030 N·mm, G^F_{II} = 10 G^F_I, σ_{dil} = 40 MPa, α_d = -2.

3.2.1 Free thermal expansion analysis

In the numerical simulation of the free thermal expansion analysis of concrete, the variable coefficient of thermal expansion for mortar is extracted from a volume expansion vs. temperature curve obtained numerically in Sec. 3.1.2 (figure 3). For aggregates, the coefficient of thermal expansion is assumed constant with value 0.0000125/ºC (same as for the sand in the mortar simulation of Sect 3.1).

Figure 8 shows the numerical and experimental results for concrete specimens, for both Cruz and Guillen [1] and Anderberg and Thelandersson [2]. Numerical results are closer to the curves reported by Cruz y Guillen [1], and do not deviate excessively from those by Anderberg y Thelandersson [2] either. Results also show that in general terms expansion of concrete is larger than of mortar subject to the same temperature.

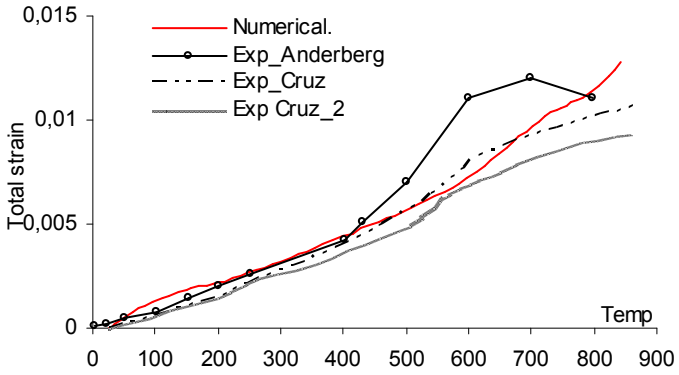

Figure 8: Total strain vs. temperature, numerical and experimental results for concrete.

3.2.2 Crack evolution and final deformation

The crack evolution trend is similar to that obtained for mortar in section 3.1.3. Figure 9 shows a detail of crack evolution for three different prescribed temperature values (157, 519 and 867ºC) and the final deformation field. We can see that, as in mortar, initially only the interface elements between aggregate and matrix are opening, while for higher temperature practically all interface elements became activated.

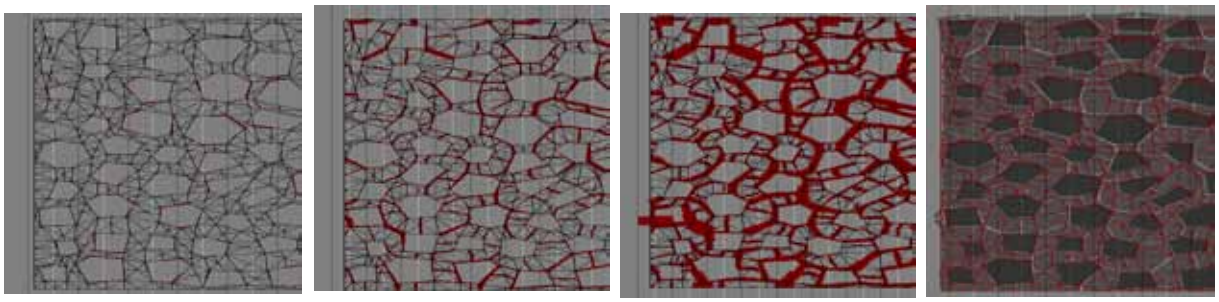

Figure 9: Crack pattern evolution of concrete in terms of the magnitude of the interface relative displacements, for increasing prescribed temperature. Max. values obtained through the mesh (x10-3): 0.1766, 5.096, and 5.970, respectively.

3.2.3 Test with thermal action under different values of vertical compressive stress

The influence of a pre-existing sustained vertical stress on the evolution of thermal expansion is analyzed. The specimens were loaded to a certain vertical stress level and then heated to 800ºC. The load level is given as a percentage of the compressive strength of the material. Three specific cases were analyzed with the three compressive vertical stresses over f'_c values of: 0.225, 0.450 and 0.675. For each cases here analyzed a constant coefficient of thermal expansion of value 0.0000125/ºC for the aggregates was used. For the mortar, a variable thermal coefficient has been extracted from the mortar expansion/contraction curves obtained in Sect. 3.1.5.

Figure 10 shows preliminary numerical results obtained in terms of overall vertical strain (positive = expansion, negative = contraction) against temperature, together with the experimental curves of Anderberg and Thelandersson [2]. For low temperature values, approximately 0-300ºC, there is a certain difference between numerical and experimental result, this is due to the fact that the experimental curves show for this range of temperatures the called transitional thermal creep which our model is not able to capture. For higher temperature values, where cracking and overall expansion are delayed for the presence of the vertical compressive stress, there is a qualitatively good agreement between results.

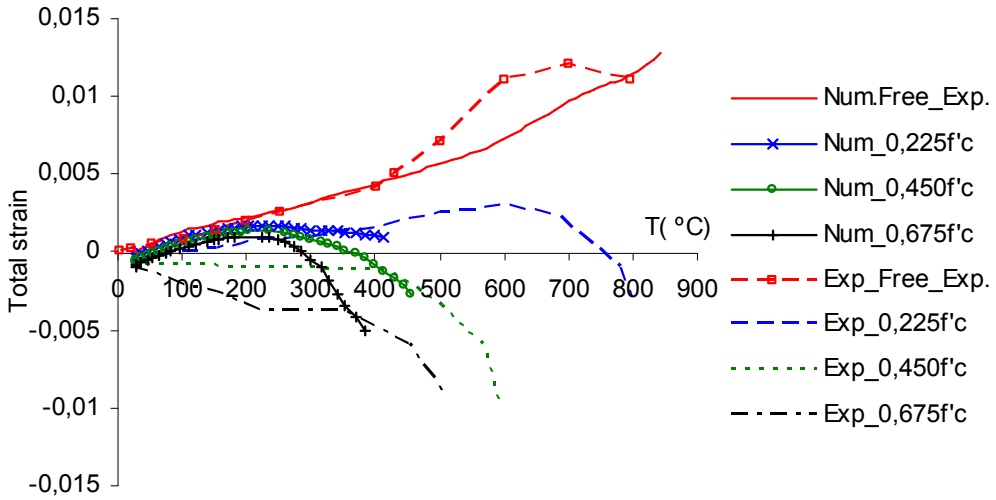

Figure 10: Total strain vs. temperature for numerical and experimental curves [2] for different load levels.

Figure 11 depicts the evolution of microcracking with increasing temperature, in the analysis under a vertical pre-compression level of $0.450f'_c$, as well as the final deformed mesh. The representation is made in terms of the magnitude of the interface relative displacements. It can be observed as cracks develop predominantly in the vertical direction, with slight lateral inclination. This is in contrast with the circumferential-radial crack patterns around aggregates observed in the case of free expansion with no vertical compression (figure 9).

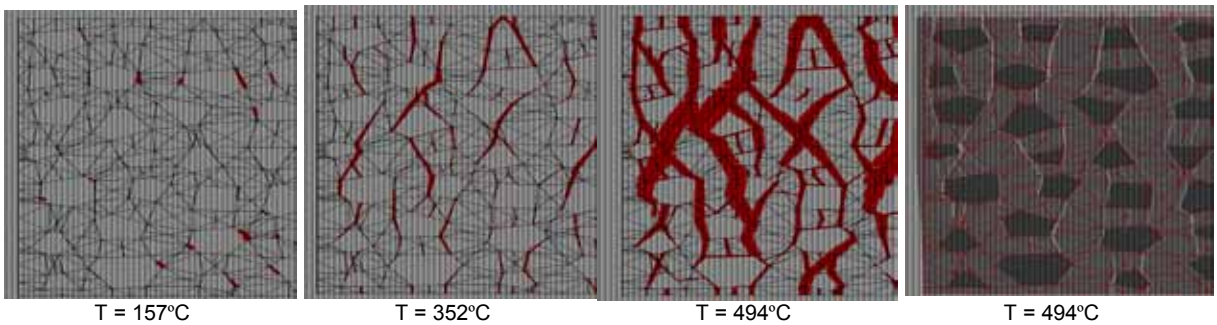

Figure 11: Crack pattern evolution in concrete in terms of magnitude of interface relative displacements, for increasing prescribed temperatures with a pre-compression stress level of $0.450f'_c$, and final deformed mesh. Max. values obtained for each diagram (x10-3): 0.020, 9.04 and 336.

4 CONCLUDING REMARKS

The purely mechanical approach employed, which is based on input data of expansion curves for individual components, plus a meso-mechanical model with interfaces for cracking, seems capable of representing the effects of temperature mismatch on the overall expansion of mortar and concrete specimens, and related degradation mechanisms of cracking and damage. On-going work is aimed at improving the material model under loading by incorporating transitional creep at high temperatures, reproducing additional results of displacement-restrained experiments, and incorporating into the model additional capabilities for temperature distribution and other diffusion-related phenomena linked to high-temperatures.

ACKNOWLEDGEMENTS

This research has been supported partially by research projects BIA2009-10491 funded by MICINN (Spain), and 2009SGR-180 from AGAUR-Generalitat de Catalunya (Barcelona). The first author is grateful to MEC, Madrid, for her FPI doctoral fellowship.

REFERENCES

[1] Cruz, C. R., and Gillen, M. Thermal expansion of Portland cement paste, mortar and concrete at high temperatures. *Fire and materials,* vol.4 nº2, pp. 66-70 (1980).
[2] Anderberg, Y., and Thelandersson, J. Stress and deformation characteristics of concrete at high temperatures. *Technical Report, Lund Institute of Technology,* Lund, Sweden (1976).
[3] Thelandersson, S. Modeling of combined thermal and mechanical action in concrete. *J. Engrg. Mech.,* ASCE 113(6), pp. 892-906, (1987).
[4] Willam, K., Rhee, I., and Shing, B. Interface damage model for thermomechanical degradation of heterogeneous materials. *Comp. Methods Appl. Mech. Engrg*. 193, pp. 3327-3350, (2004).
[5] Carol, I., Prat, P. C., López, C.M. *J.* A normal/shear cracking model. Application to discrete crack analysis. *Engng. Mech. ASCE*, 123, pp. 765–773 (1997).
[6] Carol, I., López, C.M. and Roa, O. Micromechanical analysis of quasi-brittle materials using fracture-based interface elements. *Int. J. Num. Meth. Engng.*, Vol 52, pag. 193-215 (2001).
[7] López C.M., Carol I., Aguado A. Meso-structural study of concrete fracture using interface elements. I: numerical model and tensile behaviour. *Materials and Structures*, Vol. 41, Nº 3, pag. 583-599 (2008).
[8] López C.M., Carol I., Aguado A. Meso-structural study of concrete fracture using interface element II: compression, biaxial and Brazilian test. *Materials and Structures*, Vol. 41, Nº 3, pag. 601-620 (2008).
[9] Caballero, A., Carol, I., López C. M. 3D mesomechanical analysis of concrete specimens under biaxial loading . *Fatigue and Fracture Engng. Mat. and Structures*, 30, 877-886 (2007).

XI International Conference on Computational Plasticity. Fundamentals and Applications
COMPLAS XI
E. Oñate, D.R.J. Owen, D. Peric and B. Suárez (Eds)

MESO-MACRO NUMERICAL APPROACH TO MACROSCOPIC PERMEABILITY OF FRACTURED CONCRETE – COMPLAS XI

X. Jourdain, A. Vallade, J.B. Colliat, C. De Sa, F. Benboudjema and F. Gatuingt

Laboratoire de Technologie Mécanique (LMT)
École Normale Supérieure de Cachan, Université Paris VI, CNRS
61 avenue de Président Wilson, 94235 Cachan Cedex, France
e-mail: jourdain@lmt.ens-cachan.fr, web page: http://www.lmt.ens-cachan.fr/

Key words: Permeability, Heterogeneous Material, Strong Discontinuity

Abstract. In this paper, a sequential multi-scale framework to solve mass (air or water) transfer problems is described. Numerical results are checked against mechanical and permeation experimental datas from a reinforced concrete specimen under tensile load designed by C. Desmettre and J.P. Charron [2]

1 Introduction

The durability of reinforced concrete structures is strongly linked to its porosity and moreover to its cracks pattern which can be anisotropic in many realistic contexts. Created by mechanical loading or unfavorable thermo-hydrical environment, those cracks increase the penetration of water and aggressive agents within the material which can severely weaken its mechanical behavior. It is therefore obvious that being able to compute the flow going through concrete structure is a big issue for numerous applications : concrete made bridges or CO_2 storage as well as civil nuclear industry. Thanks to a mechanical model able to represent the cracks opening in heterogeneous materials [3], we then compute a mass (air or water) transfer problem within concrete and deal with permeability on isotropic as well as anisotropic crack patterns. The experimental permeability datas obtained on a tie-specimen under uniaxial loading described by C. Desmettre and J.P. Charron in "novel water permeability device for reinforced concrete under load"[2] is then checked against our numerical results.

The section 2 of this paper focuses on the sequential multi-scale framework, dealing with the cracks FE modelling and the hydro-mechanical coupling, both at a meso scale. The section 3 briefly sum up the experimental study of C. Desmettre and J.P. Charron [2] and checks the experimental datas against our numerical results.

2 Sequential multi-scale framework

As said previously, the aim is to compute a flow problem on isotropic as well as anisotropic crack patterns on cement base materials. Firstly, it means that the mechanical model must be able to deal with heterogeneous materials. Actually, reinforced concrete is composed of steel bars and concrete, which itself is a mix of mortar and aggregates. Secondly, the flow is strongly influenced by the crack openning $[\![u]\!]$ as the Poiseuille flow Q_P going through a $[\![u]\!]$ gap between two planes is proportionnal to the cube of the opening ($Q_P \propto [\![u]\!]^3$). Therefore, the crack opening is a crucial value for the mass transfer computation.

Greatfully, the model used [3] has those two specificities :

- it represents multi-phasic materials (cement paste, aggregates and steel have different mechanical and transfer caracteristics),
- it gives the value of the opening $[\![u]\!]$ of each broken element whatever the sollicitation is.

The next part focuses on those two special features of the mechanical model before describing the permeation computation.

2.1 Crack representation : Strong discontinuities

When a concrete specimen (ie: made of cement paste and aggregates) is under a tensile sollicitation, the stress in the cement paste quickly reaches its rupture value ($f_t \approx 3MPa$) resulting in a crack initiation before its propagation. This is a dissipative phenomenon where the so-called "fracture energy" (Gf $[J.m^{-2}]$) represents the energy dissipated by a one square metre crack. Practically, it can be easily deduced from a light experimental device like a three points bending test and is therefore one of the most used caracteristics of concrete as the tensile limit stress (σ_f) or the Young modulus (E). Thence, those three parameters seems judicious to be the basis of a mechanical element able to represents the behaviour of a brittle material like concrete is.

Dealing with brittle and quasi-brittle material in computational mechanic is still a big issue and numerous models exist, each one with its benefits and its drawbacks. On one hand, discrete mesh models [6] are able to represent the crack opening, but they usually need intensive re-meshing in order to compute the crack direction. On the other hand, with a Finite Element basis, several approach exist like the smeared crack models [5]. Their main drawback is their mesh dependency, problem which can be bypasses introducing a length scale wich is mesh objective.

Recently [7], [8], [9], an elegant crack model based on FE theory has been developped. This method is mesh independent and doesn't need re-meshing but introduce a so-called strong discontinuity in the displacement field. The strong discontinuity is activated thanks to a yield function Φ written as :

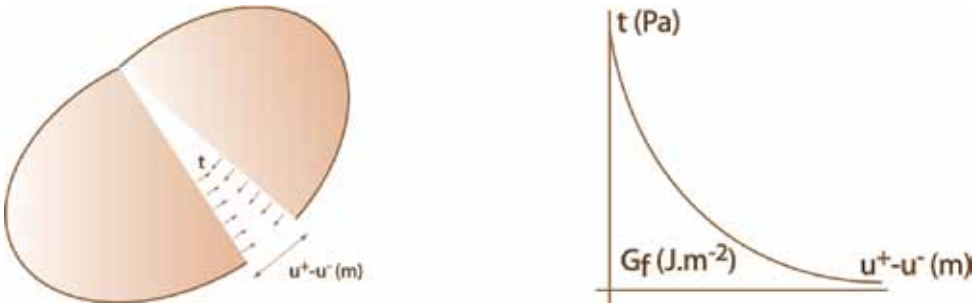

Figure 1: Strong discontinuity crack representation and crack opening process

$$\Phi(t, q) = t - (\sigma_f - q) \tag{1}$$

where t is the traction vector at the discontinuity and σ_f the limit stress. The softening is introduced through the variable $q = k([\![u]\!])$ by considering the exponential form (cf figure 1),

$$k([\![u]\!]) = \sigma_f \left(1 - exp\left(-\frac{\sigma_f}{G_f}([\![u]\!])\right)\right) \tag{2}$$

The next part focuses on the permeability part.

2.2 Mesoscopic scale flow: The Poiseuille law

Once the cracks initiates, the second step starts : the aim is to compute a mass transfer problem with the damaged mesh. Here is the key point, the material is composed of a "double porosity". At a micro-scale, the cement paste porosity is isotropic. It represents the undamaged part of the permeability (pore diametre ¡ $10\mu m$). The flow can be computed with the Darcy law (eq 3). This equation links the mass flow density $\underline{q}$ $[kg.s^{-1}.m^{-2}]$ and the pressure p.

$$\underline{q} = \rho \underline{v} = -\frac{1}{\mu}\rho.k.\underline{\underline{1}}\ \underline{grad}(p) \tag{3}$$

The permeability (k) unit is m^2.

As soon as the first crack initiates, a bigger porosity appears and the permeability rises.

If the crack pattern is isotropic, one can analytically links damage to permeability [4]. In case of anisotropy, which represents most of the realistic studies, the problem is therefore more complex to solve. Taking into accounts the anisotropy of the crack pattern is inherent to our model. It is based on a local implementation of the constitutive equation which gives the Poiseuille flow between two planes (cf figure 2 and equation 4).

$$q_{Edge} = \rho\ v_{Edge} = \rho\ \frac{w_{Edge}^3}{12\mu L_{Edge}}\ \frac{\Delta p}{L} \tag{4}$$

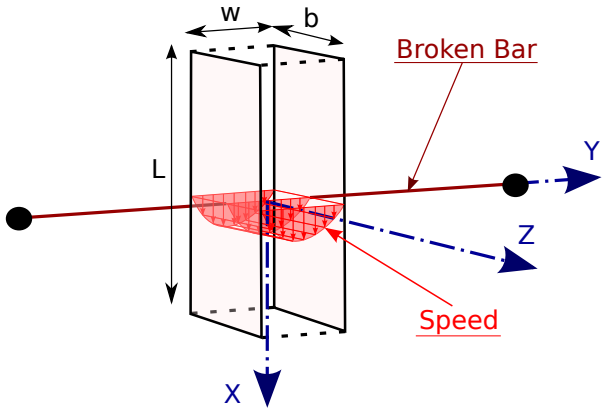

Figure 2: speed between two planes defined by the Poiseuille law

where μ is the viscosity of the studied fluid ($\mu_{water} = 8,90.10^{-4} Pa.s$ at $20\,^{\circ}$C) and ρ is a constant as this equation 4 is given for incompressible fluid.

Once the elementary permeability matrices written, the "double porosity" is easy to be written as the sum of the isotropic permeability and the anisotropic permeability due to the possible crack : $\underline{\underline{K}} = \underline{\underline{K}}_{iso} + \underline{\underline{K}}_{ani}$ where $\underline{\underline{K}}_{iso} = \frac{-k}{\mu}\underline{\underline{1}}$ and $\underline{\underline{K}}_{ani} = \frac{w^3}{L\mu}(\underline{\underline{1}} - \underline{n} \otimes \underline{n})$

As the anisotropic permeability matrix shows it, there is no flow in the colinear direction of the bar while in the two perpendicular direction, the permeability is equal to $\frac{w^3}{L\mu}$.

Once the assembly of the elementary matrices done thanks to a classical FE software, the problem can easily be solved and, as a result, the macroscopic flow can be computed. This method is an elegant way to automatically takes into account the tortuosity and the connectivity of the cracks.

2.3 Permeability of RC element under load

The multiscale framework we present here is clearly suitable dealing with mass transfers within concrete structures or their components. To that aim we focus on experimental results from [2] who designed a coupled tensile – permeability test on Reinforced Concrete (RC) specimens ($610 \times 90 \times 90$ mm^3 concrete element including a 11 mm diameter reinforcement bar). Here we aim at comparing their experimental measures to numerical results and focus on the permeability evaluation along the failure process.

The fine scale mechanical analysis of this RC tie is based on a spatial truss representation [3] built with non-adapted meshes. In order to fit to the experimental conditions, displacements are prescribed at both ends of the steel reinforcement bar. Such increasing load leads to progressive cracking of the concrete element and Figure 3 shows a typical crack pattern obtained from a numerical analysis. Three main macroscale cracks are distributed along the tie which is in accordance with experimental observations. Moreover,

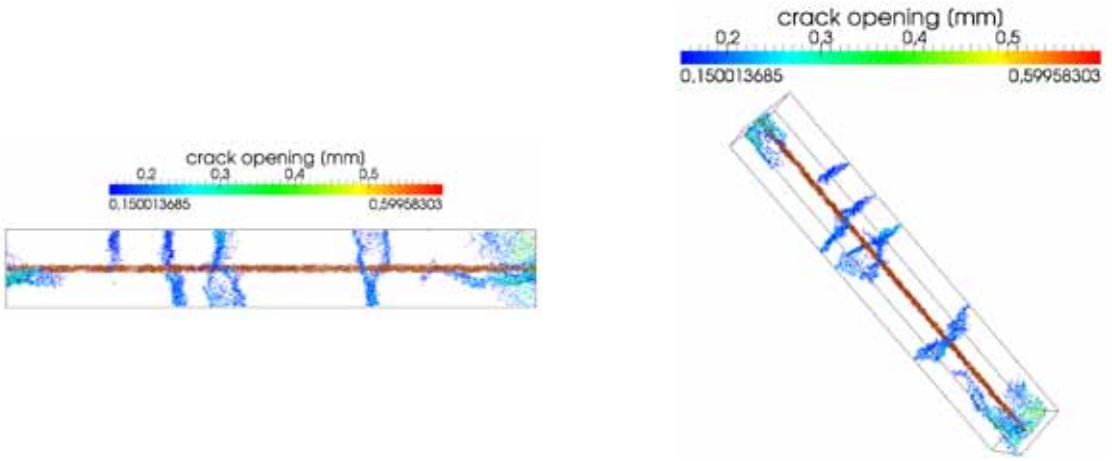

Figure 3: RC tie: numerical crack patterns

we show on Figure 4 that there is a quite good agreement between the measured values of those cracks openings during the loading process and the corresponding numerical values.

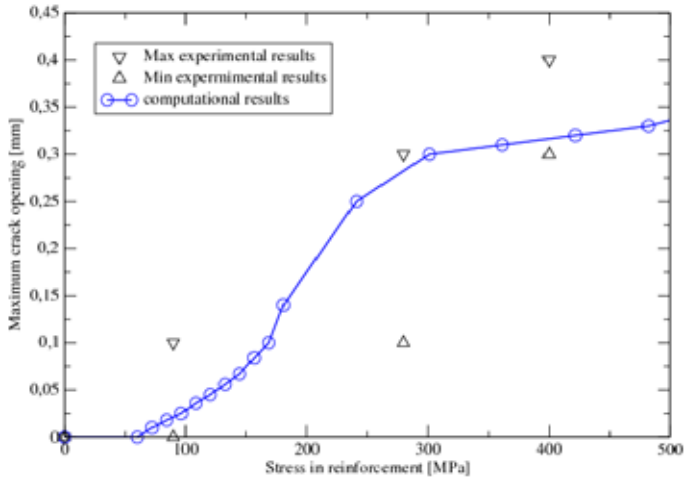

Figure 4: RC tie: maximum crack opening versus stress in reinforcement (experimental [2] vs computational results)

On the permeability assessment point of view (here the test deals with water), Figure 5 shows the norm of the mass flow vector at the end of the failure process. Although the concrete specimen contains a large number of mesoscale cracks, it is clear that the mass transfer takes place within a subset of those cracks, corresponding to several percolated paths. Thus, on the mass transfer point of view, the former may be seen as a set of

macroscale cracks. Hence, it is worth noting that, apart from considering the opening value as the pertinent criterion, this mass transfer analysis leads to an other way to determine this set of macroscale cracks. This analysis being linear and so quite simple to drive, it is a very convenient way to characterize macroscale cracks.

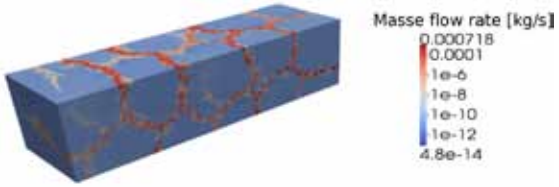

Figure 5: RC tie: numerical values of the mass flow vector norm

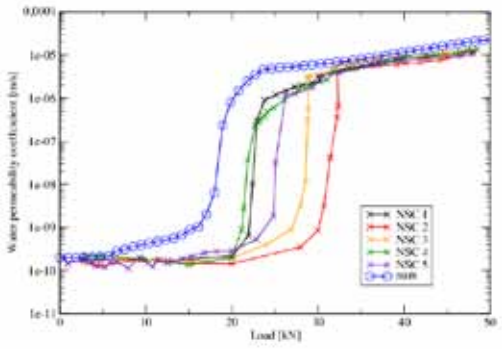

Figure 6: RC tie: numerical crack patterns

Finally, Figure 6 shows the permeability coefficient – here in [m.s^{-1}] – evolution along the load increase. The permeability increases from approximatively $2.10^{-10} m.s^{-1}$ to $1.10^{-5} m.s^{-1}$ both for numerical and experimental studies. It is also worth noting that the increasing rate is also quite well represented. Yet, the permeability rise appears for smaller loading values in the numerical study than in the experimental one. Considering the concrete heterogeneity as well as the experimental discrepancy, those results are quite promising.

3 Concluding Remarks

This paper presents the results given by a mesoscopic model able to compute the flow going through a specimen under load. Three important points have been validated :

- Cracks spacing (3 main cracks on the 610mm long specimen),
- Cracks opening (0,35mm maximum opening when the yielding stress is reach in the reinforced bar),
- Permeability values during loading (rise of 5 orders of magnitude from the original permeability for this study).

The numerical results are therefore quite promising, especially knowing that more attention can be paid on the boundary conditions and loading to fit to the experimental study.

REFERENCES

[1] X. Jourdain, J.B. Colliat, C. De Sa, F. Benboudjema and F. Gatuingt. Meso-macro numerical approach to macroscopic permeability of cracked concrete quantification.*submitted*.

[2] C. Desmettre, J. P. Charron. Novel water permeability device for reinforced concrete under load. *Mat. and Struct.*, 1-11, (29 mars 2011).

[3] N. Benkemoun, M. Hautefeuille, J. B. Colliat, A. Ibrahimbegović. Failure of heterogeneous materials: 3D meso-scale FE models with embedded discontinuities. *Int Jal for Numerical Methods in Engineering*, **82**, 1671-1688, (2010).

[4] L. Dormieux, D. Kondo. Approche micromcanique du couplage permabilit-endommagement. *C.R. Mecanique*, **332**, 135-140, (2004).

[5] A. Hillerborg. Application of the fictitious crack model to different types of materials. *International Journal of fracture*, **51**, 95-102, (1991).

[6] Toto. Tu connais un model discret qui a besoin de remaillage ou nimporte lequel fait laffaire.

[7] G.N. Wells, L.J. Sluys. Application of embedded discontinuities for softening solids. *Engineering Fracture Mechanics*, **65**, 263-281, (2000).

[8] D. Brancherie,A. Ibrahimbegovic. Novel isotropic continuum-discrete damage model capable of representing localized failure of massive structures. *Engineering Computation*, **26** . under press (2009).

[9] N. Moes, J. Dolbow, T. Belytshko. A finite element method for crack growth without remeshing. *International Journal of Numerical Methods in Engineering*, **46**, 131-150. (1999).

XI International Conference on Computational Plasticity. Fundamentals and Applications
COMPLAS XI
E. Oñate, D.R.J. Owen, D. Peric and B. Suárez (Eds)

THE INFLUENCE OF LOAD MISALIGNMENT ON FRP-CONCRETE BOND BEHAVIOUR, A NUMERICAL STUDY

P. NETO[*] AND J. ALFAIATE [†]

[*] Escola Superior de Tecnologia do Barreiro
Setubal Polytechnic Institute
Rua Stinville, nº 14, 2830-144 Barreiro, Portugal
e-mail: pedro.neto@estbarreiro.ips.pt, web page: http://www.estbarreiro.ips.pt

[†] ICIST, Department of Civil Engineering and Architecture
Instituto Superior Técnico, Technical University of Lisbon
Av. Rovisco Pais 1, 1049-001 Lisboa, Portugal
Email: alfaiate@civil.ist.utl.pt

Key words: Bond Behaviour, Fibre Reinforced Polymers (FRP), Concrete, Fracture Energy in Modes I and II.

Abstract. Various authors have used pure shear test models in order to describe the bond between FRP and concrete. However, considerable dispersion of the parameters which characterize the bond behaviour has been found. In pure shear models it is assumed that the load applied to the FRP is parallel to the axis of the concrete specimen and acts on the plane of symmetry. In this work, a numerical model is presented to analyse the influence of load misalignment on FRP-concrete bond behaviour.

1 INTRODUCTION

The use of fibre reinforced polymers (FRP) applied to the external strengthening of concrete structures, in particularly the use of laminates and sheets, has become an increasingly common practice. This is due, namely, to the mechanical properties of these composite materials, such as the ease of application and high strength-to-weight ratio. The major problems found with this reinforcement technique are the local failure modes. In the last few years, several experimental and analytical studies have been carried out, which contributed to the understanding and quantification of the phenomenon related to the bond behaviour between concrete and FRP. However, several issues still need to be clarified.

Various authors [1, 2, 3, 4, 5, 6] used pure shear test models in order to describe the bond behaviour, which contributed to the definition of constitutive relationships for the interface concrete-FRP. A considerable dispersion of the parameters adopted to characterize the bond behaviour has been found [7].

In pure shear models it is assumed that: i) the load applied to the FRP is aligned with the axis of the concrete specimen and ii) the load is applied at the symmetry axis of the strengthened material. In this work, the influence of a deviation angle of the load with respect to the element axis is analysed. A numerical model is presented, based on previous studies [7, 8, 9], in which the stress distribution long the interface concrete-FRP is evaluated. These

stresses can be both tangential and normal to the interface. In this study, unidirectional carbon fibres sheets are considered.

The bond between the FRP and the concrete is modelled using a discrete crack approach, based on Non-Linear Fracture Mechanics [10]. Interface elements with zero initial thickness are adopted. The shear and peeling stresses developed at these elements are dependent on the relative displacements measured between the strengthening material and the concrete surface, according to a local constitutive relationship under softening. The material properties that characterize the interface, namely the shear and peeling stiffness, the cohesion, the tensile strength and the fracture energy in modes I and II, are obtained from previous works [7, 8, 9]. From the analysis of the results numerically obtained, it is possible to draw conclusions concerning the relative importance of each parameters and the influence of the load slope on the obtained results. It is expected that this work may contribute to identify some aspects which should be considered in a setup of experimental tests and to clarify the interpretation of the results obtained from those tests.

2 PURE SHEAR MODEL

The pure shear model considered in this work consisted of concrete specimens in which unidirectional carbon fibres were glued, by means of resin epoxy. The specimen was subjected to a tensile load along the direction of the fibres, as shown in Figure 1. This model was used in previous studies [11]. The concrete specimens tested were 400mm long and had a rectangular cross-section of 200mm by 200mm. The strengthening material had a width of 80mm and was applied on the larger face of the specimen. The nominal values for Young's modulus and for the ultimate tensile strain of the CFRP were 240GPa and 1.55%, respectively. Mean values of 36.4MPa, 2.8MPa and 31.6GPa, for the compressive strength, tensile strength and Young's modulus of concrete, respectively, were considered.

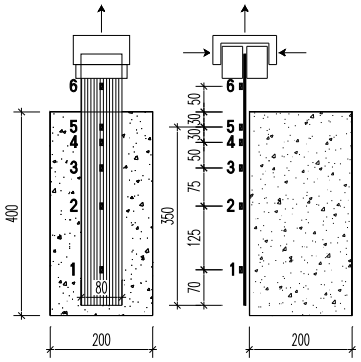

Figure 1: Shear model on concrete joint strengthened externally by CFRP [11]

3 MATERIAL MODEL

The concrete is assumed a continuum exhibiting an isotropic linear elastic behaviour. The FRP behaviour is assumed linear elastic until failure. The bond between concrete, resin and CFRP is modelled using interface elements of zero initial thickness and a discrete crack approach.

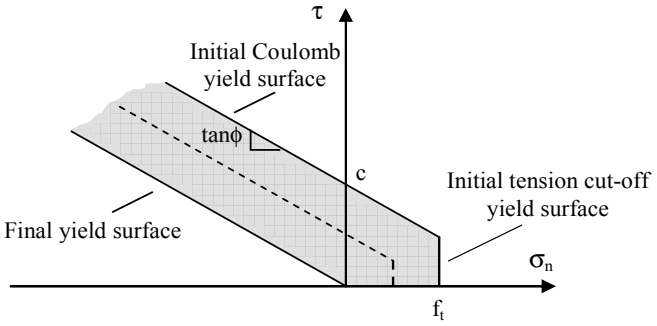

Figure 2: Yield surfaces adopted for the interface

A multi-surface plasticity model is adopted [12, 13]; two limit surfaces are considered: a tension cut-off for mode-I fracture and a Coulomb friction envelope for mode-II failure and mixed mode, as shown in Figure 2. In this figure, the horizontal axis represents the normal stress vector component and the vertical axis represents the tangential stress vector component measured at the interface. The cut-off mode-I is defined by the tensile strength of the concrete. The Coulomb friction envelope is initially characterized by the cohesion coefficient and by the internal friction angle ϕ. Both yield functions follow exponential softening flow rules (Figure 3).

The yield function associated with the normal stress is given by:

$$f_n = \sigma_n - f_t \exp\left(-\frac{f_t}{G_F^I} w\right) \tag{1}$$

where σ_n is the stress vector component measured at the interface. An associated flow rule is considered. The shear yield function reads:

$$f_s = |\tau| + \sigma_s \tan\phi - c \cdot \exp\left(-\frac{c}{G_F^{II}} s\right) \tag{2}$$

where τ is the tangential stress vector component measured at the interface. A non-associated flow rule is adopted with a plastic potential g_s given by:

$$g_s = |\tau| + \sigma_n \tan\psi - c \tag{3}$$

where ψ is the dilatancy angle. An isotropic softening criterion is adopted, meaning that both yield surfaces shrink the same relative amount in the stress space, and both keep the origin (Figure 2).

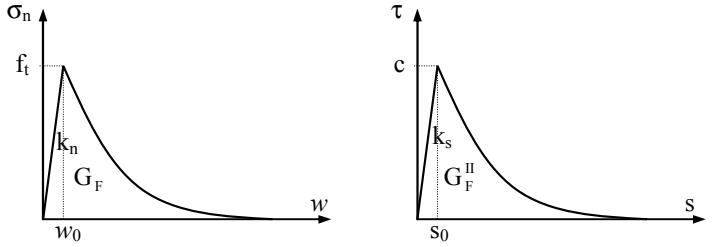

Figure 3: Normal and tangential constitutive relationships adopted for the interface

The material parameters characterizing the interface behaviour are: the elastic shear and peeling stiffness, k_s and k_n, respectively, the cohesion c, the tensile strength f_t, and the fracture energies in modes I and II, G_F and G_F^{II}, respectively (area under the curves σ_n-w and σ_s-s adopted as shown in Figure 3).

4 NUMERICAL ANALYSIS

The numerical analysis is performed using the finite element method [7]. Considering the very high stiffness of the concrete when compared to the epoxy and the FRP, this material is modelled by rigid supports. For the strengthening material, except in the reference models, 4 node isoparametric elements are adopted. These elements allow the bending stiffness of the composite to be considered. For the FRP, in the reference models, linear 2-node elements are considered [7]. The bond behaviour is modelled by linear interface elements with initial zero thickness.

The specimen response is determined under displacement control, using an incremental, iterative procedure.

As mentioned above, the constitutive relationship of the interface concrete-CFRP is defined by six parameters: the shear and peeling stiffness, the cohesion, the tensile strength and the fracture energy in modes I and II.

According with previous studies [7, 9] the following values are adopted: k_s=1500MPa/mm and k_n=4000MPa/mm, for the shear and peeling stiffness, respectively, c=5MPa for the cohesion and G_F^{II}=1.5N/mm for the fracture energy in mode II. In the case of fracture energy in mode-I there is a large variation on the values proposed in the bibliography [4, 14, 15, 16, 17], namely in the relationship between G_F^{II} and G_F. A value of G_F=0.1N/mm is considered assuming a relation G_F^{II} /G_F between 10 and 25 [4, 14, 15].

The angle α is defined between the direction of the applied force and the y axes of the model (corresponding to the fibre orientation), in order to define the load slope: α=0º, as well as values of α>0º and α<0º are adopted, meaning a counter clockwise and clockwise rotation, respectively, with respect to the fibre axis. In this study the following values are used: α=±1.0º and α=±0.5º. The load deviation with respect to the fibre orientation is implemented by means of the corresponding components: one along the direction of the fibres and the other perpendicular to the strengthening material. As a consequence, in addition to the stresses tangential to the interface, normal stresses are expected to develop.

Next, the numerical study is presented. In the analysis, the adopted thicknesses of the CFRP are: t_f=0.5mm and t_f=0.1mm. These values are typical of CFRP sheets.

4.1. CFRP thickness equal to 0.5mm

For a composite thickness of 0.5mm and α=+1.0º the interfacial stress distribution along the bond length is obtained. In Figures 4 and 5, the interfacial stresses along the bond length for several load levels are presented, for applied loads close to 20% and 90% of the maximum load registered in that model, which is circa 48kN.

For lower load levels, some values of the shear stresses are higher than the cohesion defined due to the presence of normal compressive stresses, which is in according with the yield surface adopted as shown in Figure 2. These stresses only occur along a small length, near the location where the load is applied. Apart from the region where normal stresses co-

exist, the shear stress distribution becomes similar to the one obtained in a pure shear model [7].

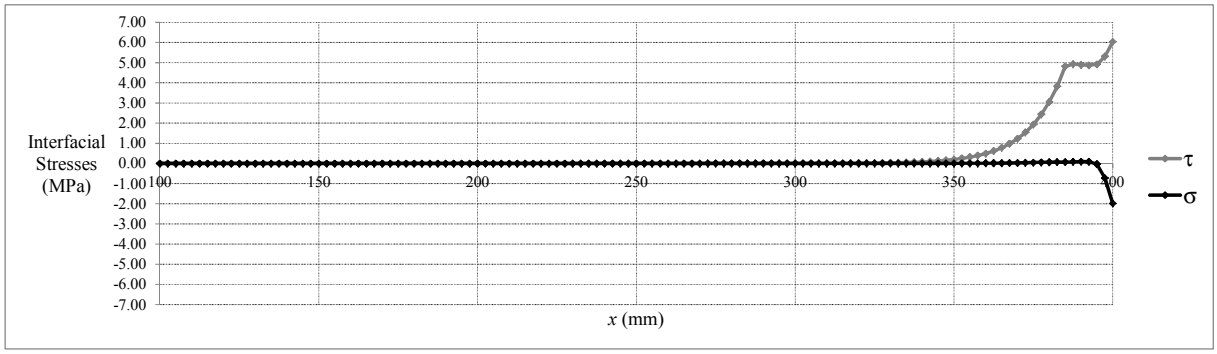

Figure 4: Interfacial stresses with t_f=0.5mm, F=10kN and α=+1.0º

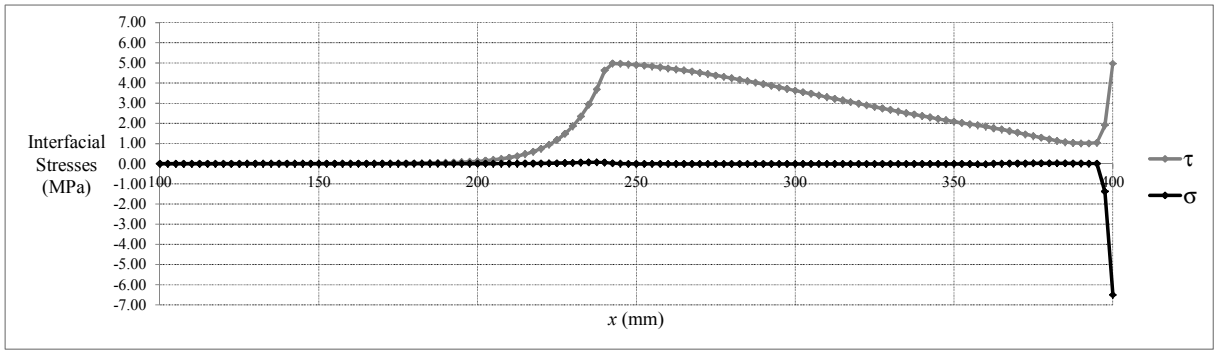

Figure 5: Interfacial stresses with t_f=0.5mm, F=43kN and α=+1.0º

In Figures 6 and 7, the interfacial stresses along the bond length for several load levels are presented, for applied loads close to 20% and 90% of the maximum load registered in that model when α=−1.0º, which was circa 25kN. Except in the region where normal stresses co-exist, the shear stress distribution becomes once more similar to the one obtained in a pure shear model [7]. Also in this case it is possible to observe normal stresses to the interface in addition to the tangential stresses. These stresses are mainly peeling stresses and also occur along a small length near the location where the load is applied. Thus, conversely to the previous case, shear stresses above the cohesion are not found.

With α=−1.0º, the maximum load is circa 52% of the maximum load obtained in the case with α=+1.0º. Theoretically, this relationship should be close to 100%. Since the evaluation of the mode-II fracture energy based on experimental tests is much dependent from the ultimate load, it is important to mention that unreliable values of this parameter will be obtained if α in the experimental setup is less than zero. This issue will be further discussed below.

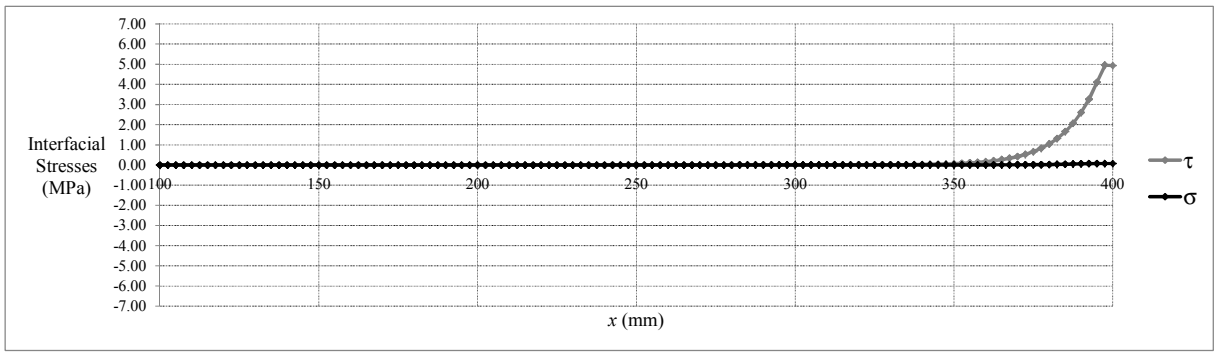

Figure 6: Interfacial stresses with t_f=0.5mm, F=5kN and α=−1.0º

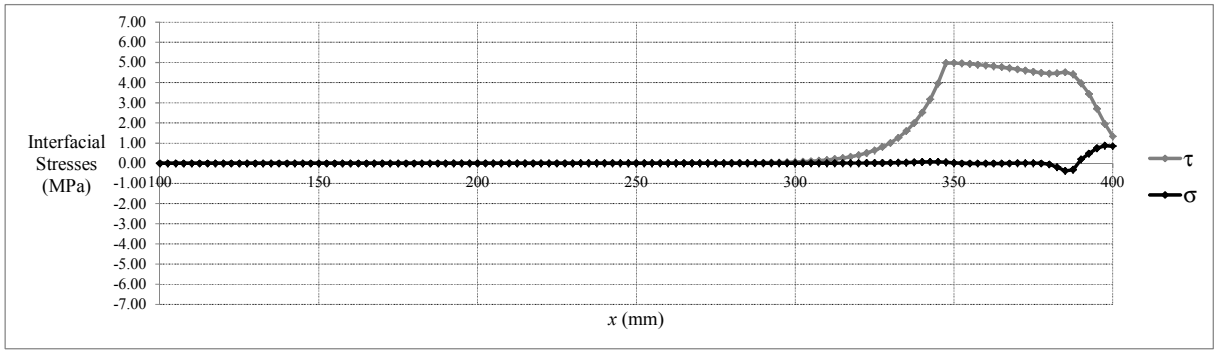

Figure 7: Interfacial stresses with t_f=0.5mm, F=22.5kN and α=−1.0º

The results obtained with α≠0º and with α=0º for a load level of 65% of the maximum load obtained with α=+1.0º and α=−1.0º, 31kN and 16kN, respectively, are compared and presented in Figures 8 and 9.

From the analysis of the results obtained from the two models, with α=+1.0º and α=0º, it is found that the corresponding maximum load and the shear stress distribution are similar, as shown in Figure 8, except along a small length near the location where the load is applied. The experimental results obtained with α=+1.0º allow for the satisfactory quantification of the material parameters that define the constitutive law of the bond behaviour between concrete and CFRP, namely: k_s, c and G_F^{II}.

The shear stress distributions obtained with both α=−1.0º and α=0º are similar, for a load of 16kN, as can be observed in Figure 9. However there are some differences which should be noticed. The relation between the maximum loads with α=−1.0º and with α=0º is about 52%. This is a very important aspect because it has direct implications on the value which could be adopted, by mistake, for G_F^{II}. The maximum load in the model with α=−1.0º is 25kN. From this result, the fracture energy in mode II was estimated according to Equation (4) [7, 18, 19]. The obtained value was 0.41N/mm, which is about 27% of the reference value, considering a pure shear model.

A new pure shear model was defined considering the above obtained value for the fracture energy in mode-II: G_F^{II}=0.41N/mm. Values of c=5.0MPa and k_s=1500MPa/mm were adopted for a complete definition of the interface behaviour. The results from this model, called α1=0, are shown in Figure 9. As expected, from this figure it is possible to observe a very good

agreement between the stress distribution and the maximum load obtained from both models: with α=−1.0º and α1=0º. However, these "corrected" values of fracture energy, obtained with α=−1.0º, are not the right ones.

$$N_u=b_f\times\sqrt{2E_f\times t_f\times G_F^{II}} \tag{4}$$

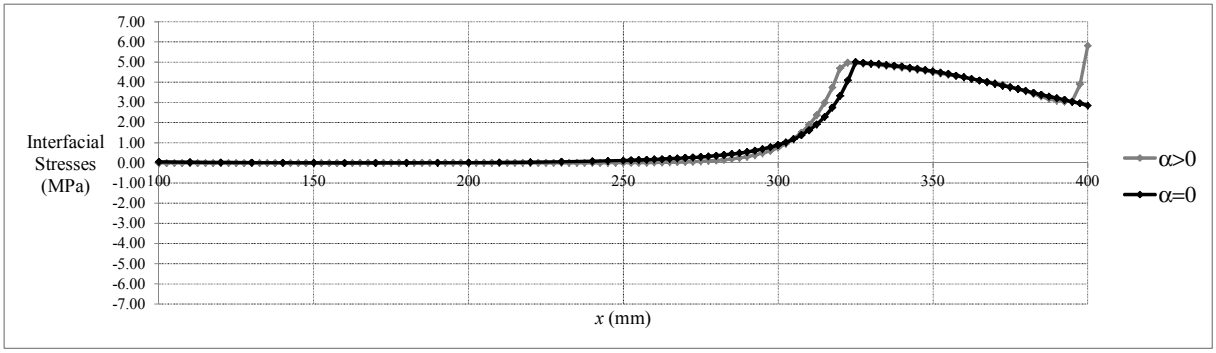

Figure 8: Shear stresses with t_f=0.5mm and F=31kN

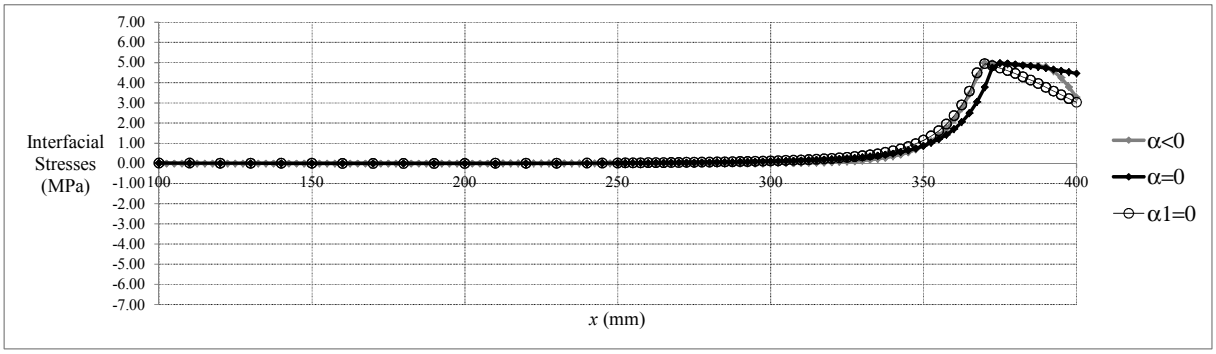

Figure 9: Shear stresses with t_f=0.5mm and F=16kN

Considering now a value of α equal to half of the previous, it is possible to note similar shear stress distribution as shown in Figure 10. However, the maximum load obtained from the model with α=−0.5º was 35kN, higher than 25kN which was obtained with α=−1.0º.

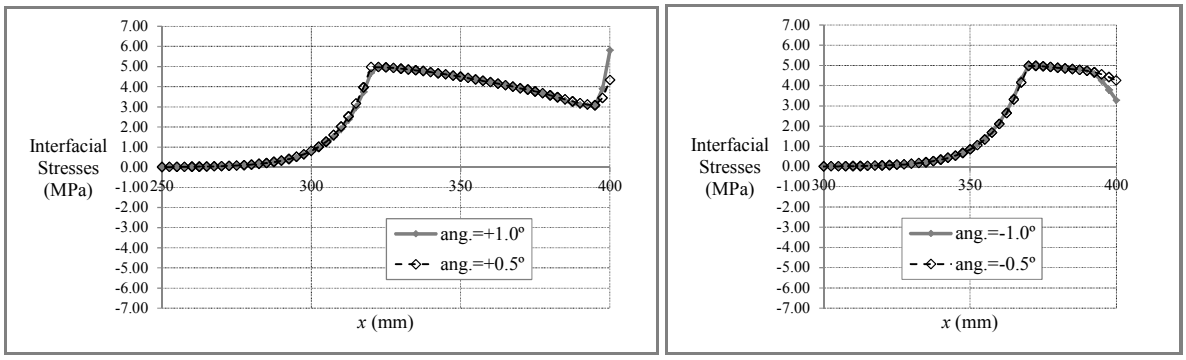

Figure 10: Shear stresses with t_f=0.5mm: F=31kN (ang.>0) and F=16kN (ang.<0)

4.2 CFRP thickness equal to 0.1mm

For a composite thickness of 0.1mm and α=+1.0º the interfacial stresses distribution along the bond length was obtained. In Figures 11 and 12, the interfacial stresses concrete-CFRP along the bond length are presented for several load levels, namely about 20% and 90% of the maximum load registered in that model, which was circa 22.5kN. From these figures it is possible to notice, as observed in the previous case with t_f=0.5mm, non-zero normal stresses. The normal stresses are compressive and occur along a smaller length than the one observed with t_f=0.5mm, next to the location where the load is applied. Except in the region where normal stresses co-exist, the shear stress distribution becomes similar to the one obtained in a pure shear model [7].

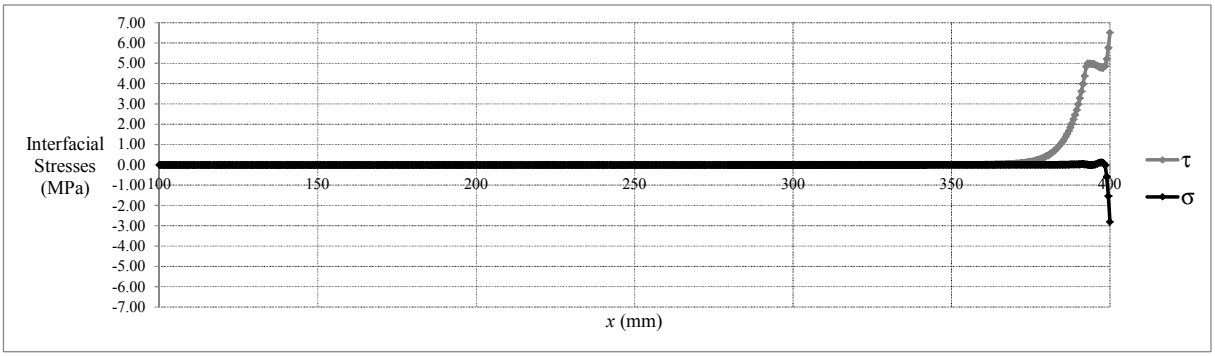

Figure 11: Interfacial stresses with t_f=0.1mm, F=5kN and α=+1.0º

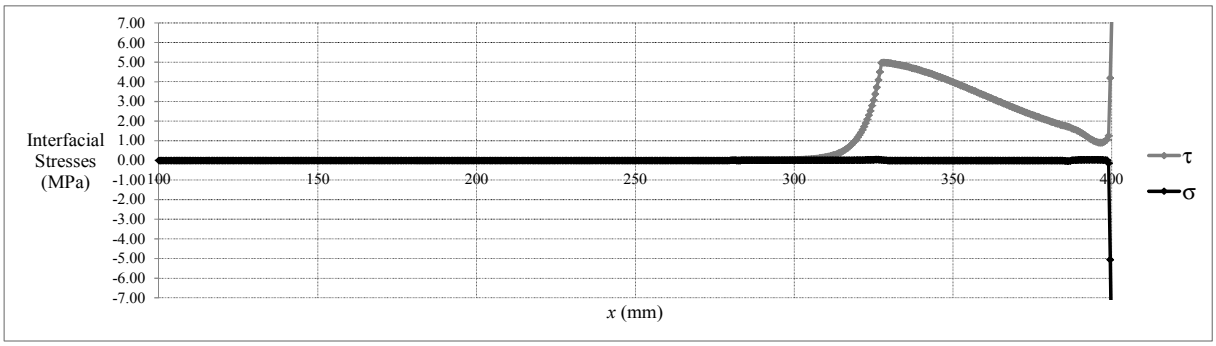

Figure 12: Interfacial stresses with t_f=0.1mm, F=20kN and α=+1.0º

In Figures 13 and 14, for α=−1.0º, the interfacial stresses along the bond length are presented for several load levels similar to the values previous adopted, namely about 20% and 90% of the maximum load registered in that model, which was circa 9.5kN. For t_f=0.1mm the relationship between the maximum load with α=−1.0º and α=0º is circa 42% and for t_f=0.5mm the corresponding ratio is 52%. Thus, compared to the case α=0º, the decrease of the maximum load under α<0º seems to become more significant when the external reinforcement thickness decreases. Similar to the case with t_f=0.5mm, the value of the fracture energy in mode-II obtained from an experimental test in these conditions will hardly match the theoretically correct one.

Except in the region where normal stresses co-exist, the shear stress distribution becomes similar to the one obtained in a pure shear model. Also in this case it is possible to observe

normal stresses to the interface in addition to the tangential stresses. The normal stresses, mainly peeling stresses, only occur along a small length, next to the location where the load is applied.

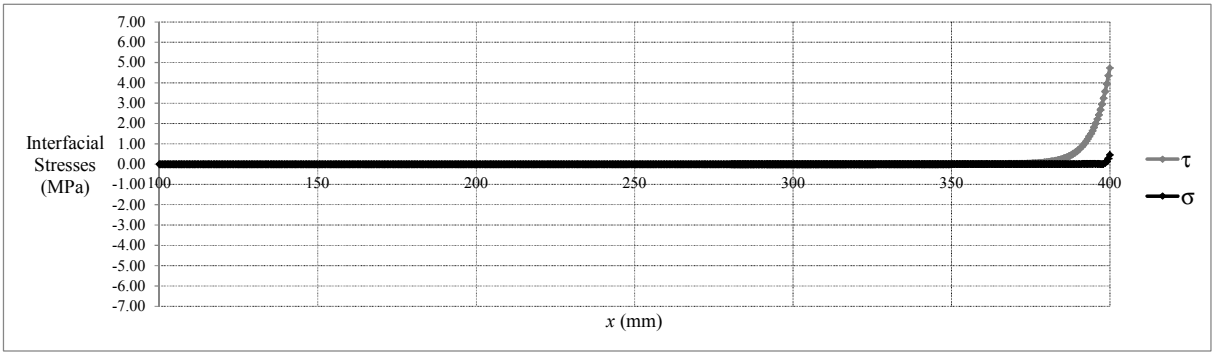

Figure 13: Interfacial stresses with t_f=0.1mm, F=2kN and α=−1.0º

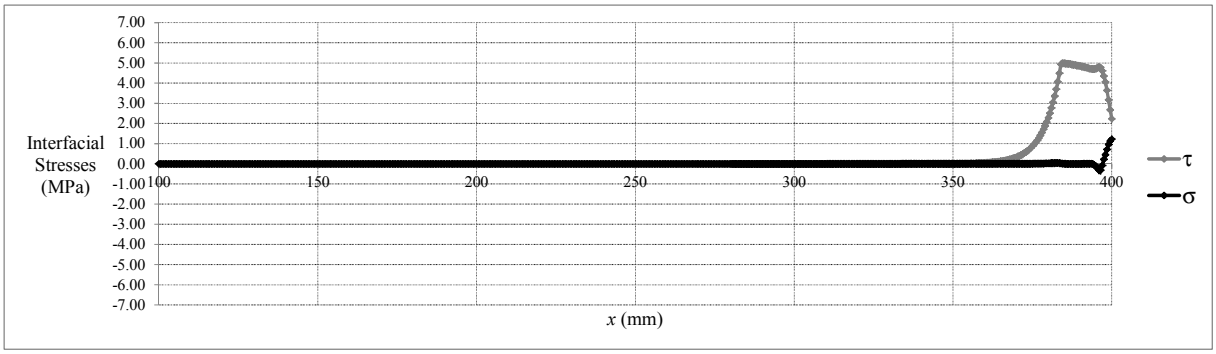

Figure 14: Interfacial stresses with t_f=0.1mm, F=8kN and α=−1.0º

An analysis similar to the previous one adopting t_f=0.5mm was performed. The results obtained with α≠0º and α=0º for a load level of 65% of the maximum load obtained with α=+1.0º and α=−1.0º, 15kN and 6kN, respectively, are presented in Figures 15 and 16.

From the analysis of the results obtained from the two models, with α=+1.0º and α=0º, it is found that the corresponding maximum load and the shear stresses distribution are almost coincident, as shown in Figure 15. Thus, in this case, the experimental results with α=+1.0º allow for a good quantification of the material parameters that define the constitutive law of the bond behaviour between concrete and CFRP, namely: k_s, c and G_F^{II}.

The shear stress distributions obtained with α=−1.0º and α=0º are similar, for a load of 6kN, as can be observed in Figure 16. However there are some differences that should be noticed. The relationship between the maximum loads with α=−1.0º and with α=0º is about 42%. As mentioned above, this is a very important aspect because it has direct implications on the value to be considered for G_F^{II}. The maximum load in the model with α=−1.0º is 9.5kN. From this result, the fracture energy in mode II was estimated according to Equation (4). The obtained value was 0.26N/mm, which is about 17% of the reference value, considering a pure shear model. In this case, the obtained G_F^{II} value would be even farther from the reference value than the value obtained considering t_f=0.5mm. A new pure shear

model was defined adopting G_F^{II}=0.26N/mm and the reference values: c=5.0MPa and k_s=1500MPa/mm. The results from this model, called by α1=0, are shown in Figure 16. As expected, from this figure it is possible to observe a good agreement between the stress distribution and the maximum loads obtained from both models: with α=−1.0º and α1=0º. Nevertheless, this "corrected" value of the fracture energy, obtained with α=−1.0º, is definitely not the right one.

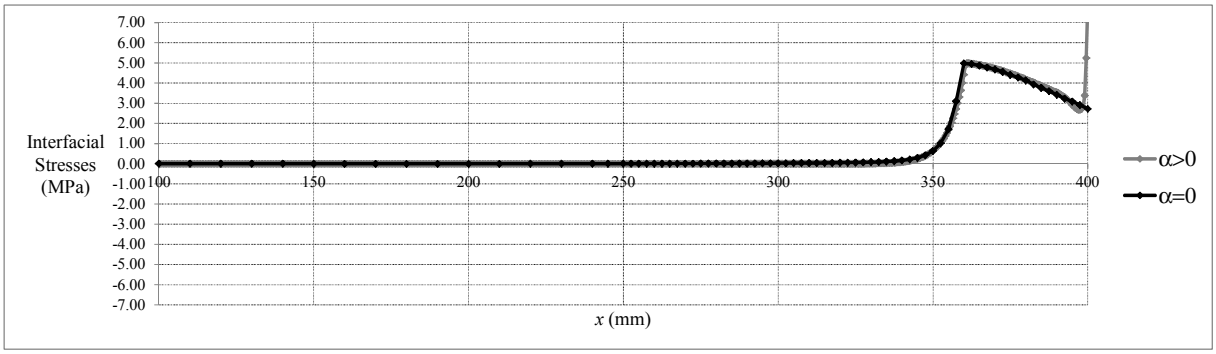

Figure 15: Shear stresses with t_i=0.1mm and F=15kN

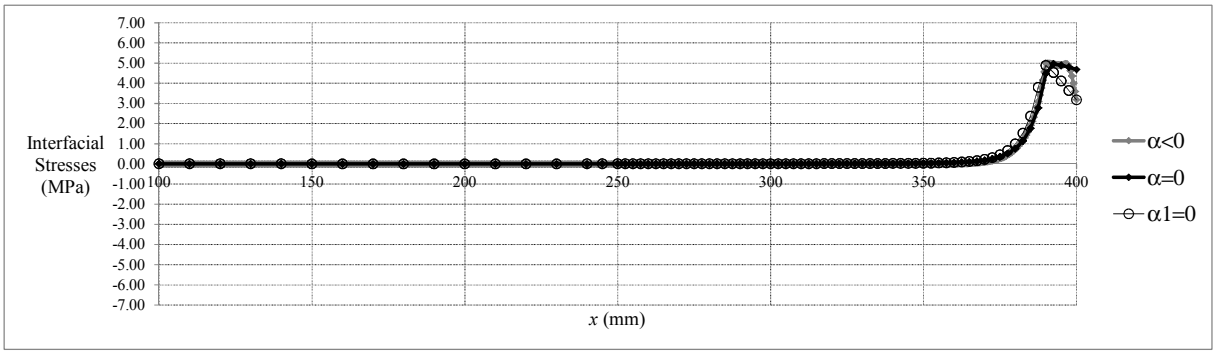

Figure 16: Shear stresses with t_i=0.1mm and F=6kN

5 CONCLUSIONS

In shear tests, adopting a deviation of the load orientation with respect to the FRP fibre orientation (α≠0º), normal stresses are obtained in addition to the stresses tangential to the interface, whereas no normal stresses occur in a pure shear model.

Considering α>0 and especially for higher thickness values, the maximum tangential stress tends to be higher than the cohesion along a small bond length, due to the existence of normal compressive stresses in the interface, in particularly for lower load levels. This small length, near to the beginning of the glued joint where the load is applied, tends to decrease with the thickness adopted.

Except in the region where normal stresses co-exist, the shear stress distribution becomes similar to the one obtained in a pure shear model.

Considering the maximum load, if α>0, its value is close to the value obtained from a pure shear test. However, if α<0, due to the existence of normal stresses at the interface, a significant reduction of the bond strength is observed, which seems to be more pronounced

using smaller FRP thickness. In this case, the measured fracture energy in mode-II is significantly different from the theoretically correct value.

The normal stresses under $\alpha<0$ are mainly peeling stresses, which occur along a small length.

With regard to the quantification of the material parameters, which define the behaviour of the bond between concrete-FRP, it is possible that these load misalignments, in an experimental shear test setup, may be responsible for the large dispersion observed in several works [7], namely:

i) the evaluation of fracture energy in mode-II based on these tests is very sensitive to the load misalignment, mainly if $\alpha<0$;
ii) the cohesion quantification from experimental tests could be accurately achieved. However, some attention should be paid to the possibility of obtaining shear stresses higher than the cohesion, along a small length, due to load misalignment;
iii) the shear stiffness appears as the parameter with the largest range of values when compared to the cohesion and the fracture energy in mode-II. However, this parameter essentially depends on the adhesive [7] and for larger values its influence, in the maximum load and in the tangential stresses, could be neglected.

It is important to stress that, if the imperfection related to the experimental test corresponds to $\alpha<0$, the obtained maximum load value can be less than half the value obtained from a test with $\alpha=0$ or $\alpha>0$.

As shown, the results obtained with $\alpha>0$ are considerably closer to the ones resulting from a pure shear test than the values obtained with $\alpha<0$.

When comparing the cases where $\alpha=+1.0^{\circ}$ and $\alpha=+0.5^{\circ}$ no significant differences are registered. However, with a negative angle, a significant difference is found, since the maximum load varies from 35kN to 25kN when the angle varies from 0.5° to 1.0°.

As a final remark, the material thicknesses considered in this study are typical from fibre carbon sheets. Thus, it is possible that the use of laminates proves to be less sensitive to the variation of the load direction.

ACKNOWLEDGEMENT

Financial support has been provided by the Portuguese Fundação para a Ciência e a Tecnologia (FCT) of the Portuguese Ministry of Science and Technology and Higher Education (PROTEC 2009).

REFERENCES

[1] Xue, W., Zenga, L. and Tana, Y. Experimental studies on bond behaviour of high strength CFRP plates, *Composites Part B: Engineering* (2008) 39(4), 592-603.
[2] Mazzotti, C., Savoiaa, M. and Ferracutia, B. An experimental study on delamination of FRP plates bonded to concrete, *Construction and Building Materials* (2008) 22(7), 1409-1421.
[3] Malek, A.M., Saadatmanesh, H. and Mohammad, R.E. Prediction of failure load of RC beams strengthened with FRP plate due to stress concentration at the plate end, *Structural Journal, ACI* (1998) 95(2), 142-152.

[4] Täljsten, B. *Plate bonding – strengthening of existing concrete structures with epoxy bonded plates of steel or fibre reinforced plastics*, Doctoral Thesis, Division of Structural Engineering, Lulea University of Technology, (1994).
[5] Chajes, M.J. and Finch jr., W.W., Januszka, T.F. and Thomson jr., T.A. Bond and force transfer of composite material plates bonded to concrete, *Structural Journal, ACI*, (1996) 93(2), 208-217.
[6] Bizindavyi, L. and Neale, K.W. Transfer lengths and bond strengths for composites bonded to concrete, *Journal of Composites for Construction, ASCE*, (1999) 3(4), 153-160.
[7] Neto, P. *Estudo numérico da ligação betão-CFRP*, Tese de Mestrado, Instituto Superior Técnico, Universidade Técnica de Lisboa, (2006).
[8] Neto, P., Alfaiate, J., Almeida, J.R. and Pires, E.B. The influence of mode-II fracture on concrete strengthened with CFRP, *Computers & Structures* (2004) 82(17-19), 1495-1502.
[9] Neto, P., Alfaiate, J. and Vinagre, J. Modelling the behaviour of reinforced concrete beams strengthened with FRP, *Proceedings of III European Conference on Computational Mechanics. Solids, Structures and Coupled Problems in Engineering, ECCM2006*, Laboratório Nacional de Engenharia Civil, Lisboa, Portugal, (2006).
[10] Hillerborg, A., Modeer, M. and Petersson, P.E. Analysis of crack formation and crack growth in concrete by means of fracture mechanics and finite elements, *Cement and Concrete Research* (1976) 6, 773-782.
[11] Travassos, N.C. *Caracterização do comportamento da Ligação CFRP-betão*, Tese de Mestrado, Documento provisório, Instituto Superior Técnico, Lisboa, Universidade Técnica de Lisboa, (2001).
[12] Lourenço, P.B. and Rots, J.G. A multi-surface interface model for the analysis of masonry structures, *Journal of Engineering Mechanics, ASCE* (1997) 123(7), 660-668.
[13] Alfaiate, J. and Almeida, J.R., Crack Evolution in Confined Masonry Walls, Idelshon, S.R., Oñate, E. and Dvorkin, E. eds. *Computational Mechanics: New Trends and Applications, CIMNE*, Barcelona, Spain, (1998).
[14] Bazant, Z.P. and Pfeiffer, P.A. Shear fracture tests of concrete, *Materials and Structures* (1986) 19, 111-121.
[15] Ozbolt, J., Reinhardt, H.W. and Xu, S. Numerical studies of the double-edge notched mode-II geometry, Mihashi, H. and Rokugo, K. eds. *FRAMCOS-3*, Japan, (1998) 2, 773-782.
[16] Alfaiate, J. and Pires, E.B. Mode-I and mixed-mode non-prescribed discrete crack propagation in concrete, Mihashi, H. and Rokugo, K. eds. *FRAMCOS-3,* Japan, (1998) 2, 739-748.
[17] Gálvez, J.C., Cendón, D.A., Planas, J., Guinea, G.V. and Elices, M. Fracture of concrete under mixed loading - experimental results and numerical prediction, Mihashi, H. and Rokugo, K. eds. *FRAMCOS-3,* Japan, (1998) 2, 729-738.
[18] Yuan, H., Wu, Z.S. and Yoshizawa, H. Theoretical solutions on interfacial stress transfer of externally bonded steel/composite laminates, *Journal of Structural Mechanics and Earthquake Engineering*, *JSCE* (2001) 675/I-55, 27-39.
[19] Wu, Z.S. and Niu, H.D Shear transfer along FRP-concrete interface in flexural members, *Journal of Material, Concrete Structures and Pavements*, *JSCE* (2000) 49(662), 231-245, 2000.

XI International Conference on Computational Plasticity. Fundamentals and Applications
COMPLAS XI
E. Oñate, D.R.J. Owen, D. Peric and B. Suárez (Eds)

A METHOD OF TWO-SCALE CHEMO-THERMAL-MECHANICAL COUPLING FOR CONCRETE

Tao Wu*, İlker Temizer†, Peter Wriggers*

*Institute of Continuum Mechanics
Leibniz Universität Hannover
Appelstraße 11, 30167 Hannover, Germany
e-mail: wu,wriggers@ikm.uni-hannover, www.ikm.uni-hannover.de/

†Department of Mechanical Engineering
Bilkent University
06800 Bilkent Ankara, Turkey
e-mail: temizer@bilkent.edu.tr, www.me.bilkent.edu.tr

Key words: Concrete, Alkali Silica Reaction, Multiscale, Homogenization, Coupling

Abstract. The Alkali Silica Reaction(ASR) is one of the most important reasons to cause damage in cementitious constructions, which can be attributed to the expansion of hydrophilic gel produced in the reaction. In this contribution, the chemical extent is described depending on the temperature and it has influences on damage parameters. Expansions of the gel are assumed to only happen in the micropores of Hardened Cement Paste. Afterwards, the homogenization of damage in the microscale is initialized and the effective damage can be applied in the mesoscale directly. Moreover, parameter identification is implemented to extract the effective inelastic consititutive equation. In all, 3D multiscale chemo-thermo-mechanical coupled model is set up to describe the damage in the concrete due to ASR.

1 INTRODUCTION

1.1 Concrete

Concrete is the most widely used construction material in the world because of its good strength and durability. However, it is a exceedingly complex material and has specific structures at different length-scales. This issue can yield stress concentrations which cause overall inelastic behavior in the material. In order to improve the reliability of numerical simulations, it is very crucial to extend the investigation to the microstructure. Concrete at the macroscale is assumed to consist of mortar, large aggregates, large pores, and a

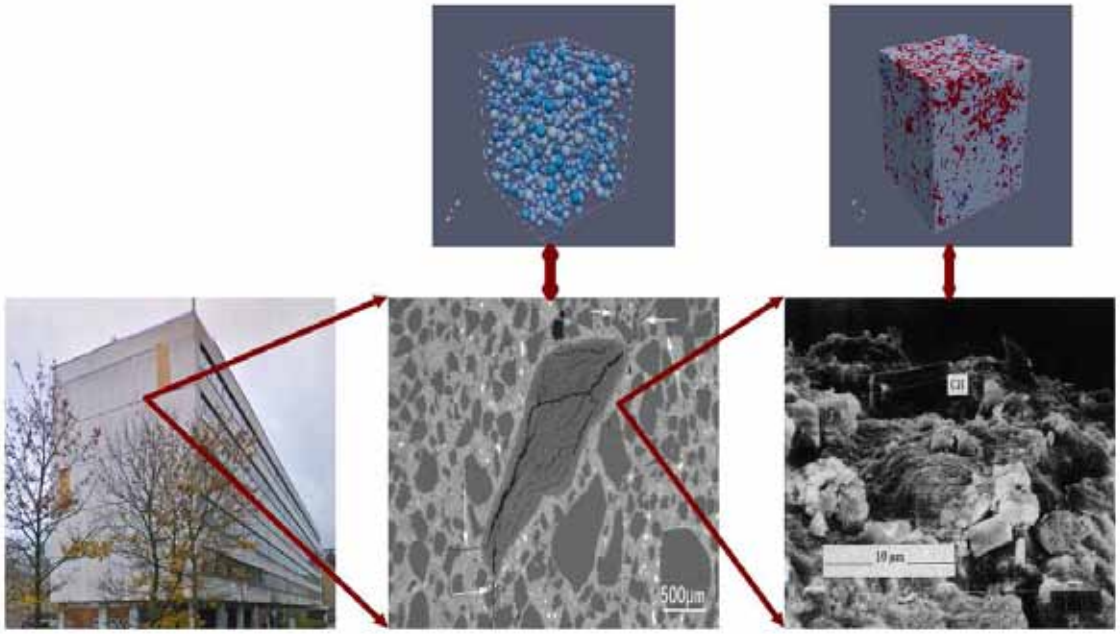

Macroscale *Mesoscale* *Microscale*

Figure 1: Multiscale Representation of the Concrete

cohesive zone between aggregates and mortar. The mortar as the mesoscale contains small aggregates, small pores, hardened cement paste(HCP) and a cohesive zone between small aggregates and HCP. At the microscale, HCP includes hydration products, unhydrated residual clinker and micropores. The whole multiscale representation of concrete is shown in Fig.1.

1.2 Alkali Silica Reaction

1.2.1 Mechanism

The issue of concrete deterioration because of the alkali silica reaction(ASR) has received numerous attentions since 1940[3]. ASR refers to a multistage process, involving non-instantaneous dissolution of silica and instantaneous swelling. The process of dissolution happens at the interface of aggregates and the alkaline solution, where hydroxyl ions attack poorly crystallized silica network. The produced ions from dissolution will combine with positively charged ions to form the gel and then the gel imbibes water and swells. As long as this free expansion space in pore is filled, the gel can exert locally a pressure on the surrounding cement paste which eventually leads the micro-crack and macro-crack of concrete. Many researchers have already agreed the dissolution mechanism of silica as the first stage of the ASR, however, there are debates how the expansion of gel works among researchers until now. The ASR model proposed by Bažant and Steffens[1] assumes that the pressure of water imbibition in the gel can push the gel to permeate the pores in the

cement paste located very near the surface of aggregate particles. Dron and Brivot[2] even go further to assume a through-solution mechanism, where the dissolved silica may diffuse away from the subsequent expansive reactions, may then happen anywhere in the connected pore space of the cement paste. On the other hand Idorn[4] indicates, that the expansive mechanism takes place directly inside the reacting aggregate particles and not in pores or cracks of the cement paste. In addition, Idorn[4] states, that gel penetrating into cracks and pores surrounding the aggregate absorbs calcium ions from the pore liquid. It makes the gel rigid and non-swelling. Up to now, there are no works regarding the alkali silica reaction implemented in the HCP, since some parameters can not be obtained from experiments directly in the microscale, and more importantly, aggregates do not exist in the HCP. The promising character of this contribution is to extend the investigation to the real microscale of concrete. So as to make the microscale model more reasonable, some assumptions have to be set up. Firstly, the expansion of gel is assumed to take place in micropores of the HCP. Secondly, the dissolution process and the expansion process are considered as a one.

1.2.2 Chemical Reaction Kinetics

A first order reaction kinetics is defined here

$$t_c \frac{d\xi}{dt} = 1 - \xi \tag{1}$$

$\xi \in [0, 1]$ is the chemical extent, where 0 indicates no reaction and 1 means the end of reaction. In addition, t_c is the characteristic time depending on the temperature and ξ. Based on experiments from Larive[11], the characteristic time is obtained as

$$t_c = \tau_{ch} \frac{1 + exp[-\tau_{lat}/\tau_{ch}]}{\xi + exp[-\tau_{lat}/\tau_{ch}]} \tag{2}$$

$$\tau_{lat}(T) = \tau_{lat}(\bar{T}) exp[U_{lat}(1/T - 1/\bar{T})]; \qquad \tau_{ch}(T) = \tau_{ch}(\bar{T}) exp[U_{ch}(1/T - 1/\bar{T})] \tag{3}$$

where τ_{lat} and τ_{ch} are the latency time and the expansion time respectively. The values of $U_c = 5400 \pm 500K$, $U_L = 9400 \pm 500K$ are from the literature[5] and afterwards, the evolution of the reaction extent ξ is obtained by integrating the ordinary differential equation (1), see equation (4) and the extent with respect to different temperatures is displayed in Fig.(2).

$$\xi(t) = \frac{1 - exp(-t/\tau_{ch})}{1 + exp(-t/\tau_{ch} + \tau_{lat}/\tau_{ch})} \tag{4}$$

For a genetric temperature history, the accumulated extent can be obtained through the backward euler scheme. In terms of different temperature inputs, the accumulation curve of extent is obtained, see Fig.(4) and Fig.(5).

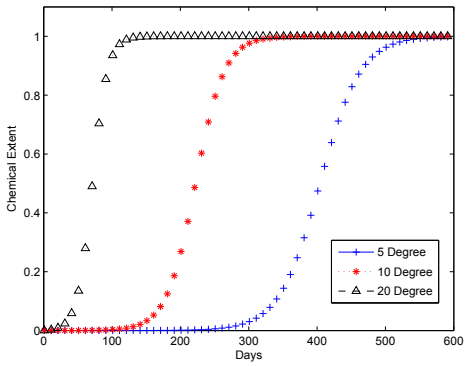

Figure 2: Chemical Extent

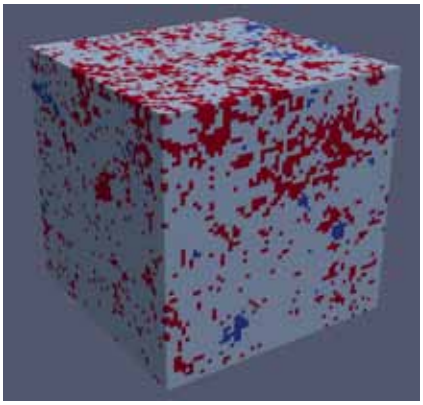

Figure 3: Hardened Cement Paste

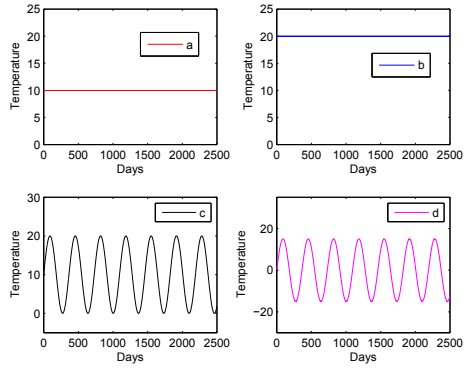

Figure 4: Different Temperatures

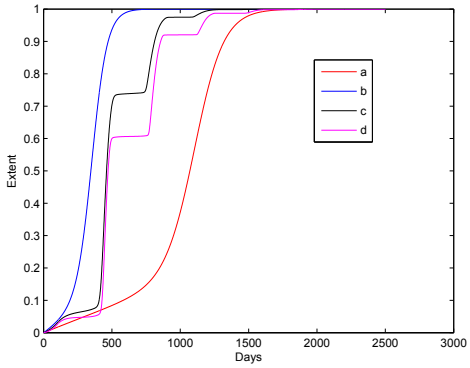

Figure 5: Chemical Extent Accumulation

2 MICROSCALE OF THE CONCRETE

2.1 Representation of the Hardened Cement Paste

The representation of HCP is obtained using three-dimensional micro-CT scans with a spatially resolved distribution of the density. Each voxel is $1\mu m^3$ with only one material identifier. According to the theory of Powers, the fractional volume of hydration products is 83.4% and the fractional volume of micropores is 14.3% when the water-cement ratio is 0.45 and the hydration degree is 0.945. Through the median filter, a final three-dimensional finite-element mesh with three different material identifiers is produced for numerical simulation, which can represent each voxel with a finite-element of hexahedron type, see Fig.(3). Pale parts are hydration products, red part are micropores and blue parts are unhydrated residual clicker.

2.2 Constitutive Equations in the HCP

2.2.1 Hydration Product

2.2.2 Gel

Since the chemistry of gel is similar to the Calcium-Silicate-Hydrate, gel is treated as a incompressible material, with a Possion ratio of 0.49975. Standard displacement elements experience locking for incompressible conditions, hence, Q1P0 is launched to solve this problem. In the case of any deformation, there are deviatoric and volumetric strain components. Deviatoric strains determine the shape change of the body and volumetric strains determine the volume change. The volume change occurs due to a hydostatic pressure. As a result, Q1P0 element determines the shape change from the deviatoric strains and the pressures from the volumetric strain, where the shape function of pressure in FEM is constant. $\sigma = 2\mu\varepsilon^D + P$ and P is the hydrostatic pressure. Herein, $P = \kappa tr\varepsilon - \kappa\beta\xi$, where β is the expansion coefficient and ξ is the chemical extent. The weak forms of the above-mentioned stress formular and the mechanical equilibrium are shown in equation (5) and equation (6).

$$\int_V r(\kappa^{-1}P - (tr\varepsilon - \beta\xi))dV = 0 \tag{5}$$

$$\int_V \varepsilon(\eta) : \sigma(u)dV = \int_V (\varepsilon^D(\eta) + \varepsilon^V(\eta)) : (\sigma^D(u) + P1)dV = \int_V \eta \cdot \rho b dV + \int_\Gamma t \cdot \eta d\Gamma \tag{6}$$

where r and η are the test function for stress and displacement. After plugging equation (5) into equation (6) and the linearization, the tangent matrix and the residual can be obtained.

2.3 Homogenization

Computational homogenization is very critical tool to bridge the microscale and the marcroscale[10]. The resulting effective material behavior can be applied to the mechanical model at the next length-scale through the volume average of representative volume elemnt(RVE). $\langle D \rangle = \frac{1}{V}\int_V D dV$, where $\langle * \rangle$ denotes the volume average of a representative volume element. The size of RVE is very critical for homogenization, which can ensure the statistical representative response under boundary conditions satisfying the HILL's energy criterion. In this contribution, the RVE of 64*64*64 is choosed from Hain[8]. Afterwards the displacement boundary condition of RVE is fixed and just consider the expansion inside of RVE. The effective damage of RVE is increased with the chemical reaction going on for different expansion ratios, see Fig.6. The damage distribution on hardened cement paste is shown in Fig.7.

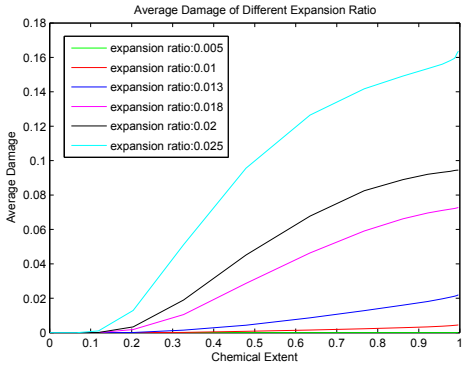

Figure 6: Effective Damage

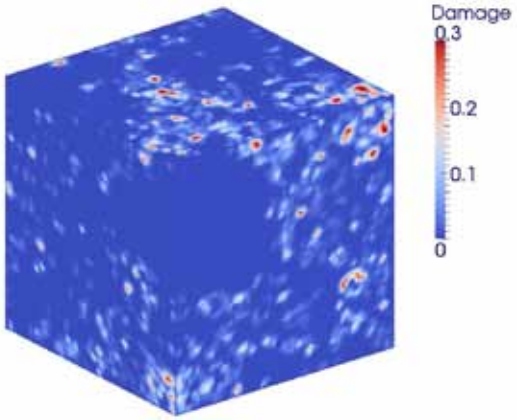

Figure 7: Damage on Hardened Cement Paste

2.4 Statistical Analysis

Because the representative volume element(RVEs) is only a different portion of the HCP, statistical analysis of a sufficient number of different three-dimensional specimens makes numerical simulation of damage more reasonable and accurate. 20 statistical tests are run with the expansion ratio of 0.02, see Fig.(8). The mean value and the standard deviation of homogenized damage-extent correlation are obtained through equation (7). Afterwards, equation (8) is used to approximate $d(\xi)^{med}$ and $d(\xi)^{std}$, which can be directly applied for the computation in the mesoscale. Table (1) demonstrates the approxmation coefficients and referring to the approximation of mean and standard deviation, see Fig.(9) and Fig.(10).

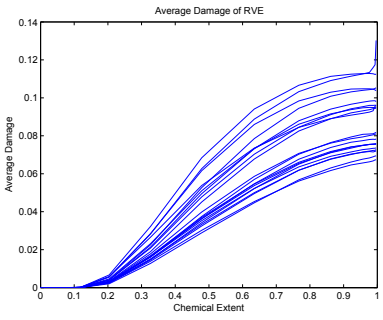

Figure 8: Statistical Tests

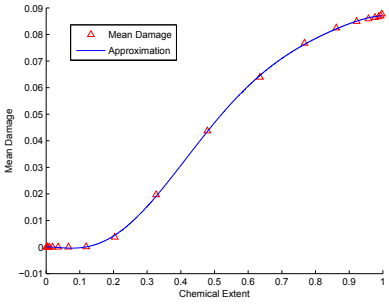

Figure 9: Mean Average

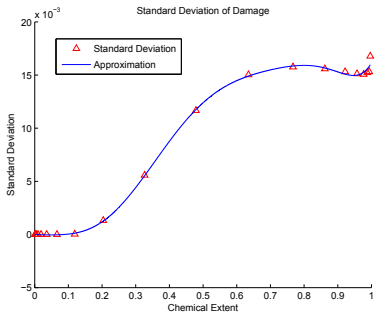

Figure 10: Standard Deviation

$$d(\xi)^{med} := \frac{1}{n}\sum_{i=1}^{n} < d(\xi_i) > \qquad d(\xi)^{std} := \sqrt{\frac{1}{n-1}\sum_{i=1}^{n}[< d(\xi)_i > -d(\xi)^{med}]^2} \tag{7}$$

$$D(\xi)^{med} := \sum_{i=0}^{i\leq 6} c_i^{med}\xi^i \quad and \quad D(\xi)^{std} := \sum_{i=0}^{i\leq 7} c_i^{std}\xi^i \tag{8}$$

i	0	1	2	3	4	5	6	7
c_i^{med}	-1.4539	4.7304	-5.5806	2.6142	-0.2205	-0.0025	0.0001	
c_i^{std}	5.5993	-20.4421	29.2301	-20.2592	6.6718	-0.8509	0.0704	-0.0033

Table 1: Coefficients of Approximation

3 MESOSCALE OF THE CONCRETE

3.1 Take and Place Algorithm

The evaluation of the mesoscale representation of concrete needs the generation of a random aggregate structure where the size and distribution of the coarse aggregates closely resemble real concrete in the statistical sense. This structure is comprised of randomly distributed aggregates particles and mortar matrix filling the space between the particles. This random principle is implemented by taking samples of aggregate particles from a source whose size distribution follows a certain given grading curve, see Fig.11 and Table (2), and then placing the aggregates one by one into the concrete in such a way, which can ensure no overlapping with particles already placed. Grading curve refers to the determination of the particle size distribution for aggregates, usually experssed in terms of cumulative percentage passing through a series of size of sieve openings. In order to place an aggregate particle at a free position within the concrete volume, two obvious conditions need to be satisfied. The whole aggregates must be completely within the boundary of the concrete volume and there must not be any overlapping with previously placed aggregates.

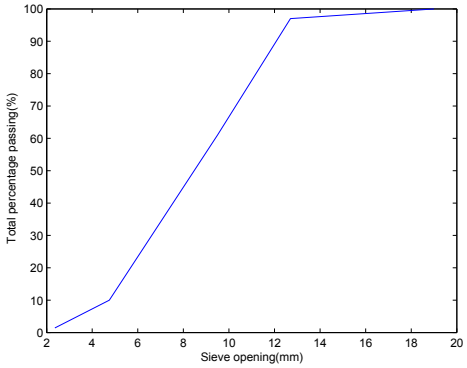

Figure 11: Grading Curve

Size(mm)	Retained(%)	Passing(%)
19.00	0	100
12.70	3	97
9.50	39	61
4.75	90	10
2.36	98.6	1.4

Table 2: Sieve Result

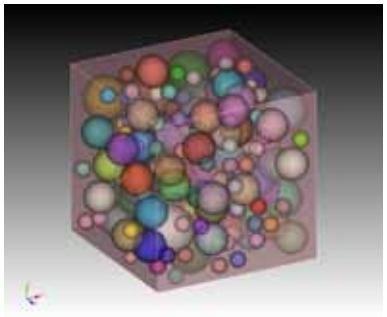

Figure 12: Mesoscale

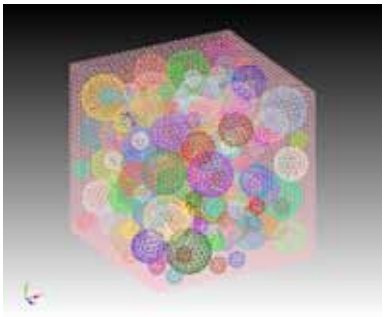

Figure 13: Descritization

3.2 Discretization

Discretization of the generated RVEs consisting of many inclusions is a tedious procedure. There are basically two approaches to mesh the microstructure of the concrete material: an unaligned or an aligned approach. In this contribution, the generated mesostructure model is translated into the commercial software CUBIT which offers the option of automatic mesh generation with tetrahedral elements, then generates the mesh and finally outputs a mesh file for the finite element analysis program (FEAP), which is a nonlinear finite element software.

3.3 Effective Inelastic Constitutive Equation

In the mesoscale, aggregates are assumed to be purely elastic and cement paste is assumed to be an inelastic damage material. Since finding an effective inelastic constitutive equation by homogenization is still an unsolved problem, an inelastic effective constitutive equation with the unknown material parameters must be defined through parameter identification. In terms of the cement paste, a visco-plastic model of PERZYNA-type combined with an isotropic damage model is choosen. Considering the definition of elas-

tic energy rate yields

$$D : 0 \leqslant \sigma : \dot{\varepsilon}^{pl} + Y\dot{D}^{u} \tag{9}$$

a constrained optimization problem combined with the Penalty-Lagrange approach can yield an unconstrained optimization problem.

$$P = -\sigma : \dot{\varepsilon}^{pl} - Y\dot{D}^{u} + \frac{1}{\eta}\phi(f) + \dot{\chi}S^{u} \rightarrow stat \tag{10}$$

where the variable $\frac{1}{\eta}$ refers to the penalty-parameter, $\phi(f)$ denotes the penalty function, and χ is the LAGRANGE multiplier. A partial differentiation of P with respct to the elastic energy rate Y yields the evolution equation of damage.

$$\dot{D} = \xi\frac{\partial S(\varepsilon^{eq})}{\partial \varepsilon^{eq}} \tag{11}$$

where $S(\varepsilon)$ is the damage surface determining whether damage increases or not. It depends on the equivalent strain ε^{eq}.

$$S(\varepsilon) := 1 - exp\left[-\left(\frac{\varepsilon^{eq} - a}{b}\right)^{c}\right] - D \leqslant 0 \tag{12}$$

The damage surface is defined by an exponential law and depends on the elastic energy ε^{eq}, in addition, the parameters $a, b, and\ c$ are the material properties of the assumed model. The partial differentiation of P with respect to the σ yields the plastic strain evolution.

$$\dot{\varepsilon}^{pl}_{n+1} = \frac{1}{\eta}\phi^{+}\frac{\partial f}{\partial \sigma} \tag{13}$$

where ϕ^{+} denotes the derivative of the penalty function $\phi(f)$ and the penalty function itself is defined the $(k+1)th$ power of the yield surface f. The material property k is assumed to take the value $k = 1$ in order to enable a nonlinear viscous behavior.

$$\phi(f) = \begin{cases} 0 & ;\text{f}\leqslant 0 \\ \frac{1}{k+1}f^{k+1} & ;\text{f}>0 \end{cases} \tag{14}$$

The abovementioned penalty function ensures that the constraint f is satisfied apprximately which is typical for visco-plastic materials. The yield surface f is assmed to be of VON-MISES-type

$$f := \alpha tr\sigma + \|dev\sigma\| - \sqrt{\frac{2}{3}}k_f \leqslant 0, \tag{15}$$

where $dev\sigma$ denotes the deviatoric part of the stress tensor, $tr\sigma$ is the trace of the stress tensor, and k_f is the material property of the model. Eventually, the equation (13) can be solved with the radial return mapping procedure based on the implicit Euler scheme.

3.4 Parameter Identification

Because the parameters in the abovementioned equation can not be obtained from experiments, parameter identification is formulated as an optimization problem, where a least-squares functional is minimized for providing the best agreement between experimental data and numerical data. The objective function is generated and then the material properties are calculated on the basis of minimization of the objective function. The objective function $A(\kappa)$ is defined as a least-square sum between the experiment[9] and the numerical result: $A(\kappa) := \sum(\langle\sigma(\kappa)\rangle_i - \sigma_i^{exp})^2 \rightarrow min$. Herein, the combination of Genetic algorithm and Levenberg-Marquardt algorithm is used. The genetic algorithm is used for pre-optimization and then the optimization will switch to the Levenberg-Marquardt method, once the object function is smaller than a certain value. It is a efficient and robust algorithm. The optimization results and resulting parameters are shown in Fig.14 and Table 3.

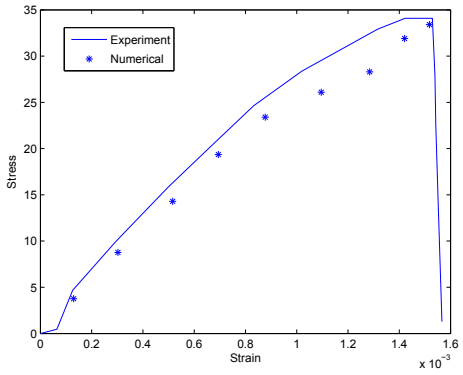

Figure 14: Optimization Result

	κ_0	κ_{min}	κ_{max}	κ^*
k_f	21	20	70	42
η	2725	1000	15000	3525
Δt	0.0015	0.001	0.2	0.0355
b	100	100	5000	4241
a	100	100	2000	718

Table 3: Optimization Parameters

4 THERMAL FIELD

The instationary thermal balance equation states that changing of the temperature is equal to the heat flux q through the surface

$$\int_V \rho c\dot{\theta} dV = -\int_\Gamma q d\Gamma \tag{16}$$

where c denotes the capacity of heat and the heat flux $q = -kgrad\theta$.

5 COUPLING

After imposing the constant temperature on top of the concrete, the heat flux continues to diffuse and then the chemical extent on each gauss point of finite elements could be updated through the backward euler scheme depending on the tempeature. Meanwhile, the chemcial extent can trigger damage which is comprised of the damage due to the alkali silica reaction and the mechanical loading. The evolution of the chemical extent and the

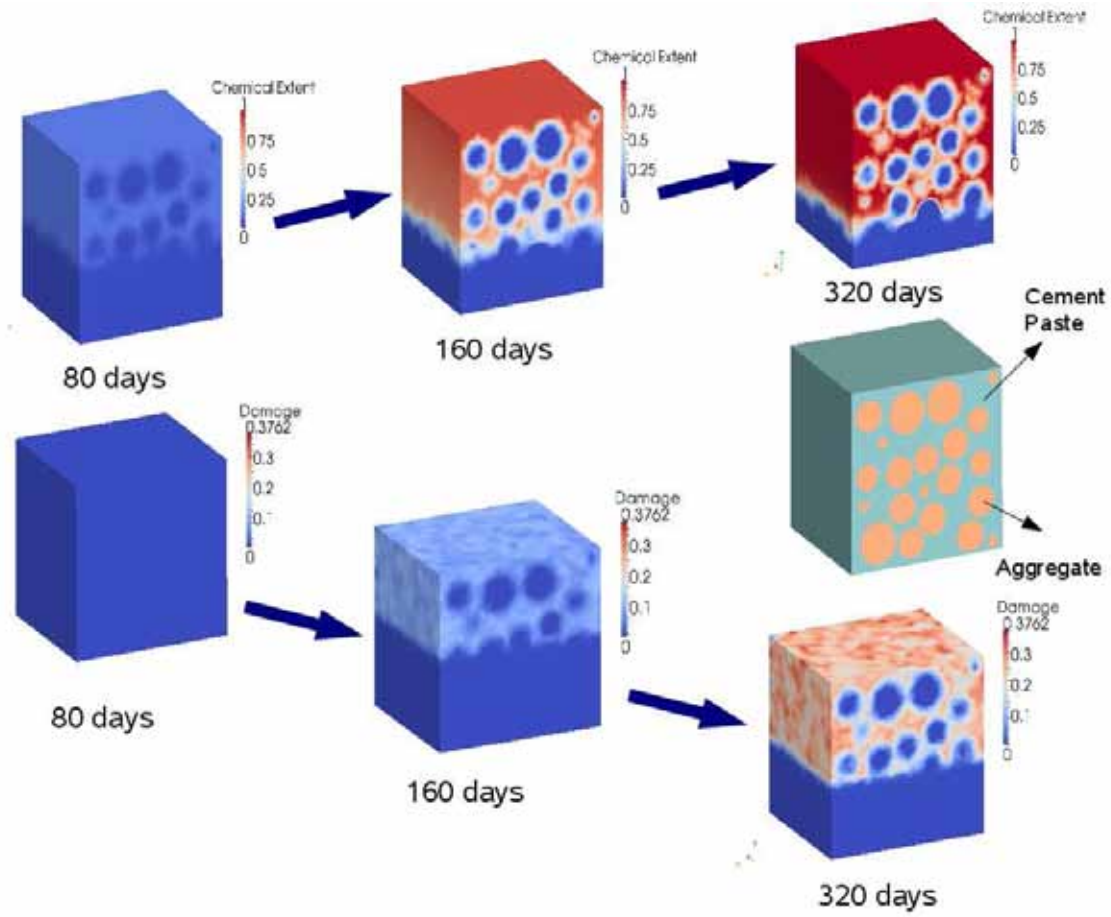

Figure 15: Coupling Result

damage with respect to time is demonstrated in Fig.15. Because aggregates are assumed to be elastic, the chemical extent and the damage do not exist in aggregates.

6 CONCLUSIONS

In this contribution, the mechanism of Alkali Silica Reaction and the representation of concrete in the microscale and mesoscale for further numerical computation are introduced. The numerical homogenization approach is set up to bridge the microscale and macroscale. Furthermore, the parameters of the effective consititutive equation are obtained through parameter identification. Eventually 3D multiscale chemo-thermo-mechanical FEM is demonstrated completely to describe damage in the concrete due to the Alkali Silica Reaction. In the future, the humidity will be incorporated and then the coupling based on the staggered method will be implemented. In addition, because the cohesive zone between aggregates and cement paste in the concrete is very week, the interfacial damage should be considered.

7 ACKNOWLEDGMENT

The first author wishes to thank Stefan Löhnert for helpful discussions.

REFERENCES

[1] Bažant, Z.P. and Steffens, A. Mathematical model for kinetics of alkali-silica reaction in concrete. Cement and Concrete Research. (2000) 30:419-428.

[2] Dorn, R. and Brivot, F. Thermodynamic and kinetic approach to the alkali-silica reaction. Part 2: experiment. Cement and Concrete Research. (1993) 23:93-103.

[3] Lemarchand, E., Dormieux, L. and Ulm, F.J. Elements of micromechanics of ASR-induced swelling in concrete structures. Concrete Science and Engineering. (2002) 4:12-22.

[4] Idorn, G.M. A discussion of the paper 'Mathematical model for kinetics of alkali-silica reaction in concrete' by Zdeněk P.Bažant and Alexander Steffen. Cement and Concrete Research. (2001) 31:1109-1110.

[5] Ulm, F.J., Coussy, O., Li, K.F. and Larive, C. Thermo-chemo-mechanics of ASR expansion in concrete structure. Journal of Engineering Mechanics. (2000) 126:233-242.

[6] Comi, C., Fedele, R. and Perego, U. A chemo-thermo-damage model for the analysis of concrete dams affected by alkali-silica reaction. (2009) 41:210-230.

[7] Wriggers, P. and Moftah, S.O, Mesoscale models for concrete: homogenisation and damage behavior. Finite Elements in Analysis and Design. (2006) 42:623-636.

[8] Hain, M. and Wriggers, P. Computational Homogenization of micro-structural Damage due to Frost in Hardened Cement Paste. Finite Elements in Analysis and Design. (2008) 44:233-244

[9] Comby-Peyrot, I., Bernard, F., Bouchard, P.O., Bay, F. and Garcia-Diaz, E. Development and validation of a 3D computational tool to describe concrete behaviour at mesoscale. Application to the alkali-silica reaction. Computational Materials Science. (2006) 46,1163-1177.

[10] Temizer, İ and Zohdi, T.I. A numerical method for homogenization in non-linear elasticity. Computational Mechanics. (2007) 40:281-298.

[11] Larive, C. Apports combinés de l'expérimentation et de la modélisation à la compréhension de l'alcali-réaction et de ses effects mécaniques. Ph.D thesis, Laboratoire Central des Ponts et Chaussées, Paris, (1998).

XI International Conference on Computational Plasticity. Fundamentals and Applications
COMPLAS XI
E. Oñate, D.R.J. Owen, D. Peric and B. Suárez (Eds)

MULTI-SURFACE DESCRIPTION OF TEMPERATURE AND STRAIN RATE-DEPENDENT DAMAGE INITIATION AND GROWTH IN DUCTILE VISCOPLASTIC MATERIALS

PATRICE LONGERE[1], ANNE-GAELLE GEFFROY[2], BRUNO LEBLE[2] AND ANDRE DRAGON[3]

[1] Université de Toulouse
Institut Supérieur de l'Aéronautique et de l'Espace - Institut Clément Ader (EA 814)
10 avenue E. Belin, BP 54032, 31055 Toulouse cedex 4, France
e-mail: patrice.longere@isae.fr

[2] DCNS NA Ingénierie
Rue de Choiseul, 56311 Lorient, France
email: anne-gaelle.geffroy@dcnsgroup.com, bruno.leble@dcnsgroup.com

[3] CNRS-Institut Pprime (UPR 3346)
Ecole Nationale Supérieure de Mécanique et d'Aérotechnique - Université de Poitiers
1 avenue C. Ader, BP 40109, 86961 Futuroscope - Chasseneuil du Poitou, France
e-mail: andre.dragon@ensma.fr

Key words: Viscoplastic metal, Ductile fracture, Void nucleation, Small triaxialities, Numerical simulation.

Abstract. A phenomenological modelling approach has been developed, based on some salient physical effects regarding void growth vs. plastic straining, to describe the transition behaviour between dense metal plasticity and micro-porous metal plasticity. Considering that void germination requires a certain amount of plastic deformation, a 'primary' hole nucleation criterion has been proposed, as well as a statistical law governing the 'secondary' hole kinetics. In a consistent way, the hole nucleation criterion accounts for the accelerating effects of stress triaxiality and, conversely, the delaying effects of temperature and strain rate. In this work, a modification of the GTN model has also been proposed, overcoming its inability to predict damage growth and fracture for zero and low triaxiality, shear-dominated deformations. In this respect the kinematic mean stress related shift mechanism has been introduced and quantified in the expression of the GTN plastic potential, enabling thus the damage growth under shear and under small negative triaxialities. The 3D constitutive equations have been implemented as user material in the engineering finite element computation code Abaqus®. Numerical simulations have been conducted considering a single finite element under simple shear on one hand and a notched cylindrical sample under remote uniaxial tensile loading on the other hand. The numerical results show clearly the influence of the hole nucleation criterion related constants on the damage and further failure of the material.

1 INTRODUCTION

Several authors have attempted to describe the consequences of micro-voiding induced damage on the bulk material behaviour. These consequences are double: a progressive loss of the overall properties of the bulk material and the appearance, in addition to the isochoric plastic deformation due to dislocation glide in the matrix material, of an inelastic dilatancy due to void growth. In order to describe this second effect in the context of standard material, BERG [1] proposed a pressure dependent plastic potential, assuming that a critical mean triaxial stress (hydrostatic stress) is required to activate the void expansion. In this approach, only a loading path involving a mean triaxial stress greater than this critical mean triaxial stress produces void growth and related dilatancy. It is noteworthy that the latter may be accompanied by plastic deformation (under moderate mean triaxial stress) or not (under high mean triaxial stress). Based on a micromechanical analysis, GURSON [2] developed a plastic potential for slightly porous and perfectly plastic metals accounting explicitly for the concentration of voids and hydrostatic stress. TVERGAARD AND NEEDLEMAN [3] modified GURSON's model in order to take notably into account isotropic strain hardening and strain rate effects. The so-called GTN (for GURSON-TVERGAARD-NEEDLEMAN) model is widely used by the community of researchers dealing with ductile damage. Using the rate type formulation coupled with physical concepts, PERZYNA [4] developed an elliptic plastic potential taking into consideration cooperative effects of void growth, strain rate sensitivity and heating.

These approaches all suppose initially the presence of micro voids, or equivalently assume mostly that void expansion starting and plastic deformation occurrence are concomitant. It is clear that such a hypothesis is not supported physically, because cavity nucleation requires a certain amount of plastic deformation. Furthermore, by construction, the plastic potentials proposed by BERG, GURSON-TVERGAARD-NEEDLEMAN and PERZYNA are not able to describe dilatancy and related cavity growth under shear loading, implying that according to their approaches shear loading cannot lead sole to fracture.

This work aims at facing up to these deficiencies concerning notably the lack of a physically satisfying description of the transition from dense metal plasticity to micro-porous metal plasticity and the incapacity of describing void growth under shear.

The principle of the modelling approach involving non-concomitant damage incipience with respect to plastic straining is described in Sect.2. The constitutive equations for an elastic-viscoplastic material undergoing the combined effects of the two stage damage formation (void nucleation) mechanism, the mean stress kinematic shift related to ductile damage growth, isotropic hardening, thermal softening, are detailed in Sect.3. The complete model has been implemented as user material in the engineering finite element computation code Abaqus® and some numerical simulations have been conducted for a single representative volume element (RVE) and a laboratory sample submitted to a remote uniaxial tensile loading. The numerical results are shown in Sect.4.

2 BASIC CONCEPTS AND PRELIMINARY CONSIDERATIONS

2.1 Principle of the sound/damaged or dense/micro-porous behavior transition

In the present approach, based in part on the concepts suggested by DRAGON AND OHJI [5], the metallic material is initially supposed to be exempt of micro-voids. Subjected to a monotonic loading involving a positive or null stress triaxiality, it behaves elastic-(visco)plastically. As soon as the condition for the germination of a given volume fraction f_0 of micro voids, involving the equivalent plastic strain κ, plastic strain rate $\dot{\kappa}$, temperature T and stress triaxiality ST, is satisfied, the material behaviour becomes pressure dependent. Consecutive damage accompanying plastic yielding may be described then using e.g. GTN and PERZYNA micro-porous plasticity oriented models. The quantity f_0 represents thus a characteristic micro-porosity initiation bunch; its occurrence does not exclude further, secondary, delayed nucleation (see Sect.3.3). According to Fig.1, where the surfaces $\Phi_0 = 0$ and $\Phi_{I_0} = 0$ represent the limits of elastic domain of the sound material and of the hole non-nucleation domain respectively, this approach is able to reproduce qualitatively the accelerating effects of the stress triaxiality $\left(ST = -\sigma_{eq} / p_m\right)$ on the hole germination.

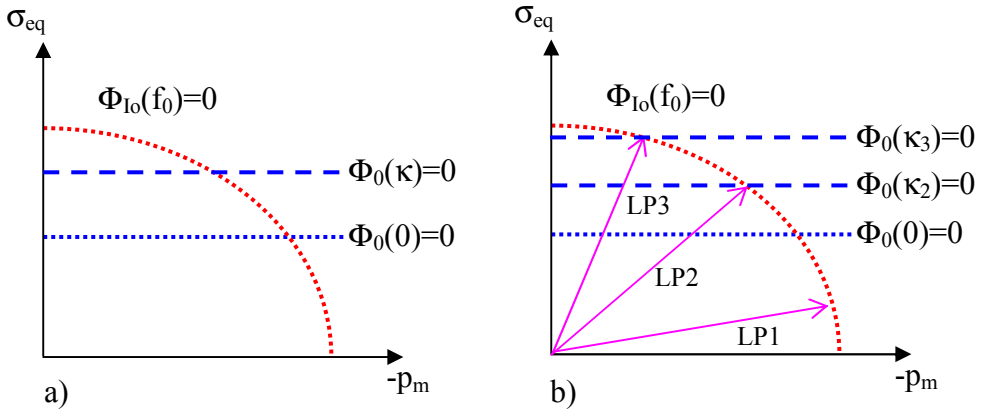

Figure 1: Principle of the approach. a) Initial and current elastic domains for the sound material and hole nucleation locus – b) Illustration of various loading paths; LP1: hole germination without plastic deformation; LP2: hole germination for a finite amount of plastic deformation (κ_2) linked to the current stress triaxiality (ST_2); LP3: hole germination for a finite amount of plastic deformation ($\kappa_3 > \kappa_2$) linked to the current stress triaxiality ($ST_3 < ST_2$) - σ_{eq} and p_m represent the equivalent stress and the pressure, respectively.

2.2 The hypothesis of a kinematical mean stress shift

It is known that viscoplastic deformation may cause brittle-like micro-damage in metals, as observed notably in creep where micro-voids and micro-cracks initiate along the grain boundaries. At an advanced stage of deformation, a material may thus contain defects potentially at the origin of brittle fracture (in the sense mentioned above) and defects potentially at the origin of ductile fracture (in the current sense). In such a material, there are thus two sources of damage induced softening, the latter being described via e.g. GTN and PERZYNA micro-porous plasticity oriented models. We are here describing the consequences of the former by introducing an effective micro porosity related softening mechanism, acting as a kinematic-like mean stress drop resulting in a shift of the yield locus centre towards

negative stress triaxiality values. Though a like shift may require more sophisticated analysis involving e.g. damage/plasticity-induced anisotropy , here, however, the purpose is limited to a modification of the GTN model. From a practical viewpoint, let denote as $\Phi\left(\sigma_{eq}, p_m; f, ...\right) = 0$ the yield surface of a material with a micro-void concentration f. The translation of the yield function Φ of the amount $-p_r$ under the micro-crack induced softening effects leads to consider the new plastic potential and corresponding yield locus $\Phi_G\left(\sigma_{eq}, p_m, p_r; f, ...\right) = 0$, such that $\Phi_G\left(\sigma_{eq}, p_m, p_r; f, ...\right) = \Phi\left(\sigma_{eq}, p_m + p_r; f, ...\right)$. The principle is illustrated in Fig.2.

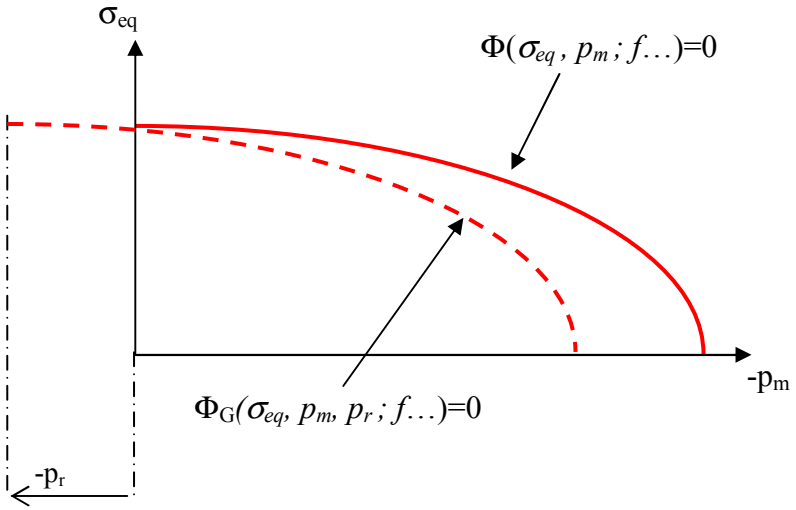

Figure 2: Shift of the micro-porous potential with kinematic mean stress

This paper aims at proposing a multi-surface approach based model accounting for the aforementioned effects.

3 CONSTITUTIVE EQUATIONS

The elastic/viscoplastic model involving two stage void nucleation mechanism and void growth related hardening/softening effects is detailed in the present section.

3.1 Constitutive equations of the sound material

The internal variable procedure has been followed to model the material behaviour. The instantaneous state of the material is described via the HELMHOLTZ free energy $\Psi\left(T; \underline{\underline{\varepsilon}}^e, \kappa\right)$, whose arguments are the absolute temperature T, the elastic strain tensor $\underline{\underline{\varepsilon}}^e$, and the isotropic strain hardening variable κ. Let us consider the following additive decomposition of Ψ :

$$\Psi\left(T; \underline{\underline{\varepsilon}}^e, \kappa\right) = \Psi_r\left(T; \underline{\underline{\varepsilon}}^e\right) + \Psi_T\left(T\right) + \Psi_s\left(T; \kappa\right) \tag{1}$$

where $\Psi_r\left(T;\underline{\underline{\varepsilon}}^e\right)$ is the recoverable part, $\Psi_T(T)$ the purely thermal part, and $\Psi_s(T;\kappa)$ the stored part. The rotational derivatives considered in the following are GREEN-NAGHDI derivatives, see GREEN AND NAGHDI [6]. Moreover, the tensor $\underline{\underline{\varepsilon}}^e$ represents here a spatial, generally small, elastic strain measure, namely $\underline{\underline{\varepsilon}}^e = \ln \underline{\underline{V}}^e$, $\underline{\underline{V}}^e$ representing pure elastic stretching resulting from the relevant multiplicative decomposition of the deformation gradient $\underline{\underline{F}}$ .The expressions of the various contributions in (1) are given by

$$\begin{cases} \rho\Psi_r\left(T;\underline{\underline{\varepsilon}}^e\right) = \dfrac{\lambda}{2}\left(Tr\underline{\underline{\varepsilon}}^e\right)^2 + \mu\underline{\underline{\varepsilon}}^e : \underline{\underline{\varepsilon}}^e - \alpha_T K Tr\underline{\underline{\varepsilon}}^e \Delta T \\ \rho\Psi_T(T) = -\dfrac{\rho C}{2T_0}\Delta T^2 \ ; \ \Delta T = T - T_0 \\ \rho\Psi_s(T;\kappa) = h(\kappa)g(T) \end{cases} \tag{2}$$

where λ and μ represent LAMÉ elastic coefficients, K is the bulk modulus $(K = \lambda + 2\mu/3)$. The quantities α_T, ρ and C represent the thermal dilatation coefficient, the mass density and the specific heat, respectively. In (2_3), $h(\kappa)$ represents the stored energy of cold work and $g(T)$ the thermal softening function. The set of thermodynamic forces connected to the state variables is given by

$$\begin{cases} \underline{\underline{\sigma}} = \rho\dfrac{\partial\Psi}{\partial\underline{\underline{\varepsilon}}^e} = \rho\dfrac{\partial\Psi_r}{\partial\underline{\underline{\varepsilon}}^e} = \left(\lambda Tr\underline{\underline{\varepsilon}}^e - \alpha_T K\Delta T\right)\underline{\underline{\delta}} + 2\mu\underline{\underline{\varepsilon}}^e \\ \rho s = -\rho\dfrac{\partial\Psi}{\partial T} = -\left(\rho\dfrac{\partial\Psi_r}{\partial T} + \rho\dfrac{\partial\Psi_T}{\partial T} + \rho\dfrac{\partial\Psi_s}{\partial T}\right) = \alpha_T K Tr\underline{\underline{\varepsilon}}^e + \dfrac{\rho C}{T_0}\Delta T - h(\kappa)g'(T) \\ r = \rho\dfrac{\partial\Psi}{\partial\kappa} = \rho\dfrac{\partial\Psi_s}{\partial\kappa} = h'(\kappa)g(T) \end{cases} \tag{3}$$

where $\underline{\underline{\sigma}}$ represent the CAUCHY stress tensor, s entropy and r isotropic hardening force. The viscoplastic yielding of the material under consideration is supposed to be well described by the plastic potential

$$\Phi_0 = \tilde{\sigma}_{eq}^2 - 1 = 0 \ ; \ \tilde{\sigma}_{eq} = \frac{\sigma_{eq}}{\bar{\sigma}_y} \ ; \ \bar{\sigma}_y = \sigma_y + \sigma_{vp} \tag{4}$$

where the quantities σ_y and σ_{vp} in (4_3) are the rate independent and rate dependent contributions to the yield stress $\bar{\sigma}_y$. The rate independent contribution σ_y in (4_3) incorporates the combined effects of strain hardening, via a VOCE type law, and thermal softening, via a power law:

$$\sigma_y = \left[R_0 + h'(\kappa)\right] g(T);\ h'(\kappa) = R_\infty \left[1 - \exp(-k\kappa)\right]^\beta\ ;\ g(T) = 1 - \left(\frac{T}{T_{melt}}\right)^m \tag{5}$$

where $(R_0, R_\infty, k, \beta)$ are isotropic hardening related constants and (T_{melt}, m) thermal softening related constants, with T_{melt} the melting point. With (5), the rate independent contribution σ_y in (4_3) and the isotropic hardening force r in (3_3) take thus the form

$$\sigma_y = \left\{R_0 + R_\infty \left[1 - \exp(-k\kappa)\right]^\beta\right\}\left[1 - \left(\frac{T}{T_{melt}}\right)^m\right]\ ;\ r = R_\infty \left[1 - \exp(-k\kappa)\right]^\beta \left[1 - \left(\frac{T}{T_{melt}}\right)^m\right] \tag{6}$$

The tensile/compressive asymmetry in the plastic behaviour is here considered as a thermally activated mechanism involving the mean stress. The strain rate induced overstress σ_{vp} in (4_3) is consequently expressed by

$$\sigma_{vp} = Y\left[\dot{\kappa}\exp\left(\frac{V_a p_m}{k_B T}\right)\right]^{1/n} \tag{7}$$

where (Y,n) are viscosity related constants and (V_a, k_B) behaviour asymmetry related constants, with $V_a = V_h \beta^3$, V_h being a constant, β Burgers vector magnitude (β=2.5Å), k_B BOLTZMANN constant (k_B=1.3804.10^{-23}J/K). The sound material satisfies the conditions of standard materials in the irreversible thermodynamics sense. Applying the normality rule yields

$$\underline{\underline{d}}^p = \Lambda \frac{\partial \Phi_0}{\partial \underline{\underline{\sigma}}} = \dot{\varepsilon}_0^{pD}\, \underline{\underline{n}}\ ;\ \dot{\varepsilon}_0^{\mathrm{pD}} = \Lambda \frac{\partial \Phi_0}{\partial \sigma_{\mathrm{eq}}} = 2\Lambda \frac{\tilde{\sigma}_{\mathrm{éq}}}{\overline{\sigma}_{\mathrm{y}}}\ ;\ \dot{\kappa} = \sqrt{\frac{2}{3}\underline{\underline{d}}^p : \underline{\underline{d}}^p} = \dot{\varepsilon}_0^{pD}\ ;\ \Lambda \geq 0 \tag{8}$$

where Λ represents the viscoplastic multiplier. Finally, heating during any adiabatic processes is supposed to proceed predominantly from dissipation, see LONGERE AND DRAGON [7] for further details, yielding

$$\rho C \dot{T} = \underline{\underline{\sigma}} : \underline{\underline{d}}^p - r\dot{\kappa} = \left(\sigma_{eq} - r\right)\dot{\kappa} \geq 0 \tag{9}$$

3.2 Constitutive equations of the damaged material

Considering slightly porous metals, we are assuming a weak damage-plasticity state coupling and strong damage-plasticity kinetic couplings, allowing us for assuming that the state potential (1)-(2) and the forces (3) still hold during the damage process considered herein. We are indeed focusing our attention on the damage-plasticity coupling intervening at the level of the yield condition, as it is mostly done when modelling micro-porous metal behaviour, see e.g. [2] – it must be noted that accounting for damage-plasticity state coupling does not imply significant changes in the present methodology. As an application of the hypothesis of a kinematical mean stress shift, see Sect.2.2, a modified version of the GTN model is proposed. Consider thus the following modified GTN potential:

$$\Phi_G = \widetilde{\sigma}_{éq}{}^2 + 2q_1 f \cosh\left[-\frac{3}{2}q_2\left(\widetilde{p}_m + \widetilde{p}_r\right)\right] - \left(1 + q_3 f^2\right) = 0 \;;\; \widetilde{p}_m = \frac{p_m}{\overline{\sigma}_y} \;;\; \widetilde{p}_r = \frac{p_r}{\overline{\sigma}_y} \tag{10}$$

where (q_1, q_2, q_3) are material constants. Let define now the 'cleavage strength' σ_{cleav} as being the critical value of the mean stress $\sigma_m = -p_m$ at the incipience of void growth under equi-triaxial stress. For the GTN model $\left(p_r = 0\right)$, the so-defined 'cleavage strength' σ_{cleav} is expressed by

$$\frac{\sigma_{cleav}}{\overline{\sigma}_y} = \frac{2}{3}\frac{1}{q_2} a\cosh\left[\frac{1 + q_3 f^2}{2q_1 f}\right] \tag{11}$$

Considering low values of f $\left(f << 1\right)$ yields

$$\sigma_{cleav} \approx -\frac{2}{3}\frac{1}{q_2}\overline{\sigma}_y \ln\left[q_1 f\right] \geq 0 \tag{12}$$

In a first approximation, we are considering the kinematic pressure p_r in a close form:

$$p_r = b\ln\left[q_1 f\right] \leq 0 \tag{13}$$

with b assumed as being a positive constant. After [1], the normality rule applies to the damaged material:

$$\underline{\underline{d}}^p = \Lambda\frac{\partial\Phi_G}{\partial\underline{\underline{\sigma}}} = \Lambda\left(\frac{\partial\Phi_G}{\partial\sigma_{eq}}\underline{\underline{n}} - \frac{1}{3}\frac{\partial\Phi_G}{\partial p_m}\underline{\underline{\delta}}\right) = \dot{\varepsilon}_G^{pD}\underline{\underline{n}} + \frac{1}{3}\dot{\varepsilon}_G^{pM}\underline{\underline{\delta}} \tag{14}$$

where the distortional and dilatational parts, namely $\dot{\varepsilon}_G^{pD}$ and $\dot{\varepsilon}_G^{pM}$, respectively, of the inelastic strain rate $\underline{\underline{d}}^p$ are given by

$$\dot{\varepsilon}_G^{pD} = \Lambda\frac{\partial\Phi_G}{\partial\sigma_{eq}} = 2\Lambda\frac{\widetilde{\sigma}_{éq}}{\overline{\sigma}_y} \;;\; \dot{\varepsilon}_G^{pM} = -\Lambda\frac{\partial\Phi_G}{\partial p_m} = 3q_1 q_2 f\Lambda\frac{\sinh\left[-\frac{3}{2}q_2\left(\widetilde{p}_m + \widetilde{p}_r\right)\right]}{\overline{\sigma}_y} \tag{15}$$

The evolution law of the isotropic hardening variable κ is deduced from the equality of the macroscopic plastic work rate with the microscopic one, see [2]:

$$\dot{\kappa} = \frac{\sigma_{eq}\dot{\varepsilon}_G^{pD} - p_m\dot{\varepsilon}_G^{pM}}{\left(1-f\right)\overline{\sigma}_y} \tag{16}$$

Adiabatic heating is accordingly evaluated from

$$\rho C\dot{T} = \underline{\underline{\sigma}} : \underline{\underline{d}}^p - r\dot{\kappa} = \sigma_{eq}\dot{\varepsilon}_G^{pD} - r\dot{\kappa} - p_m\dot{\varepsilon}_G^{pM} \geq 0 \tag{17}$$

The porosity rate $\dot{f}$ is decomposed into a contribution due to growth of existing defects and a contribution due to the formation of new defects, see (18_1). The former, namely $\dot{f}_g$, is

deduced from the classical hypothesis of matrix incompressibility, see (18_2), whereas the latter, namely $\dot{f}_n$, is the subject of the following sub section:

$$\dot{f} = \dot{f}_g + \dot{f}_n \ ; \ \dot{f}_g = (1-f)Tr\underline{\underline{d}}^p = (1-f)\dot{\varepsilon}_G^{pM} \ ; \ f_g(0) = f_0 \tag{18}$$

3.3 Micro void nucleation criterion and kinetics law

The hole nucleation criterion describes the conditions for which a specific volume fraction of 'primary' voids f_0 instantaneously germinates. A 'secondary' void initiation kinetic law is also proposed.

'Primary' micro void nucleation criterion

To ensure the instantaneous transition between dense metal plasticity and micro-porous metal plasticity, the hole nucleation criterion Φ_{I_0} is proposed in a form close to the micro-porous metal potential (10):

$$\begin{aligned} \Phi_{I_0} &= \hat{\sigma}^2 + 2q_1 f_0 \cosh\left(-\frac{3}{2}q_2(\hat{p}_m + \hat{p}_r)\right) - \left(1+q_3 f_0^2\right) = 0 \\ \hat{\sigma} &= \frac{\sigma_y}{\sigma_c} \ ; \ \hat{p}_m = \frac{p_m}{\sigma_c} \ ; \ \hat{p}_r = \frac{p_r}{\sigma_c} \end{aligned} \tag{19}$$

Hole nucleation (19) is clearly controlled by the stress triaxiality. In order to describe the delaying effects of the strain rate and the temperature in the hole nucleation process, we are assuming the following expression for the critical stress σ_c :

$$\sigma_c = \sigma_I + \sigma_{vp} \ ; \ \sigma_I = \alpha(R_0 + R_\infty) \tag{20}$$

The expression of the equivalent plastic strain at 'primary' hole nucleation $\kappa_0 = \kappa(f_0)$ may be explicitly deduced from (13) and (19) as:

$$\kappa_0 = -\frac{1}{k}\ln\left(1-\left\{\frac{\sigma_c}{R_\infty}\left[1-\left(\frac{T}{T_{fusion}}\right)^m\right]^{-1}\left[\left(1+q_3 f_0^2\right)-2q_1 f_0\cosh\left(-\frac{3}{2}q_2\left(\frac{p_m+p_r}{\sigma_c}\right)\right)\right]^{1/2}-\frac{R_0}{R_\infty}\right\}^{1/\beta}\right) \tag{21}$$

The plastic strain at 'primary' hole nucleation κ_0 in (21) is drawn in Fig.3 as a function of the stress triaxiality for various values of temperature and strain rate. The graphs in Fig.3 show clearly that the hole nucleation criterion given in (19) is able to reproduce, at least qualitatively, the accelerating effects of stress triaxiality and the delaying effects of temperature, see Fig.3.a, and strain rate, see Fig.3.b.

'Secondary' micro void formation kinetics law

In the present approach, the formation of 'secondary' voids, in addition to the 'primary' voids whose germination is controlled by the above criterion, is postulated. These 'secondary' voids include micro-voids of the same nature of the 'primary' voids but nucleating later, as

well as nano-voids germinating between macro-voids and being consequently at the origin of the coalescence by localised shearing. In agreement with this definition, the 'secondary' void nucleation kinetics is supposed to be controlled by the rate of hardening, see (22_1) below. This hypothesis is consistent with the fact that hole germination requires a certain amount of plastic deformation. Based on the works by MOLINARI AND WRIGHT [8], the kinetic law for secondary nucleation is assumed to be well described by a WEIBULL type distribution function, see (22_2):

$$\dot{f}_n = B\left\langle \dot{\sigma}_y \right\rangle \;;\; B = f_{\sup}\frac{p}{\sigma_c}\left\langle \Phi_{I_0} \right\rangle^{p-1}\exp\left(-\Phi_{I_0}^{p}\right) \;;\; f_n(0)=0 \qquad (22)$$

where p is a constant ($p=2$) and where $f_{\sup}$ represents the upper bound of the nucleated 'secondary' void volume fraction. $\langle . \rangle$ represents MCCAULAY brackets.

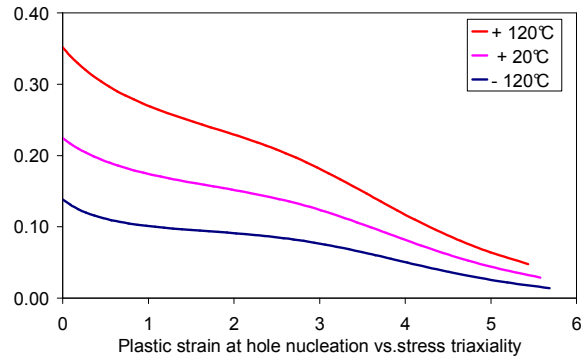

a) $\alpha=0.65$; $b=115MPa$; $f_0=10^{-4}$; $\dot{\kappa}=10^2 s^{-1}$

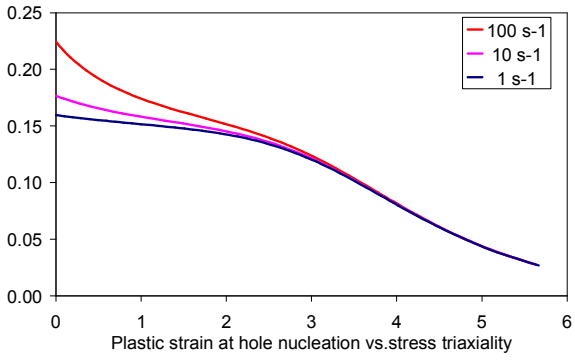

b) $\alpha=0.65$; $b=115MPa$; $f_0=10^{-4}$; $T_0=20°C$

Figure 3: Influence of temperature a) and strain rate b) on the plastic strain at hole nucleation

4 NUMERICAL SIMULATIONS AND CONFRONTATION WITH EXPERIMENTS

The model detailed in Sect.3 was implemented as user material (Vumat) in the engineering finite element computation code Abaqus®. The numerical integration is conducted in the GREEN-NAGHDI rotating frame using the classical return mapping procedure combined with the NEWTON-RAPHSON solving algorithm, see ARAVAS [9]. The thermal dilatation is supposed to be negligible in the present approach. Adiabatic conditions are furthermore assumed to be valid for plastic equivalent strain rate $\dot{\kappa}$ greater than $1s^{-1}$. In addition, failure is supposed to occur as soon as the porosity reaches the critical value f_r, leading numerically to the erosion of the concerned finite element. Some numerical simulations employing Abaqus® were conducted considering a cube under shear as well as notched structures under tension.

4.1 Case of a cube under simple shear

We are here considering a RVE submitted to a simple shearing in order to verify the ability of the model of Sect.3 to describe the consequences on the material behaviour of cavity growth under shear loading. From the numerical viewpoint, the RVE is represented by a single finite element C3D8R. The upper side is submitted to a tangential displacement at a constant velocity of 2.3m/s (leading to a plastic equivalent strain rate slightly greater than $1s^{-}$

[1]) while the lower side is constrained. The set of material constants is reported in Table 1. Shear stress-shear strain and porosity-shear strain curves are shown in Fig.4 for various values b entering the expression of the kinematic pressure softening p_r, see (13).

Table 1: Micro-porous model related constants for the numerical simulation of a cube under simple shear

q_1	q_2	q_3	f_0	α	b (MPa)	f_{sup}	f_r
1	1	1	10^{-3}	0.65	/	16.10^{-2}	1.

The graphs in Fig.4.a show the combined softening effects of adiabatic heating and cavity growth induced damage on the material behaviour – for the ETVP (ElasticThermoViscoPlastic/sound material) model adiabatic heating is solely responsible for the softening behaviour at large deformation. It is furthermore clearly visible that the loss of shear resistance of the damaged material is more significant for large values of b. As shown in Fig.4.b this softening effect is induced by cavity nucleation and growth. Cavity growth under shear loading has been made possible thanks to the introduction of the kinematic pressure softening mechanism governed by p_r in the modified GTN model, see (10).

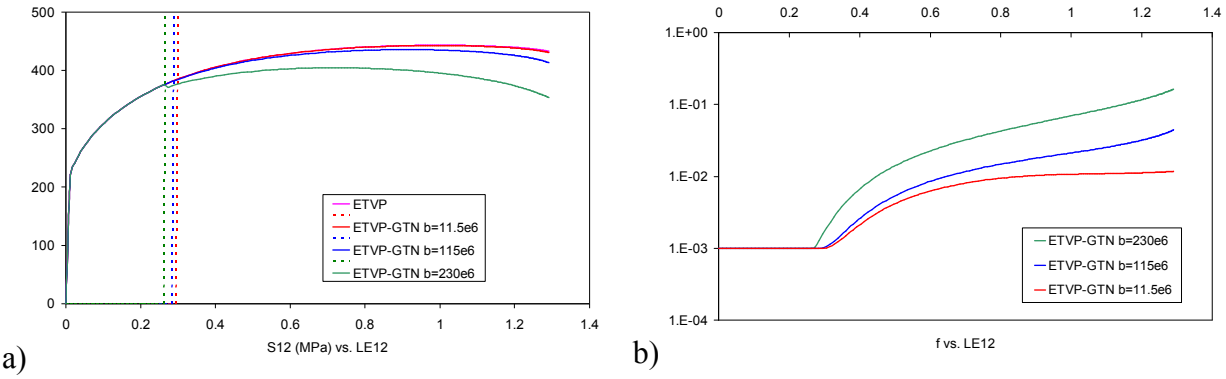

Figure 4: Influence of kinematic pressure. Simple shear on a cube.
a) Shear stress vs. shear strain. b) Volume fraction of holes vs. shear strain

4.2 Case of notched cylindrical samples under tension: simulation vs. experiment

This case deals with the tension of notched cylindrical specimens. The configurations with a notch radius value of 1.2mm (ST=1.15) and 6.2mm (ST=0.55) are considered here. Quasi-static tests were performed at room temperature and at 5mm/min on these samples. Concerning numerical simulations, the spatial discretisation consisted in meshing one eighth of the samples using solid finite elements with reduced integration C3D8R, as shown in Fig.5. The vertical translation of the lower face nodes is constrained while a vertical velocity is imposed to the upper face nodes. The sample material behaviour is described via the model detailed in Sect.3 (Vumat). The material constant values are reported in Table 2. The time integration scheme is explicit.

Experimental and numerical results are superposed in Fig.6 in the form of axial load-extensometer displacement curves. These curves allow for studying the influence of various model constants on the onset of void growth induced damage and subsequent drop in load, namely that of e.g. the ratio α in (20), see Fig.6. The influence of the secondary nucleation upper bound f_{sup}, and of the failure porosity f_r was also studied but is not shown here.

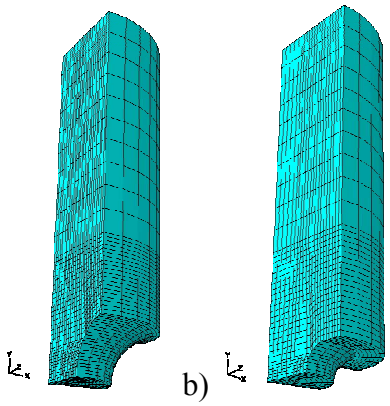

a) b)

Figure 5: Meshing of the notched cylindrical samples; a) ST=0.55 b) ST=1.15

Table 2: Microporous model related constants for the numerical simulation of notched samples under tension

q_1	q_2	q_3	f_0	α	b (MPa)	f_{sup}	f_r
1	1	1	10^{-3}	/	115	0.03	0.2

Fig.6 clearly shows the effect of the critical stress σ_c via the ratio α, see (20), on the overall response of the notched round sample. Acting on the 'primary' void germination occurrence and on the 'secondary' void nucleation rate, see (20) and (22_2), the ratio α is consequently a key parameter in the model detailed in Sect.3. For early damage conditions, the ratio α value must be low, and for late damage conditions, the ratio α value must be large. Note that a large value of α provokes a progressive drop in load, contrarily to the brutal drop in load observed for a low value of α. According to Fig.6, the set α=0.75 - f_{sup}=0.03 - f_r=0.2 may be considered as satisfying for the material at stake.

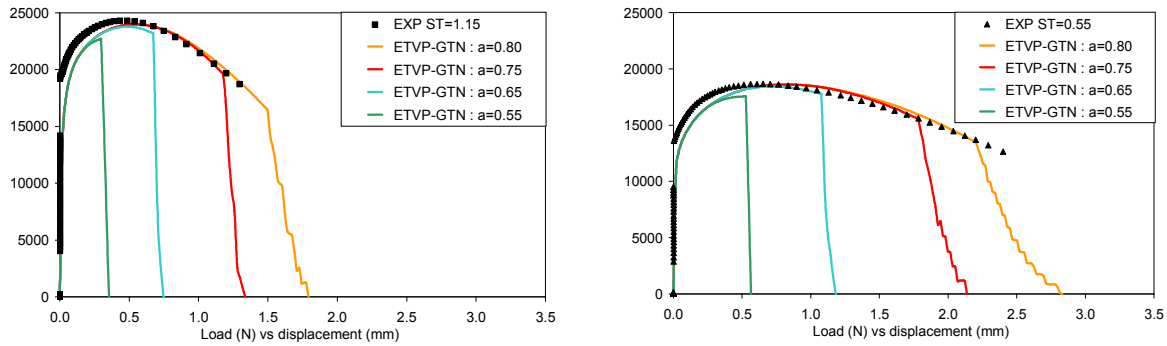

a) ST=1.15 b) ST=0.55

Figure 6: Comparison model-experiment. Influence of the ratio α. Tensile test on notched cylindrical samples ; α= / - f_{sup}=0.03 - f_r=0.2

5 CONCLUSIONS

An elastic/viscoplastic model involving two stage void nucleation mechanism and void growth related hardening/softening effects has been put forward for a class of structural steels subjected to rapid loading conditions.

A phenomenological modelling approach has been developed, based on some salient physical effects regarding void growth vs. plastic straining, to describe the transition behaviour between dense metal plasticity and micro-porous metal plasticity. Considering that void germination requires a certain amount of plastic deformation, a 'primary' hole nucleation criterion has been proposed, as well as a statistical law governing the 'secondary' hole kinetics. In a consistent way, the hole nucleation criterion accounts for the accelerating effects of stress triaxiality and, conversely, the delaying effects of temperature and strain rate. In this work, a modification of the GTN model has also been proposed, overcoming its inability to predict damage growth and fracture for zero and low triaxiality, shear-dominated deformations. In this respect the kinematic mean stress related shift mechanism has been introduced and quantified in the expression of the GTN plastic potential, enabling thus the damage growth under shear and under small negative triaxialities. The 3D constitutive equations have been implemented as user material in the engineering finite element computation code Abaqus®. Numerical simulations have been conducted considering a single finite element under simple shear on one hand and a notched cylindrical sample under remote uniaxial tensile loading on the other hand. The numerical results show clearly the influence of the hole nucleation criterion related constants on the damage and further failure of the material.

REFERENCES

[1] Berg C.A., Plastic dilation and void interaction, Proc. of the Batelle memorial institute symposium on inelastic processes in solids, pp.171-209 (1969)

[2] Gurson A.L., Continuum theory of ductile rupture by void nucleation and growth: Part I – Yield criteria and flow rules for porous ductile media, J. Eng. Mat. Tech., 99, pp.2-15 (1977)

[3] Tvergaard V., Needleman A., Analysis of the cup-cone fracture in a round tensile bar, Acta Metall., 32, 1, pp.157-169 (1984)

[4] Perzyna P., Stability of flow processes for dissipative solids with internal imperfections, J. App. Math. Phys., 35, pp.848-867 (1984)

[5] Dragon A., Ohji K., Plasticity model for inclusion-perturbed yielding and ductile fracture criterion, Research report, Japan Soc. for Promotion of Science, Osaka University (1977)

[6] Green A.E., Naghdi P.M., A general theory of an elastic-plastic continuum, Arch. Rat. Mech. Anal., 19, pp.251-281 (1965)

[7] Longère P., Dragon A., Inelastic heat fraction evaluation for engineering problems involving dynamic plastic localization phenomena, J. Mech. Mat. Struct., 4, 2, pp.319-349 (2009)

[8] Molinari A., Wright T.W., A physical model for nucleation and early growth of voids in ductile materials under dynamic loading, J. Mech. Phys. Solids, 53, pp.1476-1504 (2005)

[9] Aravas N., On the numerical integration of a class of pressure-dependent plasticity models, Int. J. Num. Meth. Eng., 24, pp.1395-1416 (1987)

Authors Index

Abdollahi A. 514
Abed F.H. 1295
Abed-Meraim F. 1072, 1380
Adámek T. 757
Akiyama M. 91, 107, 117
Alfaiate J. 1625
Alfaro I. 1466
Aliguer I. 1244
Alonso E. 1244
Ammar A. 688
Amran I. 688
Andrade Pires F.M. 66, 841, 964
Antoun B.R. 1153
Antunes J.M. 287
Aoyagi Y. 587
Arai M. 664
Arantes da Costa Júnior J.C. 932
Arfa H. 318
Arias I. 514
Ariza M.P. 1517
Arroyo M. 397, 1177
Aydogan M. 1595
Bahar O. 1063
Bahloul R. 318
Bäker M. 887
Balan T. 1072, 1380
Balzani D. 764, 1563
Bammann D.J. 1153
Bauer S. 1509
Bažant Z.P. 796
BelHadj Salah H. 318
Ben Bettaieb A. 1368
Benboudjema F. 1618
Berisha B. 1136
Biabanaki S.O.R. 1317
Biermann H. 869
Bilotta A. 1329
Böck B. 1145
Bogdan M. 1539
Bosetti P. 263
Bouchard P-O. 42
Bradford M.A. 899
Branco R.M. 1055
Brands D. 1563
Bravo R. 135
Brinkhues S. 764
Brown A.A. 1153
Bruschi S. 263
Bublik O. 776
Buchmayr B. 1145
Calloch S. 564
Canadija M. 354
Caner F.C. 796
Cardoso E.L. 295
Cardoso R. 1502
Carol I. 1233, 1244, 1607
Carter J.P. 1263
Cermak M. 1341
César de Sá J.M.A. 66, 964
Chalal H. 1072, 1380
Chalmovsky J. 1274
Charpentier I. 229
Chen J. 189
Chen Y. 999
Chenot J-L. 42
Chern S. 999
Chiesa M.L. 1153
Chinesta F. 688
Chlup H. 713, 720, 757
Cognard J-Y. 830
Colliat J.B. 1539, 1618
Créac'hcadec R. 830
Cueto E. 1466
D'hers S. 502
Das A. 1189
David S.A. 1437
Davies P. 830
De Angelis F. 1458
De la Fuente P. 1222
De Proft K. 1575
De Sa C. 1618
Defauchy D. 688
Delaplace A. 1031
Díez P. 944
Doblaré M. 700
Doca T. 964
Domínguez N. 808
Doudard C. 564
Dragon A. 1649
Drozdov A.D. 1019
Duchêne L. 221, 1368
Dufour F. 330
Dvorkin E.N. 502
Eidel B. 360
Einav I. 1189
Etse G. 342
Fernandes A. 1116
Fernandes J.V. 287, 1055
Fernandes W. 1391
Fernández-Ceniceros J. 1478
Fernández-Martínez R. 1478
Ferron G. 229
Fiala R. 1274
Filice L. 1466
Fincato R. 1165
Fortuny G. 741
Fourment L. 42
Freitag S. 676
Fukui T. 642
Gao Z. 181
Garcea G. 1329
Garolera D. 1233
Gatuingt F. 1618
Geffroy A-G. 1649

Gens A. 32, 921, 1177, 1255
Germain S. 1490
Gesto J.M. 921
Giorgio Bort C.M. 263
Giry C. 330
Gonçalves P. 1391
González N.A. 1177, 1255
Gotoh S. 126
Greco F. 1466
Gultová E. 713, 757
Habraken A.M. 1368
Hauer F. 976
Hayakawa K. 99
Hein G. 1104
Herrera B. 741
Heyens K. 422, 1575
Hild F. 564
Hinrichsen M. 881
Hirschberger C. B. 852
Hofstetter G. 442
Holzapfel G.A. 764
Hora P. 1136
Horng J. 999
Horný L. 713, 720, 757
Issa M. 56
Iwata N. 630
Izzuddin B.A. 210
Jin Y. 126
Jonasova A. 776
Jourdain X. 1618
Kainz A. 1092, 1104
Kaliske M. 676
Kang S. 552
Karaoulanis F. 1353
Kashima H. 642
Khoei A.R. 1007, 1317, 1527
Kiliclar Y. 490
Kim D-Y. 532, 552
Kim H.Y. 532, 552
Kitayama K. 1502
Koga K. 618
Konyukhov A. 147
Kostka T.D. 1153
Kozubek T. 1341
Krimpelstätter K. 1092
Kuboki T. 80, 126, 603
Kubota Y. 99
Kuhn C. 478
Kuna M. 869, 1043
Kuramae H. 594
Kuroda K. 603
Kustra P. 275
Labergère C. 56
Lackner R. 1509, 1551
Lale E. 1595
Lasne P. 42
Leblé B. 1649
Lehmann E. 1584
Lemos L.J.L. 1212
Leonetti L. 1329
Liaño C. 170
Lindgren L-E. 307, 576
Liu W.K. 576
Lloberas-Valls O. 521
Loehnert S. 1584
Lombillo I. 170
Long F. 1284
Longère P. 1649
López C.M. 1233, 1607
Lostado-Lorza R. 1478
Lucena Neto E. 1403
Lukes V. 729
Macorini L. 210
Mahdi S. 830
Makarem F.S. 1295
Malcher L. 66
Mansouri L.Z. 1072
Maranha J.R. 1201
Marcé J. 741
Margolis S.B. 1153
Marimón F. 741
Markopoulos A. 1341
Martínez M.A. 700
Martínez X. 952
Martínez-de-Pisón F.J. 1478
Martins A.X. 287
Martiny M. 229
Mata H. 1116
Matsumoto T. 126
Matthies H.G. 385, 410
Maurice J. 830
Mazars J. 330
Meirinhos G. 830
Mergheim J. 432
Metzger A. 147
Meza M. 159
Mica L. 1274
Micera S. 748
Milenin A. 275
Mirkhalaf Valashani S.M. 841
Miyagawa J. 117
Mohammadnejad T. 1527
Molins C. 944
Morimoto H. 594
Morinishi K. 642
Morozov E.V. 189
Moslemi H. 1007
Mosler J. 354, 379
Moura Belo I. 932
Mroginski J.L. 342
Müller R. 478
Munjiza A. 788
Muñoz-Rojas P.A. 295
Muramatsu M. 587
Murata M. 80, 126, 603
Murcia J. 1607
Mutrux A. 1136
Mutsukado T. 618
Nagaki S. 863
Nagel K. 869
Nakamachi E. 23, 594
Nakamura T. 99
Nakamura Y. 594
Nanba Y. 99
Natal Jorge R. 1116
Nazem M. 1263

Neto P. 1625
Nguyen G.D. 1189
Nguyen N-T. 532, 552
Nikolic 788
Nishimura M. 664
O'Connor D.T. 1153
Ohba S. 117
Okuda T. 618
Okuda Y. 107
Oliveira C. 1437
Oliveira M.C. 287, 1055
Oliver C. 1031
Oller S. 952
Ortiz M. 1517
Ostermeyer G.P. 1124
Oteo C. 1222
Otero F. 952
Pagani M. 454
Paggi M. 1082
Panagiotou K.D. 1306
Parente Azikri de Deus H. 932
Parente M. 1116
Parteder E. 1104
Peco C. 397
Peigney M. 820
Peirs J. 221
Peña E. 700
Peña F. 159
Perego U. 454
Pérez-Aparicio J.L. 135
Pérez-Mota J. 808
Peyre P. 688
Pi Y.L. 899
Pineda E. 1427
Pitts S.A. 1153
Polanco-Loria M. 881
Poncelet M. 564
Ponga M. 1517
Posch G. 1145
Prates P.A. 1055
Pros A. 944
Prüger S. 869
Puff R. 251
Qin H. 576
Qiong D. 1284
Raabe D. 1563
Ragueneau F. 1031
Rassineux A. 56
Raufi F. 1063
Reddy B. D. 852
Reese S. 490
Regnier G. 688
Richard B. 1031
Rixen D.J. 521
Roberto Ávila da Silva Júnior C. 932
Rodríguez M. 1607
Rodríguez-Ferran A. 466
Rohan E. 729
Romero I. 1517
Rosic B. 385, 410
Rosolen A. 397
Roth S. 1043
Rouainia M. 1177
Roubin E. 1539
Roux E. 42
Saanouni K. 56
Sabetamal H. 1263
Sadovskaya O. 987
Sadovskiy V. 909
Sáez P. 700
Sakamoto H. 594
Sakharova N.A. 287, 1055
Sakuma A. 863
Salahouelhadj A. 1380
Salomon O. 952
Salomoni V.A. 1165
Sánchez M. 32
Sansour C. 540
Santos A. 1116
Sanz-García A. 1478
Sato S. 587
Sawano K. 99
Scheider I. 379
Schmaltz S. 241
Schmidt U. 432
Schörkhuber K. 1104
Schröder J. 360, 1563
Schueremans L. 422
Schweizerhof K. 147
Segi T. 618
Šejnoha M. 201
Sergi P.N. 748
Setoyama D. 630
Shankar K. 189
Shizawa K. 587
Shrot A. 887
Silva A. 1391
Silveira R. 1391
Simões M.I. 287
Simões R. 841
Simon J.W. 1415
Simone A. 521
Skatulla S. 540
Sloan S.W. 1263
Sluys L.J. 521
Sodré D. 1403
Sohier L. 830
Sorace S. 1446
Spiliopoulos K.V. 1306
Srisupattarawanit T. 1124
Stahlschmidt J. 295
Stainier L. 368
Stanciulescu I. 181
Steinmann P. 432, 1490
Steinwender L. 1092
Stickle M.M. 1222
Stukowski A. 360
Su S. 368
Sueoka T. 603
Szeliga D. 1359
Tabuchi Y. 99
Takaki T. 610, 642, 652
Tamayo-Mas E. 466
Tanaka M. 618
Tang S. 576
Taylor R.L. 1458

Teaca M. 229
Temizer I. 1637
Terada K. 603
Terenzi G. 1446
Tini V. 490
Traxl R. 1551
Uchimura T. 91, 107
Uematsu S. 80
Uemor T. 1502
Valenta R. 201
Valente R. 1116
Valentini B. 442
Vallade A. 1618
Valleján B. 32
Vandoren B. 422, 1575
Vaunat J. 921
Vaz Jr. M. 251, 295
Venda Oliveira P.J. 1212
Verleysen P. 221
Veselý J. 720, 757
Vieira A. 1201
Villaseñor I. 1427
Villegas L. 170
Vimmr J. 776
Vladimirov I.N. 490
Wallner S. 1145
Watanabe I. 630
Weber B. 564
Wedberg D. 307
Wei C. 999
Wei Q. 1284
Weichert D. 1415
Widder M. 1104
Willner K. 241, 976
Wriggers P. 1082, 1584, 1637
Wu T. 1637
Yamaguchi A. 618
Yamamoto T. 91
Yamanaka A. 652
Yang N.Y.C. 1153
Yashiro K. 618, 664
Yoon J. 1502
Yoshida F. 1502
Zapata J. 1427
Zbib H. 540
Zeman K. 1092, 1104
Žitný R. 713, 720, 757
Živaljic N. 788
Zopf C. 676

This volume contains the full length papers accepted for presentation at the XI International Conference on Computational Plasticity – Fundamentals and Applications

7-9 September 2011, Barcelona, Spain

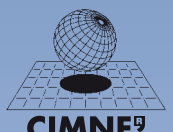

CIMNE

International Center
for Numerical Methods in Engineering